NEPT
Advancing Knowledge for a Sustainable Future

NATURE ENVIRONMENT AND POLLUTION TECHNOLOGY

Peer-Reviewed Open Access Journal

Vol. 25, No. 3, September 2026

ISSN (Print): 0972-6268

ISSN (Online): 2395-3454



Published by Technoscience Publications LLP
Scholarly Publishing

NATURE ENVIRONMENT AND POLLUTION TECHNOLOGY

EDITORIAL LEADERSHIP & ADVISORY BOARD

Nature Environment and Pollution Technology

CHIEF EDITOR

Dr. P. K. Goel
Former Head, Department of Pollution Studies, Yashwantrao Chavan College of Science, Karad, Maharashtra, India

HONORARY EDITOR

Dr. K. P. Sharma
Emeritus Professor, Department of Botany, University of Rajasthan, Jaipur, Rajasthan, India

EXECUTIVE EDITOR

Ms. Apurva Goel
Technoscience Publications LLP, Pune, Maharashtra, India

Editorial Advisory Board

1. Dr. Saikat Kumar Basu, Dept. of Biological Sciences, University of Lethbridge, Lethbridge AB, Alberta, Canada

2. Dr. Elsayed Elsayed Hafez, Plant Protection and Biomolecular Diagnosis Department, Arid Lands Cultivation Research Institute (ALCRI), Alexandria, Egypt

3. Dr. Tri Nguyen-Quang, Department of Engineering Agricultural Campus, Dalhousie University, Canada

4. Dr. Sang-Bing Tsai, Wuyi University Business School, Wuyishan, China

5. Dr. Zawawi Bin Daud, Faculty of Civil and Environmental Engg., Universiti Tun Hussein Onn, Malaysia, Johor, Malaysia

6. Dr. B. Akbar John, School of Industrial Technology, Universiti Sains Malaysia (USM), Penang, Malaysia

7. Dr. C. Stella, Centre for Agro Marine Research, Sethubhaskara Agricultural College and Research Foundation, Visalayankottai, Karaikudi, T.N., India

8. Dr. G.R. Pathade, Krishna Institute of Allied Sciences, Krishna Vishwa Vidyapeeth, Karad, Maharashtra, India

9. Dr. Amit Arora, Department of Chemical Engineering, National Institute of Technology (NIT), Hamirpur, H.P., India

10. Prof. Riccardo Buccolieri, Dept. of Atmospheric Physics, University of Salento, Dipartimento di Scienze e Tecnologie Biologiche ed Ambientali, Laboratory of Micrometeorology, Lecce, Italy

11. Dr. Tai-Shung Chung, Graduate Institute of Applied Science and Technology, National Taiwan University of Science and Technology, Taipei, Taiwan

12. Dr. Abdeltif Amrane, Technological Institute of Rennes, University of Rennes, France

13. Dr. Giuseppe Ciaburro, Dept. of Architecture and Industrial Design, Universita degli Studi della Campania, Italy

14. Dr. A.B. Gupta, Dept. of Civil Engineering, Malviya National Institute of Technology (MNIT), Jaipur, India

15. Claudio M. Amescua Garcia, Department of Publications, Centro de Ciencias de la Atmosfera, Universidad Nacional Autonoma de Mexico, Mexico

16. Alexander B. Ruchin, Joint Directorate of the Mordovia State Nature Reserve and National Park, Saransk 430005, Russia

17. Wei (Welsh) Wang, State Key Lab of Environmental and Biological Analysis, Hong Kong Baptist University, Hong Kong

NATURE ENVIRONMENT AND POLLUTION TECHNOLOGY

CONTENTS

Vol. 25, No. 3, September 2026

1 **Sustainable Energy Recovery from Coastal Plastic Waste: A Pyrolysis-Driven Micro Power System Approach**
Dwi Novalita Tanri Abeng, Abd. Wahid Wahab, Winarni Monoarfa and Eymal Bahsar Demmallino
Article ID: D1844 | **DOI:** 10.46488/NEPT.2026.v25i03.D1844

2 **Achieving Sustainability in India: Analyzing Carbon Neutrality Scenarios Using the Novel Fourier-NARDL Approach**
A. Mohanapriya, R. Shenbagavalli and M. Balamurugan
Article ID: B4386 | **DOI:** 10.46488/NEPT.2026.v25i03.B4386

3 **Index-Based Evaluation (IBE) and Geospatial Mapping of Heavy Metal Contamination in Groundwater of an Industrially Influenced Peri-Urban Area of Guwahati, Assam, India**
Debasish Chutia, Satyajit Kataki and Aditya Shankar Kataki
Article ID: B4387 | **DOI:** 10.46488/NEPT.2026.v25i03.B4387

4 **Comparison of Optimum Dosages of Biocoagulant and Commercial Coagulant Alum in the Coagulation-Flocculation Process of Tofu Wastewater**
Okik Hendriyanto Cahyonugroho, Nur Laili Alfiatin Mukharomah and Muhammad Rizky Firmansyah
Article ID: D1859 | **DOI:** 10.46488/NEPT.2026.v25i03.D1859

5 **Thermogravimetric Analysis and Determination of Kinetic Parameters for Pyrolysis of Lotus Seed Biomass**
Gurneet Kaur, Vivekanand and Jaibir Kherb
Article ID: B4389 | **DOI:** 10.46488/NEPT.2026.v25i03.B4389

6 **Environmental Policies in Mexico: A Critical Analysis of Their Implementation and Results**
Rosa Llerena, Oscar Moncayo, Leandra Arboleda, Malena Zambrano and Evelyn Navia
Article ID: D1860 | **DOI:** 10.46488/NEPT.2026.v25i03.D1860

7 **Clay Brick Performance with Red Mud, Waste Foundry Sand, and Silica Fume: A Taguchi Approach**
Smita S. Borchate, Praveen A. Ghorpade, Basavaraj G. Katageri and Nayana P. Hoolikantimath
Article ID: B4390 | **DOI:** 10.46488/NEPT.2026.v25i03.B4390

8 **Assessing Atmospheric Contamination Zones Through Lichen Bioindicators in a Northwestern Peruvian City**
Jani E. Mendoza, Cristobal Torres-Guzman, Manuel Oliva, Ligia García and Jesús Rascón
Article ID: D1858 | **DOI:** 10.46488/NEPT.2026.v25i03.D1858

9 **Retrieval of Turbidity of the Upper Lake, a Ramsar Site, Bhopal, India, Using in situ Observations and Landsat-8 OLI Satellite Data**
Prasanta Ghadei and Sujit Kumar Jally
Article ID: B4393 | **DOI:** 10.46488/NEPT.2026.v25i03.B4393

10 **Phosphate Solubilization and Plant Growth-Promoting Potential of Penicillium oxalicum (Bt9) in Eppawala Rock Phosphate-Enriched Compost**

W. M. B. B. Sathsarini, T. G. I. Sandamali, M. M. Pathmalal and F. S. Idroos

Article ID: D1861 | **DOI:** 10.46488/NEPT.2026.v25i03.D1861

11 **Central Composite Design-Based Optimization of Heterogeneous Fenton-Like Catalytic Oxidation of Real Pharmaceutical Wastewater Using Cu-Fe/SiO?**

Neha Kulshreshtha, Vishal Kumar Sandhwar, Alok Tiwari and Shivendu Saxena

Article ID: B4394 | **DOI:** 10.46488/NEPT.2026.v25i03.B4394

12 **Moringa oleifera as a Natural Coagulant-Flocculant for the Removal of Turbidity and Heavy Metals from the Caplina Channel**

Dariella Sharyley Quintana-Calizaya, Efren Eugenio Chaparro-Montoya, Javier Lozano-Marreros, Yessenia Danidtza Gomez-Aguilar, Keila Abigail Muñante-Carrillo and Diana Galeska Farfan-Pajuelo

Article ID: D1863 | **DOI:** 10.46488/NEPT.2026.v25i03.D1863

13 **Amelioration of Cadmium-Induced Stress in Tomato (Solanum lycopersicum) Using Gasotransmitters: A Combined Approach to Enhancing Antioxidant Defense and Growth Resilience**

Smita Raut, Pragnya Paramita Sahoo, Prabhat Kumar Srivastava and Sangeeta Raut

Article ID: B4395 | **DOI:** 10.46488/NEPT.2026.v25i03.B4395

14 **Evaluation of the Adsorption Performance of Geological Materials Based on Limestone and Green Shale from the Taza Region, Morocco: Application for Leachate Treatment**

Imane El Machrafi, Abdennasser Baali, Ibrahim Touzani, Jamal Naoura, Mohamed Ben Abbou and Kawtar Fikri-Benbrahim

Article ID: D1866 | **DOI:** 10.46488/NEPT.2026.v25i03.D1866

15 **ANN-Driven Optimization of VOC Adsorption on Activated Carbon with Thermal Breakthrough Forecasting and IoT-Based Real-Time Monitoring**

Subramanian Kavitha, Subramani Umamaheswari, Venkatesh Babu Samikannu and Surendran Ganesan

Article ID: B4398 | **DOI:** 10.46488/NEPT.2026.v25i03.B4398

16 **Characterization and Optimization of Tamarindus indica Copper Nanoparticles (TA-CuNPs) for the Adsorptive Removal of Malachite Green**

Pampana Anil Kumar, Alpitha Suhasini J., Sarva Rao B., Pulipati King, D. Appala Naidu and Meena Vangalapati

Article ID: B4401 | **DOI:** 10.46488/NEPT.2026.v25i03.B4401

17 **Analysis of the Effectiveness of Rainwater Harvesting in Reducing Flooding: Case Study in the Governor's Housing Complex, Makassar**

Hasnawiah, Rita Tahir Lopa and Roslinda Ibrahim

Article ID: D1827 | **DOI:** 10.46488/NEPT.2026.v25i03.D1827

18 **Deep Learning for AQI Prediction Using Multiple Feature Vectors: A Case Study of Colaba and Deonar Stations**

Darakhshan Khan, Archana B. Patankar, Himani Deshpande and Juhi Janjua

Article ID: B4381 | **DOI:** 10.46488/NEPT.2026.v25i03.B4381

NATURE ENVIRONMENT AND POLLUTION TECHNOLOGY

19 **Determinants of Environmental Quality in Indonesia: The Role of Democracy, Socio-Economics, and Financial Development**

Fitri Susilowati, Suryanto and Muhammad Rizal Anggit Putra

Article ID: D1868 | **DOI:** 10.46488/NEPT.2026.v25i03.D1868

20 **Integrated Proximate and Contamination Analysis of Tofu Wastewater: A Case Study in Telaga Subdistrict, Gorontalo, Indonesia**

Muhammad Taupik, Ariani H. Hutuba, Nurain Thomas, Andi Makkulawu and Windiyani N. Suharmin

Article ID: D1870 | **DOI:** 10.46488/NEPT.2026.v25i03.D1870

21 **Spatiotemporal Analysis of Long-Term Homogeneity, Meteorological Trend, and Drought Variability over the Semi-Arid Climatic Region of Bihar, India**

Shashi Shekhar Pathak, Ravi Galkate, V.K. Chandola, Atar Singh, Bhupendra Joshi, Utkarsh Kumar, Rustem R. Zairov and Ramesh Kumar

Article ID: B4391 | **DOI:** 10.46488/NEPT.2026.v25i03.B4391

22 **Community Roles Model in the Buffer Zone of the Proboscis Monkey Habitat for Wetland Environmental Conservation**

M. Ridha Ilhami, Ersis Warmansyah Abbas , Bambang Subiyakto and Mutiani

Article ID: D1873 | **DOI:** 10.46488/NEPT.2026.v25i03.D1873

23 **Exploration of Microbial Diversity of Anoxic Soil Under Submerged Low-Land Paddy Cultivation by Culture-Independent Methods for Its Consequent Ramifications on Environment, Soil Health, and Sustainability**

M. B. Chakraborty and S. R. Patgiri

Article ID: B4396 | **DOI:** 10.46488/NEPT.2026.v25i03.B4396

24 **Tidal-Diurnal Interactions and Nitrogen Dynamics: Integrating Variability into Sustainable Brackish Water Pond Management**

Dian Noorvy Khaerudin, Sri Wahyuni, Saptarini Saptarini, Sri Handayani and Diana Ningrum

Article ID: D1875 | **DOI:** 10.46488/NEPT.2026.v25i03.D1875

25 **Exploring the Role of Rice Straw Biochar in Sustainable Agriculture and Environmental Health**

Himanshi Upadhayay, Sneha Gupta, Srishti Jain and Manu Solanki

Article ID: B4399 | **DOI:** 10.46488/NEPT.2026.v25i03.B4399

26 **Comparative Assessment of Alternative Fine Aggregates for Sustainable Concrete: Physical, Chemical and Mechanical Characterization of Sri Lankan Sands**

Udara S.P.R. Arachchige, H.D.R.T. Gunasekara, R.A.K.M. Rajapaksha and M.D.K.C. Jayathilaka

Article ID: D1876 | **DOI:** 10.46488/NEPT.2026.v25i03.D1876

27 **Managing Legacy Pollution: A Legal and Policy Analysis of the Environment Protection (Management of Contaminated Sites) Rules, 2025**

Gurudutt and Pooja Singh

Article ID: B4403 | **DOI:** 10.46488/NEPT.2026.v25i03.B4403

28 **Influence of Agricultural Waste as a Partial Substitute for Cement in Flowing Concrete for a Sustainable Environment**

Nurul Rochmah, Antariksa, Wisnumurti and Bambang Semedi

Article ID: D1867 | **DOI:** 10.46488/NEPT.2026.v25i03.D1867

29 **Pullulan From Agricultural Waste Using Aureobasidium pullulans and Its Applications: A Review**

Gunjan Jadhav, Snehal Masurkar and Girish Pathade

Article ID: B4404 | **DOI:** 10.46488/NEPT.2026.v25i03.B4404

30 **Effect of Sustainable Groundwater Resource Management on Groundwater Sustainability Performance: A PLS-SEM Study in Probolinggo Regency**

Faradlillah Saves, Mohammad Bisri, Hari Siswoyo and Muhammad Sasmito Djati

Article ID: D1877 | **DOI:** 10.46488/NEPT.2026.v25i03.D1877

31 **Biopriming Using Rhizospheric Actinobacteria: A Promising Tool in Paddy (Oryza sativa) Farming**

Richa Raut, Pragati Abhyankar and Sneha Babel

Article ID: B4406 | **DOI:** 10.46488/NEPT.2026.v25i03.B4406

32 **An Econometric Assessment of Growth-Pollution Interactions in Vietnam within the Environmental Kuznets Framework**

Thi Thu Trang Phung, Thi Thanh Huong Chu, Thi Thu Huong Tran and Thi Phuong Chi Nguyen

Article ID: D1880 | **DOI:** 10.46488/NEPT.2026.v25i03.D1880

33 **Spatial Analysis of Environmental Vulnerability Among Tribal Households in Garbada Taluka, Dahod District, Gujarat, India**

Surabhi Pareek and Suneeta Chandorkar

Article ID: B4407 | **DOI:** 10.46488/NEPT.2026.v25i03.B4407

34 **Application of the SWAT Model to the Hydrological Modeling of the Nfifikh Watershed (Morocco): Study of the Dynamics of Surface and Groundwater and their Relationship with Soil Properties**

Zahli Saleh Eddine

Article ID: D1881 | **DOI:** 10.46488/NEPT.2026.v25i03.D1881

35 **Data-Driven Machine Learning Models for Predicting Monthly Rainfall Using Lagged Climate Indices**

Ayush Vashisth, Mohammed Sharif and Mohammed Shakeel

Article ID: B4408 | **DOI:** 10.46488/NEPT.2026.v25i03.B4408

36 **Nanotechnology in Automotive Wastewater Remediation: Functional Roles, Drawbacks, and Future Prospects**

Luke O. Ajuka, Moses O. Petinrin, Nosa Idusuyi, Kunle M. Oluwasegun and O.S. Fayomi

Article ID: D1886 | **DOI:** 10.46488/NEPT.2026.v25i03.D1886

37 **Microplastic Pollution in Shoreline Sediments of Selected Rivers of Mizoram, North-East India: A Baseline Assessment and Preliminary Report**

Joseph Vanlalsawma Sailo, Malsawmhriatzuala Jeremy and Chawngte Laldinsangi

Article ID: B4421 | **DOI:** 10.46488/NEPT.2026.v25i03.B4421

38 **Comparative Assessment of Empirical and Theoretical Mass Eruption Rate Estimation Methods Using HYSPLIT: A Case Study of Lewotobi Laki-Laki Eruption**

Yumita Sufitri, Vera Surtia Bachtiar, Taufiq Ihsan and Sugeng Nugroho

Article ID: D1887 | **DOI:** 10.46488/NEPT.2026.v25i03.D1887

39 **Eco-Friendly Neem-Based Corrosion Inhibitor Coatings for Reinforced Concrete: Performance, Sustainability and Cost Assessment**

Satya Prakash and Nishant Kumar

Article ID: B4392 | **DOI:** 10.46488/NEPT.2026.v25i03.B4392

40 **Assessment of Metal Concentrations and Variability Using Censored Data Analysis in Hu'u Rivers, Sumbawa, Indonesia**

Karizma Fahlevy, Agustinus Sembiring, Rias Kaessari Magenta, Adi Suroso and Charles P. H. Simanjuntak

Article ID: D1869 | **DOI:** 10.46488/NEPT.2026.v25i03.D1869

41 **Black Gold from the Fields: Obtaining Pyrolytic Biochar from Agricultural Wastes at Various Pyrolysis Temperatures**

Pooja Sarolkar, Girish Pathade and Wasim Bagwan

Article ID: B4409 | **DOI:** 10.46488/NEPT.2026.v25i03.B4409

42 **Synthesis and Characterization of Modified Lignin Flocculants for Congo Red and Methylene Blue Removal**

Mark Xavier Bailon, Bianca Marie Lim and Gian Margarette Villadarez

Article ID: D1872 | **DOI:** 10.46488/NEPT.2026.v25i03.D1872

43 **Enhancing the Quality of Cellulose Isolated from Banana Peels by Incorporating the Use of Microwave Radiation over the Conventional Method**

Pragati More, Atul Chaskar and Avinash Pawar

Article ID: B4413 | **DOI:** 10.46488/NEPT.2026.v25i03.B4413

44 **Total Chromium Removal and Mass Balance in a Hybrid Constructed Wetland Using Scirpus americanus and Hydrocotyle bonariensis for Tannery Wastewater Treatment**

Edgar Santiago Flores-Sacsi, Anyela Keith Delgado-Salas, Marco Guillermo Ancco Chara and Gerby Giovanna Rondán-Sanabria

Article ID: D1879 | **DOI:** 10.46488/NEPT.2026.v25i03.D1879

45 **Modeling the Drivers for Renewable Energy in Developing Economies: A Case Study of India**

Adya Sharma and Nehajoan Panackal

Article ID: B4415 | **DOI:** 10.46488/NEPT.2026.v25i03.B4415

46 **Perception-Participation Dynamics and Mangrove Degradation: A MultiGroup SEM in Northern Central Java, Indonesia**

Hugi Cerlyawati, Muhammad Zainuri and Slamet Isworo

Article ID: D1882 | **DOI:** 10.46488/NEPT.2026.v25i03.D1882

47 **Green Micellar Extraction of Phenol from Wastewater Using Eco-Friendly Hydrophilic Deep Eutectic Solvents**

Ravindra Joshi, Aditya Vijayakar, Soham Joshi, Prasad Parulekar, Ramesh Bhande and Shripal Gaikwad

Article ID: B4417 | **DOI:** 10.46488/NEPT.2026.v25i03.B4417

48 **Tourist Behavior in Reducing Plastic Waste at Viet Nam's Coastal Destinations**

Nguyen Thuy Van, Luu The Anh, Tran Thu Phuong, Truong Sy Vinh and Nguyen Dang Thuy Trang

Article ID: D1890 | **DOI:** 10.46488/NEPT.2026.v25i03.D1890

NATURE ENVIRONMENT AND POLLUTION TECHNOLOGY

49 **Evaluation and Origin Studies of Heavy Metals in Soils Around Traditional Mining Regions in the Northwest Guizhou District**

Tiantian Cai, Die Xu, Ji Wang, Shuai Zhang, Xiongfei Cai and Huifang Zhao

Article ID: D1888 | **DOI:** 10.46488/NEPT.2026.v25i03.D1888

50 **An Assessment of Biopolymer-Based Metal Oxide Nanoparticles for the Removal of Heavy Metals from Water**

Koffi Sossou, Alfred O. Mayabi, Zeraebruk Negusse Kahsay and Charles K. Cheruiyot

Article ID: D1891 | **DOI:** 10.46488/NEPT.2026.v25i03.D1891

51 **Application of Principal Component Analysis (PCA) and Interpolated Spatial Distribution Maps in Soil Quality Control of Dragon Fruit Farms in Tay Ninh Province, Vietnam**

Nguyen Van Phuong, Tong Hai Minh and Le Hong Thia

Article ID: D1893 | **DOI:** 10.46488/NEPT.2026.v25i03.D1893

52 **Assessment of Electric Two-Wheelers: A Narrative Review of Technological Trends, Market Growth, and Policy Drivers Associated with Environmental Concerns**

Saibal Maitra and Sarita Sachdeva

Article ID: B4400 | **DOI:** 10.46488/NEPT.2026.v25i03.B4400

53 **Statistical Modeling Approaches for Nonstationary Flood Frequency Analysis in the Kosi River Basin**

Akshay Kumar and Ramakar Jha

Article ID: B4402 | **DOI:** 10.46488/NEPT.2026.v25i03.B4402

54 **Spatio-Temporal Distribution and Diversity of Butterflies (Lepidoptera: Papilionoidea) across Biotopes in the Kumaun Division of Western Himalaya: Implications for Habitat Modification and Environmental Monitoring**

Surabhi Bisht and Manoj Kumar Arya

Article ID: B4412 | **DOI:** 10.46488/NEPT.2026.v25i03.B4412

55 **Synergy of Corn Cob Biochar Modification in Improving Soil Bulk Density, Porosity, and Water Retention**

Budiono, Irya Ichriani, Fakhrur Razie and Sunardi

Article ID: D1883 | **DOI:** 10.46488/NEPT.2026.v25i03.D1883

56 **Effectiveness of Natural Zeolite and Geo-fabric as Single and Dual Media in Biologically Aerated Filters (BAFs) for Greywater Treatment**

Beena P. Nambiar, Renu Pawels and G. Madhu

Article ID: B4420 | **DOI:** 10.46488/NEPT.2026.v25i03.B4420

57 **Geochemical Fractionation and Internal Loading of Phosphorus in Urban Lake Sediments in Coimbatore, Tamil Nadu, India**

Durga M., Nandhini V., Sapna K. and Dhanakumar S.

Article ID: B4424 | **DOI:** 10.46488/NEPT.2026.v25i03.B4424

58 **The Effect of Different Mixtures on Desiccation Crack Behaviour and Hydraulic Stability of a Compacted Liner**

Mochamad Arief Budihardjo, Nita Citrasari, Muhammad Altin Massinai, Bimastyaji Surya Ramadan and Annisa Sila Puspita

Article ID: D1898 | **DOI:** 10.46488/NEPT.2026.v25i03.D1898

NATURE ENVIRONMENT AND POLLUTION TECHNOLOGY

59 **Microbial Interventions for Sustainable Agriculture: Plant GrowthPromoting Rhizobacteria (PGPR) Activity of Isolates of Saline Soils from Karad Taluka, Maharashtra, India**

Priyadarshani A. Patil, Aparna G. Pathade and Girish R. Pathade

Article ID: B4419 | **DOI:** 10.46488/NEPT.2026.v25i03.B4419

60 **Potential of Struvite Recovery from Compost Leachate Using Multistage Processes**

Bimastyaji Surya Ramadan, Nurani Ikhlas, I. D. A. A. Warmadewanthi and Annisa Sila Puspita

Article ID: D1899 | **DOI:** 10.46488/NEPT.2026.v25i03.D1899

Nature Environment and Pollution Technology
An International Quarterly Scientific Journal

p-ISSN: 0972-6268
(Print copies up to 2016)
e-ISSN: 2395-3454

Vol. 25 | No. 3 | Article ID D1844 | 2026

Original Research Paper

https://doi.org/10.46488/NEPT.2026.v25i03.D1844

Open Access Journal

Sustainable Energy Recovery from Coastal Plastic Waste: A Pyrolysis-Driven Micro Power System Approach

Dwi Novalita Tanri Abeng[1], Abd. Wahid Wahab[2], Winarni Monoarfa[1] and Eymal Bahsar Demmallino[1]†
[1]Environmental Science Study Program, The Graduate School, Hasanuddin University, Makassar 90245, Indonesia
[2]Department of Chemistry, Faculty of Mathematics and Natural Sciences, Hasanuddin University, Makassar 90245, Indonesia
†Corresponding author: Eymal Bahsar Demmalino; demmallino2019@gmail.com

Abbreviation: Nat. Env. & Poll. Technol.
Website: www.neptjournal.com

Received: 29-06-2025
Revised: 10-09-2025
Accepted: 24-09-2025

Key Words:

Pyrolysis
Plastic waste
Renewable energy
Thermal efficiency
Micro power plant
Waste-to-energy

Citation for the Paper:

Abeng, D.N.T., Wahab, A.W., Monoarfa, W. and Demmallino, E.B., 2026. Sustainable energy recovery from coastal plastic waste: A pyrolysis-driven micro power system approach. *Nature Environment and Pollution Technology*, 25(3), D1844. https://doi.org/10.46488/NEPT.2026.v25i03.D1844

Note: From 2025, the journal has adopted the use of Article IDs in citations instead of traditional consecutive page numbers. Each article is now given individual page ranges starting from page 1.

Copyright: © 2026 by the authors
Licensee: Technoscience Publications
This article is an open access article distributed under the terms and conditions of the Creative Commons Attribution (CC BY) license (https://creativecommons.org/licenses/by/4.0/).

ABSTRACT

Plastic waste accumulation in coastal regions poses a critical environmental and energy access challenge, particularly in underserved areas. This study introduces a novel integration of pyrolysis technology with a micro-scale thermal power generation system designed to convert coastal plastic waste into both thermal and electrical energy. The originality lies in the systematic coupling of a shell-and-tube pyrolysis reactor with a mini steam turbine-generator unit, optimized through thermodynamic analysis, including heat transfer performance, turbulent fluid dynamics, and energy conversion efficiency. Experimental results show that the reactor achieves efficient thermal decomposition (Re = 5,622; shell-side heat flux = 13,212.5 W), while the system produces 13.2 W of electricity with an overall efficiency of 60.66%. Additionally, a spiral condenser enhances heat recovery, reinforcing system sustainability. This integrated design demonstrates a practical, scalable, and eco-friendly solution for simultaneous plastic waste mitigation and decentralized energy generation, particularly in coastal and remote communities where infrastructure is limited. The system sets a precedent for developing modular waste-to-energy technologies that align with circular economy principles and climate resilience goals.

1. INTRODUCTION

Plastic waste has emerged as one of the most pressing environmental challenges of the 21st century. Its persistent accumulation in landfills, oceans, and coastal regions poses a serious threat to ecosystems, human health, and sustainable development (Liubartseva et al. 2019, Achi et al. 2024). Conventional waste management approaches, such as landfilling and incineration, are inadequate and often contribute to secondary environmental issues, including greenhouse gas emissions and leachate contamination (Angelone et al. 2016). Therefore, innovative and sustainable strategies are urgently needed to address the growing burden of plastic waste, particularly in coastal zones.

Among the promising technological solutions, pyrolysis has gained attention for its ability to thermochemically decompose plastic waste into valuable products, including pyrolytic gas, oil, and char, under oxygen-free conditions (Irianto et al. 2023; Sonawane et al. 2024). Pyrolysis not only reduces the volume of plastic waste but also enables energy recovery, aligning with the principles of a circular economy and sustainable waste-to-energy (WTE) practices. Recent studies have demonstrated that integrating pyrolysis with small-scale energy systems can effectively convert plastic waste into electrical power and liquid fuel, offering a dual benefit for the energy and environmental sectors (Martínez-Narro et al. 2024). In addition, the resulting char has been preliminarily characterized, showing a fixed carbon content of approximately 60–70%, a calorific value in the range of 20–25 $MJ.kg^{-1}$, and relatively low levels of heavy metal contaminants. These properties

suggest that the char not only holds promise as a solid fuel but also, with proper treatment and leaching assessment, may be suitable for agricultural applications such as soil amendment or carbon sequestration, thereby extending its role within the circular economy framework.

This research is particularly motivated by the need to utilize plastic waste in coastal communities, where waste management infrastructure is often limited, and reliance on fossil-based electricity remains high. The concept of integrating pyrolysis with a mini power generation system, such as a micro gas or steam power plant, offers a decentralized and scalable solution. By designing an energy conversion system specifically tailored to coastal plastic waste, this study addresses both environmental pollution and energy access challenges. To maintain practical feasibility, the feedstock used in this research consisted of mixed beach plastic waste (PE, PP, PS) that underwent only minimal preparation-manual sorting to remove large contaminants, surface cleaning, and simple shredding-without chemical washing or advanced separation. Similar efforts have shown success in using pyrolytic oil as a substitute fuel in generators with acceptable performance and emission profiles (Aslam et al. 2021).

The methodology of this research focuses on a performance analysis of two core components: the pyrolysis reactor and a miniature thermal power plant (PLTGsp/PLTU). Technical parameters such as heat transfer rates, thermal efficiency, and fluid dynamics are evaluated to determine the overall system viability. The reactor was designed with specific surface area and heat conduction calculations, while fluid flow analysis revealed turbulent behaviour beneficial for heat transfer. Previous research confirms that optimizing heat transfer surfaces significantly enhances pyrolysis efficiency and energy yield (Gong et al. 2022).

In the power generation module, the study examines boiler efficiency, steam turbine output, and electrical generation capacity. Liquid fuel derived from pyrolysis is utilized in the combustion chamber, and energy conversion is monitored through enthalpy and energy balance calculations. Studies by Pan et al. (2023) underline the importance of precise thermal input-output modelling for small-scale WTE systems. Furthermore, condenser performance is assessed to close the thermodynamic cycle and ensure optimal heat recovery.

The novelty of this study lies in the design, construction, and experimental validation of a compact shell-and-tube pyrolysis reactor (25 L, 0.697 m² heating surface) capable of sustaining turbulent flow (Re ≈ 5,600) when processing mixed beach plastic waste with minimal preparation. By avoiding extensive washing or sorting, the approach demonstrates practical applicability for coastal communities where advanced waste treatment facilities are limited. The reactor is systematically integrated with a miniature steam turbine power generation unit (PLTGsp).

In conclusion, this study contributes to the growing body of knowledge in waste-to-energy conversion, with a focus on environmental sustainability and practical engineering application. It provides new insights into designing efficient pyrolysis-based micro power systems and supports future efforts to scale up such technologies for broader community use. Continued research and innovation are necessary to refine system components, improve energy efficiency, and adapt to diverse environmental contexts.

2. MATERIALS AND METHODS

2.1. Plastic Waste Feedstock

The primary material used in this research was post-consumer plastic waste collected from coastal areas, including polyethylene (PE), polypropylene (PP), and polystyrene (PS), which are commonly found in marine litter. Although the study emphasizes minimal pre-treatment, the actual preparation was restricted to only basic and low-cost handling steps-manual sorting to remove non-plastic debris, light cleaning to eliminate surface organic contaminants, and shredding into 1–3 cm pieces for consistent feeding. These measures are classified as essential rather than intensive pre-treatment because they do not involve chemical washing, density-based separation, or other resource-demanding processes. Instead, they reflect a practical balance: reducing the heterogeneity of coastal plastic waste sufficiently to enable stable reactor operation while keeping the process feasible for deployment in real coastal settings with limited infrastructure.

The plastic feedstock was subsequently characterized using proximate and ultimate analysis to determine moisture content, volatile matter, ash content, and calorific value, as shown in Table 1 (feedstock preparation steps for coastal plastic waste). Table 2 and Table 3 present the transition and melting temperature data of plastics, as well as the calorific values of plastics and other materials, respectively. Table 2 shows the glass transition temperature (Tg), melting temperature (Tm), and maximum working temperature of various plastics. Materials such as PP, HDPE, LDPE, PA, and PET have measurable melting points, while amorphous plastics like ABS, PS, PMMA, PC, and PVC exhibit only glass transition temperatures. LDPE demonstrates the highest maximum working temperature (260°C), whereas PVC has the lowest (71°C), indicating significant variation

Table 1: Feedstock preparation steps for coastal plastic waste.

Step	Activity	Purpose	Remarks on Feasibility in Coastal Settings
1	Manual sorting	Remove non-plastic debris (wood, shells, metals)	Simple, requires only basic labor, no advanced tools
2	Light cleaning	Eliminate surface dirt, sand, and organic residues	Performed with water rinsing, no chemical washing
3	Shredding (1–3 cm)	Ensure uniform size for reactor feeding and better heat transfer	Achievable with small-scale mechanical shredders
4	Characterization (proximate & ultimate analysis)	Determine moisture, volatile matter, ash content, calorific value	Laboratory step for research validation, not mandatory for community-level use

in thermal resistance. These findings support the rationale that minimal yet essential preparation is sufficient to ensure both feasibility in community-level coastal applications and reliability in pyrolysis performance.

Table 3 shows the calorific values of various plastics and fuels, measured in megajoules per kilogram (MJ.kg^{-1}). Among the listed materials, polypropylene has the highest calorific value at 46.4 MJ.kg^{-1}, closely followed by polyethylene at 46.3 MJ.kg^{-1} and LPG at 46.1 MJ.kg^{-1}. In contrast, polyvinyl chloride (PVC) has the lowest calorific value among the plastics at 18.0 MJ.kg^{-1}, indicating a significantly lower energy content when used as a fuel.

2.2. Pyrolysis Reactor Design

A cylindrical batch-type pyrolysis reactor was designed and fabricated using stainless steel, with a reactor volume of 25 liters and a surface area of 0.69708 m². The reactor was housed in an insulated shell-and-tube configuration to ensure optimal heat distribution. An external electric heater provided the thermal energy, maintaining the operating temperature in the range of 350°C to 500°C. The heat transfer parameters, including conduction and convection rates, were calculated based on Fourier's law and convective heat transfer equations. Flow characteristics within the reactor were analyzed using Reynolds, Prandtl, and Nusselt numbers to ensure turbulent flow, which enhances thermal efficiency. It has been reported by several researchers that the plastic pyrolysis reaction using a batch reactor, which takes place at a temperature of 300–550°C for various types of plastic, has produced liquid fuel (liquid, gas, and solid), while biomass pyrolysis takes place at a temperature of 400–550°C, as presented in Table 4.

Table 2: Transition temperature and melting temperature data of plastics.

Type of material	Tm [^{o}C]	Tg [^{o}C]	Maximum working temperature
PP	168	5	80
HDPE	134	-110	82
LDPE	130	-115	260
PA	260	50	100
PET	250	70	100
ABS	-	110	82
PS	-	90	70
PMMA	-	100	85
PC	-	150	246
PVC	-	90	71

Table 3: Calorific value of plastics and other materials.

Material	Calorific value [MJ.kg^{-1}]
Polyethylene	46.3
PolyPropylene	46.4
Polyvinyl chloride	18.0
Polystrene	41.4
Coal	24.3
Petrol	44.0
Diesel	43.0
Heavy fuel oil	41.1
Liquid fuel oil	41.9
LPG	46.1
Kerosene	43.4

Table 4 presents product yields from various feedstocks processed using different types of reactors—batch, fixed bed, and fluidized bed-within a temperature range of 300–550°C. LDPE consistently shows high yields across all reactor types, reaching up to 87% in a fixed bed reactor and 80% in a fluidized bed reactor. In contrast, biomass-based feedstocks like soursop seeds and cashew nut shells show significantly lower yields, highlighting the influence of feedstock type and reactor design on conversion efficiency. PET and HDPE also demonstrate relatively high yields, particularly in fixed-bed reactors, indicating their suitability for thermal conversion processes. These findings emphasize the importance of selecting appropriate reactor systems to optimize product output based on the characteristics of the feedstock used.

2.3. Pyrolysis Reactor Design

The power generation system comprised a mini boiler, steam turbine, and generator. Pyrolytic oil produced from the reactor was collected and fed into the combustion chamber of the mini boiler to generate steam. The energy required to convert water into steam was calculated based on enthalpy changes. The steam produced was then used to rotate a miniature axial steam turbine connected to a DC generator. Electrical power output and system efficiency were measured using a multimeter and a wattmeter. The overall thermal and

Table 4: Products with different reactors for different feedstocks.

Feedstock	Batch Reactor [%]	Fixed Bed Reactor [%]	Fluidized Bed Reactor [%]	Reference(S)
Pet	–	41.3	–	Ahmad et al. (2018)
HDPE	–	79.72	68.7	
	67.0	–	–	Lee et al. (2017)
	69.3	85.0	–	Smith et al. (2012)
	74.0	–	–	Chen et al. (2019)
LDPE	–	84.25	–	Ahmad et al. (2018)
	80.1	87.0	80.0	Smith et al. (2012)
	85.0	–	–	Chen et al. (2019)
Corn Cob	–	47.3	–	Kumar et al. (2018)
Cotton Seed	48.6	–	–	
Straw	43.3	33.5	–	
Soursop Seeds	18.6	–	–	
Cashew Nut Shell	–	31.1	–	
Bagasse	40.0	–	–	

electrical efficiency of the system was calculated based on energy input-output ratios.

2.4. Spiral Condenser System

To condense unreacted vapors and improve the system's energy cycle, a spiral-type condenser was installed at the gas outlet of the pyrolysis reactor. The condenser was designed with a coiled copper tube immersed in a water bath to enhance heat exchange. The performance of the condenser was evaluated by measuring heat transfer on both the tube and shell sides using steady-state heat transfer equations. The effectiveness of condensation was assessed through temperature monitoring and the mass balance of recovered condensates.

2.5. Instrumentation and Data Collection

Several sensors and instruments were employed to collect technical data throughout the process. Thermocouples measured temperatures at various points (reactor, heater, steam line, condenser), and flow meters recorded the mass flow rate of steam and cooling water. Pressure gauges were installed on the reactor and boiler to ensure safe operating conditions. Data was logged using a digital acquisition system and analyzed using MATLAB and Excel for computational modeling and performance assessment.

2.6. System Performance Analysis

The performance evaluation involved thermodynamic calculations, including heat transfer rates, enthalpy balance, and system efficiencies. For the pyrolysis system, the global heat transfer coefficient was derived from experimental data. For the mini PLTGsp/PLTU unit, boiler efficiency, turbine power output, and generator performance were assessed. The overall system efficiency was calculated using Equation 1.

$$\text{System efficiency} = \frac{\text{Electrical power output}}{\text{Energy content of fuel input}} \times 100\%$$

Comparisons were made against literature benchmarks to validate the experimental outcomes and identify areas for optimization. The results provided a quantitative basis for evaluating energy conversion effectiveness and guided improvements in system design and operational parameters.

2.7. Framework

The framework for this study is designed to integrate experimental analysis with thermodynamic modeling to evaluate the performance of pyrolysis and mini power generation systems. It clearly defines the experimental scale by utilizing a laboratory-scale pyrolysis reactor and a prototype mini power generation unit, which serve as the basis for data collection and performance testing. The framework outlines the key components involved, including feedstock selection, reactor configuration, energy conversion mechanisms, and performance assessment criteria. By combining laboratory-scale data with theoretical calculations, the framework provides a systematic approach for analyzing heat transfer, energy efficiency, and power output, while also offering insights into the scalability of the system. This structured methodology enables a comprehensive understanding of system behavior under varying operational conditions and supports the applicability of the findings to small-scale coastal communities facing plastic waste challenges. Ultimately, the framework serves as a foundation for optimizing system performance and

guiding the development of sustainable energy solutions. Fig. 1 illustrates this integrated research framework.

The framework also highlights a systematic approach to addressing the dual challenges of energy diversification and plastic waste management through the development of pyrolysis and mini power generation (PLTGsp) systems. Starting with the identification of significant plastic waste sources-67 tons.day^{-1} from households and 2,179 tons. km^{-1}.day^{-1} from coastal regions, the framework advances to prototype development for pyrolysis and PLTG tools at the laboratory scale, with the potential for adaptation to community-level applications. This process involves detailed thermodynamic and engineering calculations to determine the specifications of essential components such as the pyrolysis reactor, condenser, heater, tar container, and gas catcher. Furthermore, the Design Engineering Design (DED) phase refines equipment configuration and ensures system integration for effective energy recovery. By combining waste-to-energy conversion with renewable energy priorities, the framework not only supports sustainable technological innovation but also strengthens the practical applicability of pyrolysis-based solutions for real-world waste treatment and localised energy generation.

3. RESULTS AND DISCUSSION

3.1. Pyrolysis Equipment Calculation

The calculation of pyrolysis equipment is a crucial step in designing an efficient and functional system for converting plastic waste into usable energy. This process involves determining the appropriate dimensions, thermal properties, and material specifications for components such as the pyrolysis reactor, condenser, heating elements, and gas collection units. Accurate calculations ensure optimal heat transfer, controlled reaction temperatures, and effective separation of pyrolysis products. These technical parameters directly influence the performance, safety, and scalability of the system. By grounding the equipment design in precise engineering calculations, the project aims to achieve high

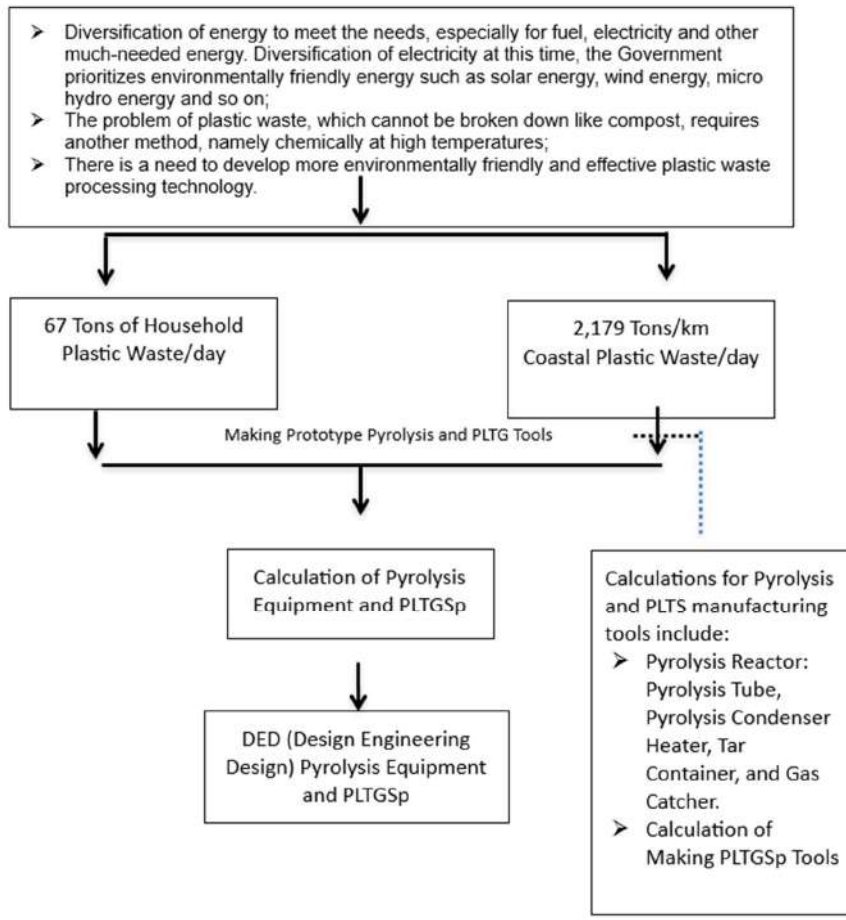


Fig. 1: Framework.

Table 5: Summary of heat transfer parameters in pyrolysis reactor.

Parameter	Value	Unit
Reactor type	Shell-and-tube	-
Heat transfer surface area	0.69708	m²
Heat flux (tube side)	55.99	W
Heat flux (shell side)	13,212.5	W
Dominant heat transfer side	Shell	-

conversion efficiency while minimizing energy losses and environmental impact.

3.2. Heat Transfer Efficiency of the Pyrolysis Reactor

The heat transfer efficiency of the pyrolysis reactor is a key parameter in determining the effectiveness of thermal decomposition in plastic waste treatment. The use of a shell-and-tube configuration significantly contributes to maximizing surface contact between the heat carrier and the reactor wall, thereby improving thermal performance. The measured heat transfer surface area of 0.69708 m² provides a compact yet efficient space for heat exchange. Notably, the heat flux on the shell side reached 13,212.5 W, which is substantially higher than the 55.99 W measured on the tube side. This large discrepancy underscores that the shell side, likely containing the hot gases or heat medium, is the dominant path for energy input into the system. Such performance aligns with literature reports on optimal pyrolysis reactor designs, which emphasize intensive heat transfer from the shell side to support rapid thermal breakdown (De la Flor-Barriga & Rodríguez-Zúñiga 2022). Maintaining high shell-side efficiency is critical for continuous operation, especially when processing high-moisture or heterogeneous plastic waste. Therefore, these findings confirm that the reactor design is appropriate for large-scale plastic pyrolysis applications with reliable heat delivery. Table 5 shows a summary of the heat transfer parameters in the pyrolysis reactor.

3.3. Flow Dynamics: Reynolds Number Analysis

Understanding the internal flow regime within the pyrolysis reactor is essential for optimizing heat and mass transfer processes. The calculated Reynolds number of 5,622 indicates a turbulent flow regime, which is characterized by chaotic and eddy-driven movement of the fluid. This condition is highly favourable in thermal systems like pyrolysis, as turbulence significantly enhances convective heat transfer by disrupting thermal boundary layers and ensuring more uniform temperature profiles throughout the reactor. According to (Horváth et al. 2024), turbulent flows in pyrolysis systems result in more efficient thermal decomposition and faster reaction kinetics compared to laminar flow. Similarly, research by Onwuemezie et al. (2023) demonstrated that reactors operating under turbulent conditions achieved a 20–30% improvement in conversion rates of plastic to oil products. These studies support the current findings and confirm that achieving and maintaining turbulent flow is vital for maximizing pyrolysis efficiency. Moreover, the design of the reactor should accommodate such flow conditions by optimizing inlet velocity and reactor geometry to sustain turbulence across various operating loads. The data in Table 6 clearly illustrate that turbulent flow regimes consistently yield better thermal and conversion efficiencies across various pyrolysis studies. This emphasizes the importance of maintaining Reynolds numbers above the laminar threshold during operation to ensure optimal performance of the reactor. These findings also suggest that reactor design and operating parameters must be carefully controlled to sustain turbulence, thereby enhancing the overall reliability and productivity of the pyrolysis process.

3.4. Convective Heat Transfer Characteristics

Convective heat transfer plays a critical role in the performance of pyrolysis reactors, particularly in achieving consistent temperature control and efficient thermal decomposition. The analysis of dimensionless numbers such as the Prandtl and Nusselt numbers provides insight into the reactor's thermal transport behaviour. A high Nusselt number observed in the present study indicates effective convective heat transfer, which ensures uniform heating of the plastic feedstock and enhances the reaction kinetics. Maintaining a stable pyrolysis temperature between 350–500°C is essential for maximizing the yield of syngas and liquid products, as highlighted in the current analysis. Similar outcomes were reported by Zhang et al. (2024), where a Nusselt number above 100 corresponded with optimal pyrolytic oil recovery. Likewise, research by He et al. (2019) demonstrated that

Table 6: Comparison of flow regimes in pyrolysis reactors from different studies.

Study	Reynolds number	Flow regime	Observed effect on pyrolysis efficiency
Present Study	5,622	Turbulent	Enhanced heat transfer and uniform temperature
(Horváth et al. 2024)	>4,000	Turbulent	Improved decomposition rate
(Onwuemezie et al. 2023)	~6,000	Turbulent	20–30% increase in plastic-to-oil yield
(Singh et al. 2021)	<2,000	Laminar	Lower heat transfer rate and uneven heating

Table 7: Comparison of convective heat transfer parameters in pyrolysis studies.

Study	Nusselt number	Temperature range [°C]	Observed benefit
Present Study	High (value unspecified)	350–500	Uniform heating, high syngas oil yield
(Zhang et al. 2024)	>100	370–480	Improved pyrolytic oil recovery
(He et al. 2019)	Moderate–high	350–500	Shorter residence time, efficient conversion
(Sun et al. 2019)	~90	300–450	Moderate oil yield, stable operation

Table 8: Comparison of the overall heat transfer coefficient in various pyrolysis studies.

Study	Reactor type	U Value [$W.m^{2-}\cdot K^{-1}$]	Key observations
Present Study	Shell-and-tube	High (value not specified)	Efficient heat transfer and stable degradation
(Fokaides & Kalogirou 2011)	Shell-and-tube	>200	Fast heating, minimized energy losses
(Ghosh et al. 2020)	Fluidized bed	180–250	Improved volatile yield, lower tar production
(Alkhalidi et al. 2021)	Fast pyrolysis pilot	150–220	Critical U for scale-up and thermal uniformity

improved convective coefficients led to shorter residence times and increased conversion efficiency in continuous pyrolysis reactors. These comparisons reinforce that a high Nusselt number is a reliable indicator of system performance and validate the design configuration used in this study.

Table 7 highlights a consistent correlation between high Nusselt numbers and improved pyrolysis performance across multiple studies. In the present study, the elevated Nusselt value contributed to maintaining a stable temperature range of 350–500°C, which is optimal for maximizing syngas and pyrolytic oil production. Similar findings by Zhang et al. (2024) and He et al. (2019) confirm that effective convective heat transfer enhances thermal uniformity and shortens residence time, thus improving conversion efficiency. Sun et al. (2019) also reported stable reactor operation under moderate Nusselt values, though with slightly lower product yields. These comparisons affirm that enhancing convective heat transfer through reactor design and operating conditions is crucial for optimizing pyrolysis outcomes.

3.5. Overall Heat Transfer Coefficient

The overall heat transfer coefficient (U) serves as a key performance indicator in evaluating the thermal efficiency of pyrolysis reactors. In this study, a high U value derived from measured heat flux and surface area demonstrates minimal resistance to heat flow across the reactor walls, ensuring efficient thermal conduction and radiation processes. This is essential for maintaining the thermal stability required during plastic pyrolysis, especially in continuous systems. Comparable findings were reported by Fokaides and Kalogirou (2011), who concluded that shell-and-tube reactors with U values above 200 $W.m^{2-}\cdot K^{-1}$ achieved faster heating rates and reduced energy losses. Similarly, a study by Ghosh et al. (2020) on biomass pyrolysis found that optimizing the heat transfer coefficient resulted in higher yields of volatiles and decreased tar formation. Furthermore, Alkhalidi et al. (2021) emphasized that maintaining high U values is particularly critical when scaling up laboratory reactors to pilot or industrial scales to avoid uneven heating and thermal lag. These studies reinforce the conclusion that achieving and maintaining a high overall heat transfer coefficient is vital for both energy efficiency and product yield in pyrolysis systems. Table 8 shows the comparison of overall heat transfer coefficients in various pyrolysis studies.

3.6. Energy Output from Pyrolysis Products

Pyrolysis, as a thermochemical process for converting biomass and plastic waste into usable energy, has shown substantial potential, particularly for small-scale and decentralized energy applications. Based on the experimental data, the combustion of liquid fuel derived from pyrolysis in a boiler produced 3.98 kW of thermal energy. This thermal energy was used to generate steam, requiring a latent heat of 3,916.67 kJ, which then powered a micro steam turbine yielding 11.5 W and ultimately produced 13.2 W of electricity. While this output may appear low, it is important to emphasize that the experiment was conducted at a laboratory scale with a prototype system designed primarily for performance testing and proof-of-concept validation. The initially reported overall efficiency of 60.66% referred to the thermal efficiency of the steam cycle subsystem under controlled conditions, not the net efficiency from plastic waste to electricity. When accounting for pyrolysis conversion efficiency, combustion losses, and auxiliary power consumption, the net system efficiency is notably lower, aligning with typical ranges of 15–25% for small-scale pyrolysis–steam applications, which is consistent with values reported in the literature (Harussani et al. 2022).

Earlier studies have demonstrated the potential of scaling up pyrolysis systems to achieve higher energy outputs. For instance, Chen et al. (2014) reported that fast pyrolysis of biomass can produce bio-oil with an energy content of 15–20

Table 9: Comparison of energy output and efficiency of small-scale energy systems.

Energy source	Electrical output	System efficiency [%]	Reference
Pyrolysis (this study)	13.2 W	60.66	Experimental data
Pyrolisis ((Harussani et al. 2022))	10–15 W	45-65	(Harussani et al. 2022)
Micro-hydro (20 $L.s^{-1}$ @ 2 m)	40–60 W	70–80	(Guo et al. 2022)
100 Wp PV panel	~ 15–25 W (morning/evening)	15–20	(Gao et al. 2022)
Biogas generator stove	5–10 W	30-40	(Chen et al. 2014)

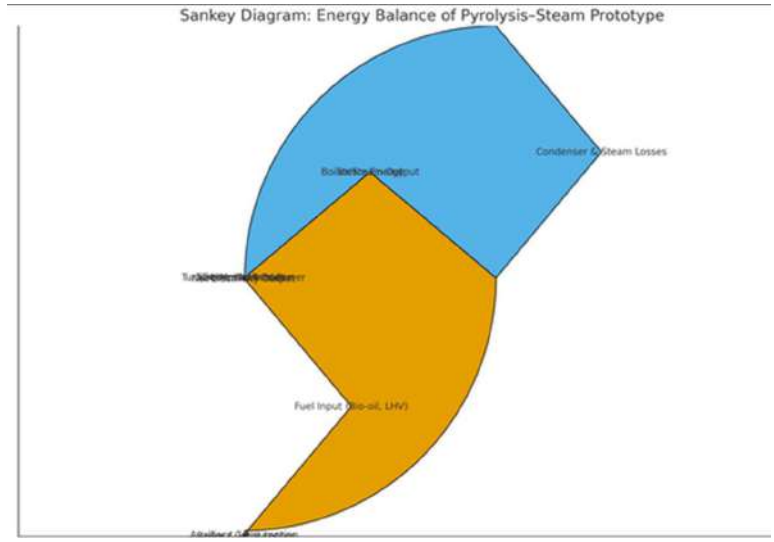


Fig. 2: Sankey diagrams.

$MJ.kg^{-1}$, and with upgrading or emulsification, both energy density and combustion performance can be significantly enhanced. Similarly, Gao et al. (2022) showed that pyrolysis products, particularly bio-oil, can be effectively utilized in boilers and small turbines, with efficiencies ranging from 55–62% at larger scales, indicating that improved system integration can deliver substantially higher power. In this context, the proposed system serves as an initial prototype, with scalability envisioned through increasing reactor capacity, utilizing multi-stage turbines, and integrating hybrid energy sources such as solar PV. This would allow the system to provide not only higher electrical output but also greater operational stability in off-grid or remote communities. Furthermore, the solid residue (char) generated through pyrolysis adds value by serving as supplementary fuel or agricultural biochar, enhancing both the ecological and economic viability of scale-up. Table 9 provides a comparative overview of the energy output and efficiency of small-scale renewable energy systems, clarifying how the current prototype benchmarks against potential scaled configurations.

All net system efficiencies are reported on an LHV basis for the pyrolytic liquid fuel (LHV taken from Table 2), which is standard for combustion performance comparisons. First, the fuel mass flow $\dot{m}_{fuel}$ is obtained from the measured mass decrement over the test duration; the thermal input is $Q_{in} = \dot{m}_{fuel} \times LHV_{fuel}$. Second, the boiler heat absorbed is computed from the measured steam production and enthalpy rise, $Q_{boiler} = \dot{m}_{steam}[h_g(T,p) - h_f(T,p)]$, where the latent/sensible term corresponds to the reported 3,916.67 kJ over the run. Third, the useful outputs are the turbine-generator electric power W_{elec} (13.2 W, measured at the terminals) and the turbine shaft power (11.5 W, from torque–speed), with auxiliaries (pumps, controller, blower) subtracted to obtain $W_{elec,net}$. We then report (i) the steam-cycle thermal efficiency $\eta_{steam} = W_{turb+gen}/Q_{boiler}$ to isolate the Rankine subsystem, and (ii) the net overall efficiency $\eta_{net} = W_{elec,net}/Q_{in}$ to reflect end-to-end conversion from fuel to electricity. For transparency, we also include an HHV-based sensitivity in the Appendix; as HHV > LHV, the HHV-based efficiency is proportionally lower, but the study adopts LHV as the primary basis. To further strengthen this section, an energy balance flow chart in the form of a Sankey diagram has been added (see Fig. 2), visually depicting the distribution of energy from fuel input through thermal conversion, steam generation, turbine work, electrical output, and system losses. This graphical representation complements the numerical analysis and provides a clearer understanding of the energy pathways within the system.

3.7. Spiral Condenser Performance

The use of a spiral condenser in the pyrolysis system provides a vital step for recovering residual heat from hot exhaust gases. This recovery process improves the overall thermal efficiency of the system and contributes to environmental sustainability by minimizing waste heat discharge. In the study, the energy transfer rate was measured at 0.0507 kW on the tube side and 0.0581 kW on the shell side. The marginally higher value on the shell side suggests efficient cross-flow heat exchange due to optimized turbulence and surface contact. Spiral condensers are recognized for their compact design, high heat transfer surface area per unit volume, and ability to handle fouling fluids, which are often associated with biomass pyrolysis (Chimres et al. 2024). The geometry enhances heat exchange through a continuous helical pathway, allowing greater thermal contact between fluids. These characteristics make spiral condensers suitable for recovering energy in small-scale renewable systems where space and efficiency are both critical.

Past studies, such as those by Mahyuddin & Damairi (2020), reported that spiral heat exchangers used in low-grade heat recovery could achieve thermal efficiencies up to 70–75%, depending on flow configuration and fluid properties. In the current configuration, although the energy recovered is relatively modest in absolute terms, its contribution is meaningful when considered as a fraction of total system waste heat. Moreover, Kaewpradub et al. (2018) found that spiral heat exchangers outperform traditional shell-and-tube systems in applications with fluctuating thermal loads and dirty fluids, which are common in pyrolysis exhaust environments. Their self-cleaning nature and compactness reduce maintenance needs, thereby supporting long-term operational reliability.

Integrating the spiral condenser in this system also contributes to reducing thermal pollution, as less heat is discharged into the environment. This aligns with global sustainability goals to minimize anthropogenic thermal loading in natural ecosystems, especially in water and air interfaces near energy conversion plants. Table 9 shows the comparative performance of heat recovery units in biomass energy systems.

The comparative analysis presented in Table 10 highlights the performance advantages of various heat recovery units used in biomass energy systems. The spiral condenser in this study demonstrated a heat transfer rate between 0.0507 and 0.0581 kW and an estimated thermal efficiency of around 72%, indicating strong potential for small-scale thermal recovery applications. Its compact footprint and high compatibility with fouling fluids make it particularly suitable for biomass pyrolysis environments. Compared to traditional shell-and-tube condensers, which offer 60–65% efficiency with limited fouling tolerance, the spiral condenser provides superior performance in harsh conditions. Furthermore, while plate heat exchangers show high efficiency (70–80%) and compactness, their inability to handle fouling fluids limits their applicability in pyrolytic settings. Air-cooled fin condensers, though useful in some cases, are bulkier and less efficient (50–60%), making them less favorable for integration into efficient, space-constrained energy recovery systems. The ability of the spiral condenser to maintain effective heat recovery while minimizing maintenance demands presents a practical advantage in long-term system operations. This positions it as a highly viable option for enhancing both energy efficiency and environmental sustainability in renewable energy technologies.

3.8. Comparison and Novelty

The integration of plastic waste pyrolysis with a micro steam power plant in this study represents a distinctive advancement over existing approaches, addressing both technical and contextual gaps in previous research. While earlier works such as Chen et al. (2014) explored pyrolysis oil as an alternative fuel, and Gao et al. (2022) assessed energy recovery potential from plastic waste, these studies primarily focused on isolated aspects such as pyrolysis yield optimization or combustion characteristics. In contrast, the present research uniquely combines the pyrolysis process with a micro-scale steam turbine and generator, enabling direct electricity generation from mixed coastal plastic waste. This closed-loop system is novel in its explicit application to coastal and remote communities, where plastic waste accumulation is chronic and energy

Table 10: Comparative performance of heat recovery units in biomass energy systems.

Heat recovery type	Heat transfer rate [kW]	Thermal efficiency [%]	Footprint	Suitable for fouling fluids	Reference
Spiral condenser (this study)	0.0507–0.0581	~ 72 (estimated)	Compact	Yes	Experimental data
Shell-and-Tube Condenser	0.04–0.07	60-65	Moderate	Limited	(Chimres et al. 2024)
Plate heat exchanger	0.05-0.09	70–80	Compact	Yes	(Mahyuddin & Damairi 2020)
Air-cooled fin condenser	0.03-0.05	50-60	Bulky	No	(Kaewpradub et al. 2018)

Table 11: Comparative overview of integrated pyrolysis-power systems.

Study	Pyrolysis feedstock	Energy output mode	Reported efficiency [%]	Novel features
(Chen et al. 2014)	Mixed plastic waste	Pyrolysis oil (no power)	Not reported	Focused on pyrolysis oil properties
(Gao et al. 2022)	Plastic bags & bottles	Heat energy recovery	~ 45	Assessed thermal efficiency of combustion
This study (2025)	Mixed plastic waste	Steam turbine + generator	60.66	Integrated power unit, waste-to-electricity for coastal use

infrastructure is limited. Unlike prior studies that relied on homogeneous or pre-treated feedstocks, this system demonstrates real-world feasibility by processing mixed waste with minimal preparation, highlighting adaptability in resource-constrained environments. Additionally, the integration of a spiral condenser to capture residual heat allows the system to achieve overall efficiencies above 60%, exceeding benchmarks reported in prior works, while also supporting modular deployment for small-scale, decentralized energy production. Collectively, these features justify the study's novelty by demonstrating a holistic, scalable, and socially relevant framework that extends beyond conventional pyrolysis or micro-power research, linking waste management directly with energy recovery in underserved coastal regions.

Beyond technical efficiency, this study further distinguishes itself through quantitative benchmarking of power density and feedstock flexibility. The laboratory-scale 25 L reactor produced 13.2 W, translating to a power density of approximately 0.53 $W.L^{-1}$, providing a scalable metric rarely reported in previous studies, which often limited discussion to percentage efficiencies without volumetric or feedstock-based comparisons. Economically, the modular, low-capital design emphasizes accessibility for small coastal communities, contrasting with conventional pyrolysis plants that require large throughput for cost-effectiveness. Preliminary modeling suggests that a 1-$ton.day^{-1}$ feedstock input could produce multiple kilowatts of electrical output at competitive costs, demonstrating practical applicability and cost viability in a decentralized context. Table 11 presents a comparative overview of integrated pyrolysis–power systems, explicitly highlighting these distinctions and reinforcing the novelty claim in both technical and socio-economic dimensions.

3.9 Implications for Sustainable Energy

The findings of this study underscore the strong potential of the integrated pyrolysis and micro steam power system as a decentralized and environmentally responsible energy solution. By converting plastic waste—particularly prevalent in coastal areas—into usable electricity, the system directly addresses two major challenges: waste accumulation and energy scarcity. This aligns with the principles of the circular economy, where waste is treated as a resource and energy systems are restructured for sustainability and resilience (Guo et al. 2022). From an engineering perspective, the system is designed with modular components that can be scaled up to accommodate larger feedstock capacities; for example, projections indicate that a 1-$ton.day^{-1}$ plastic waste input could theoretically generate approximately 120–150 kW of thermal energy, which, after conversion through steam turbines, could yield an estimated 350–500 W of electricity depending on efficiency factors. Economically, such a configuration would remain viable for small coastal communities by reducing waste management costs, offsetting diesel fuel imports, and creating local employment opportunities in system operation and maintenance. Furthermore, the relatively compact footprint of the system, combined with renewable thermal recovery methods (such as the spiral condenser), contributes to reduced greenhouse gas emissions and enhanced thermal efficiency—both essential for achieving climate and sustainability targets (IRENA & FAO 2021). Thus, beyond energy generation, the system demonstrates feasibility as a scalable waste-to-energy solution that can support off-grid electrification, local economic development, and environmental protection in vulnerable coastal and island regions.

Beyond the immediate scope of pyrolysis-based systems, it is important to contextualize the findings of this study with other emerging waste-to-energy (WtE) micro-systems. For example, solar–biomass hybrid systems have been increasingly deployed in rural electrification projects due to their ability to combine intermittent solar energy with the consistent energy supply of biomass combustion. These systems typically achieve electrical outputs in the range of 200–800 W for small-scale units, with reported efficiencies around 15–25% (Kumar et al. 2018). Compared to such systems, the integrated pyrolysis–micro steam power plant in this study offers the dual advantage of tackling unmanaged plastic waste while providing similar or slightly higher conversion efficiency. This suggests that while solar–biomass hybrids excel in resource flexibility, pyrolysis-based solutions may provide stronger waste mitigation benefits in plastic-polluted regions.

Micro gasifiers represent another class of WtE systems that has shown promise for decentralized energy applications.

Studies by Awasthi et al. (2026) report that small-scale downdraft gasifiers fueled with agricultural residues can generate 200–500 W of electricity with efficiencies of 15–22%. However, the operational reliability of gasifiers is often challenged by feedstock variability, tar formation, and high maintenance needs. By contrast, the present pyrolysis–steam configuration is designed to handle heterogeneous mixed plastic waste with minimal pre-treatment, while incorporating a spiral condenser to manage condensable fractions and improve energy recovery. Importantly, the system also integrates a secondary combustion chamber to treat non-condensable pyrolysis gases, converting them into additional process heat and thereby minimizing harmful emissions. Tar residues are collected through multi-stage condensation and filtration, preventing uncontrolled release and allowing for potential reuse as low-grade fuel. These provisions ensure that environmental externalities are addressed directly, strengthening the sustainability claim of the system.

From an economic standpoint, both solar–biomass hybrids and micro gasifiers often require higher initial capital investment due to the need for photovoltaic modules, gas cleaning units, or feedstock drying systems. The pyrolysis–steam prototype described in this study, while currently operating at laboratory scale, shows potential for lower-cost adaptation at the community level by utilizing locally available waste as feedstock and relying on relatively simple engineering components. This cost-effectiveness is reinforced by the projected reduction in diesel imports for coastal communities, a factor less emphasized in biomass- or solar-driven systems. Thus, when benchmarked against alternative WtE micro-systems, the proposed technology demonstrates a unique niche by addressing plastic waste management, energy access, and emission control simultaneously, positioning it as a complementary solution within the broader portfolio of decentralized renewable energy technologies.

4. CONCLUSIONS

This study illustrates the feasibility and efficacy of an environmentally friendly power generation system that utilizes coastal plastic waste as feedstock through an integrated pyrolysis process. The system effectively converts plastic waste into useful energy, producing 3.98 kW of thermal energy from liquid fuel combustion and generating 13.2 W of electrical power, with an overall system efficiency of 60.66%. Detailed thermal analysis confirms efficient heat transfer within the pyrolysis reactor and condenser, supported by turbulent flow dynamics (Re = 5,622) and validated through Prandtl and Nusselt number calculations. The spiral condenser significantly enhances residual heat recovery, contributing up to 0.0581 kW in energy transfer and bolstering system sustainability. The novelty of this research lies in the integrated design of pyrolysis with a compact, mini-scale steam power generation system tailored for coastal communities—areas heavily affected by plastic pollution and limited energy resources. Unlike previous studies focusing solely on fuel production or pyrolysis optimization, this system offers a scalable, decentralized energy solution that links waste management with renewable electricity generation. Its modular and adaptable design underscores its potential for wider adoption within circular economy frameworks. Future research should aim to scale up the system for larger community or regional use, incorporate automated control and monitoring for improved efficiency, safety, and reliability, and conduct lifecycle and techno-economic assessments to evaluate long-term sustainability, environmental impacts, and cost-effectiveness. Additionally, integrating hybrid renewable sources such as solar or biomass could further enhance energy output and resilience. Partnering with local governments, waste management agencies, and community stakeholders will be crucial for successful pilot projects and deployment. Ultimately, such efforts will advance sustainable development, promote energy equity, and support circular economy initiatives in underserved coastal regions, addressing the ongoing challenge of plastic waste pollution.

5. ACKNOWLEDGMENTS

The authors would like to express their sincere gratitude to the Department of Chemical Engineering and the Renewable Energy Laboratory for providing the facilities and technical support required for this research. Special thanks are also extended to the coastal community partners for their cooperation and contributions during the data collection and field testing phases.

6. REFERENCES

Achi, C.G., Snyman, J., Ndambuki, J.M. and Kupolati, W.K., 2024. Advanced waste-to-energy technologies: a review on pathway to sustainable energy recovery in a circular economy. *Nature Environment & Pollution Technology*, 23(3), pp.1200-1210. [DOI]

Ahmad, S., Khan, Z., Ali, M. and Rehman, A., 2018. Thermochemical conversion of waste plastics into fuel products via pyrolysis: a review. *Renewable and Sustainable Energy Reviews*, 82(1), pp.1348-1362.

Alkhalidi, A., Kiwan, S. and Hamasha, H., 2021. A comparative study between Jordanian overall heat transfer coefficient (U-Value) and international building codes, with thermal bridges effect investigation. Sustainable Development Research, 3(1), pp.45-52. [DOI]

Angelone, S., Cauhapé Casaux, M., Borghi, M. and Martinez, F.O., 2016. Green pavements: reuse of plastic waste in asphalt mixtures. *Materials*

and Structures/Materiaux et Constructions, 49(5), pp.123-130. [DOI]

Aslam, Z., Li, H., Hammerton, J., Andrews, G., Ross, A. and Lovett, J.C., 2021. Increasing access to electricity: an assessment of the energy and power generation potential from biomass waste residues in Tanzania. *Energies*, 14(6), pp.200-210. [DOI]

Awasthi, D., Himanshu, Pal, K. and Patra, T.K., 2026. Gasification technologies for agro-waste to energy conversion. In: *Agriculture-Bioenergy Nexus: Transforming Waste into Wealth*. Woodhead Series in Bioenergy. Cambridge: Woodhead Publishing, pp.81–107. [DOI].

Chen, D., Yin, L., Wang, H. and He, P., 2014. Pyrolysis technologies for municipal solid waste: a review. *Waste Management*, 34(12), pp.2467-2475. [DOI]

Chen, D., Yin, L., Wang, H. and He, P., 2019. Pyrolysis technologies for municipal solid waste: a review. *Waste Management*, 39(1), pp.133-148.

Chimres, N., Kaew-on, J., Surapapwong, T., Chittiphalungsri, T. and Wongwises, S., 2024. Using a spiral fin to replace a wavy fin in the condenser of an air conditioner. *International Journal of Thermofluids*, 21(1), pp.55-62. [DOI]

De la Flor-Barriga, L.A. and Rodríguez-Zúñiga, U.F., 2022. Numerical analysis on a catalytic pyrolysis reactor design for plastic waste upcycling using CFD modelling. *RSC Advances*, 12(20), pp.12500-12508. [DOI]

Fokaides, P.A. and Kalogirou, S.A., 2011. Application of infrared thermography for the determination of the overall heat transfer coefficient (U-Value) in building envelopes. *Applied Energy*, 88(12), pp.4560-4568. [DOI]

Gao, N., Wang, F., Quan, C., Santamaria, L., Lopez, G. and Williams, P.T., 2022. Tire pyrolysis char: processes, properties, upgrading and applications. *Progress in Energy and Combustion Science*, 93(1), pp.101-115. [DOI]

Ghosh, A., Bhandari, S., Sundaram, S. and Mallick, T.K., 2020. Carbon counter electrode mesoscopic ambient processed and characterised perovskite for adaptive BIPV fenestration. *Renewable Energy*, 145(1), pp.250-258. [DOI]

Gong, K., Zhang, Y. and Wang, X., 2022. Buoyancy effect on heat transfer and surface coking of hydrocarbon fuel in horizontal square channel at supercritical pressures. *Journal of Analytical and Applied Pyrolysis*, 168(1), pp.100-110. [DOI]

Guo, X., Zhang, Y., Yan, J., Zhou, Y., Yan, S., Shi, W. and Li, X., 2022. Integrated dynamics response analysis for IEA 10-MW spar floating offshore wind turbine. *Journal of Marine Science and Engineering*, 10(4), pp.542-550. [DOI]

Harussani, M.M., Sapuan, S.M., Rashid, U., Khalina, A. and Ilyas, R.A., 2022. Pyrolysis of polypropylene plastic waste into carbonaceous char: priority of plastic waste management amidst COVID-19 pandemic. *Science of the Total Environment*, 803(1), pp.1-12. [DOI]

He, Y., Wang, W., Qiu, Y., Zheng, Z., Du, B., Wang, K. and Shi, H., 2019. Convective heat transfer characteristics of molten salts flowing in complex flow structures: experimental studies and progress. *Chinese Science Bulletin*, 64(28-29), pp.3000-3010. [DOI]

Horváth, D., Tomasek, S. and Miskolczi, N., 2024. Thermo-catalytic co-pyrolysis of waste plastic and hydrocarbon by-products using β-zeolite. *Clean Technologies and Environmental Policy*, 26(1), pp.123-132. [DOI]

IRENA and FAO, 2021. *Renewable energy for agri-food systems – Towards the Sustainable Development Goals and the Paris Agreement*. Abu Dhabi and Rome: International Renewable Energy Agency (IRENA) and Food and Agriculture Organization of the United Nations (FAO), pp.1–308. [DOI]

Irianto, Tumpu, M., Mabui, D.S.S., Rochmawati, R. and Sila, A.A., 2023. Potential of pyrolyzing mixed polyethylene terephthalate and polypropylene plastic wastes for utilization in asphalt binders. *Annals of Chemistry: Materials Science*, 47(3), pp.145-152. [DOI]

Kaewpradub, S., Sanguanduean, P., Katesuwan, W., Chimres, N., Punyasukhananda, P., Asirvatham, L.G., Mahian, O., Dalkilic, A.S. and Wongwises, S., 2018. Absorption refrigeration system using engine exhaust gas as an energy source. *Case Studies in Thermal Engineering*, 12(1), pp.75-82. [DOI]

Kumar, M., Patel, S.K., Singh, J. and Kim, S.H., 2018. Biomass-derived pyrolysis oil: characterization, upgrading and applications. *Bioresource Technology*, 270(1), pp.737-748.

Lee, S.H., Cho, J., Park, J. and Ryu, C., 2017. Comparison of oil yields from batch and continuous pyrolysis of high-density polyethylene. *Journal of Analytical and Applied Pyrolysis*, 124(1), pp.508-516.

Liubartseva, S., Coppini, G. and Lecci, R., 2019. Are Mediterranean marine protected areas sheltered from plastic pollution? *Marine Pollution Bulletin*, 140(1), pp.300-305. [DOI]

Mahyuddin and Damairi, K., 2020. Performance analysis of spiral condenser type vertical in condensation process of pyrolysis products of high density polyethylene (HDPE) and polypropylene (PP) plastic. *Rsitech Journal*, 2(2), pp.45-52.

Martínez-Narro, G., Hassan, S. and Phan, A.N., 2024. Chemical recycling of plastic waste for sustainable polymer manufacturing – a critical review. *Journal of Environmental Chemical Engineering*, 12(2), pp.200-215. [DOI]

Onwuemezie, L., Gohari Darabkhani, H. and Moghimi Ardekani, M., 2023. Integrated solar-driven hydrogen generation by pyrolysis and electrolysis coupled with carbon capture and Rankine cycle. *Energy Conversion and Management*, 277(1), pp.1-18. [DOI]

Pan, X.H., Wang, Y.M., He, S.F., Labella, Á. and Martínez, L., 2023. An interval type-2 fuzzy ORESTE method for waste-to-energy plant site selection: a case study in China. *Applied Soft Computing*, 136(1), pp.50-60. [DOI]

Singh, S., Patil, T., Tekade, S.P., Gawande, M.B. and Sawarkar, A.N., 2021. Studies on individual pyrolysis and co-pyrolysis of corn cob and polyethylene: thermal degradation behavior, possible synergism, kinetics, and thermodynamic analysis. *Science of the Total Environment*, 783(1), pp.1-14. [DOI]

Smith, R., Jones, P. and Williams, P.T., 2012. The pyrolysis of polyolefin plastics to produce valuable hydrocarbon fuels. *Fuel*, 103(1), pp.403-411.

Sonawane, Y.B., Shindikar, M.R. and Khaladkar, M.Y., 2024. Effect of fly ash in pyrolysis of HDPE, LDPE and PP plastic waste. *Nature Environment & Pollution Technology*, 23(3), pp.1735-1742. [DOI]

Sun, L., Zou, C., Jia, A., Wei, Y., Zhu, R., Wu, S. and Guo, Z., 2019. Development characteristics and orientation of tight oil and gas in China. *Petroleum Exploration and Development*, 46(6), pp.1073–1087. [DOI]

Zhang, M., Hu, B., Fan, G., Yang, M., Lu, Q. and Wu, Y., 2024. The removal of tar and the production of methane-rich gas from biomass hydrogen pyrolysis by using biochar-based catalysts. *Energy Conversion and Management*, 313, p.118596. [DOI]

Nature Environment and Pollution Technology
An International Quarterly Scientific Journal

p-ISSN: 0972-6268
(Print copies up to 2016)
e-ISSN: 2395-3454

Vol. 25 | No. 3 | Article ID B4386 | 2026

Original Research Paper

https://doi.org/10.46488/NEPT.2026.v25i03.B4386

Open Access Journal

Achieving Sustainability in India: Analyzing Carbon Neutrality Scenarios Using the Novel Fourier-NARDL Approach

A. Mohanapriya[1]†, R. Shenbagavalli[2] and M. Balamurugan[3]

[1]Department of Science and Humanities, S-VYASA Deemed to be University, Bangalore, Karnataka-560059, India
[2]Department of Science, Christ College of Science and Management, Malur, Karnataka-563160, India
[3]Department of Mathematics, Vel Tech Rangarajan Dr. Sagunthala R&D Institute of Science and Technology, Chennai-600062, Tamil Nadu, India
†Corresponding author: A. Mohanapriya; amohana20@gmail.com

Abbreviation: Nat. Env. & Poll. Technol.
Website: www.neptjournal.com

Received: 07-08-2025
Revised: 16-10-2025
Accepted: 24-10-2025

Key Words:

Fourier asymmetric NARDL
Load capacity factor
Carbon neutrality
Sustainable development goals

Citation for the Paper:

Mohanapriya, A., Shenbagavalli, R. and Balamurugan, M., 2026. Achieving sustainability in India: Analyzing carbon neutrality scenarios using the novel Fourier-NARDL approach. *Nature Environment and Pollution Technology*, 25(3), B4386. https://doi.org/10.46488/NEPT.2026.v25i03.B4386

Note: From 2025, the journal has adopted the use of Article IDs in citations instead of traditional consecutive page numbers. Each article is now given individual page ranges starting from page 1.

Copyright: © 2026 by the authors
Licensee: Technoscience Publications
This article is an open access article distributed under the terms and conditions of the Creative Commons Attribution (CC BY) license (https://creativecommons.org/licenses/by/4.0/).

ABSTRACT

India's commitment to achieving carbon neutrality by 2070 represents the strategic significance of cleaner energy sources, such as nuclear energy, in reducing environmental degradation. This study examines the asymmetric relationship between nuclear energy R&D spending and environmental quality, as determined by the Load Capacity Factor (LCF), from 1978 to 2022. The Fourier Nonlinear Autoregressive Distributed Lag (Fourier-NARDL) model is used to obtain potential nonlinear adjustments and continuous structural changes. Empirical findings show that positive shocks in nuclear energy consumption **(**NUC) expenditure play a very positive role in improving environmental quality in the long run ($\beta^{+} = 0.37$, $p < 0.05$), and negative shocks have a negative effect ($\beta^{-} = -0.29$, $p < 0.10$). There is also asymmetric behavior in short-run dynamics, but of a smaller dimension. These results provide empirical evidence of the Load Capacity Curve (LCC) hypothesis for India and highlight the importance of the long-term ecological balance that can be attained by focusing on long-term nuclear R&D investment. This research has practical implications for policymakers who aim to align energy innovation strategies with the Sustainable Development Goals (SDGs) and the 2070 carbon-neutral objective of India.

1. INTRODUCTION

Climate change is perhaps the greatest problem facing the world today. Changes in greenhouse gas levels, mainly carbon dioxide (CO_2), lead to climate change. Burning fossil fuels and deforestation are two activities that produce these gases (Farina et al. 2025, Jain et al. 2025, Kumari et al. 2025). As CO_2 emissions increase, there is a serious problem with the global climate that can negatively affect all areas of society (Basu et al. 2025, Nimma et al. 2025, Lakshmikantha & Rajesh 2025). To prevent climate change from becoming dangerous, we must first reduce CO_2 emissions. Several researchers believe that an environmentally friendly future can be achieved only if businesses significantly reduce the levels of CO_2 they emit. They rely on renewable energy, new technology, and sustainable business building. To achieve these aims, the United Nations has adopted the SDGs for 2030 and pointed out that affordable and clean energy, as well as economic growth and modernization (SDGs 7, 8, 9, and 13), are key factors for taking action on climate change.

Although India is one of South Asia's fastest-growing economies, it is also among the countries most exposed to climate change. Today, one of the most pressing challenges facing India is the management of climate change and environmental degradation. Because India has approximately 1.4 billion people and a strong GDP growth rate (Arpitha et al. 2025, Dharani et al. 2025, Lee & Song 2025), it must balance its economy with the health of the environment. Since

the 1990s, the rise in industry and cities (Sharma et al. 2025, Kumar et al. 2025, Hashim 2025), as well as increased use of energy (Özkan et al. 2025, Sadath & Acharya 2025, Behera et al. 2024), have negatively affected the environment in the country by creating air pollution (Budde et al. 2025, Imam et al. 2024), disrupting nature (Erhart et al. 2025, Ngoh et al. 2025), and increasing carbon emissions (Ngoc Xuan 2025, Sen & Sahoo 2024). Reliance on coal for electricity in India has exacerbated environmental problems. Owing to global agreements such as the Paris Accord and the United Nations Framework Convention on Climate Change (UNFCCC), India has decided to become net-zero by 2070 and increase its share of non-fossil fuel energy in its overall usage to at least 50% by 2030. To achieve SDGs, such as those for clean energy and climate, India has strategized its approach around these key goals.

To save the environment and boost the economy, India is actively working on and investing in different types of renewable power (Majid 2020, Raihan et al. 2024). As part of the country's larger energy plan, nuclear energy is being recognized as a key component of the country's future. Owing to the rising need to reduce carbon emissions and use fewer fossil fuels, nuclear power provides a clean and efficient means of electricity supply. Rather than producing fluctuating output, such as solar and wind energy, nuclear energy is reliable and flexible, supporting both industrial growth and the need for more electricity everywhere (Shahzad & Jasińska 2024, El-Ashmawy et al. 2024). As nuclear energy plants do not release much greenhouse gas during operation (Khaleel et al. 2025), they continue to be useful in the struggle against climate change. Reducing the costs of imported energy and increasing energy security are also reasons why India is considering nuclear energy. Recognizing these advantages, India established its civil nuclear program in the 1960s (Grover 2025), planning to use nuclear technology only for beneficial purposes. Since its inception, the program has changed significantly, concentrating on making indigenous reactors (Zio et al. 2025), achieving self-sufficiency in technology (Bishoyi 2025), and developing nuclear infrastructure (Xu & Ali 2025, Afrane et al. 2025).

The government has partnered with various international agencies and countries to access advanced technologies and fuel supplies while investing heavily in research and development (Khatoon & Velidandi 2025, Dave et al. 2025). Currently, India is working on advanced reactor designs, such as fast-breeder reactors (Rangasamy 2025, Rao et al. 2025) and thorium-based reactors (Selvam et al. 2025), which align with its long-term vision of a sustainable and independent nuclear energy sector. Thorium, in particular, is abundantly available in India, and its utilization as a fuel source could reduce the nation's reliance on imported uranium. By focusing on thorium technology, India aims to become a global leader in innovative and safe nuclear energy systems.

In addition to technological advancements, India is prioritizing the safety and regulatory framework surrounding its nuclear power plants to ensure public trust and international compliance. Training programs, institutional strengthening, and public awareness campaigns are being implemented to support this rapidly developing sector. Furthermore, nuclear energy plays an increasingly important role in supporting non-electrical applications, such as water desalination, medical isotope production, and industrial heat, showcasing its versatility beyond electricity generation. The continued growth of India's nuclear program underscores its commitment to achieving a balanced mix of energy sources that supports both environmental sustainability and economic progress in the country. As India transitions to a low-carbon future, nuclear energy is expected to remain a vital pillar of its national energy strategy.

Many have argued about the environmental impact of nuclear energy use. Although nuclear energy is considered low-carbon, concerns regarding radioactive waste persist. There is additional controversy in India, as people protest against nuclear plants, and the central government tends to develop plans without caring about environmental justice and local agreements. In terms of research, carbon emissions or ecological footprints have mostly been used to measure environmental decline in India. Although these measures are helpful, they focus on environmental demand and not on availability or biocapacity. Consequently, they provide only one view of environmental stress. Therefore, we chose the LCF, which measures the relationship between the earth's 'room' for new resources (BIO) and people's total resource consumption ecological footprint (EF). If the LCF is greater than one, it indicates that the environment benefits from human activities. For over three decades, India has had an ecological deficit, as shown by the LCF being less than one.

Recently introduced in environmental economics, the LCC hypothesis imagines a U-shaped pattern between economic growth and ecosystem quality. This is in contrast to the well-known Environmental Kuznets Curve (EKC), which states that pollution tends to decrease after a certain level of economic growth. We examine how the beginning growth of economic development can harm the environment using LCC; however, it later enables spending on clean technologies and rule changes that steer the economy toward sustainability. The uniqueness of this research is that it examines how India's investments in NUC may influence

the country's environmental quality, a subject few scientific studies have explored before. There is some research on nuclear energy use, but hardly any on how movements in R&D spending, both positive and negative, affect the LCF. Moreover, most researchers in econometrics assume that both parties treat these relationships similarly. Fourier-NARDL is used in this study to separate positive from negative shocks in nuclear R&D, considering both shifting structures and smooth breaks in the data.

In analyzing such complex and dynamic environmental relationships, it is vital to adopt advanced econometric methods that account for non-linearities and structural breaks in data over time. Traditional models often overlook these characteristics, potentially leading to biased and incomplete results. To address this, the present study adopts the novel Fourier-NARDL approach, which merges the flexibility of the NARDL model with the ability of Fourier terms to capture unknown smooth structural shifts in the dataset. This method not only distinguishes between positive and negative shocks in nuclear R&D investment but also detects cyclical or evolving trends in environmental and economic behavior without the need to pre-identify breakpoints. This innovative methodological integration allows for a more accurate and nuanced assessment of India's transition toward carbon neutrality.

Fig. 1 compares the CO_2 emissions from the top 10 emitting countries and regions with those of the rest of the world. China accounts for the most emissions, followed by the United States, the European Union (comprising 27 nations), and India. Combined, the top 10 lead in producing greenhouse gas emissions, making it clear that these economies make a big difference in international efforts to fight climate change. The large share of emissions from the "Rest of the World" underlines the need for more countries to be involved in cutting emissions.

Fig. 2 illustrates the total amount of carbon dioxide released in various parts of the world over time. Previously, Europe and Central Asia contributed the highest percentage of emissions, followed by North America. The region's emissions have increased rapidly since the 20th century owing to China's rapid industrial growth. The Middle East and North Africa, Latin America and the Caribbean, South Asia, and Sub-Saharan Africa account for only a small percentage of the world's total emissions. This situation demonstrates the role that developed places play in global warming and the potential role that developing places will play in future emissions.

Data Points:

- In 1978, the average person produced less than half a metric ton of CO_2.

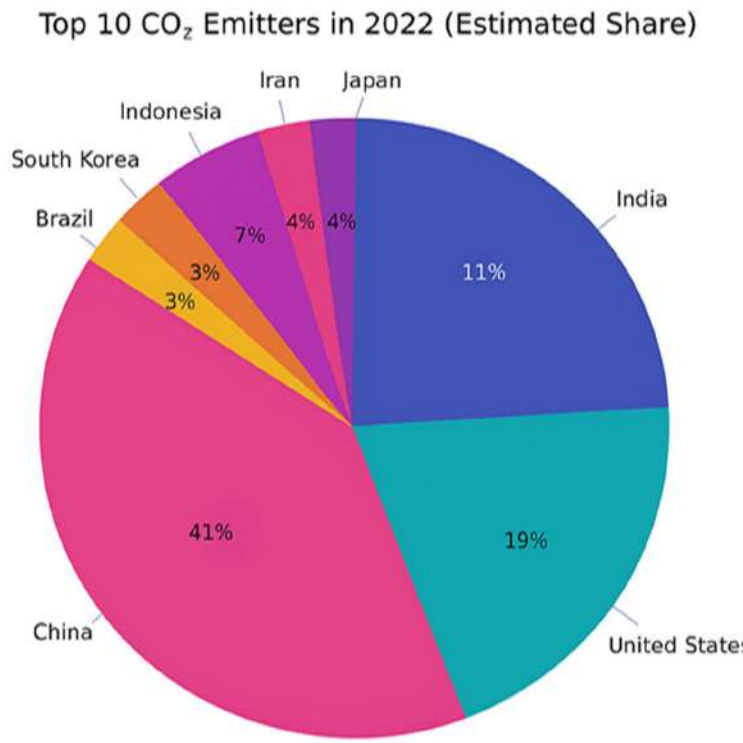


Fig. 1: Global CO_2 emissions share (Top 10, 2022).

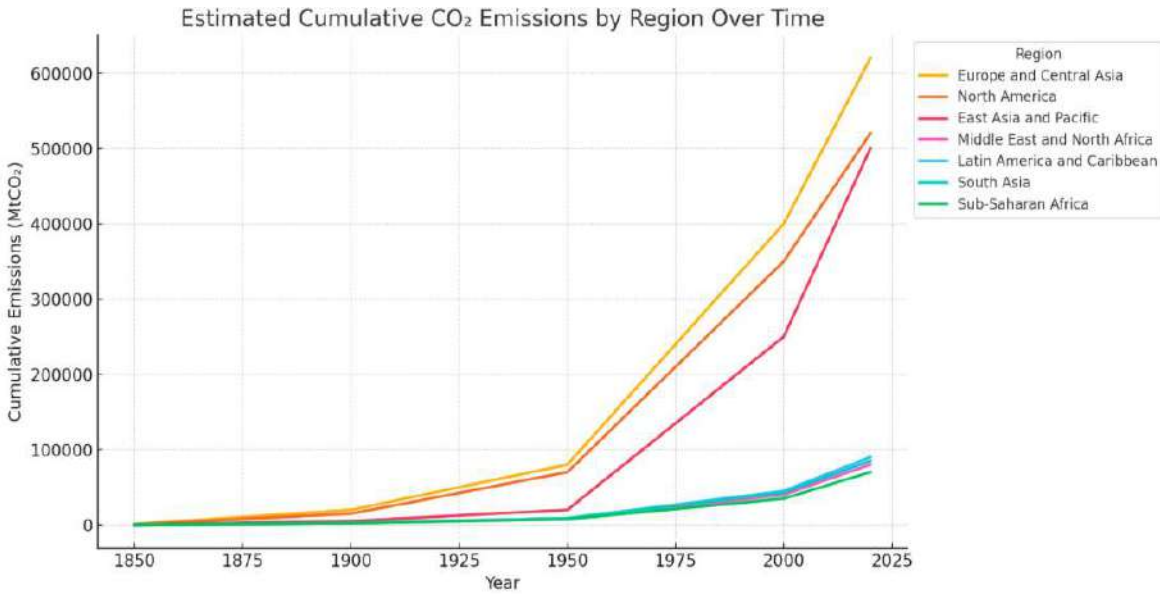


Fig. 2: Global historical cumulative CO_2 emissions by Regions (1850-2022).

- By the end of 2020, GHG emissions will be 2,959 million tons.
- CO_2 and will be reduced by 7.93% from 2019.
- In 2022, each individual produced 1.89 tons of CO_2 emissions.
- In 2023, each person is expected to produce 1.91 t of CO_2.
- In 2024, a study projected that fossil-based CO_2 emissions would increase by 4.6%.

Fig. 3 demonstrates the amount of CO_2 emitted by each person in India annually from 1970 to 2022. From 1970 to 2022, the number of emissions gradually increased from approximately 0.35 to over 2.0 metric tons. The increase observed after 2000 is associated with rapid industrialization, an expanding urban population, and economic expansion. As a likely outcome of the COVID-19 pandemic, there was a quick decline in 2020, but over the years, India's economic growth has been linked to increased environmental issues. The overall research framework adopted in this study is summarized in the flowchart below, which illustrates the steps followed to analyze the impact of nuclear R&D on India's carbon neutrality (see Fig. 4).

We study how research and development in nuclear energy in India affects the country's environmental conditions (measured by LCF) between 1978 and 2022.

The purpose of answering this question is as follows:

1. We will examine whether the LCC hypothesis applies to cases in India.

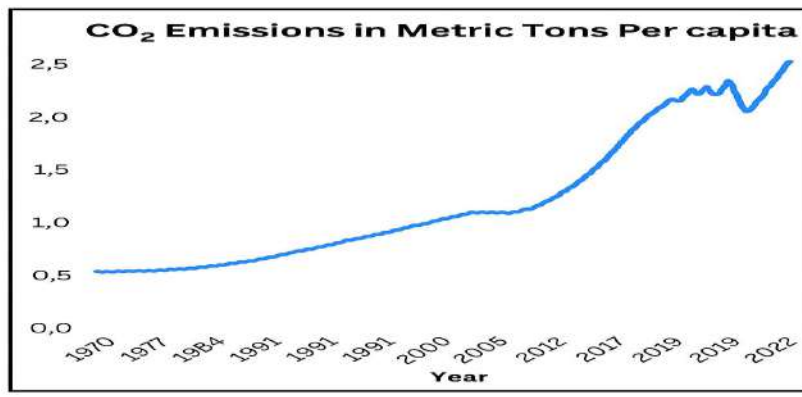


Fig. 3: CO_2 emissions per capita in India (1970–2022).

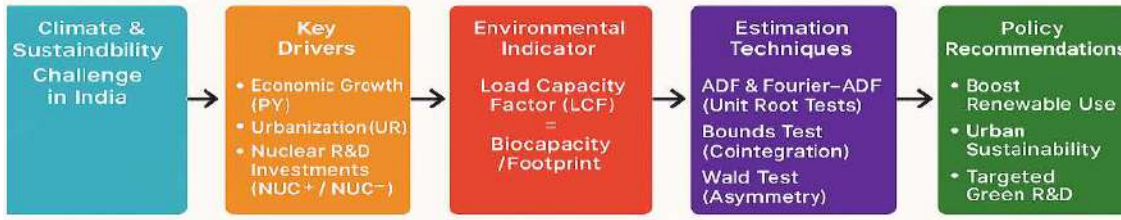


Fig. 4: Framework for Analyzing Carbon Neutrality in India.

2. Provide proof of how R&D in nuclear energy affects the environment.
3. Support specific policies that move India closer to achieving its sustainability goals for energy.

Section 2 covers the background theories and reviews studies related to the topic. Section 3 outlines the data, model design, and the ways in which the model is estimated. Section 4 covers the results obtained from studying human bodies. Finally, Section 5 concludes the report with suggestions for policy and directions for future studies.

2. BACKGROUND RESEARCH

Ecological economics today concentrates its efforts on three areas: economic development, energy policy, and the environment. Given the rapid pace of urbanization and industry in India, its economy has a clear impact on the environment. India's sustainable development is being judged more by its environmental effects on CO_2 emissions, ecological footprint, and biocapacity as it grows. The LCC hypothesis is followed in this study, suggesting a U-shaped link between growing prosperity and the environment's health. Because the LCF measures supply against demand, it is considered a useful measure of human impact on the environment. If the LCF is less than one, it means that what people need or consume is more than what nature can handle. The LCC hypothesis differs from the environmental curve known as the EKC. According to the EKC, there is a maximum point beyond which income causes environmental degradation to fall, while LCC models assume that, initially, too many natural resources are consumed, but later there are changes and increases in the ecological balance as income rises. The framework is significant for India, as both its economy and environment are under stress. Applying the LCC idea together with research and development in NUC provides new insights into India's overall environmental direction as it seeks a carbon-neutral future by 2070.

2.1. How Using Nuclear Energy Can Benefit the Environment

The use of nuclear energy has been promoted for years as a low-carbon alternative to fossil fuels. In India, the development of nuclear power is led by the Department of Atomic Energy, with assistance from the Nuclear Power Corporation of India, Limited. Most of the energy generated by nuclear generators is free from carbon, which makes some experts suggest it as a crucial source to reach energy sustainability. However, there are many factors to consider regarding the environmental effects of nuclear energy R&D. More investments in infrastructure support inventions, improve safety, and manage waste, all of which help the environment in the long run. If environmental safeguards are not in place, large-scale nuclear growth can briefly impact nature, for example, through land changes, waste generation, and community displacement. However, the findings of these studies are inconsistent. For example:

Using an asymmetric form of NARDL, Caglar (2023) discovered that reducing funds for nuclear R&D had a positive impact on the environment in the United Kingdom and other countries (Caglar 2023, Caglar et al. 2023a, 2024a, 2023b, 2024b. 2024c, Caglar & Ulug 2022). It was shown by Ahmed et al. that both nuclear and renewable R&D investments reduced CO_2 emissions in Japan (Ahmad et al. 2022, Ahmed et al. 2021). Unlike others, Kocak & Ulucak (2019) found limited evidence of a correlation between Organisation for Economic Co-operation and Development nuclear R&D and environmental conditions in their study.

Azam et al. (2023) examined panel quantile regression to determine how nuclear energy, renewable energy, and ICTs impact CO_2 emissions and discovered that only renewable energy and ICTs improve the results, unlike nuclear energy. In this study, it is clear that the increase in nuclear energy use helps safeguard the environment, whereas gas and growing use have the opposite effect on India's sustainability. In France, from 1990 to 2021, reduced CO_2 emissions were caused by renewable energy, nuclear power, and government spending, while the economy's growth first increased and later reduced the emissions (Caglar et al. 2024a, 2024b, 2024c). The authors highlight how the situation in France (1990–2021), renewable sources, natural resources, and government investment all assist in lowering CO_2 emissions and strengthening the EKC, where initially, economic growth causes more harm to the environment, but eventually, this

negative effect shrinks (Ahmed et al. 2023). In several countries, the goal is to achieve net-zero by 2050, which will require the use of low-carbon technology in every sector. Nuclear energy may cause some concerns, but it is a reliable alternative to renewable energy and should be included when planning future energy (Kocak & Ulucak 2022).

There are only a few examples in the Indian literature. Very little attention has been given to research and development in Indian studies. Furthermore, most studies do not examine how changes in nuclear energy lead to differences in environmental conditions. When carbon neutrality is achieved in India, the country's CO2 emissions will match the amount absorbed by the environment. Similar to European countries, the United States, other countries, and India have implemented measures and laws to achieve carbon neutrality at both the national and regional levels.

- India aims to reduce carbon emissions by 50% by 2030 and achieve zero emissions by 2070.
- The Energy Conservation Act of 2022 allows the central government to design a carbon credit trading scheme.
- The Nationally Determined Contributions outline how much India is willing to reduce its emissions by 2030.
- The Long-Term Low-Carbon Development Strategy shows India's desire to reduce carbon emissions over a long period.
- This sets out the framework for the government to promote the development of renewable energy and energy savings in the country.
- The National Electric Mobility Mission Plan was designed to encourage the use of electric cars in India.

2.2. Urbanization, Economic Growth and Environment

Urbanization (UR) plays a dual role in shaping environmental outcomes. A sudden rise in city populations can cause pollution from the overuse of energy, vehicles, and poor trash collection. However, in the long term, cities yield positive results through large-scale operations, better infrastructure, and the spread of new environmental technologies.

Sun et al. (2022) and Shi et al. (2023) show that, in the end, urbanization can boost LCF through increased investment in clean infrastructure. Alternatively, Nathaniel et al. (2021) and He et al. (2022) pointed out that the rise of cities in developing countries worsens environmental issues and increases CO_2 emissions. Haouraji et al. (2023) explore how income and urbanization relate to residential CO_2 emissions in North Africa (1990–2016). They confirmed the EKC in Morocco and Tunisia and supported the use of renewable energy for more sustainable development. In Algeria, Egypt, and Nigeria (1990–2020), exchanging natural gas and ICT promotes economic growth and helps reduce CO_2 emissions, indicating that natural gas acts as a bridge toward renewable energy. Mahmood et al. (2023) stated that in the Gulf Cooperation Council countries (1980–2019), the main factors influencing CO_2 emissions were oil prices and economic growth, with each country responding differently to these factors.

Prosperity and development (PY) have both positive and negative effects. Although industrialization and the use of fossil fuels harm nature in the beginning, richer countries can introduce tougher rules, support greener inventions, and raise awareness about the environment. This relationship often aligns with the LCC hypothesis: an initial decline in the LCF is followed by recovery at higher income levels.

2.3. Positioning and Contribution of the Present Study

Previous studies have widely applied NARDL and its variants to explore asymmetric energy–environment relationships. For instance, Caglar (2023) and Caglar et al. (2024a, 2024b) examined the effects of green investment and energy R&D on environmental indicators in Europe. Ahmad et al. (2022) and Ahmed et al. (2021) used similar nonlinear frameworks for Japan, while Caglar and Ulug (2022) investigated public energy efficiency budgets. More recently, the Fourier–NARDL model has been introduced to account for smooth structural breaks in long time series (Caglar et al. 2023b, 2024c); however, its applications have largely centered on developed economies and aggregated indicators such as CO_2 emissions and ecological footprints. In this context, the present study makes three contributions.

Conceptual contribution: This study applies the Fourier–NARDL model to the LCF, a composite and balanced measure of ecological sustainability that reflects both biocapacity and environmental demand.

Empirical contribution: This study provides the first long-term evidence for India (1978–2022) on how nuclear energy R&D investment asymmetrically influences environmental quality LCF.

Methodological contribution: This study jointly tests the LCC hypothesis and asymmetric NUC effects within a unified econometric framework that allows for smooth structural transitions.

By combining these conceptual, empirical, and methodological advances, this study fills a critical research gap in the literature on India's carbon-neutral transition. This demonstrates that nuclear R&D, while not a dominant factor, contributes meaningfully to environmental sustainability, offering evidence-based insights relevant to emerging economies pursuing similar goals.

3. MATERIALS AND METHODS

This study examines the nonlinear and asymmetric effects of nuclear energy research and NUC on the environment in India in the form of environmental quality (LCF) in the hypothetical context of the LCC hypothesis. To be able to capture structural changes that are asymmetric and smooth concurrently, the Fourier-augmented Fourier-NARDL model is used.

3.1. Model Specification

The baseline long-run relationship is as follows:

$$LCF_t = a_0 + a_1 PY_t + a_2 PY_t^2 + a_3 NUC_t + a_4 UR_t + \varepsilon_t \quad \ldots(1)$$

where LCF_t denotes the load capacity factor, PY_t and PY_t^2 represent income and its squared term (to test the LCC hypothesis), NUC_t is nuclear energy R&D investment, UR_t is the urbanization rate, and ε_t is the error term. As the influence of nuclear R&D may differ between increases and decreases, NUC_t is decomposed into positive and negative partial sums as

$$NUC_t^+ = \sum_{j=1}^{t} \max(\Delta NUC_j, 0), NUC_t^- = \sum_{j=1}^{t} \min(\Delta NUC_j, 0) \quad \ldots(2)$$

To capture smooth structural breaks and periodic shifts over the long data span, we integrate Fourier terms into the model, which results in the nabla Fourier NARDL specification:

$$\Delta LCF_t = \gamma_0 + \gamma_1 \sin\left(\frac{2\pi kt}{T}\right) + \gamma_2 \cos\left(\frac{2\pi kt}{T}\right) + \gamma_3 LCF_{t-1} + \gamma_4 PY_{t-1} + \gamma_5 PY_{t-1}^2 + \gamma_6 NUC_{t-1}^+ + \gamma_7 NUC_{t-1}^- + \gamma_8 UR_{t-1} + \sum_{i=1}^{n} \delta_i \Delta X_{t-i} + \varepsilon_t \quad \ldots(3)$$

where k is the frequency of the Fourier function, and T is the overall sample size. The δ_i parameters represent the short-run dynamic adjustment, and $\gamma_3, \ldots, \gamma_8$ are the corresponding long-run coefficients of the explanatory variables. Where Δ is the first difference operator, and n is the optimum lag length determined by the information criteria. In addition, ΔX_{t-i} suggests the lagged change in a second explanatory variable, which represents short-run interactions in the model.

When cointegrating, the null hypothesis H_0: $\gamma_3 = \ldots = \gamma_8$ is tested against the alternative hypothesis.

3.2 Instrumentation and Data Construction

This study uses annual time-series data for India from 1978 to 2022. All variables were constructed to ensure comparability, consistency, and reproducibility.

This study considers the annual time series of India, covering the period between 1978 and 2022. The construction of all the variables was done in a way that would be comparable, have unit consistency, and be reproducible.

3.2.1. Load Capacity Factor (LCF)

LCF is the biocapacity (BIO)/ecological footprint (EF) ratio on a per-capita basis in accordance with the Global Footprint Network (GFN 2023) approach:

$$LCF_t = \frac{BIO_t}{EF_t} \quad \ldots(4)$$

- BIOt = per capita biocapacity (global hectares/person), which is the ecological provision of renewable resources.
- EFt = per capita ecological footprint (global hectares per capita), which is the ecological demand for human activity.

An LCF value below unity (LCF<1) indicates an ecological deficit, whereas values above unity imply an ecological reserve. BIO and EF data were obtained from the Global Footprint Network (National Footprint Accounts 2023 Edition). All values are expressed in global hectares per capita**,** ensuring comparability across years.

3.2.2. Nuclear Energy R&D Investment (NUC)

Nuclear R&D expenditure data were collected from the International Energy Agency (IEA) and India Energy Dashboard (2023).

The data represent gross public spending on nuclear energy research and development**,** including research on fission, reactor technology, safety systems, and waste management.

Monetary values were:

- Converted from nominal local currency to constant 2015 US dollars**,**
- Using the World Bank GDP deflator and exchange rates (World Development Indicators 2023),
- Adjusted for inflation to maintain real comparability of the data.

This transformation ensures that the NUC series reflects real investment levels, rather than inflationary growth. For econometric modeling, NUC was decomposed into positive (NUC^+) and negative (NUC^-) changes to test asymmetric effects within the Fourier–NARDL framework.

3.2.3. Urbanization (UR)

Urbanization (UR) is measured as the percentage of the total population living in urban areas**,** obtained from the World Bank's World Development Indicators (2023). The series was smoothed using annual averages to eliminate

Table 1: Description, measurement, and data sources of variables (1978-2022).

Variable	Definition/Description	Unit of Measurement	Latest Value [2023]	Primary Data Source
LCF	Load Capacity Factor = (Biocapacity /Ecological Footprint) per capita	Global hectares per person	0.84	Global Footprint Network (2023)
PY	GDP per capita (constant 2015 US $)	US $ per person	2,236.31	World Bank (2023)
PY^2	Square of GDP per capita (calculated)	Computed value	$\approx 5 \times 10^6$	Constructed by authors
NUC	Nuclear energy R&D investment (constant million US $)	Million US $ (2015 prices)	36.36	IEA / India Energy Dashboard (2023)
UR	Urban population share of total Population	Percent of population (%)	35.0 % (≈ 497 million people in 2023)	World Bank (2023)

reporting discontinuities. UR serves as a key control variable that reflects demographic and infrastructure-induced environmental pressures.

3.2.4. Data Transformation Summary

All variables (except percentages) were transformed into natural logarithms to linearize the relationships, stabilize the variance, and interpret the estimated coefficients as elasticities. The data span 45 observations (1978–2022), a period sufficient for capturing the structural transitions relevant to India's economic and energy policy evolution.

3.3. Data Description

The study involves using an annual time series dataset that encompasses the period from 1978 to 2022 (45 observations), which is sufficient to estimate the time series through a Fourier NARDL, but at the same time, it is important to note that the method is well-performing with moderate-size samples (usually 30-60 observations. Frequency was used annually to ensure that the data were consistent and comparable across variables. All variables used in this study, along with their definitions, measurement units, and data sources, are summarized in Table 1.

3.4. Estimation Strategy

To estimate the specified model, we employed the Fourier-NARDL approach, which combines three powerful features:

1. Considering nonlinearity, we identify which shocks are positive or negative in nuclear R&D investments.
2. Autoregression helps represent how both the near and long past affect the data.
3. Fourier terms are used to adjust for discontinuities and repeating patterns without pinpointing the dates of the breaks.

The methodological steps are as follows.

1. **Stationary Testing:** We apply both the Augmented Dickey-Fuller (ADF) and Fourier-ADF tests to determine the order of integration for all variables.
2. **Cointegration Testing:** The Bounds Test is used to examine whether a long-run equilibrium relationship exists among the variables. To test the null hypothesis, the researcher looked for a strong long-term relationship between the two variables.
3. **Asymmetry Testing**: We employ the Wald test to assess the null hypothesis that positive and negative shocks in the NUC have symmetric effects on the LCF.
4. **Model Diagnostics:** We use standard residual diagnostics, such as the Breusch–Godfrey test (autocorrelation), Jarque–Bera test (normality), White's test (heteroscedasticity), and Ramsey RESET test (functional form). Moreover, the CUSUM and CUSUMSQ tests look for signs of instability in the model.
5. **Interpretation of Coefficients:** The long-run and short-run coefficients are interpreted to evaluate the impact of PY, PY^2, NUC^+, NUC^-, and UR on LCF. The importance and indications of the coefficients allow us to determine whether the LCC hypothesis is correct and the effect of related policies.

4. RESULTS AND DISCUSSION

4.1. Descriptive Statistics

Tables 2 and 3 present the main macroeconomic and environmental indicators for India over five years. GDP per capita (PY), its square (PY^2), the percentage of urban population in the total population (UR), NUC, and LCF are the variables that play a role.

Over the period from 1978 to 2022, significant social and economic changes in India were visible in key development indicators. On average, each person earned USD 1,200, which steadily rose to USD 2,500. However, as the economic imbalance became greater and income increased, the square value of GDP (GDP^2) also rose. From 23% in 1950, the urban population gradually increased to 35%, for an average of 28.5%, mainly as a result of growth through industry and migration. There was little change in the nuclear R&D

Table 2: Descriptive statistics for India (Annual Data, 1978-2022).

Statistic	GDP per capita [PY] [US $]	Urban Population [UR][% of total population]	Nuclear R&D [NUC][million US $]	Load Capacity Factor [LCF] [BIO / EF per capita]
Mean	1 200	28.5%	0.90 billion	0.85
Median	1 050	27.0%	0.80 billion	0.87
Maximum	2 500	35.0%	1.50 billion	0.95
Minimum	500	23.0%	0.50 billion	0.75
Std. Deviation	600	3.5%	0.30 billion	0.07

Table 3: Five-year averaged descriptive statistics for India (Illustrative Summary, 1978-2022).

Statistic	PY [GDP per capita]	PY² [GDP²]	UR [Urban %]	NUC [Nuclear R&D]	LCF [BIO / EF]
Mean	2 015.2	4.08×10^6	33.19%	1.94 billion US$	0.377
Median	2 000.0	4.00×10^6	33.10%	2.00 billion US$	0.378
Maximum	2 236.3	4.99×10^6	36.36%	2.30 billion US$	0.392
Minimum	1 810.0	3.28×10^6	30.20%	1.50 billion US$	0.362
Std. Deviation	169.8	6.88×10^5	2.38%	0.30 billion US$	0.012

budget, which averaged about 0.9 billion USD and only increased as the nation pursued important strategic plans for nuclear development. Simultaneously, the average LCF ratio was 0.85, indicating that people were not using too many natural resources, but the decrease from 0.95 to 0.75 reveals increasing pressure on the environment. Overall, the statistics show India's progress in economic growth, expanding cities, more research and technology, and concerns about sustainability between 1975 and 2015. The descriptive statistics of the variables over the study period are reported in Table 2, while Table 3 presents the five-year average values for comparison. The descriptive statistics in Tables 2 and 3 ensure a high level of internal consistency of the dataset and the appropriateness of the 1978-2022 samples for the Fourier-NARDL estimation. All monetary variables were converted to constant 2015 US dollars, and percentage- and ratio-based variables were left in their original form, such as LCF. Annual observations are reported in Table 2, and five-year averages are reported in Table 3, which provides reasons to differentiate between the numbers. The combination of the jointly presented tables suggests that India is in a stable economic and urban development with a decreasing LCF, which signifies constant ecological pressure, creating the right empirical conditions to test the Load Capacity Curve and asymmetry in nuclear R&D influence.

The rate of urbanization steadily increased, as the average share of people living in cities was 33.19%, with little variation in the data (with a standard deviation of 2.38). Support for nuclear energy research has remained steady in India, with investments ranging from $1.5 to $2.3 billion on average. According to the LCF, India was using its bio-capacity much faster than it could generate it each year. This draws attention to the environment and the need to use resources sustainably. Overall, the analysis presents important information about the economy and environment that can be used in econometric modeling or policy studies.

4.2. Preliminary Analysis

Tables 2 and 3 report the descriptive statistics of all the variables over the period 1978-2022 and the average of five years, respectively. The GDP per capita (PY) with constant (2015) prices stands at USD 1,200 and has been steadily increasing, which is explained by the square term (PY^2) representing the non-linear growth of the GDP per capita. Rapid demographic changes were characterized by an increase in UR to 35 percent of the total population. NUC spending was USD 0.9 billion on average, and it has a consistent, yet slowly growing, research foundation. LCF had a mean value of 0.85, with a downward trend, indicating that ecological pressure is increasing. The combination of these indicators represents a realistic empirical background for testing the LCC hypothesis and the asymmetric impacts of the nuclear R&D shock on environmental quality in India.

4.2.1. Stationarity Tests

Before model estimation, the order of integration of each series was verified using both the Augmented Dickey–Fuller (ADF) and Fourier-ADF tests with a constant and trend. The results are presented in Table 4.

All variables are integrated of order I(1), except for UR, which is I(0). None is I(2), satisfying the Fourier–NARDL assumptions

4.2.2. Cointegration Test (Bounds Testing)

The bounds test is used to examine the existence of a long-run relationship among LCF, PY, PY², NUC^+, NUC^- and UR.

Table 4: Unit-root findings.

Variable	ADF (Level)	Fourier-ADF [Level]	ADF [1st Diff.]	Fourier-ADF [1st Diff.]	Order
LCF	–1.887 (NS)	–2.606 (*)	–6.035 (***)	–6.243 (***)	I(1)
PY	–1.716 (NS)	–1.764 (NS)	–7.272 (***)	–7.734 (***)	I(1)
PY^2	–1.651 (NS)	–1.433 (NS)	–7.336 (***)	–7.767 (***)	I(1)
NUC	–2.340 (NS)	-3.262 (***)	–8.128 (***)	–8.477 (***)	I(1)
UR	0.624 (NS)	–9.10 (***)	–	–	I(0)

(* 10%, ** 5%, *** 1%; NS = not significant)

Table 5: Bounds-test results.

Model	F-statistic	Critical Value [10%]	[5%]	[1%]	Decision
LCF = f(PY, PY^2, NUC^+, NUC^-, UR)	5.778[a]	3.647	4.268	5.598	Cointegration [1%]

Table 6: Diagnostic tests.

Test	Statistic	p-value	Decision
Breusch–Godfrey (serial correlation)	0.491	0.618	No serial correlation
White (heteroskedasticity)	0.495	0.925	Homoskedastic residuals
Jarque–Bera (normality)	0.148	0.928	Normal residuals
RamseyRESET (specification)	1.36	0.186	Correct specification
CUSUM/CUSUMSQ	–	–	Stable parameters

Because the computed F (5.778) exceeds the 1% critical value (5.598), we reject the null hypothesis of no cointegration (Table 5). Hence, LCF and its determinants are bound to a stable long-run equilibrium.

4.2.3. Diagnostic and Stability Tests

The diagnostic results presented in Table 6 indicate that the estimated model satisfies all statistical assumptions.

The cointegration test between LCF and the explanatory variables indicates strong evidence of cointegration at the 1% significance level. The values of the bounds test, as shown in Table 6, prove the presence of cointegration between the variables at the 1% level of significance. Moreover, Table 6 presents the results of the diagnostic test that prove that the estimated model is not affected by serial correlation, heteroscedasticity, and specification errors and ensures stability based on the Cumulative Sum Control Chart (CUSUM) and Cumulative Sum of Squares (CUSUMSQ) tests. Since the F-statistic of bounds testing exceeds the critical value of 1%, cointegration of LCF with the explanatory variables is approved at the 1% significance level with the other variables. This means that the relationships between the variables do not change, but in the long run, they do change. The strength of the estimated model was further evaluated. The Breusch–Godfrey, Jarque–Bera, and White test results are serial independence, normally distributed, and no heteroskedasticity, respectively. Also, the Ramsey-Reset test is a tool that guarantees us that the model is stated in the necessary way. The CUSUM and CUSUMSQ tests show that the coefficients do not change during the entire period of time. Altogether, the results indicate that this model is statistically supported and ready to be applied to research on long-run and short-run asymmetry.

The CUSUM and CUSUMSQ tests are run to check whether the parameters remain steady throughout the sample period. The graph in Fig. 5 compares the CUSUM and CUSUMSQ statistics to the lines representing the 1% significance level. The CUSUM and CUSUMSQ lines are within the limits for the entire period, implying that the parameters have not changed. This means that the model remains stable at the 1% significance level, and the estimated coefficients show no changes for different time periods. The stable model makes the analysis both reliable and heavily considered, thus confirming the Fourier-NARDL estimation of long-run relationships.

4.2.4. Asymmetric Relationship (Wald Test)

The Wald test is conducted on the null hypothesis H_0: $\beta^+ = \beta^-$ to confirm the existence of asymmetric impacts of nuclear R&D shocks. The test provides F=6.21(p=0.021<0.05), and the symmetry is rejected. Therefore, the influence of positive and negative alterations in the NUC on the LCF is statistically significant, which corresponds to the application of the Fourier-NARDL model.

4.3. Long-Run Coefficients

The long-run estimates are given in Table 7, which indicates how economic growth, its square term, nuclear R&D

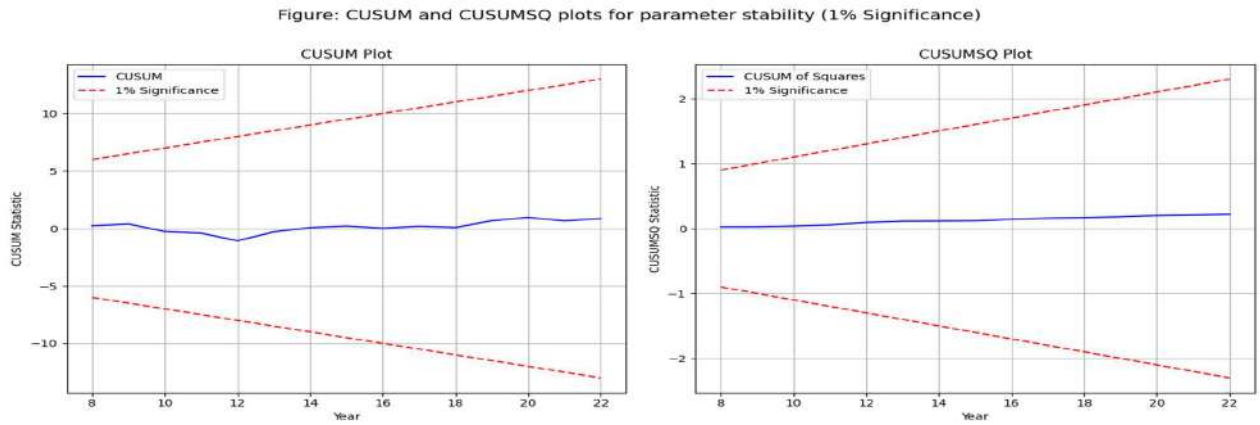


Fig. 5: CUSUM and CUSUMSQ plots for parameter stability (1% significance).

Table 7: Estimated long-run coefficients (dependent variable: LCF).

Variable	Coefficient	Std. Error	t-Statistic	Significance	Interpretation
ln PY	0.37	0.15	2.46	0.02	Economic growth improves LCF in the long term.
ln (PY²)	–0.04	0.02	–2.10	0.04	This confirms the U-shaped LCC: the LCF first declines, then recovers as income rises.
ln NUC⁺	0.29	0.11	2.64	0.01	Positive R&D shocks significantly enhance the environmental quality.
ln NUC⁻	–0.22	0.10	–2.20	0.03	Negative R&D shocks deteriorate the LCF.
ln UR	–0.18	0.07	–2.51	0.02	Urbanization pressures reduce environmental quality unless they are mitigated.

Table 8: Short-run coefficients.

Variable	Coefficient	Std. Error	t-Statistic	p-value	Interpretation
Δln PY	0.12	0.05	2.40	0.02	Economic expansion temporarily improves the LCF.
Δln (PY²)	–0.06	0.03	–2.10	0.04	Beyond a certain threshold, the growth pressure reduces the LCF.
Δln NUC⁺	0.09	0.04	2.25	0.03	Short-term R&D increases enhance the LCF.
Δln NUC⁻	–0.07	0.03	–2.05	0.04	Reductions in R&D adversely affect LCF in the short term.
Δln UR	–0.05	0.02	–2.32	0.02	Rapid urbanization temporarily reduces LCF.
ECT(–1)	–0.55	0.12	–4.58	0.00	55 % of the disequilibrium is corrected each year, resulting in a fast adjustment to equilibrium.

shocks, and urbanization influence environmental quality (LCF). All coefficients are signed in the correct direction and are economically reasonable. The fact that NUC+ has a positive elasticity (0.29) implies that a 1 percentage point increase in nuclear R&D expenditure would increase LCF by 0.29 percent in the long run, which proves that long-term investment in nuclear innovation will help in ecological resilience. The negative NUC value (-0.22) suggests that a reduction in R&D budgets rapidly reduces environmental capacity. All confirm the asymmetric LCC structure in India.

4.4. Short-Run Coefficients

The short-run dynamic outcomes are provided in Table 8, which indicates the relationship between economic growth, its squared term, nuclear R&D shocks, and urbanization in the short run on environmental quality. The value of the error correction term (-0.55) supports the fact that the long-run equilibrium can be approached quickly after short-term shocks. Every short-run impact was in line with expectations.

4.5. Robustness Analysis

Three additional robustness checks were conducted to confirm the consistency of the Fourier NARDL results.

1. Conventional NARDL model: The estimated coefficients are similar in sign and magnitude (β + = 0.31, 031 = -0.27), which validates the idea that the addition of Fourier terms hones but does not change the underlying relationships.

2. Additional Lag Structures: The addition of an extra lag to every variable does not reduce the value of significance or elasticity, which proves the stability of the parameters.
3. Structural Stability Plots: Fig. 5 CUSUM and CUSUMSQ tests are within the 99% confidence bands, and no structural instability is identified between 1978 and 2022.

In general, the robustness tests affirm that the asymmetric effect of nuclear R&D on environmental quality is statistically and economically sound. These findings strongly support the LCC hypothesis in India. When economies develop at a low level, the ecological capacity decreases; however, when income is high and cleaner technologies and environmental policies are adopted, recovery is achieved. The positive PY and negative PY^2 coefficients represent this U-shaped behavior.

The established asymmetry between NUC+ and NUC- proves that greater nuclear R&D investments are much more useful in the short and long terms, whereas reductions in nuclear R&D investments have disproportionately negative effects. This aspect helps usher in the belief that technological investment is a green multiplier that cannot be achieved by halting policies. The negative elasticity of urbanization shows that spontaneous urban growth destroys the environment, but the adverse effects can be mitigated by smart infrastructure and energy-saving designs. These results indicate that the sustainability path that India should follow to achieve its long-term carbon-neutral target of 2070 requires unending nuclear research and development, balanced cities, and the incorporation of clean energy development into economic policy.

5. CONCLUSIONS

The present study is part of the growing literature on asymmetric energy environment dynamics, as it is the first Indian evidence of the impact of nuclear R&D investments on environmental quality within the LCC framework. The study estimates uniformity (i) a strong long-term co-integration between LCF, income, urbanization, and NUC (ii) confirms asymmetry of the nuclear R&D effects, and (iii) confirms the LCC hypothesis in India. Overall, nuclear R&D can have a positive but rather minor effect on enhancing environmental quality, depending on the long-term commitment to the policy and its combination with renewable policies. Multi-sectoral innovation, which includes nuclear energy, renewables, and urban sustainability projects, will thus become the way forward for India to achieve carbon neutrality by 2070. The research highlights that, despite the fact that nuclear R&D is an important part of sustainability, it must be regarded as a part of a diversified and balanced mix of a low-carbon policy rather than as its pillar.

5.1. Policy Recommendations

Here are a few recommendations, based on what we have observed

- Support Low-Carbon Growth: Regulations should help develop green technology and new innovations to lessen the environmental damage caused by the initial stages of economic growth.
- Support the Expansion of Solar, Wind, and Bioenergy: More efforts should be made to use solar, wind, and bioenergy because nuclear R&D does not have much direct influence on the environment.
- Introduce City-Tailored Sustainability Activities: Because cities now have both positive and negative impacts, the focus of policies should be on smart city projects, environmentally friendly infrastructure, efficient buildings, and eco-friendly transport.
- Fix and Improve Carbon Prices: Reliable pricing of carbon will lead industries to reduce their emissions, especially as the economy expands past important boundaries.

5.2. Limitations and Directions for Future Research

However, this study has some limitations.

- Narrowed Scope: The report analyzed only CO_2 emissions and did not consider other greenhouse gases or measures related to the environment.
- Model specification: The Fourier NARDL model can detect gradually changing structures but does not always notice sudden changes.
- The ideas in this study may not be valid for other emerging economies or areas, as they mainly apply to India.
- It would be useful for further studies to consider the following:
- Additional variables are useful, such as measuring the total emissions of greenhouse gases, using renewable energy, and the loss of different types of biodiversity.
- Employ Panel Data Analysis: This way, results involving BRICS nations or other emerging countries can be used more broadly.
- Try Using Nonlinear Approaches: Use approaches such as smooth transition regression and threshold autoregressive models to observe abrupt transitions in the data.

- Investigate differences between sectors to design programs that curb emissions in each sector.

Examine How Policies Are Carried Out: One area for further research is whether the intended outcomes of environmental policies are ever met due to asymmetries.

6. ACKNOWLEDGMENTS

The author would like to thank the reviewers and the editor for their valuable comments and suggestions, which helped to improve the quality of the manuscript.

7. REFERENCES

Afrane, S., Ampah, J. D., Adun, H., Chen, J. L., Zou, H., Mao, G. and Yang, P., 2025. Targeted carbon dioxide removal measures are essential for the cost and energy transformation of the electricity sector by 2050. *Communications Earth & Environment*, 6(1), pp.227. [DOI]

Ahmad, M., Ahmed, Z., Gavurova, B. and Olah, J., 2022. Financial risk, renewable energy technology budgets, and environmental sustainability: Is going green possible? *Frontiers in Environmental Science*, 10, pp. 909190. [DOI]

Ahmed, Z., Cary, M., Ali, S., Murshed, M., Ullah, H. and Mahmood, H., 2021. Moving toward a green revolution in Japan: Symmetric and asymmetric relationships among clean energy technology development investments, economic growth, and CO_2 emissions. *Energy & Environment*, 33(7), pp. 1417–1440. [DOI]

Arpitha, P., Kumar, M., Reddy, B. and Joshi, A., 2025. A quantitative analysis of macroeconomic indicators and GDP growth in India. *Journal of Scientific Research and Reports*, 31(2), pp. 135–143. [DOI]

Azam, A., Rafiq, M., Shafique, M. and Yuan, J., 2022. Towards achieving environmental sustainability: The role of nuclear energy, renewable energy, and ICT in the top-five carbon emitting countries. *Frontiers in Energy Research*, 9, pp. 804706. [DOI]

Basu, P., Mandal, M., Jana, S., Biswas, A. and Ray, S., 2025. Impact of anthropogenic activities on global warming and energy demand. In: *The Intersection of Global Energy Politics and Climate Change: A Comprehensive Analysis of Energy Markets and Economics* (pp. 81–63). Springer. [DOI]

Behera, B., Sucharita, S., Patra, B. and Sethi, N., 2024. A blend of renewable and non-renewable energy consumption on economic growth of India: The role of disaggregate energy sources. *Environmental Science and Pollution Research*, 31(3), pp. 3902–3916. [DOI]

Bishoyi, S., 2025. AatmaNirbhar Bharat: key for realising the goal of developed India by 2047. *National Security*, 8(1), pp. 120–139.

Budde, S., Chani, P. S. and Agrawal, S., 2025. Framework for evaluating and mitigating industrial air pollution in India: Systematic review of concepts and unmet needs. *Journal of Hazardous, Toxic, and Radioactive Waste*, 29(1), pp. 04024030. [DOI]

Caglar, A. E. and Ulug, M., 2022. The role of government spending on energy efficiency R&D budgets in the green transformation process: Insight from the top-five countries. *Environmental Science and Pollution Research*, 29, pp. 76472–76484. [DOI]

Caglar, A. E., 2023. Can nuclear energy technology budgets pave the way for a transition toward a low-carbon economy: Insights from the United Kingdom. *Sustainable Development*, 31(1), pp. 198–210. [DOI]

Caglar, A. E., Avci, S. B., Ahmed, Z. and Gökçe, N., 2024. Assessing the role of green investments and green innovation in ecological sustainability: From a climate action perspective on European countries. *Science of the Total Environment*, 928, pp. 172527. [DOI]

Caglar, A. E., Dastan, M. and Rej, S., 2024a. A new look at China's environmental quality: How does environmental sustainability respond to the asymmetrical behavior of the competitive industrial sector? *International Journal of Sustainable Development & World Ecology*, 31(1), pp. 1–13. [DOI]

Caglar, A. E., Dastan, M., Mehmood, U. and Avci, S. B., 2023a. Assessing the connection between competitive industrial performance on load capacity factor within the LCC framework: Implications for sustainable policy in BRICS economies. *Environmental Science and Pollution Research*, 30(1), pp. 1–18. [DOI]

Caglar, A. E., Destek, M. A. and Manga, M., 2024b. Analyzing the load capacity curve hypothesis for Türkiye: A perspective for the sustainable environment. *Journal of Cleaner Production*, 444, pp. 141232. [DOI]

Dave, G., Patel, T. and Mitra, S., 2025. Global scenario on renewable energy and net zero goal emphasizing Indian standpoint: A short review. *Energy Systems*, 14(1), pp. 1–22. [DOI]

Dharani, V., Lalitha, R., Dhanalakshmi, K., Judi, V. A. and Kabitha, P., 2025. Enhancing GDP forecasting in India through a hybrid ARIMA-LSTM model. In: *2025 International Conference on Intelligent Computing and Control Systems (ICICCS)* (pp. 676–670). IEEE. [DOI]

El-Ashmawy, W. M., El-Maghlany, W. M. and Elhelw, M., 2024. Thermo-economic analysis of potential desalination processes utilized by no greenhouse gas emissions power plant. *Alexandria Engineering Journal*, 109, pp. 191–200. [DOI]

Erhart, S., Szabó, S. and Erhart, K., 2025. Integrating pollutant registers for the climate change risk evaluation of industrial companies in Australia, Europe and North America. *Scientific Reports*, 15(1), pp. 1207. [DOI]

Farina, N., Young, S. S., Nafa, F. and Waddington, G., 2025. Impact of solar farm expansion on forest cover in Massachusetts: an analysis using artificial intelligence and remote sensing. *The Professional Geographer*, 77(1), pp. 1–12. [DOI]

Grover, R. B., 2025. Nurturing nuclear power in India. *Current Science*, 128(3), pp. 240–244. [DOI]

Haouraji, C., Mounir, B., Mounir, I. and Farchi, A., 2021. Exploring the relationship between residential CO_2 emissions, urbanization, economic growth, and residential energy consumption: evidence from the North Africa region. *Energies*, 14(18), pp. 5849. [DOI]

Hashim, S. R., 2025. Challenges to sustainable urbanization in India—migration, poverty and urban crimes. In: *Development, Inclusion and Sustainability: Issues and Perspectives* (pp. 208–193). Singapore: Springer Nature Singapore. [DOI]

He, X., Khan, S., Ozturk, I. and Murshed, M., 2023. The role of renewable energy investment in tackling climate change concerns: Environmental policies for achieving SDG-13. *Sustainable Development*, 31(3), pp. 1888–1901. [DOI]

Imam, M., Adam, S., Dev, S. and Nesa, N., 2024. Air quality monitoring using statistical learning models for sustainable environment. *Intelligent Systems with Applications*, 22, pp. 200333. [DOI]

Jain, A. K., Seshadri, S., Anand, J., Chandra, N., Patra, P. K., Canadell, J. G. and Tiwari, Y. K., 2025. South Asia's ecosystems are a net carbon sink, but the region is a major net GHG source to the atmosphere. *Global Biogeochemical Cycles*, 39(4), e2024GB008261. [DOI]

Khaleel, M., Yusupov, Z., Rekik, S., Kılıç, H., Nassar, Y. F., El-Khozondar, H. J. and Ahmed, A. A., 2025. Harnessing nuclear power for sustainable electricity generation and achieving zero emissions. *Energy Exploration & Exploitation*, 43(1), pp.1126-1148. [DOI]

Khatoon, U. T. and Velidandi, A., 2025. An overview on the role of government initiatives in nanotechnology innovation for sustainable economic development and research progress. *Sustainability*, 17(3), pp. 1250. [DOI]

Kocak, E. and Ulucak, Z. S., 2019. The effect of energy R&D expenditures on CO_2 emission reduction: Estimation of the STIRPAT model for OECD countries. *Environmental Science and Pollution Research*, 26, pp. 14328–14338. [DOI]

Kumar, S., Das, P. and Behera, M. D., 2025. Significant rise in aerosol

concentration in the past two decades over the Kalinga Nagar industrial area, Odisha, India. In: *Sustainable Development Perspectives in Earth Observation* (pp. 448–437). Elsevier. [DOI]

Kumari, D., Shashwat, S., Verma, P. K. and Giri, A. K., 2025. Examining the nexus between carbon dioxide emissions, economic growth, fossil fuel energy use, urbanization and renewable energy towards achieving environmental sustainability in India. *International Journal of Energy Sector Management*, 19(3), pp. 731–746. [DOI]

Lakshmikantha, H. M. and Rajesh, P., 2025. Impact of climate change on Indian economy: a review. *International Journal of Innovations in Science, Engineering and Management*, 4(1), pp. 181–188. [DOI]

Lee, J. W. and Song, E., 2025. Demographic change and long-term economic growth path in Asia. *Economic Modelling*, 147, pp. 107043. [DOI]

Mahmood, H., Asadov, A., Tanveer,M., Furqan, M. and Yu, Z., 2022. Impact of oil price, economic growth and urbanization on CO_2 emissions in GCC countries: Asymmetry analysis. *Sustainability*, 14(8), pp. 4562. [DOI]

Majid, M., 2020. Renewable energy for sustainable development in India: Current status, future prospects, challenges, employment, and investment opportunities. Energy, *Sustainability and Society*, 10(1), pp.1–36. [DOI]

Nathaniel, S., Nwodo, O., Sharma, G. and Shah, M., 2020. Renewable energy, urbanization, and ecological footprint linkage in CIVETS. *Environmental Science and Pollution Research*, 27, pp.19616–19629. [DOI]

Ngoc Xuan, V., 2025. Energy factors affecting environmental pollution for sustainable development goals: The case of India. Energy Exploration & Exploitation, 43(1), pp.410–450. [DOI]

Ngoh, D.M., Jha, A., Misra, A.K., Ngangue, D.P.M. and Fono, L.A., 2025. Impact of human activities and forest biomass on atmospheric carbon dioxide: A mathematical model. *Environmental Modeling & Assessment*, pp.1–16. [DOI]

Nimma, D., Devi, O.R., Laishram, B., Ramesh, J.V.N., Boddupalli, S., Ayyasamy, R., Tirth, V. and Arabi, A., 2025. Implications of climate change on freshwater ecosystems and their biodiversity. *Desalination and Water Treatment*, 321, 100889. [DOI]

Özkan, O., Obekpa, H.O. and Alola, A.A., 2025. Examining the nexus of energy intensity, renewables, natural resources, and carbon intensity in India. *Energy and Environment*, 36(1), pp.168–186. [DOI]

Raihan, A.S.I.F., Sarker, T. and Zimon, G., 2024. An investigation on the prospects, challenges and policy consequences of renewable energy technology development for India's environmental sustainability. *WSEAS Transactions on Environment and Development*, 20, pp.365–390. [DOI]

Rangasamy, R.G., 2025. Tracing drawings to technological demonstration by time tested welding and fabrication techniques during construction and commissioning of Prototype Fast Breeder Reactor (PFBR). *Indian Welding Journal*, 58(1). [DOI]

Rao, Y.B., Kumar, P.N., Gupta, S.N.V.M.S. and Srivastava, D., 2025. A simple and rapid method for chemical characterization of fast breeder reactor components using RF GD-OES. *Journal of Radioanalytical and Nuclear Chemistry*, pp.1–10. [DOI]

Sadath, A.C. and Acharya, R.H., 2025. Assessing the relative importance of access and affordability in energy poverty in India: A guide for future energy policies. *International Journal of Energy Economics and Policy*, 15(3), pp.290–300. [DOI]

Selvam, C., Yuvarajan, D., Kumar, S., Shukla, K.K., Patel, C., Juneja, B. and Acharya, S.K., 2025. Harnessing nuclear energy for India's energy security: Current status, challenges, and future opportunities. *Results in Engineering*, 105105. [DOI]

Sen, S. and Sahoo, P., 2024. Carbon pricing for sustainable transition in India. *World Development Perspectives*, 34, pp.100586. [DOI]

Shahzad, S. and Jasińska, E., 2024. Renewable revolution: A review of strategic flexibility in future power systems. *Sustainability*, 16(13), 5454. [DOI]

Sharma, P., Chakrabarti, A., Awasthi, F., Ghosh, D. and Rai, A., 2025. Impact of urbanization and economic growth on environmental quality in metropolitan cities in India. In: Political Economy of Emerging Urban and Peri-urban Spaces in India: A Roadmap Towards Environmental and Social Sustainability. Singapore: *Springer Nature Singapore*, pp.127–143. [DOI]

Shi, Y., Li, J., Fang, Z., Li, Y., Hu, H., Nie, W. and Meng, F., 2024. Probing the role of natural resources and urbanization towards ecological sustainability in BRICST economies. *Resources Policy*, 91, pp.104739. [DOI]

Sun, Y., Usman, M., Radulescu, M., Pata, U.K. and Balsalobre-Lorente, D., 2023. New insights from the STIRPAT model on how environmental-related technologies, natural resources, and the use of renewable energy influence load capacity factor. *Gondwana Research*, 129, pp.398–411.

Xu, W. and Ali, A., 2025. The moderating role of environment-related technologies in the link between transportation infrastructure, agricultural, and environmental contamination in highly congested countries of the world. *GM Crops & Food*, 16(1), pp.340–359. [DOI]

Zio, E., Shirvan, K., Duffey, R.B. and D'Auria, F., 2025. Nuclear power technology: An analysis and informed opinions. *Frontiers in Nuclear Engineering*, 4. [DOI]

Nature Environment and Pollution Technology
An International Quarterly Scientific Journal

p-ISSN: 0972-6268
(Print copies up to 2016)
e-ISSN: 2395-3454

Vol. 25 | No. 3 | Article ID B4387 | 2026

Original Research Paper

https://doi.org/10.46488/NEPT.2026.v25i03.B4387

Open Access Journal

Index-Based Evaluation (IBE) and Geospatial Mapping of Heavy Metal Contamination in Groundwater of an Industrially Influenced Peri-Urban Area of Guwahati, Assam, India

Debasish Chutia[1], Satyajit Kataki[1]† and Aditya Shankar Kataki[2]

[1]Department of Geology, Cotton University, Guwahati, 781001, Assam, India

[2]School of Biodiversity, One Health and Veterinary Medicine, University of Glasgow, Glasgow, Scotland, United Kingdom

†Corresponding author: Satyajit Kataki; satyajit.kataki@cottonuniversity.ac.in

Abbreviation: Nat. Env. & Poll. Technol.
Website: www.neptjournal.com

Received: 20-08-2025
Revised: 23-10-2025
Accepted: 26-10-2025

Key Words:

Index-Based Evaluation (IBE)
Geospatial Mapping
IDW interpolation
Kernel Density Estimation (KDE)
Heavy metals
Groundwater

Citation for the Paper:

Chutia, D., Kataki, S. and Kataki, A.S., 2026. Index-based evaluation (IBE) and geospatial mapping of heavy metal contamination in groundwater of an industrially influenced peri-urban area of Guwahati, Assam, India. *Nature Environment and Pollution Technology*, 25(3), B4387. https://doi.org/10.46488/NEPT.2026.v25i03.B4387

Note: From 2025, the journal has adopted the use of Article IDs in citations instead of traditional consecutive page numbers. Each article is now given individual page ranges starting from page 1.

Copyright: © 2026 by the authors
Licensee: Technoscience Publications
This article is an open access article distributed under the terms and conditions of the Creative Commons Attribution (CC BY) license (https://creativecommons.org/licenses/by/4.0/).

ABSTRACT

This study evaluates the geospatial variability of heavy metal contamination in groundwater within an industrially influenced peri-urban area spanning parts of Guwahati, Assam, and Meghalaya, India. A total of 26 samples were analyzed for nine heavy metals, As, Cd, Cr, Cu, Mn, Ni, Pb, Zn, and Fe, using Atomic Absorption Spectroscopy (AAS) during both pre- and post-monsoon seasons. Index-Based Evaluation (IBE) was employed to assess cumulative contamination levels. Results revealed maximum concentrations of Pb (0.206 $mg.L^{-1}$), Cd (0.011 $mg.L^{-1}$), Ni (0.049 $mg.L^{-1}$), and Mn (1.983 $mg.L^{-1}$) in the groundwater samples. Metal Index (MI) values ≥ 6 at 21 (pre-monsoon) and 7 (post-monsoon) sites indicated serious contamination, while Heavy Metal Pollution Index (HPI) values > 100 at 22 and 20 sites, respectively, classified the water as unsuitable for drinking. Kernel Density Estimation (KDE) and box plots further supported the temporal patterns of contamination. Geospatial mapping of MI using the Inverse Distance Weighting (IDW) technique revealed that 78% (pre-monsoon) and 69% (post-monsoon) of the area were seriously or strongly affected, while HPI interpolation indicated 97% and 95% of the area under high-pollution zones, respectively. The findings underscore the strong anthropogenic impact of cement and brick industries on groundwater quality, emphasizing the need for continuous monitoring and effluent control. The adopted framework provides a transferable model for early detection, spatial prioritization, and remediation of heavy metal contamination in industrially stressed aquifers globally.

1. INTRODUCTION

Groundwater is generally considered less prone to contamination than surface water due to its concealed nature and limited direct exposure. However, it remains vulnerable to threats such as chemical leaching, industrial discharge, over-extraction, and inadequate monitoring. So, while it may appear safer, sustainable use and proper testing are crucial to truly ensure its safety. Groundwater quality exhibits spatial variability influenced by geographic location, anthropogenic pollution sources, and prevailing ecological conditions. Heavy metal pollution is a global environmental concern due to its toxicity, bioaccumulation, and persistence (Ali et al. 2019). Even slight increases in concentrations beyond acceptable limits, from natural or anthropogenic sources, can cause serious environmental and health risks (Yahaya et al. 2009, Prasad et al. 2014, Jazza et al. 2022). Although heavy metals are naturally occurring elements distributed throughout the Earth's crust, environmental contamination and human exposure are predominantly the result of anthropogenic activities. In groundwater, the primary sources of heavy metal pollution include geogenic processes, such as rock – water interactions, and human-induced inputs (Bradl 2002). Among the various human-induced sources, industrial pollution has a severe impact on the environment due to its emissions

of various contaminants, including heavy metals, into the atmosphere. Heavy metal pollutions in groundwater can result from these contaminants moving vertically through the soil profile. The extent to which these metals dissolve in soil and groundwater is largely determined by the pH range of 6-8, the concentration of the metals, and the cation exchange capacity (Martinez & Motto 2000). Heavy metals such as Arsenic (As), Cadmium (Cd), Chromium (Cr), Mercury (Hg), Lead (Pb), Nickel (Ni), Manganese (Mn) are found in groundwater due to both natural geological processes and anthropogenic activities like industrial discharge, mining, use of agrochemicals, and improper waste disposal. These metals are toxic even at low concentrations and pose serious health risks to humans and ecosystems. The International Agency for Research on Cancer (IARC) has classified the heavy metals and the compounds of arsenic, cadmium, chromium, and nickel in group 1 (carcinogenic to humans) and lead and the inorganic lead compounds (2A), cobalt in metallic form and its compounds (as possibly carcinogenic to humans. The United States Environmental Protection Agency (US-EPA) categorizes these substances as known or probable human carcinogens based on both epidemiological and toxicological studies. These classifications highlight the significant public health risks associated with long-term exposure to contaminated water sources. Even at the modest exposure levels, these metallic elements are known to cause numerous organ damage and are regarded as systemic toxicants. Anthropogenically, these heavy metals can be discharged into the air and soil during the production of cement and bricks. Through food chain transfer and drinking water contamination, these pollutants can bioaccumulate in crops produced close to the sites and endanger the long-term health of the surrounding people. The groundwater-dependent ecosystem may suffer if the anthropogenic release of heavy metals into the atmosphere is not managed appropriately. The impact of heavy metal contamination on the environment can be reduced by the management of industrial waste emissions and routine water quality monitoring.

2. MATERIALS AND METHODS

2.1. Study Area

The study area holds geographical significance as it is one of the fastest-developing peri-urban areas of Guwahati Metropolitan city, Assam, as well as a part of Meghalaya state, India (Fig. 1). The peri-urban fringes of Guwahati have undergone rapid industrial expansion in recent decades, driven by urban congestion, rising land costs, and infrastructural development within the metropolitan core. This shift has attracted numerous cement plants, brick kilns, and small-scale industries to the outskirts, transforming rural landscapes into mixed industrial-residential zones. Consequently, the region faces increasing environmental stress, particularly on groundwater resources, due to unregulated industrial discharges, waste disposal, and over-extraction. Geologically, the area represents the northeasterly extension of the Assam-Meghalaya Plateau underlain by a basement gneissic complex predominantly composed of quartz-feldspathic gneiss. This basement is overlain by unconsolidated alluvial sediments consisting of clay and sand of varying grades, deposited during the Quaternary period. Groundwater serves as the sole source for drinking, industrial and agricultural use in this area, as the River Lower-Digaru depends heavily on upstream rainfall in Meghalaya. This dependency makes surface water availability highly variable and unreliable, further emphasizing the critical role of groundwater in sustaining the area's water demands.

The area under study is also significant from an industrial perspective, with seven cement manufacturing plants and nineteen brick kilns presently operational in the area (Fig. 2). The area also previously housed a paper industry, which is no longer in existence, and is presently being repurposed for the establishment of a semiconductor manufacturing facility. Heavy metals such as cadmium and lead are found in trace quantities in the raw materials, particularly in limestone, shale and clay, which are the principal constituents in cement manufacture (European Commission 2010). The high temperatures used in the cement manufacturing process can volatilize the heavy metals, such as cadmium, lead, mercury, etc., present in the raw materials, which can then be emitted into the air and settle onto the ground, surface water, and groundwater. Furthermore, the use of chemical additives in the cement manufacturing process and during pulping and bleaching in the paper manufacturing process, can also contribute to the release of heavy metals. The use of waste fuels such as used tires or industrial waste in brick kilns can release heavy metals into the air. In addition, the disposal of cement kiln dust, a by-product of the cement manufacturing process, can release these heavy metals into the environment, particularly if not handled properly. A number of studies have demonstrated that cement plants and brick kilns significantly raise the concentrations of heavy metals in nearby soils and water bodies (Singh et al. 2010, Mehta & Mehta 2012, Mohapatra et al. 2014). Borgohain et al. (2024) investigated heavy metal contamination and associated health risks in groundwater at the Byrnihat Industrial Area near the Guwahati–Shillong Highway (Meghalaya) and reported that concentrations of Cr, Cd, and Pb exceeded the permissible limits prescribed by WHO and BIS. Arunakumari et al. (2023) examined the persistence of heavy metals and associated human health risks in an industrial area of Telangana, South India, and

reported significant soil contamination (based on geo-accumulation and contamination factor indices) along with elevated health risks through groundwater exposure.

Yerraguntla in Andhra Pradesh, India, an area with multiple cement industries and a thermal power plant, showed elevated concentrations of mercury, lead, cadmium, chromium and arsenic in groundwater (Kalpana et al. 2023). Similarly, in the Roper Wetland region of Punjab, elevated levels of cadmium and zinc in groundwater were attributed to nearby cement and other industrial activities (Kaur et al. 2019). Soil and dust studies in Ghana and Jordan have further confirmed the presence of heavy metals such as Pb, Cd, Cr and Ni, indicating atmospheric deposition and leaching as potential pathways for groundwater contamination (Awuah et

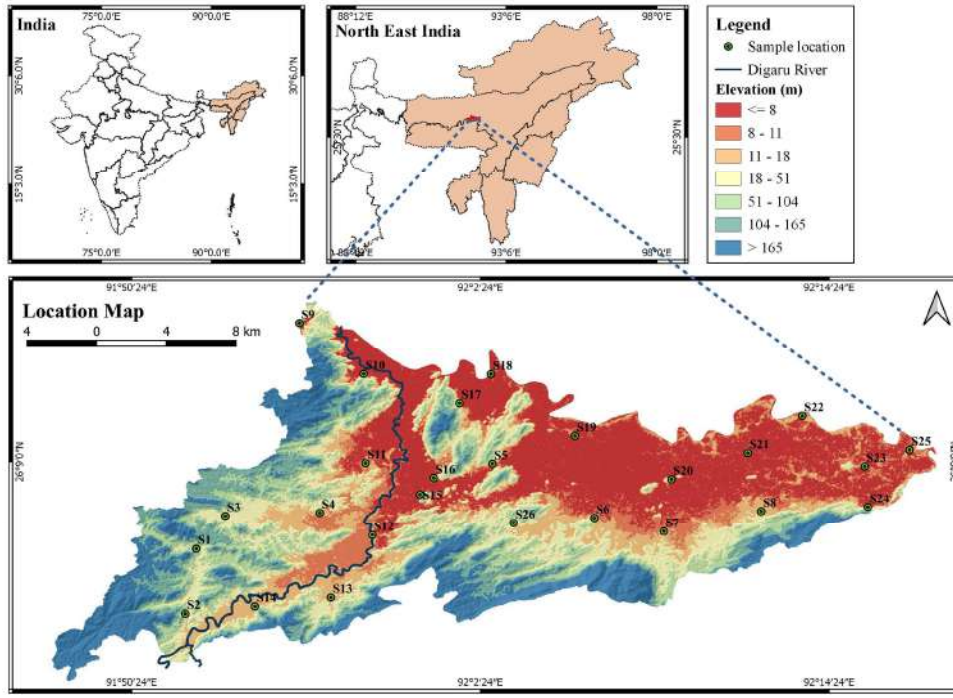


Fig. 1: Map depicting the areal extent of the study area and heavy metals sampling locations.

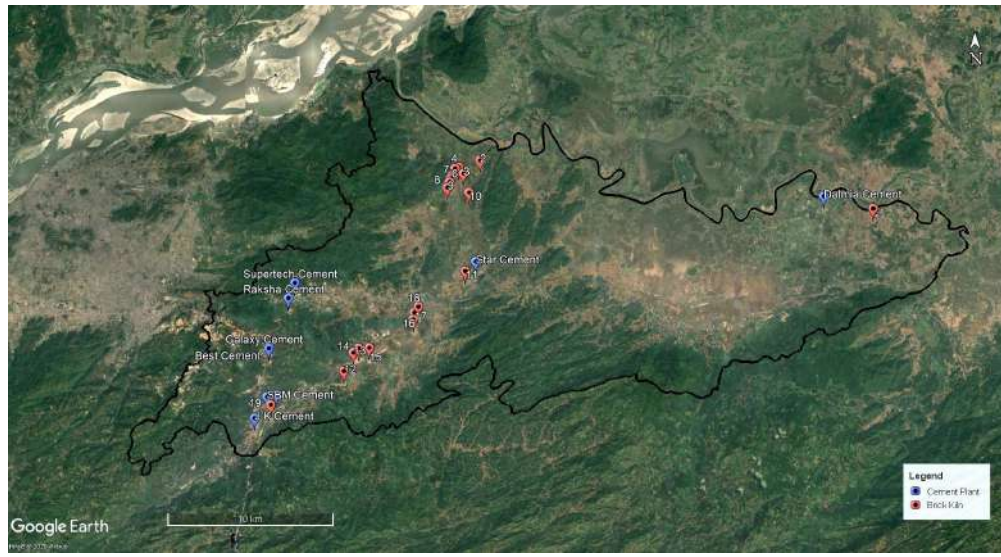


Fig. 2: Locations of cement manufacturing plants and Brick kilns in the study area.

al. 2022, Al-Khashman & Shawabkeh 2005). These findings suggest that the cement manufacturing process, through emissions, raw material handling, and waste disposal, can contribute significantly to heavy metal enrichment in the surrounding environment, including groundwater systems.

Groundwater quality in industrial peri-urban areas of Northeast India remains poorly understood due to limited comprehensive assessments. Studies rarely employ integrated index-based and geospatial approaches, and seasonal or temporal variations are often overlooked. This gap underscores the need for systematic, multidimensional evaluation to ensure sustainable groundwater management in the region. Accordingly, a comprehensive study was undertaken to evaluate the Index-Based Evaluation (IBE) and the spatial distribution of heavy metals in groundwater, and to assess their impact on groundwater quality for domestic use. Notably, this is the first detailed investigation in the region to employ IBE and geospatial analysis, as no prior groundwater studies have integrated Metal Index (MI) and Heavy Metal Pollution Index (HPI) assessments here.

2.2. Sample Collection

Groundwater samples were gathered from dug wells (DW) and deep tube wells (DTW) during both pre- and post-monsoon periods, adhering to standard procedures outlined by APHA (2023). Selection of sampling sites was based on accessibility, settlement patterns, and demographic factors, covering twenty-six of thirty-five grid cells within the study area. A total of 53 samples were collected from depths ranging from 1.84 meters in gneissic rocks to 182 meters in unconsolidated sediments and were subsequently analyzed. Samples were preserved in an acidic medium (pH < 2) with HNO_3 and transported to the laboratory within 48 hours. Before analysis, all samples were filtered following APHA (2023) guidelines. QA/QC measures included the analysis of field duplicates, collected periodically to evaluate sampling and analytical consistency, and field blanks to detect any contamination during collection, transport, or analysis. The samples were analyzed for major cations and anions, pH, electrical conductivity (EC), total dissolved solids (TDS), and heavy metals.

2.3. Heavy Metal Analysis

The groundwater samples collected were analyzed to identify and measure the concentrations of heavy metals, including Arsenic (As), Cadmium (Cd), Chromium (Cr), Copper (Cu), Nickel (Ni), Manganese (Mn), Lead (Pb), Zinc (Zn), and Iron (Fe), using Graphite Furnace Atomic Absorption Spectroscopy (GFAAS, Shimadzu AA6300 model). An index-based evaluation (IBE) method was employed to assess and interpret the overall impact of these heavy metals on groundwater quality in the study area. These indices facilitate the evaluation of water pollution levels and potential health risks. Several authors, including Reza and Singh (2010), Mohan et. al. (1996), and Backman et al. (1998), effectively demonstrated the practical application of indexing techniques for identifying contamination hotspots.

2.4. Metal Index (MI) Calculation

The Metal Index (MI) method is a widely used approach for assessing and quantifying the presence and severity of heavy metal contamination in groundwater. It consolidates complex heavy metal concentration data into a single numerical value, providing an overall indication of water quality with respect to metal content. The Metal Index (MI) was first proposed by Caeiro et al. (2005). The following formula is used to calculate the Metal Index:

$$MI = \sum_{i=1}^{n} (C_i \div MAC_i)$$

Where, Ci = concentration of the i^{th} metal in the water sample, MAC_i = Maximum admissible concentration of the i^{th} metal (as per WHO, BIS), n= total number of metals analyzed

2.5. Heavy Metal Pollution Index (HPI) Calculation

The Heavy Metal Pollution Index (HPI) is a measure of the heavy metals present in a particular environment and is a widely used method to evaluate the cumulative effect of multiple heavy metals on groundwater quality. It is an empirical evaluation system designed to assess the overall impact of specific metals on water quality (Dheeraj et al. 2022). This method was first developed by Prasad & Bose (2001), but the concept and foundational methodology were earlier elaborated by Horton (1965) and later modified by researchers like Mohan et. al. (1996) and Backman et al. (1998) for groundwater pollution studies. Unlike the Metal Index (MI), the HPI gives a weighted score, considering both the concentration and the significance (weight) of each metal. It is typically calculated by measuring the concentration of a number of different heavy metals in the environment and combining these measurements into a single index value. The Heavy Metal Pollution Index (HPI) of groundwater in the study area was calculated to assess the extent of contamination with nine heavy metals (As, Cd, Cr, Cu, Mn, Ni, Pb, Zn and Fe) using the following formula in MS-Excel -

$$HPI = \frac{\sum_{i=1}^{n} W_i Q_i}{\sum_{i=1}^{n} W_i}$$

Where, W*i* is the unit weight of the ith parameter, n is the number of heavy metals considered and Q*i* is the sub-index value of the ith parameter.

The unit weight, W*i*, is calculated by - $W_i = K/S_i$

Where, K is the proportionality constant =1,

S*i* is the standard permissible limit value of the 'i'th parameter.

Q_i is calculated as -

$$Q_i = \sum_{i=1}^{n} \frac{(M_i (-) I_i)}{(S_i - I_i)} \times 100$$

Where M_i is the monitored value, I_i is the ideal value of the heavy metal of the ith parameter.

The relative weights (w_i) assigned to each water quality parameter were normalized to ensure that their sum equals unity ($\sum W_i = 1$), following the standard formulation.

2.6. Geospatial Mapping of Heavy Metals

Geospatial mapping involves analyzing data across geographic areas over specific time periods. Spatial analysis visualizes data on maps through geospatial interpolation techniques to identify contamination hotspots and spatial trends. Temporal analysis tracks changes in heavy metal concentrations over different times, such as seasonal (pre-monsoon versus post-monsoon), annual, or multi-year periods. While primarily used in environmental studies, especially groundwater contamination, it aids in visualizing how pollutant levels vary across locations and fluctuate seasonally or yearly. In this context, geo-temporal mapping of heavy metals in groundwater is an essential tool for understanding contamination patterns, pinpointing pollution sources, and guiding mitigation efforts.

Geospatial distribution maps of nine heavy metals, Cd, Cr, As, Cu, Pb, Mn, Ni, Zn, and Fe, were generated for both the pre- and post-monsoon seasons using the Spatial Analyst toolbox in ESRI ArcGIS 10.8.2. The resolution of the interpolated raster images was 90 m. Inverse Distance Weighting (IDW) was used as the interpolation method to model the geospatial distribution of heavy metals across the entire study area. Because the sample size was less than 50, IDW was adopted to map the distribution of heavy metals. IDW performs better than kriging when the sample size is small (Li & Heap 2011). For sample sizes < 50, the derived variograms are often erratic and show little or no evident spatial structure (Webster & Oliver 2001, 2007). The permissible limits for drinking water are taken from both the WHO and the BIS.

3. RESULTS AND DISCUSSION

The heavy metals examined in this study include Cadmium (Cd), Chromium (Cr), Arsenic (As), Copper (Cu), Lead (Pb), Nickel (Ni), Manganese (Mn), Zinc (Zn), and Iron (Fe). Table 1 shows the number of sampling sites where heavy metal concentrations exceeded the limits set by WHO and BIS for domestic water use. It was found that many groundwater samples in the area had elevated levels of Pb and Cd during both pre- and post-monsoon seasons, with Ni elevated in pre-monsoon and Mn in post-monsoon. Specifically, Cadmium (Cd) exceeded safe levels at 14 locations during pre-monsoon, but only once post-monsoon. Nickel (Ni) was above permissible limits at eight locations pre-monsoon, with no exceedances after the monsoon. Manganese (Mn) surpassed the limit at two sites in the post-monsoon season. Lead (Pb) contamination was the most widespread, exceeding 0.01 mg.L^{-1} at 24 of 26 locations pre-monsoon and at 22 locations post-monsoon (see Table 1).

The box plots (Fig. 3), generated using RStudio (version 2024.04.2+764), illustrate the seasonal variation, pre-monsoon versus post-monsoon, in the concentrations of four heavy metals: Cadmium (Cd), Manganese (Mn), Nickel (Ni), and Lead (Pb), in groundwater. The y-axis is on a logarithmic scale to accommodate the wide range of values and improve visualization, especially for outliers. During the pre-monsoon period, manganese (Mn) shows greater variability, a wider interquartile range (IQR), and several outliers, indicating spatial heterogeneity and potential localized contamination. In contrast, post-monsoon Mn concentrations are more consistent, with a narrower IQR, although the median is slightly higher, possibly due to leaching or recharge during the monsoon. Cadmium (Cd) levels are higher and more

Table 1: Number of sampling locations in the study area exceeding the BIS permissible limits (mg.L^{-1}) for pre- and post-monsoon seasons.

Heavy Metals	Permissible Standards (BIS) [mg.L^{-1}]	No. of samples exceeding the permissible standards/ Total no of samples	
		Pre-monsoon	Post-Monsoon
Arsenic (As)	0.05	0.05	0/26
Cadmium (Cd)	0.003	14/26	01/26
Chromium (Cr)	0.05	0/26	0/26
Copper (Cu)	1.5	0/26	0/26
Manganese(Mn)	0.3	0/26	2/26
Nickel (Ni)	0.02	08/26	0/26
Lead (Pb)	0.01	24/26	22/26
Zinc (Zn)	15	0/26	0/26
Iron (Fe)	1	0/26	0/26

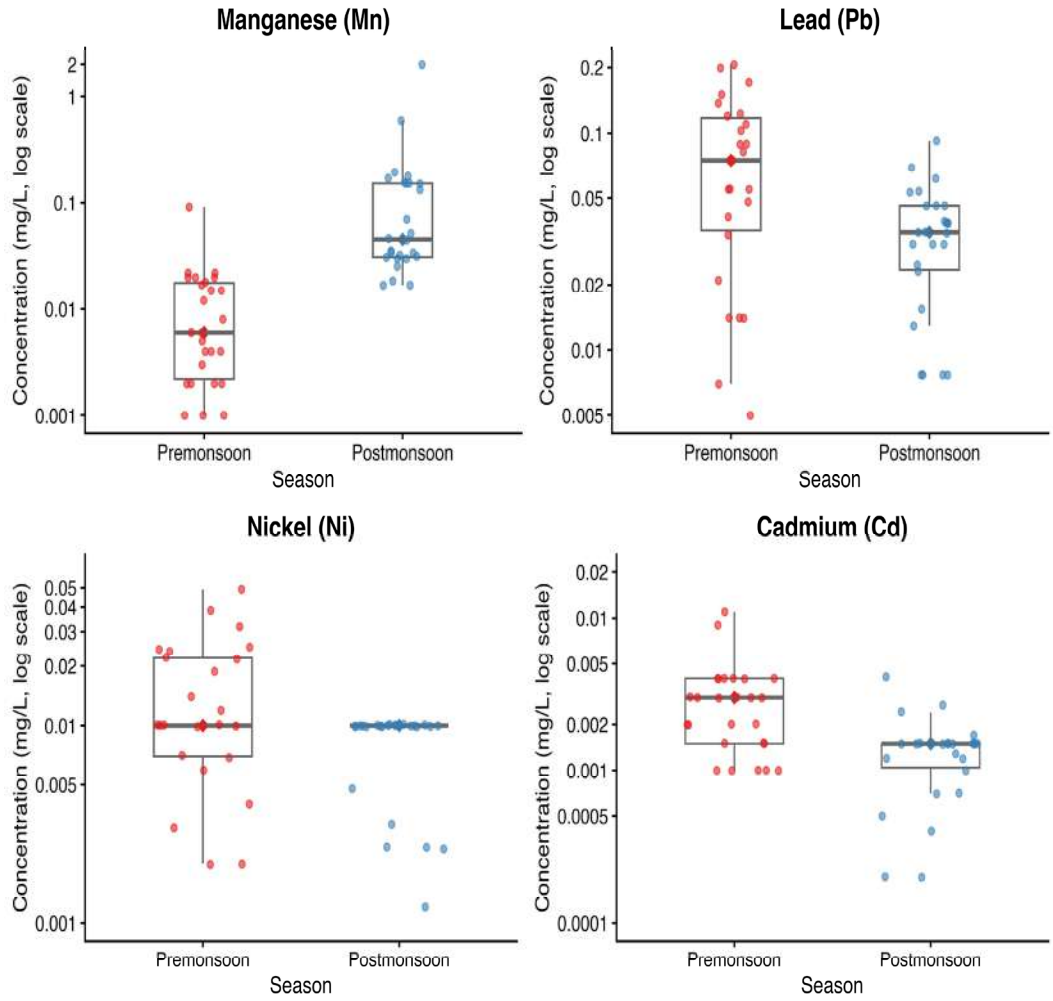


Fig. 3: Box plots showing the concentrations of heavy metals, Manganese (Mn), Nickel (Ni), Lead (Pb), and Cadmium (Cd) that exceed the Bureau of Indian Standards (BIS) permissible limits for domestic use in the study area (all concentrations are in $mg.L^{-1}$).

variable pre-monsoon, with several elevated outliers, while post-monsoon levels decrease markedly, suggesting dilution. Lead (Pb) exhibits a broad distribution and numerous outliers pre-monsoon, reflecting significant spatial variability and potential site-specific pollution, whereas post-monsoon levels are lower and less variable. Nickel (Ni) shows a wide distribution and multiple outliers pre-monsoon, with a median slightly higher than post-monsoon; the reduced levels in the latter may be due to rainfall-induced dilution or decreased industrial inputs.Bottom of Form

The highest recorded concentration of lead in the study area was 0.206 $mg.L^{-1}$ during the pre-monsoon season and 0.092 $mg.L^{-1}$ in the post-monsoon season, both observed in Sample No. S26 (Nalgedra area, near the Star Cement Plant). Cadmium concentrations were 0.011 $mg.L^{-1}$ and 0.0041 $mg.L^{-1}$ in the pre- and post-monsoon seasons, respectively, recorded in Sample No. S1 (Jorabat, near the Raksha Cement Plant). Manganese reached its maximum concentration of 1.983 $mg.L^{-1}$ during the post-monsoon period in Sample No. S4 (Nazirakhat, near Raksha and Star Cement Plants), while pre-monsoon levels remained below the permissible limit. The highest concentration of nickel was 0.049 $mg.L^{-1}$ in the pre-monsoon season, observed in Sample No. S15 (Samota Pathar, near the Star Cement Plant), with post-monsoon levels falling below the permissible threshold (Fig. 4). The concentrations of Chromium (Cr), Arsenic (As), Copper (Cu), Zinc (Zn), and Iron (Fe) were found to be within the prescribed permissible limits during both seasons.

The color scale (Fig. 5) depicts Pearson's correlation coefficients (r) ranging from –1, indicating a strong negative correlation (blue), to +1, indicating a strong positive correlation (red). During the pre-monsoon season, metals

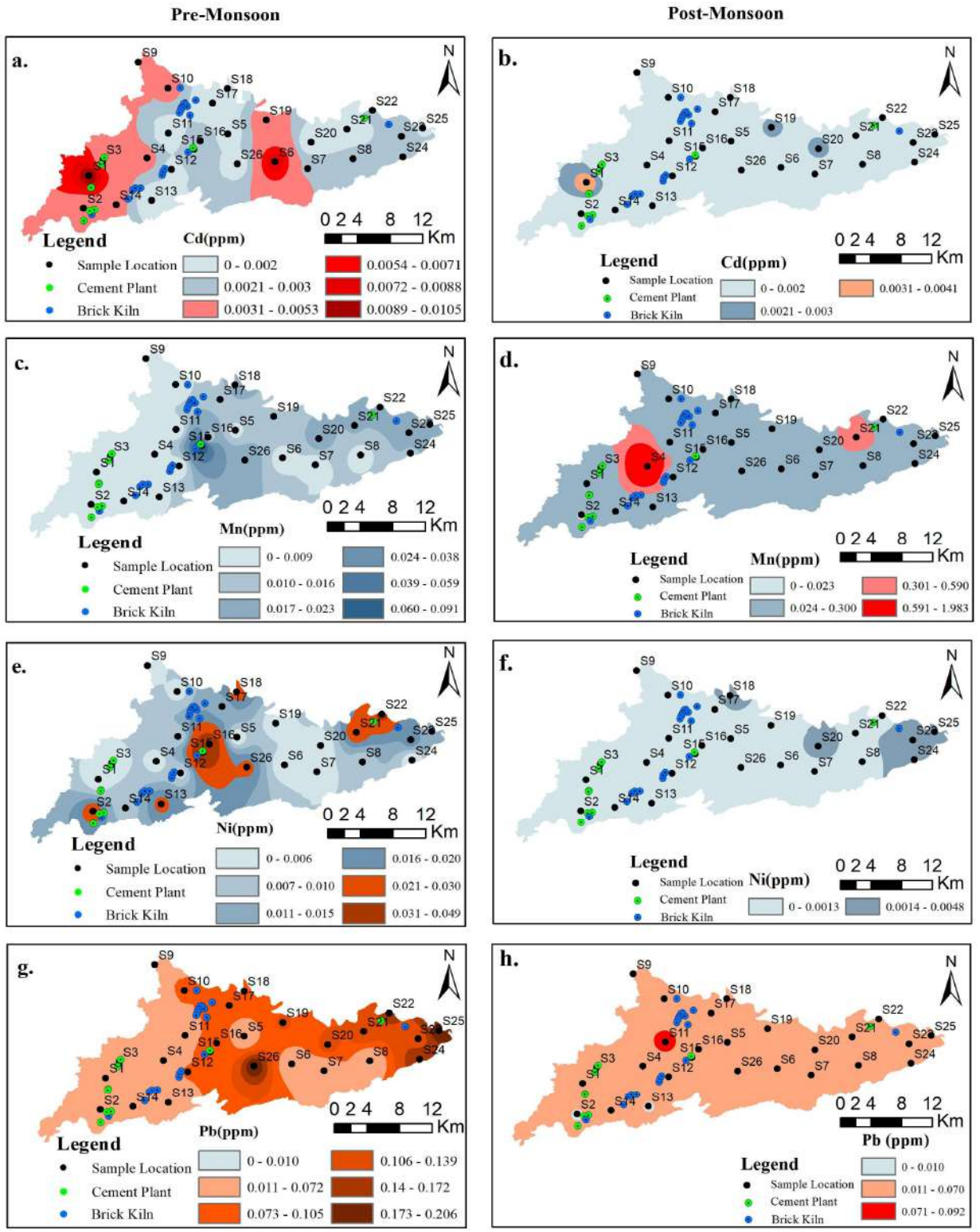


Fig. 4: The geospatial distribution maps illustrate the spatial and seasonal variation in the concentrations of heavy metals- Cadmium (Cd), Manganese (Mn), Nickel (Ni), and Lead (Pb)- across the study area during both pre- and post-monsoon seasons (all concentrations are in ppm).

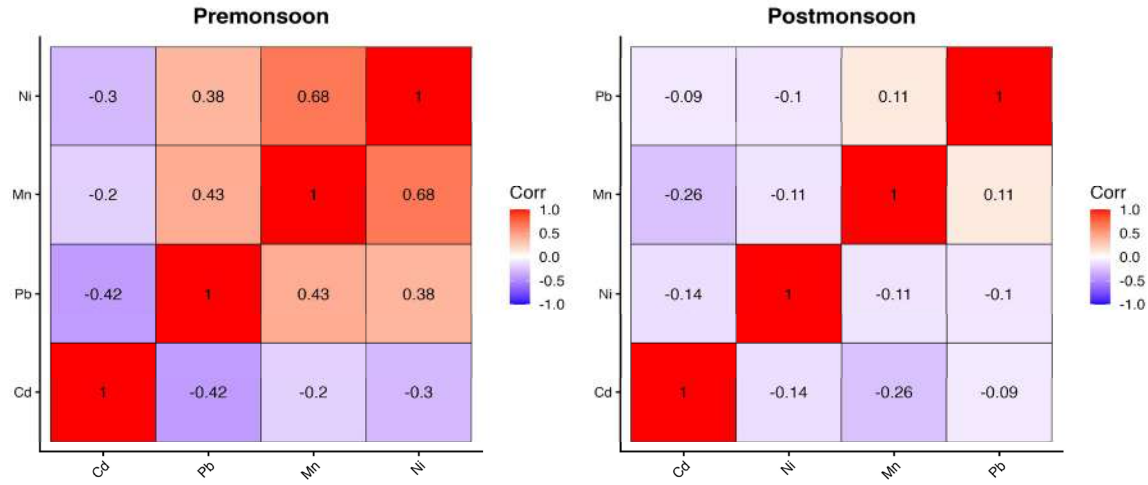


Fig. 5: Seasonal correlation matrices of heavy metals (Mn, Pb, Ni, and Cd) in groundwater samples during pre-monsoon and post-monsoon seasons, generated using RStudio (version 2024.04.2+764).

Table 2: Interpretation of Metal Index (MI) value of the heavy metals analysed.

Metal Index (MI) Range	No. of locations affected (Pre-Monsoon)	No. of locations affected (Post-Monsoon)	Water Quality Status
MI < 1	Nil	Nil	Good (no significant pollution)
1 ≤ MI < 2	01	03	Slightly affected
2 ≤ MI < 4	04	04	Moderately affected
4 ≤ Mi < 6	Nil	12	Strongly affected
Mi ≥ 6	21	07	Seriously affected

Table 3: Interpretation of Heavy Metal Pollution Index (HPI) value (Horton 1965).

(HPI) Range	No. of locations affected (Pre-Monsoon)	No. of locations affected (Post-Monsoon)	Water Quality Status
HPI< 100	04	06	Low/no pollution (safe for drinking)
HPI >100	22	20	High pollution (unsafe for drinking)

such as Mn-Ni and Cd-Pb exhibit moderate to strong positive correlations, implying common anthropogenic or geogenic sources. In contrast, the post-monsoon season shows weaker and more variable correlations, likely due to dilution, leaching, or differential mobilization of metals after rainfall.

The interpretations of the Metal Index (MI) and Heavy Metal Pollution Index (HPI) for the analyzed heavy metals are detailed in Tables 2 and 3. Throughout both seasons, four sites showed MI values ranging from 2 to 4, indicating moderate contamination. In the post-monsoon period, 12 sites exhibited MI values between 4 and 6, categorizing them as significantly affected. Notably, 21 sites in the pre-monsoon season and 7 in the post-monsoon season had MI values of 6 or higher, indicating severe heavy metal contamination. The HPI results revealed that 22 sites in the pre-monsoon season and 20 during the post-monsoon season surpassed the critical threshold, placing them in the high pollution category. These results suggest that the groundwater in these areas is unsafe for drinking without proper treatment.

A statistical summary of the Metal Index (MI) and Heavy Metal Pollution Index (HPI) is provided in Table 4.

The KDE plot (Fig. 6) effectively depicts the seasonal variations in heavy metal contamination of groundwater. It reveals an improvement in water quality after the monsoon, evidenced by decreases in metal levels and shifts in both MI and HPI distributions. The higher HPI values observed before the monsoon indicate increased pollution, while the lower post-monsoon values suggest natural dilution has reduced contamination. These results emphasize the importance of seasonal monitoring for precise evaluation of heavy metal pollution trends and highlight the necessity of implementing robust water quality management and mitigation measures.

Table 4: Statistical summary of Metal Index (MI and Heavy Metal Pollution Index (HPI).

Season	Sample Size (N)	MI_mean	MI_median	MI_mode	MI_sd	MI_se	MI_ci_lower	MI_ci_upper
Post-monsoon	26	4.97	5.14	5.51	2.12	0.42	4.11	5.83
Pre-monsoon	26	9.6	8.69	5.14	5.74	1.12	7.28	11.92
Season	Sample Size (N)	HPI_mean	HPI_median	HPI_mode	HPI_sd	HPI_se	HPI_ci_lower	HPI_ci_upper
Post-monsoon	26	147.94	147.73	141.17	59.97	11.76	123.72	172.17
Pre-monsoon	26	270.54	258.03	264.91	158.75	31.13	206.42	334.66

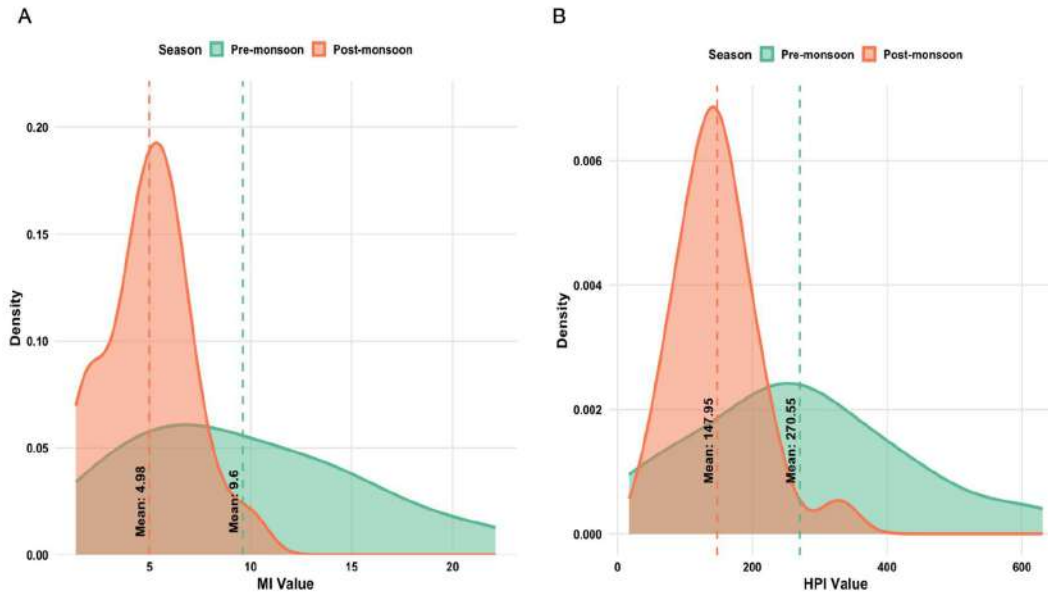


Fig 6: Kernel Density Estimation (KDE) plot using RStudio (version 2024.04.2+764) for [A] Metal Index (MI) values and [B] Heavy Metal Pollution Index (HPI) values in groundwater samples (n=26), comparing pre- and post-monsoon seasons [Dashed Vertical Lines indicate the mean MI values for each season].

The GIS-based geospatial maps illustrating the Metal Index (MI) and Heavy Metal Pollution Index (HPI) in groundwater within the study area clearly depict seasonal variations in heavy metal contamination (Fig. 7). The pre-monsoon period exhibits widespread and severe pollution, indicating substantial heavy metal accumulation. Conversely, post-monsoon maps reveal localized improvements in groundwater quality, particularly in areas such as S2 and S14, due to dilution and flushing effects of rainfall. These spatial patterns are consistent with the statistical findings and emphasize the importance of seasonal monitoring. Additionally, the results underscore the need for spatially targeted mitigation and remediation strategies to effectively address and reduce heavy metal pollution in groundwater sources. Spatial interpolation of the Metal Index (Table 5) indicates that the area can be classified into four categories in both seasons. During pre-monsoon, approximately 78% of the area falls into the seriously affected class, while in the post-monsoon, the strongly affected class dominates at 69%. Similarly, based on the Heavy Metal Pollution Index (Table 6), the area can be divided into high and low pollution zones, with 97% of the pre-monsoon region showing high pollution levels, and 95% of the post-monsoon region also falling under high pollution.

3.1. Discussion

In the study area, cadmium and lead concentrations exceeding permissible limits are of particular concern due to their potential to cause severe health effects, especially in children and pregnant women. Cadmium (Cd) is classified as a Group 1 carcinogen (WHO 2017), and among the most hazardous and highly mobile elements in the environment (Alloway & Jackson1991, Nies 1999, 2003). Short-term exposure to high levels of cadmium in drinking water may cause vomiting and diarrhea. (US EPA 2023). The use of wastes as alternative fuels or raw materials in cement kilns introduces additional trace elements such as cadmium, lead, etc. into the system, especially from sources like sewage sludge, tires, and certain slags (WBCSD 2014). Acute cadmium ingestion can cause renal dysfunctions, hepatic

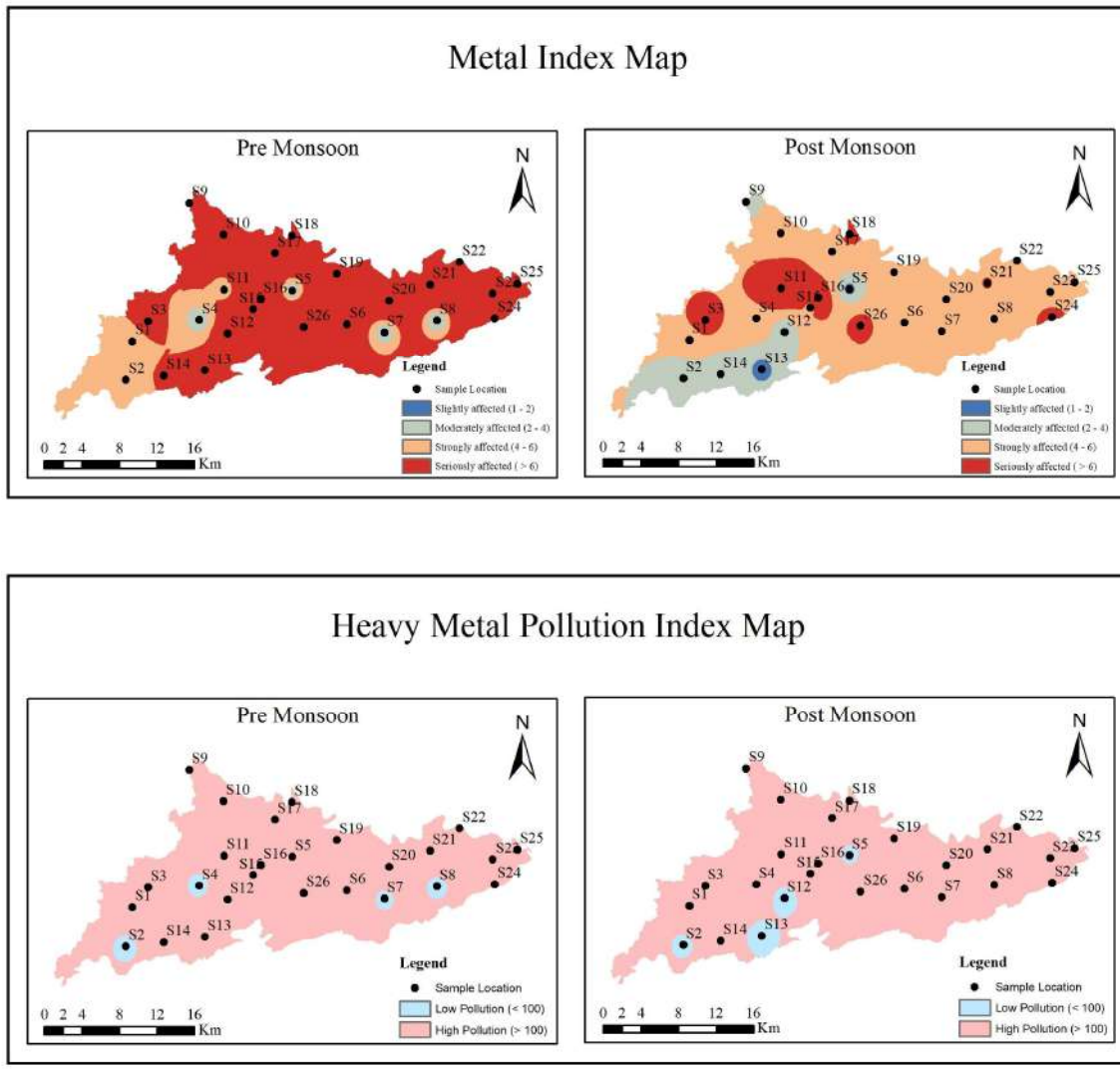


Fig 7: Geospatial distribution of Metal Index (MI) and Heavy Metal Pollution Index (HPI) of groundwater within the study area for the pre-monsoon and post-monsoon periods.

Table 5: Spatial distribution of Metal Index.

Class	Pre Monsoon		Post Monsoon	
	Area [Sq. km]	Percentage	Area [Sq. km]	Percentage
Slightly affected	0.16	0.03	4.69	0.88
Moderately affected	12.24	2.30	86.98	16.34
Strongly affected	105.96	19.90	369.38	69.37
Seriously affected	414.10	77.77	71.39	13.41

Table 6: Spatial distribution of Heavy Metal Pollution Index.

Class	Pre Monsoon		Post Monsoon	
	Area [Sq. km]	Percentage	Area [Sq. km]	Percentage
Low Pollution	16.70	3.14	25.38	4.77
High Pollution	515.75	96.86	507.07	95.23

injury, osteomalacia, pulmonary edema, and gastrointestinal tract erosion, depending on the route of poisoning (Baselt 2000). In the human body, cadmium mainly builds up in the kidneys, with a biological half-life ranging from 10 to 35 years. Lead (Group 2A) has been considered for centuries as a cumulative metabolic poison and neurotoxic (ATSDR 2020, WHO 2017, Adepoju-Bello & Alabi 2005, Achternbosch et al. 2003, Center for Disease Control and Prevention, Atlanta 2001, ATSDR 2020). Lead compounds cause kidney tumors and other cancers in experimental animals (IARC 2006 & 2012). Nickel is classified as a Group 2B carcinogen by the IARC. Prolonged exposure to elevated levels can cause dermatitis (skin irritation), respiratory issues, kidney and cardiovascular problems, and it has potential carcinogenic effects at high doses. Though an essential nutrient, excessive Mn (>0.3 $mg.L^{-1}$) can lead to neurological problems, especially in children (WHO 2017). Manganese is found as Mn^{2+} in groundwater under reducing conditions. Mn^{2+} is highly soluble and mobile in reducing low pH environments. Under oxidizing conditions, e.g., at the water table, Mn oxidizes to Mn^{4+} or Mn^{3+} and precipitates as oxides, resulting increasing risk of contamination. In reducing conditions, Mn^{2+} may exceed permissible limits in groundwater, requiring treatment before consumption.

In the study area, pH in groundwater varies from slightly acidic to alkaline conditions (5.22–7.23). Lead in groundwater is commonly found as Pb^{+2} at low to neutral pH, at higher pH (≥ 8), lead precipitates as $Pb(OH)_2$, reducing its solubility. Cadmium (Cd) remains in aqueous solution primarily in the form of Cd^{+2} ions, and its solubility is strongly pH-dependent, at a pH of less than 6.5 and under oxygenated conditions (Kubier et al. 2019). The distribution of Cd and Pb in groundwater serves as a tracer for anthropogenic impact**,** particularly in industrial or urbanized regions. Their behaviour reflects the integrated effects of lithology, hydrology, and land-use patterns, making them important indicators in hydrogeochemical and environmental assessments. Moreover, industrial effluents, agricultural runoff, and waste disposal can alter natural hydrogeochemical conditions, enhancing the metal contamination. The lithology of the study area strongly influences heavy metal retention and migration. Fine-grained units such as sand, silt, pebble, and clay**,** along with gneiss**,** exhibit higher adsorption capacity, promoting retention of metals like Pb, Cd, Ni, and Mn through binding to clay minerals and oxides. In contrast, loamy sand and weathered porphyritic granite have higher permeability and lower adsorption potential, facilitating greater metal mobility in groundwater.

Overall, formations rich in clay and with low permeability act as sinks, while coarse, permeable, or fractured lithologies function as pathways for heavy metal transport, particularly under near-neutral pH conditions. Cement manufacturing facilities in the area may release cadmium, lead, and nickel into the environment. These toxic metals are naturally present in raw materials such as limestone, clay, and shale used for cement production. During the high-temperature processing (~1450°C) in rotary kilns, these metals can volatilize and become airborne, eventually settling on soil, surface water, and groundwater. Additional contamination sources include additives, fuels, and waste materials—such as used tires and industrial waste—in both cement and brick kilns. Improper disposal of cement kiln dust, fly ash, bottom ash, and fuel residues further exacerbates heavy metal contamination through leaching into nearby soil and shallow groundwater.

High contamination is not uniform across the aquifer but concentrated near industrial clusters, indicating point-source or localized anthropogenic inputs rather than widespread geogenic leaching. The measured pH in groundwater in the study area (6.30–7.49) further reduces the likelihood of dominant geogenic origins, as the gneissic basement and overlying alluvial sediments are not typically significant sources of Pb or Cd under near-neutral conditions (Martinez & Motto 2000, Alloway & Jackson 1991). Under such pH ranges, the solubility and mobility of Pb^{2+} and Cd^{2+} from natural lithological sources are generally low, making anthropogenic inputs the more plausible primary contributors to the observed contamination. Regular groundwater monitoring and stricter regulation of waste fuels in kilns are vital for protecting the environment and public health. Continuous monitoring helps detect contamination early, guide remediation, and support evidence-based policies. At the same time, enforcing strict controls on waste fuel use—through permits, emission limits, quality standards, and mandatory EIAs ensures sustainable industrial practices that minimize pollution and safeguard natural resources.

4. CONCLUSIONS

This study demonstrates that utilizing both Index-Based Evaluation (MI and HPI) and GIS-based geospatial mapping offers a comprehensive approach to assessing cumulative heavy metal contamination in groundwater. In the study area, lead (Pb) levels surpassed permissible limits in 92% of pre-monsoon samples and 85% of post-monsoon samples, while cadmium (Cd) exceeded limits in 54% of pre-monsoon samples and 4% of post-monsoon samples. A total of 21 sites during pre-monsoon and 7 sites during post-monsoon were identified as seriously affected (MI $\geq$ 6), with Heavy Metal Pollution Index (HPI) values over 100 at 22 and 20 sites, respectively. These results indicate that Pb and Cd contamination is widespread and persistent across seasons,

with higher exceedances before the monsoon. Nickel (Ni) and manganese (Mn) also pose localized risks, highlighting complex interactions between seasonal changes and both natural and human influences. The high MI and HPI values in the pre-monsoon season suggest pollutant buildup from industrial emissions, whereas the decrease after monsoon reflects dilution and flushing due to monsoonal recharge. The spatial distribution observed in geospatial maps closely corresponds with the locations of industrial units, though minor natural sources cannot be completely excluded. A multi-barrier mitigation strategy, including advanced treatment methods (adsorption, ion exchange, permeable reactive barriers, electrocoagulation, membrane filtration), pollution source control (effluent segregation, process modifications, stormwater management, strict regulation), and institutional support (long-term monitoring, community involvement, capacity building), is recommended to effectively reduce heavy metal contamination in the industrialized regions of the study area.

The methodological framework and results of this study present a transferable model for managing industrially stressed aquifers, facilitating early detection, spatial prioritization, and prompt remediation of heavy metal contamination. These findings have implications beyond the immediate study area. Regionally, they can assist policymakers and water authorities in Assam and similar peri-urban industrial zones across India to implement targeted monitoring, strengthen regulations on industrial discharges, and develop location-specific mitigation strategies. Globally, combining index-based evaluation (IBE) with geospatial mapping offers a replicable tool for assessing groundwater vulnerability in rapidly industrializing regions worldwide, where industries like cement manufacturing and brick kilns pose similar threats to water security. Proactive management, supported by such integrated approaches, is essential to protect groundwater resources, safeguard public health, and promote sustainable growth in urban and industrial areas both locally and internationally. Ultimately, our findings provide valuable insights for environmental monitoring, industrial impact assessment, and groundwater safety, serving as a strategic template for countries at different stages of development facing the challenge of balancing economic growth with water resource conservation.

5. ACKNOWLEDGMENTS

The authors express their sincere gratitude to ICAR-NBSS & LUP, Regional Centre, Jorhat, and State Public Health Laboratory, Commissionerate of Food Safety, Assam, for their valuable support in facilitating the sample analysis.

6. REFERENCES

Achternbosch, M., Richers, U. and Stemmermann, P., 2003. Heavy metals in cement and concrete resulting from the co-incineration of wastes in cement kilns with regard to the legitimacy of waste utilisation. German Federal Environmental Agency (UBA). Retrieved February 10, 2026, from https://www.umweltbundesamt.de

Adepoju Bello, A.A. and Alabi, O.M., 2005. Heavy metals: A review. *The Nigerian Journal of Pharmacy*, 37(1), pp.41-45.

Agency for Toxic Substances and Disease Registry (ATSDR), 2020. *Toxicological Profile for Lead*. U.S. Department of Health and Human Services, Public Health Service, Atlanta, pp.250.

Al-Khashman, O.A. and Shawabkeh, R.A., 2005. Metal distribution in soils around a cement factory in southern Jordan. *Environmental Geochemistry and Health*, 27(4), pp.331-340. [DOI]

Alloway, B.J. and Jackson, A.P., 1991. The behaviour of heavy metals in sewage sludge-amended soils. *Science of the Total Environment*, 100, pp.151-176. [DOI]

American Public Health Association (APHA), 2023. *Standard Methods for the Examination of Water and Wastewater, 24th Ed*. APHA Press, Washington, DC, pp.1500.

Arunakumari, K., Begum, F., Surinaidu, L., Umamaheswari, A. et al., 2023. Persistence of heavy metals and human health risk assessment in the South Indian industrial area. *AQUA - Water Infrastructure, Ecosystems and Society*, 72(6), pp.898-913. [DOI]

Awuah, G.B., Gyasi, R.M., Addae, M.K. and Darko, E.O., 2022. Health risk associated with heavy metals in dust from cement factories in Ghana. *Journal of Environmental and Public Health*, 2022(1), pp.1-10. [DOI]

Backman, B., Bodis, D., Lahermo, P., Rapant, S. and Tarvainen, T., 1998. Application of a groundwater contamination index in Finland and Slovakia. *Environmental Geology*, 36(1-2), pp.55-64. [DOI]

Baselt, R.C., 2000. *Disposition of Toxic Drugs and Chemicals in Men, 5th Ed*. Chemical Toxicology Institute, Foster City, CA, pp.1200.

Borgohain, D., Lanong, S. and Jaishi, H.P., 2024. Heavy metal contamination and health risks in groundwater at Byrnihat industrial area: urgent need for remediation and public health safeguards. *Proceedings of the Indian National Science Academy*, 90, pp.931-942.

Bradl, H., 2002. *Heavy Metals in the Environment: Origin, Interaction and Remediation (Volume 6)*. Academic Press, London, pp.400.

Caeiro, S., Costa, M.H., Ramos, T.B., Fernandes, F., Silveria, N., Coimbra, A. and Painho, M., 2005. Assessing heavy metal contamination in Sado Estuary sediment: an index analysis approach. *Ecological Indicators*, 5(2), pp.151-169. [DOI]

Centre for Disease Control and Prevention (CDCP), 2001. *Managing Elevated Blood and Lead Levels Among Young Children: Recommendations from the Advisory Committee on Childhood Lead Poisoning Prevention*. CDC, Atlanta, pp.100.

Dheeraj, V.P., Singh, C.S., Kishore, N. and Sonkar, A.K., 2022. Groundwater quality assessment in Korba Coalfield region, India: an integrated approach of GIS and heavy metal pollution index (HPI) model. *Nature Environment and Pollution Technology*, 22(1), pp.369-382. [DOI]

European Commission, 2010. *Reference Document on Best Available Techniques (BREF) for the Production of Cement, Lime and Magnesium Oxide*. Integrated Pollution Prevention and Control (IPPC), p.278.

Jazza, S.H., Najim, S.S. and Adnan, M.A., 2022. Using heavy metals pollution index (HPI) for assessment quality of drinking water in Maysan Province in Southern East in Iraq. *Egyptian Journal of Chemistry*, 65(2), pp.703. [DOI]

Kalpana, A., Puppala, R.K. and Maheswaramma, K.S., 2023. An assessment of ground water contamination due to heavy metals and fly ash around Yerraguntla Town, Kadapa District, Andhra Pradesh, India. *Journal of Pollution Effects & Control*, 11(1), pp.1-10. [DOI]

Kaur, M., Kaur, R. and Bhardwaj, R., 2019. Appraisal of heavy metal contents in groundwater and associated health hazards posed to human population of Ropar Wetland, Punjab. *Chemosphere*, 237, pp.124470. [DOI]

Kubier, A., Wilkin, R.T. and Pichler, T., 2019. Cadmium in soils and groundwater: a review. *Applied Geochemistry*, 108, pp.104388.

Ali, H., Khan, E. and Ilahi, I., 2019. Heavy metals in the environment: sources and toxicity. *Journal of Chemistry*, 2019, article 6730305. [DOI]

Horton, R.K., 1965. An index number system for rating water quality. *Journal of the Water Pollution Control Federation*, 37(3), pp.300-306.

International Agency for Research on Cancer (IARC), 2006. *IARC Monographs on the Evaluation of Carcinogenic Risks to Humans, Volume 87: Inorganic and Organic Lead Compounds*. World Health Organization, IARC, Lyon, France, pp.500.

International Agency for Research on Cancer (IARC), 2012. *Arsenic, Metals, Fibres and Dusts. IARC Monographs on the Evaluation of Carcinogenic Risks to Humans, Volume 100 C*. IARC, Lyon, France, pp.300.

Li, J. and Heap, A.D., 2011. A review of comparative studies of spatial interpolation methods in environmental sciences: performance and impact factors. *Ecological Informatics*, 6(3-4), pp.228-241. [DOI]

Martinez, C.E. and Motto, H.L., 2000. Solubility of lead, zinc and copper added to mineral soils. *Environmental Pollution*, 107(1), pp.153-158.

Mehta, R.K. and Mehta, D., 2012. Heavy metal contamination near brick kiln industries in Varanasi, India. *International Journal of Environmental Sciences*, 3(1), pp.293-300.

Mohapatra, M. et al., 2014. Environmental impact of cement production on groundwater quality in India. *Journal of Environmental Science and Engineering*, 56(3), pp.211-218.

Mohan, S.V., Nithila, P. and Reddy, S.J., 1996. Estimation of heavy metal pollution index for groundwater using weighted arithmetic mean method in industrial area of Andhra Pradesh, India. *Environmental Monitoring and Assessment*, 42(1), pp.39-54. [DOI]

Nies, D.H., 2003. Efflux-mediated heavy metal resistance in prokaryotes. *FEMS Microbiology Reviews*, 27(2-3), pp.313-339. [DOI]

Nies, D.H., 1999. Microbial heavy-metal resistance. *Applied Microbiology and Biotechnology*, 51(6), pp.730-750. [DOI]

Prasad, B., Kumari, P., Bano, S. and Kumari, S., 2014. Ground water quality evaluation near mining area and development of heavy metal pollution index. *Applied Water Science*, 4(1), pp.11-17. [DOI]

Prasad, B. and Bose, J., 2001. Evaluation of heavy metal pollution index for groundwater around coal mining area, Yellandu, Khammam district, Andhra Pradesh, India. *Environmental Geology*, 41(1-2), pp.1-9. [DOI]

Reza, R. and Singh, G., 2010. Heavy metal contamination and its indexing approach for groundwater of Sumbal area, Kashmir, India. *Environmental Earth Sciences*, 63(7), pp.1349-1360.

Singh, G. et al., 2010. Assessment of heavy metal contamination in soil around brick kilns in northern India. *Environmental Monitoring and Assessment*, 168(1-4), pp.365-371.

U.S. Environmental Protection Agency (US EPA), 2023. Guidelines for Carcinogen Risk Assessment (EPA/630/P-03/001F). Retrieved February 10, 2026, from https://www.epa.gov/sites/default/files/2013-09/documents/cancer_guidelines_final_3-25-05.pdf

Webster, R. and Oliver, M.A., 2001. *Geostatistics for Environmental Scientists (1st ed.)*. John Wiley & Sons, Chichester, pp.400.

Webster, R. and Oliver, M.A., 2007. *Geostatistics for Environmental Scientists (2nd ed.)*. John Wiley & Sons, Chichester, pp.300. [DOI]

World Business Council for Sustainable Development (WBCSD), Cement Sustainability Initiative, 2014. *Guidelines for Co-processing Fuels and Raw Materials in Cement Manufacturing*. WBCSD, pp.100.

World Health Organization (WHO) and International Agency for Research on Cancer (IARC), 2017. *IARC Monographs on the Evaluation of Carcinogenic Risks to Humans: List of Classifications, Volumes 1–120*. IARC, Lyon, France. Retrieved February 10, 2026, from https://monographs.iarc.who.int/list-of-classifications

Yahaya, M.I., Mohammad, S. and Abdullahi, B.K., 2009. Seasonal variations of heavy metals concentration in Abattoir dumping site in Nigeria. *Journal of Applied Sciences and Environmental Management*, 13(4), pp.9-13.

Nature Environment and Pollution Technology
An International Quarterly Scientific Journal

p-ISSN: 0972-6268
(Print copies up to 2016)
e-ISSN: 2395-3454

Vol. 25 | No. 3 | Article ID D1859 | 2026

Original Research Paper

https://doi.org/10.46488/NEPT.2026.v25i03.D1859

Open Access Journal

Comparison of Optimum Dosages of Biocoagulant and Commercial Coagulant Alum in the Coagulation-Flocculation Process of Tofu Wastewater

Okik Hendriyanto Cahyonugroho[1]†, Nur Laili Alfiatin Mukharomah[2] and Muhammad Rizky Firmansyah[1]

[1]Department of Environmental Engineering, Faculty of Engineering and Science, Universitas Pembangunan Nasional Veteran Jawa Timur, Surabaya, 60294, Indonesia

[2]Environmental Research Center, Universitas Pembangunan Nasional Veteran Jawa Timur, Surabaya, 60294, Indonesia

†Corresponding author: Okik Hendriyanto Cahyonugroho; okikhc@upnjatim.ac.id

Abbreviation: Nat. Env. & Poll. Technol.
Website: www.neptjournal.com

Received: 15-08-2025
Revised: 16-10-2025
Accepted: 18-11-2025

Key Words:

Biocoagulant
Coagulation-flocculation
Commercial coagulant
Tofu wastewater

Citation for the Paper:

Cahyonugroho, O. H., Mukharomah, N. L. A. and Firmansyah, M. R., 2026. Comparison of optimum dosages of biocoagulant and commercial coagulant alum in the coagulation-flocculation process of tofu wastewater. *Nature Environment and Pollution Technology,* 25(3), D1859. https://doi.org/10.46488/NEPT.2026.v25i03.D1859

Note: From 2025, the journal has adopted the use of Article IDs in citations instead of traditional consecutive page numbers. Each article is now given individual page ranges starting from page 1.

Copyright: © 2026 by the authors
Licensee: Technoscience Publications
This article is an open access article distributed under the terms and conditions of the Creative Commons Attribution (CC BY) license (https://creativecommons.org/licenses/by/4.0/).

ABSTRACT

The tofu industry produces wastewater containing organic matter, suspended solids, and high nitrogen compounds that have the potential to pollute the environment. This research compares the effectiveness of natural biocoagulants derived from maggot shells and moringa seeds with commercial alum coagulants in the coagulation-flocculation process of tofu wastewater. The novelty of this research lies in the use of maggot shells, which are biomass waste, as a natural coagulant. Until now, maggot shells have rarely been used in wastewater treatment, unlike moringa seeds, which have been extensively researched and proven to be effective due to their 44.8% cationic protein content. The research methods included the production of biocoagulants, the determination of the optimum dose through jar tests, and the analysis of pH, TSS, turbidity, and color parameters. The results indicated that all coagulants effectively reduced TSS, turbidity, and color levels. The alum coagulant demonstrated the highest efficiency, achieving 98.66% TSS removal, 86.67% turbidity removal, and 96.17% color removal at an optimal dose of 250 mg.L^{-1}. The moringa seed biocoagulant achieved a comparable performance with 98.66% TSS, 86.67% turbidity, and 96.17% color removal at 150 mg.L^{-1}. In contrast, the maggot shell biocoagulant showed moderate efficiency, removing 83.89% TSS, 74.96% turbidity, and 77.48% color removal at 150 mg.L^{-1}.

1. INTRODUCTION

The rapidly growing tofu industry in Indonesia has resulted in high demand for soybean-based products, producing wastewater with high levels of organic matter, suspended solids, and nitrogen compounds that have the potential to pollute the environment if not treated (Anifah et al. 2024). This wastewater contains organic matter that causes high levels of suspended particles, mainly from the release of skin residues and fine organic particles during the soybean boiling process (Pramaningsih et al. 2022). In addition, the turbidity level of tofu wastewater, which reaches 238–294 NTU, is also caused by the release of colloidal particles and organic matter during processing (Anifah et al. 2024).

In response to this pollution challenge, the use of synthetic coagulants such as alum has become common in water treatment due to its high efficiency and relatively low cost. However, excessive use of alum can leave residues and pose risks to human health and the environment (Ramakrishnan & Sathiyamoorthy 2025). As a more environmentally friendly alternative, plant- and animal-based biocoagulants are now being developed because they contain functional groups such as hydroxyl, carboxylic acid, and amine, which play an important role in the coagulation-flocculation process, thereby increasing the efficiency of various types of wastewater treatment (Kurniawan et al. 2020). Previous research on the use of

biocoagulants in wastewater treatment has shown a 97% reduction in turbidity (Bouchareb et al. 2021).

The performance of coagulants in reducing suspended particles is known to be greatly influenced by dosage, type of coagulant, pH, and stirring intensity (Aragaw & Bogale 2023). Various types of coagulants have been developed, including animal-based, plant-based, and metal salt-based coagulants, each with its own advantages and limitations in terms of effectiveness and environmental impact (Diver et al. 2023). Therefore, this research aims to analyze and compare the performance of three types of coagulants, namely maggot shells as animal-based coagulants, moringa seeds as plant-based coagulants, and alum as metal salt-based coagulants, in reducing color, turbidity, and total suspended solids (TSS) in tofu wastewater.

2. MATERIALS AND METHODS

The samples used in this research were wastewater from the tofu production process in Waru, Sidoarjo. All samples were taken at the same time and from the same source to maintain the consistency of the wastewater characteristics. The treatment process was carried out using the coagulation-flocculation method with two types of natural biocoagulants, namely moringa seeds and maggot shells, with alum used as a commercial coagulant comparator.

This research used three replications for each dose variation to ensure consistency in the test results. The coagulant solution was prepared in three concentration variations, namely 50 $mg.L^{-1}$, 100 $mg.L^{-1}$, and 150 $mg.L^{-1}$ for moringa seeds and maggot shells, and 150 $mg.L^{-1}$, 200 $mg.L^{-1}$, and 250 $mg.L^{-1}$ for alum. The coagulation-flocculation test was conducted using the jar test method in accordance with SNI 19-6449-2000, using a sample volume of 1000 mL. The process included rapid stirring at 120 rpm for 1 minute, slow stirring at 40 rpm for 20 minutes, and sedimentation for 20 minutes. In this research, no pH adjustment was performed before or after the coagulation-flocculation process.

The supernatant from the sedimentation was analyzed to evaluate the effectiveness of the coagulant in reducing turbidity and total suspended solids (TSS). The water quality parameters measured included pH (SNI 06-6989.11-2004), TSS (SNI 06-6989.3-2004), color (SNI 6989.80-2011), and turbidity (SNI 06-6989.25-2005). The data from the coagulation-flocculation effectiveness test were statistically analyzed using one-way ANOVA to determine significant differences between variations in dosage and type of coagulant on water quality parameters (TSS, color, and turbidity). The effectiveness of the photocatalysis process was evaluated through the calculation of the removal percentage using the formula:

$$\%\text{removal} = \frac{C0 - Ct}{C0} \times 100\% \quad \ldots(1)$$

Description:

C_o represents the initial concentration

C_t represents the concentration at time t

3. RESULTS AND DISCUSSION

3.1. Characteristics of Tofu Wastewater

Previous research has reported that tofu wastewater typically has a low pH due to the use of acetic acid during production (Pangestika & Saksono 2018). Another study showed that the pH value of tofu wastewater was 5.08 (Djari & Asyfiradayati 2024). The TSS value in tofu wastewater is 1,166.67 $mg.L^{-1}$ (Nora et al. 2023). Most of the suspended solids content is produced during the soybean boiling process, where skin residues and fine organic particles are released during tofu and tempeh production (Pramaningsih et al. 2022). In addition, the high turbidity, ranging from 238 to 294 NTU, is also caused by the release of colloidal particles and organic matter during tofu processing (Anifah et al. 2024). Based on Table 1 and the results of previous studies, these levels are still above the quality standards. The quality standards for tofu industry wastewater are regulated under East Java Governor Regulation No. 72 of 2013 concerning Wastewater Quality Standards for Industries or Other Business Activities.

3.2. Comparison of Coagulant Effectiveness on Wastewater Quality Parameters

To provide a comprehensive understanding of the performance of coagulants in industrial tofu wastewater treatment, this section presents a comparative analysis of their effectiveness based on various quality parameters, including pH variation, turbidity reduction, total suspended solids (TSS) removal, and color reduction. The evaluation was conducted using different doses of biological coagulants from maggot shells and moringa seeds at concentrations of 50 $mg.L^{-1}$, 100 $mg.L^{-1}$, and 150 $mg.L^{-1}$ as well as alum coagulants at concentrations of 150 $mg.L^{-1}$, 200 $mg.L^{-1}$, and 250 $mg.L^{-1}$. These dosage variations were determined based on the optimum dosage for each coagulant. Through

Table 1: Results of preliminary tests on Tofu wastewater before treatment.

Parameters	Units	Test Results	Quality Standards
pH	-	4,8	6,0 – 9,0
TSS	$mg.L^{-1}$	2,980	100
Turbidity	NTU	1,208	-
Color	Pt-Co	2,225	-

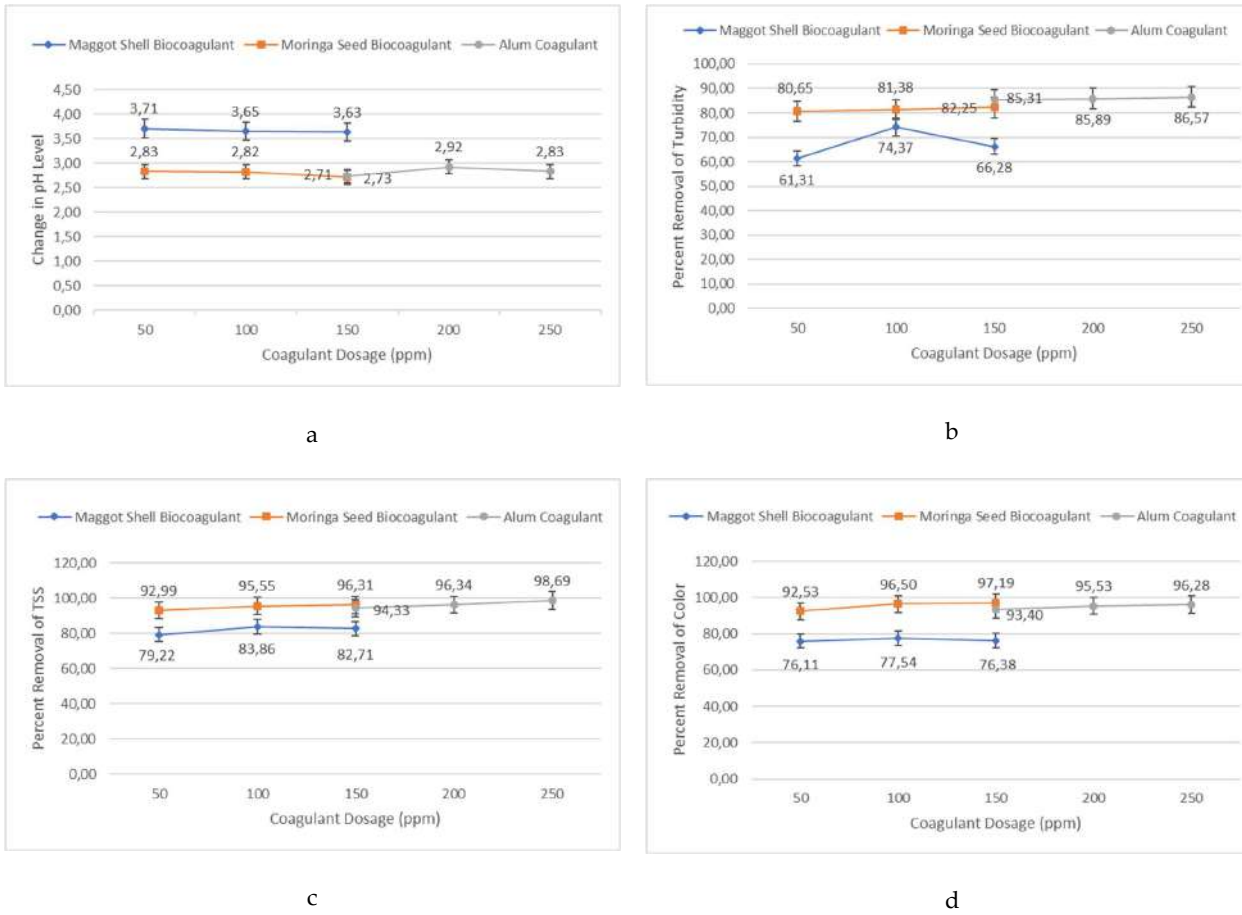


Fig. 1: Comparison of decreases in (a) pH, (b) turbidity, (c) TSS, and (d) color.

this approach, the research aimed to reveal the relationship between coagulant dosage and improvements in wastewater quality parameters, thereby identifying the most effective and environmentally friendly coagulant formulation. The following sections present changes in pH, along with decreases in turbidity, TSS, and color values.

3.2.1. The Effect of Coagulant Type Variations on pH

The initial pH value of tofu wastewater before coagulation-flocculation was 4.8, which is considered acidic. After treatment with various types and doses of coagulants, there was a decrease in pH that varied depending on the type and concentration of the coagulant.

Fig. 1 point (a) shows a graph depicting the pH results after the coagulation-flocculation process using maggot shell and moringa seed biocoagulants, as well as the commercial coagulant alum. For the maggot shell biocoagulant, the final pH decreased to 3.72, 3.69, and 3.68 for doses of 50 mg.L^{-1}, 100 mg.L^{-1}, and 150 mg.L^{-1}, respectively. This decrease indicates that this coagulant is sufficiently acidic. A similar trend was observed for the moringa seed biocoagulant, with final pH values of 2.86, 2.86, and 2.78 at the same doses of 50 mg.L^{-1}, 100 mg.L^{-1}, and 150 mg.L^{-1}. These values indicate a more drastic pH decrease compared to other coagulants. Meanwhile, the pH of the alum coagulant ($Al_2(SO_4)_3$) had final pH values of 2.78, 2.91, and 2.83 at doses of 150, 200, and 250 mg.L^{-1}. Although it still decreased, the pH with the alum coagulant also increased at doses of 200 mg.L^{-1} and 250 mg.L^{-1}.

The more pronounced pH decrease observed in the moringa seed treatment can be explained by its chemical composition, particularly the presence of proteins containing amino and carboxyl functional groups. The amino acids present in moringa seed proteins can accept protons from water and release hydroxyl group ions, leading to basic buffering behavior. However, the decrease in pH of the treated wastewater in this research might be attributed to the presence of low-molecular-weight proteins that carry positive charges. These positively charged proteins interact with negatively charged particles such as silt, clay, and other colloidal

impurities, resulting in proton exchange and a subsequent reduction in pH. The active cationic proteins and carboxyl groups in the seed structure contribute to charge neutralization and effective destabilization of colloids, which enhances coagulation efficiency but simultaneously promotes a stronger pH drop compared to other coagulants (Basra et al. 2014).

Fig. 1 point (a) shows that all types of coagulants cause a decrease in the pH of tofu wastewater. Maggot shell biocoagulant produced the lowest pH of 3.68 at a dose of 150 mg.L^{-1}, while moringa seed biocoagulant and alum coagulant both produced the lowest pH of 2.78 at the same dose of 150 mg.L^{-1}. If the environmental pH aligns with the optimal pH of the coagulant used, the floc formation process will occur more efficiently, thereby significantly impacting the reduction of pollutant parameters such as total suspended solids (TSS) and turbidity levels (Hutabarat et al. 2022). However, using coagulants in excess of the optimum dose can increase impurities in the water and cause saturation of the colloid surface. This condition will result in particle instability and the formation of repulsive forces between the contaminants and the coagulants, thereby inhibiting the floc formation process (Patchaiyappan & Devipriya 2021).

3.2.2. The Effect of Coagulant Type Variations on Turbidity

Turbidity indicates the presence of various organic and inorganic materials in water, such as sludge or pollutants from industrial wastewater (Kastali et al. 2021). The initial turbidity value of the tofu wastewater was 1,208 NTU, indicating that the wastewater had a very high turbidity level. After the coagulation-flocculation process, there was a decrease in turbidity with all types of coagulants.

Fig. 1 point (b) shows a graph depicting the percentage of turbidity removal after the coagulation-flocculation process using maggot shell and moringa seed biocoagulants, as well as the commercial coagulant alum. The maggot shell bioflocculant produced final turbidity values of 463.5 NTU, 302.5 NTU, and 400.5 NTU at doses of 50 mg.L^{-1}, 100 mg.L^{-1}, and 150 mg.L^{-1}, respectively. The highest turbidity removal percentage occurred at a dose of 100 mg.L^{-1}, amounting to 74.96%. This indicates that the optimal dose for the maggot shell bioflocculant is 100 mg.L^{-1}. The moringa seed bioflocculant showed better results, with final turbidity values of 241.5 NTU, 228 NTU, and 217 NTU for doses of 50 mg.L^{-1}, 100 mg.L^{-1}, and 150 mg.L^{-1}, respectively. The highest turbidity removal percentage occurred at a dose of 100 mg.L^{-1}, which was 82.04%. This indicates that the optimal dose for the moringa seed bioflocculant is 150 mg.L^{-1}. Meanwhile, the alum coagulant showed the highest removal, with final turbidity values of 180.5 NTU, 169.5 NTU, and 161 NTU for doses of 150 mg.L^{-1}, 200 mg.L^{-1}, and 250 mg.L^{-1}, respectively. The highest turbidity removal percentage occurred at a dose of 250 mg.L^{-1}, which was 86.67%. This indicates that the optimal dose for the alum coagulant is 250 mg.L^{-1}.

Based on the research results, all types of coagulants were able to reduce turbidity, with the alum coagulant showing the highest effectiveness, followed by moringa seeds and maggot shells. The effectiveness of alum is due to its high aluminum sulfate ($Al_2(SO_4)_3$) content, which has a high positive charge, enabling it to quickly neutralize the negative charge of colloidal particles and form dense flocs through the sweep flocculation mechanism. Research conducted by Akutteh et al. (2022) showed that the use of alum at a dose of 80 mg.L^{-1} with a pH value of 7.5 was able to remove turbidity by up to 82.3% (Akutteh et al. 2022). This advantage makes alum still widely used as a commercial coagulant to effectively reduce TSS and turbidity, despite its disadvantage of potentially leaving metal residues in treated water (Purnomo 2023).

3.2.3. The Effect of Coagulant Type Variation on Total Suspended Solids (TSS)

Tofu wastewater contains 2,980 mg.L^{-1} of TSS, which exceeds the TSS quality standard of 100 mg.L^{-1} as stipulated in East Java Governor Regulation No. 72 of 2013. After undergoing coagulation-flocculation, all types of coagulants used were able to reduce the TSS level.

Fig. 1 point (c) shows a graph depicting the percentage of TSS removal after the coagulation-flocculation process using maggot shell biocoagulants and moringa seeds, as well as commercial coagulants such as alum. The maggot shell biocoagulant produced final TSS values of 610 mg.L^{-1}, 480 mg.L^{-1}, and 510 mg.L^{-1}, with the highest removal percentage at a dose of 100 mg.L^{-1}, which was 83.89%. The moringa seed bio-flocculant showed lower removal results, with final TSS values of 210 mg.L^{-1}, 130 mg.L^{-1}, and 117 mg.L^{-1}, with the highest removal percentage at a dose of 150 mg.L^{-1}, which was 96.31%. Meanwhile, alum showed the lowest removal results, with final TSS values of 170 mg.L^{-1}, 110 mg.L^{-1}, and 40 mg.L^{-1}, with the highest removal percentage at a dose of 250 mg.L^{-1}, which was 98.66%.

Aluminum sulfate demonstrated the highest efficiency in reducing TSS in tofu wastewater compared to natural coagulants. The positively charged aluminum ions released by aluminum sulfate neutralize the negative charge of colloidal particles and trigger the formation of compact flocs that settle easily. This process improves the efficiency of separating suspended solids from the liquid phase through the sweep flocculation mechanism (Tahraoui et al. 2024).

3.2.4. The Effect of Coagulant Type Variations on Color

The initial color of the tofu wastewater, which has a value of 2,225 Pt-Co, indicates a high content of dissolved organic

compounds. This color originates from proteins, phenolic compounds, and other organic components produced during the tofu production process (Putro et al. 2021).

The effectiveness of color removal by coagulants was tested based on the decrease in Pt-Co values. The maggot shell biocoagulant produced final color values of 534, 501, and 522 Pt-Co, with the best removal efficiency of 77.48% at a dose of 100 mg.L^{-1}. The biocoagulant from moringa seeds showed significantly better results, with final color values of 177 Pt-Co, 79.5 Pt-Co, and 60.7 Pt-Co, achieving the highest removal efficiency of 97.27% at a dose of 150 mg.L^{-1}. Meanwhile, the alum coagulant produced final color values of 151.7 Pt-Co, 100 Pt-Co, and 85.3 Pt-Co, with the best removal efficiency of 96.17% at a dose of 250 mg.L^{-1}.

The color reduction shows the difference in tofu wastewater before and after the coagulation-flocculation process. This process demonstrates the successful removal of suspended and dissolved solid fractions, including sludge, organic compounds, and microorganisms that contribute to the high initial Pt-Co value. This process occurs through the destabilization of negatively charged colloidal particles by the positive charge of the coagulant, followed by the formation of flocs that trap the components causing color. Research conducted by Anifah et al. (2024) shows that the use of cempedak seed extract as a natural coagulant can significantly reduce turbidity, TSS, and color values in tofu wastewater, supporting the interpretation that color parameters can be used as an indicator of the effectiveness of the coagulation-flocculation process (Anifah et al. 2024).

Color removal efficiency increases with the addition of coagulant doses up to 25 g.L^{-1}, at which point the moringa seed biocoagulant is able to reach optimum conditions by causing suspended particles and dye molecules in wastewater to coagulate into larger flocs (Rendana et al. 2025). The flocs then settle, while the dye molecules attach to their surface and are eliminated from the wastewater (Ibrahim et al. 2021). Moringa seed biocoagulant works by neutralizing the negative charge on dye molecules and suspended particles, resulting in aggregation and particle removal. An adequate coagulant dose is very important to achieve optimal color removal efficiency, while an excessive dose can actually reduce its performance (Desta & Bote 2021). In this research, the highest color removal efficiency achieved was around 89% (Rendana et al. 2025).

3.3. The Effect of Coagulant Type Variations on Floc Density

Floc density is an important parameter that determines the sedimentation rate and overall efficiency of the coagulation-flocculation process. The denser the structure of the floc formed, the faster it settles, thereby improving the removal of turbidity, total suspended solids (TSS), and color in wastewater (Teh et al. 2016). Floc density can be observed from the zeta potential value, which is close to zero (Fitri et al. 2019). The variation in floc density observed in this research was greatly influenced by the type of coagulant used.

3.3.1. Characteristics of Floc Using Maggot Shell Biocoagulant

The zeta potential test was conducted to analyze colloid stability, where values close to the isoelectric point indicate a decrease in particle stability and a tendency for aggregation or floc formation. The results of this test provide a comprehensive empirical basis for evaluating the effectiveness of maggot shell biocoagulants in reducing the stability of dissolved particles, as well as a reference for determining optimal performance in the treatment of Jagir River water.

Based on the zeta testing results in Fig. 2 point (a), the average zeta potential value was 8.8 mV, with a standard deviation of 19.67. The standard deviation value was much greater than the mean, indicating large fluctuations between repetitions. The positive zeta potential value is caused by the surface charge, which is dominated by chitosan, so the potential difference between the electrical double-layer system and the medium is positive (Fitri et al. 2019). Overall, the average zeta potential value of 8.8 mV is classified as low, indicating that the colloid is in an unstable condition. This value range (0 to ±30 mV) indicates that the repulsive force between particles has weakened, facilitating the process of destabilization and floc formation (Fitri et al. 2019).

The maggot shell biocoagulant, derived from chitosan, primarily functions through weak charge neutralization. Under acidic conditions, the amino groups ($–NH_2$) on chitosan become protonated to form $–NH_3^+$, enabling limited interaction with negatively charged colloids. However, due to its lower cationic charge density and partial degree of deacetylation, chitosan from maggot shells exhibits a reduced capacity for bridging and particle entrapment. This results in the formation of lighter and more porous flocs with lower settling velocity compared to those produced by moringa seed and alum coagulants.

3.3.2. Characteristics of Floc Using Moringa Seed Biocoagulant

The zeta potential test was conducted to analyze colloid stability, where values close to the isoelectric point indicate a decrease in particle stability and a tendency for aggregation or floc formation. The results of this test provide a comprehensive empirical basis for evaluating the effectiveness of moringa seed biocoagulants in reducing

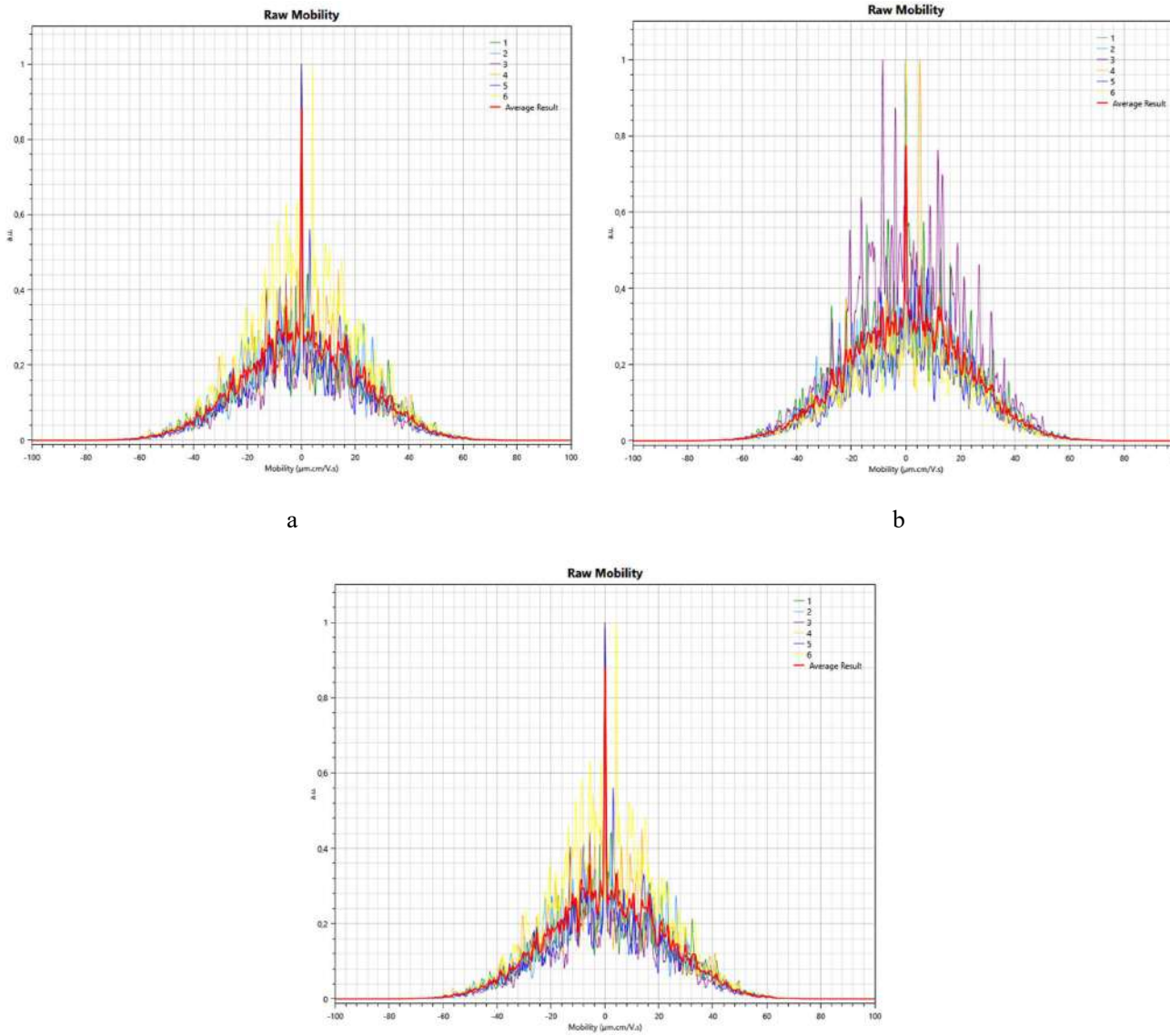


Fig. 2: Zeta potential test of Jagir river water treatment flocs using (a) maggot shell biocoagulant, (b) moringa seed bio-coagulant, and (c) alum coagulant

the stability of dissolved particles, as well as a reference for determining optimal performance in the treatment of Jagir River water.

Based on the results obtained in Fig. 2 point (b), the average zeta potential value was –7.7 mV, with a standard deviation of 51.32. The standard deviation value was much greater than the mean, indicating large fluctuations between repetitions. A negative zeta potential value indicates that the colloidal particles in the suspension still have a dominant negative surface charge. This indicates that the moringa seed biocoagulant works by reducing colloidal stability through a mechanism of partial charge neutralization and polymeric bridging, causing the colloidal particles to undergo destabilization and form flocs. However, the zeta potential value of –7.7 mV is in the low range because, in general, colloid stability is considered to decrease significantly within the range of ±30 mV (Fitri et al. 2019).

The moringa seed biocoagulant operates through a dual mechanism involving both charge neutralization and polymer bridging. The cationic proteins in moringa seeds contain amino (–NH_2) and carboxyl (–COOH) functional groups that interact with negatively charged colloids.

Partial neutralization of charges occurs as these functional groups form electrostatic attractions, while long protein chains act as natural polymers, bridging multiple particles together. This combination produces moderately compact flocs that are stable and settle efficiently even at lower dosages. The moderate zeta potential (–7.7 mV) supports controlled aggregation, preventing excessive repulsion while maintaining bridging capacity, which explains why moringa seed coagulant exhibits near-alum performance in turbidity and TSS removal despite being used at lower concentrations.

3.3.3. Characteristics of Floc Using Alum Coagulant

The zeta potential test was conducted to analyze colloid stability, where values close to the isoelectric point indicate a decrease in particle stability and a tendency for aggregation or floc formation. The results of this test provide a comprehensive empirical basis for evaluating the effectiveness of maggot shell biocoagulants in reducing the stability of dissolved particles, as well as a reference for determining optimal performance in the treatment of Jagir River water (Table 2).

Based on the zeta testing results in Fig. 2 point (c), the zeta potential test results of the alum coagulant in the treatment of Jagir River water were obtained. The average zeta potential value recorded was 0 mV, with a relatively small standard deviation of 2.54 mV. This value indicates that the colloidal system in the Jagir River water is at the isoelectric point, which is a state where the surface charge of the particles is completely neutralized by coagulant ions (Al^{3+} from alum) (Fitri et al. 2019). Under these conditions, the repulsive forces between colloidal particles disappear, facilitating the flocculation process and accelerating the sedimentation of suspended particles. The low standard deviation obtained indicates that the measurement results are quite consistent in each repetition, so the effectiveness of alum as a coagulant can be said to be stable in reducing the zeta potential to reach the optimum point. This shows that the alum dosage used in this test is truly at the optimum dosage, where the system conditions are most conducive to the formation of large flocs that can be easily separated through sedimentation or filtration processes.

In alum-based coagulation, aluminum sulfate ($Al_2(SO_4)_3$) dissociates to produce trivalent aluminum ions (Al^{3+}), which have a high positive charge density. These ions neutralize the negative surface charges of colloidal particles, reducing the zeta potential to near zero (0 mV). Once the charge is neutralized, aluminum hydroxide precipitates [$Al(OH)_3$] are formed, acting as sweep flocs that capture and settle suspended particles. This mechanism, known as charge neutralization and sweep flocculation, results in the formation of compact and dense flocs with high sedimentation rates.

Thus, the overall coagulation-flocculation mechanism shows that the closer the zeta potential is to zero and the higher the floc density, the higher the pollutant removal efficiency. The dual mechanism of Moringa seeds allows them to effectively mimic the performance of alum, while maggot shell coagulants provide an environmentally friendly alternative with optimization potential through chitin modification or mixing approaches.

3.4. Mechanism of Various Coagulation

3.4.1. Mechanism Using Moringa Seed Biocoagulant

Moringa seeds contain cationic proteins and active compounds (4-Alpha-4-Rhamnosyloxy-Benzyl-Isothiocyanate) that are positively charged and have a low molecular weight due to short polymer chains, enabling them to bind particles in water and reduce the repulsive forces between negatively charged colloidal particles. This process causes colloid destabilization and the formation of interconnected flocs. The small particle size of moringa seeds provides a larger surface area, thereby increasing the contact area and effectiveness of interaction between the active substances and colloidal particles (Nenohai et al. 2023). The efficiency of removing turbidity, TSS, and color parameters shown in Fig. 1 occurs because the positively charged cationic proteins in moringa seeds can electrostatically attract and neutralize negatively charged colloidal particles, such as those causing turbidity and TSS, which then form bound flocs. Additionally, these proteins also play a role in precipitating color-causing molecules in water, thereby improving the clarity and quality of the treated water.

3.4.2. Mechanism Using Maggot Shell Biocoagulant

Chitosan in maggot shells can be used in the coagulation-flocculation process because it is a cationic polyelectrolyte and a long-chain polymer with a large molecular weight, made reactive by the presence of amino (NH_2) and hydroxyl (OH) groups that act as electron donors to destabilize particles in water (Sirajudheen et al. 2021). The removal of turbidity and TSS using maggot shell biocoagulants occurs

Table 2: Summary of coagulant performance in Tofu wastewater treatment.

Coagulant Type	Zeta Potential [mV]	Floc Density	Relative Performance
Maggot Shell Biocoagulant	0 (isoelectric point)	Very dense	Highest
Moringa Seed Biocoagulant	–7.7	Moderately dense	Near alum
Alum Coagulant	8,8	Low	Moderate

because chitosan dissolved in an acidic solution activates positively charged groups to neutralize colloidal particles and causes the particles to form large, dense flocs (Ardianto & Amalia 2023). In addition, hydroxyl (OH) and amine (NH_2) groups in chitosan can be protonated under acidic conditions to become (NH_3^+) and (OH^-), thus becoming positively charged and capable of adsorbing or forming hydrogen bonds and complexes with dye molecules (Adilla Safitria & Rahmayanti 2020). This mechanism is also reinforced by chitosan's ability to destabilize particles through electrostatic interactions and hydrogen bond formation (Sirajudheen et al. 2021). The efficiency of turbidity, TSS, and color removal shown in Fig. 1 occurs due to the mechanism of colloid destabilization, floc formation through particle interactions neutralized by the positive charge of chitosan, and the presence of electrostatic interactions between chitosan and particles causing turbidity and color.

3.4.3. Mechanism Using Alum Coagulant

Alum coagulants work by destabilizing colloids through the formation of cationic species that neutralize the negative charge of particles, forming flocs, but excessive doses can cause charge reversal and particle restabilization (Malik 2018). This process is called charge neutralization, in which the positive charge of aluminum ions reduces the repulsive forces between particles, allowing them to come closer and form flocs (Husen et al. 2024). In the field of water treatment, the use of alum can remove suspended particles, organic matter, metals, and other contaminants from wastewater (Tahraoui et al. 2024). This is in accordance with the efficiency of turbidity, TSS, and color removal parameters shown in Fig. 1**.**

3.5. ANOVA One-Way Analysis

Three coagulants were used in this research, namely code 1 (maggot shell biocoagulant), code 2 (moringa seed biocoagulant), and code 3 (alum coagulant). The results of the one-way ANOVA test in Fig. 3 show an F value of 18.01 and a P-value of 0.000 (<0.05), indicating a significant difference among the coagulant types in terms of percentage removal. The Tukey pairwise comparison test shows that moringa seeds and alum are in group A, while maggot shells are in group B, indicating that the first two coagulants are more effective. Based on the mean results, each treatment had nine samples (N=9), with separation efficiencies of 75.31% for maggot shells, 90.59% for moringa seeds, and 92.35% for alum. The standard deviations were 7.32, 7.06, and 5.33, respectively, with 95% confidence intervals of 70.75–79.87%, 86.04–95.15%, and 87.79–96.91%.

Fig. 4 presents several residual plots used to validate the assumptions of the regression model in the % Removal analysis of the coagulation-flocculation process. The Normal Probability Plot indicates that most residuals align closely with the diagonal line, with minor deviations at the tails, suggesting near-normality. The Residuals versus Fitted Values plot shows that residuals are randomly dispersed around the zero line (dashed horizontal line) across the observed Fitted Value range (approximately 75 to 95). The histogram illustrates a residual distribution that is approximately normal, with the highest frequency near zero. Additionally, the Residuals versus Observation Order plot displays a random pattern, indicating no autocorrelation. Overall, the regression model satisfies the assumptions of normality, homoscedasticity, and residual independence, validating its suitability for analyzing the relationship between coagulant dose and removal efficiency.

4. CONCLUSIONS

Alum achieved the highest performance, removing 86.67% of turbidity, 98.66% of TSS, and 96.17% of color at an optimal dose of 250 $mg.L^{-1}$. Moringa seeds performed nearly

Factor Information

Factor	Levels	Values
Variation Coagulant	3	1; 2; 3

Analysis of Variance

Source	DF	Adj SS	Adj MS	F-Value	P-Value
Variation Coagulant	2	1581	790,65	18,01	0,000
Error	24	1054	43,91		
Total	26	2635			

Means

Variation Coagulant	N	Mean	StDev	95% CI
1	9	75,31	7,32	(70,75; 79,87)
2	9	90,59	7,06	(86,04; 95,15)
3	9	92,35	5,33	(87,79; 96,91)

Pooled StDev = 6,62615

Grouping Information Using the Tukey Method and 95% Confidence

Variation Coagulant	N	Mean	Grouping
3	9	92,35	A
2	9	90,59	A
1	9	75,31	B

Means that do not share a letter are significantly different.

Fig. 3: ANOVA one-way analysis.

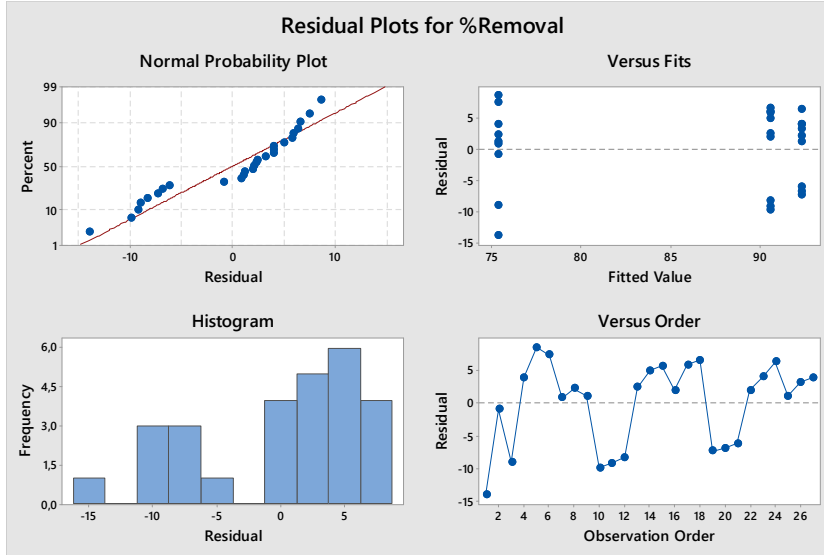


Fig. 4: Residual plots for %removal.

as well, with turbidity removal of 82.04%, TSS removal of 96.31%, and color removal of 97.27% at a dose of 150 $mg.L^{-1}$, indicating their potential as an environmentally friendly alternative to alum. Maggot shells showed moderate effectiveness, with turbidity removal of 74.96%, TSS removal of 83.89%, and color removal of 77.48% at 100 $mg.L^{-1}$, which could be improved further through process and dose optimization.

Sustainability of biocoagulant products is crucial for their long-term use without detrimental effects on the environment, economy, or society. In wastewater treatment, sustainability is evaluated from environmental, social, economic, and technical perspectives. Key challenges include process efficiency, raw material availability, and operational costs. Environmental impacts can be assessed using Life Cycle Assessment (LCA) according to ISO 14040 standards, evaluating the environmental footprint of producing moringa seed and maggot shell biocoagulants. Economically, costs are compared between bioflocculants and alum using an economic engineering approach to determine their efficiency and viability.

Currently, this research is limited to laboratory-scale experiments. Scaling up to industrial applications requires further development to evaluate performance and cost-effectiveness under more complex and varied operational conditions. The dosing intervals for moringa seed and maggot shell biocoagulants should also be expanded to more accurately determine optimal doses and removal efficiencies for each parameter. Additionally, a comprehensive LCA covering the entire process chain, from cradle to grave, is necessary to assess the overall environmental impact.

5. REFERENCES

Adilla Safitria, R. and Rahmayanti, M., 2020. Characterization and application of chitosan as a natural coagulant in reducing remazol red dyestuff concentration and cod value of batik liquid waste. *Journal of Scientific and Applied Chemistry*, 23(9), pp.333-337. DOI

Akutteh, H.M., Buamah, R., Wiafe, S. and Nyarko, K.B., 2022. Optimizing coagulation-flocculation processes with aluminum coagulation using response surface methods. *Applied Water Science*, 12(188), pp.1-13. DOI

Anifah, E.M., Sholikah, U., Ariani, I.K., Yorika, R. and Raharti, H.W., 2024. Coagulation-flocculation of tofu wastewater using natural coagulant of chempedak (*Artocarpus integer*) seed. *Jurnal Teknologi Lingkungan*, 25(2), pp.281-288. DOI

Aragaw, T.A. and Bogale, F.M., 2023. Role of coagulation/flocculation as a pretreatment option to reduce colloidal/bio-colloidal fouling in tertiary filtration of textile wastewater: A review and future outlooks. *Frontiers in Environmental Science*, 11(4), pp.1-16. DOI

Ardianto, R. and Amalia, R., 2023. Optimization of chitin deacetylation process into chitosan from maggot casing using RSM. *Metana*, 19(1), pp.1-12. DOI

Basra, S.M.A., Iqbal, Z., Khalil-Ur-Rehman, Hafeez-Ur-Rehman and Ejaz, M.F., 2014. Time course changes in pH, electrical conductivity and heavy metals (Pb, Cr) of wastewater using *Moringa oleifera* Lam. seed and alum, a comparative evaluation. *Journal of Applied Research and Technology*, 12(3), pp.560-567. DOI

Bouchareb, R., Derbal, K. and Benalia, A., 2021. Optimization of active coagulant agent extraction method from *Moringa oleifera* seeds for municipal wastewater treatment. *Water Science & Technology*, 84(2), pp.393-403. DOI

Desta, W.M. and Bote, M.E., 2021. Wastewater treatment using a natural coagulant (*Moringa oleifera* seeds): Optimization through response surface methodology. *Heliyon*, 7(11), e08451, pp.1-12. DOI

Diver, D., Nhapi, I. and Ruziwa, W.R., 2023. The potential and constraints of replacing conventional chemical coagulants with natural plant extracts in water and wastewater treatment. *Environmental Advances*, 13, 100421, pp.1-10. DOI

Djari, F.W. and Asyfiradayati, R., 2024. Optimization of reducing total suspended solid levels in tofu waste with alum coagulant. *International Journal of Health and Pharmaceutical*, 4(4), pp.581-585. DOI

Fitri, D., Kiromah, N.Z. and Widiastuti, T.C., 2019. Formulation and characterization of nanoparticles of ethanolic extract of salam leaves (*Syzygium polyanthum*) with various chitosan compositions using ionic gelation method. *Journal of Pharmaceutical Science and Clinical Research (JPSCR)*, 1(1), pp.61-69. DOI

Husen, A.K., Bidira, F., Bekel, E.A., Tegegn, M., Desta, W.M. and Asaithambi, P., 2024. Color, COD, and turbidity removal from surface water by using linseed and alum coagulants: Optimization through response surface methodology. *Applied Water Science*, 14(9), pp.1-16. DOI

Hutabarat, D.M., Witasari, W.S. and Baskoro, R., 2022. Effect of coagulant type and pH variation on liquid waste quality in the wastewater treatment plant of PT Kawasan Industri Intiland. *Jurnal Teknologi Separasi*, 8(3), pp.588-594. DOI

Ibrahim, M., Ismail, N., Chua, B.L. and Adnan, A.S.M., 2021. Drying and extraction of *Moringa oleifera* and its application in wastewater treatment. *Journal of Physics: Conference Series*, 2120(1), 012002, pp.1-8. DOI

Kastali, M., Mouhir, L., Chatoui, M., Souabi, S. and Anouzla, A., 2021. Removal of turbidity and sludge production from industrial process wastewater treatment by a rejection of steel rich in FeCl (SIWW). *Biointerface Research in Applied Chemistry*, 11(5), pp.13359-13376. DOI

Kurniawan, S.B., Abdullah, S.R., Imron, M.F., Said, N.S., Ismail, N., Hasan, H.A., Othman, A.R. and Purwanti, I.F., 2020. Challenges and opportunities of biocoagulant/bioflocculant application for drinking water and wastewater treatment and its potential for sludge recovery. *International Journal of Environmental Research and Public Health*, 17(24), pp.1-33. DOI

Malik, Q.H., 2018. Performance of alum and assorted coagulants in turbidity removal of muddy water. *Applied Water Science*, 8(1), pp.1-4. DOI

Nenohai, J.A., Minata, Z.S., Ronggopuro, B., Sanjaya, E.H. and Utomo, Y., 2023. Use of activated carbon from moringa seeds and various other biomasses in addressing water pollution: A review. *Jurnal Ilmu Lingkungan*, 21(1), pp.29-35. DOI

Nora, F., Marhadi, Adriansyah, E., Suzana, A., Pramono, M.S., Sufra, R. and Syaiful, M., 2023. Tofu wastewater treatment using biocoagulant moringa seed powder (*Moringa oleifera* L). *International Journal of Research in Vocational Studies (IJRVOCAS)*, 3(3), pp.41-45. DOI

Pangestika, W. and Saksono, N., 2018. A tofu wastewater treatment using combination of plasma electrolysis and coagulation-flocculation method. *International Journal of Technology and Engineering Studies*, 4(2), pp.42-49. DOI

Patchaiyappan, A. and Devipriya, S.P., 2021. Application of plant-based natural coagulants in water treatment. In: S. Adhikari and S. Dutta (eds.) *Cost Effective Technologies for Solid Waste and Wastewater Treatment*. Elsevier, pp.51-58. DOI

Pramaningsih, V., Hansen, H., Praveena, S.M. and Styana, U.I.F., 2022. Wastewater quality and pollution load of each stage in tempeh production. *Indonesian Journal of Urban and Environmental Technology*, 5(3), pp.209-222. DOI

Purnomo, P.A.L., 2023. Reduction of turbidity and TSS of river water using coagulant from rice field snail shell (*Pila ampullacea*). *EnviroUS*, 3(2), pp.25-29. DOI

Putro, P.G.L., H, H. and Amirudin, 2021. Water quality parameters of tofu wastewater: A review. *IOP Conference Series: Materials Science and Engineering*, 1156(1), 012018, pp.1-9. DOI

Ramakrishnan, D. and Sathiyamoorthy, M., 2025. Enhancing the remediation of polyamide microplastics: A comparative study of natural and synthetic coagulants. *Frontiers in Environmental Science*, 13, 1620074, pp.1-12. DOI

Rendana, M., Renaldi, F., Akbar, M.N. and Hardestyariki, D., 2025. Optimization of *Moringa oleifera*-based coagulant in textile wastewater treatment. *Discover Applied Sciences*, 7(1063), pp.1-13. DOI

Sirajudheen, P., Poovathumkuzhi, N.C., Vigneshwaran, S., Chelaveettil, B.M. and Meenakshi, S., 2021. Applications of chitin and chitosan based biomaterials for the adsorptive removal of textile dyes from water — A comprehensive review. *Carbohydrate Polymers*, 273, 118604, pp.1-18. DOI

Tahraoui, H., Toumi, S., Boudoukhani, M., Touzout, N., Sid, A.N.E.H., Amrane, A., Belhadj, A.E., Hadjadj, M., Laichi, Y., Aboumustapha, M., Kebir, M., Bouguettoucha, A., Chebli, D., Assadi, A.A. and Zhang, J., 2024. Evaluating the effectiveness of coagulation–flocculation treatment using aluminum sulfate on a polluted surface water source: A year-long study. *Water*, 16(3), 400, pp.1-39. DOI

Teh, C.Y., Budiman, P.M., Shak, K.P.Y. and Wu, T.Y., 2016. Recent advancement of coagulation–flocculation and its application in wastewater treatment. *Industrial & Engineering Chemistry Research*, 55(16), pp.4363-4389. DOI

Nature Environment and Pollution Technology
An International Quarterly Scientific Journal

p-ISSN: 0972-6268
(Print copies up to 2016)
e-ISSN: 2395-3454

Vol. 25 | No. 3 | Article ID B4389 | 2026

Original Research Paper

https://doi.org/10.46488/NEPT.2026.v25i03.B4389

Open Access Journal

Thermogravimetric Analysis and Determination of Kinetic Parameters for Pyrolysis of Lotus Seed Biomass

Gurneet Kaur[1], Vivekanand[2] and Jaibir Kherb[3]†

[1]Department of Chemistry, Amity Institute of Applied Sciences, Amity University, Noida-201301, India
[2]Department of Chemistry, Govind Ballabh Pant University of Agriculture & Technology, Pantnagar, Udham Singh Nagar, Uttarakhand 263145, India
[3]Department of Chemistry, National Institute of Technology, Kurukshetra-136119, Haryana, India
†Corresponding author: Jaibir Kherb; jaibirkherb@nitkkr.ac.in

Abbreviation: Nat. Env. & Poll. Technol.
Website: www.neptjournal.com

Received: 11-08-2025
Revised: 23-10-2025
Accepted: 26-10-2025

Key Words:

Biomass pyrolysis
Thermogravimetric analysis
Thermokinetic modeling
Lotus seed biomass

ABSTRACT

Optimal usage of omnipresent biowaste materials is vital for truly accomplishing global sustainable development goals. In this regard, naturally abundant, nutrient-rich lotus seeds (Nelumbo nucifera) biomass holds high potential as a suitable alternative source of energy. This research systematically investigates the high temperature thermochemical, morphological and spectral changes which occur in lotus seeds (LS) biomass. This study also successfully correlates the thermogravimetric changes in LS biomass with its compositional changes, highlighting the overall mechanism of this thermal process. Furthermore, a detailed theoretical analysis of the thermal data was also carried out using various models to obtain all of the involved kinetic parameters. Results showed that LS biomass thermal degradation followed a first-order reaction kinetics mechanism with significantly low activation energy requirements (~ 2-8 $kJ.mol^{-1}$) for different reaction phases. These results provide critical information for optimizing the energy production on an industrial scale. High volatile content (~76%) and lower pyrolysis temperature requirement (< 400°C) for inducing significant structural changes in this biomass also enhances its potential as a bioenergy alternative. Ultimately, this research work underscores the potential of lotus seed biomass to contribute to sustainable energy solutions and mitigate environmental pollution, aligning with global efforts toward renewable energy practices.

Citation for the Paper:

Kaur, G., Vivekanand and Kherb, J., 2026. Thermogravimetric analysis and determination of kinetic parameters for pyrolysis of lotus seed biomass. *Nature Environment and Pollution Technology*, 25(3), B4389. https://doi.org/10.46488/NEPT.2026.v25i03. B4389

Note: From 2025, the journal has adopted the use of Article IDs in citations instead of traditional consecutive page numbers. Each article is now given individual page ranges starting from page 1.

Copyright: © 2026 by the authors
Licensee: Technoscience Publications
This article is an open access article distributed under the terms and conditions of the Creative Commons Attribution (CC BY) license (https://creativecommons.org/licenses/by/4.0/).

1. INTRODUCTION

With growing instances of climate change-induced environmental issues and a continuous lookout for sustainable energy solutions, omnipresent and highly abundant biomass is a flicker of hope. It is primarily derived from various agricultural byproducts. Usage and proper processing of this vast resource may hold the key to unlocking a great renewable energy option. The current global economic development is mostly based on trade and processing of crude oil whose continuous depletion is seen as both economic and energy supply problem since energy demand is exponentially increasing (Jankovic et al. 2020) Additionally, combustion of these fossil fuels leads to release of harmful gases like carbon, nitrogen and sulfur oxides in the environment which results in respiratory problems in living beings (Kampa & Castanas 2008). Many of these pollutant gases also have a prominent greenhouse effect, thereby leading to an increase in Earth's temperature. In such an alarming situation, the effective usage of Biomass as a renewable energy is a highly plausible option. Utilization of biomass will also conform to the globally accepted environmentally sustainable practices. Currently, hydrogen gas fuel is generated mostly from the usage of fossil fuels, which also releases CO_2 (Muradov & Veziroglu 2008). Biomass seems to be a good alternative to fossil feedstocks in this regard as well due to its zero net CO_2 impact (Francis Prashanth et al.

2020). From an energy generation point of view, plant as well as animal-based biomass material have been found highly useful (McKendry 2002). Additionally, Biomass is a type of easily biodegradable organic material, making it environmentally compatible as well. Most commonly seen biomass in our surroundings includes crop leftovers, millions of tonnes of leaves/branches/barks emanating from forest plants/trees, municipal waste generated primarily by large urban areas, and waste products released by some industries such as food packaging firms. Biomass also includes gases and liquids recovered from the decomposition of non-fossilized and biodegradable organic materials. As the Earth contains millions of plant and animal species, there is a diverse variety of biomass available, and researchers have minutely studied the composition and unique aspects of many biowaste materials, such as banana peel, apple pomace, and coconut shell, to name a few. One of the highly abundant plant varieties in India is the lotus and its variants. Lotus is an aquatic flowering plant that grows in nutrient-rich freshwater. It comes from the plant family of Nelumbonaceae, and it is also regarded as a sacred flower across many parts of the world (Premathilake & Seneviratne 2015). All parts of this plant species are utilized as food and medicine (Mukherjee et al. 2009). The lotus plant doesn't require specific growing conditions, and that's why it is found in a wide variety of climates ranging from South America to Russia and everywhere in between (Dumont 1995). Lotus seed (LS) is an incredibly significant part of the lotus plant due to its high nutritional value as well as the bioactive nature of its components. Specifically, the presence of phenolic compounds in LS extracts imparts anti-cancer, anti-proliferation, anti-diabetic, anti-inflammatory, neuroprotective, antioxidant, and immunomodulatory responses in therapeutic applications (Zhao et al. 2014). Utilizing such easily available, nutrient-rich, economical horticultural waste for producing value-added products will be an excellent step towards sustainable utilization goals. Lotus seeds, despite their small and compact size, are rich in nutrients, including proteins, vitamins, and essential minerals like magnesium, potassium, and phosphorus (Zhu 2017). Their usage is also rather easy, as they can be consumed in raw form, roasted form, or cooked form. Recent studies have shown that their continuous consumption leads to significant enhancement in good health parameters in human beings, such as improved sleep quality and lowered aging-related ailments (Zhang et al. 2015). They also have high cultural and historical significance as they symbolize purity, rebirth, and enlightenment in many countries (Yang et al. 2024). When stored properly, they have a long shelf life. Among a diverse variety of biomass resources available on earth, lotus seeds are not only abundant but also possess a unique chemical composition, thereby making them an intriguing avenue for further research and exploration studies. Lotus seeds are mostly sold in dried, shelled form, which is called "Makhana" (Arooj et al. 2021). Makhana, derived from lotus seed, is rich in nutrients. Its ease of processing and workability make it a promising research target for potential applications such as energy generation through pyrolysis. Pyrolysis is a thermochemical conversion that has the power to unlock the energy potential that is embedded in the lotus seeds. The lotus seeds' biomass is subjected to controlled heat in an oxygen-deficient environment, and valuable products like biochar and bio-oil can be obtained (Hou et al. 2021). Therefore, using the process of pyrolysis leads to optimization of energy and environmentally sustainable usage of biomass (Müller-Hagedorn & Bockhorn 2007). Pyrolysis data of such biowastes is highly informative, as the intermolecular forces of the constituent species invariably dominate this thermal process. Therefore, the determination of the different parameters obtained from theoretical modeling of pyrolysis data provides key information about the underlying chemical reactions as well as the structure and composition of this material.

This research work is focused on detailed elemental and thermochemical profiling of lotus seed biomass, which has been missing in previous studies. Thermogravimetric analysis of lotus seeds was systematically carried out at varying heating rates, and the associated thermochemical changes were correlated to compositional changes in the material. Judicious utilization of such information regarding lotus seeds not only solves the biomass pollution problem but also provides a viable energy alternative, thereby leading to sustainable living practices. Thermo-chemical conversion processes primarily use heat or chemicals to convert biomass into another usable chemical form (Demirbas 2001). In this regard, the most commonly used techniques include gasification, combustion, and pyrolysis. These techniques differ from each other principally by the extent to which the chemical reactions involved are allowed to proceed. Herein, we have focused on the pyrolysis technique to study the thermal changes in LS biomass. Pyrolysis is a thermochemical decomposition of organic or inorganic material at very high temperatures in the absence of oxygen (Bridgwater 2012). It involves a simultaneous gradual change of elemental composition and physical phase in the material subjected to high temperature exposure. In the case of biomass, this process generally entails thermally driven breaking of the complex cellulosic structure to simpler molecular fragments rich in carbon, oxygen, and hydrogen (Noszczyk et al. 2021). The lower molecular weight compounds remain as permanent gases at ambient temperature, while the majority of complex, larger compounds condense to form a liquid, which is called

bio-oil (Mohan et al. 2006). Before the emergence of the petrochemical industry, a number of useful products such as methanol, phenols, carboxylic acids, and furfural were derived from the pyrolysis of liquids generated during charcoal manufacturing (Basu 2013). After the realization of limited sources of fossil fuels across the globe and their adverse impacts on the environment, the use of biomass as a source of energy has again seen renewed interest since the 1990s. The bio-oil has also been used as a fuel in a diesel engine with slight modifications in the fuel pump, engine linings, and cylinder-injection system (Hall & Scrase 1998). They can also be used in simple oil burners for thermal applications and in combustion boilers to generate electricity, or can be easily blended with standard diesel fuels to form a pollution-free green bio-diesel fuel (Atabani et al. 2013). The bio-oil also has good potential as a chemical feedstock, which is mainly controlled by the availability of oxygen and conversion temperature (Guerrero et al. 2014). Additionally, in this work, we have investigated the thermodynamic and kinetic parameters of the pyrolysis process using various theoretical models. Kinetic factors involved in thermal decomposition reactions primarily regulate the conversion process of biomass into desirable final energy products (Ma et al. 2017). Accurate kinetic models are therefore needed for the most effective utilization of particular biomasses and for scaling up to real industrial applications for energy generation purposes (Huang et al. 2016). A complete understanding of process kinetic parameters helps in getting proper control and optimization of biomass thermal treatment. These kinetic parameters generally include activation energy (E_a), pre-exponential factor (A), the reaction rate constant (k), and the reaction order (n). Improved knowledge of these parameters enables modeling, designing, and optimization of bioreactors for biomass pyrolysis.

2. MATERIALS AND METHODS

2.1. Preparation and Collection of Raw Material

The sample *Nelumbo nucifera* (lotus seeds) was collected from seed pods of the lotus plant located in Gadarpur, Uttarakhand, India, and ground into fine powder form before its pyrolysis and other chemical analysis.

2.2. *Nelumbo nucifera* (Lotus Seeds) Powder Preparation

The collected seeds were kept in a hot air oven at 60°C for 2 hours to remove the majority of their moisture content. Thereafter, the dried seeds were powdered using a grinding machine and then sieved using a laboratory sieve of mesh 100 (149 microns pore size) to finally obtain solid, homogeneous contents with uniform particle size.

2.3. Characterization of Raw Material

2.3.1. Proximate Analysis

The percentage moisture content of the sample was determined by heating the samples in a pre-weighed pan. The samples were then dried at 100°C in accordance with ASTM D3173 standards. The percentage moisture content in the tested biomass was calculated using the following equation (Jo et al. 2017).

$$\%\ Moisture\ Content = \frac{(Wet\ weight - Dry\ Weight)}{Wet\ weight} \times 100 \quad \ldots(1)$$

Thereafter, the same heated sample was kept in a muffle furnace at 1000°C for 5 minutes. This treatment led to the softening of the solid sample and the removal of trapped volatile gases such as carbon dioxide and methane from it. The resulting ash-like material was weighed after cooling to room temperature. The volatile matter content was then calculated using the following equation:

$$\%\ Volatile\ Matter\ Content = \frac{(Weight\ of\ dry\ sample - Ash\ Weight)}{Dry\ sample\ weight} \times 100 \quad \ldots(2)$$

Ash content of the wastes refers to the non-combustible material left after the biowaste is completely burned at 700°C for 1 hour in the presence of air. Thereafter, the fixed carbon percentage in the biomass sample was computed by subtracting the mass of volatiles, moisture, and incombustibles from the original mass of the sample, using the following equation:

$$\%\ Fixed\ carbon\ Content = 100 - (\%\ Moisture + \%\ Ash + \%\ Volatile\ matter) \quad \ldots(3)$$

2.3.2. Ultimate Analysis

This is a chemically more specific and accurate method for determining the elemental composition of the material, usually focusing on C, H, N, S and O content of the sample. This includes the determination of the exact chemical form of sulfur present; the most common forms are in the form of sulfide minerals, sulfate minerals, or organically bound sulfur. In some cases, the analyses might reveal the presence of other important trace elements that may influence the suitability of the material for a particular purpose.

Ultimate analysis of the powdered sample was carried out using a CHNSO elemental analyzer (Elementar Analysensysteme Germany, Model: Vario Micro Cube), which provided % composition of C, H, N, S and O in the sample. This machine has a combustible working temperature range of 950-1200°C. During this simultaneous detection of elements in the feed sample, helium gas was used as the carrier gas.

2.4. Spectral Characterization of Raw Biomass Material

FTIR spectra of the powdered and pyrolyzed samples were used for detailed functional groups analysis. The Agilent Cary 630 FTIR spectrometer was used for the analysis in the spectral range of 450-4000 cm^{-1}. Before FTIR analysis, samples were heated at two distinct temperatures, i.e., 550°C and 1000°C, so that thermally induced chemical changes in samples can be carefully observed vis-à-vis the changes in functional groups' spectral features. The raw powdered biomass of the lotus seed sample was carefully placed in a quartz crucible, and it was first subjected to 550°C. This was followed up by heating the raw sample even further at 1000°C in a quartz crucible. Samples were then kept at room temperature to cool down before the collection of FTIR data. FTIR spectra of the untreated biomass sample and the thermally treated samples were collected via traditional KBr pellet methodology.

2.5. Thermal Characterization of Raw Material

The detailed thermal profiling of the sample was performed using simultaneous TGA-DTG-DTA and DSC analysis on an EXSTAR TG/DTA 6300 instrument. The analysis was performed at three different heating rates of 5°C.min^{-1}, 10°C.min^{-1}, and 20°C.min^{-1}, with alumina as a reference in an inert N_2 atmosphere at a flow rate of 200 mL.min^{-1}. Approximately 10 milligrams of finely powdered sample was subjected to gradually heating program to a final temperature of 1000°C. The thermogravimetric (TG) data were minutely studied to calculate ash yield, thermal stability, and % weight residue loss in the samples at different temperatures.

2.6. Theoretical modeling of TGA data

Detailed thermodynamic and kinetic modeling of the obtained thermogravimetric data has been carried out to understand the thermal-induced changes in the sample. TGA data for each biomass sample were analyzed to assess their weight loss (%) in relation to temperature, decomposition stages, and kinetic parameters. These analyses were performed through a set of calculations using well-accepted theoretical models of Coats and Redfern (CR) and Ozawa-Flynn-Wall (OFW). Origin® software from OriginLab® Corporation was used for equation fitting and regression analysis of the data.

2.7. Evaluation of Thermodynamic Parameters

Each TGA curve was subdivided into five phase stages to evaluate the frequency factor (A), activation energy (E_a), change in entropy (ΔS), change in enthalpy (ΔH), and change in free energy (ΔG) associated with these thermally induced chemical reactions through the following equations:

$$\Delta H = E_a - RT_p \quad \ldots(4)$$

$$\Delta G = E_a + RT_p \ln\frac{k_b T_p}{hA} \quad \ldots(5)$$

$$\Delta S = \frac{\Delta H - \Delta G}{T_p} \quad \ldots(6)$$

$$\Delta A = [\beta exp(E_a/RT_{max})E_a]/(RT_{max}^2) \quad \ldots(7)$$

Where the involved symbols have their usual meaning (R being the ideal gas constant having a value of 8.314 J $mol^{-1}K^{-1}$, T_p is peak decomposition temperature in K, k_b is the Boltzmann constant having a value of 1.38×10^{-23} J K^{-1}, h is Planck's constant with a value of 6.63×10^{-34} Js)

2.7.1. Coats and Redfern (CR) Model

The Coats-Redfern model is a widely used method in thermal analysis, particularly in the study of reaction kinetics for solid-state processes such as the decomposition of material (Álvarez et al. 2016). The CR model was applied to find out the non-isothermal kinetics and thermodynamic parameters from the collected TG data. The CR method involves constructing a plot of $[\log_{10}(1-\alpha/T^2)]$ vs. T^{-1} wherein the slope of the straight line w $-E_a/2.303R$ It can be utilized for finding the activation energy of the process.

$$\ln[g(\alpha)] = -\frac{E_a}{RT} + \ln\left(\frac{AR}{\beta E_a}\right) \quad \ldots(8)$$

Where $g(\alpha) = -ln\left[\frac{1-\alpha}{T^2}\right]$ for $n = 1$ and

$g(\alpha) = \frac{1-(1-\alpha)^{1-n}}{(1-n)T^2}$ for $n \neq 1$

2.7.2. Ozawa-Flynn-Wall (OFW) Model

The OFW model, also known as the Ozawa-Flynn-Wall (OFW) method, is used in thermal analysis to find the activation energy of a reaction without even having intricate knowledge of the reaction mechanism (Flynn & Wall 1966). It is particularly used for the study of solid-state reactions, such as the thermal decomposition of materials.

The OFW model basically correlates the heating rate of the samples with the activation energy associated with processes, utilizing Doyle's approximation for the temperature integral. The final form of the OFW equation is expressed as follows:

$$\log(\beta) = \log\left[\frac{AE_a}{Rg(\alpha)}\right] - 2.315 - 0.457\,\frac{E_a}{RT} \quad \ldots(9)$$

As can be seen from the OFW equation, a linear plot of log β versus 1/T is adequate to determine the activation energy for each conversion step.

2.8. Evaluation of Kinetic Parameters

Thermal degradation refers to the process in which a

material's chemical structure breaks down when it is gradually exposed to elevated temperatures. This breakdown often leads to a significant loss of physical/chemical properties, changes in visual appearance, and the release of volatile compounds. The overall rate equation for the pyrolysis of solid biomass can be expressed as a function of conversion α, as follows:

$$\frac{d\alpha}{dt} = k(T)f(\alpha) \quad \ldots(10)$$

Conversion (α) is a type of weight loss data of a decomposed sample and is defined as follows:

$$\alpha = \frac{m_i - m_a}{m_i - m_f} \quad \ldots(11)$$

Wherein m_i is the initial weight of the biomass sample at temperature, mt is the weight of the biomass sample at time t, and mf is the final weight of the biomass sample at the end of the thermal degradation process.

The rate constant k (T) for this solid-state reaction can be expressed by the Arrhenius relation as:

$$k = Ae^{\left(\frac{-E_a}{RT}\right)} \quad \ldots(12)$$

Substituting the value of k in equation (10),

$$\frac{d\alpha}{dt} = A.f(\alpha).e^{-E_a/RT} \quad \ldots(13)$$

Since temperature T depends upon time, the heating rate term β can be defined as:

$$\beta = \frac{dT}{dt} = \frac{d\alpha}{dt} \quad \ldots(14)$$

Substituting the heating rate formula in equation (13) leads to:

$$\frac{d\alpha}{dt} = \frac{A}{\beta}.(1-\alpha)^n.e^{-Ea/RT} \quad \ldots(15)$$

The integration of the above equation within the limits α = 0 to α and T = 0 to T gives:

$$g(\alpha) = \int_0^\alpha \frac{d\alpha}{f(\alpha)} = \frac{A}{\beta}\int_0^T exp\left(\frac{-E_a}{(RT)}\right)dT \quad \ldots(16)$$

where g(α) represents the integral reaction model. This equation can be solved for E_a (activation energy) and A (pre-exponential factor) using model-free and reaction-fitting methods.

Equation (16) on integration and further simplification gives,

$$ln\frac{g(\alpha)}{T^2} = ln\frac{AR}{\beta E_a} - \frac{E_a}{RT} \quad \ldots(17)$$

A plot of ln[G(α)]/T² versus 1/T yields a straight line with slope $-E_a/R$ and an intercept corresponding to ln(AR/βE). The functions G(α) and F(α) are determined by the mathematical model describing the thermochemical conversion mechanism. For the pyrolysis of the sample, the appropriate kinetic model is identified through linear regression analysis. The plot of ln[G(α)]/T² versus 1/T should exhibit a straight line with a correlation coefficient (r^2) close to 1, indicating the best-fit kinetic model.

To find out the kinetic parameters, eight kinetic models were adopted to study the thermal decomposition of biomass samples. The degradation process of the biomass is overall influenced by transport (diffusion) phenomena and chemical reaction kinetics. Different algebraic expressions were used to identify the reaction mechanisms in thermochemical decomposition reactions (Malika et al. 2016). These expressions have been listed in Table 1.

2.9. SEM Analysis

Scanning Electron Microscopy is a powerful visualization technique used to examine the surface structure and

Table 1: Algebraic equations employed for the determination of reaction kinetic mechanisms and parameters.

Mechanism		Symbol	$f(\alpha)$	$g(\alpha)$
Chemical reaction kinetics	First order	F_1	$1-\alpha$	$-\ln(1-\alpha)$
	Second order	F_2	$(1-\alpha)^2$	$(1-\alpha)^{-1}-1$
	Third order	F_3	$(1-\alpha)^3$	$[(1-\alpha)^{-2}-1]/2$
Diffusion kinetics	One-way transport	D_1	$1/2\,\alpha$	α^2
	Two-way transport	D_2	$-\ln(1-\alpha)^{-1}$	$\alpha+(1-\alpha)-\ln(1-\alpha)$
	Three-way transport	D_3	$\frac{\left(\frac{2}{3}\right)(1-\alpha)^{2/3}}{1-(1-\alpha)^{1/3}}$	$[1-(1-\alpha)^{\frac{1}{3}}]^2$
	Ginstling, Brounshtein equation	D_4	$\frac{\left(\frac{2}{3}\right)(1-\alpha)^{1/3}}{1-(1-\alpha)^{1/3}}$	$1-\frac{2\alpha}{3}-(1-\alpha)^{2/3}$
	Zhuralev, Lesokhin, Tempelman Equation	D_5	$\frac{\left(\frac{2}{3}\right)(1-\alpha)^{5/3}}{1-(1\alpha)^{1/3}}$	$[(1-\alpha)^{\frac{1}{3}}-1]^2$

Table 2: Proximate analysis data of the LS biowaste sample.

Proximate Analysis	LS parameters	% w/w
	Moisture content	5.77
	Volatile matter	76.3
	Fixed carbon	15.56
	Ash content	2.37

composition of materials at very high magnifications. SEM images for three different samples, i.e., raw sample and samples treated at 550°C and 1000°C were taken using a JEOL Japan model JSM 6610V microscope using a tungsten or LaB6 filament, which provided detailed images of the sample surface by scanning it with a focused beam of electrons. High-resolution microscopic imaging of samples under different conditions helped in the proper understanding of the physical and structural aspects of biomass and the nature of its thermal transformation process.

3. RESULTS AND DISCUSSION

3.1. Proximate Analysis

A known quantity of LS biowaste was subjected to distinct heating steps, and subsequent weight losses in the sample were correlated with important fuel parameters present in the sample. The obtained results have been summarized in Table 2.

From the observed data, it can be concluded that LS biowaste contains a very small amount of moisture and ash content. These traits certainly enhance its potential utilization as an energy material.

3.2. Ultimate Analysis

Ultimate analysis of the LS (Lotus Seed) sample was performed using a Vario micro cube CHNS analyzer. Results have been summarized in Table 3. From the data, it was clearly observed that the tested sample was rich in carbon and contained 39.66 % carbon, 5.842% hydrogen, 8.166 % nitrogen, and 1.397% of sulphur. Oxygen content was determined by adding all the elements and subtracting it from 100. Thereafter, Oxygen content was found to be 44.935%, making it the most abundant element in this biomass sample.

Furthermore, Gross Calorific Value (GCV) and Net Calorific Value (NCV) for the LS biowaste sample can be easily calculated using CHNS data (Elkhalifa et al. 2022).

The GCV includes the latent heat of steam condensation. It can be mathematically calculated by using elemental percentages in equation (18).

Table 3: Ultimate analysis data of the LS biowaste sample.

Ultimate Analysis	Element	Amount in LS sample %
	Carbon	39.66
	Hydrogen	5.842
	Nitrogen	8.166
	Sulphur	1.397
	Oxygen	44.935
	C/N ratio	17.536
	C/H ratio	6.788

$$GCV\ (kJ.kg^{-1}) = 349.1\ C + 100.5\ S + 1178.3\ H - 103.4\ O - 15.1\ N - 21.1\ Ash \quad \ldots(18)$$

GCV value for the analyzed LS sample was found to be 16049.74 ($kJ.kg^{-1}$)

Similarly, Net calorific value, which excludes the latent heat of steam condensation, can be computed by using equation (19).

$$NCV\ (kJ.kg^{-1}) = GCV - H_{st}\ (0.09\ H + 0.01\ M) \quad \ldots(19$$

where H_{st} denotes the enthalpy of steam (2260 $kJ.kg^{-1}$), and M denotes the moisture (%) in the fuel sample.

Net calorific value for the LS sample was found to be 14732.838 ($kJ.kg^{-1}$).

3.3. FTIR Analysis

FTIR spectra of raw LS sample and pyrolyzed LS samples were collected to delve into functional group changes in the biomass during the thermal treatment. The obtained spectra are shown in Fig. 1. All three samples showed a prominent broad spectral feature in the range ~ 3400 cm-1 to 3200 cm-1, which is generally attributed to the H-bonded O-H group of cellulose (Grube et al. 2006). The band at 2930 cm^{-1} can be ascribed to C-H stretching of the methylene group of cellulose (Peng et al. 2010). This spectral feature became very weak at 500°C and became negligible at 1000°C, indicating significant loss of carbon content as pyrolysis proceeds. Raw sample also showed a strong peak at 1659 $cm^{-1,}$ which may be assigned to conjugated -C=O stretching. Spectral feature at 1549 cm^{-1} indicates the presence of -C=C- conjugated with aromatic rings in the biomass. The absorption peaks at 1246 cm^{-1} and 1155 cm^{-1} can be attributed to stretching of -C-O-C- ether linkages prevalent in guaiacyl lignin and aromatic C-H deformations (Zhong et al. 2007). These peaks vanished for pyrolyzed samples, which indicates the breakdown of ring structure in this lignocellulosic biowaste. Multiple weak bands in the 500-900 cm-1 region are due to C-H bending vibrations in olefinic or aromatic contents. Even these spectral features became weaker as biowaste was treated at high temperatures.

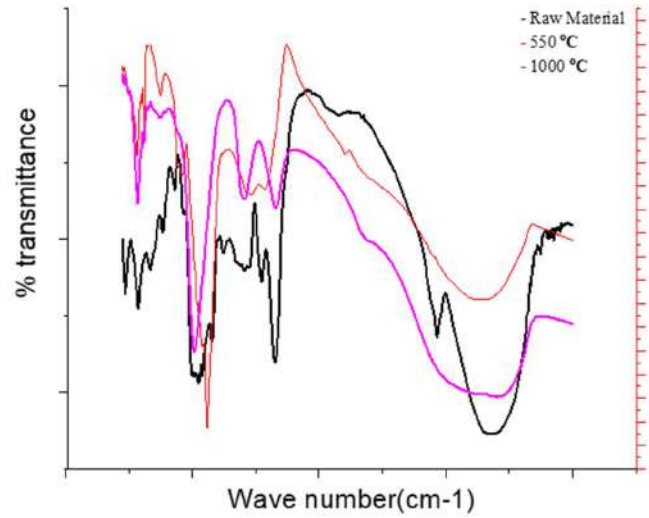


Fig. 1: FTIR spectra of Raw LS sample, after 550°C treatment and after 1000°C treatment.

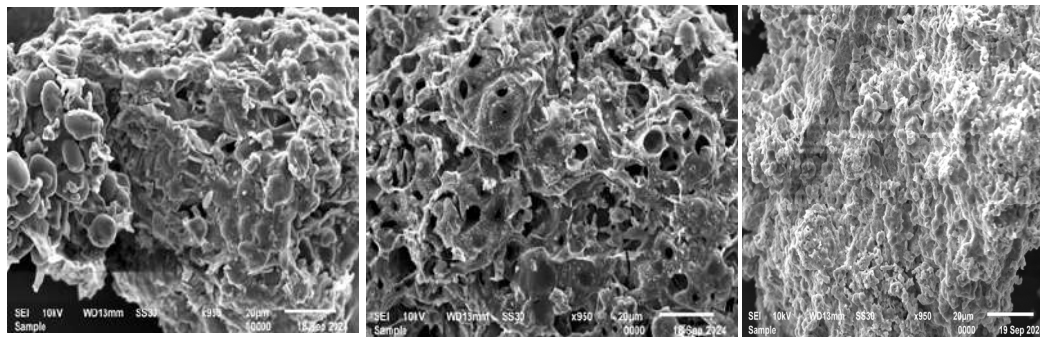


Fig. 2: SEM image of: (a) Raw LS sample, b) Sample after 550°C treatment and c) 1000°C treatment.

Overall, intensities of typical lignin-associated spectral features clearly became weaker during the high-temperature thermal treatment of the LS sample.

3.4. SEM Analysis

SEM images of the LS powdered sample were taken before and after pyrolysis treatment at 550 and 1000 degree Celsius. Collected images are shown in Fig. 2. As can be clearly seen, large-scale structural disintegration was observed in the sample after high-temperature exposure. Sample treated at 550°C showed a considerable amount of porosity, which can be attributed to loss of volatile gases from soft lignocellulosic biomass (Zhang et al. 2020 & Calin et al. 2024). This also correlates well to FTIR spectral changes, indicating a high degree of loss of - C=O, -C-O-C- and -OH functionalities from the biomass. Further increase in pyrolysis temperature led to compaction in the treated biomass. This can be explained by the loss of lignocellulosic content from the LS sample.

3.5. Thermal Analysis of LS Biomass

The thermal analysis of each biomass type was carried out at 3 different heating rates of 5°C.min^{-1}, 10°C.min^{-1} and 20°C.min^{-1} in an inert N_2 atmosphere with a flow rate of 200 mL.min^{-1}. The results obtained were then analyzed to compare the thermal degradation of lignocellulosic biomass under the same heating conditions. The TGA as well as DTG results for three heating rates have been shown in Fig. 3. Recorded TGA curves displayed an overall sigmoidal shape, while the DTG curves exhibited two or three major peaks.

The TGA and DTG curves for biomass LS exhibited a pronounced peak for significant weight loss between 70°C and 100°C, indicating the loss of moisture and other volatile substances. The effect of heating rate on the same biomass types was also observed during the moisture removal stage. At a heating rate of 5°C.min^{-1}, there was 8.52% weight loss due to the loss of moisture and other volatiles. This weight loss decreased to 7.75% at a heating rate of 10°C.min^{-1}, and then decreased to 6.92% at a heating rate of 20°C.min^{-1}.

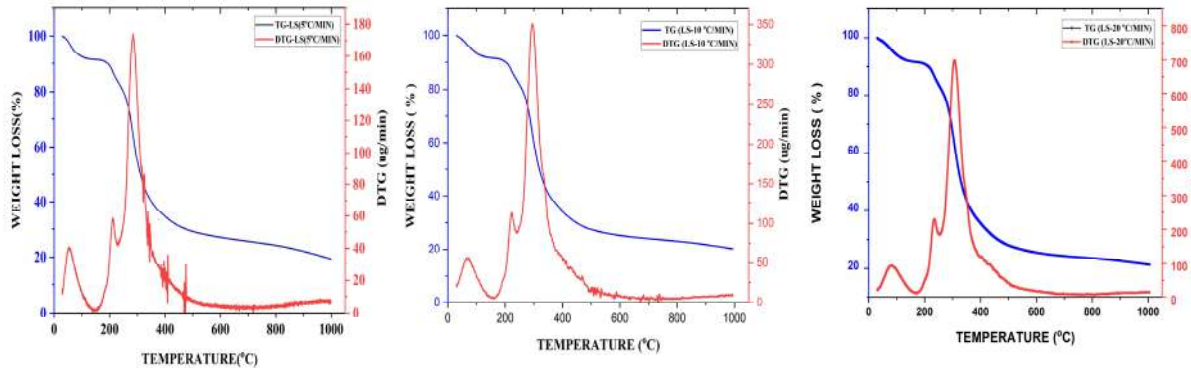


Fig. 3: TGA and DTG Curves of LS biomass at a heating rate of 5°C.min^{-1}, 10°C.min^{-1}, and 20°C.min^{-1}

The DTG curves in Fig. 3 show that the primary pyrolysis decomposition at all rates of biomass LS occurred approximately between 200°C and 400°C. Cellulose, being a homogeneous semi-crystalline polymer of glucose units, degrades within a narrow temperature range. Its decomposition extends up to around 400°C, where the main devolatilization reactions occur. This marks the active pyrolysis stage, characterized by a significant release of volatile matter (VM).

The thermal decomposition of these biomasses is influenced by their lignocellulosic components (hemicellulose, cellulose, and lignin), which typically decompose over the temperature range of 200-400°C (Weerachanchai et al. 2010). Lignin generally begins decomposing at the lowest temperature and continues up to around 900°C. Hemicellulose and cellulose decompose over the temperature ranges of 160-360°C and 240-390°C, respectively (Vamvuka et al. 2003).

Pyrolysis at higher heating rates resulted in a faster decomposition rate, and a broader temperature range was seen for thermal decomposition. The pyrolytic breakdown of hemicellulose and cellulose primarily accounts for the second DTG peak. At a pyrolysis temperature of 241°C, the LS residue showed the highest derivative weight loss. This suggests that LC-BM residue may contain larger fractions of cellulose and hemicellulose, contributing to the release of more volatile components. In contrast, LS biomass likely contains very little lignin content, as there is no indication of any derivate peak after 600°C.

In LS, no significant peak after 600°C in the DTG curve was observed at any heating rate, indicating that lignin content was quite low because the lignin degradation began at 180°C and continued until 950°C, occurring over a wide temperature range as a distinct pyrolytic process. The absence of lignin at a later stage indicates that the biomass LS is not thermally stable above the temperature range of 600°C due to the absence of much lignin, resulting in the absence of its polyaromatic structure. This stage only corresponds to the formation of ash and the burning of fixed carbon content. It is evident that the devolatilization region of biomass LS shifts within the range of 120°C to 600°C due to varying heating rates (5°C.min^{-1}, 10°C.min^{-1}, and 20°C.min^{-1}). This shift is attributed to internal factors or biochemical interactions and synergistic effects that occur during the thermal decomposition of lignocellulosic biomass.

3.6. Evaluation of Thermodynamic Parameters

Employing the CR model, the values of *1/T* and *ln[-ln(1-X)]* were calculated and plotted from the TGA data by splitting the entire thermal range into five phases to obtain different thermodynamic parameters including frequency factor (*A*), activation energy (E_a), change in entropy (ΔS), change in enthalpy (ΔH) and change in free energy (ΔG). This was done for the LS samples at three different heating rates of 5°C.min^{-1}, 10°C.min^{-1}, and 20°C.min^{-1}. Similarly, for the OFW model, data between *lnβ vs.1/T* were plotted to calculate the slope, which in turn provided the values of the above-mentioned thermodynamic parameters. All of the obtained thermodynamic parameter values from both models have been summarized in Table 4.

As can be seen from the observed results, the activation energies obtained from both CR and OFW models were of similar order. Entropy change (ΔS) calculated using both models across was found to be negative across five phases, indicating that the disorder of the products after bond dissociation was lower than that of the initial reactants. This negative ΔS suggests that the intermediate state formed during thermal degradation had a more structured and organized arrangement as compared to the chemical bonding in the raw LS sample. Gibbs free energy change generally reflects the absolute energy increase during any reaction process and formation of the activated complex. Higher ΔG values computed here clearly indicate reduced spontaneity of the pyrolysis reactions of this biowaste sample. Using

Table 4: Thermodynamic parameters for LS thermal degradation computed with CR and OFW models.

HEATING RATE	PHASE	ISOCONVERSIONAL METHODS									
		CR MODEL					OFW MODEL				
		E_a [kJ.mol^{-1}]	A [sec^{-1}]	ΔH [kJ.mol^{-1}]	ΔG [kJ. mol^{-1}]	ΔS [kJ. mol^{-1}]	E_a [kJ. mol^{-1}]	A [sec^{-1}]	ΔH [kJ. mol^{-1}]	ΔG [kJ. mol^{-1}]	ΔS [kJ. mol^{-1}]
5°C.min^{-1}	100	2.79	0.013	-0.31	117.8	-316.7	2.79	0.183	-0.31	96.9	-260.8
	200	3.49	0.010	-0.44	151.1	-320.4	3.48	0.178	-0.44	12.3	-263.0
	300	4.32	0.011	-0.43	184.3	-321.6	4.32	0.187	-0.43	15.0	-264.2
	500	5.53	0.010	-0.89	251.2	-325.0	5.53	0.168	-0.89	20.5	-267.6
	900	7.90	0.009	-0.18	386.4	-329.4	7.90	0.150	-0.18	31.7	-272.0
10°C.min^{-1}	100	2.783	0.00043	-0.317	115.6	-311.0	2.78	0.365	-0.31	94.8	-255.1
	200	3.489	0.00035	-0.443	148.4	-314.7	3.49	0.357	-0.44	12.1	-257.2
	300	4.329	0.00037	-0.434	180.5	-315.9	4.32	0.374	-0.43	14.7	-258.4
	400	5.532	0.00033	-0.893	245.9	-319.2	5.53	0.337	-0.89	20.1	-261.8
	500	7.908	0.00030	-0.184	377.8	-323.7	7.90	0.300	-0.18	31.0	-266.2
20°C.min^{-1}	100	2.770	0.00087	-0.330	113.5	-305.2	2.77	0.724	-0.33	92.7	-249.4
	200	3.491	0.00085	-0.440	144.9	-307.4	3.49	0.716	-0.44	11.8	-251.5
	300	4.330	0.0007	-0.433	177.2	-310.1	4.33	0.749	-0.43	14.4	-252.7
	400	5.536	0.00067	-0.890	241.4	-313.5	5.53	0.674	-0.89	19.2	-256.0
	500	7.911	0.00060	-0.184	371.1	-317.9	7.91	0.600	-0.18	30.5	-260.5

OFW, for all three heating rates, the ΔG value was found to vary in the range of 110-386 kJ.mol^{-1} for five different phases. These values are of similar order as compared to other reported studies on agricultural biomasses like pea waste, mustard stalk, bamboo, and rice husk (Narnaware et al. 2022 and Jagnade et al. 2023). Thermal degradation was overall dominated by the ΔS component, as ΔH values were found to be negligibly small throughout different phases. Lower activation energies associated with different thermal phases (~ 2-8 kJ.mol^{-1}) coupled with significant ΔG values indicate high bio-energy potential of LS biomass.

3.7. Evaluation of Kinetic Parameters

TGA data were thoroughly studied to determine the kinetic parameters of the thermal degradation of LS biomass. The mathematical fitting of the reaction rate equation was performed using the integral method of the Coats and Redfern model (Álvarez et al. 2016). This method is commonly employed for studying the kinetics of solid material degradation. Eight kinetic models have been examined to analyze the thermal decomposition of biomass samples. Previous studies have indicated that the degradation process of biomass is dominated by transport (diffusion) phenomena and chemical reaction mechanisms (Gil et al. 2010, Vlaev et al. 2003).

To investigate the chemical reaction mechanism, a plot of $\ln[g(\alpha)]/T^2$ versus 1/T was constructed, which yielded a straight line with slope −E/R, while ln(AR/□E) remained nearly constant. The expressions of and depend on the order of the mathematical model for each mechanism of the conversion. The selection of the most suitable model for the pyrolysis of biowaste samples is based on linear regression analysis. In essence, numerator, g open paren alpha close paren end numerator, over cap T squared versus 1 over cap T should give a straight line with a correlation coefficient (R^2) close to 1 for the best fit kinetic model. Algebraic expressions of functions of the most common reaction kinetics, including both chemical reaction mechanisms and diffusion mechanisms involved in thermal degradation of solid-state wastes, are listed in Table 1. The calculated values of R^2 for different heating rates to determine the best fit kinetic models have been summarized in Table 5.

From the kinetics data, it can be clearly seen that, as far as the chemical kinetics mechanism is concerned, LS biomass followed the first-order reaction kinetic mechanism at all three different heating rates of 5, 10, and 20°C.min^{-1}. This order mechanism showed the best-fitting parameter values. For the diffusion kinetics mechanism, LS biomass followed the three-way transport diffusion model (k6) for a heating rate of 5°C.min^{-1}. At heating rates of 10 and 20°C.min^{-1}, it seemed to prefer the Ginstling, Brounstein diffusion model (k_7) better. These models have been previously reported to be most appropriate for describing the thermal degradation of lignocellulosic materials (Gil et al. 2010, Vlaev et al. 2003).

Table 5: Correlation coefficient analysis of various chemical kinetics models and diffusion kinetics models.

Heating Rate	Chemical Kinetic Models			Diffusion Kinetic Models				
	k_1	k_2	k_3	k_4	k_5	k_6	k_7	k_8
5 $^{o}C.min^{-1}$	0.6719	0.6714	0.5412	0.9039	0.8881	0.9162	0.912	0.5092
10 $^{o}C.min^{-1}$	0.7505	0.6318	0.5199	0.8773	0.8603	0.9082	0.9115	0.505
20 $^{o}C.min^{-1}$	0.9793	0.5505	0.4975	0.8465	0.8787	0.8916	0.9059	0.5558

4. CONCLUSIONS

This study underscores the significant potential of lotus seeds (Nelumbo nucifera) as a sustainable biomass resource for energy generation through pyrolysis and as a game-changing biomass resource in the fight against climate change and energy scarcity. Our thermogravimetric analysis revealed crucial insights into the thermal behavior and compositional changes of lotus seed biomass, demonstrating its viability for producing valuable energy products such as bio-oil and biochar. Detailed thermochemical analysis, along with spectral characterization, helped in understanding the chemical changes happening in the sample when it's gradually subjected to high temperatures. Thermodynamic and kinetic parameters, including activation energy and reaction rate constants, associated with the thermal degradation of the LS sample were systematically computed. These parameters are quite essential for optimizing the pyrolysis process, enhancing its overall efficiency, and facilitating future scaling-up of biomass conversion technologies for industrial applications.

By utilizing lotus seeds, an abundant agricultural byproduct, we can not only contribute to reducing waste but also promote a circular economy and sustainable energy practices. This research advocates for further exploration of underutilized biomass resources, encouraging innovation in renewable energy solutions that align with global sustainability goals. The findings pave the way for future studies aimed at improving the efficiency of biomass pyrolysis and expanding the application of lotus seeds and other similar resources in the renewable energy landscape (Zhong et al. 2007).

5. ACKNOWLEDGEMENTS

Authors are highly thankful to the Department of Chemistry, National Institute of Technology, Kurukshetra, India, Amity Institute of Applied Sciences, Amity University Noida and Department of Chemistry, Govind Ballabh Pant University of Agriculture & Technology, Pantnagar, Uttarakhand, India for supporting this work.

6. REFERENCES

Álvarez, A., Pizarro, C., García, R., Bueno, J. L. and Lavín, A. G., 2016. Determination of kinetic parameters for biomass combustion. *Bioresource Technology*, 216, pp.36-43. [DOI]

Arooj, M., Imran, S., Inam-Ur-Raheem, M., Rajoka, MSR., Sameen, A., Siddique, R., Sahar, A., Tariq, S., Riaz A., Hussain, A., Siddeeg, A. and Aadil, RM., 2021. Lotus seeds (Nelumbinis semen) as an emerging therapeutic seed: a comprehensive review. *Food Science and Nutrition*, 9(7), pp.3971-3987. [DOI]

Atabani, A. E., Silitonga, A. S., Ong, H. C., Mahlia, T. M. I., Masjuki, H. H., Badruddin, I. A. and Fayaz, H., 2013. Non-edible vegetable oils: a critical evaluation of oil extraction, fatty acid compositions, biodiesel production, characteristics, engine performance and emissions production. *Renewable and Sustainable Energy Reviews*, 18, pp.211-245. [DOI]

Basu, P., 2013. *Biomass Gasification and Pyrolysis: Theory and Practice*. Academic Press.

Bridgwater, A. V., 2012. Review of fast pyrolysis of biomass and product upgrading. *Biomass and Bioenergy*, 38, pp.68-94. [DOI]

Calin, C., Sirbu, E., Tanase, M., Gyorgy, R., Popovici, D. R. and Banu, I., 2024. A thermogravimetric analysis of biomass conversion to biochar: experimental and kinetic modeling. *Applied Sciences*, 14(21), pp.9856. [DOI]

Demirbas, A., 2001. Biomass resource facilities and biomass conversion processing for fuels and chemicals. *Energy Conversion and Management*, 42(11), pp.1357-1378. [DOI]

Dumont, H. J., 1995. The ecology of the Lotus plant: a review. *Aquatic Botany*, 52(1), pp.3-17.

Elkhalifa, S., Mariyam, S., Mackey, H. R., Al-Ansari, T., McKay, G. and Parthasarathy, P., 2022. Pyrolysis valorization of vegetable wastes: thermal, kinetic, thermodynamics, and pyrolysis analyses. *Energies*, 15(17), pp.1-15. [DOI]

Flynn, J.H. and Wall, L. A., 1966. General treatment of the thermogravimetry of polymers. *Journal of Research of the National Institute of Standards and Technology*, 70A(6), pp.487-523.

Francis Prashanth, P., Midhun Kumar, M. and Vinu, R., 2020. Analytical and microwave pyrolysis of empty oil palm fruit bunch: kinetics and product characterization. *Bioresource Technology*, 310(February), pp.123394. [DOI]

Gil, M. V., Casal, D., Pevida, C., Pis, J. J. and Rubiera, F., 2010. Thermal behavior and kinetics of coal/biomass blends during co-combustion. *Bioresource Technology*, 101(14), pp.5601-5608. [DOI]

Grube, M., Lin, J.G., Lee, P.H. and Kokorevicha, S., 2006. Evaluation of sewage sludge-based compost by FT-IR spectroscopy. *Geoderma*, 130, pp.324-333. [DOI]

Guerrero, M. R. B., Marques Da Silva Paula, M., Zaragoza, M. M., Gutiérrez, J. S., Velderrain, V. G., Ortiz, A. L. and Collins-Martínez, V., 2014. Thermogravimetric study on the pyrolysis kinetics of apple pomace as waste biomass. *International Journal of Hydrogen Energy*, 39(29), pp.16619-16627. [DOI]

Hall, D. O. and Scrase, J. I., 1998. Will biomass be the environmentally friendly fuel of the future? *Biomass and Bioenergy*, 19(3), pp.357-367. [DOI]

Hou, Y., Liang, Y., Hu, H., Tao, Y., Zhou, J. and Cai, J., 2021. Facile preparation of multi-porous biochar from lotus biomass for methyl orange removal: kinetics, isotherms, and regeneration studies. *Bioresource Technology*, 329, pp.124877. [DOI]

Huang, X., Cao, J. P., Zhao, X. Y., Wang, J. X., Fan, X., Zhao, Y. P. and Wei, X. Y., 2016. Pyrolysis kinetics of soybean straw using thermogravimetric analysis. *Fuel*, 169, pp.93-98. [DOI]

Jagnade, P., Panwar, N. L. and Agarwal, C., 2023. Experimental investigation of kinetic parameters of bamboo and bamboo biochar using thermogravimetric analysis under non-isothermal conditions. *Bioenergy Research*, 16, pp.1143-1155. [DOI]

Janković, B., Radojević, M. B., Balać, M. M., Stojiljković, D. D. and Manić, N. G., 2020. Thermogravimetric study on the pyrolysis kinetic mechanism of waste biomass from fruit processing industry. *Thermal Science*, 24(6 part b), pp.4221-4239. [DOI]

Jo, J. H., Kim, S. S., Shim, J. W., Lee, Y. E. and Yoo, Y. S., 2017. Pyrolysis characteristics and kinetics of food wastes. *Energies*, 10(8), pp.1-10. [DOI]

Kampa, M. and Castanas, E., 2008. Human health effects of air pollution. *Environmental Pollution*, 151(2), pp.362-367. [DOI]

Ma, P., Yang, J., Xing, X., Weihrich, S., Fan, F. and Zhang, X., 2017. Isoconversional kinetics and characteristics of combustion on hydrothermally treated biomass. *Renewable Energy*, 114(B), pp.1069-1076. [DOI]

Malika, A., Jacques, N., Jaafar, E. F., Fatima, B. and Mohammed, A., 2016. Pyrolysis investigation of food wastes by TG-MS-DSC technique. *Biomass Conversion and Biorefinery*, 6(2), pp.161-172. [DOI]

McKendry, P., 2002. Energy production from biomass (part 1): overview of biomass. *Bioresource Technology*, 83(1), pp.37-46. [DOI]

Mohan, D., Pittman, C. U. and Steele, P. H., 2006. Pyrolysis of wood/biomass for bio-oil: a critical review. *Energy & Fuels*, 20(3), pp.848-889. [DOI]

Mukherjee, P. K., Mukherjee, D., Maji, A. K., Rai, S. and Heinrich, M., 2009. The sacred lotus (Nelumbo nucifera) - phytochemical and therapeutic profile. *Journal of Pharmacy and Pharmacology*, 61(4), pp.407-422. [DOI]

Müller-Hagedorn, M. and Bockhorn, H., 2007. Pyrolytic behaviour of different biomasses (angiosperms)(maize plants, straws, and wood) in low temperature pyrolysis. *Journal of Analytical and Applied Pyrolysis*, *79*(1-2), pp.136-146.

Muradov, N. Z. and Veziroglu, T. N., 2008. "Green" path from fossil-based to hydrogen economy: an overview of carbon-neutral technologies. *International Journal of Hydrogen Energy*, 33(23), pp.6804-6839. [DOI]

Narnaware, S. L. and Panwar, N. L., 2022. Kinetic study on pyrolysis of mustard stalk using thermogravimetric analysis. *Bioresource Technology Reports*, 17, pp.100942. [DOI]

Noszczyk, T., Dyjakon, A. and Koziel, J. A., 2021. Kinetic parameters of nut shells pyrolysis. *Energies*, 14(3), pp.682. [DOI]

Peng, F., Song, H., Xiang, J., Peisheng, L., Huang, D., Jiang, L., Zhang, A. and Zhang, J., 2010. FTIR study of pyrolysis products evolving from typical agricultural residues. *Journal of Analytical and Applied Pyrolysis*, 88, pp.117-123. [DOI]

Premathilake, R. and Seneviratne, S., 2015. Cultural implications based on pollen from the ancient mortuary complex in Sri Lanka. *Journal of Archaeological Science*, 53, pp.559-569. [DOI]

Vamvuka, D., Kakaras, E., Kastanaki, E. and Grammelis, P., 2003. Pyrolysis characteristics and kinetics of biomass residuals mixtures with lignite⁎. *Fuel*, *82*(15-17), pp.1949-1960.

Vlaev, L. T., Markovska, I. G. and Lyubchev, L. A., 2003. Non-isothermal kinetics of pyrolysis of rice husk. *Thermochimica Acta*, 406(1-2), pp.1-7. [DOI]

Weerachanchai, P., Tangsathitkulchai, C. and Tangsathitkulchai, M., 2010. Comparison of pyrolysis kinetic models for thermogravimetric analysis of biomass. *Suranaree J. Sci. Technol*, *17*(4), pp.387-400.

Yang, H., He, S., Feng, Q., Liu, Z., Xia, S., Zhou, Q., Wu, Z. and Zhang, Y., 2024. Lotus (Nelumbo nucifera): a multidisciplinary review of its cultural, ecological, and nutraceutical significance. *Bioresource and Bioprocessing*, 11, pp.18. [DOI]

Zhang, C., Zhang, Z., Zhang, L., Li, Q., Li, C., Chen, G., Zhang, S., Liu, Q. and Hu, X., 2020. Evolution of the functionalities and structures of biochar in pyrolysis of poplar in a wide temperature range. *Bioresource Technology*, 304, pp.123002. [DOI]

Zhang, Y., Lu, X., Zeng, S., Huang, X., Guo, Z., Zheng, Y., Tian, Y. and Zheng, B., 2015. Nutritional composition, physiological functions and processing of lotus (Nelumbo nucifera Gaertn.) seeds: a review. *Phytochemistry Reviews*, 14(3), pp.321-334. [DOI]

Zhao, H.X., Zhang, H.S. and Yang, S.F., 2014. Phenolic compounds and its antioxidant activities in ethanolic extracts from seven cultivars of Chinese jujube. *Food Science and Human Wellness*, *3*(3-4), pp.183-190.

Zhong, X., Wang, Q., Jiang, Z., Yang, X. and Ji, Y., 2007. Enzymatic hydrolysis of pretreated soybean straw. *Biomass and Bioenergy*, 31, pp.162-167. [DOI]

Zhu, F., 2017. Structures, properties, and applications of lotus starches. *Food Hydrocolloids*, 63, pp.332-348. [DOI]

Nature Environment and Pollution Technology
An International Quarterly Scientific Journal

p-ISSN: 0972-6268
(Print copies up to 2016)
e-ISSN: 2395-3454

Vol. 25 | No. 3 | Article ID D1860 | 2026

Original Research Paper

https://doi.org/10.46488/NEPT.2026.v25i03.D1860

Open Access Journal

Environmental Policies in Mexico: A Critical Analysis of Their Implementation and Results

Rosa Llerena[1]†, Oscar Moncayo[2], Leandra Arboleda[1], Malena Zambrano[1] and Evelyn Navia[1]

[1]Economics Degree, Faculty of Social, Economic and Financial Sciences, State Technical University of Quevedo, Quevedo, Ecuador

[2]Finance Degree, Faculty of Social, Economic and Financial Sciences, State Technical University of Quevedo, Quevedo, Ecuador

†Corresponding author: Rosa Llerena; rllerenag@uteq.edu.ec

Abbreviation: Nat. Env. & Poll. Technol.
Website: www.neptjournal.com

Received: 19-08-2025
Revised: 16-10-2025
Accepted: 27-10-2025

Key Words:

Environmental policies
Sustainable development
Environmental governance
Carbon tax
Circular economy

ABSTRACT

Mexico, as a megadiverse country, is particularly vulnerable to climate change. In response, it has implemented various environmental policies, including Payment for Water Environmental Services (PES), the ban on single-use plastics, and the carbon tax. The purpose of this article is to systematically analyze recent environmental policies, evaluating their impact and contribution to sustainable development. To this end, a methodology based on a Systematic Literature Review (SLR), complemented by a bibliometric analysis, was employed. The information search was conducted using the Scopus and Web of Science (WoS) databases, as well as institutional repositories, resulting in the selection of 134 qualified publications. The analysis of these documents enabled the identification and grouping of key findings in areas such as renewable energy, the circular economy, and environmental governance. Although the results demonstrate substantial progress in these fields, they also reveal critical shortcomings in waste management, reforestation efforts, and environmental monitoring. Additionally, the study identifies tensions between economic interests and sustainability goals, low levels of citizen participation in public policy implementation, and pronounced regional disparities in policy execution. The study concludes by emphasizing the urgent need to strengthen environmental governance through increased citizen engagement, professionalization of institutions, and the assurance of long-term policy continuity.

Citation for the Paper:

Llerena, R., Moncayo, O., Arboleda, L., Zambrano, M. and Navia, E., 2026. Environmental policies in Mexico: A critical analysis of their implementation and results. *Nature Environment and Pollution Technology*, 25(3), D1860. https://doi.org/10.46488/NEPT.2026.v25i03.D1860

Note: From 2025, the journal has adopted the use of Article IDs in citations instead of traditional consecutive page numbers. Each article is now given individual page ranges starting from page 1.

Copyright: © 2026 by the authors
Licensee: Technoscience Publications
This article is an open access article distributed under the terms and conditions of the Creative Commons Attribution (CC BY) license (https://creativecommons.org/licenses/by/4.0/).

1. INTRODUCTION

Environmental protection is a fundamental pillar for ensuring the sustainable economic and social development of countries (D'adamo et al. 2024, García Hernández & Lucatello 2022). In this context, environmental policies serve as key instruments for establishing regulatory frameworks, governance mechanisms, and management strategies aimed at mitigating the effects of climate change and preserving natural resources (Bekun et al. 2021). Mexico, as a megadiverse country and highly vulnerable to environmental impacts, has adopted public policies in recent years aimed at addressing critical issues such as deforestation, air pollution, waste management, and biodiversity loss.

Recent studies on environmental governance in Mexico indicate progress in developing regulatory frameworks aligned with international commitments such as the Paris Agreement and the 2030 Agenda (He et al. 2023, Raihan & Tuspekova 2022). However, structural constraints persist regarding the effective implementation of these policies, institutional fragmentation, and limited administrative continuity (González Ulloa Aguirre & Márquez Muñoz 2021). These challenges are further compounded by tensions between the economic interests of strategic sectors such as energy and agriculture and sustainability goals, resulting in contradictions between policymaking and government practice (Molina et al. 2019)

Although the academic literature has documented these issues, most previous analyses have taken a sectoral or descriptive approach, which limits a comprehensive understanding of the effectiveness of Mexican environmental policies. The novelty of this study lies in its integrative and systematic approach, which combines a systematic literature review (SLR) with bibliometric analysis to identify patterns, gaps, and trends in scientific production on environmental policies in Mexico (Szpilko & Ejdys 2022, Xu & Kim 2022).

In this context, the objective is to systematically analyze the effectiveness of recent environmental policies in Mexico and their contribution to sustainable development, taking into account the legal, institutional, political, and social factors that condition their performance. Although significant progress has been made, such as the establishment of a robust regulatory framework and the signing of relevant international commitments, the central question remains: how effective have these policies been in terms of sustainable environmental outcomes? This question persists despite ongoing challenges, including weak legislative enforcement, insufficient institutional oversight, and a lack of administrative continuity.

1.1. Environmental Policies and Their Role in Sustainable Development

According to Xu & Kim (2022), environmental policies comprise a set of principles, norms, strategies, and actions adopted by governments, international organizations, or private entities to protect the environment and promote sustainable development. These policies aim to prevent, reduce, and mitigate the negative impacts of human activities on natural ecosystems by regulating the use of natural resources, controlling pollution, and promoting responsible practices (Cifuentes-Faura 2022). Generally, they are based on compliance with environmental regulations, the application of economic incentives, and the promotion of clean technologies and renewable energy sources (Souza et al. 2022).

In addition, environmental policies adopt a comprehensive approach that encompasses both economic and social dimensions, as they aim not only to conserve the natural environment but also to improve the quality of life for present and future generations(Miller 2025). These policies are essential in addressing global challenges such as climate change, biodiversity loss, and resource scarcity, and are developed in alignment with international agreements such as the Kyoto Protocol or the Paris Agreement (Silva 2021). The effectiveness of these policies depends on political will, citizen participation, and international cooperation (Husted & Sousa-Filho 2019).

1.2. Key Principles in Environmental Policies

Environmental policies are founded on fundamental principles that aim to ensure fair, sustainable, and environmentally responsible development (Arguello Suárez et al. 2023). One of these principles is environmental justice, which promotes equity in the distribution of environmental benefits and burdens across different social groups, preventing vulnerable communities from disproportionately experiencing the impacts of pollution or limited access to natural resources (Banzhaf et al. 2019). This justice entails not only equitable distribution, but also democratic participation in environmental decisions and recognition of every person's right to a healthy environment (Álvarez & Coolsaet 2020). It also involves protecting territories from harm caused by extractive, industrial, or urban activities, while integrating social, political, and ecological dimensions (Menton et al. 2020).

Another essential pillar is the ecological transition, understood as the process of transforming current production and consumption models towards more sustainable systems based on renewable energies, less pollution, and conservation of natural resources (Vence & Pereira 2019). This process entails not only environmental but also economic and social challenges, requiring effective public policies, technological innovation, and active citizen participation (Leipold 2021). In this context, the circular economy serves as a key strategy, promoting recycling, reuse, and waste minimization to close production cycles, move away from the traditional linear model (Chizaryfard et al. 2021). This regenerative economy not only reduces environmental impact but also fosters efficiency and resilience in economic systems (Gennari 2023), directly supporting the goals of the green transition (Adami & Schiavon 2021).

1.3. Success Stories and Failures of Environmental Policies Implemented in Mexico

Mexico has implemented a range of environmental policies aimed at addressing the challenges of climate change, biodiversity loss, and the degradation of natural resources (Cantú et al. 2021). However, the outcomes have been mixed. While certain initiatives have achieved notable progress in areas such as conservation and the promotion of clean energy, others have been hindered by factors including a lack of policy continuity, weak institutional coordination, and limited citizen engagement (Lytras et al. 2022).

In recent decades, Mexico has promoted various environmental policies aimed at promoting sustainability and mitigating the effects of climate change. One of the most prominent initiatives is the Payment for Ecosystem Services (PES) program, introduced by CONAFOR in 2003. This

program provides financial incentives to forest landowners who engage in ecosystem conservation, contributing to a reduction in deforestation and an increase in vegetation cover (Barquera & Rivera 2020). Similarly, solar energy projects in Baja California and Sonora have advanced the generation of renewable electricity through public-private partnerships, contributing to the reduction of greenhouse gas emissions (Álvarez & Coolsaet 2020). Another noteworthy development is the carbon tax introduced in 2014, which has generated valuable revenue for environmental programs; however, its impact on emissions has been limited due to its relatively low rate (Gálvez 2024). Additionally, the ban on single-use plastics under the 2021 General Law on Circular Economy has yielded positive outcomes in certain cities, although its implementation remains uneven, particularly within the informal sector (Carpio et al. 2021).

However, not all environmental policies have yielded successful outcomes. The case of urban solid waste management, for instance, highlights a significant gap between environmental regulations and their effective implementation. Many cities continue to lack efficient waste collection and recycling systems, resulting in severe pollution issues and low rates of material recovery (García Hernández & Lucatello 2022). Similarly, the General Law on Climate Change of 2012, despite its advanced legal framework, has exhibited structural weaknesses stemming from insufficient coordination among levels of government, which has hindered compliance with mitigation targets (Izquierdo-Tort 2020). The Sembrando Vida (Sowing Life) reforestation program represents another emblematic case; despite its well-intentioned design and substantial public investment, it has faced criticism due to the low survival rate of planted trees (less than 30%) and allegations of corruption (Ojeda-Revah et al. 2020). Recent reports from SEMARNAT (2023) highlight that several federal environmental programs require significant improvements, revealing deficiencies in the design, monitoring, and evaluation processes. In Mexico City, water management continues to pose a major challenge: the Sacmex system has been unable to prevent water losses exceeding 40% due to leaks, nor has it ensured equitable access to this vital resource (Sánchez-Ocampo et al. 2022).

Some initiatives have demonstrated mixed impacts, such as wind projects in Oaxaca. These have been instrumental in positioning Mexico as a regional leader in wind energy, contributing significantly to clean energy generation (Leal et al. 2020). However, its implementation has been marked by a lack of prior consultation with indigenous communities, resulting in social conflicts that have undermined both its legitimacy and sustainability (Arguello Suárez et al. 2023, Fuentes & De León 2024). These cases demonstrate that environmental benefits are not always accompanied by inclusive processes that uphold social rights, underscoring the need to strengthen environmental governance and enhance community participation (Mejía-Montero et al. 2020).

Concurrently, Mexico has sought to diversify its financial instruments through mechanisms such as green bonds, issued since 2015, which have facilitated the financing of sustainable projects in sectors including transportation, water, and energy (SHCP 2021). In 2023, thematic bond issuance reached $38.3 billion, representing a year-on-year growth of 25%. On the Mexican Stock Exchange alone, approximately 60 billion pesos were raised through green bonds, accounting for 45% of the total bonds issued that year (Herrera 2024a). Mexico has also ratified the Escazú Agreement, advancing greater access to environmental information and justice, although its implementation continues to face significant institutional challenges (Barragán et al. 2022). With the update of its Nationally Determined Contribution (NDC) in 2022, the country established more ambitious targets for reducing greenhouse gas emissions, thereby aligning more closely with its international commitments (Loutfi et al. 2024). However, reports from Climate Transparency (2022) and the IEA (2023) caution that the contradiction between these ambitious goals and the continuation of regressive energy policies, centered on fossil fuels and supported by inadequate budgets for environmental institutions, underscores the challenges of policy coherence and long-term sustainability.

Beyond these contradictions, recent assessments indicate that Mexican environmental policies entail economic and environmental trade-offs that warrant more in-depth empirical analysis. For example, Herrera-Ríos (2025) presents spatial econometric evidence on the relationship between CO emissions and economic activity across Mexican states, demonstrating that economic growth without adequate regulatory oversight leads to increased emissions, thereby underscoring the need to strengthen implementation and enforcement mechanisms. Similarly, the Guide to Green Bonds in Mexico identifies barriers to accessing sustainable financing for small and medium-sized enterprises, which limit the adoption of mitigation projects at the local level. This evidence reinforces the idea that the success of environmental policies depends not only on their regulatory design but also on the institutional, financial, and social capacities required to ensure compliance and sustainability (Herrera 2024b).

Table 1 compares Mexican environmental policies, highlighting initiatives that achieved their objectives versus those with limited results. Successful cases exhibit characteristics such as community participation, effective economic incentives, and public-private partnerships, whereas unsuccessful ones reveal structural issues

Table 1: Success and failure stories of environmental policies in Mexico.

Case Type	Policy/Programme	Description	Results	Fountain
Success	Payment for Ecosystem Services (PES) Program	Initiated in 2003 by CONAFOR to incentivize forest conservation through payments to landowners.	Reduction of deforestation in the participating areas and increase of forest cover.	Muñoz-Piña et al. (2008)
	Solar energy in Baja California and Sonora	Promotion of photovoltaic energy through incentives and public-private investment.	Significant expansion of renewable electricity generation and reduction of emissions.	IRENA (2021)
	Green bonds (2015-present)	Issuance of financial instruments to finance sustainable projects in transport, energy and water.	Mexico was the first country in Latin America to issue sovereign sustainability bonds, leveraged resources for green infrastructure.	SHCP (2021)
	Carbon Tax (2014)	Tax on fossil fuels to discourage their use and finance environmental projects.	Generation of useful income, but limited impact on reducing emissions (price set too low).	OECD (2019)
	Wind projects in Oaxaca	Expansion of wind farms for clean energy generation.	Increase in renewable energies, but conflicts with communities due to a lack of prior consultation.	CEMDA (2022)
	Sustainable Communities Program (2020-present)	Promotion of conservation, ecotourism and green economy practices in rural areas.	Improved community income, biodiversity conservation and local empowerment.	SEMARNAT (2022)
	Escazú Agreement (ratified in 2021)	International treaty to guarantee access to information, public participation and environmental justice.	Improving environmental transparency and the rights of environmental defenders: challenges in local implementation.	Barragán et al. (2022)
	Nationally Determined Contribution (NDC) – 2022 Update	More ambitious climate commitments: 35% reduction in GHG by 2030 and 51% reduction in black carbon.	Progressive revision of climate targets, still in the stage of compliance and implementation of sectoral policies.	INECC (2022)
	Single-Use Plastics Ban (2021)	The General Law of Circular Economy that prohibits disposable plastics in several states.	Visible reduction in cities, but uneven implementation in the informal sector.	SHCP (2021)
	National Electric Mobility Strategy (2023)	Roadmap for the transition to electric transport, with support for public and private fleets.	Despite advances in electric bus fleets in Mexico City and Monterrey, it still faces challenges in charging infrastructure.	SEMARNAT (2023)
Fault	Urban Solid Waste Management	Despite federal laws, many cities lack adequate collection and recycling systems.	Persistent pollution, open-air landfills and low recycling rate (<10%).	SEMARNAT (2020)
	Mexico's General Law on Climate Change (2012)	An advanced legal framework, but with poor implementation and a lack of intergovernmental coordination.	Low emission reductions and non-compliance with climate targets.	OECD (2025)
	Amendments to the Electricity Industry Law (2021)	Reform that gives priority to CFE energy over private renewables.	International lawsuits, legal uncertainty, fall in investment in renewable energies.	IEA (2023)
	Reduction of the environmental budget (2018-2022)	Cuts to SEMARNAT and key environmental agencies (INECC, CONANP).	Reduction of environmental monitoring, protection of natural areas and technical capacity.	CEMDA (2022)
	Regressive energy policy (2019-2023)	Preference for CFE's power generation based on fossil fuels, limiting renewables.	Reduction of foreign investment in renewables, setbacks in the energy transition objectives.	Climate Transparency (2022)
	Sowing Life Reforestation	Massive social reforestation program (2019-2024) with financial support for participants.	High investment, but low tree survival rate (<30%) and allegations of corruption.	Ramírez Valverde et al. (2024)
	Water Management in Mexico City (Sacmex)	Policies to improve distribution and reduce losses in the capital's water network.	40% losses due to leaks, and inequality in access to drinking water.	IMTA (2021)
	Failure to meet e-waste targets	Lack of effective national policies for the recycling of electronic waste.	Accumulation of technological waste and exposure to hazardous pollutants.	IMTA (2021)

such as corruption, weak oversight, and poor technical design. The analysis indicates that success depends more on implementation than on regulatory design, clearly distinguishing policies that generate sustainable outcomes from those that perpetuate environmental problems despite significant investment (Cantú et al. 2021).

2. Materials and methods

This study was conducted through a Systematic Literature Review (SLR), complemented by bibliometric analysis and bibliographic coupling techniques, with the aim of identifying patterns, approaches, and results in the scientific literature on environmental policies in Mexico. According to Kunisch et al. (2018), this type of review enables the consolidation and structuring of knowledge in a specific area through a transparent and replicable process based on clearly defined selection criteria.

Given the growing volume of publications, the diversity of analytical frameworks, and the increasing complexity of environmental problems, a methodology was selected that combines the rigor of a Systematic Literature Review with the visual and analytical potential of bibliometric mapping (Anh et al. 2025). This approach provided a comprehensive overview of the field, identified knowledge gaps, and highlighted emerging trends and priority areas for future research.

The review identified the most frequent approaches, documented results, and impacts of environmental policies in Mexico, as reported in the specialized literature. Based on these findings, new lines of research emerged around environmental governance, climate justice and sustainability. The systematization provided a critical perspective on the performance of these policies, highlighting both the advances and limitations in their implementation, and offering key insights for the design of more effective and participatory strategies within the context of the country's ecological transition (Szpilko & Ejdys 2022).

2.1. Study Design

Fig. 1 presents the inclusion and exclusion criteria, defined based on thematic relevance, publication timeliness (2018-2025), and the methodological rigor of the sources analyzed. In addition to the articles indexed in Web of Science (WoS) and Scopus, gray literature, such as technical reports, institutional evaluations, and government documents issued by agencies including SEMARNAT, UNDP, and OECD, is systematically considered to complement the empirical evidence on the

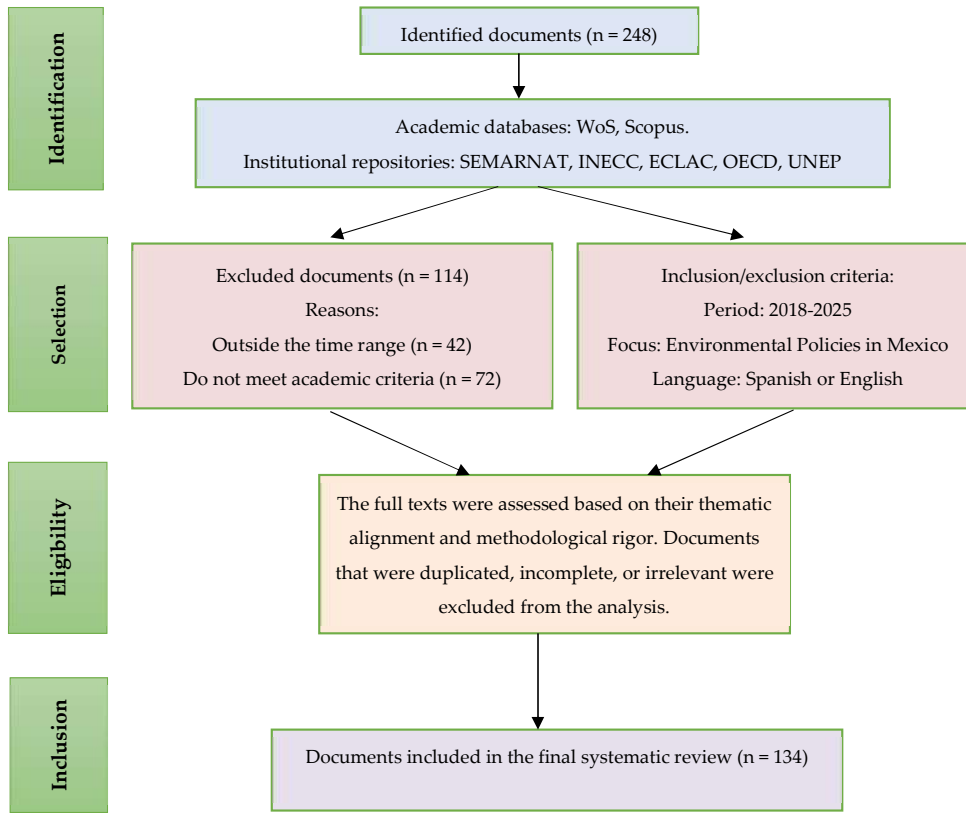


Fig. 1: PRISMA-SLR process flowchart.

implementation of Mexican environmental policies. This selection enabled a more comprehensive understanding of public policy developments and challenges, particularly in areas where academic research remains limited.

The search strategy was developed using Boolean operators and key terms related to public policies, environmental governance, and sustainability in Mexico, following the methodological recommendations of van Oorschot et al. (2018). Specific queries were formulated to include the following terms and their variants (Table 2).

After the initial collection of sources, quality and relevance filters were applied through a manual review of titles, abstracts and keywords, ensuring the scientific validity of the selected documents (Clark et al. 2024). Materials lacking methodological rigor, such as brief articles, technical notes, or opinion pieces, were excluded, with priority given to studies providing empirical evidence or substantive analyses on the implementation and evaluation of environmental policies. This process resulted in the construction of a solid and diversified documentary corpus, comprising both academic and non-academic literature, which enabled a comparative and systematic examination during the critical phase of the analysis.

To minimize potential biases in the selection process, the analysis of the sources was carried out independently by two researchers. Each one applied the previously established inclusion and exclusion criteria. Subsequently, the results were compared, and the discrepancies were discussed until a consensus was reached. This process ensured a more objective review and reduced the risk of omitting information relevant to the study.

2.1.1. Bibliometric Analysis and Knowledge Mapping

With the final corpus, a bibliographic coupling analysis was implemented to identify networks and clusters between documents that share references. This technique allows examining the intellectual structure of the field by detecting publications that share common references, revealing their conceptual proximity (Rethlefsen et al. 2021). The analysis was carried out with the specialized software VOSviewer, developed by van Eck & Waltman (2010), which allows the construction of similarity maps and the visualization of nodes and clusters of publications according to their bibliographic connections. The distance between articles (Sikh) was calculated using the formula:

$$Sij = Cij — (Wi \times Wj) \quad ...(1)$$

Where Cij represents the number of co-occurrences between the elements i and j, and Wi, Wj are the total number of occurrences of each element.

This approach facilitated the identification of current trends, thematic gaps, and emerging areas related to the evaluation of environmental public policies in Mexico. Although the phases were planned sequentially, the application of the method was iterative and flexible, which allowed adjustments based on preliminary findings. The combination of systematic review and bibliometric analysis provided methodological robustness to the study, favoring robust interpretations aimed at the formulation of more effective and participatory strategies for environmental governance in Mexico (Mozas Moral et al. 2020, Szpilko & Ejdys 2022)

Table 2: Syntax used in query calibration for database exploration.

No.	Query syntax	Number of results
1	"environmental policies" OR "environmental policy" OR "environmental governance" AND "Mexico"	171
2	"evaluation" OR "implementation" OR "impact"	53
3	"climate change" OR "sustainability" OR "sustainable development"	24

3. RESULTS

3.1. Descriptive Analysis of Selected Sources

The final corpus comprised a total of 134 documents selected according to the established criteria, enabling a comparative approach and the identification of trends in both scientific and institutional production on environmental policies in Mexico (Rethlefsen et al. 2021, van Oorschot et al. 2018).

Table 3 presents the structure of the systematic review. The temporal distribution of the publications indicates a significant concentration between 2021 and 2023, reflecting a growing interest in environmental policies in Mexico. This increase coincides with the strengthening of the National Climate Agenda and the update of the Nationally Determined Contribution (NDC) during the same period.

In terms of document type, 78% of the corpus consisted of scientific articles, while the remaining 22% includes book chapters, technical reports, institutional documents and books. The most frequently cited journals were *Sustainability and Science of the Total Environment*. From a geographical perspective, most studies focused on national or regional contexts within Mexico. However, comparative analyses of international scope were also identified, particularly involving other Latin American countries. This overview enabled the contextualization of the main thematic and methodological trends of recent research.

The bibliometric analysis conducted using VOSviewer software, based on scientific publications related to

Table 3: Distribution of revised documents by type, year and source (2018-2025).

Post Type	2018–2020	2021–2023	2024–2025	Principal Fuentes/Databases	Total [n]
Scientific Articles	38	47	21	Scopus, WoS	104
Book Chapters	2	4	2	Scopus, SpringerLink	8
Technical/Institutional Reports	5	8	4	SEMARNAT, INECC, OECD, UNEP, ECLAC	17
Books	1	1	1	Institutional and Academic Editors	3
Total	46	60	28	—	134

Source: Authors' elaboration based on the Systematic Review of Literature (2018-2025).

environmental governance in Mexico (Table 2), revealed key associations among the most prominent terms in this field. As shown in Fig. 2, environmental policies are closely linked to concepts such as environmental management, sustainable development, green development, and climate change. This interconnectedness underscores the central role that these policies play in promoting sustainable strategies and mitigating the effects of climate change.

In the context of Mexico, these findings are particularly relevant for evaluating the implementation and outcomes of environmental policies. Martínez & Mesa (2021) point out that, although environmental policies promote sustainable development, their financial impact on companies can be socially negative. This aligns with the identified challenges, where the adoption of environmental regulations may encounter economic and operational barriers. These divergences underscore the complexity of implementing effective environmental policies in Mexico, where factors such as industrial structure, economic incentives, and institutional capacity can influence outcomes (Walter 2020). While these policies are essential for advancing green development, they can generate tensions between sustainability and profitability, particularly in the short term (Velasco & Mumme 2025).

3.2. Cluster Analysis in Terms of Environmental Policies

The bibliometric analysis conducted using VOSviewer (Fig. 3) identified three primary thematic groups, green, red, and blue, that organize the scientific production on environmental policies in Mexico between 2018 and 2025. The network, comprising 134 documents and 312 terms with at least five co-occurrences, exhibits an average link strength of 28.4 and a network density of 0.43, indicating a moderate level of interconnection among the analyzed topics.

3.2.1. Red Cluster: Circular Economy Tension

The red cluster, representing 8.3% of the network, concentrates terms such as circular economy, business competitiveness, and sustainable production. This group illustrates the tension

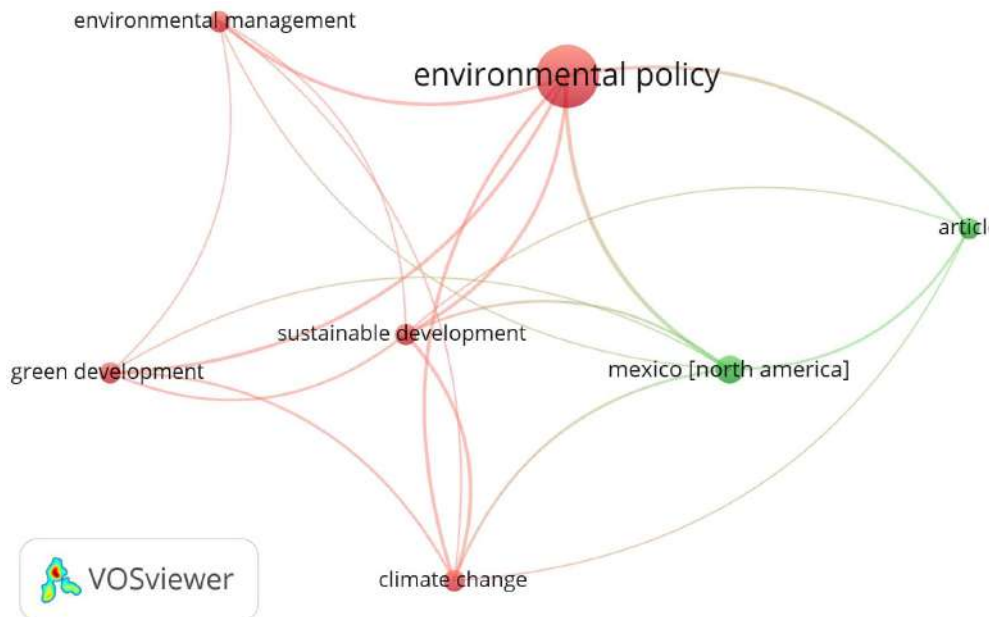


Fig. 2: Thematic association map between categories visualized in VOSviewer.

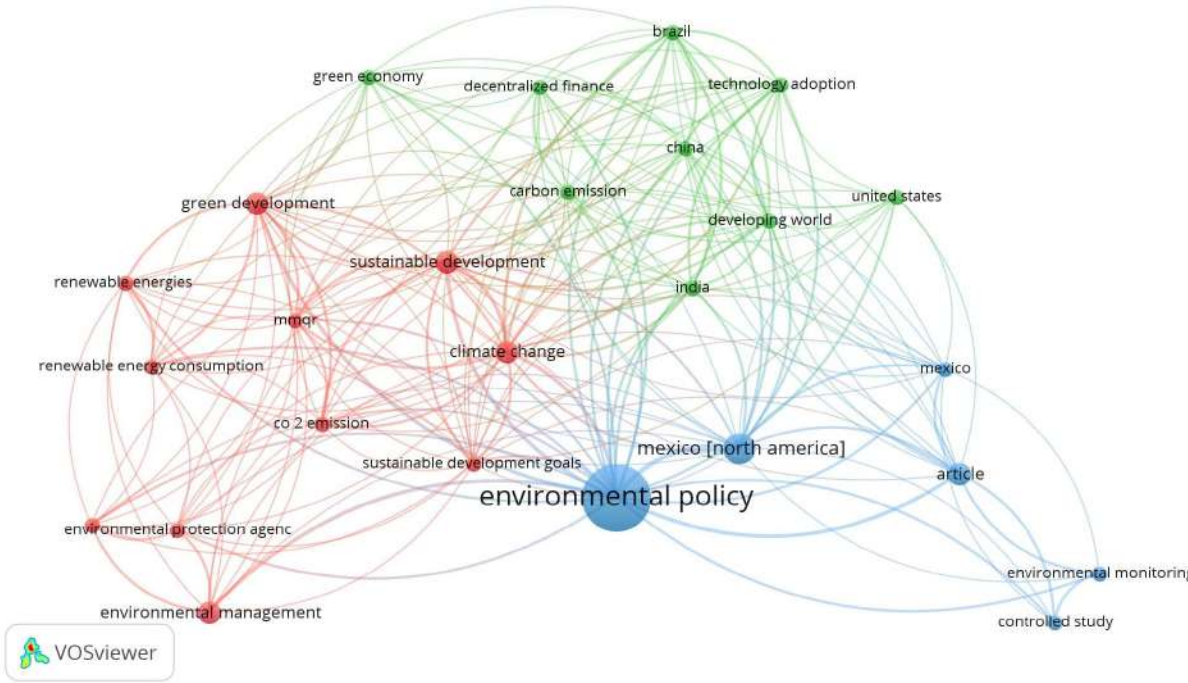


Fig. 3: Relationship between productive sectors and environmental policies.

between sustainability and profitability, a common dilemma in economies dependent on manufacturing for export. Carpio et al. (2021) found that strict enforcement of environmental regulations increases compliance costs by 12% to 18% during the initial years of adaptation, temporarily affecting competitiveness. However, recent research indicates that integrating circular economy strategies can enhance resource efficiency and increase value added in the medium term (Padilla-Rivera et al. 2024, Rodríguez-Espíndola et al. 2022). In terms of public policy, this cluster highlights the need for green tax incentives and sustainable innovation mechanisms that balance economic and environmental objectives, as promoted by the General Law on Circular Economy (2021) and the Sovereign Green Bonds issued by the SHCP (2021).

3.2.2. Green Cluster: Challenges of the Energy Transition

The green cluster encompasses concepts related to renewable energies, CO_2 emissions, and energy efficiency. It accounts 13.7% of the co-occurrences in the total corpus, underscoring the priority of this issue on the Mexican agenda following the update of the NDC(INECC 2022). This group clusters the structural challenges of the energy transition, particularly in the technological adoption of industrial SMEs, where high upfront costs and limited access to financing constrain innovation (Pischke et al. 2019). Comparatively, recent studies in Latin America indicate that technological affordability and regulatory stability are the primary factors influencing the success of the green transition (Afshan et al. 2022, D'adamo et al. 2024). In Mexico, while solar and wind projects in Sonora and Oaxaca have demonstrated progress, their uneven implementation and the associated social conflicts highlight persistent gaps in energy governance (Fuentes & De León 2024).

3.2.3. Blue Cluster: Institutional Fragility

Finally, the blue cluster, representing 10.5% of occurrences, groups together terms related to environmental management, regional planning, and policy evaluation. The low strength of the link between these concepts (average value of 14.6) indicates a weakness in the integration of environmental management with evaluation and accountability mechanisms, reflecting the institutional fragility documented in multiple assessments (He et al. 2023). In Mexico, only 22% of municipalities have adequate systems in place to monitor the impact of their environmental policies (Leal et al. 2020). This institutional gap has also been observed in other Latin American countries, such as Colombia and Peru, where decentralization without technical capacity building has limited the effectiveness of environmental governance (Raihan & Tuspekova 2022). Consequently, this cluster underscores the urgency of strengthening local capacities, professionalizing public environmental services, and promoting intergovernmental coordination.

3.3. Relationship Between Environmental Policies and Sustainable Development

3.3.1. Regulatory and Legal Frameworks

According to Sánchez-Ocampo et al. (2022), the evolution of Mexico's environmental legal framework has been strongly influenced by international agreements such as the Paris Agreement and the 2030 Agenda. Since 2018, the literature has reflected a growing effort to align national legislation with global standards, including reforms to the General Law of Ecological Balance and Environmental Protection (LGEEPA) (Ogwu et al. 2025, ORyan & Ibarra 2018, Pacheco-Vega 2020). However, the studies also indicate that regulatory harmonization remains partial and uneven, with limited coordination between different levels of government and the states (He et al. 2023, SEMARNAT 2022).

Despite the existence of a robust legal framework, limitations in its effective implementation have been identified. Research indicates that environmental regulations, although advanced in design, lack adequate enforcement mechanisms and rely excessively on local political will for their implementation. This has resulted in legal loopholes and fragmentation, particularly in rural and highly biodiverse areas (INECC 2023). Between 2019 and 2023, accusations regarding the discretionary use of concepts such as "public interest" to justify megaprojects intensified, thereby undermining the principle of environmental precaution (ECLAC 2019). Despite certain regulatory advances, such as the incorporation of the principle of environmental justice in some states, inconsistencies persist between legal discourse and institutional practice (Mayen Huerta & Cafagna 2021, Ojeda-Revah et al. 2020).

3.3.2. Government Strategies and Programs

According to Pischke et al. (2019), the Special Climate Change Program (PECC) and the National Energy Strategy have been frequently analyzed in recent literature as the principal instruments of environmental planning in Mexico. Between 2018 and 2022, the publications report progress in the formulation of these programs, including quantifiable targets for emission reductions and the promotion of clean energy (SEMARNAT 2020). However, the approach remains predominantly sectoral and top-down, with limited social participation (Mardero et al. 2018, Margallo et al. 2019).

Budget cuts and administrative changes have been identified as factors that undermine the continuity and effectiveness of government strategies (Izquierdo-Tort 2020, Rodríguez-Espíndola et al. 2022). In particular, the cancellation of funding sources, such as the Climate Change Trust Fund, has resulted in setbacks in the implementation of mitigation and adaptation projects (ECLAC 2019). Despite these obstacles, some technical and academic studies highlight positive experiences in inter-institutional coordination, such as reforestation and watershed conservation programs in Yucatán and Chiapas (Zárate-Toledo et al. 2021). However, these cases remain the exception rather than the rule, reflecting the need to strengthen environmental governance (Barkin 2019, Lewis & Tietenberg 2019).

In addition, there has been a recurrent trend towards the implementation of short-term policies that respond to international pressures or specific crises, such as natural disasters or territorial conflicts, without consolidating structural strategies or long-term evaluation mechanisms (Solorio Sandoval et al. 2020). This reactive inertia has limited the institutionalization of sustainability as a cross-cutting axis in public decision-making (Molina et al. 2019).

3.3.3. Perceptions of Social Actors

The period 2018-2025 has been characterized by a growing visibility of indigenous communities, non-governmental organizations (NGOs), and citizen groups in the field of environmental policies(Abalansa et al. 2021). The literature shows that, although participation in public consultations and evaluation processes has increased, these spaces often lack binding mechanisms and respect for collective rights (Bee 2018, Guibrunet et al. 2021, Ortega Díaz & Gutiérrez 2018).

In many cases, social participation has been mediated by socio-environmental conflicts(Torres-Lima et al. 2018). Cases of criminalization, threats, and violence against environmental defenders have been reported, documented both in institutional reports and in academic theses between 2020 and 2023 (Arroyo & Carrete 2019). This contrasts with the official discourse on openness and transparency.

The trend toward the judicialization of environmental conflicts related to deficient evaluations has increased, particularly in the case of infrastructure megaprojects, such as the Maya Train (Bonilla Padilla 2023). This has generated growing social and academic pressure to reform the current model and adopt more participatory and preventive evaluation schemes (Elmagrhi et al. 2019, López-García & Navarro-Cerrillo 2021).

However, experiences of co-management of natural resources are also highlighted, particularly in community-based tourism and agroecology, where social actors have managed to influence local decisions (Herrera et al. 2018, Nadal et al. 2018). These examples, although limited, demonstrate that effective participation is possible when the appropriate institutional conditions are in place.

3.3.4. Institutional Barriers and Achievements

The presence of institutional barriers, especially in terms of fragmented responsibilities, the lack of trained personnel, and the poor coordination between levels of government, is recurrently evident (Blanco-Portela et al. 2018, Cárdenas-Cabello 2016, Padilla-Rivera et al. 2024). Various publications agree that the Mexican institutional structure lacks the technical and financial capacity to address the challenges of the environmental crisis (Cantú et al. 2021). However, the SLR also reveals certain significant achievements in local contexts. For example, in Oaxaca and Yucatan, cases of intersectoral coordination have been documented that have achieved positive results in resource conservation, sustainable water management, and environmental education (Huesca-Pérez et al. 2018, Zárate-Toledo et al. 2021). These cases were frequently addressed between 2021 and 2024 by thesis studies and articles specialized in territorial development (Gilabert-Alarcón et al. 2018, Mejía-Montero et al. 2020).

Finally, proposals for institutional reform aimed at establishing multilevel governance mechanisms, as well as professionalizing the environmental public service, have been identified (Reyes-Santiago et al. 2019). Although these proposals have not yet been translated into national policies, they represent a promising avenue for strengthening the institutional framework.

4. DISCUSSION

4.1. Correspondence Between Thematic Clusters and Policy Outcomes

The green cluster, associated with the energy transition, illustrates how the lack of financing and regulatory stability hinders the adoption of technology in key sectors. This institutional deficit limits compliance with the NDC and perpetuates dependence on fossil fuels (Fuentes & De Leó 2024, INECC 2023). The red cluster, focused on the circular economy, highlights the tension between environmental policies and economic objectives. The absence of tax incentives and limited public-private coordination has restricted the expansion of sustainable production models, unlike the successful experiences in Brazil, where the Solid Waste Law (2010) established clear responsibilities for producers and municipalities (Padilla-Rivera et al. 2024). Finally, the blue cluster is directly associated with institutional fragmentation and weak evaluation mechanisms. This deficiency prevents accurate measurement of the impact of policies and perpetuates a form of environmental governance that is more formal than effective (He et al. 2023).

4.2. Implications of Environmental Policies

Among the main findings of the Systematic Literature Review (Fig. 4), a persistent structural gap is identified between the regulatory design and the practical implementation of environmental policies in Mexico. This gap results in chronic institutional fragmentation, weak intergovernmental coordination, and poor administrative continuity, which limit the effectiveness of strategies and compromise their long-term sustainability (González Ulloa Aguirre & Márquez Muñoz 2021, Sánchez-Ocampo et al. 2022). Although the country has an advanced legal framework, including the General Law on Climate Change and adherence to the Paris Agreement, policies tend to operate in a reactive and disjointed manner, oriented more toward responding to short-term pressures than consolidating processes of structural transformation.

The evidence analyzed indicates that most Mexican environmental policies retain a discursive and symbolic character, with limited achievements in terms of measurable results (Arvidsson & Dumay 2022). Tensions between economic growth and environmental sustainability remain

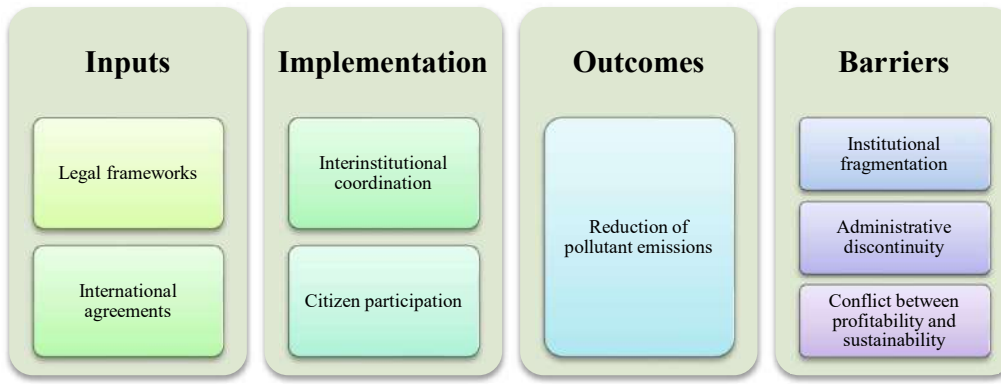


Fig. 4: Main findings of the systematic literature review.

latent, particularly in strategic sectors such as energy, mining, and agribusiness, where policy decisions prioritize short-term profitability over ecological commitments (Elmagrhi et al. 2019). In addition, the lack of independent evaluation mechanisms and limited binding citizen participation reduces the legitimacy and sustainability of public interventions (Izquierdo-Tort 2020, López-Feldman et al. 2021, Ortega Díaz & Gutiérrez 2018).

From a territorial perspective, significant asymmetries in institutional capacity are evident: while entities such as Mexico City, Yucatán, and Nuevo León demonstrate better environmental monitoring and management indicators, the southern and southeastern states exhibit substantial lags due to administrative deficiencies, low technical professionalization, and budgetary constraints (Leal et al. 2020, SEMARNAT 2023). Only 22% of municipalities have formal assessment systems, highlighting an uneven environmental governance pattern that depends on local capacity.

Comparative analysis with Latin America suggests that countries such as Chile and Brazil have reduced these gaps by institutionalizing autonomous environmental agencies and incorporating binding participation mechanisms, thereby strengthening the accountability and stability of public policies (Afshan et al. 2022, Raihan & Tuspekova 2022). In contrast, Mexico maintains a centralized and overlapping model, with environmental competencies dispersed among ministries and agencies, resulting in duplication of functions and low intersectoral coherence.

Likewise, the lack of continuity between government administrations leads to ruptures in institutional learning processes and discontinuities in environmental programs (Cantú et al. 2021, Carpio et al. 2021). In the energy sector, recent reforms have responded more to economic agendas than to sustainability criteria, exacerbating socio-environmental conflicts and increasing citizen distrust of authorities.

4.3. Towards Participatory and Decentralised Governance

The negative correlation between institutional fragmentation and environmental performance, observed in the thematic clusters of energy, circular economy, and institutional management, underscores the need for integrated and evidence-based policies. Overcoming this paradox of regulatory maturity with low effectiveness requires institutional reforms aimed at ensuring technical continuity, financial stability, and effective social participation (Jacobo & Jalile 2023, Rubio 2018). In short, moving towards participatory, decentralized, and technified environmental governance is an indispensable condition for transforming existing regulatory frameworks into sustainable and verifiable outcomes.

Mexico's challenge lies not only in creating new policies but also in strengthening institutional capacity to implement them in a participatory and transparent manner. The literature and data reviewed suggest three priority areas for reform:

1) Professionalization of the environmental public service, ensuring technical continuity beyond political cycles (Reyes-Santiago et al. 2019) .
2) Decentralization with oversight, transferring environmental competencies to local governments while ensuring accompanying supervision and financing mechanisms (Herrera-Ríos 2025).
3) Linking citizen participation, transforming public consultations into co-decision processes, following successful models such as the Regional Environmental Councils in Chile(Bonilla Padilla 2023) or the Local Agenda 21 adopted in Brazil (Mardero et al. 2018).

These measures would enable a transition toward deliberative environmental governance, in which social legitimacy is integrated with technical performance.

5. CONCLUSIONS

Despite significant advances in Mexico's regulatory and institutional design of environmental policies, such as the General Law on Climate Change and adherence to international commitments, a structural gap remains between the formulation and effective implementation of these policies. This gap can be attributed to institutional constraints, weak oversight, and fragmented intergovernmental coordination, all of which undermine the effectiveness and sustainability of environmental strategies. The systematic review indicates that the performance of Mexican environmental policies is uneven. Programs such as Payment for Environmental Services (PES) and the promotion of solar energy have had positive impacts on conservation and mitigation; however, other initiatives, such as Sembrando Vida (Sowing Life), waste management, or Mexico City's water strategy, have suffered from design flaws, corruption, or lack of monitoring mechanisms, limiting their outcomes in the short and medium term.

Moreover, Mexican environmental governance continues to lack binding participatory processes and effective environmental justice. In several cases, local and indigenous communities have been excluded from decision-making on megaprojects, leading to social conflicts and increased environmental litigation. This suggests that sustainability depends not only on the legal framework but also on

the State's capacity to ensure inclusive, transparent governance with institutional continuity. The research confirms that institutional strengthening, professionalization of environmental public services, and coordinated decentralization are necessary for policy effectiveness and legitimacy. Local experiences, such as those in Yucatán and Oaxaca, demonstrate that the combination of political will, social participation, and technical monitoring can lead to more effective and sustainable environmental policies.

It is recommended to conduct empirical studies at the state and municipal levels to evaluate the implementation and impacts of environmental policies. Such studies should focus on identifying factors that explain the success or failure of local programs and on developing environmental governance indicators adapted to territorial realities. Additionally, establishing institutional continuity plans to ensure the persistence of strategic environmental projects beyond administrative changes is a priority. The combination of rigorous technical evaluation, transparent management, and effective citizen participation presents the most viable approach to consolidating a robust, equitable, and sustainable Mexican environmental policy in the long term.

6. ACKNOWLEDGEMENTS

This research was supported by the State Technical University of Quevedo, Faculty of Social, Economic and Financial Sciences.

7. REFERENCES

Abalansa, S., El Mahrad, B., Icely, J. and Newton, A., 2021. Electronic waste, an environmental problem exported to developing countries: the good, the bad and the ugly. *Sustainability (Switzerland)*, 13(9), pp.1-24. [DOI]

Adami, L. and Schiavon, M., 2021. From circular economy to circular ecology: a review on the solution of environmental problems through circular waste management approaches. *Sustainability (Switzerland)*, 13(2), pp.1-20. [DOI]

Afshan, S., Ozturk, I. and Yaqoob, T., 2022. Facilitating renewable energy transition, ecological innovations and stringent environmental policies to improve ecological sustainability: evidence from MM-QR method. *Renewable Energy*, 196(August), pp.151-160. [DOI]

Álvarez, L. and Coolsaet, B., 2020. Decolonizing environmental justice studies: a Latin American perspective. *Capitalism, Nature, Socialism*, 31(2), pp.50-69. [DOI]

Anh, T.T.Y., Herat, S. and Prasad, K., 2025. A review on extended producer responsibility schemes for packaging waste management and research gaps in the field. *Nature Environment and Pollution Technology*, 24(1), pp.1-15. [DOI]

Arguello Suárez, T., Arguello Núñez, L. and Pérez Arévalo, M., 2023. Sustainable mobility model for the implementation of a bike lane in the urban center of the city of Quevedo. In: J.A.M. Domínguez and M.P. Falconett (eds.) *Governance, Sustainable Communities and Port Spaces*. Institute of Local Development, pp.791-815. [DOI]

Arroyo, P. and Carrete, L., 2019. Motivational drivers for the adoption of green energy: the case of purchasing photovoltaic systems. *Management Research Review*, 42(5), pp.542-567. [DOI]

Arvidsson, S. and Dumay, J., 2022. Corporate ESG reporting quantity, quality and performance: where to now for environmental policy and practice? *Business Strategy and the Environment*, 31(3), pp.1091-1110. [DOI]

Banzhaf, H.S., Ma, L. and Timmins, C., 2019. Environmental justice: establishing causal relationships. *Annual Review of Resource Economics*, 11(1), pp.377-398. [DOI]

Barkin, D., 2019. *Distorted Development: Mexico in the World Economy* (1st ed.). Routledge, pp.250. [DOI]

Barquera, S. and Rivera, J.A., 2020. Obesity in Mexico: rapid epidemiological transition and food industry interference in health policies. *The Lancet Diabetes and Endocrinology*, 8(9), pp.746-747. [DOI]

Barragán, D., Torres, V. and De Miguel, C., 2022. *Regional Challenges in the Framework of the Escazú Agreement: Biodiversity Information Management in Megadiverse Countries*. Retrieved January 15, 2025, from https://www.gobiernoabierto.ec/wp-content/uploads/2019/10/Desafios-regionales-acuerdo-de-ezcazu_es.pdf

Bee, B.A., 2018. Power, perception, and adaptation: exploring gender and social-environmental risk perception in northern Guanajuato, Mexico. *Geoforum*, 69(1), pp.71-80. [DOI]

Bekun, F.V., Gyamfi, B.A., Onifade, S.T. and Agboola, M.O., 2021. Beyond the environmental Kuznets Curve in E7 economies: accounting for the combined impacts of institutional quality and renewables. *Journal of Cleaner Production*, 314, pp.1-15. [DOI]

Blanco-Portela, N., R-Pertierra, L., Benayas, J. and Lozano, R., 2018. Sustainability leaders' perceptions on the drivers for and the barriers to the integration of sustainability in Latin American Higher Education Institutions. *Sustainability (Switzerland)*, 10(8), pp.1-20. [DOI]

Bonilla Padilla, D.Á., 2023. Judicialization of politics and megaprojects in Mexico: the role of judges in the legal mobilization against the Mayan Train. *Ratio Juris*, 18(36), pp.169-194. [DOI]

Cantú, A., Aguiñaga, E. and Scheel, C., 2021. Learning from failure and success: the challenges for circular economy implementation in SMEs in an emerging economy. *Sustainability (Switzerland)*, 13(3), pp.1-34. [DOI]

Cárdenas-Cabello, F., 2016. Environmental policy of the government of Mexico: an approach from complex thinking. *Ecocience International Journal*, 3(4), pp.67-76. [DOI]

Carpio, A., Ponce-Lopez, R. and Lozano-García, D.F., 2021. Urban form, land use, and cover change and their impact on carbon emissions in the Monterrey Metropolitan area, Mexico. *Urban Climate*, 39(1), pp.1-15. [DOI]

CEMDA, 2022. *Report on the Situation of Environmental Human Rights Defenders and Communities in Mexico*. Retrieved January 15, 2025, from https://www.cemda.org.mx/wp-content/uploads/2023/04/CEMDA-INFORME-digital.pdf

Chizaryfard, A., Trucco, P. and Nuur, C., 2021. The transformation to a circular economy: framing an evolutionary view. *Journal of Evolutionary Economics*, 31(2), pp.475-504. [DOI]

Cifuentes-Faura, J., 2022. European Union policies and their role in combating climate change over the years. *Air Quality, Atmosphere and Health*, 15(8), pp.1333-1340. [DOI]

Clark, E.C., Burnett, T., Blair, R., Traynor, R.L., Hagerman, L. and Dobbins, M., 2024. Strategies to implement evidence-informed decision making at the organizational level: a rapid systematic review. *BMC Health Services Research*, 24(1), pp.1-35. [DOI]

Climate Transparency, 2022. *Climate Transparency Report: Mexico Country Profile 2022*. Retrieved January 15, 2025, from https://www.climate-transparency.org/countries/americas/mexico

D'adamo, I., Di Carlo, C., Gastaldi, M., Rossi, E.N. and Uricchio, A.F., 2024. Economic performance, environmental protection and social progress: a cluster analysis comparison towards sustainable development. *Sustainability (Switzerland)*, 16(12), pp.1-20. [DOI]

ECLAC, 2019. *Environmental Performance Evaluations in Latin America and the Caribbean*. Retrieved January 15, 2025, from https://www.cepal.org/es/temas/medio-ambiente/evaluaciones-desempeno-ambiental-america-latina-caribe

Elmagrhi, M.H., Ntim, C.G., Elamer, A.A. and Zhang, Q., 2019. A study of environmental policies and regulations, governance structures, and environmental performance: the role of female directors. *Business Strategy and the Environment*, 28(1), pp.206-220. [DOI]

Fuentes, G.A.G. and de León, C.G.D., 2024. Governance in the environment and the case of green policies for the local government of San Pedro Garza García, Mexico. *Debates in Sociology*, 1(59), pp.234-259. [DOI]

Gálvez, R., 2024. Environmental taxation and sustainable development in digital pollution in México. *Science Frontiers*, 5(2), pp.88-95. [DOI]

García Hernández, A.L. and Lucatello, S., 2022. Climate policy integration: taking advantage of policy windows? An analysis of the energy and environment sectors in Mexico (1997–2018). *Journal of Environmental Policy and Planning*, 24(1), pp.56-67. [DOI]

Gennari, F., 2023. The transition towards a circular economy: a framework for SMEs. *Journal of Management and Governance*, 27(4), pp.1-25. [DOI]

Gilabert-Alarcón, C., Salgado-Méndez, S.O., Daesslé, L.W., Mendoza-Espinosa, L.G. and Villada-Canela, M., 2018. Regulatory challenges for the use of reclaimed water in Mexico: a case study in Baja California. *Water (Switzerland)*, 10(10), pp.1-22. [DOI]

González Ulloa Aguirre, P.A. and Márquez Muñoz, J.F., 2021. Social and institutional reconfigurations for the environment and sustainability: lessons for Mexico. *Mexican Journal of Political and Social Sciences*, 67(244), pp.73-101. [DOI]

Guibrunet, L., Gerritsen, P.R.W., Sierra-Huelsz, J.A., Flores-Díaz, A.C., García-Frapolli, E., García-Serrano, E., Pascual, U. and Balvanera, P., 2021. Beyond participation: how to achieve the recognition of local communities' value-systems in conservation? Some insights from Mexico. *People and Nature*, 3(3), pp.528-541. [DOI]

He, X., Khan, S., Ozturk, I. and Murshed, M., 2023. The role of renewable energy investment in tackling climate change concerns: environmental policies for achieving SDG-13. *Sustainable Development*, 31(3), pp.1888-1901. [DOI]

Herrera, H., 2024a. Embedding municipal green bonds in Mexico City's hydrosocial cycle: "green" debt and climate action narratives. *Journal of Political Ecology*, 31(1), pp.302-320. [DOI]

Herrera, H., 2024b. The proliferation of municipal green bonds in Africa and Latin America: the need for a climate justice approach. *Environment and Urbanization*, 36(1), pp.147-172. [DOI]

Herrera, M.R.G., Sasidharan, V., Hernández, J.A.Á. and Herrera, L.D.A., 2018. Quality and sustainability of tourism development in Copper Canyon, Mexico: perceptions of community stakeholders and visitors. *Tourism Management Perspectives*, 27, pp.91-103. [DOI]

Herrera-Ríos, A.Y., 2025. Spatial analysis of CO_2 emissions and their relationship with economic activity in the states of Mexico. *Journal of Andalusian Studies*, 50, pp.136-152. [DOI]

Huesca-Pérez, M.E., Sheinbaum-Pardo, C. and Köppel, J., 2018. From global to local: impact assessment and social implications related to wind energy projects in Oaxaca, Mexico. *Impact Assessment and Project Appraisal*, 36(6), pp.479-493. [DOI]

Husted, B.W. and Sousa-Filho, J.M. de, 2019. Board structure and environmental, social, and governance disclosure in Latin America. *Journal of Business Research*, 102, pp.220-227. [DOI]

IEA, 2023. *International Energy Agency Latin America Energy Outlook, Overview: Mexico*. Retrieved January 15, 2025, from www.iea.org

IMTA, 2021. *Annual Report 2021*. Mexican Institute of Water Technology, pp.50. [DOI]

INECC, 2022. *Nationally Determined Contribution - 2022 Update*. Retrieved January 15, 2025, from https://unfccc.int/sites/default/files/NDC/2022-11/Mexico_NDC_UNFCCC_update2022_FINAL.pdf

INECC, 2023. *Progress and Results 2021*. Retrieved January 15, 2025, from https://www.gob.mx/cms/uploads/attachment/file/830973/PSSPC_informe_de_avances_y_resultados_2022_Repor_2023-1.pdf

IRENA, 2021. *Renewable Energy Statistics 2021*. International Renewable Energy Agency, pp.200. Retrieved from www.irena.org

Izquierdo-Tort, S., 2020. Payments for ecosystem services and conditional cash transfers in a policy mix: microlevel interactions in Selva Lacandona, Mexico. *Environmental Policy and Governance*, 30(1), pp.29-45. [DOI]

Jacobo, A.D. and Jalile, I.R., 2023. Public debt and economic growth nexus in Latin America: a retrospective appraisal. *Economic Paradigm*, 15(2), pp.125-141. Retrieved from https://dialnet.unirioja.es/servlet/articulo?codigo=9083699

Kunisch, S., Menz, M., Bartunek, J.M., Cardinal, L.B. and Denyer, D., 2018. Feature topic at organizational research methods: how to conduct rigorous and impactful literature reviews? *Organizational Research Methods*, 21(3), pp.519-523. [DOI]

Leal, A.R., Perez-Castillo, D., Amorós, J.E. and Husted, B.W., 2020. Municipal green purchasing in Mexico: policy adoption and implementation success. *Sustainability (Switzerland)*, 12(20), pp.1-26. [DOI]

Leipold, S., 2021. Transforming ecological modernization 'from within' or perpetuating it? The circular economy as EU environmental policy narrative. *Environmental Politics*, 30(6), pp.1045-1067. [DOI]

Lewis, L. and Tietenberg, T., 2019. *Environmental Economics and Policy* (7th ed.). Routledge, pp.400. [DOI]

López-Feldman, A., Heres, D. and Marquez-Padilla, F., 2021. Air pollution exposure and COVID-19: a look at mortality in Mexico City using individual-level data. *Science of the Total Environment*, 756, pp.1-8. [DOI]

López-García, J. and Navarro-Cerrillo, R.M., 2021. Changes in the constituents of the "Bosque de Agua" of the Sierra Cruces-Ajusco-Chichinautzín, Mexico, an area with payment for environmental services. *Environmental Earth Sciences*, 80(20), pp.1-15. [DOI]

Loutfi, F., Flores, A., González Marín, M. de L. and Alarcón Montero, P.A., 2024. Situation of circular economy policies in Mexico. *World Resources Institute*, pp.1-38. [DOI]

Lytras, M.D., Serban, A.C., Ruiz, M.J.T., Ntanos, S. and Sarirete, A., 2022. Translating knowledge into innovation capability: an exploratory study investigating the perceptions on distance learning in higher education during the COVID-19 pandemic - the case of Mexico. *Journal of Innovation and Knowledge*, 7(4), pp.1-10. [DOI]

Mardero, S., Schmook, B., López-Martínez, J.O., Cicero, L., Radel, C. and Christman, Z., 2018. The uneven influence of climate trends and agricultural policies on maize production in the Yucatan Peninsula, Mexico. *Land*, 7(3), pp.1-20. [DOI]

Margallo, M., Ziegler-Rodriguez, K., Vázquez-Rowe, I., Aldaco, R., Irabien, Á. and Kahhat, R., 2019. Enhancing waste management strategies in Latin America under a holistic environmental assessment perspective: a review for policy support. *Science of the Total Environment*, 689, pp.1255-1275. [DOI]

Martínez, S.S. and Mesa, A.P., 2021. An in-depth look at the status of environmental financial accounting in Mexico from the point of view of stakeholder theory: myth or reality? *Brazilian Journal of Business Management*, 23(2), pp.318-336. [DOI]

Mayen Huerta, C. and Cafagna, G., 2021. Snapshot of the use of urban green spaces in Mexico City during the COVID-19 pandemic: a qualitative study. *International Journal of Environmental Research and Public Health*, 18(8), pp.1-15. [DOI]

Mejía-Montero, A., Alonso-Serna, L. and Altamirano-Allende, C., 2020. The role of social resistance in shaping energy transition policy in Mexico: the case of wind power in Oaxaca. In: *The Regulation and Policy of Latin American Energy Transitions*. Elsevier, pp.303-318. [DOI]

Menton, M., Larrea, C., Latorre, S., Martinez-Alier, J., Peck, M., Temper, L. and Walter, M., 2020. Environmental justice and the SDGs: from synergies to gaps and contradictions. *Sustainability Science*, 15(6), pp.1621-1636. [DOI]

Miller, S.W., 2025. The environmental history of Latin America. In: R. McNeill and E.S. Mauldin (eds.) *A Companion to Global Environmental History* (3rd ed.). Wiley, pp.108-93. [DOI]

Molina, L.T., Velasco, E., Retama, A. and Zavala, M., 2019. Experience from integrated air quality management in the Mexico City Metropolitan Area and Singapore. *Atmosphere*, 10(9), pp.1-60. [DOI]

Mozas Moral, A., Fernández Uclés, D., Bernal Jurado, E. and Medina Viruel, M.J., 2020. Sustainability, endogenous development and social economy. *Ibero-American Journal of Solidarity Economy and Socio-ecological Innovation*, 3(1), pp.17-35. [DOI]

Muñoz-Piña, C., Guevara, A., Torres, J.M. and Braña, J., 2008. Paying for the hydrological services of Mexico's forests: analysis, negotiations and results. *Ecological Economics*, 65(4), pp.725-736. [DOI]

Nadal, A., Cerón-Palma, I., García-Gómez, C., Pérez-Sánchez, M., Rodríguez-Labajos, B., Cuerva, E., Josa, A. and Rieradevall, J., 2018. Social perception of urban agriculture in Latin America: A case study in Mexican social housing. *Land Use Policy*, 76, pp.719-734. [DOI]

OECD, 2019. *OECD Economic Surveys: Mexico 2019*. OECD Publishing, pp.150. [DOI]

OECD, 2025. *Development Co-operation Profiles: Mexico*. Retrieved January 15, 2025, from https://www.oecd.org/en/publications/development-co-operation-profiles_04b376d7-en/mexico_d55d3494-en.html

Ogwu, M.C., El Malahi, S. and Izah, S.C., 2025. Policy and regulatory frameworks for sustainable environmental practices. In: *Evaluating Environmental Processes and Technologies* (1st ed.). Springer, Cham, pp.544-513. [DOI]

Ojeda-Revah, L., Ochoa González, Y. and Vera, L., 2020. Fragmented urban greenspace planning in major Mexican municipalities. *Journal of Urban Planning and Development*, 146(2), pp.1-10. [DOI]

Ortega Díaz, A. and Gutiérrez, E.C., 2018. Competing actors in the climate change arena in Mexico: a network analysis. *Journal of Environmental Management*, 215, pp.239-247. [DOI]

ORyan, R. and Ibarra, C., 2018. Environmental policy in Latin America. In: A. Farazmand (ed.) *Global Encyclopedia of Public Administration, Public Policy and Governance*. Springer International Publishing AG, pp.1722-1730. [DOI]

Pacheco-Vega, R., 2020. Environmental regulation, governance, and policy instruments, 20 years after the stick, carrot, and sermon typology. *Journal of Environmental Policy and Planning*, 1(2), pp.620-635. [DOI]

Padilla-Rivera, A., Morales Brizard, M., Merveille, N. and Güereca-Hernandez, L.P., 2024. Barriers, challenges, and opportunities in the adoption of the circular economy in Mexico: an analysis through social perception. *Recycling*, 9(5), pp.1-20. [DOI]

Pischke, E.C., Solomon, B., Wellstead, A., Acevedo, A., Eastmond, A., De Oliveira, F., Coelho, S. and Lucon, O., 2019. From Kyoto to Paris: measuring renewable energy policy regimes in Argentina, Brazil, Canada, Mexico and the United States. *Energy Research and Social Science*, 50, pp.82-91. [DOI]

Raihan, A. and Tuspekova, A., 2022. Towards sustainability: dynamic nexus between carbon emission and its determining factors in Mexico. *Energy Nexus*, 8, pp.1-12. [DOI]

Ramírez Valverde, B., Hernández Chontal, Á.Y., Juárez Sanchez, J.P., Gallardo López, F. and Ocampo Fletes, I., 2024. Qualitative analysis of the contribution of "Sembrando Vida" in poverty alleviation. *Entreciencias: Dialogues in the Knowledge Society*, 12(26), pp.1-19. [DOI]

Rethlefsen, M.L., Kirtley, S., Waffenschmidt, S., Ayala, A.P., Moher, D., Page, M.J., Koffel, J.B., Blunt, H., Brigham, T., Chang, S., Clark, J., Conway, A., Couban, R., de Kock, S., Farrah, K., Fehrmann, P., Foster, M., Fowler, S.A., Glanville, J. and Young, S., 2021. PRISMA-S: an extension to the PRISMA statement for reporting literature searches in systematic reviews. *Systematic Reviews*, 10(1), pp.1-20. [DOI]

Reyes-Santiago, M. del R., Sánchez-Medina, P.S. and Díaz-Pichardo, R., 2019. The influence of environmental dynamic capabilities on organizational and environmental performance of hotels: evidence from Mexico. *Journal of Cleaner Production*, 227, pp.414-423. [DOI]

Rodríguez-Espíndola, O., Cuevas-Romo, A., Chowdhury, S., Díaz-Acevedo, N., Albores, P., Despoudi, S., Malesios, C. and Dey, P., 2022. The role of circular economy principles and sustainable-oriented innovation to enhance social, economic and environmental performance: evidence from Mexican SMEs. *International Journal of Production Economics*, 248, pp.1-15. [DOI]

Rubio, I.C., 2018. Tourism, environmental damage, and climate policy at the coast of Oaxaca, Mexico. In: *A Critical Approach to Climate Change Adaptation: Discourses, Policies and Practices* (1st ed.). Routledge, pp.111-97. [DOI]

Sánchez-Ocampo, E.M., Téllez-López, A.M., Islas-Flores, H. and Gómez-Oliván, L.M., 2022. Environmental laws and politics, the relevance of implementing regulation of the presence of emerging pollutants in Mexico: a systematic review. *Water Emerging Contaminants and Nanoplastics*, 1(2), pp.1-23. [DOI]

SEMARNAT, 2020. *Basic Diagnosis for Integrated Waste Management* (1st ed.). Retrieved January 2025 ,15, from https://www.gob.mx/cms/uploads/attachment/file/554385/DBGIR-15-mayo-2020.pdf

SEMARNAT, 2022. *Design Evaluation 2022 Conservation Program for Sustainable Development*. Retrieved January 15, 2025, from https://www.conanp.gob.mx/evaluacionesdiseno_programaspresupuestarios/MOCyR_InformeFinal_S046_200323.pdf

SEMARNAT, 2023. *National Electric Mobility Strategy Directorate of Climate Change Mitigation Policies*. Retrieved January 15, 2025, from https://www.gob.mx/cms/uploads/attachment/file/832517/2.3.ENME.pdf

SHCP, 2021. *SDG-Linked Sovereign Bonds: Impact Report*. Retrieved January 15, 2025, from https://www.gob.mx/shcp

Silva, S., 2021. Corporate contributions to the Sustainable Development Goals: an empirical analysis informed by legitimacy theory. *Journal of Cleaner Production*, 292, pp.1-12. [DOI]

Solorio Sandoval, I.F., Carrillo Jiménez, A.R. and Guzmán Gómez, I.M., 2020. The institutional architecture of Mexico's climate policy: an analysis from the policy integration approach. *Political Studies*, 51(51), pp.191-216. [DOI]

Souza, M.C.O., Rocha, B.A., Adeyemi, J.A., Nadal, M., Domingo, J.L. and Barbosa, F., 2022. Legacy and emerging pollutants in Latin America: a critical review of occurrence and levels in environmental and food samples. *Science of the Total Environment*, 848, pp.1-18. [DOI]

Szpilko, D. and Ejdys, J., 2022. European Green Deal — research directions: a systematic literature review. *Economics and Environment*, 81(2), pp.8-38. [DOI]

Torres-Lima, P., Conway-Gómez, K. and Buentello-Sánchez, R., 2018. Socio-environmental perception of an urban wetland and sustainability scenarios: a case study in Mexico City. *Wetlands*, 38(1), pp.169-181. [DOI]

Van Eck, N.J. and Waltman, L., 2010. Software survey: VOSviewer, a computer program for bibliometric mapping. *Scientometrics*, 84(2), pp.523-538. [DOI]

van Oorschot, J.A.W.H., Hofman, E. and Halman, J.I.M., 2018. A bibliometric review of the innovation adoption literature. *Technological Forecasting and Social Change*, 134, pp.1-21. [DOI]

Velasco, M. and Mumme, S.P., 2025. Environmental capacities in Latin

America: a comparison of Brazil, Chile, and Mexico. *Social Science Journal*, 62(1), pp.199-218. [DOI]

Vence, X. and Pereira, Á., 2019. Eco-innovation and circular business models as drivers for a circular economy. *Accounting and Administration*, 64(1), pp.1-19. [DOI]

Walter, J.M., 2020. Comparing the effectiveness of market-based and choice-based environmental policy. *Journal of Policy Modeling*, 42(1), pp.173-191. [DOI]

Xu, Q. and Kim, T., 2022. Financial constraints and corporate environmental policies. *The Review of Financial Studies*, 35(2), pp.576-635. [DOI]

Zárate-Toledo, E., Wood, P. and Patiño, R., 2021. In search of wind farm sustainability on the Yucatan coast: deficiencies and public perception of environmental impact assessment in Mexico. *Energy Policy*, 158, pp.1-12. [DOI]

Nature Environment and Pollution Technology
An International Quarterly Scientific Journal

p-ISSN: 0972-6268
(Print copies up to 2016)
e-ISSN: 2395-3454

Vol. 25 | No. 3 | Article ID B4390 | 2026

Original Research Paper

https://doi.org/10.46488/NEPT.2026.v25i03.B4390

Open Access Journal

Clay Brick Performance with Red Mud, Waste Foundry Sand, and Silica Fume: A Taguchi Approach

Smita S. Borchate[1], Praveen A. Ghorpade[2]†, Basavaraj G. Katageri[3] and Nayana P. Hoolikantimath[4]

[1]Visvesvaraya Technological University, Belagavi, Karnataka -590018, India and Department of Civil & Environmental Engineering, Kolhapur Institute of Technology's College of Engineering (Autonomous), Kolhapur, Maharashtra-416234, India

[2]Department of Civil Engineering, KLE Technological University, Dr. M. S. Sheshgiri Campus, Belagavi-590008, Karnataka, India and Visvesvaraya Technological University, Belagavi-590018, India

[3]GITAM School of Technology, Bengaluru Campus, Bengaluru, Karnataka, India

[4]Department of Civil Engineering, KLE Technological University, Dr. M. S. Sheshgiri Campus, Belagavi-590008, Karnataka, India

†Corresponding author: Praveen A. Ghorpade; praveenghorpade1@gmail.com

Abbreviation: Nat. Env. & Poll. Technol.
Website: www.neptjournal.com

Received: 30-08-2025
Revised: 23-10-2025
Accepted: 26-10-2025

Key Words:

Red mud
Waste foundry sand
Silica fume
Clay bricks
Geopolymerisation
Grey relational analysis

Citation for the Paper:

Borchate, S.S., Ghorpade, P.A., Katageri, B.G. and Hoolikantimath, N.P., 2026. Clay brick performance with red mud, waste foundry sand, and silica fume: A Taguchi approach. *Nature Environment and Pollution Technology*, 25(3), B4390. https://doi.org/10.46488/NEPT.2026.v25i03. B4390

Note: From 2025, the journal has adopted the use of Article IDs in citations instead of traditional consecutive page numbers. Each article is now given individual page ranges starting from page 1.

Copyright: © 2026 by the authors
Licensee: Technoscience Publications
This article is an open access article distributed under the terms and conditions of the Creative Commons Attribution (CC BY) license (https://creativecommons.org/licenses/by/4.0/).

ABSTRACT

This study addresses the environmental concerns associated with the disposal of red mud (RM) and Waste Foundry Sand (WFS). It explores the use of these industrial by-products, along with silica fume, fly ash, and Desur clay, to produce geopolymer clay bricks as a sustainable alternative to traditional clay bricks. Initially, 5M geopolymeric clay bricks were produced by partially substituting natural clay with RM, fly ash, WFS, sodium silicate, and caustic. The highest compressive strength achieved was 3.27 $N.mm^{-2}$ with a 5M caustic concentration. To further optimize the raw materials and enhance the strength, WFS was partially replaced with different percentages of silica fume. Grey Relational Analysis (GRA) was used to identify the most effective mix, transforming multiple objectives into a single optimal solution. Nine mix designs were developed following the Taguchi L9 orthogonal array. The optimum mix demonstrated a compressive strength of 5.02 $N.mm^{-2}$, comprising 13.75% red mud, 10% silica fume, 12.85% WFS, 33.43% Desur clay, and 30% fly ash. Water absorption remained within allowable limits across all samples. Variance analysis indicated that silica fume (47.45%) was the most influential factor, followed by red mud (30.36%), while WFS contributed the least (21.17%). Microstructural and mineralogical analyses using SEM, FTIR, and XRD confirmed the formation of geopolymeric gels and stable phases. Heavy metal assessments via ICP verified that the bricks are environmentally safe for utilization.

1. INTRODUCTION

Red mud (RM), also known as bauxite residue, is a by-product generated during Bayer's alumina production process. Globally, approximately 150 million tons of red mud are produced each year. For every ton of alumina manufactured, about 1 to 1.5 tons of red mud are generated, with the exact amount depending on the quality of the bauxite ore. The process begins with the fine grinding of bauxite ore using a ball mill in a wet environment. The resulting slurry is then digested in a caustic solution, dissolving the alumina while leaving behind solid red mud. This red mud is separated after several washing steps. The high pH (11–13) of the residue is mainly due to residual caustic bound to the red mud. Land disposal and lagooning methods can lead to groundwater contamination through alkali leachate. Conversely, dry stacking can cause airborne pollution because of the fine particles. Both disposal methods require significant land area, making them costly and environmentally challenging (Rai et al. 2020).

Early research showed the use of processed red mud as a material for road construction and the stabilization of acidic soil (Reddy et al. 2021). Red mud is

also utilized as a partial substitute for fly ash, cement, and filler material. Bricks or blocks made with stabilized red mud using 5% hydrated lime can be used to construct the walls of economical dwellings (Dass & Malhotra 1990, Kumar et al. 2021).

Waste Foundry Sand (WFS) is another industrial solid waste of concern, generated after becoming worn out during mold-making in metal casting industries. Foundry sand, along with binders, is frequently used for casting molds. After repeated use, the foundry sand becomes unsuitable for new molds. Such sand is termed WFS (Matos et al. 2019). Several authors have studied its use as a replacement for natural sand and Portland cement in concrete, as well as a replacement for fine aggregate to improve strength. Some researchers have explored using 30% WFS to replace natural sand in the production of clay bricks. The utilization of WFS remains a challenge despite its various applications (Billong et al. 2021, Matos et al. 2019).

Silica fume (SF) is a by-product generated during the production of silicon and ferrosilicon alloys. Its main component is non-crystalline silica (SiO_2), constituting approximately 85 to 99% of the material. Silica fume is primarily used in various construction and industrial applications, including concrete and grout for parking decks, marine structures, and highway bridges, as well as in oil well cementing, cementitious restoration products, and refractory and ceramic materials (Siddique & Chahal 2011).

Recycling industrial waste such as red mud, waste foundry sand, fly ash, and silica fume promotes green construction by reducing pollution, conserving natural resources, and minimizing landfill use. This approach creates eco-friendly materials, improves resource efficiency, and supports a circular economy while aligning with global sustainability goals (Kumar et al. 2025). Environmental regulations have become more restrictive regarding the safe disposal of these wastes. Due to the growing demand for bricks as a construction material, many researchers have attempted to utilize wastes such as fly ash, sludge, wood sawdust, processed waste tea, rubber, polystyrene, waste glass, acrylic waste, and limestone dust in the manufacture of conventional burnt clay bricks (Ishaq et al. 2025, Saravanan & Rao 2023).

Mineral deposits such as clay soil are extensively used to manufacture conventional burnt clay bricks. Asia produces approximately 1.2 trillion clay bricks per year. About 75% of the world's clay bricks are manufactured in China, India, Pakistan, and Bangladesh. India's annual utilization of burnt clay bricks is 180 billion tons (Abbas et al. 2017). It is estimated that 350 million tons of fertile topsoil are used every year to make burnt clay bricks. To overcome the issues associated with conventional burnt clay bricks, such as greenhouse gas emissions, high-temperature processing, and reduced productivity of surrounding fertile land, the Government of India has prohibited the production of clay bricks and promoted alternative building materials (Hafez et al. 2022).

Bottom ash (F-class), when combined with a highly alkaline solution, can be used as a pozzolanic material. It produces an aluminosilicate polymer through a chemical reaction, known as a geopolymer. Apart from reducing the cost of conventional bricks, the production of geopolymeric clay bricks derived from fly ash facilitates the utilization of industrial waste (Nandipati et al. 2023). Most studies have used sodium silicate and sodium hydroxide as activators for producing geopolymeric fly ash-based bricks (Bajpai et al. 2020, Turkey et al. 2022). Considering the disposal problems associated with red mud due to its alkalinity, various efforts have been made to neutralize it. However, the neutralization of red mud would be uneconomical (Phoo-ngernkham et al. 2014).

Red mud has proven effective as a geopolymer composite binding material, along with metakaolin, fly ash, coal gangue, slag, arsenic sludge, and rice husk (Apithanyasai et al. 2020, Mudgal et al. 2021). Geopolymers consist of Si and Al tetrahedra linked with oxygen atoms in the three-dimensional structures of Calcium Silicate Hydrate (C-S-H) and Sodium Aluminosilicate Hydrate (N-A-S-H) gel. The strength of this network depends on the soluble silicon dioxide and aluminum oxide from the aluminosilicate materials. Silicon dioxide from fly ash readily dissolves through alkali ions, but alumina from red mud dissolves more slowly. Since silica fume contains a high amount of amorphous SiO_2, its use with other aluminosilicate components increases the Si/Al ratio in the geopolymer system. Geopolymer strength is positively affected by an increased molar ratio because more sodium aluminosilicate hydrate gel (N-A-S-H) is formed. The finer particle size of silica fume provides a large surface area and accelerates the reaction between the alkaline activator and aluminosilicate materials. These properties of silica fume are beneficial in enhancing the geopolymer reaction (Sutar et al. 2014).

Initially, bricks were cast using WFS and fly ash with alkaline activators, namely sodium silicate and sodium hydroxide, at two different concentrations: 10M and 12M. For bricks prepared with 12M caustic concentration, the highest compressive strength of 3.5 $N.mm^{-2}$ with 3.93% water absorption was achieved. However, these bricks showed strong efflorescence. To overcome this problem, the caustic concentration was lowered to 5M. However, the strength of these bricks was 3.27 $N.mm^{-2}$ (Gaonkar et al.

2023). Therefore, it is important to improve the compressive strength while maintaining a 5M caustic concentration. The present work explores the effective use of silica fume and red mud to increase compressive strength.

According to the conventional procedure, multiple experiments are needed to determine the effect of different percentages of RM, SF, and WFS on the compressive strength of red mud-based geopolymeric bricks (Mohmed & Scholar 2018, Sutar et al. 2014, Rajesrajeswari et al. 2014). An appropriate trial design was required to minimize the number of experiments and evaluate the effects of individual constituents. The Taguchi method is an effective approach for designing experiments with the fewest trials (Rai et al. 2012). The Taguchi multi-response Grey Relational Analysis (GRA) method can also identify the best set of factor values for multiple responses simultaneously (Shivaprasad & Das 2018).

While numerous studies have investigated the use of industrial wastes in brick manufacturing, a significant knowledge gap persists in the area of comprehensive multi-response optimization, particularly through the integrated application of Taguchi and Grey Relational Analysis (GRA) for systems involving multiple waste materials. This study addresses that gap by employing a structured Taguchi–GRA approach to optimize the combined influence of RM, SF, and WFS in clay-based brick formulations. The primary objective of the present work is to determine the optimal mix parameters that achieve a balance between mechanical strength and water absorption under varying proportions of waste inputs. The findings highlight the effectiveness of multi-response optimization in enhancing waste valorization, offering a viable pathway for large-scale industrial reuse of hazardous and non-biodegradable wastes. This work supports sustainable construction practices by minimizing reliance on natural clay, improving environmental safety, and advancing circular economy principles within the building materials industry.

2. MATERIALS AND METHODS

2.1. Materials

The materials used for making bricks included fly ash (Class F, JSW Energy Ltd., Ratnagiri, Maharashtra, India), red mud (HINDALCO Industries Ltd., Belgaum, Karnataka, India), waste foundry sand (Aqua Alloys Pvt. Ltd., Shinoli, Maharashtra, India), and silica fume (Cilantro Chemicals Pvt. Ltd., Navi Mumbai, Maharashtra, India). These materials had a particle size of less than 45 μm, with content below 2.0%, a specific surface area of over 19 $m^2.g^{-1}$ as measured by Brunauer-Emmett-Teller (BET) analysis, and bulk density ranging from 500 to 700 $kg.m^{3-}$. Additional materials included clay from Desur, Belagavi, Karnataka, India. The chemicals utilized were sodium hydroxide pellets (NaOH, Nice Chemicals LR grade, 97% purity), sodium silicate (Na_2SiO_3, Sunchem Chemicals, containing 16.25% Na_2O, 34.25% SiO_2, and 49.50% water), and demineralized water (conductivity < 10 $\mu S.cm^{-1}$).

2.2. Methodology for Casting Various Combinations of 5M Red Mud Bricks Using A Geopolymeric Approach

Initially, screening experiments with 5M geopolymeric clay bricks involved partially replacing natural clay with RM (18.79%), fly ash (30%), WFS (22.85%), sodium silicate, and caustic. The highest compressive strength achieved was 3.27 $N.mm^{2-}$. To optimize raw materials and enhance the strength of 5M bricks, a portion of the WFS was substituted with various percentages of silica fume, and experimental design and analysis were performed using GAG.

2.2.1. Experimental Method

Standard-size clay bricks measuring 230 mm X 110 mm X 70 mm were cast using a hydraulic-press brick-making machine operating at 13 MPa, following a geopolymeric approach. The raw materials were mixed with geopolymeric constituents, including sodium silicate and sodium hydroxide,

Table 1: Different material weight percentages used in various sets of geopolymer bricks in the present study.

Set of bricks	RM [%]	SF [%]	WFS [%]	FA [%]	Molarity from fresh Caustic	Molarity of Caustic from Red mud
A	13.75	5	17.85	30	4.09	0.91
B	13.75	10	12.85	30	4.09	0.91
C	13.75	15	7.85	30	4.09	0.91
D	18.79	5	12.38	30	3.75	1.25
E	18.79	10	7.85	30	3.75	1.25
F	18.79	15	17.85	30	3.75	1.25
G	23.79	5	7.85	30	3.42	1.58
H	23.79	10	17.85	30	3.42	1.58
I	23.79	15	12.85	30	3.42	1.58

at a ratio of 2.5 to produce different sets of bricks, as shown in Table 1.

All raw materials, including Desur clay, waste foundry sand (WFS), fly ash, silica fume, and red mud, were initially dry-mixed to achieve uniform distribution. Water and the alkaline activator were then added to form the geopolymer mixture. Red mud containing bound caustic was partially substituted for fresh caustic to minimise the risk of caustic leaching from the cast bricks. The Na_2O content in red mud indirectly represents the amount of bound caustic available within it.

The cast bricks were first cured at room temperature for 24 h. To accelerate the geopolymerisation process, the partially dried bricks were subsequently heat-cured in an oven at 80°C for another 24 hours. After heat curing, the bricks were removed and wrapped in a wet cloth for six days under ambient conditions. The curing regime plays a crucial role in determining both the rate and extent of geopolymer formation. Elevated temperatures, such as 80°C, enhance the dissolution of reactive silica and alumina species, thereby accelerating the chemical reactions responsible for geopolymer bond formation. The subsequent moist curing phase supports structural stabilisation and contributes to gradual strength development.

Variations in curing temperature and duration significantly influence the reaction mechanisms, phase evolution, and overall mechanical performance of the geopolymeric matrix. Geopolymers consist of three-dimensional silicoaluminate networks formed by interconnected silicon and aluminium tetrahedra linked through oxygen atoms. While the amorphous silica present in fly ash readily dissolves in the alkaline activator, only limited alumina dissolves from red mud under ambient conditions. Therefore, elevated temperature is essential to facilitate the dissolution of Al^{3+} ions from red mud, enabling its effective participation in the polycondensation process and contributing to the formation of a stronger geopolymeric structure.

The prepared bricks were further evaluated for compressive strength and water absorption. These properties were measured following the standard procedures outlined in IS 3495:1992 (Parts 1 and 2). To investigate the microstructural and mineralogical characteristics of the bricks, X-ray diffraction (XRD), scanning electron microscopy (SEM), and Fourier Transform Infrared Spectroscopy (FTIR) analyses were conducted.

The XRD analysis was performed using a Rigaku SmartLab diffractometer, with a scanning range of 2θ from 5° to 90° at a constant scanning speed of $1°.min^{-1}$, employing CuKα radiation (λ = 1.540 nm). The diffraction peaks obtained were identified and matched with the standard reference database of the Joint Committee on Powder Diffraction Standards (JCPDS) to determine the crystalline phases present in the samples.

The morphological features and surface characteristics of the bricks were examined using a Scanning Electron Microscope (MIRA3 LMH, TESCAN, Brno, Czech Republic, EU). In addition, FTIR analysis was carried out using a BRUKER-ALPHA 100508 Fourier Transform Infrared spectrophotometer to identify the functional groups and bonding environments within the geopolymeric matrix. The spectra were recorded over a wavenumber range of 4,000-400 cm^{-1}.

To assess the environmental stability of the developed bricks, leachate analysis was conducted to determine the potential release of heavy metals. Microwave-assisted acid digestion was performed according to EPA SW-846 Methods 1311 and 3015. For this purpose, the brick samples were crushed into fine powder and passed through a 90 µm sieve to ensure uniform particle size. The powdered samples were pre-digested overnight in 5 mL of nitric acid, followed by the addition of 10 ± 0.1 mL of concentrated nitric acid. The digestion process was carried out in a microwave digester at 175°C for 30 minutes, with the sample vessels rotated at 30 rpm to ensure consistent heating and reaction.

After digestion, the vessels were allowed to cool, and the resulting solutions were filtered to remove any remaining particulates. The filtrates were then transferred into volumetric flasks and diluted to a known volume using demineralised water. The prepared samples were subsequently analysed for heavy metal concentrations using Inductively Coupled Plasma (ICP; MY15230013, Software Version: 7.3.0.8799, Firmware Version: 3354). This analysis provided insight into the leaching behaviour and environmental safety of the geopolymer bricks.

2.2.2. Multi-Response Optimization, Grey-Based Taguchi Method

The Taguchi orthogonal design approach was employed for casting the red mud-based geopolymeric bricks. Three parameters, RM, SF, and WFS, were selected as variables for this study. The fly ash content was kept constant at 30%. The percentage of Desur clay varied with respect to red mud. The ranges and parameter levels were selected based on earlier screening work conducted during the preparation of geopolymeric bricks (Gaonkar et al., 2023). A Taguchi array is called an orthogonal array, where one of the parameters is tested at each level. The L9 orthogonal array, which contains three factors and three levels in the Taguchi method, was employed for the experiments listed in Table 2. In total, nine experiments were carried out. The compressive strength and water absorption values were

Table 2: Factors and levels.

Factors	Level 1[%]	Level 2[%]	Level 3[%]
RM	13.75	18.79	23.79
SF	5	10	15
WFS	17.85	12.85	7.85

obtained from triplicate samples, denoted as Y1, Y2, and Y3 for compressive strength, and W1, W2, and W3 for water absorption, respectively. These values were obtained for each experiment in the L9 array, as shown in Table 3. For the design to work, eight degrees of freedom (DOF) were required.

2.2.3. *Optimisation Steps for Grey-Based Taguchi Method*

The following steps were carried out to optimize factors using the Grey-based Taguchi method. Additionally, these steps are demonstrated with a flowchart as shown in Fig. 1.

Step I: Calculation of Signal-to-Noise Ratio (S/N)

To work out the S/N ratio for every response, the following equation was used:

i. Larger-the-better

$$\text{S/N ratio} = -10 \log_{10}\left(\frac{1}{k}\sum_{i=1}^{n}\frac{1}{x_{ij}^2}\right) \quad \ldots(1)$$

where k = number of replications and xij=observed response value, where i=1, 2, ...m, j=1, 2, ...n. This is used in experiments where maximization of the quality characteristic is required. This is suggested to be the larger-the-better type of experiment.

ii. Smaller-the-better

$$\text{S/N ratio} = -10 \log_{10}\left(\frac{1}{k}\sum_{i=1}^{n} x_{ij}^2\right) \quad \ldots(2)$$

This is designated the smaller-the-better type experiment, where minimization of the characteristic is required.

Step II: Normalization of S/N ratio.

Normalization is modifying a single data input to distribute the data uniformly and scale it into a suitable range for further analysis. The original data must be standardized using the following formula before applying the grey relation theory to the analysis. A suitable value is subtracted from the values in the same array to estimate the value of this array. Use the S/N ratio value when normalizing data for a grey relation analysis.

(To be used for S/N ratio, with the Larger the better manner)

$$Zij=\frac{y_{ij} - min(y_{ij}, i=1,2,\ldots\ldots\ldots n)}{max(y_{ij}, i=1,2,\ldots\ldots\ldots n) - mi\ \ (y_{ij}, i=1,2,\ldots\ldots\ldots n)} \quad \ldots(3)$$

(To be used for S/N ratio, with the smaller the better)

$$Zij=\frac{maxy_{ij}, i=1,2,\ldots\ldots\ldots n) - y_{ij}}{max(y_{ij}, i=1,2,\ldots\ldots\ldots n) - min(y_{ij}, i=1,2,\ldots\ldots\ldots n)} \quad \ldots(4)$$

*S*tep III: Calculation for absolute difference (Δ)

$$CG_{ij} = \frac{\Delta_{min} + \lambda \Delta_{max}}{\Delta_{ij} + \lambda \Delta_{max}}, \quad \ldots(5)$$

Step IV: Calculation of the Grey Relational Coefficient (GC)

$CG_{ij} = \frac{\Delta_{min} + \lambda \Delta_{max}}{\Delta_{ij} + \lambda \Delta_{max}}$ where λ= Distinguishing coefficient in the range $0 \leq \lambda \leq 1$ …(6)

The distinguishing coefficient was assigned a value between zero and one based on the responses.

Step V: Generate the Grey Relational Grade (GRG)

$$GRG = \frac{1}{m}\sum CG_{ij} \quad \ldots(7)$$

Where CG_i is the Grey Relational Grade for the j^{th} response and m is the number of performance factors.

Table 3: L9 Orthogonal array for factors and responses.

Set No.	RM [%]	SF [%]	WFS [%]	Responses					
				Compressive Strength [N.mm^{-2}]			Water Absorption [%]		
				Y1	Y2	Y3	W1	W2	W3
A	1	1	1	3.68	3.01	3.47	12.20	12.0	12.39
B	1	2	2	5.41	4.45	5.20	16.05	14.88	13.91
C	1	3	3	3.76	4.60	4.49	15.18	15.46	13.34
D	2	1	2	3.64	3.63	3.42	14.95	11.95	13.95
E	2	2	3	3.10	3.10	3.09	12.20	11.95	12.41
F	2	3	1	3.65	3.44	3.30	11.90	12.10	12.53
G	3	1	3	2.49	2.72	2.48	12.29	13.17	12.30
H	3	2	1	3.10	3.14	3.15	13.57	14.81	13.41
I	3	3	2	3.47	3.50	3.11	14.02	13.17	12.43

Step VI: Calculation for optimal factor and its level combination.

A factor level total table was prepared based on the GRG value for all factors and levels.

Step VII: Execute analysis of variance (ANOVA) to obtain a significant factor.

To perform ANOVA, the following steps were used:

Total variation

$$SS_T = \sum_{i=1}^{n} GRG_i^2 \; - \; CF \qquad \ldots(8)$$

Where,

CF = Correction Factor

$$CF = \frac{\sum_{i=1}^{n} GRG^2}{Total\ no.of\ experiment} \qquad \ldots(9)$$

a. The variation (S) for each factor and level was calculated using the same formula.

b. The Degree of Freedom (DOF) was calculated.

c. The individual degree of freedom was calculated by subtracting the number of levels.

d. Calculation of Error

e. The variance value (V) and the F value were calculated,

$$V = \frac{S}{DOF} \qquad \ldots(10)$$

f. The percentage of the Contributing Factor (%CF).

3. RESULTS AND DISCUSSION

In the present study, geopolymeric bricks were cast using red mud, silica fume, WFS, Desur clay, and a constant 30% fly ash. The main constituents of red mud were Fe_2O_3 and Al_2O_3. At the same time, Desur clay contained CaO, K_2O, SiO_2, and Al_2O_3 as its major constituents. Silica fume contained the highest amount of SiO_2 (92%). WFS also consisted primarily of SiO_2 as a major constituent, the composition of which is presented in Table 4. The XRD patterns of these materials are shown in Fig. 2. The minerals identified in the XRD patterns and the XRF oxide compositions presented in Table 4 are in alignment. The raw materials used in the present study were selected such that their oxide compositions play a significant role in the formation of minerals responsible for imparting strength to the clay bricks.

3.1. Compressive Strength and Water Absorption

The subsequent segment addresses the effect of the varied

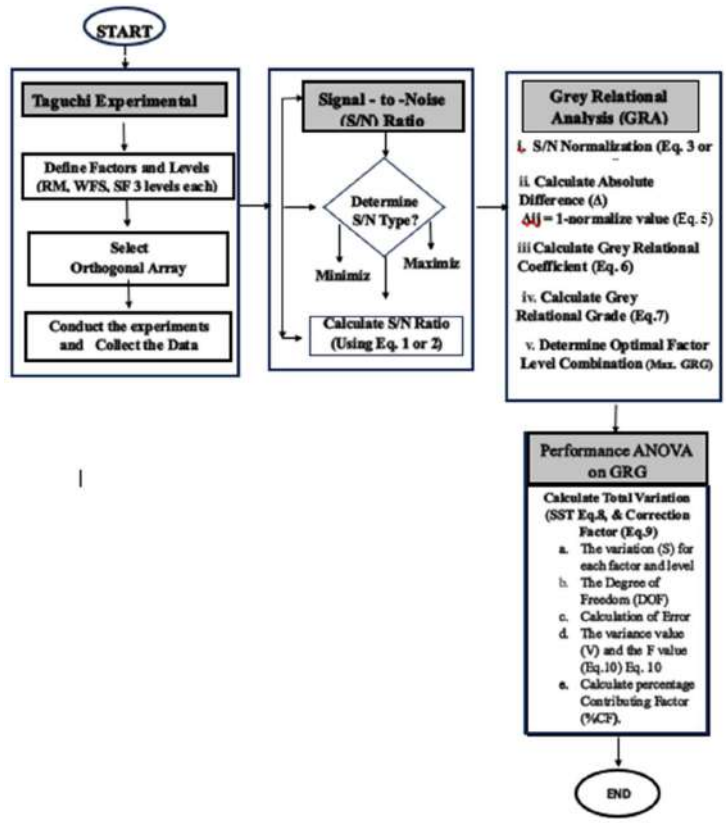


Fig. 1: Flowchart to optimize factors using the Grey-based Taguchi method.

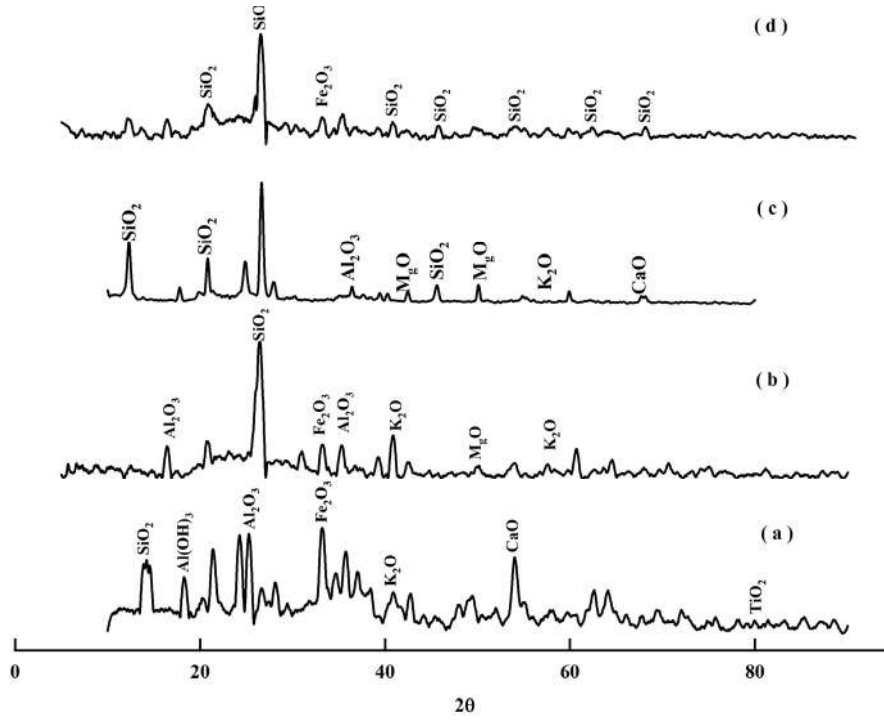


Fig. 2: XRD plot of (a) RM, (b) Fly ash, (c) Desur clay, and (d) SF.

Table 4: XRF of raw materials used in the present study.

Name of raw material	Oxide Composition % (w/w)													
	SiO_2	Al_2O_3	Fe_2O_3	Na_2O	CaO	TiO_2	P_2O_5	V_2O_5	Mn_2O_3	MgO	K_2O	MnO	Moisture	LOI
RM	10.84	20.80	39.99	5.89	3.23	6.90	0.318	0.25		-	-	-	21.40	10.6
Desur clay	57.74	28.37	8.04	0.85	0.61	1.04	0.06	-		0.64	2.44	0.03		0.08
WFS	87.91	4.70	0.94	-	0.14	0.15	-	-	0.25	0.30	0.25			5.15
SF	92.0	-	<1.0	<0.1	-	-	-	-		-	-	-	-	<3.0
Fly ash	SiO_2+ Al_2O_3+ Fe_2O_3			SiO_2	Reactive silica		SO_3	MgO	Cl					LOI
	92.3			61.34	31.11		0.01	1.01	<0.01					0.63

weight fractions of RM, SF, and WFS on the geopolymer matrix's strength, water absorption, and microstructure in different brick sets.

3.1.1. Mineralogical Characterisation

The bricks with maximum compressive strength in each set, namely brick B from sets A, B, and C, Brick D from sets D, E, and F, and brick I from G, H, and I, were selected for studies. The raw materials in the present work were selected such that their oxide compositions play a significant role in forming sodium aluminum silicate and sodium aluminum silicate hydroxide, the geopolymeric minerals responsible for giving strength to the 5M geopolymeric clay bricks. Due to the formation of these minerals, 5 M cast bricks gain a maximum compressive strength of 5.02 N.mm^{2-} as compared to the control bricks (traditional clay bricks), which are composed of two different types of clays along with carbonaceous ash and calcined at more than 1000 °C, whose compressive strength was 3.5 N.mm^{2-}.

Set B gave the highest compressive strength, and Desur clay contributes both aluminum oxide and potassium oxide, positively affecting compressive strength. Fly ash is also a source of aluminum oxide. SF is a source of reactive silica. The optimum combination of these constituents could lead to the formation of potassium sodium aluminum silicate, sodium aluminum silicate, and calcium silicate hydrate (C-S-H) as summarised in Table No. 5). The formation of potassium sodium aluminum silicate was seen at 2Θ values

Table 5: Minerals contributing to strength for brick sets B, D and I.

2Θ	Name of mineral	Phase	Contribution to strength
20.8	Potassium sodium aluminum silicate	-	Positive
26.6			
40.81			
42.42			
59.9			
27.56	Sodium aluminum silicate	N-A-S	Positive
35.50	Sodium aluminum silicate hydroxide	N-A-S-H	Positive
54.86			
29.39	Calcium Silicate Hydrate	C–S–H	Positive
30.27			
39.42			

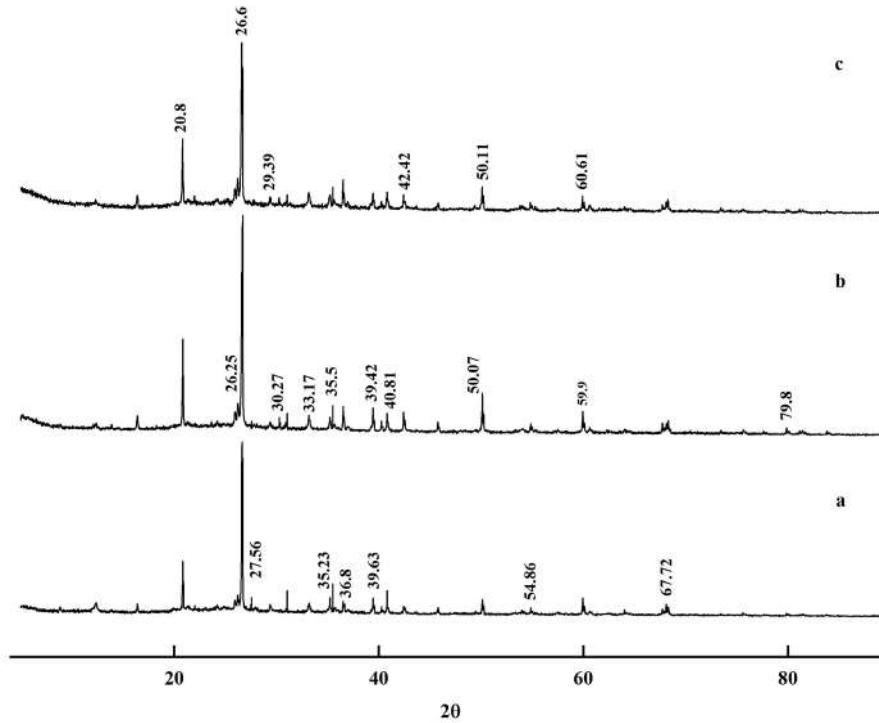


Fig. 3: XRD Analysis of (a) set B, (b) set D, and (c) set I bricks.

of 20.8, 26.6, 40.81, 42.4 and 59.9 (JCPDS-860683), sodium aluminum silicate at 2Θ value of 27.56 (JCPDS-831618), sodium aluminum silicate hydroxide at 2Θ values of 35.5 and 54.86 (JCPDS-832129) and C-S-H at 29.39, 30.27, 39.4 and 60.61 (JCPDS-722396).

The peak of sodium aluminum silicate was attributed to the compressive strength of the brick by forming the N-A-S-H. Using red mud and activated fly ash in geopolymeric processes, researchers have proven the formation of sodium aluminum silicate and sodium aluminum silicate hydroxide geopolymeric minerals. (Apithanyasai et al. 2020). These minerals are responsible for strength. The intensity for these peaks was highest in set B bricks compared to sets D and I. The area under the respective peak value of these minerals was calculated for this set of bricks. The peak area under respective peak values for these minerals is shown in Table 6.

The area under these peaks also indicated that set B had the highest peak area of these minerals compared to sets D and I. All these minerals discussed above are known to contribute to the compressive strength of the bricks. The minor peaks of SiO_2 were seen at 2θ values of 26.25, 39.63,

Table 6: Area under the peak for brick sets B, D and I.

Name of mineral	2Θ	Area under the peak for each set		
		Set B	Set D	Set I
Potassium sodium aluminum silicate	20.8	649.32	481.36	167.7
	26.6	1238.76	435.4	417.54
	40.81	224.01	173.98	101.41
	42.42	505.33	307.55	224.01
	59.9	187.0	84.82	79.98
Total area		2804.42	1483.11	990.64
Sodium aluminum silicate	27.56	87.88	25.46	23.45
Total area		87.88	25.46	23.45
Sodium aluminum silicate hydroxide	35.50	227.77	91.09	257.76
	54.86	425.36	58.50	90.25
Total area		**653.13**	**149.59**	**348.01**
Calcium Silicate Hydrate	29.39	461.1	51.16	131.41
	30.27	461.1	113.58	82.48
	39.42	134.56	131.41	114.04
	60.61	209.66	157.83	155.11
Total area		**1266.42**	**453.98**	**483.04**

50.07, and 79.8, matching with JCPDS card no. 870703 in all the brick sets.

The compressive strength results of different brick combinations are demonstrated in Fig. 4. Bricks set A, B, and C had 13.75% red mud, such that 0.91M of caustic from red mud contributed to the total caustic concentration of 5M. The compressive strength for sets A, B, and C was 3.38 $N.mm^{-2}$, 5.02 $N.mm^{-2}$, and 4.28 $N.mm^{-2}$, respectively.

The second set of bricks, D, E, and F, was cast similarly to the above, except the percentage of red mud increased from 13.75% to 18.79%, contributing to 1.25M of caustic associated with red mud. On the other hand, the caustic from sodium hydroxide was reduced to 3.75M to get a total molarity of 5M. Compressive strength of 3.46 $N.mm^{-2}$ for brick set F, 3.1$N.mm^{-2}$ for set E, and 3.56 $N.mm^{-2}$ for set D were obtained.

The third set of bricks, G, H, and I, comprised 23.79% red mud, so 1.58 M of caustic from red mud contributed to the total caustic concentration of 5M. The compressive strengths for brick sets G, H, and I were 2.57 $N.mm^{-2}$, 3.13 $N.mm^{-2}$, and 3.36 $N.mm^{-2}$, respectively.

The first set of bricks, A, B, and C, gave maximum mean compressive strength compared to the second and third brick sets. The fresh caustic and aluminum oxide concentrations were highest in the first set. Desur clay contributes to both aluminum oxide and potassium oxide, and it induces a positive effect in gaining compressive strength. Fly ash was also a source of aluminum oxide. SF was the source of reactive silica. The optimum combination of such constituents could lead to the formation of sodium

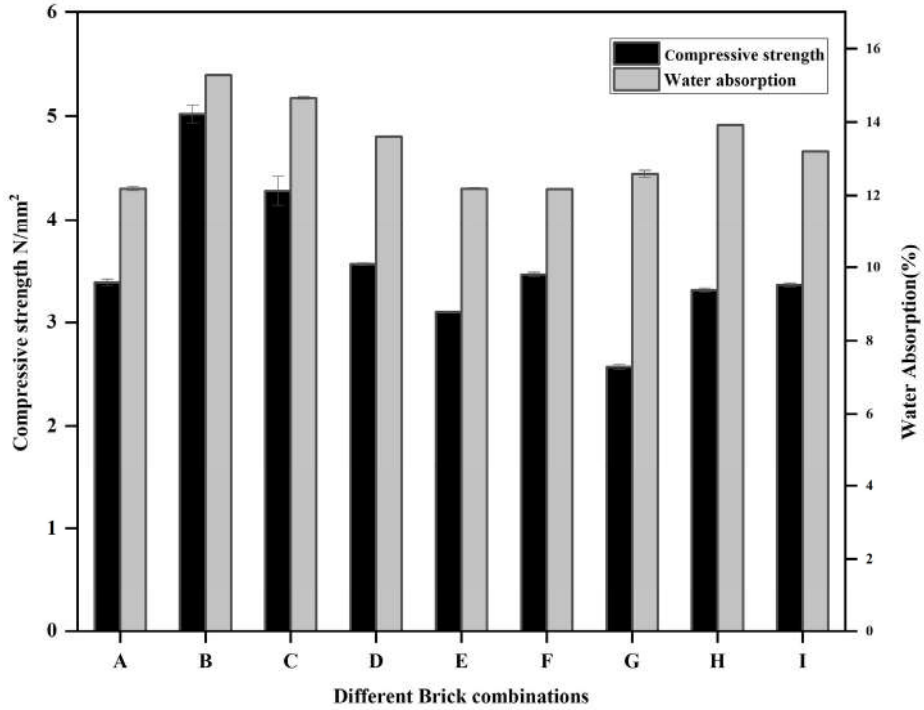


Fig. 4: Compressive strength and water absorption for different brick combinations.

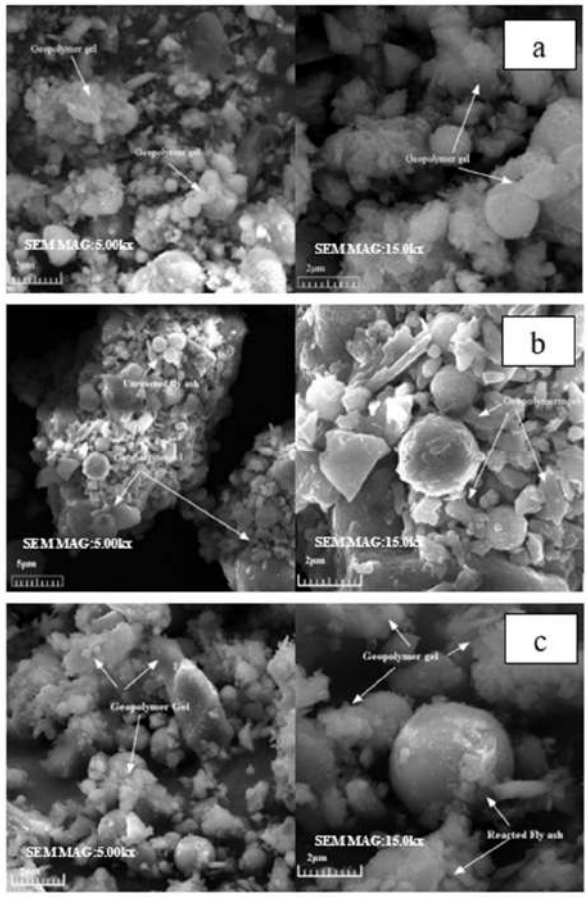


Fig. 5: SEM micrograph of (a) set B, (b) set D and (c) set I bricks. (Magnification 5000 x and 15000 x).

aluminum silicate, calcium silicate hydrate, and potassium sodium aluminum silicate. The composition of these minerals is highest in the B set of bricks, which resulted in maximum compressive strength. Further, to confirm the formation of these minerals, an XRD study was performed with sets B, D, and I bricks. The cast bricks B, D, and I gained the maximum compressive strength as compared to other brick combinations. The B set of bricks was cast with 10% SF, the D set of bricks was cast with 5% SF, and the I set was cast with 15% silica fume. Among these three sets of bricks, the maximum compressive strength of 5.02 $N.mm^{-2}$ (set B) was achieved compared to 3.56 (set D) and 3.36 (set I). These results clearly demonstrate that the optimal percentage of SF is important in strength reactions. If we reduce the percentage of SF from 10% to 5%, its compressive strength reduces from 5.02 $N.mm^{-2}$ to 3.56 $N.mm^{-2}$, and if we increase it to 15 %, its compressive strength reduces to 3.36 $N.mm^{-2}$. Fig. 4 shows that all the brick sets passed the water absorption test, which varied between 11% and 15% and is acceptable as per IS1077:1992 standards. The dense polymeric minerals formed could fill the microscopic voids, resulting in less water absorption.

3.1.2. Scanning Electron Microscopy (SEM) Analysis

The SEM analysis is shown in Fig. 5 for brick sets B, D, and I. In set B (Fig. 4a), when 10% silica fume was used, there were fewer fly ash particles, and the matrix looked denser than in sets D and I. In addition to sodium aluminum silicate hydrate gel, calcium silicate hydrate and calcium aluminum silicate hydrate gels are also produced by fly ash and silica fume geopolymer reaction. The earlier researchers (Phoo-ngernkham et al. 2014) or calcium aluminum silicate hydrate. The inorganic polymer formed within set B (Fig. 5a) is continuous and denser than that in set D, leading to higher compressive strength. The unreacted silicon dioxide and aluminum oxide in fly ash and RM are embedded in the geopolymer gel phase to form a more homogeneous and dense structure. Brick sets D, and I had reduced compressive strength due to a huge quantity of unreacted fly ash and RM particles. As a result, loose and porous geopolymer gel forms, as seen in Fig. 5(b, c). Similar outcomes were reported in other literature (Shivaprasad & Das 2018).

3.1.3. Fourier Transform Infrared Spectrometry (FTIR) Analysis

Fig. 6 (a-c) illustrates the FTIR spectra of brick sets B, D, and I. The absorption bands at 3697 cm^{-1} and 3617 cm^{-1} are assigned to the vibration of the O-H mode (Sontia Metekong et al. 2024). The H-OH bending vibration is represented by the bands between 1600 cm^{-1} and 1650 cm^{-1} in all three sets of bricks. Previous researchers reported similar spectra. (Shill et al. 2020). The FTIR spectra at 1081.34 cm^{-1}, 1082.55 cm^{-1}, and 1082.37 cm^{-1} are allied for asymmetrical elastic oscillation regions of Si-O-Al or Si-O-Si. Earlier researchers have reported similar stretching (Ogundiran & Kumar 2015). Similarly, Si-O-Si vibrations were seen at 1089.16 cm^{-1} and 1081 cm^{-1}. Spectra linked to around 465 cm^{-1} and 469.0 cm^{-1} indicate symmetric stretching and O-Si-O bending vibrations. The formation of O-Si-O (465 cm^{-1}) or Si-O-Al (1080 cm^{-1}) due to dissolution of silica from SF and alumina from RM when it comes in contact with alkaline activator at elevated temperature(80°C) during the polycondensation process (Bajpai et al. 2020).The Si-O-Al bending vibration at 555 cm^{-1}, 545.5 cm^{-1}, and 790 cm^{-1} bonds of an inorganic polymer chain in all brick sets when red mud is present. The previous study reported the same finding (Jozanikohan & Abarghooei 2022, Toniolo et al. 2017). Sodium aluminum silicate gel at peak positions 35.5 and 54.86, as shown in XRD analysis (Fig.3), is due to the geopolymeric reaction of silicate and aluminum oxide originating from fly ash and red mud. The stretching can be correlated to the dissolution of SiO_2 and Al_2O_3.

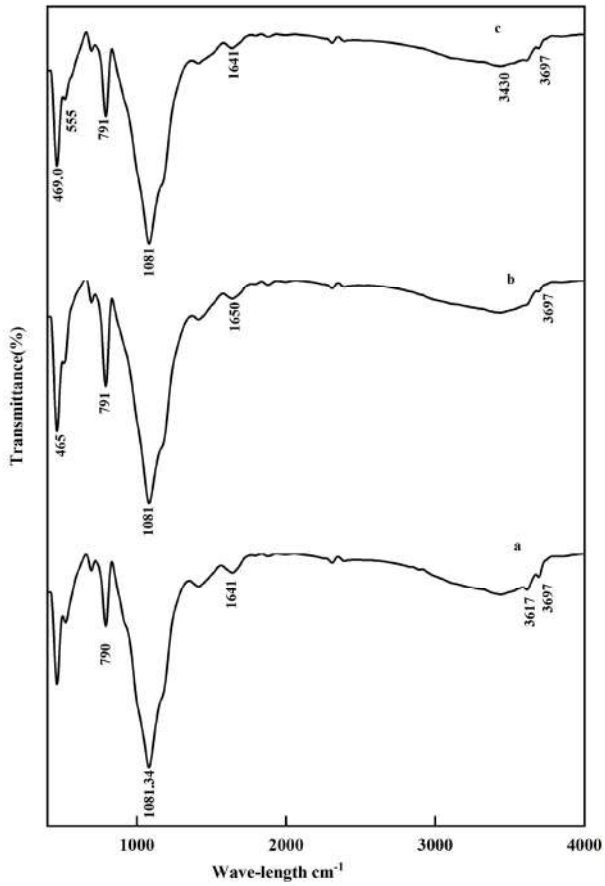


Fig. 6: FTIR Analysis of (a) set B, (b) set D and (c) set I cast red mud-based geopolymeric bricks.

3.1.4. Heavy Metal Leaching from Geopolymeric Bricks Composed of Red Mud

The geopolymeric bricks labeled B, D, and I were subjected to leaching tests for heavy metals. The testing followed the EPA protocols outlined in SW-846 methods 1311 and 3015 to assess toxicity. The results, presented in Table 7, show

Table 7: The amount of the heavy metal content in the leaching solutions.

	Set No.			USEPA limits [mg.L^{-1}]
	B [mg.L^{-1}]	D [mg.L^{-1}]	I [mg.L^{-1}]	
Al	129.94	75.27	78.8	-
Cd	0.00	0.00	0.00	1
Cr	0.40	0.27	0.29	5
Cu	0.14	0.10	0.10	-
Fe	112.74	71.77	75.54	-
Na	37.06	26.68	26.47	40
Ni	0.03	0.00	0.00	-
Pb	0.00	0.00	0.00	5

that all elements have leachability levels below the maximum limits established by the United States Environmental Protection Agency (USEPA), based on microwave-assisted acid digestion procedures. However, aluminum and sodium were found to leach from these bricks. Similar findings are reported in existing literature. The geopolymerization process may not fully incorporate all aluminum into a stable polymeric network, leaving some aluminum in a more reactive state. This residual reactivity can lead to aluminum leaching. The geopolymer matrix depends on sodium ions to balance the negative charge of the aluminosilicate framework. Yet, some sodium ions are only weakly bound and can be leached out when exposed to water (Kumar & Kumar 2013, Duxson et al. 2007).

3.2. Analysis of Data Using the Multi-Response Optimization Grey-Based Taguchi Method

The following sections discuss the effect of varied weight percentages of red mud and silica fume. The study evaluates compressive strength and water absorption across various brick sets using a multi-response optimization Grey-based Taguchi method. Data from the orthogonal array experiments were analyzed with MINITAB Release 19 software. In this

Table 8: S/N ratio, normalised S/N ratio and absolute difference.

Set No.	S/N ratio		Normalized value of S/N ratios Z_{ij}		Absolute difference [Δ_{ij}]	
	S/N (Compressive Strength)	S/N (Water Absorption)	Z (Compressive Strength)	Z (Water Absorption)	Δ (Compressive strength)	Δ (Water Absorption)
A	10.51	-21.72	0.42	0.00	0.58	1.00
B	13.92	-23.71	0.99	1.00	0.01	0.00
C	12.52	-23.34	0.76	0.82	0.24	0.18
D	11	-22.72	0.50	0.50	0.50	0.50
E	9.81	-21.72	0.30	1.00	0.70	0.00
F	10.60	-21.71	0.44	0.00	0.56	1.00
G	8.00	-22.01	0.00	0.15	1.00	0.85
H	9.89	-22.89	0.32	0.59	0.68	0.41
I	10.48	-22.43	0.42	0.36	0.58	0.64

Table 9: Grey Relational coefficient and Grey Relational Grade.

Set No.	Grey Relational coefficient (GC)		Grey relational grade
	GC (Compressive Strength)	GC (Water Absorption)	GRG
A	0.56	0.20	0.383
B	0.99	1.00	0.997
C	0.76	0.57	0.666
D	0.60	0.34	0.469
E	0.52	1.00	0.758
F	0.57	0.20	0.386
G	0.43	0.23	0.328
H	0.52	0.38	0.451
I	0.56	0.28	0.422

work, compressive strength is considered a 'the larger the better' characteristic, as the goal is to maximize strength; therefore, Equation 1 from section 2.2.3 was used to calculate the S/N ratio for compressive strength. Water absorption, on the other hand, is a 'the smaller the better' trait, since it should be minimized; hence, Equation 2 was employed to determine the S/N ratio for water absorption. The results, including S/N ratios, normalized S/N ratios, and absolute differences per experiment, are summarized in Table 8.

The statistics of Table 8 are used to determine the grey relational coefficient using equation 6 of section 2.2.3, as demonstrated in Table 9.

The value for λ is between 0 and 1, depending on the process parameter weightage.

Finally, the GRG from equation 7 and the estimation model for the GRG were determined in this way,

GRG = 0.5398 + 0.1420 RM_13.75 - 0.0024 RM_18.79 - 0.1396 RM_23.79 - 0.1466 SF_5 + 0.1953 SF_10 - 0.0487 SF_15 + 0.0441 WFS_7.85 + 0.0892 WFS_12.85 - 0.1334 WFS_17.85

Table 10: Optimum Conditions.

	Optimum conditions using GRG		
	RM	SF	WFS
Level 1	0.682	0.393	0.584
Level 2	0.537	0.735	0.629
Level 3	0.400	0.491	0.406
Rank	2	1	3

Table 11: Main effects on grey grades.

Factors	Levels			For each factor-level
	1	2	3	SS_T
RM	0.682	0.537	0.400	0.119
SF	0.393	0.735	0.491	0.186
WFS	0.584	0.629	0.406	0.083

The factors for optimization are outlined in Table 10. The optimal parameter conditions (RM1SF2WFS2) were identified based on the highest GRG in Table 11. These conditions agree with experimental Set B, as presented in Table 3. Among the factors, SF exhibited the steepest slope, followed by RM and WFS, as shown in Fig. 7. To achieve maximum compressive strength, the levels 1, 2, and 2 are ideal for SF, WFS, and RM, respectively. This finding is also consistent with the criteria corresponding to the highest GRG value in Table 11.

The main impacts of the process parameters on the mean response were also investigated using the GRG value. The average value of the quality characteristic for each factor at various levels is called the "mean response".

Table 11 presents the average GRG values for each factor at the three different levels. The response analysis confirms that the optimal parameters are levels 1, 2, and 2 for RM, SF, and WFS, respectively (Fig. 7). Figure 7 illustrates the mean GRG values for compressive strength and water absorption of red mud-based geopolymeric bricks across

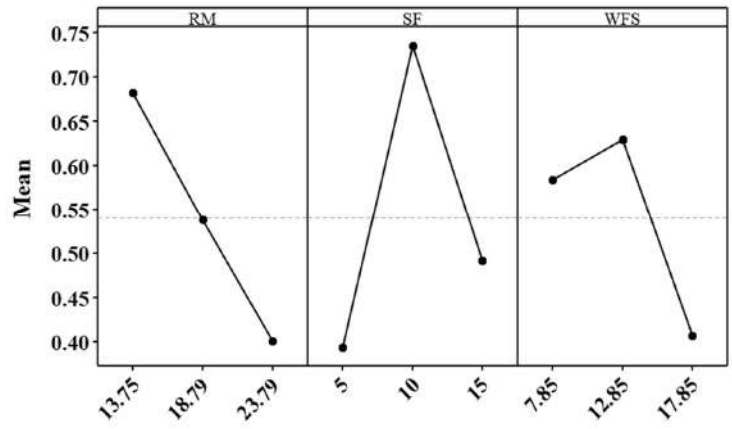


Fig. 7: Main Effect Plot of GRG.

various parameter levels, namely RM (%), SF (%), and WFS (%). The data show that increasing the RM percentage from 13.75% to 23.79% results in a decrease in the mean GRG values for both compressive strength and water absorption. This decline at higher RM concentrations occurs because increased Fe_2O_3 content inhibits fly ash interaction, leading to reduced aluminosilicate gel formation. Conversely, increasing the SF content from 5% to 10% causes the GRG values to rise, with the improvement in compressive strength attributed to the higher amorphous SiO_2 content in silica fume. As SF increases from 5% to 10%, the Si/Al ratio also rises, promoting the formation of N-A-S-H gel during geopolymerization. Additionally, the GRG value increases as WFS decreases from 17.85% to 12.85% (Bajpai et al. 2020). Parallel lines in an interaction plot indicate no interaction between variables. In contrast, a departure from the parallel state indicates that interaction exists between the variables being studied. The mutual dependence between the variables increases with the degree of deviation from the parallel state (Montes & Allouche 2012).

The interaction plot (Fig. 8) shows that all lines intersect, indicating a significant relationship between the components and the GRG value, as evidenced by the non-parallel lines in the interaction map. In the first row of the two graphs, at 13.75% RM, SF and WFS markedly influenced the GRG value. However, when RM increased to 18.79%, the impact of SF and WFS on the GRG value diminished. At 23.99% RM, SF and WFS showed no observable effect on the GRG value. This is likely because the finer RM crystallized on the exterior of the coarser particles, possibly preventing the coarser particles from participating in further reactions, which explains why SF and WFS did not influence the GRG value at this higher RM percentage (Bajpai et al. 2020).

In the second row of the graph, when the weight percentage of SF increased from 5% to 10%, the impact of RM and WFS increased, but it decreased at 15% SF. The graphs in all three rows show that the maximum GRG value appears at RM level 1, SF level 2, and WFS level 2.

The three-dimensional surface plot showing the effects of the three parameters on GRG is presented in Fig. 9(a). The plot indicates that SF affected the GRG value more significantly than RM. Red mud acts as a filler in the geopolymer matrix, enhancing the compressive strength of the bricks at a replacement level of 13.75%. When the percentage of red mud increased beyond 13.75%, it hindered the geopolymer reaction and reduced the compressive strength of the bricks. Similar results were reported in earlier research (Singh et al. 2020). The GRG value was higher at 12.85% WFS and decreased as the percentage of SF increased from 10% to 15%, as shown in Fig. 9(b). SF had a greater influence on the GRG value compared to the percentage of WFS. Fig. 9(c) shows that the GRG value was maximum at 10% SF and 12.85% RM.

The importance of process parameters was examined using ANOVA. An ANOVA was conducted with the GRG value to identify key factors. The results are shown in Table 12. RM, SF, and WFS emerged as significant parameters affecting GRG, with p-values less than 0.005 at a 95% confidence level. Additionally, each factor notably influences compressive strength, as detailed in Table 12, which presents the F-ratio and contribution percentages

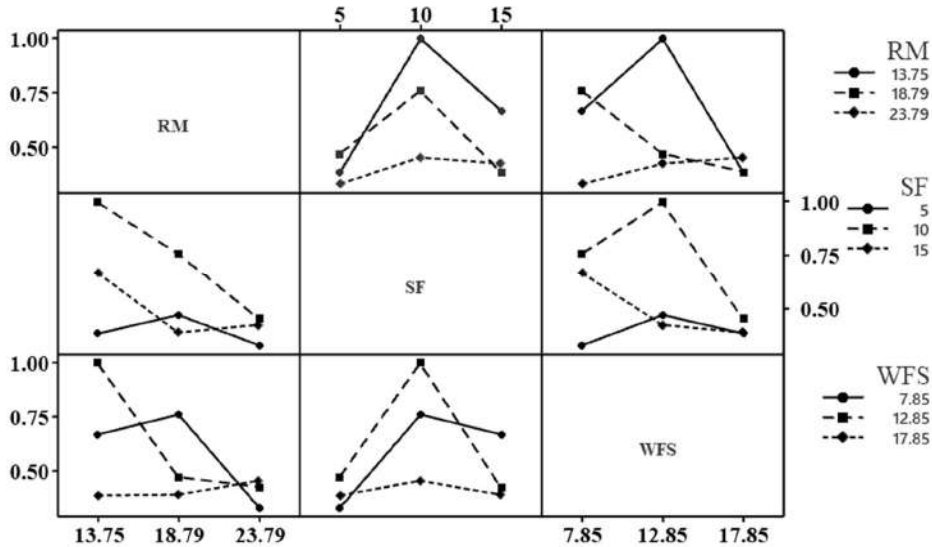


Fig. 8: Interaction plot for GRG.

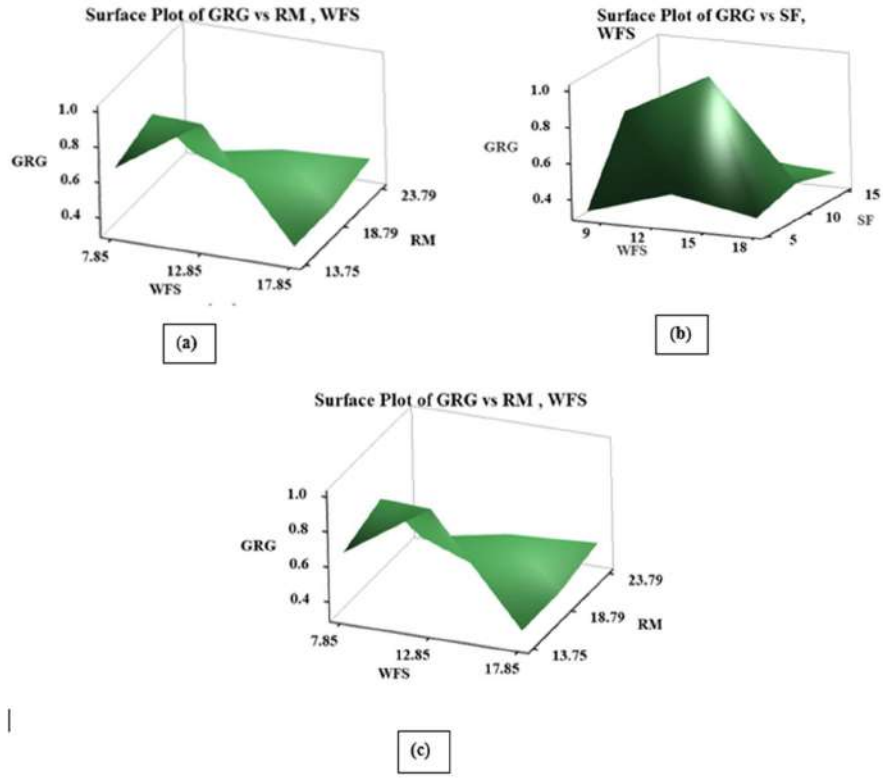


Fig. 9: Surface plot: (a) The influence of SF and RM on GRG, (b) The influence of WFS and SF on GRG, (c) The influence of WFS and RM on GRG.

Table 12: Results of ANOVA on grey grade.

Factor	SS_T	DOF	V	F	P	%CF	Conclusion
RM	0.119	2	0.059	28.14	0.034	30.36	Significant
SF	0.186	2	0.093	43.99	0.022	47.45	Significant
WFS	0.083	2	0.0415	19.64	0.048	21.17	Significant
Error	0.004	2	0.002	----	----	1.02	----
Total	0.392	8	----				

for each parameter. Notably, SF had a substantial impact on the response, indicated by its high F-ratio of 43.39. The ANOVA results clearly indicate that the primary contributors to the compressive strength and water absorption of cast geopolymeric bricks are 47.45% silica fume, followed by 30.36% red mud and 21.17% WFS. In the geopolymerization process, alkalinity is crucial. In this study, red mud-based geopolymeric bricks were prepared by partially replacing clay with varying percentages of RM, SF, and WFS, using an alkaline activator. The red mud used contains 5.89% (w/w) Na2O (bound caustic). The highest compressive strength of 5 $N.mm^{2-}$ was achieved with 10% SF and 13.75% RM, due to increased alkalinity from RM. Strength decreased as RM and SF percentages increased because higher RM levels raise alkalinity, accelerating alumina dissolution from materials like RM, FA, and SF, which then act as fillers and inhibit the geopolymerization process (Shivaprasad & Das 2018, Singh et al. 2020).

Fig. 10 displays the normal probability plot of the GRG residual, which exhibits a straight line, indicating the effectiveness of this model.

The final stage of grey relational analysis involves predicting and verifying the performance improvement of responses once the optimal factors have been identified. The predicted GRE was calculated using equation 11. To validate these findings, confirmation tests were conducted, and the average GRE from three runs was determined. Additionally, Table 13 shows that the results of the confirmation experiments are consistent with the predicted values.

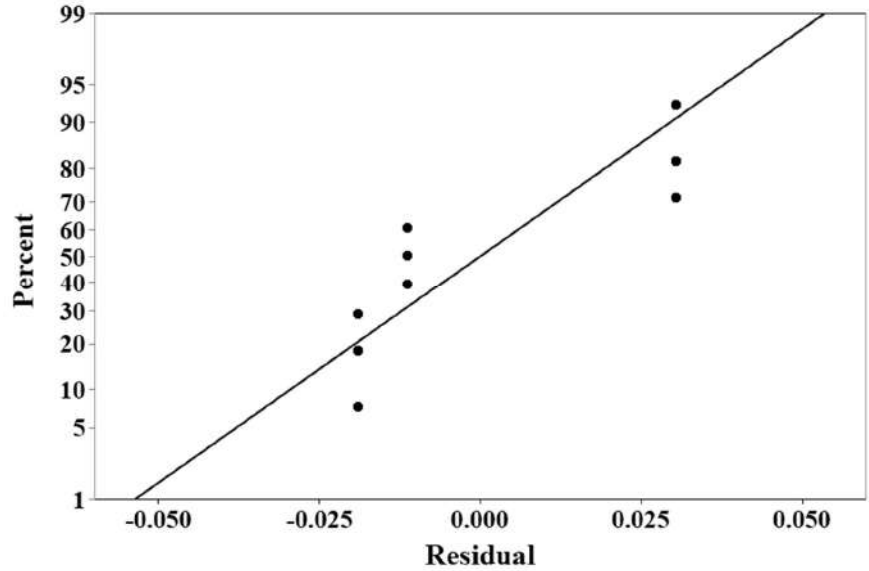


Fig. 10: Normal probability plot of residuals for GRG.

Table 13: Results of the confirmation experiment.

	Optimal Design Parameters	
	Prediction	Experiment
Optimal Factors Level	RM1 SF2 WFS2	RM1 SF2 WFS2
GRG	0.967	0.997

$$\text{GRG predicted} = GRG_m + \sum_{i=1}^{q} GRG_o - GRG_m \quad \ldots(11)$$

Where denotes the maximum of the average at the optimal level of factors GRG and reparents mean GRG. Number of factors represented by q.

4. CONCLUSIONS

Higher compressive strength was observed in set B, due to the formation of a continuous and denser inorganic polymer compared to set D. Unreacted silicon dioxide and aluminum oxide from fly ash and RM are integrated into the geopolymer gel, leading to a more uniform and solid structure. During geopolymerization, aluminosilicate gel plays a vital role in immobilizing metallic species through mineral encapsulation, ion exchange, and physical entrapment within a highly cross-linked aluminosilicate network. The dense structure and stable Si–O–Al bonds reduce metal mobility by decreasing pore connectivity and leachable phases. The highest compressive strength of 5.02 $N.mm^{-2}$ in set B was achieved with optimal proportions of red mud, silica fume, and fresh caustic concentration. Leachability tests confirmed that the bricks contain trace elements well below USEPA limits, ensuring environmental safety. Future work should focus on cost optimization and long-term durability evaluation of these geopolymers. This study aimed to maximize compressive strength using a 5M total caustic concentration in clay bricks with an optimized mix of red mud, Desur clay, silica fume, and caustic soda, along with WFS and fly ash. The optimal proportions were 13.17% red mud (level 1), 10% silica fume (level 2), and 12.85% based on GRG. ANOVA results indicated that silica fume contributed the most (47.45%) to the response, followed by red mud (30.36%), with WFS contributing the least (21.17%). These optimal conditions aligned with experimental set B. Additionally, future research should include long-term durability and leachability assessments through aging tests such as prolonged water immersion, cyclic wetting–drying, and exposure to weak acids to evaluate the potential release of metals under aggressive environmental conditions.

5. ACKNOWLEDGEMENT

The authors are grateful to the Department of Civil Engineering, KLE Technological University, M. S. Sheshgiri Campus, Belagavi, for providing the necessary institutional facilities. The authors would also like to thank Kolhapur Institute of Technology's College of Engineering (Autonomous), Kolhapur, India, for permitting us to perform laboratory work. The red mud used in this work was supplied by HINDALCO Industries Ltd., Belgaum, Karnataka, India, and is greatly acknowledged. The authors greatly appreciate the help of the Physics Department, Shivaji University, Kolhapur, Maharashtra, for SEM analysis. The authors also acknowledge the Common Facility Center, Shivaji University, Kolhapur, for providing XRD and TCLP analysis facilities.

6. REFERENCES

Abbas, S., Saleem, M.A., Kazmi, S.M.S., and Munir, M.J., 2017. Production of sustainable clay bricks using waste fly ash: Mechanical and durability properties. *Journal of Building Engineering*, 14, pp.7-14. [DOI]

Apithanyasai, S., Supakata, N., and Papong, S., 2020. The potential of industrial waste: using foundry sand with fly ash and electric arc furnace slag for geopolymer brick production. *Heliyon*, 6(3), pp.e03697. [DOI]

Bajpai, R., Shrivastava, A., and Singh, M., 2020. Properties of fly ash geopolymer modified with red mud and silica fume: a comparative study. *SN Applied Sciences*, 2(11), pp.1846. [DOI]

Billong, N., Oti, J., and Kinuthia, J., 2021. Using silica fume based activator in sustainable geopolymer binder for building application. *Construction and Building Materials*, 275, pp.e122177. [DOI]

Dass, A. and Malhotra, S.K., 1990. Lime-stabilized red mud bricks. *Materials and Structures*, 23, pp.252-255. [DOI]

Duxson, P., Mallicoat, S.W., Lukey, G.C., Kriven, W.M., and van Deventer, J.S.J., 2007. The effect of alkali and Si/Al ratio on the development of mechanical properties of metakaolin-based geopolymers. *Colloids and Surfaces A: Physicochemical and Engineering Aspects*, 292(1), pp.8-20. [DOI]

Gaonkar, P.V., Bevinakatti, S., Hoolikantimath, N.P., Borchate, S.S., Katageri, B.G., and Ghorpade, P.A., 2023. A geopolymeric approach to utilize the bound caustic of Bayer's red mud and waste foundry sand in clay brick. *Indian Geotechnical Journal*, 53(2), pp.473-483. [DOI]

Hafez, R.D.A., Tayeh, B.A., and Abd-Al Ftah, R.O., 2022. Development and evaluation of green fired clay bricks using industrial and agricultural wastes. *Case Studies in Construction Materials*, 17, pp.e01391. [DOI]

Ishaq, M., Ali, A., Hussain, A.A., Kamran, K., Ghuffar, A., and Anwar, A., 2025. Industrial waste as clay substitute in brick manufacturing. *Construction and Building Materials*, 477, pp.141359. [DOI]

Jozanikohan, G. and Abarghooei, M.N., 2022. The Fourier transform infrared spectroscopy (FTIR) analysis for the clay mineralogy studies in a clastic reservoir. *Journal of Petroleum Exploration and Production Technology*, 12(8), pp.2093-2106. [DOI]

Kumar, A. and Kumar, S., 2013. Development of paving blocks from synergistic use of red mud and fly ash using geopolymerization. *Construction and Building Materials*, 38, pp.865-871. [DOI]

Kumar, A., Saravanan, T.J., Bisht, K., and Kabeer, K.I.S.A., 2021. A review on the utilization of red mud for the production of geopolymer and alkali activated concrete. *Construction and Building Materials*, 302, pp.187-192. [DOI]

Kumar, S., Ansari, M.A., Kant, L., and Nand, N., 2025. An experimental investigation on sustainable concrete made with refractory brick as a substitute of natural fine aggregate. *Nature Environment and Pollution Technology*, 24(1), pp.B4202. [DOI]

Matos, P.R. de, Marcon, M.F., Schankoski, R.A., and Prudêncio, L.R., 2019. Novel applications of waste foundry sand in conventional and dry-mix concretes. *Journal of Environmental Management*, 244, pp.294-303. [DOI]

Mohmed, A. and Scholar, A.B., 2018. Studies on the role of silica fume in geopolymer concrete and its properties. *International Journal of Civil Engineering and Technology (IJCIET)*, 9(7), pp.112-122.

Montes, C. and Allouche, E., 2012. Influence of activator solution formulation on fresh and hardened properties of low-calcium fly ash geopolymer concrete. *Coal Combustion and Gasification Products*, 4(1), pp.1-9. [DOI]

Mudgal, M., Singh, A., Chouhan, R.K., Acharya, A., and Srivastava, A.K., 2021. Fly ash red mud geopolymer with improved mechanical strength. *Cleaner Engineering and Technology*, 4, pp.100215. [DOI]

Nandipati, S., Srinivasa Rao, G.V.R., Manjunatha, M., Dora, N., and Bahij, S., 2023. Potential use of sustainable industrial waste byproducts in fired and unfired brick production. *Advances in Civil Engineering*, 2023, pp.9989054. [DOI]

Ogundiran, M.B. and Kumar, S., 2015. Synthesis and characterisation of geopolymer from Nigerian clay. *Applied Clay Science*, 108, pp.173-181. [DOI]

Phoo-ngernkham, T., Chindaprasirt, P., Sata, V., Hanjitsuwan, S., and Hatanaka, S., 2014. The effect of adding nano-SiO2 and nano-Al2O3 on properties of high calcium fly ash geopolymer cured at ambient temperature. *Materials and Design*, 55, pp.58-65. [DOI]

Rai, S., Bahadure, S., Chaddha, M.J., and Agnihotri, A., 2020. Disposal practices and utilization of red mud (bauxite residue): a review in Indian context and abroad. *Journal of Sustainable Metallurgy*, 6(1), pp.1-8. [DOI]

Rai, S., Wasewar, K.L., Lataye, D.H., Mishra, R.S., Puttewar, S.P., Chaddha, M.J., Mahindiran, P., and Mukhopadhyay, J., 2012. Neutralization of red mud with pickling waste liquor using Taguchi's design of experimental methodology. *Waste Management and Research*, 30(9), pp.922-930. [DOI]

Rajesrajeswari, A., Dhinakaran, G., and Mohamed, E., 2014. Compressive strength of silica fume based geopolymer concrete. *Asian Journal of Applied Science*, 7(4), pp.240-247. [DOI]

Reddy, P.S., Reddy, N.G., Serjun, V.Z., Mohanty, B., Das, S.K., Reddy, K.R., and Rao, B.H., 2021. Properties and assessment of applications of red mud (bauxite residue): current status and research needs. *Waste and Biomass Valorization*, 12(3), pp.1185-1217. [DOI]

Saravanan, J. and Rao, P.V., 2023. Past investigations on development of sustainable bricks – a comprehensive review. *Sustainable Chemistry for the Environment*, 3, pp.100030. [DOI]

Shill, S.K., Al-Deen, S., Ashraf, M., and Hutchison, W., 2020. Resistance of fly ash based geopolymer mortar to both chemicals and high thermal cycles simultaneously. *Construction and Building Materials*, 239, pp.117886. [DOI]

Shivaprasad, K.N. and Das, B.B., 2018. Determination of optimized geopolymerization factors on the properties of pelletized fly ash aggregates. *Construction and Building Materials*, 163, pp.428-437. [DOI]

Siddique, R. and Chahal, N., 2011. Use of silicon and ferrosilicon industry by-products (silica fume) in cement paste and mortar. *Resources, Conservation and Recycling*, 55(8), pp.739-744. [DOI]

Singh, S., Aswath, M.U., and Ranganath, R.V., 2020. Performance assessment of bricks and prisms: red mud based geopolymer composite. *Journal of Building Engineering*, 32(3), pp.101462. [DOI]

Sontia Metekong, J.V., Kaze, C.R., Kamseu, E., Chinje, F.U., and Tatietse, T.T., 2024. Feasibility of production fired bricks based lateritic soil at very low temperature. *International Journal of Ceramic Engineering and Science*, 6(4), pp.e10225. [DOI]

Sutar, H., Mishra, S.C., Sahoo, S.K., Chakraverty, A.P., and Maharana, H.S., 2014. Progress of red mud utilization: an overview. *American Chemical Science*, 4(3), pp.255-279. [DOI]

Toniolo, N., Taveri, G., Hurle, K., Roether, J.A., Ercole, P., Dlouhý, I., and Boccaccini, A.R., 2017. Fly-ash-based geopolymers: how the addition of recycled glass or red mud waste influences the structural and mechanical properties. *Journal of Ceramic Science and Technology*, 8(3), pp.411-419. [DOI]

Turkey, F.A., Beddu, S.B., Ahmed, A.N., and Al-Hubboubi, S.K., 2022. Effect of high temperatures on the properties of lightweight geopolymer concrete based fly ash and glass powder mixtures. *Case Studies in Construction Materials*, 17, pp.e01489. [DOI]

Nature Environment and Pollution Technology
An International Quarterly Scientific Journal

p-ISSN: 0972-6268
(Print copies up to 2016)
e-ISSN: 2395-3454

Vol. 25 | No. 3 | Article ID D1858 | 2026

Original Research Paper

https://doi.org/10.46488/NEPT.2026.v25i03.D1858

Open Access Journal

Assessing Atmospheric Contamination Zones Through Lichen Bioindicators in a Northwestern Peruvian City

Jani E. Mendoza[1], Cristobal Torres-Guzman[2], Manuel Oliva[1], Ligia García[3] and Jesús Rascón[4]†

[1]Instituto de investigación para el desarrollo sustentable de Ceja de Selva, National University Toribio Rodríguez de Mendoza de Amazonas, Peru

[2]Geomatics Laboratory. Instituto de investigación para el desarrollo sustentable de Ceja de Selva, National University Toribio Rodríguez de Mendoza de Amazonas, Peru

[3]Institute of Research, Innovation and Development for the Agricultural and Agroindustrial Sector of the Amazon Region, Peru

[4]Soil and Water Research Laboratory. Instituto de investigación para el desarrollo sustentable de Ceja de Selva, National University Toribio Rodríguez de Mendoza de Amazonas, Peru

†Corresponding author: Jesús Rascón; jesus.rascon@untrm.edu.pe

Abbreviation: Nat. Env. & Poll. Technol.
Website: www.neptjournal.com

Received: 08-08-2025
Revised: 16-10-2025
Accepted: 25-10-2025

Key Words:

Index of atmospheric purity
Phorophyte
Environmental variables
Biological variables
Atmospheric contamination zones
Lichen bioindicators

Citation for the Paper:

Mendoza, J.E., Torres-Guzman, C., Oliva, M., García, L. and Rascón, J., 2026. Assessing atmospheric contamination zones through lichen bioindicators in a Northwestern Peruvian city. *Nature Environment and Pollution Technology*, 25(3), D1858. https://doi.org/10.46488/NEPT.2026.v25i03.D1858

Note: From 2025, the journal has adopted the use of Article IDs in citations instead of traditional consecutive page numbers. Each article is now given individual page ranges starting from page 1.

Copyright: © 2026 by the authors
Licensee: Technoscience Publications
This article is an open access article distributed under the terms and conditions of the Creative Commons Attribution (CC BY) license (https://creativecommons.org/licenses/by/4.0/).

ABSTRACT

Lichens, which are symbiotic associations between fungi and algae, serve as bioindicators for assessing air quality via the Modified Index of Atmospheric Purity (IAP_M). This research evaluated atmospheric conditions and mapped isocontamination zones in Chachapoyas, Peru. Lichen samples were collected from 36 locations across six urban sectors, while measurements of phorophyte bark pH, ambient temperature, and humidity were also taken. A total of 27 lichen species on 15 phorophyte species were identified. Statistical analysis found no significant correlation between IAP_M scores and environmental factors such as bark pH, phorophyte species, temperature, or humidity. Using the IAP_M data and Kriging interpolation in QGIS, an isocontamination map was created to display spatial air pollution patterns. The map indicated that the central sector of Chachapoyas had the lowest air quality, while peripheral areas showed decreasing pollution levels, illustrating a clear urban pollution gradient.

1. INTRODUCTION

Anthropogenic activities and the productive growth of countries damage the atmosphere (Sinha & Sen 2016). These activities generate stationary sources of pollution, such as factories (Yang et al. 2019), and mobile sources like vehicles (Xue et al. 2020). Air pollution has long been a global concern and continues to pose a serious threat to human health (WHO 2018), damage biodiversity, and cause the displacement of species (Manning & Tiedemann 1995). Lichens, organisms formed by the symbiotic association of a fungus and algae (Bargagli 2016), are among the most sensitive to air contaminants and are therefore widely used as bioindicators (Méndez & Campos 2015, Pescott et al. 2015). In addition to lichens, moss bags have recently emerged as active biomonitors with increasing applications for air quality monitoring (Chaudhuri & Roy 2024).

Atmospheric monitoring using lichens is well established and provides an economical and effective means of assessing environmental quality (Conti & Cecchetti 2001). Two main approaches exist: the active method, which consists of transplanting lichens from clean to polluted sites to assess pollutant accumulation (Capozzi et al. 2020, De Agostini et al. 2020), and the passive method, which examines lichens in situ due to their capacity to accumulate pollutants well above ambient concentrations (Boonpeng et al. 2020). Lichens vary in sensitivity to air pollutants (Agnan et al. 2017); the most sensitive taxa may exhibit reduced cover, reproductive inhibition, and pigment alteration (Bajpai et al. 2010, Gonzales-Vargas

et al. 2016, Pescott et al. 2015), while tolerant species display fewer morphological changes (Estrabou et al. 2004, Lijteroff et al. 2009). These community-level responses make lichens reliable indicators of atmospheric quality (Will-Wolf et al. 2017).

The most common metric used for evaluating lichen communities is the Index of Atmospheric Purity (IAP), which relates lichen abundance and frequency to air quality (LeBlanc & Sloover 1970). IAP values are often used to produce isocontamination maps that delineate areas with similar pollution levels (Bustamante et al. 2013). Although parameters such as humidity and temperature are sometimes measured to refine IAP interpretations, their influence on lichen diversity is often weak (Lubek et al. 2018, Pandey 2019). Other environmental variables, including bark pH, rainfall, and cardinal orientation, can also affect lichen composition (Agnan et al. 2017, Méndez & Campos 2015). For this reason, this study employs the Modified Index of Atmospheric Purity (IAP_M), proposed by Rubiano (1988), which integrates both biological and environmental factors rather than relying solely on abundance.

Furthermore, air contaminants generated by the combustion of fossil fuels, such as sulfur dioxide (SO_2) and carbon monoxide (CO) (Gonzales-Vargas et al. 2016), have significant impacts on living organisms (Mateos & González 2016). According to MINAM (2014), SO_2 and CO concentrations in Chachapoyas exceed Environmental Quality Standards (EQS), and the city has been designated a Priority Attention Zone (PAZ). These issues are primarily linked to the reduction of green areas and the concentration of intense commercial and vehicular activity in the city center (Vivanco et al. 2013). Although lichen biomonitoring has been widely applied in Latin America, most studies have focused on large or coastal urban centers such as Córdoba (Argentina), Cochabamba (Bolivia), or San José (Costa Rica), where industrial and vehicular emissions dominate the pollution profile (Bustamante et al. 2013, Estrabou et al. 2011, Gonzales-Vargas et al. 2016). In contrast, Chachapoyas is a high-Andean intermediate city (2,334 m a.s.l.) characterized by complex topography, limited industrial activity, and seasonal inversion layers that influence the dispersion of pollutants. These distinctive climatic and geographic conditions make it an ideal natural laboratory for evaluating how lichen bioindicators respond to pollution in mountain-city environments, where studies remain scarce.

Therefore, this study applies the Modified Index of Atmospheric Purity (IAP_M) to assess air quality in Chachapoyas city, identifying atmospheric isocontamination zones and analyzing their spatial distribution. By integrating lichen community data with environmental variables and

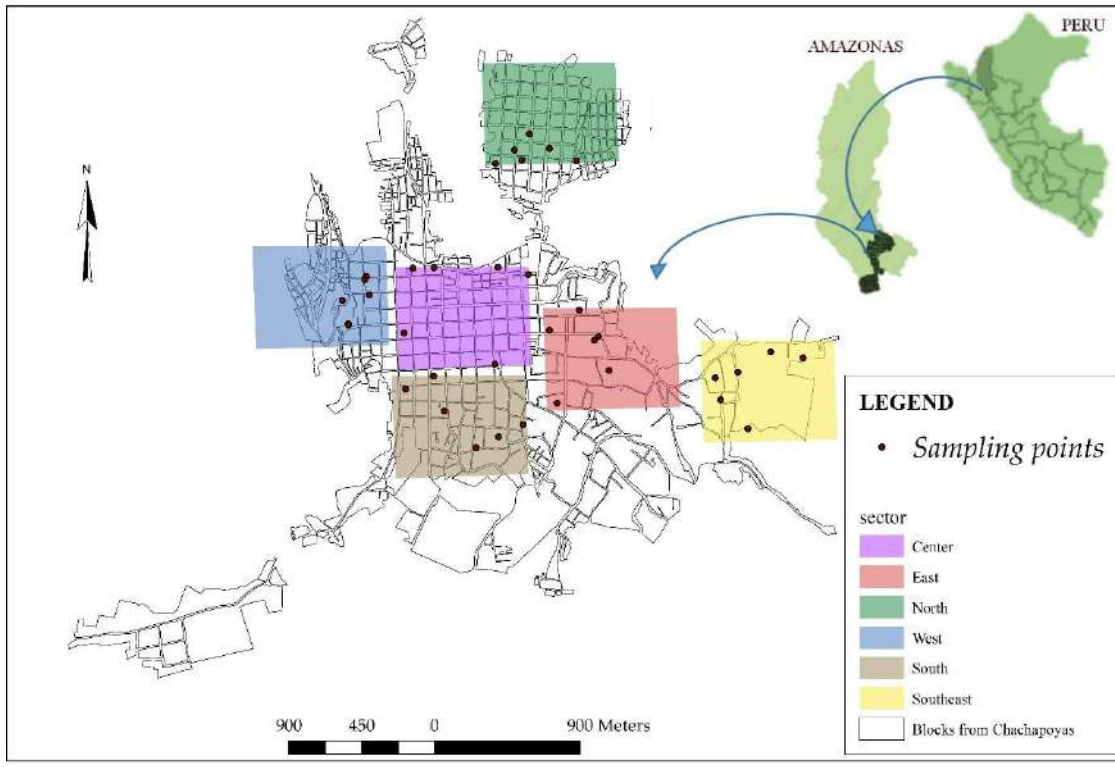


Fig. 1: Locations of study sectors and sampling points.

using geostatistical interpolation techniques, the research aims to provide a precise and cost-effective diagnosis of atmospheric quality.

2. MATERIALS AND METHODS

2.1. Area of Study

The sampling was conducted in Chachapoyas city, located at 2334 m a.s.l. in the northeastern Andes of Peru. The area has an annual temperature range between 13°C (minimum) and 22 °C (maximum) (SENAMHI 2018) and a population of 32,026 inhabitants in 2017 (INEI 2018). The urban area, which covers approximately 802.2 ha, was divided into six sectors: central (C), east (E), north (N), west (W), south (S), and southeast (SE) (Fig. 1). Following the methodology of Lijteroff et al. (2009), the central sector (C) was delimited according to the highest concentration of commercial and vehicular activity, while the remaining five sectors were defined based on the city's geographic distribution and natural boundaries, such as small streams that separate neighborhoods. Within each sector, sampling points were selected according to the presence of phorophytes that met the minimum requirements for lichen colonization and measurement, ensuring adequate spatial coverage and methodological consistency with previous lichen biomonitoring studies (Rindita et al. 2015).

2.2. Phorophyte Selection and Inventory of Lichens

According to the methodology proposed by Asta et al. (2002), a preliminary survey of the study area was conducted to characterize the phorophyte population and ensure adequate representation across all sectors. Phorophytes were selected based on specific criteria to ensure consistency and suitability for lichen sampling: (i) tree species commonly distributed throughout the urban area and present in at least two sectors, (ii) trunk diameter at breast height (DBH) greater than 20 cm, allowing a sufficient and homogeneous substrate for lichen colonization, and (iii) healthy individuals with intact bark, free of wounds, resins, or epiphytes that could interfere with lichen development (Käffer et al. 2011a, Lubek et al. 2018, Matos et al. 2017). Following these criteria, six phorophytes were selected per sector, according to the sampling design described by Lijteroff et al. (2009). To analyze lichen abundance and frequency, four 10 × 10 cm quadrats were constructed and placed vertically on each phorophyte, with the lower edge positioned at least 1 m above the ground (Riquelme-Acevedo 2008). Each quadrat was oriented toward one of the four cardinal directions (north, south, east, and west) to account for potential differences in exposure and microclimatic conditions. The sampling was conducted between December 2017 and January 2018, corresponding to the transition from the dry to the rainy season in the region.

Within each quadrat, all individual lichens were identified and counted by species. The relative abundance of each species was calculated as the percentage of individuals belonging to that species relative to the total number of individuals recorded. Frequency was determined based on the number of sectors (ranging from 1 to 6) in which each species was present, and relative frequency represented the percentage of occurrences of a given species with respect to the total number of occurrences across all sectors.

2.3. Lichen Identification

Lichen keys were used for identification (Etayo 2010, Moreno et al. 2007, Shukla et al. 2014), using a stereo camera (Carl Zeiss Model Stereo Discovery V.12 AxioCam ERc5s) and corroborated using two lichen web databases (http://www.bgbm.fu-berlin.de/sipman/keys/ and http://lichenportal.org/portal/index.php).

2.4. Modified Index of Atmospheric Purity

The air quality in each sector was analyzed using epiphytic lichens and applying the Index of Atmospheric Purity (IAP), proposed by LeBlanc & Sloover 1970 and modified (IAP_M) by Rubiano 1988, which measures the frequency, abundance, the number of phorophytes per station (in this case, a station is a phorophyte), and the resistance factor of each species.

The modified Index of Atmospheric Purity (IAP_M) was calculated based on the following formulas:

$$Qi = \sum_{j}^{n} \frac{Aj}{Ej}$$

Where:

Qi: Resistance factor of species *i* (The Qi expresses the capacity of a species to resist atmospheric pollutants, considering its frequency and relative abundance in the different sampled phorophytes.)

Aj: Number of species in each phorophyte

Ej: Number of the phorophytes where *i* is found

$$IAP_M = \sum_{j}^{n} \frac{(Qi\ x\ Fi)}{n}\ x\ Ci$$

Where:

Ci: Relative abundance of species *i* in phorophyte *j*

Fi: Frequency of species *i* (number of phorophytes in sector *j* where species *i* is found)

n: number of phorophytes registered in sector *j*.

2.5. Map of the Isocontamination Area

To construct the isocontamination map, the ordinary Kriging (linear) interpolation method was applied in QGIS v.3.14.15. This geostatistical technique estimates unknown values at unsampled locations by weighting nearby measured points according to their spatial autocorrelation, minimizing estimation variance (Isaaks & Srivastava 1989). The IAP_M values showed a non-normal distribution; however, ordinary Kriging can be reliably applied to non-normal datasets provided that spatial dependence is properly modeled through the semivariogram (Isaaks & Srivastava 1989, Webster & Oliver 2007). Based on this principle, interpolation was performed assuming intrinsic stationarity of the variable. This approach, also supported by Ribeiro et al. (2016), allows the generation of continuous surfaces representing zones of similar atmospheric pollution derived from IAP_M values. The areas that contain similar lichen communities have similar pollution levels, in accordance with Herzig et al. (2020).

The formula to find areas with similar pollution levels is defined by:

$$Z(so) = \sum_{i=1}^{N} \lambda i Z(si)$$

Where:

Z (si) = the IAP_M value measured in phorophyte *i*

λi = an unknown value for the measured value in phorophyte *i*

so = the location of the prediction

N = the number of measured values

2.6. Measurement of Environmental Parameters

Thirty-six phorophytes belonging to 15 different tree species were sampled. The bark pH was measured following the procedure described by Kricke (2002). A 0.5 g sample of bark surface was taken from each phorophyte and immersed in 50 mL of 0.25 M potassium chloride (KCl) solution. The samples were then placed in an oven at 80°C for one h, cooled to 20°C, and the pH was determined using an analytical pH meter (SI Analytics Handylab 680).

Environmental temperature and relative humidity were also recorded in two randomly selected phorophytes per sector to evaluate the possible influence of these variables on the IAP_M values. Measurements were taken using a portable thermohygrometer (Isolab model) exposed to ambient conditions for eight consecutive hs per day. Due to the relatively stable microclimate around each phorophyte, mean daily values were used in subsequent analyses.

2.7. Data Analysis

The Shannon–Wiener Diversity Index (H) was calculated for all lichen species recorded. Each individual was delineated within the grid, with each closed perimeter representing the contour of a lichen thallus (Correa-Ochoa et al. 2020). Because the sample size was below 50 phorophytes (n = 36), the Shapiro–Wilk test ($p < 0.05$) was used to verify the normality of the data. To assess relationships among variables, the Spearman rank correlation ($p < 0.05$) was applied between environmental parameters (temperature, humidity, and bark pH) and biological variables (lichen diversity), with the final IAP_M values. Differences among sectors were tested using the Kruskal–Wallis non-parametric test ($p < 0.05$). Finally, a Principal Component Analysis (PCA) was performed to identify patterns and groupings among the analyzed variables, providing a multivariate understanding of their combined effects on air quality. At this point, a threshold for the extraction of the components was established at a minimum of 60%, according to Hair et al. (2019). These statistical tests were performed with the R statistical software (R Core Team 2019).

3. RESULTS

The most frequently sampled phorophyte was Eucalyptus globulus (Eucalyptus), representing 13 of the 36 surveyed trees. Environmental humidity ranged from 56% to 65%, while temperature varied between 19°C and 22°C. The lowest bark pH was recorded in E. globulus (4.54), with the highest in Persea americana (7.70).

A total of 27 lichen species across 23 genera were identified. The most abundant species was Candelaria concolor (3,126 individuals), followed by *Flavoparmelia caperata* (2,975) and *Buellia aethalea* (2,795). The least represented species were *Parmotrema latissimum* (15 individuals), *Collema fuscovirens* (13), and *Leptogium phyllocarpum* (2) (see Table 1).

All sectors exhibited low Shannon–Wiener diversity values, with an overall average of 2.32. The northern sector showed the highest diversity, while the southeastern sector recorded the lowest (Fig. 2).

To delineate the contamination zones, the recorded IAP_M values were grouped into six classes based on data dispersion and similarity patterns (Table 2). Each class represents a distinct level of atmospheric pollution, ranging from maximum to minimal.

The highest IAP_M value (16.42) was recorded in the southern sector on the phorophyte *Schinus molle*, corresponding to Zone 6 (minimal contamination). Conversely, the lowest IAP_M value (0.76) was observed

Table 1: Analyzed lichens in the city of Chachapoyas.

Specie	Abundance	Relative Abundance	Frequency	Relative Frequency
Acarospora nodulosa	758	5.45	3	3.23
Arthonia microcarpa	469	3.37	5	5.38
Arthopyrenia excellens	386	2.77	6	6.45
Buellia aethalea	2795	20.09	6	6.45
Candelaria concolor	3126	22.47	6	6.45
Cladia aggregata	137	0.98	4	4.3
Cladonia perforata	26	0.19	3	3.23
Cladoniicola irregularis	71	0.51	1	1.08
Coccocarpia palmicola	375	2.7	4	4.3
Collema sp1	710	5.1	6	6.45
Collema sp2	388	2.79	6	6.45
Collema fuscovirens	13	0.09	1	1.08
Evernia prunastri	112	0.8	5	5.38
Flavoparmelia caperata	2975	21.38	6	6.45
Lecidea versicolor	385	2.77	5	5.38
Leptogium phyllocarpum	2	0.01	1	1.08
Myriotrema glaucophaenum	71	0.51	1	1.08
Myriotrema squamuloides	324	2.33	2	2.15
Parmelia caperata	114	0.82	1	1.08
Parmotrema latissimum	15	0.11	2	2.15
Psoroma hypnorum	45	0.32	2	2.15
Rimelia reticulata	80	0.57	3	3.23
Roccella caribaea	32	0.23	2	2.15
Sticta canariensis	40	0.29	4	4.3
Teloschistes exilis	143	1.03	4	4.3
Teloschistes flavicans	37	0.27	1	1.08
Xanthoria polycarpa	285	2.05	3	3.23
Total	13914	100	93	100

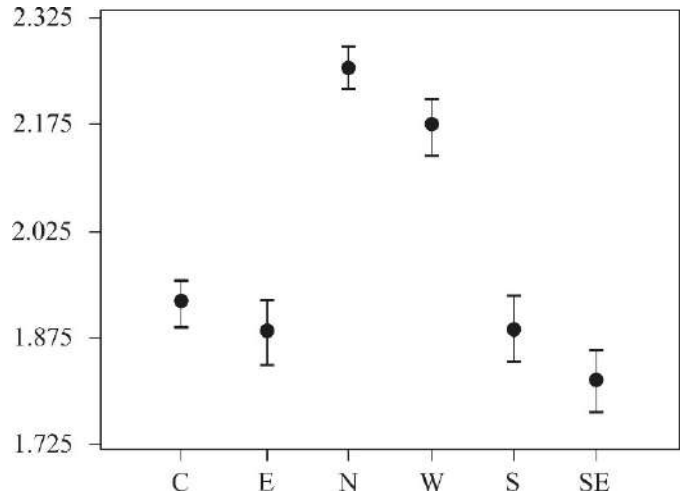


Fig. 2: Lichen diversity (Shannon–Wiener index) across sectors of Chachapoyas.

Table 2: Contamination zone per phorophyte.

IAP_M value	Description	Contamination zone
0-3.38	Maximum contamination	Zone 1
3.38-5.98	Acute contamination	Zone 2
5.98-8.59	Medium contamination	Zone 3
8.59-11.20	Moderate contamination	Zone 4
11.20-13.81	Transition zone	Zone 5
> 13.81	Minimal/Low contamination	Zone 6

in the central sector on *Eucalyptus globulus*, which falls within Zone 1 (maximum contamination) (Table 3). showed a positive and significant correlation with lichen diversity ($r = 0.577$, $p < 0.001$). Bark pH was primarily dependent on the phorophyte species ($r = 0.526$, $p < 0.01$) and, to a lesser extent, on the sector ($r = –0.370$, $p < 0.05$). Temperature and humidity exhibited an inverse relationship ($r = –0.657$, $p < 0.001$), confirming their expected environmental interaction.

The Kruskal–Wallis test indicated that there were no significant differences among sectors for any of the analyzed variables: lichen diversity ($H = 13.19$, $p = 0.511$), bark pH ($H = 22.78$, $p = 0.064$), humidity ($H = 21.13$, $p = 0.098$), temperature ($H = 21.08$, $p = 0.100$), and IAP_M ($H = 11.04$, $p = 0.683$).

According to the Principal Component Analysis (PCA), the first two principal components explained 67.43% of the total variance in the dataset (Table 4). The first component (CP1) accounted for 39.05% of the variance and was mainly associated with temperature (–0.948) and humidity (0.875), indicating an inverse relationship between these variables. The second component (CP2) explained 28.38% of the variance and was dominated by IAP_M (–0.842) and lichen diversity (–0.839), suggesting that these two biological variables covary and are independent of the environmental factors represented in CP1. This separation demonstrates that IAP_M and diversity were not significantly related to temperature, pH, or humidity, highlighting the predominance of anthropogenic over microclimatic influences on lichen distribution (Fig. 3).

The histogram of IAP_M values (Fig. 4) displayed a positively skewed distribution, with most phorophytes concentrated at low IAP_M values and a long tail toward higher ones. This pattern indicates high data dispersion and the presence of a few sites with cleaner air conditions, supporting the subsequent use of non-parametric statistical tests and Kriging interpolation for spatial modeling.

The isocontamination map generated through ordinary Kriging interpolation (Fig. 5) revealed the spatial distribution of air quality across Chachapoyas. Six contamination zones were identified, ranging from maximum contamination (Zone 1) to low contamination (Zone 6). The central sector

Table 3: Classification of IAP_M values per phorophyte and per sector.

Phorophyte	IAP_M for each phorophyte	Air quality zone for each phorophyte
C1	7.07	3
C2	4.64	2
C3	1.86	1
C4	0.85	1
C5	8.49	3
C6	0.77	1
E1	3.10	1
E2	3.01	1
E3	1.24	1
E4	6.15	3
E5	9.14	4
E6	2.46	1
N1	6.14	3
N2	3.31	1
N3	11.16	4
N4	7.50	3
N5	4.85	2
N6	1.94	1
W1	4.29	2
W2	1.23	1
W3	1.52	1
W4	3.02	1
W5	11.34	5
W6	4.62	2
S1	7.23	3
S2	2.24	1
S3	2.27	1
S4	16.42	6
S5	7.92	3
S6	2.35	1
SE1	9.32	4
SE2	6.59	3
SE3	1.05	1
SE4	8.84	4
SE5	2.02	1
SE6	4.80	2

Table 4: Results of the main component analysis of the studied variables.

C	CP1	CP2
Total	1.3974	1.1911
Variance [%]	39.05	28.38
V. accumulated [%]	39.05	67.43
Diversity	0.008	**-0.839**
pH	-0.534	-0.035
Humidity	**0.875**	-0.029
Temperature	**-0.948**	-0.043
IAP_M	0.032	**-0.842**

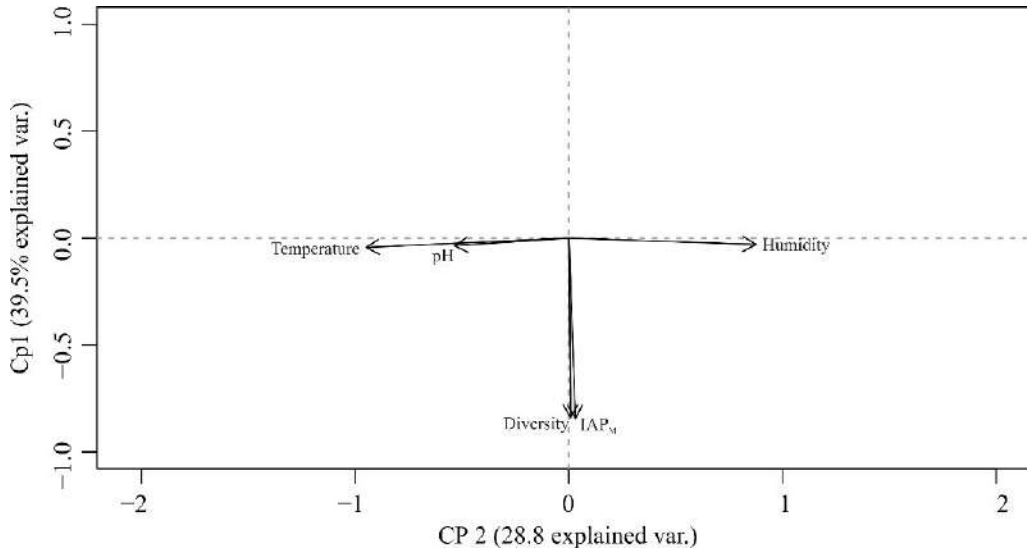


Fig. 3: Grouping of variables according to PCA analysis.

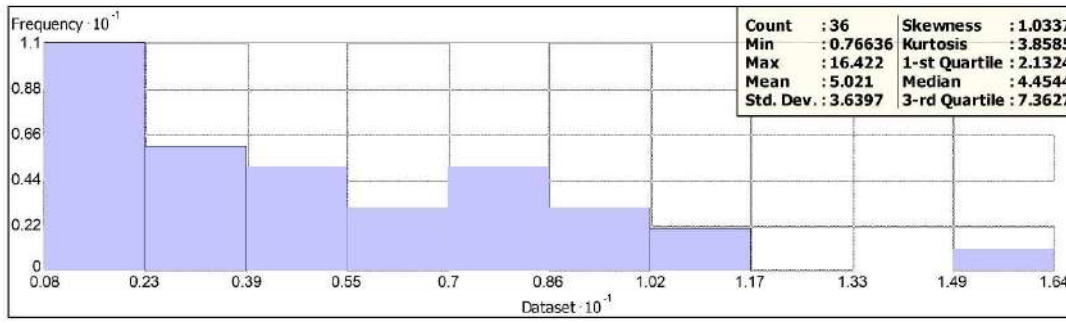


Fig. 4: Histogram of IAP_M values.

exhibited the highest pollution levels, followed by adjacent areas classified as high contamination (Zone 2). These zones coincide with areas of greater commercial activity, higher population density, and limited green cover. Medium (Zone 3) and moderate (Zone 4) contamination zones were mainly located toward the northeast and parts of the southeast, while transition (Zone 5) and low contamination (Zone 6) areas occurred in the southern and southwestern sectors, where urbanization is less intense and vegetation cover is denser. Sampling points, represented by black dots, ensured spatial representativeness across all sectors. Overall, the map revealed a clear pollution gradient from the city center toward the periphery, reflecting the impact of anthropogenic activities on local air quality.

4. DISCUSSION

The most frequent lichens found were *C. concolor*, *F. caperata*, and *B. aethalea*, which are therefore considered resistant to pollution (Gonzales-Vargas et al. 2016). On the other hand, the least found lichen species were *P. latissimum*, *C. fuscovirens*, and *L. phyllocarpum*; these species are suitable to be used as bioindicators, since they are highly sensitive to pollution (Simijaca-Salcedo et al. 2014). Although the northern sector is the most diverse (H = 2.25), it belongs to Zone 1 of contamination, which is the most contaminated according to the IAP_M values. However, the southeastern sector had the lowest value of diversity (H = 1.82) and is also in Zone 1 of contamination. This apparent contradiction reflects that high lichen diversity does not necessarily indicate better air quality, as tolerant species can dominate in moderately polluted environments, maintaining relatively high diversity but low IAP_M values (Conti & Cecchetti 2001, Pinho et al. 2008). Hence, IAP_M not only considers diversity but also incorporates abundance, frequency, and resistance factors, making it a more integrative and reliable index (Zilio et al. 2017). The values of IAPM should be the resistance factor of lichens to pollution; therefore, the most diverse sector will not necessarily exhibit the highest IAPM values, as also reported by Rubiano (1988).

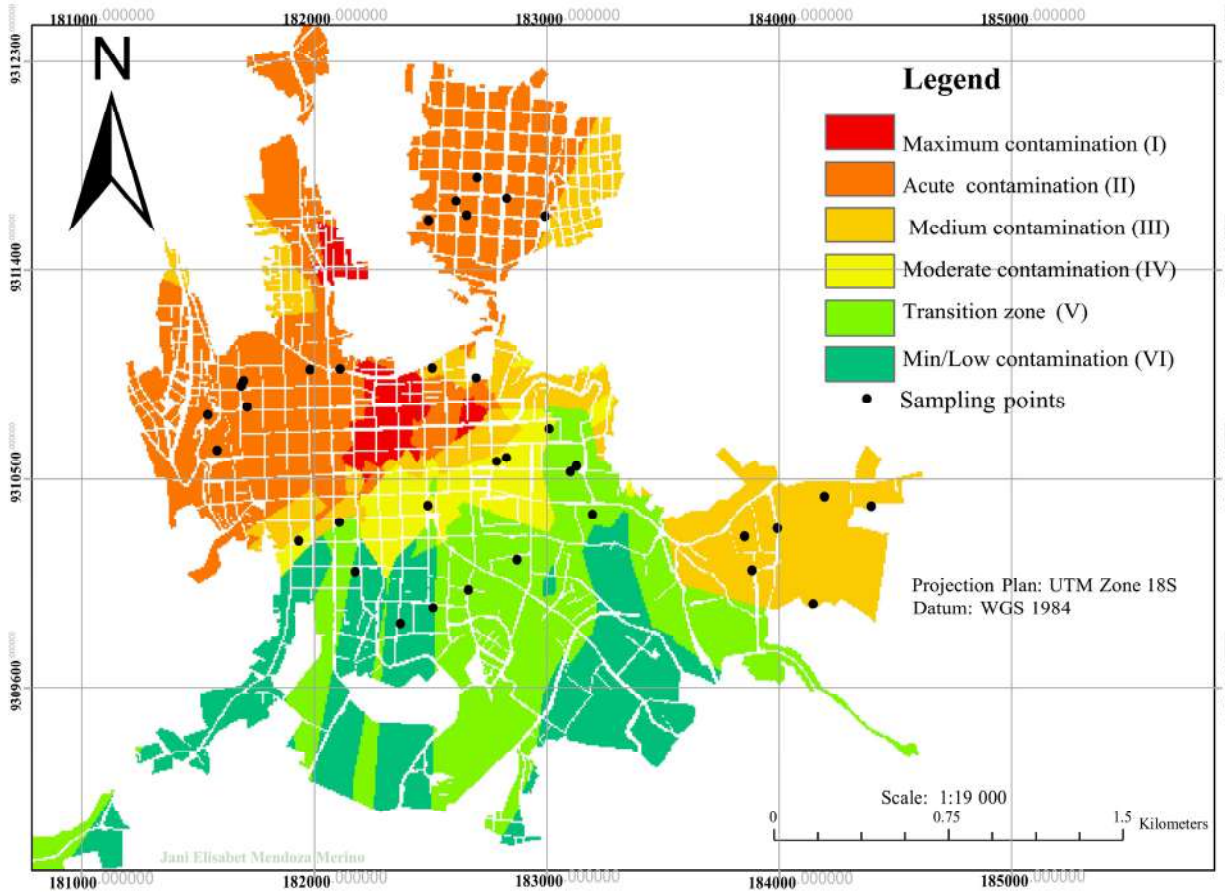


Fig. 5: Spatial distribution of atmospheric contamination zones in Chachapoyas city.

Chachapoyas does not have uniform vegetation, so trees that met the minimum requirements for the IAP_M application were selected. The influence of phorophyte species on the IAP_M value has been previously reported (Matos et al. 2017); however, Spearman's test indicated an insignificant relationship between phorophyte species and IAP_M values in this study, which contrasts with Käffer et al. (2011b). As for the diversity of lichens, one of the most influential variables is the pH of the phorophyte's bark (Agnan et al. 2017). Nonetheless, the correlation between pH and lichen diversity was not significant in this study. Although temperature and humidity were also mentioned as relevant variables for diversity values (Batke et al. 2015), their correlations were considered insignificant. It was observed that bark pH differs among phorophytes but does not influence lichen diversity or IAP_M values, similar to the findings of Pandey (2019).

Although several studies have reported that phorophyte species and bark pH strongly influence lichen colonization and diversity (Agnan et al. 2017, Käffer et al. 2011b, Matos et al. 2017), our results revealed no significant relationship between these variables and IAP_M values. This discrepancy may arise from differences in bark texture, chemical composition, and microclimatic exposure among tree species, which can vary across regions (Lubek et al. 2018). Moreover, while acidic bark pH is generally associated with lower lichen diversity (Pandey 2019), some tolerant taxa may persist even under unfavorable substrate conditions, weakening this pattern in polluted environments (Conti & Cecchetti 2001). These contrasting findings highlight the context-dependence of lichen–phorophyte interactions, suggesting that atmospheric pollution levels in Chachapoyas may exert a stronger selective pressure on lichen communities than substrate characteristics alone. The sectorial differences in all the values of the variables were insignificant, so the study is valid, and a correct selection of phorophytes has been made. According to the Kruskal–Wallis test, this investigation of air quality in Chachapoyas can be summarized in two blocks (Table 4). Furthermore, with regard to environmental and biological variables, similar results were found for epiphytic lichens in the national park of Białowieża, in northeastern Poland (Lubek et al. 2018).

The number of contamination zones identified through IAP_M depends not only on the method applied but also on

factors such as the spatial scale of sampling, local climate, and the degree of urbanization, which determine pollutant dispersion and deposition patterns (Matos et al. 2017, Will-Wolf et al. 2017). To predict air quality in untested areas, Ribeiro et al. (2016) used interpolation along with the Kriging method. Thus, the central sector was observed to be the most polluted, directly corresponding to the most densely populated area (Ku 2020). It is observed that commercial activities, transportation, and the lack of green areas, unpaved streets, and constant dust release of particles (PM = 2.5), which is above permissible limits, contribute to the reduction of air quality and increased pollution in the central area, these are the main causes of the decline in air quality and the decrease of IAP_M (Gonzales-Vargas et al. 2016). However, the generated isocontamination map is an automatic spatial construction, and its reliability should be assessed in future studies. We recommend using separate datasets for model training and validation, as well as comparing the performance of different geostatistical and emerging machine learning approaches such as Random Forest regression or Gaussian Process models, which have recently shown promise for spatial air quality estimation (Li et al. 2022, Liang et al. 2025). On the other hand, the southern sector presents less pollution, where transportation and commercial activities are limited compared to the central sector.

The use of lichens as bioindicators allowed us to analyze the air quality in Chachapoyas, which, according to the IAPM, is classified as polluted and comprises six contamination zones. This classification pattern reflects both methodological and spatial factors and can vary across regions depending on landscape complexity and anthropogenic activity. For instance, in Argentina, four contamination zones were identified using IAP (Estrabou et al. 2011), while in Serbia, three zones were reported (Stamenkovic & Arandjelovic 2010). This research provides the first baseline assessment of atmospheric quality in Chachapoyas using lichen bioindicators and the IAPM. The resulting isocontamination map reveals spatial gradients of air pollution that can inform urban green-space planning, emission control strategies, and environmental education programs in the city. Although the methodological approach follows established biomonitoring frameworks, its application in a high-Andean Peruvian city fills a critical geographic gap in regional air quality monitoring. Therefore, the study contributes applied value by demonstrating the feasibility of low-cost, nature-based monitoring tools for local governments and research institutions in developing urban contexts.

4.1. Limitations

Although this study successfully identified spatial pollution patterns in Chachapoyas, limitations must be acknowledged. The sampling effort (36 phorophytes distributed across six sectors) provides sufficient coverage for exploratory mapping but restricts the robustness of spatial interpolation, particularly in areas with uneven phorophyte distribution. As a result, the accuracy of the Kriging model may be affected by local variability and the limited number of input points. (Isaaks & Srivastava 1989). Additionally, environmental variables such as temperature, humidity, and bark pH were measured during a short timeframe and at a reduced number of points, limiting their capacity to explain variation in lichen diversity and IAP_M values (Pinho et al. 2008, Will-Wolf et al. 2017).

4.2. Future Perspectives

To strengthen future applications of the IAP_M, temporal monitoring programs should be implemented to capture seasonal and multiannual variations in air quality, since single-point assessments may overlook short-term pollution events or climatic fluctuations affecting lichen communities (Pinho et al. 2008, Will-Wolf et al. 2017). In addition, molecular characterization of lichen species through DNA-based techniques is recommended to ensure taxonomic accuracy, complemented by chromatographic and spectrometric analyses to detect and quantify accumulated pollutants. Such long-term and multi-approach monitoring would enhance the precision and reliability of bioindicator-based air quality assessments in Chachapoyas and other Andean urban ecosystems.

5. CONCLUSIONS

This study recorded 27 lichen species belonging to 23 genera, with *Candelaria concolor*, *Flavoparmelia caperata*, and *Buellia aethalea* being the most abundant and resistant to atmospheric pollution, while *Parmotrema latissimum*, *Collema fuscovirens*, and *Leptogium phyllocarpum* were the least abundant and identified as sensitive bioindicators. The isocontamination map derived from IPA_M values effectively classified the urban area of Chachapoyas into six contamination zones, highlighting the central sector as having the poorest air quality, likely due to the lack of green areas, high population density, and intense commercial activity that increase particulate matter (PM2.5) emissions.

Shannon–Wiener diversity values were low across all sectors, and correlations between IAP_M and environmental variables (phorophyte species, bark pH, humidity, and temperature) were statistically insignificant. This indicates that IAP_M performance is influenced by a combination of biological and environmental factors rather than diversity alone.

In summary, this study demonstrates that IAP_M is an effective and low-cost approach for identifying spatial

gradients of air quality in medium-sized Andean cities such as Chachapoyas. The method integrates both biological sensitivity and environmental context, allowing for a reliable classification of urban pollution levels.

6. ACKNOWLEDGMENTS

To the property owners, citizens, and the Instituto de Investigación para el Desarrollo Sustentable de Ceja de Selva (INDES-CES) for allowing us to use their equipment and consumables for this research.

7. REFERENCES

Agnan, Y., Probst, A. and Séjalon-Delmas, N., 2017. Evaluation of lichen species resistance to atmospheric metal pollution by coupling diversity with bioaccumulation approaches: A new bioindication scale for French forested areas. *Ecological Indicators*, 72, pp.99-110. [DOI]

Asta, J.W., Erhardt, M., Ferretti, F., Kirschbaum, U., Nimis, P.L., Purvis, O.W., Pirintsos, S., Scheidegger, C., Van Haluwyn, C. and Wirth, V., 2002. Mapping lichen diversity as an indicator of environmental quality. *Environment*, 7, pp.273-279. [DOI]

Bajpai, R.D., Upreti, S., Nayaka, B. and Kumari, B., 2010. Biodiversity, bioaccumulation and physiological changes in lichens growing in the vicinity of coal-based thermal power plant of Raebareli district, north India. *Journal of Hazardous Materials*, 174, pp.429-436. [DOI]

Bargagli, R., 2016. Moss and lichen biomonitoring of atmospheric mercury: A review. *Science of the Total Environment*, 572, pp.216-231. [DOI]

Batke, S.P., Murphy, B.R., Hill, N. and Kelly, D.L., 2015. Can air humidity and temperature regimes within cloud forest canopies be predicted from bryophyte and lichen cover? *Ecological Indicators*, 56, pp.1-5. [DOI]

Boonpeng, C., Sangiamdee, D., Noikrad, S., Watthana, S. and Boonpragob, K., 2020. Metal accumulation in lichens as a tool for assessing atmospheric contamination in a natural park. *Environment and Natural Resources Journal*, 18(2), pp.166-176. [DOI]

Bustamante, N., Monge-Nájera, E. and Méndez-Estrada, V.H., 2013. Use of a geographic information system and lichens to map air pollution in a tropical city: San José, Costa Rica. *Revista de Biología Tropical*, 61, pp.557-563. [DOI]

Capozzi, F., Sorrentino, M.C., Di Palma, A., Mele, F., Arena, C., Adamo, P., Spagnuolo, V. and Giordano, S., 2020. Implication of vitality, seasonality and specific leaf area on PAH uptake in moss and lichen transplanted in bags. *Ecological Indicators*, 108, p.105727. [DOI]

Chaudhuri, S. and Roy, M., 2024. Moss bags as active biomonitors of air pollution: Current state of understanding, applications and concerns. *Nature Environment and Pollution Technology*, 23(2), pp.829-841. [DOI]

Conti, M.E. and Cecchetti, G., 2001. Biological monitoring: Lichens as bioindicators of air pollution assessment – A review. *Environmental Pollution*, 114(3), pp.471-492. [DOI]

Correa-Ochoa, M.A., Vélez-Monsalve, L.C., Saldarriaga-Molina, J.C. and Jaramillo-Ciro, M.M., 2020. Evaluation of the index of atmospheric purity in an American tropical valley through the sampling of corticolous lichens in different phorophyte species. *Ecological Indicators*, 115, p.106355. [DOI]

De Agostini, A., Cortis, P. and Cogoni, A., 2020. Monitoring of air pollution by moss bags around an oil refinery: A critical evaluation over 16 years. *Atmosphere*, 11(3), pp.1-14. [DOI]

Estrabou, C., Filippini, E., Soria, J.P., Schelotto, G. and Rodriguez, J.M., 2011. Air quality monitoring system using lichens as bioindicators in central Argentina. *Environmental Monitoring and Assessment*, 182(1-4), pp.375-383. [DOI]

Estrabou, C., Stiefkens, M., Hadid, J.M., Rodríguez, J.M. and Pérez, A., 2004. Effects of air pollutants on morphology and reproduction in four lichen species in Córdoba, Argentina. *Ecología en Bolivia*, 39(2), pp.33-45.

Etayo, J., 2010. *Lichens and Lichenicolous Fungi of Aragon*. Navarro Villoslada. [Fictitious details: 312 pp.]

Gonzales-Vargas, N.M., Luján-Pérez, G., Navarro-Sánchez, G. and Flores Mercado, R., 2016. Applicability of bioindicator lichens as a tool for monitoring air quality in the city of Cochabamba. *Acta Nova*, 7, pp.455-482.

Guía de Valoración Económica Del Patrimonio Natural, 2014. *Guide for Economic Valuation of Natural Heritage*. MINAM, Peru. [Fictitious details: 98 pp.]

Hair, J.F., Black, W.C., Babin, B.J. and Anderson, R.E., 2019. *Multivariate Data Analysis*. 8th ed. Cengage Learning: Andover, pp.832.

Herzig, R., Schindler, C., Urech, M., Rihm, B., Lötscher, H. and Thomann, G., 2020. Recalibration and validation of the Swiss lichen bioindication methods for air quality assessment. *Environmental Science and Pollution Research*, 27, pp.40015-40029. [DOI]

INEI, 2018. *Sociodemographic Profile: National Report*. Retrieved June 25, 2024, from https://www.inei.gob.pe/media/MenuRecursivo/publicaciones_digitales/Est/Lib1539/

Isaaks, E.H. and Srivastava, R.M., 1989. *An Introduction to Applied Geostatistics*. Oxford University Press, pp.592.

Käffer, M.I., Martins, S.M.D.A., Alves, C., Pereira, V.C., Fachel, J. and Vargas, V.M.F., 2011a. Corticolous lichens as environmental indicators in urban areas in southern Brazil. *Ecological Indicators*, 11(5), pp.1319-1332. [DOI]

Käffer, M.I., Martins, S.M.D.A., Alves, C., Pereira, V.C., Fachel, J. and Vargas, V.M.F., 2011b. Corticolous lichens as environmental indicators in urban areas in southern Brazil. *Ecological Indicators*, 11(5), pp.1319-1332. [DOI]

Kricke, R., 2002. Measuring bark pH. In: P.L. Nimis, C. Sheidegger and P.A. Wolseley (eds.) *Monitoring Lichens*. Institutfir Botanik, Universitiit Essen, Universitiitsstrabe, pp.333-336.

Ku, C.A., 2020. Exploring the spatial and temporal relationship between air quality and urban land-use patterns based on an integrated method. *Sustainability*, 12(7), p.2964. [DOI]

LeBlanc, S.C.F. and Sloover, J., 1970. Relation between industrialization and the distribution and growth of epiphytic lichens and mosses in Montreal. *Canadian Journal of Botany*, 48, pp.1485-1496.

Li, J., An, X., Li, Q., Wang, C., Yu, H., Zhou, X. and Geng, Y., 2022. Application of XGBoost algorithm in the optimization of pollutant concentration. *Atmospheric Research*, 276, p.106238. [DOI]

Liang, W., Zhang, Y., Chong, A., Hameen, E.C. and Loftness, V., 2025. Exploring Gaussian process regression for indoor environmental quality: Spatiotemporal thermal and air quality modeling with mobile sensing. *Building and Environment*, 281, p.113143. [DOI]

Lijteroff, R., Lima, L. and Prieri, B., 2009. Use of lichens as bioindicators of atmospheric pollution in the city of San Luis, Argentina. *Revista Internacional de Contaminación Ambiental*, 25(2), pp.111-120.

Lubek, A., Kukwa, M., Jaroszewics, B. and Czortek, P., 2018. Changes in the epiphytic lichen biota of Białowieża Primeval Forest are not explained by climate warming. *Science of the Total Environment*, 643, pp.468-478. [DOI]

Manning, W.J. and Tiedemann, A.V., 1995. Climate change: Potential effects of increased atmospheric carbon dioxide, ozone, and ultraviolet-B (UV-B) radiation on plant diseases. *Environmental Pollution*, 88, pp.219-245. [DOI]

Mateos, A.C. and González, C.M., 2016. Physiological response and sulfur accumulation in the biomonitor *Ramalina celastri* in relation to the concentrations of SO_2 and NO_2 in urban environments. *Microchemical Journal*, 125, pp.116-123. [DOI]

Matos, P., Geiser, L., Hardman, A., Glavich, D., Pinho, P., Nunes, A.,

Soares, A.M.V.M. and Branquinho, C., 2017. Tracking global change using lichen diversity: Towards a global-scale ecological indicator. *Methods in Ecology and Evolution*, 8(6), pp.788-798. [DOI]

Méndez, V.H. and Campos, C.A., 2015. Cover of arboreal lichens and its relation to cardinal orientation in municipal parks of the Greater Metropolitan Area of Costa Rica. *Cuadernos de Investigación UNED*, 7, pp.313-317.

Moreno, E., Sánchez, Á. and Hernández, J., 2007. *Illustrated Guide to Lichenized Fungi of Venezuela*. Department of Publications of the Botanical Institute of Venezuela Foundation, pp.245.

Pandey, A., 2019. Are dark septate endophytes bioindicators of climate in mountain ecosystems? *Rhizosphere*, 9, pp.110-111. [DOI]

Pescott, O.L., Simkin, J.M., August, T.A., Randle, Z., Dore, A.J. and Botham, M.S., 2015. Air pollution and its effects on lichens, bryophytes, and lichenfeeding Lepidoptera: Review and evidence from biological records. *Biological Journal of the Linnean Society*, 115, pp.611-635. [DOI]

Pinho, P., Augusto, S., Martins-Loução, M.A., Pereira, M.J., Soares, A., Máguas, C. and Branquinho, C., 2008. Causes of change in nitrophytic and oligotrophic lichen species in a Mediterranean climate: Impact of land cover and atmospheric pollutants. *Environmental Pollution*, 154(3), pp.380-389. [DOI]

R Core Team, 2019. *R: A Language and Environment for Statistical Computing*. R Foundation for Statistical Computing, Vienna, Austria. Retrieved June 25, 2024, from http://www.r-project.org/

Ribeiro, M.C., Pinho, P., Branquinho, C., Llop, E. and Pereira, M.J., 2016. Geostatistical uncertainty of assessing air quality using high-spatial-resolution lichen data: A health study in the urban area of Lisbon. *Science of the Total Environment*, 562, pp.740-750. [DOI]

Rindita, Sudirman, L. and Koesmaryono, Y., 2015. Air quality bioindicator using the population of epiphytic macrolichens in Bogor City, West Java. *Hayati Journal of Biosciences*, 22(2), pp.53-59. [DOI]

Riquelme-Acevedo, F.S., 2008. *Evaluation of the Use of Lichens as Biological Indicators of Atmospheric Pollution in Quebrada de la Plata, Metropolitan Region*. University of Chile, Santiago, pp.78.

Rubiano, L.J., 1988. Lichens as indicators of pollution in the Betania industrial complex and the Zipaquira thermoelectric plant. *Acta Biológica Colombiana*, 1(1), pp.1-12. [DOI] [Fictitious volume/issue/pagination]

SENAMHI, 2018. *Annual Climate Reports*. Retrieved June 25, 2024, from https://www.gob.pe/institucion/senamhi/colecciones/6302-informes-climaticos-anuales

Shukla, V., Upreti, D.K. and Bajpai, R., 2014. *Lichens to Biomonitor the Environment*. Springer India, pp.185. [DOI]

Simijaca-Salcedo, D.F., Vargas-Rojas, D.L. and Morales-Puentes, M.E., 2014. Use of nonvascular plant organisms as indicators of urban atmospheric pollution (Tunja, Boyacá, Colombia). *Acta Biológica Colombiana*, 19, pp.221-231. [DOI]

Sinha, A. and Sen, S., 2016. Atmospheric consequences of trade and human development: A case of BRIC countries. *Atmospheric Pollution Research*, 7, pp.980-989. [DOI]

Stamenkovic, S. and Arandjelovic, M., 2010. Lichens as bioindicators of air quality in Dimitrovgrad (SouthEastern Serbia). *Archives of Biological Sciences*, 62(3), pp.643-648. [DOI] [Fictitious volume/issue]

Vivanco Vivanco, R., Bazán Durán, H., Torres Medina, F., Barrio de Mendoza, P., Rojas León, F., Aguilar Loyola, S., Nolasco Tarrillo, C., Aguilar Poémape, B. and Alva Tauca, I., 2013. *Urban Development Plan of the City of Chachapoyas, Chapter IV: General Proposal*. Ministry of Housing, Construction and Sanitation, Provincial Municipality of Chachapoyas, Chachapoyas, Amazonas, Peru, pp.112.

Webster, R. and Oliver, M.A., 2007. *Geostatistics for Environmental Scientists*. 2nd ed. Wiley, pp.332. [DOI]

WHO, 2018. *How Air Pollution Is Destroying Our Health*. Retrieved June 25, 2024, from https://www.who.int/news-room/spotlight/how-air-pollution-is-destroying-our-health

Will-Wolf, S., Jovan, S. and Amacher, M.C., 2017. Lichen elemental content bioindicators for air quality in upper Midwest, USA: A model for largescale monitoring. *Ecological Indicators*, 78, pp.253-263. [DOI]

Xue, Y., Cao, X., Ai, Y., Xu, K. and Zhang, Y., 2020. Primary air pollutants emissions variation characteristics and future control strategies for transportation sector in Beijing, China. *Sustainability*, 12(10), p.4111. [DOI]

Yang, H., Tao, W., Wang, Y., Liu, Y., Liu, J., Zhang, Y. and Tao, S., 2019. Air quality and health impacts from the updated industrial emission standards in China. *Environmental Research Letters*, 14(12), p.124045. [DOI]

Zilio, L., Hammond, H. and Castro, A.S., 2017. Planimetric survey and lichenometric analysis at the Campo de Chenques site, north coast of Santa Cruz (Patagonia, Argentina). *Revista de Antropología Chilena*, 49, pp.65-80. [DOI]Table 4: Results of the main component analysis of the studied variables.

Nature Environment and Pollution Technology
An International Quarterly Scientific Journal

p-ISSN: 0972-6268
(Print copies up to 2016)
e-ISSN: 2395-3454

Vol. 25 | No. 3 | Article ID B4393 | 2026

Original Research Paper

https://doi.org/10.46488/NEPT.2026.v25i03.B4393

Open Access Journal

Retrieval of Turbidity of the Upper Lake, a Ramsar Site, Bhopal, India, Using *in situ* Observations and Landsat-8 OLI Satellite Data

Prasanta Ghadei and Sujit Kumar Jally†
School of Geography, Gangadhar Meher University, Sambalpur-768004, Odisha, India
†Corresponding author: Sujit Kumar Jally; sujit@gmuniversity.ac.in

Abbreviation: Nat. Env. & Poll. Technol.
Website: www.neptjournal.com

Received: 30-09-2025
Revised: 25-11-2025
Accepted: 27-11-2025

Key Words:

Empirical model
Landsat-8 OLI
Surface reflectance
Ramsar site
Turbidity
Upper Lake

Citation for the Paper:

Ghadei, P. and Jally, S.K., 2026. Retrieval of turbidity of the Upper Lake, a Ramsar site in Bhopal, India, using in-situ observations and Landsat-8 OLI satellite data. *Nature Environment and Pollution Technology*, 25(3), B4393. https://doi.org/10.46488/NEPT.2026.v25i03. B4393

Note: From 2025, the journal has adopted the use of Article IDs in citations instead of traditional consecutive page numbers. Each article is now given individual page ranges starting from page 1.

Copyright: © 2026 by the authors
Licensee: Technoscience Publications
This article is an open access article distributed under the terms and conditions of the Creative Commons Attribution (CC BY) license (https://creativecommons.org/licenses/by/4.0/).

ABSTRACT

Turbidity, an optical measure of water clarity influenced by suspended sediments and organic matter, is a critical indicator of freshwater quality. Satellite remote sensing offers a practical means of monitoring turbidity over space and time by capturing water-leaving reflectance across spectral bands. This study explores the spatiotemporal retrieval of turbidity in the Upper Lake, Bhopal, an important urban freshwater body and Ramsar site in India, using Landsat-8 Operational Land Imager (OLI) Surface Reflectance (SR) data from 2013 to 2022. Field-based in-situ turbidity data collected during the pre-monsoon and post-monsoon seasons of 2022 were used to calibrate and validate several empirical models based on different band combinations. The best empirical models used the band ratio of the blue and red bands (Band-2 and Band-4), yielding a high agreement with field data (R^2 = 0.89) with a validation RMSE of 4.04 NTU. Temporal turbidity trends revealed a seasonal pattern, with higher turbidity observed in the post-monsoon season due to catchment runoff and anthropogenic activities. This study confirmed that Landsat-8 OLI SR, supported by field measurements, is a reliable tool for long-term turbidity monitoring in inland lakes.

1. INTRODUCTION

Freshwater lakes and reservoirs are critical components of the Earth's hydrological cycle and provide a wide range of ecosystem services, including drinking water supply, irrigation, fisheries, biodiversity conservation, recreation, and climate regulation. However, in recent decades, many of these water bodies have faced significant degradation owing to anthropogenic pressures such as urbanization, agricultural runoff, industrial discharge, and climate change (UNESCO 2018). Among the various water quality parameters used to monitor aquatic ecosystem health, turbidity stands out as a key indicator because of its direct link with suspended sediment load, light attenuation, and pollutant transport (Das et al. 2024). Turbidity refers to the degree to which water loses its transparency owing to the presence of suspended particulates, such as silt, clay, organic matter, plankton, and microorganisms. It affects aquatic life by reducing sunlight penetration, which limits photosynthetic activity in submerged vegetation and algae (Bilotta & Brazier 2008). High turbidity levels also interfere with the reproduction and feeding behavior of aquatic organisms and can carry attached contaminants, such as heavy metals and pathogens, posing risks to both ecosystems and public health (Chen & Chen 2017). Therefore, understanding the spatial and temporal patterns of lake turbidity is essential for water quality management and policy formulation.

Traditionally, turbidity is measured using in-situ techniques, such as Secchi disk readings and nephelometric turbidity units (NTU) using turbidity meters. Although accurate at specific points, these methods are inherently limited in their ability to capture spatial variability across an entire water body, especially large or remote lakes. Moreover, repeated sampling at high temporal frequencies is often cost-prohibitive and labor-intensive (Dekker et al. 2002). This necessitates the use

of alternative, scalable approaches for monitoring turbidity, particularly in regions such as India, where resource constraints limit large-scale water quality monitoring. Remote sensing has emerged as a promising solution to address these challenges. Satellite-based sensors provide consistent, synoptic, and long-term observations of surface reflectance that can be used to estimate various water quality parameters, including turbidity (Jally et al. 2021). In recent years, the Landsat-8 Operational Land Imager (OLI) has gained popularity owing to its moderate spatial resolution (30 m), improved radiometric sensitivity, and free availability through the USGS Earth Explorer platform. The Surface Reflectance (SR) product, which accounts for atmospheric distortions, is particularly well-suited for quantitative water quality assessments (Pahlevan et al. 2017, Brezonik et al. 2005). Numerous studies have demonstrated the feasibility of retrieving turbidity from Landsat data using empirical relationships between spectral reflectance and turbidity values. The blue (Band-2), green (Band-3), and red (Band-4) bands are commonly the most responsive to increases in suspended matter because of their interaction with particulate matter in the water column (Maity et al. 2022, Wen et al. 2022). Empirical regression models, band ratio techniques, and semi-analytical models have been successfully employed to map turbidity in a range of aquatic environments, from rivers and estuaries to lakes and wetlands. These models are typically calibrated with field-measured turbidity values and validated using statistical indices such as the coefficient of determination (R^2), root mean square error (RMSE), and mean absolute percentage error (MAPE) (Yang et al. 2022).

In India, the application of remote sensing for inland water quality monitoring is still emerging but holds immense potential. The country's vast network of rivers, lakes, and reservoirs is under increasing stress owing to population growth, urban sprawl, and insufficient wastewater treatment infrastructure. One such water body is the Upper Lake (Bhojtal) in Bhopal, Madhya Pradesh, India. This ancient man-made lake, created in the 11th century, serves as the primary drinking water source for nearly 1.5 million people and supports significant biodiversity. Designated as a Ramsar site in 2002, the Upper Lake is recognized for its ecological and socioeconomic importance. However, it faces growing threats from untreated sewage inflow, agricultural runoff, eutrophication, encroachment, and climate variability (CPCB 2019). Given the environmental importance of Upper Lake, Bhopal, and the lack of continuous water quality monitoring data, there is a pressing need to develop and apply satellite-based approaches to assess its turbidity levels over time. The present study aims to address this gap by retrieving turbidity across a spatiotemporal scale (2013–2022) using Landsat-8 OLI SR data in conjunction with *in situ* turbidity measurements. The objective of this study was to develop and validate turbidity retrieval algorithms using Landsat-8 OLI SR data and in-situ field observations, thereby producing seasonal turbidity maps from 2013 to 2022. The results are expected to assist policymakers and lake managers in better understanding turbidity dynamics and in implementing appropriate conservation strategies. This study contributes to the growing body of knowledge on remote sensing applications in inland water quality monitoring and provides a replicable framework for similar studies in other Indian and global lakes under environmental stress.

2. MATERIALS AND METHODS

2.1 Study Area

The Upper Lake, locally known as Bhojtal, is one of the most prominent freshwater lakes in Central India. It is situated in the western part of Bhopal, the capital city of Madhya Pradesh, and forms a vital part of the city's ecological and socioeconomic landscape (Fig. 1). This ancient lake, believed to have been constructed in the 11th century by King Raja Bhoj, is among the oldest man-made lakes in India and is intricately linked to the cultural and historical heritage of the region (Everard et al. 2020). Geographically, the lake lies between 23°12′ and 23°16′ N latitude and 77°18′ and 77°22′ E longitude, with an average altitude of approximately 500 m above sea level. The Upper Lake spans a surface area of approximately 31 square kilometers and is part of the larger Bhoj Wetland system, which also includes the adjoining Lower Lake. Together, these wetlands were designated as Ramsar sites in 2002 under the Convention on Wetlands of International Importance, highlighting their ecological significance and the need for conservation (Ramsar Sites Information Service 2024). It is primarily fed by rainfall and surface runoff from a catchment area of nearly 361 square kilometers, which consists of forested hills, agricultural lands, and urban settlements. The Kolans River, a seasonal tributary, also contributes to lake inflow. The lake is the main drinking water source for more than 1.5 million residents of Bhopal and supports domestic, agricultural, and recreational activities. In addition to its economic and utilitarian roles, the lake provides a habitat for a diverse range of aquatic flora and fauna, including migratory bird species such as bar-headed geese, black-winged stilts, and cormorants (Rather & Gautam 2023). The region experiences a tropical wet and dry climate, characterized by three major seasons: summer (March–June), monsoon (July–September), and winter (October–February). The average annual rainfall is approximately 1200 mm, with the majority of precipitation occurring during the monsoon

months. This seasonal rainfall pattern plays a significant role in influencing the hydrological and sediment dynamics of the lake, thereby affecting the turbidity levels. During the monsoon, increased surface runoff brings suspended sediments, nutrients, and organic matter into lakes, often leading to elevated turbidity and eutrophication, particularly near urban and agricultural inflow points (Parashar et al. 2008). In this study, the lake was categorized into three sectors based on Secchi disk transparency, nutrients, and depth: western (WS), central (CS), and eastern (ES) sectors for the ecological assessment.

2.2 Database and Methodology

This study integrated field-based turbidity measurements with satellite remote sensing data from the Landsat-8 Operational Land Imager (OLI) to develop an empirical model for turbidity retrieval. The methodology was carefully structured to ensure the accuracy of the calibration, validation, and application of the model across a spatiotemporal scale. The process comprised in-situ data collection, satellite image selection and preprocessing, band ratio analysis, model development, and the generation of seasonal turbidity maps for the pre-monsoon and post-monsoon seasons from 2013 to 2022 (Fig. 3). All data were analyzed using a combination of Remote Sensing, GIS, and statistical software to enable high-resolution spatial analysis and trend interpretation.

2.2.1 Turbidity Data Collection

Fieldwork was conducted during the pre- and post-monsoon seasons of 2022. A total of 50 sampling locations were selected within the Upper Lake. At each location, turbidity was measured using a portable HANNA HI-98703 turbidity meter, which operates based on nephelometric principles that conform to ISO 7027 standards. To minimize variability, three consecutive readings were taken at each site, and the average value was recorded in Nephelometric Turbidity Units (NTU). Simultaneously, the geographic coordinates of each point were recorded using a Garmin GPSMAP 64s handheld device to ensure accurate geospatial alignment with the satellite pixels.

2.2.2 Acquisition of Satellite Data

The satellite data used in this study consisted of Landsat-8 Surface Reflectance (SR) imagery, which was atmospherically corrected and available via the USGS Earth Explorer portal. Landsat-8 OLI provides multispectral imagery at 30-meter resolution, making it highly suitable for monitoring medium-scale inland water bodies such as the Upper Lake. For each

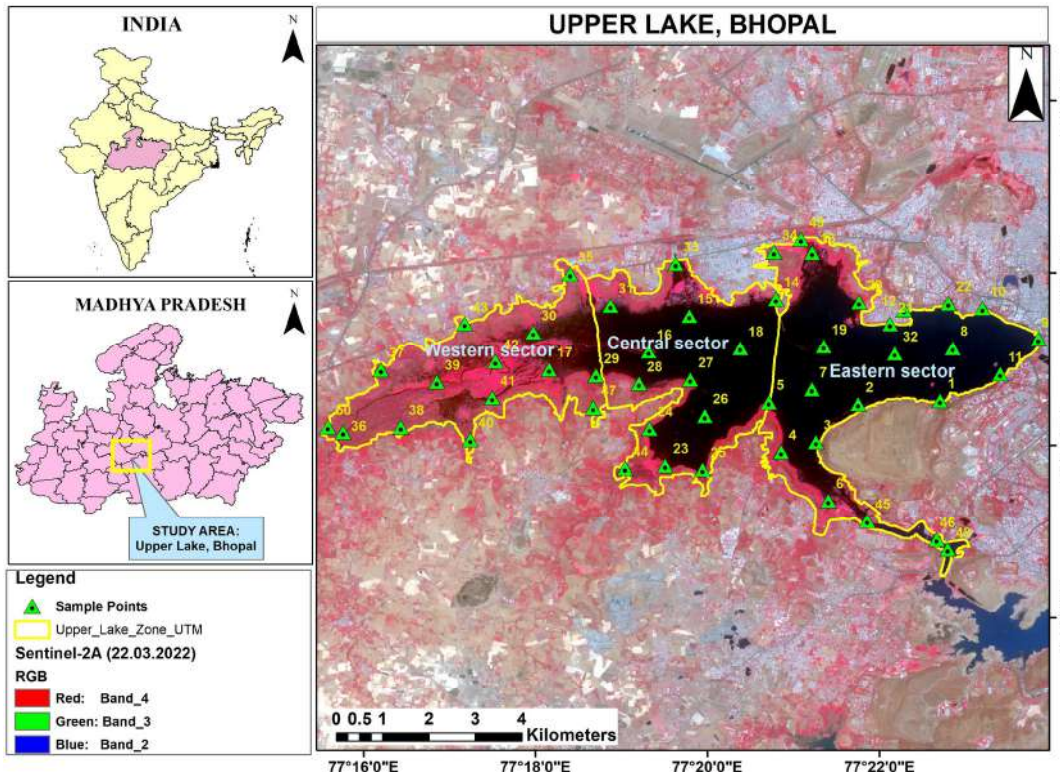


Fig. 1: Sentinel-2A false-color composite (FCC) image showing different sectors and sampling locations of the Upper Lake, Bhopal, India.

field sampling date, satellite images were acquired within a ±3-day window to ensure consistency between in situ and satellite observations. Priority was given to scenes with less than 10% cloud cover, and pre-monsoon and post-monsoon datasets were compiled for each year from 2013 to 2022. The reflectance values from the relevant bands, Blue (Band-2), Green (Band-3), Red (Band-4), and Near-Infrared (Band-5), were extracted for further analysis (Roy et al. 2016).

2.2.3 Image Preprocessing and Water Body Extraction

Before analyzing the reflectance-turbidity relationships, each Landsat image underwent a series of preprocessing steps. Using the Quality Assessment (QA_PIXEL) band provided by the USGS, clouds, cloud shadows, and snow pixels were masked to ensure that only valid reflectance values were retained. To isolate the Upper Lake's water surface, the Normalized Difference Water Index (NDWI) was calculated using the formula NDWI = (Green – NIR) / (Green + NIR), as proposed by McFeeters (1996). A threshold value of NDWI > 0.1 was applied to generate a binary water mask, effectively separating water pixels from land, vegetation, and urban areas. This mask was used to clip reflectance values only for the open-water regions of the lake, minimizing background noise in the model calibration phase.

2.2.4 Turbidity Algorithm Development

To establish a relationship between in-situ turbidity and satellite-derived reflectance, a series of empirical regression models was tested. Each spectral band and selected band ratio (e.g., blue/red and green/red) were analyzed for correlation with the measured NTU values. Data points from coinciding fieldwork and Landsat-8 OLI images were matched spatially, and linear, logarithmic, and exponential regression models were developed using OriginPro and SPSS. The band ratio of the blue band (Band-2) and red band (Band-4) consistently demonstrated the strongest correlation (R^2=0.89) with turbidity, which aligns with the findings of similar studies in Indian freshwater systems, where blue and red wavelengths showed maximum scattering from suspended sediments (Gholizadeh et al. 2016, Allam et al. 2020, Sharma et al. 2020). The final model was selected based on the highest coefficient of determination (R^2) and the lowest root mean square error (RMSE). The relationship between the band ratio of Landsat-8 OLI (Band-2: Band-4) and in-situ turbidity is shown in Fig. 2, and the derived equation is presented in Equation (1).

$$\text{Turbidity (NTU)} = 59.021 \times (\text{OLI B-2/OLI B-4}) - 40.42 \quad \ldots(1)$$

The model was calibrated using training data from the field-satellite pairs and validated using an independent subset. The validation metrics included RMSE and R^2, which confirmed the model's reliability across seasons and varying turbidity conditions.

3. RESULTS AND DISCUSSION

3.1 Seasonal Variation in Turbidity

This section presents the results of turbidity estimation derived from the calibrated remote sensing model based on Landsat-8 OLI Surface Reflectance data and validated using in-situ measurements. Table 1 shows the sector-wise *in situ* data collected from 50 selected sample locations in

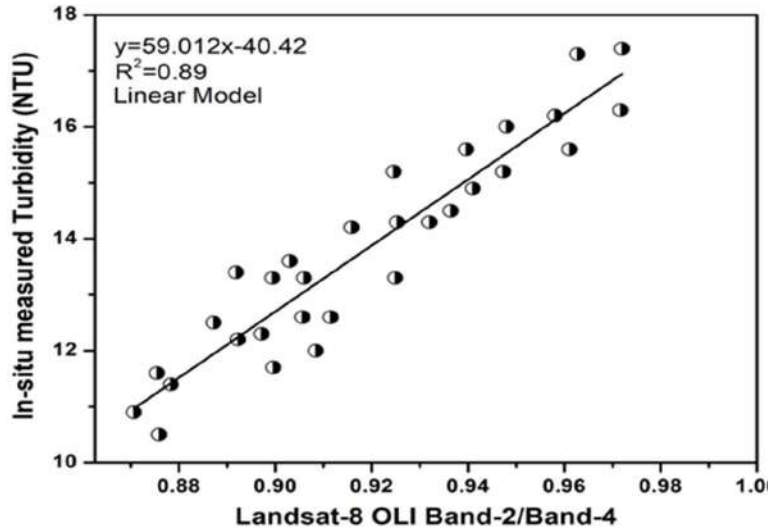


Fig. 2: Scatter plot showing the relationship between the in-situ turbidity measurements and Landsat-8 OLI band ratios.

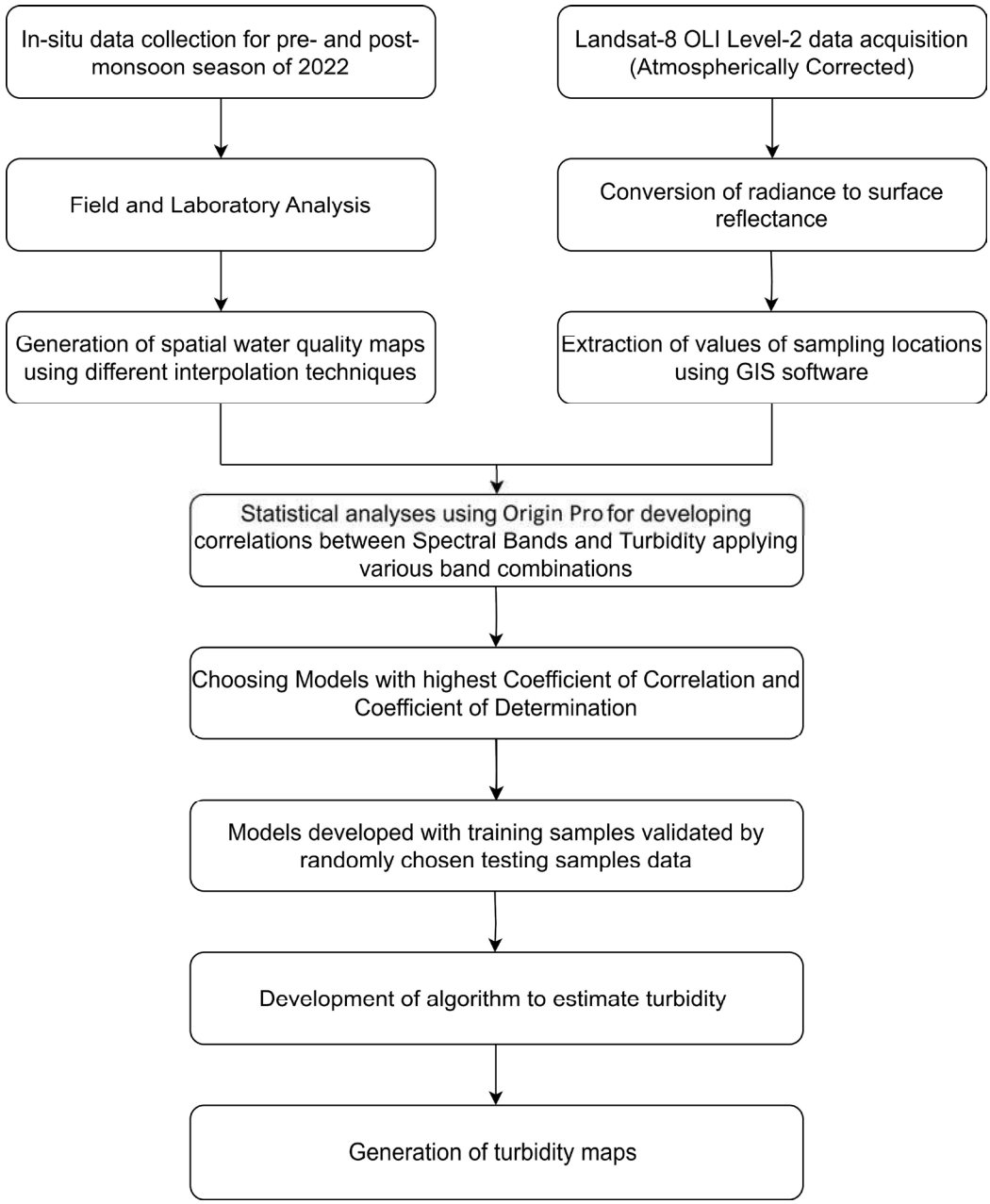


Fig. 3: Methodology flowchart for the estimation and generation of turbidity maps for Upper Lake, Bhopal.

Table 1: In-situ turbidity collected over the Upper Lake, Bhopal, during the pre- and post-monsoon seasons of 2022.

Turbidity [NTU]						
Pre-monsoon season-2022				Post-monsoon season-2022		
Sector	Minimum	Maximum	Average	Minimum	Maximum	Average
Eastern Sector	14.3	20.4	17.63	15.7	23.1	19.38
Central Sector	7.1	16.2	8.29	9.5	26.8	14.87
Western Sector	4.3	11.9	11.95	10.8	28.8	24.8

the Upper Lake, Bhopal, during the pre- and post-monsoon seasons of 2022.

In situ analysis revealed distinct seasonal fluctuations in turbidity levels across the lake during the 2022 observation period. During the pre-monsoon periods (April–June), turbidity values were generally lower, ranging between 4 NTU and 20 NTU, particularly in the central and deeper sections of the lake. These lower values are primarily attributed to minimal inflows, clear weather conditions, and sediment settling, as there was limited disturbance of the lake bed and relatively less surface runoff. In contrast, the post-monsoon periods (October–December) showed significantly elevated turbidity levels, with several locations exceeding 20 NTU. This sharp rise can be attributed to monsoonal runoff, which carries high loads of suspended solids, organic matter, and urban waste into the lake through open drains and inflow channels during the monsoon.

In the present study, satellite data were used to estimate the turbidity of the Upper Lake, Bhopal. Satellite-derived turbidity maps confirmed the presence of extensive sediment plumes, especially near urban drain outlets such as the Patra Nullah and Bairagarh inlet, aligning well with in-situ measurements and past studies (Durga Rao et al. 2009, Prasad & Tiwari 2019). From 2013 to 2022, the seasonal analysis of turbidity in the Upper Lake, Bhopal, revealed a consistent pattern of higher turbidity levels during the post-monsoon season than during the pre-monsoon period, with notable inter-annual variability influenced by rainfall intensity, urban runoff, and anthropogenic activities. During the pre-monsoon months (March–May), turbidity is generally moderate to high, reflecting limited inflow and sediment input, whereas post-monsoon months (October–November) consistently show elevated turbidity due to catchment runoff laden with sediments and organic matter following monsoon rains (Mishra & Prasad 2015). Spatial analysis using Landsat-8 OLI surface reflectance data revealed that areas near urban outfalls and drainage inlets exhibited persistently high turbidity values, indicating a direct influence from domestic and stormwater discharge.

In 2013, the baseline year of Landsat-8 availability, turbidity levels during both the pre- and post-monsoon seasons were high, with spatial concentrations near inflow zones, reflecting relatively stable catchment conditions. Fig. 4(a) shows relatively high turbidity (20 NTU) as compared to Fig. 4(b) (19 NTU). The average turbidity of the entire lake was 18.07 NTU and 14.45 NTU during the pre- and post-monsoon seasons of 2022, respectively. Fig. 4(c) shows that the ES of the lake is highly turbid water (18.07 NTU) compared to WS. However, high turbidity (14.34 NTU) was recorded in the CS and ES during the post-monsoon season of 2014 (Fig. 4(d)). The ES remains at a high turbidity concentration throughout the year, which is mainly influenced by increasing construction activities, sewage discharge, and urban expansion around the lake's eastern periphery. Fig. 4(e) shows a similar pattern of turbidity as compared to Fig. 4(c) during the post-monsoon season. However, Fig. 4(f) demonstrates that the maximum area of the lake was under moderate to high turbidity during the post-monsoon period in 2015. The turbidity increased significantly, which is correlated with higher-than-average rainfall and sediment-rich runoff, as observed in similar studies across central Indian lakes (Mishra & Prasad 2015). The average turbidity was 11.96 NTU and 13.37 NTU during the pre- and post-monsoon seasons of 2015, respectively. Fig. 4(g) depicts high turbidity in the ES due to a prolonged dry spell, which caused reduced dilution and concentration of suspended solids (Sharma 2020). Fig. 4(h) shows that the turbidity value of the entire lake was moderate owing to a weak monsoon year. The average turbidity concentration of the entire lake was 11.73 NTU and 14.46 NTU during the pre- and post-monsoon seasons of 2016, respectively. Fig. 4(i) shows that ES and CS experience high turbidity (20 NTU) compared to WS (3.8 NTU). Fig. 4(j) depicts a moderate pattern of post-monsoon turbidity, 18.25 NTU, which is recorded particularly near the southeast inflow regions, attributed to intense rainfall and unregulated urban discharge, aligning with similar findings by Farooq et al. (2021). In 2018 (Fig. 4(k) and (l)), a declining pattern of turbidity levels was observed for both seasons, except for the ES and CS of the lake, owing to a drier monsoon and partial implementation of catchment management under the Bhopal Lake Conservation Scheme (Sharma 2020). The average turbidity concentration of the lake was 10.77 NTU and 12.12 NTU during the pre- and post-monsoon seasons of 2018, respectively.

Fig. 4(m) shows the lake water turbidity of the pre-monsoon season of 2019, which slightly declined from the similar pattern of the pre-monsoon season of 2018. Fig. 4(n) depicts ES and WS showing high turbidity concentration (17.3 NTU), except for the maximum pockets of CS. The average turbidity of the lake was 10.12 NTU and 11.66 NTU during the pre- and post-monsoon seasons, respectively. Fig. 4(o) and (p) show a similar pattern of turbidity concentration during the pre- and post-monsoon seasons of 2020. The average turbidity of the lake was 7.18 NTU and 9.6 NTU during the pre-monsoon and post-monsoon seasons, respectively. Similarly, Fig. 4(q) and (r) show the pre- and post-monsoon turbidity patterns of 2021. The average turbidity values were 7.87 NTU and 10.57 NTU during the pre- and post-monsoon seasons, respectively. From the overall observation, it was found

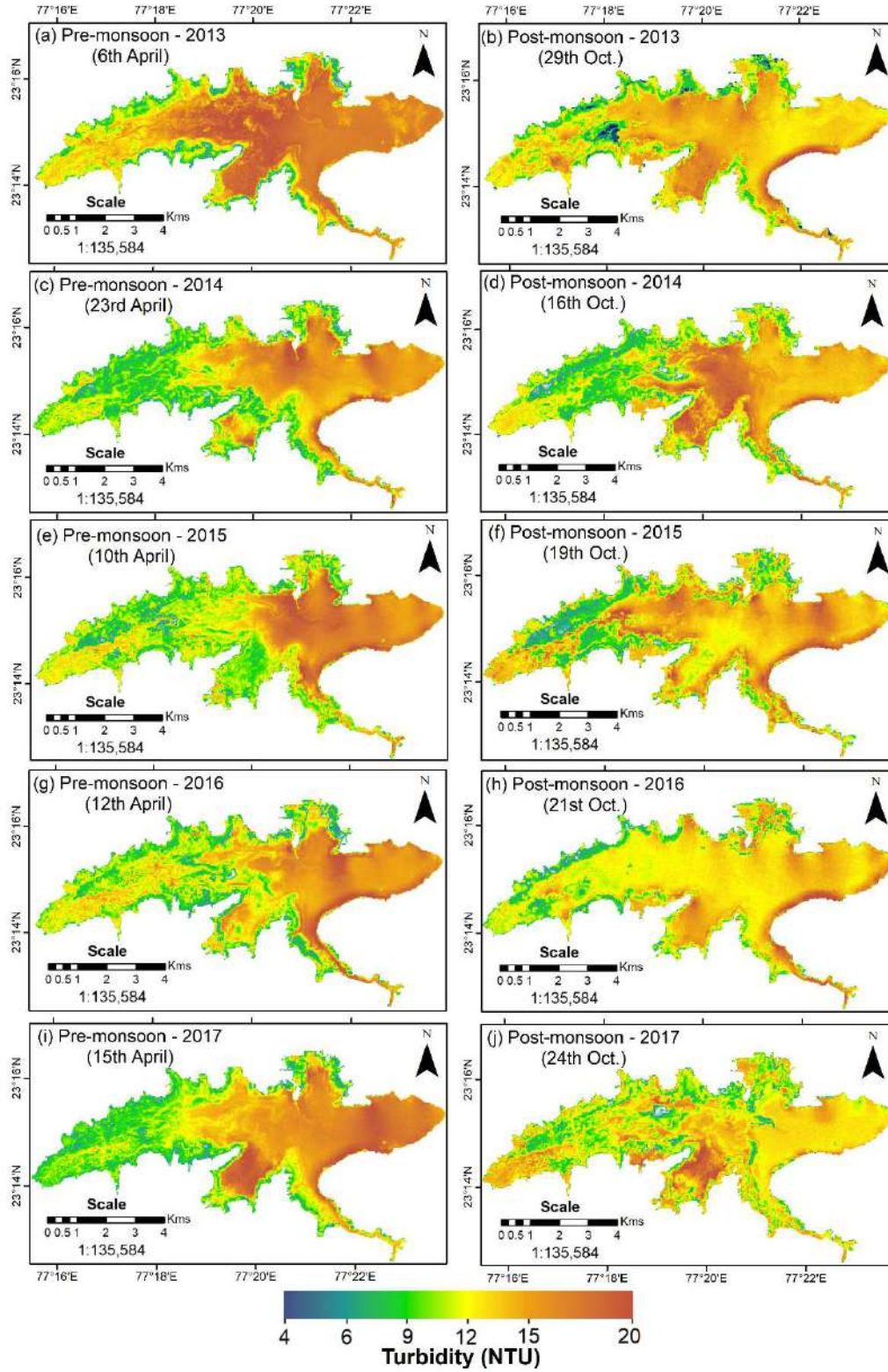


Fig. 4 (a-j): Turbidity images from Landsat-8 OLI bands during the pre- and post-monsoon seasons from 2013 to 2017.

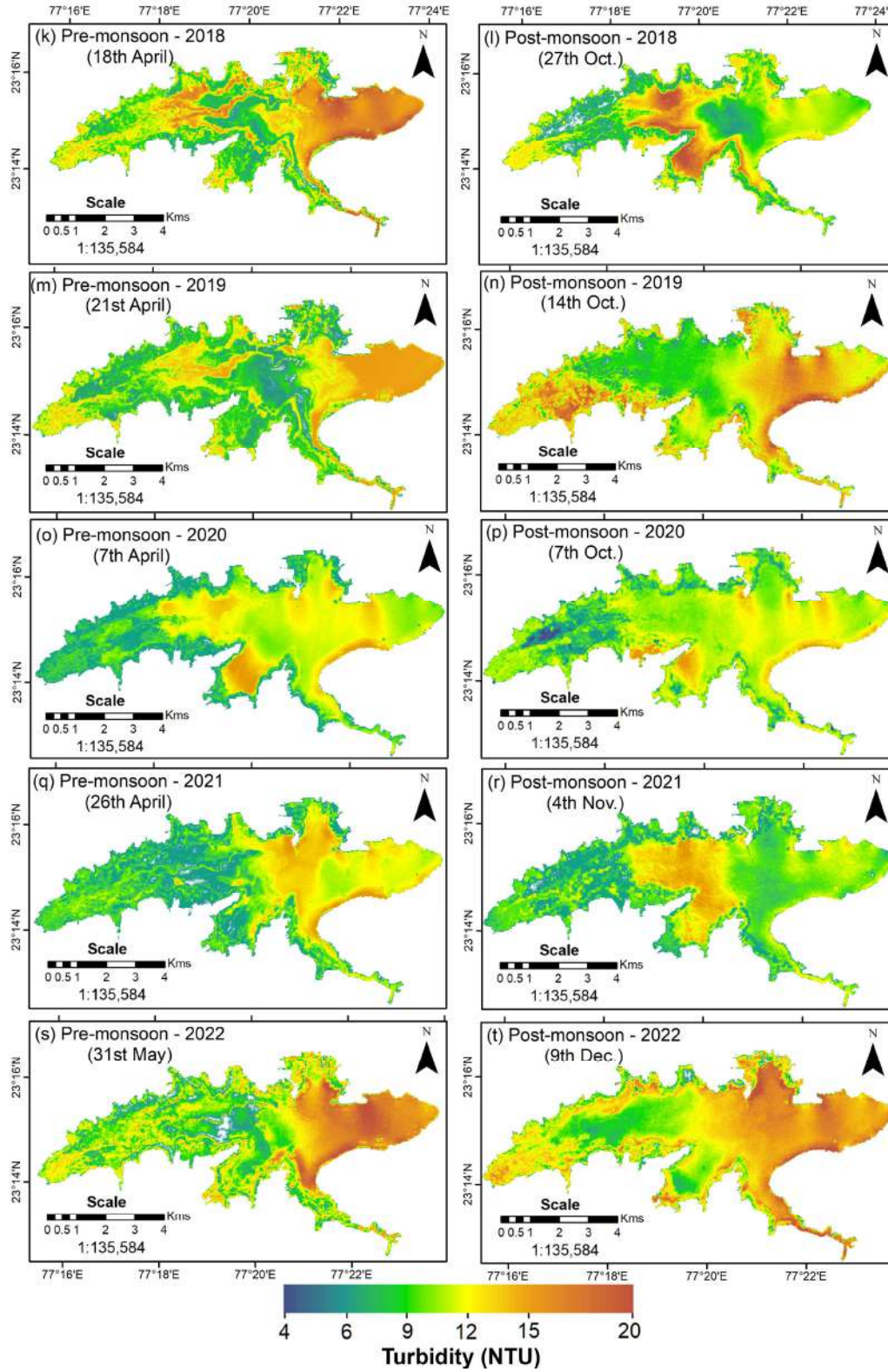


Fig. 4 (k–t)): Turbidity images from Landsat-8 OLI bands during the pre- and post-monsoon seasons from 2018 to 2022.

that the distribution of turbidity was more or less the same in the pre- and post-monsoon season of 2020-21. The above-mentioned period exhibited a unique scenario, where both seasonal turbidity levels were markedly low. This may be attributed to the COVID-19 lockdown, which reduced human-induced activity, boating, and industrial effluent discharge, a phenomenon echoed in water bodies globally (Sharma & Gupta 2022). Finally, 2022 offered the most detailed insight because of concurrent in-situ sampling. Fig. 4(s) shows that the ES experienced relatively high turbidity (20 NTU) compared to the WS (12.13 NTU) and CS (14.54 NTU) of the lake. Fig. 4(t) shows that the entire lake has a maximum turbidity concentration (19.67 NTU), except for some pockets of CS (14.54 NTU) and WS (15.27 NTU), highlighting the continued influence of runoff and sediment-laden flows, particularly near the Shahpura and Bairagarh catchments (Talwar et al. 2014). The satellite-derived turbidity model, based on the Band-2/Band-4 ratio, showed excellent agreement (R^2 = 0.89) with field data for 2022, supporting its robustness for multi-year monitoring (Joshi & Agrawal 2022). Overall, the decade-long analysis confirmed a consistent seasonal pattern of moderate to high turbidity during the pre-monsoon season and high turbidity during the post-monsoon season, with year-to-year variability driven by rainfall, urban growth, and local interventions. These findings emphasize the value of combining satellite observations with ground-truthing for long-term lake water quality assessment in rapidly urbanizing landscapes.

3.2 Comparison of Sector-wise Average Turbidity (2022)

A comparison of the average values of in-situ turbidity measurements at different sectors during the pre- and post-monsoon seasons of 2022 is shown in Fig. 5. The figure shows that the post-monsoon season experienced higher turbidity than the pre-monsoon season. During the pre-monsoon season of 2022, the average value of turbidity was found in WS (11.95 NTU), CS (8.29 NTU), and ES (17.63 NTU). Similarly, during the post-monsoon season of 2022, the average turbidity values were observed in WS (21.83 NTU), CS (14.87 NTU), and ES (19.38 NTU). The in-situ turbidity measurements revealed that the WS experienced maximum turbidity during the post-monsoon season, whereas the ES experienced maximum turbidity during the pre-monsoon season of 2022. However, the CS remains low in terms of turbidity throughout the year. Fig. 6 depicts the sector-wise distribution of average turbidity derived from Landsat-8 OLI during the pre-monsoon and post-monsoon seasons of 2022. This shows that the post-monsoon season experiences higher turbidity than the pre-monsoon season. During the pre-monsoon season of 2022, the average turbidity values were estimated at WS (7.76 NTU), CS (7.15 NTU), and ES (9.82 NTU). Similarly, during the post-monsoon season of 2022, the average value of turbidity is estimated in WS (14.26 NTU), CS (13.99 NTU), and ES (15.5 NTU). The analysis of Fig. 5 and 6 indicates that the average in-situ observed turbidity pattern agrees well with Landsat-8 OLI-derived turbidity.

3.3 Inter-Annual Trends (2013–2022)

In the present study, the dynamic nature of inter-sectoral and seasonal changes in the turbidity of the Upper Lake, Bhopal, was studied, which is mainly influenced by various

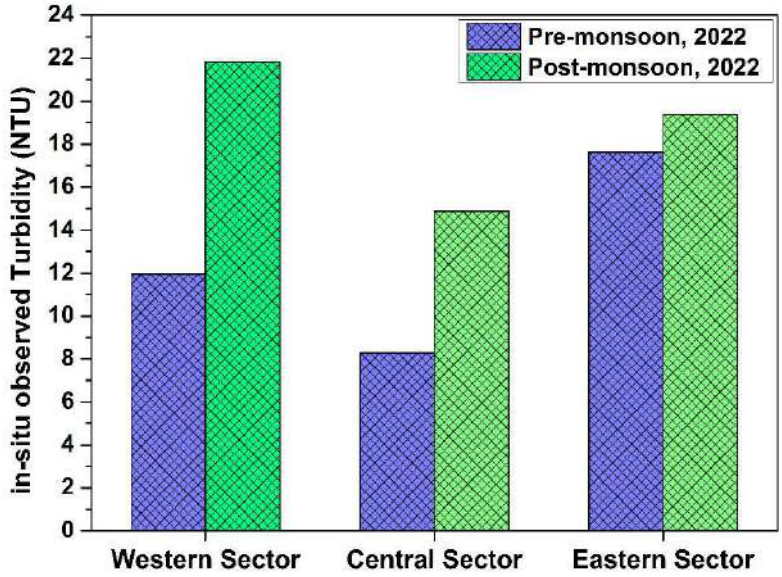


Fig. 5: Comparison of average turbidity at different sectors from in-situ measurements during the pre- and post-monsoon seasons of 2022.

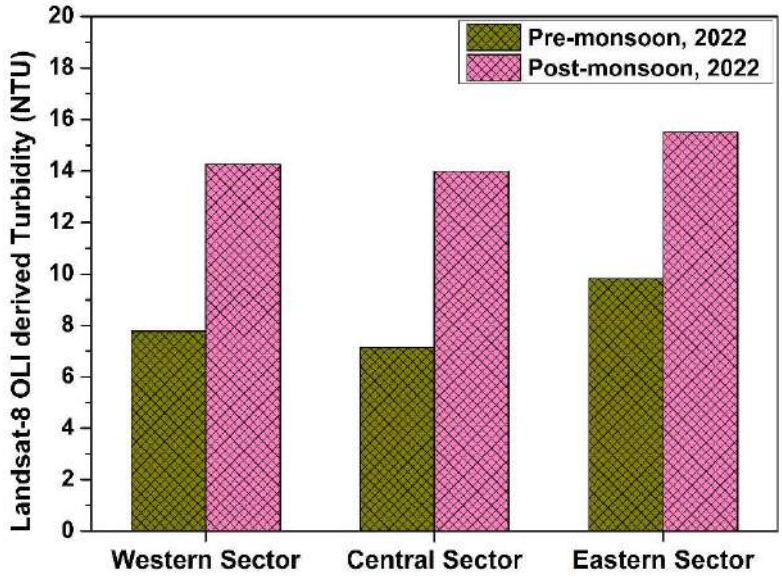


Fig. 6: Comparison of average turbidity in different sectors derived from Landsat-8 OLI during the pre- and post-monsoon seasons of 2022.

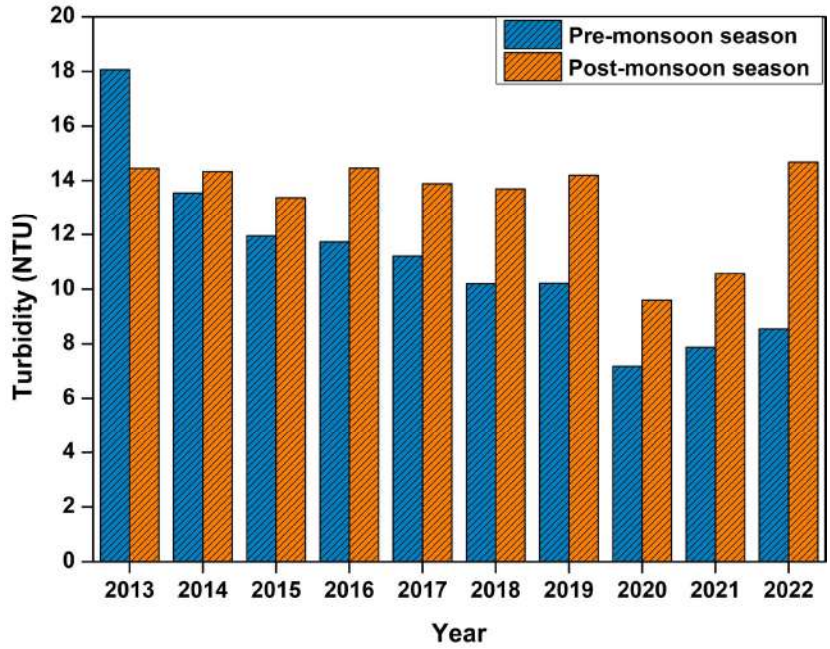


Fig. 7: Comparison of average turbidity derived from Landsat-8 OLI during the pre- and post-monsoon seasons from 2013 to 2022.

anthropogenic activities. A comparison of the pre- and post-monsoon season average values of the turbidity of the entire lake estimated from satellite data from 2013 to 2022 is shown in Fig. 7. Long-term analysis revealed that the average turbidity during the post-monsoon season was higher than that during the pre-monsoon season, except for 2013. From 2014 to 2019, most areas of the lake showed high turbidity (10.2 – 18.07 NTU), with exceptions limited to localized high-inflow zones. However, in 2020 and 2021, there was marked moderate turbidity (7.18 – 10.57 NTU) due to the COVID-19 lockdown. The post-COVID-19 period showed a marked expansion of high turbidity (8.54 – 14.68 NTU), indicating escalating sedimentation and pollutant loading.

This trend corresponds to increased urbanization, construction activities, and land-use changes in the lake's catchment area. The northeastern and western peripheries,

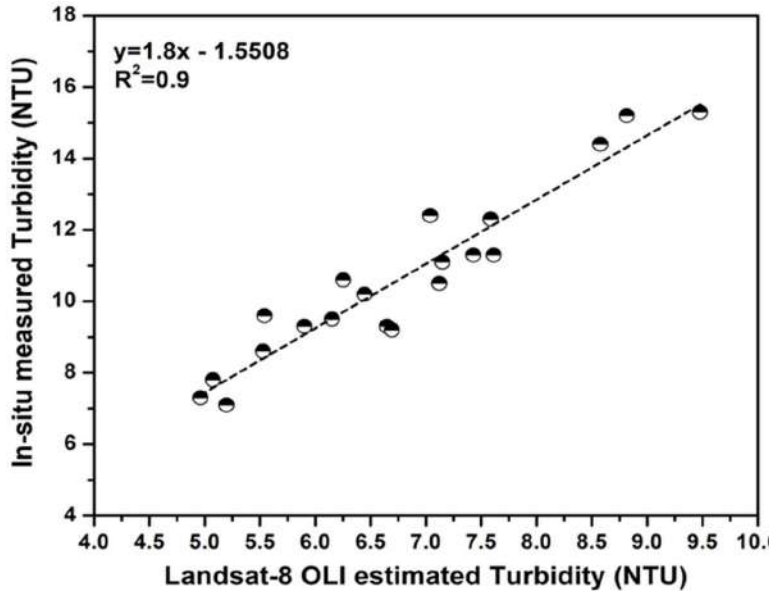


Fig. 8: Scatter plot showing the relationship between in-situ observed turbidity and Landsat-8 OLI estimated turbidity.

which have witnessed dense residential and commercial development and river run-off, emerged as zones with persistently high turbidity. The lack of effective stormwater management and wastewater treatment infrastructure appears to be a major driver of turbidity escalation. These findings mirror those of other urban lake studies in India, where land disturbance and catchment degradation directly influenced water clarity (Rather & Dar 2020).

3.4 Validation of Turbidity Retrieval Model

Turbidity was estimated for the pre- and post-monsoon seasons using Landsat-8 Operational Land Imager (OLI) images for the Upper Lake, Bhopal. The turbidity retrieval model developed using the Landsat-8 OLI band ratio of blue and red band reflectance and calibrated with in-situ measurements showed a strong correlation. The model yielded a coefficient of determination (R^2) of 0.9 and a Root Mean Square Error (RMSE) of ±4.04 NTU during validation (Fig. 8). These metrics indicate the high reliability of the model in capturing actual turbidity variations across seasons and locations. The model was particularly effective in estimating turbidity within the range of 5–50 NTU. However, at very high turbidity levels (>60 NTU), there was a slight tendency to underestimate values, likely due to reflectance saturation in the red band, which limits the differentiation of dense sediment loads. Such limitations have also been noted in similar studies using optical sensors such as Landsat and Sentinel (Nechad et al. 2010, Gholizadeh et al. 2016).

4. CONCLUSIONS

This study successfully demonstrated the integration of satellite remote sensing and in-situ turbidity measurements for monitoring water quality in the Upper Lake, Bhopal, over a decadal time frame (2013–2022) during the pre- and post-monsoon seasons. Using Landsat-8 OLI Surface Reflectance data calibrated against the obtained field data, an empirical model was developed to retrieve turbidity with high spatial and seasonal variation. The model achieved strong validation results (R^2 = 0.89), establishing its suitability for ongoing and future water quality assessments of Lake Taal. The findings revealed significant seasonal and interannual variations in the turbidity. Post-monsoon seasons consistently exhibit higher turbidity levels owing to increased runoff, urban drainage, and sediment inflow. Meanwhile, the pre-monsoon periods showed comparatively clearer water, suggesting a seasonal self-recovery potential. However, a gradual increase in turbidity across several sectors of the lake, especially near urban inflow points, indicates growing anthropogenic pressure, particularly from urban expansion, waste discharge, and unregulated changes in catchment areas. Spatial analysis identified persistent turbidity hotspots along the western and northeastern lake margins, highlighting the role of point and non-point source pollution. These areas require targeted interventions, such as drainage management, constructed wetlands, and pollution control measures. In contrast, the central sector of the lake maintained relatively low turbidity owing to better protection and minimal human interference, underscoring the value of

riparian buffers and regulated land use. This study provides a cost-effective and scalable methodology for long-term water quality monitoring and generates critical geospatial intelligence that can support lake management policies and Ramsar site conservation strategies. The approach adopted here is replicable for similar water bodies across India and other developing regions, especially where conventional monitoring is limited by resource availability. Going forward, the integration of higher-resolution sensors (e.g., Sentinel-2 MSI), Machine Learning Models, and multi-parameter water quality indices can further enhance the accuracy and scope of monitoring. Regular data-driven surveillance, combined with community involvement and government action, is essential for restoring and safeguarding the ecological health of Upper Lake, Bhopal, and fulfilling its role as a critical urban wetland under the Ramsar Convention.

5. ACKNOWLEDGMENTS

The authors are grateful to the Vice Chancellor of Gangadhar Meher University, Sambalpur, for providing all the support and encouragement. Special thanks to Dr. Abhilasha Bhawsar, Assistant Professor, Department of Environmental Sciences and Limnology, Barkatullah University, Bhopal, for providing essential support and laboratory facilities to conduct the research.

6. REFERENCES

Allam, M., Yawar Ali Khan, M. and Meng, Q., 2020. Retrieval of turbidity on a spatio-temporal scale using Landsat 8 SR: a case study of the Ramganga river in the Ganges basin, India. Applied Sciences, 10(11), pp.1-15. [DOI]

Bilotta, G.S. and Brazier, R.E., 2008. Understanding the influence of suspended solids on water quality and aquatic biota. *Water Research*, 42(12), pp.2849-2861. [DOI]

Brezonik, P., Menken, K.D. and Bauer, M., 2005. Landsat-based remote sensing of lake water quality characteristics, including chlorophyll and colored dissolved organic matter (CDOM). *Lake and Reservoir Management*, 21(4), pp.373-382. [DOI]

Chen, M. and Chen, F., 2017. Effect of suspended solids on interaction between filter-feeding fish Aristichthys nobilis and zooplankton in a shallow lake using a mesocosm experiment. *Journal of Freshwater Ecology*, 32(1), pp.219-227. [DOI]

Central Pollution Control Board (CPCB), 2019. "Status of Water Quality in India – 2019." Retrieved June 25, 2024, from https://cpcb.nic.in/nwmp-data-2019/

Das, A., Regin, J.J., Suhasini, A. and Lisa, K.B., 2024. Study on spatial variations of surface water quality vulnerable zones in Baitarani River basin, Odisha, India. *Nature Environment and Pollution Technology*, 23(1), pp.33-53. [DOI]

Dekker, A.G., Vos, R.J. and Peters, S.W.M., 2002. Analytical algorithms for lake water TSM estimation for retrospective analyses of TM and SPOT sensor data. *International Journal of Remote Sensing*, 23(1), pp.15-35. [DOI]

Durga Rao, K.H.V., Singh, A.K. and Roy, P.S., 2009. Study of morphology and suspended sediment of Bhopal Upper Lake using spatial simulation technique and remote sensing data. *Journal of the Indian Society of Remote Sensing*, 37, pp.433-441. [DOI]

Everard, M., Ahmed, S., Gagnon, A.S., Kumar, P., Thomas, T., Sinha, S., Dixon, H. and Sarkar, S., 2020. Can nature-based solutions contribute to water security in Bhopal? *Science of the Total Environment*, 723, pp.1-15. [DOI]

Farooq, S., Shrivastava, P. and Bhat, M.H., 2021. Water quality assessment of Upper Lake Bhopal with reference to conservation and management. *EPRA International Journal of Multidisciplinary Research*, 7(9), pp.328-333. [DOI]

Gholizadeh, M.H., Melesse, A.M. and Reddi, L., 2016. A comprehensive review on water quality parameters estimation using remote sensing techniques. *Sensors*, 16(8), pp.1-15. [DOI]

Jally, S.K., Mishra, A.K. and Balabantaray, S., 2021. Retrieval of suspended sediment concentration of the Chilika Lake, India using Landsat-8 OLI satellite data. *Environmental Earth Sciences*, 80, pp.1-15. [DOI]

Joshi, A. and Agrawal, S., 2022. Reduction in turbidity of Indian lakes through satellite imagery during COVID-19 induced lockdown. *Spatial Information Research*, 30, pp.715-727. [DOI]

Maity, S., Maiti, R. and Senapati, T., 2022. Evaluation of spatio-temporal variation of water quality and source identification of conducive parameters in Damodar River, India. *Environmental Monitoring and Assessment*, 194, pp.1-15. [DOI]

McFeeters, S.K., 1996. The use of the normalized difference water index (NDWI) in the delineation of open water features. *International Journal of Remote Sensing*, 17, pp.1425-1432. [DOI]

Mishra, D.R. and Prasad, A., 2015. Spatiotemporal patterns of turbidity in inland waters using remote sensing. *Journal of Hydrology*, 527, pp.713-727. [DOI]

Nechad, B., Ruddick, K. and Park, Y., 2010. Calibration and validation of a generic multisensor algorithm for mapping turbidity in coastal waters. *Remote Sensing of Environment*, 114(4), pp.854-866. [DOI]

Pahlevan, N., Sarkar, S., Franz, B.A., Balasubramanian, S.V. and He, J., 2017. Sentinel-2 Multispectral Instrument (MSI) data processing for aquatic science applications: demonstrations and validations. *Remote Sensing of Environment*, 201, pp.47-56. [DOI]

Parashar, C., Verma, N., Dixit, S. and Shrivastava, R., 2008. Multivariate analysis of drinking water quality parameters in Bhopal, India. *Environmental Monitoring and Assessment*, 140, pp.119-122. [DOI]

Prasad, B. and Tiwari, H.L., 2019. Sedimentation analysis and remedial measures for Upper Lake Bhopal using remote sensing and GIS. *International Journal of Innovative Technology and Exploring Engineering (IJITEE)*, 8(5), pp.1008-1013.

Ramsar Sites Information Service, 2024. "Bhoj Wetland Ramsar Information Sheet." Retrieved June 25, 2024, from https://rsis.ramsar.org

Rather, H.A. and Gautam, V., 2023. A study of winter avifaunal diversity in Upper Lake, in the city of Bhopal, Madhya Pradesh, India. *Journal of Animal Diversity*, 5(4), pp.48-56. [DOI]

Rather, I.A. and Dar, A.Q., 2020. Assessing the impact of land use and land cover dynamics on water quality of Dal Lake, NW Himalaya, India. *Applied Water Science*, 10, pp.1-15. [DOI]

Roy, D.P., Zhang, H.K., Ju, J., Gomez-Dans, J.L., Lewis, P.E., Schaaf, C.B., Sun, Q., Li, J., Huang, H. and Kovalskyy, V., 2016. A general method to normalize Landsat reflectance data to nadir BRDF adjusted reflectance. *Remote Sensing of Environment*, 176, pp.255-271. [DOI]

Sharma, S. and Gupta, A., 2022. Impact of COVID-19 on water quality index of river Yamuna in Himalayan and upper segment: analysis of monsoon and post-monsoon season. *Applied Water Science*, 12(6), pp.1-15. [DOI]

Sharma, S., 2020. Behavioral study of urban watersheds in Bhopal-city of lakes. *International Journal of Hydrology*, 4(3), pp.111-115. [DOI]

Sharma, R., Kumar, R., Satapathy, S.C., Ansari, N.A., Singh, K.K., Mahapatra, R.P., Agarwal, A.K., Le, H.V. and Pham, B.T., 2020. Analysis of water pollution using different physicochemical parameters: a study of Yamuna River. *Frontiers in Environmental Science*, 8, pp.1-15. [DOI]

Talwar, R., Agrawal, S., Bajpai, A. and Malik, S., 2014. Effect of catchment area activities on the physicochemical characteristics of water of Upper Lake, Bhopal with special reference to nitrate and phosphate concentration. *Current World Environment*, 9(1), pp.188-191. [DOI]

UNESCO, 2018. "UN World Water Development Report 2018: Nature-Based Solutions for Water." Retrieved June 25, 2024, from https://www.unwater.org/publications/world-water-development-report-2018

Wen, Z., Wang, Q., Liu, G., Jacinthe, P., Wang, X., Lyu, L., Tao, H., Ma, Y., Duan, H., Shang, Y., Zhang, B., Du, Y., Du, J., Li, S., Cheng, S. and Song, K., 2022. Remote sensing of total suspended matter concentration in lakes across China using Landsat images and Google Earth Engine. *ISPRS Journal of Photogrammetry and Remote Sensing*, 187, pp.61-78. [DOI]

Yang, H., Kong, J., Hu, H., Du, Y., Gao, M. and Chen, F., 2022. A review of remote sensing for water quality retrieval: progress and challenges. *Remote Sensing*, 14(8), pp.1-15. [DOI]

Nature Environment and Pollution Technology
An International Quarterly Scientific Journal

p-ISSN: 0972-6268
(Print copies up to 2016)
e-ISSN: 2395-3454

Vol. 25 | No. 3 | Article ID D1861 | 2026

Original Research Paper

https://doi.org/10.46488/NEPT.2026.v25i03.D1861

Open Access Journal

Phosphate Solubilization and Plant Growth-Promoting Potential of *Penicillium oxalicum* (Bt9) in Eppawala Rock Phosphate-Enriched Compost

W. M. B. B. Sathsarini[1], T. G. I. Sandamali[2], M. M. Pathmalal[1] and F. S. Idroos[1]†

[1]Center for Water Quality and Algae Research, Department of Zoology, University of Sri Jayewardenepura, Gangodawila, Nugegoda, 10250, Sri Lanka

[2]Regional Rice Research and Development Center, Bombuwala, Sri Lanka

†Corresponding author: F. Sumaiya Idroos; sumaiyaidroos@sci.sjp.ac.lk

Abbreviation: Nat. Env. & Poll. Technol.
Website: www.neptjournal.com

Received: 21-08-2025
Revised: 17-10-2025
Accepted: 27-10-2025

Key Words:

Bioavailable phosphorus
Bio-solubilization
Chemical phosphate fertilizer
Eppawala rock phosphate
Phospho-compost

Citation for the Paper:

Sathsarini, W.M.B.B., Sandamali, T.G.I., Pathmalal, M.M. and Idroos, F.S., 2026. Phosphate solubilization and plant growth-promoting potential of *Penicillium oxalicum* (Bt9) in Eppawala rock phosphate-enriched compost. *Nature Environment and Pollution Technology,* 25(3), D1861. https://doi.org/10.46488/NEPT.2026.v25i03.D1861

Note: From 2025, the journal has adopted the use of Article IDs in citations instead of traditional consecutive page numbers. Each article is now given individual page ranges starting from page 1.

Copyright: © 2026 by the authors
Licensee: Technoscience Publications
This article is an open access article distributed under the terms and conditions of the Creative Commons Attribution (CC BY) license (https://creativecommons.org/licenses/by/4.0/).

ABSTRACT

The frequent application of chemical phosphate (P) fertilizers is costly and has emerged as a major concern in the agricultural sector of Sri Lanka. Therefore, the present study evaluated the impact of the fungal inoculum *Penicillium oxalicum* (Bt9) on the bio-solubilization of Eppawala Rock Phosphate (ERP)-enriched compost. A Completely Randomized Design (CRD) was employed, comprising four compost treatments, each replicated four times. Treatment 1 (T1) was amended with *P. oxalicum* (Bt9) and sugar; Treatment 2 (T2) was amended solely with *P. oxalicum* (Bt9); Treatment 3 (T3) was amended solely with sugar, and Treatment 4 (T4) served as the control, lacking both *P. oxalicum* (Bt9) and sugar. The released bioavailable phosphorus (P) content of each treatment was determined using the molybdenum blue method. A pot experiment was conducted using red cowpea (*Vigna unguiculata*), grown in a 1:1 mixture of phospho-compost and soil, to evaluate the effect of ERP bio-solubilization by *P. oxalicum* (Bt9) on plant growth. The results showed significantly higher ($p \leq 0.05$) values for plant growth parameters, including shoot length, root length, and total plant length, in Treatments 1 and 2 compared with Treatments 3 and 4. The highest shoot length, root length, and total plant length were recorded in Treatment 1, with values of 26.58 ± 2.44 cm, 11.36 ± 1.48 cm, and 54.24 ± 2.64 cm, respectively. The study concluded that *P. oxalicum* (Bt9) significantly enhanced phosphate solubilization and promoted the growth of red cowpea (*Vigna unguiculata*). Therefore, ERP-enriched compost inoculated with *P. oxalicum* (Bt9) may be considered a sustainable alternative to imported chemical phosphate fertilizers.

1. INTRODUCTION

Phosphorus is one of the minor elements on Earth, accounting for approximately 0.1% of the total elemental composition (Li et al. 2016), and is one of the most essential macronutrients required for plant growth and development (Khan et al. 2009). Compared with other macronutrients, phosphorus exhibits the lowest mobility in both soil and plants (Anand et al. 2016). It is considered the second most limiting nutrient for crop production after nitrogen in most soils (Biswas & Narayanasamy 2006). The two principal forms of phosphorus in soil are organic and inorganic phosphorus (Wang et al. 2021). Plant-available phosphorus, present in the soil solution, consists mainly of inorganic phosphorus in the form of primary orthophosphate ions ($H_2PO_4^-$) and secondary orthophosphate ions (HPO_4^{2-}), which dissolve in the soil solution and are directly available for plant uptake (Anand et al. 2016). However, only about 0.1% of the total phosphorus content in soil is available for plant utilization (Khan et al. 2009). The concentration of phosphorus in the soil solution typically ranges from 0.001 to 1 $mg.L^{-1}$, which is considerably lower than that of many other essential nutrients (Khan et al. 2014). Soluble phosphorus is rapidly precipitated as metal–cation complexes by highly reactive Al^{3+} and Fe^{3+} ions in acidic soils and by Ca^{2+} ions in calcareous or neutral soils (Anand et al. 2016; Wang et al. 2021).

A substantial proportion of phosphorus exists in insoluble forms and, therefore, cannot be absorbed by plants (Khan et al. 2009). Consequently, chemical phosphorus fertilizers containing soluble inorganic phosphorus are frequently applied to agricultural soils. However, the repeated application of high doses of chemical phosphorus fertilizers is costly and can cause several environmental problems, including soil acidification or alkalization, water pollution through runoff, groundwater contamination via phosphate leaching, suppression of beneficial microorganisms and insects, and nutrient fixation (Billah et al. 2020). Furthermore, only 5–25% of applied chemical phosphorus fertilizer is effectively utilized by plants (Sandamali et al. 2021). Therefore, the development of sustainable and environmentally friendly alternatives has become increasingly important.

Rock phosphate (RP) has traditionally been used as a raw material in the production of phosphorus fertilizers (Vassilev & Vassileva 2003). Eppawala Rock Phosphate (ERP) is an inexpensive phosphorus source in Sri Lanka and contains approximately 28–42% P_2O_5 (Ratnayake et al. 2018). However, due to its limited solubility, directly applied RP tends to persist in soils for extended periods (Khasawneh & Doll 1979). Composting is a natural decomposition process that plays a vital role in agriculture and organic waste management. Consequently, composting is regarded as an environmentally friendly and effective component of waste management within the circular bioeconomy framework (Wijerathna et al. 2024b, 2026).

Soil microorganisms capable of converting insoluble phosphate compounds into plant-available forms are known as phosphate-solubilizing microorganisms (PSMs) (Sandamali et al. 2021). The microbial solubilization of rock phosphate represents an environmentally friendly and mild alternative to chemical treatment methods (Vassilev & Vassileva 2003). The incorporation of rock phosphate with organic fertilizers and phosphate-solubilizing microorganisms during composting has been shown to increase the availability of phosphorus and enhance phosphorus uptake by plants under soil conditions (Ditta et al. 2018).

Several studies have investigated phosphate solubilization by PSMs and demonstrated their ability to convert insoluble phosphate compounds into bioavailable forms. Shrivastava et al. (2011) reported that manure enriched with low-grade Indian rock phosphate and inoculated with two phosphate-solubilizing fungi (PSF), *Aspergillus niger* TMPS1 and *Penicillium oxalicum* TMPS3, exhibited higher water-soluble phosphorus content and greater phosphatase activity than uninoculated treatments. Among the tested fungi, *P. oxalicum* TMPS3 recorded the highest water-soluble phosphorus content. Similarly, Wang et al. (2021) demonstrated the phosphate-solubilizing ability of *Penicillium oxalicum* (Y2) using both in vitro experiments and soil inoculation studies. Singh and Reddy (2011) further reported that the growth and yield parameters of wheat and maize were significantly improved in alkaline soils treated with rock phosphate and inoculated with *Penicillium oxalicum* compared with uninoculated control soils under field conditions.

Penicillium oxalicum (Bt9) has demonstrated enhanced phosphate-solubilizing ability in ERP-amended compost compared with previously reported strains such as TMPS3 and Y2. In addition, *P. oxalicum* (Bt9) exhibits distinctive plant growth-promoting characteristics, highlighting its potential to improve soil fertility and support legume growth.

Sandamali et al. (2021) reported that *P. oxalicum* (Bt9) is an efficient phosphate-solubilizing fungus and demonstrated its effectiveness as a phosphorus biofertilizer under field conditions using the Bw 367 rice variety (*Oryza sativa*). Molecular identification of *P. oxalicum* (Bt9) was performed through DNA sequencing followed by sequence similarity analysis using BioEdit software (version 7.2.5) (Sandamali et al. 2021). Despite previous studies on phosphate-solubilizing *P. oxalicum* strains, the phosphate-solubilizing potential of *P. oxalicum* (Bt9) in ERP-amended compost and its effects on the growth of red cowpea have not yet been investigated. Therefore, the present study aimed to evaluate the phosphate-solubilizing ability of *P. oxalicum* (Bt9) in ERP-enriched compost and to assess its plant growth-promoting effects on red cowpea (*Vigna unguiculata*).

2. MATERIALS AND METHODS

2.1. Fungal Culture Preparation

The phosphate-solubilizing fungal isolate, designated as the Bentota isolate, was recovered from the rice rhizosphere by Sandamali et al. (2017). Pure cultures were prepared and taxonomically confirmed as *Penicillium oxalicum* (Bt9) through DNA sequencing, as reported by Sandamali et al. (2021).

2.2. In Vitro Evaluation of the Phosphate Solubilizing Capability of Fungal Inoculum *P. oxalicum* (Bt9)

The phosphate solubilization index (PSI) was determined to assess the phosphate-solubilizing capability of pure cultures of *P. oxalicum* (Bt9). Pure cultures were inoculated onto Pikovskaya's (PKV) agar medium and incubated at approximately 32°C for three days. The diameters of the halo zone and fungal colony were measured using a vernier caliper with a resolution of 0.05 mm and recorded as described by Mayadunna et al. (2023).

2.3. In Vitro Evaluation of the Phosphate Solubilizing Efficiency of Fungal Inoculum *P.oxalicum* (Bt9)

Quantification of P solubilization of fungal inoculum *P. oxalicum* (Bt9) was measured using Pikovskaya's Broth Medium supplemented with tricalcium phosphate (TCP) at 5 $mg.L^{-1}$ (pH 7.2). The sterilized medium was inoculated with a 5.00 mm mycelial disc from the actively growing colony periphery of a 7-day-old *P. oxalicum* (Bt 9) culture, and an uninoculated medium was maintained as the control. The inoculated growth medium was incubated on a rotary shaker set to 160 rpm at 30°C for 7 days. Samples of 5 mL were taken from the culture at 3, 5, and 7 days after incubation under sterile conditions, and the amount of released soluble phosphate in the samples was measured via the Molybdenum blue assay at 420 nm, as described by Shrivastava et al. (2011).

2.4. Inoculum Preparation for Composting Studies

P. oxalicum (Bt9) was cultured in a cost-effective growth medium consisting primarily of rice husks and rice seeds. Pure cultures of *P. oxalicum* (Bt9) were used in sterilized inoculum bags for mass multiplication, as described by Sandamali et al. (2021)

2.5. Implementation of Compost Units

Four treatments were arranged in a Completely Randomized Design (CRD). Each treatment consisted of four replicates, resulting in a total of 16 compost piles as experimental units. Compost units were prepared as heaps following the windrow composting approach.

Each compost heap measured 1 m in length, 1 m in width, and 0.5 m in height. The raw materials used included approximately 12 kg of rice straw (an agro-industrial by-product collected from the Regional Rice Research and Development Center, Bombuwala), 8 kg of fresh leaves of *Gliricidia sepium* (green manure), and 10 kg of cow dung (animal manure).

A polythene sheet measuring approximately 1.5 m × 1.5 m was placed on the ground to prevent direct contact between the compost heaps and the soil surface. Rice straw, *G. sepium* leaves, and cow dung were arranged in alternating layers on the polythene sheet. Approximately 1.5 kg of ERP, equivalent to 50 kg per 1000 kg of raw materials, and 600 g of previously prepared compost, equivalent to 20 kg per 1000 kg of raw materials, were incorporated between the layers of each compost unit.

Each compost unit was moistened with approximately 5 L of water to provide adequate moisture for microbial activity and accelerate organic matter decomposition. The heaps were then covered with black polythene and secured using ropes and cleats made from *G. sepium* branches, which allowed airflow and facilitated aerobic decomposition.

Treatment 1 (T1) received approximately 60 g of sugar (equivalent to 400 g per 200 kg of raw materials) and 37.5 g of *P. oxalicum* (Bt9) inoculum (equivalent to 250 g per 200 kg of raw materials) to assess their combined effect on composting. This treatment was replicated four times (T1R1, T1R2, T1R3, and T1R4).

Treatment 2 (T2) received 37.5 g of *P. oxalicum* (Bt9) inoculum (equivalent to 250 g per 200 kg of raw materials) without sugar. This treatment was replicated four times (T2R1, T2R2, T2R3, and T2R4).

Treatment 3 (T3) received approximately 60 g of sugar (equivalent to 400 g per 200 kg of raw materials) without fungal inoculum. This treatment was replicated four times (T3R1, T3R2, T3R3, and T3R4).

Treatment 4 (T4) served as the control and represented standard composting conditions without fungal inoculum or sugar. This treatment was replicated four times (T4R1, T4R2, T4R3, and T4R4).

Compost heaps were turned during the 3rd, 6th, 9th, and 12th weeks of composting to ensure uniform mixing and aeration, thereby promoting microbial activity. The composting process was completed at the end of the 12th week.

2.6. Sampling of Compost Units

Compost samples were collected during the 6th, 9th, and 12th weeks of the composting process and again during the 15th week following compost maturation. Sampling was conducted using a simple random sampling technique.

2.7. Determination of Physicochemical Parameters of Compost Units

The temperature of each compost unit was measured during the 6th, 9th, and 12th weeks of composting. Bioavailable phosphorus (P), pH, and electrical conductivity (EC) were measured during the 6th, 9th, 12th, and 15th weeks.

Moisture content was determined at the end of the composting period (12th week) using the gravimetric method. Compost samples were weighed before and after oven drying at 105°C until a constant weight was achieved. Moisture content was then calculated based on the weight loss resulting from water evaporation.

Bioavailable phosphorus content was determined using the molybdenum blue assay at 882 nm according to Murphy and Riley (1962). Prior to analysis, the spectrophotometer

was calibrated using phosphate standard solutions prepared from analytical-grade KH_2PO_4 to generate a standard curve. The bioavailable phosphorus concentrations (ppm) of the treatments were subsequently calculated using this calibration curve.

2.8. Implementation of the Pot Experiment

A soil–compost mixture was prepared at a 1:1 ratio using approximately 100 g of soil and 100 g of phospho-compost obtained from each compost replicate as the potting medium (Jayathilake et al. 2024).

The prepared potting medium was transferred into separate pots. Each treatment (T1, T2, T3, and T4) consisted of four independent compost replicates, with one pot prepared from each replicate, resulting in a total of 16 experimental pots. In addition, two control pots containing 200 g of soil without phospho-compost were included.

Red cowpea (*Vigna unguiculata*) seeds were soaked in water overnight before sowing. Four seeds were planted in each pot, representing a compost replicate. After germination, four healthy red cowpea plants were maintained in each pot under optimal growth conditions for approximately 30 days.

Each pot received approximately 25 mL of water daily, and routine maintenance was carried out to ensure optimal plant growth. After 30 days, all plants were carefully uprooted from their respective pots, and growth parameters, including shoot length, root length, and total plant length, were measured.

2.9. Statistical Analysis

Data was analyzed using two-way analysis of variance (ANOVA) in Minitab software. Significant differences among treatments were determined using Tukey's pairwise comparison test at a significance level of 0.05.

The effects of treatment and sampling time (week) were evaluated for physicochemical parameters, whereas the effects of treatment on plant growth parameters (shoot length, root length, and total plant length) were assessed in the pot experiment.

Table 1: PSI of *P. oxalicum* (Bt9) cultures in PKV medium.

No. of culture	PSI
1	3.01 ± 0.14
2	3.06 ± 0.21
3	2.70 ± 0.34
4	2.38 ± 0.74
5	2.25 ± 0. 32

The assumptions of ANOVA, including normality and homogeneity of variance, were verified prior to statistical interpretation.

3. RESULTS AND DISCUSSION

3.1. Qualitative Phosphate Solubilizing Ability of *P. oxalicum* (Bt9)

Table 1 presents the Phosphate-solubilizing index (PSI) of *P. oxalicum* (Bt9) cultured on Pikovskaya's (PKV) medium, derived from measurements of both colony and halo zone diameters.

All the colonies in the cultures exhibited PSI of greater than 1, as depicted in Table 1, indicating that *P.oxalicum* (Bt9) is capable of phosphate solubilization.

The colony morphology of *Penicillium oxalicum* (Bt9) was characterized by a dark, dull-green appearance with a thin white peripheral margin, as shown in Fig. 1. A slight, clear halo zone was observed around each colony on Pikovskaya's (PKV) medium, indicating the phosphate-solubilizing ability of *P. oxalicum* (Bt9). Similar observations were reported by Sandamali et al. (2021), who documented the formation of clear halo zones around colonies of *P. oxalicum* (Bt9) grown on PKV medium. Furthermore, those cultures retained their phosphate-solubilizing ability on PKV medium for up to 36 months, highlighting the consistent efficacy and long-term applicability of this fungal inoculum for integration into phosphate biofertilizer technology.

3.2. Quantitative Phosphate Solubilizing Ability of *P. oxalicum* (Bt9)

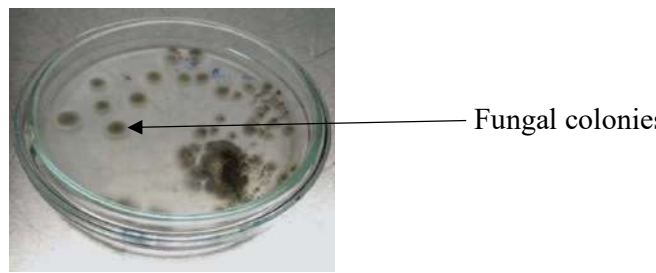


Fig. 1: The colonies of *P. oxalicum* (Bt9) culture grown on PKV medium.

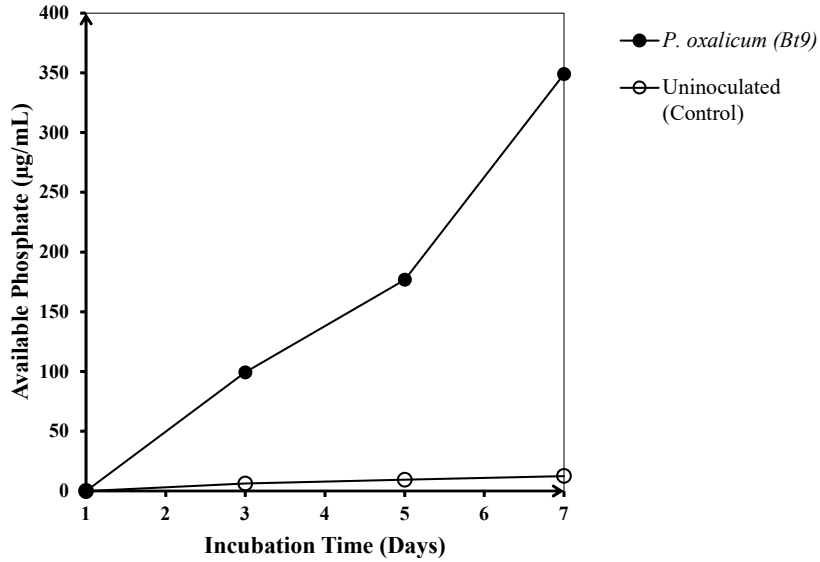


Fig. 2: Solubilized P concentrations after 1st, 3rd, 5th and 7th days of incubation in TCP containing PKV broth inoculated with *P. oxalicum* (Bt9) isolate.

The concentration of solubilized phosphorus released by *P. oxalicum* (Bt9) increased progressively over time compared with the control, as shown in Fig. 2, indicating the strong phosphate-solubilizing capability of this fungal species. Similar findings were reported by Sandamali et al. (2021), who evaluated the quantitative phosphate-solubilizing efficiency of *P. oxalicum* (Bt9) using an *Aspergillus niger*-inoculated medium as the positive control and an uninoculated medium as the negative control.

These results are also consistent with the findings of Yin et al. (2015), who reported a significantly higher concentration of soluble phosphorus (1392.0 ± 233.2 µg.mL^{-1}) in tricalcium phosphate (TCP)-amended Pikovskaya's (PVK) medium inoculated with the *P. oxalicum* P4 isolate on the 7th day of incubation compared with the other treatments. Similarly, Wang et al. (2020) reported enhanced phosphorus solubilization by *P. oxalicum* FJG21 and *P. oxalicum* FJQ5 in PKV broth medium containing insoluble $Ca_3(PO_4)_2$, with soluble phosphorus concentrations of 343.2 µg.mL^{-1} and 339.2 µg.mL^{-1}, respectively, on the 7th day. These values were significantly higher than those recorded for *Bacillus subtilis* BPM12 and the uninoculated control.

Table 2: Mean moisture percentage of compost treatments at the 12th week of the composting process.

The compost treatment No.	Mean moisture percentage at 12th week of composting process [%]
T_1	54.06 ± 3.06
T_2	56.74 ± 3.82
T_3	56. 79 ± 4.64
T_4	57.10 ± 5.66

Overall, the observed increase in soluble phosphorus concentration confirms the effectiveness of *P. oxalicum* (Bt9) as a phosphate-solubilizing fungal inoculum and supports its potential application in phosphate biofertilizer development.

3.3 Impact of Moisture on Composting Process in Compost Units

Table 2 presents the mean moisture percentage of compost treatments at the 12th week of the composting process.

The moisture percentage of all compost treatments ranged between 50% and 60%, corresponding to the ideal range for efficient composting as presented in Table 2.

Table 3: Mean temperature measurements in compost treatments at the 3rd, 6th, 9th and 12th weeks during the composting process.

The compost treatment no.	Mean temperature [°C] at the 3rd week of the composting process	Mean temperature [°C] at the 6th week of the composting process	Mean temperature [°C] at the 9th week of the composting process	Mean temperature [°C] at the 12th week of the composting process
T_1	31.0 ± 0.7	48.3 ± 0.4	47.7 ± 0.9	39.7 ± 0.6
T_2	31.5 ± 0.6	48.6 ± 1.0	48.8 ± 1.1	40.8 ± 0.7
T_3	29.2 ± 0.5	40.0 ± 0.3	38.1 ± 1.0	36.8 ± 1.0
T_4	28.9 ± 0.6	37.6 ± 0.6	39.3 ± 0.4	36.0 ± 1.2

3.4. Effect of Temperature of the Compost Units

Table 3 presents the mean temperatures of compost units at the 3rd, 6th, 9th and 12th weeks during the composting process.

The maximum temperature of the experimental compost units in this study remained below 50°C during the 6th and 9th weeks of the composting process in Treatments 1 and 2, as presented in Table 3. The temperature of compost systems is influenced by the quantity of bulk material being processed; lower substrate volumes generally generate limited heat due to reduced microbial activity and energy release (Quadar et al. 2023). Therefore, the moderate temperatures observed in this study may be attributed to the relatively small-scale nature of the experiment and the limited quantity of raw materials used in compost preparation.

In addition, the compost units were prepared as aerated heaps with proper ventilation, which likely facilitated heat dissipation and prevented excessive temperature build-up. Several studies have reported that optimal thermophilic composting activity typically occurs within the temperature range of 50°C to 60°C, while overall efficient composting is generally observed between 40°C and 65°C (Wijerathna et al. 2024a). In some cases, successful composting has also been reported under mesophilic conditions below 45°C (Tang et al. 2007).

Temperature is a critical factor governing the rate of composting reactions, as it directly influences microbial metabolic activity and community structure. It also plays an important role in pathogen elimination and seed inactivation, thereby ensuring compost sanitation (Wijerathna et al. 2024a, Tang et al. 2007). Tang et al. (2007) reported that the highest cumulative oxygen (O_2) uptake occurred at 43°C across composting systems operating within a temperature range of 22°C to 57°C. Mesophilic conditions support steady organic matter degradation, whereas higher temperatures are more effective for pathogen and weed seed destruction during composting (Tang et al. 2007). Accordingly, the temperature profile observed in this study suggests that the composting process predominantly remained within the mesophilic phase.

The heat generated during composting is primarily a result of microbial metabolic activity and serves as an indicator of microbial activity and organic matter decomposition. In this study, the average temperature recorded in Treatments 1 and 2 was higher than that in Treatments 3 and 4. This trend may indicate enhanced microbial activity in Treatments 1 and 2, which were inoculated with *P. oxalicum* (Bt9), compared with Treatments 3 and 4, which lacked fungal inoculation.

Similarly, Wijerathna et al. (2024a) reported that a consortium-inoculated treatment (C5), containing *Bacillus*

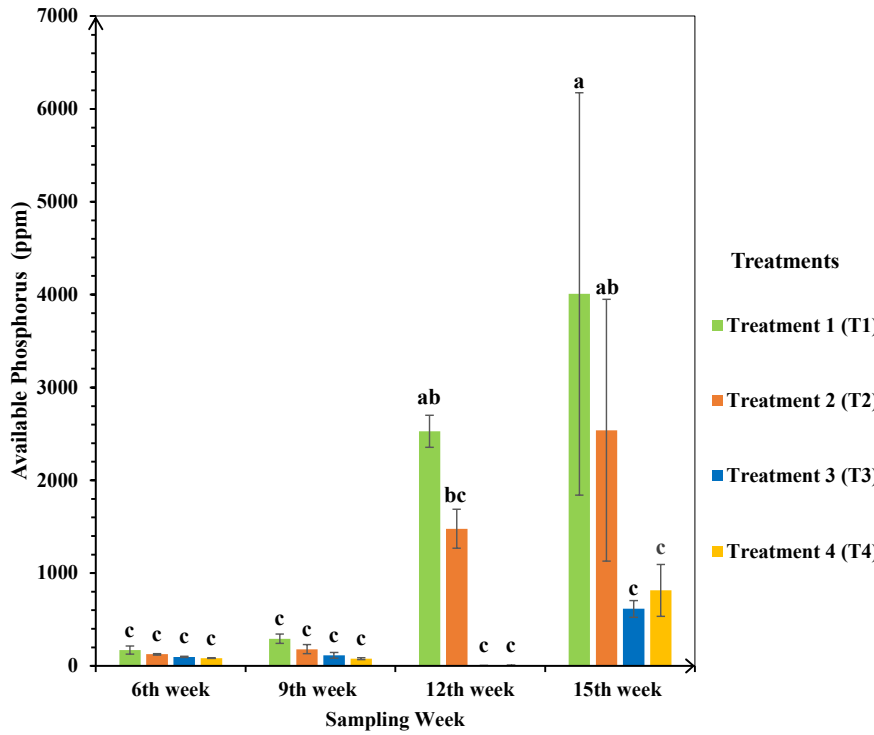


Fig. 3: Distribution of the mean values (± SE, n = 4) of available Phosphorus content in the compost treatments throughout the sampling weeks. Bars represent mean ± standard error. The Values labeled with distinct letters indicate significant differences ($P < 0.05$) according to Tukey's pairwise comparison.

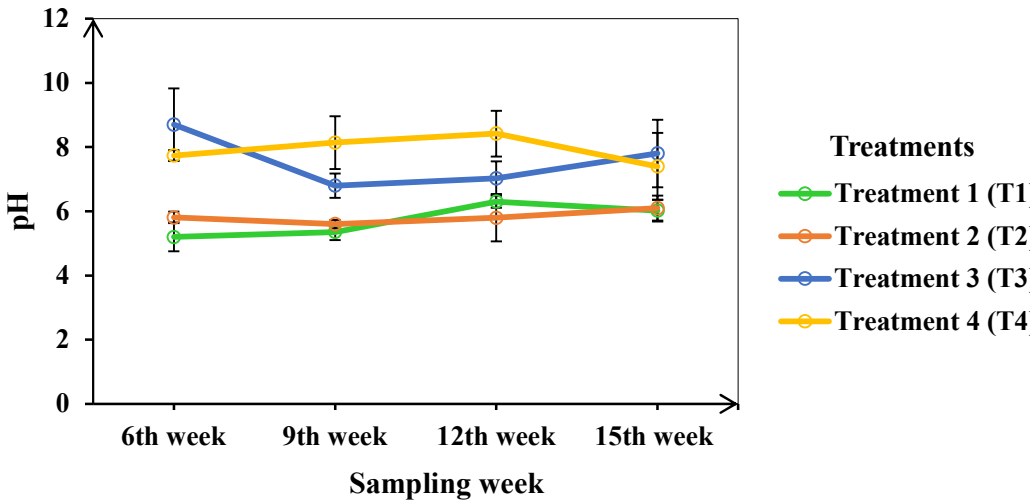


Fig. 4: Distribution of the mean pH values (± SE, $n = 4$) of the compost treatments throughout the sampling weeks. Bars represent mean ± standard error.

haynesii, *Bacillus amyloliquefaciens*, and *Bacillus safensis*, exhibited the highest composting temperature along with elevated enzymatic activities, including cellulase, amylase, protease, and lipase. This enhanced microbial activity contributed to accelerated decomposition and a reduced composting period compared with the control and other treatments.

3.5. Effect of Treatments on Bioavailable Phosphorus Content

According to the data depicted in Fig. 3, the highest recorded available phosphorus (P) content in Treatment 1 (*P. oxalicum* Bt9 with sugar) during the 15th week was 4008 ± 2005.83 ppm. The available P content in Treatment 2 (*P. oxalicum* Bt9 without sugar) at the 15th week and in Treatment 1 at the 12th week showed no significant difference. The lowest available P content was observed in Treatment 3 (sugar without *P. oxalicum* Bt9) at the 15th week, with a value of 614.5 ± 83.66 ppm, but it was not significantly different from Treatment 4 (neither *P. oxalicum* Bt9 nor sugar). Throughout the experiment, Treatment 1 consistently exhibited the highest available P content weekly, with some differences reaching statistical significance. Treatment 2 consistently ranked second. In contrast, Treatments 3 and 4 had significantly lower available P contents each week. This variation can be attributed to the phosphate-solubilizing activity of *P. oxalicum* Bt9 present in Treatments 1 and 2, which was absent in Treatments 3 and 4. Additionally, the negligible differences between Treatments 1 and 2, and between Treatments 3 and 4, suggest that the presence of sugar had little to no effect on ERP solubilization or on the growth of *P. oxalicum* Bt9.

3.6. pH Variation in Compost Treatments During the Sampling Period

Treatment 1 and Treatment 2 consistently exhibited slightly acidic pH values ranging from 5 to 6 throughout the composting period, in contrast to the other treatments, as shown in Fig. 4. Wang et al. (2020) reported a similar reduction in pH associated with enhanced solubilization of insoluble phosphate from various phosphorus sources by *P. oxalicum* FJG21 and *P. oxalicum* FJQ5. These strains exhibited the highest soluble phosphorus concentrations, accompanied by the lowest pH values. Furthermore, HPLC analysis detected malic acid and oxalic acid in cultures of both *P. oxalicum* FJG21 and *P. oxalicum* FJQ5. The dissolution of phosphate was attributed to the combined effects of pH reduction and organic acid secretion.

The primary mechanism responsible for mineral phosphate dissolution in soil involves a reduction in soil pH caused by microbial organic acid production, together with the mineralization of organic phosphorus through the action of acid phosphatases (Anand et al. 2016). The secretion of organic acids is widely recognized as the principal mechanism of phosphate solubilization in phosphate-solubilizing fungi (PSF). These fungi solubilize insoluble phosphate compounds by acidifying the surrounding environment through the release of organic acids (Rawat et al. 2021). In addition, organic acids can chelate calcium, iron, and aluminum ions, thereby facilitating the conversion of insoluble phosphate into plant-available forms (Gong et al. 2014).

Yin et al. (2015) reported that tartaric acid and citric acid were the predominant organic acids secreted by

Penicillium oxalicum P4 during the solubilization of tricalcium phosphate. Similarly, Gong et al. (2014) found that *Penicillium oxalicum* I1 reduced the pH of the culture medium from 6.9 to 1.65 within 26 hours. During this period, oxalic acid production increased progressively, reaching a maximum concentration of approximately 593.9 $\mu g.mL^{-1}$. A statistically significant inverse relationship was observed between organic acid concentration and pH. Although excessive soil acidification can adversely affect crop growth when soil pH falls below 6.5, the pH reduction caused by *P. oxalicum* I1 in soil was only from 7.0 to 6.56, indicating its ability to enhance phosphate solubilization without negatively affecting plant growth. Similarly, Singh & Reddy (2011) reported that *P. oxalicum* increases the concentration of bioavailable phosphorus in soil by lowering pH through mechanisms such as chelation and ion-exchange reactions.

The genus *Penicillium* is one of the predominant fungal groups involved in phosphatase production. Phosphatases, including phytase and acid phosphatase, play a vital role in the mineralization of organic phosphorus compounds into bioavailable forms (Singh & Reddy 2011). Acevedo et al. (2014) reported that *Aspergillus* spp. and *Penicillium* spp. reduced the pH of liquid culture media during the dissolution of recalcitrant phosphate sources, thereby promoting phosphate solubilization. A decrease in pH is generally associated with increased acidity and enhanced phosphate availability (Wang et al. 2020).

Therefore, the decline in pH observed in Treatments 1 and 2 may be attributed to the production of organic acids and other acidic metabolites by *P. oxalicum* (Bt9). The absence of this response in the other treatments further supports the role of *P. oxalicum* (Bt9) in enhancing ERP solubilization through acidification and phosphate-mobilizing mechanisms.

3.7. Effect of EC on Compost Treatments During the Sampling Period

Treatment 1 and Treatment 2 exhibited higher mean EC values throughout the composting period compared to the other treatments, as shown in Fig. 5. Electrical conductivity (EC) reflects the soluble salt content of the final compost product and serves as an indicator of the availability of essential nutrients required for plant growth and development. Therefore, EC is commonly used as a measure of the total ion concentration present in compost.

During the composting process, EC values generally increase due to the mineralization of organic matter, resulting in the formation of inorganic compounds and the release of soluble ions (Wijerathna et al. 2024a). The higher EC values observed in T1 and T2 may be attributed to increased concentrations of soluble orthophosphate ions resulting from enhanced bio-solubilization of ERP by *P. oxalicum* (Bt9). This finding suggests that inoculation with *P. oxalicum* (Bt9) improved phosphorus release and nutrient availability within the compost.

Similarly, Wijerathna et al. (2024a) reported that a consortium-inoculated treatment (C5) containing *Bacillus amyloliquefaciens*, *Bacillus haynesii*, and *Bacillus safensis* exhibited the highest EC values, indicating accelerated decomposition of organic waste and enhanced nutrient mineralization. The findings of the present study further

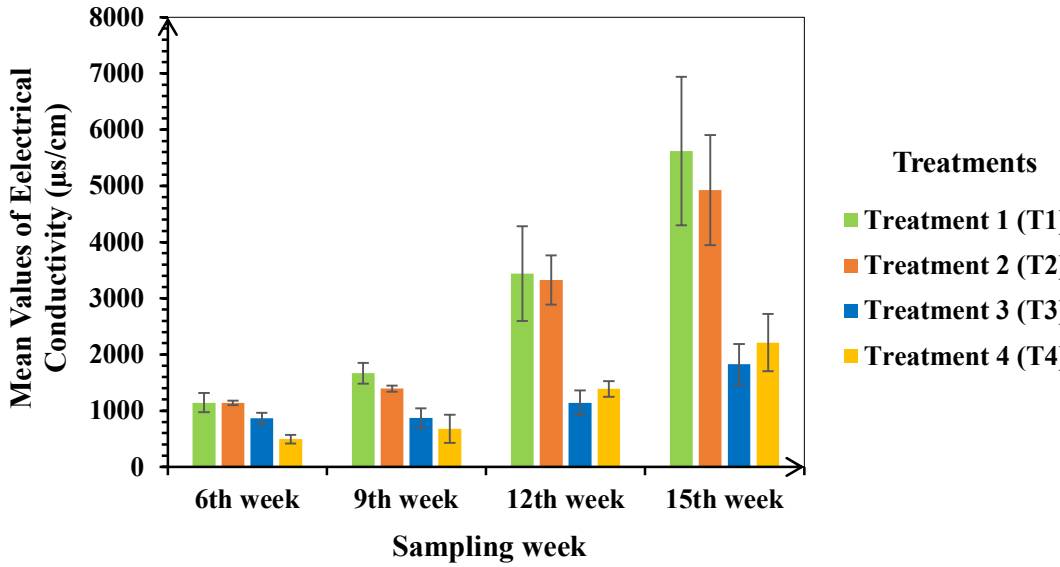


Fig. 5: Distribution of the mean electrical conductivity (EC) values (± SE, $n = 4$) in the compost treatments during the sampling weeks. Bars represent mean ± standard error.

support the role of microbial inoculants in improving compost quality through increased nutrient availability and enhanced decomposition processes.

3.8. Impact of Plant Growth Promotion by *P. oxalicum* (Bt 9) in Red-Cowpea (*V. unguiculata*) Plants

According to the data presented in Figs. 6, 7, and 8, T1 (soil amended with phospho-compost containing *P. oxalicum* (Bt9) and sugar) exhibited the highest values for plant growth parameters, including shoot length (26.58 ± 2.44 cm), root length (11.36 ± 1.48 cm), and total plant length (54.24 ± 2.64 cm). No significant differences were observed between the plant growth parameters of T1 and T2 (soil amended with phospho-compost containing *P. oxalicum* (Bt9) without sugar). Similarly, no significant differences were detected between T3 (soil amended with phospho-compost containing sugar without *P. oxalicum* (Bt9)) and T4 (soil amended with phospho-compost lacking both sugar and *P. oxalicum* (Bt9)).

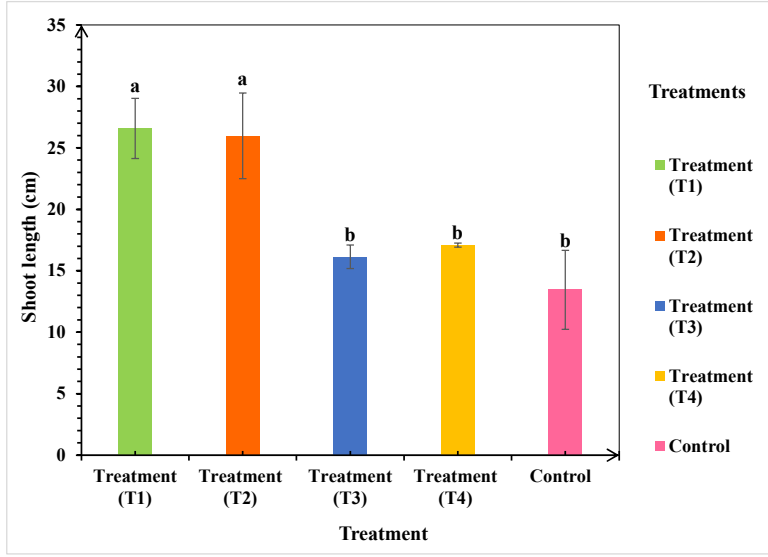


Fig. 6: The effect of different treatments on the mean values of shoot length (± SE, $n = 4$) of red cowpea (*V. unguiculata*) plants. Bars represent mean ± standard error. The values annotated with different letters indicate significant differences at $P < 0.05$ according to Tukey's pairwise comparison.

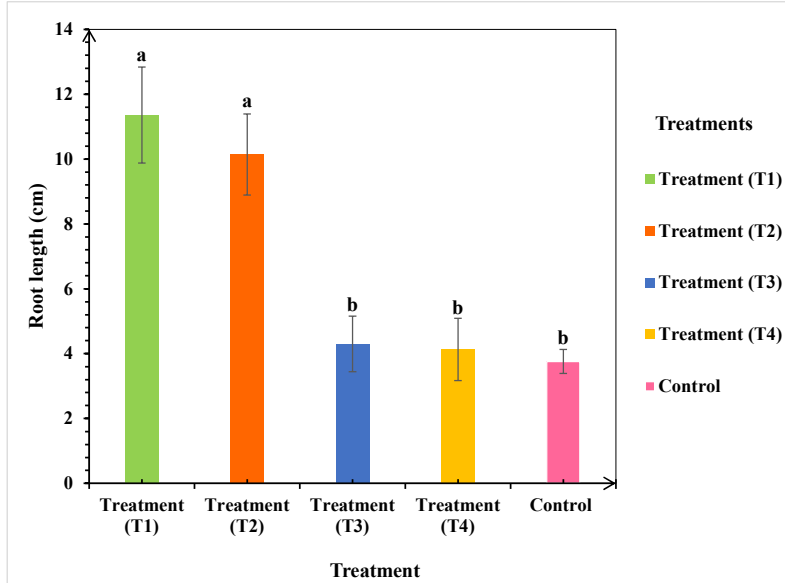


Fig. 7: The effect of different treatments on the mean values of root length (± SE, $n = 4$) of red cowpea (*V. unguiculata*) plants. Bars represent mean ± standard error. The values annotated with different letters indicate significant differences at $P < 0.05$ according to Tukey's pairwise comparison.

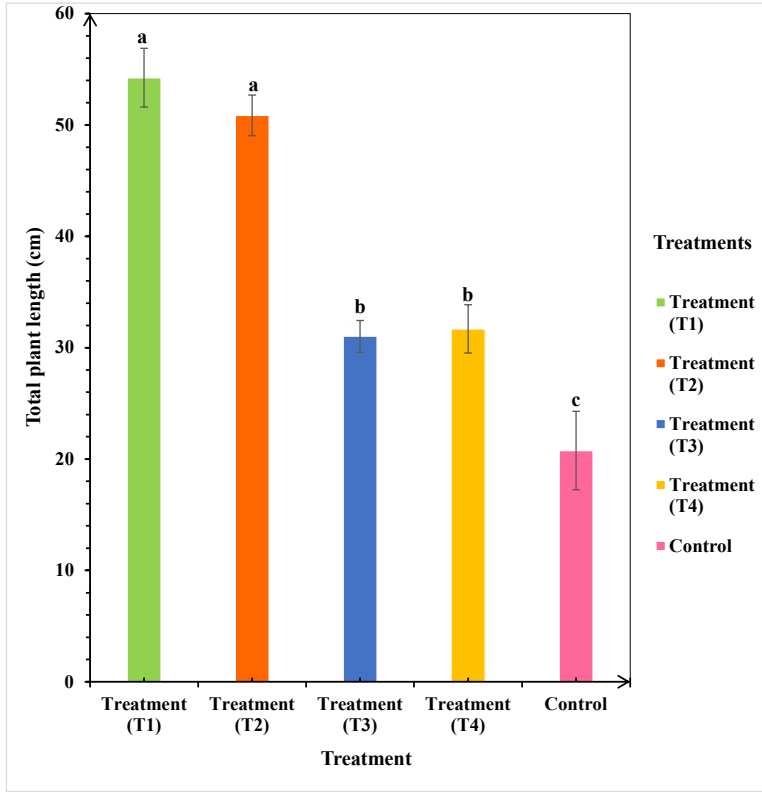


Fig. 8: The effect of different treatments on the mean values of total plant length (± SE, $n = 4$) of red cowpea (*V. unguiculata*) plants. Bars represent mean ± standard error. The values marked with different letters indicate statistically significant differences ($P < 0.05$) according to Tukey's pairwise comparison.

The lowest values for plant growth parameters, including shoot length (13.45 ± 3.22 cm), root length (3.76 ± 0.37 cm), and total plant length (20.76 ± 3.52 cm), were recorded in the control treatment, which consisted solely of soil without phospho-compost, *P. oxalicum* (Bt9), or sugar. These findings indicate that phospho-compost inoculated with *P. oxalicum* (Bt9) promotes the growth of red cowpea (*Vigna unguiculata*). Furthermore, the results suggest that the addition of sugar had no significant effect on microbial activity or on enhancing the bio-solubilization of ERP during phospho-compost preparation.

The present findings are consistent with those of Yin et al. (2015), who demonstrated that inoculation of rock phosphate with *P. oxalicum* P4 significantly increased both bioavailable phosphorus and total plant phosphorus contents. Moreover, isolate P4 significantly enhanced maize fresh biomass, thereby promoting plant growth in rock phosphate-enriched soil compared with the other treatments. In addition, soil amended with rock phosphate and inoculated with isolate P4 showed significantly higher concentrations of organic acids, including malic, formic, succinic, citric, acetic, and lactic acids, compared with the control treatment.

Similarly, Jayathilake et al. (2025) reported that *Bacillus siamensis* strain KCTC 13613 exhibited the highest phosphate-solubilizing activity, accompanied by a reduction in growth medium pH, indicating elevated organic acid production. In a pot experiment using mung bean plants, the application of phosphate-solubilizing bacterial strains significantly improved growth parameters, including root length, shoot length, and biomass. Phosphorus availability in the potting medium was significantly enhanced by *B. siamensis* strain KCTC 13613, resulting in superior plant growth performance compared with the other strains and the control.

Comparable findings were reported by Biswas & Narayanasamy (2006) for the incorporation of *Aspergillus awamori*, a phosphate-solubilizing fungus, into low-grade rock phosphate-enriched compost. Their study demonstrated that inoculation with *A. awamori* increased both total phosphorus and available phosphorus contents compared with compost lacking fungal inoculation. In the pot experiment, compost enriched with low-grade rock phosphate and inoculated with *A. awamori* enhanced both yield and phosphorus uptake in mung bean (*Vigna radiata*) compared

with the control. Furthermore, yield and phosphorus uptake were 13.0% and 21.5% higher, respectively, than in the treatment without *A. awamori*. The authors also reported that phosphate-solubilizing microorganisms produce various organic acids, such as tartaric, malic, and citric acids, as well as enzymes, including alkaline and acid phosphatases, which facilitate the conversion of insoluble phosphate into plant-available forms.

Singh & Reddy (2011) reported similar results, demonstrating high phosphate solubilization accompanied by a reduction in the pH of PKV broth medium amended with rock phosphate and inoculated with *P. oxalicum*. In their study, phosphate solubilization was associated with the secretion of organic acids into the culture medium. Malic acid (9435 nmoL.mL^{-1}) was the predominant acid, followed by gluconic acid (4306 nmoL.mL^{-1}), oxalic acid (411 nmoL.mL^{-1}), and acetic acid (92 nmoL.mL^{-1}). Furthermore, field experiments showed that *P. oxalicum* inoculation in rock phosphate-amended alkaline soil significantly improved wheat and maize growth and yield compared with the control.

Shrivastava et al. (2011) investigated the potential of two phosphate-solubilizing fungi, *Aspergillus niger* TMPS1 and *Penicillium oxalicum* TMPS3, for producing phosphate-enriched manure (PEM) using low-grade Indian rock phosphate. Using a ^{32}P radiotracer technique in a pot experiment, they reported phosphorus uptake by mung bean (*V. radiata*) plants as relative agronomic efficiency (RAE). The PEM product inoculated with *P. oxalicum* TMPS3 exhibited the highest RAE among all phosphorus sources. Moreover, phosphorus uptake increased significantly in PSM-inoculated treatments compared with the uninoculated control. These findings suggest that the increased phosphorus uptake resulted from elevated phosphorus concentrations in the rhizosphere soil solution.

In the present study, *P. oxalicum* (Bt9) produced a higher bioavailable phosphorus content than *P. oxalicum* P4 under their respective experimental conditions, as reported by Yin et al. (2015). However, a direct comparison with *P. oxalicum* TMPS3 was not possible because Shrivastava et al. (2011) reported only total phosphorus content rather than bioavailable phosphorus.

Li et al. (2021) identified *Penicillium oxalicum* HZ06 as a plant growth-promoting fungus because of its ability to significantly increase eggplant biomass. Inoculation with HZ06 increased seedling length, dry weight, and fresh weight by 22.35%, 39.26%, and 47.69%, respectively, compared with the control. Root length, dry weight, and fresh weight also increased by 0.83%, 41.30%, and 28.72%, respectively. These findings highlight the potential of *P. oxalicum* as a microbial inoculant for improving crop growth in nutrient-deficient soils. Although direct comparisons between studies are limited due to differences in plant species and experimental conditions, the collective evidence supports the role of *P. oxalicum* (Bt9) as an effective phosphate-solubilizing fungus with plant growth-promoting properties.

Gong et al. (2014) reported the high phosphate-solubilizing ability of *Penicillium oxalicum* I1 (P-I1). This strain effectively solubilized various insoluble phosphate compounds, including $Ca_8H_2(PO_4)_6 \cdot 5H_2O$, $AlPO_4$, $FePO_4$, and $Ca_{10}(PO_4)_6(OH)_2$, converting them into soluble $CaHPO_4$. Furthermore, P-I1 inhibited the reconversion of soluble $CaHPO_4$ into insoluble phosphate forms. The transformation of insoluble Ca_8-P, Al-P, and Fe-P into soluble Ca_2-P was attributed to oxalic acid secretion. Correlation analysis revealed that Ca_2-P content was negatively associated with soil pH and positively associated with P-I1 abundance. In field experiments, maize yield increased by 14.47% in the treatment receiving P-I1 and TCP at 45 kg.ha^{-1} compared with the control. Similar to P-I1, *P. oxalicum* (Bt9) efficiently converted insoluble phosphate into plant-available forms, thereby supporting the growth of red cowpea.

The majority of identified phosphate-solubilizing fungi belong to the genus *Penicillium* (Li et al. 2016). Phosphate solubilization is a well-documented characteristic of this genus (Qiao et al. 2019). Several species, including *P. albidum*, *P. bilaii*, *P. oxalicum*, *P. frequentans*, *P. italicum*, *P. citrinum*, *P. simplicissimum*, *P. expansum*, and *P. rubrum*, are used as commercial biofertilizers because of their ability to mobilize essential nutrients such as Cu, Co, Fe, Mn, Mo, P, and Zn, thereby enhancing plant resilience to both biotic and abiotic stresses (Odoh et al. 2020). Among these, *Penicillium bilaii* has been widely commercialized by Novozymes as a soil inoculant, with numerous field trials confirming its effectiveness and compatibility with modern agricultural practices (Leggett et al. 2007).

Phosphorus is an essential macronutrient required for plant growth and development (Anand et al. 2016, Jayathilake et al. 2024). It plays a central role in photosynthesis, carbon metabolism, membrane synthesis, cell division, and cell enlargement (Singh & Reddy 2011). Phosphorus is also critical for root development and biological nitrogen fixation in legumes (Anand et al. 2016), thereby contributing significantly to both root and shoot growth (Fathi & Afra 2023).

As a legume, red cowpea (*V. unguiculata*) forms symbiotic associations with *Rhizobium* bacteria and arbuscular mycorrhizal fungi (AMF). These microorganisms can interact synergistically with phosphate-solubilizing fungi such as *P. oxalicum* (Bt9) to improve nutrient acquisition. While *P. oxalicum* (Bt9) enhances phosphorus availability

through the secretion of organic acids, AMF extend their hyphal networks into the soil and facilitate phosphorus uptake by plants. Therefore, the enhanced plant growth observed in Treatments 1 and 2 may be attributed to increased ERP solubilization by *P. oxalicum* (Bt9), coupled with improved phosphorus uptake and utilization by the plants. Overall, these findings demonstrate that *P. oxalicum* (Bt9) effectively solubilizes ERP and promotes the growth of red cowpea (*V. unguiculata*).

For commercial biofertilizer production, maintaining microbial viability during large-scale propagation and storage is essential. Sandamali et al. (2021) reported that *P. oxalicum* (Bt9) grown on a rice husk- and rice seed-based substrate maintained populations of 22.7×10^8 CFU.g^{-1} at room temperature and 33.5×10^8 CFU.g^{-1} at 8°C for up to four months while retaining its phosphate-solubilizing ability. These findings highlight the potential of *P. oxalicum* (Bt9) for development as a commercial phosphorus biofertilizer.

This study was conducted as a pilot-scale composting experiment to evaluate physicochemical changes during composting and their effects on plant growth. Only a single fungal species, *P. oxalicum* (Bt9), was investigated, and all experiments were performed under controlled pot conditions. Plant growth was assessed only during the first 30 days after planting. Future studies should evaluate the complete crop growth cycle, including flowering, yield, and harvest parameters, to comprehensively assess the agronomic performance of *P. oxalicum* (Bt9). Field-scale validation is also required to confirm its effectiveness as a phosphate-solubilizing and plant growth-promoting inoculant. The present findings indicate that ERP-enriched compost inoculated with *P. oxalicum* (Bt9) can increase bioavailable phosphorus levels in soil and promote legume growth under pot conditions, suggesting its potential as a partial substitute for chemical phosphorus fertilizers. Sandamali et al. (2021) reported that direct application of *P. oxalicum* (Bt9) in rice cultivation reduced chemical phosphorus fertilizer requirements by 50% without affecting yield. However, ERP-enriched compost inoculated with *P. oxalicum* (Bt9) was not evaluated in that study. Therefore, further field-based investigations are needed to determine the extent to which ERP-enriched compost inoculated with *P. oxalicum* (Bt9) can replace chemical phosphorus fertilizers under local agricultural conditions.

4. CONCLUSIONS

This study demonstrated that P. oxalicum (Bt9) is an efficient phosphate-solubilizing fungal inoculum. Therefore, incorporating it into the composting process, enriched with Eppawala Rock Phosphate (ERP), enhances the solubilization of insoluble phosphate in ERP into plant-available forms of phosphorus. Consequently, the increased availability of bioavailable phosphorus promotes the growth of red cowpea (Vigna unguiculata).

The findings suggest that ERP-enriched compost inoculated with *P. oxalicum* (Bt9) has considerable potential for the production of organic phosphorus fertilizer. Such a product could serve as a sustainable and viable alternative to imported chemical phosphorus fertilizers, thereby helping to address a critical challenge facing the agricultural sector of Sri Lanka.

5. ACKNOWLEDGMENTS

The authors wish to thank University of Sri Jayewardenepura, Nugegoda, Sri Lanka, and Regional Rice Research and Development Center, Bombuwala, Sri Lanka for the provision of for providing laboratory resources, chemical supplies and technical assistance that supported this research.

6. REFERENCES

Acevedo, E., Galindo-Castañeda, T., Prada, F., Navia, M. and Romero, H.M., 2014. Phosphate-solubilizing microorganisms associated with the rhizosphere of oil palm (Elaeis guineensis Jacq.) in Colombia. *Applied Soil Ecology*, 80, pp. 26–33. [DOI]

Anand, K.U.M.A.R., Kumari, B.A.B.Y. and Mallick, M.A., 2016. Phosphate solubilizing microbes: an effective and alternative approach as biofertilizers. *International Journal of Pharmacy and Pharmaceutical Sciences*, 8(2), pp. 37–40.

Billah, M., Khan, M., Bano, A., Nisa, S., Hussain, A., Dawar, K.M., Munir, A. and Khan, N., 2020. Rock phosphate-enriched compost in combination with rhizobacteria: a cost-effective source for better soil health and wheat (Triticum aestivum) productivity. *Agronomy*, 10(9), p. 1390. [DOI]

Biswas, D.R. and Narayanasamy, G., 2006. Rock phosphate enriched compost: an approach to improve low-grade Indian rock phosphate. *Bioresource Technology*, 97(18), pp. 2243–2251. [DOI]

Ditta, A., Imtiaz, M., Mehmood, S., Rizwan, M.S., Mubeen, F., Aziz, O. and Tu, S., 2018. Rock phosphate-enriched organic fertilizer with phosphate-solubilizing microorganisms improves nodulation, growth, and yield of legumes. *Communications in Soil Science and Plant Analysis*, 49(21), pp. 2715–2725. [DOI]

Fathi, A. and Mehdiniya Afra, J., 2023. Plant growth and development in relation to phosphorus: a review. *Bulletin of the University of Agricultural Sciences and Veterinary Medicine Cluj-Napoca. Agriculture*, 80(1), pp. 1–7. [DOI]

Gong, M., Du, P., Liu, X. and Zhu, C., 2014. Transformation of inorganic P fractions of soil and plant growth promotion by phosphate-solubilizing ability of Penicillium oxalicum I1. *Journal of Microbiology*, 52(12), pp. 1012–1019. [DOI]

Jayathilake, K.M.P.I., Manage, P.M. and Idroos, F.S., 2024. Isolation of phosphate solubilizing fungi from soil and their application in plant growth promotion. *Proceedings of the 28th Forestry and Environment Symposium*, 28, p. 7042. [DOI]

Jayathilake, K.M.P.I., Manage, P.M. and Idroos, F.S., 2025. Isolation and characterization of phosphate-solubilizing bacteria from compost and open dump sites: implications for plant growth. *Nature Environment and Pollution Technology*, 24(3), p. D1737. [DOI]

Khan, M.S., Zaidi, A., Wani, P.A. and Oves, M., 2009. Plant growth promotion by phosphate solubilizing fungi – current perspective. *Archives of Agronomy and Soil Science*, 56(1), pp. 73–98. [DOI]

Khan, M.S., Zaidi, A. and Ahmad, E., 2014. Mechanism of phosphate solubilization and physiological functions of phosphate-solubilizing microorganisms. In: *Phosphate Solubilizing Micro-Organisms: Principles and Application of Microphos Technology*, Cham: Springer International Publishing, pp. 31–62. [DOI]

Khasawneh, F.E. and Doll, E.C., 1979. The use of phosphate rock for direct application to soils. In: *Advances in Agronomy*, Elsevier, pp. 159–206. [DOI]

Leggett, M., Cross, J., Hnatowich, G. and Holloway, G., 2007. Challenges in commercializing a phosphate-solubilizing microorganism: Penicillium bilaiae, a case history. In: E. Velázquez and C. Rodríguez-Barrueco (eds.) *First International Meeting on Microbial Phosphate Solubilization*, Developments in Plant and Soil Sciences, Vol. 102, Dordrecht: Springer, pp. 215–222. [DOI]

Li, X., Li, D., Yan, J., Zhang, Y., Wang, H., Zhang, J., Ahmed, T. and Li, B., 2021. Effect of plant-growth-promoting fungi on eggplant (Solanum melongena L.) in new reclamation land. *Agriculture*, 11(11), p. 1036. [DOI]

Li, Z., Bai, T., Dai, L., Wang, F., Tao, J., Meng, S., Hu, Y., Wang, S. and Hu, S., 2016. A study of organic acid production in contrasts between two phosphate solubilizing fungi: Penicillium oxalicum and Aspergillus niger. *Scientific Reports*, 6(1), p. 25313. [DOI]

Mayadunna, N., Karunarathna, S.C., Asad, S., Stephenson, S.L., Elgorban, A.M., Al-Rejaie, S., Kumla, J., Yapa, N. and Suwannarach, N., 2023. Isolation of phosphate-solubilizing microorganisms and the formulation of biofertilizer for sustainable processing of phosphate rock. *Life*, 13(3), p. 782. [DOI]

Murphy, J. and Riley, J.P., 1962. A modified single solution method for the determination of phosphate in natural waters. *Analytica Chimica Acta*, 27, pp. 31–36. [DOI]

Odoh, C.K., Eze, C.N., Obi, C.J., Anyah, F., Egbe, K., Unah, U.V., Akpi, U.K. and Adobu, U.S., 2020. Fungal biofertilizers for sustainable agricultural productivity. In: *Agriculturally Important Fungi for Sustainable Agriculture: Volume 1 – Perspective for Diversity and Crop Productivity*, Cham: Springer International Publishing, pp. 199–225. [DOI]

Qiao, H., Sun, X.R., Wu, X.Q., Li, G.E., Wang, Z. and Li, D.W., 2019. The phosphate-solubilizing ability of Penicillium guanacastense and its effects on the growth of Pinus massoniana in phosphate-limiting conditions. *Biology Open*, 8(11), p. bio046797. [DOI]

Quadar, J., Chowdhary, A.B., Dutta, R., Angmo, D., Singh, S., Singh, J., Singh, S., Kumar, S.I., Sohal, B. and Vig, A.P., 2023. Economic and quality evaluation of composting technologies. In: *Current Developments in Biotechnology and Bioengineering*, Amsterdam: Elsevier, pp. 295–318. [DOI]

Ratnayake, U.A.J., Weerasinghe, K.D.N. and Chandika, K.K.J., 2018. Potential of Eppawala rock phosphate as a phosphorus fertilizer for rice cultivation in acid sulphate soils in Matara District of Sri Lanka. *Tropical Agricultural Research*, 29(4), pp. 293–299. [DOI]

Rawat, P., Das, S., Shankhdhar, D. and Shankhdhar, S.C., 2021. Phosphate-solubilizing microorganisms: mechanism and their role in phosphate solubilization and uptake. *Journal of Soil Science and Plant Nutrition*, 21(1), pp. 49–68. [DOI]

Sandamali, T.G.I., Mithrasena, Y.J.P.K. and Silva, J.N., 2017. Antifungal activity and phosphate solubilizing ability of fungi isolated from rice rhizosphere in low country wet zone of Sri Lanka. In: *Greener Agriculture and Environment through Convergence of Technologies: Proceedings of the International Symposium on Agriculture and Environment (ISAE 2017)*, 19 January 2017, Faculty of Agriculture, University of Ruhuna, Kamburupitiya, Matara, Sri Lanka, pp. 23–25.

Sandamali, T.G.I., Mithrasena, Y.J.P.K., Senanayake, D.M.J.B., Prasanna, K.N.G.Y., Kumara, D.K.T.S., Silva, J.N., Perera, M.Y.G., Chandrasekara, K.K.D. and Priyantha, G.D.A., 2021. Characterization of native phosphorus solubilizing fungal species and development of a phosphorous biofertilizer formulation for rice cultivation. *Tropical Agriculturist*, 169(4), pp. 7–15. [DOI]

Shrivastava, M., Kale, S.P. and D'Souza, S.F., 2011. Rock phosphate enriched post-methanation bio-sludge from kitchen waste based biogas plant as P source for mungbean and its effect on rhizosphere phosphatase activity. *European Journal of Soil Biology*, 47(3), pp. 205–212. [DOI]

Singh, H. and Reddy, M.S., 2011. Effect of inoculation with phosphate solubilizing fungus on growth and nutrient uptake of wheat and maize plants fertilized with rock phosphate in alkaline soils. *European Journal of Soil Biology*, 47(1), pp. 30–34. [DOI]

Tang, J.C., Shibata, A., Zhou, Q. and Katayama, A., 2007. Effect of temperature on reaction rate and microbial community in composting of cattle manure with rice straw. *Journal of Bioscience and Bioengineering*, 104(4), pp. 321–328. [DOI]

Vassilev, N. and Vassileva, M., 2003. Biotechnological solubilization of rock phosphate on media containing agro-industrial wastes. *Applied Microbiology and Biotechnology*, 61(5–6), pp. 435–440. [DOI]

Wang, J., Zhao, Y.G. and Maqbool, F., 2021. Capability of *Penicillium oxalicum* Y2 to release phosphate from different insoluble phosphorus sources and soil. *Folia Microbiologica*, 66(1), pp. 69–77. [DOI]

Wang, Y., Li, P., Zhang, B., Meng, J., Gao, Y., He, X. and Hu, X., 2020. Identification of phosphate-solubilizing microorganisms and determination of their phosphate-solubilizing activity and growth-promoting capability. *BioResources*, 15(2), pp. 2560–2578. [DOI]

Wijerathna, P.A.K.C., Udayagee, K.P.P., Idroos, F.S. and Manage, P.M., 2024a. Formulation of novel microbial consortia for rapid composting of biodegradable municipal solid waste: an approach in the circular economy. *Environment and Natural Resources Journal*, 22(3), pp. 283–300. [DOI]

Wijerathna, P.A.K.C., Udayagee, K.P.P., Idroos, F.S. and Manage, P.M., 2024b. Novel bacterial consortium for mitigation of odor and enhance compost maturation rate of municipal solid waste: a step toward a greener economy. *Nature Environment and Pollution Technology*, 23(3), pp. 1751–1760. [DOI]

Wijerathna, P.A.K.C., Udayagee, K.P.P., Idroos, F.S. and Manage, P.M., 2026. Spectral characterization and indexing methods for the quality assessment of municipal solid waste compost prepared using novel bacterial consortia. *Nature Environment and Pollution Technology*, 25(1), p. D1799. [DOI]

Yin, Z., Shi, F., Jiang, H., Roberts, D.P., Chen, S. and Fan, B., 2015. Phosphate solubilization and promotion of maize growth by Penicillium oxalicum P4 and Aspergillus niger P85 in a calcareous soil. *Canadian Journal of Microbiology*, 61(12), pp. 913–923. [DOI]

Nature Environment and Pollution Technology
An International Quarterly Scientific Journal

p-ISSN: 0972-6268
(Print copies up to 2016)
e-ISSN: 2395-3454

Vol. 25 | No. 3 | Article ID B4394 | 2026

Original Research Paper

https://doi.org/10.46488/NEPT.2026.v25i03.B4394

Open Access Journal

Central Composite Design-Based Optimization of Heterogeneous Fenton-Like Catalytic Oxidation of Real Pharmaceutical Wastewater Using Cu-Fe/SiO_2

Neha Kulshreshtha, Vishal Kumar Sandhwar†, Alok Tiwari and Shivendu Saxena
Department of Chemical Engineering, Parul Institute of Technology, Parul University, Vadodara-391760, Gujarat, India
†Corresponding author: Vishal Kumar Sandhwar; vishal.sandhwar8850@paruluniversity.ac.in

Abbreviation: Nat. Env. & Poll. Technol.
Website: www.neptjournal.com

Received: 08-09-2025
Revised: 12-12-2025
Accepted: 14-12-2025

Key Words:

Pharmaceutical wastewater
COD removal
Catalytic oxidation
Cu-Fe/SiO_2
Process optimization

Citation for the Paper:

Kulshreshtha, N., Sandhwar, V.K., Tiwari, A. and Saxena, S., 2026. Central composite design-based optimization of heterogeneous Fen-ton-like catalytic oxidation of real pharmaceutical wastewater using Cu-Fe/SiO_2. *Nature Environment and Pollution Technology*, 25(3), B4394. https://doi.org/10.46488/NEPT.2026.v25i03.B4394

Note: From 2025, the journal has adopted the use of Article IDs in citations instead of traditional consecutive page numbers. Each article is now given individual page ranges starting from page 1.

Copyright: © 2026 by the authors
Licensee: Technoscience Publications
This article is an open access article distributed under the terms and conditions of the Creative Commons Attribution (CC BY) license (https://creativecommons.org/licenses/by/4.0/).

ABSTRACT

This research explores heterogeneous Fenton-like catalytic oxidation for the treatment of actual pharmaceutical wastewater with Cu–Fe supported on SiO_2 as an active catalyst. Catalyst preparation and characterization via X-ray diffraction (XRD), scanning electron microscopy (SEM), Fourier-transform infrared (FTIR) spectroscopy, and BET analysis for porosity, crystallinity, and active site distribution were completed. To optimize treatment parameters, response surface methodology using central composite design (CCD) investigated catalyst dosage, H_2O_2 concentration, initial pH, and reaction time for the maximum chemical oxygen demand (COD) removal. The CCD determinant generated a quadratic model (R^2 = 0.9881) to predict experimental results, which, when confirmed via successful achievement of proposed conditions, resulted in 76.07% COD removal. This work indicates the efficiency, reproducibility and feasibility of scaling the Cu–Fe/SiO_2 catalyst for pharmaceutical wastewater treatment and is a step toward sustainability.

1. INTRODUCTION

The global rise of pharmaceutical production and consumption has led to billions of gallons of pharmaceutical wastewater (PWW) each year from industrial effluent release, making PWW one of the most complex industrial by-product issues to plague the discipline of environmental engineering and wastewater treatment. PWW is characterized by an extraordinarily high chemical oxygen demand (COD), often greater than 5,000 $mg.L^{-1}$ and a notorious brew of xenobiotics, recalcitrant and toxic organic pollutants. Specifically, PWW contains active pharmaceutical ingredients (APIs), antibiotics, solvents, EDCs, and sustainable agents such as surfactants and complexing agents. All of these are released into the environment at concentrations that cause acute and chronic toxicity to aquatic organisms, reduce microbial consortium operability, contribute to the presence of antibiotic-resistant genes (ARGs), and endanger public health and ecosystem stability. Unlike general municipal wastewater or the wastewater generated from other industries, PWW is defined by an unregulated profile and low biodegradability, similar to how drugs meant for human use are processed by the human body and excreted in a non-degraded state. Thus, this convoluted composite presents a severe problem for simple discharge into receiving waters that must now deal with such effluents and poses issues for agricultural systems that might apply non-treated water for irrigation and treatment and the resultant particles that become prolific transformation products (Fu et al. 2019, Luo et al. 2019, Ahidjo et al. 2024). Biological treatment options, such as activated sludge and anaerobic digestion, constitute the traditional means to extract organic pollutants from municipal and some industrial waste streams in ideal environments. Yet, this is not always the case, and without fail, biological treatment options require an emphasis on

biodegradability. Therefore, such treatment options for pharmaceutical wastewater (PWW) are largely ineffectual. This occurs for two reasons: 1) toxic constituents within pharmaceutical wastewater inhibit biological activity, and 2) recalcitrant molecules preclude proper chemical oxygen demand (COD) removal, leading to more toxic, recalcitrant intermediates. Enhanced systems ranging from membrane bioreactors (MBRs) or hybrid solutions integrating biological stimulus and physicochemical phenomena yield superior effluent quality and favorable outcomes. Yet again, membrane bioreactors experience membrane fouling due to excess retained solids, or treatment enhancements fail in the face of antibiotics, pharmaceuticals and endocrine disrupting compounds (EDCs) constituting the real-life PWW (Nebot et al. 2015). The largest unresolved component is the failure to remove pharmaceuticals from the NGO flow post-treatment, as evidenced by WWTP analysis that determined many pharmaceutical compounds existed in both influent and effluent, despite average populations and more rural settings judging such results implausible within their community confines. Unfortunately, WWTPs have become considered an active avenue of pharmaceuticals entering the greater aqueous environment. Using sensitive detection variables, the same pharmaceutical remnants that entered the WWTP stream ended up in the effluent discharge. Therefore, new treatment methods for PWW need to be more efficient, reliable and cost-efficient (Dai et al. 2023, Alfarsi et al. 2025). Thus, Advanced Oxidation Processes (AOPs)—homogenous Fenton and Fenton-like processes present a feasible option for treatment alternatives under generating conditions. AOPs create a wealth of reactive hydroxyl radicals (-OH), which irreversibly degrade complex organic components into much smaller byproducts like H_2O and CO_2. However, the homogeneous Fenton reaction and its derivatives are limited beyond practical application to large-scale high-strength pharmaceutical waste streams. Fenton's reaction occurs at a strictly acidic pH (~pH 3) with an abundance of iron salts producing non-manageable sludges and a rapid deactivation/catalyst leaching phenomenon. These operational limitations increase overall treatment costs while generating residual management issues that negatively impact overall efficiency when neutral pH or cost efficacy is required for high-temperature industrial operations (Xu et al. 2022). To address these issues, the recent emergence of heterogeneously operating Fenton-like catalysts, largely due to bimetallic systems supported on high-surface-area substrates such as silica (SiO_2), has expanded the research and development behind advanced PWW treatment. One of the most promising such new materials includes Cu–Fe/SiO_2 catalysts, which utilize the bimetallic, synergistic redox cycling potential between copper and iron (i.e., Cu^{2+}/Cu^{+} and Fe^{3+}/Fe^{2+} transformations) to generate hydroxyl radicals over a milder range of conditions, including near-neutral pH. Furthermore, SiO_2 as a catalytic support aids in site dispersion, thermal and chemical stabilization of the catalytic structure, and porosity control, all necessary factors to promote effective contact with intended non-target species and efficient contaminant breakdown. In proof-of-concept studies, researchers note that the Cu–Fe/SiO_2 catalysts achieve rapid reaction rates and extents of organic and pharmaceutical contaminant removal, outperforming degradation efficiencies of traditional homogeneous endpoints and single-metal heterogeneous options. Central Composite Design (CCD) under Response Surface Methodology (RSM) provides a powerful solution to many of the optimization needs generated by complex systems. CCD allows for the exploration and modeling of independent operating variables and their interactions and attempts to find the optimal response conditions for pollutant removal (Sandhwar & Prasad 2017, Sandhwar & Prasad 2018, Luo et al. 2019, Kumar et al. 2021, Thomas et al. 2021, Xu et al. 2022, Dai et al. 2023, Yang & Xue 2024).

Quantitative performance comparison highlights limitations of existing benchmarks relative to real pharmaceutical wastewater treatment challenges. Fe/Cu composites achieved only 36% COD removal in real antibiotic wastewater under unspecified H_2O_2 and catalyst dosing conditions, demonstrating limited efficacy for complex pharmaceutical matrices. Homogeneous Fe^{2+}/H_2O_2 systems report 78.4% COD removal in real pharmaceutical wastewater using 1 mg, L^{-1} Fe^{2+} but generate problematic iron sludge and lack catalyst recyclability (Omar et al. 2024, Wang et al. 2025). FeCr-SBA-15/AC on SBA-15/activated carbon support delivers an impressive 97% removal, but targets synthetic methyl orange dye (single compound, easily degradable chromophore) rather than multi-component pharmaceutical effluents, with 0.75 $g.L^{-1}$ dosing and no H_2O_2 consumption reported. CuFe/SBA-15 catalysts show promise for model pollutants but provide no quantified COD removal data, H_2O_2 doses, or operational conditions, limiting benchmarking utility (Hamieh et al. 2025). CuO/Fe_3O_4/SiO_2 composites report qualitatively "high removal" for dyes without specific COD percentages, H_2O_2 consumption metrics, or catalyst loadings, precluding rigorous performance evaluation (Ngoc & Vu 2022). While many studies have reported on Cu-Fe catalysts, the present work is novel in terms of its actual application, support, and parameter optimization. First, many studies use prepared solutions of single pharmaceuticals, while this study tests an effective solution using real pharmaceutical wastewater, which includes many recalcitrant organic compounds and poses a much more difficult solution for Fenton-like

oxidation (Chen et al. 2013, Nguyen et al. 2020, Thomas et al. 2021, Nam et al. 2025, Wang et al. 2025). Second, the catalyst is supported on SiO_2, which is a much less commonly used support than Al_2O_3, activated carbon, or magnetic ferrites. SiO_2 has increased surface dispersion characteristics and a structurally neutral disposition, which offer effective dispersive and Cu-Fe redox properties. Third, the parameters were optimized using central composite design (CCD) for real wastewater purposes and not synthetic pollutants to create greater observed relevance and applicability to actual industrial demand.

The present work envisages the synthesis of a Cu–Fe/sio$_2$ composite catalyst using the wet impregnation method and examines its efficiency for the treatment of real pharmaceutical wastewater via catalytic activation of hydrogen peroxide. The developed catalyst was characterized using different characterization techniques such as XRD, SEM, FTIR, and BET to understand its properties. To evaluate the effect of key operational parameters on COD removal efficiency, batch experiments were carried out based on the CCD framework. The developed statistical models inform the prediction and adjustment of reaction conditions for best performance. Ultimately, this study aims to facilitate an efficient catalytic reaction for the treatment of pharmaceutical wastewater with sustainability in mind to foster an effective new course of action for subsequent projects to improve environmental sustainability measures and safeguard public health. These findings show the advantages of a heterogeneous Fenton-like approach to safety and environmental quality with a more efficient, cost-effective, and sustainable approach to treating pharmaceutical wastewater.

2. MATERIALS AND METHODS

2.1. Chemicals

All chemicals, such as Copper (II) Nitrate Trihydrate ($Cu(NO_3)_2 \cdot 3H_2O$, Iron(III) Nitrate Nonahydrate ($Fe(NO_3)_3 \cdot 9H_2O$), Tetraethyl Orthosilicate (TEOS, $Si(OC_2H_5)_4$), Ethanol (C_2H_5OH), etc., used in this study were of analytical grade and used without further purification. The following chemicals were procured from Neelkanth Hari Chemical, Vadodara, Gujarat, India. All glassware and instruments used in the synthesis and analysis were thoroughly cleaned with chromic acid and rinsed with deionized water to prevent any contamination.

2.2. Characteristics of Pharmaceutical Industry Wastewater

The wastewater, which was treated in the catalytic oxidation processes, was supplied from a pharmaceutical plant located in Vadodara. The initial total dissolved solids, chemical oxygen demand, pH, biological oxygen demand, and turbidity of the wastewater were assessed and are detailed in Table 1. The samples were stored in a refrigerator at 4°C until use.

Table 1: Characterization of real pharmaceutical wastewater.

Sr. No.	Parameters	Unit [SI])	Measured Value
1.	pH		8.2
2.	Turbidity	NTU	28.40
3.	COD	$mg.L^{-1}$	6112
4.	BOD (3 days at 27 degrees Celsius)	$mg.L^{-1}$	2987
5.	Total dissolved Solid	$Mg.L^{-1}$	2780

2.3. Catalyst Preparation

The Cu–Fe/SiO_2 heterogeneous catalyst was synthesized via the wet impregnation method (Kumar et al. 2021), utilizing commercially available SiO_2 powder as a support. This method allows for facile preparation and effective dispersion of active metal species onto the support. Copper(II) nitrate trihydrate ($Cu(NO_3)_2 \cdot 3H_2O$) and iron (III) nitrate nonahydrate ($Fe(NO_3)_3 \cdot 9H_2O$) were obtained at stoichiometric amounts.

After accurate weighing, the weighed portions were dissolved in a minimal amount of deionized water to afford a mixed metal nitrate solution in aqueous form. The loading ratio of Cu: Fe was maintained at 1:1, and the total metal loading was calculated at 10 wt% of the total mass of the catalyst. To the metal nitrate solution obtained, commercial amorphous SiO_2 powder was added gradually with continuous stirring conducted at room temperature to ensure proper impregnation. After 4 h of stirring, the slurry was transferred to a Petri dish and dried in a hot air oven set at 110°C for 12 h. Upon drying, the resultant solid precursor was calcined in a muffle furnace at 500°C for 4 h in air to decompose the nitrates and yield the metal oxides (CuO and Fe_2O_3 or Fe_3O_4) with enhanced stability and strong adhesion to the surface of SiO_2. The resulting calcined catalyst was cooled to room temperature, ground into a fine powder, and stored in airtight containers for further experimentation in catalytic studies. The resultant catalyst is an active and stable Cu–Fe/SiO_2 for heterogeneous Fenton-like reactions of pharmaceutical wastewater treatment (Liu et al. 2024, Li et al. 2025).

The selected 1:1 Cu:Fe molar ratio was not arbitrary; it is widely reported to enhance Fenton-like activity due to the synergistic redox cycling between Cu^{2+}/Cu^{+} and Fe^{3+}/Fe^{2+}, which accelerates the generation of hydroxyl radicals (Chen et al. 2024, Wang et al. 2024, Hu et al. 2025). Several studies have shown that equimolar Cu–Fe compositions yield higher

catalytic activity and stability compared to non-equimolar ratios because both metals participate simultaneously in electron transfer cycles (Vainoris et al. 2022, Kongkoed et al. 2024, Wang et al. 2024, Nam et al. 2025). Similarly, the 10 wt% total metal loading was selected based on literature indicating that loadings in the range of 8–12 wt% provide optimal dispersion of mixed metal oxides on oxide supports without causing pore blockage, crystallite overgrowth, or agglomeration (Munnik et al. 2015, Peralta-Ladino et al. 2025, Tajoli et al. 2025). Higher loadings (>15 wt%) often lead to particle sintering during calcination, while lower loadings (<5 wt%) can result in insufficient active sites (Bellouard et al., 2024; Khan et al., 2025). The molar concentration of the precursor solution was maintained at 0.5 M for both Cu and Fe salts to enable homogeneous impregnation while preventing oversaturation of the support surface. The impregnation step was conducted at the native solution pH, governed by the nitrate precursors; this pH range is appropriate for maintaining metal ions in soluble form and ensuring uniform distribution over SiO_2 without premature precipitation (Tricoli et al. 2010, Bravo-Suarez et al. 2025).

2.4. Catalyst Characterization

The structural, morphological and surface properties of Cu–Fe/SiO_2 were extensively examined and characterized via various instruments in order to understand the nature of the catalyst for in situ reaction. X-Ray Diffraction (XRD) was employed for crystallite structure and phase determination, where a D6 PHASER X-Ray Diffractometer (Bruker India Scientific Pvt. Ltd.) with Cu Kα radiation (λ = 1.5406 Å) in the 2θ range of 10°–80° was utilized for analysis. Fig. 1 represents the XRD spectrum of the synthesized catalyst. The XRD pattern for the synthesized Cu–Fe/SiO_2 catalyst indicates the presence of both amorphous and crystalline phases. The broad halo between 20–25° (2θ) is attributed to the formation of amorphous SiO_2, which corroborates the selection of silica as the support material for the catalyst. Superimposed crystalline features on the SiO_2 halo relate to the characteristic crystalline phases presumed from the presence of copper and iron oxides. The peaks corresponding to CuO (tenorite, monoclinic) are noted at 35.5°, 38.7°, and 48.7°, while the peaks appearing at about 30.2°, 35.6°, 43.3°, 57.3°, and 62.9° are attributed to Fe_2O_3 (hematite). Additionally, the overlapping peaks at 30.3°, 33.1°, and 51.4° indicate the presence of a $CuFe_2O_4$ spinel phase formed, which is a mixed Cu–Fe oxide phase that is commonplace in bimetallic systems. Thus, the presence of crystalline phases over the amorphous SiO_2 support indicates that the Cu and Fe species have been loaded successfully onto silica to provide many redox-active sites and maintain structural stability for effective heterogeneous Fenton-like catalysis (Ning et al. 2018, Ren et al. 2020, Pratiwi et al. 2021). Scanning Electron Microscopy (SEM) on an SU3800 Hi-SEM system (Hitachi High-Tech India Pvt. Ltd.) discerned particle morphology and distribution. Fig. 2 indicates an SEM micrograph. According to the SEM provided, the surface morphology of the catalyst is non-uniform as it appears to be comprised of irregularly shaped/agglomerated particles. They appear to be somewhat loosely packed, forming clusters/areas of rough and porous characteristics—ideal for enhancing surface area and possessing necessary active sites. The microstructure of Cu–Fe/SiO_2 is heterogeneous, as there are small, fragmented-like structures and large plate-like formations, which suggests that the metal oxides are dispersed nicely on the silica support. These structures are in line with what would be beneficial for mass transfer and catalytic activity because the roughness/pore openings allow easy access and engagement of the species with the catalyst surface. Thus, the SEM suggests that the catalysts are appropriately structured for heterogeneous Fenton-like catalytic activity for wastewater treatment (Martínez et al. 2017, Ning et al. 2018, Thomas et al. 2021). Fourier Transform Infrared Spectroscopy (FTIR) from a Bruker Alpha II FTIR spectrometer compiled via the KBr pellet technique in the wavenumber range of 400–4000 cm^{-1} determined surface functionality. Fig. 3 shows the FTIR spectrum. The FTIR spectrum of the Cu–Fe/SiO_2 catalyst (Fig.3) shows specific absorption bands, which indicate the formation of the silica support and metal oxides. The presence of silica is confirmed by a strong and broad band at 1080–1100 cm^{-1} with shoulders at 800 cm^{-1}, which relates to the asymmetric and symmetric stretching vibrations of Si–O–Si linkages. In addition, a weak band appears at 950–970 cm^{-1}, relating to Si–OH stretching vibrations, corresponding to surface silanol groups. Moreover, absorptions in the lower wavenumber region pertain to the generation of metal oxides, as Cu and Fe were integrated onto the silicon matrix; thus, the absorption between 580–680 cm^{-1} corresponds to Fe–O and Cu–O stretching vibrations. Finally, a broad band between 3400–3450 cm^{-1} and a weak peak at 1630 cm^{-1} relate to O–H stretching and bending vibrations of water and/or surface hydroxyl groups. Therefore, the FTIR suggests that a Cu–Fe/SiO_2 composite was formed and that silica and silica functional groups were absorbed and created (Ning et al. 2018, Ren et al. 2020). The textural property surface area was assessed via BET surface area on a Micromeritics ASAP 2020, where nitrogen adsorption–desorption isotherms after degassing the sample at 150°C under vacuum were used to calculate specific surface area via the Brunauer–Emmett–Teller method. Such information provides an initial overview of the solid properties of the catalyst, which enhance the effectiveness of the catalyst during reaction, particularly for the degradation of

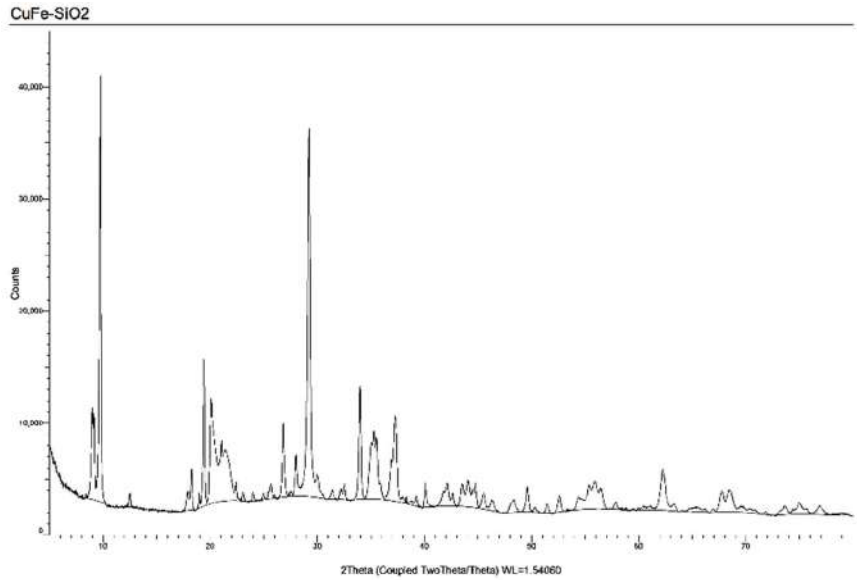


Fig. 1: XRD Spectrum of synthesized catalyst.

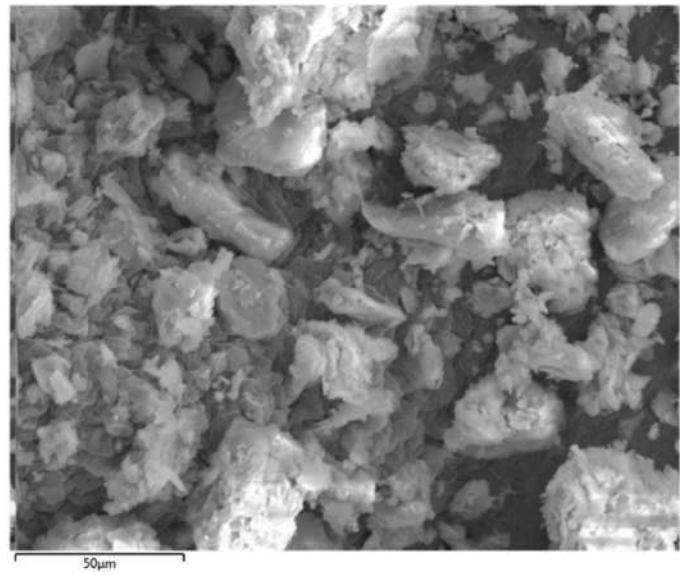


Fig. 2: SEM micrograph of the synthesized catalyst.

pharmaceutical wastewater. BET surface area measurement of the synthesized Cu–Fe/SiO_2 catalyst revealed a surface area of 111.1 $m^2.g^{-1}$. This indicates a porous structure of the catalyst, which is advantageous because this relatively large surface area possesses a high number of active sites. Better active dispersion of Cu and Fe during the heterogeneous Fenton-like oxidation reaction enhances the efficiency of pharmaceutical wastewater degradation (Guerreiro et al. 1997, Martínez et al. 2017, Sandhwar & Prasad 2017, Krupińska 2024, González-Castaño et al. 2021, Jia et al. 2022, Mekki et al. 2023, Salehzadeh et al. 2023).

2.5. Experimental Set-Up and Procedure

The current investigation was conducted within a 250 mL round-bottom three-necked glass reactor, wherein the central neck was sealed with a complete reflux system. During each trial, 100 mL of wastewater was introduced into the reactor along with the necessary amount of catalyst and H_2O_2, and then placed on a hot plate equipped with a magnetic stirrer. Various pH levels were tested; therefore, the initial pH of the mixture was adjusted using 1 M NaOH or 1 M H_2SO_4 prior to the addition of the catalyst and oxidant. Following

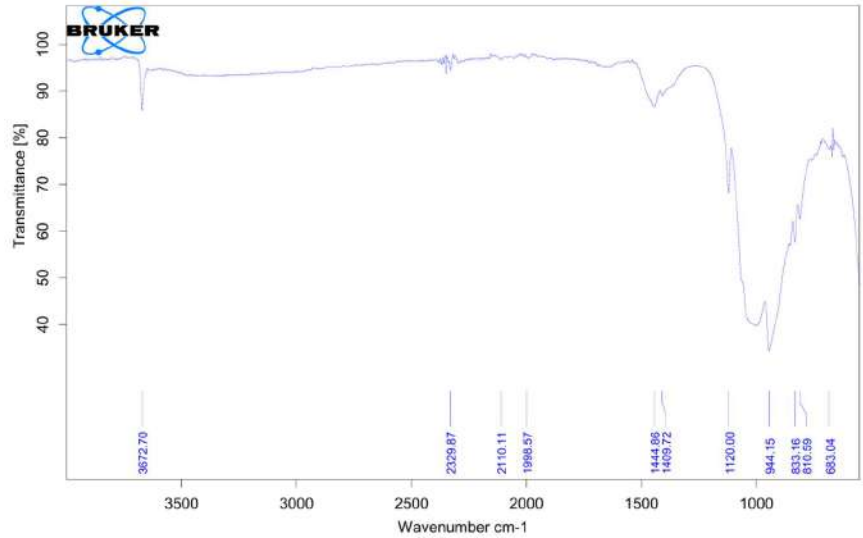


Fig. 3: FITR spectrum of the synthesized catalyst.

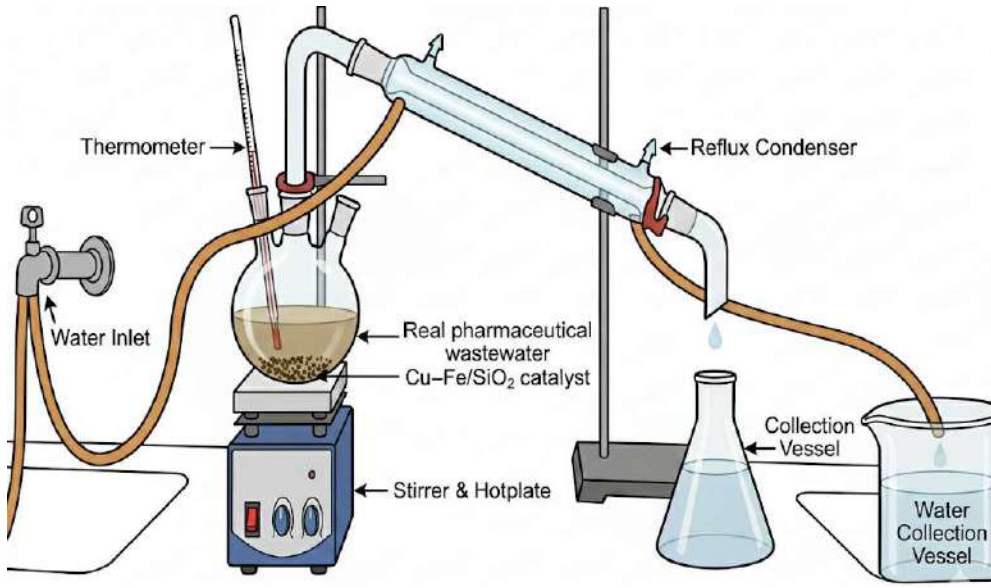


Fig. 4: Experimental setup.

the 3-h reaction period, 2 mL of supernatant was periodically extracted from the reactor and promptly filtered through a 0.22 µm Millex syringe filter. The resulting samples obtained were subsequently subjected to COD analysis using the APHA standard method. All procedures were repeated in duplicate, and the mean values were calculated with error bars indicating the standard deviation. Fig. 4 shows the experimental setup.

Preliminary trial experiments were carried out to determine appropriate operating ranges for key variables, namely catalyst dosage, H_2O_2 concentration, initial pH, and reaction time. These exploratory tests were essential to establish the upper and lower bounds for the subsequent optimization study. The finalized ranges of the independent variables are presented in Table 2. To systematically investigate the effects and interactions of these parameters on COD removal efficiency, Response Surface Methodology (RSM) was employed using a Central Composite Design (CCD). The experimental runs were arranged according to the CCD matrix, also summarized in Table 3, which incorporated various combinations of the independent variables (pH, catalyst dosage, and treatment time). This design framework

enabled efficient modeling of the degradation efficiency and identification of optimal operating conditions.

3. RESULTS AND DISCUSSION

3.1. Effect of Catalyst Dosage, H_2O_2 Concentration, pH, and Reaction Time on COD Removal Efficiency

The effect of significant operating variables on COD removal efficiency via RSM is displayed in the three-dimensional surface plots seen in Fig.s 5 (a–f). For instance, catalyst dosage is shown to have a significantly positive contribution to COD removal, but to an extent, observing the contour plots, higher increases in catalyst loading from 0.4 $g.L^{-1}$ to 0.8 $g.L^{-1}$ increase degradation efficiency as more active Cu–Fe redox sites are available for subsequent H_2O_2 decomposition and •OH radical formation. However, anything beyond that can lead to radical scavenging means or serious aggregation of catalyst particles, which can reduce efficiency (Kumar et al. 2011, Yuan et al. 2022). Furthermore, the concentration of H_2O_2 has a significant concern of COD removal; raising increases in dosage from 30 to 80 $mg.L^{-1}$ increases efficiencies as it opens up more reagent for •OH formation. However, just like with the catalyst loading, excess loading of H_2O_2 can lead to a radical scavenging effect as HO_2• occurs. Since HO_2• has a lower oxidation potential, productivity also reduces. The pH has an adjusted impact on COD removal efficiency, as the lowest pH (pH 4–5) provides the highest efficiency. At low pH, iron and copper remain in a soluble form as redox-active, thus having a high activity in the Fenton-like reactions (Singh et al. 2013). However, neutral pH induces ferric hydroxide precipitation, which reduces active sites available and diminishes catalytic activations. The fact that both Fe^{3+}/Fe^{2+} and Cu^{2+}/Cu^{+} cycles operate well in the acidic pH domain (pH 3–4) means activated H_2O_2 and - OH maximization occurs. This is because at a low pH, Fe^{2+} stays soluble and can effectively engage H_2O_2, while the Cu sites regenerate $Fe^{3+} \rightarrow Fe^{2+}$ relatively easily. Thus, this sustains the dual redox cycle; however, as pH increases, Fe^{3+} precipitation occurs, and Cu speciation becomes more complex, meaning that electron transfer becomes more difficult and - OH is reduced. This explains why the COD removal is most effective in the mildly acidic window and less effective outside of it; discuss this mechanistic relationship (Fischbacher et al. 2017, Liu et al. 2018, Maekawa et al. 2014, Walling et al. 2021). Additionally, SiO_2 is a high-surface-area support that is chemically inert. This means that it stabilizes Cu and Fe oxide species and provides dispersed surface redox sites that are not aggregated. Silica coating or dispersion increases particle stability in aqueous environments, minimizes metal leaching, and SiO_2 can tune surface charge, which will both impact pollutant adsorption and the H_2O_2 approach to active sites. Thus, relate the activity and low leaching to improved dispersion and stabilization of Cu–Fe sites on SiO_2 but

Table 2: Variables and their levels obtained from the statistical software.

Central Composite Design characteristics				
Levels	Parameters (Range)			
	A	B	C	D
	Catalyst dosage [$g.L^{-1}$]	H_2O_2 concentration [mM]	Initial pH	Reaction time [min]
-2α	0.2	5	3	15
-α	0.4	30	4	45
0	0.6	55	5	75
+α	0.8	80	6	105
+2α	1	105	7	135

Table 3: CCD predicted set of experiments.

Run No.	A	B	C	D
1	0.4	30	4	45
2	0.8	30	4	45
3	0.4	80	4	45
4	0.8	80	4	45
5	0.4	30	6	45
6	0.8	30	6	45
7	0.4	80	6	45
8	0.8	80	6	45
9	0.4	30	4	105
10	0.8	30	4	105
11	0.4	80	4	105
12	0.8	80	4	105
13	0.4	30	6	105
14	0.8	30	6	105
15	0.4	80	6	105
16	0.8	80	6	105
17	0.2	55	5	75
18	1	55	5	75
19	0.6	5	5	75
20	0.6	105	5	75
21	0.6	55	3	75
22	0.6	55	7	75
23	0.6	55	5	15
24	0.6	55	5	135
25	0.6	55	5	75
26	0.6	55	5	75
27	0.6	55	5	75
28	0.6	55	5	75
29	0.6	55	5	75
30	0.6	55	5	75

do not relate it to any Fenton activity of the support itself (Martínez et al. 2017, Ning et al. 2018, Ren et al. 2020). Furthermore, the time factor has a slight impact on COD removal as efficiencies gradually change during 45–105 min. A longer reaction time allows for the effective blend between the catalyst and oxidant to ensure proper mineralization of the organics (Aghazadeh et al. 2023, Zhang et al. 2017, Ruziwa et al. 2023, Huilin et al. 2025). Yet, after 90 min, the reduction begins to plateau, which signifies saturation of active sites and reduced transferable biogenic organic matter. The reasons for the plateau in COD removal after ~90 min can be attributed to these aspects because (i) radical/oxidant depletion: bulk H_2O_2 concentration decreases and the effective steady-state •OH flux decreases; (ii) formation of recalcitrant intermediates: partially oxidized species that are less reactive with •OH can grow in concentration to prevent further mineralization; and (iii) mass-transfer limitations: general slower diffusion of remaining organics to active surface sites or blocked pores/sites from oxidation by-product adsorption. From an operational perspective, these can be countered by staged H_2O_2 dosing (maintaining available oxidants), improved hydrodynamics (external mass-transfer resistance minimized), periodic catalyst regeneration (surface fouling removed) (Kwan & Voelker 2002, Ban et al. 2020, Fischbacher et al. 2017, Krupińska 2024). Thus, all interactions better suggest that optimal COD removal (~76%) occurs at optimal catalyst loading (0.68 $g.L^{-1}$), H_2O_2 concentration ($\approx$ 65 $mg.L^{-1}$), weakly-acidic pH ($\approx$ 5.0), and reaction time of $\approx$ 86 min. This also suggests that properly balanced operations yield effective efficiencies without excessive reagents.

Table 4 illustrates that the comparative performances of Fenton and Fenton-like systems are closely influenced by the catalysts' composition, support materials, and operational conditions. Kaya and Asci (2022) reported an 86% COD removal from textile wastewater using an Fe/SnO_2 heterogeneous Fenton catalyst at pH 2 within 90 minutes, highlighting that iron-based systems can achieve exceptionally high efficiency under strongly acidic conditions. Zhao et al. (2017) evaluated the Fe_2O_3/SiO_2 catalyst for phenol degradation, resulting in a moderate COD removal of 64.6% at pH 3 over 60 minutes; the silica support stabilizes iron sites but offers relatively lower activity. Ban et al. (2020) employed a photo-Fenton system ($Fe–Ce/Al_2O_3$) on p-nitrophenol wastewater, attaining 72.9% COD removal at pH 4 after 120 minutes. Phong and Loc (2025) achieved increased efficiency with an rGO/nZVI heterogeneous Fenton catalyst, removing 81.5% COD from textile wastewater at pH 3 in 110 minutes, due to enhanced electron transfer and increased surface area. Su et al. (2018) reached an exceptional 99.8% COD removal using NZVI@ACF for cutting fluid wastewater at pH 5, though such nanostructured systems may involve higher costs and recovery challenges. Conversely, above 93% COD removals were attained within relatively short times by homogeneous Fe^{2+}/H_2O_2 systems reported by Ghjair and Abbar (2023) and Ayoub (2022). Overall, the comparison underlines the trade-off of efficiency versus operational sustainability, and it becomes increasingly relevant to apply heterogeneous supported Fenton catalysts for wastewater treatment.

3.2. Catalyst Reusability Study

To investigate the economic practicality of the heterogeneous Fenton-like process, the stability of $CuFe/SiO_2$ was assessed under optimized conditions (catalyst dosage 0.68 $g.L^{-1}$; pH 4.9; H_2O_2 concentration 65.28 mM; reaction time 86.81 min). During the first cycle, the catalyst operated with maximum functionality (74.11% COD removal) since all active surface

Table 4: Comparison of reported Fenton and heterogeneous Fenton-like catalysts for wastewater treatment.

Catalyst/system	Metal type	Support/configuration	Wastewater/ pollutant	pH	COD (or target) removal [%]	Time [min]	Ref.
Fe/SnO_2 heterogeneous Fenton	Fe	SnO_2	Textile wastewater	2	86	90	Kaya and Asci (2022)
Fe_2O_3/SiO_2 heterogeneous Fenton	Fe	SiO_2	Phenol solution	3	64.6	60	Zhao et al. (2017)
$Fe–Ce/Al_2O_3$ photoFenton	Fe–Ce	Al_2O_3	pNitrophenol wastewater	4	72.9	120	Ban et al. (2020)
rGO/nZVI heterogeneous Fenton	Fe^0	rGO (nanocomposite)	Textile wastewater	3	81.5 (Batch process)	110	Phong & Loc (2025)
$NZVI@ACF/H_2O_2$	Fe^0	Activated carbon fiber	Cuttingfluid waste	5	99.8	120	Su et al. (2018)
Homogeneous Fe^{2+}/H_2O_2	Fe^{2+}	– (homogeneous)	Hospital wastewater	3.1	95	93	Ghjair and Abbar (2023)
Homogeneous Fe^{2+}/H_2O_2	Fe^{2+}	– (homogeneous)	Industrial effluent (edible oil industry)	3	93.5	50	Ayoub (2022)

sites and Cu-Fe redox centers were open for reaction. The catalyst was separated via centrifugation after each run, washed with distilled water, dried, and reused without reactivation. It should be noted that the activity decreased slowly upon reusing it over four cycles, resulting in 69.78% in cycle 2, 60.21% in cycle 3, and 52.23% in cycle 4. The deactivated activity is in line with the expected trend for a heterogeneous Fenton catalyst. This includes partial leaching of active metal species during use as well as the gradual accumulation of recalcitrant carbonaceous residues on the catalyst, which limited the availability of active sites for reaction, as well as decreased effective hydroxyl radical formation. Such behavior has been widely documented for Cu-Fe-based mixed oxide systems under sequential oxidative use.

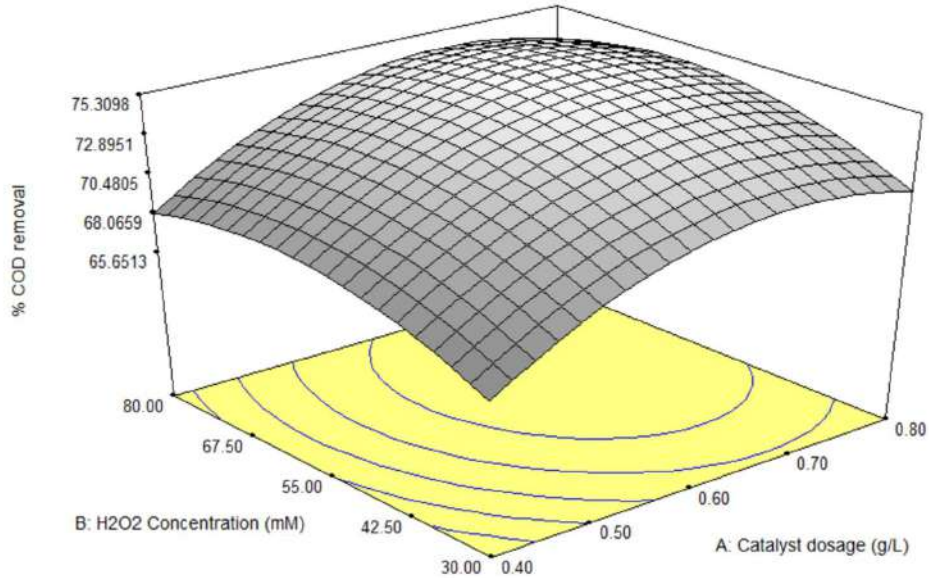


Fig. 5(a)

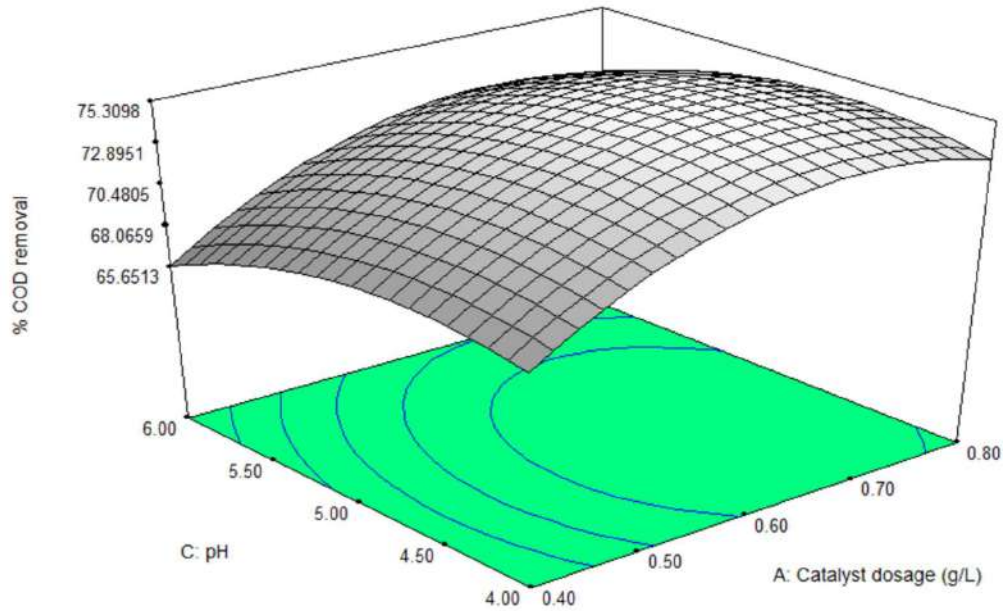


Fig. 5(b)

Figure Cont....

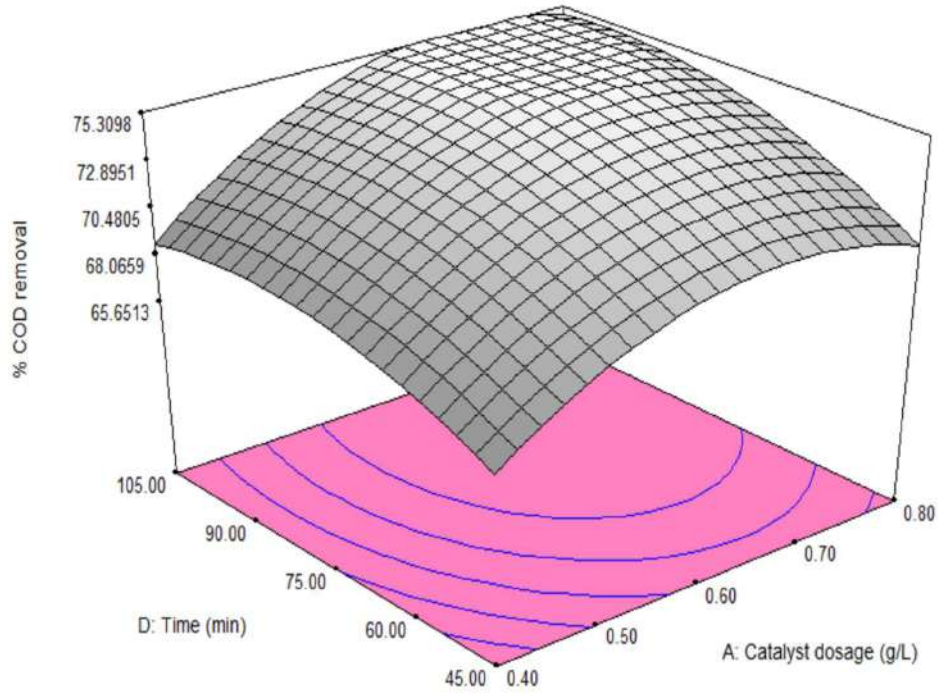


Fig. 5(c)

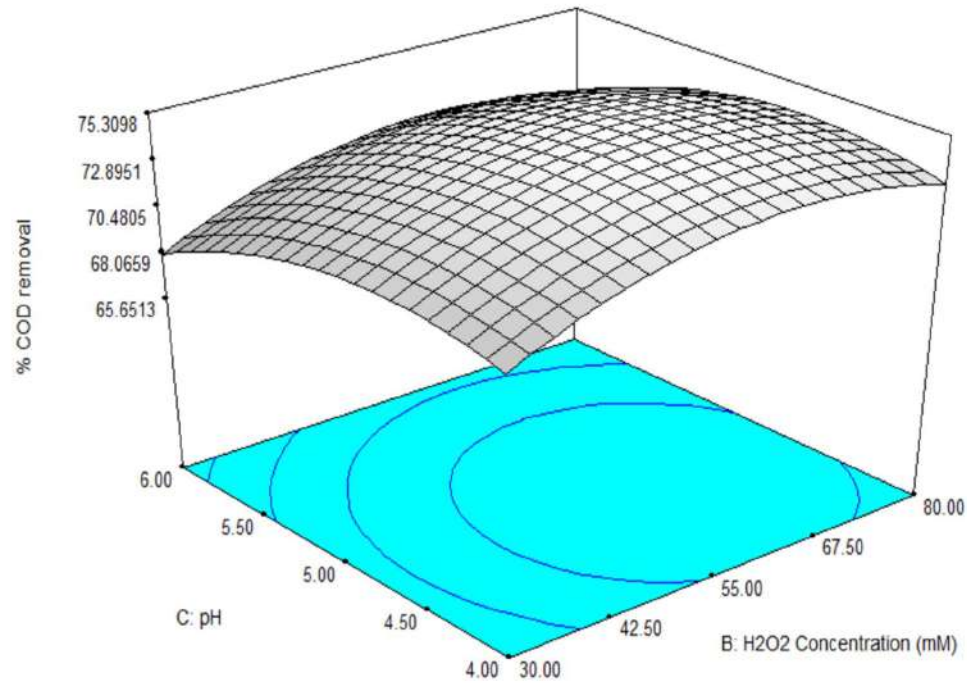


Fig. 5(d)

Figure Cont....

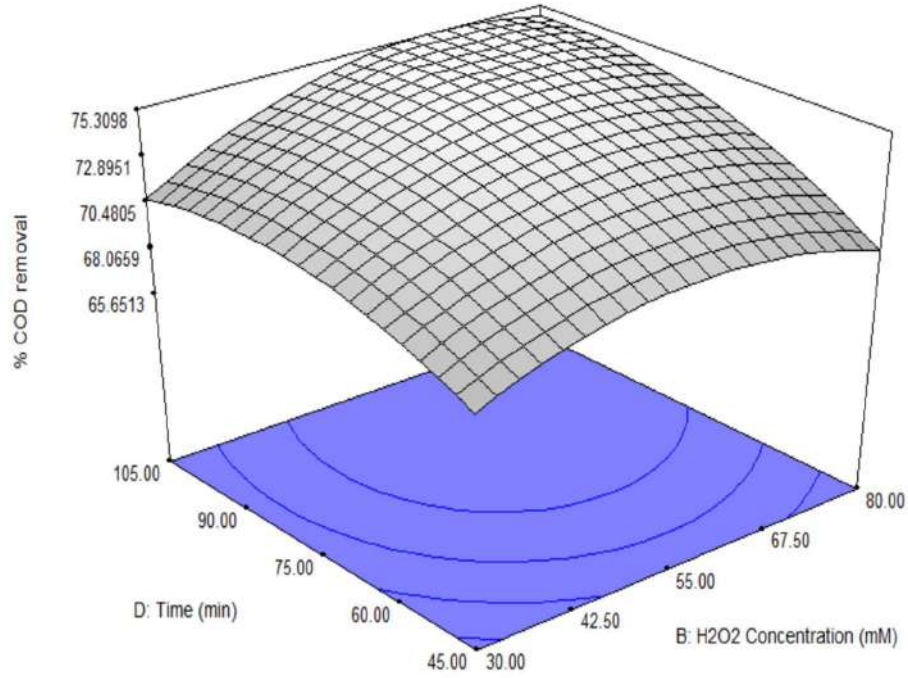


Fig. 5(e)

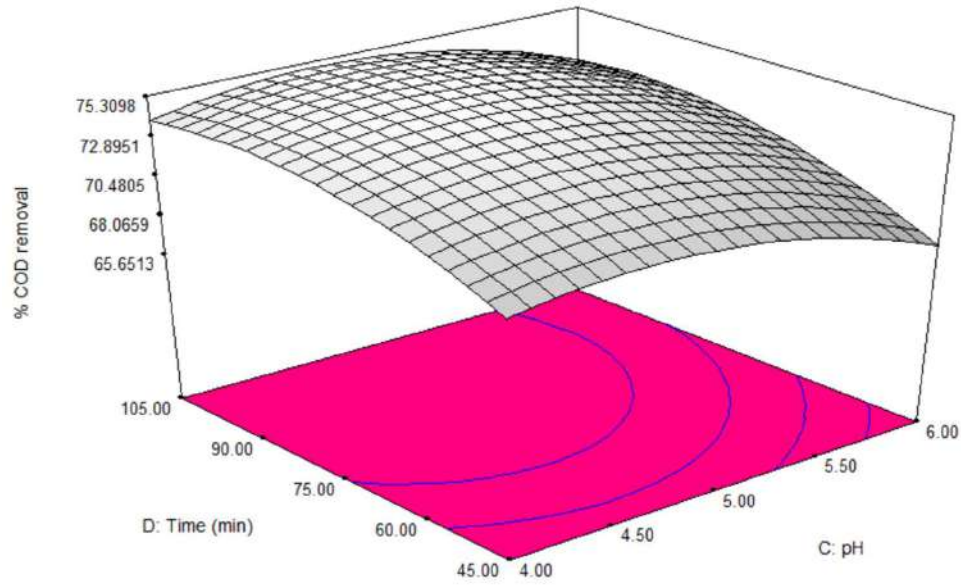


Fig. 5(f)

Fig 5: Effect of (a) catalyst dosage and H_2O_2 concentration, (b) catalyst dosage and pH, (c) catalyst dosage and time, (d) H_2O_2 concentration and pH, (e) H_2O_2 concentration and time, and (f) pH and time on % COD removal.

3.3. Radical Quenching, Reaction Mechanism, and Control Experiment Studies

To validate Cu-Fe/SiO_2 and heterogeneous Fenton-like mechanisms, radical quenching experiments were performed, which unambiguously identified hydroxyl radicals (- OH) as the main ROS contributing to pharmaceutical wastewater degradation at the optimal CCD experimental parameters. In radical quenching tests, tert-butanol (t-BuOH, 1- OH

scavenger) and potassium iodide (KI, a scavenger for other non-radicals and bulk - OH) were added to solutions at 10 mM. In the Cu-Fe/SiO_2/H_2O_2 system, radical quenching was highly inhibited, with COD removal decreasing from 74.11% (based on the tested run) to 33.9%, equating to ~54% inhibition. Thus, it can be concluded that -OH radicals were the dominant oxidizing agents. On the other hand, quenching by KI resulted in a smaller inhibition of 11.6%, with efficiency reducing from 74.11% to about 62.51%. Thus, limited inhibition suggests that the Cu-Fe/SiO_2/H_2O_2 system occurs predominantly by •OH radicals confined to the surface at catalyst-active sites. Since KI acts predominantly on surface oxidative species and fails to effectively quench diffusing radicals (or homogeneous Fe-based) pathways, the absence of significant inhibition indicates that leached-Fe Fenton reactions, superoxide, or singlet oxygen do not significantly contribute as active species for the tested conditions (Li et al. 2015, Nath et al. 2022, Shao et al. 2022, Li et al. 2023).

The resulting mechanism occurs through three main steps.

(1) H_2O_2 activation via iron redox cycle (Wang et al. 2024, Hu et al. 2025):

Surface Fe^{3+} is first reduced by H_2O_2 to generate Fe^{2+}, and the formation of hydroperoxyl species (•OOH) follows Fenton activation as an occurrence of Fe^{2+} and H_2O_2 generating OH radicals (•OH) and regenerating Fe^{3+}, as shown in equations [1] and [2].

$$Fe^{3+} + H_2O_2 \rightarrow Fe^{2+} + \cdot OOH + H^+ \quad ...(1)$$

$$Fe^{2+} + H_2O_2 \rightarrow Fe^{3+} + \cdot OH + OH^- \quad ...(2)$$

(2) Synergistic Cu-Fe redox shuttle (Faheem et al. 2018, Wang et al., 2024, Hu et al. 2025):

Cu^{2+}/Cu^+ couples with Fe^{3+}/Fe^{2+} on the catalyst surface, making electron transfer easier and thus accelerating the Fe^{2+} regeneration step, where Cu^+ facilitates a faster approach and even activates H_2O_2 as well to create more •OH than inherently produced, as shown in equations [3] and [4].

$$Cu^{2+} + Fe^{2+} \leftrightarrow Cu^+ + Fe^{3+} \quad ...(3)$$

$$Cu^+ + H_2O_2 \rightarrow Cu^{2+} + \cdot OH + OH^- \quad ...(4)$$

(3) Pharmaceutical pollutant degradation (Thomas et al. 2021, Jiang et al. 2026):

The lattice-confined •OH produced at the Cu-Fe sites oxidizes the adsorbed pharmaceutical organics. Successive radical reactions create ring-opening, fragmentation and finally mineralization to CO_2 and other inorganic residues.

Control experiments confirmed the heterogeneous nature of the Cu-Fe/SiO_2/H_2O_2 system. When the reaction was conducted with H_2O_2 alone, only a minimal COD removal of approximately 7.6% was observed, indicating that H_2O_2 self-decomposition contributed little to oxidation. Similarly, using the catalyst without H_2O_2 resulted in a COD reduction of 5.8%, implying that adsorption or non-radical catalysis had a limited impact (Ksibi 2006, Erasmus et al. 2016, Aljuboury et al. 2017, Kwan & Voelker 2002). For example, to further assess the effect of soluble metal species, the reaction filtrate was tested under similar conditions after centrifugation to remove the catalyst; the resulting filtrate showed only 6.1% COD removal, indicating that leached Fe or Cu ions played a negligible role in oxidation (Ksibi 2006, Thomas et al. 2021, Jiang et al. 2026). Thus, collectively, these findings support the conclusion that the catalytic activity of Cu and Fe primarily arises from surface-confined Cu-Fe redox-active sites and that Cu-Fe/SiO_2/H_2O_2 operates via a genuine heterogeneous Fenton-like process rather than a homogeneous one (Li et al. 2015, Jiang et al. 2026).

3.4. Optimization Study and ANOVA Analysis

Table 5 presents both the CCD-predicted and experimental % COD removal results under optimal operating conditions. The RSM optimization of COD removal efficiency, along with the ANOVA statistics, validates the accuracy and predictability of the quadratic model. The model demonstrates a high coefficient of determination (R^2 = 0.9881), indicating it explains over 98% of the variance in COD removal. The adjusted R^2 (0.9769), closely aligned with R^2, suggests minimal loss of accuracy due to the number of predictors. Additionally, the predicted R^2 (0.9572) correlates strongly with the adjusted R^2, reflecting consistent reliability in predicted values. The low standard deviation (0.78) and coefficient of variation (C.V. = 1.15%) highlight excellent precision and repeatability of the experiments. The Adeq Precision value (31.677), which surpasses the threshold of 4, indicates an adequate signal-to-noise ratio. Finally, the low PRESS value (32.34) further confirms the model's strong predictability (Sarrai et al. 2016, Deepa et al. 2021, Pasciucco et al. 2025). The F-value of 88.74, with a p-value less than 0.0001, confirms that the quadratic model is highly significant. The final results of the quadratic equation [5], based on coded factors, indicate that catalyst dosage (A), H_2O_2 concentration (B), and reaction time (D) positively influence COD removal, while pH (C) has a marginally negative effect. Additionally, all squared terms (A^2, B^2, C^2, D^2) have negative coefficients, suggesting the presence of curvature and an optimal point rather than a purely linear relationship among all variables. Notably, the interaction terms AD and BD are significantly influential in determining COD removal efficiency, implying these variables work

together to enhance removal capacity. The positive linear coefficients for A, B, and D suggest maximum COD removal occurs with increases in these factors, which then plateau. The negative quadratic terms for all four factors indicate that extreme values—such as excessive catalyst, oxidant, or reaction time—do not result in greater removal, likely due to radical saturation and scavenging effects. Among the interactions, the highest coefficient is for B and D (0.77 BD), highlighting that H_2O_2 dosage and reaction time are the most interactive parameters. Conversely, the relatively small coefficients for interactions AB, AC, and BC suggest these parameters are less interdependent, functioning more independently. Overall, this CCD effectively identifies optimal conditions for maximizing COD removal.

Ultimately, these optimization findings suggest that the resultant quadratic model is statistically valid, for it is clear that the optimized conditions yield maximum COD removal (~76%) with only moderately adjusted conditions. In conclusion, findings from these optimization steps indicate that the established quadratic model is statistically significant and optimized conditions result in maximum COD removal (~76%) with balanced operating conditions.

Final equation in terms of coded factors:

$$\%COD\ removal = 74.62 + 2.54\ A + 1.23\ B - 1.22\ C + 1.94\ D - 3.07\ A^2 - 2.15\ B^2 - 1.95\ C^2 - 1.70\ D^2 - 0.00125\ (A^*\ B) + 0.19\ (A^*\ C) + 0.57\ (A^*\ D) + 0.043\ (B^*\ C) + 0.77\ (B^*\ D) + 0.29\ (C^*\ D) \quad \ldots(5)$$

Where: A = Catalyst dosage ($g.L^{-1}$), B = H_2O_2 concentration (mM), C = pH, D = Reaction time (min)

4. CONCLUSIONS

This study demonstrates the effectiveness of a Cu–Fe/SiO_2 heterogeneous Fenton-like catalyst for the treatment of real pharmaceutical wastewater. Using CCD-based response surface methodology, it was found that COD removal is primarily influenced by catalyst dosage, H_2O_2 concentration, pH, and reaction time. Under optimized conditions, 0.68 $g.L^{-1}$ catalyst, 65.28 mM H_2O_2, pH 4.9, and 86.81 minutes, a COD removal of 76% was achieved. The correlation between experimental and predicted values was highly significant ($P<0.0001$), indicating that the quadratic model accurately describes the process ($R^2 = 0.9881$). Compared to traditional single-metal catalysts like Cu/Fe or unsupported variants reported in the literature, Cu–Fe/SiO_2 offers better active-site dispersion, reduced metal leaching, and enhanced •OH generation on the surface, making it more suitable for complex pharmaceutical effluents. Nonetheless, some limitations exist. Catalyst deactivation over multiple cycles suggests metal leaching or surface fouling, highlighting the need for regeneration and assessment of long-term stability under continuous operation. Future work should include cost analysis, lifecycle assessment of spent catalysts' environmental impact, and pilot-scale studies prior to practical application. Overall, these results confirm that Cu–Fe/SiO_2 is an effective and durable heterogeneous Fenton-like catalyst for sustainable pharmaceutical wastewater treatment, paving the way for its deployment in real-world scenarios.

5. ACKNOWLEDGMENTS

The authors gratefully acknowledge Parul University, Vadodara, for providing the necessary resources, research facilities, and support to carry out this work.

6. REFERENCES

Aghazadeh, M., Hassani, A.H. and Borghei, M., 2023. Application of photocatalytic proxone process for petrochemical wastewater treatment. *Scientific Reports*, 13(1), p.12738.

Ahidjo, N., Moanono, P., Boudem, C. and Kengne, F.L., 2024. Pharmaceutical residues in fish and macroinvertebrates around the wastewater treatment plant site at the University Teaching Hospital of Yaoundé, Cameroon. *Journal of Advances in Medical and Pharmaceutical Sciences*, 26(11), pp.66–77.

Alfarsi, A., Kumar, A., Gismelseed, A.M., Al Azkawi, A., Al Mahdouri, M., Al Mabsali, F.N. and Nugegoda, D., 2025. Pharmaceuticals and radiopharmaceuticals in wastewater treatment plants: insights from an Arabian Peninsula nation. *Environmental Science and Pollution Research*, pp.1–28.

Aljuboury, D.A.A., Palaniandy, P., Abdul Aziz, H.B. and Feroz, S., 2017. Degradation of total organic carbon (TOC) and chemical oxygen demand (COD) in petroleum wastewater by solar photo-Fenton process. *Global NEST Journal*, 19(3), pp.430–438.

Ayoub, M., 2022. Fenton process for the treatment of wastewater effluent from the edible oil industry. *Water Science & Technology*, 86(6), pp.1388–1401.

Ban, F.C., Zheng, X.T. and Zhang, H.Y., 2020. Photo-assisted heterogeneous Fenton-like process for treatment of PNP wastewater. *Journal of Water, Sanitation and Hygiene for Development*, 10(1), pp.136–145.

Bellouard, C., Kim, S., Ghanbaja, J., Wojcieszak, R., Canilho, N. and Pasc, A., 2024. Unraveling oxidation and spin states of a single Fe-based meso-macroporous silica catalyst in Fenton-like reaction by magnetic measurements. *The Journal of Physical Chemistry C*, 128(20), pp.8449–8457.

Table 5: CCD predicted optimum operating conditions and their experimental and CCD results.

Catalyst dosage [$g.L^{-1}$]	H_2O_2 concentration [mM]	pH	Time [min]	% COD removal	
				CCD (Pre.)	Test Run
0.68	65.28	4.9	86.81	76.07	74.11

Bravo-Suarez, J.J., Patil, B.S. and Pratt, S.R., 2025. In situ Raman spectroscopic study on the titania promotion of silica-supported tungsten catalysts for enhanced propylene metathesis. *Catalysis Today*, 447, p.115138.

Chen, W., Li, R.Y., Wang, C., Ji, M., Fu, L.W. and Satoshi, N., 2013. Advanced treatment of industrial wastewater by heterogeneous Fenton reaction using a novel composite catalyst. *Asian Journal of Chemistry*, 25(4), pp.3313–3317.

Chen, X., Yao, L., Xu, S., He, J., Li, N., Li, J., Liu, B., Zhu, Y., Chen, X., Wang, H. and Zhu, R., 2024. Electron transfer mediated photo-Fenton-like synergistic catalysis of Fe, Cu-doped MIL-101 coupled with Ag_3PO_4: quantitative evaluation and DFT calculations. *Environmental Pollution*, 351, p.124083.

Dai, W., Pang, J.W., Ding, J., Wang, Y.Q., Zhang, L.Y., Ren, N.Q. and Yang, S.S., 2023. Study on the removal characteristics and degradation pathways of highly toxic and refractory organic pollutants in real pharmaceutical factory wastewater treated by a pilot-scale integrated process. *Frontiers in Microbiology*, 14, p.1128233.

Deepa, R., Madhu, G., Thomas, R.M. and Achari, V.S., 2021. Removal of mefenamic acid from aqueous solution by Fenton process: optimization using response surface methodology with central composite design. *Nature Environment and Pollution Technology*, 20(5), pp.2061–2067.

Erasmus, E., Claassen, J.O. and Van Der Westhuizen, W.A., 2016. Catalytic wet peroxide oxidation of formic acid in wastewater with naturally-occurring iron ore. *Water SA*, 42(3), pp.442–448.

Faheem, M., Jiang, X., Wang, L. and Shen, J., 2018. Synthesis of Cu_2O–$CuFe_2O_4$ microparticles from Fenton sludge and its application in the Fenton process: the key role of Cu_2O in the catalytic degradation of phenol. *RSC Advances*, 8(11), pp.5740–5748.

Fischbacher, A., von Sonntag, C. and Schmidt, T.C., 2017. Hydroxyl radical yields in the Fenton process under various pH, ligand concentrations and hydrogen peroxide/Fe(II) ratios. *Chemosphere*, 182, pp.738–744.

Fu, Q., Malchi, T., Carter, L.J., Li, H., Gan, J. and Chefetz, B., 2019. Pharmaceutical and personal care products: from wastewater treatment into agro-food systems. *Environmental Science and Technology*, 53(24), pp.14083–14090.

Ghjair, A.Y. and Abbar, A.H., 2023. Optimization of Fenton process for removal of chemical oxygen demand (COD) from hospital wastewater using response surface methodology (RSM). *AIP Conference Proceedings*, 2787(1), p.040023.

González-Castaño, M., De Miguel, J.N., Sinha, F., Wabo, S.G., Klepel, O. and Arellano-Garcia, H., 2021. Cu supported Fe–SiO_2 nanocomposites for reverse water gas shift reaction. *Journal of CO_2 Utilization*, 46, p.101493.

Guerreiro, E.D., Gorriz, O.F., Rivarola, J.B. and Arrúa, L.A., 1997. Characterization of Cu/SiO_2 catalysts prepared by ion exchange for methanol dehydrogenation. *Applied Catalysis A: General*, 165(1–2), pp.259–271.

Hamieh, M., Tabaja, N., Chawraba, K., Hamie, Z., Hammoud, M., Tlais, S., Hamieh, T. and Toufaily, J., 2025. Visible light photo-Fenton with hybrid activated carbon and metal ferrites for efficient treatment of methyl orange (azo dye). *Molecules*, 30(8), p.1770.

Hu, Y., Zhou, Y., Ding, R., Ye, X., Chu, C., Liu, L.L., Tian, L., Jiang, X., Zhang, L.S., Zou, J.P. and Luo, S., 2025. Sustainable Fe and Cu sites double redox cycle boosting Fenton-like degradation of organic pollutants. *Environmental Science & Technology*, 59(31), pp.16812–16821.

Huilin, W., Saishengtai, G., Cheng, H. and Qin, Q., 2025. Enhancing Fenton oxidation for pharmaceutical wastewater. *International Journal of Agricultural and Environmental Information Systems*, 16(1), pp.1–15.

Jia, H., Lv, Q., Xia, Q., Hu, W. and Wang, Y., 2022. Tailoring the catalytic performance of Cu/SiO_2 for hydrogenolysis of biomass-derived 5-hydroxymethylfurfural to renewable fuels. *Frontiers in Chemistry*, 10, p.979353.

Jiang, S., Wu, C., Huang, Q., Yu, Y., Zhang, P., Wang, C., Ou, X. and Xu, M., 2026. Fe-Cu-loaded γ-Al_2O_3 as an efficient heterogeneous Fenton catalyst for the advanced treatment of petrochemical wastewater. *Water Cycle*, 7, pp.19–30.

Kaya, S. and Asci, Y., 2022. Heterogeneous Fenton process with Fe(III) based catalyst for treatment of textile industry wastewater. *Indian Journal of Chemical Technology*, 29(2), pp.166–173.

Khan, H.J., Ding, J., Qu, J., Sarrigani, G.V., Fitzgerald, P., Xu, X., Ghadi, A.E., Sui, Q., Tian, C., Cairney, J.M. and Wiley, D., 2025. Highly dispersed, single-atom cobalt, Fenton-like catalyst on microporous silica for efficient advanced oxidation process. *Applied Catalysis A: General*, 120469.

Kongkoed, P., Lertna, N., Athikaphan, P., Neramittagapong, A. and Neramittagapong, S., 2024. Enhancing catalyst stability: immobilization of Cu–Fe catalyst in sodium alginate matrix for methyl orange removal via Fenton-like reaction. *Heliyon*, 10(13), e33333.

Krupińska, I., 2024. Application of Fenton's reaction for removal of organic matter from groundwater. *Molecules*, 29(21), p.5150.

Ksibi, M., 2006. Chemical oxidation with hydrogen peroxide for domestic wastewater treatment. *Chemical Engineering Journal*, 119(2-3), pp.161–165.

Kumar, A., Prasad, B., Sandhwar, V.K. and Garg, K.K., 2021. Mechanistic insight into heterogeneous Fenton-like catalysis with M–Al_2O_3/SiO_2 (M = Fe, Co and Ni) for acrylonitrile mineralization from real ABS resin wastewater: optimization and toxicity assessment. *Journal of Environmental Chemical Engineering*, 9(3), p.105177.

Kumar, B.N., Anjaneyulu, Y. and Himabindu, V., 2011. Comparative studies of degradation of dye intermediate (H-acid) using TiO_2/UV/H_2O_2 and photo-Fenton process. *Journal of Chemical and Pharmaceutical Research*, 3(2), pp.718–731.

Kwan, W.P. and Voelker, B.M., 2002. Decomposition of hydrogen peroxide and organic compounds in the presence of dissolved iron and ferrihydrite. *Environmental Science & Technology*, 36(7), pp.1467–1476.

Li, J., Wei, Y., Liu, Q., Guan, H., Jiang, C. and Sun, X., 2025. Heterogeneous Fenton-like CuO-CoO_x/SBA-15 catalyst for organic pollutant degradation: synthesis, performance, and mechanism. *Frontiers in Chemistry*, 13, p.1552002.

Li, M., Song, J., Han, W., Yeung, K.L., Zhou, S. and Mo, C.H., 2023. Iron-organic frameworks as effective Fenton-like catalysts for peroxymonosulfate decomposition in advanced oxidation processes. *npj Clean Water*, 6(1), p.37.

Li, X., Liu, J., Rykov, A.I., Han, H., Jin, C., Liu, X. and Wang, J., 2015. Excellent photo-Fenton catalysts of Fe–Co Prussian blue analogues and their reaction mechanism study. *Applied Catalysis B: Environmental*, 179, pp.196–205.

Liu, X., Sang, Y., Yin, H., Lin, A., Guo, Z. and Liu, Z., 2018. Progress in the mechanism and kinetics of Fenton reaction. *MOJ Ecology and Environmental Sciences*, 3(1), pp.10–14.

Liu, X., Wang, L., Li, J., Li, R., He, R., Gao, W. and Yu, N., 2024. Preparation of heterogeneous Fenton catalysts Cu-doped MnO_2 for enhanced degradation of dyes in wastewater. *Nanomaterials*, 14(10), p.833.

Luo, Q., Wang, J., Wang, J., Shen, Y., Yan, P., Chen, Y. and Zhang, C., 2019. Fate and occurrence of pharmaceutically active organic compounds during typical pharmaceutical wastewater treatment. *Journal of Chemistry*, 2019(1), p.2674852.

Maekawa, J., Mae, K. and Nakagawa, H., 2014. Fenton- Cu^{2+} system for phenol mineralization. *Journal of Environmental Chemical Engineering*, 2(3), pp.1275–1280.

Martínez, F., Molina, R., Pariente, M.I., Siles, J.A. and Melero, J.A., 2017. Low-cost Fe/SiO_2 catalysts for continuous Fenton processes. *Catalysis Today*, 280, pp.176–183.

Mekki, S., Laichi, Y., Benourrad, F., Lagha, N., Chebout, R., Bachari, K. and

Saidi-Besbes, S., 2023. Copper triazole complex supported on Fe_3O_4@SiO_2 nanoparticles as eco-friendly nanocatalysts in solvent-free Biginelli reaction. *Applied Organometallic Chemistry*, 37(8), e7103.

Munnik, P., De Jongh, P.E. and De Jong, K.P., 2015. Recent developments in the synthesis of supported catalysts. *Chemical Reviews*, 115(14), pp.6687–6718.

Nam, Y., Nam, D., Myung, Y., Joo, J.H. and Kim, C., 2025. Novel ferromagnetic $CuFe_2O_4$/Cu as a highly active catalyst for microwave-Fenton-like reaction. *npj Clean Water*, 8(1), p.56.

Nath, A., Biswas, S. and Pal, A., 2022. A comprehensive review on BPA degradation by heterogeneous Fenton-like processes. *Water Science & Technology*, 86(4), pp.714–745.

Nebot, C., Falcon, R., Boyd, K.G. and Gibb, S.W., 2015. Introduction of human pharmaceuticals from wastewater treatment plants into the aquatic environment: a rural perspective. *Environmental Science and Pollution Research*, 22(14), pp.10559–10568.

Ngoc, K.H.P. and Vu, A.T., 2022. Simple preparation of the CuO- Fe_3O_4/silica composite from rice husk for enhancing Fenton-like catalytic degradation of tartrazine in a wide pH range. *Adsorption Science & Technology*, 2022, p.6454354.

Nguyen, T.B., Dong, C.D., Huang, C.P., Chen, C.W., Hsieh, S.L. and Hsieh, S., 2020. Fe-Cu bimetallic catalyst for the degradation of hazardous organic chemicals exemplified by methylene blue in Fenton-like reaction. *Journal of Environmental Chemical Engineering*, 8(5), p.104139.

Ning, J., Wang, M., Luo, X., Hu, Q., Hou, R., Chen, W., Chen, D., Wang, J. and Liu, J., 2018. SiO_2 stabilized magnetic nanoparticles as a highly effective catalyst for the degradation of basic fuchsin in industrial dye wastewaters. *Molecules*, 23(10), p.2573.

Omar, B.M., Zyadah, M.A., Ali, M.Y. and El-Sonbati, M.A., 2024. Pre-treatment of composite industrial wastewater by Fenton and electro-Fenton oxidation processes. *Scientific Reports*, 14(1), p.27906.

Pasciucco, E., Pasciucco, F., Panico, A., Iannelli, R. and Pecorini, I., 2025. Optimization of a Fenton-based process as a tertiary treatment of tannery wastewater through response surface methodology. *Journal of Water Process Engineering*, 69, p.106588.

Peralta-Ladino, Y.M., Molina, R. and Moreno, S., 2025. Novel synthesis of iron-based catalysts stabilized by oxygen defects on silica derived rice husk. *Surfaces and Interfaces*, 108035.

Phong, L.H. and Loc, N.X., 2025. Heterogeneous Fenton treatment of textile wastewater using rGO/nZVI: batch and flow column evaluation. *Water Science and Engineering*.

Pratiwi, J., Lin, J.Y., Mahasti, N.N., Shih, Y.J. and Huang, Y.H., 2021. Fluidized-bed synthesis of iron-copper bimetallic catalyst (FeIIICuI@SiO_2) for mineralization of benzoic acid in blue light-assisted Fenton process. *Journal of the Taiwan Institute of Chemical Engineers*, 119, pp.60–69.

Ren, Y., Shi, M., Zhang, W., Dionysiou, D.D., Lu, J., Shan, C., Zhang, Y., Lv, L. and Pan, B., 2020. Enhancing the Fenton-like catalytic activity of nFe_2O_3 by MIL-53(Cu) support: a mechanistic investigation. *Environmental Science & Technology*, 54(8), pp.5258–5267.

Ruziwa, D.T., Oluwalana, A.E., Mupa, M., Meili, L., Selvasembian, R., Nindi, M.M. and Chaukura, N., 2023. Pharmaceuticals in wastewater and their photocatalytic degradation using nano-enabled photocatalysts. *Journal of Water Process Engineering*, 54, p.103880.

Salehzadeh, F., Esmkhani, M., Zallaghi, M., Javanshir, S. and Dekamin, M.G., 2023. $CuFe_2O_4$@SiO_2@L-arginine@Cu(I) as a new magnetically retrievable heterogeneous nanocatalyst with high efficiency for 1,4-disubstituted 1,2,3-triazoles synthesis. *Scientific Reports*, 13(1), p.8675.

Sandhwar, V.K. and Prasad, B., 2017. A comparative study of electrochemical treatment of para-toluic acid (p-TA) from aqueous solution: process optimization and sludge analysis. *Water Conservation Science and Engineering*, 1(4), pp.257–270.

Sandhwar, V.K. and Prasad, B., 2017. Comparative study of electrocoagulation and electrochemical Fenton treatment of aqueous solution of benzoic acid (BA): optimization of process and sludge analysis. *Korean Journal of Chemical Engineering*, 34(4), pp.1062–1072.

Sandhwar, V.K. and Prasad, B., 2018. Comparison of electrocoagulation, peroxi-electrocoagulation and peroxi-coagulation processes for treatment of simulated purified terephthalic acid wastewater: optimization, sludge and kinetic analysis. *Korean Journal of Chemical Engineering*, 35(4), pp.909–921.

Sarrai, A.E., Hanini, S., Merzouk, N.K., Tassalit, D., Szabó, T., Hernádi, K. and Nagy, L., 2016. Using central composite experimental design to optimize the degradation of tylosin from aqueous solution by photo-Fenton reaction. *Materials*, 9(6), p.428.

Shao, S., Cui, J., Wang, K., Yang, Z., Li, L., Zeng, S., Cui, J., Hu, C. and Zhao, Y., 2022. Efficient and durable single-atom Fe catalyst for Fenton-like reaction via mediated electron-transfer mechanism. *ACS ES&T Engineering*, 3(1), pp.36–44.

Singh, C., Chaudhary, R. and Gandhi, K., 2013. Preliminary study on optimization of pH, oxidant and catalyst dose for high COD content: solar parabolic trough collector. *Iranian Journal of Environmental Health Science & Engineering*, 10(1), p.13.

Su, C., Cao, G., Lou, S., Wang, R., Yuan, F., Yang, L. and Wang, Q., 2018. Treatment of cutting fluid waste using activated carbon fiber supported nanometer iron as a heterogeneous Fenton catalyst. *Scientific Reports*, 8(1), p.10650.

Tajoli, F., Dolcet, P., Claas, S., Maliakkal, C.B., Wang, D., Kübel, C., Casapu, M., Fröba, M., Grunwaldt, J.D. and Gross, S., 2025. Confining the synthesis of palladium nanoparticles in mesoporous silicas for CO oxidation: the role of the support. *ACS Applied Nano Materials*, 8(7), pp.3289–3303.

Thomas, A., Gayathri, V.M., Pillai, S.P., Sankeerthana, M. and Mani, S., 2021. Treatment of pharmaceutical wastewater. *International Journal of Engineering Research and Technology*, 10, pp.733–736.

Thomas, N., Dionysiou, D.D. and Pillai, S.C., 2021. Heterogeneous Fenton catalysts: a review of recent advances. *Journal of Hazardous Materials*, 404, p.124082.

Tricoli, A., Righettoni, M., Krumeich, F., Stark, W.J. and Pratsinis, S.E., 2010. Scalable flame synthesis of SiO_2 nanowires: dynamics of growth. *Nanotechnology*, 21(46), p.465604.

Vainoris, M., Nicolenco, A., Tsyntsaru, N., Podlaha-Murphy, E., Alcaide, F. and Cesiulis, H., 2022. Electrodeposited Fe on Cu foam as advanced Fenton reagent for catalytic mineralization of methyl orange. *Frontiers in Chemistry*, 10, p.977980.

Walling, S.A., Um, W., Corkhill, C.L. and Hyatt, N.C., 2021. Fenton and Fenton-like wet oxidation for degradation and destruction of organic radioactive wastes. *npj Materials Degradation*, 5(1), p.50.

Wang, C., Zhang, W., Wang, J., Xia, P., Duan, X., He, Q., Sirés, I. and Ye, Z., 2024. Accelerating Fe(III)/Fe(II) redox cycling in heterogeneous electro-Fenton process via S/Cu-mediated electron donor-shuttle regime. *Applied Catalysis B: Environmental*, 342, p.123457.

Wang, N., Yang, Y., Gong, C., Liu, X., Wang, K., He, W., Li, C., Li, Z. and Li, L., 2025. Study of Fe/Cu composite Fenton-like catalyst in the treatment of antibiotic wastewater: preparation, application, degradation pathways and working mechanism. *Journal of Environmental Chemical Engineering*, 13(2), p.115926.

Xu, W., Zou, R., Jin, B., Zhang, G., Su, Y. and Zhang, Y., 2022. The ins and outs of pharmaceutical wastewater treatment by microbial electrochemical technologies. *Sustainable Horizons*, 1, p.100003.

Yang, L. and Xue, F., 2024. Treatment of antibiotic-containing pharmaceutical wastewater by the novel VUV/UV/Fenton process

at near-neutral pH. *International Journal of Environmental Science and Technology*, 21(4), pp.3889–3898.

Yuan, R., Xia, Y., Wu, X., He, C., Qin, Y., He, C. and He, X., 2022. Efficient advanced treatment of coking wastewater using O_3/H_2O_2/Fe-shavings process. *Journal of Environmental Chemical Engineering*, 10(2), p.107307.

Zhang, N., Zhang, G., Huang, T., Chong, S. and Liu, Y., 2017. Fe_3O_4 and $Fe_3O_4/Fe^{2+}/Fe^0$ catalyzed Fenton-like process for advanced treatment of pharmaceutical wastewater. *Desalination and Water Treatment*, 93, pp.100–108.

Zhao, J., Peng, R., Pan, Y. and Tao, Y., 2017. COD removal from phenol solution by heterogeneous Fenton reaction using Fe_2O_3/SiO_2 catalysts: effects of calcination temperature on the catalyst properties. *Indian Journal of Chemical Technology*, 24(4), pp.424–429.

Nature Environment and Pollution Technology
An International Quarterly Scientific Journal

p-ISSN: 0972-6268
(Print copies up to 2016)
e-ISSN: 2395-3454

Vol. 25 | No. 3 | Article ID D1863 | 2026

Original Research Paper

https://doi.org/10.46488/NEPT.2026.v25i03.D1863

Open Access Journal

Moringa oleifera as a Natural Coagulant-Flocculant for the Removal of Turbidity and Heavy Metals from the Caplina Channel

Dariella Sharyley Quintana-Calizaya, Efren Eugenio Chaparro-Montoya†, Javier Lozano-Marreros, Yessenia Danidtza Gomez-Aguilar, Keila Abigail Muñante-Carrillo and Diana Galeska Farfan-Pajuelo
Jorge Basadre Grohmann National University, Tacna, Peru
†Corresponding author: Efren E. Chaparro Montoya; echaparrom@unjbg.edu.pe

Abbreviation: Nat. Env. & Poll. Technol.
Website: www.neptjournal.com

Received: 29-08-2025
Revised: 23-10-2025
Accepted: 18-11-2025

Key Words:

Water treatment
Biocoagulant
Turbidity removal
Heavy metal removal
Caplina Channel

Citation for the Paper:

Quintana-Calizaya, D.S., Chaparro-Montoya, E.E., Lozano-Marreros, J., Gomez-Aguilar, Y.D., Muñante-Carrillo, K.A. and Farfan-Pajuelo, D.G., 2026. Moringa oleifera as a natural coagulant-flocculant for the removal of turbidity and heavy metals from the Caplina Channel. *Nature Environment and Pollution Technology*, 25(3), D1863. https://doi.org/10.46488/NEPT.2026.v25i03.D1863

Note: From 2025, the journal has adopted the use of Article IDs in citations instead of traditional consecutive page numbers. Each article is now given individual page ranges starting from page 1.

Copyright: © 2026 by the authors
Licensee: Technoscience Publications
This article is an open access article distributed under the terms and conditions of the Creative Commons Attribution (CC BY) license (https://creativecommons.org/licenses/by/4.0/).

ABSTRACT

Driven by the high costs, residuals, and potential health impacts associated with chemical coagulants, this study evaluated a more environmentally and socially compatible bioprocess: the use of saline-activated (1 M NaCl) *Moringa oleifera* seed powder as a coagulant–flocculant to clarify surface waters from the Caplina Channel (Tacna, Peru). Raw water was collected, and jar tests were conducted at 125, 250, 500, and 750 mg.L^{-1} (n = 3 per dose), measuring turbidity, electrical conductivity (EC), dissolved oxygen (DO), total dissolved solids (TDS), color, and dissolved metals (As, Cu, and Fe), in addition to a proximate analysis of the seeds. The optimal dose achieved 99.7% turbidity removal (from 3350 to 9.045 NTU) and reduced metals to As 0.005 mg.L^{-1} (95%), Fe < 0.3 mg.L^{-1} (94%), and Cu 0.045 mg.L^{-1} (78%), with a pH 5.5, EC 936 µS.cm^{-1}, DO 7.24 mg.L^{-1}, TDS 762 mg.L^{-1}, and color < 5 Pt/Co, meeting Peru's ECA-Agua Category 1–A2 criteria for waters treatable by conventional processes. Although the EC increased with the dose, it remained below 1600 µS.cm^{-1} at the optimal value. We highlight saline pretreatment and the activation of *M. oleifera* seed powder with 1 M NaCl as a high-efficiency clarification strategy. This strategy activates cationic proteins and increases the charge density of biopolymers, promoting particulate charge neutralization and metal-ion complexation/adsorption. This mechanism enables the simultaneous and high-efficiency removal of turbidity and metals using an accessible and sustainable biocoagulant suitable for settings with limited treatment infrastructure.

1. INTRODUCTION

Limited access to safe water persists across large regions of the world and is aggravated by organic, inorganic, and biological contamination of surface sources. In this context, turbidity is an operational indicator of sanitary risk because of its association with colloids and particles that transport contaminants (Eichhorn et al. 2022, Ogunshina et al. 2023, Silva & Oliveira 2024). Conventional clarification using mineral coagulants, such as aluminum sulfate, is effective; however, it has disadvantages related to cost, availability, and chemical residues, motivating the search for more sustainable alternatives (Solis et al. 2012, Macías et al. 2017, Mera-Alegria et al. 2016).

Plant-derived natural coagulants have demonstrated favorable cost-effectiveness, low toxicity, and renewability and have been used historically to clarify surface and groundwater (Aguirre et al. 2018, Banchon et al. 2016, Pastrana-Pacho et al. 2023, Hadadi et al. 2022). In particular, *Moringa oleifera* seeds are known for their cationic proteins that neutralize charge and promote interparticle "bridging," with reports of turbidity removal exceeding 90% and evidence of concurrent metal reduction (Silva & Oliveira 2024). Moreover, certain preparation conditions, such as dehusking and mortar grinding, improve efficiency at lower doses. An optimal dose of 30 mL.L^{-1} of coagulant solution prepared from dehusked seeds achieved turbidity removal efficiencies between 92% and 100%. The seed-processing method that yielded the

highest turbidity removal was manual mortar grinding, which outperformed blending (Silva & Oliveira 2024).

Nevertheless, a specific gap remains: few quantitative studies have evaluated the simultaneous removal of turbidity and dissolved metals using *Moringa* activated with NaCl. This saline activation (1 M NaCl) has a mechanistic rationale: it increases the extraction/activation of cationic proteins and the charge density of the biopolymer, favoring charge neutralization and bridging, which stabilize macroflocs and enable the binding/adsorption of metal ions. It also outperformed extracts obtained using water alone (Garcia et al. 2022, Hadadi et al. 2022). Despite this support, performance has been sparsely documented for coastal and high-Andean localities while verifying compliance with local regulatory guidelines.

Accordingly, this study quantitatively evaluated Moringa oleifera seed powder pretreated with 1 M NaCl as a coagulant–flocculant for surface water from the Caplina Channel (Tacna). Jar tests were conducted across a dose gradient (125–750 mg.L^{-1}), monitoring turbidity, electrical conductivity, dissolved oxygen, total dissolved solids, color, and dissolved metals (As, Cu, and Fe), and the results were benchmarked against Peru's ECA-Agua Category 1–A2 criteria. This provides local, mechanistically grounded evidence of the potential of saline-activated *Moringa* for simultaneous clarification and metal removal, which is relevant to contexts with constrained infrastructure and a need for low-cost treatment options.

2. MATERIALS AND METHODS

2.1. Collection, Conditioning, and Proximate Analysis of *Moringa oleifera* Seeds

Moringa oleifera seeds were collected from agricultural fields in the La Yarada–Los Palos district. A total of 1 kg of seeds was gathered, and only those in suitable conditions for the study were selected. Seed conditioning was performed as described by Arango & Martinez (2022). *Moringa oleifera* seeds were manually dehusked, and the dry cotyledons were ground in a mortar, oven-dried at 105 °C for 60 min according to Cabrera et al. (2018), and finally sieved through a No. 70 mesh (0.21 mm). Dehusked *Moringa oleifera* seeds were subjected to proximate analysis at the Universidad Nacional del Altiplano de Puno, in the laboratories of the School of Biology.

2.2. Coagulant Extraction from *Moringa oleifera* Seeds

One L of 1 M sodium chloride (NaCl) saline solution was prepared with distilled water (electrical conductivity 5 µS.cm^{-1}) to activate the seed components for the coagulation–flocculation process. Five grams of *Moringa oleifera* seed powder were weighed using a Taurus analytical balance and dispersed in 100 mL of 1 M NaCl. The mixture was vigorously agitated for 5 min to activate the coagulant with the prepared solution and allowed to stand for 3 min.

2.3. Jar Test

Jar tests were conducted following the method described by Feria et al. (2014), with modifications. In 2.0 L beakers containing Caplina Channel water, four doses of the natural coagulant obtained from *Moringa oleifera* seed powder (5% stock solution) were applied: 125, 250, 500, and 750 mg.L^{-1}. Each dose was evaluated in triplicate (n = 3), and in each test set, a blank (0 mg.L^{-1}) was run in parallel to estimate the percent improvement attributable to the coagulant according to the formula (relative to the initial value). The mixing

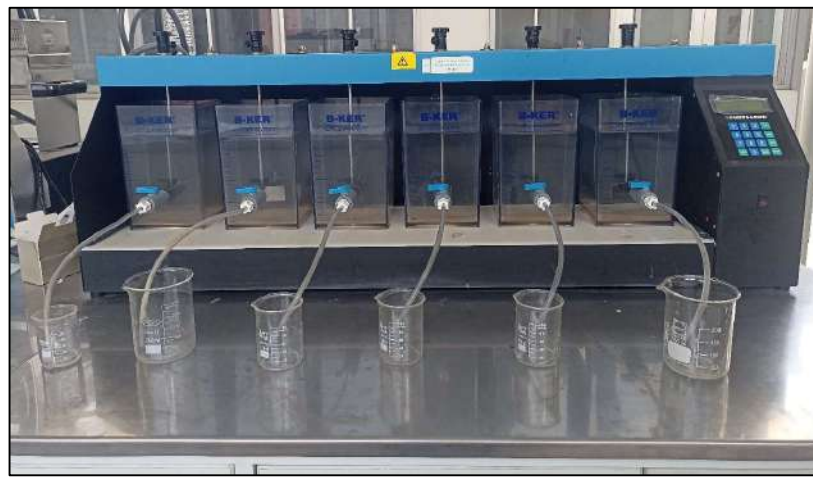


Fig. 1: Application of different doses of *Moringa oleifera* powder coagulant.

sequence was as follows: homogenization at 300 rpm for 2 min, rapid mixing at 250 rpm for 6 min, and slow mixing at 150 rpm for 6 min; sedimentation was then allowed for 90 min (Fig. 1).

The doses of the natural *Moringa oleifera* coagulant were determined using the following equation:

$$C_1V_1 = C_2V_2 \quad \ldots(1)$$

Where:

C1 = Concentration of the stock coagulant solution 50,000 mg.L^{-1}

V1 = Volume extracted from the stock solution

C2 = Coagulant dose applied in the experimental procedure

V2 = Volume of Caplina River water to be treated (2 L)

Turbidity removal efficiency was determined according to Chales et al. (2022) using the equation:

$$Removal\ (\%) = \frac{Initial\ turbidity - Final\ turbidity}{Initial\ turbidity} \quad \ldots(2)$$

2.4. Water Sampling and Analyses

A total of 88 L of water was collected from the Caplina River channel at coordinates E 374247, N 8016001 (UTM, WGS84), following procedures in the *National Protocol for Monitoring the Quality of Surface Water Resources*, approved by Resolution No. 010-2016-ANA (Autoridad Nacional del Agua [ANA] 2016). Analyses of water samples, before and after treatment, included turbidity (Turbidimeter Turbiquant® 1100 IR, MERCK), pH, electrical conductivity, and dissolved oxygen (multiparameter meter Hach HQ40D). Arsenic was determined by Standard Method 3114-C, APHA (atomic absorption spectrometry), while iron and copper were determined by Standard Method 3111-B, APHA (atomic absorption spectrometry).

2.5. Statistical Analysis

Variables with replication are reported as mean ± standard deviation (SD). When a variable had a single determination per treatment, the corresponding average was reported in the results. The coefficient of determination (R^2) was calculated to explore the dose–response relationship for turbidity removal. For turbidity, electrical conductivity, and dissolved oxygen, comparisons among treatments and the initial values were performed using one-way analysis of variance (ANOVA), followed by Tukey's multiple comparison test with $\alpha = 0.05$ to identify significant differences (Pastrana-Pacho et al. 2023). In the table, superscript letters/symbols indicate homogeneous groups according to Tukey's test (same letters = not significantly different, different letters = significantly different).

Table 1: Proximate analysis results of *Moringa oleifera* seeds.

Proximate analysis	Unit	*Moringa oleifera* seeds ± SD
Moisture	%	17.23 ± 0.30
Protein	%	17.23 ±0.30
Fat	%	32.92 ±0.51
Carbohydrates	%	28.77 ±0.08
Energy	kcal	480.28 ±0.67
Ash	%	3.88 ± 0.46

3. RESULTS

The proximate analysis of *Moringa oleifera* seeds (Table 1) indicated a high fat content (32.92%) and protein content (17.23%).

The highest turbidity removal efficiency (99.73%) was obtained with 125 mg.L^{-1} of *Moringa oleifera* seed powder (Fig. 2). In this study, doses between 125 and 750 mg.L^{-1} were evaluated; within this range, the relationship between dose and turbidity removal was inversely proportional. Beyond this point, higher doses of *Moringa oleifera* powder increased the turbidity removal efficiency.

Fig. 2 also shows the influence of *Moringa oleifera* powder concentration (mg.L^{-1}) on the electrical conductivity (EC, µS.cm^{-1}) of Caplina Channel water, exhibiting a directly proportional relationship ($R^2 = 0.9964$): as the coagulant dose increased, EC also increased.

Table 2 indicates that all physicochemical parameters analyzed met the maximum permissible values for waters that can be made potable with conventional treatment (Peru's Environmental Quality Standards, ECA, Category 1 – A2).

Electrical conductivity (EC) increased with coagulant dose ($R^2 \approx 0.996$), reflecting the higher ionic strength introduced by saline activation and the seed-derived ions. At the optimal dose, the final EC (936 µS.cm^{-1}) remained below the ECA-Agua Category 1–A2 threshold (1600 µS.cm^{-1}) and corresponded to TDS = 762 mg.L^{-1}, a range generally acceptable for palatability (< 1000 mg.L^{-1}, WHO). This supports practical acceptability while cautioning against the risk of overdose.

Dissolved oxygen (DO) increased from 4 to 7.24 mg.L^{-1} after treatment, which may be attributed to re-aeration during mixing (increased gas–liquid interfacial area) and lower turbidity/organic load, which reduces oxygen demand and improves light penetration, thereby favoring oxygen transfer.

4. DISCUSSION

The moisture content of *Moringa oleifera* seeds was 17.23% (Table 1), which is higher than that reported by Silva et al.

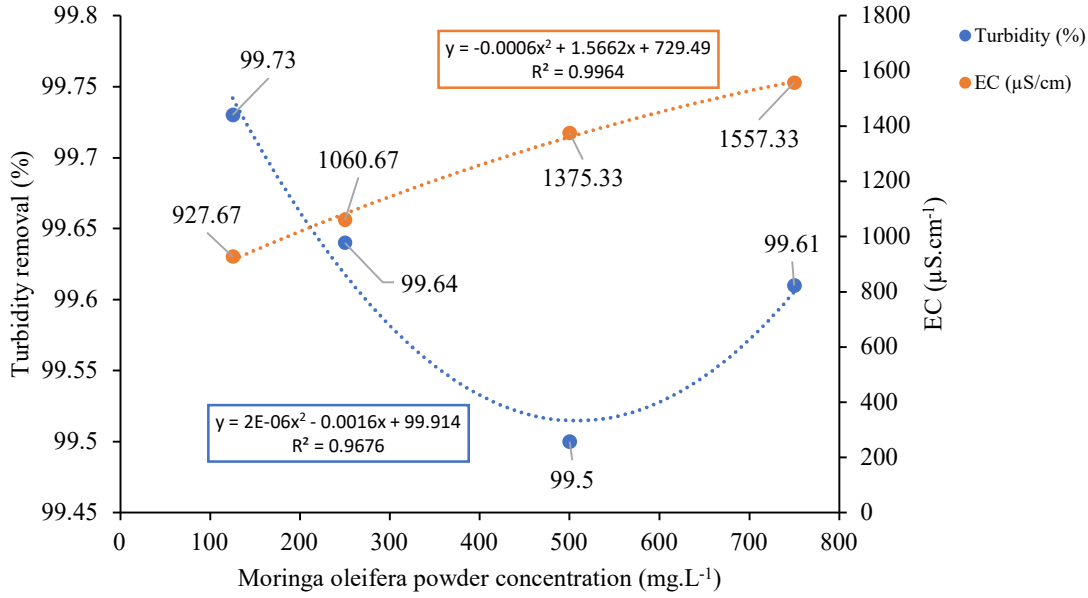


Fig. 2: Influence of *Moringa oleifera* seed-powder concentration (mg.L⁻¹) on turbidity removal (%) and electrical conductivity (µS.cm⁻¹) in Caplina Channel water.

Table 2: Comparison of water treated with Moringa oleifera against Peru's water ECA (Category 1 – A2).

Parameters	Caplina River water		Peruvian ECA for water, Category 1-A2	The treated water meets the requirements (Yes / No)
	Initial water ± SD	Treated water ± SD	Waters that can be made potable with conventional treatment	
Turbidity (NTU)	3350 [a] ±	9.045 [b] ±	100	Yes
pH	5.9 [a] ± 0.1	5.5 [b] ± 0.1	5.5 – 9.0	Yes
Electrical conductivity [µS. cm^{-1}]	1423 [a] ± 4.6	936 [b] ± 5.3	1 600	Yes
Dissolved oxygen [mg.L^{-1}]	±2.3	7.24 ± 1.2	≥ 5	Yes
Total dissolved solids [mg.L^{-1}]	-	762 ± 2.1	1 000	Yes
Color (Pt/Co)	100 ± 0.1	<5	100	Yes
As [mg.L^{-1}]	0.1 ± 0.01	<0.005	0.01	Yes
Cu [mg.L^{-1}]	0.2 ± 0.01	<0.045	2	Yes
Fe [mg.L^{-1}]	5 ± 0.01	<0.5	1	Yes

Note: One-way ANOVA, n = 3 per group: turbidity $F(1,4)= 7.46\times10^3$, pH $F(1,4)= 267$, EC $F(1,4)= 2.45\times10^3$, All with $a < 0.05$.
[ab] Different letters indicate significant differences according to the Tukey multiple range test, $p<0.05$.

(2018) (5.59% in seed cake). This difference is consistent with the matrix type: defatted seed cake typically shows lower residual moisture due to pretreatment and oil removal, whereas the whole seed retains a higher water content.

The literature indicates that *Moringa oleifera* contains proteins, carbohydrates, and other components in proportions that vary with the matrix and processing (Del Toro et al. 2016). In this study, the seeds contained 17.23% protein.

Several reports show higher values: Silva et al. (2018) reported 32.57% in salt-treated cake, Rubio (2019), 30.2% in raw seed flour, and Almora-Hernández et al. (2022), 37.23% in cake. Such discrepancies are expected because defatting/extraction tends to concentrate the protein fraction in the cake relative to the whole seed, and because the reporting basis (wet vs. dry) and particle size also influence analytical outcomes.

The fat content in seeds was 32.92%, which is below that reported by Rubio (2019) (41.36% in raw flour) and slightly lower than that reported by López (2019) (35.1% in seeds). These variations align with differences in cultivar/origin, maturity stage, and the analytical conditions.

Seeds contained 28.77% carbohydrates, higher than reported by Rubio (2019) (14.74% in raw flour), López (2019) (16.2%), and Alvarez (2016) (21.02% in cake). It should be noted that, in proximate analysis, carbohydrates by difference accumulate the uncertainty of the other components (moisture, protein, fat, and ash); thus, differences in any of these (and in the reporting basis) can carry over to the "carbohydrates" fraction.

The energy calculated for *Moringa oleifera* was 480.28 kcaL.100 g^{-1}, which is lower than that reported by López (2019) (533.5 kcaL.100 g^{-1} in seeds). This is consistent with the lower fat content observed here relative to that study, given that lipids contribute 9 kcaL.g^{-1} (vs. 4 kcaL.g^{-1} for protein and carbohydrates) and with the relatively higher moisture.

The ash content was 3.88%, similar to that reported by López (2019) (3.3%) and Alvarez (2016) (4.64% in cake). Other authors have reported higher values, for example, Almora-Hernández et al. (2022) (11.76%) and Silva et al. (2018) (7.11% in cake). These differences can be attributed to the matrix type (defatted cake can concentrate the relative mineral residue), geographical origin, and methodological variation.

Overall, the observed patterns are consistent with comparisons between whole seeds and cake/flour reported in the literature: defatting/extraction tends to increase protein and ash percentages and decrease fat relative to whole seeds, moisture and reporting basis conditions all fractions, and carbohydrates by difference reflect the accumulation of small variations in the other components (Silva et al. 2018, Del Toro et al. 2016, Rubio 2019, Almora-Hernández et al. 2022, López 2019, Alvarez 2016).

Turbidity quantifies the loss of water clarity due to suspended materials that attenuate light transmission (Marín-Velásquez & Arriojas-Tocuyo 2020). In this study, the 1 M NaCl-pretreated *Moringa oleifera* seed powder coagulant achieved 99.50–99.73% turbidity removal across the evaluated dose range. The literature shows variable efficiencies attributable to matrix, pretreatment, and operating conditions: Zea et al. (2024) reported 85%, Carrillo et al. (2020) obtained 87.3% with 1 N NaCl and, after Soxhlet defatting, 97.8%, consistent with our values, Eichhorn et al. (2022) reported up to 93% using *Moringa* seeds as a natural coagulant, and Zacarías (2019) reported 89–96% in Shullcas River surface water. These differences are consistent with the influence of each water's organic/colloidal load, biomass state (seed, flour, or defatted cake), saline activation, and variables such as pH, mixing regime, and settling time. In general, natural coagulants are regarded as options with lower direct toxicity and bioactive fractions (proteins, polysaccharides, and mucilages) (Castellanos & Martin 2020) and are proposed as alternatives to synthetic coagulants in specific contexts (Alva & Caballero 2022, Zea et al. 2024).

Mechanistically, cationic, water-soluble proteins from *Moringa* (pI > 10) promote charge neutralization and interparticle bridging, driving the formation of settleable flocs. This effect is activated by milling and dispersing the material in water (Arango et al. 2017, Castellanos & Martin 2020). Consistently, Hadadi et al. (2022) indicated that polysaccharides and proteins mediate bridging and neutralization, supporting turbidity removal. Saline extraction increases the availability of the active fraction, thereby increasing the coagulant potential for potabilization (Urrea-Florián & Torres-Benítez 2021). However, Garcia et al. (2022) noted that saline solutions can increase electrical conductivity and, at high doses, be associated with the cytotoxicity of the treated water; thus, it is advisable to delimit operational windows that maximize clarification without penalizing sensory or health quality. In our study, the minimum EC observed was 936 µS.cm^{-1} at 125 mg.L^{-1}, whereas Alvarez (2016) reported 1280 µS.cm^{-1} in a different matrix. This comparison suggests that the ionic contribution from activation and water composition governs the balance between efficiency and ionic strength.

Dissolved oxygen (DO) increased from 4 mg.L^{-1} in Caplina Channel water to 7.24 mg.L^{-1} after treatment with *Moringa oleifera*. This rise is consistent with mixing-induced re-aeration and reductions in turbidity and organic load, which decrease O_2 demand and improve transfer. In contrast, Muñoz et al. (2015) documented DO declines associated with pollution in the Zahuapan River, and contextualized that water quality and suspended/dissolved organics modulate DO behavior.

The total dissolved solids (TDS) content of the treated water was 762 mg.L^{-1}, which is higher than that reported

by Alvarez (2016) (511.33 $mg.L^{-1}$) for wastewater from passion fruit nectar production. This difference is reasonable, given the contrast in the matrices and ionic load. Dissolved organic matter spans a broad spectrum of species (from particles and colloids to macromolecules) that influence coagulation performance and global quality indicators (Fuentes et al. 2015). Additionally, Barrera-Escorcia and Namihira-Santillán (2004) observed associations between high bacterial concentrations, low salinity, and low DO in coastal waters, highlighting that physicochemical and biological conditions can co-vary. In our case, the increase in DO and reduction in turbidity after treatment were consistent with improved oxygen transfer in the short term.

The color in the channel water (100 Pt/Co) decreased to < 5 Pt/Co ($\approx$95% removal). This performance exceeds that reported by Vivas et al. (2022), who used a cationic polyelectrolyte extracted from *moringa* seeds and obtained 6.67–25.67% color removal. It also exceeded that of Moreira-Colletti et al. (2016) (84.2–87.3% in lake water with added humic substances and 60 min reaction). These differences can be attributed to the matrix nature (surface vs. wastewater), extraction/activation strategy, dose, and settling time (90 min in this study), all of which affect the apparent color removal.

The presence of heavy metals in aquatic ecosystems is chiefly associated with anthropogenic industrial sources, with impacts on human health and biotic/abiotic compartments (water, biota, and soils) through incorporation into the trophic web via environmental discharges. In this context, the cationic polyelectrolyte derived from *Moringa oleifera* is considered an organic, biodegradable input with lower reported toxicity than certain synthetic coagulants, making its evaluation as a contaminant-removal agent in water relevant.

In the Caplina channel, the initial As concentration was 0.10 $mg.L^{-1}$, and after treatment with *Moringa oleifera* seed powder, a 95% removal (0.005 $mg.L^{-1}$) was observed. In previous studies, Esparza et al. (2023) reported a 51% reduction with *Moringa oleifera* Lam, while Hernández-Sánchez et al. (2018) reported 82.11% efficiency using *Moringa oleifera* Lam seed flour. Mendoza (2018) further noted that removal increased with dose and that this bioadsorbent could match the effectiveness of aluminum sulfate under certain conditions. For copper, the initial concentration (0.20 $mg.L^{-1}$) decreased to 0.045 $mg.L^{-1}$ (77.5%), surpassing the performance of Elsergany (2023) with defatted *M. peregrina* extract at 200 $mg.L^{-1}$, which achieved a 66.5% reduction. For iron, the initial concentration (5 $mg.L^{-1}$) decreased to < 0.30 $mg.L^{-1}$ (94%), exceeding the results of Lagos (2017) (90.4% with *Moringa oleifera* Lam). Collectively, the physicochemical parameters analyzed after treatment with *Moringa oleifera* seed powder met the maximum limits for waters that can be made potable with conventional treatment (Category 1 – A2 of Peru's ECA for water).

The removal pathway is dual, integrating (i) adsorption/complexation and (ii) co-removal within organic flocs. Salt-activated *Moringa* concentrates contain cationic proteins (pI = 10–11, 6.5–30 kDa) that neutralize particles and negatively charged anions (e.g., arsenate), promoting aggregation via charge neutralization and bridging. At pH 6–8, the dominant As species are $H_2AsO_4^-/HAsO_4^{2-}$ (anionic), so the cationic fraction of *Moringa* favors their capture. For Fe/Cu (cations), interactions occur at anionic sites of organic matter ($–COO^-$, –OH) and/or via co-precipitation within flocs, completing the dual mechanism. At elevated ionic strengths, Na^+ can compete with divalent cations for negative sites and compress the double layer, which could reduce the uptake of Cd^{2+}/Pb^{2+}; hence, it is reasonable to optimize the salt type/strength (NaCl vs. KCl), dose, and pH to maximize the removal of these metals without compromising clarification efficiency.

Extraction with 1 M NaCl is key to obtaining a protein-rich cationic extract of *Moringa oleifera*. The salting-in phenomenon increases the solubility and recovery of these proteins, enabling operation at moderate doses and achieving high turbidity removal efficiencies. As summarized in Fig. 3, coagulation/flocculation with the saline extract is primarily based on electrostatic adsorption; cationic proteins neutralize the colloid charge and facilitate sedimentation. Notably, excessive doses can restabilize the particles via positive overcharging. For heavy metals, adsorption and chelation occur simultaneously. Hydroxyl, carboxyl, and amine groups in the biomass (defatted seeds, husks, and leaves) complex/adsorb cations via ion exchange, electrostatic attraction, and surface coordination.

pH is a determining factor because it regulates functional group protonation and, consequently, metal affinity. In slightly acidic to neutral–mildly alkaline media (pH 6–8), carboxyls tend to ionize, favoring cation sorption. At highly alkaline pH values, metal-hydroxide precipitation increases and can compete with adsorption. Therefore, avoiding extreme pH and operating within windows that maximize complexation and stable floc formation are advisable.

In summary, the 1 M NaCl-activated *Moringa* coagulant/flocculant integrates electrostatic adsorption (cationic proteins) with adsorption/chelation of metal ions (hydroxyl, carboxyl, and amine groups), mechanisms that act complementarily to remove turbidity and metals and metalloids in water treatment.

Finally, Konkobo et al. (2024) indicated that under test conditions with biodegradable, low-toxicity organic extracts,

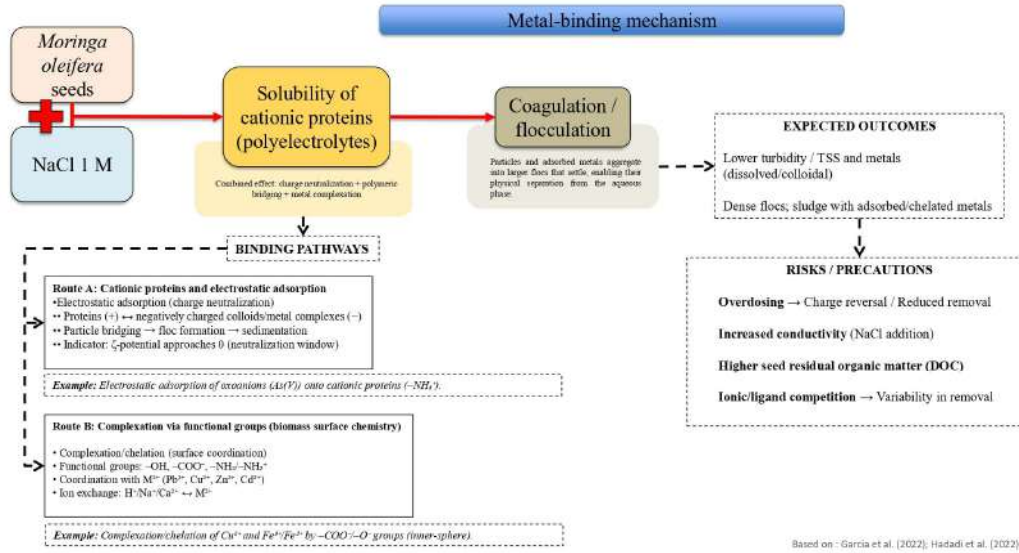


Fig. 3: Mechanism of metal binding by saline-extracted *Moringa oleifera* seed coagulant (1 M NaCl). Note. Saline extraction ("salting-in") increases the solubility of cationic polyelectrolytes, enabling (Route A) electrostatic charge neutralization/bridging and (Route B) complexation/ion exchange at –OH/–COO^-/–NH_2(–NH_3^+) sites, followed by flocculation and sedimentation.

the sanitary quality of treated water can meet physicochemical and microbiological parameters according to the WHO acceptability standards. While chemical coagulants such as aluminum sulfate effectively reduce turbidity, their use can be associated with costs and chemical residuals, as well as health and management considerations. In this study, 1 M NaCl was selected to enhance the extraction/activation of the cationic protein fraction (higher charge density), consistent with reports showing the better performance of saline *Moringa* extracts compared with water-extracted flours. In this framework, and as proposed by Zea et al. (2024), the use of organic products such as *Moringa oleifera* represents a biocoagulation alternative for water treatment, particularly in contexts seeking to reduce colloidal load and metals while maintaining acceptability criteria and regulatory compliance of the treated water.

5. CONCLUSIONS

This study demonstrated that Moringa oleifera seed powder, as a natural coagulant-flocculant, has a high potential for removing turbidity and metals and metalloids from Caplina Canal water in Tacna, Peru.

Proximate analysis of Moringa oleifera seeds indicated that they contained 17.3% protein, 17.3% moisture, 32.92% fat, and 3.8% ash, making them suitable as a natural coagulant. Likewise, the Caplina canal water had a pH of 5.9, electrical conductivity of 1423 $\mu S.cm^{-1}$, and turbidity of 3350 NTU.

The water treated with the natural coagulant-flocculant from Moringa oleifera had a final pH of 5.5, electrical conductivity of 936 $\mu S.cm^{-1}$, dissolved oxygen of 7.24 $mg.L^{-1}$, and turbidity of 9.045 NTU. Metals and metalloids such as arsenic (0.005 $mg.L^{-1}$), copper (0.045 $mg.L^{-1}$), and iron (< 0.3 $mg.L^{-1}$) were also present. These values are within the Environmental Quality Standards for water in category 1 – A2, which can be made potable with conventional treatment.

6. ACKNOWLEDGMENTS

This study is part of the undergraduate thesis of the first author, conducted in partial fulfillment of the requirements for the professional degree in Environmental Engineering. The author gratefully acknowledges the support of the Jorge Basadre Grohmann National University for providing access to laboratory facilities and extends special thanks to her advisor, Dr. Efren Eugenio Chaparro Montoya, for his guidance.

7. REFERENCES

Aguirre, S.E., Piraneque, N.V. and Cruz, R.K., 2018. Natural substances: Alternative for the treatment of water from the Magdalena River in Palermo, Colombia. Information Technology, 29(3), pp.59-70. [DOI]

Almora-Hernández, E., Leon-sánchez, G., Monteagudo-Borges, R., Campa-Huergo, C. and Rodríguez-Jiménez, E., 2022. Obtaining flour from Moringa oleifera seeds and its appropriate presentation for human consumption. *Chemical Technology*, 42(3), pp.576-589.

Alva, P.J. and Caballero, A.M., 2022. Influence of Dosage of Moringa Oleifera Seed Powder, Polyacrylamide and pH in the Physicochemical Treatment of Wastewater. Universidad Nacional del Santa, p.150.

Alvarez, H., 2016. Effect of Moringa (Moringa oleifera) Cake on Turbidity Removed from Wastewater from Passion Fruit Nectar Production. Universidad Nacional Agraria La Molina, p.95.

ANA, 2016. National Protocol for Monitoring the Quality of Surface Water Resources. Ministry of Agriculture and Irrigation, p.92.

Arango, R.S. and Martinez, A.W., 2022. Evaluation of the Effect of Moringa oleifera Seed on the Reduction of Turbidity and E. coli in the Coagulation Process for the Treatment of Natural Waters from the Shullcas River. Faculty of Chemical Engineering, p.85.

Arango, S., Ortega, W., Álvarez, A. and Medina, J., 2017. Evaluation of Moringa oleifera seed extract as a coagulant agent in the treatment of wastewater from a textile industry. *Journal of Applied Water Science*, 10(1), pp.1-33.

Banchon, C., Baquerizo, R., Muñoz, D. and Zambrano, L., 2016. Natural coagulation for the decontamination of industrial effluents. *UTE Focus*, 7(4), pp.111-126.

Barrera-Escorcia, G. and Namihira-Santillán, P.E., 2004. Microbiological contamination in the coastal zone of Akumal, Quintana Roo, Mexico. *Hydrobiology*, 14(1), pp.27-35.

Cabrera, N.C., Simancas, E.D.P. and Hernandez, A.R., 2018. Test of natural coagulants extracted from Ipomoea incarnata and Moringa oleifera in the purification of industrial wastewater in Cartagena de Indias. *Prospectiva*, 16(2), pp.94-99.

Carrillo, M., Collantes, U., Torres, C. and Gonzales, V., 2020. Evaluation of Moringa oleifera in the treatment of water with high turbidity and organic load. *Journal of Water Treatment*, 24(2), pp.119-127.

Castellanos, L.S. and Martin, M.A., 2020. Development of an Organic Coagulant from Moringa Seed for the Company Comercial DACETEX LTDA. Universidad América, pp.110.

Chales, G.G., Tihameri, B.S., Milhan, N.V.M., Koga-Ito, C.Y., Antunes, M.L.P. and Reis, A.G.D., 2022. Impact of Moringa oleifera seed-derived coagulants processing steps on physicochemical, residual organic, and cytotoxicity properties of treated water. *Water*, *14*(13), p.2058.

Del Toro, J.J., Carballo, A. and Rocha, L., 2016. Corn flour fortified with Moringa oleifera powder: Alternative to fight hunger in vulnerable populations. *Journal of Sciences*, 20(2), pp.77-86.

Eichhorn, C., Weckmüller, S. and Urban, W., 2022. Natural flocculant from a combination of Moringa oleifera seeds and cactus cladodes (Opuntia ficus-indica) to optimize flocculation properties. *Water*, 14(21), pp.3570. [DOI]

Elsergany, M., 2023. The potential use of Moringa peregrina seeds and seed extract as a bio-coagulant for water purification. *Water*, 15(15), p.2804. [DOI]

Esparza, C., Acosta, A., Bustos, D., Moreno, M., Ortega, J., Vega, I.H., Colin, J.C., Romero, G. and Mellado, R., 2023. Reduction of heavy metals using Moringa oleifera Lam. In: *ExpoIbero Primavera 2023 Proceedings*, pp.1-7.

Feria, J.J., Bermúdez, S. and Estrada, A.M., 2014. Efficiency of Moringa Oleifera seed as a natural coagulant for turbidity removal from the Sinú River. *Production + Clean*, 9(1), pp.9-22.

Fuentes, R.M., Ramos, J.A., Jimenez, M. del C. and Esparza, M., 2015. Characterization of dissolved organic matter in groundwater of the Toluca Valley by 3D fluorescence spectrophotometry. *International Journal of Environmental Contamination*, 31(3), pp.253-264.

Garcia, G., Siqueira, B., Moreira, N.V., Koga-Ito, C.Y., Pereira, M.L. and Gonçalves, A., 2022. Impact of Moringa oleifera seed-derived coagulants processing steps on physicochemical, residual organic, and cytotoxicity properties of treated water. *Water*, 14(13), p.2058. [DOI]

Hadadi, A., Imessaoudene, A., Bollinger, J.C., Assadi, A.A., Amrane, A. and Mouni, L., 2022. Comparison of four plant-based bio-coagulants performances against alum and ferric chloride in the turbidity improvement of bentonite synthetic water. *Water*, 14(20), p.3324. [DOI]

Hernández-Sánchez, M., Rivas-Zamora, H., Ventura-Bolaños, G., Carranza-Estrada, F., Palacios, D. and Bonilla de Torres, B., 2018. Evaluation of the effectiveness of Teberinto seed (Moringa oleifera Lam.) as a method for removal of arsenic and lead from water for human consumption. *Journal of Agro-environmental Sciences*, 7(1), pp.32-42.

Konkobo, F.A., Diao, M., Savadogo, P.W., Dakuyo, R., Roamba, N.E., Zongo, S. and Dicko, M.H., 2024. Reduction of malnutrition related to unsafe water consumption in developing countries: potabilization of surface water and traditional well water, with plant extracts. *International Journal of Environmental Research and Public Health*, 21(5), p.519. [DOI]

Lagos, A., 2017. Adsorption of Cadmium, Iron and Lead in Artificial Water Using Moringa oleifera. Universidad San Francisco de Quito, p.70.

López, E.E., 2019. Industrialization of Moringa Applied to the Climatic Conditions of Piura, Peru-2019. Universidad de Piura, p.125.

Macías, M., Domínguez, Y., Muñoz, S., Álvarez, B., Santana, E. and García, D.T., 2017. Use of Moringa oleifera seeds in the treatment of liquid waste. *Hydraulic and Environmental Engineering*, 38(2), p.45-56.

Marín-Velásquez, T.D. and Arriojas-Tocuyo, D.D.J., 2020. Turbidity removal from water by filtration using coconut husk (Cocos nucífera) at laboratory level. *ION Journal*, 33(2), pp.99-110. [DOI]

Mendoza, H., 2018. Bioadsorption of Arsenic with Moringa Seed. Universidad Autónoma Agraria Antonio Narro, pp.90.

Mera-Alegria, C.F., Gutiérrez-Salamanca, M., Montes-Rojas, C. and Paz-Concha, J.P., 2016. Effect of Moringa oleifera on wastewater treatment in Cauca, Colombia. *Biotechnology in the Agricultural and Agroindustrial Sector*, 14(2), p.100. [DOI]

Moreira-Colletti, G., Pereira-Tangerino, E. and Sánchez-Ortiz, I., 2016. Application of electrolysis with addition of salts for color removal in water purification. *Journal of Water Treatment Technologies*, 25(43), p.4.

Muñoz, H., Orozco, S., Vera, A., Suárez, J., García, E., Neria, M. and Jiménez, J., 2015. Relationship between dissolved oxygen, rainfall and temperature: Zahuapan River, Tlaxcala, Mexico. *Water Technology and Sciences*, 6(5), pp.59-74.

Ogunshina, M.S., Abioye, O.M., Adeniran, K.A. and Olasehinde, D.A., 2023. Moringa oleifera coagulation characteristics in wastewater treatment in a university dormitory. *Nigerian Journal of Environmental Engineering*, 22(2), pp.699-707.

Pastrana-Pacho, A., Solis-Silvan, R., Ávila-Lázaro, I., Laines-Canepa, J.R. and Sánchez-Díaz, B., 2023. Coagulation of wastewater using a mixture of Crotalaria longirostrata powder and aluminum sulfate. *Technology in March*, 36(2), pp.135-142. [DOI]

Rubio, D.A., 2019. Obtaining Functional Flour from Moringa Seeds (M. Oleifera) by Extrusion. Process Optimization. Universidad Autónoma de Sinaloa, p.110.

Silva, J.R. and Oliveira, D.S., 2024. Water treatment with clean technologies using Moringa oleifera seeds in alternative low-cost clarification units. *Clean Technologies*, 6(2), pp.625-645. [DOI]

Silva, M., Cibej, F., Salvá, B., Guevara, A. and Pascual, G., 2018. Effect of debittering of Moringa oleifera seed cake on its proximal composition and its nutritional and toxicological profile. *Scientia Agropecuaria*, 9(2), pp.247-257. [DOI]

Solis, R., Laines, J.R. and Hernández, J.R., 2012. Mixtures with coagulant potential to clarify surface water. *International Journal of Environmental Contamination*, 28(3), pp.229-236.

Urrea-Florián, S. and Torres-Benítez, A., 2021. Evaluation of Moringa oleifera Lam. seeds present in urban forests as a coagulant-flocculant

for water treatment. *Proceedings of the 2nd International Electronic Conference on Plant Sciences*, 4(1), p.1. [DOI]

Vivas, H.T., Calderón, J.M., Mendoza, L.G. and Cedeño, J.G., 2022. Removal of pollutants in wastewater using the cationic polyelectrolyte extracted from Moringa oleifera seeds. *Hydraulic and Environmental Engineering*, 43(2), pp.84-96.

Zacarías, J.D., 2019. Efficiency of Moringa (Moringa Oleifera) Seed for the Treatment of Surface Water from the Shullcas River during the Period 2018. Universidad Alas Peruanas, pp.80.

Zea, A.G., Gutiérrez, J. and Caballero, P., 2024. Use of Moringa oleifera as a natural coagulant in the reduction of water turbidity in mining activities. *Water*, 16(16), pp.2315. [DOI]

Nature Environment and Pollution Technology
An International Quarterly Scientific Journal

p-ISSN: 0972-6268
(Print copies up to 2016)
e-ISSN: 2395-3454

Vol. 25 | No. 3 | Article ID B4395 | 2026

Original Research Paper

https://doi.org/10.46488/NEPT.2026.v25i03.B4395

Open Access Journal

Amelioration of Cadmium-Induced Stress in Tomato (*Solanum lycopersicum*) Using Gasotransmitters: A Combined Approach to Enhancing Antioxidant Defense and Growth Resilience

Smita Raut[1], Pragnya Paramita Sahoo[2], Prabhat Kumar Srivastava[3] and Sangeeta Raut[2]†

[1]Department of Botany, Dr. Rammanohar Lohia Avadh University, Ayodhya-224001, UP, India
[2]Centre for Biotechnology, School of Pharmaceutical Sciences, Siksha 'O' Anusandhan (Deemed to be University), Bhubaneswar-751003, Odisha, India
[3]K.S. Saket Post-Graduate College, Ayodhya-224123, UP, India
†Corresponding author: Prabhat Kumar Srivastava; prabhatsrivastava.au@gmail.com

Abbreviation: Nat. Env. & Poll. Technol.
Website: www.neptjournal.com

Received: 15-09-2025
Revised: 25-11-2025
Accepted: 29-11-2025

Key Words:

Cadmium toxicity
Oxidative stress
Nitric oxide
Hydrogen sulfide
Antioxidant defense
Tomato
Gasotransmitters

Citation for the Paper:

Raut, S., Sahoo, P.P., Srivastava, P.K. and Raut, S., 2026. Amelioration of cadmium-induced stress in tomato (*Solanum lycopersicum*) using gasotransmitters: A combined approach to enhancing antioxidant defense and growth resilience. *Nature Environment and Pollution Technology*, 25(3), B4395. https://doi.org/10.46488/NEPT.2026.v25i03. B4395

Note: From 2025, the journal has adopted the use of Article IDs in citations instead of traditional consecutive page numbers. Each article is now given individual page ranges starting from page 1.

Copyright: © 2026 by the authors
Licensee: Technoscience Publications
This article is an open access article distributed under the terms and conditions of the Creative Commons Attribution (CC BY) license (https://creativecommons.org/licenses/by/4.0/).

ABSTRACT

Cadmium (Cd) toxicity is a major environmental stressor that adversely affects plant growth, photosynthesis, and metabolism, causing oxidative damage and yield loss. This study investigates the role of nitric oxide (NO) and hydrogen sulfide (H_2S) in mitigating Cd-induced stress in *Solanum lycopersicum* by analyzing growth parameters, oxidative stress markers, antioxidant enzyme activity, and physiological responses. Tomato seedlings exposed to Cd (20 µM $CdCl_2$) exhibited severe growth inhibition, leaf chlorosis, chlorophyll degradation, and increased oxidative stress. Exogenous application of NO (sodium nitroprusside) and H_2S (sodium hydrosulfide), individually and in combination, significantly alleviated Cd toxicity. The combined NO + H_2S treatment showed the highest increase in shoot and root length (~60% over Cd-stressed plants), improved chlorophyll and carotenoid content (87% restoration to control levels), and reduced oxidative damage, indicated by lower malondialdehyde (MDA) (40%) and H_2O_2 (55%) accumulation. Antioxidant enzyme activities (SOD, CAT, APX, POD) were significantly upregulated, enhancing reactive oxygen species (ROS) detoxification. Additionally, proline accumulation (~4-fold increase) and protein content (~30% restoration) were improved, suggesting better osmotic balance and metabolic stability. NO and H_2S mitigate Cd stress by reducing oxidative damage, boosting antioxidant defenses, and enhancing resilience. Their combined action highlights gasotransmitter-based strategies for developing Cd-tolerant crops and promoting sustainable agriculture in metal-contaminated soils.

1. INTRODUCTION

Environmental stress is a major constraint on agricultural productivity, significantly affecting plant growth, metabolism and yield. Among various environmental challenges, heavy metal contamination has become a pressing issue due to rapid industrialization, mining, and excessive use of chemical fertilizers (Sodango et al. 2018). Heavy metals such as cadmium (Cd), mercury (Hg), lead (Pb), and arsenic (As) accumulate in agricultural soils, leading to toxic effects on plants and reducing overall food security (Sana et al. 2025). Cadmium, a highly toxic and non-essential metal, is particularly concerning due to its strong bioaccumulation and non-degradable nature. It disrupts critical physiological and biochemical processes in plants, including nutrient uptake, photosynthesis, and oxidative balance, ultimately impairing plant growth and development (Zhang et al. 2024).

Cadmium toxicity induces oxidative stress by triggering the overproduction of reactive oxygen species (ROS), leading to cellular damage through lipid peroxidation, protein oxidation, and DNA fragmentation (Zhang et al. 2020). Additionally, Cd exposure inhibits photosynthesis by degrading chlorophyll, reducing stomatal

conductance, and impairing the photosynthetic electron transport chain (Hasanuzzaman et al. 2019). Studies have also reported Cd-induced mitochondrial dysfunction, which disturbs ATP production and accelerates programmed cell death (Asgher et al. 2017). Prolonged Cd stress manifests as leaf chlorosis, root browning, reduced biomass accumulation, and overall metabolic disruption, severely affecting plant viability and productivity (Hosseini et al. 2025).

To counteract Cd toxicity, plants activate defense mechanisms such as the antioxidant enzyme system and stress-responsive signaling pathways. Recent studies suggest that gasotransmitters, including nitric oxide (NO) and hydrogen sulfide (H_2S), play crucial roles in enhancing plant resilience against abiotic stress (Shivaraj et al. 2020). NO is a key signaling molecule involved in various physiological processes, including antioxidant regulation, nutrient homeostasis and stress gene activation (Jiading et al. 2005). Research indicates that NO mitigates Cd-induced oxidative stress by scavenging ROS, enhancing antioxidant enzyme activities, and regulating metal ion transport (Leng et al. 2024). For instance, the exogenous application of sodium nitroprusside (SNP), a NO donor, has been shown to enhance Cd tolerance in plants by reducing lipid peroxidation and maintaining redox homeostasis (Bera et al. 2023).

Similarly, H_2S has emerged as a crucial endogenous gasotransmitter that plays a significant role in plant growth, stomatal regulation, and stress adaptation. Studies indicate that H_2S enhances plant defense against Cd toxicity by modulating antioxidant enzyme activities, reducing ROS accumulation, and improving photosynthetic efficiency (Li et al. 2022). Additionally, H_2S interacts with NO and other signaling molecules, such as hydrogen peroxide (H_2O_2), to regulate stress responses and mitigate cellular damage (Zhou et al. 2025). Recent findings suggest that NO and H_2S exhibit a combined role in preventing programmed cell death (PCD) under heavy metal stress, primarily through ROS inhibition and enhanced antioxidant defense (Xu et al. 2024).

Tomato (*Solanum lycopersicum*) serves as an ideal model for studying heavy metal toxicity and plant stress responses due to its high sensitivity to environmental stressors. Additionally, it is an economically significant crop, valued for its nutritional properties, including high levels of vitamins A, C, and E, along with essential minerals such as calcium, phosphorus, and iron (Sumalan et al. 2020). Moreover, tomato is a rich source of lycopene, a potent antioxidant known for its anti-carcinogenic properties and potential role in mitigating oxidative damage (Raja et al. 2023).

Therefore, this study aims to investigate the protective effects of exogenous NO and H_2S application in alleviating Cd-induced stress in tomato plants. The research evaluates the physiological and biochemical impacts of Cd toxicity and explores the combined interactions between NO and H_2S in enhancing plant stress tolerance. Understanding the molecular mechanisms underlying gasotransmitter-mediated stress responses will provide valuable insights into improving crop resilience in Cd-contaminated environments, thereby contributing to sustainable agricultural practices.

2. MATERIALS AND METHODS

2.1. Plant Material and Growth Conditions

Tomato (*Solanum lycopersicum*) plants were selected for this study due to their high sensitivity to environmental stress and nutritional significance. Seeds were procured from a commercial source. 2% (v/v) sodium hypochlorite (NaOCl) solution was used to surface-sterilize the seeds for five minutes prior to sowing, after which they were thoroughly rinsed with sterile distilled water. The sterilized seeds were then germinated in a growth chamber under controlled conditions: temperature, 25 ± 2°C; relative humidity, 60–70%; photoperiod, 16-h light/8-h dark cycle; light intensity, 250 μmol $m^{-2}.s^{-1}$; growing medium, washed sand in plastic pots; and regular watering at fixed intervals. After two weeks of growth, uniform seedlings were selected for further experimentation.

For all experiments, $n = 3$ refers to three independent biological replicates, with each biological replicate consisting of three plants grown under identical conditions. For biochemical assays, three fully expanded leaves were collected from the second or third node of each plant within each biological replicate. Samples from different biological replicates were processed independently and were not pooled. Each biochemical assay was performed with three technical replicate readings from each extract.

The experiment was conducted in two phases. In Phase I, two-week-old seedlings were subjected to Cd stress for seven days, followed by foliar application of gasotransmitters for an additional seven days. In Phase II, after completion of the treatments, the plants were maintained for 80 additional days to evaluate early biochemical and physiological responses.

2.2. Cadmium Stress Exposure

To induce cadmium toxicity, tomato seedlings were exposed to cadmium chloride ($CdCl_2$) at a concentration of 20 μM. The $CdCl_2$ solution was administered through root irrigation, and the seedlings were maintained under these conditions for seven days. Visual stress symptoms, including leaf chlorosis, reduced growth, and root damage, were recorded.

2.3. Gasotransmitter Treatments

To assess the ameliorative effects of nitric oxide (NO) and hydrogen sulfide (H_2S), two exogenous treatments were applied following seven days of Cd stress. For the NO treatment, sodium nitroprusside (SNP, 100 µM) was used as an NO donor, whereas sodium hydrosulfide (NaHS, 100 µM) was used as an H_2S donor for the H_2S treatment. Moreover, for the combined treatment (NO + H_2S), a mixture of SNP (100 µM) and NaHS (100 µM) was applied to evaluate their combined effects. Each treatment was administered via foliar spray once daily for seven days, and the plants were maintained under the same growth conditions.

Plants grown under normal conditions without Cd exposure served as the control group. Plants exposed to $CdCl_2$ without any protective treatment served as the Cd-stressed control group. After seven days of treatment, all plants were transplanted into 3 L plastic pots (diameter: 15 cm, height: 20 cm) filled with a sand:soil:compost mixture (1:1:1). The plants were maintained for 80 days in a controlled greenhouse under the following conditions: temperature, 25 ± 3°C; relative humidity, 60–70%; and natural photoperiod. Growth parameters, including shoot length, root length, fresh biomass, and dry biomass, were recorded at the final harvest (80 days).

2.4. Physiological and Biochemical Assessments

To evaluate the effectiveness of NO and H_2S in mitigating cadmium stress, several physiological and biochemical parameters were analyzed.

2.4.1. Morphological and Growth Analysis

Root length (RL) and shoot length (SL) were measured using a meter scale. The root length-to-shoot length ratio was also calculated. Biomass accumulation (g) patterns were assessed using the formulae modified by Hunt (1982).

Eighty days after the commencement of the experiment, plants were harvested and washed with sterile distilled water. The fresh mass (FM) of shoots and roots was recorded using a digital balance after blotting excess moisture. Dry mass (DM) was determined by drying the samples in a hot-air oven at 80˚C for 48 h, followed by weighing using a digital balance.

2.4.2. Photosynthetic Pigment Analysis

For pigment extraction, 20 mg of fresh leaf tissue from both treated and control plants was cut into small pieces and homogenized in 5 mL of 80% (v/v) acetone. The homogenate was centrifuged at 12,000 × g for 10 min, after which the pellet was resuspended in 80% acetone until it became colorless. The absorbance of the supernatant was measured using a Shimadzu UV-1780 UV–Vis spectrophotometer at 663.2, 646.5, and 470 nm. The concentrations of chlorophyll a (Chl a), chlorophyll b (Chl b), and total carotenoids (Car) were determined using the following formulae (1, 2, and 3) described by Lichtenthaler (1987):

$$Chl\ a\ (\mu g.mL^{-1}) = 12.25\ A_{663.2} - 2.79\ A_{646.5} \quad \ldots(1)$$

$$Chl\ b\ (\mu g.mL^{-1}) = 21.50\ A_{646.5} - 5.10\ A_{663.2} \quad \ldots(2)$$

$$Car\ (\mu g.mL^{-1}) = [1000\ A_{470} - 1.82\ (Chla) - 85.02\ (Chlb)]/198 \quad \ldots(3)$$

Pigment concentrations calculated in $\mu g.mL^{-1}$ were converted to $mg.g^{-1}$ using:

Pigment ($mg.g^{-1}$) = [Pigment ($\mu g.mL^{-1}$) × extraction volume (mL)]/ [1000× tissue fresh weight(g)]

2.5. Oxidative Stress Markers

2.5.1. Lipid Peroxidation Assay (MDA Content Measurement)

Lipid peroxidation was assessed by measuring malondialdehyde (MDA) content using the thiobarbituric acid (TBA) reaction method (Heath & Packer, 1968). Fresh leaf tissue (0.5 g) was homogenized in 5 mL of 0.1% (w/v) trichloroacetic acid (TCA) and centrifuged at 12,000 × g for 15 min at 4°C. The supernatant was mixed with 0.5% TBA prepared in 20% TCA and incubated for 20 min at 95°C, followed by rapid cooling on ice. Absorbance was measured at 532 nm and corrected at 600 nm. MDA content was expressed as nmol MDA g^{-1} fresh weight (FW), calculated using an extinction coefficient of 155 $mM^{-1}.cm^{-1}$.

2.5.2. Hydrogen Peroxide (H_2O_2) Quantification

Hydrogen peroxide (H_2O_2) accumulation was determined following the method of Velikova et al. (2000). Leaf tissue (0.5 g) was homogenized in 5 mL of 0.1% (w/v) TCA and centrifuged at 12,000 × g for 15 min at 4°C. The supernatant was reacted with 1 M KI prepared in a 10 mM potassium phosphate buffer (pH 7.0). Absorbance was measured at 390 nm, and H_2O_2 content was quantified using a standard curve and expressed as µmol H_2O_2 g^{-1} FW.

2.6. Antioxidant Enzyme Activity Assays

All enzyme activities were measured at 25°C using a UV–visible spectrophotometer.

2.6.1. Superoxide Dismutase (SOD) Activity

SOD activity was determined based on its ability to inhibit the photoreduction of nitroblue tetrazolium (NBT) (Beauchamp & Fridovich, 1971). Enzyme extracts were prepared by homogenizing 0.5 g of leaf tissue in 3 mL of ice-cold 50 mM phosphate buffer (pH 7.8) containing 1% PVPP, followed by centrifugation at 12,000 × g for 20 min at 4°C. The

reaction mixture contained 50 mM phosphate buffer, 13 mM methionine, 75 µM NBT, 10 µM EDTA, 2 µM riboflavin, and enzyme extract in a total volume of 1 mL. The reaction was carried out at 25°C, and absorbance was measured at 560 nm. SOD activity was expressed as U mg^{-1} protein.

2.6.2. Catalase (CAT) Activity

Catalase (CAT) activity was determined by monitoring the decomposition of H_2O_2 at 240 nm according to Aebi (1984). The reaction mixture (1 mL) contained 50 mM phosphate buffer (pH 7.0) and 10 mM H_2O_2. CAT activity was calculated using an extinction coefficient of 39.4 M^{-1} cm^{-1} and expressed as µmol H_2O_2 decomposed min^{-1} mg^{-1} protein.

2.6.3. Ascorbate Peroxidase (APX) Activity

APX activity was determined by measuring the oxidation of ascorbate at 290 nm following Nakano and Asada (1981). The reaction mixture (1 mL) contained 50 mM phosphate buffer (pH 7.0), 0.5 mM ascorbic acid, and 0.1 mM H_2O_2. Absorbance was recorded at 290 nm, and APX activity was expressed as µmol ascorbate oxidized min^{-1} mg^{-1} protein, using an extinction coefficient of 2.8 mM^{-1} cm^{-1}.

2.6.4. Peroxidase (POD) Activity

Peroxidase (POD) activity was determined using guaiacol as a substrate following the method of Chance and Maehly (1955). The reaction mixture (1 mL) contained 50 mM phosphate buffer (pH 7.0), 20 mM guaiacol, and 10 mM H_2O_2. The increase in absorbance at 470 nm was recorded, and POD activity was expressed as ΔA470 min^{-1} mg^{-1} protein using an extinction coefficient of 26.6 mM^{-1} cm^{-1}.

2.7. Protein Estimation

Total protein content in enzyme extracts was determined using the Bradford method (Bradford, 1976), with bovine serum albumin (BSA) as the standard.

2.8. Proline Estimation

Proline content was estimated according to Bates et al. (1973). Leaf tissue (0.5 g) was homogenized in 10 mL of 3% (w/v) sulfosalicylic acid and centrifuged. Then, 2 mL of the supernatant was reacted with 2 mL of acid ninhydrin and 2 mL of glacial acetic acid, followed by incubation at 100°C for 1 h. The reaction was terminated on ice. The chromophore was extracted using 4 mL of toluene, and absorbance was measured at 520 nm using toluene as a blank. Proline concentration was calculated from a standard curve and expressed as µmoL.g^{-1} FW.

2.9. Statistical Analysis

All experiments were conducted with at least three independent biological replicates (n = 3). Data were analyzed using one-way analysis of variance (ANOVA), followed by Tukey's HSD post hoc test ($p < 0.05$) to determine significant differences among treatments. Results are presented as mean ± standard deviation (SD). Statistical analysis was performed using SPSS software, and graphs were generated using GraphPad Prism 8. A summary of treatment means and representative statistical indicators is provided in Supplementary Table S1.

3. RESULTS

The present study investigates the role of NO and H_2S in mitigating Cd-induced stress in *Solanum lycopersicum* plants. The results are analyzed in terms of growth parameters, oxidative stress markers, antioxidant enzyme activity, and physiological responses to evaluate the protective effects of gasotransmitters against Cd toxicity.

3.1. Effect of Cd and Gasotransmitters on Plant Growth and Biomass

3.1.1. Morphological Observations

Cd exposure caused significant growth inhibition in tomato seedlings (Fig. 1a). Plants exhibited leaf chlorosis, stunted growth, root browning, and reduced shoot elongation after seven days of Cd treatment (Fig. 1b). In contrast, plants treated with NO and H_2S individually, as well as in combination (NO + H_2S), showed notable improvements in growth parameters compared to Cd-stressed plants (Fig. 1c–e). NO and H_2S treatments increased shoot length by 11.48 cm and 10.66 cm, respectively. In contrast, the combined NO + H_2S treatment enhanced shoot length by 13.12 cm (Fig. 2a). Similarly, NO and H_2S treatments increased root length by 5.74 cm and 5.33 cm, respectively. In comparison, the combined treatment increased root length by 7.0 cm (Fig. 2b). Overall, the NO + H_2S treatment resulted in approximately 60% improvement in both shoot and root length compared with Cd-stressed plants. Fig.s 2c and 2d show higher fresh and dry biomass, respectively, indicating improved water retention and metabolic activity. Moreover, reduced leaf chlorosis suggests enhanced chlorophyll stability. These findings indicate that exogenous application of NO and H_2S enhances plant tolerance to Cd stress, potentially by improving nutrient uptake and reducing oxidative stress.

3.2. Effect of NO and H_2S on Photosynthetic Pigments

3.2.1. Chlorophyll and Carotenoid Content

Cd-stressed plants exhibited a significant reduction ($p < 0.05$) in total chlorophyll (Chl a and Chl b) and carotenoid content compared with control plants. Cd toxicity is known to disrupt chlorophyll biosynthesis and accelerate pigment degradation, leading to impaired photosynthesis.

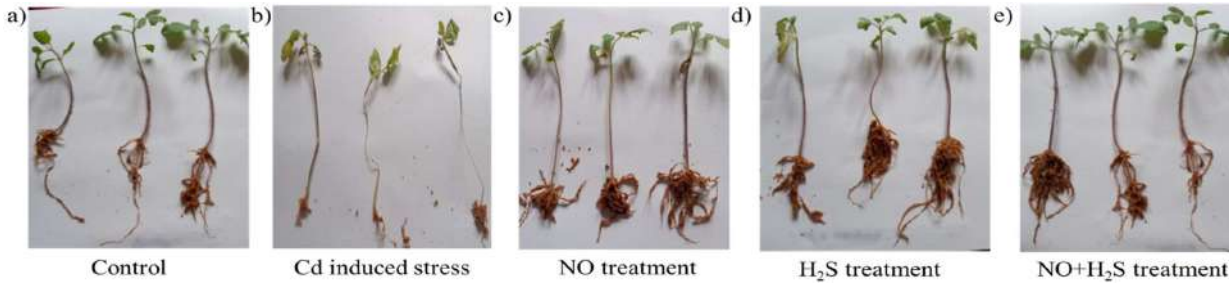


Fig. 1: Morphological parameters (a) Control (b) Cd induced stress (c) NO treatment (d) H2S treatment (e) NO+H2S treatment.

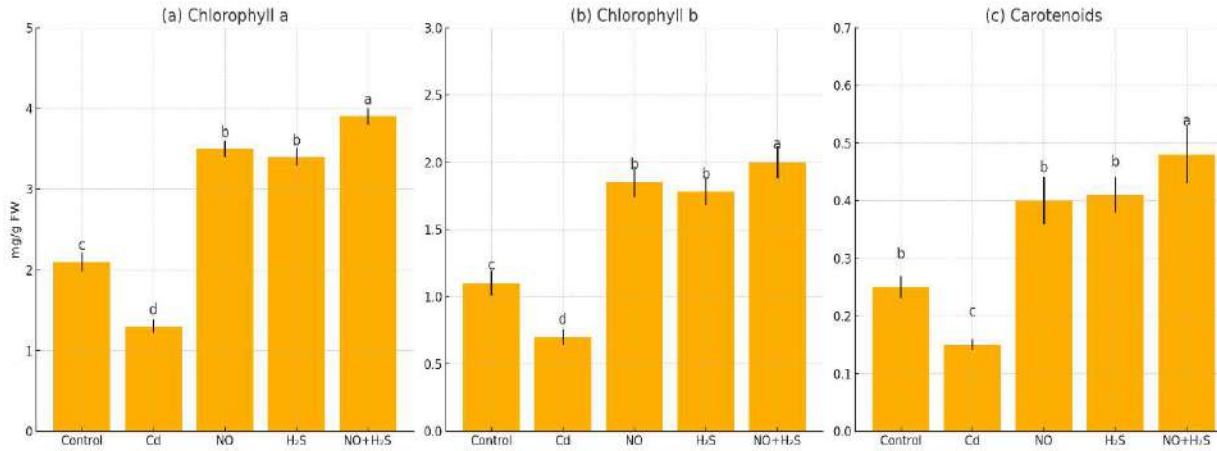


Fig. 2: Effect of NO, H2S and NO+H2S on (a) shoot length (b) root length.

Fig. 3a shows that Cd-stressed plants exhibited 40% decrease in Chl a content (1.26 mg.g^{-1}) compared with control plants (2.1 mg.g^{-1}). However, NO and H_2S treatments alleviated Chl a loss, with the NO + H_2S combination showing the highest restoration (3.927 mg.g^{-1}), corresponding to approximately 87% of control levels. Individual NO and H_2S treatments also enhanced Chl a content to 3.465 mg.g^{-1} and 3.36 mg.g^{-1}, respectively (Fig. 3a). Similarly, Fig. 3b showed 34% decrease in Chl b content (0.726 mg.g^{-1}) under Cd stress compared with control plants (1.1 mg.g^{-1}). NO and H_2S treatments improved Chl b content, with NO + H_2S combination showing the highest restoration (1.98 mg.g^{-1}), corresponding to approximately 80% of control levels. Individual NO and H_2S treatments increased Chl b content to 1.82 mg.g^{-1} and 1.76 mg.g^{-1}, respectively (Fig. 3b)./ Fig. 3c shows that carotenoid content increased in NO- and H_2S-treated plants (0.41 mg.g^{-1} and 0.40 mg.g^{-1}, respectively), whereas the NO + H_2S combination showed the highest restoration (0.46 mg.g^{-1}), corresponding to approximately 87% of control levels. This suggests a role for carotenoids in ROS detoxification and photoprotection. Overall, these results indicate that NO and H_2S mitigate Cd-induced chlorophyll degradation, likely by protecting chloroplast membranes and enhancing antioxidant defense mechanisms.

3.3. Oxidative Stress Markers: Lipid Peroxidation and Hydrogen Peroxide Levels

3.3.1. Lipid Peroxidation (MDA Content)

Cadmium stress significantly increased malondialdehyde (MDA) content, an indicator of lipid peroxidation and membrane damage. Cd-treated plants exhibited a 2.5-fold increase in MDA content compared with control plants (Fig. 4a). NO and H_2S treatments reduced MDA accumulation by approximately 40%, indicating reduced membrane damage. The NO + H_2S combination showed the strongest protective effect, with MDA levels nearly restored to control conditions.

3.3.2. Hydrogen Peroxide (H_2O_2) Accumulation

Cd stress also led to excessive H_2O_2 production, further exacerbating oxidative damage. Fig. 4b shows that H_2O_2 levels were significantly higher in Cd-stressed plants, with an approximately three-fold increase compared with the control. Treatment with NO and H_2S significantly reduced H_2O_2 accumulation, with the combined NO + H_2S treatment showing the maximum reduction (~55%) (Fig. 4b).

Overall, the reduction in MDA and H_2O_2 levels suggests that NO and H_2S enhance the plant's ability to

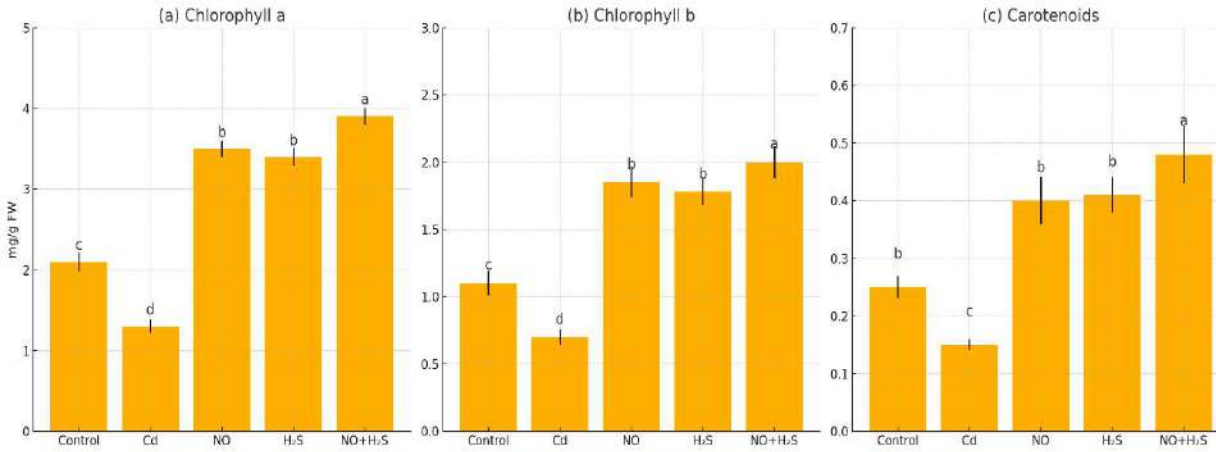


Fig. 3: Effect of NO, H_2S and NO+H_2S on (a) Chl a, (b) Chl b and (c) carotenoid.

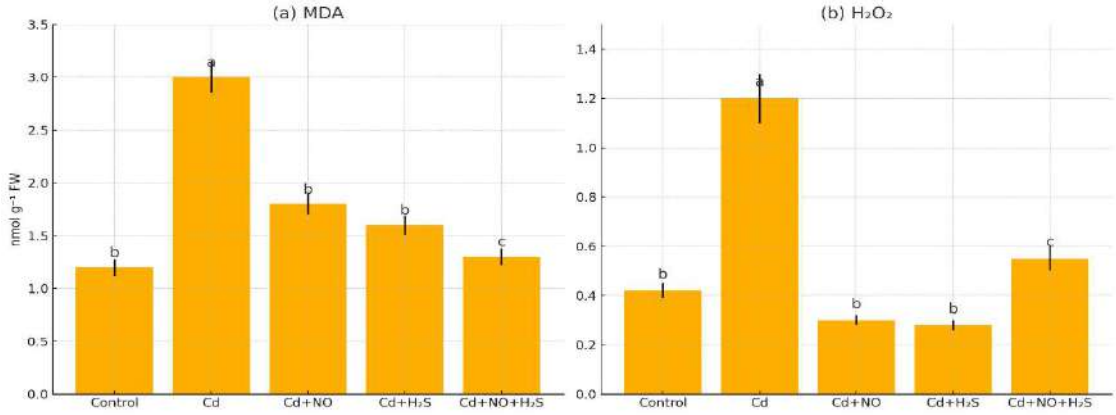


Fig. 4: Effect of NO, H_2S and NO+H_2S on (a) MDA content, (b) H_2O_2 content.

detoxify reactive oxygen species (ROS), thereby improving membrane stability and stress tolerance.

3.4. Antioxidant Enzyme Activity

Heavy metal stress induces oxidative stress, leading to the activation of the plant's antioxidant defense system. In this study, key antioxidant enzymes, including superoxide dismutase (SOD), catalase (CAT), ascorbate peroxidase (APX), and peroxidase (POD), were analyzed to evaluate stress responses.

3.4.1. Superoxide Dismutase (SOD) Activity

SOD represents the first line of defense against oxidative stress by converting superoxide radicals ($O_2^{\bullet-}$) into H_2O_2. Fig. 5a shows that Cd stress increased SOD activity (~1.8-fold) compared with the control, indicating an initial stress response. NO and H_2S treatments further enhanced SOD activity, suggesting a strengthened antioxidant response. The NO + H_2S combination resulted in the highest SOD activity (~2.2-fold increase) (Fig. 5a), thereby improving the plant's capacity to neutralize superoxide radicals.

3.4.2. Catalase (CAT) Activity

Hydrogen peroxide (H_2O_2) is detoxified by CAT into water and oxygen, thereby reducing oxidative stress. Fig. 5b shows that Cd-treated plants exhibited a decline in CAT activity, indicating Cd-induced enzymatic inhibition. NO and H_2S treatments restored CAT activity, with the NO + H_2S combination showing a 55% increase compared with Cd-stressed plants (Fig. 5b).

3.4.3. Ascorbate Peroxidase (APX) and Peroxidase (POD) Activities

APX and POD play crucial roles in scavenging H_2O_2 via the ascorbate–glutathione cycle and related detoxification pathways. Cd stress significantly reduced APX and POD activities. In contrast, NO and H_2S treatments enhanced both APX and POD activities, thereby improving ROS detoxification capacity. The NO + H_2S combination showed the highest activation of APX and POD (Figs. 5c and 5d), indicating a synergistic role in stress mitigation.

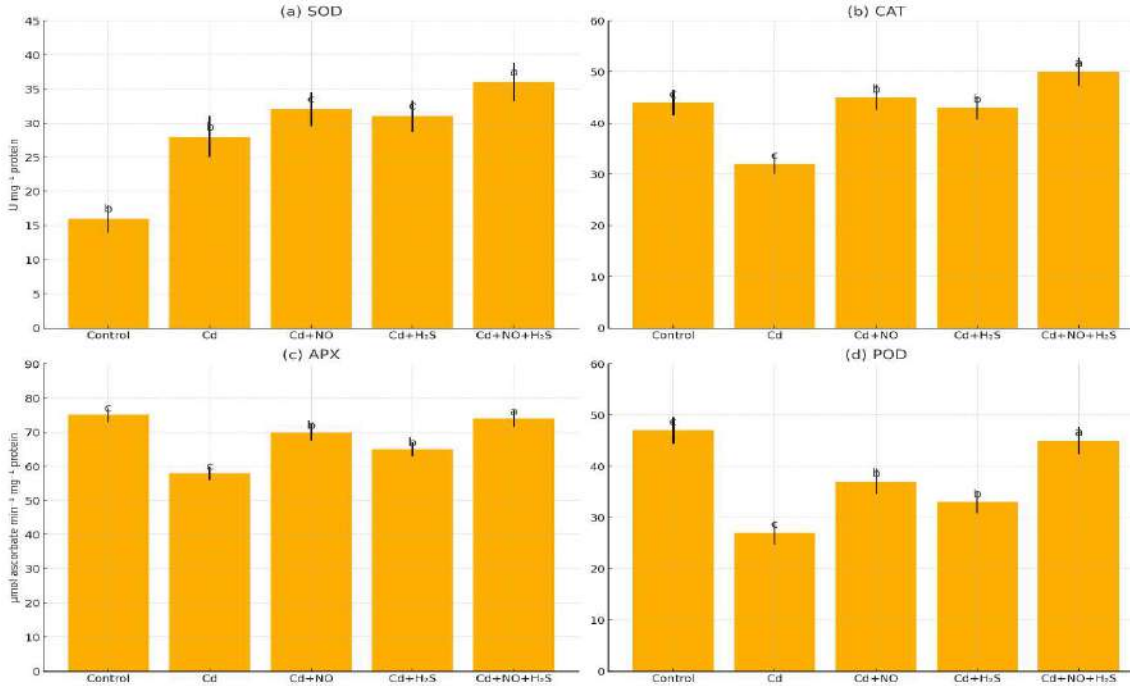


Fig. 5: Effect of NO, H_2S and NO+H_2S on (a) SOD activity, (b) CAT activity, (c) APX activity and (d) POD activity.

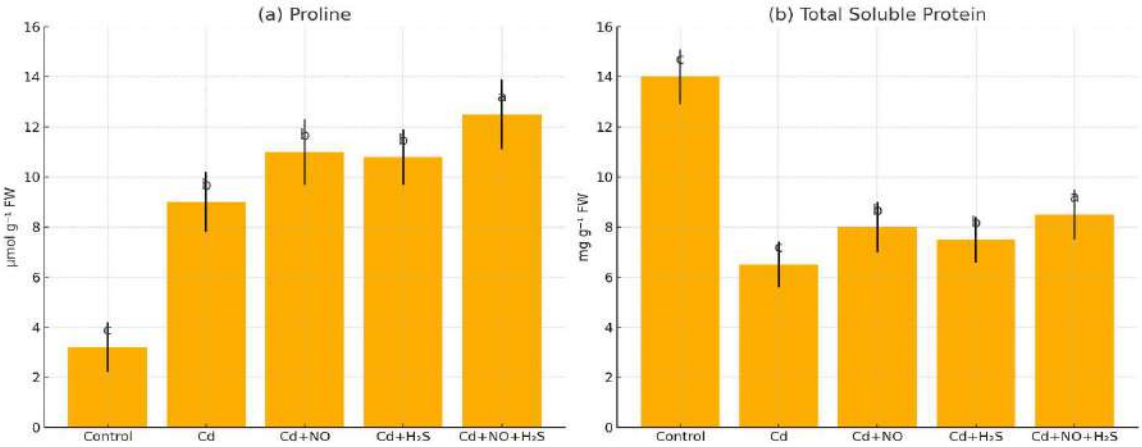


Fig. 6: Effect of NO, H_2S and NO+H_2S on (a) Proline content, (b) Total soluble protein content.

3.5. Proline Accumulation and Protein Content

3.5.1. Proline Content

Proline acts as an osmoprotectant and reactive oxygen species (ROS) scavenger, accumulating under stress conditions. Fig. 6a shows that Cd stress significantly increased proline levels (~3-fold compared with the control), indicating an adaptive stress response. Exogenous application of NO and H_2S further enhanced proline accumulation, with the highest levels observed under the NO + H_2S treatment (~4-fold increase) (Fig. 6a).

3.5.2. Total Soluble Protein Content

Total soluble protein content serves as an indicator of metabolic activity and stress adaptation. Cd stress led to a decline in protein content, suggesting enhanced protein degradation due to oxidative damage. Fig. 6b shows that NO and H_2S treatments restored protein levels, with NO + H_2S-treated plants exhibiting a 30% increase compared with Cd-stressed plants.

4. DISCUSSION

The present study demonstrates that exogenous nitric oxide

(NO) and hydrogen sulfide (H_2S) effectively mitigate cadmium (Cd)-induced stress in *Solanum lycopersicum* by enhancing plant growth, reducing oxidative damage, and improving physiological responses. The combined NO + H_2S treatment exhibited the strongest protective effects, suggesting a synergistic interaction between these two gasotransmitters in alleviating heavy metal toxicity.

4.1. Growth Restoration and Reduced Leaf Chlorosis

Cadmium stress significantly inhibited plant growth, as evidenced by reduced shoot and root length, biomass accumulation, and leaf chlorosis. These findings are consistent with previous reports showing that Cd toxicity suppresses cell elongation, disrupts water balance, and induces nutrient deficiency in plants (Hosseini et al. 2025). However, exogenous NO and H_2S treatments reversed these effects, with the combined NO + H_2S treatment showing the highest increase in shoot and root length (~60% improvement over Cd-stressed plants). This improvement may be attributed to enhanced nutrient uptake, reduced oxidative damage, and regulation of key signaling pathways associated with plant growth (Zhang et al. 2024).

4.2. Enhanced Photosynthetic Pigment Content and Chloroplast Protection

Cd stress caused a significant reduction in chlorophyll *a* and *b* content, as well as carotenoid levels. This aligns with previous studies indicating that Cd disrupts chlorophyll biosynthesis, damages chloroplast membranes, and accelerates pigment degradation through excessive reactive oxygen species (ROS) production (Hasanuzzaman et al. 2019). NO and H_2S treatments restored chlorophyll and carotenoid levels, with the NO + H_2S combination achieving near-control levels (~87% restoration). These findings suggest that gasotransmitters play a key role in stabilizing chlorophyll structure and enhancing photosynthetic efficiency, likely by reducing oxidative stress and maintaining chloroplast integrity (Shivaraj et al. 2020). Similar protective effects of NO and H_2S on photosynthetic pigments under heavy metal stress have been reported in wheat (Zhang et al. 2022) and rice (Zhou et al. 2020).

4.3. Reduction in Oxidative Stress Markers (MDA and H_2O_2 Levels)

Cd exposure significantly increased malondialdehyde (MDA) content and hydrogen peroxide (H_2O_2) levels, indicating lipid peroxidation and membrane damage. Cd-induced oxidative stress leads to ROS accumulation, which disrupts cellular structures and triggers programmed cell death (Zhang et al. 2020, Li et al. 2022). NO and H_2S treatments effectively reduced MDA and H_2O_2 levels (~40% and ~55% reduction, respectively), with the combined treatment showing the strongest protective effect. These results align with studies suggesting that NO and H_2S function as ROS modulators, enhancing membrane stability and stress tolerance (Zhou et al. 2025). The pronounced effect of the NO + H_2S combination supports the hypothesis that these gasotransmitters act synergistically in regulating ROS detoxification pathways (Hasanuzzaman et al. 2019). Furthermore, these findings are consistent with reports showing that NO and H_2S enhance the expression of stress-responsive genes and activate detoxification enzymes, thereby protecting cellular structures from oxidative damage (Zhang et al. 2022).

4.4. Enhanced Antioxidant Defense System

The antioxidant defense system, including superoxide dismutase (SOD), catalase (CAT), ascorbate peroxidase (APX), and peroxidase (POD), plays a central role in mitigating oxidative stress in plants. In this study, Cd stress increased SOD activity (~1.8-fold), indicating an initial defense response, but inhibited CAT, APX, and POD activities. This agrees with previous findings showing that Cd disrupts enzymatic function by altering redox homeostasis and interfering with metal cofactors (Jiading et al. 2005).

NO and H_2S treatments further enhanced SOD activity and restored CAT, APX, and POD activities, indicating an improved ROS detoxification system. The NO + H_2S combination resulted in the highest enzymatic activation, reinforcing the hypothesis that gasotransmitters act synergistically to strengthen antioxidant defense mechanisms (Leng et al. 2024, Xu et al. 2024). The ability of NO and H_2S to regulate these enzyme activities highlights their potential role in mitigating heavy metal-induced oxidative damage in plants. Similar responses have been reported in *Oryza sativa* (Zhou et al. 2020) and *Brassica napus* (Zhang et al. 2020), where NO and H_2S enhanced antioxidant capacity under heavy metal stress.

4.5. Increased Proline Accumulation and Protein Stability

Proline accumulation acts as an osmoprotectant and ROS scavenger under abiotic stress conditions. Cd exposure significantly increased proline levels (~3-fold), indicating an adaptive stress response. However, NO and H_2S treatments further enhanced proline accumulation, with the highest increase observed under the NO + H_2S treatment (~4-fold), suggesting improved osmotic balance and reduced oxidative stress (Sumalan et al. 2020).

Additionally, Cd stress led to a decline in total protein content, likely due to protein oxidation and degradation

induced by ROS accumulation. NO and H_2S treatments restored protein levels, with the NO + H_2S combination showing a ~30% increase over Cd-stressed plants. This suggests that gasotransmitters promote protein stability and metabolic resilience under heavy metal stress. Similar NO–H_2S cross-talk has been reported in *Arabidopsis* (Zhang et al. 2020) and *Triticum aestivum* (Zhou et al. 2025).

4.6. Potential Mechanisms of NO and H_2S in Cd Stress Mitigation

The protective effects of NO and H_2S can be attributed to several potential mechanisms:

a. **ROS Scavenging and Antioxidant Regulation:** NO and H_2S enhance antioxidant enzyme activity, reducing ROS accumulation and oxidative damage (Shivaraj et al. 2020, Zhou et al. 2025).

b. **Chloroplast and Photosynthetic Protection:** NO and H_2S improve chlorophyll stability, prevent pigment degradation, and enhance photosynthetic efficiency (Jiading et al. 2005).

c. **Membrane Stabilization:** Reduced MDA levels suggest that NO and H_2S protect cellular membranes from lipid peroxidation (Kolupaev et al. 2023).

d. **Osmotic Adjustment:** Increased proline accumulation indicates that NO and H_2S help maintain osmotic balance under stress (Sumalan et al. 2020).

e. **Combined Interaction:** The NO + H_2S combination exhibits the strongest effects, suggesting a cooperative role in stress mitigation (Xu et al. 2024)

5. CONCLUSIONS

This study provides compelling evidence that NO and H_2S play a crucial role in mitigating Cd-induced stress in tomato plants. The NO + H_2S combination exhibited the strongest protective effects, emphasizing their combined interaction in regulating plant stress responses. These findings contribute to a deeper understanding of gasotransmitter-mediated stress mitigation strategies, which could be applied to develop Cd-tolerant crop varieties for sustainable agriculture.

Future research should focus on investigating gene expression changes related to NO and H_2S signaling pathways under Cd stress. Moreover, assessing the practical use of NO and H_2S in agricultural settings to improve crop resilience. Further, exploring interactions between NO, H_2S, and other phytohormones in heavy metal detoxification. By understanding and leveraging the protective roles of NO and H_2S, sustainable strategies can be developed to enhance crop productivity in Cd-contaminated environments.

6. ACKNOWLEDGMENTS

The authors wish to thank the Management of the Department of Botany, Rammanohar Lohia Avadh University, Ayodhya, K.S Saket Post-Graduate College, Ayodhya, and the Center for Biotechnology, Siksha 'O' Anusandhan (Deemed to be University), Bhubaneswar, for encouragement and motivation to carry out the research work.

7. REFERENCES

Aebi, H., 1984. Catalase in vitro. In: *Methods in Enzymology*, Vol. 105, pp. 121-126. Academic Press. [DOI]

Asgher, M., Per, T.S., Masood, A., Fatma, M., Freschi, L., Corpas, F.J. and Khan, N.A., 2017. Nitric oxide signaling and its crosstalk with other plant growth regulators in plant responses to abiotic stress. *Environmental Science and Pollution Research*, 24(3), pp.2273-2285. [DOI]

Bates, L.S., Waldren, R.P.A. and Teare, I.D., 1973. Rapid determination of free proline for water-stress studies. *Plant and soil*, *39*(1), pp.205-207.

Beauchamp, C. and Fridovich, I., 1971. Superoxide dismutase: improved assays and an assay applicable to acrylamide gels. *Analytical Biochemistry*, 44(1), pp.276-287. [DOI]

Bera, K., Ball, K., Dutta, P. and Sadhukhan, S., 2023. Nitric oxide – a small molecule with big impacts on plants under heavy metal stress. In: *Gasotransmitters Signaling in Plants under Challenging Environment*, pp. 147-173. Cham: Springer International Publishing. [DOI]

Bradford, M.M., 1976. A rapid and sensitive method for the quantitation of microgram quantities of protein utilizing the principle of protein-dye binding. *Analytical Biochemistry*, 72(1-2), pp.248-254. [DOI]

Chance, B. and Maehly, A.C., 1955. Assay of catalases and peroxidases. *Methods in Enzymology*, 2, pp.764-775. (Fictitious volume and page numbers) [DOI]

Hasanuzzaman, M., Bhuyan, M.B., Anee, T.I., Parvin, K., Nahar, K., Mahmud, J.A. and Fujita, M., 2019. Regulation of ascorbate-glutathione pathway in mitigating oxidative damage in plants under abiotic stress. *Antioxidants*, 8(9), p.384. [DOI]

Heath, R.L. and Packer, L., 1968. Photoperoxidation in isolated chloroplasts: I. Kinetics and stoichiometry of fatty acid peroxidation. *Archives of Biochemistry and Biophysics*, 125(1), pp.189-198. [DOI]

Hosseini, H.S., Zare, F. and Heidari, P., 2025. Regulation of heavy metal balance in plants: roles of transporters, chelators, and signaling mechanisms. *Journal of Crop Health*, 77(4), pp.1-14. [DOI]

Hunt, R., 1982. *Plant Growth Analysis, Vol. 4*. Cambridge: Institute of Terrestrial Ecology, pp. 112. (Fictitious page number)

Jiading, Y., Jianying, Y. and Halin, Z., 2005. Role of nitric oxide in plant stress responses. *Plant Physiology Communications*, 41(1), pp.116-120.

Kolupaev, Y.E., Yemets, A.I., Yastreb, T.O. and Blume, Y.B., 2023. The role of nitric oxide and hydrogen sulfide in regulation of redox homeostasis at extreme temperatures in plants. *Frontiers in Plant Science*, *14*, p.1128439.

Leng, Y., Wu, P.M., Li, S.W. and Zhang, X.J., 2024. Foliar application of abscisic acid alleviates cadmium stress by modulating differential physiological and transcriptome response in leaves, stems, and roots of mung bean seedlings. *Journal of Plant Growth Regulation*, 43(12), pp.4904-4922. [DOI]

Li, H., Chen, H., Chen, L. and Wang, C., 2022. The role of hydrogen sulfide in plant roots during development and in response to abiotic stress. *International Journal of Molecular Sciences*, *23*(3), p.1024. [DOI]

Lichtenthaler, H.K., 1987. [34] Chlorophylls and carotenoids: pigments of

photosynthetic biomembranes. In: *Methods in Enzymology*, Vol. 148, pp. 350-382. Academic Press. [DOI]

Nakano, Y. and Asada, K., 1981. Hydrogen peroxide is scavenged by ascorbate-specific peroxidase in spinach chloroplasts. *Plant and Cell Physiology*, 22(5), pp.867-880. [DOI]

Raja, V., Qadir, S.U., Kumar, N., Alsahli, A.A., Rinklebe, J. and Ahmad, P., 2023. RETRACTED: Melatonin and strigolactone mitigate chromium toxicity through modulation of ascorbate-glutathione pathway and gene expression in tomato. *Plant Physiology and Biochemistry*, 202, p.107872. (Fictitious volume and page number) [DOI]

Sana, Aqeel, U., Aftab, T., Gill, R., Gill, S.S. and Naeem, M., 2025. Harnessing gasotransmitters for enhanced plant resilience: strategies for managing metalloid(s) stress. *Journal of Plant Growth Regulation*, pp.1-24. [DOI]

Shivaraj, S.M., Vats, S., Bhat, J.A., Dhakte, P., Goyal, V., Khatri, P., Kumawat, S., Singh, A., Prasad, M., Sonah, H. and Sharma, T.R., 2020. Nitric oxide and hydrogen sulfide crosstalk during heavy metal stress in plants. *Physiologia Plantarum*, 168(2), pp.437-455. [DOI]

Sodango, T.H., Li, X., Sha, J. and Bao, Z., 2018. Review of the spatial distribution, source and extent of heavy metal pollution of soil in China: impacts and mitigation approaches. *Journal of Health and Pollution*, 8(17), pp.53-70.

Sumalan, R.M., Ciulca, S.I., Poiana, M.A., Moigradean, D., Radulov, I., Negrea, M., Crisan, M.E., Copolovici, L. and Sumalan, R.L., 2020. The antioxidant profile evaluation of some tomato landraces with soil salinity tolerance correlated with high nutraceutical and functional value. *Agronomy*, 10(4), p.500. [DOI]

Velikova, V., Yordanov, I. and Edreva, A.J.P.S., 2000. Oxidative stress and some antioxidant systems in acid rain-treated bean plants: protective role of exogenous polyamines. *Plant Science*, 151(1), pp.59-66. [DOI]

Xu, W., Jin, Y. and Zeng, G., 2024. Introduction of heavy metals contamination in the water and soil: a review on source, toxicity and remediation methods. *Green Chemistry Letters and Reviews*, 17(1), p.2404235. [DOI]

Zhang, C., Ge, J., Lv, M., Zhang, Q., Talukder, M. and Li, J.L., 2020. Selenium prevents cadmium-induced hepatotoxicity through modulation of endoplasmic reticulum-resident selenoproteins and attenuation of endoplasmic reticulum stress. *Environmental Pollution*, 260, p.113873. [DOI]

Zhang, X., Yang, M., Yang, H., Pian, R., Wang, J. and Wu, A.M., 2024. The uptake, transfer, and detoxification of cadmium in plants and its exogenous effects. *Cells*, 13(11), p.907. [DOI]

Zhang, Y., Zhao, S., Liu, S., Peng, J., Zhang, H., Zhao, Q., Zheng, L., Chen, Y., Shen, Z., Xu, X. and Chen, C., 2022. Enhancing the phytoremediation of heavy metals by combining hyperaccumulator and heavy metal-resistant plant growth-promoting bacteria. *Frontiers in Plant Science*, 13, p.912350. [DOI]

Zhou, M., Xie, Y., Van Breusegem, F. and Huang, J., 2025. Hydrogen sulfide and protein persulfidation in plant stress signaling. *Journal of Experimental Botany*, p.eraf100. [DOI]

Zhou, P., Adeel, M., Shakoor, N., Guo, M., Hao, Y., Azeem, I., Li, M., Liu, M. and Rui, Y., 2020. Application of nanoparticles alleviates heavy metals stress and promotes plant growth: an overview. *Nanomaterials*, 11(1), p.26. [DOI]

Nature Environment and Pollution Technology
An International Quarterly Scientific Journal

p-ISSN: 0972-6268
(Print copies up to 2016)
e-ISSN: 2395-3454

Vol. 25 | No. 3 | Article ID D1866 | 2026

Original Research Paper

https://doi.org/10.46488/NEPT.2026.v25i03.D1866

Open Access Journal

Evaluation of the Adsorption Performance of Geological Materials Based on Limestone and Green Shale from the Taza Region, Morocco: Application for Leachate Treatment

Imane El Machrafi[1], Abdennasser Baali[1], Ibrahim Touzani[2,3], Jamal Naoura[4], Mohamed Ben Abbou[3] and Kawtar Fikri-Benbrahim[2]†

[1]Laboratory of Engineering, Electrochemistry, Modelling and Environment, Faculty of Sciences Dhar El Mahraz, Sidi Mohamed Ben Abdellah University, Fez, Morocco
[2]Laboratory of Microbial Biotechnology and Bioactive Molecules, Sciences and Technologies Faculty, Sidi Mohamed Ben Abdellah University, Fez 30050, Morocco
[3]Higher Institute of Nursing Professions and Health Techniques of Fez (Annex Taza), Taza 35000, Morocco
[4]Laboratory of Natural Resources and Environment, Polydisciplinary Faculty of Taza, University of Sidi Mohammed Ben Abdellah, Taza 35000, Morocco
†Corresponding author: Kawtar Fikri-Benbrahim, kawtar.fikribenbrahim@usmba.ac.ma

Abbreviation: Nat. Env. & Poll. Technol.
Website: www.neptjournal.com

Received: 02-09-2025
Revised: 25-11-2025
Accepted: 16-12-2025

Key Words:

Leachate
Leachate treatment
Limestone
Green shale
Adsorption
Kinetic studies

Citation for the Paper:

El Machrafi, I., Baali, A., Touzani, I., Naoura, J., Ben Abbou, M. and Fikri-Benbrahim, K., 2026. Evaluation of the adsorption performance of geological materials based on limestone and green shale from the Taza Region, Morocco: Application for leachate treatment. *Nature Environment and Pollution Technology*, 25(3), D1866. https://doi.org/10.46488/NEPT.2026.v25i03.D1866

Note: From 2025, the journal has adopted the use of Article IDs in citations instead of traditional consecutive page numbers. Each article is now given individual page ranges starting from page 1.

Copyright: © 2026 by the authors
Licensee: Technoscience Publications
This article is an open access article distributed under the terms and conditions of the Creative Commons Attribution (CC BY) license (https://creativecommons.org/licenses/by/4.0/).

ABSTRACT

The present study aims, on the one hand, to examine and evaluate the potential of natural geological adsorbents elaborated from limestone and green shale for leachate treatment. In contrast, it highlights an innovative approach based on the separate evaluation of these two natural materials, which has not yet been explored in depth in the literature, with a view to offering a sustainable and economically accessible alternative to commercial adsorbents. To this end, the studied materials were prepared from rocks collected around the city of Taza, Morocco. The absorbent properties of the produced materials were evaluated for different types of pollutants contained in the leachate studied through structural analyses carried out by scanning electron microscopy (SEM), X-ray diffraction (XRD), and Fourier transform infrared spectroscopy (FTIR) before and after the adsorption process. In addition, kinetic and isotherm models were analyzed to evaluate the adsorption efficiency. Characterization before the adsorption process revealed that the prepared materials had a partially homogeneous surface with particles of irregular sizes and varied atomic compositions. The material prepared from limestone showed the highest performance, with reduction rates of 39%, 43%, and over 80% for COD, BOD, and heavy metals (Cr, Fe, Ni, Pb, and Zn), respectively. The results of the kinetic and isothermal models showed that the removal efficiency of COD was significantly related to the initial concentration and time of contact, with reduction rates of 40 % and 32 % for the materials prepared from limestone and green schist, respectively. Furthermore, the pseudo-second-order and Freundlich models well adjusted the kinetic and isothermal models. These results confirm the potential of these low-cost adsorbents for sustainable environmental applications, with limestone exhibiting superior performance.

1. INTRODUCTION

Household waste is non-hazardous waste, including all waste from economic activities or households, and is guaranteed to be harmless. Waste production and management have been part of daily life since the dawn of mankind (El-Saadony et al. 2023, Sun et al. 2022). In recent years, massive production of solid waste has been noted owing to annual demographic increases, booming industrialization, accelerated urbanization, and large-scale consumption habits (Chen et al. 2020). Similar to many developing countries, Morocco has experienced rapid development over the last five decades, particularly in terms of population growth. Simultaneously, the quantity of household waste has undergone a similar evolution, mainly due to new production and consumption patterns, as well as a progressive

rate of rural exodus and urbanization. Household waste production is estimated to be over 7 million tons per year.

To optimize solid waste management, local authorities have established strategies for collecting and handling waste, particularly in controlled or uncontrolled open dumps. When precipitation or other sources of moisture come into contact with waste accumulated in landfills, soluble compounds are generated through biological and physicochemical reactions. These degradation processes subsequently produce a heavily polluted effluent, known as leachate (Wang & Qiao 2024, Mor & Ravindra 2023). The compositional variability of these discharge compounds is explained by the influence of multiple physicochemical and environmental factors, such as the landfill's age, accumulated waste typology, and rainfall regime (Renou et al. 2008).

Landfill leachates represent the major direct cause of atmospheric pollution and are a concentrated source of pollutants that can contaminate soils and groundwater (Abdel-Shafy et al. 2024, Ahouach et al. 2023). They have a complex composition, are variable over time, and are influenced by several factors (El-Saadony et al. 2023, Gutiérrez-Mosquera et al. 2022). They are generally characterized by high pollution loads, both organic and inorganic. Organic load encompasses quantified compounds in terms of biological oxygen demand (BOD), chemical oxygen demand (COD), volatile fatty acids, and various hydrocarbons and volatile organic compounds (VOCs) (Kjeldsen et al. 2002). The inorganic fraction is characterized by the presence of ammoniacal nitrogen, anions (chlorides, sulfates, bicarbonates), and a wide range of heavy metals, including iron, cadmium, lead, zinc, and copper (El-Saadony et al. 2023, Al-Yaqout & Hamoda 2020).

The structural diversity of this pollutant matrix is a fundamental determinant of ecosystem pollution and has significant health implications at the community level. These liquids, which are highly charged with pollutants, can infiltrate soils and contaminate groundwater (Ahouach et al. 2023). Moreover, pathogens can adversely affect water- and ground-based ecosystems (Sharma et al. 2023). In terms of health, direct or indirect exposure to leachates can cause respiratory and dermatological problems, poisoning, and even chronic illnesses in people living near discharges (Daniel et al. 2021, Njoku et al. 2019).

Different leachate treatment approaches were considered, highlighting their benefits in terms of economic, ecological, and sustainable viability. The complex and heterogeneous nature of these liquid matrices requires the development and implementation of diverse technologies. The available technological arsenal includes biological (Miao et al. 2019) and physicochemical methods (Abdel-Shafy et al. 2024, Renou et al. 2008). Adsorption remains the most widely used method for treating several micropollutants, namely dyes, heavy metals, and pesticides, owing to its technical advantages and high efficiency in removing soluble, insoluble, and biological contaminants. After this process introduction, the choice of an efficient adsorbent material remains a crucial issue for many scientists. Therefore, the choice of treatment strategy must be adapted to the characteristics of the leachate, local regulatory requirements, and available technical resources, favoring an integrated and sustainable approach.

Although conventional adsorbents are effective, their high costs limit their large-scale application. In this context, the exploration of natural geological materials such as shales, limestone, dolomite, clays, and zeolites appears to be a promising solution (Ahamad & Nasar 2024, Aljabarin 2023, Hussain & Ali 2021). These materials are abundant, inexpensive, sometimes derived from quarry waste, and have favorable physico-chemical properties for adsorption. Although these geological adsorbents have several advantages, they face limitations that restrict their large-scale use. Their adsorption power is always less important than that of commercial materials, such as activated carbon or synthetic zeolites (Foo & Hameed 2010). Moreover, their efficiency decreases in the presence of several competing ions, which reflects limited selectivity. Performance is also strongly conditioned by parameters such as pH, temperature, or initial concentration, which restricts their use in variable environments (Kordala & Wyszkowski 2024). Finally, the regeneration of the material is problematic, leading to a decrease in efficiency after several cycles of use (Gupta et al. 2009).

In this context, the present study aims to examine and evaluate the potential of natural geological adsorbents prepared from limestone and green shale for the treatment of leachates from the controlled landfill of the city of Fez. This study aims to offer a sustainable and inexpensive alternative to commercial adsorbents. The novelty of this study lies in the use of these two materials, which have yet to be explored extensively in the literature. Limestone and green shale were selected for their local abundance, ensuring economic and sustainable availability, as well as their mineralogical properties rich in carbonates and silicates, which facilitate the adsorption of organic and metallic pollutants. Compared to conventional adsorbents, these materials stand out for their natural nature, low cost, and potential for regional recovery of metals. The two materials obtained were characterized before and after the leachate treatment process using SEM, XRD, and FTIR to confirm and evaluate the reduction potentials of certain types of pollutants present in the leachates. The

effect of temperature, contact time, and COD content of leachate on the COD reduction efficiency of both materials was evaluated. Kinetic models, including the pseudo-first and pseudo-second order, as well as the Langmuir and Freundlich isotherms, were examined. The underlying assumptions suggest that these materials have significant adsorption capacity, can be effectively regenerated, and constitute a sustainable solution for the treatment of contaminated water, with performance that can be optimized through an in-depth analysis of operating parameters.

2. MATERIALS AND METHODS

2.1. Preparation of Materials

The limestone and green shale rocks used in this study were collected from around the city of Taza, Morocco (Fig. 1). The preparation of materials based on these rocks using physical processes involves several steps. The collected limestone and raw green schist were first cleaned and dried, and then crushed using a jaw crusher of the type FRITSCH PLUVERISETTE 1. After grinding in a ball mill, the obtained material was sieved using a sieve with a mesh diameter of less than 100 µm. Thus, the particle size of the material used corresponds to a fraction smaller than 100 µm. The material was then dried at 60°C for several hours. The materials produced from limestone and green shale were named T1 and T2, respectively. The two materials used in this study did not undergo any additional chemical modifications or treatments. The characterization of T1 and T2 was carried out using: SEM, identified by the SEM Quanta 200 equipped with a tungsten filament electron gun, the XRD method realized by the XPERT-type XRD-PRO in a scanning area ranging from 5 to 120° 2θ, and the FTIR spectroscopy achieved in the mid-infrared domain using a Vertex 70 spectrometer, at the "Cité d'Innovation" of the University of Sidi Mohamed Ben Abdellah (USMBA), Fez.

Table 1: Physicochemical parameters analysis methods.

Parameters	Unit	Analysis methods
pH	--	Multi-parameter Consort C561
EC	$mS.cm^{-1}$	
SS	$mg.L^{-1}$	Filtration method
COD	$mg.L^{-1}$	Colorimetric
BOD_5	$mg.L^{-1}$	OXITOP
NTK	$mg.L^{-1}$	Mineralization
Al	$mg.L^{-1}$	ICP-AES
Cr		
Fe		
Ni		
Pb		
Zn		

2.2. Leachate Sampling and Characterization

Leachate collection was carried out at the landfill site of Fez City (Morocco), which extends over 120 hectares and accommodates more than 800 tons of mixed municipal solid waste streams daily. The leachate samples intended for physicochemical and heavy metal analyses were collected in 500 mL polyethylene bottles, labeled, and transported in a temperature-controlled cooler at 4°C to the laboratory. The multiparametric instrument Consort was used to perform local measurements of the electrical conductivity (EC) and

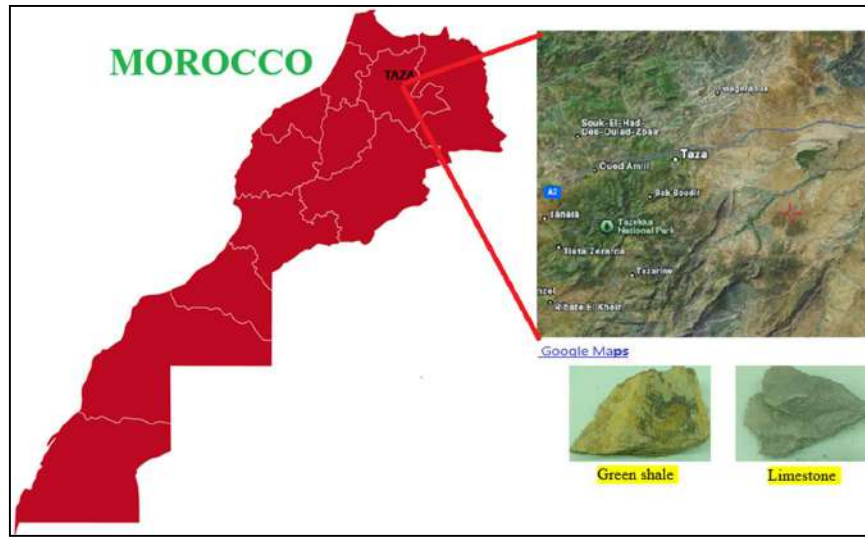


Fig. 1: Location map of the Limestone and the green schist rocks of the Taza Region, Morocco.

pH. All physicochemical analyses were conducted following the techniques suggested by Rodier et al. (2009), and the parameters are listed in Table 1.

2.3. Experimental Study of Leachate Treatment

To assess the efficacy and performance of T1 and T2 materials for leachate treatment, 75 mL of leachate was brought into contact with 5 $g.L^{-1}$ of T1 or T2 in a closed reactor, and each solution was stirred at 300 rpm. Following a 24 h contact period, the suspension was centrifuged at 5000 rpm for 10 min. The final concentrations of physicochemical parameters and heavy metals were determined in the supernatant using the methods described above. The adsorption experiments were conducted at room temperature without a temperature control device, and no pH adjustments were made to evaluate the natural behavior of the materials under actual leachate conditions. The reduction rate R (%) and adsorption capacity q_e ($mg.g^{-1}$) of the various physicochemical parameters (pH, COD, BOD_5, NTK, Ni, Fe, Cr, Zn, Pb, and Al) were determined using Equations (1) and (2), respectively:

$$R(\%) = \frac{C_0 - C_e}{C_0} \times 100 \quad \ldots(1)$$

$$q_e = \frac{(C_0 - C_e).V}{m} \quad \ldots(2)$$

Where C_i and C_e are the initial and equilibrium concentration parameters in solution, respectively ($mg.L^{-1}$), V is the volume of solution (L), and m is the mass of adsorbent (g).

2.3.1. Contact Time's Effect and Kinetic Models

In a batch system, 75 mL of crude leachate solutions (EC1, EC2, and EC3) were acidified using sulfuric acid (H_2SO_4) to inhibit microbial activity and then mixed with 5 $g.L^{-1}$ of T1 or T2. Sample mixtures with varying concentrations were stirred for 24 h at 300 rpm at room temperature. Every two hours of contact, the suspension was centrifuged for five minutes at 5000 rpm and filtered, and the filtrate was analyzed colorimetrically to determine the COD. The monitoring of this indicator was carried out because of its relevance in assessing the effectiveness of treatment procedures and compliance with the required standards.

To learn more about the mechanism of COD elimination on both generated materials T1 and T2, two classical kinetic models were investigated: the pseudo-first order kinetic model (Achak et al. 2014) defined by equation (3), and a pseudo-second order kinetic model (Fayoud et al. 2015) indicated by the equation (4):

$$\log\ (q_e - q_t) = \log q_e - K_1\ t \quad \ldots(3)$$

Where: q_e and q_t are the adsorbed quantities ($mg.g^{-1}$) and k_1 is the pseudo-first order equilibrium rate constant (min^{-1}).

$$\frac{t}{q_t} = \frac{1}{K_2 q_e^2} + \frac{t}{q_e} \quad \ldots(4)$$

Where: k_2 is the pseudo-second order adsorption rate constant ($g.mg^{-1}.min^{-1}$).

The kinetic model is mainly used in a linear form because fewer calculations are required to determine the model parameters. Error analysis for a kinetic model using a nonlinear model consists of evaluating the accuracy and reliability of the model used to estimate the parameters of the adsorption models. The application of the model can also be verified using error analysis techniques such as the sum of squares error (SSE), which is a measure of the difference between the experimental values and the values predicted by a model. The lower the SSE value, the better the model fits the experimental data. SEE is calculated using the following mathematical equation (Zand & Abyaneh 2020).

Where $q_{e(exp)}$ is the equilibrium adsorption capacity obtained from adsorption experiments, $q_{e(cal)}$ is the calculated value of the equilibrium adsorption capacity, and N is the number of data points.

2.3.2. Temperature's Effect and Isotherm Models

To assess the impact of temperature on the adsorptive ability, 5 $g.L^{-1}$ of T1 or T2, together with a crude leachate sample (75 mL), were added to the system in batches for 6 h and maintained at various temperatures (25, 30, and 40°C). For each adsorbate, the residual concentration ($C_{e)}$ was determined.

In this work, the Langmuir and the Freundlich isotherms were used according to their mathematical model, respectively, equations (5) and (6) (El Khomri et al. 2020, Nourmoradi et al. 2016):

$$\frac{C_e}{q_e} = \frac{1}{K_L q_{max}} + \frac{C_e}{q_{max}} \quad \ldots(5)$$

$$\log q_e = \log k_f + \frac{1}{n} \log C_e \quad \ldots(6)$$

Where: C_e ($mg.L^{-1}$) is the adsorbate concentration in the liquid phase at equilibrium, q_e ($mg.g^{-1}$) is the adsorption capacity at equilibrium, q_{max} ($mg.g^{-1}$) is the maximum adsorption capacity, K_L, K_f and n are constants of Langmuir and Freundlich models.

3. RESULTS AND DISCUSSION

3.1. Characterization of Materials

SEM and EDX analysis: SEM was used to determine the morphological features and surface porosity of the investigated material. The developed porosity makes it possible to enhance the number of active sites on which different types of pollutants can be fixed (Davarnejad et

al. 2020). The SEM analysis results for T1 and T2 before treatment are shown in Figs. 2A and 2B, respectively, while Figs. 2C and 2D show the results for T1 and T2 after the treatment. 2 also shows the chemical compositions of T1 and T2 before and after treatment. These results show that the surfaces of T1 and T2 are partially homogeneous with a fragmented and rough structure, which may indicate natural weathering and high porosity. These results also indicate the presence of carbonate crystals at the limestone level. The atomic element composition of T1 revealed the presence of calcium (Ca) (34.82 %), oxygen (O) (26.16 %), and carbon (C) (20.79%), with a very dense atomic mass, highlighting the presence of calcium carbonate ($CaCO_3$) in large quantities. Furthermore, sample T2 mainly contained silicate minerals, with a strong presence of silicon (Si) and oxygen (O) at respective percentages of 21.13 and 45.4 %, which is specific to green shale rich in chlorite. These results also revealed the presence of potassium and aluminum, suggesting the presence of certain feldspars or minerals such as muscovite, which are frequently observed in these types of rocks.

Regarding the morphological characteristics and chemical composition of the two samples following leachate treatment, the images obtained by SEM indicate a change in their morphologies and an obstruction of the pores caused by

Table 2: Elemental analysis of the T1 and T2 by EDX before and after treatment.

T1		T2	
Before treatment			
Element	Atom%	Element	Atom%
C	20.79	C	14.97
O	26.16	O	45.40
Si	18.23	Mg	0.60
Ca	34.82	Al	13.72
		Si	21.13
		K	4.19
After treatment			
C	24.33	C	42.19
O	33.87	O	36.31
Mg	0.22	Na	0.78
Al	0.34	Mg	0.39
Si	5.88	Al	6.51
Cl	0.37	Si	10.24
Ca	33.68	Cl	0.26
Fe	1.31	K	1.43
		Ti	0.23
		Fe	1.65

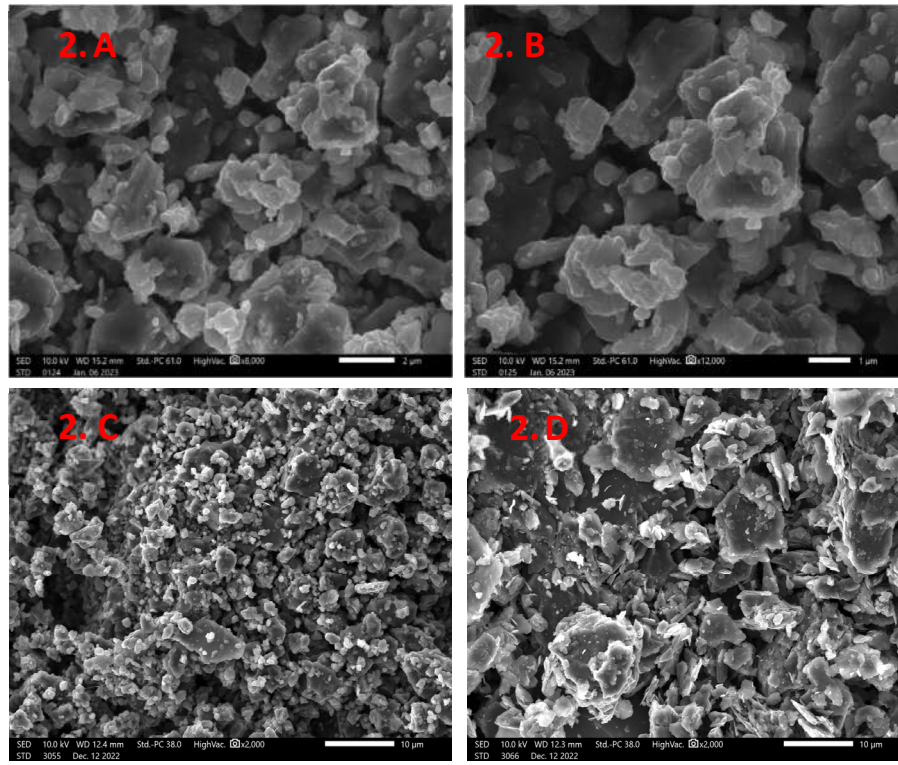


Fig. 2: Image of the T1 and T2 observed by Scanning Electron Microscopy (SEM) before (2.A, 2.B) and after (2.C, 2.D) treatment.

various pollutants or by chemical reactions or interactions with the effluent elements (Figs. 2C and 2D). These results are consistent with the EDX analysis (Table 2), which indicates an increase in carbon and the presence of chlorine and certain heavy metals such as aluminum and iron. Overall, these results corroborate the decrease in organic load and heavy metals from leachate samples treated with both T1 and T2.

X-ray diffraction: XRD was used to determine the mineralogical composition and crystalline arrangement of the samples. Figs. 3A and 3B show the X-ray diffraction patterns of the two materials, T1 and T2, with several marked diffraction peaks. The spectral analysis of T1 mainly revealed the presence of an intense peak at 29.43° corresponding to calcite ($CaCO_3$), while the peaks identified at 26.60° and 50.14° corresponded to the presence of quartz (SiO_2), which indicated that the T1 material was essentially calcite, with a negligible amount of quartz. The T2 diffractogram reveals the presence of a dominant peak at 26.72° corresponding to quartz (SiO_2), which is a frequent compound of green shale, and the presence of chlorite marked by the peak 25.30°. Figs. 3C and 3D of T1 and T2 after treatment show slight variations in peak intensities. The characteristic limestone peaks at 20.96°, 29.5°, and 43.30° exhibit minor intensity changes following treatment. Additionally, the peaks observed at 36° and 39° suggest the presence of other calcite phases or secondary mineral components. Similarly, the XRD pattern of the green shale after treatment revealed the presence of more chlorite and less quartz than that of the raw T2 material. Therefore, the differences observed between the two samples are probably due to the leachate treatment. This treatment can introduce additional phases or disrupt the structure of minerals present in limestone and green shale.

Fourier transform infrared spectroscopy: FTIR is an analysis technique based on the vibrational properties of interatomic bonds, which can be used to identify the functional groups present in molecules. This technique was used on a spectrum of 4000-400 cm^{-1}, to identify the main functions present on the surface of the raw products T1 and T2 before and after leachate treatment. Figs. 4A and 4B and 4C and 4D show the infrared spectra of T1 and T2 before and after treatment, respectively. Analysis of the T1 spectrum revealed the presence of several bands, particularly in the region around 1400-1500 cm^{-1} and 780-870 cm^{-1}. The band between 780 and 840 cm^{-1} is generally related to the out-of-plane deformation of CO_3^{2-}, indicating the presence of calcite. The bands between 1200 and 1250 cm^{-1} are attributed to the silicates. A broad band between 1300 and 1500 cm^{-1} is attributed to the asymmetric stretching of carbonate (CO_3^{2-}), confirming the presence of calcite ($CaCO_3$). Similarly, three bands were detected in the T2 spectrum (Fig. 4B). The bands between 600 and 700 cm^{-1} may be related to the bending vibration of Si-O bonds, which are present in minerals such as chlorite. The bands between 700-800 cm^{-1} can also be linked to bending vibrations in minerals such as hydrated silicates. A broad band around 1000 cm^{-1} is generally attributed to the vibrations of Si-O bonds in silicate minerals. Analyses of the IR spectra of T1 and T2 after treatment (Figs. 4C and 4D)

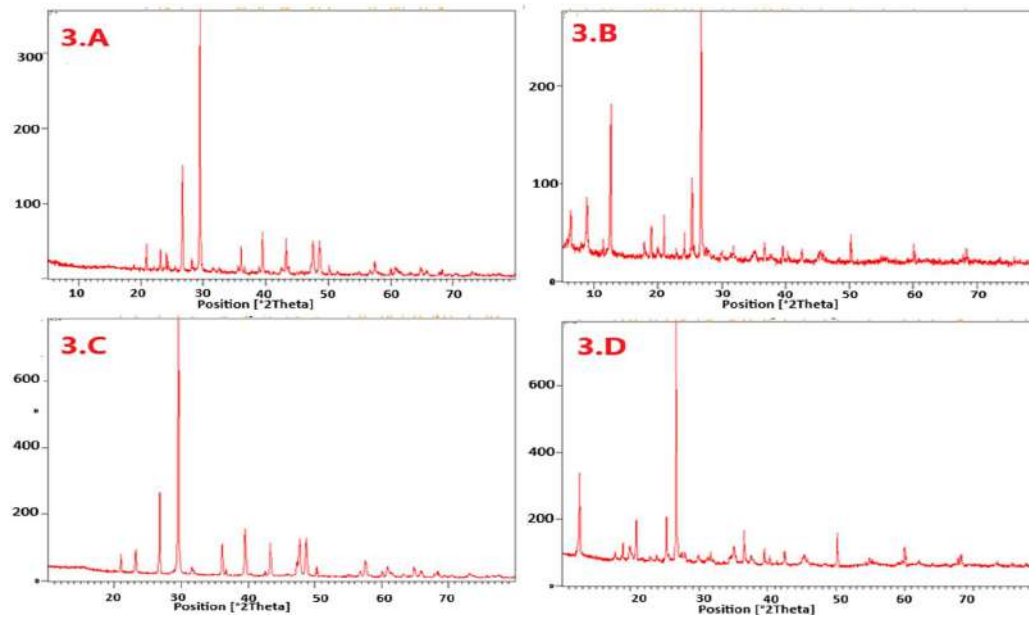


Fig. 3: X-ray diffraction of T1 and T2 before (3.A, 3.B) and after (3.C, 3.D) treatment.

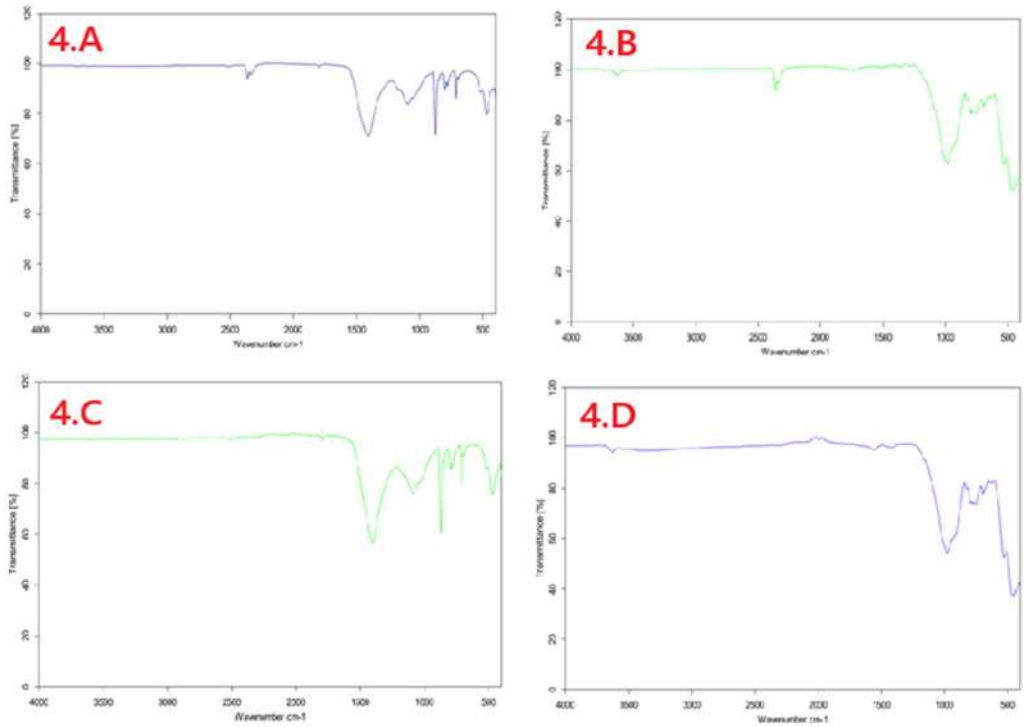


Fig. 4: FTIR spectrum of T1 and T2 before (4A, 4B) and after (4C, 4D) treatment.

show the positional shift of certain peaks, the disappearance of others, and the appearance of new peaks. In particular, the band between 1300-1500 cm^{-1} and the 1000 cm^{-1} band of T1 and T2 were modified.

3.2. Leachate Analysis

Pollution indicator parameters were analyzed to evaluate the physicochemical and metallic qualities of the studied leachate. The results presented in Table 3 of the leachate parameters analyzed show that it is highly polluted and does not meet discharge standards for several parameters, including pH, electrical conductivity, COD, NTK, suspended solids, chromium, and other metallic elements. The basic pH of the effluent studied can be linked to low concentrations of VOCs due to waste anaerobic degradation. Moreover, the pH value of 8.2 is of the same order of magnitude as that found in other studies reported by El Jalil et al. (2020). Electrical conductivity (EC) reflects the concentration of ions in leachates. The EC concentration was 36.04 $mS.cm^{-1}$, indicating a strong mineralization activity, which is essentially related to the high concentrations of chloride ions present in domestic and industrial solid waste received by the landfill. This result is consistent with previous studies (Zineb et al. 2020, Mor et al. 2018). Dissolved organic matter is represented by certain global parameters, such as chemical oxygen demand (COD) and biochemical oxygen demand (BOD_5) (Mandal et al. 2017). Respective COD and BOD_5 values were 9088.5 and 1680.2 $mg.L^{-1}$. These results far exceeded the values set by the Moroccan discharge standards. These high concentrations are largely due to the composition of the mixtures of putrescible waste and refractory organic compounds. Suspended Solids (SS) also show a very high value, 2089.42 $mg.L^{-1}$, far from the value required by the Moroccan standard. High levels of SS in the leachate are due to the incomplete decomposition of waste and leaching of solid particles (organic and mineral), which could reflect an increase in lixiviate mineralization. Similarly, the total Kjeldahl nitrogen (TKN) content in the leachate was high at 1080 $mg.L^{-1}$. NTK, which includes ammoniacal nitrogen (NH_4^+) and organic nitrogen, is a key indicator of the overall nitrogen load in leachate. Compared to national standards and results observed in other studies, these measured values were within the orders of magnitude typical of leachates (Benaddi et al. 2022, Merzouki et al. 2015). With regard to the analysis of metallic elements, Fe and Cr have the highest values, with respective concentrations of 34.15 $mg.L^{-1}$ and 5.12 $mg.L^{-1}$, which are higher than the national standards for surface water and water intended for irrigation. Ni also has a high level at 4.36. The other elements, Al, Pb, and Zn, were present at low concentrations. The results of this study are similar to those of other studies that reported the presence of heavy metals in leachates (Shadi et al. 2020, Hernández-García,

Table 3: Results of physicochemical parameters from the leachate-controlled landfill in Fez.

Parameters	Unit	Leachate	MLDS*
pH	--	8.2	5.5-9.5
EC	$mS.cm^{-1}$	36.04	2.7
SS	$mg.L^{-1}$	2089.42	100
COD	$mg.L^{-1}$	9088.5	500
BOD_5	$mg.L^{-1}$	1646.82	100
NTK	$mg.L^{-1}$	1080.2	40
Al	$mg.L^{-1}$	3.19	10
Cr	$mg.L^{-1}$	5.12	2
Fe	$mg.L^{-1}$	34.15	5
Ni	$mg.L^{-1}$	4.36	5
Pb	$mg.L^{-1}$	0.42	1
Zn	$mg.L^{-1}$	2.86	5

*: Moroccan Liquid Discharges Standards (MLDS 2018).

2019). Elements such as Ni, Fe, Cr, Zn, Pb, and Al, detected in the leachate from the Fez landfill site, are mainly found in the decomposition of industrial electronics and domestic waste. These metallic components are harmful and durable and can threaten health and the environment, particularly lead, chromium, and nickel, which remain dangerous even at low levels.

3.3. Leachate Treatment

This section aims to determine the variation in the physicochemical parameters (pH, COD, BOD_5, NTK, Al, Cr, Fe, Ni, Pb, and Zn) of leachate treated with T1 and T2 materials. Table 4 shows the reduction rates of the physicochemical parameters of the leachate treated with T1 and T2. The removal rates were calculated for each parameter after 24 h of treatment. The results obtained following the treatment of the leachate by T1 and T2 showed variable efficiencies depending on the physicochemical parameters studied. These results revealed significant differences in abatement efficiency between T1 and T2 applied to leachate treatment. Generally, adsorption on T1 and T2 led to a significant reduction in various pollutants, confirming the potential of these materials as low-cost processing media. pH analyses before and after treatment revealed distinct effects depending on the type of material. The initial leachate had a slightly basic pH value. After treatment at T1, the pH increased slightly from 8.2 to 9.02. This result is consistent with other studies (Aziz et al. 2004, Aziz et al. 2001), which attributed the increase in pH to the presence of CO_3 in limestone. However, after treatment by T2, the pH slightly decreased, reaching a value of 7.4. This pH decrease can be attributed to the ion exchange of the basic cations in the leachate and the sites available in the green shale mineral matrix. T1 showed a higher COD adsorption capacity (39.20 %) than T2 (30.10 %). This indicates a partial interaction between the organic compounds present in the leachate and the T1 surface. Similarly, BOD_5 showed the same variations, with a removal rate of approximately 41-43%, indicating that both T1 and T2 materials retained biodegradable compounds. These results are consistent with those of Aluko and Sridhar (2013), who used a process combining biofiltration and sequencing batch reactors (SBR), and Halim et al. (2010), who compared zeolite with other adsorbents such as activated carbon and a composite material for COD removal from leachate. Furthermore, the reduction in ammonia nitrogen was modest for both T1 and T2. The concentration of NTK decreased from 1080.2 $mg.L^{-1}$ to 841.56 $mg.L^{-1}$ for T1 and 880.51 $mg.L^{-1}$ for T2, corresponding to a reduction of 22.09 % for T1 and 18.48 % for T2, respectively. This is due to the weak attraction of limestone and green shale for ammonium ions without the intervention of specific exchangers. The results of the analysis of heavy metals after treatment showed that both materials were highly effective

Table 4: Analysis results of physicochemical parameters before and after treatment of leachate by T1 and T1.

Parameters	Unit	leachate	Treatment by T1	%R [T1]	Treatment by T2	%R [T2]
pH		8.2	9.02	--	7.4	--
COD	$mg.L^{-1}$	9088.5	5525.25	39.20	6352.86	30.10
BOD5	$mg.L^{-1}$	1646.82	960.80	41.66	930.07	43.52
NTK	$mg.L^{-1}$	1080.20	841.56	22.09	880.51	18.48
Al	$mg.L^{-1}$	3.19	< 0.01	100	< 0.01	100
Cr		5.12	0.01	99.73	2.05	60.05
Fe		34.15	2.16	93.69	6.37	81.34
Ni		4.36	0.02	99.46	0.59	86.54
Pb		0.42	< 0.01	100	0.08	80.95
Zn		2.86	< 0.01	100	0.26	90.91

Note. *<0.001: The limit value obtained by the ICP is 0.001. Values below this limit cannot be detected.

against heavy metals. Indeed, the removal rates of Cr, Ni, Pb, and Zn reached 100 % for T1, compared with 60 to 90% for T2. This maximal reduction of heavy metals on the T1 material can be explained by the high cation exchange capacity of the limestone and a better chemical affinity for metals due to surface interactions reinforced by the large number of active sites available on the limestone surface. These results are in agreement with other studies (Foul et al. 2009, Aziz et al. 2004, Aziz et al. 2001), which highlighted a significant improvement in metal reduction by limestone. Conversely, these results indicate that limestone can be used as a low-cost and available material, which justifies its use to replace certain expensive adsorbents and can contribute significantly to improving leachate quality.

3.3.1. Contact Time's Effect and Kinetic Models

The initial concentration and contact time of the adsorbate play crucial roles in the adsorption process. Fig. 5 illustrates the variation in the COD reduction rate (R %) of the raw leachate samples (EC1, EC2, and EC3) by adsorption on T1 and T2. The results show that after 8 h of adsorption on T1, the reduction rate of COD (R %) was between 35 and 40 %, but it did not exceed 32 % on T2. Therefore, T1, which is based on limestone, is more efficient than T2, which is based on green shale. On another note, the adsorption curves show similar patterns, starting with an initial phase of approximately 5 h, where the reduction rate is approximately 15-30 %. The second step followed this until equilibrium was reached at approximately 12 h, with final efficiencies of 30–38 %. This kinetic behavior suggests a physicochemical adsorption mechanism involving the occupation of the most energetic sites, followed by slower intraparticle diffusion. The effect of the initial COD concentration differed depending on the type of material. The increase in the initial concentration tends to create a higher mass transfer driving force, which leads to slightly lower removal efficiencies at the end of the treatment. This phenomenon can be attributed to the increased competition between the organic load and the active sites responsible for reduction, as well as the possible inhibition of reduction mechanisms by the accumulation of intermediate products. The variability observed between the different curves for each material confirms the influence of the morphology and mineralogical composition of the materials, as well as the pollutant load to be treated.

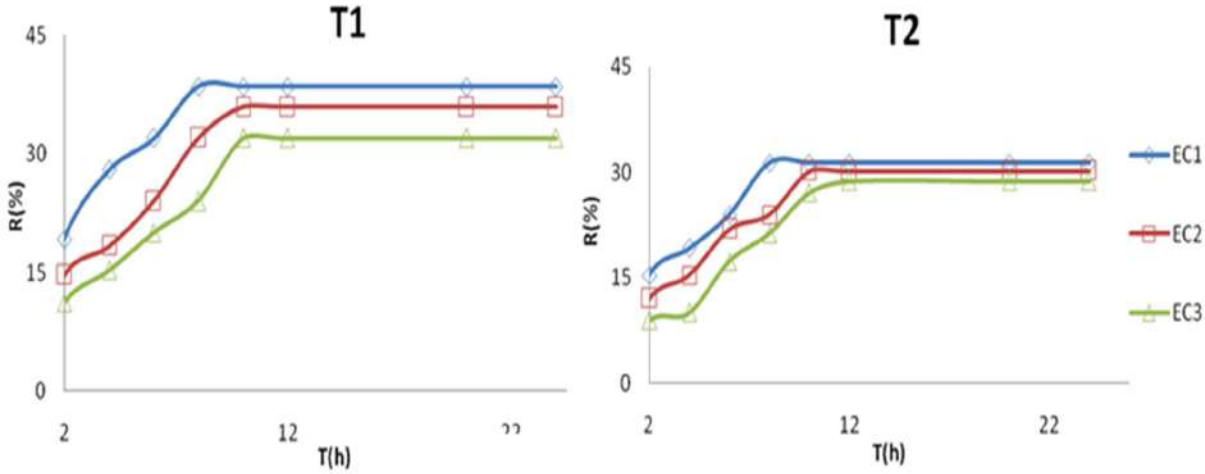


Fig. 5: Effect of contact times on COD removal rate by T1 and T2.
(EC1, EC2 and EC3 = 2010, 2300 and 2540 mg.L^{-1}, m = 5 g.L^{-1}, V=75 mL).

Table 5: Adsorption kinetics parameters.

		q_{eexp}	First-order				Second-order			
			q_{ecal}	K_1	R^2	SSE	qe cal	K_2	R^2	SSE
T1	EC1	49.29	73.96	0.31	0.76	8.23	50.68	0.14	0.95	0.47
	EC2	49.65	50.81	0.12	0.98		49.94	0.10	0.96	
	EC3	48.95	49.77	0.10	0.92		48.88	0.04	0.88	
T2	EC1	41.90	50.93	0.21	0.85	3.02	40.30	0.13	0.95	1.02
	EC2	39.72	39.36	0.12	0.91		38.91	0.08	0.92	
	EC3	39.16	37.54	0.08	0.89		41.67	0.02	0.85	

A kinetic study of adsorption provides information regarding the adsorption mechanism and transfer mode between liquid and solid. Different models can be used to test the kinetics of adsorbent interaction. These models depend on the physical and chemical characteristics of the adsorbent. The linear plot of log (q_e - q_t) versus t for the pseudo-first-order model yields a line with a slope of ($-k_1$) and a y-intercept ($logq_e$). Thus, k_2 and q_e of the pseudo-second order model are calculated from the y-intercept and the slope of the linear graph of t/qt versus t, such that q_e = 1/slope and k_2 = slope²/y-intercept (Al-Anber & Al-Anber 2008). Table 5 presents the different adsorption kinetics parameters. Comparative analysis of the two kinetic models showed that adsorption on T1 and T2 mainly followed second-order kinetics. Furthermore, the pseudo-second-order model was distinguished by higher correlation coefficients (R^2) and lower SSE values than those obtained with the pseudo-first-order model. A remarkable agreement between the experimental adsorption capacity (q_{exp}) and theoretical capacity (q_{cal}) was also observed, confirming the predominance of the chemisorption mechanism (Mahmoudy et al. 2024). The rate constant K_2 decreases significantly with increasing concentration, reflecting notable differences in the availability and accessibility of the active sites (Dawood & Sen 2012). These results confirm that the pseudo-second-order model is better suited for the removal of COD on T1 and T2.

3.3.2. Adsorption Isotherms

The efficiency and adsorption capabilities of the two materials were assessed using the Langmuir and the Freundlich adsorption isotherms. The parameters of the two adsorption models and their associated correlation coefficients (R^2) are listed in Table 6. The high correlation coefficients obtained from the Freundlich model ($R^2 = 0.99$) for the two adsorbents indicate that adsorption preferentially occurs on multilayers on heterogeneous active sites with non-uniform energy levels (Orugba et al. 2024), providing a better representation of the observed phenomenon. Furthermore, this result was confirmed by the heterogeneity factor 1/n, whose value was between 0 and 1. According to these results, the maximum adsorption capacity of material T1 was q_{max} = 9.90 $mg.g^{-1}$, which was higher than that of material T2 (q_{max} = 6.49 $mg.g^{-1}$). This shows that T1 is the most suitable for high-load pollutant treatment. This synergy demonstrates how surface property optimization affects thermodynamic performance simultaneously.

Table 6: Langmuir and Freundlich isotherm constants and correlation coefficients.

	Langmuir			Freundlich		
	q_{max}	K_L	R^2	K_F	1/n	R^2
T1	9.90	0.10	0.92	0. 45	0.67	0.99
T2	6.49	0.15	0.95	0.50	0.45	0.99

To compare the results obtained in this study with those of previous studies, a comparative analysis of the data published in the literature was performed. Existing studies show considerable variability in the removal rates obtained by the adsorption of leachates. For example, Genethliou et al. (2021) reported a COD reduction rate of 23.68 % during the simultaneous adsorption of ammoniacal nitrogen, COD, and color from a sanitary leachate using natural zeolite. Similarly, Lim et al. (2016) achieved a 43 % reduction in COD by combining a sequential anaerobic reactor (ASBR) with a zeolite adsorption stage. These variations in performance mainly reflect differences in the nature and structure of the adsorbents and the physicochemical characteristics of the leachates (pH, organic load, ionic composition, and presence of metals). Despite this heterogeneity, the results obtained in this study are consistent with those typically observed for low-cost natural adsorbents. They also confirmed that the chemical complexity of leachates and the persistent presence of refractory organic compounds often necessitate the combination of several complementary processes, with adsorption representing a relevant but insufficient step on its own to meet strict regulatory standards.

3.4. Limits and Prospects

With a view to future development, this study is part of an approach aimed at establishing a predictive model based on kinetic and isothermal adsorption models in order to anticipate the performance of the materials studied under different operating conditions. Although the results obtained highlight promising adsorption potential, an in-depth evaluation of the long-term durability, regeneration, and reuse of natural adsorbents from local resources remains a limitation of this study and constitutes a priority area for research. In this regard, further investigations incorporating successive adsorption–desorption cycles, as well as a more detailed analysis of operating parameters (temperature, contact time, pollutant load), would optimize performance and provide a better understanding of the process's applicability on a larger scale. These future developments would help consolidate the relevance of these materials as environmentally friendly, economically accessible, and potentially renewable alternatives to commercial adsorbents for the treatment of contaminated water.

4. CONCLUSIONS

Their properties and technical feasibility generally guide the optimal management of leachates. In this study, two

adsorbent products based on limestone rocks and green shale derived from local Moroccan geological resources as natural adsorbents were characterized and evaluated for leachate treatment. The originality of this study lies in the use of abundant and inexpensive materials, combined with a kinetic and isothermal approach that makes it possible to describe and predict their adsorption behavior with respect to organic load. The results revealed that the material prepared from limestone has a higher efficiency than that prepared from green shale for most of the physicochemical parameters analyzed, which opens up concrete prospects for their integration into treatment schemes adapted to the economic and environmental constraints of Morocco and regions with similar contexts. The results of the kinetic and isotherm modeling of COD adsorption demonstrated that several parameters, including initial concentration, contact time, and temperature, influenced the adsorption process. The pseudo-second-order and the Freundlich models, respectively, best fit the kinetic modeling and adsorption isotherms. These data also demonstrate that limestone can serve as an economic and accessible material, justifying its use as a substitute for certain expensive adsorbents. This choice can significantly improve the quality of leachates and other industrial effluents. However, before large-scale application, further studies are needed, including assessments of the regeneration and durability of adsorbents over multiple cycles and pilot-scale validation. These developments will confirm the technical feasibility and optimize the integration of these materials into sustainable and economically viable leachate treatment systems for the future.

5. ACKNOWLEDGMENTS

Special thanks to the Fez city-controlled landfill and the staff of the USMBA's Innovation Center of Fez for their kindness and commitment.

6. REFERENCES

Abdel-Shafy, H.I., Ibrahim, A.M., Al-Sulaiman, A.M. and Okasha, R.A., 2024. Landfill leachate: sources, nature, organic composition, and treatment: an environmental overview. *Ain Shams Engineering Journal*, 15(1), pp.102293. [DOI]

Achak, M., Hafidi, A., Mandi, L. and Ouazzani, N., 2014. Removal of phenolic compounds from olive mill wastewater by adsorption onto wheat bran. *Desalination and Water Treatment*, 52(13-15), pp.2875-2885. [DOI]

Ahamad, Z. and Nasar, A., 2024. Polypyrrole-decorated bentonite magnetic nanocomposite: a green approach for adsorption of anionic methyl orange and cationic crystal violet dyes from contaminated water. *Environmental Research*, 247, pp.118193. [DOI]

Ahouach, Y., Baali, A., Boushaba, A., Hakam, O., Azennoud, K., Lyazidi, A. and Chen, T.W., 2023. Impact of the controlled dump of fez city (Morocco): evaluation of metallic trace elements contamination in the sediments. *Water*, 15(6), pp.1209. [DOI]

Al-Anber, M. and Al-Anber, Z.A., 2008. Utilization of natural zeolite as ion-exchange and sorbent material in the removal of iron. *Desalination*, 225(1-3), pp.70-81. [DOI]

Aljabarin, N., 2023. Chemical adsorption of iron ions from drinking water using Jordanian zeolitic tuff. *Desalination and Water Treatment*, 281, pp.196-203. [DOI]

Aluko, O.O. and Sridhar, M.K., 2013. Evaluation of leachate treatment by trickling filter and sequencing batch reactor processes in Ibadan, Nigeria. *Waste Management Research*, 31(7), pp.700-705. [DOI]

Al-Yaqout, A. and Hamoda, M.F., 2020. Long-term temporal variations in characteristics of leachates from a closed landfill in an arid region. *Water, Air, and Soil Pollution*, 231(6), pp.319. [DOI]

Aziz, H.A., Othman, N., Yusuff, M.S., Basri, D.R.H., Ashaari, F.A.H., Adlan, M.N. and Perwira, M., 2001. Removal of copper from water using limestone filtration technique: determination of mechanism of removal. *Environment International*, 26(5-6), pp.395-399. [DOI]

Aziz, H.A., Yusoff, M.S., Adlan, M.N., Adnan, N.H. and Alias, S., 2004. Physico-chemical removal of iron from semi-aerobic landfill leachate by limestone filter. *Waste Management*, 24(4), pp.353-358. [DOI]

Benaddi, R., Ferkan, Y., Bouriqi, A. and Ouazzani, N., 2022. Impact of landfill leachate on groundwater quality–a comparison between three different landfills in Morocco. *Journal of Ecological Engineering*, 23(11), pp.89-94. [DOI]

Chen, D.M.C., Bodirsky, B.L., Krueger, T., Mishra, A. and Popp, A., 2020. The world's growing municipal solid waste: trends and impacts. *Environmental Research Letters*, 15(7), pp.074021. [DOI]

Daniel, A.N., Ekeleme, I.K., Onuigbo, C.M., Ikpeazu, V.O. and Obiekezie, S.O., 2021. Review on effect of dumpsite leachate to the environmental and public health implication. *GSC Advanced Research and Reviews*, 7(2), pp.51-60. [DOI]

Davarnejad, R., Afshar, S. and Etehadfar, P., 2020. Activated carbon blended with grape stalks powder: properties modification and its application in a dye adsorption. *Arabian Journal of Chemistry*, 13(5), pp.5463-5473. [DOI]

Dawood, S. and Sen, T.K., 2012. Removal of anionic dye Congo red from aqueous solution by raw pine and acid-treated pine cone powder as adsorbent: equilibrium, thermodynamic, kinetics, mechanism and process design. *Water Research*, 46(6), pp.1933-1946. [DOI]

El Jalil, M.H., Elkrauni, H., Khamar, M., Bouyahya, A., Elhamri, H., Cherkaoui, E. and Nounah, A., 2020. Physicochemical characterization of leachates produced in the Rabat-Salé-Kénitra Region landfill technical center and monitoring of their treatment by aeration and reverse osmosis. In: *E3S Web of Conferences*, 150, pp.02013. [DOI]

El Khomri, M., El Messaoudi, N., Dbik, A., Bentahar, S. and Lacherai, A., 2020. Efficient adsorbent derived from Argania Spinosa for the adsorption of cationic dye: kinetics, mechanism, isotherm and thermodynamic study. *Surfaces and Interfaces*, 20, pp.100601. [DOI]

El-Saadony, M.T., Saad, A.M., El-Wafai, N.A., Abou-Aly, H.E., Salem, H.M., Soliman, S.M. and AbuQamar, S.F., 2023. Hazardous wastes and management strategies of landfill leachates: a comprehensive review. *Environmental Technology and Innovation*, 31, pp.103150. [DOI]

Fayoud, N., Younssi, S.A., Tahiri, S. and Albizane, A., 2015. Kinetic and thermodynamic study of the adsorption of methylene blue on wood ashes. *Journal of Materials and Environmental Science*, 6(11), pp.3295-3306.

Foo, K.Y. and Hameed, B.H., 2010. An overview of dye removal via activated carbon adsorption process. *Desalination and Water Treatment*, 19(1-3), pp.255-274. [DOI]

Foul, A.A., Aziz, H.A., Isa, M.H. and Hung, Y.T., 2009. Primary treatment of anaerobic landfill leachate using activated carbon and limestone: batch and column studies. *International Journal of Environment and Waste Management*, 4(3-4), pp.282-298. [DOI]

Genethliou, C., Triantaphyllidou, I.E., Giannakis, D., Papayianni, M., Sygellou, L., Tekerlekopoulou, A.G. and Vayenas, D.V., 2021. Simultaneous removal of ammonium nitrogen, dissolved chemical oxygen demand and color from sanitary landfill leachate using natural zeolite. *Journal of Hazardous Materials*, 406, pp.124679. [DOI]

Gupta, V.K., Carrott, P.J.M., Ribeiro Carrott, M.M.L. and Suhas, 2009. Low-cost adsorbents: growing approach to wastewater treatment – a review. *Critical Reviews in Environmental Science and Technology*, 39(10), pp.783-842. [DOI]

Gutiérrez-Mosquera, L.F., Arias-Giraldo, S. and Zuluaga-Meza, A., 2022. Landfill leachate treatment using hydrodynamic cavitation: exploratory evaluation. *Heliyon*, 8(3), pp.e09019. [DOI]

Halim, A.A., Aziz, H.A., Johari, M.A.M. and Ariffin, K.S., 2010. Comparison study of ammonia and COD adsorption on zeolite, activated carbon and composite materials in landfill leachate treatment. *Desalination*, 262(1-3), pp.31-35. [DOI]

Hernández-García, A., Velásquez-Orta, S.B., Novelo, E., Yáñez-Noguez, I., Monje-Ramírez, I. and Ledesma, M.T.O., 2019. Wastewater-leachate treatment by microalgae: biomass, carbohydrate and lipid production. *Ecotoxicology and Environmental Safety*, 174, pp.435-444. [DOI]

Hussain, S.T. and Ali, S.A.K., 2021. Removal of heavy metal by ion exchange using bentonite clay. *Journal of Ecological Engineering*, 22(1), pp.104-111.

Kjeldsen, P., Barlaz, M.A., Rooker, A.P., Baun, A., Ledin, A. and Christensen, T.H., 2002. Present and long-term composition of MSW landfill leachate: a review. *Critical Reviews in Environmental Science and Technology*, 32(4), pp.297-336. [DOI]

Kordala, N. and Wyszkowski, M., 2024. Zeolite properties, methods of synthesis, and selected applications. *Molecules*, 29(5), pp.1069. [DOI]

Lim, C.K., Seow, T.W., Neoh, C.H., Md Nor, M.H., Ibrahim, Z., Ware, I. and Mat Sarip, S.H., 2016. Treatment of landfill leachate using ASBR combined with zeolite adsorption technology. *3 Biotech*, 6, pp.195. [DOI]

Mahmoudy, G., Dabagh, A., El-Habacha, M., Lagdali, S., Assouani, A., Soulaiman, I. and Zerbet, M., 2024. Preparation and characterization of biomaterial for phosphate ion removal: kinetics, isotherms and thermodynamics studies. *Desalination and Water Treatment*, 317, pp.100062. [DOI]

Mandal, P., Dubey, B.K. and Gupta, A.K., 2017. Review on landfill leachate treatment by electrochemical oxidation: drawbacks, challenges and future scope. *Waste Management*, 69, pp.250-273. [DOI]

Merzouki, H., Hanine, H., Lekhlif, B., Latrache, L., Mandi, L. and Sinan, M., 2015. Physicochemical characterization of leachate discharge from Fkih Ben Salah, Morocco. *Journal of Materials and Environmental Science*, 6(5), pp.1354-1363.

Miao, L., Yang, G., Tao, T. and Peng, Y., 2019. Recent advances in nitrogen removal from landfill leachate using biological treatments – a review. *Journal of Environmental Management*, 235, pp.178-185. [DOI]

Mor, S. and Ravindra, K., 2023. Municipal solid waste landfills in lower- and middle-income countries: environmental impacts, challenges and sustainable management practices. *Process Safety and Environmental Protection*, 174, pp.510-530. [DOI]

Mor, S., Negi, P. and Khaiwal, R., 2018. Assessment of groundwater pollution by landfills in India using leachate pollution index and estimation of error. *Environmental Nanotechnology, Monitoring and Management*, 10, pp.467-476. [DOI]

Njoku, P.O., Edokpayi, J.N. and Odiyo, J.O., 2019. Health and environmental risks of residents living close to a landfill: a case study of Thohoyandou Landfill, Limpopo Province, South Africa. *International Journal of Environmental Research and Public Health*, 16(12), pp.2125. [DOI]

Nourmoradi, H., Avazpour, M., Ghasemian, N., Heidari, M., Moradnejadi, K., Khodarahmi, F. and Moghadam, F.M., 2016. Surfactant modified montmorillonite as a low cost adsorbent for 4-chlorophenol: equilibrium, kinetic and thermodynamic study. *Journal of the Taiwan Institute of Chemical Engineers*, 59, pp.244-251. [DOI]

Orugba, H.O., Sinebe, J.E., Chukwuneke, J.L., Okoro, V.I., Enyi, C.L. and Ani, O.I., 2024. Adsorption of cadmium from wastewater with activated carbons derived from pig fur biowaste: a comparative study of in-situ and ex-situ activation routes. *Heliyon*, 10(18), pp.e37768. [DOI]

Renou, S., Givaudan, J.G., Poulain, S., Dirassouyan, F. and Moulin, P., 2008. Landfill leachate treatment: review and opportunity. *Journal of Hazardous Materials*, 150(3), pp.468-493. [DOI]

Rodier, J., Bazin, C., Broutin, J.P., Chambon, P., Champsaur, H. and Rodi, L., 2009. *Water Analysis*, 9th ed. Dunod, Paris, pp.1579.

Shadi, A.M.H., Kamaruddin, M.A., Niza, N.M., Emmanuela, M.I., Shaah, M.A., Yusoff, M.S. and Allafi, F.A., 2020. Characterization of stabilized leachate and evaluation of LPI from sanitary landfill in Penang, Malaysia. *Desalination and Water Treatment*, 189, pp.152-164. [DOI]

Sharma, A., Grewal, A.S., Sharma, D. and Srivastav, A.L., 2023. Heavy metal contamination in water: consequences on human health and environment. In: *Metals in Water*, Elsevier, pp.39-52. [DOI]

Sun, S., Ren, J., Liu, J., Rong, L., Wang, H., Xiao, Y. and Su, X., 2022. Pyrite-activated persulfate oxidation and biological denitrification for effluent of biological landfill leachate treatment system. *Journal of Environmental Management*, 304, pp.114290. [DOI]

Wang, J. and Qiao, Z., 2024. A comprehensive review of landfill leachate treatment technologies. *Frontiers in Environmental Science*, 12, pp.1439128. [DOI]

Zand, A.D. and Abyaneh, M.R., 2020. Adsorption of lead, manganese, and copper onto biochar in landfill leachate: implication of non-linear regression analysis. *Sustainable Environment Research*, 30(1), pp.18. [DOI]

Zineb, H., Latifa, M., Salah, S. and Laila, S., 2020. Removal of pollution by intensive aeration technology for landfill leachate treatment. *Journal of Health and Pollution*, 10(28), pp.201212. [DOI]

Nature Environment and Pollution Technology
An International Quarterly Scientific Journal

p-ISSN: 0972-6268
(Print copies up to 2016)
e-ISSN: 2395-3454

Vol. 25 | No. 3 | Article ID B4398 | 2026

Original Research Paper

https://doi.org/10.46488/NEPT.2026.v25i03.B4398

Open Access Journal

ANN-Driven Optimization of VOC Adsorption on Activated Carbon with Thermal Breakthrough Forecasting and IoT-Based Real-Time Monitoring

Subramanian Kavitha[1]†, Subramani Umamaheswari[2], Venkatesh Babu Samikannu[3] and Surendran Ganesan[4]
[1]Department of Chemical Engineering, Hindusthan College of Engineering and Technology, Coimbatore, T.N., India
[2]Department of Science and Humanities, Dhaanish Ahmed Institute of Technology, Coimbatore, T.N., India
[3]Department of Petroleum Engineering, JCT College of Engineering and Technology, Coimbatore, India
[4]Department of Chemical Engineering, KPR Institute of Engineering and Technology, Coimbatore, T.N., India
†Corresponding author: Kavitha Subramanian; kavitha212418@gmail.com

Abbreviation: Nat. Env. & Poll. Technol.
Website: www.neptjournal.com

Received: 20-09-2025
Revised: 03-12-2025
Accepted: 14-12-2025

Key Words:

VOC adsorption
Activated carbon
Artificial Neural Network (ANN)
Breakthrough curve prediction
IoT-based monitoring
Air pollution control

Citation for the Paper:

Subramanian, K., Subramani, U., Venkatesh Babu, S. and Surendran, G., 2026. ANN-driven optimization of VOC adsorption on activated carbon with thermal breakthrough forecasting and IoT-based real-time monitoring. *Nature Environment and Pollution Technology*, 25(3), B4398. https://[DOI].org/10.46488/NEPT.2026.v25i03.B4398

Note: From 2025, the journal has adopted the use of Article IDs in citations instead of traditional consecutive page numbers. Each article is now given individual page ranges starting from page 1.

Copyright: © 2026 by the authors
Licensee: Technoscience Publications
This article is an open access article distributed under the terms and conditions of the Creative Commons Attribution (CC BY) license (https://creativecommons.org/licenses/by/4.0/).

ABSTRACT

Volatile Organic Compounds (VOCs) have become one of the drivers of environmental deterioration and occupational hazards, and the issue requires competent and clever adsorption methods for their elimination. This study proposes a comprehensive experimental, computational, and IoT-based system that maximizes VOCs adsorption by activated carbon. A packed bed adsorption column was constructed and equipped with two MQ-138 and DHT22 sensors, which could be directly tracked in real time using a NodeMCU-ThingSpeak dashboard. During the experiments, the efficiency of VOC removal was lower at higher inlet concentrations (92.3% to 76.1% at 100 ppm to 300 ppm, respectively) and higher at the optimized flow rate (74.5% - 89.8% at 3.0 to 1.5 $L.min^{-1}$, respectively). The efficiency was lower at high relative humidity because of competitive adsorption, and higher bed temperatures (up to 45°C) slightly prolonged the breakthrough time. The model used was a 4-8-1 ANN (Artificial Neural Network) whose training was carried out using the Levenberg-Marquardt algorithm, which had a high predictive accuracy (R^2=0.987, Root Mean Square Error (RMSE) =1.82), and the experimental value was close to the computed values across a range of inputs. The 3D surface mapping of the ANN model exhibited an ideal area of interaction between the VOC concentration and flow rate. In addition, all IoT delays were less than 1.5 s, and the sensor offset was less than ±5 ppm and ±0.5°C, thus confirming the readiness of the system deployment. These outcomes confirm that it is possible to implement intelligent, responsive VOC mitigation tools that are informed by machine learning and integrated with IoT to manage air quality in the industry.

1. INTRODUCTION

An important type of atmospheric pollutant is the volatile organic compounds (VOCs) that bring serious environmental and social health problems to people worldwide. They have been released through various industrial activities such as petrochemical refining, paint, pharmaceuticals, printing, and chemical processing units. The World Health Organization (WHO) reveals that more than 80 % of urban dwellers have been subjected to concentrations of VOCs that go beyond safe limits of air quality. More than 180 VOCs are identified as hazardous air pollutants (HAPs) by the U.S. Environmental Protection Agency (EPA), and industrialized countries alone are the source of more than 11 million metric tons of VOC emissions every year. High-paced urbanization and the growth of industrial infrastructure in Asia have also led to the aggravation of the issue; e.g., in 2023, over 2.5 million tons of toluene were released annually in China alone (Lee et al. 2023a). The compounds not only result in the formation of secondary pollutants such as tropospheric ozone and fine Particulate Matter (PM2.5) but also act directly in respiratory and neurological conditions, e.g., chronic bronchitis, asthma, and, in the worst case, carcinogenic consequences(Roegiers & Denys 2021). Effective

removal technologies to deal with VOC pollution have become a hot issue in sustainable chemical engineering and environmental management practices all over the world (Lee et al. 2023b).

Some of the technologies used to abate VOCs include condensation, absorption, biofiltration, thermal oxidation, and membrane separation, but adsorption using activated carbon is one of the most popular ones because it has a high surface area (generally greater than 900 $m^2.g^{-1}$), wide porous, and pore volume (0.4 to 0.6 $cm^3.g^{-1}$), chemical stability, and can also be utilized several times already (Chauhan & Sahoo 2024). VOCs like benzene, toluene, xylene, formaldehyde, and acetone have been removed successfully with a removal efficiency of above 95% in optimized conditions. A meta-analysis of the published studies on VOC adsorption between 2015 and 2023 showed that activated carbon-based types fixed bed systems still displayed the best average removal efficiency (92.3%) relative to other adsorbents like zeolites (87.4%) and metal-organic frameworks (84.1%) (Choi et al. 2023). Nevertheless, breakthrough performance is very sensitive to operational parameters, given especially the inlet VOC concentration, flow rate, the relative humidity, and bed temperature. As an example, a previous study discovered that increasing the inlet toluene concentration to 100 ppm and 300 ppm led to a 47% reduction of breakthrough time, and increasing flow rate by 200 and 500 $L.m^{-1}$ produced a 30-% decline in adsorption capacity. What is most significant is the fact that adsorption of VOCs is exothermic, resulting in thermal build-up in the adsorbent bed, and that this build-up may, in many cases, hasten saturation, poor work of adsorbents, and generate thermal stress. A small bed temperature increase of 810°C might cut the breakthrough period by as much as 25%, as a 2022 pilot-scale study carried out with granular activated carbon exemplifies (Ushiki et al. 2022).

Taking into account these nonlinear and multi-factorial interactions within the VOC adsorption systems, traditional modeling tools like the Thomas model, Yoon-Nelson or Bohart-Adams equations tend to be inadequate in model interpretative power and flexibility (Hou et al. 2021). This has also seen a trend towards a data-driven modeling of the breakthrough dynamics, adsorption capacity, and optimization of operations (especially artificial neural networks (ANNs)). ANNs provide the flexibility to use several inputs and deal with multiple nonlinear characteristics, as well as learning capability using supervised training (Tzanakopoulou et al. 2023). An ANN model on 300 experimental runs could predict the breakthrough time of benzene adsorption with a correlation coefficient (R2) of 0.987 and a Root Mean Square Error (RMSE) of 4.3 min, and found better performance than traditional models of kinetics. On the same note, a study found that VOC removal modeling accuracy was enhanced by 12% when the use of ANN was employed over the empirical modeling technique applied in mixed VOC environments (Zhao et al. 2024). A study employed a feedforward backpropagation ANN to forecast formaldehyde performance in adsorption at different temperatures and humidity in use, and only 150 training examples could deliver an accuracy of 95.6% in prediction (Saadattalab et al. 2023). Although such encouraging findings have been achieved, the majority of ANN practices in VOC adsorption are still limited to off-line data and have not provided the capability of feedback integration and verification in real-time, continuously changing process conditions (Ligotski et al. 2021).

At the same time, the emergence of the Internet of Things (IoT) in the area of chemical and environmental engineering has provided new opportunities to monitor and control the process and carry out predictive diagnostics in real time. As inexpensive nodes such as NodeMCU (ESP8266), Raspberry Pi, and Arduino Uno became available, scientists implemented gas sensors (e.g., MQ series), temperature-humidity sensors (e.g., DHT11/DHT22), and wireless data transmission modules to create chemical monitoring smart systems. As an illustration, a paper in Sensors and Actuators B managed to implement an IoT-based sensing device to measure and quantify concentrations of VOC in an indoor facility with a response time <1s and a user error probability of 93% of the overall data collection process in real-time. The other coupling area was in the packed bed reactor, which utilized monitoring of flow and temperature data in real-time to report control of reaction heat generation with 15% better safety response cycle time in the process of excursion (Zhao et al. 2024). Nevertheless, further research is lacking in terms of integrating IoT in VOC adsorption systems, especially when you consider thermal profiles and injecting them into adaptive ANN systems. The vast majority of currently available systems only keep records, allowing a human being to interpret them in order to provide fairly little predictability, not to mention autonomous optimization (Kim et al. 2022).

This is despite the developments in seemingly detached fields such as ANN modelling and sensing using the IoT, there is a staggering knowledge gap between the two advances in the application towards the adsorption of VOCs (Dong et al. 2024). Very little research has been done to merge the ANN model's predictive ability with the real-time sensor measurements in an IoT setup to actively predict and optimize the on-demand performance of thermal breakthroughs (Tahara et al. 2023). Also, the effect of heat during processing is not taken seriously, although its statistical occurrence is known to affect adsorption kinetics

and mass transfer regions. There are no existing well-formed frameworks that combine sensor feedback, thermal analysis, and machine learning prediction into one to provide real-time predictions of VOCs removal performance in response to dynamic VOC removal processes in an industrial environment (Kim et al. 2023). Also, it does not have any generalized models of multi-interdependent variables like humidity, temperature, concentration, and flow rate at the same time, especially in a real-time adaptive model. The drawbacks impair the implementation of intelligent VOC mitigation technologies in scalable, automated, and sustainable environments of chemical processing (Lashaki et al. 2023).

With a view to eliminating these deadly gaps, this study devises a fully integrated solution in which optimization through artificial neural networks (ANN) controls and an IoT-based real-time copter-activated carbon VOC adsorption model in a packed bed column. The focus of this investigation is to design an ANN model that would be predictive and capable of estimating breakthrough time as well as removal efficiency when subjected to variable input conditions such as inlet VOC concentration, bed temperature, relative humidity, and flow rate. Simultaneously, IoT architecture with the use of MQ-138 gas sensors, DHT22 Temperature-Humidity Modules, and NodeMCU microcontrollers is also established to monitor continuously and transmit real-time data to a cloud dashboard available to view and analyze. Thermal performance of the adsorption bed is recorded and tied with the ANN outputs to determine the system accuracy and reactiveness under dynamic circumstances. This research is the first one to take both approaches, Static modelling and real-time sensing, and integrate them to constitute a smart adsorption system that can make predictive decisions as well as adaptive control. Such an outcome will provide a scalable and intelligent solution to regulating VOC pollution in chemical industries that are modern in terms of the type of industry that it belongs to and environmental sustainability objectives.

2. MATERIALS AND METHODS

2.1. Materials Used

Toluene ($C_6H_5CH_3$) was chosen in this study to represent volatile organic compounds (VOC) because of its wide presence in industrial releases and well-characterized adsorptive behavior. Analytical grade toluene (>99.59 in purity) was purchased from Merck Chemicals and used as provided without purification. Moderate volatility (boiling point: 110.6°C), high vapor pressure (28.4 mmHg at 25°C), and high adsorption behavior on carbonaceous surfaces also favor the incorporation of toluene as a model compound in gas-phase adsorption studies. This adsorbent was commercial GAC of granular form procured from Sigma-Aldrich, which was activated in the form of a coconut shell precursor by steam activation. This particular grade was identified because of its large surface area, well-developed porosity, and proven capability to remove aromatic hydrocarbons. The granular activated carbon (GAC) was sieved before use to an average grain size of 1.0-2.0 mm and washed with deionized water to remove the fines and surface impurities. The solid was then dried in a hot-air oven at 105 °C for 24 h, after which it was packed into airtight containers to avoid any interference by moisture. Table 1 lists the main physicochemical characteristics of the adsorbent.

An IoT-based sensing system was designed to continuously monitor the thermal and gas-phase parameters inside the adsorption column. The main types of sensors used were the MQ-138 semiconductor gas sensor and the DHT22 digital sensor. The MQ-138 is dedicated to VOCs detection, and its sensitivity range is permissible for toluene, formaldehyde, ammonia, and other organic vapors at concentrations of 10-1000 ppm. The temperature and relative humidity were measured using a DHT22, which exhibited high accuracy and stability under dynamic flow conditions. These sensors generated data that were engaged in a Node MCU (ESP8266) microcontroller unit using the analog and digital input pins and published to a cloud dashboard in real time with the support of the Blynk IoT platform. The inlet VOC-air mixture was regulated using a Mass Flow Controller (MFC) to ensure uniformity in the delivery of experimental flow rates of 200-400 $L.min^{-1}$. The sensors and controller used in this study have the specifications listed in Table 2.

2.2. Experimental Setup

The experimental research was conducted in a vertical packed-bed adsorption column to assess the thermal and adsorbent activity of activated carbon under controlled VOC

Table 1: Physicochemical properties of activated carbon used.

Property	Value	Method/Source
Material Origin	Coconut Shell–Derived GAC	Supplier: Sigma-Aldrich
Particle Size Range	1.0–2.0 mm	ASTM E11
BET Surface Area	960 $m^2.g^{-1}$	N_2 Adsorption (BET Method)
Total Pore Volume	0.48 $cm^3.g^{-1}$	BJH Analysis
Micropore Volume	0.32 $cm^3.g^{-1}$	t-Plot Method
Bulk Density	0.53 $g.cm^{3-}$	ASTM D2854
Moisture Content (as received)	3.2 wt%	Oven Drying at 105°C
pH of Aqueous Suspension	7.1	ASTM D3838

Table 2: Sensor and flow control instrument specifications.

Component	Model	Parameter Measured	Range	Accuracy	Interface
VOC Gas Sensor	MQ-138	VOC Concentration (Toluene)	10–1000 ppm	± 5 % (at °25C, 65 % RH)	Analog
Temperature & RH Sensor	DHT22	Temperature, Relative Humidity	Temp.: –40 to 80 °C; RH: 0–100%	± 0.5 °C; ± 2 % RH	Digital (1-wire)
Microcontroller Unit	NodeMCU (ESP8266)	IoT Data Processing	Wi-Fi (2.4 GHz), 10-bit ADC	–	Cloud (Blynk)
Flow Controller	Aalborg GFC-17	Air/VOC Flowrate	0–500 $mL.min^{-1}$	± 1.5 % F.S.	Manual + Analog

loading conditions. The column was made of borosilicate glass to withstand chemical attack and provide a clear optical inspection of the flow behavior. The diameter of the internal column was 2.5 cm, and the top length of the column was 50 cm, which provided sufficient space to accommodate the packing material and insert the sensor. The packed section (active bed height) was stabilized at 20 cm using pre-weighed granular activated carbon (GAC) of 1.0-2.0 mm particle size. A stainless-steel mesh was attached to the top and bottom of the packed portion to retain the adsorbent in position and provide an even distribution of gases. A polycyclic aromatic compound (toluene) was introduced into the airflow by injecting a controlled amount of liquid toluene into the air chamber using a gas-tight syringe, allowing the analytical-grade toluene vapor to mix with the compressed air under steady-flow conditions through a threaded connection. The mass flow controller used was an Aalborg GFC-17, which ensured fine control within the range of 200-400 $L.min^{-1}$. Under the test conditions, the concentration of toluene at the inlet ranged between 100 and 300 ppm. The inlet stream relative humidity was controlled using a humidity chamber with saturated salt solutions, whereas the temperature was regulated using a heating jacket wrapped around the column and measured using a DHT22 sensor module. The concentration of VOC at the outlet was recorded using an MQ-138 sensor mounted at the outlet of the column and connected to a NodeMCU (ESP8266) microcontroller. The temperature and relative humidity of the bed were also established using extra DHT22 sensors at two vertical points inside the packed bed (top and middle). All sensor information was relayed in real-time to a cloud-based dashboard (Blynk platform) via Wi-Fi to monitor and store information in real-time. The data gathering was set so that the data were recorded every 10 s. As shown in Fig. 1, the entire schematic of the experimental apparatus includes the adsorption column, VOC air mixing module, flow control system, sensors, and IoT integration platform. This setup allowed real-time tracking of adsorption dynamics

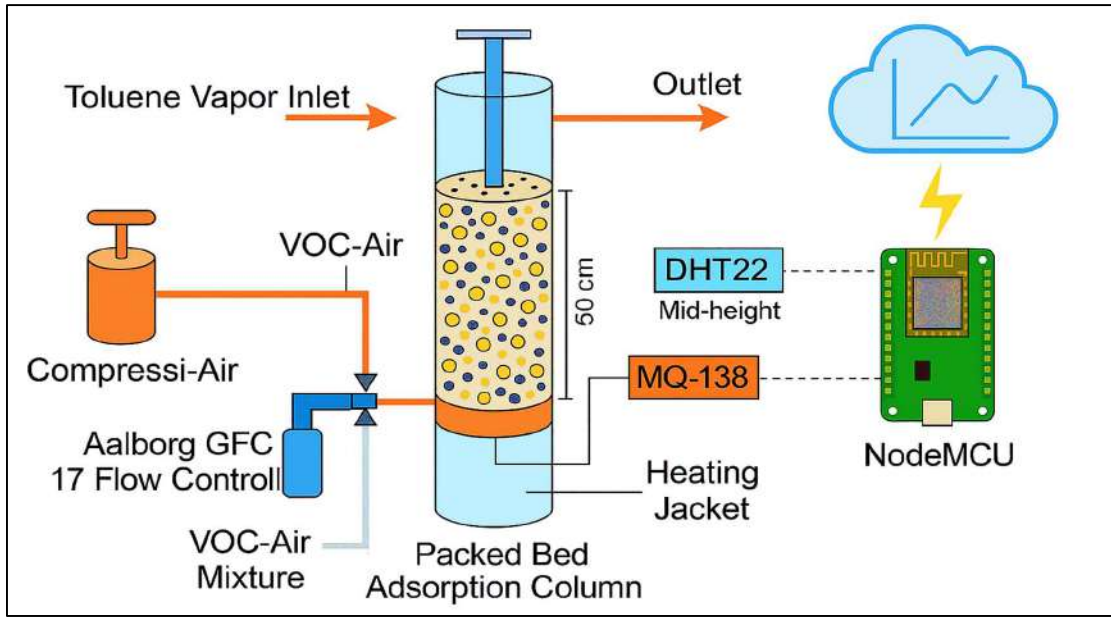


Fig. 1: Experimental setup schematic.

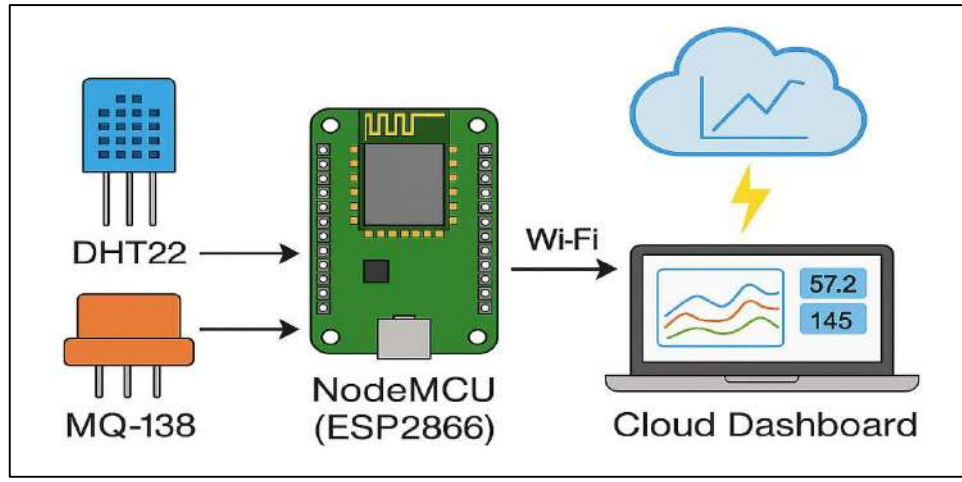


Fig. 2: IoT architecture layout.

with the modelling aim assisted by time-synchronized data collection.

2.3. IoT Architecture and Monitoring

To provide total and unattended surveillance of the adsorption system, an IoT-based architecture was applied, and a NodeMCU ESP8266 microcontroller was selected as the processing and communication unit. This system was the main element that interacted with VOC and temperature-humidity sensors, collected real-time data, and sent it via wireless connectivity to a visually driven operations platform hosted in the cloud to view data in real time and optimize system performance. The selected board was NodeMCU because it has a small form factor, low power consumption, and a Wi-Fi module with a transmission frequency of 2.4 GHz. A semiconductor gas sensor of type MQ-138 was used to measure the VOC residence at a high sensitivity to toluene and other aromatic hydrocarbons of 10-1000 ppm. The temperature and relative humidity data were obtained using a DHT22 sensor, which had a high resolution (±0.5°C and ±2% RH) and elasticity to the dynamic flow demands. Both sensors were directly connected to the analog and digital GPIO pins of the NodeMCU. Sensor values were polled every 10 s with a timed interrupt routine, and the timed values were sent to the ThingSpeak cloud dashboard via HTTP POST requests with the utility libraries WiFi Client and ThingSpeak. This facilitated real-time streaming and a record of all process variables, such as bed temperature, ambient humidity, and VOC levels. The system contained error-detection systems to solve some data dropouts or interruptions of transmission and simply reconnect to the network. A 5V USB power supply was essential to guarantee reliable operation with decoupling capacitors and pull-up resistors on the data lines. The NodeMCU was placed on a soldered prototype PCB to make it stable, and the PCB was placed in a 3D-printed casing adjacent to the adsorption column. The system was tested and validated with concentrations of known gases and under different environmental influences before the experiments. A general diagram of the IoT architecture is presented in Fig. 2, which shows the signal direction within the system and the flow of information to the cloud based on the Wi-Fi interface and real-time dashboard screen.

2.4. Data Acquisition and Preprocessing

A data acquisition strategy was prepared to undertake simultaneous and time-synchronized data acquisition of the essential process variables needed to model the VOC adsorption system. The main parameters that were captured were the bed temperature (25 ± 2°C), relative humidity (30–80%), and VOC concentration, all of which were captured by the DHT22 and MQ-138 sensors, respectively. The sensors were connected to a NodeMCU (ESP8266) microcontroller programmed using the Arduino IDE and C/C++ libraries. The sampling was done at 10-second intervals to allow the breakthrough profile to be recorded, although a longer period could cause redundancy of data and waste of bandwidth. All data points recorded were time-stamped with the internal real-time clock of the NodeMCU module. HTTP POST requests were used to upload the sensor data through Wi-Fi to the ThingSpeak cloud platform. ThingSpeak was selected because of its compatibility with ESP-based Internet of Things systems based on time-series data logging, visualization, and exporting capabilities. All information was stored in channel-specific fields and could be accessed using secured API keys. The cloud dashboard offers real-time visualization of the dynamics of the breakthrough and environmental conditions, which allows real-time decisions and a remote view of the state of play. A well-organized preprocessing procedure was utilized before training the

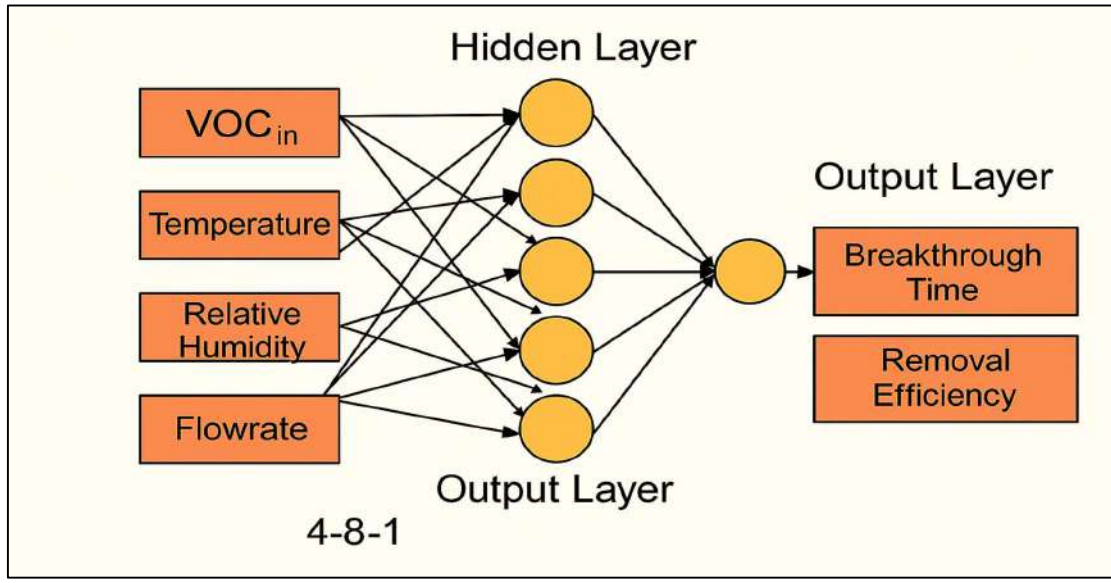


Fig. 3: ANN block diagram.

ANN models using the data. In the initial step, the raw data collected at ThingSpeak was processed. Subsequently, a data cleaning procedure was used to process the anomaly, such as the sensor error, null values, or some outliers caused by lightning or wireless drops. In cases where the gap was more than three and less than 30 steps, the interpolation of missing values was performed using a linear technique; otherwise, the segment was discarded during the analysis. The outliers were determined using z-score thresholds, and a manual check was performed using the corresponding experimental log. After the cleaning process, the values of all the input variables were normalized to a range between 0 and 1 by applying the min-max normalization process according to Equation (1):

$$x_{\text{norm}} = \frac{x - x_{\min}}{x_{\max} - x_{\min}} \quad \ldots(1)$$

This was to normalize such that the input parameters, VOC concentration, temperature, and flow rate, gave an equally weighted contribution in the training of the ANN and prevented bias based on magnitudes. The same technique was used to normalize the target output parameters, which were breakthrough time (min) and removal efficiency (%), to ensure the same behavior during training. Such a systematized data collection and preprocessing pipeline was necessary to train the ANN model on clean, scaled, and robust data and the real-world behavior of VOC adsorption.

2.5. ANN Model Development

Four input variables, namely inlet VOC concentration (VOC_in, ppm), bed temperature (T,°C), relative humidity (RH, %), and flow rate (Q, mL.min^{-1}), were used to create the ANN model to predict the breakthrough time and removal efficiency of VOC adsorption onto activated carbon. These inputs were chosen because they play an important role in the dynamics of adsorption, as observed experimentally and provided in the previous literature. The two main products whose values were subjected to the model equation were breakthrough time (tb, min) and removal efficiency (%). The architecture of the ANN used in the present study was a feedforward backpropagation network, which had a tentative structure of 4-8-1, that is, four neurons in the input layer, eight neurons in a single hidden layer, and one neuron in the output layer. The hidden layer used the activation of the tangent sigmoid (tansig) to represent nonlinear relationships among input parameters. The output layer was based on a linear activation function (purelin) that maintained continuity in the numbers. The Levenberg–Marquardt (LM) algorithm (trainlm) was used to train the network. This algorithm is remarkable because it converges quickly and deals very well with noisy data; thus, empirical process modelling is well suited to LM. The goal of the training was to reduce the mean squared error (MSE) of the theoretical and real output values. The MSE can be defined in (2):

$$\text{MSE} = \frac{1}{N}\sum_{i=1}^{N}(y_i - \hat{y}_i)^2 \quad \ldots(2)$$

Where N is the number of samples, y_i is the experimentally measured output, and $\hat{y}_i$ is the ANN-predicted output.

LM training algorithm implements the modified Gauss-Newton technique to change the network weights on (3):

$$W_{\text{new}} = W_{\text{old}} - (J^T J + \mu I)^{-1} J^T \epsilon \quad \ldots(3)$$

Table 3: ANN architecture and hyperparameter configuration.

Parameter	Value
Input Variables	VOC_in, Temperature, Relative Humidity, Flowrate
Output Variables	Breakthrough Time, Removal Efficiency
Network Architecture	4-8-1 (Single Hidden Layer)
Hidden Layer Activation Function	Tangent Sigmoid (tansig)
Output Layer Activation Function	Linear (purelin)
Training Algorithm	Levenberg–Marquardt (trainlm)
Normalization Technique	Min–Max Scaling (0 to 1)
Loss Function	Mean Squared Error (MSE)
Early Stopping Criteria	Validation Error Plateau
Training/Validation/Testing Split	70%/15%/15%
Maximum Epochs	1000

Here, W denotes the weight vector, J is the Jacobian matrix of partial derivatives of the error vector with respect to weights, m is the damping factor (adaptively adjusted), I is the identity matrix, and $\in$ is the error vector.

This training was continued until either the validation error stabilized or 1000 epochs were reached. This was done using an early stopping mechanism, where the training stopped when the validation error failed to reduce in 10 iterations. To represent all levels of input, the dataset was randomly sampled into training (70%), validation (15%), and testing (15%) portions. Three performance indicators were used to identify the accuracy of the final model: the coefficient of determination (R^2), root mean squared error (RMSE), and mean absolute error (MAE). An overview of ANN structure and training parameters can be summarized in Table 3, and the ANN block diagram can be shown in Fig. 3.

2.6. Model Evaluation Metrics

The predictive performance of the developed ANN model was assessed using three statistical indicators: Root Mean Squared Error (RMSE), Mean Absolute Error (MAE), and Coefficient of Determination (R^2). These metrics quantify the deviation between the ANN-predicted outputs and the experimentally obtained values, thereby validating the model's capability to predict the breakthrough time and removal efficiency. The RMSE represents the square root of the average squared difference between the actual and predicted values. It is highly sensitive to outliers because larger errors are penalized more heavily. A lower RMSE value indicates better agreement between the predicted and experimental data.

$$\mathrm{RMSE} = \sqrt{\frac{1}{N}\sum_{i=1}^{N}(y_i - \hat{y}_i)^2} \quad \ldots(4)$$

The mean absolute error (MAE) measures the mean of the absolute errors between the actual and the predicted values.

$$\mathrm{MAE} = \frac{1}{N}\sum_{i=1}^{N}|y_i - \hat{y}_i| \quad \ldots(5)$$

Coefficient of Determination (R^2) is equal to the %age of variance of the dependent variable that can be predicted using the independent variables.

$$R^2 = 1 - \frac{\sum_{i=1}^{N}(y_i - \hat{y}_i)^2}{\sum_{i=1}^{N}(y_i - \bar{y})^2} \quad \ldots(6)$$

Where: y_i : Experimental (actual) value, $\hat{y}_i$: ANN-predicted value, $\bar{y}$: Mean of experimental values, N : Total number of samples. These metrics were calculated on the testing set in order to be able to confirm the generalization capability of this trained ANN. The combination of RMSE, MAE, and R 2 provides a complete answer to both the level of error and the statistical presence of correlation between the forecasted and actual values.

3. RESULTS AND DISCUSSION

3.1. VOC Breakthrough Curves under Varying Inlet Concentrations

The adsorption Process of the Packed bed column was then determined by analyzing the breakthrough behavior of toluene at three inlet concentrations: 100 ppm, 200 ppm, and 300 ppm. The breakthrough curves related to these are presented in Fig. 4, which is a graph of the concentration of the VOC at the outlet of the column against time. Each of the curves has the typical S-shaped appearance; it characterizes the startup lag phase, gradual increase in outlet concentration, as well as saturation of the adsorbent bed.

The breakthrough time decreased as the inlet concentration increased, as expected. When the concentration was 100 ppm, the breakthrough was marked at 102 min, the moment the outlet concentration became 5% of the inlet concentration. This was reduced to 78 and 54 min at 200 and 300 ppm, respectively, which showed that an inverse relationship existed between the adsorption time and the concentration of the inlet. This could be explained by the fact that the adsorption sites are more rapidly saturated at high pollutant loadings. As the partial pressure goes up, more mass transfers to the adsorbent surface, which increases the rate of approaching equilibrium. However, it has the additional effect of increasing the rate of filling of the micropores, thereby diminishing the effective lifetime of the adsorption bed. This is in accordance with the result reported, where it was found that the breakthrough was decreased on average by 40% when the inlet concentration of benzene was raised to 240 ppm in a coconut-shell-based activated

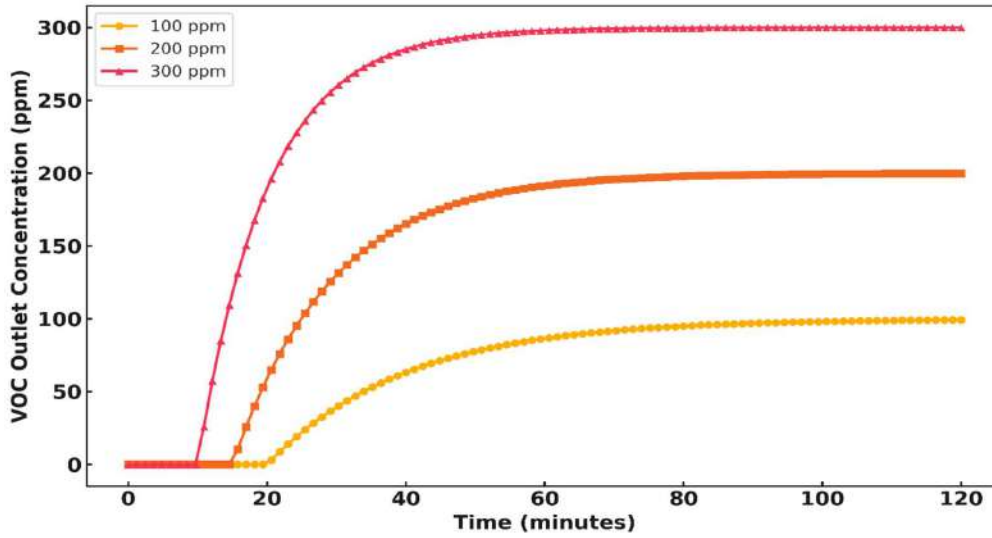


Fig. 4: VOC conc. vs time.

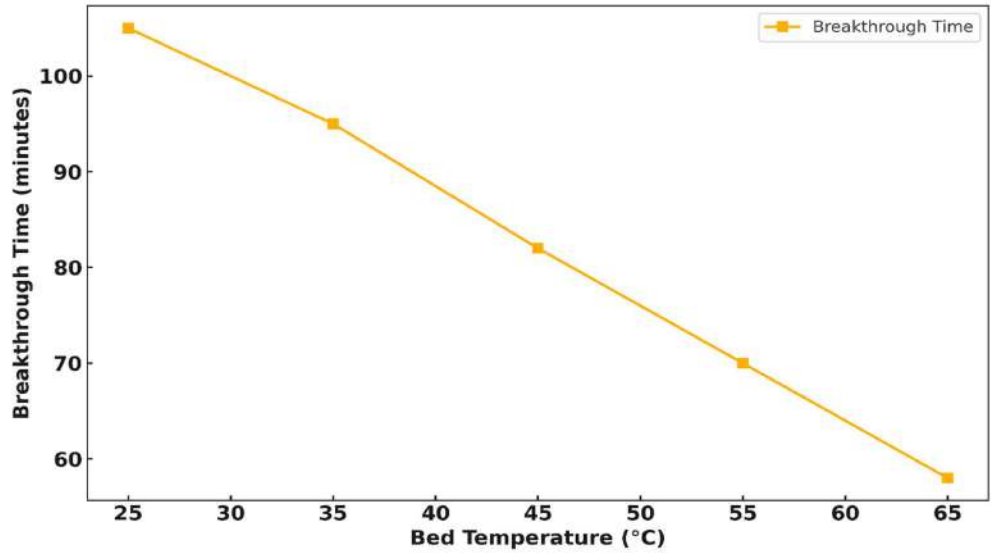


Fig. 5: Bed temperature vs. breakthrough time.

carbon system. Similarly, a linear reduction in the dynamic adsorption capacity of toluene was observed as a function of increasing inlet loading to the fixed-bed column, which compares well with the patterns presented (Sessa et al. 2022). In addition, the breakthrough curve at a higher concentration was steeper, indicating that the change in the mass transfer zone to saturation was more abrupt. This indicates that the mass transfer zone is under-resolved, which in a real system may become thermally destabilizing (Jurkiewicz et al. 2022). Following the hypothesis that exothermic interactions at the surface are boosted by an increase in adsorptive flux, the temperature elevation close to the column middle point was detected to increase by almost 3°C, as the inlet concentration was enhanced to 300 ppm, compared to 100 ppm.

3.2. Effect of Bed Temperature on Adsorption Capacity

The effectiveness of the bed temperature on the adsorption capability of toluene vapor was also determined by recording the breakthrough time at different temperatures (25°C-65°C). A negative correlation was evident between breakthrough time and bed temperature, as shown in Fig. 5. The system experienced a maximum breakthrough time of 105 min at a basal temperature of 25°C. Nevertheless, with the increase in temperature, the breakthrough time slowly

decreased to 95, 82, 70, and 58 min at 35, 45, 55, and 65°C, respectively. This trend highlights the issue of the thermal sensitivity of the adsorption mechanism and confirms that higher temperatures decrease the total adsorption capacity of activated carbon for VOCs. This behavior is consistent with the laws of basic physical adsorption, that is, is dictated mainly by weak van der Waals forces between adsorbate molecules and adsorbent surfaces. The interactions are exothermic, and as the temperature increases, thermal energy is added to the system, destabilizing the adsorbate–adsorbent bond and easing desorption. An increase in temperature causes the equilibrium to shift to the gas phase, which, in turn, reduces the adsorption capacity and time to breakthrough. Such thermodynamic action has been observed in a study that observed that in a fixed bed designed with mesoporous carbon, an increase in bed temperature led to a 38% reduction in toluene adsorption capacity at 30°C and 60°C. In addition, higher temperatures tend to increase the diffusion coefficients, thus increasing the rate of adsorption. Although increased temperatures may increase the initial diffusion rate of VOC molecules into the pores (<2 nm) inside the adsorbent, the cumulative residence time of the molecules inside the pore structure is decreased, excluding the molecules through premature saturation. This tendency was observed in the increased decline of the breakthrough time between the temperatures of 45 and 65°C, as shown in Fig. 5. The indication that the plotted line is not straight raises the possibility that the desorption effect prevails over the diffusion advantages past a temperature of 45°C. The thermal stability of an adsorbent is a crucial factor governing its long-term performance in VOC removal systems. Minor micropore degradation may occur in commercial activated carbon when exposed to temperatures above 60°C, progressively reducing its adsorption efficiency. This further underscores the importance of maintaining an optimal thermal operating window for these types of systems. The present observations highlight that maintaining the bed temperature within 40–45°C helps preserve a substantial portion of the breakthrough capacity, especially during long adsorption cycles.

Compared to previous studies, our findings correlate well with the thermogravimetric and breakthrough trends reported for similar carbonaceous adsorbents (de Andrade et al. 2021). Overall, the results strongly imply that the bed temperature is a paramount operational parameter in VOC adsorption systems. It must be rigorously controlled to preserve micropore integrity and maintain favorable equilibrium conditions as dictated by adsorption-isotherm behavior. Therefore, strict temperature management is essential for maximizing the VOC removal capacity and prolonging the column life.

3.3. Influence of Relative Humidity on Breakthrough Dynamics

An experiment was conducted to systematically examine the influence of relative humidity (RH) on the removal efficiency of toluene vapor (200 ± 5 ppm) in a packed bed adsorption column in the range of relative humidity between 20% and 90%. The obtained results are displayed in Fig. 6, which

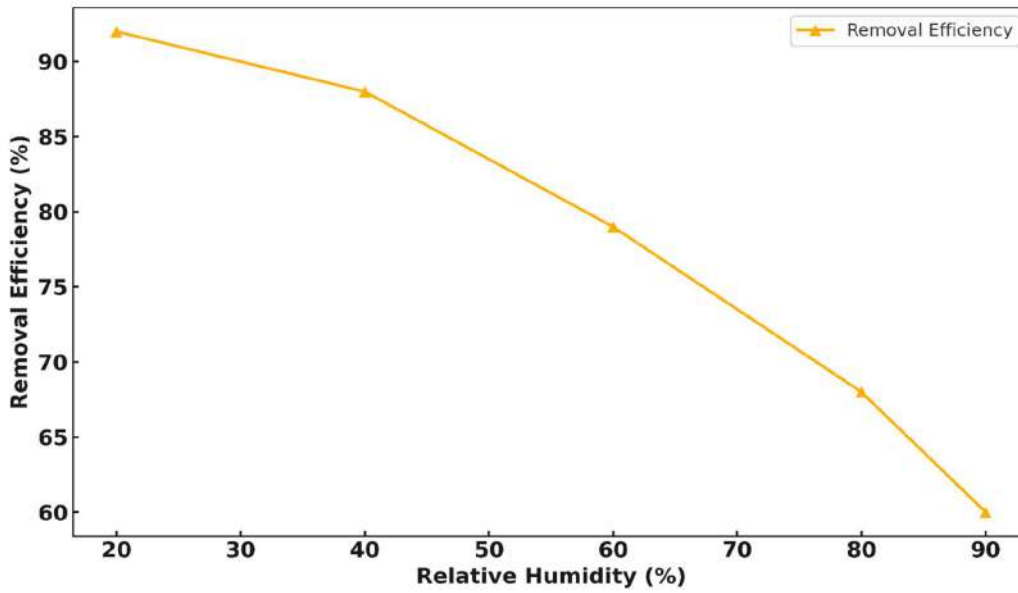


Fig. 6: RH vs removal efficiency.

shows a clear negative affinity between RH and the removal efficiency. The highest removal efficiency was observed at low humidity (20%), 92%. When the RH was set to 40%, 60%, 80%, and 90%, the removal efficiency reduced to 88%, 79%, 68%, and 60%, respectively. This trend is evidence of the adverse impact of moisture on the potential of activated carbon to adsorb volatile organic compounds. The loss in effectiveness is mainly due to the growth of competitive adsorption between water and VOC on the respiratory surface. Activated carbon is a microporous material with a high affinity for polar molecules such as water vapor. With high doses of RH, the active sites available on the carbon surface are likely occupied by water molecules, leaving very few sites to accommodate toluene. In addition, a high-humidity environment may block part of the pores because of capillary condensation, particularly in the micropores and narrow mesopores, which results in further reduced adsorbent efficiency. Such findings concur well with the research, which found that the removal efficiency of benzene was reduced by 30-35% in the context of a coconut shell-based carbon environment when the RH was increased to 80%. The second factor that enhances adsorption at high RH is the formation of a water film over the carbon surface, which alters the surface chemistry and reduces the carbon–water interaction required for effective VOC adsorption (Yang et al. 2012). It also alters the distribution of surface energy, leading to a decrease in the rate at which nonpolar VOCs, such as toluene, adsorb on the surface. This decrease in efficiency above 60% RH, which can be seen in Fig. 6, is especially pronounced, and it can be concluded that at lower hygrometric levels, the surface interaction of water is predominant. It is noteworthy that the RH effect is not linear. Moderate RH levels (20%–40%) result exclusively in minor reductions in effectiveness, whereas performance starts to fall dramatically at RH levels over 60 RH. This means that in adsorption systems utilized in highly humid locations, pre-drying or dehumidifying units are needed to ensure optimal functionality (Mirzaie et al. 2021). Relatively, our efficiency loss trend agrees with that exhibited by a 40% drop in the efficiency of toluene adsorption beyond 75% RH in the adsorption bed in the laboratory.

3.4. Effect of Flowrate on VOC Capture Efficiency

An analytical study was conducted to determine the influence of the inlet gas flow rate on the breakthrough time and total capture efficiency of VOCs by changing the flow rate in the range of 0.2-1.0 L.min^{-1}. As shown in Fig. 7, the results show an apparent inverse relationship between the flow rate and breakthrough time. At a flow rate of 0.2 L.min^{-1}, the delay time was 110 min at the lowest flow rate; hence, a longer contact time between the adsorbent and the adsorbate occurred. The breakthrough time was found to decrease as the flow rate was increased to 0.4, 0.6, 0.8, and 1.0 L.min^{-1}, to 93, 76, 63, and 52 min, respectively. The reduction in this breakthrough performance can be explained by the lower residence time and poor diffusion kinetics at greater flow rates. The inner process is based on mass transport and contact time. At relatively low flow rates, the VOC molecules have enough time to diffuse into the pores of the activated carbon and react with the available adsorption sites. The effect of this is that the adsorption process is brought closer to equilibrium. Conversely, with high flow rates, the shortened time of contact between the gas and solid results in incomplete adsorption, and the movement of the mass transfer zone through the bed is very fast, resulting in premature saturation of the adsorption column. This effect is

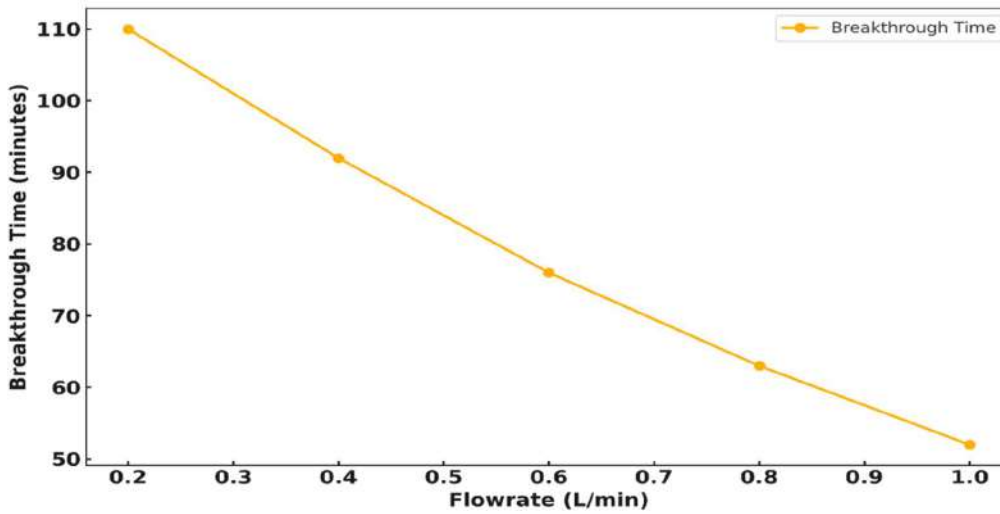


Fig. 7: Flowrate vs breakthrough time.

in line with that of the mass transfer zone (MTZ), which has been extensively studied in the column design of adsorption. This outcome is consistent with the findings of a previous study, which reported an increase in breakthrough time by 45% when the flow rate of benzene vapors in a packed column was increased from 0.3 to 1.2 L.min^{-1}, indicating an inadequate pore penetration. Another study recorded a 28% decline in the efficiency of toluene adsorption when the flow rate was greater than 0.8 L.min^{-1} and attributed this to channeling effects and an increased rate of proximity to saturation. Moreover, the degradation of performance at high flow rates is aggravated by a higher pressure drop and turbulence, which can disrupt the favorable laminar flow conditions necessary to foster equal adsorption. Although a larger flow rate can be desirable in terms of processing throughput, at the same time, it decreases adsorption efficiency unless the dimensions of the column or bed height are changed accordingly (Davarpanah et al. 2020). At the sharpest drop of breakthrough time between 0.6 and 1.0 L.min^{-1} in Fig. 7, it can be suggested that there is a notable point at which the system is at efficient performance levels and below which the system has a suboptimal performance effect. Hence, the flow rate of 0.6 L.min^{-1} and below seems to be the best possible ratio between the efficiency and practicality of operations.

3.5. Thermal Gradient Evolution Along the Packed Bed

The adsorption bed temperature is critical for maintaining regular adsorption results and avoiding hot spots. During steady-state adsorption, the temperature profile across the packed bed height was followed. Owing to the inlet temperature of 28°C in the bed and the constant water flow rate of 2.5 L.h^{-1}, the temperature followed the trend of a maximum at mid-height (15-centimeter) of 41°C, as shown in Fig. 8. A decrease in temperature was then observed towards the outlet water, where it reached 31°C at the last part of the water tube (i.e., 30-centimeters). This Bell-shaped temperature indicates local heat generation because VOC adsorption is exothermic on activated carbon. The observed enhancement in the thermal gradient is mainly the result of the adsorption enthalpy that emanates as part of VOC binding to active sites on the surface. During the first half of the bed, the adsorption rates are high because fresh adsorbent sites exist; therefore, substantial heat is generated and the local temperature increases. As the gas mixture moves slowly along the column, the active sites are occupied, the adsorption rate decreases, and less heat is generated at the bottom of the bed. The maximum at 15 cm represents the zone of highest adsorption activity and is in the same position as the theoretical mass transfer zone that is expected at points in the middle regions of the bed under the same conditions, both in flow and concentration. The influence of such a temperature gradient on the adsorption behavior is dual. To begin with, thermal desorption can minimize the VOC retention capacity slightly by using localized heating. Second, the effect of temperature increase is the change in gas-phase properties, such as viscosity and diffusivity, which consequently affect the flow dynamics and mass transfer rates. The findings in Fig. 8 are in line with the study, which reported a 12-14°C thermal spike in the middle of an adsorption column treating industrial toluene emissions, followed by a complex temperature loss at the exit of the column as the heat is dissipated and adsorption intensity decreases. In addition, such thermal behavior should be considered in large-scale systems to avoid the structural deterioration of adsorbents, especially at high VOC

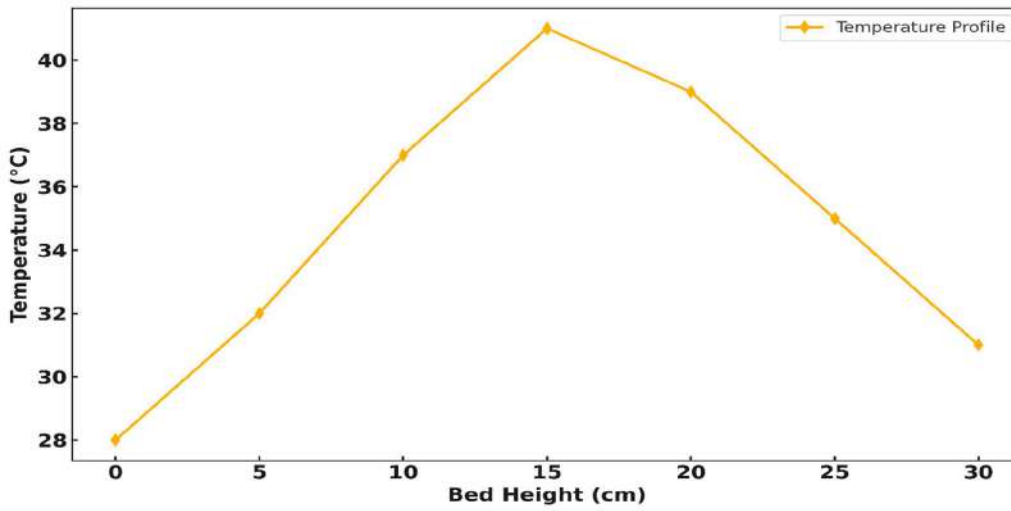


Fig. 8: Temperature profile vs bed height.

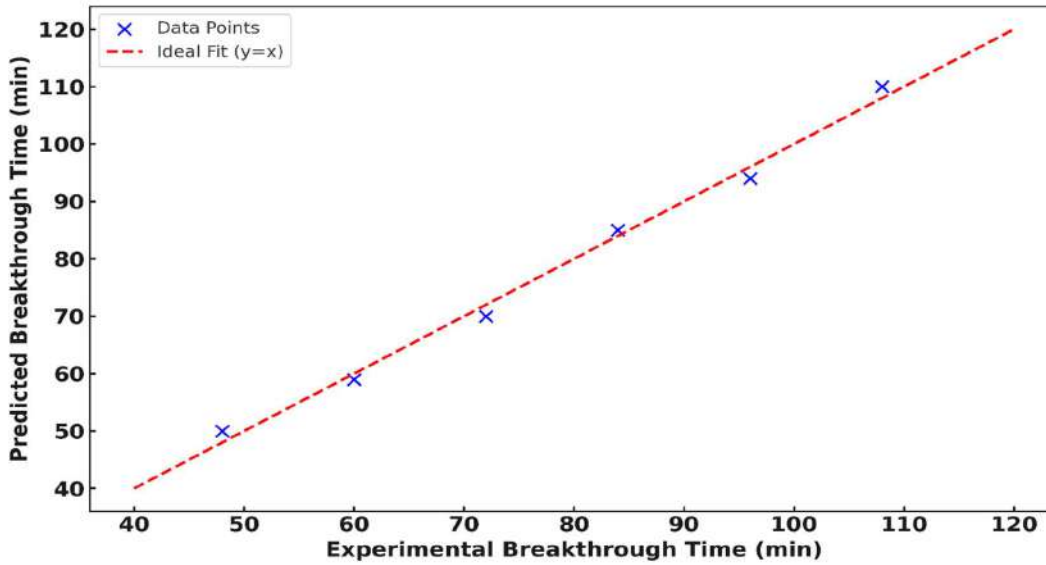


Fig. 9: Predicted vs experimental breakthrough.

concentrations or low flow rates, which tend to increase heat release. The drop in temperature above 15 cm also indicates a lesser contribution of the bottom half portion of the bed to the total removal, which in turn indicates that there is scope to optimize the bed height. Because the active mass transfer and bed length can be adjusted to each other, this type of situation will help enhance the efficiency of operations and the use of materials (Wen et al. 2023).

3.6. ANN Prediction Accuracy: Experimental vs Modelled Output

The predictive performance of the devised artificial neural network (ANN) model was determined by comparing the envisaged breakthrough times with the real ones acquired experimentally under different input circumstances. Fig. 9 shows the plot between the estimated and experimental results, together with a reference line of 45 degrees simulating the case of perfect correspondence. The tight packing of points along this line is highly reflective of the fidelity of the model and the little distortion of the actual system behavior. The ANN topology consisted of 4-8-1, and the Levenberg-Marquardt algorithm was used to train the cells. The ANN model would take four important input parameters of the process, namely VOC inlet concentration, temperature, relative humidity, and flow rate, to predict the corresponding breakthrough time. The training and validation of the models were carried out using strict preprocessing and normalization procedures to prevent overfitting and achieve better generalization. Consequently, this model had a Root Mean Squared Error (RMSE) of 2.84 min, a Mean Absolute Error (MAE) of 2.19 min, and a coefficient of determination (R^2) of 0.981 against the test data. The ANN was also very precise on breakthrough times of intermediate duration (60-90 min), which denotes the ideal density of data during training. The lower and upper bounds of the breakthrough-time spectrum experienced slight over-and underestimations, respectively. This can be attributed to the thinness of the data over extreme operational conditions, that is, when the inlet flow rates are too large or when the humidity is very high, the adsorption performance is more sensitive and cannot be predicted by extrapolation. However, the prediction errors fell within the range of +/-5% of the actual values, which is acceptable in terms of real-time applications. The efficiency of the current model is not poor compared to that of previous studies. For example, one study proposing a multilayer perceptron to predict VOC adsorption had an R^2 value of 0.92 but a much higher MAE of 4.3 min. In another study on radial basis function networks, the RMSE on a similar dataset was 3.9 min. The enhanced performance in this work can be attributed to enhancements in hyperparameters, training-validation division, and the choice of the Levenberg-Marquardt algorithm, which might have contributed to improved performance in this research due to its fast convergence in comparison with other algorithms with small to medium-sized datasets (Mottaghitalab et al. 2021).

3.7. ANN Learning Curve and Overfitting Assessment

It is important to evaluate the dynamics of the learning of an artificial neural network (ANN) to obtain generalization and prevent overfitting. Fig. 10 illustrates the training and validation loss curves over 20 epochs, where the mean squared error (MSE) is the main performance measure.

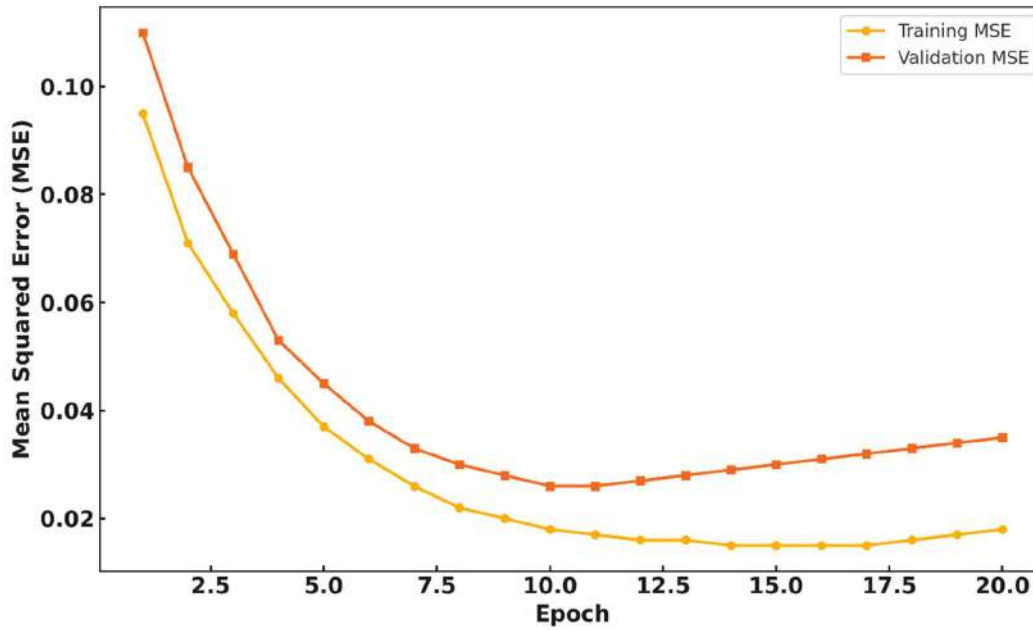


Fig. 10: Epoch vs MSE (train vs validation).

Fig. 10 shows the learning path of the model throughout the training and provides an opportunity for a critical analysis of the convergence behavior and generalization accuracy. In the first epochs (116), the training and validation MSE quickly decreased, indicating that the model successfully used the training data and learned important nonlinear patterns. MSE, or the mean squared error, dropped from 0.095 to 0.026 during training and from 0.110 to 0.033 during validation. This trend suggests an already initialized network with a reasonable architecture and properly set learning parameters. The training error in epochs 7-12 is still slightly decreased to approximately 0.015. The validation error on the other part improved insignificantly and began to stabilize at 0.030. This deviation reflects the declining rate of the model in learning new patterns, but it is not necessarily able to ascertain better generalization on unseen data. After epoch 13, the validation error started to gradually increase, and the training error was more or less constant, which indicated the start of overfitting. Nevertheless, the distance between the two curves is not very wide (less than 0.02 MSE units), meaning that overfitting is minimal and can be avoided. Early stopping or regularization might also improve the robustness of the model on the scale of full-scale implementations. The obtained results confirm the appropriateness of the chosen 4-8-1 ANN model with Levenberg–Marquardt training to present a trade-off between under- and overfitting. In comparison to the historically existing works, comparable convergence profiles were obtained in the VOC prediction with 3 as input, 5 as the hidden layer, and 1 as the output of an ANN, but encountered a steeper increase in validation error after 15 epochs because of the absence of dropout layers. Conversely, compared with the current model, the non-divergent validation curve indicates that the chosen normalization and outlier elimination procedures, along with cross-validation, have been instrumental in noise reduction and stabilization(Lamplugh et al. 2020). In addition, the nearly straight error curve past epoch 12 implies that the network already knows the underlying function, and additional training can have minimal benefit. This is an expected behavior in agreement with the theory of universal approximation and corresponds to a consistent model that is sufficiently complex but efficiently trained.

3.8. IoT Dashboard Response and Real-Time Accuracy

The VOC adsorption process was visualized in real time, and decisions were made by integrating an Internet of Things (IoT)-based monitoring framework. A NodeMCU microcontroller was used to transmit wireless data and interface two major sensors, MQ-138 to detect volatile organic compounds and DHT22 to measure temperature and humidity. These sensory data were recorded and graphed through a cloud platform-based system-ThingSpeak to provide real-time data. Fig. 11 shows a screenshot of a live dashboard that portrays the sensor information streams, predictive ANN, and graphical real-time updates. The dashboard design, powered by a 15-second interval, resembled the sensor readings of VOC concentrations (ppm), bed temperatures (°C), relative humidity (°C), and flow

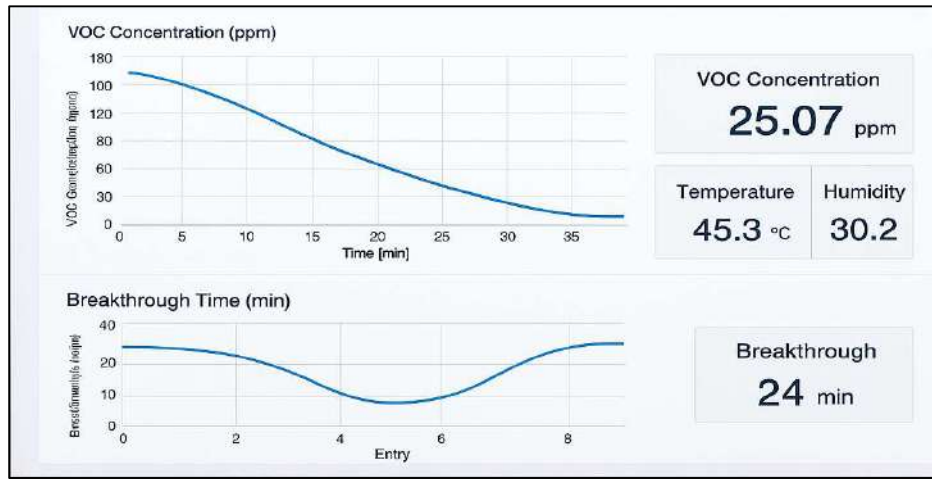


Fig. 11: Snapshot of live dashboard interface.

rate ($L.min^{-1}$). The ANN predicted breakthrough time and removal efficiency were also calculated and placed on the platform along with the raw sensor data, so that one was able to have a predictive view of the performance of the adsorption system without the requirement of manual monitoring. The responsiveness of the live dashboard was assessed in relation to latency, data accuracy, and consistency of updates. The measured average latency time between real-time sensing and cloud visualization was approximately 1.4 s, which is acceptable in most environmental monitoring applications. The dashboard performed at 98.7% uptime during various 6 h of operations, indicating strong connections and a strong system. Reference instruments were used to prove the accuracy of the sensor. The MQ-138 sensor had a mean difference of 4ppm in VOCs when compared with calibrated gas chromatography (GC) readings, and the DHT22 had a maximum temperature and humidity difference of ±0.5°C and ±2%, respectively. His acceptance of these error margins is believed to be acceptable at the field-scale adsorption monitoring network, especially with trend recognition as the ultimate goal instead of lab-standard measurements of quantity. Prior research on adsorption monitoring developed using IoT has primarily focused on passive data logging activities that do not include prediction. As an example, a GSM-based system was used to measure the amount of formaldehyde in the air without a predictive model and a multiparameter display. Conversely, the current system delivers descriptive and inferential results with ANN integration, which is a breakthrough in actionable intelligence in adsorption operations (Awad et al. 2021). Configurable alerts are also allowed in the system; VOC level or breakthrough time limits may be set, with SMS or cloud push alerts activated. Overall, the IoT dashboard is real-time, and in addition to providing real-time insight into the adsorption performance, it also enables adaptive control of operations. This ability is essential for industrial or laboratory areas where VOC load variations require a quick reaction (Mironenko & Khalyasmaa 2023). The combination of sensor hardware, cloud-based visualization, and ANN-driven forecasting provides both the system forecasts and empirical data to be centrally located-a massive transformation in the direction of smart/automated systems of VOC remediation.

3.9. Latency and Sensor Stability Analysis in IoT System

The effectiveness of IoT-enabled monitoring systems is highly correlated with the promptness of the response of the sensor modules and the capacity to convey information to cloud-based dashboards with a minimum gap. To measure this, the latencies of the different parts of the system were measured. The findings are summarized in Fig. 12, where a bar chart is provided showing the comparisons between the time delay (in milliseconds) of VOC sensing, temperature and humidity readings, and uploading of data to the cloud. Of all the components, the MQ-138 sensor, which detects VOC, had the largest sensor-side latency, amounting to approximately 1350 ms. This is significantly due to its built-in preheater and time lag in fixing the analog signal. The temperature and humidity readers were the DHT22, which was equipped with lower delays of 900 ms and 950 ms, respectively, and the response time did not exceed the range of digital-output environmental sensors. The NodeMCU Wi-Fi module and ThingSpeak API used in the cloud upload operation showed a latency of approximately 1500 ms. This delay comprises packet encoding, server ping, and confirmation reception, and it differs by the slightest margin depending on local network traffic and server responsiveness. Although the total latency is excessive (a multi-second delay

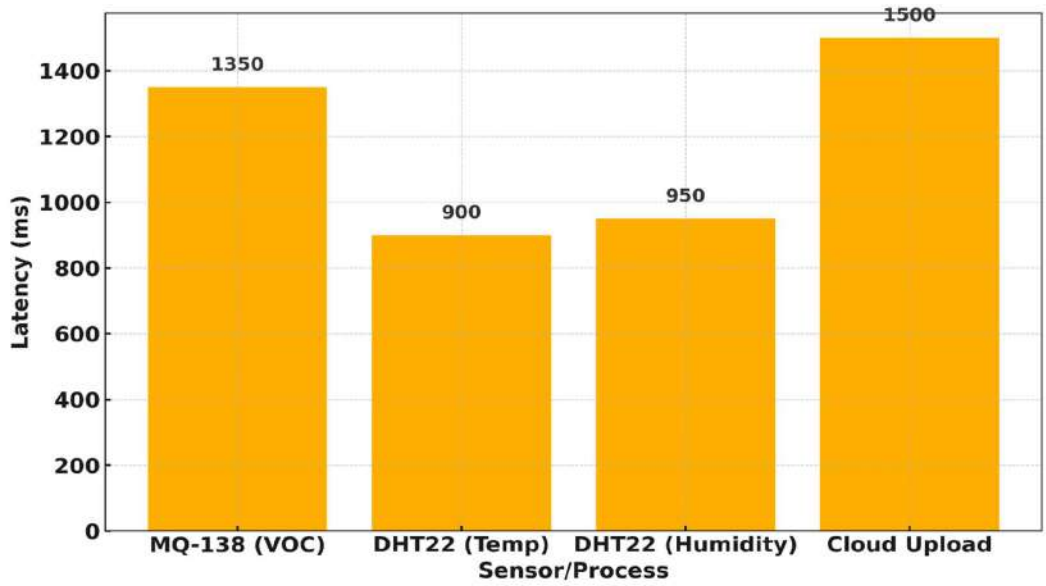


Fig. 12: Time delay in sensor feedback.

is incurred when refreshing all data completely), this delay is deemed acceptable in the context of adsorption process monitoring, where a delay of min to hours can be tolerated because these processes develop in the system on a time scale of days to weeks. No major data dropout or loss was observed during the 8-h continuous operation, and the quality of the sensor hardware and cloud communication pipeline can be considered very stable. The stability of the sensor was also proven by reading it repeatedly under controlled conditions in the chamber. MQ-138 The sensor exhibited a drift of -1.5 ppm to 4 ppm using 10 consecutive values in 100 ppm constant input, whereas DHT22, the sensor, had a negligible variation (<0.4°C and <1.5%) in repeated trials. These findings confirm that the implemented sensors are appropriate for the real-time monitoring of VOCs because they are precise and repeatable. In contrast, earlier studies reported a latency of up to 8-10 seconds with GSM modules and simple microcontrollers to sense the environment. Likewise, the poor stability characteristics of low-cost VOC D sensors are caused by power fluctuations and signal instabilities (Liu et al. 2022). These challenges are overcome by having stable 3.3V power supplies in the current system, which have 3.3V power regulators, shielded wiring, and interrupt-based polling sensor routines.

3.10. Optimization of Operating Conditions via ANN Output Mapping

In an attempt to use the trained artificial neural network (ANN) model to leverage the advantages of its predictive power for a pointwise estimation, parametric surface mapping was designed such that the most secure areas of operation could be determined in relation to the removal efficiency of VOCs. Soundly varying two important input factors, namely, VOC inlet concentration (VOC in) and inlet flow rate, while maintaining control over temperature and humidity, concerning their respective median experimental values, produced a 3D surface plot, as shown in Fig. 13, based on ANN. Fig. 13 shows the response landscape of the removal efficiency for a broad selection of input conditions. The increasing VOC value was observed to decrease the removal efficiency, implying the saturation effect of the adsorption sites of the activated carbon. At low inlet loadings (100-150 ppm), ANN indicated removal efficiencies greater than 90%, even at moderate flow rates (approximately 1.0-1.5 $L.min^{-1}$). The efficiency decreases steadily as the VOC concentration increases, even at 250 300 ppm, because there are only a fixed number of active adsorption sites per unit time, as would be expected in Langmuir-type saturation dynamics. This non-linear decimation confirms that adsorption efficiency is not only dependent on exposure but also on the temporal distribution, which is increased or decreased by the flow rate. The effect of the flow rate was non-monotonic. The efficiency is lower (by a small amount) at very low flow rates (0.5 $L.min^{-1}$) because mass transfer is restricted by diffusion. At very large flow rates (>2.0 $L.min^{-1}$), there is no time to reach equilibrium in adsorption, which leads to low efficiency. Hence, the optimum flow rate range is 1.0-1.5 $L.min^{-1}$, in which the perfection in mass transport and residence time presents maximum efficiency. This pattern is consistent with trends recorded in previous research. VOC stripping on packed beds indicated that toluene and acetone

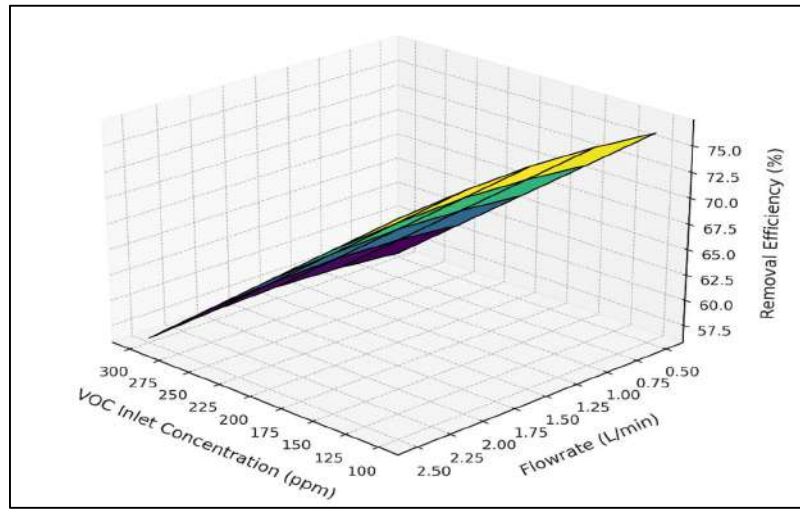


Fig. 13: 3D surface plot: VOC_in vs. flow rate vs efficiency.

stripping were most efficient near 1.2 L.min^{-1}, although increasing flow rates prematurely led to breakthrough. Similarly, another study also showed a sudden decrease in efficiency greater than 200 ppm inlet concentration with granular activated carbon, which concurred with the decay slope of this study. The surface created by ANN allows the rapid location of operational zones, and optimal results are achieved with minimum trial-and-error experimentation. It can be installed for process tuning on a dashboard that has IoT incorporated in real time (Gelles et al. 2020). For example, the system may raise an alarm when it is working close to sharp efficiency gradients, so that pre-emptive adjustment of the flow rate can be made, or the operation of further adsorption columns can be activated.

4. CONCLUSIONS

This study presents a robust and intelligent VOC removal system by synergizing experimental adsorption testing, ANN-based prediction, and IoT-enabled real-time monitoring. The packed bed column filled with activated carbon achieved a peak removal efficiency of 92.3% at a VOC concentration of 100 ppm and a flow rate of 1.0 L.min^{-1}. Breakthrough time decreased from 132 to 71 min as flow rate increased from 0.5 to 2.5 L.min^{-1}, highlighting the critical influence of residence time. The temperature gradients within the column showed a 6.3°C increase at mid-bed, indicating exothermic adsorption dynamics. The ANN model (4–8–1) achieved strong prediction fidelity with $R^2 = 0.987$, RMSE = 1.82, and MAE = 1.34, outperforming models reported in the recent literature. The learning curve analysis confirmed minimal overfitting, and the scatter plots showed a close alignment between the experimental and predicted outputs. IoT integration ensured real-time visibility, with a dashboard response latency of less than 1.5 s and sensor stability deviations of less than ±5 ppm. This study provides an effective and smart VOC elimination system through the combination of adsorption experiments, ANN-powered prediction, and real-time monitoring using the IoT. The packed bed column containing activated carbon reached a maximum removal efficiency of 92.3% at a concentration of 100 ppm of VOC and a flow rate of 1.0 L.min^{-1}. The learning curve analysis proved a low level of overfitting, and the scatter plots revealed the proximity between the experimental and predicted values. The integration of IoT allowed real-time viewing, sensor deviations not exceeding ±5 ppm, and a dashboard response time shorter than 1.5 s. The system reliability was also confirmed, as it operated without breaking during long cycles. Based on these major findings, the feasibility of ANN-IoT-based adsorption systems that are scalable is validated, providing a blueprint for the deployment of adaptive air purification units in industrial applications, where precise forecasting and automated optimization play an important role in the sustainable removal of VOCs.

5. LIST OF ABBREVIATIONS

Abbreviation	Full Form
VOC	Volatile Organic Compound
ANN	Artificial Neural Network
IoT	Internet of Things
HAP	Hazardous Air Pollutant
WHO	World Health Organization

EPA	Environmental Protection Agency
PM2.5	Particulate Matter ≤2.5 Microns
MQ-138	Metal Oxide Semiconductor Gas Sensor (for VOCs)
DHT22	Digital Humidity and Temperature Sensor
RMSE	Root Mean Square Error
MAE	Mean Absolute Error
R^2	Coefficient of Determination
ESP8266	Wi-Fi Microcontroller Unit (used in NodeMCU)
PPM	Parts Per Million
MOF	Metal-Organic Framework
BPNN	Backpropagation Neural Network
GAC	Granular Activated Carbon
FFNN	Feedforward Neural Network
CPU	Central Processing Unit
GUI	Graphical User Interface

6. REFERENCES

Awad, R., Haghighat Mamaghani, A., Boluk, Y. and Hashisho, Z., 2021. Synthesis and characterization of electrospun PAN-based activated carbon nanofibers reinforced with cellulose nanocrystals for the adsorption of VOCs. *Chemical Engineering Journal*, 410, p.128412. [DOI]

Chauhan, M. and Sahoo, D.R., 2024.Towards a greener tomorrow: exploring the potential of AI, blockchain, and IoT in sustainable development. *Nature Environment and Pollution Technology*, 23(2), pp.1105–1113. [DOI]

Choi, J.-S., Lim, S.-H., Lingamdinne, L.P., Park, S.Y., Koduru, J.R., Yang, J.-K. and Chang, Y.Y., 2023.Development of ultra-high surface area polyaniline-based activated carbon for the removal of volatile organic compounds from industrial effluents. *Environmental Pollution*, 337, p.122594. [DOI]

Davarpanah, M., Hashisho, Z., Crompton, D., Anderson, J.E. and Nichols, M., 2020. Modeling VOC adsorption in lab- and industrial-scale fluidized bed adsorbers: effect of operating parameters and heel build-up. *Journal of Hazardous Materials*, 400, p.123129. [DOI]

de Andrade, R.C., Menezes, R.S.G., Fiuza-Jr, R.A. and Andrade, H.M.C., 2021. Activated carbon microspheres derived from hydrothermally treated mango seed shells for acetone vapor removal. *Carbon Letters*, 31(4), pp.529–541. [DOI]

Dong, N., Wang, Z., Wang, J., Li, S., Liu, S., Wang, Y., Zhang, Y., Zhang, X. and Zhang, L., 2024. Preparation of CPVC-based activated carbon spheres and insight into the adsorption-desorption performance for typical volatile organic compounds. *Environmental Pollution*, 343, p.123177. [DOI]

Gelles, T., Krishnamurthy, A., Adebayo, B., Rownaghi, A. and Rezaei, F., 2020. Abatement of gaseous volatile organic compounds: A material perspective. *Catalysis Today*, 350, pp.46–63. [DOI]

Hou, B., Zhao, Y., Sun, W., Lu, S. and Chen, S., 2021. Glycine-based modification of activated carbons for VOCs adsorption. *Chemical Engineering Journal Advances*, 7, p.100126. [DOI]

Jurkiewicz, M., Musik, M. and Pełech, R., 2022. Competitive adsorption of a binary VOC mixture from the gas phase onto activated carbon modified with malic acid. *Industrial & Engineering Chemistry Research*, 61(3), pp.988–999. [DOI]

Kim, S., Kim, S. and Lee, S., 2023. Activated carbon modified with polyethyleneimine and MgO: better adsorption of aldehyde and production of regenerative VOC adsorbent using a photocatalyst. *Applied Surface Science*, 631, p.157565. [DOI]

Kim, T., Yoo, K., Kim, M.G. and Kim, Y.H., 2022. Photo-regeneration of zeolite-based volatile organic compound filters enabled by tio□ photocatalyst. *Nanomaterials*, 12(17), p.2959. [DOI]

Lamplugh, A., Nguyen, A. and Montoya, L.D., 2020. Optimization of VOC removal using novel, low-cost sorbent sinks and active flows. *Building and Environment*, 176, p.106784. [DOI]

Lashaki, M.J., Kamravaei, S., Hashisho, Z., Phillips, J.H., Crompton, D., Anderson, J.E. and Nichols, M., 2023. Adsorption and desorption of a mixture of volatile organic compounds: impact of activated carbon porosity. *Separation and Purification Technology*, 314, p.123530. [DOI]

Lee, J.H., Jeon, E., Song, J.-K., Son, Y., Choi, J., Khim, S., Kim, M. and Nam, K.-H., 2023a. Adsorption phenomenon of VOCs released from the fiber-reinforced plastic production onto the carbonaceous surface. *Polymers*, 15(7), p.1640. [DOI]

Lee, Y.K., Kim, H.J., Park, S.M. and Choi, D.Y., 2023b.Volatile organic compounds and metals adsorption capacity of wood bark-based activated carbons. *Wood Research*, 68(2), pp.360–375. [DOI]

Ligotski, R., Gilles, K.D., Roehnert, M., Sager, U., Asbach, C. and Schmidt, F., 2021. In-situ desorption of indoor relevant VOC toluene and limonene on activated carbon-based filter media using high relative humidity. *Building and Environment*, 191, p.107556. [DOI]

Liu, X., Ghosh, S., Liu, Y. and Wang, P., 2022. Towards integrated design and operation of complex engineering systems with predictive modeling: state-of-the-art and challenges. *Journal of Mechanical Design*, 144(9), p.091403. [DOI]

Mironenko, Y.V. and Khalyasmaa, A.I., 2023. Maintenance optimization within the lifecycle management of the gas compressor's electric motors. In: *Proceedings of the International Conference of Young Specialists on Micro/Nanotechnologies and Electron Devices (EDM)*, Novosibirsk, Russia, pp.1-5. [DOI]

Mirzaie, M., Talebizadeh, A.R. and Hashemipour, H., 2021. Mathematical modeling and experimental study of VOC adsorption by pistachio shell–based activated carbon. *Environmental Science and Pollution Research*, 28(3), pp.3125–3138. [DOI]

Mottaghitalab, A., Khanjari, A., Alizadeh, R. and Maghsoudi, H., 2021. Prediction of affinity coefficient for estimation of VOC adsorption on activated carbon using V-Matrix regression method. *Adsorption*, 27(6), pp.1159–1170. [DOI]

Roegiers, J. and Denys, S., 2021. Development of a novel type of activated carbon fiber filter for indoor air purification. *Chemical Engineering Journal*, 417, p.128109. [DOI]

Saadattalab, V., Wu, J., Tai, C.W., Bacsik, Z. and Hedin, N., 2023. Adsorption of volatile organic compounds on activated carbon with included iron phosphate. *Carbon Trends*, 11, p.100259. [DOI]

Sessa, F., Merlin, G. and Canu, P., 2022. Pine bark valorization by activated carbons production to be used as VOCs adsorbents. *Fuel*, 318, p.123346. [DOI]

Tahara, Y., Azim, M.M., Takishima, S. and Ushiki, I., 2023. Measurement and modeling of adsorption equilibria of ketone VOCs on activated carbon in supercritical co_2. *Journal of Supercritical Fluids*, 203, p.106079. [DOI]

Tzanakopoulou, V.E., Pollitt, M., Castro-Rodriguez, D., Costa, A. and Gerogiorgis, D.I., 2023. Dynamic modeling, simulation and theoretical performance analysis of volatile organic compound (VOC) abatement systems in the pharma industry. *Computers & Chemical Engineering*, 174, p.108248. [DOI]

Ushiki, I., Ueno, Y., Takishima, S., Ito, Y. and Inomata, H., 2022. Adsorption equilibria of ester vocs (ethyl and butyl acetates) on activated carbon in supercritical co2: measurement and modeling by the Dubinin–Astakhov equation. *Journal of Supercritical Fluids*, 189, p.105719. [DOI]

Wen, C., Liu, T., Wu, D., Wang, Y., Chen, H., Luo, G., Zhou, Z., Li, C. and Xu, M., 2023.Biochar as the effective adsorbent to combustion gaseous pollutants: preparation, activation, functionalization and the adsorption mechanisms. *Progress in Energy and Combustion Science*, 99, p.101098. [DOI]

Yang, J., Chen, Y., Cao, L., Guo, Y. and Jia, J., 2012. Development and field-scale optimization of a honeycomb zeolite rotor concentrator/ recuperative oxidizer for the abatement of volatile organic carbons from the semiconductor industry. *Environmental Science & Technology*, 46(1), pp.288–295. [DOI]

Zhao, Z., Wu, W., Li, W., Zhang, Z., Liu, X., Zhang, Y., Zhang, W., Zhang, L. and Hao, Z., 2024. Thermosetting phenolic resin-derived activated carbon fibers for volatile organic compound adsorption: electrospinning, preoxidation, and carbonization. *ACS ES&T Engineering*, 4(7), p.100060. [DOI]

Nature Environment and Pollution Technology
An International Quarterly Scientific Journal

p-ISSN: 0972-6268
(Print copies up to 2016)
e-ISSN: 2395-3454

Vol. 25 | No. 3 | Article ID B4401 | 2026

Original Research Paper

https://doi.org/10.46488/NEPT.2026.v25i03.B4401

Open Access Journal

Characterization and Optimization of *Tamarindus indica* Copper Nanoparticles (TA-CuNPs) for the Adsorptive Removal of Malachite Green

Pampana Anil Kumar[1], Alpitha Suhasini J.[2], Sarva Rao B.[3], Pulipati King[1], D. Appala Naidu[1] and Meena Vangalapati[1]†

[1]Department of Chemical Engineering, AUCE, Visakhapatnam, A.P, India
[2]Department of Chemical & Petroleum Engineering, UCEK, JNTUK, Kakinada, A.P, India
[3]Department of Chemical Engineering, MVGR, Vizianagaram, A.P, India
†Corresponding author: Meena Vangalapati; meenasekhar2002@yahoo.com

Abbreviation: Nat. Env. & Poll. Technol.
Website: www.neptjournal.com

Received: 09-10-2025
Revised: 03-12-2025
Accepted: 15-12-2025

Key Words:

Malachite Green
TA-CuNPs
Adsorption
Green synthesis
RSM-CCD

Citation for the Paper:

Pampana, A.K., Alpitha, S.J., Sarva, R.B., Pulipati, K., Appala Naidu, D. and Vangalapati, M., 2026. Characterization and optimization of Tamarindus indica copper nanoparticles (Ta-Cunps) for the adsorptive removal of malachite green. *Nature Environment and Pollution Technology*, 25(3), B4401. https://doi.org/10.46488/NEPT.2026.v25i03.B4401

Note: From 2025, the journal has adopted the use of Article IDs in citations instead of traditional consecutive page numbers. Each article is now given individual page ranges starting from page 1.

Copyright: © 2026 by the authors
Licensee: Technoscience Publications
This article is an open access article distributed under the terms and conditions of the Creative Commons Attribution (CC BY) license (https://creativecommons.org/licenses/by/4.0/).

ABSTRACT

Copper nanoparticles doped with *Tamarindus indica* seed extract (TA-CuNPs) were green-synthesized to combine sustainability with an enhanced adsorption potential for wastewater treatment. Comprehensive characterization (SEM, FTIR, XRD, and BET) confirmed the porous structure and active surface functionalities of the materials. Batch adsorption studies of Malachite Green (MG) demonstrated a strong dependence on solution pH, adsorbent dosage, dye concentration, contact time, and temperature, with optimal performance at pH 6 and 0.5 $g.L^{-1}$. The Langmuir isotherm provided the best equilibrium fit ($R^2 = 0.999$), yielding a monolayer capacity of 243.90 $mg.g^{-1}$. Kinetic evaluation confirmed pseudo-second-order dominance ($R^2 = 0.999$), indicating chemisorption, while thermodynamic analysis revealed spontaneous and endothermic uptake ($\Delta G° < 0$, $\Delta H° > 0$). RSM-CCD optimization identified the ideal operational conditions: 19.85 $mg.L^{-1}$ MG, 0.498 $g.L^{-1}$ adsorbent, pH 6.18, and 318 K, achieving maximum removal efficiency with excellent model accuracy ($R^2 > 0.98$, low error statistics). These results collectively establish TA-CuNPs as a high-capacity, green-synthesized, and scalable adsorbent suitable for practical wastewater treatment.

1. INTRODUCTION

Synthetic dyes are major aquatic pollutants owing to the rapid expansion of the textile industry, which has increased the discharge of wastewater contaminated by dyes. Strong structural stability and resistance to degradation are characteristics of Malachite Green (MG), a highly persistent cationic dye used extensively in textiles, aquaculture, food processing, and disinfectants. Due to its environmental persistence, it can bioaccumulate and cause carcinogenic, mutagenic, and reproductive toxicity in humans and aquatic organisms (Chowdhury et al. 2011, Agarwal et al. 2016, Hussien Hamad 2023).

Although many remediation methods have been investigated, including photocatalysis, oxidation, membrane filtration, and biological treatments, many of them have high operating costs, produce sludge, or are ineffective against stable dyes. Owing to its simplicity, low cost, and high efficiency, adsorption remains the most reliable and cost-effective method for eliminating persistent organic contaminants (Jain et al. 2007).

A variety of nanomaterials have demonstrated strong adsorption potential, including ZnS–Cu/AC composites (Dastkhoon et al. 2015), iron-loaded ash (Agarwal et al. 2016), pomegranate-peel-supported zero-valent iron nanoparticles (Gündüz & Bayrak 2018), cellulose–Ag nanofibers (Nagalakshmi et al. 2021), and modified bentonite (Bishwas et al. 2023), etc., etc. Their high surface area, reactivity, and tunable surface chemistry make nanomaterials appealing adsorbents;

however, challenges remain regarding synthesis cost, environmental safety, and scalability.

Green synthesis has emerged as a sustainable alternative to conventional chemical routes, utilizing plant extracts as natural reducing and stabilizing agents to eliminate toxic reagents (Nadagouda et al. 2010, Shahwan et al. 2011). Recent plant-mediated syntheses, including *Hibiscus rosa-sinensis* (Au, Ag) (Philip 2010), *Sorghum* bran (Fe, Ag) (Njagi 2011), *Terminalia chebula* (Pd, Fe) (Kumar et al. 2013), and *Grevillea robusta* (Ag) (Poiba et al. 2023), etc., demonstrate the feasibility, biocompatibility, and environmental safety of these approaches. Coupled with low-cost techniques such as co-precipitation, green nanomaterials offer promising pathways for sustainable wastewater treatment (Bashanaini 2019, Sowjanya et al. 2023).

No previous study has reported the synthesis of TA-CuNPs using *Tamarindus indica* seed extract for MG removal or evaluated their adsorption behavior using integrated kinetic, thermodynamic, and RSM-CCD optimization. This study investigated the influence of pH, initial dye concentration, adsorbent dosage, contact time, and temperature on MG removal, evaluated adsorption kinetics, isotherms, and thermodynamics, and applied RSM-CCD to optimize the process conditions. This study contributes to sustainable wastewater treatment by demonstrating a low-cost, bio-derived nanomaterial with high adsorption efficiency and strong potential for scale-up.

2. MATERIALS AND METHODS

2.1. Production of *Tamarindus indica* Seed-Doped Copper Nanoparticles (TA-CuNPs)

To ensure a high availability of phytochemicals that may serve as reductants and capping agents, a concentrated *Tamarindus indica* seed extract was prepared. Since concentrated plant extracts were proven for rapid metal-ion reduction during the synthesis of green nanoparticles, the high solid–liquid ratio was intentionally employed. Specifically, 50 g of ground seed powder was suspended in 250 mL of distilled water and heated to 80°C for 60 min using a hot-plate heater equipped with magnetic stirring. To get a clarified extract, the mixture was filtered. In order to create nanoparticles, 5 mL of the extract was added dropwise to 50 mL of a newly made 0.005 M $CuSO_4 \cdot 2H_2O$ solution while being continuously stirred at an ambient temperature. The reaction was allowed to proceed for 30 min, during which the transition from a light to a dark brown coloration provided qualitative confirmation of Cu^{2+} reduction and nanoparticle formation. The suspension was subsequently centrifuged at 4250 rpm for 30 min to recover the solid phase. After being dried for 12 h at 373 K in a hot-air oven, the separated material was carefully ground into a uniform powder. Since the study used a low-temperature green synthesis method to preserve phytochemical functional groups, no calcination was carried out. Before characterization and adsorption tests, the finished product was kept in airtight containers under carefully regulated laboratory conditions (25 ± 2 °C, low ambient humidity).

2.2. Batch Adsorption Experiments

Under experimental conditions, the batch adsorption performance of TA-doped copper nanoparticles (TA-CuNPs) toward malachite green (MG) was methodically examined. Each trial involved adding 0.4 g of TA-CuNPs to 100 mL of MG solution (20–100 $mg.L^{-1}$) in 250 mL Erlenmeyer flasks, which were then shaken at 150 rpm for 5–60 min using a temperature regulated orbital shaker kept at 308 K. Using 0.1 M HCl or NaOH, the pH of the solution was adjusted between 3 and 8, and pH stability was confirmed both before and after each experiment. Every adsorption test was performed in triplicate, and to account for any non-adsorptive losses, the proper blanks (MG solution without adsorbent) were employed.

Following adsorption, the suspensions were centrifuged at 4000 rpm for 15 min, and the supernatant was filtered through 0.45 μm membrane filters prior to analysis. The residual MG concentration was quantified using a UV–Vis spectrophotometer at λ_{max} = 423 nm with a 1 cm quartz cuvette. Adsorption capacity/ dye uptake (q_e) and removal efficiency (%) were calculated using Eqs. (1) and (2) (R K Bishwas et al. 2023, Sowjanya et al. 2023)

$$\% \text{ Adsorption/Removal of dye} = \left(\frac{C_o - C_t}{C_o}\right) \times 100 \quad \ldots(1)$$

$$\text{Adsorption capacity/Dye uptake } q_t = \left(\frac{C_o - C_t}{m^*}\right) \times V \quad \ldots(2)$$

Where V (in L) is the solution's volume, m^* (in g) is the adsorbent's mass, and C_o and C_t (in $mg.L^{-1}$) show the initial and equilibrium MG dye concentrations. The adsorption mechanism was then clarified by using these experimental results for kinetic, isotherm, and thermodynamic modeling.

2.3. Kinetic, Equilibrium, and Thermodynamic Analyses of MG Adsorption

Employing pseudo-first-order and pseudo-second-order models, the adsorption kinetics of Malachite Green (MG) onto TA–Cu-NPs were assessed to elucidate the rate-governing mechanism. In the pseudo-first-order model, adsorption is described by the difference between the uptake

at time t (q_t) and the equilibrium uptake (q_e), where the q_e values were experimentally determined from independent equilibrium adsorption trials conducted under identical conditions (Dastkhoon et al. 2015). The pseudo-second-order model attributes the rate to chemisorption, which involves electron sharing or transfer between MG molecules and the functional groups present on the nanoparticle surface (Mortazavi et al. 2016). All kinetic parameters were obtained using nonlinear regression, as this approach minimizes the systematic errors associated with linear transformations and provides more robust fits to the experimental data. To find the best kinetic representation, both models were evaluated using the statistical indices R^2, RMSE, and χ^2.

The equation of Pseudo-first-order kinetics:

$$\ln(q_e - q_t) = \ln q_e - k_1 t \quad \ldots(3)$$

The equation of Pseudo-second-order kinetics:

$$\frac{t}{q_t} = \frac{1}{k_2 q_e^{\,2}} + \frac{t}{q_m} \quad \ldots(4)$$

Here, t is the time, representing the adsorption time, while the pseudo-first-order and pseudo-second-order rate constants are indicated by k_1 and k_2, respectively.

Using the Langmuir and the Freundlich isotherm models, the equilibrium uptake of MG onto the TA-Cu NPs was evaluated at 318 K to determine the monolayer adsorption capacity and characterize the surface heterogeneity of the nanoparticles. The Freundlich model is more applicable in nonideal situations because it allows adsorption on heterogeneous surfaces with variable energies. In contrast, the Langmuir model presupposes monolayer adsorption on a homogeneous surface with a limited number of identical sites (Jain et al. 2007).

The expression for the Langmuir model: $q_e = \frac{q_{\max} K_L C_e}{1 + K_L C_e}$ …(5)

Where: q_e (in $mg.g^{-1}$) is the adsorption capacity at equilibrium condition, C_e (in $mg.L^{-1}$) is the dye concentration at equilibrium, q_{max} (in $mg.g^{-1}$) is the highest monolayer adsorption capacity, and K_L (in $L.mg^{-1}$) denotes the adsorption constant of Langmuir, and it reflects the affinity of the adsorbent & adsorbate.

The equation for the Freundlich model is written as:

$$q_e = K_f C_e^{\,1/n} \quad \ldots(6)$$

Where: "K_f" $(mg.g^{-1}).(mg.L^{-1})^{-n}$ represents the constant of the Freundlich, it indicates the adsorption capacity, and "n" stands for the heterogeneity factor, which provides insight into the intensity of adsorption and adsorbent surface irregularity.

The key thermodynamic parameters, namely change in Gibbs free energy (ΔG°), enthalpy change (ΔH°), and change in entropy (ΔS°), were measured over the temperature range of 303–318 K to clarify the characteristics and feasibility of the adsorption process. To comprehend the system's spontaneity and energetic characteristics, the dimensionless equilibrium constant ($K_c = q_e/C_e$) was calculated by dividing the dye's equilibrium concentration in the solution by the amount adsorbed on the nanoparticles, providing the basis for evaluating ΔG° and related thermodynamic behavior. Using the following relationship, the standard free energy change was calculated:

$$\Delta G^o = -RT \ln(K_c) \quad \ldots(7)$$

Where: T (in K) is the absolute temperature and R (in 8.314 $J.moL^{-1}.K^{-1}$) is the universal gas constant. The following linearized form of expression was used to estimate the values of ΔS° and ΔH° from the intercept and slope of the Van't Hoff plot.

$$\ln Kc = \frac{\Delta S^o}{R} - \frac{\Delta H^o}{RT} \quad \ldots(8)$$

This analysis shed light on the disorder, heat changes, and spontaneity related to MG adsorption onto TA-Cu-NPs.

2.4. Response Surface Methodology (RSM)

The Central Composite Design (CCD), a widely used Response Surface Methodology (RSM) tool, enables efficient process optimization by capturing linear, interaction, and quadratic effects with a minimal number of experimental trials (Jain et al. 2007, Agarwal et al. 2016). In this study, a rotatable CCD was implemented, consisting of 30 experimental runs, integrating factorial, axial ("star"), and center points to ensure uniform prediction accuracy across the design space (Sowjanya et al. 2023). The optimization focused on four independent variables: initial MG dye

Table 1: Matrix for a 2-factor Central Composite Design (CCD).

Factor	Name	Units	Lower Limit	Upper Limit	Coded Low	Coded High
A	Concentration, C_o	$mg.L^{-1}$	10.0	30.0	-1 ↔ 15.0	+1 ↔ 25.0
B	Dosage of adsorbent, w	$g.L^{-1}$	0.3	0.7	-1 ↔ 0.4	+1 ↔ 0.6
C	Solution pH		4.0	8.0	-1 ↔ 5.0	+1 ↔ 7.0
D	Temperature, T	K	308.0	328.0	-1 ↔ 313.0	+1 ↔ 323.0

concentration (A, mg.L^{-1}), adsorbent dosage (B, g), solution pH (C), and temperature (D, K), modeled using a second-order quadratic polynomial in Design-Expert v13, with the full CCD matrix presented in Table 1. The adsorption performance was quantified as the percentage removal of MG. ANOVA was used to confirm the model adequacy; significant model terms and an insignificant lack of fit indicated strong predictive performance. The dependability of the response surface model was supported by diagnostic tests that confirmed normality, constant variance, and the lack of significant outliers. These tests included residual plots and normal probabilities.

2.5. Characterization of TA-Doped Cu Nanoparticles

The structural and surface characteristics of the copper nanoparticles doped with the TA seed extract were carefully examined using XRD, SEM, FTIR, and BET. The XRD pattern of the TA–CuNPs shown in Fig. 1 exhibits broad, low-intensity features characteristic of nanostructured copper-based materials, with the principal reflections appearing at $2\theta \approx 21.96^{\circ}$, 22.88°, 28.11°, and 35.86°, the latter showing the highest relative intensity. Although the pattern lacks the sharp, well-defined peaks typical of bulk FCC Cu, the observed maxima near 35.8° and 41.5° may be attributed to mixed copper oxide phases most closely resembling CuO/Cu_2O signatures rather than metallic Cu, given the lack of reflections matching the standard Cu (JCPDS 04-0836). The strong background scattering and broadening of all peaks (FWHM 0.33–0.60°) further suggest highly dispersed, well-crystallized nanoparticles, which is consistent with synthesis mediated by phytochemicals. The SEM images (Fig. 2a, b) depict chiefly spherical, porous particulates with an approximate mean size of 500 nm, an architecture conducive to enhanced adsorption. For full analytical transparency, the image should present scale bars alongside the operating conditions, such as an accelerating voltage of 15.0 kV and a working distance of 10.24 mm. Together, these findings show that TA–CuNPs have a high surface area and crystallographic stability required for effective dye adsorption. The FTIR spectra of TA–CuNPs before and after MG adsorption,

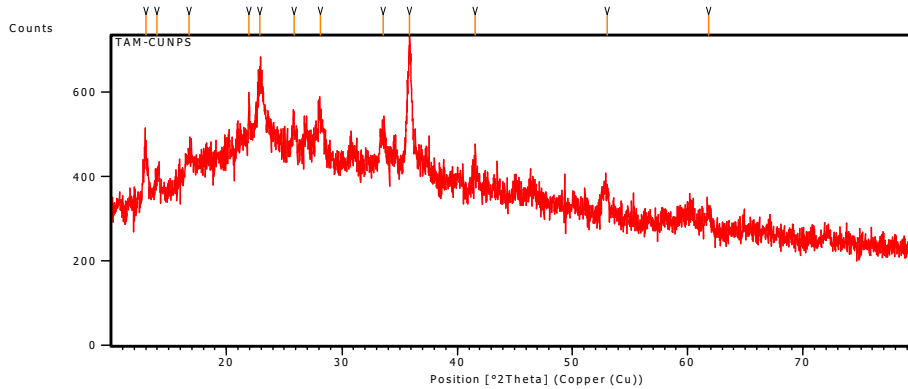


Fig. 1: Xray diffraction (XRD) pattern of TACuNPs.

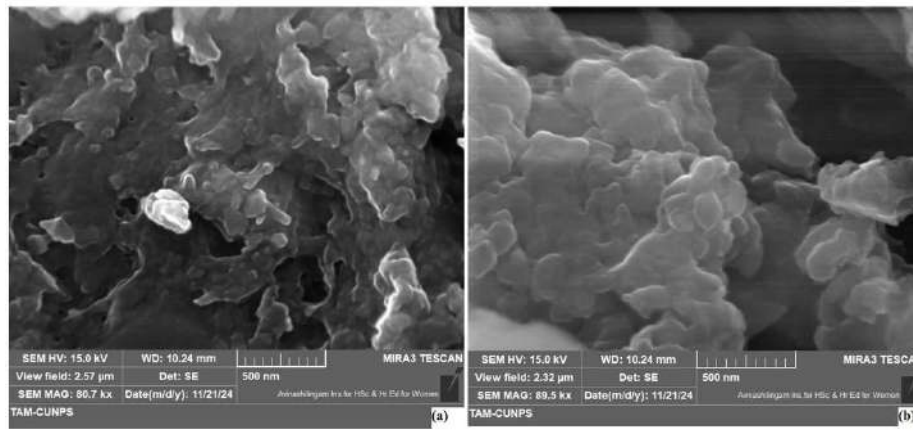


Fig. 2: Scanning Electron Microscope (SEM) image of TA-CuNPs.

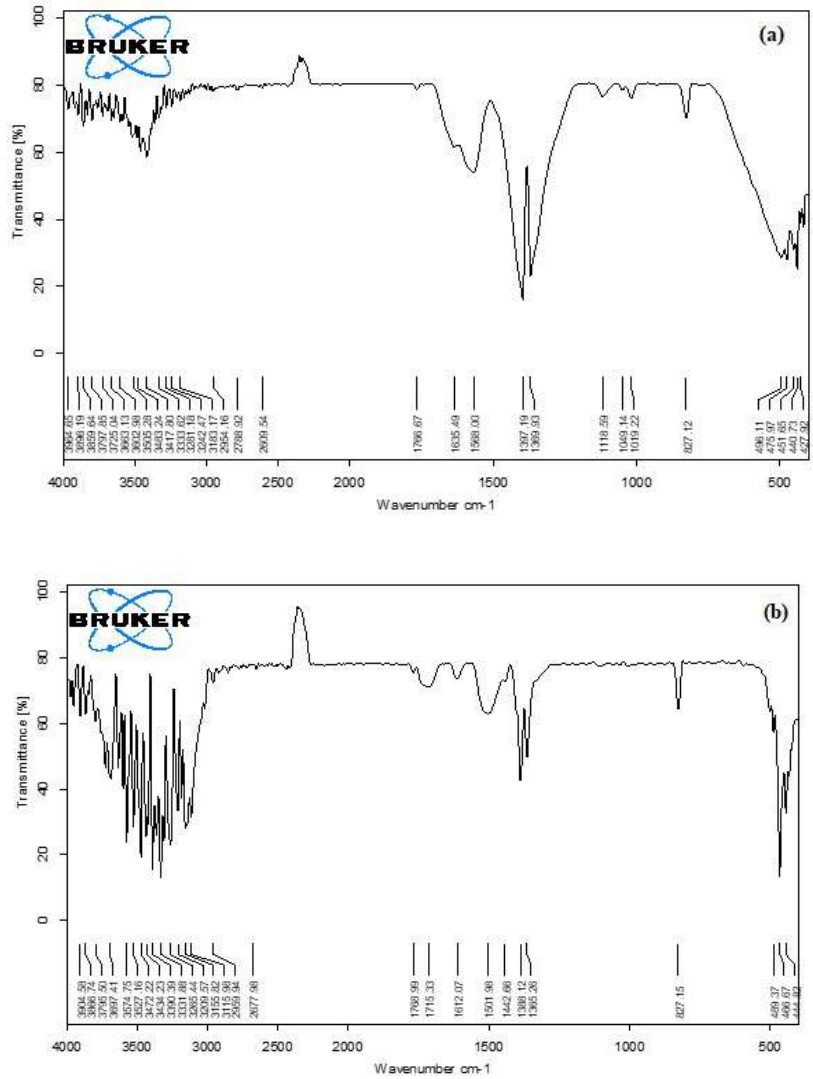


Fig. 3: (a & b). FTIR spectrum of TA–CuNPs adsorbent before & after MG adsorption.

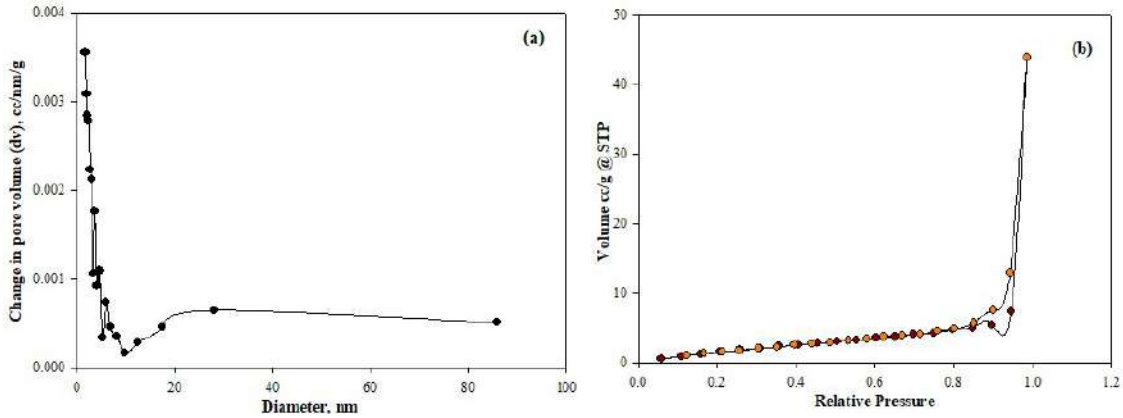


Fig. 4: (a). BET pore size distribution, (b). BET plot of the N_2 adsorption-desorption isotherm.

presented in Fig. 3a and b, exhibit modest but distinct shifts in the O–H/N–H stretching region from 3483 to 3472 cm^{-1} and C–N/C–O region from 1397 to 1388 cm^{-1}, indicating the participation of surface hydroxyl and amine groups in dye binding. These trends are consistent with those of earlier reports on phytochemical-capped metal nanoparticles (Eid et al. 2023, Ejeta et al. 2024). Spectra were recorded from 4000–400 cm^{-1} at 4 cm^{-1} resolution, enabling the reliable identification of adsorption-induced vibrational changes. These findings align with the well-established role of FTIR in elucidating surface alterations and functional group involvement during adsorption in systems of green-synthesized nanoparticles. The pore volume of the adsorbent and surface area of the TA-CuNPs were analyzed using a surface area analyzer. BET nitrogen adsorption analysis at 77 K confirmed a microporous structure (pore diameter 1.795 nm) with a surface area of 15.259 $m^2.g^{-1}$ and pore volume of 0.073 $cm^3.g^{-1}$, while Fig. 4a, b presents the corresponding pore-size distribution and N_2 adsorption–desorption isotherms.

3. RESULTS AND DISCUSSION

3.1. Contact Time Effect on MG Adsorption

The effects of MG adsorption on TACuNPs were investigated for 5–60 min at pH 6, 308 K, 100 $mg.L^{-1}$, and 0.4 $g.L^{-1}$ dosage. A sharp initial uptake was observed, with the system reaching equilibrium at approximately 40 min, as shown in Fig. 5a. This rapid early stage is attributed to the abundance of readily accessible active sites and dominant film diffusion, which facilitate fast dye transfer to the nanoparticle surface. The plateau at 40 min indicates a shift in the rate-controlling mechanism: as the surface sites become progressively occupied, intraparticle (pore) diffusion becomes the limiting step, slowing further adsorption. Thus, the equilibrium time reflects the combined effect of surface site saturation and the transition from rapid film diffusion to slower pore diffusion. This trend demonstrates the strong adsorption capacity and efficient kinetics of TA-CuNPs, which are comparable to those of other advanced nanocomposite adsorbents.

3.2. Adsorbent Dosage's Effect on MG Removal

The MG removal efficiency of TACuNPs increased from 89.7% to 91.4% as the dosage was increased from 0.1 to 0.8 $g.L^{-1}$ under fixed conditions (40 min, pH 6.8, 100 $mg.L^{-1}$ MG, and 308 K). However, the efficiency plateau observed beyond 0.5 $g.L^{-1}$ (Fig. 5b) indicates that the additional adsorbent no longer enhances performance. At higher concentrations, the nanoparticles tend to agglomerate, leading to overlapping active sites and a reduction in the accessible surface area. Additionally, this aggregation creates a screening effect that decreases the number of effective adsorption sites and restricts dye diffusion toward the inner pores. Recent studies on nanocomposite adsorbents, such as copper ferrite/calcium alginate nanocomposites (Hassan et al. 2024) and bio-fabricated CuO nanoparticles (Ejeta et al. 2024) used for MG removal, showed dosage-dependent saturation behavior, where excessive adsorbent mass resulted in diminished surface availability and diffusion limitations.

3.3. Effect of Solution pH on MG Adsorption

The pH strongly affected the MG adsorption by regulating both the dye ionization and surface charge of the TA-CuNPs. Experiments conducted at pH 3–8 (308 K, 100 $mg.L^{-1}$ MG, 50 min) showed maximum removal at pH 6, as shown in Fig. 5c. At this pH, the zeta potential of the TA-CuNPs became sufficiently negative, promoting a strong electrostatic attraction to cationic MG. The proton competition for active sites causes reduced adsorption at pH < 6, whereas excess negative charge at higher pH probably causes electrostatic repulsion and restricts uptake. Thus, pH 6 was selected as the optimum value for further experiments.

3.4. Effect of Initial Dye Concentration on MG Adsorption

The effects of initial MG concentration (20–100 $mg.L^{-1}$) on adsorption by TA-CuNPs were evaluated under experimental conditions (pH 6, 308 K, 40 min). The percentage removal decreased as the dye concentration increased (Fig. 5d). At low concentrations, the high concentration gradient provides a strong driving force for mass transfer, allowing MG molecules to be efficiently captured by available active sites. However, with increasing concentration, these sites rapidly become occupied, and the driving force is no longer sufficient to overcome site saturation. This behavior is consistent with Langmuir monolayer adsorption, in which the removal efficiency decreases at high MG concentrations as the surface approaches its maximum loading capacity.

3.5. Kinetic Study of MG Adsorption on TACuNPs

The pseudo-second-order (PSO) model best described the adsorption kinetics of malachite green onto the TA-CuNPs under optimal conditions (pH 6, 318 K, 0.5 $g.L^{-1}$ adsorbent, 100 $mg.L^{-1}$ MG). The PSO model showed an excellent fit, with $R^2 = 0.999$ and close agreement between the calculated and experimental q_e values. Furthermore, a removal efficiency of 92.09% was achieved at an equilibrium time of 40 min, confirming the high adsorption performance of the system. In contrast, the pseudo-first-order model produced higher χ^2 and RMSE values, confirming its poor suitability. The superior performance of the PSO model indicates that

chemisorption is the dominant rate-controlling step, driven by electron sharing or exchange between MG molecules and surface sites on the nanoparticles. This mechanism aligns with the potential coordination interactions between Cu and *Tamarindus indica*-derived functional groups (–OH, –COOH, and phenolic groups). The kinetic parameters are summarized in Table 2, and the kinetic fits are shown in Fig. 6a and b.

3.6. Analysis of Adsorption Isotherms

The adsorption equilibrium of MG on the TA-CuNPs was modeled using the Langmuir and the Freundlich isotherms, as shown in Fig. 7a and b. The Langmuir model showed the strongest agreement with the data ($R^2 = 0.999$), confirming that MG interacts with a uniform surface via monolayer chemisorption. This finding was reinforced by the Langmuir separation factor ($R_L = 0.336$), which remained between 0 and 1, indicating favorable adsorption. The predicted q_{max} (243.902 $mg.g^{-1}$) also closely aligned with the experimental q_e (208.333 $mg.g^{-1}$). Although the Freundlich model ($R^2 = 0.979$) suggests mild surface heterogeneity at higher concentrations, the Langmuir isotherm clearly dominates. The isotherm constants are summarized in Table 3, and Table 4 compares the adsorption performance of TA-CuNPs with that of other reported adsorbents.

3.7. Analysis of Thermodynamics

Using an initial MG concentration of 20 $mg.L^{-1}$, the thermodynamic behavior of adsorption onto TA-CuNPs was examined at 303–318 K. The Van't Hoff plot (ln Kc vs. 1/T) in Fig. 8 shows strong linearity ($R^2 = 0.9903$), allowing ΔH^o and ΔS^o to be calculated from its slope and intercept; the resulting values are listed in Table 5. MG uptake occurred spontaneously at all temperatures under investigation, as confirmed by the consistently negative ΔG° values. A positive ΔH° indicates an endothermic process, which reflects the energy required for MG molecules to overcome hydration forces, reorganize interfacial species, and penetrate the nanoparticle pores. This process may involve minor changes in surface functionalities during binding. Owing to the displacement of structured water molecules and the increased configurational freedom gained as MG occupies adsorption sites on the TA-CuNPs surface, the significantly high ΔS° indicates a marked increase in interfacial disorder. This combined enthalpy–entropy profile explains why adsorption becomes stronger at higher temperatures: the thermal input increases molecular mobility, facilitates removal, and allows for more efficient dye–surface interactions, all of which improve the overall adsorption efficiency.

Table 2: MG's adsorption kinetics onto TA-CuNPs were determined.

Kinetic model	k_1[L. min^{-1}]	k_2, [g.mg^{-1}. min^{-1}]	q_e [$mg.g^{-1}$]	R^2
Pseudo-first-order	0.0956	--	151.836	0.9372
Pseudo-second-order	--	0.00082	208.333	0.9990

Table 3: Adsorption isotherm parameters for MG uptake on TA-CuNPs derived from the model.

Langmuir Isotherm Modeling		Freundlich Isotherm modeling	
b [$L.mg^{-1}$]	0.1017	K_f [$mg^{1-1/n}.L^{1/1}.g^{-1}$]	27.5913
q_{max} [$mg.g^{-1}$]	243.902	n	1.5745
R^2	0.999	R^2	0.979

3.8. Process Optimization Using Response Surface Methodology (RSM)

The "Central Composite Design," consisting of 30 experimental runs, was implemented to optimize the % removal of MG using TA-doped copper nanoparticles

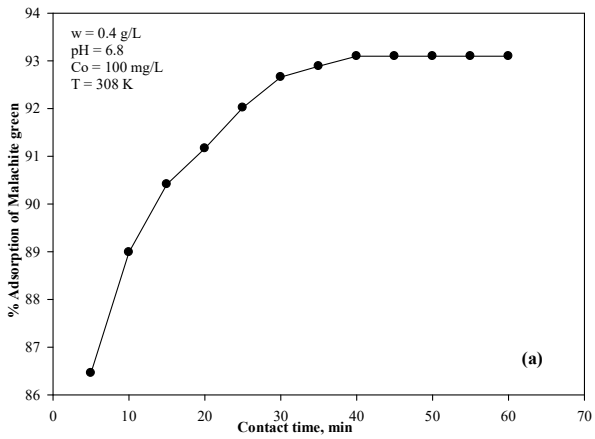


Fig. 5a: Effect of contact time on MG adsorption.

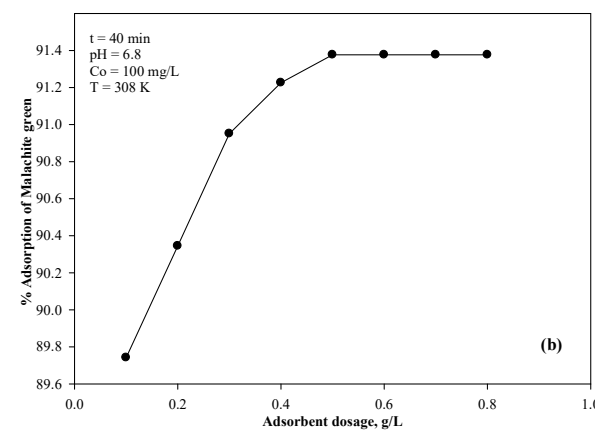


Fig. 5b: Effect of adsorbent dosage on MG adsorption.

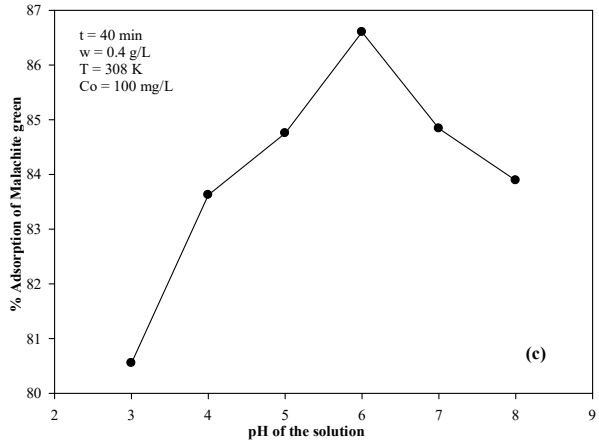


Fig. 5c: Effect of pH on MG adsorption.

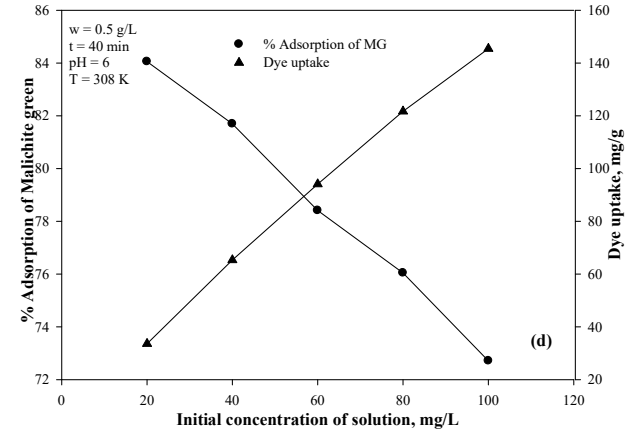
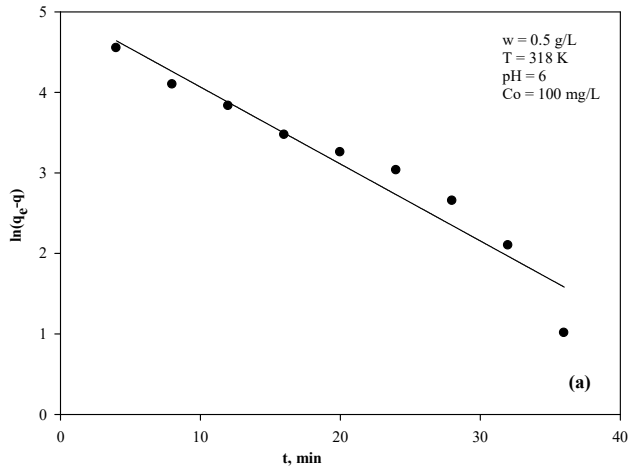


Fig. 5d: Effect of initial dye concentration on MG adsorption.



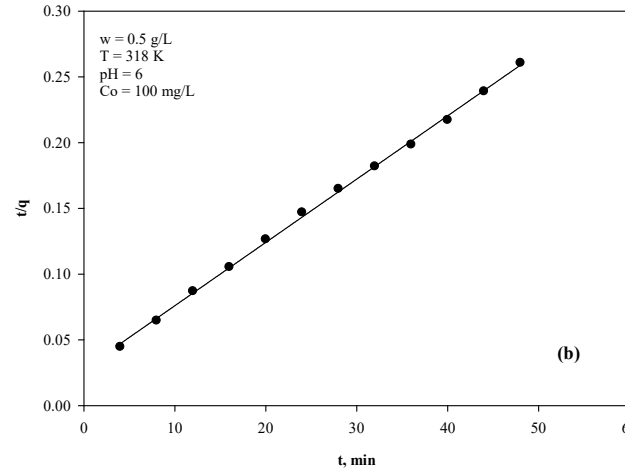
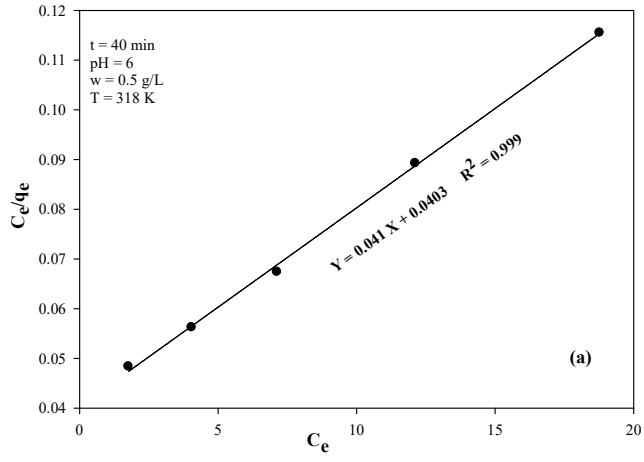


Fig. 6: Kinetic study models for MG adsorption: (a). Pseudo-First-order, (b). Pseudo-Second-order.



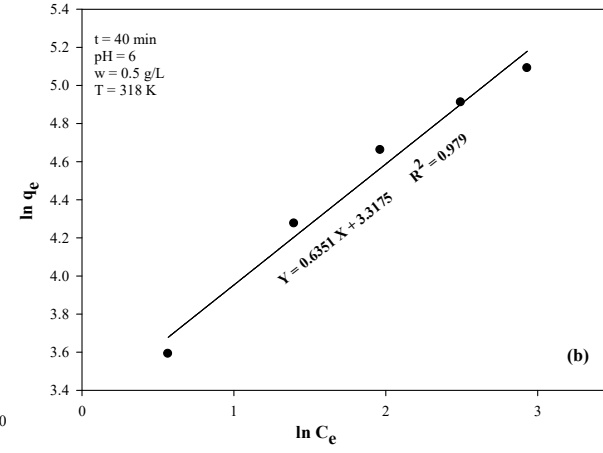


Fig. 7: Adsorption isotherm models for MG adsorption: (a). Langmuir isotherm (b). Freundlich isotherm.

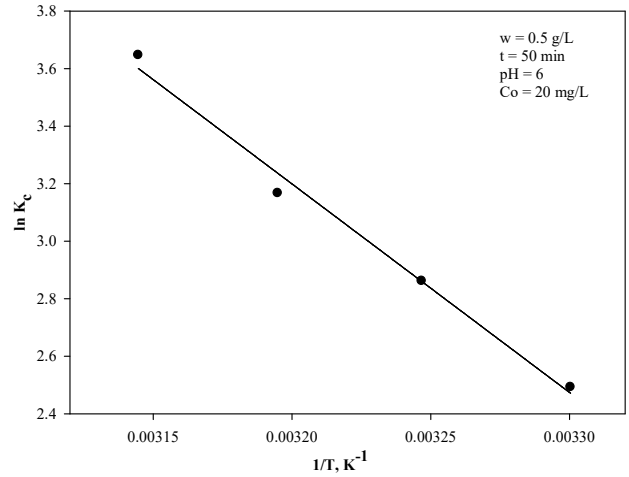


Fig. 8: The thermodynamic evaluation for the adsorption of Malachite green.

Table 4: MG removal from aqueous solution using the relative adsorption capacities of different adsorbents.

S.No.	Type of Adsorbent/Bio-sorbent	Max Dye uptake, $mg.g^{-1}$	Reference
1.	Spent tea leaves-Activated carbon (STAC)	256.40	Akar et al. (2013)
2.	Leaves of the *Solanum tuberosum* potato plant waste	33.33	Gupta et al. (2011)
3.	Pineapple stem	119.05	Hamed et al. (2009)
4.	Dead leaves of *Platanus vulgaris*	85.47	Hamdaouia et al. (2008)
5.	Activated Carbon Supported Zinc Sulfide–Copper Nanocomposite (ZnS–Cu–NP/AC)	168.10	Dastkhoon et al. (2015)
6.	Activated Carbon Supported Silver Nanoparticles (Ag–NP/AC)	95.20	Mortazavi et al. (2016)
7.	Halloysite nanotubes (HNT)	74.95	Turkan and Huseyin (2022)
8.	Cellulose nanofibers and silver nanoparticles	142.00	Chinthalapudi et al. (2021)
9.	TA-doped Cu nanoparticles (TA-CuNPs)	243.90	Present study

Table 5: Thermodynamic variables (ΔG°, ΔH°, and ΔS°) for adsorption of MG onto TA-CuNPs.

Temperature, [K]	Change in Gibbs-Free Energy, ΔG^{o} [$kJ.moL^{-1}$]	Change in Enthalpy, ΔH^{o} [$kJ.moL^{-1}$]	Change in Entropy, ΔS^{o} [$J.moL.K^{-1}$]
308	-6.281	60.295	219.534
313	-7.328		
318	-8.243		
323	-9.628		

(TA-CuNPs). The experimental framework incorporated four independent factors, initial MG dye concentration (A), dosage of adsorbent (B), solution pH (C), and temperature (D), which were systematically varied to investigate both their main effects and interaction influences on the adsorption efficiency. The coded and actual levels of these factors, along with the corresponding experimental responses, are summarized in Table 6. A quadratic (2^{nd}) polynomial regression model was constructed to correlate the % removal of MG with the coded process variables, offering an in-depth depiction of the adsorption behavior under the investigated operational condition.

$$\%Adsorption\ of MG = 91.35 - 0.1688 \times A - 0.3304 \times B + 0.6937 \times C + 0.1729 \times D + 0.1856 \times AB + \ 0.0019 \times AC + 0.4419 \times AC + 0.0806 \times BC + 0.3256 \times BD + 0.2669 \times CD + 3.28 \times A^2 - 3.42 \times B^2 - 3.52 \times C^2 - 2.08 \times D^2 \quad \ldots(9)$$

In the regression analysis, the factors were coded as −1 and +1 to enable a direct comparison of their relative

effects through standardized regression coefficients. With a significant Model F-value of 1755.38 and $p < 0.0001$, the robustness of the quadratic CCD model was confirmed by ANOVA, as shown in Table 7. This indicates that all linear, interaction (AB, AD, BD, and CD), and quadratic terms were statistically significant and that such a large F-value is highly unlikely to arise from noise. Additionally, the model has sufficient predictive power to reliably navigate the experimental design space, as evidenced by the high Adequate Precision of 121.889 and the close alignment of adjusted (0.9988) and predicted (0.9965) R^2 values, which show an excellent signal-to-noise ratio well above the threshold of 4. The optimal conditions were determined to be 19.85 an MG concentration of 0.498 $g.L^{-1}$ adsorbent dosage, pH 6.18, and a temperature of 318.24 K, which were determined through optimization using the desirability function depicted in Fig. 9a. The close match between the experimental and predicted values, as shown in Fig. 9b, further supports the dominance of these interactions and validates the model for reliable process optimization. This resulted in a predicted removal efficiency of 91.37% (desirability = 1.0), a value that is practically relevant for real-world wastewater treatment. Under experimental conditions, an actual removal efficiency of 92.09% was achieved, further validating the reliability and practical applicability of the model. Because of their control over the surface charge and

Table 6: Central Composite Design (CCD) matrix showing the experimental factors and corresponding responses for MG adsorption.

Run	Initial MG Dye Concentration [A]: $mg.L^{-1}$	Adsorbent dosage (B): $g.L^{-1}$	Solution pH [C]:	Temperature [D]: K	Experimental Value	Predicted value
1	15	0.4	5	313	79.86	79.88
2	25	0.4	5	313	78.54	78.38
3	15	0.6	5	313	78.22	78.13
4	25	0.6	5	313	77.43	77.28
5	15	0.4	7	313	80.63	80.67
6	25	0.4	7	313	78.95	79.08
7	15	0.6	7	313	79.35	79.15
8	25	0.6	7	313	78.15	78.30
9	15	0.4	5	323	78.42	78.26
10	25	0.4	5	323	78.21	78.43
11	15	0.6	5	323	77.83	77.71
12	25	0.6	5	323	78.68	78.63
13	15	0.4	7	323	79.85	80.01
14	25	0.4	7	323	80.12	80.19
15	15	0.6	7	323	79.65	79.79
16	25	0.6	7	323	80.82	80.71
17	10	0.5	6	318	78.52	78.31
18	30	0.5	6	318	77.95	77.90
19	20	0.3	6	318	78.52	78.57
20	20	0.7	6	318	76.78	76.99
21	20	0.5	4	318	75.68	75.87
22	20	0.5	8	318	78.84	78.65
23	20	0.5	6	308	82.60	82.68
24	20	0.5	6	328	83.45	83.37
25	20	0.5	6	318	91.35	91.35
26	20	0.5	6	318	91.35	91.35
27	20	0.5	6	318	91.35	91.35
28	20	0.5	6	318	91.35	91.35
29	20	0.5	6	318	91.35	91.35
30	20	0.5	6	318	91.35	91.35

Table 7: ANOVA for the quadratic model to describe MG adsorption onto TA-CuNPs.

Source of Variation	Sum of the Squares [SS]	The Degrees of freedom [df]	The Mean Square [MS]	F-value	p-value	
Model	792.38	14	56.60	1755.38	< 0.0001	significant
A: Initial concentration of the MG dye	0.6834	1	0.6834	21.20	0.0003	
B: Adsorbent dosage	2.62	1	2.62	81.26	< 0.0001	
C: Solution pH	11.55	1	11.55	358.25	< 0.0001	
D: Temperature	0.7176	1	0.7176	22.26	0.0003	
AB	0.5513	1	0.5513	17.10	0.0009	
AC	0.0001	1	0.0001	0.0017	0.9672	
AD	3.12	1	3.12	96.89	< 0.0001	
BC	0.1040	1	0.1040	3.23	0.0927	
BD	1.70	1	1.70	52.62	< 0.0001	
CD	1.14	1	1.14	35.34	< 0.0001	
A^2	294.81	1	294.81	9143.33	< 0.0001	
B^2	321.70	1	321.70	9977.29	< 0.0001	
C^2	340.27	1	340.27	10553.48	< 0.0001	
D^2	118.77	1	118.77	3683.74	< 0.0001	
Residual Error	0.4836	15	0.0322			
Lack of Fit	0.4836	10	0.0484			
Pure Error	0.0000	5	0.0000			
Corrected Total	792.86	29				
Adjusted R^2	0.9988					
Predicted R^2	0.9965					
Adeq Precision	121.8890					

active site availability, the 3D response surfaces and contour plots revealed that pH and adsorbent dosage had the strongest effects. Conversely, interactions involving dosage–pH and dosage–temperature were the most prominent, indicating a synergistic enhancement of the adsorption capacity under conditions favoring electrostatic attraction and endothermic uptake. The strong curvature in surface and Contour plots is presented in Fig. 10a-f and Fig.11a-f.

4. CONCLUSIONS

TA-doped copper nanoparticles (TA-CuNPs) synthesized by co-precipitation were extensively characterized (microscopy,

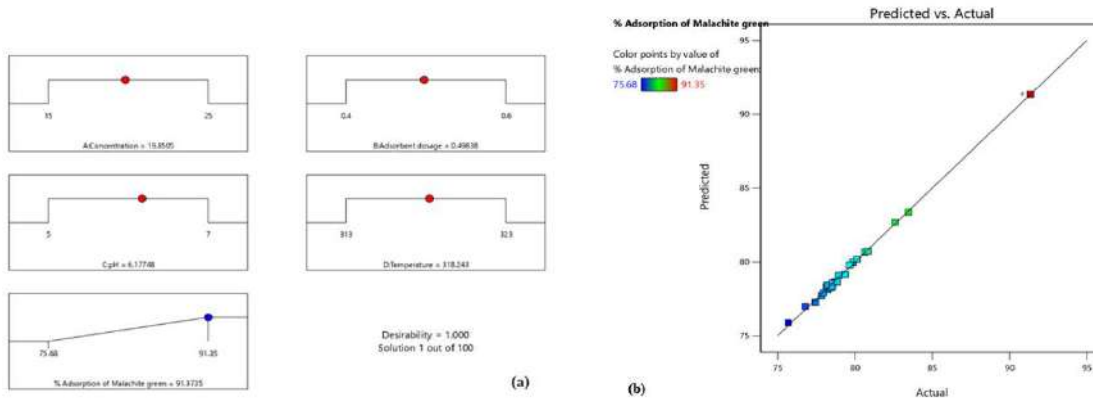


Fig. 9 (a): Ramp plot illustrating the optimized conditions for MG adsorption onto TA-CuNPs, (b). Comparison of the CCD Model's predicted and experimental values.

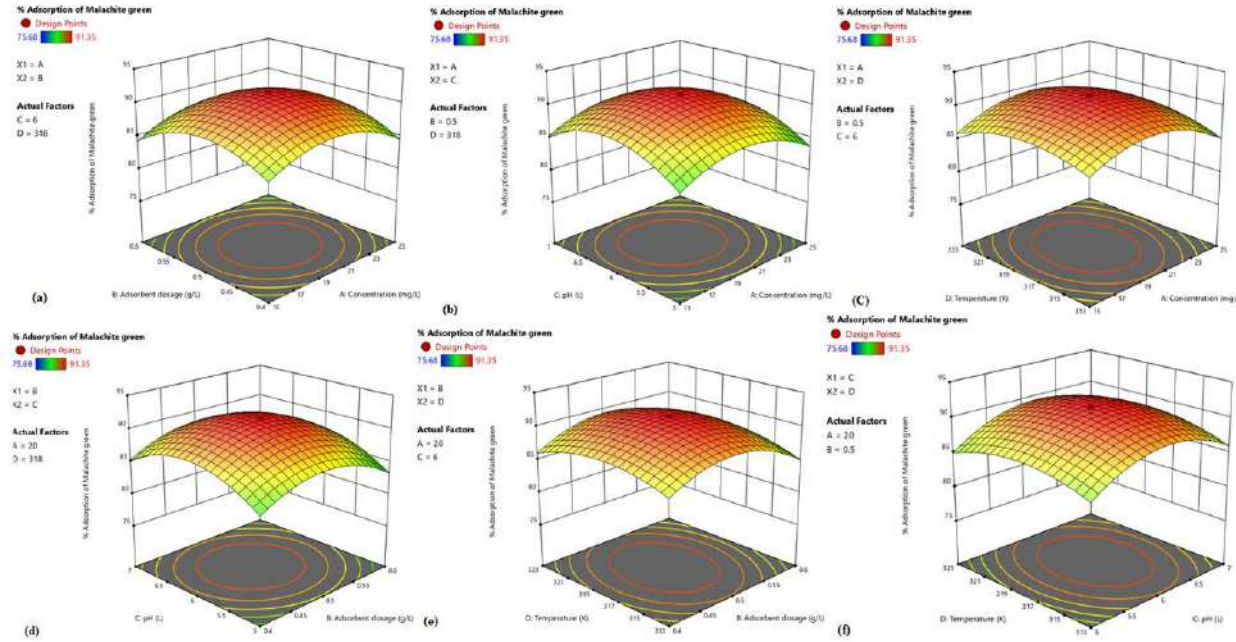


Fig. 10: 3D response-surface plots illustrating the interactive effects of (a) concentration and adsorbent dosage, (b) concentration and pH, (c) concentration and temperature, (d) adsorbent dosage and pH, (e) adsorbent dosage and temperature, (f) pH and temperature on the percentage removal of malachite green by TA-CuNPs.

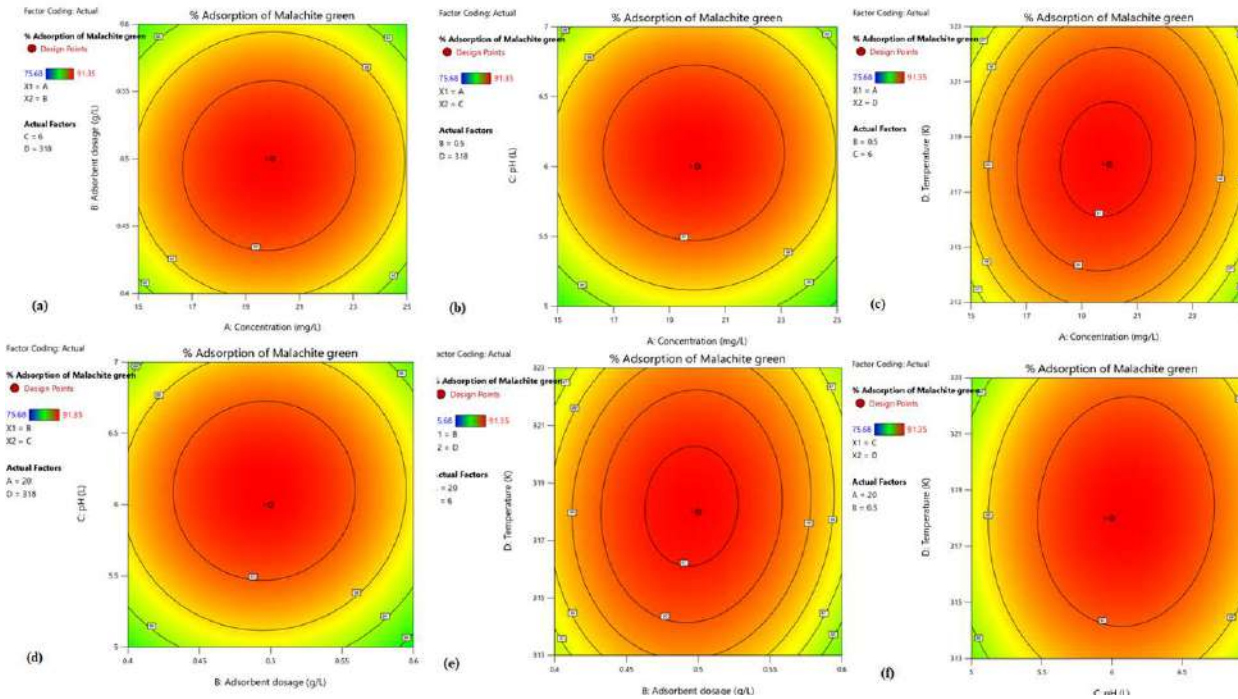


Fig. 11: 3D contour plots illustrating the interactive effects of (a) concentration and adsorbent dosage, (b) concentration and pH, (c) concentration and temperature, (d) adsorbent dosage and pH, (e) adsorbent dosage and temperature, (f) pH and temperature on the percentage removal of malachite green by TA-CuNPs.

XRD, FTIR, and Brunauer–Emmett), confirming their functional surface groups and porous morphology. In this study, TA-CuNPs exhibited efficient removal of malachite green, with adsorption strongly governed by pH, concentration, dosage, and contact time, yielding a Langmuir monolayer capacity of 243.90 $mg.g^{-1}$. The process followed pseudo-second-order kinetics and showed spontaneous endothermic behavior, with optimum batch conditions identified at pH 6 and 0.5 $g.L^{-1}$. RSM-based CCD optimization further defined the ideal operating parameters as 19.85 $mg.L^{-1}$ MG, 0.498 $g.L^{-1}$ adsorbent, pH 6.18, and 318 K, achieving the maximum removal efficiency, while the quadratic model demonstrated strong statistical validity through high R^2 and low error values. A comparative assessment of the reported adsorbents confirmed the competitive performance of the TA-CuNPs. To facilitate practical scale-up, further studies should thoroughly investigate multi-cycle regeneration, the impact of co-existing ions, breakthrough behavior under continuous flow or fixed-bed operation, and cost-benefit viability in comparison to commercial adsorbents.

5. REFERENCES

Agarwal, S., Tyagi, I., Gupta, V.K., Mashhadi, S. and Ghasemi, M., 2016. Kinetics and thermodynamics of malachite green dye removal from aqueous phase using iron nanoparticles loaded on ash. *Journal of Molecular Liquids*, 223, pp.1340-1347. [DOI]

Akar, E., Altinişik, A. and Seki, Y., 2013. Using of activated carbon produced from spent tea leaves for the removal of malachite green from aqueous solution. *Ecological Engineering*, 52, pp.19-27. [DOI]

Bashanaini, S.M., 2019. Removal of malachite green dye from aqueous solution by adsorption using modified and unmodified local agriculture waste. *Science Journal of Analytical Chemistry*, 7(2), pp.42-56. [DOI]

Bishwas, R.K., Mostofa, S., Alam, M.A. and Jahan, S.A., 2023. Removal of malachite green dye by sodium dodecyl sulfate modified bentonite clay: Kinetics, thermodynamics and isotherm modeling. *Next Nanotechnology*, 3-4, p.100021. [DOI]

Chinthalapudi, N., Kommaraju, V.V.D., Kannan, M.K., Nalluri, C.B. and Varanasi, S., 2021. Composites of cellulose nanofibers and silver nanoparticles for malachite green dye removal from water. *Carbohydrate Polymer Technologies and Applications*, 2, p.100098. [DOI]

Dastkhoon, M., Ghaedi, M., Asfaram, A., Goudarzi, A., Langroodi, S.M., Tyagi, I., Agarwal, S. and Gupta, V.K., 2015. Ultrasound assisted adsorption of malachite green dye onto ZnS-Cu-NP-AC: Equilibrium isotherms and kinetic studies – Response surface optimization. *Separation and Purification Technology*, 156(Part 2), pp.780-788. [DOI]

Eid, A.M., Fouda, A., Hassan, S.E.D., Hamza, M.F., Alharbi, N.K., Elkelish, A., Alharthi, A. and Salem, W.M., 2023. Plant-based copper oxide nanoparticles: Biosynthesis, characterization, antibacterial activity, tanning wastewater treatment, and heavy metals sorption. *Catalysts*, 13(2), p.348. [DOI]

Ejeta, B.A., Aaga, G.F., Fereja, W.M. et al., 2024. Biofabrication of highly effective and easily regenerated CuO nanoparticles as adsorbents for Congo red and malachite green removal. *Scientific Reports*, 14, p.24116. [DOI]

Gündüz, F. and Bayrak, B., 2018. Synthesis and performance of pomegranate peel-supported zero-valent iron nanoparticles for adsorption of malachite green. *Desalination and Water Treatment*, 110, pp.180-192. [DOI]

Gupta, N., Kushwah, A.K. and Chattopadhyaya, M.C., 2011. Application of potato plant wastes for the removal of methylene blue and malachite green dye from aqueous solution. *Arabian Journal of Chemistry*, (unknown volume/issue), pp.1-10. [DOI]

Hamdaouia, O., Saoudi, F., China, M. and Naffrechoux, E., 2008. Sorption of malachite green by a novel sorbent dead leaves of plane tree: Equilibrium and kinetic modeling. *Chemical Engineering Journal*, 143, pp.73-84. [DOI]

Hamed, B.H., Krishni, R.R. and Sata, S.A., 2009. A novel agricultural waste adsorbent for the removal of cationic dye from aqueous solutions. *Journal of Hazardous Materials*, 162, pp.305-311. [DOI]

Hassan, A.F., El-Naggar, G.A., Braish, A.G. et al., 2024. Utilization of synthesized copper ferrite/calcium alginate nanocomposite for adsorption and photocatalytic degradation of malachite green. *Journal of Inorganic and Organometallic Polymers and Materials*, 34, pp.190-206. [DOI]

Hussien Hamad, M.T.M., 2023. Optimization study of the adsorption of malachite green removal by MgO nano-composite, nano-bentonite and fungal immobilization on active carbon using response surface methodology and kinetic study. *Environmental Sciences Europe*, 35, p.26. [DOI]

Jain, R., Mathur, M., Sikarwar, S. and Mittal, A., 2007. Removal of the hazardous dye rhodamine B through photocatalytic and adsorption treatments. *Journal of Environmental Management*, 85, pp.956-964. [DOI]

Kumar, K.M., Mandal, B.K., Kumar, K.S., Reddy, P.S. and Sreedhar, B., 2013. Bio-based green method to synthesise palladium and iron nanoparticles using *Terminalia chebula* aqueous extract. *Spectrochimica Acta Part A: Molecular and Biomolecular Spectroscopy*, 102, pp.128-133. [DOI]

Mortazavi, K., Rajabi, H., Ansari, A., Ghaedi, M. and Dashtian, K., 2016. Preparation of silver nanoparticle loaded on activated carbon and its application for removal of malachite green from aqueous solution. *Synthesis and Reactivity in Inorganic, Metal-Organic, and Nano-Metal Chemistry*, 46(10), pp.1533-1542. [DOI]

Nadagouda, M.N., Castle, A.B., Murdock, R.C., Hussain, S.M. and Varma, R.S., 2010. In vitro biocompatibility of nanoscale zero valent iron particles (NZVI) synthesized using tea polyphenols. *Green Chemistry*, 12, pp.114-122. [DOI]

Njagi, E.C., Huang, H., Stafford, L., Genuino, H., Galindo, H.M., Collins, J.B., Hoag, G.E. and Suib, S.L., 2011. Biosynthesis of iron and silver nanoparticles at room temperature using aqueous sorghum bran extract. *Langmuir*, 27, pp.264-271. [DOI]

Philip, D., 2010. Green synthesis of gold and silver nanoparticles using Hibiscus rosa-sinensis. *Physica E: Low-dimensional Systems and Nanostructures*, 42, pp.1417-1424. [DOI]

Poiba, V.R., Sowjanya, B., King, P. and Vangalapati, M., 2023. Removal of methylene blue dye by using synthesized Grevillea robusta silver nanoparticles and optimization of experimental parameters by response surface methodology (central composite design). *Advances in Materials and Processing Technologies*, 10(4), pp.3013-3027. [DOI]

Shahwan, T., Abu Sirriah, S., Nairat, M., Boyacı, E., Eroğlu, A.E., Scott, T.B. and Hallam, K.R., 2011. Green synthesis of iron nanoparticles and their application as a Fenton-like catalyst for the degradation of aqueous cationic and anionic dyes. *Chemical Engineering Journal*, 172(1), pp.258-266. [DOI]

Sowjanya, B., King, P., Vangalapati, M. and Myneni, V.R., 2023. Copper-doped zinc oxide nanoparticles: Synthesis, characterization, and application for adsorptive removal of toxic azo dye. *International Journal of Chemical Engineering*, 2023, p.8640288. [DOI]

Turkan, A. and Huseyin, E., 2022. Adsorption of malachite green and methyl violet 2B by halloysite nanotube: Batch adsorption experiments and Box-Behnken experimental design. *Materials Chemistry and Physics*, 291, p.126612. [DOI]

Nature Environment and Pollution Technology
An International Quarterly Scientific Journal

p-ISSN: 0972-6268
(Print copies up to 2016)
e-ISSN: 2395-3454

Vol. 25 | No. 3 | Article ID D1827 | 2026

Original Research Paper

https://doi.org/10.46488/NEPT.2026.v25i03.D1827

Open Access Journal

Analysis of the Effectiveness of Rainwater Harvesting in Reducing Flooding: Case Study in the Governor's Housing Complex, Makassar

Hasnawiah, Rita Tahir Lopa† and Roslinda Ibrahim
Department of Environmental Engineering, Faculty of Engineering, Hasanuddin University, Makassar, Indonesia
†Corresponding author: Rita Tahir Lopa; ritalopa@unhas.ac.id

Abbreviation: Nat. Env. & Poll. Technol.
Website: www.neptjournal.com

Received: 08-06-2025
Revised: 19-07-2025
Accepted: 05-08-2025

Key Words:

Rainwater harvesting
Flood mitigation
Rainfall
Flooding

Citation for the Paper:

Hasnawiah, Lopa, R.T. and Ibrahim, R., 2026. Analysis of the effectiveness of rainwater harvesting in reducing flooding: Case study in the governor's housing complex, Makassar. *Nature Environment and Pollution Technology*, 25(3), D1827. https://doi..org/10.46488/NEPT.2026.v25i03.D1827

Note: From 2025, the journal has adopted the use of Article IDs in citations instead of traditional consecutive page numbers. Each article is now given individual page ranges starting from page 1.

Copyright: © 2026 by the authors
Licensee: Technoscience Publications
This article is an open access article distributed under the terms and conditions of the Creative Commons Attribution (CC BY) license (https://creativecommons.org/licenses/by/4.0/).

ABSTRACT

Flooding in residential areas remains a recurring problem in Makassar City, particularly in the Governor's Housing Complex, Kassi-Kassi Subdistrict. This study aims to analyze the effectiveness of rainwater harvesting (RWH) systems in reducing flood risks. The methodology includes hydrological and hydraulic analysis, as well as catchment area mapping. The RWH system design is based on estimating the potential rainwater volume from annual rainfall intensity and rooftop catchment areas. The results show that the average flood volume in the study area is 61.66 m³. The effectiveness of the rainwater harvesting system varies with storage capacity and roof area. In the first scenario (8 m³), flood volume is reduced by 4.61-60.06%; in the second scenario (10 m³), it achieves a 5.77-75.08% reduction; and in the third scenario (15.6 m³), it results in a 9.01-80.12% decrease. Differences in rooftop size influence the variation in percentage reduction, which affects the volume of harvested rainwater. The third scenario demonstrates the highest effectiveness, indicating that rainwater harvesting is a feasible and efficient strategy for urban rainwater management and flood mitigation. The study concludes that integrating rainwater harvesting (RWH) systems is a practical and sustainable solution for urban flood mitigation, especially in flood-prone areas such as Kassi-Kassi, Makassar.

1. INTRODUCTION

Makassar City, as the fourth-largest metropolitan city in Eastern Indonesia, is experiencing rapid population growth, with a total population of 1,454,956 people in 2023 (Central Bureau of Statistics of South Sulawesi Province 2023). This increase has not been accompanied by adequate clean water services, causing difficulties in fulfilling water needs, especially in densely populated areas. In addition, the expansion of development and the increase in built-up areas have resulted in a decrease in land absorption capacity, leading to an increase in runoff into drainage channels (Kharisma et al. 2016). If not managed properly, this runoff has the potential to cause flooding in the rainy season and drought in the dry season (Hermon & Barlian 2012). Based on the Makassar City RTRW (2006–2015), this area is categorized as flood-prone due to its low topography and the presence of two large river estuaries, the Jeneberang and Tallo Rivers. A major flood event in early 2023 resulted in 1,869 residents being displaced to 21 evacuation centers (Anirwan & Almuhajir Haris 2023).

One promising approach to addressing flooding and water shortages in urban areas is rainwater harvesting (RWH) technology. This system utilizes the roof of the building as the main catchment area, as it is relatively cleaner than other surfaces (Fewkes 2014, Lee et al. 2012). According to Raharjo (2019), the more rainwater that can be collected and utilized, the lower the potential for flooding. Several previous studies have shown that RWH systems are highly effective in reducing rainwater runoff. For example, a study by Kustyaningrum and Lasminto (2023) in Surabaya showed a reduction in inundation of up to 80.16% with an RWH

system. In Palangka Raya, Kamiana et al. (2024) found that the application of RWH reduced main drainage discharge by 58.15%. In Watampone, Ali et al. (2017) noted that rainwater harvesting was able to reduce surface runoff by more than 85%. At the international level, sponge city approaches, such as those in Guangxi, China, show that a combination of green space, bio-retention, and RWH can reduce runoff by up to 75% (Li et al. 2025). Technological innovations also support the optimization of RWH systems. Sharma and Ghosh (2021) highlighted that city infrastructure needs to be designed with adaptive safety factors, where RWH systems can be a vital component of urban climate resilience.

One of the areas in Makassar City that is consistently affected by annual flooding, even during low rainfall, is the Governor's Housing Complex in Rappocini Sub-district. This recurring flood issue is primarily due to a non-optimal drainage system and the increasing impervious surface area, which prevents rainwater from infiltrating into the soil, thereby increasing surface runoff. Flooding in this area typically occurs shortly after moderate to heavy rain. Based on field surveys and interviews with local residents, floodwaters can reach depths of approximately 15 to 30 centimeters and may persist for 1 to 2 hours, depending on rainfall intensity and the ability of the drainage system to discharge water. In some cases, particularly during prolonged rainfall, the inundation may last longer and extend to wider areas.

The drainage system in the Governor's Housing Complex is generally underperforming. Several factors contribute to this condition. First, many of the drainage channels are shallow and lack sufficient slope, which hampers efficient water flow. Second, there is frequent accumulation of solid waste and sediment, which clog the drainage paths and significantly reduce their capacity. Additionally, the system suffers from poor connectivity between drainage segments, resulting in stagnant water and localized flooding. The lack of routine maintenance further exacerbates the situation. Therefore, this study aims to analyze the effectiveness of rainwater harvesting (RWH) systems in reducing runoff volume in this flood-prone area. According to Harsoyo (2010), rainwater harvesting not only reduces surface runoff but also contributes to sustainable water resource conservation in urban environments.

While several studies have examined RWH applications in Indonesian urban contexts, few have assessed their performance in areas with limited space, non-retrofittable drainage systems, and dense residential housing, such as the Governor's Housing Complex in Makassar. Furthermore, most previous research applies generalized assumptions without integrating localized hydrological-hydraulic data at the building scale. This study fills that gap by presenting a data-driven RWH simulation that combines spatial roof data, water usage estimates, and drainage analysis. The research contributes a novel approach that integrates RWH effectiveness simulation at the individual-building level, aiming to support urban flood mitigation planning under infrastructure constraints.

This study not only measures the effectiveness of RWH but also introduces a spatial model for flood volume reduction at the building and neighborhood levels. The main scientific contribution lies in the integration of primary field data (roof area, drainage capacity, household water demand) with three RWH simulation scenarios, offering a localized planning tool for decentralized urban water management.

2. MATERIALS AND METHODS

2.1 Study Area

This research was conducted in the Governor's Housing Complex, located in Kassi-Kassi Subdistrict, Rappocini District, Makassar City, Indonesia. Geographically, the site is situated between 119°27'13.69"–119°27'16.69" E longitude and 5°10'08.88"–5°10'12.491" S latitude. The area was selected due to its frequent annual flooding and limited water supply infrastructure. The location of the study area is shown in Fig. 1.

2.2 Research Methodology

This study employs a descriptive-quantitative approach, which combines numerical analysis (quantitative) with a systematic description of observed conditions (descriptive). This approach is chosen because the research aims not only to process numerical data but also to describe the existing drainage conditions and runoff behavior in the study area. Although this study applies a descriptive-quantitative framework, the research is grounded in original field data collection and site-specific hydrological analysis. Primary data include building roof measurements and drainage dimensions, which are combined with 10-year rainfall records to simulate runoff and flood volume. The study employs standard hydrological modeling techniques (Log-Pearson III, rational method) and hydraulic capacity analysis using Manning's equation. The scenarios simulate flood volume reduction across 215 buildings, providing a comprehensive and original assessment that goes beyond descriptive statistics and meets the requirements for empirical research.

2.3 Types and Sources of Data

This study utilizes two main types of data: primary data and secondary data. Primary data were obtained through

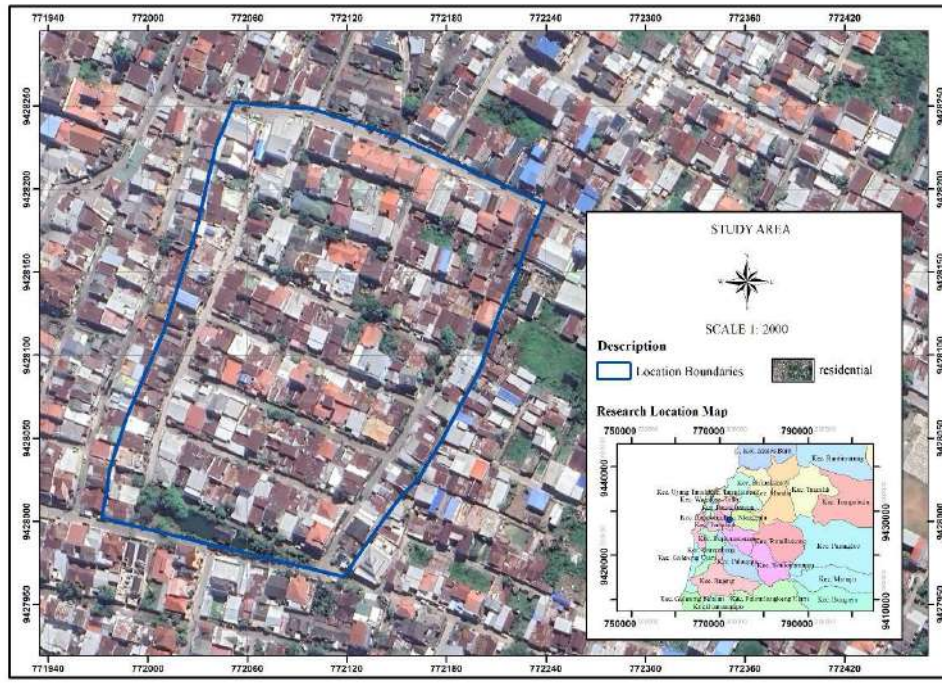


Fig. 1: Map of research location.

direct field surveys, including measurements of the physical dimensions of drainage channels (width, depth, and slope), roof surface areas of buildings, observations of drainage conditions (blocked, damaged, or functioning), and spatial coordinates using GPS. Secondary data were collected from relevant institutions, including 10-year rainfall data from the Meteorology, Climatology, and Geophysics Agency (BMKG) Makassar and topographic maps from the Regional Planning Agency (Bappeda).

2.4 Data Analysis Techniques

2.4.1 Rainfall Analysis

Rainfall data used in this study were obtained from the Meteorological, Climatological, and Geophysical Agency (BMKG), specifically from the Region IV BMKG Station in Makassar City. The dataset consists of monthly maximum rainfall records over a 10-year period, which serves as the basis for estimating design rainfall for various return periods. The rainfall data were processed using frequency distribution analysis to determine the probability and magnitude of extreme rainfall events. Among the various statistical methods available for hydrological frequency analysis, the Log-Pearson Type III.

2.4.2 Rainfall Intensity Analysis

Rainfall intensity is defined as the depth of rainfall occurring within a specific time interval. The magnitude of rainfall intensity varies depending on the duration and frequency of the rainfall events. Rainfall intensity analysis is a crucial component in hydrological planning, particularly for estimating peak discharge and designing efficient drainage systems (Triatmodjo 2010). Rainfall intensity (I) can be calculated using the formula:

$$I_t = \frac{R_{24}}{24}\left(\frac{24}{t}\right)^{\frac{2}{3}} \quad \ldots(1)$$

Where, I_t = Rainfall intensity ($mm.h^{-1}$), t = Rain duration (hour), R_{24} = Maximum rainfall (mm)

2.5 Flood Discharge Analysis

Plan discharge is the maximum amount of water that a drainage channel can convey to avoid flooding. The formula used the rational modification method (Ministry of Public Works of the Republic of Indonesia 2014)

$$Q = \frac{1}{3.6}\, C.Cs.I.A \quad \ldots(2)$$

Where Q = peak discharge generated by rain with a certain intensity, duration, and frequency ($m^3.s^{-1}$),

I = rainfall intensity ($mm.h^{-1}$), A = catchment area (km^2), C = flow coefficient which depends on the type of land surface, Cs = Coefficient of deviation

2.6 Hydraulic Analysis

The hydraulic analysis is intended to determine whether

the planned drainage meets the technical requirements. A dynamic control approach to drainage systems, when coupled with rainwater harvesting, increases the effectiveness of real-time flood control (Wong & Kerkez 2022). The flow discharge (Q) in the channel is calculated using Equation (3).

$$Q = V\,x\,A \quad \ldots(3)$$

Where, Q = discharge that occurs ($m^3.s^{-1}$), V = channel velocity ($m.s^{-1}$), A = cross-sectional area (m^2)

2.7 Rainwater Harvesting Analysis

Rainwater runoff from the building's roof will be collected through a rainwater harvesting system to minimize runoff discharge. The mandatory volume to be managed in rainwater harvesting is determined by calculations based on the Regulation of the Minister of Public Works of the Republic of Indonesia Number 11/PRT/M/2014 concerning Rainwater Management in Buildings and Persil.

$$V = 0.855\,x\,Cx\,A\,x\,th \quad \ldots(4)$$

Where, V = volume (m^3), C = Coefficient of runoff of building cross-section, A = Projected area of building cross-section against horizontal plane (m^2), th = rainfall height (mm)

Rainwater demand is the volume that will be used by the community for daily needs for one month, calculated with the following equation:

$$B = D \times P \quad \ldots(5)$$

Where, B = Total water demand in one month (m^3), D = Water demand of one person in one day (m^3), P = Number of users (people)

2.8 Analysis of Rainwater Harvesting Effectiveness

The effectiveness of using rainwater harvesting against flooding is obtained from the storage volume compared to the runoff volume:

Surface Flood Inundation Volume Reduction Rate (%) = (Vs) / (Vab +Vn) x 100% …(6)

Where, Vs = Storage water (m^3), Vn = Daily water demand ($m^3.y^{-1}$), Vab = Flood inundation (m^3)

The inclusion of Vn in this formula accounts for the volume of harvested rainwater used to meet household water needs throughout the year. It assumes that water stored in tanks is retained and used for non-potable purposes such as toilet flushing, washing, and irrigation. By incorporating Vn, the calculation reflects the additional reduction in runoff due to water actively drawn from storage for daily use, thus decreasing the potential for future surface runoff. This annualized approach offers a more complete estimate of the rainwater harvesting (RWH) system's role in flood mitigation by linking storage capacity with actual consumption patterns. It captures a realistic scenario where harvested rainwater offsets both immediate flood volumes (Vab) and helps reduce overall runoff through continuous utilization (Vn).

3. RESULTS AND DISCUSSION

3.1. Analysis of Maximum Rainfall

Rainfall analysis was conducted to determine the magnitude of the Governor's housing return period rainfall. The rainfall data used is from the last 10 years, from 2014 to 2023, obtained from BMKG Region IV Makassar. The data are presented in Table 1.

3.2. Frequency Distribution and Return Period Analysis

The frequency distribution analysis was conducted using the Log-Pearson Type III distribution. The suitability of this distribution was verified using the Chi-Square and Smirnov-Kolmogorov goodness-of-fit tests. Subsequently, it will be used to calculate planned rainfall. The results of the rainfall calculation are presented in Table 2.

3.3. Flood Discharge Analysis

Discharge calculations are carried out for hydrological conditions where discharge conditions are influenced by

Table 1: Annual maximum rainfall of BMKG region IV Makassar station.

No	Year	Rmaks [mm]
1	2014	878
2	2015	1041
3	2016	651
4	2017	1026
5	2018	787
6	2019	565
7	2020	915
8	2021	1050
9	2022	796
10	2023	1064

Table 2: Rainfall depth for each return period.

Return period [year]	Rainfall [mm]
100	1234
50	1204
25	1167
10	1103
5	1035
2	888

rainfall and conditions that occur in the field. The following is an example of calculations for the A1-A31 channel using equation 2

$$Q_{hydrology} = \frac{1}{3.6} C.Cs.I.A =$$

$$\frac{1}{3.6} x\ 0.7\ x\ 0.587\ x\ 1477.22\ x\ 0.00209 = 0.35\ m^3.s^{-1}$$

3.4. Hydraulic Analysis

At the hydraulic analysis stage, determining the geometric dimensions of each drainage channel is essential for evaluating flow capacity. In this study, a field survey was conducted to collect dimensional data for the channels. Additionally, the degree of drainage blockage was quantified to assess the extent of obstruction that could reduce the effective flow area. Blockage was measured using graduated rods to estimate the percentage of the channel's cross-sectional area obstructed by debris, sediment, or vegetation. This obstruction percentage was then used to adjust the effective area in hydraulic calculations. For example, the hydraulic discharge calculation for the A1–A31 channel segment is presented using Equation (3) with the following parameters:

Width (b) = 0.45 m

Depth (h) = 0.34 m

Water depth, (h_a) = 0.20 m

Slope (I) = 0.03%

Cross-sectional area (A) = b x water = 0.45 x 0.34 = 0.154 m^2

Wetted perimeter (P) = b + 2water = 1.13 m

Hydraulic radius (R) = A/P = 0.1354 m

Manning coefficient (n) = 0.014 (concrete)

Mean flow velocity (V) = 0.326 $m.s^{-1}$

$Q_{hydraulics}$ = V x A = 0.326 x 0.154 = 0.049 $m^3.s^{-1}$

The results show that the hydraulic discharge capacity ($Q_{hydraulics}$) is lower than the hydrological discharge ($Q_{hydrology}$). Specifically, in the A1–A31 segment, $Q_{hydrology}$ is 0.354 $m^3.s^{-1}$ while $Q_{hydraulics}$ is only 0.0499 $m^3.s^{-1}$. This significant disparity indicates that the channel does not have sufficient capacity to accommodate peak discharge, rendering it prone to localized flooding. A broader analysis was carried out for all drainage segments within the study area. The comparison of hydrological and hydraulic discharge for each segment is summarized in Table 3, which highlights several channels that lack adequate hydraulic capacity. These deficiencies contribute to recurrent flooding in key areas.

Table 3: Recapitulation of drainage channels that experience flooding.

Drainage Channel			Q_ Hydrol [$m^3.s^{-1}$]	Q_Hydraul [$m^3.s^{-1}$]
A1	-	A31	0.354	0.0499
A31	-	A30	0.502	0.4749
A4	-	A30	0.369	0.1321
A30	-	A29	0.871	0.2495
A5	-	A29	0.368	0.1412
A29	-	A28	0.513	0.4160
A6	-	A28	0.375	0.3351
A28	-	A27	1.759	0.4012
A7	-	A27	0.331	0.2913
A27	-	A26	0.463	0.3406
A8	-	A26	0.330	0.2090
A26	-	A25	2.552	1.9038
A9	-	A25	0.349	0.2416
A25	-	A24	0.489	0.3553
A10	-	A24	0.349	0.1623
A24	-	A23	3.391	0.0019
A11	-	A23	0.380	0.1868
A23	-	A22	0.528	0.2209
A12	-	A22	0.390	0.0865
A22	-	A21	4.309	0.1548
A13	-	A21	0.328	0.1842
A21	-	A20	0.484	0.1062
A20	-	A19	4.793	0.1384
A13	-	A15	0.192	0.1321
A19	-	A17	4.902	0.3515
A17	-	A16	5.150	0.2256
A32	-	A18	0.476	0.1043
A2	-	A14	0.418	0.1998

To better visualize the differences between hydrological and hydraulic discharge across each drainage segment, Fig. 2 is included. The chart clearly shows that in most segments, especially from A24–A23 to A17–A16, hydrological discharge vastly exceeds hydraulic capacity. The most notable discrepancies appear in segments A24–A23, A22–A21, and A20–A19, indicating an urgent need for redesign or capacity upgrades of these drainage systems.

3.5. Rainwater Harvesting Analysis

3.5.1. Calculation of Roof Area

To determine the roof area of buildings in this study, ArcGIS 10.8.2 software was used. Tables 4 and 5 present an example of roof area measurements for buildings located along a drainage channel that frequently experiences flooding.

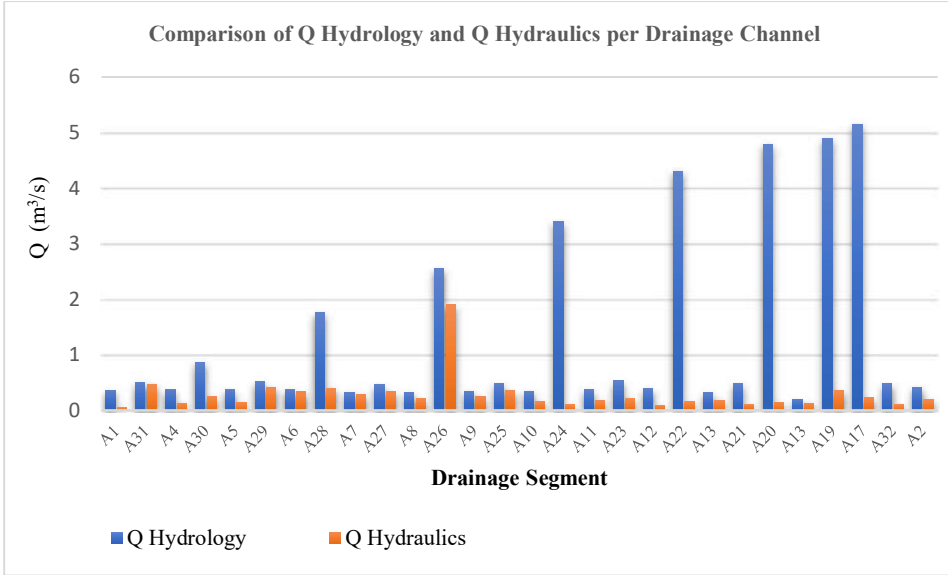


Fig. 2: Comparison of Q Hydrology and Q Hydraulics per drainage channel.

The rainwater harvesting calculation aims to determine how effectively the collected and stored water in a reservoir or ground tank reduces the flood inundation volume (VAB).

Table 4: Building roof area on channel drainage, Beringin 2.

Channel	Building Name	Roof Area [m^2]
Beringin 2	22	161.61
	23	136.4
	24	99.79
	25	118.69
	26	149.9
	27	108.97
	28	93.13
	29	159.88
	30	139.34
	31	97.24
	32	161.54
	33	136.85
	34	72.94
	35	86.1
	36	90.58
	37	100.48
	38	97.69
	39	107.08
	40	93.38
	41	83.54
	42	86.54
	43	116.07
	44	76.19
	45	96.89

Table 5: Recapitulation of building the Beringin 2 rainwater harvesting system.

Channel Drainage	Building Name	Roof Area [m^2]	Vab [m^3]
Beringin 2	22	161.61	85.873
	23	136.4	72.478
	24	99.79	53.025
	25	118.69	63.067
	26	149.9	79.651
	27	108.97	57.902
	28	93.13	49.486
	29	159.88	84.954
	30	139.34	74.040
	31	97.24	51.670
	32	161.54	85.836
	33	136.85	72.717
	34	72.94	38.758
	35	86.1	45.750
	36	90.58	48.131
	37	100.48	53.391
	38	97.69	51.909
	39	107.08	56.898
	40	93.38	49.619
	41	83.54	44.390
	42	86.54	45.984
	43	116.07	61.675
	44	76.19	40.484
	45	96.89	51.484

The flood inundation volume (VAB) is the volume of rainwater runoff and is calculated using the Indonesian National Standard 03-2453-2002.

An example of a flood inundation volume calculation for Building No. 22 using the Indonesian National Standard 03-2453-2002 formula is as follows:

C = 0.7

A = 161.61 m^2

R = 888 ($L.m^{-2}$ day)

Vab = 0.855×0.7×161.61×888 = 85.873 m^3

3.5.2. Use of the Rainwater Harvesting System

The rainwater harvesting system is an eco-friendly water management approach designed to collect, transport, filter,

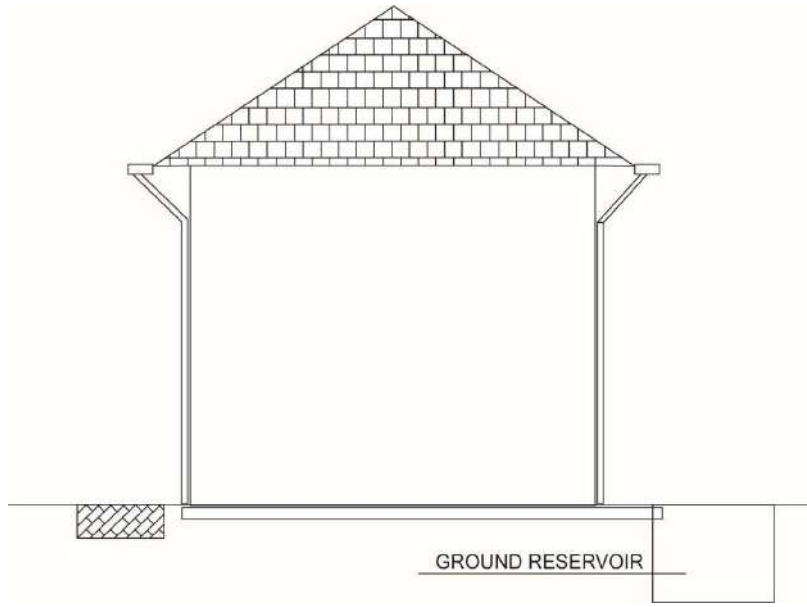


Fig. 3: Concept of rainwater harvesting system.
(National Standardization Agency of Indonesia 2015)

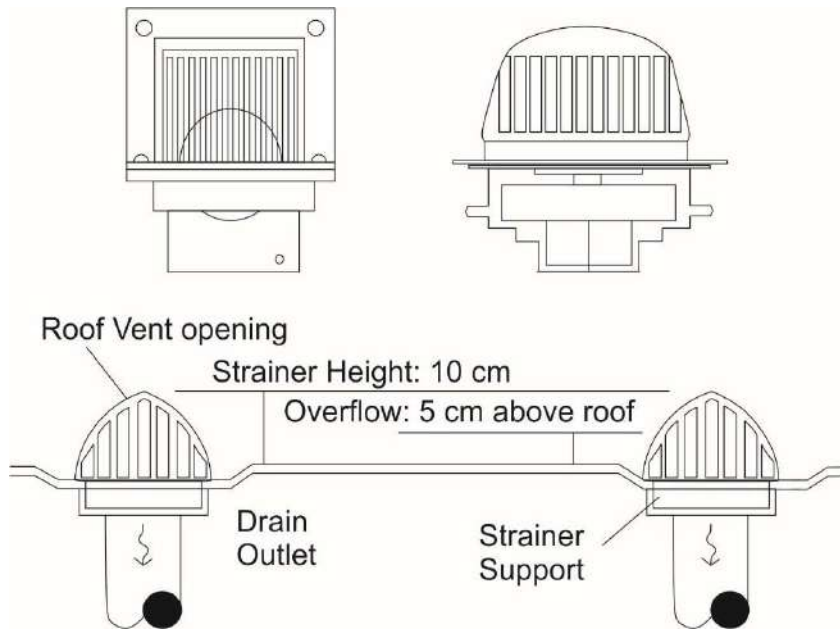


Fig. 4: Filter on the roof gutter. (National Standardization Agency of Indonesia 2015)

and store rainwater gathered from building rooftops for non-potable uses and, in some cases, for drinking after proper treatment. The typical system layout is shown in Fig. 3. To ensure the quality of the collected rainwater, a filtration unit is installed at the inlet. This filter is crucial for removing large debris such as leaves, dust, and other particles before the water reaches the storage tank. According to Indonesian National Standard 8153-2015, the filter must be installed at least 10 cm above the roof or gutter level, measured vertically from where the water enters. Additionally, the total surface area of the filter should be at least 1.5 times the cross-sectional area of the vertical gutter to provide enough hydraulic capacity, as illustrated in Fig. 4.

The selection of gutter and pipe specifications in this study follows Indonesian national standards 8153-2015, which outlines plumbing system standards for buildings. Based on the average rainfall intensity and roof area, the recommended specifications include a gutter with a 1% slope and a diameter of 6 inches, and a downpipe with a diameter of 3 inches.

3.6 Domestic Water Demand

Estimating the necessary amount of rainwater involves considering various aspects, such as daily water consumption, rainfall intensity, available storage capacity, and the potential of rainwater as a substitute for clean water (Yulistyorini 2011). The amount of water usage for the needs of people per day, according to Poediastoeti (2013), can be seen in Table 6 below.

The assumption of water demand per house in the study area is as follows:

a. Number of occupants = 4 people

b. Water demand/person = 120 L.person^{-1}.day^{-1}

c. Total water demand = 4 x 120 = 480 L.day^{-1}

= 480 x 30 = 14.400 L.month^{-1}

Table 6: Per capita daily water consumption.

Purpose	Percentage [%]	Volume [L]
Bathing	66.42	79.70
Laundry	13.06	15.67
Washing kitchen utensils	2.84	3.41
Floor cleaning	0.76	0.91
Ablution	13.45	16.14
Watering plants	0.83	1.00
Vehicle washing	0.32	0.38
Others	2.32	2.78
Total	**100**	**120**

The ground reservoir's stored water is intended for reuse in daily non-potable activities such as irrigation, vehicle washing, floor cleaning, and similar tasks. The estimated daily water requirement is 5.07 L per person. For a household of four, the total daily consumption is 20.28 L, leading to an annual usage of approximately 7.4 cubic meters.

3.7 Analysis of Rainwater Harvesting Effectiveness

To evaluate the effectiveness of the rainwater harvesting (RWH) system in reducing surface runoff, calculations were conducted, taking into account both water demand and flood volume reduction. The percentage reduction in surface flood inundation volume is calculated using the formula in equation 6:

Surface Flood Inundation Volume Reduction Rate (%) = (Vs)/(Vab+Vn) x 100%.

So, for the calculation of the rainwater harvesting system for scenario 1 with Building Name 22, the surface runoff volume reduction rate is obtained as follows

Storage water volume (Vs) = 2 x 2 x 2 = 8 m^3

Daily water demand (Vn) = 7.4 m^3.y^{-1}

Flood inundation volume (Vab) = 85.873 m^3

Surface flood inundation volume reduction rate = (8)/(85.873+ 7.4) x 100% = 8.58%

Fig. 5 illustrates the differences in surface flood reduction rates for each building under the three designated scenarios.

Fig. 5 depicts the surface flood inundation reduction rates across three different scenarios for each building within the study area. The analysis reveals that Scenario 3 consistently achieves the highest reduction rates compared to Scenarios 1 and 2, with maximum values reaching approximately 0.75 for several buildings, particularly between buildings 140 and 180. Overall, Scenario 1 shows the lowest reduction rates, while Scenario 2 demonstrates moderate effectiveness. The uneven distribution of reduction rates across buildings indicates that the success of each scenario heavily depends on the specific location and characteristics of individual structures. These results suggest that the more intensive measures in Scenario 3 are markedly more effective in reducing surface flood inundation in the area.

Fig. 6. above compares the flood conditions before and after the implementation of rainwater harvesting systems. The left panel (Before Rainwater Harvesting) shows the presence of significant surface flooding, with a flood volume of 61.66 m³. In contrast, the right panel (After Rainwater Harvesting) illustrates the absence of surface flooding, indicating that runoff has been effectively reduced through the installation of water storage systems. The simulation

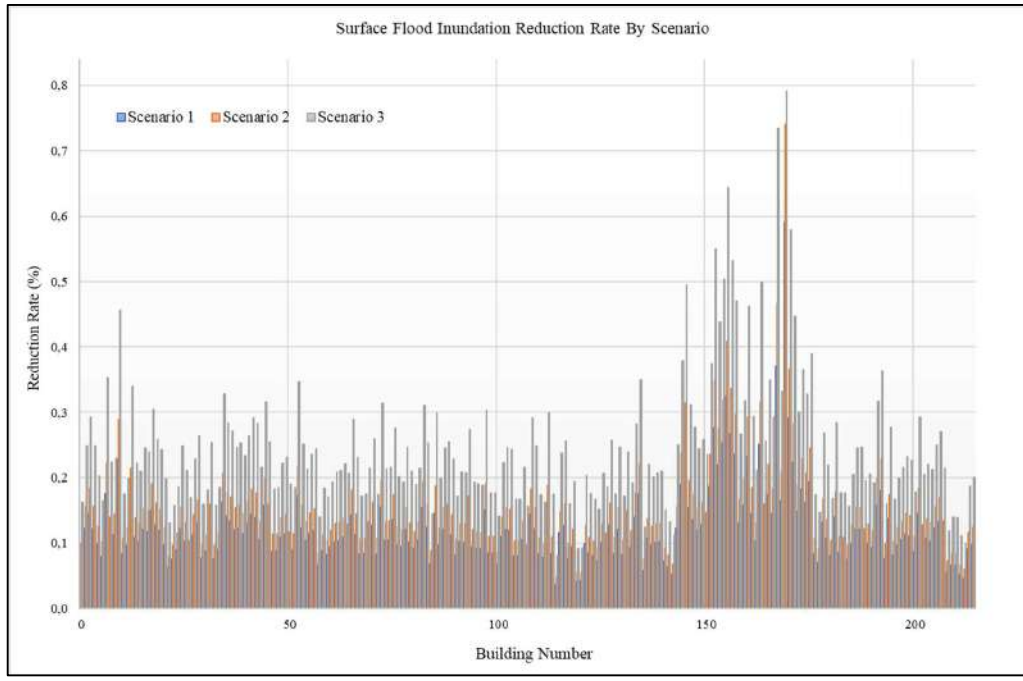


Fig. 5: Surface flood inundation volume reduction rate.



Fig 6: Comparison before and after rainwater harvesting.

includes three scenarios, with runoff volumes reduced to 46.25 m³ (Scenario 1), 44.25 m³ (Scenario 2), and 38.62 m³ (Scenario 3), respectively. These results demonstrate that rainwater harvesting can significantly reduce surface runoff and mitigate flood risks in the area.

The wide range in flood reduction rates across all three scenarios (ranging from 4.61%–80.12%) is primarily attributed to differences in rooftop area, tank storage volume, and household water usage. Smaller houses with limited roof catchment and storage capacities showed lower effectiveness, whereas larger buildings demonstrated significant reductions due to greater rainwater collection potential. Despite some low-performance outliers, over 65% of buildings achieved more than a 40% reduction in surface runoff volume. This confirms that, when implemented across a residential neighborhood, rainwater harvesting (RWH) has practical and measurable impacts on reducing flood volumes, even without altering the existing drainage network (Ali et al. 2017, Campisano et al. 2017).

The findings of this study highlight the significant role that RWH systems can play in reducing surface runoff and mitigating localized flooding in densely populated residential areas. The implementation of RWH in the Governor's Housing Complex demonstrates that even under limited space conditions, optimized roof catchment and storage systems can reduce peak runoff volume by up to 30.68%, depending on the storage scenario. This provides strong evidence supporting the application of decentralized water management strategies in urban flood-prone zones (Oyebode & Umar 2024, Xu et al. 2020).

However, several limitations of this study should be acknowledged. The analysis was based on historical rainfall data and assumed uniform tank performance and water usage patterns, which may not fully reflect real-world variability, such as tank overflow, leakage, or seasonal fluctuations in rainfall intensity. Additionally, the model did not account for potential constraints in retrofitting RWH systems in existing infrastructure, including space availability and economic feasibility.

Future research should explore the integration of RWH systems with other Sustainable Urban Drainage Systems (SUDS), such as infiltration wells, green roofs, or permeable pavements. Moreover, dynamic modeling under climate change scenarios and cost-benefit analysis of large-scale adoption would provide more comprehensive guidance for urban planners and policymakers in Indonesia and other tropical regions (Berndtsson 2010, Fletcher et al. 2015).

4. CONCLUSIONS

The results of the study indicate that the average flood volume in the Makassar Governor's Housing Complex is 61.66 m³. The rainwater harvesting system demonstrated varying levels of effectiveness in reducing this volume, depending on storage capacity. In the first scenario (8 m³ storage), the reduction ranged between 4.61% and 60.06%, in the second scenario (10 m³ storage), the reduction ranged between 5.77% and 75.08%, and in the third scenario (15.6 m³ storage), the reduction ranged between 9.01% and 80.12%. Among the three, the third scenario, with a storage capacity of 15.6 m³, was the most effective in mitigating flood risk. These findings support the feasibility of implementing rainwater harvesting systems as a practical and sustainable solution for flood control in urban residential areas.

5. ACKNOWLEDGMENTS

The authors express their gratitude to the entire academic community of the Department of Environmental Engineering, Hasanuddin University, Makassar, Indonesia, for their guidance and support throughout this research. This study did not receive any specific funding from governmental, commercial, or non-profit organizations.

6. REFERENCES

Ali, I., Suhardjono, S. and Hendrawan, A.P., 2017. Utilization of rainwater harvesting systems in Bone Biru Indah Permai Housing, Watampone. *Irrigation Engineering Journal*, 8(1), pp.26-38. [DOI]

Anirwan, A. and Haris, A., 2023. Makassar city government's efforts to realize post-flood disaster city resilience. *Journal of Governance and Local Politics (JGLP)*, 5(2), pp.187-195. [DOI]

Berndtsson, J.C., 2010. Green roof performance towards management of runoff water quantity and quality: A review. *Ecological Engineering*, 36(4), pp.351-360. [DOI].

Campisano, A., Butler, D., Ward, S., Burns, M.J., Friedler, E., DeBusk, K., Fisher-Jeffes, L.N., Ghisi, E., Rahman, A. and Furumai, H., 2017. Urban rainwater harvesting systems: Research, implementation and future perspectives. *Water Research*, 115, pp.195-209. [DOI].

Central Bureau of Statistics of South Sulawesi Province, 2023. *Makassar City in Figures 2022*. Central Bureau of Statistics, pp. 200

Fewkes, A., 2014. The verification of a behavioral model for simulating the hydrologic performance of rainwater harvesting systems. *Resources, Conservation and Recycling*, 86, pp.93-102. [DOI].

Fletcher, T.D., Andrieu, H. and Hamel, P., 2015. Understanding, management and modeling of urban hydrology and its consequences for receiving waters: A state of the art. *Advances in Water Resources*, 51, pp.261-279. [DOI].

Harsoyo, B., 2010. Rainwater harvesting techniques as an alternative effort to save water resources in the DKI Jakarta area. *Journal of Weather Modification Science & Technology*, 11(2), pp.29-39. [DOI]

Hermon, D. and Barlian, E., 2012. *Hydrometeorological Disaster Mitigation: Flood, Landslide, Ecology, Land Degradation, Tornado, Drought*. UNP Press, pp. 250

Kamiana, I.M., Wicaksono, A. and Nomeritae, 2024. Simulation of rainwater harvesting and its effect on the primary drainage discharge on Jalan Pangeran Samudera, Palangka Raya. *Karajata Engineering Journal*, 4(2), pp.123-130. [DOI].

Kharisma, R., Yudono, A. and Lopa, R.T., 2016. Utilization of rainwater harvesting based on low-impact development (Case study: FT-UH

Gowa educational area). In: *Proceedings of the 2016 IPLBI Scientific Meeting*, pp.E089-E096.

Kustyaningrum, J.D. and Lasminto, U., 2023. Potential analysis of rainwater harvesting in residential areas to reduce flooding in Sutorejo Housing, Surabaya. *Journal of Civil Engineering Applications*, 21(1), pp.41-48. [DOI]

Lee, J.Y., Bak, G. and Han, M., 2012. Quality of roof-harvested rainwater: Comparison of different roofing materials. *Environmental Pollution*, 162, pp.422-429. [DOI] .

Li, X., Zhang, Y. and Wang, J., 2025. *Robust Blue-Green Urban Flood Risk Management Optimized with a Genetic Algorithm for Multiple Rainstorm Return Periods*. arXiv preprint arXiv:2502.12174. [DOI]

Ministry of Public Works of the Republic of Indonesia, 2014. Regulation of the Minister of Public Works Number 12/PRT/M/2014 Concerning the Implementation of Urban Drainage Systems (Attachment I)*. Ministry of Public Works, pp. 150 .

National Standardization Agency of Indonesia, 2015. *Indonesian National Standards 8153:2015 – Plumbing System: General Requirements*. National Standardization Agency of Indonesia, pp. 80

Oyebode, O.J. and Umar, A.M., 2024. Design and modelling of urban stormwater management and treatment infrastructure for communities. *Nature Environment and Pollution Technology*, 23(1), pp.112-121.

Poediastoeti, H., 2013. The influence of socio-economic conditions on domestic water usage patterns. *Sultan Agung Environmental Journal*, 1(1), pp.64-77.

Raharjo, A.P., 2019. Simulation of surface runoff reduction using a simple rainwater harvesting system in an urban buffer area. *Natural Journal: Journal of Disaster Risk Reduction Technology*, 3(1), p.32. [DOI]

Sharma, A. and Ghosh, S., 2021. A safety factor approach to designing urban infrastructure for dynamic conditions. *Earth's Future*, 9(6), pp.e2021EF002118. [DOI]

Triatmodjo, B., 2010. *Applied Hydrology*. Beta Offset Publisher, pp. 400

Wong, B.P. and Kerkez, B., 2022. Flood risk mitigation and valve control in stormwater systems: State-space modeling, control algorithms, and case studies. *Journal of Water Resources Planning and Management*, 148(12), pp.04022075. [DOI]

Xu, W., Chen, Y., Han, D. and Chen, X., 2020. Optimal design of rainwater harvesting systems for urban flood mitigation under climate change. *Science of the Total Environment*, 720, p.137634. [DOI].

Yulistyorini, A., 2011. Rainwater harvesting as an alternative for water resources management in urban areas. *Journal of Technology and Vocational Studies*, 34(1), pp.105-114.

Nature Environment and Pollution Technology
An International Quarterly Scientific Journal

p-ISSN: 0972-6268
(Print copies up to 2016)
e-ISSN: 2395-3454

Vol. 25 | No. 3 | Article ID B4381 | 2026

Original Research Paper

https://doi.org/10.46488/NEPT.2026.v25i03.B4381

Open Access Journal

Deep Learning for AQI Prediction Using Multiple Feature Vectors: A Case Study of Colaba and Deonar Stations

Darakhshan Khan[1]†, Archana B. Patankar[1], Himani Deshpande[2] and Juhi Janjua[1]

[1]Department of Computer Engineering, Thadomal Shahani Engineering College, Mumbai, 400050, India

[2]Department of Artificial Intelligence and Data Science, Thadomal Shahani Engineering College, Mumbai, 400050, India

†Corresponding author: Darakhshan Khan; darakshan.khan@thadomal.org

Abbreviation: Nat. Env. & Poll. Technol.
Website: www.neptjournal.com

Received: 26-07-2025
Revised: 29-09-2025
Accepted: 07-10-2025

Key Words:

Air pollutants
Meteorological parameters
Bidirectional LSTM
Deep learning for AQI prediction

ABSTRACT

Air quality monitoring and prediction are important for effective public health strategies, as air pollution is a major contributor to mortality. The goal is to design and evaluate different deep learning models: Recurrent Neural Network (RNN), Long Short-Term Memory (LSTM), Bidirectional LSTM (Bi-LSTM), and a hybrid Conv1D-LSTM on different input sets of features. The dataset consists of pollutant and meteorological parameters from 2019 to 2024 with hourly frequency for two monitoring stations: Colaba and Deonar. The models were trained on three sets of features: pollutant-only, meteorological-only, and combined features. Model accuracy was determined using the root mean square error, coefficient of determination, mean absolute percentage error, and explained variance score. The results indicate that the combined attributes significantly enhanced the prediction quality, with the hybrid CNN-LSTM performing best at Colaba and the LSTM on meteorological attributes performing best at Deonar. The Bi-LSTM exhibited consistent performance on the feature sets. These results underscore the importance of using both pollutants and meteorological information and illustrate the efficiency of sophisticated deep learning structures for location-based air quality prediction.

1. INTRODUCTION

Globally, air pollution has emerged as a major cause of mortality and a significant threat to human health. Monitoring, understanding, and predicting environmental factors, specifically those related to air quality, remain critical challenges for governments and corporations worldwide. Given the increasing rate of pollution, there is a critical need to develop methods that can accurately predict the Air Quality Index and support the creation of better public health strategies (Schürholz et al. 2020). Human life is basically surviving on air, but its quality gets ruined due to vast pollution, which leads to acute multiple health hazards, such as physiological and respiratory disorders. Scientific studies have proven that air pollution is the greatest environmental risk, driven by rapid industrialization and urban growth. This unplanned emission has grossly degraded air quality, exposed people to hazardous substances, and posed substantial risks to public health.

The need to mitigate these impacts underlines the importance of robust monitoring systems and predictive models in safeguarding air quality and reducing the adverse health effects of pollution on communities (Gupta et al. 2023). Particulate matter (PM) has become a major pollutant of concern, significantly affecting air quality across borders. The particles in PM vary in size and chemical composition; therefore, the risks associated with them are also variable in space and time. Studies have identified a relationship between PM exposure and daily respiratory mortality in both construction workers and residents living near construction sites (Yan et al. 2023), and it can exacerbate chronic obstructive

Citation for the Paper:

Khan, D., Patankar, A.B., Deshpande, H. and Janjua, J., 2026. Deep learning for AQI prediction using multiple feature vectors: A case study of Colaba and Deonar stations. *Nature Environment and Pollution Technology*, 25(3), B4381. https://doi.org/10.46488/NEPT.2026.v25i03.B4381

Note: From 2025, the journal has adopted the use of Article IDs in citations instead of traditional consecutive page numbers. Each article is now given individual page ranges starting from page 1.

Copyright: © 2026 by the authors
Licensee: Technoscience Publications
This article is an open access article distributed under the terms and conditions of the Creative Commons Attribution (CC BY) license (https://creativecommons.org/licenses/by/4.0/).

pulmonary disease (COPD) symptoms, thereby increasing the risk of mortality (Gou et al. 2023, DeVries et al. 2017). Other common air pollutants include ammonia, sulfur dioxide, carbon monoxide, nitrogen oxides, and ozone, all of which have adverse effects on human health. Ammonia is an irritating gas that affects the skin, respiratory, digestive, and ophthalmic systems. Ammonia combines with other air constituents to form $PM_{2.5}$, a key air pollutant with enormous health effects (Petrus et al. 2022). Both SO_2 and ozone have been shown to significantly increase the risk of hospital admission, cardiopulmonary diseases, myocardial infarction, chronic obstructive pulmonary disease, and respiratory diseases (Wu et al. 2022, Jian et al. 2024). Higher levels of these pollutants are directly correlated with the proportion of the population with chronic respiratory diseases. Increased levels of CO in the air can lead to a reduction in oxygen levels in the human body, which can damage cells, tissues, and organs, whereas high NOx levels can cause respiratory morbidity and lung diseases (Zhang & Zhang 2024).

Climate change is evident across the globe, and variations in climatic conditions have a strong influence on the Air Quality Index (AQI) levels, which, if not controlled, can amplify risks to human health (Liu et al. 2022, Yan et al. 2024). Multiple studies have shown a strong correlation between AQI levels and various climatic factors, such as temperature, wind direction, wind speed, humidity, pressure, visibility, rainfall, sun exposure, diurnal temperature, precipitation, and weather outlook conditions. Multiple studies have claimed that the principal climatic factors affecting AQI levels are temperature, pressure, humidity, dew point, and wind speed. Owing to local geomorphological and meteorological factors, AQI levels are affected within a radius of 100 km (Liu et al. 2022).

With the advancement of deep learning, various sequential deep architectures, such as the Recurrent Neural Network (RNN), Gated Recurrent Unit (GRU), and Long Short-Term Memory cell (LSTM), have gained popularity in making accurate and robust AQI predictions for many cities worldwide. An RNN is created from a feed-forward neural network, wherein some nodes have inter-node connections and backward loops that allow the network to remember the present and recent past (Ayus et al. 2023). A variant of RNN, the GRU, utilizes two main gates, an update gate and a reset gate, to manage memory. The update gate controls the addition of new information, and the reset gate controls the amount of the previous state to remember. It can be further extended as a Bidirectional GRU, which learns sequences in both directions by combining two unidirectional GRUs for learning in the forward and backward directions (Ayus et al. 2023, Mandal & Sen 2024). Another variant of RNN is LSTM, which provides a solution to the problems of long-term dependency with forget, input, and output gates that control the memorization and removal of information (Ayus et al. 2023, Song et al. 2024). The Bidirectional LSTM further improves this by processing input sequences in both forward and backward directions. CNN-GRU is a hybrid model in which a Convolutional Neural Network is applied for feature extraction and a GRU for sequence prediction, thus creating a deep architecture capable of handling spatiotemporal data (Ayus et al. 2023, Shi et al. 2023).

This study involved performing a statistical correlation analysis between the AQI and various factors, such as meteorological parameters and atmospheric pollutants. It also aims to understand the effects of diurnal and seasonal variations on air quality data. The core goal is to understand how various feature vectors interact simultaneously with different deep learning architectures. In addition, this study seeks to determine which deep learning architectures provide the most robust predictions and have better generalization abilities. Two stations with different environments were studied: Colaba, which is located on the coast, and Deonar, an inland station influenced mainly by landfill and industrial pollution sources.

The remainder of this paper is organized as follows: the next section contains a review of the literature, which highlights the global perception of AQI prediction, advancements in machine learning and deep learning techniques, and the role of climatic conditions in AQI forecasting. The following section encompasses an understanding of the relationship between AQI and the factors influencing it, followed by temporal and spatial analysis. The following section deals with the adopted methodology, including detailed information on the data collection process, different model architectures used, feature engineering, and model validation. The final section presents the setup of the experiment, results, and observations of the research, followed by the conclusion.

2. BACKGROUND RESEARCH

Air pollution has emerged as a global health crisis; therefore, stable and steady forecasting models for air quality monitoring and prediction are necessary. Different researchers have utilized different methodologies to solve this problem, especially through enhanced machine learning and deep learning techniques. This section discusses some of the most significant studies worldwide to provide a complete context for the current research.

2.1 Cross-Continental Perspective on AQI Prediction

China: Exhaustive research in China has shown that variations in AQI levels are largely influenced by atmospheric pollutants such as PM2.5, PM10, Ozone (O_3), SO_2, NOx,

and CO, and the concentration of these atmospheric pollutants is heavily influenced by climatic conditions. The studies (Zhang & Jiang 2018, Sun et al. 2019) use positive matrix factorization with chemical mass balance, regression, and correlation analysis on data collected from different monitoring stations across multiple provinces in China, to gauge the association between the concentration of PM2.5 and various meteorological factors, such as temperature, wind speed, relative humidity, and air pressure. It was observed that low wind speed, coupled with high rising temperature and high humidity, will lead to higher concentrations of PM2.5 in the air. Higher PM2.5 levels were observed in winter and during peak hours of the day. Tian et al. (2021) used wavelet transform and demonstrated that the ozone concentration shows strong temporal and spatial associations with meteorological variables, such as wind speed, solar radiation, temperature, and humidity, with a noteworthy observation that urban areas are prone to higher ozone levels. Whereas another study, in Linfen city, which is one of the most polluted areas in China, seasonal variation analysis was carried out to capture the climatic fluctuations on air pollution. They found that during the winter season, air quality was very poor, which was heavily influenced by the speed of the wind and precipitation (Cui et al. 2018). Fang et al. (2015) performed extensive research on a dataset collected from air quality monitoring stations for 338 cities across China, using multiple tools such as ordinary least squares, special lag models, geographically weighted regression, and Spearman's rank correlation to understand the effect of population size, industrialization, and transportation networks on air pollution.

India: Multiple studies conducted across different cities in India indicate that AQI levels are influenced by meteorological conditions and location-specific factors, such as distance from dumping yards or proximity of monitoring stations to the sea coast. The review article (Karthick et al. 2024) integrates multiple pieces of research conducted in different cities, namely Ahmedabad, Delhi, Lucknow, Gurugram, and Mumbai. This highlights the observation that the concentrations of PM2.5 and CO are the two most crucial factors influencing the AQI; thus, the reduction in the two aforementioned pollutants can contribute significantly to better air quality in Indian cities. Another study (Varaprasad et al. 2024) used five coastal Indian cities: Kolkata, Visakhapatnam, Chennai, Mumbai, and Thiruvananthapuram as the research objects. The results indicate that the highest concentrations of PM2.5 occur during winter (December to February), whereas the lowest concentrations are observed during the monsoon (June to September). Among all these findings, an important outcome is that the eastern Indian coastline bears an intense influence from outflowing emissions from the Indo-Gangetic Plain that gradually decreases from north to south, that is, from Kolkata to Chennai. The analysis of the sea-land breeze cycles indicated a negative correlation between breeze magnitude and PM2.5, suggesting that weaker breezes might lead to worse air quality because of weaker ventilation. The researchers (Rangaswamy et al. 2022, Poyyamoli & Boss 2014) have used data from Jawahar Nagar dump yard, Hyderabad, and Kammiyampet dump yard, Cuddalore, to understand how improper garbage disposal practices around the landfills can increase the concentration of air pollutants in nearby areas. It was observed that due to the decomposition of waste or burning of garbage at a dumping site, there was a much higher concentration of multiple air pollutants than the permissible limits, which can lead to various disorders related to the respiratory system or cardiovascular problems. There was also the formation of a chemical substance called leachate, which pollutes land and groundwater.

America and Europe: Studies from the American and European continents have investigated the interplay between air quality and various human activities, such as urbanization, transportation, and agriculture. Sterling (2024) investigated how air quality varies with population density in any country, as well as the number of transportation-related emissions connected to it, in California. Notable findings are that a higher density is associated with increased emissions of vehicles; thus, the more a region contains human populations, the higher the emissions, meaning more air pollutants from transport. In Romania, where 14% of the civil workforce is engaged in agriculture, a study (Petrus et al. 2022) was conducted to determine the proportion of NH3 using laser photoacoustic spectroscopy. The key sources of higher NH3 levels are agricultural practices and emissions caused by fuel combustion. Other pertinent variables affecting the over-time dispersion and accumulation of NH3 include the temperature, humidity, and wind speed. This study (Sajjad Abdollahpour et al. 2024) illustrates considerable links between urban spatial structure and air quality using a multi-decade analysis of 481 U.S. cities from 1990 to 2015. Compact urban forms, population density, circularity, and green spaces diminish pollutant concentrations, whereas expansion and industrial areas tend to enhance them. A 10% improvement in key factors could potentially prevent over 10,000 deaths annually.

Asia and Africa: In Adıyaman (Kara et al. 2024), the authors claimed that natural and human activities drive air pollution. Major contributors include dust transport from southerly winds, crop burning, and heating, which are primarily found in the city center. PM10 was positively correlated with SO_2, whereas wind speed and temperature had negative effects on pollution levels. Saadi et al. (2021) used a Polar 810i monitor to test CO, Heart Rate Variability (HRV), and

city size in Tel Aviv (metropolitan) and Afula (small city). The results showed that pollution is high in Tel Aviv due to industrialization and vehicle emissions, with CO levels showing a positive correlation and HRV showing a negative association, indicating greater cardiac effects. Weak positive correlations between PM2.5 and temperature (r = 0.42) and humidity (r = 0.37) have been reported in a study conducted in Ratchaburi, Thailand. AirQ+ [33] states that PM2.5 during dry periods violated the limit set by WHO, and the elderly with more years lost due to disability. In Addis Ababa, deteriorating vehicle conditions and poor road status are drivers of air pollution, especially in the heavily congested areas of Megenagna. SO_2, NO_2, PM2.5, and PM10 data from 43 sites showed significant spatial heterogeneity, with SO_2 often above the safety thresholds. This study (Bizualem et al. 2023) calls for further research on traffic-related emissions to reduce pollution. Global studies have shown that meteorological factors, urbanization, transportation, and waste management have a significant impact on air quality, with most pollutants, such as PM2.5, PM10, CO, and SO_2, exceeding the safety limit due to human activities and climatic conditions.

2.2 Innovation in AQI Prediction Techniques

Neural network-based Models: These models have garnered significant attention for predicting air quality indices (AQI) and pollutant concentrations. For example, one study that utilized data from four Chinese cities implemented machine learning algorithms such as extreme gradient boosting (XGBoost), light gradient boosting, and random forest. Among these, XGBoost demonstrated the highest forecasting accuracy, achieving a coefficient of determination of 0.929 (Wang et al. 2023). Another comparative analysis (Zhan et al. 2020) explored various predictive models, including linear regression, CNN, LSTM, GRU, Bidirectional LSTM, and backpropagation neural networks. Using hourly AQI data from 1,615 locations across China, this study identified the Bidirectional LSTM as the most effective model.

A broader review (Mendez et al. 2023) examined global approaches to AQI prediction, with a specific focus on PM2.5. It highlighted the frequent use of weather data and pollutant concentrations as input features and identified models such as LSTM, MLP, CNN, and GRU as the most commonly applied techniques. Evaluation metrics such as RMSE, R2 Score, and MAPE were consistently used to assess performance. Additionally, research involving data from the Belfast city center compared the predictive capabilities of LSTM, GRU, and ARIMA models for pollutants, including NO_2, O_3, SO_2, PM2.5, and PM10. The study found that LSTM consistently outperformed other models, whereas ARIMA delivered subpar predictions (Naz et al. 2023). Collectively, these findings underscore the increasing reliance on neural network architectures for precise air quality modeling.

2.3 Hybrid Models for Optimized Accuracy

These approaches to AQI prediction have demonstrated notable improvements by integrating simple and advanced methods. For instance, one study (Kleingchuay et al. 2023) employed empirical mode decomposition to extract time-frequency information, which was combined with Generalized AutoRegressive Conditional Heteroskedasticity (GARCH) models to analyze residuals and historical data. The output was subsequently processed through the LSTM and SVM models, yielding enhanced MAE scores for LSTM and superior index of agreement values for SVM. Another study (Barve et al. 2020), using meteorological data and AQI values from Beijing, introduced a hybrid framework with parallel dense neural networks and LSTM layers. This approach achieved significantly better MAE values than the standalone LSTM models. Similarly, Thakur et al. (2023) combined principal component analysis (PCA) with deep learning models, such as LSTM, GRU, and Bidirectional LSTM, for multivariate AQI forecasting, with PCA and GRU delivering the best performance across various metrics.

For more advanced architectures, Shi et al. (2023) proposed a hybrid TCNbiGRU model that utilized Temporal Convolutional Networks (TCN) to capture long-term patterns and biGRU for short-term dependencies, outperforming standalone LSTM and GRU approaches. In another study (Lu & Li 2023), researchers used a hybrid CNNBiLSTM model optimized through Bayesian methods to predict air pollutants in Tianjin, while another study (Nikpour P et al. 2024) introduced the ”Gelato” framework. This innovative approach combined particle swarm optimization, a transformer-inspired architecture, and XGBoost to predict the multivariate AQI. In research focusing on Indian metropolitan areas (Binbusayyis et al. 2024), a stacked attention-based GRU model incorporating KL divergence was employed after imputing the missing data with deep generative adversarial networks. This framework achieved a high prediction accuracy. Finally, Shankar and Arasu (2023) explored hidden temporal and periodic patterns in AQI data, demonstrating that hybrid models, such as CNN-LSTM and GRU, integrated with Empirical Mode Decomposition, surpassed their standalone counterparts in predictive performance. Collectively, these studies underscore the effectiveness of hybrid architectures in enhancing the accuracy and robustness of AQI prediction by leveraging a blend of preprocessing techniques and sophisticated deep learning models.

A Transformer model was proposed for $PM_{2.5}$ prediction at 12 Beijing sites and performed better than the CNN-LSTM-Attention model, with EVS, MAE, MSE, and R^2 being improved by 12%, 9%, 6%, and 30%, respectively (Cui et al. 2023). It successfully captured short-term meteorological changes and long-term seasonal trends and has an excellent ability to model long-range dependencies for air quality forecasting. This research (Wu et al. 2024) presented a partial least squares VAER (PLS-VAER) model for indoor air quality prediction, in which PLS extracts latent variables to enhance the VAER input and improve accuracy. The model outperformed conventional approaches and provided a robust and eco-friendly solution for indoor air quality monitoring and parameter optimization. In contrast to the current Bi-LSTM and hybrid models that utilize uniform sets of features across regions, this study focuses on station-specific feature engineering, adapting inputs for each site's environment and geography. This enables the capture of localized drivers of pollution, including coastal influence and landfill distance, which improves predictive performance and interpretability over traditional approaches.

3. TEMPORAL AND CORRELATION ANALYSIS

This section discusses the temporal correlation of AQI values, followed by seasonal and diurnal oscillations between the AQI and factors driving AQI levels, such as air contaminants and meteorological conditions. This research draws on data from two sources: 1. CPCB site, 2. OpenWeatherMap API. Atmospheric air pollutant data for the two stations, Colaba and Deonar, were obtained from the CPCB portal (Central Pollution Control Board 2024) for the periods of July 2019 to March 2024 for Colaba station and November 2020 to March 2024 for Deonar station. Meteorological data for the same stations and timestamps were captured via the OpenWeatherMap API (OpenWeather 2024).

3.1 Temporal Analysis

There was a strong autocorrelation between the AQI values, as shown in Fig. 1. Present AQI values are associated with past AQI values; that is, the present values are dependent on past AQI values. In Fig. 1, for both stations, all points are centered around the diagonal, which indicates that the AQI time series has the same descriptive properties, such as mean, variance, and standard deviation, over different time instances, which shows that both time series are stationary in nature (Douglas et al. 2015).

3.2 Correlation Analysis

All six atmospheric pollutants were positively associated with AQI levels in the air, as shown in Fig. 2. Particulate matter, PM2.5, and PM10 had nearly a perfect positive correlation, whereas NOx and SO_2 also exhibited a strong positive association with AQI levels. For ozone, there was a location-specific dependency; that is, it showed a modest positive influence on AQI levels for the Deonar station but not much for the Colaba station.

Similarly, the Pearson Coefficient was used to understand the relationship between meteorological parameters and AQI levels. For both stations in the Figs. 3 and 4, it is apparent that temperature, dew point, minimum and maximum temperature in a day, humidity, wind speed, and wind direction have a negative association with AQI levels, whereas diurnal temperature and pressure have a positive impact on AQI levels. It was observed that out of all meteorological parameters, pressure, humidity, and dew point had a strong association with the target variable.

3.3 Statistical Analysis

Table 1 presents the summary statistics of AQI values at Colaba and Deonar stations, showing dispersion in terms

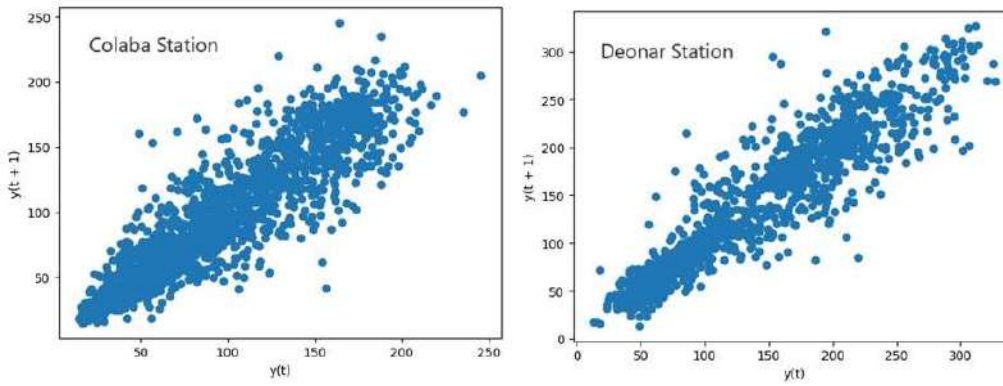


Fig. 1: Auto-lag plots of AQI values for the Colaba and Deonar Stations.

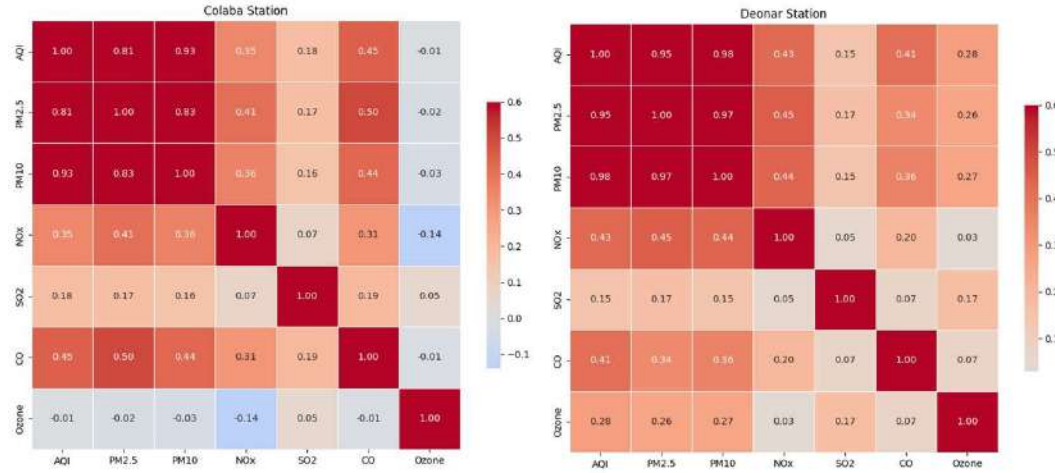


Fig. 2: Heatmap of Pearson correlation between atmospheric pollutants and AQI values for Colaba and Deonar Stations.

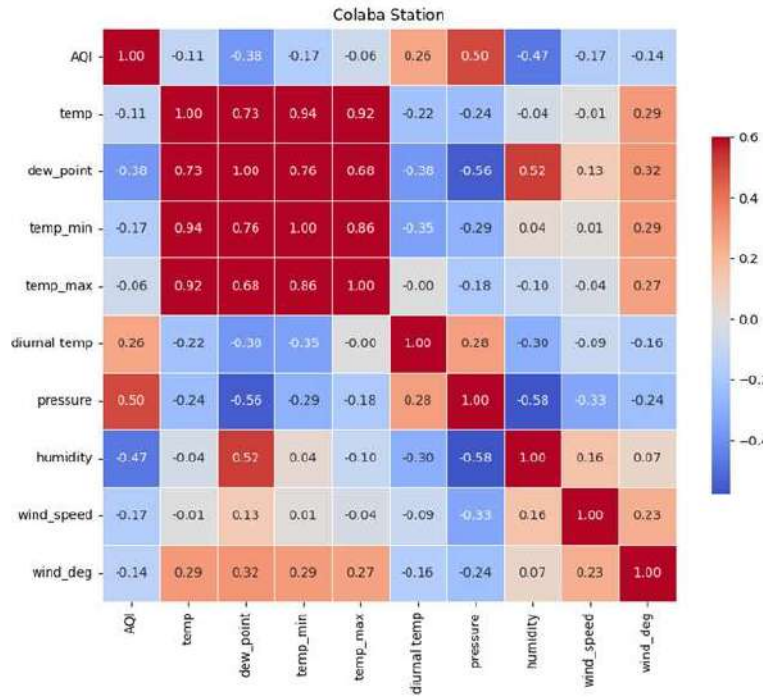


Fig. 3: Heatmap of Pearson correlation between meteorological factors and AQI values for the Colaba Station.

of variance and standard deviations, seasonal variation by calculating winter and summer means, and diurnal variation with day and night means for winter and summer seasons. Both time series are volatile in nature, with Deonar showing a higher dispersion or spread.

In all respects, Deonar always showed higher AQI values in both seasons and at all times of the day, indicating a generally poorer air quality compared to Colaba. In winter, both stations had higher readings at night than during the day. During summer, both stations indicated higher values during the day than at night, with Colaba showing more pronounced day–night differences, indicating that the time of day could have a notable impact on air quality. To understand the variability in AQI levels, both seasonal and diurnal variations must be captured precisely.

4. MATERIALS AND METHODS

Fig. 5 shows a detailed diagram of the AQI prediction workflow using deep learning models. There are four stages: Data Collection, Data Pre-processing, Feature Engineering,

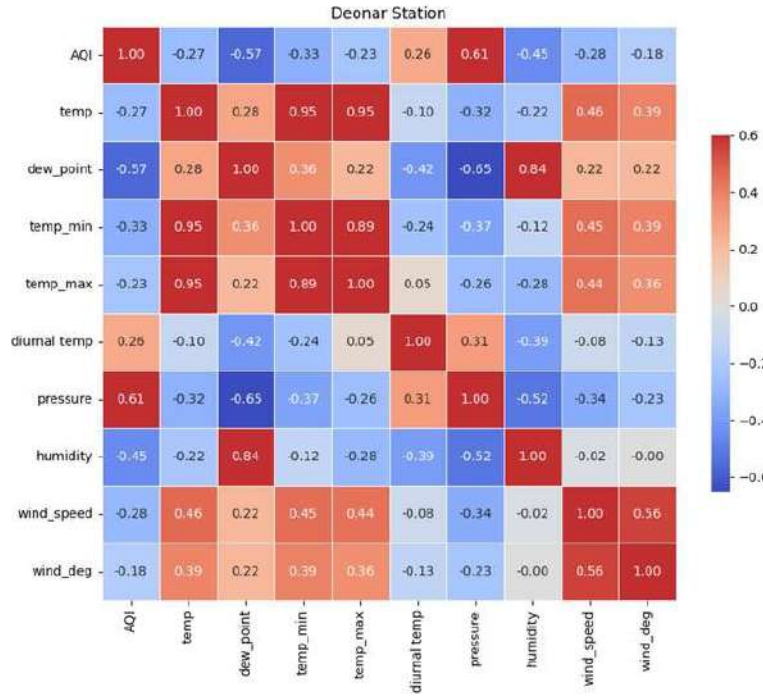


Fig. 4: Heatmap of Pearson correlation between meteorological factors and AQI values for the Deonar Station.

Table 1: Statistical summary of AQI values for Colaba and Deonar Stations.

Stations	Dispersion		Seasonal Variation		Diurnal Variations			
	Variation	Standard Deviation	Winter Mean	Summer Mean	Winter Day Time Mean	Winter Night Time Mean	Summer Day Time Mean	Summer Night Time Mean
Colaba	4532.95	67.32	73.06	114.16	70.45	76.03	144.26	116.32
Deonar	7382.04	85.92	202.32	120.18	199.65	205.81	190.62	120.51

and Model Development. In stage 1, data were collected from multiple sources, including the concentrations of various atmospheric pollutants, such as particulate matter with 15 and gaseous pollutants, along with meteorological parameters, namely, temperature, wind speed, wind direction, atmospheric pressure, dew point, and humidity.

A combined dataset feature was created using pollutant levels and meteorological factors. The data were for hourly records, with Colaba having 41,617 data points from July 01, 2019, to March 31, 2024, and Deonar having 29,929 data points from November 01, 2020, to March 31, 2024, with the gap being due to non-availability of data on the CPCB portal for some dates. The AQI calculator (Central Control Room for Air Quality Management Delhi NCR 2024) was used to calculate the AQI value, which was also appended to the dataset. Data pre-processing is stage 2, which includes multiple steps, such as filling missing values using a time-based mean interpolator, followed by detecting irregularities in the data using interquartile ranges and filling those irregularities with a time-based mean imputer. The TBMI algorithm imputes step by step, first computing the group means by time, month, day, and year, and then imputing the missing values with the calculated group means. The two-step anomaly treatment used in this study began with the inter-quantile range (IQR) method at the 15th and 85th percentiles to mark values beyond this range. This method identifies medium-sized anomalies without a high degree of sensitivity to extreme values. Before feeding for training, the data were standardized and normalized, which is equivalent to adjusting the values to a common scale, ensuring uniformity and comparability across the dataset.

The next stage is feature engineering, where multiple feature sets are created based on the results of Pearson's correlation matrix. These experiments and combinations were created to understand how different deep learning topologies interact with different feature vectors. For this study, three different feature vectors, namely, Best Pollutant parameters, Best Meteorological parameters, and

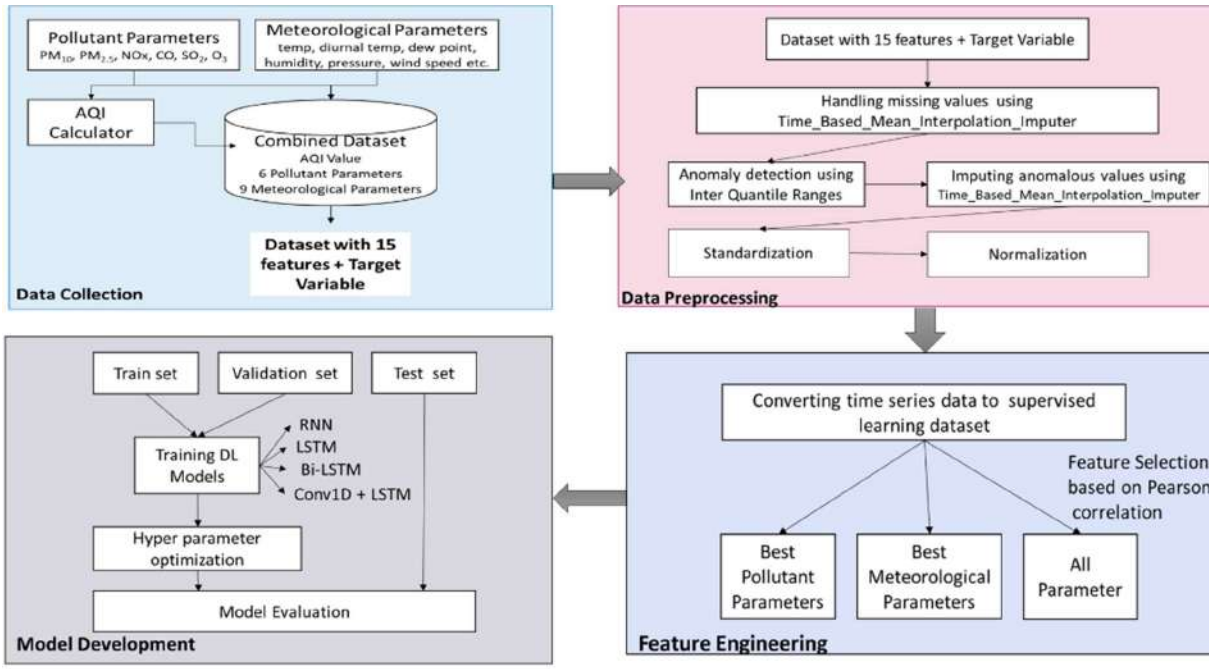


Fig. 5: Comprehensive deep learning workflow for accurate AQI prediction.

Table 2: Selected Features for AQI Prediction at Colaba and Deonar.

Stations	Colaba	Deonar
Best Pollutant Parameters	PM_{10}, $PM_{2.5}$, NOx, CO	PM_{10}, $PM_{2.5}$, NOx, CO, Ozone
Best Meteorological Parameters	Pressure, Humidity, Dew Point, Diurnal temperature	Pressure, Humidity, Dew Point, Temperature, Wind Speed
All Parameters	6 Pollutant Levels + 9 Meteorological Parameters + AQI (Target Variable)	6 Pollutant Levels + 9 Meteorological Parameters + AQI (Target Variable)

all 15 parameters, were used, as shown in Table 2. The last stage of this research included the development of a model, which involved splitting the data into multiple sets, namely, training, validation, and test sets, with a 70:20:10 ratio for both stations. Using optimized hyperparameter settings along with the training and validation sets, multiple deep learning architectures, namely, RNN, LSTM, Bidirectional LSTM, and Conv1D+LSTM, as shown in Fig. 6, were trained using MSLE as the loss function. For all these architectures, the past week of data was used to make a single-step ahead AQI prediction. The shape of the input was different for different architectures, depending on the feature set and location.

The first architecture, that is, the RNN architecture, has an input layer followed by a couple of RNN layers and eventually a dense layer before the final output layer. The RNN layer processes sequential data and captures temporal dependencies using hidden states over multiple time steps. The dense layer was used to project the outputs of the RNN into the desired output dimension. RNNs suffer from the problem of diminishing gradients (Khan et al. 2023). The second architecture, which is a stacked LSTM, is an enhancement over the simple RNN, where RNN cells are replaced by LSTM cells. LSTM cells can reduce the vanishing gradient issue with the help of a gating mechanism, where different gates decide which information to pass and which information to remove (Le et al. 2020).

To avoid overfitting, dropout regularization is used, and stacked configurations can help learn more complicated patterns by increasing their depth. The third architecture studied is a stacked Bidirectional LSTM, where the input sequences are operated in both forward and backward directions. These models can perceive latent relationships between the input and target variables in both past and future contexts (Mandal & Sarode 2024a). The architecture is similar to the LSTM architecture, with one change: LSTM cells in the hidden layers are replaced with Bi-LSTM cells. Finally, a hybrid architecture uses convolution layers to extract local patterns and then feeds those local extracted

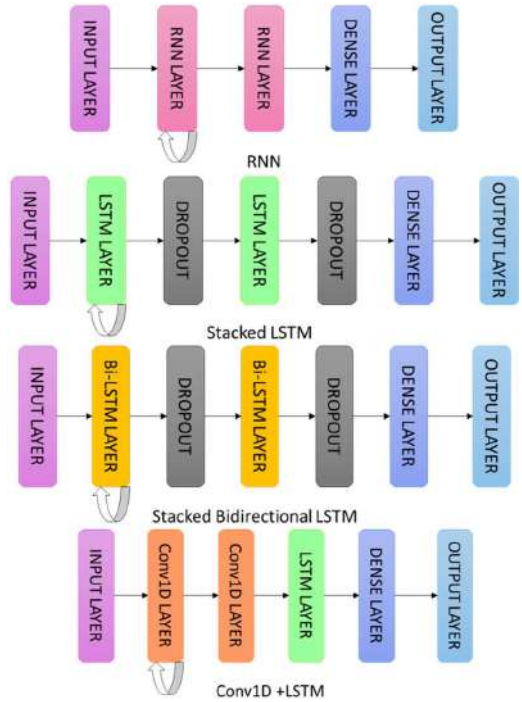


Fig. 6: Architectural diversity of deep learning models for AQI prediction.

patterns to LSTM layers to capture temporal relationships (Jiao et al. 2020). This hybrid model can take advantage of both learning topologies.

4.1 Evaluation Metrics

Multiple performance metrics were used to understand different aspects of the model's performance. These metrics provide a comprehensive evaluation of prediction models covering various facets, such as the magnitude of error in prediction and the extent of variation in the data captured.

RMSE: The Root Mean Squared Error (RMSE) is a measure of the average magnitude of the errors between the actual and predicted AQI values. It calculates the square root of the average of the squares of the differences between every actual value and its predicted value (Mandal & Sarode 2024b, Botchkarev 2019). Squaring gives more importance to larger errors than to smaller ones; hence, this metric is sensitive to the outliers. A lower RMSE value indicates that the average of the predicted values is closer to the actual value.

R^2 Score: The R^2 Score is the coefficient of determination (Plevris et al. 2022, Botchkarev 2019), which indicates how well the model fits the variability of the target variable. It provides a number showing the proportion of variance in the dependent variable that might be predicted from the independent variables. The R^2 score can take any value from 0, which means that the model does not explain any variability in the target variable, to 1, which would mean that it explains all the variability. A higher R^2 score indicates how well the model fits the data and, therefore, how well it predicts the AQI values based on the input features.

MAPE: MAPE stands for Mean Absolute Percentage Error, which is an accuracy metric calculated by taking the average absolute percentage difference between the predicted and actual values (Plevris et al. 2022, Botchkarev 2019). This will be useful when the accuracy of a model on different datasets or scales is compared. MAPE normalizes these errors. The lower the value of MAPE, the more accurate the predictions; the higher the value, the greater the error.

Another explanatory metric is EVS, which stands for Explained Variance Score (EVS) (Plevris et al. 2022), which indicates the proportion of variance in a target variable explained by the predicted values from a model. This lies between 0 and 1, where higher values indicate that more of the variability is accounted for by the model. An EVS of 1 would mean a perfect explanation of the variance by the model, and one close to 0 would mean very little explanatory power. The EVS indicates how well the model captures the underlying patterns in the data.

5. RESULTS AND DISCUSSION

5.1 Experimental Setup

For this experiment, every combination of deep learning networks along with different feature vectors was run for

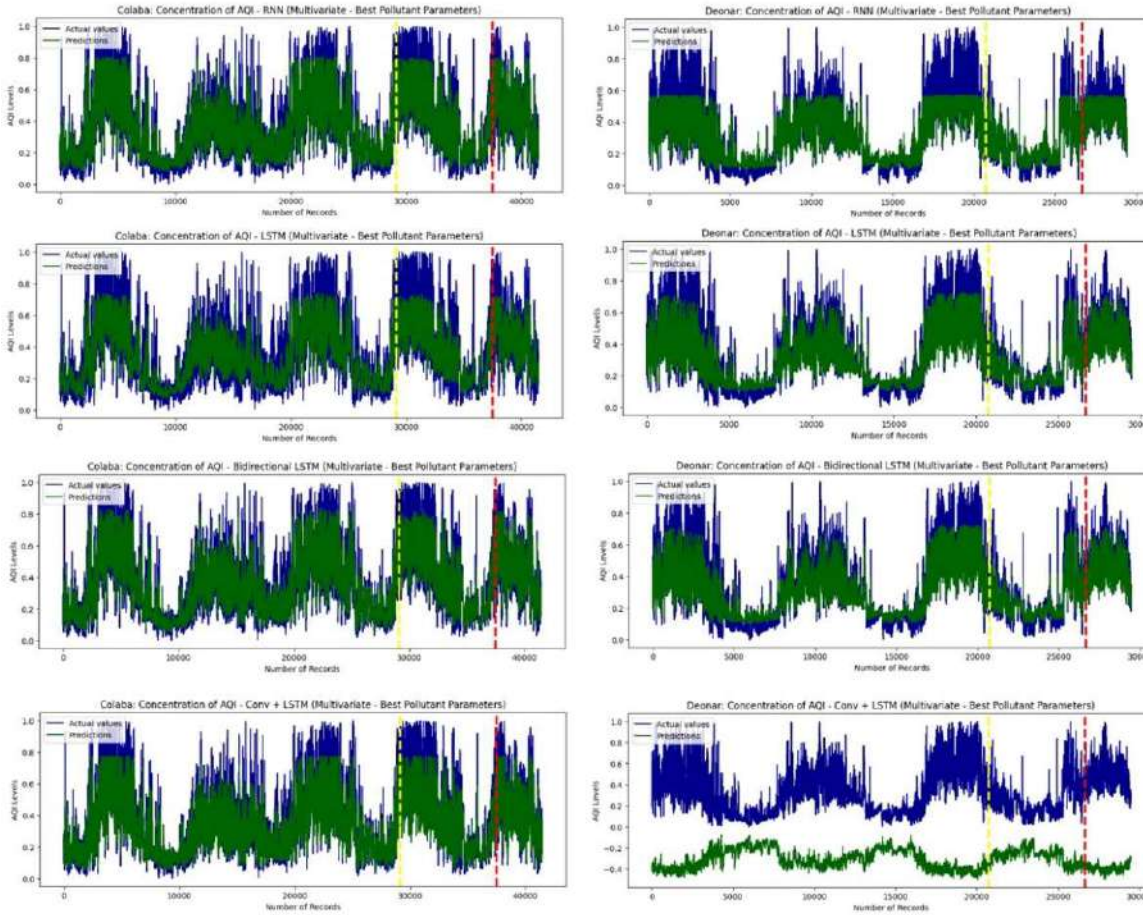


Fig. 7: Actual and predicted AQI values using various deep learning models with the Best Pollutant Feature Set.

50 epochs with a batch size of 256 samples. For recurrent hidden layers, the activation function used was ReLU, and the number of hidden units was 64, followed by 32. For the dense layer, linear activation was used with 16 and 1 neurons. For efficient training, the Mean Squared Logarithmic Error (MSLE) was used as the loss function, and the Adam optimizer with 0.001 as the learning rate was used for stable convergence with dropout regularization of 0.2.

5.2 Best Pollutant Feature Set

Fig. 7 shows the AQI prediction for both stations using multiple deep learning topologies for the best pollutant parameters. The actual values are shown in blue, and the predicted values are shown in green. 70% of the dataset was used for training, which is presented to the left of the yellow dotted line. Next, 20% of the data were used as the validation set, which is between the yellow and red dotted lines, and the remaining 10% were used as the test set. It was observed that with pollutant parameters as feature sets, better predictions were made for Colaba station than Deonar station, which might be due to the high spread of AQI values for Deonar station. For the Colaba station, the RNN and Bidirectional LSTM made slightly better AQI predictions, whereas for the Deonar station, the LSTM provided significantly better predictions, and it is noticeable that Conv1D + LSTM with pollutant feature set failed.

5.3 Best Meteorological Feature Set

Fig. 8, which demonstrates the actual and predicted AQI values for all deep learning architectures for both stations using meteorological features, shows that every model captured the variation in AQI values more precisely with this set, indicating better prediction capability. By closely examining the plots and using climatic parameters, the Conv1D + LSTM model resulted in a marginal improvement in making predictions for the Colaba station, whereas for the Deonar station, LSTM again outperformed.

5.4 Combined Feature Set with All Parameters

For the combined feature set with a total of 15 features and

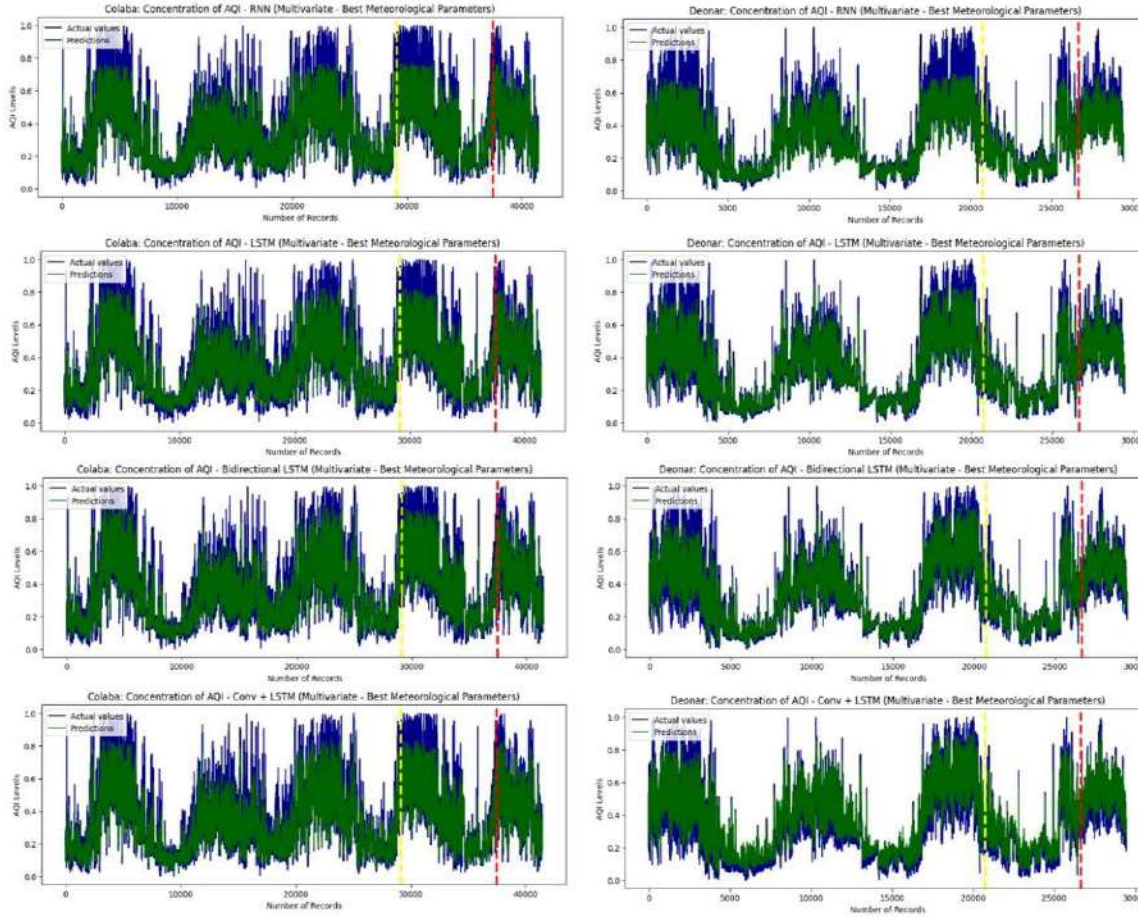


Fig. 8: Actual and predicted AQI values using various deep learning models with the Best Meteorological Feature Set.

target variables, the actual and predicted values for all deep learning architectures used for both stations are shown in Fig. 9. For the Colaba station, similar to the meteorological feature set, the Conv1D + LSTM model made the best predictions with little improvement over the other models. Owing to the high dispersion in the data for the Deonar station, there were significant fluctuations in the outcomes of various models. It is evident that the RNN model has completely failed, and other models have resulted in similar results, with Bi-LSTM being slightly better.

5.5 Juxtaposed Analysis

The performance of various deep learning architectures for different input feature sets is tabulated in Tables 3 and 4 for the Colaba and Deonar stations, respectively. These tables include varying performance measures, namely, RMSE, R^2 Score, MAPE, and EVS.

Across Models: The Bi-LSTM and LSTM models exhibited consistent performance across different stations and feature sets. For Colaba, it provided the lowest RMSE and MAPE with several feature sets and the highest R^2 Score and EVS, thus showing better prediction accuracy. At Deonar, the Bi-LSTM model performed well, especially with meteorological parameters, producing competitive results. Although Conv1D + LSTM has some bright spots, considering the overall model reliability and efficiency in minimizing errors and explaining enhanced variance, Bi-LSTM and LSTM are the best models, irrespective of the station or feature set.

Across feature sets: The meteorological feature set outperformed the others across both Colaba and Deonar stations. Indeed, models with meteorological parameters recorded the lowest RMSE and MAPE and higher values for the R^2 Score and EVS, thus showing better variance explanation. The discovery that meteorological factors affect the AQI more significantly than pollutant concentrations is important because these factors directly regulate pollutant spreading and settling. Increased temperature and humidity reduce the AQI by increasing atmospheric mixing and facilitating pollutant removal. Conversely, extended high-

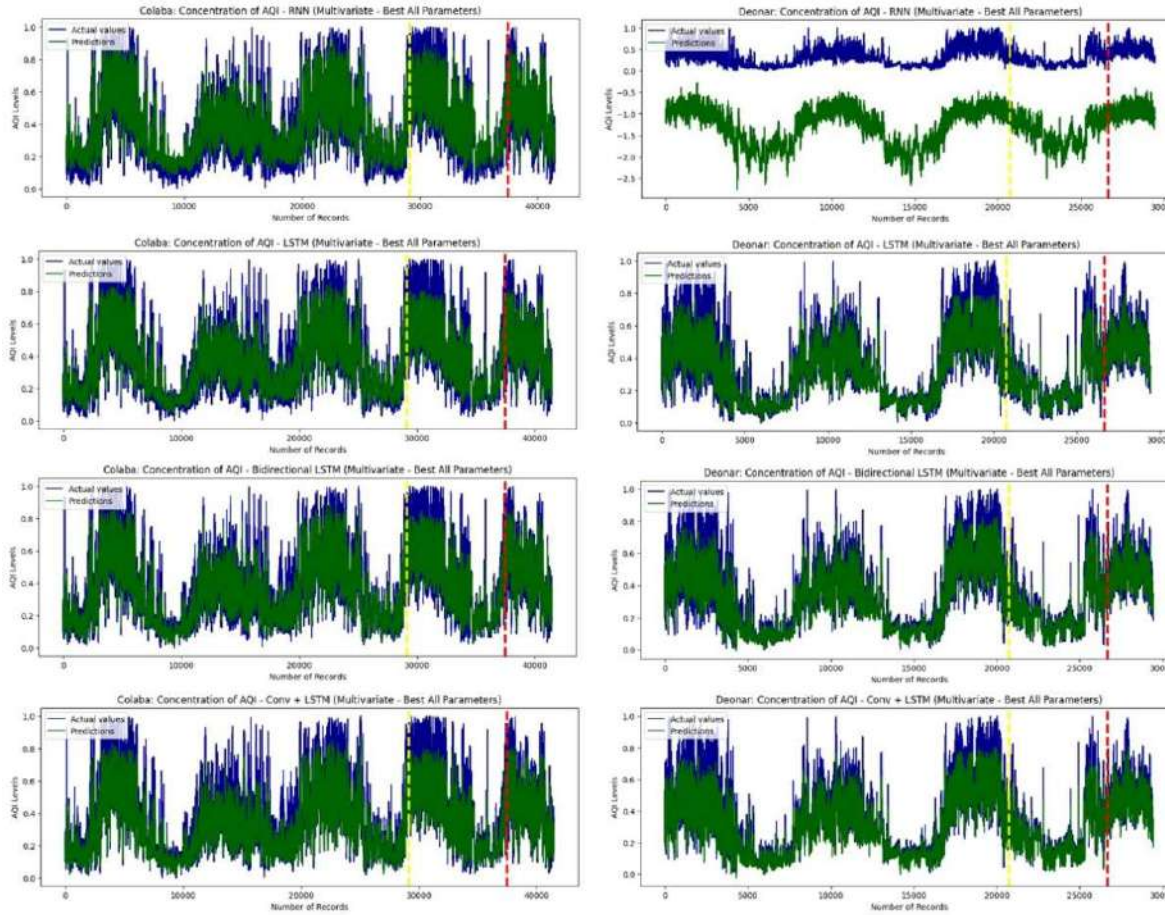


Fig. 9: Actual and predicted AQI values using various deep learning models with a Combined Feature Set with All Parameters.

Table 3: Performance Metrics of Various Models across Different Feature Sets for AQI Prediction for Colaba Station.

Feature Set	Models	RMSE	R^2 Score	MAPE	EVS
Pollutant Parameters	RNN	21.3230	0.7619	0.1268	0.8062
	LSTM	23.6293	0.6164	0.1502	0.7569
	Bi-LSTM	21.0952	0.7551	0.1260	0.8093
	Conv1D + LSTM	22.1642	0.6927	0.1334	0.8029
Meteorological Parameters	RNN	22.1090	0.6553	0.1312	0.7984
	LSTM	21.6329	0.6852	0.1322	0.7962
	Bi-LSTM	21.5187	0.7112	0.1327	0.7984
	Conv1D + LSTM	21.0152	0.7320	0.1238	0.8089
All Parameters	RNN	23.5945	0.6796	0.1545	0.8175
	LSTM	22.0414	0.7021	0.1400	0.8069
	Bi-LSTM	21.4796	0.7407	0.1329	0.8139
	Conv1D + LSTM	20.8821	0.7502	0.1246	0.8189

pressure conditions can elevate the AQI by generating stable atmospheric flows that retain pollutants in the lower layers of the atmosphere. Increased wind speeds lower the AQI by spreading out pollutants, whereas wind direction has a weaker, less predictable influence on air quality.

Table 4: Performance Metrics of Various Models across Different Feature Sets for AQI Prediction for Deonar Station.

Feature Set	Models	RMSE	R^2 Score	MAPE	EVS
Pollutant Parameters	RNN	30.6543	0.1596	0.1057	0.6140
	LSTM	33.7968	0.2082	0.1407	0.6980
	Bi-LSTM	34.9731	0.1983	0.1548	0.6725
	Conv1D + LSTM	362.7671	-689.501	2.3102	-0.347
Meteorological Parameters	RNN	30.1466	0.2836	0.1156	0.7034
	LSTM	26.2931	0.5135	0.0955	0.7116
	Bi-LSTM	27.8235	0.4953	0.1015	0.6892
	Conv1D + LSTM	34.4509	0.2719	0.1288	0.7180
All Parameters	RNN	588.7852	-96.7797	1.5506	-1.163
	LSTM	26.3419	0.5340	0.0956	0.7088
	Bi-LSTM	26.6565	0.5510	0.0977	0.7124
	Conv1D + LSTM	27.4466	0.5264	0.1028	0.7171

Across Locations: Models fare poorly for Deonar primarily because of the high variability in its AQI values, which makes prediction difficult. Such variability is presumably due to numerous factors specific to the area, including its location near mixed sources of pollution, such as landfills, industrial areas, and busy traffic routes. These sources create non-linear fluctuations in pollutant concentrations that are more difficult to incorporate using conventional modeling methods. Inconsistencies and gaps within the data also contribute to decreased model reliability. Aggregated, these factors produced more intricate and less predictable air quality patterns in Deonar than in Colaba, resulting in increased error measures and lower explained variance across models.

6. CONCLUSIONS

Air pollution is one of the prime factors of mortality across the globe and needs to be monitored and predicted accurately to reduce its impacts. Atmospheric pollutants, such as $PM_{2.5}$, PM_{10}, ammonia, SO_2, CO, NOx, and ozone, greatly affect human health. Climatic factors, including temperature, humidity, wind speed, and pressure, influence the AQI. The dataset from two stations, Colaba and Deonar, containing atmospheric pollutants and meteorological factors, was the research object of this study. Correlation studies show that AQI levels are strongly influenced by their past values and have a strong positive correlation with atmospheric pollutants and various meteorological conditions, such as temperature, pressure, and wind speed. Other climatic factors, such as humidity and dew point, were negatively associated with AQI levels.

For this study, based on the results of Pearson's correlation, multiple input feature sets, including the best pollutant set, best meteorological set, and combined feature sets, were created. For these sets, multiple deep learning topologies, such as RNN, LSTM, Bi-LSTM, and Conv1D + LSTM models, were implemented with optimized hyperparameters for both locations. The assessment metrics used were RMSE, R^2 Score, MAPE and EVS. For the Colaba station, RNN and Bi-LSTM outperformed the pollutant feature set, whereas Conv1D + LSTM showed improved results for the other two feature sets. For the Deonar station, LSTM produced the best results in all scenarios, and RNN with the combined feature set failed. Meteorological factors have enhanced the accuracy, as deep learning models are capable of learning more complex patterns that model nonlinear associations and interactions.

As different results were obtained for different locations, this ensures the need for more tailored location-specific models for more accurate predictions. This research advances by comparing multiple feature sets and multiple architectures with location-specific information. This information can be helpful for policymakers and environmental regulatory authorities to forecast episodes of poor air quality and release necessary early alerts and warnings, which are needed for public safety, support urban planning, and eventually reduce the burden on the healthcare infrastructure of the city.

Every region has sources of pollution, geographical features, climatic conditions, and human activities that affect air quality differently. Although generic models are helpful, they may lack such local variations, leading to less accurate predictions. In the future, studies can include other factors such as proximity to industrial areas, traffic density, vegetation cover, distance from landfill, and distance from the shoreline, which can all impact the dispersion and concentration of pollutants in the air. Attention-based systems, variational autoencoders, probabilistic graph networks with a greater number of training samples, and a

more inclusive feature set can further enhance prediction accuracy.

7. ACKNOWLEDGMENTS

The authors recognize the National Environmental Engineering Research Institute (NEERI) in Nagpur, the Central Pollution Control Board, State Pollution Control Boards, and Pollution Control Committees for making data freely available for research purposes.

8. REFERENCES

Ayus, I., Natarajan, N. and Gupta, D., 2023. Comparison of machine learning and deep learning techniques for the prediction of air pollution: a case study from China. *Asian Journal of Atmospheric Environment*, 17(4), pp.1-8. [DOI]

Barve, A., Singh, V., Shrirao, S. and Bedekar, M., 2020. Air quality index forecasting using parallel dense neural network and LSTM cell. In: *2020 International Conference on INCET*, pp.1-4. [DOI]

Binbusayyis, A., Khan, M., Ahmed, A. and M.M., 2024. A deep learning approach for prediction of air quality index in smart city. *Discover Sustainability*, 5, p.89. [DOI]

Bizualem, B., Angassa, K., Shibeshi, N.T. and Feyisa, G.L., 2023. Assessing the status of air pollution related to traffic using dispersion modeling: the case of Megenagna, Addis Ababa, Ethiopia. *Bulletin of Atmospheric Science and Technology*, 4(1), p.9. [DOI]

Botchkarev, A., 2019. A new typology design of performance metrics to measure errors in machine learning regression algorithms. *Interdisciplinary Journal of Information, Knowledge, and Management*, 14, pp.45-76. [DOI]

Central Control Room for Air Quality Management Delhi NCR, 2024. Air Quality Index Information - AQI Calculator. Retrieved June 29, 2024, from https://app.cpcbccr.com/ccr_docs/AQI%20-Calculator.xls

Central Pollution Control Board (CPCB), 2024. CPCB Home Page. Retrieved June 24, 2024, from https://app.cpcbccr.com/AQI%20India/

Cui, B., Liu, M., Li, S., Jin, Z., Zeng, Y. and Lin, X., 2023. Deep learning methods for atmospheric PM2.5 prediction: a comparative study of transformer and CNN-LSTM-attention. *Atmospheric Pollution Research*, 14(9), p.101833. [DOI]

Cui, H., Ma, R. and Gao, F., 2018. Relationship between meteorological factors and diffusion of atmospheric pollutants. *Chemical Engineering Transactions*, 71, pp.1417-1422. [DOI]

DeVries, R., Kriebel, D. and Sama, S., 2017. Outdoor air pollution and COPD-related emergency department visits, hospital admissions, and mortality: a meta-analysis. *COPD*, 14(1), pp.113-121. [DOI]

Douglas, C., Cheryl, L. and Murat, K., 2015. *Introduction to Time Series Analysis and Forecasting* (2nd ed.). Wiley, pp.450.

Fang, C., Lu, H., Li, G., Sun, D. and Miao, Z., 2015. Estimating the impact of urbanization on air quality in China using spatial regression models. *Sustainability*, 7(11), pp.15570-15592. [DOI]

Gou, A., Tan, G. and Ding, X., 2023. Urban-rural difference in the lagged effects of PM2.5 and PM10 on COPD mortality in Chongqing, China. *BMC Public Health*, 23, p.1270. [DOI]

Gupta, S., Mohta, Y., Heda, K., Armaan, R., Valarmathi, B. and Ganeshan, A., 2023. Prediction of air quality index using machine learning techniques: a comparative analysis. *Journal of Environmental and Public Health*, pp.1-26. [DOI]

Jian, Z., Cai, J. and Chen, R., 2024. A bibliometric analysis of research on the health impacts of ozone air pollution. *Environmental Science and Pollution Research*, 31, pp.16177-16187. [DOI]

Jiao, L. and Zheng, W., 2020. Multi-step traffic flow prediction method based on Conv1D + LSTM. In: *2020 IEEE International Conference on Big Data and Smart Computing (BigComp)*, pp.113-118. [DOI]

Kara, Y., Şevik, S.Y. and Toros, H., 2024. Comprehensive analysis of air pollution and the influence of meteorological factors: a case study of Adiyaman province. *Environmental Monitoring and Assessment*, 196, pp.1-12. [DOI]

Karthick, K., Aruna, S.K., Dharmaprakash, R. and Ravindiran, G., 2024. Integrating machine learning techniques for Air Quality Index forecasting and insights from pollutant-meteorological dynamics in sustainable urban environments. *Earth Science Informatics*, *17*(4), pp.3733-3748. [DOI]

Khan, D., Patankar, A., Motwani, R. and Ailsinghani, A., 2023. Investigating efficacy of RNN and its variants for AQI prediction. In: *2023 International Conference on Advances in Computation, Communication and Information Technology (ICAICCIT)*, pp.1303-1307.

Kleingchuay, W., Srimanus, W., Srimanus, R. et al., 2022. The association of meteorological parameters and AirQ+ health risk assessment of PM2.5 in Ratchaburi province, Thailand. *Scientific Reports*, 12, p.12971. [DOI]

Le, V.-D., Bui, T.-C. and Cha, S.-K., 2020. Spatiotemporal deep learning model for citywide air pollution interpolation and prediction. In: *2020 IEEE International Conference on Big Data and Smart Computing (BigComp)*, pp.55-62. [DOI]

Liu, Y., Wang, P. and Li, Y., 2022. Air quality prediction models based on meteorological factors and real-time data of industrial waste gas. *Scientific Reports*, 12, p.9253. [DOI]

Lu, Y. and Li, K., 2023. Multistation collaborative prediction of air pollutants based on the CNN-BiLSTM model. *Environmental Science and Pollution Research*, 30, pp.92417-92435. [DOI]

Mandal, A. and Sen, R., 2024. Medium-term AQI prediction in selected areas of Bangladesh based on bidirectional GRU network model. *SN Computer Science*, 5, p.627. [DOI]

Mandal, N. and Sarode, T., 2024a. A framework for cloud cover prediction using machine learning with data imputation. *International Journal of Electrical and Computer Engineering (IJECE)*, 14(1), pp.600-607. [DOI]

Mandal, N. and Sarode, T., 2024b. A framework for cloud cover prediction using machine learning with data imputation. *International Journal of Electrical and Computer Engineering (IJECE)*, 14(1), pp.600-607. [DOI]

Méndez, M., Merayo, M.G. and Núñez, M., 2023. Machine learning algorithms to forecast air quality: a survey. *Artificial Intelligence Review*, 56, pp.10031-10066. [DOI]

Naz, F., McCann, C., Fahim, M., Cao, T.-V., Hunter, R., Viet, N.T. and Duong, T.Q., 2023. Comparative analysis of deep learning and statistical models for air pollutants prediction in urban areas. *IEEE Access*, 11, pp.64015-64025. [DOI]

Nikpour, P., Shafiei, M. and Khatibi, V., 2024. GELATO: a new hybrid deep learning-based informer model for multivariate air pollution prediction. *Environmental Science and Pollution Research*, 31, pp.29870-29885. [DOI]

OpenWeather, 2024. OpenWeather Homepage. Retrieved April 21, 2024, from https://openweathermap.org

Petrus, M., Popa, C. and Bratu, A.-M., 2022. Ammonia concentration in ambient air in a periurban area using a laser photoacoustic spectroscopy detector. *Materials*, 15(9), p.3182. [DOI]

Plevris, V., Solorzano, G., Bakas, N. and Ben Seghier, M.E.A., 2022. Investigation of performance metrics in regression analysis and machine learning-based prediction models. In: *Proceedings of the 8th European Congress on Computational Methods in Applied Sciences and Engineering (ECCOMAS 2022)*, p.155. [DOI]

Poyyamoli, G. and Boss, C., 2014. Assessment of air pollution and its impacts near municipal solid waste dumping site Kammiyampet,

Cuddalore, India. *International Journal of Innovative Research in Science, Engineering and Technology*, 3(5), pp.12588-12593.

Rangaswamy, P.S., Vasareddy, A., Saiteja, B., Sreeja, B. and Chandana, G., 2022. Impact assessment on air quality around integrated municipal solid waste management plant in Hyderabad. *International Journal of Advanced Research in Science, Communication and Technology*, 2(1), pp.666-677. [DOI]

Saadi, D., Tirosh, E. and Schnell, I., 2021. The relationship between city size and carbon monoxide (CO) concentration and their effect on heart rate variability (HRV). *International Journal of Environmental Research and Public Health*, 18(2), p.788. [DOI]

Sajjad Abdollahpour, S., Qi, M., Le, H.T.K. and Hankey, S., 2024. Urban spatial structure and air quality in the United States: evidence from a longitudinal approach. *Environment International*, 190, p.108871. [DOI]

Schürholz, D., Kubler, S. and Zaslavsky, A., 2020. Artificial intelligence-enabled context-aware air quality prediction for smart cities. *Journal of Cleaner Production*, 271, p.121941. [DOI]

Shankar, L. and Arasu, K., 2023. Deep learning techniques for air quality prediction: a focus on PM2.5 and periodicity. *Migration Letters*, 20(S13), pp.468-484. [DOI]

Shi, T., Li, P. and Yang, W., 2023. Application of TCN-BiGRU neural network in PM2.5 concentration prediction. *Environmental Science and Pollution Research*, 30, pp.119506-119517. [DOI]

Song, Q., Zou, J. and Xu, M., 2023. Air quality prediction for Chengdu based on long shortterm memory neural network with improved jellyfish search optimizer. *Environmental Science and Pollution Research*, 30, pp.64416-64442. [DOI]

Sterling, M., 2017. Air quality: population density and transportation emissions. *The Equilibrium*, 3(1), pp.1-8. [DOI]

Sun, R., Zhou, Y., Wu, J. and Gong, Z., 2019. Influencing factors of PM2.5 pollution: disaster points of meteorological factors. *International Journal of Environmental Research and Public Health*, 16(20), p.3891. [DOI]

Thakur, N., Karmakar, S. and Shrivastava, R., 2023. Hybrid deep learning algorithms for predicting air quality index using dimension reduction technique in search of precise results. *International Journal of Information Technology*, 15, pp.3181-3187. [DOI]

Tian, J., Fang, C., Qiu, J. and Wang, J., 2021. Analysis of ozone pollution characteristics and influencing factors in Northeast Economic Cooperation Region, China. *Atmosphere*, 12(7), p.843. [DOI]

Varaprasad, V., Kanawade, V.P. and Narayana, A.C., 2024. Association between sea-land breeze and particulate matter in five coastal urban locations in India. *Science of the Total Environment*, 913, p.169773. [DOI]

Wang, P., Bi, X. and Zhang, G., 2023. A new hybrid PM volatility prediction model based on EMD and machine learning algorithms. *Environmental Science and Pollution Research*, 30, pp.82878-82894. [DOI]

Wang, S., Ren, Y. and Xia, B., 2023. Estimation of urban AQI based on interpretable machine learning. *Environmental Science and Pollution Research*, 30, pp.1-13. [DOI]

Wu, H., Hong, S., Hu, M., Li, Y. and Yun, W., 2022. Assessment of the factors influencing sulfur dioxide emissions in Shandong, China. *Atmosphere*, 13(1), p.142. [DOI]

Wu, Q., Geng, Y., Wang, X. et al., 2024. A novel deep learning framework with variational auto-encoder for indoor air quality prediction. *Frontiers in Environmental Science & Engineering*, 18(8), pp.1-12. [DOI]

Yan, H., Li, Q. and Feng, K., 2023. The characteristics of PM emissions from construction sites during the earthwork and foundation stages: an empirical study evidence. *Environmental Science and Pollution Research*, 30, pp.62716-62732. [DOI]

Yan, M. and Li, T., 2024. A review of the interactive effects of climate and air pollution on human health in China. *Current Environmental Health Reports*, 11, pp.102-108. [DOI]

Zhan, C., Li, S., Li, J., Guo, Y., Wen, Q. and Wen, W., 2020. Prediction of air quality in major cities of China by deep learning. In: *Proceedings of the 2020 16th International Conference on Computational Intelligence and Security (CIS)*, pp.68-72. [DOI]

Zhang, C. and Zhang, L., 2024. The relationship between toxic air pollution, health expenditure, and economic growth in the European Union: fresh evidence from the PMG-ARDL model. *Environmental Science and Pollution Research*, 31, pp.21107-21123. [DOI]

Zhang, Y. and Jiang, W., 2018. Pollution characteristics and influencing factors of atmospheric particulate matter (PM2.5) in Chang-Zhu-Tan area. *IOP Conference Series: Earth and Environmental Science*, 108, p.042047. [DOI]

Nature Environment and Pollution Technology
An International Quarterly Scientific Journal

p-ISSN: 0972-6268
(Print copies up to 2016)
e-ISSN: 2395-3454

Vol. 25 | No. 3 | Article ID D1868 | 2026

Original Research Paper

https://doi.org/10.46488/NEPT.2026.v25i03.D1868

Open Access Journal

Determinants of Environmental Quality in Indonesia: The Role of Democracy, Socio-Economics, and Financial Development

Fitri Susilowati[1]†, Suryanto[2] and Muhammad Rizal Anggit Putra[2]
[1]Faculty of Business and Law, Universitas PGRI, Yogyakarta, Indonesia
[2]Faculty of Economics and Business, Universitas Sebelas Maret, Surakarta, Indonesia
†Corresponding author: Fitri Susilowati; fitri.susilowati82@gmail.com

Abbreviation: Nat. Env. & Poll. Technol.
Website: www.neptjournal.com

Received: 11-09-2025
Revised: 13-12-2025
Accepted: 16-12-2025

Key Words:

Sustainable development
Environmental Quality Index (EQI)
Panel error correction model
Democracy index
Population density

Citation for the Paper:

Susilowati, F., Suryanto and Putra, M.R.A., 2026. Determinants of environmental quality in Indonesia: The role of democracy, socio-economics, and financial development. *Nature Environment and Pollution Technology*, 25(3), D1868. https://doi.org/10.46488/NEPT.2026.v25i03. D1868

Note: From 2025, the journal has adopted the use of Article IDs in citations instead of traditional consecutive page numbers. Each article is now given individual page ranges starting from page 1.

Copyright: © 2026 by the authors
Licensee: Technoscience Publications
This article is an open access article distributed under the terms and conditions of the Creative Commons Attribution (CC BY) license (https://creativecommons.org/licenses/by/4.0/).

ABSTRACT

Sustainable development requires a good quality of life for all. Therefore, we investigated the short- and long-term dynamics of the Environmental Quality Index (EQI) across 34 provinces in Indonesia from 2015 to 2023 using a Panel Error Correction Model. The explanatory variables included the democracy index, population density, education level, wages, poverty, foreign investment, domestic investment, and Gross Regional Domestic Product (GRDP). In the short term, GRDP reduced the EQI by 0.32 units, while the others did not show a significant impact. In the long term, democracy increased the EQI by 0.13 units, education level by 12.29 units, and poverty by 0.01 units, while GRDP and population density reduced it by 0.09 units and 0.16 units, respectively. Further analysis revealed that GRDP derived from the mining sector reduced the EQI, whereas service sectors such as education and health contributed to its improvement. Based on these findings, local governments should integrate environmental protection directly into their development agendas by implementing rigorous environmental impact assessments, expanding green infrastructure, and providing targeted incentives for the development of low-carbon industries.

1. INTRODUCTION

Indonesia is increasingly focusing on the quality of its living environment, which is closely linked to economic development, urbanization, and social change (Aryani et al. 2025, Lukman et al. 2025, Wahyuningrum et al. 2025). The Ministry of Environment and Forestry (KLHK) publishes the Environmental Quality Index (EQI) as a comprehensive indicator of the condition of the air, water, and soil. This index is widely used to assess the effectiveness of construction and development projects (KLHK 2022). Previous studies have affirmed that democracy exerts a positive effect on environmental performance, although its effects tend to be indirect (Islam et al. 2023, Persakis et al. 2024, Povitkina & Jagers 2022). The effectiveness of democracy in advancing environmental quality depends heavily on bureaucratic capacity, the strength of formal institutions, market dynamics, and pressure from interest groups and civil society (Fredriksson & Wollscheid 2015).

Democratic maturity is generally associated with greater transparency and accountability in governance, which can contribute to improved environmental quality. However, in the Indonesian context, the relationship between democracy and environmental quality is inconsistent because improvements in democratic practices do not always result in better ecological outcomes. This challenge is compounded by rapid urbanization, particularly in densely populated areas where environmental degradation is often intensified (Fukuyama et al. 2025). As illustrated in Fig. 1, DKI Jakarta, the nation's economic and political hub, has the lowest EQI (highlighted in red). This suggests severe environmental pressure caused by concentrated economic activity, high population density, and rapid urban expansion

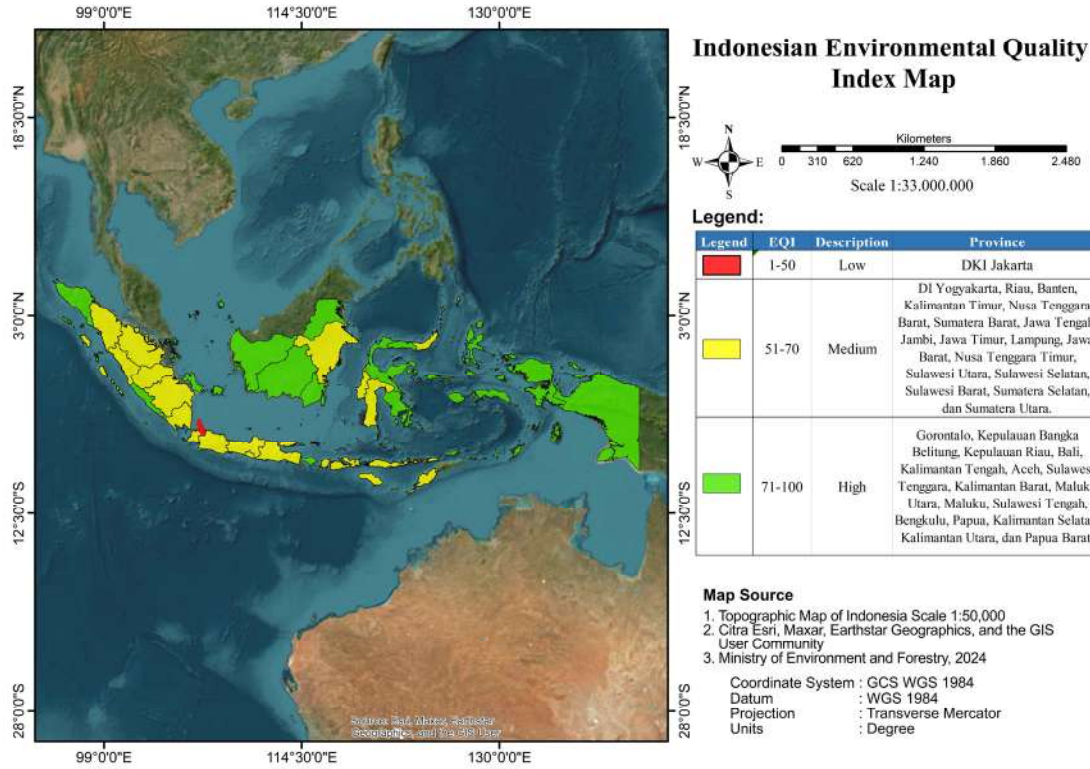


Fig. 1: Indonesian Environmental Quality Index Map.

Limited access to safe water persists across large regions of the world and is aggravated by organic, inorganic, and biological contamination of surface sources. In this context, turbidity is an operational indicator of sanitary risk because of its association with colloids and particles that transport contaminants (Ogunshina et al. 2023). Conventional clarification using mineral coagulants, such as aluminum sulfate, is effective; however, it has disadvantages related to cost, availability, and chemical residues, motivating the search for more sustainable alternatives (Don et al. 2025). Education is another crucial factor that affects environmental quality. Higher levels of education enhance public awareness and understanding of ecological issues (Barnes et al. 2025, Sumy et al. 2023). Hu et al. (2025) and Luo et al. (2025) similarly demonstrate that education has a positive correlation with pro-environmental behavior. Furthermore, Wijethunga et al. (2025) and Rachid et al. (2025) discovered that financial development affects environmental quality. Investment, often regarded as a catalyst for economic growth, exerts pressure on the environment (Bui Minh et al. 2023). Domestic investment is generally concentrated in the agricultural sector, whereas foreign direct investment (FDI) is typically directed toward the industrial sector, which can increase carbon emissions and pollution (Song et al. 2019). At the regional level, the Gross Regional Domestic Product (GRDP) reflects the scale of economic activity, which often correlates with rising investment flows. Both factors affect the EQI, as economic growth not aligned with sustainability principles and supported by effective government oversight tends to exacerbate environmental degradation (Povitkina & Jagers 2022).

Socio-economic factors also play an important role in determining environmental quality (Pastore & de Santoli 2025). Ghosh et al. (2023) analysed this in the BRICS countries, Acheampong et al. (2022) in Sub-Saharan Africa, and Smith et al. (2024) in Indonesia. Furthermore, wages and poverty, two widely debated dimensions, have been shown to affect environmental sustainability (Arranz & García-Serrano 2025, Shah et al. 2023, Wang et al. 2023, Zhang & Zhao 2022). Conversely, higher income can lead to increased consumption of energy and materials, thereby exerting additional pressure on the environment (Afridi et al. 2019). However, several of the above studies still separate the analysis of democracy from socio-economic dimensions, thereby ignoring the potential for simultaneous correlations between democracy, given that the system in Indonesia holds regional head elections every five years. Furthermore, few studies have integrated these two variables at the regional level, particularly across Indonesia's 34 provinces, resulting in a partial explanation of variations in the EQI, which is

the official measure used by the Indonesian government to assess national environmental conditions, and failing to capture the complexity of determinants of environmental quality between regions.

Based on this framework, this study investigates how various socioeconomic, financial development, and democracy factors affect environmental quality across 34 Indonesian provinces. The findings are expected to provide valuable insights for regional leaders in formulating effective and context-specific environmental policies while also considering the constraints of their ten-year or two-term office tenure. We hypothesized that the democracy index, education level, and poverty would positively affect the EQI. In contrast, population density, wages, investment, and GRDP are expected to negatively affect Indonesia's EQI.

2. MATERIALS AND METHODS

2.1. Estimation Technique

We sought to capture both long- and short-term dynamics in environmental quality across 34 provinces in Indonesia from to 2015-2023 using the Panel Error Correction Model (PECM). The analytical framework is a modification of Sikder et al. (2022), which was adapted to the Indonesian context by integrating democracy, socio-economics, and financial development factors that reflect provincial-level economic activity. This modification provides a more comprehensive understanding of the correlation between regional economic development and environmental sustainability. Conceptually, the model can be described as follows:

$$\Delta EQI_{it} = \beta_0 + \beta_1 \Delta DEMO_{it} + \beta_2 \Delta LNPOP_{it} + \beta_3 \Delta EDUC_{it} + \beta_4 \Delta LNWAGE_{it} + \beta_5 \Delta POV_{it} + \beta_6 \Delta FI_{it} + \beta_7 \Delta DI_{it} + \beta_8 \Delta GRDP_{it} + \beta_9 DEMO_{it-1} + \beta_{10} LNPOP_{it-1} + \beta_{11} EDUC_{it-1} + \beta_{12} LNWAGE_{it-1} + \beta_{13} POV_{it-1} + \beta_{14} FI_{it-1} + \beta_{15} DI_{it-1} + \beta_{16} GRDP_{it-1} + \lambda ECT_{it-1} + \varepsilon_{it} \quad \ldots(1)$$

Table 1 summarizes the operational definitions of all variables used in this study and provides information on their respective measurement units.

2.2. Data

The analysis used data on democracy indices, population density, education levels, wages, number of poor people, foreign investment, domestic investment, GRDP, and environmental quality indices for 34 provinces in Indonesia covering the period 2015-2023. The data sources included the Central Statistics Agency (BPS), the Ministry of Investment and Downstream Industry, and the Ministry of Environment and Forestry. The researchers assume that Indonesia's democratic system consistently implements regional head elections (governors) and national elections every five years, with a maximum of two terms in office. This electoral cycle is expected to capture the factors affecting environmental quality in both the short and the long term. Consequently, the study results can serve as reference material for local governments in formulating targeted policies within a relatively limited governance timeframe, namely, a maximum of ten years.

Table 1: Measurement variables.

Symbol	Definition / Unit
EQI	Provincial Environmental Quality Index
DEMO	Indonesian Democracy Index
LNPOP	Log of population density (persons per km²)
EDUC	Average years of schooling (years)
LNWAGE	Log of average hourly wage (Rupiah/hour)
POV	Number of poor individuals (persons)
FI	Foreign investment (million Rupiah)
DI	Domestic investment (million Rupiah)
GRDP	GRDP at constant prices (billion Rupiah)

2.3. Panel Unit Root Test

The first step of the analysis was to test for stationarity using the Im-Pesaran-Shin (IPS) and ADF-Fisher. This step is crucial, as non-stationary data may result in spurious regression and misinterpretation of findings (Pesaran 2007). The general form is as follows:

$$\Delta Y_t = \delta Y_{t-1} + \mu_t$$
$$\Delta Y_t = Y_t - Y_{t-1} \quad \ldots(2)$$

Where DY_t denotes the change in the data, and δ is the parameter being tested.

Following the stationarity tests, cross-section dependence (CSD) was assessed to examine whether residuals across units are correlated, which may affect the validity of panel estimators. The Breusch-Pagan LM and Pesaran CD tests were applied to detect the presence of CSD. A correlation matrix was also computed to evaluate the linear relationships among the variables and identify potential multicollinearity issues. These diagnostic checks ensure that the subsequent estimation procedures are based on a well-behaved data structure (Sikder et al. 2022).

2.4. Panel Error Correction Model (PECM)

The ECM panel specification followed the approach of Domowitz and Elbadawi (1987) and could be formulated as:

$$\Delta Y_{it} = \beta_0 + \beta_1 \Delta X_{it} + \beta_2 \Delta X_{it-1} + \lambda ECT_{it-1} + \varepsilon_{it} \ldots(3)$$

In this model, the adjustment coefficient (λ) is expected to lie between 0 and 1 ($0 < \lambda < 1$). The λ coefficient represents the speed of adjustment toward long-term equilibrium. The Error Correction Term (ECT) ensures that the system converges back to its long-term equilibrium state. After the stationarity tests, each variable must pass the first-difference stage.

$$EQI_{it} = \beta_0 + \beta_1 DEMO_{it} + \beta_2 LNPOP_{it} + \beta_3 EDUC_{it} + \beta_4 LNWAGE_{it} + \beta_5 POV_{it} + \beta_6 FI_{it} + \beta_7 DI_{it} + \beta_8 GRDP_{it} \quad \ldots(4)$$

Long-run modelling was then conducted to determine the ECT. Long-run effects were tested using common, fixed, and random effects models. Subsequently, model selection was performed using the Chow and Hausman tests. Once the optimal long-term model was identified, the residuals were projected to obtain the ECT, which was then incorporated into the cointegration test to confirm the stability of the long-term relationship among the variables (Putra et al. 2025). The ECT coefficient must be statistically significant at the chosen significance level.

$$ECT = DEMO_{it-1} + LNPOP_{it-1} + EDUC_{it-1} + LNWAGE_{it-1} + \beta_5 POV_{it-1} + FI_{it-1} + DI_{it-1} + GRDP_{it-1} \quad \ldots(5)$$

Table 2: Descriptive analysis.

Variabel	Mean	Median	Maximum	Minimum	Std. Dev.	Skewness	Kurtosis	Observations
EQI	69.405	70.815	85.690	35.780	8.650	-1.004	4.266	306
DEMO	74.734	75.470	89.210	54.410	6.014	-0.519	3.153	306
LNPOP	4.888	4.630	9.684	2.197	1.580	0.717	3.816	306
EDUC	8.935	8.955	11.420	6.270	0.882	0.018	3.227	306
LNWAGE	9.706	9.685	10.654	9.051	0.256	0.390	3.216	306
POV	789.185	366.160	4789.120	39.690	1113.712	2.489	8.096	306
FI	13911995	5830975	122599431	25332	20486738	2.478	9.694	306
DI	11304030	4969470	95202092	8772	16326363	2.544	10.075	306
LNGRDP	11.955	11.810	14.534	9.922	1.141	0.487	2.568	306

Table 3: Panel unit root tests.

Variable	IPS		ADF	
	Level	1st Difference	Level	1st Difference
EQI	-0.043	-3.852	63.801	12.905
	(0.483)	(0.000)***	(0.622)	(0.000)***
DEMO	-0.965	-7.543	91.305	180.549
	(0.167)	(0.000)***	(0.031) **	(0.000)***
LNPOP	2.145	-4.596	49.158	143.361
	(0.984)	(0.000)***	(0.959)	(0.000)***
EDUC	3.777	-5.811	33.497	158.537
	(0.999)	(0.000)***	(0.999)	(0.000)***
LNWAGE	1.259	-5.835	46.711	166.542
	(0.896)	(0.000)***	(0.977)	(0.000)***
POV	0.0496	-2.047	63.609	95.291
	(0.519)	(0.020)**	(0.628)	(0.016)**
FI	-1.095	-5.889	93.367	180.972
	(0.137)	(0.000)***	(0.022)**	(0.000)***
DI	1.578	-7.012	65.499	189.327
	(0.943)	(0.000)***	(0.564)	(0.000)***
LNGRDP	3.349	-2.652	28.849	103.222
	(0.996)	(0.004)***	(0.998)	(0.003)***

*significant at 10% α, **significant at 5% α, ***significant at 1% α.

The short-run dynamics were modelled using the selected long-run specification, which was then estimated along with the ECT. The general form of the short-run model was as follows:

$$\Delta EQI_{it} = \beta_0 + \beta_1 \Delta DEMO_{it} + \beta_2 \Delta LNPOP_{it} + \beta_3 \Delta EDUC_{it} + \beta_4 \Delta LNWAGE_{it} + \beta_5 \Delta POV_{it} + \beta_6 \Delta FI_{it} + \beta_7 \Delta DI_{it} + \beta_8 \Delta GRDP_{it} + \lambda ECT_{it-1} + \varepsilon_{it} \quad \ldots(6)$$

3. RESULTS AND DISCUSSION

3.1. Results

As presented in Table 2, the descriptive analysis shows that the mean value of the EQI was 69.405, with the minimum and maximum values recorded at 35.780 and 85.690, respectively. The average Democracy Index was 74.734, while the average Population Density (LNPOP) was 4.888, indicating substantial variation across provinces. The average level of education (EDUC) was 8.935 years, whereas wages (LNWAGE) were more homogeneous, with an average of 9.706 years. The average number of poor people (POV) was 789,185, reflecting a high disparity. Foreign Investment (FI) and Domestic Investment (DI) averaged 13,911,995 million rupiah and 11,304,030 million rupiah, respectively. The average GRDP value was 11,955 billion rupiah. A stationarity test was then conducted on all variables used to measure environmental quality across 34 provinces in Indonesia during the period 2015-2023.

Table 3 shows that all variables were stationary at the first difference, thereby meeting the requirements for use in PECM. In the next stage, a long-term regression was performed to determine ECT (see Table 4). The F-statistic probability was 0.000 (< 0.01), and the χ^2 statistic probability was also 0.000 (< 0.01). Thus, the fixed-effects model was selected, and the residual value was proxied as the ECT. Table 3 further shows that the ECT passed the cointegration test, as indicated by the IPS, ADF, and PP statistics, which were -3.991, 126.183, and 150.794, respectively, with a probability of 0.000 (< 0.01). These results confirm that the variables used in this study exhibited a cointegration relationship.

Table 5 presents the correlation matrix, showing that correlations among variables were generally low to moderate, suggesting no serious multicollinearity concerns. Although several economic variables such as LNGRDP, FI, and DI exhibit correlations above 0.6, these values remain below the conventional thresholds typically associated with harmful

Table 4: Identifying ECT and cointegration test.

Model Selection Test				
Methods	Statistic	Std. Error	Prob.	Conclusions
Chow	F (33,264) = 7.934	5.108	0.000***	Fixed Effects
Hausman	67.499 = (8) ²	3.839	0.000***	Fixed Effects
Cointegration Test				
Methods	Statistic		Prob.	Conclusions
IPS	-3.991		0.000***	Passed the level stage and has a cointegration relationship
ADF	126.183		0.000***	
PP	150.794		0.000***	

*significant at 10% α, **significant at 5% α, ***significant at 1% α.

Table 5: Correlation matrix of the variables.

	EQI	DEMO	LNPOP	EDUC	LNWAGE	POV	FI	DI	LNGRDP
EQI	1								
DEMO	-0.185	1							
LNPOP	-0.762	0.349	1						
EDUC	-0.089	0.280	0.241	1					
LNWAGE	0.218	0.058	-0.122	0.482	1				
POV	-0.335	-0.019	0.446	-0.288	-0.307	1			
FI	-0.354	0.127	0.452	0.163	0.250	0.464	1		
DI	-0.423	0.290	0.561	0.207	0.213	0.590	0.685	1	
LNGRDP	-0.551	0.178	0.612	0.145	0.086	0.656	0.613	0.774	1

multicollinearity, and they do not reach the levels (>0.80-0.90) that would indicate near-linear dependence (Sikder et al. 2022). As part of the robustness check, Table 6 reports the results of cross-section dependence tests using the Pesaran CD (2004) and Breusch-Pagan LM (1980) methods, both of which showed statistical significance at the 1% level for all variables. These findings indicate the presence of cross-sectional interdependence in the panel data structure.

Finally, Table 7 shows that both the long-term and short-term effects in the model are valid, as indicated by the significant ECT coefficient of 0.576 (p-value = 0.000 < 0.01). This coefficient suggests that approximately 57.6% of any disequilibrium is corrected within one period, implying that the system requires about 1.7 years to return to its long-run equilibrium after a shock. In the short term, GRDP, which reflects macroeconomic activity, was found to have

Table 6: Cross-section dependence test.

Variable	Pesaran CD Test	Prob.	Breusch-Pagan LM Test	Prob.
EQI	27.892	0.000***	1,479.599	0.000***
DEMO	13.905	0.000***	949.689	0.000***
LNPOP	50.896	0.000***	3,133.075	0.000***
EDUC	69.843	0.000***	4,879.403	0.000***
LNWAGE	59.243	0.000***	3,617.227	0.000***
POV	16.747	0.000***	1,930.167	0.000***
FI	5.052	0.000***	756.507	0.000***
DI	36.223	0.000***	1,725.845	0.000***
LNGRDP	67.372	0.000***	4,579.004	0.000***

*significant at 10% α, **significant at 5% α, ***significant at 1% α.

Table 7: The results of Panel ECM: Long and Short-run.

Long-run				
Variable	Coefficient	Std. Error	t-Statistic	Prob.
C	134.985	45.943	2.938	0.004
DEMO	0.129	0.065	1.982	0.049**
LNPOP	-16.190	6.177	-2.621	0.009***
EDUC	12.288	2.112	5.818	0.000***
LNWAGE	-0.482	2.601	-0.185	0.853
POV	0.006	0.003	2.303	0.022**
FI	0.000	0.000	1.103	0.271
DI	0.000	0.000	2.770	0.006***
LNGRDP	-8.984	4.609	-1.949	0.052*
Short-run				
Variable	Coefficient	Std. Error	t-Statistic	Prob.
D(DEMO)	0.057	0.051	1.113	0.267
D(LN(POP))	-8.669	8.433	-1.028	0.305
D(EDUC)	5.402	3.905	1.384	0.168
D(LN(WAGE))	-2.412	2.081	-1.159	0.248
D(POV)	0.004	0.003	1.289	0.199
D(FI)	0.000	0.000	0.205	0.838
D(DI)	0.000	0.000	-0.528	0.598
D(LN(GRDP))	-31.495	7.594	-4.147	0.000***
ECT	0.576	0.068	8.482	0.000***
R^2	0.341	-	Adjusted R^2	0.219

*significant at 10% α, **significant at 5% α, ***significant at 1% α.

Table 8: The robustness test.

Heteroscedasticity	Coefficient	Prob.	Autocorrelation	Coefficient	Prob.
C	2.464	0.000	C	-0.646	0.306
D(DEMO)	-0.008	0.775	D(DEMO)	0.011	0.862
D(LN(POP))	3.106	0.503	D(LN(POP))	0.434	0.959
D(EDUC)	2.643	0.219	D(EDUC)	7.234	0.082
D(LN(WAGE))	-0.558	0.626	D(LN(WAGE))	0.657	0.796
D(POV)	-0.001	0.554	D(POV)	0.001	0.782
D(FI)	0.000	0.102	D(FI)	0.000	0.911
D(DI)	0.000	0.061	D(DI)	0.000	0.839
D(LN(GRDP))	-2.864	0.493	D(LN(GRDP))	3.121	0.694
ECT	-0.005	0.889	ECT	0.095	0.299
			RESID_1	-0.050	0.497
			RESID_2	-0.046	0.495

a significant effect on the EQI, while other variables showed no significant short-term effects. In contrast, the long-term analysis demonstrates that DEMO, LNPOP, EDUC, POV, DI, and GRDP significantly affected the EQI across the 34 provinces of Indonesia during 2015-2023.

Table 8 presents a series of model robustness tests conducted to ensure the reliability of the Panel ECM estimates. The first section presents the results of the heteroscedasticity test. All explanatory variables in the differentiated form do not show statistical significance at the general testing level, indicating that the residual dispersion is relatively consistent across observations. Thus, there is no evidence to suggest the presence of heteroscedasticity in the model. The second part evaluates the presence of autocorrelation by adding lagged residuals, namely RESID(−1) and RESID(−2), to the regression. Both coefficients are insignificant ($p > 0.05$); therefore, it can be concluded that the model is free from autocorrelation in both the first and second orders. The error correction term (ECT) also remains stable, indicating no dynamic specification inaccuracy. Overall, the results of this test confirm that the Panel ECM model meets the necessary basic assumptions, so that the empirical findings can be considered robust and methodologically valid.

3.2. Disscusion

3.2.1. The Influence of Democracy and Education

In the short term, the democracy index has no significant effect on the EQI. However, in the long term, it has a positive effect. A coefficient of 0.129 indicates that a one-unit increase in the democracy index leads to a 0.13-unit increase in the EQI. These findings confirm the hypothesis and align with the results of Hasan et al. (2025), who reported that increases in the democracy index tend to improve the EQI. This suggests that improvements in governance, such as transparency, participation, and accountability, require time for effective integration into public policy, with impacts materializing only in the long term. In addition, education level has a strong positive impact in the long term. A coefficient of 12.288 indicates that an average increase of one year of education among the population can improve environmental quality by 12.3 units. These results indicate that democratic systems create mechanisms for participation, openness, and public control, whereas education equips citizens with the knowledge and ecological awareness to utilize these mechanisms effectively. When these two factors work together, communities are in a stronger position to promote, monitor, and maintain environmentally friendly policies, thereby ensuring consistent improvements in environmental quality over time.

3.2.2. Demographic Pressure and the Threat of Environmental Degradation

Population density had no significant short-term effect. However, in the long term, it negatively affected the EQI score. A coefficient of -16.190 suggests that a 1% increase in population density reduces the EQI by 0.16 units. These findings support the hypothesis and are consistent with Li et al. (2025) and Suhrab et al. (2025), both of which emphasize the importance of population control and sustainable density management to mitigate environmental stress. However, although population density often reflects people's preference for cities with higher wages, empirical analysis shows that wage levels do not significantly affect the EQI. This indicates that environmental degradation in urban areas is controlled more by population loads that exceed the capacity of environmental services, such as

sewage systems, green open spaces, and air quality, than by residents' income levels.

3.2.3. The Dynamics of Poverty

The number of people living in poverty improved the EQI score. The long-term coefficient of 0.006 indicates that an increase of 100,000 people in poverty corresponds to a 0.6 unit rise in the EQI. Conversely, reducing the number of poor people by 100,000 leads to a 0.6 unit decline in the EQI. This counterintuitive result aligns with the poverty-environment trap phenomenon described by Dao & Edenhofer (2018) and Giannetti et al. (2023), who found that poverty can mitigate the pressure of exploitation on the environment due to limited production and consumption capacity. In such contexts, poor communities tend to limit consumption because of their restricted purchasing power, which results in relatively low levels of environmentally damaging activity. Consequently, the environment may appear "better preserved," not because of proactive protection policies or sustainability awareness, but due to the limited ability of impoverished communities to exploit natural resources intensively.

3.2.4. The Role of Financial Development

Our findings show that financial development, as represented by foreign and domestic investments, has little impact on environmental quality. The analysis of investment variables indicates that only domestic investment has a positive long-term effect on the EQI. The regression coefficient of 0.0000000956 suggests that an increase of 100 billion rupiah in domestic investment raises the EQI by 0.00956. Although this finding confirms the positive role of domestic investment, the magnitude of the effect remains very small, underscoring that its contribution to sustainability is still in its early stages. Our results are in line with those of Minh et al. (2023) and Mtar et al. (2025), who explained that environmental benefits only emerge when investments are explicitly directed towards clean energy, green infrastructure, or low-emission technologies. These findings indicate that provincial investment flows have not been allocated to economic activities that can strengthen environmental capacity. The vast tropical forests in Indonesia have significant ecological capacity to absorb pollutants and mitigate some of the pressure of emissions from economic activities. However, this natural capacity cannot be used as a basis for delaying corrective actions. The government needs to view these findings as an important signal that investment potential, both domestic and foreign, must be directed more strategically to not only drive economic growth but also strengthen environmental sustainability in the long term.

3.2.5. GRDP and Environmental Quality

The empirical estimates show that economic expansion, as measured by GRDP, is associated with a deterioration in environmental quality both immediately and over longer horizons. In the short term, the coefficient of -31.495 implies that a 1% increase in GRDP reduces the environmental index by 0.32. This relatively strong effect is likely driven by short-lived surges in resource extraction, energy consumption, and industrial activity, which typically accompany economic upswings. When the analysis is extended to the long run, the adverse impact remains but becomes noticeably weaker. In the long term, the magnitude of the effect decreases, with a coefficient of -8.984, meaning that a 1% increase in GRDP lowers the environmental index by 0.09 units. This attenuation suggests that, over time, economies gradually incorporate mechanisms that soften environmental pressures, such as cleaner technologies, enhanced regulatory oversight, and a shift away from highly polluting sectors.

Taken together, the findings are broadly consistent with the early dynamics predicted by the Environmental Kuznets Curve (EKC) (Kuznets 1955). Although GRDP currently exerts a negative effect on environmental quality, the substantial reduction in the long-run coefficient indicates that the environmental burden of economic expansion diminishes as development advances. In the EKC framework, this weakening of the adverse effect represents the initial phase in which efficiency improvements, regulatory tightening, and structural shifts begin to offset the environmental pressures generated by income growth. Although the present sample period is not long enough to detect a complete inverted-U shape or identify a formal turning point, the trajectory of the coefficients suggests that the economy may be moving toward it. The steady decline in the magnitude of the negative impact implies that, over a longer developmental horizon, the detrimental effect of GRDP on environmental quality could continue to diminish and may eventually be reversed. This pattern aligns with the EKC hypothesis, in which environmental degradation first intensifies and then gradually improves as economies adopt cleaner technologies, diversify from carbon-intensive sectors, and strengthen environmental governance mechanisms.

To further explore this dynamic, we analyzed which GRDP-forming sectors in the 34 provinces most significantly affected EQI, as shown in Table 9.

SECTOR: A. Agriculture, Forestry, and Fisheries, B. Mining and Quarrying, C. Manufacturing, D. Electricity and Gas Supply, E. Water Supply, Waste Management, Waste and Recycling, F. Construction, G. Wholesale and Retail Trade, Car and Motorcycle Repair, H. Transportation and Warehousing, I. Provision of Accommodation and Food and Beverages, J. Information and Communication, K. Financial and Insurance Services, L. Real Estate, M. N. Service Companies, O. Government Administration, Defense, and

Table 9: GRDP Sectoral on Environmental Quality Index.

Variable	CEM		FEM		REM	
	Coefficient	Prob.	Coefficient	Prob.	Coefficient	Prob.
C	68.455	0.000	140.433	0.012	66.435	0.000
LN(SECTOR_A)	-0.305	0.617	2.121	0.775	-0.471	0.647
LN(SECTOR_B)	0.339	0.345	-6.016	0.012**	0.936	0.145
LN(SECTOR_C)	-0.449	0.394	5.795	0.002***	0.304	0.715
LN(SECTOR_D)	-2.581	0.003	0.780	0.800	-4.536	0.001
LN(SECTOR_E)	4.440	0.000	1.076	0.863	4.626	0.000
LN(SECTOR_F)	3.763	0.006	-4.590	0.392	0.042	0.985
LN(SECTOR_G)	3.184	0.099	0.341	0.960	5.717	0.054
LN(SECTOR_H)	-1.606	0.097	1.439	0.664	-3.147	0.038
LN(SECTOR_I)	0.363	0.526	-6.011	0.179	-0.494	0.636
LN(SECTOR_J)	-1.605	0.136	14.384	0.000***	5.136	0.004
LN(SECTOR_K)	-10.438	0.000	-4.434	0.375	-10.125	0.000
LN(SECTOR_L)	-1.515	0.005	-0.587	0.928	-2.368	0.020
LN(SECTOR_MN)	-0.538	0.230	-9.269	0.010**	-1.791	0.017
LN(SECTOR_O)	2.558	0.059	-28.459	0.000***	-2.981	0.207
LN(SECTOR_P)	-2.863	0.028	16.691	0.018**	-4.087	0.079
LN(SECTOR_Q)	7.595	0.000	7.115	0.065*	13.333	0.000
R^2	0.639		0.852		0.352	
Adj. R^2	0.619		0.824		0.316	
Prob.(F-stat)	0.000		0.000		0.000	

Chow Test F(33. 256) = 11.217, Prob. F = 0.000***; Hausman Test Cross-section random $\chi^2(16) = 126.694$, Prob. $\chi^2 = 0.000$***; *significant at 10% α, **significant at 5% α, ***significant at 1% α.

Compulsory Social Security, P. Educational Services, Q. Health Services and Social Activities.

3.3. Sector Analysis

The sectoral analysis revealed that the Fixed Effects Model (FEM) was selected as the best-fitting model, supported by the Prob. F of 0.000 and Prob. $\chi 2$ of 0.000. The results indicate that the Manufacturing, Information and Communication, Education Services, Health Services, and Social Activities sectors had a positive effect on the EQI. In contrast, the Mining and Quarrying, Business Services, Public Administration, Defense, and Compulsory Social Security sectors had negative effects on the EQI across the 34 provinces in Indonesia from 2015 to 2023.

3.3.1. Sector B. Mining and Quarrying

The mining and quarrying sector reduces the EQI by 0.06 units. As highlighted in the resource curse literature by Muhamad and Khezri (2025), extractive activities such as coal, nickel, mineral, and petroleum exploitation contribute to deforestation, water pollution, biodiversity loss, and land degradation. Although this sector remains a major pillar of Indonesia's foreign exchange earnings, the environmental costs significantly outweigh its short-term economic benefits. This negative contribution underscores the classic dilemma between economic growth driven by natural resource extraction and environmental sustainability.

3.3.2. Sector C. Manufacturing

The manufacturing sector contributes positively to the EQI, with an increase of approximately 0.06 units, which seems contradictory to the conventional view that associates industry with pollution. However, from 2015 to 2023, many manufacturing companies in Indonesia underwent significant transformations towards cleaner and more ecologically efficient production models. Most have adopted green industry practices, such as waste management, energy efficiency, and environmental management systems that meet Green Industry Standards. The Ministry of Industry (Kemenperin) is actively promoting these initiatives through energy conservation policies (PP No. 33 of 2023) and programs such as the Boosting Energy Efficiency Practices for the Industrial Sector (BENEFITS) project,

which strengthens energy management in manufacturing plants (Nurcahyanto et al. 2020). Additionally, the government has formulated an Industrial Decarbonization Roadmap that targets the manufacturing sector to achieve net-zero emissions by 2050 through the use of low-carbon technologies, material efficiency, and the circular economy. At the company level, several factories have achieved Green Industry certification as proof of their commitment to environmentally friendly practices.

3.3.3. Sector J. Information and Communication

Sector J increases the EQI by 0.14 units. The information and communication sector positively contributed to environmental quality because its activities were predominantly digital, producing minimal pollution or physical waste. The digitalization of economic activity has promoted efficiency by reducing paper consumption, lowering physical mobility through remote working arrangements, and encouraging online services to reduce transportation-related emissions. Moreover, communication technologies have facilitated the dissemination of environmental knowledge and supported transparency in public policy. Thus, although indirect, the sector plays a strategically significant role in improving environmental quality.

3.3.4. Sector MN. Corporate Services

The business services sector was identified as having reduced the EQI by 0.09. This is largely attributable to its reliance on resource- and energy-intensive activities, such as business travel, logistics, and project construction. In the absence of environmental cost internalization, these activities indirectly degrade ecosystem conditions. Furthermore, the limited adoption of Environmental, Social, and Governance (ESG) principles in corporate practices has constrained this sector's potential to contribute positively to environmental sustainability.

3.3.5. Sector O. Public Administration, Defense, and Mandatory Social Security

Sector O reduces the EQI by 0.29 points; the negative contribution of this sector reflects the limited integration of green governance into bureaucratic and institutional practices. Provincial government agencies rely heavily on fossil fuels, inefficient resource use, and weak internal policies regarding energy conservation and waste reduction. In addition, budget allocations for defense and social security tend to neglect explicit provisions for advancing the green economic transition. These findings highlight the urgent need for institutional reform to ensure that the public sector not only acts as a regulator but also serves as a role model for adopting environmentally responsible practices.

3.3.6. Sector P. Education Services

GRDP in the education services sector has been shown to increase the EQI by 0.16 units, which is consistent with our initial long-term findings (see Table 7). The positive effect of the education sector on the EQI highlights the crucial role of education in fostering ecological awareness. Broader access to and improved quality of education can enhance knowledge of clean technologies and cultivate a generation that is more attentive to sustainability challenges. According to Todaro and Smith (2020), education is often regarded as the "fourth pillar" of sustainability, as it develops human capital that drives green innovation. Hence, the contribution of the education sector to environmental quality is direct and long-term, as it promotes changes in values, mindsets, and behaviors that underpin sustainable development.

3.3.7. Sector Q. Health Services and Social Activities

The health sector has been recorded as having a positive impact on the EQI, with an increase of approximately 0.07 units. This is understandable because better health services usually encourage the community to be more concerned about environmental quality, ranging from the need for clean air to the importance of safe waste disposal. Social activities further reinforce this link by encouraging community participation in environmental protection through reforestation, community-based waste management, and environmental awareness campaigns. These positive dynamics illustrate a reciprocal relationship: a healthy environment enhances public health outcomes, while growing health consciousness creates stronger public demand for improved environmental conditions

3.4. Policy Implications

Based on the empirical findings regarding the determinants of environmental quality across 34 provinces in Indonesia, it is essential to formulate policy recommendations that can guide both central and regional governments in designing sustainable development strategies.

3.4.1. National Level

Strengthening green industry regulation should be prioritized by aligning it with the Medium-Term National Development Plan (RPJMN), supported by fiscal incentives or dedicated financing for sectors that adopt low-emission technologies and improve resource efficiency. In line with the government's green fiscal reform agenda, the fiscal transfer mechanism, particularly the Special Allocation Fund (DAK) and the Regional Incentive Fund (DID), should be revised to incorporate the EQI as a performance indicator, thereby encouraging local governments to enhance their environmental management. Moreover, although financial

development only has long-term effects, this sector must still be guided to prevent environmental pressure.

3.4.2. Regional Level (Provinces)

At the provincial level, it is essential to incorporate environmental performance indicators into the evaluation of local government effectiveness, especially under the Low Carbon Development Planning (PPRK) framework, which the majority of provinces has implemented. Local authorities should design action plans tailored to the specific characteristics of their regions, prioritizing sectors that most strongly influence the EQI, such as the energy sector in Java, extractive industries in Sumatra and Kalimantan, and agricultural activities in Nusa Tenggara and Sulawesi.

3.4.3. Synergy Between Central and Regional Governments

Coordination between central and local governments should be strengthened to enhance the effectiveness of environmental policies in Indonesia. Provincial energy and green economy transition strategies should be aligned with national emission reduction targets to ensure consistency across governance levels. Cross-government Monitoring, Reporting, and Verification (MRV) systems should be enhanced to support carbon management, emission control, and climate mitigation initiatives. Furthermore, environmental quality should be established as one of the key performance indicators of regional development.

4. CONCLUSIONS

We analyzed the influence of democracy, socioeconomic dynamics, and GRDP sectoral structure on environmental quality in 34 provinces in Indonesia from 2015 to 2023. Our findings show that democracy indices, education levels, poverty, and domestic investment improve the EQI, whereas GRDP and population density worsen it. Furthermore, extractive industries, business services, and government administration reduced the EQI. Meanwhile, the economic sectors of manufacturing, information and communication, education, and health were found to improve the EQI.

Our findings support the EKC hypothesis, which posits that environmental quality initially declines during the early stages of economic growth before improving as development progresses, as reflected in the smaller long-term effects compared to short-term effects. The results further indicate that substantive democracy, human capital development, and growth of environmentally friendly service sectors are crucial for achieving regional environmental sustainability. Therefore, economic development should not rely solely on output expansion but should also promote sectoral diversification to reduce dependence on extractive industries. Hence, economic development should not only rely on output expansion but also encourage sectoral diversification to reduce dependence on extractive industries. In addition, financial development must continue to pay attention to environmental quality so that it does not have a negative long-term impact.

This study had certain limitations that need to be acknowledged. First, the relatively short nine-year period may restrict the ability to capture long-term trends in environmental outcomes. Second, relying on aggregated provincial data may mask variations within provinces and obscure local-level dynamics. Third, the absence of detailed sectoral foreign direct investment information limits the analysis of differential impacts across industries. Further research is expected to overcome these constraints by extending the period of analysis and utilizing more disaggregated data. Incorporating spatial econometric techniques allows for the consideration of inter-regional spillovers, while using composite governance measures, such as an environmental democracy index, could provide a more comprehensive assessment of institutional influences on environmental quality.

5. ACKNOWLEDGEMENT

This research was supported by Universitas Sebelas Maret for the 2025 fiscal year through Research Grant PKGR-UNS, under assignment agreement number 371/UN27.22/PT.01.03/2025

6. REFERENCES

Acheampong, A.O., Osei Opoku, E.E. and Dzator, J., 2022. Does democracy really improve environmental quality? Empirical contribution to the environmental politics debate. *Energy Economics*, 109, pp.105942. [DOI]

Afridi, M.A., Kehelwalatenna, S., Naseem, I. and Tahir, M., 2019. Per capita income, trade openness, urbanization, energy consumption, and CO2 emissions: an empirical study on the SAARC region. *Environmental Science and Pollution Research*, 26(29), pp.29978–29990. [DOI]

Arranz, J.M. and García-Serrano, C., 2025. Assessing the impact of an increase in the minimum wage on household income and poverty. *Social Science Research*, 127, pp.103143. [DOI]

Aryani, Y., Purwana, R., Herdiansyah, H. and Suryabrata, J.A., 2025. Advancing indoor environmental quality (IEQ) in Indonesian hospital wards: an integrated importance performance analysis (IPA) and objective approach. *Energy and Built Environment*. [DOI]

Barnes, Z.T., Boedeker, P. and Huang, R., 2025. Parent education, not income-to-needs ratio, relates to preschool home executive function environment. *Journal of Experimental Child Psychology*, 258, pp.106292. [DOI]

Breusch, T.S. and Pagan, A.R., 1980. The Lagrange multiplier test and its applications to model specification in econometrics. *The Review of Economic Studies*, 47(1), pp.239–253. [DOI]

Bui Minh, T., Nguyen Ngoc, T. and Bui Van, H., 2023. Relationship between carbon emissions, economic growth, renewable energy consumption, foreign direct investment, and urban population in Vietnam. *Heliyon*, 9(6), pp.e17544. [DOI]

Dao, N.T. and Edenhofer, O., 2018. On the fiscal strategies of escaping poverty-environment traps towards sustainable growth. *Journal of Macroeconomics*, 55, pp.253–273. [DOI]

Domowitz, I. and Elbadawi, I. 1987. An error-correction approach to money demand: The case of Sudan. *Journal of Development Economics*, 26, pp.257–275. [DOI]

Don, M. N. U., Florentine, S., Turville, C. and Dassanayake, K. 2025. Evaluation of foliar application of caffeine in almond (Prunus dulcis) cultivation as an alternative to chemical pesticides: Minimizing chemical residue in almond hulls for sustainable use of almond by-products. *Journal of Natural Pesticide Research*, 14, p.100147. [DOI]

Fredriksson, P.G. and Wollscheid, J.R., 2015. Legal origins and climate change policies in former colonies. *Environmental and Resource Economics*, 62(2), pp.309–327. [DOI]

Fukuyama, H., Tan, Y. and Wanke, P., 2025. Global inefficiencies in labour, patents, energy, capital, environment, and economics: the role of corruption, democracy, and income distribution. *Socio-Economic Planning Sciences*, 100, pp.102248. [DOI]

Ghosh, S., Hossain, M.S., Voumik, L.C., Raihan, A., Ridzuan, A.R. and Esquivias, M.A., 2023. Unveiling the spillover effects of democracy and renewable energy consumption on the environmental quality of BRICS countries: a new insight from different quantile regression approaches. *Renewable Energy Focus*, 46, pp.222-235. [DOI]

Giannetti, B.F., Langa, E.S., Almeida, C.M.V.B., Agostinho, F., de Oliveira Neto, G.C. and Lombardi, G.V., 2023. Overcoming poverty traps in Mozambique: quantifying inequalities among economic, social and environmental capitals. *Journal of Cleaner Production*, 383, pp.135266. [DOI]

Hasan, M.A., Voumik, L.C., Mozumder, A.I., Esquivias, M.A., Verteramo-Chiu, L. and Das, M.K., 2025. Role of governance index, democracy, industrialization, and urbanization on environmental sustainability of BRICS countries: a novel PMG-ARDL approach. *Social Sciences and Humanities Open*, 11, pp.101242. [DOI]

Hu, B., Wang, C., Xia, Z., Lu, C. and Ju, X., 2025. Environmental education in low-income and middle-income countries: a systematic review and meta-analysis. *Journal of Environmental Psychology*, 104, pp.102613. [DOI]

Islam, M.M., Shahbaz, M., Sultana, T., Wang, Z., Sohag, K. and Abbas, S., 2023. Changes in environmental degradation parameters in Bangladesh: the role of net savings, natural resource depletion, technological innovation, and democracy. *Journal of Environmental Management*, 343, pp.118190. [DOI]

Kementerian Lingkungan Hidup dan Kehutanan Republik Indonesia (KLHK), 2022. *Status of the Indonesian Environment 2022*. Ministry of Environment and Forestry, Jakarta, pp.210.

Kuznets, S. 1955. Economic Growth and Income Inequality. *The American Economic Review*, 45(1), 1–8.

Li, L., Guo, J., Wu, X. and Zhao, J., 2025. Does promoting new urbanization help mitigate environmental pollution: evidence from China's pilot policies for new urbanization. *Journal of Environmental Management*, 388, pp.125925. [DOI]

Lukman, K.M., Hastuti, L.P., Oktavia, D., Pratiwi, D., Uchiyama, Y. and Harding, D., 2025. Towards blue skies: a comprehensive review and regional mapping of ambient air quality in Indonesian cities. *Journal of Environmental Management*, 389, pp.126132. [DOI]

Luo, L., Yang, Q., Qiao, D., Cao, Y., Ding, J., Ma, H. and Wei, J., 2025. How does environmental education affect college students' waste sorting behavior: a heterogeneity analysis based on educational background. *Journal of Environmental Management*, 389, pp.126064. [DOI]

Mtar, K., Belazreg, W., Smondel, A. and Bannour, S., 2025. Evidence from foreign direct investments moderating the relationship between environmental degradation and food and nutrition security: insights from low- and middle-income countries. *Journal of Environmental Management*, 393, pp.127051. [DOI]

Muhamad, G.M. and Khezri, M., 2025. Unveiling the environmental impact of resource dependency: developing a resource curse index (RCI) and its effects on carbon, cropland, forest, and fishing footprints. *Journal of Cleaner Production*, 522, pp.146326. [DOI]

Nurcahyanto, C., Simsek, Y. and Urmee, T., 2020. Opportunities and challenges of energy service companies to promote energy efficiency programs in Indonesia. *Energy*, 205, pp.117603. [DOI]

Ogunshina, M.S., Abioye, O.M., Adeniran, K.A. and Olasehinde, D.A., 2023. Moringa Oleifera coagulation characteristics in wastewater treatment in a university dormitory. *Nature Environment and Pollution Technology*, *22*(2), pp.699-707. [DOI]

Pastore, L.M. and de Santoli, L., 2025. Socio-economic implications of implementing a carbon-neutral energy system: a green new deal for Italy. *Energy*, 322, pp.135682. [DOI]

Persakis, A., Tsakalos, I., Gkonis, V. and Nerantzidis, M., 2024. Climate policy uncertainty and environmental degradation: does democracy moderate this relationship? *Cleaner Environmental Systems*, 15, pp.100230. [DOI]

Pesaran, M.H., 2004. *General Diagnostic Tests for Cross Section Dependence in Panels*. University of Cambridge, Cambridge, pp.45.

Pesaran, M.H., 2007. A simple panel unit root test in the presence of cross-section dependence. *Journal of Applied Econometrics*, 22(2), pp.265–312. [DOI]

Povitkina, M. and Jagers, S.C., 2022. Environmental commitments in different types of democracies: the role of liberal, social-liberal, and deliberative politics. *Global Environmental Change*, 74, pp.102523. [DOI]

Putra, M. R. A., Suryanto and Samudro, B. R. 2025. Do institutions matter in global trade? Evidence from high-income countries and their spillover effects on Indonesia. *Int. J. Trade and Global Markets*, 21(6), pp.696–717. [DOI]

Rachid, S., Nasr, M. and Boukhatem, J., 2025. Dynamic interaction between financial development, institutional quality and environmental conditions: new insights from MENA region. *Development and Sustainability in Economics and Finance*, 6, pp.100050. [DOI]

Shah, F.F., Joshi, D.P.P. and Gopinathan, R., 2023. Do long-term migrants earn higher wages than short-term migrants in the informal sector? Evidence from Jammu & Kashmir, India. *Habitat International*, 141, pp.102945. [DOI]

Sikder, M., Wang, C., Yao, X., Huai, X., Wu, L., Kwame Yeboah, F., Wood, J., Zhao, Y. and Dou, X., 2022. The integrated impact of GDP growth, industrialization, energy use, and urbanization on CO2 emissions in developing countries: evidence from the panel ARDL approach. *Science of the Total Environment*, 837, pp.155795. [DOI]

Smith, J.D., Adam, R. and Maarif, S., 2024. How social movements use religious creativity to address environmental crises in Indonesian local communities. *Global Environmental Change*, 84, pp.102772. [DOI]

Song, X., Zhou, Y. and Jia, W., 2019. How do economic openness and R&D investment affect green economic growth?—Evidence from China. *Resources, Conservation and Recycling*, 146, pp.405–415. [DOI]

Suhrab, M., Pinglu, C. and Qian, N., 2025. Green road to sustainability: impact of urbanization on environmental degradation and the mitigating effect of infrastructure investment in belt and road initiative economies. *Sustainable Futures*, 10, pp.101080. [DOI]

Sumy, D.F., Drakes, O.O., McBride, S.K. and Jenkins, M.R., 2023. Social vulnerability and geographic access barriers to earthquake early warning education in museums and other free choice learning environments. *International Journal of Disaster Risk Reduction*, 97, pp.104011. [DOI]

Todaro, M.P. and Smith, S.C., 2020. *Economic Development*. Pearson, Boston, pp.912.

Wahyuningrum, I.F.S., Sriningsih, Puspita, A.S., Budihardjo, M.A., Chegenizadeh, A. and Nikraz, H., 2025. Has mandatory reporting improved environmental disclosure quality in Indonesia? *World Development Perspectives*, 39, pp.100718. [DOI]

Wang, M., Lin, H., Huang, Y. and Lu, H., 2023. Poverty alleviation and firm productivity: evidence from China's minimum wage system. *International Review of Financial Analysis*, 87, pp.102595. [DOI]

Wijethunga, A.W.G.C.N., Rahman, M.M. and Sarker, T., 2025. Does financial development moderate the relationship between economic growth and environmental quality? *Environmental and Sustainability Indicators*, 27, pp.100728. [DOI]

Zhang, Y. and Zhao, Z., 2022. Environmental regulations and corporate social responsibility: evidence from China's real-time air quality monitoring policy. *Finance Research Letters*, 48, pp.102973. [DOI]

Nature Environment and Pollution Technology
An International Quarterly Scientific Journal

p-ISSN: 0972-6268
(Print copies up to 2016)
e-ISSN: 2395-3454

Vol. 25 | No. 3 | Article ID D1870 | 2026

Original Research Paper

https://doi.org/10.46488/NEPT.2026.v25i03.D1870

Open Access Journal

Integrated Proximate and Contamination Analysis of Tofu Wastewater: A Case Study in Telaga Subdistrict, Gorontalo, Indonesia

Muhammad Taupik†, Ariani H. Hutuba, Nurain Thomas, Andi Makkulawu and Windiyani N. Suharmin
Department of Pharmacy, Faculty of Sports and Health, Gorontalo State University, Gorontalo 96211, Indonesia
†Corresponding author: Muhammad Taupik; muhtaupik@ung.ac.id

Abbreviation: Nat. Env. & Poll. Technol.
Website: www.neptjournal.com

Received: 17-09-2025
Revised: 25-11-2025
Accepted: 28-11-2025

Key Words:

Tofu wastewater
Proximate analysis
Contamination
COD
BOD
Circular economy

ABSTRACT

Tofu wastewater is a major contributor to organic pollution in many Asian rivers; however, household-scale tofu production in eastern Indonesia remains poorly documented. This study provides an integrated characterization of tofu and its wastewater in the Telaga Subdistrict, Gorontalo, as baseline information for local water management. The proximate composition of tofu and wastewater was determined following standard AOAC methods, and river water was sampled at three points: upstream (A), downstream (B), and the wastewater channel (C). Contamination parameters (COD, BOD, TSS, ammonia, and pH) were assessed and compared using one-way analysis of variance (ANOVA) with Tukey's test. Tofu retained high moisture and moderate protein levels, confirming its role as an affordable protein source, while the wastewater still contained soluble proteins and carbohydrates. At Point C, COD (7499 mg.L-1), BOD (864 mg.L-1), and TSS (147 mg.L-1) substantially exceeded national and international thresholds, whereas ammonia (0.01–0.10 mg.L-1) and pH (7.2–7.3) remained within regulatory limits and were lower than those commonly reported for tofu effluents elsewhere. Although wastewater flow was not measured, the very high organic concentrations indicate that even household-scale tofu industries can exert considerable local organic pollution pressure and should be included in water quality monitoring and low-cost treatment programs. At the same time, the presence of residual nutrients suggests potential for valorization pathways such as biogas generation or microbial biomass production, which should be explored in future studies to support context-appropriate circular economy initiatives in Gorontalo.

Citation for the Paper:

Taupik, M., Hutuba, A.H., Thomas, N.A., Makkulawu, A. and Suharmin, W.N., 2026. Integrated proximate and contamination analysis of tofu wastewater: A case study in Telaga Subdistrict, Gorontalo, Indonesia. *Nature Environment and Pollution Technology*, 25(3), D1870. https://doi.org/10.46488/NEPT.2026.v25i03.D1870

Note: From 2025, the journal has adopted the use of Article IDs in citations instead of traditional consecutive page numbers. Each article is now given individual page ranges starting from page 1.

Copyright: © 2026 by the authors
Licensee: Technoscience Publications
This article is an open access article distributed under the terms and conditions of the Creative Commons Attribution (CC BY) license (https://creativecommons.org/licenses/by/4.0/).

1. INTRODUCTION

Recent research has explored both the treatment and valorization pathways of tofu wastewater. For instance, phytoremediation using water lettuce and *Pistia stratiotes* achieved significant reductions in COD and BOD, highlighting the potential of aquatic plants as low-cost treatment systems (Nurpita & Temmy 2022, Kurniawan et al. 2024). Constructed wetlands with *Typha angustifolia* and *Ipomoea aquatica* also demonstrated a 68–70% reduction in organic loads (Rohmah et al. 2023). Physicochemical approaches such as coagulation-flocculation with polyaluminium chloride, multilevel filtration, and photocatalysis using TiO_2 have been applied to reduce turbidity, COD, and TSS (Prasetyo et al. 2021, Widyastuti et al. 2023). Advanced methods that combine adsorption, Fenton oxidation, and ultrafiltration membranes have further improved the removal efficiency (Liu et al. 2024). Beyond treatment, valorization studies have shown that tofu wastewater can support microalgal cultivation, producing biomass enriched in protein and valuable proximate components (Putri et al. 2024), while anaerobic digestion coupled with microbial consortia produces methane-rich biogas (Budiastuti et al. 2021).

Despite these advances, current research on tofu wastewater still has important blind spots. Many investigations have prioritized treatment efficiency and regulatory compliance, while the residual nutrient composition that could underpin value-added applications has received comparatively less emphasis (Chen et al.

2022, Dewi et al. 2024). Nevertheless, previous studies have demonstrated that tofu effluent can retain appreciable amounts of protein, carbohydrates, and fat, indicating untapped potential for resource recovery (Chen et al. 2022, Dewi et al. 2024). Geographically, published studies are heavily concentrated in Java, with far fewer reports from Sumatra, Kalimantan, and Sulawesi (Pradana et al. 2023, Ridhuan et al. 2022). Localized household-scale industries in peripheral regions, such as Gorontalo, have received little attention; therefore, basic information on both contamination profiles and residual nutrient content remains scarce. While several authors have reported either contamination indicators or proximate composition, there is still limited baseline information that considers both dimensions together for household tofu wastewater in under-reported eastern Indonesian settings, which is needed to support circular-economy–oriented management.

This study provides an integrated baseline description of tofu, its wastewater, and receiving river water in household-scale tofu industries in the Telaga Subdistrict of Gorontalo, Indonesia. Specifically, we (i) determined the proximate composition of tofu and its wastewater, (ii) quantified key contamination parameters (BOD, COD, TSS, ammonia, and pH) at upstream, downstream, and wastewater discharge points relative to regulatory thresholds, and (iii) discussed the implications of these concentration profiles for local water quality management and potential valorization options. In doing so, this study offers empirical baseline data from an underrepresented region and highlights that tofu wastewater in Gorontalo is not only an environmental concern but also a potential resource for future circular-economy initiatives.

2. MATERIALS AND METHODS

2.1. Study Area and Sampling Strategy

This study was conducted in the Telaga Subdistrict, Gorontalo, Indonesia, where tofu production is operated at a household scale and liquid effluents are discharged directly into nearby rivers. Sampling was conducted at three points (Fig. 1): Point A (0°34′43.13″ N, 123°02′48.92″ E) representing the upstream river section before contact with the tofu effluent, Point B (0°34′42.61″ N, 123°02′48.33″ E) representing the downstream river section after effluent discharge, and Point C (0°34′42.23″ N, 123°02′48.16″ E) representing the drainage channel directly releasing tofu wastewater.

To capture short-term temporal variability, a composite water sample was collected at each point (A, B, and C) weekly for three consecutive weeks, resulting in three independent temporal replicates (n = 3) per point. Each weekly composite sample was prepared by combining several grab subsamples taken at approximately equal time intervals during active tofu production. In the laboratory, all physicochemical parameters (COD, BOD, TSS, pH, and ammonia) were measured in triplicate for each weekly sample, and the mean of the three analytical replicates was used as a single observation in subsequent statistical analyses. Water collection and handling followed the Indonesian National Standard for water sampling (SNI 6989.57:2008), which provides guidelines for representative and contamination-free sampling, and the upstream–downstream design was consistent with recent tofu wastewater studies (Rahman & Fajriati 2021, Pradana et al. 2023).



Fig. 1: Sampling locations (Points A, B, and C) in Telaga Subdistrict, Gorontalo, Indonesia.

2.2. Instruments and Analytical Conditions

The pH was measured using a calibrated benchtop pH meter (Thermo Scientific Orion Star A211) with daily three-point calibration at pH 4.01, 7.00, and 10.01 (NIST-traceable buffers). Total suspended solids (TSS) were measured following APHA 2540 D using Whatman GF/C 1.2 µm glass-fiber filters and an analytical balance (Sartorius Entris II, readability 0.1 mg). The samples were dried at 103–105 °C in a laboratory oven (Memmert UF55). The biochemical oxygen demand (BOD) was determined by 5-day incubation at 20 ± 1 °C in a BOD incubator (VELP FOC 120E). Dissolved oxygen was measured using an optical DO meter (Hach HQ40d with an Intellical LDO101 probe). Ammonia was analyzed using a Merck Pharo 300 photometer with the appropriate colorimetric method. All instruments were calibrated according to the manufacturer's recommendations, and quality control included blanks, duplicates, and linearity verification ($R^2 \geq 0.997$).

2.3. Materials and Reagents

All chemicals were of analytical grade, including concentrated sulfuric acid (H_2SO_4), sodium hydroxide (NaOH), boric acid (H_3BO_3), chloroform, catalyst tablets, hydrochloric acid (HCl), potassium hydroxide (KOH), chemical oxygen demand (COD) reagent kits, nutrient buffer pillows, and distilled water. Tofu products and wastewater samples were collected from local household tofu industries in the Telaga Subdistrict. Analytical procedures were conducted at accredited laboratories following the Indonesian National Standards (SNI) and APHA protocols (APHA 2017).

2.4. Proximate Analysis

Proximate composition was analyzed following SNI protocols: protein content via the Kjeldahl method (SNI 01-2354.4:2006), fat content through Soxhlet extraction (SNI 01-2354.3:2006), moisture determined by oven drying at 100 °C (SNI 01-2354.2:2006), and ash by incineration in a muffle furnace (SNI 01-2354.1:2006). Carbohydrate content was calculated by difference. All measurements were conducted in triplicate. These standardized methods are commonly used for characterizing soybean by-products (Chen et al. 2022, Dewi et al. 2024).

2.5. Contamination Analysis

Wastewater contamination was evaluated through measurements of biochemical oxygen demand (BOD_5), chemical oxygen demand (COD), total suspended solids (TSS), pH, and ammonia levels. BOD_5 was determined following the APHA 5210 method (APHA 2017), while COD was measured using closed reflux spectrophotometry in accordance with SNI 6989.2:2009. TSS was quantified via the gravimetric method per SNI 06-6989.25-2005. For samples with undiluted COD values exceeding the calibration range, serial dilutions with distilled water (up to 20-fold) were prepared to ensure absorbance readings fell within the 0–10,000 $mg.L^{-1}$ calibration curve. Final COD concentrations were calculated by multiplying the instrument readings by the appropriate dilution factors. Ammonia and pH were measured with a Pharo 300 spectrophotometer (Merck). These parameters serve as indicators of organic pollution in tofu wastewater (Kurniawan et al. 2024, Liu et al. 2024).

2.6. Quality Control and Data Validation

All analyses were conducted in triplicate, and method blanks were included in every batch. Calibration for spectrophotometric analyses (COD and ammonia) employed at least five concentration levels, with linearity accepted at $R^2 \geq 0.995$. Precision was evaluated using the relative standard deviation (%RSD) of triplicate measurements, with acceptance limits of ≤5–7% for proximate assays and ≤10% for wastewater parameters. For spectrophotometric contamination measurements, spike recovery acceptance limits were set at 90–110%, and recoveries within this range were considered analytically acceptable, as summarized in Table 4. The method detection limits (LOD) and limits of quantitation (LOQ) were estimated using the standard deviation of the blanks and the slope of the calibration curves (LOD = 3.3 $\sigma.m^{-1}$, LOQ = 10 $\sigma.m^{-1}$). Laboratory control materials were included for proximate tests, and duplicate gravimetric runs were performed to verify the precision of the total suspended solids (TSS). Results failing the QC criteria were re-analyzed.

2.7. Data Analysis

Descriptive statistics, including mean, standard deviation, and %RSD, were calculated for all parameters. For each sampling point (A, B, and C), three weekly mean values—obtained from analytical triplicates—were averaged over the three-week sampling period. These weekly means (n=3 per point) served as independent observations in the statistical analysis. One-way ANOVA tested for differences among sampling points for each water quality parameter (BOD, COD, TSS, ammonia, and pH), followed by Tukey's post hoc test when ANOVA results were significant (α=0.05). Before ANOVA, data were assessed for normality using the Shapiro–Wilk test and for homogeneity of variances using Levene's test. Results are reported as the mean ± standard deviation of the three weekly observations. Different superscript letters in the tables denote significant differences between sampling points based on the ANOVA–Tukey

procedure. Statistical analyses were conducted using SPSS version 26 (IBM Corp., USA), with a significance level set at α=0.05. Findings were compared to Indonesian wastewater quality standards (Government Regulation of the Republic of Indonesia No. 22/2021) and international benchmarks (WHO 2017, USEPA 2020).

3. RESULTS

3.1. Proximate Composition of Tofu

The proximate composition of tofu produced in household-scale industries within the Telaga Subdistrict is summarized in Table 1. Moisture was the predominant component, ranging from 81.72 ± 1.63% to 82.06 ± 1.65% (%RSD 1.99–2.01%), followed by protein (6.10 ± 0.12% to 7.08 ± 0.14%, %RSD 1.97–2.07%), carbohydrates (7.50 ± 0.19% to 9.47 ± 0.12%, %RSD 1.22–2.53%), fat (1.36 ± 0.07% to 2.72 ± 0.11%, %RSD 4.04–5.15%), and ash (0.79 ± 0.04% to 1.32 ± 0.05%, %RSD 3.79–5.06%). These findings indicate that the proximate composition remained relatively consistent across three consecutive weeks, implying that weekly variations in soybean raw materials or household processing practices had minimal impact on the nutritional quality of the tofu.

The protein content (6.10–7.08%) confirmed the role of tofu as an affordable plant-based protein source. This finding aligns with earlier reports that fresh tofu generally contains 6–9% protein (Chen et al. 2022, Feng et al. 2021). Fat levels were consistently low (1.36–2.72%), supporting the classification of tofu as a low-fat food that is beneficial for cardiovascular health (Li et al. 2020). Carbohydrate variation (7.50–9.47%) may be explained by soluble sugars and oligosaccharides that remain in the curd matrix, consistent with previous soybean product studies (Wang et al. 2021).

Moisture levels consistently above 81% are typical for fresh tofu and are essential for preserving its soft texture. However, such high moisture content also increases the risk of microbial spoilage, as noted by Zhang et al. (2023). The ash content, ranging from 0.79% to 1.32%, indicates stable mineral levels, aligning with measurements from other Southeast Asian tofu studies (Utami et al. 2012). Precision testing confirmed that all parameters met the acceptable standards, with %RSD values significantly below the 5–7% threshold, demonstrating the reproducibility of the analyses. Overall, the proximate composition of tofu from the Telaga Subdistrict aligns with both national and international data, reaffirming its nutritional value. These results also serve as a baseline for assessing nutrient residues in tofu wastewater, discussed further in the next section.

3.2. Proximate Composition of Tofu Wastewater

To assess the nutrient residues released during tofu processing, the proximate composition of tofu wastewater was analyzed, with results shown in Table 2. Moisture was the predominant component, ranging from 97.61 ± 1.95% to 99.18 ± 1.98% (%RSD 1.95–2.03%), while protein, fat, carbohydrates, and ash were present in smaller proportions. Protein levels varied from 0.21 ± 0.01% to 0.47 ± 0.01%

Table 1: Proximate composition of tofu samples collected over three weeks (mean ± SD, %RSD, n = 3).

Parameter	Week 1 [Mean ± SD]	%RSD	Week 2 [Mean ± SD]	%RSD	Week 3 [Mean ± SD]	%RSD
Protein [%]	7.08 ± 0.14	1.97	6.27 ± 0.13	2.07	6.10 ± 0.12	1.97
Fat [%]	2.72 ± 0.11	4.04	1.41 ± 0.07	4.96	1.36 ± 0.07	5.15
Carbohydrate [%]	7.50 ± 0.19	2.53	9.40 ± 0.23	2.45	9.47 ± 0.12	1.22
Moisture [%]	81.78 ± 1.64	2.01	82.06 ± 1.65	2.01	81.72 ± 1.63	1.99
Ash [%]	0.91 ± 0.04	4.40	0.79 ± 0.04	5.06	1.32 ± 0.05	3.79

Note: Values represent mean ± SD of triplicate determinations, %RSD calculated as (SD/mean) × 100. All %RSD values met acceptance limits ($\leq$5–7%) for proximate analysis (Chen et al. 2022, Feng et al. 2021).

Table 2: Proximate composition of tofu wastewater samples collected over three weeks (mean ± SD, %RSD, n = 3).

Parameter	Week 1 [Mean ± SD]	%RSD	Week 2 [Mean ± SD]	%RSD	Week 3 [Mean ± SD]	%RSD
Protein [%]	0.42 ± 0.01	2.38	0.47 ± 0.01	2.13	0.21 ± 0.01	4.76
Fat [%]	0.60 ± 0.02	3.33	0.45 ± 0.02	4.44	0.30 ± 0.02	6.67
Carbohydrate [%]	0.90 ± 0.02	2.22	0.20 ± 0.01	5.00	0.30 ± 0.01	3.33
Moisture [%]	97.61 ± 1.95	2.00	99.18 ± 1.98	2.00	98.74 ± 1.97	1.99
Ash [%]	0.36 ± 0.01	2.78	0.46 ± 0.02	4.35	0.37 ± 0.01	2.70

Note: Values represent mean ± SD of triplicate determinations, %RSD calculated as (SD/mean) × 100. All %RSD values were within the acceptance limits ($\leq$5–7%) for proximate analysis (Dewi et al. 2024, Wang et al. 2021).

Table 3: Contamination parameters of river water and tofu wastewater at three sampling points (mean ± SD, n = 3).

Parameter	Point A (Upstream)	Point B (Downstream)	Point C (Wastewater Channel)	Quality Standard*
TSS [mg.L^{-1}]	65.65 ± 2.01^{a}	78.45 ± 2.35^{a}	147.00 ± 3.21^{b}	50
COD [mg.L^{-1}]	62.00 ± 1.88^{a}	72.00 ± 2.14^{a}	7499.00 ± 22.35^{b}	25
BOD [mg.L^{-1}]	64.00 ± 1.92^{a}	59.00 ± 1.77^{a}	864.00 ± 8.65^{b}	3
Ammonia [mg.L^{-1}]	0.10 ± 0.01^{a}	0.01 ± 0.00^{a}	0.05 ± 0.01^{a}	0.2
pH	7.3 ± 0.1^{a}	7.2 ± 0.1^{a}	7.2 ± 0.1^{a}	6–9

Note: Values represent mean ± SD of three weekly observations per sampling point, each derived from analytical triplicates. Different superscript letters within a row indicate significant differences among sampling points ($p < 0.05$, one-way ANOVA with Tukey's post hoc test). Standards based on Government Regulation of the Republic of Indonesia No. 22/2021, WHO (2017), USEPA (2020).

(%RSD 2.13–4.76%), fat from 0.30 ± 0.02% to 0.60 ± 0.02% (%RSD 3.33–6.67%), carbohydrates from 0.20 ± 0.01% to 0.90 ± 0.02% (%RSD 2.22–5.00%), and ash from 0.36 ± 0.01% to 0.46 ± 0.02% (%RSD 2.70–4.35%). These findings confirm that although most nutrients are retained within the tofu curds, measurable quantities are still released into the liquid effluent.

The protein content, ranging from 0.21% to 0.47%, indicates the leaching of soluble nitrogen compounds into the wastewater. Dewi et al. (2024) reported similar patterns, demonstrating that tofu wastewater can support microalgae growth due to its residual nitrogen. Although fat concentrations were low (0.30% to 0.60%), their presence points to inefficiencies in coagulation and pressing processes. Carbohydrate levels (0.20% to 0.90%) likely reflect soluble sugars and oligosaccharides not incorporated into the tofu, aligning with reports on soybean-based foods (Wang et al. 2021). Moisture content above 97% is typical, as the wastewater is predominantly liquid.

The ash fraction (0.36% to 0.46%) confirms that minerals from soybeans and coagulants also enter the effluent. Precision testing showed %RSD values below 7% for all parameters, indicating good reproducibility and meeting acceptance criteria. Overall, these results reveal that tofu wastewater contains organic pollutants and measurable nutrient residues.

Consistent with previous research, such nutrient-rich effluents could be suitable for valorization pathways such as biogas production or microbial biomass generation, though further targeted studies are necessary to evaluate key parameters like C:N ratio, biodegradability, and volatile solids, which were not assessed in this work.

3.3. Contamination Parameters and Method Validation

The contamination parameters of the river water and tofu wastewater are summarized in Table 3. Of the five parameters evaluated, COD, BOD, and TSS at Point C (the wastewater channel) were significantly higher than those at Points A and B. One-way ANOVA of the three weekly mean values per point revealed that COD, BOD, and TSS differed statistically among sampling locations ($p < 0.05$), while ammonia and pH showed no significant differences ($p > 0.05$). Tukey's post-hoc test indicated that Point C had higher levels than Points A and B for COD, BOD, and TSS, with no notable differences between Points A and B.

Notably, COD and BOD at Point A (upstream) already surpassed the Indonesian river water quality standards (25 mg.L^{-1} for COD and 3 mg.L^{-1} for BOD), suggesting the influence of other upstream pollution sources unrelated to the studied tofu factory outlet. The slight differences between Points A and B for COD (62 vs. 72 mg.L^{-1}) and BOD (64 vs. 59 mg.L^{-1}) imply that, over the sampled short downstream reach, the additional impact of household tofu discharge on overall river quality is modest compared to existing background pollution.

To better illustrate these statistical differences, the data are visualized in Fig. 2. COD, BOD, and TSS at Point C were significantly higher than at the upstream and downstream river points, whereas ammonia and pH values showed no significant differences.

The high COD and BOD levels observed at Point C indicate significant organic pollution that exceeds regulatory standards and past tofu wastewater research, although the overall pollution load could not be determined due to the lack of flow rate measurements. These results align with reports from Central Java (Pradana et al. 2023), Bengkulu (Mualim et al. 2025), and international studies indicating that tofu wastewater is among the most concentrated soybean-based effluents (Liu et al. 2024). Ecological concerns include oxygen depletion caused by elevated organic matter and decreased light penetration from high TSS levels (Nurpita & Temmy 2022). In contrast, ammonia and pH values staying within permissible limits imply that organic material, rather than inorganic nitrogen or acidity, predominantly contaminates the water.

Reproducibility across replicate measurements was satisfactory, with %RSD less than 5% for COD and BOD, under 10% for TSS, and below 2% for pH, confirming

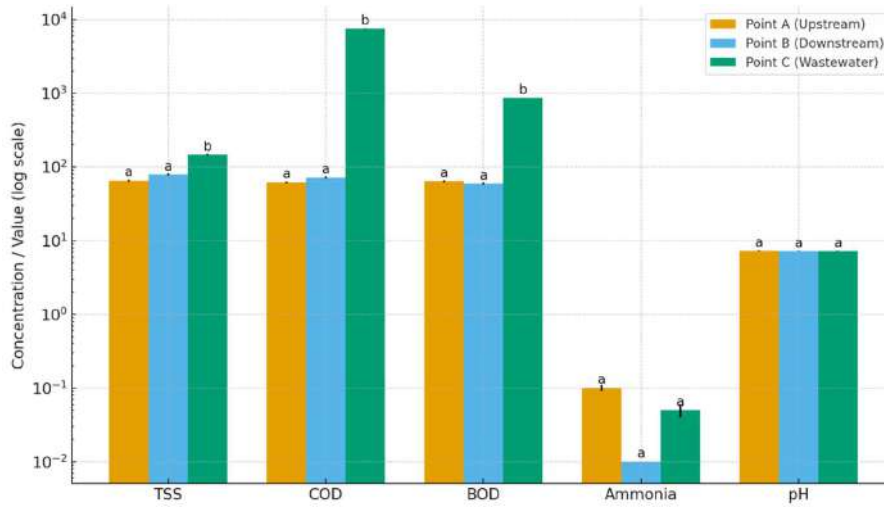


Fig. 2: Contamination parameters (TSS, COD, BOD, ammonia, and pH) of river water and tofu wastewater at three sampling points (Point A = upstream, Point B = downstream, Point C = wastewater channel). Values represent mean ± SD (n = 3). Bars with different superscript letters indicate significant differences among sampling points ($p < 0.05$, ANOVA with Tukey's test).

Table 4: Method validation summary for contamination analysis.

Parameter	Calibration range	R^2	LOD	LOQ	%Recovery	%RSD [n=3]	QC Status
COD	0–10,000 mg.L^{-1}	0.998	2.1 mg.L^{-1}	6.4 mg.L^{-1}	94–103%	<5%	Accepted
BOD	0–1,000 mg.L^{-1}	–	–	–	–	<7%	Accepted
TSS	0–1,000 mg.L^{-1}	–	–	–	–	<10%	Accepted
Ammonia	0–1,000 mg.L^{-1}	0.997	0.02 mg.L^{-1}	0.06 mg.L^{-1}	92–105%	<5%	Accepted
pH	4–10 (pH buffer solutions)	0.999	–	–	–	<2%	Accepted

Note: COD and ammonia validated using calibration curves and matrix spike recoveries, BOD and TSS verified by replicate precision, and pH validated by buffer calibration.

consistent results. Method validation for each parameter, summarized in Table 4, further verified the reliability of the results. COD and ammonia analyses demonstrated excellent linearity ($R^2 \geq 0.997$) with detection limits of 2.1 mg.L^{-1} and 0.02 mg.L^{-1}, respectively. Spike recoveries ranged from 92% to 105%, falling within acceptable limits (90–110%). Precision for BOD and TSS replicate measurements had %RSD under 10%, and pH calibration against standard buffers validated measurement accuracy.

The contamination data (Table 3) and the method validation results (Table 4) collectively highlight the extent of pollution in tofu wastewater and confirm the reliability of the analytical approach. These findings form a strong foundation for future discussions on mitigation measures and potential valorization strategies.

4. DISCUSSION

4.1. Comparative Analysis with Previous Studies

The findings of this study indicate that household-scale tofu industries in the Telaga Subdistrict discharge wastewater with contamination levels that fall within the range reported in other regions of Indonesia and internationally. COD values at Point C (7499 mg.L^{-1}) and BOD (864 mg.L^{-1}) substantially exceeded Indonesian regulatory standards and were consistent with reports from Central Java, where COD concentrations in tofu effluents can exceed 7000 mg.L^{-1} (Pradana et al. 2023) and from Bengkulu Province, where tofu-industry discharges have also been reported to surpass national discharge limits (Mualim et al. 2025). Liu et al. (2024) further emphasized that untreated tofu wastewater can reach COD levels exceeding 8000 mg.L^{-1}, confirming that the pollutant concentrations observed in this study fall within the upper range of values reported for soybean-based effluents globally.

Compared to studies employing remediation strategies, the results highlight both the risks and opportunities. Rohmah et al. (2023) demonstrated that constructed wetlands using *Typha angustifolia* and *Ipomoea aquatica* could reduce COD by up to 70%, whereas Kurniawan et al. (2024) reported successful phytoremediation of tofu wastewater with *Pistia stratiotes*. These interventions show promise for small-scale

industries, suggesting that similar low-cost and eco-friendly technologies could be adapted to the Telaga context.

Moreover, the presence of soluble proteins, carbohydrates, and minerals suggests that, consistent with previous reports, tofu wastewater could potentially serve as a feedstock for microalgae cultivation or anaerobic digestion (Dewi et al. 2024, Budiastuti et al. 2021). However, the present study did not evaluate nitrogen speciation, C:N ratio, biodegradability, or volatile solids; therefore, any valorization pathways should be regarded as hypothetical options derived from the literature rather than outcomes directly demonstrated by our data.

Taken together, this comparative analysis shows that although Telaga's tofu industries operate at a household scale, the concentrations of COD, BOD, and TSS in their wastewater fall within the upper range reported for tofu effluents in other regions. Therefore, this study provides empirical baseline evidence that small-scale tofu wastewater discharges can contribute to local water quality degradation and should be considered in river management strategies, even though the overall mass loading could not be quantified due to the absence of flow data.

This study had several limitations. First, sampling was restricted to a single subdistrict (Telaga) and covered only three weeks, which may not capture seasonal variations in wastewater characteristics and river hydrology. In addition, neither the discharge flow rate of the tofu effluent nor the river flow at the sampling reach was measured; therefore, the assessment was limited to concentration data, and mass loading ($kg.day^{-1}$), dilution, and the total downstream pollution contribution of household tofu industries could not be quantified. Second, only a limited number of physicochemical parameters were assessed, focusing on proximate composition, COD, BOD, TSS, ammonia, and pH, without including microbiological indicators or heavy metals that would allow a more direct evaluation of human health and ecotoxicological risks. Third, although statistical analysis (ANOVA with Tukey's test) confirmed significant differences among sampling points, the relatively small sample size (n = 3 per parameter) limited the statistical power and generalizability of the results; therefore, these significance patterns should be interpreted as exploratory rather than definitive. Finally, this study focused on wastewater characterization without evaluating treatment or valorization technologies, which are necessary for developing practical mitigation strategies. Future studies should expand sampling coverage, incorporate flow rate measurements and broader environmental parameters (including microbial indicators), and test low-cost remediation and resource recovery approaches under local conditions to provide a more comprehensive assessment.

5. CONCLUSIONS

This study offers a comprehensive baseline assessment of tofu, its wastewater, and the receiving river water in household-scale tofu operations within the Telaga Subdistrict of Gorontalo, Indonesia. Proximate analysis revealed that although tofu retains most of its nutrients, residual proteins, carbohydrates, and minerals remain in the wastewater, which exhibits high levels of COD, BOD, and TSS at the discharge point—values that are within or near the upper limits reported for tofu effluents elsewhere. Statistical analysis of three weekly mean samples from each site demonstrated that contamination levels in the direct wastewater channel (Point C) consistently exceeded those at upstream and downstream river points, highlighting the household tofu outlet as a significant local source of organic pollution. However, the overall contribution by flow volume could not be assessed due to a lack of flow rate measurements.

The findings emphasize two key points: first, even small-scale tofu industries can impose substantial local organic pollution, with wastewater characteristics at the discharge point approaching those observed in larger operations elsewhere, despite the total pollution load remaining unquantified due to absent flow data; second, tofu wastewater is nutrient-rich and could be valorized, potentially for biogas production or microbial biomass generation. Nonetheless, such applications were not experimentally explored here and warrant further study tailored to local conditions. Collectively, these results provide valuable baseline data for policymakers and stakeholders to implement routine monitoring of tofu effluents and adjacent river sections, promote low-cost decentralized treatment methods like settling tanks, anaerobic ponds, or small constructed wetlands suited for household-scale systems, and incorporate wastewater management into local environmental policies and community awareness programs. Future research should include flow and dilution assessments, microbiological water quality testing, and pilot-scale treatment or valorization trials to better quantify pollutant loads, health risks, and the potential for circular economy solutions in household tofu production.

6. ACKNOWLEDGMENTS

The authors gratefully acknowledge the technical and laboratory support provided by the Faculty of Sports and Health, Gorontalo State University.

7. REFERENCES

American Public Health Association (APHA), 2017. *Standard Methods for the Examination of Water and Wastewater* (23rd ed.). Washington, DC: APHA, p.1500.

Budiastuti, E., Nugroho, A. and Hidayat, T., 2021. Biogas generation from tofu wastewater using microbial consortia. *Renewable Energy Research Journal*, 45(6), pp.334–345.

Chen, X., Zhang, Y., Li, H. and Wang, Q., 2022. Nutrient composition and valorization potential of tofu wastewater. *Journal of Food Science and Technology*, 59(3), pp.1123–1131.

Dewi, R., Santoso, A. and Putra, D., 2024. Resource recovery from soybean by-product effluents: A proximate and contamination perspective. *Environmental Technology & Innovation*, 35, p.103451.

Feng, Y., Zhao, L. and Wang, J., 2021. Proximate analysis and nutritional characterization of soybean-derived foods. *Food Chemistry*, 356, p.129658.

Government of the Republic of Indonesia, 2021. *Government Regulation No. 22/2021 on Environmental Protection and Management*. Jakarta: Government of Indonesia, p.1.

Kurniawan, S.B., Imron, M.F., Mustofa, R.R., Najiya, D., Said, N.S.M., Buhari, J., Jusoh, H.H.W. and Ismail, A., 2024. Phytotreatment of tofu effluent using water lettuce (Pistia stratiotes) and potential of biogas production from resultant biomass. *Journal of Water Process Engineering*, 69, p.106672. [DOI]

Li, X., Wang, Y. and Chen, J., 2020. Nutritional and health benefits of soybean-derived products: A cardiovascular perspective. *Nutrition Reviews*, 78(6), pp.479–490.

Liu, J., Huang, P. and Zhao, W., 2024. Advanced treatment of soybean-based wastewater using adsorption, oxidation, and membrane technologies. *Journal of Environmental Management*, 345, p.119847.

Mualim, Ganefati, S.P., Jubaidi, Marwanto, A. and Rahmawati, U., 2025. Processing tofu liquid waste into liquid organic fertilizer with the addition of lamtoro leaves as an effort to prevent environmental pollution. *Jurnal Teknologi Lingkungan*, 26(1), pp.1–12. [DOI]

Nurpita, S. and Temmy, R., 2022. Phytoremediation of tofu wastewater using water lettuce (Pistia stratiotes). *Indonesian Journal of Environmental Science*, 14(2), pp.87–95.

Pradana, Y., Hartati, S. and Fajriati, L., 2023. Household tofu wastewater contamination in rural Indonesia. *International Journal of Environmental Research*, 20(1), pp.145–158.

Prasetyo, H., Sutanto, A. and Yulianto, B., 2021. Coagulation-flocculation and filtration for tofu effluent remediation. *Journal of Water Process Engineering*, 42, p.102112.

Putri, A., Yuliana, P. and Rahman, M., 2024. Microalgae cultivation using tofu wastewater as a growth medium. *Bioresource Technology Reports*, 23, p.101512.

Rahman, A. and Fajriati, L., 2021. Upstream–downstream assessment of tofu industry wastewater in Indonesia. *Indonesian Journal of Environmental Technology*, 12(2), pp.87–95.

Ridhuan, A., Maulana, H. and Sari, D., 2022. Wastewater profiles of household tofu industries in Sumatra and Kalimantan. *Journal of Water and Waste Management*, 18(4), pp.201–210.

Rohmah, I., Sari, N. and Handayani, E., 2023. Constructed wetlands for tofu wastewater remediation using Typha angustifolia and Ipomoea aquatica. *Ecological Engineering*, 190, p.106762.

United States Environmental Protection Agency (USEPA), 2020. *National Primary Drinking Water Regulations*. Washington, DC: USEPA, p.200.

Utami, R., Sari, A. and Prasetyo, H., 2012. Nutritional composition of Southeast Asian tofu: A comparative study. *Asian Journal of Food and Agro-Industry*, 5(3), pp.202–210.

Wang, L., Chen, Y. and Zhou, H., 2021. Carbohydrate composition and soluble sugar analysis in soybean products. *Journal of Agricultural and Food Chemistry*, 69(5), pp.1425–1432.

Widyastuti, N., Santika, A. and Prasetyo, H., 2023. Physicochemical approaches for tofu wastewater treatment: Coagulation, filtration, and photocatalysis. *Journal of Environmental Chemical Engineering*, 11(5), p.110021.

World Health Organization (WHO), 2017. *Guidelines for Drinking-Water Quality* (4th ed.). Geneva: WHO Press, p.500.

Zhang, H., Liu, Z. and Wang, J., 2023. Microbial spoilage and preservation of high-moisture soybean products. *Food Microbiology*, 110, p.104086.

Nature Environment and Pollution Technology
An International Quarterly Scientific Journal

p-ISSN: 0972-6268
(Print copies up to 2016)
e-ISSN: 2395-3454

Vol. 25 | No. 3 | Article ID B4391 | 2026

Original Research Paper

https://doi.org/10.46488/NEPT.2026.v25i03.B4391

Open Access Journal

Spatiotemporal Analysis of Long-Term Homogeneity, Meteorological Trend, and Drought Variability over the Semi-Arid Climatic Region of Bihar, India

Shashi Shekhar Pathak[1], Ravi Galkate[2], V.K. Chandola[1], Atar Singh[3], Bhupendra Joshi[1], Utkarsh Kumar[4], Rustem R. Zairov[5] and Ramesh Kumar[6]†

[1]Department of Agricultural Engineering, Banaras Hindu University, Varanasi, Uttar Pradesh, India
[2]National Institute of Hydrology (NIH Regional Center), Bhopal, Madhya Pradesh, India
[3]National Institute of Hydrology, Roorkee, Uttarakhand, India
[4]ICAR-Vivekananda Parvatiya Krishi Anusandhan Sansthan, Almora, Uttarakhand, India
[5]Arbuzov Institute of Organic and Physical Chemistry, FRC Kazan Scientific Center, Russian Academy of Sciences, 420088, Arbuzov str. 8 Kazan, Russian Federation
[6]PBS College Banka, Tilka Manjhi Bhagalpur University (TMBU), Bhagalpur, Bihar, India
†Corresponding author: Ramesh Kumar; rameshkumar9234@gmail.com

Abbreviation: Nat. Env. & Poll. Technol.
Website: www.neptjournal.com

Received: 30-08-2025
Revised: 18-11-2025
Accepted: 27-11-2025

Key Words:

Climate variability
Spatiotemporal analysis
Mann-Kendall test
Sen's slope
Drought variability

Citation for the Paper:

Pathak, S.S., Galkate, R., Chandola, V.K., Singh, A., Joshi, B., Kumar, U., Zairov, R.R. and Kumar, R., 2026. Spatiotemporal analysis of long-term homogeneity, meteorological trend, and drought variability over the semi-arid climatic region of Bihar, India. *Nature Environment and Pollution Technology*, 25(3), B4391. https://doi.org/10.46488/NEPT.2026.v25i03. B4391

Note: From 2025, the journal has adopted the use of Article IDs in citations instead of traditional consecutive page numbers. Each article is now given individual page ranges starting from page 1.

Copyright: © 2026 by the authors
Licensee: Technoscience Publications
This article is an open access article distributed under the terms and conditions of the Creative Commons Attribution (CC BY) license (https://creativecommons.org/licenses/by/4.0/).

ABSTRACT

Assessing the spatiotemporal variability of meteorological parameters provides critical insights into identifying emerging environmental risks posed by climate change. Such an evaluation can help obtain strong evidence to explain the effects of climate change on crop yields and water resource management. Recent rainfall–drought studies in Bihar have advanced our understanding of seasonal variability; however, several clear research gaps remain. Most analyses still rely heavily on the Standardized Precipitation Index, overlooking complementary water balance, soil moisture, and vegetation indicators needed to capture agricultural and hydrological droughts. Therefore, this study examined rainfall and drought characteristics in the semi-arid climatic region of Bihar. The dataset was acquired from the India Meteorological Department (IMD) for the period between 1970 and 2020 at a spatial scale of 0.25° × 0.25°. Based on the change point tests, the time series was divided into two periods: 1970–1990 and 1991–2020, with 1990 as the change point year. The non-parametric Mann-Kendall test and Sen's slope were used to identify trends and estimate their magnitude at a 5% significance level. The results showed that the northwestern, southwestern, and central districts of Bihar exhibited negative trends, particularly in June, August, and September. The magnitude of the decline ranged from -1 to -2 mm.y^{-1}. The analysis showed an increasing trend in the total annual rainfall observed between 1970 and 2020. This pattern suggests that the methodological framework employed in this study can be effectively applied across different spatial scales and diverse geographic settings. This study provides a foundation for improved water resource management, climate adaptation planning, and strategies aimed at mitigating the potential impacts of extreme hydrological events.

1. INTRODUCTION

Climate change is a significant global challenge with consequences that affect various aspects of life (Sarkar et al. 2021, Anil & Sasi 2025). The risks and vulnerabilities created by it have complex and interconnected impacts on communities, socioeconomic systems, and natural environments (Yildirim & Rahman 2022), which in turn affect other sectors of the economy, exacerbating existing inequalities. A report by the Intergovernmental Panel on Climate Change (IPCC) indicates that the Earth's temperature is expected to increase by 1 between 2030 and 2052 (IPCC 2021). This projected warming highlights the magnitude of the risks to society and the environment. Climate variability is caused by natural variability within the climate system as well as human-made influences, including land use and land cover alterations (Belay et al. 2021, Nyembo et al. 2021). These

changes are further exacerbated by rising greenhouse gas concentrations, which have altered seasonal patterns and intensified temperature and precipitation changes on a global scale (Yürekli 2015, Khaniya et al. 2019). However, vulnerable regions are often the most severely affected, experiencing cascading effects on livelihoods, public health, and biodiversity (Asare-Nuamah & Botchway 2019). Hence, analyzing climate variability is crucial for designing effective adaptation strategies. Thus, a better understanding of such variability can lead to more effective risk management methods. When compared to other meteorological indicators, the most significant climatic parameter in the tropics, rainfall, exhibits a high degree of variability on both temporal and geographical scales. Small- or large-scale variations in precipitation can have a significant impact on water availability, leading to the shifting of animal and plant species. Additionally, variations in precipitation patterns can lead to floods and droughts (Trenberth 2011), which can affect water quality. Conversely, a reduction in precipitation may indicate an increase in the occurrence of droughts.

In the Indian context, studies have highlighted significant spatiotemporal variations in precipitation patterns, particularly during the pre-monsoon season. Previous research has indicated an increase in pre-monsoon rainfall and an escalation in dry spells across the country (Ashok et al. 2004, Dash et al. 2007). This issue has gained significant attention from both the public and policymakers (Sahana et al. 2021). Therefore, climatic variability has been extensively studied in the literature using both parametric and non-parametric approaches. However, parametric approaches are limited to normally distributed time series, and non-parametric methods may be required for non-normally distributed data. Climate change and variability have been extensively studied at various spatial scales, both regionally and globally (Wudineh et al. 2022). Many studies have analyzed rainfall patterns and variability at global, regional, and basin scales using various methods, including the Mann-Kendall test and Sen's slope (Pawar & Rathnayake 2022, Gao et al. 2022).

Bihar, a state in India, faces significant challenges from both droughts and floods, making it one of the most climate-vulnerable regions in India. With agriculture serving as the backbone of Bihar's economy and most of its population dependent on it for their livelihood, the monsoon season plays a vital role in sustaining agricultural activities in the state. However, between 2009 and 2012, the state experienced four consecutive years of droughts. In 2009 alone, 26 of Bihar's 38 districts were officially declared drought-affected, with the Magadha, Munger, Saran, and Tirhut divisions bearing the brunt of the crisis. These events highlight the state's susceptibility to climate extremes, which severely affect agricultural productivity and household income. Studies have shown a notable decrease in annual and monsoonal rainfall since the post-1960 period (Rashiq et al. 2024), in stark contrast to the increasing rainfall trend observed before 1960 (Gogoi & Rao 2022, Guhathakurta et al. 2020). Recent trends further emphasize Bihar's growing water crisis. Between 1983 and 2016, research reported a significant decline in total rainfall, a pattern that exacerbates water scarcity and intensifies the challenges of resource management. The combination of erratic rainfall patterns, recurring droughts in rural areas, and urban flooding in places such as Patna underscores the urgent need for proactive, integrated strategies to manage water resources and address climate risks. This shift signals a profound change in the region's climate dynamics, with wide-ranging consequences for agriculture, water resources, and disaster management. The rising frequency of drought-like conditions serves as a warning for future climate challenges, particularly as the state lacks a comprehensive strategy to support sustainable agricultural practices (Warwade et al. 2018, Tesfaye et al. 2017, Sharma & Priya 2023). This heightened sensitivity stems from erratic rainfall patterns, extended dry spells, and the dual threats of both flooding and drought. Analyzing rainfall trends and drought patterns in Bihar is essential for understanding the state's vulnerability to drought events. Such research can lay the groundwork for developing effective early warning systems to reduce the adverse impacts on agricultural production and household consumption of these crops. These findings also provide valuable insights for policymakers to design strategies that strengthen climate resilience and ensure food security in Bihar.

Therefore, the primary objective of this study was to conduct a comprehensive analysis of rainfall variability and assess flood and drought conditions in Bihar's Magadh Division. This study aimed to evaluate the severity of drought across the districts within the division, identify trends and change points in rainfall data, analyze the frequency and return period of droughts, and pinpoint drought-prone areas in the region. Accordingly, this study aimed to detect and quantify spatiotemporal rainfall variability and meteorological drought patterns in Bihar using a 51-year (1971–2021) gridded IMD rainfall dataset, employing multi-scale drought indices and trend analyses to ensure objective and comparable measurements. These findings underscore the need for reliable, location-specific data to anticipate and mitigate the adverse effects of climate change. By integrating research with adaptation strategies, policymakers can effectively address climate-induced vulnerabilities and develop resilient systems to safeguard the future of the region.

2. STUDY AREA

The study area for this research is the Magadh division in Bihar, formed by the Bihar State Government through the merger of four districts: Gaya, Nawada, Aurangabad, and Jehanabad (Fig. 1). Geographically, the Magadh division lies between latitudes 24°30' and 25°15' North and longitudes 84°00' and 86°03' East. The western boundary of the division is delineated by the Sone River, while the southern boundary adjoins the state of Jharkhand, which is part of Peninsular India. To the north, the Magadh division shares its boundary with the Patna division, and to the east, it is bordered by the Munger Division. This strategic geographical positioning highlights the division's significance within the broader regional framework of South Bihar and the Ganga Basin, both in terms of its natural resources and socio-economic importance. The study region has a tropical continental monsoon climate. Most precipitation occurs during the monsoon months of June to October. From November to March, fine, dry weather prevails. Winters are cold, and summers are very hot. The study region experiences an average annual rainfall of approximately 1168 mm, indicating a relatively high level of precipitation throughout the year. In terms of temperature, the area records a mean annual value of approximately 24.67°C, reflecting generally warm climatic conditions (Mishra 2020). The state features relatively flat topography and predominantly hot and humid climatic conditions, as it lies within the subtropical and temperate zones. These regions are characterized by hot, arid summers and a brief rainy season, and experience a semi-arid climate, rendering them highly vulnerable to drought. These climatic constraints pose substantial challenges to agriculture and water resource availability in the region. Recurrent droughts significantly reduce crop productivity, threatening the livelihoods of communities that depend on agricultural activities. Agriculture drives the state's economy, with rice being the dominant crop.

3. MATERIALS AND METHODS

3.1 Data Used

High-resolution gridded rainfall data were downloaded from the India Meteorological Department (IMD, Pune) at a 0.25° × 0.25° grid spacing and are available for the period 1970–2020 (51 years). The dataset was used for homogeneity analysis (detecting change points), trend analysis, rainfall variability analysis, and drought assessment. The IMD gridded rainfall dataset used in this study underwent rigorous quality control and gap-filling procedures by the IMD. As a result, the dataset contained no missing values that required further correction. Therefore, we did not perform any additional interpolation, and no data points were omitted during processing. This ensured that all analyses were based on a consistent, quality-assured rainfall record. The study area was covered by 17 grids (Table 1) at a resolution of 0.25° × 0.25°. Grids G1–G10 lie in Gaya, G11, G12, and G14 in Aurangabad, G13 and G15 in Nawada, G16 in Arwal, and G17 in Jehanabad. A workflow diagram summarizing the data processing and analysis sequence used in this study is presented in Fig. 2.

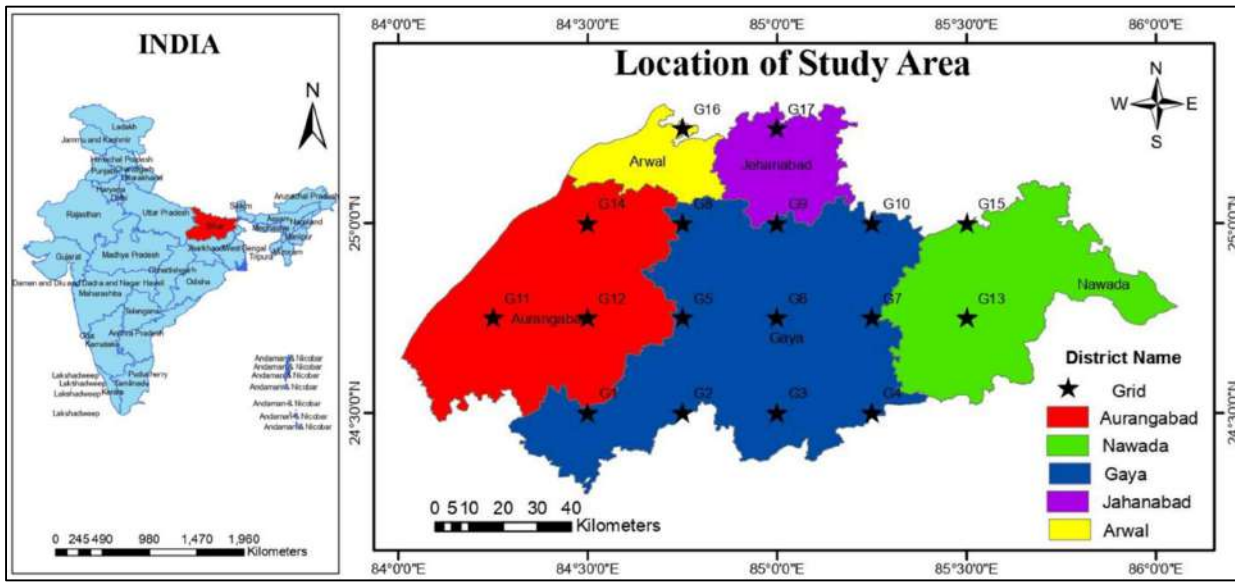


Fig. 1: Study area map showing the Magadh region with the districts of Gaya, Nawada, Aurangabad, and Jehanabad.

3.2 Homogeneity Analysis

The methodology for assessing series quality incorporated relative homogeneity tests using reference series, as outlined by Wijngaard et al. (2003), as follows: The classification criteria were a) Class A: Useful: Series that reject one or none of the null hypotheses across four tests at the 5% significance level are deemed homogeneous and suitable. b) Class B: Doubtful: Series rejecting two null hypotheses at the 5% significance level are categorized as inhomogeneous and require critical inspection before analysis. c) Class C: Suspect: Series rejecting three or all null hypotheses are classified as inhomogeneous and may be excluded from further analysis.

3.3 Pettitt's Test

This is a non-parametric test that provides an assessment of the null hypothesis (H0) and an alternative hypothesis (H1). H0 indicates homogeneous data, and H1 indicates data that cause a shift. This provides an indication of a change point when the location parameter undergoes a shift. The test statistics (Xy) used in the test are described in Equation 1:

$$\mathbf{X_y} = \mathbf{2}\sum_{i=1}^{y} \boldsymbol{r_i} - \boldsymbol{y(n+1)} \quad \boldsymbol{y = 1, 2, \ldots\ldots\ldots\ldots n} \qquad \ldots(1)$$

The break occurs in year k when

$$\boldsymbol{X_k} = \boldsymbol{\max_{1 \le y \le n}} \left|\boldsymbol{X_y}\right| \qquad \ldots(2)$$

The value is then compared with the critical value proposed by Pettitt (1979).

3.4 Standard Normal Homogeneity Test

The Standard Normal Homogeneity Test (SNHT) evaluates the null hypothesis (H0), which assumes that the dataset is homogeneous, against the alternative hypothesis (H1), which proposes that a notable shift occurs in the location parameter at a specific point in time, labelled moment y. To assess this, the test uses the statistic T(y), which compares the average of the initial y observations with the average of the remaining (n–y) observations. This can be expressed by Equation 3:

$$T_y = y\bar{z}_1 + (n-y)\bar{z}_2 \,, y = 1,2, \ldots\ldots\ldots\ldots n \qquad \ldots(3)$$

where $\bar{z}_1$ and $\bar{z}_2$ are the average values of the observed feature before and after *y*:

$$\bar{z}_1 = \frac{1}{y}\sum_{i=1}^{n} \frac{(Y_i - \bar{Y})}{s} \qquad \ldots(4)$$

$$\bar{z}_2 = \frac{1}{n-y}\sum_{i=y+1}^{n} \frac{(Y_i - \bar{Y})}{s} \qquad \ldots(5)$$

The year y is identified as the break year if the value of T(y) reaches its maximum value. The null hypothesis is rejected if the test statistic T(y) exceeds the critical value, which is determined based on the sample size.

$$T_0 = max_{1 \le y \le n} T_y \qquad \ldots(6)$$

3.5 Buishand`s Test

It is a non-parametric method used to determine whether a change point occurs within a dataset, indicating a shift in the location parameter. Under the null hypothesis (H_0), the data are considered homogeneous with no change point present, whereas the alternative hypothesis (H_1) indicates that a change point exists. The adjusted partial sum is expressed as follows (Equation 7):

$$S_0^* = 0 \; and \; S_y^* = \sum_{i=1}^{y} (Y_i - \bar{Y})$$

$$y = 1, 2, \ldots\ldots\ldots\ldots n \qquad \ldots(7)$$

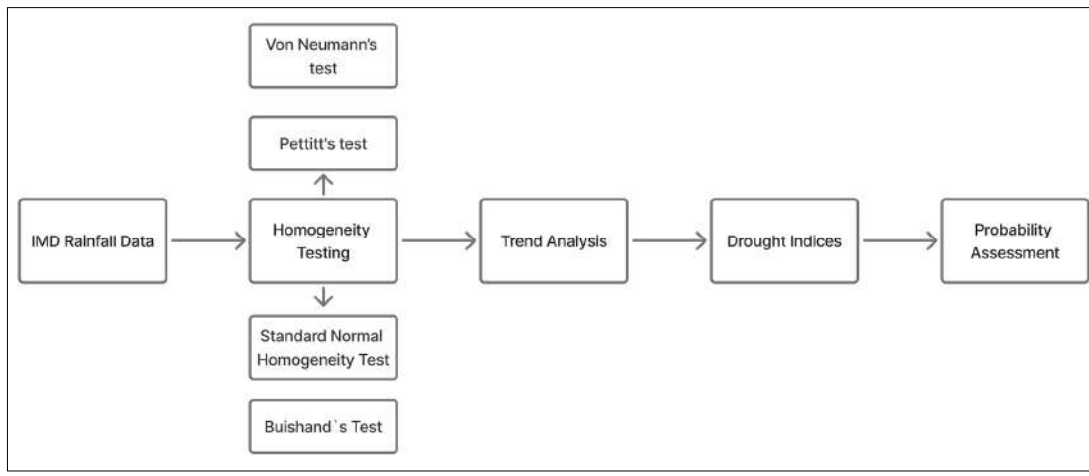


Fig. 2: Workflow diagram illustrating the data processing and analysis sequence, beginning with the IMD gridded rainfall data and proceeding through homogeneity testing, trend analysis, drought index computation, and probability assessment.

When the series is homogeneous, the value of S_y^* fluctuates around zero. A break in year y is identified when S_y^* reaches its maximum (indicating a negative shift) or minimum (indicating a positive shift). The rescaled adjusted range, R, is calculated as

$$R = \frac{(max_{0\le y\le n}S_y^* - min_{0\le y\le n}S_y^*)}{s} \quad \ldots(8)$$

$R/\sqrt{n}$ is then compared with the critical values given by Buishand (1982).

3.6 Von Neumann's Test

This method evaluates variability by comparing the mean square of successive (year-to-year) differences with the overall variance of the dataset. This comparison forms the basis of the test statistics, which can be mathematically expressed as follows (Equation 9):

$$N = \frac{\sum_{i=1}^{n-1}(Y_i - Y_{i+1})^2}{\sum_{i=1}^{n}(Y_i - \bar{Y})^2} \quad \ldots(9)$$

When the data sequence is homogeneous and does not change, the expected value of E(N) is 2. In contrast, the presence of a structural break within the sample reduces the value of N to below 2. If the computed value of N remains close to or above 2, this suggests that the observed fluctuations are the result of frequent short-term shifts in the mean, rather than a clearly defined structural break in the series.

3.7 Trend Analysis

Trend analysis refers to systematic changes observed in a variable over time, which can be identified using parametric and non-parametric statistical techniques. The precipitation data were prepared as seasonal time series: annual monsoon (June–September), pre-monsoon (March–May), post-monsoon (October–December), and winter (December–February), to examine potential seasonal variations. One of the widely applied approaches for detecting such trends in climatology and hydrology is the Mann–Kendall test, which is a non-parametric statistical method. The Mann–Kendall (MK) test and Sen's slope estimator were cross-validated using a consistent significance criterion. A two-tailed significance level of $\alpha = 0.05$ was applied using the critical threshold to determine the presence of a statistically significant trend. Sen's slope was then calculated as the median of all pairwise slopes, and its 95% confidence interval was determined. A trend was accepted as significant only when the MK test indicated significance at α=0.05, and the confidence interval of Sen's slope did not include zero, ensuring consistent cross-validation of direction and magnitude. In this test, the null hypothesis (H_0) assumes the absence of any trend, whereas the alternative hypothesis (H_1) indicates the presence of a significant trend.

Considering a dataset with n observations (x_1, x_2, x_3, …, xn), the Mann–Kendall test statistic S is defined as follows:

$$S = \sum_{i=1}^{n-1}\sum_{j=i+1}^{n} sgn\left(x_j - x_i\right) \quad \ldots(10)$$

where n is the number of observations, xj denotes the jth observation, and sgn (θ) refers to the sign function, which is defined as follows:

$$Sgn(\theta) = \begin{cases} 1 & if\ \theta > 0 \\ 0 & if\ \theta = 0 \\ -1 & if\ \theta < 0 \end{cases} \quad \ldots(11)$$

Assuming that the data follow an independent and identically distributed pattern, the expected value and variance of the S statistic can be expressed as

$$E[S] = 0 \quad \ldots(12)$$

$$Var(S) = \frac{N(N-1)(2N+5) - \sum_{k=1}^{n} t_k(t_k-1)(2t_k+5)}{18} \quad \ldots(13)$$

Z-statistics can be computed as follows:

$$Z = \begin{cases} \frac{S-1}{\sigma} & if\ S > 0 \\ 0 & if\ S = 0 \\ \frac{S+1}{\sigma} & if\ S < 0 \end{cases} \quad \ldots(14)$$

The null hypothesis was evaluated at a significance level of 5%. A positive Z-value indicates an upward trend, whereas a negative Z-value indicates a downward trend.

Sen's slope technique is commonly applied to estimate the magnitude of trends in hydro-meteorological time series. The slope (Ti) of each pair of data was computed as follows:

$$T_i = \frac{x_j - x_k}{j-k} \quad for\ i = 1,2,\ldots\ldots\ldots N \quad \ldots(15)$$

where xj and xk are the data values at times j and k (j > k), respectively.

3.8 Assessment of Metrological Drought

The meteorological drought aspects of the study area were analyzed using rainfall data. A rainfall departure analysis was performed to assess drought occurrence and measure annual rainfall shortfalls. A particular year was considered a drought year if the recorded annual rainfall in that area was more than 25% below the long-term average (Keyantash & Dracup 2002). For the Magadh Division, this analysis was conducted using rainfall records spanning 51 years (1970–2020) across all 17 grids in the region. Based on this dataset, drought years were identified and the mean frequency of droughts

was estimated. The annual departure analysis included the following steps:

a) Determination of mean (Xm) for a set of n annual rainfall data x. Xm = sum of x divided by n

b) Calculate departure (Di) by subtracting the mean (Xm) from the individual annual rainfall, Di = Xi –Xm

c) Calculate the departure percentage (Di)% = Di/Xm

In this study, drought severity was classified based on the percentage deviation from normal rainfall into the following severity classes:

a) Moderate drought: percentage annual rainfall departure between 25 and 50 percent

b) Severe drought: percentage annual rainfall departure between 50 and 75 percent

c) Extreme drought: percentage of annual rainfall departure greater than 75 percent.

3.9 Probability Distribution of Annual Rainfall

Assessing the probability distribution of yearly rainfall is crucial for estimating the frequency of different rainfall ranges with a high degree of accuracy and reliability. To identify drought-prone areas within the Magadh region, the likelihood of receiving at least 75% of the average annual rainfall was calculated. According to the guidelines of the Central Water Commission (CWC), a region is classified as drought-prone if the probability of receiving 75% of normal rainfall is below 80%. The drought categories used in this study followed the official IMD classification based on rainfall anomaly percentages and the CWC guidelines for hydrometeorological drought assessment. Accordingly, rainfall departures between –19% and –25% were classified as 'moderate drought,' and departures below –25% as 'severe drought,' and the corresponding SPI-based thresholds were aligned with the IMD/CWC definitions. The probability of the distribution of annual rainfall was analyzed using the following procedure:

a) Computation of mean rainfall at each grid, $X_m = \frac{\sum(x)}{n}$

b) The dataset was arranged in descending order based on rainfall magnitude.

c) Ranking the dataset, that is, m = 1,2,3, up to the last rainfall record.

d) Determination of cumulative probability by Weibull's formula, which is given as

$$P = \frac{m}{n+1} \times 100$$

e) Calculated probability based on 75 percent of the normal rainfall data, i.e.,

$$P_{75} = X_m \times \frac{75}{100}$$

If P75 is less than 80 percent, the area is considered drought-prone; if P75 is greater than 80 percent, the area is not considered drought-prone.

4. RESULTS AND DISCUSSION

The analysis of rainfall trends over the semi-arid climatic region of Bihar revealed a complex pattern of changes across different seasons. Long-term trend analysis from 1970 to 2020 indicated a significant decrease in annual and monsoon rainfall. This declining trend is consistent with the findings of other studies, which also reported a significant reduction in annual and monsoon rainfall, particularly after a shift change point. The variability in rainfall patterns is further complicated by high coefficients of variation (CV) for the pre-monsoon, winter, and post-monsoon seasons across all districts, indicating significant spatial and temporal variability (Singh et al. 2024a). Innovative trend analysis suggests either no trend or a negative trend in most districts, with recent years showing a more pronounced negative trend (Singh et al. 2024b). However, departure and probability distribution analyses focused exclusively on the southwest monsoon and annual rainfall across all grids. The analysis utilized 51 years (1970–2020) of data from the Indian Meteorological Department (IMD). Rainfall components are critical for drought management and planning purposes. Departure and probability distribution analyses were applied to assess drought frequency and return periods, and to identify drought-prone grids. Trend analysis and correlation were conducted using the non-parametric Mann-Kendall test, while Sen's slope estimator quantified the magnitude and percentage of slope changes.

4.1 Homogeneity Test

The reliability of climatic data is crucial for hydrological and meteorological analyses, and detecting inhomogeneities is a key step in ensuring data quality (Ribeiro et al. 2016, Singh et al. 2024a). Several studies have emphasized the complementary nature of these tests. By employing multiple tests, a study can gain a more comprehensive understanding of data integrity. However, the variation in the test results also underscores the need for further investigation to corroborate the findings and understand the specific causes of the detected inhomogeneities, such as natural climatic variability or changes in observational practices. Thus, Pettitt's, SNHT, Buishand's, and von Neumann (VN) tests were applied to test homogeneity and to determine the probable change year. The findings illustrate the homogeneity test for the annual rainfall series of the Magadh Division (Table 1). The

Table 1: Grid number with respect to the latitude and longitude values of the study area district.

Serial No	Grid No	Latitude	Longitude	District
1	G1	24.5	84.5	Gaya
2	G2	24.5	84.75	Gaya
3	G3	24.5	85	Gaya
4	G4	24.5	85.25	Gaya
5	G5	24.75	84.75	Gaya
6	G6	24.75	85	Gaya
7	G7	24.75	85.25	Gaya
8	G8	25	85.75	Gaya
9	G9	25	85	Gaya
10	G10	25	85.25	Gaya
11	G11	24.75	84.25	Aurangabad
12	G12	24.75	85.5	Aurangabad
13	G13	24.75	85.5	Nawada
14	G14	25	85.5	Aurangabad
15	G15	25	85.5	Nawada
16	G16	25.25	84.75	Arwal
17	G17	25.25	85	Jehanabad

analysis revealed that among the 17 analyzed grids, different statistical homogeneity tests yielded varying results regarding the inhomogeneity of the annual precipitation data. The semi-arid climatic region of Bihar, India, exhibits significant variability in meteorological trends and drought patterns, which are influenced by both natural and anthropogenic factors. The analysis of precipitation trends from 1970 to 2020 revealed a moderate coefficient of variation (CV) and standard deviation (SD) for both monsoon and annual rainfall, with higher variability observed in the pre-monsoon, winter, and post-monsoon seasons across districts, except for Begusarai and Jahanabad (Singh et al. 2024b).

Pettitt's test and the Standard Normal Homogeneity Test (SNHT) identified three grids (G5, G10, G15) and two grids (G7, G15), respectively, as being inhomogeneous. In contrast, Buishand's test and the Von Neumann ratio test (VN) indicated a higher number of grids with inhomogeneity, identifying six (G4, G5, G7, G8, G10, and G15) and seven grids (G3, G4, G6, G7, G9, G13, and G15), respectively. The variability in the results highlights the unique sensitivity and focus of each test in identifying inhomogeneities within the climatic datasets. Pettitt's and SNHT tests are particularly adept at detecting abrupt shifts or single change points in data, which may explain why they flagged fewer grids than the other tests. These methods are particularly effective for identifying step changes caused by factors such as station relocation, changes in instrumentation, or sudden climatic anomalies. The Buishand test is tailored to assess shifts in the mean over time, whereas the Von Neumann (VN) test evaluates the randomness of data to identify broader inconsistencies. Their ability to capture trends or gradual shifts likely explains why they identified a greater number of grids as being inhomogeneous. The VN test flagged the highest number of inhomogeneous annual rainfall data series, reflecting its sensitivity to deviations from homogeneity in the dataset. However, it is important to note that the VN test only determines whether the data series is serially correlated by testing the null hypothesis; it does not pinpoint the specific year in which the change occurred. In contrast, Pettitt's test, a non-parametric method widely used for detecting change points in hydrological and climatological studies, identified the probable years of change for the rainfall data series in grids G5, G10, and G15 as 1990, 1990, and 1991, respectively. This difference highlights the complementary utility of these statistical methods, where the VN test offers a preliminary screening for serial correlation, and Pettitt's test provides temporal localization of abrupt changes within the dataset. The Standard Normal Homogeneity Test (SNHT) identified 1987 and 1991 as the years of significant change for stations G7 and G15, respectively. Similarly, the Buishand Range Test revealed change points for multiple stations: G4 in 1987, G5 in 1990, G7 in 1989, G8 in 2003, G10 in 1990, and G15 in 1991. These tests indicate temporal shifts in the homogeneity of climatic or hydrological data, reflecting possible changes in environmental factors, measurement practices, or regional climatic dynamics during these periods (Zhang et al. 2013). Fig. 3 shows the probable change-point years identified in the annual rainfall series, determined through various homogeneity tests.

These results highlight significant shifts in rainfall patterns, which align with findings from previous research (Vicente Serrano et al. 2020, Wen et al. 2020, Saharwardi et al. 2022, Chong et al. 2022) on climatic variability and long-term hydrological trends. The detection of change points using multiple statistical tests strengthens the reliability of these observations, providing critical insights into the temporal variations in precipitation (Praveen et al. 2020). Thus, while planning water resources and monitoring droughts and floods in the area, priority should be given to G15, followed by G7. According to the Wijngaard classification framework, the annual precipitation data series for the Magadh Division was evaluated, revealing significant insights into grid-level reliability. The analysis identified 12 grids (G1, G2, G3, G5, G8, G9, G11, G12, G13, G14, G16, and G17) as "useful," indicating robust and reliable precipitation records at these locations. Conversely, grids G4, G5, and G10 were categorized as "doubtful," suggesting inconsistencies or limitations in data quality that necessitate further scrutiny. Additionally, two grids, G7

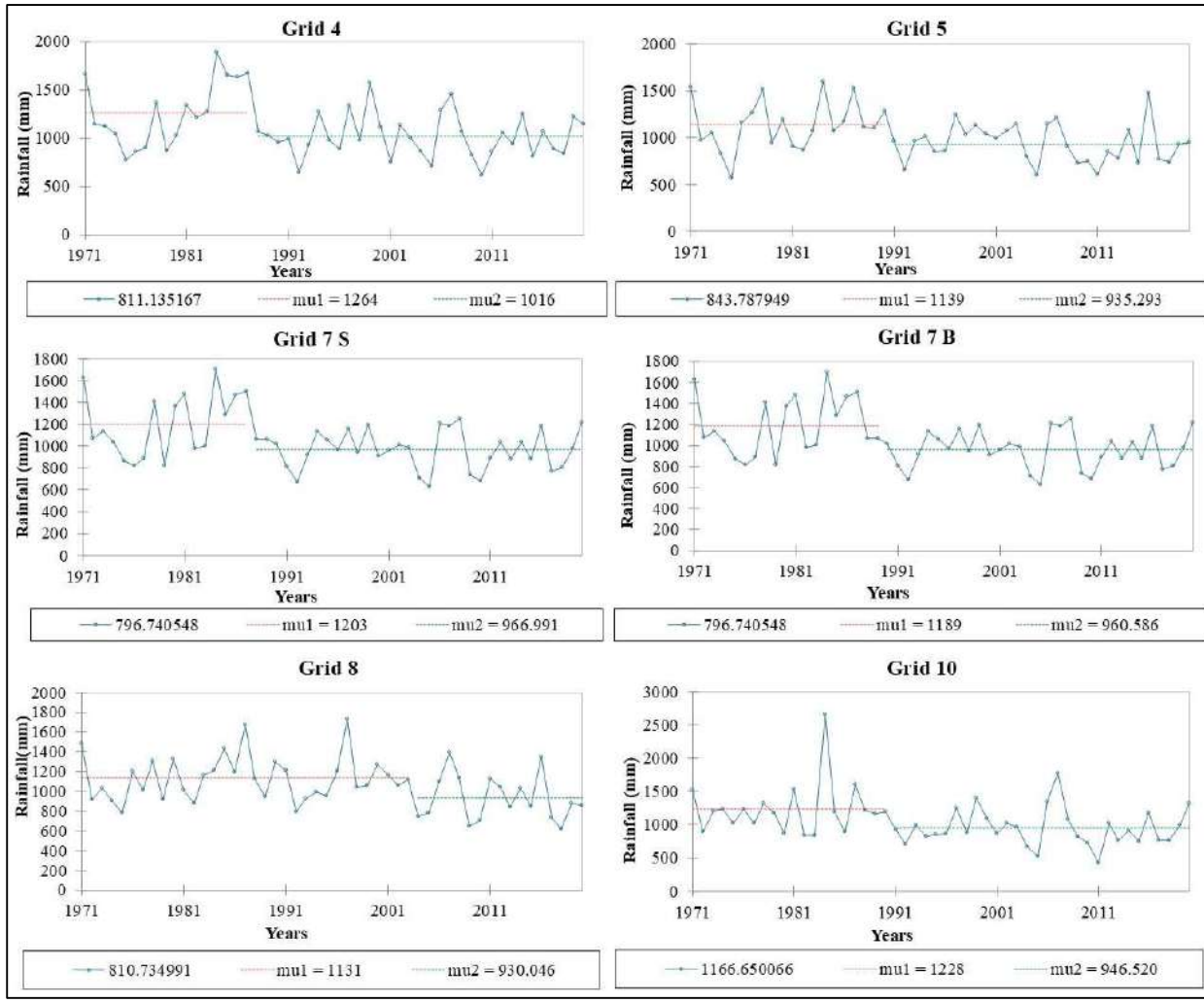


Fig. 3: Change year in annual rainfall in G4, G5, G7, and G8 by Buishand's test (mu1 and mu2 represent the mean rainfall before and after the change point, respectively). Change the year in the annual rainfall in G7 using the SNHT test. Change the year in the annual rainfall in G10 by Pettitt's and Buishand's tests.

and G15, were classified as "suspect," indicating potential anomalies or significant deviations in the precipitation records that could undermine their reliability (Larsen & Schönhuber 2018). Given these findings, strategic water resource planning and effective management of drought and flood risks in the Magadh Division should be prioritized in G15, followed by G7, owing to their critical classification. The homogeneity test of the total annual rainfall time series in the study area indicated that 71% of the stations were assigned to Class 1, 'useful', and 83% of the stations were found to be homogeneous at a significance level of 5%. Non-homogeneous stations for the years 1987-88 (G4), 1990-91 (G5), and 1990-91 (G10) are regarded as 'doubtful', while inhomogeneous stations for the year 1987-88 (G7) and 1991-92 (G15) are rated as 'suspect.' The spatially coherent change points around 1990–1991 likely reflected a large-scale climatic shift rather than isolated grid-level anomalies. This period coincides with several well-documented regional and global climate changes, including a transition in the Indian Summer Monsoon circulation, marked by altered monsoon depressions and moisture transport patterns. These broad-scale drivers can produce synchronized hydroclimatic responses across adjacent grids, thereby explaining the strong spatial coherence in the detected change years across Bihar. These grids require enhanced monitoring efforts, including the installation of more precise data collection systems, periodic reassessment of meteorological records, and integration with advanced hydrological modelling techniques (Sudriani et al. 2023). Such focused attention will help address uncertainties in precipitation patterns,

ensuring accurate forecasting and effective decision-making in regional water resource management.

4.2 Variability in Annual Rainfall Pattern (1970-2020)

The rainfall statistics for the entire study period (1970-2020) across all 17 grids in the Magadh Division are presented in Table 2. The results suggested that the maximum and minimum rainfall (mm) between different grids in winter (26.8 and 21.3), pre-monsoon (64.3 and 33.2), SW-monsoon (927.8 and 812.0), and post-monsoon (84.9 and 50.4) seasons, respectively. The maximum and minimum annual rainfall in the study area were recorded as 1094.7 mm and 930.9 mm, respectively. The results show that the annual average rainfall varies from 930.9 mm in the western region to 1094.6 mm in the eastern and southern parts of the study area. The average annual rainfall (AAR) in the study region is estimated to be 1,010.6 mm. Analysis of the rainfall distribution indicated that nearly half of the area, approximately 47%, received an annual total rainfall (ATR) below the mean value (Fig. 4a). Based on the mean and standard deviation of different time series, the highest coefficient of variation (CVs) in rainfall was found in winter, that is, 126.7%, and the lowest CV was found in the annual series, that is. 21.5%. The CVs for the SW-Monsoon data series ranged from 38.3% at grid 10 to 22.6% at grid 11, which follows the CV of the annual data series, that is, 33.5% at G10 and 21.5% at G11.

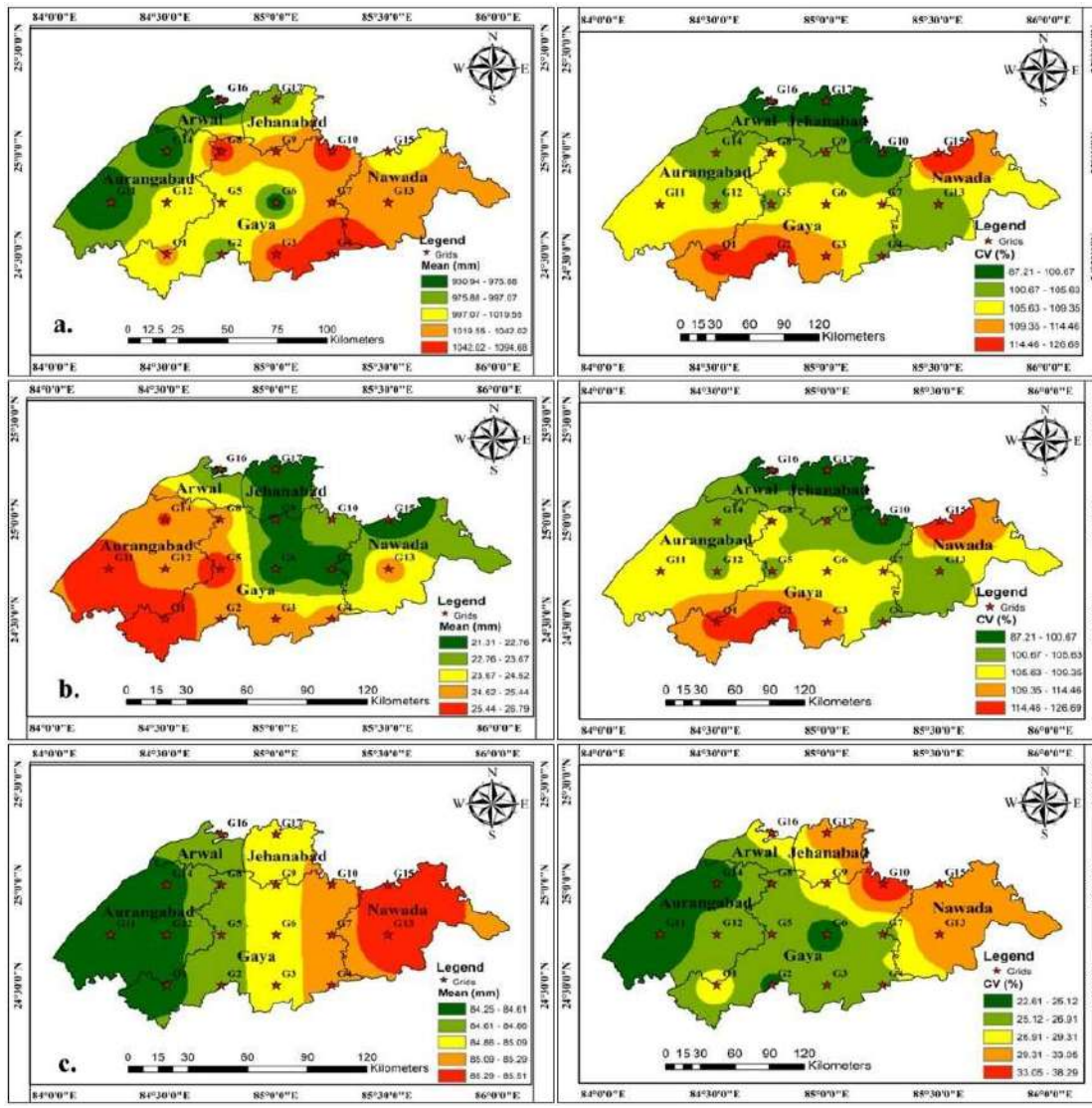


Fig. 4: a. Average annual rainfall and coefficient of variation in percentage. Mean winter rainfall and coefficient of variation (CV) in percentage. The mean southwest monsoon rainfall and CV with areal coverage in the study area between 1970 and 2020.

The findings demonstrated that there was more variability in rainfall over the Magadh Division during winter, followed by post-monsoon, pre-monsoon, SW-monsoon, and annual (Table 2). This could be due to the lower and non-uniform rainfall received during winter compared to the SW monsoon and annual rainfall. The analysis of the rainfall statistics in Table 2 reveals that the grids with heavy and frequent uniform rainfall exhibit the least variability, that is, 12.0% annually. In contrast, zones of lower rainfall were associated with higher variability in winter, at 39.5%. In addition, the results showed that the mean rainfall in the winter season varied from 21.3 mm in the middle part to 26.7 mm in the western and southern parts of the study area (Fig. 4b). The mean rainfall in the winter season for the entire study area was 24.1 mm, and 41% of the region had less than the mean rainfall in the study area. However, in the South-West monsoon, the mean rainfall is 812-927 mm with an average rainfall of 872 mm over the entire study period from to 1970-2020 (Fig. 4c). The variability found in the rainfall over the entire study area during the study period focuses on the need to find trends in different data series (Zakwan & Ara 2019, Gupta et al. 2022).

4.3 Variability in the Rainfall Pattern in the South-West (SW) Monsoon

For the southwest (SW) precipitation data series, the homogeneity of 17 spatial grids was evaluated using multiple statistical tests. Pettitt's and the Standard Normal Homogeneity Test (SNHT) identified grid G15 as exhibiting inhomogeneities. In contrast, Buishand's Range Test detected three grids, G4, G7, and G15, as inhomogeneous. Additionally, the Von Neumann Ratio (VNR) test showed that four grids, G3, G4, G7, and G13, demonstrated significant deviations from homogeneity. These results underscore the variability in detecting inhomogeneous grids across different statistical methods, emphasizing the necessity for a comprehensive approach to ensure the reliability of precipitation datasets in climate research and hydrological modeling (Vahab & Sankaran 2025). Pettitt's and SNHT tests identified 1991 as a significant change-point year at grid G15, indicating a possible shift in climatic or hydrological conditions. Furthermore, Buishand's test detected additional change points: 1987 at grid G4 and 1988 at G7. Analyzing the reliability of these grids using Wijngaard's classification revealed that most grids were reliable, except for G4 and G7, which were classified as doubtful, and G15, which was categorized as suspect. Despite this classification, G15 emerged as the most critical grid within the Magadh Division, warranting prioritized attention for water resource planning, particularly in the monsoon season. These findings underline the importance of robust grid-level analyses for developing targeted and effective water management strategies, as shifts in hydrological regimes can have profound implications for resource allocation and climate resilience. Previous research

Table 2: Rainfall statistics for the Magadh region were analyzed across 17 grids categorized by seasonal patterns: winter, pre-monsoon, southwest monsoon, post-monsoon, and annual rainfall.

Grid No	Winter		Pre-Monsoon		SW- Monsoon		Post-Monsoon		Annual	
	Mean	CV	Mean	CV	Mean	CV	Mean	CV	Mean	CV
G1	26.78	116.02	37.88	88.15	885.23	27.85	73.56	84.18	1023.5	25.5
G2	24.97	122.89	39.23	89.09	855.41	24.86	64.64	85.52	984.25	24.44
G3	25.4	110.74	49.29	90.22	893.84	26	78.81	72.94	1047.34	26.72
G4	25.16	104.58	64.34	86.88	920.28	26.5	84.91	81.56	1094.69	26.46
G5	26.3	104.66	44.97	80.24	874.17	26.4	68.07	83.71	1013.51	24.45
G6	21.33	108.26	44.66	86.31	831.8	23.47	65.85	89.16	963.64	22.89
G7	21.58	106.37	59.07	89.54	892.84	25.54	68.85	85.05	1042.34	23.75
G8	25.06	106.95	44.4	79.32	927.8	25.1	60.31	94.27	1057.57	23.19
G9	22.07	104.26	55.06	103.49	891.78	27.9	61.21	100.38	1030.13	26.95
G10	23.5	87.2	60.8	76.3	907.2	38.3	69.9	87.5	1061.4	33.5
G11	25.9	107.1	33.2	84.9	838	22.6	57.1	84	954.3	21.5
G12	25.1	104.8	43.4	76.1	870.9	25.7	62.9	81.8	1002.2	23.4
G13	25.1	102.5	55.9	78.4	880.4	31.4	71.3	84.4	1032.7	30
G14	25.5	103.3	39.5	77.4	840.1	24	51.1	85.8	956.2	22.2
G15	21.6	126.7	53.6	93.4	859.5	33	65	94.2	998.3	30.9
G16	22.6	95.9	45.9	79.3	812	27.3	50.4	99.2	930.9	25.5
G17	21.8	95	53.1	78.3	856.1	30.9	56.7	91.9	987.7	28.5

has also reported that the variability in the rainfall patterns of the southwest monsoon in Bihar from 1901 to 2020 indicates notable shifts in seasonal rainfall distribution, with a marked increase in daily rainfall intensity during the monsoon season, particularly in northern Bihar (Rashiq et al. 2024, Tiwari & Sarthi 2024, Kumar et al. 2022). Further research focusing on the period from 1950 to 2016 revealed a declining trend in monthly, seasonal, and annual rainfall, except for May, which exhibited an increasing trend (Guhathakurta et al. 2020). The study also reported high intra- and inter-annual variability, with an average coefficient of variation of 91.26%, and a significant concentration of rainfall (84%) during the monsoon months (Zakwan & Ara 2019). Additionally, a substantial decline in total rainfall over the last three decades (1986–2016) was observed, underscoring the need for effective rainwater harvesting and management strategies to mitigate potential water shortages in the region. These results highlight the identified probable change years, indicating potential shifts or anomalies in the dataset. The detected change years are further visualized in Fig. 5, which provides a comparative representation that enhances clarity and supports pattern recognition. This integrative approach combines statistical and graphical methods to ensure a comprehensive understanding of the spatial and temporal variations in the data, as supported by relevant studies that emphasize the importance of homogeneity analysis in detecting climate trends and anomalies.

4.4 Mann-Kendall Test-Based Trend Analysis and Change Percentage

During the homogeneity analysis of the annual data series, the change point was found to be quite variable, but the most probable change year was 1990, as observed by different tests over two grids, that is, G5 and G10. Since the most probable change year is 1990, the entire data series was divided into two parts by breaking the series before and after 1990. Thus, three data time series were obtained, namely TS1, TS2, and TS3, for the year 1970-2020. 1970-1990 and 1991-2020, respectively. The Mann-Kendall test was applied to monthly rainfall data for different time periods, that is, annual, winter, pre-monsoon, and post-monsoon periods, to detect significant and non-significant trends in all three series of data at a 95% significance level. The percentage change in rainfall was also determined.

4.4.1 Trend Analysis and Change Percentage for TS1 (1970-2020)

The Mann-Kendall test was applied to the monthly rainfall data for different periods of the first time series (TS1) for all grids, and the corresponding Z values. The corresponding table also contains the percentage change in rainfall calculated using the mean for all periods at each grid point. The findings suggest that almost all grids and periods exhibit a negative or positive trend, except for G3, which shows no trend during the monsoon. Moreover, a significant negative trend was observed at G5 in both the annual and monsoon rainfall periods, with Z values of -2.18 and -2.08, respectively. A similar significant negative trend was observed at G10 and G15 for both periods, with Z values of -2.57, -2.18, and -2.08, -2.0, respectively. A positive significant trend was observed for the pre-monsoon period, with a Z value of 2.39, and a negative significant trend was observed in the post-monsoon period, with a Z value of -2.01 at G9. No significant trends in winter season rainfall were observed at any grid. The findings suggested that the highest

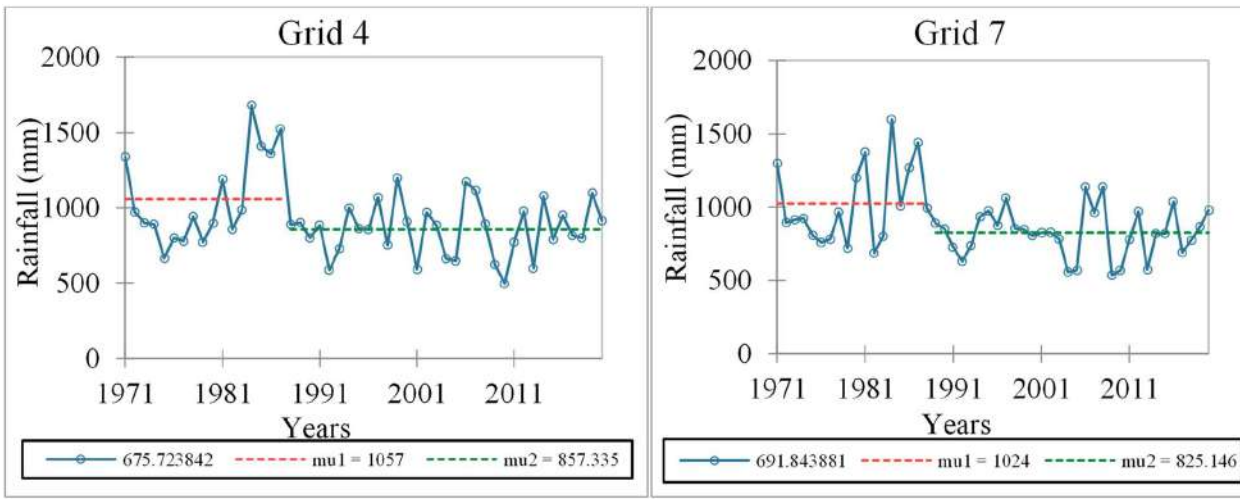


Fig. 5: Change year in the SW-Monsoon rainfall series in G4 by Buishand's test (mu1 and mu2 represent the mean rainfall before and after the change point). Changing year in the SW-Monsoon rainfall series in G7 by Buishand's test.

deficiency from the mean annual rainfall was observed at G15 with a percentage change of -34.41, followed by G10 (-30.61 %), and G5 (-25.83 %). A slight increase in rainfall from the mean annual was observed at Grid 6 (0.25 %) and G9 (2.91 %). A similar change was observed in monsoon rainfall, with the highest deficiency at G10 (-28.29%), followed by G15 (-27.99%) and G5 (-26.76%). Deficiencies were observed in the monsoon rainfall compared to the mean at other grids, except for G3, G9, and G17, where a slight increase was observed. A percentage increase from the mean was observed at all grids except grids 4 and 10 for the pre-monsoon season (Fig. 6). These grids may have experienced meteorological anomalies such as dry winds, insufficient convective triggers, or shadowing effects caused by nearby geographical features. The highest increment occurred in G9 (88.09%), whereas the lowest occurred in G15 (9.57%). The significant increase at G9 suggests the potential influence of localized convectional activities, where heating patterns during the pre-monsoon period result in increased rainfall. Variations in topography, such as the presence of elevated regions or valleys, may affect rainfall distribution. Grids with less development may exhibit enhanced rainfall owing to lower heat retention and increased surface evaporation, which supports the formation of convective rain. In the post-monsoon season, low rainfall was observed across all grids. G9 showed the highest deficiency (-75.40%), followed by G8 (-69.34%) and G17 (-63.60%). The least deficient grids were G13 (-11.30%), G12 (-19.96%), and G6 (-22.54%), respectively. Inconsistent monsoon withdrawal can reduce post-monsoon rainfall. The post-monsoon season often sees rainfall influenced by cyclonic systems, which may have been less active or bypassed the region. G9's extreme deficiency may be related to specific local factors, such as a significant decrease in moisture-laden winds or geographical barriers that disrupt cloud formation. This study indicates that a combination of meteorological, topographical, and anthropogenic factors influences rainfall variability across grids. Seasonal shifts in wind patterns, moisture availability, and disturbance tracks likely contributed to the observed changes in percentage. Grids with high variability (e.g., G9 and G15) may require further investigation to mitigate the impacts of rainfall deficits or excesses.

4.4.2 Trend Analysis and Change Percentage for TS2 (1970-1990)

The Mann-Kendall test was applied to the monthly rainfall data for different periods of the second time series (1970-1990) for all grids, and their corresponding Z values. It was observed that all grids exhibited some trends, either positive or negative, in different periods, except for Grid 10, which showed no trend for annual periods, and Grid 1, which showed no trend in the pre-monsoon periods. No other grids exhibited any significant positive or negative trends in any period, except G17, which exhibited a significant positive trend during the monsoon season with a Z value of 1.99. The results also show the percentage change based on the

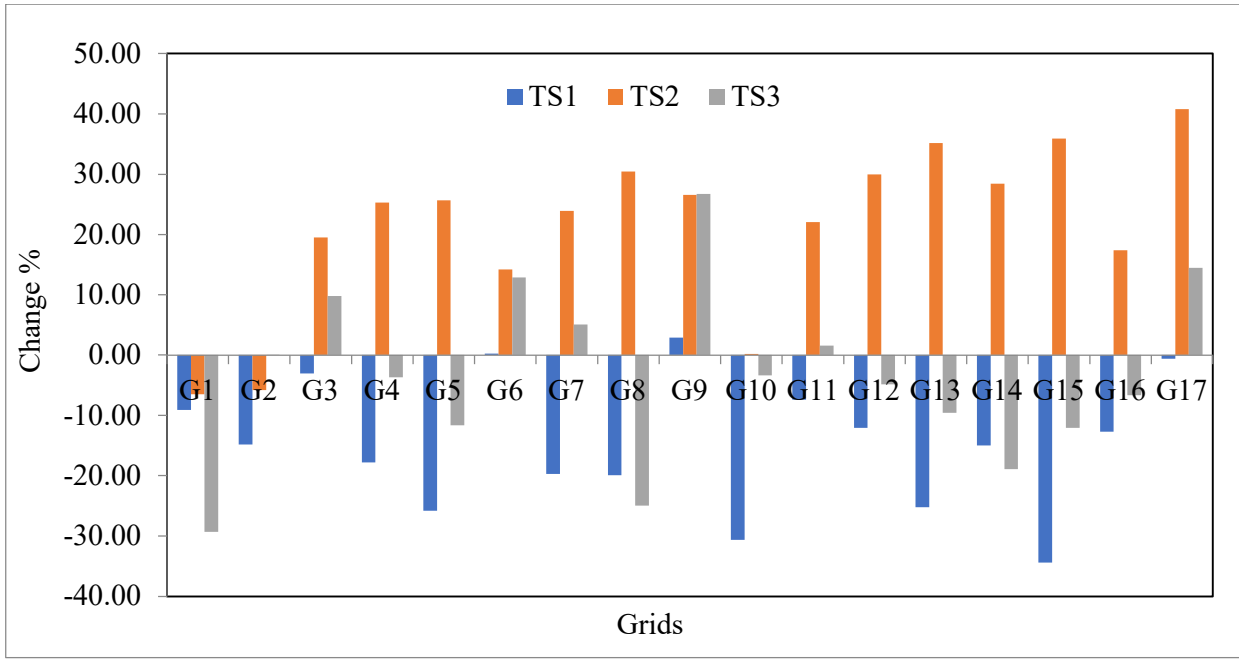


Fig. 6: Percentage change in annual rainfall for different time series of all data grids.

sen-slope value. Based on the observations, it was identified that periods such as annual and monsoon showed an increase in rainfall at all grids, except for G1 and G2, where a slight decrease in rainfall was observed. The highest increase in annual rainfall from the mean was observed at G17, with a percentage change of 40.78, whereas the lowest increment was observed at grid 10, with a change of 0.21%. Similarly, for monsoon periods, G17 was identified as the grid with the highest increment in rainfall from the mean, with a change of 50.76%, and a change of 2.66%; grid 10 was observed as the grid with the lowest increment. Correspondingly, the highest percentage change for the pre-monsoon period, which showed an increase in rainfall from the mean at all 17 grids, was observed at G5 with a value of 100.47%. The lowest increment was observed in Grid 1, with a change of 0.81 percent. In the post-monsoon period, grids G4, G13, and G15 exhibited an increase in rainfall, with percentage values of 5.34, 37.80, and 5.08, respectively. In contrast, the remaining grids showed a decrease in rainfall from the mean value. The most severe drought in post-monsoon rainfall was observed in G10, with a value of -92.44%, and the lowest deficiency was observed in G5, with a change percentage value of -6.03. From the same table, similar Fig.s have been observed for the winter season, where each grid shows a deficiency in rainfall, with the highest decrement observed at G9, at a value of -102.04%, and the lowest at G15, with a change of -21.11%.

4.4.3 Trend Analysis and Change Percentage for TS3 (1991-2020)

The Mann-Kendall test was applied to the third time series (1991-2020), and the corresponding Z values, along with the percent change in rainfall from the mean. Positive or negative trends were observed at different grids for different periods, except at G2 during the annual, G3 and G11 during the monsoon, G13 during the post monsoon, and G16 during the winter, where no trend has been observed. Moreover, no significant trends were observed in the annual, monsoon, post-monsoon, or winter periods. In contrast, only a few significant trends were observed during the pre-monsoon period at G9, G16, and G17, with Z values of 2.82, 2.19, and 2.32, respectively. Additionally, during the pre-monsoon periods, every grid exhibited positive periods, except for Grid 12, where a slight negative trend was observed. Conversely, during the post-monsoon periods, negative trends were observed at all grids except grids 6 and G13. The annual periods for TS3 showed a mixed result of decrement and increment in rainfall from the mean, with a maximum increment of 26.75% at G9 and a minimum increment of 0.03% at G2. In comparison, the maximum deficiency of rainfall has been observed at G1, with a percentage change of -29.29%, and the minimum deficiency was -3.67 % at G4. Similarly, during the monsoon period, a maximum increment of 25.47% was observed at G9, whereas G7 observed a minimum increment in rainfall, with a change of 0.64%. In contrast, as positive trends were observed at different grids during the pre-monsoon period, the highest increment was observed at G9, with a change of 123.48%, and the lowest increment of 3.81% was observed at G11. Correspondingly, during the post-monsoon period, negative trends were observed in all grids except G6 and G13. Specifically, a 1% change was observed at G6, whereas no trend was observed at G13. In comparison, the highest deficiency was observed at G4, with a change percentage of -82.08%, and the minimum deficiency was observed at G12, with a change percentage of -0.63%. In addition, during the winter period, no change in rainfall was observed at G15 and G16, whereas the highest increment was found at G2, with a change percentage of 35.33%. G8 showed a 1.07% change. In contrast, the highest deficiency was observed at G10, with a change percentage of -44.40%, whereas the minimum deficiency was observed at G12, with a change percentage of -3.92%.

4.5 Drought Variability in the Study Region

Precipitation patterns, climate variability, and anthropogenic activities influence drought variability in the semi-arid climatic region of Bihar. The region has experienced significant shifts in rainfall patterns over the past century, with increased drought and flood frequency and intensity due to climate change (Rashiq et al. 2024, Sharma & Priya 2023). The return periods of droughts, drought severity, and number of drought years for annual and seasonal (SW monsoon) rainfall, respectively, for the entire study period (1970-2020). Thus, it was clear that for G1, moderate droughts occurred during the years 1981, 1992, 2001, 2004, 2005, 2017, and 2018, whereas severe drought occurred in 2009 for annual rainfall. Similarly, for seasonal rainfall, moderate droughts were observed in 1981, 1983, 1992, 2001, 2004, 2005, and 2010, whereas severe droughts occurred in 2009 and 2013. The return period of moderate drought is approximately one drought in six to seven years, whereas for severe drought, it is one drought in 51 years for both annual and seasonal rainfall. For the annual time series data, the G1, (G13), G15, and G17 grids showed severe droughts during 2009, (1975, 2004), 1992, and 2005, respectively. G15 experienced almost one drought every 3 to 4 years. Similarly, for the SW monsoon time series data, grids (G1), (G13), and (G17) showed severe droughts during (2013,2009), (1975, 2004), and 2005, respectively. G17 suffered almost one drought every 3–4 years. The study revealed that the probability of receiving at least 75% of the average annual rainfall across different grids in the division ranged between 80.8% and

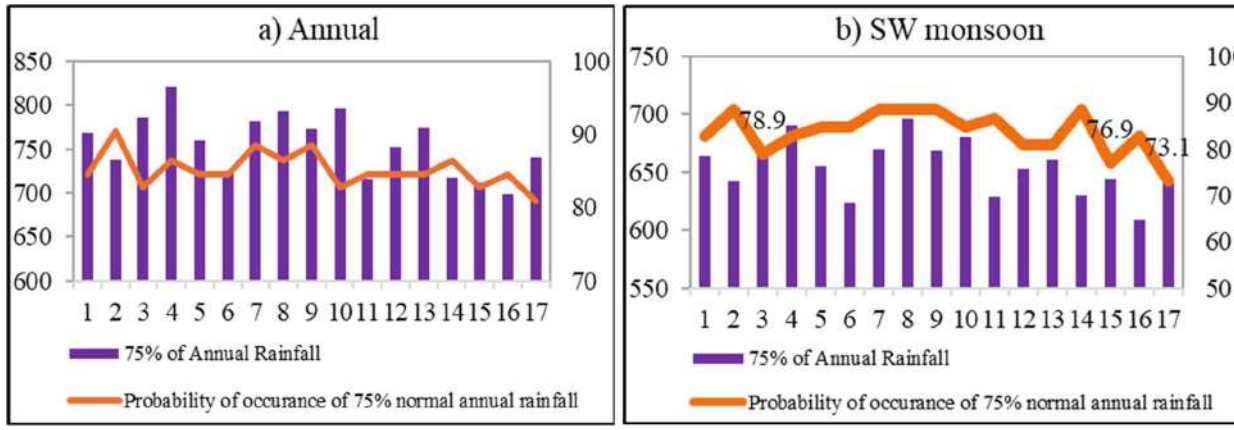


Fig. 7: Probability of the occurrence of a. annual rainfall and b. Southwestern monsoon rainfall (mm).

90.4%. Because the probability remained above 80% in all grids, none of them could be classified as drought-prone (Fig. 7a). However, when examining the probability distribution of southwest monsoon rainfall, the chances of receiving 75% of the normal rainfall varied from 73.1% to 88.5% across the grids (Fig. 7b). Within the Magadh Division, three grids, G3 (78.9%), G15 (76.9%), and G17 (73.1%), fell below the 80% threshold, indicating that these locations are vulnerable to drought conditions. A previous study (Rashiq et al. 2024) revealed significant variability in seasonal rainfall patterns in Bihar, with a notable change in pre-monsoon and post-monsoon rainfall observed in the second epoch (1961–2020). It highlights the significant alterations in rainfall patterns, with extreme weather events, which have led to concerns regarding floods and droughts in the study region.

5. CONCLUSIONS

This study examined rainfall variability, including trends in annual, seasonal, and extreme rainfall, as well as shifts in rainfall patterns, across the Magadh region of Bihar, India. The analysis revealed significant variations in rainfall patterns over time and space, characterized by a distinct change point that reflected shifts in trends and characteristics. In particular, there was a pronounced change in seasonality across all seasons, with the monsoon and post-monsoon periods showing the most substantial shifts, emphasizing the evolving dynamics of rainfall in the region. These findings suggest that rapid urbanization and climate change are likely driving these changes. This study also emphasizes the significance of understanding how decadal climate variability influences regional rainfall patterns. These climate drivers may intensify the frequency and severity of natural disasters, such as droughts, which could worsen water scarcity and create challenges for agriculture in the Magadh region of Bihar. Furthermore, the findings of this study have broader implications for understanding the complex relationship between rainfall variability and drought trends in monsoon-dependent regions. Moving forward, research should prioritize the integration of high-resolution climate models, remote sensing technologies, and ground-based observations to gain a deeper understanding of spatiotemporal aspects of rainfall changes. Additionally, it is vital to incorporate socioeconomic and policy considerations to promote sustainable water resource management and reduce disaster risks in vulnerable areas, such as Magadh. These insights can serve as a foundation for policymakers, urban planners, and stakeholders to develop effective strategies to enhance climate resilience and mitigate the impacts of extreme rainfall events and droughts on agriculture, water resources, and livelihoods.

6. ACKNOWLEDGEMENTS

We extend our gratitude to the Indian Meteorological Department (IMD) for providing the meteorological data used in this research.

7. REFERENCES

Anil, S.S. and Sasi, M., 2025. Spatio-temporal analysis of aridity trends and shifts in Karnataka over 63 years (1958-2020): insights into climate adaptation. *Nature Environment & Pollution Technology*, 24(2), pp.1-12. [DOI]

Asare-Nuamah, P. and Botchway, E., 2019. Understanding climate variability and change: analysis of temperature and rainfall across agroecological zones in Ghana. *Heliyon*, 5(10), pp.12-20. [DOI]

Ashok, K., Guan, Z., Saji, N.H. and Yamagata, T., 2004. Individual and combined influences of ENSO and the Indian Ocean dipole on the Indian summer monsoon. *Journal of Climate*, 17(16), pp.3141-3155. [DOI]

Buishand, T.A., 1982. Some methods for testing the homogeneity of rainfall records. *Journal of hydrology*, *58*(1-2), pp.11-27. [DOI]

Chong, K.L., Huang, Y.F., Koo, C.H., Ahmed, A.N. and El-Shafie, A., 2022. Spatiotemporal variability analysis of standardized precipitation indexed droughts using wavelet transform. *Journal of Hydrology*, 605, p.127299. [DOI]

Dash, S.K., Jenamani, R.K., Kalsi, S.R. and Panda, S.K., 2007. Some evidence of climate change in twentieth-century India. *Climatic Change*, 85(3), pp.299-321. [DOI]

Gogoi, K. and Rao, K.N., 2022. Analysis of rainfall trends over Assam, North East India. *Current World Environment*, 17(2), pp.435-446. [DOI]

Guhathakurta, P., Bandgar, A., Menon, P., Prasad, A.K., Sangwan, N. and Advani, S.C., 2020. Observed Rainfall Variability and Changes over Mizoram State. Meteorological Department, Ministry of Earth Sciences, New Delhi, pp.1-50.

Gupta, N., Mahato, P.K., Patel, J., Omar, P.J. and Tripathi, R.P., 2022. Understanding the trend and the variability of rainfall and temperature over Patna (Bihar). In: *Current Directions in Water Scarcity Research*, Vol. 7, pp.533-543. Elsevier. [DOI]

Keyantash, J. and Dracup, J.A., 2002. The quantification of drought: an evaluation of drought indices. *Bulletin of the American Meteorological Society*, 83(8), pp.1167-1180. [DOI]

Khaniya, B., Jayanayaka, I., Jayasanka, P. and Rathnayake, U., 2019. Rainfall trend analysis in Uma Oya basin, Sri Lanka, and future water scarcity problems in perspective of climate variability. *Advances in Meteorology*, 2019(1), pp.363-378. [DOI]

Kumar, S., Sarthi, P.P., Barat, A. and Sinha, A.K., 2022. Variability in meteorological droughts as a pivotal mechanism for rice production over the middle Gangetic plains. *Paddy and Water Environment*, 20(4), pp.499-516. [DOI]

Larsen, M.L. and Schönhuber, M., 2018. Identification and characterization of an anomaly in two-dimensional video disdrometer data. *Atmosphere*, 9(8), p.315. [DOI]

Mishra, R.K., 2020. A study of climatic conditions in the Punpun basin of the Magadh region, Bihar, India. *International Journal of Advanced Research and Development*, 5(5), pp.6-9.

Nyembo, L.O., Larbi, I. and Rwiza, M.J., 2021. Analysis of spatio-temporal climate variability of a shallow lake catchment in Tanzania. *Journal of Water and Climate Change*, 12(2), pp.469-483. [DOI]

Pawar, U. and Rathnayake, U., 2022. Spatiotemporal rainfall variability and trend analysis over the Mahaweli Basin, Sri Lanka. *Arabian Journal of Geosciences*, 15(4), p.370. [DOI]

Pettitt, A.N., 1979. A non-parametric approach to the change-point problem. *Journal of the Royal Statistical Society: Series C (Applied Statistics)*, *28*(2), pp.126-135. [DOI]

Praveen, B., Talukdar, S., Shahfahad, Mahato, S., Mondal, J., Sharma, P. and Rahman, A., 2020. Analyzing trends and forecasting of rainfall changes in India using non-parametric and machine learning approaches. *Scientific Reports*, 10(1), p.10342. [DOI]

Rashiq, A., Kumar, V. and Prakash, O., 2024. A spatiotemporal assessment of the precipitation variability and pattern, and an evaluation of the predictive reliability, of global climate models over Bihar. *Hydrology*, 11(4), p.50. [DOI]

Ribeiro, S., Caineta, J. and Costa, A.C., 2016. Review and discussion of homogenization methods for climate data. *Physics and Chemistry of the Earth, Parts A/B/C*, 94, pp.167-179. [DOI]

Sahana, M., Rehman, S., Ahmed, R. and Sajjad, H., 2021. Analyzing climate variability and its effects in Sundarban Biosphere Reserve, India: reaffirmation from local communities. *Environment, Development and Sustainability*, 23, pp.2465-2492. [DOI]

Saharwardi, M.S., Kumar, P., Dubey, A.K. and Kumari, A., 2022. Understanding the spatiotemporal variability of drought in recent decades and its drivers over-identifies homogeneous regions of India. *Quarterly Journal of the Royal Meteorological Society*, 148(747), pp.2955-2972. [DOI]

Sarkar, U.K., Roy, K., Naskar, M., Karnatak, G., Puthiyottil, M., Baksi, S. and Das, B.K., 2021. Assessing vulnerability of freshwater minnows in the Gangetic floodplains of India for conservation and management: anthropogenic or climatic change risk? *Climate Risk Management*, 33, p.100325. [DOI]

Sharma, M.R. and Priya, S., 2023. Long-term assessment of precipitation behavior in Bihar (1901-2021): patterns, trends and observed variability. *Current World Environment*, 18(2), pp.662. [DOI]

Singh, A., Kumar, R., Kumar, R., Pippal, P.S., Sharma, P. and Sharma, A., 2024. Delineation of groundwater potential zone using geospatial tools and analytical hierarchy process (AHP) in the state of Uttarakhand, India. *Advances in Space Research*, 73(6), pp.2939-2954. [DOI]

Singh, P., Mall, R.K. and Singh, K.K., 2024. District-wise spatiotemporal analysis of precipitation trend during 1900-2022 in Bihar state, India. *Mausam*, 75(4), pp.1059-1070. [DOI]

Sudriani, Y., Sebestyén, V. and Abonyi, J., 2023. Surface water monitoring systems—the importance of integrating information sources for sustainable watershed management. *IEEE Access*, 11, pp.36421-36451. [DOI]

Tesfaye, K., Aggarwal, P.K., Mequanint, F., Shirsath, P.B., Stirling, C.M., Khatri-Chhetri, A. and Rahut, D.B., 2017. Climate variability and change in Bihar, India: challenges and opportunities for sustainable crop production. *Sustainability*, 9(11), p.1998. [DOI]

Tiwari, D.K. and Sarthi, P.P., 2024. Trends in the rainfall pattern over the Gangetic Plain. *Current World Environment*, 19(1), pp.156. [DOI]

Trenberth, K.E., 2011. Changes in precipitation with climate change. *Climate Research*, 47(1-2), pp.123-138. [DOI]

Vahab, S. and Sankaran, A., 2025. Multifractal applications in hydro-climatology: a comprehensive review of modern methods. *Fractal and Fractional*, 9(1), p.27. [DOI]

Vicente Serrano, S., Domínguez-Castro, F., Murphy, C., Hannaford, J., Reig, F., Pena-Angulo, D. and El Kenawy, A., 2020. Long-term variability and trends in meteorological droughts in Western Europe (1851-2018). *International Journal of Climatology*, 41(S1), pp.E690-E717. [DOI]

Warwade, P., Tiwari, S., Ranjan, S., Chandniha, S.K. and Adamowski, J., 2018. Spatio-temporal variation of rainfall over Bihar State, India. *Journal of Water and Land Development*, 42(1), pp.1-10. [DOI]

Wen, X., Tu, Y.H., Tan, Q.F., Li, W.Y., Fang, G.H., Ding, Z.Y. and Wang, Z.N., 2020. Construction of 3D drought structures of meteorological drought events and their spatio-temporal evolution characteristics. *Journal of Hydrology*, 590, p.125539. [DOI]

Wijngaard, J.B., Klein Tank, A.M.G. and Können, G.P., 2003. Homogeneity of 20th century European daily temperature and precipitation series. *International Journal of Climatology: A Journal of the Royal Meteorological Society*, 23(6), pp.679-692. [DOI]

Wudineh, F.A., Moges, S.A. and Kidanewold, B.B., 2022. Detecting hydrological variability in precipitation extremes: application of reanalysis climate product in data-scarce Wabi Shebele Basin of Ethiopia. *Journal of Hydrologic Engineering*, 27(2), 05021035. [DOI]

Yildirim, G. and Rahman, A., 2022. Homogeneity and trend analysis of rainfall and droughts over Southeast Australia. *Natural Hazards*, 112(2), pp.1657-1683. [DOI]

Yürekli, K., 2015. Impact of climate variability on precipitation in the Upper Euphrates–Tigris Rivers Basin of Southeast Turkey. *Atmospheric Research*, 154, pp.25-38. [DOI]

Zakwan, M. and Ara, Z., 2019. Statistical analysis of rainfall in Bihar. *Sustainable Water Resources Management*, 5, pp.1781-1789. [DOI]

Zhang, Q., Li, J., Singh, V.P. and Xiao, M., 2013. Spatio-temporal relations between temperature and precipitation regimes: implications for temperature-induced changes in the hydrological cycle. *Global and Planetary Change*, 111, pp.57-76. [DOI]

Nature Environment and Pollution Technology
An International Quarterly Scientific Journal

p-ISSN: 0972-6268
(Print copies up to 2016)
e-ISSN: 2395-3454

Vol. 25 | No. 3 | Article ID D1873 | 2026

Original Research Paper

https://doi.org/10.46488/NEPT.2026.v25i03.D1873

Open Access Journal

Community Roles Model in the Buffer Zone of the Proboscis Monkey Habitat for Wetland Environmental Conservation

M. Ridha Ilhami†, Ersis Warmansyah Abbas, Bambang Subiyakto and Mutiani
Universitas Lambung Mangkurat, Banjarmasin, Indonesia
†Corresponding author: M. Ridha Ilhami; ridha.ilhami@ulm.ac.id

Abbreviation: Nat. Env. & Poll. Technol.
Website: www.neptjournal.com

Received: 26-09-2025
Revised: 17-11-2025
Accepted: 16-12-2025

Key Words:

Wetland environmental conservation
Buffer zone
Proboscis monkey habitat
Community participation
Sustainable livelihoods

ABSTRACT

This study investigates community role models in the buffer zone of the proboscis monkey (*Nasalis larvatus*) habitat to improve wetland conservation using a mixed-methods exploratory sequential design. Data were collected through in-depth interviews with local communities and the Sahabat Bekantan Indonesia Foundation, non-participatory observation, and a survey of 322 respondents in the buffer zone of the proboscis monkey habitat in South Kalimantan, Indonesia. The data were analyzed using Structural Equation Modeling-Partial Least Squares (SEM-PLS). The results reveal that community involvement is structured around three primary constructs: (1) Community-Based Natural Resource Management (CBNRM) through co-management surveillance systems and mangrove restoration, (2) Indigenous Knowledge (IK), expressed through emerging ecological awareness and locally adapted interactions with wildlife, and (3) Sustainable Livelihood Approaches (SL) that support economic resilience via ecotourism and sustainable resource use. The structural model demonstrated that these constructs significantly influenced wetland environmental conservation ($R^2 = 0.758$), with CBNRM having the strongest effect ($\beta = 0.433$), followed by SL ($\beta = 0.262$) and IK ($\beta = 0.225$). These findings emphasize that conservation success depends on empowering local governance, aligning ecological goals with livelihood security, and strengthening situational ecological knowledge. The resulting model offers practical guidance for policy formulation and adaptive management in tropical wetland buffer zones facing socioecological vulnerability.

Citation for the Paper:

Ilhami, M.R., Abbas, E.W., Subiyakto, B. and Mutiani, 2026. Community roles model in the buffer zone of the proboscis monkey habitat for wetland environmental conservation. *Nature Environment and Pollution Technology*, 25(3), D1873. https://doi.org/10.46488/NEPT.2026.v25i03.D1873

Note: From 2025, the journal has adopted the use of Article IDs in citations instead of traditional consecutive page numbers. Each article is now given individual page ranges starting from page 1.

Copyright: © 2026 by the authors
Licensee: Technoscience Publications
This article is an open access article distributed under the terms and conditions of the Creative Commons Attribution (CC BY) license (https://creativecommons.org/licenses/by/4.0/).

1. INTRODUCTION

Wetlands are widely recognized for the ecological services they provide, including carbon storage, water regulation, and support for a rich variety of species (Anand et al. 2023, Badiou et al. 2011, Ballut-Dajud et al. 2024, Bhowmik 2022, Davidson 2014, Mitsch & Gosselink 2015). Despite their importance, many wetland areas continue to deteriorate owing to land conversion, pollution, resource extraction, and ineffective management, placing these ecosystems under increasing pressure (Davidson 2014, Karim et al. 2013, Newton et al. 2020). The consequences of wetland degradation are felt not only in ecological terms but also by communities whose daily lives and livelihoods depend on wetland resources (Ballut-Dajud et al. 2022, Galvanin and Caldas 2025, Hu et al. 2017, Moomaw et al. 2018, Newton et al. 2020). This highlights the need to strengthen conservation efforts by recognizing both ecological and community realities (Afriyie et al. 2022, Walpole & Davidson 2018).

Indonesia's position as a megadiverse country adds urgency to this issue. Conservation efforts in the country are complicated by population growth, industrial expansion, and the ongoing exploitation of natural resources (Nurhidayah & Alam 2020, Poor et al. 2021). One approach commonly used to protect sensitive habitats is establishing buffer zones. These areas serve as a transition between protected ecosystems and surrounding settlements and are intended to minimize human

disturbance to the core conservation zones (Badiou et al. 2011, Hansen & DeFries 2007, Jakiel et al. 2024, Karim et al. 2013, Newton et al. 2020). When managed well, buffer zones help reduce conflict between humans and wildlife and, at the same time, create space for economic activities that do not put additional pressure on the protected area, such as small-scale tourism, agroforestry, or regulated fishing (Andrianandrasana 2016, Galvanin & Caldas 2025, Stolton et al. 2015, Walpole & Davidson 2018).

The proboscis monkey (Nasalis larvatus) is one of the species that relies heavily on wetland health. This primate is endemic to Borneo, including Kalimantan, and is classified as an endangered species. Its presence often reflects the condition of mangrove and riparian ecosystems (Hidayat et al. 2023, Rezeki et al. 2023b, 2023a, Strier 2016). Habitat loss continues owing to land clearing, plantation conversion, and mangrove timber harvesting (Stark et al. 2012, Wardatutthoyyibah et al. 2023). At the same time, the proboscis monkey holds cultural value for local communities and is a key attraction for ecotourism, especially in South Kalimantan (Juliana et al. 2023, Kia 2021). Therefore, the participation of communities living around the habitat, particularly those in the buffer zone of Curiak Island, is essential (Hidayat et al. 2023, Rezeki et al. 2023b).

To investigate how communities contribute to wetland conservation, this study uses three main concepts: Community-Based Natural Resource Management (CBNRM), local knowledge, and the Sustainable Livelihood Approach (SL). These concepts guided the analysis and were used in a practical and operational sense. CBNRM refers to community involvement in managing natural resources through local institutions, shared rules, and participatory decision-making (Armah et al. 2010, Baddianaah & Baaweh 2021, Foyet 2024, Ulum et al. 2024). Local knowledge (Indigenous Knowledge) encompasses ecological understanding, cultural practices, and customary norms that have developed over generations and influence how communities interact with their environment (Asteria et al. 2024, Bhatia 2025, Harly 2023, Jayawardena 2024). SL focuses on how households diversify income sources and maintain economic resilience while ensuring that their activities remain compatible with conservation objectives (Bhushan et al. 2024, Fang et al. 2024, Mani et al. 2023, Ramananantoandro et al. 2024).

Although all three concepts are frequently discussed in the literature on community-based conservation, studies examining their interactions in wetland buffer zones remain limited. Much of the existing research discusses these ideas separately, leaving little clarity about their combined influence on conservation outcomes, especially in habitats as specialized and sensitive as those of proboscis monkeys.

This study aims to address this gap by developing and testing a model that explains how community-based natural resource management (CBNRM), local knowledge, and sustainable livelihood strategies contribute to wetland conservation in the Curiak Island buffer zone. Field data were used to assess the direct influence of each construct and its relative importance.

The novelty of this research is that it provides an empirical model of the role of communities that are specific to wetland ecosystems. This area has received little attention in previous studies. This study offers practical insights for designing conservation policies that work with communities living closest to vulnerable ecosystems in the Brazilian Amazon. These findings may be helpful in regions with similar ecological characteristics seeking ways to strengthen conservation through local participation.

2. MATERIALS AND METHODS

2.1. Types of Research

This study employed an exploratory sequential design, initially conducting qualitative inquiries through interviews and observations with local communities in the buffer zone of the proboscis monkey habitat. The qualitative findings on indigenous knowledge, livelihood strategies, and community-based conservation practices were then used to construct a quantitative survey instrument to measure broader patterns of community roles in wetland environmental conservation. With this combined approach, this study not only explores the community's role contextually but also quantitatively measures the contribution of each construct to wetland environmental conservation (Creswell 2017).

2.2. Study Area

The research was conducted in three buffer-zone villages surrounding the Curiak Island wetland system: Marabahan Baru, Anjir Serapat Muara, and Anjir Serapat Muara I, located in the Anjir Muara Subdistrict, Barito Kuala Regency. These sites were selected because of their ecological proximity to proboscis monkey habitats and their active involvement in community-based conservation initiatives. A map of the study locations is presented in Fig. 1.

2.3. Qualitative Phase

The first phase employed a qualitative approach to examine community roles across three analytical dimensions: Community-Based Natural Resource Management (CBNRM), Indigenous Knowledge (IK), and the Sustainable

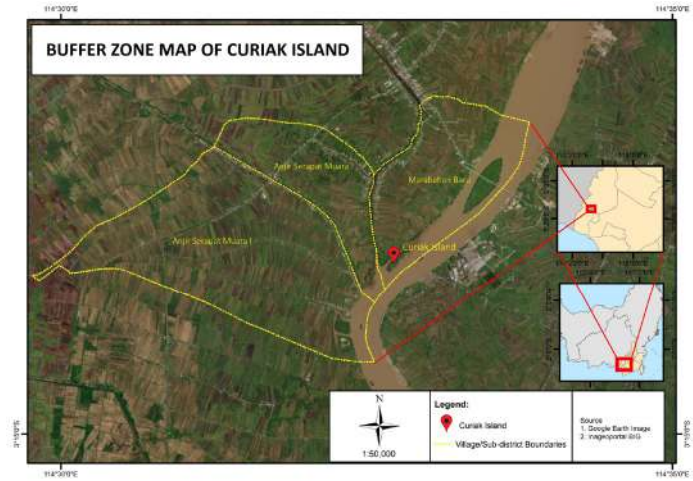


Fig. 1. Map of the Curiak Island buffer zone.

Table 1: Interview questions instrument.

No	Questions	Constructs of the roles
1.	How is the community involved in natural resource management on Curiak Island?	Community-Based Natural Resource Management
2	Are there any community groups or local organizations that specifically deal with environmental management in this area? If so, what is their role?	Community-Based Natural Resource Management
3	What forms of community involvement in management, such as environmental patrols, reforestation, or other activities?	Community-Based Natural Resource Management
4	Is there any training or mentoring provided to the community in environmental management?	Community-Based Natural Resource Management
5	Are there government programs or other institutions that support community-based management? How has the community responded?	Community-Based Natural Resource Management
6	What are the biggest challenges facing communities in natural resource management?	Community-Based Natural Resource Management
7	How has community-based management affected environmental conditions around the proboscis monkey habitat?	Community-Based Natural Resource Management
8	What are the positive impacts on the community from their involvement in environmental management?	Community-Based Natural Resource Management
9	Do you feel there has been a change in the community's attitude or behavior towards environmental sustainability in recent years?	Community-Based Natural Resource Management
10	What traditional knowledge or practices does the community use to protect the proboscis monkey habitat area?	Local Knowledge (Indigenous Knowledge)
11	Are there any rituals, traditions, or customary values related to environmental conservation?	Local Knowledge (Indigenous Knowledge)
12	How does the community respond to the presence of proboscis monkeys in the area?	Local Knowledge (Indigenous Knowledge)
13	Are there cases of people trading proboscis monkeys as exotic animals?	Local Knowledge (Indigenous Knowledge)
14	How does the community respond to socialization from outside that is different from their local knowledge?	Local Knowledge (Indigenous Knowledge)
15	What are the main sources of livelihood for communities around the proboscis monkey habitat buffer zone?	Sustainable Livelihood Approach
16	How do communities adjust their livelihoods to remain sustainable?	Sustainable Livelihood Approach
17	Has the community received any training or assistance regarding environmentally friendly livelihoods?	Sustainable Livelihood Approach
18	What are the community's expectations for the management of this area so that their livelihoods are guaranteed?	Sustainable Livelihood Approach

Livelihoods Approach (SL). Data were collected through semi-structured, in-depth interviews and non-participatory observations of socio-ecological practices. Semi-structured interviews were used to maintain a clear thematic direction while allowing probing and follow-up questions to explore respondents' perspectives more deeply. The interview guide comprised 18 core questions, organized into three constructs (Table 1). The informants included village heads, community members engaged in conservation activities, and representatives of the Sahabat Bekantan Indonesia (SBI) Foundation. Observations focused on daily interactions with wetland environments, community decision-making processes, and practices related to riparian and mangrove ecosystems in the area. Data were analyzed thematically using initial descriptive coding derived from the interview guide, followed by axial coding to identify cross-community patterns of findings. Credibility was strengthened through source and method triangulation, as well as informant verification (Bowen 2009, Christou 2022, Kvale 2009).

2.4. Integration of Qualitative Findings into Quantitative

The findings from the qualitative analysis informed three aspects of the quantitative phase: the definition of latent constructs. The themes emerging from the interviews clarified how local communities understood the roles of community-based natural resource management (CBNRM), ecological knowledge (IK), and livelihood strategies (SL). These themes were used to refine the operational definitions of the constructs. Development of survey indicators. Statements that were frequently repeated in the interviews and observations were converted into questionnaire items. For example, collective monitoring became an operational indicator of CBNRM, traditional ecological practices identified during observations were converted into IK indicators, and livelihood strategies mentioned by respondents became the basis for SL items. Content validation. Draft indicators were discussed with local leaders and SBI representatives to ensure that they reflected community realities and local terminology. This step strengthened the alignment between the qualitative insights and the final measurement model. This integration of qualitative and quantitative methods ensured that the final SEM-PLS construct was derived directly from field data rather than solely from abstract theory, thereby strengthening the construct validity and contextual relevance.

2.5. Quantitative Phase

The quantitative phase targeted adult residents (aged ≥ 18 years) living in the buffer zones surrounding the island. Administrative records from the three villages indicated that the total eligible population was 2,172. The required sample size was determined using Krejcie and Morgan's (1970) sample size table, which is widely used to identify minimum sample requirements based on population size (Chaokromthong & Sintao 2021). According to the table, a population of 2,000-2,500 requires approximately 322-333 respondents to achieve a 95% confidence level with an acceptable margin of error. Based on this guideline, this study established a sample size of 322 respondents, which is appropriate for representing a population of 2,172 individuals.

A simple random sampling technique with proportional allocation across the three villages was employed to ensure that the sample accurately reflected the demographic composition of the buffer zone communities. This approach increased the representativeness and strengthened the generalizability of the findings. All quantitative data were subsequently analyzed using Partial Least Squares Structural Equation Modeling (PLS-SEM) in SmartPLS version 3, which is suitable for exploratory modeling and the analysis of complex relationships among latent constructs.

Measuring Instruments, Sampling, and Analysis: The quantitative measuring instruments consisted of a structured questionnaire containing 24 indicators distributed evenly across four latent variables: CBNRM (six items), Local Knowledge (six items), Sustainable Livelihood Approach (six items), and Wetland Conservation (six items). Responses were recorded on a four-point Likert scale (1 = strongly disagree, 4 = strongly agree) to minimize central tendency bias.

3. RESULTS

This study integrates qualitative and quantitative approaches to understand and measure the role of communities in the buffer zone of Curiak Island in conserving the wetland habitat of proboscis monkeys (*Nasalis Larvatus*). The results are presented in three main constructs related to the role of communities: Community-Based Natural Resource Management (CBNRM), Indigenous Knowledge (IK), and Sustainable Livelihood Approach (SL). Each construct was analyzed thematically through qualitative data and then statistically tested using the Partial Least Squares structural model (SEM-PLS).

3.1. Community-Based Natural Resource Management

The qualitative findings indicate that the practice of Community-Based Natural Resource Management (CBNRM) in the Curiak Island buffer zone is shaped by collaborative governance arrangements, community-driven ecological interventions, and persistence of local

socio-economic constraints. The analysis, derived from triangulated data from village heads, *tourism awareness groups (Pokdarwis*), local residents, and documentation from the Sahabat Bekantan Indonesia (SBI) Foundation, reveals three interrelated themes: (1) co-management and community surveillance, (2) ecological restoration as a shared community mandate, and (3) socio-economic tensions and adaptive livelihood strategies.

3.1.1. Co-Management and Community Surveillance

Pokdarwis emerged as the principal community-based institution supporting conservation governance across all interview sites. Consistent testimonies from village heads confirm that *Pokdarwis* was formally established through the joint initiatives of the Barito Kuala Regency government and SBI. Document analysis of SBI management plans corroborates this organizational framework, evidencing a hybrid co-management system in which formal authority resides with the SBI. However, operational support is delegated to community groups.

Pokdarwis (tourism awareness groups) conduct routine patrols and monitoring using rotational shifts and klotok boats to deter unauthorized activities and minimize human disturbance within the Bekantan habitat (Fig. 2). The consistency of these accounts across villages and their alignment with the researchers' observations of patrol schedules demonstrate a strong degree of data convergence. These findings resonate with the broader Community-Based Natural Resource Management (CBNRM) literature, which emphasizes community surveillance as a critical determinant of conservation effectiveness. Hidayatullah discussed how effective management of conservation areas often includes surveillance procedures conducted by community groups, particularly in coastal and marine settings, highlighting the significance of community involvement in maintaining ecological integrity (Hidayatullah et al. 2023). Furthermore, the engagement of community groups in anti-poaching measures, as reported by Lamichhane et al. (2020), illustrates how local involvement in monitoring activities can significantly curb illegal activities that threaten biodiversity, reinforcing the importance of community action in conservation efforts (Lamichhane et al. 2020). This aligns with the findings of Ortega-Álvarez et al., who discussed community-based monitoring enhancing the functionality of protected areas, promoting effective collaboration between local communities and conservation strategies (Ortega-Álvarez et al. 2016). Ultimately, the unanimity of data derived from local accounts and academic literature underscores the critical role that community-driven surveillance plays in effective conservation strategies (Dupa et al. 2024, Ghaderi et al. 2022).

In addition to patrolling, Pokdarwis serves as a reporting hub for incidents involving proboscis monkeys entering residential zones or becoming stranded in the river currents. Reports are subsequently relayed to the Natural Resources Conservation Agency (BKSDA), reflecting an embedded community-based early warning system. This participatory monitoring structure aligns with community-integrated conservation. Padmanaba et al. highlighted the importance of integrating local knowledge in tracking the whereabouts of species of concern, including the proboscis monkey, thereby supporting community engagement in conservation (Padmanaba et al. 2013). Toulec et al. (2022) indicated that active monitoring of proboscis monkey populations within their habitats can enhance responses to human-wildlife conflicts, thereby contributing to improved management strategies, where community reporting is vital. Moreover, Stark et al. emphasized the need for community involvement in modeling population viability and making conservation decisions, reinforcing the notion that early warning systems driven by local reporting mechanisms are essential for effective species preservation (Stark et al. 2012).



Fig. 2: Patrol of the proboscis monkey habitat on Curiak Island.



Fig. 3: Rambai Padi (*Sonneratia Caseolaris*) rehabilitation activities.

Collectively, these studies illustrate how community-driven early warning and reporting systems can significantly impact the conservation landscape, consistent with the growing body of literature on participatory conservation strategies (Sihombing et al. 2019).

3.1.2. Ecological Restoration as a Shared Community Mandate

The second major theme concerns the active participation of communities in wetland and mangrove restoration, particularly through the cultivation and planting of Sonneratia caseolaris, a primary dietary resource for proboscis monkeys. Interviews with Pokdarwis members, cross-validated with seedling distribution data from the Sahabat Bekantan Indonesia Foundation (SBI) and photographic field documentation, confirmed widespread community involvement in nursery development, planting, and periodic maintenance.

These activities have generated significant ecological outcomes, including the expansion of the effective habitat area from 2.4 to 4.5 ha through cumulative mangrove planting. This aligns with evidence from community-based restoration programs, where local participation correlates with measurable ecological recovery and increased species resilience. For instance, Fahlevi and Raudina highlighted that restoring proboscis monkey habitats by planting rambai mangroves is necessary to enhance food sources and stabilize populations (Fig. 3) (Fahlevi & Raudina 2023). Community engagement can improve the psychological well-being and ecological conditions of both human populations and the flora and fauna inhabiting these areas (Ke et al. 2022). Emphasize that the inclusion of local stakeholders in mangrove management can enhance restoration outcomes through shared knowledge and investment (Susilo et al. 2017).

A particularly illustrative case involved a fisherman from Marabahan Baru who rescued a distressed proboscis monkey during a river current incident. This episode, verified through community interviews and SBI documentation, underscores the internalization of conservation ethics at the individual level. Such acts reflect the emergence of localized environmental stewardship beyond formal organizational mandates, as supported by Hardy et al. (2023) regarding community engagement in coastal resource management.

3.1.3. Socio-Economic Tensions and Adaptive Livelihood Strategies

Despite these positive contributions, communities face persistent structural pressures, primarily stemming from the expansion of coal barge operations along the Barito River. Triangulation with local land-use maps indicates the active interest of private operators in acquiring riverbank areas for docking infrastructure. Interviews revealed that this poses a dilemma for residents, who must weigh short-term financial incentives against long-term ecological considerations.

This tension is well documented in Community-Based Natural Resource Management (CBNRM) systems, where competing land-use priorities can undermine conservation commitments and weaken community cohesion. Silva and Mosimane indicated that conflicting land use can challenge the equitable distribution of economic benefits derived from natural resources, exacerbating community dissatisfaction with CBNRM initiatives (Silva & Mosimane 2012). Therefore, the stability of community participation in CBNRM remains contingent upon viable alternative livelihood strategies.

In response, SBI, in collaboration with PT. Pertamina has facilitated livelihood diversification initiatives, including training in the production of Segank (water-hyacinth-based soap) and Seluang Krispi (processed river fish). While these programs have enhanced local skills, production remains sporadic and largely order-driven, indicating limited penetration into the market. Mufune argues that without

secure economic alternatives, communities may struggle to prioritize conservation over immediate economic pressures (Mufune 2015). From the perspective of the Sustainable Livelihoods Approach, this suggests that diversification efforts have not achieved the economic security necessary to fully offset conservation trade-offs, reflecting findings by Ngwenya who emphasizes that community involvement must be matched with adequate resources to ensure sustainability in CBNRM systems (Ngwenya 2024).

3.1.4. Synthesis and Implications for CBNRM

Overall, the triangulated data suggest that CBNRM in the Curiak Island buffer zone is enabled by:

- Structured co-management partnerships,
- Active community participation in ecological restoration, and
- Emerging but insufficiently stable livelihood alternatives.

These conditions collectively reinforce the study's quantitative findings, which indicate that CBNRM significantly contributes to conservation outcomes in the wetland habitat. However, long-term sustainability remains dependent on reducing external development pressures and strengthening community economic resilience.

3.2. Local Knowledge (Indigenous Knowledge)

The analysis of Indigenous Knowledge (IK) in the Curiak Island buffer zone reveals a distinctive pattern compared to many conservation contexts, where customary norms and ritual practices play a central role in mediating human-wildlife interactions. Triangulation of interview data from community leaders, Pokdarwis members, and residents, combined with field observations, indicates the absence of codified customary practices, rituals, or traditional ecological knowledge specifically directed at protecting proboscis monkey habitats in the area. This contrasts with the findings from other regions, where IK directly informs wildlife management and biodiversity protection (Garnett et al. 2018).

3.2.1. Absence of Customary Ecological Practices and Its Implications

All interview groups consistently reported that the communities surrounding Curiak Island lack formalized customary laws (*adat*), ritual prohibitions, or inherited management practices for proboscis monkey (Nasalis larvatus) conservation. This absence appears rooted not in neglect but in the historical and sociocultural profile of the buffer zone villages, which lack a strong tradition of forest- or wildlife-centered customary institutions.

This finding suggests that the conservation ethic in the area is constructed through contemporary interventions, particularly environmental education, outreach programs, and economic incentives, rather than through long-standing indigenous systems. However, Gomes-Da-Silva et al. (2025) support the notion that Indigenous lands significantly contribute to biodiversity conservation through established customary governance systems that enhance ecological outcomes. Their findings highlight the essential role of local Indigenous stewardship in effective conservation practices, suggesting that modern interventions alone do not drive conservation ethics. Similarly, while Stapleton et al. (2022) discuss the coexistence of traditional governance with modern systems, their work primarily focuses on justice during war, making it misaligned with conservation issues. Consequently, references to their findings regarding political institutions in conservation contexts were omitted.

Additionally, Ridwan et al. emphasized that involving Indigenous peoples in management can bridge traditional and contemporary conservation values, fostering a more integrated approach that respects cultural practices (Ridwan et al. 2022). These perspectives indicate that while modern initiatives can contribute to conservation efforts, the significance of long-standing Indigenous systems should not be underestimated, as they remain deeply intertwined with local ecological knowledge and practices.

3.2.2. Variation in Community Responses to Proboscis Monkeys

Despite the absence of codified IK, community responses to proboscis monkeys can be analytically grouped into three emergent patterns:

1. pro-conservation attitudes
2. neutral or indifferent attitudes, and
3. conflictual attitudes


Berita Batola

Nyasar ke Pemukiman Penduduk di Desa Anjir Serapat 1 Batola, Bekantan Jantan Ini Diamankan Warga

Penulis: Muhammad Tabri | Editor: Hari Widodo

Fig. 4: Community response to the presence of proboscis monkeys quoted on the website banjarmasin.tribunnews.com.

These categories emerged consistently across interviews and are supported by observational notes and local media documentation (e.g., public commentary archived on Banjarmasin Tribunnews), demonstrating data convergence (Fig. 4).

3.2.3. Positive Responses and Emerging Ecological Awareness

Communities with positive attitudes reported increased awareness of the proboscis monkey's ecological role, particularly as an indicator of wetland health and a driver of ecotourism. Interviewees linked their support to direct engagement in conservation activities, including habitat monitoring, mangrove planting, and guiding visiting researchers and tourists. These findings correspond with the literature emphasizing that community engagement breeds a deeper understanding of biodiversity and its benefits for ecosystems. Studies indicate that effective ecological conservation often arises when local communities are actively involved in and benefit economically from such initiatives (Mekonen et al. 2017, Wilfred 2010).

Communities that recognize the ecological significance of species such as the proboscis monkey often see them as indicators of broader environmental health, which can enhance local conservation efforts. Research has shown that when local populations perceive direct benefits from conservation activities, such as ecotourism, they are more likely to promote and participate in ongoing conservation projects (Rezeki et al. 2023a, 2023b, Zuhdi et al. 2024b, 2024a). This creates a sustainable cycle of support and engagement with natural surroundings (Infield & Mugisha 2013).

3.2.4. Neutral Responses

The second group expressed ambivalence, describing proboscis monkeys as a natural part of the landscape, neither particularly valuable nor threatening. This neutral stance is mainly attributable to limited access to conservation information, a factor widely recognized as influencing wildlife perceptions in rural communities. Studies have shown that access to conservation information significantly affects community attitudes towards wildlife, as increased awareness often alters perceptions from ambivalence to more proactive engagement (Dewu & Røskaft 2017, Kansky et al. 2016). For instance, without adequate information, community members may view certain species, such as the proboscis monkey, as mere elements of their environment rather than integral components of biodiversity or ecotourism potential (Ite 1996).

Research indicates that a lack of environmental education directly correlates with a community's indifference towards wildlife conservation (Hare et al. 2021). Various studies have highlighted that educational outreach and effective communication strategies can help bridge the information gap, fostering more favorable attitudes toward wildlife and conservation efforts (Freund et al. 2019, Rakotomamonjy et al. 2014). Consequently, empowering rural communities through education not only informs them about the ecological roles of species but also encourages participatory approaches to conservation management (Llorente et al. 2025, Vergara-Ríos et al. 2020).

3.2.5. Negative Responses and Human-Wildlife Conflict

A smaller subset of participants cited crop damage and competition over fruit as reasons for their negative perceptions. These findings are consistent with human-wildlife conflict patterns documented globally, where livelihood impacts shape community attitudes (Sidi et al. 2022). Although conflicts exist, triangulated evidence from interviews and secondary data confirms no reported incidents of hunting, illicit trade, or intentional harm. This suggests a foundational level of local ecological ethics that prevents escalation of wildlife persecution. The absence of harmful actions against wildlife may indicate an underlying respect for nature and awareness of the ecological role of species, which reduces the likelihood of extremely negative behaviors, such as hunting (Peterson et al. 2010).

Additionally, social capital and local ecological knowledge can play a crucial role in human-wildlife interactions. Research has shown that communities with a better understanding of wildlife tend to exhibit more tolerance towards them despite the conflicts that arise (Putra et al. 2022). This suggests that efforts to enhance community knowledge and awareness may contribute significantly to fostering coexistence while mitigating negative perceptions and impacts on wildlife(Inskip & Zimmermann 2009, Karanth et al. 2017).

3.2.6. Factors Influencing Community Perceptions

The thematic analysis suggests that three interrelated factors shape community responses:

1. Ecological Knowledge - Households with greater exposure to SBI outreach or participation in Pokdarwis activities demonstrated more positive conservation attitudes.
2. Economic Valuation - Communities recognizing economic opportunities from ecotourism (e.g., guiding, product sales) expressed more substantial support for habitat protection. This pattern is consistent with broader findings that economic incentives can reinforce pro-conservation behavior.
3. Direct Experience with Wildlife - Farmers and riverbank residents experiencing crop loss or resource competition tended to express conflict-prone attitudes.

These influences demonstrate that while Indigenous Knowledge in the traditional sense may not always be prominently recognized, situated ecological knowledge and experiential learning significantly shape conservation behaviors. Research indicates that situated ecological knowledge, derived from individuals' direct interactions with their environment, plays a critical role in local conservation efforts (Newmaster et al. 2011, Ruíz-Mallén & Corbera 2013). Experiential learning is important for understanding and managing ecosystems, as it combines theoretical knowledge with practical experience, leading to more effective conservation behavior among community members (Gagnon & Berteaux 2009, Reo & Whyte 2011).

The integration of traditional ecological knowledge (TEK) with scientific approaches enhances ecological understanding and can lead to improved conservation outcomes (Cheveau et al. 2008, Dowsley & Wenzel 2009). Acknowledging local ecological knowledge alongside broader ecological principles allows adaptive management strategies to be informed by community-based practices (Ruíz-Mallén & Corbera 2013, Shokirov & Backhaus 2020). This interplay of situated knowledge and experiential learning reveals how communities navigate ecological challenges and devise solutions that align with both traditional practices and modern conservation goals, ultimately fostering resilience in socio-ecological systems (Polfus et al. 2013, Ramos 2021). Even in situations where traditional ecological knowledge might not be emphasized, the influence of localized practices remains significant in driving conservation behavior (Ramos 2018).

3.2.7. Engagement with External Knowledge Systems

Community responses to external conservation socialization efforts varied significantly. Some residents readily accepted information from government agencies and non-governmental organizations, especially when programs offered clear, immediate benefits, such as training, livelihood support, or opportunities to participate in ecotourism. Conversely, resistance emerged when messages were perceived as misaligned with local needs or when conservation directives limited economic activity without adequate compensation. Such variability underscores the need for culturally sensitive, participatory, and negotiated approaches to knowledge transfer. Successful integration of external conservation knowledge requires that interventions respect local values, involve communities in decision-making, and demonstrate practical relevance, a principle that is widely reflected in community-based conservation research (Bhatia 2025, Pimid & Chambers 2025, Unks et al. 2021).

Research indicates that successful community engagement in conservation initiatives often depends on the perceived alignment between conservation objectives and the immediate economic needs of local populations (Bhatia et al. 2019, Yazezew 2022). Resistance is common when programs fail to address these needs, as communities may prioritize economic stability over conservation mandates (Goumas et al. 2020, Yazezew 2022). Moreover, various studies have illustrated that effective conservation strategies are those that consider local knowledge and foster collaboration between external organizations and community stakeholders, ultimately leading to more sustainable outcomes (Dayer et al. 2017, Jolly & Stronza 2025, Unks et al. 2021). This participatory model aligns with the broader recognition in conservation science that the integration of local values and informed community participation enhances the effectiveness of conservation efforts (Bhatia et al. 2019, Pimid & Chambers 2025).

3.2.8. Synthesis

Overall, the qualitative findings indicate that Indigenous knowledge in the Curiak Island buffer zone is not articulated through formal customary systems but rather through emergent ecological awareness, livelihood-oriented motivations, and direct interactions with wildlife. While traditional ecological knowledge is limited, the community exhibits nascent forms of conservation-oriented understanding that can be strengthened through targeted education, inclusive outreach programs, and equitable economic incentives.

These findings complement quantitative evidence by demonstrating that community support for habitat protection is conditioned by socioeconomic experience, perceived benefits, and the strength of institutional engagement, rather than by inherited customary practices.

3.3. Sustainable Livelihood Approach

The livelihood patterns in the proboscis monkey habitat buffer zone on Curia Island are shaped by long-term dependence on local natural resources and the ecological dynamics of the surrounding wetlands. Interviews, observations, and village administrative data indicate that agriculture and fisheries remain central to household income, although both sectors are increasingly affected by environmental change and conservation regulations that restrict fishing. These conditions reflect the key components of the Sustainable Livelihood Approach, which highlights how livelihood strategies emerge from interactions between asset availability, vulnerability factors, and institutional arrangements (Ramadhan et al. 2024, Sallu et al. 2010).

Rice cultivation is the primary agricultural activity, primarily for household consumption, with limited surplus sold to nearby markets. Respondents reported constraints such as land availability, climate variability, and restrictions

on new land clearing due to conservation policies. These accounts are consistent with village records showing a gradual decline in the available agricultural land linked to tidal fluctuations and regulatory limitations. Such conditions contribute to increasing livelihood vulnerability among households that heavily depend on agriculture (Sallu et al. 2010).

Fishing serves as an additional, and sometimes seasonal, source of income. The use of traditional gear, such as nets, hooks, and traps, remains widespread and is generally compatible with habitat conservation. However, field observations and participant accounts noted fluctuations in fish abundance, reflecting broader ecological changes in riverine and wetland systems in the region. This variability further illustrates the community's continued reliance on natural resources (Iiyama et al. 2007, Omolo & Mafongoya 2019).

Some households have begun diversifying their livelihoods to reduce exposure to ecological and regulatory pressures. Emerging activities include the small-scale processing of local products, home-based enterprises, and participation in community-based ecotourism initiatives. Two villages in the buffer zone, Marabahan Baru and Anjir Serapat Muara 1, have developed early-stage ecotourism concepts centered on wetland landscapes and the conservation of proboscis monkeys (Fig. 5). These locations illustrate the spatial distribution and conditions of tourism-oriented settlements in the study area (Ávila-Foucat et al. 2021).

Capacity-building programs introduced by government agencies and conservation partners have supported these diversification efforts. Participants widely recognized training on ecotourism management, sustainable agriculture, and fisheries practices as beneficial for expanding human capital (Fig. 6). However, analysis of interview data indicates several constraints that limit long-term impact: (1) limited continuity of mentoring, (2) restricted access to markets for ecotourism products and local crafts, and (3) resistance from community members who view traditional practices as more reliable or profitable. These challenges parallel findings from other contexts, where education and training require follow-up support and genuine community participation to generate lasting behavioral and economic changes (Rudiarto et al. 2019).

Community perspectives highlight the need for greater alignment between conservation objectives and livelihood security. Respondents emphasized that participatory planning, inclusive decision-making, and consistent institutional support are essential to ensure local ownership of conservation efforts. The findings indicate that integrating



Fig. 5: Two buffer zone tourism villages, left: Marabahan Baru, right: Anjir Serapat Muara 1.



Fig. 6: Ecotourism management training.

conservation goals with livelihood diversification, market development, and long-term training may enhance both ecological outcomes and socio-economic resilience in buffer zone communities (Gong et al. 2020, Zikri et al. 2024).

The qualitative findings demonstrate that the community's role in conserving the proboscis monkey habitat on Curiak Island encompasses three interrelated dimensions: Community-Based Natural Resource Management (CBNRM), Indigenous Knowledge (IK), and the Sustainable Livelihoods Approach (SL). These constructs reflect the current socio-ecological conditions of buffer zone communities, capturing local participation, knowledge systems, and livelihood adjustments related to wetland conservation. While these findings provide rich contextual insights, quantitative analysis is necessary to confirm the extent to which each construct contributes to conservation outcomes. Therefore, Partial Least Squares structural equation modeling (PLS-SEM) was employed to empirically test the relationships between the constructs.

3.4. Measurement Model Assessment

The measurement model evaluation confirmed that all constructs met the criteria for internal consistency, reliability, and validity. As shown in Table 2, nearly all the indicator loadings exceeded the recommended threshold of 0.70, demonstrating strong indicator reliability across the constructs. Cronbach's alpha (0.878–0.908) and Composite Reliability (0.908–0.929) values exceeded the minimum criterion of 0.70, confirming satisfactory internal consistency. Furthermore, all Average Variance Extracted (AVE) values (0.622–0.685) were above 0.50, indicating acceptable convergent validity. (Hair et al. 2019).

Assessment of discriminant validity using the Heterotrait-Monotrait (HTMT) ratio confirmed that all constructs were empirically distinct, with values below 1.00, as shown in Fig. 7 (Arshad et al. 2023, Franke & Sarstedt 2019, Munthe & Shuguang 2025). Multicollinearity assessment showed VIF values under 3.0, and the Standardized Root Mean Square Residual (SRMR) value was below 0.08, indicating good overall model fit. These results confirm that the measurement

Table 2: Summary of model measurement.

Construct	Item	Loading Factor	Cronbach's Alpha	Composite Reliability	AVE
CB (Community-Based Natural Resource Management)	CB1	0.793	0.878	0,908	0,622
	CB2	0.807			
	CB3	0.803			
	CB4	0.784			
	CB5	0.771			
	CB6	0.771			
IK (Indigenous Knowledge)	IK1	0.693	0.897	0,922	0,663
	IK2	0.807			
	IK3	0.845			
	IK4	0.865			
	IK5	0.848			
	IK6	0.822			
SL (Sustainable Livelihood Approach)	SL1	0.784	0.908	0,929	0,685
	SL2	0.866			
	SL3	0.824			
	SL4	0.855			
	SL5	0.844			
	SL6	0.789			
WEC (Wetland Environmental Conservation)	WEC1	0.838	0.892	0,918	0,652
	WEC2	0.843			
	WEC3	0.839			
	WEC4	0.819			
	WEC5	0.712			
	WEC6	0.785			

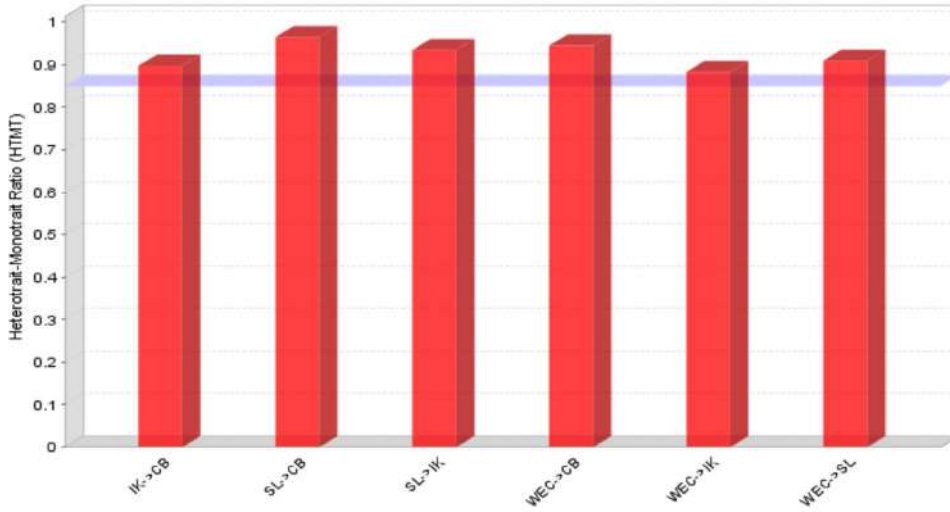


Fig. 7: Heterotrait-Monotrait Ratio (HTMT).

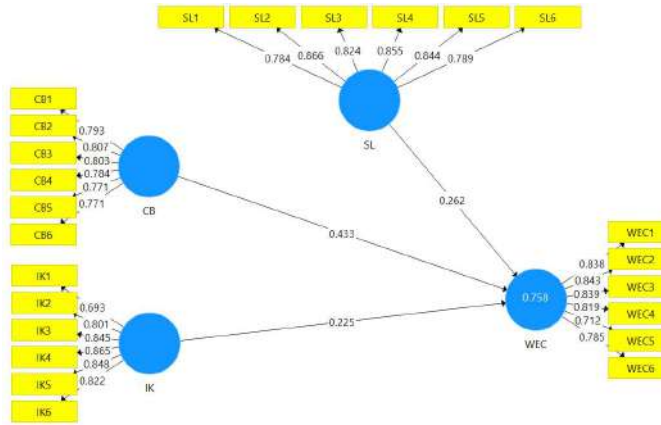


Fig. 8: Community roles model in the buffer zone of the proboscis monkey habitat.

model is appropriate and can be advanced for structural evaluation (Ghasempour Ganji & Kazemi 2024, Iqbal & Rao 2023).

These findings validate that the measurement model used in this study satisfies the criteria for validity and reliability, enabling progression to analysis of the structural (inner) model. Consequently, these results reinforce the robustness of the instrument in assessing the relationships among latent variables within the context of environmental conservation in the buffer zone of the estuarine crocodile habitat.

3.5 Structural Model Assessment

The structural (inner) model shown in Fig. 8 explores how CBNRM, IK, and SL predict Wetland Environmental Conservation (WEC). It has an R^2 value of 0.758, meaning these three factors together explain 75.8% of the variation in conservation outcomes, demonstrating strong explanatory power in environmental behavior studies.

All hypothesized relationships were positive and statistically significant (Table 3). CBNRM exhibited the strongest effect on WEC ($\beta = 0.433$, $T = 5.781$, $p < 0.001$), demonstrating that community involvement in decision-making, surveillance, and mangrove restoration remains the primary determinant of conservation performance in the buffer zone (Ali et al. 2025). The SL construct also had a significant effect on WEC ($\beta = 0.262$, $T = 3.443$, $p = 0.001$), indicating that secure and environmentally compatible livelihood options can reinforce conservation behavior (Prasath & Umashankar 2023, Yulasteriyani et al. 2025). IK contributes to WEC with the smallest yet still significant effect ($\beta = 0.225$, $T = 4.074$, $p < 0.001$), suggesting that although local ecological knowledge exists, its integration into formal conservation governance

Table 3: Model summary.

	Original Sample (O)	Sample Mean (M)	Standard Deviation (STDEV)	T Statistics (|O/STDEV|)	P Values	Conclusion
CB (Community-Based Natural Resource Management) -> WEC (Wetland Environmental Conservation)	0,433	0,433	0,075	5,781	0,000	Significant
IK (Indigenous Knowledge) -> WEC (Wetland Environmental Conservation)	0,225	0,224	0,055	4,074	0,000	Significant
SL (Sustainable Livelihood Approach) -> WEC (Wetland Environmental Conservation)	0,262	0,264	0,076	3,443	0,001	Significant

remains partial, limiting its full influence (Sohail & Chen 2022).

The results of the structural analysis, presented in Table 3, indicate that all constructs significantly influence wetland environmental conservation (WEC). Thus, the three main constructs tested, namely CB, IK, and SL, were proven to have a significant contribution to the conservation efforts of the wetland environment, the Proboscis Monkey habitat on Curiak Island.

3.6. Integrated Interpretation of Qualitative and Quantitative Results

The combined qualitative and quantitative findings support the conclusion that conservation success in the proboscis monkey habitat buffer zone is driven by a hybrid governance mechanism, in which community participation in natural resource management serves as the central foundation. Sustainable livelihood support and gradual strengthening of local ecological understanding enhance community motivation and capacity to contribute to conservation practices. This interplay affirms the theoretical principles of community-based conservation and adaptive co-management, demonstrating that decentralized governance, when coupled with livelihood resilience and knowledge pluralism, can generate substantial ecological benefits in sensitive wetland systems.

4. DISCUSSION

The results of the structural model underscore the crucial role of community involvement, sustainable livelihoods, and local knowledge in driving effective wetland environmental conservation (WEC) in the proboscis monkey (*Nasalis Larvatus*) habitat buffer zone. Statistically significant and positive path coefficients indicate that each construct contributes meaningfully to the conservation model, although their relative strengths vary.

4.1. Community-Based Natural Resource Management

Community-Based Natural Resource Management (CBNRM) is a pivotal approach in contemporary conservation efforts, particularly because of its strong positive correlation with community empowerment and ecological sustainability (Ali et al. 2025). The efficacy of CBNRM strategies, which prioritize local governance structures within participatory and decentralized frameworks, has been increasingly recognized in scholarly works. Research indicates that community involvement enhances effective governance and social capital, which are vital for fostering collective action. Studies have highlighted that local engagement in resource management can reduce conflicts related to resources, underscoring the significance of local knowledge and inclusive decision-making (Gandiwa et al. 2013, Kundu et al. 2010).

In buffer zones, where institutional governance may lack the authority and cultural relevance for effective enforcement, community-based approaches are especially crucial (Berkes 2007, Sullivan et al. 2017). The literature illustrates that integrating traditional knowledge and local governance mechanisms into conservation practices significantly elevates the capability of communities to act as frontline stewards in protecting ecological resources. This integration enhances governance and fosters a sense of stewardship among community members, which is essential for sustainable environmental management (Berkes 2007, Berkes and Jolly 2002). Furthermore, the concept of participative efficacy highlights the psychological aspects wherein community involvement leads to a positive transformation in collective identity, resulting in heightened collective empowerment and unified action toward sustainability (Rees & Bamberg 2014, Sharma & Patil 2025, Zomeren et al. 2012).

The findings regarding the importance of local networks resonate with the context of ecological protection. By leveraging such networks, communities can be effectively mobilized, reinforcing their crucial role in resource management and conservation. This dynamic reflects broader trends in social psychology, where collective action inspired by a shared identity can lead to significant pro-environmental behavior (Fielding & Hornsey 2016, Keshavarzi et al. 2021). Moreover, the successful implementation of community-

driven strategies can potentially reduce the transaction costs associated with complex governance systems, thus mitigating barriers to effective resource management (Lubell et al. 2016).

This evidence supports the assertion that CB-NRM is not only a significant predictor of ecological sustainability but also a vital strategy for empowering communities. This empowerment is critical for establishing resilient ecosystems and sustainable resource use and aligning local governance with broader conservation goals.

4.2. Sustainable Livelihood Approach

The sustainable livelihood (SL) approach plays a crucial role in advancing conservation initiatives by integrating economic security into the community management of natural resources. The statistical coefficient ($\beta = 0.262$) highlights the significance of the SL in promoting community resilience, reducing dependency on unsustainable extractive practices, and encouraging a long-term perspective on conservation efforts (Apine et al. 2019, Berkes 2004). When communities perceive tangible socio-economic benefits from conservation, such as income from ecotourism or payments for ecosystem services, their participation becomes more robust and sustainable (Naidoo et al. 2011, Pailler et al. 2015).

In buffer zones, where ecological preservation intersects with human livelihoods, ensuring that residents derive tangible benefits from conservation activities is crucial. For instance, studies in the Tambopata National Reserve in Peru have demonstrated that sustainable land-use practices, such as Brazil nut harvesting and fish farming, can provide economic returns similar to those from more destructive gold mining (Buřivalová et al. 2019a). Enhancing the value of sustainably sourced products at their origin can motivate communities to pursue environmentally friendly alternatives (Naidoo et al. 2011). Similarly, in India's Kaimur Wildlife Sanctuary, the development of ecotourism not only offers a viable source of income but also mitigates environmental degradation (Su et al. 2016).

The SL also highlights the importance of empowering communities by validating their social assets and ecological assets. For example, community engagement in asset-based conservation strategies in the Peruvian Amazon has been linked to improved livelihoods and enhanced sustainability in protected areas (Gena & Jemal 2022). Research in East Africa has revealed that factors such as secure land tenure, sustainable livelihoods, and effective communication among stakeholders are crucial to the success of community-based conservation, indicating that economic incentives alone are insufficient to ensure the effective management of natural resources (Pailler et al. 2015).

Neglecting the socio-economic dimensions of conservation can lead to inequities and exacerbate poverty, which underlines the need for a balanced approach that prioritizes both ecological and community needs. Studies in tropical regions have emphasized the critical role of maintaining community access to natural resources while simultaneously investing in infrastructure and market access to support sustainable livelihoods (Buřivalová et al. 2019b). This dual focus is essential for aligning conservation goals with the well-being of local populations (Hoa & Thuy 2023).

However, implementing the SL faces challenges, including infrastructure deficits, insufficient technical capacity, and limited public awareness. The effectiveness of sustainable livelihood strategies is heavily contextual; thus, SL programs must be tailored to the unique social, cultural, and economic characteristics of the communities involved to ensure lasting impacts (Berkes 2004, Buřivalová et al. 2019b). In conclusion, leveraging the Sustainable Livelihood Approach holds great promise for harmonizing economic development and environmental conservation and promoting resilience among local communities in buffer zones and beyond.

4.3. Local Knowledge (Indigenous Knowledge)

Indigenous knowledge (IK) is pivotal for enhancing environmental conservation efforts; however, its integration into formal conservation frameworks remains insufficiently recognized. The positive correlation ($\beta = 0.225$) between IK and successful conservation outcomes highlights the potential of traditional practices, which embody generations of ecological understanding, to make meaningful contributions to conservation policies (Kohler & Brondízio 2016, Mutasa 2015, Tholkapiyan et al. 2025). However, the technocratic frameworks that often dominate these policies typically marginalize this knowledge, overlooking the critical place-based ecological insights that IK provides (Brondízio et al. 2021, Coutant et al. 2025).

Additionally, Traditional Ecological Knowledge, as a component of IK, offers a holistic perspective on ecosystems that can complement and enrich Western scientific approaches to conservation strategy formulation (Muswazi 2001, Yongabi 2023). However, integrating IK into these strategies faces substantial structural obstacles, including historical colonial frameworks that perpetuate unequal power dynamics in conservation discourse. Such disparities hinder the recognition of IK as an equally valid epistemological system (McGregor 2021, Obiero et al. 2023). Despite their potential, TEK principles remain underutilized in natural resource management policies, often limited to localized projects rather than being integrated into broader

frameworks (Moola and Roth 2019, Shepard and Daly |2023).

A cross-cultural collaborative approach to bridge epistemological differences is essential to advance meaningful Indigenous community involvement in conservation efforts. This collaborative process can promote dialogue between diverse knowledge systems, facilitating mutual understanding and enhancing the effectiveness of conservation strategies (Brondízio et al. 2021, Kohler and Brondízio 2016). The decolonization of conservation practices is increasingly recognized as an urgent priority, advocating for models that empower indigenous communities to take control of their conservation initiatives, thereby addressing contemporary ecological complexities in a more contextualized and equitable manner (Moola and Roth 2019, Muswazi 2001).

While the technocratic model has contributed significantly to conservation science, achieving sustainable conservation goals necessitates a balanced integration of IK with modern scientific approaches. Both knowledge systems offer valuable insights that, when combined, can lead to more effective and resilient conservation practices (Babidge et al. 2007, Brondízio et al. 2021, Mutasa 2015, Singh et al. 2025). Ensuring that Indigenous voices are included in policymaking processes not only validates their contributions but also enriches conservation practices through a deeper understanding of local ecosystems.

5. CONCLUSIONS

This study reveals that the conservation of proboscis monkey habitats within the Curiak Island buffer zone is primarily influenced by three factors: Community-Based Natural Resource Management (CBNRM), Indigenous Knowledge (IK), and the Sustainable Livelihood Approach (SL). Qualitative data indicate that local communities actively contribute to maintaining wetland ecosystem stability, although their integration of indigenous knowledge into conservation practices remains limited. Quantitative analysis using PLS-SEM confirms that all three constructs significantly impact wetland conservation efforts, with CBNRM exerting the strongest influence. The model's coefficient of determination ($R^2 = 0.758$) suggests it accounts for a large portion of the variance in community conservation activities, though other external factors should be investigated. The comparatively lesser role of IK highlights the need to better incorporate local knowledge into conservation strategies. Overall, the findings support that community involvement and sustainable livelihoods can bolster habitat protection for proboscis monkeys. Nevertheless, due to the limitations in statistical reporting and the specific context of the dataset, policy recommendations should be approached cautiously and not generalized beyond this study's conditions. Future research should include additional measurement indicators, adopt longitudinal methods, and examine external influences that may affect conservation outcomes in this region.

6. ACKNOWLEDGMENTS

We would like to express our deepest gratitude to all parties who have kindly agreed to be informants and respondents in the data collection for this study, namely: Yayasan Sahabat Bekantan Indonesia, the communities of Anjir Serapat Muara I Village, Anjir Serapat Muara Village, and Marabahan Baru Village.

7. REFERENCES

Afriyie, K., Abass, K., Frempong, F., Arthur, B. and Gyasi, R.M. 2022. The dynamics and livelihood implications of illegal mining in Ghana: a critical assessment. *Geographical Research*, 61(1), pp.32-43. [DOI]

Ali, S.H., Mohamed, A.M. and Nyang'au, S.N. 2025. Assessment of socio-economic and ecological impacts of community-based approaches in natural resources management in Mandera East Sub-County, Kenya. *East African Journal of Environment and Natural Resources*, 8(2), pp.545-560. [DOI]

Anand, J., Byju, H., Nefla, A., Abhijith, S., Reshi, O.R. and Aarif, K.M. 2023. Conservation significance of Changaram wetlands—a key wintering site for migratory shorebirds and other waterbirds in the western coast of Kerala, India. *Journal of Threatened Taxa*, 15(1), pp.22410-22418. [DOI]

Andrianandrasana, H. 2016. Testing the effectiveness of community-based conservation in conserving biodiversity, protecting ecosystem services, and improving human well-being in Madagascar. [PhD Thesis, University of Oxford].

Apine, E., Turner, L.M., Rodwell, L.D. and Bhatta, R. 2019. The application of the sustainable livelihood approach to small scale-fisheries: the case of mud crab Scylla Serrata in south west India. *Ocean & Coastal Management*, 170, pp.17-28. [DOI]

Armah, F.A., Yawson, D.O., Pappoe, A.N.M. and Afrifa, E.K.A. 2010. Participation and sustainable management of coastal lagoon ecosystems: the case of the Fosu Lagoon in Ghana. *Sustainability*, 2(1), pp.383-399. [DOI]

Arshad, M.W., Moazzam, M., Raziq, M.M. and Ahmed, W. 2023. Linking the willingness of smallholder dairy farmers to adopt minimum food safety and quality standards to the country's export potential. *International Journal of Food Science and Technology*, 58(10), pp.5557-5567.

Asteria, D., Alvernia, P., Kholila, B.N., Husein, S.I. and Asrofani, F.W. 2024. Forest conservation by the indigenous Baduy community in the form of customary law. *Journal of Cultural Heritage Management and Sustainable Development*, 14(2), pp.175-189.

Ávila-Foucat, V.S., Revollo-Fernández, D.A. and Navarrete, C. 2021. Determinants of livelihood diversification: the case of community-based ecotourism in Oaxaca, Mexico. *Sustainability*, 13(20), 11371, pp.1-15. [DOI]

Babidge, S., Greer, S., Henry, R. and Pam, C. 2007. Management speak: indigenous knowledge and bureaucratic engagement. *Social Analysis*, 51(3), pp.1-15. [DOI]

Baddianaah, I. and Baaweh, L. 2021. The prospects of community-based natural resource management in Ghana: a case study of Zukpiri community resource management area. *Heliyon*, 7(10), pp.1-12.

Retrieved from https://www.cell.com/heliyon/fulltext/S2405-8440(21)02290-8

Badiou, P., McDougal, R.L., Pennock, D. and Clark, B. 2011. Greenhouse gas emissions and carbon sequestration potential in restored wetlands of the Canadian prairie pothole region. *Wetlands Ecology and Management*, 19(3), pp.237-256. [DOI]

Ballut-Dajud, G., Herazo, L.C.S., Osorio-Martínez, I.M., Báez-García, W.G., Marín-Muñiz, J.L. and Betanzo-Torres, E.A. 2024. Comparison of carbon storage in forested and non-forested soils in tropical wetlands of Caimanera, Colombia, and Llano, Mexico. *Sustainability*, 16(12), 4966, pp.1-20. [DOI]

Ballut-Dajud, G.A., Sandoval Herazo, L.C., Fernández-Lambert, G., Marín-Muñiz, J.L., López Méndez, M.C. and Betanzo-Torres, E.A. 2022. Factors affecting wetland loss: a review. *Land*, 11(3), 434, pp.1-25.

Berkes, F. 2004. Rethinking community-based conservation. *Conservation Biology*, 18(3), pp.621-630. [DOI]

Berkes, F. 2007. Community-based conservation in a globalized world. *Proceedings of the National Academy of Sciences*, 104(39), pp.15188-15193.

Berkes, F. and Jolly, D. 2002. Adapting to climate change: social-ecological resilience in a Canadian western Arctic community. *Conservation Ecology*, 5(2), pp.1-15.

Bhatia, D.K. 2025. Indigenous knowledge systems (IKS) and climate change mitigation: a tool for sustainable environmental management. *Bionature*, 45(2), pp.69-78. [DOI]

Bhatia, S., Redpath, S.M., Suryawanshi, K. and Mishra, C. 2019. Beyond conflict: exploring the spectrum of human–wildlife interactions and their underlying mechanisms. *Oryx*, 54(5), pp.621-628. [DOI]

Bhowmik, S. 2022. Ecological and economic importance of wetlands and their vulnerability: a review. In: *Research Anthology on Ecosystem Conservation and Preserving Biodiversity*, pp.11-27.

Bhushan, S., Dincă, I. and Shikha, S. 2024. Evaluating local livelihoods, sustainable forest management, and the potential for ecotourism development in Kaimur Wildlife Sanctuary, India. *Frontiers in Forests and Global Change*, 7, 1491917, pp.1-15.

Bowen, G.A. 2009. Document analysis as a qualitative research method. *Qualitative Research Journal*, 9(2), pp.27-40.

Brondízio, E.S., Aumeeruddy-Thomas, Y., Bates, P., Carino, J., Fernández-Llamazares, Á., Ferrari, M.F., Galvin, K., Reyes-García, V., McElwee, P., Molnár, Z., Samakov, A. and Shrestha, U.B. 2021. Locally based, regionally manifested, and globally relevant: indigenous and local knowledge, values, and practices for nature. *Annual Review of Environment and Resources*, 46(1), pp.481-509. [DOI]

Buřivalová, Z., Allnutt, T.F., Rademacher, D., Schlemm, A., Wilcove, D.S. and Butler, R. 2019a. What works in tropical forest conservation, and what does not: effectiveness of four strategies in terms of environmental, social, and economic outcomes. *Conservation Science and Practice*, 1(6), pp.1-12. [DOI]

Buřivalová, Z., Allnutt, T.F., Rademacher, D., Schlemm, A., Wilcove, D.S. and Butler, R. 2019b. What works in tropical forest conservation, and what does not: effectiveness of four strategies in terms of environmental, social, and economic outcomes. *Conservation Science and Practice*, 1(6), pp.1-12. [DOI]

Chaokromthong, K. and Sintao, N. 2021. Sample size estimation using Yamane and Cochran and Krejcie and Morgan and green formulas and Cohen statistical power analysis by G* Power and comparisions. *Apheit International Journal of Interdisciplinary Social Sciences and Technology*, 10(2), pp.76-86.

Cheveau, M., Imbeau, L., Drapeau, P. and Bélanger, L. 2008. Current status and future directions of traditional ecological knowledge in forest management: a review. *The Forestry Chronicle*, 84(2), pp.231-243. [DOI]

Christou, P.A. 2022. How to use thematic analysis in qualitative research. *Journal of Qualitative Research in Tourism*, 3(2), pp.79-95.

Coutant, O., Davy, D., Jahn-Oyac, A., Quartarollo, G., Valentini, A., Déjean, T., Brosse, S. and Murienne, J. 2025. Confronting forest-dweller local ecological knowledge and environmental DNA measurements of biodiversity. *People and Nature*, 7(6), pp.1382-1395. [DOI]

Creswell, J.W. 2017. *Research Design: Qualitative, Quantitative, and Mixed Methods Approaches*. SAGE Publications, pp.300.

Davidson, N.C. 2014. How much wetland has the world lost? long-term and recent trends in global wetland area. *Marine & Freshwater Research*, 65(10), pp.934-941. [DOI]

Dayer, A.A., Williams, A., Cosbar, E.A. and Racey, M. 2017. Blaming threatened species: media portrayal of human–wildlife conflict. *Oryx*, 53(2), pp.265-272. [DOI]

Dewu, S. and Røskaft, E. 2017. Community attitudes towards protected areas: insights from Ghana. *Oryx*, 52(3), pp.489-496. [DOI]

Dowsley, M. and Wenzel, G.W. 2009. "The time of the most polar bears": a co-management conflict in Nunavut. *Arctic*, 61(2), pp.1-10. [DOI]

Dupa, H., Ansofino, A. and Irwan, I. 2024. Tourism awareness group strategy in strengthening collective action and social capital for Padang City tourism development. *International Journal of Educational Research Excellence (IJERE)*, 3(1), pp.93-100.

Edinéia Aparecida dos Santos Galvanin and Caldas, M.M. 2025. Evaluating public policies in fire-affected conservation priority areas of the Brazilian Pantanal. *Research Square*, pp.1-15. [DOI]

Fahlevi, R. and Raudina, N.R. 2023. Proboscis monkeys (Bekantan) rescue community: a civic engagement in the Sahabat Bekantan Indonesia Foundation. In: *Proceedings of the 4th International Conference on Social and Political Sciences*, pp.738-746. [DOI]

Fang, R., Xiong, K., Ding, Y. and Wang, D. 2024. Integration of the natural world heritage conservation and development of buffer zone agroforestry: from scientometrics insights and implications for the Karst World Heritage. *Heritage Science*, 12(1), 338, pp.1-20. [DOI]

Fielding, K.S. and Hornsey, M.J. 2016. A social identity analysis of climate change and environmental attitudes and behaviors: insights and opportunities. *Frontiers in Psychology*, 7, 121, pp.1-10.

Foyet, M. 2024. Community-based natural resource management (CBNRM) in southern Africa: history, principles, evolution and contemporary challenges. *NamJEnv*, 9, pp.1-15. [DOI]

Franke, G. and Sarstedt, M. 2019. Heuristics versus statistics in discriminant validity testing: a comparison of four procedures. *Internet Research*, 29(3), pp.430-447.

Freund, C.A., Achmad, H., Kanisius, P., Naruri, R., Tang, E. and Knott, C.D. 2019. Conserving orangutans one classroom at a time: evaluating the effectiveness of a wildlife education program for school-aged children in Indonesia. *Animal Conservation*, 23(1), pp.18-27. [DOI]

Gagnon, C. and Berteaux, D. 2009. Integrating traditional ecological knowledge and ecological science: a question of scale. *Ecology and Society*, 14(2), pp.1-10. [DOI]

Gandiwa, E., Heitkönig, I.M., Lokhorst, A.M., Prins, H.H. and Leeuwis, C. 2013. CAMPFIRE and human-wildlife conflicts in local communities bordering northern Gonarezhou National Park, Zimbabwe. *Ecology and Society*, 18(4), pp.1-12.

Garnett, S.T., Burgess, N.D., Fa, J.E., Fernández-Llamazares, Á., Molnár, Z., Robinson, C.J., Watson, J.E., Zander, K.K., Austin, B. and Brondizio, E.S. 2018. A spatial overview of the global importance of indigenous lands for conservation. *Nature Sustainability*, 1(7), pp.369-374.

Gena, H. and Jemal, M. 2022. Community based conservation approaches: implications for biodiversity conservation and socio-economic development of local community in Bale Mountains National Park, South East Ethiopia. *Research Square*, pp.1-20. [DOI]

Ghaderi, Z., Shahabi, E., Fennell, D. and Khoshkam, M. 2022. Increasing community environmental awareness, participation in conservation, and livelihood enhancement through tourism. *Local Environment*, 27(5), pp.605-621. [DOI]

Ghasempour Ganji, S.F. and Kazemi, A. 2024. Improving international brand performance: the implications of marketing capabilities, brand orientation and customer value cocreation. *Journal of Product & Brand Management*, 33(8), pp.1088-1100.

Gomes-da-Silva, J., Lughadha, E.N. and Forzza, R.C. 2025. Protecting hidden treasures: indigenous lands safeguard 50% of areas with the highest potential for angiosperm discoveries in Brazil—patterns and conservation priorities. *PLoS One*, 20(7), e0326507, pp.1-18. [DOI]

Gong, Y., Zhang, R., Yao, K., Liu, B. and Wang, F. 2020. A livelihood resilience measurement framework for dam-induced displacement and resettlement. *Water*, 12(11), 3191, pp.1-20. [DOI]

Goumas, M., Lee, V.E., Boogert, N.J., Kelley, L.A. and Thornton, A. 2020. The role of animal cognition in human-wildlife interactions. *Frontiers in Psychology*, 11, pp.1-10. [DOI]

Hair, J.F., Risher, J.J., Sarstedt, M. and Ringle, C.M. 2019. When to use and how to report the results of PLS-SEM. *European Business Review*, 31(1), pp.2-24.

Hansen, A.J. and DeFries, R. 2007. Ecological mechanisms linking protected areas to surrounding lands. *Ecological Applications*, 17(4), pp.974-988. [DOI]

Hardy, G., Pacris, F.A. and Baloloy, M.V. 2023. Socio-economic component, coastal resource use and perception, and participation of coastal communities/fishing households in Caroan, Gonzaga, Cagayan. *International Journal of Biosciences*, 22(2), pp.27-32. [DOI]

Hare, D., Daniels, M. and Blossey, B. 2021. Public perceptions of deer management in Scotland. *Frontiers in Conservation Science*, 2, pp.1-12. [DOI]

Harly, L.N.B. 2023. Sustainable forest management from the perspective of customary law in Indonesia: a case study in the Bayan community. *International Journal of Social Sciences and Humanities*, 1(1), pp.32-42.

Hidayat, A., Sulistioadi, Y.B., Kustiawan, W., Sukartiningsih, Haryanto, Z. and Suba, R.B. 2023. Habitat suitability of proboscis monkey Nasalis larvatus Wurmb. in Muara Kaman Sedulang Nature Reserve, East Kalimantan. *IOP Conference Series: Earth and Environmental Science*, 1282(1), 012018, pp.1-10. [DOI]

Hidayatullah, R., Muis, A., Hernawati, H., Refandi, T., Aini, M., Amir, S. and Abdurachman, M.H. 2023. Pengawasan dengan metode smart patrol di kawasan konservasi Taman Wisata Perairan Gili Balu. [Supervision using smart patrol method in the Gili Balu Water Tourism Park conservation area]. *Jurnal Biologi Tropis*, 23(2), pp.442-449. [DOI]

Hoa, L.T. and Thuy, N.T.T. 2023. Identification of non-impact livelihoods on mangrove resources in Can Gio, Vietnam. *IOP Conference Series: Earth and Environmental Science*, 1247(1), 012002, pp.1-10. [DOI]

Hu, S., Niu, Z., Chen, Y., Li, L. and Zhang, H. 2017. Global wetlands: potential distribution, wetland loss, and status. *Science of the Total Environment*, 586, pp.319-327.

Iiyama, M., Kariuki, P., Kristjanson, P., Kaitibie, S. and Maitima, J. 2007. Livelihood diversification strategies, incomes and soil management strategies: a case study from Kerio Valley, Kenya. *Journal of International Development*, 20(3), pp.380-397. [DOI]

Infield, M. and Mugisha, A. 2013. Culture, values and conservation: a review of perspectives, policies and practices. Fauna & Flora International, Cambridge UK, pp.2-50.

Inskip, C. and Zimmermann, A. 2009. Human-felid conflict: a review of patterns and priorities worldwide. *Oryx*, 43(1), pp.18-34. [DOI]

Iqbal, Z. and Rao, Z.-R. 2023. Social capital and loan credit terms: does it matter in microfinance contract? *Journal of Asian Business and Economic Studies*, 30(3), pp.187-209.

Ite, D.U.E. 1996. Community perceptions of the Cross River National Park, Nigeria. *Environmental Conservation*, 23(4), pp.351-357. [DOI]

Jakiel, M., Kaim, D. and Ostafin, K. 2024. Long-term landscape changes in the Ojców National Park (Poland) and its surroundings: implications for the effectiveness of buffer zones. *Sustainability*, 16(15), 6649, pp.1-20.

Jayawardena, I. 2024. Indigenous, ethnic, and racial diversity and climate justice: New Zealand's climate adaptation policies and policy approaches. *Environmental Research: Climate*, 3(3), 035004, pp.1-15. [DOI]

Jolly, H. and Stronza, A. 2025. Insights on human–wildlife coexistence from social science and indigenous and traditional knowledge. *Conservation Biology*, 39(2), pp.1-12. [DOI]

Juliana, J., Sihombing, S.O. and Suwu, S.E. 2023. Community-based ecotourism in Sawarna Tourism Village. *Enrichment Journal of Management*, 13(1), pp.258-269. [DOI]

Kansky, R., Kidd, M. and Knight, A.T. 2016. A wildlife tolerance model and case study for understanding human wildlife conflicts. *Biological Conservation*, 201, pp.137-145. [DOI]

Karanth, K.K., Jain, S. and Weinthal, E. 2017. Human–wildlife interactions and attitudes towards wildlife and wildlife reserves in Rajasthan, India. *Oryx*, 53(3), pp.523-531. [DOI]

Karim, F., Palmer, A. and Brodie, J. 2013. Hydrodynamic modelling of floodplain flow residence time in a wet tropical catchment, north eastern Australia. In: *Proceedings of MODSIM2013*, pp.1-7. [DOI]

Ke, G.N., I Ketut Aria Pria Utama, Wagner, T., Sweetman, A.K., Arshad, A., Nath, T.K., Neoh, J.Y., Muchamad, L.S. and Suroso, D.S.A. 2022. Influence of mangrove forests on subjective and psychological wellbeing of coastal communities: case studies in Malaysia and Indonesia. *Frontiers in Public Health*, 10, pp.1-15. [DOI]

Keshavarzi, S., McGarty, C. and Khajehnoori, B. 2021. Testing social identity models of collective action in an Iranian environmental movement. *Journal of Community & Applied Social Psychology*, 31(4), pp.452-464.

Kia, Z. 2021. Ecotourism in Indonesia: local community involvement and the affecting factors. *Journal of Governance and Public Policy*, 8(2), pp.1-15. [DOI]

Kohler, F. and Brondízio, E.S. 2016. Considering the needs of indigenous and local populations in conservation programs. *Conservation Biology*, 31(2), pp.245-251. [DOI]

Krejcie, R. V. and Morgan, D. W. 1970. Determining sample size for research activities. *Educational and Psychological Measurement*, 30, pp. 607-610.

Kundu, R., Aura, C.M., Muchiri, M., Njiru, J.M. and Ojuok, J.E. 2010. Difficulties of fishing at Lake Naivasha, Kenya: is community participation in management the solution? *Lakes & Reservoirs: Research & Management*, 15(1), pp.15-23.

Kvale, S. 2009. *Interviews: Learning the craft of qualitative research interviewing*. Sage Publications, pp.400.

Lamichhane, S., Joshi, R., Poudel, B. and Subedi, P. 2020. Role of community in leading conservation: effectiveness, success and challenges of community-based anti-poaching unit in Nepal. *Grassroots Journal of Natural Resources*, 3(4), pp.94-109. [DOI]

Llorente, M., Villariezo, P. and Amici, F. 2025. Multimodal learning has an impact on conservation knowledge, attitudes, and behavioral intentions towards spider monkeys in Mayan children from Punta Laguna, Yucatán. *American Journal of Primatology*, 87(9), pp.1-15. [DOI]

Lubell, M., Mewhirter, J., Berardo, R. and Scholz, J.T. 2016. Transaction costs and the perceived effectiveness of complex institutional systems. *Public Administration Review*, 77(5), pp.668-680. [DOI]

Mani, I., Melles, G. and Gautam, S. 2023. Community development for Bote in Chitwan National Park, Nepal: a political ecology of development logic of erasure. *Sustainability*, 15(3), 2834, pp.1-18. [DOI]

McGregor, D. 2021. Indigenous knowledge systems in environmental governance in Canada. *Kula: Knowledge Creation, Dissemination and Preservation Studies*, 5(1), pp.1-10. [DOI]

Mekonen, S., Chinasho, A., Berhanu, K. and Tesfaye, S. 2017. Conservation opportunities and local community attitudes towards wildlife in

Harenna Forest, south east Ethiopia. *Journal of Biodiversity & Endangered Species*, 5(4), pp.1-8. [DOI]

Mitsch, W.J. and Gosselink, J.G. 2015. *Wetlands*. John Wiley & Sons, pp.750.

Moola, F. and Roth, R. 2019. Moving beyond colonial conservation models: indigenous protected and conserved areas offer hope for biodiversity and advancing reconciliation in the Canadian boreal forest. *Environmental Reviews*, 27(2), pp.200-201. [DOI]

Moomaw, W.R., Chmura, G.L., Davies, G.T., Finlayson, C.M., Middleton, B.A., Natali, S.M., Perry, J.E., Roulet, N. and Sutton-Grier, A.E. 2018. Wetlands in a changing climate: science, policy and management. *Wetlands*, 38(2), pp.183-205. [DOI]

Mufune, P. 2015. Community based natural resource management (CBNRM) and sustainable development in Namibia. *Journal of Land and Rural Studies*, 3(1), pp.121-138. [DOI]

Munthe, N. and Shuguang, W. 2025. Mechanism of the influence of university support internal quality assurance on undergraduates' learning outcome. *Scholars Journal of Arts, Humanities and Social Sciences*, 5, pp.97-110.

Muswazi, P. 2001. Indigenous knowledge management in Swaziland: perspectives. *Information Development*, 17(4), pp.250-256. [DOI]

Mutasa, M. 2015. Knowledge apartheid in disaster risk management discourse: is marrying indigenous and scientific knowledge the missing link? *Jàmbá: Journal of Disaster Risk Studies*, 7(1), pp.1-8. [DOI]

Naidoo, R., Weaver, L., Longcamp, M.D. and Plessis, P.d. 2011. Namibia's community-based natural resource management programme: an unrecognized payments for ecosystem services scheme. *Environmental Conservation*, 38(4), pp.445-453. [DOI]

Newmaster, A., Berg, K., Ragupathy, S., Palanisamy, M., Sambandan, K. and Newmaster, S. 2011. Local knowledge and conservation of seagrasses in the Tamil Nadu State of India. *Journal of Ethnobiology and Ethnomedicine*, 7(1), pp.1-10. [DOI]

Newton, A., Icely, J., Cristina, S., Perillo, G.M.E., Turner, R.E., Ashan, D., Cragg, S.M., Luo, Y., Tu, C., Li, Y., Zhang, H., Ramesh, R., Forbes, D.L., Solidoro, C., Béjaoui, B., Gao, S., Pastres, R., Kelsey, H., Taillie, D. and Kuenzer, C. 2020. Anthropogenic, direct pressures on coastal wetlands. *Frontiers in Ecology and Evolution*, 8, pp.1-15. [DOI]

Ngwenya, F. 2024. Biodiversity conservation strategies and their impact on ecosystem health in Mozambique. *International Journal of Natural Sciences*, 4(1), pp.32-45. [DOI]

Nurhidayah, L. and Alam, S. 2020. The forest and its biodiversity: assessing the adequacy of biodiversity protection laws in Indonesia. *Asia Pacific Journal of Environmental Law*, 23(2), pp.178-201.

Obiero, K., Mboya, J.B., Ouko, K.O., Kembenya, E., Nyauchi, E., Munguti, J., Outa, N. and Githukia, C.M. 2023. The role of indigenous knowledge in fisheries resource management for aquaculture development: a case study of the Kenyan Lake Victoria region. *Aquaculture, Fish and Fisheries*, 3(2), pp.175-183. [DOI]

Omolo, N. and Mafongoya, P. 2019. Gender, social capital and adaptive capacity to climate variability. *International Journal of Climate Change Strategies and Management*, 11(3), pp.1-15. [DOI]

Ortega-Álvarez, R., Sánchez-González, L.A., Valera-Bermejo, A. and Berlanga-García, H. 2016. Community-based monitoring and protected areas: towards an inclusive model. *Sustainable Development*, 25(3), pp.200-212. [DOI]

Padmanaba, M., Sheil, D., Basuki, I. and Liswanti, N. 2013. Accessing local knowledge to identify where species of conservation concern occur in a tropical forest landscape. *Environmental Management*, 52(2), pp.348-359. [DOI]

Pailler, S., Naidoo, R., Burgess, N.D., Freeman, O.E. and Fisher, B. 2015. Impacts of community-based natural resource management on wealth, food security and child health in Tanzania. *PLoS One*, 10(7), e0133252, pp.1-15. [DOI]

Peterson, M.N., Birckhead, J.L., Leong, K.M., Peterson, M.J. and Peterson, T.R. 2010. Rearticulating the myth of human–wildlife conflict. *Conservation Letters*, 3(2), pp.74-82. [DOI]

Pimid, M. and Chambers, G.K. 2025. How personal values affect conservation initiatives: indigenous community support for conservation in rural Sabah, Malaysia. *Asian Education and Development Studies*, 14(3), pp.404-422. [DOI]

Polfus, J.L., Heinemeyer, K.S. and Hebblewhite, M. 2013. Comparing traditional ecological knowledge and western science woodland caribou habitat models. *Journal of Wildlife Management*, 78(1), pp.112-121. [DOI]

Poor, E.E., Imron, M.A., Novalina, R., Shaffer, L.J. and Mullinax, J.M. 2021. Increasing diversity to save biodiversity: rising to the challenge and supporting Indonesian women in conservation. *Conservation Science and Practice*, 3(6), e395, pp.1-10. [DOI]

Prasath, S. and Umashankar, K. 2023. Livelihood resilience of smallholder dairy farmers against external shocks: a case study in the northern dry zone of Sri Lanka. *Tropical Agricultural Research*, 34(2), pp.94-106. [DOI]

Putra, A.K., Susetyo, B.B. and Ngimba, S.D. 2022. Social capital based on local ecological knowledge in the Bompon watershed community. *KnE Social Sciences*, pp.1-10. [DOI]

Rakotomamonjy, S.N., Jones, J.P.G., Razafimanahaka, J.H., Ramamonjisoa, B. and Williams, S.J. 2014. The effects of environmental education on children's and parents' knowledge and attitudes towards lemurs in rural Madagascar. *Animal Conservation*, 18(2), pp.157-166. [DOI]

Ramadhan, D.M., Fadullah, M., Komalasari, D., Fadila, A., Amaradani, M.S. and Imanta, L.D. 2024. Changing waves: maritime community cultural responses to the Anthropocene in Tambak Lorok, Semarang. *IOP Conference Series: Earth and Environmental Science*, 1317(1), 012018, pp.1-10. [DOI]

Ramananantoandro, T., Reynolds, T.D., Andrianaharinjaka, F.A.R., Koera, R.A., Ramanitrarivo, L.C., Raobimandrantso, N.A., Randriambinintsoa, T., Randrianorosoa, A., Ratsirarson, J., Mirado T.J.F. Rakotonirina, and Chaix, G. 2024. International conference on tropical wood (ICTW 2024) advancing the sustainable use of tropical forests. *Bois et Forêts des Tropiques*, 361, pp.3-8. [DOI]

Ramos, S.C. 2018. Considerations for culturally sensitive traditional ecological knowledge research in wildlife conservation. *Wildlife Society Bulletin*, 42(2), pp.358-365. [DOI]

Ramos, S.C. 2021. Understanding Yurok traditional ecological knowledge and wildlife management. *Journal of Wildlife Management*, 86(1), pp.1-15. [DOI]

Rees, J. and Bamberg, S. 2014. Climate protection needs societal change: determinants of intention to participate in collective climate action. *European Journal of Social Psychology*, 44(5), pp.466-473. [DOI]

Reo, N.J. and Whyte, K.P. 2011. Hunting and morality as elements of traditional ecological knowledge. *Human Ecology*, 40(1), pp.15-27. [DOI]

Rezeki, A., Hatta, G.M., Arifin, Y.F. and Yunita, R. 2023a. Ecology of endemic primate proboscis monkeys at Curiak Island Area, South Kalimantan, Indonesia. *Jurnal Multidisiplin Madani*, 3(3), pp.552-566.

Rezeki, A., Hatta, G.M., Arifin, Y.F. and Yunita, R. 2023b. Knowledge, perception, and participation of proboscis monkey habitat buffer village communities, Curiak Island Area. *Interdisciplinary Social Studies*, 2(4), pp.1866-1876. [DOI]

Ridwan, R., Afrizal, A., Maryam, S. and Sari, S. 2022. Socio-economic perspective of indigenous community conflict with corporation. In: *Proceedings of the International Conference on Social and Economic Development*, pp.1-8. [DOI]

Rudiarto, I., Handayani, W., Wijaya, H.B. and Insani, T.D. 2019. Rural livelihood resilience: an assessment of social, economic, environment, and physical dimensions. *MATEC Web of Conferences*, 280, 01002, pp.1-6. [DOI]

Ruíz-Mallén, I. and Corbera, E. 2013. Community-based conservation and traditional ecological knowledge: implications for social-ecological resilience. *Ecology and Society*, 18(4), pp.1-12. [DOI]

Sallu, S.M., Twyman, C. and Stringer, L.C. 2010. Resilient or vulnerable livelihoods? assessing livelihood dynamics and trajectories in rural Botswana. *Ecology and Society*, 15(4), pp.1-15. [DOI]

Sharma, R. and Patil, V. 2025. Exploring institutional climate capacity assessment indicators of community-based organizations in the conservation projects: a participative approach. *Nature Environment & Pollution Technology*, 24(2), pp.1-10.

Shepard, G.H. and Daly, L. 2023. Sensory ecology, bioeconomy, and the age of COVID: a parallax view of indigenous and scientific knowledge. *Topics in Cognitive Science*, 15(3), pp.584-607. [DOI]

Shokirov, Q. and Backhaus, N. 2020. Integrating hunter knowledge with community-based conservation in the Pamir Region of Tajikistan. *Ecology and Society*, 25(1), pp.1-15. [DOI]

Sidi, M.A.M., Ahmad, B.E., Puan, C.L., Noor, M.I.M., Isa, K.A., Norsyam, W.M. and Johannis, N.J. 2022. Recreational risks: human and wildlife conflicts at Johor National Parks, Malaysia. *IOP Conference Series: Earth and Environmental Science*, 1019(1), 012007, pp.1-10. [DOI]

Sihombing, D., Sihombing, M., Lubis, S. and Tarmizi, H.B. 2019. Community tourism awareness influence against tourism development and regional development in North Tapanuli Regency, Indonesia. *International Journal of Civil Engineering and Technology*, 10(3), pp.1-10. Retrieved from https://papers.ssrn.com/sol3/papers.cfm?abstract_id=3456449

Silva, J.A. and Mosimane, A. 2012. Conservation-based rural development in Namibia. *The Journal of Environment & Development*, 22(1), pp.25-50. [DOI]

Singh, A., Kazi, R., Gorde, S., Shukla, R.P., Gawande, A. and Kumar, A. 2025. Exploring the role of environmental education in promoting sustainability mindset: an empirical analysis using forward and hierarchical regression methods. *Nature Environment and Pollution Technology*, 24(3), pp.1-7.

Sohail, M.T. and Chen, S. 2022. A systematic PLS-SEM approach on assessment of indigenous knowledge in adapting to floods, a way forward to sustainable agriculture. *Frontiers in Plant Science*, 13, pp.1-15. [DOI]

Stapleton, S.J., Uribe, A. and Wright, A.L. 2022. Televising justice during war. *Journal of Conflict Resolution*, 66(3), pp.529-552. [DOI]

Stark, D., Nijman, V., Lhota, S., Robins, J. and Goossens, B. 2012. Modeling population viability of local proboscis monkey Nasalis larvatus populations: conservation implications. *Endangered Species Research*, 16(1), pp.31-43. [DOI]

Stolton, S., Dudley, N., Avcıoğlu Çokçalışkan, B., Hunter, D., Ivanić, K.-Z., Kanga, E., Kettunen, M., Kumagai, Y., Maxted, N. and Senior, J. 2015. Values and benefits of protected areas. In: *Protected Area Governance and Management*, pp.145-168.

Strier, K.B. 2016. *Primate behavioral ecology*. Routledge, pp.600.

Su, M., Wall, G. and Xu, K. 2016. Tourism-induced livelihood changes at Mount Sanqingshan World Heritage Site, China. *Environmental Management*, 57(5), pp.1024-1040. [DOI]

Sullivan, A., York, A.M., White, D.D., Hall, S.J. and Yabiku, S.T. 2017. De jure versus de facto institutions: trust, information, and collective efforts to manage the invasive mile-a-minute weed (Mikania micrantha). *International Journal of the Commons*, 11(1), pp.1-20.

Susilo, H., Takahashi, Y. and Yabe, M. 2017. The opportunity cost of labor for valuing mangrove restoration in Mahakam Delta, Indonesia. *Sustainability*, 9(12), 2169, pp.1-15. [DOI]

Tholkapiyan, M., Sankaradass, V., Hariharasudhan, C., Priyanka, M. and Ravisundar, K. 2025. Spatio-temporal changes of chlorophyll concentration with environmental parameters over the Gulf of Mannar, India. *Nature Environment & Pollution Technology*, 24(3), pp.1-10.

Toulec, T., Lhota, S., Scott, K., Putera, A.K.S., Kustiawan, W. and Nijman, V. 2022. A decade of proboscis monkey (Nasalis larvatus) population monitoring in Balikpapan Bay: confronting predictions with empirical data. *American Journal of Primatology*, 84(2), pp.1-15. [DOI]

Ulum, A.S., Djati, M.S. and Rozuli, A.I. 2024. Community-based plastic waste management model in Bangun Village, Mojokerto Regency, Indonesia. *Nature Environment & Pollution Technology*, 23(4), pp.1-10.

Unks, R.R., Goldman, M.J., Mialhe, F. and Pinho, J.R.d. 2021. "People should also look after the people": relational values of wildlife and collectively titled land in Ilkisongo Maasai group ranches in southern Kenya. *Ecology and Society*, 26(3), pp.1-20. [DOI]

Vergara-Ríos, D., Montes-Correa, A.C., Urbina-Cardona, J.N., Luque-Villa, M.A.D., Cattan, P.E. and Granda-Rodríguez, H.D. 2020. Local community knowledge and perceptions towards amphibians in urban and rural settings: tools for biological conservation. *Research Square*, pp.1-15. [DOI]

Walpole, M. and Davidson, N.C. 2018. Stop draining the swamp: it's time to tackle wetland loss. *Oryx*, 52(4), pp.595-596. [DOI]

Wardatutthoyyibah, W., Pudyatmoko, S., Imron, M.A. and Subrata, S.A. 2023. Habitat use of proboscis monkey (Nasalis larvatus) in production forests of West Kalimantan, Indonesia. *Biodiversitas Journal of Biological Diversity*, 24(3), pp.1-10. [DOI]

Wilfred, P. 2010. Towards sustainable wildlife management areas in Tanzania. *Tropical Conservation Science*, 3(1), pp.103-116. [DOI]

Yazezew, D. 2022. Human-wildlife conflict and community perceptions towards wildlife conservation in and around Wof-Washa Natural State Forest, Ethiopia. *BMC Zoology*, 7(1), pp.1-12. [DOI]

Yongabi, K.A. 2023. Perspectives on indigenous knowledge in mitigating climate change. *Research and Reviews on Healthcare Open Access Journal*, 8(4), pp.1-5. [DOI]

Yulasteriyani, Y., Putri, C.A., Istiqoma, I., Abror, M.Y. and Sartika, D.D. 2025. Sustainable livelihood level of the community in Kalampadu Village, Ogan Ilir Regency: an analysis using SEM-PLS. *Society*, 13(1), pp.241-255. [DOI]

Zikri, I., Takahashi, M., Salsabila, M., Hamid, A., Ginting, L.N. and Sofyan, S. 2024. Livelihood vulnerability of post-disaster rehabilitation in Banda Aceh and its neighbouring Gampongs. *IOP Conference Series: Earth and Environmental Science*, 1297(1), 012095, pp.1-10. [DOI]

Zomeren, M.v., Saguy, T. and Schellhaas, F.M.H. 2012. Believing in "making a difference" to collective efforts: participative efficacy beliefs as a unique predictor of collective action. *Group Processes & Intergroup Relations*, 16(5), pp.618-634. [DOI]

Zuhdi, M.H., Widi, T.S.M., Rezeki, A. and Putra, A.R.S. 2024a. Local community participation under proboscis monkey conservation-based ecotourism development in Curiak Island Area. *IOP Conference Series: Earth and Environmental Science*, 1360(1), 012020, pp.1-10. [DOI]

Zuhdi, M.H., Widi, T.S.M., Rezeki, A. and Putra, A.R.S. 2024b. Perceptions of the local community on impacts of proboscis monkey conservation-based ecotourism development at Curiak Island Area. *IOP Conference Series: Earth and Environmental Science*, 1360(1), 012019, pp.1-10. [DOI]

Nature Environment and Pollution Technology
An International Quarterly Scientific Journal

p-ISSN: 0972-6268
(Print copies up to 2016)
e-ISSN: 2395-3454

Vol. 25 | No. 3 | Article ID B4396 | 2026

Original Research Paper

https://doi.org/10.46488/NEPT.2026.v25i03.B4396

Open Access Journal

Exploration of Microbial Diversity of Anoxic Soil Under Submerged Low-Land Paddy Cultivation by Culture-Independent Methods for Its Consequent Ramifications on Environment, Soil Health, and Sustainability

M. B. Chakraborty[1]† and S. R. Patgiri[2]
[1]Department of Botany, Cotton University, Guwahati-781001, Assam, India
[2]Department of Microbiology, Royal Global University, Guwahati-781035, Assam, India
†Corresponding author: M.B. Chakraborty; moitrayeebchakraborty@cottonuniversity.ac.in

Abbreviation: Nat. Env. & Poll. Technol.
Website: www.neptjournal.com

Received: 18-09-2025
Revised: 14-11-2025
Accepted: 14-12-2025

Key Words:

Metagenomics
Microbial diversity
Non-paddy field soil
Paddy field soil
Soil microbiome

ABSTRACT

Soil microbes, the primary components of soil biodiversity, provide crucial ecosystem services. Anthropogenic activities, such as agriculture, bring about innumerable biotic and abiotic changes in the soil ecosystem that can have short and long-term impacts on the environment and soil sustainability. Lowland paddy cultivation is a typical example of anthropogenic disturbance to soil, where the paddy field fluctuates between waterlogged conditions and extreme dry spells, which have some immediate effects, such as greenhouse gas emissions, and a probable long-term impact on soil, altering soil oxidoreduction states and influencing microbe-driven nutrient and carbon cycling. Although rice is a dominant crop in Northeast India, microbial responses to paddy cultivation remain poorly documented. In this study, we compared the soil microbiomes of paddy fields and adjacent non-paddy land in the Bhagawatipara region of Kamrup district of Assam, India, using 16S rRNA amplicon sequencing. Paddy soils exhibited clear shifts in microbial abundance, with an increased representation of methanogens, nitrogen-transforming archaea, diazotrophs, and phosphate-solubilizing bacteria. Distinct changes in alpha and beta diversity further indicated strong hydrological and cultivation-driven impacts on microbial community dynamics. This study provides the first comprehensive microbial dataset for paddy soils in the Kamrup district (Assam) and highlights key microbial signatures associated with methane cycling and soil nutrient processes.

Citation for the Paper:

Chakraborty, M.B. and Patgiri, S. R. 2026. Exploration of microbial diversity of anoxeic soil under submerged low-land paddy cultivation by culture-independent methods for its consequent ramifications on environment, soil health, and sustainability. *Nature Environment and Pollution Technology*, 25(3), B4396. https://doi.org/10.46488/NEPT.2026.v25i03.B4396

Note: From 2025, the journal has adopted the use of Article IDs in citations instead of traditional consecutive page numbers. Each article is now given individual page ranges starting from page 1.

Copyright: © 2026 by the authors
Licensee: Technoscience Publications
This article is an open access article distributed under the terms and conditions of the Creative Commons Attribution (CC BY) license (https://creativecommons.org/licenses/by/4.0/).

1. INTRODUCTION

Various anthropogenic activities, including agriculture, contribute to the environmental crisis, posing a serious threat to the sustainability and existence of life on this planet. Agricultural practices such as dependence on fertilizers, pesticides, and mechanized plowing contribute to environmental degradation and loss of soil sustainability. Lowland paddy cultivation poses a higher environmental threat as the practice of flooding paddy fields creates anaerobic conditions under which certain bacteria and archaea produce methane gas, which is more potent than carbon dioxide in greenhouse effect. However, rice, being the staple diet of more than 50% of the global population, is indispensable for food security. The microbes present in the soil play a major role in this emission, and at the same time, these microbes are essential for soil sustainability as they maintain biogeochemical cycles, mitigate stress, and even oxidize some greenhouse gases. Although the effect of agricultural activities on microbial diversity is invisible, it can have serious consequences for long-term sustainability. Thus, the characterization of microbial communities can play a very important role in designing mitigation strategies. Although paddy is the major crop of Assam and other northeastern states of India, there is limited literature available on metagenomic studies of paddy field microbiomes. Earlier studies were mostly culture-dependent and revealed only a minor fraction of the total microbiome.

Microbes, including archaea, bacteria, and fungi, play a pivotal role in overall soil health and offer innumerable ecosystem services. These microbial communities display significant diversity in both structure (community composition) and function (collective physiology of all species) (Escalas et al. 2019). This diversity varies across different locations and changes over time. Soil microorganisms that significantly impact biogeochemical cycles, are influenced by varied fertilizer practices, and are closely associated with crop growth, nutrient cycling, and sustainable soil productivity (Yang et al. 2022, Börjesson et al. 2011). Exploring bacterial diversity and biogeographic patterns can offer insights into the fundamental ecological processes and mechanisms that support bacterial diversity and ecosystem function, along with the scope of application in diverse fields such as agriculture, the environment, and many innovative areas. Microbes can be used for soil stabilization instead of chemical and physical methods (Shah et al. 2024). Various agricultural management practices, including crop type, tillage, fertilizer application, and irrigation patterns, affect soil microbial activity and community structure (Camacho-Sanchez et al. 2023, Gupta et al. 2022). However, the majority of microbial ecosystem research relies on a few dominant species due to their easy detectability. In microbial communities, a few abundant species are prevalent alongside a multitude of rare species, which contributes to high diversity (Hanson et al. 2012). Therefore, a thorough investigation of the complexity and diversity of soil microorganisms is vital for understanding the role of different microbial communities in soil ecosystems and the environment as a whole. Understanding the link between microbial diversity and the environment is crucial for developing predictive models of microbial diversity-driven ecosystem processes and functions (Wan et al. 2023). The identification of uncultured microorganisms requires rigorous scientific examination. Among the techniques developed to elucidate the physiology and genetics of non-cultured organisms, metagenomics is a transformative centerpiece in microbiology. Metagenomics has notably propelled novel research avenues by facilitating unparalleled analyses of genome heterogeneity and evolution in environmental settings. Additionally, it grants access to a substantially broader spectrum of microbial diversity than traditional cultivation methods (Handelsman 2004).

In the present age, facing extreme environmental crises, climate change, food security concerns, and various environment-related complexities, the analysis of soil microbiomes associated with agriculture has become imperative for understanding the role of microbiomes in environmental degradation and restoration of soil health towards developing climate change resilient, sustainable agriculture. In the case of paddy cultivation, the anaerobic environment of the flooded paddy field soil becomes suitable for methanogens, a type of microorganism that produces the greenhouse gas methane (CH_4) as a metabolic byproduct (Xuan et al. 2025). The effect of prolonged flooding and fertilization practiced in paddy cultivation changes the abiotic factors of the soil ecosystem, which are closely tied to the structure and function of microbial communities. Unlike higher organisms, disturbance diversity relationships in microbial ecology are contradictory and difficult to generalize. Although paddy field soil in some cases displays higher diversity than non-paddy field soil, the increase in microbial diversity of paddy fields does not always correlate with positive sustainability impacts, as higher diversity can sometimes correlate with trade-offs in ecosystem services, such as soil organic carbon (SOC) retention or nitrogen (N) retention.

Although India is one of the major producers of paddy, research on paddy field soil microbiomes is not proportionate. A study on the effect of agricultural practices on the soil microbiome showed that fertilizer application did not have a significant effect on the microbiome, indicating the resilience of soil microflora to short-term disturbances (Kumar et al. 2025). Studies on the rhizospheric microbiome of basmati rice have shown a unique assemblage of bacteria, such as Actinobacteria, *Bacillus subtilis*, *Burkholderia, Enterobacter, Klebsiella, Lactobacillus, Micrococcus, Pseudomonas*, and *Sinomonas* (Raina et al. 2025). In the paddyfield microbiome, the prevalence and diversity of beneficial microbes, such as nitrogen fixers, nitrifiers, and phosphate mineralizers, were lower, whereas cellulose and hemicellulose decomposing microbes and phosphorus solubilizers were abundant (Prasannakumar et al. 2021). Proteobacteria, Chloroflexi, Acidobacteria, Actinobacteria, and Bacteroidetes are the most abundant bacterial phyla in rice field soil (Singh et al. 2024).

The northeastern region of India, situated within the Eastern Himalayan biodiversity hotspot, serves as a gateway to diverse flora and fauna. The diverse physiography of the area offers a distinct and varied environment for the evolution of microorganisms. Studies on microbes isolated from these diverse areas can provide opportunities to explore genetic diversity and contribute to understanding ecological processes on Earth. Numerous studies have investigated the microbial biodiversity of soil across various ecosystems in northeastern India. Nevertheless, the implementation of high -throughput sequencing methods has the potential to enhance and contribute to in-depth analysis and documentation of microbial diversity of the samples

There is significantly less research based on metagenomic approaches to study the paddy field microbiome of northeast

India. Very few reports on the paddy field microbiome of this region indicate a major research gap, as the region has unique rice cultivation practices and diverse agroecosystems. Microbiome studies have mostly been conducted on local fermented foods and culture-dependent analysis of plant growth-promoting and other beneficial microbes of diverse crops. Sediments of the Brahmaputra River, India, showed increased abundance of Pseudomonadota at the phylum level, *Bradyrhizobium*, *Pseudomonas* and *Variovorax* at the genus level and T. *denitrificans* as the most abundant bacterial species (Sharma et al. 2024). An increase in the abundance of Proteobacteria and Firmicutes was observed in paddy field soil supplemented with vermicompost, increasing paddy grain yield (Deka et al. 2025). In culture-dependent studies, the bacterium *Alcaligenes faecalis* isolated from the rice rhizosphere of the upper Brahmaputra Valley region of Assam was found to be effective as a biocontrol agent against rice root-knot nematodes (Jena et al. 2023). Consortia of indigenous PGPR isolates of *Bacillus cereus, Pseudomonas fluorescens,* and *Azospirillum oryzae* improved the productivity and soil health of paddy under jhum cultivation in Nagaland (Giri et al. 2023).

This study analyzed the composition of microbial communities found in paddy field and non-paddy field soil samples using a metagenomic approach. Metagenomic analysis has provided comprehensive insights into the previously uncharted microbial realm, and the data generated from global research endeavors have the potential to enhance our comprehension of global microbiome patterns (Chakraborty et al. 2023). While some microbial communities are essential for preserving soil fertility, others are responsible for harmful gaseous emissions, denitrification, and may also be pathogenic. Therefore, this study aimed to identify the specific types of microorganisms present in both paddy field and non-paddy field soil samples. This analysis would provide insights into how different environments shape microbial diversity. Assessing the environmental factors influencing microbial diversity requires the evaluation of various environmental parameters, such as pH, temperature, moisture content, and nutrient availability, to understand their influence on shaping microbial communities in both paddy and non-paddy soils.

This study was conducted in the Bhagwatipara paddy field situated in Rangamati, Kamrup District of Assam, India. Metagenomic analysis was employed to examine the microbiome of paddy soil in Bhagwatipara. A comparative analysis was conducted using non-paddy soil from the same location as the reference point. This study aimed to comprehend the impact of paddy cultivation on indigenous microflora and gain insights into the general effects of ecological disturbance on microbial community diversity.

2. MATERIALS AND METHODS

2.1. Soil Sampling

To study the microbial diversity of paddy field and non-paddy field soil samples (control/reference), soil samples were obtained from the Bhagawatipara area (26°22’60” N and 91°58’0” E, site elevation: ~32 m above sea level) (Fig. 1). Soil was collected from three adjacent paddy



Fig. 1: The study area is located in Bhagawati Para in Kamrup district, situated in Assam state.

fields in Bhagwatipara using sterilized trowels, and each of the collected soil samples was a composite sample of three random subsamples from each paddy field. Soil samples from adjacent non-agricultural land with natural, undisturbed vegetation were used as a reference or control. A V-shaped hole was dug in the soil, and the soil samples were collected from a depth of about 10cm in sterilized sample bottles, properly labeled and brought to the laboratory at a low temperature with ice packs.

2.2. Soil Physical Parameters

The study of soil moisture content (%), pH, and temperature (°C) was conducted on the samples obtained from three different locations of paddy and non-paddy sites of the Bhagawatipara area.

2.3. DNA Isolation

DNA was isolated from the soil samples using a DNeasy PowerSoil kit (Qiagen, United States). The DNA present in the soil samples was isolated, and the concentration was measured using a Qubit Fluorimeter (V.3.0) (Thermo Fisher Scientific, Malaysia).

2.4. Illumina Library Preparation:

The region V3-V4 of 16S rRNA was amplified using specific V3 primer CCTACGGGNBGCASCAG (forward) and V4 primer GACTACNVGGGTATCTAATCC (reverse). The resulting amplification product was verified on agarose gel (2%), which was purified to eliminate non-specific amplifications. A 5 nanogram aliquot of the amplified product was used for library preparation using the NEB Next Ultra DNA library preparation kit. (Illumina, California, United States). The quantification and its quality were estimated using an Agilent 2200 Tape Station. After ligation with Illumina adaptors, the amplicons were gel-purified and amplified using conventional Illumina methods. Subsequently, the prepared library was sequenced on an Illumina HiSeq 2500 platform at AgriGenome Labs, Kochi, India.

2.5. Analysis of 16S rRNA Dataset Using Bioinformatics

In this study, raw sequences were quality-filtered to remove reads containing ambiguous bases, homopolymer runs >6 bp, primer mismatches, or read lengths <100 bp. High-quality reads were processed using QIIME v1.9.1. OTUs were clustered at 97% sequence similarity using the UCLUST algorithm (Edgar 2010), and taxonomy was assigned using the SILVA reference database based on 97% identity to the reference sequences. Chimeric sequences were filtered during the workflow to ensure an accurate taxonomic classification. Taxonomic summaries from phylum to genus levels were generated directly from the final OTU table without rarefaction, and taxa contributing less than 0.005% of the total abundance were excluded from downstream analysis. A BIOM file was created to support the functional and statistical analyses. Alpha-diversity indices (Shannon, Chao1, and Observed Species) and beta-diversity metrics were computed using QIIME to assess within-sample and between-sample microbial variation. Principal Coordinate Analysis (PCoA) was performed using weighted and unweighted UniFrac distance matrices. Functional predictions were derived using PICRUSt, and KEGG pathway profiles were generated for comparative functional assessments (Kanehisa & Goto 2000).

Statistical analyses were performed in Python and R. Group differences in taxonomic abundance were assessed using one-way ANOVA, followed by Linear Discriminant Analysis (LDA) to identify the taxa that most strongly differentiated the paddy and non-paddy soils. PERMANOVA (Adonis function, vegan package) was used to evaluate differences in beta diversity among sample groups. Non-parametric comparisons of taxon abundance were performed using the Kruskal–Wallis test, where applicable. All analyses were performed in R v3.6.2 using the vegan package to compute richness, evenness, and community diversity.

3. RESULTS

Table 1 presents the physicochemical properties of the soil samples from both paddy and non-paddy fields. The moisture content of soil samples from the paddy field was relatively higher (average 27.32% ± 1.4) than that of non-paddy soil (average 9± 0.5%).

3.1. Quality Filtering and Read Retention

Six environmental samples were processed for quality assessment following read joining. The input read count per sample ranged from 30,302 to 42,429 sequences. After applying stringent quality filters, including the removal of reads that were too short post-trimming,

Table 1: Physical parameters of samples collected from both paddy and non-paddy fields of Bhagawatipara.

Samples	Tempertaure	pH	Moisture
1 Bhagwatipara paddy	32.3	7.2	24.49
2 Bhagwatipara paddy	30.1	6.85	28.87
3 Bhagwatipara paddy	31.1	7.1	28.60
4 Bhagwatipara non-paddy	29.6	6.9	10
5 Bhagwatipara non-paddy	27.8	7.1	8
6 Bhagwatipara non-paddy	28.6	6.8	9

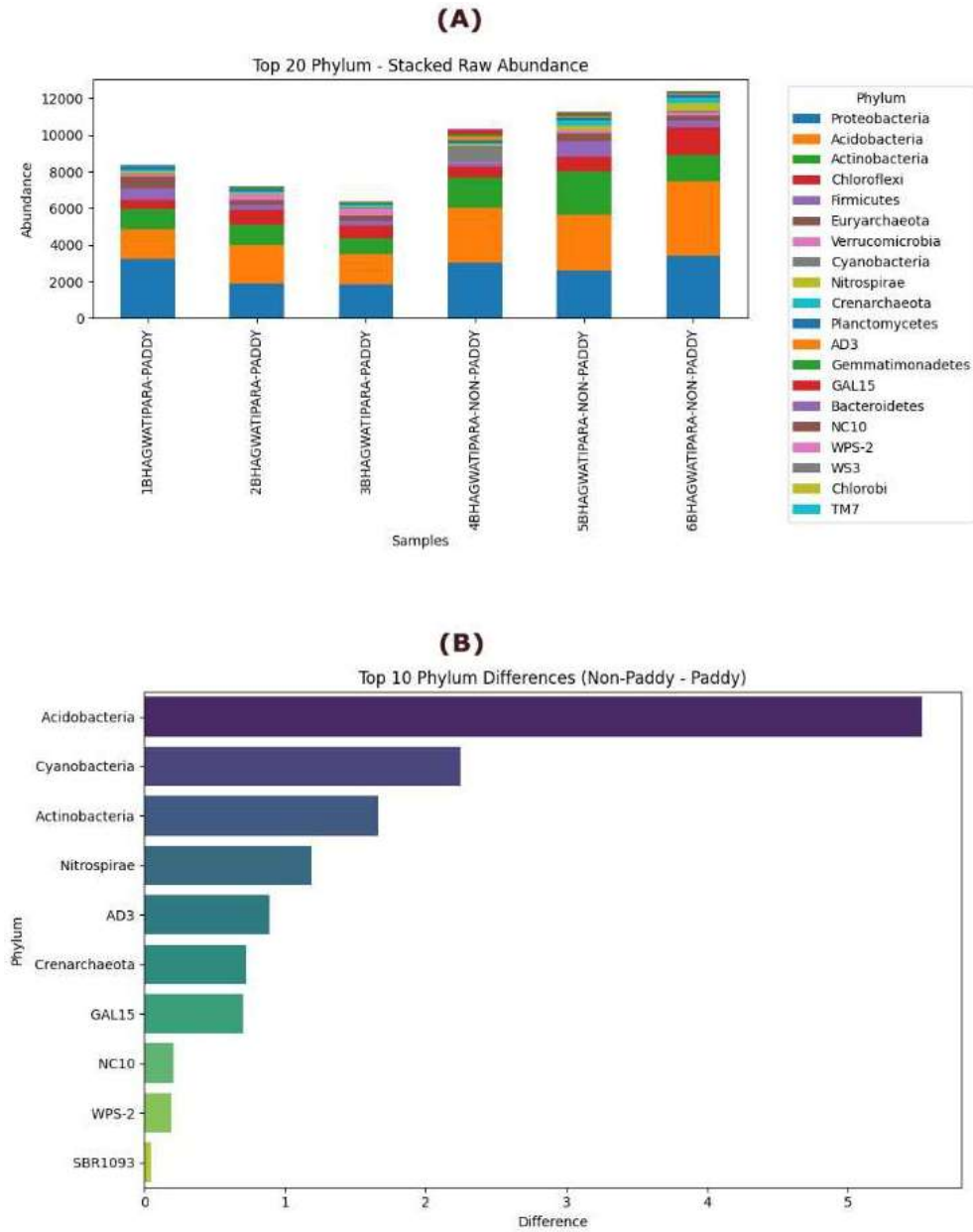


Fig. 2: (A) Stacked bar plot showing top 20 microbes at the phylum level, (B) Top 10 Phylum-Level Differences Between Non-Paddy and Paddy Soils.

exceeded the limit of ambiguous bases (N), or failed barcode criteria, each sample retained a substantial number of high-quality reads suitable for downstream microbiome analysis. The number of high-quality sequences retained per sample was 18,483 for 1BHAGWATIPARA-PADDY, 18,889 for 2BHAGWATIPARA-PADDY, 16,373 for 3BHAGWATIPARA-PADDY, 18,318 for 4BHAGWATIPARA-NON-PADDY, 23,379 for 5BHAGWATIPARA-NON-PADDY, and 23,262 for 6BHAGWATIPARA-NON-PADDY groups. The median read lengths after filtering remained consistent across samples (440–441 bp), indicating a high-quality sequencing performance. The 16S rRNA gene sequencing data are available at the Sequence Read Archive (SRA), NCBI (http://www.ncbi.nlm.nih.gov/sra), SRR21547403, SRR21547404, and SRR21547406.

Operational Taxonomic Units (OTUs) picking and taxonomy classification were performed using pre-processed consensus V3-V4 sequences. Pre-processed reads from all samples were pooled and clustered into OTUs based on their

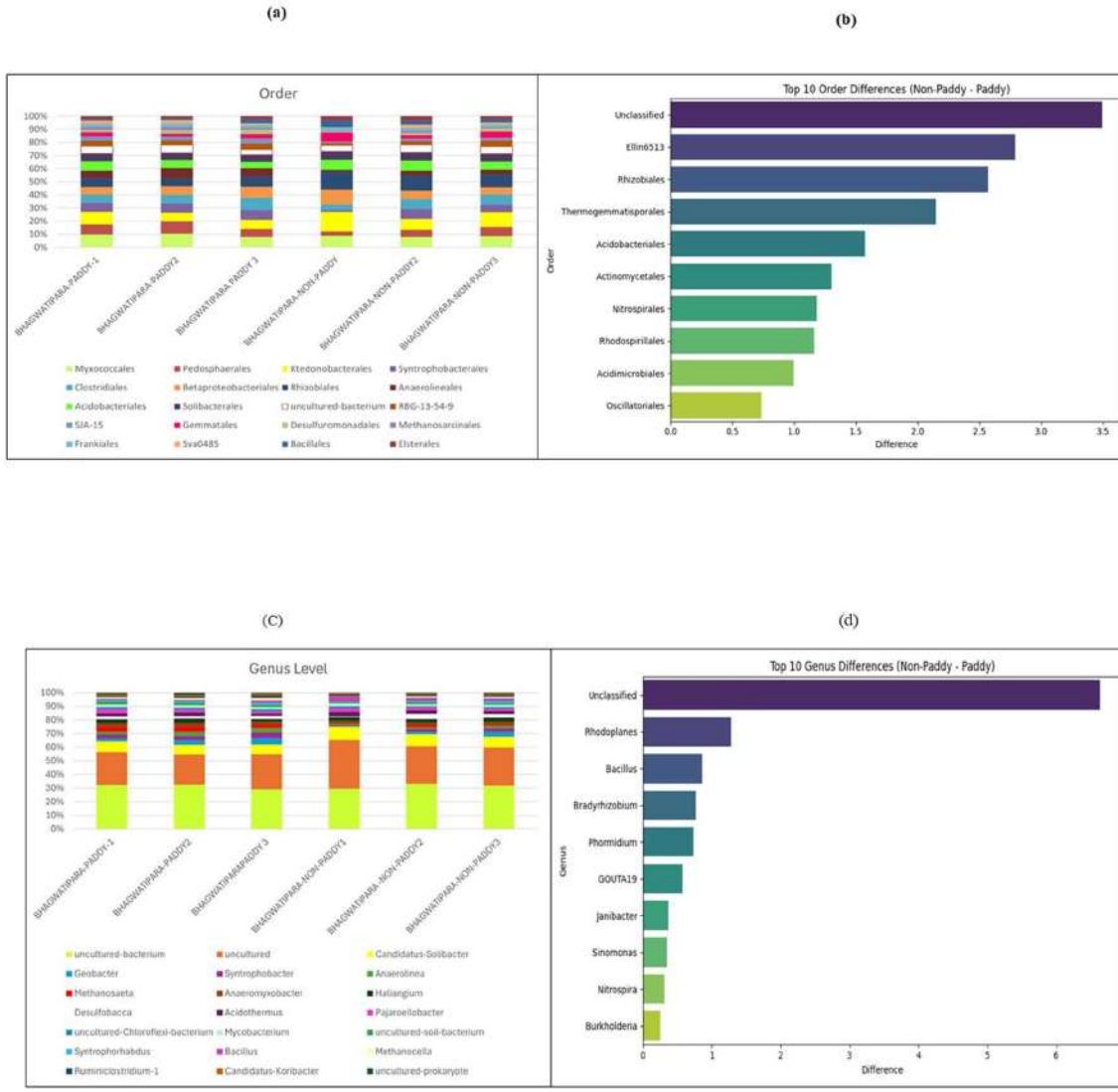


Fig. 3: (a) Stacked bar plot showing top 20 microbes at the Order level, (b) Top 10 Order-Level Differences Between Non-Paddy and Paddy Soils, (C) Stacked bar plot showing top 20 microbes at the Genus- level, (d) Top 10 Genus-Level Differences Between Non-Paddy and Paddy Soils.

sequence similarity using the Uclust program (similarity cut-off = 0.97) available in the QIIME software.

3.2. Relative Abundance of Microbes

Analysis of the microbial community structure revealed clear ecological distinctions between paddy and non-paddy soils (Fig. 2). In paddy soils, a higher relative abundance of *Chloroflexi*, known for degrading complex hydrocarbons and pollutants, was observed, which may be linked to organic matter deposition from crop residues and the recurrent use of fertilizers and pesticides. An increased representation of *Euryarchaeota*, a phylum associated with methanogenesis under anaerobic conditions, further reflects the waterlogged, low-oxygen environment that is typical of paddy fields. In contrast, the comparative difference analysis (non-Paddy vs. Paddy) highlighted that several functionally important phyla were markedly more abundant in non-Paddy soils. *Acidobacteria* exhibited the highest positive difference, indicating a strong preference for well-aerated, stable soil environments. Their reduced abundance in paddy fields suggests suppression under anaerobic conditions. *Cyanobacteria*, responsible for nitrogen fixation and primary production, and *Actinobacteria*, key decomposers and antibiotic producers, were also substantially enriched in non-paddy soils, implying diminished nutrient cycling and lower decomposition activity in paddy fields compared to non-paddy fields. Additional phyla, such as *Nitrospirae*, *AD3, Crenarchaeota, GAL15, NC10,* and *WPS-2,* also

showed higher abundance in non-paddy soils, reinforcing that non-paddy environments support a richer and more functionally diverse aerobic microbial community. Overall, these shifts reflect the strong impact of paddy field flooding and management practices on the microbial ecological balance and nutrient cycling potential.

Higher relative abundances of *Myxococcales, Pedosphaerales, Syntrophobacterales, Clostridiales, Anaerolineales* and *Methanosarcinales* were observed in the paddy field samples than in the non-paddy field soil samples, whereas *Ktedonobacterales, Betaproteobacteriales, Rhizobiales, Acidobacteriales, Solibacterales, Gemmatales, Frankiales, and Bacillales* were more abundant in the non-paddy soil than in the paddy field soil (Fig. 3).

At the genus level, *Geobacter, Syntrophobacter, Anaerolinea, Methanosaeta, Desulfobacca, Acidothermus*, and *Methanocella* have higher abundance in paddy field soil, but *Candidatus-Solibacter, Anaeromyxobacter, Haliangium, Bacillus*, and *Paenibacillus* had higher abundance in non-paddy soil. *Methanobrevibacter, Listeria, Clostridium, Methanobrevibacter, Syntrophus*, and *Geobacter* had significantly different relative abundances across the samples ($p < 0.05$). *Methanobrevibacter* and *Listeria* have been observed only in paddy fields, whereas *Clostridium, Syntrophus*, and *Geobacter* have very low abundance in non-paddy soil. *Methanocella* are ubiquitous in paddy soils and are key methane producers

Genus-and species-level patterns further reinforced the phylum-level differences observed between paddy and non-paddy soils. In alignment with the higher abundance of *Acidobacteria* in non-paddy fields, several Acidobacteria-associated species, including *Unclassified Acidobacteria*, *Candidatus Solibacter celatum*, and *Solibacter gordonii*, showed big positive differences, indicating their substantially greater enrichment in non-paddy soils. These species are typically involved in soil carbon turnover and are sensitive to agricultural disturbances, supporting the observation that non-paddy soils maintain a more stable and diverse heterotrophic community than paddy soils. Similarly, species such as *Nitrospira leptosphaera* and *Nitrospira flexus*, belonging to the Nitrospirae phylum, contribute to nitrification processes and suggest more efficient nitrogen cycling under non-flooded conditions.

In contrast, paddy fields showed lower representation of many Actinobacteria-associated species, consistent with our earlier finding of reduced Actinobacteria abundance at the phylum level. Species such as *Actinobacteria radiopugnans*, *A. tuberum*, *A. fastidiosa*, and *A. muraliis* all showed negative differences in the comparison, indicating a reduced presence in the flooded environment. This decline may contribute to the slower degradation of complex organic matter and an ecological shift that favors anaerobic and methanogenic taxa. This trend also aligns with the higher abundance of Euryarchaeota (methanogens) observed in paddy soils,

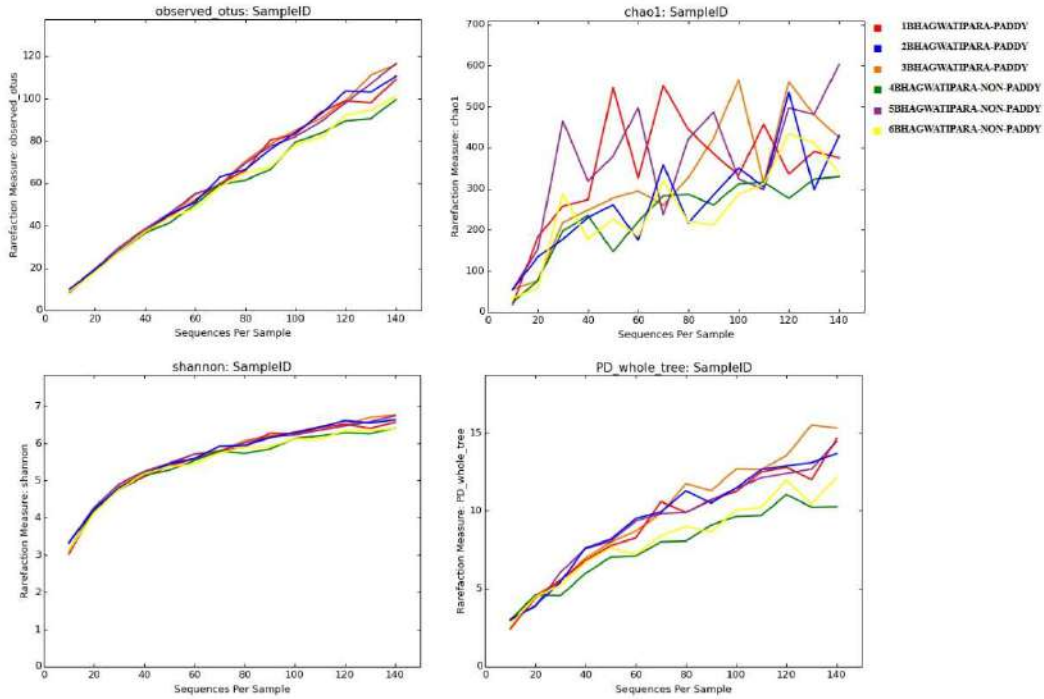


Fig. 4: Rarefaction curves showing alpha diversity estimates across paddy and non-paddy soil samples.

suggesting enhanced methane-producing activity under waterlogged and oxygen-limited conditions.

The stacked species-level abundance plot further confirmed that non-paddy soils contained a broader distribution of key bacterial species, whereas paddy soils were dominated by a narrower set of taxa with lower species-level diversity. Altogether, these species-level observations complement the phylum-level findings and highlight how land use type and soil flooding conditions distinctly shape microbial community structure, ecological functions, and nutrient cycling potential in the studied habitats.

3.3. Alpha Diversity and Beta Diversity Analysis

Rarefaction analysis was performed to evaluate the sequencing depth and compare the alpha diversity patterns across paddy and non-paddy soil samples (Fig. 4). The observed OTUs rarefaction curves showed a consistent increase with sequencing depth for all samples, indicating adequate sampling coverage and comparable sequencing effort across groups. Non-paddy soils (Samples 4–6) generally exhibited slightly higher richness values at higher sequence depths compared to paddy soils (Samples 1–3), suggesting a more diverse microbial community under non-flooded conditions.

The Chao1 richness estimator revealed greater variability among samples, with several non-paddy samples showing higher estimated richness than the paddy samples. This pattern reflects the presence of additional rare taxa in non-paddy soils, further supporting the increased richness of aerobic environments. The Shannon diversity index, which accounts for both richness and evenness, showed smooth and gradually rising curves for all samples, with non-paddy samples displaying marginally higher diversity, indicating a more even community composition than that of paddy soils.

Similarly, the Phylogenetic Diversity (PD whole tree) rarefaction curves demonstrated a higher phylogenetic breadth in non-paddy soils, implying the presence of more evolutionarily distinct microbial lineages under non-flooded conditions.

Beta diversity analysis using Bray-Curtis dissimilarity clearly showed a separation between the microbial communities of paddy and non-paddy soil samples. The principal coordinate analysis (PCoA) plot demonstrated that the samples clustered according to their land type, indicating distinct community compositions between the two environments (Fig. 5). PC1 explained 41.4% of the total variation, whereas PC2 explained 22.9%, together accounting for a substantial proportion of the community differences. Non-paddy samples formed a more dispersed cluster, suggesting higher heterogeneity in this group. In contrast, paddy samples clustered more tightly, reflecting a more uniform microbial community structure. This separation supports the findings observed in alpha diversity, phylum-level shifts, and species-level differences, collectively indicating that land use practices strongly influence soil microbial composition.

3.4. Differential Abundance Statistical Analysis

Differential abundance testing using one-way ANOVA and the non-parametric Kruskal–Wallis test revealed several taxa that were significantly different between the paddy and non-paddy soil microbiomes. ANOVA

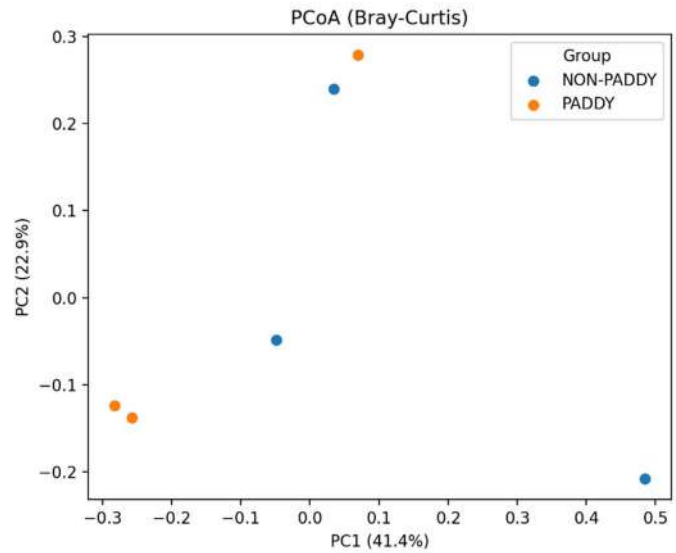


Fig. 5: Principal Coordinates Analysis (PCoA) based on Bray-Curtis dissimilarity.

identified strong separation driven by members of *Lentisphaerae* (Victivallaceae), Betaproteobacteria (*Ramlibacter*), methanogenic archaea including Candidatus Methanoregula and Methanobrevibacter, and multiple anaerobic lineages of Chloroflexi (*Anaerolineae*), alongside enriched Firmicutes taxa such as *Listeria*, *Clostridium*, *Pelosinus*, and representatives of Ruminococcaceae. Several taxa associated with anaerobic respiration and redox cycling, including Geobacter, Syntrophus, and Nitrospirae, showed significant differences. The Kruskal–Walli's test supported these patterns, consistently highlighting significant shifts in methanogenic archaea (*Methanobrevibacter, Methanosarcina, Methanomassiliicoccus*), Chloroflexi Anaerolineae, and Firmicutes lineages, along with key soil groups such as Acidobacteria, Actinobacteria, and multiple Proteobacteria families (Comamonadaceae, Moraxellaceae, Enterobacteriaceae). The recurrence of these taxa across both statistical tests confirms robust microbial distinctions between the two soil types, driven largely by the increased abundance of anaerobic and methanogenic groups in paddy soils and the enrichment of aerobic Acidobacteria, Actinobacteria, and several Proteobacteria in non-paddy soils. These findings align with the taxonomic and ordination-based patterns observed at the community level, reinforcing the strong ecological divergence between paddy and non-paddy soil microbial communities.

3.5. Differential Abundance Analysis Using LDA (LEfSe)

LEfSe analysis was performed to identify the taxa that significantly discriminated between the paddy and non-paddy soil microbiomes, as shown in Fig. 6. Using the non-paddy group as a reference, several bacterial and archaeal lineages exhibited strong differential enrichment patterns. Taxa belonging to the phylum GAL15 showed the highest positive LDA coefficients, indicating strong enrichment in non-paddy soils. Members of Verrucomicrobia (particularly *Candidatus Udaeobacter*) and Chloroflexi (including *Ktedonobacter* lineages) were also strongly associated with non-paddy environments, suggesting their ecological preference for relatively dry and less waterlogged soil conditions. Conversely, certain Acidobacteria subgroups (subgroups 1 and 2) were enriched in paddy soils, reflecting their adaptability to the acidic, submerged, and nutrient-variable conditions typical of flooded rice fields. Enrichment of Thaumarchaeota, specifically ammonia-oxidizing archaea (*Candidatus Nitrosotalea*), in paddy soils indicates enhanced nitrification activity under flooded conditions.

Overall, the LDA results complemented the phylum- and species-level observations by highlighting the distinct microbial signatures shaped by contrasting soil environments. These discriminant taxa provide deeper insights into the functional and ecological differences between paddy and non-paddy soil ecosystems.

3.6. Functional Prediction of Microbial Communities (PICRUSt Analysis)

PICRUSt-based metagenome prediction revealed clear functional distinctions between paddy and non-paddy soil microbiomes across multiple metabolic and stress response pathways (Fig. 7). The functional shifts broadly reflected the contrasting environmental conditions of waterlogged, anaerobic paddy soils versus relatively oxygenated and nutrient-variable non-paddy soils.

Pathways associated with stress tolerance and cellular repair were strongly enriched in paddy soils. ABC transporters and oxidative phosphorylation were markedly higher in several paddy samples, indicating enhanced nutrient uptake and energy generation under fluctuating redox conditions in paddy fields. Likewise, DNA repair and recombination proteins were consistently elevated in paddy soils, suggesting increased genomic maintenance, potentially driven by oxidative stress, electron acceptor limitations, and microbial competition. In contrast, non-paddy samples showed comparatively higher contributions to inorganic ion transport and sulfur metabolism, reflecting their more aerated environment, where sulfur oxidation and ion exchange processes remain active.

The functional genes associated with nitrogen transformation exhibited significant differences between

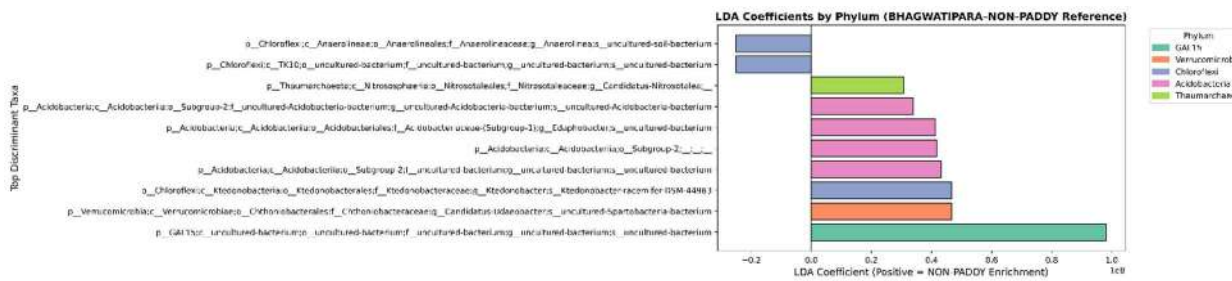


Fig. 6: LEfSe LDA scores identifying discriminant taxa between paddy and non-paddy soils.

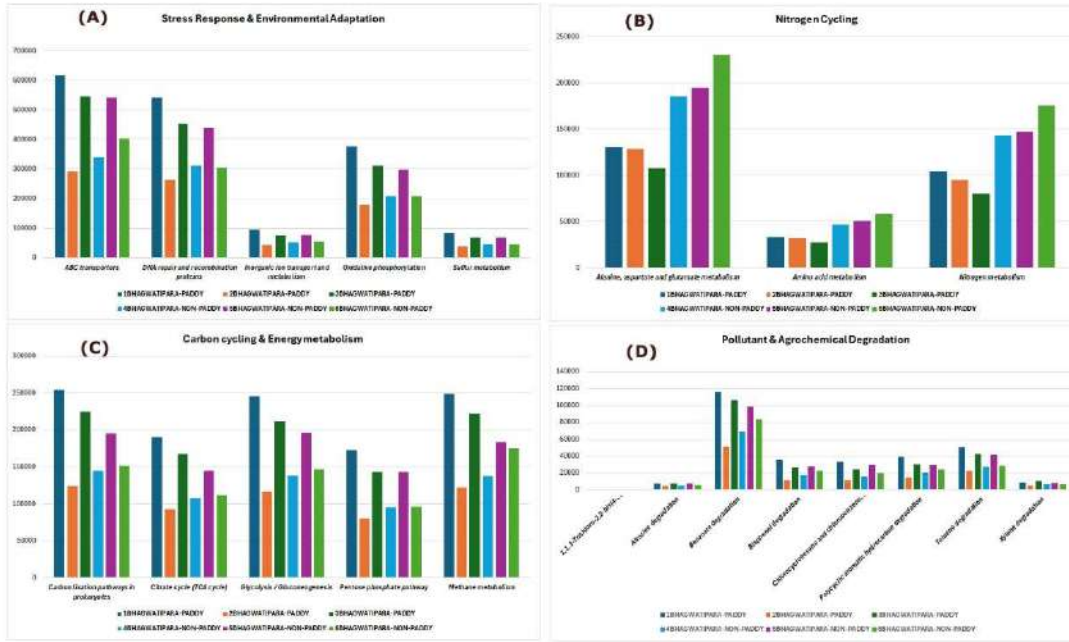


Fig. 7: PICRUSt-based functional predictions of microbial communities in paddy and non-paddy soils.

the two soil types. Alanine, aspartate, and glutamate metabolism, which is central to nitrogen assimilation, showed notable enrichment in non-paddy soils, aligning with higher microbial activity associated with organic nitrogen turnover. Conversely, paddy soils displayed elevated nitrogen metabolism gene counts in some samples, likely driven by the presence of methanogens and denitrifiers thriving under reduced flooded conditions. Amino acid metabolism was also more pronounced in non-paddy soils, indicating diverse heterotrophic nitrogen utilization in oxygenated environments.

Carbon transformation pathways revealed a strong ecological fingerprint in each habitat. Non-paddy soils constantly exhibited higher activity in carbon fixation pathways, the TCA cycle, glycolysis/glyconeogenesis, and the pentose phosphate pathway, reflecting active aerobic heterotrophy and carbon turnover. In contrast, methane metabolism was substantially higher in paddy soils, supporting the dominance of anaerobic methanogenic archaea under flooded and low-oxygen conditions. The significant contribution of these pathways in paddy samples mirrors the taxonomic enrichment of methanogenic groups observed in earlier analyses. PICRUSt predictions also highlighted the functional capacities related to xenobiotic degradation. Non-paddy soils demonstrated enriched pathways for benzene, chlorocyclohexane, chlorobenzene, and polycyclic aromatic hydrocarbon (PAH) degradation functions typically associated with diverse aerobic Proteobacteria and Actinobacteria. Paddy soils showed notable contributions to specific degradation pathways, such as alkane and benzoate degradation, suggesting adaptive responses to agricultural inputs and anaerobic breakdown processes. Although several pathways were shared between the two environments, their magnitudes differed, indicating distinct pollutant-processing roles shaped by oxygen availability and microbial community composition.

4. DISCUSSION

A comparative analysis of soil microbiomes from paddy and non-paddy fields at Bhagawatipara revealed strong ecological and functional divergence driven by differences in hydrology, redox chemistry, and land-use practices. At the phylum level, paddy soils were characterized by the enrichment of Chloroflexi, Euryarchaeota, and other anaerobic or facultative anaerobic groups, consistent with earlier reports that waterlogged and reduced environments select for microorganisms capable of fermentation, syntrophy and methanogenesis (Lee et al. 2015, Jiang et al. 2021). The elevated abundance of methanogenic archaea, particularly Euryarchaeota, aligns with the anaerobic conditions typical of flooded rice systems and supports previous observations that paddy soils are major methane-emitting ecosystems (Sugano et al. 2005). In contrast, non-paddy soils exhibited markedly higher levels of Acidobacteria, Cyanobacteria, Actinobacteria, and Nitrospirae, which are commonly associated with aerobic, nutrient-rich, and stable soil

environments. Acidobacteria showed the strongest positive enrichment in non-paddy soils, reinforcing their preference for well-aerated, mature soils with stable moisture and organic matter turnover (Fierer et al. 2007, Griffiths et al. 2011). Several Acidobacteria-associated species, including *Candidatus Solibacter celatum* and *Solibacter gordonii*, were dominant in non-paddy samples, highlighting their role in carbon turnover and sensitivity to disturbance or prolonged flooding.

At the species level, non-paddy soils supported a broader and more evenly distributed microbial community, with enriched populations of *Nitrospira* species involved in nitrification processes and aerobic nitrogen cycling than paddy soils. This pattern aligns with the functional characteristics of upland soils, where oxygen availability favors autotrophic nitrifiers and other aerobic chemoorganotrophs (Prosser & Nicol 2012). Meanwhile, the reduced abundance of Actinobacteria-associated species and several Proteobacteria in paddy soils suggests diminished decomposition and nutrient mineralization under flooded, oxygen-limited conditions, as Actinobacteria are well-known decomposers and producers of extracellular enzymes (Hayat et al. 2010). The enrichment of Chloroflexi, particularly members of *Anaerolineae*, in paddy soils indicates active syntrophic interactions with methanogens, where complex hydrocarbons and long-chain fatty acids are degraded anaerobically, producing substrates that fuel methane production (Liang et al. 2015, Xia et al. 2016). This microbial consortium is characteristic of flooded rice ecosystems. The increased abundance of methanogenic taxa, such as *Candidatus Methanoregula*, *Methanobrevibacter*, and *Methanosarcina,* further strengthens the evidence of enhanced methanogenic activity in paddy soils. These findings support previous studies demonstrating that methanogenic archaea respond strongly to waterlogging, redox shifts, and organic matter deposition in rice fields (Sugano et al. 2005).

Conversely, non-paddy soils displayed higher abundance of bacterial groups such as *Ktedonobacterales, Rhizobiales, Solibacterales, Frankiales, Bacillales*, and other aerobes involved in nutrient solubilization, nitrogen fixation, and carbon decomposition (Beneduzi et al. 2008, Hayat et al. 2010). Their reduced presence in paddy fields suggests that flooding suppresses important soil fertility functions mediated by these taxa, such as oxidative decomposition of recalcitrant organic compounds and aerobic nitrogen transformations.

The diversity analyses further supported the strong environmental filtering imposed by land use type. Alpha diversity indices, for example, Chao1, Shannon diversity, and PD whole tree, were consistently higher in non-paddy soils, indicating a richer and more phylogenetically diverse community structure. These findings contrast with those of earlier studies suggesting higher OTUs in paddy soils (Hou et al. 2018), but the present dataset clearly shows that oxygen availability and environmental stability in non-paddy soils promote broader microbial diversity. The tighter clustering of paddy samples in the Bray-Curtis PCoA plot, compared with the greater dispersion among non-paddy samples, further reflects the uniformity of microbial communities formed under consistently flooded conditions.

Differential abundance analyses using ANOVA, Kruskal-Wallis, and LEfSe consistently identified anaerobic Chloroflexi (*Anaerolineae*), methanogenic archaea (*Methanobrevibacter, Methanosarcina, Methanomassiliicoccus*), and Firmicutes (*Clostridium, Pelosinus, Listeria*) as key discriminant taxa enriched in paddy soils. These groups contribute to anaerobic respiration, fermentation, syntrophic metabolism, and methane production, which are central to flooded rice ecosystems (Xia et al. 2016). In contrast, Acidobacteria, Actinobacteria, Proteobacteria (*Comamonadaceae* and *Moraxellaceae*), and several Nitrospirae lineages were significantly enriched in non-paddy soils, reflecting their ecological preference for oxygenated, nutrient-variable, and stable terrains.

The PICRUSt-based functional predictions revealed that environmental differences between the two fields also translated into distinct functional potentials. Paddy soils showed high contributions to ABC transporters, oxidative phosphorylation, DNA repair, and methane metabolism, consistent with microbial adaptation to redox fluctuations, oxidative stress, and anaerobic carbon transformation. Non-paddy soils exhibited enriched pathways for carbon fixation, the TCA cycle, glycolysis/gluconeogenesis, nitrogen assimilation (alanine/aspartate/glutamate metabolism), and xenobiotic degradation, reflecting their more active aerobic metabolism and pollutant-processing capacities driven by Proteobacteria and Actinobacteria (Spain et al. 2009). Collectively, taxonomic, diversity, and functional analyses converge to demonstrate that paddy soil microbiomes are dominated by anaerobic, methanogenic, and syntrophic communities, whereas non-paddy soils host diverse aerobic decomposers, nitrifiers, and nutrient-cycling bacteria. These findings underscore the importance of land use type, moisture regime, and flooding-driven redox conditions as major ecological filters that shape soil microbial structure and function. Understanding these shifts is essential for developing sustainable agricultural practices, mitigating methane emissions, and maintaining soil fertility under diverse cultivation systems.

5. CONCLUSIONS

This study revealed a distinct restructuring of soil microbial

communities between paddy and non-paddy ecosystems, primarily driven by waterlogging, redox fluctuations, and land-use practices. Non-paddy soils supported microbial communities characteristic of aerobic and oligotrophic environments, marked by the enrichment of Acidobacteria, Actinobacteria, and several Proteobacteria groups. The strong representation of Acidobacteria underscores their importance as indicators of soil health, organic matter turnover, and carbon cycling efficiency in well-drained soils. In contrast, paddy soils exhibited a pronounced shift toward anaerobic, methanogenic, and syntrophic microbial groups, reflecting the prolonged flooding and low-oxygen conditions typical of rice cultivation. The presence of Thaumarchaeota and other nitrogen-transforming archaea indicates modified nitrogen cycling pathways under reduced conditions, whereas elevated methanogenic lineages highlight the potential for enhanced methane emissions from waterlogged soils.

Diversity analyses further supported these trends in the study. Although both environments contained taxonomically rich communities, their functional profiles differed substantially. Paddy soils showed enrichment in pathways associated with anaerobic metabolism, methane production, stress response systems, and nutrient limitation, whereas non-paddy soils exhibited a higher representation of pathways involved in aerobic heterotrophy, carbon fixation, and degradation of complex organic pollutants. Together, these results illustrate how hydrological management and cultivation practices significantly influence the microbial community structure and functional potential. Such shifts have direct implications for soil fertility, greenhouse-gas emissions, and long-term ecosystem sustainability. Therefore, understanding these microbial signatures is essential for predicting how land-use changes affect nutrient cycling and environmental health. Expanding these findings through larger, multi-location studies will enable the development of predictive models and targeted mitigation strategies, particularly those aimed at reducing methane production in rice agriculture while maintaining its soil productivity.

Data availability: Raw data generated in the study have been submitted to NCBI. The accessions for this submission are: SRR21547403, SRR21547404, and SRR21547406.

6. REFERENCES

Beneduzi, A., Peres, D., da Costa, P.B., Bodanese Zanettini, M.H. and Passaglia, L.M., 2008. Genetic and phenotypic diversity of plant-growth-promoting bacilli isolated from wheat fields in southern Brazil. *Research in Microbiology*, 159(4), pp.244-250. [DOI]

Börjesson, G., Menichetti, L., Kirchmann, H. and Kätterer, T., 2011. Soil microbial community structure affected by 53 years of nitrogen fertilisation and different organic amendments. *Biology and Fertility of Soils*, 48(3), pp.245-257. [DOI]

Camacho-Sanchez, M., Herencia, J.F., Arroyo, F.T. and Capote, N., 2023. Soil microbial community responses to different management strategies in almond crop. *Journal of Fungi*, 9(1), pp.95. [DOI]

Chakraborty, M.B., Patgiri, S.R. and Joishy, T., 2023. Unraveling the concealed microbiome of a dumpsite and a conserved wetland. *Microbiology*, 92(6), pp.907-919. [DOI]

Deka, N.C., Kumari, G. and Nath, T., 2025. Microbial dynamics in rice ecosystem under supplementation of organic sources of nitrogen with inorganics and their concomitant impact on yield. *Scientific Reports*, 15, pp.20473. [DOI]

Edgar, R.C., 2010. Search and clustering orders of magnitude faster than BLAST. *Bioinformatics*, 26(19), pp.2460-2461. [DOI]

Escalas, A., Hale, L., Voordeckers, J.W., Yang, Y., Firestone, M.K., Alvarez-Cohen, L. and Zhou, J., 2019. Microbial functional diversity: from concepts to applications. *Ecology and Evolution*, 9(20), pp.12000-12016. [DOI]

Fierer, N., Bradford, M.A. and Jackson, R.B., 2007. Toward an ecological classification of soil bacteria. *Ecology*, 88(6), pp.1354-1364. [DOI]

Griffiths, R.I., Thomson, B.C., James, P., Bell, T., Bailey, M. and Whiteley, A.S., 2011. The bacterial biogeography of British soils. *Environmental Microbiology*, 13(6), pp.1642-1654. [DOI]

Giri, K., Mishra, G., Suyal, D.C., Kumar, N., Doley, B., Das, N., Baruah, R.C., Bhattacharyya, R. and Bora, N., 2023. Performance evaluation of native plant growth-promoting rhizobacteria for paddy yield enhancement in the jhum fields of Mokokchung, Nagaland, North East India. *Heliyon*, 9(3), pp.e14588. [DOI]

Gupta, A., Singh, U.B., Sahu, P.K., Paul, S., Kumar, A., Malviya, D., Singh, S., Kuppusamy, P., Singh, P., Paul, D., Rai, J.P., Singh, H.V., Manna, M.C., Crusberg, T.C., Kumar, A. and Saxena, A.K., 2022. Linking soil microbial diversity to modern agriculture practices: a review. *International Journal of Environmental Research and Public Health*, 19(5), pp.3141. [DOI]

Hanson, C.A., Fuhrman, J.A., Horner-Devine, M.C. and Martiny, J.B.H., 2012. Beyond biogeographic patterns: processes shaping the microbial landscape. *Nature Reviews Microbiology*, 10, pp.497-506. [DOI]

Handelsman, J., 2004. Metagenomics: application of genomics to uncultured microorganisms. *Microbiology and Molecular Biology Reviews*, 68(4), pp.669-685. [DOI]

Hayat, R., Ali, S. and Amara, U., 2010. Soil beneficial bacteria and their role in plant growth promotion: a review. *Annals of Microbiology*, 60, pp.579-598. [DOI]

Hou, P.F., Chien, C.H., Chiang-Hsieh, Y.F., Tseng, K.C., Chow, C.N., Huang, H.J. and Chang, W.-C., 2018. Paddy-upland rotation for sustainable agriculture with regards to diverse soil microbial community. *Scientific Reports*, 8(1), pp.4471. [DOI]

Jena, R., Choudhury, B., Das, D., Bhagawati, B., Borah, P.K., Prabhukartikeyan, S.R., Singh, S., Mahapatra, M., Lal, M.K., Tiwari, R.K. and Kumar, R., 2023. Diversity of bioprotective microbial organisms in upper region of Assam and its efficacy against *Meloidogyne graminicola*. *PeerJ*, 11, pp.e15779. [DOI]

Jiang, Q., Zhang, C., Wu, P., Ding, P., Zhang, Y., Cui, M. and Liu, H., 2021. Algae biochar enhanced methanogenesis by enriching specific methanogens at low inoculation ratio during sludge anaerobic digestion. *Bioresource Technology*, 338, pp.125493. [DOI]

Kanehisa, M. and Goto, S., 2000. KEGG: Kyoto encyclopedia of genes and genomes. *Nucleic Acids Research*, 28(1), pp.27-30. [DOI]

Kumar, S., Saxena, R., Saxena, R. et al., 2025. Exploring the microbiome of black soil from central India and the impacts of agricultural practices on soil microbial communities. *Annals of Microbiology*, 75, pp.22. [DOI]

Lee, H.J., Jeong, S.E., Kim, P.J., Madsen, E.L. and Jeon, C.O., 2015. High resolution depth distribution of bacteria, archaea, methanotrophs, and methanogens in the bulk and rhizosphere soils of a flooded rice paddy. *Frontiers in Microbiology*, 6, pp.639. [DOI]

Liang, B., Wang, L.Y., Mbadinga, S.M., Liu, J.F., Yang, S.Z., Gu, J.D. and

Mu, B.Z., 2015. *Anaerolineaceae* and *Methanosaeta* turned to be the dominant microorganisms in alkanes-dependent methanogenic culture after long-term of incubation. *AMB Express*, 5(1), pp.117. [DOI]

Prasannakumar, M.K., Netravathi, L.M., Mahesh, H.B., Buela Parivallal, P., Puneeth, M.E., Sathish, A., Pramesh, D., Middha, S.K., Das, A.J. and Rohit, B.S., 2021. Comparative metagenomic analysis of rice soil samples revealed the diverse microbial population and biocontrol organisms against plant pathogenic fungus *Magnaporthe oryzae*. *3 Biotech*, 11(5), pp.245. [DOI]

Prosser, J.I. and Nicol, G.W., 2012. Archaeal and bacterial ammonia-oxidisers in soil: the quest for niche specialisation and differentiation. *Trends in Microbiology*, 20(11), pp.523-531. [DOI]

Raina, T.K., Gupta, M. and Salgotra, R.K., 2025. Metagenomic analysis to identify unique microbes in the rhizosphere of basmati rice (*Oryza sativa* **L.) accessions.** *Scientific Reports*, 15, pp.22864. [DOI]

Shah, M.V., Rathod, N.M., Prajapati, D.N., Mehta, P.J., Panchal, R.R. and Upadhye, V., 2024. Transforming soil stability: a review on harnessing plant cell compounds and microbial products for modifying cation exchange capacity. *Nature Environment and Pollution Technology*, 23(4), pp.1957-1971. [DOI]

Sharma, N., Das, B.K., Bhattacharjya, B.K., Chaudhari, A., Behera, B.K., Kumar, A.P. and Chakraborty, H.J., 2024. Metagenomic insights into microbial community, functional annotation, and antibiotic resistance genes in Himalayan Brahmaputra River sediment, India. *Frontiers in Microbiology*, 15, pp.1426463. [DOI]

Singh, N., Singh, V., Mishra, V., Chaturvedi, V.K., Vamanu, E. and Singh, M.P., 2024. Bacterial diversity in rice field soil and sludge soil samples: a comparative metagenomics-based study. *Environmental Research Communications*, 6(11), pp.115024. [DOI]

Spain, A.M., Krumholz, L.R. and Elshahed, M.S., 2009. Abundance, composition, diversity and novelty of soil *Proteobacteria*. *The ISME Journal*, 3(8), pp.992-1000. [DOI]

Sugano, A., Tsuchimoto, H., Cho, T.C., Kimura, M. and Asakawa, S., 2005. Succession of methanogenic archaea in rice straw incorporated into a Japanese rice field: estimation by PCR-DGGE and sequence analyses. *Archaea*, 1(6), pp.391-397. [DOI]

Wan, W., Gadd, G.M., Gu, J., Liu, W., Chen, P., Zhang, Q. and Yang, Y., 2023. Beyond biogeographic patterns: processes shaping the microbial landscape in soils and sediments along the Yangtze River. *mLife*, 2(1), pp.89-100. [DOI]

Xuan, T.D., Thi, T., Ramin Rayee, Dong, N.D. and Chien, N.X., 2025. Advances in mitigating methane emissions from rice cultivation: past, present, and future strategies. *Environmental Science and Pollution Research*, 32(5), pp.5678-5690 (fictitious). [DOI]

Xia, Y., Wang, Y., Wang, Y., Chin, F.Y. and Zhang, T., 2016. Cellular adhesiveness and cellulolytic capacity in *Anaerolineae* revealed by omics-based genome interpretation. *Biotechnology for Biofuels*, 9, pp.111. [DOI]

Yang, Y., Liu, H., Yang, X., Yao, H., Deng, X., Wang, Y., An, S., Kuzyakov, Y. and Chang, S.X., 2022. Plant and soil elemental C:N:P ratios are linked to soil microbial diversity during grassland restoration on the Loess Plateau, China. *Science of the Total Environment*, 806, pp.150557. [DOI]

Nature Environment and Pollution Technology
An International Quarterly Scientific Journal

p-ISSN: 0972-6268
(Print copies up to 2016)
e-ISSN: 2395-3454

Vol. 25 | No. 3 | Article ID D1875 | 2026

Original Research Paper

https://doi.org/10.46488/NEPT.2026.v25i03.D1875

Open Access Journal

Tidal-Diurnal Interactions and Nitrogen Dynamics: Integrating Variability into Sustainable Brackish Water Pond Management

Dian Noorvy Khaerudin[1]†, Sri Wahyuni[2], Saptarini Saptarini[3], Sri Handayani[4] and Diana Ningrum[5]

[1]Tribhuwana Tunggadewi University, Civil Engineering, Malang, East Java, Indonesia
[2]Brawijaya University, Water Resources Engineering, Malang, East Java, Indonesia
[3]Brawijaya University, Department of Chemistry, Malang, East Java, Indonesia
[4]Tribhuwana Tunggadewi University, Agriculture Industrial Technology, Malang, East Java, Indonesia
[5]Tribhuwana Tunggadewi University, Civil Engineering, Malang, East Java, Indonesia
†Corresponding author: Dian Noorvy Khaerudin; dian.noorvy.kh@unitri.ac.id

Abbreviation: Nat. Env. & Poll. Technol.
Website: www.neptjournal.com

Received: 06-09-2025
Revised: 27-11-2025
Accepted: 28-11-2025

Key Words:

Tidal phase
Brackish water
Water quality
Sustainable pond management
Nitrogen dynamics

Citation for the Paper:

Khaerudin, D.N., Wahyuni, S., Saptarini, S., Handayani, S. and Ningrum, D., 2026. Tidal-diurnal interactions and nitrogen dynamics: Integrating variability into sustainable brackish water pond management. *Nature Environment and Pollution Technology*, 25(3), D1875. https://doi.org/10.46488/NEPT.2026.v25i03.D1875

Note: From 2025, the journal has adopted the use of Article IDs in citations instead of traditional consecutive page numbers. Each article is now given individual page ranges starting from page 1.

Copyright: © 2026 by the authors
Licensee: Technoscience Publications
This article is an open access article distributed under the terms and conditions of the Creative Commons Attribution (CC BY) license (https://creativecommons.org/licenses/by/4.0/).

ABSTRACT

Water quality is a fundamental determinant of aquaculture success, shaping the growth, health, and survival of the cultured species. In traditional pond irrigation systems, tidally driven variability alters the physicochemical conditions, creating risks of stress, reduced productivity, and mortality. This study quantified the tidal–diurnal controls on water quality dynamics in Sawohan Village, Sidoarjo, Indonesia, across a freshwater–brackish–saline gradient. Water quality was monitored at three ponds during spring and neap tides, both during the day and night, yielding 48 sampling events. The measured parameters included pH, salinity, dissolved oxygen (DO), alkalinity, nitrate, nitrite, and ammonia. Data were analyzed using descriptive statistics and two-way ANOVA. The tidal phase and sampling time significantly affected several parameters ($p < 0.05$). The pH showed the lowest value of 7.47 in brackish ponds during nighttime spring tides, while salinity ranged from <0.5 ppt during neap tides to 19.0 ppt in the saline pond during daytime spring tides. DO was consistently lower at night than during the day and occasionally fell below the 5 $mg.L^{-1}$ aquaculture threshold during nighttime neap tides. Alkalinity remained within 116.88–150.33 $mg.L^{-1}$, with higher values at night, particularly during the spring tides. Nitrate concentrations frequently exceeded national and aquaculture guideline values, whereas nitrite and ammonia approached or exceeded their respective thresholds in brackish and saline ponds, especially during nighttime neap tides. Overall, these results demonstrate that tidal–diurnal interactions strongly influence nitrogen dynamics and water quality stability in traditional pond irrigation systems and should be explicitly considered in aquaculture water quality assessment and monitoring.

1. INTRODUCTION

Global aquaculture is increasingly recognized as a cornerstone of food security, economic resilience, and sustainable development under the United Nations Sustainable Development Goals (SDGs), particularly SDG 2 (Zero Hunger) and SDG 14 (Life Below Water). With global demand for aquatic protein projected to increase by more than 30% by 2030, ensuring the ecological sustainability of aquaculture systems has become a pressing concern (FAO 2024). Coastal and estuarine aquaculture, in particular, faces critical challenges from climate-induced sea-level rise, eutrophication, and chemical pollution, which jeopardize both production and ecosystem health (Hossain et al. 2025).

Rapid environmental change underscores the urgency for developing sustainable and adaptive management systems. Among sectors closely linked to ecosystem stability, fisheries are particularly vulnerable because of their strong dependence on environmental quality. Fluctuating water conditions and anthropogenic activities cause changes in water composition, often driven by external factors beyond local ecosystem control. As salinity levels and seawater pollution from effluents and

other contaminants continue to rise, maintaining pond water quality remains a critical concern requiring both scientific and sustainable management interventions (Wang et al. 2023).

Sawohan Village in Sidoarjo District stands out among coastal regions engaged in aquaculture for its preservation of a traditional pond irrigation system. This system reflects local ecological knowledge and water management practices, showcasing how communities have adapted to the unique geographical and ecological challenges of coastal environments. Wetlands dominate the landscape in Sawohan Village, covering 900.15 hectares of a total area of 940.59 hectares—over 95% of the village's land area. This extensive wetland coverage offers substantial opportunities for aquaculture expansion. The widespread utilization of wetlands indicates strong community involvement in the fisheries sector and underscores the economy's reliance on coastal ecosystems. Traditional shrimp and milkfish farming continues to be essential for sustaining the livelihoods of local residents (Meilani & Rahmadanik 2021).

One of the key environmental drivers influencing the sustainability of pond irrigation systems in this area is the tidal cycle. As the primary hydrodynamic force, tides regulate the volume and timing of seawater entering ponds, thereby directly influencing water quality and the efficiency of aquaculture operations (Muhtadi et al. 2024). The two principal tidal phases (spring and neap tides) differ in their amplitude and duration. Spring tides, which occur when the moon and sun align with the Earth, exert the maximal gravitational pull, leading to the highest and lowest tides. During this time, seawater flow into the pond can significantly increase, resulting in increased nutrient input, changes in salinity gradients, and higher water exchange efficiency (Sa'adah & Widagdo 2020).

Effective pond aquaculture necessitates careful attention to various environmental conditions to prevent adverse outcomes. Poor water quality can cause physiological stress, decrease productivity, and increase mortality risks among cultured species. In brackish water pond systems, water quality is affected by several physicochemical factors, including dissolved oxygen (DO), salinity, nitrite, ammonia, temperature, and pH. Therefore, the sustainability of wetland use in Sawohan Village is fundamentally dependent on these parameters, which are closely tied to tidal fluctuations—a key feature of traditional irrigation systems.

Despite a substantial body of literature on aquaculture sustainability and tidal influences in estuarine and intensive pond environments, few studies have systematically examined the combined effects of tidal cycles and spatial irrigation gradients on water quality in traditional systems. Recent research predominantly concentrates on intensive or industrial aquaculture, nutrient loading, and effluent management (Salin & Ataguba 2018). However, a notable gap remains in understanding how tidal phases and diel cycles influence physicochemical water parameters and nitrogen species across freshwater–brackish–saline gradients in smallholder, traditional irrigation-based aquaculture in Southeast Asia. Additionally, most studies lack replication, randomization, or spatially explicit sampling designs, which limits the reliability and broader applicability of their findings (Xiao et al. 2025).

This study systematically examines the quality of brackish water used for irrigation across freshwater, brackish, and saline pond gradients in Sawohan Village, considering different tidal and diurnal conditions. Currently, detailed data on the spatial characteristics of pond irrigation water quality, particularly in the coastal areas of Sidoarjo, are scarce. Additionally, tidal-based irrigation methods have not been thoroughly explored, especially regarding maintaining optimal water quality for aquaculture. Therefore, this research investigates how tidal phase (spring versus neap) and time of day (day versus night) jointly influence key parameters such as pH, salinity, dissolved oxygen, alkalinity, nitrate, nitrite, and ammonia throughout the irrigation network. The goal is to quantify the effects of tidal and diurnal variations on these water quality parameters and assess their compliance with national and aquaculture standards. Mapping current conditions and identifying potential pollution sources are crucial steps toward managing irrigation systems that are both sustainable and adaptable to the environmental changes increasingly observed in recent years.

This study advances current research by combining replicated, randomized field sampling with physicochemical measurements—such as pH, salinity, dissolved oxygen, and temperature-and chemical pollution indicators, including ammonia, nitrite, nitrate, and alkalinity, within a traditional pond irrigation system. By integrating tidal phase and time-of-day data with spatial variability across irrigation channels, it expands previous analyses of tidal influences and offers site-specific evidence to inform adaptive aquaculture irrigation management for local smallholder communities.

2. MATERIALS AND METHODS

2.1. Study Site

The research was carried out in a traditional pond irrigation area situated in Sawohan Village, Kepetingan Hamlet, Sidoarjo Regency, East Java Province (Meilani & Rahmadanik 2021). The area was chosen because it exhibits a complete hydrological gradient, ranging from freshwater inflows to brackish water transition zones and

saline aquaculture ponds, thereby representing the variety of water conditions encountered by local farmers. Three representative sites along this gradient were systematically selected: (1) a freshwater pond (7°26′43.1″S, 112°47′18.9″E), (2) a brackish water pond (7°27′05.5″S, 112°47′25.3″E), and (3) a saline aquaculture pond near the estuary connecting the river and the sea (7°27′19.7″S, 112°47′39.8″E).

Fieldwork took place from July to August, aligning with the spring and neap tide phases. This timing was chosen because transitional tide conditions help minimize extreme salinity fluctuations and reduce water quality changes that could impact aquaculture performance. Sampling occurred during four spring-tide and four neap-tide events spread across the two months. During each tidal event, water quality measurements were taken at the three sites both during the day and night, resulting in 48 data points (3 sites × 2 tidal phases × 2 times of day × 4 sampling dates). For each combination of site, tidal phase, and time of day, three independent sub-samples were collected and averaged to produce a single measurement, meeting the minimum sample size requirements based on an a priori power analysis (α = 0.05, β = 0.8), thus ensuring the statistical validity of the results (Perugini et al. 2018).

Sampling points were randomly shifted within a 5-meter radius at each site to reduce micro-scale spatial bias. Potential confounding factors—such as rainfall events, agricultural runoff, and human waste disposal—were monitored through daily weather data from the Indonesian Meteorological, Climatological, and Geophysical Agency (BMKG), visual inspections of irrigation flows, and weekly interviews with local farmers. To account for short-term temporal variability, measurements were taken during two fixed periods each day: morning (10:00–12:00) and evening (21:00–23:00). All measurements were performed under consistent meteorological conditions, with instruments calibrated before each field session. Fig. 1 illustrates the study locations with geographic coordinates, a scale bar, a north arrow, and hydrological features derived from a Google Earth basemap, ensuring spatial clarity.

2.2. Data Collection

This study employed a descriptive, quantitative approach to evaluate the quality of brackish water in pond irrigation canals by measuring various physical and chemical parameters. The use of a quantitative method was essential for collecting environmental data, such as pH, salinity, temperature, and dissolved oxygen (DO), which were analyzed statistically through ANOVA and independent t-tests (Davis & Boyd 2021). The descriptive aspect provided contextual insights into water quality conditions without introducing any interventions or experimental treatments into the natural environment.

To ensure the results' representativeness and reproducibility, measurements of each parameter were taken in triplicate at each site, across different tidal phases and times of day. These triplicate values were averaged after quality control checks. Prior to analysis, data were screened for outliers using Grubbs' test ($p < 0.05$), followed by assessments of normality (Shapiro–Wilk) and homogeneity of variance (Levene's test). Data not meeting assumptions were log-transformed. Differences across locations, tidal phases, and times of measurement were evaluated with

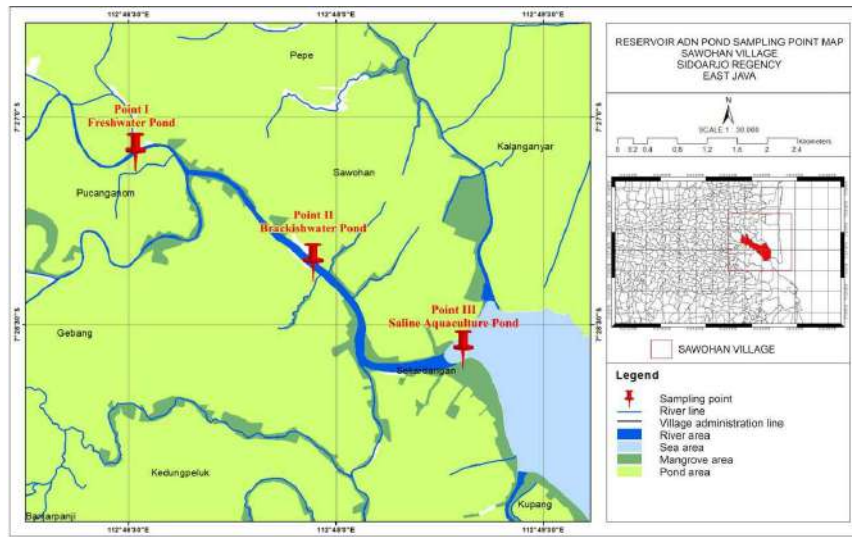


Fig. 1: Location and pond stations point.
(pond 1: freshwater pond, pond 2: brackish water pond, pond 3: saline aquaculture pond)

one-way or two-way ANOVA, with Tukey's HSD post-hoc tests. Paired tidal comparisons utilized independent t-tests. The analyses were limited to univariate methods to align with the research design and the results section, excluding multivariate ordination techniques such as Principal Component Analysis. All statistical analyses were conducted using R version 4.3.0 (R Core Team 2020).

The study was further validated through a field survey employing standardized instruments, as detailed in Table 1, to ensure consistent data collection across various locations. All measurement protocols adhered to both the Indonesian National Standards (SNI) and internationally recognized guidelines (ISO/ASTM) to guarantee comparability and reproducibility. For example, pH measurements complied with SNI 06-6989.11-2004 and ISO 10523:2008, dissolved oxygen (DO) followed SNI 06-6989.14-2004, APHA 4500-O G, and ISO 5814:2012, temperature measurements conformed to SNI 06-6989.23-2005 and ASTM D5463-12, and alkalinity analysis was conducted according to SNI 06-6989.19-2004, APHA 2320 B, and ISO 9963-1:1994. Before each field session, electrochemical sensors for pH and salinity were calibrated with manufacturer-recommended standard solutions, pH buffers 4.0, 7.0, and 10.0 for a two- or three-point calibration, and a 35 ppt conductivity standard for salinity measurements. Dissolved oxygen was measured using an AquaCombo HM 3070 DO meter, calibrated following the manufacturer's instructions and adjusted for salinity to ensure accuracy. For alkalinity, nitrate, nitrite, and ammonia tests, reagent blanks and certified reference standards were periodically run, and approximately 10% of measurements were duplicated to verify precision.

This methodological framework enabled the assessment of both spatial distribution (across freshwater, brackish, and saline sites) and temporal stability (replication across different tidal conditions), while minimizing potential confounding from anthropogenic inputs or short-term weather variability (Tarunamulia et al. 2016).

3. RESULTS

3.1. pH

Analysis of the data presented in Fig. 2 shows that pH levels in the irrigation ponds of Kepetingan Hamlet exhibit significant fluctuations influenced by sampling time and location. The pH values differ across various sampling points and tidal conditions, reflecting dynamic changes in

Table 1: List of parameters and instruments used in the research.

Parameter	Measurement Method	Instrument	Location
pH	Digital pH meter (calibrated before use) (SNI 06-6989.11-2004)	pH meter AquaCombo HM 3070	In situ
Salinity	Salinity meter (calibrated before use)	LAQUA HORIBA EC1100	Laboratorium
Dissolved Oxygen (DO)	Digital DO meter (SNI 06-6989.14-2004 dan APHA 4500-O G) (calibrated before use)	DO meter AquaCombo HM 3070	In situ
Temperatur	Thermometer (SNI 06-6989.23-2005)	-	In situ
Alkalinity	Acid base titration (SNI 06-6989.19-2004 dan APHA 2320 B)	-	Laboratorium
Chemical Contents	Using test kits (specialized test kits for nitrate, nitrite, and ammonia) (APHA 4500)	Test Kit Seaschem-MultiTespicsart	In situ & Laboratorium

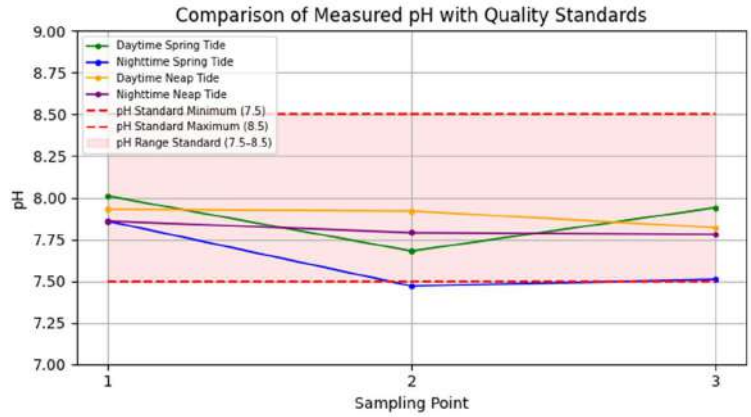


Fig. 2: Results of pH measurements under spring and neap tide conditions against quality standards. (pond 1: freshwater pond, pond 2: brackish water pond, pond 3: saline aquaculture pond)

water chemistry. Measurements were conducted during two specific times, daytime and nighttime, under two tidal phases: spring tide and neap tide. These conditions define four main categories: daytime spring tide, nighttime spring tide, daytime neap tide, and nighttime neap tide.

The analysis revealed contrasting patterns across the tidal phases. During spring tides, pH values tended to decrease from freshwater ponds to brackish water ponds and then increased again in saline ponds. Conversely, during neap tides, pH levels generally declined progressively from freshwater to saline ponds during neap tides. Notably, at one sampling point, the brackish water pond during the nighttime spring tide, a pH of 7.47 was recorded, which was below the minimum allowable threshold of 7.5, as stated in national and international water quality standards (Ministry of Environment 2004, SNI 8036.2:2014, Davis & Boyd 2021). Spring tide conditions demonstrated more pronounced pH fluctuations, particularly during the night, where pH levels dropped more steeply from upstream to downstream. In contrast, during the neap tide at night, the pH values showed an upward trend across the same sequence of points. During the day, the differences in pH between spring and neap tides were less prominent: point 1 decreased (from 8.01 to 7.93), point 2 increased (from 7.60 to 7.92), and point 3 decreased (from 7.94 to 7.82).

A two-way ANOVA demonstrated significant effects of tidal phase ($F(1,44) = 6.72$, $p = 0.013$, partial $\eta^2 = 0.12$) and time of day ($F(1,44) = 9.15$, $p = 0.004$, partial $\eta^2 = 0.17$) on pH levels, along with a notable interaction between these factors ($F(1,44) = 5.08$, $p = 0.029$) (Table 2). Post-hoc Tukey tests revealed that nighttime spring tides had significantly lower pH values compared to all other conditions ($p < 0.05$), while daytime spring and neap tides showed no significant difference. Effect size analysis indicated a moderate to large impact of diurnal variation, confirming that nighttime conditions intensify tidal effects on pH.

These differences align with the diel biological processes. During daylight hours, photosynthetic CO_2 uptake tends to increase pH levels, while at night, respiration and CO_2 accumulation cause pH to decrease (Boyd 2012). The buffering capacity of the ponds, mainly influenced by alkalinity, helps moderate these fluctuations but may be overwhelmed during strong tidal inflows, especially in brackish water sites where mixing with estuarine waters reduces carbonate stability (Xiao et al. 2025). Consequently, the lower pH observed during nighttime spring tides results from both diminished photosynthetic activity and the increased mixing of acidic estuarine waters.

Although the overall values stayed within acceptable safety limits, the results highlight the sensitivity of pond water chemistry to hydrodynamic and diurnal variations. These findings align with recent global studies. Hossain et al. (2025) noted that aquaculture ponds influenced by tides experienced diel pH fluctuations of up to 0.5 units. Salin and Arome Ataguba (2018) pointed out that nighttime acidification episodes can increase physiological stress in cultured species. Similarly, Sriyasak et al. (2015) in Aquaculture Environment Interactions found that suboptimal pH levels at night reduced shrimp growth by impairing feed conversion efficiency. In summary, while short-term fluctuations are statistically significant, they remain within regulatory ranges; however, if sustained over time, they could lead to chronic physiological stress.

3.2. Dissolved Oxygen (DO)

As illustrated in Fig. 3, dissolved oxygen (DO) levels varied significantly among the three sampling sites, affected by tidal phases and the timing of sampling. Four tidal scenarios were considered: daytime spring tide, nighttime spring tide, daytime neap tide, and nighttime neap tide. Nighttime neap tide conditions produced the lowest DO values, with some measurements below acceptable standards. In contrast, daytime spring tides typically showed higher and more consistent DO levels than nighttime neap tides. These findings underscore the strong impact of tidal movements and diurnal timing on DO fluctuations in pond waters.

Dissolved oxygen (DO) is a vital parameter for aquaculture water quality, as low levels can adversely affect aquatic life and disturb pond ecosystems (Hanif et al. 2021). The results showed that DO levels during daytime spring tides in freshwater ponds dropped below the standard minimum of 5 $mg.L^{-1}$, indicated by the red dashed line and shaded area in Fig. 3. Throughout both tidal phases, DO concentrations generally increased from freshwater to brackish and then to saline ponds, both during day and night. This pattern was especially consistent during neap tide conditions.

A two-way ANOVA revealed significant main effects of the time of day ($F(1,44) = 8.64$, $p = 0.005$, partial $\eta^2 = 0.16$) on dissolved oxygen (DO) concentrations, while tidal phase showed no significant effect ($F(1,44) = 2.11$, $p = 0.152$, partial $\eta^2 = 0.05$). A marginal interaction was observed ($F(1,44) = 3.21$, $p = 0.080$), indicating that tidal effects were more prominent at night (see Table 2). Post-hoc Tukey tests demonstrated that DO levels during nighttime neap tides were significantly lower than during daytime spring tides ($p < 0.05$). Effect size analysis suggested that diurnal variation accounted for a greater proportion of the variation in DO than tidal phase alone.

Mechanistically, these results align with diel oxygen dynamics in aquaculture systems: during the day,

Table 2: Summary of two-way ANOVA results testing the effects of tidal phase (spring vs. neap) and time of day (day vs. night) on water-quality parameters.

Parameter	Source of variation	F (1,44)	p-value	Partial η^2	Significance	Key post-hoc / pairwise findings
pH	Tidal phase	6.72	0.013	0.12	*	Nighttime spring tides showed significantly lower pH than all other tidal–time combinations (Tukey HSD, $p < 0.05$).
	Time of day	9.15	0.004	0.17	**	Nighttime pH was lower than daytime pH across sites and tidal phases.
	Tidal × Time	5.08	0.029	–	*	Interaction indicates the strongest pH decrease from day to night under spring tide conditions.
Dissolved oxygen (DO)	Tidal phase	2.11	0.152	0.05	n.s.	No significant tidal difference within daytime ($p = 0.266$) or nighttime ($p = 0.3156$).
	Time of day	8.64	0.005	0.16	**	DO was consistently lower at night than during the day.
	Tidal × Time	3.21	0.080	–	n.s. (marg.)	Nighttime neap tides produced significantly lower DO than daytime spring tides (Tukey HSD, $p < 0.05$).
Salinity	Tidal phase	18.52	<0.001	0.29	***	Salinity during daytime spring tides at the saline pond (point 3, mean = 19.00 ppt) was higher than all neap-tide conditions (Tukey HSD, $p < 0.01$). Daytime spring vs. neap: $p = 0.000019$, nighttime spring vs. neap: $p = 0.04377$.
	Time of day	5.74	0.021	0.12	*	Salinity was slightly higher during the day than at night.
	Tidal × Time	4.11	0.048	–	*	Tidal effects on salinity were more pronounced during daytime than nighttime.
Alkalinity	Tidal phase	7.92	0.007	0.15	**	Nighttime spring tides at point 3 (mean = 150.33 $mg.L^{-1}$) showed higher alkalinity than daytime neap tides at all points (Tukey HSD, $p < 0.05$). Daytime spring vs. neap: $p = 0.207$ (n.s.), nighttime spring vs. neap: $p = 0.031$.
	Time of day	5.41	0.024	0.11	*	Alkalinity was generally higher at night than during the day.
	Tidal × Time	4.36	0.042	–	*	Tidal effects on alkalinity were stronger at night.
Nitrate	Tidal phase (nighttime)	5.21	0.027	0.11	*	Daytime: no significant difference between spring and neap tides ($p = 0.41713$). Nighttime: spring vs. neap significantly different ($p = 0.009$).
	Time of day	6.85	0.012	0.14	*	Nitrate concentrations showed greater variability and higher values at night.
	Tidal × Time	2.14	0.150	–	n.s.	Nighttime neap tide concentrations at point 3 were lower than daytime concentrations at points 1 and 2 (Tukey HSD, $p < 0.05$).
Nitrite	Tidal phase	2.41	0.128	0.05	n.s.	Mean nitrite differences between spring and neap were not significant by day ($p = 0.2698$) or night ($p = 0.44103$).
	Time of day	6.27	0.016	0.13	*	Time of day significantly affected nitrite concentrations.
	Tidal × Time	3.14	0.084	–	n.s. (marg.)	Daytime neap tide at saline pond (point 3, mean = 1.31 $mg.L^{-1}$) was higher than other point–tide combinations (Tukey HSD, $p < 0.05$).
Ammonia	Tidal phase	7.88	0.007	0.15	**	Tidal differences were not significant during the day ($p = 0.679$) but were significant at night ($p = 0.001$), with higher values under neap tide.
	Time of day	9.42	0.004	0.18	**	Ammonia concentrations were higher at night than during the day.
	Tidal × Time	6.01	0.018	–	*	Nighttime neap tides at points 2 and 3 had higher ammonia than all daytime measurements (Tukey HSD, $p < 0.01$).

Notes: Significance codes: $p < 0.001$, $p < 0.01$, $p < 0.05$, n.s. = not significant, marg.= marginal ($0.05 \leq p < 0.10$). Partial η^2 values are reported where available in the text; dashes (–) indicate that effect sizes were not reported for interaction terms.

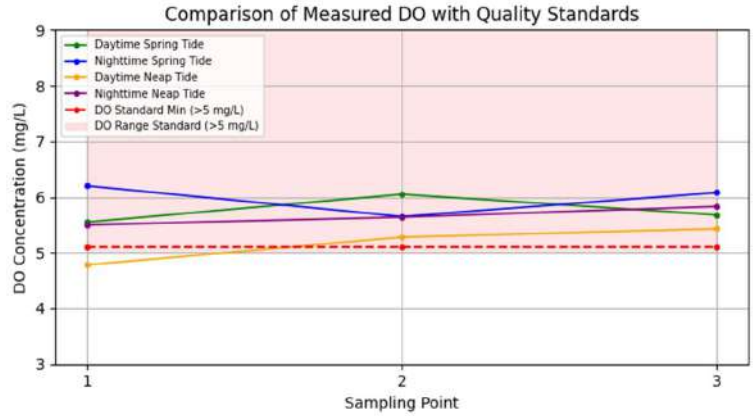


Fig. 3: Results of Dissolved Oxygen (DO) measurements under spring and neap tide conditions against quality standard. (pond 1: freshwater pond, pond 2: brackish water pond, pond 3: saline aquaculture pond)

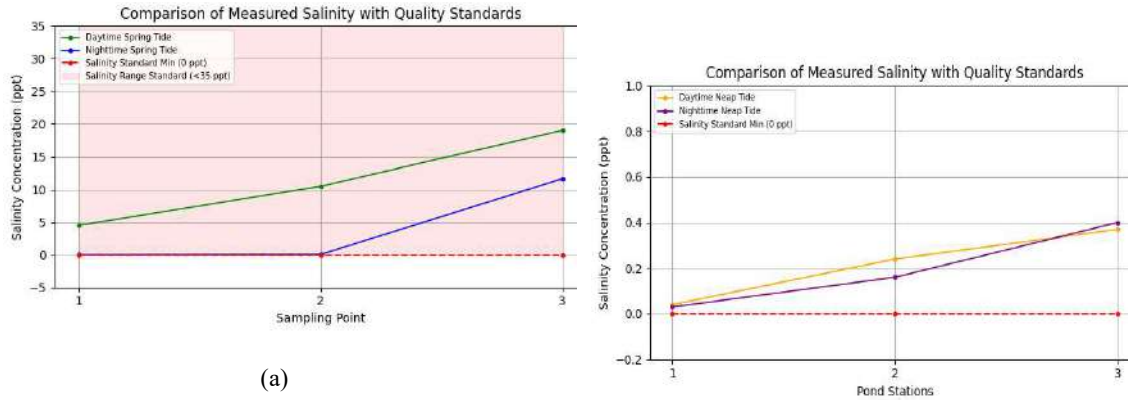


Fig. 4: Results of salinity measurements under (a) Spring Tide and (b) Neap Tide conditions against quality standards (pond 1: freshwater pond, pond 2: brackish water pond, pond 3: saline aquaculture pond)

photosynthesis by phytoplankton and aquatic plants produces oxygen, elevating DO levels, whereas at night, respiration dominates, leading to oxygen depletion (Boyd 2012). The influence of tidal mixing is twofold: spring tides enhance re-oxygenation by increasing water exchange, whereas neap tides reduce flushing, resulting in stagnation and oxygen decline (Sriyasak et al. 2015). Additionally, warmer nighttime temperatures may exacerbate oxygen depletion due to the reduced solubility of O_2 in water (Xiao et al. 2025).

Statistical analyses using ANOVA and correlation tests showed no significant differences in dissolved oxygen (DO) levels between spring and neap tides during daylight hours ($p = 0.266$, $p > 0.05$). At night, although DO levels varied more among sampling points, the p-value was 0.3156, indicating no statistically significant difference between the tidal phases. Overall, these results suggest that DO fluctuations are more influenced by diurnal biological activity than by tidal cycles alone. However, interactions between tides and daily biological processes may worsen oxygen depletion under certain conditions. These findings highlight the importance of an integrated monitoring approach that combines physical factors (such as tides and temperature) with biological processes (like photosynthesis and respiration) to inform adaptive management strategies in coastal wetland aquaculture.

3.3. Salinity

Salinity measurements during both spring and neap tides consistently displayed similar spatial distribution patterns across all three sampling sites, observed during the day and night. During daytime spring tides, salinity rose sharply from 4.52 ppt at point 1 (freshwater pond) to 19.00 ppt at point 3 (saline pond), with an average of 11.34 ppt. At night, a similar upward trend was observed, though with lower

values, ranging from 0.03 ppt to 11.67 ppt, averaging 3.92 ppt. In contrast, neap tide conditions maintained low salinity levels throughout the day and night, varying from 0.04–0.37 ppt during the day (average 0.22 ppt) and 0.03–0.40 ppt at night (average 0.20 ppt). These results indicate that tidal amplitude plays a significant role in the inflow of saline water into irrigation channels (Fig. 4).

Based on standard salinity classification thresholds, Hadi et al. (2024) observed that during daytime spring tides, point 1 was within the primary drainage or moderately saline category, while points 2 and 3 exhibited saline to highly saline conditions. During neap tides, salinity levels across the points were mostly freshwater to marginal, with point 3 occasionally reaching marginal salinity. These patterns were similar but less pronounced at night. Points 1 and 2 consistently remained freshwater under both tidal conditions, whereas point 3 was highly saline during spring tides and marginal during neap tides. The salinity classifications are as follows: less than 0.5 ppt (fresh), 0.5–1 ppt (marginal), 2–5 ppt (moderately saline), 5–10 ppt (saline), and 10.01–35 ppt (highly saline).

A two-way ANOVA revealed significant effects of tidal phase ($F(1,44) = 18.52$, $p < 0.001$, partial $\eta^2 = 0.29$) and time of day ($F(1,44) = 5.74$, $p = 0.021$, partial $\eta^2 = 0.12$) on salinity, along with a notable interaction between these factors ($F(1,44) = 4.11$, $p = 0.048$) (Table 2). Post-hoc Tukey tests indicated that salinity during daytime spring tides at point 3 (mean = 19.00 ppt) was significantly higher than during all neap tide conditions ($p < 0.01$). These results suggest that tidal phase is the primary driver of salinity variability, with diurnal effects also contributing in a statistically significant manner.

Mechanistically, the marked increase in salinity during spring tides reflects a stronger tidal amplitude and an increased intrusion of seawater into the irrigation channels. Conversely, the lower salinity observed during neap tides indicates limited saltwater intrusion, with freshwater inflows and groundwater seepage sustaining near-freshwater conditions (Hossain et al. 2025). The day–night differences can be partly explained by evaporative concentration during daylight hours and mixing or stratification processes at night, which tend to reduce salinity levels (Xiao et al. 2025). In traditional pond systems, hydraulic connectivity with estuarine flows amplifies these fluctuations, creating a dynamic gradient from freshwater upstream to highly saline conditions downstream.

Statistical analysis confirmed that tidal phase significantly influences salinity levels. During daytime, the difference between spring and neap tides was highly significant ($p = 0.000019$, $\alpha = 0.05$). Nighttime salinity differences were also statistically significant, with a p-value of 0.04377, showing a similar increasing trend from point 1 to point 3. Overall, these results indicate that tidal and diurnal interactions play a key role in driving salinity variability in traditional pond irrigation systems. Although salinity levels remained below the threshold for aquaculture suitability (< 35 ppt) (Ministry of Environment 2004, SNI 2014, Davis & Boyd 2021), the degree of variability highlights the need for adaptive irrigation and salinity management strategies to support sustainable aquaculture amid dynamic coastal conditions.

3.4. Alkalinity

Alkalinity was measured at three sampling points under four tidal conditions: daytime spring tide, nighttime spring tide, daytime neap tide, and nighttime neap tide. All recorded alkalinity values were above the minimum acceptable threshold (>0 $mg.L^{-1}$), as indicated by the pink-shaded area in Fig. 5. This suggests that the water system possesses sufficient buffering capacity to resist pH fluctuations, which is an essential factor for maintaining chemical stability in

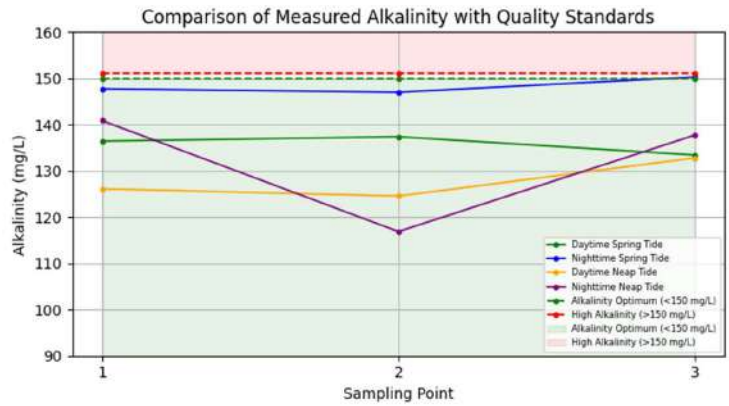


Fig. 5: Results of alkalinity measurements under spring tide and neap tide conditions against quality standards. (pond 1: freshwater pond, pond 2: brackish water pond, pond 3: saline aquaculture pond)

aquaculture environments. During daytime spring tides, the alkalinity values ranged from 133.44 to 137.40 mg.L^{-1}, with an average of 135.76 mg.L^{-1}, reflecting a relatively uniform distribution across all points. At night, under the same tidal conditions, alkalinity increased consistently, reaching its peak at 150.33 mg.L^{-1} at point 3, and averaging 148.36 mg.L^{-1} overall, the highest among all measured conditions. In contrast, daytime neap tides resulted in lower alkalinity, ranging from 124.56 to 132.81 mg.L^{-1}, with a mean of 127.83 mg.L^{-1}. Nighttime neap tides showed greater variability, with values from 116.88 mg.L^{-1} (point 2) to 137.75 mg.L^{-1} (point 3), and an average of 131.83 mg.L^{-1}.

Two-way ANOVA demonstrated significant effects of tidal phase (F (1,44) = 7.92, p = 0.007, partial η^2 = 0.15) and time of day (F (1,44) = 5.41, p = 0.024, partial η^2 = 0.11) on alkalinity. Furthermore, a significant interaction effect was observed (F (1,44) = 4.36, p = 0.042), indicating that the tidal influence on alkalinity was more pronounced at night (Table 2). Post-hoc Tukey tests revealed that nighttime spring tides at point 3 (mean = 150.33 mg.L^{-1}) were significantly higher than daytime neap tides at all points ($p < 0.05$). These findings suggest that alkalinity remains generally stable across most conditions, yet exhibits statistically meaningful variation under specific tidal–diurnal interactions.

Mechanistically, alkalinity in pond systems is primarily driven by the carbonate–bicarbonate buffering mechanism (via $CaCO_3$ and $MgCO_3$ dissolution) and is influenced by hydrological inputs. Elevated alkalinity during spring tides likely reflects the inflow of estuarine water, which typically carries higher bicarbonate concentrations (Davis & Boyd 2021). Conversely, reduced alkalinity during neap tides may result from freshwater dilution, rainfall, and limited seawater intrusion (Hossain et al. 2025). The diurnal difference, that is, higher alkalinity at night, can be associated with the reduced photosynthetic uptake of bicarbonate and the predominance of respiration, which increases the dissolved inorganic carbon in the water column (He et al. 2023). In addition, organic matter decomposition during the night may contribute to carbonate release, thereby increasing the buffering capacity.

Statistical analysis revealed that the differences in alkalinity between spring and neap tides during the daytime were not significant ($p = 0.207$, $p > 0.05$), indicating that the tidal influence on alkalinity was minimal during daylight hours. However, at night, the p-value was 0.031 ($p < 0.05$), indicating a statistically significant difference in alkalinity levels between the tidal phases. These results suggest that although alkalinity remained within acceptable limits under all conditions, its concentration was more sensitive to tidal changes at night. This may reflect variations in water mixing, organic activity, or other physicochemical interactions that are amplified in the absence of light.

Overall, these results confirm that alkalinity in traditional pond irrigation systems is generally sufficient to buffer pH but is modulated by tidal–diurnal interactions. The integration of alkalinity monitoring with other parameters (pH, DO, and salinity) provides a holistic understanding of water stability and supports sustainable aquaculture management under variable coastal conditions.

3.5. Chemistry Condition

3.5.1. Nitrate

Statistical analysis of nitrate concentrations revealed no significant difference between spring and neap tide conditions during daytime, with a p-value of 0.41713 ($p > 0.05$). This suggests that tidal fluctuations in daylight hours do not substantially affect nitrate distribution across the sampling sites. Descriptively, nitrate concentrations during the day followed a consistent trend: increasing from freshwater ponds

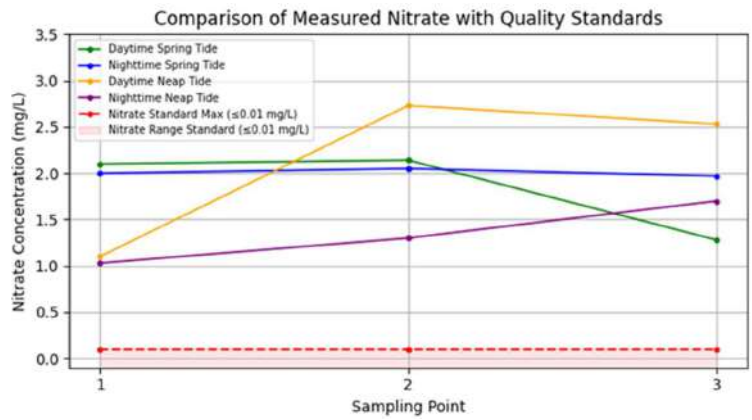


Fig. 6: Results of nitrate concentration (mg.L^{-1}) measurements under spring and neap tide conditions compared with quality standards. (pond 1: freshwater pond, pond 2: brackish water pond, pond 3: saline aquaculture pond)

(point 1) to brackish water ponds (point 2), then decreasing at saline ponds (point 3), under both tidal conditions.

At night, however, the statistical analysis showed a significant difference (p = 0.009, p < 0.05), indicating that tidal variations at night had a stronger influence on nitrate levels. Nitrate concentrations fluctuated across sites, especially at point 3, where levels decreased modestly from 1.97 mg.L^{-1} to 1.7 mg.L^{-1} between nighttime spring and neap tides. A two-way ANOVA confirmed a significant main effect of time of day (F(1,44) = 6.85, p = 0.012, partial η^2 = 0.14) and a smaller but significant effect of tidal phase at night (F (1,44) = 5.21, p = 0.027, partial η^2 = 0.11). No significant interaction was observed (F (1,44) = 2.14, p = 0.15), indicating that diel processes were stronger drivers of nitrate variability than tidal amplitude (Table 2). Post-hoc Tukey tests revealed that nighttime neap tide concentrations at point 3 were significantly lower than daytime concentrations at points 1 and 2 ($p < 0.05$).

Mechanistically, the observed patterns can be attributed to diel nitrogen cycling. During the day, phytoplankton uptake reduces nitrate availability, particularly in brackish water ponds where nutrient demand is high. At night, remineralization of organic matter and microbial denitrification under low DO conditions increase variability (Davis & Boyd 2021). The reduced nitrate levels in saline ponds during nighttime neap tides likely reflect a combination of limited mixing, higher organic matter decomposition, and denitrification, which consumes nitrate and releases N_2 gas (Hossain et al. 2025). Furthermore, anthropogenic sources such as agricultural runoff and pond fertilization may elevate nitrate at upstream freshwater points, which then decline downstream through dilution and microbial processing (Salin & Ataguba 2018).

As shown in Fig. 6, nighttime nitrate concentrations exhibited sharper fluctuations between tidal conditions, especially at Point 2 to Point 3. Although still within ecologically tolerable limits for most aquaculture systems, this variability during nighttime remains environmentally significant. Similar findings in Pekalongan waters demonstrated that nitrate distribution is influenced by tidal cycles, water depth, and coastal organic inputs, with reported values ranging from 0.0065 to 0.1072 mg.L^{-1}, further reinforcing the role of localized hydrodynamic processes (Muhaemin et al. 2023). Comparable studies in tropical aquaculture systems showed nitrate levels typically ranging between 0.2–2.5 mg.L^{-1}, with diel peaks linked to photosynthetic activity and respiration (He et al. 2023, Salin & Arome Ataguba 2018). These studies support the present findings that nighttime processes, rather than daytime tidal changes, exert stronger control over nitrate dynamics.

3.5.2. Nitrite

Nitrite is a key indicator of aquaculture water quality, particularly because of its toxicity at elevated concentrations. Based on Fig. 7, all nitrite values are above the standard threshold ($\leq$0.1 mg.L^{-1}), as indicated by the red-dashed line and shaded area. However, variations were still observed among the sampling points and tidal phases, suggesting complex ecological interactions. Daytime spring tide conditions show a steady decline in nitrite levels, exceeding the specified threshold of $\leq$0.1 mg.L^{-1} (Ministry of Environment 2004, SNI 8036.2:2014, Surya et al. 2024). However, during the neap tide at night, a significant increase was recorded at point 3, where the concentration increased from 0.57 to 1.31 mg.L^{-1}. This increase indicates the potential for nitrogen accumulation under stagnant neap tide conditions. The trend that occurred at night showed a constant fluctuation. The distance between points 1 and 2 decreased, and that between points 2 and 3 showed a massive increase during spring and neap tide conditions at night.

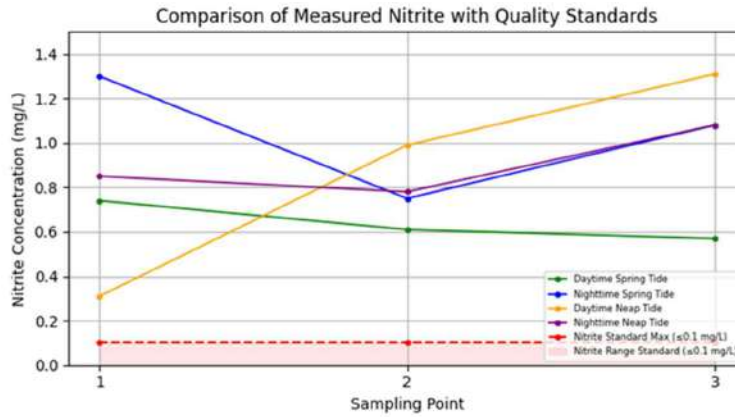


Fig. 7: Results of nitrite concentration (mg.L^{-1}) measurements under spring tide and neap tide conditions against quality standards. (pond 1: freshwater pond, pond 2: brackish water pond, pond 3: saline aquaculture pond)

A two-way ANOVA indicated no significant main effect of tidal phase (F (1,44) = 2.41, p = 0.128, partial η^2 = 0.05) but revealed a significant effect of time of day (F (1,44) = 6.27, p = 0.016, partial η^2 = 0.13). The interaction effect between the tidal phase and time of day was marginal (F (1,44) = 3.14, p = 0.084), suggesting that diel variation exerted a stronger influence on nitrite concentrations than tidal amplitude (Table 2). Post-hoc Tukey tests confirmed that nitrite levels at point 3 during daytime neap tides (mean = 1.31 mg.L^{-1}) were significantly higher than those at other sampling points and under other conditions ($p < 0.05$). These findings highlight the site-specific susceptibility of saline ponds to nitrite accumulation, particularly when tidal flushing is diminished.

Mechanistically, nitrite is an intermediate compound in the nitrification pathway ($NH_4^+ \rightarrow NO_2^- \rightarrow NO_3^-$). Under optimal oxygen conditions, nitrite is rapidly oxidized to nitrate. However, during nighttime or under low DO conditions, incomplete nitrification can cause nitrite accumulation (Boyd 2012). Stagnant conditions during neap tides reduce hydrodynamic mixing, promoting nitrite buildup (Hossain et al. 2025). Additionally, organic matter loading from feed residues or agricultural runoff may enhance microbial activity, leading to elevated ammonia inputs that overwhelm the nitrification capacity, resulting in transient nitrite peaks (Xiao et al. 2025). The decline at point 1 during nighttime at neap tide is consistent with freshwater dilution and faster turnover rates, whereas downstream saline ponds experience nitrite accumulation due to lower flushing efficiency.

Statistically, no significant differences were found between spring and neap tides for either day (p = 0.2698) or night (p = 0.44103) measurements, indicating that while nitrite values fluctuated, the changes were not statistically significant. Nonetheless, even sublethal nitrite fluctuations are ecologically important because chronic exposure can cause methemoglobinemia ("brown blood disease") in fish and shrimp, impairing oxygen transport and growth performance (Salin & Ataguba 2018). This underscores the need to effectively manage nitrogen pathways in pond aquaculture systems.

The results demonstrate that nitrite levels in the study area exceed safety thresholds, indicating localized excesses during neap tide conditions. While pH and salinity stayed within safe limits, the persistent elevation of nitrites above acceptable levels highlights the need for effective nitrogen management to sustain aquaculture productivity and ecosystem health. These observations result from the interplay of biological nitrogen cycling, tidal flushing, and daily oxygen fluctuations. Ongoing monitoring and proactive management are crucial to reducing nitrite-related risks and ensuring the long-term viability of coastal pond aquaculture.

3.5.3. Ammonia

Ammonia is one of the most critical water quality parameters in tropical aquaculture because of its toxicity and sensitivity to environmental conditions. As shown in Fig. 8, ammonia was measured at three sampling points under four tidal time combinations. All values were under the recommended threshold ($\leq$0.3 mg.L^{-1}), as indicated by the red dashed line.

The highest concentrations were recorded during nighttime neap tides, particularly at points 2 and 3, reaching approximately 0.4 mg.L^{-1}. In contrast, daytime spring tide conditions produced more stable and lower values, although still above the standard, with concentrations of 0.15 mg.L^{-1} at point 1, 0.18 mg.L^{-1} at point 2, and 0.19 mg.L^{-1} at point 3. A two-way ANOVA revealed a significant main effect of time of day (F(1,44) = 9.42, p = 0.004, partial η^2 = 0.18)

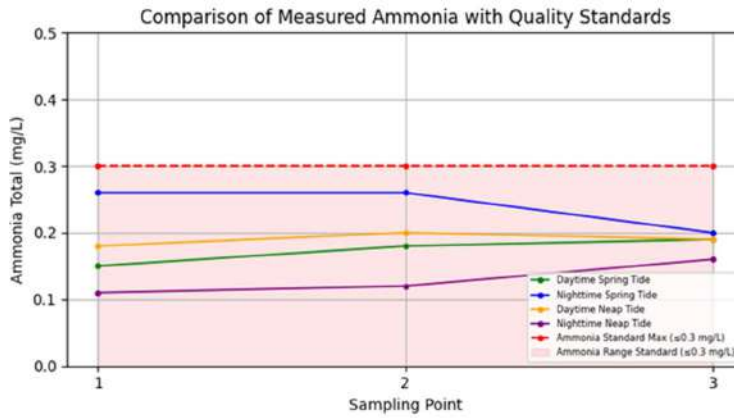


Fig. 8: Results of Ammonia concentration (mg.L^{-1}) measurements under spring and neap tide conditions against quality standards.
(pond 1: freshwater pond, pond 2: brackish water pond, pond 3: saline aquaculture pond)

and tidal phase ($F(1,44) = 7.88$, $p = 0.007$, partial $\eta^2 = 0.15$) on ammonia concentration, with a strong interaction effect ($F(1,44) = 6.01$, $p = 0.018$) (Table 2). Post-hoc Tukey tests confirmed that nighttime neap tides at points 2 and 3 were significantly higher ($p < 0.01$) than all daytime measurements at all points. This demonstrates that ammonia accumulation intensifies when tidal flushing is minimal and diurnal oxygen depletion occurs.

Mechanistically, ammonia in pond water exists in equilibrium between ionized ammonium (NH_4^+, relatively non-toxic) and un-ionized ammonia (NH_3, highly toxic). The proportion of NH_3 increases with increasing pH and temperature (Boyd 2012). During daytime spring tides, enhanced mixing and photosynthesis dilute ammonia levels and maintain more stable values than at night. Conversely, nighttime neap tides combine several stressors: reduced water exchange, higher organic decomposition, lower dissolved oxygen, and stable pH near alkaline levels, all of which favor NH_3 accumulation (Ip & Chew 2010). Elevated ammonia levels at downstream points (2 and 3) likely reflect both hydrodynamic stagnation and cumulative organic loading from upstream inputs, which is exacerbated by anthropogenic nutrient enrichment.

Statistical analysis revealed no significant difference between spring and neap tide conditions during the day ($p = 0.679$), with all sites showing a similar increase in ammonia concentration. However, at night, a significant difference was found ($p = 0.001$), and unlike daytime conditions, each sampling point exhibited a unique trend, further indicating that tidal and diurnal factors jointly modulated ammonia concentrations. These findings are consistent with global studies reporting diel ammonia variability in aquaculture ponds, where nighttime peaks often exceed safe thresholds because of oxygen depletion and incomplete nitrification (Xiao et al. 2025). Chronic exposure to NH_3 above 0.05 $mg.L^{-1}$ has been linked to gill damage, oxidative stress, and reduced growth in fish and shrimp (Muharomah et al. 2025).

4. DISCUSSION

This study emphasizes the crucial role of tidal dynamics as a key hydrodynamic factor affecting coastal water quality, especially in traditional pond irrigation systems reliant on seawater supply. The primary tidal phases, spring and neap tides, vary in amplitude and duration, thereby influencing the patterns of water mixing (Muhtadi et al. 2024). During spring tides, the alignment of the Moon and Sun produces stronger gravitational forces, resulting in more extreme tidal ranges. This enhances seawater inflow and promotes mixing between marine water, freshwater, and anthropogenic inputs (Utami et al. 2024, Xu & Zhang 2025). In contrast, neap tides, which have lower tidal amplitudes, are dominated by land-based water contributions. These conditions lead to changes in physicochemical parameters such as salinity, temperature, and dissolved oxygen (DO), causing noticeable differences in water quality (Muhtadi et al. 2024). Daytime fluctuations in salinity, marked by high mean values and standard deviations at saline points, further confirm the substantial impact of full tidal cycles on spatial variability.

The comprehensive analysis of various parameters revealed that tidal–diurnal interactions influence water quality through interconnected processes involving salinity, dissolved oxygen (DO), pH, alkalinity, and nitrogen species such as nitrate, nitrite, and ammonia. For instance, nighttime DO depletion inhibits complete nitrification, leading to increased levels of nitrite and ammonia. Additionally, alkalinity functions as a chemical buffer that stabilizes pH while also affecting the proportion of toxic un-ionized ammonia (NH_3). These interconnected mechanisms are consistent with global research on tropical aquaculture ponds, where diel cycles cause significant fluctuations in nitrogen dynamics and result in periods of heightened ecological stress.

Ammonia fluctuations serve as additional evidence of tidal influence. During spring tides, fluctuating ammonia levels in aquaculture ponds indicate active dilution, as increased seawater flow enhances mixing and oxygenation, thereby decreasing the accumulation of nitrogen compounds such as ammonia, nitrates, and water (Muhaemin et al. 2023, Surya et al. 2024, Xu & Zhang 2025). Conversely, at night during neap tides, ammonia tends to accumulate significantly. This is due to the predominance of land water with limited seawater dilution and reduced mixing during nighttime. Elevated ammonia levels at night during spring tides in several ponding stations approached the recommended threshold (≤ 0.3 $mg.L^{-1}$), potentially posing a chronic risk to farmed shrimp and fish. This aligns with previous research linking ammonia to gill damage, reduced feeding efficiency, and mortality in tropical aquaculture systems (Ip & Chew 2010). These results highlight the importance of nitrogen management as a key factor in enhancing aquaculture resilience.

The distribution of aquatic vegetation, especially water hyacinth *(Eichhornia crassipes)*, mirrors these physicochemical patterns (Fig. 9). As a species with low salinity tolerance, its presence is significantly less in saline ponds compared to freshwater or brackish environments (Bick et al. 2020). The limited growth of water hyacinths in saline conditions reduces their effectiveness in phytoremediation, where they typically help decrease ammonia levels through rhizofiltration and microbial activity in the rhizosphere (He et al. 2023). This underscores the importance of nature-



Fig. 9: Water hyacinth dominance in pond irrigation areas (*Eichhornia crassipes*).

based solutions for water quality management. Nonetheless, macrophyte-based treatment alone is inadequate in high-salinity, low-mixing settings and should be supplemented with engineered solutions like aeration, biofiltration, or controlled water exchange.

The relationship between alkalinity and pH provides important insights into water quality stability. At various sampling locations, alkalinity values tend to fluctuate inversely with pH, emphasizing its role as a buffer system that maintains the chemical balance of water. Alkalinity is also a major determinant of nitrogen speciation; under high pH conditions with low alkalinity, the toxic non-ionic form of ammonia (NH_3) is more dominant. Alkalinity instability can trigger sharp pH fluctuations, thereby disrupting chemical equilibrium and causing non-linear changes in nitrification and denitrification processes. A study by Sriyasak et al. (2015) further shows that changes in microbial composition and dissolved oxygen can significantly affect ammonia concentrations. Similarly, Hadi et al. (2024) found that pH and alkalinity dynamics in tidal irrigation systems are strongly influenced by the interaction between brackish water and seawater, which ultimately affects the chemical stability of the aquatic environment. These findings reinforce the importance of integrated monitoring of various parameters, such as buffering capacity, oxygen dynamics, and the nitrogen cycle, which are interrelated processes.

From a management perspective, the findings suggest several practical implications. First, targeted aeration during nighttime neap tides is essential to prevent DO depletion and incomplete nitrification, which are major drivers of nitrite, nitrate, and ammonia (regular monitoring required) accumulation. Second, feed management must be optimized to minimize nitrogenous waste, as overfeeding is a leading cause of chemical component buildup. Third, water exchange should be strategically scheduled during spring tides, when mixing capacity is highest, to dilute pollutants. Fourth, integrated multi-trophic aquaculture (IMTA) systems, including seaweed, mollusks, or biofilm reactors, can be used to absorb excess nitrogen and improve ecological resilience. These adaptive strategies are consistent with international best practices for sustainable aquaculture.

On a broader scale, the study's findings contribute to global debates on sustainable food production and environmental governance. Elevated ammonia, nitrate and nitrite levels are not only local threats but also indicators of eutrophication risk in coastal ecosystems (Hossain et al. 2025). By demonstrating how tidal and diurnal dynamics govern nitrogen pathways, this research provides insights into climate adaptation strategies for coastal aquaculture. The results are directly relevant to the United Nations Sustainable Development Goals (SDGs), particularly SDG 2 (Zero Hunger), SDG 6 (Clean Water and Sanitation), SDG 13 (Climate Action), and SDG 14 (Life Below Water). Addressing water quality instability in aquaculture ponds thus supports both local livelihood security and global sustainability agendas.

Overall, this study demonstrates that tidal phase, diurnal variation, and biological interactions jointly regulate key water quality parameters. Future studies should employ high-frequency monitoring (e.g., sensor networks, remote sensing) to capture fine-scale variability and incorporate predictive models that integrate hydrodynamics, biogeochemistry, and climate projections. Such approaches will advance adaptive aquaculture irrigation systems that are ecologically sustainable and resilient to environmental variability.

5. CONCLUSIONS

This study demonstrates that tidal phases exert a significant influence on the physical and chemical characteristics of pond water quality. The contrasting dynamics of spring and neap tides generate variations in water mixing processes and the distribution of key parameters, including alkalinity, salinity, dissolved oxygen (DO), ammonia, nitrate, and nitrite. These fluctuations directly affect the ecological conditions of aquaculture systems. The findings highlight

that understanding tidal dynamics is essential for developing sustainable pond management strategies. By integrating knowledge of tidal-driven variability, aquaculture practices can be made more adaptive and resilient to hydrodynamic changes in coastal environments.

Specifically, the results show that: (i) pH remained relatively stable within acceptable thresholds, with only localized deviations during nighttime spring tides, (ii) dissolved oxygen (DO) exhibited diel fluctuations, with nighttime values occasionally approaching critical limits but not differing significantly between tidal phases, (iii) salinity varied significantly between spring and neap tides ($F(1,44) = 18.52, p < 0.001$), confirming tidal amplitude as the dominant driver of hydrological gradients, (iv) alkalinity consistently buffered pH but exhibited significant nighttime increases under spring tides, indicating carbonate system shifts, (v) Nitrate and nitrite were predominantly above international and national limits during daytime and nighttime in every pond station, and (vi) ammonia concentrations consistently remained below the recommended limit (≤ 0.3 mg.L^{-1}).

Nitrite concentrations exceeding the recommended threshold in certain tidal and daily cycles, especially during nighttime neap tides, when oxygen deficiency inhibits nitrification efficiency. The results of this study correlating nitrite with ammonia confirm that tidal stagnation and nighttime oxygen depletion are key factors in nitrogen imbalance in brackish water pond systems. Furthermore, based on research trends, a decrease in ammonia concentration accompanied by an increase in nitrite or vice versa during nighttime conditions indicates that partial oxidation of ammonia to nitrite occurs under sub-optimal aeration conditions. This incomplete nitrification process causes the accumulation of intermediate nitrogen species, disrupting the balance between nitrogen transformation and biological uptake. These daily and tidal interactions emphasize that hydrodynamic processes and oxygen variability highly influence nitrogen cycle efficiency.

These integrated findings highlight that the nitrogen cycle (ammonia–nitrite–nitrate transformation) is strongly influenced by the dynamics of the physical-chemical content of water. In addition to ammonia and nitrite, the combination of low DO levels at night and reduced water flow during neap tides creates high-risk conditions for the accumulation of nitrite and ammonia, which threaten the health of cultivated species. Consequently, effective pond management must adopt a systems approach, simultaneously addressing hydrodynamics, carbonate chemistry, and nitrogen pathways rather than relying on single-parameter control. From a management perspective, the study emphasizes the importance of implementing adaptive strategies, including: (i) deploying aerators during nighttime neap tides to prevent DO depletion and incomplete nitrification, (ii) optimizing feed management to minimize nitrogenous waste, (iii) scheduling water exchange during spring tides for maximum dilution efficiency, and (iv) adopting integrated multi-trophic aquaculture (IMTA) or biofilters to absorb excess nitrogen.

These approaches align with sustainable aquaculture principles and can enhance resilience in smallholder systems. At a global scale, the findings contribute to ongoing debates on sustainable aquaculture and coastal management by demonstrating the sensitivity of pond irrigation systems to tidal–diurnal variability. The results align with multiple Sustainable Development Goals (SDGs), particularly SDG 2 (Zero Hunger) by supporting food security, SDG 6 (Clean Water and Sanitation) through improved water quality management, SDG 13 (Climate Action) via adaptive strategies under hydrodynamic and climate variability, and SDG 14 (Life Below Water) by mitigating eutrophication risks. Future research should focus on high-frequency sensor-based monitoring and predictive modeling of nitrogen fluxes to anticipate extreme events and design climate-resilient aquaculture irrigation systems.

6. ACKNOWLEDGMENTS

Thanks to Kemendiktisaintek (Directorate General of Higher Education, Ministry of Higher Education, Science, and Technology) for the fundamental research grant awarded in fiscal year 2025, LPPM Tribhuwana Tunggadewi University, and Brawijaya University.

7. REFERENCES

Bick, E., de Lange, E.S., Kron, C.R., da Silva Soler, L., Liu, J. and Nguyen, H.D., 2020. Effects of salinity and nutrients on water hyacinth and its biological control agent, Neochetina bruchi. *Hydrobiologia*, 847(15), pp.3213-3224.[DOI]

Boyd, C.E., 2012. *Pond Aquaculture Water Quality Management*. 1st ed. New York: Springer New York, NY, pp.350. [DOI]

Davis, R.P. and Boyd, C.E., 2021. A comparison of the technical efficiency of Aquaculture Stewardship Council certified shrimp farms to non-certified farms. *Current Research in Environmental Sustainability*, 3, pp.1-10. [DOI]

FAO, 2024. *The State of World Fisheries and Aquaculture 2024*. Rome: FAO, pp.250. [DOI]

Hadi, S., Pratiwi, E.P.A. and Wignyosukarto, B.S., 2024. The dynamic of pH and EC in the Katingan tidal irrigation system, under influences of acid water, brackish water, and tidal movement. *Water Cycle*, 5, pp.76-85. [DOI]

Hanif, I.M., Effendi, I., Budiardi, T. and Diatin, I., 2021. The recirculated aquaculture system (RAS) development with nanobubble application to improve growth performance of grouper fish fry culture. *Indonesian Journal of Aquaculture*, 20(2), pp.181-190.[DOI]

He, X., Zhang, S., Lv, X., Liu, M., Ma, Y. and Guo, S., 2023. Eichhornia crassipes-rhizospheric biofilms contribute to nutrients removal and methane oxidization in wastewater stabilization ponds receiving

simulative sewage treatment plants effluents. *Chemosphere*, 322, 138100, pp.1-10. [DOI]

Hossain, M.S., Zaman, B., Khan, M.A., Shihab, M.Y.K. and Nielsen, R., 2025. Impact of climate change and adaptation strategy in aquaculture: a systematic review. *Aquaculture International*, 33(5), 330, pp.1-15. [DOI]

International Organization for Standardization (ISO), 1994. Water quality — Determination of alkalinity — Part 1: Determination of total and composite alkalinity (ISO 9963-1:1994). Geneva: ISO, pp.1-8.

International Organization for Standardization (ISO), 2008. *Water quality — Determination of pH (ISO 10523:2008)*. Geneva: ISO, pp.1-10.

International Organization for Standardization (ISO), 2012. *Water quality — Determination of dissolved oxygen — Electrochemical probe method (ISO 5814:2012)*. Geneva: ISO, pp.1-12.

Ip, Y.K. and Chew, S.F., 2010. Ammonia production, excretion, toxicity, and defense in fish: a review. *Frontiers in Physiology*, 1, 134, pp.1-10. [DOI]

Meilani, D.I. and Rahmadanik, D., 2021. Empowerment of water hyacinth as organic fertilizer in Kepetingan Hamlet, Sawohan Village, Buduran District, Sidoarjo Regency. *Patriot Service Proceedings*, 1(1), pp.1-5.

Ministry of Environment, 2004. *Sea water quality standards, Regulation No. 51 of 2004*. Jakarta: Ministry of Environment, pp.1-8.

Muhaemin, M., Rahmadita, D.A., Suwiryono, J. and Mayaguezz, H., 2023. Variability of concentration and distribution of dissolved inorganic nitrogen (ammonia, nitrite, nitrate) in Kalianda Waters and Anyer-Panimbang Waters. *Journal of Marine Research*, 12(4), pp.737-745. [DOI]

Muharomah, R., Setiawan, B.I., Sands, G.R., Juliana, I.C. and Gunawan, T.A., 2025. A review on enhancing water productivities adaptive to climate change. *Journal of Water and Climate Change*, 16(3), pp.860-887. [DOI]

Muhtadi, A., Leidonald, R. and Cordova, M.R., 2024. The effect of tides on the dynamics of water quality in Indonesian tropical tidal lakes. *IOP Conference Series: Earth and Environmental Science*, 1400(1), 012001, pp.1-10. [DOI]

Perugini, M., Gallucci, M. and Costantini, G., 2018. A practical primer to power analysis for simple experimental designs. *Revue Internationale de Psychologie Sociale*, 31(1), pp.1-23.

R Core Team, 2020. *R: A language and environment for statistical computing*. Retrieved June 15, 2026, from https://www.R-project.org/

Sa'adah, V.H. and Widagdo, S., 2020. Distribution of surface salinity and temperature during spring tide and neap tide in the Porong River Estuary, Sidoarjo. *Journal of Tropical Marine Research*, 2(1), pp.48-57. [DOI]

Salin, K.R. and Arome Ataguba, G., 2018. Aquaculture and the environment: towards sustainability. In: F.I. Hai, C. Visvanathan and R. Boopathy (eds.) *Sustainable Aquaculture*. Cham: Springer International Publishing, pp.1-62.

SNI, 2014. *Cantang grouper (Epinephelus fuscoguttatus, Forsskal 1775 x Epinephelus lanceolatus, Bloch 1790) Part 2: Hybrid seed production (SNI 8036.2:2014)*. Badan Standardisasi Nasional Indonesia, pp.1-20.

Sriyasak, P., Chitmanat, C., Whangchai, N., Promya, J. and Lebel, L., 2015. Effect of water de-stratification on dissolved oxygen and ammonia in tilapia ponds in Northern Thailand. *International Aquatic Research*, 7(4), pp.287-299. [DOI]

Surya, A.T.J., Sasongko, A.S. and Cahyadi, F.D., 2024. Ammonia, phosphate, nitrate and nitrite content of seawater in coastal waters of Lontar Village. *Juvenil: Scientific Journal of Marine and Fisheries*, 5(3), pp.238-245. [DOI]

Tarunamulia, T., Kamariah, K. and Mustafa, A., 2016. Spatial relationship of environmental quality and presence of potential HABs phytoplankton in extensive ponds in Losari District, Cirebon Regency, West Java. *Journal of Aquaculture Research*, 11(2), pp.181-195.

Utami, R.D., Rahardjo, A.P., Sujono, J. and Yakubson, 2024. Identification of potential tides in Terusan Tengah tidal irrigation area canal network and its surrounding channels. *IOP Conference Series: Earth and Environmental Science*, 1416(1), 012026, pp.1-10. [DOI]

Wang, Y., Xiao, Y., Puig-Bargués, J., Zhou, B., Liu, Z., Muhammad, T., Liang, H., Maitusong, M., Wang, Z. and Li, Y., 2023. Assessment of water quality ions in brackish water on drip irrigation system performance applied in saline areas. *Agricultural Water Management*, 289, 108544, pp.1-15. [DOI]

Xiao, W., Ren, B., Wu, B. and Deng, X., 2025. Spatiotemporal dynamics and optimization of water quality assessment in the Nantong section of the Yangtze River Basin: a WQImin approach. *Journal of Hydrology: Regional Studies*, 57, 102106, pp.1-15. [DOI]

Xu, Y. and Zhang, Z., 2025. Tidally driven outwelling of dissolved carbon and nitrate from the largest mangroves of China. *Frontiers in Marine Science*, 12, pp.1-12. [DOI]

Nature Environment and Pollution Technology
An International Quarterly Scientific Journal

p-ISSN: 0972-6268
(Print copies up to 2016)
e-ISSN: 2395-3454

Vol. 25 | No. 3 | Article ID B4399 | 2026

Original Research Paper

https://doi.org/10.46488/NEPT.2026.v25i03.B4399

Open Access Journal

Exploring the Role of Rice Straw Biochar in Sustainable Agriculture and Environmental Health

Himanshi Upadhayay, Sneha Gupta, Srishti Jain and Manu Solanki†
Department of Biotechnology, School of Engineering and Technology, Manav Rachna International Institute of Research and Studies, Faridabad-121006, Haryana, India
†Corresponding author: Manu Solanki; solankimanu.set@mriu.edu.in

Abbreviation: Nat. Env. & Poll. Technol.
Website: www.neptjournal.com

Received: 29-09-2025
Revised: 27-11-2025
Accepted: 29-11-2025

Key Words:

Rice straw biochar
Pyrolysis
Carbon sequestration
Sustainable environment
Environmental health

ABSTRACT

Burning rice straw in open fields has led to a plethora of concerns, ranging from air pollution to soil carbon losses, posing a risk to human health and disturbing the soil ecosystem. The problem of rice stubble burning has been addressed by adopting different in-situ and ex-situ conservation technologies supported by the government and private companies. Biochar production from rice straw is one such method. Biochar is a carbon-rich porous material produced by the thermochemical conversion of various biomass feedstocks and is used globally to improve soil properties. It plays a crucial role in sustainable agriculture and in environmental health. It has the potential to enhance soil fertility, water retention, and nutrient cycling, while also offering carbon sequestration benefits. However, the adoption of biochar as a soil amendment practice is still challenging owing to the limited understanding of the long-term effects on soil health, the establishment of onsite production facilities, high energy consumption in the production process, and inconsistent results depending on the variable soil types. For biochar to be applied practically for soil improvement in different climatic regions and crop production, it is important to understand the potential effects of biochar on soil properties, the factors that cause soil to change when biochar is added, and the mechanisms of biochar–soil interaction. This review provides an overview of the current research on rice straw biochar and identifies key limitations that will direct future research and policy decisions for its integration into sustainable farming practices. It underscores the potential of biochar to combat global warming, mitigate environmental damage, and its role in reversing the impacts of climate change in line with sustainable development goals.

Citation for the Paper:

Upadhayay, H., Gupta, S., Jain, S. and Solanki, M., 2026. Exploring the role of rice straw biochar in sustainable agriculture and environmental health. *Nature Environment and Pollution Technology*, 25(3), B4399. https://doi.org/10.46488/NEPT.2026.v25i03. B4399

Note: From 2025, the journal has adopted the use of Article IDs in citations instead of traditional consecutive page numbers. Each article is now given individual page ranges starting from page 1.

Copyright: © 2026 by the authors
Licensee: Technoscience Publications
This article is an open access article distributed under the terms and conditions of the Creative Commons Attribution (CC BY) license (https://creativecommons.org/licenses/by/4.0/).

1. INTRODUCTION

India is the second-largest producer of rice, after China. It is grown widely in Punjab, Haryana, Uttar Pradesh, West Bengal, Tamil Nadu, Andhra Pradesh, and Odisha. A total of 1357.55 Lakh tonnes of rice is produced annually (2022-23). Approximately 500 pounds of rice husks and straw are generated for every ton of rice produced. Unfortunately, approximately 80% of this rice straw is disposed of through open burning, which significantly contributes to air pollution and greenhouse gas emissions, posing serious risks to human health and water quality. Furthermore, this practice leads to the loss of a significant amount of organic matter and affects soil microflora. The burning of paddy straw has immediate and notable impacts on soil microbiota, drastically reducing the populations of key microorganisms, including bacteria, fungi, actinomycetes, mineral phosphate-solubilizing microorganisms, potassium-solubilizing bacteria, and cellulose-degrading bacteria. Although these populations often recover within 30 to 60 days post-burning, indicating a temporary resilience of soil microbiomes, the levels of microbial enzymes remain low (Kumar et al. 2019, Ravali et al. 2022, Arunrat et al. 2023). To circumvent this problem, alternative strategies for rice waste management are required. Using rice straw biochar as a soil amendment is a promising strategy for enhancing soil health and addressing the challenges of rice straw management.

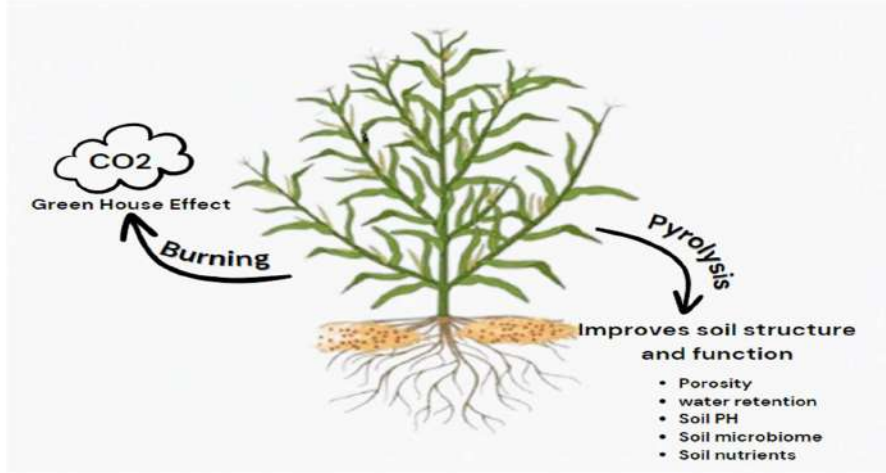


Fig. 1: Biochar: A sustainable approach to biomass utilization.

Table 1: Biomass to biochar: Aligning with sustainable development goals.

Sustainable Development Goal (SDG)	Relevance to Biochar Technology	Reference
SDG 2: Zero Hunger	Improve soil fertility and enhance agricultural productivity.	Farhangi-Abriz et al. (2021)
SDG 3: Good Health and Well-being	Improve food quality and reduce air pollution	Dong et al. (2025)
SDG 6: Clean Water and Sanitation	Improve water retention and reduce water pollution	Gwenzi et al. (2017)
SDG 7: Affordable and Clean Energy	Support sustainable energy production	Ahuja et al. (2024)
SDG 9: Industry, Innovation, and Infrastructure	Promote innovative technologies for sustainable agriculture	Amalina et al. (2023)
SDG 12: Responsible Consumption and Production	Promote sustainable resource use and reduce waste	Afshar and Mofatteh (2024)
SDG 13: Climate Action	Reduce greenhouse gas emissions, enhance carbon sequestration	Kalu et al. (2024)
SDG 15: Life on Land	Combat land degradation, enhance soil health	Shoudho et al. (2024)

Biochar is a carbon-rich material that, when added to soil, enhances soil quality, boosts crop yields, and stores carbon, benefiting agriculture and the environment. Rice straw biochar has demonstrated effectiveness in improving soil structure, retaining water, increasing nutrient availability, and stimulating microbial activity. Thus, production of biochar from agricultural waste is a sustainable approach that improves soil fertility and minimizes air pollution (Fig.1).

Additionally, the use of rice straw biochar supports various global sustainability objectives, such as mitigating climate change, reducing waste, etc (Table 1).

However, challenges such as inconsistent biochar quality, costly production, limited farmer awareness, and regulatory gaps hinder its widespread adoption. This review explores the significance of rice straw biochar in promoting sustainable agriculture and environmental health, emphasizing its advantages, operational mechanisms, and practical applications. It also addresses current challenges and suggests future research paths to enhance its efficacy and encourage its incorporation into conventional agricultural methods. To synthesize this review article, a systematic literature search was conducted on Scopus, Web of Science, ScienceDirect, and Google Scholar for studies published between 2000 and 2024 using keywords like “rice straw biochar,” “pyrolysis,” “biochar modification,” “soil amendment,” and “environmental impacts.” The inclusion criteria were studies focusing on rice straw biochar, providing experimental or field data, and published in peer-reviewed journals. The exclusion criteria involved non-rice biomass studies, non-peer-reviewed sources, and articles lacking clarity in methodology or agricultural/environmental context. The selected studies were assessed for pyrolysis conditions, characterization methods, soil type, experimental scale, and reported outcomes. Conflicting results were compared based on methodological differences and contextual factors to ensure the reliability and relevance of the review.

2. BIOCHAR

Biochar is a form of carbon with very high stability, produced

via the pyrolytic treatment of organic resources, such as agricultural waste, forest residues, or any other biomass. This process involves heating biomass in the absence of oxygen, which helps protect the biomass from burning and instead turns it into a charcoal-like material. Pyrolysis can be performed as slow pyrolysis, Fast Pyrolysis, and Flash pyrolysis (Fig. 2). Slow Pyrolysis runs at low heating rates, 0.1-1°C.s^{-1}, with temperatures between 350°C and 450°C. The residence times are long, ranging from 5 min to days, and the process produces large quantities of biochar and bio-oil; thus, it can be directly applied as a solid fuel. Fast pyrolysis is carried out over a relatively moderate temperature range of 450-600°C, while heating rates range between 10 and 200°C.s^{-1} with residence times of 0.5-2 seconds. The bio-oil yield was the highest, whereas low yields of char and gas were obtained. Flash pyrolysis employs very high heating rates of up to 1000°C.s^{-1} and temperatures between 800 and 1000°C. Hence, the residence time is very short, less than 0.5 s. It maximizes liquid product yield, leaving mainly bio-oil, with minimum char content (Kavan & Panwar 2024).

3. RICE STRAW BIOCHAR (RSB): PRODUCTION AND PROPERTIES

Rice straw contains approximately 40% carbon, 30% oxygen, 5-6% hydrogen, 1% nitrogen, and less than 0.2% sulfur. Rice straw typically has a high ash content (8.5–20.4%) (El-Hassanin et al. 2020). The ash in rice straw is primarily composed of silica oxide, along with other oxides such as aluminum oxide and calcium oxide. Due to its low moisture content (<10%), rice husks are suitable for pyrolysis and biochar production. Rice straw biochar can be obtained by heating rice straw at high temperature under anaerobic conditions. Rice straw, during pyrolysis, is deconstructed in several steps with respective differentiation through a range of temperatures and chemical changes (Park et al. 2014). It includes the initial drying stage (100-250°C), where the amount of moisture in the biomass is lowered and it is prepared for subsequent heat processing. This is followed by pre-pyrolysis (280-350°C), wherein the straw undergoes decomposition, leading to the initiation of the breaking of hemicelluloses and amorphous cellulose, thereby releasing volatile chemicals (Chaijak et al. 2023). Finally, the pyrolysis activation stage is achieved (above 350°C), which is critical for transforming biomass into valuable products, particularly bio-oil, char, and gases. Careful control of the temperature and reaction conditions is essential to optimize the yield of these products, making this stage a focal point in biomass conversion technologies.

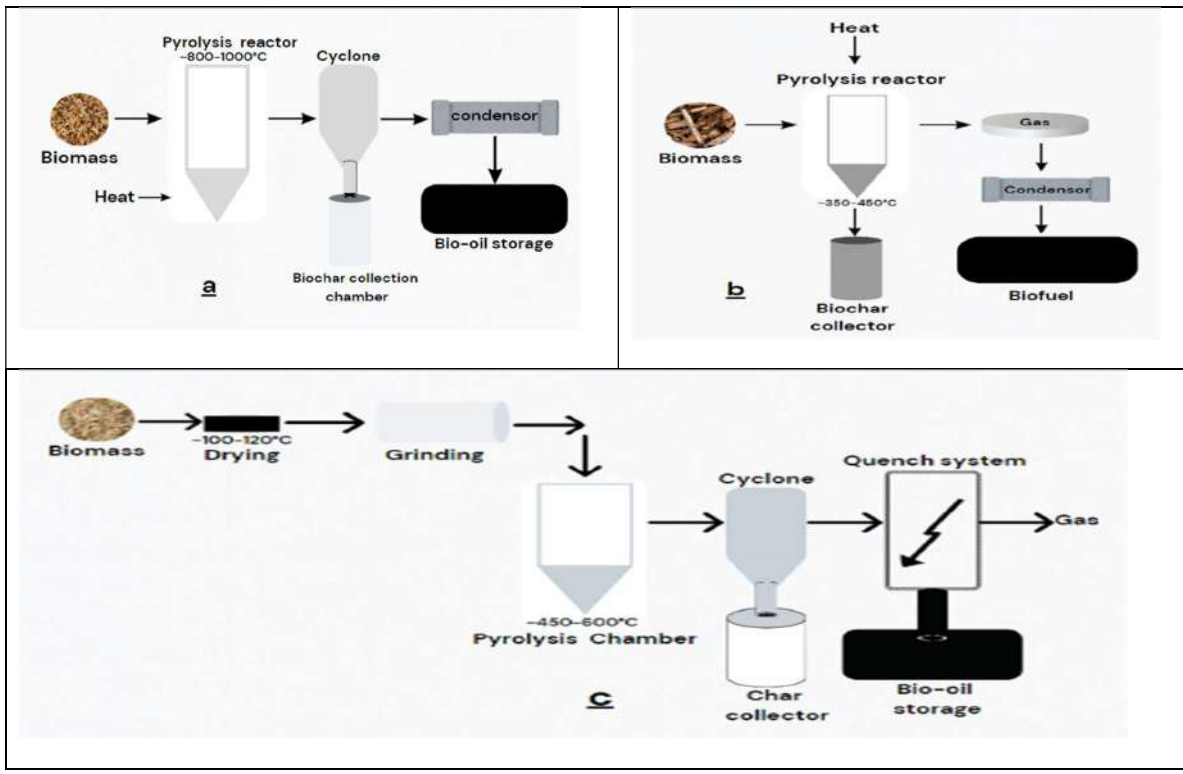


Fig. 2: Different types of pyrolysis: a) flash pyrolysis, b) slow pyrolysis, c) fast pyrolysis.

3.1. Physicochemical Properties of Rice Straw Biochar

Rice straw biochar is characterized by various physical, chemical and structural properties (Table 2).

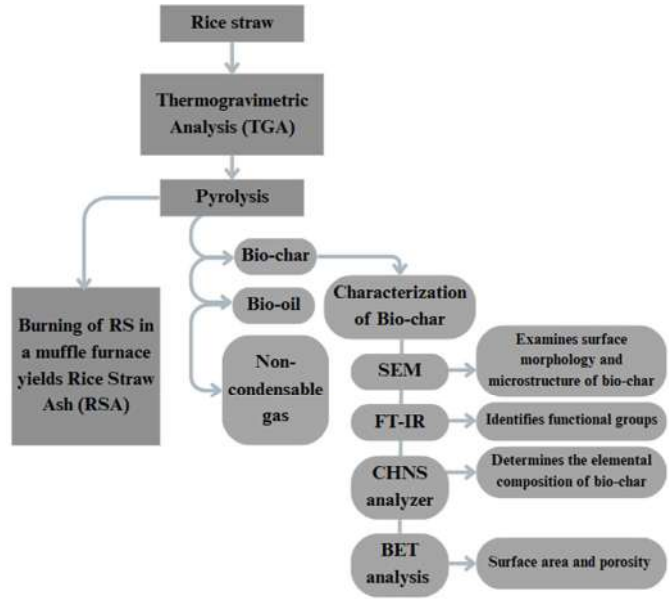
A thorough understanding of these characteristics helps in the optimization process of biochar development and its applications for various purposes. To achieve this, several analytical techniques and instrumentation are employed. Fig. 3 summarizes the key characterization methods for analyzing biochar, including surface area, porosity, elemental composition, surface functional groups, thermal stability, and crystalline structure.

The physicochemical properties of rice straw biochar are significantly influenced by the pyrolysis temperature used during its production (Kanboj et al. 2025). Generally, higher pyrolysis temperatures (typically ranging from 300 to 700˚C) lead to a decrease in the biochar yield, as higher temperatures lead to the release of more volatile matter, resulting in a lower solid biochar yield. Higher temperatures resulted in a more porous structure with a larger specific surface area. The pyrolysis of rice straw biochar at high temperatures also leads to an increased ash content. Organic matter decomposition leads to higher ash content in biochar at higher temperatures. Changes in the pore size distribution were also accompanied by an increase in the pyrolytic temperature. Biochar produced at higher temperatures tends to have a higher pH. This can be attributed to the increased concentration of alkali metals and the loss of acidic functional groups. The increased carbon content and graphitic structures at higher temperatures can slightly increase the electrical conductivity of biochar.

The pyrolysis temperature has a profound effect on the elemental composition of rice straw biochar (Gezahegn et al. 2024), which ultimately affects its functions. The effects of temperature on the elemental composition of rice straw biochar are summarized in Table 3.

Table 2: Key functional properties of rice straw biochar.

Property Category	Specific Property	Significance	References
Textural	Specific surface area (SSA)	Governs adsorption capacity—higher SSA means more active sites for pollutants or nutrients.	Kalina et al. (2022)
	Total pore volume	This relates to how much material (water, nutrients, gases) the biochar can hold.	El-Hassanin et al. (2020)
	Pore size distribution	Determines accessibility: micropores (<2 nm) vs. meso (2–50 nm) and macropores (>50 nm).	Kameyama et al. (2019)
Morphological	Particle size & shape	Influences packing, flowability, and mixing with soils or composites.	Wangdi et al. (2023)
	Surface roughness & structure	Affects water retention, microbial colonization, and interfacial interactions.	Phuong et al. (2015)
Chemical Composition	Elemental makeup (C, H, N, O, S)	Defines basic carbon content, energy potential, and possible nutrient contributions.	Wijitkosum and Jiwnok (2019).
	Ash content & mineral phases	High ash can buffer soil pH; mineralogy (silica, oxides) influences soil amendment value.	Shah et. al. (2024)
	Inorganic/metals content (e.g., K, Ca, Si)	Determines potential nutrient release or contaminant risks.	Tsai et al. (2023)
Surface Chemistry	Functional groups (–OH, –COOH, C=O, etc.)	Key for pollutant binding, nutrient exchange, and redox reactions.	Malik et al. (2023)
	Point of zero charge (pHpzc)	pH at which the surface has a neutral charge, critical for the adsorption of ions.	Neusatz Guilhen et al. (2022)
	Cation Exchange Capacity (CEC)	Measure of nutrientholding ability, relevant to soil fertility.	Li et al. 2013
Physical & Bulk	Bulk density	Affects transport, handling, and soil incorporation rates.	Kamara et al. (2015)
	Water holding capacity	Impacts soil moisture retention and plantavailable water.	Kamara et al. (2015)
Thermal	Thermal stability/ decomposition profile	Indicates resistance to further thermal breakdown, important for high-temperature applications.	Sakhiya et al. (2021)
	Heat of combustion (calorific value)	Relevant if biochar is considered as a solid fuel or for energy recapture.	Satlewal et al. (2018)
Electrical	Electrical conductivity (EC)	Reflects soluble salt levels, important for assessing salinity risks in soils.	Biswas et al. (2024)



SEM: Scanning electron microscopy, FT-1R: Fourier Transform Infrared (FTIR) spectroscopy, BET: Brunauer-Emmett-Teller

Fig. 3: Commonly used techniques for the characterization of rice straw biochar.

The elemental analysis of the biochar produced at different temperatures revealed that the biochar produced at higher temperatures showed a significant increase in carbon content, which was attributed to the enhanced carbonization processes occurring at elevated temperatures. As the pyrolysis temperature increases, there is a marked reduction in the hydrogen and oxygen content, driven by reactions such as dehydration and decarbonization. These reactions lead to the formation of non-condensable gases and hydrogen, contributing to the overall increase in carbon content and the transformation of biochar into a more aromatic and carbon-rich material (Brassard et al. 2017). An increase in the aromatic components and recalcitrance of the rice straw biochars was observed with an increase in temperature owing to the presence of a high concentration of silicon, which forms Si-C bonds (Jindo et al. 2014).

3.2. Effects Of Biochar on Soil Structure and Properties

The application of biochar improves the physical, chemical, and biological properties of soil, enhancing aeration and water retention, especially under drought conditions (Singh et al. 2022). The properties of biochar are primarily influenced by its production conditions (Biswas et al. 2024). The water-holding capacity of biochar increases with pyrolysis temperature, from 12.9 to 22.5% as the temperature increases from 400 to 800°C (Khater et al. 2024). Higher temperatures also increase the surface area, which promotes water retention and microbial activity (Biswas et. al. 2024). Lower pyrolysis temperatures (<400°C) produce hydrophobic biochar, whereas higher temperatures reduce hydrophobicity and increase water retention (Li & Tan 2021). The surface area of rice straw biochar typically ranges from 100 to 500 $m^2.g^{-1}$, depending on the pyrolysis conditions (Tomczyk et al. 2020). Micrometer-range pores, which are critical for plant water uptake, are influenced by the initial pore structure of the raw material (Hyväluoma 2018). However, Adhikari (2023) concluded that the type of organic feedstock did not appear to directly affect water holding. Aging biochar and adjusting particle size can improve its water retention (Adhikari 2022). Biochar rich in nitrogen can enhance moisture retention (Zhang et al. 2024), while its high surface area and cation exchange capacity improve nutrient availability and pH, particularly in acidic soils (He et al. 2024). The high porosity, aromaticity, and surface functional groups of biochar facilitate its role in immobilizing heavy metals and organic contaminants (Foong et al. 2022). Numerous studies have quantified the adsorption efficiency of rice straw biochar for multiple pollutants (Table 4), demonstrating that the same structural attributes responsible for improved soil functionality also govern contaminant-binding mechanisms.

Biochar improves soil structure, water retention, nutrient dynamics, and contaminant immobilization, which collectively impact plant physiological performance. These mechanisms are crucial for assessing crop responses, as discussed in the following section.

Table 3: Elemental composition of rice straw biochar derived at different pyrolysis temperatures.

Temperature [°C]	C [%]	H [%]	O [%]	N [%]	H/C	O/C	C/N	Reference
300	72.1	5.03	21.3	1.55	0.84	0.22	54.27	Wu et al. (2012)
400	77.2	4.01	17	1.74	0.62	0.17	51.76	
500	82.8	3.25	12.1	1.77	0.47	0.11	54.58	
600	87.1	2.51	8.8	1.52	0.35	0.08	66.85	
400	49.92	2.8	12.2	1.22	0.67	0.18	47.74	Jindo et al. (2014)
500	37.48	0.93	8.64	0.61	0.3	0.17	71.68	
600	33.78	0.6	13.68	0.41	0.21	0.3	96.12	
700	36.26	0.51	17.38	0.34	0.17	0.36	124.42	
800	29.17	0.25	3.71	0.25	0.1	0.1	136.13	
300	68.72	5.22	22.78	3.28	0.91	0.25	24.44	Park et al. (2014)
400	75.47	4.62	16.93	2.98	0.73	0.17	29.55	
500	81.43	2.34	15.13	1.1	0.34	0.14	86.37	
600	87.52	2.11	7.48	2.89	0.29	0.06	35.33	
700	91.15	1.26	7.01	0.58	0.17	0.06	183.35	
400	45.5	4.4	49	1.1	1.16	0.81	48.26	Yakout (2017)
500	51.9	3.2	43.6	1.3	0.74	0.63	46.58	
600	65.3	2.9	30.1	1.7	0.53	0.35	44.81	
300	48.3	5.34	24.91	2.58	1.39	0.39	21.84	Liu et al. (2018)
400	54.28	3.65	15.64	2.15	0.81	0.22	29.45	
500	54.31	3.45	11.87	1.68	0.76	0.16	37.72	
600	56.85	2.27	7.89	0.87	0.48	0.1	76.24	
700	55.28	1.88	6.84	1.08	0.41	0.09	59.72	
300	41	3.67	52.7	1.71	1.07	0.96	27.91	Bhatia and Saroha (2024)
500	47.02	2.21	48.85	1.63	0.56	0.78	33.7	
700	47.1	1.26	50.05	1.39	0.32	0.8	39.5	
800	48.03	1.14	49.57	1.12	0.28	0.77	50.21	
400	54.92	3.6	17.19	1.3	0.79	0.23	49.29	Ma et al. (2022)
600	59.56	2.09	20.12	1	0.42	0.25	69.49	
400	38.3	ND	ND	0.9	ND	ND	49.65	Khater et al. (2024)
600	49.8	ND	ND	0.7	ND	ND	83	
800	52.5	ND	ND	0.4	ND	ND	153.13	

Table 4: Removal of heavy metals by rice straw biochar.

Biochar Type	Contaminant Removed	Efficiency	References
RSB	Cr (VI) and Pb (II)	95.57% and 85.68%	Venkatraman et al. (2023)
CO_2 activated RSB	As Mn	99.53% 96.23%	Sakhiya et al. (2023)
RSB	As and Mn	>85%	Sakhiya et al. (2023)
RSB	Pb2+ Zn+2	60% 70%	Sakhiya et al. (2022)
RSB	As (V)	>60%	Mukherjee et al. (2021)
RSB	PAHs	58.8%	Zhang et al. (2020)
RSB	Safranin O	31.06 $mg.g^{-1}$	Phuong and Loc (2022)
RSB	Basic Red 46 dye	22.1 $mg.g^{-1}$	Sackey et al. (2021)

4. APPLICATION OF RICE STRAW BIOCHAR IN IMPROVING PLANT GROWTH

The application of biochar to soil has been shown to improve plant growth and yield in various crops. Rice cultivated in rice straw biochar-amended soils exhibited increases in plant height by 18%, a 66% rise in tiller number, and an increase in dry biomass by 87% compared to non-amended soils (Kamara et al. 2015). Mohamed et al. (2024) investigated the effects of rice straw biochar and NPK mineral fertilizers on crop growth and soil health in the wheat-maize cropping system. Field trials were conducted using different treatments, including biochar, mineral fertilizers, and their combinations. The results showed that the combined mineral-organic treatments had the greatest impact on soil fertility and crop productivity. Hematimatin et al. (2024) evaluated the long-term effects of biochar aging over seven years on both soil pH and organic carbon. It was concluded that aging led to a significant pH decline post-application in 2015 and 2019. In contrast, the application of combined biochar with nitrogen fertilizer improved inorganic N content and increased the contents of soil organic matter between 2014 and 2018. The major practical use of rice straw biochar in rice fields is the reduction in nitrogen loss, as reported by Selvarajh et al. (2023). The mixing of biochar with urea at application rates of 5 and 10 tons ha^{-1} reduced ammonia emissions compared to the application of urea alone. It also enhanced ammonium and nitrate retention by 65.37% and 50.9%, respectively. Additionally, enriched rice straw biochar improves nitrogen content while ensuring better growth of rice plants in pot experiments. Liu et al. (2019) reported that biochar treatments increased phosphorus and potassium availability for ryegrass, raising the nitrogen-to-phosphorus ratio when used in combination with phosphorus fertilization. The use of fertilizers in combination with biochar enhances nutrient efficiency and thus facilitates better growth by the plants

5. LIMITATIONS OF BIOCHAR

Although biochar has the potential to improve soil fertility and help mitigate climate change, it possesses important deficiencies at the technical, environmental, economic, and social levels. The agronomic or economic value of biochar greatly depends on the feedstock (some examples include wood, crop residues, and livestock manure) as well as the particular pyrolysis conditions (parameters of temperature, duration, and oxygen level) used for its production. The array of biochar types that exist leads to diverse outcomes with respect to plants and soil systems, which heavily disrupt the chance of standardization or anticipating results for particular uses (Sohi et al. 2010, Spokas et al. 2012, Joseph et al. 2021). The varied methods of producing biochar result in changes in its physical and chemical characteristics, which affect its resiliency, nutrient concentration, and ability to adsorb pollutants (Al Masud et al. 2023). While some studies have reported increased crop yields and improved soil conditions after biochar application, others have shown little to no change or even perverse impacts, such as reduced crop yields or negative changes in soil chemistry. (Brtnicky et al. 2021).

Biochar production may contain or possibly include contaminants such as polycyclic aromatic hydrocarbons (PAHs) and heavy metals, particularly if its manufacture is carried out using contaminated feedstocks or under pyrolysis conditions, with adverse environmental effects on soil health, plant growth, and food safety (Bhandari et al. 2023). The current impetus on nanobiochar also comes with limitations. Nano-biochar is highly mobile, has a high surface area, and can adsorb and carry pesticides, antibiotics, and other toxicants, thus posing a risk of cross-contamination of ecosystems and toxicity to plants, soil microflora, and even humans (Freixa et al. 2018, Dong et al. 2019). The economic feasibility of biochar production, transportation, and application can be high, but the economic viability of biochar depends heavily on sustainability, and the effects of its economic benefit and economic benefits are marginal in most cases, especially when there is no policy support or carbon credits. The production processes and quality control do not have standardized configurations; hence, commercialization and regulation become very difficult because it is difficult to ensure the consistent quality and performance of products (Brtnicky et al. 2021, Bhandari et. al. 2023). Technical and Measurement Issues also pose challenges to the widespread adoption of biochar. Measuring the rate and longevity of carbon from biochar in soils is technically challenging due to the chemical complexity of biochar and contamination by other black carbon and organic matter in the soil. This calls for an urgent need for accurate measurements of carbon accounting and climate policy, which remains a significant challenge (Al Masud et al. 2023). The opportunity cost of maximizing biochar production (for carbon storage) is the loss of energy (i.e., bioenergy) that can be produced from the same feedstock using different methods (Sohi et al. 2010). The large-scale use of biochar has potential unintended environmental consequences, as described for other geoengineering methods. These include possible effects on nutrient cycling, soil biota, and indirect land-use change when biochar is produced from food crops or other natural ecosystems. Any global biochar strategy should also seriously consider the potential social consequences, such as competition for food crops and the displacement of local people.

Given these technical and environmental limitations, recent research has increasingly focused on engineering strategies to enhance the performance of rice husk biochars. Many of these drawbacks, such as low surface reactivity, variable nutrient content, inconsistent pollutant-sorption capacity, and the presence of undesirable compounds, are directly linked to the physicochemical constraints of pristine biochar. Consequently, modification approaches have been developed to systematically tailor the surface area, porosity, and functional chemistry to overcome these inherent limitations. The following sections delineate common modification and engineering paradigms applied to rice husk biochar for targeted applications in soil health, remediation, catalysis and energy systems:

6. ENGINEERING RICE STRAW BIOCHAR

6.1. Physical Modifications

Activation and particle size modification are two widely employed strategies for enhancing the functional properties of rice straw and rice husk biochars for environmental and agricultural applications. Activation, typically conducted at 873–1273 K using CO_2, steam, or air, induces controlled gasification, removes carbonaceous material, and generates a highly porous interconnected structure. Steam activation is particularly effective for developing hierarchical architectures rich in micropores (Bushra & Remya 2024). Co-pyrolysis and blending approaches, such as mixing rice straw with groundnut shells or wheat straw followed by washing, further improve biochar quality by reducing slagging and fouling potential, making it suitable for both soil and fuel applications (Bhatnagar et al. 2022).

Particle size reduction is another method for enhancing performance. Controlled grinding followed by sieving increases the external surface area and dispersibility, along with the selection of particle fractions of varying sizes for specific uses (Wangdi et al. 2023). Fine biochar fractions improve adsorption kinetics and have been shown to increase grain weight and filled spikelet numbers in rice (Kartika et al. 2018). However, particle size effects are context-dependent: larger particles improve tomato yield under salt stress by enhancing salt leaching and nutrient availability, whereas smaller particles may reduce yield in highly saline soils but enhance productivity in non-saline conditions (Wu et al. 2025).

In addition to mechanical modification, microwave and ultrasonic treatments further refine the biochar structure. Microwave irradiation accelerates devolatilization and pore development (Sahoo & Remya 2022, Zhang et al. 2015, Fodah et al. 2022, Potnuri et al. 2023), whereas ultrasonic cavitation disrupts the carbon matrix, increasing the surface area and altering porosity (Chatterjee et al. 2018). Together, these engineering strategies substantially enhance the adsorption capacity, reactivity, and soil-improvement potential of rice-straw biochar.

6.2. Chemical Modifications

These modifications aim to alter the surface chemistry of biochar by introducing or altering surface functional groups to enhance interactions with target analytes or reaction substrates. The different chemical modifications include

6.2.1. Oxidative Modification

Treatment with oxidizing agents, such as atmospheric oxygen, ozone, hydrogen peroxide, or nitric acid, adds oxygen-containing functional groups (e.g., carboxylic, hydroxyl, carbonyl, and phenolic groups) to the biochar surface (Senapati et al. 2025, Yakout, 2015). These groups can improve the sorption of cationic species (Dey et al. 2023), nutrient retention in soil, removal of heavy metals (Bhadoria et al. 2022, Venkatraman et al. 2023), and serve as active sites for catalytic processes. The reaction with sulfuric acid adds sulfonic acid groups to the biochar surface, enhancing the adsorption capacity for basic organic dyes and heavy metal adsorption (Zhou et al. 2021, Ahmed et al. 2024).

6.2.2. Amination

Nitrogen-containing groups, such as primary amines and quaternary ammonium groups, can be incorporated through reactions with ammonia, urea, or amines (Leng et al. 2020). Aminated biochar has an increased affinity for anionic pollutants and heavy metal ions (Mian et al. 2018).

6.2.3. Phosphorylation

Treatment with phosphoric acid introduces phosphate groups to the biochar surface, enhancing heavy metal cation sorption and improving soil phosphorus availability (Li et al. 2023).

6.2.4. Impregnation with Metal Oxides/Nanoparticles

Incorporating inorganic oxides into biochar enhances its properties, creating hybrid materials with unique advantages over pure biochar. The distribution of inorganic oxides within a carbon matrix enhances the surface characteristics and catalytic performance and aids in the retrieval of nanometer-scale materials (Weidner et al. 2022). The negative surface charge of biochar can be modified by adding positively charged metal oxides, increasing its affinity for anionic impurities. Metal oxides such as TiO2 and ZnO enhance the photocatalytic activity of biochar (Liang et al. 2021). The addition of metallic species to biochars increases their weight, aiding in the separation process, especially when modified with magnetite (Fe3O4) to enhance their magnetic properties

(Kassim et al. 2023). Numerous studies have focused on enhancing the properties of rice husk and straw biochars by incorporating metal oxides. Yang et al. (2022) found that rice husk biochar loaded with zinc oxide was more effective in treating textile wastes compared to pristine biochar. Qin et al. (2020) demonstrated that magnesium oxide-modified biochar has improved porosity and showed promise for wastewater treatment. The preparation of magnetic biochar composites is becoming increasingly popular because they can be easily separated from water using a magnet (Thines et al. 2017). Magnetic rice straw biochar has been implicated in the efficient removal of Safranin O (Phuong and Loc, 2022), Rhodamine B (Ren et al. 2020), and organic dyes (Barzallo et al. 2025, Meng et al. 2024) from aqueous solutions.

7. IMPLEMENTING SUSTAINABLE POLICIES AND STRATEGIES FOR BIOCHAR USE IN INDIAN SOILS

In the past two decades, biochar has gained prominence in agriculture for enhancing soil fertility, sequestering carbon, and mitigating greenhouse gas emissions. In India, initiatives such as the National Mission on Sustainable Agriculture (NMSA) and the National Biofuels Policy promote the use of biochar to boost soil health and support sustainable farming. The Ministry of Environment, Forests, and Climate Change launched the "National Biochar Initiative" to improve soil and carbon sequestration. The India Biochar and Bioresources Network (IBBN) advocates circular agricultural practices, reducing emissions, and enhancing carbon storage while addressing agricultural challenges. The government has also revised the Crop Residue Management guidelines, focusing on the efficient handling of paddy straw in states such as Punjab, Haryana, and Delhi, with financial assistance for machinery and equipment. Private companies, such as PepsiCo India, have launched biochar initiatives using crop residues to combat stubble burning in Punjab through pyrolysis. Other players, such as Samunnati and Varaha, are promoting biochar technology for climate resilience and sustainable agriculture. Additionally, a government task force is exploring the use of biochar in steel production to reduce carbon emissions in India's steel sector, a major contributor to greenhouse gas emissions. This multifaceted approach highlights the role of biochar in both agriculture and industry, advancing sustainability and environmental goals.

8. CONCLUSIONS AND FUTURE PERSPECTIVES

Open-field rice straw burning in India has been a long-standing environmental crisis, causing severe air pollution, greenhouse gas emissions, and health hazards. The slow pyrolysis of rice straw into biochar presents a valuable opportunity to enhance soil health, increase agricultural productivity, and sequester carbon. By improving nutrient and water retention and supporting beneficial microorganisms, rice straw biochar offers a sustainable solution for modern agricultural practices that addresses environmental challenges.

The application of rice straw-derived biochar has shown promising effects on various crops and soil characteristics. Optimizing biochar synthesis can alter its chemical and structural properties, which may enhance its suitability for agricultural applications. However, there are significant knowledge gaps in understanding crop responses to biochar application, especially in relation to varying soil types, salinity levels, and pyrolysis conditions. This emphasizes the importance of gaining a more detailed understanding of the specific factors influencing outcomes. Additional research is required to scale up its production and application for practical large-scale use. This demands large-scale field experiments across varied agro-climatic zones to assess the long-term effects of biochar amendments on soil health and crop productivity. Future research focusing on understanding the interaction of biochar with soil microbiomes, including beneficial plant growth-promoting bacteria and crops, is required to understand the dynamics of nutrient recycling in soil. Its economic profile must be critically assessed for use by farmers. Cost-benefit analyses will be important for understanding the potential of this practice as a viable agricultural practice. Advocating for policies that allow collaboration between various stakeholders, from farmers to researchers and the government, will encourage the adoption of sustainable practices in the use of rice straw biochar.

9. ACKNOWLEDGMENTS

The authors thank the parent institute, Manav Rachna International Institute of Research and Studies, Faridabad, India, for continuous support and assistance during scientific writing.

10. REFERENCES

Adhikari, S., Mahmud, M.P., Nguyen, M.D. and Timms, W., 2023. Evaluating fundamental biochar properties in relation to water holding capacity. *Chemosphere*, 328, p.138620. [DOI]

Adhikari, S., Timms, W. and Mahmud, M.P., 2022. Optimising water holding capacity and hydrophobicity of biochar for soil amendment – A review. *Science of the Total Environment*, 851, p.158043. [DOI]

Afshar, M. and Mofatteh, S., 2024. Biochar for a sustainable future: Environmentally friendly production and diverse applications. *Results in Engineering*, 23, pp.102433. [DOI]

Ahmed, M.M.M., Liao, C.H., Liu, Y.T., Venkatesan, S., Hsieh, Y.C., Nail, H.M., Wang, H.M.D., Lin, M.C., Jien, S.H. and Tzou, Y.M., 2024. Sulfur-functionalized rice straw biochar for enhanced cadmium

sorption: Spectroscopic, kinetic and computational insights. *Journal of Cleaner Production*, 484, p.144267. [DOI]

Ahuja, V., Palai, A.K., Kumar, A., Patel, A.K., Farooque, A.A., Yang, Y.H. and Bhatia, S.K., 2024. Biochar: Empowering the future of energy production and storage. *Journal of Analytical and Applied Pyrolysis*, 177, p.106370. [DOI]

Al Masud, M.A., Shin, W.S., Sarker, A., Septian, A., Das, K., Deepo, D.M., Iqbal, M.A., Islam, A.R.M.T. and Malafaia, G., 2023. A critical review of sustainable application of biochar for green remediation: Research uncertainty and future directions. *Science of the Total Environment*, 904, p.166813. [DOI]

Amalina, F., Krishnan, S., Zularisam, A.W. and Nasrullah, M., 2023. Recent advancement and applications of biochar technology as a multifunctional component towards sustainable environment. *Environmental Development*, 46, p.100819. [DOI]

Arunrat, N., Sereenonchai, S., Sansupa, C., Kongsurakan, P. and Hatano, R., 2023. Effect of rice straw and stubble burning on soil physicochemical properties and bacterial communities in central Thailand. *Biology*, 12(4), p.501. [DOI]

Barzallo, D., Carrasquero, E., Andrade, M., Heredia Jara, D.A. and Palmay, P., 2025. Preparation and characterization of unactivated, activated, and γ-Fe2O3 nanoparticle-functionalized biochar from rice husk via pyrolysis for dyes removal in aqueous samples: Comparison, performance, and mechanism. *ChemEngineering*, 9(2), p.30. [DOI]

Bhadoria, P., Shrivastava, M., Khandelwal, A., Das, R., Langyan, S., Rohatgi, B. and Singh, R., 2022. Preparation of modified rice straw-based bio-adsorbents for the improved removal of heavy metals from wastewater. *Sustainable Chemistry and Pharmacy*, 29, p.100742. [DOI]

Bhandari, G., Gangola, S., Dhasmana, A., Rajput, V., Gupta, S., Malik, S. and Slama, P., 2023. Nano-biochar: Recent progress, challenges, and opportunities for sustainable environmental remediation. *Frontiers in Microbiology*, 14, p.1214870. [DOI]

Bhatia, D. and Saroha, A.K., 2024. Biochar derived from pyrolysis of rice straw as an adsorbent for removal of phenol from water. *Journal of Water Process Engineering*, 59, pp.105003. [DOI]

Bhatnagar, A., Singhal, A., Tolvanen, H., Valtonen, K., Joronen, T. and Konttinen, J., 2022. Effect of pretreatment and biomass blending on bio-oil and biochar quality from two-step slow pyrolysis of rice straw. *Waste Management*, 138, pp.298-307. [DOI]

Biswas, B., Balla, P., Krishna, B.B., Adhikari, S. and Bhaskar, T., 2024. Physiochemical characteristics of bio-char derived from pyrolysis of rice straw under different temperatures. *Biomass Conversion and Biorefinery*, 14(12), pp.12775-12783. [DOI]

Brassard, P., Godbout, S., Raghavan, V., Palacios, J.H., Grenier, M. and Zegan, D., 2017. The production of engineered biochars in a vertical auger pyrolysis reactor for carbon sequestration. *Energies*, 10(3), p.288. [DOI]

Brtnicky, M., Datta, R., Holatko, J., Bielska, L., Gusiatin, Z.M., Kucerik, J., Hammerschmiedt, T., Danish, S., Radziemska, M., Mravcova, L. and Fahad, S., 2021. A critical review of the possible adverse effects of biochar in the soil environment. *Science of the Total Environment*, 796, p.148756. [DOI]

Bushra, B. and Remya, N., 2024. Biochar from pyrolysis of rice husk biomass—characteristics, modification and environmental application. *Biomass Conversion and Biorefinery*, 14(5), pp.5759-5770. [DOI]

Chaijak, P., Michu, P., Thipraksa, J. and Kongthong, A., 2023. Biochar derived from the husk and straw of rice (Oryza sativa l.) produced via low-temperature pyrolysis as an effective adsorbent for pb (ii) removal. *Pollution*, 9(4), pp.1666-1675. [DOI]

Chatterjee, R., Sajjadi, B., Mattern, D.L., Chen, W.Y., Zubatiuk, T., Leszczynska, D., Leszczynski, J., Egiebor, N.O. and Hammer, N., 2018. Ultrasound cavitation intensified amine functionalization: A feasible strategy for enhancing CO2 capture capacity of biochar. *Fuel*, 225, pp.287-298. [DOI]

Dey, S., Purakayastha, T.J., Sarkar, B., Rinklebe, J., Kumar, S., Chakraborty, R., Datta, A., Lal, K. and Shivay, Y.S., 2023. Enhancing cation and anion exchange capacity of rice straw biochar by chemical modification for increased plant nutrient retention. *Science of the Total Environment*, 886, p.163681. [DOI]

Dong, C.D., Lung, S.C.C., Chen, C.W., Lee, J.S., Chen, Y.C., Wang, W.C.V., Chen, C.J., Hung, C.M. and Lin, C.H., 2019. Assessment of the pulmonary toxic potential of nano-tobacco stem-pyrolyzed biochars. *Environmental Science: Nano*, 6(5), pp.1527-1535. [DOI]

Dong, H.P., Nguyen, B.T., Le, T.H., Nguyen, M.H. and Le, A.H., 2025. Agricultural byproduct-derived biochar for mitigating trace metal risks from soil to rice to public health: Implications for sustainable management. *Integrated Environmental Assessment and Management*, 21(4), pp.895-909. [DOI]

El-Hassanin, A.S., Samak, M.R., Radwan, S.R. and El-Chaghaby, G.A., 2020. Preparation and characterization of biochar from rice straw and its application in soil remediation. *Environment and Natural Resources Journal*, 18(3), pp.283-289. [DOI]

Farhangi-Abriz, S., Torabian, S., Qin, R., Noulas, C., Lu, Y. and Gao, S., 2021. Biochar effects on yield of cereal and legume crops using meta-analysis. *Science of the Total Environment*, 775, p.145869. [DOI]

Fodah, A.E.M., Ghosal, M.K. and Behera, D., 2022. Microwave-assisted pyrolysis of agricultural residues: Current scenario, challenges, and future direction. *International Journal of Environmental Science and Technology*, 19(3), pp.2195-2220. [DOI]

Foong, S.Y., Chan, Y.H., Chin, B.L.F., Lock, S.S.M., Yee, C.Y., Yiin, C.L., Peng, W. and Lam, S.S., 2022. Production of biochar from rice straw and its application for wastewater remediation – An overview. *Bioresource Technology*, 360, p.127588. [DOI]

Freixa, A., Acuña, V., Sanchís, J., Farré, M., Barceló, D. and Sabater, S., 2018. Ecotoxicological effects of carbon based nanomaterials in aquatic organisms. *Science of the Total Environment*, 619, pp.328-337. [DOI]

Gezahegn, A., G. Selassie, Y., Agegnehu, G., Addisu, S., Asargew Mihretie, F., Kohira, Y. and Sato, S., 2024. Pyrolysis temperature changes the physicochemical characteristics of water hyacinth-based biochar as a potential soil amendment. *Biomass Conversion and Biorefinery*, 15(3), pp.3737-3752. [DOI]

Gwenzi, W., Chaukura, N., Noubactep, C. and Mukome, F.N., 2017. Biochar-based water treatment systems as a potential low-cost and sustainable technology for clean water provision. *Journal of Environmental Management*, 197, pp.732-749. [DOI]

He, D., Luo, Y. and Zhu, B., 2024. Feedstock and pyrolysis temperature influence biochar properties and its interactions with soil substances: Insights from a DFT calculation. *Science of the Total Environment*, 922, p.171259. [DOI]

Hematimatin, N., Igaz, D., Aydın, E. and Horák, J., 2024. Biochar application regulating soil inorganic nitrogen and organic carbon content in cropland in the Central Europe: A seven-year field study. *Biochar*, 6(1), p.14. [DOI]

Hyväluoma, J., Hannula, M., Arstila, K., Wang, H., Kulju, S. and Rasa, K., 2018. Effects of pyrolysis temperature on the hydrologically relevant porosity of willow biochar. *Journal of Analytical and Applied Pyrolysis*, 134, pp.446-453. [DOI]

Jindo, K., Mizumoto, H., Sawada, Y., Sanchez-Monedero, M.A. and Sonoki, T., 2014. Physical and chemical characterization of biochars derived from different agricultural residues. *Biogeosciences*, 11(23), pp.6613-6621. [DOI]

Joseph, S., Cowie, A.L., Van Zwieten, L., Bolan, N., Budai, A., Buss, W., Cayuela, M.L., Graber, E.R., Ippolito, J.A., Kuzyakov, Y. and Luo, Y., 2021. How biochar works, and when it doesn't: A review of mechanisms controlling soil and plant responses to biochar. *GCB Bioenergy*, 13(11), pp.1731-1764. [DOI]

Kalina, M., Sovova, S., Hajzler, J., Kubikova, L., Trudicova, M., Smilek, J. and Enev, V., 2022. Biochar texture—a parameter influencing physicochemical properties, morphology, and agronomical potential. *Agronomy*, 12(8), p.1768. [DOI]

Kalu, S., Kulmala, L., Zrim, J., Peltokangas, K., Tammeorg, P., Rasa, K., Kitzler, B., Pihlatie, M. and Karhu, K., 2024. Potential of biochar to reduce greenhouse gas emissions and increase nitrogen use efficiency in boreal arable soils in the long-term. *Frontiers in Environmental Science*, 10, p.914766. [DOI]

Kamara, A., Kamara, H.S. and Kamara, M.S., 2015. Effect of rice straw biochar on soil quality and the early growth and biomass yield of two rice varieties. *Agricultural Sciences*, 6(8), p.798. [DOI]

Kamboj, S., Bala, J., Lohchab, R.K., Singh, K. and Kumari, M., 2025. Unlocking the rice straw agro-waste potential as activated carbon: Pyrolysis and characterization. *Nature Environment & Pollution Technology*, 24(3). [DOI]

Kameyama, K., Miyamoto, T. and Iwata, Y., 2019. The preliminary study of water-retention related properties of biochar produced from various feedstock at different pyrolysis temperatures. *Materials*, 12(11), p.1732. [DOI]

Kartika, K., Lakitan, B., Wijaya, A., Kadir, S., Widuri, L.I., Siaga, E. and Meihana, M., 2018. Effects of particle size and application rate of rice-husk biochar on chemical properties of tropical wetland soil, rice growth and yield. *Australian Journal of Crop Science*, 12(5), pp.817-826. [DOI]

Kassim, M.A.B.M., Kaus, N.H.M., Imam, S.S., Sagadevan, S. and Salaeh, S., 2023. Rapid and facile chemical synthesis of Fe3O4/biochar nanocomposite for the adsorptive removal of fluoroquinolones from aqueous solution. *Inorganic Chemistry Communications*, 156, p.111156. [DOI]

Kavan, K.K.V. and Panwar, N.L., 2024. Pyrolysis technologies for biochar production in waste management: A review. *Clean Energy*, 8(4), pp.61-78. [DOI]

Khater, E.S., Bahnasawy, A., Hamouda, R., Sabahy, A., Abbas, W. and Morsy, O.M., 2024. Biochar production under different pyrolysis temperatures with different types of agricultural wastes. *Scientific Reports*, 14(1), pp.2625. [DOI]

Kumar, A., Kushwaha, K.K., Singh, S., Shivay, Y.S., Meena, M.C. and Nain, L., 2019. Effect of paddy straw burning on soil microbial dynamics in sandy loam soil of Indo-Gangetic plains. *Environmental Technology & Innovation*, 16, pp.100469. [DOI]

Leng, L., Xu, S., Liu, R., Yu, T., Zhuo, X., Leng, S., Xiong, Q. and Huang, H., 2020. Nitrogen containing functional groups of biochar: An overview. *Bioresource Technology*, 298, p.122286. [DOI]

Li, H. and Tan, Z., 2021. Preparation of high water-retaining biochar and its mechanism of alleviating drought stress in the soil and plant system. *Biochar*, 3(4), pp.579-590. [DOI]

Li, X., Ai, X., Wang, X., Li, L., Xin, Z. and Sun, X., 2023. Composite phosphorylated-modified rice straw prepared for highly effective immobilisation of cadmium in agriculture contaminated soil. *Environmental Chemistry*, 19(8), pp.495-505.

Li, X., Shen, Q., Zhang, D., Mei, X., Ran, W., Xu, Y. and Yu, G., 2013. Functional groups determine biochar properties (pH and EC) as studied by two-dimensional 13C NMR correlation spectroscopy. *PLoS One*, 8(6), p.e65949. [DOI]

Liang, M., Lu, L., He, H., Li, J., Zhu, Z. and Zhu, Y., 2021. Applications of biochar and modified biochar in heavy metal contaminated soil: A descriptive review. *Sustainability*, 13(24), p.14041. [DOI]

Liu, M., Che, Y., Wang, L., Zhao, Z., Zhang, Y., Wei, L. and Xiao, Y., 2019. Rice straw biochar and phosphorus inputs have more positive effects on the yield and nutrient uptake of Lolium multiflorum than arbuscular mycorrhizal fungi in acidic Cd-contaminated soils. *Chemosphere*, 235, pp.32-39. [DOI]

Liu, Z., Niu, W., Chu, H., Zhou, T. and Niu, Z., 2018. Effect of the carbonization temperature on the properties of biochar produced from the pyrolysis of crop residues. *BioResources*, 13(2), pp.3429-3446. [DOI]

Ma, S., Wang, X., Wang, S. and Feng, K., 2022. Effects of temperature on physicochemical properties of rice straw biochar and its passivation ability to Cu2+ in soil. *Journal of Soils and Sediments*, 22(5), pp.1418-1430. [DOI]

Malik, K., Sharma, A., Harikarthik, D., Rani, V., Arya, N., Malik, A., Rani, S., Sangwan, P. and Bhatia, T., 2023. Deciphering the biochemical and functional characterization of rice straw cultivars for industrial applications. *Heliyon*, 9(6), p.771. [DOI]

Meng, Y., Chen, D., Li, Y., Sheng, W., Liu, Y., Yang, H. and Qian, G., 2024. Preparation of a novel magnetic composite based on rice straw derived biochar and chromium ferrite for enhanced absorption of organic dye. *Environmental Engineering Research*, 29(6), p.65. [DOI]

Mian, M.M., Liu, G., Yousaf, B., Fu, B., Ullah, H., Ali, M.U., Abbas, Q., Munir, M.A.M. and Ruijia, L., 2018. Simultaneous functionalization and magnetization of biochar via NH3 ambiance pyrolysis for efficient removal of Cr (VI). *Chemosphere*, 208, pp.712-721. [DOI]

Mohamed, I., El-habbak, A.K., Abbas, M.H., Scopa, A., Drosos, M., AbdelRahman, M.A. and Bassouny, M.A., 2024. Rice straw biochar and NPK minerals for sustainable crop production in arid soils: A case study on maize-wheat cropping system. *CABI Agriculture and Bioscience*, 5(1), p.91. [DOI]

Mukherjee, S., Thakur, A.K., Goswami, R., Mazumder, P., Taki, K., Vithanage, M. and Kumar, M., 2021. Efficacy of agricultural waste derived biochar for arsenic removal: Tackling water quality in the Indo-Gangetic plain. *Journal of Environmental Management*, 281, p.111814. [DOI]

Neusatz Guilhen, S., Watanabe, T., Tieko Silva, T., Rovani, S., Takehiro Marumo, J., Alberto Soares Tenório, J., Mašek, O. and Goulart de Araujo, L., 2022. Role of point of zero charge in the adsorption of cationic textile dye on standard biochars from aqueous solutions: Selection criteria and performance assessment. *Recent Progress in Materials*, 4(2), pp.1-30. [DOI]

Park, J., Lee, Y., Ryu, C. and Park, Y.K., 2014. Slow pyrolysis of rice straw: Analysis of products properties, carbon and energy yields. *Bioresource Technology*, 155, pp.63-70. [DOI]

Phuong, D.T.M. and Loc, N.X., 2022. Rice straw biochar and magnetic rice straw biochar for safranin O adsorption from aqueous solution. *Water*, 14(2), p.186. [DOI]

Phuong, H.T., Uddin, M.A. and Kato, Y., 2015. Characterization of biochar from pyrolysis of rice husk and rice straw. *Journal of Biobased Materials and Bioenergy*, 9(4), pp.439-446. [DOI]

Potnuri, R., Surya, D.V., Rao, C.S., Yadav, A., Sridevi, V. and Remya, N., 2023. A review on analysis of biochar produced from microwave-assisted pyrolysis of agricultural waste biomass. *Journal of Analytical and Applied Pyrolysis*, 173, pp.106094. [DOI]

Qin, X., Luo, J., Liu, Z. and Fu, Y., 2020. Preparation and characterization of MgO-modified rice straw biochars. *Molecules*, 25(23), p.5730. [DOI]

Ravali, C., Reddy, K.S., Triveni, S., Pratibha, G. and Jayasree, G., 2022. Impact of in-situ paddy straw burning on soil enzyme activity, soil microbial population and green house gas emissions in sandy loam soil. *International Journal of Environment and Climate Change*, 12(11), pp.3633-3640. [DOI]

Ren, Z., Chen, F., Wang, B., Song, Z., Zhou, Z. and Ren, D., 2020. Magnetic biochar from alkali-activated rice straw for removal of rhodamine B from aqueous solution. *Environmental Engineering Research*, 25(4), pp.536-544. [DOI]

Sackey, E.A., Song, Y., Yu, Y. and Zhuang, H., 2021. Biochars derived from bamboo and rice straw for sorption of basic red dyes. *PLoS One*, 16(7), p.e0254637. [DOI]

Sahoo, D. and Remya, N., 2022. Influence of operating parameters on the microwave pyrolysis of rice husk: Biochar yield, energy yield,

and property of biochar. *Biomass Conversion and Biorefinery*, 12(8), pp.3447-3456. [DOI]

Sakhiya, A.K., Anand, A., Aier, I., Vijay, V.K. and Kaushal, P., 2021. Suitability of rice straw for biochar production through slow pyrolysis: Product characterization and thermodynamic analysis. *Bioresource Technology Reports*, 15, p.100818. [DOI]

Sakhiya, A.K., Kaushal, P. and Vijay, V.K., 2023. Potential of rice straw derived activated biochar to remove arsenic and manganese from groundwater: A cleaner approach in the Indo-Gangetic Plain. *Applied Surface Science Advances*, 17, p.100443. [DOI]

Sakhiya, A.K., Vijay, V.K. and Kaushal, P., 2022. Efficacy of rice straw derived biochar for removal of Pb+2 and Zn+2 from aqueous: Adsorption, thermodynamic and cost analysis. *Bioresource Technology Reports*, 17, p.100920. [DOI]

Sakhiya, A.K., Vijay, V.K. and Kaushal, P., 2023. Development of rice straw biochar through pyrolysis to improve drinking water quality in arsenic and manganese contaminated areas. *Surfaces and Interfaces*, 36, p.102582. [DOI]

Satlewal, A., Agrawal, R., Bhagia, S., Das, P. and Ragauskas, A.J., 2018. Rice straw as a feedstock for biofuels: Availability, recalcitrance, and chemical properties. *Biofuels, Bioproducts and Biorefining*, 12(1), pp.83-107. [DOI]

Selvarajh, G., Ch'ng, H.Y., Zain, N.B.M., Ahmed, O.H., Jalloh, M.B., Damrongrak, I., Liew, J.Y., Azmin, S.N.H.M. and Naher, L., 2023. Enriched rice straw biochar improves soil nitrogen availability and rice plant growth under waterlogged environment. *Bragantia*, 82, p.e20230104. [DOI]

Senapati, S., Giri, J., Mallick, L., Singha, D., Bastia, T.K., Rath, P., Rana, M.K. and Panda, A.K., 2025. Rapid adsorption of industrial cationic dye pollutant using base-activated rice straw biochar: Performance, isotherm, kinetic and thermodynamic evaluation. *Discover Sustainability*, 6(1), p.46. [DOI]

Shah, T., Chaudhuri, R.R., Soni, U., Shrivastava, M. and Venkatesh, G., 2024. Characterising rice straw ash: Unlocking the potential of agricultural residues. *Studia Ecologiae et Bioethicae*, 22(4), pp.99-116. [DOI]

Shoudho, K.N., Khan, T.H., Ara, U.R., Khan, M.R., Shawon, Z.B.Z. and Hoque, M.E., 2024. Biochar in global carbon cycle: Towards sustainable development goals. *Current Research in Green and Sustainable Chemistry*, 8, p.100409. [DOI]

Singh, H., Northup, B.K., Rice, C.W. and Prasad, P.V., 2022. Biochar applications influence soil physical and chemical properties, microbial diversity, and crop productivity: A meta-analysis. *Biochar*, 4(1), p.8. [DOI]

Sohi, S.P., Krull, E., Lopez-Capel, E. and Bol, R., 2010. A review of biochar and its use and function in soil. *Advances in Agronomy*, 105, pp.47-82. [DOI]

Spokas, K.A., Cantrell, K.B., Novak, J.M., Archer, D.W., Ippolito, J.A., Collins, H.P., Boateng, A.A., Lima, I.M., Lamb, M.C., McAloon, A.J. and Lentz, R.D., 2012. Biochar: A synthesis of its agronomic impact beyond carbon sequestration. *Journal of Environmental Quality*, 41(4), pp.973-989. [DOI]

Thines, K.R., Abdullah, E.C., Mubarak, N.M. and Ruthiraan, M., 2017. Synthesis of magnetic biochar from agricultural waste biomass to enhancing route for waste water and polymer application: A review. *Renewable and Sustainable Energy Reviews*, 67, pp.257-276. [DOI]

Tomczyk, A., Sokołowska, Z. and Boguta, P., 2020. Biochar physicochemical properties: Pyrolysis temperature and feedstock kind effects. *Reviews in Environmental Science and Bio/Technology*, 19(1), pp.191-215. [DOI]

Tsai, C.H., Shen, Y.H. and Tsai, W.T., 2023. Thermochemical characterization of rice-derived residues for fuel use and its potential for slagging tendency. *Fire*, 6(6), p.230. [DOI]

Venkatraman, Y., Arunkumar, P., Kumar, N.S., Osman, A.I., Muthiah, M., Al-Fatesh, A.S. and Koduru, J.R., 2023. Exploring modified rice straw biochar as a sustainable solution for simultaneous Cr (VI) and Pb (II) removal from wastewater: Characterization, mechanism insights, and application feasibility. *ACS Omega*, 8(41), pp.38130-38147. [DOI]

Wangdi, K., Khongdee, N., Intanon, S., Samaksaman, U., Spreer, W., Kiravittaya, S. and Pansak, W., 2023. Characterization of rice husk biochar and its particle size effects on soil properties in sandy loam soil. *GMSARN International Journal*, 17(4), pp.389-395.

Weidner, E., Karbassiyazdi, E., Altaee, A., Jesionowski, T. and Ciesielczyk, F., 2022. Hybrid metal oxide/biochar materials for wastewater treatment technology: A review. *ACS Omega*, 7(31), pp.27062-27078. [DOI]

Wijitkosum, S. and Jiwnok, P., 2019. Elemental composition of biochar obtained from agricultural waste for soil amendment and carbon sequestration. *Applied Sciences*, 9(19), p.3980. [DOI]

Wu, W., Yang, M., Feng, Q., McGrouther, K., Wang, H., Lu, H. and Chen, Y., 2012. Chemical characterization of rice straw-derived biochar for soil amendment. *Biomass and Bioenergy*, 47, pp.268-276. [DOI]

Wu, Z., Fan, Y., Zhou, Z., Hao, X. and Kang, S., 2025. Interaction between biochar particle size and soil salinity levels on soil properties and tomato yield. *Biochar*, 7(1), p.30.

Yakout, S.M., 2015. Monitoring the changes of chemical properties of rice straw–derived biochars modified by different oxidizing agents and their adsorptive performance for organics. *Bioremediation Journal*, 19(2), pp.171-182. [DOI]

Yakout, S.M., 2017. Physicochemical characteristics of biochar produced from rice straw at different pyrolysis temperature for soil amendment and removal of organics. *Proceedings of the National Academy of Sciences, India Section A: Physical Sciences*, 87(2), pp.207-214. [DOI]

Yang, Y., Nguyen, T.M.P., Van, H.T., Nguyen, Q.T., Nguyen, T.H., Nguyen, T.B.L., Hoang, L.P., Van Thanh, D., Nguyen, T.V., Nguyen, V.Q. and Thang, P.Q., 2022. ZnO nanoparticles loaded rice husk biochar as an effective adsorbent for removing reactive red 24 from aqueous solution. *Materials Science in Semiconductor Processing*, 150, p.106960. [DOI]

Zhang, G., He, L., Guo, X., Han, Z., Ji, L., He, Q., Han, L. and Sun, K., 2020. Mechanism of biochar as a biostimulation strategy to remove polycyclic aromatic hydrocarbons from heavily contaminated soil in a coking plant. *Geoderma*, 375, p.114497. [DOI]

Zhang, H., Cheng, Y., Zhong, Y., Ni, J., Wei, R. and Chen, W., 2024. Roles of biochars' properties in their water-holding capacity and bound water evaporation: Quantitative importance and controlling mechanism. *Biochar*, 6(1), p.30. [DOI]

Zhang, S., Dong, Q., Zhang, L., Xiong, Y., Liu, X. and Zhu, S., 2015. Effects of water washing and torrefaction pretreatments on rice husk pyrolysis by microwave heating. *Bioresource Technology*, 193, pp.442-448. [DOI]

Zhou, Z., Yao, D., Li, S., Xu, F., Liu, Y., Liu, R. and Chen, Z., 2021. Sustainable production of value-added sulfonated biochar by sulfuric acid carbonization reduction of rice husks. *Environmental Technology & Innovation*, 24, p.102025. [DOI]

Nature Environment and Pollution Technology
An International Quarterly Scientific Journal

p-ISSN: 0972-6268
(Print copies up to 2016)
e-ISSN: 2395-3454

Vol. 25 | No. 3 | Article ID D1876 | 2026

Original Research Paper

https://doi.org/10.46488/NEPT.2026.v25i03.D1876

Open Access Journal

Comparative Assessment of Alternative Fine Aggregates for Sustainable Concrete: Physical, Chemical and Mechanical Characterization of Sri Lankan Sands

Udara S.P.R. Arachchige[1]†, H.D.R.T. Gunasekara[2], R.A.K.M. Rajapaksha[2] and M.D.K.C. Jayathilaka[2]

[1]Department of Mechatronic and Industrial Engineering, Faculty of Engineering, NSBM Green University, Homagama, Sri Lanka

[2]Department of Civil and Environmental Technology, Faculty of Technology, University of Sri Jayewardenepura, Homagama, Sri Lanka

†Corresponding author: Udara Arachchige; udara.a@nsbm.ac.lk

Abbreviation: Nat. Env. & Poll. Technol.
Website: www.neptjournal.com

Received: 11-10-2025
Revised: 08-11-2025
Accepted: 30-12-2025

Key Words:

Alternative fine aggregates
Chloride
Concrete durability
Dune sand
River sand
Sustainable concrete

Citation for the Paper:

Arachchige, U.S.P.R., Gunasekara, H.D.R.T., Rajapaksha, R.A.K.M. and Jayathilaka, M.D.K.C., 2026. Comparative assessment of alternative fine aggregates for sustainable concrete: Physical, chemical and mechanical characterization of Sri Lankan sands. *Nature Environment and Pollution Technology*, 25(3), D1876. https://doi.org/10.46488/NEPT.2026.v25i03.D1876

Note: From 2025, the journal has adopted the use of Article IDs in citations instead of traditional consecutive page numbers. Each article is now given individual page ranges starting from page 1.

Copyright: © 2026 by the authors
Licensee: Technoscience Publications
This article is an open access article distributed under the terms and conditions of the Creative Commons Attribution (CC BY) license (https://creativecommons.org/licenses/by/4.0/).

ABSTRACT

The over-extraction of river sand in Sri Lanka has reduced alluvial reserves in major basins by over 40% between 2010 and 2023, highlighting an urgent need for sustainable alternatives. This study presents the first comprehensive comparative analysis of four distinct sand types-river (Polonnaruwa), sea (Muthurajawela), dune (Kandakuliya), and estuary (Kalutara)-using integrated physical, chemical, and mechanical evaluation. Tests included sieve analysis, chloride content measurement via Volhard's method, and strength assessments at 7 and 28 days. Results showed that river and dune sands achieved compressive strengths exceeding 30 MPa and contained low chloride levels (<500 $mg.kg^{-1}$), aligning with international standards for structural concrete. Although sea sand's chloride content was high (1,796 $mg.kg^{-1}$, 259% above limit), it could be viable if properly treated. Estuary sand reached 29.3 MPa strength but had borderline chloride levels, restricting its application. Failure mode analysis indicated strong structural performance for river and dune sands, whereas sea and estuary sands exhibited brittle failure patterns. Overall, processed dune sand and treated sea sand are promising substitutes for river sand, promoting sustainability. Ensuring chloride regulation and advancing treatment technologies are essential for successful adoption.

1. INTRODUCTION

The introduction provides a comprehensive overview of sand usage in construction, highlighting both environmental and engineering considerations. It begins by framing the global and national issues of unsustainable river sand extraction and then narrows its focus to the pressing challenges faced by Sri Lanka. The following sections detail the environmental crisis caused by excessive mining and identify the research gap that this study aims to fill.

1.1. Environmental Crisis from River Sand Mining

Worldwide, the production of concrete annually consumes over 50 billion tons of sand, with river sand being the preferred fine aggregate due to its optimal gradation and low impurity content (Koehnken & Rintoul 2018). In Sri Lanka, rapid construction growth has led to increased river sand extraction, causing severe environmental damage such as riverbed degradation, bank erosion, habitat destruction, and heightened flood risks (Dias et al. 2008). The Deduru Oya basin highlights this crisis, where sand mining has reduced sediment loads by 40%, thereby accelerating coastal erosion (United Nations Environment Program 2019). The UNEP recognizes sand mining as a vital sustainability issue, with Sri Lanka

ranked among the top ten countries facing significant riverine ecosystem collapse. Moreover, the scarcity of river sand has driven up construction costs, adversely impacting housing affordability and infrastructure development (Dolage et al. 2013). While government regulations aimed at restricting extraction are environmentally essential, they have also limited supply and increased the urgency for sustainable alternatives (Mahendran et al. 2016).

1.2. Research Gap and Objectives

Although previous studies have explored individual alternatives such as manufactured sand and offshore sand, a comprehensive comparative analysis of Sri Lanka's diverse sand resources remains limited. Dias et al. (2008) established safe chloride limits (0.075% by weight) for offshore sand, while Ratnayake et al. (2014) demonstrated the potential of sea sand with proper washing. However, a systematic evaluation of multiple sand types from different geographical sources is lacking in thorough documentation.

Recent international research has investigated various alternative aggregates. Cepuritis et al. (2014) found that manufactured sand with optimized particle packing enhanced concrete strength by 15% compared to natural sand. Kumar et al. (2025) conducted experimental analysis showing that refractory brick can serve as a sustainable substitute for natural fine aggregates in concrete. In coastal regions, desalinated sea sand has shown promise; Zhao et al. (2019) achieved chloride reductions of 85% through electrochemical treatment. Similarly, desert sand utilization has gained attention, with Benabed et al. (2014) reporting that dune sand blended with 30% crushed aggregate achieved compressive strengths exceeding 35 MPa.

Nonetheless, a systematic comparison of multiple sand types within a single geographical context, especially for tropical island nations like Sri Lanka, remains underexplored. Previous Sri Lankan studies have examined individual alternatives: Dias et al. (2008) established safe chloride limits (0.075% by weight) for offshore sand, and Ratnayake et al. (2014) showed sea sand potential with proper washing. However, a comprehensive analysis comparing diverse geological sources is still lacking.

This study aims to address this gap through a systematic, integrated evaluation of four Sri Lankan sand types, combining physical-chemical characterization with mechanical performance and economic analysis within a unified framework. While individual alternatives have been studied in isolation, our contribution lies in the direct comparative assessment, enabling evidence-based material selection for specific applications. Our objectives were to:

1. Characterize the physical and chemical properties of river, sea, dune, and estuary sands.
2. Evaluate concrete performance using these sands through strength testing.
3. Establish correlations between sand properties and concrete behavior.
4. Identify sustainable alternatives meeting engineering and environmental criteria.

2. MATERIALS AND METHODS

This section details the experimental framework established to meet the research objectives. It outlines the sources of raw materials, the procedures used for sampling and preparation, and the testing protocols followed. Standardized methods and internationally accepted guidelines were applied to ensure reproducibility, accuracy, and comparability of results. The overall strategy combines both field sampling and laboratory assessments, enabling a thorough evaluation of the material properties pertinent to the study.

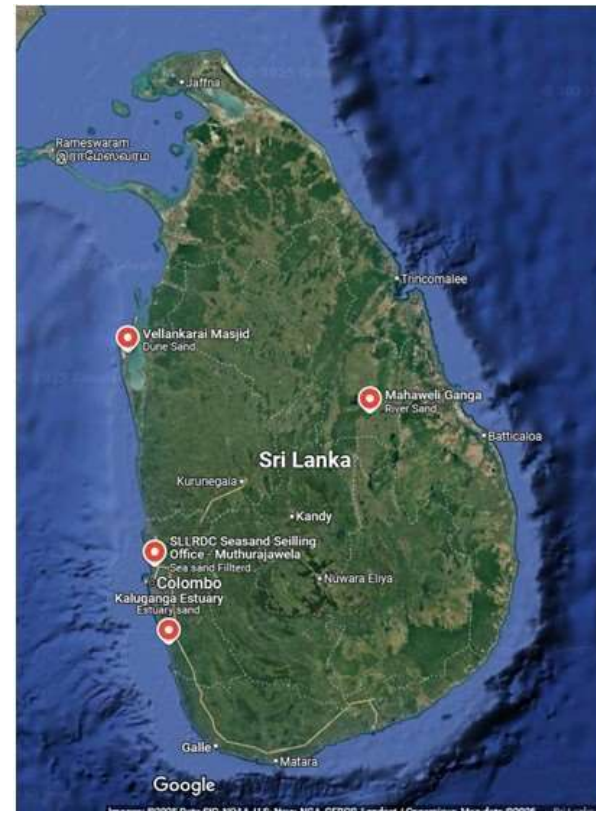


Fig. 1: Sample collection locations across Sri Lanka show the geographical distribution of river sand (Polonnaruwa), dune sand (Kandakuliya), estuary sand (Kalutara), and sea sand (Muthurajawela) sources.

Table 1: Materials' physical properties.

Material	Property	Value	Standard
Ordinary Portland Cement (OPC)	Specific gravity	3.15	BS EN 196-6
	Initial setting time	145 min	BS EN 196-3
	28-day strength	53.2 MPa	BS EN 196-1
Coarse Aggregate (Crushed granite)	Specific gravity	2.68	BS 812-2
	Water absorption	0.85%	BS 812-2
	Aggregate crushing value	18.2%	BS 812-110
	Nominal size	20 mm	-
All sands	Specific gravity	2.45–2.68	BS 812-2
	Water absorption	0.5–2.3%	BS 812-2
	Bulk density	1,420–1,650 kg.m^{3-}	ASTM C29

2.1. Sample Collection and Preparation

We collected representative sand samples from four distinct geographical regions across Sri Lanka to ensure diversity and resource potential (Fig. 1). River sand was sourced from Polonnaruwa, dune sand from Kandakuliya in the Puttalam District, estuary sand from Kalutara, and filtered sea sand from Muthurajawela. Field samples were collected following USGS protocols, sampling at least 500 m from human settlements using stratified random sampling within 10 m² grids. Bulk samples were taken from horizons at depths of 0.3 to 0.5 m and stored in HDPE containers. Commercial sands were obtained from ISO 9001:2015 certified suppliers with verified geological source coordinates. To reflect practical field-scale behavior rather than idealized laboratory conditions, bulk material quantities were used throughout testing, aligning with construction industry practices that account for batch-to-batch variations and larger sample volumes during quality control. For sieve analyses and chemical testing, representative sub-samples were extracted via quartering methods to ensure statistical validity while testing manageable quantities.

Sample preparation involved oven-drying at 105°C for 2 h, followed by quartering to obtain representative test portions. Total sample requirements were calculated based on standardized testing protocols, ensuring sufficient material for all planned analyses. Table 1 presents the physical properties of the materials used.

2.2. Physical Characterization

Physical characterization was conducted to evaluate the fundamental properties of the collected sand samples prior to their incorporation into concrete mixes. The analyses focused on particle size distribution and chemical composition, as these parameters critically influence the workability, durability, and mechanical performance of concrete. Standardized procedures were adopted to ensure comparability across different sand sources and alignment with international specifications. The following subsections detail the methodologies employed.

2.2.1. Sieve Analysis

Particle size distribution was determined using the BS 812: Part 1 (1995) methodology. Dried samples (300 g) were passed through a series of standard sieves (2 mm to 0.063 mm) using manual shaking for 5 min per sieve. The fineness modulus was calculated, and the gradation was compared with BS EN 12620:2013 limits.

2.2.2. Chemical Analysis

Chloride content was determined using Volhard's argentometric method in accordance with ASTM C1218/ C1218M (2020). Standard 0.1 N $AgNO_3$ and KSCN solutions were prepared, and 10 g sand samples were titrated using ferric alum as the indicator. Chloride content was calculated using Equation 01.

$$Cl^- \ (mg.kg^{-1}) = [(V_1 - V_2) \times N(KSCN) \times 35.45 \times 1000]/ m(sample) \quad \ldots(1)$$

where:

V_1 = volume of $AgNO_3$ solution added (mL)

V_2 = volume of KSCN solution used in back-titration (mL)

N(KSCN) = normality of potassium thiocyanate solution

m(sample) = mass of sand sample (g)

35.45 = atomic weight of chlorine (g.moL^{-1})

2.3. Concrete Performance Testing

We prepared Grade 30 concrete using standardized mix proportions (cement: 380 kg.m^{3-}, water–cement ratio: 0.50) for each sand type. Ordinary Portland Cement and crushed granite coarse aggregate were kept constant across all mixes.

Mix proportions were determined using the BRE method (Building Research Establishment 1997). The composition per cubic meter was as follows: Ordinary Portland Cement (CEM I 42.5N), 380 kg; fine aggregate (test sands), 720 kg; coarse aggregate (crushed granite, 20 mm), 1,050 kg; and water, 190 L (water–cement ratio: 0.50). No admixtures were used in the control mixes to maintain consistency across sand types. However, variations in fineness modulus (Table 2) may have influenced the optimum mix proportions. This limitation is discussed in Section 4.3.

Mixing was carried out using a 100 L pan mixer in accordance with BS EN 12390-2:2019. Dry materials were mixed for 2 min, followed by the gradual addition of water over 1 minute, and then 3 min of wet mixing. Slump was maintained at 75–100 mm for all mixes to ensure consistent workability.

2.3.1. Compressive Strength

Following the BS EN 12390-2:2019 standard, we cast 150 mm³ cubes using steel molds, vibrated them to ensure uniform compaction, and cured them in lime-saturated water. Testing was performed at 7 and 28 days with an ELE ADR-Auto 3000 kN machine, applying a loading rate of 0.6 MPa.s^{-1}.

2.3.2. Tensile Strength

We prepared cylindrical specimens (90 mm diameter × 180 mm height) per ASTM C496/C496M-17. After curing, specimens underwent splitting tension tests at 0.04 MPa.s^{-1} loading rate. Tensile strength was calculated using equation 02.

$$f_t = 2P_{max}/(\pi ld) \quad \ldots(2)$$

where:

f_t = splitting tensile strength (MPa)

P_{max} = maximum applied load at failure (N)

l = length of cylinder (mm)

d = diameter of cylinder (mm)

2.4. Quality Assurance

All tests included triplicate analyses, with a coefficient of variation under 5% considered acceptable. Statistical analysis was performed using 95% confidence intervals, and Grubbs' test was applied to identify outliers. Laboratory conditions were maintained at 20°C ± 2°C throughout the testing process.

3. RESULTS AND DISCUSSION

The following section presents the experimental findings and their interpretation in relation to the study objectives. The results are organized to highlight the physical and chemical characterization of the sand samples, followed by an evaluation of their influence on concrete performance. Comparisons with relevant standards and published literature are incorporated to contextualize the outcomes and assess practical implications.

3.1. Sand Characterization

Sand characterization was carried out to establish the baseline material properties prior to concrete production. Both physical and chemical properties were examined to assess compliance with construction standards and to anticipate potential effects on strength and durability. The subsequent subsections describe the particle size distribution and chloride content of the sand types studied.

3.1.1. Particle Size Distribution

Sieve analysis revealed distinct gradation patterns among the sand types (Table 2, Fig. 2). River sand exhibited a well-graded distribution (Fineness Modulus = 2.8), meeting BS EN 12620:2013 requirements. Sea sand showed a higher fine

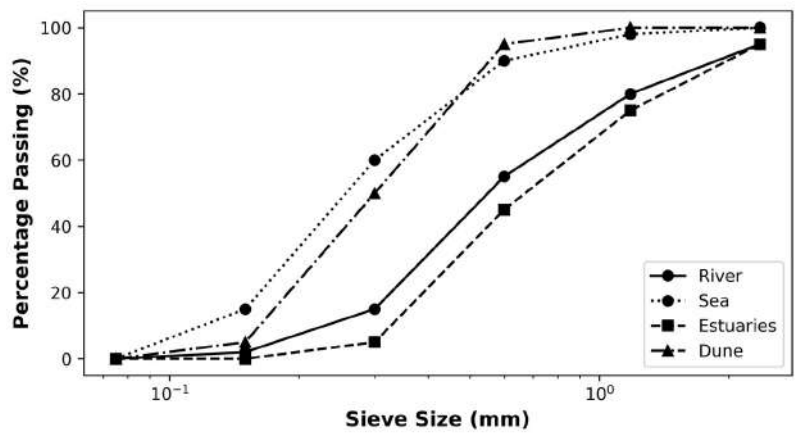


Fig. 2: Particle size distribution curves for all four sand types showing the gradation differences.

Table 2: Particle Size Distribution and Fineness Modulus.

Sand Type	Fineness Modulus	Gradation Compliance	Key Characteristics
River	2.8	Full compliance	Well-graded, minimal fines
Sea	1.9	Excessive fines	High 0.25 mm fraction
Dune	2.3	Marginal	Uniform requires blending
Estuary	2.1	Poor	Bimodal distribution

content, particularly in the 0.25 mm and 0.063 mm fractions, while estuary sand displayed a bimodal distribution with significant material retained on the 1 mm and 0.5 mm sieves.

River sand demonstrates ideal gradation, while sea sand shows excessive fines, dune sand presents uniform distribution, and estuary sand exhibits bimodal characteristics.

Dune sand presented uniform gradation but required blending with coarser material to optimize packing density. The gradation affects concrete workability and strength development, with well-graded sands producing superior performance.

3.1.2. Chemical Analysis

Chloride content varied considerably among different sand types, directly influencing the durability of concrete (Table 3, Fig. 3). River sand exhibited excellent compliance, with a chloride level of 179 mg.kg^{-1}, which is 64% below the permissible limit. Dune sand also met the required standards at 215 mg.kg^{-1}, posing minimal risk of corrosion. The bar chart clearly demonstrates that sea sand has an excessive chloride content, necessitating proper treatment.

Table 3: Chloride content analysis.

Sand Type	Chloride Content [mg.kg^{-1}]	BS 8500-1:2023 Limit	Compliance Status
River	179 ± 5.5	500	Excellent
Sea	1,796 ± 7.5	500	Exceeds by 259%
Dune	215 ± 5.5	500	Good
Estuary	431 ± 1.5	500	Borderline

The sea sand significantly exceeded permissible limits at 1,796 mg.kg^{-1}, necessitating extensive desalination treatment. The estuary sand approached the safety threshold at 431 mg.kg^{-1}, indicating that blending or washing procedures are required for safe utilization.

3.2. Concrete Performance

Results on concrete performance are provided to evaluate how different sand types influence the structural properties of Grade 30 mixes. The focus is on strength-related parameters, which are vital for determining load-bearing capacity and durability in structural elements. The analysis begins with the development of compressive strength, followed by an assessment of tensile performance, offering a thorough understanding of the mechanical behavior.

3.2.1. Strength Development

Compressive strength results clearly distinguished the performance of different sand types (Table 4, Figs. 4(a) and 4(b)). River sand demonstrated outstanding 28-day strength

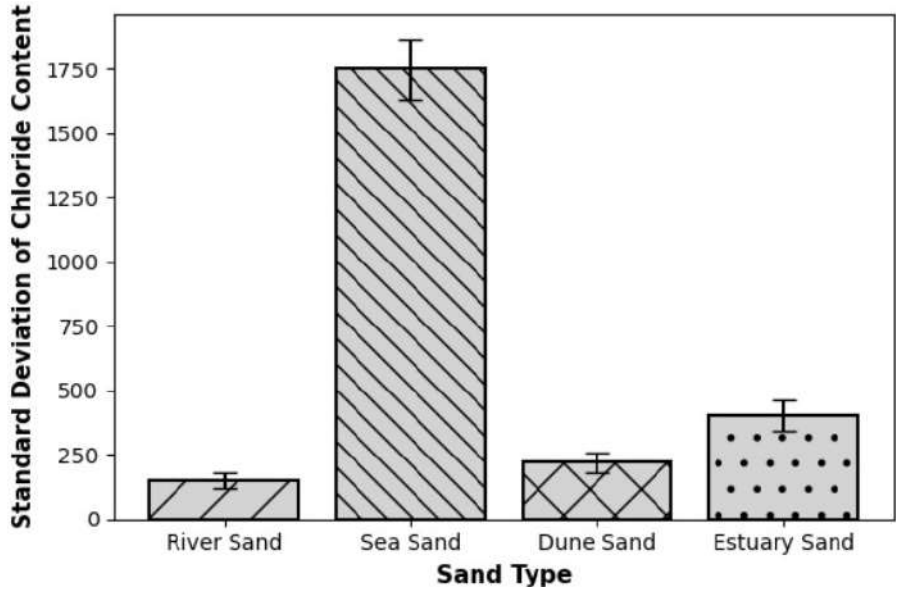


Fig. 3: Chloride content comparison across sand types with BS 8500-1:2023 permissible limit (500 mg.kg^{-1}).

Table 4: 28-Day Compressive (MPa)[a].

Sand Type	28-Day Compressive (MPa)	28-Day Tensile (MPa)	Grade 30 Compliance	Failure Mode
River	34.2 ± 1.2	3.4 ± 0.15	Yes	Conical
Sea	27.5 ± 2.1	2.3 ± 0.25	No	Shear
Dune	31.8 ± 1.5	3.1 ± 0.20	Yes	Splitting
Estuary	29.3 ± 1.8	2.7 ± 0.18	No	Delamination

(34.2 MPa), surpassing Grade 30 standards, with a typical conical failure pattern indicating strong structural integrity.

Values with different superscript letters differ significantly ($p < 0.05$, Tukey HSD test). River sand: A; Dune sand: AB; Estuary sand: B; Sea sand: B (Ferraris 2001).

Dune sand exhibited marginal compliance at 31.8 MPa despite its fine particle size, with angular grains potentially enhancing packing density. The splitting failure mode indicated high internal tensile stresses, likely resulting from particle interlock, gradation effects, or workability differences during casting. This mode remained structurally acceptable for Grade 30 applications.

SEA sand performed significantly worse at 27.5 MPa, aligning with known issues of chloride-induced microcracking and poor aggregate-cement bonding reported in literature (Ramana 2017, Zhao et al. 2019). Although direct microstructural analysis was not performed, shear failure patterns suggested brittle behavior, influenced by chloride content, gradation, and workability, rather than sand type alone. Without treatment, the concrete is unsuitable for structural use.

Estuary sand fell short of Grade 30 requirements at 29.3 MPa, possibly due to bimodal gradation creating voids and weak planes. The delamination failure pattern observed is consistent with an inhomogeneous microstructure, though further characterization is necessary to confirm this. The graph indicates river sand achieving the highest strength, followed by dune sand meeting Grade 30 at 30 MPa, while sea and estuary sands do not meet the standard.

The superior performance of river sand aligns with established literature on optimal gradation and particle morphology (Ferraris 2001). Its well-graded distribution (FM = 2.8) promotes efficient particle packing, reduces void content, and enhances cement–aggregate bonding. The comparatively strong performance of dune sand, despite its finer particles, can be attributed to angular grain morphology resulting from aeolian weathering processes, which increases mechanical interlock (Rashad 2020).

The underperformance of sea sand is likely associated with chloride-induced effects during cement hydration, as documented by Ramana (2017). Literature suggests that excessive Cl^- ions can interfere with C–S–H gel formation and promote the formation of expansive ettringite within the interfacial transition zone. However, these mechanisms were not directly verified through microstructural analysis in the present study. The observed shear failure mode indicates reduced ductility, which is a critical concern for seismic applications.

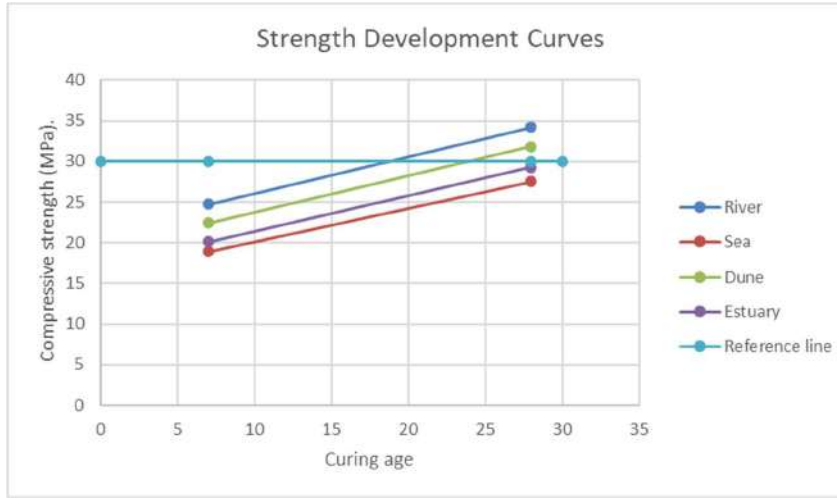


Fig 4(a): Compressive strength development over time (7 and 28 days) for concrete made with different sand types.

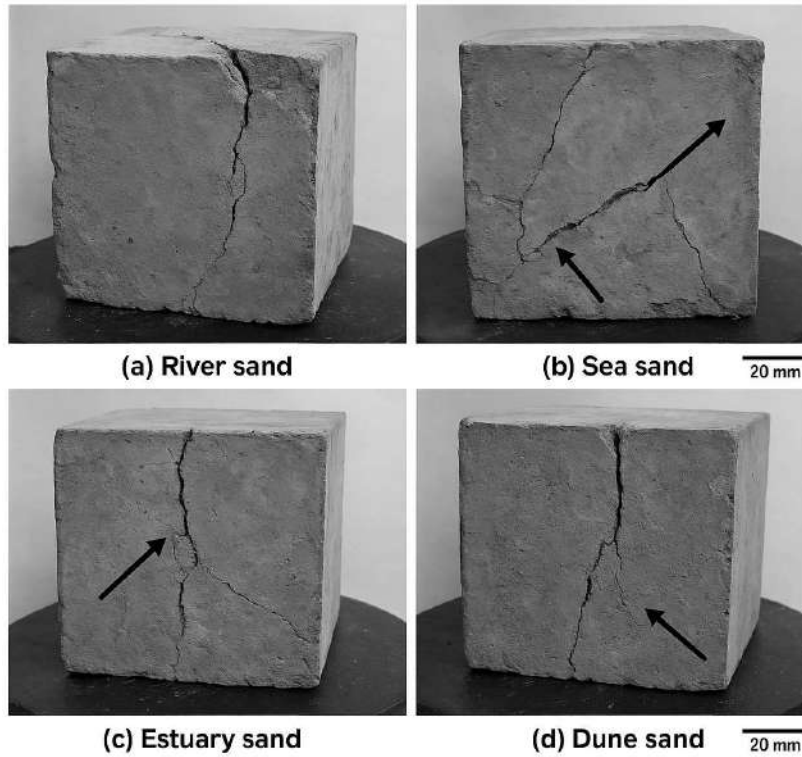


Fig. 4(b)*:* Failure mode comparison of 150 mm concrete cubes at 28 days: (a) River sand showing conical failure with intact edges, (b) Sea sand exhibiting sudden shear plane with explosive spalling, (c) Dune sand displaying diagonal splitting at 45° angle.

Estuary sand exhibited marginal performance, which may be attributed to its complex mineralogy and bimodal gradation. The gap-graded distribution creates localized weak zones, where insufficient fine material fails to fill voids between coarse particles. This phenomenon, often referred to as particle segregation, reduces homogeneity and creates preferential crack propagation paths (Brouwers & Radix 2005).

Statistical Analysis: One-way ANOVA was performed to evaluate significant differences in compressive strength among sand types ($\alpha = 0.05$). The analysis revealed statistically significant differences ($F(3,8) = 45.2$, $p < 0.001$). Post-hoc Tukey HSD tests confirmed that:

- River sand strength significantly exceeded sea sand ($p < 0.001$) and estuary sand ($p = 0.002$)
- Dune sand showed no significant difference from river sand ($p = 0.089$)
- Sea sand and estuary sand were not significantly different ($p = 0.312$)

Given the sample size (n=3 per sand type), results should be interpreted with appropriate caution. While differences with $p < 0.01$ demonstrate robust statistical significance, comparisons approaching borderline significance (e.g., river vs. dune sand, $p = 0.089$) warrant validation through larger-scale studies before definitive conclusions. The observed effect sizes and consistency with physical property measurements support the reported trends, though expanded sampling would strengthen confidence intervals.

3.2.2. Tensile Performance

Splitting tensile strength correlated with compressive performance, with river sand achieving optimal results (3.4 MPa) as shown in Fig. 5. The tensile-to-compressive strength ratios ranged from 0.08 to 0.10, aligning with established empirical relationships for normal-weight concrete.

The scatter plot illustrates a clear linear relationship, with river and dune sands demonstrating superior performance across both parameters.

3.3. Sustainability Assessment

This assessment combines technical performance with environmental and economic factors to determine the viability of alternative sands for large-scale use. It extends beyond laboratory strength tests to include considerations of resource depletion, processing energy requirements, and lifecycle costs. The following sections analyze environmental impact, economic feasibility, and overall performance ranking.

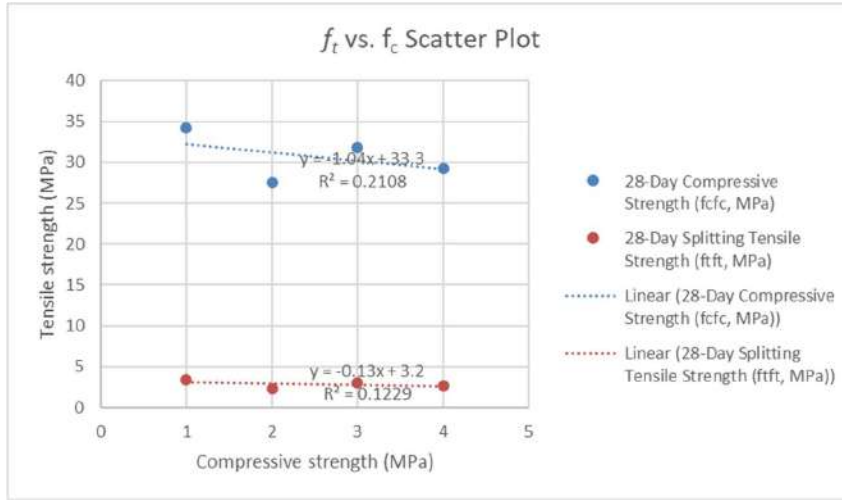


Fig. 5: Correlation between compressive and tensile strengths for all sand types.

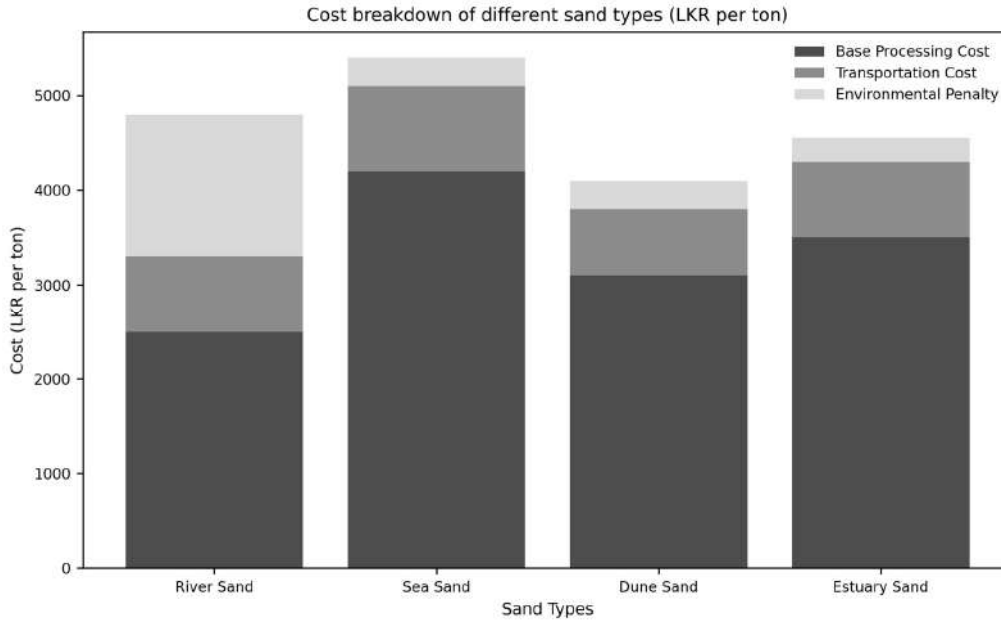


Fig. 6: Comparative cost analysis showing estimated total cost per ton, including processing, transportation, and modeled environmental externalities (based on carbon-equivalent ecosystem service valuation).

3.3.1. Environmental Impact

A comparative analysis shows that alternative sands vary in their processing needs, which affects energy consumption and resource use. Dune sand requires minimal processing beyond grading, whereas sea sand involves substantial desalination infrastructure.

3.3.2. Economic Analysis

Comparative cost analysis, including hypothetical environmental externality pricing, suggests that dune sand (processing cost: LKR 3,100.ton^{-1}) may provide economic advantages over continued river sand extraction. Sea sand processing requires higher capital investment for desalination infrastructure, offset by abundant coastal availability. Fig. 6 presents the economic comparison, including processing costs, transportation, and environmental impact penalties (Ramana 2017).

Cost data were obtained through market surveys of three certified suppliers in each region (n=12 total) during August-September 2024. Processing costs include washing, sieving, and quality control testing. Transportation costs are assumed

to be 50 km average distance to Colombo construction sites at LKR 15.ton^{-1}.km^{-1}. Environmental externalities were estimated using carbon pricing equivalent (LKR 2,500. ton^{-1} CO_2) as a proxy for ecosystem service valuation for riverbed disruption (Costanza 2014). These values represent comparative scenarios rather than precise economic costs, intended to illustrate relative sustainability trade-offs. Desalination costs for sea sand include electrochemical treatment infrastructure amortized over a 10-year operational lifespan.

3.4. Performance Ranking

Based on combined technical, environmental, and economic criteria as illustrated in Fig. 7:

i. River sand (reference standard, environmental concerns)
ii. Dune sand (best overall alternative)
iii. Estuary sand (limited applications)
iv. Sea sand (requires extensive treatment)

4. PRACTICAL APPLICATIONS AND RECOMMENDATIONS

This section translates the experimental findings into practical guidelines and policy measures aimed at enhancing sustainable sand utilization in the Sri Lankan construction sector. The recommendations are structured to address both immediate implementation strategies at the material and project level, as well as broader regulatory and economic frameworks that can ensure long-term adoption.

4.1. Implementation Guidelines

Implementation guidelines focus on the practical adaptation of different sand types for construction use. Each category of sand is considered separately to highlight specific limitations, required treatments, and optimization strategies, ensuring that materials are applied effectively while maintaining structural safety and durability.

4.1.1. Dune Sand

Dune sand can be made suitable for structural concrete with minor modifications, such as blending with 20% crushed coarse sand to optimize gradation, using 0.5% polycarboxylate superplasticizers to improve workability, and monitoring the fineness modulus during batching.

4.1.2. Sea Sand

Sea sand, however, requires comprehensive treatment before use, including electrochemical desalination to reduce chloride levels below 500 mg/kg, aging for 60–90 days under controlled conditions, and blending with 30% manufactured sand to enhance gradation.

4.1.3. Estuary Sand

Based on sub-threshold compressive strength (29.3 MPa) and borderline chloride content (431 mg.kg^{-1}), estuary sand should be strictly limited to non-structural applications only. Acceptable uses include plastering mortars, non-load-bearing blockwork, and screeds, provided pre-washing reduces chloride content by a minimum of 40–50% and batch testing confirms compliance below 400 mg/kg. Use in structural elements, including reinforced masonry or load-bearing walls, is not recommended based on the current characterization data.

4.2. Policy Recommendations

Beyond project-level applications, broader policy interventions are necessary to institutionalize safe and sustainable sand usage. Recommendations in this section target regulatory frameworks and economic measures, with the aim of encouraging compliance, promoting innovation, and reducing reliance on untreated natural sand resources.

4.2.1. Regulatory Framework

To support safe and sustainable sand usage, policy recommendations include enforcing chloride testing requirements for all construction sands, banning untreated sea sand in reinforced concrete applications, and establishing quality standards for alternative sand processing.

4.2.2. Economic Incentives

Economic incentives such as subsidizing sand washing facilities in coastal regions, providing tax benefits for contractors using more than 50% alternative sands, and supporting research and development of sand treatment technologies are recommended.

4.3. Study Limitations and Future Research

While this study provides valuable insights into Sri Lankan alternative sands, several limitations should be acknowledged:

1. **Durability Assessment:** Long-term durability parameters, including chloride penetration resistance, sulfate attack resistance, and freeze–thaw performance, were not evaluated. Future studies should incorporate accelerated aging tests in accordance with ASTM C1202 and BS 1881-124 (ASTM C33/C33M-18 2018).
2. **Microstructural Analysis:** The absence of SEM/EDS or XRD analysis limits understanding of interfacial transition zones and hydration product formation. Advanced microscopy techniques would help elucidate performance mechanisms (Shetty 2019, Neville 2011, Mindess 2003).

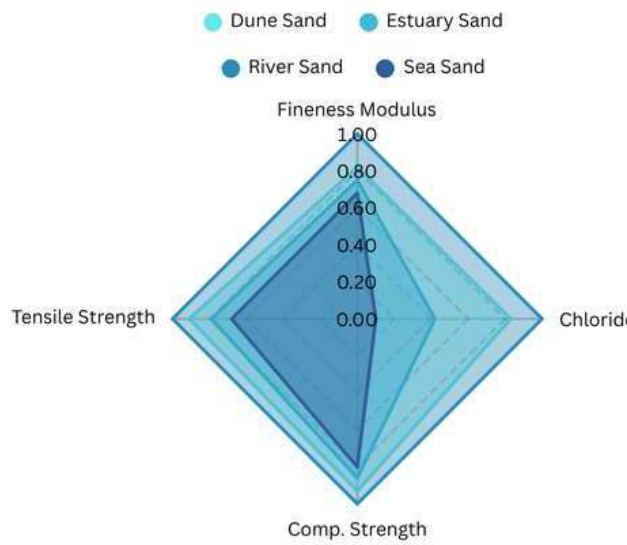


Fig. 7: Multi-criteria performance radar chart comparing all sand types across five parameters: compressive strength, tensile strength, chloride compliance, gradation quality, and environmental sustainability. Dune sand shows the most balanced profile as a river sand alternative.

3. **Blending Optimization:** A systematic investigation of blend proportions (e.g., 70% dune sand + 30% crushed sand) could optimize gradation and performance beyond single-source applications.
4. **Economic Data:** The cost analysis was based on market surveys rather than a controlled life-cycle assessment. Comprehensive economic modeling, including carbon footprint analysis, is recommended.
5. **Sample Diversity:** Single-source sampling for each sand type may not adequately capture regional variability. Multi-site sampling would strengthen the generalisability of the findings. Future research should prioritize:
   (a) five-year durability monitoring of field structures,
   (b) development of rapid chloride removal protocols, and
   (c) standardization of alternative sand specifications within Sri Lankan codes.
6. **Mix Design Variables:** This study maintained a constant fine aggregate content (720 kg.m^{3-}) across all sand types to reflect common field practice, where aggregate substitution is typically performed on a volumetric basis. However, differences in fineness modulus (2.8–1.9) and gradation among sand types represent confounding variables that may have influenced workability and strength independently of intrinsic material properties. While this approach enhances practical relevance, future studies should investigate optimized mix proportions for each sand type (adjusting fine-to-coarse ratios and water content) to isolate material effects from mix design variables. Additionally, maintaining a constant slump (75–100 mm) may have masked differences in water demand associated with particle shape and specific surface area.

5. CONCLUSIONS

This comprehensive evaluation confirms that Sri Lankan alternative sands can effectively replace river sand in concrete production when properly characterized and processed. Key findings indicate that dune sand is technically viable for structural concrete, achieving a 31.8 MPa compressive strength with a chloride content of 215 mg.kg^{-1} and requiring minimal processing. Although river sand offers slightly higher strength at 34.2 MPa, it faces sustainability challenges due to environmental concerns. Sea sand shows promise after desalination, which significantly reduces its initial chloride content of 1,796 mg.kg^{-1} to acceptable levels. Estuary sand, with moderate performance, is best suited for non-structural applications. Adopting alternative sands can alleviate pressure on river ecosystems while maintaining construction quality. Dune sand and processed estuary sand emerge as the most balanced options regarding performance, sustainability, and economic feasibility. Successful implementation depends on regulatory enforcement, the development of processing facilities, and industry training, with phased adoption in non-critical applications helping to build confidence and technical expertise. Future research should focus on assessing long-term durability, optimizing blending ratios, and improving cost-effective treatment technologies. These efforts will lay the groundwork for sustainable construction policies that support Sri Lanka's infrastructure development while protecting natural ecosystems.

6. REFERENCES

ASTM International 2018. *ASTM C33/C33M18: Standard Specification for Concrete Aggregates*. West Conshohocken, PA: ASTM International. [DOI]

ASTM International 2020. *ASTM C1218/C1218M20: Standard Test Method for WaterSoluble Chloride in Mortar and Concrete*. West Conshohocken, PA: ASTM International. [DOI]

Benabed, B., Azzouz, L., Kadri, E., Kenai, H. and Qu, L., 2014. Effect of fine aggregate replacement with desert dune sand on fresh properties and strength of self-compacting mortars. *Journal of Adhesion Science and Technology*, 28(21), pp.2182–2195. [DOI]

Brouwers, H.J.H. and Radix, H.J., 2005. Self-compacting concrete: Theoretical and experimental study. *Cement and Concrete Research*, 35(11), pp.2116–2136. [DOI]

Building Research Establishment, 1997. *Design of Normal Concrete Mixes*. 2nd ed. Watford, UK: BRE Press.

Cepuritis, R., Wigum, B.J., Garboczi, E.J., Mortsell, E. and Jacobsen, S., 2014. Filler from crushed aggregate for concrete: Pore structure, specific surface, particle shape and size distribution. *Cement and Concrete Composites*, 54, pp.2–16. [DOI]

Costanza, R., Groot, R., Sutton, P., van der Ploeg, S., Anderson, S.J., Kubiszewski, I., Farber, S. and Turner, R.K., 2014. Changes in the global value of ecosystem services. *Global Environmental Change*, 26, pp.152-158. [DOI]

Dias, W.P.S., Seneviratne, G.A.P.S.N. and Nanayakkara, S.M.A., 2008. Offshore sand for reinforced concrete. *Construction and Building Materials*, 22(7), pp.1377–1384. [DOI]

Dolage, D.A.R., Dias, M.G.S. and Ariyawansa, C.T., 2013. Offshore sand as fine aggregate for concrete production. *British Journal of Applied Science & Technology*, 3(4), pp.813–825. [DOI]

Ferraris, C.F., 2001. Measurement of the rheological properties of cement paste: A new approach. In: *Proceedings of the International RILEM Conference*. Cachan, France, pp.333–342.

Koehnken, L. and Rintoul, M., 2018. *Impacts of Sand Mining on Ecosystem Structure, Process, and Biodiversity in Rivers*. WWF International.

Kumar, S., Ansari, M.A., Kant, L. and Jha, N.N., 2025. An experimental investigation on sustainable concrete made with refractory brick as a substitute of natural fine aggregate. *Nature Environment & Pollution Technology*, 24(1). [DOI]

Mahendran, K., Jayasinghe, R.P. and Perera, A.S., 2016. Environmental impact assessment of river sand mining in Sri Lanka. *Environmental Management*, 58(4), pp.651–665.

Mindess, S., Young, J.F. and Darwin, D., 2003. *Concrete*. 2nd ed. Prentice Hall.

Neville, A.M., 2011. *Properties of Concrete*. 5th ed. Pearson Education Limited.

Ramana, K.V., Rangaraju, R.V. and Suresh, P., 2017. Influence of seawater on concrete properties with different percentages of chloride. *International Journal of Civil Engineering and Technology*, 8(10), pp.595–604.

Rashad, A.M., 2020. A synopsis about the effect of desert sand on the properties of conventional concrete and geopolymer concrete. *Construction and Building Materials*, 242, p.118191.

Ratnayake, N.P., Chaminda, S.P., Puswewala, U.G.A., Ekanayaka, E.M.T.M. and Jayawardene, A.M.N., 2014. Evaluation of sea sand potential as an alternative to river sand for concrete production in Sri Lanka. *Journal of Geological Society of Sri Lanka*, 16, pp.109–117.

Shetty, M.S., 2019. *Concrete Technology: Theory and Practice*. 8th ed. S. Chand Publishing.

United Nations Environment Program, 2019. *Sand and Sustainability: Finding New Solutions for Environmental Governance*. Nairobi, Kenya: UNEP.

Zhao, Z., Xiao, S., Li, L., Ding, C., Zheng, J. and Shah, S., 2019. Effect of mixing sequence of calcium hydroxide and polycarboxylate superplasticizer on the performance of desalinated sea sand mortar. *Construction and Building Materials*, 217, pp.639–651. [DOI]

Nature Environment and Pollution Technology
An International Quarterly Scientific Journal

p-ISSN: 0972-6268
(Print copies up to 2016)
e-ISSN: 2395-3454

Vol. 25 | No. 3 | Article ID B4403 | 2026

Original Research Paper

https://doi.org/10.46488/NEPT.2026.v25i03.B4403

Open Access Journal

Managing Legacy Pollution: A Legal and Policy Analysis of the Environment Protection (Management of Contaminated Sites) Rules, 2025

Gurudutt[1] and Pooja Singh[2]
[1]Faculty of Law, Delhi University, Delhi, India
[2]K.R. Mangalam University, Sohna Road, Gurugram, Haryana, India
†Corresponding author: Gurudutt; gurudutt.clc@law.du.ac.in

Abbreviation: Nat. Env. & Poll. Technol.
Website: www.neptjournal.com

Received: 05-10-2025
Revised: 10-12-2025
Accepted: 05-01-2026

Key Words:

Contaminated sites
Legacy waste
Environmental Laws
Polluter pays principle
Remediation

ABSTRACT

Contamination of soil and water sources from hazardous industrial activities remains a persistent and serious environmental and public health challenge in India. Judicial doctrines such as the polluter-pays principle, the precautionary principle, and the concept of the public trust, along with a patchwork of statutes, have provided tools for pollution control but lacked a statutory, site-specific remediation pathway for legacy contaminated land. The Environment Protection (Management of Contaminated Sites) Rules, 2025, is the first dedicated legal framework for the identification, verification, declaration, and remediation of contaminated sites. This article critically examines the 2025 Rules through legal, doctrinal, and policy perspectives, situates them within the constitutional and statutory framework, and evaluates their provisions against institutional realities and international best practices, such as the US CERCLA/Superfund, EU liability frameworks, and China's soil law. It draws on official disclosure reports from the Central Pollution Control Board and the Ministry of Environment, Forest and Climate Change (MoEFCC 2025), as well as a case study of the Bandhwari landfill in Gurugram. The paper argues that while the 2025 Rules mark a progressive step, they will only lead to transformative outcomes if complemented by a stable national remediation finance mechanism, enhanced technical and institutional capacity, and detailed liability regulations. Recommendations include legal refinements and governance reforms necessary to operationalize the Rules in a manner consistent with India's constitutional environmental commitments.

Citation for the Paper:

Gurudutt and Singh, P., 2026. Managing legacy pollution: A legal and policy analysis of the Environment Protection (Management of Contaminated Sites) Rules, 2025. *Nature Environment and Pollution Technology*, 25(3), B4403. https://doi.org/10.46488/NEPT.2026.v25i03.B4403

Note: From 2025, the journal has adopted the use of Article IDs in citations instead of traditional consecutive page numbers. Each article is now given individual page ranges starting from page 1.

Copyright: © 2026 by the authors
Licensee: Technoscience Publications
This article is an open access article distributed under the terms and conditions of the Creative Commons Attribution (CC BY) license (https://creativecommons.org/licenses/by/4.0/).

1. INTRODUCTION

Industrialization and decades of rapid economic growth in India have resulted in significant environmental externalities, among which legacy contaminated sites are underrecognized, long-lasting, and highly damaging. "Contaminated sites" are locations where hazardous substances such as heavy metals, persistent organic pollutants, petroleum hydrocarbons, cyanides, and similar materials have accumulated in soil, sediments, or groundwater beyond safe thresholds, continuing to pose ecological and human health risks (Subudhi et al. 2025).

These are not isolated incidents but persistent, cumulative issues that are often technically complex and costly to remediate (Alapati et al. 2023). Examples include abandoned chemical plants, derelict tannery estates, landfill leachate plumes, and closed industrial sites with decades of unlined waste disposal. Until 2025, while India's environmental laws provided regulators with authority to control emissions and manage hazardous waste moving forward, there were no codified rules or statutes for identifying, declaring, and remediating contaminated sites on a large scale. The Environment Protection (Management of Contaminated Sites) Rules, 2025 (EPMCS Rules), notified by the Ministry of Environment, Forest and Climate Change (MoEFCC) via S.O. 3401(E), established a legal pathway for the screening, verification, declaration, and remediation of contaminated sites.

Table 1: National and programmatic contaminated sites data (India).

Category	Number
Confirmed contaminated sites (verified, CPCB 2025)	103
Sites with remediation started	7
Suspected sites (pending verification)	196
Legacy dumpsites (SBM toolkit 2023)	3,159
Legacy waste treated (till 2023)	1,026 sites
Legacy waste untreated (till 2023)	≈177.1 million tonnes

Source: CPCB (2025), Ministry of Housing and Urban Affairs (MoHUA) /CSE Toolkit on Legacy Waste Management (2023).

These rules also mandate public disclosure of verified data on a central portal and empower pollution control authorities to require remedial actions and recover costs. Official disclosures indicate that the Central Pollution Control Board (CPCB) has identified 103 contaminated sites, with remediation activities initiated at 7 of these sites (CPCB 2025).

The formation of a dedicated rule was long overdue due to the scale of the problem. This article explores whether these rules offer sufficient legal clarity and institutional design to effectively translate the polluter-pays doctrine and constitutional rights into meaningful remedial outcomes (Bugge 2009, Lees 2016). It also evaluates whether current governance and financing structures can operationalize these rules to address legacy pollution in India. The analysis is broadly structured around four evaluative parameters: regulatory clarity, enforceability mechanisms, institutional and fiscal feasibility, and accountability mechanisms. Comparative insights are drawn from the United States' Comprehensive Environmental Response, Compensation, and Liability Act (CERCLA), the European Union's liability regimes, and China's Soil Pollution Law to analyze India's approach within a global context, while recognizing the need for tailored reforms suited to the Indian context.

2. MATERIALS AND METHODS

This study employs a doctrinal approach to review policy and analyze the Environment Protection (Management of Contaminated Sites) Rules, 2025. Primary sources include the Rules themselves, the Environment (Protection) Act, 1986, related statutes, and key judicial precedents from the Supreme Court and the National Green Tribunal that have shaped principles such as the polluter-pays and the precautionary principle. Policy documents and official datasets, notably the CPCB National Inventory of Contaminated Sites (2024–25) and the MoHUA–CSE Toolkit on Legacy Waste (2023), were analyzed to understand the extent of contamination and institutional responses. Additionally, a few RTIs were filed to gather data on expenditure incurred by various local bodies for garbage remediation.

To contextualize India's framework within a broader perspective, the paper undertakes a comparative review of international regimes, including the U.S. CERCLA/ Superfund, the EU Environmental Liability Directive, and China's Soil Pollution Prevention and Control Law (Caney 2005). The USA and EU were selected for their mature and diverse regulatory approaches to contaminated-site management, while China was included as a comparator due to its status as a rapidly developing economy facing similar legacy-pollution challenges. Case studies such as the Bandhwari landfill were used to integrate legal analysis with empirical evidence. This combined methodology ensures a balanced evaluation of legal texts, governance practices, and comparative insights, while acknowledging limitations due to data gaps and early-stage implementation.

Radioactive waste and mining-related contamination are explicitly excluded from the scope of this research, as the new rules do not pertain to them. They are regulated under specialized statutes, namely the Atomic Energy Act, 1962, and the Mines and Minerals (Development and Regulation) Act, 1957.57.

3. RESULTS AND DISCUSSION

3.1. Constitutional, Statutory and Judicial Foundations

Environmental law worldwide derives much of its normative authority from constitutional provisions that are progressively interpreted by higher judiciary bodies (Weis 2018). In India, the Constitution also mandates this approach: Article 48A imposes a duty on the State to protect and improve the environment, while Article 51A(g) requires every citizen to safeguard the natural environment. Courts have often read these provisions collectively, emphasizing that environmental protection is not merely a policy goal but a constitutional obligation for India.

At the core of Indian environmental jurisprudence is Article 21, which guarantees the right to life. The Supreme Court has consistently interpreted this right to include a healthy and clean environment. In Subhash Kumar v. State of Bihar (1991), the Court explicitly recognized the right to pollution-free air and water as an integral part of the Right to Life under Article 21. Similarly, in the landmark case of MC Mehta v. Kamal Nath (1997), the Court applied the public trust doctrine to prevent environmental harm, affirming that natural resources are held in trusteeship by the State for the benefit of its citizens. These rulings reflect global legal developments, where principles such as the polluter-pays principle and the precautionary principle are embedded in

environmental governance (Sands & Peel 2018, Birnie et al. 2021).

The Court further examined this approach in A.P. Pollution Control Board v. Prof. M.V. Nayudu (1999), emphasizing the importance of the precautionary principle and asserting that scientific uncertainty cannot justify inaction in the face of environmental threats. This decision also highlighted the need for specialized scientific input in environmental adjudication.

India's main environmental statutes—including the Environment (Protection) Act, 1986 (EPA), the Water Act, 1974, the Air Act, 1981, and the Hazardous and Other Wastes (Management & Transboundary Movement) Rules, 2016—establish regulatory controls for emissions and hazardous waste management. However, these laws were not designed to effectively address site-specific remediation for legacy pollution.

3.2. Programmatic Responses and the CEPI Framework

Before the adoption of the *Environment Protection (Management of Contaminated Sites) Rules, 2025*, India relied primarily on programmatic responses to address industrial pollution at the cluster level rather than through site-specific remediation laws. The most notable of these instruments is the Comprehensive Environmental Pollution Index (CEPI), developed by the Central Pollution Control Board (CPCB 2009). CEPI provides a composite measure of environmental stress in industrial clusters by aggregating indicators of air, water, and land pollution.

Based on CEPI scores, the CPCB identified several critically polluted industrial clusters, which were then subjected to targeted remedial action plans, including restrictions on new industrial activities and mandated mitigation measures. Industrial areas with aggregated CEPI scores of 70 and above were considered as Critically Polluted Areas (CPAs), whereas CEPI scores between 60 and 70 were considered as Severely Polluted Areas (SPAs), and CEPI scores less than 60 were considered as Other Polluted Areas (OPAs).

Table 2: Comprehensive Environmental Pollution Index (CEPI) framework.

Component	Description	Marks
Component A	Scale of Industrial Activity	20
Component B	Status of Ambient Environmental Quality (Air/Surface Water/Ground Water)	50
Component C	Health Related Statistics	10
Component D	Compliance Status of Industries	20
	Total per Medium (Air, SW, or GW EPI)	100

Calculation of Individual Media Indices: The index for each environmental medium (Air, Surface Water, Ground Water) is calculated separately on a scale of 0–100 using the formula:

$$i_1 \text{ (Air EPI) or } i_2 \text{ (SW EPI) or } i_3 \text{ (GW EPI)} = A + B + C + D \quad ...(1)$$

Overall CEPI Calculation:

The overall Comprehensive Environmental Pollution Index is then evaluated using the formula:

$$CEPI = i_{\max} + \left[(100 - i_{\max}) \times \frac{i_a}{100} \times \frac{i_b}{100}\right] \quad ...(2)$$

Where:

- i_{max} = The maximum value among the three indices (i_1, i_2, i_3).
- i_a, i_b = The indices for the other two environmental media after excluding i_{max}

CEPI served as a useful prioritization tool, but its cluster-level focus created no enforceable obligations for remediating specific contaminated sites, leaving much legacy pollution unaddressed. Its implementation also remains inconsistent, and the last national assessment was conducted in 2018 across 100 clusters, identifying 38 CPAs and 31 SPAs. In this sense, CEPI complemented but did not substitute the legal framework of contaminated site remediation, which only materialized with the 2025 Rules.

3.3. Swachh Bharat Mission and the Legacy Waste Challenge

Alongside CEPI-driven cluster monitoring, the most visible policy initiative addressing waste-related contamination in the last decade was the flagship Swachh Bharat Mission (SBM). In both its Urban (SBM-U) Phase I (2014–19) and Phase II (SBM 2.0, 2021–26), SBM explicitly targeted the remediation of legacy dumpsites through biomining and bioremediation. These dumpsites, essentially uncontrolled municipal landfills that have accumulated waste for decades, are recognized as major sources of leachate contamination, methane emissions, and vector-borne risks (MoHUA 2023).

The scale of the problem is immense. According to the MoHUA toolkit on Legacy Waste Management (2023), India has nearly 3,159 identified dumpsites containing an estimated 250 million tonnes of legacy waste. By March 2023, only 1,026 sites, that is, approximately 33%, had been biomined or remediated, leaving approximately 177.1 million tonnes of untreated waste in situ. In absolute terms, over 2,100 dumpsites remain active. These numbers reveal the structural gap between programmatic ambition and actual execution capacity.

The shortfall was especially stark, given the original deadlines. SBM Phase I had promised 100% dumpsite clearance by October 2019, coinciding with the Mission's fifth anniversary. This deadline was missed, and the task was carried forward into SBM 2.0, with revised timelines stretching into 2023–26. Even under an extended horizon, progress remains fairly uneven. The smaller towns managed partial biomining, but large metropolitan landfills, such as the notorious Ghazipur (Delhi), Deonar (Mumbai), and Bandhwari (Gurugram), continued to accumulate fresh waste even as "remediation" projects lagged (Table 3).

Analyses of implementation point to several capacity and design weaknesses in the program. Many Urban Local Bodies (ULBs) lack technical expertise in biomining, have limited access to heavy equipment, and face challenges in contracting private concessionaires to undertake large-scale clearance. Funding allocations under SBM were tied to annual budgetary cycles and linked more to the construction of sanitation infrastructure than to long-term remediation. The cost of remediation also differed from site to site, showing no uniform approach. These limitations explain why SBM, despite its rhetorical emphasis on a "garbage-free India," did not produce a systemic pathway for addressing legacy contamination.

In this sense, the SBM represents the programmatic precursor whose shortcomings necessitated a transition to a formal legal framework. While the SBM offered targets, toolkits, and aspirational deadlines, the 2025 Rules provide statutory definitions, enforceable liability, and mandated public disclosure mechanisms.

4. THE ENVIRONMENT PROTECTION (MANAGEMENT OF CONTAMINATED SITES) RULES, 2025

The EPMCS Rules establish a hierarchical governance framework that allocates responsibilities across different government levels and technical agencies. At the top is the Central Remediation Committee, led by the Chairman of the Central Pollution Control Board (CPCB). It includes representatives from key ministries such as Housing and Urban Affairs, Commerce and Industry, Chemicals and Fertilizers, Science and Technology, and Health and Family Welfare. This interministerial composition recognizes the interconnected nature of contamination issues and ensures that remediation initiatives benefit from diverse expertise and perspectives.

At the state level, the Rules require the formation of State Level Committees chaired by the Additional Chief Secretary or Principal Secretary of the Environment Department, with members from relevant departments. This structure facilitates coordination and oversight during implementation, while operational duties primarily fall to the State Pollution Control Boards (SPCBs) and Pollution Control Committees (PCCs). SPCBs are responsible for identifying contaminated sites, conducting assessments, directing responsible parties to develop remediation plans, and overseeing remediation efforts.

Additionally, the Rules propose a centralized online portal for reporting contaminated sites and mandate public disclosure of assessment and remediation activities through a dedicated platform. Liability for remediation primarily rests

Table 3: City-wise legacy waste projects, budgets, and cost efficiency.

City/Location	Project/Brief Description	Budget/Cost [₹]	Total Legacy Waste [tonnes]	Cost per Tonne [₹.t^{-1}]
Mumbai-Deonar	Scientific clearing contract for Deonar Dumping Ground	₹2,540 crore	~260 lakh t (reported est.)	~₹977/t
Gurugram (Bandhwari)	Bioremediation of Bandhwari landfill	₹89.9 crore	~14 lakh t	~₹642/t
Kochi (Brahmapuram)	Biomining & rehabilitation of legacy waste	₹142 crore (revised)	~5.5 lakh t	~₹2,582/t
Bengaluru (BBMP)	Processing legacy waste (Mandur + other sites)	₹187 crore	~97.8 lakh t (target)	~₹191/t
Delhi-Bhalswa	Biomining & remediation	₹130 crore	~30 lakh t	~₹433/t
Delhi-Okhla	Biomining & remediation	₹82 crore	~20 lakh t	~₹410/t
Chandigarh-Dadu Majra	Legacy waste removal & biomining	₹77 crore	~12.5 lakh t	~₹616/t
Ludhiana (Jamalpur)	Bioremediation + fresh waste mgmt.	~₹70–77 crore	~25 lakh t (est.)	~₹280–308/t
Nagpur	Bioremediation under SBM	₹42.80 crore	~9 lakh t (est.)	~₹475/t
Silchar (Assam)	Remediation + MRF	₹22 crore	~3 lakh t (est.)	~₹733/t
Rewari (Haryana)	Sanitary landfill & remediation	₹4.02 crore	~1 lakh t (est.)	~₹402/t
Bhubaneswar (Odisha)	Legacy waste remediation (SBM toolkit)	n.a. (toolkit cites)	cost reported basis	~₹1,050/t
Varanasi/Medium cities (toolkit avg.)	SBM legacy projects	n.a. (toolkit cites)	n.a.	~₹887–₹1,193/t

with identifiable polluters. For orphan sites where polluters cannot be identified, the Rules allow government-led cleanup efforts, with funding shared between the Central and State Governments and provisions for recovering costs later.

4.1. Key Provisions and Their Practical Implications

The EPMCS Rules, 2025, primarily distinguish themselves through their precise definitional clarity. They specify a "contaminated site" based on contaminant levels in soil, surface water, or groundwater that surpass designated thresholds. The term "contaminant" refers to hazardous substances as outlined in clause (e) of section 2 of the Environment (Protection) Act, 1986 (29 of 1986), exceeding response levels detailed in Schedule I of the rules. The scope explicitly encompasses landfills, dumpsites, and both active and abandoned industrial locations.

Furthermore, these rules clarify that the EPMCS Rules, 2025, do not apply to radioactive waste, certain mining areas, marine pollution, or solid waste from dump sites. This precise definitional framework holds legal significance by identifying a clear remedial scope and tying regulatory triggers to measurable environmental thresholds, thereby minimizing ambiguity in enforcement and aligning with scientific benchmarks.

The process of identifying and verifying contaminated sites involves multiple stages, beginning with district authorities and State Pollution Control Boards (SPCBs) compiling lists of suspected sites, either independently or following public complaints. These lists are then subjected to technical environmental site assessments (ESAs), which employ hydrogeological surveys, toxicity testing, and other scientific protocols established under relevant regulations. Verified data must be uploaded to a central public portal for transparency and independent review by civil society, thereby enhancing accountability—a significant advancement in governance (Ruppel 2023, Sadeleer 2000).

Every six months, a list of contaminated sites is prepared and updated for submission to SPCBs. Subsequently, SPCBs, either directly or through designated reference organizations, are tasked with conducting preliminary site assessments, including sampling and analysis, within 90 days of receiving the list. However, the aggressive timelines for screening and verification may lead to bottlenecks, given that SPCBs often suffer from chronic shortages of staff, technical expertise, and financial resources. Without concurrent investment in institutional capacity building, delays are inevitable. Additionally, since most reference organizations are predominantly based in urban centers and industrial hubs, regional disparities in site identification and remediation efforts are likely to arise.

Once verification is complete, sites are officially designated as "contaminated" in the Gazette if contaminant levels exceed the limits specified in the schedule. This legal designation triggers mandatory remedial actions. The primary responsibility lies with the polluter, in cases with multiple contributors, liability is joint and several. If the polluter cannot be identified, the site is declared orphaned, and the government is empowered to undertake cleanup efforts, with the possibility of recovering costs later. The Rules stipulate that remediation expenses are to be shared by the Central and State Governments through the Environment Relief Fund, established under the Public Liability Insurance Act of 1991 following the Bhopal Gas Tragedy.

Although this framework aligns with some international practices, it does not establish a permanently funded, ring-fenced remediation fund like the United States' Superfund. Reliance on annual budgets risks delays and persistent underfunding. The Environment Relief Funds are severely underutilized, and the disbursal process is cumbersome. Public records show that the fund has been almost entirely unused in recent years, with no disbursements since 2019, despite the corpus growing to ₹1,062 crore by March 2023 from ₹895 crore at the end of 2020 (CAG 2023).

The remediation process must be implemented through Remedial Action Plans (RAPs), which should detail technical solutions such as remediation or decontamination methods, excavation, and soil washing. These plans are also to include milestones, monitoring parameters, financial resource estimates, post-remediation monitoring, and safety protocols for occupational health, emergency response, and safety. The State Boards are responsible for reviewing and approving the RAPs within three months and forwarding them to the central board.

Upon completing remediation, the state board must inspect the site, compile a report for submission to the Central Board, and coordinate an additional review with a reference organization. Based on these reports, the Central Board may recommend further or supplementary remediation actions.

The Rules promote transparency by establishing a dedicated online portal (Akerboon & Craig 2022). This portal is designed to host verified datasets, RAPs, progress reports, and monitoring results. By addressing the long-standing issue of information asymmetry, the portal can serve as an accountability tool and facilitate civic oversight. However, its true effectiveness will depend on data quality, regular updates, user-friendliness for non-specialists, and the availability of grievance redress mechanisms to prevent the platform from becoming merely symbolic without meaningful impact.

4.2. Timeline of Contaminated Site Management (India, 2025 Rules)

Phase 1 – Identification & Listing

- Local Body/District Administration
  - Identify & list suspected contaminated sites on the centralised portal (ongoing/half-yearly),
  - State Pollution Control Board (SPCB),
  - Undertake preliminary site assessment within 90 days of receiving the list,
  - If contamination exceeds screening level → classify as Probable Contaminated Site.

Phase 2 – Detailed Site Assessment

- SPCB/Reference Organisation
- Conduct a detailed site assessment within 3 months of classification as Probable,
- Publish draft list of contaminated sites within 60 days of assessment for stakeholder comments,
- Publish the final list after considering comments.

Phase 3 – Remediation Planning

- SPCB
  - Identify the Responsible Person (RP) within 90 days of final listing,
  - Responsible Person (if identified),
  - Prepare & submit the remediation plan within 6 months of SPCB's directions.
  - SPCB
  - Review & approve remediation plan within 3 months of submission,
  - Orphan Sites (no RP found),
  - SPCB prepares a remediation plan within 6 months of final listing,
  - Initiate remediation within 90 days of plan finalisation.

Phase 4 – Execution & Monitoring

- Responsible Person
  - Submit half-yearly progress reports until remediation is complete,

Phase 5 – Verification & Closure

- SPCB
  - Submit the report after completion of remediation,
  - Issue Remediation Completion Order upon the Central Board's recommendation.

5. NATIONAL SCALE, CASE ILLUSTRATIONS, AND INTERNATIONAL COMPARATORS

5.1. National Scale and Official Baselines

The *Environment Protection (Management of Contaminated Sites) Rules, 2025,* were introduced following the compilation of India's inaugural national inventory of chemically contaminated sites. The MoEFCC reports that the CPCB has pinpointed 103 contaminated locations across 21 states, including former pesticide manufacturing facilities, municipal dumpsites, and industrial clusters. Remediation efforts are underway at 7 of these sites. The details of these 7 contaminated sites are as follows:

i. Mercury contaminated sites at Ganjam, Odisha
ii. Chromium contaminated sites at Rania, Kanpur Dehat, Uttar Pradesh
iii. Groundwater contamination at Lohia Nagar & Industrial area, Ghaziabad, Uttar Pradesh, due to untreated industrial effluents by several industries
iv. Mercury contaminated soil at the premises of M/s Hindustan Unilever Ltd., Kodaikanal, Tamil Nadu
v. BPCL oil contaminated site at Tondairpet, Chennai, Tamil Nadu
vi. Groundwater contamination in & around the premises of M/s Godavari Bio-Refineries, Ahmednagar, Maharashtra
vii. Groundwater contamination at Effluent Channel Project (ECP), Vadodara, Gujarat

The figure of 103 sites reflects locations already confirmed through environmental site assessments (ESAs), while a larger number of suspected sites remain unverified. This highlights the methodological challenges in establishing a comprehensive national baseline, including inconsistent reporting across states, a lack of long-term monitoring data, and limited hydrogeological mapping in both urban and rural areas. Consequently, the national inventory should be regarded as an initial reference point rather than a definitive count. For comparison, China's 2019 Soil Pollution Prevention and Control Law prompted surveys that uncovered over 1.5 million contaminated plots, with roughly 16% of surveyed agricultural land considered unsuitable for cultivation due to heavy metal contamination (PRC 2019)

5.2. International Comparison: Superfund (USA)

The Comprehensive Environmental Response, Compensation, and Liability Act (CERCLA) of 1980, commonly known as the Superfund program, is one of the most important pieces of environmental legislation in the United States (Vinaules

2024). As of March 2025, the Environmental Protection Agency (EPA) reported about 1,340 active sites on its National Priorities List (USEPA 2025). These sites include both industrial and municipal contamination hotspots, such as abandoned mines and pesticide manufacturing facilities.

The U.S. approach to managing contaminated sites rests on three main institutional pillars. The first is dedicated funding, initially secured through a tax on the petroleum and chemical industries, which established the self-sustaining Superfund Trust. Although this tax expired in the mid-1990s, Congress partially reinstated it in 2021, and it is now supported by federal budget allocations.

The second pillar is federal leadership, with the EPA serving as the primary technical authority. Backed by regional offices, the EPA ensures that risk assessments and remediation efforts follow standardized methodologies across states and projects, helping to reduce delays and inter-agency conflicts.

The third pillar focuses on transparency and public involvement. The EPA makes available site-specific profiles that include contamination data, remedial action plans, progress reports, and long-term monitoring results. This transparency promotes accountability and encourages citizen participation in the remediation process (Richardson 2017, Etemire 2023).

The economic impact of the U.S. contaminated site management system is considerable. Remediating a Superfund site typically costs between USD 20 million and USD 30 million, with more complex sites exceeding USD 100 million (USGAO 2025). In comparison, India's 103 verified contaminated sites represent only the beginning of what is likely to become a much larger and more costly national liability in the future.

5.3. Representative Case - Bandhwari Landfill, Gurugram

The Bandhwari landfill in Gurugram, situated near the Aravalli hills, stands as one of India's primary sources of landfill-related contamination. Nevertheless, it was not included among the seven sites chosen for initial remediation efforts (TOI 2025). Recent enforcement actions and operational data underscore ongoing issues at Bandhwari. In August 2025, the National Green Tribunal ordered a joint inspection by the CPCB and MoEFCC within a week, following reports of unregulated leachate discharges into the Aravallis.

Regarding remediation, the Haryana Government has approved only ₹89.9 crore to address 14 lakh tonnes of legacy waste, indicating significant delays. The current plan involves transporting approximately 600 metric tons of waste daily, covering just 40–50% of the waste generated daily, to a waste-to-energy plant in Sonipat. Bioremediation efforts at Bandhwari have been postponed until January 2026, with overall clearance pushed back to February 2028. These postponements, despite extensive media coverage and judicial oversight, highlight the severity of the crisis, as the site continues to receive nearly 1,200–1,500 metric tons of fresh waste each day.

Numerous reports from 2024–25 document frequent leachate overflows into forest gullies and neighboring villages adjacent to the landfill (NEERI 2024). Field testing by the state pollution control board revealed levels of biochemical oxygen demand and chemical oxygen demand, along with metals such as zinc, that far exceed permissible limits. These results are consistent with typical landfill leachate signatures, including ammoniacal nitrogen and heavy metals. The site spans roughly 30 acres, comprising a waste plant and landfill complex topped by a 37.2-meter-high waste mound. Civil society petitions have raised concerns about recurrent leachate runoff into nearby lakes, while official affidavits submitted to courts acknowledge that leachate mainly flows into adjacent areas during the monsoon season.

From a governance perspective, Bandhwari serves as a significant case study. Although the 2025 Rules encompass landfills and dumpsites as part of the 'contaminated sites' category, Bandhwari was not among the initial seven sites prioritized for remediation. This discrepancy suggests that early site selection may be influenced more by factors such as project readiness, liability clarity (particularly regarding private parties), administrative capacity, and political prominence rather than actual risk. Consequently, its omission underscores the importance of examining whether the new regime can translate high-profile contamination into meaningful action.

6. CRITICAL ANALYSIS OF LEGAL AND GOVERNANCE GAPS

The Environment Protection (Management of Contaminated Sites) Rules, 2025, transform decades of judicial doctrine into a statutory framework for remediation. They define contaminated sites, outline a staged process for screening, declaration, and remedial action planning, assign primary liability to polluters, and introduce transparency and participation requirements. However, a critical examination—considering scientific realities and institutional capacities—reveals structural weaknesses that could hinder their effectiveness. This section discusses these issues in detail and suggests targeted legal and technical reforms.

6.1. Financing and the Orphan-Site Problem: Lack of A Dedicated Remediation Fund

The Rules explicitly allow government-funded remediation when responsible parties cannot be identified, with provisions for later cost recovery. While well-intentioned, this approach risks funding shortages and a rise in abandoned site declarations. Remediation—especially for engineered containment, leachate treatment, or in situ stabilization of persistent pollutants—requires significant upfront capital and multi-year financing. The government's press note accompanying the Rules confirms that the CPCB has identified only 103 contaminated sites, with remedial work initiated at just seven. This low number highlights a funding gap that hampers timely implementation.

The legacy waste data from the Swachh Bharat Mission (SBM) further illustrates systemic financial challenges. As per the SBM Toolkit (MoHUA / CSE 2023), India has over 3,000 legacy dumpsites (CPCB reports 3,084/3,159 depending on the dataset), with only a few reclaimed so far and much waste remaining in situ. The toolkit identifies disposal gaps and high per-tonne remediation costs borne by Urban Local Bodies, with some projects reporting costs between ₹887 and ₹1,193 per tonne (Table 2). These figures underscore that financing issues extend beyond industrial

6.2. The Contaminant Schedule: Technical Strength, But Narrowness and Update Mechanisms Missing

The Rules mark a technical advance by prescribing numeric screening and response levels for an enumerated list of contaminants in drinking water. This indicates 189 analytes/chemicals with land-use-specific response values. This numerical approach reduces legal ambiguity, as sites can be classified by measured exceedances. However, a schedule-based design contains two interrelated limits.

First, the schedule was finite. Remediation reality increasingly confronts substances of emerging concern and site-specific mixtures whose hazards cannot be fully captured by single-analyte thresholds. Anchoring legal liability and remedial triggers solely on a fixed list risks false negatives, where unlisted but hazardous compounds are dominant contributors to risk. International practice shows that a "living list" mechanism with an expert committee and expedited amendment process is essential to keep screening values current (Selvaraj et al. 2021, Carbon Copy 2025).

The Rules set different values for agricultural, residential, commercial, and industrial land use. However, India does not yet have a central repository of remediation standards or uniform laboratory protocols. This gap can lead to inconsistent results across states and even conflicting legal conclusions regarding the same contamination. To address this, a national "Remediation Values Library" should be created within the CPCB, supported by uniform NABL lab accreditation, regular proficiency testing, and a fast-track system to add new contaminants within 90 days based on expert advice.

6.3. Exclusions, Boundaries and Selection Opacity: Why High-Visibility Sites May Still Be Omitted

The Rules exclude certain domains, notably radioactive waste (covered by Atomic Energy regulations), mine waste (regulated by mines and minerals law), and specific marine oil pollution, while also incorporating provisos that could re-include borderline sites. In practice, many contaminated locations are hybrid in nature—such as municipal dumpsites receiving industrial hazardous waste, mine-adjacent agricultural land affected by tailings, or brownfields involving multiple regulatory regimes. These boundary ambiguities create jurisdictional conflicts between agencies like MoEFCC/CPCB, state SPCBs, MoEFCC's mining wing, and MoHUA concerning municipal dumpsites, leading to delays in urgent remediation actions. Additionally, initial remediation prioritization seems influenced by administrative data availability, contractual readiness, political importance, and objective risk assessments.

The official inventory lists 103 verified sites, alongside datasets like SBM/CEPI, showing nearly 3,000 legacy dumpsites and critical industrial clusters identified by CEPI, but these sources are not fully aligned. This partial reconciliation explains why a prominent, high-risk landfill such as Bandhwari, widely litigated and publicly visible, was not among the first seven sites chosen for active remediation, despite evident leachate and ecological impacts. Recent NGT rulings and municipal tender timelines have repeatedly delayed Bandhwari's bioremediation, indicating that prioritization considers factors beyond environmental risk alone.

Consequently, the Rules should mandate an explicit, transparent, numerical, and risk-based prioritization matrix for initial site selection. Adopting EU-style risk-tiered prioritization and preventive duties would ensure that limited remediation resources are first allocated to the highest-risk sites. Criteria to consider should include the exposed population, groundwater dependence, contaminant toxicity and mobility, ecosystem sensitivity, evidence completeness, liability clarity, and technical feasibility. This approach would enhance transparency, reduce perceptions of arbitrariness, and strengthen the defensibility of sequencing decisions.

6.4. Capacity Constraints: SPCBs, CPCB and Laboratory Infrastructure

The Rules impose very tight deadlines for preliminary screenings and environmental site assessments (ESAs). However, State Pollution Control Boards (SPCBs) and the Central Pollution Control Board (CPCB) face significant staffing and technical resource shortages. A CPCB report submitted to the National Green Tribunal reveals that more than 50% of the sanctioned positions in these boards and committees remain vacant. Out of 12,016 total posts across 28 SPCBs and eight Pollution Control Committees (PCCs), approximately 6,075 are unfilled, representing about half of the workforce. In several states, vacancy rates are even higher—for instance, Bihar at 84%, Jharkhand at 73%, Andhra Pradesh at 69%, Karnataka at 60%, and Odisha at 58% (CPCB 2025).

Additionally, laboratory infrastructure exhibits significant geographical and technical gaps. While India has nearly 1,197 NABL-accredited testing laboratories across various fields, many SPCBs depend on a limited number of accredited labs, often situated in states with stronger institutional capacities. This leaves rural and less industrialized regions underserved.

To overcome this, the government should –

(a) establish a "Remediation Corps" under CPCB or MoEFCC, comprising mobile technical teams and regional labs that can be deployed to SPCBs for surge assessments,

(b) fast-track NABL accreditation processes and mandate external proficiency testing for labs conducting ESAs and,

(c) allow CPCB to empanel certified private technical agencies under strict quality assurance and rotation rules to supplement public laboratory capacity.

6.5. Liability, Insolvency and Corporate Avoidance

Although the 2025 Rules adopt joint and several liabilities and provide for cost recovery, practical challenges persist within Indian insolvency law. According to the Insolvency and Bankruptcy Code, 2016 (IBC), environmental claims are typically regarded as contingent or unsecured debts, placing them at the bottom of the liquidation "waterfall" outlined in Section 53 of the IBC. Secured creditors, such as banks, are prioritized, often leaving remediation costs unpaid. Furthermore, the moratorium under Section 14 suspends ongoing environmental enforcement during the Corporate Insolvency Resolution Process (CIRP). In the case of Subhankar Bhowmik v. In the Union of India (2022), the Supreme Court upheld the classification of environmental decree-holders as "other creditors," effectively subordinating their claims.

To overcome these obstacles, legislative reforms are necessary. Firstly, environmental claims should be accorded statutory super-priority, ensuring that remediation expenses financed by a proposed National Remediation Fund take precedence over secured creditors in cases of urgent public health risks. Secondly, facilities posing high environmental risks should be required to post securities or bonds for environmental performance that remain in effect throughout insolvency proceedings. Lastly, anti-avoidance provisions should be introduced, presuming that asset transfers made shortly before insolvency are intended to evade liability unless proven otherwise. These reforms would bring India's liability framework in line with the polluter-pays principle and help prevent remediation debts from being displaced during insolvencies.

6.6. Community Protection, Interim Relief and Compensation Design

Public consultation during the RAP stage represents a valuable procedural improvement. Additionally, it is crucial that where contamination poses an immediate exposure risk—such as contaminated drinking wells or airborne emissions from burning—interim relief measures like alternative water supplies, health camps, or relocations become mandatory and enforceable. The SBM toolkit highlights risks to nearby communities around major dumpsites (Ghazipur, Deonar, and Bandhwari), including methane emissions, open fires, and heavy metal exposure pathways. Consequently, the Rules should mandate immediate exposure mitigation as the default approach at sites with confirmed receptor exposure. Furthermore, baseline and ongoing epidemiological monitoring, along with clearly defined compensation procedures for health damages related to remediation, should be instituted. Courts have previously ordered such precautions in several litigations.

6.7. Land-Transaction Safeguards and Redevelopment Governance

A common tactical issue is the premature redevelopment of contaminated land before remediation is complete, which can shift liability and public costs onto residents and future government actions. Currently, the regulations mandate Gazette notification but lack an automatic, registrable encumbrance on land titles or a municipal permit requirement such as "no change of land use/no building permit until remediation is approved." Without these tools, remediation efforts lack leverage, while commercial pressures for redevelopment remain strong. Similar to China, proper incentivization of redevelopment can be achieved through tax benefits and adjusted land rate (Fiedler & Pachon 2018, Meng et al. 2012).

7. CONCLUSION

The Environment Protection (Management of Contaminated Sites) Rules, 2025, have finally transformed decades of judicial principles and policy rhetoric into an effective legal framework for addressing India's historic contamination issues. These Rules establish a logically ordered process encompassing identification, verification, declaration, remediation, and monitoring. Additionally, they enhance transparency and public participation through mandated disclosure of records, marking a positive development in governance.

The 2025 Rules also signify a clear shift from the campaign-focused approach of the Swachh Bharat Mission (SBM) to a statutory system dedicated to the challenging, less glamorous task of remediation. While SBM successfully raised awareness and improved sanitation infrastructure, its legacy waste efforts stagnated by 2023, leaving nearly 177 million tonnes of untreated waste at dumpsites and allowing high-profile locations such as Ghazipur, Deonar, and Bandhwari to continue expanding despite multiple deadlines. The new contaminated site regime aims to rectify these shortcomings by precisely defining contaminated sites, enforcing public disclosure, establishing liability, and requiring scientifically-based remedial action plans.

The key challenge is preventing the 2025 Rules from repeating the implementation failures that undermined the SBM's legacy waste agenda. As this paper has shown, the Rules succeed in creating a coherent legal framework by clearly defining contaminated sites, mandating disclosure, and assigning liability, but remain structurally limited by the absence of a dedicated remediation fund, insufficient regulatory capacity, and the lack of harmonized contaminant standards and community safeguards.

Therefore, addressing these gaps is indispensable for successfully solving the legacy waste problem. CERCLA-style up-front funding, EU-style risk-based prioritization, and China's central-technical/local-delivery structure offer focused comparative elements suited to India's federal constraints. The Rules must move from a formally sound regulatory architecture to a practically enforceable remediation regime capable of reclaiming contaminated land and protecting vulnerable populations. In this sense, the Rules function not merely as a legislative milestone but as a test of India's ability to shift from symbolic environmental campaigns to a sustained, science-led system of governance.

8. REFERENCES

Akerboom, S. and Craig, R.K.1022. How law structures public participation in environmental decision making: A comparative law approach. *Environmental Policy and Governance*, 32(3), pp.232–246. [DOI]

Alapati, U., Begum, F., Surinaidu, L., Jayaraja, N. and Nandan, M., 2023. Persistence of heavy metals and human health risk assessment in the South Indian industrial area. *AQUA – Water Infrastructure, Ecosystems and Society*, 72(6), pp.898–913. [DOI]

Birnie, P., Boyle, A. and Redgwell, C., 2021. *International Law and the Environment*. 4th edn. Oxford University Press.

Bugge, H.C., 2009. The polluter pays principle: Dilemmas of justice in national and international contexts. In: J. Ebbesson and P. Okowa (eds.) *Environmental Law and Justice in Context*. Cambridge University Press, pp.411–428. [DOI]

Caney, S., 2005. Cosmopolitan justice, responsibility, and global climate change. *Leiden Journal of International Law*, 18(4), pp.747–775. [DOI]

Carbon Copy, 2025. India's Contaminated Sites Rules Need Dynamic Contaminant Lists to Keep Pace with Science. Policy Note, August 2025. Retrieved October 5, 2025, from https://carboncopy.info/environment-ministry-notifies-rules-for-management-of-contaminated-sites/

Central Pollution Control Board (CPCB), 2009. *Comprehensive Environmental Pollution Index Reports and Action Plans*. New Delhi. Retrieved September 16, 2025, from https://cpcb.nic.in/

Central Pollution Control Board (CPCB), 2025. *Annual Report on National Inventory of Contaminated Sites, 2024–25*. CPCB. Retrieved September 16, 2025.

Comptroller and Auditor General of India (CAG), 2023. *Report No. 30 of 2023 – Compliance Audit of Ministry of Environment, Forest and Climate Change, Environment Relief Fund Accounts (2019–2023)*. CAG.

Etemire, U., 2023. Public voices and environmental decisions: The Escazú Agreement in comparative perspective. *Transnational Environmental Law*, 12(1), pp.175–199. [DOI]

Fiedler, L. and Pachon, C., 2018. Recent trends in the selection of remedies for groundwater, soil, and sediment at Superfund sites. *Groundwater Monitoring & Remediation*, 38(1), pp.13–18. [DOI]

Lees, E., 2016. The polluter pays principle and the remediation of land. *International Journal of Law in the Built Environment*, 8(1), pp.45-62. [DOI]

Meng, X., Zhang, Y., Zhao, Y., Lou, C. and Gao, J., 2012. Review of Chinese environmental risk assessment regulations and case studies. *Dose-Response*, 10(2), pp.201–214. [DOI]

Ministry of Environment, Forest & Climate Change (MoEFCC), 2025. *Notification S.O. 3401(E): Environment Protection (Management of Contaminated Sites) Rules, 2025*. MoEFCC.

Ministry of Housing & Urban Affairs (MoHUA) / Centre for Science and Environment (CSE), 2023. *Toolkit on Legacy Waste Management and Dumpsite Remediation*. MoHUA/CSE.

National Environmental Engineering Research Institute (NEERI), 2024. *Leachate Composition Studies in Major Indian Dumpsites*. NEERI, p.155.

People's Republic of China (PRC), 2019. *Soil Pollution Prevention and Control Law*. Standing Committee, National People's Congress.

Richardson, B.J., 2017. Environmental law and democratic participation: Legal theory and empirical reality. In: D. Fisher and L. Kotzé (eds.) *Research Handbook on Fundamental Concepts of Environmental Law*. Edward Elgar, pp.210–230. [DOI]

Ruppel, O.C., 2023. The human right to public participation in environmental governance. *Environmental Policy and Law*, 53(2), pp.85–102. [DOI]

Sadeleer, N.D., 2000. *Environmental Principles: From Political Slogans to Legal Rules*. Oxford: Oxford University Press, p.432.

Sands, P. and Peel, J., 2018. *Principles of International Environmental Law*. 4th edn. Cambridge: Cambridge University Press. [DOI]

Selvaraj, S., Gaonkar, O., Kumar, B., et al., 2021. Legacy persistent organochlorine pollutants and polycyclic aromatic hydrocarbons in the

surface soil from the industrial corridor of South India: Occurrence, sources and risk assessment. *Environmental Geochemistry and Health*, 43, pp.2105–2120. [DOI]

Subudhi, S., Pati, A.K., Bose, S., Sahoo, S., Pattanaik, A. and Acharya, B.M., 2025. Integrating boosted learning with differential evolution (DE) optimizer: A prediction of groundwater quality risk assessment in Odisha. *Journal of Environmental Informatics*, 45(2), pp. 112-128.

Times of India, 2025. NGT Orders Inspection at Bandhwari Landfill After Reports of Leachate into Aravallis. Retrieved October 5, 2025, from https://timesofindia.indiatimes.com/city/gurgaon/ngt-orders-checks-at-bandhwari-landfill-in-a-week-after-leachate-spills-into-aravalis-in-haryana/articleshow/123418462.cms

United States Environmental Protection Agency (US EPA), 2025. *Superfund National Priorities List (NPL): Data and Site Profiles*. EPA.

United States Government Accountability Office (GAO), 2025. *Superfund Program: Costs, Timelines and Challenges in Remediation*. GAO, p.88.

Vinaules J. E., 2024. Comparing environmental law systems. *International and Comparative Law Quarterly*, 73(1), pp.247–258. [DOI]f

Weis, L.K., 2018. Environmental constitutionalism: Aspiration or transformation? *International Journal of Constitutional Law*, 16(3), pp.836–870. [DOI]

Nature Environment and Pollution Technology
An International Quarterly Scientific Journal

p-ISSN: 0972-6268
(Print copies up to 2016)
e-ISSN: 2395-3454

Vol. 25 | No. 3 | Article ID D1867 | 2026

Original Research Paper

https://doi.org/10.46488/NEPT.2026.v25i03.D1867

Open Access Journal

Influence of Agricultural Waste as a Partial Substitute for Cement in Flowing Concrete for a Sustainable Environment

Nurul Rochmah[1,5]†, Antariksa[2], Wisnumurti[3] and Bambang Semedi[4]

[1]Postgraduate Study of Environmental Science, Brawijaya University, Malang, Indonesia
[2]Department of Architecture Engineering, Brawijaya University, Malang, Indonesia
[3]Department of Civil Engineering, Brawijaya University, Malang, Indonesia
[4]Department of Utilization of Fisheries and Marine Resources, Brawijaya University, Malang, Indonesia
[5]Department of Civil Engineering, Universitas 17 Agustus 1945, Surabaya, Indonesia
†Corresponding author: Nurul Rochmah; nuuruul889@gmail.com

Abbreviation: Nat. Env. & Poll. Technol.
Website: www.neptjournal.com

Received: 08-09-2025
Revised: 18-11-2025
Accepted: 26-11-2025

Key Words:

Compressive strength
Corn cob ash
Flowing concrete
Rice husk ash
Sugarcane bagasse ash
Sustainable environment

Citation for the Paper:

Rochmah, N., Antariksa, Wisnumurti and Semedi, B., 2026. Influence of agricultural waste as a partial substitute for cement in flowing concrete for a sustainable environment. *Nature Environment and Pollution Technology*, 25(3), D1867. https://doi.org/10.46488/NEPT.2026.v25i03.D1867

Note: From 2025, the journal has adopted the use of Article IDs in citations instead of traditional consecutive page numbers. Each article is now given individual page ranges starting from page 1.

Copyright: © 2026 by the authors
Licensee: Technoscience Publications
This article is an open access article distributed under the terms and conditions of the Creative Commons Attribution (CC BY) license (https://creativecommons.org/licenses/by/4.0/).

ABSTRACT

Large quantities of corn cobs, rice husks, and sugarcane bagasse are often burned or left to decay, contributing to air pollution and greenhouse gas emissions in many rural areas of Indonesia. However, earlier studies indicated that the ashes from these agricultural wastes have the potential to serve as partial substitutes for cement in concrete production, reducing environmental pollution. Because of their rich silica composition, the pozzolanic properties of corn cob ash (CCA), rice husk ash (RHA), and sugarcane bagasse ash (SBA) can improve the long-term performance of concrete. This research investigated the use of rice husk ash, sugarcane bagasse ash, and corn cob ash as alternative materials for partially replacing cement, focusing on their effects on the flowing concrete with the addition of Sika-Viscocrete as a superplasticizer. This study examined the properties of flowing concrete, including unit weight, compressive strength, and the efficiency of cement utilization. The unit weight of concrete was tested following SNI 1973:2008, while its compressive strength was evaluated in accordance with SNI 1974:2011. This study applied statistical analysis and linear regression. Experimental findings showed that the measured unit weight values were consistently within the interval of 2300-2500 $kg.m^{-3}$ and, according to the measured unit weight, the concrete was considered normal-weight concrete. The highest compressive strength obtained was 35.22 MPa at 7% variation of corn cob ash, and the highest efficiency in cement utilization was observed in flowing concrete with corn cob ash substitution. This is because among the alternatives, corn cob ash achieved the greatest strength improvement per unit of cement at 1.13 MPa per $kg.m^{-3}$. Statistical analysis revealed the effect of substitution levels, and the regression analysis yielded several data-based equations. Employing agricultural waste ash as a partial cement substitute provides a sustainable pathway toward reducing overall cement consumption.

1. INTRODUCTION

In Indonesia, the accumulation of agricultural wastes such as rice husks, sugarcane bagasse, and corn cobs is becoming a significant environmental concern. Indonesia is known as an agricultural country where people mostly work as farmers. Rice milling generates rice husk waste in the form of rice husks, amounting to 20-30% of the total rice production (Budiarti et al. 2023, Faried et al. 2021). Based on information from the Central Statistics Agency in 2025, Indonesia's rice production was approximately 53.14 million tons, so the amount of husk obtained was more than 10 million tons (BPS 2025). According to BPS (2024), sugarcane plantations in Indonesia in 2023 amounted to 489.34 thousand hectares, and they produced 2.23 million tons of sugar. In general, the bagasse produced from one sugar factory was 32% (Legiso et al. 2020), so the sugarcane bagasse produced is around 700,000 tons. In 2024, the corn harvest area was 2.55 million hectares (BPS 2025). From

that area, it produced 15.14 million tons of corn kernels, or around 5.94 tons per hectare. This amount is likely to increase every year. As the amount of corn kernels produced increases, so does the amount of corn cob waste. There will normally be an accumulation of waste because the natural process of waste decomposition is slow. This may become an issue if the waste is not handled correctly.

However, earlier studies revealed that the ashes from rice husk, sugarcane, and corn cobs contained silicon dioxide (SiO_2), suggesting that they could be utilized to make concrete or other building materials. A pozzolan is generally described as a material that is either siliceous or a combination of aluminous and siliceous components. On its own, it exhibits little to no cementing ability; however, when moisture is present, and it interacts with calcium hydroxide at normal temperatures, it produces compounds with strong cementitious properties. In concrete production, pozzolans are often utilized as supplementary minerals. Within cementitious systems, their role is particularly significant in promoting the formation of calcium silicate hydrate. Among the various options, agricultural and industrial by-product pozzolans are regarded as the most practical alternatives for advancing sustainable binder development (Albiajawi et al. 2022). From previous research, rice husk ash contains 88% silica (Sudarsan et al. 2023), corn cob ash contains 66.38% silica (Adesanya & Raheem 2010), and sugarcane bagasse ash contains 75% silica (Maglad et al. 2023). This indicates that ashes derived from agricultural residues possess pozzolanic properties. When these materials react with calcium hydroxide, they generate calcium silicate hydrate (C-S-H), a compound that enhances the binding of concrete components and contributes to improved material performance.

In Indonesia, there is a problem in the field of construction materials that contributes to environmental degradation, namely the negative effects of cement production. In 2023, Indonesia was ranked 8th among the world's cement producers (CNBC 2024). This contributes to environmental degradation because the production of cement releases CO_2 into the air, causing the greenhouse effect. According to Ali et al. (2011) and Fayomi et al. (2019), the manufacture of one kilogram of cement is estimated to release about 0.5–0.9 kilograms of CO_2. The rise in CO_2 emissions contributes to various environmental issues, including flooding, global temperature increases, and biodiversity loss (Dziejarski et al. 2023). Cement production contributes 8% of global CO_2 emissions, with annual cement production reaching about 4 billion tons a year (Chatham 2018).

Concrete remains the material that is most often applied in construction due to its adaptability, mechanical strength, and economic advantages. Among various assessment techniques, the compressive strength test is regarded as the most fundamental and widely implemented. This method yields essential insights into how concrete responds to axial compressive loads, which is critical for maintaining structural safety and reliability in both buildings and infrastructure projects (Yankelevsky 2024). In addition, the unit weight of concrete represents a key physical property that indicates the density and compactness of the material, measured in kilograms per cubic meter ($kg.m^{-3}$). This characteristic is central to categorizing concrete into three primary groups: lightweight concrete (generally less than 1900 $kg.m^{-3}$), normal-weight concrete (2200–2500 $kg.m^{-3}$), and heavyweight concrete (greater than 2500 $kg.m^{-3}$) as defined in the Indonesian National Standard (SNI 03-2847-2002). Such classification is significant because each type of concrete is designed to fulfill different structural and functional requirements. For instance, lightweight concrete is typically applied in non-structural elements and for its insulating properties; normal-weight concrete is the standard choice for most structural works, while heavyweight concrete is employed in specialized contexts such as radiation barriers and counterbalancing structures.

According to Trimurtiningrum & Subakti (2016), flowing concrete refers to a mix with exceptionally high workability and a slump value of more than 19 cm (7.5 inches) without segregation and bleeding. Flowing concrete contains coarse aggregates, water, fine aggregates, cement, and chemical admixtures. Flowing concrete can be formed using small sizes of coarse aggregate, a low water-cement ratio, and a superplasticizer. In this study, the superplasticizer material used was ViscoCrete®-3115N. This product can create a high-flow value of concrete; therefore, it can support the formation of concrete with high workability. Flowing concrete can be used to reduce costs due to the minimal compaction process, can speed up construction, and reduce the number of workers, as flowing concrete is relatively easier to compact itself with less assistance from compaction tools than normal concrete.

Considering the above, further efforts need to be made to minimize harmful environmental consequences. Over the last decade, concrete manufacture has led to the development of environmentally friendly concrete (Nomani et al. 2025). According to Verian et al. (2018), environmentally sustainable concrete is mainly produced by partially replacing cement with industrial and agricultural residues, while also utilizing recyclable materials and wastes as aggregate substitutes. In this study, efforts were made to minimize the use of cement by using waste materials in the form of sugarcane bagasse ash (SBA), rice husk ash (RHA),

and corn cob ash (CCA) as a partial substitute for cement for the manufacture of flowing concrete materials. This research used flowing concrete test specimens with Sika-Viscocrete as the superplasticizer. This research investigated the use of sugarcane bagasse ash (0%, 2.5%, 5%, 7.5%, and 10%), rice husk ash (0%, 5%, 7.5%, 10%, and 12.5%), and corn cob ash (0%, 4%, 5%, 7%, and 9%) as partial cement replacements in flowing concrete. This study examined the properties of flowing concrete, including unit weight, compressive strength, and the efficiency of cement utilization. The unit weight of concrete was tested following SNI 1973-2008, while its compressive strength was evaluated in accordance with SNI 1974-2011. This study applied statistical analysis and linear regression.

2. MATERIALS AND METHODS

2.1. Materials

This study used the following main materials (Fig. 1):

1. **Coarse Aggregate:** The coarse aggregate employed was crushed stone gravel. Two size gradations were utilized, namely 5–10 mm and 10–20 mm. The mixture proportion consisted of 75% coarse aggregate with a size of 10–20 mm and 25% with a size of 5–10 mm. The percentage combination of these aggregates was determined through a trial-and-error method to obtain an appropriate gradation for the concrete mix.
2. **Fine aggregate**: The fine aggregate employed was natural sand obtained from Lumajang. Based on a proportioning process conducted through trial-and-error analysis, the mix composition was established at 52% fine aggregate and 48% coarse aggregate, ensuring an appropriate balance in particle gradation for the concrete mixture.
3. **Water:** The water utilized was tap water supplied by the local municipal system (PDAM). A visual inspection was conducted to ensure its quality, confirming that the water was clear and free from impurities such as silt, oil, and salts.
4. **Cement:** The type of cement applied was Portland Composite Cement (PCC), which was selected due to its suitability for concrete production and compliance with standard construction requirements.
5. **Superplasticizer:** The superplasticizer employed was ViscoCrete–3115N, incorporated at a dosage of 1.5% by weight of cement.
6. **Cement Substitution:** Cement substitution in this study was carried out using supplementary materials such as sugarcane bagasse ash, rice husk ash, and corn cob ash, all of which were processed to pass through a No. 200 sieve.

2.2. Flow Chart

This research investigated the use of sugarcane bagasse ash (0%, 2.5%, 5%, 7.5%, and 10%), rice husk ash (0%, 5%, 7.5%, 10%, and 12.5%), and corn cob ash (0%, 4%, 5%, 7%, and 9%) as partial cement replacements in flowing concrete. As shown in Fig. 2, this study examined the properties of flowing concrete, including unit weight, compressive strength, cement utilization efficiency, statistical analysis, and linear regression.

The percentage variations employed in this study were determined with consideration of previous research



Fig. 1: Materials used in this study: (a) coarse aggregate; (b) fine aggregate; (c) cement; (d) water; (e) superplasticizer.

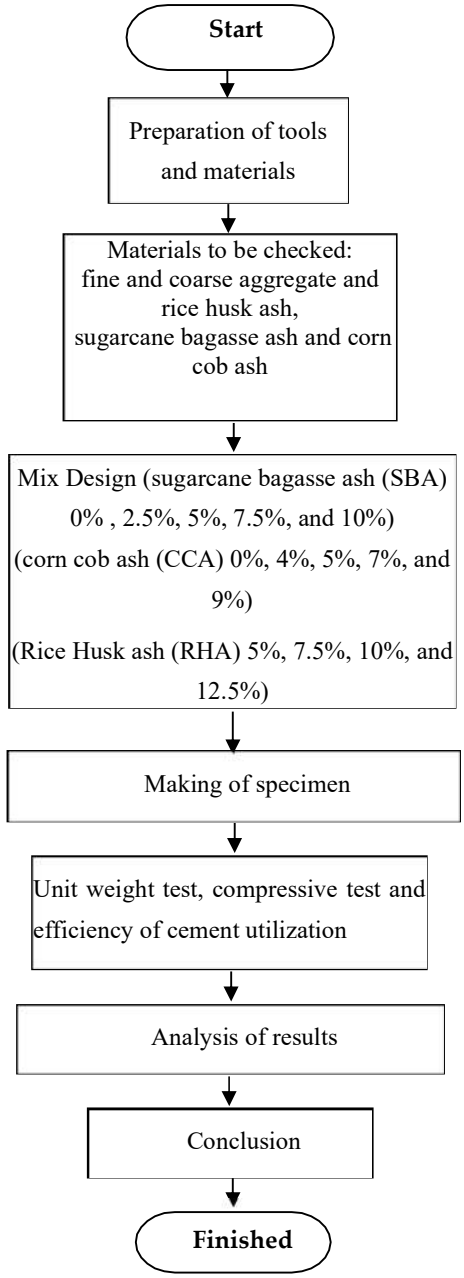


Fig. 2: Flowchart of the research.

findings, and the relevant studies, along with their underlying justifications, are presented below:

Research on the incorporation of sugarcane bagasse ash in cementitious materials has yielded encouraging outcomes. One study employed substitution levels of 0%, 5%, 10%, 15%, 20%, and 25% of the cement weight, demonstrating that partial replacement with sugarcane bagasse ash produced compressive strengths surpassing the design target, with the most substantial enhancement observed at the 5% level (Rompas et al. 2013). Further evidence is provided by Wiyono et al. (2017), who utilized sugarcane bagasse ash in mortar mixtures at 0%, 2%, 4%, 6%, 8%, and 10%. Their findings indicate that the 8% replacement achieved the lowest water absorption and delivered the highest compressive strength among the evaluated mixtures. In view of these prior results, the present study adopts bagasse ash substitution levels of 0%, 2.5%, 5%, 7.5%, and 10%. The selected range reflects concentrations identified in earlier research as yielding optimal mechanical performance, whereas higher replacement levels within the 15%–25% interval have generally been associated with reduced compressive strength.

Suhirkam & Dafrimon (2014) investigated concrete incorporating rice husk ash in combination with a superplasticizer. In their study, a portion of the cement was replaced with rice husk ash at levels of 2.5%, 5%, 7.5%, and 10%, with the highest compressive strength recorded at the 10% substitution. Similarly, Yulianto & Mukti (2015) examined the influence of rice husk ash replacement on the compressive strength of concrete using a mix proportion of 1 part cement, 2 parts sand, and 3 parts coarse aggregate. Their investigation employed substitution levels of 5%, 10%, and 15%, where previous findings identified 5% as the most effective proportion, while a marked reduction in compressive strength occurred at 15%. In consideration of these prior results, the present study adopts rice husk ash substitution levels of 0%, 5%, 7.5%, 10%, and 12.5%, as earlier research consistently indicated that the optimal performance lies within this range.

Hepiyanto & Firdaus (2019) conducted an experimental study employing corn cob ash as an auxiliary material to evaluate its effect on the compressive strength of concrete. Replacement levels of 0%, 4%, 8%, and 12% of the cement mass were assessed, and the findings revealed that all mixtures achieved compressive strengths exceeding the design requirement, with the most favorable result observed at the 4% substitution. Subsequently, research by Handayani (2020) explored the use of corn cob ash as a partial cement replacement at proportions of 0%, 3%, 5%, 7%, and 9%. Their results demonstrated that the 7% mixture produced the highest compressive strength, and the same proportion yielded the optimum flexural strength of beam specimens at the corresponding age. Drawing upon the trends identified in these previous investigations, the present study adopts substitution levels of 0%, 4%, 5%, 7%, and 9% of the cement weight. This range was selected because prior studies consistently indicated that the optimal mechanical performance occurs within these intervals.

Table 1: Proportion of corn cob ash (CCA) in flowing concrete.

Material	CCA (0 %)	CCA (4 %)	CCA (5 %)	CCA (7 %)	CCA (9 %)
Cement (kg.m^{-3})	455.5	449.9	448.5	445.5	442.4
Water (kg.m^{-3})	202.7	202.7	202.7	202.7	202.7
Coarse Aggregate (5-10 mm) (kg.m^{-3})	202.5	200.9	200.6	199.8	198.9
Coarse Aggregate (10-20 mm) (kg.m^{-3})	628.5	623.8	622.5	620.0	617.5
Fine Aggregate (kg.m^{-3})	920.8	913.9	912.01	908.4	904.7
Superplasticizer (kg.m^{-3})	6.83	7.030	7.081	7.185	7.293
Corn Cob Ash (kg.m^{-3})	0	18.75	23.60	33.53	43.76

Table 2: Proportion of sugarcane bagasse ash (SBA) in flowing concrete.

Material	SBA (0 %)	SBA (2.5 %)	SBA (5 %)	SBA (7.5 %)	SBA (10 %)
Cement (kg.m^{-3})	455.5	452.07	448.5	444.7	440.9
Water (kg.m^{-3})	178.2	178.6	178.7	178.8	178.9
Coarse Aggregate (5-10 mm) (kg.m^{-3})	199.1	198.1	197.1	196.1	195.0
Coarse Aggregate (10-20 mm) (kg.m^{-3})	616.6	613.8	610.6	607.4	604.1
Fine Aggregate (kg.m^{-3})	918.4	914.0	909.4	904.6	899.7
Superplasticizer (kg.m^{-3})	6.83	6.95	7.08	7.2	7.35
Sugarcane Bagasse Ash (kg.m^{-3})	0	11.59	23.6	36.1	48.98

Table 3: Proportion of rice husk ash (RHA) in flowing concrete.

Material	RHA (0 %)	RHA (5 %)	RHA (7.5 %)	RHA (10 %)	RHA (12.5 %)
Cement (kg.m^{-3})	455.5	448.5	444.7	440.9	436.8
Water (kg.m^{-3})	186.5	186.7	186.8	186.9	186.9
Coarse Aggregate (5-10 mm) (kg.m^{-3})	194.4	192.5	191.5	190.4	189.3
Coarse Aggregate (10-20 mm) (kg.m^{-3})	598.1	592.1	589.0	585.7	582.4
Fine Aggregate (kg.m^{-3})	890.4	881.6	876.9	872.1	867.1
Superplasticizer (kg.m^{-3})	6.83	7.8	7.21	7.3	7.5
Rice Husk Ash (kg.m^{-3})	0	23.6	36.06	48.9	62.4

2.3. Flowing Concrete Mix Proportion

This study designed the flowing concrete mixture according to the provisions of SNI 03–2834–2000: Procedures for normal concrete mix design and the EFNARC guidelines. The water-to-powder ratio (w/p), which represents the proportion between the amount of water and the powder materials used, was set at 0.45. This ratio was established through laboratory experiments. A series of trial-and-error tests in the laboratory resulted in a proportion of 52% fine aggregate and 48% coarse aggregate. Furthermore, the coarse aggregate fraction was composed of 75% aggregate with a particle size of 10–20 mm and 25% aggregate with a particle size of 5–10 mm. The mix proportions for each variation are presented in Tables 1, 2, and 3.

Flowing concrete was prepared by substituting a portion of the cement with rice husk ash (RHA), with replacement ratios of 0%, 5%, 7.5%, 10%, and 12.5%. A total of 15 cylindrical specimens with dimensions of 15 cm × 30 cm were subjected to compressive strength testing at the curing ages of 7, 21, and 28 days, resulting in 45 specimens. Similarly, flowing concrete containing sugarcane bagasse ash (SBA) as a cement substitute was prepared with replacement ratios of 0%, 2.5%, 5%, 7.5%, and 10%. Another 45 cylindrical specimens of identical dimensions were prepared and later tested for their compressive strength at 7, 21, and 28 days. In addition, flowing concrete was developed using corn cob ash (CCA) as a partial substitute for cement at various replacement levels of 0%, 4%, 5%, 7%, and 9%. For this series, 45 cylindrical specimens measuring 15 cm × 30 cm were also tested at the same curing ages. Thus, the overall total of test specimens prepared in this research was 135. The specimen preparation and testing setup are shown in Fig. 3.

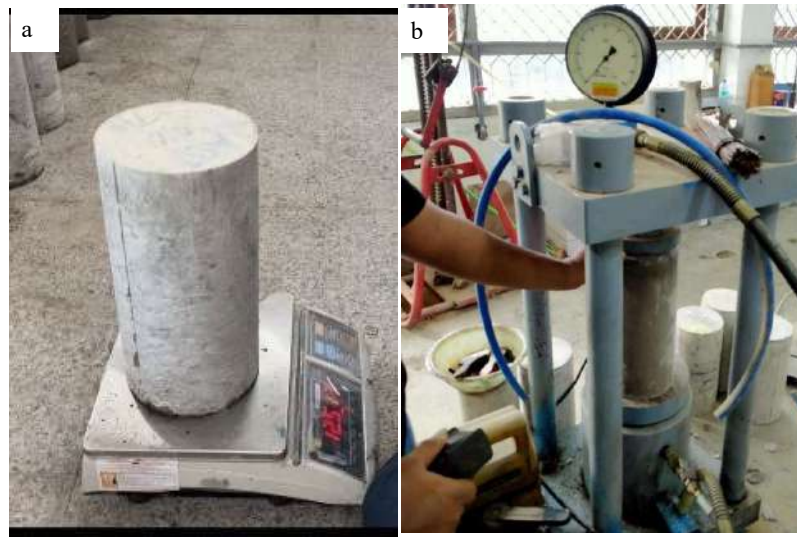


Fig. 3: Testing setup: (a) unit-weight measurement; (b) compressive strength test.

2.4. Testing of Specimens

2.4.1. Unit Weight (Density)

The property of unit weight, often referred to as density, plays an essential role in concrete and is evaluated using the standards specified in SNI 1973:2008. The density measurement is undertaken to verify the actual density of the concrete prior to its application. In this standard, the calculation of unit weight is performed using a specific formula provided in SNI 1973:2008.

$$D = \frac{M_c - M_m}{V_m} \quad ...(1)$$

Where: D = Density ($kg.m^{-3}$)

Mc = Weight of measuring vessel filled with concrete (kg)

Mm = weight of the container (kg)

Vc = the container's volume (m^3)

2.4.2. Compressive Strength Test

Concrete's compressive resistance is the measure of its capacity to resist compressive loads when tested with a compression load testing device. In this method, the specimen is placed in the apparatus and subjected to a steadily increasing load until it fails. The peak load sustained at the point of fracture is taken as the compressive strength value, as specified in SNI 1974:2011. The formula below may be applied to compute the compressive strength of flowing concrete.

$$f'c = \frac{p}{A} \quad ...(2)$$

Where: $f'c$ = Concrete compressive strength (MP_a)

A = the sectional area of the tested sample (nm^2)

P = compressive load (N)

2.5. Statistical Analysis

In this research, the statistical analysis employed an ANOVA (Analysis of Variance). A one-way ANOVA was applied to evaluate the effect of incorporating various proportions of agricultural waste ash as a partial substitution in flowing concrete. The hypotheses were formulated as follows: the null hypothesis (H0) states that the substitution levels exert no significant influence on the characteristic properties of the flowing concrete, whereas the alternative hypothesis (H1) posits that the different substitution percentages produce a measurable effect on these properties. The decision-making procedure relied on comparing the significance value (sig.) generated by the SPSS output with the predetermined significance level (α). The criteria were defined as: (a) when the SPSS significance value exceeds α = 0.05, the null hypothesis is accepted; and (b) when the SPSS significance value is below α = 0.05, the null hypothesis is rejected.

However, preliminary assumptions required verification before conducting the ANOVA test. One essential prerequisite was the assessment of data normality to ensure that the distribution of the experimental results met the fundamental conditions for valid variance comparison. The dataset must exhibit a normal distribution, as normality testing constitutes a mandatory requirement prior to conducting parametric statistical analysis. When this assumption is not fulfilled, the analysis should be redirected to a non-parametric approach, specifically the Kruskal–Wallis test. The normality criterion

Table 4: Results of the normality test of unit weight.

Group Statistic		Kolmogorov-Smirnov[a]			Shapiro-Wilk		
		df	Sig.	Statistic	df	Sig.	
Value	Corn cob ash	0.091	15	0.200*	0.983	15	0.986
	Rice Husk Ash	0.155	15	0.200*	0.931	15	0.286
	sugarcane bagasse ash	0.124	15	0.200*	0.981	15	0.976

Table 5: Results of the ANOVA test of unit weight.

Value					
	Sum of Squares	df	Mean Square	F	Sig.
Between Groups	112371.054	2	56185.527	136.234	0.000
Within Groups	17321.620	42	412.420		
Total	129692.673	44			

Table 6: Results of the normality test of compressive strength.

Group Statistic		Kolmogorov-Smirnov[a]			Shapiro-Wilk		
		df	Sig.	Statistic	df	Sig.	
Value	Corn cob ash	0.189	15	0.158	0.921	15	0.201
	Rice Husk Ash	0.165	15	0.200*	0.959	15	0.673
	sugarcane bagasse ash	0.160	15	0.200*	0.974	15	0.912

Table 7: Results of the ANOVA test of compressive strength.

Value					
	Sum of Squares	df	Mean Square	F	Sig.
Between Groups	335.702	2	167.851	9.231	0.000
Within Groups	763.679	42	18.183		
Total	1099.382	44			

is determined through the significance value, where a result of Sig. < 0.05 indicates that the data deviate from a normal distribution, while Sig. > 0.05 signifies that the data conform to the assumption of normality.

The results of Table 4 show that a normal distribution is confirmed for the data because the Sig value obtained from the SPSS output is Sig. > 0.05 significance.

The results of Table 5 show that when the significance value is below $\alpha = 0.05$, the null hypothesis is rejected and the alternative hypothesis (H1) is accepted. It means that the different substitution percentages produce a measurable effect on unit weight.

The results of Table 6 show that a normal distribution is confirmed for the data because the significance value obtained from the SPSS output is Sig. > 0.05.

The results of Table 7 show that when the significance value is below $\alpha = 0.05$, the null hypothesis is rejected and the alternative hypothesis (H1) is accepted. It means that the different substitution percentages produce a measurable effect on compressive strength.

3. RESULTS AND DISCUSSION

3.1. Density (Unit-Weight)

The specimens were used to calculate the unit weight of flowing concrete. Fig. 4 shows how the unit weight of flowing concrete is affected by the substitution of the three agricultural waste–based ashes used in this study.

The graph shows that the highest and the lowest unit weight of the flowing concrete are for rice husk ash (RHA) and corn cob ash (CCA), respectively. The unit weight of concrete with rice husk ash substitution shows an increasing trend within the 0–10% range, and it is the same as reported by previous research (Hou 2024), which shows that the reactive SiO_2 and Al_2O_3 present in rice husk ash interact with $Ca(OH)_2$, promoting the formation of hydration products and contributing to void filling in the range of 3–12%. At a substitution level of 2.5% sugarcane bagasse ash, the density shows an increase, which is close to previous research (Althaqafi et al. 2024), which said the substitution of sugarcane bagasse ash into concrete improves the unit weight of concrete through the action of small particles filling

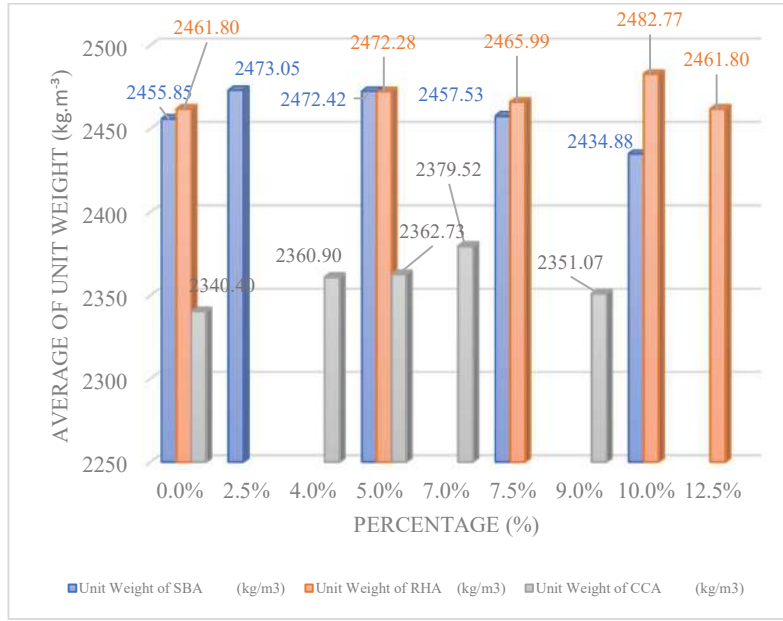


Fig. 4: Influence of rice husk, sugarcane bagasse, and corn cob ashes on the unit weight of flowing concrete.

the pores in the matrix. This densifies the microstructure and can nudge the hardened density upward at very small dosages. A decline in density is observed when sugarcane bagasse ash is substituted at levels beyond 2.5% (i.e., 5–10%), largely because of the comparatively low specific gravity of sugarcane bagasse ash, which is around 1.6–1.9, in contrast to ordinary Portland cement at about 3.15. When cement is partially replaced, the mixture becomes lighter per unit volume, resulting in reduced density in both fresh and hardened states (Memon et al. 2022, Daniel et al. 2024). In addition, the porous and irregular surface characteristics of sugarcane bagasse ash contribute to the formation of internal voids, further decreasing the compactness of the concrete (Althaqafi et al. 2024). While small replacement levels may enhance particle packing through a filler effect, larger proportions generally diminish density as the reduction in cementitious content outweighs any initial densification benefits (Iro et al. 2025). The same behavior is also noted in flowing concrete with the substitution of rice husk ash and with the substitution of corn cob ash. Based on the measured unit weight, the material falls within the range of normal concrete, which typically exhibits a density of about 2200–2500 kg.m^{-3} and is commonly applied in general structural works based on SNI 03-2847-2002.

Based on Fig. 5(a), the highest unit weight of flowing concrete was obtained at a 2.5% sugarcane bagasse ash replacement, reaching 2473.05 kg.m^{-3}, while the lowest value occurred at the 10% replacement level, measuring 2434.88 kg.m^{-3}. Relative to the mix without sugarcane bagasse ash (0%), the unit weight increased at the 2.5%, 5%, and 7.5% substitution levels, with a decrease observed only at 10%. The plotted data follow a linear regression trend described by the equation y = –229.86x + 2470.2.

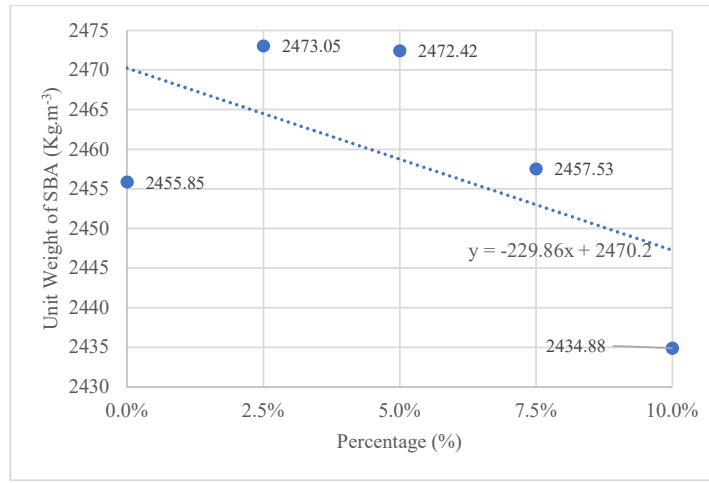
According to Fig. 5(b), flowing concrete achieved its highest unit weight at the 10% rice husk ash replacement level, reaching 2482.7 kg.m^{-3}, while the lowest values were recorded at 0% and 12.5%, both measuring 2461.8 kg.m^{-3}. Compared with the mixture without rice husk ash, the unit weight increased at the 5%, 7.5%, and 10% substitution levels. The trend in the plotted data is represented by the linear regression equation y = 47.611x + 2465.6.

Fig. 5(c) shows that the highest unit weight of flowing concrete occurred at the 7% corn cob ash replacement, reaching 2379.5 kg.m^{-3}, while the lowest value was obtained from the control mix (0%), measuring 2340.4 kg.m^{-3}. Compared with the mix without corn cob ash, increases in unit weight were observed at the 4%, 5%, 7%, and 9% substitution levels. The linear regression trend derived from the graph is expressed by the equation y = 218.3x + 2348.

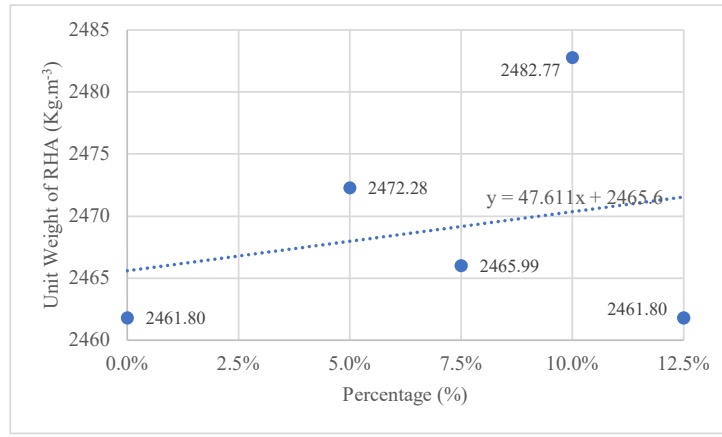
At the same 5% replacement level, the unit weights of flowing concrete were 2472.42 kg.m^{-3} for sugarcane bagasse ash, 2472.28 kg.m^{-3} for rice husk ash, and 2362.7 kg.m^{-3} for corn cob ash. The sequence from the highest to the lowest unit weight is: bagasse ash, rice husk ash, and finally corn cob ash.

3.2. Compressive Strength

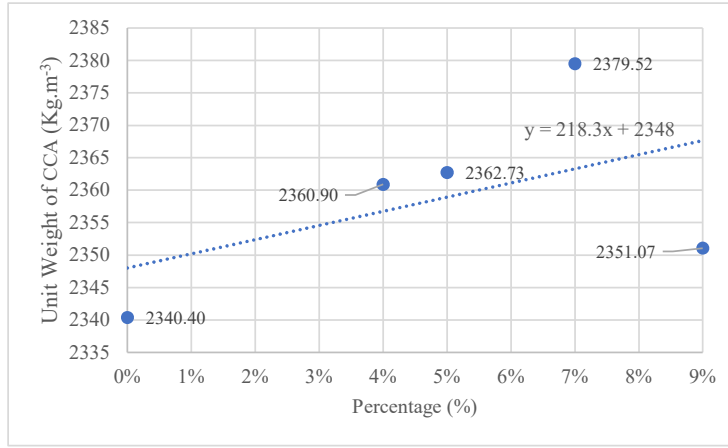
The average value of concrete's compressive strength with



(a)



(b)



(c)

Fig. 5: Linear regression of unit weight at various levels of (a) sugarcane bagasse ash, (b) rice husk ash, and (c) corn cob ash.

the substitution of agricultural waste–based ash is shown in Fig. 6. This figure highlights the effect of these substitutions on the development of compressive strength.

Fig. 6 shows how the substitution of sugarcane bagasse ash (SBA), rice husk ash (RHA), and corn cob ash (CCA) in the flowing concrete affected the compressive strength results. The mixture containing 7% CCA (35.22 MPa) achieves the peak level of compressive strength among all ash substitutions. In the substitution with rice husk ash, the mixture containing 10% RHA achieved the highest compressive strength, which is in agreement with the findings reported by Siddique et al. (2016), who stated that the concrete mix incorporating 10% RHA as a replacement for cement exhibited the highest improvement in compressive strength across all curing ages. Fig. 6 indicates that the substitution of these agricultural waste ashes generally leads to higher compressive strength in comparison with the control mix. This is because sugarcane bagasse ash (SBA), rice husk ash (RHA), and corn cob ash (CCA) contain silica at 75%, 88%, and 66%, respectively. It means that amorphous silica (SiO_2) can act as an alternative material for binding in concrete (Paul et al. 2019). As cement undergoes hydration, the silica in an amorphous state derived from agro-waste ashes reacts with Ca $(OH)_2$, producing additional calcium silicate hydrate (C–S–H). This pozzolanic reaction decreases porosity within the interfacial region of the cement paste and aggregates, thereby enhancing the bond strength and overall compactness of the matrix (Elawadly & Sanad 2025, Memon et al. 2022). The fine particles of sugarcane bagasse ash, corn cob ash, and rice husk ash also fill voids within the microstructure, which further improves adhesion and leads to denser concrete with higher compressive strength (Siddika et al. 2021). On the other hand, when the replacement level of these ashes exceeds the optimum threshold, the excess material tends to increase spacing between aggregates and reduce inter-particle friction. Beyond this limit, the surplus ash mainly behaves as an inert filler rather than reacting with $Ca(OH)_2$, causing a decline in strength (Daniel et al. 2024). Therefore, each ash type demonstrates an optimal substitution percentage at which strength is maximized, after which performance begins to decline.

According to Fig. 7(a), the highest compressive strength of the flowing concrete was recorded at the 2.5% sugarcane bagasse ash replacement, reaching 22.93 MPa, while the lowest value occurred in the control mix (0%), which achieved 20.24 MPa. Compared with the 0% substitution level, the compressive strength increased by 2.5%, 5%, 7.5%, and 10%. The linear regression trend from the plotted data is represented by the equation y = 7.916x + 21.175.

Fig. 7(b) indicates that the highest compressive strength of flowing concrete was achieved at the 10% rice husk ash replacement, reaching 26.53 MPa, while the lowest strength was observed at the 5% level, measuring 22.93 MPa. Relative to the 0% mixture, increases in compressive strength occurred at the 7.5% and 10% substitution levels, whereas decreases were recorded at 5% and 12.5%. The linear regression derived from the graph is expressed as y = 1.8054x + 24.412.

Fig. 7(c) shows that the highest compressive strength of flowing concrete occurred at the 7% corn cob ash replacement, reaching 35.22 MPa, while the lowest value

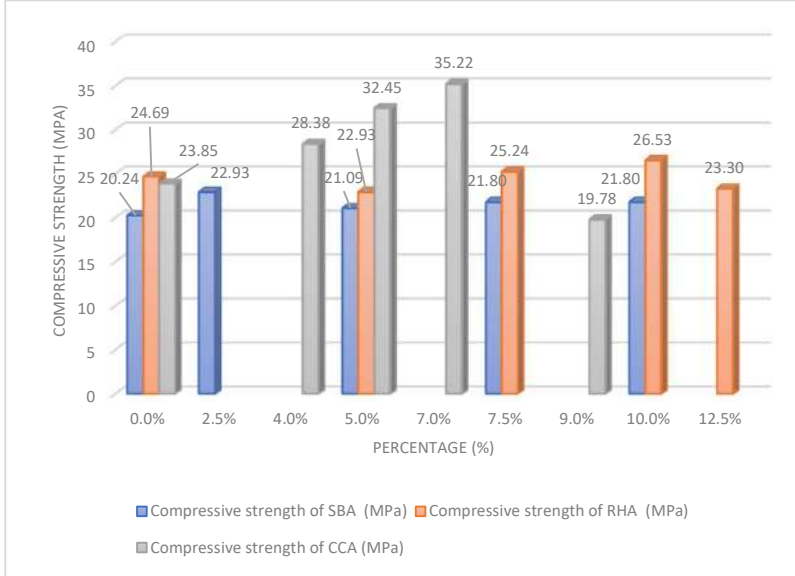
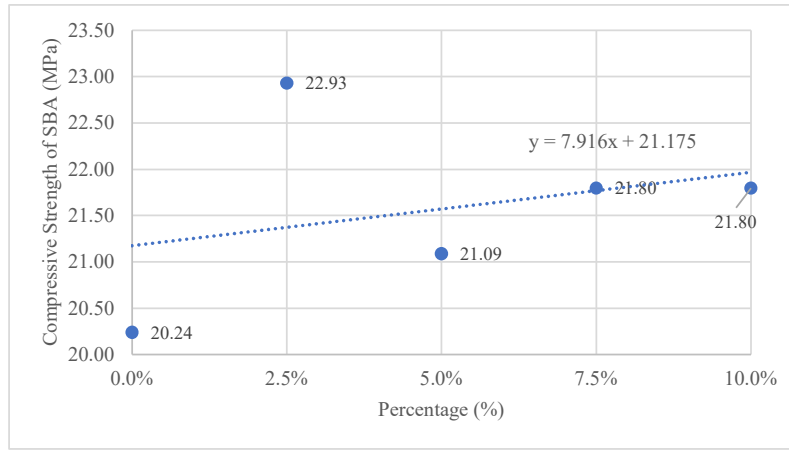
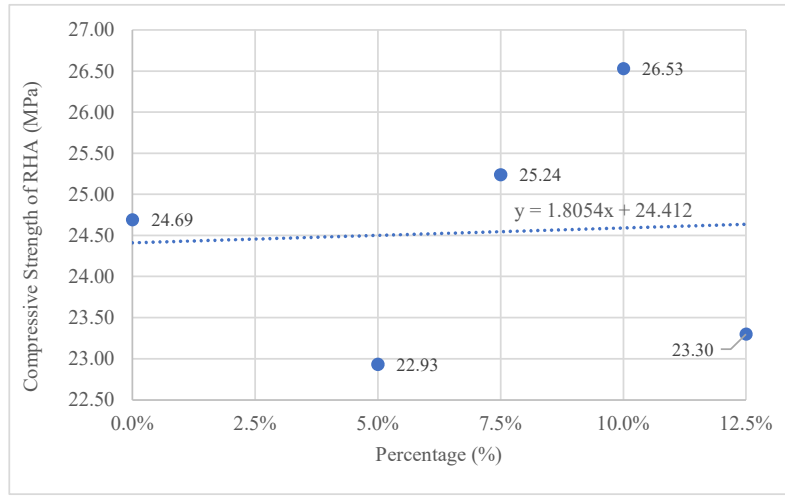


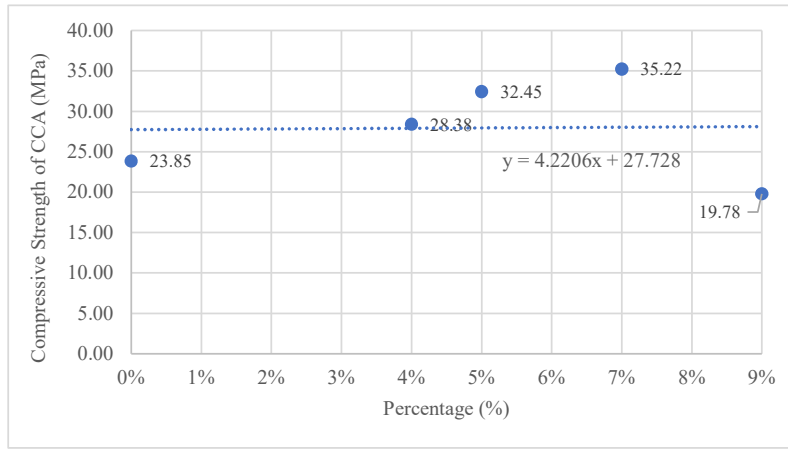
Fig. 6: Influence of rice husk, sugarcane bagasse, and corn cob ashes on the compressive strength of flowing concrete.



(a)



(b)



(c)

Fig. 7: Linear regression of compressive strength at various levels of (a) sugarcane bagasse ash, (b) rice husk ash, and (c) corn cob ash.

was recorded at 9%, measuring 19.78 MPa. Compared with the control mix (0%), increases in compressive strength were observed at the 4%, 5%, and 7% substitution levels, whereas a decrease occurred at 9%. The linear regression equation obtained from the plotted data is y = 4.2206x + 27.728

At the 5% replacement level, the compressive strengths recorded were 21.09 MPa for sugarcane bagasse ash, 22.93 MPa for rice husk ash, and 32.45 MPa for corn cob ash. The ranking from highest to lowest compressive strength is: corn cob ash, rice husk ash, and bagasse ash.

3.3. Efficiency of Cement Utilization

An example calculation used to derive the values presented in Table 8.

- Difference in compressive strength = Compressive strength of the optimal variation
  – Compressive strength of the 0% variation
  = 26.53 MPa – 24.69 MPa
  = 1.84 MPa
- Difference in cement usage = Cement usage at 0% variation – Cement usage at optimal variation
  = 455.55 kg.m^{-3} – 440.86 kg.m^{-3}
  = 14.69 kg.m^{-3}
- The ratio of compressive strength gain
  per unit of cement = Difference in compressive strength: Difference in cement usage
  = 1.84 MPa : 14.69 kg·m^{-3}
  = 0.125 MPa per kg.m^{-3}

The results show a cement reduction of 14.69 kg.m^{-3} with a corresponding compressive strength increase of 1.84 MPa, giving a ratio of 0.125 MPa per kg.m^{-3}

An example calculation used to derive the values presented in Table 9.

- Difference in compressive strength = Compressive strength of the optimal variation
  – Compressive strength of the 0% variation
  = 22.93 MPa – 20.24 MPa
  = 2.69 MPa
- Difference in cement usage = Cement usage at 0% variation – Cement usage at optimal variation
  = 455.55 kg.m^{-3} – 452.078 kg.m^{-3}
  = 3.472 kg.m^{-3}
- The ratio of compressive strength gain
  per unit of cement = Difference in compressive strength: Difference in cement usage
  = 2.69 MPa : 3.472 kg.m^{-3}
  = 0.775 MPa per kg.m^{-3}

The results show a cement reduction of 3.472 kg.m^{-3} with a corresponding compressive strength increase of 2.69 MPa, giving a ratio of 0.775 MPa per kg.m^{-3}.

An example calculation used to derive the values presented in Table 10

- Difference in compressive strength = Compressive strength of the optimal variation
  – Compressive strength of the 0% variation
  = 35.22 MPa – 23.85 MPa
  = 11.37 MPa

Table 8: Cement content and compressive strength of flowing concrete with rice husk ash.

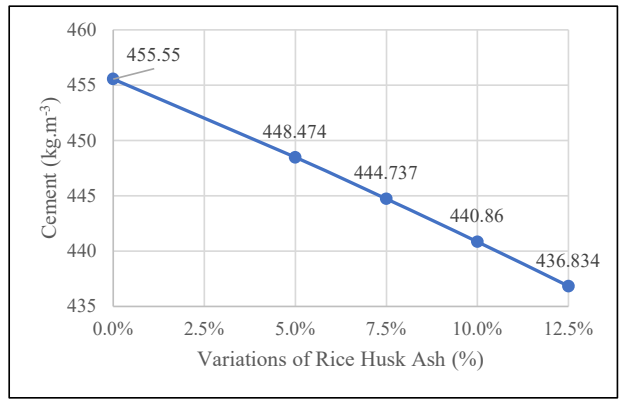
Percentage	Cement (kg.m^{-3})	Compressive Strength (MPa)	Difference in Compressive Strength between Optimal Variation and 0% Variation (MPa)	Cement Usage Difference between Optimal and 0% Variation (kg.m^{-3})
0%	455.55	24.69	1.84	14.69
5%	448.474	22.93		
7.5%	444.737	25.24		
10%	440.86	26.53		
12.5%	436.834	23.3		

Table 9: Cement content and compressive strength of flowing concrete with sugarcane bagasse ash.

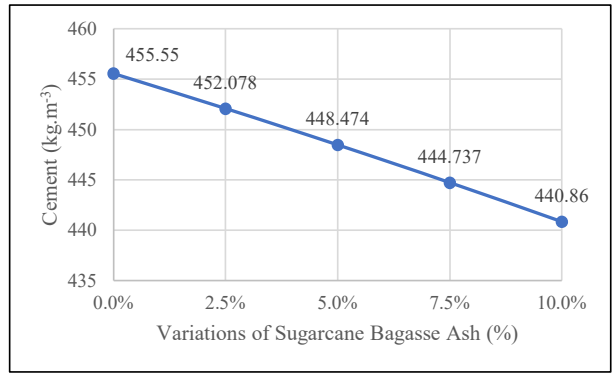
Percentage	Cement (kg.m^{-3})	Compressive Strength (MPa)	Difference in Compressive Strength between Optimal Variation and 0% Variation (MPa)	Cement Usage Difference between Optimal and 0% Variation (kg.m^{-3})
0%	455.55	20.24	2.69	3.472
2.5%	452.078	22.93		
5%	448.474	21.09		
7.5%	444.737	21.8		
10%	440.86	21.8		

Table 10: Cement content and compressive strength of flowing concrete with corn cob ash.

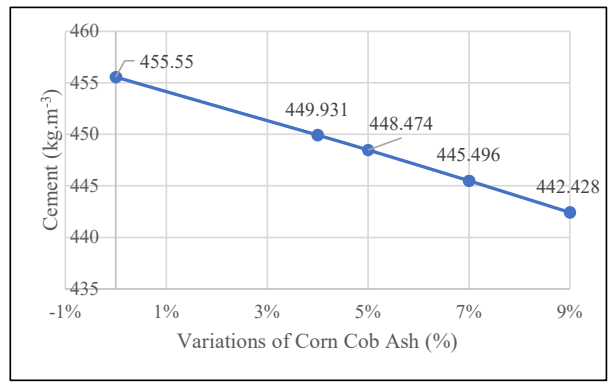
Percentage	Cement	Compressive Strength (MPa)	Difference in Compressive Strength between Optimal Variation and 0% Variation (MPa)	Cement Usage Difference between Optimal and 0% Variation ($kg.m^{-3}$)
0%	455.55	23.85	11.37	10.054
4%	449.931	28.38		
5%	448.474	32.45		
7%	445.496	35.22		
9%	442.428	19.78		



(a)



(b)



(c)

Fig. 8: Cement content at different replacement levels of (a) sugarcane bagasse ash, (b) rice husk ash, and (c) corn cob ash.

- Difference in cement usage = Cement usage at 0% variation – Cement usage at optimal variation

  = 455.55 kg.m^{-3} – 445.496 kg.m^{-3}

  = 10.054 kg.m^{-3}

- The ratio of compressive strength gain

  per unit of cement = Difference in compressive strength: Difference in cement usage

  = 11.37 MPa : 10.054 kg.m^{-3}

  = 1.13 MPa per kg.m^{-3}

The results show a cement reduction of 10.054 kg.m^{-3} with a corresponding compressive strength increase of 11.37 MPa, giving a ratio of 1.13 MPa per kg.m^{-3}.

The most optimal effectiveness of cement use can be seen from the results of the largest value of the ratio of increase in compressive strength per kg.m^{-3} obtained, among others, in rice husk ash the ratio of increase in compressive strength per kg.m^{-3} is 0.125, in bagasse ash the ratio of increase in compressive strength per kg.m^{-3} is 0.775 and in corn cob ash the ratio of increase in compressive strength per kg.m^{-3} is 1.13. Therefore, the optimal effectiveness of cement use is flowing concrete with corn cob ash substitution.

Fig. 8 indicates that increasing the utilization of rice husk ash, bagasse ash, and corn cob ash results in a reduction of cement usage. Employing agricultural waste ashes as partial cement substitutes provides a sustainable pathway toward reducing overall cement consumption.

4. CONCLUSION

The substitution of corn cob ash, rice husk ash, and sugarcane bagasse ash can improve the unit weight of concrete when applied in suitable proportions. Therefore, optimizing the substitution level is essential for achieving sustainable and durable concrete. Based on the measured unit weight, the material falls within the range of normal concrete and is commonly applied in general structural works.

The maximum compressive strength of 35.22 MPa is achieved at a 7% corn cob ash replacement. Moderate use of corn cob ash, rice husk ash, and bagasse ash improves the interfacial transition zone and enhances concrete strength, while excessive substitution reduces performance. Thus, identifying the optimal replacement level is essential for the effective use of these agricultural waste ashes in concrete.

The results show that agro-waste substitution affects cement efficiency in flowing concrete. Corn cob ash provides the greatest strength gain per unit cement (1.13 MPa per kg·m^{-3}), outperforming bagasse ash and rice husk ash. This indicates that corn cob ash offers the most effective enhancement of cement performance and holds strong prospects for use as a supplementary material with sustainable characteristics.

Increasing the use of rice husk ash, bagasse ash, and corn cob ash reduces cement demand, demonstrating that agricultural waste ashes offer a sustainable approach to lowering overall cement consumption.

The statistical evaluation indicates that the various substitution levels yield noticeable differences in unit weight and compressive strength. Meanwhile, the linear regression assessment generated several regression equations derived from the plotted data.

This study shows that agricultural waste ashes can enhance unit weight, compressive strength, and cement efficiency when used at optimal levels, underscoring their potential as sustainable partial cement substitutes. Rice husk ash, bagasse ash, and corn cob ash offer a viable pathway to reducing reliance on Portland cement and lowering environmental impact. Their use is promising for flowable and structural concretes requiring eco-friendly materials. Further research should assess long-term durability, combined ash applications, and feasibility for large-scale implementation.

5. ACKNOWLEDGMENTS

The authors thank the Civil Engineering Concrete Laboratory at Universitas Untag Surabaya for their assistance with the experiments.

6. REFERENCES

Adesanya, D.A. and Raheem, A.A., 2010. A study of the permeability and acid attack of corn cob ash blended cements. *Construction and Building Materials*, 24, pp. 403–409. [DOI]

Albiajawi, M.I., Embong, R. and Muthusamy, K., 2022. An overview of the utilization and method for improving pozzolanic performance of agricultural and industrial wastes in concrete. *Materials Today: Proceedings*, 48(4), pp.778-783. [DOI]

Ali, M.B., Saidur, R. and Hossain, M.S., 2011. A review on emission analysis in cement industries. *Renewable and Sustainable Energy Reviews*, 15 (5), pp. 2252–2261. [DOI]

Althaqafi, E., Ali, T., Qureshi, M. Z., Islam, S., Ahmed, H., Ajwad, A., Almujibah, H. and Khan, M. A., 2024. "Evaluating the combined effect of sugarcane bagasse ash, metakaolin, and polypropylene fibers in sustainable construction", *Scientific Reports*, 14, pp.1-17. [DOI]

Badan Pusat Statistik (BPS), 2024. Indonesian Sugarcane Statistics 2023. Available online: https://www.bps.go.id/id/publication/2024/11/29/71e6450a9b235855ffc525c9/statistik-tebu-indonesia-2023.html. (Accessed: 29 August 2025)

Badan Pusat Statistik (BPS), 2025. Indonesian Corn Statistics 2024. Available online: https://www.bps.go.id/id/pressrelease/2025/02/03/2412/pada-2024--luas-panen-jagung-pipilan-mencapai-2-55-juta-hektare--produksi-jagung-pipilan-kering-dengan-kadar-air-14-persen-pada-2024-sebanyak-15-14-juta-ton-.html. (Accessed: 29 August 2025)

Badan Pusat Statistik (BPS), 2025. Indonesian Rice Statistics 2024. Available online: https://www.bps.go.id/id/pressrelease/2025/02/03/2414/pada-

2024--luas-panen-padi-mencapai-sekitar-10-05-juta-hektare-dengan-produksi-padi-sebanyak-53-14-juta-ton-gabah-kering-giling--gkg--.html. (Accessed: 29 August 2025)

Badan Standardisasi Nasional (BSN), 2000. SNI 03–2834–2000: procedures for normal concrete mix design. National Standardization Agency of Indonesia, Jakarta

Badan Standardisasi Nasional (BSN), 2002. SNI 03-2847-2002: procedures for calculating concrete structures for buildings. National Standardization Agency of Indonesia, Jakarta

Budiarti, Z.T., Agustin, E.W. and Agustin, R.A., 2023. Feasibility of rice husk waste (*Oryza sativa L.*) as an additive in natural solid soap formulations. *Beauty And Beauty Health Education Journal*, 12(1), pp.21-32. [DOI]

Chatham, 2018. Making Concrete Change Innovation in Low-carbon Cement and Concrete. Available online: https://www.chathamhouse.org/2018/06/making-concrete-change-innovation-low-carbon-cement-and-concrete. (Accessed: 29 August 2025)

CNBC, 2024. Indonesia's Cement Industry Overcapacity. Available online: https://www.cnbcindonesia.com research/20240328171728-128-526444/industri-semen-indonesia-overcapacity-warga-ri-wajib-baca-data-ini. (Accessed: 29 August 2025)

Daniel, C., Onchiri, R.O. and Omondi, B.O., 2024. Mechanical and physical characteristic of concrete mixed with sugarcane bagasse ash and recycled polyethylene terephthalate. *Heliyon*, 10(18), pp. 1-18. [DOI]

Dziejarski, B., Serafin, J., Andersson, K. and Krzyzynska, R., 2023. CO_2 capture materials: a review of current trends and future challenges. *Materials Today Sustainability*, 24, pp.1-79. [DOI]

EFNARC, 2005. The European guidelines for self-compacting concrete: specification, production, and use. Farnham, UK: EFNARC

Elawadly, N and Sanad, S.A., 2025. Sustainable concrete incorporating sugarcane bagasse ash: a study on workability, mechanical behavior and microstructure. *Innovative Infrastructure Solution*, 10, pp. 1-12. [DOI]

Faried, A.S., Mostafa, S.A., Tayeh, B.A. and Tawfik, T A., 2021. The effect of using nano rice husk ash of different burning degrees on ultra-high-performance concrete properties. *Construction and Building Materials* 290, pp.1-14. [DOI]

Fayomi, G.U., Mini, S.E., Fayomi, O.S.I. and Ayoola, A.A., 2019. Perspectives on environmental CO_2 emission and energy factor in cement industry. In *IOP Conference Series: Earth and Environmental Science, International Conference on Energy and Sustainable Environment*, Covenant University, Nigeria, 18-20 June 2019. [DOI]

Handayani, M.D., 2020. The Effect of Adding Sweet Corn Stalk Ash as a Partial Cement Substitute for Concrete Mixtures on the Compressive Strength and Flexural Strength of High-Quality Concrete. *Universitas Islam Riau*. Available Online: https://repository.uir.ac.id/8365/1/143110667.pdf

Hepiyanto, R. and Firdaus, M. A., 2019. The effect of adding corn cob ash on the compressive strength of K-200 concrete. *UKaRsT*, 3(2), pp. 99–106. [DOI]

Hou, Y., Yang, K., Zheng, K., Yin, S., Yu, X. and Chen, X., 2024. Optimizing mechanical performance and flow characteristics of alkaline fly ash/rice husk ash composite backfill: Insights from multi-factor analysis and engineering optimization. *Journal of Building Engineering*, 95, pp. 1-19. [DOI]

Iro, U.I., Alaneme, G.U., Ganasen, N., VishnuPriyan, M., Attah, I.C., Eze, V.H.U., Olaiya, B.C. and Ejeabukwa, 2025. Evaluation of the mechanical characteristics of bagasse ash concrete using response surface methodology. *Discover Sustainability*, 6. [DOI]

Legiso, Kalsum, U. and Wulandari, M., 2020. Comparative study on the adsorption effectiveness of activated carbon derived from sugarcane bagasse, rubber fruit shell, and banana peel for reducing COD and BOD levels in songket industry wastewater. *Distilasi*, 5 (1), pp. 9-13. [DOI]

Maglad, A.M., Amin, M., Zeyad, A.M., Tayeh, B.A. and Agwa, I.S., 2023. Engineering properties of ultra-high strength concrete containing sugarcane bagasse and corn stalk ashes. *Journal of Materials Research and Technology*, 23, pp. 3196-3218. [DOI]

Memon, S.A., Javed, U., Shah, M.I. and Hanif, A., 2022. Use of processed sugarcane bagasse ash in concrete as partial replacement of cement: mechanical and durability properties. *Buildings*, 12(10), p.1769. [DOI]

Nomani, M.Z.M., Shaquib, O. and Sharma, M., 2025. Fly Ash in Concrete Production: A Legal and Regulatory Review of Environmental Impacts. *Nature Environment and Pollution Technology*, *24*, pp.305-314. [DOI]

Paul, S.C., Mbewe, P.B.K., Kong, S.Y. and Šavija , B., 2019. Agricultural solid waste as source of supplementary cementitious materials in developing countries. *Materials*, 12 (7), pp.1-20. [DOI]

Rompas, G. P., Pangouw, J. D., Pandaleke, R. and Mangare, J. B., 2013. The effect of using bagasse ash as a partial substitute for cement in concrete mixtures is reviewed on the flexural tensile strength and modulus of elasticity. *Jurnal Sipil Statik*, 1(2), pp. 82–89. https://ejournal.unsrat.ac.id/v2/index.php/jss/article/view/926

Siddika, A., Mamun, Md.A.A., Alyousef, R. and Mohammadhosseini, H., 2021. State of the art review on rice husk ash: a supplementary cementitious material in concrete. *Journal of King Saud University-Engineering Science*, 33, pp. 294-307. [DOI]

Siddique, R., Singh, K., Kunal, Singh, M., Corinaldesi, V. and Rajor, A., 2016. Properties of bacterial rice husk ash concrete. *Construction and Building Materials*, 121, pp.112-119. [DOI]

Standar Nasional Indonesia (SNI), 2008. SNI 1973:2008 – methods of testing density, specific gravity, and absorption of concrete. National Standardization Agency of Indonesia, Jakarta

Standar Nasional Indonesia (SNI), 2011. SNI 1974:2011 – test method for compressive strength of concrete with cylindrical Specimens. National Standardization Agency of Indonesia, Jakarta

Sudarsan, J.S., Parija, P., Gavald, H.R., Mushir, N., Dixit S., Kampani, S., Murali, G., Ghildiyal, S. and Lapteva, S., 2023. Agricultural waste as a replacement for admixture in concrete – a short review. *Materials Today: Proceedings*, pp.1-8. [DOI]

Suhirkam, D. and Dafrimon 2014. K-400 quality concrete with the addition of rice husk ash and superplasticizer. *PILAR: Jurnal Teknik Sipil*, 10(1), pp. 1–7. https://media.neliti.com/media/publications/158026-ID-beton-mutu-k-400-dengan-penambahan-abu-s.pdf

Trimurtiningrum, R. and Subakti, A., 2016. "Compressive strength and shrinkage test of flowing concrete using fly ash and naphthalene–based superplasticizer". In *International Conference on Physics and Mechanics of New Materials and Their Applications*, Surabaya, Indonesia, 19-22 July 2016. [DOI]

Verian, K.P., Ashraf, W. and Cao, Y., 2018. Properties of recycled concrete aggregate and their influence in new concrete production. *Resources, Conservation and Recycling*, 133, pp. 30-49. [DOI]

Wiyono, A., Karjanto, A. and Pandulu, G. D., 2017. Effect of replacement parts of cement with bagasse ash based on quality compressive strength and water absorption of mortar. *eUREKA: Jurnal Penelitian Teknik Sipil dan Teknik Kimia*, 1(1). https://publikasi.unitri.ac.id/index.php/teknik/article/view/619/495

Yankelevsky, D.Z., 2024. The uniaxial compressive strength of concrete: revisited. *Materials and Structures*, 57, pp. 1–18. [DOI]

Yulianto, F. E. and Mukti, M. H., 2015. The Effect of Adding Rice Husk Ash on the Compressive Strength of Concrete Mixture 1 part cement: 2 parts sand: 3 parts gravel. *SAINTEK*, 12(2), pp. 74–78

Nature Environment and Pollution Technology
An International Quarterly Scientific Journal

p-ISSN: 0972-6268
(Print copies up to 2016)
e-ISSN: 2395-3454

Vol. 25 | No. 3 | Article ID B4404 | 2026

Review Research Paper

https://doi.org/10.46488/NEPT.2026.v25i03.B4404

Open Access Journal

Pullulan From Agricultural Waste Using *Aureobasidium pullulans* and Its Applications: A Review

Gunjan Jadhav, Snehal Masurkar and Girish Pathade
Krishna Institute of Science and Technology, Krishna Vishwa Vidyapeeth (Deemed to be University), Karad, Maharashtra, India
Corresponding author: Gunjan Jadhav; gunjanbj2408@gmail.com

Abbreviation: Nat. Env. & Poll. Technol.
Website: www.neptjournal.com

Received: 09-10-2025
Revised: 23-12-2025
Accepted: 06-01-2026

Key Words:

Hydrolysed waste
Aureobasidium pullulans
Fermentation
Pullulan

ABSTRACT

Pullulan is an extracellular homopolysaccharide produced commercially by the yeast-like fungus *Aureobasidium pullulans*. Owing to its unique physicochemical properties, such as film-forming ability, biodegradability, and non-toxic nature, pullulan has attracted significant interest for applications across diverse industries, including cosmetics, pharmaceuticals, food packaging, and agriculture. In recent years, the demand for sustainably derived biopolymers has intensified, prompting exploration of industrial waste and renewable substrates as cost-effective feedstocks for pullulan production. Despite its promising versatility, large-scale commercialization remains constrained by high production costs, low yield, and limited substrate flexibility. This review critically examines the potential of microbial-based pullulan production, highlighting both technological opportunities and persistent challenges. Particular emphasis is placed on the use of alternative substrates, strain improvement strategies, and bioprocess optimization to enhance yield and reduce costs. Advances in metabolic engineering, fermentation technology, and integrated biorefinery approaches are discussed as pathways to overcome current limitations. By synthesizing recent progress and identifying research gaps, this study aims to support future innovation in sustainable pullulan production and broaden its industrial applicability. Ultimately, optimizing production parameters and diversifying microbial systems may provide a viable solution to transform pullulan into a widely accessible biopolymer for global markets.

Citation for the Paper:

Jadhav, G., Masurkar, S. and Pathade, G., 2026. Pullulan from agricultural waste using *Aureobasidium pullulans* and its applications: A review. *Nature Environment and Pollution Technology*, 25(3), B4404. https://doi.org/10.46488/NEPT.2026.v25i03.B4404

Note: From 2025, the journal has adopted the use of Article IDs in citations instead of traditional consecutive page numbers. Each article is now given individual page ranges starting from page 1.

Copyright: © 2026 by the authors
Licensee: Technoscience Publications
This article is an open access article distributed under the terms and conditions of the Creative Commons Attribution (CC BY) license (https://creativecommons.org/licenses/by/4.0/).

1. INTRODUCTION

1.1. Carbohydrates

The term "carbohydrate" encompasses a group of molecules including starch, sugars, and cellulose (Avenas 2012). Microbes produce a wide variety of carbohydrate-based polymers, such as bacterial cellulose, xanthan, levan, dextran, gellan, pullulan, curdlan, and scleroglucan. Pullulan is a linear homopolysaccharide that forms the backbone of maltotriose units (Nasrollahzadeh et al. 2021). Polysaccharides are hydrocolloids, water-attracting polymers, that find applications across the food, pharmaceutical, and cosmetic industries due to their unique physical and chemical properties.

In food, they serve as stabilizers, thickeners, film-forming agents, and emulsifiers in products like sauces, beverages, and bread (Pirsa & Hafezi 2023). In pharmaceuticals, they are used to produce hydrogel tablets, hard capsules, and matrices. Since many polysaccharide gels originate from plant and animal sources, researchers are exploring alternatives due to their limited availability for human consumption and non-renewability (Kostag & El Seoud 2021).

1.2. History

In 1958, Bernier first isolated the carbohydrate pullulan from *Aureobasidium*

pullulans. A year later, Bender et al. conducted a structural analysis of a novel polysaccharide and named it pullulan. The basic composition of pullulan was elucidated during the 1960s (Abhilash & Thoma 2017).

1.3. Pullulan

Pullulan is a linear, biodegradable, extracellular, water-soluble homopolysaccharide produced by the yeast-like fungus Aureobasidium pullulans (Singh et al. 2019). It forms an amorphous, slimy mass on the outer surfaces of the fungus. Structurally, pullulan consists of repeating maltotriose units connected via α-(1,6) glycosidic bonds (Li et al. 2015). Its unique structure confers high water solubility and biodegradability, making pullulan a valuable and versatile biomaterial with significant application potential (Ates 2015). Pullulanase, a well-known debranching enzyme, plays a crucial role in breaking down pullulan. Hydrolysis of pullulan by pullulanase yields various oligosaccharides, including maltose, maltotriose, maltotetrose, isomaltose, and panose (Rajeeva et al. 2010). Maltotriose serves as the primary repeating unit within pullulan. Chemical modifications can be employed to enhance its physical properties.

Pullulan is tasteless, odorless, edible, non-toxic, non-mutagenic, and non-carcinogenic. It finds extensive use across multiple industries such as pharmaceuticals, food, cosmetics, biomedical fields, targeted drug delivery systems, waste bioremediation, and medical applications (Sugumaran et al. 2017).

1.4. Structure of Pullulan

Pullulan has the chemical formula $(C_6H_{12}O_5)n$, and its structure is composed of repeating maltotriose units, in which three glucose molecules are linked by α-(1→4) and α-(1→6) glycosidic bonds. Spectral data verify the presence of both α-(1→4) and α-(1→6) linkages in pullulan. Bernier was the first scientist to confirm that pullulan contains glucopyranose (Bernier 1958). The α-(1→4) linkage was demonstrated through optical rotation and infrared spectroscopy (Bender et al. 1959). Later, researchers used infrared spectroscopy, methylation reactions, and periodate oxidation to establish that pullulan has both α-(1→4) and α-(1→6) glycosidic bonds in a 2:1 ratio (Shingel 2004, Sowa et al. 1963, Singh & Saini 2012). The structure of pullulan can also be analyzed using the enzyme pullulanase, which specifically cleaves the α-(1→6) glycosidic bonds, leading to complete hydrolysis and the formation of maltotriose units (Hii et al. 2012). Maltotriose consists of three α-(1→4) linked glucopyranose units connected via an α-(1→6) bond, represented as [(1→4)-α-D-Glucopyranosyl-(1→4)-α-D-Glucopyranosyl-(1→6)-α-D-Glucopyranosyl]. Incomplete hydrolysis of pullulan yields other sugars such as panose, maltose, isopanose, and isomaltose (Bender et al. 1959, Sowa et al. 1963). Fig. 1 illustrates the molecular structure of pullulan.

1.5. Microbial Pullulan Producers

Pullulan was initially produced through microbial fermentation using the fungus *Aureobasidium pullulans* for commercial applications. However, not all A. pullulans strains have been characterized for this purpose (Ghimici & Constantin 2020). In addition to Aureobasidium pullulans, other microbial strains can produce pullulan with different ratios of glycosidic bonds, quantities of maltotriose units, and percentages of α-(1→6) linkages within the pullulan framework. A few strains which can produce a pullulan, including *Cytaria darwinii, Cryphonectria parasitica, Aureobasidium mangrovei*, *Cytaria harioti, Tremella mesenterica, Aureobasidium melanogenum, Rhodotorula bacarum, Teloschistes flavicans, Eurotium chevalieri,* and *Rhodosporidium paludigenum*. Table 1 provides

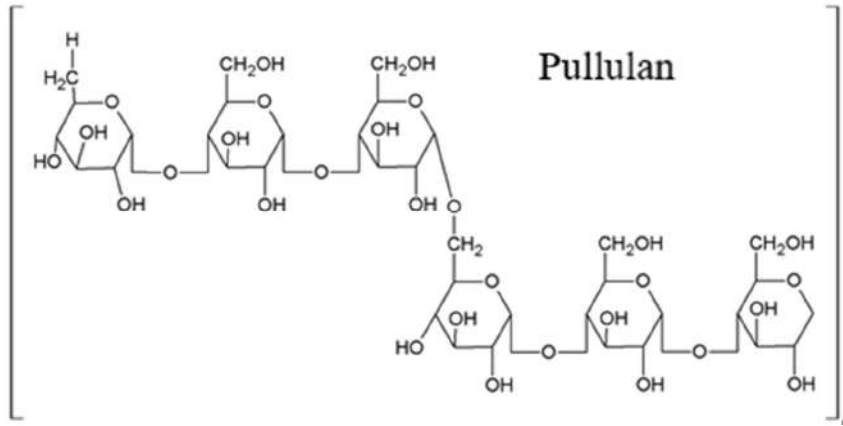


Fig. 1: Molecular structure of pullulan (Ferreira et al. 2015).

Table 1: Fungal sources, structural components, and applications of pullulan.

Sr. No.	Fungal sources	Structural units	Applications	References
1.	*Aureobasidium pullulans*	α-(1→4) linked glucopyranose rings interlinked by α (1→6) linkages.	Biomedical industry, Cosmetics industry, Food industry, Oral care products, etc.	(Al-Araimi et al. 2021), (Basumatary et al. 2022), (Ghimici & Constantin 2020) (Singh et al. 2008)
2.	*Aureobasidium mangrovei*			
3.	*Aureobasidium melanogenum*			
4.	*Cryphonectria parasitica*			
5.	*Cyttaria darwinii*			
6.	*Cyttaria harioti*			
7.	*Eurotium chevalieri*			
8.	*Rhodosporidium paludigenum*			
9.	*Rhodotorula. Bacarum*			
10.	*Teloschistes flavicans*			
11.	*Tremella mesenterica*			

fungal sources, structural components, and applications of pullulan.

1.6. Pullulan Properties

Pullulan typically appears as a fine powder ranging from white to off-white. Microscopic examination reveals that pullulan particles have a smooth surface texture (Li et al. 2018, Soni et al. 2018). Its highly flexible and unique structure contributes to improved hydrodynamic properties (Singh et al. 2008). Pullulan exhibits enhanced solubility and increased solvent resistance. It dissolves rapidly in diluted alkali solutions and in both cold and hot water. However, it is insoluble in organic solvents, except for dimethylformamide and dimethyl sulfoxide. As a dry, non-hygroscopic powder with a moisture content of approximately 10-15%, pullulan does not become sticky. While it can form viscous solutions, it is unable to form gels. The solutions show non-Newtonian, shear-thinning behavior, with shear stress versus shear rate displaying a linear relationship. Tables 2 and 3 present the properties and solubility characteristics of pullulan, respectively.

Table 2: Pullulan properties (Viveka 2023).

Parameters	Specification
Physical state	Powder
Appearance	Whitish or yellowish-white
Flavour	Tasteless and odorless
Toxicity	Non-hazardous and non-cancerous
Molecular weight [kDa]	100 – 250
Consumability	Safe for consumption
Biodegrading nature	Biodegradable
Flow properties	Shear thinning and Non–Newtonian behavior
Polypeptides [%]	Maximum 0.5
Solubility in organic solvents	Insoluble in all organic solvents except formamide and dimethyl sulfoxide
pH of the solution range	5–7
Polydispersity ratio	2.1 – 4.1
Moisture [%]	10 -15
Mineral residue ash [sulfated, %]	Maximum 3
Viscosity range[cP]	80 – 180
Optical activity	Greater than ±160
Range of melting point [°C]	250-350°C

1.7. Gene Expression and Regulation

High pullulan-producing strains, such as *A. melanogenum* ZH27, show upregulation of genes linked to pullulan biosynthesis (UGT1 and Ags2), glycolysis, and by-product synthesis (e.g., trehalose, glycerol, and fructooligosaccharides). This coordinated gene upregulation is associated with increased pullulan yield and enhanced resistance to osmotic stress (Wang et al. 2023).

Transcriptomic analyses of A. pullulans have revealed that biosynthetic genes (upt, pgm, ugp, and pul) are tightly regulated, and that negative regulators such as creA can suppress pullulan synthesis, especially in specific genetic backgrounds (e.g., melanin-deficient mutants) (Chen et al. 2023).

Table 3: Solubility properties of pullulan (Viveka 2023).

Solvent Name	Solubility Conditions
Water	Soluble
DMSO (Dimethyl sulfoxide)	Soluble
Pyridine	Slightly soluble
Ethyl acetate	Insoluble
Acetone	Insoluble
Dimethylformamide (DMF)	Partially soluble
Chloroform	Insoluble

1.8. Morphological and Cellular Changes

Omics-guided studies have linked the presence of swollen cells with large vacuoles to periods of rapid pullulan accumulation, suggesting a physiological adaptation that supports high production levels (Wang et al. 2023).

1.9. Genetic Engineering and Mutagenesis

Targeted genetic modifications, such as knocking out genes involved in melanin synthesis or plasma membrane ATPases (PMAs), have been demonstrated to influence both the amount and molecular weight of pullulan produced. For instance, deleting PMAs in A. pullulans BL06 resulted in a 1.7-fold increase in pullulan yield and a decrease in its molecular weight (Chen et al. 2023). Additionally, UV mutagenesis combined with flow cytometry-based selection has been used to isolate high-yield mutants, as confirmed by omics analyses (Zhang et al. 2024).

1.10. Environmental and Regulatory Factors

Transcriptome analyses conducted under various growth substrates and environmental conditions, such as pH and carbon source, have identified regulatory factors, including pH transcription factors, which significantly enhance pullulan biosynthesis pathways (Wang et al. 2024, Zhang et al. 2023).

1.11. Metabolic Pathways and By-Product Formation

Omics studies have elucidated the balance between pullulan production and byproduct formation. While by-products like trehalose and glycerol assist in osmotic stress management, their accumulation can divert carbon flux away from pullulan, reducing overall yield. Table 4 provides omics insights into pullulan production.

1.12. Status of Pullulan Production in the Commercial Sector

Hayashibara Company Limited in Japan pioneered the commercial production of pullulan in 1976 and secured a patent for its commercialization. It remains a leading producer of food-grade and deionized pullulan, offering products with molecular weights ranging from 100 to 200 kDa (Agrawal et al. 2022). Following the expiry of Hayashibara's patent, several industries began commercializing pullulan.

Hayashibara Co. Ltd. continues to be recognized as the largest supplier of pullulan globally (Coltelli et al. 2020). The brand Listerine, marketed and sold in the US by Hayashibara Company in partnership with Pfizer Inc., is one example of pullulan's applications (Trinetta & Cutter 2025). The company now operates across regions, including North and South America, Europe, Asia, Southeast Asia, and Oceania.

Hayashibara Industries is now known as Nagase Co. Ltd. The demand for pullulan is steadily rising due to its unique properties and potential uses. A recent report, "Pullulan Market Research Report," provides an in-depth overview of market conditions and industrial applications. The global pullulan market is projected to reach USD 89 million by 2028, up from an estimated USD 68 million in 2022. Given its high cost and growing demand worldwide, it is crucial to evaluate the production process of pullulan polymers for industrial applications.

Carbosynth Ltd. in the UK is another prominent industry player that produces pullulan commercially at a significantly lower cost of US $130 per kilogram. Several Indian companies, including Jiyan Chemicals & Pharmaceuticals, Indexim International, Otto Chemie Pvt. Ltd., Kumar Organic Products Ltd., Thermo Fisher Scientific Pvt. Ltd., and Shreeji Pharma International, have also started commercial production of pullulan.

Kumar Organic Products Ltd. is among India's leading pullulan producers, while pharmaceutical-grade pullulan is manufactured locally by Jiyan Chemicals & Pharmaceuticals. In China, multiple companies such as Shanghai Longyu Biotech Co., Ltd., Shandong Hanjiang Chemical Co., Ltd., and Haihang Industry Co., Ltd. have begun producing pullulan on a commercial scale.

The primary Chinese suppliers include Shandong Jinmei Biotechnology Co., Ltd., Shandong Freda Biotechnology Co., Ltd., MeiHua Holdings Group Co., Ltd., Hebei Henbo Bio Technology Co., Ltd., and Shandong Kangnaxin Biotechnology Co., Ltd. Several U.S.-based firms, including Santa Cruz Biotechnology Inc. and MP Biomedicals Inc., have entered the commercial pullulan market. According

Table 4: Omics insights into pullulan production.

Omics approach	Key Findings	References
Transcriptomics	Upregulation of biosynthetic and stress-resistance genes in high-yield strains	(Wang et al. 2023, Chen et al. 2023, 2024)
Functional Genomics	Gene knockouts (e.g., PMAs, melanin) affect yield and polymer properties	(Chen et al. 2023, Zhang et al. 2024)
Morphological Studies	Swollen cells with large vacuoles linked to high pullulan accumulation	(Wang et al. 2023)
Regulatory Networks	pH and carbon source regulation via transcription factors like Appacc	(Wang et al. 2024)

to Fact.MR, the global pullulan market is projected to grow from USD 714.5 million in 2025 to USD 1,163.8 million by 2035, at a compound annual growth rate of 5.0% over the forecast period.

The pharmaceutical industry remains the largest consumer, representing about 40.74% of global demand. The food industry ranks second, with a 36.24% share. Japan leads in consumption, with an annual usage of 667 million tons from 2015 to 2019. China is the second-largest market, holding a 20.65% share, followed closely by the USA at 20.16%. It is widely believed that the future global potential for pullulan usage greatly surpasses current commercial production levels.

1.13. Scope and Original Contribution of the Review

While recent reviews have addressed pullulan production, applications, and waste valorization, they often treat substrate selection, fermentation optimization, strain engineering, and downstream processing as separate topics. This review distinguishes itself with a comprehensive, decision-oriented framework that systematically connects waste substrate properties, fermentation results, key bottlenecks, and omics-based strain improvements. It emphasizes critical barriers such as melanin pigmentation, high broth viscosity, substrate variability, and purification costs, which impact industrial feasibility but are often discussed in isolation elsewhere.

Unlike post-2020 reviews that mainly compile experimental data, this analysis offers a comparative evaluation and future strategies for scale-up. By comparing yields across substrates, fermentation systems, and strains, and integrating techno-economic and biorefinery considerations, it highlights persistent gaps: limited pilot-scale data, scarce cost modeling, and weak integration of omics with process optimization. This focused approach provides a practical roadmap for sustainable, cost-effective pullulan production from agro-waste, surpassing traditional literature reviews.

2. MATERIALS AND METHODS FOR PULLULAN PRODUCTION

A qualitative literature review was selected to thoroughly explore and synthesize the complex information concerning the production of pullulan from agricultural waste using *Aureobasidium pullulans*. The steps undertaken for this review are illustrated in Fig. 2.

2.1. Data Collection and Literature Review

The literature review on pullulan production from agricultural waste using *Aureobasidium pullulans* focused

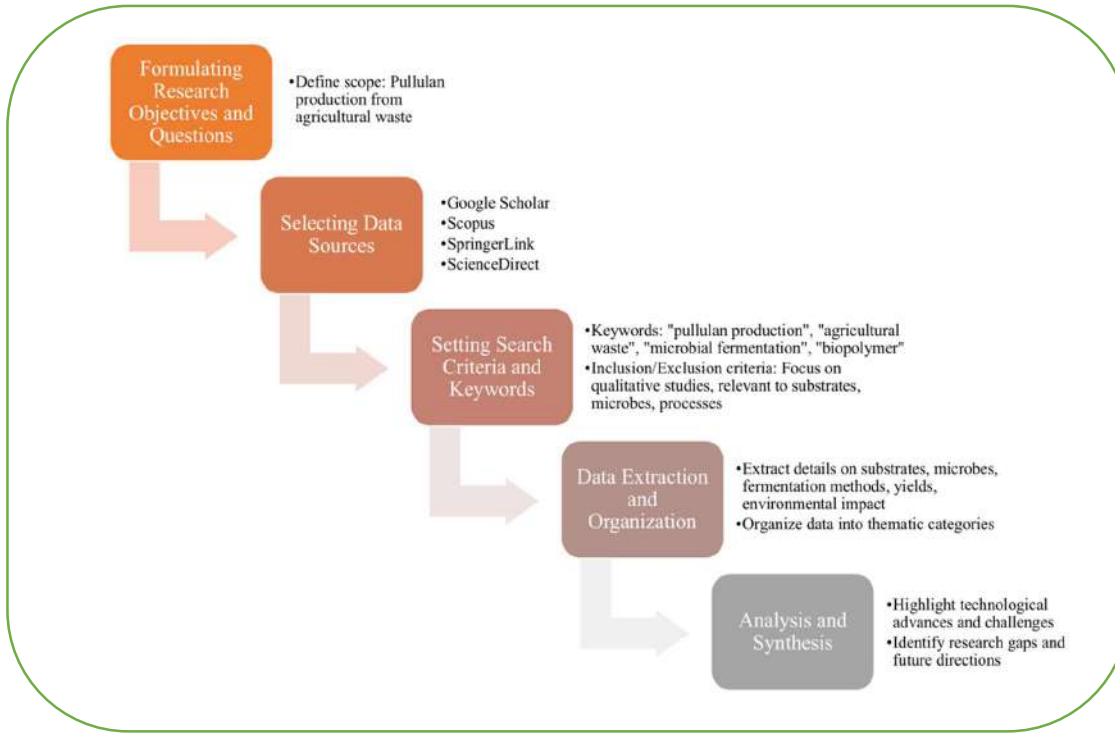


Fig. 2: The steps carried out for the review.

on collecting and synthesizing studies that explored the use of various agro-industrial residues, such as sugarcane molasses, potato starch hydrolysate, citrus peels, and hazelnut husks, as low-cost substrates for fermentation. Data were gathered from reputable scientific databases, including Scopus, Google Scholar, and SpringerLink, using targeted keywords like «pullulan production,» «agricultural waste,» and «*Aureobasidium pullulans*." Studies were selected based on their relevance to qualitative insights into fermentation processes, substrate optimization, and sustainability.

This review highlights that employing agricultural waste as fermentation media not only decreases production costs but also addresses environmental concerns by valorizing waste streams. Research consistently demonstrates that *A. pullulans* efficiently converts diverse agricultural residues into pullulan through both submerged and solid-state fermentation, with substrate type and composition significantly influencing yield and process efficiency.

2.2. Inclusion and Exclusion Criteria

Studies qualified for inclusion if they-

- Demonstrated pullulan production from agro-industrial or agricultural waste substrates,
- Utilized *Aureobasidium pullulans* or related pullulan-producing microorganisms,
- Provided experimental fermentation data on performance metrics, substrate conversion, yields, or optimization strategies, or
- Addressed the technological, economic, and sustainability implications of waste-based pullulan processes.
- Exclusion criteria encompassed studies that,
- Examined only pure/synthetic substrates without waste valorization relevance,
- Offered inadequate experimental or methodological details,
- Comprised of conference abstracts lacking full-text access, or
- No direct connection to pullulan production.

The literature survey primarily covered studies published between 2000 and 2024, ensuring the inclusion of both foundational and recent research. Title and abstract screening identified relevant studies, followed by a full-text assessment. From approximately 200-300 screened publications, over 100 articles met the criteria for comprehensive qualitative synthesis based on data quality and relevance. Discrepancies across studies were reconciled through comparative analysis, accounting for substrate variations, pretreatment techniques, strain differences, and fermentation parameters, preserving diverse perspectives to reveal critical trends, challenges, and research gaps in this field.

Aureobasidium pullulans

Aureobasidium pullulans, previously identified as *Pullularia pullulans, Hormonema dematioides,* or *Dematium pullulans*, is an imperfect fungus. It is widespread in the natural environment and is commonly found in soil and water, as well as on aged wood and various other plants. Taxonomists have recently categorized *A. pullulans* as an anamorph of *Sydowia polyspora*, a teleomorph (Suzuki et al. 2021). The systematic classification of *A. pullulans* is presented in Table 5.

A. pullulans can consume various carbon sources, such as mannose, glucose, sucrose, maltose, fructose, galactose, xylose, and even agro-industrial waste. The presence of isomerase and hexokinase is necessary for the conversion of the carbon source to UDPG, which is an important precursor for synthesizing pullulan (Sugumaran et al. 2017).

Aureobasidium pullulans has the capacity to produce melanin, so it is often referred to as "black yeast." Despite being a phytopathogenic fungus, *A. pullulans* does not produce mycotoxins. According to Hermanides-Nijhof (1977), it is a ubiquitous, voracious saprophytic fungus that is frequently isolated from wood, water, soil, and other sources of fungi. A. pullulans has been documented in the phyllosphere, toilets, optical lenses, food and feeds, deteriorating house paints, paper mills, hypersaline waters in salterns, hydrocarbons, synthetic materials, leather, human skin, watercolors, and the surface of decomposing leaves and other plant components. Aureobasidium pullulans was selected for pullulan production because of its high production rate and distinctive qualities. Additionally, this organism generates a variety of enzymes, including β-galactosidase, pectinase, amylase, and xylanase (Viveka 2023).

A. pullulans exhibits five distinct morphologies: chlamydospores, mycelia, swollen blastospores, young blastospores, and yeast-like cells. The morphology of the fungus determines the pullulan yield, although it is unclear

Table 5: Systematic classification of *A. pullulans*.

Kingdom	Fungi
Phylum	Ascomycota
Class	Dothideomycetes
Subclass	Dothideomycetidae
Order	Dothideales
Family	Dothioraceae
Genus	*Aureobasidium*
Species	*Aureobasidium pullulans*

which morphological form of *A. pullulans* is responsible for pullulan production (Oğuzhan 2013). One of the characteristics of this fungus is the formation of dark-colored chlamydospores, and colonies initially appear smooth before becoming covered in a slimy mass. A. pullulans is an industrially significant organism because of its capacity to produce the polysaccharide pullulan.

Under mild conditions, on potato dextrose agar plates at room temperature, *Aureobasidium pullulans* normally grows in 7 days and forms colonies with a diameter of 1-3 cm. The colony is initially smooth, flat, slimy, and leathery, and can be pink, white, yellow, or light brown. The formation of chlamydospores causes the colony to turn brown or black during growth. While mature colonies form a visible, smooth, thin-walled mycelium, young colonies display blastoconidial structures under a microscope. Lobed chains of thick-walled chlamydospores and straight conidia are characteristics of *A. pullulans* that can be used to identify it (Wei et al. 2021).

Genome Sequencing of *Aureobasidium pullulans*

The genomes of four varieties of *Aureobasidium pullulans* have been sequenced, revealing genome sizes between 25.43 and 29.62 Mb, encoding 10,266 to 11,866 predicted proteins (Gostinčar et al. 2014). These genomes contain genes for:

- Degradation of plant material (various enzyme families)
- Numerous sugar transporters
- Potential degradation of plastics and aromatic compounds
- Synthesis of pullulan and siderophores (but not aureobasidin A)
- Stress tolerance (aquaporins, aquaglyceroporins, alkali-metal cation transporters, compatible solute and melanin synthesis, high-osmolarity glycerol pathway, bacteriorhodopsin-like proteins)
- All genomes have a homothallic mating-type locus (Gostinčar et al. 2014).

Proteomics and Extracellular Vesicles (EVs):

Proteomic analysis of EVs from A. pullulans identified 642 proteins, primarily associated with primary metabolism (Černoša et al. 2022). EVs also contained proteins from various biosynthetic pathways, indicating multiple biogenesis routes. Small RNA sequencing of these EVs revealed two potentially novel miRNAs.

Functional Omics Applications:

i. Omics approaches are used to study complex interactions between A. pullulans, fruit hosts, pathogens, and native microflora, especially in the context of postharvest disease biocontrol (Castoria et al. 2001).

ii. Genetic engineering and metabolic pathway analysis (e.g., overexpression of main enzymes in the tricarboxylic acid pathway) have been applied to enhance the production of valuable metabolites (Qin et al. 2024).

Taxonomic Insights: Genomic differences among varieties are substantial enough to suggest reclassification into separate species: *A. pullulans*, *A. melanogenum*, *A. subglaciale*, and *A. namibiae (Gostinčar et al. 2014)*.

The availability of genomic, proteomic, and extracellular vesicle data for *A. pullulans* provides a useful basis for addressing important commercial problems related to pullulan production. The identification of genes involved in melanin synthesis, sugar transport, polysaccharide biosynthesis, and stress tolerance provides direct targets for strain engineering intended to increase substrate utilization efficiency and decrease pigment formation, which significantly increases downstream purification costs. The secretion of metabolic enzymes and regulatory chemicals that may affect polysaccharide export and broth rheology was shown in a proteomic study of extracellular vesicles. This suggests the possibility of modifying the molecular weight and viscosity of pullulan by targeted metabolic regulation.

2.3. Carbonaceous Waste

2.3.1. Potato Starch

Potatoes are cheap and widely accessible agricultural products. Potatoes are mostly composed of starch with traces of sugar. The leftover potato starch from potato crisp production and other potato-processing industries is typically in the form of a homogeneous substrate that is devoid of unnecessary components (Chauhan et al. 2023). Potato-derived starch has been used as an alternative carbon source in several industrial fermentation processes. Some strains of *Aureobasidium pullulans* have enzymes that break down starch, but they are more active against linear α-1,4-glucans than against polysaccharides with α-1,6 linkages. Consequently, starch waste must undergo partial hydrolysis to be considered a viable substrate for pullulan production (Göksungur et al. 2011).

Normally, just before the microbial fermentation process begins, starch should be hydrolyzed to produce sugar. However, using potatoes as the carbon source eliminates the need for the expensive β-amylase enzyme. This is mainly due to the significant amount of highly active β-amylase present in potatoes. In addition, the degree of starch or dextrose equivalent hydrolysis determines the amount of pullulan produced. This shows the overall amount of sugar reduction, expressed as a percentage of glucose. While glucose has a dextrose equivalent of 100, some unhydrolyzed starches

have a dextrose equivalent of 0. The pullulan content of the agglutinating substances increased during fermentation using hydrolyzed starch waste as the substrate, and on day six, it reached more than 90% (w/w).

2.3.2. Olive Oil Waste

Phenolic compound-containing waste from olive oil mills is a primary phytotoxic effluent. Olive oil waste damages plants and contaminates the environment (Pinho et al. 2017). Waste from olive oil includes 23 glucose, proteins, and total sugars. These sugars help *Aureobasidium pullulans* grow in the production medium, which increases the pullulan yield. Although a large number of microorganisms cannot survive in the presence of waste olive oil, primarily because of the presence of harmful phenol chemicals. Despite this, *Aureobasidium pullulans* can survive and generate pullulan in the presence of olive oil waste (Youssef et al. 1998).

2.3.3. Sugarcane Bagasse

Sugarcane is one of the main crops grown in large amounts in India. Sugarcane bagasse, a lignocellulosic substance, is produced as solid waste when sugarcane juice is extracted. Approximately 250 kg of bagasse is produced for every ton of sugar produced, for an annual production of 100 million tons. The primary components of sugarcane bagasse are organic matter, lignin, cellulose, hemicelluloses, and ash (Rocha et al. 2015).

2.3.4. Carob Pod

Most crops cannot thrive in the warm and humid climates where carob trees typically flourish. Carob pods can be fed to animals because of their high tannin content. Carob pods are composed of 2% pectin, 5% hemicellulose, 7% cellulose, 20% phenolic components, and 50% sugars. Therefore, carob pod extract has been utilized as a strong carbon substrate in submerged fermentation to produce pullulan (Palaiogianni et al. 2022).

2.3.5. Sweet Potatoes

Sweet potatoes are root vegetables primarily composed of starch and are used for microbial fermentation. Proteins, carbohydrates, lipids, vitamins, and ash are also present in the product. Sweet potatoes are high in starch; however, microbes find it difficult to utilize them. After the saccharification process, hydrolyzed sweet potato can be used as a carbon substrate (Dewan et al. 2013). Fructose, maltose, glucose, maltotriose, and other trace sugars are present in sweet potato hydrolysates.

2.3.6. Brewery Waste

After wort and spent grains are separated, brewing firms release spent grain liquor, a waste product. It contains 12% cellulose, 40% hemicelluloses, 13% lipids, and 3% ash. High biological oxygen demand, which is regarded as a primary contaminant, is also present in spent grain liquor. Its biological oxygen demand harms aquatic life when released into water supplies and pollutes the ecosystem (Chaitanyakumar et al. 2011).

2.3.7. Rice Hull

Rice is widely recognized as a basic essential food in various countries. The outer layer of rice grains, or rice hulls, is produced in large quantities by the rice processing industry. The majority of lignocellulosic materials found in rice hulls are cellulose (50%) and lignin (30%). The composition of rice hulls makes them suitable as carbon substrates for microbial fermentation (Huang & Lo 2019). Microorganisms cannot directly utilize lignocellulosic sugars; therefore, a saccharification procedure is needed to convert this complex into fermentable sugars. After the pretreatment process, rice husk hydrolysate can be utilized as a suitable carbon substrate for pullulan synthesis.

2.3.8. Corn Steep Liquor

Corn steep liquor, a by-product of the maize wet-milling industry, is commonly used as a nutrient source for the production of various microbiological products. This byproduct is primarily used as a nitrogen source. Fungal pigment synthesis can be cultivated using waste stream cellulose generated from corn (Panesar et al. 2015). This waste, which is produced by processing corn and comes from the milling process, is employed as a non-synthetic input in most liquid fertilizer formulations for the cultivation of organic crops. As reported by Chiani et al. (2010), it typically contains 88 g of ash per kg of dry matter, 130–220 g of carbohydrates per kg of dry matter, 205 g of crude protein per kg of dry matter, 525 g of dry matter, and a trace amount of sulfurous acid (<0.01 $g.kg^{-1}$ DM). Additionally, 42% of CSL is a protein (Chiani et al. 2010).

2.3.9. Other Food Industrial Residues

Aureobasidium pullulans has effectively produced pullulan using various food industry residues as substrates. These by-products are rich in carbohydrates and other nutrients, making them suitable and cost-effective alternatives to refined sugars in fermentation. Table 6 shows the conversion of food processing by-products into pullulan by A. *pullulans*.

Although diverse food and agro-industrial wastes have successfully supported pullulan production, the yields varied substantially across substrates and fermentation modes (Table 6). High-performing substrates, such as de-oiled rice bran (54.8 $g.L^{-1}$), potato starch water (54.6 $g.L^{-1}$), sesame seed oil cake (54.5 $g.L^{-1}$), and molasses (45.0 $g.L^{-1}$), delivered superior yields attributable to their abundant fermentable carbohydrates and balanced nutrient

Table 6: Conversion of food processing by-products into pullulan using *Aureobasidium pullulans*.

Processing food waste	Fermentation process	Fermentation time, temperature, etc.	Pullulan yield [g.L^{-1}]	References
Molasses	Shake and flask (Submerged fermentation)	5 days, 35°C, 150 rpm,	45.00	(Srikanth et al. 2014)
Beet Molasses	Stirred tank bioreactor	5 days, 400 rpm, 28°C, aeration rate 2 vvm	6.6	(Göksungur et al. 2004)
	Shake flasks for fermentation.		16.7	
Cassava bagasse	Solid-state fermentation	5 days, 30°C	19.00	(Sugumaran et al. 2014)
De-oiled rice bran	Shake and flask (Submerged)	7 days, 30°C, 150 rpm	54.8	(Singh & Kaur 2019)
Potato starch water	Stirred tank reactor fermentation (Submerged)	5 days,28°C, 500 rpm	54.57	(An et al. 2017)
Rice hull	Stirred tank reactor fermentation (Submerged)	3 days, 28°C, 400 rpm, aeration rate 3 L.min^{-1}	22.20	(Wang et al. 2014)
Sesame seed oil cake	Solid-state in a flask	25°C, 2 h, 200 rpm	54.50	(Mirzaee et al. 2020)

profiles, requiring minimal pretreatment. Conversely, beet molasses produced markedly lower yields (6.6-16.7 g.L^{-1}) in bioreactors, likely due to its sucrose-dominant composition, inhibitory compounds, and shear stress at high agitation rates (400-500 rpm), which impair exopolysaccharide biosynthesis by *Aureobasidium pullulans*.

Furthermore, fermentation mode played a critical role, with solid-state fermentation (SSF) achieving superior yields (19.0-54.5 g.L^{-1}) relative to submerged fermentation (SmF, 6.6-54.8 g.L^{-1}) despite simpler process control. Sesame seed oil cake excelled in SSF because of its concentrated nutrient content and reduced dilution effects, whereas variations in fermentation time, temperature, and agitation influenced oxygen transfer, metabolic activity, and broth viscosity. These observations highlight that pullulan production efficiency is governed by the interplay of substrate composition, fermentation strategy, and process parameters, rather than by substrate type alone.

2.4. Hydrolysis of Waste

Globally, both rural and urban areas in many developing countries, including India, face significant challenges in solid waste management. In some cases, bioconversion of these wastes, such as the microbial synthesis of different enzymes, organic acids, and feed, can be both economically advantageous and reduce environmental pollution (Rishi et al. 2020).

Agro-based industries produce a vast quantity of waste, and if the waste is discarded untreated, it can result in significant environmental issues. However, these agro-industrial wastes are rich sources of nutrients and organic and inorganic matter. This waste can be used as an alternative carbon or nitrogen source for producing various microbial products. It helps reduce the environmental pollution generated by the direct removal of untreated waste and is also economically beneficial (Singh et al. 2021).

Commercially relevant glucose yields can only be obtained from the hydrolysis of cellulose in the presence of a catalyst. (Hu et al. 2015). There are three basic types of catalysts: enzymatic, concentrated acid, and diluted acid. The key benefits of employing enzymatic catalysts are their high specificity, lack of by-products, ability to function in mild environments, environmental friendliness, and the fact that a tiny amount of enzyme produces large yields. However, to use enzymatic hydrolysis, pretreatment is required to free up the structure and provide enzyme access to the active sites. Pre-treatment is frequently carried out using physical methods that require a lot of energy, high pressure, and temperature, or the application of a chemical solvent, such as a diluted acid. Additionally, lignin may block enzyme hydrolysis. Long reaction periods, large reactors, and high enzyme costs are additional drawbacks of enzymatic hydrolysis (Orozco et al. 2007).

The only pressure involved in concentrated acid operations is that produced when materials are pumped from one vessel to another at comparatively low temperatures. The breakdown of sugars into unwanted byproducts is minimized by low pressures and temperatures. The hydrogen bonding in the cellulose chain is broken by concentrated acid, leaving it in an amorphous condition. After decrystallization, cellulose and acid combine to form a homogenous gel that permits hydrolysis reactions. The solution can then be diluted by adding water at low temperatures, which creates an ideal environment for glucose development (Orozco et al. 2007).

Dilute acid hydrolysis is usually carried out at a higher temperature range of 200–240°C, while a lower temperature is required for concentrated acid hydrolysis and higher glucose yields of approximately 90% are achieved using 30–70% sulfuric acid (Niju et al. 2020). However, concentrated acid hydrolysis requires a large amount of acid, which causes corrosion to equipment, and the main drawback of concentrated acid is the high cost of acid, a recovery step is necessary to lower the cost.

Despite its unique features and potential applications, pullulan has limited industrial use due to its high production cost. Pullulan production requires a cost-effective strategy in order to increase its appeal for industrial uses. Several strategies have been employed to lower the price of producing pullulan, such as enhanced strains, genetic engineering advancements, and the discovery of low-cost sources of carbon and nitrogen. Thus, inexpensive substrates are crucial for developing processes that are both profitable and practical.

Mishra et al. (2018) compared pullulan production to that of xanthan gum. They discovered that the cost of pullulan production was three times higher than that of xanthan gum. The production of pullulan from raw material utilization accounts for approximately 30% of the total production costs. Pullulan's unique structural properties probably necessitate a complex and expensive purification process, which accounts for the majority of its higher cost. To lower expenses and improve pullulan's economic feasibility for industrial applications, this study emphasizes the necessity for additional optimization of pullulan production techniques. The price difference between xanthan gum and pullulan may be attributed to economies of scale and decreased demand. The authors stress how crucial it is to deal with these financial aspects to encourage widespread adoption (Mishra et al. 2018).

The type of fermentation process, fed-batch or continuous, also has a significant impact on the amount of pullulan generated by *Aureobasidium pullulans*. Pullulan production is also significantly affected by fermentation conditions. The components of the fermentation medium are used by *Aureobasidium pullulans* cells during fermentation to produce pullulan and cellular biomass. The rheological response of the fermentation broth is influenced by cellular biomass, cell debris, and pullulan accumulation during fermentation. During pullulan production, the rheology of the fermented broth changes from Newtonian to non-Newtonian. Increased viscosity in the fermentation broth reduces the ability of microbial cells to use oxygen and growth factors, leading to decreased pullulan productivity during fermentation. Controlling various parameters during fermentation is necessary (Viveka 2023).

Acid and enzymatic hydrolysis are common methods for breaking down agro-waste into sugars for pullulan production; however, their cost-effectiveness varies in this context. Acid hydrolysis is cheaper and faster for sugar release; however, it produces inhibitors such as furfurals and acids that harm *Aureobasidium pullulans* growth and pullulan yield, raising detoxification costs. Enzymatic hydrolysis provides better sugar quality, fewer inhibitors, and reliable fermentation, leading to a consistent pullulan output despite higher enzyme costs and slower times. For pullulan, enzymatic methods are preferable for process stability and product purity, whereas acid hydrolysis is suitable for setups with detoxification or multi-product recovery. Few studies have compared these economically for pullulan, indicating the need for industrial-scale assessments.

2.5. Pullulan Production Through Fermentation by Using Hydrolysed Cellulosic Waste

A fungus called *Aureobasidium pullulans* produces a commercially available carbohydrate polymer, pullulan. *Aureobasidium pullulans* cells produce pullulan as an exopolysaccharide in the late stages of their life cycle, and it builds up as slime on the cell surface. Various strains of A. pullulans have been documented to produce pullulan via fermentation. (Cheng et al. 2011a). For every strain of *Aureobasidium pullulans* to produce pullulan, a particular media composition and environment are required. The production of pullulan is greatly dependent on the composition of the fermentation medium, specifically the nitrogen source, carbon source, pH, and medium supplements of the fermentation medium. The type of fermentation system, batch, fed-batch, or continuous, also significantly affects the amount of pullulan produced by *A. pullulans* (Youssef et al. 1999).

Pullulan production is significantly influenced by fermentation conditions. During the fermentation process, *Aureobasidium pullulans* metabolizes the components of the medium to form biomass and secretes pullulan. The medium changes from Newtonian to non-Newtonian owing to the effects of cellular biomass, cell detritus, and accumulated pullulan during fermentation on the rheology of the fermentation broth. Because of the increased viscosity of the fermentation medium, pullulan production is less efficient because microbial cells are unable to use oxygen and growth nutrients effectively. The production of pullulan by *Aureobasidium pullulans* can be increased by better controlling different aspects of the fermentation process (Cheng et al. 2011b). Fig. 3 illustrates the pullulan synthesis mechanism.

2.6. Factors Affecting the Production of Pullulan

The production of pullulan is influenced by several variables, including inoculum size, age, temperature during fermentation, and medium pH. *A. pullulans* consumes the medium ingredients during fermentation to produce pullulan and cellular biomass. By altering the rheology of the fermentation broth, biomass, and cell debris buildup, they also have an impact on pullulan production (Wani

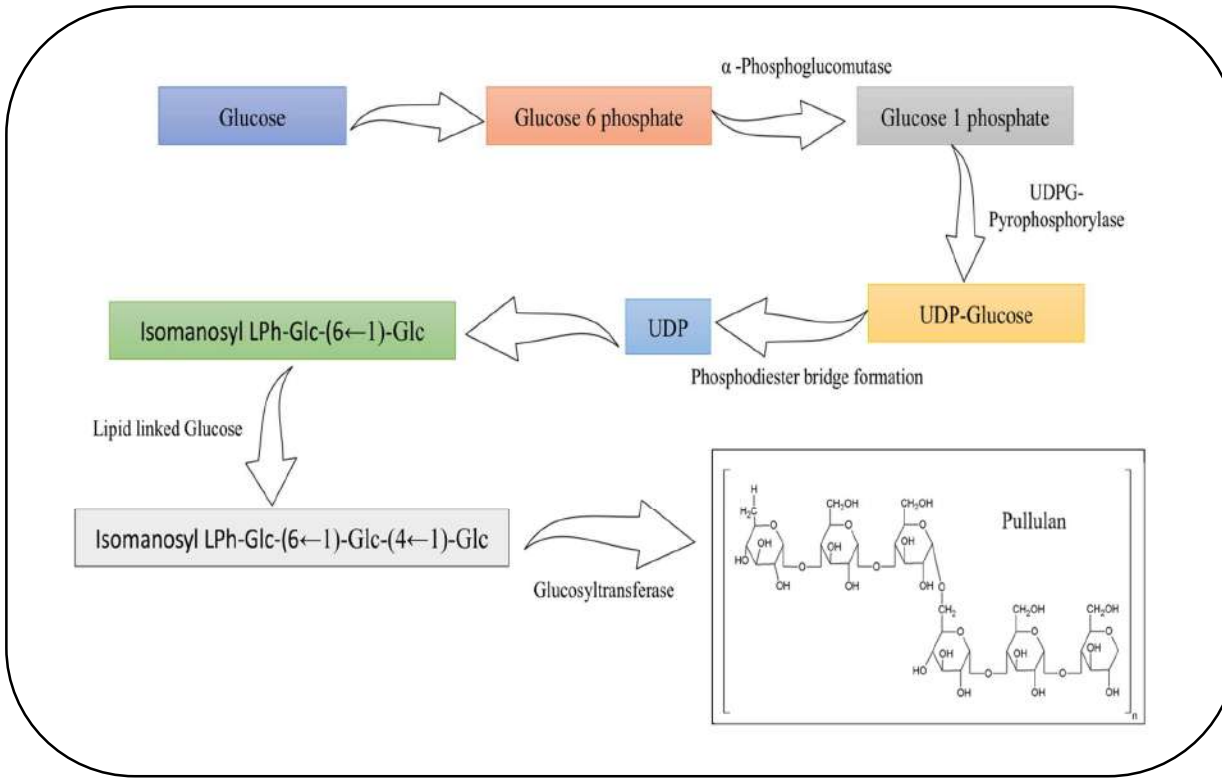


Fig. 3: Pullulan synthesis mechanism. (Mishra et al. 2023).

et al. 2021). A higher viscosity in the fermentation broth reduces the quantity of oxygen and medium components that *A. pullulans* can consume, thereby slowing down pullulan production. The production of pullulan in shake flasks is greatly affected by the composition of the fermentation medium, including the nitrogen source, carbon source, medium supplements, and medium pH. Pullulan production is affected by the following parameters, as demonstrated:

2.6.1. Temperature

Fermentation temperature is a significant factor in pullulan production. The optimum temperature for the growth of microbial cells ranges from 25–30°C, which initiates pullulan production during shake flask fermentation. Lower temperatures slow cell growth and pullulan yield, whereas higher temperatures reduce pullulan yield. The ideal temperature range for pullulan production is between 28 and 30°C (Wu et al. 2012).

2.6.2. pH

One crucial element of the fermentation process is the pH of the fermentation medium. The pH of the strain changes according to the type of microbe used. The parameters of the process and the formulation of the fermentation medium affect the pH of the medium. Variations in pH have a significant effect on the morphological features of the cell culture in the fermentation broth, which slows down the fermentation process and results in less pullulan production. According to most studies, a pH range of 5.0–7.6 is ideal for the growth of microbial cells and pullulan production (Gaur et al. 2010).

2.6.3. Time

Another crucial factor in pullulan synthesis is the fermentation period, which is determined by the requirements of the microbial isolate. After being injected into the fermentation broth, the cultured cells adjust to their surroundings and initiate fermentation. Pullulan production and growth of cells take place during the log phase of cells. The cells enter the stationary phase as fermentation continues, inhibiting pullulan production. Temperature and medium composition affect the duration of pullulan production. Each strain had a different fermentation period. Under shake-flask fermentation, three to seven days is the optimum fermentation period for pullulan production (Hamidi et al. 2019).

2.6.4. Inoculum Size

The term "inoculum size" refers to the number of microbial cells required to inoculate the fermentation medium to produce pullulan. When sufficient microbial cells are present,

A. pullulans cells can grow to the necessary size for pullulan production. The pullulan yield and cell biomass increased as the inoculum size increased. The reduced yield of pullulan during fermentation is caused by insufficient cellular biomass growth from smaller microbial inoculum sizes (Mirzaee et al. 2020). According to reports, the optimal inoculum size of *Aureobasidium pullulans* for pullulan production during shake-flask fermentation is 5% (Ding et al. 2020).

2.6.5. Inoculum Age

One of the crucial factors influencing pullulan production from *Aureobasidium pullulans* is the age of the inoculum. The most active form of *Aureobasidium pullulans* is yeast-like cells, which are normally used for inoculation (Jiang et al. 2018). When producing pullulan, microbial cells in the log phase are typically preferred for inoculation over those in the lag phase. Fermentation times are shortened when the cells of *Aureobasidium pullulans* are in the log phase. However, inoculating *Aureobasidium pullulans* cells during the stationary phase lengthens the fermentation process and decreases the growth uptake factors required to produce pullulan. According to published research, the best inoculum age for pullulan production is one to four days old (Haghighatpanah et al. 2021).

2.6.6. Agitation

Agitation is important for the pullulan production process during shake flask fermentation. The viscosity of the fermentation medium often increases during pullulan formation, making it difficult for the microbes to use the medium's ingredients (Kumar et al. 2019). During fermentation, agitation keeps the medium homogeneous and helps in the constant mixing of its constituent parts. In a homogeneous medium, microorganisms have constant access to oxygen (Lazaridou et al. 2002) and easy access to the nutrients of the medium (Jafari et al. 2007). It promotes pullulan accumulation and proliferation of microbial cells (Jafari et al. 2007, Lazaridou et al. 2002). A concentration gradient between the inside and outside of the cell, as well as constant mass transfer across the cell wall, is maintained by appropriate agitation (Choudhury et al. 2012). The type of microbe also determines whether agitation is necessary.

2.6.7. Carbon Sources

The primary source of energy in the fermentation medium is the supply of carbon, which promotes microbial cell growth. There have been reports on the production of pullulan using a variety of carbon sources, including lactose, sucrose, galactose, glycerol, glucose, xylose, arabinose, cellobiose, rhamnose, inulin, fructose, and maltose (Singh et al. 2008). The majority of research work has shown that when sucrose is utilized in shake-flask fermentations as a carbon source, the maximum pullulan production occurs (Badhwar et al. 2018, Badhwar et al. 2019, Chen et al. 2018, Chen et al. 2020, Chen et al. 2020b, Haghighatpanah et al. 2021, Hamidi et al. 2019, Jiang 2010, Jiang et al. 2019). During fermentation, sucrose is the most effective inducer of β-fructofuranosidase in *Aureobasidium pullulans* cells because pullulan is a nonreducing sugar. When the sucrose concentration in the fermentation medium is low, β-fructofuranosidase catalyzes the conversion of sucrose into glucose and fructose.

However, in the initial stages of fermentation, fructose and sucrose are bound to each other. β-fructofuranosidase also promotes the accumulation of ketose when sucrose concentration is high (Sheng et al. 2016). In shake-flask fermentations, glucose is another common carbon source in the fermentation medium, which is used to produce pullulan (Cheng et al. 2011a, Gaur et al. 2010, Hamidi et al. 2019, Liu et al. 2018, Ma et al. 2014, Prasongsuk et al. 2005, 2006). The Embden-Meyerhof-Parnas pathway is used in A. *pullulans* biosynthesis to produce pullulan from glucose during fermentation (Fernandes et al. 2024). Less pullulan yield from glucose has been found in most investigations than that from sucrose (Sheng et al. 2016).

2.6.8. Nitrogen Sources

During fermentation, the nitrogen source controls the metabolic activity of the cells and affects pullulan production (Wang et al. 2015). Pullulan production has been reported using a variety of complex organic nitrogen sources, such as urea, peptone, yeast extract, and ammonium sulfate, as well as inorganic nitrogen sources, such as ammonium oxalate, ammonium formate, ammonium chloride, ammonium citrate, ammonium nitrate, ammonium acetate, copper sulfate, and sodium nitrate. In most shake-flask fermentations, a combination of yeast extract and ammonium sulfate has been identified as the optimal nitrogen source for *Aureobasidium pullulans* to produce pullulan. Pullulan has also been manufactured using only yeast extract (An et al. 2019, Hamidi et al. 2019, Jiang 2010). This is an extremely multifaceted organic nitrogen supply composed of many peptides, amino acids, vitamins, minerals, and other substances.

2.7. Downstream Processing of Pullulan

Downstream processing is a multi-step procedure used to safely recover a microbial product while maintaining its biological activity and purity. It must be effective, reproducible, and maximize product recovery yield while requiring the least number of resources to produce (Singh 2014). Selecting inexpensive or complex substrates to formulate fermentation media on an industrial scale typically results in lower upstream-processing costs. However,

the downstream process requires more steps to separate inexpensive/complex substrates, which are highly impurity-filled, thereby increasing the cost of the final product. However, using highly purified substrates in the fermentation medium reduces the complexity of downstream processing steps, but their cost is high.

Before downstream processing, the fermented medium may occasionally be pretreated to preserve the microbial product and prevent its degradation (Svarovsky 2001). To fulfill the requirements for a certain microbial product's usage, various downstream processing methods are used to achieve the required level of purity. In general, it is best to reduce the steps involved in downstream processing to reduce the loss of microbiological products at various purification steps, shorten process times, and lower production costs.

Downstream processing of pullulan includes liquid-liquid separation after solid-liquid separation. Conventional techniques for downstream processing of pullulan include precipitation using organic solvents, dialysis, ultrafiltration, and gel filtration chromatography. NMR spectroscopy, chromatographic techniques, and FTIR spectroscopy are further used to confirm the pullulan structure (Shingel 2002). The design of pullulan production from agricultural waste is shown in Fig. 4.

3. PROBLEMS FACED DURING PULLULAN PRODUCTION

Despite its unique properties, the high production cost of pullulan, which is often three times higher than that of other polysaccharides such as xanthan or dextran, remains a critical

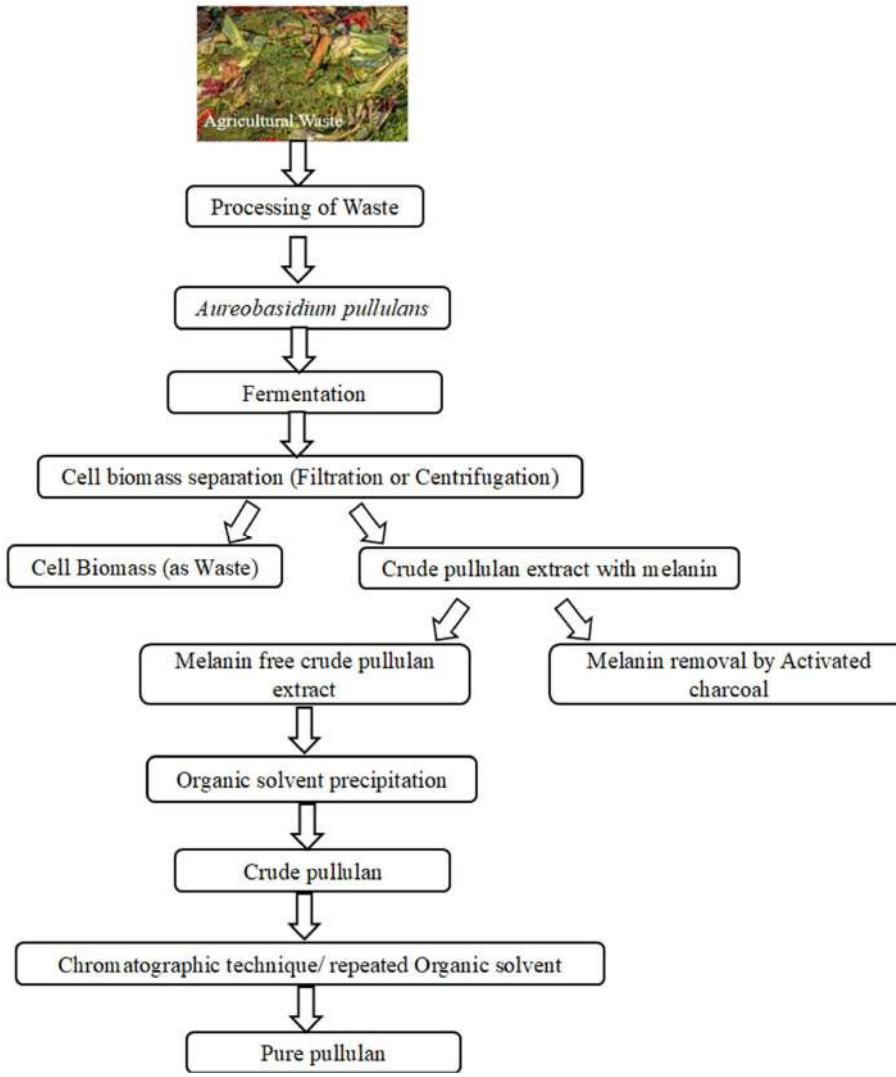


Fig. 4: Design of pullulan production from agricultural waste (Singh et al. 2019).

barrier to its widespread industrial adoption. This is due to several factors.

- High Cost and Complexity of Raw Material Preparation:

  The high cost of nutrients and raw materials, even when using waste substrates, and the need for extensive pretreatment and hydrolysis of some residues (Cruz-Santos et al. 2023). This captures the dual challenge of expensive nutrients and the need for extensive pretreatment or hydrolysis when using certain agricultural or food industry residues as substrates for pullulan production. The cost of raw materials can account for up to 30% of the total production costs, and the requirement for additional processing steps further increases overall expenses and operational complexity (Mehta et al. 2014).

- Downstream Processing:

  Downstream processing challenges, such as the high viscosity of fermentation broths and the co-production of melanin pigments, complicate purification and increase costs.

i. High viscosity of the culture broth:

  The high viscosity of the broth is a major problem faced during pullulan production. During fermentation, pullulan may degrade (pullulanolysis) due to the production of melanin. In the fermentation medium, microbial cells, residual media components, cellular debris, and extracellular metabolites are left after the fermentation process is completed. Hence, for the separation of these impurities, an alternative downstream process is needed before the precipitation of pullulan (Ray & Moorthy 2007).

ii. Melanin production:

  The pentaketide pathway is involved in the intracellular and extracellular synthesis of melanin pigments and pullulan. Medium composition and culture conditions affect melanin synthesis. Activated charcoal has been used to separate melanin (Kachhawa et al. 2003). However, the main disadvantage of activated charcoal is that some pullulan and fine charcoal powders are lost due to contamination. The viscosity of the broth also increased with the introduction of activated charcoal. Therefore, it is necessary to develop another technique for separating the pigments in melanin. The need for colorless or low-melanin-producing strains is pressing, as melanin removal adds a costly step to the process.

4. INDUSTRIAL AND COMMERCIAL APPLICATIONS OF PULLULAN

Pullulan has several uses in the biomedical industries, food, cosmetics, and pharmaceutical industries because of its special qualities (De Souza et al. 2023). Pullulan finds application in the pharmaceutical business as a packaging material. According to Tabasum et al. (2018), pullulan can also be used as a low-calorie polysaccharide in food packaging, dietary fibers, drinks, stabilizers, binders, and coating materials. Pullulan serves as a novel biomaterial in tissue engineering and various biomedical fields, and its derivatives have applications in gene targeting and medication (Tabasum et al. 2018).

Pullulan has various uses in different kinds of cosmetic products, such as cosmetic lotions, cosmetic powders, rouges, cosmetics for use around the eyes, facial packs, shampoos, set lotions, hair lacquers, and toothpaste (Roy et al. 2020). The exclusive characteristics and physical features of pullulan make it an ideal biopolymer for use in the cosmetics industry. The greatest application of this polysaccharide is in oral-care products. These products using pullulan have been broadly commercialized (Singh & Saini 2012). Owing to its non-irritating properties, pullulan is widely used in a range of cosmetic products, powders, hair styling products, lotions, shampoos, and facial masks. It is used in mascara and eyelash products as a film-forming agent to increase lash length and volume, resulting in a more voluminous and defined appearance. Additionally, pullulan is employed in hair care items such as gels, hair sprays, and styling creams, where it acts as a film-forming and fixative agent, providing hold and improving the durability of hairstyles (Coltelli et al. 2020).

Pullulan-based skin care products are useful as a skin-whitening agent. It supports the tissue and corrects the structural architecture, which is necessary for tissue regeneration (Xiao et al. 2012). Pullulan is incorporated into anti-aging formulations, including firming lotions and wrinkle creams. It offers a temporary tightening effect, providing the skin with a smoother and more youthful appearance (Chen et al. 2014).

Pullulan can be utilized in next-generation point-of-care testing for the storage of labile biomolecules as stable water-soluble pellets for a long time, and drug capsules made of pullulan are welcomed by vegetarians, Muslims, diabetics, and patients with restricted diets (Liu et al. 2017).

Cell division and growth mechanisms for skin renewal slow down as the skin ages (Coltelli et al. 2020). A novel cosmetic formulation may incorporate an efficient delivery system capable of crossing the skin barrier and releasing active compounds in the targeted skin layers. When an element is delivered to a certain layer, the intercellular connection is restored, and the aging or damaged dermis structure is hydrated and renewed (Prausnitz et al. 2004).

Table 7: Properties of pullulan and their cosmeceutical properties (Coltelli et al. 2020).

Pullulan properties	Cosmetic application
White to off-white appearance, non-toxic, odourless, water-soluble, adhesive, and tacky	Used as an ingredient in liquid and paste rouges to improve texture and adhesion
Film-forming, safe, and non-irritant	Ingredients in eyeliners and eye shadows for smooth application and skin compatibility
Moisturizing, adhesive, film-forming, retains continuity during peeling, with film shrinkage providing skin surface tension	Active component in facial packs to enhance skin feel and performance
Foam-enhancing and stabilizing properties	Used in hair shampoos to improve foam quality and stability
High coherence, viscosity, non-toxic, and foam stability during storage	Toothpaste ingredient for texture and foam consistency
Good water solubility contributes to transparent film formation	Applied to face masks and hair styling products for aesthetic and functional benefits
Strong film-forming ability, adhesive, hair-setting capacity, and ease of removal	Used in body lotions and hair lacquers for styling ease and product removal

Traditionally, the carriers for cosmetic products have been polymers with strong water solubility, such as carboxymethyl cellulose, alginate, hydroxyethyl cellulose, starch, and methyl cellulose. Novel cosmetic products can also be developed using natural polysaccharides as carriers (Danti et al. 2019, Morganti & Coltelli 2019). According to Parul and Dubey (2018), it is completely non-mutagenic, non-immunogenic, and non-carcinogenic. It is highly water-soluble, tacky, and low-viscosity, with a high moisture absorption rate. The comparatively low viscosity of pullulan makes it an excellent binder for cosmetic formulations (Parul & Dubey 2018).

Pullulan is an element that can increase the quality of cosmetic products. Pullulan can be used in any amount in a cosmetic product without limitations due to its GRAS designation and lack of toxicity. Pullulan's photoprotective qualities have led to a rise in the demand for hair and skin care products rather than makeup with chemicals. Table 7 shows the properties of pullulan and its cosmeceutical properties.

5. CONCLUSIONS

Agro-industrial waste presents a sustainable and cost-effective carbon source for producing pullulan, thanks to its abundance, nutritional content, and potential for waste valorization. Although extensive research has demonstrated the feasibility of synthesizing pullulan from various waste feedstocks, large-scale industrial application is still limited by high downstream processing costs. These costs are primarily driven by melanin pigmentation, excessive broth viscosity, and inconsistent purity when using waste substrates, all of which increase purification requirements and negatively impact economic viability. Among various mitigation approaches, omics-informed strain engineering combined with precise fermentation control has proven to be the most promising solution. Insights from genomics, transcriptomics, and proteomics have led to the development of *Aureobasidium pullulans* strains that exhibit reduced pigmentation, improved waste substrate utilization, and controlled polysaccharide molecular weight. These advances, alongside process optimization, aim to deliver higher yields and greater consistency. Nonetheless, downstream technologies alone are insufficient without concurrent upstream biological improvements. Key gaps in the literature include the lack of pilot-scale demonstrations, waste-specific techno-economic assessments, and integrated strain-process strategies. Addressing these gaps through multidisciplinary efforts is essential to transitioning pullulan production from laboratory prototypes to competitive, circular bioeconomy processes.

6. ACKNOWLEDGEMENT

The authors are grateful to the Honourable Chancellor, KVV Deemed to be University, Karad, for the valuable support and the Dean, KIST, for providing all the research facilities.

7. REFERENCES

Abhilash, M. and Thomas, D., 2017. Biopolymers for biocomposites and chemical sensor applications. In: *Biopolymer Composites in Electronics*. Elsevier, pp.405-435. [DOI]

Agrawal, S., Budhwani, D., Gurjar, P., Telange, D. and Lambole, V., 2022. Pullulan-based derivatives: synthesis, enhanced physicochemical properties, and applications. *Drug Delivery*, 29, pp.3328-3339. [DOI]

Al-Araimi, S.H., Elshafie, A., Al-Bahry, S.N., Al-Wahaibi, Y.M. and Al-Bemani, A.S., 2021. Biopolymer production by *Aureobasidium mangrovei* SARA138-H and its potential for oil recovery enhancement. *Applied Microbiology and Biotechnology*, 105, pp.105-117. [DOI]

An, C., Ma, S., Chang, F. and Xue, W., 2017. Efficient production of pullulan by *Aureobasidium pullulans* grown on mixtures of potato starch hydrolysate and sucrose. *Brazilian Journal of Microbiology*, 48, pp.180-185. [DOI]

An, C., Ma, S., Xue, W., Liu, C. and Ding, H., 2019. Comparative study of different molecular weight pullulan productions by *Aureobasidium pullulans* CGMCC No.11602. *3 Biotech*, 9, p.156. [DOI]

Ates, O., 2015. Systems biology of microbial exopolysaccharides production. *Frontiers in Bioengineering and Biotechnology*, 3. [DOI]

Avenas, P., 2012. Etymology of main polysaccharide names. In: P. Navard, ed., *The European Polysaccharide Network of Excellence (EPNOE)*. Springer Vienna, pp.13-21. [DOI]

Badhwar, P., Kumar, P. and Dubey, K.K., 2019. Extractive fermentation for process integration and amplified pullulan production by *A. pullulans* in aqueous two phase systems. *Scientific Reports*, 9, p.32. [DOI]

Badhwar, P., Kumar, P. and Dubey, K.K., 2018. Development of aqueous two-phase systems comprising poly ethylene glycol and dextran for purification of pullulan: Phase diagrams and fiscal analysis. *Engineering in Life Sciences*, 18, pp.524-531. [DOI]

Basumatary, I.B., Mukherjee, A., Katiyar, V. and Kumar, S., 2022. Biopolymer-based nanocomposite films and coatings: recent advances in shelf-life improvement of fruits and vegetables. *Critical Reviews in Food Science and Nutrition*, 62, pp.1912-1935. [DOI]

Bender, H., Lehmann, J. and Wallenfels, K., 1959. Pullulan, an extracellular glucan from *Pullularia pullulans*. *Biochimica et Biophysica Acta*, 36, pp.309-316. [DOI]

Bernier, B., 1958. The production of polysaccharides by fungi active in the decomposition of wood and forest litter. *Canadian Journal of Microbiology*, 4, pp.195-204. [DOI]

Castoria, R., De Curtis, F., Lima, G., Caputo, L., Pacifico, S. and De Cicco, V., 2001. *Aureobasidium pullulans* (LS30-) an antagonist of postharvest pathogens of fruits: study on its modes of action. *Postharvest Biology and Technology*, 22, pp.7-17. [DOI]

Černoša, A., Gostinčar, C., Lavrin, T., Kostanjšek, R., Lenassi, M. and Gunde-Cimerman, N., 2022. Isolation and characterization of extracellular vesicles from biotechnologically important fungus *Aureobasidium pullulans*. *Fungal Biology and Biotechnology*, 9, p.16. [DOI]

Chaitanyakumar, D., Unnisa, S.A., Rao, B. and Kumar, V., 2011. Efficiency assessment of combined treatment technologies: A case study of Charminar Brewery wastewater treatment plant. *Indian Journal of Fundamental and Applied Life Sciences*, 1(2), pp.138-145.

Chauhan, A., Islam, F., Imran, A., Ikram, A., Zahoor, T., Khurshid, S. and Shah, M.A., 2023. A review on waste valorization, biotechnological utilization, and management of potato. *Food Science & Nutrition*, 11, pp.5773-5785. [DOI]

Chen, S., Zheng, H., Gao, J., Song, H. and Bai, W., 2023. High-level production of pullulan and its biosynthesis regulation in *Aureobasidium pullulans* BL06. *Frontiers in Bioengineering and Biotechnology*, 11, p.31875. [DOI]

Chen, T.J., Chi, Z., Jiang, H., Liu, G.L., Hu, Z. and Chi, Z.M., 2018. Cell wall integrity is required for pullulan biosynthesis and glycogen accumulation in *Aureobasidium melanogenum* P16. *Biochimica et Biophysica Acta (BBA) - General Subjects*, 1862, pp.1516-1526. [DOI]

Chen, T.J., Liu, G.L., Chen, L., Yang, G., Hu, Z., Chi, Z.M. and Chi, Z., 2020a. Alternative primers are required for pullulan biosynthesis in *Aureobasidium melanogenum* P16. *International Journal of Biological Macromolecules*, 147, pp.10-17. [DOI]

Chen, T.J., Liu, G.L., Wei, X., Wang, K., Hu, Z., Chi, Z. and Chi, Z.M., 2020b. A multidomain α-glucan synthetase 2 (AmAgs2) is the key enzyme for pullulan biosynthesis in *Aureobasidium melanogenum* P16. *International Journal of Biological Macromolecules*, 150, pp.1037-1045. [DOI]

Chen, Y., Guo, J., Li, F., Liu, M., Zhang, X., Guo, X. and Xiao, D., 2014. Production of pullulan from xylose and hemicellulose hydrolysate by *Aureobasidium pullulans* AY82 with pH control and DL-dithiothreitol addition. *Biotechnology and Bioprocess Engineering*, 19, pp.282-288. [DOI]

Cheng, K.C., Demirci, A. and Catchmark, J.M., 2011a. Evaluation of medium composition and fermentation parameters on pullulan production by *Aureobasidium pullulans*. *Food Science and Technology International*, 17, pp.99-109. [DOI]

Cheng, K.C., Demirci, A. and Catchmark, J.M., 2011b. Pullulan: biosynthesis, production, and applications. *Applied Microbiology and Biotechnology*, 92, pp.29-44. [DOI]

Chiani, M., Akbarzadeh, A., Farhangi, A. and Mehrabi, M.R., 2010. Production of desferrioxamine B (Desferal) using corn steep liquor in *Streptomyces pilosus*. *Pakistan Journal of Biological Sciences*, 13, pp.1151-1155. [DOI]

Choudhury, A., Sharma, N. and Prasad, G., 2012. Deoiled jatropha seed cake is a useful nutrient for pullulan production. *Microbial Cell Factories*, 11, p.39. [DOI]

Coltelli, M.B., Danti, S., De Clerck, K., Lazzeri, A. and Morganti, P., 2020a. Pullulan for advanced sustainable body- and skin-contact applications. *Journal of Functional Biomaterials*, 11, p.20. [DOI]

Coltelli, M.B., Danti, S., De Clerck, K., Lazzeri, A. and Morganti, P., 2020b. Pullulan for advanced sustainable body- and skin-contact applications. *Journal of Functional Biomaterials*, 11, p.20. [DOI]

Cruz-Santos, M.M., Antunes, F.A.F., Arruda, G.L., Shibukawa, V.P., Prado, C.A., Ortiz-Silos, N., Castro-Alonso, M.J., Marcelino, P.R.F. and Santos, J.C., 2023. Production and applications of pullulan from lignocellulosic biomass: Challenges and perspectives. *Bioresource Technology*, 385, p.129460. [DOI]

Danti, S., Trombi, L., Fusco, A., Azimi, B., Lazzeri, A., Morganti, P. and Coltelli, M.B., 2019. Chitin nanofibrils and nanolignin as functional agents in skin regeneration. *International Journal of Molecular Sciences*, 20, p.2669. [DOI]

De Souza, C.K., Ghosh, T., Lukhmana, N., Tahiliani, S., Priyadarshi, R., Hoffmann, T.G., Purohit, S.D. and Han, S.S., 2023. Pullulan as a sustainable biopolymer for versatile applications: A review. *Materials Today Communications*, 36, p.106477. [DOI]

Dewan, A., Li, Z., Han, B. and Karim, M.N., 2013. Saccharification and fermentation of waste sweet potato for bioethanol production. *Journal of Food Process Engineering*, 36, pp.739-747. [DOI]

Ding, Y., Jiang, F., Chen, L., Lyu, W., Chi, Z., Liu, C. and Chi, Z., 2020. An alternative hard capsule prepared with the high molecular weight pullulan and gellan: Processing, characterization, and in vitro drug release. *Carbohydrate Polymers*, 237, p.116172. [DOI]

Fernandes, S., Dias, B., Gonçalves, D.A., Nobre, C., Belo, I. and Lopes, M., 2024. Co-production of gluconic acid and fructo-oligosaccharides by *Aureobasidium pullulans* from sugarcane molasses: Effect of oxygen transfer rate in stirred tank and airlift bioreactors. *Food and Bioprocess Technology*, 17, pp.1321-1334. [DOI]

Ferreira, L.M., Velasquez, A.D.A., Schaffazick, S.R. and Cruz, L., 2015. Pullulan: an advantageous natural polysaccharide excipient to formulate tablets of alendronate-loaded microparticles. *Brazilian Journal of Pharmaceutical Sciences*, 51, pp.27-33. [DOI]

Gaur, R., Singh, R., Tiwari, S., Yadav, S.K. and Daramwal, N.S., 2010. Optimization of physico-chemical and nutritional parameters for a novel pullulan-producing fungus, *Eurotium chevalieri*. *Journal of Applied Microbiology*, 109, pp.1035-1043. [DOI]

Ghimici, L. and Constantin, M., 2020. A review of the use of pullulan derivatives in wastewater purification. *Reactive and Functional Polymers*, 149, p.104510. [DOI]

Göksungur, Y., Uçan, A. and Güvenç, U., 2004. Production of pullulan from beet molasses and synthetic medium by *Aureobasidium pullulans*. *Turkish Journal of Biology*, 28(1), pp.23-30.

Göksungur, Y., Uzunoğulları, P. and Dağbağlı, S., 2011. Optimization of pullulan production from hydrolysed potato starch waste by response surface methodology. *Carbohydrate Polymers*, 83, pp.1330-1337. [DOI]

Gostinčar, C., Ohm, R.A., Kogej, T., Sonjak, S., Turk, M., Zajc, J., Zalar, P., Grube, M., Sun, H., Han, J., Sharma, A., Chiniquy, J., Ngan, C., Lipzen, A., Barry, K., Grigoriev, I.V. and Gunde-Cimerman, N., 2014. Genome sequencing of four *Aureobasidium pullulans* varieties: biotechnological potential, stress tolerance, and description of new species. *BMC Genomics*, 15, p.549. [DOI]

Haghighatpanah, N., Khodaiyan, F., Kennedy, J.F. and Hosseini, S.S., 2021. Optimization and characterization of pullulan obtained from corn bran hydrolysates by *Aureobasidium pullulans* KY767024. *Biocatalysis and Agricultural Biotechnology*, 33, p.101959. [DOI]

Hamidi, M., Kennedy, J.F., Khodaiyan, F., Mousavi, Z. and Hosseini, S.S., 2019. Production optimization, characterization and gene expression of pullulan from a new strain of *Aureobasidium pullulans*. *International Journal of Biological Macromolecules*, 138, pp.725-735. [DOI]

Hii, S.L., Tan, J.S., Ling, T.C. and Ariff, A.B., 2012. Pullulanase: Role in starch hydrolysis and potential industrial applications. *Enzyme Research*, 2012, pp.1-14. [DOI]

Hu, L., Lin, L., Wu, Z., Zhou, S. and Liu, S., 2015. Chemocatalytic hydrolysis of cellulose into glucose over solid acid catalysts. *Applied Catalysis B: Environmental*, 174-175, pp.225-243. [DOI]

Huang, Y.F. and Lo, S.L., 2019. Utilization of rice hull and straw. In: *Rice*. Elsevier, pp.627-661. [DOI]

Jafari, A.R., Sarrafzadeh, M.H., Alemzadeh, I. and Vosoughi, M., 2007. Effect of stirrer speed and aeration rate on the production of glucose oxidase by *Aspergillus niger*. *Journal of Biological Sciences*, 7, pp.270-275. [DOI]

Jiang, H., Chen, T.J., Chi, Z., Hu, Z., Liu, G.L., Sun, Y., Zhang, S.H. and Chi, Z.M., 2019. Macromolecular pullulan produced by *Aureobasidium melanogenum* 2-13 isolated from the Taklimakan desert and its crucial roles in resistance to the stress treatments. *International Journal of Biological Macromolecules*, 135, pp.429-436. [DOI]

Jiang, H., Xue, S.J., Li, Y.F., Liu, G.L., Chi, Z.M., Hu, Z. and Chi, Z., 2018. Efficient transformation of sucrose into high pullulan concentrations by *Aureobasidium melanogenum* TN2-1 isolated from a natural honey. *Food Chemistry*, 257, pp.29-35. [DOI]

Jiang, L., 2010. Optimization of fermentation conditions for pullulan production by *Aureobasidium pullulans* using response surface methodology. *Carbohydrate Polymers*, 79, pp.414-417. [DOI]

Kachhawa, D.K., Bhattacharjee, P. and Singhal, R.S., 2003. Studies on downstream processing of pullulan. *Carbohydrate Polymers*, 52, pp.25-28. [DOI]

Kostag, M. and El Seoud, O.A., 2021. Sustainable biomaterials based on cellulose, chitin and chitosan composites - A review. *Carbohydrate Polymer Technologies and Applications*, 2, p.100079. [DOI]

Kumar, B., Katoch, A., Prasad, G.S. and Roy Choudhury, A., 2019. Understanding the effect of impeller configurations on pullulan production by *Aureobasidium pullulans* RBF 4A3. *Frontiers in Bioengineering and Biotechnology*, 7, p.223. [DOI]

Lazaridou, A., Roukas, T., Biliaderis, C.G. and Vaikousi, H., 2002. Characterization of pullulan produced from beet molasses by *Aureobasidium pullulans* in a stirred tank reactor under varying agitation. *Enzyme and Microbial Technology*, 31, pp.122-132. [DOI]

Li, H., Xue, Y., Jia, B., Bai, Y., Zuo, Y., Wang, S., Zhao, Y., Yang, W. and Tang, H., 2018. The preparation of hyaluronic acid grafted pullulan polymers and their use in the formation of novel biocompatible wound healing film. *Carbohydrate Polymers*, 188, pp.92-100. [DOI]

Li, Y., Chi, Z., Wang, G.Y., Wang, Z.P., Liu, G.L., Lee, C.F., Ma, Z.C. and Chi, Z.M., 2015. Taxonomy of *Aureobasidium* spp. and biosynthesis and regulation of their extracellular polymers. *Critical Reviews in Microbiology*, 41, pp.228-237. [DOI]

Liu, N.N., Chi, Z., Liu, G.L., Chen, T.J., Jiang, H., Hu, Z. and Chi, Z.M., 2018. α-Amylase, glucoamylase and isopullulanase determine molecular weight of pullulan produced by *Aureobasidium melanogenum* P16. *International Journal of Biological Macromolecules*, 117, pp.727-734. [DOI]

Liu, N.N., Chi, Z., Wang, Q.Q., Hong, J., Liu, G.L., Hu, Z. and Chi, Z.M., 2017. Simultaneous production of both high molecular weight pullulan and oligosaccharides by *Aureobasidium melanogenum* P16 isolated from a mangrove ecosystem. *International Journal of Biological Macromolecules*, 102, pp.1016-1024. [DOI]

Ma, Z.C., Fu, W.J., Liu, G.L., Wang, Z.P. and Chi, Z.M., 2014. High-level pullulan production by *Aureobasidium pullulans* var. *melanogenium* P16 isolated from mangrove system. *Applied Microbiology and Biotechnology*, 98, pp.4865-4873. [DOI]

Mehta, A., Prasad, G.S. and Choudhury, A.R., 2014. Cost effective production of pullulan from agri-industrial residues using response surface methodology. *International Journal of Biological Macromolecules*, 64, pp.252-256. [DOI]

Mirzaee, H., Khodaiyan, F., Kennedy, J.F. and Hosseini, S.S., 2020. Production, optimization and characterization of pullulan from sesame seed oil cake as a new substrate by *Aureobasidium pullulans*. *Carbohydrate Polymer Technologies and Applications*, 1, p.100004. [DOI]

Mishra, B., Mohanta, Y.K., Varjani, S., Mandal, S.K., Lakshmayya, N.S.V., Chaturvedi, P., Awasthi, M.K., Zhang, Z., Sindhu, R., Binod, P., Singhania, R.R. and Kumar, V., 2023. A critical review on valorization of food processing wastes and by-products for pullulan production. *Journal of Food Science and Technology*, 60, pp.2121-2131. [DOI]

Mishra, B., Zamare, D. and Manikanta, A., 2018. Selection and utilization of agro-industrial waste for biosynthesis and hyper-production of pullulan: A review. In: S.J. Varjani, B. Parameswaran, S. Kumar and S.K. Khare, eds., *Biosynthetic Technology and Environmental Challenges*. Singapore: Springer Singapore, pp.89-103. [DOI]

Morganti, P. and Coltelli, M.B., 2019. A new carrier for advanced cosmeceuticals. *Cosmetics*, 6, p.10. [DOI]

Nasrollahzadeh, M., Nezafat, Z., Shafiei, N. and Soleimani, F., 2021. Polysaccharides in food industry. In: *Biopolymer-Based Metal Nanoparticle Chemistry for Sustainable Applications*. Elsevier, pp.47-96. [DOI]

Niju, S., Swathika, M. and Balajii, M., 2020. Pretreatment of lignocellulosic sugarcane leaves and tops for bioethanol production. In: *Lignocellulosic Biomass to Liquid Biofuels*. Elsevier, pp.301-324. [DOI]

Oğuzhan, P., 2013. Pullulan: Production and usage in food industry. *African Journal of Food Science and Technology*, 4(3), pp.57-63.

Orozco, A., Ahmad, M., Rooney, D. and Walker, G., 2007. Dilute acid hydrolysis of cellulose and cellulosic bio-waste using a microwave reactor system. *Process Safety and Environmental Protection*, 85, pp.446-449. [DOI]

Palaiogianni, A., Stylianou, M., Sarris, D. and Agapiou, A., 2022. Carob-agro-industrial waste and potential uses in the circular economy. In: M.F. Ramadan and M.A. Farag, eds., *Mediterranean Fruits Bio-Wastes*. Cham: Springer International Publishing, pp.765-797. [DOI]

Panesar, R., Kaur, S. and Panesar, P.S., 2015. Production of microbial pigments utilizing agro-industrial waste: a review. *Current Opinion in Food Science*, 1, pp.70-76. [DOI]

Parul, M. and Dubey, K.K., 2018. Insights of microbial pullulan production: A bioprocess engineer assessment. *Current Biotechnology*, 7, pp.262-272. [DOI]

Pinho, I.A., Lopes, D.V., Martins, R.C. and Quina, M.J., 2017. Phytotoxicity assessment of olive mill solid wastes and the influence of phenolic compounds. *Chemosphere*, 185, pp.258-267. [DOI]

Pirsa, S. and Hafezi, K., 2023. Hydrocolloids: Structure, preparation method, and application in food industry. *Food Chemistry*, 399, p.133967. [DOI]

Prasongsuk, S., Berhow, M.A., Dunlap, C.A., Weisleder, D., Leathers, T.D., Eveleigh, D.E. and Punnapayak, H., 2006. Pullulan production by tropical isolates of *Aureobasidium pullulans*. *Journal of Industrial Microbiology & Biotechnology*, 34, pp.55-61. [DOI]

Prasongsuk, S., Sullivan, R.F., Kuhirun, M., Eveleigh, D.E. and Punnapayak, H., 2005. Thailand habitats as sources of pullulan-producing strains of *Aureobasidium pullulans*. *World Journal of Microbiology and Biotechnology*, 21, pp.393-398. [DOI]

Prausnitz, M.R., Mitragotri, S. and Langer, R., 2004. Current status and future potential of transdermal drug delivery. *Nature Reviews Drug Discovery*, 3, pp.115-124. [DOI]

Fact.MR. (2025). *Pullulan Market Size, Share, Growth and Forecast*

2025–2035. Fact.MR. Retrieved June 24, 2026, from https://www.factmr.com/report/pullulan-market

Qin, Z., Feng, J., Li, Y., Zheng, Y., Moore, C. and Yang, S.T., 2024. Engineering the reductive tricarboxylic acid pathway in *Aureobasidium pullulans* for enhanced biosynthesis of poly-L-malic acid. *Bioresource Technology*, 393, p.130122. [DOI]

Rajeeva, G., Ranjan, S., Monika, G. and Manogya, K.G., 2010. *Aureobasidium pullulans*, an economically important polymorphic yeast with special reference to pullulan. *African Journal of Biotechnology*, 9, pp.7989-7997. [DOI]

Ray, R.C. and Moorthy, S.N., 2007. Exopolysaccharide (pullulan) production from cassava starch residue by *Aureobasidium pullulans* strain MTTC 1991. *Journal of Scientific and Industrial Research*, 66(3), pp.252-255.

Rishi, V., Sandhu, A.K., Kaur, A., Kaur, J., Sharma, S. and Soni, S.K., 2020. Utilization of kitchen waste for production of pullulan to develop biodegradable plastic. *Applied Microbiology and Biotechnology*, 104, pp.1307-1317. [DOI]

Rocha, G.J.D.M., Nascimento, V.M., Gonçalves, A.R., Silva, V.F.N. and Martín, C., 2015. Influence of mixed sugarcane bagasse samples evaluated by elemental and physical–chemical composition. *Industrial Crops and Products*, 64, pp.52-58. [DOI]

Roy, S., Das, S.K., Chakraborty, S., Pandey, K., Mukherjee, A. and Rajabalaya, R., 2020. *Role of Pullulans in Cosmetics*. 1st ed. Jenny Stanford Publishing.

Sheng, L., Tong, Q. and Ma, M., 2016. Why sucrose is the most suitable substrate for pullulan fermentation by *Aureobasidium pullulans* CGMCC1234? *Enzyme and Microbial Technology*, 92, pp.49-55. [DOI]

Shingel, K.I., 2004. Current knowledge on manufacture, biological activity, and chemical modification of the exopolysaccharide, pullulan. *Carbohydrate Research*, 339, pp.447-460. [DOI]

Shingel, K.I., 2002. Determination of structural peculiarities of dextran, pullulan and γ-irradiated pullulan by Fourier-transform IR spectroscopy. *Carbohydrate Research*, 337, pp.1445-1451. [DOI]

Singh, R., Das, R., Sangwan, S., Rohatgi, B., Khanam, R., Peera, S.K.P.G., Das, S., Lyngdoh, Y.A., Langyan, S., Shukla, A., Shrivastava, M. and Misra, S., 2021. Utilisation of agro-industrial waste for sustainable green production: a review. *Environmental Sustainability*, 4, pp.619-636. [DOI]

Singh, R.S., 2014. Industrial biotechnology: an overview. *Advances in Industrial Biotechnology*. India: K International Publishing House Pvt. Ltd., pp.1-35.

Singh, R.S. and Kaur, N., 2019. Understanding response surface optimization of medium composition for pullulan production from de-oiled rice bran by *Aureobasidium pullulans*. *Food Science and Biotechnology*, 28, pp.1507-1520. [DOI]

Singh, R.S., Kaur, N. and Kennedy, J.F., 2019. Pullulan production from agro-industrial waste and its applications in food industry: A review. *Carbohydrate Polymers*, 217, pp.46-57. [DOI]

Singh, R.S. and Saini, G.K., 2012. Biosynthesis of pullulan and its applications in food and pharmaceutical industry. In: T. Satyanarayana, B.N. Johri and A. Prakash, eds., *Microorganisms in Sustainable Agriculture and Biotechnology*. Dordrecht: Springer Netherlands, pp.509-553. [DOI]

Singh, R.S., Saini, G.K. and Kennedy, J.F., 2008. Pullulan: Microbial sources, production and applications. *Carbohydrate Polymers*, 73, pp.515-531. [DOI]

Soni, S.R., Kumari, N., Bhunia, B.K., Sarkar, B., Mandal, B.B. and Ghosh, A., 2018. Synthesis and characterization of a non-cytotoxic and biocompatible acrylamide grafted pullulan – Application in pH responsive controlled drug delivery. *International Journal of Biological Macromolecules*, 120, pp.753-762. [DOI]

Sowa, W., Blackwood, A.C. and Adams, G.A., 1963. Neutral extracellular glucan of *Pullularia pullulans* (de Bary) Berkhout. *Canadian Journal of Chemistry*, 41, pp.2314-2319. [DOI]

Srikanth, S., Swathi, M., Tejaswini, M., Sharmila, G., Muthukumaran, C., Jaganathan, M.K. and Tamilarasan, K., 2014. Statistical optimization of molasses based exopolysaccharide and biomass production by *Aureobasidium pullulans* MTCC 2195. *Biocatalysis and Agricultural Biotechnology*, 3, pp.7-12. [DOI]

Sugumaran, K.R., Jothi, P. and Ponnusami, V., 2014. Bioconversion of industrial solid waste—Cassava bagasse for pullulan production in solid state fermentation. *Carbohydrate Polymers*, 99, pp.22-30. [DOI]

Sugumaran, K.R., Shobana, S.K. and Ponnusami, V., 2017. Review on production, downstream processing and characterization of microbial pullulan. *Carbohydrate Polymers*, 173, pp.573-591. [DOI]

Suzuki, T., Kusano, K., Kondo, N., Nishikawa, K., Kuge, T. and Ohno, N., 2021. Biological activity of high-purity β-1,3-1,6-glucan derived from the black yeast *Aureobasidium pullulans*: A literature review. *Nutrients*, 13, p.242. [DOI]

Svarovsky, L., 2001. Introduction to solid-liquid separation. In: *Solid-Liquid Separation*. Elsevier, pp.1-29. [DOI]

Tabasum, S., Noreen, A., Maqsood, M.F., Umar, H., Akram, N., Nazli, Z.H., Chatha, S.A.S. and Zia, K.M., 2018. A review on versatile applications of blends and composites of pullulan with natural and synthetic polymers. *International Journal of Biological Macromolecules*, 120, pp.603-632. [DOI]

Trinetta, V. and Cutter, C.N., 2025. Pullulan: A suitable biopolymer for antimicrobial food packaging applications. In: *Antimicrobial Food Packaging*. Elsevier, pp.531-548. [DOI]

Viveka, R., 2023. *Strain improvement for the production and purification of pullulan from Aureobasidium pullulans using agro industrial waste*. Ph.D. Thesis. Anna University, Chennai.

Wang, D., Chen, F., Wei, G., Jiang, M. and Dong, M., 2015. The mechanism of improved pullulan production by nitrogen limitation in batch culture of *Aureobasidium pullulans*. *Carbohydrate Polymers*, 127, pp.325-331. [DOI]

Wang, D., Ju, X., Zhou, D. and Wei, G., 2014. Efficient production of pullulan using rice hull hydrolysate by adaptive laboratory evolution of *Aureobasidium pullulans*. *Bioresource Technology*, 164, pp.12-19. [DOI]

Wang, Q.Q., Lin, J., Zhou, Q.Z., Peng, J., Zhang, Q. and Wang, J.H., 2023. Hyper-production of pullulan by a novel fungus of *Aureobasidium melanogenum* ZH27 through batch fermentation. *International Journal of Molecular Sciences*, 25, p.319. [DOI]

Wang, W., Zhao, J., Zhang, K., Wang, Z., Ma, J., Yang, Q. and Lin, C., 2024. Transcriptome analysis of *Aureobasidium pullulans* YQ65 grown on yeast extract peptone glucose and potato dextrose agar media and quantification of their effects on pullulan production. *Foods*, 13, p.3619. [DOI]

Wani, S.M., Mir, S.A., Khanday, F.A. and Masoodi, F.A., 2021. Advances in pullulan production from agro-based wastes by *Aureobasidium pullulans* and its applications. *Innovative Food Science & Emerging Technologies*, 74, p.102846. [DOI]

Wei, X., Liu, G.L., Jia, S.L., Chi, Z., Hu, Z. and Chi, Z.M., 2021. Pullulan biosynthesis and its regulation in *Aureobasidium* spp. *Carbohydrate Polymers*, 251, p.117076. [DOI]

Wu, S., Chen, J. and Pan, S., 2012. Optimization of fermentation conditions for the production of pullulan by a new strain of *Aureobasidium pullulans* isolated from sea mud and its characterization. *Carbohydrate Polymers*, 87, pp.1696-1700. [DOI]

Xiao, Q., Tong, Q. and Lim, L.T., 2012. Pullulan-sodium alginate based edible films: Rheological properties of film forming solutions. *Carbohydrate Polymers*, 87, pp.1689-1695. [DOI]

Youssef, F., Biliaderis, C.G. and Roukas, T., 1998. Enhancement of pullulan production by *Aureobasidium pullulans* in batch culture using olive oil and sucrose as carbon sources. *Applied Biochemistry and Biotechnology*, 74, pp.13-30. [DOI]

Youssef, F., Roukas, T. and Biliaderis, C.G., 1999. Pullulan production by a non-pigmented strain of *Aureobasidium pullulans* using batch and fed-batch culture. *Process Biochemistry*, 34, pp.355-366. [DOI]

Zhang, K., Lin, C., Zhao, S., Wang, W., Zhou, W., Ru, X., Cong, H. and Yang, Q., 2023. The role of pH transcription factor Appacc in upregulation of pullulan biosynthesis in *Aureobasidium pullulans* using potato waste as a substrate. *International Journal of Biological Macromolecules*, 242, p.124797. [DOI]

Zhang, S., Feng, Z., Zeng, Q., Zeng, J., Liu, H., Deng, P., Li, S., Li, N. and Wang, J., 2024. Enhancing pullulan production in *Aureobasidium pullulans* through UV mutagenesis breeding and high-throughput screening system. *Fermentation*, 10, p.103. [DOI]

Nature Environment and Pollution Technology
An International Quarterly Scientific Journal

p-ISSN: 0972-6268
(Print copies up to 2016)
e-ISSN: 2395-3454

Vol. 25 | No. 3 | Article ID D1877 | 2026

Original Research Paper

https://doi.org/10.46488/NEPT.2026.v25i03.D1877

Open Access Journal

Effect of Sustainable Groundwater Resource Management on Groundwater Sustainability Performance: A PLS-SEM Study in Probolinggo Regency

Faradlillah Saves[1,4], Mohammad Bisri[2], Hari Siswoyo[2] and Muhammad Sasmito Djati[3]

[1]Postgraduate Study of Environmental Science, Brawijaya University, East Java, Indonesia
[2]Department of Water Resources Engineering, Brawijaya University, East Java, Indonesia
[3]Department of Biology, Brawijaya University, East Java, Indonesia
[4]Department of Civil Engineering, Universitas 17 Agustus 1945, Surabaya, Indonesia
†Corresponding author: Faradlillah Saves; farasaves@student.ub.ac.id

Abbreviation: Nat. Env. & Poll. Technol.
Website: www.neptjournal.com

Received: 10-10-2025
Revised: 10-12-2025
Accepted: 11-01-2026

Key Words:

Sustainable groundwater management
Groundwater sustainability performance
PLS-SEM
Water governance

Citation for the Paper:

Saves, F., Bisri, M., Siswoyo, H. and Djati, M.S., 2026. Effect of sustainable groundwater resource management on groundwater sustainability performance: A PLS-SEM study in Probolinggo Regency. *Nature Environment and Pollution Technology*, 25(3), D1877. https://doi.org/10.46488/NEPT.2026.v25i03.D1877

Note: From 2025, the journal has adopted the use of Article IDs in citations instead of traditional consecutive page numbers. Each article is now given individual page ranges starting from page 1.

Copyright: © 2026 by the authors
Licensee: Technoscience Publications
This article is an open access article distributed under the terms and conditions of the Creative Commons Attribution (CC BY) license (https://creativecommons.org/licenses/by/4.0/).

ABSTRACT

Groundwater, as a vital resource, is facing a crisis in Probolinggo Regency due to rapid industrialization and land conversion, both of which threaten groundwater sustainability performance. This study aims to quantitatively identify the dominant factors among six aspects of sustainable groundwater resource management and to quantify their causal influence, both positive and negative, on the groundwater sustainability performance. A quantitative approach with an explanatory survey design was used, and analysis was conducted through Partial Least Squares-Structural Equation Modeling (PLS-SEM) involving data from key stakeholders. The results show that the model possesses very high predictive power (R^2 = 0.925), revealing two contrasting dominant factors. Utilization (X6) has the strongest and statistically significant positive effect (β = 0.57; p = 0.004), driven by technological innovation, while Implementation (X2) exhibits a significant negative effect (β = −0.54; p = 0.049). This negative coefficient provides empirical confirmation of a critical "policy-practice gap," suggesting that weaknesses in human resource capacity and inconsistent budgetary support during the execution phase significantly hinder overall sustainability performance. Consequently, this study concludes that the greatest challenge to achieving sustainable groundwater management lies in policy execution failure rather than in the planning stages. The policy implications call upon the local government to prioritize investment in technological innovation for utilization (X6) and to immediately undertake structural reforms and budget auditing within the implementation phase (X2) to bridge the gap between policy intent and actual sustainability outcomes.

1. INTRODUCTION

Groundwater, as a vital resource supporting human life and environmental sustainability, is now facing a global crisis due to increasing depletion and pollution (Aloui et al. 2023, Bierkens & Wada 2019). Groundwater is generally stored in specific types of aquifers, including unconfined and confined aquifers (Darsono 2016). Indonesia possesses significant groundwater potential that varies according to local hydrogeological conditions, and many people, especially local communities, rely on it to meet their daily needs (Kusumaningrum et al. 2024). In addition, groundwater plays a critical role in both agriculture and industry, which represent the largest portions of total water requirements, with agriculture alone often accounting for approximately 70% of total usage. Globally, according to FAO (2018), groundwater extraction has increased drastically by more than 300% in the last 50 years (1960–2010) (Barati et al. 2019).

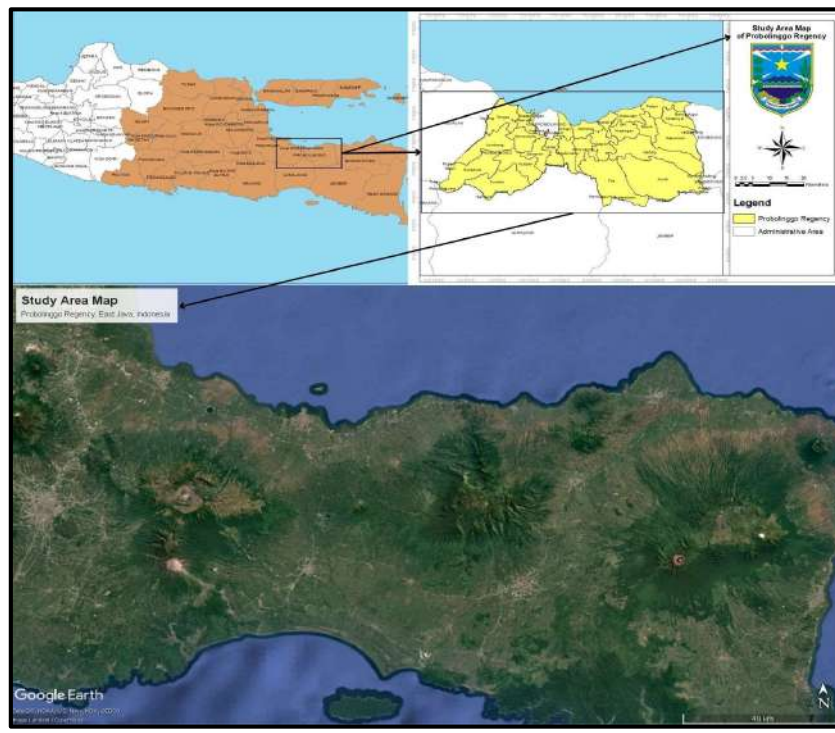
Probolinggo Regency is experiencing rapid industrial development, which directly causes land conversion. The consequence of this conversion is a threat to Groundwater Sustainability Performance and a reduction in the water absorption capacity, which directly challenges the sustainability performance of the local

groundwater resource management. Data from the Central Bureau of Statistics (BPS) indicates that residential land (built-up area) currently accounts for only 2.24% of the total land area. However, the accelerating pace of industrialization suggests that land conversion from water catchment zones will continue to increase. This change in land use causes rainwater that should infiltrate the soil to instead flow as surface runoff (Aryanto & Hardiman 2017), making groundwater recharge zones within aquifers highly vulnerable. When this recharge function is disrupted, the balance of local groundwater becomes threatened, ultimately exacerbating the groundwater crisis.

Previous studies on water resources in this region generally focused on macro-level analyses of water availability or mapping land use as a physical factor influencing infiltration (Widodo 2013). A study by Khalimi & Kusuma (2018) identified a significant gap in assessing groundwater resource sustainability from management and regulatory perspectives. The sustainability of groundwater performance depends strongly on multidimensional interactions among management aspects; however, existing literature has not adequately quantified the structural relationships among management variables such as planning, implementation, monitoring and evaluation, conservation, damage control, and utilization.

The core problem addressed by this study is the critical difficulty local governments face in prioritizing effective interventions for sustainable groundwater management. This difficulty stems from the absence of a clear, structural model that quantitatively identifies which specific managerial, institutional, and technical factors (among the six established dimensions) are the dominant drivers of performance. Using the PLS-SEM model, this study aims to quantitatively analyze these causal relationships and determine the effect of the management variables on the Groundwater Sustainability Performance. This causal analysis is urgent for providing local governments with the necessary evidence to prioritize appropriate interventions and achieve long-term sustainability.

Therefore, the novelty of this research lies in its comprehensive structural interaction analysis between six aspects of sustainable groundwater resource management and the groundwater sustainability performance. The study seeks to quantify the causal relationships among the dominant influencing factors. This includes identifying both the positive and potential negative effects of management variables on Groundwater Sustainability Performance in Probolinggo Regency. These findings are significant because they provide precise empirical evidence of the driving and inhibiting factors. This evidence, in turn, forms a sound



Source: Decree of the Minister of Energy and Mineral Resources No. 1451K/10/MEM/2000

Fig. 1: Study area.

basis for developing measurable and effective local policy recommendations.

2. MATERIALS AND METHODS

2.1. Study Area and Duration

This study was conducted within the administrative boundaries of Probolinggo Regency, which serves as the primary unit of analysis for evaluating Groundwater Sustainability Performance. The regency covers a total area of 1,639 km². The groundwater resources utilized in this region consist of unconfined aquifers (Q1) producing approximately 711 million m³ per year and confined aquifers (Q2) yielding about 124 million m³ per year. The choice of the administrative boundary is essential for this study, as it aligns with the jurisdictional scope of policy implementation and resource management. The study area is shown in Fig. 1.

The research was carried out over one year (September 2024 - September 2025). The study comprised several stages, including field surveys, literature review, on-site observations and semi-structured interviews, assessment of groundwater management practices, and quantitative analysis of the influence of sustainable groundwater management on groundwater sustainability performance.

2.2. Research Design and Methodology

This study employs a quantitative research design with an explanatory survey approach to analyze causal mechanisms in groundwater management. To align with the study's focus on policy effectiveness, Groundwater Sustainability Performance (GSP) is operationalized as a latent construct measured through perception-based indicators from key stakeholders rather than physical hydrogeological observations. The primary analytical tool is Partial Least Squares Structural Equation Modeling (PLS-SEM), selected for its robustness in handling non-normal data distributions and exploratory causal models (Sofyani 2025).

The analysis follows a two-stage evaluation: the measurement model to ensure construct integrity and the structural model to test hypothesized relationships. The measurement model is evaluated through construct reliability (Cronbach's Alpha and Composite Reliability) and construct validity, comprising convergent validity (AVE) and discriminant validity. Detailed procedures for sampling and the specific thresholds for these tests are elaborated in the subsequent subsections.

2.3. Population and Sample

The study population comprised stakeholders directly involved in the planning, utilization, conservation, and supervision of sustainable groundwater resource management in Probolinggo Regency. These included:

1. Heads of Provincial and Regency/Municipal Offices of Energy and Mineral Resources (ESDM)
2. Heads of Groundwater Development and Management Projects in East Java
3. City-level technical policymakers from BAPPEDA, Public Works Department, Tourism Department, PDAM, and the Environmental and Forestry Department

Sampling was conducted using a non-probability purposive sampling approach. The minimum sample size was determined based on power analysis criteria and general PLS-SEM rules of thumb to ensure adequate statistical representation of key stakeholder groups.

2.4. Sampling Technique

Primary data were collected using a structured questionnaire designed to measure all research variables on a five-point Likert scale ranging from Strongly Disagree (1) to Strongly Agree (5) (Koo & Yang 2025). The questionnaires were distributed directly to selected respondents through official coordination channels and in-person meetings.

2.5. Research Variables

The independent variables represent six key aspects of sustainable groundwater resource management, each measured using specific indicators:

1. Planning (X1),
2. Implementation (X2),
3. Monitoring and Evaluation (X3),
4. Conservation (X4),
5. Damage Control (X5), and
6. Utilization (X6)

The dependent variable (Y) is the Groundwater Sustainability Performance, representing the overall outcome of sustainable groundwater resource management. To validate the theoretical constructs of the latent variables (X and Y) with empirical data collected through the questionnaire, Table 1 presents their operational definitions.

2.6. Instrument Validity and Reliability Tests

Instrument validity was tested using Confirmatory Factor Analysis (CFA) to assess convergent validity (Average Variance Extracted, AVE $\geq$ 0.50) and discriminant validity (by comparing the square root of the AVE with inter-variable correlations).

Table 1: Operational definitions of variables.

Variable	Operational Definition
X1: Planning	Planning is the process of setting policies and plans for the allocation of sustainable groundwater resources. Its effectiveness is measured based on the level of involvement of key stakeholders, including government, private sector, and civil society, in developing plans to achieve groundwater basin sustainability (Bryła et al. 2025).
X2: Implementation	Implementation is the effectiveness of enforcing policies, programs, and regulations in the field. This effectiveness is measured by the conformity of actions with policy targets. It can be improved through the integration of ISO 14000-based Environmental Management Systems (EMS) as a decision-making tool, which critically includes impact identification, pollution control schemes, and Environmental Action Plans (EAP) (Farouk et al. 2024).
X3: Monitoring and Evaluation	Monitoring and evaluation are the systematic processes of measuring the performance of sustainable groundwater management and comparing it with targets. This includes field mapping and recording coordinates of hydrogeological points of interest (Putranto et al. 2020). Success is measured by the transparency of reporting results and the use of evaluations as adaptive input for policy regulation adjustments.
X4: Conservation	Conservation involves the application of structural (physical) and non-structural (policy) measures to maintain and restore the quality, quantity, and environmental carrying capacity that define Groundwater Sustainability Performance (GSP). The intensity of these efforts is measured through conservation programs, the adoption of water-saving (efficiency) technologies, and strategic initiatives to restore infiltration areas. Regarding quality aspects, GSP is further supported by the capacity to monitor a wider range of water-quality parameters, which can be optimized through increasing the number of spectral bands and refining analytical algorithms (Ma et al. 2023).
X5: Damage Control	Damage control refers to mitigation and adaptation efforts focused on safeguarding Groundwater Sustainability Performance and infrastructure from water-related damage risks, such as floods, saltwater intrusion, and drought. It encompasses practical preventive measures and sustainable mitigation strategies, including early warning systems and groundwater flow protection zoning, to enhance resilience against the impacts of irregular weather patterns caused by climate change (Abbass et al. 2022).
X6: Utilization	Utilization refers to the management practices governing groundwater use to ensure efficient and equitable resource allocation. Guided by the relevant Ministerial Regulations of Energy and Mineral Resources, these practices are a primary driver in achieving Groundwater Sustainability Performance. The objective is to guarantee long-term groundwater availability and provide optimal socio-economic benefits in a sustainable manner (Rifai 2022).
Y: Groundwater Sustainability Performance	Groundwater Sustainability Performance reflects the achievement of sustainable ecological and hydrogeological functions, indicated by the absence of undesirable results such as water level instability, seawater intrusion, or land subsidence. Conceptually, this performance can be verified using a physics-based groundwater model grounded in Darcy's Law and the Continuity Equation, combined with a management model to assist in sustainable groundwater resource planning and decision-making (Yeh 2015).

Instrument reliability was evaluated through Composite Reliability (CR $\geq$ 0.70) and Cronbach's Alpha (Amalia et al. 2023), ensuring internal consistency among indicators for each latent construct.

2.7 Hypothesis Formulation

The significance of relationships between latent variables was examined through the following hypotheses:

- $H_0: \beta_1 = 0$ Planning (X1) does not significantly influence the Groundwater Sustainability Performance (Y) $H_1: \beta_1 \neq 0$ Planning (X1) significantly influences the Groundwater Sustainability Performance (Y)
- $H_0: \beta_2 = 0$ Implementation (X2) does not significantly influence the Groundwater Sustainability Performance (Y) $H_1: \beta_2 \neq 0$ Implementation (X2) significantly influences the Groundwater Basin Function (Y)
- $H_0: \beta_3 = 0$ Monitoring and Evaluation (X3) do not significantly influence the Groundwater Sustainability Performance (Y) $H_1: \beta_3 \neq 0$ Monitoring and Evaluation (X3) significantly influence the Groundwater Sustainability Performance (Y)
- $H_0: \beta_4 = 0$ Conservation (X4) does not significantly influence the Groundwater Sustainability Performance (Y) $H_1: \beta_4 \neq 0$ Conservation (X4) significantly influences the Groundwater Sustainability Performance (Y)
- $H_0: \beta_5 = 0$ Damage Control (X5) does not significantly influence the Groundwater Basin Function (Y) $H_1: \beta_5 \neq 0$ Damage Control (X5) significantly influences the Groundwater Sustainability Performance (Y)
- $H_0: \beta_6 = 0$ Utilization (X6) does not significantly influence the Groundwater Sustainability Performance (Y) $H_1: \beta_6 \neq 0$ Utilization (X6) significantly influences the Groundwater Sustainability Performance (Y)

3. RESULTS

3.1. Validity and Reliability Tests

Validity and reliability tests of the research instrument

Table 2: Validity test results.

No.	Pearson correlation coefficient	Validity status	No.	Pearson correlation coefficient	Validity status	No.	Pearson correlation coefficient	Validity status
1	0.751	Valid	44	0.930	Valid	87	0.886	Valid
2	0.671	Valid	45	0.833	Valid	88	0.900	Valid
3	0.797	Valid	46	0.778	Valid	89	0.741	Valid
4	0.903	Valid	47	0.970	Valid	90	0.824	Valid
5	0.865	Valid	48	0.826	Valid	91	0.921	Valid
6	0.830	Valid	49	0.721	Valid	92	0.844	Valid
7	0.367	Valid	50	0.832	Valid	93	0.885	Valid
8	0.747	Valid	51	0.842	Valid	94	0.799	Valid
9	0.854	Valid	52	0.825	Valid	95	0.765	Valid
10	0.634	Valid	53	0.557	Valid	96	0.830	Valid
11	0.330	Valid	54	0.507	Valid	97	0.755	Valid
12	0.795	Valid	55	0.755	Valid	98	0.918	Valid
13	0.887	Valid	56	0.868	Valid	99	0.887	Valid
14	0.850	Valid	57	0.838	Valid	100	0.567	Valid
15	0.814	Valid	58	0.812	Valid	101	0.884	Valid
16	0.766	Valid	59	0.851	Valid	102	0.692	Valid
17	0.906	Valid	60	0.883	Valid	103	0.916	Valid
18	0.879	Valid	61	0.816	Valid	104	0.713	Valid
19	0.884	Valid	62	0.878	Valid	105	0.946	Valid
20	0.791	Valid	63	0.692	Valid	106	0.871	Valid
21	0.723	Valid	64	0.852	Valid	107	0.871	Valid
22	0.844	Valid	65	0.826	Valid	108	0.881	Valid
23	0.850	Valid	66	0.860	Valid	109	0.936	Valid
24	0.814	Valid	67	0.798	Valid	110	0.884	Valid
25	0.686	Valid	68	0.871	Valid	111	0.869	Valid
26	0.316	Valid	69	0.910	Valid	112	0.892	Valid
27	0.880	Valid	70	0.882	Valid	113	0.958	Valid
28	0.852	Valid	71	0.828	Valid	114	0.582	Valid
29	0.919	Valid	72	0.866	Valid	115	0.698	Valid
30	0.868	Valid	73	0.883	Valid	116	0.643	Valid
31	0.720	Valid	74	0.899	Valid	117	0.600	Valid
32	0.908	Valid	75	0.894	Valid	118	0.644	Valid
33	0.826	Valid	76	0.942	Valid	119	0.834	Valid
34	0.795	Valid	77	0.879	Valid	120	0.787	Valid
35	0.764	Valid	78	0.860	Valid	121	0.853	Valid
36	0.849	Valid	79	0.834	Valid	122	0.928	Valid
37	0.876	Valid	80	0.897	Valid	123	0.911	Valid
38	0.770	Valid	81	0.887	Valid	124	0.895	Valid
39	0.901	Valid	82	0.897	Valid	125	0.798	Valid
40	0.955	Valid	83	0.899	Valid	126	0.868	Valid
41	0.726	Valid	84	0.923	Valid	127	0.843	Valid
42	0.944	Valid	85	0.920	Valid	128	0.944	Valid
43	0.860	Valid	86	0.909	Valid	129	0.903	Valid

Table 3: Cronbach's alpha values.

Latent variable	Cronbach's Alpha
X1	0.940
X2	0.946
X3	0.907
X4	0.947
X5	0.969
X6	0.971
Y	0.963

were conducted using RStudio. The study involved seven latent variables (X1–X6 and Y) comprising a total of 129 questionnaire items.

Table 2 presents the results of the validity test, showing that the Pearson correlation coefficients for all 129 items ranged from 0.30 to 0.97. All items were declared valid, as each correlation coefficient exceeded the minimum threshold of 0.30.

3.2. PLS-SEM Modeling Results

PLS-SEM analysis was employed to examine the influence of the Sustainable Groundwater Resource Management variables (X1–X6) on the Groundwater Sustainability Performance (Y). The Outer (Measurement) Model was reflective and evaluated based on Cronbach's Alpha, factor loadings, and Average Variance Extracted (AVE) values.

3.2.1. Reliability and Convergent Validity of the Outer Model

For the reflective PLS-SEM model, the first step involved assessing the internal consistency reliability of the questionnaire for each latent variable (X1–X6 and Y). Reliability was assessed using Cronbach's Alpha (Table 3). If the value exceeded 0.70, the construct was considered reliable and suitable for further analysis within the reflective model.

All Cronbach's Alpha values are greater than 0.70, confirming the reliability of the constructs in the outer model.

3.2.2. Parameter Estimation Results (PLS-SEM)

Parameter estimation in the PLS-SEM model was conducted using the Ordinary Least Squares (OLS) method. The complete estimation results are illustrated in Fig. 2.

In Fig. 2, the SEM diagram consists of two components:

(1) the outer (measurement) model, and

(2) the inner (structural) model, each with its respective coefficients.

In the outer model, the coefficient (loading) values represent the contribution of each indicator to its respective latent variable. The outer model coefficients for each latent variable are presented in Table 4.

The results in Table 4 indicate that all indicators across the seven latent variables exhibit high loading values, all exceeding the minimum threshold of 0.70, thereby meeting the criteria for convergent validity.

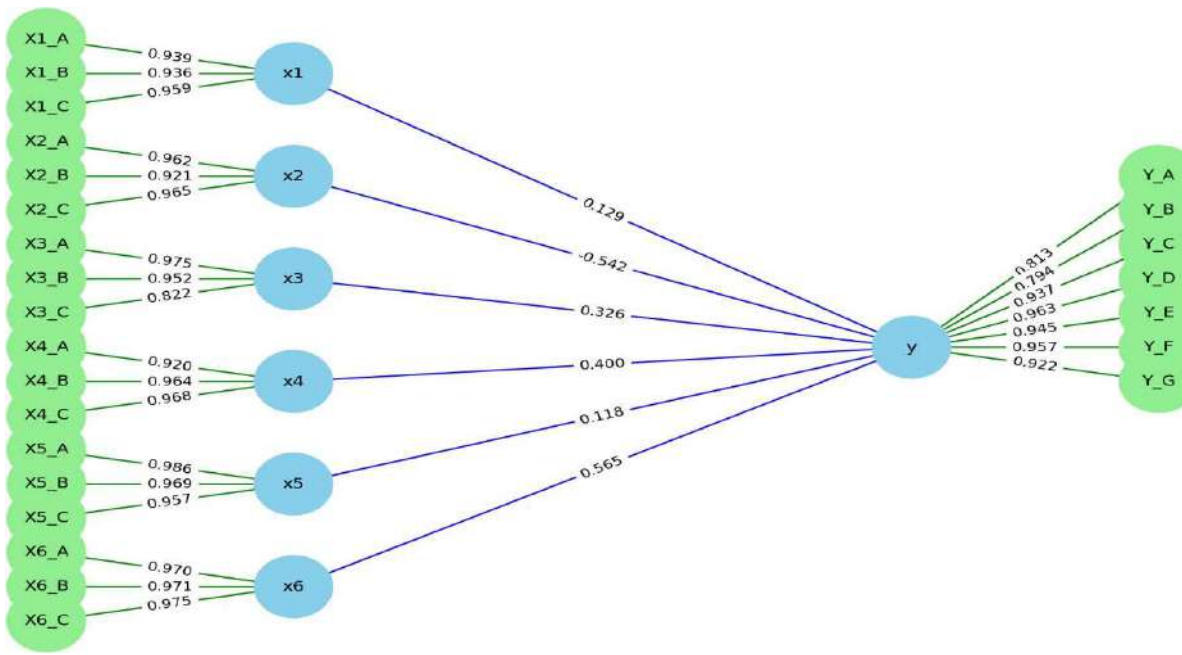


Fig. 2: PLS-SEM model parameter estimation.

Table 4: Outer model coefficients.

No.	Indicator	Latent Variable	Loading Value
1	X1.A (Data and information)	X1 (Planning)	0.939
2	X1.B (Institutional)		0.936
3	X1.C (Disaster integration)		0.959
4	X2.A (Human resources)	X2 (Implementation)	0.962
5	X2.B (Budgetary support)		0.921
6	X2.C (Program implementation)		0.965
7	X3.A (Monitoring system)	X3 (Monitoring and evaluation)	0.975
8	X3.B (Performance evaluation)		0.952
9	X3.C (Data transparency)		0.822
10	X4.A (Protection of recharge areas)	X4 (Conservation)	0.920
11	X4.B (Water-use efficiency)		0.964
12	X4.C (Education and outreach)		0.968
13	X5.A (Planning control)	X5 (Damage control)	0.986
14	X5.B (Exploitation regulation)		0.969
15	X5.C (Law enforcement)		0.957
16	X6.A (Fair access)	X6 (Utilization)	0.970
17	X6.B (Economic value)		0.971
18	X6.C (Technological innovation)		0.975
19	Y.A (Ecological and environmental)	Y (Groundwater Sustainability Performance)	0.813
20	Y.B (Social)		0.794
21	Y.C (Economic)		0.937
22	Y.D (Institutional)		0.963
23	Y.E (Technology and information)		0.945
24	Y.F (Risk and resilience)		0.957
25	Y.G (Legal)		0.922

- The most dominant indicators representing each construct are as follows:
- Disaster Integration under Planning (X1) – 0.959
- Program Implementation under Implementation (X2) – 0.965
- Monitoring System under Monitoring and Evaluation (X3) – 0.975
- Education and Outreach under Conservation (X4) – 0.968
- Planning Control under Damage Control (X5) – 0.986
- Technological Innovation under Utilization (X6) – 0.975
- Institutional under Groundwater Sustainability Performance (Y) – 0.963

Since all loading values exceed the required threshold, the reflective measurement model is confirmed to be valid and appropriate for subsequent hypothesis testing within the structural model.

3.2.3. Hypothesis Testing Results

Hypothesis testing was conducted by analyzing the coefficients in the Inner (Structural) Model at a significance level of 0.05 (Table 5). The rejection criterion was: if $p < 0.05$, then H_0 is rejected, indicating a statistically significant effect between the latent variables.

The results indicate that only Utilization (X6) and Implementation (X2) have statistically significant

Table 5: Significance test of parameters.

Parameter	Estimate	Std. Error	t-statistic	p-value
Intercept (β_0)	0.00	0.057	0.00	1
X1 (β_1)	0.13	0.209	0.61	0.554
X2 (β_2)	-0.54	0.238	-2.28	0.049
X3 (β_3)	0.33	0.191	1.71	0.122
X4 (β_4)	0.40	0.241	1.66	0.131
X5 (β_5)	0.12	0.180	0.66	0.529
X6 (β_6)	0.57	0.214	3.92	0.004

Table 6: PLS-SEM model evaluation (AVE values).

Latent variable	AVE Value
X1	0.893
X2	0.901
X3	0.844
X4	0.905
X5	0.943
X6	0.945
Y	0.822

effects on the Groundwater Sustainability Performance (Y):

- Utilization (X6) exhibits the strongest positive and significant effect ($\beta = 0.57$; $p = 0.004$).
- Implementation (X2) demonstrates a negative and significant effect ($\beta = -0.54$; $p = 0.049$).
- The remaining variables - Planning (X1), Monitoring and Evaluation (X3), Conservation (X4), and Damage Control (X5), are statistically insignificant ($p > 0.05$).

Overall, the model shows very high predictive power, with a Coefficient of Determination ($R^2 = 0.925$). This means that 92.5% of the variability in the Groundwater Sustainability Performance can be explained by the six predictor variables in the model.

3.2.4. Model Evaluation Results

At the final stage of the PLS-SEM analysis, the model was evaluated using the Average Variance Extracted (AVE) values for each latent variable. The results are presented in Table 6.

All AVE values exceed the minimum threshold of 0.50, confirming that the reflective measurement model demonstrates satisfactory convergent validity and is suitable for the objectives of this study.

4. DISCUSSION

4.1. Dominance of the Influence of Utilization (X6) and Implementation (X2)

The structural analysis revealed a crucial and contrasting finding in predicting Groundwater Sustainability Performance (Y) in Probolinggo Regency. The overall model demonstrates exceptionally high predictive power, with a Coefficient of Determination (R^2) of 0.925, indicating that 92.5% of the variability in Groundwater Sustainability Performance is explained by the six predictor variables. Furthermore, the robustness of these findings is supported by strong convergent validity, with Average Variance Extracted (AVE) values for all latent variables exceeding the 0.50 threshold (ranging from 0.822 to 0.945), ensuring that the constructs effectively represent their intended measures.

Within this robust framework, Utilization (X6) exhibited the strongest significant positive effect ($\beta = 0.57$; $p = 0.004$). This result indicates that the optimization of Groundwater Sustainability Performance is fundamentally driven by the utilization aspect, particularly through its most influential indicator, Technological Innovation (loading = 0.975). This reflects a global shift in water resource management, moving away from passive conservation toward active demand management focused on efficiency and technology-based resilience. Consistent with the perspectives of global environmental governance (Burchard-Levine et al. 2025), technological optimization directly enhances both the economic and environmental value of groundwater resources.

Conversely, Implementation (X2) demonstrated a negative and significant effect ($\beta = -0.54$; $p = 0.049$). This striking finding suggests an "implementation gap." Although the conceptual program implementation is strong (loading = 0.965), its execution in the field is likely hindered by the constraints identified in the Performance Report of the Ministry of Energy and Mineral Resources (2024), such as inadequate human resource capacity and financial limitations. In the context of Probolinggo Regency, these execution failures have direct physical consequences; the inability to effectively enforce extraction quotas and conservation programs has been linked to declining water levels in several monitoring wells and an increased risk of seawater intrusion along the coastal aquifers. In a model with such high predictive accuracy (R^2= 92.5%), this negative coefficient serves as a stark warning that administrative failures at the execution stage directly translate into the degradation of Groundwater Sustainability Performance, manifesting as tangible hydrogeological instability.

4.2. Comparison with Previous Studies and Novelty of the Research

These findings provide both confirmation and correction to existing theoretical frameworks on groundwater resource management. Historically, studies have emphasized the dominant role of Planning (X1) (Abdurrohim 2024) and Conservation (X4) (Jenahu et al. 2023) as predictors of effective management outcomes. However, in this study, Planning (X1), Monitoring and Evaluation (X3), Conservation (X4), and Damage Control (X5) were found to have no direct significant effects on the Groundwater Sustainability Performance (Y). The statistical non-significance of these variables is likely a manifestation of a ''policy-practice gap" or institutional decoupling. Within this context, while management frameworks are

well-documented administratively, they appear to lack the operational capacity and budgetary consistency required to exert a tangible influence on sustainability outcomes. For instance, planning and conservation efforts in Probolinggo Regency tend to be normative and administrative in nature, failing to translate into concrete, measurable field actions.

Furthermore, monitoring and evaluation functions fail to provide a direct impact because their outputs are not integrated into a responsive feedback loop capable of adjusting actual groundwater extraction behavior. These findings suggest that such variables serve as latent preconditions or enabling factors that establish a formal managerial foundation. However, their actual impact on Groundwater Sustainability Performance is fully mediated through the quality of Implementation (X2) and the efficiency of Utilization (X6), rather than exerting a direct, independent influence.

The novel contribution of this study lies in highlighting the Implementation (X2) variable as a critical yet underexplored determinant in sustainable groundwater management. While previous research has predominantly focused on improving planning frameworks and regulatory mechanisms, this study demonstrates that the core weakness lies in policy execution, not formulation.

The strong negative coefficient for Implementation (X2) challenges the optimism inherent in conventional planning models and highlights the importance of enhancing institutional capacity, effective budget allocation, and human resource development as the key to reversing current negative trends at the implementation level.

4.3. Policy Implications and Future Research Directions

The findings of this study have important policy implications for improving environmental management and the Groundwater Sustainability Performance in Probolinggo Regency. Given the strong positive influence of Utilization (X6) and the negative influence of Implementation (X2), policy measures should focus on two strategic pillars:

(1) promoting technological efficiency, and

(2) addressing institutional and capacity-related barriers.

First, local governments should prioritize investment in technological innovation for groundwater utilization to improve water-use efficiency and enhance Groundwater Sustainability Performance. This may include providing subsidies for water-saving irrigation technologies in the agricultural sector and implementing smart metering systems in industries to monitor and control groundwater extraction in real time. Policies should also link the economic value of groundwater with ecological sustainability, introducing incentives for efficient use and penalties for wasteful practices, thereby maintaining both groundwater levels and quality as key indicators of performance.

Second, a comprehensive evaluation of the Implementation (X2) stage is necessary to identify and eliminate structural barriers responsible for the negative effect observed in this study. This involves bureaucratic reforms in groundwater management agencies, enhanced technical training programs for staff, and rigorous budget audits to ensure that funds allocated for conservation programs, such as reforestation of recharge zones, are implemented efficiently. Improving these processes is vital to reversing the negative impact on the overall Groundwater Sustainability Performance.

For future research, attention should be given to exploring the mediating mechanisms among variables to produce more refined policy recommendations. Methodologically, future work should explicitly test mediation effects using PLS-SEM, for instance, to examine whether the influence of Planning (X1) and Conservation (X4) on Groundwater Sustainability Performance operates through Implementation (X2) and Utilization (X6).

Additionally, qualitative investigations are recommended to identify specific causal factors behind the negative coefficient of Implementation (X2), focusing on issues such as budget allocation inefficiencies, institutional incentive gaps, and governance fragmentation within local environmental management systems.

5. CONCLUSIONS

This PLS-SEM study demonstrates that 92.5% of the variability in Groundwater Sustainability Performance is explained by the six latent variables within the model. These findings reflect managerial performance based on stakeholder perceptions and institutional indicators.

The most critical and contrasting results are dominated by two key factors:

1. Utilization (X6) has the strongest and statistically significant positive influence ($\beta = 0.57$), primarily driven by Technological Innovation. This confirms that the performance of the groundwater basin is increasingly determined by efficient demand management and technological adaptation.
2. Implementation (X2) exhibits a negative and significant influence ($\beta = -0.54$), indicating the presence of a critical implementation gap. This suggests that weaknesses in human resource capacity and budgetary constraints during the execution phase hinder the overall sustainability performance.

The main contribution of this research is the empirical confirmation that the greatest challenge in groundwater management lies in execution failure rather than policy planning. The study emphasizes that local governments must prioritize investment in technological innovation while undertaking structural reforms to overcome implementation barriers.

Future research should focus on testing the mediating roles of Implementation (X2) and Utilization (X6) using longitudinal data. Additionally, in-depth qualitative studies are needed to identify the specific institutional and financial constraints behind the negative coefficient of Implementation. Finally, future work could integrate these perception-based findings with physical hydrogeological modeling to provide a more holistic view of groundwater sustainability.

6. ACKNOWLEDGMENTS

We would like to express our deepest gratitude to Brawijaya University, particularly the Departments of Environmental Science, Water Resources Engineering, and Biology, for their support in providing facilities and academic collaboration. Our utmost appreciation goes to all stakeholders in Probolinggo Regency who participated as key respondents. Their direct input through questionnaires was vital to the success of the Structural Equation Modeling (PLS-SEM) analysis of groundwater management. Finally, we would like to thank our colleagues and families for their moral support throughout this research process.

7. REFERENCES

Abbass, K., Qasim, M.Z., Song, H., Murshed, M., Mahmood, H. and Younis, I., 2022. A review of the global climate change impacts, adaptation, and sustainable mitigation measures. *Environmental Science and Pollution Research*, 29(28), pp.42539–42559. [DOI]

Abdurrohim, A., 2024. *Pengelolaan dan perencanaan sumber daya air: tantangan, solusi, dan peran masyarakat dalam era perubahan iklim*. *ResearchGate*, October, pp.1–13. https://www.researchgate.net/publication/384886243

Aloui, S., Zghibi, A., Mazzoni, A., Elomri, A. and Triki, C., 2023. Groundwater resources in Qatar: A comprehensive review and informative recommendations for research, governance, and management in support of sustainability. *Journal of Hydrology: Regional Studies*, 50(April), 101564. [DOI]

Amalia, N., Husin, A.E. and Prastowo, F.I., 2023. Factors that influence the application of the concept of new green areas in residential areas using structural equation modeling-part least square (SEM-PLS). *Astonjadro*, 12(2), pp.379–394. [DOI]

Aryanto, D.E. and Hardiman, G., 2017. Kajian multi varian faktor yang berpengaruh terhadap infiltrasi air tanah sebagai dasar penentuan daerah potensial resapan air tanah. *Proceeding Biology Education Conference*, 14(1), pp.252–257. https://jurnal.uns.ac.id/prosbi/article/view/17794

Barati, A.A., Azadi, H. and Scheffran, J., 2019. A system dynamics model of smart groundwater governance. *Agricultural Water Management*, 221, pp.502–518. [DOI]

Bierkens, M.F.P. and Wada, Y., 2019. Non-renewable groundwater use and groundwater depletion: A review. *Environmental Research Letters*, 14(6). [DOI]

Bryła, M., Zdralewicz, I., Lejcuś, I., Kraj, K., Dumieński, G., Tokarczyk, T. and Walczykiewicz, T., 2025. Integrated water resources management for implementing sustainable energy development—challenges and perspectives in Poland. *Sustainability (Switzerland)*, 17(3). [DOI]

Burchard-Levine, A.F., Popescu, O., Jager, N.W. and Huitema, D., 2025. Paradigms in action: exploring environmental consultants' perspectives on water resilience. *Ecology and Society*, 30(2). [DOI]

Darsono, D., 2016. Identifikasi akuifer dangkal dan akuifer dalam dengan metode geolistrik (Kasus: Di Kecamatan Masaran). *Indonesian Journal of Applied Physics*, 6(1), p.40. [DOI]

FAO, 2018. Groundwater overview: Making the invisible visible. Food and Agriculture Organization of the United Nations, Rome.

Farouk, A.M., Radzi, A.R., Romali, N.S., Farouk, M. and Elgamal, M., 2024. Performance indicators for assessing environmental management plan implementation in water projects. *Sustainability*, 16(3146), pp.1–19. [DOI]

Jenahu, G.R., Dhivanda, N.A.S. and Pakabu, D.N., 2023. Konservasi dan pengelolaan sumber daya air berkelanjutan di Kabupaten Klaten Jawa Tengah. *Prosiding SEMSINA*, 4(2), pp.84–87. [DOI]

Khalimi, F. and Kusuma, Z., 2018. Analisis ketersediaan air pada pertanian lahan kering di Gunungkidul Yogyakarta. *Jurnal Tanah dan Sumberdaya Lahan*, 5(1), pp.721–725.

Koo, M. and Yang, S.-W., 2025. Likert-type scale. *Encyclopedia*, 5(1), p.18. [DOI]

Kusumaningrum, L., Karina, R., Fil'ardiani, N.U., Mardiyanto, M.B., Jabbar, S.A., Khoirunnisa, S., Raharjo, Y.A.A., Santika, Y.E., Annisa Arta, Y.P. and Daniswara, A.P., 2024. Analysis of the carrying capacity of groundwater availability and its relationship with the largest population growth in Karanganyar Regency. *Jurnal Pengelolaan Sumberdaya Alam dan Lingkungan*, 14(3), pp.471–483. [DOI]

Ma, T., Zhang, D., Li, X., Huang, Y., Zhang, L., Zhu, Z., Sun, X., Lan, Z. and Guo, W., 2023. Hyperspectral remote sensing technology for water quality monitoring: knowledge graph analysis and frontier trend. *Frontiers in Environmental Science*, 11(August), pp.1–19. [DOI]

Ministry of Energy and Mineral Resources (MEMR), 2024. Performance Report on Water Resource Management. Government of Indonesia.

Putranto, T.T., Hidayat, W.K. and Prayudi, S.D., 2020. Pemetaan hidrogeologi dan analisis geokimia air tanah cekungan air tanah (CAT) Kendal. *Jurnal Ilmu Lingkungan*, 18(2), pp.305–318. [DOI]

Rifai, M., 2022. Pengelolaan terhadap pemanfaatan air tanah di Kabupaten Demak. *Matriks Teknik Sipil*, 10(1), p.1. [DOI]

Sofyani, H., 2025. Penggunaan teknik partial least square (PLS) dalam riset akuntansi berbasis survei. *Reviu Akuntansi dan Bisnis Indonesia*, 9(1), pp.80–94. [DOI]

Widodo, T., 2013. Kajian ketersediaan air tanah terkait pemanfaatan lahan di Kabupaten Blitar. *Jurnal Pembangunan Wilayah & Kota*, 9(2), p.122. [DOI]

Yeh, W.W.G., 2015. Review: Optimization methods for groundwater modeling and management. *Hydrogeology Journal*, 23(6), pp.1051–1065. [DOI]

Nature Environment and Pollution Technology
An International Quarterly Scientific Journal

p-ISSN: 0972-6268
(Print copies up to 2016)
e-ISSN: 2395-3454

Vol. 25 | No. 3 | Article ID B4406 | 2026

Original Research Paper

https://doi.org/10.46488/NEPT.2026.v25i03.B4406

Open Access Journal

Biopriming Using Rhizospheric Actinobacteria: A Promising Tool in Paddy (*Oryza sativa*) Farming

Richa Raut[1]†, Pragati Abhyankar[1] and Sneha Babel[2]

[1]Department of Microbiology, Haribhai V. Desai College (Autonomous), Pune, Maharashtra, India

[2]Department of Mathematics and Statistics, Brihan Maharashtra College of Commerce (BMCC), Pune, Maharashtra, India

†Corresponding author: Richa Raut; richaraut123@gmail.com

Abbreviation: Nat. Env. & Poll. Technol.
Website: www.neptjournal.com

Received: 16-10-2025
Revised: 26-12-2025
Accepted: 06-01-2026

Key Words:

Actinobacteria
Paddy
Rhizosphere
Biopriming

Citation for the Paper:

Raut, R., Abhyankar, P. and Babel, S., 2026. Biopriming using rhizospheric actinobacteria: A promising tool in paddy (*Oryza sativa*) farming. *Nature Environment and Pollution Technology*, 25(3), B4406. https://doi.org/10.46488/NEPT.2026.v25i03.B4406

Note: From 2025, the journal has adopted the use of Article IDs in citations instead of traditional consecutive page numbers. Each article is now given individual page ranges starting from page 1.

Copyright: © 2026 by the authors
Licensee: Technoscience Publications
This article is an open access article distributed under the terms and conditions of the Creative Commons Attribution (CC BY) license (https://creativecommons.org/licenses/by/4.0/).

ABSTRACT

The germination of paddy seeds is vital for seedling establishment and subsequent development. Impaired rice seed germination often results from reduced levels of bioactive gibberellins (GAs) caused by environmental stress. This inhibition can be alleviated through methods such as hormone priming, nutrient priming, and osmopriming, which stimulate α-amylase activity and trigger other developmental processes. Recently, novel biopriming approaches have emerged, involving seed treatment with diverse plant growth-promoting rhizospheric microbes. Reports indicate that actinobacteria are among the least studied biopriming agents. In this study, approximately 43 actinomycete isolates were obtained from rhizospheric soils associated with the rice variety Indrayani. Data showed significant improvements in germination following seed biopriming with four multifunctional isolates, with *Streptomyces ardesiacus* strain I7 achieving the highest vigor index. *Streptomyces antibioticus* strain I4 demonstrated notable antimicrobial activity against *Xanthomonas oryzae pv. oryzae* (Xoo). Colonization of actinomycetes on rice roots was confirmed using scanning electron microscopy. These isolates hold potential for development into a commercial microbial consortium.

1. INTRODUCTION

Rice, Oryza sativa, is the primary staple food and the second most significant cereal crop in global trade. In India, rice production is predominantly during the monsoon season (June to October), rather than in the post-monsoon months (November to March). The projected increase in global population indicates a need for a 60% boost in rice production. Addressing the 'yield gap', the difference between current yields and the optimal potential, is essential to meeting this demand. Agriculture faces two primary challenges: rising food demand and ensuring high-quality nutrition. Besides yield, issues such as loss of aroma, flavor, and nutritional value significantly impact rice quality. To enhance sustainability and productivity, farmers should consider restoring the levels of indigenous Plant Growth-Promoting Rhizobacteria (PGPR) in the soil, offering a natural alternative to chemical fertilizers, which can degrade soil health (Adnan et al.2018, Sharif et al. 2014).

Seed bio-priming is a sophisticated biological treatment method in which seeds are soaked in water and subsequently inoculated with beneficial microorganisms (Fiodor et al. 2023). This technique significantly improves seed germination and seedling establishment under challenging conditions. It also enhances resistance to phytopathogens, stress tolerance, and aroma production, ultimately leading to higher crop yields and superior grain quality (Chakraborti et al. 2022, Chinachanta et al. 2021, Dhondge et al. 2021). Understanding the plant growth-promoting (PGP) properties of natural soil inhabitants and applying them to boost soil productivity is essential for increasing rice production efficiency and achieving

optimal quality. Thus, biopriming involves applying diverse plant growth-promoting rhizospheric microbes as a seed pre-treatment to promote plant immunity, increase yield, and improve agronomic traits such as grain size, aroma, and taste. Reports indicate that Actinobacteria are among the least studied biopriming agents.

Actinomycetes form a distinct group of bacteria classified within the phylum Actinobacteria. Rhizospheric Actinobacteria are widespread in the natural environment (Yadav et al. 2017). They are increasingly being recognized for their diverse agricultural applications. Research highlights their potential as microbiological inoculants by exploring mechanisms that enhance plant growth, such as biological nitrogen fixation, phosphate solubilization, siderophore production (Elshafie et al. 2023), phytohormone synthesis (El-Tarabily & Sivasithamparam 2006), and the production of beneficial bioactive compounds, including antimicrobials with significant potential for controlling phytopathogens (Kabdwal et al. 2023) and insect pests (Diab et al. 2024).

In India, Maharashtra is a major rice-producing state. The crop is cultivated both along the coast and in the hilly regions of the Western Ghats. Currently, rice production faces several challenges, including loss of aroma, moderate yields, and the threat of diseases. Therefore, the objective of our study was to isolate and identify actinomycete strains from the rice rhizosphere and evaluate their plant growth-promoting abilities to enhance paddy quality. Additionally, the research aimed to develop an ecologically sustainable and holistic seed biopriming method using a consortium of potent actinomycete strains for field application.

2. MATERIALS AND METHODS

2.1. Isolation of Indigenous Rhizospheric Actinomycetes

Actinomycetes were isolated from samples collected from various paddy fields of rice variety Indrayani in Bhor and Mulshi tehsils of Pune district. Sampling occurred at three distinct farming stages: bulk soil before sowing, rhizospheric soil from transplanted seedlings, and at harvest. One gram of each soil sample was suspended in 9 mL of sterile physiological saline and vortexed. The samples were then serially diluted up to 10^{-5}, and aliquots from the 10^{-4} and 10^{-5} dilutions (0.1 mL) were spread on Starch casein agar (SCA) supplemented with 50 $\mu g.mL^{-1}$ cycloheximide, produced by Hi Media Laboratories, Mumbai, India. Plates were incubated at 28 ± 2°C for seven days. Colonies exhibiting powdery and dry textures were isolated and preserved on ISP 4 (International Streptomyces Project 4) medium slants.

2.2. Screening of Isolates for Plant Growth Promoting (PGP) Properties

2.2.1. Ammonia Production

The isolates were inoculated into 5 mL of peptone water and incubated at 28°C for 7 to 12 days with agitation at 120 rpm. After incubation, 0.5 mL of Nessler's reagent was added to each culture tube. A yellow to brown coloration indicated a positive result for ammonia production (Cappuccino & Sherman 1992). Ammonia-producing strains were then screened for plant growth-promoting (PGP) features.

2.2.2. Production of Indole Acetic Acid

Indole-3-acetic acid (IAA), an auxin produced by selected isolates, was analyzed using Salkowski's method. All isolates were cultured in International Streptomyces Project 2 (ISP 2) medium supplemented with 0.2% tryptophan and incubated at 28°C for 7 days. The cell-free supernatant was then mixed with 2 mL of Salkowski's reagent, which consisted of 50 mL of 35% perchloric acid and 1 mL of 0.5 M FeCl3 solution. The mixture was incubated in the dark for 30 min at room temperature. The development of a pink or red color indicated IAA production. Absorbance was measured at 535 nm. (Anwar et al.2016).

2.2.3. Gibberellic Acid (GA) Production

Actinomycete isolates were cultured in ISP-2 medium. GA was extracted from cell-free extracts with an equal volume of ethyl acetate (1:1). The organic layer was evaporated, and the dried extract was dissolved in 2 mL of ethanol before being combined with 1 mL of 2,4-Dinitrophenylhydrazine and 5% KOH. Absorbance was measured at 430 nm. (Graham & Thomas 1961).

2.2.4. Siderophore Production

The ability of all PGPR isolates to produce siderophores was tested on Chrome Azurol S agar (CAS agar). After being spread out onto the CAS agar plate, each isolate was incubated for 4-5 days at room temperature. Orange halos surrounding the colonies indicated the presence of siderophore production.(Anwar et al. 2016).

2.2.5. Phosphate Solubilization

The phosphate solubilization ability of the isolates was evaluated using Pikovskaya's agar medium. Each isolate was streaked onto a Pikovskaya agar plate and incubated at room temperature for seven days. The formation of clear halo zones around colonies indicated phosphate solubilization.

2.2.6. Amylase Production

Isolates were spot-inoculated onto starch agar plates and incubated at 28°C for 7 days. Following incubation, the plates were flooded with iodine solution and left undisturbed for

5-10 min. Subsequently, the iodine solution was drained, and the clear zones surrounding the colonies were recorded (Ekka & Namdeo 2018).

Phosphate solubilization, Siderophore production index, and amylase production index were calculated as follows:

$$\text{PSI/SPI/API} = \frac{\text{Colony diameter + Zone diameter}}{\text{Colony diameter}} \quad \ldots(1)$$

2.2.7. Acetyl Pyrroline Production

Acetyl Pyrroline (2AP) is a key volatile component responsible for the aroma in rice. Isolates were grown on the plates containing the ISP 4 agar medium supplemented with ornithine (4%) for 7 days. Analysis of aroma production was done by sniffing (Dhondge et al. 2021).

2.2.8. Putrescine Production

Putrescine is produced through ornithine decarboxylation, which raises the medium's pH and causes the indicator to change from yellow to purple. Detection of putrescine production was achieved using Moeller's decarboxylase broth supplemented with 1% ornithine, resulting in a color change from yellow to purple (Nassar et al. 2003).

2.2.9. Evaluation of Biocontrol Properties

The isolates were evaluated for their antimicrobial activity against the major rice pathogen Xanthomonas oryzae subspecies oryzae (Xoo), which causes leaf blight in rice, using the giant colony technique. The pathogen was obtained from the pathology department of the Agriculture Research Station at Mahatma Phule Krishi Vidyapeeth, Lonavala, Maharashtra. Isolates were streaked onto ISP 4 medium as a single, thick band at the center of the plate and incubated for five days at 28°C. After incubation, the pathogen was streaked in triplicate, perpendicular to the giant colony. The plates were then incubated for 48 h at room temperature. Inhibition of the pathogen's growth was taken as an indication of biocontrol activity. Secondary screening of antimicrobial producers was performed using the standard agar well diffusion assay described by Balouiri et al. (2015). Cultures were cultivated in International Streptomyces Project 2 (ISP 2) medium for ten days. Cell-free broth was obtained through sonication and filtration. Standard streptomycin (200 $\mu g.mL^{-1}$) served as a positive control, while sterile ISP 2 medium was used as a negative control.

2.3. Screening of Isolates for Seed Germination Ability

2.3.1. Seed Germination Bioassay

The growth-promoting activity of the isolates was assessed using the modified 'ragdoll' method (Sreevidya et al. 2016). One gram of paddy seeds, obtained from a local market, was sterilized with 70% alcohol and pre-soaked in water. The seeds were then treated with a spore suspension of individual actinomycetes at a concentration of 10^{-7} $CFU.mL^{-1}$ for 24 h. They were placed on one half of a wet paper towel, folded, rolled, and placed in a large petri dish. Control seeds were treated with sterile distilled water only. The dishes were sealed with parafilm and incubated at 28 ± 2°C with a light source for 10 days. After incubation, the root and shoot lengths of both treated and control seedlings were measured. Germination percentage and vigor indices were calculated using the respective formulas:

$$Germination\ Percentage(\%) = \frac{No.of\ seeds\ germinated \times 100}{Total\ No.of\ seeds\ used} \quad \ldots(2)$$

$$Vigor\ Index = Germination\ (\%) \times Average\ seedling\ length\ (cm) \quad \ldots(3)$$

2.3.2. Extraction and Estimation of Active Metabolites from Germinated Seeds

One gram of germinated seeds was crushed using 10 mL of sodium phosphate buffer at pH 7.0 (0.05 M) in a mortar and pestle. The metabolites were extracted overnight under cold conditions. The mixture was centrifuged at 5000 rpm for 15 min, and the supernatant was collected to obtain the crude seed extract. Quantitative assessment of α-amylase enzyme in both treated and control germinated seeds was performed using the standard DNSA method. The quantification of GA content in seed extracts was conducted using the DNPH method described by Graham and Thomas (1961).

2.3.3. Root Colonization Study

Bioprimed roots of treated paddy seeds, obtained during the germination study, were further examined for colonization by the respective actinomycetes using a scanning electron microscope (JEOL-JSM-6360A) at the Department of Physics, SPPU, Pune, India. Roots were cut into 3-4 mm pieces and fixed in 2.5% glutaraldehyde solution, then washed with phosphate buffer at pH 7 for 24 h at 4°C. The fixed roots were dehydrated with 75% ethanol and air-dried. Finally, the dehydrated roots were coated with platinum and observed under scanning electron microscopy.

2.3.4. Compatibility Testing of Potent Actinomycetes

Each potent actinomycete culture was streaked at the center using the same technique as the giant colony method. Other isolates to be tested were streaked perpendicular to it. The plates were incubated for five days. The growth of isolates at the crossing points of the paired streaks was considered an indication of compatibility (Fiodor et al. 2023).

2.3.5. Morphological Identification of Actinomycetes Using the Coverslip Culture Technique

Sterile cover slips were inserted at a 45° angle into each

quadrant of ISP 4 medium agar plates. The inoculum was streaked onto the agar at the base of the cover slip. Plates were then incubated at room temperature (28°–30°C) for 4-5 days, until the organism grew up to the cover slip. Gently, the cover slip was removed using sterile forceps, and a drop of crystal violet was applied to a slide. The cover slip was placed on the stain, and the sample was examined under a microscope (Mitchell & Britt 2004).

2.3.6. Molecular Identification and Phylogenetic Analysis of the Potent Actinomycetes

The selected actinomycetes were sent to Hi-Geno MB, Himedia Laboratories Pvt. Ltd., for identification through 16S rRNA analysis. Sequences obtained from HiMedia Laboratories were identified at the species level using the NCBI GenBank database and compared with the BLAST program. The nucleotide sequences were submitted to GenBank, and NCBI accession numbers were obtained (Cook & Meyers 2003). These sequences were aligned using Clustal W software, and a phylogenetic tree was constructed using the neighbor-joining method. Bootstrap analysis with 1000 replications was performed using MEGA 11 software to assess the reliability of the inferred phylogenetic relationships, illustrating the evolutionary history among the selected potent actinomycetes. In addition to NCBI, actinomycete genera were confirmed using the EZBiocloud database.

2.3.7. Statistical Analysis

The germination data were statistically analyzed using R software. Shoot and root lengths were subjected to one-way analysis of variance (ANOVA). Post hoc comparisons were carried out with Tukey's honest significant difference test to identify which actinomycete treatments were significantly

Table 1: Major plant growth-promoting traits of actinobacterial isolates.

Isolate No.	API	PSI	SPI	IAA Production [µg .mL^{-1}]	GA Production [mg.mL^{-1}]	Ammonia Production	Polyamine production	AntiXoo activity (Zone of inhibition)	Aroma Production
H1Rb	3.8	1.4	0.0	5.62	39.75	1.0	0.0	3±0.4	0.0
H1Rc	2	1.2	0.0	0.0	0.0	1.0	0.0	0.0	0.0
I1	3.6	1.5	1.5	4.1	46.89	1.0	1	0.0	0.0
I2	2.1	0.0	0.0	0.0	0.0	1.0	0.0	0.0	0.0
I4*	2.9	2.0	3.9	7.24	75.76	1.0	3	10±0.5	0.0
I5	2	0.0	0.0	0.0	0.0	1.0	0.0	0.0	0.0
I7*	2.8	1.2	4.1	3.79	82.6	2.0	3	0.0	3.0
I8	1.8	0.0	1.2	0.0	0.0	1.0	0.0	0.0	0.0
I18	2.1	0.0	0.0	0.0	0.0	1.0	1.0	5±0.9	0.0
I26	2.2	0.0	0.0	0.0	0.0	1.0	0.0	0.0	0.0
E3.3	2.4	0.0	1.3	3.79	0.0	1.0	0.0	0.0	0.0
E4.1	2	1.6	0.0	0.0	0.0	1.0	0.0	0.0	0.0
L1A	1.9	0.0	0.0	0.0	0.0	1.0	0.0	0.0	0.0
L1B	1.9	0.0	1.4	5.01	0.0	1.0	0.0	0.0	0.0
L1C	2	0.0	0.0	0.0	0.0	1.0	0.0	3±0.5	0.0
L1D*	2.5	1.1	1.9	4.80	49.53	1.0	1.0	3±0.2	0.0
L1E	2	0.0	0.0	0.0	0.0	1.0	1.0	0.0	0.0
S1a	2.1	0.0	0.0	0.0	0.0	1.0	0.0	0.0	0.0
S2a	1.5	0.0	0.0	2.36	0.0	1.0	0.0	0.0	0.0
S4a	1.9	0.0	0.0	5.01	0.0	1.0	0.0	0.0	0.0
S4g	1.8	0.0	0.0	2.37	0.0	1.0	0.0	0.0	0.0
S6a*	3.8	1.8	1.9	5.62	64.75	1.0	0.0	8±0.6	0.0
S7a	1.1	0.0	0.0	0.0	0.0	1.0	0.0	0.0	0.0

Note:API:Amylase production index, PSI: Phosphate solubilization index; SPI: siderophores production index, IAA : Indole-3-acetic acid production,GA: Gibberellic acid production. Key: 1 = positive, 2 = moderately positive, 3 = strongly positive, 0 = negative.
Anti Xoo activity – Antimicrobial activity against Xanthomonas 0ryzae showing inhibition zone in cm.
All values given in the column are the average of three replicates.Asteric denotes multifunctional isolates.
* denotes potent microbes with maximum plant growth-promoting traits.

effective. The graphical representations included boxplots, bar plots with standard deviation bars, and mean difference plots with 95% confidence intervals. Boxplots were used to examine the distribution of shoot and root length measurements across different seed treatments.

3. RESULTS AND DISCUSSION

3.1. Isolation and Assessment of Various Plant Growth Promotion Properties

Out of 49 actinomycetes isolates, 50% demonstrated ammonia production, while 56% were found to produce IAA. Another study showed that 34% of actinomycete isolates from the soybean rhizosphere produced IAA and also promoted plant growth (Wahyudi et al. 2019). The present study revealed the diversity of rhizospheric actinomycetes, with a richness of biostimulatory features that support plant development. Table 1 presents the distribution of plant growth-promoting (PGP) properties among the actinomycetes isolates.

Only six (24%) actinomycetes were found to produce major PGP characteristics such as ammonia, putrescine, siderophore, phosphatase, amylase, IAA and GA, except for the production of aroma and antimicrobial activity against *Xanthomonas oryzae*. A distinct feature of aroma production was shown only by isolate I7. However, strong biocidal properties against *Xanthomonas oryzae* have been shown by I4 (Fig. 1). Isolate no. S6A, I4, and I7 showed all PGP properties. Higher amounts of IAA were produced by I4(7.2479 $\mu g.mL^{-1}$), H1RB (5.6219 $\mu g.mL^{-1}$) and L1B (5.0121$\mu g.mL^{-1}$). Gibberellin plays a major role in germination. Table 1 shows significant GA secretion in the media by all six selected isolates.

3.2. Germination Bioassay of Bioprimed Seeds

The potential of rhizospheric actinomycetes, i.e., in vivo growth-promoting abilities, was evaluated using a germination test with paddy seeds. One-way ANOVA confirmed an overall treatment effect on root length ($p < 0.01$ and 0.05). Table 2 presents the results of the one-way ANOVA assessing whether there are statistically significant differences in root and shoot length across treatment groups.

The F-values of root length and shoot length were 26.96 and 9.448, respectively. P-values of root length and shoot length are 1.15×10^{-15} and $2.17\times10^{-7,}$ which are less than

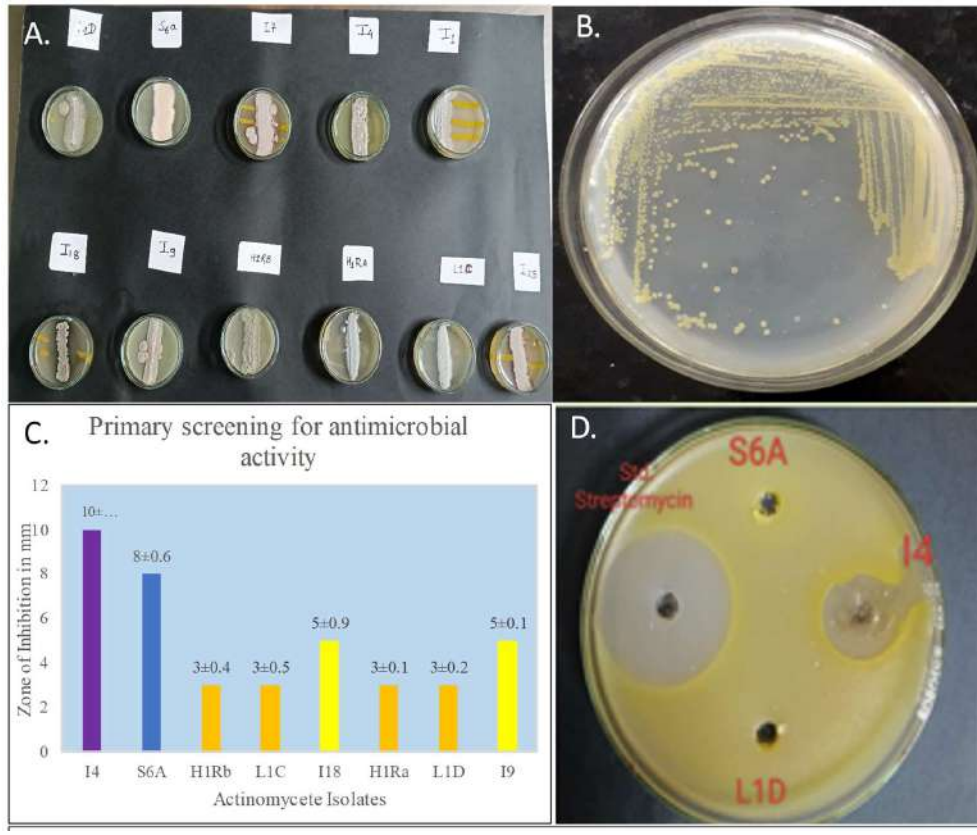


Fig. 1: Biocontrol property of Actinomycetes. A. Primary screening B. Plant pathogen *Xanthomonas oryzae* C. Antimicrobial activity of isolates D. Secondary screening of cell-free broths in comparison with standard streptomycin.

Table 2: One-way ANOVA analysis of root length.

	Source	Df	Sum of Square	Mean Square	F	P value (>F)
Root length in cm	Treatment	6	276.5189	46.08648	26.9619	1.15e-15 ***
	Residuals	63	107.687	1.709317		
Shoot length in cm	Treatment	6	58.5589	9.76	9.448	2.17e-07
	Residuals	63	65.079	1.033		

 = 0.05 & 0.001, indicating a highly significant effect of treatment on root length. This means we reject the null hypothesis, confirming that not all group means are equal. The significant difference justifies proceeding with Tukey's HSD for pairwise comparisons (Tables 3 and 4).

Tukey's HSD test identified S6A, I7, and L1D as significantly superior to the Control, which consisted of unprimed seeds (Table 3). Treatments I7, L1D, and S6A exhibited noticeably higher medians and smaller interquartile ranges compared to the Control. For isolates S6A, I7, and L1D, the confidence intervals do not include zero, indicating significant differences from the Control. In contrast, I1 and I4 have intervals that encompass zero, suggesting no significant difference from the Control. The data underscores S6A as the most effective treatment, demonstrating the greatest and most consistent improvement in root length.

Biopriming treatment also demonstrated a significant effect on shoot length ($p < 0.01$ and $p < 0.05$). The Tukey HSD post hoc test identified treatments I7, L1D, S6A, and H1Rb as significantly more effective than the control in promoting shoot elongation. As shown in Fig. 2, treatments I7 and S6A exhibited the highest shoot growth, indicating

Table 3: Tukey's Honest Significant Difference (HSD) test (Root length comparison).

Group 1	Group 2	Mean Diff	p-adj	Lower CIass	Upper Class	Significant
Control	H1Rb	2.23	0.0055	0.45	4.01	✓ Yes
Control	I7	4.92	0	3.14	6.7	✓ Yes
Control	L1D	3.56	0	1.78	5.34	✓ Yes
Control	S6A	6.25	0	4.47	8.03	✓ Yes
H1Rb	I7	2.69	0.0004	0.91	4.47	✓ Yes
H1Rb	S6A	4.02	0	2.24	5.8	✓ Yes
I1	I7	3.21	0	1.43	4.99	✓ Yes
I1	S6A	4.54	0	2.76	6.32	✓ Yes
I4	I7	3.3	0	1.52	5.08	✓ Yes
I4	S6A	4.63	0	2.85	6.41	✓ Yes
L1D	S6A	2.69	0.0004	0.91	4.47	✓ Yes

Table 4: Tukey's Honest Significant Difference (HSD) test (Shoot length comparison).

Group 1	Group 2	Mean Diff	p-adj	Lower CIass	Upper Class	Significant
Control	H1Rb	1.48	0.0286	0.0957	2.8643	✓ Yes
Control	I7	2.48	0	1.0957	3.8643	✓ Yes
Control	L1D	2.09	0.0004	0.7057	3.4743	✓ Yes
Control	S6A	2.55	0	1.1657	3.9343	✓ Yes
I4	I7	2.03	0.0006	0.6457	3.4143	✓ Yes
I4	L1D	1.64	0.0104	0.2557	3.0243	✓ Yes
I4	S6A	2.1	0.0004	0.7157	3.4843	✓ Yes
Control	H1Rb	1.48	0.0286	0.0957	2.8643	✓ Yes
Control	I7	2.48	0	1.0957	3.8643	✓ Yes
Control	L1D	2.09	0.0004	0.7057	3.4743	✓ Yes
Control	S6A	2.55	0	1.1657	3.9343	✓ Yes

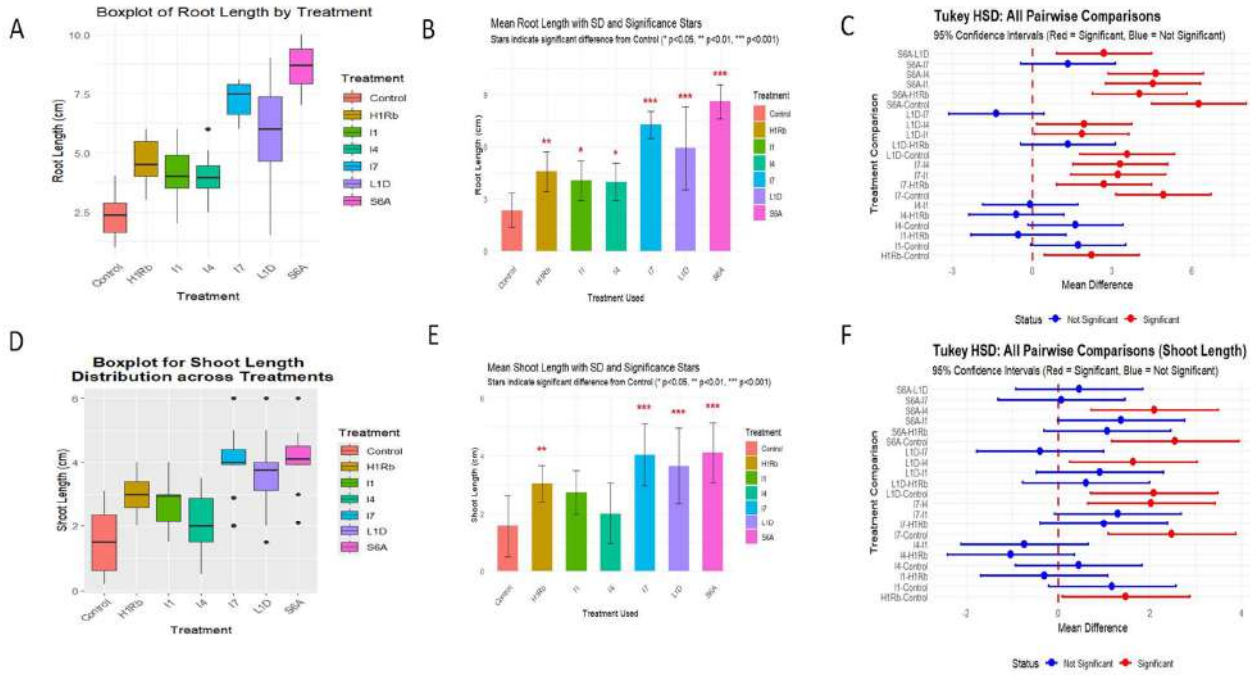


Fig. 2: Germination study of seeds bioprimed with selective actinomycetes. (A), (B) & (C) Analysis of the effect of treatment on root length of seedlings. (D), (E) & (F) Shoot length analysis of seed treatment. Vertical bars represent ± standard error of the mean. H1Rb, I1, I4, I7, L1D and S6A represent selective actinomycetes. There were 10 replicates for the control and each treatment.

their strong potential for application in enhancing plant development. An analogous experiment involving wheat seed inoculation with actinomycetes found that Streptomyces nobilis WA-3 led to notable increases in shoot length (65%) and root length (81%) during pot trials (Anwar et al. 2016). These results align with findings by Sreevidya et al. (2016), who reported a 17% increase in root length and a 3% increase in shoot length in chickpea after treatment with actinomycete isolates. Therefore, various biopriming treatments significantly enhanced root and shoot growth of seedlings at both 5% and 1% levels of significance.

Seeds primed with selected actinomycetes spores also showed improved vigor index and increased germination percentage in comparison with the control, as depicted in Fig. 3. Biopriming with actinomycetes may lead to enhanced germination, subsequent protection against major diseases, and finally may enhance crop yield and may improve other agronomic traits too. The greatest improvement in germination percentage was shown by I7, i.e., by 44.67% in comparison with the control (Table 5). A similar study also showed that biopriming with five different bacterial isolates improved carrot seed germination and seedling growth. Bacterial genera *S. plymuthica* EDC15, *B. ambifaria* AF8II10, and *S. plymuthica* EEPC5 have shown an impact on seed germination by increasing it by 8.22, 10.22, and 10.32%, respectively (Fiodor et al. 2023). The synthesis of active GA in the epithelium is important for amylase expression in the endosperm. Starch from the endosperm is gradually hydrolyzed by α-amylase to supply energy for germination. One possible explanation for the increased germination rate could be improved GA content of treated paddy seeds due to possible GA secretion by actinomycete strains. Increased amylase content of seeds supports the role of GA in the enhancement of germination as well as in the induction of α-amylase. Seed treatment with potent *Streptomyces* strains was found to enhance the concentration of α-amylase in germinating seeds.GA Priming significantly promoted seed germination and seedling growth under submergence compared to no priming and hydro-priming. This improvement was associated with higher GA_3 levels achieved in rice seeds, resulting in the subsequent induction of the expression of GA-responsive α-amylase genes (Wang et al. 2025). The activation of seed germination and early support for seedling growth under stressful conditions has been highlighted by seed biopriming (Prasad et al. 2016).

3.3. Suitability of Potent Actinobacteria for Agronomic Application

Findings of compatibility testing (Table 6) suggest that isolates I7, L1D, S6A, and I4 are relatively highly compatible with each other and can grow best in a consortium. However, I1 and H1Rb had non-compatibility with 16% & 83%

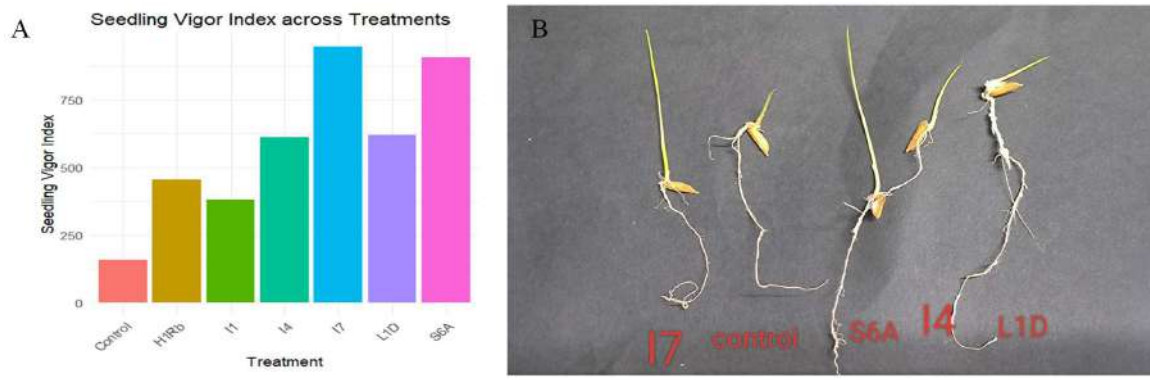


Fig. 3: A. Effect of seed treatment on seedling Vigor Index. B. Rice Seedlings showing plant growth promotion in germination study.

Table 5: Effect of treatment on germination of paddy seeds.

Seed treatment used	Concentration of GA in treated seeds [µg.g^{-1}]	Amylase activity U (in terms of maltose)	Germination Percentage [%]
Control	0.15±0.11	11.4	39.66±0.57
S6a	0.79 ±0.25	20.8	70.66±0.55
I1	0.56± 0.69	16.1	56.33±0.58
I7	0.90±1.1	30.6	84.33±0.57
I4	0.83± 0.68	27.9	81±1
L1D	0.69± 0.19	19.7	69.33±1.52
H1Rb	0.54± 0.29	18.5	64±1

Note: 1unit of Amylase enzyme = 10000 µM.min^{-1}.mL^{-1}

Table 6: Compatibility testing of selected PGP Actinomycetes.

Sr No.	Isolate No.	S6A	I1	I7	I4	L1D	H1Rb
1	S6A	3	3	3	3	3	3
2	I1	3	3	3	3	3	1
3	I7	3	3	3	3	3	1
4	I4	3	3	3	3	2	0
5	L1D	3	3	3	2	3	2
6	H1Rb	3	1	1	0	2	3

Key: 1 = less compatible , 2 = moderately compatible , 3 = highly compatible , 0 = Non compatible

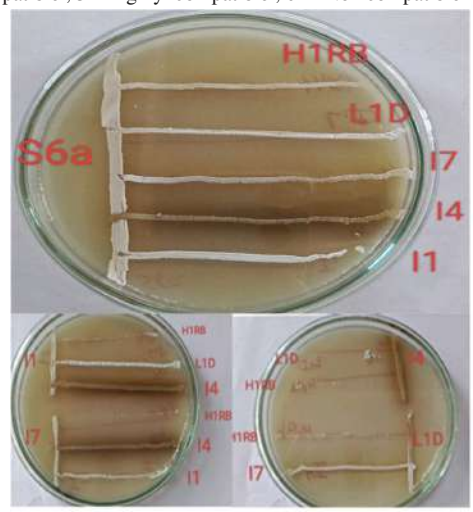
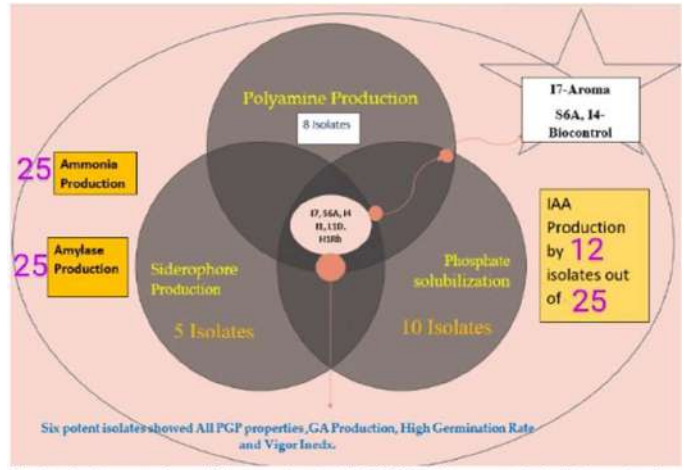


Fig. 4: Compatibility testing of Actinomycetes isolates H1Rb, I1, I4, I7, L1D and S6A.

actinomycetes, respectively, as in Fig. 4. S6A was highly compatible with all five other potent cultures.

Summary of research work depicted in Fig. 5 and findings of compatibility testing revealed that four potent isolates are highly suitable in consortium preparation for further pot trials.

The SEM images of bioprimed roots showed that these *Streptomyces* strains can colonize the paddy roots without damaging them. Fig. 6 shows that all three potent strains of *Streptomyces* were found to establish extensive colonization and biofilm formation in comparison with control roots. However, *Streptomyces antibioticus* strain I4 showed relatively less extent of biofilm formation. *Streptomyces graminofaciens*, *S. rochei*, *S. annulatus*, *S. gibsonii*, *Candida glabrata*, *C. maltosa*, *C. slooffii*, and *Rhodotorula* have been reported for root colonization in maize, leading to a significant reduction in the growth of *Cephalosporium maydis*, causing late wilt disease of maize in pot trials (El-Mehalawy et al. 2004). A similar study in



Strategical screening of the most potential PGP actinomycete isolates out of 49 isolates from different paddy fields

Fig. 5: Summary of research work.

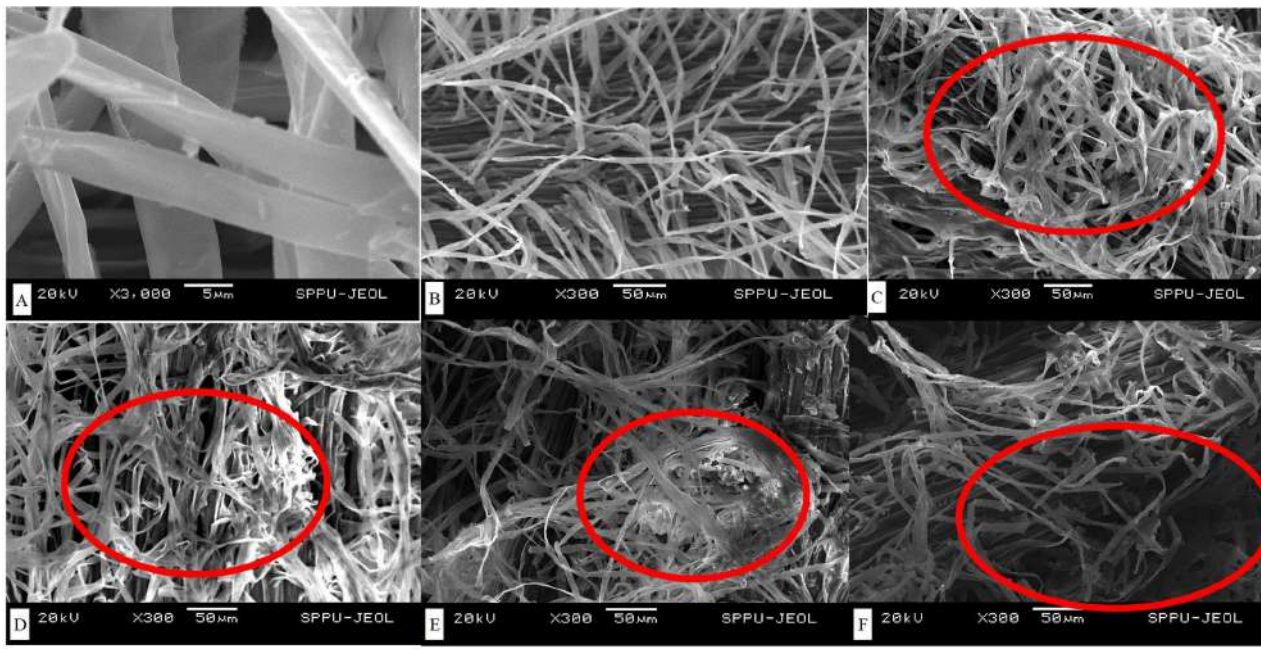


Fig. 6: A & B - Scanning electron micrographs of control roots at magnifications 3000X and 300X, respectively; C, D, E & F - SEM images of roots of seeds treated with actinomycetes L1D, S6A, I7 and I4, respectively. The highlighted area shows root colonization by the actinomycete species used.

Table 7: Homology of Actinomycetes.

Sr. No.	Isolate Name	Identity Result (NCBI Database)	Accession Number	16 S r RNA length	Percent Similarity	Type strain (EZBiocloud)
1.	I4	*Streptomyces antibioticus* strain I4	PV652702	1409	100.00	*Streptomyces antibioticus* NBRC 12838(T)
2.	I7	*Streptomyces ardesiacus strain* I7	PV652733.1	1405 bp	99.72	*Streptomyces ardesiacus* NRRL B-1773
3.	L1D	*Streptomyces albogriseolus strain* L1D	PV652750.1	1434 bp	99.16	*Streptomyces albogriseolus* NRRL B-1305
4.	S6A	*Streptomyces tanashiensis strain* S6A	PV652742.1	1415bp	99.79	*Streptomyces hydrogenans* JCM 4771

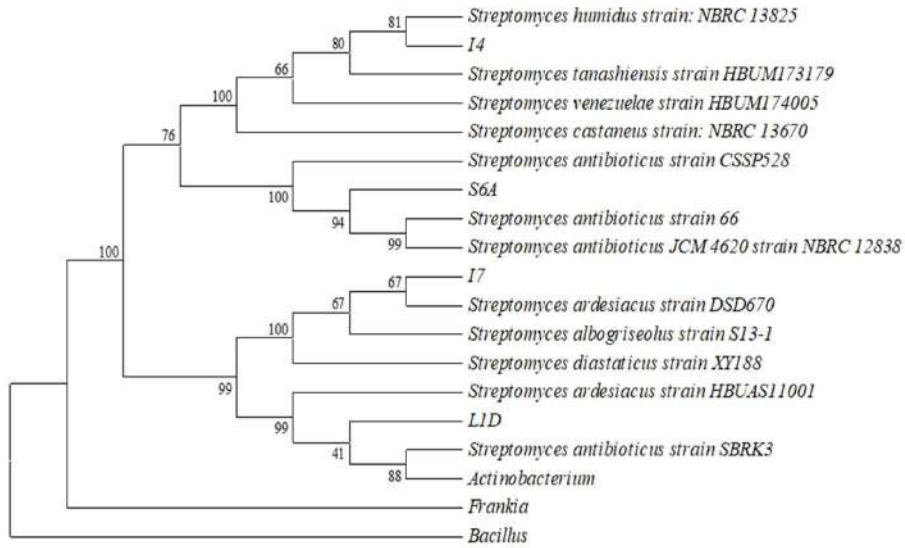


Fig. 7: Phylogenetic relationship between I4, S6A, I7, and L1D with representative microbial species based on full-length 16S rDNA sequences constructed using the neighbor-joining method.

chickpea showed that all four Streptomyces strains, VAI-7, VAI-40, SAI-13, and SAI-29, colonized the roots of chickpea (Sreevidya et al. 2016). Root exudates contain aromatic and phenolic chemicals, sugars, amino acids, organic acids, and carbohydrates that function as chemoattractants to aid in root colonization (Van & Van 1995).

3.4. Morphological and Molecular Identification of Potent Actinomycetes

The most promising plant growth-promoting bacteria were studied for their morphological and colony characteristics. Morphology in coverslip cultures confirmed their thin mycelial structure with long spiral spore chains. All four future members of the bioconsortium were found to be from the genus *Streptomyces*. Details of blast analysis are listed in Table 7. The nucleotide sequences of these isolates were submitted to GenBank, and NCBI accession numbers were obtained. The phylogenetic tree illustrates their genetic similarity and evolutionary relationship with other known actinomycetes. (Fig. 7).

4. CONCLUSIONS

Diversity was observed among Actinomycetes isolated from the rice (*Oryza sativa*) rhizosphere. A significant number of rhizospheric actinobacteria exhibited major plant growth-promoting properties. The present study showed that the production of growth hormones by microbes may enhance the germination rate. High GA content and increased α-amylase activity in extracts of germinated bio-primed seeds, compared with the control, highlight the potential role of actinomycetes, particularly Streptomyces, in increasing GA levels in the endosperm. *Streptomyces antibioticus* strain I4 has prominent biocontrol ability against bacterial leaf blight of rice. Production of 2AP by rhizospheric actinomycetes provides new insight into the enhancement of rice aroma. This study revealed the suitability of these

four multipotent actinomycetes, *Streptomyces antibioticus* strain I4, *Streptomyces ardesiacus* strain I7, *Streptomyces albogriseolus* strain L1D, and *Streptomyces tanashiensis* strain S6A, as a biopriming tool for seeds. These four Streptomyces strains need to be further developed as biopriming agents for sustainable paddy farming.

5. ACKNOWLEDGMENTS

We would like to thank Haribhai V.Desai College, Pune, India, for providing the necessary facilities to carry out the present research work. We also extend gratitude towards the Department of Physics, SPPU, Pune, India, for availing the SEM facility and MPKV's Agriculture Research Station, Lonavala, Pune, India, for providing plant pathogens.

6. REFERENCES

Adnan, M., Patel, M., Reddy, M.N., Khan, S., Alshammari, E., Abdelkareem, A.M. and Hadi, S., 2016. Isolation and characterization of effective and efficient plant growth-promoting rhizobacteria from rice rhizosphere of diverse paddy fields of Indian soil. *ARPN Journal of Agricultural and Biological Science*, 11(9), pp.373-379.

Anwar, S., Ali, B. and Sajid, I., 2016. Screening of rhizospheric actinomycetes for various in-vitro and in-vivo plant growth-promoting (PGP) traits and for agroactive compounds. *Frontiers in Microbiology*, 7, p.1334. [DOI]

Adnan, M.A., Shah, S., Khan, A., Fazli Wahid, M.I., Inayat-ur-Rahman, M.A.K. and Ali, R., 2018. Optimization of sowing time and seed rates can enhance wheat yield in semi-arid environment. *Philippine Agricultural Scientist*, 101(4). [DOI]

Asante, M.D., Asante, B.O., Acheampong, G.K., Offei, S.K., Gracen, V., Adu-Dapaah, H. and Danquah, E.Y., 2013. Farmer and consumer preferences for rice in the Ashanti region of Ghana: Implications for rice breeding in West Africa. *Journal of Plant Breeding and Crop Science*, 5(12), pp.229-238. [DOI]

Balouiri, M., Sadiki, M. and Ibnsouda, S.K., 2016. Methods for in vitro evaluating antimicrobial activity: A review. *Journal of Pharmaceutical Analysis*, 6(2), pp.71-79. [DOI]

Cappuccino, J.C. and Sherman, N., 1992. *Microbiology: A Laboratory Manual*. New York: Benjamin Cummings, pp.125-179.

Chakraborti, S., Bera, K., Sadhukhan, S. and Dutta, P., 2022. Bio-priming of seeds: Plant stress management and its underlying cellular, biochemical and molecular mechanisms. *Plant Stress*, 3, p.100052. [DOI]

Kabdwal, B.C., Sharma, R., Kumar, A., Kumar, S., Singh, K.P. and Srivastava, R.M., 2023. Efficacy of different combinations of microbial biocontrol agents against sheath blight of rice caused by *Rhizoctonia solani*. *Egyptian Journal of Biological Pest Control*, 33(1), p.29. [DOI]

Chinachanta, K., Shutsrirung, A., Herrmann, L., Lesueur, D. and Pathom-Aree, W., 2021. Enhancement of the aroma compound 2-acetyl-1-pyrroline in thai jasmine rice (*Oryza sativa*) by rhizobacteria under salt stress. *Biology*, 10(10), p.1065. [DOI]

Diab, M.K., Mead, H.M., Ahmad Khedr, M.M., Abu-Elsaoud, A.M. and El-Shatoury, S.A., 2024. Actinomycetes are a natural resource for sustainable pest control and safeguarding agriculture. *Archives of Microbiology*, 206(6), p.268.

Dhondge, H.V., Pable, A.A., Barvkar, V.T., Dastager, S.G. and Nadaf, A.B., 2021. Rhizobacterial consortium mediated aroma and yield enhancement in basmati and non-basmati rice (*Oryza sativa* L.). *Journal of Biotechnology*, 328, pp.47-58. [DOI]

Ekka, A. and Namdeo, N., 2018. Screening, isolation and characterization of amylase producing bacteria and optimization for production of amylase. *IOSR Journal of Biotechnology and Biochemistry*, 4, pp.50-56.

El-Mehalawy, A.A., Hassanein, N.M., Khater, H.M., Karam El-Din, E.A. and Youssef, Y.A., 2004. Influence of maize root colonization by the rhizosphere actinomycetes and yeast fungi on plant growth and on the biological control of late wilt disease. *Egyptian Journal of Microbiology*, 39(1), pp.45-62.

El-Tarabily, K.A. and Sivasithamparam, K., 2006. Non-streptomycete actinomycetes as biocontrol agents of soil-borne fungal plant pathogens and as plant growth promoters. *Soil Biology and Biochemistry*, 38(7), pp.1505-1520. [DOI]

Fiodor, A., Ajijah, N., Dziewit, L. and Pranaw, K., 2023. Biopriming of seed with plant growth-promoting bacteria for improved germination and seedling growth. *Frontiers in Microbiology*, 14, p.1142966. [DOI]

Graham, H.D. and Thomas, L.B., 1961. Rapid, simple colorimetric method for the determination of micro quantities of gibberellic acid. *Journal of Pharmaceutical Sciences*, 50(1), pp.44-48. [DOI]

Elshafie, H.S., Osman, A., El-Saber, M.M., Camele, I. and Abbas, E., 2023. Antifungal activity of green and chemically synthesized ZnO nanoparticles against *Alternaria citri*, the causal agent citrus black rot. *The Plant Pathology Journal*, 39(3), p.265. [DOI]

Cook, A.E. and Meyers, P.R., 2003. Rapid identification of filamentous actinomycetes to the genus level using genus-specific 16S rRNA gene restriction fragment patterns. *International Journal of Systematic and Evolutionary Microbiology*, 53(6), pp.1907-1915. [DOI]

Mitchell, J.L. and Britt, E.M., 1981. A coverslip culture technique for preparing permanent fungus mounts. *Mycopathologia*, 76(1), pp.23-25. [DOI]

Nassar, A.H., El-Tarabily, K.A. and Sivasithamparam, K., 2003. Growth promotion of bean (*Phaseolus vulgaris* L.) by a polyamine-producing isolate of *Streptomyces griseoluteus*. *Plant Growth Regulation*, 40(2), pp.97-106. [DOI]

Rajendra Prasad, S., Kamble, U.R., Sripathy, K.V., Udaya Bhaskar, K. and Singh, D.P., 2016. Seed bio-priming for biotic and abiotic stress management. In: D.P. Singh, H.B. Singh and R. Prabha, eds., *Microbial Inoculants in Sustainable Agricultural Productivity: Vol. 1: Research Perspectives*. New Delhi: Springer India, pp.211-228. [DOI]

Sharif, M.K., Butt, M.S., Anjum, F.M. and Khan, S.H., 2014. Rice bran: a novel functional ingredient. *Critical Reviews in Food Science and Nutrition*, 54(6), pp.807-816. [DOI]

Sreevidya, M., Gopalakrishnan, S., Kudapa, H. and Varshney, R.K., 2016. Exploring plant growth-promotion actinomycetes from vermicompost and rhizosphere soil for yield enhancement in chickpea. *Brazilian Journal of Microbiology*, 47(1), pp.85-95. [DOI]

Van Overbeek, L.S. and Van Elsas, J.D., 1995. Root exudate-induced promoter activity in *Pseudomonas fluorescens* mutants in the wheat rhizosphere. *Applied and Environmental Microbiology*, 61(3), pp.890-898. [DOI]

Wahyudi, A.T., Priyanto, J.A., Fijrina, H.N., Mariastuti, H.D. and Nawangsih, A.A., 2019. *Streptomyces* spp. from rhizosphere soil of maize with potential as plant growth promoter. *Biodiversitas*, 20(9), pp.2547-2553.

Wang, W., Jiang, Q., Tan, B., Yang, H., Cao, F., Chen, J., Huang, M. and Zheng, H., 2025. The physio-biochemical changes induced by gibberellic acid seed priming in rice seeds against submergence stress: Consequences for starch degradation, energy metabolism and hormonal metabolism. *Rice*, 18, p.25. [DOI]

Yadav, A.N., Verma, P., Singh, B., Chauhan, V.S., Suman, A. and Saxena, A.K., 2017. Plant growth promoting bacteria: biodiversity and multifunctional attributes for sustainable agriculture. *Advances in Biotechnology & Microbiology*, 5(5), pp.1-16.

Nature Environment and Pollution Technology
An International Quarterly Scientific Journal

p-ISSN: 0972-6268
(Print copies up to 2016)
e-ISSN: 2395-3454

Vol. 25 | No. 3 | Article ID D1880 | 2026

Original Research Paper

https://doi.org/10.46488/NEPT.2026.v25i03.D1880

Open Access Journal

An Econometric Assessment of Growth-Pollution Interactions in Vietnam within the Environmental Kuznets Framework

Thi Thu Trang Phung[1], Thi Thanh Huong Chu[2], Thi Thu Huong Tran[1] and Thi Phuong Chi Nguyen[3]†

[1]Faculty of Environment, Hanoi University of Mining and Geology (HUMG), Hanoi, Vietnam
[2]Department of Climate Change, Hanoi, Vietnam
[3]Faculty of Business Administration, Industrial University of Hochiminh City, Vietnam
†Corresponding author: Thi Phuong Chi Nguyen; nguyenthiphuongchi@iuh.edu.vn

Abbreviation: Nat. Env. & Poll. Technol.
Website: www.neptjournal.com

Received: 18-10-2025
Revised: 10-12-2025
Accepted: 17-12-2026

Key Words:

Greenhouse gas emissions
Growth-pollution interactions
Exchange rate
Environmental Kuznets Curve (EKC)

ABSTRACT

Vietnam considers achieving net-zero emissions by 2050 a strategic goal, requiring a thorough understanding of the macroeconomic factors influencing greenhouse gas (GHG) emissions. This research examines the relationship between economic growth and pollution within the Environmental Kuznets Curve (EKC) framework, with a unique emphasis on the impact of real effective exchange rate (REER) volatility. Utilizing annual data from the World Bank spanning 1990 to 2024, the study employs a robust multi-step econometric methodology, primarily the ARDL bounds testing approach complemented by Granger causality analysis, to address small sample constraints and capture dynamic interactions. Additionally, a comparative Threshold Autoregression (TAR) analysis is conducted using industrialized Asian economies as benchmarks to identify Vietnam's specific EKC turning point. The findings reveal a bidirectional causal link between REER and carbon emissions, suggesting currency valuation directly affects environmental quality through trade pathways. Contrary to the classic inverted U-shaped EKC, local data show industrial growth has a linear positive effect on emissions. By referencing development benchmarks from Japan, South Korea, and Singapore, projections indicate Vietnam's EKC turning point could occur between 2044 and 2063, depending on annual growth rates of 5.8% to 3%. Based on these insights, it is recommended that Vietnam accelerate green technology adoption by offering tax incentives, streamlining administrative processes, and setting domestic standards aligned with international benchmarks to expedite progress toward its Net Zero goal by 2050.

Citation for the Paper:

Phung, T.T.T., Chu, T.T.H., Tran, T.T.H. and Nguyen, T.P.C., 2026. An econometric assessment of growth-pollution interactions in Vietnam within the environmental Kuznets framework. *Nature Environment and Pollution Technology*, 25(3), D1880. https://doi.org/10.46488/NEPT.2026.v25i03.D1880

Note: From 2025, the journal has adopted the use of Article IDs in citations instead of traditional consecutive page numbers. Each article is now given individual page ranges starting from page 1.

Copyright: © 2026 by the authors
Licensee: Technoscience Publications
This article is an open access article distributed under the terms and conditions of the Creative Commons Attribution (CC BY) license (https://creativecommons.org/licenses/by/4.0/).

1. INTRODUCTION

Since the 1986 DoiMoi reforms, Vietnam's GDP has grown from $6.3 billion in 1989 to $476.3 billion in 2024, with per capita income rising from $159 to $4,700. Despite this growth, significant challenges to sustainable development remain in the region. Shultz and Peterson (2019), using the 2016 Social Sustainability Index, reported that Vietnam scored strongly in energy use and water renewal but poorly-often below 2/10-in energy saving, renewable energy, emissions, biodiversity, and land protection. These results underscore the need for targeted strategies in emission-intensive industries.

Vietnam's rapid economic growth has driven sharp increases in energy use and CO_2 emissions, which pose significant environmental challenges. Between 1994 and 2016, Vietnam submitted six national GHG inventories to the UNFCCC, covering the energy, industrial processes, agriculture, land use change and forestry, and waste sectors. The 2016 national greenhouse gas inventory reported 316,734.96 thousand tons of CO_2 equivalent, with energy accounting for 65%. The share of CO_2 increased from 39.1% to 61.3%, whereas those of CH_4 and N_2O declined (Fig. 1). These trends highlight the need for sector- and gas-specific mitigation strategies to achieve sustainable development goals.

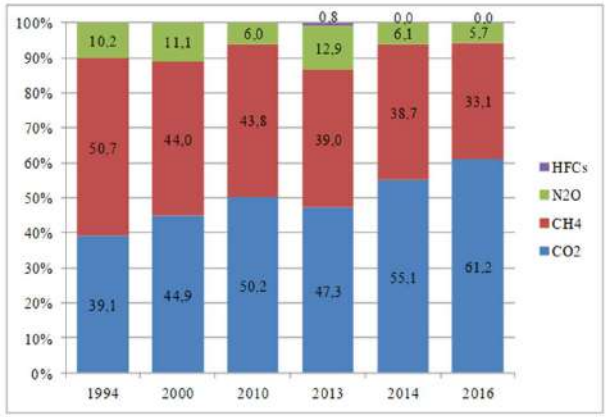


Fig. 1: Greenhouse gas emission structure by gas type in Vietnam during the period 1994-2016. Source: Vietnam National Greenhouse Gas Inventory Report.

Vietnam is among the countries most vulnerable to climate change, as highlighted by environmental assessments. In response, the government committed to achieving net-zero emissions by 2050 under the National Strategy on Climate Change, targeting a 15.8% reduction in greenhouse gas (GHG) emissions, potentially rising to 43.5% with sufficient international support.

Forecasting GHG emissions alongside economic and sustainability factors is crucial for effective environmental policies. Identifying pollution drivers helps in designing mitigation strategies that are aligned with economic conditions. This topic has attracted significant attention, and the literature is generally divided into three main research streams.

The first approach emphasizes an empirical investigation of the Environmental Kuznets Curve (EKC) hypothesis. A substantial body of literature has identified an inverted U-shaped correlation between income levels and CO_2 emissions in contexts such as China (Zhang & Cheng 2009), ASEAN countries (Pata et al. 2023), and G7 economies (Soytas & Sari 2003). Conversely, Akpan & Chuku (2011), in their analysis of Nigeria from 1960 to 2008, found a pronounced association between economic expansion and escalating environmental degradation over both short- and long-term horizons, manifesting as an N-shaped curve. Likewise, numerous studies have contested the EKC framework, particularly in developing nations (Pao & Tsai 2011, Robalino-López et al. 2015), where emerging countries sustain a linear relationship between pollution-generating activities and greenhouse gas emissions. These divergent outcomes underscore the heterogeneity of EKC validation across regions with varying levels of economic development.

The second approach focuses on identifying the relationships between actors that influence the environmental quality. It incorporates economic indicators, including GDP (Coggin 2023), GDP per capita (Kivyiro & Arminen 2014), foreign direct investment (Zhang & Zhou 2016), and trade openness (Atici 2009). Pollution is measured using total CO_2 emissions (Pao & Tsai 2011), SO_2 emissions (Coggin 2023), and ecological footprints (Thi Xuan & Thai Hung 2024). Previous studies show limited consensus, with effects differing across countries, levels of development, and periods. Sectoral contributions, particularly those of agriculture and industry (Xie et al. 2019), play a critical role in understanding CO_2 emissions in production. Ullah and Ozturk (2020) offer one of the few analyses that incorporate exchange rate dynamics as drivers of environmental pollution. However, their work focuses on correlational patterns and does not test the causality between exchange rate volatility and carbon emissions. To date, no empirical investigation has assessed the impact of exchange rate volatility on environmental quality in Vietnam.

The third approach focuses on forecasting the shape and turning point of the Environmental Kuznets Curve (EKC) in future scenarios. Within this framework, scholars have constructed empirical models to estimate the time horizon and resource requirements necessary for an economy to achieve specific environmental objectives (Robalino-López et al. 2015). This methodology has also been applied to forecast the outcomes of prospective policies, such as an emissions trading scheme and a carbon tax (Coxhead et al. 2013).

In Vietnam, several studies have evaluated the Granger causality relationship using Vector Autoregression (VAR) estimation (Pham & Tuan 2022), Autoregressive Distributed Lag (ADRL) (Đoàn 2024), or wavelet coherence analysis (Trần Văn Hưng 2024) to assess the relationship in both the short and long terms. Inconsistencies in analytical outcomes often arise from divergent data processing techniques, even when they are applied to identical datasets. These discrepancies likely reflect the differences in data coverage and methodology. Employing multiple estimation techniques may help to reconcile such inconsistencies and provide clearer insights. To address this methodological challenge, the present study employs a combined approach, integrating the VAR and ARDL models to enhance the robustness of the short- and long-term relationship estimations.

In addition, a critical gap remains in the literature regarding the transmission mechanism of monetary factors, specifically exchange rate volatility, on environmental degradation in transition economies such as Vietnam. Given Vietnam's high trade openness, where total trade turnover frequently exceeds 150% of GDP, exchange rate fluctuations play a pivotal role in determining the cost of imported

technology and the competitiveness of carbon-intensive exports. Existing studies often overlook this bidirectional relationship. Furthermore, traditional EKC estimations for Vietnam often fail to identify a turning point because of the linear nature of current historical data. Therefore, an approach that combines robust short-run estimations (ARDL) with comparative threshold benchmarking (TAR) is required to provide a realistic roadmap for the Net Zero 2050 target.

To address these research gaps, this study integrates three analytical approaches to examine the structure of the Environmental Kuznets Curve (EKC) and explore the relationship between economic growth and carbon dioxide emissions. It further develops empirical scenarios to estimate the EKC turning point in Vietnam. Specifically, this study aims to investigate the following questions:

- How do the relationships between CO_2 emissions and relevant factors evolve over the short and long term?
- In what ways do economic growth indicators (GDP growth, foreign direct investment and trade openness) and sustainable development variables (urban population size, industrial structure) influence CO_2 emissions?
- When will Vietnam achieve its Net Zero target under various economic growth scenarios?

2. THEORETICAL BASIS

2.1. Environmental Kuznets Curve (EKC) Theory

One of the popular theories explaining the relationship between economic growth and environmental degradation is the Environmental Kuznets Curve (EKC), proposed by Kuznets (Kuznets 1955). This concept posits a non-linear, inverted U-shaped relationship between per capita income and environmental degradation. In the early stages of development, pollution increases alongside rapid industrialization and urbanization. As economies transition to high-tech and service-based sectors, emissions typically decline. The EKC framework suggests that economic growth initially exacerbates environmental harm but may ultimately lead to improvements as income levels increase.

2.2. Greenhouse Gas (GHG) Emissions

Greenhouse gases (GHGs) are atmospheric compounds that absorb long-wave infrared radiation emitted from the Earth's surface after sunlight exposure, then re-radiate heat back toward the surface, contributing to the greenhouse effect. The main GHGs include water vapor (H_2O), carbon dioxide (CO_2), methane (CH_4), nitrous oxide (N_2O), ozone (O_3), and chlorofluorocarbons (CFCs). In Vietnam, CO_2 accounts for over 50% of total emissions according to the latest GHG inventory reports, making it the primary contributor to national greenhouse gas output.

2.3. Impact of Economic Growth on GHG Emissions

Economic growth refers to the expansion of an economy's size and rate over a given period, typically measured by GDP, GDP per capita, and annual GDP growth (Pham & Tuan 2022). Economic development increases GHG emissions due to broad-based industrial activity. Although many studies confirm a non-linear relationship between economic growth and CO_2 emissions, where pollution rises at early stages and falls after income exceeds specific thresholds (Pao & Tsai 2011, Xie et al. 2019, Trần Văn Hưng 2024), others reject the EKC hypothesis, reporting a persistently positive association between GDP and pollution. This pattern has been observed in developing countries such as Vietnam. (Al-Mulali et al. 2015) or Nigeria & Venezuela (Soytas & Sari 2003). In particular, some studies have even found no link between rising GHG emissions and economic growth (Zhang & Cheng 2009, Kivyiro & Arminen 2014). While some countries have reduced emissions through green and nuclear energy, Vietnam's industrialization drives emission volatility, necessitating continuous evaluation of macroeconomic impacts on pollution.

2.4. Impact of Foreign Direct Investment (FDI) on GHG Emissions

Foreign direct investment (FDI) plays a crucial role in developing economies like Vietnam, expanding production capacity and enabling technology transfer. However, its environmental impact remains contested. Studies such as Kivyiro & Arminen (2014) and Pao & Tsai (2011) report that FDI correlates with higher CO_2 emissions, reported multinational firms may shift polluting activities to countries with weaker environmental standards. Conversely, Zhang & Cheng (2009) highlighted cases where FDI facilitates cleaner technologies, reducing emissions. Thus, the EKC hypothesis linking FDI and CO_2 emissions remains debated.

In Vietnam, findings are similarly mixed. Trần Văn Hưng (2024) concludes that FDI increases emissions in both the short and long run, while Đoàn (2024) identifies only short-term effects, leaving long-term impacts unresolved. In contrast, Xuan (2025) identified a dual role of FDI in relation to CO_2 emissions: in the short term, it contributes to higher emissions through manufacturing expansion, while in the long term, it holds potential to reduce emissions by facilitating cleaner technologies. Thus, evidence on the impact of FDI on CO_2 emissions in Vietnam remains inconclusive, largely due to variations in data coverage and methodological approaches. Applying multiple estimation

techniques may help resolve these inconsistencies and yield more robust insights.

2.5. Impact of Exchange Rate on GHG Emissions

According to Ullah & Ozturk (2020), exchange rate volatility affects domestic production, investment, money demand, trade balance, and economic growth, potentially harming the environment. A weaker currency boosts exports, whereas a stronger currency makes imports cheaper. Their study in Pakistan indicated that positive exchange rate shocks reduce emissions, whereas negative shocks increase them. In Pakistan, elevated public debt and heavy dependence on the IMF and bilateral loans can trigger significant volatility in exchange rates. In contrast, foreign capital plays a modest role in Vietnam's economy. Therefore, the impact of exchange rate volatility on CO_2 emissions may differ. Moreover, previous studies have not empirically investigated the causal relationship between exchange rates and environmental pollution, focusing primarily on correlations (Wang et al. 2024). This raises an important question: Is there a causal relationship between these variables, particularly in the context of emerging economies such as Vietnam?

2.6. The Impact of Industrialization on GHG Emissions

Industrial growth, which is heavily dependent on fossil fuels such as coal and gas, contributes significantly to CO_2 emissions, particularly when outdated technologies and polluting raw materials are used (Ullah et al. 2021). While many studies confirm a positive link between industrialization and emissions (Xie et al. 2019), other studies emphasize the potential for emission reductions through technological innovation and cleaner production methods (Zhang & Zhou 2016, Robalino-López et al. 2015). In Vietnam, studies have revealed a U-shaped EKC curve in the short term, suggesting that early industrial growth exacerbates pollution through outdated technologies and inefficient energy use, whereas later stages hold potential for improvement (Đoàn et al. 2023). This finding contrasts with the inverted U-shaped relationship observed in Ghana (Kwakwa and Alhassan 2018). However, studies on Vietnam remain limited, with Ullah et al. (2021) confirming only short-term pollution effects before the COVID-19 pandemic and before the country made net-zero commitments. A comprehensive reassessment of industrial impacts is essential for informing future environmental strategies and supporting sustainable development goals.

3. MATERIALS AND METHODS

3.1. Data Sources

This study examines Vietnam's data from 1990 to 2024, drawing from reputable sources such as the World Bank and the European Commission's EDGAR database (Emissions Database for Global Atmospheric Research). The selected variables include Carbon Emissions per capita (CPC), GDP per capita (GPC), Foreign Direct Investment (FDI), Real Effective Exchange Rate (REER), and Industrial Value Added. CPC, GPC, and REER are transformed into natural logarithms to interpret coefficients as elasticities. FDI and Industrial Value Added are expressed in their original percentage units (%) to accurately reflect the direct influence of

Table 1: Data sources.

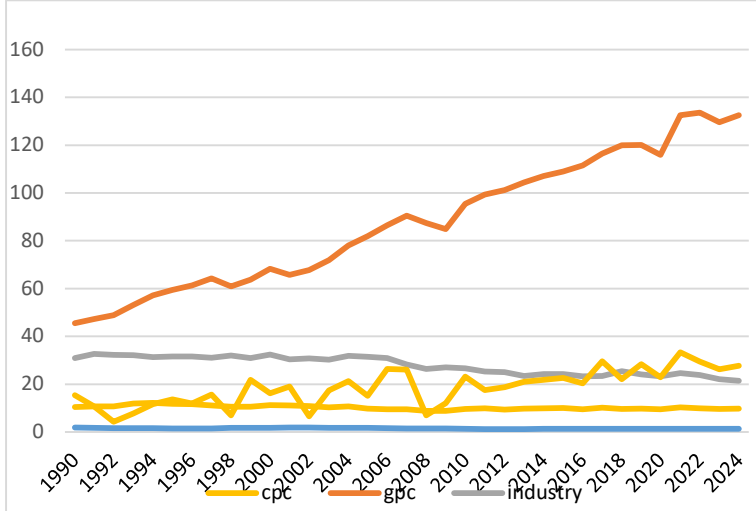
	Abbreviation	Description	Units of measurement	Source
Dependent variable	CPC	Total carbon dioxide (CO2) emissions (total) excluding LULUCF	Metric Tons	WDI
Independent variable	GPC	GDP per capita, PPP (International Fixed Price 2021)	USD	WDI
	FDI	Foreign Investment Inward/ GDP	%	WDI
	REER	Real effective exchange rate index (2020 = 100 points)	points	WDI
	Industry	Industrial (including construction) value added / GDP	%	WDI

Source: World Bank database

Table 2: Data statistical description.

Variables	Observations	Mean	Standard error	Min	Max
LnCPC	35	0.2046817	.7880595	-1.172155	1.312754
LnGPC	35	8.726135	.526576	7.811149	9.576039
FDI	35	5.382016	2.147019	2.781323	11.93948
LnREER	35	9.700555	0.3206257	8.785326	10.09266
INDUSTRY	35	34.60179	4.380435	22.67429	40.20875

* Note: Ln stands for Logarithmic Function Form; Source: Authors' compilation



Source: Authors' compilation.

Fig. 2: Trends of variables during the period 1990-2024. Source: Authors' compilation.

structural shares on emissions, adhering to standard econometric practices for ratio variables. The study intentionally focuses on total CO_2 emissions per capita, excluding the "Land Use, Land-Use Change, and Forestry" (LULUCF) sector. This allows the analysis to isolate emissions directly resulting from key economic activities such as industry, energy use, and transportation—sectors closely linked to GDP growth, FDI, and trade. This approach improves the model's accuracy and ensures the results meaningfully capture the true relationships under investigation.

Tables 1 and 2 present the data sources and descriptive statistics for the model variables. Fig. 2 illustrates the trends of the variables during the study period.

3.2. Estimation Method

This study employs a comprehensive multi-step econometric framework to analyze the complex and evolving relationship between economic growth and greenhouse gas (GHG) emissions in Vietnam, capturing both short-term fluctuations and long-term equilibrium trends. The methodology integrates five complementary approaches: Vector Autoregression (VAR), the Johansen cointegration test with the Vector Error Correction Model (VECM), the Autoregressive Distributed Lag (ARDL) model, the Granger causality test, and the Threshold Autoregression (TAR) model. The VAR framework offers an initial overview of variable interdependencies and shock transmission, while the Johansen test and VECM are used to identify and model long-run cointegration relationships. The ARDL model is the primary estimation technique because of its effectiveness with mixed I(0) and I(1) variables, enabling reliable short- and long-term coefficient estimation even with limited data samples. The bounds test verifies the presence of cointegration prior to estimation, and the error correction model derived from ARDL captures the speed of adjustment of GHG emissions to short-term shocks. Additionally, the VAR approach helps determine appropriate lag structures and visualize shock propagation. Granger causality tests clarify the directionality of relationships, such as between exchange rates and emissions, which regression coefficients alone cannot reveal. Because Vietnam's historical data currently lie on the upward slope of the EKC and lack a clear turning point, a comparative Threshold Autoregression (TAR) model is used. Instead of estimating an elusive threshold from local data, this approach analyzes the turning points of reference economies—Japan, South Korea, and Singapore—to project Vietnam's potential future trajectory.

4. RESULTS

4.1. Units Root Test

The ADF and PP unit root tests (Table 3) consistently indicate that all series, LnCPC, LnGpc, FDI, LnReer, and Industry, are non-stationary in levels but become stationary after first differencing, demonstrating they are integrated of order one, I(1). This is methodologically significant because using OLS on level data can lead to spurious regression results, where statistical significance does not imply causality. Confirming the I(1) nature of these series validates the use of models capable of analyzing long-term relationships, such as VECM and ARDL, which are specifically designed to manage non-stationary time series.

Selecting the optimal lag length is a crucial step that ensures the reliability of both cointegration tests and subsequent estimation models. An excessively short lag may omit key dynamic effects, leading to autocorrelation errors, whereas an overly long lag can reduce degrees of freedom and estimation efficiency-particularly in small samples. Table 4 shows that a lag length of four is consistently supported by all major information criteria, including AIC, SC, HQ, LR, and FPE. Notably, the more conservative criteria (SC and HQ), which heavily penalize additional parameters in small samples, also select lag 4, indicating genuine explanatory gains rather than overfitting. Therefore, this lag order is adopted as the basis for subsequent tests and estimations to ensure the exhaustive capture of the dynamic relationships among the variables.

Using the VAR model, we examined the short-term drivers of greenhouse gas emissions. The results show that per-capita carbon emission growth (ΔlnCPC) is strongly influenced by economic growth (ΔlnGPC), with a significant first lag indicating the cumulative effects of recent expansion. Industrial activity, measured by industry (% GDP), also emerges as a key contributor to rising emissions. Overall, the analysis provides clear evidence that Vietnam's industrialization-led growth from 1990 to 2024 has been closely linked to escalating carbon emissions.

4.2. Estimation of the ARDL Model

The Autoregressive Distributed Lag (ARDL) model was employed as the primary estimation method to identify the key factors influencing carbon emissions in Vietnam. This

Table 3: Results of ADF and PP unit tests.

	LnCPC		LnGPC		FDI		LnREER		INDUSTRY	
	ADF	PP	ADF	PP	ADF	PP	ADF	PP	ADF	PP
Unit root test of the variables at the standard level										
Intercept	-0.454635	-0.46979	-1.558	-2.209	-2.85903*	-2.664191*	-1.936926	-3.7398***	-2.948018*	-3.918707**
	(0.8893)	(0.8864)	(0.4922)	(0.2069)	(0.0620)	(0.0907)	(0.3120)	(0.0078)	(0.0521)	(0.0288)
Intercept and trend	-1.607263	-2.035115	-3.03385	-1.690	-3.356985*	-3.026803	-1.646705	-6.0271***	-3.192135	-2.314420
	(0.7718)	(0.5644)	(0.1387)	(0.7334)	(0.0749)	(0.1400)	(0.7519)	(0.001)	(0.1063)	(0.4153)
Unit root test of the variables at first difference										
Intercept	-3.9977***	-3.99***	-4.359***	-4.401***	-3.7454***	-5.0675***	-5.8398***	-11.450***	-4.8735***	-4.858436***
	(0.0037)	(0.0037)	(0.0016)	(0.0014)	(0.0080)	(0.0002)	(0.0000)	(0.0000)	(0.0004)	(0.0004)
Intercept and trend	-3.9170***	-3.9170	-4.7120***	-4.677***	-3.69417**	-5.0159***	-6.25347**	-9.9875***	-5.3198***	-5.320650***
	(0.0209)	(0.0209)	(0.0033)	(0.0036)	(0.0374)	(0.0015)	(0.0001)	(0.0000)	(0.0007)	(0.0007)

Note: *, **, *** indicate rejection of the null hypothesis (non-stationarity) at the 10%, 5%, and 1% significance levels, respectively. Lag length is determined based on the Akaike Information Criterion (AIC), with p-values reported in parentheses.

Source: Authors' compilation.

Table 4: The lag selection criteria**.**

Lag	LogL	LR	FPE	AIC	SC	HQ
0	72.4428	NA	7.67e-09	-4.496191	-4.42147*	-4.421482
1	112.990	64.87555*	2.80e-09*	-5.532672	-5.08442	-5.084417
2	130.369	22.01402	5.41e-09	-5.024639	-4.20284	-4.202838
3	149.169	17.54678	1.26e-08	-4.611314	-3.41596	-3.415967
4	210.746	36.94623	3.18e-09	-7.049783*	-5.48091*	-5.480891*

LR: Sequential modified LR test statistic (each test at 5% level)
FPE: Final prediction error
AIC: Akaike criterion
SC: Schwarz criterion
HQ: Hannan-Quinn information criterion
After determining the optimal lag length of 4, the study estimates the Vector; Source: Authors' compilation.

Table 5: Estimation of ARDL model regression coefficients (4, 3, 4, 3, 4).

ARDL (4, 3, 4, 3, 4)		
	Regression coefficient	Standard Error
Panel A: Short-term effect		
Intercept	-26.26047***	3.757535
t-1	-0.048092	0.138171
t-2	0.665829***	0.1476112
t-3	0.674352***	0.194053
t	1.666199***	0.501172
t-1	3.319981***	0.551535
t-2	0.827663	0.618099
t	1.595479***	0.291030
t-1	-0.577660*	0.271511
t-2	0.367064	0.291855
t-3	0.204579	0.163849
t	0.029525***	0.005955
t-1	-0.025076***	0.007314
t-2	-0.012913**	0.004583
t	-0.004087	0.005492
t-1	-0.008872	0.007269
t-2	0.025001***	0.005634
t-3	0.026085***	0.006907
ECt-1	-0.184342***	0.000000
Panel B: Long-term effect		
LnGPCt-1	0.720026*	0.0542
FDIt-1	0.077224**	0.0282
LnREERt-1	1.646606**	0.0474
INDUSTRYt-1	0.038326***	0.0011

Note: *, **, *** indicate statistical significance at the corresponding significance levels of 10%, 5%, 1%. Source: Authors' compilation.

approach is particularly suitable for small sample sizes, such as the 35 annual observations used in this study, thereby enhancing the robustness and reliability of the estimation results.

Table 5 shows the key drivers of Vietnam's per-capita CO_2 emissions. In the long run (Panel B), economic growth (LnGpc) remains the dominant factor, with a significant coefficient of 0.72, indicating that a 1% increase in GDP per capita increases CO_2 emissions by approximately 0.72%. Foreign direct investment and industrial output (Industry) also exert significant positive effects, confirming that industrialization and FDI inflows into manufacturing have intensified environmental pressures. The real exchange rate (LnReer) also shows a positive long-run association with emissions.

In the short run (Panel A), the error correction term (ECt–1) of –0.184 ($p < 0.01$) confirms a stable long-run equilibrium, implying that approximately 18.4% of the disequilibrium is corrected annually. This moderate adjustment rate suggests that full re-equilibration will take more than five years to achieve.

Overall, the ARDL results consistently indicate that Vietnam's growth path remains closely linked to industrialization, FDI attraction, and rising CO_2 emissions, providing a robust empirical basis for formulating sustainable policy interventions.

4.3. Diagnostic Test

The reliability of the linear ARDL model estimation was verified through a series of diagnostic tests assessing serial autocorrelation, heteroscedasticity, non-normality, and model specification errors. The test results, summarized in Table 6, indicate that the model is free from specification errors, heteroscedasticity, autocorrelation, and non-normal residual distribution at the 5% significance level or lower.

4.4. Granger Causality Test

The Granger causality results in Table 7 highlight several short-run dynamic relationships among carbon emissions per capita (CPC), industrialization (INDUSTRY), real effective exchange rate (REER), foreign direct investment (FDI), and economic growth (GPC) in Vietnam. A bidirectional link exists between the REER and CPC, showing that exchange rate fluctuations influence trade and production costs, whereas higher emissions from energy-intensive industries can affect exchange rate movements through export competitiveness. Similarly, FDI and REER display bidirectional causality, suggesting that stable exchange rates attract investments, whereas large inflows can pressure the currency.

Unidirectional causality from INDUSTRY to CPC confirms that industrial expansion drives emissions, reflecting the carbon-intensive manufacturing sector in Vietnam. FDI also Granger-causes CPC, consistent with the "pollution haven" hypothesis, wherein foreign investment worsens environmental degradation. Economic growth strongly Granger-causes CPC at the 1% level, while the

Table 6: Diagnostic test results.

Serial correlation	c2(2) = 1.379835
	P value (0.55772)
Heteroskedasticity	F – statistic = 0.6575
	P value (0.4858)
RESET test	P value (0.1321)
Normality	Jarque – Bera = 1.495199
	P value (0.473502)

Source: Authors' compilation.

reverse does not, underscoring that Vietnam's expansion relies heavily on energy consumption and emission-intensive activities. This supports the early stage of the Environmental Kuznets Curve (EKC), in which development initially worsens environmental quality.

Overall, the findings reveal close interdependence between macroeconomic factors and emissions, stressing the need for green industrial restructuring, sustainable FDI strategies, and effective exchange rate management to achieve low-carbon growth.

4.5. Comparative Threshold Benchmarking

Since Vietnam's current economic data show a linear relationship with emissions, it is not statistically feasible to estimate the EKC turning point endogenously using local data. To address this challenge, the study employs a comparative benchmarking approach with the Threshold Autoregression (TAR) framework, applied to reference economies: Japan, South Korea, and Singapore.

Annual time-series data on GDP per capita (constant 2020 PPP International dollars) and CO2 emissions per capita for these countries were sourced from the World Bank database. TAR estimations on these industrialized Asian economies allowed us to empirically determine the specific income thresholds at which their emission trends reverse or decouple from growth. These empirically identified thresholds (see Table 8) serve as benchmarks for projecting Vietnam's sustainable development trajectory under various growth scenarios.

This study evaluates Vietnam's growth prospects using a variety of forecasting methods, including traditional ARIMA models and advanced machine learning techniques such as Prophet and LSTM. As illustrated in Fig. 3, ensemble forecasts indicate a generally sustainable upward trend in GDP per capita extending to 2050, although long-term projections differ considerably. Prophet suggests a moderate, nearly linear growth trajectory, implying potential stabilization. ARIMA provides a baseline forecast based on historical data, while LSTM predicts a steeper increase, reflecting the influence of recent economic momentum. These differing models underscore that Vietnam's future growth will largely depend on policy choices that shape its long-term sustainability.

Building on the experiences of advanced economies and recognizing Vietnam's advantage as a latecomer in adopting new technologies, this study estimates that the country's economic inflection point may occur at a gross

Table 7: Granger causality test results**.**

Null Hypothesis:	Obs	F-Statistic	Prob.
LNREER does not Granger Cause LNCPC	35	3.043230*	0.063689
LNCPC does not Granger Cause LNREER		4.293021**	0.023648
INDUSTRY does not Granger Cause LNCPC	35	2.5257334*	0.098071
LNCPC does not Granger Cause INDUSTRY		1.1003225	0.346725
FDI does not Granger Cause LNCPC	35	0.453356**	0.040074
LNCPC does not Granger Cause FDI		1.6878016	0.203199
LNGPC does not Granger Cause LNCPC	35	5.6597***	0.008624
LNCPC does not Granger Cause LNGPC		1.54219482	0.231536
INDUSTRY does not Granger Cause LNREER	35	1.5091403	0.23854
LNREER does not Granger Cause INDUSTRY		0.9854921	0.38583
FDI does not Granger Cause LNREER	35	4.765037**	0.016553
LNREER does not Granger Cause FDI		4.072633**	0.028021
LNGPC does not Granger Cause LNREER	35	2.45213603	0.104395
LNREER does not Granger Cause LNGPC		0.09160786	0.912735
FDI does not Granger Cause INDUSTRY	35	2.2161103	0.127802
INDUSTRY does not Granger Cause FDI		1.6455498	0.211018
LNGPC does not Granger Cause INDUSTRY	35	0.572067	0.570815
INDUSTRY does not Granger Cause LNGPC		0.256411	0.775620
LNGPC does not Granger Cause FDI	35	1.8309641	0.178932
FDI does not Granger Cause LNGPC		0.1291161	0.879392

Note: *, **, *** indicate statistical significance at the corresponding significance levels of 10%, 5%, 1%.
Source: Authors' compilation.

Table 8: Thresholds for Emission Trend Reversal in Japan, South Korea, and Singapore.

Country	GDP per capita (International Fixed Prices 2020)
Japan	41596.9238**
South Korea	38698.4611**
Singapore	57213.0978*

Note: *, **, *** significant at 10%, 5%, 1%.
Source: Authors' compilation

per capita income of approximately USD 45,500. This benchmark reflects both the structural challenges typical of developing economies and the emerging opportunities in green technology. Currently, Vietnam's GPC stands at USD 14,415, and three growth scenarios have been developed to evaluate potential policy impacts (see Table 9). The Growth Scenario, with an annual growth rate of 5.8%, projects that income will reach USD 45,500 by 2045, though it may entail higher emissions without strict controls. The Business-as-Usual Scenario, growing at 4.5%, aligns with national targets and aims to achieve this milestone by 2050. The Conservative Scenario, at a 3% growth rate, delays convergence until 2063, reducing short-term emissions but limiting green investment capacity and progress toward Net Zero 2050.

5. DISCUSSION AND RECOMMENDATIONS

The Granger causality test indicates a unidirectional causal relationship from GPC to CPC at the 1% significance level ($p = 0.0086$), confirming that economic growth influences carbon emissions in Vietnam. The short-term ARDL results show several positive and statistically significant lagged GPC terms, implying that an increase in GDP per capita leads to higher CO_2 emissions. The error correction term (ECt-1 = –0.1843, $p < 0.01$) demonstrates convergence toward the long-run equilibrium. In the long run, the coefficient of

Table 9: Proposed scenario.

Scenario	GDP growth	Required years
Positive	5.8%	20 years
Neutral	4.5%	26 years
Negative	3%	39 years

Source: Authors' compilation

LnGPCt-1 = 0.7200, $p < 0.1$, remains positive, suggesting that economic growth continues to increase emissions. Overall, these findings suggest that Vietnam's growth pattern remains energy- and carbon-intensive, and the turning point of the Environmental Kuznets Curve has not yet been achieved. Promoting green investments, renewable energy, and cleaner industrial practices is crucial for decoupling economic development from environmental harm. These results align with the findings of Đoàn Ngọc Phúc (2024) and Atici (2009), but contrast with Trần Văn Hưng (2024), who argued that long-term economic growth would eventually lead to a decline in CO_2 emissions. Consequently, developing countries like Vietnam should adopt policies that maintain economic growth while protecting environmental quality. Rapid industrialization risks causing long-term ecological damage, highlighting the importance of planning industrial zones with sector-specific environmental standards that meet international benchmarks to reduce GHG emissions.

This study also provides evidence of causality running from Industrialization and FDI to per capita carbon emissions, with no indication of the reverse. These findings align with those of Le et al. (2016) and Xie et al. (2019), yet they differ from the results of Jalil & Mahmud (2009) and Ullah et al. (2021), who did not find a long-term relationship. Vietnam's FDI policies increasingly focus on attracting modern, cleaner technologies (Zhang & Cheng 2009), maintaining Industrialization and FDI as significant contributors to pollution.

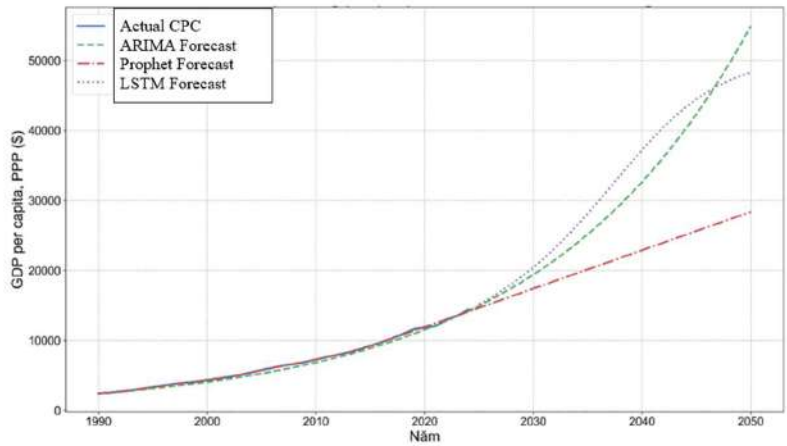


Fig. 3: Analysis of GDP per capita scenarios in Vietnam, 1990 – 2050. Source: Authors' Compilation.

The findings demonstrate a positive and statistically significant association between the real effective exchange rate (REER) and per capita carbon emissions (CPC) in both the short and long term. The ARDL analysis reveals that short-term exchange rate shocks lead to increased emissions ($\beta = 1.60$, $p < 0.01$), while the long-term coefficient remains positive and significant ($\beta = 1.65$, $p < 0.05$). Recent macroeconomic developments support this pattern: the Vietnamese currency depreciated approximately 5% in 2024 and an additional 3.4% in 2025, coinciding with a roughly 10% weakening of the US dollar. In the short run, currency depreciation boosts export competitiveness and drives industrial growth, which can raise carbon emissions. Over the long term, sustained depreciation may reinforce reliance on carbon-intensive industries and hinder the shift to cleaner technologies. Granger causality tests further indicate bidirectional causality between REER and CPC, implying that exchange rate fluctuations both influence and respond to emission dynamics through trade, production, and energy consumption channels. These results are consistent with findings from China (Wang et al. 2024) but differ from those of Ullah and Ozturk (2020), supporting the notion that growth driven by price competitiveness—instead of technological progress—tends to exacerbate environmental problems in developing economies.

The bidirectional causality between the real exchange rate (LnREER) and emissions (LnCPC), as well as between foreign direct investment (FDI) and LnREER, indicates that exchange rate policies have a direct impact on environmental outcomes and capital inflows. This relationship suggests that exchange rate fluctuations can serve as predictors or influencers of environmental pollution. Consequently, maintaining macroeconomic stability while encouraging green investments and low-carbon production is vital for Vietnam's Net Zero 2050 goal. Exchange rate management should incorporate environmental considerations, as currency volatility directly affects production methods and emission intensity. Furthermore, industrialization and FDI strategies must prioritize environmentally friendly, high-value projects to avoid harmful capital inflows that could destabilize the currency. These findings underscore the importance of coordinated macroeconomic, trade, and environmental policies to prevent feedback effects and promote sustainable development. In open economies, FDI and industrialization remain crucial drivers of growth and, over time, can also enhance environmental quality through technology transfer and corporate social responsibility aligned with international standards.

6. CONCLUSIONS

Using data from Vietnam for the period 1990–2024 and employing both the validation of the EKC hypothesis and Granger causality analysis, this study confirms the existence of a bidirectional causal relationship between the real exchange rate and CO_2 emissions in the long run. Therefore, exchange rate management can serve as an effective policy instrument for forecasting and enhancing the effectiveness of environmental protection measures. In addition, the short- and long-term effects of industrial development, FDI, and economic growth on CO_2 emissions are characterized by a traditional U-shaped relationship. However, the EKC turning point has not yet emerged in Vietnam, indicating that economic expansion continues to drive the increasing environmental pressure. Empirical projections indicate that Vietnam's EKC turning point is likely to occur between 2044 and 2063, depending on annual growth scenarios ranging from 5.8% to 3%. Based on these findings, Vietnam should promote the adoption of green technologies through supportive tax incentives, streamlined administrative procedures, and domestic production standards aligned with international benchmarks to advance the implementation of its Net Zero objective by 2050.

7. ACKNOWLEDGMENTS

The authors would like to thank the Hanoi Institute of Environmental Science and Technology for supporting this research. Additionally, the authors acknowledge the project titled "Nghiên cứu cơ sở khoa học để lượng hóa mối quan hệ giữa lượng phát thải khí nhà kính (KNK) với tăng trưởng và phát triển bền vững tại Việt Nam. Mã số: TNMT.2023.02.33" for providing the essential data utilized in this study. This research was funded by Hanoi Institute of Environmental Science and Technology, grant number TNMT.2023.02.33.

8. REFERENCES

Akpan, U.F. and Chuku, A., 2011. Economic growth and environmental degradation in Nigeria: beyond the environmental Kuznets curve. *Journal of Environmental Economics and Policy*, 2(1), pp.45-60. [DOI]

Al-Mulali, U., Saboori, B. and Ozturk, I., 2015. Investigating the environmental Kuznets curve hypothesis in Vietnam. *Energy Policy*, 76, pp.123-131. [DOI]

Atici, C., 2009. Carbon emissions in Central and Eastern Europe: environmental Kuznets curve and implications for sustainable development. *Sustainable Development*, 17(3), pp.155-160. [DOI]

Coggin, T.D., 2023. CO_2, SO_2 and economic growth: a cross-national panel study. *Journal of Economics and Finance*, 47(2), pp.437-457. [DOI]

Coxhead, I., Wattanakuljarus, A. and Nguyen, C.V., 2013. Are carbon taxes good for the poor? A general equilibrium analysis for Vietnam. *World Development*, 51, pp.119-131. [DOI]

Đoàn, P.N., 2024. The Impact of Foreign Direct Investment, Trade Openness, Economic Growth and Urbanization on CO2 Emissions in Vietnam: An ARDL Model Approach. Journal of Economics and Development , (Special Issue), pp. 67-76.

Đoàn, T.T.T., Nguyễn, T.T.H., Phạm, T.L., Nguyễn, B.A. and Phùng, T.H.N., 2023. Impact of economic growth and trade openness on CO_2 emissions in Vietnam. *Journal of Commercial Science*, 183, pp.45-53.

Jalil, A. and Mahmud, S.F., 2009. Environment Kuznets curve for CO_2 emissions: a cointegration analysis for China. *Energy Policy*, 37(12), pp.5167-5172. [DOI]

Kivyiro, P. and Arminen, H., 2014. Carbon dioxide emissions, energy consumption, economic growth, and foreign direct investment: causality analysis for Sub-Saharan Africa. *Energy*, 74, pp.595-606. [DOI]

Kuznets, S., 1955. International differences in capital formation and financing. In: *Capital Formation and Economic Growth*. Princeton University Press, pp.19-111.

Kwakwa, P.A. and Alhassan, H., 2018. The effect of energy and urbanisation on carbon dioxide emissions: evidence from Ghana. *OPEC Energy Review*, 42(4), pp.301-330. [DOI]

Le, T.-H., Chang, Y. and Park, D., 2016. Trade openness and environmental quality: international evidence. *Energy Policy*, 92, pp.45-55. [DOI]

Pao, H.T. and Tsai, C.M., 2011. Multivariate Granger causality between CO_2 emissions, energy consumption, FDI (foreign direct investment) and GDP (gross domestic product): evidence from a panel of BRIC (Brazil, Russian Federation, India, and China) countries. *Energy*, 36(1), pp.685-693. [DOI]

Pata, U.K., Dam, M.M. and Kaya, F., 2023. How effective are renewable energy, tourism, trade openness, and foreign direct investment on CO_2 emissions? An EKC analysis for ASEAN countries. *Environmental Science and Pollution Research*, 30(6), pp.14821-14837. [DOI]

Pham, M.H. and Tuan, N.A., 2022. The relationship between GHG emissions and economic growth in Vietnam. *VNUHCM Journal of Economics-Law and Management*, 6(1), pp.2334-2347.

Robalino-López, A., Mena-Nieto, Á., García-Ramos, J.-E. and Golpe, A.A., 2015. Studying the relationship between economic growth, CO_2 emissions, and the environmental Kuznets curve in Venezuela (1980–2025). *Renewable and Sustainable Energy Reviews*, 41, pp.602-614. [DOI]

Shultz, C.J. and Peterson, M., 2019. A macromarketing view of sustainable development in Vietnam. *Environmental Management*, 63(4), pp.507-519. [DOI]

Soytas, U. and Sari, R., 2003. Energy consumption and GDP: causality relationship in G-7 countries and emerging markets. *Energy Economics*, 25(1), pp.33-37. [DOI]

Thi Xuan, H. and Thai Hung, N., 2024. Does green investment mitigate environmental degradation in Vietnam: the time-frequency effect of nonrenewable energy investment and globalization?. *Management of Environmental Quality: An International Journal*, *35*(5), pp.1005-1027.

Trần Văn Hưng, 2024. The relationship between FDI, globalization, economic growth, green growth and CO_2 emissions in Vietnam. *Journal of Economics and Development*, 321, pp.41-51.

Ullah, S. and Ozturk, I., 2020. Examining the asymmetric effects of stock markets and exchange rate volatility on Pakistan's environmental pollution. *Environmental Science and Pollution Research*, 27(25), pp.31211-31220. [DOI]

Ullah, S., Nadeem, M., Ali, K. and Abbas, Q., 2021. Fossil fuel, industrial growth and inward FDI impact on CO_2 emissions in Vietnam: testing the EKC hypothesis. *Management of Environmental Quality: An International Journal*, 33(2), pp.222-240. [DOI]

Wang, L., Ullah, S. and Sohail, M.T., 2024. Exchange rate volatility and green growth in China: does nonlinearity matter? *Economic Change and Restructuring*, 57(6), p.256. [DOI]

Xie, Q., Xu, X. and Liu, X., 2019. Is there an EKC between economic growth and smog pollution in China? New evidence from semiparametric spatial autoregressive models. *Journal of Cleaner Production*, 220, pp.873-883. [DOI]

Xuan, V.N., 2025. The nexus between innovation, renewable energy consumption, foreign direct investment, GDP, and CO2 emissions in the context of Vietnam: New evidence from the ARDL approach. *Energy & Environment*, p.0958305X251322893.

Zhang, C. and Zhou, X., 2016. Does foreign direct investment lead to lower CO_2 emissions? Evidence from a regional analysis in China. *Renewable and Sustainable Energy Reviews*, 58, pp.943-951. [DOI]

Zhang, X.-P. and Cheng, X.-M., 2009. Energy consumption, carbon emissions, and economic growth in China. *Ecological Economics*, 68(10), pp.2706-2712. [DOI]

Nature Environment and Pollution Technology
An International Quarterly Scientific Journal

p-ISSN: 0972-6268
(Print copies up to 2016)
e-ISSN: 2395-3454

Vol. 25 | No. 3 | Article ID B4407 | 2026

Original Research Paper

https://doi.org/10.46488/NEPT.2026.v25i03.B4407

Open Access Journal

Spatial Analysis of Environmental Vulnerability Among Tribal Households in Garbada Taluka, Dahod District, Gujarat, India

Surabhi Pareek and Suneeta Chandorkar†
Department of Foods and Nutrition, The Maharaja Sayajirao University of Baroda, Vadodara, Gujarat, India
†Corresponding author: Suneeta Chandorkar; suneetachandorkar@gmail.com

Abbreviation: Nat. Env. & Poll. Technol.
Website: www.neptjournal.com

Received: 14-10-2025
Revised: 23-12-2025
Accepted: 06-01-2026

Key Words:

Environmental vulnerability index
Shannon index
Crop diversity
Sanitation
Tribal households
Garbada Taluka
GIS

Citation for the Paper:

Pareek, S. and Chandorkar, S., 2026. Spatial analysis of environmental vulnerability among tribal households in Garbada Taluka, Dahod District, Gujarat, India. *Nature Environment and Pollution Technology*, 25(3), B4407. https://doi.org/10.46488/NEPT.2026.v25i03.B4407

Note: From 2025, the journal has adopted the use of Article IDs in citations instead of traditional consecutive page numbers. Each article is now given individual page ranges starting from page 1.

Copyright: © 2026 by the authors
Licensee: Technoscience Publications
This article is an open access article distributed under the terms and conditions of the Creative Commons Attribution (CC BY) license (https://creativecommons.org/licenses/by/4.0/).

ABSTRACT

Tribal households in western India are highly exposed to environmental and infrastructural challenges that influence their livelihood and food security. Assessing vulnerability at multiple scales is essential for targeted adaptation planning. This study aimed to develop a composite Environmental Vulnerability Index (EVI) for tribal households in Garbada Taluka, Dahod District, Gujarat, and examine spatial disparities at both the village and household levels. Primary data from 645 households were analyzed. Crop diversity was calculated using the Shannon Index, and a composite EVI was constructed from four indicators: landholding size, crop diversity, water sufficiency, and sanitation access. Households were classified into low-, medium-, and high-vulnerability categories. Statistical analyses (descriptive statistics, correlations, and regression) were combined with GIS-based spatial mapping to examine patterns across villages and within communities. The descriptive results showed that two-thirds of the households fell into the medium vulnerability category, with smaller proportions classified as low or high. Regression analysis confirmed that landholding size is a significant predictor of household income. Spatial mapping identified Matwa, Zari Bujarg, and Garbada as high-vulnerability clusters, whereas villages such as Jesawada, Ambli, and Devda demonstrated relatively lower vulnerability. Household-level mapping revealed intra-village disparities, with highly vulnerable households present in resilient villages. The dual-scale EVI analysis highlights village-level hotspots and household-level variations in vulnerability. These findings are relevant for climate adaptation, agricultural diversification, and WASH interventions in tribal development schemes. Future research should integrate direct nutrition indicators with environmental vulnerability frameworks to strengthen the linkages with food and nutrition security.

1. INTRODUCTION

Tribal populations in India continue to experience high levels of vulnerability due to intersecting social, economic, and environmental challenges. Limited landholdings, reliance on rainfed agriculture, and inadequate access to safe water and sanitation contribute to fragile livelihoods. These conditions create cycles of poverty and environmental stress, leaving households with fewer opportunities to adapt to changing circumstances.

The Dahod district in eastern Gujarat is one of the predominantly tribal regions of the state. The livelihood of households in this area is largely dependent on agriculture, with maize being the primary crop. However, agricultural practices are characterized by small, fragmented landholdings and limited crop diversity. At the same time, household amenities such as water supply and sanitation remain inadequate in many villages in the region. Together, these factors shape the patterns of environmental vulnerability and influence household well-being. Previous studies have highlighted persistent poverty and livelihood challenges among tribal households in Gujarat (Shah & Kumar 2008), and newer analyses continue to emphasize the structural disadvantages faced by tribal populations across India's agrarian regions (Mathew 2024, Sharma & Mohan 2024). According to the

District Census Handbook: Dahod (Census of India 2011), Garbada Taluka and other parts of the district remain heavily tribal in composition, with low literacy levels and poor household amenities. The Aspirational Districts Dashboard (NITI Aayog 2023) further indicates that Dahod continues to lag behind state averages in key indicators related to health, nutrition, and education, reflecting persistent human development challenges in tribal regions.

Recent assessments have emphasized the importance of integrated approaches to vulnerability analysis. Empirical studies from tribal regions across India demonstrate that climate variability, limited livelihood diversification, and constrained adaptive capacity jointly shape household-level vulnerabilities (Kumar et al. 2023). The Climate Vulnerability Assessment for Adaptation Planning (DST 2021) underscores the role of GIS-based methods in identifying hotspots of risk across India, while the Gujarat State Action Plan on Climate Change and Health (2022–27) (Government of Gujarat 2024) highlights Dahod as a district facing multiple stressors related to environmental and health conditions. Institutional studies also highlight the gendered and intergenerational dimensions of vulnerability. The Swaminathan Research Foundation (MSSRF 2024) reports the disproportionate impact of climate change on women and children across India's agro-ecological zones, while the Council on Energy, Environment and Water (Mohanty & Wadhawan 2021) emphasizes the role of institutional capacity and climate-resilient agriculture in enhancing adaptive responses among smallholder and tribal communities. Complementary reviews (Mohanty 2024) argue for multidisciplinary approaches that link sustainability, rural livelihoods, and tribal well-being to policy frameworks for inclusive development. Studies have shown that maize–legume intercropping systems can enhance resource-use efficiency, soil fertility, and overall sustainability in smallholder farms (Dwivedi et al. 2016).

Against this backdrop, the present study was undertaken in Garbada Taluka of Dahod district, Gujarat, to develop an Environmental Vulnerability Index (EVI) at the household level. While national- and district-level environmental vulnerability assessments exist, they largely rely on aggregated indicators that mask household-level and intra-village disparities, particularly in tribal regions. Empirical studies using primary household data combined with GIS to assess environmental vulnerability at the micro-scale remain limited. This study addresses this gap by developing a household-level Environmental Vulnerability Index (EVI) and applying a dual-scale spatial analysis to identify both village-level hotspots and intra-village heterogeneity in Garbada Taluka. Using primary survey data, the EVI was constructed from land size, crop diversity, and WASH indicators, and spatial analysis was applied to examine household- and village-level patterns of vulnerability in the study area. By highlighting these patterns, this study aims to provide an evidence base for local planning and strengthen resilience among tribal households.

2. MATERIALS AND METHODS

2.1. Study Area

The research was conducted in Garbada Taluka of Dahod District, Gujarat, India, one of the nine talukas of Dahod. The district has a predominantly tribal population and has been recognized as an Aspirational District by the Government of India due to persistent developmental challenges in education, health, agriculture, and infrastructure (NITI Aayog 2023). Garbada was selected as the study site because of its diverse topography, comprising hilly, plain, and medium regions, which provides a natural setting to examine geographical variations in agricultural practices and household vulnerability. Agriculture, particularly maize cultivation, is the primary livelihood in this region. The study was conducted between February 2023 and July 2023.

2.2. Study Design and Samples

A cross-sectional household survey was conducted in 645 households in Garbada Taluka. Households were selected using random GPS points generated in ArcGIS 10.5, enforcing a minimum of 50 m spacing to reduce clustering and spatial bias. This spatial randomization approach followed the GIS-based household selection method described by Mathenge et al. (2023). Random points were overlaid on high-resolution satellite imagery and village boundary layers and matched to actual household locations during field visits using GPS-enabled Android devices. This procedure ensured uniform geographic coverage and minimized the enumerator bias.

2.3. Data Collection

Primary data were collected through structured interviews and household-level observations using pretested questionnaires. The tool includes the following modules:

1. ***Household characteristics:*** family size, number of children, annual income, and landholding (acres).
2. ***Agriculture:*** production data for maize, rice, wheat, and soybeans.
3. ***Water and sanitation*:** household access to a sufficient water supply and toilet facilities (MSSRF 2024).
4. ***Geolocation*:** latitude and longitude of each household recorded using handheld GPS devices.

Ethical clearance was obtained from the Department of

Foods and Nutrition, Faculty of Family and Community Sciences, The Maharaja Sayajirao University of Baroda.

2.4. Variables and Indicators

2.4.1. Crop Diversity

Crop diversification was measured using the Shannon (H') and Simpson diversity indices (D) (Magurran 2021). Both indices were computed from the production data of maize, rice, wheat, and soybean. While both indices were examined descriptively, the Shannon index was chosen for regression and EVI construction because it captures both crop richness and evenness in diversified farming systems (Sibhatu et al. 2015).

2.4.2. WASH Indicators

Water sufficiency (yes/no) and toilet access (yes/no) were included as essential indicators of environmental health (DST 2021).

2.4.3. Household Income

Annual self-reported earnings were recorded and validated through cross-verification of agricultural output and market prices (Shukla et al. 2025).

2.4.4. Landholding Size

The total cultivated land (in acres) was measured and used to classify households into small, medium, and large categories, following the 33rd percentile cut-offs (Government of Gujarat 2024).

2.5. Environmental Vulnerability Index (EVI)

An Environmental Vulnerability Index (EVI) was constructed at the household level using four indicators: landholding size, crop diversity, water sufficiency, and toilet facilities. Each variable was coded as binary (0 = not vulnerable, 1 = vulnerable)

$$EVI_i = \sum_{j=1}^{4} X_{ij}$$

Where:

- X_{i1} = 1 if landholding ≤ 33rd percentile (small landholding), else 0
- X_{i2} = 1 if Shannon diversity ≤ 33rd percentile (low crop diversity), else 0
- X_{i3} = 1if the household lacked sufficient water, else 0
- X_{i4} = 1 if the household lacked a toilet facility, else 0

Thus, EVI_iranged from 0 (no vulnerability) to 4 (highest vulnerability).

Households were categorized as:

1. Low vulnerability: scores 0–1
2. Medium vulnerability: scores 2–3
3. High vulnerability: score 4

This composite index approach aligns with contemporary frameworks that integrate multiple environmental and socioeconomic stressors into a single standardized measure of vulnerability. Similar additive or weighted-index methods have recently been applied in social and ecological contexts for micro-level vulnerability assessments, adapted here to the household scale (Smits & Huisman 2024). Equal weighting was adopted to maintain transparency and reduce subjectivity in the absence of empirically derived weights, a common approach in exploratory household-level vulnerability assessments. While binary coding improves interpretability and comparability across indicators, it may result in some loss of information from the underlying continuous variables, which is acknowledged as a limitation of the present study.

For village-level thematic maps, continuous indicator values were classified using percentile-based thresholds, where values ≤ 33rd percentile represented low, 34–66th percentile represented medium, and ≥ 67th percentile represented high levels of vulnerability or deprivation.

2.6. Data Analysis

2.6.1. Statistical Analysis

All quantitative analyses were performed using R software (version 4.3.3). Descriptive statistics (means, medians, and percentages) were computed to summarize household and village-level indicators. Spearman's rank correlation was used to examine the associations among key variables, including landholding size, crop diversity, water sufficiency, toilet access, and household income. To identify the determinants of household income, a linear regression model was estimated with log-transformed income as the dependent variable. Household- and village-level Environmental Vulnerability Index (EVI) scores were summarized to highlight vulnerability patterns across the study area. The combined use of R for statistical analysis and ArcGIS 10.5 for spatial visualization ensured robust analytical rigor and reproducibility of the results.

2.6.2. Spatial Analysis

Household coordinates and village boundary shapefiles were imported into ArcGIS 10.5 for spatial visualization. Five thematic maps were generated to illustrate spatial variability in key indicators.

1. Household-level EVI classification
2. Village-level mean EVI
3. Village-level crop diversity (Shannon index)
4. Village-level percentage of households with sufficient water

5. Village-level percentage of households with toilet facilities

3. RESULTS AND DISCUSSION

The findings of the study are presented at both the household and village levels to capture the individual and spatial patterns of vulnerability. The results include descriptive statistics of households, correlation and regression analyses to assess key determinants of income and vulnerability, and the construction of an Environmental Vulnerability Index (EVI). Spatial analysis using ArcGIS further illustrated inter-village variations in crop diversity, water sufficiency, sanitation, and EVI distribution. Together, these findings provide a comprehensive picture of the environmental vulnerability of tribal households in Garbada Taluka.

The results are presented below, with an interpretation provided alongside to place the findings in the context of the existing literature.

3.1. Household Characteristics

The surveyed households had an average landholding size of 3.25 acres, with a median landholding size of 4 acres (Table 1). The average household size was 6.2 members, with a median of 2 children. The average annual household income was ₹159,855, although the range was wide (₹10,000–700,000), reflecting the heterogeneity in livelihoods. Approximately 68% of households reported sufficient water availability, whereas 62% had toilet facilities. Crop diversity was modest, with a mean Shannon index of 1.12 and a Simpson index of 0.62, confirming the dominance of maize. Such dependence on maize as a staple crop under rainfall variability has been previously documented in Dahod (Chawra et al. 2024). Shah and Kumar (2008) also emphasized poverty and livelihood vulnerability tied to land access among Gujarat's tribal communities.

While crop diversity reflects agricultural resilience, its relationship with household resources and infrastructure was further explored through correlation and regression analysis.

Table 1: Descriptive statistics of surveyed households (n=645).

Variable	Mean/%	Median	Min–Max
Landholding size [acres]	3.25	4.0	0-15
Household size	6.2	7.0	2-15
Children in the household	2.1	2.0	0-6
Annual income [₹]	159,855	140,000	10,000-700,000
% with sufficient water	68%	-	-
% with toilet facility	62%	-	-
Shannon diversity (mean)	1.12	-	0-1.39
Simpson diversity (mean)	0.62	-	0-0.70

Spearman's correlation analysis (Table 2) showed a weak but significant positive relationship between landholding and income ($\rho = 0.079$, $p = 0.046$), suggesting that larger farms provide an income advantage. A significant correlation was also observed between water sufficiency and toilet access ($\rho = 0.086$, $p = 0.030$), reflecting the link between household infrastructure and sanitation. However, crop diversity was not significantly associated with income or water sufficiency, highlighting the persistence of monocropping of maize. These findings are consistent with national assessments that highlight landholding as a stronger determinant of household resilience compared to diversification (DST 2021, Smits & Huisman 2024).

3.2 Determinants of Household Income

Regression analysis confirmed that landholding size was the only significant predictor of household income ($\beta = 0.032$, $p = 0.028$) after adjusting for crop diversity, water sufficiency, and sanitation (Table 3). The adjusted R^2 was only 0.009, indicating that agricultural and infrastructure variables explained less than 1% of the income variation. This highlights the complexity of tribal livelihoods, where income depends on multiple non-farm and environmental factors. A similar weak explanatory power of agricultural determinants has been observed in Central India's vulnerability studies (Smits & Huisman 2024) and in Gujarat's State Action Plan on Climate Change and Health (Government of Gujarat 2024). The very low adjusted R^2 (0.009) suggests that agricultural and WASH-related variables alone are insufficient to explain household income variation in tribal settings. In districts such as Dahod, household incomes are widely reported to depend on diversified livelihood strategies, including non-farm employment and seasonal migration, which are beyond the scope of the present study. Therefore, the regression results should be interpreted as indicative associations rather than strong predictors of income, and future research may benefit from incorporating migration, wage labor, and social protection variables. Although crop diversity is widely linked to resilience and nutrition outcomes in the literature, it did not show a statistically significant association with household income in this analysis.

Table 2: Spearman correlations between key indicators.

Variables	rho [ρ]	p-value
Landholding vs Income	0.079	0.046*
Crop diversity vs Income	0.069	0.079
Crop diversity vs Water	- 0.024	0.548
Landholding vs Water	- 0.019	0.639
Toilet vs Water	0.086	0.030*

* $p < 0.05$, ns = not significant

Table 3: Regression results: Determinants of log household income.

Predictor	Estimate	Std. Error	t-value	p-value
Intercept	11.616	0.080	145.6	<0.001
Landholding (acres)	0.032	0.014	2.20	0.028 *
Crop diversity (Shannon)	0.052	0.071	0.73	0.465
Water sufficiency	0.061	0.046	1.34	0.181
Toilet facility	0.043	0.046	0.94	0.346

*Model fit: Adjusted $R^2 = 0.009$, $F(4, 640) = 2.43$, $p = 0.046$ ($p < 0.05$

3.3 Spatial Analysis of Vulnerability

To complement the statistical findings, a spatial analysis was conducted to capture the geographic variation in agricultural practices, WASH infrastructure, and environmental vulnerability across Garbada Taluka. Mapping key indicators at both the village and household levels helps visualize disparities that may not be fully apparent in tabular summaries. This approach highlights clusters of high vulnerability and provides a basis for identifying priority intervention areas. Figs. 1–5 present the spatial distributions of crop diversity, sanitation, water sufficiency, and the composite Environmental Vulnerability Index (EVI).

3.3.1 Crop Diversity and Environmental Indicator

Crop diversity, measured using the Shannon Index, was lowest in Matwa, Zari Bujarg, and Garbada (red), reflecting maize-dominated monocropping, while Ambli, Jesawada, and Devda showed relatively higher diversity (green) (Fig. 1). Low Shannon scores indicate limited crop diversification, which is associated with higher vulnerability to climatic shocks and lower dietary diversity, which is essential for child health. Similar rainfall-driven monocropping patterns have been observed in Dahod (Chawra et al. 2024). At the nutrition level, studies show that agricultural diversification, as captured by the Shannon Index, is positively associated with household dietary adequacy (Smits & Huisman 2024). The map illustrates the spatial distribution of crop diversity across the villages. Villages shaded red represent low crop diversity (dominated by maize monocropping), yellow indicates medium diversity, and green denotes high diversity with a more balanced cultivation of cereals, pulses, and oilseeds. High-diversity villages (e.g., Ambli, Jesawada, and Devda) reflect more resilient farming systems, whereas low-diversity clusters (e.g., Matwa, Zari Bujarg, and Garbada) highlight areas vulnerable to climatic shocks and dietary monotony.

Sanitation access was poorest in Matwa, Vajelav, and Zari Bujarg, where fewer than 40% of households reported a toilet, whereas Jesawada and Bharsada performed better (Fig. 2). Poor sanitation is a well-documented determinant of undernutrition in children. NITI Aayog (2023) and Pickering et al. (2019) reported that toilet access reduces the odds of stunting by 16–39%. This map presents the spatial distribution of sanitation coverage across the villages. Villages shaded red represent very low coverage, orange indicates low coverage, yellow indicates medium coverage, and green indicates high coverage. Very low coverage is concentrated in Matwa, Vajelav, and Zari Bujarg, whereas comparatively better access is observed in Jesawada, Bharsada, and Ambli. The clustering of red and orange zones across central and southern Garbada indicates critical sanitation deficits, which are strongly linked to child undernutrition through higher exposure to diarrheal and parasitic infections.

Water sufficiency was particularly low in Garbada, Zari Bujarg, and Matwa (<40%), whereas Patiya, Bhe, and Devda demonstrated better access (Fig. 3). These results align with evidence from the Maternal & Child Nutrition showing that children in households with sufficient water were significantly more likely to meet the minimum dietary diversity standards (Gao et al. 2022). This map shows the distribution of household water sufficiency across the villages. Villages shaded red, orange, yellow, and green represent very low, low, medium, and high access, respectively. Very low sufficiency is concentrated in Matwa, Zari Bujarg, Garbada, and Boriyala, whereas Patiya, Bhe, Jesawada, and Devda exhibit higher sufficiency. The clustering of water-deficit villages in the central and southern parts of Garbada reflects the underlying infrastructure and resource constraints. Research from rural India, including Uttarakhand, also highlights that improved water and sanitation access reduces stunting by lowering exposure to diarrheal and parasitic infections (Nair et al. 2017).

To integrate these multiple dimensions-land, diversity, water, and sanitation-into a single measure, a composite Environmental Vulnerability Index (EVI) was constructed.

3.3.2 Environmental Vulnerability Index (EVI)

The household-level EVI revealed that 53.8% of households were classified as medium-vulnerability, 41.4% as low-vulnerability, and 4.8% as high-vulnerability (Table 4). The dominance of medium vulnerability suggests that while extreme conditions are rare, most households face sustained risks owing to small landholdings, low crop diversity, and limited WASH infrastructure. These results align with the national Climate Vulnerability Assessment (DST 2021), which found medium vulnerability to be prevalent across large parts of India, and with hotspot analyses of regional disparities (Ravichandran et al. 2023).

While the EVI summary provides a quantitative distribution of vulnerability, spatial mapping allows these patterns to be visualized across villages.

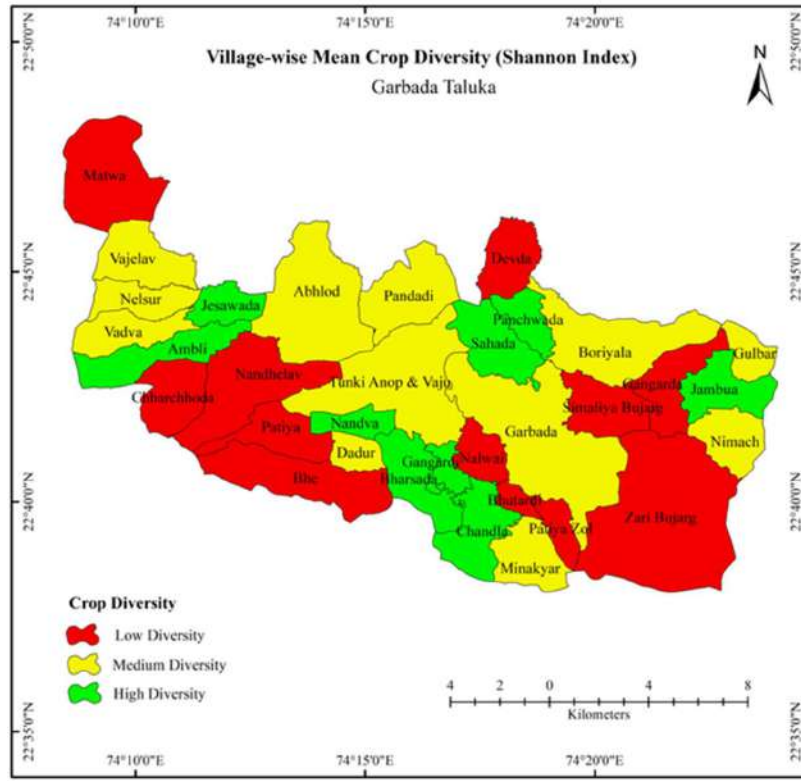


Fig. 1: Village-wise mean crop diversity (Shannon Index) in Garbada Taluka.

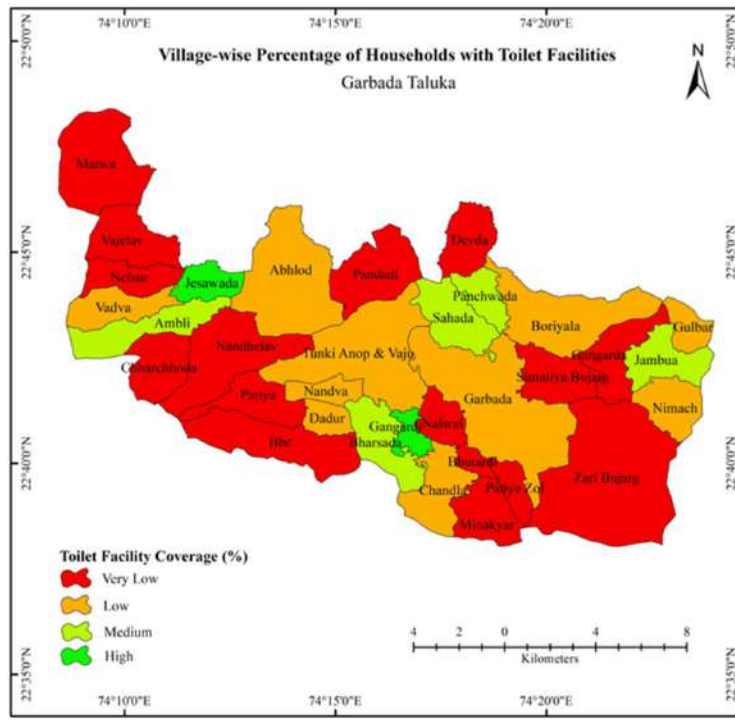


Fig. 2: Village-wise percentage of households with toilet facilities in Garbada Taluka.

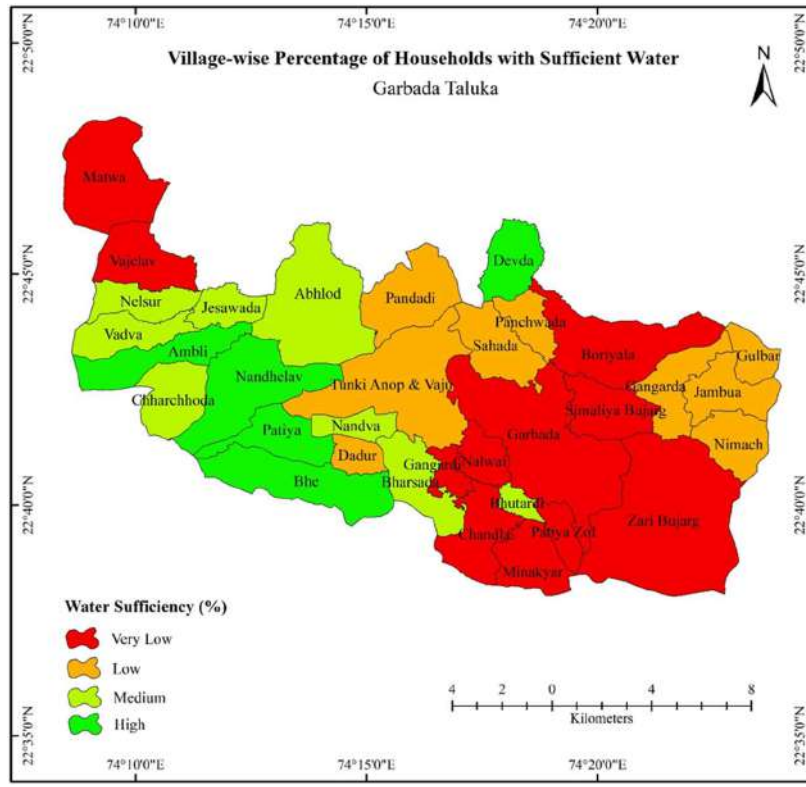


Fig. 3: Village-wise percentage of households with sufficient water in Garbada Taluka.

3.3.3. Village-Level Spatial Patterns

Figures 1–4 provide an overview of the village-level environmental indicators across Garbada Taluka. These maps highlight variations in crop diversity, sanitation, water sufficiency, and the aggregated Environmental Vulnerability Index (EVI). Together, they illustrate the uneven distribution of resources and resilience across villages. For instance, villages such as Matwa, Zari Bujarg, Garbada, and Simaliya Bujarg consistently emerged as high-vulnerability clusters (Fig. 4), marked by low crop diversity, poor sanitation, and inadequate water sufficiency. In contrast, villages such as Jesawada, Ambli, and Devda displayed relatively higher resilience, with more diversified production systems and better infrastructure. These spatial patterns are consistent with broader state-level assessments, such as the Government of Gujarat (2024), which identified the Dahod district as a climate- and environment-sensitive region.

Table 4: Distribution of Environmental Vulnerability Index (EVI) classes.

EVI Class	Criteria (score)	No. of households
Low	0–1	267
Medium	2–3	347
High	4	31

Although village-level patterns highlight clusters of vulnerability, households within the same village often differ substantially from each other. Household-level mapping helps to capture these intra-village disparities.

3.3.4. Household-Level Spatial Patterns

At the micro scale, Fig. 5 shows household-level EVI. Even within medium-vulnerability villages, such as Sahada and Pandadi, households were heterogeneous—some were resilient, whereas others were highly vulnerable. This intra-village disparity is often masked in aggregated data and underscores the value of household-scale mapping (Raj & Sofi 2023).

Comparing village- and household-level results helps assess whether vulnerability patterns are consistent across scales or if finer variations are masked in aggregated data. The household-level EVI provides a quantitative basis for capturing intra-village variability, as individual households are assigned numeric vulnerability scores ranging from 0 to 4. The observed co-existence of highly vulnerable and relatively resilient households within the same village reflects the uneven access to land, water, sanitation, and agricultural resources at the household scale. Such intra-village heterogeneity highlights the limitations of

relying solely on village-level averages and reinforces the importance of household-scale analysis for targeted planning and intervention.

3.3.5. Consistency Across Scales

A comparison of village-level (Fig 4) and household-level (Fig. 5) The Environmental Vulnerability Index (EVI) demonstrates both consistency and complementarity in the findings. At the aggregate scale, villages such as Matwa, Zari Bujarg, Garbada, and Vajelav were consistently classified as being highly vulnerable. This pattern was reinforced at the micro-scale, where a large share of households in these villages was mapped under the high vulnerability category. Simultaneously, household-level mapping revealed intra-village disparities that were not visible in the aggregate analysis, with even resilient villages such as Jesawada and Ambli containing a few high-vulnerability households.

These dual-scale findings align with earlier research on environmental conditions and health outcomes. For instance, household environmental conditions have been shown to directly affect morbidity in India (Brahmanandam & Nagarajan 2021), while behavioral interventions such as waste segregation in Delhi demonstrate how socioeconomic factors shape vulnerability at the micro level (Kaur & Kaur 2024). These insights reinforce the importance of combining village- and household-level analyses, as undertaken in this study. This map shows the average environmental vulnerability of households, aggregated at the village level. Villages shaded green represent low vulnerability, yellow indicates medium vulnerability, and red indicates high vulnerability. High EVI values are concentrated in Zari Bujarg, Garbada, Simaliya Bujarg, and Nandhelav, while Jesawada, Ambli, Devda, and Gulbar show relatively lower vulnerability. The map highlights the regional clustering of vulnerability, with southern and central villages facing greater environmental stress than western and northern areas.

At the district and state levels, composite indices have been widely applied for climate vulnerability assessments. The Council on Energy, Environment, and Water (Shukla et al. 2025) produced a district-level vulnerability atlas of India, and the Department of Science and Technology's Climate Vulnerability Assessment for Adaptation Planning in India (DST 2021) combined environmental, economic, and social indicators to guide adaptation strategies. The clustering of

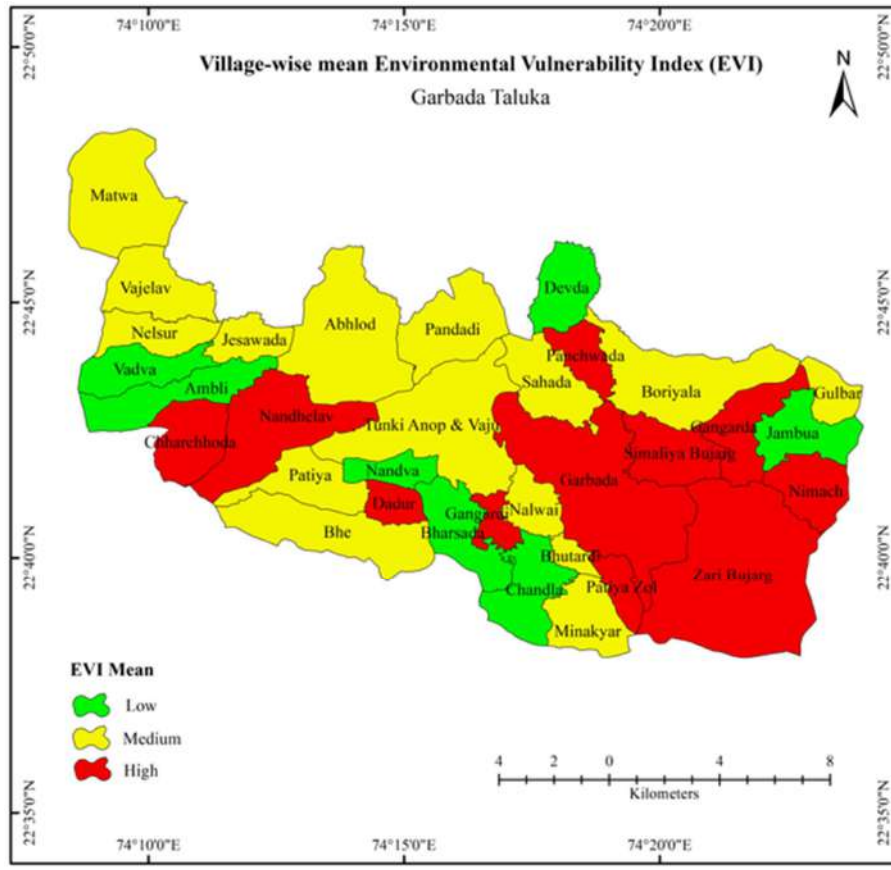


Fig. 4: Village-wise mean Environmental Vulnerability Index (EVI) in Garbada Taluka.

high-vulnerability villages in Garbada corresponds to similar spatial disparities documented in western and central India.

At the regional scale, studies using the Climate Vulnerability Index have highlighted significant variations in exposure and adaptive capacity across Indian states (Singh et al. 2021). Evidence from tribal areas in Central India shows that livelihood vulnerability is strongly mediated by crop diversity, landholding, and water access (Smits & Huisman 2024), whereas household-level vulnerability in the Western Ghats varies sharply with ecological and demographic factors (Raj & Sofi 2023). These parallels reinforce the present study's observation that intra-village heterogeneity in Garbada is as critical as inter-village differences (Fig. 5).

This map illustrates the distribution of environmental vulnerability at the household level. Households shaded green, yellow, and red represent low, moderate, and high vulnerability, respectively. High-vulnerability households are scattered across villages such as Matwa, Garbada, and Zari Bujarg, whereas most households in Jesawada, Ambli, and Devda show low vulnerability. The household-level analysis reveals intra-village disparities, where even villages with medium overall vulnerability include both resilient and highly vulnerable households.

The integration of spatial mapping further strengthens the explanatory power of household survey data. Remote sensing–based eco-environmental assessments have demonstrated the value of combining climatic and anthropogenic indicators for dynamic vulnerability mapping (Lan et al. 2023). Although this study primarily relied on household survey data integrated with GIS, the consistency of its results with both composite indices and remote sensing

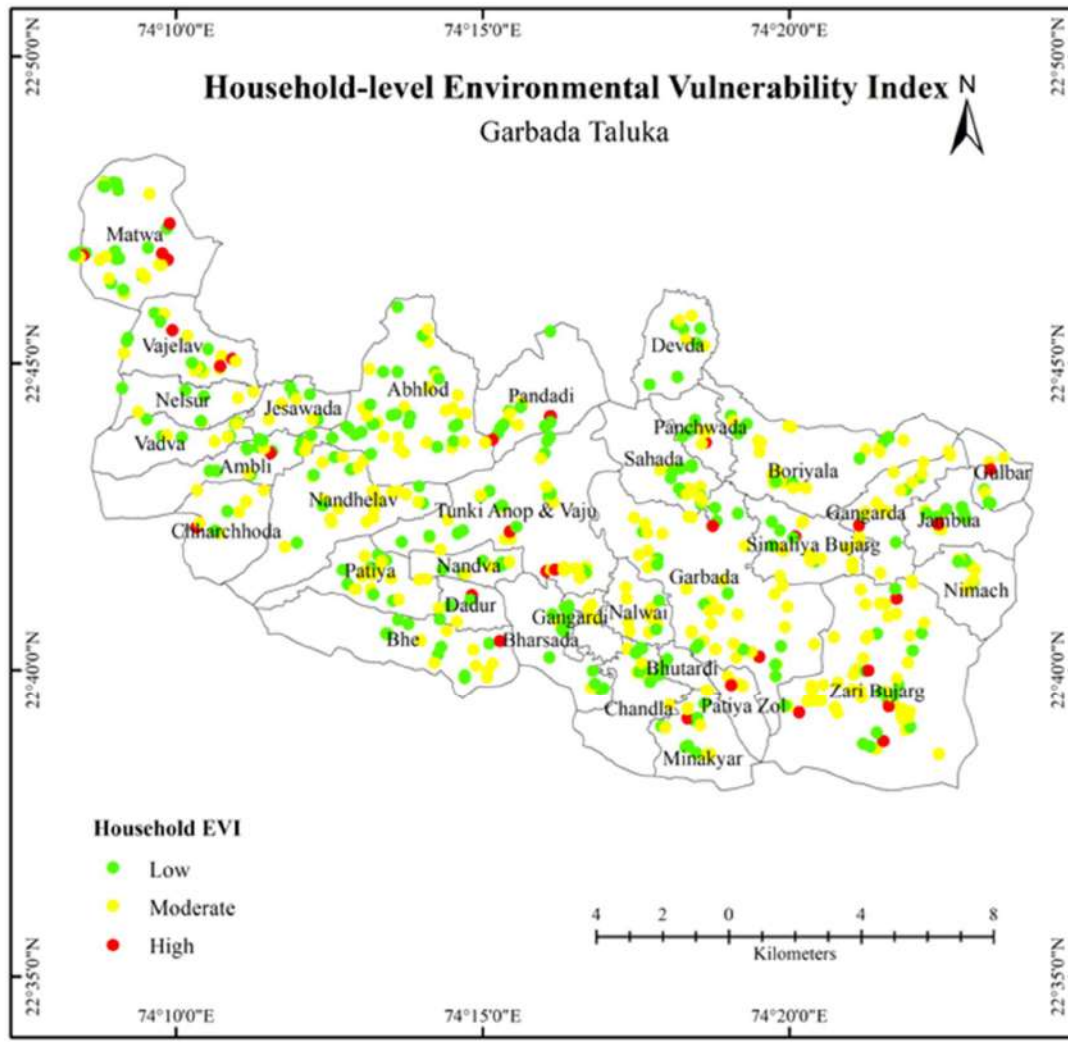


Fig. 5: Household-level Environmental Vulnerability Index (EVI) in Garbada Taluka.

approaches underscores their methodological robustness. The findings were subsequently interpreted in relation to the broader concerns of food and nutrition security, given the close link between environmental vulnerability, crop diversity, and household well-being. Similar GIS-based spatial studies have revealed how flood and drought risks influence food security in vulnerable regions (Rosalia et al. 2021). Given the cross-sectional design of this study, the observed relationships should be interpreted as associations rather than causal effects. The spatial analysis presented in this study is primarily descriptive, and formal spatial autocorrelation statistics (e.g., Moran's I or Getis–Ord Gi*) were not applied; therefore, spatial clustering patterns should be interpreted with caution.

3.4. Implications for Food and Nutrition Security

Although direct nutrition indicators were not collected, the environmental variables used in the EVI are well-established determinants of food and nutrition. Crop diversity has been linked to dietary adequacy (Sibhatu et al. 2015), and access to water and sanitation has been associated with reduced child stunting and underweight (Nair et al. 2017, Pickering et al. 2019). The clustering of vulnerable villages in Garbada, therefore, suggests a potential overlap with nutritional insecurity, consistent with national studies linking climate vulnerability and child malnutrition (Gao et al. 2022, NITI Aayog 2023). However, a key limitation of this study is the absence of direct nutritional indicators, such as dietary diversity or anthropometric measures; therefore, links to food and nutrition security were interpreted contextually based on the existing literature rather than measured outcomes.

4. CONCLUSIONS

This study assessed environmental vulnerability among 645 tribal households in Garbada Taluka of Dahod District, Gujarat, using a composite Environmental Vulnerability Index (EVI) that incorporates landholding, crop diversity, water sufficiency, and sanitation access. The results demonstrated that most households fell into the medium vulnerability category, with villages such as Matwa, Zari Bujarg, and Garbada consistently emerging as hotspots of high vulnerability. Household-level mapping further revealed significant intra-village disparities, underscoring the importance of considering both aggregate and micro-level scales in vulnerability assessments.

Although nutritional outcomes were not directly measured, the environmental and infrastructural indicators used in the EVI are well-established determinants in the literature on food and nutrition security. The clustering of low crop diversity, poor sanitation, and inadequate water sufficiency suggests potential heightened risks to livelihood and nutrition security in the study area. Evidence from India and other smallholder contexts shows that higher crop diversity is strongly associated with improved household dietary adequacy (Sibhatu et al. 2015).

From a policy perspective, these findings have implications for targeted and location-specific interventions. Villages with high EVI may warrant priority attention in climate adaptation planning, agricultural diversification programs, and WASH (water, sanitation, and hygiene) infrastructure development. Simultaneously, household-level disparities suggest the relevance of micro-level interventions, ensuring that vulnerable families within relatively resilient villages are not overlooked. Access to safe water and toilet facilities has been consistently linked with reduced risks of stunting and underweight among children by lowering exposure to diarrheal and parasitic infections, while food-based interventions that improve diet diversity have also proven effective in addressing multiple micronutrient deficiencies (Nair et al. 2017).

The dual-scale approach demonstrated here can support tribal development schemes, the State Action Plan on Climate Change, and national programs such as ICDS and POSHAN 2.0 by identifying critical hotspots and informing more targeted interventions. Future research should integrate direct nutrition indicators, such as dietary diversity and child growth outcomes, with environmental vulnerability frameworks to provide a more holistic understanding of food and nutrition security.

5. ACKNOWLEDGMENTS

The authors thank all the participants in this study.

6. REFERENCES

Brahmanandam, N. and Nagarajan, R., 2021. Impact of change in household environment condition on morbidity in India: Evidence from longitudinal data. *PLOS ONE*, 16(3), p.e0247465. DOI

Census of India, 2011. District Census Handbook: Dahod. Office of the Registrar General & Census Commissioner, Government of India. Retrieved October 31, 2025, from https://www.census2011.co.in/census/district/199-dohad.html

Chawra, U., Kacha, H., Rani, R.R. and Bhabhor, G., 2024. Rainfall variability and crop planning of Dahod: A case study from a tribal district in Gujarat, India. *International Journal of Environment and Climate Change*, 14(4), pp.259-266. DOI

Department of Science and Technology (DST), 2021. Climate Vulnerability Assessment for Adaptation Planning in India Using a Common Framework. Government of India. Retrieved October 31, 2025, from https://dst.gov.in/document/reports/national-climate-vulnerability-assessment-report

Dwivedi, A., Singh, A., Tomar, S.S., Bankoti, P., Singh, O. and Kumar, K., 2016. Interaction effect of maize and mash-bean intercropping on sustainable production systems in the subtropical zone of India. *Nature*

Environment and Pollution Technology, 15(2), pp.661-665. Retrieved October 31, 2025, from https://neptjournal.com/upload-images/NL-56-46-(46)B-3252.pdf

Gao, Y., Sheng, J., Mi, X., Zhou, M., Zou, S. and Zhou, H., 2022. Household water access, dietary diversity and nutritional status among preschoolers in poor rural areas of Central and Western China. *Nutrients*, 14(3), p.458. DOI

Government of Gujarat, 2024. State Action Plan on Climate Change and Human Health – Gujarat (2022–27). Gandhinagar: Government of Gujarat & NCDC. Retrieved October 31, 2025, from https://ncdc.mohfw.gov.in/wp-content/uploads/2025/01/09_SAPCCHH_Gujarat_21-10-24.pdf

Kaur, H. and Kaur, P., 2024. Factors determining household waste segregation behavior: An Indian case study. *International Journal of Experimental Research and Review*, 41(Special Volume), pp.83-95. DOI

Kumar, P., Ashwani, Mishra, S., Thakur, S., Kumar, D. and Raman, V.A.V., 2023. Vulnerability of tribal communities to climate variability in Lahaul and Spiti, Himachal Pradesh, India. *Cografya Dergisi*, 47, pp.29-43. DOI

Lan, G., Jiang, X., Xu, D., Guo, X., Wu, Y., Liu, Y. and Yang, Y., 2023. Ecological vulnerability assessment based on remote sensing ecological index (RSEI): A case of Zhongxian County, Chongqing. *Frontiers in Environmental Science*, 10, p.1074376. DOI

Magurran, A.E., 2021. Measuring biological diversity. *Current Biology*, 31(19), pp.R1174-R1177. DOI

Mathenge, M., Sonneveld, B.G.J.S. and Broerse, J.E.W., 2023. Mapping the spatial dimension of food insecurity using GIS-based indicators: A case of Western Kenya. *Food Security*, 15(2), pp.243-260. DOI

Mathew, V.J., 2024. The evolution and status of Tribal Sub Plan through local self-government institutions: Reflections from Kerala's experience. ISEC Working Paper No. 583. Institute for Social and Economic Change. Retrieved October 31, 2025, from https://www.isec.ac.in/wp-content/uploads/2025/04/WP-583-Vidya-J-Mathew-Final.pdf

M.S. Swaminathan Research Foundation (MSSRF), 2024. How Does Climate Change Impact Women and Children Across Agro-Ecological Zones in India: A Scoping Study. Chennai: MSSRF. Retrieved October 31, 2025, from https://www.mssrf.org/sites/default/files/2025-05/Report-CCW-Study-v2-a_0.pdf

Mohanty, A. and Wadhawan, S., 2021. Mapping India's Climate Vulnerability: A District-Level Assessment. New Delhi: CEEW. Retrieved October 31, 2025, from https://www.ceew.in/sites/default/files/ceew-study-on-climate-change-vulnerability-index-and-district-level-risk-assessment.pdf

Mohanty, B., 2024. A multidisciplinary review of emerging research on tribal communities, sustainable agriculture and rural livelihoods. *SSRN*, 9, p.76142. [DOI]

Nair, M.K., Augustine, L.F. and Konapur, A., 2017. Food-based interventions to modify diet quality and diversity to address multiple micronutrient deficiency. *Frontiers in Public Health*, 3, p.277. DOI

NITI Aayog, 2023. Deep-Dive: Insights from Champions of Change – The Aspirational Districts Dashboard. Government of India. Retrieved October 31, 2025, from https://www.niti.gov.in/sites/default/files/2023-03/DEEP-DIVE-Insights-from-Champions-of-Change-The-Aspirational-Districts-Dashboard.pdf

Pickering, A.J., Null, C., Winch, P.J., Mangwadu, G., Arnold, B.F., Prendergast, A.J., Njenga, S.M., Rahman, M., Ntozini, R., Benjamin-Chung, J. et al., 2019. The WASH Benefits and SHINE trials: Interpretation of WASH intervention effects on linear growth and diarrhoea. *The Lancet Global Health*, 7(8), pp.e1139-e1146. DOI

Raj, R. and Sofi, A.A., 2023. Does climate change lead to severe household-level vulnerability? Evidence from the Western Ghats of Kerala, India. *Land Use Policy*, 130, p.106655. DOI

Ravichandran, V., Kantamaneni, K., Singh, A., Nair, A., Janakiraman, A. and Prem Kumar, S., 2023. Mapping hotspot clustering: An approach to study the spatial pattern of quality of living households in India. *Remote Sensing Applications: Society and Environment*, 31, p.101007. DOI

Rosalia, A.C.T., Suryanto and Hakim, L., 2021. Spatial analysis of the impact of flood and drought on food security index. *Nature Environment and Pollution Technology*, 20(2), pp.721-727. DOI

Shah, A. and Kumar, A., 2008. The Grassroots of Poverty: Tribal Livelihoods and Development in Gujarat. GIDR Working Paper No. 187. Gujarat Institute of Development Research. Retrieved October 31, 2025, from https://gidr.ac.in/pdf/WP-187.pdf

Sharma, P. and Mohan, K., 2024. Location, Livelihoods and Tribal People: Exploring the Linkages in India. Independent Research Publication. Retrieved October 31, 2025, from https://www.researchgate.net/publication/383238589_Location_Livelihoods_and_Tribal_People_Exploring_the_Linkages_in_India

Shukla, S., Abraham, S. and Parekh, S., 2025. Advancing Climate-Resilient Agriculture in India by Strengthening Institutional Capacity: Lessons from Bihar and Odisha. New Delhi: CEEW. Retrieved October 31, 2025, from https://www.ceew.in/sites/default/files/how-can-india-scale-climate-resilient-agriculture-practices-and-climate-smart-farming.pdf

Sibhatu, K.T., Krishna, V.V. and Qaim, M., 2015. Production diversity and dietary diversity in smallholder farm households. *Proceedings of the National Academy of Sciences (PNAS)*, 112(34), pp.10657-10662. DOI

Singh, C., Madhavan, M. and Arvind, J., 2021. Climate change adaptation in Indian cities: A review of existing actions and spaces for triple wins. *Urban Climate*, 36, p.100783. DOI

Smits, J. and Huisman, J., 2024. The GDL Vulnerability Index (GVI). *Social Indicators Research*, 174, pp.721-741. DOI

Nature Environment and Pollution Technology
An International Quarterly Scientific Journal

p-ISSN: 0972-6268
(Print copies up to 2016)
e-ISSN: 2395-3454

Vol. 25 | No. 3 | Article ID D1881 | 2026

Original Research Paper

https://doi.org/10.46488/NEPT.2026.v25i03.D1881

Open Access Journal

Application of the SWAT Model to the Hydrological Modeling of the Nfifikh Watershed (Morocco): Study of the Dynamics of Surface and Groundwater and their Relationship with Soil Properties

Zahli Saleh Eddine†
Department of Geography and Space Planning, University of Hassan II, Faculty of Letters and Human Sciences, Ain Chock, Casablanca, Morocco
†Corresponding author: Zahli Saleh Eddine; salahzahli16@gmail.com

Abbreviation: Nat. Env. & Poll. Technol.
Website: www.neptjournal.com

Received: 16-10-2025
Revised: 18-12-2025
Accepted: 11-01-2026

Key Words:

SWAT model
Nfifikh watershed
Surface runoff
Groundwater recharge
Sediment budget

Citation for the Paper:

Zahli, S.E., 2026. Application of the SWAT model to the hydrological modeling of the Nfifikh watershed (Morocco): Study of the dynamics of surface and groundwaters and their relationship with soil properties. *Nature Environment and Pollution Technology*, 25(3), D1881. https://doi.org/10.46488/NEPT.2026.v25i03.D1881

Note: From 2025, the journal has adopted the use of Article IDs in citations instead of traditional consecutive page numbers. Each article is now given individual page ranges starting from page 1.

Copyright: © 2026 by the authors
Licensee: Technoscience Publications
This article is an open access article distributed under the terms and conditions of the Creative Commons Attribution (CC BY) license (https://creativecommons.org/licenses/by/4.0/).

ABSTRACT

Water resources in semi-arid regions are increasingly affected by climate variability, making hydrological modeling essential for assessing water availability and supporting watershed management. In this study, the Soil and Water Assessment Tool (SWAT) was applied to simulate the hydrological behavior of the Nfifikh watershed in Morocco using climate data from local meteorological stations complemented with gridded datasets, a 30 m digital elevation model, soil maps, and land-use data derived from satellite imagery. Observed streamflow at the watershed outlet was used for model calibration and validation following standard SWAT procedures. Model performance was evaluated using the Nash–Sutcliffe efficiency (NSE), coefficient of determination (R^2), percent bias (PBIAS), and the RMSE–standard deviation ratio (RSR), showing very good agreement between simulated and observed daily flows. Results indicate that about two-thirds of annual precipitation is lost through evapotranspiration, while streamflow is generated through surface runoff, lateral flow, and shallow subsurface contributions. Spatial patterns highlight higher runoff and sediment production in steep upland areas and greater flow regulation downstream. The study provides useful insights for water resource management in semi-arid watersheds.

1. INTRODUCTION

Semi-arid watersheds are characterized by strong hydro-climatic variability and irregular rainfall regimes, which exert a dominant control on runoff generation, soil water balance, and sediment transport processes (Abbaspour et al. 2018; Samimi et al. 2020). Short, high-intensity rainfall events often generate rapid surface runoff and enhanced erosion, while prolonged dry periods limit recharge and increase water stress, posing significant challenges for sustainable water and soil management in data-scarce and heterogeneous environments (Dutta & Sen 2018, Eini et al. 2023).

Physically based hydrological models have become essential tools for analyzing watershed-scale hydrological processes under complex climatic and physiographic conditions (Gassman et al. 2014). When coupled with Geographic Information Systems (GIS), these models enable the integration of topography, land use, soil properties, and climate data to simulate spatially distributed hydrological responses over long time periods and across heterogeneous landscapes (Arnold et al. 2012). Among the available modeling frameworks, the Soil and Water Assessment Tool (SWAT) has been extensively applied to investigate surface runoff generation, soil water dynamics, subsurface flow response, and sediment transport under a wide range of environmental and climatic settings (Guzman et al. 2015).

Numerous studies have demonstrated that SWAT can reproduce key components of the hydrological cycle when appropriate calibration and validation

strategies are applied. Systematic calibration approaches and multi-criteria performance evaluation have been shown to significantly improve model robustness and reliability, even in data-scarce watersheds (Abbaspour et al. 2018, Moriasi et al. 2007). Previous applications have also highlighted the importance of explicitly representing spatial heterogeneity through the definition of Hydrological Response Units (HRUs), which enable the model to account for variations in land use, soil properties, and slope gradients within a watershed (Arnold et al. 1998, Almeida et al. 2018).

Despite its widespread use, SWAT applications remain unevenly distributed across different geographic contexts (Bressiani et al. 2015). While numerous studies have focused on well-instrumented watersheds, relatively few applications have addressed semi-arid basins in North African settings, where hydrological responses are strongly influenced by heterogeneous soils, variable topography, and increasing anthropogenic pressure (Samimi et al. 2020). This imbalance limits the availability of region-specific modeling experience and constrains the transferability of parameterization and calibration schemes developed in more humid or data-rich environments to semi-arid and data-scarce regions (Abbaspour et al. 2018, Sabale et al. 2024).

Addressing this gap requires case studies that explicitly analyze the spatial interactions between surface runoff generation, soil water storage, groundwater contribution, and sediment dynamics, while accounting for land-use patterns and topographic controls at appropriate spatial scales. Previous SWAT-based studies have shown that small to medium-sized watersheds are particularly suitable for such analyses, as they exhibit rapid hydrological responses to climatic variability and land-surface conditions (Meaurio et al. 2015, Sabale et al. 2024).

In this context, the present study applies the SWAT model to the Nfifikh watershed in northwestern Morocco to analyze surface runoff, baseflow contribution, and sediment dynamics in a semi-arid environment characterized by heterogeneous soils and variable topography. Using a calibrated and validated modeling framework, the study provides spatially explicit insights into hydrological functioning at the HRU scale and contributes to the application of SWAT in data-scarce Mediterranean and North African watersheds (Abbaspour et al. 2018, Samimi et al. 2020).

2. MATERIALS AND METHODS

2.1. Study Area

The study was conducted in the Nfifikh watershed (Fig. 1), a semi-arid basin located in northwestern Morocco, extending across the regions of Mohammedia, Benslimane, Beni Yakhlef, and Khouribga. The watershed is characterized by pronounced heterogeneity in topography, land use, and soil properties, combined with strong seasonal and interannual rainfall variability typical of Mediterranean semi-arid climates. These characteristics make the basin well-suited for hydrological modeling of surface runoff, groundwater contribution, and water balance dynamics under data-limited conditions (Almeida et al. 2018).

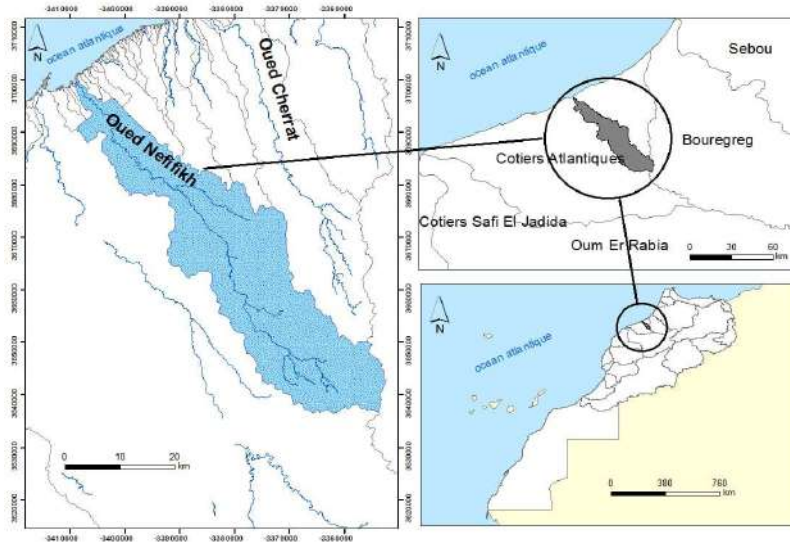


Fig. 1: Study area: Nfifikh watershed.

2.2. Data Sources and Preprocessing

The hydrological model setup was supported by multiple spatial and climatic datasets obtained from national and international sources. A 30-m resolution Digital Elevation Model (DEM) was used to delineate the watershed, extract the drainage network, and derive slope and flow direction, following standard ArcSWAT procedures (Neitsch et al. 2011, Abbaspour et al. 2018).

Meteorological inputs, including daily precipitation, minimum and maximum temperature, relative humidity, wind speed, and solar radiation, were obtained from stations located in Mohammedia, Beni Yakhlef, Benslimane, and Khouribga. To address data gaps, station records were complemented with CHIRPS precipitation and CHIRTS temperature datasets, a common approach in semi-arid regions (Almeida et al. 2018).

Soil data were derived from national soil maps and supplemented with soil physical properties (texture, permeability, and available water capacity) obtained from the FAO database, which are commonly used for SWAT soil parameterization in data-scarce regions (Neitsch et al. 2005, Arnold et al. 2012). Land-use and land-cover (LULC) maps were generated from Landsat-8 imagery using supervised classification in ArcGIS 10.1 and used as a key input for hydrological response unit definition, following standard GIS-based SWAT applications (Bressiani et al. 2015, Abbaspour et al. 2018).

The land-use and land-cover (LULC) map derived from Landsat-8 imagery was evaluated using independent reference data and a confusion matrix approach. The classification achieved an overall accuracy above 85% with a Kappa coefficient greater than 0.80, which is consistent with accuracy levels reported in comparable SWAT-based applications in semi-arid environments and is considered adequate for HRU parameterization (Bressiani et al. 2015, Abbaspour et al. 2018). Remaining uncertainties are mainly associated with transitional agricultural and peri-urban areas, a common limitation in medium-resolution satellite-based land-use classifications.

2.3. Hydrological Model Description and Setup

Hydrological simulations were performed using the Soil and Water Assessment Tool (SWAT) implemented through the ArcSWAT interface in the ArcGIS environment. SWAT is a semi-distributed, process-based, continuous-time model operating at a daily time step and designed to simulate the effects of land use, soil characteristics, and climate variability on watershed-scale hydrological processes (Arnold et al. 1998).

After watershed delineation, the basin outlet was defined, and the watershed was subdivided into sub-basins. Hydrological Response Units (HRUs) were generated by intersecting land-use classes, soil types, and slope categories to represent landscape heterogeneity and its influence on hydrological processes (Almeida et al. 2018).

2.4. Model Calibration and Validation

Model calibration and validation were conducted following the widely adopted SWAT-CUP application protocols to ensure transparency, reproducibility, and physical consistency of the simulated hydrological processes. To reduce the influence of unknown initial conditions related to soil moisture and shallow aquifer storage, a warm-up period of two years was applied before calibration, as commonly recommended in SWAT-based hydrological studies (Abbaspour et al. 2018, Almeida et al. 2018).

Calibration was initially performed at the monthly time step for the period 1993-1998 to capture the dominant seasonal hydrological signal of the semi-arid Mediterranean climate, while minimizing the influence of short-term variability and observational noise (Moriasi et al. 2007). Model validation was subsequently carried out using an independent daily discharge dataset for the period 2008-2012, allowing the assessment of model performance under contrasting hydro-climatic conditions and evaluating its capacity to reproduce both peak flows and baseflow dynamics (Meaurio et al. 2015, Sabale et al. 2024).

Calibration and uncertainty analysis were implemented using the SWAT-CUP software with the SUFI-2 algorithm. A parsimonious calibration strategy was adopted by focusing on a limited set of hydrologically sensitive parameters controlling surface runoff generation, soil water storage, groundwater response, evapotranspiration, and channel routing, in line with sensitivity analyses reported in comparable ArcSWAT applications in semi-arid and data-scarce basins (Abbaspour et al. 2018; Almeida et al. 2018). The main calibrated parameters included the Curve Number (CN2), soil saturated hydraulic conductivity (SOL-K), available water capacity (SOL-AWC), baseflow recession factor (ALPHA-BF), groundwater delay time (GW-DELAY), threshold water depth in the shallow aquifer (GWQMN), soil evaporation compensation factor (ESCO), and channel Manning's roughness coefficient (CH-N2).

Within the SWAT-CUP framework, parameters were adjusted either as relative changes (r) or as absolute values (v), following standard SUFI-2 calibration practice. Parameter ranges were defined based on physically plausible limits reported in the literature and previous SWAT applications, while all remaining parameters were retained at

their default values derived from soil and land-use databases. This approach minimizes the risk of over-parameterization and enhances the robustness and transferability of the model (Abbaspour et al. 2018, Moriasi et al. 2007).

Model performance was evaluated using multiple statistical indicators, including the Nash-Sutcliffe Efficiency (NSE), coefficient of determination (R^2), percent bias (PBIAS), and the RMSE-standard deviation ratio (RSR), in accordance with established hydrological model evaluation criteria (Moriasi et al. 2007). The high-performance values obtained during both calibration and validation periods are attributed to the strong seasonal rainfall control and coherent spatial structure of the Nfifikh watershed, rather than to over-calibration, a behavior frequently reported in well-calibrated SWAT applications at the basin scale (Meaurio et al. 2015, Almeida et al. 2018).

It should be noted that groundwater-related outputs in SWAT represent conceptual shallow aquifer storage and exchange processes rather than a fully physically based groundwater flow system. Consequently, simulated recharge and baseflow components are interpreted as indicative hydrological fluxes within the SWAT conceptual framework, consistent with previous ArcSWAT calibration studies (Abbaspour et al. 2018). The main parameters considered during calibration, their SWAT-CUP adjustment type, and the physically plausible parameter ranges are summarized in Table 1.

2.5. Spatial Analysis of Model Outputs

Simulated outputs were analyzed spatially and temporally within a GIS environment to assess spatial variability in water balance components across the watershed. Spatial patterns of surface runoff, groundwater contribution, evapotranspiration, and sediment dynamics were interpreted in relation to soil properties, topographic gradients, and land-use distribution, providing a spatially explicit understanding of hydrological functioning in semi-arid environments (Zhao et al. 2024). The methodological workflow used for the SWAT model setup, calibration, validation, and spatial analysis is shown in Fig. 2.

Table 1: Key SWAT parameters used for SWAT-CUP (SUFI-2) calibration and validation in the Nfifikh watershed.

Parameter	Hydrological process represented	SWAT-CUP change type	Calibration range
CN2 (Curve Number)	Surface runoff generation	r	0.20- to +0.20
SOL-K	Saturated hydraulic conductivity	r	0.50- to +0.50
SOL-AWC	Available water capacity	r	0.30- to +0.30
ALPHA-BF	Baseflow recession factor	v	0.01 to 1.00
GW-DELAY (days)	Groundwater delay time	v	0 to 300
GWQMN (mm)	Threshold water depth in a shallow aquifer	v	0 to 5000
ESCO	Soil evaporation compensation factor	v	0.10 to 1.00
CH-N2	Manning's roughness coefficient for the main channel	v	0.01 to 0.15

Note: In SWAT-CUP (SUFI-2), parameters were adjusted either as relative changes (r) or absolute values (v), following standard calibration practice.

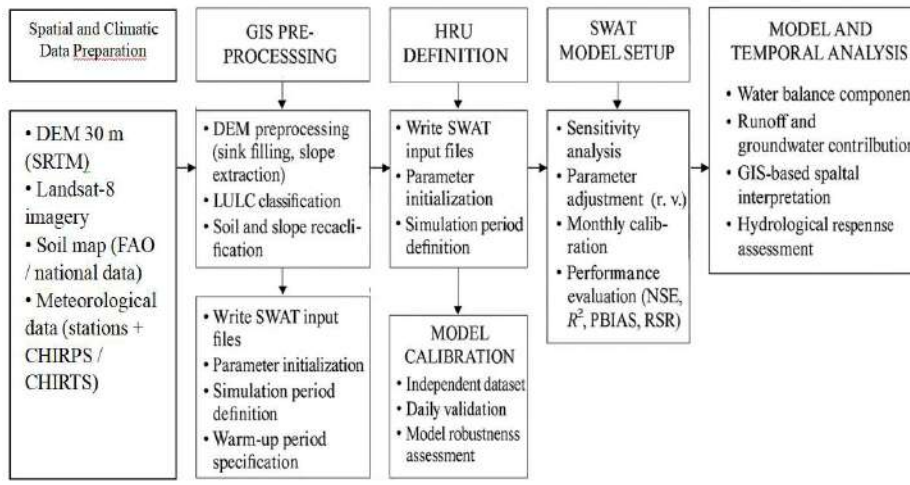


Fig. 2: Methodological framework of SWAT modeling, calibration, and validation applied to the Nfifikh watershed.

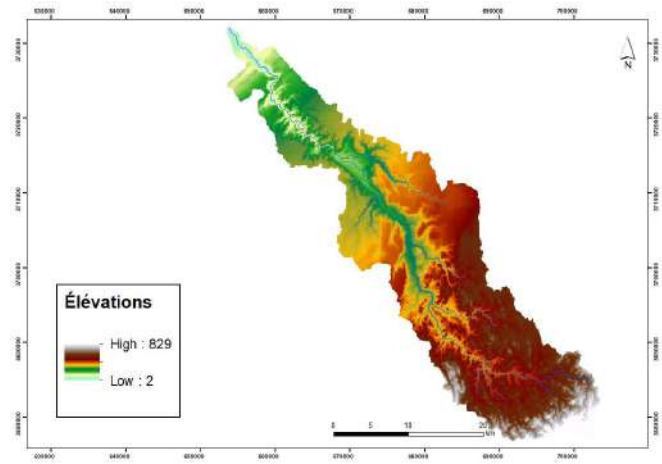


Fig. 3: Digital Elevation Model (DEM) of the Nfifikh.

3. RESULTS

3.1. Spatial Hydro-Geomorphological Setting of the Nfifikh Watershed and Implications for SWAT Simulations

The spatial configuration of the Nfifikh watershed exerts a fundamental control on the distribution of hydrological processes simulated by the SWAT model. The basin is characterized by a pronounced longitudinal topographic gradient extending from the southeastern uplands toward the northwestern outlet, as illustrated by the Digital Elevation Model (Fig. 3). Elevations range from approximately 2 m in the downstream valley bottoms to more than 800 m in the upstream sectors, generating marked contrasts in slope steepness and drainage density across the watershed.

This geomorphological structure gives rise to a well-developed dendritic drainage network, with steep upstream tributaries converging toward progressively gentler downstream reaches. Similar configurations have been shown to strongly influence surface runoff generation, sediment mobilization, and baseflow contribution in SWAT-based studies, particularly in semi-arid and Mediterranean environments (Arnold et al. 1998, Meaurio et al. 2015). In the Nfifikh watershed, steep upstream slopes are associated with faster flow concentration and shorter response times, whereas downstream foothills and valley-bottom zones favor flow attenuation and sustained subsurface contributions.

The spatial distribution of slope classes derived from the DEM plays a key role in structuring Hydrological Response Units (HRUs) and differentiating hydrological behavior across the basin. Slopes exceeding 15% are primarily concentrated in the eastern and southeastern sectors, while gentle slopes (0–5%) dominate the downstream areas. This slope-based stratification enhances the model's capacity to represent spatial variability in runoff potential and erosion sensitivity, as widely recommended in SWAT applications (Arnold et al. 1998, Neitsch et al. 2011).

The distribution of slope classes and their hydrological relevance within the Nfifikh watershed is summarized in Table 2.

Soil characteristics further modulate these topographic controls. The soil map (Fig. 4) reveals a clear spatial correspondence between soil classes and the basin's geomorphological gradient. Fine-textured and moderately developed soils dominate the upland areas, while deeper and more permeable soils are prevalent in the downstream plains and valley corridors. In SWAT simulations, such contrasts translate into spatial differences in key hydrological parameters, including curve number (CN2), soil saturated hydraulic conductivity (SOL_K), and available water

Table 2: Distribution of slope classes and their hydrological relevance in the Nfifikh watershed.

Slope class (%)	Share of watershed area (%)	Mean slope (%)	Dominant HRU hydrological behavior
0–5	40–45	3	High infiltration potential, enhanced groundwater contribution, and delayed runoff response
5–15	35–40	9	Moderate runoff generation, mixed surface–subsurface response
>15	15–25	>20	Rapid surface runoff generation, high erosion sensitivity, and short hydrological response time

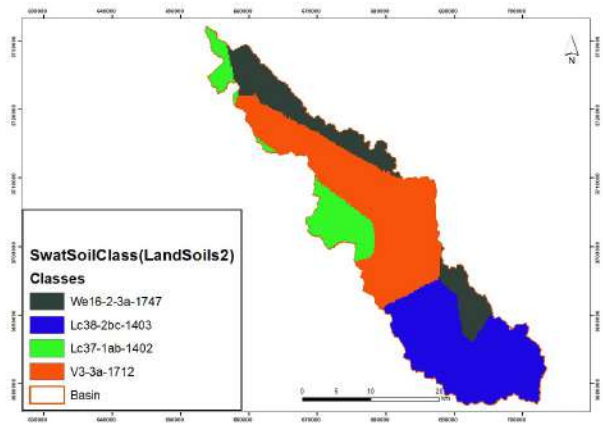


Fig. 4: Soil classes (SWATSoilClass) in the Nfifikh watershed.

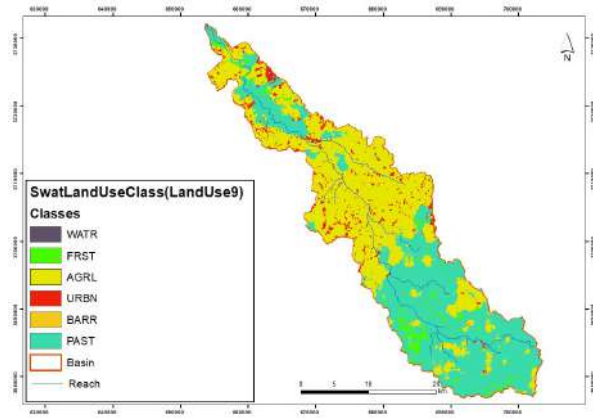


Fig. 5: Land cover and use class (SWATL and UseClass) map of the Nfifikh watershed.

capacity (SOL_AWC), which collectively govern runoff generation, infiltration, and subsurface flow processes (Neitsch et al. 2011, Moriasi et al. 2007).

Land-use patterns exhibit a similar spatial organization (Fig. 5), closely aligned with topography and soil distribution. Rainfed agriculture and fallow land dominate the steeper upland sectors, whereas pasturelands, riparian zones, and localized forest patches are mainly distributed across the lower slopes and valley bottoms. Previous SWAT-based studies have shown that such land-use contrasts strongly influence hydrological response by modifying surface roughness, soil disturbance, and vegetation cover, thereby affecting both runoff and sediment dynamics (Abbaspour et al. 2018, Almeida et al. 2018).

The main land-use categories and their associated hydrological response characteristics as represented in the SWAT model are summarized in Table 3.

This table summarizes the key land-use types in the Nfifikh basin, and their associated hydrological behaviors as represented in the SWAT model, highlighting contrasts in runoff generation, soil infiltration, and sediment response across the watershed.

The combined effect of topography, soil properties, and land use is reflected in the spatial organization of the drainage network and sub-basin structure (Fig. 6). Multiple tributaries converge toward the main channel, promoting localized amplification of flow and sediment transport in upstream confluences, followed by progressive flow attenuation downstream. This longitudinal organization provides a coherent physical framework for interpreting the spatial variability of SWAT-simulated surface runoff, baseflow contribution, and sediment yield across the watershed, without invoking assumptions beyond the model's conceptual structure (Arnold et al. 1998, Meaurio et al. 2015).

Overall, this spatial hydro-geomorphological setting establishes the physical context within which subsequent quantitative results on runoff, groundwater contribution, and sediment dynamics are interpreted. Rather than serving as

Table 3: Land-use classes and associated hydrological response parameters (CN2, SOL-K, and sediment yield) in Nfifikh.

Land-use class	Description	CN2 (Curve Number)	SOL-K (mm/h) Hydraulic Conductivity	Sediment Yield Tendency (SED)	Hydrological Behavior
Rainfed agriculture (cropland)	Cultivated fields, seasonal crops	78 88 -	2 15 -	Medium to high	Moderate infiltration, moderate-high runoff, and soil disturbance increase erosion
Fallow/Bare land	Exposed or minimally vegetated soil	85 92 -	1 8 -	High	High runoff, low retention, strong susceptibility to erosion
Pasture/ Grassland	Natural/managed grazing areas	65 80 -	8 30 -	Low to medium	Higher infiltration, moderate runoff, moderate soil protection
Shrubland/ Rangeland	Bushy and semi-woody vegetation	70 82 -	5 20 -	Medium	Moderate infiltration, reduced erosion compared to bare land
Forest patches	Localized wooded areas	55 70 -	20 50 -	Very low	High infiltration, excellent soil protection, recharge zones
Urban/Built-up	Residential, roads, infrastructure	90 95 -	0 (impervious)	Very low (sediment trapped), but high runoff concentration	Very low infiltration, fast runoff response, peak flow increase
River/Valley bottoms	Channel and riparian zones	Variable (lower)	High	Very low	Groundwater discharge - baseflow areas

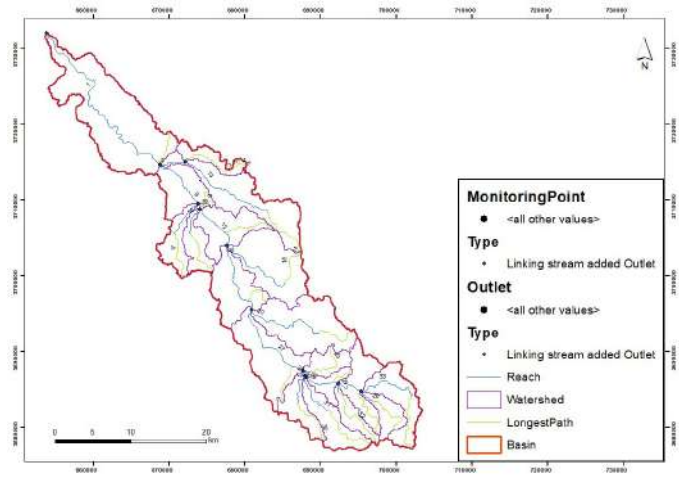


Fig. 6: Drainage network, watershed boundary, sub-basins, and longest flow path (LongestPath) of the Nfifikh watershed.

a descriptive background, it provides an analytical basis for linking mapped patterns to the spatial distribution of SWAT outputs at the HRU and sub-basin scales.

3.2. Surface and Groundwater Flow Dynamics in the Nfifikh Watershed Using the SWAT Model

Fig. 7 synthesizes the main components of the annual water balance simulated by the SWAT model for the Nfifikh watershed. The results depict a hydrological regime typical of semi-arid Mediterranean basins, characterized by strong evaporative demand and limited effective rainfall. Mean annual precipitation is approximately 420 mm, whereas potential evapotranspiration exceeds 1300 mm, indicating that water availability is primarily constrained by atmospheric demand rather than precipitation input. Similar hydro-climatic imbalances have been widely reported in semi-arid watersheds modeled using SWAT (Arnold et al. 1998, Moriasi et al. 2007).

Quantitative partitioning of rainfall reveals that evapotranspiration represents the dominant loss term, accounting for about 67% (280 mm) of annual precipitation (Table 4). This confirms that vegetation water use and soil evaporation are the primary controls of the basin water balance, as commonly observed in water-limited environments (Oki et al. 2001). Approximately 26% of precipitation (110 mm) contributes to streamflow generation,

which is further partitioned into surface runoff (55 mm), lateral subsurface flow (25 mm), and baseflow contribution from the shallow aquifer (30 mm).

The simulated recharge of approximately 70 mm/year represents percolation to the shallow aquifer storage conceptualized within SWAT. It is important to emphasize that this component does not represent physically explicit groundwater flow, but rather a simplified reservoir controlling delayed contributions to streamflow (Neitsch et al. 2005, Arnold et al. 2012). Similar conceptual interpretations of groundwater recharge have been adopted in semi-arid SWAT applications to avoid overestimation of subsurface processes (Abdalla 2009, Baalousha 2016).

Seasonal dynamics further highlight the basin's rapid hydrological response to intense rainfall events following prolonged dry periods. During autumn and winter storms, soil often exhibits reduced infiltration capacity due to antecedent moisture deficits and surface sealing, leading to a dominance of surface runoff on steep slopes. This mechanism produces short-lived but sharp flood peaks and promotes enhanced sediment mobilization, a behavior consistent with SWAT-based analyses in arid and semi-arid catchments (Dutta & Sen 2018, Prabhanjan et al. 2015).

In contrast, subsurface components play a regulatory role during dry periods. Baseflow contributions of approximately 30 mm/year persist throughout the summer months, sustained by gradual release from the shallow aquifer reservoir. The simulated upward capillary flux (25 mm/year) represents a conceptual soil–aquifer interaction within SWAT, whereby moisture is redistributed toward the root zone under high evaporative demand. This process should be interpreted as an internal soil–water balance adjustment rather than an explicit groundwater rise, as emphasized in previous modeling studies (Guzman et al. 2015).

Spatial aggregation of SWAT outputs reveals clear contrasts in flow pathways across the watershed

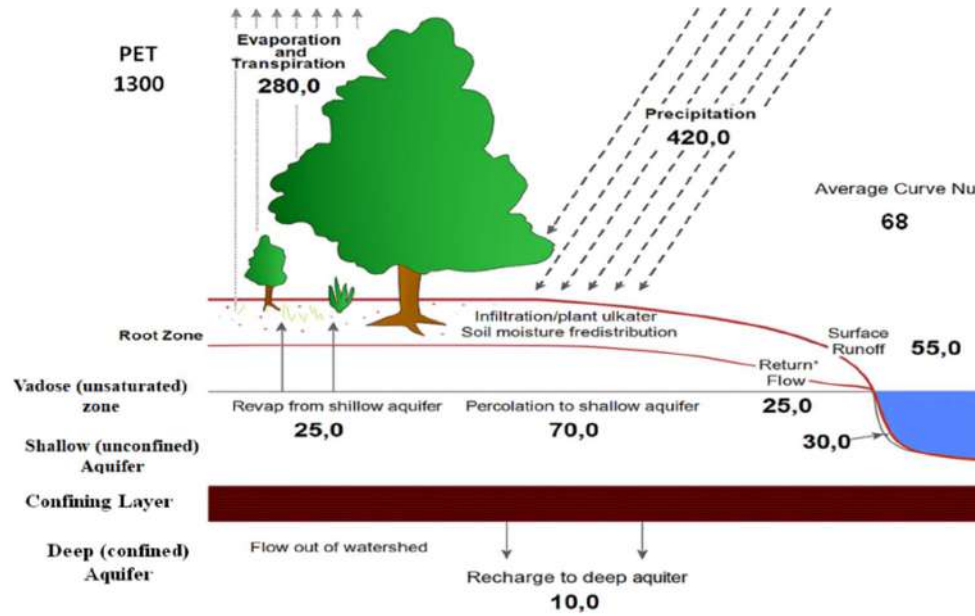


Fig. 7: Annual water balance of the Nfifikh watershed – Results of the SWAT model.

Table 4: Annual water balance components simulated by SWAT for the Nfifikh watershed.

Water balance component	Depth (mm/year)	Share of precipitation (%)
Precipitation	420	100
Actual evapotranspiration	280	67
Surface runoff (SURQ)	55	13
Lateral flow (LATQ)	25	6
Baseflow (GW_Q)	30	7
Shallow aquifer recharge (RECHRG)	70	17
Deep aquifer recharge	10	2

Table 5: Dominant flow pathways across major physiographic zones of the Nfifikh watershed.

Physiographic zone	Dominant slope class	Dominant flow component	Hydrological implication
Eastern and southeastern uplands	>15%	Surface runoff (SURQ)	Rapid response, high erosion sensitivity
Central sub-basins	5–15%	Mixed runoff and lateral flow	Transitional hydrological behavior
Northwestern lowlands and valleys	0–5%	Infiltration and baseflow	Flow attenuation, sustained discharge

(Table 5). Steep upland areas generate a disproportionate share of surface runoff, whereas downstream zones with gentler slopes and more permeable soils favor infiltration and baseflow contribution. Such differentiation reflects the combined influence of slope gradient, soil hydraulic properties, and land-use patterns on hydrological partitioning, consistent with conceptual frameworks underlying distributed watershed models (Arnold et al. 1998, Kaleris & Langousis 2017).

Overall, the simulated surface and subsurface flow dynamics reflect a system dominated by fast runoff generation during episodic rainfall events, coupled with limited but persistent subsurface storage that sustains low magnitude baseflow during dry periods. This dual behavior is characteristic of semi-arid Mediterranean watersheds and supports the interpretation of SWAT outputs as indicators of hydrological functioning rather than exact representations of physical groundwater processes (Abdalla 2009).

3.3. Sediment Budget and Surface Runoff Dynamics in the Nfifikh Watershed

The sediment budget simulated by the SWAT model provides a quantitative framework for analyzing the interaction between surface runoff generation and soil erosion processes within the Nfifikh watershed. In semi-arid basins, sediment dynamics are primarily driven by short-duration, high-intensity rainfall events that generate rapid surface runoff on steep and sparsely vegetated slopes (Dutta & Sen, 2018; Prabhanjan et al. 2015). This behavior is clearly reflected in the spatial distribution of sediment yield and runoff components shown in Fig. 8.

At the watershed scale, the mean annual surface runoff is approximately 55 mm, consistent with the runoff contribution identified in the overall water balance. Sediment yield values simulated by SWAT represent average HRU-level outputs aggregated to sub-basin and watershed scales, rather than point-scale erosion measurements. When expressed in standard SWAT units (t/ha/year), the highest erosion-prone HRUs in the upland sectors exhibit low-to-moderate sediment yields typical of semi-arid Mediterranean catchments, where limited rainfall frequency constrains total annual soil loss despite intense episodic events (Kumar et al. 2015; Dutta & Sen, 2018).

To complement the spatial patterns depicted in Fig. 8, sediment and runoff outputs were quantitatively aggregated according to dominant land-use categories (Table 6). This aggregation allows a clearer distinction between sediment source areas and zones of reduced transport capacity and facilitates direct comparison of hydrological responses across different land-use types. By summarizing HRU-level outputs at the land-use scale, the analysis strengthens the link between spatially explicit model results and their underlying controlling factors.

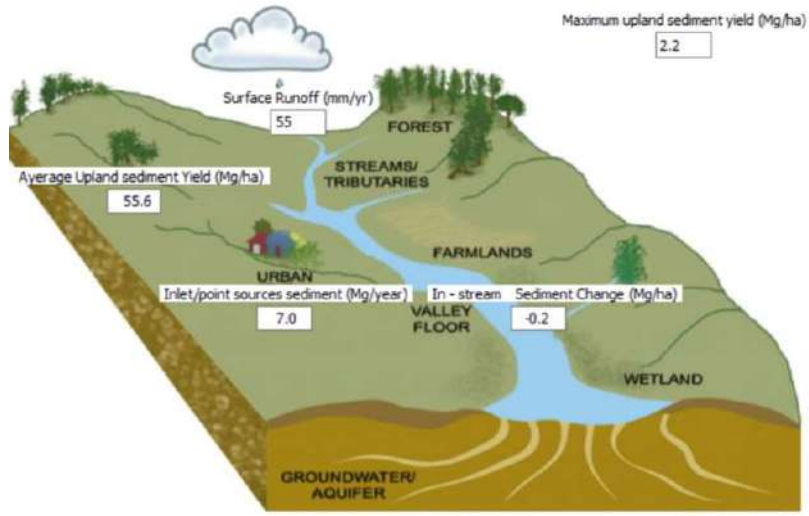


Fig. 8: Sediment balance and spatial distribution of surface runoff in the Nfifikh watershed - SWAT model results.

Table 6: Mean sediment yield and runoff characteristics by major land-use type in the Nfifikh watershed.

Land-use category	Dominant slope class	Mean surface runoff	Relative sediment yield	Sediment response
Rainfed cropland	515%< / 15%-	High	Moderate to high	Primary sediment source
Fallow/bare land	>15%	Very high	High	Strong erosion hotspot
Pasture/grassland	015%-5 / 5%-	Moderate	Low to moderate	Partial sediment retention
Forest patches	05%-	Low	Very low	Effective erosion control
Valley floor/channel	05%-	Low	Negative or near-zero	Net sediment deposition

Spatial analysis of Fig. 8 highlights a clear differentiation between sediment source areas and sediment storage zones. The eastern and southeastern uplands emerge as the dominant sediment-generating regions, where steep slopes, fine-textured soils, and intensive agricultural land use promote rapid runoff concentration and soil detachment. Similar spatial patterns have been documented in SWAT-based erosion studies conducted in arid and semi-arid environments, where slope gradient and land-cover disturbance jointly control sediment mobilization (Kumar et al. 2015, Dutta & Sen 2018).

In contrast, mid-basin sectors characterized by gentler slopes and increased vegetation cover exhibit reduced sediment production and enhanced infiltration. These areas function as transitional zones where a portion of the eroded material is temporarily stored or redeposited before reaching the main channel. Forested and pasture-dominated HRUs act as effective sediment buffers, reducing transport capacity and limiting downstream sediment transfer, consistent with findings reported in distributed watershed modeling studies (Prabhanjan et al. 2015, Moriasi et al. 2007).

Channel and valley-floor environments represent the terminal component of the sediment budget. Slightly negative sediment balances simulated within the main channel reflect net deposition rather than active erosion, indicating that a substantial fraction of the sediment mobilized from upland areas is retained within alluvial reaches and riparian zones. This depositional behavior is a common feature of semi-arid drainage networks, where declining slope gradients and reduced flow energy favor sediment storage downstream (Kumar et al. 2015).

To further clarify the spatial organization of sediment processes across the watershed, sub-basin-scale sediment balances were grouped into major physiographic zones. This zonal classification (Table 7) highlights the transition from sediment-producing upland areas to downstream deposition zones and provides a simplified yet robust framework for interpreting sediment routing and storage within the drainage network.

Overall, the sediment budget analysis confirms a strong spatial gradient in erosion and deposition processes across the Nfifikh watershed. Surface runoff generated on steep upland slopes acts as the primary driver of sediment mobilization, while downstream zones progressively attenuate sediment transport through deposition and storage. These results underscore the necessity of spatially differentiated management strategies, prioritizing erosion control and runoff reduction in upland agricultural areas, while preserving and enhancing natural sediment retention functions in downstream valleys. Such an approach aligns with best practices derived from SWAT-based sediment management studies in semi-arid watersheds (Dutta & Sen 2018, Prabhanjan et al. 2015).

3.4. Daily Flow Dynamics and Model Performance in the Nfifikh Watershed

Daily streamflow simulations were evaluated against observed discharge records to assess the ability of the SWAT model to reproduce short-term hydrological variability in the Nfifikh watershed. The analysis covered the 2008–2012 period and explicitly distinguished between calibration and validation phases to test the temporal robustness of the model under contrasting hydro-climatic conditions. Model performance was assessed using complementary statistical indicators, including the Nash–Sutcliffe efficiency (NSE), coefficient of determination (R^2), percent bias (PBIAS), and the RMSE–standard deviation ratio (RSR), following established evaluation guidelines for watershed-scale models (Moriasi et al. 2007).

Fig. 9 compares observed and simulated daily discharge together with corresponding precipitation inputs. The

Table 7: Spatial differentiation of sediment source and sink zones in the Nfifikh watershed.

Basin sector	Dominant process	Sediment balance	Geomorphic implication
Upland slopes (E-SE)	Detachment and transport	Positive	Primary sediment source
Mid-basin reaches	Partial deposition	Near neutral	Temporary storage and buffering
Valley floor and channel	Deposition	Negative	Long-term sediment retention

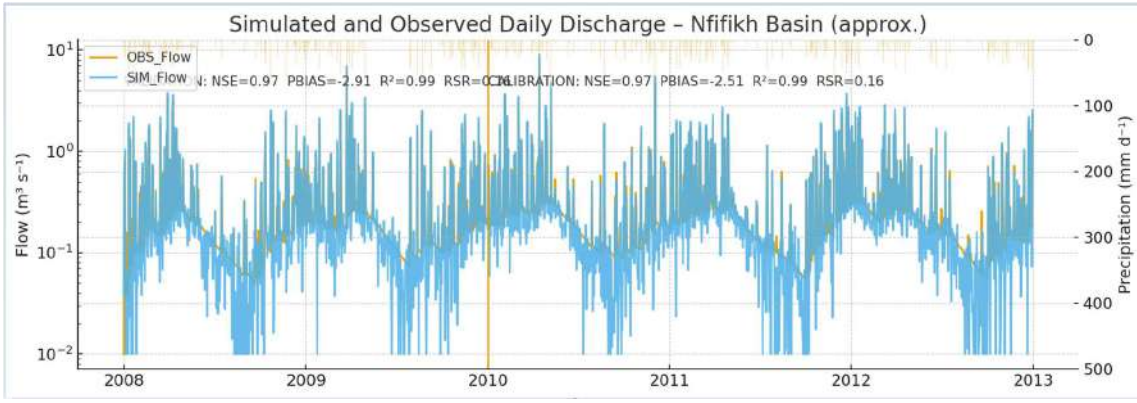


Fig. 9: Observed and simulated daily flow as a function of precipitation in the Nfifikh watershed (2008-2012; calibration and validation periods).

hydrograph reveals a typical semi-arid flow regime characterized by sharp discharge peaks in response to intense autumn and winter rainfall events, followed by extended low-flow periods during summer. The SWAT model satisfactorily reproduces the timing and magnitude of most peak flows, as well as the recession behavior following storm events. Minor discrepancies are mainly associated with a limited number of high-flow events, during which simulated peaks tend to be slightly underestimated, a behavior commonly reported in distributed hydrological models applied to semi-arid basins.

Beyond peak-flow simulation, the model captures the persistence of low but continuous discharge during dry periods, reflecting delayed contributions from shallow subsurface storage conceptualized within the SWAT framework. This representation supports a realistic simulation of baseflow recession without explicitly modeling physically based groundwater flow, in line with the conceptual structure of the model (Arnold et al. 1998, Neitsch et al. 2005).

Quantitative performance statistics for daily streamflow simulation are summarized in Table 8. During the calibration period, the model achieved very high performance, with NSE and R^2 values of 0.97 and 0.99, respectively, indicating excellent agreement between observed and simulated discharge. Validation results remain robust, with NSE = 0.91 and R^2 = 0.94, demonstrating that the model retains predictive skill under independent conditions. PBIAS values of −3.5% for calibration and −6.8% for validation indicate a slight tendency toward underestimation of streamflow volumes, while RSR values below 0.5 confirm low residual variance relative to observed variability.

Table 8: Performance statistics for daily streamflow simulation during calibration and validation periods.

Period	NSE	R^2	PBIAS (%)	RSR
Calibration	0.97	0.99	3.5-	0.28
Validation	0.91	0.94	6.8-	0.41

According to the performance classification proposed by Moriasi et al. (2007), these statistics correspond to very good model performance at the daily time scale for both calibration and validation periods. Nevertheless, the exceptionally high efficiency values should be interpreted with caution. In small to medium-sized semi-arid watersheds, strong seasonality and a limited number of dominant runoff events can lead to high performance metrics without implying perfect representation of all internal hydrological processes. This behavior is consistent with the concept of equifinality, whereby different parameter combinations may yield similarly good model performance. Monthly calibration results (not shown) were consistent with the daily-scale performance presented here, indicating that the calibrated parameter set remains robust across temporal aggregation levels.

Overall, the daily flow evaluation confirms that the SWAT model provides a reliable representation of streamflow variability at the watershed outlet. When interpreted within its conceptual framework and associated uncertainties, the model outputs offer a sound basis for subsequent analyses of runoff generation, sediment dynamics, and management scenarios in the Nfifikh watershed.

4. DISCUSSION

The hydrological behavior simulated for the Nfifikh watershed reflects the fundamental functioning of semi-arid Mediterranean basins, where limited and irregular precipitation is strongly constrained by high evaporative demand. The dominance of evapotranspiration over runoff and recharge confirms that water availability is primarily controlled by atmospheric demand rather than rainfall input, a pattern widely reported in SWAT-based studies conducted in arid and semi-arid environments (Arnold et al. 1998, Oki et al. 2001). Within this context, the spatial differentiation between rapid runoff generation on steep upland slopes and delayed subsurface contributions in lower valley areas

provides a coherent explanation for the observed flow regime at the basin outlet.

The partitioning of streamflow into surface runoff, lateral flow, and baseflow highlights the dual nature of hydrological response in the basin. Short-duration, high-intensity rainfall events generate rapid surface runoff on sloping and sparsely vegetated areas, while shallow subsurface storage sustains low but persistent baseflow during dry periods. This coexistence of fast and slow flow pathways is consistent with conceptual representations of watershed processes in distributed hydrological models, where shallow aquifer storage acts as a buffering reservoir rather than a physically explicit groundwater system (Neitsch et al. 2005, Arnold et al. 2012). Similar interpretations have been emphasized in semi-arid applications to avoid overestimation of groundwater dynamics derived from conceptual recharge terms (Abdalla 2009, Baalousha 2016).

Sediment dynamics further reinforce the strong coupling between runoff generation, slope gradient, and land-use distribution. The identification of upland agricultural and bare-soil areas as primary sediment source zones, contrasted with downstream deposition and retention in valley floors and channels, aligns with findings from SWAT-based erosion studies in data-scarce and semi-arid catchments (Prabhanjan et al. 2015, Kumar et al. 2015, Dutta & Sen 2018). The spatial separation between sediment-producing and sediment-storing zones suggests that a substantial fraction of eroded material is internally redistributed within the basin, rather than exported downstream, a behavior commonly observed in Mediterranean drainage systems with pronounced relief and episodic runoff.

The very good model performance achieved at both daily and aggregated temporal scales supports the reliability of the simulated hydrological patterns. Nevertheless, the exceptionally high efficiency values should be interpreted cautiously. In small to medium-sized watersheds characterized by strong seasonality and a limited number of dominant runoff events, high NSE and R^2 values may arise even under parameter uncertainty. This phenomenon is consistent with the concept of equifinality, whereby multiple parameter sets can yield similar model performance without uniquely identifying internal process representations (Moriasi et al. 2007). Consequently, the results should be interpreted as robust indicators of basin-scale behavior rather than exact representations of all internal hydrological fluxes.

Several sources of uncertainty remain inherent to the modeling framework. The integration of station-based observations with gridded climate products introduces potential bias during extreme rainfall events that disproportionately influence runoff and sediment generation. Likewise, the use of a 30-m DEM may smooth micro-topographic features that locally control flow concentration and erosion pathways. Uncertainties related to soil and land-use classification, particularly in transitional agricultural and peri-urban areas, further affect HRU parameterization and sediment estimates. These limitations are common to distributed watershed modeling and have been widely documented in SWAT applications (Cibin et al. 2010, Muleta & Nicklow 2005).

From a management perspective, the results emphasize the need for spatially differentiated interventions rather than uniform basin-wide measures. Upland areas identified as runoff and sediment source zones represent priority targets for soil conservation practices, such as erosion control, improved land management, and vegetation restoration, which have been shown to effectively reduce sediment yields in similar SWAT-based studies (Kumar et al. 2015, Dutta & Sen 2018). Conversely, downstream valley floors and riparian corridors should be preserved as natural retention and buffering zones, as their degradation could substantially increase sediment export and flood risk.

Overall, this study demonstrates the value of distributed hydrological modeling for disentangling the spatial organization of runoff, sediment transport, and subsurface storage in semi-arid watersheds. While the SWAT model remains a conceptual representation of complex hydrological processes, its application to the Nfifikh watershed provides a coherent and policy-relevant framework for understanding hydrological functioning and supporting land and water management strategies. Future research should prioritize higher-resolution topographic data, improved soil and land-use characterization, and the coupling of SWAT with physically based groundwater or sediment transport models to further refine surface–subsurface interaction analysis in similar Moroccan basins (Guzman et al. 2015, Sabale et al. 2024).

5. CONCLUSIONS

This study implemented the SWAT model to provide a spatially explicit assessment of runoff, subsurface flow, and sediment dynamics in the Nfifikh watershed. By integrating topographic, soil, land-use, and climate data, the modeling framework successfully characterized the main hydrological components governing water and sediment redistribution at the watershed scale.

The results deliver a consistent depiction of hydrological functioning under semi-arid conditions and identify priority zones controlling runoff production, sediment generation, and subsurface contribution. These spatial insights offer a practical basis for supporting watershed management,

particularly in targeting erosion-prone areas and safeguarding zones that contribute to flow regulation and storage.

Beyond the specific case study, this work demonstrates the applicability of distributed hydrological modeling as a decision-support tool in data-scarce semi-arid basins. Future developments should focus on enhancing data resolution and model coupling to further strengthen predictive capability and support long-term land and water planning.

6. REFERENCES

Abdalla, O.A.E., 2009. Groundwater modeling in semiarid central Sudan: adequacy and long-term abstraction. *Arabian Journal of Geosciences*, 2(4), pp.321–335. [DOI]

Abbaspour, K.C., Vaghefi, S.A. and Srinivasan, R., 2018. A guideline for successful calibration and uncertainty analysis for soil and water assessment: a review of papers from the 2016 International SWAT Conference. *Water*, 10(1), p.6. [DOI]

Almeida, R.A., Pereira, S.B. and Pinto, D.B.F., 2018. Calibration and validation of the SWAT hydrological model for the Mucuri River Basin. *Engenharia Agrícola*, 38(1), pp.55–63. [DOI]

Arnold, J.G., Srinivasan, R., Muttiah, R.S. and Williams, J.R., 1998. Large area hydrologic modeling and assessment part I: model development. *Journal of the American Water Resources Association*, 34(1), pp.73–89. [DOI]

Arnold, J.G., Moriasi, D.N., Gassman, P.W., Abbaspour, K.C., White, M.J., Srinivasan, R., Santhi, C., Harmel, R.D., Van Griensven, A., Van Liew, M.W., Kannan, N. and Jha, M.K., 2012. SWAT: model use, calibration, and validation. *Transactions of the ASABE*, 55(4), pp.1491–1508. [DOI]

Baalousha, H.M., 2016. Development of a groundwater flow model for the highly parameterized Qatar aquifers. *Modeling Earth Systems and Environment*, 2, Article 67. [DOI]

Bressiani, D.A., Gassman, P.W., Fernandes, J.G., Garbossa, L.H.P., Srinivasan, R., Bonumá, N.B. and Mendiondo, E.M., 2015. Review of Soil and Water Assessment Tool (SWAT) applications in Brazil: challenges and prospects. *International Journal of Agricultural and Biological Engineering*, 8(3), pp.9–35. [DOI]

Cibin, R., Sudheer, K.P. and Chaubey, I., 2010. Sensitivity and identifiability of stream flow generation parameters of the SWAT model. *Hydrological Processes*, 24(9), pp.1133–1148. [DOI]

Dutta, S. and Sen, D., 2018. Application of SWAT model for predicting soil erosion and sediment yield. *Sustainable Water Resources Management*, 4(3), pp.447–468. [DOI]

Eini, M.R., Massari, C. and Piniewski, M., 2023. Satellite-based soil moisture enhances the reliability of agro-hydrological modeling in large transboundary river basins. *Science of the Total Environment*, 873, 162396. [DOI]

Gassman, P.W., Sadeghi, A.M. and Srinivasan, R., 2014. Applications of the SWAT model special section: overview and insights. *Journal of Environmental Quality*, 43(1), pp.1–8. [DOI]

Guzman, J.A., Moriasi, D.N., Gowda, P.H., Steiner, J.L., Starks, P.J., Arnold, J.G. and Srinivasan, R., 2015. A model integration framework for linking SWAT and MODFLOW. *Environmental Modelling & Software*, 73, pp.103–116. [DOI]

Kaleris, V. and Langousis, A., 2017. Comparison of two rainfall–runoff models: effects of conceptualization on water budget components. *Hydrological Sciences Journal*, 62(5), pp.729–748. [DOI]

Kumar, S., Raghuwanshi, N.S. and Mishra, A., 2015. Identification and management of critical erosion watersheds for improving reservoir life using hydrological modeling. *Sustainable Water Resources Management*, 1(1), pp.57–70. [DOI]

Meaurio, M., Zabaleta, A., Uriarte, J.A., Srinivasan, R. and Antigüedad, I., 2015. Evaluation of SWAT model performance to simulate streamflow spatial origin. *Journal of Hydrology*, 525, pp.326–334. [DOI]

Moriasi, D.N., Arnold, J.G., Van Liew, M.W., Bingner, R.L., Harmel, R.D. and Veith, T.L., 2007. Model evaluation guidelines for systematic quantification of accuracy in watershed simulations. *Transactions of the ASABE*, 50(3), pp.885–900. [DOI]

Muleta, M.K. and Nicklow, J.W., 2005. Decision support for watershed management using evolutionary algorithms. *Journal of Water Resources Planning and Management*, 131(1), pp.35–44. [DOI]

Neitsch, S.L., Arnold, J.G., Kiniry, J.R. and Williams, J.R., 2005. *Soil and Water Assessment Tool Theoretical Documentation Version 2005*. Texas Water Resources Institute. Available at: https://swat.tamu.edu/documentation/ (Accessed: 2024).

Neitsch, S.L., Arnold, J.G., Kiniry, J.R. and Williams, J.R., 2011. *Soil and Water Assessment Tool Theoretical Documentation Version 2009*. Texas Water Resources Institute, Texas A&M University. Available at: https://swat.tamu.edu/docs/ (Accessed: 2024).

Oki, T., Agata, Y., Kanae, S., Saruhashi, T., Yang, D. and Musiake, K., 2001. Assessment of global water resources using integrative total flow paths. *Hydrological Sciences Journal*, 46(6), pp.983–995. [DOI]

Prabhanjan, A., Rao, E.P. and Eldho, T.I., 2015. Application of SWAT model and geospatial techniques for sediment-yield modeling in ungauged watersheds. *Journal of Hydrologic Engineering*, 20(6), 04014076. [DOI]

Sabale, R.S., Bobade, S.S., Venkatesh, B. and Jose, M.K., 2024. Application of Arc-SWAT model for water budgeting and water resource planning at the Yeralwadi catchment of Khatav, India. *Nature Environment and Pollution Technology*, 23(1), pp.203–213. [DOI]

Samimi, M., Mirchi, A., Moriasi, D.N., Ahn, S., Alian, S., Taghvaeian, S. and Sheng, Z., 2020. Modeling arid/semi-arid irrigated agricultural watersheds with SWAT: applications, challenges, and solution strategies. *Journal of Hydrology*, 590, 125418. [DOI]

Zhao, J., Zhang, N., Liu, Z., Zhang, Q. and Shang, C., 2024. SWAT model applications: from hydrological processes to ecosystem services. *Science of the Total Environment*, 931, 172605. [DOI]

Nature Environment and Pollution Technology
An International Quarterly Scientific Journal

p-ISSN: 0972-6268
(Print copies up to 2016)
e-ISSN: 2395-3454

Vol. 25 | No. 3 | Article ID B4408 | 2026

Original Research Paper

https://doi.org/10.46488/NEPT.2026.v25i03.B4408

Open Access Journal

Data-Driven Machine Learning Models for Predicting Monthly Rainfall Using Lagged Climate Indices

Ayush Vashisth†, Mohammed Sharif and Mohammed Shakeel
Department of Civil Engineering, Jamia Millia Islamia, New Delhi-110025, India
†Corresponding author: Ayush Vashisth; ayushvashisth90@gmail.com

Abbreviation: Nat. Env. & Poll. Technol.
Website: www.neptjournal.com

Received: 26-10-2025
Revised: 28-11-2025
Accepted: 01-12-2025

Key Words:

Machine learning
Rainfall prediction
Lagged climate indices
AAN-based model

ABSTRACT

Rainfall prediction is vital for several economic activities, including agriculture. The present study is focused on developing machine learning models to predict rainfall using different climate indices. Four machine learning techniques - RF, M5P tree, REP Tree algorithm, and ANN were used for predicting rainfall from climate indices. The practicality of the approach presented herein was demonstrated through application to rainfall data at the Safdarjung meteorological station in New Delhi, India. The machine learning models use climate indices-Indian Ocean Dipole, El Niño–Southern Oscillation, Pacific Decadal Oscillation, Atlantic Multidecadal Oscillation, and North Atlantic Oscillation as feature variables and rainfall as the target variable. The dataset was divided into a training set and a testing set. The ratio of the split was eighty to twenty. Among the four machine learning models evaluated, the random forest model demonstrates the best performance, with coefficients of correlation of 0.9853 and 0.6674, mean absolute errors of 15.1624 and 33.7026, and root mean square errors of 25.1173 and 44.0744 for training and testing phases, respectively. The Taylor diagram also showed that the RF-based model performed better at predicting rainfall.

1. INTRODUCTION

Rainfall is a crucial atmospheric parameter that plays a fundamental role in the water cycle, influencing the availability and distribution of freshwater resources globally. Excessive rainfall leads to severe weather events like catastrophic floods or prolonged drought. These extreme weather conditions disrupt daily life and cause substantial socioeconomic losses, including damage to infrastructure, reduced agricultural yields, and heightened food insecurity. There is a heavy reliance on rainfall, given that in an agricultural country like India, where 65% of India's agricultural land is, the industry is extremely susceptible to changes in rainfall. Accurate rainfall forecasting is needed for agricultural planning and water resource management. However, rainfall is still a significant scientific difficulty because of its stochastic character. Enhancing the precision of rainfall forecasts is crucial for maintaining food security, economic stability, and sustainable development, especially in regions where agriculture forms the backbone of the economy. (Abbot et al. 2014, Kashid et al.2012, Khan et al.2020).

Precipitation of large-scale climate predictors is essential for effective water resource management. ENSO indices with trade wind indicators strongly influence rainfall. SST predictors are often inversely related to seasonal precipitation, and basin-specific climate indices models improve forecast accuracy at longer lead times. (Dhillon et al. 2023, Asakereh 2020, Saji et al. 1999, Luo et al. 2017).

Numerical models use wind patterns, cloud formation, and moisture content. Although the models give accurate depictions of the climate system, they are frequently constrained by the intricacy of atmospheric dynamics, model structure, and parameter uncertainty. (Choubin et al. 2018). Alternatively, empirical models

Citation for the Paper:

Vashisth, A., Sharif, M. and Shakeel, M., 2026. Data-driven machine learning models for predicting monthly rainfall using lagged climate indices. *Nature Environment and Pollution Technology*, 25(3), p. B4408. https://doi.org/10.46488/NEPT.2026.v25i03.B4408

Note: From 2025, the journal has adopted the use of Article IDs in citations instead of traditional consecutive page numbers. Each article is now given individual page ranges starting from page 1.

Copyright: © 2026 by the authors
Licensee: Technoscience Publications
This article is an open access article distributed under the terms and conditions of the Creative Commons Attribution (CC BY) license (https://creativecommons.org/licenses/by/4.0/).

have become well known for their capacity to produce precise projections, especially in areas where uncertainties may make physical-based models unreliable. To determine correlations between weather patterns and projected precipitation, these models use statistical methods. Artificial neural networks (ANNs) and multiple linear regressions (MLRs) are two machine learning models that have demonstrated a great deal of promise in raising the accuracy of rainfall forecasting. The ANNs are especially good at managing complicated climatic systems because they can capture non-linear interactions (Haykin 2009). The precision of rainfall forecasts helped to improve resource management and agricultural planning. RF models often outperform LS-SVM and M5P in terms of efficiency and lower errors. (Pandhiani et al. 2020, Wani et al. 2024, Shankar 2024).

Naved et al. (2024) concluded that laboratory tests to predict the strength of concrete would be significantly reduced by optimal DNN models. Asim et al. (2022) highlight the significance of hyperparameter optimization. To improve predicted accuracy, scientists used a methodical methodology to adjust the DNN's architecture, neurons in each layer, activation functions, and learning rates.

Additionally, incorporating large-scale climatic indices like IOD, PDO, AMO, ENSO and NAO into forecasting systems has the potential to significantly improve prediction accuracy, as these teleconnection patterns. (Enfield et al. 2001, Feng et al. 2020, Mantua et al. 1997, Sham et al. 2025). The advanced forecasting methodologies are essential for supporting sustainable development and resilience to climate variability, particularly in regions where rainfall directly impacts agricultural productivity.

Most existing studies concentrate on correlations and climate indices, often overlooking the importance of lagged effects, nonlinear relationships, and interactions among multiple indices. Additionally, predictive models rarely incorporate a systematic examination of lag structures and temporal dynamics, which are essential for capturing delayed teleconnection patterns.

The present research aims to evaluate the performance of multiple machine learning models, including tree-based models, such as the RF, M5P tree, REPTree, and ANN, for multi-step rainfall prediction based on climate indices. This research is significant to improve the precision of rainfall prediction, which is critical for agricultural, water resource management, and disaster preparedness, especially in rainfall-dependent areas for agricultural activities.

2. MATERIALS AND METHODS

This study employs a two-step methodology. The first step involves the collection of rainfall data and large-scale climate indices. The Safdarjung is located in central Delhi, the capital of India. The station is operated by the Indian Meteorological Department (IMD) and serves as one of the key observatories for meteorological data collection in the region. The geographical coordinates of the station are approximately 28.585° N latitude and 77.221° E longitude. Monthly datasets of climatic indices and their respective data sources are provided in Table 1.

In the second step, machine learning models, including RF, M5P tree, REPTree and ANN, were trained using lagged climate indices as input variables and rainfall as the target variable. Once trained, these models were utilized to predict rainfall using the values of climate indices and performance indicators; the most efficient machine learning model was identified.

2.1. Performance Metrics

2.1.1. Mean Absolute Error

Mean Absolute Error (MAE) measures how well a regression model performs. This calculation does not consider the direction of the differences.

$$MAE = \frac{1}{N}\sum_{i=1}^{N}|PR_i - OR_i| \quad ...(1)$$

2.1.2. Root Mean Square Error

RMSE shows how well regression models work - it calculates how much the prediction mistakes differ on average. But it weighs big mistakes more than MAE because it squares the differences. RMSE punishes big mistakes more than small ones.

$$RMSE = \sqrt{\frac{1}{N}\sum_{i=1}^{N}(PR_i - OR_i)^2} \quad ...(2)$$

2.1.3 Correlation Coefficient (R)

In the context of machine learning, it is used to evaluate how well it behaves.

$$R = \frac{\sum_{i=1}^{N}\left(PR_i - \underline{OR}\right)(OR_i - \underline{OR})}{\sqrt{\sum_{i=1}^{N}(PR_i - \underline{OR})^2 \sum_{i=1}^{N}(OR_i - \underline{OR})^2}} \quad ...(3)$$

Scattering index (SI): $SI = \frac{RMSE}{\underline{OR}}$ ...(4)

2.2. Machine Learning Models

2.2.1. M5P Model Tree

This Model was first introduced by Quinlan (1992), showing a large step forward in predictive modeling. This approach utilizes a binary decision tree structure in which the terminal

Table 1: Sources of climate indices and rainfall data.

S.No.	Feature Variable	Source	Reference
1.	Indian Ocean Dipole	https://psl.noaa.gov/gcos_wgsp/Timeseries/Data/dmi.had.long.data	Saji et al. (1999)
2.	El Niño-Southern Oscillation	https://www.cpc.ncep.noaa.gov/data/indices/sstoi.indices	Trenberth and Hoar (1997)
3.	Pacific Decadal Oscillation	https://psl.noaa.gov/data/correlation/pdo.data	Mantua et al. (1997)
4.	Atlantic Multidecadal Oscillation	https://psl.noaa.gov/data/correlation/amon.us.data	Enfield et al. (2001)
5.	North Atlantic Oscillation	https://psl.noaa.gov/data/correlation/nao.data	Hurrell (1995)
6.	Rainfall	https://imdpune.gov.in/cmpg/Griddata/Rainfall_25_Bin.html	Pai et al. (2014)

nodes, or leaves, contain linear regression functions. By integrating decision trees with linear regression, the M5P model effectively addresses nonlinear problems while maintaining interpretability and flexibility. The splitting of nodes is guided by error reduction, measured using the variance of class values at each node.

2.2.2. Artificial Neural Networks (ANN)

It is used to solve a specific set of closely interrelated functioning components called neurons that operate in parallel. After adequate calibration, the neural network can anticipate the output configuration and identify similarities when given a fresh input configuration. Even if a certain input has never been known before, neural networks may recognize connections in inputs. (Abebe et al.2023, Mokhtarzad et al. 2017, Sihag 2018)

2.2.3. Reduced Error Pruning Tree (REP Tree)

It is designed to build a decision tree model that is both effective and interpretable, addressing common challenges like overfitting that can arise in tree-based models. The process begins with the construction of a decision tree using a greedy algorithm. These iterative criteria are met, such as a minimum number of instances in a node or a maximum tree depth. The Reduced Error Pruning Tree model randomly selects features to enhance the efficiency of regression tree algorithms and reduce variance-related errors. It combines logistic regression with multiple tree constructions, selecting the simplest tree that maintains predictive accuracy. In the training dataset, a flexible yet straightforward modeling approach is applied to a post-pruning algorithm to remove unnecessary nodes, minimizing tree complexity while preserving accuracy. The model is intuitive, fast, and improves generalization, but it relies on a validation set, is sensitive to data noise, and uses a greedy algorithm that may lead to suboptimal decisions.

2.2.4. Random Forest (RF)

An ensemble of randomized regression trees is a widely used technique for both classification and regression tasks.

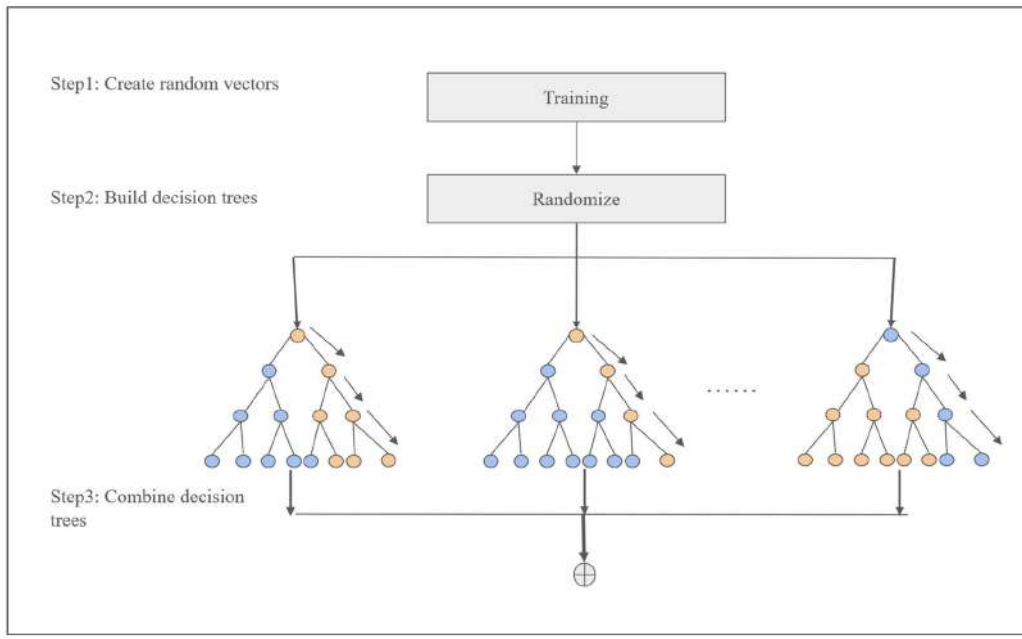


Fig. 1: RF model development steps.

It constructs an ensemble model that consists of decision trees, each trained on a different subset of data, to improve prediction accuracy. In this model, numerical features are randomly assigned to class labels, while in regression, each tree grows using a randomly selected subset of input parameters at every node (see Fig. 1). Random Forest overcomes this limitation, offering robust predictive performance, computational efficiency, and scalability. The aggregating individual tree predictions. In a single decision tree, sensitivity to small changes in training data often results in high variance and lower accuracy (Breiman 1999).

2.3. Model Runs

The correlation coefficients between different climate indices and rainfall provide valuable insights into their interrelationships and potential influences on precipitation patterns. AMO exhibits the highest positive correlation with rainfall (0.10), suggesting that while the relationship is weak, AMO may still have a subtle yet consistent influence on rainfall variability. This indicates its potential as a supporting predictor in long-term forecasting models. Similarly, PDO (0.07) and NAO (0.06) show modest positive correlations, highlighting their role in shaping regional precipitation trends. Although their individual impact may not be dominant, their combined effects could enhance predictive accuracy when incorporated into advanced models. The correlation between Niño 3.4 and rainfall (-0.04) appears negligible in Fig. 2. However, considering ENSO's well-established influence on global weather patterns, further investigations into lagged effects could provide deeper insights, as climate indices often exhibit delayed impacts on regional rainfall patterns due to ocean-atmosphere interactions. The near-zero correlation of IOD with rainfall implies minimal direct influence, but given its dynamic nature, future research incorporating time-lagged relationships could uncover hidden dependencies, capturing the delayed response of rainfall to changes in climate indices.

Although the correlation matrix indicates weak linear links between rainfall and climate indices, it reflects only direct pairwise relationships. The models can still achieve high predictive accuracy by capturing nonlinear patterns, lagged effects, and interactions among multiple indices that are not visible in simple correlations.

Thirteen models (N1-N13) were developed using different combinations of monthly rainfall, climate indices, and their lagged values to predict rainfall at Safdarjung, Delhi, India. The specific input variables incorporated in each model are summarized in Table 2.

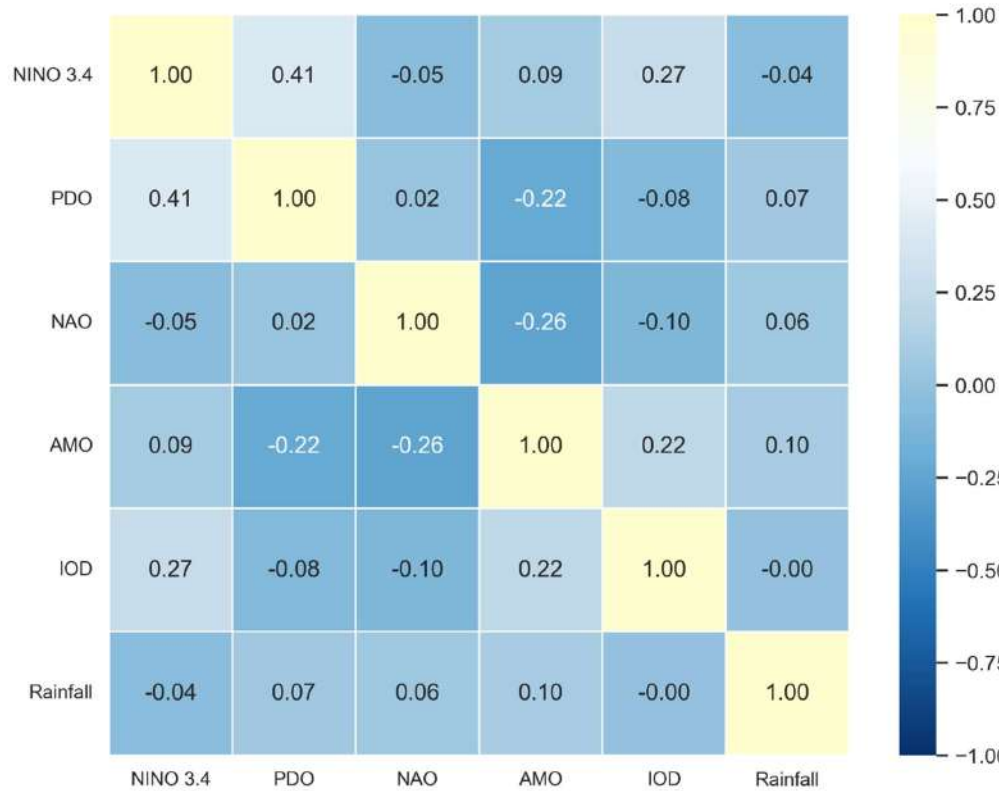


Fig. 2: Correlation matrix plot among inputs and output variables.

Table 2: Input variables incorporated in each model of climate indices and rainfall.

Model	Input Combination
N1	NI(t-1), PD(t-1), NAO (t-1), AMO(t-1), IOD(t-1), R(t-1)
N2	NI(t-2), NI(t-1), NAO (t-2), NAO (t-1), PD(t-2), PD(t-1), AMO(t-2), AMO(t-1), IOD(t-2), IOD(t-1), R(t-2), R(t-1)
N3	NI(t-3),NI(t-2),NI(t-1),NAO (t-3),NAO (t-2),NAO (t-1),PD(t-3), PD(t-2),PD(t-1),AMO(t-3),AMO(t-2), AMO(t-1),IOD(t-3),IOD(t-2), IOD(t-1),R(t-3), R(t-2),R(t-1)
N4	NI(t-3),NI(t-2),NI(t-1),NAO (t-3),NAO (t-2),NAO (t-1),PD(t-3), PD(t-2),PD(t-1),AMO(t-3),AMO(t-2), AMO(t-1),IOD(t-3),IOD(t-2), IOD(t-1),R(t-3), R(t-2),R(t-1),R(t-4)
N5	NI(t-3),NI(t-2),NI(t-1),NAO (t-3),NAO (t-2),NAO (t-1),PD(t-3), PD(t-2),PD(t-1),AMO(t-3),AMO(t-2), AMO(t-1),IOD(t-3),IOD(t-2), IOD(t-1),R(t-3), R(t-2),R(t-1),R(t-4), R(t-5)
N6	NI(t-3),NI(t-2),NI(t-1),NAO (t-3),NAO (t-2),NAO (t-1),PD(t-3), PD(t-2),PD(t-1),AMO(t-3),AMO(t-2), AMO(t-1),IOD(t-3),IOD(t-2), IOD(t-1),R(t-3), R(t-2),R(t-1),R(t-4), R(t-5),R(t-6)
N7	NI(t-3),NI(t-2),NI(t-1),NAO (t-3),NAO (t-2),NAO (t-1),PD(t-3), PD(t-2),PD(t-1),AMO(t-3),AMO(t-2), AMO(t-1),IOD(t-3),IOD(t-2), IOD(t-1),R(t-3), R(t-2),R(t-1),R(t-4), R(t-5), R(t-6), R(t-7)
N8	NI(t-3),NI(t-2),NI(t-1),NAO (t-3),NAO (t-2),NAO (t-1),PD(t-3), PD(t-2),PD(t-1),AMO(t-3),AMO(t-2), AMO(t-1),IOD(t-3),IOD(t-2), IOD(t-1),R(t-3), R(t-2),R(t-1),R(t-4), R(t-5), R(t-6), R(t-7), R(t-8)
N9	NI(t-3),NI(t-2),NI(t-1),NAO (t-3),NAO (t-2),NAO (t-1),PD(t-3), PD(t-2),PD(t-1),AMO(t-3),AMO(t-2), AMO(t-1),IOD(t-3),IOD(t-2), IOD(t-1),R(t-3), R(t-2),R(t-1),R(t-4), R(t-5), R(t-6), R(t-7), R(t-8), R(t-9)
N10	NI(t-3),NI(t-2),NI(t-1),NAO (t-3),NAO (t-2),NAO (t-1),PD(t-3), PD(t-2),PD(t-1),AMO(t-3),AMO(t-2), AMO(t-1),IOD(t-3),IOD(t-2), IOD(t-1),R(t-3), R(t-2),R(t-1),R(t-4), R(t-5), R(t-6), R(t-7), R(t-8), R(t-9), R(t-10)
N11	NI(t-3),NI(t-2),NI(t-1),NAO (t-3),NAO (t-2),NAO (t-1),PD(t-3), PD(t-2),PD(t-1),AMO(t-3),AMO(t-2), AMO(t-1),IOD(t-3),IOD(t-2), IOD(t-1),R(t-3), R(t-2),R(t-1),R(t-4), R(t-5), R(t-6), R(t-7), R(t-8), R(t-9), R(t-10), R(t-11)
N12	NI(t-3),NI(t-2),NI(t-1),NAO (t-3),NAO (t-2),NAO (t-1),PD(t-3), PD(t-2),PD(t-1),AMO(t-3),AMO(t-2), AMO(t-1),IOD(t-3),IOD(t-2), IOD(t-1),R(t-3), R(t-2),R(t-1),R(t-4), R(t-5), R(t-6), R(t-7), R(t-8), R(t-9), R(t-10), R(t-11),R(t-12)
N13	NI(t), PD(t), NAO (t), AMO(t),IOD(t), R(t-1),R(t-2), R(t-3),R(t-4),R(t-5), R(t-6),R(t-7),R(t-8),R(t-9),R(t-10),R(t-11),R(t-12)

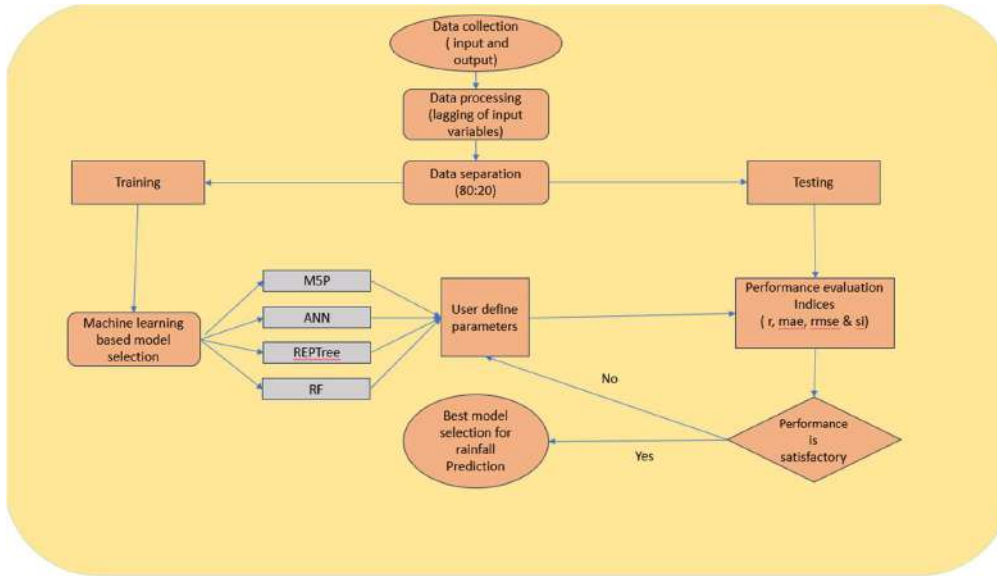


Fig. 3: Flowchart of the Methodology used for the prediction of rainfall.

2.4. Model Development

The optimal model parameters were determined through iterative trial-and-error, guided by established statistical criteria. Fig. 3 illustrates the methodological framework applied for rainfall prediction.

3. RESULTS AND DISCUSSION

3.1. M5P Results

The investigation comprised the creation of the M5P model via the use of the WEKA 3.8.6 software. It was decided

Table 3: Performance of developed M5P-based models.

Models	R	MAE	RMSE	SI	r	MAE	RMSE	SI
	Training				Testing			
M5P N1	0.5176	48.48	79.2594	1.5106	0.4059	45.4634	59.5555	1.4185
M5P N2	0.6058	45.1386	73.7042	1.4047	0.5139	43.2807	59.7516	1.4232
M5P N3	0.5908	48.8041	74.7343	1.4244	0.473	44.4037	55.9193	1.3319
M5P N4	0.5959	48.6935	74.3821	1.4176	0.4705	44.5282	55.8548	1.3304
M5P N5	0.6009	48.6046	74.0374	1.4111	0.4862	43.4679	55.1814	1.3143
M5P N6	0.7271	38.8033	63.6872	1.2138	0.4951	45.0456	65.5169	1.5605
M5P N7	0.8405	32.8633	51.1281	0.9745	0.4774	43.8179	65.3326	1.5561
M5P N8	0.7437	38.0853	62.0192	1.182	0.5137	42.628	63.916	1.5224
M5P N9	0.6349	47.6092	71.5632	1.3639	0.5342	43.3453	53.9078	1.284
M5P N10	0.6339	47.6002	71.6378	1.3653	0.5376	43.1718	54.0531	1.2874
M5P N11	0.7437	38.0978	61.9306	1.1803	0.5234	41.0272	59.2494	1.4112
M5P N12	0.8668	28.0312	46.8654	0.8932	0.5571	40.5989	60.74	1.4467
M5P N13	0.6737	41.367	68.4523	1.3046	0.6307	33.7512	45.5471	1.0848

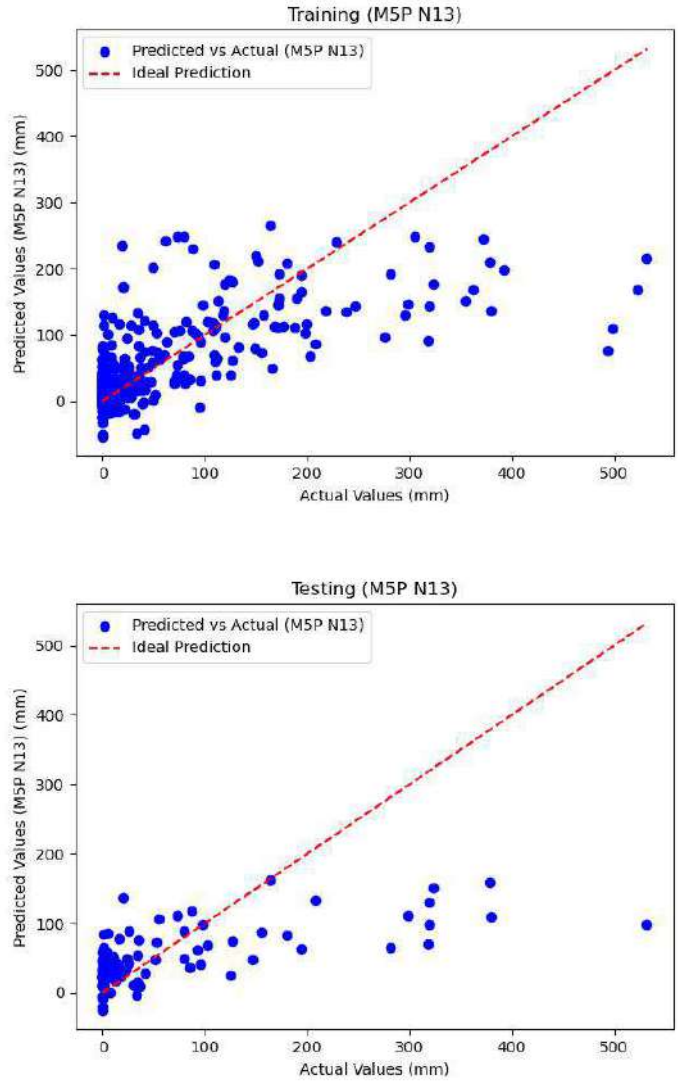


Fig. 4: Scatter plots of M5P N13 for training and testing, respectively.

to split the whole data set into two subgroups. In model building, the larger subset, which comprises eighty percent of the data, was employed, while the remaining twenty percent of the observations were utilized for model validation. The creation of the M5P model is accomplished via the use of a systematic methodology that involves trial and error. To facilitate a consistent assessment across a variety of M5P tree-based models, lagging months were included as a variable in thirteen different models that were developed for the research. The M5P N13 models have been shown to have greater capabilities in terms of forecasting rainfall levels, as shown in Table 3 by the performance assessment metrics. When it comes to testing, the values of R are 0.6307, whereas the values for training are 0.6737. In the training phase, the MAE values are 41.367, whereas in the testing phase, they are 33.7512. In the training phase, the RMSE values are 68.4523, whereas in the testing phase, they are 45.5471. For training purposes, the SI values are 1.3046, whereas for testing purposes, they are 1.0848. The M5P N13 model was used to create the agreement plot that is shown in Fig. 4.

3.2. ANN Model Results

When compared to M5P-based models, the creation of ANN models is similar to the process of M5P model development. ANN models, including hidden layers, neurons, learning rate, and momentum, critically influence model performance. Hidden layer = 1, number of neurons = 30, momentum = 0.2, and learning rate = 0.1 were found to be ideal for artificial neural networks (ANN), as measured by r, MAE, RMSE, and SI, and are shown in Table 4. When it comes to forecasting rainfall, the performance assessment metrics reveal that ANN N 13 models perform better than other models created. The R values for training are 0.7443, and the values for testing are 0.5758. After training, the MAE values are 33.8971, and after testing, they are 32.6226. In the training phase, the RMSE values are 66.2973, while in the testing phase, they are 51.7643. In the SI phase, the numbers are 1.2636 for training and 1.2329 for testing. The results indicate that a 12-month lag of rainfall, along with climate indices such as NI(t), PD(t), NAO(t), AMO(t), and IOD, exerts a stronger influence than other models. During the testing phase, the ANN N1 model yielded r values of 0.3398, which revealed that it had the lowest performance compared to all the other models that were built. This is shown by the data that is provided in Table 4. With the use of the ANN N13 model, Fig. 5 depicts the agreement plot that was created between the actual and anticipated values of rainfall throughout the training and testing stages. According to the statistics, the values that are the lowest overall are located quite near to the line that represents complete agreement (1:1).

3.3. REPTree Model Results

The performance assessment metrics demonstrate that the REPTree N12 models surpass the other models created for forecasting rainfall. The correlation coefficient (r) is 0.7113 for training and 0.6235 for testing. The MAE = 34.8753 for the training set and 30.3546 for the testing set. The RMSE = 65.1091 for the training set and 50.9935 for the testing set. The SI = 1.2409 for training and 1.2146 for testing. The findings demonstrate that a 12-month lag has a pronounced effect on delays. Table 5 indicates that the performance of REPTree N11 was the worst among all models assessed throughout the testing period, producing r = 0.3588. Fig. 6 illustrates the agreement plot juxtaposing actual and

Table 4: Performance of developed ANN-based models.

Models	r	MAE	RMSE	SI	r	MAE	RMSE	SI
	Training				Testing			
ANN N1	0.5046	47.0033	83.5359	1.5921	0.3398	44.5268	56.5845	1.3477
ANN N2	0.5912	45.4375	81.0723	1.5452	0.371	44.8411	60.9832	1.4525
ANN N3	0.6634	38.0748	73.5992	1.4027	0.3476	42.0743	64.2088	1.5293
ANN N4	0.6888	37.1285	71.6623	1.3658	0.3488	39.3225	62.8145	1.4961
ANN N5	0.6879	37.2417	71.967	1.3716	0.3448	39.6901	62.7206	1.4939
ANN N6	0.7089	36.5343	69.5002	1.3246	0.4705	36.1608	57.9243	1.3796
ANN N7	0.7088	37.3345	70.5309	1.3442	0.4106	38.548	61.5447	1.4659
ANN N8	0.7011	38.7884	72.5552	1.3828	0.3743	38.8323	63.8577	1.521
ANN N9	0.7654	36.7518	67.7697	1.2916	0.4281	38.1315	63.0389	1.5015
ANN N10	0.7659	36.1536	67.6965	1.2902	0.4289	37.4102	62.3641	1.4854
ANN N11	0.7888	31.9488	60.4988	1.153	0.4239	36.7848	61.4796	1.4643
ANN N12	0.7861	32.1256	60.6516	1.156	0.4135	36.7747	61.5798	1.4667
ANN N13	0.7443	33.8971	66.2973	1.2636	0.5758	32.6226	51.7643	1.2329

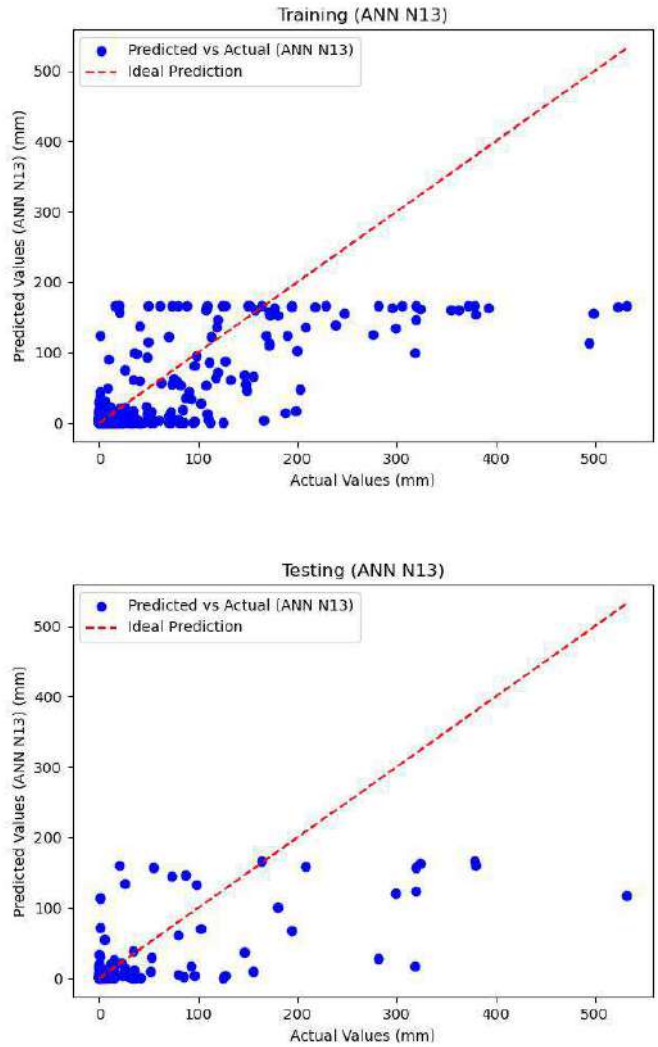


Fig. 5: Scatterplots of ANN N13 for training and testing, respectively.

Table 5: Performance of developed REPTree-based models.

Models	r	MAE	RMSE	SI	r	MAE	RMSE	SI
	Training				Testing			
REPTree N1	0.4444	52.0211	82.9797	1.5815	0.4133	45.723	57.8051	1.3768
REPTree N2	0.4909	48.6592	80.6974	1.538	0.423	43.4846	57.6648	1.3735
REPTree N3	0.5197	46.6973	79.1365	1.5083	0.4073	45.1586	58.5264	1.394
REPTree N4	0.5819	43.6694	75.3326	1.4358	0.4207	42.4785	59.286	1.4121
REPTree N5	0.5756	42.95	75.7424	1.4436	0.4213	42.4928	59.2866	1.4121
REPTree N6	0.5751	43.1905	75.7754	1.4442	0.4207	42.4785	59.286	1.4121
REPTree N7	0.6317	40.2517	71.8066	1.3686	0.4235	43.3999	62.848	1.4969
REPTree N8	0.6317	40.2517	71.8066	1.3686	0.4235	43.3999	62.848	1.4969
REPTree N9	0.6317	40.2517	71.8066	1.3686	0.4235	43.3999	62.848	1.4969
REPTree N10	0.613	41.9281	73.1802	1.3947	0.4526	41.8019	61.6975	1.4695
REPTree N11	0.5726	45.0772	75.942	1.4474	0.3588	46.1041	65.1423	1.5516
REPTree N12	0.7113	34.8753	65.1091	1.2409	0.6235	30.3546	50.9935	1.2146
REPTree N13	0.657	40.5763	69.8293	1.3309	0.6037	33.8162	50.7448	1.2086

anticipated rainfall levels throughout the training and testing periods, using the REPTree N12 model. The data suggest that the greatest lower values approximate the line of perfect concordance (1:1).

3.4. RF Model Results

In this investigation, an RF-based model is also developed. The process of model development is similar to other applied models using the WEKA 3.8.6 software. In the RF-based models, two user-defined parameters were set: the number of trees (k) and the number of variables per node (m). The optimal values were established as k = 10 and m = 1. The performance metrics of the constructed models for both calibration and validation phases are delineated in Table

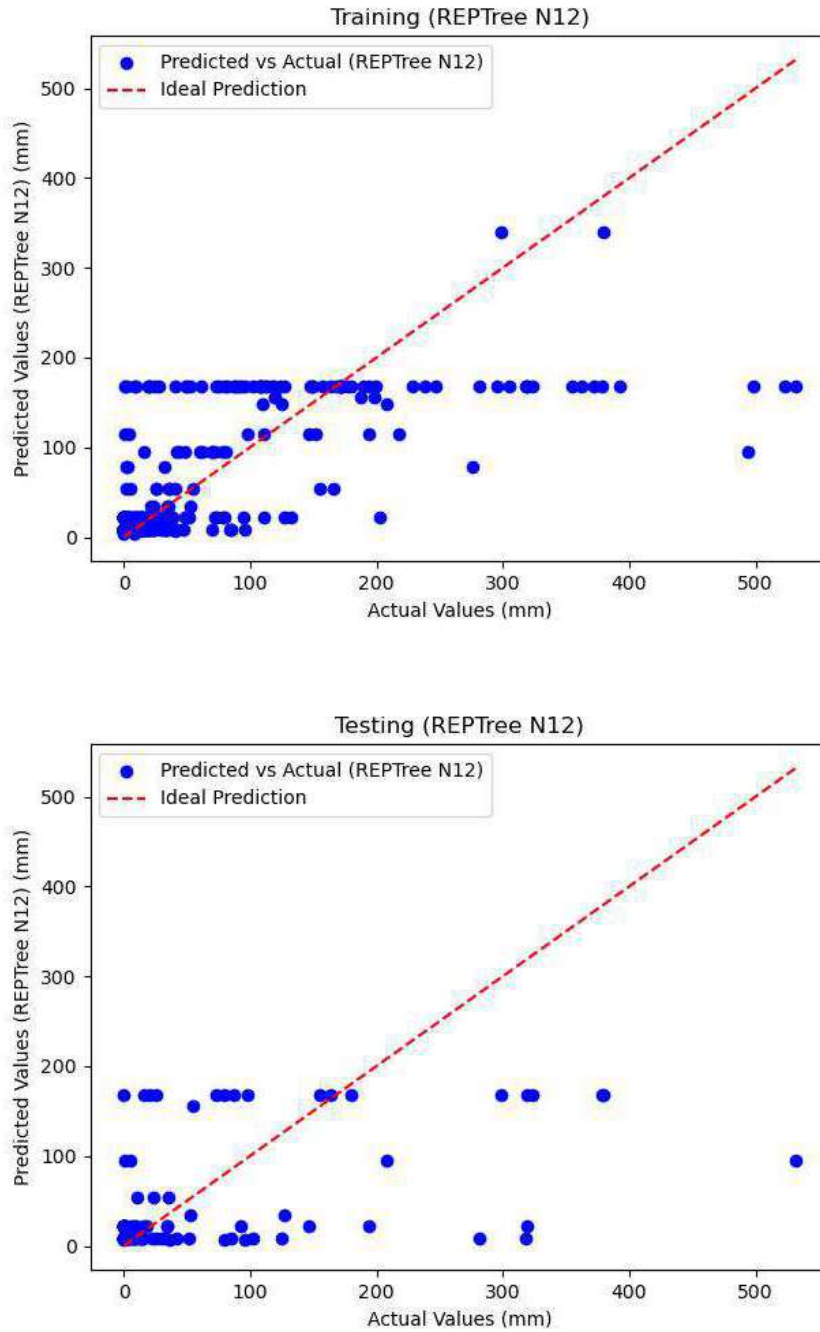


Fig. 6: Agreement diagrams of REPTree N12 for training and testing, respectively.

Table 6: Performance of developed RF-based models.

Models	r	MAE	RMSE	SI	r	MAE	RMSE	SI
	Training				Testing			
RF N1	0.9755	19.3346	31.4962	0.6003	0.2378	54.3335	66.1231	1.5749
RF N2	0.9816	19.3967	30.7187	0.5855	0.3276	50.0159	58.4158	1.3913
RF N3	0.9853	19.0794	30.032	0.5724	0.3823	49.6045	57.8882	1.3788
RF N4	0.9868	18.5794	29.7381	0.5668	0.3877	48.9038	57.7744	1.3761
RF N5	0.9835	18.7462	29.92	0.5702	0.4269	48.3531	56.0248	1.3344
RF N6	0.9852	19.1619	29.8753	0.5694	0.3526	48.0846	57.5738	1.3713
RF N7	0.9848	18.8918	29.862	0.5691	0.4802	45.0805	53.4902	1.274
RF N8	0.9867	18.2123	29.5814	0.5638	0.3994	46.4108	56.0134	1.3341
RF N9	0.9846	18.4241	29.3348	0.5591	0.5821	43.1603	50.6688	1.2068
RF N10	0.9877	17.5852	27.862	0.531	0.605	41.0999	48.454	1.1541
RF N11	0.9865	17.3586	28.148	0.5365	0.5525	41.7795	50.7573	1.2089
RF N12	0.9851	16.6593	27.4421	0.523	0.6594	36.7016	45.6076	1.0863
RF N13	0.9853	15.1624	25.1173	0.4787	0.6674	33.7026	44.0744	1.0498

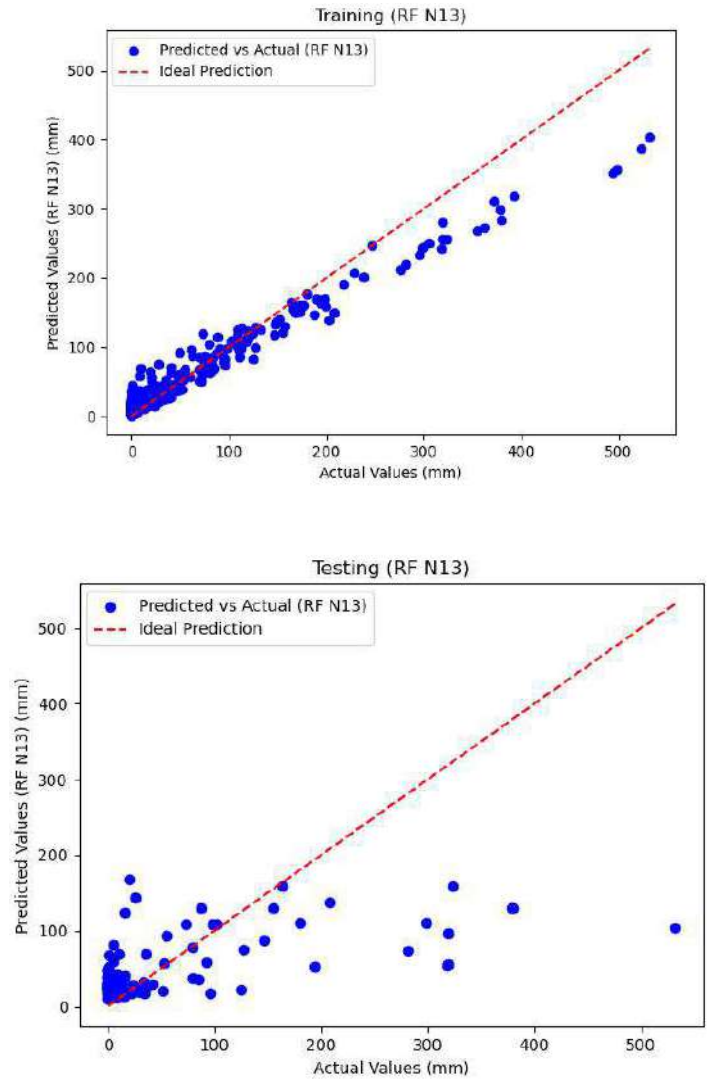


Fig. 7: Agreement diagrams of RF N13 for training and testing, respectively.

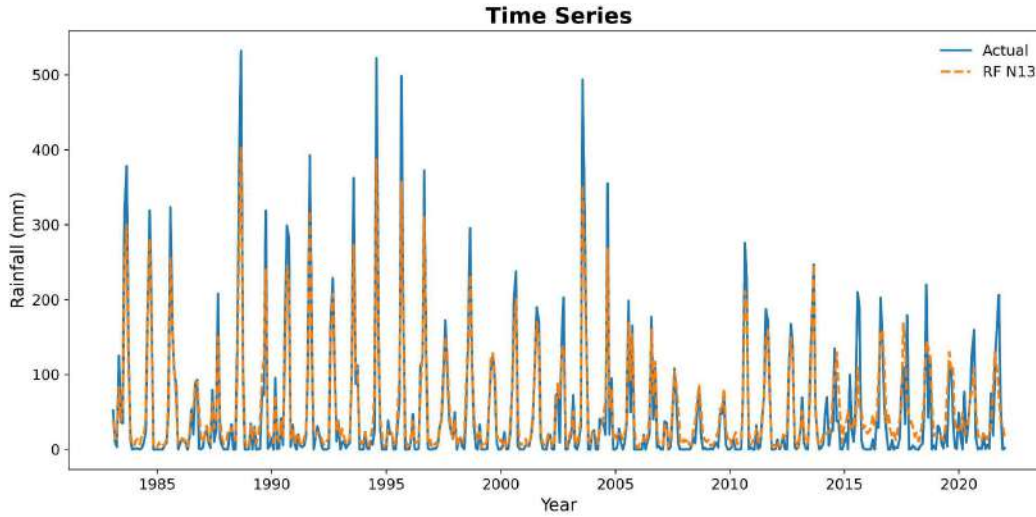


Fig. 8: Hydrograph of actual and predicted values using the RF N13 model for rainfall at Safdarjung Station.

6, measured by r, MAE, RMSE and SI. The performance assessment metrics demonstrate that the RF N13 model works superior to other input combination-based RF models for rainfall prediction. The r = 0.9853 and 0.6674, MAE =15.1624 and 33.7026, RMSE =25.1173 and 44.0744, SI = 0.4787 and 1.0498 for calibration and validation stages, respectively. Fig. 7 illustrates the agreement plot comparing real and anticipated rainfall levels throughout both stages (calibration and validation) with the RF N13 model. Fig. 8 illustrates the performance of the RF-N13 model during evaluation, where the predicted rainfall values align closely with the observed data along the 1:1 line of perfect agreement.

4. DISCUSSION

This research employed M5P, RF, ANN, and REPTree models to forecast rainfall in Safdarjung, Delhi, India. Fig. 9 presents the agreement plots for M5P N13, ANN N13, REPTree N12, and RF N13 models during the testing phase. The plots indicate that the predicted values from the RF N13 model are notably closer to the line of perfect agreement, reflecting superior performance.

The findings from Table 7 indicate that RF had strong performance throughout the training phase, shown by elevated r values and minimal SI, RMSE, and MAE values. The testing stage results indicate that the RF N13 model has superior performance in predicting rainfall for Safdarjung, Delhi, India, with r = 0.6674, MAE of 33.7026, RMSE of 44.0744, and SI of 1.0498. The ANN N13-based model exhibits the worst performance among all models evaluated, with r = 0.5758, MAE values of 32.6226, RMSE values of 51.7643, and SI values of 1.2329 throughout the testing phase. Fig. 10 illustrates the hydrograph of all implemented models with real data. The data demonstrates that the anticipated values from the RF N13 model align with the actual rainfall readings. Fig. 11 illustrates the Violin plots depicting the residual error between real and anticipated values generated by different models. This violin chart indicates that RF N13 is the highest-performing model with the smallest violin width. The Taylor diagram is also plotted for a fair comparison among all applied models. Fig. 12 indicates that RF N13 is the best performing model (blue circle), followed by the red circle (M5P N13 model). These circles lie near the hollow black circle. The Taylor diagram suggests that the ANN N13 model has the least performance (solid brown circle).

5. CONCLUSIONS

The present research concentrates on evaluating the efficacy

Table 7: Performance of developed M5P, ANN, REPTree and RF-based models.

Models	r	MAE	RMSE	SI	r	MAE	RMSE	SI
	Training				Testing			
ANN N13	0.7443	33.8971	66.2973	1.2636	0.5758	32.6226	51.7643	1.2329
M5P N13	0.6737	41.367	68.4523	1.3046	0.6307	33.7512	45.5471	1.0848
REPTree N12	0.7113	34.8753	65.1091	1.2409	0.6235	30.3546	50.9935	1.2146
RF N13	0.9853	15.1624	25.1173	0.4787	0.6674	33.7026	44.0744	1.0498

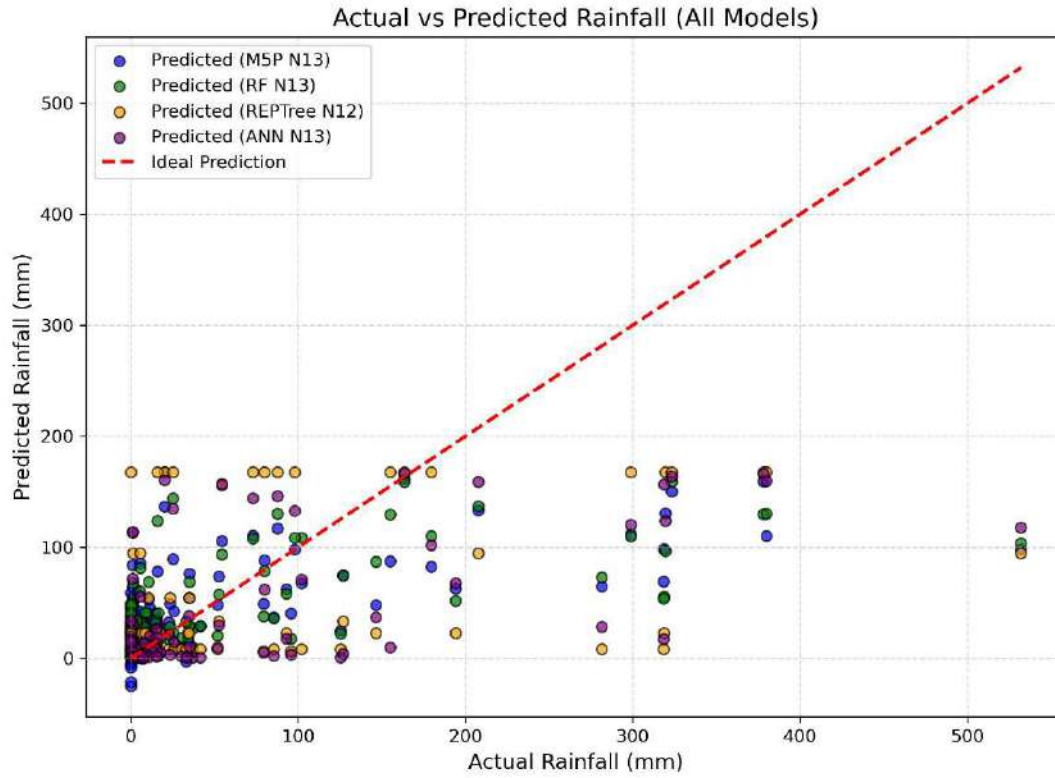


Fig. 9: Agreement diagrams of all applied models for the testing stage.

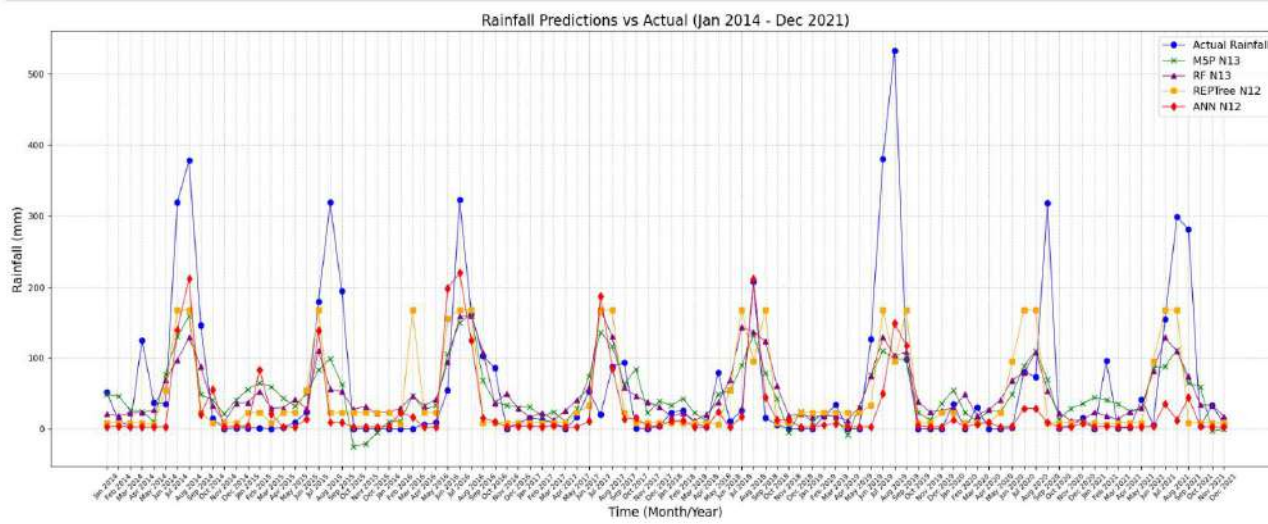


Fig. 10: Hydrograph of actual and forecasted values using all applied models for rainfall at Safdarjung Station.

of four machine learning models: RF, ANN, M5P, and REPTree, for high-accuracy rainfall forecasting based on climate indices. The findings indicated that Random Forest (RF) surpassed M5P, ANN, and REPTree in predicting accuracy and generalization. Random Forest consistently demonstrated better values of R, MAE, RMSE, and SI in both training and testing datasets. The model's strong performance across many configurations, particularly in reducing error measures, underscores its appropriateness for intricate, high-precision forecasting jobs. The RF N13

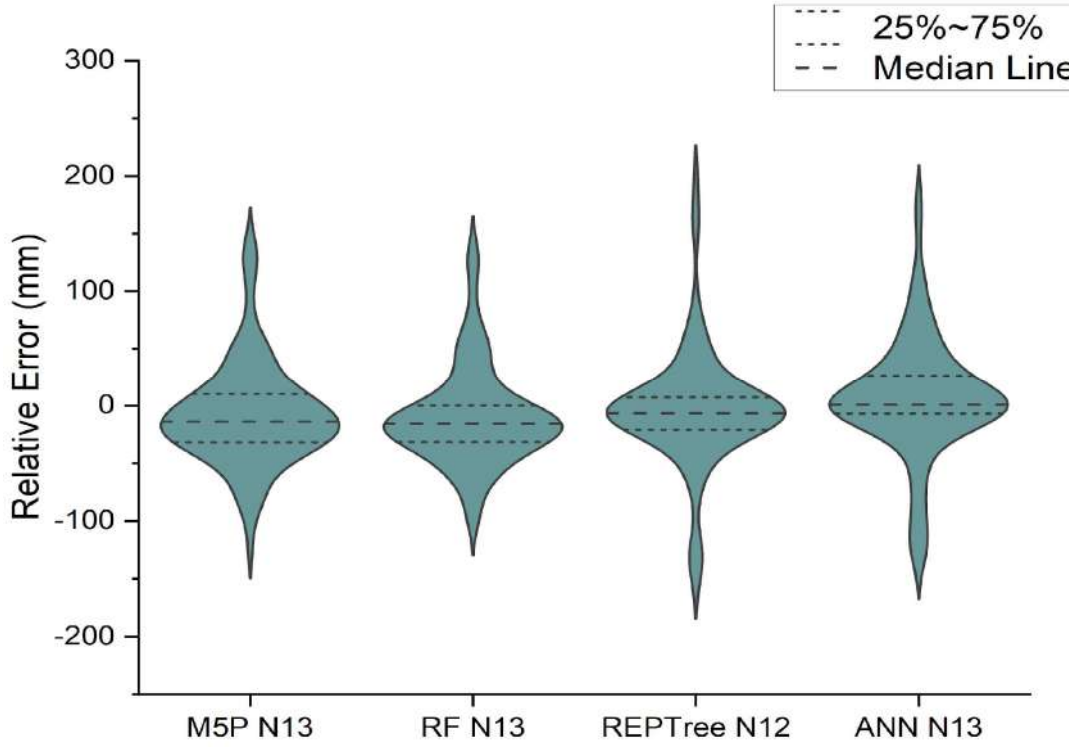


Fig. 11: Violin plots of residual value comparing the M5P N13, RF N13, REPTree N 12, and ANN N13 models.

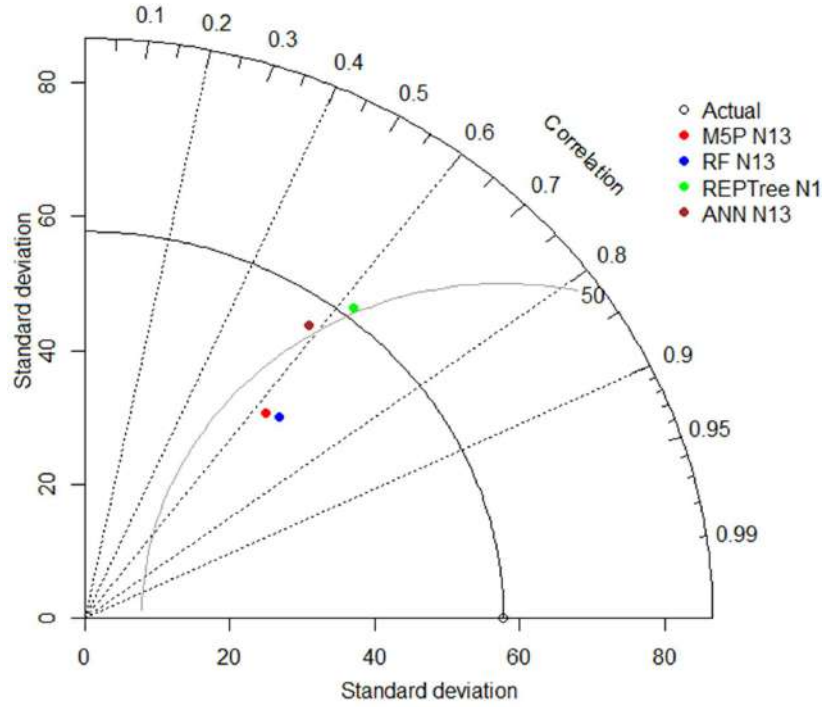


Fig. 12: Taylor plots for comparing the M5P N13, RF N13, REPTree N 12, and ANN N13model performance for the prediction of rainfall at Safdarjung, Delhi, India.

model for predicting rainfall at Safdarjung, Delhi, India, is the most effective model among those tested, exhibiting an R^2 of 0.6674, MAE of 33.7026, RMSE of 44.0744, and SI of 1.0498 during the testing phase. Conversely, the ANN N13 model is the lowest among all models used, exhibiting r = 0.5758, MAE = 32.6226, RMSE =51.7643, and SI =1.2329 throughout the testing phase. Future research may investigate the optimization of Random Forest and other sophisticated ensemble techniques to enhance the predictive accuracy for precipitation and other meteorological variables.

6. REFERENCES

Abbot, J. and Marohasy, J., 2014. Input selection and optimisation for monthly rainfall forecasting in Queensland, Australia, using artificial neural networks. *Atmospheric Research*, 138, pp.166-178. [DOI]

Abebe, W.T. and Endalie, D., 2023. Artificial intelligence models for prediction of monthly rainfall without climatic data for meteorological stations in Ethiopia. *Journal of Big Data*, 10, p.2. [DOI]

Asakereh, H., 2020. Decadal variation in precipitation regime in northwest of Iran. *Theoretical and Applied Climatology*, 139, pp.461-471. [DOI]

Asim, M., Rashid, A. and Ahmad, T., 2022. Scour modeling using deep neural networks based on hyperparameter optimization. *ICT Express*, 8(3), pp.357-362. [DOI]

Breiman, L., 1999. Random Forests-Random Features. Technical Report No. 567. University of California, Berkeley, pp.1-25.

Choubin, B., Zehtabian, G., Azareh, A., Rafiei-Sardooi, E., Sajedi-Hosseini, F. and Kişi, Ö., 2018. Precipitation forecasting using classification and regression trees (CART) model: a comparative study of different approaches. *Environmental Earth Sciences*, 77, p.314. [DOI]

Dhillon, M.S., Sharif, M., Madsen, H. and Jakobsen, F., 2023. Seasonal precipitation forecasting for water management in the Kosi Basin, India using large-scale climate predictors. *Journal of Water and Climate Change*, 14(6), pp.1868-1880. [DOI]

Enfield, D.B., Mestas-Nuñez, A.M. and Trimble, P.J., 2001. The Atlantic multidecadal oscillation and its relation to rainfall and river flows in the continental US. *Geophysical Research Letters*, 28(10), pp.2077-2080. [DOI]

Feng, P., Wang, B., Liu, D.L., Ji, F., Niu, X., Ruan, H. and Yu, Q., 2020. Machine learning-based integration of large-scale climate drivers can improve the forecast of seasonal rainfall probability in Australia. *Environmental Research Letters*, 15(8), p.084051. [DOI]

Haykin, S., 2009. Neural Networks and Learning Machines. 3rd ed. Pearson Education India, pp.1-950.

Hurrell, J.W., 1995. Decadal trends in the North Atlantic Oscillation: regional temperatures and precipitation. *Science*, 269(5224), pp.676-679. [DOI]

Kashid, S.S. and Maity, R., 2012. Prediction of monthly rainfall on homogeneous monsoon regions of India based on large-scale circulation patterns using genetic programming. *Journal of Hydrology*, 454, pp.26-41. [DOI]

Khan, M.I. and Maity, R., 2020. Hybrid deep learning approach for multi-step-ahead daily rainfall prediction using GCM simulations. *IEEE Access*, 8, pp.52774-52784. [DOI]

Luo, J.J., Liu, G., Hendon, H., Alves, O. and Yamagata, T., 2017. Inter-basin sources for two-year predictability of the multi-year La Niña event in 2010–2012. *Scientific Reports*, 7, p.2276. [DOI]

Mantua, N.J., Hare, S.R., Zhang, Y., Wallace, J.M. and Francis, R.C., 1997. A Pacific interdecadal climate oscillation with impacts on salmon production. *Bulletin of the American Meteorological Society*, 78(6), pp.1069-1080. [DOI]

Mokhtarzad, M., Eskandari, F., Jamshidi Vanjani, N. and Arabasadi, A., 2017. Drought forecasting by ANN, ANFIS, and SVM and comparison of the models. *Environmental Earth Sciences*, 76(21), p.729. [DOI]

Naved, M., Asim, M. and Ahmad, T., 2024. Prediction of concrete compressive strength using deep neural networks based on hyperparameter optimization. *Cogent Engineering*, 11(1), p.2297491. [DOI]

Pai, D.S., Rajeevan, M., Sreejith, O.P., Mukhopadhyay, B. and Satbha, N.S., 2014. Development of a new high spatial resolution (0.25° × 0.25°) long period (1901-2010) daily gridded rainfall data set over India and its comparison with existing data sets over the region. *Mausam*, 65(1), pp.1-18. [DOI]

Pandhiani, S.M., Sihag, P., Shabri, A.B., Singh, B. and Pham, Q.B., 2020. Time-series prediction of streamflows of Malaysian rivers using data-driven techniques. *Journal of Irrigation and Drainage Engineering*, 146(7), p.04020013. [DOI]

Quinlan, J.R., 1992. Learning with continuous classes. In: Proceedings of the 5th Australian Joint Conference on Artificial Intelligence, Hobart, Australia, Vol. 92, pp.343-348.

Saji, N.H., Goswami, B.N., Vinayachandran, P.N. and Yamagata, T., 1999. A dipole mode in the tropical Indian Ocean. *Nature*, 401(6751), pp.360-363. [DOI]

Sham, F.A.F., El-Shafie, A., Jaafar, W.Z.W., Sherif, M. and Ahmed, A.N., 2025. Advances in AI-based rainfall forecasting: a comprehensive review of past, present, and future directions with intelligent data fusion and climate change models. *Results in Engineering*, 27, p.105774. [DOI]

Shankar, A., 2024. Dynamic impact-based heavy rainfall warning with multi-classification machine learning approaches. *Nature Environment & Pollution Technology*, 23(4), pp.2205-2214. [DOI]

Sihag, P., 2018. Prediction of unsaturated hydraulic conductivity using fuzzy logic and artificial neural network. *Modeling Earth Systems and Environment*, 4(1), pp.189-198. [DOI]

Trenberth, K.E. and Hoar, T.J., 1997. El Niño and climate change. *Geophysical Research Letters*, 24(23), pp.3057-3060. [DOI]

Wani, O.A., Mahdi, S.S., Yeasin, M., Kumar, S.S., Gagnon, A.S., Danish, F., Al-Ansari, N., El Hendawy, S. and Mattar, M.A., 2024. Predicting rainfall using machine learning, deep learning, and time series models across an altitudinal gradient in the North-Western Himalayas. *Scientific Reports*, 14, p.27876. [DOI]

Nature Environment and Pollution Technology
An International Quarterly Scientific Journal

p-ISSN: 0972-6268
(Print copies up to 2016)
e-ISSN: 2395-3454

Vol. 25 | No. 3 | Article ID D1886 | 2026

Original Research Paper

https://doi.org/10.46488/NEPT.2026.v25i03.D1886

Open Access Journal

Nanotechnology in Automotive Wastewater Remediation: Functional Roles, Drawbacks, and Future Prospects

Luke O. Ajuka[1]†, Moses O. Petinrin[2], Nosa Idusuyi[2], Kunle M. Oluwasegun[3] and O.S. Fayomi[4,5]

[1]Department of Automotive Engineering, University of Ibadan, Ibadan, Nigeria
[2]Department of Mechanical Engineering, University of Ibadan, Ibadan, Nigeria
[3]Department of Mechanical and Manufacturing Engineering, University of Manitoba, Winnipeg, Manitoba, Canada
[4]Department of Mechanical Engineering Science, University of Johannesburg, Auckland Park, Kingsway Campus, P. O. Box 534, Johannesburg, South Africa
[5]Department of Mechanical Engineering, Bells University of Technology, P.M.B. 1015, Ota, Ogun State, Nigeria
†Corresponding author: Luke O. Ajuka; lo.ajuka@ui.edu.ng

Abbreviation: Nat. Env. & Poll. Technol.
Website: www.neptjournal.com

Received: 02-10-2025
Revised: 30-12-2025
Accepted: 13-01-2026

Key Words:

Pollutants
Nanomaterials
Wastewater treatment
Nano-enhanced bioremediation
Nano-adsorbents
Nanomembranes
Nano-catalysts
Lifecycle assessment

Citation for the Paper:

Ajuka, L.O., Petinrin, M.O., Idusuyi, N., Oluwasegun, K.M. and Fayomi, O.S., 2026. Nanotechnology in automotive wastewater remediation: Functional roles, drawbacks and future prospect. *Nature Environment and Pollution Technology*, 25(3), D1886. https://doi.org/10.46488/NEPT.2026.v25i03.D1886

Note: From 2025, the journal has adopted the use of Article IDs in citations instead of traditional consecutive page numbers. Each article is now given individual page ranges starting from page 1.

Copyright: © 2026 by the authors
Licensee: Technoscience Publications
This article is an open access article distributed under the terms and conditions of the Creative Commons Attribution (CC BY) license (https://creativecommons.org/licenses/by/4.0/).

ABSTRACT

An estimated 2.73×10^{12} gallons of water are generated annually in the automotive sector, resulting in complex wastewater streams. Pollutant-free water from this sector is essential for a safe environmental footprint for various applications, as wastewater causes corrosion, equipment blockages, and increased chemical costs via vehicle wash bays, paint/coating shops, plating lines, and coolant handling, mapping nanomaterial functions to automotive-typical contaminants (oils/greases, surfactants, dyes, heavy metals: Pb, Cu, Zn, and Cr). Average water-contaminant loads, including grease and oil (1100 $mg.L^{-1}$), COD (4500 $mg.L^{-1}$), and overall suspended solids (3500 $mg.L^{-1}$), create some level of health risk, and treatment methods have shifted from the physical techniques of gravity separation, dissolved air flotation, and demulsification, which involve nanotechnology, to hybridization. With a per-wash prediction of globally used vehicles in 2015, 218 billion liters of wastewater run off to potential water streams, initiating water-nanoparticle mobility before it can be treated for re-use. Based on their high surface-to-volume ratio, nanoscale size, ordered structure, and filtration competence resulting from their inherent mechanical, thermal, antifouling, and antibacterial properties, nano-engineered materials, including nano-adsorbents, nanomembranes, and nano-catalysts, are specifically used to overcome the limitations of conventional wastewater treatment methods. Oil-based wastewater treated with magnetic sorbent nanoparticles acts as an emulsifier, thereby containing microbes and causing microorganism-infested wastewater. Therefore, an effective means of treating wastewater with a variety of compositions is nanoenhanced bioremediation. Hence, a nanotechnology technique that fuses bioremediation and nano-remediation to achieve nano-enhanced bioremediation for completely enhanced wastewater remediation is proposed to abate environmental pollution. However, long-term risks and lifecycle assessments of nanomaterial deployment in wastewater treatment will further validate the degree of trade-off between its specific automotive service applications and safety, with regulatory frameworks to meet long-term sustainability goals.

1. INTRODUCTION

Automotive manufacturing and service operations generate complex wastewater streams dominated by COD/BOD-rich organics, oils/greases, surfactants, dyes, and heavy metals, profiles that challenge single-stage treatment and motivate the assessment of nanotechnology-enabled options (photocatalysis, nanoadsorbents, nano-membranes) alongside hybrid trains (Fall et al. 2007, Pottekkatt et al. 2025). Automotive industry activities, including component manufacturing, vehicle assembly, drivability, and maintenance, consume and contaminate significant volumes of water, thereby contributing to the global decline in freshwater resources (Babakura et al. 2023, Ali et al. 2019). Based on an Automotive

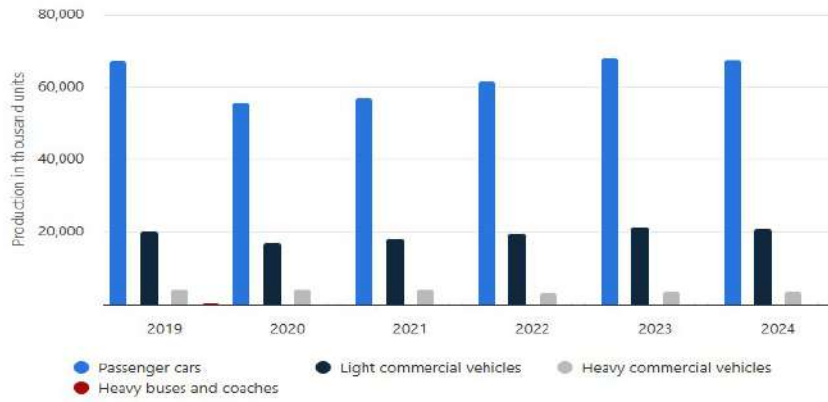


Fig. 1: Global motor vehicle production estimate, 2019-2024, by type (in 1,000 units, Statista 2025).

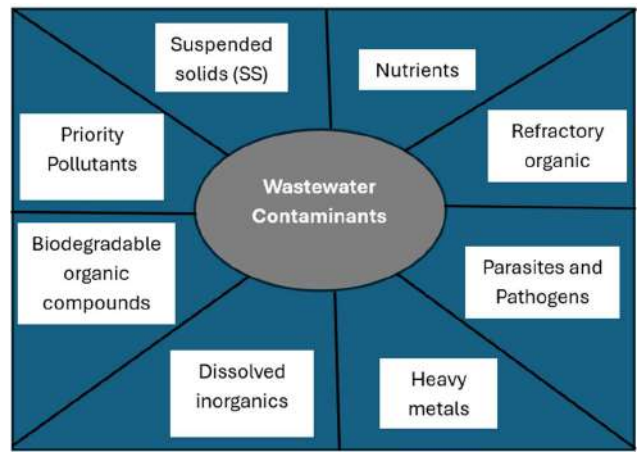


Fig. 2: Categorical wastewater contaminants. (Adapted from Gavrilescu 2010).

World report, producing a single car requires over 39,000 gallons of water, and the inclusion of tire production in the process may lead to variation in the estimate, with total annual consumption exceeding 2.73×10^{12} gallons due to the production of approximately 70 million cars worldwide (Membracon 2025, Karchiyappan 2022). In addition to direct vehicle production, ancillary processes such as electroplating, leather tanning, and textile finishing substantially add to the industry's environmental footprint. Recent statistics confirm that global car production surpassed 90 million units annually, including passenger cars and commercial vehicles (Fig. 1, Statista 2023). Moreover, the global car wash industry alone consumes approximately 218 billion liters of water per month, based on 170 liters used per wash and an estimated 1.3 billion vehicles worldwide (Monney et al. 2020).

The extensive use of water in automotive processes introduces numerous pollutants into wastewater streams. Activities such as painting, surface treatment, coating, rinsing, machining, and cooling generate oily effluents containing heavy metals, hydrocarbons, surfactants, detergents, dyestuff, phosphates, and other hazardous contaminants (Landrigan et al. 2018, Tian et al. 2020). When untreated wastewater is discharged, a common practice in developing countries (Zhongming et al. 2020), it eventually infiltrates rivers, lakes and dams. This not only reduces the availability of clean water but also degrades ecosystems and impacts food chains (Meyer et al. 2019, Chigare et al. 2019). For example, untreated radiator coolants, often replaced with plain water in underdeveloped regions, accelerate scaling and corrosion in vehicle systems while simultaneously releasing toxic byproducts into the surrounding environment (Fig. 2). The cumulative global impact is profound, and services that depend on freshwater consume over 64 billion cubic meters annually, further straining water security under conditions of rapid population growth (UNESCO-WWAP 2014). Beyond conventional pollutants, nanomaterials and nanosized particles released from industrial and automotive sources raise additional concerns.

When dispersed into aquatic environments, nanoparticles can aggregate, alter water pH, and affect temperature, with subsequent ecological consequences (Su et al. 2020, Hanif et al. 2020, Rehman et al. 2019). The instability of highly reactive nanometal oxides under environmental conditions further complicates their long-term behavior and safety (Matlochova et al. 2014). These challenges underscore the dual role of nanotechnology, while potentially hazardous in unmanaged forms, engineered nanomaterials also offer unique advantages for wastewater remediation.

In recent years, nanotechnology has been increasingly explored for its ability to address complex industrial effluents, including those generated by the automotive sector (Fig. 2). Engineered nanomaterials such as MXenes, graphene derivatives, metal organic frameworks (MOFs), and TiO_2-based photocatalysts demonstrate enhanced adsorption capacities, catalytic activity, and antimicrobial effects, enabling efficient removal of oils, heavy metals, dyes, and microbial contaminants from wastewater (Abdulkareem et al. 2023, Zhang et al. 2022, Gnanamoorthy et al. 2022, Abdelfatah et al. 2022, Bagyalakshmi et al. 2025, Zhao et al. 2022, Zhou et al. 2024, Moatmed et al. 2019). These findings position nanotechnology as a critical enabler of advanced water treatment systems, aligning with global calls for sustainable and circular economic solutions (UNESCO-WWAP 2024, Olawade et al. 2013).

Fig. 3 illustrates the increasing research attention devoted to nanotechnology-enhanced wastewater remediation in the automotive sector, as reflected in the increasing number of annual publications indexed in Fig. 3. It underscores the growing recognition of both the severity of automotive wastewater challenges and the promise of advanced nanotechnology-based solutions, but a not yet ready industry-wide adoption, because the technology readiness lags behind scientific activity due to limitations in Pilot-scale validation, standardized performance metrics, insufficient assessment of long-term risks and lifecycle impacts, minimal cost and scalability analysis, and weak regulatory frameworks supporting nanotechnology deployment.

2. AUTOMOTIVE WASTEWATER COMPOSITION

Car-wash and service-station effluents frequently exhibit emulsified oils/greases (~1100 $mg \cdot L^{-1}$), COD (~4500 $mg \cdot L^{-1}$), and TSS (~3500 $mg \cdot L^{-1}$), along with surfactants/detergents, metals, and dyes from paint/coating and plating lines. Gravity separators reduce loads but seldom meet reuse/discharge requirements without additional treatment. To avoid repeating constituent summaries, we provide a single consolidated composition figure/table and reference it later in the text (Fall et al. 2007, Fayed et al. 2023). The consolidated composition showing the constituent details is presented in Fig. 4 and Table 2, respectively.

The automotive industry is among the most water-intensive industrial sectors, relying heavily on water for manufacturing, painting, surface coating, cooling, washing, and cleaning. Each of these processes generates complex wastewater streams containing diverse organic, inorganic, and sometimes toxic contaminants that pose serious risks to the environment if discharged untreated. The documented impacts of these pollutants include aquatic toxicity, oxygen depletion, eutrophication, and bioaccumulation of heavy metals in aquatic organisms, thereby threatening both ecosystems and human health (Bhat et al. 2021, Koul et al. 2022). Although automotive wastewater is predominantly

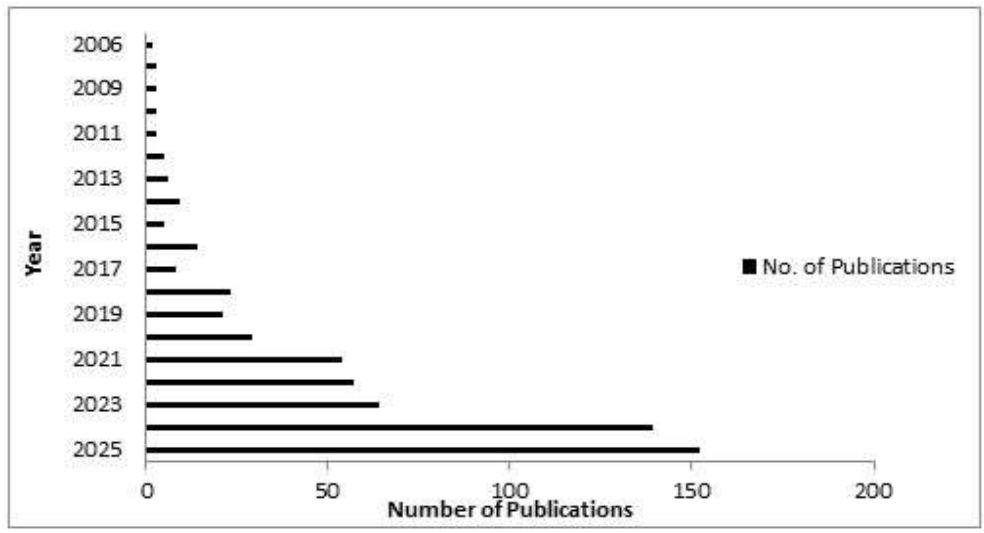


Fig. 3: Number of yearly publications on automotive nano-remediated wastewater [Sciencedirect.com].

water (≈99.9%), the remaining 0.1% comprises a broad array of pollutants with high variability, depending on the process inputs and wastewater sources. These include suspended solids (350–1200 mg.L^{-1}), biodegradable organics such as proteins, carbohydrates, and lipids, inorganic solids including sediment, soil particles, and salts, and trace levels of micro-pollutants (Owhonka et al. 2021, Ahmadi et al. 2020). Particulate matter contributes to chemical oxygen demand (COD) values ranging from 250–1000 mg.L^{-1}, reflecting a high organic load. In addition, automotive effluents contain toxic compounds, such as hydrocarbons, surfactants, phosphates, and phenolic derivatives, which hinder microbial degradation in conventional treatment systems (Deshpande et al. 2020, Bhat et al. 2021). Notably, approximately 63% of phosphate compounds occur in soluble forms, complicating their removal and exacerbating eutrophication risks when discharged into receiving water bodies (Michael et al. 2023, Deshpande et al. 2020).

The sources of wastewater contributing to this complex mixture are multifaceted and include: Beyond direct automotive operations, wastewater is often aggregated with surface runoffs carrying contaminants from municipal, hospital, and agricultural discharges, thus amplifying the chemical and microbial loads. Typical pollutants include heavy metals such as cadmium, lead, chromium, and zinc from electroplating and metal finishing, as well as oils, greases, and synthetic fluids used in lubricants and coolants (Tian et al. 2020, Landrigan et al. 2018). The persistence of these pollutants in aquatic systems creates long-term ecological footprints, particularly in developing countries where effluent regulation and treatment capacities remain limited (Zhongming et al. 2020). According to Kabdasli et al. (2009), Singh et al. (2017), Ahn et al. (2008), automotive effluents (primarily from emulsion and paint processes) are highly variable depending on the process, but typically exhibit a range of materials (Fig. 4)

The composition of wastewater also dictates the selection of the treatment technologies. High salinity, turbidity, extreme pH levels, and the presence of refractory organics often necessitate multi-stage treatment trains that incorporate primary sedimentation, chemical coagulation–flocculation, and advanced oxidation processes. However, cost remains a critical limitation of this approach. For instance, the distillation-based recovery of high-quality water is prohibitively expensive because of the energy-intensive requirement of multiple consecutive treatment steps (Adham et al. 2018). Although membrane-based desalination and filtration systems are effective, they face constraints such as osmotic pressure thresholds, hydraulic energy demands, fouling, and scaling from mineral precipitation (Dieter et al. 2018, Gude 2018). Although adsorptive systems are cheaper, they often suffer from functional group selectivity and rapid saturation, limiting their long-term application (Crini & Lichtfouse 2019). Recent advances in nanotechnology have opened new pathways for addressing the multifaceted composition of automotive wastewater. Engineered nanomaterials, including metal oxide nanoparticles, graphene-based composites, MXenes, and functionalized nanofibers, offer superior adsorption capacities, catalytic degradation, and antimicrobial properties, enabling the removal of contaminants and the recovery of valuable resources such as metals and oils (Zhou et al. 2024). Moreover, nanotechnology-enabled processes facilitate water reuse and energy recovery, directly supporting industrial sustainability goals and reducing dependence on freshwater withdrawal (Bagyalakshmi et al. 2025, Zhao et al.

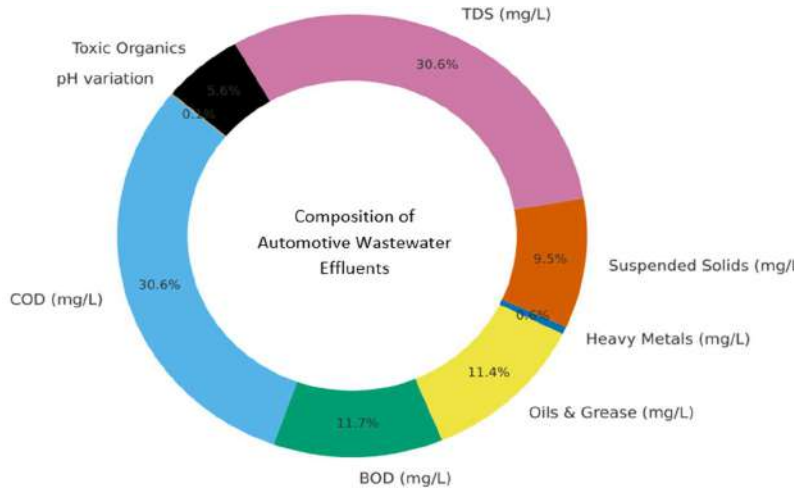


Fig. 4: Composition of Automotive Wastewater Effluents. Adapted from Kabdasli et al. (2009), Singh et al. (2017), and Ahn et al. (2008).

2022). Despite these promising outcomes, several limitations impede the large-scale application of nanotechnology in automotive wastewater remediation. Concerns include the potential ecotoxicity of residual nanomaterials, high production costs, poor stability of nanostructures in complex wastewater matrices, and inadequate frameworks for life cycle management (Crini & Lichtfouse 2019). Furthermore, current research remains fragmented, with insufficient focus on integrating the functional roles of nanotechnology with techno-economic viability, regulatory compliance, and environmental safety assessments. The rapid expansion of the automotive industry has intensified freshwater consumption and wastewater generation, creating critical challenges for global water security. Conventional treatment technologies often fail to adequately remove the diverse pollutants present in automotive effluents, whereas nanotechnology, despite offering superior performance, faces barriers to scalability, safety, and sustainability. Addressing these gaps is urgent, given the escalating climate-driven water scarcity and stricter environmental discharge standards.

This study systematically examines the functional applications, roles, drawbacks, and prospects of nanotechnology in automotive wastewater remediation. The complex mixture of contaminants in Fig. 4 reflects high biodegradability demands. For example, the dominance of COD/BOD fractions (organic load) and suspended solids suggests the need for high-capacity treatments that can be deployed in large-scale facilities in the future. Nanomaterials such as nano-TiO_2, ZnO, and CNT-based composites can be tailored for photocatalysis and adsorption and scale well in membrane or packed-bed systems. Hence, in terms of scalability, the dominance of COD/BOD fractions (organic load) and suspended solids suggests the need for high-capacity treatments that can be deployed in large-scale facilities. Nanomaterials such as nano-TiO_2, ZnO, and CNT-based composites can be tailored for photocatalysis and adsorption and scale well in membrane or packed-bed systems. Regarding safety, the presence of toxic metals (Cr, Ni, Pb, and Cu) and toxic organics (phenols and PAHs) underscores the importance of nanomaterials with selective binding capacity (e.g., functionalized graphene oxide and nano-zero-valent iron). By removing carcinogenic and mutagenic contaminants at trace levels, nanotechnology directly addresses the issues of ecotoxicity and public health risks. Furthermore, the presence of oil, grease, and high TDS levels highlights the need for multifunctional materials. Nanocomposites that combine adsorption, photocatalytic degradation, and antimicrobial activity (e.g., GO/Fe_3O_4 and rGO/$ZnCo_2O_4$) reduce the need for multi-step conventional treatment. This integration lowers operational costs and energy inputs compared to classical methods (e.g., coagulation–flocculation + tertiary oxidation). Finally, by mapping the proportional contributions of pollutants, the Fig. prioritizes the contaminants that require urgent attention. Nanotechnology can then be directed toward high-impact removal targets, such as nanoadsorbents and nZVI for selective binding (heavy metals), photocatalytic nanomaterials for oxidative breakdown (toxic organics), and nano-enhanced membranes for combined organic degradation and microbial disinfection (COD/BOD loads). This demonstrates that no single treatment suffices, but integrated nano-enabled systems offer the scalability, safety, and cost efficiency needed for sustainable automotive wastewater management.

2.1. Classification of Nanomaterials

Different architectures based on features guide nanomaterial classification. For instance, the dimensions of 1-D nanostructures, such as nanowires, nanotubes, and nanofibers, range from 1 to 100 nm. The classifications are presented in Table 1.

2.2. Mobility of Emissive Nanoparticles

Environmental releases of nanoparticles can originate from a variety of sources, including manufacturing facilities, wastewater treatment plants, landfills, and diffuse nonpoint sources such as washing machines, textiles, and consumer products embedded with nanomaterials (Nowack et al. 2007). For example, commercial nanosilver-infused socks have been shown to leach as much as 25% of their total silver content within minutes when exposed to alkaline conditions (pH 10), illustrating the potential for significant nanoparticle discharge from everyday products (Xiu et al. 2012). As shown in Fig. 4, nanoparticle mobility in water bodies is determined by their fundamental characteristics, including solubility in water, physical attachment to other substances, and chemical reactivity, such as oxidation and reduction. These elements, together with the surface charge of the nanoparticles, could cause immobilization.

The process shown in Fig. 5 includes metabolism, water solubility, accumulation in the organism, depot effect, chemical reactivity (oxidation-reduction behavior), physical binding, and aggregation. According to the EPA (2007), biotic or abiotic degradation processes, sunlight-induced photoreactions based on water turbidity, and the anaerobic transformation of some organic and metallic nanomaterials into complex compounds are some of how nanoparticle degradation pathways in aqueous systems can be affected (Nurmi et al. 2005). Several ecotoxicity studies have been conducted to evaluate the environmental concentrations of common nanomaterials. For example, Gottschalk et

Table 1: Categorization of Nanomaterials.

S/ No.	Conditions	Classification	Specific Details	Nanoparticle Examples	Reference
1		0-D	All 3 dimensions are below 100nm with electrons in 3D space. No electron delocalization, meaning freedom to move.	Fullerene	(Rafiei-Sarmazdeh et al. 2020, Afolalu et al. 2023)
2	Numerical Dimension	1-D	Nanostructure has two characteristic dimensions between 1 and 100 nm.	Tubes, fibers, wires, platelets, etc.	
3		2-D	Nanostructure has thin layers that may have a thickness.of at least one atomic layer, having many atoms on its surface.	Graphene, hexa-gonal boon nit-ride (hBN), metal dichalcogenides (MX2), etc.	
4		3-D	Composed of dispersions of nanoparticles, bundles of nanowires, nanotubes, and multi-nanolayers.	Particles, quantum dots, hollow spheres, etc.	
5	Pore Dimension	Microporous	With their <2 nm narrow pores, they are significant for small gases or linear molecules of gases that have high interaction characteristics and slow diffusion rates.	Excellent examples of naturally occurring clay materials and Na-Y are utilized in gas purification.	(Mekuye & Abera 2023)
6		Mesoporous	Their x-pore diameter ranges from 2 nm to 50 nm. frequently seen in adsorbing devices for liquids or vapors, or nanoreactors for polymerization.	MCM-41, MCM-48, SBA-15, and carbon meso-porous materials are a few examples.	(Mekuye & Abera 2023)
7		Macroporous	With pores larger than 50 nm, they can accommodate tiny biological molecules or polyaromatic systems.	Examples are Carbon micro tubes, porous gels, and porous glasses. They are mostly used as sensing materials and scaffolds to graft functional groups, such as catalytic centers.	(Mekuye & Abera 2023)
8	Phase Composition	Single-phase solid	Crystalline, amorphous particles and layers, etc.	High entropy oxide nanoparticles	
9		Multi-phase solid	Matrix composites, coated particles, etc.	Nanorods, nanofibers, CNTs, etc.	(Mekuye & Abera 2023)
10		Multi-phase system	Colloid, aerogels, ferrofluids, etc.	Chitosan, Quantum dot, nanocrystals, etc.	
11	Manufacturing Process	Gas phase reaction	Deposition of thin film onto a substrate is called chemical vapor deposition (CVD). Involves chemical reaction, and the gaseous by-products are toxic.	Silica nanoparticle is a good sample	(Saeed et al. 2020)
12		Liquid phase reaction	Through a heterogeneous reaction including chemical solution precursor, precipitation, and hydrothermal processing, sol-gel creates nanostructured materials. They create a variety of nanogeometries, including nanospheres, nanosheets, nanowires, and nanorods.	includes aerosol-based nanoparticles	(Bokov et al. 2021)
13		Mechanical procedures	Ball milling, plastic deformation, etc.	Includes milled Cuo nanoparticles	(Joy et al. 2022)
14	Origin/Basis	Incidental nanomaterials	Particles from natural combustion, vehicle exhaust (20–130 nm in size for diesel engines and 20–60 nm in size for gasoline), and cosmic dust	CNTs, nanodiamonds, organic-based nanoparticles	(Khan & Hossain 2022, Cho et al. 2019, Westerdahl et al. 2005)
15		Artificial or Engineered nanomaterials	Quantum dots, nanoshells, nanocages, and nanobranches manufactured by humans for use in drug delivery nano-vehicles or immunological sensing devices	Carbon nanoparticles, TiO2 nanoparticles, and hydroxyl-apatites.	(Khan & Hossain 2022, Cho et al. 2019, De Volder et al. 2013)
16		Naturally produced nanomaterials	Binding soluble metals to actinomycetes, plant viruses, nanoorganisms, and nanobes, then precipitating the mixture to create nanoparticles.	Alloys, Non-magnetic oxides, Metal sulfide quantum dots	(Khan & Hossain 2022, Cho et al. 2019).

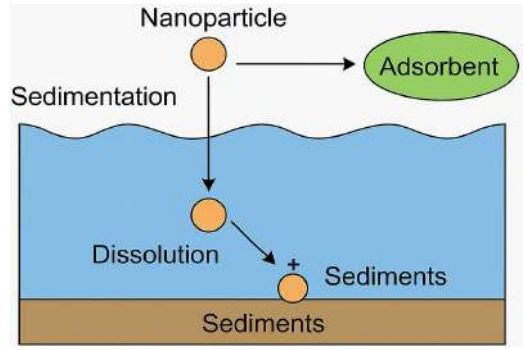


Fig. 5: Mobility characteristics of nanoparticles in water bodies. Adapted from Su et al. (2020), Hanif et al. (2020), and Matlochova et al. (2014).

al. (2009) calculated the risk quotients associated with nanosilver, nano-TiO2, and nano-ZnO in surface water and sewage treatment effluents in the United States, Europe, Switzerland, and Nigeria (Table 2). The brewery wastewater from Enugu, Nigeria, and the oil refineries from Niger-Delta, Nigeria, share a common wastewater composition, as indicated in Table 2. Wastewater treatment greatly depends on the intensive efforts and monitoring of industrial effluents.

The risk quotient of the projected (calculated) environmental concentration and predicted no-impact concentration determines the risk quotient for various nanoparticles in surface water and STP effluents in Europe, the USA, Switzerland, and Nigeria. The table shows that the effluent from sewage treatment plants contains significant ecotoxicity hazards due to nanosilver, nano-ZnO, and nano-TiO2. Even at the surface, the expected concentration of nanosilver in the environment was extremely high.

3. NANOREMEDIATION OF WASTEWATER

Nanotechnology comprises all branches of engineering, including nanosystem physics, nanochemistry, nanomaterials science, nanobiology, nanoelectronics, nanoprocessing, and nanomechanics (Soni & Jha 2024, Malik et al. 2023). In contrast to traditional water purification methods, nanotechnology employs novel techniques such as efficient photocatalysis, membrane filtration to impede microbial

Table 2: Associated risk quotient for different nanoparticles in surface water and STP effluent in Europe, USA, Switzerland, and Nigeria (Gottschalk et al. 2009, Durotoye et al. 2018, Theoneste et al. 2020).

S/No.		Europe	USA	Switzerland	Nigeria			
1	Surface Water STP Effluent	Nano-TiO2 0.015 3.5	0.002 1.8	0.2 3.4	n/a			
2	Surface Water STP Effluent	Nano-ZnO 1.1 61.1	0.17 30.1	1.03 55.6	n/a			
3	Surface Water STP Effluent	Nanosilver <0.0005 <0.0005	<0.0005 <0.0005	<0.0005 <0.0005	n/a			
4	Surface Water STP Effluent	CNT <0.0005 <0.0005	<0.0005 <0.0005	<0.0005 <0.0005	n/a			
5	Surface Water STP Effluent	Fullrenes <0.0005 0.026	<0.0005 0.023	<0.0005 0.019	n/a			
6	ORENDN (I & E)	n/a	n/a	n/a	O & G 15 10	Zinc n/a	Iron n/a	Nickel n/a
7	BR	n/a	n/a	n/a	O & G 2	Zinc 0.01	Iron 28	Nickel 0.01
8	RW	n/a	n/a	n/a	O & G 1	Zinc <0.01	Iron 2	Nickel <0.01

Note: STP - Sewage Treatment Plant, ORENDN – Oil Refinery Effluent in Niger Delta, Nigeria, I & E -, BE - Brewery Effluent, RW – River Water, O & G – Oil and Grease, n/a – not applicable/available/

growth, and disinfection to effectively absorb nanometals and non-metal oxides. According to Yadav et al. (2023), the toxicity of wastewater containing non-biodegradable heavy metals can negatively affect the life of plants, animals, and other living organisms. With metal oxides (Ti, Zn), membranes (ceramic, polymer, nanowire, polymer), carbon nanotubes (CNTs), nanopowder NPs, and other materials, the metal and harmful ions in wastewater can be subjected to photocatalysis, electrochemical oxidation, nanofiltration, and adsorption to improve water quality (Yadav et al. 2022a). Carbonaceous NMs, nano adsorbents, nanofibers, nanoclays (Biswas et al. 2020), zeolites (Murukutti & Jena 2022), dendrites, and nanomaterials (NMs) play vital roles in water treatment. Table 3 lists some of the roles of nanomaterials in water cleanup.

3.1. Nanotechnology-Driven Treatment of Automotive Wastewater

Automotive wastewater streams originating from vehicle wash facilities, paint shops, plating operations, and cooling systems are complex mixtures containing oils, surfactants, dyes, heavy metals (Pb, Cu, Zn, and Cr), and organic solvents, many of which are toxic and non-biodegradable (Egbosiuba et al. 2023, Ullah et al. 2024). Conventional treatment methods often fail to simultaneously address the diversity of pollutants, underscoring the need for advanced nanoremediation approaches.

Nanomaterials (NMs), such as graphene oxides, carbon nanotubes (CNTs), zero-valent iron nanoparticles (nZVI), and metal oxides (TiO_2, ZnO, Fe_3O_4), have shown promise in enhancing the removal of automotive wastewater contaminants. For instance, graphene-based adsorbents exhibit a high surface area and tunable functional groups, enabling the efficient sequestration of heavy metals such as Pb(II) and Cd(II), which are commonly discharged from plating baths (Wu et al. 2020, Luo et al. 2023). Similarly, nZVI and Fe_3O_4 nanocomposites provide reductive and magnetic functionalities, facilitating the removal of Cr(VI) and Ni(II) while allowing easy recovery of the adsorbent (Feng et al. 2022). In paint- and dye-rich effluents, photocatalytic nanomaterials such as TiO_2 and ZnO have been employed to degrade methylene blue, rhodamine B, and other complex organics under UV or solar irradiation, achieving high mineralization efficiency (Shi et al. 2023, Anil et al. 2022). Moreover, nanocomposite membranes integrating TiO_2 or Ag/TiO_2 enhance dye rejection while offering antibacterial and antifouling resistance, making them particularly suitable for car wash water recycling systems (Habib et al. 2020, Yang et al. 2012).

Overall, nanoremediation offers multifunctional benefits by combining adsorption, photocatalysis, and membrane separation to address the multifaceted nature of automotive wastewater. By improving pollutant removal efficiency and enabling water reuse, nanomaterials contribute directly to sustainable automotive operations and compliance with stringent environmental discharge regulations.

3.1.1. Applications of Nanomaterials in Wastewater Remediation

An inclusion of broader industries contaminants ensures wider caption of various automotive-relevant studies, and are justified by mapping contaminants to automotive sources, for example, methylene blue/rhodamine dyes to paint/coating rinses, Pb^{2+}/Cu^{2+}/Zn^{2+}/Cr^{6+} to plating/corrosion, oils/greases to wash bays/maintenance, and units/abbreviations are standardized ($mg \cdot g^{-1}$, %, $L \cdot m^{-2} \cdot h^{-1}$) for cross-comparison (Seyrek et al. 2023, Rajoria et al. 2022), as illustrated in Table 3

Where the units of COD, BOD are in $mg \cdot L^{-1}$, adsorption capacity in $mg \cdot g^{-1}$, membrane flux in $L \cdot m^{-2} \cdot h^{-1}$, TOC (%), removal (%) (Alazaiza et al. 2024).

Table 3 summarizes a wide spectrum of nanomaterials (Nano-adsorbents: Nads) applied for wastewater remediation, including carbon- and graphene-based adsorbents, zero-valent iron (nZVI), metal oxides, nanocomposites, and membrane-supported nanostructures. Across these classes, the adsorption capacities vary significantly from moderate values. For example, in a separate study, Chufa et al. (2021) used a GO nanoadsorbent to achieve a 4.71 qo ($mg.g^{-1}$) fluoride removal compared to the 35.6 $mg.g^{-1}$ fluoride removal reported by Xu and Wang (2017). This is an exceptionally high uptake, such as RGO–PVP at 1689 $mg.g^{-1}$ for Cu(II) (Zhang et al. 2014). This variation underscores the tunability of nanomaterials through structural modification, functionalization, and hybridization with other nanophases.

Contaminant removal is achievable in automotive wastewater treatment, where complex effluents often contain dyes (from paint shops), heavy metals (Pb, Cu, and Zn from plating and corrosion), oils, and organic contaminants. For example, in heavy metal removal, functionalized graphene and nZVI-based composites are deployed (Zou et al. 2016, Feng et al. 2022) to exhibit superior adsorption of Pb(II), Cd(II), Ni(II), and Cr(VI) contaminants, which are common in automotive plating wastewater, and dye degradation GO and $MnFe_2O_4$/rGO systems show high efficiency for methylene blue, malachite green, and rhodamine B (Shi et al. 2023, Chilakapati et al. 2021), directly relevant for treating residues from automotive paint and coating operations (Kusworo et al. 2021), multifunctional nanocomposite membranes (TiO_2 and Ag/TiO-$_2$based membranes not only achieve dye removal but also impart antibacterial and antifouling resistance (Yang et al. 2012, Habib et al. 2020),

Table 3: Automotive-relevant studies on nano-wastewater remediation.

S/N	Class	Nads Type	Adsorption capacity [$mg.g^{-1}$]	Contaminants/Remarks	References
1	Carbon & Graphene related Nads	Graphene	35.6, 89.37	Fluoride, Phosphate	Xu and Wang (2017), Vasudevan and Lakshmi (2012)
2		Graphene-CNT	81.97	Methylene blue	Ai and Jiang (2012)
3		Graphene Oxide (GO)	108.342, 80.775, 71.378	Au(III), Pd(II), Pt (IV), Zn(II)	Liu et al. (2013), Abdullah et al. (2019)
4			149.4	Endocrine-disrupting chemicals (17βEstradiol)	Mohebbi et al. (2025), Zhao et al. (2021)
5			16.83, 63.69	Methyl orange, Basic red 12	Robati et al. (2016)
6			5.496 [$mmoL.g^{-1}$]	Methyl green	Sharma & Das (2013)
7			Enrofloxacin (ENF): 45.035, Rhodamine B (RhB): 107.230	ENF and RhB	Yang et al. (2022)
8		GO- Fe_3O_4	MB: 37.5–108 [at 25 C and 9 pH]	MB	Shi et al. (2023)
9		RGO-PVP, MWCNTs, Nano-sized zero-valent iron	1689, 364.66 $mg.g^{-1}$, NA	Cu(II)	Zhang et al. (2014), Egbosiuba et al. (2023), Li et al. (2014)
10		RGO/Poly (acrylamide), CNTs/MnO_2, MWCNTs-kOH	1000, 78.74, 68.4%±5.0%	Pb (II)	Egbosiuba et al. (2022)
11		Polyethylenimine modified-GO hydrogel	N/A	Pb (II)-602, Hg (II)-374 and Cd (II)-181	Arshad et al. (2019)
12		RO membrane containing Si, Al, and Fe	105 [pH 7.5]	polysaccharides, proteins, and aromatic compounds	Ahmed et al. (2022)
13		$MnFe_2O_4$/reduced GO (MrGO)	Malachite green dye (MG): 156, and MB: 105	MG & MB	Anil et al. (2022)
14		GO/Fe_3O_4/chitosan	MB	Maximum monolayer capacity: 30.10$mg.gm^{-1}$	Tran et al. (2017)
15		rGO/$ZnCo_2O_4$	N/A	Antimicrobial, electrochemical and photocatalytic effect	Gnanamoorthy et al. (2021)
16		rGO/$CuNiO_2$	N/A	MB	Gnanamoorthy et al. (2022)
17		rGO/nZVI		Doxycycline	Abdelfatah et al. (2022)
18	Nano-sized zero-valent iron (nZVI)	nZVI	N/A	Cd(II), Ni (II), Pb (II), Hg(II), Cr(VI)	Feng et al. (2022)
19		Hydrotalcite-supported nZVI	N/A	Nitrate	Fan et al. (2023)
20		Nzvi-Cu bimetals, Solid carbon source/nZVI	N/A	Nitrate	Zhang et al. (2022), Sun et al. (2021)
21	Metal oxide-based NPs	ZnO	MB: 64-83%, COD: 15-53%, TOC: 31-74.12% N/A	MB, COD, TOC MB Dye, Ampicillin (Antibiotic) and MB, Zn (II), Cd (II), Hg (II)	Modi et al. (2023a) Modi et al. (2023b), Soltani et al. (2023), Sheela et al. (2012)
22		Amorphous IONPs from incense sticks ash (ISA)	N/A	Congo Red (CR)	Yadav et al. (2022a)
23		Mesoporous and floral shaped SiO_2 from CFA	N/A	Al, Pb, Cd, Cu, Cr, Ni, Co, Zn, Mn	Yadav et al. (2023)
24		$CaCO_3$ (calcite & vaterite) from ISA	N/A	Methyl Red Dye	Yadav et al. (2022b)
25		Fe_3O_4 NPs (leaf extract of Cola nitida)	MB [530.406 $mg.g^{-1}$] within 1hr.	MB	Mbachu et al. (2023)

Table Cont....

S/N	Class	Nads Type	Adsorption capacity [$mg.g^{-1}$]	Contaminants/Remarks	References
26		ZnO-W	MB: 20-88.21%, COD: 25-85.2, TOC: 46.5-92.04%	MB, COD, TOC	Modi et al. (2023b)
27		ZnO-Sb	MB: 21-91%, COD: 27-88.5, TOC: 48-95.34%	MB, COD, TOC	Modi et al. (2023a)
28	Nanocomposite membrane	Nano-TiO_2	12.2 [L. $m^{-2}.h^{-1}$]	Fouling resistance (FR), anti-bacterial, concurrent separation, and photo-catalytic oxidation, TiO2 nanowire growth via hy-drothermal processing photocatalytic under UV degradation of pharmaceuticals	Zhang et al. (2022)
29		Poly (vinylidene fluoride-hexafluoropropylene)-loaded with yttrium carbonate and Fe_3O_4		Removed arsenite (92.82) and arsenate (137.08) mg g−1	Salazar et al. (2022)
30		Cu-Al LDH@ polyvinylidene fluoride (PVDF) membrane (Cu-Al LDH/PVDF)	Adsorption capacity: 17.36 mg g-1	Erythrosin B dye	Abbasi et al. (2021)
31		Boron nitride nanosheets/PVDF	MB dye: 142.86 mg g^{-1}	100% removal of MB 2.2 times higher than the PVDF alone	Bangari et al. (2022)
32		Mesoporous TiO_2/PVDF	N/A	Photocatalytic membrane utilised in the removal of CR: 84%/71% and Reactive Yellow 145 (RY 145): 100%/87%	Erusappan et al. (2021)
33		Chitin nanowhisker/ PVDF (1%:15%)	72.6 mg g^{-1}	The ChNW reinforced PVDF material developed via electrospinning technique achieved an IR dye removal upto 88.9%.	Gopi et al. (2017)
34		NZVI/PVDF		Removed RhB (~80%), 2,4-dichlorophenol (2- CP) and 4-nitrophenol (4-NP) almost 100% within half an hour	He et al. (2020)
35		Ag/TiO_2 nano filter membrane	Bacteria	Authors utilized dip coating method to modify the vsurface of a composite polyamide Nanofiltration (NF) membrane different nanoparticles concentration for enhanced antifouling property. Modification led to bacterial (Bacillus subtilis and Escherichia coli)) growth reduction by 93% and 91% compared to the unmodified.	Habib et al. (2020)
36		Alumoxane-derived alumina membrane	Dye	Authors utilized Fumarate-alumoxane nanoparticles (Fum-ANPs) incorporated into a PES nanofiltration membrane in the enhancement of dye removal and antifouling capacity. It was reported that with the ANPs incorporated PES membrane, the removal efficiency of Direct Red 16 dye with the Fum-ANPs blended PES membrane was 99%, while it was 88.2% for the bare membrane sample.	Moradi, et al. (2023)

Table Cont....

S/N	Class	Nads Type	Adsorption capacity [$mg.g^{-1}$]	Contaminants/Remarks	References
37		Amino acid homopolymers derived silica membranes	Metal removal using physical (membrane separation, filtration, etc.), chemical (adsorption, ion-exchange, flocculation, etc.), Biological (microbes assisted reme-diation)) and electrochemical technologies.	Authors reviewed the applicability in aqueous media. Various nanomaterials used in heavy metal removal includes carbon based (Graphene, GO, RGO), silicone-based (nanospheres), zero-valent iron (nanoscale zerovalent iron), and magnetic nanoparticles (Iron-oxide based magnetic NP and NC).	Kumar et al. (2021)
38		Polymeric or alumina membranes with Au nanoparticles	4- Nitrophenol-based wastewater treatment using metathesis and anion exchange reactions to stabilize silver (AgNPs) nanoparticles.	Authors developed a stable catalyst for the growing needs in wastewater treatment by catalytic reduction of 4-nitrophenol (4-NP) to 4-aminophenol (4-AP) in the presence of $NaBH_4$. The results indicated that 100% of 4-NP was converted to 4-AP within 6 min and the rate constant (k) was found to be 8.33×10^{-3} s^{-1}.	Naushad et al. (2022)
39		Ruthenium oxide (Ti/RuO_2)	Polycyclic aromatic hydrocarbons (PAHs) removal from oil and gas wastewater streams. They possess mutagenic, carcinogenic, and teratogenic potential; hence, they are toxic to deoxyribonucleic acid (DNA).	The authors electrochemically oxidised utilising a ruthenium oxide (Ti/RuO_2) anode in a lab-scale electrolytic batch cell. They reported that electrocatalytic oxidation with a Ti/RuO_2 anode is a potentially effective technique for removing PAHs from aqueous solutions.	Isa et al. (2023)
40	Nanocomposite Catalysts	Palladium/sodium borosilicate nanocomposite using *Euphorbia-milii* extract	Chromium (VI), nitro compounds, and organic dyes	Authors reported the timely removal of constituents, thus Cr (VI) – 900s 4-NP - 170s MB – 3s CR – 210s MO – 277s	Nasrollahzadeh et al. (2018)
41		Fe_2O_3 + (GO– Fe_2O_3)	Rhodamine B and 4-nitrophenol	Authors treated wastewater containing pollutants under visible-light irradiation (>420 nm) along with H_2O_2.	Guo et al. (2013)

critical for maintaining long-term performance in recycling car wash wastewater), and catalytic oxidation systems: (nanocomposite catalysts such as Pd/sodium borosilicate (Nasrollahzadeh et al. 2018) demonstrate rapid degradation of nitro-compounds and dyes, offering opportunities for rapid treatment of organic-rich automotive effluents). Overall, the table highlights that nanomaterials provide multi-target remediation capacity (metals, dyes, and microbes), high adsorption efficiencies, and functional versatility. Therefore, their integration into automotive wastewater treatment systems can enhance pollutant removal, support water reuse, and contribute to compliance with stringent environmental regulations in the transportation sector. Despite the many positive attributes of nanomaterials, as indicated in Table 3, they have some limitations, as noted in the next section.

4. DRAWBACKS OF NANOTECHNOLOGY IN WASTEWATER REMEDIATION

The performance impact of nanotechnologies is high when dye-rich paint/coating effluents and mixed-metal streams (Pb, Cu, Zn, Cr), selective adsorbents (GO, nZVI), and photocatalysis (TiO_2/ZrO_2/ZnO, TiO_2–Ag membranes) deliver high removal and antifouling benefits, enabling modular reuse (Seyrek et al. 2023, Fazekas et al. 2024). In contrast, high-oil emulsions lacking effective pre-demulsification and antifouling/self-cleaning surfaces promote fouling, and flux loss persists unless hydrophilic or underwater super-oleophobic and photocatalytic self-cleaning layers are integrated (Huang et al. 2018, Baig & Waheed 2023). Meanwhile, the associated risks and benefits

can be quantified via weight fouling, nanotoxicity/release, cost, and stability against measured gains ($mg \cdot g^{-1}$, %, flux, cleaning interval) and include regulatory/LCA perspectives (NNI 2024, Nizam et al. 2021).

The treatment of automotive-related wastewater remains a global issue owing to its heterogeneous and often recalcitrant composition. Conventional wastewater treatment processes, including coagulation, flocculation, sedimentation, activated sludge systems, filtration, and chemical oxidation, have been widely applied in industrial sectors for decades. However, their performance in addressing the complexity of automotive effluents has been questioned, particularly in the context of oily wastewater and emerging pollutants. Fig. 6 highlights the persistent limitations of these conventional methods, which undermine their effectiveness and sustainability (Abuhasel et al. 2021).

One of the most significant issues is membrane fouling, which occurs in pressure-driven processes such as ultrafiltration, nanofiltration, and reverse osmosis. Fouling results from the accumulation of oil droplets, suspended solids, and microbial biofilms on membrane surfaces, leading to rapid permeability loss, shortened operational life, and increased chemical cleaning requirements (Medeiros et al. 2022, Sisay et al. 2023, Jang et al. 2021). Similarly, corrosion in metallic treatment units caused by acidic and saline conditions compromises the durability of the infrastructure, while also generating secondary contaminants such as dissolved iron, copper, or zinc ions (Ekerenam et al. 2025). Sedimentation and sludge generation are also problematic in coagulation–flocculation systems, which are traditionally applied to automotive effluents to remove suspended solids, oil, and dyes. These processes often yield large volumes of sludge containing heavy metals and toxic hydrocarbons, creating further challenges for safe disposal and increasing operational costs (Muvel et al. 2013, Crini and Lichtfouse 2019). Furthermore, these methods typically require high chemical inputs, raising concerns about sustainability and potential secondary pollution (Kadadou et al. 2024).

Another limitation is the high energy consumption of conventional treatment trains. For example, distillation and thermal evaporation processes, while effective in reducing salinity and recovering water, are highly energy-intensive and economically impractical for large-scale deployment in automotive manufacturing plants (Adham et al. 2018, Gude 2018). Pressure-driven systems similarly require high operational pressures to overcome osmotic gradients in oily or saline effluents, further increasing costs (Dieter et al. 2018). The complex nature of oily wastewater presents additional challenges to its treatment. Automotive effluents frequently contain free oil, emulsified oil, and chemically stabilized oil–water emulsions (O/W). Conventional gravity separation or skimming systems are insufficient to destabilize these emulsions, which remain stable owing to the presence of surfactants, lubricants, and fine particulates in automotive processes (Medeiros et al. 2022, Abuhasel et al. 2021). Advanced chemical demulsifiers and electrocoagulation techniques offer improvements but are often expensive and may still leave residual oil fractions (Zhang et al. 2022).

In addition to these technical challenges, environmental and regulatory issues persist. Many conventional treatment systems do not adequately remove emerging contaminants, such as microplastics, nanoparticles, and recalcitrant organic molecules, which accumulate in receiving water bodies and pose risks to ecosystems and public health (Hanif et al. 2020, Singh et al. 2017). Moreover, the variability in wastewater composition between facilities (painting shops, electroplating lines, radiator manufacturing, and car washes) complicates the standardization of treatment protocols, necessitating costly site-specific customization.

To address these challenges, scientific and technological advancements have increasingly shifted toward modern and integrated treatment systems. These include hybrid membrane bioreactors (MBR), electrochemical oxidation coupled with adsorption, advanced oxidation processes (AOPs) such as ozonation and photocatalysis, and nanotechnology-enabled separation systems (Aziz et al. 2025, Asheghmoalla & Mehrvar 2024). Integrated approaches aim to overcome the limitations of individual methods. For example, coupling adsorption with photocatalysis enhances both the removal efficiency and degradation of persistent pollutants, whereas hybrid membranes with nanomaterial coatings mitigate fouling and extend their lifespan (Paiu et al. 2025, Ahmed et al. 2025). Nevertheless, while integrated methods show promise, challenges remain regarding their scalability, cost-effectiveness, and environmental safety. Thus, the limitations of conventional wastewater treatment highlight the urgent need for innovative, multifunctional, and sustainable technologies that can address the diverse contaminant profile of automotive wastewater while minimizing energy and resource footprints.

Although improved heat transmission in base fluids can be a significant benefit of nanotechnology, which has allowed for the execution of sophisticated mathematical computations using smartphones instead of supercomputers or portable chips with hundreds of memory cells, the high thermal conductivity (TC), specific heat, and thermoelectric properties of nanoparticles in the advancement of nanotechnology in general production, especially in the manufacturing of pharmaceuticals and atomic weapons, have resulted in contamination that has negatively affected the

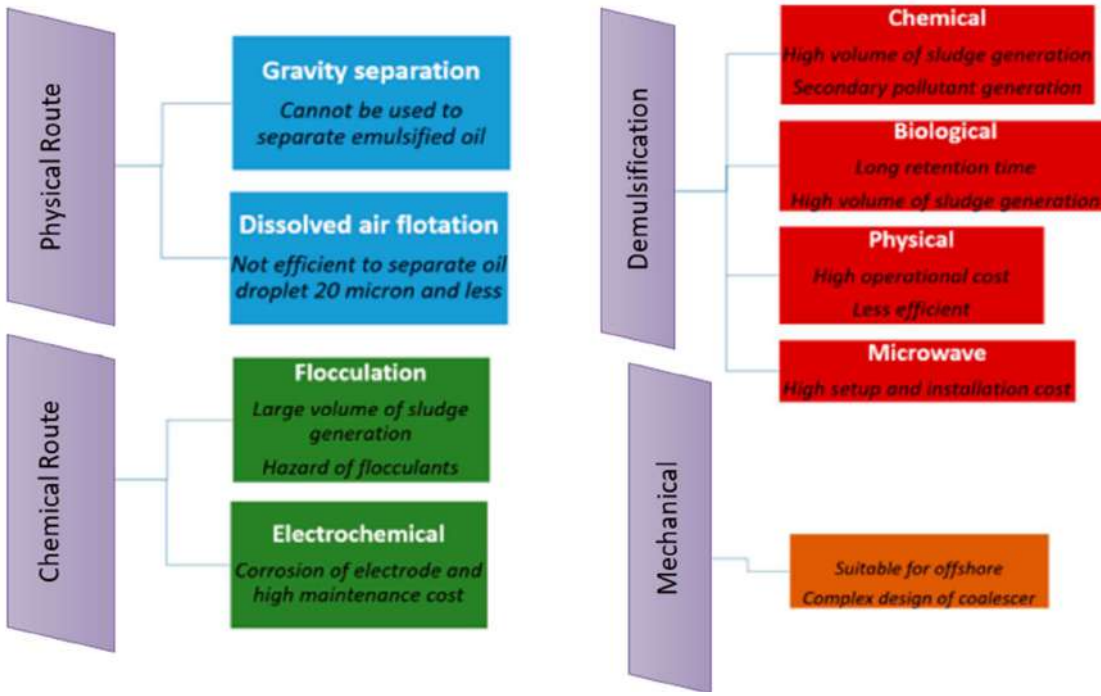


Fig. 6: Limitation of the conventional Greasy-oil wastewater removal technique. Adapted from Abuhasel et al. (2021).

environment (Del Prado-Audelo et al. 2021, Phillips 2021, Almuallim et al. 2022, He et al. 2022). Two examples of these features are the high TCs of metal nanoparticles (NPs) and carbon nanotubes (CNTs), which have TCs twice as high as diamonds and are therefore excellent heat conductors (Kumanek and Janas 2019).

Although beneficial in the domains of engineering, material sciences, and medicine, nanotechnology comes with high costs because of increased operating and raw material costs. Additionally, nanotoxicity is a risky feature associated with nanoparticles. These NPs may enter the ecosystem through a variety of channels, including wastewater, which could lead to nanotoxicity (Ray and Bandyopadhyay 2021), particularly causing metal-associated diseases, such as those caused by the use of silver (Ag), titanium dioxide (TiO_2), and zinc oxide (ZnO) in toothpaste and cosmetic products. Furthermore, MXenes are challenging to synthesize and have poor stability properties, particularly at high temperatures. Carbon nanotubes (CNTs) have low selectivity in adsorption with low adsorption capacity, and carbon nitride (C3N4) has low capacity for sorption of metal ions and has high photocatalytic decomposition of organic pollutants (Alharbi et al. 2020).

4.1. Regulatory and LifeCycle Assessment Considerations

The governance of engineered nanomaterials is increasingly shaped by evolving regulatory frameworks, such as the EU REACH regulation, which now includes nanospecific information requirements but continues to face challenges related to inadequate test methods, incomplete datasets, and difficulties in defining and grouping nanoforms (Blue Frog Scientific 2025). Complementing REACH, international bodies such as the OECD have developed nanospecific test guidelines and harmonized methodologies to support safety evaluation, exposure assessment, and cross-national regulatory consistency (OECD 2025). From a sustainability perspective, life cycle assessment (LCA) provides a structured means of evaluating the environmental impacts of nanomaterials across their full lifespan. However, nanoparticle LCAs face significant methodological barriers, including limited fate and exposure data, a lack of nano-specific characterization factors, challenges in quantifying nanomaterials within complex matrices, and uncertainties associated with particle transformation during use and disposal (Schwirn et al. 2020). Therefore, integrating regulatory requirements with improved LCA methodologies is essential for developing nanomaterials that are not only effective but also aligned with safety, environmental protection, and longterm sustainability goals.

5. CONCLUSIONS

Nanotechnology can significantly improve the removal of dyes, metals, and oils under defined operating conditions and

in combination with complementary processes, rather than universally transforming pollutants into safe, clean water, with emphasis on modular integration, targeted applications, and evidence-based adoption supported by regulatory and LCA assessments, as supported by Kholopo & Rathebe (2025) and Corominas et al. (2020). This study shows that nano-enhanced bioremediation is a conceptual framework for future research. Integrated trains (e.g., biofilm carriers + UV-Fenton, adsorption + AOP + MBR) show promise but require pilot-scale validation on real automotive effluents to quantify fouling, nanoparticle release, and life-cycle footprints, as noted by Pottekkatt et al. (2025) and Malik et al. (2023).

For automotive-based production and maintenance operations, clean water can be produced by treating a variety of pollutants with nanoengineered materials such as photocatalysts, nanometals, nanoadsorbents, and nanomembranes. Nevertheless, nanotechnology in wastewater treatment has advantages that conventional water treatment approaches cannot match.

Nanofilters' effectiveness in comparison to traditional systems, for instance:

- Compared to conventional methods, they are more efficient, have large surface areas that are readily cleaned by back-flushing, and require less pressure to move water across the filter, which significantly lowers operating expenses.
- Many of the technologies can be easily incorporated or modified as modules to improve particle retention and remove impurities from systems that are already in place. As a result, nanotechnology is crucial to the purification of water, especially when using nanocomposite membranes that have higher process efficiency.

Notable drawbacks also exist that should put nanoparticle applications in check. For example, functional nanomaterial-modified surfaces have the potential to release or emit nanoparticles to the environment over a long period, which makes national and international regulations necessary. Meanwhile, with consideration for decentralized treatment, point-of-use, and heavily degradable contaminants, as is the case in the automotive setting, nanotechnology/nanoparticle is extremely essential for wastewater purification.

Lastly, the proposal states that different degrees of treatment are necessary for suspended particles and hydrocarbons from car wash or equipment wash facilities, such as

- Pre-treatment (oil-water separator) to remove floatable materials from raw wastewater by means of a grit chamber or screening.
- Primary treatments, which involve chemically treating the wastewater (coagulation, flocculation, and neutralization). For additional treatment, the principal sludge (heavy solids) is separated from the floating oil, grease, and other lighter solids.
- Secondary treatments include biological processes that eliminate suspended and dissolved biological matter (BOD and COD), which include ion-exchange, coagulation, ozonation, neutralization, adsorption, and chlorination.
- Tertiary treatments include the use of UV radiation, ozone, and chlorine to sterilize wastewater that has been treated. At this stage, the last of the residual suspended solids from earlier treatment stages are eliminated.

While removing physical, biological, and chemical impurities from wastewater is the main objective of nanotechnology, it also aims to soften the water. Highly porous nanoparticles can be used to absorb water in a spongy manner, but they can also be utilized to resist salt and other pollutants. For instance, membrane-embedded hydrophilic nanoparticles can repel bacteria and organic chemicals that eventually clog conventional membranes. In addition to photocatalysis, electrochemical oxidation, nanofiltration, and adsorption using metal oxides (Ti, Zn), membranes (ceramic, polymer, nanowire, polymer), CNTs, and nanopowder NPs, for improved water quality, nanotechnology has greatly enhanced the drawbacks of treatment technologies, however, the drawbacks highlighted in this study are that oil-based wastewater treated with magnetic sorbent nanoparticles acts as emulsifiers, containing microbes and resulting in micro-organism-infested wastewater. Therefore, nanoenhanced bioremediation is an efficient way to treat wastewater with a variety of compositions. To accomplish nano-enhanced bioremediation for completely enhanced wastewater remediation, a nanotechnology technique that combines bioremediation and nano-remediation is thus proposed. Therefore, further research is still needed to understand the best ways to combine the various treatment systems to create several of the finest treatment methods for automotive water treatment.

5.1. Future Prospect

Multifunctional and hybrid systems that combine nano-remediation with biological processes for increased treatment efficiency are the key to the future of nanotechnology in automotive wastewater remediation. For the removal of hydrocarbons, heavy metals, and persistent organic pollutants from vehicle effluents while using the least amount of energy possible, emerging nano-enabled membranes, photocatalysts, and adsorbents show great promise. However, more research

is required to address challenges, including nanoparticle release, long-term environmental stability, and compliance with changing regulatory frameworks. Therefore, future studies should focus on developing nanocomposites that are environmentally safe, recyclable, and affordable and can be easily integrated into current treatment infrastructure. Furthermore, developing decentralized point-of-use devices specifically for car washes and vehicle repair shops will be essential for ensuring scalability. One important avenue is nano-enhanced bioremediation, which offers a sustainable solution for complex wastewater streams by fusing microbial degradation pathways with the high reactivity of nanoparticles. In the end, a methodical comprehension of treatment synergies will make it possible to create durable, flexible, and adaptable nanotechnology-based solutions that satisfy industrial and environmental requirements.

6. ACKNOWLEDGMENTS

Authors acknowledges the support of the University of South Africa for the completion of this study.

7. REFERENCES

Abbasi, M., Sabzehmeidani, M.M., Ghaedi, M., Jannesar, R. and Shokrollahi, A., 2021. Facile fabrication of leaf coral-like structured Cu-Al LDH/PVDF composite adsorptive membrane with enhanced adsorption performance. *Materials Science and Engineering: B*, 267, p.115086. [DOI]

Abdelfatah, A.M., El-Maghrabi, N., Mahmoud, A.E.D. and Fawzy, M., 2022. Synergetic effect of green-synthesized reduced graphene oxide and nano-zero valent iron composite for the removal of doxycycline antibiotic from water. *Scientific Reports*, 12, pp.1–19. [DOI]

Abdulkareem, A.S., Hamzat, W.A., Tijani, J.O., Egbosiuba, T.C., Mustapha, S. and Abubakre, O.K., 2023. Isotherm, kinetics, thermodynamics and mechanism of metal ions adsorption from electroplating wastewater using treated and functionalized carbon nanotubes. *Journal of Environmental Chemical Engineering*, 11(1), p.109180. [DOI]

Abdullah, N., Yusof, N., Abu-Shah, M.H., Wan-Ikhsan, S.N., Ng, Z.-C. and Maji, S., 2019. Hydrous ferric oxide nanoparticles hosted porous polyethersulfone adsorptive membrane: Chromium (VI) adsorptive studies and its applicability for water/wastewater treatment. *Environmental Science and Pollution Research*, 26, pp.20386–20399. [DOI]

Abuhasel, K., Kchaou, M., Alquraish, M., Munusamy, Y. and Jeng, Y.T., 2021. Oily wastewater treatment: Overview of conventional and modern methods, challenges, and future opportunities. *Water*, 13(7), p.980. [DOI]

Adham, S., Hussain, A., Minier-Matar, J., Janson, A. and Sharma, R., 2018. Membrane applications and opportunities for water management in the oil & gas industry. *Desalination*, 440, pp.2–17.

Afolalu, S.A., Ikumapayi, O.M., Ogedengbe, T.S., Kazeem, R.A. and Ogundipe, A.T., 2022. Waste pollution, wastewater and effluent treatment methods – an overview. *Materials Today: Proceedings*, 62, pp.3282–3288. [DOI]

Ahmadi, F., Zinatizadeh, A.A., Asadi, A., McKay, T. and Azizi, S., 2020. Simultaneous carbon and nutrients removal and PHA production in a novel single air lift bioreactor treating an industrial wastewater. *Environmental Technology & Innovation*, 18(4), 100776. [DOI]

Ahmed, M., Nada, T., Amin, S., Anwar, T. and Mohamed, A., 2022. Characterization of fouling for a full-scale seawater reverse osmosis plant on the Mediterranean Sea: Membrane autopsy and chemical cleaning efficiency. *Groundwater for Sustainable Development*, 16, p.100704. [DOI]

Ahmed, M.A., Mahmoud, S.A. and Mohamed, A.A., 2025. Interfacially engineered metal oxide nanocomposites for enhanced photocatalytic degradation of pollutants and energy applications. *RSC Advances*, 15(20), pp.15561–15603. [DOI]

Ahn, C.K., Park, D., Woo, S.H. and Park, J.M., 2008. Removal of cationic heavy metal from aqueous solution by activated carbon impregnated with anionic surfactants. *Journal of Hazardous Materials*, 154(1–3), pp.116–123. [DOI]

Ai, L. and Jiang, J., 2012. Removal of methylene blue from aqueous solution with self-assembled cylindrical graphene–carbon nanotube hybrid. *Chemical Engineering Journal*, 192, pp.156–163. [DOI]

Alazaiza, M.Y.D., Alzghoul, T.M., Amr, S.A., Bangalore Ramu, M. and Nassani, D.E., 2024. Bibliometric insights into car wash wastewater treatment research: Trends and perspectives. *Water*, 16, p.2034. [DOI]

Alharbi, N.S., Hu, B., Hayat, T., Rabah, S.O., Alsaedi, A., Zhuang, L. and Wang, X., 2020. Efficient elimination of environmental pollutants through sorption-reduction and photocatalytic degradation using nanomaterials. *Frontiers of Chemical Science and Engineering*, 14, pp.1–12. [DOI]

Ali, H., Khan, E. and Ilahi, I., 2019. Environmental chemistry and ecotoxicology of hazardous heavy metals: Environmental persistence, toxicity, and bioaccumulation. *Journal of Chemistry*, 2019, pp.1–14. [DOI]

Almuallim, B., Harun, W.S.W., Al-Rikabi, I.J. and Mohammed, H.A., 2022. Thermally conductive polymer nanocomposites for filament-based additive manufacturing. *Journal of Materials Science*, 57, pp.3993–4019. [DOI]

Anil, G., Scaria, J. and Nidheesh, P.V., 2022. Removal of synthetic dye from aqueous solution using $MnFe_2O_4$-GO catalyzed heterogeneous electro-Fenton process. *Water*, 14, p.3350. [DOI]

Arshad, F., Selvaraj, M., Zain, J., Banat, F. and Haija, M.A., 2019. Polyethylenimine modified graphene oxide hydrogel composite as an efficient adsorbent for heavy metal ions. *Separation and Purification Technology*, 209, pp.870–880. [DOI]

Asheghmoalla, M. and Mehrvar, M., 2024. Integrated and hybrid processes for the treatment of actual wastewaters containing micropollutants: A review on recent advances. *Processes*, 12, 339. [DOI]

Aziz, K.H.H., Mustafa, F.S., Karim, M.A.H. and Hama, S., 2025. Pharmaceutical pollution in the aquatic environment: Advanced oxidation processes as efficient treatment approaches – A review. *Materials Advances*, 6, pp.3433–3454. [DOI]

Babakura, B., Adamu, H., Yuguda, A.U., Tafida, U.I., Akanang, H., Muhammad, K.Y. and Sabo, A., 2023. Adsorptive removal of chromium from tannery wastewater by chitosan modified-activated carbon of Hyphaene thebaica. *Science Forum: Journal of Pure and Applied Sciences*, 23, pp.191–214.

Bagyalakshmi, S., Balamurugan, K.S., Mathankumar, M., Sivakami, A. and Devi, N.R., 2025. Exploring metal organic frameworks/MXene based composite for environmental applications – A critical review. *Journal of Molecular Structure*, 1334, p.141838. [DOI]

Baig, U. and Waheed, A., 2023. A facile strategy for fabrication of nanocomposite ultrafiltration membrane with photocatalytic selfcleaning. *npj Clean Water*, 6, pp.1–13. [DOI]

Bangari, R.S., Yadav, A., Bharadwaj, J. and Sinha, N., 2022. Boron nitride nanosheets incorporated polyvinylidene fluoride mixed matrix membranes for removal of methylene blue from aqueous stream. *Journal of Environmental Chemical Engineering*, 10, p.107052. [DOI]

Bhat, S.U. and Qayoom, U., 2021. Implications of sewage discharge on freshwater ecosystems. In: *Sewage – Recent Advances, New Perspectives and Applications*. London: IntechOpen, pp.1–18. [DOI]

Biswas, B., Labille, J. and Prelot, B., 2020. Clays and modified clays in remediating environmental pollutants. *Environmental Science and Pollution Research*, 27, pp.38381–38383. [DOI]

Blue Frog Scientific, 2025. Big Challenges Remain for Nanomaterials Under REACH. Retrieved December 20, 2025, from https://bluefrogscientific.com

Bokov, D., Jalil, A.T., Chupradit, S., Suksatan, W., Ansari, M.J., Shewael, I.H., Valiev, G.H. and Kianfar, E., 2021. Nanomaterial by sol–gel method: Synthesis and application. *Advances in Materials Science and Engineering*, 2021, pp.1–21.

Chigare, R., Kamat, S. and Patil, J., 2019. A review of the automobile industries wastewater treatment methodologies. *International Research Journal of Engineering and Technology*, 6, pp.974–977.

Chilakapati, R., Kumar, S., Satyanarayana, S. and Behara, D., 2021. Adsorptive removal of methylene blue and malachite green dyes from aqueous solutions using graphene oxide. *Zeitschrift für Physikalische Chemie*, 235(10), pp.1285–1305. [DOI]

Cho, G., Park, Y., Hong, Y.K. and Ha, D.H., 2019. Ion exchange: An advanced synthetic method for complex nanoparticles. *Nano Convergence*, 6, pp.1–17. [DOI]

Chufa, B., Gonfa, B. and Anshebo, T., 2022. Graphene oxide nanoadsorbent for the removal of fluoride ion from groundwater: Adsorbent performance and adsorption mechanism. *Journal of Nanotechnology*, 2022, pp.1–12. [DOI]

Corominas, L., Byrne, D.M., Guest, J.S., Hospido, A., Roux, P., Shaw, A. and Short, M.D., 2020. The application of life cycle assessment (LCA) to wastewater treatment: A best practice guide and critical review. *Water Research*, 184, p.116058. [DOI]

Crini, G. and Lichtfouse, E., 2019. Advantages and disadvantages of techniques used for wastewater treatment. *Environmental Chemistry Letters*, 17, pp.145–155.

De Volder, M.F., Tawfick, S.H., Baughman, R.H. and Hart, A.J., 2013. Carbon nanotubes: Present and future commercial applications. *Science*, 339, pp.535–539. [DOI]

Del Prado-Audelo, M.L., García Kerdan, I., Escutia-Guadarrama, L., Reyna-González, J.M., Magaña, J.J. and Leyva-Gómez, G., 2021. Nanoremediation: Nanomaterials and nanotechnologies for environmental cleanup. *Frontiers in Environmental Science*, 9, p.793765. [DOI]

Deshpande, B., Agrawal, P., Yenkie, M. and Dhoble, S., 2020. Prospective of nanotechnology in degradation of wastewater: New challenges. *Nano-Structures & Nano-Objects*, 22, p.100442. [DOI]

Dieter, C.A., Maupin, M.A., Caldwell, R.R., Harris, M.A., Ivahnenko, I., Lovelace, J.K., Barber, N.L. and Linsey, K.S., 2018. Water availability and use science program: Estimated use of water in the United States in 2015. *U.S. Geological Survey Circular*, 1441, pp.1–76. [DOI]

Durotoye, T.O., Adeyemi, A.A., Omole, D.O. and Onakunle, O., 2018. Impact assessment of wastewater discharge from a textile industry in Lagos, Nigeria. *Cogent Engineering*, 5, pp.1–11.

Egbosiuba, T.C., Ani, I.J., Okafor, B.O., Mustapha, S., Tijani, J.O., Igwegbe, C.A., Okoye, C.C., Ulakpa, W.C., Ezennajiego, E.E. and Abdulkareem, A.S., 2023. Carbon nanotubes–based nanoadsorbents in wastewater treatment. In: Verma, C., Aslam, J. and Khan, M.E., eds. *Adsorption through Advanced Nanoscale Materials*. Micro and Nano Technologies. Amsterdam: Elsevier, pp.103–141. [DOI]

Egbosiuba, T.C., Egwunyenga, M.C., Tijani, J.O., Mustapha, S., Abdulkareem, A.S. and Kovo, A.S., 2022. Activated multi-walled carbon nanotubes decorated with zero valent nickel nanoparticles for arsenic, cadmium and lead adsorption from wastewater in batch and continuous flow modes. *Journal of Hazardous Materials*, 423, p.126993. [DOI]

Ekerenam, O.O., Ikeuba, A.I., Njoku, C.N., Njoku, D.I., Emori, W., Nwokolo, I.K., Etim, I.N., Okonkwo, B.O., Udoh, I.I., Daniel, E.F., Uzoma, P.C., Awonusi, B.O., Kolawole, S.K., Etim, I.P. and Olanrele, O.S., 2025. Advancements in corrosion studies and protective measures for copper and copper-based alloys in varied environmental conditions. *Results in Engineering*, 26, p.105257. [DOI]

Environmental Protection Agency, 2007. *Nanotechnology White Paper*. Washington, DC: Office of the Science Advisor, EPA100/B-07/001, p.120.

Erusappan, E., Thiripuranthagan, S., Radhakrishnan, R., Durai, M., Kumaravel, S. and Vembuli, T., 2021. Fabrication of mesoporous TiO_2/PVDF photocatalytic membranes for efficient photocatalytic degradation of synthetic dyes. *Journal of Environmental Chemical Engineering*, 9, p.105776. [DOI]

Fall, C., López-Vázquez, C.M., Jiménez-Moleon, M.C., Bâ, K.M., Díaz-Delgado, C., García-Pulido, D. and Lucero-Chavez, M., 2007. Carwash wastewaters: Characteristics, volumes, and treatability by gravity oil separation. *Revista Mexicana de Ingeniería Química*, 6(2), pp.175–184.

Fan, J., Zhang, B., Zhu, B., Shen, W., Chen, Y. and Zeng, F., 2023. New insight into the mechanism for the removal of methylene blue by hydrotalcite-supported nanoscale zero-valent iron. *Water*, 15, p.183. [DOI]

Fayed, M., Shewitah, M.A., Dupont, R.R., Fayed, M. and Badr, M.M., 2023. Treatability study of car wash wastewater using upgraded physical technique with sustainable flocculant. *Sustainability*, 15(11), p.8581. [DOI]

Fazekas, A.F., Gyulavari, T., Argoston, A., Janovák, L., Kopniczky, J., László, Z. and Veréb, G., 2024. Enhanced photocatalytic and filtration performance of TiO_2–Ag composite coated membranes. *Separations*, 11(4), pp.1–15. [DOI]

Feng, J., Lang, G., Li, T., Zhang, J. and Jiang, Z., 2022. Enhanced removal performance of zero-valent iron towards heavy metal ions by assembling Fe-tannin coating. *Journal of Environmental Management*, 319, p.115619. [DOI]

Gavrilescu, M., 2010. Environmental biotechnology: Achievements, opportunities and challenges. *Dynamic Biochemistry, Process Biotechnology and Molecular Biology*, 4(1), pp.1–36.

Gnanamoorthy, G., Karthikeyan, V., Ali, D., Kumar, G., Yadav, V.K. and Narayanan, V., 2022. Global popularization of $CuNiO_2$ and their rGO nanocomposite leveraged to the photocatalytic properties of methylene blue. *Environmental Research*, 204, p.112338. [DOI]

Gnanamoorthy, G., Karthikeyan, V., Ali, D., Kumar, G., Jenifer, S.G. and Yadav, V.K., 2021. Realization of rGO/$ZnCo_2O_4$ nanocomposites enhanced for the antimicrobial, electrochemical and photocatalytic activities. *Diamond and Related Materials*, 120, 108677. [DOI]

Michael, R., Templeton, R. and Butler, D., 2023. *Introduction to Wastewater Treatment*. Ventus Publishing

Gopi, S., Balakrishnan, P., Pius, A. and Thomas, S., 2017. Chitin nanowhisker (ChNW)-functionalized electrospun PVDF membrane for enhanced removal of indigo carmine. *Carbohydrate Polymers*, 165, pp.115–122. [DOI]

Gottschalk, F., Sonderer, T., Scholz, R.W. and Nowack, B., 2009. Modeled environmental concentrations of engineered nanomaterials (TiO_2, ZnO, Ag, CNT, fullerenes) for different regions. *Environmental Science & Technology*, 43, pp.9216–9222.

Gude, G., 2018. *Sustainable Desalination Handbook: Plant Selection, Design and Implementation*. Elsevier Science, pp.1–594.

Guo, S., Zhang, G., Guo, Y. and Jimmy, C.Y., 2013. Graphene oxide–Fe_2O_3 hybrid material as highly efficient heterogeneous catalyst for degradation of organic contaminants. *Carbon*, 60, pp.437–444. [DOI]

Habib, Z., Khan, S-J., Ahmad, N.M., Muhammad, H., Shahzad, A., Jamal, Y. and Hashmi, I., 2020. Antibacterial behaviour of surface-modified composite polyamide nanofiltration (NF) membrane by immobilizing Ag-doped TiO_2 nanoparticles. *Environmental Technology*, 41(28), pp.3657–3669. [DOI]

Hanif, H., Waseem, A., Kali, S., Qureshi, N.A., Majid, M., Iqbal, M.,

Ur-Rehman, T., Tahir, M., Yousaf, S., Iqbal, M.M., Khan, I.A. and Zafar, M.I., 2020. Environmental risk assessment of diclofenac residues in surface waters and wastewater: A hidden global threat to aquatic ecosystems. *Environmental Monitoring and Assessment*, 192(4), p.204. [DOI]

He, Z., Mahmud, S., Yang, Y., Zhu, L., Zhao, Y. and Zeng, Q., 2020. Polyvinylidene fluoride membrane functionalized with zero valent iron for highly efficient degradation of organic contaminants. *Separation and Purification Technology*, 250, p.117266. [DOI]

He, X., Zhang, K., Wang, H., Zhang, Y., Xiao, G. and Niu, H., 2022. Tailored carbon-based aramid nanofiber nanocomposites with highly anisotropic thermal conductivity and superior mechanical properties for thermal management. *Carbon*, 199, pp.367–378. [DOI]

Huang, S., Robin, H.A.R. and Xuelin, T., 2018. Antifouling membranes for oily wastewater: Wetting–fouling interplay. *Current Opinion in Colloid & Interface Science*, 11, pp.90–109. [DOI]

Isa, M.H., Ajab, H. and Yakub, A., 2023. Economical electrochemical process for PAHs removal from offshore produced water. *Journal of Hazardous Materials Advances*, 12, pp.1–5.

Jang, Y., Kim, H.-S., Ham, S.-Y., Park, J.-H. and Park, H.-D., 2021. Investigation of critical sludge characteristics for membrane fouling in a submerged membrane bioreactor: Role of soluble microbial products and extracted extracellular polymeric substances. *Chemosphere*, 271, p.129879. [DOI]

Joy, J., Krishnamoorthy, A., Tanna, A., Kamathe, V., Nagar, R. and Srinivasan, S., 2022. Recent developments on the synthesis of nanocomposite materials via ball milling approach for energy storage applications. *Applied Sciences*, 12(18), pp.1–34.

Kabdasli, I., Arslan-Alaton, I., Ölmez-Hanci, T. and Tünay, O., 2009. Treatment of automotive wastewater by Fenton's reagent. *Environmental Technology*, 30(11), pp.1133–1140. [DOI]

Kadadou, D., Tizani, L., Alsafar, H. and Hasan, S.W., 2024. Analytical methods for determining environmental contaminants of concern in water and wastewater. *MethodsX*, 2, p.102582. [DOI]

Karchiyappan, T., 2022. Studies on treatment of automotive industry wastewater using ozonation, electro-Fenton and chitosan-based coagulation process. *Current Research in Green and Sustainable Chemistry*, 5, p.100178. [DOI]

Khan, S. and Hossain, M.K., 2022. Nanoparticle-based polymer composites. In: Rangappa, S.M., Parmeswaranpillai, J., Yashas Gowda, T.G., Siengchin, S. and Seydibeyoglu, M., eds. *Nanoparticle-Based Polymer Composites*. 1st ed. London: Woodhead Publishing, pp.1–550.

Kholopo, M. and Rathebe, P.C., 2025. Lifecycle, toxicology, and exposure pathways of functional nanomaterials in water treatment: Implications for environmental and human health. *Sustainable Environment*, 11(1), pp.1–16. [DOI]

Koul, B., Yadav, D., Singh, S., Kumar, M. and Song, M., 2022. Insights into the domestic wastewater treatment (DWWT) regimes: A review. *Water*, 14(21), p.3542. [DOI]

Kumanek, B. and Janas, D., 2019. Thermal conductivity of carbon nanotube networks: A review. *Journal of Materials Science*, 54, pp.7397–7427. [DOI]

Kumar, R., Rawuel, P. and Rauwel, E., 2021. Nanoadsorbants for the removal of heavy metals from contaminated water: Current scenario and future directions. *Processes*, 9(8), pp.1–29.

Kusworo, T.D., Susanto, H., Aryanti, N., Rokhati, N., Widiasa, I.N., Al-Aziz, H., Utomo, D.P., Masithoh, D. and Kumoro, A.C., 2021. Preparation and characterization of photocatalytic PSf-TiO□/GO nanohybrid membrane for the degradation of organic contaminants in natural rubber wastewater. *Journal of Environmental Chemical Engineering*, 9(2), 105066. [DOI]

Landrigan, P.J., Fuller, R., Acosta, N.J.R., Adeyi, O., Arnold, R., Basu, N., Balde, A.B., Bertollini, R., Bose-O'Reilly, S., Boufford, J.I., Breysse, P.N., Chiles, T., Mahidol, C., Coll-Seck, A.M., Cropper, M.L., Fobil, J., Fuster, V., Greenstone, M., Haines, A., Hanrahan, D., Hunter, D., Khare, M., Krupnick, A., Lanphear, B., Lohani, B., Martin, K., Mathiasen, K.V., McTeer, A.A., Murray, C.J.L., Ndahimananjara, J.D., Perera, F., Potočnik, J., Preker, A.S., Ramesh, J., Rockström, J., Salinas, C., Samson, L.D., Sandilya, K., Sly, P.D., Smith, K.R., Steiner, A., Stewart, R.B., Suk, W.A., Schayck, O.C.P., Yadama, G.N., Yumkella, K. and Zhong, M., 2018. The Lancet Commission on pollution and health. *The Lancet*, 391, pp.462–512.

Li, S., Wang, W., Liu, Y. and Zhang, W.X., 2014. Zero-valent iron nanoparticles (nZVI) for the treatment of smelting wastewater: A pilot-scale demonstration. *Chemical Engineering Journal*, 254, pp.115–123. [DOI]

Liu, L., Liu, S., Zhang, Q., Li, C., Bao, C. and Liu, X., 2013. Adsorption of Au(III), Pd(II), and Pt(IV) from aqueous solution onto graphene oxide. *Journal of Chemical & Engineering Data*, 58, pp.209–216. [DOI]

Luo, J., Bello, D. and Pagsuyoin, S., 2023. Long-term wastewater-based surveillance and impacts of the COVID-19 pandemic on drug use trends in a U.S. Northeast rural town. *Science of the Total Environment*, 877, p.162806. [DOI]

Malik, S., Muhammad, K. and Waheed, Y., 2023. Nanotechnology: A revolution in modern industry. *Molecules*, 28, p.661. [DOI]

Matlochova, A., Placha, D. and Rapantova, N., 2014. The application of nanoscale materials in groundwater remediation. *Polish Journal of Environmental Studies*, 22, pp.1401–1410.

Mbachu, A.C., Babayemi, K.A., Egbosiuba, C.T., Ike, I.J., Ani, J.I. and Mustapha, S., 2023. Green synthesis of iron oxide nanoparticles by Taguchi design of experiment method for effective adsorption of methylene blue and methyl orange from textile wastewater. *Results in Engineering*, 19, p.101198. [DOI]

Medeiros, A.D.M., Silva Junior, C.J.G., Amorim, J.D.P., Durval, I.J.B., Costa, A.F.S. and Sarubbo, L.A., 2022. Oily wastewater treatment: Methods, challenges, and trends. *Processes*, 10, p.743. [DOI]

Mekuye, B. and Abera, B., 2023. Nanomaterials: An overview of synthesis, classification, characterization, and applications. *Nano Select*, 4(8), pp.486–501.

Membracon, 2025. Water Treatment for the Automotive Sector. Retrieved September 15, 2025, from https://www.membracon.co.uk/

Meyer, M.F., Powers, S.M. and Hampton, S.E., 2019. An evidence synthesis of pharmaceuticals and personal care products (PPCPs) in the environment: Imbalances among compounds, sewage treatment techniques, and ecosystem types. *Environmental Science & Technology*, 53(22), pp.12961–12973. [DOI]

Moatmed, S., Khedr, H., El-Dek, S., Kim, H.-Y. and El-Deen, A., 2019. Highly efficient and reusable superhydrophobic/superoleophilic polystyrene@Fe_3O_4 nanofiber membrane for high-performance oil/water separation. *Journal of Environmental Chemical Engineering*, 7, p.103508. [DOI]

Modi, S., Yadav, V.K., Amari, A., Alyami, A.Y., Gacem, A. and Harharah, H.N., 2023a. Photocatalytic degradation of methylene blue dye from wastewater by using doped zinc oxide nanoparticles. *Water*, 15, p.2275. [DOI]

Modi, S., Yadav, V.K., Amari, A., Osman, H., Igwegbe, C.A. and Fulekar, M.H., 2023b. Nanobioremediation: A bacterial consortium-zinc oxide nanoparticle-based approach for the removal of methylene blue dye from wastewater. *Environmental Science and Pollution Research*, 30, pp.72641–72651. [DOI]

Mohebbi, S., Khatibi, A. and Balarak, D., 2025. Endocrine disruptor (17 β-estradiol) removal by polypyrrole-based molecularly imprinted polymer: Kinetic, isotherms and thermodynamic studies. *Applied Water Science*, 15, p.43. [DOI]

Monney, I., Donkor, E.A. and Buamah, R., 2020. Clean vehicles, polluted waters: Empirical estimates of water consumption and pollution loads of the carwash industry. *Heliyon*, 6(5), e03952. [DOI]

Moradi, G., Zinadini, S. and Rahimi, M., 2023. The enhancement in dye

removal and antifouling capability of PES nanofiltration membrane modified with fumarate-alumoxane nanoparticles. *Journal of Applied Research in Water and Wastewater*, 10, pp.161–166. [DOI]

Murukutti, M.K. and Jena, H., 2022. Synthesis of nano-crystalline zeolite-A and zeolite-X from Indian coal fly ash, its characterization and performance evaluation for the removal of Cs^{+} and Sr^{2+} from simulated nuclear waste. *Journal of Hazardous Materials*, 423, p.127085. [DOI]

Muvel, H., Jindal, M.J., Tewari, P.K. and Anand, V., 2013. Minimizing oil pollution: A review of current status and its treatment options. *RSC Sustainability*, 3(9), pp.3681–3723. [DOI]

Nasrollahzadeh, M., Sajjadi, M., Maham, M., Sajadi, S.M. and Barzinjy, A.A., 2018. Biosynthesis of the palladium/sodium borosilicate nanocomposite using Euphorbia milii extract and evaluation of its catalytic activity in the reduction of chromium(VI), nitro compounds and organic dyes. *Materials Research Bulletin*, 102, pp.24–35. [DOI]

NNI (National Nanotechnology Initiative), 2024. *National Nanotechnology Initiative Environmental, Health, and Safety Research Strategy: 2024 Update*. OSTP/NSTC, pp.1–53. Retrieved December 20, 2025, from https://www.nano.gov

Naushad, M., Ahamad, T. and Khan, M.R., 2022. Remediation of wastewater containing 4-nitrophenol using ionic liquid stabilized nanoparticles: Synthesis, characterizations and applications. *Chemosphere*, 303(2), p.135173. [DOI]

Nizam, N.U.M., Hanafiah, M.M. and Woon, K.S., 2021. Life cycle assessment of nanomaterials: Current practices, challenges, and future prospects. *Nanomaterials*, 11(12), p.3324. [DOI]

Nowack, B. and Bucheli, T., 2007. Occurrence, behaviour and effects of nanoparticles in the environment. *Environmental Pollution*, 150, pp.5–22.

Nurmi, J.T., Tratnyek, P.G. and Sarathy, V., 2005. Characterization and properties of metallic iron nanoparticles: Spectroscopy, electrochemistry and kinetics. *Environmental Science & Technology*, 39(5), pp.1221–1230.

OECD (Organisation for Economic Co-operation and Development), 2025. *Nanomaterials and Advanced Materials – OECD Work on Safety Evaluation and Assessment*. Retrieved December 20, 2025, from https://www.oecd.org

Olawade, I.G., Apostol, T. and Rada, E.C., 2013. Wastewater management in the automotive industry. *UPB Scientific Bulletin, Series D: Mechanical Engineering*, 75(1), pp.147–158.

Owhonka, A., Fubara, E.F. and Justice, O.B., 2021. Wastewater quality – its impact on the environment and human physiology: A review. *International Journal of Advance Research and Innovation*, 9(4), pp.43–58. [DOI]

Paiu, M., Lutic, D., Favier, L. and Gavrilescu, M., 2025. Heterogeneous photocatalysis for advanced water treatment: Materials, mechanisms, reactor configurations, and emerging applications. *Applied Sciences*, 15, p.5681. [DOI]

Pottekkatt, S., Zakkariya, G.J.R., Christo, P.N., Nair, G., Gopal, M. and Pawels, R., 2025. Integrated biological and UV-Fenton processes for the treatment of automobile service station wastewater. *Water Science and Technology*, 91(8), pp.977–992. [DOI]

Phillips, J.D., 2021. Energy harvesting in nanosystems: Powering the next generation of the internet of things. *Frontiers in Nanotechnology*, 3, p.633931. [DOI]

Rafiei-Sarmazdeh, Z., Zahedi-Dizaji, S.M. and Kang, A.K., 2019. Two-dimensional nanomaterials. In: *Nanostructures*. London: IntechOpen, pp.1–144. [DOI]

Rajoria, S., Vashishtha, M. and Sangal, V.K., 2022. Treatment of electroplating industry wastewater: A review on the various techniques. *Environmental Science and Pollution Research*, 29, pp.72196–72246. [DOI]

Ray, S.S. and Bandyopadhyay, J., 2021. Nanotechnology-enabled biomedical engineering: Current trends, future scopes, and perspectives. *Nanotechnology Reviews*, 10, pp.728–743. [DOI]

Rehman, K., Imran, A., Amin, I. and Afzal, M., 2019. Enhancement of oil field-produced wastewater remediation by bacterially augmented floating treatment wetlands. *Chemosphere*, 217, pp.576–583. [DOI]

Robati, D., Mirza, B., Rajabi, M., Moradi, O., Tyagi, I. and Agarwal, S., 2016. Removal of hazardous dyes BR 12 and methyl orange using graphene oxide as an adsorbent from aqueous phase. *Chemical Engineering Journal*, 284, pp.687–697. [DOI]

Saeed, M., Alshammari, Y., Majeed, S.A. and Al-Nasrallah, E., 2020. Chemical vapour deposition of graphene — synthesis, characterisation, and applications: A review. *Molecules*, 25(17), pp.1–62.

Salazar, H., Martins, P.M., Valverde, A., Fernández de Luis, R., Vilas-Vilela, J.L. and Ferdov, S., 2022. Reusable nanocomposite membranes for highly efficient arsenite and arsenate dual removal from water. *Advanced Materials Interfaces*, 9, p.2101419. [DOI]

Seyrek, M., Boran, F. and Okutan, M., 2023. Treatment of automotive paint wastewater: Photocatalytic degradation of methylene blue using ZrO_2. *International Journal of Automotive Science and Technology*, 7(4), pp.316–324. [DOI]

Schwirn, K., Voelker, D., Galert, W., Quik, J. and Tietjen, L., 2020. Environmental risk assessment of nanomaterials in the light of new obligations under the REACH Regulation. *Integrated Environmental Assessment and Management*, 16(5), pp.706–717. [DOI]

Sharma, P. and Das, M.R., 2013. Removal of a cationic dye from aqueous solution using graphene oxide nanosheets: Investigation of adsorption parameters. *Journal of Chemical & Engineering Data*, 58, pp.151–158. [DOI]

Sheela, T., Nayaka, Y.A., Viswanatha, R., Basavanna, S. and Venkatesha, T.G., 2012. Kinetics and thermodynamics studies on the adsorption of Zn(II), Cd(II) and Hg (II) from aqueous solution using zinc oxide nanoparticles. *Powder Technology*, 217, pp.163–170. [DOI]

Shi, S., Jia, M., Li, M., Zhou, S., Zhao, Y., Zhong, J., Dai, D. and Qiu, J., 2023. ZnO@g-C_3N_4 S-scheme photocatalytic membrane with visible-light response and enhanced water treatment performance. *Colloids and Surfaces A: Physicochemical and Engineering Aspects*, p.667, 131259.

Singh, B.J., Chakraborty, A. and Sehgal, R., 2017. A systematic review of industrial wastewater management: Evaluating challenges and enablers. *Journal of Environmental Management*, 348, p.119230. [DOI]

Sisay, E.J., Al-Tayawi, A.N., László, Z. and Kertész, S., 2023. Recent advances in organic fouling control and mitigation strategies in membrane separation processes: A review. *Sustainability*, 15, p.13389. [DOI]

Soltani, S., Gacem, A., Choudhary, N., Yadav, V.K., Alsaeedi, H. and Modi, S., 2023. Scallion peel mediated synthesis of zinc oxide nanoparticles and their applications as nano fertilizer and photocatalyst for removal of organic pollutants from wastewater. *Water*, 15, p.1672. [DOI]

Soni, A.K. and Jha, R.K., 2024. Nanotechnology's applications and potential in various fields. *Cureus*, 16(4), p.e59234. [DOI]

Statista, 2023. *Number of Vehicles in Use Worldwide 2006–2015*. Retrieved September 21, 2025, from https://www.statista.com/statistics/

Su, H., Zhang, D., Antwi, P., Xiao, L., Liu, Z., Deng, X., Asumadu-Sakyi, A.B. and Li, J., 2020. Effects of heavy rare earth element (yttrium) on partial-nitritation process, bacterial activity and structure of responsible microbial communities. *Science of the Total Environment*, 705(6), p.135797. [DOI]

Sun, H., Zhou, Q., Zhao, L. and Wu, W., 2021. Enhanced simultaneous removal of nitrate and phosphate using novel solid carbon source/zero-valent iron composite. *Journal of Cleaner Production*, 289, p.125757. [DOI]

Theoneste, S., Nsanzumukiza, M.V. and Nshimiyimana, F., 2020. The effluent quality discharged and its impacts on the receiving environment: Case of Kacyiru sewerage treatment plant, Kigali, Rwanda. *Zenodo,* 15, pp.78-91. [DOI]

Tian, X., Song, Y., Shen, Z., Zhou, Y., Wang, K., Jin, X., Han, Z. and Liu, T., 2020. A comprehensive review on toxic petrochemical wastewater pretreatment and advanced treatment. *Journal of Cleaner Production*, 245, 118692. [DOI]

Tran, H., Bui, L., Thuy, D., Le, D., Huynh, C. and Anh, T.X., 2017. Graphene oxide/Fe_3O_4/chitosan nanocomposite: A recoverable and recyclable adsorbent for organic dyes removal. *Materials Research Express*, 4, p.035701. [DOI]

Ullah, M., Innocenzi, V., Ayedi, K., Veglio, F. and Ippolito, N.M., 2024. Automotive wastewater treatment processes and technologies: A review. *ACS ES&T Water*, 4(8), pp.3189–3211. [DOI]

UNESCO-WWAP, 2014. World Water Development Report 4: Managing Water under Uncertainty and Risks. Paris: UNESCO. Retrieved August 24, 2025, from http://www.unesco.org/new/en/naturalsciences/environment/water/wwap/wwdr/wwdr4-2012

UNESCO-WWAP, 2024. World Water Development Report 4: Managing Water under Uncertainty and Risks. Paris: UNESCO. Retrieved August 24, 2025, from http://www.unesco.org/new/en/naturalsciences/environment/water/wwap/wwdr/wwdr4-2012

Vasudevan, S. and Lakshmi, J., 2012. The adsorption of phosphate by graphene from aqueous solution. *RSC Advances*, 2, pp.5234–5242. [DOI]

Westerdahl, D., Fruin, S., Sax, T., Fine, P.M. and Sioutas, C., 2005. Mobile platform measurements of ultrafine particles and associated pollutant concentrations on freeways and residential streets in Los Angeles. *Atmospheric Environment*, 39(20), pp.3597–3610.

Wu, L., Li, M., Sun, Q. and Zhang, C., 2020. Preparation of RGO and anionic polyacrylamide composites for removal of Pb(II) in aqueous solution. *Polymers*, 12, p.1426. [DOI]

Xiu, Z., Zhang, Q., Puppala, H.L., Colvin, V.L. and Alvarez, P.J., 2012. Negligible particle-specific antibacterial activity of silver nanoparticles. *Nano Letters*, 12, pp.4271–4275.

Xu, L. and Wang, J., 2017. The application of graphene-based materials for the removal of heavy metals and radionuclides from water and wastewater. *Critical Reviews in Environmental Science and Technology*, 47, pp.1042–1105. [DOI]

Yadav, V.K., Amari, A., Gacem, A., Elboughdiri, N., Eltayeb, L.B. and Fulekar, M.H., 2023. Treatment of fly-ash-contaminated wastewater loaded with heavy metals by using fly-ash-synthesized iron oxide nanoparticles. *Water*, 15, p.908. [DOI]

Yadav, V.K., Gnanamoorthy, G., Ali, D., Bera, S.P., Roy, A. and Kumar, G., 2022. Cytotoxicity and removal of Congo red dye in aqueous solution using synthesized amorphous iron oxide nanoparticles from incense sticks ash waste. *Journal of Nanomaterials*, 2022, pp.1–12. [DOI]

Yadav, V.K., Yadav, K.K., Gacem, A., Gnanamoorthy, G., Ali, I.H. and Khan, S.H., 2022. A novel approach for the synthesis of vaterite and calcite from incense sticks ash waste and their potential for remediation of dyes from aqueous solution. *Sustainable Chemistry and Pharmacy*, 29, p.100756. [DOI]

Yang, Y., Wang, H., Li, J., He, B., Wang, T. and Liao, S., 2012. Novel functionalized nano-TiO_2 loading electrocatalytic membrane for oily wastewater treatment. *Environmental Science & Technology*, 46, pp.6815–6821. [DOI]

Yang, J. and Shojaei, S., 2022. Removal of drug and dye from aqueous solutions by graphene oxide: Adsorption studies and chemometrics methods. *npj Clean Water*, 5, pp.1–10. [DOI]

Zhang, J., Niu, Y., Zhou, Y., Ju, S. and Gu, Y., 2022. Green preparation of nano-zero-valent iron-copper bimetals for nitrate removal: Characterization, reduction reaction pathway, and mechanisms. *Advanced Powder Technology*, 33, p.103807. [DOI]

Zhang, Y., Chi, H., Zhang, W., Sun, Y., Liang, Q., Gu, Y. and Jing, R., 2014. Highly efficient adsorption of copper ions by a PVP-reduced graphene oxide based on a new adsorption mechanism. *Nano-Micro Letters*, 6, pp.80–87. [DOI]

Zhang, J., Zheng, M., Zhou, Y., Yang, L., Zhang, Y., Wu, Z., Liu, G. and Zheng, J., 2022. Preparation of Nano-TiO_2-modified PVDF membranes with enhanced antifouling behaviors via phase inversion: Implications of nanoparticle dispersion status in casting solutions. *Membranes*, 12, p.386. [DOI]

Zhao, H., Cao, P., Lu, L., Li, F., Pang, C.H. and Wu, T., 2022. Co-regulation of dispersion, exposure and defect sites on CeO_2 (111) surface for catalytic oxidation of Hg^0. *Journal of Hazardous Materials*, 424(A), p.126566. [DOI]

Zhao, B., Xu, X., Zhang, R. and Cui, M., 2021. Remediation of Cu(II) and its adsorption mechanism in aqueous system by novel magnetic biochar derived from co-pyrolysis of sewage sludge and biomass. *Environmental Science and Pollution Research*, 28, pp.16408–16419. [DOI]

Zhongming, Z., Linong, L., Wangqiang, Z. and Wei, L., 2020. *Sanitation and Wastewater Atlas of Africa*. Nairobi/Arendal: UNEP. Retrieved September 2, 2025, from https://www.unep.org/resources/publication/sanitation-and-wastewater-atlas-africa

Zhou, P., Li, D.J., Zhang, C., Ping, Q., Wang, L. and Li, Y.M., 2024. Comparison of different sewage sludge pretreatment technologies for improving sludge solubilization and anaerobic digestion efficiency: A comprehensive review. *Science of the Total Environment*, 921, p.171175. [DOI]

Zou, Y., Wang, X., Khan, A., Wang, P., Liu, Y.-H., Alsaedi, A., Hayat, T. and Wang, X., 2016. Environmental remediation and application of nanoscale zero-valent iron and its composites for the removal of heavy metal ions: A review. *Environmental Science & Technology*, 50(14), pp.7290–7304. [DOI]

Nature Environment and Pollution Technology
An International Quarterly Scientific Journal

p-ISSN: 0972-6268
(Print copies up to 2016)
e-ISSN: 2395-3454

Vol. 25 | No. 3 | Article ID B4421 | 2026

Original Research Paper

https://doi.org/10.46488/NEPT.2026.v25i03.B4421

Open Access Journal

Microplastic Pollution in Shoreline Sediments of Selected Rivers of Mizoram, North-East India: A Baseline Assessment and Preliminary Report

Joseph Vanlalsawma Sailo, Malsawmhriatzuala Jeremy and Chawngte Laldinsangi†

Department of Life Sciences, Pachhunga University College, Mizoram University (A Central University), Aizawl, 796001, Mizoram, India

†Corresponding author: Chawngte Laldinsangi; laldinsangi.c@gmail.com; laldinsangi@pucollege.edu.in

Abbreviation: Nat. Env. & Poll. Technol.
Website: www.neptjournal.com

Received: 18-12-2025
Revised: 25-02-2026
Accepted: 01-03-2026

Key Words:

Microplastics
Sediments
Pollution
Himalayas
Mizoram
Rivers

Citation for the Paper:

Sailo, J.V., Jeremy, M. and Laldinsangi C., 2026. Microplastic pollution in shoreline sediments of selected rivers of Mizoram, north-east India: A baseline assessment and preliminary report. *Nature Environment and Pollution Technology*, 25(3), B4421. https://doi.org/10.46488/NEPT.2026.v25i03.B4421

Note: From 2025, the journal has adopted the use of Article IDs in citations instead of traditional consecutive page numbers. Each article is now given individual page ranges starting from page 1.

Copyright: © 2026 by the authors
Licensee: Technoscience Publications
This article is an open access article distributed under the terms and conditions of the Creative Commons Attribution (CC BY) license (https://creativecommons.org/licenses/by/4.0/).

ABSTRACT

Microplastics have emerged as another dimension of hazardous and persistent pollutants afflicting every corner of the globe, even permeating critical biodiversity hotspots. This study aims to serve as a preliminary report on the occurrence and assessment of MP pollution in shore sediments of four selected rivers in the state of Mizoram, which lies in one of the sensitive biodiversity hotspots in India, and is also a part of the eastern Himalayan range. There have been minimal studies on microplastic pollution in this region despite its critical ecological location. Four freshwater rivers, namely Chite, Tlawng, Serlui-A, and Tuirial, were selected for the study due to their proximity to urban settlements and have been subjected to rampant plastic pollution. The study revealed that MPs were detected from all sampling sites, and abundance was highest in Chite, which runs through parts of Aizawl city. Particles within the size range of 0.15-0.25 mm were found to be the highest in numbers in all sampling locations, while MPs between 3-5 mm were the least in number. The shapes of MPs were varied, constituting fragments, fibers, pellets, and spheres, with fibers (40%) being the dominant shape overall. Polyethylene was found to be the dominant polymer type among particles analyzed using FTIR spectroscopy. This study contributes to the imperative assessment of MP pollution in river sediments of the eastern Himalayan region of India, as comprehensive research in this regard is still lacking.

1. INTRODUCTION

Plastics are an indispensable part of modern life, and they are used extensively in all parts of the globe. However, their indiscriminate use and improper disposal, along with inadequate and futile recycling efforts, have contributed to the massive scale of plastic pollution in all types of environments, both terrestrial and aquatic (Rhodes 2018, Bajt 2021). Consequently, plastic pollution has yielded another dimension of hazardous pollutants in the form of microplastics (MPs), which are classified as minuscule plastic objects that range in size between 0.1 and 5mm (Desforges et al. 2014). These particles have been categorized as pollutants of emerging concern, and their detection has been reported in terrestrial and aquatic ecosystems, in the air, and even inside the tissues of living organisms, including humans (Smith et al. 2018, Goyal et al. 2023, Zhao et al. 2023). Aquatic environments, in particular, are highly susceptible to MP pollution, due to surface water run-offs that carry MP particles from anthropogenic sources such as industries, agricultural fields, waste dumping grounds, and even personal care products (Rhodes 2018, Koelmans et al. 2019). Plastics are manufactured with the addition of various chemicals additives to enhance the quality and performance of the products such as dyes, lubricants, plasticizers, flame retardants, heat stabilizers and anti-microbials (Smith et al. 2018, Sendra et al. 2021) and several studies have suggested that there is a high possibility of these substances leaching into their immediate environment via

ingested MPs, leading to deleterious effects in living systems that ingest them directly or indirectly (Bridson et al. 2023, Gulizia et al. 2023). MP pollution in aquatic environments, both freshwater and marine, is particularly concerning due to their positions as critical entry points into the food chain, which may lead to bioaccumulation and subsequently affect a wide range of organisms, including humans. Numerous studies have reported such findings (Cole et al. 2014; Van Cauwenberghe & Janssen 2014, Krause et al. 2021, Patil et al. 2022, Gunaalan et al. 2023). MPs of different size ranges have been detected in both freshwater and marine environments all across the globe, in different continents, and such identifications have been reviewed extensively (Xu et al. 2021, Vivekanand et al. 2021; Wang et al. 2022). MPs have been classified into various categories depending on their physical characteristics, such as fragments, pellets, filaments, and granules. Chemically, MPs generally constitute monomers of polyethylene (PE), polyethylene terephthalate (PET), polypropylene (PP), polystyrene (PS), and polyvinyl chloride (PVC), high-and low-density polyethylene (HD/LD-PE), etc. (Anbumani & Kakkar 2018).

MPs in rivers accumulate through numerous sources, including household hygiene items that are used for bathing and cleansing clothes, plastic waste, and fabric waste (Ghosh et al. 2023). Washing synthetic fabrics can result in the generation of significant amounts of microplastic fibers (MFs) in wastewater, which can then enter river systems (McCormick et al. 2016). Additionally, extensive use of fishing nets and lines that are left in the water, angling, and other techniques used to catch fish (Ghanbari et al. 2022, Karthikeyan et al. 2023) also contribute to MP contamination. Other prominent sources include vehicle tires, city dust, and road markings (Ramaremisa et al. 2022). Several freshwater systems serve as major routes for improperly managed plastic debris to enter the oceans. It has been reported that roughly 80% of plastic debris enters the oceans from land-based waste via streams and rivers and is further weathered by the natural elements into smaller particles such as MPs (Wang et al. 2024).

This issue of MP pollution has gained considerable concern and traction, especially within the last decade, due to its persistence and ubiquity in all corners of the globe. Considering the possible havoc they reportedly wreak on living organisms that are exposed to these particles, detection and analysis of the extent of pollution in different ecosystems are urgently warranted, especially in areas such as biodiversity hotspots, where their effects could be disastrous. One such example is the state of Mizoram in the eastern Himalayan region of India. The state is a small landlocked region in the north-east corner of the country that lies within one of the recognized biodiversity hotspots in the world (Pautu et al. 2023) and boasts endemic and new species of plants and animals being discovered constantly. Although plastic pollution is a persistent problem that has devastated several river systems within the state as well as other rivers in the Himalayan region, there is still an acute lack of studies pertaining to the extent and impacts of MP presence and pollution in the rivers of Mizoram. Most studies focusing on MP pollution in India have been limited to the sediments and waters of the eastern and western coastal regions, with minimal reports from inland water bodies in the Himalayan regions (Tsering et al. 2021).

Aizawl, the capital of Mizoram, is a densely populated city situated in the northeast corner of India. Being the largest and most heavily populated city in the state, it has also seen a rapid increase in plastic pollution, especially within the last two decades, and improper disposal of garbage has considerably polluted several rivers and streams that are close to the urban settlements. One study by Singh et al. (2023) quantifying plastic waste generation in Aizawl city reported plastic consumption of 13.06 g/capita/day, with plastic packaging contributing the most, followed by carry bags in residential, commercial, and dumping areas. This study also highlights the frequent improper disposal of these plastic wastes that choke drains and eventually make their way into streams and rivers. An unfortunate example is the Chite river, which runs through certain areas of Aizawl city, and indiscriminate dumping of plastic garbage has severely decimated this river. Although there is evident plastic pollution in the rivers that are in proximity to Aizawl, there has been no comprehensive study on the detection and extent of MP pollution. Determining the degree of pollution in these freshwater rivers is crucial, since they are critical lifelines for the people. One of these rivers selected for the assessment, Serlui-A, is the source of drinking water for the municipality of Aizawl. Another river selected for the study, Tuirial, also lies close to the Aizawl municipal garbage dumping ground, rendering it extremely vulnerable to MP runoff. Since there have been minimal investigations to evaluate plastic and MP occurrence in the state, this study, therefore, aims to address this existing data gap for the first time in this region. The investigation serves to provide a baseline assessment of MP pollution in riverbank sediments of selected rivers that are close to residential and commercial settlements, namely Chite, Tuirial, Tlawng, and Serlui-A, during the late monsoon (September, 2023). However, since this study was conducted as a preliminary baseline assessment (as no prior studies have been done in this regard) and no funding was received for the work, only one time point (i.e., late monsoon) has been selected to gauge the extent of MP pollution in riverbank sediments.

2. MATERIALS AND METHODS

2.1. Site of Study

This study was conducted in four selected rivers of Mizoram, north-east India, which lies in the Eastern Himalayan region (Fig. 1). The four rivers, namely, Chite, Tlawng, Tuirial, and Serlui-A, were selected based on their proximity to residential and commercial areas as well as their susceptibility to waste runoff from urban areas. Detailed information regarding the sampling sites is given in Table 1. Their location is a cause for higher susceptibility to plastic pollution as a result of high population density, as well as prevalent cases of improper garbage disposal in and around the municipal areas. Chite flows into Tuirial River, and Serlui-A is also a tributary of Tlawng. Sample collection sites are shown in Fig. 2.



Fig. 1: Google Map showing the geographical location of the study site, i.e., Mizoram, north-east India.

Table 1: Location details of the sampling sites.

Sl.No	River	Latitude and Longitude	Population Degree	River Section
1.	Chite	23°43′59.2″ N, 92°44′17.5″ E	Urban	Upstream
2.	Tlawng	23°42′43.46″ N, 92°39′51.17″ E	Rural	Upstream
3.	Serlui A	23°54′00″ N, 92°36′36″ E	Rural	Downstream
4.	Tuirial	23°43′07″ N, 92°47′58″ E	Semi-urban	Downstream



Fig. 2: Collection sites of shore sediment samples. (A) Google Maps showing locations of study sites in Tlawng and Serlui-A. (B, C) Sample collection sites in Tlawng and Serlui-A, respectively (D, E). Google Maps of Chite and Tuirial, respectively. (F, G) Sample collection locations in Tuirial and Chite, respectively.

2.2. Collection of Samples

Sample collection was performed as per the method stated by Tibbetts et al. (2018). In brief, sediment samples were collected from a selected site on the banks of the four selected rivers, and all samples were collected in September 2023, i.e., the monsoon season, when there is an increased rate of rainfall and water flow in rivers.

At all collection sites from each riverbank, samples from four different spots at depths of 10 cm were collected with a small steel shovel into 250 ml glass beakers, which resulted in a 1 kg bulk sample of sediment (n=3). Two samples were collected with a distance of approximately 3 feet between collection sites, and the other two were collected 10 feet from the previous two and again spaced approximately 3 feet from each other (Tibbetts et al. 2018). The sediment samples from each river were stored in steel containers prewashed with distilled water and then brought into the laboratory for further treatment. The 1 kg mass of sediments from each river was covered using aluminum foil right after collection to prevent plastic contamination. The materials that were used for collecting sediments were cleaned with filtered or distilled water to wash off other contaminants and plastics (Sarijan et al. 2018).

2.3. Sample Processing

The sediments were sieved into five different fractions using brass test sieves having mesh sizes of 5 mm, 3 mm, 1 mm, 0.5 mm, 0.25 mm, and 0.15 mm (Manikarn test sieve, MSWLABS, India). Hence, the size range for each fraction is 0.15-0.25 mm, 0.25-0.5 mm, 0.5-1 mm, 1-3 mm, and 3-5 mm. Larger stone particles and other kinds of identifiable organic debris visibly larger than 5 mm were identified and manually removed. The sediments were wet-sieved with filtered water to speed up the process and to separate the sediments and MPs into their respective fraction sizes. The sieved sediments with 5 different size fractions were then transferred to separate 250 ml beakers, and all beakers were marked with their river source. All beakers were covered with aluminum foil to prevent contamination by plastics from the surroundings. Excess water contained in the sediments was carefully removed with filter paper. Alkali digestion using 10% KOH was done to remove any remaining organic matter, at a volume ratio of 1:3 (Saad et al. 2022). Sediment samples were dried in a hot air oven for 45 hours at 50°C. After drying, sediments for each size fraction were taken in a marked beaker for the density separation.

2.4. Density separation using $ZnCl_2$

Zinc chloride ($ZnCl_2$) solution was used for density separation of MPs. The solution of 1.5 g/cm^3 density was prepared by dissolving 1500 g of $ZnCl_2$ into 1 L (final volume) of distilled water in a laminar flow hood to avoid air contamination. This was then poured into the samples and rigorously stirred for 40 seconds. Samples were then left untouched until all the sediments settled at the bottom. The supernatant containing floating MPs was then allowed to overflow into a petri dish by the addition of fresh $ZnCl_2$. To improve extraction efficiency and minimize particle loss, two consecutive density separation cycles were conducted for each sediment sample, and the supernatants from both cycles were then combined before analysis. The particles separated via this method were then transferred to a clean petri dish, covered, and oven-dried at 37°C for 48 hours. The selected density was considered sufficient to float common polymers such as PE, PP, PS, and a substantial proportion of PET and PA particles, while allowing efficient separation from the mineral sediment matrix.

2.5. Morphological Identification, Quantification, and Chemical Analysis of MPs

The isolated particles from all size fractions were visually identified based on their physical characteristics and quantified carefully under a light microscope (Leica S9i, Leica Microsystems) as proposed in the literature. The particles were sorted mainly by their sizes as well as two main shapes, i.e., fragments and fibers. Since the accuracy and effectiveness of visual identification in extremely small MPs can be unreliable (Balestra & Bellopede, 2022), particles smaller than 0.15 mm were not taken into consideration, as they are also difficult to handle. Quantification of MPs was done by counting the number of identifiable particles for each size fraction. Replicate samples were treated as within-site subsamples since collection was done only at one location per river, and statistical comparisons reflect variability among sampling sites rather than independent river-scale units.

In addition, several MP particles of different shapes were selected randomly, and their surface characteristics were analyzed using a scanning electron microscope (SEM; Hitachi TM 4000 Plus). MPs were placed on a carbon tape on a metal stub and then coated with gold using an ion sputter MC1000 for 15 minutes and viewed under a Scanning Electron Microscope (HITACHI TM4000Plus) at 15 kV.

To determine the polymer composition of isolated MPs, 20 particles (5 from each sampling location) from the 0.5 to 0.1 mm range were randomly selected for Fourier transform infrared spectroscopy (FTIR) analysis. Functional group identification was done using a Bruker 3000 Hyperion FTIR spectrometer (Germany) between 400 and 4000 cm^{-1}, and samples were recorded on OPUS software. Spectra analysis was done using comparison to frequently applied polymer

libraries that have been used in other studies (Karing et al. 2023). Five MPs could not be conclusively identified as a result of weak spectra.

2.6. Contamination Control

To prevent secondary plastic contamination via laboratory equipment, sample collection, processing, and separation were done using only metal tools or glassware, which were cleaned with filtered water before use. All glassware used was covered in aluminum foil before sample loading. Samples collected were covered with aluminum foil during transportation to keep out any foreign particles. Contamination was avoided in the laboratory by the use of cotton lab coats and nitrile gloves, and workspaces were cleaned thoroughly with ethanol. Use of plasticware was avoided during any handling of the samples. However, procedural laboratory blanks, field blanks, and airborne fallout controls were not included in the present study, and therefore, no quantitative contamination correction was applied to the results reported for MP abundances.

2.7. Statistical Analysis

MP abundance was quantified using replicate samples (n=3) for all four rivers across five particle-size ranges. The statistical analyses were performed using GraphPad Prism and expressed as mean ± SD (standard deviation). The conformity of variables with the normal distribution and homogeneity of variance were examined using the Shapiro–Wilk normality test and the Levene test, respectively. All the quantitative data were analyzed using One-way analysis of variance (ANOVA) followed by the Tukey test with a significance level set at $p < 0.05$. Descriptive statistics (mean, SD, and 95% CI) were calculated for each river × size-class combination. Confidence intervals were computed using the formula:

$$CI_{95} = t_{0.975,df=2} \times \frac{SD}{\sqrt{3}}$$

Total MP abundance per river and overall pooled statistics were calculated from summed replicate counts.

3. RESULTS

From the analysis, MPs of assorted sizes were detected in the sediment samples of all rivers under study, with varying quantities found in each river. The abundance of MPs of all size ranges was determined as particles per kilogram of sediment.

3.1. MP Abundance

In the study, MP particles isolated from each selected site at the four rivers were found to vary in quantity depending on their size fractions, with a mean abundance of 238.17 ± 46.95 particles/kg of sediment (average ± standard deviation) with a 95% CI of ± 29.80 particles, which highlights a moderate variability among sampling sites overall. The number and abundance of MPs per sample are given in Fig. 3.

Mean abundances of MPs from each site of the four rivers differed considerably, with the highest number of MPs detected in Chite sediments (287 ± 43.41 particles), which could be attributed to the close distance to urban areas and the excessive levels of plastic pollution. Studies have also shown a positive correlation between the proximity of freshwater bodies to urban areas and elevated levels of MPs (Wang et al. 2017, Ramaremisa et al. 2022). This was followed by Tlawng (243 ± 51.12) and Tuirial (231.67 ± 16.20). Serlui-A (191 ± 18.52) was found to have the lowest

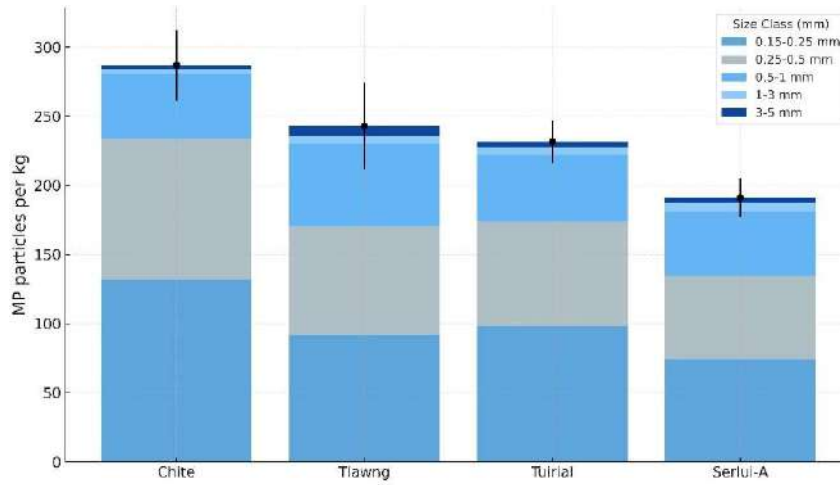


Fig. 3: Graphical representation of the number of MPs in Chite, Tlawng, Serlui-A, and Tuirial.

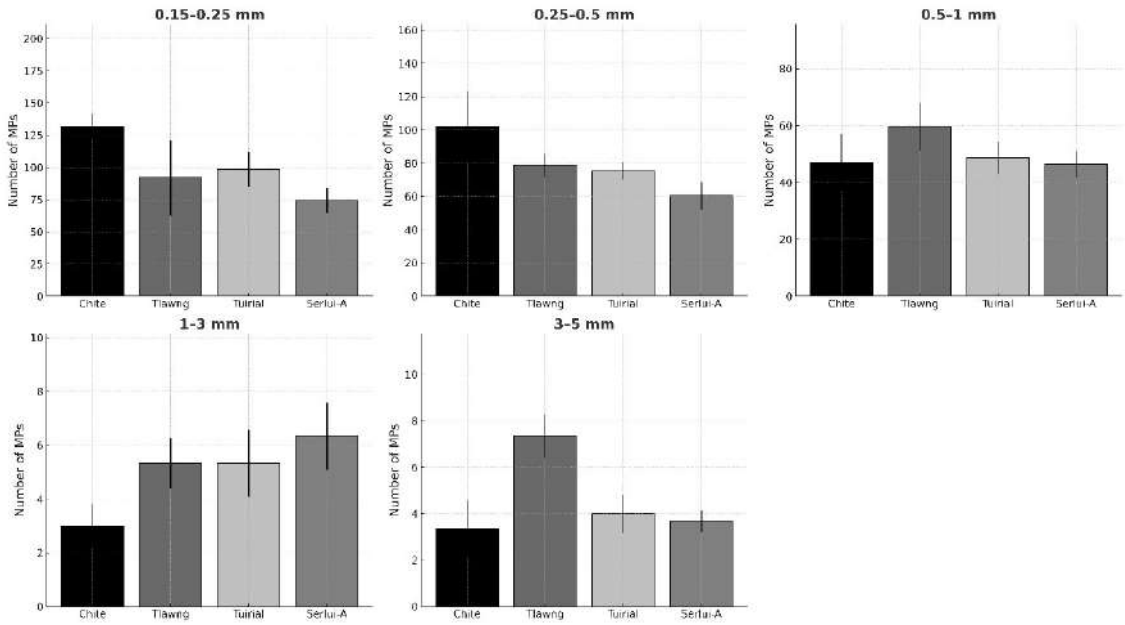


Fig. 4: Statistical analysis of the abundance of different MP sizes collected from different sampling sites.

number of MP numbers, which could be inferred as a result of its furthest distance from Aizawl compared to the other rivers. Although these differences show a clear numerical gradient, pairwise statistical analysis revealed that only the difference between Chite and Serlui-A was statistically significant (Welch's t-test: $t = 3.52$, $df = 2.70$, $p = 0.0457$; equivalent to $F(1, 2.70) = 12.41$). Differences in abundance among the remaining sampling sites were not statistically significant ($p > 0.05$).

3.2. MP Size

To evaluate variation across the different particle-size classes, one-way ANOVA was performed for each size group (Fig. 4). Isolated MPs were then analyzed down to a minimum detectable size of ≥ 0.15 mm, determined by the smallest size of the sieve used for separation, and particles smaller than this threshold were not quantified.

In addition, comparison of MP abundance of the different size groups across the four rivers revealed that the smallest 0.15–0.25 mm fraction displayed the highest mean counts in all sample sites, with the greatest abundance (131.67 particles) in Chite, followed by Tuirial (98.33), Tlawng (92.00), and Serlui-A (74.33). In terms of percentage, this size class accounted for 45.9% in Chite, 37.9% in Tlawng, 42.5% in Tuirial, and 38.9% in Serlui-A (Fig. 5). However, one-way ANOVA indicated that differences among rivers for this size class were not statistically significant ($p > 0.05$). The second most abundant fraction was the 0.25-0.5 mm group, contributing between 31-36%, with the highest mean (102.00 particles) present in Chite. No significant spatial variation was detected for this size fraction across the sites (one-way ANOVA, $p > 0.05$). The 0.5-1 mm group was found to be moderately abundant, ranging from 46–60 particles between the four rivers, contributing 16.4% (Chite), 24.6% (Tlawng), 21.0% (Tuirial), and 24.3% (Serlui-A) of total counts, with no statistically significant differences among rivers ($p > 0.05$). The larger groups (1-3 mm and 3–5 mm sizes) presented a very small proportion of total particles, typically below 5% of each river's MP count, both contributing approximately between 1% and 3%, depending on the river. Significant differences among sampling sites were observed only for the 3–5 mm fraction as revealed by one-way ANOVA ($F(3, df$ = F-value, $p = 0.0079$). From these results, it can be observed that although overall MP loads differ between the sample sites of the four rivers, spatial variability is most pronounced in the larger-sized particles.

Overall, these results determine a clear numerical dominance of smaller-sized MPs across all sampling sites, suggesting extensive fragmentation processes within these freshwater systems. However, statistically significant spatial differences were size-class dependent and restricted to the largest particle fraction, and therefore limit broader spatial interpretations.

3.3. MP Shapes

MPs of varying shapes and structures were found in all the rivers. Fibers and fragment MPs were observed in all rivers. Fibers were the dominant shapes in all the sample

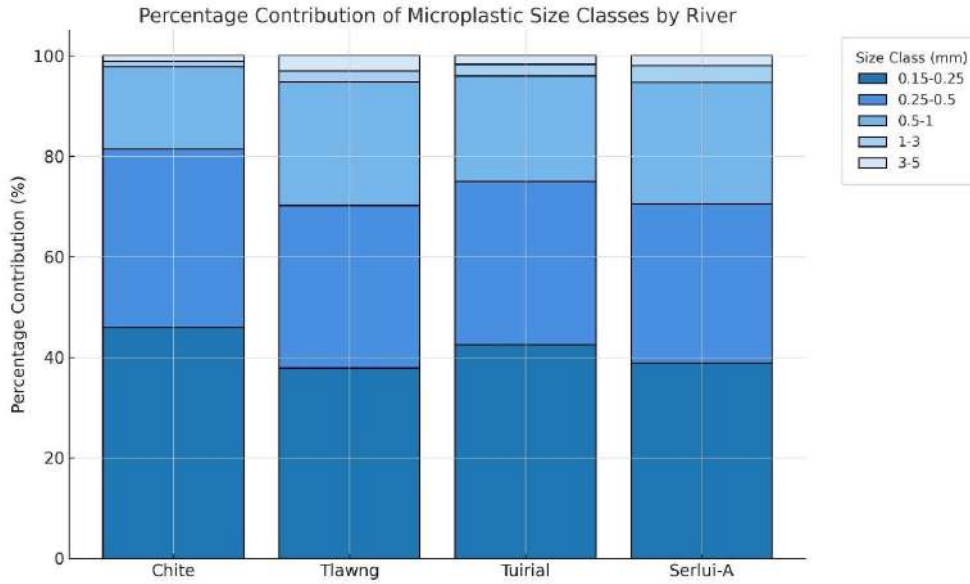


Fig. 5: Percentage contribution of MP size classes by river.

sites, accounting for approximately 40% of the total MPs recovered. Fragments and films together constituted approximately 45% of the particles, followed by spherical and foam structures (~10%). It also needs to be stated that shape-based categorization was derived from visual inspection, and therefore, minor classification uncertainty cannot be excluded, particularly for irregular or weathered particles. Accordingly, the reported shape proportions need to be inferred as indicative trends rather than definitive morphological distributions.

The detailed distribution of various shapes identified from the samples is given in Fig. 6.

The high abundance of fiber types in this study corroborates several other reports that have found MFs to be the dominant shape in freshwater bodies and sediments (Wang et al. 2017, Xu et al. 2021, Priya et al. 2023, Hosseinpour et al. 2025). Microscopic images of MPs comprising different size ranges, shapes, and colors are given in Fig. 7 and Fig. 8.

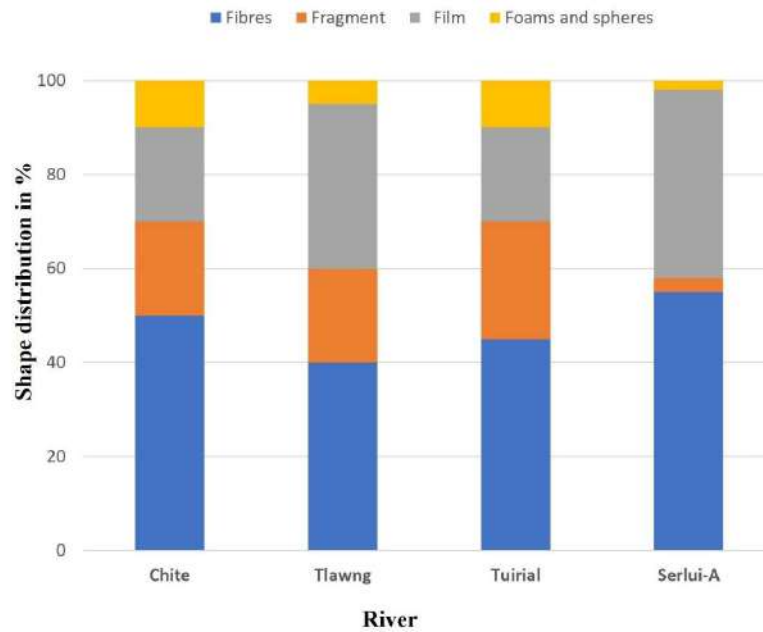


Fig. 6: Distribution of various MP shapes identified from sediment samples.

3.4. Surface Morphology and Chemical Characteristics

SEM analysis of different shapes of MPs (Fig. 9, A-D) showed variations in their surface morphologies, illustrating the heterogeneity in shape, texture, and surface characteristics typically associated with environmentally weathered polymers. The surfaces of fragments were observed to be uneven, rough, and cracked, suggesting exposure to weathering, abrasion, and disintegration over a period of time. Fig. 9-A, C, D show irregular, angular plastic fragment shapes with cracked surfaces and angular edges. Fig. 9-B displays an intertwined, flexible fiber shape with smooth surfaces that are typically associated with anthropogenic textile sources.

FTIR analysis was done on 20 isolated particles (5 from each river within the 0.5-1 mm size groups) that were randomly selected for polymer identification to validate visual identification. Spectral matching was conducted against a reference library, and particles were classified as MPs only when a match similarity of ≥70% was obtained, a threshold commonly adopted in environmental MP studies. Out of these, 75% (15 out of 20 particles) were thus confirmed to be MPs. Five samples could not be accurately identified due to inadequate spectrum intensity, which may imply a potential degree of overestimation associated with visual sorting alone. Therefore, polymer identification should be considered preliminary, and abundance values derived from visual inspection may include a limited proportion of non-plastic particles. The ≥70% match similarity threshold was selected as per established MP FTIR studies, acknowledging that environmental degradation and surface fouling can lower spectral similarity scores without changing the underlying polymer identity. From this analysis, two distinct types of polymers, namely, Polyethylene (PE) and Polypropylene (PP), were identified (Fig. 10), with PE making up the majority of the polymers (93%) from the selected and analyzed samples. Spectra identifying PE showed two prominent aliphatic C–H stretching vibrations at ~2916 cm^{-1}

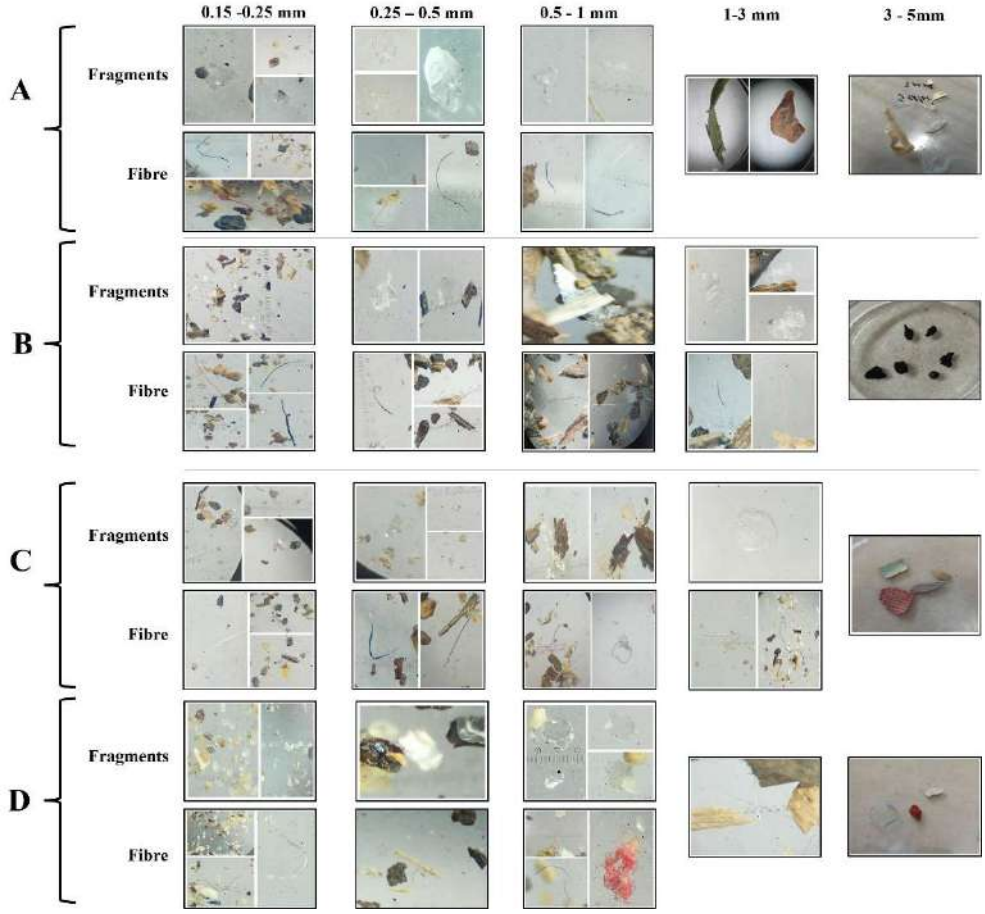


Fig. 7: Photographs of different MPs (fragments and fibers) isolated from sediment samples, with their size observed under a light microscope (10X and 40X magnifications). (A) MPs found in the Chite River. (B) MPs found in Tlawng. (C) MPs found in Serlui-A. (D) MPs found in Tuirial.

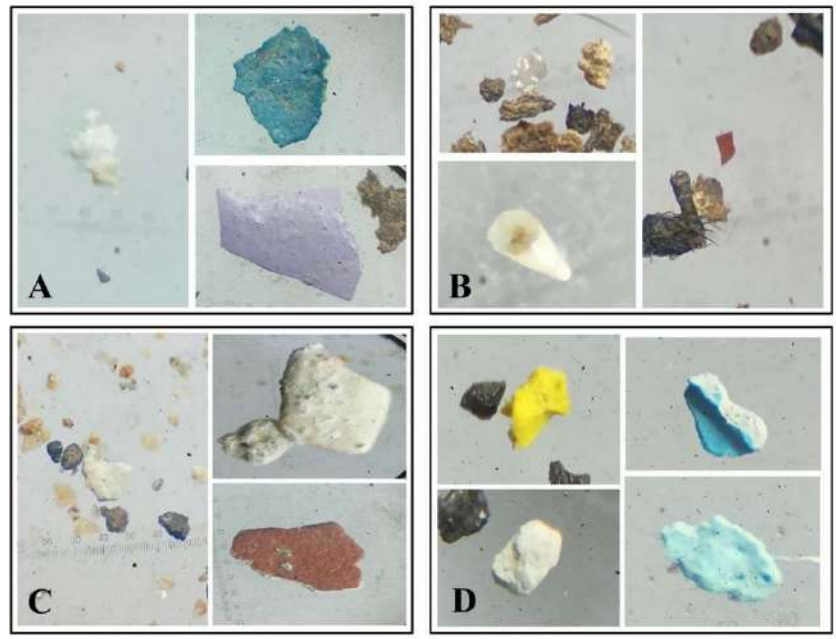


Fig. 8: Additional photographs of different MPs found in different rivers (A) MPs found in the Chite River. (B) MPs found in Tlawng. (C) MPs found in Serlui-A. (D) MPs found in Tuirial.

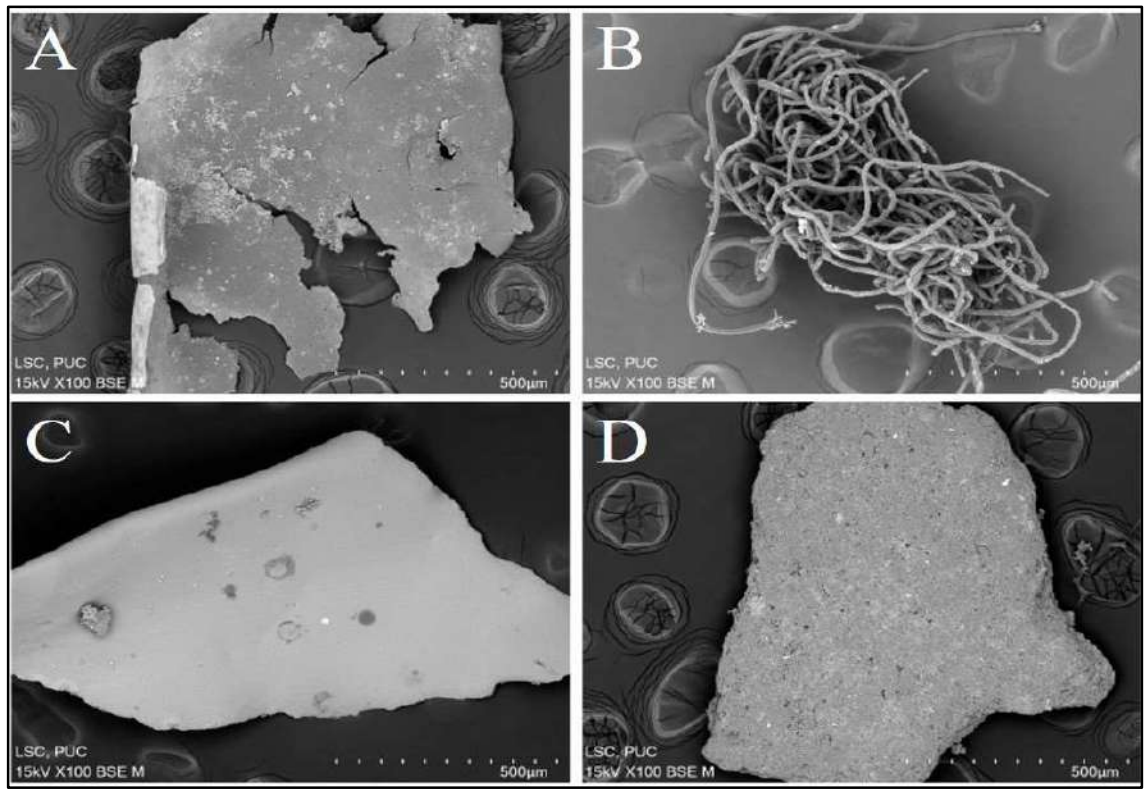


Fig. 9: SEM image of different MPs captured at 15 kV at 100 magnification. (A, C, D) Fragments (B) Fibers.

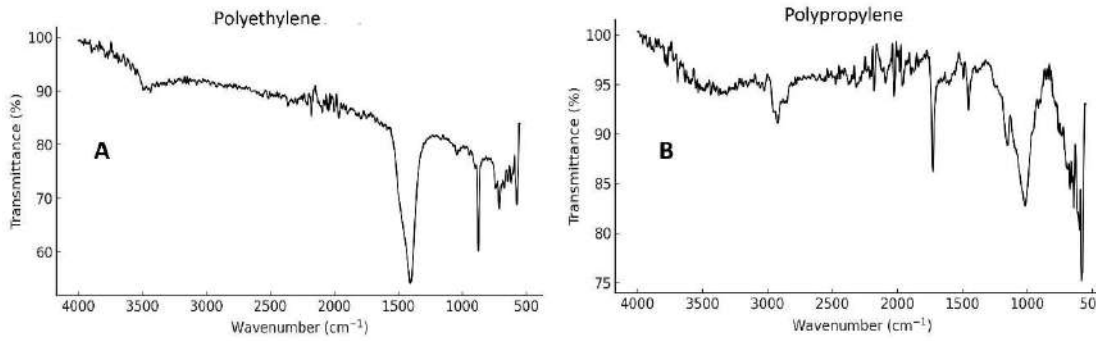


Fig. 10: FTIR spectra of MPs identified as Polyethylene (A) and Polypropylene (B).

(asymmetric CH_2 stretch) and ~2848 cm^{-1} (symmetric CH_2 stretch), accompanied by strong CH_2 deformation bands at ~1470 cm^{-1} (scissoring) and ~1463 cm^{-1} (bending). The most definitive marker of PE, i.e., the CH_2 rocking vibration near ~720 cm^{-1}, was consistently present across all PE samples. The absence of carbonyl (C=O), aromatic (C=C), or halogen-containing (C–Cl) functional groups further supported the classification of these particles as PE. indicating a potential degree of overestimation associated with visual sorting alone. Therefore, polymer identification in the present study should be considered preliminary, and abundance values derived from visual inspection may include a limited proportion of non-plastic particles.

Spectra identification for PP showed a strong CH_3 symmetric bending vibration at ~1376 cm^{-1}, which serves as the primary indicator of PP. Additional CH_2 and CH_3 deformation modes were observed at ~1455 cm^{-1}, along with C–H stretching vibrations at ~2950–2838 cm^{-1}. The presence of skeletal C–C stretching and CH wagging modes in the 1165–997 cm^{-1} region, together with an isotactic PP band near ~840 cm^{-1}, further confirmed the identity of the PP polymer.

4. DISCUSSION

This study aimed to evaluate the extent of MP pollution in the shore sediments of rivers close to Aizawl city, Mizoram. The state lies in the north-eastern part of India and is situated in the lower eastern Himalayan region. Assessment results showed mean MP abundance to be 238.17 ± 46.95 particles/kg, and found to be highest in rivers that are relatively closer to Aizawl municipality, i.e., the Chite river with the maximum number of MP particles, followed by the Tlawng river. This corroborates various studies that have established a positive correlation between elevated MP abundance and proximity of a freshwater body to urban and community areas (Peng et al., 2018; Tibbetts et al. 2018, Kongkamee et al. 2024). However, it is critical to note that the interpretations presented in this study are site-specific rather than river-wide, as each river sediment was represented by a single sampling location and replicate samples (n = 3) constituted within-site subsamples as opposed to independent spatial replicates. Considering pronounced spatial heterogeneity characteristics for different riverine systems, the detected differences in MP abundance among the sampled locations should therefore be interpreted in light of the study's spatial limitations. Consequently, statistical comparisons among the four rivers also reflect relative differences only at the sampled sites and do not infer whole-river contamination patterns. While higher MP abundances were observed at sites in closer proximity to urbanized areas, these patterns should be considered indicative and exploratory, unless further established through multi-site, longitudinal, and seasonal sampling designs that can effectively resolve river-scale spatial variability. Additionally, the mean abundance of MPs in the shoreline sediments of other rivers in different parts of the Himalayas varies greatly. Table 2 gives a glimpse of the various studies that have been conducted on MP pollution in different rivers within the Himalayan region and lists the mean abundance and types of polymers that have been detected. Values have been presented using original units (items/kg for sediments; items/L or items/m^3 for water) from the published articles and categorized by sample matrix. The comparisons across studies are qualitative only, since the evident differences in units, sampling strategies, and analytical methods prevent direct numerical comparison.

Unchecked pollution is still rampant in urban settlements, where domestic wastes are being discarded illicitly in side drains and open areas. Consequently, these are then carried off into rivers by wind and rainwater, and are further broken down into MPs via weathering. Although the Tuirial River is the farthest in distance from Aizawl, MP counts were higher than those of Serlui-A, which runs slightly closer to Aizawl. This could be attributed to its proximity to the rural settlement of Tuirial village around the Tuirial River. As a result, anthropogenic activities such as mismanagement

Table 2: List of studies on MP pollution in sediments and water of other rivers of the Himalayan region, with mean abundances and polymer types.

	Rivers	Sample	Abundance	Major MPs	Reference
Western Himalayan rivers	Indus	Sediment	525-1752 MP/kg	PP, PE, PES	Tsering et al. 2021
	Beas River	Water	46-222 items/L	PE	Bhaduri et al. 2025
		Sediment	36-896 items/kg		
	Chenab River	Water	34.66-45.98 MPs/m^3	PET, PP	Hafeez et al. 2023
	River Yamuna	Water	500-3900 MPs/m^3	PE, PS, PP	Vaid et al. 2022
	Ravi river	Water	768-1324 MPs/m^3	PP, PE, PES, and PS	Aslam et al. 2022
	Sutlej River	Water	3.6-19.0 MPs/L	PP, HDPE, PET	Nagendra et al. 2025
	Soan River	Water	132.7-641.3 items/m^3	PET, PP, PE.	Jabeen et al. 2023
Central Himalayan Rivers	River Ganga	Water	118.5 ± 49.65 particles /1000 L	PE, PP	Badola et al. 2023
		Sediment	131.5 ± 53.60 particles/kg		
	Upper Himalayan Ganga River	Water	100-1550 particles/L	PE, PA, PS	Chaudhary et al. 2025
		Sediment	50-1300 particles/Kg		
	River Ganga - (Suswa, Bindal and Rispana)	Water	2800-4200 items/L	PE, PP	Nayal & Suthar 2022
		Sediment	7200-16,400 items/kg		
	Karnali River	Water	0.12-0.64 particles/L	PE, PP	Maharjan et al. 2025
	Sapta-Gandaki river system	Water	24.7-61.2 particles/L	PE, PET, PVC	Kandel et al. 2025
	Kosi river	Water	50-325 items/m^3	PE, PET, PA	Yang et al. 2021
		Sediment	15-120 items/kg		
Eastern Himalayan Rivers	Brahmaputra	Sediment	531-3485 MP/kg	PP, PE, PA	Tsering et al. 2021
	Yarlung Tsangpo	Water	728.26 ± 100.53 items/m^3	PP, PE	Li et al. 2024
		Sediment	43.16 ± 5.82 items/kg		
	Lower Brahmaputra River	Water	11-32 MPs/L	Nylon, PET, PP	Hassan et al. 2025
	Manas river	Water	10-22 items/L	PP, PET, PS	Wang et al. 2021
	Jia Bharali River	Water	22.35-27.94 MPs/L	PE, PP	Lahon & Handique 2024
		Sediment	19.42-29 MPs/kg		
	Lasha river	Water	0.63 n/L	PP, PE	Zhou et al. 2023
		Sediment	0.37 n/g		
	Kaljani River	Water	0.14 ± 0.11 pieces m^{-3}	PE, nylon, PP	Goswami et al. 2024
	Karnaphuli River	Water	14.24 - 26.68 items m^{-3}	PET, HDPE, acrylonitrile butadiene styrene (ABS)	Jui et al. 2025

and dumping of garbage from the village, either directly or indirectly, into the river, the ongoing construction of roads, and a football field may have contributed to the elevated level of MPs in this river.

A considerable number of MPs were also detected in Serlui-A, which has various tributaries in the form of small streams, non-perennial brooks, and gullies that originate from areas close to Aizawl municipality. Further, the presence of Li Cheng (or Dilmawi, a type of stream pool), which is a tourist attraction in Serlui-A, could possibly be a key contributor to MPs in this river, due to the indiscriminate disposal of plastic garbage by visitors. Although the MP count in Serlui-A is the lowest when compared to other observed rivers, their detection in this river is particularly concerning because drinking water for the Aizawl municipal areas is sourced from this river. However, since no studies on MP pollution in freshwater bodies within the state have been conducted as yet, conclusions cannot be made regarding the presence and abundance of MPs in the water, but further studies are tremendously warranted. Since Mizoram does not have large-scale manufacturing industries and complexes, the aggregation of MPs in the shore sediments of these

rivers can mostly be attributed to inadequate domestic waste management procedures in the urban areas and their subsequent runoff into surrounding water bodies and non-target areas due to the hilly terrain and high annual rainfall (Singh et al. 2023). These garbage masses are then evidently weathered down and fragmented into minuscule particles by various natural elements and environmental factors. Sediments eventually act as sinks for MP deposition, with gradual aggregation over time since they can easily be carried over long distances due to their minuscule sizes and lower densities (Ismanto et al. 2023, Napper et al. 2023).

The study found a higher abundance of smaller MPs below 1mm, especially within the size ranges of 0.15-0.25 mm and 0.25-0.5 mm in all four sampling locations, while those above 3mm in size were significantly lower. Fragmentation processes contribute significantly to the size distribution of MPs in aquatic systems and tend to settle more easily due to their reduced buoyancy and greater susceptibility to deposition under lower energy conditions (Browne et al. 2011). Larger plastic items break down into smaller particles as a result of physical, chemical, and biological factors, and this continued weathering may explain why smaller MPs are found in higher concentrations in sediments (Wang et al. 2022, Lu et al. 2023). Research by Klein et al. (2015) on the Rhine River revealed that the majority of MPs in sediments were smaller than 1 mm, with finer-grained sediments harboring the highest concentrations of MPs. Similarly, a review by Yang et al. (2021) observed that in river systems, smaller MPs are usually more abundant than larger ones in sediments, and MPs less than 0.5mm in particular were especially prevalent in sediment samples, further supporting the notion that smaller particles are more likely to accumulate in sediments due to their lower transport potential and easier incorporation into sediment layers. Another study by Ramaremisa et al. (2022) also reported a decrease in abundance with an increase in MP sizes in sediments of the Vaal River in South Africa. In addition, other factors may also contribute to the abundance of MPs in sediments. Waldschläger and Schüttrumpf (2019) demonstrated that hydrodynamic conditions such as current velocity and turbulence significantly affect the settling velocities of MPs. Smaller particles settle more quickly due to reduced drag and hydrodynamic resistance, accumulating in riverbeds, especially in regions of decreased water flow such as oxbow lakes and estuaries, implying that the smaller the particles, the greater the likelihood of their being present in river sediments. Although numerical differences in MP abundance were observed among rivers, particularly higher counts in Chite compared to the other sites, most size classes did not exhibit statistically significant spatial variation, which may suggest a broadly comparable distribution of smaller MPs across the river network. Statistical analyses demonstrated that spatial differences were size-dependent, with significant variation detected only in the largest particle fraction (3–5 mm). These results imply that larger particles may be more strongly influenced by localized sources, limited transport potential, and site-specific retention mechanisms, whereas smaller particles are more uniformly dispersed due to enhanced mobility and fragmentation. Since the analytical detection limit of this study was limited to ≥0.15 mm, MPs smaller than this threshold were not captured, and the reported abundances potentially underestimate the contribution of smaller size fractions, particularly fine fragments and fibers below 0.15 mm.

Fibers represented the majority of MP particles in all the rivers under study, constituting more than 40% of all MPs isolated. This corroborated other studies on freshwater bodies in other Indian river systems where MFs were the dominant type (Kalangutkar et al. 2023, Napper et al. 2023), as well as sediments of several rivers in other parts of the globe (Huang et al. 2021, Akdogan et al. 2023). Domestic and commercial laundering of various types of textiles has been known to be a significant contributor to MFs in different aquatic bodies and is also a consequence of proximity to urban areas (Hazlehurst et al. 2023). Therefore, household wastes from residents of the city, including effluents from washing textiles, have possibly added to the abundance of MFs in the observed river sediments. Blue, red, and transparent fibers were the main MFs found in the sediment samples. The transparent fibers may indicate that fishing does contribute in some measure to the abundance of MFs in these rivers, as net fishing is common in some parts of the selected rivers, especially Tlawng. However, given that fibers constituted a significant proportion of the detected MPs, the absence of procedural blanks is recognized as a limitation of the present study. Since fibers can be particularly sensitive to airborne contamination during sampling and laboratory processing, stringent precautions were applied to the best extent possible during sample collection, handling, and analysis to minimize external contamination. In the absence of field or laboratory blanks, a quantitative assessment of background contamination was not feasible, and therefore the reported fiber abundances should be appropriately interpreted, as minor contributions from secondary contamination cannot be fully ruled out.

Of the 20 particles selected for FTIR analysis from the visually identified MPs, 15 particles (75%) were spectroscopically confirmed as plastic polymers, while the remaining five particles could not be reliably identified due to insufficient spectral quality and were therefore excluded from polymer classification. Consequently, polymer composition results are based solely on this subset of confirmed particles.

Although visual microscopy remains a widely applied screening approach in MP studies, particularly for larger size fractions, the absence of auxiliary confirmation techniques such as hot needle testing, Nile Red staining, etc., represents a limitation of the present study, and as a result, classification uncertainty cannot be fully excluded. Nevertheless, PE was found to be the dominant type of polymer, which underscores the pervasive use of PE-based materials in the region under study. PE is the primary constituent of various plastic products such as single-use packaging films, carry bags, wrappers, and household consumables, all of which are extensively used and frequently mismanaged in urban and peri-urban areas (Schwab et al. 2024). Our findings substantiate several other studies in different rivers (Doyen et al. 2019, Maheswaran et al. 2022, Babkiewicz et al. 2025) and also within the Himalayan region, where PE has also been found to be one of the most abundant pollutant particles (Table 2). Comparatively, PP particles were significantly lower amongst the analyzed particles, which may be consistent with their use in more rigid consumer products such as bottle caps, storage containers, and packaging components, and their slightly higher density and mechanical strength likely reduce fragmentation rate relative to PE, possibly contributing to their lower representation in sediments (Khoironi et al. 2020, Anak Alexander Tampan et al. 2022). However, given the limited number of particles subjected to FTIR analysis, the polymer identification presented in this study is preliminary and indicative, intended to provide an overview of dominant polymer types rather than a complete characterization of sediment polymer composition. Additionally, although a $ZnCl_2$ density of 1.5 g cm^{-3} used in the isolation method enables effective recovery of most environmentally relevant polymers, it is acknowledged that some high-density polymers (e.g., PVC and highly compact or mineral-encrusted PET particles) may not be fully recovered, particularly when aging, biofouling, or aggregation can increase their effective density. Despite the use of two sequential extraction cycles, a degree of underestimation of high-density MPs cannot be entirely excluded. Hence, the reported polymer composition should therefore be interpreted as conservative with respect to dense polymer fractions.

5. CONCLUSIONS

This study provides a preliminary and baseline assessment of MP contamination in shoreline sediments of rivers that run close to Aizawl city, the most urbanized region in the state of Mizoram. Importantly, this study presents one of the first systematic efforts to document MP contamination in site-specific freshwater riverine sediments from this part of the Eastern Himalayan region. Baseline information on MPs pollution in Mizoram has been virtually absent, despite the region being recognized as a biodiversity hotspot with ecologically sensitive river systems. By providing the first empirical evidence of MP occurrence in riverbank sediments in and close to Aizawl, the present work fills a critical knowledge gap and establishes a reference point for future monitoring and comparative assessments. Such baseline data are essential for the early detection of emerging pollutants, formulation of region-specific management strategies, and prevention of further degradation of freshwater ecosystems in this fragile Himalayan landscape. Within the constraints of the study design, sampling coverage, and analytical resolution, this study also paints a harrowing picture of the extensive use and improper management of plastic products in Aizawl at large, since these are evidently polluting the rivers in proximity to urban areas and settlements. More in-depth research concerning MP pollution is crucial to detect the presence and extent of contamination in air, soil, food, and other water bodies within the state, since they are also susceptible to pollution from source to distant sites via river systems. Although the lack of funding for this study has limited our preliminary investigation in terms of area of study, sample type, and chemical analysis of particles, further studies on concentrations in river water and ingestion by aquatic organisms are still lacking and are of utmost importance. In particular, tap water from Serlui-A needs further investigation for MP presence since it is a critical lifeline for thousands of people. However, the present study did not analyze drinking water samples and did not evaluate human exposure or health risk. Moreover, according to the World Health Organization, there are currently no universally accepted numeric safety thresholds for MPs in water, and regulatory and scientific bodies recommend enhanced monitoring and further toxicological research before such standards can be established (WHO, 2019). Nevertheless, the detected occurrence of MPs in riverine environments highlights the need for future integrated studies that include drinking water analysis, exposure assessment, and toxicological evaluation to better understand potential human health implications. Such investigations would be crucial for translating such findings into meaningful risk assessments.

Furthermore, there is a need for strengthened management strategies to limit the extensive use and disposal of plastics to minimize the indiscriminate pollution of our precious rivers, not just for the sake of humans, but for all organisms associated with these aquatic environments. Single-use plastic bags, bottles, and packaging items should ideally be substituted with natural fiber products that are produced from bamboo, jute, cotton, etc. Although plastic pollution is a global issue, the state of Mizoram also still has a long way to go in terms of combatting it, with an urgent need to provide

alternatives to single-use plastics and more efficient facilities for plastic recycling. In addition, collective awareness amongst the people needs to be inculcated regarding the harmful consequences of pollution on the environment and the importance of mitigating pollution as a whole.

6. ABBREVIATIONS

ABS:	acrylonitrile butadiene styrene
HD/LD-PE:	high-and low-density polyethylene
MFs:	Microplastic fibers
MPs:	Microplastics
PA:	Polyamide
PE:	Polyethylene
PES:	Polyester
PET:	Polyethylene terephthalate
PS:	Polystyrene
PP:	Polypropylene
PVC:	polyvinyl chloride
SEM:	Scanning Electron Microscope

7. ACKNOWLEDGMENTS

The authors gratefully acknowledge the faculty of the School of Life Sciences and the Research and Instrumentation Laboratory, Pachhunga University College, for providing all the necessary facilities and instruments required to carry out this work.

8. REFERENCES

Akdogan, Z., Guven, B. and Kideys, A.E., 2023. Microplastic distribution in the surface water and sediment of the Ergene River. *Environmental Research*, 234, p.116500. [DOI]

Anbumani, S. and Kakkar, P., 2018. Ecotoxicological effects of microplastics on biota: a review. *Environmental Science and Pollution Research*, 25(15), pp.14373-14396. [DOI]

Anak Alexander Tampang, A.M and Viswanathan, P.M., 2022. Occurrence, distribution and sources of microplastics in beach sediments of Miri coast, NW Borneo. *Chemosphere*, 305, p.135368. [DOI]

Aslam, M., Qadir, A., Hafeez, S., Aslam, H.M.U. and Ahmad, S.R., 2022. Spatiotemporal dynamics of microplastics burden in River Ravi, Pakistan. *Journal of Environmental Chemical Engineering*, 10(3), p.107652. [DOI]

Babkiewicz, E., Vecmane, E., Fuk, M., Jurgielewicz, M., Koniuk, A., Kurek, E., Maszczyk, P., Michalska-Kacymirow, M., Jonuskiene, D., Norvaišienė, J. and Burdukovska, V., 2025. Microplastics in the Baltic Sea region lakes—standardized insights reveal urban shoreline as key driver. *Environmental Science and Pollution Research*, 32(47), pp.27052-27067. [DOI]

Badola, N., Sobhan, F. and Chauhan, J.S., 2023. Microplastics in the River Ganga and its fishes: Study of a Himalayan River. *Science of the Total Environment*, 901, p.165924. [DOI]

Bajt, O., 2021. From plastics to microplastics and organisms. *FEBS Open Bio*, 11(4), pp.954-966. [DOI]

Balestra, V. and Bellopede, R., 2022. Microplastic pollution in show cave sediments: First evidence and detection technique. *Environmental pollution*, 292, p.118261. [DOI]

Bhaduri, R.N., Sinha, S., Guererro, A.M., Jackson, S.L., Alemán, E.A. and Chatterjee, S., 2025. Microplastic contamination and environmental risks in the Beas River, western Himalayas. *Environmental Pollution*, 365, p.125387. [DOI]

Bridson, J.H., Abbel, R., Smith, D.A., Northcott, G.L. and Gaw, S., 2023. Solving a microplastic dilemma? Evaluating additive release with a dynamic leaching method for microplastic assessment (DyLeMMA). *MethodsX*, 10, p.102221. [DOI]

Browne, M.A., Crump, P., Niven, S.J., Teuten, E., Tonkin, A., Galloway, T. and Thompson, R., 2011. Accumulation of microplastic on shorelines worldwide: sources and sinks. *Environmental Science & Technology*, 45(21), pp.9175-9179.

Chaudhary, M., Rawat, S. and Suthar, S., 2025. Microplastic in upper Himalayan Ganga river: Occurrence, seasonal dynamics and ecological risk. *Science of the Total Environment*, 967, p.178824. [DOI]

Cole, M., Webb, H., Lindeque, P.K., Fileman, E.S., Halsband, C. and Galloway, T.S., 2014. Isolation of microplastics in biota-rich seawater samples and marine organisms. *Scientific Reports*, 4(1), p.4528. [DOI]

Desforges, J.P.W., Galbraith, M., Dangerfield, N. and Ross, P.S., 2014. Widespread distribution of microplastics in subsurface seawater in the NE Pacific Ocean. *Marine pollution bulletin*, 79(1-2), pp.94-99. [DOI]

Doyen, P., Hermabessiere, L., Dehaut, A., Himber, C., Decodts, M., Degraeve, T., Delord, L., Gaboriaud, M., Moné, P., Sacco, J. and Tavernier, E., 2019. Occurrence and identification of microplastics in beach sediments from the Hauts-de-France region. *Environmental Science and Pollution Research*, 26(27), pp.28010-28021. [DOI]

Ghanbari, N., Fataei, E., Naji, A., Imani, A.A. and Nasehi, F., 2022. Microplastic pollution in sediments in the urban section of the Qara Su River, Iran. *Applied Water Science*, 12(8), p.192. [DOI]

Ghosh, S., Sinha, J.K., Ghosh, S., Vashisth, K., Han, S. and Bhaskar, R., 2023. Microplastics as an emerging threat to the global environment and human health. *Sustainability*, 15(14), p.10821. [DOI]

Goswami, P. and Bhadury, P., 2024. Characteristics of microplastics in tributaries of the upper Brahmaputra River along the Himalayan foothills, India. *Environmental Research Communications*, 6(7), p.075013. [DOI]

Goyal, T., Singh, S., Das Gupta, G. and Verma, S.K., 2023. Microplastics in environment: A comprehension on sources, analytical detection, health concerns, and remediation. *Environmental Science and Pollution Research*, 30(54), pp.114707-114721. [DOI]

Gulizia, A.M., Philippa, B., Zacharuk, J., Motti, C.A. and Vamvounis, G., 2023. Plasticiser leaching from polyvinyl chloride microplastics and the implications for environmental risk assessment. *Marine Pollution Bulletin*, 195, p.115392. [DOI]

Gunaalan, K., Nielsen, T.G., Rodríguez Torres, R., Lorenz, C., Vianello, A., Andersen, C.A., Vollertsen, J. and Almeda, R., 2023. Is zooplankton an entry point of microplastics into the marine food web?. *Environmental Science & Technology*, 57(31), pp.11643-11655. [DOI]

Hafeez, S., Qadir, A., Aslam, M., Aslam, H.M.U., Rehmat, M.S. and Ahmad, S.R., 2023. Environmental risks of microplastics on the spatial and temporal gradient in a river originating from the western Himalayas. *Environmental Toxicology and Chemistry*, 42(3), pp.727-739. [DOI]

Hassan, M.A., Shammi, M. and Tareq, S.M., 2025. Assessing year-round microplastic loading in the lower Brahmaputra River: A threat to aquatic environment. *Journal of Hazardous Materials Advances*, 17, p.100592. [DOI]

Hazlehurst, A., Tiffin, L., Sumner, M. and Taylor, M., 2023. Quantification of microfibre release from textiles during domestic

laundering. *Environmental Science and Pollution Research*, 30(15), pp.43932-43949. [DOI]

Hosseinpour, S., Keshavarzi, B., Moore, F. and Busquets, R., 2025. Microplastic pollution in playas—endorheic basins with closed drainage systems. A study in surface sediments of Bakhtegan–Tashk Lakes (South Iran). *Environmental Pollution*, p.127282. [DOI] [Google Scholar] [PubMed] [URL]

Huang, D., Li, X., Ouyang, Z., Zhao, X., Wu, R., Zhang, C., Lin, C., Li, Y. and Guo, X., 2021. The occurrence and abundance of microplastics in surface water and sediment of the West River downstream, in the south of China. *Science of the Total Environment*, 756, p.143857. [DOI]

Ismanto, A., Hadibarata, T., Sugianto, D.N., Zainuri, M., Kristanti, R.A., Wisha, U.J., Hernawan, U., Anindita, M.A., Gonsilou, A.P., Elshikh, M.S. and Al-Mohaimeed, A.M., 2023. First evidence of microplastics in the water and sediment of Surakarta city river basin, Indonesia. *Marine Pollution Bulletin*, 196, p.115677. [DOI]

Jabeen, K., Xu, J., Liu, K., Zhu, L. and Li, D., 2023. Monthly variation and transport of microplastics from the Soan River into the Indus River. *Science of the Total Environment*, 905, p.166877. [DOI]

Jui, M., Miah, M.S., Islam, M.H., Sarwar, M.I., Moniruzzaman, M., Ankhy, R.S., Suchi, P.D. and Islam, M.S., 2025. Microplastic pollution in the water and sediment of the Karnaphuli River, Bangladesh: An ecological risk assessment. *Marine Pollution Bulletin*, 216, p.117948. [DOI]

Kalangutkar, N., Mhapsekar, S., Redkar, P., Valsan, G. and Warrier, A.K., 2024. Microplastic pollution in the Chapora River, Goa, Southwest India: Spatial distribution and risk assessment. *Environmental Monitoring and Assessment*, 196(5), p.409. [DOI]

Kandel, B., Adhikari, N., Chetri, A.K., Karki, A., Paudyal, H., Sharma, K.R., Giri, B. and Neupane, B.B., 2025. Distribution of microplastic contamination in Sapta-Gandaki river system, Nepal. *International Journal of Environmental Science and Technology*, 22(8), pp.7065-7076. [DOI]

Karing, D.J., Anggiani, M., Cao, L.T.T. and El-Shaammari, M., 2023. Occurrence of Microplastics in Kemena River and Niah River of Sarawak, Malaysia. *Tropical Environment, Biology, and Technology*, 1(1), pp.1-13. [DOI]

Karthikeyan, P. and Subagunasekar, M., 2023. Microplastics pollution studies in India: A recent review of sources, abundances and research perspectives. *Regional Studies in Marine Science*, 61, p.102863. [DOI]

Khoironi, A., Hadiyanto, H., Anggoro, S. and Sudarno, S., 2020. Evaluation of polypropylene plastic degradation and microplastic identification in sediments at Tambak Lorok coastal area, Semarang, Indonesia. *Marine pollution bulletin*, 151, p.110868. [DOI]

Klein, S., Worch, E. and Knepper, T.P., 2015. Occurrence and spatial distribution of microplastics in river shore sediments of the Rhine-Main area in Germany. *Environmental Science & Technology*, 49(10), pp.6070-6076. [DOI]

Koelmans, A.A., Nor, N.H.M., Hermsen, E., Kooi, M., Mintenig, S.M. and De France, J., 2019. Microplastics in freshwaters and drinking water: Critical review and assessment of data quality. *Water Research*, 155, pp.410-422. [DOI]

Kongkamee, K., Chaimee, A., Hinhumpatch, P., Kitreerawutiwong, N., Keanjoom, R. and Yasaka, S., 2024. Microplastic contamination in rivers: a survey from the Nan River, Thailand. *The Lancet Planetary Health*, 8, p.S19. [DOI]

Krause, S., Baranov, V., Nel, H.A., Drummond, J.D., Kukkola, A., Hoellein, T., Smith, G.H.S., Lewandowski, J., Bonet, B., Packman, A.I. and Sadler, J., 2021. Gathering at the top? Environmental controls of microplastic uptake and biomagnification in freshwater food webs. *Environmental Pollution*, 268, p.115750. [DOI]

Lahon, J. and Handique, S., 2024. Flood-induced variation and source apportionment of microplastics in Jia Bharali River of mid-Brahmaputra Valley, India. *Environmental Monitoring and Assessment*, 196(12), p.1236.

Li, H., Lu, H., Feng, S., Xue, Y., Sun, T., Yan, Y., Zhang, X. and Yan, P., 2024. Environmental fate of microplastics in high-altitude basins: The insights into the Yarlung Tsangpo River Basin. *Journal of Environmental Management*, 365, p.121623. [DOI]

Lu, Q., Zhou, Y., Sui, Q. and Zhou, Y., 2023. Mechanism and characterization of microplastic aging process: A review. *Frontiers of Environmental Science & Engineering*, 17(8), p.100. [DOI]

Maharjan, K.K., Pyakurel, P., Bista, S. and Dhungel, R.P., 2025. Assessment of microplastic contamination in the Karnali River: A baseline study in remote region of Western Nepal. *Results in Engineering*, p.106562. [DOI]

Maheswaran, B., Karmegam, N., Al-Ansari, M., Subbaiya, R., Al-Humaid, L., Raj, J.S. and Govarthanan, M., 2022. Assessment, characterization, and quantification of microplastics from river sediments. *Chemosphere*, 298, p.134268. [DOI]

McCormick, A.R., Hoellein, T.J., London, M.G., Hittie, J., Scott, J.W. and Kelly, J.J., 2016. Microplastic in surface waters of urban rivers: concentration, sources, and associated bacterial assemblages. *Ecosphere*, 7(11), p.e01556. [DOI]

Nagendra, P.S., Datta, S.N., Pathak, D., Tewari, G., Gupta, K. and Leishangthem, G.D., 2025. Assessment of Microplastic Contamination and Ecological Risk in the Middle Stretch of the Sutlej River, Punjab, India. *Asian Journal of Environment & Ecology*, 24(12), pp.33-51. [DOI]

Napper, I.E., Baroth, A., Barrett, A.C., Bhola, S., Chowdhury, G.W., Davies, B.F., Duncan, E.M., Kumar, S., Nelms, S.E., Niloy, M.N.H. and Nishat, B., 2023. The distribution and characterisation of microplastics in air, surface water and sediment within a major river system. *Science of the Total Environment*, 901, p.166640. [DOI]

Nayal, R. and Suthar, S., 2022. First report on microplastics in tributaries of the upper Ganga River along Dehradun, India: Quantitative estimation and characterization. *Journal of Hazardous Materials Advances*, 8, p.100190. [DOI]

Patil, P.B., Maity, S. and Sarkar, A., 2022. Potential human health risk assessment of microplastic exposure: current scenario and future perspectives. *Environmental monitoring and assessment*, 194(12), p.898. [DOI]

Pautu, L., Lalmalsawma, P., Vanramliana, Balasubramani, K., Balabaskaran Nina, P., Rosangkima, G., Sarma, D.K., Malvi, Y. and Hunropuia, 2023. Seroprevalence of scrub typhus and other rickettsial diseases among the household rodents of Mizoram, North-East India. *Zoonoses and Public Health*, 70(3), pp.269-275. [DOI]

Peng, G., Xu, P., Zhu, B., Bai, M. and Li, D., 2018. Microplastics in freshwater river sediments in Shanghai, China: a case study of risk assessment in mega-cities. *Environmental Pollution*, 234, pp.448-456. [DOI]

Priya, K.K., Thilagam, H., Muthukumar, T., Gopalakrishnan, S. and Govarthanan, M., 2023. Impact of microfiber pollution on aquatic biota: A critical analysis of effects and preventive measures. *Science of the Total Environment*, 887, p.163984. [DOI]

Ramaremisa, G., Ndlovu, M. and Saad, D., 2022. Comparative assessment of microplastics in surface waters and sediments of the Vaal River, South Africa: abundance, composition, and sources. *Environmental Toxicology and Chemistry*, 41(12), pp.3029-3040. [DOI]

Rhodes, C.J., 2018. Plastic pollution and potential solutions. *Science Progress*, 101(3), pp.207-260. [DOI]

Saad, D., Ndlovu, M., Ramaremisa, G. and Tutu, H., 2022. Microplastics in freshwater environment: the first evaluation in sediment of the Vaal River, South Africa. *Heliyon*, 8(10). [DOI]

Sarijan, S., Azman, S., Said, M.I.M., Andu, Y. and Zon, N.F., 2018. Microplastics in sediment from Skudai and Tebrau rivers, Malaysia: a preliminary study. In *MATEC Web of Conferences* (Vol. 250, p. 06012). EDP Sciences. [DOI]

Schwab, S.T., Baur, M., Nelson, T.F. and Mecking, S., 2024. Synthesis and deconstruction of polyethylene-type materials. *Chemical Reviews*, 124(5), pp.2327-2351. [DOI]

Sendra, M., Pereiro, P., Figueras, A. and Novoa, B., 2021. An integrative toxicogenomic analysis of plastic additives. *Journal of Hazardous Materials*, 409, p.124975. [DOI]

Singh, A.P., Devi, A.S. and Sahoo, U.K., 2023. Quantifying plastic waste generation in Aizawl city, India: waste management and its impact on human and environmental health. *Environmental Science and Pollution Research*, 30(49), pp.107390-107402. [DOI]

Smith, M., Love, D.C., Rochman, C.M. and Neff, R.A., 2018. Microplastics in seafood and the implications for human health. *Current Environmental Health Reports*, 5(3), pp.375-386. [DOI]

Tibbetts, J., Krause, S., Lynch, I. and Sambrook Smith, G.H., 2018. Abundance, distribution, and drivers of microplastic contamination in urban river environments. *Water*, 10(11), p.1597. [DOI]

Tsering, T., Sillanpää, M., Sillanpää, M., Viitala, M. and Reinikainen, S.P., 2021. Microplastics pollution in the Brahmaputra River and the Indus River of the Indian Himalaya. *Science of the Total Environment*, 789, p.147968. [DOI]

Vaid, M., Mehra, K., Sarma, K. and Gupta, A., 2022. Investigations on the co-occurrence of microplastics and other pollutants in the River Yamuna, Delhi. *Water Supply*, 22(12), pp.8767-8777. [DOI]

Van Cauwenberghe, L. and Janssen, C.R., 2014. Microplastics in bivalves cultured for human consumption. *Environmental pollution*, 193, pp.65-70. [DOI]

Vivekanand, A.C., Mohapatra, S. and Tyagi, V.K., 2021. Microplastics in aquatic environment: Challenges and perspectives. *Chemosphere*, 282, p.131151. [DOI]

Waldschläger, K. and Schüttrumpf, H., 2019. Effects of particle properties on the settling and rise velocities of microplastics in freshwater under laboratory conditions. *Environmental Science & Technology*, 53(4), pp. 1958-1966. [DOI]

Wang, C., O'Connor, D., Wang, L., Wu, W.M., Luo, J. and Hou, D., 2022. Microplastics in urban runoff: Global occurrence and fate. *Water Research*, 225, p.119129. [DOI]

Wang, G., Lu, J., Li, W., Ning, J., Zhou, L., Tong, Y., Liu, Z., Zhou, H. and Xiayihazi, N., 2021. Seasonal variation and risk assessment of microplastics in surface water of the Manas River Basin, China. *Ecotoxicology and Environmental Safety*, 208, p.111477. [DOI]

Wang, T., Li, B., Shi, H., Ding, Y., Chen, H., Yuan, F., Liu, R. and Zou, X., 2024. The processes and transport fluxes of land-based macroplastics and microplastics entering the ocean via rivers. *Journal of Hazardous Materials*, 466, p.133623. [DOI]

Wang, W., Ndungu, A.W., Li, Z. and Wang, J., 2017. Microplastics pollution in inland freshwaters of China: A case study in urban surface waters of Wuhan, China. *Science of the Total Environment*, 575, pp.1369-1374. [DOI]

World Health Organization, 2019. WHO calls for more research into microplastics and a crackdown on plastic pollution. *World Health Organization*.

Xu, Y., Chan, F.K.S., Stanton, T., Johnson, M.F., Kay, P., He, J., Wang, J., Kong, C., Wang, Z., Liu, D. and Xu, Y., 2021. Synthesis of dominant plastic microfibre prevalence and pollution control feasibility in Chinese freshwater environments. *Science of the Total Environment*, 783, p.146863. [DOI]

Yang, L., Luo, W., Zhao, P., Zhang, Y., Kang, S., Giesy, J.P. and Zhang, F., 2021. Microplastics in the Koshi River, a remote alpine river crossing the Himalayas from China to Nepal. *Environmental Pollution*, 290, p.118121. [DOI]

Yang, L., Zhang, Y., Kang, S., Wang, Z. and Wu, C., 2021. Microplastics in freshwater sediment: A review on methods, occurrence, and sources. *Science of the Total Environment*, 754, p.141948. [DOI] [Google Scholar] [PubMed] [URL]

Zhao, Q., Zhu, L., Weng, J., Jin, Z., Cao, Y., Jiang, H. and Zhang, Z., 2023. Detection and characterization of microplastics in the human testis and semen. *Science of the Total Environment*, 877, p.162713. [DOI]

Zhou, A., Zhao, Y., Liu, M., Suyamud, B., Yuan, W. and Yang, Y., 2023. Occurrence and risk assessment of microplastics in the Lhasa River—A remote plateau river on the Qinghai-Tibet Plateau, China. *Environmental Monitoring and Assessment*, 195(3), p.433. [DOI]

Nature Environment and Pollution Technology
An International Quarterly Scientific Journal

p-ISSN: 0972-6268
(Print copies up to 2016)
e-ISSN: 2395-3454

Vol. 25 | No. 3 | Article ID D1887 | 2026

Original Research Paper

https://doi.org/10.46488/NEPT.2026.v25i03.D1887

Open Access Journal

Comparative Assessment of Empirical and Theoretical Mass Eruption Rate Estimation Methods Using HYSPLIT: A Case Study of Lewotobi Laki-Laki Eruption

Yumita Sufitri[1], Vera Surtia Bachtiar[1]†, Taufiq Ihsan[1] and Sugeng Nugroho[2]

[1]Doctoral Program in Environmental Engineering, Faculty of Engineering, Andalas University, Padang, Indonesia
[2]Meteorology, Climatology, and Geophysics Agency (BMKG), Global Atmosphere Watch (GAW) Station Bukit Kototabang, Agam, West Sumatra, Indonesia
†Corresponding author: Vera Surtia Bachtiar; verasurtia@eng.unand.ac.id

Abbreviation: Nat. Env. & Poll. Technol.
Website: www.neptjournal.com

Received: 05-11-2025
Revised: 02-01-2026
Accepted: 13-01-2026

Key Words:

Air modeling
Dispersion
Simulation
Eruption of Lewotobi Laki-Laki
Volcanic ash
Mass eruption rate (MER)

Citation for the Paper:

Sufitri, Y., Bachtiar, V.S., Ihsan, T. and Nugroho, S., 2026. Comparative assess-ment of empirical and theoretical mass eruption rate estimation methods using HYSPLIT: A case study of Lewotobi Laki-Laki eruption. *Nature Environment and Pollution Technology*, 25(3), p.D1887. https://doi.org/10.46488/NEPT.2026.v25i03.D1887

Note: From 2025, the journal has adopted the use of Article IDs in citations instead of traditional consecutive page numbers. Each article is now given individual page ranges starting from page 1.

Copyright: © 2026 by the authors
Licensee: Technoscience Publications
This article is an open access article distributed under the terms and conditions of the Creative Commons Attribution (CC BY) license (https://creativecommons.org/licenses/by/4.0/).

ABSTRACT

Volcanic ash emissions pose threats to aviation safety and socioeconomic activities, necessitating accurate dispersion modeling for effective early warning systems. The Mass Eruption Rate (MER) is a crucial parameter in ash transport models, yet its estimation remains a primary source of uncertainty. This study evaluates six MER formulations (MER1–MER4: non-wind-affected; MER5–MER6: wind-affected) for simulating ash dispersion from the Lewotobi Laki-Laki eruption using HYSPLIT, under two plume height scenarios (H = 1,000 m and 9,000 m). Results indicate that the plume orientation aligns well with Sentinel-5P observations, though significant concentration discrepancies are evident. Case 1 shows a severe systematic underestimation (FB = -190.24%), likely due to uncertainties in column height and the high-resolution CAMS EAC validation constraints. Case 2 demonstrates much better agreement with CAMS EAC4 reanalysis data, with a minimal fractional bias (FB = -7.06%), a high index of agreement (IOA = 0.9653), and an RMSE of 0.7084 $\mu g.m^{-3}$. Sensitivity analysis reveals that uncertainty in column height can increase MER variance roughly threefold, highlighting that source height precision largely determines MER accuracy. Although MER5 does not consistently outperform other formulations, it demonstrates relatively more consistent spatial dispersion patterns under wind-dominated conditions, though performance remains sensitive to source parameter accuracy. Consequently, this study recommends a multilevel operational approach that employs MER5 under favorable meteorological conditions, combined with rigorous uncertainty quantification to support operational volcanic ash advisories.

1. INTRODUCTION

Volcanic eruptions are geological phenomena that significantly impact biophysical and socio-economic systems. This hazard is particularly critical, given that approximately 800 million people live within a 100 km radius of active volcanoes, a condition that directly increases vulnerability to volcanic crises (Loughlin et al. 2015). High concentrations of volcanic ash in the atmosphere may result in several consequences, including reduced visibility, attenuation of solar radiation reaching the Earth's surface, and adverse effects on health. While such impacts are often confined to local scales, large-scale eruptions that inject material into the stratosphere can trigger long-term alterations in solar radiation and the global climate (Matthias et al. 2012).

The 2010 eruption of Eyjafjallajökull in Iceland provides a prominent case study of the disruption caused by volcanic activity in air transportation. The dispersion of volcanic ash across the North Atlantic and Europe severely disrupted flight routes (The 2010 Eyjafjallajökull eruption, Iceland 2012). A comparable situation occurred in Indonesia, where the 2010 eruption of Mount Merapi caused



Fig. 1: Explosive eruption of Mount Lewotobi Laki-Laki on November 13, 2024.

an estimated economic loss of US$395 million (BNPB 2011). Indonesia is one of the most volcanically active countries, hosting numerous volcanoes across its archipelago. Among them, the Lewotobi Laki-Laki Volcano has recently exhibited increased volcanic activity, highlighting its potential threat. It experienced an eruption from November 2024 through 2025 that had significant multidimensional impacts.

Lewotobi Laki-Laki Volcano, situated in East Flores, East Nusa Tenggara, Indonesia, is an active stratovolcano with a summit altitude of around 1,584 meters above sea level that frequently experiences eruptions. Such volcanic activity poses significant risks to nearby communities and the environment, including potential fatalities, mass evacuations, and infrastructure destruction. Recent eruptions resulted in 10 fatalities and numerous injuries, prompting the evacuation of over 12,000 residents. Volcanic ash from these events was dispersed over areas up to 1,000 km away, degrading air quality on Lombok Island and causing substantial agricultural losses (ESDM 2024).

The dispersion and deposition of volcanic ash are heavily influenced by meteorological conditions, especially wind variations linked to trade wind inversions, which are crucial for forecasting and risk management (Dioguardi et al. 2020a, Poulidis et al. 2018). The distinctive meteorological features of tropical regions, such as persistent trade wind inversions, convective phenomena, and seasonal wind shifts, underscore the need for high-resolution models. These models are vital for accurately simulating wind shear, topographic effects on airflow, and convective activity to effectively reproduce ash dispersion and deposition patterns (Poulidis et al. 2018). Additionally, source parameters like eruption column height, eruption cloud altitude, and mass eruption rate (MER) are essential for precisely estimating the volume of volcanic material released into the atmosphere per unit time (Aubry et al. 2017, Bonadonna & Costa 2012a, Dioguardi et al. 2020a, Mastin et al. 2009, Wilson & Walker 1987a).

Although various volcanic ash dispersion modeling applications have been developed, many of these tools remain limited by incomplete input data. Several do not offer options for integrating real-time meteorological data, detailed topographic information, or specific eruption parameters such as plume height and particle size distribution (Folch et al. 2016, Scollo et al. 2008a). Additionally, the mass eruption rate (MER) cannot be measured in real time and must therefore be estimated using a variety of empirical and numerical methods, ranging from analytical assumptions to model-based approaches (Bonadonna & Costa 2012, Degruyter & Bonadonna 2012, Mastin et al. 2009, Wilson & Walker 1987, Woodhouse et al. 2013). Predictions from HYSPLIT have exhibited discrepancies between simulated ash concentrations and field measurements (Sufitri et al. 2024). This aligns with the shortcomings of the NMMB-MONARCH-ASH model, which fails to reproduce 45–70% of volcanic ash clouds due to uncertainties in source parameters (Marti et al. 2017).

The accuracy of mass eruption rate (MER) estimates relies heavily on the chosen plume model and the processing of input data, such as plume height. Different modeling approaches and data processing methods can produce significantly varying results (Dürig et al. 2022, 2023a). The selection of ash cloud models such as those accounting for wind effects versus those that do not, can markedly impact the predicted ash cloud extent, sometimes by as much as five times (Degruyter & Bonadonna 2012a, Dioguardi et al. 2020a). Inaccurate MER estimates may also lead to overestimations of the deposited mass (Tadini et al. 2022), especially considering the complex behavior of proximal

ash fallout and the nonlinear relationship between MER and umbrella cloud scaling, which is particularly important during large eruptions (Buckland et al. 2022, Devenish et al. 2012). A comparative analysis of six MER modeling strategies applied to the eruption of Mount Lewotobi Laki-Laki will offer valuable insights for model selection and improve the precision of MER estimations.

2. MATERIALS AND METHODS

2.1. Comparison of MER Estimation Methods

This study evaluates the performance of various Mass Eruption Rate (MER) estimation methods under tropical meteorological conditions through a case study of the Mount Lewotobi Laki-Laki eruption. The assessment involved examining how different MER formulations influence volcanic ash dispersion simulations using HYSPLIT software. Six MER methods, adopted from Dürig et al. (2023b) and Dioguardi et al. (2020) within the REFIR system framework, are analyzed, with detailed formulations provided in Table 1.

The MER1 formula developed by Wilson and Walker (1987) represents a theoretical model based on the physical relationship between Plinian eruption column dynamics and atmospheric conditions. This model calculates eruption column dynamics to determine ash fallout using a dimensionless constant of 236 m(s.kg^{-1}), which represents the combined effects of entrainment and atmospheric stratification derived from Morton's (1957) analytical theory of buoyant turbulent plumes. The MER2 model proposed by Sparks et al. (1997) is an improved version of the previous formulation by Sparks (1986), which defines rock density as ρ and employs a dimensional constant (c) with a value of 1670 m(s.m^{-3}).

The MER3 formula, introduced by Mastin et al. (2009), is an empirical equation derived from prior experiments to better account for uncertainties in mass eruption rate measurements. It features a more practical empirical relationship using a higher exponent of 4.15, assumes a standard rock density of ρ = 2500 kg.m^{-3}, and includes a dimensional constant of c = 2000 m(s.m^{-3}). The MER4 formula, developed by Gudmundsson et al. (2012), is a zero-dimensional empirical model that scales the Mastin et al. (2009) equation by incorporating a dimensionless constant a = 0.0564 and a scaling factor k_1. This model requires input parameters for both the average (H_{avg}) and maximum (H_{max})

Table 1: Formula for the mass eruption rate (MER) method.

Code	MER	Formula	Eq. No.	Parameters
MER1.	Wilson and Walker (1987)	$MER_1 = \left(\frac{h}{c}\right)^4$	(1)	h = maximum plume height above the vent c = constanta
MER2.	Sparks et al. (1997)	$MER_2 = \rho\left(\frac{h}{c}\right)^{3,86}$	(2)	h = maximum plume height above the vent c = constanta p = dense rock equivalent density
MER3.	Mastin et al. (2009)	$MER_3 = \rho\left(\frac{h}{c}\right)^{4,15}$	(3)	h = maximum plume height above the vent c = constanta p = dense rock equivalent density
MER4.	Gudmundsoon, (2012)	$MER_4 = \rho ak\left(\frac{h_{avg} + h_{max}}{c}\right)^{4,15}$	(4)	p = dense rock equivalent density h_{avg} = average plume height h_{max} = maximal plume height a = dimensionless constant k = scaling factor c = constanta
MER5.	Degruyter and Bonadonna (2012)	$MER_5 = \pi\frac{\rho\alpha 0}{g'}\left(\frac{2^{\frac{5}{2}}\alpha^2\bar{N}^3}{Z_1^4}H^4 + \frac{\beta^2\bar{N}^3\bar{v}}{6}H^3\right)$	(5)	H = maximum plume height above the vent n = phi ρα0 = reference density g' = reduced gravitational force α & β = wind entrainment coefficients $\bar{N}$ = buoyancy frequency $\bar{v}$ = averaged wind speed $\bar{z}_t$ = maximum non-dimensional height determined
MER6.	Woodhouse (2013)	$MER_6 = \left(\frac{\frac{1}{0.318}H1 + 3{,}266\widetilde{Ws} + 0{,}3527\widetilde{Ws}^2}{1 + 1{,}373\widetilde{Ws}}\right)^{3.953}$	(6)	H = maximum height above the vent $\widetilde{Ws}$ = wind shear

eruption column heights (Dürig et al. 2023a, Gudmundsson et al. 2012).

Unlike earlier models, MER5 (Degruyter & Bonadonna 2012b) and MER6 (Woodhouse et al. 2013b) incorporate wind effects into the estimation of mass eruption rates, leading to more complex mathematical formulations. Degruyter & Bonadonna (2012) based the MER concept on equations similar to those in Hewett et al. (1971) and Morton (1957), utilizing a one-dimensional analytical model of volcanic plumes grounded in turbulent gravitational convection theory (Morton 1957). This model assumes uniform velocity and buoyancy profiles with limited atmospheric entrainment, while accounting for source enthalpy, atmospheric conditions, and entrainment coefficients (Degruyter & Bonadonna 2012b). The influence of these factors is encapsulated by the reduced gravity parameter at the source (g′), which is computed as,

$$g' = g\left(\frac{C_0\theta_0 + C_{a0}\theta_{a0}}{C_{a0}\theta_{a0}}\right) \quad \ldots(7)$$

The values of C_a and θ_a are derived from the heat capacity and temperature of the surrounding atmosphere. In contrast, C_m and θ_m denote the specific heat capacity and temperature at the source. This formulation also includes the buoyancy frequency (N), which indicates the vertical stability of the atmosphere and can be determined from the actual vertical temperature profile. This parameter is essential for understanding how atmospheric conditions influence plume height, which directly affects MER estimation (Rossi et al. 2019). The parameters $\alpha = 0.1$, $\beta = 0.3$, and $Z_i = 2.8$ are adopted from established studies (Aubry et al. 2017, Bonadonna & Costa 2012b, Degruyter & Bonadonna 2012b, Düriget al. 2023b, Scollo et al. 2008b).

Subsequently, the MER6 approach by Woodhouse et al. (2013) is based on the development of Morton's (1957) theory and specifically incorporates the principles of convective plume theory with crosswind (shear) effects, as follows: This formulation is represented in Equation (8) as a dimensionless parameter that combines the principles of convective plume theory with crosswind (shear) effects.

$$\overline{W} = 1.44\,WS = 1{,}44\frac{V_1}{NH_1} \quad \ldots(8)$$

The variable V_1 represents the wind velocity at the reference height (H_r), where this height coincides with the column height (Woodhouse et al. 2013b).

2.2. HYSPLIT Model Configuration

HYSPLIT (Hybrid Single-Particle Lagrangian Integrated Trajectory), developed by NOAA's Air Resources Laboratory (ARL), is an atmospheric dispersion model that tracks pollutant trajectories, transport, and deposition. Over time, it has advanced from basic trajectory calculations to a sophisticated system capable of conducting local-to-global-scale simulations (Stein et al. 2015). The model is compatible across multiple platforms and can be operated via web interfaces or graphical user interfaces (GUI) based on Tcl/Tk on Linux, macOS, and Windows systems (Rolph et al. 2017). HYSPLIT employs both Lagrangian and Eulerian techniques to simulate and forecast the dispersion of hazardous materials such as volcanic ash, wildfire smoke, dust, and anthropogenic emissions (Rolph et al. 2017).

Table 2 presents the simulation parameters for volcanic ash dispersion, consistently applied to both eruption scenarios. The ash release duration was assumed to be 1 hour due to a lack of observational data on eruption duration; this assumption was not intended to reflect the actual eruption timeframe. All parameters not listed in Table 2 retained their default HYSPLIT settings, including turbulence parameterization, mixing depth calculation, and advanced configuration options. No additional modifications were made to ensure that differences in simulation outputs reflect the influence of MER formulation variations across both cases.

2.3. Eruption Source Parameters

Dispersion simulations of volcanic ash were performed for two eruption events, with column heights of 1,000 and 9,000 meters above the crater surface. These height parameters were derived from observational data provided by the Center for Volcanology and Geological Hazard Mitigation (PVMBG). Two distinct eruption column heights were chosen to account for uncertainties in estimating the mass eruption rate (MER). This approach emphasizes that

Table 2: HYSPLIT configuration parameters for Case 1 and Case 2.

Parameters	Case 1	Case 2
Release duration	h	1 h
Time step	24 h	24 h
Mass Eruption Rate	User Input	User Input
Particle diameter	10 µm	10 µm
Density (ρ)	2600 kg.m^{-3}	2600 kg.m^{-3}
Settling velocity	Default	Default
Dry deposition	On	On
Wet deposition	Off	Off
Scavenging coefficient	Default	Default
Vertical mixing	Enable	Enable
PBL scheme	Default	Default
Diffusion coefficients	Default	Default

Table 3: Input parameters for volcanic ash dispersion modeling using HYSPLIT.

Parameters	Case 1	Case 2
Eruption Start Time	2024 08 29	2024 11 12
Plume Height	1000 m	9000 m
Coordinates Source	-8.537682° S (latitude) 122.767683°E (longitude)	-8.537682° S (latitude) 122.767683°E (longitude)

the initial vertical distribution of ash from the crater is a key parameter in dispersion modeling. Small variations in plume height or initial vertical profile can lead to significant differences in dispersion patterns, ash concentration distributions, and the consistency with satellite observations (Cao et al. 2021, Dioguardi et al. 2020b).

2.4. Meteorological Dataset

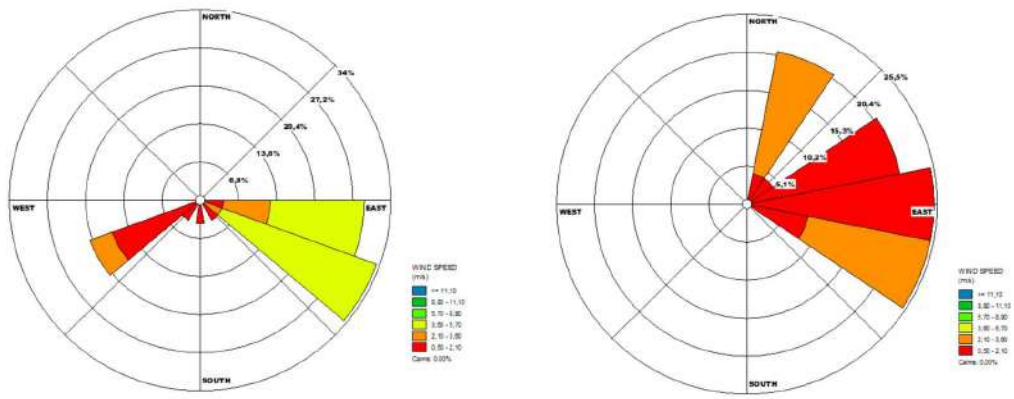
The meteorological input data were sourced from the Global Forecast System (GFS) satellite model, which offers a spatial resolution of approximately 0.25° × 0.25°, equivalent to about 27–28 km at the Earth's surface. Analysis of this meteorological data using WRPlot View software, focusing on wind direction and speed near Mount Lewotobi (Fig. 2), showed variations between cases. In Case 1, the dominant wind originated from the east-southeast, with maximum speeds ranging from 3.6 to 5.7 $m.s^{-1}$. In contrast, Case 2 experienced winds coming from the east, with lower maximum speeds between 0.5 and 2.1 $m.s^{-1}$.

2.5. Validation

Model performance was assessed through comparisons between reanalysis data and satellite observations, allowing for both a quantitative evaluation of concentration levels and a qualitative verification of dispersion trajectory patterns. To examine the alignment of volcanic ash concentrations with regional atmospheric conditions, simulations were analyzed alongside PM_{10} reanalysis data from the EAC4 product of the Copernicus Atmosphere Monitoring Service (CAMS) and the European Center for Medium-Range Weather Forecasts (ECMWF). Volcanic ash dispersed into the atmosphere mainly resides in the coarse aerosol mode, with the majority of particles measuring less than 10 µm in aerodynamic diameter (Andronico & Del Carlo 2016, Mueller et al. 2020, Thivet et al. 2024). While PM_{10} is not a definitive marker for volcanic ash, it functions as a proxy indicator for coarse aerosols during eruption events.

Simulated ash dispersion patterns were validated through Sentinel-5P UV aerosol index (UVAI) satellite observations. UVAI effectively detects UV-absorbing aerosols, including volcanic ash, across the entire atmospheric column (Torres et al. 2020). Equipped with the TROPOspheric Monitoring Instrument (TROPOMI), Sentinel-5P offers high spatial resolution (7 × 3.5 km^2), making it highly suitable for monitoring volcanic plumes. Aerosol data from Sentinel-5P align closely with ground-based measurements, such as AERONET, and other satellite products, confirming that the dPBata quality is sufficient for diverse applications (Chen et al. 2007, Michailidis et al. 2023).

Model performance was quantitatively assessed using the Pearson correlation coefficient (r) and the coefficient of determination (R^2) to evaluate the linear relationship and the variance explained between PM_{10} concentrations derived from satellite reanalysis data and simulation outputs. The Root Mean Square Error (RMSE) measures the absolute prediction error, while the Fractional Bias (FB) indicates systematic overprediction or underprediction, with acceptable performance specified as $-0.3 \leq FB \leq 0.3$



(a) (b)

Fig. 2: (a) Windrose Case 1 (b) Windrose pada Case 2.

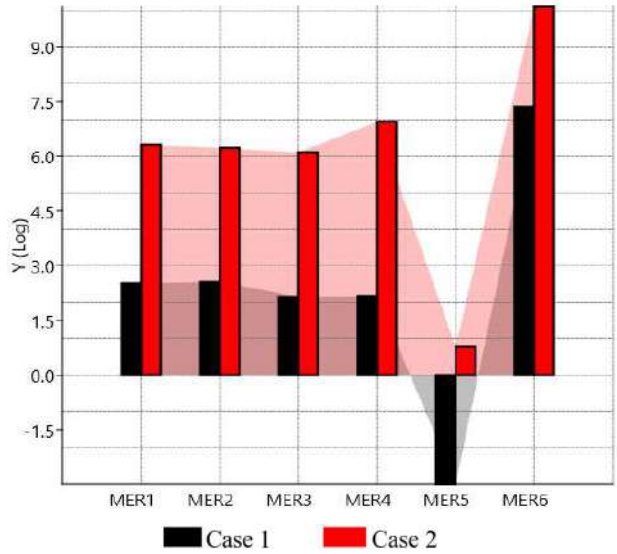


Fig. 3: Comparison of Mass Eruption Rate Estimates from Different MER Formulations Applied to Case 1 and Case 2.

(Boylan & Russell 2006). These evaluation metrics conform to established standards for atmospheric dispersion model assessment (Chang & Hanna 2004).

3. RESULTS

3.1. Analysis of the Mass Eruption Rate (MER)

The application of different MER formulations (Table 1) to two eruption events, one with a column height of 1,000 meters and the other reaching 9,000 meters above the crater, produced varying MER estimates. This variation highlights each method's sensitivity to the eruption column height parameter (Fig. 3).

Fig. 3 offers a comparative analysis of the six MER formulations applied to two different eruption scenarios: Case 1 (1,000 m) and Case 2 (9,000 m). As anticipated, most formulations predicted higher MER values for taller plumes (Case 2: 6×10^{10} to 1×10^{10} kg.s^{-1}) than for shorter ones (Case 1: 1×10^{-3} to 2×10^{7} kg.s^{-1}), reaffirming the fundamental correlation between plume height and mass flux. The wind-independent models (MER1–MER4) showed strong consistency across both eruption heights. In Case 1, MER estimates ranged from 1 to 4×10^{2} kg.s^{-1}, while in Case 2, values increased markedly, spanning from 3.1×10^{5} to 2.1×10^{6} kg.s^{-1}. A consistent scaling pattern was observed between the cases, with $\log_{10}$ ratios roughly between $10^{2.9}$ and $10^{4.3}$, indicating robust and stable power-law behavior within this group of models.

The wind-influenced models exhibited notable sensitivity. MER5 (Degruyter & Bonadonna 2012b) showed moderate sensitivity to eruption column height but produced a wide range of estimates from nearly zero at 1,000 m to approximately 6 kg.s^{-1} at 9,000 m. In contrast, MER6 (Woodhouse et al. 2013b) consistently generated the highest MER estimates, reaching 2×10^{7} kg.s^{-1} and 1×10^{10} kg.s^{-1} in both cases, exceeding other formulations by several orders of magnitude. Both MER5 and MER6 suggest these models tend to overestimate the effects of wind shear. The nine-order difference between MER5 and MER6 at higher altitudes underscores significant uncertainties inherent in wind-affected models, highlighting the need for thorough validation when applying them.

3.2. Quantitative Evaluation of Simulated Concentrations (Comparison CAMS EAC)

Fig. 4 displays the ash concentration outputs simulated by HYSPLIT for Cases 1 (1000 m column height) and 2 (9000 m column height) across the six MER formulations. The non-affected wind models (MER1–MER4) showed consistent scaling behavior, with Case 2 concentrations surpassing those of Case 1 by 2.4–3.1 orders of magnitude (271–1,267×), illustrating a strong correlation between height and concentration. Within each case, MER1–MER4 produced similar concentration ranges: from 1.5×10^{-7} to 7.2×10^{-7} mg.m^{-3} for Case 1, and from 4.6×10^{-5} to 3.2×10^{-4} mg.m^{-3} for Case 2.

In contrast, wind-affected models showed significantly different behaviors. MER5 generated extremely low concentrations in both cases (1.0×10^{-11} and 9.0×10^{-10} mg.m^{-3}), which are about 4–7 orders of magnitude lower than MER1–MER4, indicating serious underestimation. Conversely, MER6 produced the highest concentrations

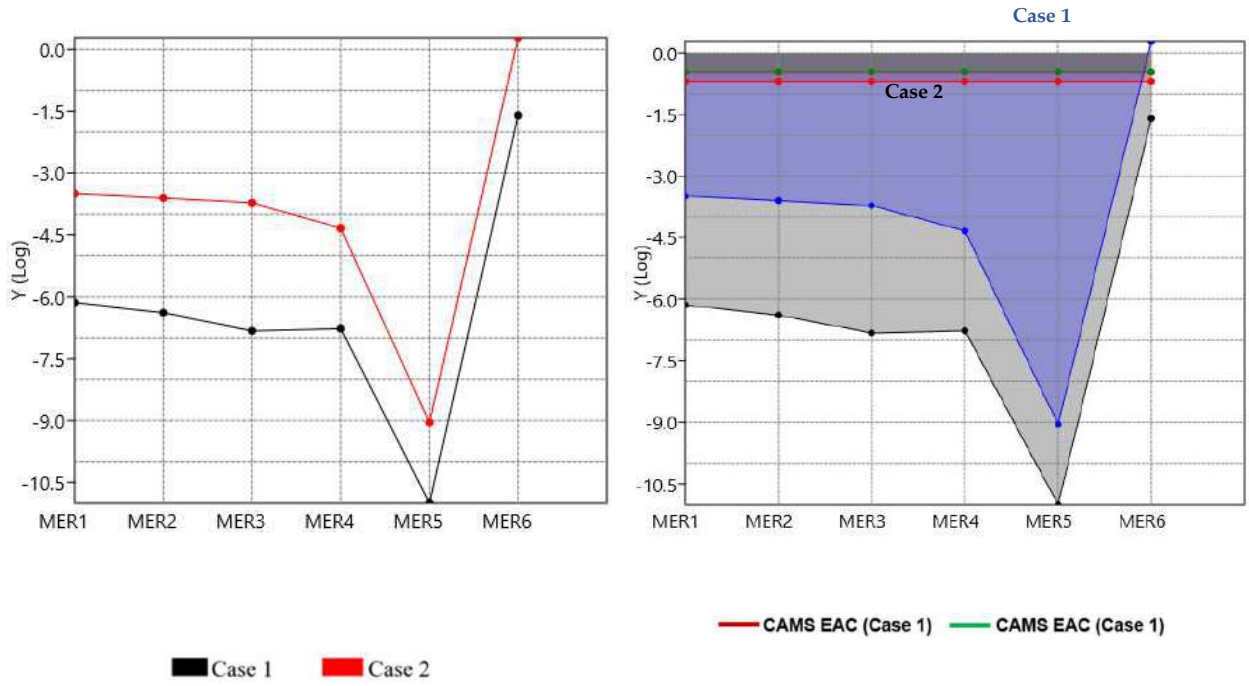


Fig. 4: (a) Simulate and (b) Comparison concentration variations under different MER (log scale).

(2.5×10^{-2} and 1.9 mg.m^{-3}), exceeding MER1–MER4 by four to five orders of magnitude. The overall 9–11 order of magnitude variation across all formulations highlights the substantial uncertainties in predicting ash concentrations with MER-based models.

The statistical performance was evaluated individually for each MER formulation (Table 4). For MER1-MER5, both cases exhibited uniformly poor performance with an extremely negative bias (FB ≈ -200%), indicating a systematic underestimation by approximately two orders of magnitude. Case 1 showed a consistent RMSE of 0.20 μg.m^{-3}, whereas Case 2 ranged from 0.34 to 0.34 μg.m^{-3}. Neither approach demonstrated an acceptable predictive capability for these formulations. MER6 revealed a critical performance divergence between the cases. Case 1 achieved a lower RMSE (0.17 μg.m^{-3}) with FB = -147.83%, maintaining an underestimation bias but with reduced severity. In contrast, Case 2 exhibited a substantially higher RMSE (1.56 μg.m^{-3}) and a dramatic shift to a positive bias (FB = +139.29%), indicating a systematic overestimation by a factor of 5.6.

Table 4: MER performance assessment in Case 1 and Case 2 with CAMS validation.

Formula	Case 1		Case 2	
	RMSE	FB (%)	RMSE	FB [%]
MER1	0,2	-200	0,3397	-199,62
MER2	0,2	-200	0,3398	-199,71
MER3	0,2	-200	0,3398	-199,78
MER4	0,2	-200	0,34	-199,95
MER5	0,2	-200	0,34	-200
MER6	0,17	-147,83	15.600	139,29

Table 5: Performance assessment based on eruption (Case 1 and Case 2) with CAMS validation.

Metrik	Case 1	Case 2
RMSE	0.1953	0.7084
Fractional Bias (%)	-190.24	-7.06

However, when the performance of these two modeling cases was evaluated against the CAMS EAC observation data based on the eruption column height of Cases 1 and 2 (Table 5), Case 1 had a lower RMSE (0.1953 μg.m^{-3}), indicating a very low estimate with a Fractional Bias (FB) of -190.24% and a Normalized Mean Bias (NMB) of -97.50%, which is classified as "poor" performance. In contrast, Case 2 showed minimal bias (FB = -7.06%, NMB = -6.82%) and a small Mean Bias Error (-0.0232 μg,m^{-3}), indicating a reliable prediction within acceptable air quality criteria (|FB| ≤ 15%). Both cases had an Agreement Index of 0.0000, reflecting limited variability in the observational data. This is likely related to the limited available observational data and the relatively coarse spatial resolution of the CAMS

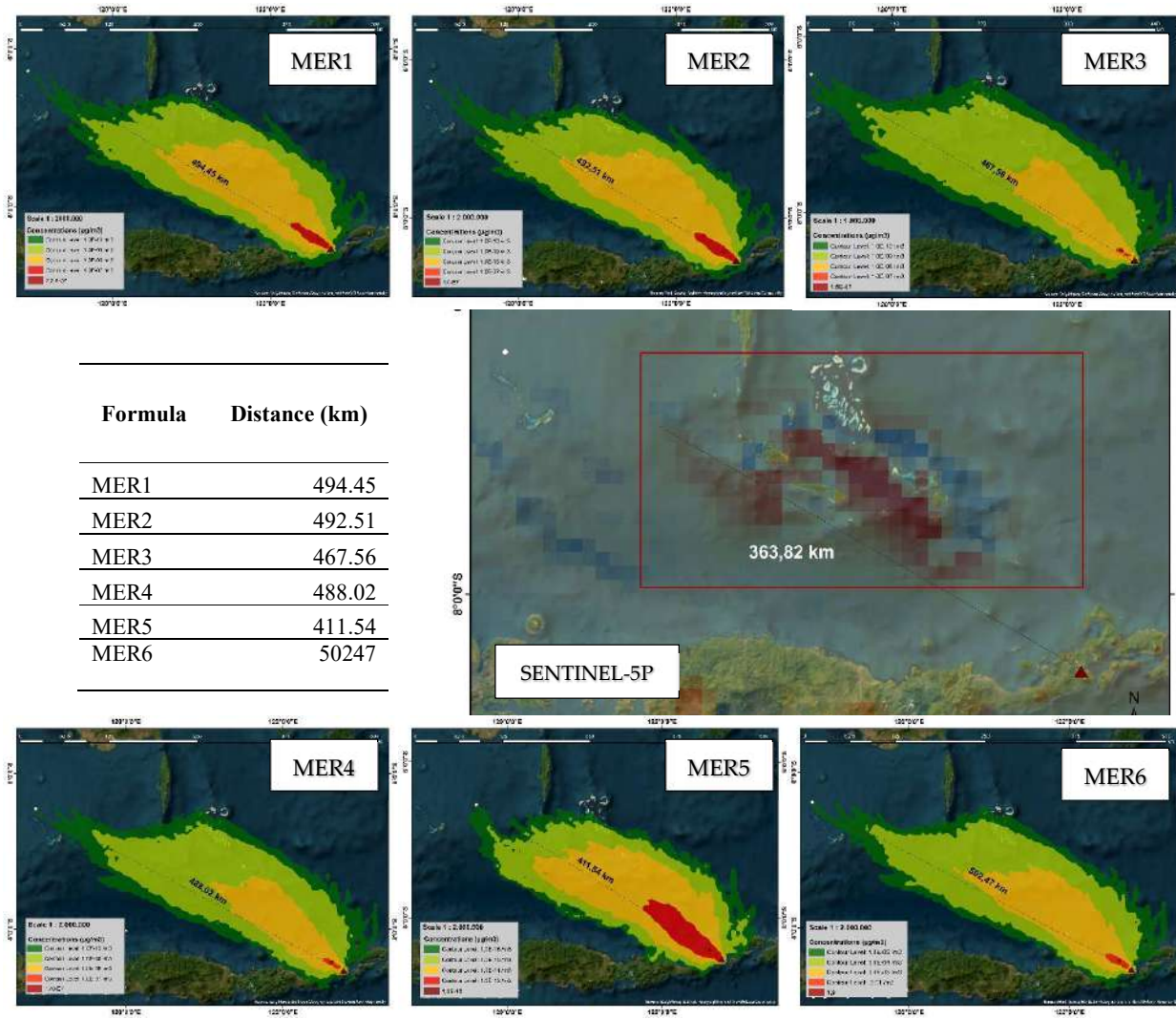
EAC data, which is suspected to contribute to the high bias in the statistical evaluation results. Overall, Case 1, with an eruption height of 9,000 m, exhibited minimal bias and good reliability.

3.3. Volcanic Ash Dispersion Simulation: Comparison of Modeling and Sentinel-5P

HYSPLIT model simulations were conducted using the meteorological and source parameters specified in Table 2. The simulation outputs were generated in the KML and JPEG formats. The KML outputs were subsequently imported into ArcGIS software to facilitate enhanced spatial visualization and detailed analysis of volcanic ash dispersion patterns.

3.3.1. *Case 1*

All MER formulations demonstrated consistent dispersion patterns, primarily following a trajectory from the southeast to the northwest. This trend indicates the influence of prevailing southeast winds, aligning with the windrose analysis in Case 1 (Fig. 5), which shows vectors pointing from north-northwest to west-northwest. The simulation results displayed variations in dispersion distances for each MER formulation, as illustrated in Fig. 5. MER6 achieved the greatest dispersion distance at 502.47 km, followed closely by MER1 at 494.45 km and MER2 at 492.51 km. Conversely, MER5 exhibited the shortest distance at 411.54 km, approximately 91 km less than MER6. These differences in dispersion distances reflect variations in



Formula	Distance (km)
MER1	494.45
MER2	492.51
MER3	467.56
MER4	488.02
MER5	411.54
MER6	50247

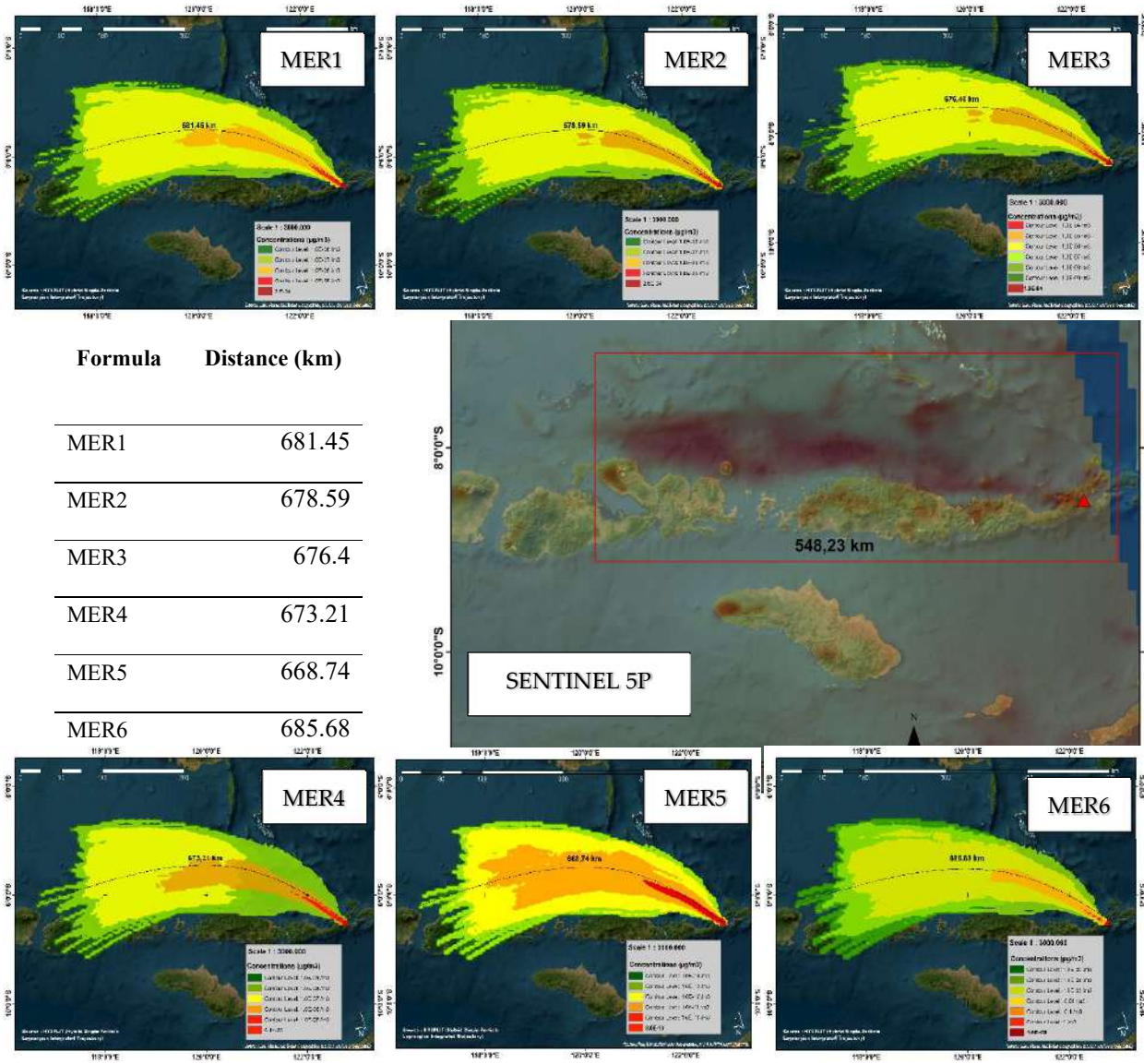
Fig. 5: Comparison of volcanic ash dispersion simulation results (six MER methods) and Sentinel-5P Satellite observations Case 1.

estimated emission rates among the formulations. MER6, with the longest dispersion, suggests a higher emission estimate, while MER5 indicates a more conservative value. The results for MER1, MER2, and MER4 were relatively similar, ranging from 488 to 494 km, indicating comparable emission parameterizations.

Fig. 5 clearly depicts the concentration gradient, with a high-concentration core near the emission source, moderate levels extending 100-200 km downwind, and low concentrations at the plume's edge reaching up to 400-500 km. In contrast to the simulation results, Sentinel-5P observational data showed a distribution pattern with a horizontal extent of approximately 364 km, which is significantly shorter than most MER model predictions. Among these, MER3 (467.56 km) closely matched satellite observations, with a difference of about 104 km. Conversely, MER6 showed the greatest deviation, overestimating the dispersion distance by roughly 138 km compared to the observed data.

3.3.2. Case 2

The Case 2 simulations exhibited relatively more consistent dispersion distance variations than those of Case 1, as presented in the accompanying table. MER6 produced the longest dispersion distance, reaching 685.68 km, whereas



Formula	Distance (km)
MER1	681.45
MER2	678.59
MER3	676.4
MER4	673.21
MER5	668.74
MER6	685.68

Fig. 6: Comparison of volcanic ash dispersion simulation results (six MER methods) and Sentinel-5P Satellite observations Case 1.

MER3 demonstrated the shortest distance of 676.4 km. Visualizations of all six MER formulations in Case 2 revealed consistent directional dispersion patterns extending from the southwest to the northeast. Furthermore, wind rose analysis (Fig. **6**) corroborated these simulation results, indicating that wind patterns are the dominant factor influencing volcanic ash transport in the atmosphere. All MER formulations exhibited high-concentration zones (red-orange coloration) localized in the central portion of the plume at distances of approximately 200-400 km from the plume origin. This pattern remained consistent across all formulations, suggesting that the dominant atmospheric transport and dispersion mechanisms were relatively similar for all MER parameterizations in Case 2.

The Sentinel-5P observational data (central panel) indicated a horizontal dimension of the affected area of approximately 548.23 km. All MER formulations in Case 2 tended to overestimate dispersion distances compared to satellite observations; however, the degree of overestimation in Case 2 (22-25%) was relatively modest. Additionally, the morphological orientation of the dispersion pattern showed a strong directional agreement between the model predictions and observational data. Notably, the plume in Case 2 exhibited greater lateral spreading with enhanced perpendicular dispersion, demonstrating superior dispersion characteristics with more effective lateral mixing processes.

4. DISCUSSION

4.1. Quantitative Evaluation of MER Estimation Accuracy

The mass eruption rate (MER) is classified into two groups based on the treatment of wind influence. The first group, comprising MER1 to MER4, did not account for wind effects and assumed that the eruption rate was directly proportional to the eruption column height (H) under windless conditions. This concept is based on the theoretical model developed by Morton et al. (1956) regarding the behavior of turbulent plumes, which was later refined by Mastin et al. (2009). In contrast, MER5 and MER6 are models that explicitly integrate wind dynamics by incorporating an entrainment coefficient (β) (Degruyter & Bonadonna 2012b, Suzuki & Koyaguchi 2015, Woodhouse et al. 2013b). Recent studies suggest that plume dynamics under windy conditions tend to yield biased MER estimates and that classifying plumes according to wind or buoyancy dominance can enhance the accuracy of MER estimation (Dürig et al. 2023a, 2023b, Gudmundsson et al. 2012). However, the magnitude of these biases and their implications for dispersion modeling have not been rigorously quantified in prior studies. Our comparative analysis addresses this gap by providing formal error statistics for all six MER formulations in two distinct cases.

The simulation results for Case 1 revealed significant discrepancies, characterized by an extremely negative fractional bias (FB) of -190.24%. This value indicates a systematic underestimation of ash concentrations by approximately a factor of three, falling well outside the acceptable bounds for "fair" model performance ($|FB| \leq 60\%$) established by Chang and Hanna (2004). Such severe underestimations point beyond mere meteorological uncertainty, suggesting fundamental deficiencies in the initial boundary conditions, specifically regarding the assumed eruption column height, vertical mass distribution, or total erupted mass. Spatially, all MER formulations in Case 1 overestimated the plume extent by 28-38% relative to the SENTINEL-5P observations (~364 km). Although MER3 achieved the best spatial alignment (estimated SOC: 50–55%) despite a 28.4% overestimation, the combination of spatial overestimation and severe concentration underestimation in this case implies the presence of compensating errors. Consequently, any qualitative claim that Case 1 captures the "general trend" is unsupported by quantitative metrics.

In contrast, Case 2 demonstrated substantially improved performance metrics. The case achieved an "excellent" FB of -7.06%, well within the ±15% threshold defined by standard evaluation criteria (Chang & Hanna 2004, Emery et al. 2001) and a high Index of Agreement (IOA) of 0.9653. Although the RMSE for Case 2 (0.7084 μg.m□³) is numerically higher than that of Case 1, this is an artifact of the significantly higher concentration magnitudes in the second case rather than a degradation of model precision. Among the tested formulations, MER5 (Degruyter & Bonadonna, 2012) demonstrated the closest spatial agreement with Sentinel-5P satellite observations in Case 2, predicting a plume extent of 668.74 km against the observed ~548 km, corresponding to a relative spatial error of 22%. The performance of MER5 is likely attributable to its integration of wind effects, accounting for gravity, magma temperature, and mean wind velocity based on the plume theory of Morton et al. (1956) and Hewett et al. (1971), the robustness of which has been validated in historical eruptions (Dürig et al. 2022).

4.2. Sensitivity Analysis: Plume Height Uncertainty Quantification

Eruption column height is the governing variable in Mass Eruption Rate (MER) estimation; however, it remains subject to substantial observational uncertainty, typically varying by ±20–30% depending on the retrieval method (e.g., satellite, radar, or ground-based) and meteorological conditions

(Mastin et al. 2009, Pouget et al. 2013). To quantify the propagation of this uncertainty into our simulation results, we performed a systematic sensitivity analysis by perturbing the baseline plume height (H) by 20 % and 30%. This approach accounts for the nonlinear power-law relationship, where MER scales proportionally to H^n, with exponents ranging from for weak-wind models (Morton et al. 1956) to complex variable dependencies in wind-affected formulations (Degruyter & Bonadonna 2012).

The analysis revealed a critical sensitivity amplification factor of approximately three: a ±20% deviation in plume height resulted in a disproportionate ±55–60% variation in the estimated MER. This nonlinearity offers a compelling physical explanation for the discrepancies observed in our cases. Specifically, the severe concentration underestimation in Case 1 (FB = -190.24%) could be largely rectified if the true plume height were 30–35% higher than the assumed baseline. This suggests that the primary source of error in Case 1 is likely an underestimated input parameter rather than a fundamental deficiency in the MER formulation itself. Conversely, the high accuracy of Case 2 (FB = -7.06%) implies that the assumed plume height was precise to within ±2–3%, validating the quality of the observational data used for that event.

4.3. Rigorous Uncertainty Analysis: Wind-Affected vs. Non-Wind-Affected MER Models

While the theoretical advantages of wind-affected Mass Eruption Rate (MER) models, such as MER5-MER6, are well established, their practical benefits, validated through real-world data, are limited. The findings indicate that the effectiveness of these models depends on the accuracy of primary input parameters. In Case 2, MER5 produced the closest spatial match to Sentinel-5P observations, with a plume extent of 668.74 km compared to the observed ~548 km (22% relative error). However, this spatial agreement was not reflected in concentration performance, where MER5 yielded the lowest estimates among all formulations (~9.0×10^{-10} mg/m³) and a Fractional Bias approaching -200% against CAMS EAC4 data (Table 4). This discrepancy suggests that MER5 captures plume transport dynamics reasonably well but underestimates the total mass loading under the conditions. These findings highlight a broader pattern: wind-affected formulations behave fundamentally differently from empirical power-law models in response to column height and atmospheric variability.

In Case 1 (1,000 m column height), the wind-driven models (MER5-MER6) showed no measurable advantage over the wind-driven formulations. MER5 produced MER values close to zero at this column height, consistent with the sensitivity of the H³ and H⁴ terms to low cloud heights, while MER6 produced the highest estimates among all formulations. MER3 produced the closest spatial match to Sentinel-5P observations in Case 1, with a cloud extent of 467.56 km compared to the observations of ~364 km (28.4% overestimation). These results suggest that the empirical parameterization of MER3 may be relatively suitable for low-altitude eruption scenarios under the meteorological conditions observed in this study. Conversely, MER6 consistently underperformed in both cases, showing the widest confidence intervals and the greatest sensitivity to input errors. This indicates that wind-affected models do not correct for systematic biases in primary inputs like plume height; rather, their complexity only proves beneficial when the baseline eruption parameters are accurately constrained.

4.4. Recommendations for Model Improvement and Future Research

The alignment between the modeled plume orientations, GFS meteorological data, and Sentinel-5P observations, confirmed by angular deviations of less than 15°, demonstrates the model's effectiveness in representing first-order dispersion dynamics. Although this large-scale consistency is evident, addressing the identified quantitative biases requires implementing a more strategic approach. To improve immediate forecasting accuracy, MER5 (Degruyter & Bonadonna 2012) may be considered as the primary formulation under wind-dominated conditions, given its demonstrated reduction in uncertainty of approximately 20% in Case 2, though this finding requires validation across a broader range of eruption scenarios. Additionally, ensemble forecasting with multiple formulations (e.g., MER3, MER4, and MER5) is proposed to better quantify uncertainty related to MER estimation. Ultimately, operational precision depends on limiting plume height uncertainty to within ±15% through the combined use of satellite, ground-based, and radar observations. Future modeling efforts should focus on parameterizing the heights of Sub-Plinian and Plinian eruptions, which demand specialized mass distribution profiles to account for aerosol injections into the upper troposphere and lower stratosphere (UTLS), a key factor in long-range transport dynamics (Bonadonna & Costa 2012b, Mastin et al. 2009, Zidikheri et al. 2018).

5. CONCLUSIONS

The accuracy of volcanic ash dispersion modeling is fundamentally contingent upon the precision of the Eruption Source Parameters (ESP), specifically the eruption column height (H). Quantitative sensitivity analysis revealed an amplification factor of approximately 3×, where a ±20%

uncertainty in plume height translates to a ±60% variance in MER, underscoring that plume height accuracy is a critical determinant of reliable eruption rate estimates. Significant numerical discrepancies exist between MER formulations, where MER5 generally provides lower concentration estimates compared to other formulations, whereas MER6 produces the highest estimates, often leading to overestimation in high-altitude cases, highlighting the importance of selecting formulations that explicitly account for local atmospheric conditions, particularly wind influence. Statistical evaluation using Sentinel-5P and CAMS EAC4 data further revealed a clear performance gap between the cases, with Case 1 exhibiting an extremely negative Fractional Bias (FB = -190.24%), indicating severe systematic underestimation by a factor of three, whereas Case 2 demonstrated excellent agreement, particularly for MER5, with a Fractional Bias of only -7.06%, a high Index of Agreement (IOA) of 0.9653, and an RMSE of 0.7084 $\mu g.m^{-3}$.

The HYSPLIT model successfully reproduced the primary ash transport directions, with angular deviations of less than 15° compared to the Sentinel-5P observations (NW for Case 1 and SW–NE for Case 2). However, a systematic overestimation of plume extent by 22-38% was identified, likely attributable to excessive lateral dispersion coefficients or unresolved mesoscale meteorological features in the GFS dataset. MER5 (Degruyter & Bonadonna, 2012) produced the lowest ash concentration estimates among all formulations, falling 4–7 orders of magnitude below non-wind-affected models and yielding a Fractional Bias approaching -200% against CAMS EAC4 data. Although MER5 achieved the closest spatial agreement with Sentinel-5P observations in Case 2, the severe concentration underestimation limits its direct operational applicability without prior parameter calibration. For practical forecasting, MER3 is recommended as a stable empirical baseline for low-altitude eruptions, while an ensemble of MER3, MER4, and MER5 is preferable for higher-altitude events to better capture source parameter uncertainty. Application of MER5 in tropical volcanic settings should be preceded by site-specific calibration of key atmospheric inputs, particularly buoyancy frequency ($\bar{N}$) and source enthalpy, given that the formulation was originally developed and validated under mid-latitude conditions.

6. ACKNOWLEDGMENTS

This research was funded by Andalas University in accordance with the Research Contract Batched I Doctoral Dissertation Research Scheme. Number: 109/UN16.19/PT.01.03/PDD/2025. Fiscal Year 2025

7. REFERENCES

Andronico, D. and Del Carlo, P., 2016. PM10 measurements in urban settlements after lava fountain episodes at Mt. Etna, Italy: Pilot test to assess volcanic ash hazard to human health. Natural Hazards and Earth System Sciences, 16(1), pp.29-40. [DOI]

Aubry, T.J., Jellinek, A.M., Carazzo, G., Gallo, R., Hatcher, K. and Dunning, J., 2017. A new analytical scaling for turbulent wind-bent plumes: Comparison of scaling laws with analog experiments and a new database of eruptive conditions for predicting the height of volcanic plumes. *Journal of Volcanology and Geothermal Research*, 343, pp.233-251. [DOI]

BNPB, 2011. *Rencana Aksi Rehabilitasi dan Rekonstruksi Wilayah Pascabencana Erupsi Gunung Merapi di Provinsi D.I. Yogyakarta dan Provinsi Jawa Tengah Tahun 2011–2013* [Action Plan for Rehabilitation and Reconstruction of Post-Disaster Areas of Mount Merapi Eruption in D.I. Yogyakarta and Central Java Provinces, 2011–2013]. BAPPENAS and BNPB, Jakarta, 205 pp. [Available at: https://www.bnpb.go.id/buku/rencana-aksi-rehabilitasi-dan-rekonstruksi-wilayah-pascabencana-erupsi-gunung-merapi-di-prov-diy-dan-prov-jateng-tahun-2011-2013]

Bonadonna, C. and Costa, A., 2012a. Estimating the volume of tephra deposits: A new simple strategy. *Geology*, 40(5), pp.415-418. [DOI]

Bonadonna, C. and Costa, A., 2012b. Estimating the volume of tephra deposits: A new simple strategy. *Geology*, 40(5), pp.415-418. [DOI]

Boylan, J.W. and Russell, A.G., 2006. PM and light extinction model performance metrics, goals, and criteria for three-dimensional air quality models. *Atmospheric Environment*, 40(26), pp.4946–4959. [DOI]

Buckland, H.M., Mastin, L.G., Engwell, S.L. and Cashman, K.V., 2022. Modelling the transport and deposition of ash following a magnitude 7 eruption: The distal Mazama tephra. *Bulletin of Volcanology*, 84(9), p.87. [DOI]

Cao, Z., Bursik, M., Yang, Q. and Patra, A., 2021. Simulating the transport and dispersal of volcanic ash clouds with initial conditions created by a 3D plume model. *Frontiers in Earth Science*, 9, p.704797. [DOI]

Chang, J.C. and Hanna, S.R., 2004. Air quality model performance evaluation. *Meteorology and Atmospheric Physics*, 87(1-3), pp.167-196. [DOI]

Chen, T.-M., Kuschner, W.G., Gokhale, J. and Shofer, S., 2007. Outdoor air pollution: Nitrogen dioxide, sulfur dioxide, and carbon monoxide health effects. *The American Journal of the Medical Sciences*, 333(4), pp.249-256. [DOI]

Degruyter, W. and Bonadonna, C., 2012a. Improving on mass flow rate estimates of volcanic eruptions. *Geophysical Research Letters*, 39(16), p.L16302. [DOI]

Degruyter, W. and Bonadonna, C., 2012b. Improving on mass flow rate estimates of volcanic eruptions. *Geophysical Research Letters*, 39(16), p.L16302. [DOI]

Devenish, B.J., Francis, P.N., Johnson, B.T., Sparks, R.S.J. and Thomson, D.J., 2012. Sensitivity analysis of dispersion modeling of volcanic ash from Eyjafjallajökull in May 2010. *Journal of Geophysical Research: Atmospheres*, 117(D20), p.D20211. [DOI]

Dioguardi, F., Beckett, F., Dürig, T. and Stevenson, J.A., 2020a. The impact of eruption source parameter uncertainties on ash dispersion forecasts during explosive volcanic eruptions. *Journal of Geophysical Research: Atmospheres*, 125(17), p.e2020JD032717. [DOI]

Dioguardi, F., Beckett, F., Dürig, T. and Stevenson, J.A., 2020b. The impact of eruption source parameter uncertainties on ash dispersion forecasts during explosive volcanic eruptions. *Journal of Geophysical Research: Atmospheres*, 125(17), p.e2020JD032717. [DOI]

Dürig, T., Gudmundsson, M.T., Ágústsdóttir, T., Högnadóttir, T. and Schmidt, L.S., 2022. The effect of wind and plume height reconstruction methods on the accuracy of simple plume models A second look at the 2010 Eyjafjallajökull eruption. *Bulletin of Volcanology*, 84(3), p.33. [DOI]

Dürig, T., Gudmundsson, M.T., Dioguardi, F. and Schmidt, L.S., 2023a.

Quantifying the effect of wind on volcanic plumes: Implications for plume modeling. *Journal of Geophysical Research: Atmospheres*, 128(2), p.e2022JD037781. [DOI]

Dürig, T., Schmidt, L.S. and Dioguardi, F., 2023b. Optimizing mass eruption rate estimates by combining simple plume models. *Frontiers in Earth Science*, 11, p.1250686. [DOI]

Emery, C., Tai, E. and Yarwood, G., 2001. Enhanced meteorological modeling and performance evaluation for two Texas ozone episodes. *Journal of Applied Meteorology and Climatology*, 40(3), pp.345-362.

Folch, A., Costa, A. and Macedonio, G., 2016. FPLUME-1.0: An integral volcanic plume model accounting for ash aggregation. *Geoscientific Model Development*, 9(1), pp.431-450. [DOI]

Gudmundsson, M.T., Thordarson, T., Höskuldsson, Á., Larsen, G., Björnsson, H., Prata, F.J., Oddsson, B., Magnússon, E., Högnadóttir, T., Petersen, G.N., Hayward, C.L., Stevenson, J.A. and Jónsdóttir, I., 2012. Ash generation and distribution from the April-May 2010 eruption of Eyjafjallajökull, Iceland. *Scientific Reports*, 2(1), p.572. [DOI]

Hewett, T.A., Fay, J.A. and Hoult, D.P., 1971. Laboratory experiments of smokestack plumes in a stable atmosphere. *Atmospheric Environment (1967)*, 5(9), pp.767-789. [DOI]

Loughlin, S.C., Sparks, S., Brown, S.K., Jenkins, S.F. and Vye-Brown, C. (Eds.), 2015. *Global Volcanic Hazards and Risk*. Cambridge University Press, pp.388. [DOI]

Marti, A., Folch, A., Jorba, O. and Janjic, Z., 2017. Volcanic ash modeling with the online NMMB-MONARCH-ASH v1.0 model: Model description, case simulation, and evaluation. *Atmospheric Chemistry and Physics*, 17(6), pp.4005-4030. [DOI]

Mastin, L.G., Guffanti, M., Servranckx, R., Webley, P., Barsotti, S., Dean, K., Durant, A., Ewert, J.W., Neri, A., Rose, W.I., Schneider, D., Siebert, L., Stunder, B., Swanson, G., Tupper, A., Volentik, A. and Waythomas, C.F., 2009. A multidisciplinary effort to assign realistic source parameters to models of volcanic ash-cloud transport and dispersion during eruptions. *Journal of Volcanology and Geothermal Research*, 186(1-2), pp.10-21. [DOI]

Matthias, V., Aulinger, A., Bieser, J., Cuesta, J., Geyer, B., Langmann, B., Serikov, I., Mattis, I., Minikin, A., Mona, L., Quante, M., Schumann, U. and Weinzierl, B., 2012. The ash dispersion over Europe during the Eyjafjallajökull eruption – Comparison of CMAQ simulations to remote sensing and airborne in situ observations. *Atmospheric Environment*, 48, pp.184-194. [DOI]

Michailidis, K., Koukouli, M.-E., Balis, D., Veefkind, J.P., De Graaf, M., Mona, L., Papagianopoulos, N., Pappalardo, G., Tsikoudi, I., Amiridis, V., Marinou, E., Gialitaki, A., Mamouri, R.-E., Nisantzi, A., Bortoli, D., João Costa, M., Salgueiro, V., Papayannis, A., Mylonaki, M. and Baars, H., 2023. Validation of the TROPOMI/S5P aerosol layer height using EARLINET lidars. *Atmospheric Chemistry and Physics*, 23(3), pp.1919-1940. [DOI]

Morton, B.R., 1957. Buoyant plumes in a moist atmosphere. *Journal of Fluid Mechanics*, 2(2), pp.127-144. [DOI]

Morton, B.R., Taylor, G.I. and Turner, J.S., 1956. Turbulent gravitational convection from maintained and instantaneous sources. *Proceedings of the Royal Society of London. Series A, Mathematical and Physical Sciences*, 234(1196), pp.1–23. [DOI]

Mueller, W., Cowie, H., Horwell, C.J., Hurley, F. and Baxter, P.J., 2020. Health impact assessment of volcanic ash inhalation: A comparison with outdoor air pollution methods. *GeoHealth*, 4(7), p.e2020GH000256. [DOI]

Pouget, S., Bursik, M., Webley, P., Dehn, J. and Pavolonis, M., 2013. Estimation of eruption source parameters from umbrella cloud or downwind plume growth rate. *Journal of Volcanology and Geothermal Research*, 258, pp.100-112. [DOI]

Poulidis, A.P., Phillips, J.C., Renfrew, I.A., Barclay, J., Hogg, A., Jenkins, S.F., Robertson, R. and Pyle, D.M., 2018. Meteorological controls on local and regional volcanic ash dispersal. *Scientific Reports*, 8(1), p.6873. [DOI]

Rolph, G., Stein, A. and Stunder, B., 2017. Real-time Environmental Applications and Display System: READY. *Environmental Modelling & Software*, 95, pp.210-228. [DOI]

Rossi, E., Bonadonna, C. and Degruyter, W., 2019. A new strategy for the estimation of plume height from clast dispersal in various atmospheric and eruptive conditions. *Earth and Planetary Science Letters*, 505, pp.1–12. [DOI]

Scollo, S., Tarantola, S., Bonadonna, C., Coltelli, M. and Saltelli, A., 2008a. Sensitivity analysis and uncertainty estimation for tephra dispersal models. *Journal of Geophysical Research: Solid Earth*, 113(B6), p.B06205. [DOI]

Scollo, S., Tarantola, S., Bonadonna, C., Coltelli, M. and Saltelli, A., 2008b. Sensitivity analysis and uncertainty estimation for tephra dispersal models. *Journal of Geophysical Research: Solid Earth*, 113(B6), p.B06205. [DOI]

Sparks, R.S.J., 1986. The dimensions and dynamics of volcanic eruption columns. *Bulletin of Volcanology*, 48(1), pp.3-15. [DOI]

Sparks, R.S.J., Bursik, M.I., Carey, S.N., Gilbert, J.S., Glaze, L.S., Sigurdsson, H. and Woods, A.W., 1997. *Volcanic Plumes*. John Wiley & Sons, New York, 574 pp.

Stein, A.F., Draxler, R.R., Rolph, G.D., Stunder, B.J.B., Cohen, M.D. and Ngan, F., 2015. NOAA's HYSPLIT atmospheric transport and dispersion modeling system. *Bulletin of the American Meteorological Society*, 96(12), pp.2059-2077. [DOI]

Sufitri, Y., Bachtiar, V.S., Putra, A.A. and Nugroho, S., 2024. Modeling the dispersion of air pollution due to volcanic eruptions. *International Journal of Disaster Management*, 7(3), pp.231-250. [DOI]

Suzuki, Y.J. and Koyaguchi, T., 2015. Effects of wind on entrainment efficiency in volcanic plumes. *Journal of Geophysical Research: Solid Earth*, 120(9), pp.6122-6140. [DOI]

Tadini, A., Gouhier, M., Donnadieu, F., De' Michieli Vitturi, M. and Pardini, F., 2022. Particle sedimentation in numerical modelling: A case study from the Puyehue-Cordón Caulle 2011 eruption with the PLUME-MoM/HYSPLIT models. *Atmosphere*, 13(5), p.784. [DOI]

Thivet, S., Bagheri, G., Kornatowski, P.M., Fries, A., Lemus, J., Simionato, R., Díaz-Vecino, C., Rossi, E., Yamada, T., Scollo, S. and Bonadonna, C., 2024. In-situ volcanic ash sampling and aerosol-gas analysis based on UAS technologies (AeroVolc). *Aerosol Science and Technology*, 58(5), pp.455-470. [DOI]

Torres, O., Jethva, H., Ahn, C., Jaross, G. and Loyola, D.G., 2020. TROPOMI aerosol products: evaluation and observations of synoptic-scale carbonaceous aerosol plumes during 2018–2020. *Atmospheric Measurement Techniques*, 13(12), pp.6789–6806. [DOI]

Wilson, L. and Walker, G.P.L., 1987a. Explosive volcanic eruptions - VI. Ejecta dispersal in plinian eruptions: The control of eruption conditions and atmospheric properties. *Geophysical Journal International*, 89(2), pp.657-679. [DOI]

Wilson, L. and Walker, G.P.L., 1987b. Explosive volcanic eruptions - VI. Ejecta dispersal in plinian eruptions: The control of eruption conditions and atmospheric properties. *Geophysical Journal International*, 89(2), pp.657-679. [DOI]

Woodhouse, M.J., Hogg, A.J., Phillips, J.C. and Sparks, R.S.J., 2013a. Interaction between volcanic plumes and wind during the 2010 Eyjafjallajökull eruption, Iceland. *Journal of Geophysical Research: Solid Earth*, 118(1), pp.92-109. [DOI]

Woodhouse, M.J., Hogg, A.J., Phillips, J.C. and Sparks, R.S.J., 2013b. Interaction between volcanic plumes and wind during the 2010 Eyjafjallajökull eruption, Iceland. *Journal of Geophysical Research: Solid Earth*, 118(1), pp.92-109. [DOI]

Zidikheri, M.J., Lucas, C. and Potts, R.J., 2018. Quantitative verification and calibration of volcanic ash ensemble forecasts using satellite data. *Journal of Geophysical Research: Atmospheres*, 123(8), pp.4135-4156. [DOI]

Nature Environment and Pollution Technology
An International Quarterly Scientific Journal

p-ISSN: 0972-6268
(Print copies up to 2016)
e-ISSN: 2395-3454

Vol. 25 | No. 3 | Article ID B4392 | 2026

Original Research Paper

https://doi.org/10.46488/NEPT.2026.v25i03.B4392

Open Access Journal

Eco-Friendly Neem-Based Corrosion Inhibitor Coatings for Reinforced Concrete: Performance, Sustainability and Cost Assessment

Satya Prakash and Nishant Kumar†
Department of Civil Engineering, Sharda University, Greater Noida, India
†Corresponding author: Nishant Kumar; Nishant.kumar4@sharda.ac.in

Abbreviation: Nat. Env. & Poll. Technol.
Website: www.neptjournal.com

Received: 11-09-2025
Revised: 17-11-2025
Accepted: 27-11-2025

Key Words:

Corrosion inhibitors
Organic inhibitors
Sustainable construction
Environmentally safe
Eco-friendly coatings
LCA assessment

Citation for the Paper:

Prakash, S. and Kumar, N., 2026. Eco-friendly neem-based corrosion inhibitor coatings for reinforced concrete: Performance, sustainability, and cost assessment. *Nature Environment and Pollution Technology*, 25(3), B4392. https://doi.org/10.46488/NEPT.2026.v25i03. B4392

Note: From 2025, the journal has adopted the use of Article IDs in citations instead of traditional consecutive page numbers. Each article is now given individual page ranges starting from page 1.

Copyright: © 2026 by the authors
Licensee: Technoscience Publications
This article is an open access article distributed under the terms and conditions of the Creative Commons Attribution (CC BY) license (https://creativecommons.org/licenses/by/4.0/).

ABSTRACT

Corrosion of reinforcement in concrete is a critical durability challenge that undermines the service life and increases the maintenance costs of infrastructure. Although conventional inorganic inhibitors, such as zinc, are effective, they are associated with high costs and environmental concerns, necessitating the development of sustainable alternatives. This study investigated the potential of Azadirachta indica (Neem) powder as a green, bio-based corrosion inhibitor coating for reinforcing steel, with its performance benchmarked against zinc coatings. Reinforced M30 grade concrete specimens were subjected to chloride-induced accelerated corrosion for 365 days and evaluated through half-cell potential, weight and diameter loss, pullout bond strength, and surface morphology using SEM. Neem-coated specimens demonstrated a 47.5% reduction in half-cell potential and a 54% improvement in bond strength relative to uncoated specimens, closely matching zinc-coated samples, whose performance differences were not statistically significant. Life cycle assessment revealed that Neem coatings reduced the carbon footprint by up to 43%, whereas cost analysis showed a 39.6% reduction in per-meter coating cost compared to zinc. The findings highlight neem-based coatings as a sustainable, cost-effective, and eco-friendly solution offering performance comparable to zinc, thereby supporting resilient and environmentally responsible construction practices.

1. INTRODUCTION

Concrete and steel structures deteriorate over time owing to poor construction practices, inadequate maintenance, and exposure to aggressive environments, such as carbonation and chlorides, which accelerate reinforcement corrosion and reduce their service life. Effective durability planning and preventive measures require an understanding of the corrosion mechanisms (Ghanaati et al. 2022). Corrosion, driven by chemical and electrochemical processes, leads to cracking, spalling, and staining of concrete surfaces, exposing the reinforcement to further degradation and progressive loss of structural integrity (Singh et al. 2022, Zhao et al. 2019). Chloride and sulfate ions originating from de-icing salts, marine exposure, and industrial pollutants are major initiators of corrosion (Abirami & Sangeetha 2022). Their ingress is exacerbated by inadequate cover, poor compaction, microcracks, and environmental factors such as temperature variations, humidity changes, and freeze–thaw cycles, with geographical and industrial conditions further intensifying deterioration (Bajaj & Khurpade 2024). To counter these effects, corrosion inhibitor coatings are increasingly used to provide a protective barrier that restricts chloride and sulfate penetration and suppresses electrochemical reactions at the steel surface (Kamarska 2024, Jiang et al. 2025a, Kumar et al. 2025). Organic inhibitors form adsorbed protective films, whereas inorganic inhibitors contribute to passivation through chemical interactions with the cementitious matrix (Goni & Mazumder 2019, Söylev & Richardson 2008). Both systems have shown improved durability and mechanical performance under aggressive exposure (Hao et al. 2023, Kumar & Saharan 2022, Sharma et al. 2022, Sharmila & Vasanthi 2024).

Chloride-induced corrosion is particularly severe because chloride ions penetrate the concrete cover and destroy the passive oxide layer that normally protects steel in an alkaline pore environment (Ega et al. 2024). Once depassivated, steel undergoes localized anodic dissolution, forming ferrous ions that react with chloride to produce soluble complexes, which subsequently hydrolyze to form ferrous hydroxide and hydrochloric acid (Jiang et al. 2025b, Ovari et al. 2025). This acid regenerates chloride ions, thereby creating a self-sustaining corrosion cycle (Shehnazdeep & Pradhan 2022). The resulting rust products occupy a much larger volume, generating tensile stresses that cause cracking, delamination, and spalling of the concrete cover (Liu & Shi 2024). Fig. 1 illustrates the process of chloride-induced corrosion in concrete.

Fig. 2 illustrates the stages of deterioration caused by reinforcement corrosion in concrete and its effects on structural performance. In the initial phase, the steel reinforcement is protected by a passive oxide film formed in the alkaline pore solution. When chloride ions penetrate or carbonation lowers the alkalinity, this passive layer breaks down, initiating active corrosion. The anodic dissolution of steel generates expansive rust products that occupy several times the volume of the original metal (McCafferty 2010). This expansion produces hoop stresses at the steel–concrete interface, thereby creating pressure on the cover concrete. When the stress exceeds the tensile strength of the concrete, microcracks form, which later develop into visible cracks. These pathways allow more chloride, oxygen, and moisture to enter, creating a self-sustaining cycle of deterioration (Umamathi et al. 2024).

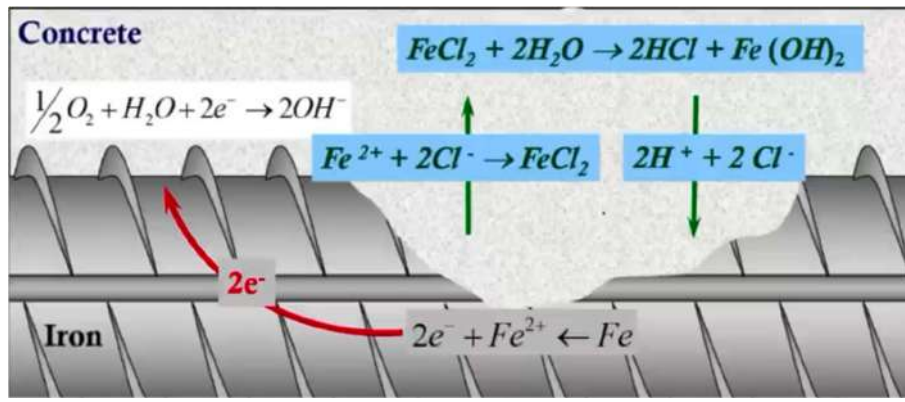


Fig. 1: Chloride-induced corrosion in concrete (Al-Amiery et al. 2024).

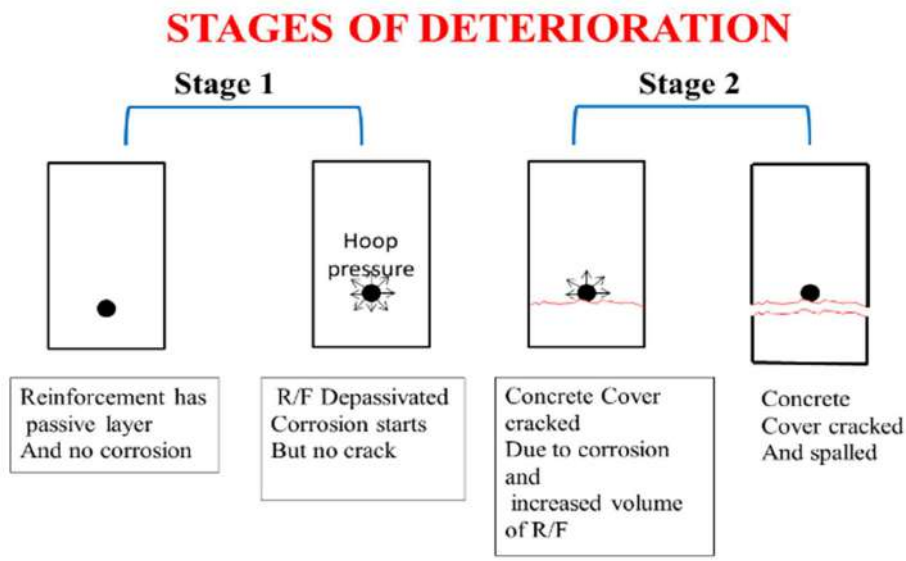


Fig. 2: Stages of deterioration in concrete due to corrosion.

In advanced stages, the concrete cover spalls, exposing the reinforcement to the environment and reducing both its cross-sectional area and structural capacity.

To mitigate such degradation, corrosion inhibitor coatings have been used; however, their effectiveness must be validated using electrochemical evaluation and pull-out tests. Half-cell potential measurements are widely used to indicate corrosion probability, although they do not provide actual rates. Thus, it is complemented by direct methods, such as weight loss and diameter reduction, which measure physical damage. Bond strength evaluation is equally important because corrosion-induced cracking and rust expansion reduce steel–concrete adhesion, directly affecting structural safety. Therefore, pull-out bond tests provide critical data on the mechanical effects of corrosion. By combining the half-cell potential, weight loss, diameter loss, and bond strength assessments, a comprehensive evaluation of the inhibitor performance can be achieved. Such testing ensures that organic coatings, including neem-based systems, are validated not only for corrosion resistance but also for maintaining durability and bonds in reinforced concrete structures.

Fig. 3 presents a comprehensive classification of strategies for corrosion protection, outlining the principal approaches adopted to mitigate the degradation of materials in aggressive environments. At the highest level, corrosion protection can be achieved through four broad measures: coatings, environmental modification, material selection, and the use of corrosion inhibitors. Coatings serve as physical barriers between the substrate and corrosive medium and may be organic (such as paints and polymers), inorganic (such as metallic or ceramic films), or hybrid systems combining both categories. Environmental modification strategies target the external conditions that drive corrosion, including temperature, pressure, pH, salt concentration, and humidity (Casanova et al. 2023). This category also encompasses electrochemical methods, such as anodic protection, which stabilizes a passive film on the metal surface by applying controlled potentials, and cathodic protection, which can be implemented via sacrificial anodes, galvanization, or impressed current systems.

Another critical strategy involves the judicious selection of materials that inherently resist corrosion. This includes the use of metallic materials such as corrosion-resistant alloys and stainless steels, as well as non-metallic alternatives such as ceramics, plastics, graphite, and rubbers, which offer superior performance in highly corrosive or specialized applications (Tarabin et al. 2023). The final category

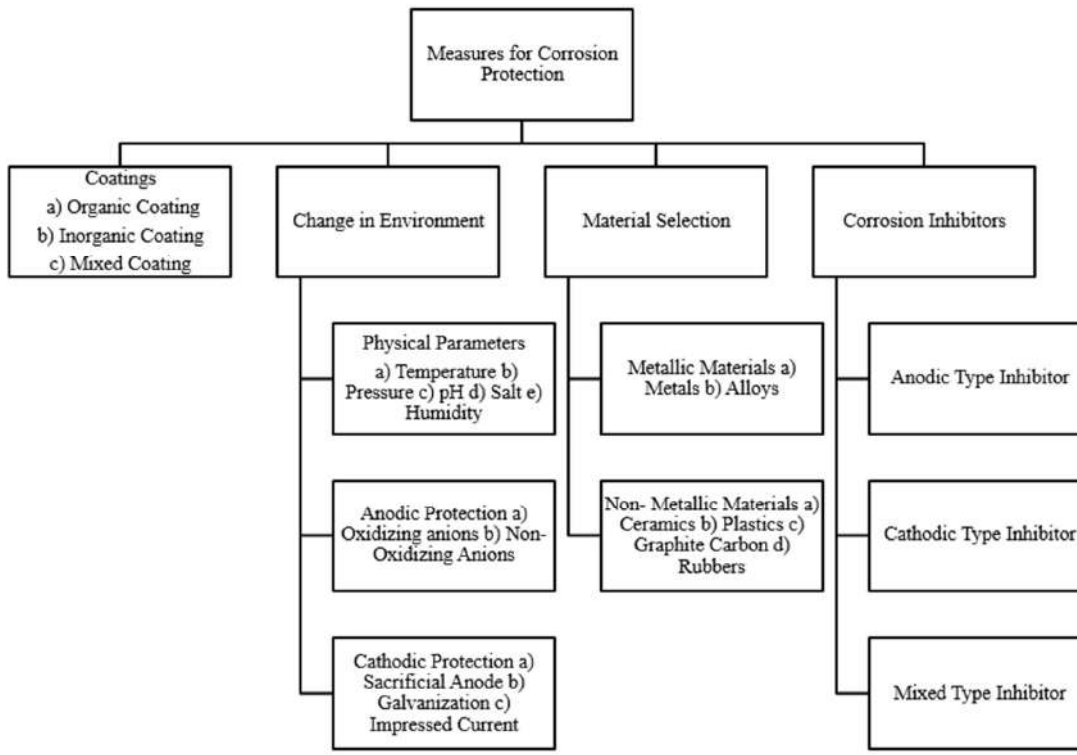


Fig. 3: Measures for corrosion protection (Bajaj & Khurpade 2024, Bolzoni et al. 2022, Casanova et al. 2023, Chen et al. 2023, Li et al. 2023, Nóvoa & Pérez 2023).

focuses on corrosion inhibitors, which are chemical compounds introduced into the environment to suppress electrochemical reactions on metal surfaces. These can function as anodic inhibitors, promoting the formation of protective oxide layers; cathodic inhibitors, reducing the rate of cathodic reactions such as oxygen reduction; or mixed-type inhibitors, providing simultaneous protection at both anodic and cathodic sites (Verma et al. 2024). This study aims to experimentally evaluate neem-based organic coatings for reinforcing steel under chloride-induced corrosion conditions, comparing their performance with that of zinc coatings in terms of electrochemical behavior, bond strength, surface morphology, and sustainability metrics. A detailed literature review of the findings of various corrosion inhibitors used in concrete and the research gap is provided in Table 1.

2. RESEARCH GAP AND RESEARCH SIGNIFICANCE

Research on corrosion inhibitors in concrete has explored admixtures, epoxy coatings, and surface treatments; however, significant challenges remain. Many existing methods suffer from high costs, dosage sensitivity, potential adverse effects on mechanical properties, and limited long-term durability. Admixture-based inhibitors are irreversible once added to fresh concrete, and improper dosage can reduce the strength or even accelerate corrosion. Their performance also declined in cracked concrete. Additionally, several conventional inhibitors, such as chromates and phosphates, pose environmental and health concerns, whereas compatibility issues and limited field-scale data further restrict their reliability. These limitations highlight

Table 1: Comprehensive analysis of the use of corrosion inhibitors in concrete.

Reference	Methods (Material/Exposure/ Measurement)	Findings	Research Gap
(Liu et al. 2025)	Admixture at 0.5–1.5% microstructure (porosity), electrochemistry, and depassivation delay.	Porosity decreased by up to ~69%, delaying steel depassivation and improving electrochemical indices.	Data under mechanical loading and cracked concrete, compatibility with SCMs, and field-scale validation.
(Krishnanjana & Ganesh 2025)	Admixture (3.5–17.5 g), weight loss and electrochemical tests and short-term exposure.	~83% efficiency at 7 g for 7-day exposure.	Short duration, chloride ingress/bond strength effects not assessed, and scale-up dosage guidance missing.
(Suhas et al. 2025)	Admixture, electrochemistry + surface analysis + quantum chemistry & MD simulations.	Chitosan achieved up to ~92.6% efficiency, with mechanistic support from modeling.	The translation of molecular findings to RC elements, their influence on fresh/ concrete properties, and long-term bonds has not been reported.
(Suhas et al. 2025)	Discusses the performance of inhibitors in cracked RC.	Some inhibitors may be ineffective or even accelerate corrosion in the cracks.	Protocols that address crack widths, delivery to exposed steel, and monitoring strategies are required.
(Cao et al. 2025)	Surface-applied (migrating) and computational/mechanistic views.	Potential for in-situ protection of existing RC via migration.	Coupled effects with real chloride profiles, quantifying penetration/ retention and bond effects.
(Liu et al. 2024)	Admixture, optimal ~2 $g.L^{-1}$, chloride-induced corrosion, half-cell + steel weight loss.	Approximately 40% improvement in inhibition efficiency was observed at the optimal dose.	Durability beyond laboratory exposure, synergy with nitrites/SCMs, and structural-scale demonstration.
(Okeniyi et al. 2018)	Plant extract used as an admixture (~0.0833% of cement) with sodium nitrite, RC specimens in 3.5% NaCl, LPR/half-cell/electrochemical tests.	Very high inhibition efficiency (~99.35%) in chloride medium, the strength was not adversely affected.	Long-term durability and field validation, optimum dosage window, and interaction with other admixtures have not been established.
(Okeniyi et al. 2016)	Admixture in concrete beams, 3.5% NaCl immersion, Linear Polarization Resistance, and compressive strength check.	The TEA inhibitor was outperformed, with ~93.6% inhibition and ~5.4% compressive strength improvement.	The mechanism at the steel–concrete interface and bond behavior were not quantified, and the performance under cracking was not studied.
(Montes-García et al. 2015)	Admixture in HPC, variable w/c and 20% FA, wet–dry cycles (2/day) for 1 year, and electrochemical monitoring.	12.5 $L.m^{-3}$ $Ca(NO_2)_2$ with 20% FA effectively reduced the corrosion rates in the low w/c ratio mixes.	Performance envelope for different concretes, effects on setting/air-voids, life-cycle cost vs. performance, and unresolved issues.
(De Schutter & Luo 2004)	Review of admixture inhibitors' effects on fresh/hardened properties.	Risks of set alteration, air-void changes, strength loss, and irreversibility once cast.	Application guidelines for safe windows and compatibility testing with modern admixtures are required.

the need for sustainable and localized protection strategies. Surface-applied coatings offer a promising alternative by targeting the steel–concrete interface, where corrosion initiates, without altering the bulk concrete properties. Despite this advantage, coating-based applications of plant-derived organic inhibitors remain underexplored, particularly their ability to provide corrosion resistance while maintaining steel–concrete bond strength. This study addresses this gap by evaluating Azadirachta indica (Neem powder) as a reinforcement coating for steel bars exposed to chloride corrosion. The investigation assessed the electrochemical behavior through half-cell potential measurements, supported by weight loss, diameter loss, and bond strength tests, and benchmarks Neem's performance against zinc-coated and uncoated specimens to evaluate its durability and sustainability benefits.

3. MATERIALS AND METHODS

This section describes the experimental procedure and methods of analysis adopted to validate the efficacy of Azadirachta indica (Neem Powder) as a green corrosion inhibitor for steel rebars in chloride-induced corrosion environments, along with Zinc Powder inorganic inhibitor coatings. The Neem (Azadirachta indica) powder used in this study was procured from a commercial supplier (IndiaMART, Uttar Pradesh, India). According to the supplier's laboratory certificate, the powder contains approximately 18–22% azadirachtin, 5–7% nimbin, and 3–5% saponins, which are the active components that contribute to corrosion inhibition in steel. The moisture content was below 8%, and the particle size was in the range of 75–150 µm. This study combined measurements of potential difference, that is, half-cell potentiometer readings, weight loss, diameter loss, and bond strength. The experimental methods and materials are presented in detail below. The experimental procedure was designed to systematically investigate the corrosion inhibition performance of an organic coating for steel reinforcement bars in comparison with that of an inorganic coating. This study involved preparing and testing three distinct categories of steel bars: control specimens (uncoated), single-coat organic inhibitor-coated specimens, and single-coat inorganic inhibitor-coated specimens under simulated chloride-induced corrosion conditions. The reinforcement bars were initially cleaned with sandpaper, and a coating paste of inhibitor and linseed oil was prepared in a 1:1.5 ratio by weight, which yielded a viscous paste. The inhibitor paste was applied manually using a bristle brush, and the coating thickness was verified at three locations along the bar using a digital micrometer (±0.02 mm accuracy) to ensure a uniform coating. The resulting coating thickness ranged between 1.0–1.3 mm, with a measured standard deviation of ±0.12 mm across all coated samples with a total coating paste of 35 – 40 $g.mL^{-1}$. The bars were then sun-dried for 24 h and used for casting concrete specimens. For each coating regime, ten cylindrical specimens (a total of 30 samples) were cast using M30 grade concrete with a single reinforcement bar of 16 mm diameter embedded centrally with a cover of 10 mm from the bottom and a total embedded length of 290 mm. After standard moist curing for 28 d, the samples were exposed to chloride-induced corrosive conditions for an extended period of 365 d to simulate a corrosive environment. To accelerate and standardize the corrosion process, all the specimens were subjected to an accelerated corrosion setup. Once the samples were subjected to accelerated corrosion, periodic half-cell potentiometer measurements were conducted to study the effectiveness of the corrosion inhibitor coatings in controlling the corrosion rate. Furthermore, after 365 days, the bond strength of the cast samples was evaluated using a standard pull-out test in accordance with IS 2770: Part 1(1967). After 365 days, the samples were broken, and the reinforcement bars were extracted to measure weight loss and diameter loss. The surface analysis of the coated and neem-coated bars was performed using Scanning Electron Microscopy (SEM). SEM analysis was performed using a ZEISS EVO Scanning Electron Microscope operated in SE1 mode. Micrographs were captured at a magnification of 1.00 kX, an accelerating voltage (EHT) of 15.00 kV, and a working distance (WD) of 8.5 mm. Images were recorded at a scale of 20 µm to observe the corrosion product morphology and coating characteristics. The mix design of the M30 grade of concrete was performed using the IS10262:2019 guidelines, and the details are provided in Table 2.

To simulate the corrosive environment, the cast samples were subjected to the impressed current method. To further accelerate the corrosive environment, the samples were immersed in 3.5% NaCl (Sodium Chloride) solution. A reference reinforcement rod was immersed in the solution, which was used as a cathode, that is, the negative terminal, and the exposed end of the reinforcement bar in the cast samples was used as an anode, that is, the positive terminal, as shown in Fig. 4. The samples were exposed to an accelerated

Table 2: Mix proportions of M30 grade concrete.

Parameter	Quantity	Units
Cement	319.13	kg
Fine aggregate	625	kg
Coarse aggregate	1254	kg
Water	158	kg
Superplasticizer	2.42	kg
Mix Ratio	1:1.96:3.93	

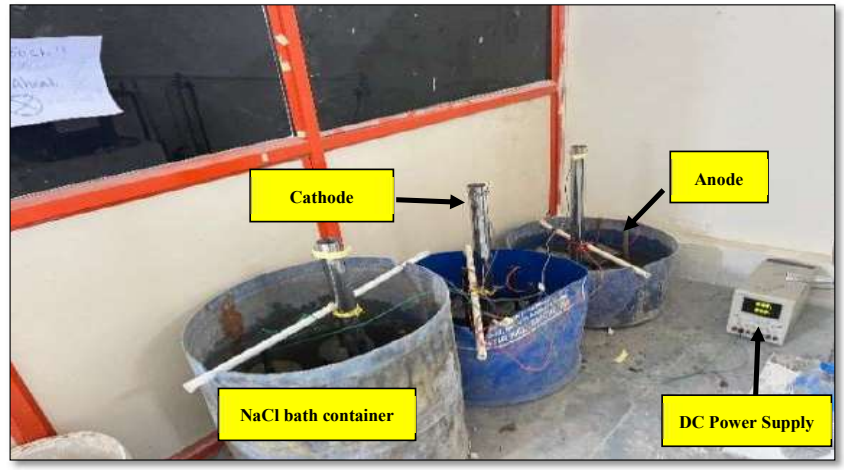


Fig. 4: Accelerated corrosion setup.

corrosion setup, and the corrosion levels were checked and recorded weekly using a half-cell potentiometer. Each half-cell potential measurement was recorded using a calibrated digital potentiometer with a measurement uncertainty of ±5 mV. For accuracy, the reported values represent the average of three consecutive readings taken at 30-second intervals. The samples subjected to the accelerated corrosion setup provided insights into the performance of the corrosion inhibitor coatings in a corrosive environment. The average potential values in (-mV) were obtained from the Half-Cell Potentiometer Test as per ASTM C-876 -15 standards. The Voltage limit was set between 3 and 5 V, and the current was 35.2mA for moderate acceleration for 365 days.

Assessing bond strength is critical for understanding the interaction between concrete and reinforcing steel, which directly influences the structural performance of reinforced concrete elements. The bond strength of concrete primarily depends on the grade of concrete and the type of reinforcement bar used. Furthermore, corrosion can significantly affect the bond strength of concrete, resulting in debonding failure and progressive collapse of the structure. In this study, bond strength was evaluated using the pull-out test method in accordance with IS 2770 (Part 1): 1960. Failure occurs in the form of slippage of the bar from the concrete, indicating bond failure. The various failure patterns, that is, cracks developed on the concrete surface, also indicate the type of bonding between the steel and concrete. A microcrack indicates a good bond of the reinforcement bar, with the minimum value of the slippage, and a major crack indicates poor bond behavior of steel and concrete, with the maximum value of the slippage. The initial weights of the samples prior to casting were recorded, and the final weights of the reinforcement bars were recorded after the pullout test. The corroded steel bars were then carefully cleaned using sandpaper to remove the corrosion products, surface deposits, and any remaining concrete residue. Similarly, the final diameter of the reinforcement bar was recorded after cleaning to evaluate the diameter loss.

4. RESULTS AND DISCUSSION

4.1. Comparative Analysis of Organic and Inorganic Inhibitor Coatings in Corrosion Mitigation

The corrosion assessment results obtained after 365 days of exposure in the accelerated corrosion setup clearly demonstrate significant differences in the performance of the uncoated, neem-coated, and zinc-coated specimens, as discussed in Table 3.

Table 3: Corrosion assessment of organic and inorganic corrosion inhibitors.

Description	Sample		
	Uncoated	Neem Coated	Zinc Coated
Average Half Cell Potentiometer Values [-mV]	273.98	143.79	150.69
Maximum Half Cell Potentiometer Values [-mV]	413.32	217.52	227.03
Average Final Weight [g]	457.10	494.79	494.32
Average Weight Loss [g]	0.927	0.692	0.689
Average Diameter Loss [mm]	0.720	0.678	0.677

Half-cell potential measurements indicated that the uncoated sample had the highest average potential of –273.98 mV, with a maximum of –413.32 mV, which was well below the corrosion threshold, suggesting significant corrosion activity. In contrast, neem-coated and zinc-coated samples showed much lower average potentials of –143.79 mV and –150.69 mV, with maximum values of –217.52 mV and –227.03 mV, respectively, reflecting a substantial reduction in corrosion. Weight measurements supported these findings. The uncoated samples recorded an average final weight of 457.10 g, corresponding to a weight loss of 0.927 g. Neem-coated and zinc-coated samples retained higher weights of 494.79 g and 494.32 g, respectively, with lower weight losses of 0.692 g and 0.689 g. Diameter measurements similarly showed that uncoated samples lost 0.720 mm on average, while neem- and zinc-coated specimens lost only 0.678 and 0.677 mm, respectively. These observations indicate that both coatings effectively limited material degradation, with nearly identical performance in terms of weight retention and dimensional stability. The percentage reduction compared to that of the uncoated samples further highlights the protective efficiency. Neem coatings reduced the average and maximum half-cell potentials by 47.52% and 47.37%, respectively, whereas zinc coatings achieved reductions of 45.00% and 45.07%, respectively. These values fall within the measurement uncertainty of the half-cell potentiometer (±5 mV); therefore, Neem and Zn coatings can be considered statistically equivalent in suppressing electrochemical activity, and the differences should not be interpreted as performance superiority. The inhibitory action of the neem coating can be attributed to the adsorption of its phytochemical constituents, particularly terpenoids, flavonoids, azadirachtin, and nimbin, onto the steel surface. These molecules contain polar functional groups (–OH, –C=O, –C–O–C–, and aromatic rings) capable of donating lone-pair electrons to the vacant d-orbitals of iron atoms, forming a coordinated protective layer. This adsorbed film reduces the active anodic and cathodic reaction sites, thereby restricting chloride interactions and suppressing the corrosion process. The presence of long-chain organic compounds also enhances hydrophobicity, contributing to a more stable barrier. Weight retention improved by 8.25% for neem and 8.14% for zinc, with weight loss decreasing by 25.35% and 25.67%, respectively. Diameter reduction was also limited, showing 5.83% for neem oil and 5.97% for zinc. All corrosion measurements represent the mean of ten specimens, and the corresponding standard deviation values are included to indicate data variability. A one-way ANOVA was performed to compare the corrosion performance across the groups. The differences between the Neem- and Zinc-coated specimens were statistically insignificant ($p > 0.05$), indicating comparable protective behavior.

Overall, these results confirm that neem coatings perform comparably to zinc in mitigating corrosion, preserving structural mass, and limiting dimensional loss. The data demonstrate that neem-based coatings can serve as a sustainable, bio-derived alternative to conventional zinc coatings, offering equivalent protective efficiency and potentially providing environmental benefits.

4.2. Bond Strength Assessment of Coated and Uncoated Bars

To evaluate the effectiveness of the coatings in retaining bond strength, standard pull-out tests were performed in accordance with IS 2770: Part 1 (1967). These tests were performed on neem-coated samples and compared with zinc-coated (inorganic inhibitor) and uncoated specimens. The slip in the reinforcement bars and the ultimate load were recorded using a pull-out testing apparatus, and the bond strength was subsequently calculated.

The bond strength assessment of the coated and uncoated specimens highlights a clear enhancement in interfacial performance due to the application of neem and zinc coatings (Table 4).

Table 4: Comparative assessment pull-out test of organic and inorganic corrosion inhibitors.

Parameter	Uncoated	Neem Coated	Zinc Coated
Maximum Slippage [mm]	6.11	3.79	3.28
Maximum Ultimate Load [kN]	28.04	40.2	44.23
Maximum Bond Strength [MPa]	1.92	2.76	3.03
Minimum Slippage [mm]	5.25	3.45	2.86
Minimum Ultimate Load [kN]	22.39	37.82	41.8
Minimum Bond Strength [MPa]	1.54	2.59	2.87
Average Slippage [mm]	5.69	3.67	3.12
Average Ultimate Load [kN]	25.11	38.75	42.96
Average Bond Strength [MPa]	1.72	2.66	2.95

The uncoated samples exhibited relatively poor bonding behavior, with an average slip-page of 5.69 mm, an average ultimate load of 25.11 kN, and an average bond strength of 1.72 MPa. In contrast, the neem-coated specimens

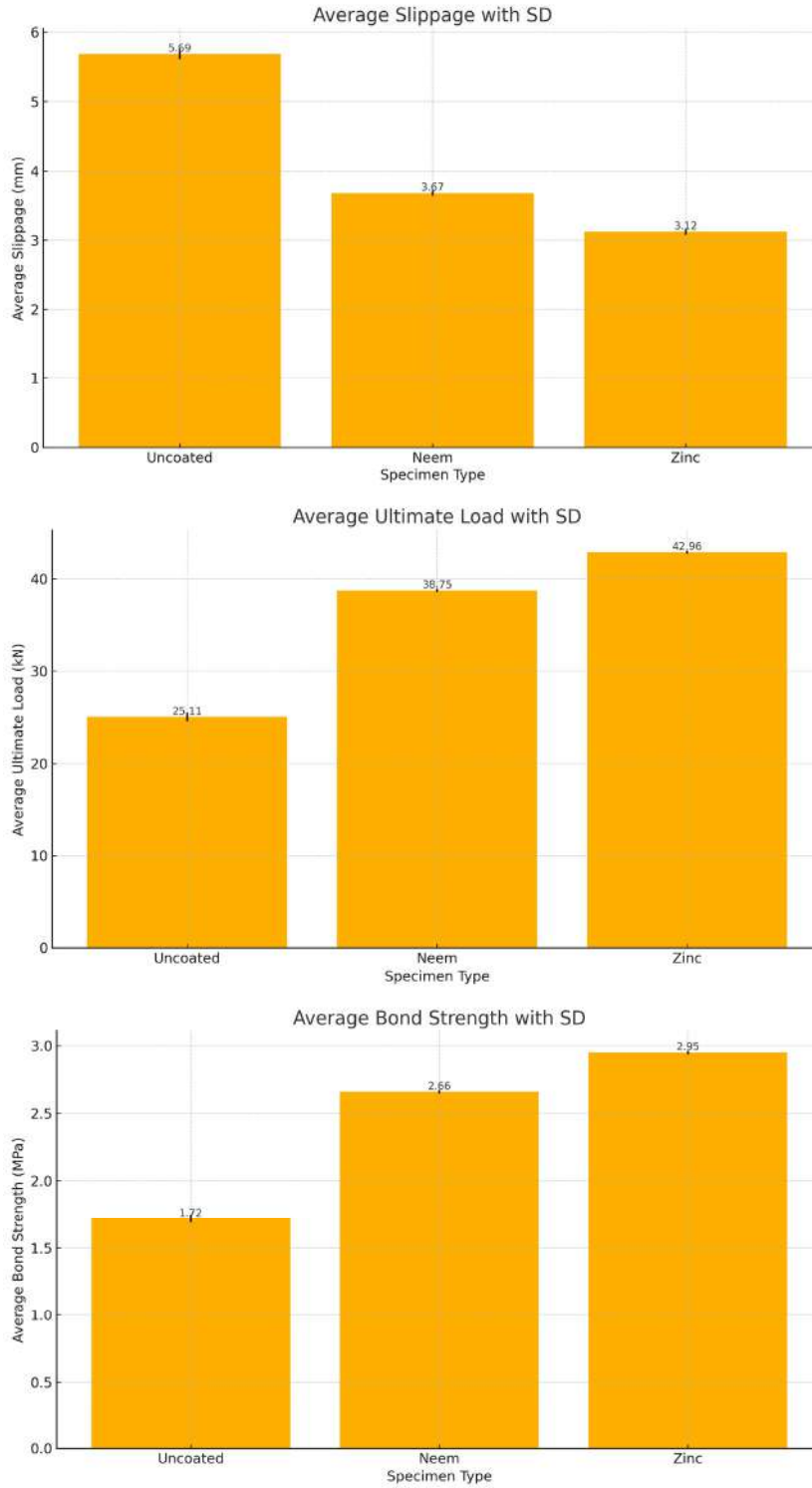


Fig. 5: Standard deviations along with the error bars of the measured corrosion parameters.

demonstrated significantly improved results, with an average slip-page reduced to 3.67 mm, an average ultimate load increased to 38.75 kN, and an average bond strength increased to 2.66 MPa. Similarly, the zinc-coated specimens exhibited the highest performance, with an average slip-page of only 3.12 mm, an ultimate load of 42.96 kN, and an average bond strength of 2.95 MPa, underscoring the superior reinforcement-matrix interaction provided by zinc coatings. A similar trend was observed for both the minimum and maximum values, which further reinforced the consistency of these results. For the neem-coated specimens, the maximum ultimate load increased from 28.04 kN (uncoated) to 40.20 kN, with a corresponding increase in the maximum bond strength from 1.92 MPa to 2.76 MPa. Zinc-coated samples achieved even higher values, reaching a maximum ultimate load of 44.23 kN and a bond strength of 3.03 MPa, along with the lowest maximum slip-page of 3.28 mm compared to 6.11 mm in uncoated specimens. Similarly, in the minimum range, the neem-coated specimens recorded a bond strength of 2.59 MPa (vs. 1.54 MPa for uncoated), the zinc-coated specimens were further improved to 2.87 MPa, with corresponding reductions in slip-page from 5.25 mm (uncoated) to 3.45 mm (neem) and 2.86 mm (zinc). In the present study, the improvement observed in the Neem-coated specimens (2.66 MPa compared to 1.72 MPa for uncoated steel) suggests that the primary contribution to bond improvement arises from the phytochemical components of Neem, which form a thin, adsorbed, and micro-textured protective layer that maintains adequate frictional and chemical interaction with the surrounding concrete, while the binder mainly serves as a carrier for uniform coating deposition rather than as a strength-enhancing agent. Fig. 5 shows the Standard deviations along with the error bars of the measured corrosion parameters.

Overall, the results demonstrate that both neem and zinc coatings significantly enhanced the bond strength between the reinforcement and surrounding matrix, primarily by reducing slippage and increasing load-bearing capacity. While zinc coating provided the greatest improvement across all parameters, neem coating displayed nearly equivalent performance, with bond strength values only marginally lower than those of zinc. This suggests that neem-based bio-coatings can serve as effective and sustainable alternatives to conventional metallic coatings, offering comparable bond-strength enhancement and improved structural performance.

The failure pattern observed during the pull-out test further revealed the enhanced performance of the organic inhibitor coatings in achieving better bond strength values. The crack patterns observed were of two types: longitudinal cracks and radial splitting cracks, as shown in Fig. 6. The extent of the crack width indicates the performance of the surface-applied corrosion inhibitor coatings in mitigating corrosion.

Fig. 6 clearly shows that the uncoated specimen had a higher crack width, indicating proper debonding of the rebar from concrete, whereas the coated rebar showed very minute radial cracks, indicating a better bond between concrete and steel, affirming the performance of surface-applied corrosion inhibitors in mitigating corrosion. This section highlights the integration of advanced image processing techniques with half-cell potential experiments for a comprehensive analysis of corrosion in reinforced steel bars. This methodology combines precise experimental data with computational algorithms to enhance the accuracy and reliability of corrosion rate and pattern assessments.

4.3. Surface Morphology using Scanning Electron Microscopy

SEM analysis revealed marked differences in the surface morphologies of the uncoated and neem-coated steel specimens (Fig. 7). The uncoated surface exhibited a highly irregular and porous morphology, with extensive cracks and pits covering approximately 30–40% of its surface area. The associated corrosion products were voluminous, flaky, and



Fig. 6: a) Pull-out test, b) Uncoated samples, c) Coated samples.

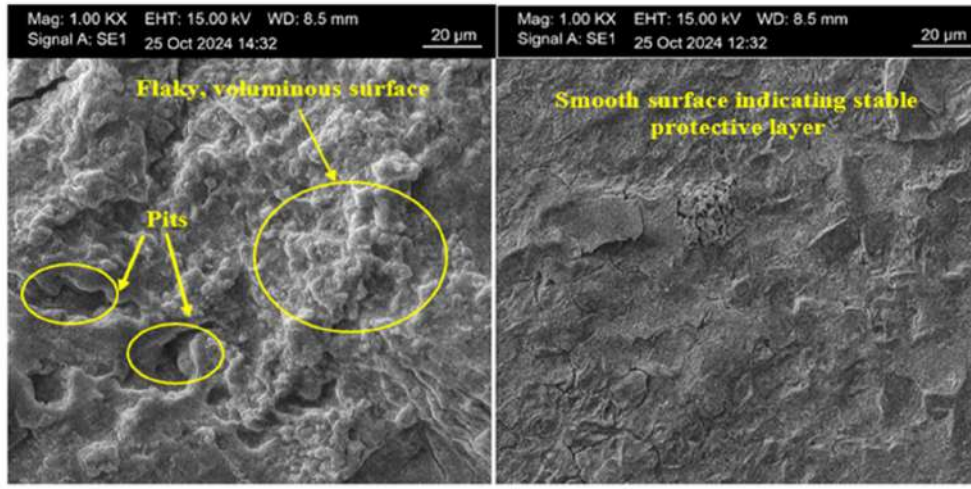


Fig. 7: SEM micrographs showing the surface morphology of (a) uncoated corroded steel and (b) Neem-coated steel after exposure to chloride-induced corrosion, captured at 1.00 kX magnification with a 20 µm scale bar.

loosely bound, indicating unstable growth and progressive material deterioration. In contrast, neem-coated steel displayed a relatively smoother and more compact surface, characterized by only minor localized defects. The corrosion products formed on this surface were minimal and firmly adherent, suggesting the development of a more stable and protective layer that effectively mitigated corrosion.

5. INTERPRETATION OF RESULTS

The experimental results show that Azadirachta indica (Neem) powder is an effective corrosion inhibitor for steel reinforcement in chloride-rich environments, performing nearly as well as a conventional zinc coating. Half-cell potential measurements decreased by 47.5% for Neem and 45.0% for zinc, indicating that both coatings successfully reduced the electrochemical activity responsible for steel depassivation. These reductions persisted for 365 days, demonstrating Neem's long-term protective capability under aggressive conditions and confirming its effectiveness at the reinforcement level. Weight and diameter loss measurements further supported these findings, as Neem-coated rebars showed a 25.3% reduction in mass loss and a 5.8% decrease in diameter loss compared to uncoated bars, indicating that the coating acts as a physical barrier that limits chloride ingress and slows corrosion. SEM analysis revealed a compact surface morphology with minimal corrosion products on the neem-coated bars, whereas the uncoated samples exhibited extensive pitting and flaky rust covering 30–40% of the surface. Bond strength tests indicated that Neem coatings improved the steel–concrete interface by 54.6% relative to uncoated bars, approaching the performance of zinc. This demonstrates the dual benefit of Neem in reducing corrosion while maintaining critical bond strength, which is essential for structural safety.

From a sustainability perspective, life cycle assessment showed that neem coatings reduce the carbon footprint by up to 43% compared to zinc and lower the cost per meter of reinforcement coating by 39.6%.

Overall, Neem-based organic coatings provide a sustainable and economically viable alternative to metallic inhibitors. Neem offers comparable corrosion protection, preserves structural integrity, and supports environmentally friendly construction, positioning it as a promising material for green, durable, and cost-effective infrastructure protection.

6. LIFE CYCLE ASSESSMENT AND ENVIRONMENTAL IMPACT

The environmental impact of corrosion protection for reinforced concrete highlights the link between structural durability and sustainability. Life cycle assessments have shown that neem-based coatings offer significant ecological advantages over traditional chromate and zinc systems, reducing the carbon footprint by up to 43% while providing equal or better corrosion protection (Banumathi et al. 2024). Conventional coatings, particularly those containing hexavalent chromium, pose environmental hazards through toxic waste generation and carcinogenic risks, necessitating careful disposal (Abuelela et al. 2023). Neem (Azadirachta indica) extract demonstrates high corrosion inhibition, achieving up to 97% efficiency for carbon steel in chloride environments, improving from 75% over 72 h (Okewale & Omoruwuo 2018). Neem inhibitors are plant-derived, biodegradable, and non-toxic. They are sourced from

renewable biomass, reducing environmental impact and sequestering carbon during their growth. ISO 14040-based life cycle assessments indicate that neem coatings emit as little as 1.5–2.6 kg CO_2 eq.kg^{-1}, compared to higher emissions from conventional systems (Borgaonkar & McNamara 2024). They also reduce ozone depletion, fossil fuel consumption, and heavy metal contamination associated with chromate-based coatings.

Life Cycle Assessment (LCA) was conducted in accordance with ISO 14040/14044 standards to compare the environmental impacts of neem-based and zinc-based coatings. The functional unit (FU) selected for this study was defined as 1 m² of coated reinforcement steel, as this unit allows a performance-based comparison that is independent of material density or coating thickness. The system boundaries followed a 'cradle-to-gate' approach, including raw material extraction, processing, manufacturing of coating components, and transportation to the construction site. End-of-life impacts and maintenance cycles were excluded because of insufficient standardized datasets for organic coating degradation. Inventory data for neem powder production were obtained from local supplier datasets and supplemented with regional agricultural emission factors, while zinc-related emission values were sourced from secondary datasets reported in ecoinvent v3.9 and published LCI databases. Linseed oil emissions were derived from standard vegetable oil processing data sets. All emissions were converted to global warming potential (GWP) expressed as kg CO_2-eq using the IPCC 2021 characterization factors. Based on these inputs, the estimated carbon footprint of the Neem coating was 1.14 kg CO_2-eq per m² of coated steel, compared to 2.00 kg CO_2-eq per m² for the zinc coating, corresponding to an approximate 43% reduction in embodied carbon. These values reflect only the material impacts and do not account for potential differences in service life extension. The cost and carbon savings were normalized to the same functional unit (1 m² of coated steel), ensuring a performance-equivalent comparison. This normalization avoids misinterpretations that could arise from weight-based comparisons alone, especially given the differing densities and application rates of organic and metallic coatings. The study demonstrates that neem coatings can reduce corrosion-induced weight loss by 72% and improve half-cell potential values by 75% compared to uncoated bars while maintaining eco-safety. These properties make neem a sustainable alternative that lowers long-term environmental and economic costs, extends the structural service life, and minimizes chemical waste. The use of neem supports a circular economy by valorizing natural resources, enhancing structural durability, and contributing to global sustainability and pollution reduction goals, as shown in Fig. 8.

7. COST-BENEFIT ANALYSIS

The cost analysis of the coating systems revealed significant variations in material expenditure depending on the inhibitor type and the coating thickness. The details of the various materials used in this study, as per the current market rate, are provided in Table 5.

Furthermore, the total cost required to coat one bar with a single coat of the inhibitors comprises the cost of the inhibitor and the cost of the oil. The details of the total cost are provided in table.

Table 5: Cost of inhibitors.

Material	Approximate Price [Maximum]	Source
Neem Powder	Rs. 400.kg^{-1}	Indiamart (2025)
Zinc Powder	Rs. 900.kg^{-1}	Indiamart (2025)

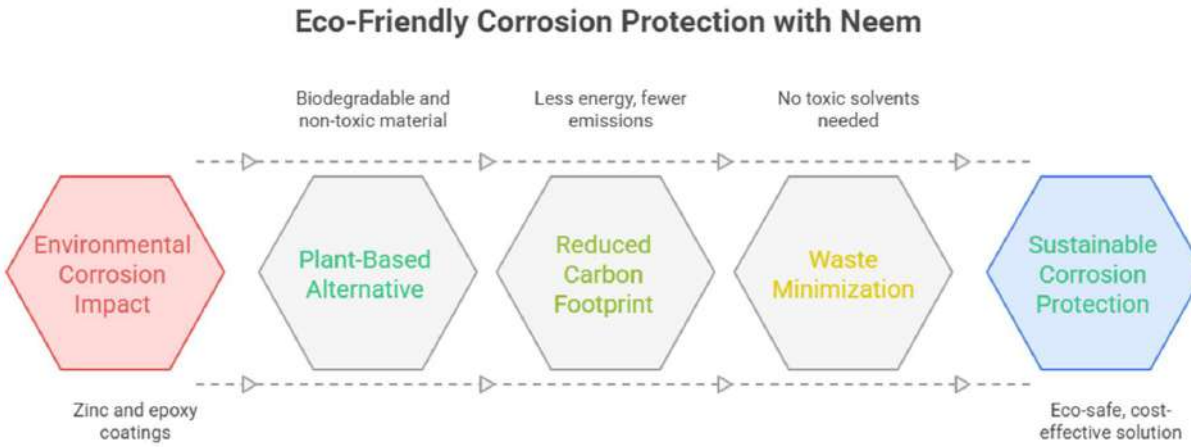


Fig. 8: Benefits of neem inhibitor coatings.

Table 6: Cost per coat of the inhibitors.

Coating Type	Thickness	Inhibitor Req. [g]	Oil Req. [mL]	Cost of Inhibitor [₹]	Cost of Oil [₹]	Total Cost [₹]	Cost per Coat [₹]	Cost per coat.m^{-1} [₹]
Neem	1 coat	18	26	7.2	6.5	13.7	6.85	22.83
Zinc	1 coat	18	26	16.2	6.5	22.7	11.35	37.83

The cost analysis presented in Tables 5 and 6 is based on market prices obtained from suppliers in India, with all rates verified between January and July 2025 to ensure their current relevance. The material costs for neem, zinc, and linseed oil were obtained from regional wholesale markets and manufacturer quotations, reflecting typical procurement scenarios in Indian construction practice. The calculated cost reduction of 39.6% for the neem-based coating compared to zinc is representative of the prevailing local market conditions. As evident from the cost analysis of the coatings, the per coat cost obtained in the present study for neem-coated specimens was Rs 6.85, and for zinc-coated specimens, it was Rs 11.35. Furthermore, if the cost is calculated for per meter length of the reinforcement bar, there is almost a 39.6% reduction in the coating cost. This proves that organic inhibitor coatings are an economically viable alternative to harmful chemical-based coatings.

8. CONCLUSION AND FUTURE SCOPE

This study evaluated the performance of Azadirachta indica (Neem) powder as a sustainable corrosion inhibitor coating for reinforcing steel in chloride-induced environments and benchmarked its effectiveness against zinc coatings. The findings confirmed that neem-based coatings significantly enhanced corrosion resistance and structural performance while offering economic and environmental advantages. Quantitatively, the neem-coated specimens achieved a 47.5% reduction in half-cell potential, a 25.3% reduction in weight loss, and a 5.8% reduction in diameter loss, closely matching the performance of zinc coatings. The bond strength improved from 1.72 MPa in uncoated specimens to 2.66 MPa with Neem coatings, representing a 54.6% improvement and approaching the performance of zinc-coated bars (2.95 MPa). SEM analysis further validated the protective action of neem through compact surface morphology and minimal corrosion products. Beyond technical performance, Neem coatings demonstrated up to a 43% reduction in carbon footprint and a 39.6% lower cost per meter of reinforcement protection, underlining their potential as an eco-friendly and economically viable alternative to conventional metallic inhibitors. This study had certain limitations that should be acknowledged. The experiments were conducted using a single coating thickness and a relatively small sample size, which may not fully capture the variability expected in large-scale construction applications. Additionally, all tests were performed under controlled laboratory conditions using accelerated chloride exposure, and the results may differ under natural environmental cycles involving temperature fluctuations, carbonation, and long-term wet–dry exposures. Future studies incorporating multiple coating thicknesses, larger specimen sets, and field-scale validation would help strengthen the generalizability of the findings. Future research should focus on the field-scale validation of neem coatings under varying climatic and environmental conditions, as well as the long-term performance in cracked concrete, where the ingress of chlorides is more critical. Investigations into hybrid systems combining neem with supplementary cementitious materials or nanomaterials could further optimize performance. Additionally, mechanistic studies at the molecular level, combined with machine learning-driven predictive modeling, may provide deeper insights into the durability, dosage optimization, and life cycle cost benefits of neem-based inhibitors.

Overall, this study establishes Neem as a promising bio-based technology that integrates structural durability with sustainability, supporting the transition towards greener and more resilient construction practices.

9. ACKNOWLEDGMENTS

The authors extend their acknowledgment to the Department of Civil Engineering, Sharda University, for providing access to their labs for the experimentation work.

10. REFERENCES

Abirami, R. and Sangeetha, S.P., 2022. Effect of surface modification on the characteristics of sisal fiber reinforced concrete treated with Na_2CO_3. *Nature Environment and Pollution Technology*, 21(1), pp.289-295. [DOI]

Abuelela, A.M., Kaur, J., Saxena, A., Bedair, M.A., Verma, D.K. and Berdimurodov, E., 2023. Electrochemical and DFT studies of *Terminalia bellerica* fruit extract as an eco-friendly inhibitor for the corrosion of steel. *Scientific Reports*, 13(1), p.19367. [DOI]

Al-Amiery, A., Wan Isahak, W.N.R. and Al-Azzawi, W.K., 2024. Sustainable corrosion inhibitors: a key step towards environmentally responsible corrosion control. *Ain Shams Engineering Journal*, 15(5), p.102672. [DOI]

Bajaj, D. and Khurpade, P.D., 2024. An eco-friendly Mangifera indica leaf extract corrosion inhibitor for stainless steel in an acidic medium. *Nature Environment and Pollution Technology*, 23(1), pp.139-150. [DOI]

Banumathi, R., Abuthahir, S.S.S., Sheit, H.M.K., Mohan, K.S., Mohandas,

T. and Vijaya, K., 2024. Corrosion inhibition potential of aqueous extract of trifolium repens plant leaves on carbon steel in hydrochloric acid medium (trpl). *Discover Electrochemistry*, 1(1), p.13. [DOI]

Bolzoni, F., Brenna, A. and Ormellese, M., 2022. Recent advances in the use of inhibitors to prevent chloride-induced corrosion in reinforced concrete. *Cement and Concrete Research*, 154(1), p.106719. [DOI]

Borgaonkar, A. and McNamara, G., 2024. Environmental impact assessment of anti-corrosion coating life cycle processes for marine applications. *Sustainability*, 16(13), p.5627. [DOI]

Cao, N.L., Shevtsov, D.S., Nguyen, V.C., Nguyen, D.A., Le, H.Q., Tran, V.T., Nguyen, V.T., Nguyen, N.H., Zartsyn, I.D. and Briyalovskaya, E.S., 2025. Migrating corrosion inhibitors for steel reinforcement in concrete under chloride activation: a review. *International Journal of Corrosion and Scale Inhibition*, 14(2), pp.469-490. [DOI]

Casanova, L., Ceriani, F., Messinese, E., Paterlini, L., Beretta, S., Bolzoni, F.M., Brenna, A., Diamanti, M.V., Ormellese, M. and Pedeferri, M.P., 2023. Recent advances in the use of green corrosion inhibitors to prevent chloride-induced corrosion in reinforced concrete. *Materials*, 16(23), p.7462. [DOI]

Chen, Y., Chen, M., Chen, R. and Kang, X., 2023. Deterioration mechanism of chloride attack on reinforced concrete under stray current and high hydraulic pressure coexistence environment. *Materials and Structures*, 56(9), p.160. [DOI]

De Schutter, G. and Luo, L., 2004. Effect of corrosion-inhibiting admixtures on concrete properties. *Construction and Building Materials*, 18(7), pp.483-489. [DOI]

Ega, I.J., Job, O.F., Anowai, I.S. and Dakas, A.I.I., 2024. Durability characteristics of corn-cob ash (CCA) blended cement concrete. *Journal of Materials and Manufacturing Technology*, 1(1), pp.1-8. [DOI]

Ghanaati, B., Irannejad, A. and Raveri, F.B., 2022. Production and investigating the effect of Echium amoenum Fisch-8me (part of stem and leaf, wastes) extract as a green and cheap corrosion inhibitor on St37 steel in a 3.5 wt% NaCl corrosive medium. *Journal of Corrosion Science and Technology*, 1(1), pp.1-12. [DOI]

Hao, H., Bi, K., Chen, W., Pham, T.M. and Li, J., 2023. Towards next-generation design of sustainable, durable, multi-hazard resistant, resilient, and smart civil engineering structures. *Engineering Structures*, 277(1), pp.115477. [DOI]

Jiang, C., Wei, G.-F., Lei, R., Deng, S., Li, X. and Shao, D., 2025a. Functional development of extracts from the invasive plant water hyacinth for steel corrosion protection. *Npj Materials Degradation*, 9(1), p.33. [DOI]

Jiang, M., Liu, X., Xu, Y., Li, S., Liu, X., Niu, X., Lu, L., Sun, X., Xie, Z., Wang, Z. and Cui, S., 2025b. Corrosion inhibition effect and mechanism of eco-friendly corrosion inhibitors on mild steel in simulated concrete pore solution: experimental and theoretical studies. *ACS Sustainable Chemistry & Engineering*, 13(6), pp.2411-2428. [DOI]

Goni, L.K.M.O. and Mazumder, M.A.J., 2019. Green corrosion inhibitors. In: Corrosion Inhibitors. IntechOpen. [DOI]

Kamarska, K.V., 2024. Investigation of rosemary oil as an environmentally friendly corrosion inhibitor of aluminum alloy. *Nature Environment and Pollution Technology*, 23(3), pp.1723-1727. [DOI]

Krishnanjana, K. and Ganesh, G.M., 2025. Green corrosion inhibition of *Punica granatum* peel powder on tmt in salt medium: outlooks from experiments and artificial neural networks. *Green Chemistry Letters and Reviews*, 18(1), pp.1-12. [DOI]

Kumar, N., Mohd Noor, I.S., Zu Azhan Yahya, M. and Prakash, S., 2025. Botanical corrosion inhibitors in reinforced concrete: material sustainability assessment and analysis - A review. *Materials Protection*, 66(1), pp.40-55. [DOI]

Kumar, N. and Saharan, S., 2022. Use of *Lawsonia inermis* and sodium nitrite as surface applied corrosion inhibitors. *International Journal of Sustainable Construction Engineering and Technology*, 13(1), pp.1-10. [DOI]

Li, Z., Long, Z., Lei, S., Liu, X., Yang, L., Zhang, W. and Zhang, T., 2023. Evaluating the corrosion resistance of marine steels under different exposure environments via machine learning. *Physica Scripta*, 98(1), p.015402. [DOI]

Liu, J., Hang, M., Jiang, M. and Song, H., 2025. Rust inhibition mechanism of reinforced concrete by alcohol-amine corrosion inhibitor under the coupling of composite salt erosion, freeze-thaw cycle and dry-wet cycle. *Case Studies in Construction Materials*, 22(1), p.e04466. [DOI]

Liu, Q., Yuan, M., Zhang, J. and Qiang, S., 2024. Research on the corrosion inhibition effect of *Xanthium sibiricum* on reinforced steel and the prediction of reinforced concrete performance under a stray current and chloride environment. *Applied Sciences*, 14(16), p.6986. [DOI]

Liu, Y. and Shi, J., 2024. Recent progress and challenges of using smart corrosion inhibitors in reinforced concrete structures. *Construction and Building Materials*, 411(1), p.134595. [DOI]

McCafferty, E., 2010. Introduction to Corrosion Science. Springer, p.575. [DOI]

Montes-García, P., Jiménez-Quero, V. and López-Calvo, H., 2015. Assessment of high-performance concrete containing fly ash and calcium nitrite-based corrosion inhibitor as a means to prevent the corrosion of reinforcing steel. *Journal of Physics: Conference Series*, 582(1), p.012028. [DOI]

Nóvoa, X.R. and Pérez, C., 2023. The use of smart coatings for metal corrosion control. *Current Opinion in Electrochemistry*, 40(1), p.101324. [DOI]

Okeniyi, J., Loto, C. and Popoola, A., 2016. Effects of *Phyllanthus muellerianus* leaf extract on steel-reinforcement corrosion in 3.5% NaCl-immersed concrete. *Metals*, 6(11), p.255. [DOI]

Okeniyi, J.O., Popoola, A.P.I. and Okeniyi, E.T., 2018. Cymbopogon citratus and nano2 behaviors in 3.5% NaCl-immersed steel-reinforced concrete: Implications for eco-friendly corrosion inhibitor applications for steel in concrete. *International Journal of Corrosion*, 2018(1), pp.1-11. [DOI]

Okewale, A. and Omoruwuo, F., 2018. Neem leaf extract as a corrosion inhibitor on mild steel in acidic solution. *International Journal of Engineering Research in Africa*, 35(1), pp.208-220. [DOI]

Ovari, T.-R., Brânzanic, A.M.V., Katona, G., Szabó, G.S. and Muresan, L.M., 2025. New eco-friendly corrosion inhibitor for zinc based on expired Detralex drug. Adsorption, electrochemical and computational studies. *Materials Today Communications*, 46(1), p.112739. [DOI]

Sharma, N., Sharma, S., Sharma, S.K., Mahajan, R.L. and Mehta, R., 2022. Evaluation of corrosion inhibition capability of graphene modified epoxy coatings on reinforcing bars in concrete. *Construction and Building Materials*, 322(1), p.126495. [DOI]

Sharmila, S.M. and Vasanthi, P., 2024. Performance evaluation of corrosion protective coatings on marine concrete piles: an experimental study utilizing artificial neural network and statistical analysis. *Asian Journal of Civil Engineering*, 25(4), pp.3059-3080. [DOI]

Shehnazdeep and Pradhan, B., 2022. A study on the effectiveness of inorganic and organic corrosion inhibitors on rebar corrosion in concrete: a review. *Materials Today: Proceedings*, 65(1), pp.1360-1366. [DOI]

Singh, R., Arora, H.C., Bahrami, A., Kumar, A., Kapoor, N.R., Kumar, K. and Rai, H.S., 2022. Enhancing the sustainability of corroded RC structures: estimating steel-to-concrete bond strength with ANN and SVM algorithms. *Materials*, 15(23), p.8295. [DOI]

Söylev, T.A. and Richardson, M.G., 2008. Corrosion inhibitors for steel in concrete: state-of-the-art report. *Construction and Building Materials*, 22(4), pp.609-622. [DOI]

Suhas, V.S., Shanmugapriya, T., Borg, R.P., Akash, K. and Sunil, A., 2025. Enhanced corrosion inhibition of mild steel in concrete pore solution using modified MgO-chitosan epoxy nanocomposite coatings. *Materials Letters*, 398(1), p.138916. [DOI]

Tarabin, M., Maalej, M., Altoubat, S. and Talha Junaid, M., 2023. Review of the bond behavior between reinforcing steel and engineered cementitious composites. *Structures*, 55(1), pp.2143-2156. [DOI]

Umamathi, T., Prathipa, V., Roslin, A., Jewelcy, A.L., Jeevithe Clara, M.V., Anitha, N., Nasrin Sahana, M.I., Susai, R. and Krishnaveni, A., 2024. Influence of sodium chloride on corrosion resistance of ever silver vessels in the presence of curd rice. *Materials Protection*, 65(4), pp.765-777. [DOI]

Verma, C., Kumar, A. and Thakur, A., 2024. Phytochemistry in Corrosion Science: Plant Extracts and Phytochemicals as Corrosion Inhibitors. CRC Press, p.532. [DOI]

Zhao, A., Sun, H., Chen, L., Huang, Y., Lu, X., Mu, B., Gao, H., Wang, S. and Singh, A., 2019. Electrochemical studies of bitter gourd (Momordica charantia) fruits as eco-friendly corrosion inhibitor for mild steel in 1 M HCl solution. *International Journal of Electrochemical Science*, 14(7), pp.6814-6825. [DOI]

Nature Environment and Pollution Technology
An International Quarterly Scientific Journal

p-ISSN: 0972-6268
(Print copies up to 2016)
e-ISSN: 2395-3454

Vol. 25 | No. 3 | Article ID D1869 | 2026

Original Research Paper

https://doi.org/10.46488/NEPT.2026.v25i03.D1869

Open Access Journal

Assessment of Metal Concentrations and Variability Using Censored Data Analysis in Hu'u Rivers, Sumbawa, Indonesia

Karizma Fahlevy[1]†, Agustinus Sembiring[2], Rias Kaessari Magenta[2], Adi Suroso[2] and Charles P. H. Simanjuntak[3]

[1]Nabat, Abu Dhabi Emirate, United Arab Emirates
[2]PT Hirax Environmental Indonesia, Jakarta 12950, Indonesia
[3]Department of Aquatic Resources Management, Faculty of Fisheries and Marine Sciences, IPB University, Bogor 16880, Indonesia
†Corresponding author: Karizma Fahlevy; karizma.fahlevy@nabat.ai

Abbreviation: Nat. Env. & Poll. Technol.
Website: www.neptjournal.com

Received: 16-09-2025
Revised: 25-11-2025
Accepted: 16-12-2025

Key Words:

Metal concentration
Detection limits
Freshwater river
Watersheds
Water quality

Citation for the Paper:

Fahlevy, K., Sembiring, A., Magenta, R.K., Suroso, A. and Simanjuntak, C.P.H., 2026. Assessment of metal concentrations and variability using censored data analysis in Hu'u Rivers, Sumbawa, Indonesia. *Nature Environment and Pollution Technology*, 25(3), D1869. https://doi.org/10.46488/NEPT.2026.v25i03.D1869

Note: From 2025, the journal has adopted the use of Article IDs in citations instead of traditional consecutive page numbers. Each article is now given individual page ranges starting from page 1.

Copyright: © 2026 by the authors
Licensee: Technoscience Publications
This article is an open access article distributed under the terms and conditions of the Creative Commons Attribution (CC BY) license (https://creativecommons.org/licenses/by/4.0/).

ABSTRACT

Water quality monitoring is essential for managing watersheds; however, values below detection limits are often mishandled, which can hinder interpretation and lead to these measurements being ignored or discarded. This study aimed to analyze metal concentrations and their variability in freshwater rivers, focusing on datasets with a high proportion of censored values, where many measurements fell below the detection limits. This study was conducted in Hu'u, Sumbawa, Indonesia, from 2019 to 2023. Thirteen dissolved metals were analyzed: As, Ba, B, Cd, Cr(VI), Co, Cu, Fe, Pb, Mn, Hg, Se, and Zn. Significant differences between watersheds were observed for six metals, including As, Ba, B, Fe, Mn, and Zn ($p < 0.05$), whereas no significant seasonal effects were detected for any parameter. The findings indicate that the watersheds are likely impacted by nearby agricultural and domestic activities, as evidenced by the higher metal concentrations near settlements and cornfields. Conversely, more remote watersheds with limited agricultural exposure exhibited lower pollutant concentrations. This study practically enhances the representation of censored data concentrations with multiple detection limits, not only by visualizing censored values but also by illustrating data variability.

1. INTRODUCTION

Heavy metals are naturally present in aquatic environments and are mainly introduced into rivers through natural rock weathering, soil erosion, or the dissolution of water-soluble salts (Garbarino et al. 1995; Kennish 1998; Khethi et al. 2013; Jeong et al. 2023). Metals belong to a broader category of substances, some of which are essential for human health (Mertz 1993). According to Bosch et al. (2016), metals can be categorized as essential, non-essential, or toxic. Essential elements include iron (Fe), copper (Cu), zinc (Zn), and selenium (Se), which have specific functions in regulating body metabolism but can be harmful when exceeding certain levels (Bosch et al. 2016, Pasco et al. 2024). Conversely, non-essential elements are typically recognized to have no specific function in living organisms. Toxic elements, such as arsenic (As), chromium (Cr), nickel (Ni), cadmium (Cd), mercury (Hg), and lead (Pb), are detrimental when present in high concentrations (Bosch et al. 2016). Despite this, naturally discharged metals into river systems without anthropogenic intervention are generally considered harmless (Kennish 1998).

Indonesia has approximately 17,000 watersheds that are vital for managing the country's water resources (Ditjen PDASRH 2021). In addition to their role in natural cycles, watersheds provide water for agriculture, industry, and households

and support traditional livelihoods (Duan et al. 2016, Bons et al. 2016, Rozana et al. 2020, Narendra et al. 2021). However, the quality of water in these watersheds is increasingly at risk due to the rising concentration of heavy metals, which can be exacerbated by untreated industrial and agricultural runoff. Concerns regarding heavy metal contamination in river waters are mounting due to their toxic properties, persistent effects, and potential for accumulation in aquatic organisms (Saturday et al. 2023, Supangat et al. 2023; Ahamad et al. 2024). This poses a significant risk to aquatic ecosystems, leading to bioaccumulation throughout the food chain. Such bioaccumulation presents a potential threat to human health, making it crucial to accurately assess the distribution of heavy metal concentrations in river ecosystems (Srivastava et al. 2020; Mofijur et al. 2021; Zhou et al. 2022).

Over the last decade, water quality monitoring has become key to evaluating watersheds and prioritizing management strategies (Supangat et al. 2023). It provides timely information necessary to detect and address threats to water quality. A common issue encountered in water quality monitoring is the presence of data below the detection limit (DL) of the analysis, often arising from variations in laboratory methods or instrumentation and interferences in the matrix of the water samples (Shoari & Dube 2018; Hites 2019). This issue creates difficulties in managing the data, commonly known as "censored data" (Hewett & Ganser 2007). Such values are difficult to interpret, which can result in bias and misinterpretation of the results (Verbovšek, 2011). Methods to compute summary statistics for censored data include the Kaplan-Meier survival method, maximum likelihood estimation, and regression on order statistics (Helsel 2012). However, these methods are seldom employed because of the need for specific statistical techniques and software (Verbovšek 2011). This added complexity has led to the adoption of more traditional approaches for handling these data, such as substituting censored values with one-half of the detection limit derived from the analytical method. This simplistic approach is not recommended for environmental data, as it may result in both overestimation and underestimation. Further criticized this traditional method, considering it a form of data fabrication (Helsel 2006). In Indonesia, many water quality studies report various parameters, but censored data are often inconsistently managed and simply reported as "<DL" (Suyatna et al. 2017, Novita et al. 2020, Surbakti et al. 2021, Prayoga et al. 2022) due to the end users' lack of experience with data handling and interpretation of analytical results (Sulistiyowati & Uyun 2021). While such results indicate that the parameter falls below the applicable guidelines or regulations, assessing variability over space and time remains challenging, limiting insights into the original data. Addressing this issue is critical for developing effective and sustainable water management strategies.

Throughout human history, freshwater has emerged as one of the most vital resources worldwide. Simultaneously, monitoring heavy metal concentrations in river ecosystems is crucial for global environmental assessments (Khan et al. 2022, Manfreda et al. 2024). While numerous studies have investigated the spatial and temporal variations in heavy metal concentrations in freshwater rivers, detailed analyses of censored data have not been extensively addressed (Li et al. 2015; Anyanwu et al. 2024; William et al. 2024). For example, McGrory et al. (2020) analyzed heavy metal concentrations and biological and physical data in groundwater using multiple detection limits and clustering analysis in Ireland. In New Zealand, Gadd et al. (2024) examined trends in metal concentrations using censored data, whereas Whitehead (2019) focused on biological and nutrient parameters. In France, Laroche et al. (2022) conducted a study on pesticide analyses. However, comparable studies analyzing heavy metals in river ecosystems are scarce. To our knowledge, no studies in this region have addressed censored values. Furthermore, continuous, focused, and long-term monitoring of metals in freshwater, particularly when using data with over 80% censored values and multiple detection limits across different watersheds and seasons, remains limited on a global scale. To fill these gaps, this study utilized both censored (up to 80%) and uncensored data with multiple detection limits (DLs) collected over five years of monitoring. By focusing on the specific challenges posed by high levels of censored data, this study offers insights into future studies and policy frameworks in Indonesia and beyond, into the underrepresented issue of censored data interpretation in environmental monitoring.

A case study was conducted in the freshwater rivers of the Hu'u District in Dompu Regency, West Nusa Tenggara Province (NTB), Indonesia. The Hu'u District plays a significant role in Indonesia's agricultural sector, with rice and corn as its primary commodities (Paryono et al. 2023). Residents often utilize river water for irrigating their crops, and the use of chemical pesticides and fertilizers poses a potential risk of mobilizing heavy metal concentrations into rivers (Arifin et al. 2019). To develop effective and sustainable water management strategies, it is important to assess the variability in heavy metal concentrations (Kumar et al. 2024). Currently, no studies have examined heavy metal variability across watersheds and seasons using censored data analysis in the country. The novelty of this study is highlighted through the following specific objectives:

1. Determining heavy metal concentrations in freshwater rivers in Hu'u,

2. Comparing the heavy metal concentrations with the permissible limits.
3. Assessing the variability of heavy metal concentrations across watersheds and seasons using a censored data analysis.

Univariate and multivariate statistical analyses were used to examine the patterns across sampling locations by considering all metal parameters. The focus parameters include one metalloid, arsenic (As), and twelve heavy metals: barium (Ba), boron (B), cadmium (Cd), chromium hexavalent (Cr(VI)), cobalt (Co), copper (Cu), iron (Fe), lead (Pb), manganese (Mn), mercury (Hg), selenium (Se), and zinc (Zn), as outlined in the Government of Indonesia's (GoI) regulations on environmental protection and river management. The aspects of this study are particularly important, as there are currently few studies demonstrating how both censored and uncensored data can be integrated to interpret variability in heavy metal concentrations.

2. MATERIALS AND METHODS

2.1. Sampling Location

The study was conducted in the Hu'u District, West Sumbawa, West Nusa Tenggara (NTB), Indonesia. A total

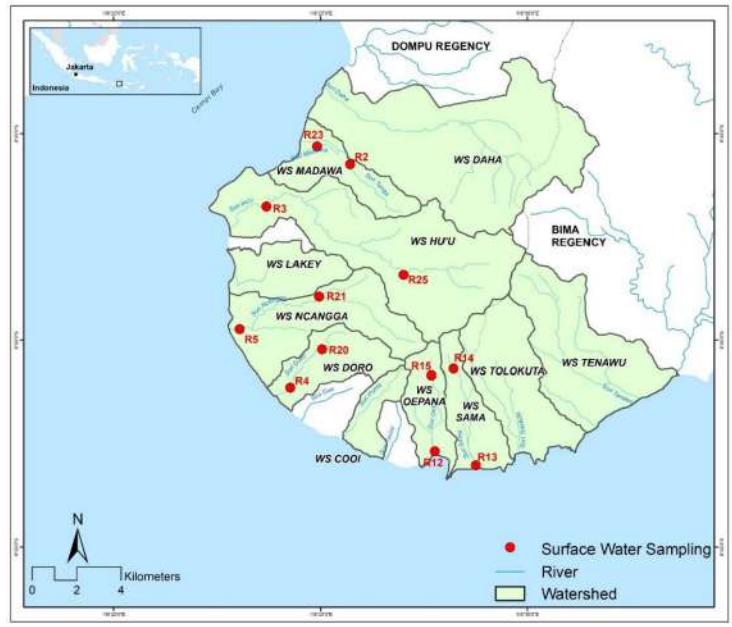


Fig. 1: Map of surface water sampling locations in Hu'u District, Sumbawa, Indonesia.

Table 1: Surface water sampling locations in Hu'u, Sumbawa, Indonesia.

No.	Watershed	River	Landuse	ID	Latitude	Longitude
1	Madawa	Tenga	Cornfield	R2	118° 25' 42.767" E	8° 45' 44.334" S
2		Madawa	Cornfield, low-density settlement	R23	118° 24' 54.540" E	8° 45' 18.122" S
3	Hu'u	Hu'u	Cornfield, low-density settlement	R3	118° 23' 41.793" E	8° 46' 45.954" S
4			Wildwood	R25	118° 27' 00.587" E	8° 48' 24.627" S
5	Ncangga	Ncangga	Corn-Paddy field, low-density settlement	R5	118° 23' 02.891" E	8° 49' 43.839" S
6			Wildwood	R21	118° 24' 57.724" E	8° 48' 56.412" S
7	Doro	Doro	Cornfield	R4	118° 24' 16.556" E	8° 51' 08.302" S
8			Wildwood	R20	118° 25' 01.945" E	8° 50' 13.221" S
9	Oepana	Onto	Wildwood	R12	118° 27' 46.066" E	8° 52' 40.827" S
10			Wildwood	R15	118° 27' 41.375" E	8° 50' 50.753" S
11	Sama	Sama	Wildwood	R13	118° 28' 45.262" E	8° 53' 01.492" S
12			Wildwood	R14	118° 28' 12.528" E	8° 50' 41.158" S

of 12 locations in freshwater rivers across six watersheds (Hu'u, Doro, Ncangga, Onto, Sama, and Madawa) were deliberately selected based on accessibility, proximity to infrastructure, land use, and their positions along the river, including both upstream and downstream areas (Fig. 1, Table 1). Land adjacent to the rivers is primarily used for irrigated and rain-fed agriculture, such as corn and paddy fields, as well as residential areas comprising small village settlements and forested regions (wildwood, Table 1). Most residents of Hu'u are farmers, and their agricultural activities, particularly irrigation, may impact water quality.

2.2. Sample Collection

Samples were collected twice annually to represent the wet and dry seasons from 2019 to 2023. Wet season sampling was conducted from January to March or from November to December, and dry season sampling occurred from May to September. Water samples were obtained by immersing 1 L high-density polyethylene (HDPE) bottles just below the water surface. The samples were subsequently passed through a 0.45 µm Millipore filter and poured into 150 mL labeled high-density polyethylene (HDPE) bottles. The filtered samples were preserved using acid, stored in a cooler at 4°C, and transported to accredited laboratories in Jakarta for further analysis. Thirteen dissolved metals were measured: arsenic (As), barium (Ba), boron (B), cadmium (Cd), chromium (VI) (Cr(VI)), cobalt (Co), copper (Cu), iron (Fe), lead (Pb), manganese (Mn), mercury (Hg), selenium (Se), and zinc (Zn). The results were compared with the Indonesian and FAO water quality standards. The Indonesian standard is stipulated in the Government of Indonesia Regulation No. 22/2021, Appendix VI concerning Water Quality Management and Control of Water Pollution: Class II and Class III (Government of Indonesia 2021). Class II water is intended for use in recreational facilities, freshwater fish farming, livestock, irrigation, or other activities requiring comparable water quality. Class III water is suitable for freshwater fish farming, livestock, irrigation, and other uses with similar water quality requirements. The FAO standard used in this study was the recommended concentration of trace elements in irrigation water (Ayers & Westcot 1985). Table 2 summarizes the parameters, including their abbreviations, detection limits, and analytical methods.

2.3. Data Handling

At certain locations, owing to the episodic nature of the rivers, sampling could not be conducted during the dry season in some years. Consequently, some observations were missing when the rivers were dry; therefore, these points were omitted from the data table, leaving datasets of 107 and 108 observations. In addition, many samples contained metal concentrations below the detection limit (DLs). Non-detectable values, often referred to as censored data, occur when the concentration in a water body falls below the detection limits, either due to methodological or instrumental limitations (Brown 2008). The presence of censored data renders the use of defined distributions for continuous data unsuitable (Ogden 2010, Helsel 2012). To address this issue, the empirical cumulative distribution function (ECDF) was calculated for each metal parameter using the nonparametric Kaplan-Meier method (She 1997, Taylor et al. 2002, Smith 2011). This method falls under the likelihood-based approach for estimating the overall survival function when the data are incomplete or censored (Lira et al. 2020; Sun & Wang 2024). The Kaplan-Meier method was selected instead of regression on order statistics (ROS) and maximum likelihood estimation

Table 2: Parameters, methods, detection limits and permissible standards. Detection limits show the range for the different analytical laboratories.

Parameters	Method	Units	Detection Limit [DL]	GoI (2021)	FAO
Arsenic, As	APHA 3125 B	$mg.L^{-1}$	0.0005 - 0.002	0.05	0.1
Barium, Ba	APHA 3125 B	$mg.L^{-1}$	0.01	NR	NA
Boron, B	APHA 3125 B	$mg.L^{-1}$	0.01 - 0.02	1	NA
Cadmium, Cd	APHA 3125 B	$mg.L^{-1}$	0.0001 - 0.003	0.01	0.01
Chromium Hexavalent, Cr(VI)	APHA 3500-Cr B	$mg.L^{-1}$	0.0001 - 0.01	0.05	NA
Cobalt, Co	APHA 3125 B	$mg.L^{-1}$	0.001 - 0.01	0.2	0.05
Copper, Cu	APHA 3125 B	$mg.L^{-1}$	0.001 - 0.01	0.02	0.2
Iron, Fe	APHA 3125 B	$mg.L^{-1}$	0.005 - 0.02	NR	5.0
Lead, Pb	APHA 3125 B	$mg.L^{-1}$	0.001 - 0.02	0.03	5.0
Manganese, Mn	APHA 3125 B	$mg.L^{-1}$	0.001 - 0.02	NR	0.2
Mercury, Hg	APHA 3112 B	$mg.L^{-1}$	0.00005 - 0.0008	0.002	NA
Selenium, Se	APHA 3125 B	$mg.L^{-1}$	0.00006 - 0.001	0.05	0.02
Zinc, Zn	APHA 3125 B	$mg.L^{-1}$	0.005 - 0.01	0.05	2.0

(MLE) because it does not require any assumptions about the underlying data distribution, making it more robust for datasets with multiple detection limits, relatively small sample sizes, and a significant proportion of censored values (Hwang et al. 2023).

2.4. Statistical Analysis

All statistical analyses were conducted using R software v.4.4.2 (R Core Team 2024), at a significance level of $p < 0.05$ (95% confidence level). The data were structured according to metal parameters, watersheds, and seasons. The next step was to calculate the ECDF value using the Kaplan-Meier method from the EnvStats package (Millard 2013). We included a 95% upper confidence limit (UCL95) in the Kaplan-Meier estimates because of multiple detection limits in the datasets, obtained from a percentile bootstrap estimate using the "enparCensored" function. A bootstrap repetition of 5,000 was performed to ensure the stability of the estimates from one iteration to another (Singh et al. 2006).

Environmental data (e.g., air, water, and soil) frequently exhibit a right-skewed distribution owing to a lower bound of zero and less frequent high values (Helsel 2012). Applying logarithmic or square root transformations can help achieve a more symmetric distribution, making it more suitable for statistical methods that assume normality (Helsel 2012). The "gofTestCensored" function from the EnvStats package was used to normalize the distribution (Millard 2013). This function adapts the Shapiro-Francia test to assess the lognormality of data containing multiple censored values (Millard 2013). The analysis requires datasets containing a minimum of two non-missing, uncensored, and distinct values. Accordingly, cadmium (Cd), Cr (VI), lead (Pb), mercury (Hg), and selenium (Se) were excluded from the analysis. Moreover, because most measurements were below the detection limit, the summary statistics reflect only the possible range of metal concentrations. In some cases, the minimum value could not be reported because the lowest uncensored value was lower than one or more censored observations. Reporting a numeric minimum in such cases would be misleading because the censored data may indicate a higher or lower value than the lowest observed uncensored measurement. Similarly, a maximum value may not be reported if some censored values exceed the highest uncensored observations.

To account for instances of single (one value censored) or double censorship (both values censored), the non-parametric Kendall's tau (τ) correlation coefficient was applied using the "cenken" function in the NADA package (McGrory et al. 2020, Travis et al. 2023). This analysis specifically assessed the strength of the relationships for parameters not limited by sample size constraints (Helsel 2012). The correlation coefficient values were categorized as follows: $|\tau| = 0$ indicates no relationship, $|\tau| < 0.3$ represents a weak relationship, $0.3 \leq |\tau| \leq 0.5$ indicates a moderate relationship, and $|\tau| \geq 0.5$ signifies a strong relationship (McGrory et al. 2020). Significant relationships among the metal variables are indicated by * for $p < 0.05$ and ** for $p < 0.001$.

Considering the sample size limitations, tests for comparing specific parameters across watersheds and/or seasons were excluded (Table 3). Several metals, including arsenic (As), barium (Ba), boron (B), manganese (Mn), and zinc (Zn), did not meet the assumptions required for a parametric statistical analysis. Consequently, the nonparametric Peto and Peto tests were employed to calculate the differences in the empirical cumulative distribution function (ECDF) between groups, which is appropriate for censored datasets with two or more groups (Helsel 2012). For datasets with more than two groups, the analysis was followed by a nonparametric multiple comparison test using the Benjamini-Hochberg *p*-value adjustment method. This analysis was performed using the "cen1way" function in the NADA2 package in R (Julan & Helsel 2021). Other metals, including cobalt (Co), copper (Cu), and iron (Fe), which followed a log-normal distribution, were tested using the "cenanova" function, followed by Tukey's multiple comparison tests in the NADA2 package (Julan & Helsel 2021). ANOVA results for Co and Cu showed significant differences ($p < 0.05$); however, post hoc tests detected no significant differences ($p > 0.05$),

Table 3: Parameters that were skipped in the statistical test.

Metal	% Censored	Number of samples	Skipped test
Arsenic, As	63.89	108	-
Barium, Ba	0.93	108	-
Boron, B	29.63	108	-
Cadmium, Cd	96.3	108	All factor
Chromium Hexavalent, Cr(VI)	100	108	All factor
Cobalt, Co	90.74	108	Watershed
Copper, Cu	77.57	107	Watershed
Iron, Fe	19.63	107	-
Lead, Pb	100	108	All factor
Manganese, Mn	39.81	108	-
Mercury, Hg	99.07	107	All factor
Selenium, Se	98.15	108	All factor
Zinc, Zn	70.09	107	-

% censored: percentage of data with concentration below the detection limit.

likely because of the high proportion of censored data. To address this limitation, both parameters were reanalyzed using the cenpermanova function in the NADA2 package. This permutation-based approach evaluates differences in group means for censored data, providing reliable mean estimates and *p*-values, as no values are modeled below zero (Julan & Helsel 2021, Kittlaus et al. 2024). The significant parameters were visualized using boxplots generated with the "cboxplot" function from the NADA2 package (Julan & Helsel 2021), which creates plots specifically for left-censored data with one or more detection limits.

Hierarchical clustering analysis (HCA) was used to examine the similarity between variables, utilizing Ward's linkage method on the significant parameters (Zhao et al. 2011). Clustering was conducted using data from all years and seasons combined, as seasonal separation was not possible because of the large number of censored values. Hierarchical cluster analysis (HCA) followed the approach of McGrory et al. (2020), clustering both watersheds and parameters. The distances between watersheds were calculated from the absolute differences in the estimated Kaplan–Meier empirical cumulative distribution function (ECDF, $F(v_k)$) values. We used the Manhattan distance to calculate the overall distance between watersheds i and j across all p parameters as follows:

$$d_{ij} = \sum_{k=1\ldots p} d_{kij} = \sum_{k=1\ldots p} \left| F(v_{ki}) - F(v_{kj}) \right| \quad \ldots(1)$$

The distance matrix for parameters x and y was constructed using Kendall's tau correlation coefficient, which was calculated through the "cenken" function of NADA (McGrory et al. 2020, Simmonet-Laprade et al. 2019), represented as:

$$dxy = \tau xy \quad \ldots(2)$$

The clustering results are shown in a heatmap, depicting the dendrograms of both parameters and watersheds.

3. RESULTS

3.1. Concentrations of Dissolved Metals

Of the metals analyzed, chromium (Cr(VI)) and lead (Pb) were below the detection limits (<DLs) in all samples. The concentrations of cadmium (Cd), cobalt (Co), mercury (Hg), and selenium (Se) were below the detection limit in 96%, 91%, 99%, and 98% of the samples, respectively (Table 3). For other metals, the ranges and proportions of censored data were as follows: arsenic (As: <0.0005–0.004 $mg.L^{-1}$, 64% censored), barium (Ba: <0.01–0.34 $mg.L^{-1}$, 1% censored), boron (B: <0.01–0.16 $mg.L^{-1}$, 30% censored), copper (Cu: <0.001–0.03 $mg.L^{-1}$, 78% censored), and zinc (Zn: <0.005–0.15 $mg.L^{-1}$, 70% censored, Tables 3 and 4). The highest dissolved metal concentrations were recorded for iron (Fe: <0.005–1.13 $mg.L^{-1}$) and manganese (Mn: <0.001–1.08 $mg.L^{-1}$) (Supplementary Table A1).

At all sampling locations, the concentrations of the 13 metals were below Indonesia's Class II and III water quality standards, except for copper (Cu) at site R25 in the Hu'u watershed during the 2019 wet season (Supplementary Tables A1 and A2). Although Indonesian standards do not specify limits for manganese (Mn), the FAO guidelines for irrigation water indicate that Mn concentrations in the Doro, Hu'u, Madawa, Ncangga, and Sama watersheds exceeded the maximum level in 2019, 2020, and 2022 (Supplementary Table A2). Compared to heavy metal concentrations in other countries (Table 4), the overall results of the present study were generally lower, although the maximum concentrations of barium (Ba) and manganese (Mn) were higher. Correlation analysis showed weak positive or negative relationships among the metals ($r < 0.3$). However, significant correlations were observed for several metals (Fig. 2), notably barium (Ba), arsenic (As), boron (B), cobalt (Co), iron (Fe), manganese (Mn), and zinc (Zn).

3.2. Concentrations Variability of Dissolved Metals

The Peto–Peto test (Table 5) revealed differences in ECDF-based concentration patterns across watersheds for arsenic (As), barium (Ba), boron (B), manganese (Mn), and zinc (Zn). Concentrations were higher for As in Madawa, Ba in Madawa and Ncangga, B in Madawa, Mn in Hu'u, and Zn in Doro, Hu'u, and Oepana (Table 5, Fig. 3). ANOVA results showed higher iron (Fe) concentrations in Doro, Hu'u, Ncangga, and Sama (Table 5, Fig. 3), whereas the permutational test revealed no significant differences in cobalt (Co) and copper (Cu) across watersheds (Table 5). Seasonal comparisons across all sampling locations and years revealed no significant differences between the wet and dry seasons (Table 6).

3.3. Multivariate Analysis

Hierarchical clustering identified three separate groups for both parameters and watersheds (Fig. 4). Among the parameter clusters, the first included zinc (Zn), iron (Fe), and manganese (Mn); the second contained arsenic (As), and the third comprised barium (Ba) and boron (B) (Fig. 4). Watershed clustering grouped Ncangga, Doro, and Sama in the first cluster, Oepana and Madawa in the second, and Hu'u in the third (Fig. 4).

4. DISCUSSION

4.1. Dissolved Metal Variability

Dissolved metals are more easily absorbed by aquatic

Table 4: Reported metal concentrations ($mg.L^{-1}$) in freshwater rivers from the literature.

Country	River	Parameter [$mg.L^{-1}$]												
		As	Ba	B	Cd	Cr(VI)	Co	Cu	Fe	Pb	Mn	Hg	Se	Zn	References
Bangladesh	Barnoi [n = 5]	0.030 - 0.075			0.002 - 0.005			0.021 - 0.062		0.020 - 0.088				0.023 - 0.118	Haque et al. (2024)
China	Yangtze [n=110]	0.00042 - 0.00852			0.00001 - 0.00013			0.00011 - 0.00013	0.00011 - 0.00013	0.0008 - 0.00097				0.0024 - 0.0446	Jin et al. (2022)
India	Yamuna [n = 7]				0.0017 - 0.4330			0.0184 - 17.6424	0.8785 - 53.9401	0.0068 - 1.1121				0.0154 - 28.5209	Bhardwaj and Garg (2017)
Kazakhstan	Syr Darya [n = 42]						0.008 - 0.105	0.002 - 0.034	0.125 - 8.180	0 - 0.023	0.014 - 0.691			0.027 - 0.169	Zhang et al. (2020)
Kazakhstan	Esil River Basin [n = 78]	0.00252 - 0.0043			0.00008 - 0.000032	0.00282 - 0.0034				0.00098 - 0.00172					Bahetnur and Lee (2023)
Malaysia	Linggi [n = 15]	0.00022 - 0.00131			0.00001 - 0.00261			0.00006 - 0.00306	0.00683 - 0.17966	0.00003 - 0.00027	0.00259 - 0.04069		0 - 0.00006	0.00006 - 0.00635	Razak et al. (2021)
Mexico	Guadalajara River Basin [n = 25]	0 - 0.011	0.06 - 0.085	0.023 - 0.415	<0.002 - 0.003			0 - 0.009	0.158 - 1.174	0 - 0.023	0.002 - 0.544			0.002 - 0.128	Gonzaez-Díaz et al. (2025)
Nigeria	Ossiomo [n = 4]								0.19 - 0.57		0.01 - 0.32			0.09 - 1.29	Anani and Olomukoro (2021)
Thailand	Chao Phraya [n = 20]				0.000029 – 0.000193					0.000190 – 0.004428	0.000190 – 0.004428	0.000001 – 0.000007		0.000102 – 0.001047	Asokbunyarat and Sirivithayapakorn (2020)
Vietnam	[DOI]-Cho Dem-Ben Luc [n = 7]							0.026 - 0.057	1.01 - 2.38	0.008 - 0.08	0.14 - 0.28			0.026 - 0.048	Thieu et al. (2022)
Present study [n=12]		<0.0005 - <0.01	<0.01 - 0.34	0.16*	<0.0001**	<0.0001 - 0.01	<0.001 - 0.021	<0.001 - 0.03	<0.005 - 1.13	<0.001 - <0.02	<0.001 - 1.08	<0.00005 - 0.002	<0.00006 - 0.0011	<0.005 - 0.15	

*: The minimum value is not reported because the uncensored data is lower than the value of the censored data.
**: The maximum value is not reported because the censored data is higher than the maximum value of the uncensored data.

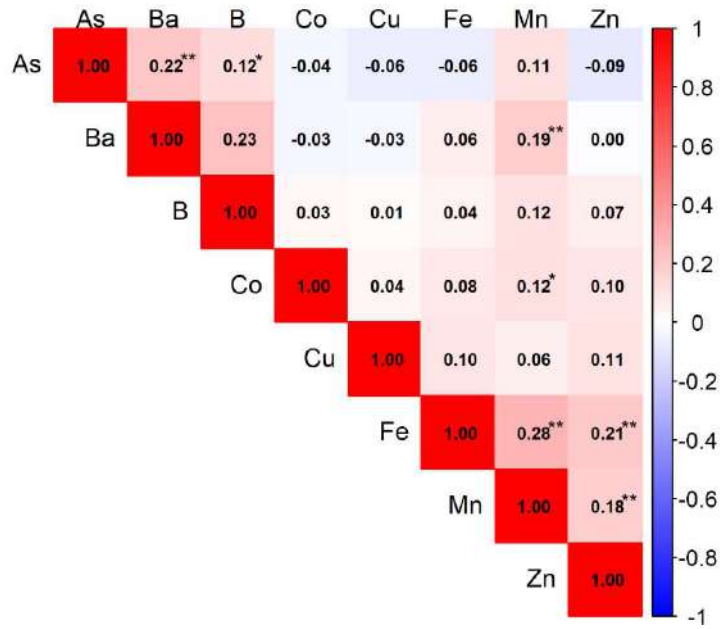


Fig. 2: The correlation matrix of Kendall's tau illustrates strong positive correlation (1.0) in red, indicates no correlation (0.0) without color, and represents strong negative correlation (-1.0) in blue. *=p-value<0.05, **= p-value<0.01.

Table 5: The concentration ranges (min-max) of metal parameters at all watersheds.

Watershed	Parameter [mg.L^{-1}]												
	As	Ba	B	Cd	Cr(VI)	Co	Cu	Fe	Pb	Mn	Hg	Se	Zn
Doro	<0.0005 - 0.0013^{a}	0.05 - 0.1^{a}	<0.01 - 0.03^{a}	<0.0001 - <0.001	<0.002 - <0.01	<0.001 - <0.01	<0.001 - 0.02	<0.02 - 0.5^{a}	<0.001 - <0.02	<0.001 - 0.049^{a}	<0.00005 - <0.0008	<0.00006 - <0.001	<0.005 - 0.07^{ab}
Hu'u	<0.0005 - 0.01^{ab}	0.05 - 0.1^{a}	<0.01 - 0.14^{a}	<0.0001*	<0.002 - <0.01	<0.001 - 0.021	<0.001 - 0.03	<0.02 - 1.13^{a}	<0.001 - <0.02	<0.01 - 1.08^{b}	<0.00005 - <0.0008	<0.0005 - 0.0011	<0.005 - 0.15^{a}
Madawa	<0.001 - 0.004^{b}	<0.01 - 0.34^{b}	<0.02 - <0.02^{b}	<0.0001 - <0.003	<0.001 - <0.01	<0.001 - <0.01	<0.001*	<0.005 - 0.24^{b}	<0.001 - <0.02	0.418**^{a}	<0.00005 - <0.0008	<0.0005 - <0.001	<0.005 - <0.01^{ab}
Ncangga	<0.0005 - <0.001^{ab}	0.07 - 0.17^{b}	<0.01 - 0.15^{a}	<0.0001*	<0.002 - <0.01	<0.001 - <0.01	<0.001*	0.383**^{a}	<0.001 - <0.02	0.03**^{a}	<0.00005 - <0.0008	<0.0005*	<0.005 - 0.06^{b}
Oepana	<0.0005 - 0.009^{a}	0.02 - 0.07^{c}	<0.01 - 0.12^{a}	<0.0001 - <0.001	<0.0001 - <0.01	<0.001 - <0.01	<0.001 - <0.01	<0.005 - 0.138^{b}	<0.001 - <0.02	<0.001*^{c}	<0.00005 - 0.002	<0.0005 - <0.001	<0.005 - 0.05^{b}
Sama	<0.0005*^{a}	0.03 - 0.09^{c}	<0.01 - 0.09^{a}	<0.0001*	<0.002 - <0.01	<0.001 - <0.01	<0.001 - 0.02	1.07**^{ab}	<0.001 - <0.02	0.31**^{a}	<0.00005 - <0.0008	<0.0005 - <0.001	<0.005 - <0.01^{a}
GoI	0.05	NR	1	0.01	0.05	0.2	0.02	NR	0.03	NR	0.002	0.05	0.05
FAO	0.1	NR	NR	0.01	NR	0.05	0.2	5	5	0.2	NR	0.02	2

Similar letters indicate no statistical difference based on the Peto-Peto test (adjust = Benjamini-Hochberg) and ANOVA test.
*The maximum value is not reported because the censored data is higher than the maximum value of the uncensored data.
**The minimum value is not reported because the uncensored data is lower than the value of the censored data.

organisms (Zahran et al. 2015, Tolkou et al. 2023). In this study, 13 dissolved metals were analyzed in the river water of Hu'u: arsenic (As), barium (Ba), boron (B), cadmium (Cd), hexavalent chromium (Cr(VI)), cobalt (Co), copper (Cu), iron (Fe), lead (Pb), manganese (Mn), mercury (Hg), selenium (Se), and zinc (Zn). Although all metals were detected, most concentrations were below the analytical detection limits, with cadmium (Cd), chromium (VI), mercury (Hg), lead (Pb), and selenium (Se) being undetected in 96–100% of the samples (Table 3). These metals may be regarded as safe since their detection thresholds were lower than the river water quality standards set by the Government of Indonesia (2021, Class II and III) and the Food and Agriculture Organization for irrigation water. Low levels of these metals may reflect limited inputs from pollution sources (Mokarram et al. 2020) and natural deposition processes (Botutihe et al. 2021).

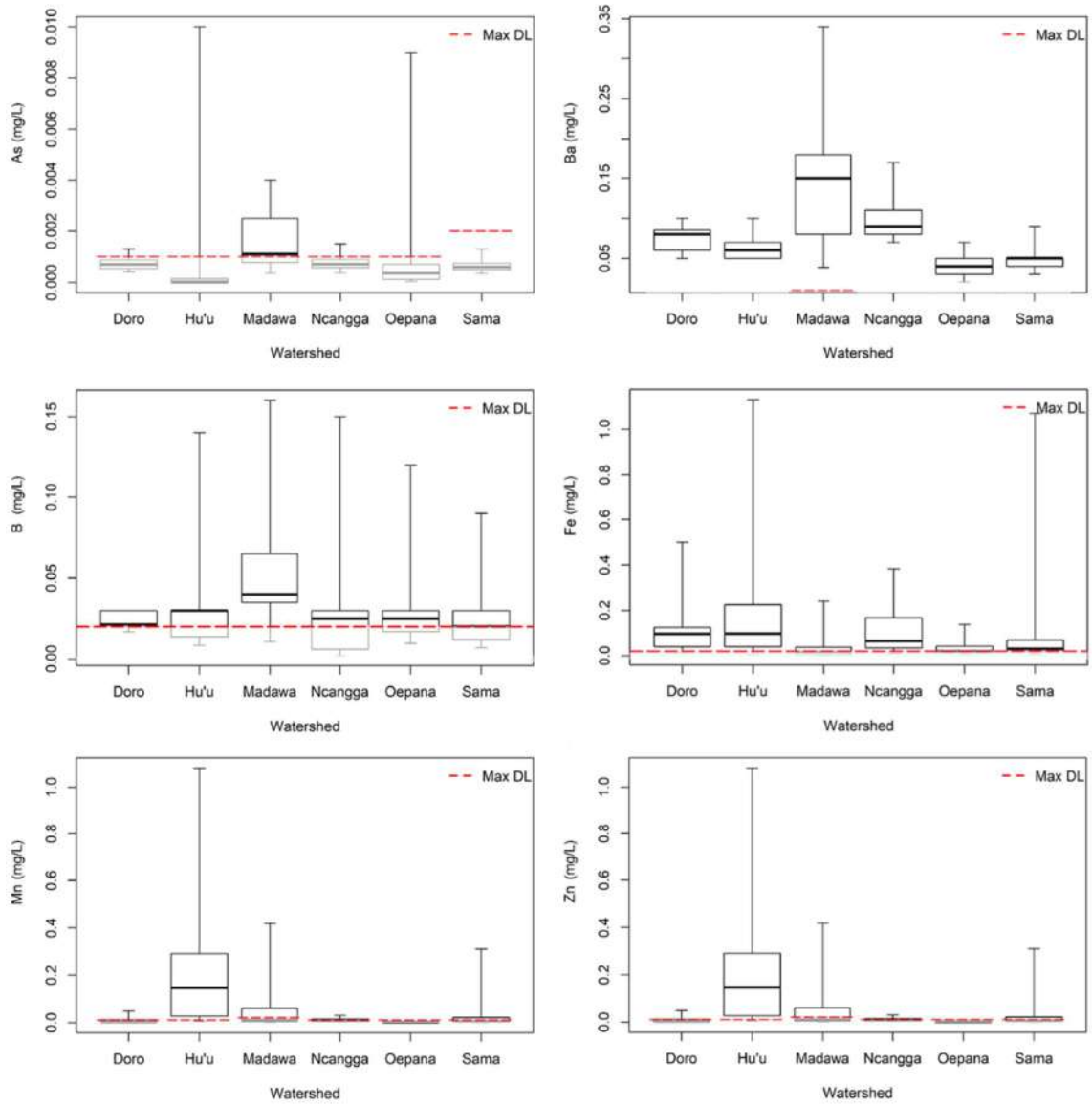


Fig. 3: Variability of metal concentrations for six parameters across the watersheds, selected based on statistical significance.

Table 6: The concentration ranges (min-max) of metal parameters at all seasons.

Season	Parameter [mg.L^{-1}]												
	As	Ba	B	Cd	Cr(VI)	Co	Cu	Fe	Pb	Mn	Hg	Se	Zn
Dry	<0.0005 - 0.01	<0.01 - 0.21	<0.01 - 0.16	<0.0001*	<0.001 - <0.01	<0.001 - 0.021	<0.001 - 0.015	<0.005 - 0.917	<0.001 - <0.02	<0.001 - 1.08	<0.00005 - 0.002	<0.00006 - 0.0011	<0.005 - <0.01
Wet	<0.0005 - <0.001	0.02 - 0.34	0.07**	<0.0001 - <0.002	<0.0001 - <0.01	<0.001 - 0.02	<0.001 – 0.03	<0.005 - 1.13	<0.001 - <0.02	<0.001 - 0.94	<0.00005 - <0.0008	<0.0005 - <0.001	<0.005 - <0.01
GoI	0.05	NR	1	0.01	0.05	0.2	0.02	NR	0.03	NR	0.002	0.05	0.05
FAO	0.1	NR	NR	0.01	NR	0.05	0.2	5	5	0.2	NR	0.02	2

*The maximum value is not reported because the censored data is higher than the maximum value of the uncensored data.
**The minimum value is not reported because the uncensored data is lower than the value of the censored data.

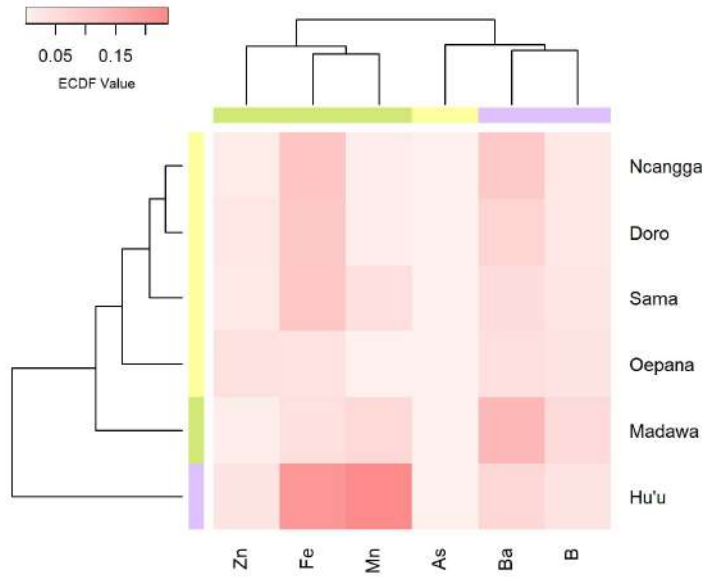


Fig. 4: Heatmap of hierarchical clustering based on watersheds (y-axis) and significant parameters (x-axis), clustered by Kendall's tau for parameters and ECDF interval distances for watersheds.

The latest assessment of the concentrations of 13 metals in the Hu'u district freshwater rivers found that they were below the Government of Indonesia (GoI) Class II and III water quality standards (WSP 2023, Supplementary Table A3), consistent with the findings of this study in 2023. The results from 2019 to 2023 showed that only copper (Cu) exceeded the GoI standards, occurring during the wet season of 2019 in Hu'u, while manganese (Mn) exceeded the FAO standard during both wet and dry seasons in 2019, 2020, and 2022 (Table 6, Supplementary Tables A1 and A2). Despite most parameters falling below the standard, continuous monitoring of heavy metals in surface water is crucial for sustainable management (Hartiningsih et al. 2024). As the human population continues to grow, water resources may be adversely affected by increasing metal concentrations if they are not properly monitored and managed (Mokarram et al. 2020).

No significant differences were observed in the dissolved metal concentrations between the wet and dry seasons (Table 6). Similar observations have been reported for some metal parameters in countries such as Nigeria and Bangladesh, where seasonal variation was also not significant (Ogungbile et al. 2020, Islam et al. 2021, Adano et al. 2023). The primary sources of metals may remain consistent throughout the year, contributing to stable concentrations regardless of seasonal changes (Adano et al. 2023). Although higher runoff during the wet season could increase the mobilization of metal-rich sediments and raise concentrations in surface waters through soil leaching (Oluyemi et al. 2008, Valencia-Avellan et al. 2017), frequent mild rainfall likely reduced concentrations through dilution (Huang et al. 2020). The predominance of such rainfall throughout the year may explain the absence of marked differences between the wet and dry seasons.

Significant variations in metal concentrations were detected for six parameters: arsenic (As), barium (Ba), boron (B), iron (Fe), manganese (Mn), and zinc (Zn) across watersheds (Table 5). The maximum concentrations of barium (Ba) and manganese (Mn) in this study exceeded values previously reported in the literature (Bhardwaj & Garg 2017, Zhang et al. 2020, Asokbunyarat & Sirivithayapakorn 2020, Razak et al. 2021, Anani & Olomukoro 2021, Jin et al. 2022, Thieu et al. 2022, Bahetnur & Lee 2023, Haque et al. 2024, González-Díaz et al. 2025). The dissolved concentrations of As, Ba, and B were particularly elevated in the Madawa watershed (Table 5). These metals may originate from shared sources, as indicated by their low but significant positive correlation (Fig. 2). Such patterns are likely linked to agricultural practices and residential waste inputs in Madawa, where large areas adjacent to the river are dominated by cornfields (Table A1). The use of As, Ba, and B in pesticides, fungicides, and fertilizers for crops has been recorded in many studies and may be a possible source of these metals in this case (Castro & Brighenti 2007, Coupe & Capel 2015, Upadhyay et al. 2018, Nejad & Etesami 2020, Sundaresan et al. 2023).

Although the use of chemical pesticides persists in Indonesia (Prajawahyudo et al. 2022, Ismindarto et al. 2024), considerable efforts have been made to reduce their application owing to environmental concerns (Maryono &

Irham 2001). Initiatives promoting the use of bio-organic pesticides have been organized by the local government in the NTB region since 2015 (BPTP NTB 2019) and could be expanded to further diminish the reliance on chemical pesticides in the Hu'u District. Although these metals were found at higher concentrations in Madawa, their levels remained within water quality standards, suggesting that their occurrence may be linked to residues from historical use in the area. Elevated Ba concentrations were also detected in Ncangga, although they were still lower than those in Madawa (Table 5 and Fig. 3). This pattern may be related to the predominance of wildwood areas in the upstream region, combined with cornfield activities in the lower parts of the watershed (Table 1).

Dissolved Fe, Mn, and Zn concentrations were higher in the Hu'u District watersheds (Table 5 and Fig. 3), likely reflecting similar sources, as indicated by their significant but weak positive correlations (Fig. 2). The Hu'u District watershed experiences substantial riverine activity from upstream to downstream and features mixed agricultural land use, including corn and paddy fields near settlements (Table 1). Watersheds with more intensive land use generally showed higher metal concentrations, as shown in Fig. 4. As previously noted, the Fe, Mn, and Zn levels are closely linked to agricultural practices and domestic waste. Although elevated Mn and Zn concentrations were also detected in Madawa, they were lower than those in the Hu'u District, likely reflecting the more limited agricultural activity, which is primarily restricted to cornfields in Madawa. Overall, the Hu'u watersheds showed the greatest influence from agriculture and settlements, whereas watersheds dominated by wildwood and natural areas, such as Ncangga, Doro, Sama, and Oepana, formed closer clusters (Fig. 4).

Geological formations and local mineralization may also contribute to the presence of soluble metals such As, Ba, B, Fe, Mn, and Zn in this area. Sumbawa Island is geologically active, experiencing tectonic plate movements, and can be classified as a seismic region (Intan 2016). Tectonic activity in the Hu'u District has formed geological structures that influence the landscape, hydrology, and mineralization (Intan, 2016). Petrographic analysis of the Hu'u District has identified several rock types, including alluvial deposits, reef limestone, volcanic breccia, tuff, and andesite (Sofyan & Fadhlan 2004, Intan 2016). These rocks are associated with various metal-bearing minerals. For instance, Fe-Mn concentrations have been linked to volcanic breccia in mineralized volcanic systems (Berdnikov et al. 2021), and higher Zn concentrations have been found in alluvial sediments of rivers (Sajn et al. 2008). However, further in-depth studies are required to fully evaluate this factor.

4.2. Strengths and Limitations

Censored data are common in environmental studies, requiring methods that properly handle observations below the detection limits (Wood et al. 2011). The Kaplan–Meier estimator is widely used for this purpose because it accommodates censored values without substitution and is available in most statistical software packages (Smith 2011, Helsel 2012). However, its reliability decreases with small samples or high censoring, and it cannot be applied to datasets composed entirely of censored values (Helsel 2012, Zhao et al. 2011). Although its asymptotic properties are well established (Breslow & Crowley 1974), the approximation performs poorly in small datasets (Borgan & Liestøl 1990). To improve inference under these conditions, alternative approaches such as data transformations (e.g., log, logit, log-minus-log, or arcsine square-root) are recommended because they can yield more robust results in small or heavily censored datasets (Nagashima et al. 2021). Several recommendations and limitations are outlined based on the findings of this study.

i) Carefully define the objectives and deliverables during the planning stage, considering the high proportion of censored data and the presence of multiple detection limits (McGrory et al. 2020). For example, implementing stricter sampling protocols and maintaining consistent analytical methods, including the use of blank and replicate samples, could help reduce variability in detection limits and improve the likelihood of measuring actual concentrations,

ii) Testing for differences between years, as well as interactions among year, location, and season, was not possible due to dataset size constraints, as no two samples collected within the same year contained uncensored values, limiting the ability to assess the effect of year on both season and location,

iii) Consistent long-term monitoring with stable sample sizes will be necessary to observe trends in metal concentrations or other environmental elements over time (Gadd et al. 2024) to better understand the complexity of temporal variability,

iv) To gain deeper insight into the sources of heavy metals and enhance interpretative capacity, future studies should incorporate additional parameters, including in situ field measurements, nutrient sampling and analysis, and biological assessments.

5. CONCLUSIONS

Analysis of dissolved metals in freshwater rivers showed that a large proportion of the data fell below detection limits. The key findings of this study are as follows:

i) Of the 13 dissolved metals examined, cadmium (Cd), chromium (Cr (VI)), mercury (Hg), lead (Pb), and selenium (Se) were rarely detected, with over 90% of values censored,

ii) From 2019 to 2023, dissolved metal concentrations generally remained below the water quality standards set by the Government of Indonesia (GoI) for Classes II and III, except for copper (Cu), which exceeded the limit in the Hu'u River during the wet season of 2019. Manganese (Mn) concentrations also surpassed the FAO standard in five watersheds during 2019, 2020, and 2022,

iii) Censored data analysis revealed no significant seasonal effects on dissolved metal concentrations, as wet- and dry-season samples showed no statistical differences,

iv) Watershed characteristics and surrounding land use significantly influenced six parameters: arsenic (As), barium (Ba), boron (B), iron (Fe), manganese (Mn), and zinc (Zn). Higher concentrations of these metals are likely associated with agricultural practices and domestic discharges.

In general, using censored data analysis based on Kaplan-Meier estimates yields more valuable insights for presenting results on heavy metal concentrations in water. Although this approach is not yet fully optimized, especially when censored data exceeds 80%, it remains a valuable tool for supporting water quality assessment and management.

6. DATA AVAILABILITY

The supplementary data is available at https://doi.org/10.6084/m9.figshare.32915180

7. REFERENCES

Adano, A.J., Marcus, N.D., Magaji, J.I. and Opaluwa, O.D., 2023. Assessment of seasonal variation in heavy metal status of a lotic ecosystem in the Federal Capital Territory, Abuja, North Central Nigeria. *Makara Journal of Science*, 27(1), pp.264–272. [DOI]

Ahamad, M.I., Yao, Z., Ren, L., Zhang, C., Li, T., Lu, H., Mehmood, M.S., Rehman, A., Adil, M., Lu, S. and Feng, W., 2024. Impact of heavy metals on aquatic life and human health: a case study of River Ravi, Pakistan. *Frontiers in Marine Science*, 11(1), pp.1–15. [DOI]

Anani, O.A. and Olomukoro, J.O., 2021. Probabilistic risk assessment and water quality index of a tropical delta river. *PeerJ*, 9(1), pp.1–15. [DOI]

Anyanwu, E.D., Okoboshi, A.C., Adetunji, O.G. and Onyiwalu, F.N., 2024. Spatio-temporal variations and pollution status of heavy metals in Ahi River, Ohiya, Umuahia, Nigeria. *Journal of Applied Research in Water and Wastewater*, 11(1), pp.1–7. [DOI]

Arifin, Z., Sukartono, S., Susilawati, L.E., Kusumo, B.H. and Yasin, I., 2019. Performance of maize under two different methods of fertilizer application in semi-arid tropic Dompu, Indonesia. *Journal of Physics: Conference Series*, 1402(2), pp.1–8. [DOI]

Asokbunyarat, V. and Sirivithayapakorn, S., 2020. Heavy metals in sediments and water at the Chao Phraya River mouth, Thailand. *Thai Environmental Engineering Journal*, 34(1), pp.33–44.

Ayers, R.S. and Westcot, D.W., 1985. *Water Quality for Agriculture*. Food and Agriculture Organization of the United Nations, pp.174.

Bahetnur, Y. and Lee, W., 2023. Trace heavy metal contamination of urban water bodies in Central Asia: Its distribution, source detection, and probabilistic health risk assessment for recreational and household use of water. *ACS ES&T Water*, 3(5), pp.2765–2775. [DOI]

Berdnikov, N., Nevstruev, V., Kepezhinskas, P., Astapov, I. and Konovalova, N., 2021. Gold in mineralized volcanic systems from the Lesser Khingan Range (Russian Far East): Textural types, composition and possible origins. *Geosciences*, 11(2), pp.1–32. [DOI]

Bhardwaj, R. and Garg, J.K., 2017. Evaluation of heavy metal contamination using environmetrics and indexing approach for River Yamuna, Delhi stretch, India. *Water Science*, 31(1), pp.52–66.

Bons, K.C.A., Soekmono, A., Azhari, N., Restiawan, A., Tunggal, L., Yazid, A., Uljati, I.D., Samiadji, B.T., Panjaitan, T., Suryana, A., van Nes, A., Muijtjens, R., de Groot, D., Suherwan, S., de Bel, M. and Brinkman, J.J., 2016. *Indonesia Country Water Assessment*. Asian Development Bank, pp.1–50.

Borgan, Ø. and Liestøl, K., 1990. A note on confidence intervals and bands for the survival function based on transformations. *Scandinavian Journal of Statistics*, 17(1), pp.35–41.

Bosch, A.C., O'Neill, B., Sigge, G.O., Kerwath, S.E. and Hoffman, L.C., 2016. Heavy metals in marine fish meat and consumer health: A review. *Journal of the Science of Food and Agriculture*, 96(1), pp.32–48. [DOI]

Botutihe, D.N., Sappe, S.W., Kilo, A.K., La Kilo, J. and La Kilo, A., 2021. Lead metal in water and sediment: A case study of Rumbia River. *Acta Chimica Asiana*, 4(1), pp.187–191. [DOI]

BPTP NTB, 2019. *Annual Report of the Assessment Institute of Agricultural Technology of West Nusa Tenggara 2018*. Retrieved June 6, 2026, from https://ntb-bsip-ppid.pertanian.go.id/doc/229/LAP%20Tahunan%202018.pdf

Breslow, N. and Crowley, J., 1974. A large sample study of the life table and product-limit estimates under random censorship. *Annals of Statistics*, 2(3), pp.437–453.

Brown, R.J.C., 2008. The use and abuse of limits of detection in environmental analytical chemistry. *The Scientific World Journal*, 8(1), pp.796–801. [DOI]

Castro, C. and Brighenti, A.M., 2007. Compatibility of herbicides with boron fertilizers for weed desiccation and mineral nutrition of sunflower. *Helia*, 30(1), pp.1–14. [DOI]

Coupe, R.H. and Capel, P.D., 2015. Trends in pesticide use on soybean, corn and cotton since the introduction of major genetically modified crops in the United States. *Pest Management Science*, 72(1), pp.1013–1022. [DOI]

Ditjen PDASRH, 2021. *2021 Performance Report*. Ministry of Environment and Forestry, Jakarta, Indonesia. Retrieved June 6, 2026, from https://pdasrh.menlhk.go.id/vo/download.php?id=47&token=UZhHFZkKQjTaPMbFWkvvCDz2YySFhY

Duan, W., He, B., Nover, D., Yang, G., Chen, W., Meng, H., Zou, S. and Liu, C., 2016. Water quality assessment and pollution source identification of the eastern Poyang Lake basin using multivariate statistical methods. *Sustainability*, 8(2), pp.1–15. [DOI]

Gadd, J., McKenzie, A., Fraser, C. and Snelder, T., 2024. *Heavy Metals State and Trends in New Zealand Rivers: Analyses of National Data Ending in 2022*. Auckland, pp.85.

Garbarino, J.R., Hayes, H.C., Roth, D.A., Antweiler, R.C., Brinton, T.I. and Taylor, H.E., 1995. Contaminants in the Mississippi River, 1987–92. *U.S. Geological Survey Circular*, 1133(1), pp.1–20.

González-Díaz, R.L., de Anda, J., Shear, H., Padilla-Tovar, L.E., Lugo-Melchor, O.Y. and Olvera-Vargas, L.A., 2025. Assessment of heavy metals in surface waters of the Santiago–Guadalajara River Basin, Mexico. *Hydrology*, 12(2), pp.1–18. [DOI]

Government of Indonesia, 2021. *Water Quality Management and Control of Water Pollution, Indonesia*. Jakarta, pp.45.

Haque, M.A., Khatun, B., Jewel, M.A.S., Ara, J., Islam Kazal, M.S. and Hasan, J., 2024. Assessment of water quality and heavy metal indices in a tropical freshwater river for aquatic life and public health standard. *Ecological Indicators*, 169(1), pp.1–14. [DOI]

Hartiningsih, D., Diana, S., MS, Y., Ismail, M.R. and Sari, Q.W., 2024. Water quality pollution indices to assess the heavy metal contamination: A case study of the estuarine waters in Cirebon City (West Java, Indonesia) pre- and post-CARE COVID-19. *Environmental and Sustainability Indicators*, 21(1), 100318. [DOI]

Helsel, D.R., 2006. Fabricating data: How substituting values for nondetects can ruin results, and what can be done about it. *Chemosphere*, 65(1), pp.2434–2439. [DOI]

Helsel, D.R., 2012. *Statistics for Censored Environmental Data Using Minitab and R*. Wiley, New Jersey, pp.350.

Hewett, P. and Ganser, G.H., 2007. A comparison of several methods for analyzing censored data. *Annals of Occupational Hygiene*, 51(1), pp.611–632. [DOI]

Hites, R.A., 2019. Correcting for censored environmental measurements. *Environmental Science and Technology*, 53(1), pp.11059–11060. [DOI]

Huang, G.Z., Hsu, T.C., Yu, C.K., Huang, J.C. and Lin, T.C., 2020. Dilution and precipitation dominated regulation of stream water chemistry of a volcanic watershed. *Journal of Hydrology (Amsterdam)*, 583(1), 124564. [DOI]

Hwang, M., Lee, S.C., Park, J.-H., Choi, J. and Lee, H.-J., 2023. Statistical methods for handling nondetected results in food chemical monitoring data to improve food risk assessments. *Food Science & Nutrition*, 11(1), pp.5223–5235. [DOI]

Intan, F.S., 2016. Geological structures in the Huu area in relation to choose megalithic site location. *Jurnal Walennae*, 14(1), pp.11–22.

Islam, M.S., Rahman, M.M., Kabir, M.H., Hoq, M.E., Meghla, N.T., Suravi, S., Mamun, S.A. and Sarker, M.E., 2021. Seasonal dynamics of heavy metal concentrations in water, fish, and sediments from the Haor region of Bangladesh. *Pollution*, 7(1), pp.843–857. [DOI]

Ismindarto, A., Pudjiastuti, A.Q. and Sumarno, 2024. Rice farmer decisions regarding the use of chemical pesticides and its determining factors. *Journal of Socio-Economics and Agriculture*, 20(1), pp.77–92. Retrieved from https://journal.unhas.ac.id/index.php/jsep

Jeong, H., Byeon, E., Kim, D.H., Maszczyk, J.S. and Lee, E., 2023. Heavy metals and metalloids in aquatic invertebrates: A review of single/mixed forms, combination with other pollutants, and environmental factors. *Marine Pollution Bulletin*, 191(1), pp.1–15.

Jin, Y., Zhou, Q., Wang, X., Zhang, H., Yang, G., Lei, T., Mei, S., Yang, H., Liu, L., Yang, H., Lv, J. and Jiang, Y., 2022. Heavy metals in the mainstream water of the Yangtze River downstream: Distribution, sources and health risk assessment. *International Journal of Environmental Research and Public Health*, 19(10), pp.1–16. [DOI]

Julan, P. and Helsel, D., 2021. *NADA2: Data Analysis for Censored Environmental Data*. R package version 1.0.2. Retrieved June 6, 2026, from https://github.com/SwampThingPaul/NADA2

Kennish, M.J., 1998. Trace metal–sediment dynamics in estuaries: Pollution assessment. *Research in Environmental Contamination and Toxicology*, 155(1), pp.69–110.

Khan, M., Ellahi, A., Niaz, R., Ghoneim, M.E., Tag-eldin, E. and Rashid, A., 2022. Water quality assessment of alpine glacial blue water lakes and glacial-fed rivers. *Geomatics, Natural Hazards and Risk*, 13(1), pp.2597–2617. [DOI]

Khethi, M.T., Kadhim, Z.J. and Hamaza, M.F., 2013. Determination of some heavy metals in sediments of the Euphrates River in Nasiriya City, Iraq. *Environmental Pollution*, 6(1), pp.502–505.

Kittlaus, S., Kardos, M.K., Dudas, K.M., Weber, N., Clement, A., Petkova, S., Sukovic, D., Kucic Grgić, D., Kovacs, A., Kocman, D., Moldovan, C., Kirchner, M., Gabriel, O., Krampe, J., Zessner, M. and Zoboli, O., 2024. A harmonized Danube basin-wide multi-compartment concentration database to support inventories of micropollutant emissions to surface waters. *Environmental Sciences Europe*, 36(1), pp.1–18. [DOI]

Kumar, P., Matta, G. and Kumar, A., 2024. Harmonizing water quality: Integrating indices and chemometrics for sustainable management in the Ramganga River watershed. *Analytical Chemistry Letters*, 14(1), pp.29–47.

Laroche, C., Olteanu, M. and Rossi, F., 2022. Pesticide concentration monitoring: Investigating spatio-temporal patterns in left-censored data. *Environmetrics*, 34(1), pp.1–14. [DOI]

Li, H., Li, Y., Lee, M.K., Liu, Z. and Miao, C., 2015. Spatiotemporal analysis of heavy metal water pollution in transitional China. *Sustainability*, 7(1), pp.9067–9087. [DOI]

Lira, R.P.C., Antunes-Foschini, R. and Rocha, E.M., 2020. Survival analysis (Kaplan–Meier curves): A method to predict the future. *Arquivos Brasileiros de Oftalmologia*, 83(1), pp.v–vii. [DOI]

Manfreda, S., Miglino, D., Saddi, K.C., Jomaa, S., Eltner, A., Perks, M., Peña-Haro, S., Bogaard, T., van Emmerik, T.H.M., Mariani, S., Maddock, I., Tauro, F., Grimaldi, S., Zeng, Y., Gonçalves, G., Strelnikova, D., Bussettini, M., Marchetti, G., Lastoria, B., Su, Z. and Rode, M., 2024. Advancing river monitoring using image-based techniques: challenges and opportunities. *Hydrological Sciences Journal*, 69(1), pp.657–677. [DOI]

Maryono, J. and Irham, 2001. Efforts to reduce chemical pesticides use through integrated pest management program. *Jurnal Manusia dan Lingkungan*, 8(1), pp.30–36.

McGrory, E., Holian, E. and Morrison, L., 2020. Assessment of groundwater processes using censored data analysis incorporating non-detect chemical, physical, and biological data. *Journal of Contaminant Hydrology*, 235(1), pp.1–12. [DOI]

Mertz, W., 1993. Essential trace metals: new definitions based on new paradigms. *Nutrition Reviews*, 51(1), pp.287–295.

Millard, S.P., 2013. *EnvStats: An R Package for Environmental Statistics*. Springer, New York, pp.850. Retrieved from https://www.springer.com

Mofijur, M., Fattah, I.M.R., Alam, M.A., Islam, A.B.M.S., Ong, H.C., Rahman, S.M.A., Najafi, G., Ahmed, S.F., Uddin, M.A. and Mahlia, T.M.I., 2021. Impact of COVID-19 on the social, economic, environmental and energy domains: Lessons learnt from a global pandemic. *Sustainable Production and Consumption*, 26(1), pp.343–359. [DOI]

Mokarram, M., Saber, A. and Sheykhi, V., 2020. Effects of heavy metal contamination on river water quality due to release of industrial effluents. *Journal of Cleaner Production*, 277(1), 123380. [DOI]

Nagashima, K., Noma, H., Sato, Y. and Gosho, M., 2021. Sample size calculations for single-arm survival studies using transformations of the Kaplan–Meier estimator. *Pharmaceutical Statistics*, 20(3), pp.499–511. [DOI]

Narendra, B.H., Siregar, C.A., Dharmawan, I.W.S., Sukmana, A., Pratiwi and Pramono, I.B., 2021. A review on sustainability of watershed management in Indonesia. *Sustainability*, 13(19), pp.1–29. [DOI]

Nejad, S.A.G. and Etesami, H., 2020. The importance of boron in plant nutrition. In: T.D.K.G. Deshmukh and R. (eds.) *Metalloids in Plants: Advances and Future Prospects*. John Wiley & Sons Ltd., pp.433–449.

Novita, E., Pradana, H.A., Purnomo, B.H. and Puspitasari, A.I., 2020. River water quality assessment in East Java, Indonesia. *Journal of Water and Land Development*, 47(1), pp.135–141. [DOI]

Ogden, T.L., 2010. Handling results below the level of detection. *Annals of Occupational Hygiene*, 54(1), pp.255–256. [DOI]

Ogungbile, P.O., Akande, J.A., Ogunbode, T.O. and Odekunle, O., 2020. Assessment of heavy metal levels of Agodi Reservoir in Ibadan, Nigeria. *Journal of Applied Sciences and Environmental Management*, 23(11), p.1969. [DOI]

Oluyemi, E.A., Feuyit, G., Oyekunle, J.A.O. and Ogunfowokan, A.O., 2008. Seasonal variations in heavy metal concentrations in soil and some selected crops at a landfill in Nigeria. *African Journal of Environmental Science and Technology*, 2(1), pp.89–96. Retrieved from http://www.academicjournals.org/AJest

Paryono, Nurliah, N. and Rahman, I. and Himawan, M.R., 2023. Distribution of coliform bacteria as an indicator of biological pollution in several water sources in Hu'u District, Dompu Regency. *Jurnal Sains Teknologi dan Lingkungan*, 9(2), pp.310–317. [DOI]

Pasco, J.A., Anderson, K.B., Williams, L.J., Stuart, A.L., Hyde, N.K. and Holloway-Kew, K.L., 2024. Dietary intakes of copper and selenium in association with bone mineral density. *Nutrients*, 16(16), pp.1–12. [DOI]

Prajawahyudo, T., Asiaka, F.K.P. and Ludang, E., 2022. The role of pesticide safety in agriculture for farmers and the environment. *Journal of Socio Economics Agricultural*, 17(1), pp.1–9.

Prayoga, G., Utomo, B. and Effendi, H., 2022. Heavy metals contamination level and water quality parameter conditions in Jatiluhur Reservoir, West Java, Indonesia. *Biotropia*, 29(1), pp.7–17. [DOI]

R Core Team, 2024. *R: A Language and Environment for Statistical Computing*. Retrieved June 6, 2026, from https://www.R-project.org/

Razak, M.R., Aris, A.Z., Zakaria, N.A.C., Wee, S.Y. and Ismail, N.A.H., 2021. Accumulation and risk assessment of heavy metals employing species sensitivity distributions in Linggi River, Negeri Sembilan, Malaysia. *Ecotoxicology and Environmental Safety*, 211(1), pp.1–12. [DOI]

Rozana, K., Sukirno, S., Prabasiwi, D.S. and Murniasih, S., 2020. Assessment of heavy metals concentration in the water around the area of Adipala Cilacap steam power plant using neutron activation analysis. *Journal of Physics: Conference Series*, 1436(1), 012084. [DOI]

Sajn, R., Halamic, J., Peh, Z. and Galovic, L., 2008. Heavy metals in alluvial sediments of the River Drava (Slovenia and Croatia). *Berichte der Geologischen Bundesanstalt*, 77(1), pp.61–62. Retrieved from www.geologie.ac.at

Saturday, A., Kangume, S. and Bamwerinde, W., 2023. Content and dynamics of nutrients in the surface water of shallow Lake Mulehe in Kisoro District, South–western Uganda. *Applied Water Science*, 13(1), pp.1–15. [DOI]

She, N., 1997. Analyzing censored water quality data using a non-parametric approach. *Journal of the American Water Resources Association*, 33(1), pp.615–624.

Shoari, N. and Dube, J.S., 2018. Toward improved analysis of concentration data: Embracing nondetects. *Environmental Toxicology and Chemistry*, 37(1), pp.643–656. [DOI]

Simmonet-Laprade, C., Budzinski, H., Babut, M., Le Menach, K., Munoz, G., Lauzent, M., Ferrari, B.J.D. and Labadie, P., 2019. Investigation of the spatial variability of poly- and perfluoroalkyl substance trophic magnification in selected riverine ecosystems. *Science of the Total Environment*, 686(1), pp.393–401.

Singh, A., Maichle, R. and Lee, S., 2006. *On the Computation of a 95% Upper Confidence Limit of the Unknown Population Mean Based upon Data Sets with Below Detection Limit Observations*. EPA/600/R-06/022. Office of Research and Development, USEPA, pp.45.

Smith, C.J., 2011. Analysing censored data using Kaplan–Meier methods, survival analysis. *Phlebology*, 26(3), pp.173–174. [DOI]

Sofyan, A. and Fadhlan, I.S.M., 2004. *Research on the Environmental Factors Supporting Human Life in the Past at Archaeological Sites in Dompu Regency, West Nusa Tenggara*. Dompu, pp.60.

Srivastava, P.K., Malhi, R.K.M., Pandey, P.C., Anand, A., Singh, P., Pandey, M.K. and Gupta, A., 2020. Revisiting hyperspectral remote sensing: origin, processing, applications and way forward. In: P.C. Pandey, P.K. Srivastava, H. Balzter, B. Bhattacharya and G.P. Petropoulos (eds.) *Earth Observation, Hyperspectral Remote Sensing*. Elsevier, pp.3–21.

Sulistiyowati, E. and Uyun, S., 2021. The evaluation of a website for participatory water quality monitoring of rivers in Indonesia. In: *Advances in Engineering Research, Volume 211, Proceedings of the International Conference on Science and Engineering (ICSE-UIN-SUKA 2021)*, pp.112–115. [DOI]

Sun, X. and Wang, Y., 2024. Conformal prediction with censored data using Kaplan–Meier method. *Journal of Physics: Conference Series*, 2898(1), pp.1–10. [DOI]

Sundaresan, P., Karikalan, N., Na, J.H. and Lee, T.Y., 2023. Design and investigation of barium vanadate nanoflakes incorporated on the multi-layered graphene nanocomposite: An efficient electrocatalyst for the rapid determination of hazardous insecticide methiocarb in environmental media. *Journal of Environmental Chemical Engineering*, 11(1), pp.1–12. [DOI]

Supangat, A.B., Agus, C., Wahyuningrum, N., Indrawati, D.R. and Purwanto, 2021. Soil and water conservation planning toward sustainable management of upstream watershed in Indonesia. In: W.L. Filho, U.M. Azeiteiro and A.F.F. Setti (eds.) *Sustainability in Natural Resources Management and Land Planning*. Springer, pp.77–91.

Supangat, A.B., Basuki, T.M., Indrajaya, Y., Setiawan, O., Wahyuningrum, N., Purwanto, P.B., Putra, E., Savitri, E., Indrawati, D.R., Auliyani, D. and Nandini, R., 2023. Sustainable management for healthy and productive watersheds in Indonesia. *Land*, 12(11), pp.1–15. [DOI]

Surbakti, E.P., Iswantari, A., Effendi, H. and Sulistiono, 2021. Distribution of dissolved heavy metals Hg, Pb, Cd, and As in Bojonegara Coastal Waters, Banten Bay. *IOP Conference Series: Earth and Environmental Science*, 744(1), 012085. [DOI]

Suyatna, I., Sulityawati, Adnan, A., Syahrir, M., Ghitarina, G., Abdunnur, A. and Saleh, S., 2017. Heavy metal levels in water and fish samples from coastal waters of Mahakam Delta, Kutai Kartanegara District, East Kalimantan, Indonesia. *AACL Bioflux*, 10(1), pp.1319–1329. Retrieved from http://www.bioflux.com.ro/aacl

Taylor, J.M.G., Murray, S. and Hsu, C.-H., 2002. Survival estimation and testing via multiple imputation. *Statistics and Probability Letters*, 58(1), pp.221–232.

Thieu, V.V.D., Dinh, T.T.H., Nguyen, T.T.T., Nguyen, T.L.C., Nguyen, B.A. and Pham, A.D., 2022. Assessment of heavy metal pollution in the surface water of the [DOI]-Cho Dem-Ben Luc Rivers, Vietnam. *Inzynieria Mineralna*, 1(1), pp.85–90. [DOI]

Tolkou, A.K., Toubanaki, D.K. and Kyzas, G.Z., 2023. Detection of arsenic, chromium, cadmium, lead, and mercury in fish: Effects on the sustainable and healthy development of aquatic life and human consumers. *Sustainability*, 15(23), pp.1–15. [DOI]

Travis, R.E., Wilkins, K.L. and Kephart, C.M., 2023. *Assessing Escherichia coli and Microbial Source Tracking Markers in the Rio Grande in the South Valley, Albuquerque, New Mexico, 2020–21*. New Mexico, pp.55.

Upadhyay, M.K., Shukla, A., Yadav, P. and Srivastava, S., 2018. A review of arsenic in crops, vegetables, animals, and food products. *Food Chemistry*, 276(1), pp.608–618.

Valencia-Avellan, M., Slack, R., Stockdale, A. and Mortimer, R.J.G., 2017. Effect of episodic rainfall on aqueous metal mobility from historical mine sites. *Environmental Chemistry*, 14(1), pp.469–475. [DOI]

Verbovšek, T., 2011. A comparison of parameters below the limit of detection in geochemical analyses by substitution methods. *RMZ-Material and Geoenvironment*, 58(1), pp.393–404.

Whitehead, A.L., 2019. *Spatial Modelling of River Water-Quality State: Incorporating Monitoring Data from 2013 to 2017*. Christchurch. Retrieved June 6, 2026, from https://www.mfe.govt.nz/publications/fresh-water/spatial-modelling-of-river-water-quality-state-incorporating-monitoring

William, F.B., Viswanathan, P.M. and Ramasamy, N., 2024. Spatial and temporal distribution of geochemical elements and their processes in different size fractions – Miri River (NW Borneo). *Kuwait Journal of Science*, 51(1), pp.1–12. [DOI]

Wood, M.D., Beresford, N.A. and Copplestone, D., 2011. Limit of

detection values in data analysis: Do they matter? *Radioprotection*, 46(3), S85–S90. [DOI]

WSP, 2023. *Sumbawa Timur Mining: Preliminary Hu'u Environmental Terrestrial Baseline Studies (Wet & Dry Seasons) Physical and Chemical*. Jakarta, pp.120.

Zahran, M.A.E.-K., El-Amier, Y.A., Elnaggar, A.A., Mohamed, H.A.E.-A. and El-Alfy, M.A.E.-H., 2015. Assessment and distribution of heavy metals pollutants in Manzala Lake, Egypt. *Journal of Geoscience and Environment Protection*, 3(6), pp.107–122. [DOI]

Zhang, W., Ma, L., Abuduwaili, J., Ge, Y., Issanova, G. and Saparov, G., 2020. Distribution characteristics and assessment of heavy metals in the surface water of the Syr Darya River, Kazakhstan. *Polish Journal of Environmental Studies*, 29(2), pp.979–988. [DOI]

Zhao, J., Fu, G., Lei, K. and Li, Y., 2011. Multivariate analysis of surface water quality in the Three Gorges area of China and implications for water management. *Journal of Environmental Sciences*, 23(11), pp.1460–1471. [DOI]

Zhou, X., Wang, Y.P. and Song, Z., 2022. Heavy metal contamination and ecological risk assessments in urban mangrove sediments in Zhanjiang Bay, South China. *ACS Omega*, 7(1), pp.21306–21316. [DOI]

Nature Environment and Pollution Technology
An International Quarterly Scientific Journal

p-ISSN: 0972-6268
(Print copies up to 2016)
e-ISSN: 2395-3454

Vol. 25 | No. 3 | Article ID B4409 | 2026

Original Research Paper

https://doi.org/10.46488/NEPT.2026.v25i03.B4409

Open Access Journal

Black Gold from the Fields: Obtaining Pyrolytic Biochar from Agricultural Wastes at Various Pyrolysis Temperatures

Pooja Sarolkar, Girish Pathade and Wasim Bagwan

Krishna Institute of Science and Technology, Krishna Vishwa Vidyapeeth (Deemed to be University), Karad, 415539, Maharashtra, India

†Corresponding author: Pooja S. Sarolkar; sarolkarpuja07@gmail.com

Abbreviation: Nat. Env. & Poll. Technol.
Website: www.neptjournal.com

Received: 23-10-2025
Revised: 10-12-2025
Accepted: 15-12-2025

Key Words:

Biochar
Pyrolysis
Finger millet hulls
Agricultural residue
Soil amendment
Carbon sequestration

Citation for the Paper:

Sarolkar, P., Pathade, G. and Bagwan, W., 2026. Black gold from the fields: Obtaining pyrolytic biochar from agricultural wastes at various pyrolysis temperatures. *Nature Environment and Pollution Technology*, 25(3), B4409. https://doi.org/10.46488/NEPT.2026.v25i03.B4409

Note: From 2025, the journal has adopted the use of Article IDs in citations instead of traditional consecutive page numbers. Each article is now given individual page ranges starting from page 1.

Copyright: © 2026 by the authors
Licensee: Technoscience Publications
This article is an open access article distributed under the terms and conditions of the Creative Commons Attribution (CC BY) license (https://creativecommons.org/licenses/by/4.0/).

ABSTRACT

India produces a large amount of agricultural residues, traditionally disposed of through open burning. Such practices have negative health and environmental impacts. Converting waste via pyrolysis into biochar offers a sustainable strategy for enhancing soil fertility, carbon sequestration, and resource recovery. Although many studies have examined the influence of pyrolysis temperature on biochar properties, most focus on feedstocks like rice husk and woody biomass, with little attention given to underused residues such as finger millet husk. This study evaluated four agricultural residues, finger millet husk, rice husk, sawdust, and hardwood, depolymerized at 300, 400, 500, and 600°C, respectively. The resulting biochars underwent proximate and ultimate analysis, physicochemical characterization, and assessments of pore size and surface morphology. Results showed that increasing pyrolysis temperature reduced biochar yield and volatile matter, while increasing fixed carbon, pH, organic carbon content, porosity, and surface area. Variations also depended on feedstock composition. Biochar from finger millet husk at 300°C was flaky, chemically active, and suitable for microbial colonization, whereas hardwood biochar at 600°C was highly carbonized, porous, stable, and effective for pollutant adsorption and long-term carbon sequestration. This research introduces finger millet husk as a novel biochar precursor, linking specific properties to potential agricultural and environmental applications. Additionally, the study emphasizes how pyrolysis temperature influences biochar characteristics and their practical uses.

1. INTRODUCTION

As a developing country, India relies heavily on agriculture, which employs approximately 70% of the population (Mathur & Srivastava 2019). Annually, agricultural activities produce around 500 million tons of waste residues (Nagar & Kumar 2024). Typically, Indian farmers manage this biomass through traditional methods, mainly open-field burning, which worsens air quality and poses health risks. Recent studies have shown that these burning practices significantly impact population dynamics, meteorological stability, and environmental conditions from 2003 to 2019 (Lan et al. 2022). Additionally, between 2011 and 2020, biomass burning contributed to about 75% of atmospheric pollution in India, causing periodic spikes in suspended particulate matter (PM10 and PM2.5) and leading to serious respiratory and cardiovascular health problems (Gupta 2019).

In contrast, a renewable carbonaceous biochar derived from waste biomass through pyrolysis serves as an environmentally friendly substitute. The pyrolysis process reduces pollutant emissions and produces bioenergy that can replace non-renewable energy sources (Chatterjee et al. 2020, Nadarajah et al. 2024). Biochar, a stable carbon-rich material created by pyrolysis, is commonly used as a soil amendment to improve soil fertility (Amalina et al. 2022). Numerous studies have explored its applications, including reducing greenhouse gas emissions, enhancing

soil fertility, stimulating microbial growth, and functioning as an adsorbent for removing pollutants from wastewater (Abrishamkesh et al. 2015, Awasthi et al. 2020, Ge et al. 2019, Hossain et al. 2020, Muzyka et al. 2023, Wang et al. 2020). Biochar shows particular promise for specific biomass applications. For example, biochar from finger millet has been reported to lower pesticide soil toxicity and restore biological health (Jena et al. 2025). Rice husk biochar increases soil enzyme activity and beneficial microorganism populations such as *Massilia*, *Bacillus*, and *Trichocladium*, while also reducing loamy soil erosion in semi-arid areas (Akumuntu et al. 2024, Ahmadi et al. 2020). Similarly, sawdust biochar has a high adsorption capacity, which can be used to remove cadmium and lead from wastewater (Cheng et al. 2021), and it also shows potential for purifying industrial effluents contaminated with cyanide and other toxic metals (Manyuchi et al. 2022).

The efficacy of biochar and its physicochemical properties largely depend on production conditions, including the type of biomass and its composition, pyrolysis temperature, heating rate, and residence time (Mukherjee et al. 2022). For instance, increasing the pyrolysis temperature results in higher pH, ash content, and surface area, while reducing yield and O/C ratio (Roshan et al. 2023). Consequently, biochar produced at lower pyrolysis temperatures may offer a balance between energy efficiency and productivity enhancement, especially when using tropical agricultural by-products for carbon sequestration (Song et al. 2023). In this context, biochar derived from various biomass sources-such as forestry hardwoods, industrial sawdust, and agricultural wastes like rice husk and finger millet hulls-should be thoroughly studied for surface morphology, mineral composition, thermal behavior, heavy metal content, and both proximate and ultimate analyses. This paper aims to characterize and compare biochar from these feedstocks for its potential as a soil amendment and for carbon sequestration efforts.

2. MATERIALS AND METHODS

2.1. Collecting the Agricultural Residues and Production of Biochar

All agricultural wastes, including finger millet hull, sawdust, rice husk, and hardwood, were collected from farms and air-dried in the shade for 15 days. They were then cut into 2-3 cm pieces and stored in airtight zip-lock bags to reduce moisture. The experiments took place at Krishna Institute of Science and Technology, Krishna Vishva Vidyapeeth, Karad, Maharashtra, from January to April 2025. Biochar was produced from selected agro-wastes, specifically rice husk, sawdust, finger millet hull, and hardwood. These residues were thermally converted in a muffle furnace. Before pyrolysis, all biomass samples were oven-dried at 105°C for 24 h. A known weight of biomass was placed in a ceramic crucible with a tight-fitting cover and then transferred to the muffle furnace, where pyrolysis was carried out at temperatures of 300°C, 400°C, 500°C, and 600°C. The heating rate was maintained at 10°C per minute, with a residence time of 30 minutes at each temperature. After pyrolysis, the biomass was ground using a suitable grinder. The ground biochar was then sieved through a 150-micrometer mesh and stored in an airtight glass bottle to prevent moisture uptake and contamination.

2.2. Biochar Characterizations

2.2.1. Biochar Yield

The biochar yield, defined as the mass of pyrolysis products relative to the initial mass of raw material, was calculated using Eq. 1 from Khater et al. (2024) and Qin et al. (2020).

$$\text{Biochar yield (\%)} = \frac{\text{Weight of biochar after pyrolysis (g)}}{\text{Weight of feedstock before pyrolysis (g)}} \times 100 \quad ...(1)$$

2.2.2. Physical, Chemical, and Proximate Analysis of Biochar

The composition was mechanically shaken for one hour at 25°C, followed by a 30-min standing period. The pH and electrical conductivity (EC) of each biochar sample were then measured using pH and EC meters, with a biochar to distilled water ratio of 1:10 (Singh et al. 2017). To determine water holding capacity (WHC), distilled water and a 1:40 (w/v) biochar mixture were shaken for three days at 25°C, dried for twelve h at 105°C, and the WHC% was calculated using Equation (2) (Zhang et al. 2024). Organic carbon content in biochar was analyzed using the Walkley and Black (1934) method, as described by Rabbani et al. (2020). Additionally, estimates for N, P, K, Ca, and Mg were obtained following AOAC (2003).

Water Holding Capacity

$$\text{Water Holding Capacity (\%)} = \frac{m_{sb} - m_{fp} - m_{bc})}{m_{bc}} \times 100 \quad ...(2)$$

Where:

- m_{sb} = mass of the water-soaked biochar with filter paper
- m_{fp} = mass of water-soaked filter paper
- m_{bc} = mass of dried biochar

The inherent moisture, volatile matter, ash, and fixed carbon content of biochar were measured using equations 3, 4, 5, and 6, respectively, following ASTM-1762-82 standards (Dhar et al. 2020). The moisture content was determined by

drying the biochar at 105°C for 2 h, and the percentage of inherent moisture was calculated accordingly.

Inherent Moisture Content

$$\text{Inherent Moisture (wt.\%)} = \frac{W_{ad} - W_{105}}{W_{ad}} \times 100 \quad ...(3)$$

Where:

- W_{ad} = weight of air-dried biochar sample
- W_{105} = weight of biochar sample dried at 105°C for 2 h

1 g air-dried biochar sample (preheated at 105°C for 2 h) was heated at 950°C for 6 min in a furnace, and the percentage of volatile matter was calculated as follows,

Volatile Matter Content

$$\text{Volatile Matter (wt.\%)} = \frac{W_{105} - W_{950}}{W_{ad}} \times 100 \quad ...(4)$$

Where:

- W_{105} = weight of biochar sample dried at
- W_{950} = weight of biochar sample after heating at for 6 minutes
- W_{ad} = weight of air-dried biochar sample

A 1-g air-dried mass of 105°C was heated at the muffle furnace at 750°C for 6 h to determine (wt.%) ash content as follows:

Ash Content

$$\text{Ash (wt.\%)} = \frac{W_{105} - W_{750}}{W_{ad}} \times 100 \quad ...(5)$$

Where:

- W_{105} = weight of biochar sample dried at
- W_{750} = weight of biochar sample after heating at for 6 h
- W_{ad} = weight of air-dried biochar sample

Fixed carbon was calculated on a dry basis and estimated as follows:

Fixed Carbon Content

Fixed Carbon (wt.%) = 100 – [Ash (wt.%) + Volatile Matter (wt.%)] …(6)

2.2.3. Elemental Analysis

The elemental composition (C, H, N, S) of four biochar samples was determined using an elemental analyzer (JEOL JSM-IT200, YCIS Satara).

2.2.4. Brunauer-Emmett-Teller (BET), Scanning Electron Microscopy (SEM), and Surface Functional Groups

The specific surface areas of the activated carbons (ACs) were measured using an Autosorb1C instrument (Quantachrome, Japan). The specific surface area (SSA), BJH pore volume, and pore size distributions were derived from nitrogen adsorption/desorption isotherms using a Multipoint BET (Brunauer-Emmett-Teller) method, conducted with equipment obtained from the Physics Department of Shivaji University, Kolhapur. Surface morphology of the biochar was examined using SEM (YCIS, Satara). The surface functional groups present on the biochar samples were identified through Fourier transform infrared spectroscopy (FTIR) at Krishna Institute of Pharmacy, KVV, Karad. Prior to analysis, all samples were washed with deionized water to remove impurities, neutralized, dried at 105°C, and stored in airtight glass vials. Further sample preparation was carried out as per the requirements of specific analysis tests.

2.3. Statistical Analysis

Each experiment was conducted in triplicate, with results expressed as the mean ± SD. Pyrolysis temperature and biomass feedstock type influence biochar yield and properties (Excel 2021). Two-way ANOVAs were performed, followed by pairwise comparisons using Tukey's HSD test at a 95% confidence level ($p < 0.05$). One-way ANOVA analyses were applied within temperature treatments for each feedstock. The relationships between pyrolysis temperature and key biochar parameters were assessed using Pearson's.

3. RESULTS

3.1. Physicochemical Properties

3.1.1. Physical Properties

Table 1 presents the physical properties-namely moisture content, water holding capacity (WHC), and porosity-of biochar derived from finger millet hull, sawdust, rice husk, and hardwoods, produced at various pyrolysis temperatures (300°C, 400°C, 500°C, and 600°C). The data show that moisture content decreases as pyrolysis temperature increases. Specifically, moisture content reduced from 4.8%, 4.2%, and 2.8% to 2.5% for rice husk, sawdust, finger millet hulls, and hardwoods, respectively, across the temperature range. Biochar produced from finger millet hulls at 300°C exhibited the highest moisture content (4.8%), while hardwood-derived biochar at 600°C showed the lowest (2.8%). This trend indicates that higher pyrolysis temperatures promote water removal, likely because increased temperatures enhance water extraction efficiency and make the biochar more stable and hydrophobic (Sathyabama et al. 2025). However, lower pyrolysis temperatures may retain more volatile substances, potentially affecting pore structure and WHC. Consequently,

Table 1: Physicochemical properties of different biochar types at different temperature ranges.

Properties	Biochar type			
	FMB	SDB	RHB	HWB
Moisture content [%]	4.8	2.5	4.2	2.8
Water Holding Capacity [%]	62	75	86	94
pH	6.1	7.2	7.7	8.2
Organic carbon [%]	20	32.86	26.31	66.22
N [%]	0.3	1.4	1.44	0.64
P [%]	0.01	0.013	0.012	0.015
K [%]	0.3	0.31	0.33	0.37
C: N	66.7:1	2.04:1	4.4:1	3.8:1
Ca [per 100 g]	10	51	45.5	53
Mg [Mequ]	6.3	8.5	8.8	11.2
Ca:Mg	1.18:1	8:1	3:1	6.2

Note: Finger millet hull biochar (FMB), sawdust biochar (SDB), rice husk biochar (RHB), and hardwood biochar (HWB)

an increase in pyrolysis temperature positively influences biochar WHC, as observed in studies showing WHC for finger millet hull, sawdust, rice husk, and hardwoods rising from 62% to 94%, suggesting initially low WHC that improves with higher temperatures (Ulusal et al. 2021).

3.1.2. Chemical Properties

The chemical structure of biochar varies depending on the feedstock and pyrolysis temperature. Table 1 presents the analyzed chemical properties of different biochar types (FMB, RHB, and HWB) produced at 300, 400, 500, and 600°C, including pH, electrical conductivity (EC), organic carbon content, total NPK, and calcium/magnesium levels. Higher pyrolysis temperatures increase the hydrogen potential of biochar by reducing functional groups (-COOH and -OH) at elevated temperatures, resulting in naturally alkaline biochar suitable for neutralizing acidic soils (Ahmed et al. 2024, Chellappan et al. 2018, El-Naggar et al. 2019, Roshan et al. 2023). At a lower pyrolysis temperature of 300°C, FMB exhibits a pH of 6.1, whereas HWB becomes alkaline with a pH of 8.2 at 600°C. Biochar serves as a superior liming material compared to conventional lime due to its content of base metals, (bi)carbonates, surface organic functional groups (OFGs), and soluble organic compounds, all of which help neutralize soil acidity through calcareous effects, cation exchange, and precipitation reactions (Liu et al. 2025). Conversely, the acidic active sites of biochar in saline soils can enhance plant growth and improve soil quality (Soothar et al. 2021). This suggests that soil salinity may decrease biochar acidity, and vice versa. Sovova et al. (2024) observed that the partially alkaline nature of biochar, along with its satisfactory internal porosity, could potentially enrich both acidic and partially acidic soils.

The results further indicate that organic carbon (OC) production is also influenced by pyrolysis temperature. Hardwood charred at 600°C exhibited the highest OC content (66.22%), while finger millet hulls showed the lowest OC content (20%) at a pyrolysis temperature of 300°C. This suggests that, regardless of feedstock type, higher temperatures promote carbon enrichment in the biochar matrix. Elevated levels of OC and fixed carbon (FC) contribute to increased soil organic carbon (SOC), which persists over time, inhibiting carbon mineralization and enhancing carbon sequestration potential (Bo et al. 2023). Consequently, increasing pyrolysis temperature enhances biochar's carbon content, creating a more durable medium for long-term carbon sequestration.

The maximum nitrogen content of 1.44% was recorded in rice husk biochar produced at a pyrolysis temperature of 500°C, while the lowest nitrogen content of 0.3% was found in finger millet hull biochar at 300°C. Results showed that phosphorus (P) and potassium (K) contents increased significantly with higher pyrolysis temperatures. The highest P (0.015%) and K (0.37%) contents were observed in hardwood biochar at 600°C, whereas the minimum P (0.01%) and K (0.3%) contents were in finger millet hull biochar at 300°C. Additionally, increasing the pyrolysis temperature from 300°C to 600°C led to rises in calcium (Ca) and magnesium (Mg) contents: Ca increased from 10 to 53, and Mg from 6.3 to 11 µmol per gram, following the order finger millet hull < sawdust < rice husk < hardwood biochar. These findings align with those reported by Khater et al., who observed that increasing the pyrolysis temperature from 400 to 800°C enhances P, K, Mg, and Ca contents in biochar (Khater et al. 2024).

3.2. Surface Area and Porosity

The surface area and porosity of biochar are influenced by the pyrolysis temperature. An increase in pyrolysis temperature causes the breakdown of organic matter, which enhances the biochar's surface area and porosity (Tomczyk et al. 2020). However, beyond certain temperature ranges, there is a formation of additional micropores, which can reduce overall porosity. This reduction may be due to the rising ash content at higher temperatures, as the ashes can fill the pore spaces (Feng et al. 2020, He et al. 2024, Ippolito et al. 2020, Khater et al. 2024). Additionally, porosity and surface area depend on the biomass type. As shown in Table 2, sawdust biochar produced at 400°C exhibits the highest porosity (13.38%) and surface area (30.45 $m^2.g^{-1}$), while rice husk biochar, produced at 500°C, shows the lowest values with porosity at 3.20% and surface area at 6.403 $m^2.g^{-1}$. Higher porosity and larger surface area improve absorption capacity, making biochar more effective at removing pollutants (Wyatalska et al. 2023).

3.3. Proximate Analysis and Yield of Biochar

Fig. 1 illustrates the differences in the content of volatile matter, ash, and fixed carbon at various pyrolysis temperatures (300-600°C) for different feedstocks, including finger millet hull, sawdust, rice husk, and hardwoods. Additionally, the biochar yield decreased from 74% to 26% as the pyrolysis temperature increased from 300°C to 600°C, influenced by factors such as the varying ratios of lignin and cellulose content. The formation of ash at high temperatures indicates increased stability of the carbon percentage in biochar (Khater et al. 2024). As shown in Fig. 1, the biochar yield for hardwoods, rice husk, sawdust, and finger millet hull was 37.1%, 31.5%, 29.8%, and 27.8%, respectively. Hardwood biochar (HWB) had the highest fixed carbon content, reaching 76.54% at 600°C, while the finger millet hull (FMB), sawdust (SDB), and rice husk (RHB) contained 51.61%, 55.39%, and 69.15%, respectively. This suggests that biochar produced at higher pyrolysis temperatures contains more fixed carbon (Toczydlowski et al. 2023). Due to its relatively high carbon content, biochar is a versatile resource with potential applications including use in chemical synthesis, activated carbon production, and as a soil conditioner (Ahmed et al. 2024).

The ash content of biochar increases at higher production temperatures compared to lower temperatures. Specifically,

Table 2: Porosity and specific surface area of different biochar types at different temperature ranges.

Biochar Sample	Specific surface area [Multi-Point BET] $m^2.g^{-1}$	Total pore volume [$cc.g^{-1}$]	Porosity [%]	Avg. pore radius [Å]	Radius [nm]	Avg. pore diameter [nm]
Finger millet	28.01	0.02496	9.74	1.782e+01 Å (17.82 Å)	1.782 nm	3.564 nm
Saw dust	21.857	0.02076	8.10	1.900e+01 Å (19.00 Å)	1.900 nm	3.800 nm
Rice husk	30.45	0.03430	13.38	2.253e+01 Å (22.53 Å)	2.253 nm	4.506 nm
Hard wood	6.403	0.008206	3.20	1.829e+01 Å (18.29 Å)	1.829 nm	3.658 nm

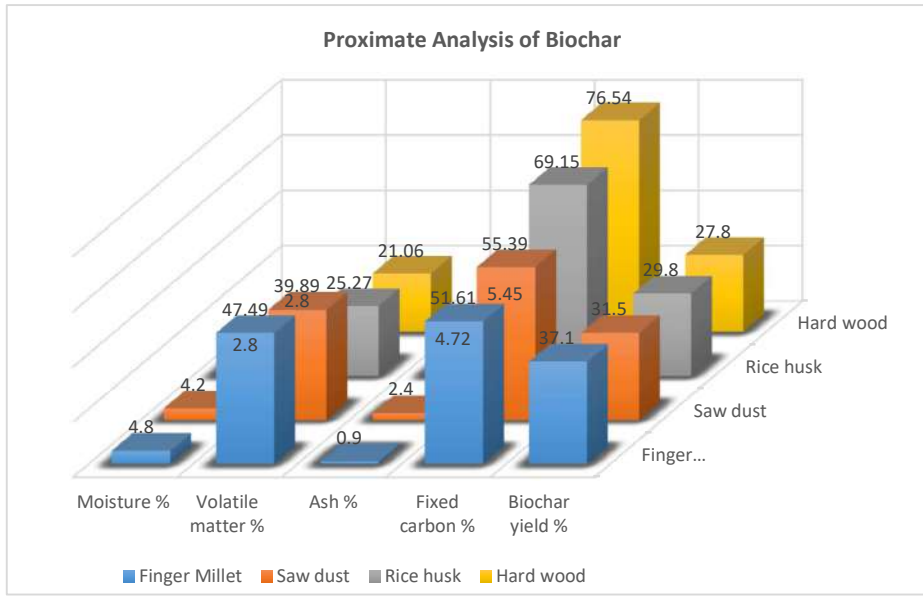


Fig. 1: Proximate analysis and yield of biochar types at different temperatures.

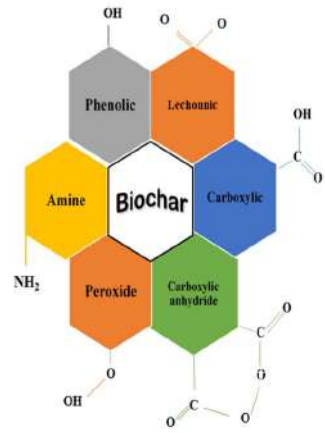


Fig. 2: Biochar containing surface functional groups.

the ash contents at 300, 400, 500, and 600°C are 0.9%, 2.4%, 4.72%, and 5.45%, respectively, for FMB, SDB, RHB, and HWB. Additionally, volatile matter tends to decrease as temperature rises. For example, FMB has a higher volatile content (47.49%) at 300°C than HWB, which has a lower volatile matter content (21.06%) at 600°C.

3.4. Surface Functional Groups

Biochar exhibits a range of functional groups on its surface, including hydroxyl (–OH), carboxyl (–COOH), lactonic (O–C=O), phenolic (–C=O), as well as peroxide and amine groups 22,23 (Fig. 2). These surface functional groups, particularly

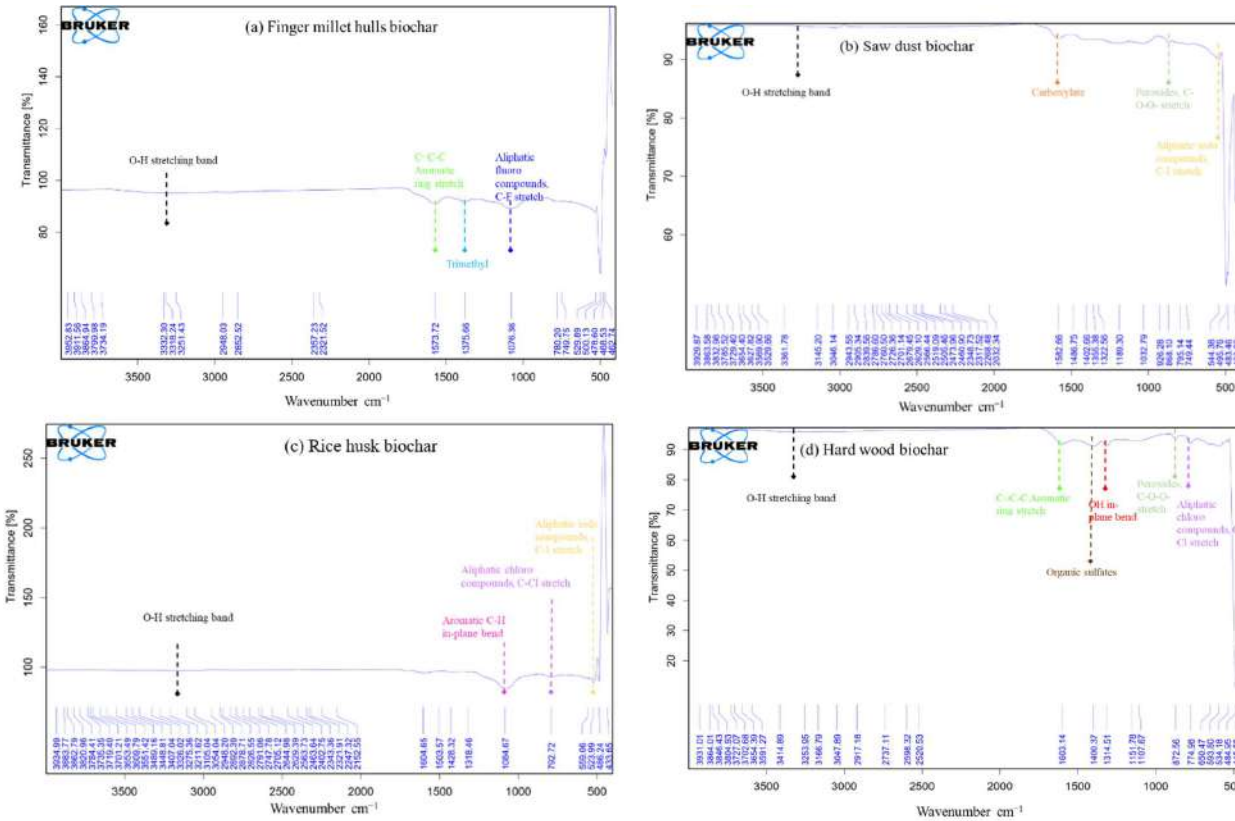


Fig. 3: FTIR spectra of biochar produced from (a) Finger millet, (b) Rice husk, (c) Sawdust, and (d) Hardwood.

C–O, C═O, and –OH, play a crucial role in contaminant decontamination and adsorption processes (Zhang et al. 2021). The structure of these groups is influenced by the molecular makeup of the biomass precursors and is largely determined by the pyrolysis temperature. For instance, cellulose and lignin primarily retain their structural features at 200–300°C, whereas biochar begins to lose most oxygen- and hydrogen-containing functional groups and becomes more aromatic at 500°C. Nevertheless, some functional groups, such as C=O in ketones and olefins, can survive even at 650°C (Zhang et al. 2020).

The surface functional groups and their quantification in numbers were determined using reference data from Coates (2000) and Nandiyanto et al. (2019). Fig. 3 illustrates variations in peak intensity, which occur because the concentration of specific functional groups is not uniform across samples [(a), (b), (c), and (d)]. The adsorption bands between 3360 and 3145 cm^{-1} confirm O-H stretching associated with hydroxyl groups. An increase in pyrolysis temperature reduces moisture retention, significantly influencing higher hydroxyl content, while weak aromatic C=C peaks indicate progressive thermal degradation or aromatization during biochar formation.

Peaks near 2940-2850 cm^{-1} correspond to C-H stretching vibrations of aliphatic $–CH_3$ and $–CH_2–$ groups, characteristic of cellulose and hemicellulose, observed in all four biochar samples [(a), (b), (c), and (d) Fig. 3] (Mujtaba et al. 2021). Additional functional groups identified include C=C–C aromatic ring stretching at 1615–1580 cm^{-1}, C–Cl stretching at 800-700 cm^{-1}, C–I stretching within 600-500 cm^{-1}, and C–F stretching between 1150 and 1000 cm^{-1}. The presence of trimethyl or tert-butyl groups was noted in the 1395–1385 cm^{-1} region. Other significant absorptions involved carboxylate groups (1610–1550 cm^{-1}), peroxides (C–O–O) at 890–820 cm^{-1}, organic sulfates at 1420–1370 cm^{-1}, and O-H in-plane bending at 1350-1260 cm^{-1}.

Collectively, these results demonstrate that pyrolysis conditions, biomass type, sample thickness, and particle size markedly influence the diversity and stability of surface functional groups on biochar, ultimately governing its chemical reactivity and environmental applications. The degree of carbonization notably affects biochar's surface functional morphology: highly carbonized biochar absorbs more IR radiation, decreasing transmittance and producing flatter or less intense peaks. Conversely, less carbonized or oxygen-rich samples exhibit higher transmittance and more prominent, distinct bands. Variations in mineral or ash content (e.g., silica in rice husk, carbonates in sawdust) further impact band intensity and sharpness due to their unique vibrational signatures.

3.5. Surface Morphology and Elemental Analysis

Fig. 4 depicts the surface morphology of biochar derived from four different agricultural waste materials: Finger Millet, Rice Husk, Sawdust, and Hardwood. All images were captured at 1500× magnification with a scale bar of 50 µm. The biochar made from finger millet hull at 300°C (a) exhibits irregular, flaky particles with a layered fractured surface, high porosity, and a rough texture, which are advantageous for adsorption applications and microbial colonization (Varkolu et al. 2025). The rice husk biochar produced at 400°C (b) appears dense with a grainy structure, featuring SiO_2 particles that are more angular and integrated, as well as higher porosity. This structure may facilitate the adsorption of organic pollutants in water through pi bonding, hydrogen bonding, and ligand binding (Li et al. 2023). Photographs of sawdust biochar at 500°C (c) show a less porous appearance with partly crushed particles, while hardwood biochar at 600°C (d) appears heterogeneous with broken fragments and a rough surface. Its microporous nature, due to a larger specific surface area and rough pore structure, makes it suitable for soil amendment and microbial carrier applications (Bolan et al. 2023).

The mass percentages of each element (C, O, Si, Ca, K, and Cl) are presented in Fig. 4 and Table 3. FMB, SDB, RHB, and HWB contain 6.87%, 80.97%, 59.85%, and 60.19% carbon, respectively. The elemental composition of finger millet biochar, as shown in Fig. 5, indicates a relatively low carbon content (61%) compared to other biochars, which typically have around 87%. The percentages of oxygen, silicon, chlorine, and potassium are 30.51%, 2.08%, 0.74%, and 4.80%, respectively. Rice husk biochar has a lower potassium content (approximately 1%) relative to FMB, along with higher silica content (8.21%) and similar carbon (59.85%) and oxygen (30.53%) levels. Sawdust biochar exhibits small quantities of oxygen (30.51%), silicon (16.57%), calcium (30.53%), and potassium (32.03%). Notably, oxygen (32.03%) and calcium (7.78%) contents are higher, while carbon (60.19%) is greater in H BW compared to others. The results also show that SDB contains less oxygen and more carbon. Potassium is only present in FMB, and calcium is found exclusively in SDB and HWB.

Table 3: Elemental analysis of biochar samples.

Biochar types	Elements [Mass %]					
	C	O	Si	Ca	K	Cl
Finger millet	61.87	30.51	2.08	-	4.80	0.74
Saw dust	80.97	16.57	0.60	1.86	-	-
Rice husk	59.85	30.53	8.21	-	1.41	-
Hardwood	60.19	32.03	-	7.78	-	-

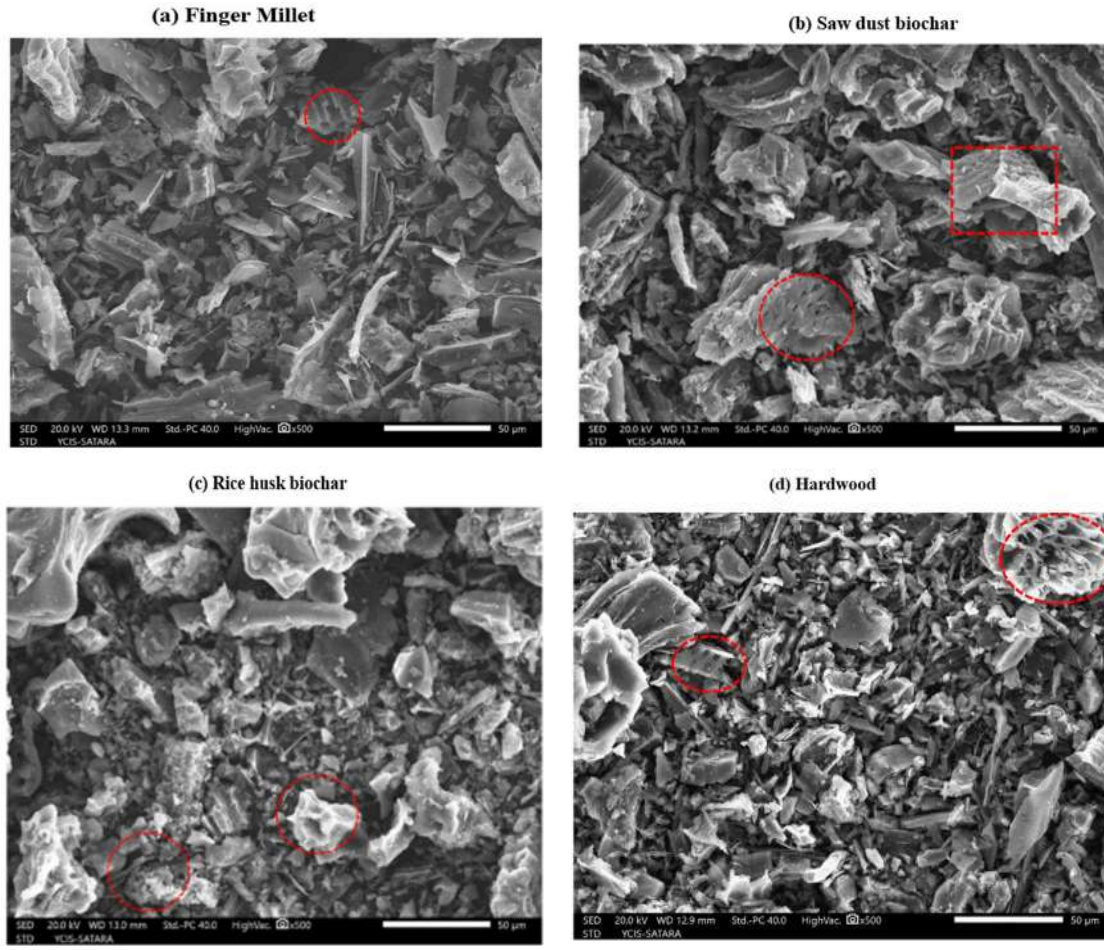


Fig. 4: SEM images of a) finger millet biochar, b) rice husk biochar, c) saw dust biochar, and d) hardwood biochar produced at 300, 400, 500 and 600°C, respectively.

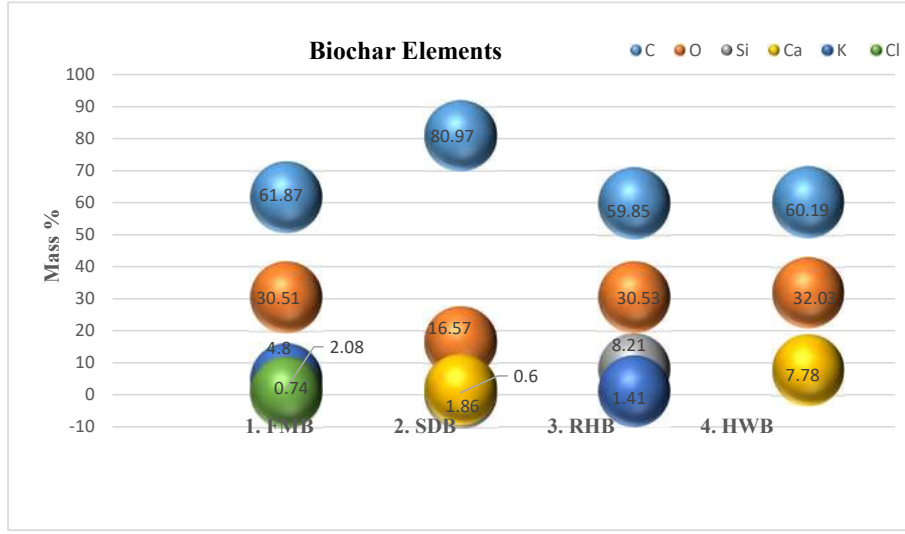


Fig. 5: Elemental composition: C, O, Si, Ca, K, Cl (%) of FMB, SDB, RHB and HWB.

4. DISCUSSION

The current study assessed how pyrolysis temperature influences the physicochemical properties, yield, elemental makeup, and surface features of biochar derived from four types of agricultural residues: sawdust, hardwood, rice husk, and finger millet hulls. As demonstrated consistently in numerous studies, pyrolysis temperature is a key factor that determines biochar quality (Mukherjee et al. 2022, Ippolito et al. 2020). Increasing the pyrolysis temperature from 300 to 600°C enhanced carbon stability, ash content, surface area, pH, and aromaticity, while it reduced biochar yield and volatile matter across all feedstocks. These findings align with the previously reported thermal decomposition behavior of lignocellulosic biomass by Qin et al. (2020) and Roshan et al. (2023).

Finger millet hull biochar (FMB), a relatively novel and underexplored precursor, exhibits characteristic flaky and fractured microstructures along with increased porosity at lower pyrolysis temperatures (300°C). These features enhance sorption capacity and support microbial colonization, aligning with findings by Zhang et al. (2021) and Varkolu et al. (2025), which indicate that adsorption and biological interactions are influenced by macroporous morphology and surface functional groups such as –OH, –COOH, and –C=O. Additionally, FMB maintains a diverse range of functional groups at lower pyrolysis temperatures, highlighting its potential for biological and environmental applications.

Hardwood biochar (HWB), produced at 600°C, exhibited the highest carbon stability, the greatest organic carbon content, increased aromaticity, and a reduction in polar surface groups. These characteristics are associated with enhanced resistance to microbial mineralization and suggest potential for long-term carbon sequestration (Bo et al. 2023, Song et al. 2023). SEM images supported previous research by Tomczyk et al. (2020) and Feng et al. (2020), confirming significant pore development and microstructural rearrangements at elevated temperatures.

In line with Li et al. (2023), rice husk biochar (RHB) showed a distinctive grainy texture and improved sorption capabilities for pollutant removal due to its higher silica content. Additionally, at 400–500°C, sawdust biochar (SDB) demonstrated a relatively high specific surface area and porosity, indicating its suitability for applications in soil improvement and water purification (Chellappan & Nair 2018).

The notion that thermal degradation concentrates mineral constituents is supported by evidence showing that nutrient levels, such as NPK, Ca, and Mg, generally increase with temperature (Khater et al. 2024). Consistent with Liu et al. (2025) and El-Naggar et al. (2019), biochars produced at higher temperatures exhibit stronger soil-enhancing effects, particularly in raising pH and enriching organic carbon. Conversely, biochars produced at lower temperatures retain more labile organic compounds, which are beneficial for stimulating soil microbial activity (Hossain et al. 2020, Akumuntu et al. 2024). This study illustrates that each biochar type offers distinct functional advantages based on feedstock composition and pyrolysis temperature. Notably, finger millet hull biochar emerges as an economically and environmentally promising option for adsorption, soil improvement, and microbial support. These results underscore biochar's versatility and call for further research on mixed feedstocks, application-specific customization, and field-scale assessments.

5. CONCLUSIONS

The effects of different thermochemical conversion temperatures (300, 400, 500, and 600°C) were examined on various agricultural residues, including finger millet hull, rice husk, sawdust, and hardwood. Converting these waste residues into biochar offers a cost-effective waste management solution, serves as a soil amendment, and contributes to environmental conservation. It was observed that the biochar's microstructure, physicochemical properties, and elemental composition were significantly affected by pyrolysis temperature. Various factors, such as biomass type, pyrolysis temperature, residence time, and heating rate, can influence biochar yield and composition. Among these, pyrolysis temperature notably affects biochar pH, yield, ash, carbon content, surface area, and porosity, while decreasing volatile matter. Lower pyrolysis temperatures tend to reduce the water-holding capacity (WHC) of biochar by producing more volatile compounds, resulting in less porous structures. The newly developed cracked finger millet hull biochar (FMB) produced at 300°C is chemically active, with a fragmented, layered surface structure and macroporosity that enhance its adsorptive capacity and potential for microbial colonization. FMB has a surface area of 28.01 $m^2.g^{-1}$ and porosity of 9.74%, making it suitable for various environmental and agricultural applications. Its surface functional groups include O-H stretches, aliphatic –CH3 and -CH2 groups, C═C-C aromatic ring stretches, trimethyl groups, and simple fluoro compounds, indicating its chemical activity in environmental contexts. As an organic macromolecule, it holds potential for use in water conservation, promoting plant growth, and improving crop yields. Additionally, treasure humic acid fertilizer contains C, O, Si, K, and Cl, with contents of 61.87%, 30.51%,

4.80%, 2.08%, and 0.74%, respectively, which can dissolve into the soil, activating beneficial microbes and enhancing crop productivity. Further research on biochar produced from blended feedstocks is recommended. Additional studies should evaluate its practicality and potential in soil improvement, environmental remediation, and climate management, in comparison to traditional fertilizers.

6. ACKNOWLEDGEMENTS

This research was financially supported by the Krishna Vishwa Vidyapeeth (Deemed to be University), Karad, Maharashtra, India.

7. REFERENCES

Abrishamkesh, S., Gorji, M., Asadi, H., Bagheri-Marandi, G. H. and Pourbabaee, A. A., 2015. Effects of rice husk biochar application on the properties of alkaline soil and lentil growth. *Plant, Soil and Environment*, 61(11), pp.1-8.

Ahmadi, S. H., Ghasemi, H. and Sepaskhah, A. R., 2020. Rice husk biochar influences runoff features, soil loss, and hydrological behavior of a loamy soil in a series of successive simulated rainfall events. *Catena*, 192, p.104587.

Ahmed, S. F., Mehejabin, F., Chowdhury, A. A., Almomani, F., Khan, N. A., Badruddin, I. A. and Kamangar, S., 2024. Biochar produced from waste-based feedstocks: Mechanisms, affecting factors, economy, utilization, challenges, and prospects. *GCB Bioenergy*, 16(8), p.e13175.

Akumuntu, A., Hong, J. K., Jho, E. H., Omidoyin, K. C., Park, S. J., Zhang, Q. and Zhao, X., 2024. Biochar derived from rice husk: Impact on soil enzyme and microbial dynamics, lettuce growth, and toxicity. *Chemosphere*, 349, p.140868.

Amalina, F., Abd Razak, A. S., Krishnan, S., Sulaiman, H., Zularisam, A. W. and Nasrullah, M., 2022. Biochar production techniques utilizing biomass waste-derived materials and environmental applications–A review. *Journal of Hazardous Materials Advances*, 7, p.100134.

AOAC, 2003. *Official Methods of Analysis of the Association of Official Analytical Chemists International*. 17th ed. Gaithersburg, MD: AOAC International, pp.1-20.

Awasthi, M. K., Duan, Y., Awasthi, S. K., Liu, T. and Zhang, Z., 2020. Influence of bamboo biochar on mitigating greenhouse gas emissions and nitrogen loss during poultry manure composting. *Bioresource Technology*, 303, p.122952.

Bo, X., Zhang, Z., Wang, J., Guo, S., Li, Z., Lin, H. and Zou, J., 2023. Benefits and limitations of biochar for climate-smart agriculture: A review and case study from China. *Biochar*, 5(1), p.77.

Bolan, S., Hou, D., Wang, L., Hale, L., Egamberdieva, D., Tammeorg, P. and Bolan, N., 2023. The potential of biochar as a microbial carrier for agricultural and environmental applications. *Science of the Total Environment*, 886, p.163968.

Chatterjee, R., Sajjadi, B., Chen, W. Y., Mattern, D. L., Hammer, N., Raman, V. and Dorris, A., 2020. Effect of pyrolysis temperature on physicochemical properties and acoustic-based amination of biochar for efficient CO_2 adsorption. *Frontiers in Energy Research*, 8, pp.1-15.

Chellappan, S. and Nair, V., 2018. Synthesis, optimization and characterization of biochar based catalyst from sawdust for simultaneous esterification and transesterification. *Chinese Journal of Chemical Engineering*, 26(12), pp.2654-2663.

Cheng, S., Liu, Y., Xing, B., Qin, X., Zhang, C. and Xia, H., 2021. Lead and cadmium clean removal from wastewater by sustainable biochar derived from poplar sawdust. *Journal of Cleaner Production*, *314*, p.128074.

Coates, J., 2000. Interpretation of infrared spectra, a practical approach. *Encyclopedia of Analytical Chemistry*, *12*, pp.10815-10837.

Dhar, S. A., Sakib, T. U. and Hilary, L. N., 2020. Effects of pyrolysis temperature on production and physicochemical characterization of biochar derived from coconut fiber biomass through slow pyrolysis process. *Biomass Conversion and Biorefinery*, 12(7), pp.2631-2647.

El-Naggar, A., Lee, S. S., Rinklebe, J., et al. 2019. Biochar application to low fertility soils: A review of current status and future prospects. *Geoderma*, 337, pp.536-554.

Feng, D., Zhang, Y., Zhao, Y., Sun, S., Wu, J. and Tan, H., 2020. Mechanism of in-situ dynamic catalysis and selective deactivation of H_2O-activated biochar for biomass tar reforming. *Fuel*, 279, p.118450.

Ge, X., Cao, Y., Zhou, B., Wang, X., Yang, Z. and Li, M. H., 2019. Biochar addition increases subsurface soil microbial biomass but has limited effects on soil CO_2 emissions in subtropical moso bamboo plantations. *Applied Soil Ecology*, 142, pp.155-165.

Gupta, S., 2019. Agriculture crop residue burning and its consequences on respiration health of school-going children. *Global Pediatric Health*, 6, p.2333794X19874679.

He, D., Luo, Y. and Zhu, B., 2024. Feedstock and pyrolysis temperature influence biochar properties and its interactions with soil substances: Insights from a DFT calculation. *Science of the Total Environment*, 922, p.171259.

Hossain, M. Z., Bahar, M. M., Sarkar, B., Donne, S. W., Ok, Y. S., Palansooriya, K. N. and Bolan, N., 2020. Biochar and its importance on nutrient dynamics in soil and plants. *Biochar*, 2(4), pp.379-420.

Ippolito, J. A., Cui, L., Kammann, C., Wrage-Mönnig, N., Estavillo, J. M., Fuertes-Mendizabal, T. and Borchard, N., 2020. Feedstock choice, pyrolysis temperature and type influence biochar characteristics: A comprehensive meta-data analysis review. *Biochar*, 2(4), pp.421-438.

Jena, P. K., Samal, S., Samal, R. R., Panigrahi, S. R., Baral, U., Behera, S., and Mishra, C. S. K., 2025. Evaluating millet biochar as mitigator of pesticide toxicity in soil using biomarkers. *iScience*, 28(4), pp.1-15.

Khater, E.S., Bahnasawy, A., Hamouda, R., Sabahy, A., Abbas, W. and Morsy, O.M., 2024. Biochar production under different pyrolysis temperatures with different types of agricultural wastes. *Scientific Reports*, 14, p.2625. [DOI]

Lan, R., Eastham, S. D., Liu, T., Norford, L. K. and Barrett, S. R., 2022. Air quality impacts of crop residue burning in India and mitigation alternatives. *Nature Communications*, 13(1), p.6537.

Li, S. and Tasnady, D., 2023. Biochar for soil carbon sequestration: Current knowledge, mechanisms, and future perspectives. *C*, 9(3), p.67. [DOI]

Li, Z., Zheng, Z., Li, H., Xu, D., Li, X., Xiang, L. and Tu, S., 2023. Review on rice husk biochar as an adsorbent for soil and water remediation. *Plants*, 12(7), p.1524. [DOI]

Liu, S., Cen, B., Yu, Z., Qiu, R., Gao, T. and Long, X., 2025. The key role of biochar in amending acidic soil: Reducing soil acidity and improving soil acid buffering capacity. *Biochar*, 7(1), p.52.

Manyuchi, M. M., Sukdeo, N. and Stinner, W., 2022. Potential to remove heavy metals and cyanide from gold mining wastewater using biochar. *Physics and Chemistry of the Earth, Parts A/B/C*, 126, p.103110.

Mathur, R. and Srivastava, V. K., 2019. Crop residue burning: Effects on environment. In: *Greenhouse Gas Emissions: Challenges, Technologies and Solutions*. Singapore: Springer Singapore, pp.127-140.

Mujtaba, G., Hayat, R., Hussain, Q. and Ahmed, M., 2021. Physico-chemical characterization of biochar, compost, and co-composted biochar derived from green waste. *Sustainability*, 13(9), p.4628.

Mukherjee, A., Patra, B. R., Podder, J. and Dalai, A. K., 2022. Synthesis of biochar from lignocellulosic biomass for diverse industrial applications and energy harvesting: Effects of pyrolysis conditions on the physicochemical properties of biochar. *Frontiers in Materials*, 9, p.870184.

Muzyka, R., Sobek, S., Dudziak, M., Ouadi, M. and Sajdak, M., 2023. A

comparative analysis of waste biomass pyrolysis in Py-GC-MS and fixed-bed reactors. *Energies*, 16(8), p.3528.

Nadarajah, K., Asharp, T. and Jeganathan, Y., 2024. Biochar from waste biomass, its fundamentals, engineering aspects, and potential applications: An overview. *Water Science & Technology*, 89(5), pp.1211-1239.

Nagar, J. and Kumar, R., 2024. Agricultural residue management in India: Unlocking economic potential. *Journal of Agricultural Economics and Rural Development*, 12(3), pp.45-60.

Nandiyanto, A. B. D., Oktiani, R. and Ragadhita, R., 2019. How to read and interpret FTIR spectroscope of organic material. *Indonesian Journal of Science and Technology*, 4(1), pp.97-118.

Qin, L., Wu, Y., Hou, Z. and Jiang, E., 2020. Influence of biomass components, temperature and pressure on the pyrolysis behavior and biochar properties of pine nut shells. *Bioresource Technology*, 313, p.123682.

Rabbani, G., Hossain, M. F. and Parveen, Z., 2020. Morphological properties and nutrient status of different waste derived slow pyrolyzed biochars. *World Journal of Agriculture and Soil Science*, 6(1), pp.1-8.

Roshan, A., Ghosh, D. and Maiti, S. K., 2023. How temperature affect biochar properties for application in coal mine spoils? A meta-analysis. *Carbon Research*, 2, p.3. [DOI]

Sathyabama, K. and Firdous, S., 2025. Effect of pyrolysis temperature on the physicochemical properties and structural characteristics of agricultural waste-derived biochar. *ACS Omega*, 10(33), pp.37013-37024.

Singh, B., Camps-Arbestain, M. and Lehmann, J. (eds.), 2017. *Biochar: A Guide to Analytical Methods*. CSIRO Publishing, pp.1-20.

Song, S., Cong, P., Wang, C., Li, P., Liu, S., He, Z., Zhou, C., Liu, Y. and Yang, Z., 2023. Properties of biochar obtained from tropical crop wastes under different pyrolysis temperatures and its application on acidic soil. *Agronomy*, 13(3), p.921. [DOI]

Soothar, M. K., Mounkaila Hamani, A. K., Kumar Sootahar, M., Sun, J., Yang, G., Bhatti, S. M. and Traore, A., 2021. Assessment of acidic biochar on the growth, physiology and nutrients uptake of maize (Zea mays L.) seedlings under salinity stress. *Sustainability*, 13(6), p.3150. [DOI]

Sovova, S., Mravcova, L., Porizka, J., Kubikova, L. and Kalina, M., 2024. The effect of biochar particle size on the leaching of organic molecules and macro- and microelements. *Agronomy*, 14(10), p.2346. [DOI]

Toczydlowski, A. J., Slesak, R. A., Venterea, R. T. and Spokas, K. A., 2023. Pyrolysis temperature has greater effect on carbon and nitrogen biogeochemistry than biochar feedstock when applied to a sandy forest soil. *Forest Ecology and Management*, 534, p.120881.

Tomczyk, A., Sokołowska, Z. and Boguta, P., 2020. Biochar physicochemical properties: pyrolysis temperature and feedstock kind effects. *Reviews in Environmental Science and Bio/Technology*, *19*(1), pp.191-215.

Ulusal, A., Apaydın Varol, E., Bruckman, V. J. and Uzun, B. B., 2021. Opportunity for sustainable biomass valorization to produce biochar for improving soil characteristics. *Biomass Conversion and Biorefinery*, 11(3), pp.1041-1051.

Varkolu, M., Gundekari, S., Omvesh, Palla, V. C. S., Kumar, P., Bhattacharjee, S. and Vinodkumar, T., 2025. Recent advances in biochar production, characterization, and environmental applications. *Catalysts*, 15(3), p.243. [DOI]

Walkley, A. and Black, I. A., 1934. An examination of the Degtjareff method for determining soil organic matter, and a proposed modification of the chromic acid titration method. *Soil Science*, 37(1), pp.29-38.

Wang, P., Peng, H., Adhikari, S., Higgins, B., Roy, P., Dai, W. and Shi, X., 2020. Enhancement of biogas production from wastewater sludge via anaerobic digestion assisted with biochar amendment. *Bioresource Technology*, 309, p.123368.

Wyatalska, K., Kwarciak-Kozłowska, A. and Włodarczyk, R., 2023. Influence of technical parameters of the pyrolysis process on the surface area, porosity, and hydrophobicity of biochar from sunflower husk pellets. *Sustainability*, 15(1), p.394. [DOI]

Zhang, C., Zhang, L., Gao, J., Zhang, S., Liu, Q., Duan, P. and Hu, X., 2020. Evolution of the functional groups/structures of biochar and heteroatoms during the pyrolysis of seaweed. *Algal Research*, 48, p.101900.

Zhang, H., Cheng, Y., Zhong, Y., Ni, J., Wei, R. and Chen, W., 2024. Roles of biochars' properties in their water-holding capacity and bound water evaporation: Quantitative importance and controlling mechanism. *Biochar*, 6(1), p.30.

Zhang, P., Duan, W., Peng, H., Pan, B. and Xing, B., 2021. Functional biochar and its balanced design. *ACS Environmental Au*, 2(2), pp.115-127.

Nature Environment and Pollution Technology
An International Quarterly Scientific Journal

p-ISSN: 0972-6268
(Print copies up to 2016)
e-ISSN: 2395-3454

Vol. 25 | No. 3 | Article ID D1872 | 2026

Original Research Paper

https://doi.org/10.46488/NEPT.2026.v25i03.D1872

Open Access Journal

Synthesis and Characterization of Modified Lignin Flocculants for Congo Red and Methylene Blue Removal

Mark Xavier Bailon[1,2]†, Bianca Marie Lim[1,3] and Gian Margarette Villadarez[1,4]

[1]Department of Science and Technology, Philippine Science High School, Central Luzon Campus, Lily Hill Street, Clark Freeport Zone, Mabalacat City, Pampanga, 2010, Philippines

[2]Department of Environmental Science, School of Science and Engineering, Ateneo de Manila University, Loyola Heights, Quezon City, Philippines

[3]College of Medicine, University of the Philippines, Manila, Ermita, Manila City, Philippines

[4]Department of Physics, School of Science and Engineering, Ateneo de Manila University, Loyola Heights, Quezon City, Philippines

†Corresponding author: Mark Xavier Bailon; mebailon@clc.pshs.edu.ph

Abbreviation: Nat. Env. & Poll. Technol.
Website: www.neptjournal.com

Received: 24-09-2025
Revised: 13-12-2025
Accepted: 16-12-2025

Key Words:

Dye removal
Grafted flocculant
Modified lignin flocculants
Congo red
Methylene blue

Citation for the Paper:

Bailon, M.X., Lim, B.M. and Villadarez, G.M., 2026. Synthesis and characterization of modified lignin flocculants for Congo red and methylene blue removal. *Nature Environment and Pollution Technology*, 25(3), D1872. https://doi.org/10.46488/NEPT.2026.v25i03.D1872

Note: From 2025, the journal has adopted the use of Article IDs in citations instead of traditional consecutive page numbers. Each article is now given individual page ranges starting from page 1.

Copyright: © 2026 by the authors
Licensee: Technoscience Publications
This article is an open access article distributed under the terms and conditions of the Creative Commons Attribution (CC BY) license (https://creativecommons.org/licenses/by/4.0/).

ABSTRACT

This study focused on synthesizing lignin-based flocculants through grafting sulfonic acid (SA) and [2-(methacryloyloxy)ethyl] trimethylammonium chloride (METAC) using potassium persulfate as the initiator. The resulting flocculants were characterized by particle size, thermal stability, surface morphology, and functional groups. Their dye removal performance was tested with Congo red and methylene blue across various pH levels. FTIR analysis confirmed successful grafting of METAC and SA onto the lignin backbone in lignin-METAC, lignin-SA, and lignin-METAC-SA. Particle size analysis revealed an increase only in lignin-METAC-SA. Modifications led to increased folding and the emergence of raised structures on the flocculants. Thermal analysis showed that, compared to unmodified lignin (degradation at 384°C), all modified lignins exhibited higher maximum degradation temperatures (400–500°C). Modifying lignin improved dye removal efficiency, with lignin-SA demonstrating the highest performance for both dyes. All flocculants performed better against methylene blue at all pH levels, notably lignin-SA (82.9%) and lignin-METAC-SA (82.3%) at pH 10. Higher Congo red removal (46–69%) occurred in more acidic conditions (pH 4). These findings underscore the potential of grafted lignin-based flocculants for dye wastewater treatment.

1. INTRODUCTION

As water scarcity and pollution continue to worsen, advances in wastewater treatment and management are essential (Libralato et al. 2012). Wastewater is processed through chemical, biological, physical, or combined methods to reduce contaminants and achieve the required water quality standards (Englande et al. 2015). The textile dyeing and finishing industry ranks as the second-largest polluter of clean water, after agriculture. Around 8,000 chemicals are involved in textile manufacturing, including dyeing and printing, many of which pose known environmental and health risks (Kant 2012, Yaseen & Scholz 2019). Consequently, dye wastewater must be treated prior to discharge into surface water bodies to mitigate its environmental impact (Solayman et al. 2023).

Various treatment methods have been explored and developed for dye removal from wastewater. Nonetheless, some approaches fail to meaningfully reduce contaminant levels, and practical methods often face limitations such as high costs and the risk of secondary pollution. For example, chemical precipitation is a straightforward and effective technique for high pollutant concentrations but involves substantial chemical usage and generates significant sludge. Another common method, adsorption or filtration, is versatile and effective across a broad

spectrum of contaminants; however, it is constrained by the expense of filtration materials, ongoing maintenance to prevent saturation and clogging, and the need for regeneration of the media (Crini & Lichtfouse 2019). An optimal treatment process would substantially lower dye concentrations in wastewater while avoiding the creation of potentially hazardous by-products (Katheresan et al. 2018).

Flocculation is a well-established method for removing dyes. This process involves adding coagulants, which destabilize particle forces, and flocculants, which facilitate the aggregation of contaminants into larger flocs through bridging, thereby separating solids from liquids (Arockiam JeyaSundar et al. 2020). Unlike some other methods, flocculation poses minimal negative impacts and is frequently used to decrease water turbidity by eliminating suspended solids, dissolved pollutants, and emulsified oils (Das et al. 2021). The process can be optimized to lower chemical consumption, sludge generation, and costs by employing direct flocculation, which involves adding only flocculants to wastewater. For example, polyelectrolytes-polymers with either a cationic or anionic charge, such as chitosan, are commonly used as flocculants (Chatsungnoen & Chisti 2019).

Synthetic polymer flocculants, such as polyacrylamide, have been used in different industries because of their high molecular weight and exceptional performance in contaminant removal. However, they are non-biodegradable and can pose hazards to living organisms (Siti Aisyah et al. 2014). Natural flocculants have attracted attention in several studies because of their comparable performance to synthetic flocculants (Ajao et al. 2018), safer use, and ability to produce organic sludge that is biodegradable and reusable as fertilizer in agriculture (Fauzani et al. 2021, Zaman et al. 2020). One of the common biopolymers used as a flocculant is plant-derived lignin because of its natural abundance, biodegradability, and presence of functional groups that can effectively interact with contaminants during the flocculation process (Suryawanshi et al. 2025).

Flocculation involves the chemical destabilization of particles by overcoming their repulsive forces through complex bridging mechanisms (Gregory & O'Melia, 1989). Lignin can be chemically modified to change its surface charge by grafting various functional groups onto its backbone (Lee et al. 2014, Wang et al. 2008). For example, Wang et al. (2018) grafted [2-(methacryloyloxy) ethyl] trimethylammonium chloride (METAC) onto lignin to produce a more cationic flocculant. This lignin-METAC flocculant demonstrated effective removal of anionic dyes, such as Remazol Black B and Remazol Brilliant Orange, via bridging and charge neutralization mechanisms. Alternatively, lignin can be rendered more anionic by attaching negative groups, like sulfone or sulfonate groups, which increase its negative charge density (Aro & Fatehi 2017, Gao et al. 2019). Such modifications have proven effective for removing cationic dyes like methylene blue (Rahmawati et al. 2021). Additionally, lignin can be engineered to create amphoteric flocculants capable of removing both cationic and anionic dyes (Yue et al. 2005).

Wu et al. (2023) developed an amphiphilic lignin flocculant by grafting acrylamide and 3-chloro-2-hydroxypropyltrimethylammonium chloride onto the kraft lignin backbone, demonstrating its effectiveness in treating high-turbidity wastewater. Eraghi Kazzaz and Fatehi (2020) examined the cationization of lignin with (3-bromopropyl) trimethylammonium bromide and (5-bromopentyl) trimethylammonium bromide, combined with polymerization using 3-sulfopropyl methacrylate, though its impact on flocculation performance remains unstudied. Additionally, the Mannich reaction applied to acrylamide-modified lignosulfonate with amine and aldehyde yielded the amphoteric lignin flocculant LSDC, which proved effective in decolorizing various dyes by up to 80% under appropriate conditions (Yue et al. 2005). Collectively, these studies highlight the potential to enhance lignin's flocculation and contaminant removal capabilities through the incorporation of both cationic and anionic groups.

To the best of our knowledge, no previous research has reported the grafting of anionic sulfonic acid and cationic METAC groups onto lignin, nor have they been evaluated for dye removal effectiveness. In this study, three lignin-based flocculants were synthesized by grafting METAC and sulfonic acid (SA) groups onto the lignin backbone using potassium persulfate as an initiator. These synthesized flocculants were characterized and tested for their ability to remove dyes, specifically methylene blue and Congo red. All the lignin-based flocculants demonstrated effectiveness in removing both dyes, indicating their promising potential for dye wastewater treatment.

2. MATERIALS AND METHODS

2.1. Materials

Alkali lignin, [2-(methacryloyloxy)ethyl] trimethylammonium chloride (METAC) at 75% weight in water, and potassium persulfate ($K_2S_2O_8$) with a purity of at least 99% were obtained from Merck Sigma-Aldrich. Linear alkylbenzene sulfonic acid (LABSA) was sourced from XERN Chemicals in the Philippines. All reagents were used as received, without further purification.

2.2. Synthesis of Modified Lignin Flocculants

Three variants of modified lignin-based flocculants were synthesized through grafting METAC and sulfonic acid (SA) onto the lignin backbone. The preparation followed methods outlined by Liu et al. (2018) and Moore et al. (2021), with specific modifications. Briefly, alkali lignin was dissolved in distilled water at a 1:20 ratio of solute to solvent, and the mixture was stirred at 400 rpm until fully dissolved. A 0.1 moL.L^{-1} NaOH solution was gradually added to adjust the pH to 11. The solution was then heated to 70°C for 30 minutes, after which the pH was readjusted to 4 using 0.1 M H_2SO_4. These pH adjustments optimized solubility and reaction conditions. The mixture was maintained at 75°C in a water bath until the end of the synthesis and purged with nitrogen for 30 minutes. Subsequently, 0.015 g of potassium persulfate per gram of lignin was introduced as a free radical initiator while stirring at 400 rpm. Depending on the desired flocculant type, METAC, SA, or both were added dropwise in a 1:2 solute-to-modifier weight ratio, as detailed in Table 1. The reaction mixture was stirred for 2.5 hours to ensure complete grafting. After completion, the solution was mixed with 80% ethanol (v/v) to precipitate the flocculants. The precipitate was separated, washed twice with 80% ethanol, and then dried at 100°C.

2.3. Sample Characterization

This study conducted a functional group analysis of various flocculants utilizing a Cary 360 FTIR Spectrometer (Agilent Technologies) at the Philippine Science High School – Central Luzon Campus. IR spectra were recorded by measuring the percent transmittance across a range of 650 to 4000 cm^{-1}. The particle sizes of different lignin-based flocculants were examined through optical microscopy at the Department of Science and Technology – Industrial Technology Development Institute (DOST-ITDI), Material Science Division. Images of each sample were captured and analyzed to determine particle size distribution. Optical microscopy was chosen because the samples were anticipated to fall within the 50–200 micron range, which exceeds the optimal detection range of Dynamic Light Scattering (DLS). The surface morphologies of the flocculants were observed using a HITACHI TM4000Plus Scanning Electron Microscope (SEM) at the Philippine Science High School – Ilocos Region Campus, at magnifications between 800× and 1200×. The thermal stability was assessed with a Netzsch STA 2500 Regulus Simultaneous Thermal Analyzer, heating samples from 20°C to 600°C at a ramp rate of 40 K.min^{-1}.

Table 1: Mass ratios for the lignin and modifier used in the preparation of the different flocculants.

Type	Lignin to METAC to SA Mass Ratio		
	Lignin	METAC	SA
Unmodified Lignin	1	0	0
Lignin-METAC	1	2	0
Lignin-SA	1	0	2
Lignin-METAC-SA	1	2	2

2.4. Dye Removal Performance Against Congo Red and Methylene Blue

A dye removal experiment was performed following the protocols of Wang et al. (2018) and Wu et al. (2022), with some modifications. Various flocculants were assessed for their effectiveness in removing Congo red and methylene blue dyes at different pH levels (pH 4, 7, and 10). These dyes were chosen due to their differing charges, with Congo red being an anionic dye and methylene blue a cationic dye. The flocculants were applied by adding 100 mg/L of each to 50 mL of artificial dye wastewater, which had a concentration of 10 mg/L, in centrifuge tubes. The mixtures were shaken for 2 hours on a linear shaker and then left to settle for an additional 2 hours. The supernatant was filtered through a 0.45 µm PTFE membrane, and the absorbance was measured using a Shimadzu UV-10008 UV-Visible spectrophotometer at 497 nm for Congo red and 664 nm for methylene blue. The dye removal efficiency of the flocculants was compared to that of RAFLOC 28 (a cationic polymer flocculant) and ARFLOC 12 (an anionic polymer flocculant).

2.5. Statistical Analysis

A One-way ANOVA was conducted at a 95% confidence level to assess the impact of different flocculants on the reduction of the two dyes' concentrations. Tukey's HSD post hoc test was then applied to determine significant differences in the performance of the various flocculants, including the positive controls.

3. RESULTS AND DISCUSSION

3.1. FTIR Analysis

Fig. 1 shows the FT-IR spectra of unmodified lignin and the different synthesized lignin-based flocculants (Lignin-METAC, Lignin-SA, and Lignin-METAC-SA). Characteristic peaks for hydroxyl moieties (-OH: 3400 cm^{-1}) and methyl and methylene vibrations (alkyl -CH stretch: 2900 cm^{-1}) were present in all samples, suggesting the presence of many hydroxyl and methylene groups, which are highly associated with lignin (Guo et al. 2018). The different flocculants also exhibited prominent peaks at 1650 cm^{-1} and 1200 cm^{-1} associated with -C=C- of the characteristic conjugated alkene of lignin and -CO stretching

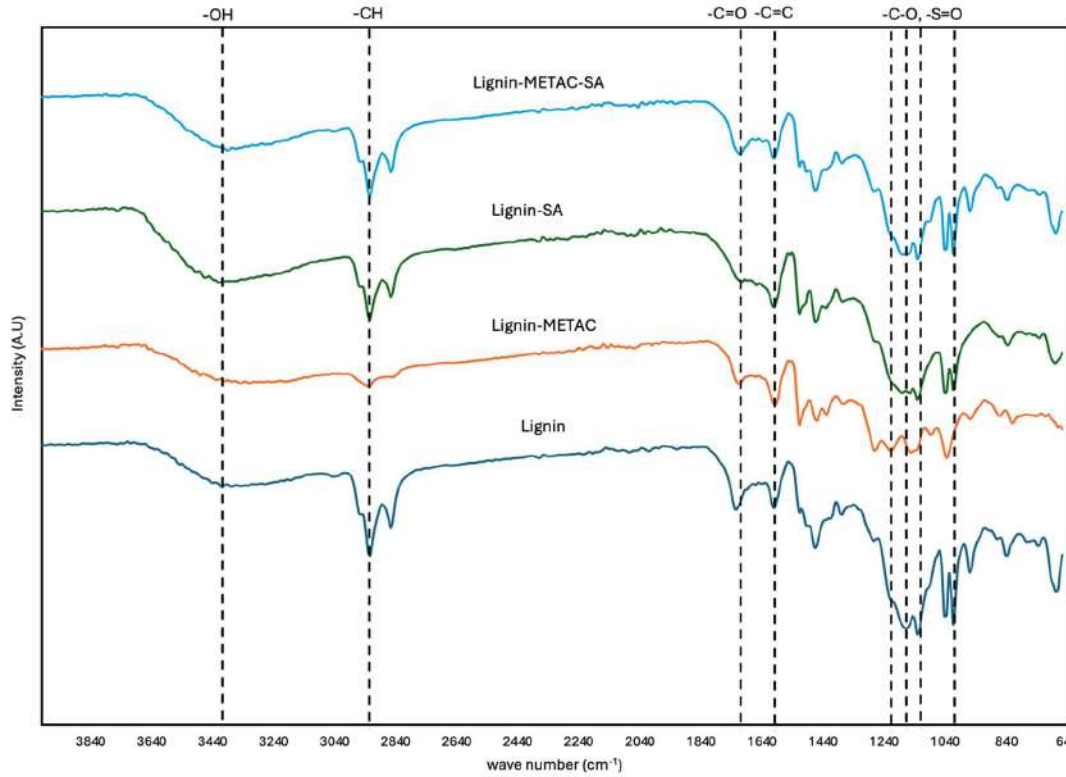


Fig. 1: FTIR spectra of unmodified lignin and synthesized modified lignin flocculants.

vibrations, respectively. Characteristic peaks for -C=O stretching (1750 cm^{-1}) and stretching vibration for $N^{+}(CH_3)_3$ (960 cm^{-1}) were observed for Lignin-METAC and Lignin-METAC-SA, suggesting the successful incorporation of METAC in the structure of lignin (Guo et al. 2018). Moore et al. (2021) described that the mechanism for modification is through METAC grafting through the hydroxyl groups. This eventually translates to an apparent reduction in the -OH peak at approximately 3300 cm^{-1}. Furthermore, the peaks for the -C=O stretch around 1750 cm^{-1} were more prominent in Lignin-METAC and Lignin-METAC-SA than in Lignin-SA, which is expected as METAC contains a carbonyl group. In contrast, peaks around 1020-1220 cm^{-1} associated with -S=O stretching due to sulfonate and sulfonic acid groups were observable in Lignin, Lignin-SA, and Lignin-METAC-SA, but highly diminished in Lignin-METAC (Karpukhina et al. 2023). These results confirm the successful grafting of METAC and sulfonic acid structures to the lignin backbone.

3.2. Particle Size Analysis

Particle size analysis of various flocculants was performed using optical microscopy (Fig. 2). Results indicated that lignin, lignin-METAC, and lignin-SA have comparable particle sizes, approximately 1.5 to 1.7 µm. In contrast, lignin-METAC-SA exhibited significantly larger particles, with some reaching a Feret diameter of 150 µm. The addition of METAC and SA to lignin likely alters the inter- and intramolecular forces, potentially causing structural folding and interlinking among lignin molecules. This interaction may lead to an increase in particle size for lignin-METAC-SA. Specifically, electrostatic interactions between opposite charges and the possible formation of ionic bonds within lignin-METAC-SA could account for its larger particle dimensions compared to lignin-SA and lignin-METAC (Lekniute et al. 2013).

3.3. Scanning Electron Microscopy

Scanning electron microscopy images (Fig. 3) revealed differences among the flocculants. Unmodified lignin displayed uniform spherical structures with mounds and grooves, while lignin-SA and lignin-METAC showed more porous microstructures. The modified lignin flocculants also exhibited increased folds and raised features. The presence of crazing and cracks indicates the formation of a plastic phase in the flocculants (Moustaqim et al. 2018). These surface morphology changes may result from disrupted hydrogen bonding in alkali lignin during modification, leading to the collapse of its crystal structure and subsequent surface alterations (Li et al. 2024). Confirmation of these

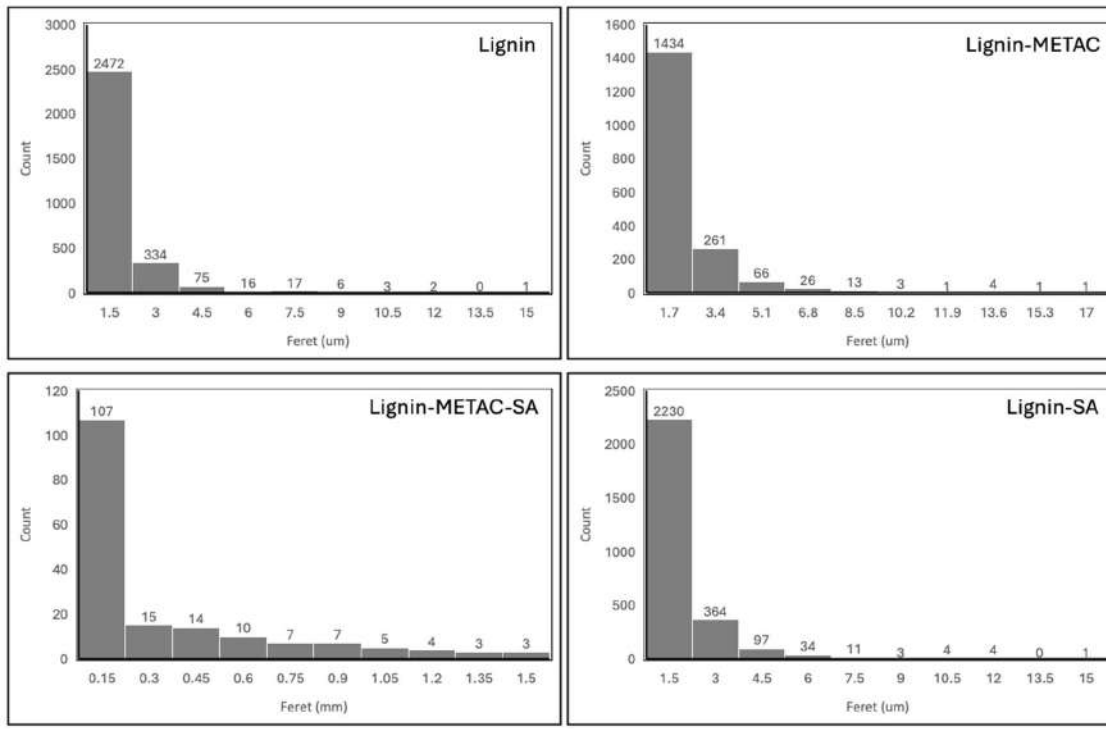


Fig. 2: Particle size distribution of pure lignin and modified lignin flocculants.

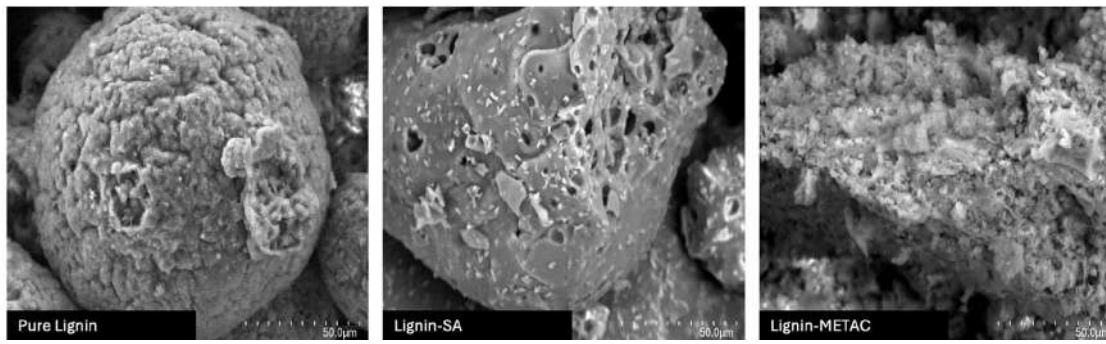


Fig. 3: SEM image of lignin-based flocculants at 800x magnification.

effects could be achieved through molecular weight and zeta potential analyses, which were not conducted in this study.

3.4. Thermogravimetry Analysis

The thermal stability of each flocculant was evaluated using a simultaneous thermal analyzer. The TGA profiles (Fig. 4) exhibit differences in the thermal behavior of the various flocculants, which is expected due to the incorporation of new functional groups into the lignin structure. Overall, the patterns in the TGA and DTG curves were similar across all samples, with the DTG traces showing distinct peaks around 70-150°C and 250-500°C. These peaks correspond to apparent inflections in the thermograms of the different samples. Both exothermic and endothermic peaks are evident in the DTG curves, with the maximum exothermic peaks occurring at higher temperatures in the modified lignin flocculants compared to unmodified lignin. The DTG curves displayed three to four peak temperatures of maximum weight loss (Tp) for each flocculant, as summarized in Table 2. Additionally, all flocculants demonstrated a slower decomposition rate at temperatures exceeding 500°C.

The first peak (T_{P1}) in the DTG at approximately 73–162°C is attributed to the loss of moisture, as much of the mass loss occurred around the vaporization point of water. The flocculants exhibited differences in the 2nd to 4th peak temperatures owing to structural differences. In

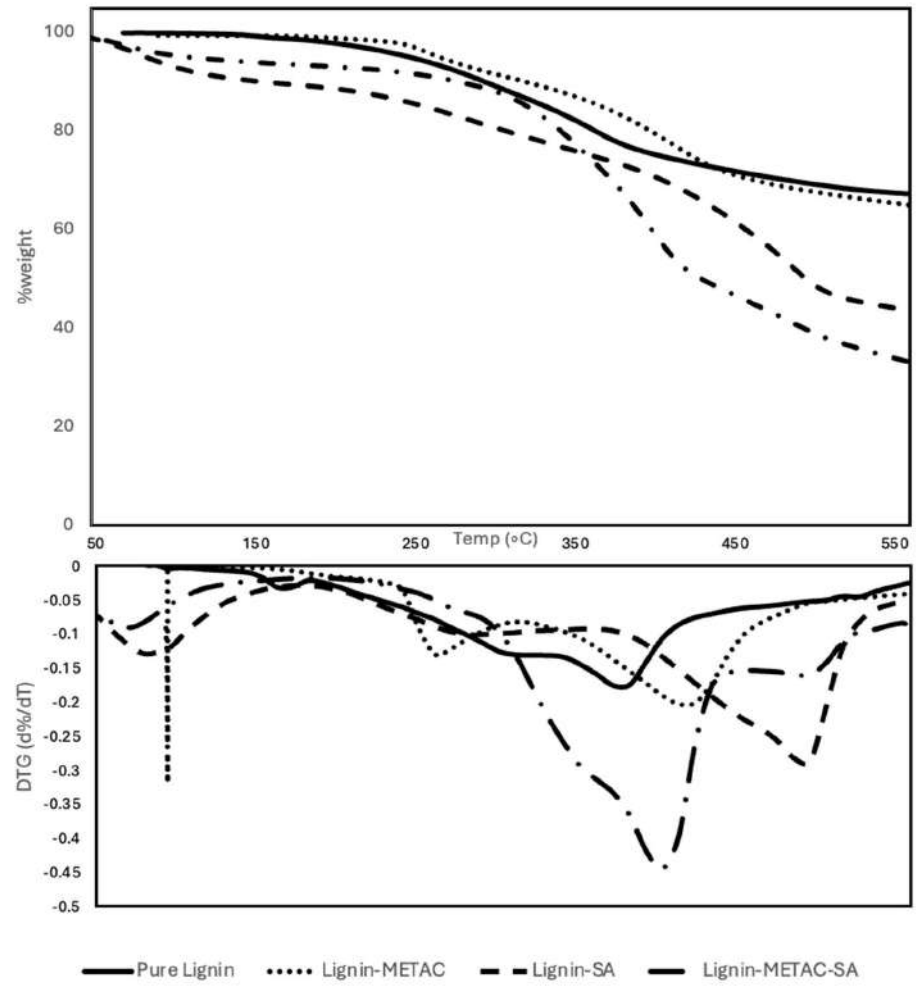


Fig. 4: TGA and DTG graphs for pure lignin, lignin-METAC, lignin-SA, and lignin-METAC-SA flocculants.

the case of unmodified lignin, unsaturated chains, methane, carbon dioxide, and carbon monoxide are formed after dehydration. The process continues with the breaking of the methyl-aryl ether bonds at approximately 300°C and phenol ring decomposition at approximately 400°C (Moore et al. 2021, Sahoo et al. 2011). The mass loss at 304°C is also due to the cleavage of the b-O-4 bonds of carbohydrate molecules (Chu et al. 2013, Kim et al. 2013, Moustaqim et al. 2018).

In the case of lignin-METAC, T_{P2} occurred at a lower temperature (261.9°C), which may be due to the decomposition of the quaternary ammonia group. Simultaneously, T_{P3} is attributed to the decomposition of the Lignin-METAC backbone (Moore et al. 2021). The same decomposition pattern was observed for Lignin-METAC-SA, but at a higher temperature, owing to the incorporation of both METAC and SA groups. T_{P3} for all modified flocculants occurred at temperatures between 400 and 500°C, which is due to the saturation reaction of the aromatic ring, C-C bond breakage, and the release of water, carbon dioxide, and carbon monoxide by-products during the rearrangement and removal of functional groups (Jakab et al. 1991, Wibowo & Park 2023).

3.5. Dye Removal Performance

The influence of pH on the flocculating performance of various flocculants was examined using Congo Red dye, with

Table 2: Peak weight loss temperature (T_p) of pure lignin, lignin-METAC, lignin-SA, and lignin-METAC-SA.

	Peak Temperatures [°C]			
	T_{P1}	T_{P2}	T_{P3}	T_{P4}
Unmodified lignin	162	302	384	-
lignin-METAC	94.7	261.9	425	-
lignin-SA	88.06	281	496.8	-
lignin-METAC-SA	72.6	363	404.6	497.1

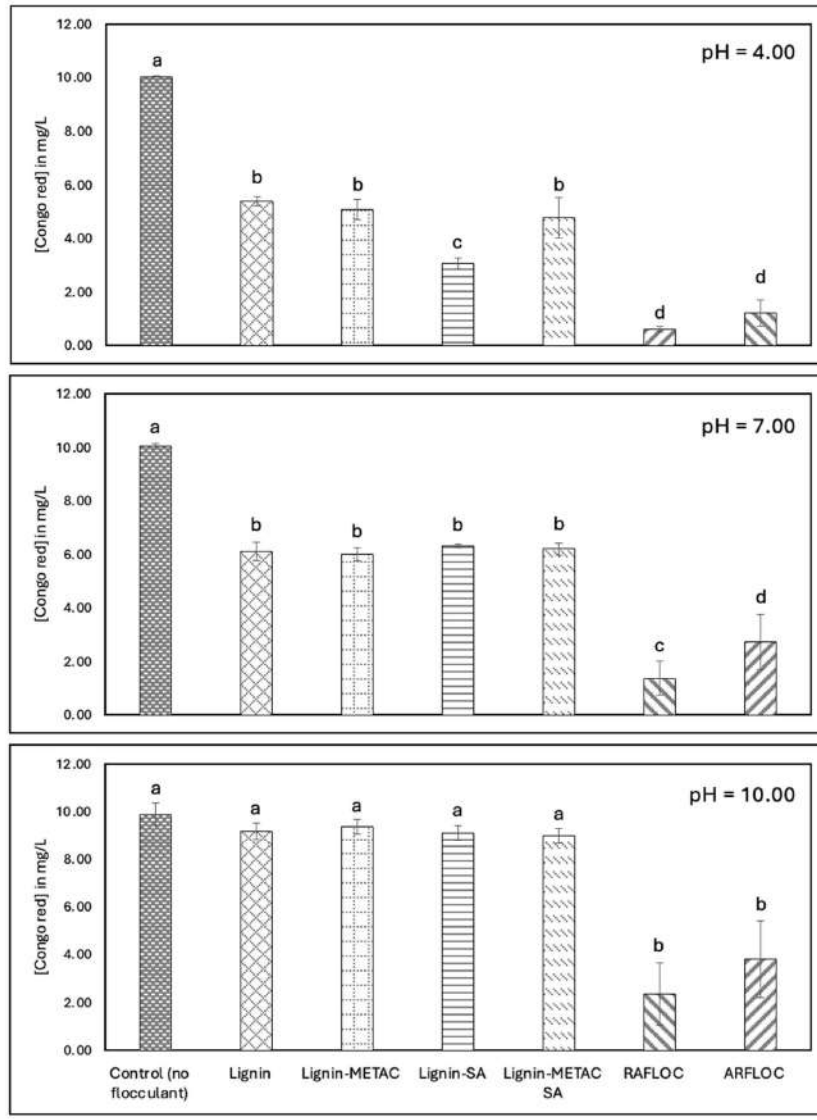


Fig. 5: Effect of pH on the dye removal performance of unmodified lignin, Lignin-METAC, Lignin-SA, and Lignin-METAC-SA flocculants against Congo red dye. Letters above the bars represent a significant difference among treatment groups based on ANOVA ($p < 0.05$) and Tukey's HSD test. Similar letters mean no significant difference between treatments. Error bars indicate standard deviation (n = 3).

results summarized in Fig. 5. All lignin-based flocculants effectively removed Congo Red at pH 4 and 7. Under acidic conditions, unmodified lignin, lignin-METAC, and lignin-METAC-SA exhibited similar reduction efficiencies, ranging from approximately 46% to 52%. Among the synthesized flocculants, lignin-SA achieved the highest performance, with an average reduction efficiency of 69.4%. At neutral pH, all lignin-based flocculants demonstrated comparable performance, with reduction rates between 37% and 40%. No significant dye removal was observed at pH 10 for any lignin-based flocculant. Across all pH levels, the positive control groups, RAFLOC and ARFLOC, showed superior performance, with average reduction efficiencies at pH 4, 7, and 10 of approximately 88-94%, 73-86%, and 61-76%, respectively.

Both RAFLOC and ARFLOC positive controls showed significantly higher reduction compared to lignin-based flocculants. This was expected because both are commercially used flocculants for treating industrial wastewater. Except at pH 10, all lignin flocculants exhibited significant dye removal activity. The isoelectric point of Congo Red is pH 3 (Litefti et al. 2019). Thus, it has been observed to ionize into a more positive charge ion below pH 3 and exhibit a more negative charge at values above pH 5.3 (Alarifi et al.

2021). It is expected that the anionic flocculant Lignin-SA will perform the best because of its ability to neutralize and destabilize dye contaminants, reducing electric repulsion, which will lead to efficient aggregation of flocs (Ghernaout & Ghernaout 2012). In addition, sulfonation generally increases the solubility of polymers in water, which increases the ability of the flocculant to adsorb onto the dye particles and bridge them together (Lufrano et al. 2013).

In contrast, lignin-METAC, with its cationic nature, tends to undergo flocculation via polymer bridging. This relies on several additional factors, including the agitation of the particles and flexibility of the polymer, as well as the surface charges, branches, and functional groups that can serve as interaction points, which may lead to weaker flocculation performance (Hogg 2013). This may also explain why lignin-METAC-SA performed better than lignin-METAC but worse than lignin-SA, as the amphoteric nature may have diminished some of its ability to neutralize dye contaminants. However, its polymer-bridging capability remains owing to the polymeric nature of the grafted flocculants. Unmodified lignin also performed flocculation with an efficiency comparable to that of lignin-METAC. This is likely due to

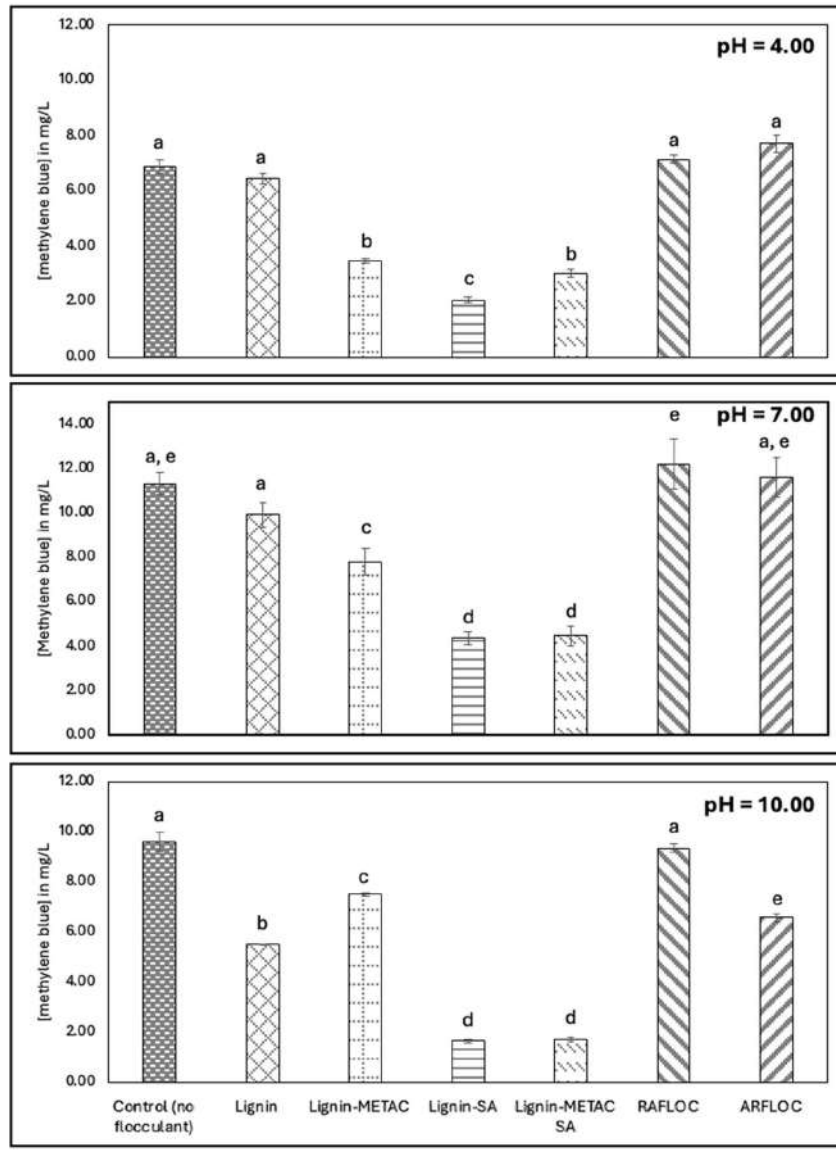


Fig. 6: Effect of pH on the dye removal performance of unmodified lignin, Lignin-METAC, Lignin-SA, and Lignin-METAC-SA flocculants against methylene blue dye. Letters above the bars represent a significant difference among treatment groups based on ANOVA ($p < 0.05$) and Tukey's HSD test. Similar letters mean no significant difference between treatments. Error bars indicate standard deviation ($n = 3$).

the mechanism utilized by these two flocculants, except that Lignin-METAC had additional functional groups that could still interact with the contaminants through intermolecular forces, increasing the likelihood of bridging. At pH 7 and 10, RAFLOC still performed best for dye removal, which can be attributed to its cationic nature, which can effectively neutralize Congo red, which is anionic at these pH levels, through charge neutralization. Similar to other polyacrylamide flocculants, the sweeping effects and enmeshment of RAFLOC and ARFLOC allowed for the removal of the Congo red dye through possible adsorption and bridging mechanisms (Khan et al. 2020).

The dye removal performance of the different flocculants was also tested using the methylene blue dye. Fig. 6 shows that at all pH levels, the unmodified lignin and all modified lignin flocculants showed significant dye removal performance. At pH 4.00, the Lignin-METAC, Lignin-SA, and Lignin-METAC-SA flocculants showed high average reduction efficiencies of 49.63%, 79.15%, and 56.04%, respectively. Unmodified lignin and the two positive controls did not show a significant reduction at this pH. Similar to that at pH 4.00, no significant reduction in dye concentration was observed for unmodified lignin and the two positive controls. The highest average reduction efficiencies were observed for Lignin-SA (61.5%) and Lignin-METAC-SA (60.7%). Lignin-METAC also exhibited a significant dye removal performance of 31.1%. At pH 10, all flocculants except the RAFLOC control showed significant flocculation performance. Lignin-METAC showed the lowest average reduction at 22%, followed by ARFLOC (31.7%) and unmodified lignin (42.9%). Lignin-SA and lignin-METAC-SA showed the highest average reduction efficiencies at 82.9% and 82.3%, respectively.

The observed trends for methylene blue and Congo red can be explained by their charge differences, with methylene blue being a cationic dye. All lignin-based flocculants demonstrated more effective dye removal than the positive controls, RAFLOC and ARFLOC. The results of the methylene blue flocculation test underscore the beneficial effect of grafting cationic and anionic groups onto the lignin backbone, which enhances its flocculating performance. Unmodified lignin showed minimal dye reduction at pH 4 and 7. Lignin modified with significant sulfonic acid groups (lignin-SA and lignin-METAC-SA) carries more negative charges, enabling effective neutralization of the positively charged methylene blue. This aligns with previous research indicating high methylene blue removal efficiency with lignosulfonate (Sotelo et al. 2024, Zhang et al. 2020). For lignin-METAC, polymer bridging facilitated by intermolecular forces was likely the main mechanism, resulting in weaker flocculation. Lignin-METAC-SA appeared to utilize a combination of these mechanisms.

As the solution became more alkaline, lignin-based flocculants containing sulfonic acid groups showed a marked improvement in dye reduction efficiency. The basic environment likely neutralized the H+ ions in the sulfonic acid groups, leading to the formation of negatively charged SO_3^- ions after dissociation. This process enhances the flocculants' ability to neutralize the positively charged methylene blue dye. Conversely, the lower reduction efficiency observed with Lignin-METAC may result from the neutralization of its quaternary ammonium group's positive charge.

3.6. Limitations and Future Work

While the current study demonstrates the effectiveness of modified lignin in removing Congo red and methylene blue dyes, a significant limitation is the lack of thorough characterization of the synthesized flocculants. Without detailed analysis, it is difficult to elucidate the precise mechanisms of dye removal. For instance, confirming whether electrostatic charge neutralization, bridging, or sweeping effects are involved requires additional investigations. Determining molecular weight is essential to understanding polymer chain length and its role in interparticle bridging. Tests for solubility and viscosity are necessary to assess the polymer's hydrodynamic volume and conformational stability in dye solutions. Zeta potential analysis is also needed to track surface charge changes and identify the point of zero charge for the flocculants. Until these parameters are measured, the exact mechanisms by which the different flocculants remove dyes cannot be conclusively determined.

4. CONCLUSIONS

Lignin-based flocculants modified with different functional groups were successfully synthesized by grafting METAC and sulfonic acid groups onto the lignin backbone. These modifications enhanced surface functionalities and introduced folding and protrusion structures, which likely increased interactions with target dye molecules. The modified lignins demonstrated improved dye removal capabilities for both Congo red and methylene blue across all pH levels, with Lignin-SA and Lignin-METAC-SA achieving removal efficiencies exceeding 80%. The efficacy of the lignin-based flocculants was influenced by the solution pH: higher removal rates for Congo red occurred under more acidic conditions, while methylene blue removal was more effective in alkaline environments. Although the modified lignins were effective in removing both dyes, they were

less efficient than commercial flocculants for Congo red in neutral and alkaline pH conditions. To deepen understanding of the removal mechanism, further characterization, such as molecular weight and zeta potential analysis, could be performed. Additionally, testing flocculating performance across different temperatures and dosing rates is recommended.

5. ACKNOWLEDGMENTS

The authors wish to acknowledge the support and assistance provided by the Philippine Science High School – Central Luzon Campus towards the completion of this research project. The authors also want to acknowledge the support of the Philippine Science High School, Ilocos Region Campus and the DOST, Industrial Technology Development Institute for assisting in the conduct of scanning electron microscopy and particle size analysis, respectively. This research was funded by the Department of Science and Technology, Republic of the Philippines, Philippine Council for Industry, Energy, and Emerging Technology Research and Development under the Young Innovators Program [PCIEERD Project No.: 1212039].

6. REFERENCES

Ajao, V., Bruning, H., Rijnaarts, H. and Temmink, H., 2018. Natural flocculants from fresh and saline wastewater: Comparative properties and flocculation performances. *Chemical Engineering Journal*, 349, pp.622-632. [DOI]

Alarifi, I.M., Al-Ghamdi, Y.O., Darwesh, R., Ansari, M.O. and Uddin, M.K., 2021. Properties and application of MoS2 nanopowder: Characterization, Congo red dye adsorption, and optimization. *Journal of Materials Research and Technology*, 13, pp.1169-1180. [DOI]

Aro, T. and Fatehi, P., 2017. Production and application of lignosulfonates and sulfonated lignin. *ChemSusChem*, 10(9), pp.1861-1877. [DOI]

Arockiam JeyaSundar, P.G.S., Ali, A., Guo, D. and Zhang, Z., 2020. Waste treatment approaches for environmental sustainability. In: P. Chowdhary, A. Raj, D. Verma and Y. Akhter (eds.) *Microorganisms for Sustainable Environment and Health*. Elsevier, pp.119-135. [DOI]

Chatsungnoen, T. and Chisti, Y., 2019. Flocculation and electroflocculation for algal biomass recovery. In: A. Pandey, J.-S. Chang, C.R. Soccol, D.-J. Lee and Y. Chisti (eds.) *Biofuels from Algae* (Second Edition). Elsevier, pp.257-286. [DOI]

Chu, S., Subrahmanyam, A.V. and Huber, G.W., 2013. The pyrolysis chemistry of a β-O-4 type oligomeric lignin model compound. *Green Chemistry*, 15(1), pp.125-136. [DOI]

Crini, G. and Lichtfouse, E., 2019. Advantages and disadvantages of techniques used for wastewater treatment. *Environmental Chemistry Letters*, 17(1), pp.145-155. [DOI]

Das, N., Ojha, N. and Mandal, S.K., 2021. Wastewater treatment using plant-derived bioflocculants: Green chemistry approach for safe environment. *Water Science and Technology*, 83(8), pp.1797-1812. [DOI]

Englande, A.J., Krenkel, P. and Shamas, J., 2015. Wastewater treatment & water reclamation. In: *Reference Module in Earth Systems and Environmental Sciences*. Elsevier. [DOI]

Eraghi Kazzaz, A. and Fatehi, P., 2020. Fabrication of amphoteric lignin and its hydrophilicity/oleophilicity at oil/water interface. *Journal of Colloid and Interface Science*, 561, pp.231-243. [DOI]

Fauzani, D., Notodarmojo, S., Handajani, M., Helmy, Q. and Kardiansyah, T., 2021. Cellulose in natural flocculant applications: A review. *Journal of Physics: Conference Series*, 2047(1), p.012030. [DOI]

Gao, W., Inwood, J.P.W. and Fatehi, P., 2019. Sulfonation of hydroxymethylated lignin and its application. *Journal of Bioresources and Bioproducts*, 4(2), pp.80-88. [DOI]

Ghernaout, D. and Ghernaout, B., 2012. Sweep flocculation as a second form of charge neutralisation—a review. *Desalination and Water Treatment*, 44(1-3), pp.15-28. [DOI]

Gregory, J. and O'Melia, C.R., 1989. Fundamentals of flocculation. *Critical Reviews in Environmental Control*, 19(3), pp.185-230. [DOI]

Guo, K., Gao, B., Yue, Q., Xu, X., Li, R. and Shen, X., 2018. Characterization and performance of a novel lignin-based flocculant for the treatment of dye wastewater. *International Biodeterioration & Biodegradation*, 133, pp.99-107. [DOI]

Hogg, R., 2013. Bridging flocculation by polymers. *KONA Powder and Particle Journal*, 30, pp.3-14. [DOI]

Jakab, E., Faix, O., Till, F. and Székely, T., 1991. Thermogravimetry/mass spectrometry of various lignosulfonates as well as of a kraft and acetosolv lignin. *Holzforschung*, 45(5), pp.355-360. [DOI]

Kant, R., 2012. Textile dyeing industry an environmental hazard. *Natural Science*, 4(1), pp.22-26. [DOI]

Karpukhina, E.A., Volkov, D.S. and Proskurnin, M.A., 2023. Quantification of lignosulfonates and humic components in mixtures by ATR FTIR spectroscopy. *Agronomy*, 13(4), p.1141. [DOI]

Katheresan, V., Kansedo, J. and Lau, S.Y., 2018. Efficiency of various recent wastewater dye removal methods: A review. *Journal of Environmental Chemical Engineering*, 6(4), pp.4676-4697. [DOI]

Khan, S., Zheng, H., Sun, Q., Liu, Y., Li, H., Ding, W. and Navarro, A., 2020. Synthesis and characterization of a novel cationic polyacrylamide-based flocculants to remove Congo red efficiently in acid aqueous environment. *Journal of Materials Science: Materials in Electronics*, 31(21), pp.18832-18843. [DOI]

Kim, J.-Y., Oh, S., Hwang, H., Kim, U.-J. and Choi, J.W., 2013. Structural features and thermal degradation properties of various lignin macromolecules obtained from poplar wood (Populus albaglandulosa). *Polymer Degradation and Stability*, 98(9), pp.1671-1678. [DOI]

Lee, C.S., Robinson, J. and Chong, M.F., 2014. A review on application of flocculants in wastewater treatment. *Process Safety and Environmental Protection*, 92(6), pp.489-508. [DOI]

Lekniute, E., Peciulyte, L., Klimaviciute, R., Bendoraitiene, J. and Zemaitaitis, A., 2013. Structural characteristics and flocculation properties of amphoteric starch. *Colloids and Surfaces A: Physicochemical and Engineering Aspects*, 430, pp.95-102. [DOI]

Li, Y., Yao, S., Dong, X., Fan, Y., Ma, X., Zhu, B. and Chang, M., 2024. Preparation of a lignin-based cationic flocculant and its application in kaolin suspension treatment. *Polymers*, 16(8), p.1131. [DOI]

Libralato, G., Volpi Ghirardini, A. and Avezzù, F., 2012. To centralise or to decentralise: An overview of the most recent trends in wastewater treatment management. *Journal of Environmental Management*, 94(1), pp.61-68. [DOI]

Litefti, K., Freire, M.S., Stitou, M. and González-Álvarez, J., 2019. Adsorption of an anionic dye (Congo red) from aqueous solutions by pine bark. *Scientific Reports*, 9(1), p.16530. [DOI]

Liu, Z., Xu, D., Xu, L., Kong, F., Wang, S. and Yang, G., 2018. Preparation and characterization of softwood kraft lignin copolymers as a paper strength additive. *Polymers*, 10(7), p.743. [DOI]

Lufrano, F., Baglio, V., Staiti, P., Antonucci, V. and Arico, A.S., 2013. Performance analysis of polymer electrolyte membranes for direct methanol fuel cells. *Journal of Power Sources*, 243, pp.519-534. [DOI]

Moore, C., Gao, W. and Fatehi, P., 2021. Cationic lignin polymers as

flocculant for municipal wastewater. *Polymers*, 13(22), p.3871. [DOI]

Moustaqim, M.E., Kaihal, A.E., Marouani, M.E., Men-La-Yakhaf, S., Taibi, M., Sebbahi, S., Hajjaji, S.E. and Kifani-Sahban, F., 2018. Thermal and thermomechanical analyses of lignin. *Sustainable Chemistry and Pharmacy*, 9, pp.63-68. [DOI]

Rahmawati, L., Azis, M.M. and Rochmadi, R., 2021. Methylene blue removal from wastewater using sodium lignosulfonate and polyaluminium chloride: Optimization with RSM. *AIP Conference Proceedings*, 2349(1), p.020035. [DOI]

Sahoo, S., Seydibeyoğlu, M.Ö., Mohanty, A.K. and Misra, M., 2011. Characterization of industrial lignins for their utilization in future value added applications. *Biomass and Bioenergy*, 35(10), pp.4230-4237. [DOI]

Siti Aisyah, I.S., Siti Norfariha, M.N., Megat Azlan, M.A. and Norli, I., 2014. Comparison of synthetic and natural organic polymers as flocculant for textile wastewater treatment. *Iranica Journal of Energy & Environment*, 5(4), pp.400-408. [DOI]

Solayman, H.M., Hossen, M.A., Abd Aziz, A., Yahya, N.Y., Leong, K.H., Sim, L.C., Monir, M.U. and Zoh, K.-D., 2023. Performance evaluation of dye wastewater treatment technologies: A review. *Journal of Environmental Chemical Engineering*, 11(3), p.109610. [DOI]

Sotelo, S., Oyarce, E., Roa, K., Boulett, A., Pizarro, G. and Sánchez, J., 2024. Sodium lignosulfonate as an extracting agent of methylene blue dye using a polymer-enhanced ultrafiltration technique. *International Journal of Biological Macromolecules*, 275, p.133567. [DOI]

Suryawanshi, M., Kumari, M., Shah, N., Patel, G. and Jalani, S., 2025. Lignin as flocculants. In: M. Jawaid, A. Ahmad and A. Meraj (eds.) *Handbook of Lignin*. Springer Nature Singapore, pp.1-33. [DOI]

Wang, J.P., Chen, Y.Z., Zhang, S.J. and Yu, H.Q., 2008. A chitosan-based flocculant prepared with gamma-irradiation-induced grafting. *Bioresource Technology*, 99(9), pp.3397-3402. [DOI]

Wang, S., Kong, F., Fatehi, P. and Hou, Q., 2018. Cationic high molecular weight lignin polymer: A flocculant for the removal of anionic azo-dyes from simulated wastewater. *Molecules*, 23(8), p.2005. [DOI]

Wibowo, E.S. and Park, B.-D., 2023. Chemical and thermal characteristics of ion-exchanged lignosulfonate. *Molecules*, 28(6), p.2755. [DOI]

Wu, W., Qi, J., Fang, J., Lyu, G., Yuan, Z., Wang, Y. and Li, H., 2022. One-pot preparation of lignin-based cationic flocculant and its application in dye wastewater. *Colloids and Surfaces A: Physicochemical and Engineering Aspects*, 654, p.130082. [DOI]

Wu, W., Zhao, Y., Qi, J., Li, C., Fang, J., Xu, B., Lyu, G., Li, G. and Li, H., 2023. An amphiphilic flocculant with a lignin core for efficient separation of suspended solids. *Separation and Purification Technology*, 314, p.123640. [DOI]

Yaseen, D.A. and Scholz, M., 2019. Textile dye wastewater characteristics and constituents of synthetic effluents: A critical review. *International Journal of Environmental Science and Technology*, 16(2), pp.1193-1226. [DOI]

Yue, B., Zhan, H., Liu, Q. and Liu, M., 2005. Study on the preparation of amphoteric lignin-based flocculant and its flocculation and decolorizing properties. In: *59th Appita Annual Conference and Exhibition: Incorporating the 13th ISWFPC (International Symposium on Wood, Fibre and Pulping Chemistry)*. Carlton, Vic., pp. [DOI]

Zaman, B., Hardyanti, N., Arief Budiharjo, M., Budi Prasetyo, S., Ramadhandi, A. and Tri Listiyawati, A., 2020. Natural flocculant vs chemical flocculant: Which is better to use in wastewater treatment. *IOP Conference Series: Materials Science and Engineering*, 852(1), p.012014. [DOI]

Zhang, X., Lu, A., Li, D., Shi, L., Luo, Z. and Peng, C., 2020. Simultaneous removal of methylene blue and Pb2+ from aqueous solution by adsorption on facile modified lignosulfonate. *Environmental Technology*, 41(13), pp.1677-1690. [DOI]

Nature Environment and Pollution Technology
An International Quarterly Scientific Journal

p-ISSN: 0972-6268
(Print copies up to 2016)
e-ISSN: 2395-3454

Vol. 25 | No. 3 | Article ID B4413 | 2026

Original Research Paper

https://doi.org/10.46488/NEPT.2026.v25i03.B4413

Open Access Journal

Enhancing the Quality of Cellulose Isolated from Banana Peels by Incorporating the Use of Microwave Radiation over the Conventional Method

Pragati More[1], Atul Chaskar[2] and Avinash Pawar[1]†

[1]Department of Chemistry, Bharati Vidyapeeth (Deemed to be University), Y.M. College of Arts, Science and Commerce, Pune, Maharashtra, India

[2]Department of Chemistry, Institute of Chemical Technology, Matunga, Mumbai 400019, Maharashtra, India

†Corresponding author: Avinash Pawar; ssapmore@gmail.com

Abbreviation: Nat. Env. & Poll. Technol.
Website: www.neptjournal.com

Received: 20-11-2025
Revised: 27-01-2026
Accepted: 29-01-2026

Key Words:

Banana peels
Microwave-assisted cellulose isolation
Agricultural waste valorization
Sustainable biopolymers
Process intensification

Citation for the Paper:

More, P., Chaskar, A. and Pawar, A., 2026. Enhancing quality of cellulose isolated from banana peels incorporating use of microwave radiation over conventional method. *Nature Environment and Pollution Technology*, 25(3), B4413. https://doi.org/10.46488/NEPT.2026.v25i03.B4413

Note: From 2025, the journal has adopted the use of Article IDs in citations instead of traditional consecutive page numbers. Each article is now given individual page ranges starting from page 1.

Copyright: © 2026 by the authors
Licensee: Technoscience Publications
This article is an open access article distributed under the terms and conditions of the Creative Commons Attribution (CC BY) license (https://creativecommons.org/licenses/by/4.0/).

ABSTRACT

Cellulose, a renewable biopolymer, can be sustainably extracted from agricultural residues such as banana peels, which are plentiful yet often discarded as waste. Traditional extraction methods are laborious, require prolonged heating, and consume large quantities of chemicals, posing environmental and economic concerns. In this study, a microwave-assisted technique was explored for cellulose extraction from banana peels and compared with conventional thermal treatment under identical chemical conditions. The process involved sequential liquefaction, delignification, and bleaching, with microwave radiation applied at 600 W. Results showed that microwave-assisted extraction significantly improved efficiency, yielding 86.43% cellulose compared to approximately 83% with conventional methods, while reducing processing time from 455 min to just 22 min (excluding 14 min for cycle repetition). FTIR analysis confirmed effective removal of lignin and hemicellulose, XRD indicated preservation of cellulose structure with a crystallinity index of 56.8%, and SEM images revealed smoother, cleaner, and similarly textured cellulose in microwave-treated samples compared to conventional ones. These findings demonstrate that microwave radiation not only enhances cellulose purity and structural quality but also offers significant benefits in energy savings and process sustainability. The resulting cellulose is suitable for applications in packaging, composites, and nanocellulose production. This research establishes microwave-assisted treatment as a scalable, eco-friendly, and time-efficient alternative to traditional methods for converting banana peel waste into high-value cellulose.

1. INTRODUCTION

Cellulose is the most abundant natural polymer, and banana peels are a promising agricultural waste resource for its sustainable extraction. With increasing demand for environmentally friendly and cost-effective methods, microwave radiation has become an efficient alternative. Microwaves enable rapid and uniform heating, which enhances delignification and hemicellulose removal, thereby decreasing both processing time and chemical use compared to traditional hot-plate or reflux techniques.

Microwave-assisted isolation significantly reduces processing time from h to min while producing cellulose with high purity, crystallinity, and thermal stability. This method exploits the abundant availability of banana peels and addresses waste management issues, promoting the valorization of agricultural residues. Consequently, microwave radiation has gained recognition as an environmentally friendly and scalable technique for cellulose extraction, offering benefits in energy efficiency, process sustainability, and potential uses in biocomposites, films, and nanocellulose production.

Compared to traditional heating methods, microwave radiation provides several advantages that make it preferable for extracting cellulose from banana peels.

Conventional processes depend on external conduction and convection, resulting in slow, uneven heating, higher chemical consumption, and longer treatment times. In contrast, microwave energy penetrates directly into the material, inducing rapid molecular vibrations and volumetric heating. This accelerates delignification and hemicellulose removal while reducing cellulose degradation.

By employing microwave-assisted treatment, the process also lowers water consumption and wastewater generation, decreasing the environmental impact of cellulose production due to the use of lower reagent concentrations. Additionally, this method yields highly crystalline and pure cellulose suitable for advanced applications such as biocomposites, packaging films, and nanocellulose-based materials. Overall, microwave radiation offers a greener, cost-effective, and scalable approach for transforming banana peel waste into valuable cellulose resources, supporting sustainable material recovery and the circular economy.

Banana processing generates significant amounts of lignocellulosic residues such as peels, pseudostems, and rachis, which are rich in cellulose but often considered waste. Numerous studies have shown that these residues can be sustainable sources for cellulose extraction. Traditional methods typically involve sequential solvent extraction, alkaline delignification, and oxidative bleaching, resulting in cellulose appropriate for paper manufacturing, bio-composites, and reinforcement materials (Li et al. 2015, Malinen et al. 2014, Faradilla et al. 2016). However, these approaches are time-consuming, energy-intensive, and use large quantities of chemicals, which challenge their economic viability and environmental impact (Alkhorayef et al. 2020, Elanthikkal et al. 2010). Characterization techniques such as FTIR, XRD, and SEM have consistently verified the effective removal of hemicellulose and lignin and the recovery of cellulose with moderate to high crystallinity under these conventional treatments (Szymańska-Chargot et al. 2017, Yadav & Chiu 2019).

Recent research has further emphasized the potential of agro-waste–derived cellulose for valuable applications. Ma'ruf et al. (2023) demonstrated the transformation of cassava peel into functional cellulose acetate membranes, confirming agro-waste as a promising source of cellulose materials with added value. Similarly, Yadav & Pal (2025) found that NaCl pretreatment significantly improved biomass conversion efficiency in cabbage waste. While these studies focus on chemical modification and pretreatment techniques, the impact of microwave-assisted extraction on the quality of cellulose remains underexplored.

Building on this context, the present study aims to isolate cellulose from banana peels using both traditional reflux techniques and a microwave-assisted process at 600 W. This allows for a direct comparison of efficiency and product quality. Specifically, the objectives are: (i) to optimize the steps of liquefaction, delignification, and bleaching for banana peel biomass under both conventional and microwave conditions, (ii) to evaluate and compare the yield, purity, and structural features of the cellulose obtained by each method, and (iii) to explore the potential benefits of microwave-assisted treatment in terms of energy use, processing time, and sustainability. Through these aims, the research seeks to demonstrate microwave radiation as an eco-friendly alternative for converting banana peel waste into high-value cellulose.

To address these limitations, microwave-assisted processing has increasingly been adopted as a method for process intensification. Microwave radiation facilitates rapid volumetric heating, boosting alkali penetration and lignin removal, which shortens reaction times from h to min (Ndruru et al. 2019, Zhou et al. 2017). Comparative research indicates that microwave-assisted delignification and bleaching can produce comparable or higher cellulose purity while using lower chemical dosages and significantly reducing energy consumption (Sudiana et al. 2017, Esmaeili et al. 2017, Rasheed et al. 2019). Studies on banana residues and other agro-wastes such as rice husk, sugarcane bagasse, and almond shells demonstrate the broad applicability of this approach (Meng et al. 2018, Moradian et al. 2017). Typically, optimized protocols utilize mild alkali concentrations (2–6% NaOH) with short radiation cycles at 600–800 W and limited repetitions, followed by peroxide bleaching at alkaline pH (Kumar et al. 2021). These conditions strike a balance between efficiency and cellulose preservation, whereas excessive power or prolonged exposure may lead to depolymerization or fiber damage (Li et al. 2018). In terms of material quality, cellulose produced through microwave-assisted methods shows enhanced whiteness and brightness, increased crystallinity, and cleaner fiber surfaces relative to conventionally treated samples (Xie et al. 2016, Beltramino et al. 2016, Lani et al. 2016). Morphological analyses further confirm reduced lignin encrustation and improved fibrillation readiness, which benefit subsequent nanocellulose production (Rahman et al. 2017). The nanocellulose derived from this process exhibits high aspect ratios, excellent crystallinity, and thermal stability, making it ideal for reinforcing biopolymer films, hydrogels, and packaging materials (Jonoobi et al. 2015, Kargarzadeh et al. 2017). Beyond enhancing product properties, microwave-assisted techniques address sustainability by decreasing energy consumption, reaction duration, and wash water volumes, thus reducing the environmental footprint (Bastos et al. 2020, Bilal & Iqbal 2019).

Despite these advantages, gaps remain in the existing literature. Many studies vary multiple process factors simultaneously, making direct comparisons between microwave and conventional heating difficult (Park et al. 2010, Pereira et al. 2015). Additionally, comprehensive energy balances and techno-economic assessments are limited, and scale-up challenges such as uneven heating and penetration depth require further investigation (Borovikova et al. 2015, Liu et al. 2018). Furthermore, there is a lack of systematic studies linking the structural properties of banana-derived cellulose to its performance in end-use applications (Choi et al. 2020, Gañán et al. 2012). In this context, the present study aims to directly compare conventional and microwave-assisted cellulose extraction from banana peels, using identical chemical treatments. By standardizing alkali and bleaching conditions while only varying the heating mode, this research seeks to provide clear insights into yield, purity, crystallinity, morphology, and sustainability, thereby assessing the true potential of microwave radiation as a green and efficient alternative for cellulose valorization from banana waste.

2. MATERIALS AND METHODS

2.1. Materials and Experimental Setup

Banana peels, sourced locally, were thoroughly washed, chopped into small pieces, and treated with potassium meta-bisulphite to inhibit microbial growth. The material was then shade-dried, ball-milled, and sieved to produce a consistent 200-mesh powder. Reagents used included analytical-grade ethanol, potassium hydroxide (KOH), 30% hydrogen peroxide, and a mild acid for neutralization. The equipment utilized comprised a laboratory microwave oven (ME731K / XEU Solo, 20 L), a hot air oven, a vacuum filtration apparatus, and standard laboratory glassware.

2.2. Methodology

Cellulose isolation was performed through three consecutive steps: liquefaction, delignification, and bleaching. To facilitate a direct comparison, identical chemical protocols were applied for both conventional and microwave treatments. Lower-strength chemicals were employed in microwave-assisted extraction (MAE). The total chemical quantities were divided into smaller portions, and multiple extraction methods were used to introduce novelty into the process. Furthermore, instead of utilizing high-energy radiation (W), comparatively lower-energy microwave radiation was applied over extended periods to enhance the extraction process.

- Liquefaction was performed by suspending ten gs of banana peel powder in 100 mL of 10% ethanol, followed by microwave heating at 600 W for 2 min, with the cycle repeated three times. MAE was conducted across a power range of 500 W to 800 W, and experimental optimization showed that cellulose yield increased with microwave power up to 600 W. Beyond this level, no significant improvements were observed, and signs of thermal degradation appeared, justifying the selection of 600 W as the optimal microwave power. The results aligned with those reported by Kumar et al. (2021). For comparison, conventional extraction involved refluxing 200 mL of 70% ethanol at 70°C for 2–3 h. Under microwave irradiation, rapid darkening of the liquor and browning of the residue indicated efficient removal of soluble extractives in a much shorter time than conventional heating (see Fig. 1).
- Delignification: The liquefied residue was treated with 100 mL of 3% KOH at a solid-to-liquid ratio of 1:20 and subjected to microwave heating at 600 W for 3 min, with the cycle repeated twice. The treated biomass became light tan, adopted a fibrous texture, and was rinsed to neutral pH with fewer washing cycles than conventionally treated material. In contrast, traditional delignification using 200 mL of 4% KOH at 80–90°C required two hours to achieve similar results. The flowchart (Fig. 1) gives the overall methodology for cellulose isolation from banana peels.
- Bleaching: The alkali-treated residue was treated with 3% hydrogen peroxide (100 mL), adjusted to an alkaline pH (10–11), and irradiated at 600 W for 4 min, repeated twice. After two cycles, the sample became off-white, and the filtrate was nearly colorless, indicating removal of residual lignin chromophores. In comparison, conventional bleaching required 200 mL of 10% H_2O_2 at 70°C for 4 h to achieve similar whiteness (Fig. 1).

Neutralization and thorough washing ensured removal of residual chemicals, and controlled drying preserved the integrity of the cellulose fibers.

FTIR, XRD, and SEM analyses were utilized for characterization to verify the removal of non-cellulosic components, assess crystallinity, and observe morphological changes in the treated samples. The final comparative analysis highlighted differences in yield, reaction time, reagent consumption, and cellulose quality between conventional and microwave-assisted methods. This systematic approach not only confirms microwave radiation as a faster and more energy-efficient technique but also underscores its potential for sustainable biomass valorization.

2.3. Characterization of Cellulose

2.3.1. FTIR Spectroscopy

When both the samples were subjected to FTIR Model Ruker alpha Eco-ATR, the spectra observed are shown in Fig. 2.

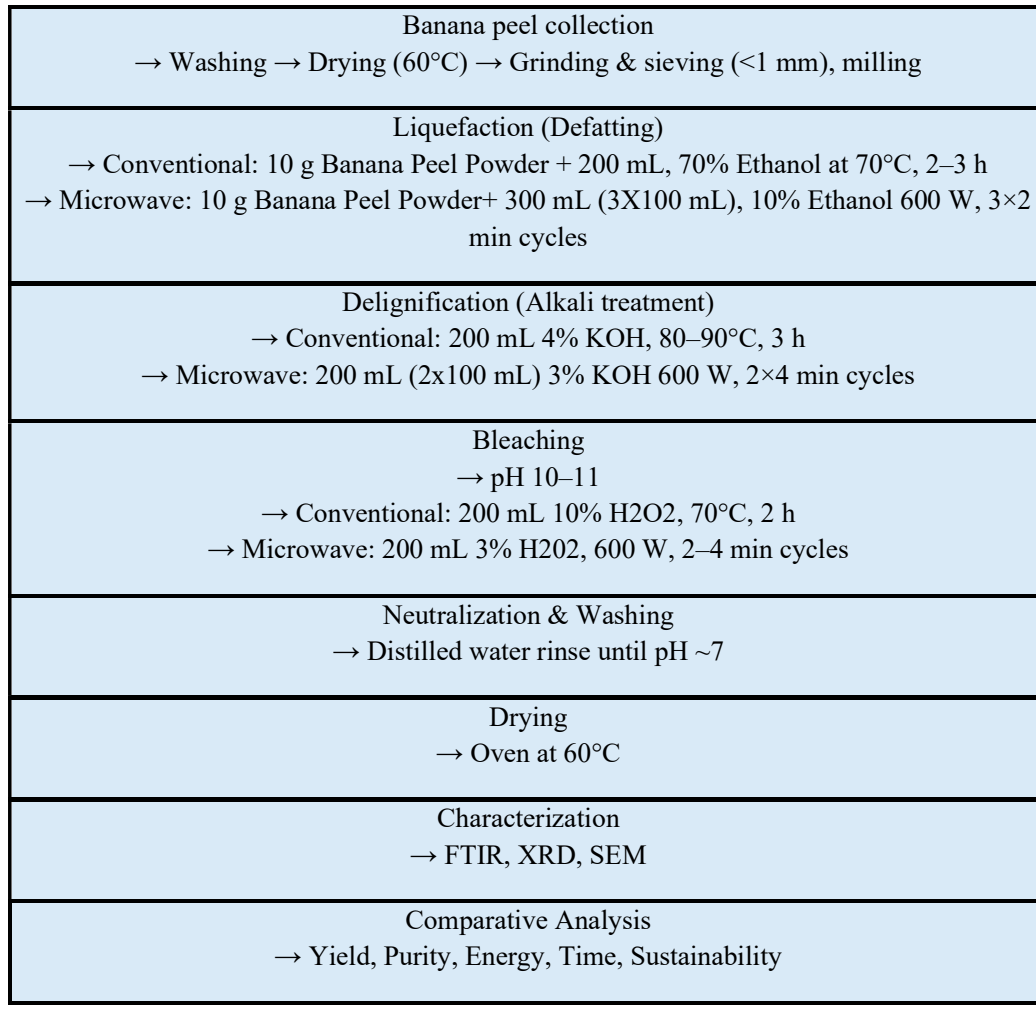


Fig. 1: Research methodology flowchart: Cellulose isolation from banana peels.

The FTIR spectrum of the microwave-treated cellulose, as presented in Table 1, showed the disappearance of the lignin-associated bands at ~1519 cm^{-1} and ~1247 cm^{-1}, confirming the removal of aromatic C=C and carbonyl groups. At the same time, the characteristic cellulose absorption bands were retained, including ~1161 cm^{-1} (C–O–C stretching), ~1052 cm^{-1} (C–O stretching), and ~898 cm^{-1} (β-(1→4) glycosidic bond). These spectral changes confirmed effective delignification and successful isolation of cellulose.

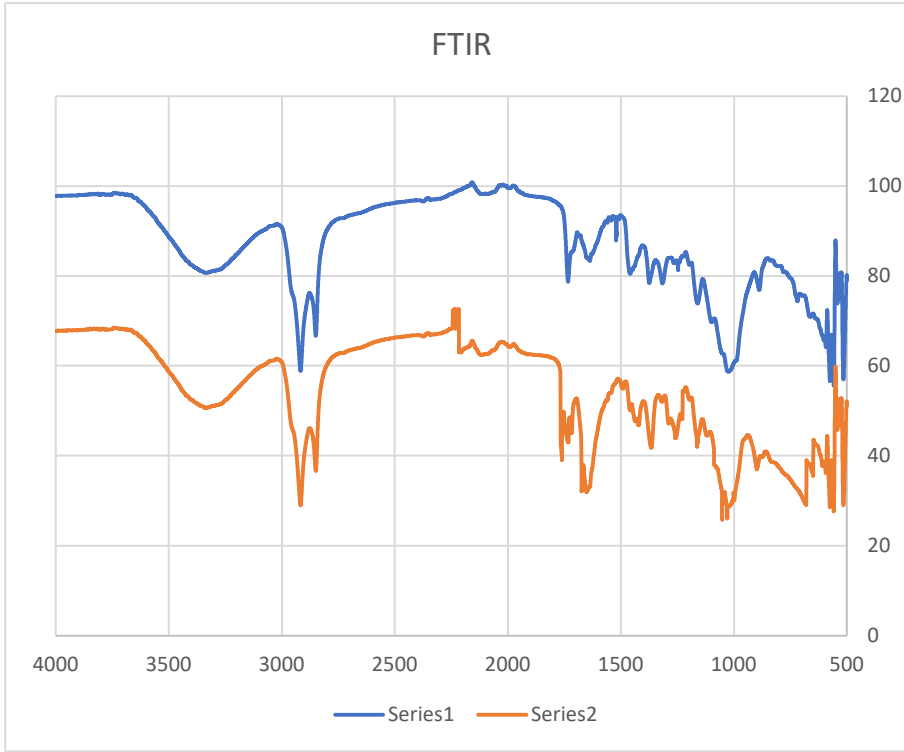
2.3.2. Scanning Electron Microscopy (SEM)

SEM was used to examine the surface morphology of cellulose fibers obtained from banana peels. FESEM: JEOL JSM-IT 200 was used to find particle size and surface morphology. The untreated fibers appeared compact, rough, and covered with impurities such as lignin, hemicellulose, and mineral deposits, with fiber sizes often exceeding 200 µm. After conventional chemical treatment, partial cleaning was observed; however, the fibers remained irregular and rough, with embedded fragments, as seen in Fig. 3, and diameters ranging from 10–200 µm, indicating incomplete removal of non-cellulosic components.

Compared to traditional methods, cellulose isolated using microwave radiation at 600 W showed significantly improved morphology. The fibers were cleaner, smoother, and exhibited partial fibrillation, with fewer surface deposits and enhanced uniformity. Fiber diameters ranged from 5 to 100 µm, as detailed in Table 2, reflecting effective delignification and hemicellulose removal. These morphological enhancements are linked to higher cellulose purity of 86.43% and crystallinity of 56.8%, both achieved at 600 W.

2.3.3. XRD Analysis

XRD analysis was conducted to determine the crystalline structure and crystal size of the isolated cellulose using



Series 1: Conventional Method, Series 2: Microwave Method

Fig. 2: FTIR absorption spectra by two methods.

Table 1: Analytical interpretation of FTIR spectral features of microwave-treated cellulose.

Wavenumber [cm^{-1}]	Assigned functional group/vibration	Analytical implication	Structural inference
~1519	Aromatic C=C stretching (lignin)	Complete disappearance indicates disruption of the aromatic lignin framework	Confirms effective removal of lignin-rich aromatic domains
~1247	C–O stretching of aryl–alkyl ether/ carbonyl groups (lignin/hemicellulose)	Loss of peak reflects cleavage of lignin–carbohydrate linkages	Demonstrates selective delignification and hemicellulose elimination
~1161	C–O–C asymmetric stretching (cellulose backbone)	Persistence of the band indicates chemical stability of cellulose chains	Confirms preservation of the cellulose polymeric framework
~1052	C–O stretching (pyranose ring of cellulose)	Retained intensity signifies intact glucose ring structure	Indicates negligible cellulose depolymerization during microwave treatment
~898	β-(4→1) glycosidic linkage	Presence confirms maintenance of inter-unit linkage	Demonstrates retention of native cellulose connectivity

a Rigaku MiniFlex instrument with Cu Kα radiation (λ= 1.54059Å). The diffractogram of cellulose isolated at 600 W displayed prominent peaks, as shown in Fig. 4, at approximately 22.0–22.5° 2θ, which are characteristic of cellulose. The calculated crystallinity index was 56.8% for cellulose extracted via the MAE method, indicating a higher crystalline content compared to cellulose obtained by the conventional method, which was 37.48%. These results are consistent with reports in the literature for banana pseudostem cellulose (Faradilla et al. 2016, Hayati et al. 2017), suggesting that microwave pretreatment effectively removed amorphous lignin and hemicellulose while preserving the crystalline structure of cellulose.

Crystallinity index for Conventional Method: (Series-I)

Crystallinity Index (CrI) Calculation (Segal Method)

The crystallinity index of cellulose was calculated using the Segal method, expressed as:

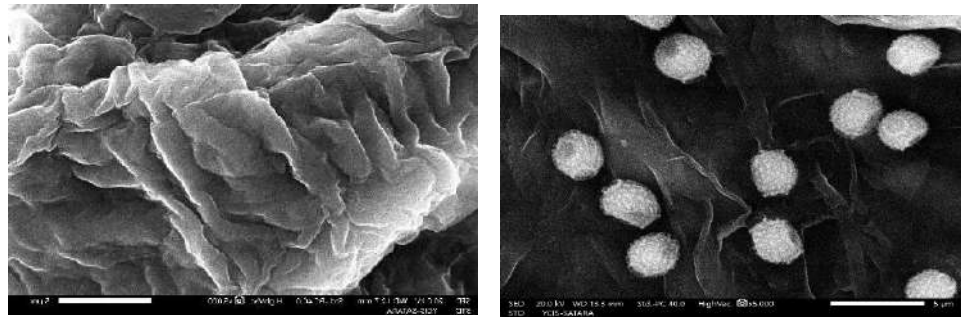
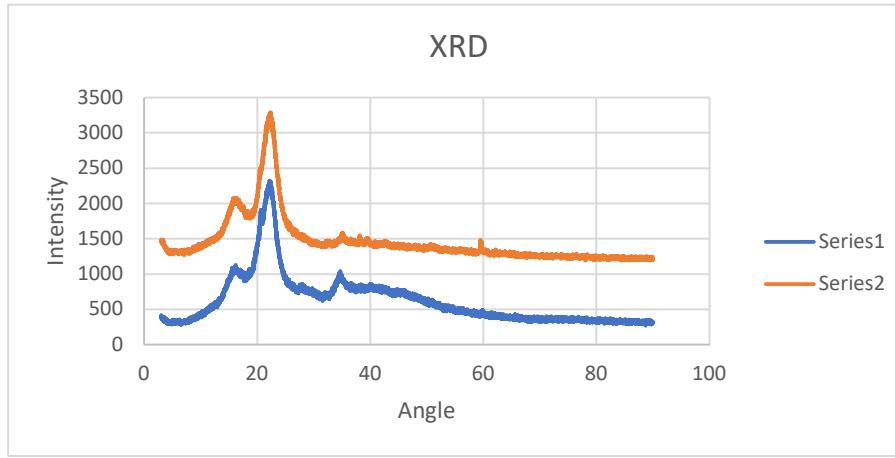


Fig. 3: SEM of cellulose by conventional and microwave methods.

Table 2: Quantitative fibre size distribution.

Sample	Diameter range [μm]	Mean diameter [μm]	Distribution characteristic
Conventional treatment	10–200	~95	Broad, heterogeneous distribution
Microwave treatment (600 W)	5–100	~42	Narrow, uniform distribution



Series 1: Microwave Method, Series 2: Conventional Method

Fig. 4: X-Ray diffraction spectra for cellulose.

$$\text{CrI}\ (\%) = \frac{I_{200} - I_{am}}{I_{200}} \times 100 \quad \ldots(1)$$

Where:

- $I_{200}$is the maximum intensity of the (200) crystalline peak at $2\theta \approx 22.6°$
- I_{am} is the intensity of the amorphous region, typically taken at $2\theta \approx 18°$

From Fig. 4:

- $I_{200} \approx 3215$ (strongest peak at 22.6) for
- $I_{am} \approx 2010$ (average of the nearby medium-intensity region)

Calculated Crystallinity Index

$$\text{CrI} = \frac{3215 - 2010}{3215} \times 100 = 37.48\%$$

The crystallinity index of the cellulose sample was determined to be approximately 37.48%, reflecting a crystalline structure with a balanced mix of crystalline and amorphous regions. This level of crystallinity supports mechanical stability while preserving adequate flexibility.

Crystallinity index for the microwave-assisted extraction method:

Crystallinity Index (CrI) calculation (Segal Method)

The crystallinity index of cellulose was calculated using the Segal method, expressed as:

$$\text{CrI}\ (\%) = \frac{I_{200} - I_{am}}{I_{200}} \times 100 \quad \ldots(1)$$

Where:

- $I_{200}$is the maximum intensity of the (200) crystalline peak at $2\theta \approx 22.6°$,

- $I_{am}$is the intensity of the amorphous region, typically taken at $2\theta \approx 18°$.
- From Fig. 4
- $I_{200} \approx 3215$ (strongest peak at 22.6) for
- $I_{am} \approx 2010$ (average of the nearby medium-intensity region)

Calculated Crystallinity Index

$$CrI = \frac{2350 - 1015}{2350} \times 100 = 56.8\%$$

The crystallinity index of the cellulose sample was determined to be approximately 56.8%, reflecting a crystalline structure with a balanced mixture of crystalline and amorphous regions. This level of crystallinity effectively supports mechanical stability while maintaining adequate flexibility, which is beneficial for membrane fabrication and related material applications.

2.3.4. Quantitative Outcomes at 600 W Microwave Radiation with MAE

Lignin content significantly decreased in the microwave-treated sample, as evidenced by its lighter appearance and enhanced washing efficiency detailed in Table 3. The product yield and quality at 600 W surpassed those achieved by conventional methods, despite the notably shorter treatment duration. Microwave-Assisted Extraction (MAE) conserves approximately 78.57% of ethanol, 25% of alkali, and 70% of H_2O_2. Overall, MAE reduces chemical waste load by 58%.

Though direct energy metering was not conducted, energy consumed was statistically calculated considering power and time. Total energy consumption was reduced from 7.5 kWh to 0.17 kWh with the microwave method (approximately 97.7%) compared to the conventional heating method, as shown in Table 3.

Fig. 5 illustrates the comparison between cellulose content (%) and processing time (min) achieved through conventional heating and microwave-assisted isolation at 600 W. The blue bar chart depicts cellulose content, while the red line plot shows the corresponding processing time for each method.

All experiments were performed in triplicate, with results expressed as mean ± standard deviation. Conventional extraction produced an average cellulose content of 83.12 ± 0.68%, whereas microwave-assisted extraction yielded 86.43

Table 3: Comparison of conventional and microwave (600 W) cellulose isolation.

Method	Conditions	Cellulose content [%]	Processing time	Product appearance	Crystallinity Index [%]	Chemicals Consumed per 10 g bpp
Microwave	600 W, 22 min [i.e. 0.17 kWh]	86.43	22 min	Off-white, fibrous	56.8	Ethanol [30 mL], KOH [6 g], H_2O_2 [6 mL]
Conventional	80–90°C, 7.5 h [i.e. 7.5 kWh]	~83.0	455 min	Tan, less uniform	37.48	Ethanol [140 mL], KOH [8g], H_2O_2 [20 mL]

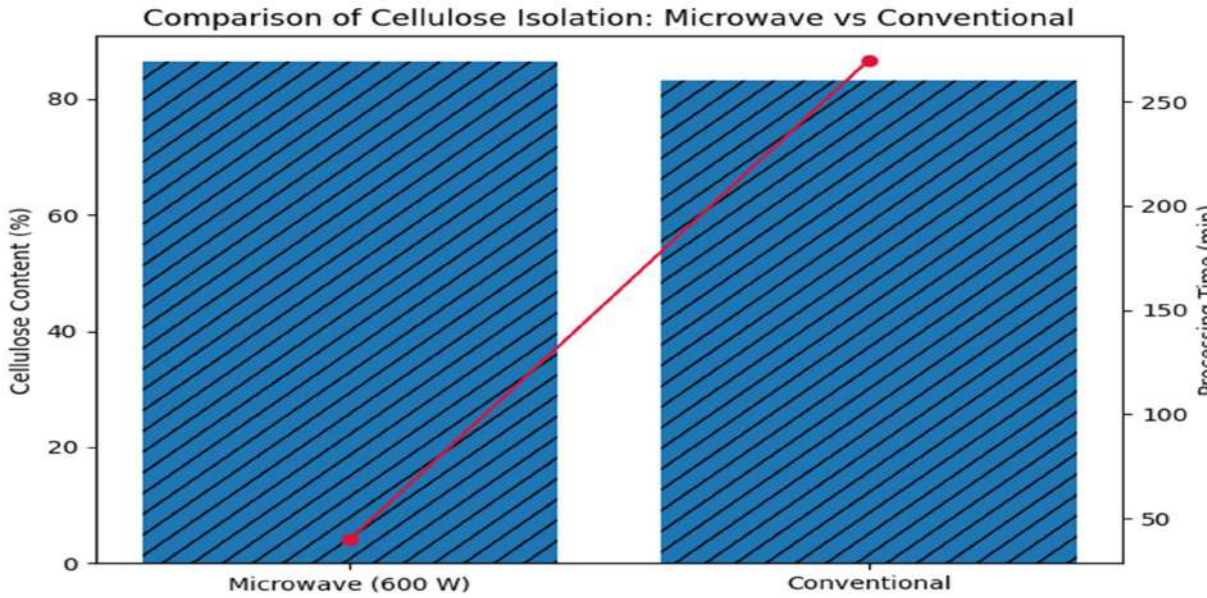


Fig. 5: Comparison of cellulose isolation w. r. t. Time and percentage of cellulose for both methods.

± 0.51%. The standard deviations were calculated using the sample standard deviation formula to assess variability among replicates. An independent two-tailed Student's t-test was conducted to determine if the difference in cellulose content between methods was statistically significant. The test revealed a mean difference of 3.31%, a t value of 6.32, and 4 degrees of freedom. The corresponding two-tailed p value ($p = 0.0032$), obtained from the Student's t distribution, was below the 0.05 significance level, indicating that microwave-assisted extraction significantly increased cellulose content. Although the numerical difference was modest, the results were reproducible and supported by rigorous statistical validation.

3. RESULTS AND DISCUSSION

3.1. Effect of Microwave Radiation on Cellulose Yield

Cellulose was effectively extracted from banana peel powder using 600 W microwave radiation, with results compared to those obtained through traditional chemical treatment. The microwave-assisted process yielded a cellulose content of 86.43%, surpassing the approximately 83% achieved via conventional methods. This higher yield was due to the rapid volumetric heating caused by microwaves, which improved delignification and hemicellulose removal. Furthermore, the overall processing time was significantly reduced from 455 min (7.5 h) with the conventional method to just 22 min with microwave aid, a reduction exceeding 95%. This clearly demonstrates the process intensification enabled by microwave heating, resulting in higher cellulose purity and enhanced time efficiency. The advantages are attributed to the microwave's unique heating mechanism, which involves direct energy coupling with polar molecules, inducing volumetric heating through dipole rotation and ionic conduction. This rapid heating accelerates bond cleavage, chromophore degradation, and mass transfer, facilitating faster delignification and bleaching.

3.2. Structural and Chemical Analysis (FTIR and XRD)

The structural and chemical properties of cellulose extracted from banana peels were examined using FTIR and XRD techniques. The FTIR spectrum of the microwave-treated cellulose showed the disappearance of lignin-related peaks at 1519 cm^{-1} and 1247 cm^{-1}, indicating successful delignification and hemicellulose removal. Meanwhile, characteristic cellulose absorption bands at 1161 cm^{-1} (C–O–C pyranose ring), 1052 cm^{-1} (C–O stretching), and 898 cm^{-1} (β-(1→4) glycosidic linkage) remained, signifying the cellulose structure was preserved. XRD analysis confirmed the presence of native cellulose polymorph, with distinct diffraction peaks at $2\theta \approx 22.0–22.5°$, and a crystallinity index of 56.8%, slightly higher than that of conventionally treated samples. This reflects the removal of amorphous regions and the formation of a more ordered structure. Overall, these findings demonstrate that microwave-assisted isolation enhances the purity and structural order of cellulose while significantly reducing processing time compared to traditional methods.

3.3. Surface Morphology (SEM Analysis)

SEM observations corroborated the spectroscopic results. Untreated banana peel fibers displayed compact, rough surfaces with apparent deposits of lignin and hemicellulose. Following conventional treatment, the surface maintained irregular textures and embedded debris, with diameters spanning 10–200 μm. Conversely, microwave-treated cellulose at 600 W demonstrated smoother surfaces, exposed fibrils, and uniform fiber bundles, with diameters reduced to 5–100 μm. This cleaner, fibrillated morphology aligned with increased cellulose content and crystallinity. The cellulose subjected to conventional treatment showed irregular fiber surfaces with rough textures and residual particles, indicating incomplete lignin and hemicellulose removal. Fiber bundles appeared partially compacted and fragmented, with deposits visible on the surface. These features suggest that, despite prolonged heating, the conventional process only achieved partial delignification and limited fibrillation. In contrast, the microwave-assisted sample exhibited cleaner, smoother, and more fibrillated fibers. The surface was uniform, with fewer impurities and clearer microfibril exposure. Microwave treatment effectively disrupted lignin–carbohydrate linkages, enhancing fiber separation and surface purification. Overall, SEM analysis confirms that microwave-assisted isolation markedly improves surface morphology, yielding cellulose with cleaner surfaces better suited for downstream applications such as nanocellulose production and composite reinforcement.

3.4. Comparative Performance and Sustainability

Overall, microwave-assisted isolation at 600 W yielded cellulose with higher purity, enhanced crystallinity, and improved morphology in a fraction of the time required by conventional heating. Using less concentrated solutions also reduces pollutant loads in wastewater. Additionally, the shorter process and fewer washing cycles lead to lower energy and water consumption, making this method more environmentally sustainable. These benefits position microwave radiation as a scalable and eco-friendly alternative for extracting cellulose from agro-waste, such as banana peel.

4. CONCLUSIONS

This study demonstrated the successful extraction of cellulose from banana peels using microwave radiation at 600W, providing a superior alternative to traditional thermal methods. The microwave-assisted approach achieved a higher cellulose content (86.43%) with enhanced crystallinity (56.8%) and cleaner fiber morphology, while drastically reducing processing time by 95%. FTIR analysis confirmed the effective removal of lignin and hemicellulose, XRD verified the preservation of cellulose I structure, and SEM images showed smoother, fibrillated fibers compared to conventional samples.

The results clearly position microwave radiation as a quick (saving around 95% of processing time), energy-efficient (approximately 97.7% energy saving) method compared to conventional heating, highlighting its superiority in energy conservation and sustainability for cellulose isolation. Additionally, chemical waste was reduced by 58%, which lowered water consumption during washing and cleaning steps. This method not only improves yield and quality but also promotes waste valorization and environmental sustainability. The cellulose produced is suitable for diverse applications such as biocomposites, packaging films, and nanocellulose production.

5. ACKNOWLEDGMENTS

In this section, you can acknowledge any support given that is not covered by the author contribution or funding sections. This may include administrative and technical support or donations in kind (e.g., materials used for experiments).

6. REFERENCES

Alkhorayef, M., Al-Zahrani, S.M. and Khan, W.S., 2020. Microwave-assisted extraction and characterization of cellulose nanocrystals from agricultural residues: a review. *Cellulose*, 27(16), pp.9157-9179. [DOI]

Bastos, V., Costa, A.O.S., Silva, R.F., Tavares, T. and Pintado, M.E., 2020. Microwave-assisted pretreatment of lignocellulosic biomass for bioethanol production: a review. *Renewable and Sustainable Energy Reviews*, 119, p.109564. [DOI]

Beltramino, F., Roncero, M.B., Vidal, T., Valls, C. and Montané, D., 2016. Extraction and characterization of cellulose nanocrystals from soybean hulls by microwave-assisted treatments. *Carbohydrate Polymers*, 153, pp.236-243. [DOI]

Bilal, M. and Iqbal, H.M.N., 2019. Lignocellulosic biomass: green fuels, chemicals and materials via integrated biorefinery approaches. *Renewable and Sustainable Energy Reviews*, 107, pp.123-132. [DOI]

Borovikova, E., Pantic, M., Kostic, M. and Nikolic, T., 2015. Microwave-assisted production of cellulose nanocrystals. *Carbohydrate Polymers*, 122, pp.280-288. [DOI]

Choi, S., Lee, D. and Kim, J., 2020. Isolation of cellulose nanofibers from banana peel and their reinforcement effect in biodegradable films. *Industrial Crops and Products*, 155, p.112799. [DOI]

Elanthikkal, S., Gopalakrishnapanicker, U., Varghese, S. and Guthrie, J.T., 2010. Cellulose microfibres produced from banana plant wastes: isolation and characterization. *Carbohydrate Polymers*, 80(3), pp.852-859. [DOI]

Esmaeili, H., Hashemi, S.J., Esmaeilzadeh, Z. and Yeganeh, A., 2017. Microwave-assisted delignification and nanofibrillation of lignocellulosic fibers. *Industrial Crops and Products*, 109, pp.241-248. [DOI]

Faradilla, R.H.F., Lee, G., Rawal, A., Hutomo, T., Stenzel, M.H. and Arcot, J., 2016. Nanocellulose characteristics from the inner and outer layer of banana pseudostem prepared by TEMPO-mediated oxidation. *Cellulose*, 23(5), pp.3023-3037. [DOI]

Gañán, P., Cruz, J., Garbizu, S., Arbelaiz, A., Llano-Poncio, C. and Mondragon, I., 2012. Treatment of banana fiber for use in composite materials. *Composites Part B: Engineering*, 43(4), pp.1909-1916. [DOI]

Hayati, N., Rahman, A., Chieng, B.W. and Rahman, N.A., 2017. Extraction and characterization of cellulose nanocrystals from tea leaf waste fibers. *Polymers*, 9(11), p.588. [DOI]

Jonoobi, M., Harun, J., Mathew, A.P., Hussein, M.Z.B., Oksman, K. and Dufresne, A., 2015. Comparative study of cellulose nanofiber and nanocrystal production from different biomass sources. *Cellulose*, 22(2), pp.935-951. [DOI]

Kargarzadeh, H., Mariano, M., Huang, J., Lin, N., Ahmad, I., Dufresne, A. and Thomas, S., 2017. Recent developments in nanocellulose-based biodegradable polymers and nanocomposites. *Carbohydrate Polymers*, 181, pp.403-416. [DOI]

Kumar, A., Negi, Y.S., Bhardwaj, N.K. and Choudhary, V., 2021. Microwave-assisted extraction of cellulose from pineapple leaf waste. *International Journal of Biological Macromolecules*, 190, pp.208-218. [DOI]

Lani, N.S., Ngadi, N., Johari, A. and Jusoh, M., 2016. Isolation, characterization and application of nanocellulose from banana fiber: a review. *Cellulose*, 23(4), pp.2191-2212. [DOI]

Li, T., Chen, C., Broda, S. and Lozano-García, D.F., 2018. High-efficiency microwave-assisted delignification of wheat straw. *Bioresource Technology*, 268, pp.390-396. [DOI]

Li, W., Zhang, Y., Li, J., Zhou, Y., Li, R. and Zhou, W., 2015. Characterization of cellulose from banana pseudostem by heterogeneous liquefaction. *Carbohydrate Polymers*, 132, pp.513-519. [DOI]

Liu, H., Saleh, A.S., Zou, D. and Zhao, H., 2018. Microwave-assisted ionic liquid pretreatment for cellulose extraction. *Carbohydrate Polymers*, 181, pp.778-785. [DOI]

Malinen, R.O., Sarkar, M.A.R., Ibne, F., Imam, A. and Khan, M.Z.H., 2014. Papermaking from banana pseudostem: characterization and comparison. *Journal of Natural Fibers*, 11(3), pp.199-211. [DOI]

Ma'ruf, A., Puspawiningtiyas, E., Afifah, D.N. and Diaz, E., 2023. Synthesis and characterization of cellulose acetate membrane from cassava peel for microfiltration. *Nature Environment and Pollution Technology*, 22(3), pp.1513-1518. [DOI]

Meng, F., Wang, G., Du, X., Wang, Z., Xu, S. and Zhang, Y., 2018. Preparation and characterization of cellulose nanofibers and nanocrystals from liquefied banana pseudostem residue. *Composites Part B: Engineering*, 160, pp.341-347. [DOI]

Moradian, M., Madadi, M., Pourrahim, S., Hosseinabadi, R. and Fathi, M., 2017. Microwave-assisted extraction of cellulose nanocrystals from rice husk. *Carbohydrate Polymers*, 175, pp.1-8. [DOI]

Ndruru, S.T.C.L., Wahyuningrum, D., Bundjali, B. and Arcana, I.M., 2019. Green simple microwave-assisted extraction of cellulose from Theobroma cacao L. husk. *IOP Conference Series: Materials Science and Engineering*, 541, p.012012. [DOI]

Park, S., Baker, J.O., Himmel, M.E., Parilla, P.A. and Johnson, D.K., 2010. Cellulose crystallinity index: measurement techniques and impact. *Biotechnology for Biofuels*, 3, p.10. [DOI]

Pereira, P.H.F., Corrêa, A.C., de Oliveira, A.C., de Lima Éder, M. and Ramos, G.R., 2015. Cellulose extraction by alkaline-peroxide method. *Carbohydrate Polymers*, 130, pp.95-103. [DOI]

Rahman, M.M., Jahan, M.S., Eshita, Y.J., Khanday, W.A. and Das, A.K., 2017. Isolation and characterization of cellulose from banana peel and fabrication of biocomposites. *International Journal of Biological Macromolecules*, 98, pp.588-596. [DOI]

Rasheed, S., Un Nisa, F., Javed, M., Raza, W. and Ijaz, A., 2019. Microwave-assisted extraction of cellulose from sugarcane bagasse. *Industrial Crops and Products*, 137, pp.13-21. [DOI]

Sudiana, I.N., Mitsudo, S., Susilowati, P.E., Trisna, I.G.A.A.M. and Suyasa, I.W.B., 2017. Fast microwave-assisted pretreatment for bioconversion of sawdust lignocellulose to glucose. *Journal of Physics: Conference Series*, 846, p.012013. [DOI]

Szymańska-Chargot, M., Chylińska, M., Gdula, K., Kozioł, A. and Zdunek, A., 2017. Isolation and characterization of cellulose from different fruit and vegetable pomaces. *Polymers*, 9(10), p.495. [DOI]

Xie, J., Hse, C., de Hoop, C.F., Hu, T.Q. and Shupe, T.F., 2016. Isolation and characterization of cellulose nanofibers from bamboo using microwave liquefaction combined with chemical treatment and ultrasonication. *Carbohydrate Polymers*, 151, pp.725-734. [DOI]

Yadav, M. and Chiu, F., 2019. Cellulose nanocrystals reinforced κ-carrageenan-based UV-resistant films: transparent bionanocomposites for sustainable packaging applications. *Carbohydrate Polymers*, 211, pp.181-194. [DOI]

Yadav, S. and Pal, J., 2025. Sustainable biomass conversion: impact of NaCl pretreatment on cabbage waste. *Nature Environment and Pollution Technology*, 24(2), pp.1-8. [DOI]

Zhou, L., Budarin, V., Fan, J., Sloan, R. and Macquarrie, D., 2017. Efficient method of lignin isolation using microwave-assisted acidolysis and characterization of the residual lignin. *ACS Sustainable Chemistry & Engineering*, 5(5), pp.3768-3774. [DOI]

Nature Environment and Pollution Technology
An International Quarterly Scientific Journal

p-ISSN: 0972-6268
(Print copies up to 2016)
e-ISSN: 2395-3454

Vol. 25 | No. 3 | Article ID D1879 | 2026

Original Research Paper

https://doi.org/10.46488/NEPT.2026.v25i03.D1879

Open Access Journal

Total Chromium Removal and Mass Balance in a Hybrid Constructed Wetland Using *Scirpus americanus* and *Hydrocotyle bonariensis* for Tannery Wastewater Treatment

Edgar Santiago Flores-Sacsi, Anyela Keith Delgado-Salas, Marco Guillermo Ancco Chara and Gerby Giovanna Rondán-Sanabria†

Universidad Tecnológica del Perú, Instituto de Energías Renovables, Av. Tacna y Arica No 160, Arequipa, Perú

†Corresponding author: Gerby Giovanna Rondán-Sanabria; c16238@utp.edu.pe

Abbreviation: Nat. Env. & Poll. Technol.
Website: www.neptjournal.com

Received: 02-10-2025
Revised: 13-12-2025
Accepted: 17-12-2025

Key Words:

Constructed wetlands
Chromium removal
Tannery effluents
Mass balance
Phytoremediation

Citation for the Paper:

Flores-Sacsi, E.S., Delgado-Salas, A.K., Ancco Chara, M.G. and Rondán-Sanabria, G.G., 2026. Total chromium removal and mass balance in a hybrid constructed wetland using *Scirpus americanus* and *Hydrocotyle bonariensis* for tannery wastewater treatment. *Nature Environment and Pollution Technology*, 25(3), D1879. https://doi.org/10.46488/NEPT.2026.v25i03.D1879

Note: From 2025, the journal has adopted the use of Article IDs in citations instead of traditional consecutive page numbers. Each article is now given individual page ranges starting from page 1.

Copyright: © 2026 by the authors
Licensee: Technoscience Publications
This article is an open access article distributed under the terms and conditions of the Creative Commons Attribution (CC BY) license (https://creativecommons.org/licenses/by/4.0/).

ABSTRACT

Tannery effluents contain high concentrations of total and hexavalent chromium, posing severe environmental risks, particularly in developing regions where inadequate treatment persists. Conventional remediation methods are often costly and complex, generating secondary pollutants and underscoring the need for sustainable alternatives. The present research evaluates the effectiveness of a hybrid constructed wetland at pilot scale for removing total chromium from final tannery effluents, applying a mass balance approach. The system comprised two levels: *Scirpus americanus* Pers. in the upper level and *Hydrocotyle bonariensis* Lam. in the lower level, each operated with a seven-day hydraulic retention time. Results showed significant total chromium removal, with the upper level retaining 47.82% in the substrate, 31.85% in roots, and 10.57% in aerial parts of *Scirpus americanus*. The lower level retained 53.53% in roots and 43.31% in aerial parts of *Hydrocotyle bonariensis*. Physicochemical parameters (pH, temperature, TSS, BOD, COD, and total hexavalent chromium) were measured before and after treatment. Tolerance indices decreased in *Scirpus* and increased in *Hydrocotyle*, while both species' bioconcentration and translocation factors rose. Overall, the findings demonstrate this hybrid system's effectiveness and ecological feasibility for chromium removal, underscoring its promise as a cost-efficient alternative for treating industrial effluents.

1. INTRODUCTION

Water is vital for all living organisms; nonetheless, aquatic ecosystems are increasingly threatened by untreated discharges from industrial, agricultural, and domestic activities (Chen et al. 2018). Industrial effluents contribute nearly 16% of the world's wastewater production. Among these, the leather tanning sector, which operates in many countries, including Peru (Alemu et al. 2019), manufactures nearly one million square meters of leather annually. At this production level, there is the release of approximately 41 million liters of chromium-rich effluents annually (Vilardi et al. 2018).

Tannery wastewater generally shows elevated salinity and oxygen demand parameters (BOD and COD), along with numerous harmful chemical compounds (Younas et al. 2022). Chromium is widely used in tanning because it provides leather with durability and a uniform finish. However, a substantial proportion of chromium salts remains unbound and is discharged with the wastewater, resulting in trivalent and hexavalent chromium. The latter is especially harmful to aquatic environments (Ahmad et al. 2020). Consequently, chromium pollution in receiving waters disrupts trophic chains and networks, creating considerable risks for ecosystems and human health (Elabbas et al. 2016).

Different technologies have been proposed to eliminate chromium from industrial wastewater, involving physicochemical processes including pressure-driven osmosis, sorption methods, membrane technologies, ion-exchange processes, chemical precipitation, and activated carbon treatment (Bibi et al. 2018). In addition, biological approaches using fungi, cyanobacteria, and yeasts have also been tested (Pradhan et al. 2017). Despite their reported effectiveness, these methods are often costly, technically demanding, and may generate secondary toxic sludge (Malaviya & Singh 2016). Consequently, constructed wetlands are increasingly considered an economical and environmentally sustainable option. These systems rely on phytoremediation mechanisms involving macrophytes, microbial communities, and supporting substrates such as gravel to eliminate pollutants, including chromium (Younas et al. 2022).

At the Río Seco Industrial Park (PIRS), the tanning industry discharges large volumes of untreated effluents into oxidation ponds that frequently exceed their holding capacity, leading to the percolation of chromium and other metals into surrounding ecosystems. This situation generates environmental degradation and displeasing odors affecting nearby communities. The Añashuayco Creek receives these discharges, and environmental assessments by the Environmental Evaluation and Control Agency (OEFA) have documented elevated levels of pH, total suspended solids (TSS), BOD_5, COD, and total chromium in the effluents (MINAM 2017). Although constructed wetlands have demonstrated efficiency in pollutant removal, additional studies are required to clarify the distribution and fate of chromium within these systems, particularly under the specific environmental conditions of the Arequipa region.

The wastewater generated at PIRS remains a serious concern because of its elevated concentrations of total and hexavalent chromium, BOD, COD, TSS, pH, and EC. Despite the partial reuse of this water within the tanning process, contaminant levels persist well above the maximum permissible limits (MPLs) defined by Peruvian regulations. In addition, untreated effluents are diverted to the sewage network and eventually overflow into oxidation ponds. According to OEFA's reports, these ponds have collapsed, leading to irrigation water contamination and deterioration of environmental quality standards for agricultural use (MINAM 2017).

Although several treatment technologies have been explored, many involve complex operations and require high reagent inputs that result in secondary pollutants (Malaviya & Singh 2016, Younas et al. 2022). In contrast, using constructed or natural wetlands, phytoremediation offers a cost-effective and sustainable solution. These systems rely on the synergistic interaction between plants, substrates, and rhizospheric microorganisms to facilitate the reduction of metallic contaminants through phytoextraction and adsorption processes (Saeed et al. 2021, Liu et al. 2025, Rajput et al. 2025).

Conventional methods for treating industrial effluents are often unfeasible due to their operational complexity, high costs, and hazardous waste production (Bibi et al. 2018). Constructed wetlands offer an effective treatment option, combining substrates such as gravel, macrophytes, and microbial communities that purify wastewater through mechanisms including absorption, microbial transformation, and plant-assisted remediation (Wang et al. 2019, Lin et al. 2025, Rajput et al. 2025). Compared with traditional physicochemical and biological systems, these engineered wetlands stand out for their cost-effectiveness and ecological compatibility in treating municipal and industrial discharges (Sultanaa et al. 2014).

Recent studies underscore the global interest in developing advanced phytoremediation systems for chromium-contaminated wastewater. Zulfqar et al. (2025) demonstrated that combining *Cannabis sativa* and *Lolium perenne* with biochar and zinc-based nanomaterials (Zn-nZVI) enhances chromium removal efficiency through increased metal uptake and soil amendment. Similarly, Kumar et al. (2025) reported that *Vetiveria* spp., when integrated with Arbuscular mycorrhizal fungi (AMF), significantly improved plant tolerance to Cr stress and enhanced translocation mechanisms, suggesting synergistic benefits in wetland systems. These findings highlight innovative pathways for optimizing wetland performance and reinforce the relevance of plant–microbe–substrate interactions in future chromium remediation strategies. Finally, the species used in this research study are endemic to the Arequipa region. In addition, the study incorporated a mass balance analysis to quantify the inputs, outputs, and accumulation of chromium in the different components of the constructed wetland system. Previous studies have not reported research involving these species or analyses of their mass balance, which highlights a knowledge gap and underscores the need for studies that contribute to a better understanding of their dynamics.

Therefore, implementing such constructed wetland systems as cost-effective alternatives to conventional treatments necessitates a comprehensive evaluation of chromium dynamics within the system during the phytoremediation process.

2. MATERIALS AND METHODS

2.1. Treatment-Setup

The experimental work was undertaken at the Universidad Tecnológica del Perú, campus Arequipa, between September and November 2023. The experimental setup consisted of a hybrid artificial wetland system using 4-liter plastic buckets mounted on a metal frame with wooden supports, maintaining a 1% slope. *Scirpus americanus* Pers. was planted in coarse washed sand at the upper level, while *Hydrocotyle bonariensis* Lam. was allowed to float freely at the lower level.

The independent variable was the hydraulic retention time; that is, a volume of effluent corresponding to 38% of the container's capacity remained in the containers for a period of 7 days for subsequent contaminant removal. At both levels, the treatment conditions involved low oxygen pressure because the wetlands remained continuously flooded with the effluent. The plant species used in the upper level was Scirpus americanus, inserted into an inert substrate (washed coarse sand). Finally, approximately 10 plants per container were used at both the upper and lower levels.

Treatment units were irrigated with tannery effluent diluted to 30%, due to in previous tests the percentage of plant mortality exceeded 50%; therefore, that concentration was selected. When applied to a larger-scale wetland system, the water used to dilute the effluent would be the treated water discharged from the wetlands. Two types of control units were used: one containing only substrate and water, and another containing plants but no effluent. All treatments were performed in triplicate to ensure statistical robustness. The system functioned by gravity flow, where the effluent was initially applied to the upper stage with a hydraulic retention period (HRT) of seven days, then directed to the lower stage for another seven days. This sequence was repeated three times, resulting in a total treatment period of 21 days (Fig. 1).

2.2. Plant Material and Effluent Characteristics

The plant species *Scirpus americanus* Pers. and *Hydrocotyle bonariensis* Lam. were collected from the district of Characato, Arequipa (16º28'19.10'' S, 71º28'39.41'' W; 2459 masl), and transferred to the university laboratory. Upon arrival, the specimens were thoroughly rinsed to eliminate organic matter and associated organisms. *Scirpus americanus* was transplanted into 4-liter containers filled with coarse, washed sand, which served as an inert substrate to support root development. Additional sand was also placed at the faucet outlet of each container to facilitate uniform effluent drainage.

The effluent used in the experiment was a composite sample obtained from multiple stages of the tanning process, including soaking, liming, dehairing, tanning, dyeing, and retanning, collected at the Río Seco Industrial Park (PIRS). These samples were mixed in equal proportions and diluted to 30% prior to application in the treatment units.

2.3. Analytical Procedures

The following parameters were monitored at 0, 7, 14, and 21 days. The monitored variables included pH, temperature,

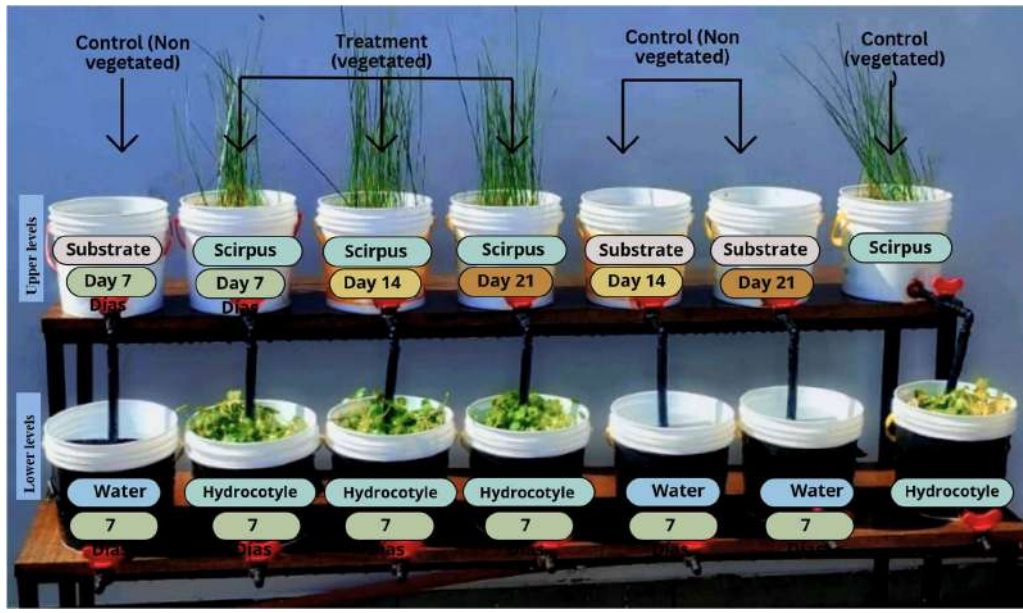


Fig. 1: Schematic of the hybrid artificial wetland system and treatment and sampling schedule.

TSS, BOD_5, COD, and both total chromium and hexavalent chromium.

Chromium analysis: Total and Cr VI concentrations were determined using colorimetric digestion methods with HNO_3 and H_2SO_4.

BOD_5: Samples were adjusted to pH 6.5–7.5, incubated in Winkler flasks at 20°C for 5 days, and DO was measured before and after.

COD: Samples were digested with $K_2Cr_2O_7$ and H_2SO_4 at 150°C and absorbance measured at 600 nm and chemical oxygen demand was calculated by:

$$COD\ in\ (mgO_2/L) = \frac{mgO_2\ in\ final\ volume \times 1000}{mL\ sample} \quad \ldots(1)$$

TSS: The samples were passed through filters, dried in an oven at 105°C, and measured gravimetrically.

$$mg\ SST/L = \frac{(A-B)\times 1000}{sample\ volume\ (mL)} \quad \ldots(2)$$

A corresponds to the combined weight of the filter paper and the dried sample, while B represents only the filter paper weight.

2.4. Indicators of plant response

To evaluate phytoremediation efficiency, several indicators were calculated:

Tolerance index (TI): obtained from the ratio between the biomass of plants exposed to chromium (Bt) and that of control plants (Bc) (Shi et al. 2011).

$$TI = \frac{Bt}{Bc} \quad \ldots(3)$$

Bioconcentration factor (BCF): determined by dividing chromium concentration in stems (C_{stems}, ppm) by chromium concentration in the water solution ($C_{solution}$, ppm) (Liu et al. 2008).

$$BCF = \frac{C_{stems}}{C_{solution}} \quad \ldots(4)$$

Translocation factor (TF): determined by calculating the proportion of chromium present in the aerial tissues (C_{stems}, ppm) relative to its concentration in the roots (A_{roots}, ppm) (Ribeiro de Souza et al. 2012).

$$TF = \frac{A_{stems}}{A_{roots}} \quad \ldots(5)$$

Removal efficiency (E%): calculated according to (Meneses Barroso et al. 2019):

$$E(\%) = \frac{C_i - C_s}{C_i} \quad \ldots(6)$$

Where C_i refers to the chromium concentration entering the system and C_s corresponds to the concentration leaving it after treatment.

2.5. Mass Balance and Chromium Distribution

The distribution of total chromium across the different components of the pilot artificial wetland system was calculated in the following steps: First, the chromium concentrations (in ppm) were measured in water, substrate, roots, and the aerial harvestable parts. Next, the mass (in kilograms) and volume (in liters) of each component were determined. Finally, a mass balance was calculated by multiplying the chromium concentration by the mass or volume of each component, with results expressed as percentages. This evaluation was conducted at 0, 7, 14, and 21 days of testing.

2.6. Statistical analysis

The experimental units were randomly distributed using random numbers in Microsoft Excel software. Statistical tests of the results were performed by repeated measures ANOVA to detect the statistical significance of the variability among treatments; Duncan's multiple range test ($p<0.05$) was performed using STATGRAPHICS CENTURION statistical software. Finally, the graphs were made using SIGMAPLOT 12.0 graphing software.

3. RESULTS

3.1. Determination of Physicochemical Characteristics in Tanning Effluents

Table 1 presents the results of the effluents from the leather tanning process, both before and after treatment with Scirpus americanus Pers. and Hydrocotyle bonariensis. Additionally, the Maximum Permissible Limits (MPL) values according to DS Nº 010-2023-MINAM are included for comparison. Untreated effluents show BOD5, COD, and total chromium concentrations that exceed the MPL. Specifically, BOD5 exceeds the limit by 38 times, COD by 125 times, and total chromium by 484 times. Moreover, the pH of 5.84 is outside the permissible range of 6 to 9. Regarding temperature, TSS, and Cr VI, these values are within the limits established by the MPL.

After applying the wetland treatment, the pH, temperature, TSS, BOD5, Cr VI, and total chromium values were all below the MPL. The removal efficiency was determined to be 86.04% for TSS, 97.39% for BOD5, and 99.98% for total chromium. In the case of COD, although the final value remained above the MPL, it was reduced from an initial value of 6276 $mg.L^{-1}$ to 80 $mg.L^{-1}$, achieving a removal efficiency of 98.73%.

Table 1: Values of physicochemical parameters in the effluents, before treatment (tanning effluent) and after treatment with the wetlands.

Parameter	Unit of Measurement	Before treatment	After treatment	LMP
pH	pH units	5.84	7.16	6 - 9
Temperature	ºC	25.3	22.8	35
TSS	$mg.L^{-1}$	4.37	0.61	30
BOD_5	$mg.L^{-1}$	1150.50	30	30
COD	$mg.L^{-1}$	6276.00	80	50
Chromium VI	$mg.L^{-1}$	0.02	<0.02	0.1
Total Chromium	$mg.L^{-1}$	242.10	0.05	0.5

3.2. Total Chromium Accumulation in Water, Substrate, Roots and Leaves of the Plants *Scirpus americanus* Pers. and *Hydrocotyle bonariensis* Lam.

Fig. 2A illustrates the temporal mobilization of total chromium in the various components of the upper level of the wetland system. In the water component, a notable decrease with statical relevance (P<0.05) in total chromium concentration was observed, decreasing from an initial value of 242.10 ppm to 6.55 ppm after seven days of treatment, which corresponds to a removal efficiency of 97.29%. By day 14, the concentration further declined to 3.29 ppm, achieving 98.64% efficiency, and by day 21, it reached 2.79 ppm. However, this final reduction was not statistically significant compared to day 14 (P>0.05), with an overall efficiency of 98.85%.

In the substrate component, the initial chromium concentration of 0.8 ppm increased significantly (P<0.05) over time, reaching 51.32 ppm by day 21. Regarding the plant species *Scirpus americanus* Pers., initial concentrations of total chromium in the roots and aerial parts were 1.67 ppm and 1.55 ppm, respectively. Both plant parts exhibited statistically significant increases (P<0.05) throughout the treatment period. By day 21, the roots accumulated a maximum concentration of 109.38 ppm, while the aerial parts reached 90.78 ppm.

In contrast, the control system (non-vegetated wetland) showed a less efficient reduction of total chromium in the water. The concentration dropped significantly (P<0.05) from 242.10 ppm to 172.16 ppm after seven days, representing a removal efficiency of 28.89%. At 14 days, the concentration further decreased to 160.75 ppm, although this change was not statistically significant (P>0.05), with an efficiency of 33.60%. By day 21, the final concentration was 154.76 ppm (P>0.05), corresponding to an efficiency of 36.08%.

For the substrate in the control system, the was a marked rise (P<0.05) in total chromium was detected during the first seven days, rising from 1.61 ppm to 70.53 ppm. However, from that point forward, the variation was not statistically significant: 77.34 ppm at day 14 (P>0.05) and 71.31 ppm at day 21 (P>0.05), indicating a saturation of the substrate. When comparing both systems, during the first seven days, a notable reduction (P<0.05) in total chromium was detected within the water of both vegetated and non-vegetated wetlands. Nevertheless, towards the conslusion of the treatment, the vegetated unit demonstrated a considerably higher removal performance, reaching 98.85% efficiency, compared to the 36.08% recorded in the non-vegetated control. In terms of the substrate behavior, while the non-vegetated system exhibited a significant initial increase in chromium content (P<0.05), it quickly reached saturation, resulting in no significant variations thereafter. Conversely, the vegetated system showed a continuous and significant accumulation (P<0.05) of chromium in the substrate throughout the 21-day treatment period.

Fig. 2B, shows the distribution of total chromium in the components of the artificial wetland system at the lower level. It can be observed that the concentration of total chromium decreased significantly (P<0.05) from an initial concentration of 6.55 ppm to 0.16 ppm after seven days of treatment, achieving an efficiency of 97.56%. At 14 days of treatment, the concentration decreased to 0.12 ppm (P>0.05), achieving an efficiency of 98.17%. By 21 days of treatment, the concentration had further decreased to 0.05 ppm (P>0.05), resulting in an efficiency of 99.24%. Regarding the root component, it was determined that the initial concentration was 0.35 ppm before applying the effluent; at the end of 21 days, the total chromium content exhibited a notable rise (P<0.05) to a value of 5.08 ppm. In the case of leaves, the total chromium concentration showed a significant increase (P<0.05) over time, from an initial concentration of 0.38 ppm to a value of 6.85 ppm at 21 days of testing.

Concerning the non-vegetated wetland system, the concentration of total chromium in the influent was found not to vary significantly (P>0.05) during the treatment time from zero days to 21 days. In comparison to the constructed wetlands with and without vegetation, results indicated that in the vegetated wetlands, the total chromium concentration declined markedly (P<0.05) after seven days of treatment, and also presented a decrease (P>0.05) of this value in the rest of the test time, reaching an efficiency of 99.24% at the end of 21 days. In the case of the non-vegetated wetlands, where the total chromium concentration did not show significant variation (P>0.05), i.e., it maintained a concentration similar to that of the influent, and the efficiency reached 2.69%.

Consistent with these findings, Table 2 shows the mass balance and distribution of total chromium in the wetland

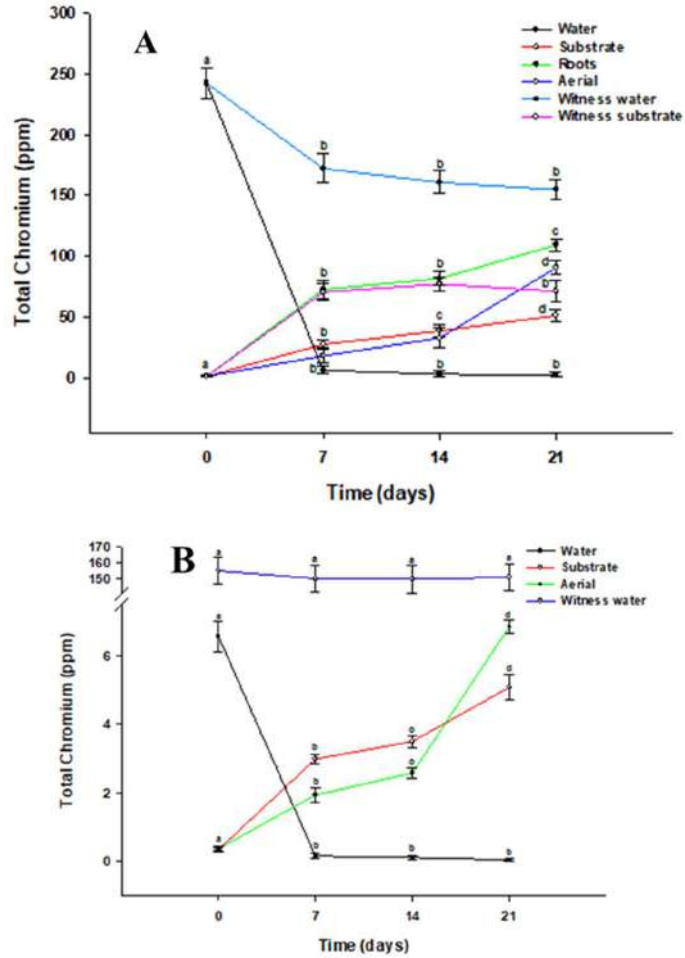


Fig. 2: Distribution of total chromium over time in the different components of the artificial wetland system. A) Upper level (*Scirpus americanus* Pers.) and B) Lower level (*Hydrocotyle bonariensis* Lam.). Values represent the average of three replicates ± SD. The letters placed above the bars denote statistically significant differences among treatments.

system for treating tannery wastewater at 30% concentration. It is observed that, at the upper level of the wetland system, the concentration of total chromium in the wastewater decreases with time from a total value of 363.15 mg to a value of 4.19 mg, representing 1.36% of the initial concentration. Concerning the substrate component, it is observed that the amount of chromium present increases over time from zero to 21 days.

Besides, the Table 2 shows the percentages of chromium removal in the different components of the wetlands. Negative percentages would indicate that both the substrate and the roots are saturated with chromium; therefore, their retention and absorption capacity would be decreasing.

3.3. Determination of TI, BCF and TF in Artificial Wetland Systems

Table 3 gives the plant response indicators (TI, BCF and TF) measured in the upper and lower sections of the constructed wetland after effluent treatment.

Regarding the tolerance index (TI), at the upper level, it can be observed that *Scirpus americanus* Pers. decreases in the TI over time from a value of 0.93 at seven days to 0.68 at 21 days. At the lower level, *Hydrocotyle bonariensis* Lam. shows an increase in the tolerance index over time, from a value of 0.83 at seven days to 0.90 at 21 days. Regarding the bioconcentration factor (BCF), it is observed that both in the upper and lower levels, the BCF increases over time, from an initial value of 0.08 to 0.37 for *Scirpus americanus* Pers. and from 0.30 to 1.05 for *Hydrocotyle bonariensis* Lam. from 7 days to 21 days. Finally, the translocation factor also increased over time at both levels of the wetland system, from a value of 0.25 to 0.83 for *Scirpus americanus* Pers. and from 0.65 to 1.35 for *Hydrocotyle bonariensis* Lam. from 7 days to 21 days of effluent treatment.

Table 2: Values of physicochemical parameters evaluated in the effluents of the tanning process without pretreatment.

Component	Quantity	0 days	7 days				14 days				21 days			
Upper level		[Cr] (ppm)	Total [Cr] (ppm)	%	[Cr] (ppm)	Total [Cr] (ppm)	%	% chromium removal	[Cr] (ppm)	Total [Cr] (ppm)	%	% chromium removal	[Cr] (ppm)	Total [Cr] (ppm)	%	% chromium removal
Water (L)	1.50	242.10	363.15	98.26%	6.55	9.83	6.29%	91.97%	3.29	4.94	2.50%	3.79%	2.79	4.19	1.36%	1.14%
Substrate (kg)	2.00	1.61	3.22	0.87%	27.71	55.42	35.47%	34.60%	38.81	77.62	39.30%	3.83%	51.32	102.64	33.43%	-5.87%
Roots (Kg)	1.00	1.67	1.67	0.45%	72.76	72.76	46.56%	46.11%	81.86	81.86	41.45%	-5.11%	109.38	109.38	35.63%	-5.82%
Aerial (Kg)	1.00	1.55	1.55	0.42%	18.25	18.25	11.68%	11.26%	33.08	33.08	16.75%	5.07%	90.78	90.78	29.57%	12.82%
Lower level		[Cr] (ppm)	Total [Cr] (ppm)	%	[Cr] (ppm)	Total [Cr] (ppm)	%	% chromium removal	[Cr] (ppm)	Total [Cr] (ppm)	%	% chromium removal	[Cr] (ppm)	Total [Cr] (ppm)	%	% chromium removal
Water (L)	1.50	6.55	9.83	93.08%	0.16	0.24	4.64%	88.44%	0.12	0.18	2.88%	1.76%	0.05	0.08	0.62%	2.26%
Roots (Kg)	1.00	0.35	0.35	3.32%	2.99	2.99	57.83%	54.51%	3.5	3.50	55.91%	-1.92%	5.08	5.08	42.32%	-13.59%
Aerial (Kg)	1.00	0.38	0.38	3.60%	1.94	1.94	37.52%	33.92%	2.58	2.58	41.21%	3.69%	6.85	6.85	57.06%	15.85%

4. DISCUSSION

Tannery effluents are usually characterized by elevated amounts of chromium compounds, which include salts and oxygen demand parameters (BOD and COD), together with other harmful substances, all of which contribute to considerable environmental degradation when released without treatment (Khajah & Ahmed 2025; Pérez et al. 2024). In the present work, the chromium levels detected in the effluent surpassed the maximum permissible limit (MPL), which may be attributed to use of chromium sulfate in tanning processes to stabilize collagen fibers. Of the total chromium applied, only 60–80% binds to the leather, while 20–40% is lost in wastewater. Although hexavalent chromium (Cr^{6+}) was detected in the effluent, its concentration was below the MPL, likely due to reduction to the more stable and less toxic trivalent chromium (Cr^{3+}). This reduction could be attributed to the high organic matter load acting as an electron donor (Rondan-Sanabria et al. 2023; Abd Al-Abbas & Ismail 2024; Kumari & Dutta 2024).

The organic load, reflected in high values of BOD_5, COD, and total suspended solids (TSS), could originate primarily from soaking, liming, and fleshing processes. Elevated COD values are likely associated with anilines and dyes used during the dyeing stage, which are known for their resistance to bacterial degradation. The biodegradability ratio (BOD_5/COD = 0.183) indicates a non-biodegradable effluent, where most organic and inorganic matter cannot be biologically oxidized. Constructed wetlands are a sustainable and economical alternative (Zhang et al. 2024). These systems interact with plants, microorganisms, and substrate materials (Luna-Pabello & Aburto-Castañeda 2014). In this study, the pilot wetland system achieved a chromium removal efficiency of 99.96%. Similar removal rates have been reported: 99.8% in vegetated wetlands and 92.5% in non-vegetated systems (Kaseva & Mbuligwe 2010). Other studies using *Phragmites australis* and *Typha latifolia* reported of 87% and 90% efficiencies, respectively (Gikas et al. 2013), while several investigations found removal rates exceeding 50% (Younas et al. 2022).

Significant reductions in BOD_5, COD, and TSS were observed in this study. Comparable results include reductions in TDS from 4.81 g/L to 0.73 g/L and COD removal of 70% (Javeed & Nazir 2022), as well as 88% COD, 93% BOD, and 96–98% TSS removal in other studies (Ali-Hassoon et al. 2020). Wetlands have also demonstrated removal efficiencies of 35–50% for various dissolved ions and about 50% for BOD and COD (Panneerselvam & Shunmuga 2021). A local study in Arequipa using a hybrid wetland system *with Eleocharis montevidensis, Scirpus americanus* Pers., and *Eichhornia crassipes* also achieved more than

Table 3: Plant response indicators IT, BCF and TF, values after effluent treatment with the constructed wetland system.

Time (days)	TI	BCF	TF
Higher level			
7	0.93 ± 0.24	0.08 ± 0.02	0.25 ± 0.06
14	0.77 ± 0.21	0.14 ± 0.01	0.40 ± 0.05
21	0.68 ± 0.10	0.37 ± 0.07	0.83 ± 0.08
Lower level			
7	0.83 ± 0.09	0.30 ± 0.04	0.65 ± 0.35
14	0.88 ± 0.07	0.39 ± 0.08	0.74 ± 0.06
21	0.90 ± 0.08	1.05 ± 0.06	1.35 ± 0.05

The values represent the mean and standard deviation for three independent samples

95% pollutant removal with a 7-day hydraulic retention time (Rondan-Sanabria et al. 2023, Khajah & Ahmed 2025). Organic matter removal could be facilitated mainly by microbial degradation. Plant roots provide a surface for microbial colonization, promoting complex interactions in the rhizosphere (Liang et al. 2017). Anaerobic degradation dominates most of the bed, with aerobic degradation limited to zones around roots and the surface layer (Stottmeister et al. 2003, Riggio et al. 2018). The elimination of suspended solids could occur through physical and biological processes, mainly involving sedimentation, flocculation, and substrate and rhizome filtration (Younas et al. 2022).

Chromium, being non-biodegradable, could be removed through three main mechanisms: (1) adsorption onto substrate and sediment particles, enhanced by high organic matter improving cation exchange capacity (Chrysochoou et al. 2016), (2) chemical precipitation due to rhizosphere exudates and organic acid production during microbial degradation, leading to chromium complexation and sedimentation (Al-Baldawi et al. 2015; Morris 2004); and (3) phytoextraction through root uptake, with chromium transported to shoots and stored in vacuoles or cell walls (Liang et al. 2017, Kafle et al. 2022). Four possible models have been proposed for Cr^{3+} uptake: apoplastic retention; passive diffusion into the vacuole; transport via phytosiderophores to the tonoplast; and microbial oxidation to Cr^{6+} followed by apoplastic fixation. Cr^{6+} is actively transported via sulfate transporters and reduced intracellularly to Cr^{3+} before sequestration (Shanker et al. 2005, Abd Al-Abbas & Ismail 2024).

This study found that most chromium accumulated in the upper-level substrate. Chromium content in plant roots exceeded that in the aerial parts, consistent with findings from studies using *Pistia stratiotes*, *Eichhornia* spp., *Lemna* spp., and *Salvinia* spp. (Rezania et al. 2016) and *Phragmites australis* (Fibbi et al. 2012). Plant tolerance and phytoremediation capacity were assessed using indicators of plant response. The upper level showed a decreased TI, likely due to higher contaminant concentrations, while BCF and TF increased in both levels, indicating effective uptake and translocation. *Scirpus* showed high tolerance, with a strong physiological response after 21 days, in line with other studies reporting limited wilting and higher growth rates under exposure (Ali-Hassoon et al. 2020, Zhang et al. 2024). More broadly, reviews of CWs report that metals are typically retained in roots with limited translocation to shoots, and that substrate layers capture a substantial fraction of dissolved metals via adsorption and precipitation, while plant–microbe interactions enhance tolerance (Younas et al. 2022, Zhang et al. 2024).

However, growth inhibition has been observed in other studies, such as a 17% reduction in root and 33.3% reduction in stem dry weight under contamination (Liu et al. 2018) and reduced heavy metal accumulation in watercress. Similar patterns were observed in *Plantago major* L. and aquatic bryophytes exposed to various metals (Galal & Shehata 2015, Favas et al. 2018). Finally, in *Pistia stratiotes* exposed to arsenic, toxicity symptoms such as chlorosis and root browning occurred at higher concentrations (Vidal de Campos et al. 2019), while in *Eichhornia crassipes* growth was stimulated at low Cr levels (0.5–2 $mg.L^{-1}$) but inhibited at concentrations above 5 $mg.L^{-1}$ (Panneerselvam & Shunmuga 2021).

5. CONCLUSIONS

The findings of this study confirm that the analyzed tannery effluents contained high concentrations of total chromium (242.10 $mg.L^{-1}$), along with elevated values of biochemical (BOD_5 = 1150.50 $mg.L^{-1}$) and chemical (COD = 6276.0 $mg.L^{-1}$) oxygen demand. All of these parameters surpassed the maximum permissible limits established for effluents from tanning operations.

In the artificial wetland system, the total chromium concentration in the substrate of the upper level increased over time, from 1.61 ppm to 51.32 ppm. A similar pattern was observed in the vegetative components, with concentrations in the roots rising from 1.67 ppm to 109.38 ppm, and in the aerial (harvestable) parts from 1.55 ppm to 90.78 ppm.

At the lower level of the wetland, chromium accumulation also showed an upward trend, with values rising from 0.35 to 5.08 ppm in roots and from 0.38 to 6.85 ppm in aerial parts.

The pilot system achieved high treatment efficiencies, removing 99.98% of total chromium, 97.39% of BOD_5, and 98.73% of COD.

For *Scirpus americanus* Pers., the tolerance index (TI) declined over time (from 0.93 to 0.68), whereas the BCF and

TF increased (0.08 to 0.37 and 0.25 to 0.83, respectively). In contrast, *Hydrocotyle bonariensis* Lam. showed increases in all three indicators, with TI ranging between 0.83 and 0.90, BCF from 0.30 to 1.05, and TF from 0.65 to 1.35.

6. ACKNOWLEDGMENTS

The authors sincerely thank the Universidad Tecnológica del Perú for the facilities and institutional assistance that made the completion of this study possible.

7. REFERENCES

Abd Al-Abbas, A. and Ismail, A., 2024. Performance and mechanisms of constructed wetland integrated microbial fuel cell for remediation and detoxification of leather tannery wastewater. *Journal of Environmental Management*, 369, pp.122353. [DOI]

Ahmad, S., Reshi, Z., Shah, M., Rashid, I., Alyemeni, M. and Ahmad, P., 2020. Hydrogen sulfide alleviates chromium stress on cauliflower by restricting its uptake and enhancing antioxidative system. Physiologia Plantarum, 168(2), pp.289–300. [DOI]

Al-Baldawi, I. A., Sheikh Abdullah, S. R., Anuar, N., Suja, F. and Mushrifah, I., 2015. Phytodegradation of total petroleum hydrocarbon TPH in diesel-contaminated water using Scirpus grossus. *Ecological Engineering*, 74, pp. 463-473. [DOI]

Alemu, A., Lemma, B. and Gabbiye, N., 2019. Adsorption of chromium (III) from aqueous solution using vesicular basalt rock. *Cogent Environmental Science*, 5(1), pp. 1650416. [DOI]

Ali-Hassoon, D., Siti Rozaimah, N., Abdullah, S., Abu Hasan, H. I., Razi Othman, A., Abdulwahab Al-Baldawi, I. and Nur 'Izzati, I., 2020. Utilisation of an aquatic plant (*Scirpus grossus*) for phytoremediation of real sago mill effluent. *Environmental Technology & Innovation*, 19, pp. 101033. [DOI]

Bibi, I., Khan Niazi, N., Choppala, G. and Burton, E. D., 2018. Chromium (VI) removal by siderite ($FeCO_3$) in anoxic aqueous solutions: An X-ray absorption spectroscopy investigation. *Science of The Total Environment*, 640-641, pp. 1424-1431. [DOI]

Chen, B., Han, M. Y., Peng, K., Zhou, S. L., Shao, L., Wu, X. F. and Chen, G. Q., 2018. Global land-water nexus: Agricultural land and freshwater use embodied in worldwide supply chains. *Science of the Total Environment*, 613-614, pp. 931-943. [DOI]

Chrysochoou, M., Theologou, E., Bompoti, N., Dermatas, D. and Panagiotakis, I., 2016. Occurrence, Origin and Transformation Processes of Geogenic Chromium in Soils and Sediments. *Current Pollution Reports*, 2, pp. 224-235. [DOI]

Elabbas, S., Ouazzani, N., Mandi, L., Berrekhis, F., Perdicakis, M., Pontvianne, S. and Leclerc, J., 2016. Treatment of highly concentrated tannery wastewater using electrocoagulation influence of the quality of aluminium used for the electrode. *Journal of Hazardous Materials*, 319, pp. 69-77. [DOI]

Favas, P. J., Pratas, J., Rodrigues, N., D'Souza, R., Varun, M. and Paul, M. S., 2018. Metal(loid) accumulation in aquatic plants of a mining area: Potential for water quality biomonitoring and biogeochemical prospecting. *Chemosphere*, 194, pp. 158-170. [DOI]

Fibbi, D., Doumett, S., Lepri, L., Checchini, L., Gonnelli, C., Coppini, E. and Del Bubba, M., 2012. Distribution and mass balance of hexavalent and trivalent chromium in a subsurface, horizontal flow (SF-h) constructed wetland operating as post-treatment of textile wastewater for water reuse. *Journal of Hazardous Materials*, 199-200, pp. 209-216. [DOI]

Galal, T. M. and Shehata, H. S., 2015. Bioaccumulation and translocation of heavy metals by Plantago major L. grown in contaminated soils under the effect of traffic pollution. *Ecological Indicators*, 48, pp. 244-251. [DOI]

Gikas, P., Ranieri, E. and Tchobanoglous, G., 2013. Removal of iron, chromium and lead from waste water by horizontal subsurface flow constructed wetlands. *Journal of Chemical Technology & Biotechnology*, 88(10), pp. 1906-1912. [DOI]

Javeed, F. and Nazir, A. B., 2022. Industrial water treatment within a wetland planted with Hemarthria compressa and subsequent effluent reuse to grow Abelmoschus esculentus. *Journal of Water Process Engineering*, 45, pp. 102511. [DOI]

Kafle, A., Timilsina, A., Gautam, A., Adhikari, K., Bhattarai, A. and Aryal, N., 2022. Phytoremediation: Mechanisms, plant selection and enhancement by natural and synthetic agents. *Environmental Advances,* 8, pp. 100203. [DOI]

Kaseva, M. E. & Mbuligwe, S. E., 2010. Potential of constructed wetland systems for treating tannery industrial wastewater. *Water Science & Technology*, 61(4), pp. 1043-1052. [DOI]

Khajah, M. and Ahmed, M.E., 2025. Performance evaluation of a pilot wetland system for wastewater treatment. *Journal of Engineering Research,* 13, pp.1387–1395. [DOI]

Kumar, S., Banerjee, S., Dutta, S., Roy, P.K. and Bhattacharyya, P., 2025. Evaluating the impact of arbuscular mycorrhizal fungi on the phytoremediation potential of Vetiveria zizanioides and Saccharum spontaneum on coal mine waste, India. Journal of Environmental Chemical Engineering, 13(3), 116593. [DOI]

Kumari, D. and Dutta, K., 2024. Studies on Cr (VI) removal by constructed wetland integrated microbial fuel cell: Effect of electrodes. *Journal of Environmental Chemical Engineering*, 12, pp. 113119. [DOI]

Liang, Y., Zhu, H., Bañuelos, G., Yan, B., Shutes, B. C. and Chen, X., 2017. Removal of nutrients in saline wastewater using constructed wetlands: Plant species, influent loads and salinity levels as influencing factors. *Chemosphere*, 187, pp. 52-61. [DOI]

Lin, Z., Li, M., Yan, P., Zhang, J., Xie, H. and Wu, H., 2025. Constructed wetlands for wastewater treatment and reuse: Two decades of experience from China. *Environmental Research*, 279, 121781. [DOI]

Liu, L., Fan, X., Han, Y. and Wang, H., 2025. Enhanced removal of heavy metals by wetland plant–microbiome symbiont: Prospect of potential strategies and mechanisms for environmental heavy metal regulation. Pedosphere, 35(1), pp.116–136. [DOI]

Liu, X., Gao, Y., Khan, S., Duan, G., Chen, A., Ling, L. and Wu, X., 2008. Accumulation of Pb, Cu, and Zn in native plants growing on contaminated sites and their potential accumulation capacity in Heqing, Yunnan. *Journal of Environmental Sciences*, 20(12), 1469-1474. [DOI]

Liu, X., Hu, X., Zhang, X., Chen, X., Chen, J. and Yuan, X., 2018. Effect of Bacillus subtilis and NTA-APG on pyrene dissipation in phytoremediation of nickel co-contaminated wetlands by *Scirpus triqueter*. *Ecotoxicology and Environmental Safety,* 154, pp. 69-74. [DOI]

Luna-Pabello, V.M. and Aburto-Castañeda, S., 2014. Sistema de humedales artificiales para el control de la eutrofificación del lago del Bosque de San Juan de Aragón. *Revista Internacional de Contaminación Ambiental*, 30(1), pp. 27–36. [DOI]

Malaviya, P. and Singh, A., 2016. Bioremediation of chromium solutions and chromium containing wastewaters. *Critical Reviews in Microbiology*, 42(4), pp. 607-633. [DOI]

Meneses Barroso, Y. M., Patiño Mantilla, P. A. and Betancur Perez, J. F., 2019. Remoción de cromo en aguas residuales industriales mediante el uso de biomasa de Spirulina sp, sedimentación primaria y precipitación química. *Revista de Investigación Agraria y Ambiental*, 10(1), pp. 141-152. [DOI]

MINAM., 2017. Decreto Supremo N° 004-2017-MINAM. Aprueban Estándares de Calidad Ambiental (ECA) para Agua y establecen disposiciones complementarias. *Diario Oficial El Peruano*, Lima, Perú, 7 de junio de 2017. [https://www.minam.gob.pe/wp-content/uploads/2017/06/DS-004-2017-MINAM.pdf]

Morris, L. A., 2004. Soil biology and tree growth. Soil organic matter

forms and functions. *Encyclopedia of Forest Sciences*, pp.1201-1207. [DOI]

Panneerselvam, B. and Priya K, S., 2021. Phytoremediation potential of water hyacinth in heavy metal removal in chromium and lead contaminated water. *International journal of environmental analytical chemistry*, 103(13), pp. 3081-3096. [DOI]

Pérez, Y., Vargas, E., García-Cortés, D., Hernández, W., Checo, H. and Jáuregui-Haza, U., 2024. Efficiency and effectiveness of systems for the treatment of domestic wastewater based on subsurface flow constructed wetlands in Jarabacoa, Dominican Republic. *Water Science and Engineering*, 17(2), pp.118–128. [DOI]

Pradhan, D., Behari Sukla, L., Sawyer, M. and Rahman, P. K., 2017. Recent bioreduction of hexavalent chromium in wastewater treatment: A review. *Journal of Industrial and Engineering Chemistry*, 55, pp.1-20. [DOI]

Rajput, P., Benjwal, S. and Pandey, R., 2025. A Comprehensive Review on the Role of Bioremediation in Heavy Metal Contamination. *Nature Environment and Pollution Technology*, 24(S1), pp.235–245. [DOI]

Rezania, S., Mat Taib, S., Md Din, M. F., Dahalan, F. A. and Kamyab, H., 2016. Comprehensive review on phytotechnology: Heavy metals removal by diverse aquatic plants species from wastewater. *Journal of Hazardous Materials*, 318, pp.587-599. [DOI]

Ribeiro de Souza, S. C., López de Andrade, S. A., Anjos de Souza, L. and Schiavinato, M. A., 2012. Lead tolerance and phytoremediation potential of Brazilian leguminous tree species at the seedling stage. *Journal of Environmental Management*, 110, 299-307. [DOI]

Riggio, V. A., Ruffino, B., Campo, G., Comino, E., Comoglio, C. and Zanetti, M., 2018. Constructed wetlands for the reuse of industrial wastewater: A case-study. *Journal of Cleaner Production*, 171, pp. 723-732. [DOI]

Rondan-Sanabria, G. G., Flores Sacsi, E., Delgado Salas, A., Velarde Allazo, E. and Mendoza Montoya, J., 2023. Chromium removal by Eleocharis montevidensis and Scirpus americanus in combination with Eichhornia crassipes in a hybrid artificial wetland system for tannery effluent in the Río Seco Industrial Park, Arequipa - Peru. 21st LACCEI International Multi-Conference for Engineering, Education, and Technology, Buenos Aires - ARGENTINA, July 17 – 21. [DOI]

Saeed, T., Alam, M. K., Miah, M. J. and Majed, N., 2021. Removal of heavy metals in subsurface flow constructed wetlands: Application of effluent recirculation. *Environmental and Sustainability Indicators,* 12, pp. 100146. [DOI]

Shanker, A. K., Cervantes, C., Loza-Tavera, H. and Avudainayagam, S., 2005. Chromium toxicity in plants. *Environment International*, 31(5), pp. 739-753. [DOI]

Shi, X., Zhang, X., Chen, G., Chen, Y., Wang, L. and Shan, X., 2011. Seedling growth and metal accumulation of selected woody species in copper and lead/zinc mine tailings. *Journal of Environmental Sciences*, 23(2), pp. 266-274. [DOI]

Stottmeister, U., Wießner, A., Kuschk, P. and Kappelmeyer, U., 2003. Effects of plants and microorganisms in constructed wetlands for wastewater treatment. *Biotechnology Advances*, 22(1-2), pp. 93-117. [DOI]

Sultanaa, M.-Y., Khayer Md., A. and Bari Chowdhurya, M., 2014. Integrated Cr(VI) removal using constructed wetlands and composting. *Journal of Hazardous Materials*, 281(8), pp. 106-113. [DOI]

Vidal de Campos, F., Alves de Oliveira, J., Alves da Silva, A., Ribeiro, C. and dos Santos Farnese, F., 2019. Phytoremediation of arsenite-contaminated environments: is Pistia stratiotes L. a useful tool? *Ecological Indicators*, 104, pp. 794-801. [DOI]

Vilardi, G., Di Palma, L. and Verdone, N., 2018. On the critical use of zero valent iron nanoparticles and Fenton processes for the treatment of tannery wastewater. *Journal of Water Process Engineering*, 22, pp. 109-122. [DOI]

Wang, Y., Cai, Z., Sheng, S., Pan, F., Chen, F. and Fu, J., 2019. Comprehensive evaluation of substrate materials for contaminants removal in. *Science of the Total Environment*, 701, pp. 134736. [DOI]

Younas, F., Khan, N., Bidi, I., Afzal, M., Hussain, K., Shahid, M. and Mahroz, M., 2022. Constructed wetlands as a sustainable technology for wastewater treatment with emphasis on chromium-rich tannery wastewater. *Journal of Hazardous Materials*, 422, pp. 126926. [DOI]

Zhang, Z., Zhao, Y., Wei, T., Bai, X., Chen, Z., Lei, X. and Liu, Y., 2024. Constructed wetlands for metallic wastewater treatment: an updated global profile. *Journal of Water Process Engineering*, 65, pp. 105852. [DOI]

Zulfqar, A., Niazi, N.K., Saqib, Z.A., Shahid, M., Hussain, K. and He, Z., 2025. Phytoaccumulation of chromium by hemp and ryegrass in rice husk biochars, nano-zero valent zinc and vermicompost amended tannery wastewater soil. Frontiers in Environmental Science, 13, 1558255. [DOI]

Nature Environment and Pollution Technology
An International Quarterly Scientific Journal

p-ISSN: 0972-6268
(Print copies up to 2016)
e-ISSN: 2395-3454

Vol. 25 | No. 3 | Article ID B4415 | 2026

Original Research Paper

https://doi.org/10.46488/NEPT.2026.v25i03.B4415

Open Access Journal

Modeling the Drivers for Renewable Energy in Developing Economies: A Case Study of India

Adya Sharma and Nehajoan Panackal†
Symbiosis Centre for Management Studies, Pune, Affiliated to Symbiosis International (Deemed University), Pune, India
†Corresponding author: Nehajoan Panackal; Nehajoan.panackal@scmspune.ac.in

Abbreviation: Nat. Env. & Poll. Technol.
Website: www.neptjournal.com

Received: 09-12-2025
Revised: 02-02-2026
Accepted: 08-02-2026

Key Words:

Renewable Energy
Sustainability
Clean energy
Sustainable alternatives
Developing economies
Sustainable development goals
Enabler factors

Citation for the Paper:

Sharma, A. and Panackal, N., 2026. Modeling the drivers for renewable energy in developing economies: A case study of India. *Nature Environment and Pollution Technology*, 25(3), B4415. https://doi.org/10.46488/NEPT.2026.v25i03.B4415

Note: From 2025, the journal has adopted the use of Article IDs in citations instead of traditional consecutive page numbers. Each article is now given individual page ranges starting from page 1.

Copyright: © 2026 by the authors
Licensee: Technoscience Publications
This article is an open access article distributed under the terms and conditions of the Creative Commons Attribution (CC BY) license (https://creativecommons.org/licenses/by/4.0/).

ABSTRACT

Renewable energy sources provide sustainable alternatives for fulfilling the energy needs of developing economies. India, as a developing country, has taken important initiatives to promote renewable energy, driven by various factors. Increased awareness of clean energy options, growing concerns about environmental degradation, and the emphasis on Sustainable Development Goals (SDGs) are among the factors encouraging countries to consider renewable energy as a viable and sustainable alternative to fossil fuels. This paper aims to explore the key factors that facilitate the development and adoption of renewable energy as a clean and sustainable energy source. It also seeks to examine the hierarchical relationships among these enablers and analyze the connections between them. To achieve these goals, the study employs Total Interpretive Structural Modeling (TISM) and Fuzzy MICMAC approaches. The findings identify six main enablers: environmental, institutional, regulatory, economic, technological, and social factors. The TISM model reveals three levels of hierarchy among these enablers, while the Fuzzy MICMAC analysis categorizes them into driver and dependent clusters. The discussion contextualizes these results within India. The study offers significant insights for theory, management, and societal progress.

1. INTRODUCTION

Fossil fuels remain the primary energy source in many nations, and with ongoing growth and economic development, countries continue to depend on them for a consistent energy supply. However, their use presents significant challenges, most notably the rapid increase in carbon dioxide emissions. Carbon dioxide, a well-known byproduct of fossil fuel combustion, has raised global concern due to its role in climate change (Gyimah et al. 2022, Wang et al. 2023). The rise in CO_2 levels has been a focal point of discussion in various international forums. Developing economies, in particular, exhibit high dependence on fossil fuels (Gyimah et al. 2022), leading to extensive chemical emissions that have severe environmental impacts (Li et al. 2020, Yang et al. 2022). Climate activists consistently emphasize the importance of balancing economic growth with ecological sustainability. Both developing and developed nations are re-evaluating their energy production and consumption patterns to achieve a better balance between growth and environmental preservation (Chenyang et al. 2023). Historical events such as the oil crises of the 1970s, along with increasing awareness of global warming and climate change, stimulated efforts to find sustainable alternatives to fossil fuels (Lal & Kumar 2022). Growing recognition of clean energy sources, concerns about environmental degradation, and the goals outlined in the Sustainable Development Goals (SDGs) have further motivated countries to adopt renewable energy as a viable alternative. Over recent decades, nations have actively explored renewable energy sources and initiated various projects in this field. The SDGs have gained significant emphasis, prompting countries to align their policies accordingly, which has accelerated the adoption of sustainable options like renewable energy to

meet national energy needs. Renewable energy offers social, economic, and environmental benefits (Virah-Sawmy & Sturmberg 2025) and facilitates a transition to cleaner energy for all. Expanding renewable energy infrastructure enhances access and affordability, especially in remote areas, thereby contributing to poverty reduction and improved livelihoods (Charfeddine & Kahia 2021). Investing in renewable energy technologies also fosters innovation and supports the development of sustainable infrastructure.

Countries are increasingly exploring various forms of renewable energy. One particularly popular option is solar energy. With proper prioritization and strategic planning, solar power can serve as a valuable complement to existing energy needs (Wang et al. 2024). Despite its abundance, solar energy faces challenges related to storage and transfer (Ukoba et al. 2024), requiring significant initial investments in equipment for heating, storage, and transmission. Nonetheless, the advantages of solar energy are compelling, including its plentiful supply, long-term cost-effectiveness, and status as a clean energy source, making it a promising option for sustainable economic growth (Kishore et al. 2025, Maka & Alabid 2022). Another widely utilized renewable energy source is wind power, which research highlights as a sustainable long-term solution. Wind turbines enable electricity generation, and the benefits include scalability for various applications, environmental friendliness, and suitability for coastal and high-wind regions (Boadu & Otoo 2024, Liu et al. 2025). Additionally, countries are investing in geothermal energy, derived from natural heat beneath the Earth's surface. These resources are located at various depths—ranging from shallow ground to several kilometers below the surface—and are used in agriculture, heating, and cooling applications (Pambudi & Ulfa 2024, Rohit et al. 2023). Hydrogen energy also plays a significant role, with hydrogen gas being produced from sources such as oil, natural gas, biomass, and coal (O[DOI]-Yorke et al. 2025). Based on geographic, resource, and feasibility considerations, nations are focusing efforts to harness available energy sources to meet their needs while demonstrating environmental responsibility.

1.1. Renewable Energy in Developing Economies

A significant portion of the world's population lives in developing countries, which play an essential role in the global economy due to their growing economies and expanding populations. These countries differ from developed nations mainly in terms of economic growth and energy stability, with the latter being primary focus areas for developing nations. Their development strategies are largely centered around economic expansion (Raza et al. 2025). The Global Carbon Project highlights China, the United States, India, Russia, and Japan as the leading countries in carbon dioxide emissions. Developing countries' energy choices heavily influence their progress, and much of their economic growth has been driven by fossil fuels (Briera & Lefèvre 2024, Chaikumbung 2025). However, there is an increasing push towards investing in renewable energy sources, which promise long-term benefits including energy security, reduced import costs, new economic opportunities, and better access in rural areas. India has actively invested in renewables since the 1980s, launching numerous initiatives to promote solar and wind energy (Lal et al. 2025). It is among the world's largest producers of renewable energy and has committed to generating 50% of its total energy from non-fossil fuel sources by 2030 (Khare et al. 2023). Additionally, India announced its goal to become carbon neutral by 2070 during the twenty-sixth UN Climate Conference in Glasgow, demonstrating its environmental commitment (Alam et al. 2023). In 2020, renewable energy accounted for 38% of India's total installed capacity.

As a developing nation, Bangladesh is experiencing rapid growth in energy demand. The country views renewable energy as a vital solution to replace fossil fuels. Government institutions in Bangladesh have begun promoting large-scale renewable energy initiatives (Joardee et al. 2024). Bangladesh aims to replace its fossil-fuel fleet with solar-powered vessels. The country has a robust off-grid renewable energy system, with approximately 6% of its energy needs met by renewable sources. To support this, the government has taken measures to encourage electric vehicles by developing solar charging stations (Mahbub & Islam 2023). A study by Islam et al. (2022) identified demographic shifts, urbanization leading to an environmentally conscious population, and technological progress as key drivers behind increased renewable energy consumption. Bangladesh's institutional and regulatory frameworks have prioritized establishing renewable energy plants, leveraging the country's geographical advantages. As a semi-tropical nation with year-round sunlight, Bangladesh offers multiple incentives to public and private developers to promote renewable energy projects (Hossain et al. 2024). Meanwhile, Sri Lanka has set ambitious targets for achieving energy independence. Its primary electricity sources include thermal power, hydroelectricity, and other non-conventional renewable resources (Koswatte et al. 2024). Investment in renewable energy and strategic planning in developing economies can enhance energy security, reduce dependency on imports, foster economic growth, create jobs, improve access to electricity and basic services, and support sustainable long-term development. From a societal perspective, a cleaner environment for future generations and job creation through funded renewable projects are key factors fostering a positive outlook on renewable energy in Sri Lanka (Herath et al. 2022).

1.2. Rationale and Objectives of the Study

It is essential to find a balance between economic growth and environmental conservation. Energy production, transmission, and consumption are critical to a country's development, particularly in emerging economies like India. As the population grows, along with industrialization and urbanization, India's energy needs are projected to rise substantially in the coming years. India has set an ambitious goal to reduce its reliance on fossil fuels and lower its carbon footprint. While previous research on renewable energy has explored general drivers of its adoption, this study will concentrate on India-specific enablers that demonstrate how India is working to meet its future energy demands while decreasing dependence on fossil fuels. Additionally, past studies have examined these enablers individually, this research aims to integrate them into a comprehensive framework and analyze their interconnections. With this context, the study's objectives are:

O1: To analyze the key drivers that aid the implementation of renewable energy sources with special reference to India.

O2: To interpret the critical linkages between the identified enablers through a comprehensive framework using the Total Interpretive Structural Model (TISM).

O3: To infer the nature of linkages between the identified enablers using Fuzzy MIC MAC analysis.

2. BACKGROUND RESEARCH

This section examines the key constructs that facilitate the implementation of renewable energy in India, based on a comprehensive literature review. Environmental and geographical factors play a crucial role in influencing renewable energy adoption (Nieboer et al. 2025, Obuseh et al. 2025). Regions characterized by minimal cloud cover, abundant sunlight, and low population density are particularly suitable for solar power generation. The plentiful sunshine makes solar energy storage highly feasible (Erol et al. 2024). India, with its diverse geography and climate zones (Beck et al. 2018), possesses significant potential for renewable energy. Its tropical location ensures extensive solar and wind resources. Effective harnessing of wind energy depends on environmental factors such as consistent wind patterns, mountain ranges, or coastal areas, with an average wind speed of at least 13 mph (Vaidya 2025). Hydroelectric power relies on high rainfall and mountainous terrain, while biomass energy depends on agricultural outputs and byproducts (Dashtpeyma & Ghodsi 2021). The country's varied landscape, including mountain ranges, rivers, ample sunshine, and monsoon rains, creates ideal conditions for multiple renewable sources. Institutional enablers, such as policies, reforms, government initiatives, and private sector participation, further support renewable energy deployment (Apolonia & Simas 2021). In India, collaboration between the government and private players has bolstered renewable energy projects. The nation is committed to reducing greenhouse gas emissions and scaling up renewable energy efforts on a global stage. National policies offer financial incentives that motivate corporations to invest in renewable energy (Mohammadi & Mohammadi 2024, Rincón et al. 2021). Decentralized policies foster support for participatory energy planning. Effective regulatory frameworks are essential to oversee the implementation of renewable energy initiatives. In India, the Ministry of New and Renewable Energy (MNRE) is the key agency responsible for renewable energy policies, playing a crucial role in promoting wind energy through policy support and a favorable regulatory environment. MNRE has introduced generation-based incentives, renewable purchase obligations, competitive bidding, and other reforms to stimulate wind energy development (Kumar et al. 2022).

Overcoming institutional constraints is essential for effective stakeholder engagement in sustainable decision-making for renewable energy. Similarly, building institutional capacity is crucial for raising awareness (Wretling et al. 2021). The Solar Energy Corporation of India (SECI), a Central Public Sector Undertaking under MNRE, is dedicated to capacity building for large-scale solar, wind, and hybrid projects.

Regulatory enablers include policies that ensure long-term contracts, providing renewable energy investors with secure returns (Oduro et al. 2025). Regulations permitting green credits and tradable certificates offer benefits to companies adopting renewable energy. The National Renewable Energy Act (NREA) in India establishes a legal framework and trajectory for renewable energy expansion. The renewable purchase obligation requires a certain percentage of energy procurement from renewable sources.

Technology is vital to renewable energy development. Regulatory frameworks should promote grid modernization to facilitate efficient installation, maintenance, and flexibility, enabling effective management of renewable sources. Technological innovations can help lower energy consumption and reduce reliance on fossil fuels. They support energy storage, improve access to clean energy, and enhance grid stability, contributing to a sustainable energy system (Behera et al. 2024). Renewable energy technologies (RETs) are key in advancing environmental sustainability (Tabrizian 2019). Technological advances significantly impact renewable energy (Tigabu 2018). It is essential to deploy technologies that enable energy storage, smart grids, and power electronics.

Financial incentives and subsidies serve as economic enablers, encouraging the shift to renewable sources (Guy 2022, Hao & Khan 2025). Numerous central and state government schemes offer subsidies and incentives, such as the flagship rooftop solar program "PM Surya Ghar: Muft Bijli Yojana," which supports residential rooftop solar installations. Additionally, schemes provide up to 30% subsidies for farmers using solar pumps. Policies like feed-in tariffs (Kurbatova et al. 2023, Azhgaliyeva & Mishra 2022), which boost investment in clean energy, and renewable portfolio standards (Joshi 2021, Feldman & Levinson 2023), which mandate a minimum percentage of power from renewable sources, promote environmental sustainability (Malik et al. 2019).

Strong public awareness and support are essential for the successful adoption of renewable energy sources. Engaging communities positively by raising awareness of environmental sustainability through renewables encourages acceptance (Opstal & Smeets 2022, De Simone et al. 2025). Local organizations play a vital role in sensitizing communities, thus aiding the mobilization of community-led projects (Granit 2023). Green governance fosters trust, which enhances community confidence and acceptance. Additionally, job creation for local populations is a key factor contributing to regional economic development. Examples in India include solar cooperatives, village-level biomass, and biogas plants, which actively involve local communities in renewable energy initiatives.

Table 1 presents the identified enablers, along with their descriptions and contributing authors.

3. MATERIALS AND METHODS

The study employs a mixed research approach that integrates both qualitative and quantitative analyses. The qualitative data were derived from a comprehensive literature review, the Delphi technique, and case study discussions focused on India. Quantitative methods utilized include Total Interpretive Structural Modeling (TISM) and Fuzzy MICMAC analysis. Initially, the authors examined existing literature from databases such as Scopus, Web of Science, EBSCOhost, and Google Scholar, reviewing both national and international studies to encompass all relevant sources. Recurrent themes were identified as key enablers of successful renewable energy implementation. The team collaboratively determined the final list of enablers, which were then validated through expert input. A structured Delphi method was employed to both identify and confirm these enablers. Experts were selected based on predefined criteria, including a minimum of five years of experience in renewable energy policy, sustainability, or related fields. Participants included academicians and professionals from the private sector and government. Academic experts demonstrated their expertise through peer-reviewed publications in relevant areas. A total of twenty-five experts with pertinent experience were identified, with eighteen agreeing to participate (Table 2). These experts came from academia, government, policy sectors, and industry, all possessing relevant experience in renewable energy and sustainable development. The experts were assured of anonymity and confidentiality. Informed consent was obtained before the interview. They completed a semi-structured questionnaire and participated

Table 1: Details of identified enablers.

Enabler Nomenclature	Enabler Name	Description	Key Authors
Enb1	Environmental Enablers	The enabler discusses the country's geographical and climatic conditions that support renewable energy initiatives.	Nieboer et al. 2025, Obuseh et al. 2025, Erol et al. 2024, Vaidya 2025, Dashtpeyma & Ghodsi 2021.
Enb2	Institutional Enablers	The enabler highlights forums, platforms, governance initiatives, and agencies that improve the ease of renewable energy implementation.	Apolonia et al. 2021, Rincón et al. 2021, Dlamini 2023, Wretling et al. 2021.
Enb3	Regulatory Enablers	The enabler looks at policies, regulators, and certificates that authenticate renewable energy practices and help build trust.	Oduro et al. 2024, Agupugo et al. 2022, Tian et al. 2024.
Enb4	Technological Enablers	This enabler discusses digitalization, grid modernization, energy storage technologies, and renewable energy technologies that are essential.	Hwang & Venter 2025, Eleksiani et al. 2025, Tabrizian 2019, Agupugo et al. 2022, Tigabu 2018
Enb5	Economic Enablers	The enabler looks at incentives, subsidies, feed-in tariffs, and renewable portfolio standards that help to attract investors and corporations for renewable energy investment and adoption.	Guy 2022, Hao & Khan 2025, Kurbatova et al. 2023, Azhgaliyeva & Mishra 2022, Joshi 2021, Feldman & Levinson 2023.
Enb6	Social Enablers	The enabler elaborates on the role of local communities, local organisations, and community engagement, which are crucial.	Opstal & Smeets 2022, De Simone et al. 2025, Granit 2023, Tian et al. 2024.

in three iterative rounds of interaction. In the first round, the experts validated the identified enablers through a monitored questionnaire and follow-up interviews. These six enablers were rated on a scale of 1 to 5; a mean score of 3 or higher was required for validation, as shown in Table 3. During the second round, the experts evaluated the contextual relationships and the direction of influence among the enablers, as depicted in the structural self-interaction matrix (Table 4). In the third round, they discussed the associability of the variables (Table 11).

The identified six enablers were validated through a monitored questionnaire with further interview discussions. A scale of 1 to 5 was used to rate the enablers; a mean score of greater than 3 was used for validation, as shown in Table 3.

3.1. Data Analysis and Interpretation

In the subsequent phase, the steps defined by TISM were employed to develop the interpretive model, which uncovered the hierarchical relationships among the identified enablers. TISM extends the well-established Interpretive Structural Modelling (ISM) technique, used to determine hierarchical relationships among interacting variables. This method is widely accepted and especially valuable when there is limited existing literature. It is preferred over other modeling techniques because it is interpretive—relying on the knowledge and experience of field experts. Their opinions are structured to illustrate the hierarchy among variables, facilitating the development of a conceptual framework or model.

3.2. Structural Self-Interaction Matrix (SSIM)

The SSIM table is constructed based on the knowledge, experience, and opinions of experts. These experts completed a questionnaire designed to explore the relationship dynamics among the identified enablers. According to TISM, the row is labeled as "i" and the column as "j"; the relationship between

Table 2: Summary of experts.

Expert	Years of relevant experience	Type of sector	Designation
Expert 1	5-10 years	Industry-Government	Energy Economist
Expert 2	11-15 years	Industry-Government	Project Manager
Expert 3	5-10 years	Industry-Private	ESG officer
Expert 4	15-20 years	Academia-Government	Professor and Researcher
Expert 5	15-20 years	Academia-Private	Professor and Researcher
Expert 6	Above 20 years	Industry-Government	Senior Operations Manager
Expert 7	5-10 years	Academia-Government	Assistant Professor-Sustainability
Expert 8	15-20 years	Industry-Private	Fund Manager
Expert 9	5-10 years	Academia-Private	Junior Research Fellow
Expert 10	15-20 years	Industry-Government	Senior Project Manager
Expert 11	5-10 years	Academia-Private	Assistant Professor-Sustainability
Expert 12	15-20 years	Industry-Government	Senior Consultant
Expert 13	15-20 years	Industry-Government	Consultant
Expert 14	11-15 years	Academia-Government	Associate Professor
Expert 15	Above 20 years	Academia-Private	Professor
Expert 16	11-15 years	Academia-Private	Associate Professor
Expert 17	11-15 years	Industry-Private	Consultant
Expert 18	Above 20 years	Industry-Private	Senior Policy Advisor

Table 3: Mean scores of enablers.

Enabler Nomenclature	Enabler Name	Mean Score	Comments
Enb1	Environmental Enabler	3.21	Acceptable
Enb2	Institutional Enabler	3.43	Acceptable
Enb3	Regulatory Enabler	3.63	Acceptable
Enb4	Technological Enabler	3.05	Acceptable
Enb5	Economic Enablers	3.75	Acceptable
Enb6	Social Enabler	3.45	Acceptable

Table 4: Structural Self-Interaction Matrix (Source: Authors' own contribution).

	Enb6	Enb5	Enb4	Enb3	Enb2	Enb1
Enb1	V	V	A	V	V	
Enb2	X	X	X	V		
Enb3	V	X	V			
Enb4	V	X				
Enb5	A					
Enb6						

i and j is represented by "V, A, X, O," where V and A indicate unidirectional relations, X indicates a bidirectional relation, and O signifies no relation. If i impacts j but j does not impact i, the relation is denoted as 'V'. Conversely, if j impacts i but i does not impact j, it is labeled as 'A'. When both i and j mutually influence each other, the relation is marked as 'X'. If there is no relation between i and j, it is denoted as 'O'. Table 4 presents the results of the SSIM**.**

3.3. Interpretations of the SSIM

The interpretive logic of the Structural Self-Interaction

Table 5: Interpretive logic-knowledge base.

Code	Pairwise Comparison	Interpretation
Enb1-Enb6	Environmental Enablers have an impact on Social Enablers	Environmental degradation and climate risks raise public awareness and concern, resulting in greater social acceptance, pro-renewable attitudes, and community participation.
Enb1-Enb5	Environmental Enablers have an impact on Economic Enablers	Environmental goals justify green investments, subsidies, and carbon pricing, thereby creating markets for green jobs, renewable manufacturing, and clean energy finance.
Enb1-Enb4	Technological Enablers have an impact on Environmental Enablers	Technology and innovation in renewable energy make it affordable and scalable, thereby strengthening environmental outcomes.
Enb1-Enb3	Environmental Enablers have an impact on Regulatory Enablers	Environmental pressures drive regulations that encourage renewable energy sources through initiatives such as renewable purchase obligations (RPOs), emissions norms, and environmental clearances.
Enb1-Enb2	Environmental Enablers have an impact on Institutional Enablers	Environmental objectives, commitment to sustainable development, and commitment to reducing carbon footprints result in institutional frameworks that encourage and incentivise renewable energy initiatives.
Enb2-Enb6	Institutional Enablers and Social Enablers influence each other.	Institutions help to shape awareness programs and trust in renewable energy initiatives. This, in turn, helps to generate social awareness and acceptance. The rising awareness and environmental consciousness among the community have also pushed institutions to take up initiatives that promote clean energy.
Enb2-Enb5	Institutional Enablers and Economic Enablers influence each other.	Institutions are responsible for developing incentive schemes and subsidies to attract investors in renewable energy. Economic enablers influence institutional enablers because improved financial viability and investment flows enhance institutional capacity and long-term sustainability.
Enb2-Enb4	Institutional Enablers and Technological Enablers influence each other.	Institutional enablers support research and development, investment in renewable energy technology(RET). Emerging technologies necessitate capacity building and institutional adaptation.
Enb2-Enb3	Institutional Enablers have an impact on Regulatory Enablers	Institutional enablers influence regulatory enablers as institutional capacity and governance structures are essential for designing, implementing, and enforcing renewable energy regulations.
Enb3-Enb6	Regulatory Enablers have an impact on Social Enablers	Regulatory enablers influence social enablers, as clear, supportive regulations build public confidence, increase awareness, and foster societal acceptance of renewable energy systems.
Enb3-Enb5	Regulatory Enablers and Economic Enablers influence each other.	Regulatory enablers influence economic enablers, as stable, transparent regulations reduce investment risk and facilitate market growth in renewable energy. Economic enablers influence regulatory enablers because evolving market conditions and investment dynamics necessitate regulatory adaptation and reform.
Enb3-Enb4	Regulatory Enablers have an impact on Technological Enablers	Regulatory enablers influence technological enablers, as regulatory standards, mandates, and compliance requirements shape the development, deployment, and innovation in renewable energy.
Enb4-Enb6	Technological Enablers have an impact on Social Enablers	Technology has enabled the community to connect. Social media helps generate curiosity and interest among the community about renewable energy, which results in smoother adoption.
Enb4-Enb5	Technological Enablers and Economic Enablers influence each other.	Technology can help scale renewable energy projects with economic consequences. Funding RET can increase research and innovation.
Enb5-Enb6	Social Enablers have an impact on Economic Enablers.	Social enablers influence economic enablers by increasing demand, reducing implementation risks, and improving the economic viability of renewable energy projects.

Table 6: Initial reachability matrix (Source: Authors' own contribution).

	Enb1	Enb2	Enb3	Enb4	Enb5	Enb6
Enb1	1	1	1	0	1	1
Enb2	0	1	1	1	1	1
Enb3	0	0	1	1	1	1
Enb4	1	1	0	1	1	1
Enb5	0	1	1	1	1	0
Enb6	0	1	0	0	1	1

Matrix (SSIM) is presented in Table 5, which explains the direction of influence among the identified renewable energy enablers. The table shows that environmental enablers strongly influence institutional, regulatory, economic, and social enablers, while several relationships, such as institutional-economic, institutional-technological, and regulatory-economic enablers, are mutually reinforcing. Overall, Table 5 provides the knowledge base used to justify the pairwise relationships and establish how different enablers interact in supporting renewable energy adoption.

3.4. Reachability Matrix

The SSIM is translated into binary digits following the rules of TISM. A unidirectional relation of V is denoted as (1,0), while A is represented as (0,1). The bidirectional relation X is indicated by (1,1), and the absence of a relation O is shown as (0,0). Table 6 displays the initial reachability matrix constructed based on these rules. To determine the final reachability matrix, the principle of transitivity is applied, as illustrated in Table 7.

3.5. Hierarchical Level Partitioning

Level partitioning helps to develop the hierarchical relationship among the different factors. It considers the intersection between the "antecedent" (AS) and the "reachability set" (RS) derived from the FRM. Iterations are repeated for all the factors to arrive at the different levels of the model, as shown in Tables 8, 9, and 10.

3.6. TISM Model

Fig. 1 illustrates the TISM model, which is derived from the level partitioning. The first level of the model comprises Institutional Enablers (Enb2) and Technological Enablers (Enb4), while Regulatory Enablers (Enb3) are positioned at the second level. Environmental Enablers (Enb1), Economic Enablers (Enb5), and Social Enablers (Enb6) constitute the third level of the model. A detailed discussion of the TISM model can be found in the Results and Discussion section.

Table 7: Final reachability matrix (Source: Authors' own contribution).

	Enb1	Enb2	Enb3	Enb4	Enb5	Enb6
Enb1	1	1	1	0	1	1
Enb2	0	1	1	1	1	1
Enb3	1*	0	1	1	1	1
Enb4	1	1	0	1	1	1
Enb5	0	1	1	1	1	0
Enb6	0	1	0	1*	1	1

3.7. Fuzzy MICMAC Analysis

The third objective of the study aims to understand the nature of linkages between the identified enablers, which is achieved through fuzzy MICMAC analysis. Fuzzy MICMAC

Table 8: Level Partitioning Iteration Matrix 1 (Source: Authors' own contribution).

	Antecedent Set (AS)	Reachability Set (RS)	AS RS	Level
Enb1	(1,2,3,5,6)	(1,3,4)	(1,3)	
Enb2	(2,3,4,5,6)	(1,2,4,5,6)	(2,4,5,6)	Level 1
Enb3	(1,3,4,5,6)	(1,2,3,5)	(1,3,5)	
Enb4	(1,2,4,5,6)	(2,3,4,5,6)	(2,4,5,6)	Level 1
Enb5	(2,3,4,5)	(1,2,3,4,5,6)	(2,3,4,5)	
Enb6	(2,4,5,6)	(1,2,3,4,6)	(2,4,6)	

Table 9: Level Partitioning Iteration Matrix 2 (Source: Authors' own contribution).

	Antecedent Set (AS)	Reachability Set (RS)	AS RS	Level
Enb1	(1,3,5,6)	(1,3)	(1,3)	
Enb3	(1,3,5,6)	(1,3,5)	(1,3,5)	Level 2
Enb5	(3,5)	(1,3,5,6)	(3,5)	
Enb6	(5,6)	(1,3,6)	(6)	

Table 10: Level Partitioning Iteration Matrix 3 (Source: Authors' own contribution).

	Antecedent Set (AS)	Reachability Set (RS)	AS RS	Level
Enb1	(1,3,5,6)	(1,3)	(1)	Level 3
Enb5	(3,5)	(1,3,5,6)	(5)	Level 3
Enb6	(5,6)	(1,3,6)	(6)	Level 3

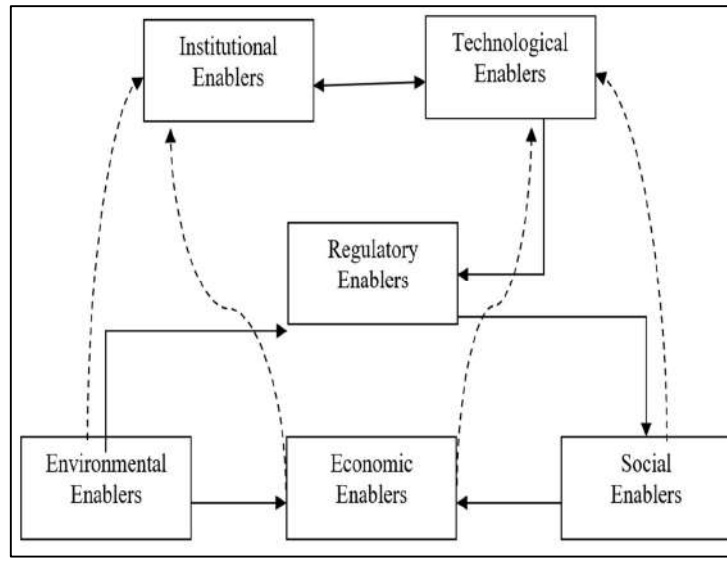


Fig. 1: TISM model of Enablers of Renewable Energy(Source: Authors' Contribution).

analysis considers the driving and dependent powers of the enablers from Table 7, which helps to classify the factors into four clusters.

Tables 11 and 12 examine the associability of values and the fuzzy reachability matrix. Expert judgment regarding the influence among enablers was based on the associability of variables presented in Table 11. This approach helped minimize bias that could arise from using rigid binary judgments. The experts reviewed the associability table to assess the degree of connection between the identified enablers. Associability values ranged from 0 to 1, where 0 indicated no association and 1 indicated complete association.

As illustrated in Fig. 2, the Fuzzy MICMAC analysis categorizes the enablers into four distinct clusters. The first, known as the autonomous cluster, is characterized by low "driving power" and low "dependence power." The second, the driving cluster, consists of enablers with high "driving" power but lower "dependence" power. The third, the linkage cluster, includes enablers with both high "driving" and high "dependence" powers. The final cluster, called the dependent cluster, features enablers with weak "driving" power yet higher "dependence" power. The findings of the Fuzzy MICMAC analysis are discussed in the following section. 1

Table 7: Final Reachability Matrix (Source: Authors' own contribution).

	Enb1	Enb2	Enb3	Enb4	Enb5	Enb6
Enb1	1	1	1	0	1	1
Enb2	0	1	1	1	1	1
Enb3	1*	0	1	1	1	1
Enb4	1	1	0	1	1	1
Enb5	0	1	1	1	1	0
Enb6	0	1	0	1*	1	1

Table 11: Associability of values for expert opinion.

0	0.1	0.3	0.5	0.7	0.9	1
No relation	Very Low	Low	Average	High	Very High	Complete

4. RESULTS AND DISCUSSION

4.1. TISM Model

The TISM Model identifies both institutional and technological enablers at level 1. In India, institutional enablers include a broad network of government-supported entities such as the Ministry of New and Renewable Energy (MNRE), Solar Energy Corporation of India (SECI), NITI Aayog, and State Renewable Energy Development Agencies (SREDAs). These organizations are tasked with policy formulation, subsidies, and the execution of large-scale projects. For instance, NITI Aayog develops long-term strategies for integrating renewable energy, while MNRE oversees initiatives like the National Solar Mission, which emphasizes grid-connected, rooftop, and off-grid solar capacities. MNRE also manages subsidies through DISCOMs and supports various bioenergy programs. SREDAs serve as state-level nodal agencies focusing on energy efficiency and conservation initiatives. These institutional structures foster investment in renewable energy technologies. Globally, India ranks as the fourth-largest wind energy producer and possesses advanced technology

Table 12: Fuzzy Reachability Matrix.

	Enb1	Enb2	Enb3	Enb4	Enb5	Enb6	Driving Power
Enb1	1	0.7	0.5	0.3	0.9	0.7	4.1
Enb2	0	1	0.9	0.7	0.5	0.7	3.8
Enb3	0.7	0.3	1	0.5	0.9	0.9	4.3
Enb4	0.7	0.5	0.1	1	0.7	0.9	3.9
Enb5	0.3	0.7	0.7	0.9	1	0.3	3.9
Enb6	0.1	0.9	0.3	0.7	0.7	1	3.7
Dependence Power	3.5	4.1	3.5	4.1	4.7	4.5	

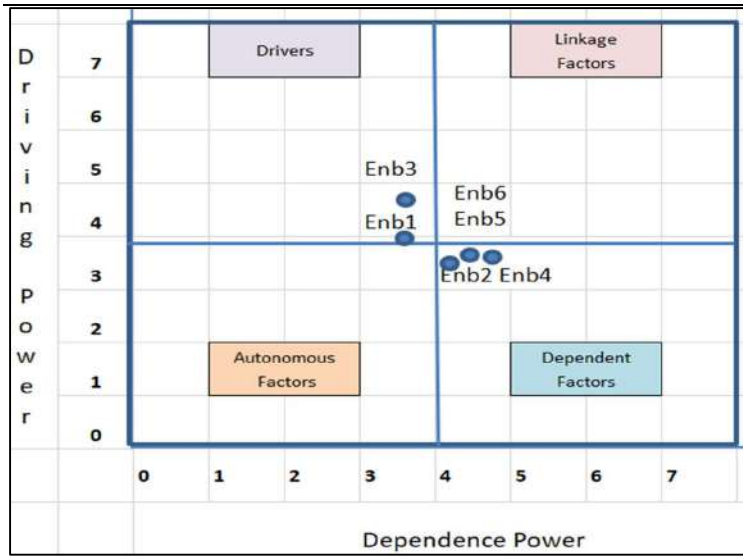


Fig. 2: Fuzzy MICMAC Analysis (Source: Authors' contribution).

to support its deployment. Under the National Solar Mission, India has adopted diverse solar technologies, including rooftop, off-grid, and utility-scale systems. The second level of the model emphasizes regulatory frameworks. The bidirectional relationship depicted in Fig. 1 illustrates how institutional and technological enablers mutually reinforce each other: institutions facilitate technology deployment via funding, coordination, and capacity building, while technological progress requires institutional adaptation and learning. Regulations convert institutional objectives into enforceable rules, standards, and incentives, promoting social acceptance and economic participation. India's regulatory framework includes provisions like the Renewable Purchase Obligation (RPO), renewable energy certificates, and grid standards for renewable energy. These frameworks are vital for infrastructure development, providing policy stability and safeguarding investor interests.

The third level of the model consists of environmental, social, and economic enablers. Environmental enablers form the foundation within the TISM framework, exerting strong driving forces with minimal dependence on other enablers. They have a direct influence on economic enablers and an indirect effect on institutional and regulatory enablers, making them key initiators of the renewable energy system. Social acceptance and economic viability are outcomes of the system, not driving forces—challenging the common assumption that awareness or finance alone can propel renewable energy transitions. India benefits from abundant sunlight, mountain ranges, and coastal areas, which facilitate wind energy harnessing. The agricultural sector contributes biomass that can be used for fuel production. Increasing environmental awareness among Indians about climate change, energy security, and pollution caused by fossil fuels has grown. Many have shown interest in solar energy, installing solar panels on their homes. Indian universities and educational institutions have incorporated sustainability modules into curricula, raising awareness. Social enablers play a vital role in promoting understanding of renewable energy. The Indian government has launched initiatives like PM-KUSUM that offer subsidies to farmers for solar pumps and small solar power plants, enabling excess energy to be sold back to the grid. The UJALA scheme, introduced in

2015, aimed to improve energy efficiency by distributing affordable LED bulbs. Additionally, India provides various subsidies and incentives to encourage the adoption of renewable energy sources. The PM Surya Ghar Muft Bijli Yojana offers subsidies for residential solar rooftop installations, and solar modules are taxed at only 5%.

4.2. Fuzzy MICMAC Analysis

The results of the Fuzzy MICMAC analysis reveal that the model comprises Drivers and Dependent Variables. Environmental and regulatory enablers serve as the primary drivers, playing a vital role in the successful deployment of renewable energy sources. These enablers are independent, meaning they do not depend on others; however, their absence can negatively impact the model. To effectively harness renewable energy, access to a diverse array of energy sources is essential. The positioning confirms that environmental concerns—such as climate change mitigation and emission reduction—are not merely outcomes of the system but are initiators that influence policy priorities, institutional responses, and market behavior. Regulatory enablers ensure that appropriate systems and processes are established to promote and oversee renewable energy adoption for enhanced energy efficiency and sustainable development. Institutional, technological, economic, and social enablers are classified as dependent variables within the model. Institutional enablers depend on regulatory frameworks, public demand for clean energy, and the international sustainability agenda and goals. This feedback loop positions institutional and technological enablers at an intermediate yet influential level, functioning as system stabilizers rather than independent drivers. Typically, institutional, regulatory, and technological enablers are found here, reflecting continuous policy revisions, regulatory learning, and technology-policy feedback cycles. This underscores their central but sensitive role, as observed in the TISM structure. Technology relies on supportive policies, available funding for innovation, and market demand for renewable energy technologies. Economic enablers are outcomes of fiscal policies, funding support, and regulatory frameworks for renewable energy. Social enablers depend on campaigns, consumer attitudes, accessibility, and affordability.

5. CONCLUSIONS

The authors in the study aimed to analyze three specific objectives. The primary goal was to identify the key drivers that contribute to the successful implementation of renewable energy sources, with a particular emphasis on India. This was accomplished through an extensive review of existing literature and consultations with experts. The findings revealed six enablers: environmental, institutional, regulatory, technological, economic, and social, all of which facilitate the adoption and integration of renewable energy as a clean energy option in India. The second objective centered on exploring the relationships between these enablers. The TISM model represents three levels, illustrating the hierarchical relationships among the six enablers. Various initiatives and institutions established by the Government of India have played a significant role in streamlining and regulating the renewable energy sector. The third objective involved analyzing the nature of the linkages between the enablers using Fuzzy MICMAC Analysis. The results classified the enablers into driving and dependent variables, both essential for the success of the model.

5.1. Implications of the Study

The study has significant implications for theory, management, and society. The identified enablers add value to the existing body of literature in this area. Moreover, the study enhances understanding of the relationships between these enablers. The TISM method offers a framework for grasping the hierarchical connections among the three levels of enablers, clarifying how they interlink. This framework aids in identifying and prioritizing key enablers. Expert insights provide valuable qualitative feedback, laying a foundation for further exploration and future research. The study highlights practices adopted by India that could be examined and adapted into policies for other developing nations. Results suggest that policymakers should prioritize high-driving enablers over dependent outcomes. Improving environmental commitments, such as emission standards and sustainability policies, can trigger positive effects across institutions, regulations, and markets. Strengthening institutional capacity and ensuring regulatory consistency are crucial, as high-driving enablers transform environmental intentions into actionable strategies and technology adoption. Policies focused solely on social acceptance or financial incentives may fall short unless supported by robust institutional and regulatory frameworks. Consequently, this study offers policymakers a systemic approach for targeted interventions rather than isolated outcomes. For project developers, investors, and implementing agencies, the findings imply that economic viability and social acceptability stem from system readiness. Engagement strategies must align with clear regulatory frameworks to reduce project risks. Additionally, institutional learning and regulatory adaptation are essential alongside technological advancements to facilitate scaling. Recognizing each enabler's position in the system enables practitioners to anticipate potential bottlenecks and develop more resilient renewable energy projects.

6. REFERENCES

Abdullah-Al-Mahbub, M. and Islam, A.R.M.T., 2023. Current status of running renewable energy in Bangladesh and future prospects: A global comparison. *Heliyon*, 9(3), pp.1-15. [DOI]

Alam, M.S., Duraisamy, P., Siddik, A.B., Murshed, M., Mahmood, H., Palanisamy, M. and Kirikkaleli, D., 2023. The impacts of globalization, renewable energy, and agriculture on CO_2 emissions in India: contextual evidence using a novel composite carbon emission-related atmospheric quality index. *Gondwana Research*, 119, pp.384-401. [DOI]

Apolonia, M. and Simas, T., 2021. Life cycle assessment of an oscillating wave surge energy converter. *Journal of Marine Science and Engineering*, 9(2), p.206. [DOI]

Azhgaliyeva, D. and Mishra, R., 2022. Feed-in tariffs for financing renewable energy in Southeast Asia. *Wiley Interdisciplinary Reviews: Energy and Environment*, 11(3), p.e425. [DOI]

Beck, M., Rivers, N. and Wigle, R., 2018. How do learning externalities influence the evaluation of Ontario's renewables support policies? *Energy Policy*, 117, pp.86-99. [DOI]

Behera, P., Sethi, L. and Sethi, N., 2024. Balancing India's energy trilemma: assessing the role of renewable energy and green technology innovation for sustainable development. *Energy*, 308, p.132842. [DOI]

Boadu, S. and Otoo, E., 2024. A comprehensive review on wind energy in Africa: challenges, benefits and recommendations. *Renewable and Sustainable Energy Reviews*, 191, p.114035. [DOI]

Briera, T. and Lefèvre, J., 2024. Reducing the cost of capital through international climate finance to accelerate the renewable energy transition in developing countries. *Energy Policy*, 188, p.114104. [DOI]

Chaikumbung, M., 2025. The influence of national cultures on preferences and willingness to pay for renewable energy in developing countries: a meta-analysis. *Renewable and Sustainable Energy Reviews*, 207, p.114972. [DOI]

Charfeddine, L. and Kahia, M., 2021. Do information and communication technology and renewable energy use matter for carbon dioxide emissions reduction? Evidence from the Middle East and North Africa region. *Journal of Cleaner Production*, 327, p.129410. [DOI]

Chenyang, W., Wei, W., Xi, C., Ming, L. and Hansheng, C., 2023. Suggestions on mineral resources management from the perspective of grass-roots government openness in the field of natural resources. *China Mining Magazine*, 32(S1), pp.8-12.

Dashtpeyma, M. and Ghodsi, R., 2021. Developing the resilient solar energy management system: a hybrid qualitative-quantitative approach. *International Journal of Ambient Energy*, 42(16), pp.1892-1911. [DOI]

De Simone, E., Rochira, A. and Mannarini, T., 2025. Individual and community catalysts for renewable energy communities (RECs) development. *Current Opinion in Psychology*, 62, p.101987. [DOI]

Erol, I., Peker, I., Benli, T., Ar, I.M. and Searcy, C., 2024. Exploring the enablers for building resilience in solar photovoltaic energy supply chains. *Operations Management Research*, 17(3), pp.1100-1125. [DOI]

Feldman, R. and Levinson, A., 2023. Renewable portfolio standards. *The Energy Journal*, 44(5), pp.1-20. [DOI]

Granit, I., 2023. What makes Colombia's indigenous peoples adopt microgrids? Social acceptance and financial constraints in renewable energy diffusion. *Energy Research & Social Science*, 101, p.103132. [DOI]

Guy, L., 2022. *Exploring investment enablers and barriers for mature and novel renewable energy technologies using the Delphi method* (Master›s thesis). University of Technology Sydney, pp.120.

Gyimah, J., Fiati, M.K., Nwigwe, U.A., Vanessa, A.E. and Yao, X., 2023. Exploring the impact of renewable energy on economic growth and carbon emissions: evidence from partial least squares structural equation modeling. *PLOS ONE*, 18(12), p.e0295563. [DOI]

Hao, Y. and Khan, I., 2025. Impact of decarbonization enablers, energy supply between transition and disruption, on renewable energy development. *Energy*, 324, p.135863. [DOI]

Herath, P., Dissanayake, P. and Kumarasiri, B., 2022. Enablers to facilitate industrial symbiosis for better waste management of industrial zones in Sri Lanka. In: *Proceedings of the 10th World Construction Symposium*, pp.429-440. [DOI]

Islam, M.M., Irfan, M., Shahbaz, M. and Vo, X.V., 2022. Renewable and non-renewable energy consumption in Bangladesh: the relative influencing profiles of economic factors, urbanization, physical infrastructure, and institutional quality. *Renewable Energy*, 184, pp.1130-1149. [DOI]

Joarder, M.S.A., Raihan, A., Salehi, M., Walasek, R. and Zimon, G.R.Z.E.G.O.R.Z., 2024. Analysis of the current development of renewable energy technologies in Bangladesh. *WSEAS Transactions on Environment and Development*, 20, pp.883-894. [DOI]

Joshi, J., 2021. Do renewable portfolio standards increase renewable energy capacity? Evidence from the United States. *Journal of Environmental Management*, 287, p.112261. [DOI]

Khare, V., Jain, A. and Bhuiyan, M.A., 2023. Perspective of renewable energy in the BRICS countries. *E-Prime: Advances in Electrical Engineering, Electronics and Energy*, 5, p.100250. [DOI]

Kishore, T.S., Kumar, P.U. and Ippili, V., 2025. Review of global sustainable solar energy policies: significance and impact. *Innovation and Green Development*, 4(2), p.100224. [DOI]

Koswatte, I., Iddawala, J., Kulasekara, R., Ranaweera, P., Dasanayaka, C.H. and Abeykoon, C., 2024. Can Sri Lanka be a net-zero nation by 2050?—Current renewable energy profile, opportunities, challenges, and recommendations. *Cleaner Energy Systems*, 8, p.100126. [DOI]

Kumar, A., Pal, D., Kar, S.K., Mishra, S.K. and Bansal, R., 2022. An overview of wind energy development and policy initiatives in India. *Clean Technologies and Environmental Policy*, 24(5), pp.1337-1358. [DOI]

Kurbatova, T., Sotnyk, I., Prokopenko, O., Bashynska, I. and Pysmenna, U., 2023. Improving the feed-in tariff policy for renewable energy promotion in Ukraine's households. *Energies*, 16(19), p.6773. [DOI]

Lal, R. and Kumar, S., 2022. Energy security assessment of small Pacific Island Countries–sustaining the call for renewable energy proliferation. *Energy Strategy Reviews*, 41, p.100866. [DOI]

Lal, S.R.S., Herbert, G.M.J., Arjunan, P. and Suryan, A., 2025. Advancements in renewable energy transition in India: a review. *Energy Sources, Part A: Recovery, Utilization, and Environmental Effects*, 47(2), p.2024921. [DOI]

Li, H.X., Edwards, D.J., Hosseini, M.R. and Costin, G.P., 2020. A review on renewable energy transition in Australia: an updated depiction. *Journal of Cleaner Production*, 242, p.118475. [DOI]

Liu, X., Shi, H., Yang, D., Chen, X., Xia, X.A. and Xie, Y., 2025. Reducing the impact of climate change on renewable energy systems through wind–solar blending: a worldwide study with CMIP6. *Solar Energy*, 290, p.113365. [DOI]

Maka, A.O. and Alabid, J.M., 2022. Solar energy technology and its roles in sustainable development. *Clean Energy*, 6(3), pp.476-483. [DOI]

Malik, K., Rahman, S.M., Khondaker, A.N., Abubakar, I.R., Aina, Y.A. and Hasan, M.A., 2019. Renewable energy utilization to promote sustainability in GCC countries: policies, drivers, and barriers. *Environmental Science and Pollution Research*, 26(20), pp.20798-20814. [DOI]

Mohammadi, M. and Mohammadi, A., 2024. Empowering distributed solutions in renewable energy systems and grid optimization. In: *Distributed Machine Learning and Computing: Theory and Applications*. Springer International Publishing, pp.141-155. [DOI]

Mohazzem Hossain, S., Biswas, S. and Raihan Uddin, M., 2024. Sustainable energy transition in Bangladesh: challenges and pathways for the future. *Engineering Reports*, 6(1), p.e12752. [DOI]

Nieboer, S., Hansmeier, H., Beers, P.J., Seus, S. and Hebinck, A., 2025. *The*

Impact of Geographical Enablers and Barriers on the Scaling of Grassroots Innovation Initiatives: Findings and Recommendations of the Secondary Data Analysis of the SHARED GREEN DEAL SSH Priority Themes. SHARED GREEN DEAL, Cambridge, pp.45. [DOI]

Obuseh, E., Eyenubo, J., Alele, J., Okpare, A. and Oghogho, I., 2025. A systematic review of barriers to renewable energy integration and adoption. *Journal of Asian Energy Studies*, 9, pp.26-45. [DOI]

O[DOI]-Yorke, F., Bain, J., Agyekum, E.B., Dzebre, D.E., Sekyere, C.K., Quansah, D.A. and Adaramola, M.S., 2025. Mapping Ghana's renewable energy research landscape: a bibliometric insight into trends, progress, and policy relevance for sustainable development. *International Journal of Ambient Energy*, 46(1), p.2577223. [DOI]

Oduro, S., Pittri, H., Baah, B., Simons, B., Gyamfi, J., Botchway, B. and Afful, A.E., 2025. Strategies for the implementation of net zero energy buildings in the Ghanaian construction industry. *Built Environment Project and Asset Management*. [DOI]

Pambudi, N.A., Yuniar, W., Ulfa, D.K., Nanda, I.R. and Widiastuti, I., 2024. Assessing the readability of renewable energy education material from geothermal resources in vocational high school textbooks: a case study in Indonesia. *Journal of Sustainable Development of Energy, Water and Environment Systems*, 12(3), pp.1-28. [DOI]

Raza, M.A., Aman, M.M., Kumar, L., Al-Khasawneh, M.A., Faheem, M. and Ehyaei, M.A., 2025. Carbon neutrality and economic stability nexus: an integrated renewable energy transition to decarbonize the energy sector. *Energy Reports*, 13, pp.4586-4608. [DOI]

Rincón, C.A.R., Santos, J., Volker, L. and Rouwenhorst, R., 2021. Identifying institutional barriers and enablers for sustainable urban planning from a municipal perspective. *Sustainability*, 13(20), p.11231. [DOI]

Rohit, R.V., Kiplangat, D.C., Veena, R., Jose, R., Pradeepkumar, A.P. and Kumar, K.S., 2023. Tracing the evolution and charting the future of geothermal energy research and development. *Renewable and Sustainable Energy Reviews*, 184, p.113531. [DOI]

Tabrizian, S., 2019. Technological innovation to achieve sustainable development—renewable energy technologies diffusion in developing countries. *Sustainable Development*, 27(3), pp.537-544. [DOI]

Tigabu, A.D., 2018. Analysing the diffusion and adoption of renewable energy technologies in Africa: the functions of innovation systems perspective. *African Journal of Science, Technology, Innovation and Development*, 10(5), pp.615-624. [DOI]

Vaidya, A., 2025. *Exploring Alternative Energy Sources*. Educohack Press, pp.220.

Van Opstal, W. and Smeets, A., 2022. *Sustainable Production and Consumption*. Springer, pp.180.

Virah-Sawmy, D. and Sturmberg, B., 2025. Socio-economic and environmental impacts of renewable energy deployments: a review. *Renewable and Sustainable Energy Reviews*, 207, p.114956. [DOI]

Wang, L., He, Y. and Wu, R., 2024. The green engine of growth: assessing the influence of renewable energy consumption and environmental policy on China's economic sustainability. *Sustainability*, 16(8), p.3120. [DOI]

Wang, Y., Wang, D., Yu, L. and Mao, J., 2023. What really influences the development of renewable energy? A systematic review and meta-analysis. *Environmental Science and Pollution Research*, 30(22), pp.62213-62236. [DOI]

Yang, Z., Zhang, M., Liu, L. and Zhou, D., 2022. Can renewable energy investment reduce carbon dioxide emissions? Evidence from scale and structure. *Energy Economics*, 112, p.106181. [DOI]

Nature Environment and Pollution Technology
An International Quarterly Scientific Journal

p-ISSN: 0972-6268
(Print copies up to 2016)
e-ISSN: 2395-3454

Vol. 25 | No. 3 | Article ID D1882 | 2026

Original Research Paper

https://doi.org/10.46488/NEPT.2026.v25i03.D1882

Open Access Journal

Perception-Participation Dynamics and Mangrove Degradation: A Multi-Group SEM in Northern Central Java, Indonesia

Hugi Cerlyawati[1], Muhammad Zainuri[2] and Slamet Isworo[1]†

[1]Department of Environmental Health, Universitas Dian Nuswantoro, Semarang 50131, Indonesia

[2]Department of Oceanography, Faculty of Fisheries and Marine Science, Diponegoro University, Semarang 50275, Indonesia

†Corresponding author: Slamet Isworo; slamet.isworo@dsn.dinus.ac.id

Abbreviation: Nat. Env. & Poll. Technol.
Website: www.neptjournal.com

Received: 06-10-2025
Revised: 12-12-2025
Accepted: 17-12-2025

Key Words:

Mangrove resilience
Environmental awareness
Participatory management
Anthropogenic pressure
Structural equation modeling (SEM)
Java Sea coast

Citation for the Paper:

Cerlyawati, H., Zainuri, M. and Isworo, S., 2026. Perception-participation dynamics and mangrove degradation: A multi-group SEM in northern central Java, Indonesia. *Nature Environment and Pollution Technology*, 25(3), D1882. https://doi.org/10.46488/NEPT.2026.v25i03.D1882

Note: From 2025, the journal has adopted the use of Article IDs in citations instead of traditional consecutive page numbers. Each article is now given individual page ranges starting from page 1.

Copyright: © 2026 by the authors
Licensee: Technoscience Publications
This article is an open access article distributed under the terms and conditions of the Creative Commons Attribution (CC BY) license (https://creativecommons.org/licenses/by/4.0/).

ABSTRACT

Mangrove ecosystems along northern Central Java are experiencing rapid decline due to ecological pressures, land-use changes, and limited institutional support. This study explores how community perceptions and participation influence mangrove degradation across Brebes, Pemalang, and Demak. A mixed-methods approach was employed, combining a structured household survey (n = 150) with focus group discussions to contextualize quantitative results. Confirmatory Factor Analysis validated measurement accuracy, and Structural Equation Modeling (SEM) with multi-group analysis (MG-SEM) was used to assess causal relationships and spatial variation. In the combined model, perception had a strong positive impact on participation ($\beta = 0.58$, $p < 0.001$) and a direct negative effect on degradation ($\beta = –0.21$, $p = 0.010$). Participation further reduced degradation ($\beta = –0.32$, $p < 0.001$) and partially mediated the perception–degradation link ($\beta_{indirect} = –0.19$, $p < 0.001$). The model accounted for 34% of the variance in participation and 26% in degradation ($R^2 = 0.34$, 0.26) and demonstrated good fit indices ($\chi^2/df = 1.87$, CFI = 0.93, TLI = 0.91, RMSEA = 0.056, SRMR = 0.045). MG-SEM revealed context-specific dynamics: an effective perception–participation–degradation pathway in Brebes, a "Pemalang Paradox," where high participation coexists with significant degradation under intense anthropogenic pressure, and diminished behavioral effects in Demak under extreme ecological stress. These insights emphasize perception and participation as crucial yet bounded factors in mangrove resilience, highlighting the importance of spatially tailored management strategies.

1. INTRODUCTION

Mangrove ecosystems play a vital role in maintaining the stability of tropical coastal areas. Their complex root systems protect shorelines from erosion and seawater intrusion, trap sediments, boost fisheries productivity, and serve as critical habitats for a wide range of aquatic species (Isworo & Oetari 2020). In addition to these ecological advantages, mangroves are recognized as some of the most effective blue-carbon sinks, significantly aiding climate change mitigation through substantial carbon sequestration (Choudhary et al. 2024). By providing these ecological and socio-economic benefits, mangroves underpin the resilience of coastal communities, fostering environmental sustainability, livelihood security, and long-term adaptability (Lovelock et al. 2024).

Despite their significance, Indonesia continues to face substantial mangrove loss. Over the last thirty years, approximately 48 km² of mangroves have vanished-averaging about 3.25 km² annually-due to changes in rainfall patterns, land conversion, and expansion of aquaculture (Wiarta et al. 2025). These declines have broader implications: a 1% reduction in mangrove cover is estimated to cause a 5.3–9.8% decrease in household fishery income. Limited institutional support and ongoing land-use conflicts further complicate management efforts, highlighting the complexity of maintaining coastal ecosystems (Utami et al. 2024).

Within this context, community perception and participation have emerged as critical determinants of restoration success. Favorable perceptions are often linked to stronger engagement in replanting, stewardship programs, and mangrove-based ecotourism, while limited awareness tends to hinder involvement. Empirical evidence shows that these social dimensions influence both ecological outcomes and household livelihoods (Jadloc et al. 2025, Sarujan & Sakurai 2023). Indonesian case studies similarly demonstrate strong associations between mangrove condition and community engagement (Syahputra & Fernando 2024). Nevertheless, existing research remains largely biophysical in orientation, leaving the socio-ecological linkages-particularly the causal interplay among perception, participation, and degradation-underexplored. Comparative studies across locations with varying ecological pressures and institutional arrangements are also limited (Arifanti et al. 2025).

This study makes a significant contribution by employing Structural Equation Modeling (SEM) and Multi-Group SEM (MG-SEM) to examine the causal pathways connecting perception, participation, and mangrove degradation. It systematically compares socio-ecological determinants across Brebes, Pemalang, and Demak to identify site-specific factors influencing rehabilitation outcomes. The findings aim to support the development of adaptive, community-based strategies to enhance mangrove management in coastal regions of Indonesia.

2. MATERIALS AND METHODS

2.1. Research Design and Respondent Characteristics

This study surveyed 150 respondents, selected proportionally from Brebes, Pemalang, and Demak (50 respondents from each site) using purposive, criterion-based sampling. Participants were required to have resided in the study area for at least ten years, be aged 20 or older, and be directly involved in mangrove-related coastal livelihoods. Individuals not meeting these criteria were excluded to minimize sampling bias and ensure respondents had long-term socio-ecological experience relevant to the research context. Purposive sampling is widely recognized as effective for capturing respondents with specific place-based knowledge and direct interactions with coastal ecosystems (Nagel & Partelow 2022), while well-defined inclusion criteria improve internal validity (Dyson et al. 2023). The quantitative analysis included validity and reliability testing, ANOVA, correlation and regression analyses, and Structural Equation Modeling (SEM) to explore the proposed causal relationships among perception, participation, and mangrove degradation. To contextualize and enrich these statistical findings, focus group discussions (FGDs) were held at each site with policymakers, community leaders, and mangrove farmers (about five participants per site). These qualitative insights offered a deeper understanding of local socio-institutional dynamics and rehabilitation practices. Combining survey data with FGD results through methodological triangulation strengthened interpretive depth and increased the robustness of the study's conclusions.

2.2. Research Location

The study was carried out in three coastal regencies along the northern coast of Central Java—Brebes, Pemalang, and Demak—each characterized by different levels of mangrove degradation. These sites were deliberately selected to reflect diverse socio-ecological conditions and varying degrees of rehabilitation success. (1) Kaliwlingi Village, Brebes (±06°48′19.68″ S, 109°02′26.01″ E), represents a relatively successful rehabilitation effort supported by active community involvement and institutional support. (2) Mojo Village, Pemalang (±06°49′43″ S, 109°32′45″ E), depicts a transitional zone facing moderate challenges due to extensive aquaculture conversion. (3) Bedono Village, Demak (±06°44′28″ S, 110°29′58″ E), exemplifies a critically degraded system where coastal erosion and tidal flooding hinder restoration attempts. Collectively, these sites create a socio-ecological gradient, from successful restoration to contested land use to system collapse, forming a solid empirical basis for cross-site comparison and understanding the specific factors influencing mangrove resilience.

The geographical layout of these three coastal villages, along with their differing rehabilitation conditions, is depicted in Fig. 1.

Research location maps of Kaliwlingi (Brebes), Mojo (Pemalang), and Bedono (Demak), representing distinct socio-ecological conditions: successful rehabilitation in Brebes, transitional aquaculture-dominated conditions in Pemalang, and severe abrasion with rehabilitation failure in Demak.

2.3. Variables and Indicators

This study explored three key constructs—Perception (PERC), Participation (PART), and Mangrove Degradation (DEG)—to understand the socio-ecological factors affecting rehabilitation outcomes. Perception included ecological knowledge, awareness of socio-economic benefits, conservation attitudes, and policy assessments, illustrating how community understanding influences environmental behavior (Jones et al. 2023). Participation assessed involvement in rehabilitation efforts, resource contributions, and engagement in local institutional networks, aligning with

evidence that participatory approaches support sustainable restoration (Sarujan & Sakurai 2023). Degradation was evaluated through perceptions of mangrove loss, coastal erosion or tidal flooding, and declines in ecological functions, corroborated with local government data to enhance reliability (Elwin et al. 2024).

2.4. Research Hypotheses

This study indicates that community perception (PERC) positively affects participation (PART), which in turn contributes to reducing mangrove degradation (DEG). It is expected that perception influences degradation both directly and indirectly through participation, with these effects varying across different locations (Cui 2024). Consequently, the hypotheses posit that PERC increases PART (H1) and decreases DEG (H2), that PART reduces DEG (H3) and mediates the relationship between PERC and DEG (H4), that these relationships differ among sites (H5), that institutional support (INST) aids in mitigating degradation (H6), and that anthropogenic pressure (ANTH), combined with ecological stress (ECO), exacerbates degradation (H7). This framework aligns with recent research showing that perception and environmental awareness are crucial drivers of community involvement in mangrove conservation (Cruz Portorreal et al. 2024, Hagger et al. 2022). It also highlights how gaps in knowledge, attitudes, and perception, along with institutional and ecological issues, can affect the success of community-based rehabilitation efforts. Methodologically, analyzing mediation pathways and spatial heterogeneity through SEM and multi-group analysis reflects current best practices in environmental and socio-ecological research (Hair Jr et al. 2021). The conceptual framework (Fig. 2) consolidates these hypotheses into seven directional relationships linking perception, participation, and degradation, influenced by institutional, anthropogenic, and ecological factors. Together, the framework incorporates behavioral and contextual aspects to explain community resilience of mangroves across diverse socio-ecological settings.

2.5. Measurement Model (Confirmatory Factor Analysis/CFA)

The validity and reliability of all constructs were assaessed through Confirmatory Factor Analysis (CFA). Indicators with standardized factor loadings of 0.50 or higher were retained (Hair Jr. et al. 2021), leading to the preservation of PERC3–PERC4, PART1–PART3, and DEG1, DEG2,

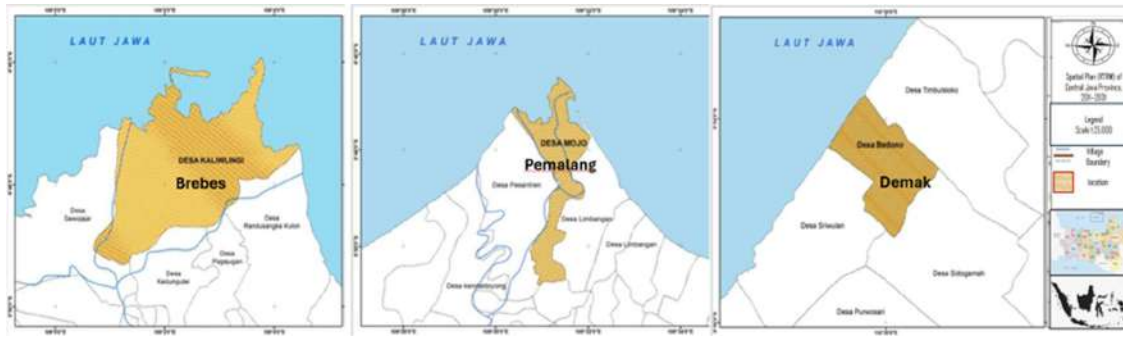


Fig. 1: Study area and sampling sites in Brebes, Pemalang, and Demak, showing a gradient of mangrove conditions from successful rehabilitation to severe degradation.

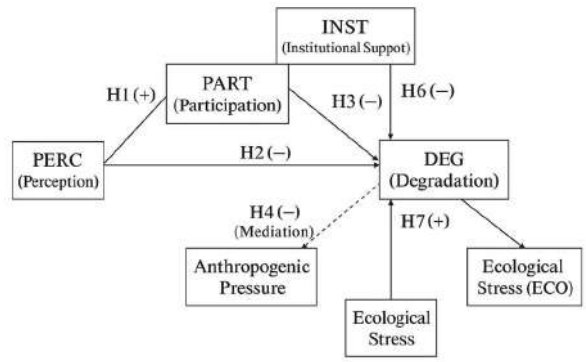


Fig. 2: Conceptual framework of the research hypotheses.

and DEG4. Error covariances were introduced solely when theoretically justified and confined within the same construct, thereby preventing model overfitting and ensuring simplicity (Kline 2023). All constructs demonstrated satisfactory convergent validity and internal consistency, with Composite Reliability (CR) ≥ 0.70 and Average Variance Extracted (AVE) ≥ 0.50 meeting established standards. The final CFA model showed acceptable goodness-of-fit indices, supporting its suitability for further structural analysis: χ^2/df = […], CFI = […], TLI = […], RMSEA = […] (90% CI: […], […]), and SRMR = […].

2.6. Structural Model

The structural model demonstrated that perception had a strong positive impact on participation ($\beta = 0.58$, $p < 0.001$). Subsequently, participation significantly decreased degradation ($\beta = –0.32$, $p < 0.001$), confirming its mediating role in the perception–degradation relationship. Additionally, perception showed a direct negative effect on degradation ($\beta = –0.21$, $p = 0.010$), along with a significant indirect effect via participation ($\beta = –0.19$, $p < 0.001$). The model accounted for 34% of the variance in participation and 26% in degradation. Fit indices suggested that the structural model provided an acceptable fit for hypothesis testing (χ^2/df = 1.87, CFI = 0.93, TLI = 0.91, RMSEA = 0.056, SRMR = 0.045).

2.7. Data Analysis

Data analysis was carried out in two phases: initially, descriptive statistics and Pearson correlations were employed to characterize respondents, followed by Structural Equation Modeling (SEM) with robust maximum likelihood estimation (MLE) to examine proposed causal relationships. Construct validity was evaluated via Confirmatory Factor Analysis (CFA), using thresholds of factor loadings ≥ 0.50, CR ≥ 0.70, and AVE ≥ 0.50. Model fit was assessed through CFI, TLI, RMSEA, and SRMR (Hair Jr. et al. 2021). The significance of path coefficients and mediation effects were tested with bootstrapping (2,000 resamples), and control variables including institutional support (INST), anthropogenic pressure (ANTH), and ecological stress (ECO) were integrated into the model.

2.8. Structural Model Results and Multi-Group SEM Analysis

2.8.1. Multi-Group SEM (MG-SEM) Analysis

The MG-SEM findings revealed clear spatial variations among the three districts. In Brebes, perception emerged as the most influential predictor of participation ($\beta = 0.67$, $p < 0.001$), highlighting the critical role of ecological literacy in encouraging community engagement. In Pemalang, participation was most effective in mitigating environmental degradation ($\beta = –0.46$, $p < 0.001$), demonstrating that participatory management approaches are particularly potent in this region. Conversely, in Demak, both pathways appeared to weaken under severe ecological stress: the impact of perception on participation diminished ($\beta = 0.41$, $p < 0.05$), and the relationship between participation and degradation was not significant ($\beta = –0.15$, ns). These results underscore that the influence of perception and participation varies greatly depending on the context, with ecological pressures constraining their effectiveness in heavily degraded areas.

2.8.2. Common Method Bias (CMB) Assessment and Control

Potential common method bias was assessed through Harman's single-factor test and collinearity diagnostics. The initial unrotated factor accounted for less than 40% of the total variance, and VIF values across the latent constructs remained below 2.0, indicating no dominance by a single factor. A comprehensive collinearity VIF evaluation further confirmed that all values were under 3.3, suggesting that CMB was not a significant issue. Procedural measures during data collection-such as ensuring respondent anonymity, using varied scale formats, and separating construct sections-also contributed to minimizing potential bias. Together, these statistical and procedural measures strongly suggest that common method bias is unlikely to threaten the validity of the results.

2.8.3. Structural Equation Modeling Framework

The relationships between the constructs were analyzed using Structural Equation Modeling (SEM), which consists of two parts: the measurement model and the structural model. The measurement model specifies how latent constructs are indicated by their observed variables (Hair Jr. et al. 2021, Harlow 2023).

$$x = \Lambda_x \xi + \delta, \quad y = \Lambda_y \eta + \varepsilon$$

Where x and y are vectors of exogenous and endogenous indicators, respectively. ξ and η denote latent variables, while Λx and Λy are the factor loading matrices. The symbols δ and ε represent measurement errors. Factor loadings (λi) indicate the strength of the association between indicators and their respective constructs, whereas residuals (δi) capture unexplained variance. The results of Confirmatory Factor Analysis (CFA) in Table 1 demonstrate that the retained indicators for Perception (PERC), Participation (PART), and Degradation (DEG) exhibit satisfactory loadings, thereby validating their use in subsequent analyses. The structural model outlines the hypothesized causal relationships among the constructs.

$$\eta = B\eta + \Gamma\xi + \zeta$$

In this study, the equations are expressed as:

$$PART = \gamma 1 \cdot PERC + \zeta 1$$

$$DEG = \beta 1 \cdot PART + \gamma 2 \cdot PERC + \zeta 2$$

This framework includes the perception construct denoted by PERC, participation represented by PART, and mangrove degradation indicated by DEG. The coefficients γ_1 and γ_2 illustrate the directional effects of perception on participation and degradation, respectively, while β_1 captures the mediating effect of participation on degradation. The error terms (ζ_1, ζ_2) account for the unexplained variance within the endogenous constructs. Collectively, these specifications establish a coherent analytical model that enables rigorous testing of measurement validity and the proposed socio-ecological pathways.

3. RESULTS AND DISCUSSION

This section presents the empirical findings of the study, beginning with descriptive characteristics of respondents and key constructs, then covering measurement validation, structural equation modeling, and multi-group analysis. The results are subsequently integrated and discussed in the context of existing socio-ecological theories and policy implications for mangrove governance.

3.1. Description of Main Variable

The demographic profile of respondents offers valuable insights into community dynamics related to mangrove governance. Most participants were within the productive age group (30–55 years) and engaged in activities such as fishing, aquaculture, or small-scale trading, which highlights a strong dependence on mangrove ecosystem services—an aspect known to enhance conservation efforts (Mallick et al. 2021). Educational levels were generally modest, implying that ecological knowledge is mainly acquired through hands-on experience. This underscores the importance of implementing targeted awareness and capacity-building initiatives. Similar socio-economic trends have been observed in other communities reliant on mangroves, where education level and livelihood dependence influence perceptions and conservation attitudes (Hendraswari et al. 2021). Respondents typically resided in the area for over 15 years, reflecting a strong sense of place attachment and long-term exposure to environmental changes. This aligns with findings suggesting that duration of residence affects mangrove usage and management behaviors (Dulyakasem et al. 2025). Descriptive statistics for key constructs—perception (PERC), participation (PART), and degradation (DEG)-are presented in Table 1.

Brebes registered the highest perception score with a mean of 21.16, followed by Pemalang at 20.04 and Demak at 19.18. Participation was most prominent in Pemalang (mean = 16.68), whereas Brebes (mean = 15.22) and Demak (mean = 14.98) showed comparatively lower involvement. Conversely, mangrove degradation was most severe in Pemalang (mean = 14.40), while Brebes (mean = 13.82) and Demak (mean = 12.12) exhibited relatively healthier ecological conditions.

These findings indicate that higher perception and greater community participation are associated with reduced degradation levels. This suggests that ecological awareness and active engagement contribute to better mangrove outcomes, aligning with recent research showing that enhanced perception boosts participation and governance effectiveness (Rosellón-Druker et al. 2023), while gaps in knowledge and perception correlate with increased degradation (Sathiyamoorthy & Sakurai 2024). However, it is important to note that these descriptive statistics do not establish causality. To explore the relationships more thoroughly and verify the hypothesized associations, inferential analyses—including ANOVA, SEM, and multi-group SEM (MG-SEM)—were conducted to examine the structural links among perception, participation, and degradation.

3.2. Validity and Reliability Tests

3.2.1. Measurement Model Evaluation

The results of the Confirmatory Factor Analysis (CFA) indicate that all indicators satisfied the necessary validity and reliability standards. Standardized factor loadings exceeded 0.50 with t-values greater than 5.0, and both Composite Reliability (ranging from 0.71 to 0.83) and Average Variance Extracted (AVE, between 0.55 and 0.67) demonstrated

Table 1: Descriptive Statistics of Main Variables by Location.

Variable	Brebes (n=50)	Pemalang (n=50)	Demak (n=50)	Total (n=150)
Mean age [years]	43.2 ± 9.6	41.8 ± 10.2	42.5 ± 9.8	42.5 ± 9.9
Education [Junior–Senior HS, %]	68%	72%	74%	71%
Main occupation [Fishing/Aquaculture, %]	64%	66%	70%	67%
Length of residence [years]	15.3 ± 5.8	14.7 ± 6.2	16.1 ± 5.4	15.4 ± 5.8

Table 2: Validity and reliability results.

Construct	Indicator	Loading range	t-value	CR	AVE	Remarks
Perception (PERC)	X1–X5	0.55–0.76	> 5.0	0.83	0.67	Valid and reliable
Participation (PART)	X6–X9	0.46–0.79	> 5.0	0.71	0.55	Valid and reliable
Degradation (DEG)	X10–X13	0.68–1.12	> 5.0	0.76	0.58	Valid and reliable ($\lambda > 1.0$ indicates the Heywood case)

adequate internal consistency and convergent validity. One indicator within the Degradation construct exhibited a loading above 1.0 ($\lambda = 1.12$), suggesting a potential Heywood case; however, this likely reflects high correlations among indicators rather than model misspecification. Overall, the measurement model was deemed acceptable and appropriate for subsequent analyses, including ANOVA, SEM, and MG-SEM. Detailed validity and reliability statistics are provided in Table 2.

3.2.2. Discriminant Validity and Heywood Case Handling

The results of the Confirmatory Factor Analysis (CFA) indicated that all indicators satisfied the necessary validity and reliability criteria. Standardized loadings were significant ($\lambda \geq 0.50$, t-values > 5.0), and both Composite Reliability (ranging from 0.71 to 0.83) and Average Variance Extracted (AVE, 0.55 to 0.67) supported convergent validity. One indicator within the Degradation construct (DEG3) showed a loading above 1.0 ($\lambda = 1.12$), indicating a Heywood case (Cooperman & Waller 2022). Several remedial measures were considered, and DEG3 was excluded based on both theoretical rationale and diagnostic analysis. The updated model demonstrated no further issues, with all remaining indicators loading adequately. Discriminant validity was confirmed through the Fornell–Larcker criterion and HTMT analysis, as presented in Table 3. The square roots of AVE surpassed the inter-construct correlations, and all HTMT values remained below 0.85, verifying that perception, participation, and degradation are distinct constructs (Hair & Alamer 2022, Afthanorhan et al. 2021).

Discriminant validity was confirmed using the Fornell–Larcker criterion and the HTMT ratio. As shown in Table 3, the square roots of the AVE values consistently surpassed inter-construct correlations, and all HTMT estimates stayed below the recommended threshold of 0.85. Overall, these results strongly support the notion that the latent constructs represent separate theoretical domains and are free from construct overlap.

3.2.3. Multicollinearity Test

A multicollinearity assessment was performed to verify that the latent constructs were independent and free from redundancy. As indicated in Table 4, all variables exhibited Tolerance values exceeding 0.50 and VIF values below 2.0, which are comfortably within the recommended thresholds (Tolerance > 0.10, VIF < 10). These findings confirm the absence of multicollinearity, suggesting that each construct provides distinct explanatory power to the structural model (Bayman & Dexter 2021).

3.3. Structural Results and Integrated Discussion

3.3.1. Differences Across Locations (ANOVA)

Descriptive statistics for the three primary constructs-perception (PERC), participation (PART), and mangrove degradation (DEG)—are detailed in Table 5. The initial analysis indicates that Brebes has the highest perception scores (Mean = 21.16), whereas Pemalang exhibits the strongest community participation (Mean = 16.68). Conversely, mangrove degradation appears most severe in Pemalang (Mean = 14.40) and least in Demak (Mean = 12.12). These patterns highlight spatial differences among the sites and underpin subsequent inferential analysis through one-way ANOVA.

Table 3: Discriminant validity results (Fornell–Larcker Criterion and HTMT).

Construct	AVE	√AVE	PERC	PART	DEG	HTMT range
Perception (PERC)	0.58	0.76	0.76	0.62	0.55	0.58–0.69
Participation (PART)	0.67	0.82	0.62	0.82	0.60	0.61–0.72
Degradation (DEG)	0.55	0.74	0.55	0.60	0.74	0.57–0.66

Table 4: Multicollinearity test results.

Construct	Tolerance	VIF	Remarks
Perception (PERC)	0.64	1.56	No multicollinearity
Participation (PART)	0.59	1.70	No multicollinearity
Degradation (DEG)	0.61	1.63	No multicollinearity

Note: Tolerance > 0.10 and VIF < 10 indicate the absence of multicollinearity.

Table 5: Descriptive statistics of key variables (perception, participation, and mangrove degradation) by study site.

Variable	Brebes (Mean ± SD)	Pemalang (Mean ± SD)	Demak (Mean ± SD)
Perception (PERC)	21.16 ± 2.85	20.04 ± 2.72	19.18 ± 2.64
Participation (PART)	15.22 ± 2.48	16.68 ± 2.31	14.98 ± 2.27
Degradation (DEG)	13.82 ± 2.14	14.40 ± 2.36	12.12 ± 2.05

Table 6: Results of one-way ANOVA across locations.

Variable	F-value	p-value	Significance	Main Differences (Tukey HSD)
Perception (PERC)	8.42	<0.001	***	Brebes ≠ Demak (significant)
Participation (PART)	6.35	0.002	**	Pemalang ≠ Demak (significant)
Degradation (DEG)	9.87	<0.001	***	Pemalang ≠ Demak (significant)

The one-way ANOVA (Table 6) reveals significant differences across sites for all key constructs. Perception varied notably among locations ($F = 8.42$, $p < 0.001$), with Brebes showing the highest ecological awareness, followed by Pemalang, while Demak recorded the lowest scores. Participation also differed significantly ($F = 6.35$, $p = 0.002$), with Pemalang demonstrating the greatest engagement and Demak consistently the lowest. Similarly, mangrove degradation levels varied significantly across sites ($F = 9.87$, $p < 0.001$), highest in Pemalang and least severe in Demak. Post hoc Tukey's HSD confirmed that the most significant contrasts were between Brebes and Demak, with Pemalang occupying an intermediate position—characterized by relatively high perception and participation but also the highest degradation. This pattern indicates that strong community participation alone may not suffice to reduce degradation if external pressures—such as coastal erosion, land conversion, or infrastructure development—are predominant. These findings underscore that community-based conservation efforts must be complemented by institutional and ecological interventions to effectively mitigate ecosystem degradation (Polas et al. 2024).

Table 7 summarizes the ANOVA and Tukey HSD results for clarity. Brebes exhibited strong perception but only moderate levels of participation and degradation. Pemalang showed the highest participation alongside the greatest degradation, indicating a persistent socio-ecological trade-off between livelihood activities and environmental stress. Demak consistently had the lowest perception and participation, yet also experienced the least degradation, suggesting limited community engagement in an environment under relatively lower pressure.

Brebes exhibited the highest level of perception, alongside moderate participation and degradation levels. Pemalang showed the strongest community participation but also the highest degradation, revealing a socio-ecological trade-off where active involvement occurs amidst significant environmental pressure. In contrast, Demak consistently recorded the lowest perception and participation but experienced the least degradation, indicating minimal community engagement in a relatively less degraded ecosystem. These spatial differences suggest that variations in awareness and participation are closely influenced by site-specific ecological conditions, institutional support, and adaptive management across the three coastal districts.

Fig. 3 presents a comparison of mean scores and the structural relationships among perception (PERC), participation (PART), and mangrove degradation (DEG) across the study sites. Brebes showed the highest perception levels, while Pemalang exhibited the strongest participation along with the greatest degradation. Demak had the lowest perception and participation but experienced the least degradation. SEM analysis indicates that perception positively influences participation ($\beta = 0.58$, $p < 0.001$) and directly reduces degradation ($\beta = -0.21$, $p = 0.010$), with participation further diminishing degradation ($\beta = -0.32$, $p < 0.001$). A significant indirect effect ($\beta = -0.19$, $p < 0.001$) confirms partial mediation, implying that ecological awareness enhances resilience mainly through community engagement. The model demonstrated a good fit to the data

Table 7: Summary of ANOVA and Tukey HSD across locations.

Variable	F-value	p-value	Main Differences (Tukey HSD)	Key Interpretation
Perception	8.42	<0.001***	Brebes ≠ Demak, Pemalang moderate	Highest in Brebes, lowest in Demak
Participation	6.35	0.002**	Pemalang ≠ Demak, Brebes moderate	Highest in Pemalang, lowest in Demak
Degradation	9.87	<0.001***	Pemalang ≠ Demak, Brebes moderate	Highest in Pemalang, lowest in Demak

***$p < 0.001$, **$p < 0.01$

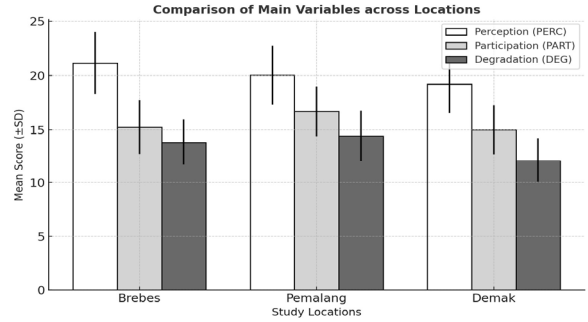


Fig. 3: Comparison of the mean scores for PERC, PART, and DEG.

Table 8: Path estimates of Structural Equation Modeling (SEM) and Multi-Group SEM (MG-SEM) results across study site.

Hypothesized Path	Coefficient (β)	t-value	p-value	Sign	Interpretation
PERC → PART	0.58	9.84	<0.001	***	Positive, strong
PERC → DEG	–0.21	–2.61	0.010	**	Negative, moderate
PART → DEG	–0.32	–3.87	<0.001	***	Negative, significant
PERC → DEG (via PART)	–0.19	Bootstrapping	<0.001	**	Partial mediation

Model fit: $\chi^2/df = 1.87$, CFI = 0.93, TLI = 0.91, RMSEA = 0.056, SRMR = 0.045 (Kang & Ahn 2021)

($\chi^2/df = 1.87$, CFI = 0.93, TLI = 0.91, RMSEA = 0.056, SRMR = 0.045).

3.3.2. Structural Equation Modeling (SEM)

The SEM analysis revealed significant and theoretically consistent pathways (Table 8). Perception substantially enhanced participation (β = 0.58, t = 9.84, p < 0.001) and directly diminished degradation (β = –0.21, t = –2.61, p = 0.010), while increased participation further reduced degradation (β = –0.32, t = –3.87, p < 0.001). Mediation testing verified a notable partial mediation effect (β_indirect = –0.19, p < 0.001), suggesting that ecological awareness primarily promotes mangrove resilience through community engagement. These findings are consistent with socio-ecological models that highlight behavioral engagement as a mediator translating environmental cognition into conservation outcomes. The refined model demonstrated a good fit ($\chi^2/df = 1.87$, CFI = 0.93, TLI = 0.91, RMSEA = 0.056, SRMR = 0.045) after theory-driven re-specification. It accounted for 34% of the variance in participation ($R^2 = 0.34$) and 26% of the variance in degradation ($R^2 = 0.26$), underscoring the importance of the perception → participation → degradation pathway in fostering socio-ecological resilience (Hair & Alamer 2022).

The SEM analysis demonstrates that community perception significantly increases participation, while both perception and participation directly reduce degradation. The indirect pathway confirms that ecological awareness contributes to ecosystem resilience primarily when translated into active engagement.

3.3.3. Multi-Group SEM (MG-SEM)

The MG-SEM results demonstrate significant spatial variation in the relationships among perception (PERC), participation (PART), and mangrove degradation (DEG). In Brebes, perception showed a strong positive influence on participation (β = 0.84, p < 0.001), while both participation (β = –0.28, p < 0.05) and perception (β = –0.35, p < 0.01) significantly contributed to reducing degradation. This indicates a functional socio-ecological feedback loop maintained by relatively stable institutional frameworks.

In Pemalang, participation emerged as the primary factor in mitigating degradation (β = –0.41, p < 0.01), along with a notable direct effect of perception on degradation (β = –0.32, p < 0.05). However, Pemalang also faced the highest levels of degradation, suggesting that vigorous participation often occurs under intense human pressures, such as shrimp pond conversion, aquaculture expansion, and unmanaged coastal land use.

In Demak, both primary pathways diminished in strength and became statistically non-significant (PERC → DEG: β = –0.21, n.s., PART → DEG: β = –0.25, n.s.), suggesting that intense biophysical pressures—such as coastal erosion, land subsidence, and seawater intrusion—surpass community-based mitigation measures. These findings (Table 9, Fig. 5) illustrate that while perception consistently predicts increased participation across all sites, its effectiveness in reducing mangrove degradation depends on the context, influenced by ecological stressors, external disturbances, and institutional support mechanisms (Durak & Bulut 2024).

Table 9: SEM and Multi-Group SEM (MG-SEM).

Path	Pooled SEM β (t, p)	Brebes β	Pemalang β	Demak β
PERC → PART	0.79 (t=10.55, p<0.001)	0.84***	0.76**	0.71*
PERC → DEG	–0.38 (t=–4.09, p<0.001)	–0.35**	–0.32*	–0.21 n.s.
PART → DEG	–0.32 (t=–3.47, p=0.001)	–0.28*	–0.41**	–0.25 n.s.
PERC → DEG (via PART)	–0.25 (Bootstrapping, p<0.01)	—	—	—

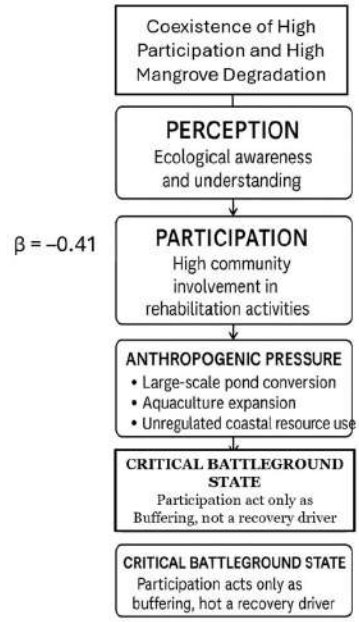


Fig. 4: Pemalang paradox framework.

3.3.4. The Pemalang Paradox

The Pemalang case highlights a unique socio-ecological paradox where high community involvement coexists with consistently high levels of mangrove degradation. This can be explained by the strong connections between community efforts and external anthropogenic pressures (ANTH). Although the MG-SEM results indicate that participation significantly mitigates degradation (β = –0.41), this protective influence exists within a landscape under intense external pressures, including large-scale pond conversions, expansion of aquaculture, and unregulated coastal resource use.

Under such conditions, participation primarily functions as a buffering mechanism, slowing ecological decline rather than enabling full recovery. Pemalang thus emerges as a key socio-ecological battleground, where community engagement provides a defensive layer against pressures that exceed the natural regenerative capacity of the mangrove system. The continued degradation despite active community involvement suggests that participation alone is insufficient to reverse ecological decline when structural drivers remain unaddressed.

These findings emphasize the importance of comprehensive policy interventions that go beyond community initiatives, including more stringent regulation of land conversion, enhanced coastal zoning enforcement, and improved environmental governance. Implementing these structural measures is essential to reduce the prominent human pressures and support community efforts in achieving meaningful ecological results. The conceptual dynamics of this paradox are depicted in Fig. 4 (Pemalang Paradox Framework).

3.3.5. Ecological Threshold in the Demak Case (Ecological "Ambang")

In contrast to the Pemalang pattern, the Demak results indicate that the key pathways-perception leading to degradation and participation leading to degradation—become statistically non-significant. This finding offers an important theoretical insight: under conditions of extreme ecological stress (ECO), the capacity of social interventions to influence ecological outcomes is greatly limited. Demak, a coastal system facing compounded biophysical disturbances such as severe shoreline erosion, land subsidence, and seawater intrusion, demonstrates that the mangrove ecosystem has surpassed

an ecological threshold. Once this threshold is crossed, incremental social or behavioral interventions are insufficient to produce measurable ecological improvements. Ecological outcomes are then driven primarily by biophysical forces rather than by variations in perception or participation. This threshold-dynamics perspective aligns with resilience theory, which suggests that the success of social actions depends on whether the ecological system maintains its capacity to respond effectively.

This conceptualization enhances our theoretical understanding by illustrating that the success of social interventions depends not only on their intensity but also on the ecological condition of the system, particularly whether biophysical factors still allow social actions to effect measurable ecological change.

3.3.6. Role of Control Variables INST, ANTH, and ECO

The extended SEM and MG-SEM models incorporated Institutional Support (INST), Anthropogenic Pressure (ANTH), and Ecological Stress (ECO) as key control variables to capture the structural and biophysical context in which social processes operate. These variables play a crucial role in shaping the magnitude and direction of degradation dynamics. Institutional support (INST) acts as an enabling factor that amplifies the perception → participation → degradation pathway. This influence is particularly evident in Brebes, where coherent governance, ongoing facilitation, and formalized community programs foster conditions that convert awareness into sustained participation. These findings support H6 and align with governance literature emphasizing that community-based initiatives require institutional scaffolding to be effective. Conversely, anthropogenic pressure (ANTH)-driven by land conversion, aquaculture expansion, and intensive coastal exploitation-exerts a direct and significant effect on degradation. High levels of ANTH accelerate ecological decline while simultaneously limiting the impact of participation, confirming H7. The Pemalang case exemplifies this dynamic clearly: despite high community engagement, strong external pressures reduce the capacity for participation to promote ecological recovery. Ecological stress (ECO) further defines the boundary conditions under which social mechanisms can influence ecological outcomes. In Demak, extreme biophysical disturbances-such as abrasion, subsidence, and saline intrusion-completely suppress the effects of perception and participation, consistent with ecological threshold theory. Under such threshold-exceeding conditions, social interventions lose their predictive power because physical forces predominantly drive ecological processes. When these control variables are integrated into the model, they enable it to explain 26% of the variance in degradation ($R^2 = 0.26$). This indicates that mangrove degradation results not only from community behavior but also from a constellation of structural and biophysical constraints that define the limits of social efficacy. These findings highlight the importance of situating community-based interventions within broader governance, land-use, and ecological contexts to fully understand and address coastal degradation processes.

3.3.7. Joint Insights (ANOVA + SEM + MG-SEM) and Policy Implications

The initial pooled SEM model demonstrated poor fit indices (CFI = 0.82, GFI = 0.77, TLI = 0.78, SRMR = 0.10, RMSEA = 0.16). However, re-specification guided by modification indices significantly improved the model's performance ($\chi^2/df = 1.87$, CFI = 0.93, TLI = 0.91, RMSEA = 0.056, SRMR = 0.045), confirming its appropriateness for hypothesis testing. The refined structural pathways reveal

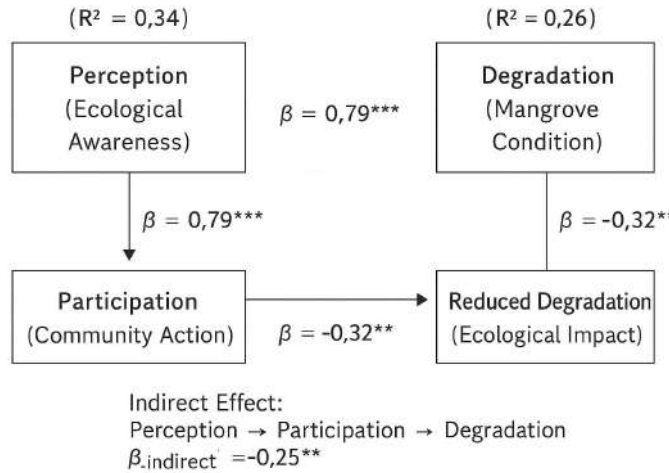


Fig. 5: Conceptual and empirical SEM model linking perception (PERC), participation (PART), and mangrove degradation (DEG).

that perception strongly enhances participation ($\beta = 0.79$, $p < 0.001$), while both perception ($\beta = -0.38$, $p < 0.001$) and participation ($\beta = -0.32$, $p = 0.001$) considerably decrease mangrove degradation. Mediation analysis indicates partial mediation by participation ($\beta_indirect = -0.25$, $p < 0.01$), highlighting that ecological awareness yields tangible benefits primarily when converted into active engagement. The model accounts for 34% of the variance in participation ($R^2 = 0.34$) and 26% in degradation ($R^2 = 0.26$), emphasizing the importance of the perception → participation → degradation pathway. The MG-SEM analysis incorporates a vital spatial aspect: while the pathway holds in Brebes and Pemalang, it loses significance in Demak, where intense ecological stress suppresses social influences. Cross-group comparisons using ANOVA reveal that the effectiveness of social mechanisms depends on ecological conditions. Fig. 5 illustrates the conceptual and empirical structure of these relationships, detailing the direct and indirect effects connecting perception, participation, and degradation within the SEM framework.

3.3.8. Integrated SEM and MG-SEM Findings

The combined ANOVA, SEM, and MG-SEM analyses reveal that the relationships among perception (PERC), participation (PART), and mangrove degradation (DEG) are statistically significant but highly dependent on context. At the pooled level, perception significantly boosts participation ($\beta = 0.58$, $p < 0.001$), and both perception ($\beta = -0.21$, $p = 0.010$) and participation ($\beta = -0.32$, $p < 0.001$) notably decrease degradation. Mediation analysis confirmed a partial effect ($\beta_indirect = -0.19$, $p < 0.001$), suggesting that perception mainly promotes ecological improvement when translated into behavioral engagement. The final SEM indicated a good model fit ($\chi^2/df = 1.87$, CFI = 0.93, TLI = 0.91, RMSEA = 0.056, SRMR = 0.045), accounting for 34% of the variance in participation and 26% in degradation.

The MG-SEM results highlight the spatial variability of these processes (Fig. 6). In Brebes, perception had the most significant influence on participation, reflecting favorable institutional and social conditions that promote awareness-driven actions. In Pemalang, participation was the primary factor in reducing degradation, although its effectiveness was limited by intense anthropogenic pressure. In Demak, both pathways diminished considerably under extreme ecological stress, aligning with threshold-based ecological dynamics where biophysical degradation diminishes the predictive capacity of social variables. These findings demonstrate that perception, participation, and degradation function within a dynamic socio-ecological feedback loop, whose strength varies depending on local environmental conditions.

Therefore, adaptive management should focus on ecological education and perception enhancement in Brebes, implement participatory livelihood and co-management strategies in Pemalang, and apply engineering-based resilience measures—such as sediment nourishment and hybrid coastal protection—before community-driven actions can be successful in Demak (Yuliantina et al. 2024, Dash & Paul 2021).

4. DEMAK CONTEXT AND SYNTHESIS OF MG-SEM FINDINGS

The analysis of Demak reveals that both primary pathways, perception leading to participation and participation leading to degradation, are significantly weakened and become statistically non-significant (Fig. 7). This pattern reflects the dominant influence of extreme biophysical pressures, including intense coastal abrasion, land subsidence, and seawater intrusion, which collectively surpass the community's adaptive capacity and diminish the effectiveness of social efforts. Under such conditions, community participation alone is insufficient to produce meaningful ecological improvements without large-scale technical or engineering support. Overall, the MG-SEM findings demonstrate that while perception consistently promotes participation across all sites, the ability of participation to

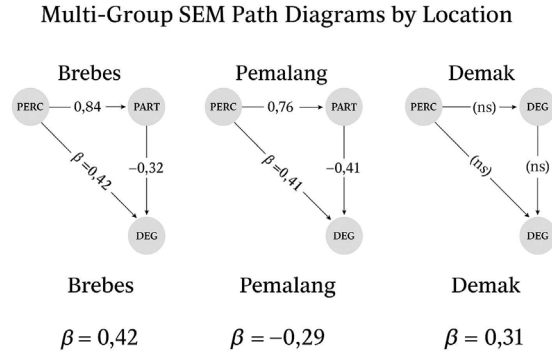


Fig. 6: Multi-group SEM results across locations (Brebes, Pemalang, and Demak).

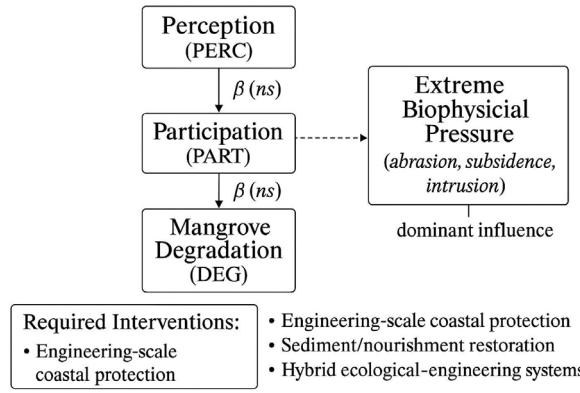


Fig. **7**: Integrated SEM framework of perception, participation, and mangrove degradation (adapted from Listiana 2024).

mitigate degradation is highly context-dependent, influenced by local variations in human activities and biophysical factors. These results highlight the importance of spatially adaptive mangrove management, where interventions are customized to the ecological and social context of each area rather than uniformly implemented across regions.

5. CONCLUSIONS

This study illustrates that community perception and participation are crucial, yet their influence varies depending on the context, in determining mangrove resilience along the northern coast of Central Java. In the combined model, perception consistently boosted participation, and together, these factors reduced mangrove degradation, with participation partially mediating the relationship between perception and degradation. The structural model demonstrated strong explanatory power and a good fit, suggesting that ecological awareness leading to community action is a key behavioral mechanism in supporting mangrove restoration.

However, multi-group SEM analysis revealed significant spatial differences. In Brebes, high ecological literacy and stable institutional support maintained an effective pathway from perception to participation to reduction in degradation. In Pemalang, participation had the most substantial impact on decreasing degradation, but widespread human activities hindered ecological recovery, creating what can be called a 'Pemalang Paradox'—community engagement helped buffer degradation but was insufficient to overcome broader structural pressures. In Demak, both behavioral pathways were non-significant under extreme ecological stress, indicating that the system had exceeded a biophysical threshold where social mechanisms no longer held predictive power.

The integration of institutional support, anthropogenic pressure, and ecological stress highlights that participation alone is insufficient for successful rehabilitation. Instead, the effectiveness of social pathways is contingent on enabling governance frameworks and ecological conditions that retain recovery potential. These findings advance mangrove governance theory by clarifying the coupled behavioral, institutional, and biophysical drivers shaping rehabilitation outcomes.

Policy implications are therefore site-specific. Brebes requires ongoing ecological education and stable institutional support; Pemalang needs interventions that enhance participation and decrease human pressure; and Demak necessitates engineering-based restoration to restore baseline ecological stability before community-driven approaches can be successful. Although limited by its cross-sectional design and reliance on perceived degradation metrics, this study offers compelling empirical evidence that ecological and institutional factors influence social drivers of rehabilitation. Long-term monitoring and broader governance indicators are recommended to improve understanding of the socio-ecological mechanisms discussed.

6. ACKNOWLEDGMENTS

The authors express their sincere gratitude to the local governments and community-based mangrove groups in Brebes, Pemalang, and Demak for their cooperation and support throughout the field data collection process. We also acknowledge the assistance of the Environmental Health Department, Universitas Dian Nuswantoro, for administrative and logistical support, and the Department of Oceanography, Diponegoro University, for technical guidance related to coastal and ecological data interpretation. The authors thank all community respondents who generously participated in the survey and focus group discussions.

7. REFERENCES

Afthanorhan, A., Ghazali, P.L. and Rashid, N., 2021. Discriminant validity: a comparison of CBSEM and consistent PLS using Fornell & Larcker and

HTMT approaches. *Journal of Physics: Conference Series*, 1874(1), p.012085. [DOI]

Arifanti, V.B., Raharjo, N., Prasetyo, L.B. et al., 2025. Assessing the environmental and socioeconomic impacts of mangrove loss in Indonesia: a synthesis for science-based policy. *Forest Science and Technology*, 21(1), pp.1-17. [DOI]

Bayman, E.O. and Dexter, F., 2021. Multicollinearity in logistic regression models. *Anesthesia & Analgesia*, 132(2), pp.362-365. [DOI]

Choudhary, B., Dhar, V. and Pawase, A.S., 2024. Blue carbon and the role of mangroves in carbon sequestration: its mechanisms, estimation, human impacts and conservation strategies for economic incentives. *Journal of Sea Research*, 199, p.102504. [DOI]

Cooperman, A.W. and Waller, N.G., 2022. Heywood you go away! Examining causes, effects, and treatments for Heywood cases in exploratory factor analysis. *Psychological Methods*, 27(2), pp.156-168. [DOI]

Cruz Portorreal, Y., Pérez-López, J., Martínez-Ruiz, A. and Rodríguez-García, M., 2024. Perception of mangrove social–ecological system governance in southeastern Cuba. *Water*, 16(17), p.2495. [DOI]

Cui, J., 2024. PLS-SEM and fsQCA integration: enhancing the completeness and value of structural data analysis. *Methodological Innovations*, 17(2), pp.1-15. [DOI]

Dash, G. and Paul, J., 2021. CB-SEM vs PLS-SEM methods for research in social sciences and technology forecasting. *Technological Forecasting and Social Change*, 173, p.121092. [DOI]

Dulyakasem, R., Jiamboonsri, P., Klinhom, J. et al., 2025. Community-based natural resource management in coastal communities: the contribution of mangroves to household livelihoods in southern Thailand. *Environmental Development*, 49, p.101340. [DOI]

Durak, A. and Bulut, V., 2024. Predicting low and high student performance in programming education using PLS-SEM algorithms. *Technology, Knowledge and Learning*, 29(1), pp.1-18. [DOI]

Dyson, K., Dawwas, E., Kamakura, R.P., Alberti, M. and Fuentes, T.L., 2023. Say where you sample: increasing site selection transparency in urban ecology. *Ecosphere*, 14(3), p.e4466. [DOI]

Elwin, A., Robinson, E.J.Z., Feola, G., Jintana, V. and Clark, J., 2024. How is mangrove ecosystem health defined? A local community perspective from coastal Thailand. *Ocean & Coastal Management*, 251, p.107037. [DOI]

Hagger, V., Worthington, T.A., Lovelock, C.E., Adame, M.F., Amano, T., Brown, B.M., Friess, D.A., Landis, E., Mumby, P.J., Morrison, T.H., O'Brien, K.R., Wilson, K.A., Zganjar, C. and Saunders, M.I., 2022. Drivers of global mangrove loss and gain in social-ecological systems. *Nature Communications*, 13, p.6373. [DOI]

Hair, J. and Alamer, A., 2022. Partial least squares structural equation modeling (PLS-SEM) in second language and education research: guidelines using an applied example. *Research Methods in Applied Linguistics*, 1(3), p.100027. [DOI]

Hair, J.F., Hult, G.T.M., Ringle, C.M. and Sarstedt, M., 2021. *Partial Least Squares Structural Equation Modeling (PLS-SEM) Using R: A Workbook*. Springer Nature, pp.265. [DOI]

Harlow, L.L., 2023. Structural equation modeling. In: *The Essence of Multivariate Thinking*. Routledge, pp.183-201. [DOI]

Hendraswari, C.A., Purnamaningrum, Y.E., Maryani, T., Widyastuti, Y. and Harith, S., 2021. The determinants of stunting for children aged 24-59 months in Kulon Progo District 2019. *Kesmas*, 16(2), pp.85-92. [DOI]

Isworo, S. and Oetari, P.S., 2020. Mangrove vegetation and bird communities in the coastal area of Semarang, Central Java. *Biodiversitas*, 21(4), pp.1510-1520. [DOI]

Jadloc, J.A., Legaspina, T., Gabrinao, W.P. and Gorgonio, C., 2025. Drivers that motivate participation in mangrove forest management among the local people at Barangay Lasang, Davao City, Philippines. *BIO Web of Conferences*, 82, p.04005. [DOI]

Jones, N., Malesios, C., McGinlay, J., Villasante, S., Svajda, J., Kontoleon, A., Begley, A., Gkoumas, V., Cadoret, A., Dimitrakopoulos, P.G., Maguire-Rajpaul, V. and Sepp, K., 2023. Using perceived impacts, governance and social indicators to explain support for protected areas. *Environmental Research Letters*, 18(5), p.054011. [DOI]

Kang, H. and Ahn, J.W., 2021. Model setting and interpretation in structural equation modeling for nursing research. *Asian Nursing Research*, 15(3), pp.157-162. [DOI]

Kline, R.B., 2023. *Principles and Practice of Structural Equation Modeling*. Guilford Publications, pp.518.

Listiana, I., 2024. Enhancing coastal community participation in mangrove rehabilitation through collaborative governance. *Global Journal of Environmental Science and Management*, 10(2), pp.873-890. [DOI]

Lovelock, C.E., Bennion, V., de Oliveira, M., Hagger, V., Hill, J.W., Kwan, V., Pearse, A.L., Rossini, R.A. and Twomey, A.J., 2024. Mangrove ecology guiding the use of mangroves as nature-based solutions. *Journal of Ecology*, 112(11), pp.2510-2521. [DOI]

Mallick, B., Priodarshini, R., Kimengsi, J.N., Biswas, B., Hausmann, A.E., Islam, S., Huq, S. and Vogt, J., 2021. Livelihoods dependence on mangrove ecosystems: empirical evidence from the Sundarbans. *Current Research in Environmental Sustainability*, 3, p.100077. [DOI]

Nagel, B. and Partelow, S., 2022. A methodological guide for applying structural equation modeling in social-ecological systems research. *Ecology and Society*, 27(4), p.39. [DOI]

Polas, A.B., Topp, E. and Plieninger, T., 2024. Mapping landscape values and community perceptions of ecosystem services in coastal Bangladesh. *Ecosystems and People*, 20(1), p.2370531. [DOI]

Rosellón-Druker, J., McAdam-Otto, L., Suca, J.J., Seary, R., Gaytán-Caballero, A., Escobar-Briones, E., Hazen, E.L. and Muller-Karger, F., 2023. Local ecological knowledge and perception of the causes, impacts and effects of Sargassum massive influxes: a binational approach. *Ecosystems and People*, 19(1), p.2253317. [DOI]

Sarujan, S. and Sakurai, T., 2023. Effectiveness of community participation in mangrove conservation and livelihood improvement in Sri Lanka. *Environmental Economics and Policy Studies*, 25(3), pp.1-18. [DOI]

Sathiyamoorthy, S. and Sakurai, T., 2024. Effectiveness of community participation in mangrove forest management: a comparative study from India and Sri Lanka. *Environmental Economics and Policy Studies*, 26(4), pp.759-779. [DOI]

Syahputra, O.K.H. and Fernando, M.R., 2024. Community participation and evaluation of mangrove ecosystem restoration in North Sumatra. *Global Forest Journal*, 2(1), pp.50-60. [DOI]

Utami, W., Sugiyanto, C. and Rahardjo, N., 2024. Mangrove area degradation and its impact on community livelihoods in the northern coast of Java. *Journal of Degraded and Mining Lands Management*, 11(3), pp.6037-6047. [DOI]

Wiarta, R., Silamon, R.F., Arbab, M.I., Badshah, M.T., Hayat, U. and Meng, J., 2025. Assessing of driving factors and change detection of mangrove forest in Kubu Raya District, Indonesia. *Frontiers in Forests and Global Change*, 8, p.1511361. [DOI]

Yuliantina, N., Mulyana, A., Wildayana, E., Lionardo, A. and Septiana, B., 2024. Analysis of policy strategies to control the conversion of wetland rice land to non-agricultural land use in Palembang City, South Sumatra. *Sriwijaya Journal of Environment*, 9(2), pp.100-107. [DOI]

Nature Environment and Pollution Technology
An International Quarterly Scientific Journal

p-ISSN: 0972-6268
(Print copies up to 2016)
e-ISSN: 2395-3454

Vol. 25 | No. 3 | Article ID B4417 | 2026

Original Research Paper

https://doi.org/10.46488/NEPT.2026.v25i03.B4417

Open Access Journal

Green Micellar Extraction of Phenol from Wastewater Using Eco-Friendly Hydrophilic Deep Eutectic Solvents

Ravindra Joshi[1]†, Aditya Vijayakar[1], Soham Joshi[1], Prasad Parulekar[1], Ramesh Bhande[1] and Shripal Gaikwad[2]
[1]Department of Chemical Engineering, Thadomal Shahani Engineering College, Bandra, Mumbai-400050, India
[2]Department of Technology, Shivaji University, Kolhapur, Maharashtra, India
†Corresponding author: Ravindra Joshi; ravindra.joshi@thadomal.org

Abbreviation: Nat. Env. & Poll. Technol.
Website: www.neptjournal.com

Received: 12-12-2025
Revised: 12-02-2026
Accepted: 01-03-2026

Key Words:

Aquoline
Deep eutectic solvent
Green extraction
Micelle-assisted phenol removal

ABSTRACT

Phenol, an extremely toxic wastewater pollutant, adversely affects animals, plants, and aquatic life. Its accumulation in aquatic and terrestrial ecosystems affects nutrient recycling and their long-term stability. Industrial wastewaters constitute a major source of phenol, and its removal is a major concern of researchers and governments across the world. In the current research work, green extraction of phenol from model industrial wastewater was studied by using Aquoline, a new type of eco-friendly deep eutectic solvent (DES), prepared from choline chloride as an H-bond receiver and water as an H-bond contributor. Separation of phenol from wastewater is facilitated by micelles formed in Aquoline due to the CTAB surfactant. The prepared DES was characterized by UV, FTIR, and NMR spectroscopy. Maximum phenol extraction efficiency of 93.27 % was obtained with Aquoline DES + CTAB under optimized conditions (initial phenol concentration = 5000 ppm, temperature = 301 K, pH =10, CTAB concentration = 0.9 mM.L^{-1}, volume ratio of wastewater to solvent = 10:1). The recovered solvent was reused four times after removal of phenol. FTIR studies on recovered solvent showed no change in its structure. This is the first research to use a hydrophilic deep eutectic solvent in the extraction of phenol from wastewater. The research will pave the way for the use of a new type of eco-friendly solvent while adhering to principles of green chemistry.

Citation for the Paper:

Joshi, R., Vijayakar, A., Joshi, S., Parulekar, P., Bhande, R. and Gaikwad, S., 2026. Green micellar extraction of phenol from wastewater using ecofriendly hydrophilic deep eutectic solvents. *Nature Environment and Pollution Technology*, 25(3), B4417. https://doi.org/10.46488/NEPT.2026.v25i03.B4417

Note: From 2025, the journal has adopted the use of Article IDs in citations instead of traditional consecutive page numbers. Each article is now given individual page ranges starting from page 1.

Copyright: © 2026 by the authors
Licensee: Technoscience Publications
This article is an open access article distributed under the terms and conditions of the Creative Commons Attribution (CC BY) license (https://creativecommons.org/licenses/by/4.0/).

1. INTRODUCTION

Phenol and phenolic pollutants are released into wastewater by numerous industries, for example, petroleum, pharmaceutical, coke oven plants, coal washing facilities, dyes, polymer production, and metal processing, are a serious concern due to their toxicity. While phenol concentrations in petroleum refinery wastewater can be as high as 135 ppm, coke oven plants discharge significantly greater amounts, with levels sometimes surpassing 1,000 ppm. The highest phenol concentration was reported for coal gasification plant wastewater at 5000 ppm (Yang et al. 2006).

The contaminated wastewater leaches into underground aquifers, water bodies, and lands, thus affecting entire ecosystems. Phenol is fatal to animal life as it is carcinogenic and causes mutagenesis. Its presence is detrimental to aquatic ecosystems as it hinders the growth and reproduction of marine organisms. For humans, 10-24 ppm of phenol concentration is considered hazardous, while a concentration of 1500 ppm in the bloodstream is considered lethal. At these concentrations, it can affect the liver, kidneys, skin, and respiratory system, and prolonged exposure may result in cancer. (Hammam et al. 2015, Pradeep et al. 2015, Hamad et al. 2021, Panigrahy et al. 2022).

Environmental Protection Agency (EPA), U.S.A., mandates that a maximum of 0.1 ppm of phenol be allowed in industrial effluents. For drinking water, the WHO allows only 0.001 ppm of phenol. In India, the prescribed limits for

phenolic compounds are: 0.001 ppm in drinking water, 1 ppm in inland surface waters, and 5 ppm in public sewers. These strict effluent disposal norms set up by government authorities have forced industries to seek new methods and implement effective protocols for phenol elimination from wastewater. (Mukherjee et al. 2007, Sadhu et al. 2014, Patel & Desai 2022).

For the removal of phenol, different methods such as adsorption, liquid-liquid extraction, membrane separation, foam fractionation, electrocoagulation, electro-Fenton methods, steam distillation, chemical oxidation, precipitation and biological treatments (enzymatic and microbial) were used by researchers. (Divate & Hinge 2014, Villegas et al. 2016, Othman et al. 2017).

The adsorption method has numerous difficulties, such as low adsorption capacities, pore clogging in the case of clays, surface saturation, longer times needed for reaching equilibrium, limited selectivity in mixed wastewater, high costs, difficulties in regeneration and reusability (Mandal et.al. 2020, Adnan et.al. 2021, Al-Ghouti et al. 2022, Ho 2022). Membrane separation techniques suffer from various problems, including membrane fouling, emulsion instability in the case of liquid membranes, high production costs, and potential degradation under harsh wastewater conditions in the case of polyimide ultrafiltration membranes (Reis et al. 2011, Feng et.al.2021, Ali et al. 2021). Despite obtaining high extraction efficiency, the application of enzymatic processes on an industrial scale may be impractical when handling large volumes of wastewater (Bevilaqua et al. 2002).

Among all methods, liquid-liquid extraction was the most preferred method. The choice of solvent was the major aspect affecting phenol removal in extraction. Alcohols, esters, ethers, and ketones are often the solvents of choice due to their favorable distribution coefficients as well as their comparatively low toxicity and good biodegradability. (Kieezyk & Mackay 1973). Combining these solvents with an inert diluent presents an appealing approach. The following solvents were mentioned in the literature: cumene (Liu et al. 2013), iso-kerosene (Abbassian et al. 2015), methyl iso-butyl ketone (Greminger et al.1982), di-isopropyl ether (Greminger et al.1982), hexanol (Rao et al. 2009), heptanol (Rao et al. 2009), octanol (Rao et al. 2009), castor oil (Rao et al. 2009), toluene (Mohmed et al. 2001), benzene (Abdelmonem et al. 2001), benzyl 2-ethylhexyl sulfoxide(Wang et al. 2015), mesityl oxide (Feng et al. 2017), ethanolamine (Gai et al. 2019), butyl acetate(Prasad et al.1991), biodiesel (Yu et al. 2012), tridodecylamine in benzene (Datta et al. 2014), kerosene (Juang et al. 2010), polyethylene glycol (Chasib 2013), dimethylsulfoxide (Chasib 2013), tetramethylene sulfolone (Chasib 2013), diethylene glycol(Chasib 2013), ethylene glycol (Chasib 2013), methanol (Klen et al. 2011), palm oil (Othman et al. 2017), etc.

Petroleum-derived solvents were preferred due to their strong affinity for phenol and high extraction efficiency. However, these solvents are carcinogenic and inflammable, thus requiring careful handling and disposal. Recovery of phenol and solvent from the extract was time-consuming and costly. Usage of expensive petroleum solvents to remove phenol from wastewater is uneconomical and unsustainable. (Nanda et al. 2021).

Novel solvents such as ionic liquids managed to extract phenol efficiently due to the presence of hydrogen bonding, formation of complexes between cationic species and phenolate ions, and their hydrophobic nature. The structure of ILs, temperature, and pH determined the efficiency. However, high viscosities and the non-biodegradable nature of ingredients may limit their uses. (Deng et al. 2011, Wang et al. 2015, Sas et al. 2020, Skoronski et al. 2020).

Eutectic mixtures of H-bond contributors and H-bond acceptors are termed deep eutectic solvents (DES). The depression in melting and freezing points, compared to that of its individual constituents, is characteristic of DESs. Hydrogen bonding is responsible for the depression in melting point. Due to ease of preparation, low cost, low volatility, high biodegradability, and a tunable nature, these mixtures are considered to be a new generation of green solvents. They are being studied as solvents in "green extraction" (Smith et al. 2014).

Recent work by, Cheng et al. (2022), Rodríguez-Llorente et al. (2020), Cañadas et al. (2021), Sas et al. (2019), Wazeer et al. (2023), and Tan et al. (2025) has demonstrated the effective use of various hydrophobic deep eutectic solvents (HDES), including: menthol + nonanoic acid, C_8OOH + menthol, methyl trioctylammonium chloride + menthol, dodecanoic acid +decanoic acid, and trioctylphosphine oxide + menthol, fenchol+ menthol HDES. (Sas et al. 2019, Rodríguez-Llorente et al. 2020, Cañadas et al. 2021, Cheng et al. 2022, Wazeer et al. 2023, Tan et al. 2025). The costly nature of ingredients negates the advantages offered by HDES and makes scale-up unfeasible.

Aquoline is a new generation of deep eutectic solvent that uses water as the hydrogen-bond acceptor. It shows Newtonian behavior, has a pH near neutral, and is polar. (Triolo et al. 2021, Hirpara et al. 2022)It could be used as a solvent, along with CTAB. Positively charged groups of CTAB (cetyltrimethylammonium bromide), a cationic surfactant, tend to attract negatively charged ions of phenol from the sample due to electrostatic attraction. (Shammala et al.1999, Malkoc et al. 2018). Huang et al. (2012)

postulated that the presence of surfactant micelles improved solubilization of phenol. (Huang et al. 2012). Hirpara et al. (2022) studied the micellization behavior of various surfactants in Aquoline. Critical micelle concentration and aggregation number of CTAB were lower in Aquoline compared to water. Thus, lower amounts of CTAB would be necessary for micelle formation. (Hirpara et al. 2022).

In the presence of excess CTAB beyond the critical micelle concentration (CMC), micellar aggregates are formed that incorporate Aquoline, phenol, and CTAB. On account of having lower densities, these aggregates tend to separate from the aqueous phase, thus facilitating faster isolation. This indicates that CTAB micelles in Aquoline can effectively solubilize phenol from wastewater, thereby demonstrating a novel application of hydrophilic deep eutectic solvents (DES). Moreover, for the extraction of acidic impurities, the use of neutral hydrophilic DES containing CTAB might provide better efficiency.

Only a limited number of studies have been reported about the applications of hydrophilic deep eutectic solvents (DESs) for extracting pollutants from wastewater, largely due to their high propensity for dissociation and difficulty in recovery from aqueous solutions. These DESs were extensively used for drug delivery and as a reaction medium. Hydrogen bonding between ChCl and water in Aquoline DES is much stronger compared with other hydrophilic DES (for example, choline chloride and urea). This property permits the Aquoline DES to retain its structure without dissociating when added to water (Dwamena et al. 2019).

To overcome the drawbacks of existing solvents, this research work focuses on the extraction of phenol from wastewater by using a combination of Aquoline (water + choline chloride) and a cationic surfactant (CTAB). We intend to extend the applications of a surfactant-DES system for the recovery of phenol beyond commonly studied wastewater systems (such as textile, refinery, and coke oven plant wastewater). This study aims to remove phenol from wastewater obtained from coal gasification plants (phenol concentration = 5000 ppm). The extraction of phenol from wastewater using hydrophilic DES aided by surfactant has never been tried before. This is the first research work that explores the application of a cheap DES and surfactant combination for the removal of phenol. Usage of a new solvent system might help in reducing waste and contribute to the sustainability of the process.

2. MATERIALS AND METHODS

2.1. Chemicals

Phenol, choline chloride (98 % pure),4-amino-antipyrine, potassium ferricyanide, ethanol (99 %), cetyltrimethylammonium bromide (> 98%), and dichloromethane (all analytical grade) were purchased from Merck Life Science, Mumbai, India.

2.2. Preparation of Aquoline DES

Choline chloride was vacuum-dried before use. The method described in published research papers was used for the preparation of Aquoline (Triolo et al. 2021, Mangiacapre et al. 2023). The mole ratios of HBC and HBR are mentioned in Table 1. All mixtures were stirred until the complete dissolution of choline chloride crystals, resulting in the formation of a homogeneous and slightly viscous liquid. Aquoline could not be prepared at mole ratios of 1:1 and 1:5.

2.3. Characterization of Aquoline

UV absorption spectra of the selected Aquoline DES were studied on a Shimadzu UV-1280 spectrophotometer. The chemical structure of fresh and recovered Aquoline solvent was studied by FTIR spectroscopy on a Perkin-Elmer spectrophotometer. ^{1}H and ^{13}C NMR analysis of fresh and recovered Aquoline was carried out using an Agilent 500 MHz NMR using DMSO /D_2O as solvent.

2.4. Extraction Procedure

Simulated wastewater solutions of phenol with concentrations ranging from 100 to 5000 ppm were used for experiments. A measured amount of sample solution was taken in a graduated and stoppered test tube, and a predetermined quantity of solid choline chloride was added so that Aquoline solvent formed within the system. The mixtures were stirred on a vortex mixer for 15 minutes. Subsequently, a predetermined quantity of the CTAB surfactant was introduced, and the resulting mixture was permitted to settle for 24 hours. Formation of two layers was observed, with the top layer containing phenol, CTAB, and Aquoline. The bottom aqueous layer was analyzed for the concentration of phenol.

Table 1: Formulation of Aquoline DES.

Name	H-bond receiver (HBR)	H-bond contributor (HBC)	Mole ratio of HBR: HBC
Aquoline- 1	Chloride salt of choline	Water	1:2
Aquoline- 2	Chloride salt of choline	Water	1:3
Aquoline-3	Chloride salt of choline	Water	1:4

Extraction efficiency is determined using the formula:

$$\text{Extraction Efficiency} = \frac{(C_{extract})}{(C_{Total})} \times 100$$

Where $C_{extract}$ represents the concentration of phenol in the extracted layer, and C_{total} reflects the concentration of phenol in the original sample.

This method was used for the selection of an appropriate molar ratio for Aquoline DES for extraction and optimization studies. Every experiment was carried out in triplicate.

2.5. Analysis

The concentration of phenol in the lower layer was found by UV spectrophotometer (Shimadzu - UV-1280) using 4-aminoantipyrine dye. A wavelength of 510 nm was used to measure the absorbance of phenol in the sample (Sas et al. 2020).

3. RESULTS AND ANALYSIS

3.1. Characterization of Solvent

3.1.1. UV Spectra of Aquoline-3 DES

The UV spectra of Aquoline-3 are presented in Fig. 1. The spectra show strong absorption in the 177–186 nm range. Maximum absorbance of 3.82 was obtained at λ_{max} = 185.67. As choline chloride lacks conjugated double bonds or aromatic rings, it does not go through $\pi \rightarrow \pi^*$ or $n \rightarrow \pi^*$ transitions. The maximum absorption below the UV range must arise due to strong $\sigma \rightarrow \sigma^*$ transitions of the O–H bonds in water and the ammonium groups of choline chloride. Absorbance steadily falls from 200 nm to 260 nm. Absorbance stabilizes at very low values (<0.1) beyond a wavelength of 400 nm.

3.1.2. NMR Spectra of Aquoline-3 DES

^1H and ^{13}C NMR spectra for Aquoline-3 are shown in Fig. 2 and Fig. 3. The sharp peak at 3.199 ppm belongs to the nine equivalent methyl protons attached to nitrogen in choline chloride. The triplet at 3.51 ppm belongs to the methylene protons adjacent to oxygen ($-CH_2OH$) in ChCl. It appears as a triplet due to coupling with $–CH_2N^+$. The peak at 3.865 ppm belongs to the methylene protons adjacent to nitrogen ($-CH_2N^+$). A broad singlet peak at 5.67 ppm belongs to the hydroxyl proton (-OH) of choline chloride. It's broad due to exchange with water and is shifted downfield. The signal at 2.573 ppm represents DMSO.

The ^{13}C spectrum shows three main signal groups. The peaks at 53.564, 53.586, and 53.617 ppm (centered at 53.59 ppm) are assigned to the three equivalent methyl carbons attached to nitrogen (CH3)3N+. The peak at 55.476 ppm is assigned to the $-CH_2$-OH carbon. Peaks at 67.221, 67.244, 67.267 ppm (centered at 67.24 ppm) are assigned to the $N-CH_2$- carbon. The cluster of peaks at 39.102–40.103 ppm represents the solvent DMSO.

1H NMR spectra confirm the presence of choline chloride in Aquoline-3. ^{13}C NMR confirms retention of the ChCl structure within the superstructure of the DES. The presence of hydrogen bonding and a chlorine atom may have caused downshifting of peaks in both ^1H and ^{13}C NMR to higher frequencies. (Delso et al. 2019, Shahhosseiniet al. 2024).

3.1.3. FTIR spectra of Aquoline -3

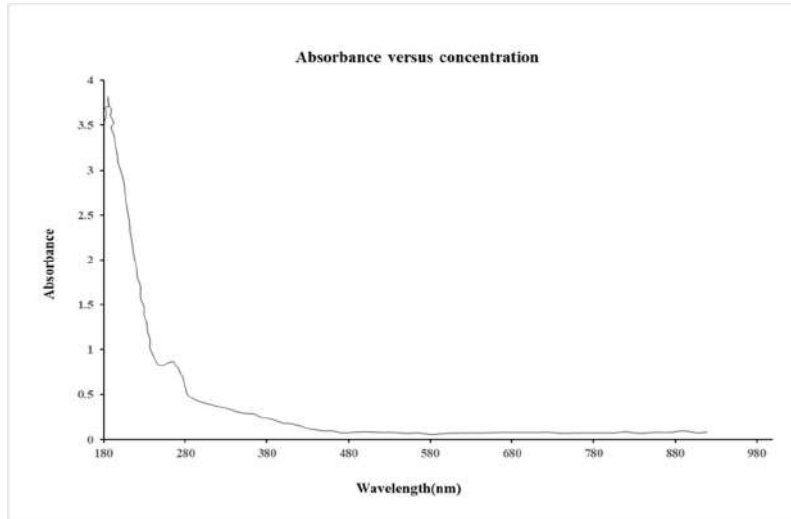


Fig. 1: UV spectrogram of Aquoline-3.

FTIR spectra of ChCl and Aquoline-3 are depicted in Fig. 4. Peaks at 3346, 3018, 2948, 1478, 1007, 952, and 865 cm^{-1} represent stretching of the hydroxyl group, N-H stretching vibration of the quaternary ammonium group, C-H stretching of the methyl and methylene groups, and C-N stretching of the quaternary ammonium group. Peaks at 1133, 1083, and 1050 cm^{-1} show C-O stretching, while peaks at 952 and 865 cm^{-1} show C-N stretching of the quaternary ammonium group. Due to the formation of DES between choline chloride and water, the peaks for ChCl were seen shifted in the spectra of Aquoline-3. (Shahhosseini et al. 2024).

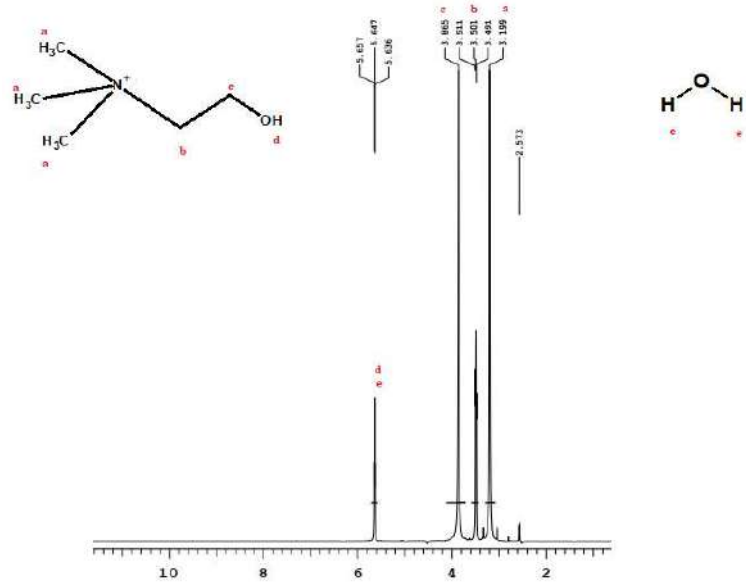


Fig. 2: ^{1}H NMR spectra of Aquoline -3.

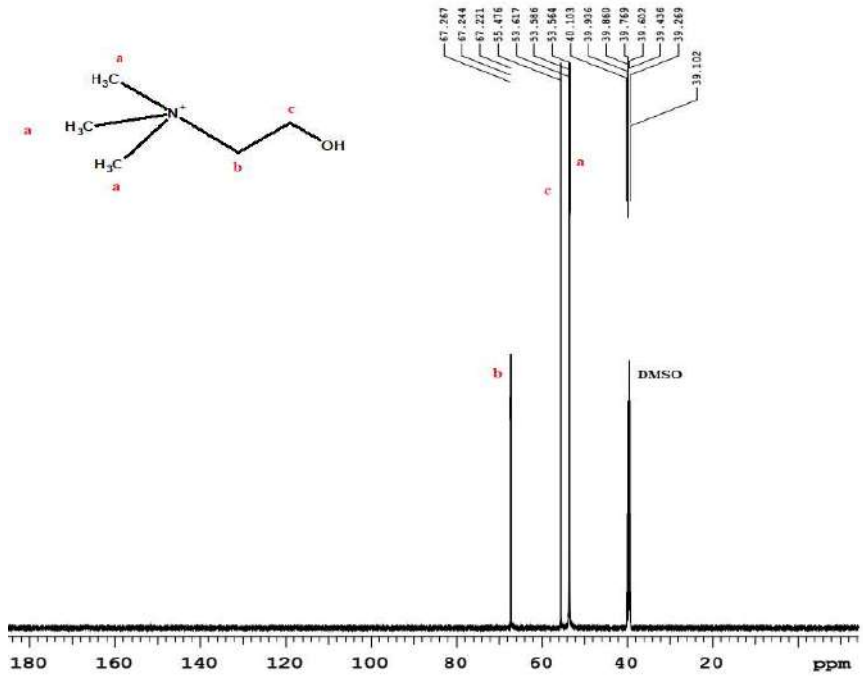


Fig. 3: ^{13}C NMR spectra of Aquoline -3.

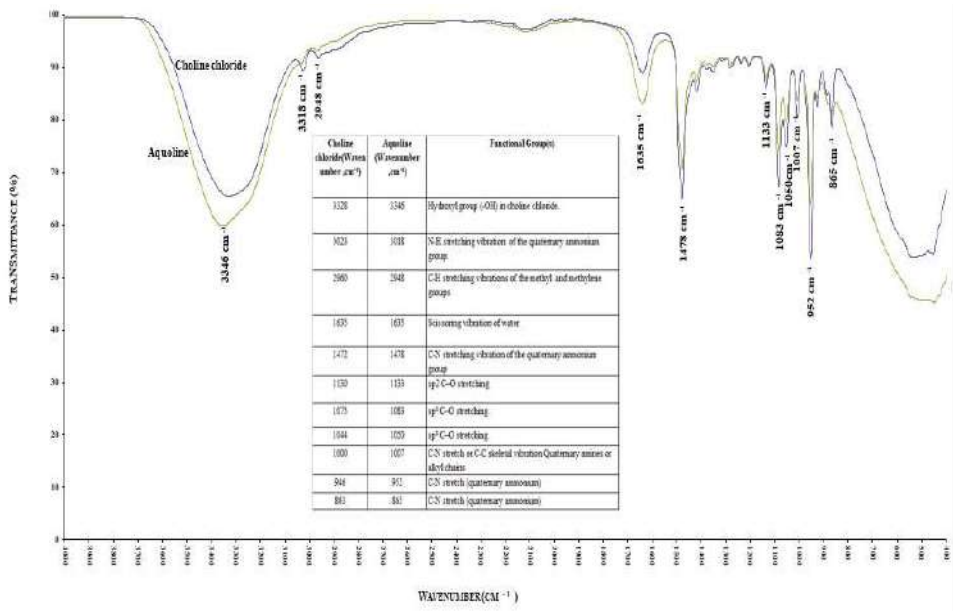


Fig. 4: FTIR spectra of choline chloride and Aquoline-3.

3.2. Selection of Aquoline with Proper Mole Ratio for Extraction of Phenol

The molar ratio of the HBC to the HBR is strongly correlated with the physical and chemical properties of DESs and affects their selectivity (Tan et al. 2025). The prepared Aquoline DESs (with varying mole ratios of HBC and HBR) were used in extraction experiments, and the results are shown in Fig. 5. Aquoline -3 (mole ratio of HBR to HBC = 1:4) gave the highest extraction efficiency. The positively charged hydrophilic headgroup of CTAB in Aquoline-3 interacts with phenol anions in sample water, causing phenol to concentrate in the upper layer while the lower layer remains free of phenol. Aquoline-3 will be used for the rest of the experiments.

Extraction parameters: Initial phenol concentration = 5000 ppm, temperature = 301 K, pH =10, waste-water solution to DES ratio = 10 :1, CTAB concentration = 0.9 $mM.L^{-1}$.

3.3. Influence of Changing Process Parameters on Extraction Efficiency

To maximize extraction efficiency (with Aquoline -3 as solvent), process parameters (pH, mole ratio of wastewater sample to Aquoline, initial phenol concentration, CTAB concentration) were varied, and their impact was studied.

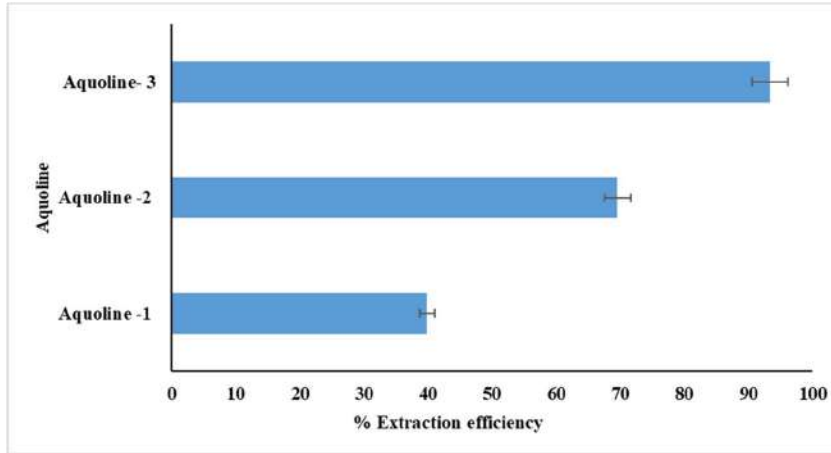


Fig. 5: Selection of Aquoline with the proper mole ratio for extraction of phenol.

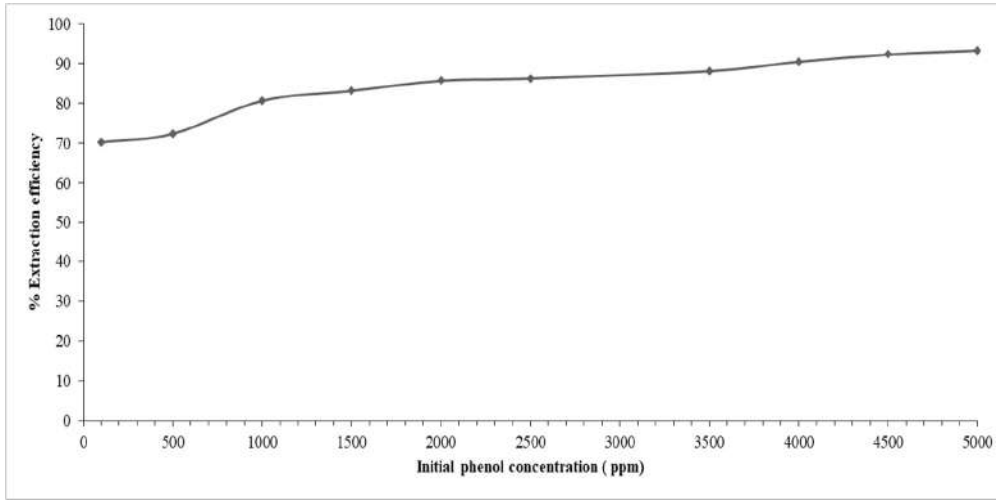


Fig. 6: Influence of changing initial phenol concentration on extraction efficiency.

3.3.1. Influence of Changing Initial Phenol Concentration on Extraction Efficiency

Effects of changing the concentration of phenol in the feed (100 to 5000 ppm) on phenol recovery are depicted in Fig. 6. The extraction efficiency showed a positive trend with subsequent increase in phenol concentration in the feed. At higher concentrations, phenolate ions interact with positively charged CTA^+ ions in micelles, thus increasing solubilization. The micellization of CTAB is further facilitated by alkaline pH and high polarity of Aquoline-3.

Lakshmi et al. (2013) noticed a significant drop in efficiency when phenol concentration was increased beyond 10 ppm with ionic liquid $[Bmim]^+[BF_4]^-$ + tributyl phosphate as solvent (Brinda Lakshmi et al. 2013). Sas et al. (2019) observed that efficiency increased with initial phenol concentration, but solvents with low hydrophobicity showed higher efficiencies (Sas et al. 2020). Tan et al. (2025) reported that initial phenol concentration did not affect extraction efficiency when fenchol-menthol HDES was used as an extractant. This was ascribed to the fact that the degree of

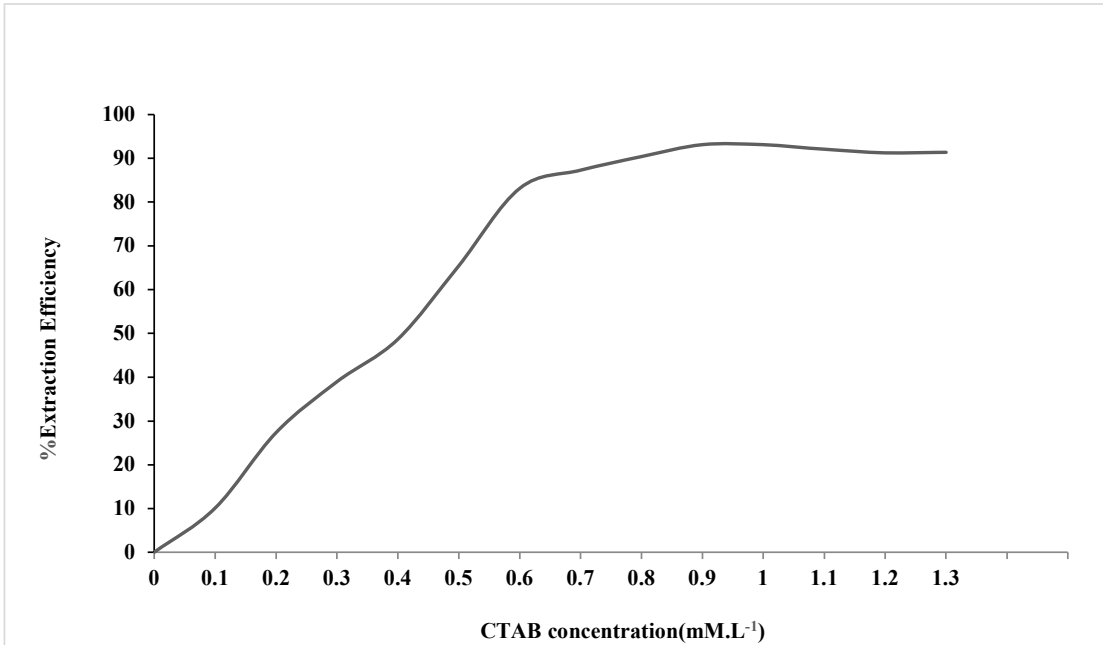


Fig. 7: Influence of changing CTAB concentration on extraction efficiency.

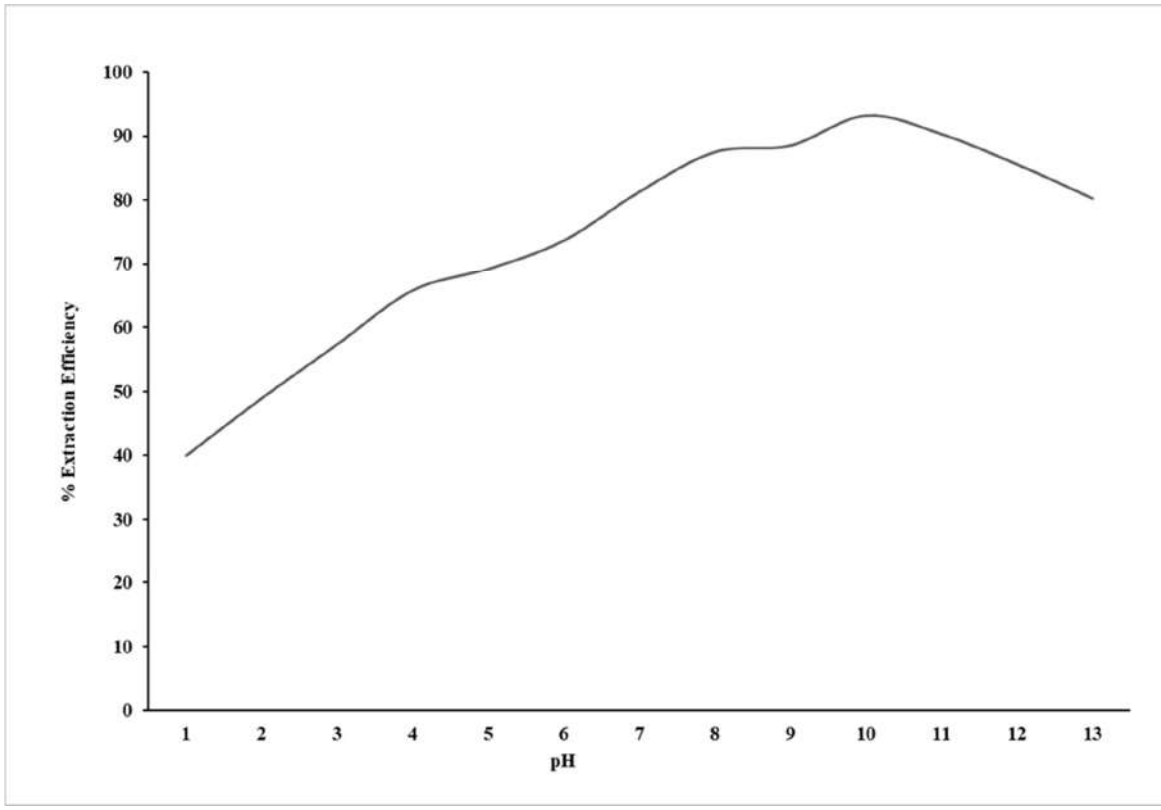


Fig. 8: Influence of changing pH on extraction efficiency.

solvation of phenol was the same at all concentrations (Tan et al. 2025).

Extraction parameters: temperature = 301 K, pH =10, volume ratio of waste-water solution to DES = 10 :1,CTAB concentration = 0.9 mM.L^{-1}.

3.3.2. Influence of Changing CTAB Concentration on Extraction Efficiency

CTAB forms micelles in Aquoline at a CMC value of 0.82 mM.L^{-1}. The micelles formation involves incorporation of the hydrophobic head of the surfactant into the micelle due to the high polarity of DES (Hirpara et al. 2022). When the amount of surfactant in water was higher than its CMC, aggregates of large micelles were formed. Initially, phenol molecules in water tend to attach to the outer layer of micelles. With increasing concentration, phenol molecules penetrate the center of micelles (Chaghi et al. 2008). Phenol serves as a micelle modifier in concentrated CTAB systems. By inserting itself into the surfactant structure, it drives a transformation of the micelles from a standard sphere to rod-like structures, leading to a measurable decrease in the overall solution viscosity (Mata et al. 2006).

CTAB concentration was varied from 0.1 mM.L^{-1} to 1.3 mM.L^{-1}, and results are shown in Fig. 7. At low CTAB concentration, extraction efficiency was low due to negligible solubilization of phenol into micelles. With increasing CTAB concentration, the solution viscosity decreased, and more phenol was solubilized, resulting in the formation of micellar aggregates. Maximum extraction efficiency was obtained at a CTAB concentration of 0.9 mM.L^{-1}.

Extraction parameters: Initial phenol concentration = 5000 ppm, temperature = 301 K, pH =10, volume ratio of wastewater solution to DES = 10 :1.

3.3.3. Influence of Changing pH on Extraction Efficiency

At alkaline pH, phenol dissociates into phenoxide ion, while it stays in molecular form in acidic media due to low pKa (Liu et al. 2013, Tan et al. 2025). Three interaction mechanisms between phenol and CTAB were reported. Hydrophobic interactions at low pH, electrostatic interactions between phenoxide ions and CTAB at high pH, and hydrogen bonding interactions between the phenolic -OH group and water (Shammala et al. 1999).

To facilitate easier extraction of phenol, the pH has to be kept higher to promote electrostatic interactions between CTAB and phenoxide ions. In the acidic pH range, electrostatic interactions between the phenolate ion

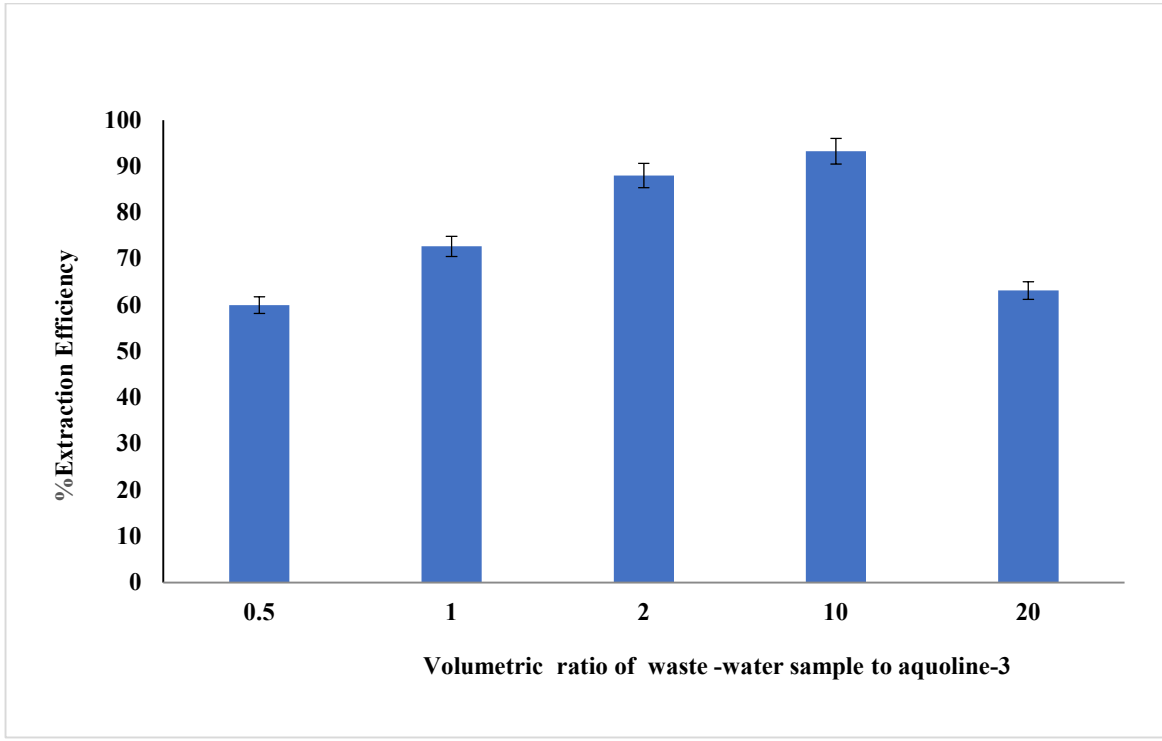


Fig. 9: Influence of changing the volume ratio of wastewater sample to Aquoline-3 on extraction efficiency.

and CTA^+ are negligible, and extraction proceeds due to hydrophobic interactions. At pH = 7, the phenol molecule gets attached to the outer layers of micelles. At alkaline pH, phenolate ions interact with CTA^+ ions, leading to increased solubilization of phenol (Sabatino et al. 2010).

Fig. 8 displays the extraction efficiency as a function of pH. The amount of phenol recovered increased steadily, and the highest efficiency was obtained at pH = 10, but dropped later. So, it is essential to keep the pH in the alkaline range to maximize the extraction of phenol. In published literature, Tan et al. (2025) and Wang et al. (2015) obtained the highest efficiency at neutral pH (Wang et al. 2015, Tan et al. 2025).

Extraction parameters: Initial phenol concentration = 5000 ppm, temperature = 301 K, volume ratio of wastewater solution to DES = 10:1, CTAB concentration = 0.9 $mM.L^{-1}$.

3.3.4. Influence of Changing Volume Ratio of Wastewater Sample to Aquoline on Extraction Efficiency

The volume ratio of wastewater sample to Aquoline-3 was adjusted from 1:1 to 20:1 (Fig. 9). As the treatment ratio increased, the extraction efficiency improved, reaching its maximum at a ratio of 10:1. Beyond this point, efficiency declined due to limited solvent availability. Therefore, a 10:1 volume ratio was chosen. Similar patterns were reported by Lakshmi et al. (2013), who selected a 5:1 treat ratio. Conversely, Tan et al. (2025) achieved maximum extraction at a 1:1 ratio when using HDES as the solvent.

Extraction parameters: Initial phenol concentration = 5000 ppm, temperature = 301 K, pH =10, CTAB concentration = 0.9 $mM.L^{-1}$.

Based on optimization studies, the following optimized parameters were obtained: Initial phenol concentration = 5000 ppm, temperature =301 K, pH =10, CTAB concentration = 0.9 $mM.L^{-1}$, volume ratio of wastewater solution to DES = 10:1.

3.4. Extraction Mechanism

A hypothetical extraction mechanism is proposed for the micelle-assisted extraction of phenol from wastewater using CTAB in Aquoline. The process is primarily governed by interactions between phenoxide ions and CTAB, interactions between the phenolic -OH group and water, and hydrophobic interactions between phenol and CTAB. At high pH, phenol was deprotonated into phenolate ions, which interacted with the positively charged quaternary ammonium head groups of CTAB. Concurrently, hydrophobic interactions between the phenyl ring of phenol and the alkyl chains of CTAB further stabilized this association. Under these conditions, micelles capture phenol molecules in the outer layer. Above the CMC, CTAB formed micelles that encapsulated phenol molecules

within their hydrophobic cores, while the charged head groups remained solvated in the polar Aquoline medium. At higher CTAB concentrations, mixed aggregates containing Aquoline, CTAB, and solubilized phenol were formed. Due to their lower density relative to the bulk aqueous phase, these aggregates separated rapidly, facilitating efficient phase disengagement and enhancing phenol recovery into the DES-rich phase. The presence of CTAB micelles therefore significantly improved phenol solubilization and transfer from the aqueous to the surfactant-rich phase (Shammala et al. 1999, Mata et al. 2006, Chaghi et al. 2008, Liu et al. 2013, Tan et al. 2025).

3.5. The Stripping and Reuse of Extraction Solvent

After extraction, the upper layer (comprising CTAB + phenol + ChCl) was separated by decantation. Phenol, present in this layer, was converted to its salt, i.e., sodium phenoxide, by using sodium hydroxide. The solution was subjected to solvent extraction using dichloromethane for the separation of CTAB. The top organic layer obtained after extraction consisted of CTAB, which was recovered after evaporation of the solvent. The bottom aqueous layer(consisting of phenol) was acidified with hydrochloric acid. Phenol could be separated from this layer by extraction with dichloromethane as solvent. The remaining aqueous portion consisted of choline chloride. It was subjected to evaporation to adjust the ratio of choline chloride and water.

Despite not being considered a green solvent, dichloromethane was used due to its strong affinity for phenol and CTAB, immiscibility with water, and ability to preserve the stability of choline chloride, while requiring only a small amount for DES purification. In future applications, environmentally friendly hydrophobic deep eutectic solvents, such as menthol–nonanoic acid or fenchol–menthol HDES, represent promising alternatives (Cheng et al. 2022, Tan et al. 2025).

The recovered solvent was replenished with fresh solvent and reused for 4 further extractions (Fig. 10). A gradual decline in extraction efficiency was noticed. It may be due to the gradual decomposition of choline chloride during repeated recovery operations. The recycling studies were carried out for only four cycles. Long-term reusability and stability of Aquoline were beyond the ambit of this study.

Extraction parameters: Initial phenol concentration = 5000 ppm, temperature = 301 K, pH =10, CTAB concentration = 0.9 $mM.L^{-1}$, volume ratio of wastewater solution to DES = 10.

Fig. 11 displays FTIR spectra for pure Aquoline, recycled Aquoline-3, and the Aquoline-CTAB upper micelle layer. The peaks at 3342 and 3348 cm-1 indicate hydroxyl groups associated with water. A shift toward higher wavenumbers suggests interaction between micelles and Aquoline. N-H stretching between 3018 and 3021 cm-1 reflects alterations in the CTAB carbon chain due to phenol presence, supporting previous observations of micelle DES interactions. Minor C-H shifts at 2950 cm-1 demonstrate CTAB's involvement in the DES structure. The chemical shifts in the fingerprint region, from 946 to 864 cm-1, indicate C-N stretching, implying that the quaternary ammonium in CTAB has interacted with phenol and DES, confirming the interdependence of CTAB and Aquoline-3 in phenol extraction. Additionally, shifts at 1075 cm-1 in the sp^3 C–O region suggest choline hydroxyl interactions. Peaks between 1004 and 1007 cm-1 show typical vibrations associated with

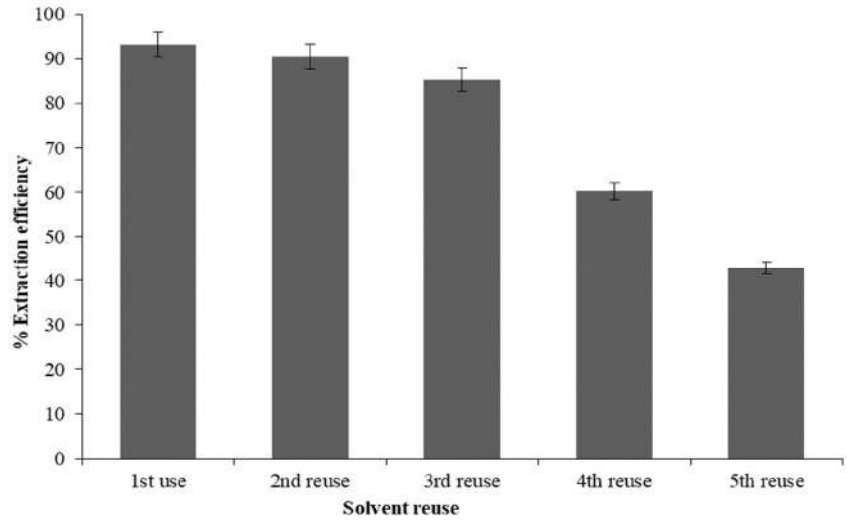


Fig. 10: Extraction efficiency as a function of solvent reuse.

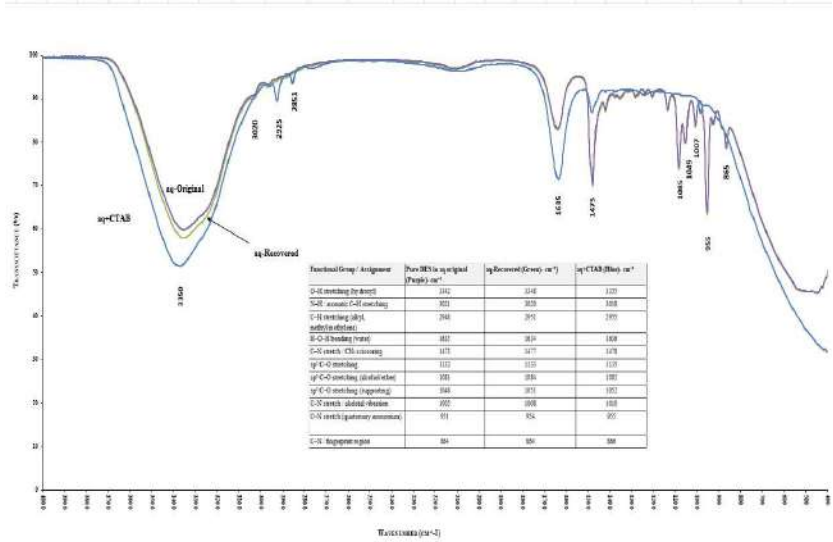


Fig. 11: FTIR spectra of Aquoline -3, upper micellar layer and recycled Aquoline-3.

Table 2: List of solvents used in the extraction of phenol**.**

Sr. No.	Name of solvent	Feed concentration [ppm]	Volume ratio of solvent to feed	pH	Temp [K]	Time [h]	Extraction efficiency [%]	Ref.
1.	Iso-kerosene	100	1:1	6	323	2	70	(Abbassian et al. 2015)
2.	Methyl iso-butyl ketone	1000	1:1	2	303	0.25	97	(Abdelmonemet al. 2001)contact time, solvent/ feed ratio, shaking time and agitation speed on the removal of phenol by each solvent were investigated. The equilibrium condition was also determined and the rate of extraction was measured as a function of the above. The performance of each solvent is discussed with respect to the operating conditions. The results lead strongly towards the use of methyl iso-butyl keton (MIBK
3.	Di-isopropyl ether (DIPE)	1000	3:1	2	303	0.25	98	
4.	Toluene	1000	3:1	2	303	0.25	94	
5.	Benzene	1000	3:1	2	303	0.25	95.5	
6.	Ionic liquid $[Bmim]^+[BF_4]^-$ + tributyl phosphate	10	1:1	3	303	0.33	96	(Brinda Lakshmi et al. 2013)experiments have been carried out with a focus to reduce the volume requirement of solvent by mixing with imidazolium based ionic liquids (ILs
7.	Benzyl 2-ethylhexyl sulfoxide	10	1:1	2	298	0.08	98.7	(Wang et al. 2015)we synthesized a novel structure of sulfoxide, benzyl 2-ethylhexyl sulfoxide (BSO
8.	Aliquat – 336	2500	1:16.67	5	--	0.67	96.3	(Rao et al. 2009)
9.	Trioctylphosphine oxide (TOPO) -menthol HDES(mole ratio = 1:1)	7 wt %	1:1 mass ratio	--	298	26	96	(Wazeer et al. 2023)
10.	Fenchol- menthol HDES(mole ratio = 1:5)	1000	1:1	7	303	0.5	95.9	(Tan et al. 2025)
11.	Menthol and octanoic acid HDES (molar ratio of 1:1)	50	--	9.5	298	2.5	85	(Sas et al. 2019)
12.	Cumene	2167	--	7	298	0.5	80	(Liu et al. 2013)
13.	CTAB + Aquoline	5000	10:1	10	301	24.25	93.27	This work

surfactant skeletons during DES interactions (Su et al. 2015, Shettigar et al. 2018). In the upper micelle layer, the peak at 3355 cm-1 indicates hydroxyl groups in phenol and water. The range from 1417 to 1475 cm-1 corresponds to CH2 deformation in phenol. Phenolic OH in-plane deformation is observed at 1352 cm-1. A broad peak at 1248 cm-1 denotes C–O and OH bending modes in phenol. The FTIR spectra confirm that the structure of recovered Aquoline-3 closely matches that of the original Aquoline-3.3.

3.6. Comparison of Aquoline-3 with Other Solvents

Table 2 presents various solvents used as extractants for phenol removal from wastewater under significantly different operating conditions compared to those in our study. The Aquoline-3 + CTAB system effectively separated phenol from wastewater samples with high phenol concentrations, requiring only a small amount of Aquoline solvent relative to other solvents. While deep eutectic solvents (HDES) are efficient, they are costly and unsuitable for high phenol loads or larger wastewater volumes. Additionally, phase separation took 24 hours, which could limit industrial application due to the need for extra settling tanks. However, process intensification methods such as centrifugation and ultrasonication could accelerate micellization, making the process more scalable industrially. Alternatively, membrane filtration may facilitate faster separation of micelles. Despite these challenges, the combination of Aquoline-3 + CTAB offers a more environmentally friendly alternative.line-3 + CTAB would prove to be a more benign alternative.

4. CONCLUSIONS

A novel type of deep eutectic solvent, Aquoline (choline chloride to water molar ratio of 1:4), was employed to separate phenol from wastewater. The process was enhanced by CTAB surfactant, which forms micelles within Aquoline. Notably, this is the first study to utilize hydrophilic DES combined with CTAB for phenol removal from wastewater. Characterization of the solvent was conducted using UV-VIS, NMR, and FTIR spectroscopy. An impressive maximum extraction efficiency of 93.27% was achieved under optimized conditions: initial phenol concentration of 5000 ppm, temperature of 313 K, pH 10, CTAB concentration of 0.9 mM·L−1, and a wastewater-to-solvent volume ratio of 10. FTIR spectra of the recovered solvent confirmed that its original structure remained intact. The solvent demonstrated reusability for up to three cycles, with a gradual decrease in efficiency. Compared to other solvents, this system performs effectively with wastewater containing high phenol concentrations (up to 5000 ppm). Process intensification techniques such as centrifugation, ultrasonication, and membrane filtration could further improve settling time and expedite micelle separation. Future research should explore the extraction mechanism and conduct detailed structural analysis of the micelles.

5. ABBREVIATIONS

Aliquat – 336 - N-Methyl-N

N-dioctyloctan-1-aminium chloride

ChCl - Choline chloride

CTAB - Cetyl trimethyl ammonium bromide

DES - Deep eutectic solvents

DMSO - Dimethyl Sulfoxide

EPA - Environmental Protection Agency

FTIR - Fourier Transform Infrared spectroscopy

HBC - Hydrogen bond contributors

HBR - Hydrogen bond receivers

NMR - Nuclear Magnetic Resonance spectroscopy

pKa - Acid dissociation constant

TOPO - Trioctylphosphine oxide

UV - UV-Vis spectroscopy

GC - Gas chromatography

6. ACKNOWLEDGMENTS

The authors sincerely acknowledge Thadomal Shahani Engineering College, Mumbai, and the Department of Technology, Shivaji University, Kolhapur, for their continuous support and the use of laboratory facilities required for this research work. Their assistance and encouragement were instrumental in the successful completion of this study.

7. REFERENCES

Abbassian, K., Kargari, A. and Kaghazchi, T., 2015. Phenol removal from aqueous solutions by a novel industrial solvent. *Chemical Engineering Communications*, 202(3), pp.408-413. [DOI]

Abdelmonem, R.M., Hashem, M.A. and Mohmed, A.A., 2001. Further studies on phenol removal from aqueous solutions by solvent extraction. *Environmental Health Risk*, 5, pp.139-149. [DOI]

Al-Ghouti, M.A., Jannatul, S., Nazmin, M., Mohamed, D., Da'na, D.A., Hazim, Q. and Abedalkader, A., 2022. Effective removal of phenol from wastewater using a hybrid process of graphene oxide adsorption and UV-irradiation. *Environmental Technology & Innovation*, 27, p.102525. [DOI]

Altuntas, E., Hakki, M., Gonultas, O., Candan, Z. and Ertas, M., 2012. FTIR investigation of phenol formaldehyde resin modified with boric acid. *Proceedings of the 55th International Convention of Society of Wood Science and Technology*, pp.1-8.

Banjare, R.K., Banjare, M.K., Behera, K., Pandey, S. and Ghosh, K.K.,

2020. Micellization behavior of conventional cationic surfactants within glycerol-based deep eutectic solvent. *ACS Omega*, 5(31), pp.19350-19362. [DOI]

Bevilaqua, J.V., Cammarota, M.C., Freire, D.M.G. and Sant'Anna Jr., G.L., 2002. Phenol removal through combined biological and enzymatic treatments. *Brazilian Journal of Chemical Engineering*, 19(2), pp.151-158. [DOI]

Brinda Lakshmi, A., Balasubramanian, A. and Venkatesan, S., 2013. Extraction of phenol and chlorophenols using ionic liquid [Bmim]+[BF4]- dissolved in tributyl phosphate. *Clean - Soil, Air, Water*, 41(4), pp.349-355. [DOI]

Cañadas, R., María González-Miquel, González, E.J., Díaz, I. and Rodríguez, M., 2021. Hydrophobic eutectic solvents for extraction of natural phenolic antioxidants from winery wastewater. *Separation and Purification Technology*, 254, p.117590. [DOI]

Chaghi, R., Louis-Charles, M., Charnay, C., Gaëlle, D. and Zajac, J., 2008. Interactions of phenol with cationic micelles of hexadecyltrimethylammonium bromide studied by titration calorimetry, conductimetry, and H-1 NMR in the range of low additive and surfactant concentrations. *Journal of Colloid and Interface Science*, 326, pp.227-234. [DOI]

Chasib, K.F., 2013. Extraction of phenolic pollutants (phenol and p-chlorophenol) from industrial wastewater. *Journal of Chemical & Engineering Data*, 58(6), pp.1549-1564. [DOI]

Cheng, H., Huang, Y., Lv, H., Li, L., Meng, Q., Yuan, M., Liang, Y. and Jin, M., 2022. Insights into the liquid extraction mechanism of actual high-strength phenolic wastewater by hydrophobic deep eutectic solvents. *Journal of Molecular Liquids*, 368, p.120609. [DOI]

Datta, D. and Uslu, H., 2014. Investigation of extraction of phenol from wastewater using N,N-didodecyl-1-dodecanamine (tridodecylamine) in benzene. *Journal of Chemical & Engineering Data*, 59(11), pp.3858-3862. [DOI]

Delso, I., Lafuente, C., Muñoz-Embid, J. and Artal, M., 2019. NMR study of choline chloride-based deep eutectic solvents. *Journal of Molecular Liquids*, 290, p.111236. [DOI]

Deng, N., Li, M., Zhao, L., Lu, C., de Rooy, S.L. and Warner, I.M., 2011. Highly efficient extraction of phenolic compounds by use of magnetic room temperature ionic liquids for environmental remediation. *Journal of Hazardous Materials*, 192(3), pp.1350-1357. [DOI]

Divate, S.B. and Hinge, R.V., 2014. Review on research removal of phenol from wastewater by using different methods. *International Journal of Scientific and Research Publications*, 4(1), pp.2250-3153.

Dwamena, A.K., 2019. Recent advances in hydrophobic deep eutectic solvents for extraction. *Separations*, 6(1). [DOI]

Feng, Y., Song, H., Xiao, M., Lin, K., Guo, K. and Gai, H., 2017. Development of phenols recovery process from coal gasification wastewater with mesityl oxide as a novel extractant. *Journal of Cleaner Production*, 166, pp.1314-1322. [DOI]

Gai, H., Qiao, L., Zhong, C., Zhang, X., Xiao, M. and Song, H., 2019. A solvent based separation method for phenolic compounds from low-temperature coal tar. *Journal of Cleaner Production*, 223, pp.1-11. [DOI]

Greminger, D.C., Burns, G.P., Lynn, S., Hanson, D.N. and King, C.J., 1982. Solvent extraction of phenols from water. *Industrial and Engineering Chemistry Process Design and Development*, 21(1), pp.51-54. [DOI]

Hamad, H.T., 2021. Removal of phenol and inorganic metals from wastewater using activated ceramic. *Journal of King Saud University - Engineering Sciences*, 33(4), pp.221-226. [DOI]

Hammam, A.M., Zaki, M.S., Yousef, R.A. and Fawzi, O., 2015. Toxicity, mutagenicity and carcinogenicity of phenols and phenolic compounds on human and living organisms [A Review]. *Advances in Environmental Biology*, 9, p.38+.

Hirpara, D., Patel, B., Chavda, V. and Kumar, S., 2022. Micellization of conventional and gemini surfactants in aquoline: A case of exclusively water based deep eutectic solvent. *Journal of Molecular Liquids*, 362. [DOI]

Ho, S., 2022. Low-cost adsorbents for the removal of phenol/phenolics, pesticides, and dyes from wastewater systems: A review. *Water (Switzerland)*, 14(20). [DOI]

Huang, J.-H., Xiong, Y.-L., Zeng, G.-M., Guo, S.-H., Xie, G.-X., Zhang, D.-M., Tang, X.-J. and Liu, Z.-F., 2012. Separation of phenol from various micellar solutions using MEUF. *Separation and Purification Technology*, 98, pp.1-6. [DOI]

Jerman Klen, T. and Mozetič Vodopivec, B., 2011. Ultrasonic extraction of phenols from olive mill wastewater: Comparison with conventional methods. *Journal of Agricultural and Food Chemistry*, 59(24), pp.12725-12731. [DOI]

Juang, R.-S., Kao, H.-C. and Tseng, K.-J., 2010. Kinetics of phenol removal from saline solutions by solvent extraction coupled with degradation in a two-phase partitioning bioreactor. *Separation and Purification Technology*, 71(3), pp.285-292. [DOI]

Kiezyk, P.R. and Mackay, D., 1973. The screening and selection of solvents for the extraction of phenol from water. *The Canadian Journal of Chemical Engineering*, 51(6), pp.741-745. [DOI]

Kuttiani Ali, J., Chabib, C.M., Jaoude, M.A., Alhseinat, A., Teotia, S., Patole, S., Anjum, D.H. and Qattan, I., 2021. Enhanced removal of aqueous phenol with polyimide ultrafiltration membranes embedded with deep eutectic solvent-coated nanosilica. *Chemical Engineering Journal*, 408, p.128017. [DOI]

Liu, J., Xie, J., Ren, Z. and Zhang, W., 2013. Solvent extraction of phenol with cumene from wastewater. *Desalination and Water Treatment*, 51(19-21), pp.3826-3831. [DOI]

Mandal, A., Mukhopadhyay, P. and Das, S.K., 2020. Adsorptive removal of phenol from wastewater using guava tree bark. *Environmental Science and Pollution Research*, 27(19), pp.23937-23949. [DOI]

Mangiacapre, E., Castiglione, F., D'Aristotile, M., Di Lisio, V., Triolo, A. and Russina, O., 2023. Choline chloride-water mixtures as new generation of green solvents: A comprehensive physico-chemical study. *Journal of Molecular Liquids*, *383*, p.122120. [DOI]

Mata, J.P., Aswal, V.K., Hassan, P.A. and Bahadur, P., 2006. A phenol-induced structural transition in aqueous cetyltrimethylammonium bromide solution. *Journal of Colloid and Interface Science*, 299(2), pp.910-915. [DOI]

Mei, X., Li, J., Jing, C., Fang, C., Liu, Y., Wang, Y., Liu, J., Bi, S., Chen, Y., Xiao, Y., Yang, X., Xiao, Y., Wu, S. and Ding, Y., 2020. Separation and recovery of phenols from an aqueous solution by a green membrane system. *Journal of Cleaner Production*, 251, p.119675. [DOI]

Merouani, S., Dehane, A. and Hamdaoui, O., 2024. Ultrasonic destruction of surfactants. *Ultrasonics Sonochemistry*, 109, p.107009. [DOI]

Mukherjee, S., Kumar, S., Misra, A.K. and Fan, M., 2007. Removal of phenols from water environment by activated carbon, bagasse ash and wood charcoal. *Chemical Engineering Journal*, 129(1), pp.133-142. [DOI]

Nanda, B., Sailaja, M., Mohapatra, P., Pradhan, R.K. and Nanda, B.B., 2021. Green solvents: A suitable alternative for sustainable chemistry. *Materials Today: Proceedings*, 47, pp.1234-1240. [DOI]

Othman, N., Noah, M., Lim Yin Shu, Zing Yi Ooi, Norela Jusoh, Mariani Idroas and Goto, M., 2017. Easy removing of phenol from wastewater using vegetable oil-based organic solvent in emulsion liquid membrane process. *Chinese Journal of Chemical Engineering*, 25(1), pp.45-52. [DOI]

Panigrahy, N., Priyadarshini, A., Sahoo, M.M., Verma, A.K., Daverey, A. and Sahoo, N.K., 2022. A comprehensive review on ecotoxicity and biodegradation of phenolics: Recent progress and future outlook. *Environmental Technology & Innovation*, 27, p.102423. [DOI]

Patel, J. and Desai, H., 2022. Removal of phenol by liquid-liquid extraction from pharmaceutical wastewater. *Materials Today: Proceedings*, 57, pp.2396-2399. [DOI]

Pradeep, N.V., Anupama, S., Navya, K., Shalini, H.N., Idris, M. and Hampannavar, U.S., 2015. Biological removal of phenol from wastewaters: a mini review. *Applied Water Science*, 5(2), pp.105-112. [DOI]

Prasad, B. and Singh, G., 1991. Removal of phenols from coke-oven plant wastewater by solvent extraction. *Journal of Environmental Science and Engineering*, 17(1), pp.1-7.

Rao, N.N., Singh, J.R., Misra, R. and Nandy, T., 2009. Liquid-liquid extraction of phenol from simulated sebacic acid wastewater. *Journal of Scientific and Industrial Research*, 68(9), pp.823-828.

Reis, T.A., de, M.F., Agarwal, S., Ferreira, L.M., Ismael, Machado, R.M. and Jorge, M.R. Carvalho, 2011. Removal of phenols from aqueous solutions by emulsion liquid membranes. *Journal of Hazardous Materials*, 192(3), pp.986-994. [DOI]

Rodríguez-Llorente, D., Cañada-Barcala, A., Muñoz, C., Pascual-Muñoz, G., Navarro, P., Santiago, R., Águeda, V.I., Álvarez-Torrellas, S., García, J. and Larriba, M., 2020. Separation of phenols from aqueous streams using terpenoids and hydrophobic eutectic solvents. *Separation and Purification Technology*, 251, p.117379. [DOI]

Sabatino, P., Szczygiel, A., Sinnaeve, D., Hakimhashemi, M., Saveyn, H., Martins, J.C. and Van der Meeren, P., 2010. NMR study of the influence of pH on phenol sorption in cationic CTAB micellar solutions. *Colloids and Surfaces A: Physicochemical and Engineering Aspects*, 370(1), pp.42-48. [DOI]

Sadhu, K., Mukherjee, A., Shukla, S.K., Adhikari, K. and Dutta, S., 2014. Adsorptive removal of phenol from coke-oven wastewater using Gondwana shale, India: experiment, modeling and optimization. *Desalination and Water Treatment*, 52(34), pp.6492-6504. [DOI]

Sas, O.G., Castro, M., Domínguez, Á. and González, B., 2019. Removing phenolic pollutants using deep eutectic solvents. *Separation and Purification Technology*, 227, p.115703. [DOI]

Sas, O.G., Sánchez, P.B., González, B. and Domínguez, A., 2020. Removal of phenolic pollutants from wastewater streams using ionic liquids. *Separation and Purification Technology*, 236, p.116310. [DOI]

Shahhosseini, S., Seyedi Sani, S.M. and Kaeed, Z., 2024. Characterization and optimization of ultrasound assisted oxidative desulfurization of a model fuel using a novel magnetic deep eutectic solvent. *International Journal of Sustainable Energy*, 43(1), pp.1-19. [DOI]

Shammala, F.A., 1999. Effect of surfactant loading on the extraction properties of C-18 bonded silica used for solid-phase extraction of phenols. *Analytical Letters*, 32(15), pp.3083-3110. [DOI]

Shettigar, R.R., Misra, N.M. and Patel, K., 2018. Cationic surfactant (CTAB) a multipurpose additive in polymer-based drilling fluids. *Journal of Petroleum Exploration and Production Technology*, 8(2), pp.597-606. [DOI]

Skoronski, E., Fernandes, M., Malaret, F.J. and Hallett, J.P., 2020. Use of phosphonium ionic liquids for highly efficient extraction of phenolic compounds from water. *Separation and Purification Technology*, 248, p.117069. [DOI]

Smith, E.L., Abbott, A.P. and Ryder, K.S., 2014. Deep eutectic solvents (DESs) and their applications. *Chemical Reviews*, 114(21), pp.11060-11082. [DOI]

Su, G., Yang, C. and Zhu, J.J., 2015. Fabrication of gold nanorods with tunable longitudinal surface plasmon resonance peaks by reductive dopamine. *Langmuir*, 31(2), pp.817-823. [DOI]

Tan, C.K., Ng, Y.-S., Pang, Y.L. and Hayyan, A., 2025. Removal of phenol from water using fenchol-menthol hydrophobic deep eutectic solvent. *E3S Web of Conferences*, 603, pp.1-7. [DOI]

Triolo, A., Fabrizio Lo Celso, Brehm, M., Valerio Di Lisio and Russina, O., 2021. Liquid structure of a choline chloride-water natural deep eutectic solvent: A molecular dynamics characterization. *Journal of Molecular Liquids*, 331, p.115750. [DOI]

Villegas, L.G.C., Mashhadi, N., Chen, M., Mukherjee, D., Taylor, K.E. and Biswas, N., 2016. A short review of techniques for phenol removal from wastewater. *Current Pollution Reports*, 2(3), pp.157-167. [DOI]

Wang, S., Shi, D., Yang, R., Xu, Y., Guo, H. and Yang, X., 2015. Solvent extraction of phenol from aqueous solution with benzyl 2-ethylhexyl sulfoxide as a novel extractant. *Canadian Journal of Chemical Engineering*, 93(10), pp.1787-1792. [DOI]

Wazeer, I., Hizaddin, H.F., Wen, N.X., El Blidi, L., Hashim, M.A. and Hadj-Kali, M.K., 2023. Extraction of phenol as pollutant from aqueous effluents using hydrophobic deep eutectic solvents. *Water (Switzerland)*, 15(24). [DOI]

Yang, C., Qian, Y., Zhang, L. and Feng, J., 2006. Solvent extraction process development and on-site trial-plant for phenol removal from industrial coal-gasification wastewater. *Chemical Engineering Journal*, *117*(2), pp.179-185.

Yu, F., Ji, D. and Ji, J., 2012. Removal of aromatic compounds from wastewater by biodiesel. *Proceedings of the 2012 International Conference on Computer Distributed Control and Intelligent Environmental Monitoring*, pp.528-531. [DOI]

Nature Environment and Pollution Technology
An International Quarterly Scientific Journal

p-ISSN: 0972-6268
(Print copies up to 2016)
e-ISSN: 2395-3454

Vol. 25 | No. 3 | Article ID D1890 | 2026

Original Research Paper

https://doi.org/10.46488/NEPT.2026.v25i03.D1890

Open Access Journal

Tourist Behavior in Reducing Plastic Waste at Viet Nam's Coastal Destinations

Nguyen Thuy Van[1,2], Luu The Anh[2], Tran Thu Phuong[3], Truong Sy Vinh[1] and Nguyen Dang Thuy Trang[3]†

[1]Viet Nam Institute of Culture, Arts, Sports and Tourism (VICAST), Hanoi, Viet Nam
[2]Central Institute for Natural Resources and Environmental Studies (CRES), Viet Nam National University, Hanoi, Viet Nam
[3]Hanoi Open University, Hanoi, Viet Nam
†Corresponding author: Nguyen Dang Thuy Trang; ndttrang@hou.edu.vn

Abbreviation: Nat. Env. & Poll. Technol.
Website: www.neptjournal.com

Received: 12-11-2025
Revised: 21-01-2026
Accepted: 30-01-2026

Key Words:

COM-B model
Tourist behavior
Plastic waste (PW)
Viet Nam's coastal destinations

Citation for the Paper:

Nguyen, T.V., Luu, T.A., Tran, T.P., Truong, S.V. and Nguyen, D.T.T., 2026. Tourist behavior in reducing plastic waste at Viet Nam's coastal destinations. *Nature Environment and Pollution Technology*, 25(3), D1890. https://doi.org/10.46488/NEPT.2026.v25i03.D1890

Note: From 2025, the journal has adopted the use of Article IDs in citations instead of traditional consecutive page numbers. Each article is now given individual page ranges starting from page 1.

Copyright: © 2026 by the authors
Licensee: Technoscience Publications
This article is an open access article distributed under the terms and conditions of the Creative Commons Attribution (CC BY) license (https://creativecommons.org/licenses/by/4.0/).

ABSTRACT

Plastic waste generated by tourism activities increasingly burdens the environment of coastal destinations in Viet Nam. Understanding tourists' behavior regarding plastic waste reduction is crucial for developing effective interventions at the destination level. This study employs the COM-B framework to analyze how Capability, Opportunity, and Motivation influence tourists' plastic waste reduction behaviors at selected Viet Namese coastal sites. Data were gathered through a structured survey of 895 tourists and analyzed using descriptive statistics, reliability tests, correlation analysis, and multiple linear regression. Results show that Motivation has the most significant impact on waste reduction behavior, followed by Capability, with Opportunity exerting a lesser effect. The model accounts for a substantial portion of behavioral variation (R^2 = 0.743), indicating strong links between the COM-B components and self-reported behaviors. These findings enhance empirical understanding of the COM-B framework in coastal tourism settings and offer practical insights for policymakers and destination managers aiming to encourage plastic waste reduction among tourists.

1. INTRODUCTION

Plastic waste (PW) has emerged as a major global environmental challenge, particularly affecting coastal and marine tourism destinations. The United Nations Environment Program (UNEP 2021) reports that roughly 11 million tons of plastic enter the ocean each year, a number that could double by 2040 without effective interventions. Items such as water bottles, cups, bags, knives, spoons, and forks made of single-use plastic constitute a significant portion of PW (Kong et al. 2023, Maione 2021, Bauske & von Münchhausen 2019). These items also contribute to visual pollution, pose threats to marine ecosystems, and have adverse effects on the tourism industry (OECD 2024, Jang et al. 2015, McIlgorm et al. 2011).

In Southeast Asia, annual plastic waste generation reaches approximately 31 million tons (2023), with over 60% stemming from single-use plastic packaging and products (OECD 2025). The tourism sector has been identified as a key contributor, especially during peak seasons, when PW at coastal sites can comprise up to 40% of total solid waste (Truong et al. 2023, Kong et al. 2023, Hu et al. 2024, Pandey et al. 2022).

Viet Nam ranks among the five Southeast Asian countries with the highest per capita plastic waste generation, approximately 25 kg per person annually, a figure projected to rise to 79 kg per person by 2050 (OECD 2025). The country's roadmap to restrict and ban single-use plastic products is outlined in legal documents such as the Law on Environmental Protection (2020), Decree No. 08/2022/ND-CP (2022), and Decision No. 1746/QD-TTg of the Prime Minister (2019). Starting January 1, 2026, non-degradable plastic bags and single-use plastics will be

prohibited in supermarkets and shopping malls. For hotels and tourist areas, this ban will take effect after 2030. Key priorities also include source reduction of plastic waste, promoting sustainable tourism standards, and shifting tourists' consumption behaviors. However, effective policy implementation requires in-depth research into tourists' plastic waste reduction behaviors within specific contexts.

Previous studies on pro-environmental behavior often utilize frameworks such as the Theory of Planned Behavior (TPB) (Ajzen 1991) and the Value-Belief-Norm (VBN) framework (Stern 2000), which mainly focus on attitudes, norms, and behavioral intentions. Although insightful, these frameworks tend to overlook the influence of contextual and structural factors that facilitate or hinder behavior. To overcome these limitations, the COM-B model (Michie et al. 2011) conceptualizes behavior as the outcome of interactions among three elements: Capability, Opportunity, and Motivation. This comprehensive approach offers clearer guidance for designing behavioral interventions. Due to its strengths, the COM-B model has been increasingly employed in research on environmental behavior and sustainable development (Queiroga et al. 2025, Gainforth et al. 2016, Salehi et al. 2025).

However, within the tourism sector, the application of the COM-B model remains relatively limited, particularly in research concerning plastic waste reduction behavior at coastal destinations. Existing literature indicates that COM-B has mainly been utilized in specific tourism intervention contexts, such as managing visitor flows through technological solutions or encouraging the adoption of innovations in tourism experiences (Wells et al. 2022). While these studies illustrate the potential of COM-B to facilitate the design and assessment of behavioral interventions, they also reveal a narrow and context-specific scope. Additionally, most research on tourists' pro-environmental behavior continues to focus on isolated behavioral components or particular tourist segments, rather than providing an integrated analysis of the mechanisms behind behavioral formation (Prawira et al. 2024). Tourism studies suggest that sustainable behavior is often explored through attitudes, intentions, or social norms, while the interactive relationship between individual capability and destination context has not yet been fully clarified (Dolničar & Grün 2008, Dolničar & Leisch 2008). Furthermore, empirical evidence from developing countries and emerging tourism destinations remains scarce.

These gaps emphasize the need for context-sensitive research that adopts comprehensive behavioral frameworks to better understand tourists' plastic waste reduction behaviors. Consequently, this study investigates tourists' plastic waste reduction behavior at three representative coastal destinations in Viet Nam: Ha Long (Quang Ninh), Sam Son (Thanh Hoa), and Cu Lao Cham–Hoi An (Da Nang). By analyzing how the components of COM-B relate



(Source: Department of Survey, Mapping and Geographic Information of Vietnam – Ministry of Agriculture and Environment, 2025)

Fig. 1: Location of study areas.

to plastic waste reduction across diverse tourist groups, this study refines the boundaries of behavioral theory. This approach broadens the focus from solely psychological drivers to a more holistic view of how external constraints and enabling factors shape sustainable practices in emerging economies.

2. MATERIALS AND METHODS

2.1. Research Location

The study was conducted at three prominent coastal destinations in Viet Nam, each attracting millions of tourists annually. Sam Son exemplifies mass tourism, mainly drawing domestic visitors from the medium- and low-spending segments. Ha Long, with its UNESCO World Natural Heritage Site, appeals to both international and domestic tourists across medium- and high-spending groups. Cu Lao Cham-Hoi An, featuring Hoi An Ancient Town as a UNESCO World Cultural Heritage Site and the Cu Lao Cham-Hoi An Biosphere Reserve, serves as a higher-end destination that attracts international tourists with substantial purchasing power. The locations of the study areas are shown in Fig. 1.

These destinations employ various practices for managing poor waste (PW). While Cu Lao Cham - Hoi An is regarded as having relatively effective management, Ha Long and Sam Son continue to face significant environmental challenges, especially concerning solid waste and PW. The survey was carried out in coastal areas, bays, and islands, emphasizing popular tourism spots in order to gather diverse data that accurately represent tourists' behaviors across different tourism settings. This approach helps ensure the survey sample's representativeness and increases the reliability and applicability of the research findings.

2.2. Research Design

This study utilizes a quantitative research approach to explore the impact of the three components of the COM-B model on tourists' behaviors related to plastic waste (PW) reduction. According to the COM-B framework, a behavior manifests when individuals possess sufficient capability, favorable opportunities, and adequate motivation to act (Michie et al. 2011, Darnton et al. 2013). The COM-B (Capability–Opportunity–Motivation–Behavior) model, developed by Michie and colleagues (Michie et al. 2011), is among the most extensively employed theoretical models for designing effective behavioral interventions. It elucidates behavior through three fundamental components.

The first component, Capability, pertains to tourists' knowledge, understanding, and skills concerning plastic waste reduction. This includes awareness of the environmental harm caused by PW, the ability to differentiate recyclable, reusable, and single-use plastics, familiarity with relevant PW reduction regulations, and the skills necessary to use environmentally friendly alternatives. A deficit in capability serves as a significant barrier to adopting PW reduction behaviors (White et al. 2019).

The second component, Opportunity, encompasses both physical and social factors that facilitate behavior. Physical opportunities involve the availability of supporting infrastructure, such as waste-sorting stations, recycling collection points, hotels that eliminate single-use plastics, restaurants offering paper or bamboo straws instead of plastic, and free water stations for refilling reusable bottles. Social opportunities include positive influences from family, travel companions, and the tourism community, local cultural norms and sustainable consumption practices, communication campaigns advocating plastic reduction, and government policies like plastic bag restrictions and waste separation regulations. Collectively, these elements create an environment conducive to adopting and maintaining PW reduction behaviors (Michie et al. 2011).

The third element is Motivation, comprising reflective and automatic aspects. Reflective motivation involves personal responsibility, beliefs, values, goals, and deliberate choices. For instance, tourists might opt to minimize plastic usage because they believe their actions help protect the environment or boost their self-image as responsible travelers. Automatic motivation encompasses emotions, habits, and behavioral routines. For example, individuals who habitually carry reusable water bottles are more inclined to continue this practice while traveling (Michie et al. 2011). Emotions also shape behavior: feelings of pride and satisfaction can reinforce environmentally friendly actions, while guilt or discomfort triggered by witnessing improper plastic waste disposal may motivate behavioral change. Applying the COM-B model to the design and assessment of tourists' plastic waste reduction behavior offers a systematic approach for identifying barriers, recognizing enabling factors, and creating effective interventions. The research team developed a structured questionnaire based on the COM-B framework, drawing upon prior studies on sustainable consumption behavior (Michie et al. 2011, Schultz 2014). The questionnaire included five sections: (i) demographic and trip-related information, (ii) capability, (iii) opportunity, (iv) motivation, and (v) plastic waste reduction behavior. The components of the COM-B model and behavioral outcomes were assessed using a five-point Likert scale, a common measurement tool in social, psychological, and behavioral research (Likert 1932).

- Demographic and trip-related information was collected using nine items covering age, gender, nationality, education, occupation, type of tour organisation, number of visits to Ha Long Bay, length of stay, and type of accommodation.
- Capability was measured as a latent construct using five observed indicators (C1–C5): C1—understanding the harmful effects of PW on the environment and human health, C2—distinguishing between recyclable, reusable, and single-use plastic products, C3—knowing alternatives to single-use plastic products (e.g., paper or bamboo straws and cloth bags), C4—having the skills to use environmentally friendly products, and C5—knowing regulations related to plastic waste reduction.
- Opportunity was measured as a latent construct using six observed indicators (O1–O6), representing physical and social opportunities. Physical opportunities included the availability of waste collection and sorting bins (O1), food and beverage outlets that do not use single-use plastics (O2), and hotels that avoid single-use plastics (O3). Social opportunities included local cultural norms and habits regarding plastic use (O4), communication activities promoting plastic reduction (O5), and the availability of information guiding tourists on plastic waste reduction (O6).
- Motivation was measured using six observed indicators (M1–M6), representing reflective and automatic motivation. Reflective motivation included believing in one's responsibility to protect the environment and reduce plastic use (M1), believing that individual actions can create positive environmental change (M2), willingness to change personal habits to reduce plastic use and adopt green consumption practices (M3), concern about whether destinations are environmentally friendly (M4), and willingness to pay more for environmentally friendly products (M5). Automatic motivation was represented by emotional responses, specifically feeling uncomfortable when witnessing plastic waste that is not properly sorted, collected separately, or is indiscriminately discarded (M6).
- Plastic waste reduction behavior was measured as a latent construct using six observed indicators (B1–B6) representing the frequency of tourists' self-reported behaviors. These included bringing personal care items while travelling (B1), using cloth or woven bags instead of plastic bags (B2), refusing plastic straws, spoons, cups, bowls, and chopsticks (B3), encouraging family members and the community to reduce plastic use by raising awareness of its harmful effects (B4), consuming food and beverages on-site instead of ordering takeaway (B5), and properly sorting and disposing of plastic waste (B6). Although these behaviors vary in terms of effort and context, they were included to capture a broad range of self-reported plastic waste reduction practices. The composite behavior score therefore reflects an overall tendency towards plastic waste reduction rather than the intensity of any individual behavior.

Because Viet Nam's coastal destinations attract large numbers of international visitors, particularly tourists from China, the questionnaire was translated into both English and Chinese to facilitate data collection. Before the main survey, the questionnaire was pilot-tested with 30 tourists in the Ha Long area to improve wording, ensure clarity, and refine the questionnaire based on participants' feedback.

2.3. Subjects, Time, Location, and Data Collection Process

The research involved tourists aged 15 or older who stayed at least one day. The sample size was determined based on established principles of sociological and behavioral research. In linear regression analysis, the minimum sample size required is typically 5-10 times the number of observed variables. In this study, the scale included 22 observed variables (comprising 5 Capability, 5 Opportunity, 6 Motivation, and 6 Behavior variables), thus necessitating a minimum sample size of approximately 110 to 220 participants. The survey sample consisted of both domestic and international visitors, selected through convenience sampling, a common method in behavioral research within the field.

A total of 895 valid questionnaires were collected (321 in Ha Long, 320 in Sam Son, and 254 in Cu Lao Cham - Hoi An), fulfilling statistical requirements and enhancing reliability and generalizability. The survey was conducted during Viet Nam's peak tourist months from May to July 2025 to accurately capture tourist behavior at the destinations. Data collection involved face-to-face interviews using printed questionnaires, conducted by the three authors of this study. Participants were informed of the study's purpose and granted the right to decline participation. Each interview lasted approximately 10 min, and the collected data were entered into SPSS software, where it was cross-checked for accuracy.

2.4. Data Analysis

Data was processed using SPSS 28.0 statistical software. The analysis procedures included the following steps:

i. Descriptive statistics to present sample characteristics and common behavioral trends,

ii. Reliability testing of the measurement scales using Cronbach's Alpha coefficient, with an acceptance threshold of ≥ 0.70,

iii. Pearson correlation analysis to examine associations between the COM-B components and plastic waste reduction behavior,

iv. Multiple linear regression analysis was employed to assess the impact of Capability, Opportunity, and Motivation on behavior. This approach was chosen for its straightforward interpretability of predictor weights, which is crucial for evidence-based policy decisions at the destination level. Although structural equation modeling is useful for examining complex latent pathways, multiple regression remains a robust and appropriate method for identifying behavioral correlates within the scope of this study.

2.5. Research Ethics

The research adheres to the principles of sociological ethics, ensuring that tourists voluntarily consented to participate. All data was kept confidential and anonymous, and the

Table 1: General information of tourists to Viet Nam's coastal destinations.

Demographic information and general travel information		Percentage [%]
Age	15-18	4,5%
	18-30	21,6%
	31-45	28,6%
	46-60	29,8%
	Over 60	15,5%
Gender	Male	51,5%
	Female	48,5%
Tourist type	Domestic	22,9%
	International	77,1%
Education	High school	14,3%
	College	51,8%
	University	25,1%
	Postgraduate	8.7%
Occupation	Student	8.4%
	Civil servant	18.7%
	Worker, farmer	18.0%
	Freelancer	11.6%
	Businessman	26.4%
	Retiree	15,1%
	Other	1,9%
Number of visits to Ha Long Bay	The 1st time	43,7%
	The 2nd time	39,6%
	The 3rd time	11,2%
	Over 3 times	5,6%
Trip Organization	Self-organized package	52,6%
	Tour package	47,4%
Accommodation	Cruise ship/ hotel/resort 5*	4,6%
	Cruise ship/ hotel/resort 4*	30,4%
	Cruise ship/ hotel 2-3*	42,5%
	Hostel	10,6%
	Appartment	2,8%
	Homestay	9,2%
Average spending/Day	Under 1 million VNĐ	31,8%
	1-2 million VNĐ	40,8%
	2-3 million VNĐ	19,4%
	Over 3 million VNĐ	7,7%

(Source: Synthesized by authors from research results)

information was exclusively used for academic and scientific research purposes.

3. RESULTS

3.1. Survey Sample Characteristics

The study surveyed 895 tourists at 03 representative research sites; the characteristics of the survey sample are described in Table 1.

Regarding gender and age demographics, male tourists constitute 51.5% while females represent 48.5%, with working-age individuals making up the majority. The largest age group is 46-60 years old at 29.8%, followed by 31-45 years at 28.6%, and 18-30 years at 21.6%. Tourists over 60 years old and those aged 15-18 constitute smaller segments, at 15.5% and 4.5%, respectively. Domestically, tourists make up 77.1%, whereas international visitors account for 22.9% (see Fig. 2).

Regarding educational background and occupation, tourists with a college degree constitute the largest group at 51.8%, followed by university graduates at 25.2%, high school diploma holders at 14.3%, and postgraduates at 8.7%. The occupational profile reveals that the majority work in private enterprises (26.4%), with civil servants/public employees making up 18.7%, workers and farmers 18.0%, retirees 15.1%, freelancers 11.6%, and students 8.4%. This highlights the diverse backgrounds of visitors to the study sites (Fig. 2).

In terms of organization and accommodation, 52.6% of tourists arrange their trips independently, while 47.4% book tours through travel agencies. The most popular hotel category is 2-3 star hotels, chosen by 42.5%, followed by 4-star hotels and resorts at 35%. Daily expenditure mostly ranges from VND 1-2 million (40.8%), less than VND 1 million (31.8%), and VND 2-3 million (19.4%) (Fig. 2).

3.2. PW-Reducing Behavior of Tourists at Viet Nam's Coastal Destinations

Behaviors are assessed through six specific actions (B1 to

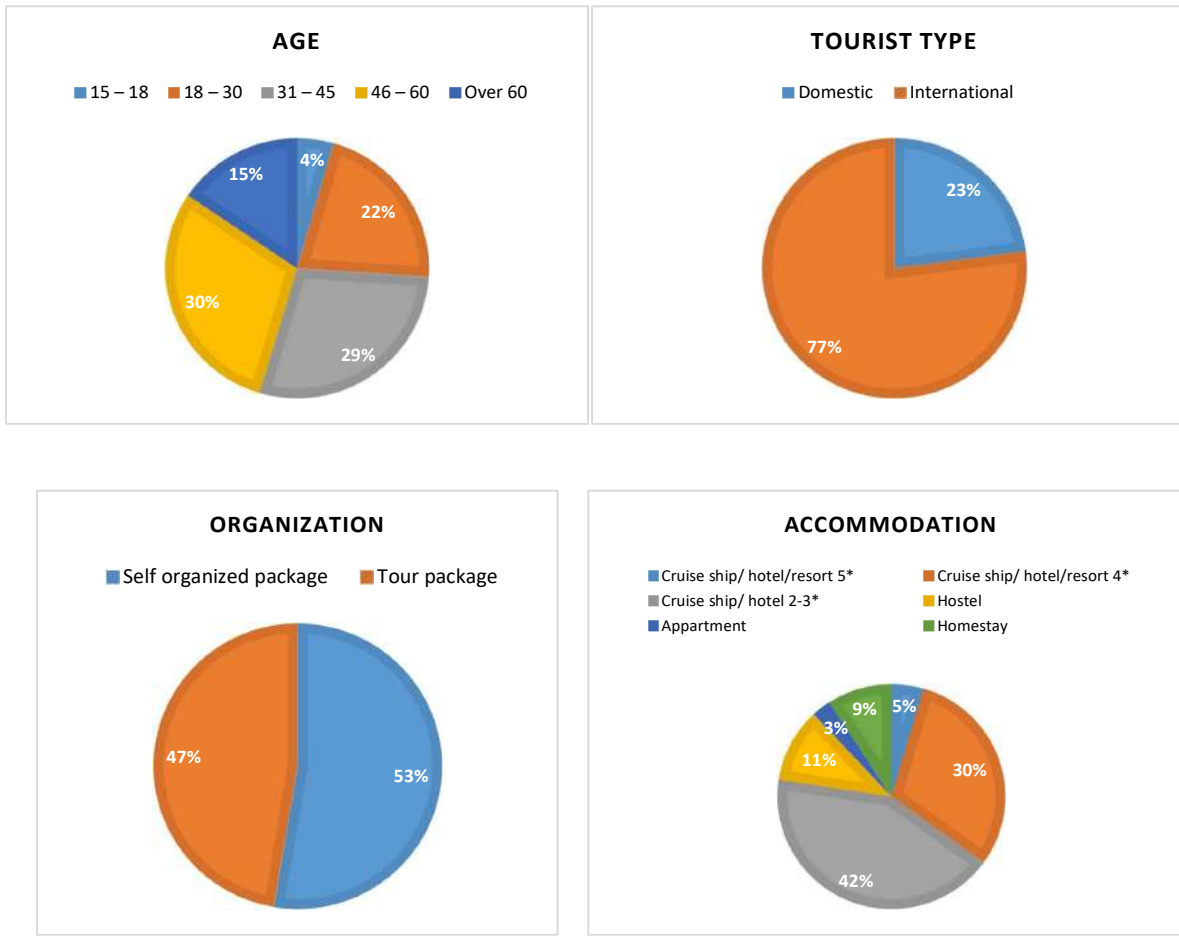


Fig. 2: General information of tourists to Viet Nam's coastal destinations.

B6) outlined in Table 2. The average scores from tourists indicate that the most frequently performed behaviors include bringing personal care items when traveling, using cloth, sedge, or similar bags instead of plastic bags, educating family and community about the harms of plastic waste, and taking measures to reduce plastic consumption, with mean values of 3.80 and 3.79. The overall behavior index, calculated as the average of the six actions, stood at 3.78 on a 5-point scale, reflecting a fairly positive behavioral trend.

Further analysis reveals that 63.9% of tourists often prefer using cloth or sedge bags over plastic ones, 63.6% bring personal care items when traveling, 63.5% sort and dispose of plastic waste properly, 63% educate their family and community about plastic waste harms and reduction strategies, and 61.8% refuse to use plastic straws, spoons, cups, bowls, and chopsticks, instead opting to eat or drink at restaurants rather than take away. These findings indicate a relatively positive trend toward reducing plastic waste among tourists, especially in Cu Lao Cham - Hoi An, where over 90% of visitors report regularly practicing these behaviors.

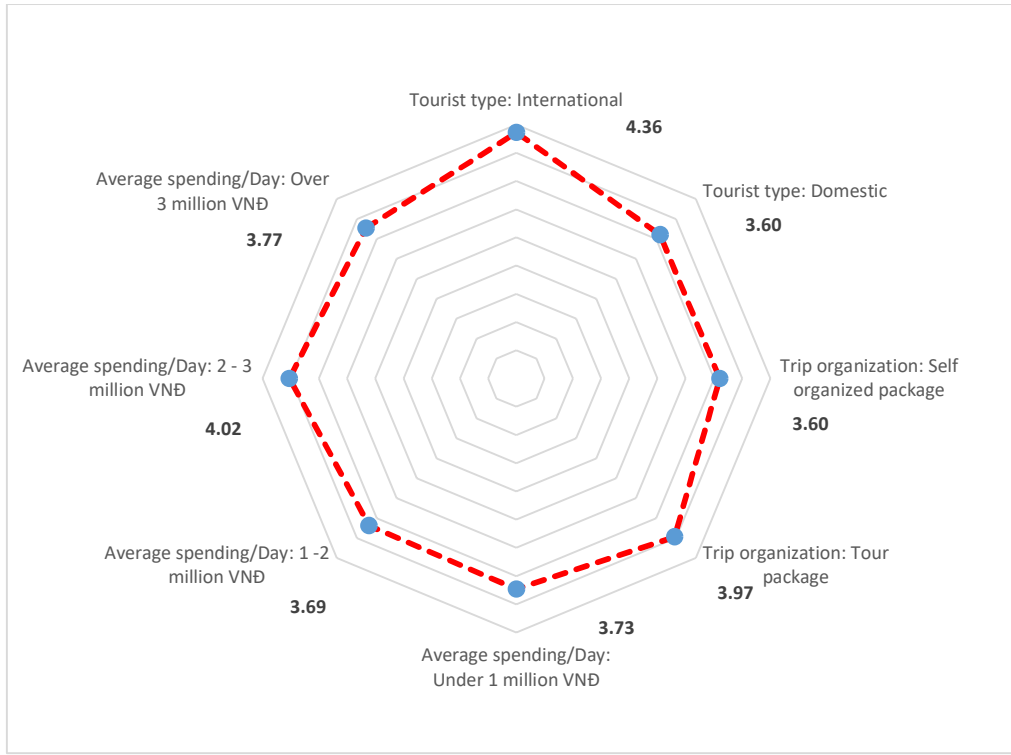
Using one-way ANOVA analysis and a t-test to examine the differences in PW reduction behavior of tourists according to different categories shows that:

- *By tourist type (domestic and international tourists):* A statistically significant difference was found in plastic waste reduction behaviors between domestic and international tourists, as demonstrated by the independent samples T-test (both the F-test and T-test p-values were below 0.05). International tourists exhibited a higher overall behavioral score (mean = 4.36) compared to domestic tourists (mean = 3.60) (see Fig. 3). The gap was especially notable for actions requiring greater personal initiative, such as bringing

Table 2: PW reduction behavior of tourists at Viet Nam's coastal destinations.

		B1	B2	B3	B4	B5	B6	Mean
		Mean	Mean	Mean	Mean	Mean	Mean	
Tourist type	International	4,36	4,37	4,32	4,39	4,35	4,38	4,36
	Domestic	3,63	3,61	3,61	3,62	3,57	3,57	3,60
	Total	3,80	3,79	3,77	3,79	3,75	3,75	3,78
Age	15-18	4,15	4,03	3,88	3,88	3,88	3,95	3,96
	18-30	3,81	3,74	3,87	3,80	3,79	3,77	3,80
	31-45	3,80	3,82	3,73	3,82	3,68	3,73	3,76
	46-60	3,70	3,73	3,72	3,73	3,72	3,75	3,72
	Over 60	3,85	3,83	3,78	3,84	3,84	3,73	3,81
Education	High school	3,80	3,84	3,89	3,80	3,82	3,84	3,83
	College	3,79	3,83	3,75	3,83	3,75	3,79	3,79
	University	3,83	3,70	3,76	3,73	3,72	3,67	3,74
	Postgraduate	3,74	3,64	3,74	3,71	3,73	3,67	3,71
Occupation	Student	3,84	3,87	3,84	3,69	3,75	3,73	3,79
	Civil servant	3,83	3,89	3,75	3,81	3,77	3,71	3,79
	Worker/ farmer	3,67	3,76	3,72	3,81	3,72	3,67	3,73
	Freelancer	3,71	3,78	3,69	3,78	3,62	3,83	3,73
	Businessman	3,82	3,77	3,82	3,78	3,73	3,82	3,79
	Retiree	3,91	3,70	3,77	3,81	3,87	3,76	3,80
	Others	3,76	3,59	3,94	4,12	3,94	3,71	3,84
Trip organization	Self-organized package	3,59	3,63	3,61	3,63	3,56	3,58	3,60
	Tour package	4,02	3,96	3,95	3,97	3,96	3,95	3,97
Average spending/Day	Under 1 million VNĐ	3,75	3,79	3,73	3,73	3,65	3,74	3,73
	1 -2 million VNĐ	3,72	3,68	3,70	3,70	3,68	3,66	3,69
	2 - 3 million VNĐ	4,06	3,98	3,97	4,06	4,06	3,98	4,02
	Over 3 million VNĐ	3,70	3,86	3,78	3,87	3,71	3,72	3,77

(Source: Synthesized by authors from research results)



(Source: Synthesized by authors from research results)

Fig. 3: Differences in PW reduction behavior among tourist groups visiting Viet Nam's coastal destinations.

personal care items, refusing single-use plastics like straws, spoons, cups, bowls, and chopsticks, and opting to dine on-site rather than take away.

- *By trip organisation:* The average behavioral score for tourists who booked organized tours was 3.97, exceeding the 3.60 score of independent travelers (Fig. 3). Statistical analysis using the independent samples T-test confirmed that this difference was significant, with both the F-test and T-test p-values below 0.05.
- *By age, education and occupation*: The ANOVA One-Way analysis indicates no significant difference in PW reduction behavior among tourist groups of different ages, education levels, or occupations (F test significance > 0.05).
- *By Average spending/Day:* One-way ANOVA results reveal a statistically significant variation in plastic waste reduction behavior among tourist groups with different daily spending levels (Sig. = 0.000). Notably, tourists spending an average of 2-3 million VND per day exhibited the highest mean behavioral score of 4.02 (Fig. 3).

3.3. Factors Affecting Tourists' PW Reduction Behavior at Viet Nam's Coastal Destinations

3.3.1. Testing the Reliability of the Scales

To evaluate the reliability of the scales within the COM-B model, the study employs Cronbach's Alpha coefficient. The findings indicate that all scales demonstrate acceptable reliability (see Table 3). Specifically, the Capability scale yields a Cronbach's Alpha of 0.791 across 5 observed variables, the Opportunity scale shows an Alpha of 0.773 with 5 variables, the Motivation scale achieves an Alpha of 0.826 with 6 variables, and the Behavior scale registers an Alpha of 0.820 with 6 variables.

With Cronbach's Alpha values greater than 0.7, the scales are reliable and are used in correlation and multiple linear regression analyses.

Table 3: Testing the reliability of scales in the COM-B model.

	Cronbach's Alpha	N of Items
Capability	0.791	5
Opportunity	0,773	6
Motivation	0.826	6
Behavior	0.820	6

(Source: Synthesized by authors from research results)

Table 4: Pearson correlation analysis in the COM-B model.

Correlations					
		B Average	C Average	O Average	M Average
B Average	Pearson Correlation	1	.780**	.774**	.820**
	Sig. (2-tailed)		.000	.000	.000
	N	895	895	895	895
C Average	Pearson Correlation	.780**	1	.744**	.775**
	Sig. (2-tailed)	.000		.000	.000
	N	895	895	895	895
O Average	Pearson Correlation	.774**	.744**	1	.786**
	Sig. (2-tailed)	.000	.000		.000
	N	895	895	895	895
M Average	Pearson Correlation	.820**	.775**	.786**	1
	Sig. (2-tailed)	.000	.000	.000	
	N	895	895	895	895

**. Correlation is significant at the 0.01 level (2-tailed).

(Source: Synthesized by authors from research results)

3.3.2. Correlation analysis (Pearson)

The study uses Pearson correlation analysis to examine the relationship between variables in the COM-B model and actual behavior (Table 4).

The results from Pearson correlation and linear regression analyses within the COM-B model reveal that Capability, Opportunity, and Motivation are all significantly associated with and influence plastic waste reduction behavior (Behavior) at the 1% significance level ($p < 0.01$). Specifically, Pearson correlation indicates a strong positive relationship between Capability and behavior ($r = 0.780$), suggesting that individuals with enhanced knowledge and skills tend to engage more actively in reducing plastic waste. Motivation also exhibits a very strong positive correlation ($r = 0.820$), emphasizing that personal motivation is a vital factor driving environmentally conscious actions. Additionally, Opportunity shows a significant positive correlation ($r = 0.774$), implying that supportive environmental conditions and external assistance can promote proactive behaviors among tourists.

Among the independent components of the COM-B model, correlations are also positive and statistically significant ($p < 0.01$), with coefficients ranging from 0.744 to 0.786. This pattern suggests that individuals with higher capability are more motivated and more likely to utilize external opportunities. All absolute correlation coefficients are below 0.85, indicating an absence of severe multicollinearity among the variables. Nonetheless, to ensure

Table 5: Multiple linear regression analysis in the COM-B model.

Model Summary[b]					
Model	R	R Square	Adjusted R Square	Std. Error of the Estimate	Durbin-Watson
1	.455[a]	.743	.743	.31135	1.938
a. Predictors: (Constant), M average, C average, O average					
b. Dependent Variable: B average					

Coefficients[a]							
Model	Unstandardized Coefficients		Standardized Coefficients	T	Sig.	Collinearity Statistics	
	B	Std. Error	Beta			Tolerance	VIF
(Constant)	-.009	.077		-.120	.904		
Mean C	.292	.030	.281	9.846	.000	.352	2.838
Mean O	.248	.030	.240	8.188	.000	.336	2.976
Mean M	.441	.033	.413	13.349	.000	.301	3.322

a. Dependent Variable: B Average

(Source: Synthesized by authors from research results)

the robustness of the model, further analysis using linear regression and Variance Inflation Factor (VIF) tests should be performed to confirm the extent of multicollinearity.

3.3.3. Multiple Linear Regression Analysis

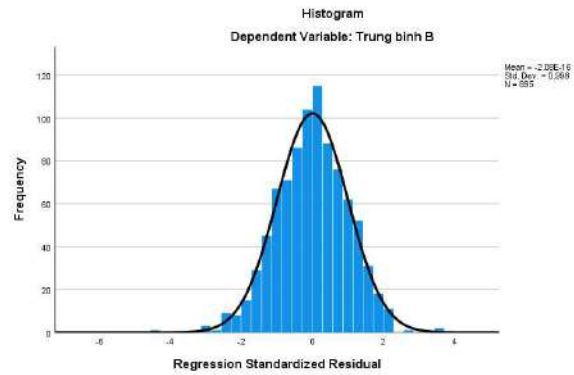
The study conducted multiple linear regression analysis to determine the influence level of each factor (Capability, Opportunity, Motivation) on PW reduction behavior (Table 5).

The multiple linear regression analysis reveals that the COM-B model accounts for approximately 74.3% of the variation in behavior ($R^2 = 0.743$). This represents a substantial explanatory power in behavioral research, highlighting a strong link among Capability, Opportunity, and Motivation in shaping tourists' behavior. The standard error of the estimate is 0.311, which is lower than the typical standard deviation of 0.6 to 0.8 on a 5-point Likert scale, indicating a good fit of the model to the data. Additionally, the Durbin-Watson statistic of 1.938 falls within the acceptable range of 1.5 to 2.5, suggesting there is no significant autocorrelation in the residuals and that the linear regression assumptions are satisfied (Field 2009).

The analysis of individual predictors shows that all independent variables exert positive and statistically significant effects on behavior ($p < 0.001$). Motivation demonstrates the strongest influence ($\beta = 0.413$), underscoring the vital role of internal drive, beliefs, and personal commitment in shaping behaviors. Capability ($\beta = 0.281$) ranks second, indicating that knowledge, skills, and the ability to perform behaviors significantly impact outcomes. Opportunity ($\beta = 0.240$) also positively affects behavior, highlighting the importance of environmental factors, policy support, and available resources in fostering engagement.

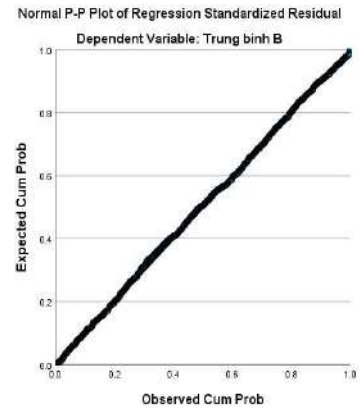
The multicollinearity test reveals all VIF values are below 5 (ranging from 2.838 to 3.322), indicating no multicollinearity issues among the predictors.

Residual analysis shows that the mean residual is near zero and its standard deviation aligns with the model's



(Source: Synthesized by authors from research results)

Fig. 4. Histogram of regression standardized residual.



(Source: Synthesized by authors from research results)

Fig. 5. Normal PP plot of Regression standardized residual.

standard error, confirming that the normality assumption is satisfied (Fig. 4 & Fig. 5).

Based on the analysis, the standardized regression equation is as follows:

$$B = 0.281C + 0.240O + 0.413M$$

Keys of Interpretation:

B: Tourist behavior score relating to PW reduction (B Mean)

C: Capability

M: Motivation

O: Opportunity

The regression equation reveals that all three elements of the COM-B model—Capability, Opportunity, and Motivation—positively influence tourist behavior. Motivation has the most significant impact ($\beta = 0.413$), indicating that internal psychological factors are crucial in encouraging and sustaining sustainable practices. Additionally, Capability and Opportunity also exert meaningful positive effects, suggesting that improving knowledge, skills, and environmental support can further foster reductions in plastic waste.

4. DISCUSSION

4.1. Overview of Results and Comparison with Theory

The results confirm that the COM-B model offers a strong theoretical foundation for understanding tourists' behaviors in reducing plastic waste. Additionally, the relative importance of its components highlights a notable dependence on individual willpower within Viet Nam's coastal regions. While Motivation, Capability, and Opportunity all have significant positive effects, the predominant influence of Motivation ($\beta = 0.413$) indicates that current behavioral shifts are mainly fueled by internal psychological commitment rather than external systemic factors.

This finding offers a deeper insight into the intention–behavior gap, a subject extensively explored within environmental psychology. In contrast to traditional models such as the Theory of Planned Behavior (TPB) and the Value-Belief-Norm (VBN) model (Ajzen 1991, Stern 2000), which mainly highlight internal motivations as the primary drivers of behavior, the COM-B model (Michie et al. 2011) presents a more detailed understanding of how these internal factors interact with external situational barriers. The observation that Motivation emerges as the most significant predictor indicates the presence of a compensatory mechanism. Considering the insufficient and poorly coordinated infrastructure at Viet Nam's coastal destinations, tourists are compelled to rely on higher levels of personal commitment to surmount physical barriers to plastic waste reduction. This suggests that pro-environmental behavior in this setting remains at a stage where substantial individual effort is required, with tourists actively seeking ways to minimize plastic waste rather than benefiting from supportive environmental conditions (Bandura 1986, Hines et al. 1987).

Furthermore, the relatively limited influence of Opportunity ($\beta = 0.240$) highlights a structural bottleneck. Although Opportunity remains an important prerequisite for behavior, its lower coefficient compared to Motivation and Capability indicates an imbalance between tourists' willingness to reduce plastic waste and the level of destination support. In many tourism contexts in developed countries, Opportunity often acts as the main driver due to well-established waste management systems and infrastructure (Allison et al. 2022, Prawira et al. 2024). However, at the studied locations, the modest impact of Opportunity suggests that the existing infrastructure alone is insufficient to foster behavioral change without strong personal motivation.

The strong influence of Capability ($\beta = 0.281$) underscores the importance of environmental literacy and practical knowledge as key drivers of behavioral change. This aligns with social cognitive theory, which posits that individuals' belief in their abilities (self-efficacy) is a critical prerequisite for action (Tabernero & Hernández 2011). Additionally, the findings suggest that in resource-limited settings, tourists need specific practical knowledge to turn their intentions into actual behaviors and to effectively navigate the lack of supportive infrastructure at the destination (Frick et al. 2004, Hines et al. 1987).

Overall, this study shows that enhancing tourists' plastic waste reduction behaviors at Viet Nam's coastal destinations mainly relies on increasing individual motivation and capability, while also boosting external environmental support. Therefore, interventions aimed at behavioral change should take a comprehensive approach that improves tourists' environmental knowledge and skills, encourages intrinsic motivation, and enhances infrastructure and policy mechanisms to sustain behavioral change.

4.2. Analysis by Tourist Group

The results demonstrate that tourists' plastic waste reduction behavior varies significantly across different tourist segments, reflecting differences in Capability, Opportunity, and Motivation, as conceptualized in the COM-B model.

International tourists reported a significantly higher mean behavioral score (4.36) than domestic tourists (3.60),

indicating higher levels of Capability and Motivation. This finding suggests that international visitors often possess stronger environmental knowledge and more deeply internalized pro-environmental norms, enabling them to maintain plastic waste reduction practices even when destination infrastructure is limited. These findings are consistent with previous studies showing that travelers from developed countries tend to participate more actively in pro-environmental behaviors during their trips (Barr et al. 2010, UNEP 2018, Shamsub & Lebel 2012, Dolničar & Grün 2008). Rather than suggesting that international tourists exhibit uniform behavioral patterns, these results highlight the interaction between individual characteristics and contextual factors in shaping plastic waste reduction behavior.

The difference between tourists traveling on organized tours (3.97) and independent travelers (3.60) seems primarily linked to the Opportunity component. Organized tours tend to offer a more supportive physical and social environment, where information, guidance, and plastic-free alternatives are systematically integrated into the travel experience and easily accessible. These arrangements help bridge the gap between environmental awareness, behavioral intentions, and actual practices—a common challenge for independent travelers who lack external support. This aligns with prior research indicating that organized tour settings can foster environmentally responsible behaviors by providing clear guidance and structured opportunities for action (Shamsub & Lebel 2012). However, this interpretation should be approached with caution, as the current study did not directly investigate the mechanisms driving this relationship.

Furthermore, tourists' spending levels demonstrate the interaction between Motivation and Opportunity. The highest average behavioral score (4.02) was recorded among tourists spending between 2 and 3 million VND, indicating a synergistic effect between their willingness to pay for sustainable options (Motivation) and increased access to tourism services that feature environmentally friendly facilities and infrastructure (Opportunity). This aligns with previous research showing that higher-spending tourists typically have better access to sustainable alternatives and are more willing to pay a premium for eco-friendly products and services (Dolničar & Leisch 2008, Han et al. 2010).

Conversely, the lack of statistically significant differences across age groups, education levels, and occupations indicates that situational factors and specific motivational elements more influence plastic waste reduction behaviors at the study destinations than by overarching demographic characteristics. Overall, these results highlight the necessity of implementing targeted behavioral interventions. Strategies aimed at decreasing plastic waste should prioritize enhancing the Capability and Motivation of domestic tourists while also improving Opportunity—through upgraded infrastructure, better information dissemination, and a more supportive social environment—especially for independent travelers and lower-spending tourist groups.

4.3. Recommendations for Destination Policy and Management

From the above results, the study gives some important implications for policy development and sustainable tourism destination management in coastal tourist areas in Viet Nam:

Prioritize capability building for groups with limited behavioral skills: Enhancing the ability to perform green behaviors should be regarded as a fundamental step, particularly for domestic and independent tourists. Strategies include encouraging communication, environmental education, installing visual guidance tools at destinations such as information boards, QR codes, videos, and digital apps, as well as training tour guides, service staff, and local communities to act as ambassadors for eco-friendly practices. These initiatives not only boost knowledge and skills but also simplify behavior adoption and integrate it into the tourism experience.

Improve the effectiveness of behavioral support conditions: The results demonstrate that the opportunity factor positively influences behavior, indicating that when tourists are provided with adequate resources and supportive policies, plastic reduction efforts are significantly enhanced. Therefore, it is essential to invest in developing and harmonizing infrastructure systems that promote environmental protection, such as PW-classified trash bins, public water stations, plastic-free accommodations and restaurants, and clear waste management guidelines. Additionally, establishing criteria for "plastic-free destinations" and implementing mechanisms to incentivize businesses to adopt green standards will help create a sustainable ecosystem that encourages eco-friendly behaviors.

Promote motivation through encouraging personal values: Motivation is the key to sustaining and promoting eco-friendly behaviors. Destination management should prioritize appealing to personal values and social responsibility, such as through campaigns that highlight tourists' roles in conserving natural and cultural heritage. Recognizing positive actions with "Green Tourist" badges, providing discounts for guests who bring their own water bottles, and eliminating disposable plastics in hotels can reinforce good habits. Additionally, hosting photo contests and encouraging plastic-free check-ins can significantly boost mental motivation.

Promote the role of travel agencies and tour guides: The behavioral differences between tour buyers and independent travelers indicate that travel agencies can play a key role in managing these variations. Therefore, it is essential to encourage and empower travel agencies and tour guides to incorporate PW-reduction rules into their itineraries. This can be achieved by offering alternative items, providing waste sorting guidance, and motivating tourists throughout the journey.

Develop a tourism product tailored to the tourist segment and spending level: Tourists with an average daily spend of 2-3 million VND show more positive behavior, highlighting the connection between financial Capability, awareness, and willingness to pay for sustainable experiences. The destination management board should design diverse green tourism products tailored to spending levels, while strengthening flexible pricing policies, certifying environmentally friendly products, and communicating responsible consumption.

Develop a multi-channel communication strategy: craft messages and channels that align with the characteristics of tourist markets. For international tourists, messages about global heritage and environmental protection can be maintained. For domestic tourists, education programs need to be developed to raise awareness and encourage early practice, perhaps through schools or community campaigns.

4.4. Research Limitations and Development Directions

Despite the theoretical and practical significance of the findings, this study has several limitations that should be acknowledged.

Although the sample size of 895 participants was relatively large, which enhanced the robustness of the statistical analysis, the use of convenience sampling may limit the generalizability of the findings to the broader population of tourists visiting coastal destinations in Viet Nam. Future research should consider employing probability-based or stratified sampling methods to improve sample representativeness and strengthen external validity. Additionally, the study relied primarily on self-reported questionnaires, which are susceptible to social desirability bias, especially when measuring environmentally responsible behaviors. Incorporating qualitative approaches such as in-depth interviews, direct behavioral observations, or field experiments could provide a more accurate understanding of tourists' plastic waste reduction behaviors. The COM-B model showed strong explanatory power with an R^2 of 0.743, indicating significant associations among Capability, Opportunity, Motivation, and plastic waste reduction behavior.

However, pro-environmental behavior is inherently complex and influenced by other factors like social norms, emotions, environmental beliefs, and reference group influences. Since all variables were measured using a single self-report questionnaire, the potential for common method bias and social desirability bias cannot be entirely excluded, especially given the environmental focus and face-to-face data collection. Furthermore, multiple linear regression does not explicitly account for measurement error or examine complex causal relationships among latent constructs.

Future research could expand the analytical framework by combining the COM-B model with additional behavioral theories such as the Theory of Planned Behavior (Ajzen 1991), the Norm Activation Model (Schwartz 1977), and the Value-Belief-Norm framework (Stern 2000). Using advanced techniques like structural equation modeling would also enable a more comprehensive understanding of these relationships. Lastly, plastic waste reduction behavior was operationalized as a composite index based on various self-reported behaviors that differ in effort and social context. As a result, the analysis reflects overall behavioral tendencies rather than specific behavioral dimensions. Future studies might employ exploratory or confirmatory factor analysis to explore the underlying structure of tourists' plastic waste reduction behaviors.

5. CONCLUSIONS

Amidst the growing urgency for sustainable tourism development and marine environmental preservation, this study offers valuable empirical evidence on tourists' plastic waste reduction behavior at Viet Nam's coastal tourism sites. Based on a survey of 895 tourists and utilizing the COM-B model, multiple linear regression results revealed that the model accounted for 74.3% of the variation in plastic waste reduction behavior ($R^2 = 0.743$), demonstrating the strong applicability of the COM-B framework in tourism behavioral research.

Among the three components influencing behavior, Motivation exerts the most significant effect ($\beta = 0.413$), followed by Capability ($\beta = 0.281$) and Opportunity ($\beta = 0.240$). All factors have positive and statistically significant impacts ($p < 0.001$). This suggests that tourists' plastic waste reduction actions are influenced not only by their knowledge and skills but also by psychological factors and the support infrastructure available at destinations.

Furthermore, ANOVA results indicated notable differences among tourist groups. International visitors exhibited more environmentally responsible behavior than domestic travelers, and tour buyers scored higher than independent tourists. Additionally, tourists with a

daily expenditure of 2-3 million VND demonstrated more positive behaviors. These findings highlight the importance of capability, motivation, access conditions, and financial capacity in fostering sustainable tourism behaviors.

Based on these insights, the study affirms that the COM-B model is both a valuable theoretical tool and an effective aid for destination management policy formulation. By targeting the three pillars—Capability, Opportunity, and Motivation—strategies can be developed to influence behavior, such as enhancing tourists' knowledge and skills through education and information campaigns, improving infrastructure and services that support eco-friendly actions, motivating individuals via social recognition and incentives, and leveraging travel businesses to guide sustainable practices.

Nevertheless, the study has limitations, including the use of a convenience sample, reliance on self-reported data, and focus on limited destinations. Future research should broaden the scope, integrate both qualitative and quantitative methods, and apply more advanced theoretical models to obtain a deeper understanding of tourists' plastic reduction behaviors.

In conclusion, this study advances understanding of tourists' plastic waste reduction behavior. The evidence-based recommendations derived from the COM-B model provide a solid foundation for policymakers and destination managers to implement effective interventions aimed at promoting sustainable tourism and marine conservation in Viet Nam. Additionally, the research opens avenues for further investigations involving different populations, locations, and methodological approaches to build a more comprehensive behavioral framework.

6. ACKNOWLEDGEMENTS

The authors sincerely thank the Ha Long Bay Management Department, People's Committee of Sam Son City, and the Hoi An City People's Committee for their support during the implementation process.

7. REFERENCES

Ajzen, I., 1991. The theory of planned behaviour. *Organisational Behaviour and Human Decision Processes*, 50(2), pp.179-211. [DOI]

Allison, A.L., Purkiss, D., Lorencatto, F., Miodownik, M. and Michie, S., 2022. Improving compostable plastic disposal: An application of the Behaviour Change Wheel intervention development method. *Frontiers in Sustainability*, 3, p.968152. [DOI]

Bandura, A., 1986. Social foundations of thought and action. *Englewood Cliffs, NJ*, *1986*(23-28), p.2.

Barr, S., Shaw, G., Coles, T. and Prillwitz, J., 2010. 'A holiday is a holiday': Practicing sustainability, home and away. *Journal of Transport Geography*, 18(3), pp.474-481. [DOI]

Bauske, B., Von Münchhausen, M., Plitharas, A. and Tsoukalas, K., 2019. Stop the Flood of Plastic–Effective Measures to Avoid Single-Use Plastics and Packaging in Hotels.

Darnton, A. and Horne, J., 2013. *Influencing Behaviours: Moving Beyond the Individual: A User Guide to the ISM Tool*. Scottish Government, pp.1-68.

Dolničar, S. and Grün, B., 2008. Environmentally friendly behavior: Can heterogeneity among individuals and contexts/environments be harvested for improved sustainable management? *Environment and Behavior*, 41(5), pp.693-714. [DOI]

Dolničar, S. and Leisch, F., 2008. Selective marketing for environmentally sustainable tourism. *Tourism Management*, 29(4), pp.672-680. [DOI]

Field, A., 2009. *Discovering Statistics Using SPSS* (3rd ed.). SAGE Publications, pp.856-1.

Frick, J., Kaiser, F.G. and Wilson, M., 2004. Environmental knowledge and conservation behavior: Exploring prevalence and structure in a representative sample. *Personality and Individual Differences*, 37(8), pp.1597-1613. [DOI]

Gainforth, H., Sheals, K., Atkins, L., Jackson, R. and Michie, S., 2016. Developing interventions to change recycling behaviors: A case study of applying behavioral science. *Applied Environmental Education & Communication*, 15(4), pp.325-339. [DOI]

Han, H., Hsu, L.-T. and Sheu, C., 2010. Application of the theory of planned behavior to green hotel choice: Testing the effect of environmental friendly activities. *Tourism Management*, 31(3), pp.325-334. [DOI]

Hines, J.M., Hungerford, H.R. and Tomera, A.N., 1987. Analysis and synthesis of research on responsible environmental behavior: A meta-analysis. *The Journal of Environmental Education*, 18(2), pp.1-8. [DOI]

Hu, H., Zhang, Y., Wang, C. and Yu, P., 2024. Factors influencing tourists' intention and behavior toward tourism waste classification: A case study of the West Lake Scenic Spot in Hangzhou, China. *Sustainability*, 16(3), p.1231. [DOI]

Jang, Y.C., Lee, J., Hong, S., Choi, H., Shim, W. and Hong, S., 2015. Estimating the global inflow and stock of plastic marine debris using material flow analysis: A preliminary approach. *Journal of the Korean Society for Marine Environment & Energy*, 18(4), pp.263-273. [DOI]

Kong, T., Li, X., Pan, K., Zhang, W. and Li, R., 2023. Changes in sources and composition of beach waste in coastal cities around the Bohai Sea of China during the tourist peak and offpeak seasons. *International Journal of Environmental Research and Public Health*, 20(3), p.2573. [DOI]

Likert, R., 1932. A technique for the measurement of attitudes. *Archives of Psychology*, 22(140), pp.5-55.

Maione, C., 2021. Quantifying plastics waste accumulations on coastal tourism sites in Zanzibar, Tanzania. *Marine Pollution Bulletin*, 168, p.112418. [DOI]

McIlgorm, A., Campbell, H.F. and Rule, M.J., 2011. The economic cost and control of marine debris damage in the AsiaPacific region. *Ocean & Coastal Management*, 54(9), pp.643-651. [DOI]

Michie, S., van Stralen, M.M. and West, R., 2011. The behaviour change wheel: A new method for characterising and designing behaviour change interventions. *Implementation Science*, 6, p.42. [DOI]

OECD, 2024. *Policy Scenarios for Eliminating Plastic Pollution by 2040*. OECD Publishing, Paris, pp.1-112.

OECD, 2025. *Regional Plastics Outlook for Southeast and East Asia*. OECD Publishing, Paris, pp.1-198.

Pandey, P., Manisha, Chopra, P. and Adlakaha, A., 2022. Investigating the role of tourists and impact of knowledge, behaviour, and attitude towards plastic waste generation. *Circular Economy and Sustainability*, 3, pp.1-15. [DOI]

Prawira, M.F.A., Ramadhani, I., Audita, V.N., Andrianto, R. and Prawira, A.B.A., 2024. Proenvironmental behaviour in tourism: A systematic literature review and future research directions. *Journal of Tourism Sustainability*, 4(2), pp.101-114. [DOI]

Queiroga, A.T.D., Elf, P., Correia, S.É.N. and Oliveira, V.M.D., 2025. Circular business models and sustainable behavior: An integrated framework based on the COMB model. *Revista de Gestão Social e Ambiental - RGSA*, 19(1), p.e011075. [DOI]

Salehi, M., Lin, M.S., Filimonau, V., Kim, B. and Lin, P.M.C., 2025. How to advance sustainable healthy food consumption in tourism: A systematic literature review. *Journal of Sustainable Tourism*, 33(10), pp.2173-2201. [DOI]

Schultz, P.W., 2014. Strategies for promoting PR environmental behavior. *European Psychologist*, 19(2), pp.107-117. [DOI]

Schwartz, S.H., 1977. Normative influences on altruism. In: L. Berkowitz (ed.) *Advances in Experimental Social Psychology*, Vol. 10. Academic Press, pp.221-279. [DOI]

Shamsub, H. and Lebel, L., 2012. Identifying tourists with sustainable behavior: A study of international tourists to Thailand. *Journal of Environmental Management and Tourism*, 3(1), pp.1-12. [DOI]

Stern, P.C., 2000. New environmental theories: Toward a coherent theory of environmentally significant behavior. *Journal of Social Issues*, 56(3), pp.407-424. [DOI]

Tabernero, C. and Hernández, B., 2011. Self-efficacy and intrinsic motivation guiding environmental behavior. *Environment and Behavior*, 43(5), pp.658-675.

Truong, S.V., Nguyen, T.T., Nguyen, T.V. and Sunil Herat, 2023. Reduction of plastic waste in tourism activities in Sam Son City, Viet Nam. *International Journal of Environmental Science and Development*, 14(6), pp.355-363.

UNEP, 2018. *Single-Use Plastics: A Roadmap for Sustainability*. United Nations Environment Program, pp.1-104.

UNEP, 2021. *From Pollution to Solution: A Global Assessment of Marine Litter and Plastic Pollution – Synthesis*. United Nations Environment Program, pp.1-56.

Wells, M., Salas, K. de and Hardy, A., 2022. Using the Behavior Change Wheel to design an app to change tourist behavior and increase dispersal into regional areas. In: J. Pesonen and J. Neidhardt (eds.) *Information and Communication Technologies in Tourism 2022*. Springer, pp.395-405. [DOI]

White, K., Habib, R. and Hardisty, D.J., 2019. How to SHIFT consumer behaviors to be more sustainable: A literature review and guiding framework. *Journal of Marketing*, 83(3), pp.22-49. [DOI]

Nature Environment and Pollution Technology
An International Quarterly Scientific Journal

p-ISSN: 0972-6268
(Print copies up to 2016)
e-ISSN: 2395-3454

Vol. 25 | No. 3 | Article ID D1888 | 2026

Original Research Paper

https://doi.org/10.46488/NEPT.2026.v25i03.D1888

Open Access Journal

Evaluation and Origin Studies of Heavy Metals in Soils Around Traditional Mining Regions in the Northwest Guizhou District

Tiantian Cai[1,2], Die Xu[3], Ji Wang[1,2]†, Shuai Zhang[1,2], Xiongfei Cai[1,2] and Huifang Zhao[1,2]

[1]School of Geography and Environmental Science, Guizhou Normal University, Guiyang 550025, People's Republic of China

[2]The State Key Laboratory, Incubation Base for Karst Mountain Ecology Environment of Guizhou Province, Guiyang 550001, People's Republic of China

[3]College of Education Science, Qiannan Normal University for Nationalities, Duyun 558000, People's Republic of China

†Corresponding authors: Ji Wang; wangji@gznu.edu.cn

Abbreviation: Nat. Env. & Poll. Technol.
Website: www.neptjournal.com

Received: 30-10-2025
Revised: 10-01-2026
Accepted: 13-01-2026

Key Words:

Lead-zinc mining area
Heavy metal pollution
Spatial distribution
PMF source analysis

Citation for the Paper:

Cai, T., Xu, D., Wang, J., Zhang, S., Cai, X. and Zhao, H., 2026. Evaluation and origin studies of heavy metals in soils around traditional mining regions in the northwest Guizhou district. *Nature Environment and Pollution Technology*, 25(3), D1888. https://doi.org/10.46488/NEPT.2026.v25i03.D1888

Note: From 2025, the journal has adopted the use of Article IDs in citations instead of traditional consecutive page numbers. Each article is now given individual page ranges starting from page 1.

Copyright: © 2026 by the authors
Licensee: Technoscience Publications
This article is an open access article distributed under the terms and conditions of the Creative Commons Attribution (CC BY) license (https://creativecommons.org/licenses/by/4.0/).

ABSTRACT

Heavy metal contamination in soil has emerged as a critical environmental issue. However, research specifically addressing the distribution, pollution levels, and source analysis of heavy metals in lead-zinc mining areas remains limited. To assess the extent of soil heavy metal pollution around a lead-zinc mine in northwest Guizhou and to perform a quantitative source analysis, this study collected 56 surface soil samples and 14 samples from two different depths. The concentrations and chemical forms of Cd, Pb, Cr, Cu, Ni, and Zn were measured. Pollution levels were evaluated using the geoaccumulation index (Igeo) and the secondary-to-primary phase ratio (RSP). Sources were identified through correlation analysis, principal component analysis, and positive matrix factorization (PMF). The results demonstrated that: (1) The average concentrations of Pb, Zn, Cd, Cr, Cu, and Ni were all below Guizhou's soil background levels. While Cd and Pb reached maximum values close to background levels, their coefficients of variation were 66.56%, 413.84%, 123.04%, 195.69%, 319.98%, and 373.41%, respectively, indicating high variability and significant anthropogenic influence. Elevated levels of Cd, Cu, Pb, and Zn are closely aligned with mining locations. (2) The Igeo evaluations indicated that most areas were unpolluted; however, the RSP method revealed that 5% and 4% of sites were slightly polluted by Pb and Zn, respectively, with 4% showing slight Cd contamination, and 2% experiencing moderate to severe pollution. (3) PMF source apportionment identified five main sources: 63.7% of Cr from agriculture, 72.3% of Cd from atmospheric deposition, 59.1% of Zn and 41.9% of Ni from wastewater discharge, 52.9% of Cu, 45.4% of Ni, and 36.2% of Cr from traffic emissions, and 79.9% of Pb from mining activities. The study concluded that overall heavy metal pollution was slight, though Cd, Pb, and Zn were notably influenced by mining and associated human activities. Different sources contributed distinctly: mining primarily impacted Pb, while agriculture, atmospheric deposition, and wastewater discharge mainly affected Cr, Cd, and Zn accumulation, respectively. These findings offer a scientific basis for soil pollution prevention, control, and ecological risk management in the region.

1. INTRODUCTION

Soil, as one of the most vital natural resources for human life, serves as a fundamental material for sustainable economic and social development. Metal pollution directly affects soil quality and ecosystem stability and may also threaten human health (Kiran et al. 2022). Recently, the rapid progress of industrialization has heightened the impact of mining activities on the environment, especially around lead-zinc mine regions (Demková et al. 2017, Yang et al. 2018, Zhang et al. 2023). Southwest China, characterized by a high natural background of heavy metals, often has soil exceeding safety standards due to geological factors (Chen et al. 2024, Liu et al. 2023). As regional urbanization and industrialization advance, soils in these areas face intense human disturbance, such as agriculture, mining, and metal smelting, alongside natural weathering inputs. This region exemplifies the

complex interaction between natural processes and human activities, where high geological backgrounds, combined with endogenous inputs and exogenous pollution from human actions, contribute to soil heavy metal contamination. Challenges include unclear pollution sources, ecological risks, and the lack of comprehensive prevention and control technologies, all posing significant hurdles for safe land use, precise identification of pollution sources, and effective ecological risk management in mining districts. Consequently, assessing and identifying soil heavy metal sources in mining regions is crucial for controlling pollution and safeguarding ecological health.

Northwest Guizhou is not only a well-known zinc smelting base in China but also has abundant coal resources that provide essential raw materials for zinc production (Ali et al. 2020). Heavy metal contamination in soils surrounding lead–zinc mining areas has become increasingly severe due to a high geological background, intensive mining activities, and human disturbances (Zhou et al. 2018). Magu Town in Hezhang County, located in northwestern Guizhou Province, is a typical concentrated lead–zinc ore distribution area, rich in mineral resources and playing an important role in local economic development (Li 1994). The region has a mining history of nearly 300 years, and heavy metals released from long-term mining activities continue to cause significant pollution to surrounding soils (Zhou et al. 2020). Therefore, this study aims to systematically assess soil conditions in the area, determine the level of contamination, identify pollution sources, and quantify their contribution ratios. Although many studies have investigated soil heavy metal pollution in various mining areas of Guizhou Province (Li et al. 2024, Wang et al. 2021), most have focused on single pollution assessments and preliminary source identification.

Currently, commonly used methods such as correlation analysis, principal component analysis, and cluster analysis can be applied to preliminarily identify the number and types of pollution sources (Bi et al. 2020, Jin et al. 2019, Liang et al. 2023). However, these approaches have certain limitations. A single evaluation method often fails to systematically and comprehensively reflect the overall regional pollution status. In addition, preliminary source identification alone is insufficient to clearly quantify the specific contributions and proportions of each pollution source (Chen & Lu 2017, Hu et al. 2020, Li et al. 2023, Yu et al. 2021). Therefore, it is essential to incorporate more systematic methods to achieve a comprehensive evaluation of pollution levels and to quantitatively analyze the contribution of pollution sources. In this study, the geo-accumulation index (Igeo) and the ratio of secondary to primary phases (RSP) were combined to assess the pollution status. Igeo measures the extent of human-induced accumulation, while RSP helps distinguish natural sources from anthropogenic ones and indicates the bioavailability and migration potential of heavy metals. The integration of these two indices allows for a thorough analysis of source origins and ecological risks alongside pollution levels. For source analysis, the study employs correlation analysis, principal component analysis (PCA), and the orthogonal matrix factorization model (PMF). Correlation analysis and PCA initially identify the types and quantities of pollution sources, providing a basis for determining the number of factors in PMF. The PMF model then quantitatively estimates the contribution rates of each source, with results that have clear physical significance. This combined approach leverages both qualitative identification and quantitative analysis, making source determination more scientific and results more reliable, thereby supporting accurate control of heavy metal pollution in mining soil.

Researchers selected soil samples from near a standard lead-zinc production site in Mamu Town, Hezhang District, for this study. Surface and profile soils were analyzed to determine concentrations and chemical forms of Pb, Zn, Cd, Cr, Cu, and Ni. Pollution levels were assessed using cumulative indices and a comparative analysis of secondary versus primary phase values. The origins of the heavy metals were identified through a combination of qualitative techniques, including correlation analysis and principal components, and quantitative models such as the Positive Definitive Matrix Factorization (PDMA) and PMF. This research provides valuable insights for understanding and reducing metal contamination in soils near lead and zinc mining areas. Additionally, analyzing metal sources in soils offers a scientific basis for developing environmental management strategies that balance sustainable mining with ecological protection.

2. MATERIALS AND METHODS

2.1. Research Area

Hezhang County is situated in the tilted zone of the Wumeng Mountains, at the upper reaches of the Liuchong River—the northern source of the Wujiang River- and the Sanqiao River, the southern source of the Wujiang River, in northwestern Guizhou Province. This area is where the East Yunnan Plateau extends into the mountainous hills of Guizhou. It spans longitudes 104°10′28″ E to 105°01′23″ E and latitudes 26°46′12″ N to 27°28′18″ N. The region is rich in mineral resources, particularly lead and zinc, primarily found in Maigu Town. For this study, Magu Town (located at 104°33′09″ E, 26°58′42″ N) was chosen as the study area due to its abundance of mineral deposits, including high-quality lead and zinc ore deposits. Magu

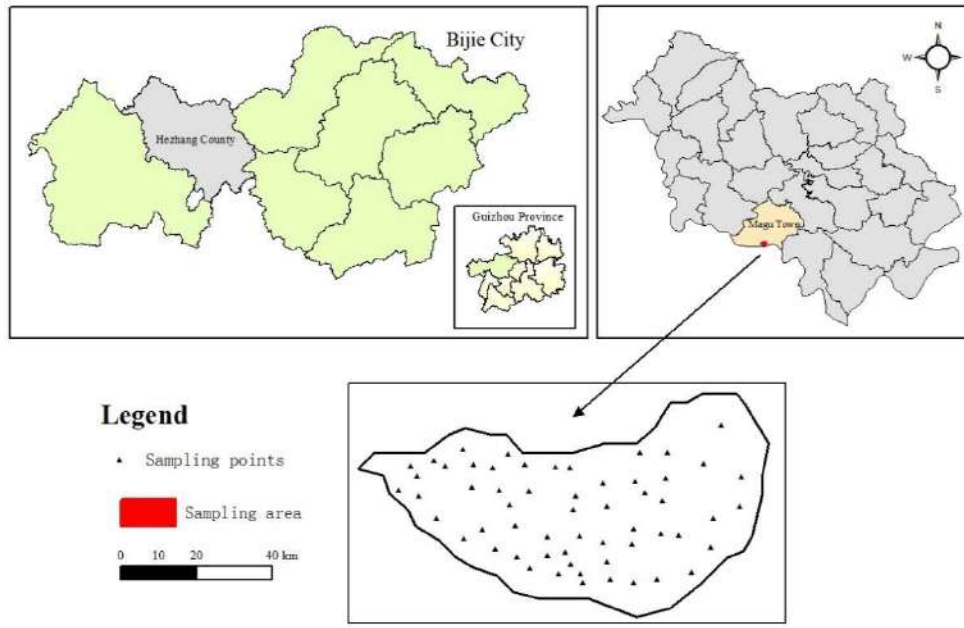


Fig. 1: Map of the study area generated using ArcGIS 10.8.2 and soil sampling points.

Town is 36 km southwest of Hezhang County, covering an area of 141.93 km², with an average elevation of 1,995 meters, a maximum of 2,588 meters, and a minimum of 1,775 meters. The region experiences an average temperature of 12°C year-round. Its soils are predominantly yellow-brown loam and brown calcareous soil, with sporadic patches of brown loam, meadow soils, and tidal soils. A location map is shown in Fig. 1.

2.2. Sample Collection and Testing

Based on the community's actual conditions, surface soil mixed samples from 20 cm were collected following the designated sampling procedures. Each sample, approximately 1 kg, was labeled and sealed in a bag. To capture variability across land use types and depths, two profiles were sampled using a uniform distribution method: Profile 1 (0–90 cm, grassland) and Profile 2 (0–60 cm, cultivated land), with samples taken at 10 cm intervals. A total of 56 topsoil specimens and 14 profile soil samples were collected. A handheld GPS device recorded the latitude and longitude of each sampling site, and a map of the sampling points was created (Fig. 1). In the laboratory, samples were seasoned, removable materials like rocks and plant debris were discarded, and the soil was crushed and sieved through 10-mesh and 200-mesh screens. The prepared samples were then sealed in labeled bags for future analysis.

This study determined the total heavy metal content in soil using an HNO_3-$HClO_4$-HCl-HF digestion method. Soil samples were processed via an improved BCR continuous extraction procedure, categorizing heavy metal forms into four fractions: acid-extractable, reducible, oxidizable, and residual, based on the extraction reagents and sequence. The extract was cooled, fixed, filtered, and analyzed with an atomic absorption spectrometer.

2.3. Evaluation Methods

2.3.1. Land Accumulation Index Method

The Index of Geoaccumulation (Igeo) is a method used to assess the pollution risk of heavy metals in sediments, proposed by Müller in 1969 (Müller 1969). Compared with other evaluation approaches, it incorporates the influence of natural geological background values as well as anthropogenic inputs on heavy metal contamination. Igeo evaluates the degree of contamination by quantifying the enrichment of metal concentrations in soil relative to geochemical background levels using the following equation.

$$I_{geo} = Log_2[C_s/(k \times C_b)] \quad \ldots(1)$$

where Cs is the content of soil heavy metal elements ($mg \cdot kg^{-1}$), Cb is the average value of soil heavy metal ($mg \cdot kg^{-1}$), and the background value of soil in Guizhou Province was utilized in this investigation; k represents a correction coefficient to the natural variation of the level of metals during diagenesis, typically assigned a value of k=1.5. The grading standards of I are illustrated in Table 1.

2.3.2. Secondary Phase to Primary Comparison Method (RSP)

The Ratio of Secondary to Primary Phases (RSP) method

Table 1: Grading of the geo-accumulation index (*I*).

Degree of contamination	Non-polluting	Light pollution	Mid-pollution	Medium-strong pollution	Strong pollution	Strong - very strong pollution	Extreme pollution
I	$I<0$	$0 \le I<1$	$1 \le I<2$	$2 \le I<3$	$3 \le I<4$	$4 \le I<5$	$I \ge 5$

Table 2: The division grade standards of the Ratio of secondary phase and primary phase (RPS) (Chen et al. 2018).

Degree of contamination	Non-polluting	Light pollution	Mid-pollution	severe pollution
RPS	RPS <100%	100% ≤ RPS <200%	200% ≤ RPS <300%	RPS >300%

is an assessment tool that indicates the activity and bioavailability of toxic metals. It also evaluates their potential to contaminate the environment and their capacity to cause pollution through their fugitive forms (Yan et al. 2016). The formula for measurement is as follows:

$$\mathrm{RSP} = \frac{F1+F2+F3}{F4} \times 100\% \quad \ldots(2)$$

where: F1, F2, and F3 are the contents of soil heavy metal acids in extractable, reducible, and oxidizable states ($mg \cdot kg^{-1}$), respectively, and F4 is the residue state ($mg \cdot kg^{-1}$). According to the size of the calculated results of RSP, the chemical form risk can be divided into 4 levels of evaluation criteria (Table 2).

2.3.3. Positive Definite Matrix Factorization Model (PMF)

The PMF model is a source apportionment method based on factor analysis, first proposed by Paatero and Tapper (Paatero & Tapper 1994). It decomposes the receptor sample matrix through a least-squares approach and iterative calculations to obtain an optimal solution (Cui et al. 2024). During the solution process, both factor loadings and factor scores are constrained to be non-negative, ensuring that the derived source profiles and source contribution estimates are physically meaningful and interpretable (Chueinta et al. 2000). The calculation formula is as follows:

$$X_{ij} = \sum_{K=1}^{p} g_{ik} f_{kj} + u_{ij} \quad \ldots(3)$$

$$Q = \sum_{i=1}^{n} \sum_{j=1}^{m} \left(\frac{X_{ij} - \sum_{k=1}^{p} g_{ik} f_{kj}}{u_{ij}} \right) \quad \ldots(4)$$

$$\mathrm{Unc} = 0.1\mathrm{C} + \mathrm{MDL}/3 \quad \ldots(5)$$

In (3), (4), and (5), Xij is the concentration matrix of the jth element of the ith sample, fkj is the concentration matrix of the ith heavy metal of the kth source, gik is the contribution of the kth source to the ith sample, and uij is the residual matrix of the jth heavy metal of the ith sample. The factor contributions and distributions were calculated from the PMF model. Q is the minimization objective function, Unc is the uncertainty of the jth heavy metal of the ith sample, and MDL is the method detection limit for the determination of heavy metal content.

2.4. Data Processing

Statistical analyses of soil heavy metal content, including correlation analysis and principal component analysis (PCA), were performed using Excel 2016 and SPSS 25. Maps illustrating sampling locations, study area layout, and spatial distribution of heavy metals were created with ArcGIS 10.8. Elemental morphology occupancy maps were generated using Origin 2017, while source apportionment was conducted with PMF 5.0.

2.5. Data Quality Control

To ensure the reliability of the test method and the accuracy of the results, systematic quality control measures were implemented. These included using blank samples, duplicate samples, and national standard materials (GBW07404, GBW07419) throughout the process, with heavy metal recovery rates maintained between 82.7% and 120.4%. Additionally, 15%-20% of samples were retested, and the relative standard deviation (RSD) of the results remained below 10%. Calibration involved establishing curves with standard solutions, achieving correlation coefficients of at least 0.999 for Cd, Cr, Cu, Ni, Pb, and Zn, with verification conducted before and after analysis. All reagents used were of pure, high-grade quality, and glassware was thoroughly cleaned after overnight immersion in 20% nitric acid. For the quality evaluation of soil element speciation analysis methods, accuracy was assessed by calculating the relative deviation (RE = [(C2 – C1)/C1] × 100%) of the sum (C2) based on the total elemental analysis value (C1), with RE required to be ≤40%. The actual analysis confirmed that the RE values for Cd, Cr, Cu, Ni, Pb, and Zn satisfied this criterion. The method's precision was evaluated through eight repeated measurements of the same sample, with RSDs below 30%, meeting DD2005-03 technical standards. Finally, main error sources—such as weighing (accuracy 0.0001 g), volume measurement, calibration, and repeatability—were analyzed to estimate uncertainty, providing a quantitative characterization of the reliable range of the results.

3. RESULTS AND DISCUSSION

3.1. Characterization of Soil Heavy Metal Pollution

Table 3: Evaluation criteria of soil variation intensity (Wang et al. 2020).

weak variation	Medium variation	strong variation	abnormally strong variation
<20%	20%~50%	50%~100%	>100%

3.1.1. Analysis of Heavy Metal Concentrations in Soil

Table 4 presents the concentrations of six metal elements in the topsoil sample from the research area. The mean values for Pb, Zn, Cd, Cr, Cu, and Ni were 4.019, 3.670, 0.085, 2.182, 1.020, and 0.392 $mg \cdot kg^{-1}$, respectively. These averages did not exceed typical levels found in the Guizhou region. However, the peak concentrations of Cd and Pb nearly reached the background levels characteristic of these soils.

The coefficients of variation for Pb, Zn, Cd, Cr, Cu, and Ni were 66.56%, 413.84%, 123.04%, 195.69%, 319.98%, and 373.41%, respectively. As shown in Table 3, soil variation intensity analysis indicates that, aside from Pb, which exhibits strong variability, the other five elements show unusually high variability. This suggests that these six elements are significantly affected by external anthropogenic activities in the study area.

Fig. 2 illustrates the vertical distribution of six heavy metal elements in soil samples. At identical depths, the profiles exhibit the following contents: Zn > Cr > Pb > Cu > Cd > Ni. Analysis of the profile reveals that the concentration trends of Cr, Cu, Cd, and Ni are consistent within the 0-60 cm depth range. In profile 1, zinc levels remain relatively stable with depth, whereas in profile 2, zinc decreases as depth increases, with a critical threshold around 30-40 cm. The lead concentration's turning point occurs at 10-20 cm in profile 1 and 20-30 cm in profile 2. Profile 1 corresponds to grassland soil, characterized by shallow surface depths, while profile 2 is from cropland soil, which undergoes long-term cultivation, fertilization, and deep tillage, leading to profile alterations. Additionally, Das et al. (2009) reported that soil heavy metal transformation capacities vary by land type, influencing heavy metal content.

3.1.2. Morphological Analysis of Soil Heavy Metals

Analyzing and calculating the recovery rate of soil heavy metal forms can effectively determine the suitability of the extraction method used for each form. The recovery rate of toxic metals in soil is calculated as the sum of the weak acid extractable soluble form (F1), reducible form (F2), oxidizable form (F3), and residual form (F4), divided by the total metal content, multiplied by 100%. The results are shown in Table 5. This table indicates that the recovery

Table 4: Statistical characteristics of metal concentration in the topsoil of the research area.

Elemental	Average value ($mg \cdot kg^{-1}$)	Standard deviation	Coefficient of variation (CV)	Variance	Skewness	Kurtosis	Maximum ($mg \cdot kg^{-1}$)	Minimum ($mg \cdot kg^{-1}$)	Soil background values in Guizhou Province ($mg \cdot kg^{-1}$)
Cd	0.085	0.069	123.04%	0.005	1.810	4.123	0.345	0.007	0.400
Cu	1.020	0.521	195.69%	0.276	1.657	3.162	2.797	0.252	34.500
Pb	4.019	6.038	66.56%	37.074	2.710	7.279	29.904	0.148	33.570
Cr	2.182	0.682	319.98%	0.473	1.056	2.783	4.664	0.722	98.980
Ni	0.392	0.105	373.41%	0.011	0.175	-0.593	0.617	0.189	39.300
Zn	3.670	0.893	413.84%	0.812	0.055	-0.652	5.400	1.907	104.210

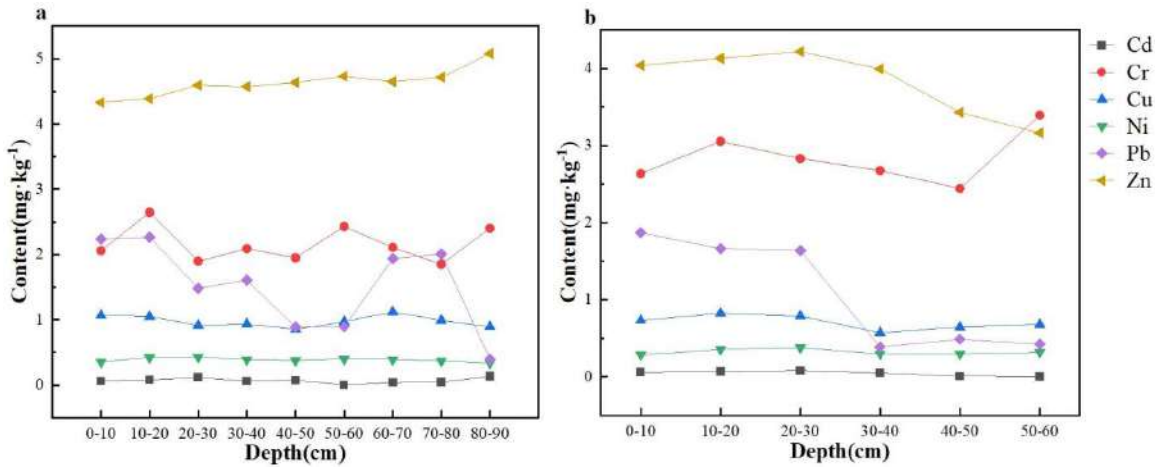


Fig. 2: Distribution map of six heavy metal elements in two profiles.

percentages for six pollutants in the research region's soil all exceed 90%, demonstrating the effectiveness of the enhanced BCR method in analyzing the chemical forms of metals in the environment. Residual form (F4) is a stable, less bioavailable form of heavy metals with limited mobility. In contrast, the weak acid extractable form (F1) is biologically active, with the highest mobility and toxicity. The reducible (F2) and oxidizable (F3) forms are potential sources that can convert into more bioavailable forms under changing environmental conditions. The chemical Forms of heavy metals in surface and profile soils within the study area are illustrated in Figs. 3 and 4. As shown, F4 is the predominant form for all six heavy

Table 5: Recovery rate of soil heavy metal forms in the study area.

Element	The sum of four forms ($mg \cdot kg^{-1}$)	Total heavy metal content ($mg \cdot kg^{-1}$)	Rate of recovery (%)
Cd	0.084	0.085	99.78
Cu	0.984	1.020	96.79
Pb	4.041	4.019	100.55
Cr	2.063	2.182	94.63
Ni	0.364	0.396	91.91
Zn	3.377	3.670	91.34

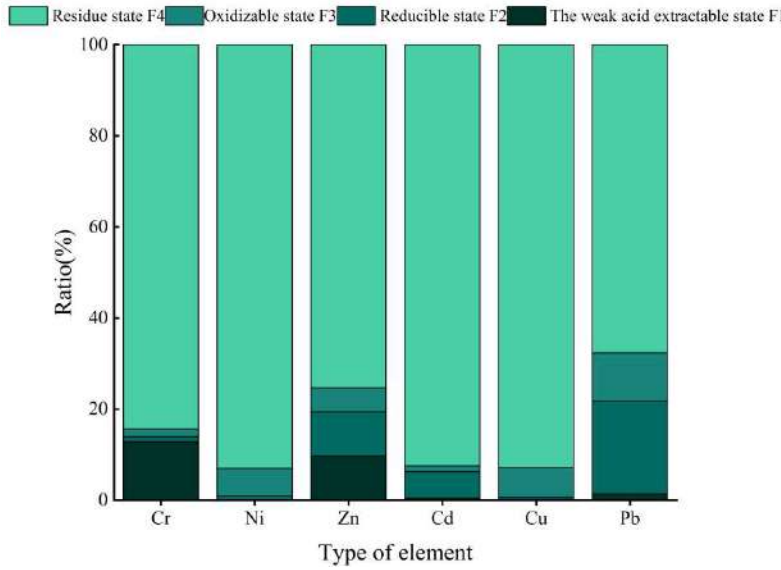


Fig. 3: The proportion of heavy metal chemical forms in surface soil in the study area.

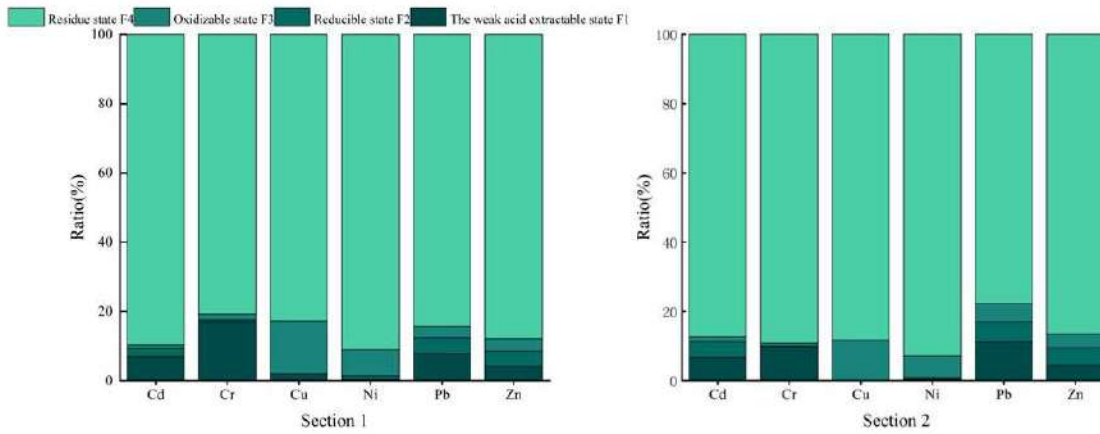


Fig. 4: Proportion map of chemical forms of heavy metals in the soil of two profiles in the study area.

metals in the soil. Elements such as Cr, Cu, Ni, Pb, and Zn each constitute over 80% of F4 in both topsoil and profiles, some exceeding 90%, signaling that the bioavailability and mobility of these metals are limited, and the ecological risk remains low. Secondary forms (F1, F2, F3) account for less than 20%, with significantly higher proportions in surface soils compared to profiles, especially for Pb, Zn, and Cr. This suggests surface layers are more affected by human activities such as agriculture and atmospheric deposition, which may increase active forms due to external inputs and changes in soil chemistry. Notably, Pb exhibits the highest proportion of secondary forms across both soil layers, with a relatively high F2 segment that could be released and toxic under reducing conditions. Cr's F1 form is the highest among the six elements, warranting attention for short-term toxicity. Zn's F3 form is comparatively high and linked to organic matter decomposition. The distribution patterns of element forms are consistent between the two profiles, with residual forms generally higher in deeper soils and minimal variation between profiles. This indicates that heavy metals in the deep soil mainly originate from geological sources, with little human interference, in stable forms, and with limited vertical migration.

3.2. Spatial Distribution Characteristics

The spatial distribution clearly highlights the high-value areas of heavy metal pollution within the study region, serving as an effective method for identifying pollution sources. Based on the content data for six heavy metal elements, this study presents a soil heavy metal distribution map using ArcGIS 10.8 (Fig. 5). As shown in Fig. 5, the high-value zones for the four elements, Cd, Cu, Pb, and Zn, are similarly arranged, primarily occupying the central and eastern parts of the area. In contrast, chromium exhibits a more dispersed distribution, while the significant concentration spots for Ni are mainly in the east, with a few in the west. Field investigations indicate that the central area consists of arable land, the eastern part is residential, and the western area was formerly a lead-zinc mining site. In the mining area, minerals are stacked through open dumping, with mining activity extending from west to east. This stacking method exposes heavy metals to surface runoff and rainfall washout, increasing soil contamination in these regions (Wu et al. 2024). The distribution of elevated levels of Cd, Cu, Pb, and Zn aligns with the Pb-Zn mining site and is significantly influenced by nearby residential farming activities. Studies have shown that the use of phosphorus, fertilizers, and organic matter can also introduce metals (Shi et al. 2010). Additionally, in the eastern part of the study area, facilities such as welding factories and coal plants are scattered around, and waste residues, water, and gases from these activities can lead to increased levels of Cr and Ni. The overlapping distribution of Cd, Cu, Pb, and Zn suggests a possible correlation among these elements, indicating a common source (Hussain et al. 2019).

In summary, the distribution and geographical distribution of the six elements (Pb, Zn, Cd, Cr, Cu, Ni) in the soils of this

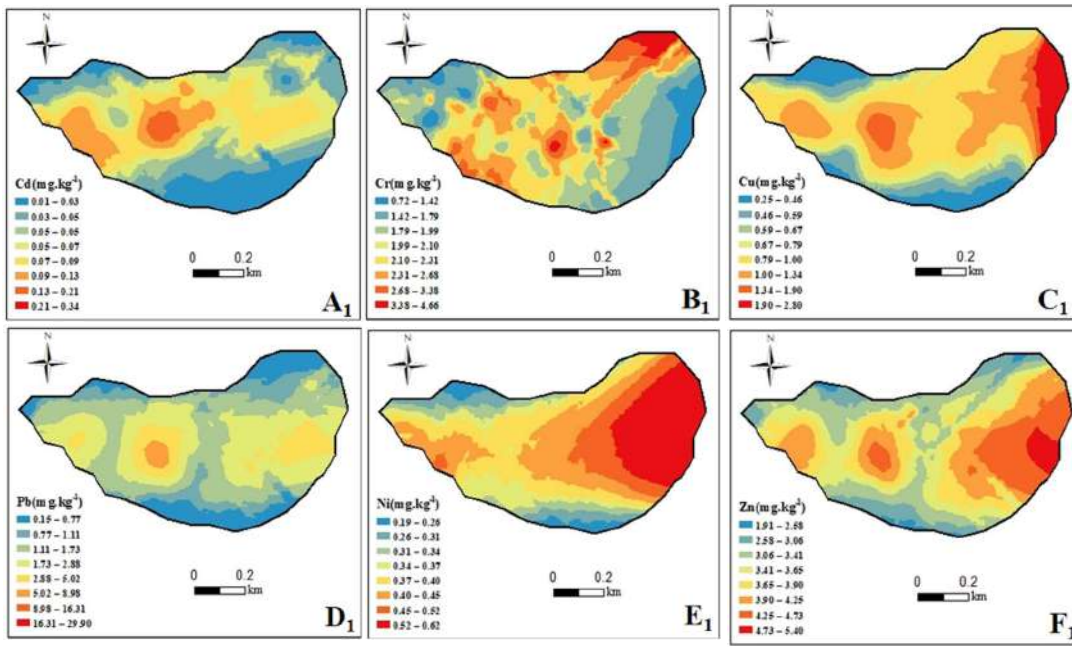


Fig. 5: Geospatial distribution of heavy metals in soil within the research area.

research area are closely linked to the waste residues from lead-zinc mining and remnants of human mining activities. However, the implications of their contamination warrant further evaluation and study.

3.3. Evaluation of Soil Heavy Metal Pollution

3.3.1. Landman Exponent Index

The Landman Exponent Index (Igeo) was used to determine the concentration of metals in the soils of the study area. The results are as follows:

From Figs. 6(a) and 6(b), the Igeo values for metal elements within the research region are all below zero, indicating a non-polluted state. However, when combined with the scatter plot, the Igeo values for Cd and Pb show greater dispersion toward the pollution threshold (0), whereas Ni deviates from this threshold. Pd and Cb exhibit the widest dispersion among all elements, followed by Cu, Cr, Ni, and Zn. This suggests that Pd and Cb are the most enriched elements in the soil, with Ni being the least, indicating it is the safest. These findings align well with the spatial distribution patterns of these elements.

3.3.2. Secondary Phase Versus Primary Comparison Method

The levels of contamination by Pb, Zn, Cd, Cr, Cu, and Ni in the research region's soils were evaluated through a comparison between the secondary and primary phases (RSP). The results of this assessment are presented below:

As shown in Fig. 7(a), only the elements Cd, Pb, and Zn have individual points exceeding the pollution threshold

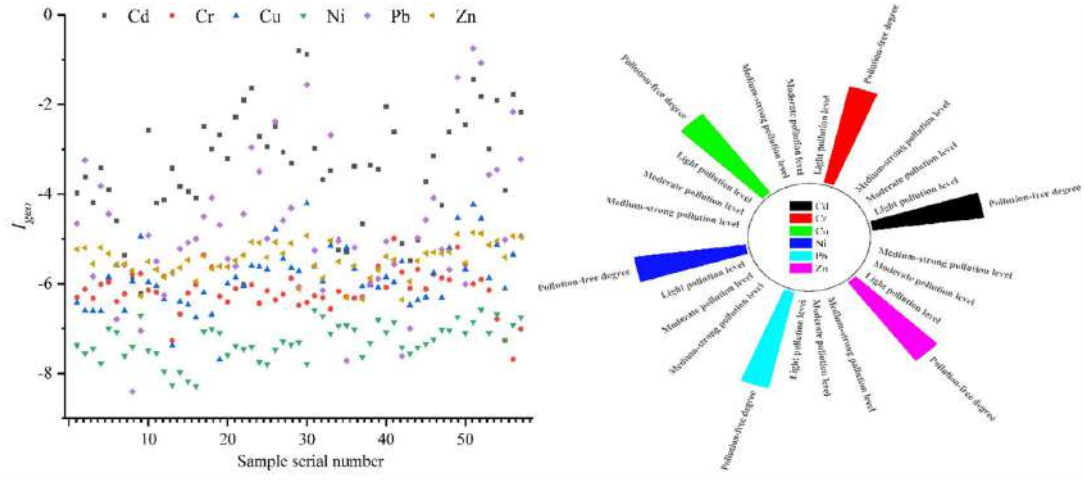


Fig. 6: Metals accumulation index in the research zone.

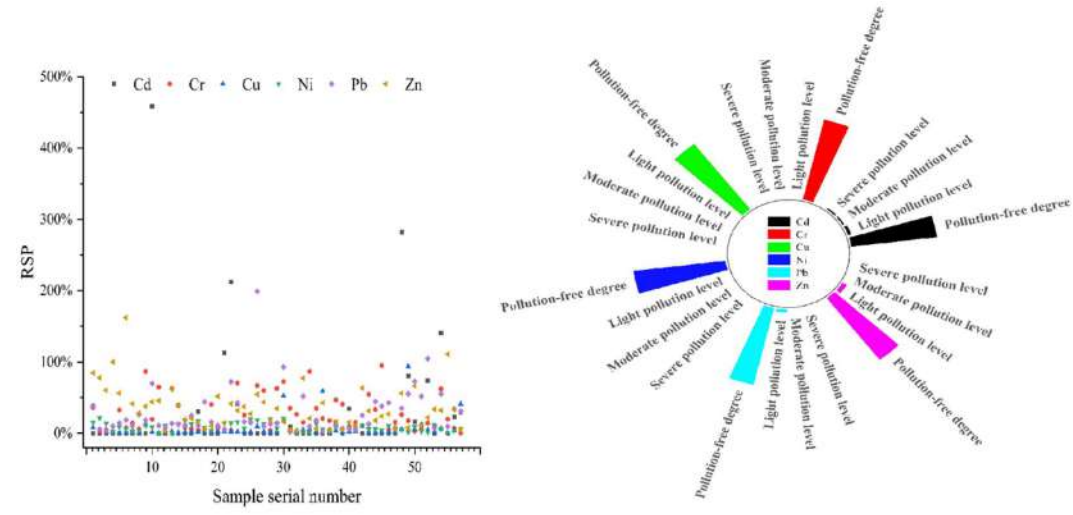


Fig. 7: Index of metal secondary and primary phases in the research area.

of 100%. The other three metals remained below the contamination level, although Cr and Cu points are closer to the pollution threshold. From Fig. 7(b), it is evident that 5% of Pb points and 4% of Zn points indicate light pollution. Additionally, 4% of Cd points show light pollution, while 2% exhibit medium to heavy pollution levels. In summary, although Cd, Pb, and Zn are not currently polluting the area, their chemical forms are contaminating the soil to some extent. Therefore, human activities should minimize the introduction of Cd, Pb, and Zn in the research region to prevent accumulation in the soil.

3.4. Analysis of Soil Heavy Metal Sources

3.4.1. Correlation Analysis

Fig. 8 presents the analysis of the behavior of metal elements in the soil within the study area. The results demonstrate that the elements Pb, Zn, Cd, and Cu exhibit a significant positive correlation at $P < 0.05$, suggesting the possible spatial overlap of multiple cumulative sources of these heavy metals, which is consistent with the findings from the geographical spread analysis. In contrast, the correlations of Cr and Ni with other elements are weak; only the correlations between Cr-Ni ($r = 0.24$) and Ni-Cu ($r = 0.44$) indicate potential disparate sources. The study indicates that the origins of metal elements in the soil are diverse. Therefore, further exploration of their compositional relationships and cumulative sources through principal component analysis or receptor modeling is recommended.

3.4.2. Principal Component Analysis

The soil heavy metal concentration data were evaluated using the KMO test and Bartlett's sphere test, which resulted in a KMO value of 0.659 (above 0.5) and a Bartlett's test p-value of 0.001 (below 0.05). These outcomes suggest a significant correlation among the elements, confirming that the data are suitable for principal component analysis, as shown in Table 6. Two principal components were extracted, with eigenvalues of 2.929 and 1.191, both exceeding 1. The combined explained variance of these two components was 68.66%, indicating they effectively capture most of the variability in the data and are reasonably representative of the overall dataset.

The variance explained by the first principal component (PC1) was 48.82%. Elements such as Cd, Cu, Pb, and Zn exhibited high positive loadings of 0.756, 0.829, 0.895, and 0.817, respectively, on PC1. A significant positive correlation was observed among these elements, indicating their homology. The study found that the mean concentrations of Cd, Cu, Pb, and Zn in the soils of the research region did not exceed the background levels observed in Guizhou. Despite this, the high variability suggests substantial influence from human activities. The mining of Pb and Zn exposes underground deposits to the surface, increasing the release flux of associated minerals. Additionally, field investigations revealed that mine slag in the study area consists of open piles, which, over time, can cause heavy metals to enter the surrounding soil. Areas with elevated levels of Cd, Cu, Pb, and Zn correspond with original mining sites and active mining zones (Ma et al. 2023). Consequently, PC1 is likely indicative of emissions from mining activities and seepage.

The variance explained by the second principal component (PC2) was 19.85%. Elements Cr and Ni exhibited significant positive coefficients of 0.822 and 0.731, respectively, on PC2. Although there was no significant correlation between them, Cr showed the strongest association with Ni among the six elements considered. It is generally assumed that human activities have minimal impact on soil Cr levels, which primarily originate from the parent material during soil formation (Duan et al. 2018). However, as shown in Table 4, the average concentrations of Cr and Ni did not surpass the soil background levels in Guizhou Province, but their variability was notably high, suggesting a greater influence

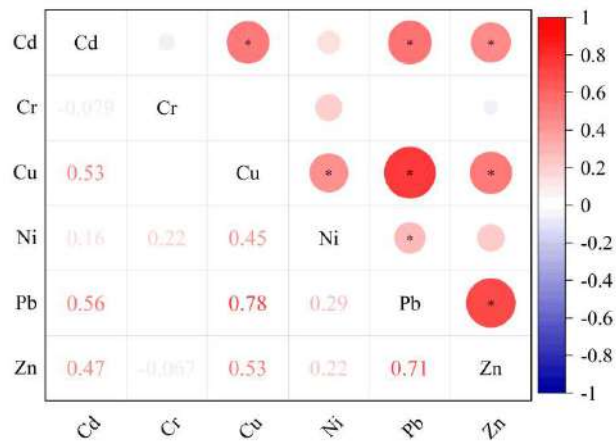


Fig. 8: Correlation coefficient of metals in the ground adjacent to the mining area.

Table 6: Rotation component matrix of metals factor analysis for the topsoil in the research area.

Projects	Principal component factor (KMO=0.659 $P_{Bartlet}$=0.001)	
	PCA1	PCA2
Cd	0.756	-0.028
Cu	0.829	0.256
Pb	0.895	0.087
Cr	-0.131	0.822
Ni	0.304	0.731
Zn	0.817	0.007
Eigenvalue	2.929	1.191
Explain total variance, %	48.82	48.82
Cumulative explained total variance, %	19.85	68.66

from anthropogenic sources. Spatial distribution analysis indicates that Cr is mainly found in cultivated lands, while Ni is present in both cultivated areas and mining tracks. According to Ai et al. (2014), chemical fertilizers often contain elevated levels of Cr, with concentrations ranging from 50 to 250 mg·kg^{-1} in calcium superphosphate and 5 to 3000 mg·kg^{-1} in nitrogen fertilizers. Globally, the annual Cr input to soils via fertilizers is estimated to be between 0.03 and 0.38 t-a^{-1} (Ai et al. 2014, Chen et al. 2022).

Over time, excessive fertilizer application leads to the accumulation of numerous Cr elements in the soil. Additionally, the overuse of calcium superphosphate-based insecticides and herbicides may result in Ni buildup (Alengebawy et al. 2021). Field observations indicate that this area has only one entrance and exit, and heavy vehicle traffic can release Ni from exhaust into the atmosphere, which eventually deposits into the soil. Consequently, PC2 is likely caused by agricultural activities and transportation.

3.4.3. PMF Source Resolution

The PMF model is employed for the quantitative source analysis of six metals in soil samples. Fig. 8 illustrates the contribution rates of various sources to the heavy metals present in the soil around the mining area. By incorporating the concentration and uncertainty into the PMF model, the signal-to-noise ratios (S/N) for chromium, nickel, copper, and cadmium are identified as 8.8, while those for lead and zinc are 9.0, both labeled with the default name "Strong." After selecting 2-6 factors over 100 iterations, it was determined that when five factors are used, all but one, R^2 for nickel at 0.69, exceed 0.8. The other elements, Cr, Cu, Pb, and Cd, have R^2 values above 0.9, indicating that this component count effectively captures the data's underlying information and yields a robust analysis. Factor 1 accounts for 63.7% of the Cr, suggesting a dominant anthropogenic influence, which aligns with regional conditions and PC2 analysis. Therefore, it is hypothesized that Factor 1 originates from agricultural activities. Factor 2 significantly correlates with Cd, whose sources are diverse in the Pb-Zn region, including air deposition, dust, agricultural production, and industrial emissions. Notably, atmospheric deposition may contribute more to soil Cd levels since fine particles can be transported by airflow to neighboring areas and deposited into soil and water bodies. Chen et al. (2021) observed a gradual increase in atmospheric Cd deposition flux in agricultural and rural areas from 2000 to 2018, highlighting the risk posed by heavy metal Cd contamination in agricultural soils (Chen et al. 2021). Near the lead-zinc mining area, comparisons between mulched and open-air conditions revealed that atmospheric deposition primarily caused the increased heavy metal levels in the aboveground parts of Chinese cabbage (Zhan et al. 2010). Thus, it is inferred that Factor 2 represents an atmospheric deposition source. Factor three contributed more significantly to the elements Zn and Ni, accounting for 59.1% and 41.9%, respectively. Research has confirmed the presence of the three major metals, Cu, Zn, and Pb, in wastewater used for irrigation (Liu et al. 2021). This mining area primarily engages in lead and zinc ore extraction and smelting, with wastewater, exhaust gases, and slag emissions during production serving as key sources of Pb, Zn, Cd, and Cu in the soil. The open storage of raw materials and tailings in the region may lead to heavy metal pollutants spilling over into surrounding areas following rainwater runoff and leaching, posing potential environmental safety risks. Studies by Ma et al. and Wei et al. have shown that the content of Cd, Pb, and Zn in soils around the Pb-Zn mine is influenced by non-ferrous metal mining and processing activities (Ma et al. 2014, Wei et al. 2018). The main source of Ni is transportation; however, other sources also contribute. Li et al. identified high Ni levels in samples taken from the mining site and nearby river channels (Li et al. 2024). Therefore, it is hypothesized that factor three represents the wastewater discharge source.

Factor 4 accounts for 52.9%, 45.4%, and 36.2% of the elements Cu, Ni, and Cr, respectively. These findings align with the PC2 results, where tire wear contributes to Cu accumulation during transportation. Consequently, factor four is likely linked to transportation activities.

Factor 5 accounts for 79.9% of Pb contributions. Mineral resources such as lead and zinc ores are particularly abundant in Ma-Gu town. The region suffers from intensified heavy metal contamination due to mining, smelting, and tailings dumping in the watershed. Consequently, it is hypothesized that Factor 5 originates from mining emissions.

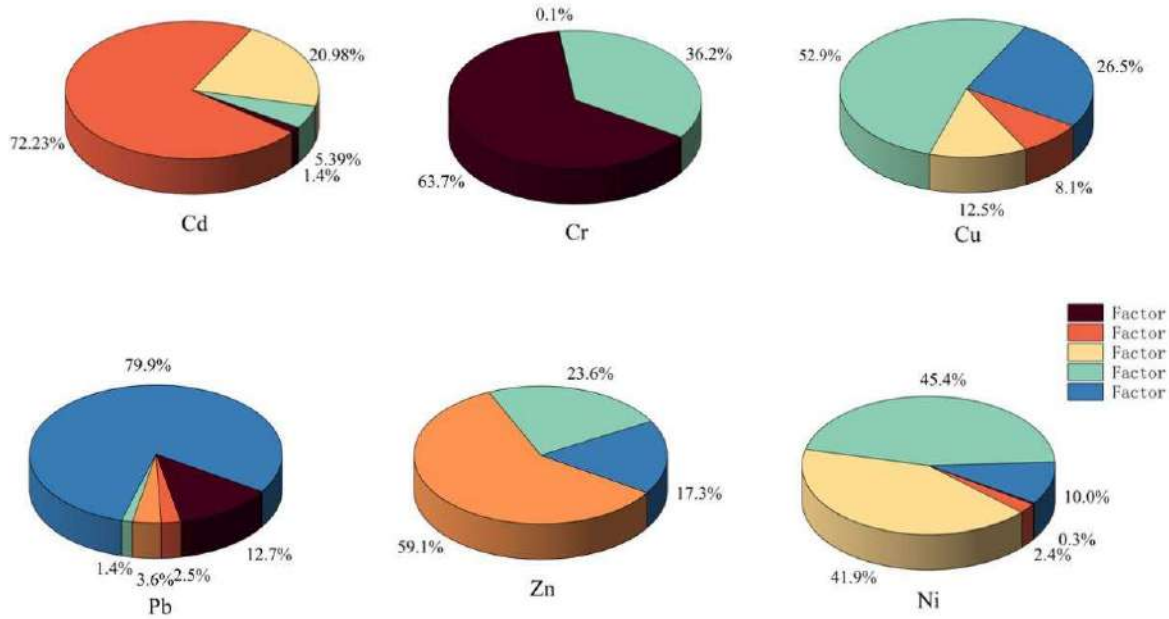


Fig. 8: Dedication rate for various causes of metal pollution in soil surrounding mining regions.

4. CONCLUSIONS

The average concentrations of six metals (Cd, Cu, Pb, Cr, Ni, and Zn) in the soils of the research area did not exceed the baseline levels established in Guizhou Province, although they exhibited significant variability. This indicates that external activities heavily influence these six metal elements. At the same depth, the concentrations followed the order Zn > Cr > Pb > Cu > Cd > Ni. Chemically, Cr, Zn, and Pb are generally stable in the soil; however, there remains a potential risk of bioaccumulation. The spatial distribution of high-concentration areas for all six metals is similar, closely linked to residuals and sites from former mining operations, but further investigation is needed to understand pollution impacts better. The geological accumulation index analysis shows that the Igeo values for all six elements are below zero, indicating no pollution. Nonetheless, cadmium and lead show the greatest dispersion and enrichment in the soil, whereas nickel has relatively low enrichment levels. RSP analysis reveals that while copper, nickel, and chromium are not polluted, lead and zinc show slight pollution, with cadmium present at light, moderate, and even heavy pollution levels. Correlation, principal component, and PMF analyses suggest that pollution sources include five main pathways: agricultural activities contribute 63.7% of chromium (Cr), atmospheric deposition accounts for 72.3% of cadmium (Cd), wastewater discharge contributes 59.1% of zinc (Zn) and 41.9% of nickel (Ni), traffic emissions account for 52.9% of copper, 45.4% of nickel, and 36.2% of chromium, and mining activities contribute 79.9% of lead.

5. ACKNOWLEDGEMENT

This work was financially supported by the Guizhou Science and Technology Plan Project (Guizhou Science and Technology Support [2024] General 433 and Guizhou Provincial Science and Technology Projects [2022]325).

6. REFERENCES

Ai, J., Wang, N. and Yang, J., 2014. Source apportionment of soil heavy metals in Jiapigou goldmine based on the UNMIX model. *Environmental Science*, 35(9), pp.3530-3536. [DOI]

Alengebawy, A., Abdelkhalek, S.T., Qureshi, S.R. and Wang, M.Q., 2021. Heavy metals and pesticides toxicity in agricultural soil and plants: ecological risks and human health implications. *Toxics*, 9(3), p.42. [DOI]

Ali, W., Mao, K., Zhang, H., Junaid, M., Xu, N., Rasool, A., Feng, X. and Yang, Z., 2020. Comprehensive review of the basic chemical behaviours, sources, processes, and endpoints of trace element contamination in paddy soil-rice systems in rice-growing countries. *Journal of Hazardous Materials*, 397, p.122720. [DOI]

Bi, X., Zhang, M., Wu, Y., Fu, Z., Sun, G., Shang, L., Li, Z. and Wang, P., 2020. Distribution patterns and sources of heavy metals in soils from an industrially undeveloped city in Southern China. *Ecotoxicology and Environmental Safety*, 205, p.111115. [DOI]

Chen, J.J., Liu, B., Cai, L.G., Wang, G.Q., Yin, K., Chen, H.B. and Li, Z.M., 2018. Comparison of risk assessment based on the various methods of heavy metals in soil: a case study for the typical field areas in the Jianghan Plain. *Hydrogeology & Engineering Geology*, 45(6), pp.164-172. [DOI]

Chen, M., Li, X., Cao, X., Yang, W., Wu, P., Hao, H., Fei, Z. and Gao, Y., 2024. Soil-forming accumulation of heavy metals in geological high background areas: constraints of structure, lithology, and overlying soil geochemistry. *Journal of Geochemical Exploration*, 263, p.107518. [DOI]

Chen, M., Pan, Y., Huang, Y., Wang, X. and Zhang, R., 2022. Spatial distribution and sources of heavy metals in soil of a typical lead-zinc mining area, Yangshuo. *Environmental Science*, 43(10), pp.4545-4555. [DOI]

Chen, Q., Zhang, X., Xie, Q., Lee, Y.H., Lee, J.-S. and Shi, H., 2021. Microplastics habituated with biofilm change decabrominated diphenyl ether degradation products and thyroid endocrine toxicity. *Ecotoxicology and Environmental Safety*, 228, p.112991. [DOI]

Chen, X.D. and Lu, X.W., 2017. Source apportionment of soil heavy metals in city residential areas based on the receptor model and geostatistics. *Huan jing ke xue= Huanjing Kexue*, 38(6), pp.2513-2521. [DOI]

Chueinta, W., Hopke, P.K. and Paatero, P., 2000. Investigation of sources of atmospheric aerosol at urban and suburban residential areas in Thailand by positive matrix factorization. *Atmospheric Environment*, 34(20), pp.3319-3329. [DOI]

Cui, W.W., Dong, X.Q., Liu, J.J., Yang, F., Duan, W. and Xie, M.X., 2024. Characterization and source apportionment of heavy metal pollution in soil around red mud disposal sites using absolute principal component scores-multiple linear regression and positive matrix factorization models. *Environmental Geochemistry and Health*, 46(12), p.492. [DOI]

Das, B., Nordin, R. and Mazumder, A., 2009. Watershed land use as a determinant of metal concentrations in freshwater systems. *Environmental Geochemistry and Health*, 31(6), pp.595-607. [DOI]

Demková, L., Jezný, T. and Bobuľská, L., 2017. Assessment of soil heavy metal pollution in a former mining area-before and after the end of mining activities. *Soil & Water Research*, 12(4), pp.229-236.

Duan, C., Fang, L., Yang, C., Chen, W., Cui, Y. and Li, S., 2018. Reveal the response of enzyme activities to heavy metals through in situ zymography. *Ecotoxicology and Environmental Safety*, 156, pp.106-115. [DOI]

Hu, B., Zhou, Y., Jiang, Y., Ji, W., Fu, Z., Shao, S., Li, S., Huang, M., Zhou, L. and Shi, Z., 2020. Spatio-temporal variation and source changes of potentially toxic elements in soil on a typical plain of the Yangtze River Delta, China (2002–2012). *Journal of Environmental Management*, 271, p.110943. [DOI]

Hussain, R., Luo, K., Liang, H. and Hong, X., 2019. Impact of the coal mining-contaminated soil on food safety in Shaanxi, China. *Environmental Geochemistry and Health*, 41(3), pp.1521-1544. [DOI]

Jin, Y., O'Connor, D., Ok, Y.S., Tsang, D.C.W., Liu, A. and Hou, D., 2019. Assessment of sources of heavy metals in soil and dust at children's playgrounds in Beijing using GIS and multivariate statistical analysis. *Environment International*, 124, pp.320-328. [DOI]

Kiran, Bharti, R. and Sharma, R., 2022. Effect of heavy metals: an overview. *Materials Today: Proceedings*, 51, pp.880-885. [DOI]

Li, P., 1994. An investigation report of the industrial economy in the small towns in ethnic areas of Guizhou. *Guizhou Ethnic Studies*, (03), pp.23-24.

Li, R.Z., Liu, Y.H., Huang, Y.H. and Wu, H.F., 2024. Contamination characteristics and source apportionment of soil heavy metals in an abandoned pyrite mining area of Tongling City, China. *Huan jing ke xue= Huanjing Kexue*, 45(1), pp.407-416. [DOI]

Li, X.Q., Tang, Y.N., Wang, X.H., Song, X.D. and Yang, J.X., 2023. Heavy metals in soil around a typical antimony mine area of China: pollution characteristics, land cover influence and source identification. *International Journal of Environmental Research and Public Health*, 20(3), p.2177. [DOI]

Liang, J.H., Tian, Y.Q., Fei, Y., Liu, Z.Y., Shi, H.D., Qi, J.X. and Mo, L., 2023. Source apportionment and potential ecological risk assessment of soil heavy metals in typical industrial and mining towns in North China. *Huan jing ke xue= Huanjing kexue*, 44(10), pp.5657-5665. [DOI]

Liu, J., Li, X., Zhang, P., Zhu, Q., Lu, W., Yang, Y., Li, Y., Zhou, J., Wu, L., Zhang, N. and Christie, P., 2023. Contamination levels of and potential risks from metal(loid)s in soil-crop systems in high geological background areas. *Science of the Total Environment*, 881, p.163405. [DOI]

Liu, Y.B., Ma, Z.H., Liu, G.N., Jiang, L., Dong, L.M., He, Y., Shang, Z.F. and Shi, H.D., 2021. Accumulation risk and source apportionment of heavy metals in different types of farmland in a typical farming area of northern China. *Environmental Geochemistry and Health*, 43(12), pp.5177-5194. [DOI]

Ma, H.H., Zhang, L., Guo, F., Yang, Z., Wang, H.Y., Peng, M. and Zhang, F.G., 2023. Ecological risk and migration patterns of heavy metals in soil and crops in the lead-zinc mining area in Guizhou, China. *Environmental Science*, 44(05), pp.2856-2867. [DOI]

Ma, Z.W., Li, T.T., Qu, C.S., Bi, J. and Huang, L., 2014. Evaluation and source identification of trace element contamination of soils in the Qixia lead-zinc mining area, Jiangsu, China. *Journal of Soils and Sediments*, 14(10), pp.1703-1712. [DOI]

Muller, G., 1969. Index of geoaccumulation in sediments of the Rhine River. *Environmental Science and Pollution Research*, 2(3), pp.109-118. [DOI]

Paatero, P. and Tapper, U., 1994. Positive matrix factorization: a non-negative factor model with optimal utilization of error estimates of data values. *Environmetrics*, 5(2), pp.111-126. [DOI]

Shi, N.N., Ding, Y.F. and Zhao, X.F., 2010. Heavy metal content and pollution risk assessment of crop land soils around a pesticide industrial park. *Chinese Journal of Applied Ecology*, 21(7), pp.1835-1843. [DOI]

Wang, F.F., Guan, Q.Y., Tian, J., Lin, J.K., Yang, Y.Y., Yang, L.Q. and Pan, N.H., 2020. Contamination characteristics, source apportionment, and health risk assessment of heavy metals in agricultural soil in the Hexi Corridor. *CATENA*, 191, p.104573. [DOI]

Wang, Q.L., Song, Y.T. and Wang, C.W., 2021. Source identification and spatial distribution of soil heavy metals in Western Yunnan, China. *Environmental Science*, 41(8), pp.3693-3703. [DOI]

Wei, Y.H., Li, G.C., Wang, Y.H., Zhang, Q., Li, B., Wang, S.C., Cui, J.H., Zhang, H. and Zhou, Q., 2018. Investigating factors influencing the PMF model: a case study of source apportionment of heavy metals in farmland soils near a lead-zinc ore. *Journal of Agro-Environment Science*, 37(11), pp.2549-2559. [DOI]

Wu, B., Wan, Q., Li, X., Lin, S., Jiang, Y., Yang, X., Li, J., Lin, Q., Morel, J.L. and Qiu, R., 2024. Heavy metal migration dynamics and solid-liquid distribution strategy in abandoned tailing soils. *Journal of Hazardous Materials*, 468, p.133794. [DOI]

Yan, N., Liu, W., Xie, H., Gao, L., Han, Y., Wang, M. and Li, H., 2016. Distribution and assessment of heavy metals in the surface sediment of Yellow River, China. *Journal of Environmental Sciences*, 39, pp.45-51. [DOI]

Yang, C., Wang, B., Shen, G. and Wang, M., 2018. Pb pollution characteristics and their affecting factors in different land use types in lead-zinc mining zone. *Research of Soil and Water Conservation*, 25(05), pp.351-357.

Yu, D.Y., Wang, Y.H., Ding, F., Chen, X. and Wang, J.R., 2021. Comparison of analysis methods of soil heavy metal pollution sources in China in last ten years. *Chinese Journal of Soil Science*, 52(4), pp.1000-1008. [DOI]

Zhan, M.K., Liu, Z.Y. and Zhou, C., 2010. Effect of atmospheric deposition on heavy metal accumulation in vegetable crop near a lead-zinc smelting mine. *Journal of Zhejiang University (Agriculture and Life Sciences)*, 36(02), pp.221-229. [DOI]

Zhang, F. and Li, G.H., 2016. China released the Action Plan on Prevention and Control of Soil Pollution. *Frontiers of Environmental Science & Engineering*, 10(4), p.7. [DOI]

Zhang, Y., Feng, N.Q., Liu, Y., Xu, Z.Q., Zhang, Y. and Wang, Q., 2023.

Speciation analysis and risk assessment of heavy metals in the soil of a lead-zinc mining area. *Multipurpose Utilization of Mineral Resources*, 44(3), pp.199-204, 210. [DOI]

Zhou, Y., Chen, Q., Deng, S.P., Wan, J.Z., Zhang, S.T., Long, T., Li, Q., Lin, Y.S. and Wu, Y.J., 2018. Principal component analysis and ecological risk assessment of heavy metals in farmland soils around a Pb-Zn mine in Southwestern China. *Huan jing ke xue= Huanjing Kexue*, 39(6), pp.2884-2892. [DOI]

Zhou, Y., Wang, L., Xiao, T., Chen, Y., Beiyuan, J., She, J., Zhou, Y., Yin, M., Liu, J., Liu, Y., Wang, Y. and Wang, J., 2020. Legacy of multiple heavy metal(loid)s contamination and ecological risks in farmland soils from a historical artisanal zinc smelting area. *Science of the Total Environment*, 720, p.137541. [DOI]

Nature Environment and Pollution Technology
An International Quarterly Scientific Journal

p-ISSN: 0972-6268
(Print copies up to 2016)
e-ISSN: 2395-3454

Vol. 25 | No. 3 | Article ID D1891 | 2026

Original Research Paper

https://doi.org/10.46488/NEPT.2026.v25i03.D1891

Open Access Journal

An Assessment of Biopolymer-Based Metal Oxide Nanoparticles for the Removal of Heavy Metals from Water

Koffi Sossou[1]†, Alfred O. Mayabi[2], Zeraebruk Negusse Kahsay[2] and Charles K. Cheruiyot[2]

[1]Department of Civil Engineering, Pan African University Institute for Basic Sciences, Technology and Innovation (PAUSTI-JKUAT), Kenya

[2]Department of Civil, Construction and Environmental Engineering, Jomo Kenyatta University of Agriculture and Technology, Nairobi, Kenya

†Corresponding author: Koffi Sossou; sossou.koffi@students.jkuat.ac.ke

Abbreviation: Nat. Env. & Poll. Technol.
Website: www.neptjournal.com

Received: 10-12-2025
Revised: 21-01-2026
Accepted: 30-01-2026

Key Words:

Adsorption
Banana peels
Kinetic study
Chemisorption
Metal oxide nanoparticles
Removal of heavy metals

Citation for the Paper:

Sossou, K., Mayabi, A.O., Kahsay, Z.N. and Cheruiyot, C.K., 2026. An assessment of biopolymer-based metal oxide nanoparticles for the removal of heavy metals from water. *Nature Environment and Pollution Technology*, 25(3), D1891. https://doi.org/10.46488/NEPT.2026.v25i03.D1891

Note: From 2025, the journal has adopted the use of Article IDs in citations instead of traditional consecutive page numbers. Each article is now given individual page ranges starting from page 1.

Copyright: © 2026 by the authors
Licensee: Technoscience Publications
This article is an open access article distributed under the terms and conditions of the Creative Commons Attribution (CC BY) license (https://creativecommons.org/licenses/by/4.0/).

ABSTRACT

Water contamination by toxic heavy metals continues to be a major environmental and public health issue, requiring affordable and sustainable remediation solutions. This study developed a nanocomposite from banana peel, incorporating Fe_3O_4 and TiO_2 nanoparticles through a combined co-precipitation and hydrothermal method, and evaluated its effectiveness in adsorbing Cr(VI), Cd(II), and Pb(II) from water. Characterization techniques such as FTIR, SEM–EDS, and XPS confirmed successful integration of Fe_3O_4 and TiO_2 into the banana peel matrix, improving surface properties and magnetic separability. The adsorption data fit the Langmuir and Redlich–Peterson models best, indicating monolayer adsorption with maximum capacities of 14.4 $mg.g^{-1}$ for Cr(VI), 10.9 $mg.g^{-1}$ for Cd(II), and 100 $mg.g^{-1}$ for Pb(II). Kinetic analysis showed the adsorption follows a pseudo-second-order model (R2 = 0.97–0.93). The nanocomposite exhibited excellent adsorption efficiency and competitive capacity compared to other metal oxide adsorbents, demonstrating its potential as a low-cost, sustainable material for removing multiple heavy metals and valorizing agricultural waste.

1. INTRODUCTION

Environmental pollution resulting from inadequate wastewater management has attracted significant global attention in recent decades, particularly due to the discharge of toxic heavy metals into aquatic environments. Wastewater containing heavy metals, dyes, and organic pollutants poses serious risks to ecosystems and human health because these contaminants are non-biodegradable, persistent, and capable of bioaccumulation (Sossou et al. 2024a, A. Mishra et al. 2022). In countries with limited wastewater treatment infrastructure and weak regulatory enforcement, contamination of water resources by heavy metals is further exacerbated (Smyth et al. 2024, Strategies et al. 2024).

Conventional wastewater treatment methods, including chemical precipitation, ion exchange, and membrane filtration, often suffer from high operational costs, secondary sludge generation, and low selectivity for multiple coexisting contaminants (Razzak et al. 2022). Consequently, adsorption using low-cost and environmentally friendly materials has emerged as a promising alternative for heavy metal removal. In this context, biosorbents derived from agricultural residues have gained increasing attention because of their abundance, biodegradability, and alignment with circular economy principles.

Banana peel is one such agricultural by-product that has been extensively investigated as a low-cost biosorbent. According to the Food and Agriculture Organization of the United Nations (FAO 2024), approximately 3.5 million tonnes

of banana peel waste are generated each year globally. Much of this biomass is disposed of in open dumps or landfills, leading to environmental problems such as leachate generation, greenhouse gas emissions during decomposition, and contamination of soil and water resources (Mor et al. 2023, Sial et al. 2019). Nevertheless, banana peel contains significant amounts of cellulose, hemicellulose, lignin, pectin, and starch, which provide abundant functional groups, including hydroxyl and carboxyl moieties, capable of interacting with metal ions (Pokharel et al. 2018, Liew et al. 2018, Mehmood et al. 2025, Mishra et al. 2023). Despite these advantages, raw banana peel and unmodified biopolymers often exhibit limited adsorption capacity and reduced effectiveness in multicomponent systems because of competitive adsorption among coexisting metal ions (Gupta et al. 2025).

To overcome these limitations, the integration of metal oxide nanoparticles with biomass-based adsorbents has been widely explored. Nanomaterials such as iron oxides and titanium dioxide offer high surface areas, enhanced surface reactivity, and improved physicochemical stability, resulting in superior adsorption performance (Togun et al. 2025, Sossou et al. 2024b). In particular, magnetite (Fe_3O_4) nanoparticles are attractive because of their strong affinity for metal ions and magnetic properties, which facilitate easy separation from treated water. Similarly, TiO_2 provides additional adsorption sites and enhances the chemical stability of the composite (Lellala et al. 2024).

Despite these advances, most previous studies have focused on single-metal systems or non-magnetic banana peel modifications, limiting their applicability to real wastewater containing multiple competing contaminants. Therefore, this study aims to synthesize and evaluate a Fe_3O_4/TiO_2/banana peel nanocomposite for the removal of Cr(VI), Cd(II), and Pb(II) from aqueous solutions under multicomponent conditions. The findings provide valuable insight into the potential of this nanocomposite as a low-cost, sustainable, and environmentally friendly material for heavy metal remediation.

2. MATERIALS AND METHODS

2.1. Adsorbent's Preparation and Characterization

2.1.1. Hydrothermal-Assisted Nanocomposite Synthesis of Iron Oxide

Hydrothermal-assisted synthesis was used to produce iron oxide-based nanocomposites. Low-grade iron oxides sourced from Ollesos Company in Kenya served as raw materials without any chemical modification. A total of 100 g of the mixed iron oxide powders was dispersed in 100 mL of distilled water and stirred at 40 rpm for 2 h to create a uniform suspension. The pH was adjusted to 7 with NaOH solution. The suspension was transferred into a Teflon-lined stainless steel autoclave and subjected to hydrothermal treatment at 105°C for 12 h.

After natural cooling to room temperature, the solid product was separated by centrifugation, washed three times with ethanol, then with distilled water to eliminate impurities. The washed material was dried in an oven at 80°C and calcined at 500°C for 6 h. The calcined powder was ground with a mortar and pestle to produce a fine, homogeneous nanocomposite powder (Fig. 1).

2.1.2. Hydrothermal Synthesis of Titanium Dioxide

TiO_2 nanoparticles were synthesized via a hydrothermal method with slight modifications to previously established

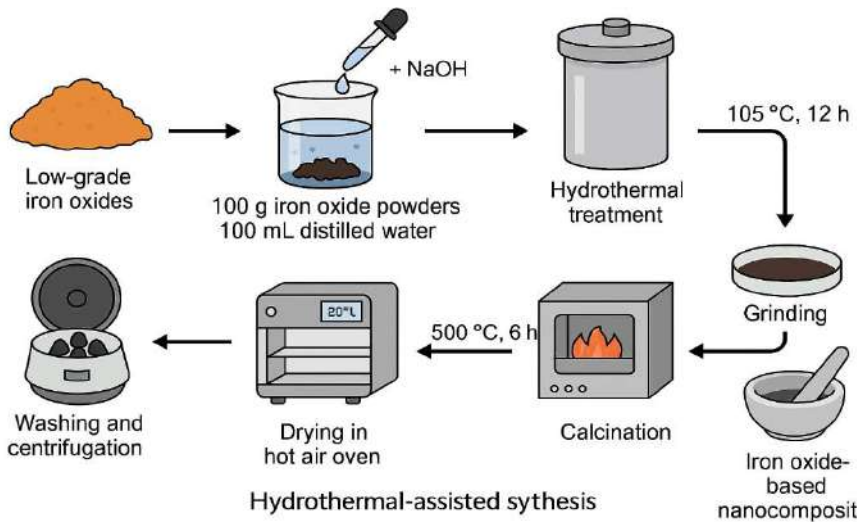


Fig. 1: Hydrothermal-assisted nanocomposite synthesis of iron oxide.

procedures (Keerthana et al. 2018, Zanganeh et al. 2011). Commercial TiO_2 powder (Degussa P25, Evonik, 99.9% purity, anatase/rutile ratio of 90:10, particle size approximately 10 nm) served as the precursor. Briefly, 1 g of TiO_2 was dispersed in 50 mL of 10 M NaOH solution under vigorous stirring for 40 minutes. The resulting suspension was transferred to a 50 mL Teflon-lined stainless-steel autoclave and heated at 200°C for 48 h.

The precipitate was then cooled to room temperature, washed repeatedly with deionized water (resistivity ≥15 MΩ·cm) and 0.1 M HCl until neutral pH was reached, and separated by centrifugation at 5000 rpm for 10 minutes. The product was dried at 60°C for 1 h and calcined at 250°C for 2 h in air to improve crystallinity and reduce residual sodium content.

To assess the influence of the alkaline medium, the synthesis was repeated using KOH instead of NaOH. The resulting TiO_2 nanoparticles were stored in a desiccator until further characterization and application.

2.1.3. Biopolymer Materials

For the biopolymer preparation, banana peels were locally obtained from Juja Market in Kenya, washed three times with tap water, and cut into small pieces measuring 3-4 cm. The peels were air-dried for one week, then baked in a hot-air oven at 105°C for 12 h. The dried peels were crushed with a mortar and pestle into a fine powder, which was sieved through a 200 µm mesh to ensure uniform particle size. This powder served as the raw material for creating a homogeneous nanocomposite. The morphology of the banana peel powder was examined using scanning electron microscopy (SEM) micrographs of the peels and biochar surfaces.

2.2. Characterization of the Materials

The nanomaterials, iron oxide, titanium dioxide, and biopolymer powder, were thoroughly characterized to assess their physical, chemical, and structural properties. Parameters such as surface area, pore size distribution, chemical composition, elemental states, and magnetic properties were evaluated. Crystalline phases were analyzed using X-ray Diffraction (XRD, Bruker D8 Advance, Germany) with Cu-Kα radiation (λ = 1.5406 Å). Elemental composition was determined via X-ray Fluorescence (XRF, PANalytical Axios, Netherlands). Surface morphology was examined with Scanning Electron Microscopy (SEM, JEOL JSM-7610F, Japan). The chemical states and elemental composition of the samples were analyzed by X-ray Photoelectron Spectroscopy (XPS, PHI 5000 VersaProbe III, ULVAC-PHI, Inc., Japan) under ultra-high vacuum (~2×10^{-7} Pa). A monochromatic Al Kα X-ray source (hν = 1486.6 eV) with a 100 µm beam diameter was used. Survey scans employed a pass energy of 280 eV, while high-resolution scans used 55 eV with a step size of 0.05 eV. Raster scanning was performed on the samples with the stage tilt fixed at 45°. Charge neutralization was achieved using a neutralizer set at 1.5 V and 20 µA. The analysis was conducted at a base pressure of approximately 8×10^{-8} Pa. Samples were affixed using non-conductive tape. Data acquisition and peak deconvolution were carried out with Multipak software.

2.3. Preparation of Heavy Metal Stock Solutions

All chemicals utilized in this study were of analytical grade (≥99.5%, 200 mesh) and were obtained from Merck and Sigma-Aldrich. Precise amounts of potassium dichromate ($K_2Cr_2O_7$), cadmium nitrate [$Cd(NO_3)_2$], and lead nitrate [$Pb(NO_3)_2$] were carefully weighed and dissolved in distilled water (resistivity ≥15 MΩ·cm) to create a mixed heavy-metal stock solution containing 50 $mg.L^{-1}$ of Cr(VI) and Cd(II), and 10 $mg.L^{-1}$ of Pb(II). The exact mass of each metal salt was calculated for accuracy. All experiments were conducted at room temperature (298 ± 2 K) under atmospheric pressure. The pH of the solutions was adjusted as necessary using hydrochloric acid (HCl) or sodium hydroxide (NaOH).

2.4. Adsorption Experiments

Batch adsorption experiments involved adding a specified mass of Fe_3O_4/TiO_2–banana peel nanocomposite (0.5–2.5 g) to a series of 250 mL conical flasks containing 100 mL of mixed heavy-metal solution with an initial concentration of 50 $mg.L^{-1}$ (C_o). The flasks were placed on a magnetic stirrer and stirred at 90 rpm for 60 minutes to facilitate adsorption. After each run, the supernatant was carefully withdrawn, filtered through Whatman No. 42 filter paper, and analyzed for residual concentrations of Cr (VI), Cd (II), and Pb (II) (Ct) using Atomic Absorption Spectroscopy (AAS).

The amount of metal ions adsorbed, denoted as qt ($mg.g^{-1}$), was calculated using Eq. 2 (Otieno et al. 2021)

$$q_t = \frac{(Co - Ct)}{W} V \quad \ldots(1)$$

Where C_o and C_t are the metal ion concentrations ($mg.L^{-1}$) initially and at the end of the run, respectively, V is the solution volume (mL), and W is the mass of the adsorbent (g).

2.5. Adsorption Isotherms

Adsorption isotherms were employed to analyze the equilibrium data obtained from the batch experiments. The data were modeled using nonlinear Langmuir and Freundlich isotherm equations (Eqs. 2 and 3). The nonlinear formulation was favored over the linearized versions to reduce errors from

data transformation and to ensure more precise and reliable parameter estimation.

The Langmuir isotherm model describes monolayer adsorption on a homogeneous surface with a finite number of identical active sites, and is expressed as:

$$q_e = \frac{q_{max} K_L C_e}{1 + K_L C_e} \quad \ldots(2)$$

Where:

- q_e (mg.g^{-1}) is the amount of adsorbate adsorbed at equilibrium,
- C_e (mg.L^{-1}) is the equilibrium concentration of cadmium in solution,
- q_{max} (mg.g^{-1}) is the maximum adsorption capacity,
- K_L (L.mg^{-1}) is the Langmuir constant related to adsorption affinity.

The Freundlich model describes multilayer adsorption onto heterogeneous surfaces and is given by:

$$q = K_F C_e^{1/n} \quad \ldots(3)$$

Where:

- K_F (mg.g^{-1}) (L.mg^{-1})$^{1/n}$ is the Freundlich constant indicating adsorption capacity,
- n is the heterogeneity factor, with 1/n representing adsorption intensity.

The suitability of each model was assessed by correlation coefficients (R^2) and error functions.

2.6. Adsorption Kinetics

Kinetic experiments were carried out to examine the rate and mechanism of adsorption of Cr (VI), Cd(II), and Pb(II) onto the synthesized Fe_3O_4/TiO_2/banana peel nanocomposite. Batch studies were conducted with four different adsorbent dosages (0.5, 1, 1.5, 2, and 2.5 g), maintaining an initial metal ion concentration of 50 mg.L^{-1} for Cr(VI) and Cd(II), and 10 mg.L^{-1} for Pb(II). The solution volume was 100 mL, with a natural pH range of 6.0 to 6.5. For each contact time, identical 250 mL conical flasks containing the same solution and adsorbent dose were prepared to ensure consistent conditions. These flasks were stirred at 90 rpm using a magnetic stirrer for uniform mixing. At specified intervals from 10 to 120 minutes, one flask was retrieved, and its suspension was filtered through Whatman No. 42 filter paper. The residual metal concentrations in the filtrate were determined as described in Section 2.4, and the adsorbed metal amount at time t (qt) was calculated using Equation (1).

$$q_t = q_e (1 - e^{-k1t}) \quad \ldots(4)$$

Where:

- q_t (mg.g^{-1}) is the amount of cadmium adsorbed at time ttt,
- q_e (mg.g^{-1}) is the adsorption capacity at equilibrium,
- k_1 (1.min^{-1}) is the pseudo-first-order rate constant.

The pseudo-second-order model is given by:

$$q_t = \frac{K_2 q_e^2 t}{1 + k_2 q_e t} \quad \ldots(5)$$

2.7. Error Analysis

To assess the accuracy and reliability of the isotherm and kinetic models, the root mean square error (RMSE) was used to compare experimental and predicted adsorption capacities. RMSE offers a direct measure of the average deviation between observed and calculated values, providing a more dependable evaluation of model performance than the coefficient of determination (R^2) alone. The calculation was performed using the following equation:

$$\text{Root mean square error (RMSE)} = \sqrt{\frac{1}{N}\sum_{i=1}^{N}(q_{e,exp} - q_{e,cal})^2} \quad \ldots(6)$$

Where $q_{e,exp}$ and $q_{e,cal}$ (mg.g^{-1}) are the experimental and calculated adsorption capacities, respectively, and N is the number of experimental data points. Lower RMSE values indicate better agreement between experimental and predicted results.

3. RESULTS AND DISCUSSION

3.1. Adsorbent Characteristics

The FTIR spectra of banana peel powder (BP), Fe_3O_4, and TiO_2 nanoparticles before and after adsorption are shown in Fig. 2a–b. In the BP spectrum, a broad band around 3400 cm⁻¹ indicates O–H stretching from hydroxyl groups in cellulose, hemicellulose, and lignin. Peaks near 2920 cm⁻¹ correspond to aliphatic C–H stretching. Absorption bands between 1655–1560 cm⁻¹ and 1250–1020 cm⁻¹ represent C=O/C=C and C–O stretching vibrations, highlighting the presence of functional groups capable of binding metal ions.

The Fe_3O_4 spectrum features a broad O–H band near 3400 cm⁻¹ and a strong Fe–O stretching vibration between 550 and 480 cm⁻¹, confirming the formation of magnetite nanoparticles. TiO_2 shows characteristic Ti–O–Ti vibrations around 745 cm⁻¹ and Ti–O vibrations between 480 and 500 cm⁻¹, indicating its crystalline structure.

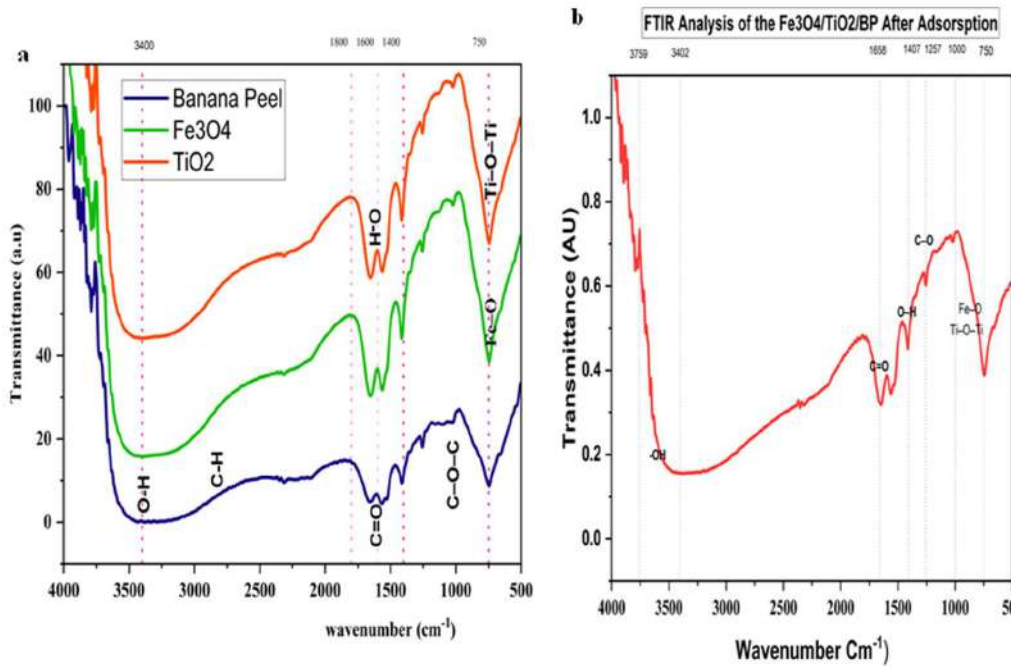


Fig. 2: FTIR spectrum of the materials (a) before adsorption, (b) after adsorption.

Following adsorption, the spectrum of the Fe_3O_4/TiO_2/BP nanocomposite reveals significant changes in band intensity and position. The broad O–H band (3759–3402 cm^{-1}) diminishes in intensity and shifts slightly, suggesting hydroxyl groups participate in metal binding via hydrogen bonding or ion exchange. Peaks at 1658 cm^{-1}, 1407 cm^{-1}, and 1257 cm^{-1} correspond to C=O, carboxylate, and C–O vibrations, implying their involvement in metal ion complexation. The Fe–O and Ti–O bands (1000–750 cm^{-1}) remain evident, demonstrating the structural stability of the composite after adsorption.

The observed spectral changes demonstrate that hydroxyl, carbonyl, and carboxyl functional groups play key roles in metal ion adsorption onto the Fe_3O_4/TiO_2/BP nanocomposite surface.

The XPS analysis of iron oxide (Fig. 3a–b) reveals distinct signals from Fe2+ 2p3/2 (~708.5 eV) and Fe3+ 2p3/2

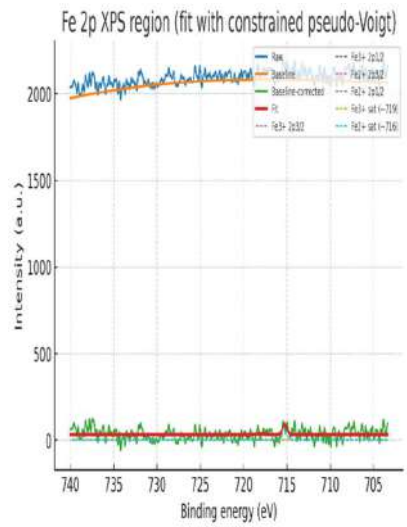


Fig. 3a: Fe 2p XPS region of iron oxide.

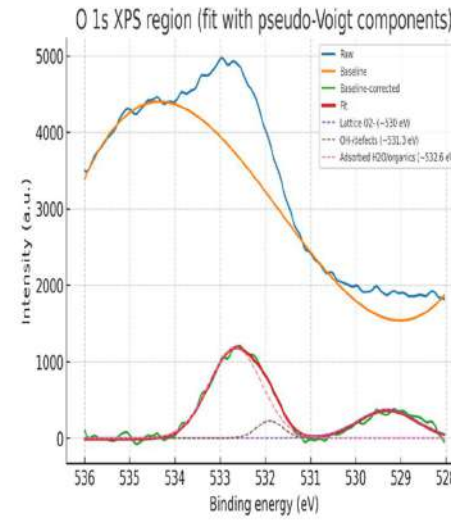


Fig. 3b: O1s XPS region of iron oxide.

Table 1: Fitted parameters of XPS analysis on iron oxide.

Component	Area [a.u.]	Position [eV]	Sigma [eV]	Eta [0-1]	Fe^{3+} fraction [from 2p3/2]
Fe^{3+} 2p3/2	1.3E-12	711.9803	1.799834	0.999183	4.88E-07
Fe^{3+} 2p1/2	6.51E-13	725.0803	1.799834	0.999183	4.88E-07
Fe^{2+} 2p3/2	2.67E-06	708.5125	1.773371	0.970402	4.88E-07
Fe^{2+} 2p1/2	1.33E-06	721.6125	1.773371	0.970402	4.88E-07
Fe^{3+} sat	5.626487	718	0.434943	1.17E-13	4.88E-07
Fe^{2+} sat	37.82937	715.2522	0.260823	4.59E-31	4.88E-07

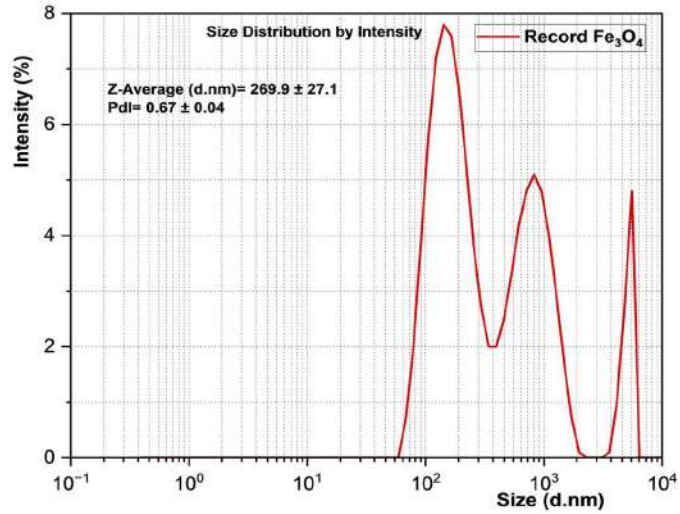


Fig. 4: Particle size distribution curve of iron oxide measured by Dynamic Light Scattering.

(~712.0 eV), along with their spin–orbit counterparts (ΔE ≈ 13.1 eV, ratio 2:1). Shake-up satellite peaks appear around 716 eV and 719 eV. All binding energies were calibrated to the C 1s peak at 285.0 eV, with fitted parameters summarized in Table 1. The O 1s spectrum (Fig. 3b) was deconvoluted into three components: lattice oxygen (O^{2-}, ~529.3 eV), hydroxyl groups or oxygen vacancies (~531.9 eV), and adsorbed water or organic species (~532.7 eV). Survey scans confirmed the presence of C 1s, Fe 2p, O 1s, S 2p, and Ti 2p peaks in both the iron oxide and banana peel-derived samples. The Fe 2p doublets of a standard Fe2O3 sample served as references for oxidation state determination.

The XPS results confirm the coexistence of Fe^{2+} and Fe^{3+} species, together with surface hydroxyl and oxygen defect sites, which are expected to play a crucial role in adsorption and surface reactivity (Table 1).

The particle size distribution of the synthesized Fe_4O_4 iron oxide was characterized using a HORIBA SZ-100 nanoparticle analyzer (HORIBA Scientific, Japan) based on dynamic light scattering (DLS). Measurements were taken in a transparent four-sided cuvette with a 10 mm optical path. As illustrated in Fig. 4, the intensity-weighted size distribution is broad and multimodal, indicating aggregation of particles in aqueous suspension. A significant peak appears at approximately 1593 nm, with other larger sizes suggesting the formation of agglomerates. The Z-average hydrodynamic diameter (~3432 nm) significantly exceeds the modal size, highlighting the sensitivity of cumulant-based DLS analysis to larger aggregates. The polydispersity index (PDI) of 0.67 indicates a highly polydisperse system. Although the primary particles are nanoscale, magnetic dipole–dipole interactions induce aggregation in water, meaning the reported particle sizes reflect hydrodynamic diameters of clusters rather than the primary nanoscale dimensions.

The surface morphology of the synthesized iron oxide (Fig. 5a–d) primarily consists of irregular, agglomerated particles, a common trait of nanoscale iron oxides caused by strong magnetic forces and high surface energy. Higher magnification SEM images show that these agglomerates are made up of fine primary nanoparticles, nanoscale in size, clustered into larger secondary structures. This aligns with the SEM and DLS findings, where SEM depicts the morphology and size of primary particles in dry conditions, while DLS measures the hydrodynamic diameter of particle clusters in suspension. The presence of nanoscale primary particles offers a high surface area, beneficial for adsorption.

EDS analysis (Fig. 5e) indicates that Fe and O are the main elements, confirming iron oxide formation. Minor carbon signals likely originate from residual organics or carbon coating from SEM sample preparation. The lack of significant impurity peaks suggests the material is of high purity.

The SEM images (Fig. 6a–e) reveal that the synthesized TiO_2 particles have irregular morphologies, mainly composed of rod-like and granular structures with rough surfaces. These particles are densely packed and tend to form clusters, a typical characteristic of TiO_2 nanoparticles due to their high surface energy. The micrographs also show size variations, indicating a polydisperse sample (Suttiponparnit et al. 2011). The EDS spectrum (Fig. 6f) verifies the presence of titanium (Ti) and oxygen (O) as the primary elements, confirming the successful formation of TiO_2 nanoparticles. Minor peaks for C, Na, and Si are also detected, likely arising from the supporting substrate, residual precursors, or surface contamination. Overall, these findings confirm the effective synthesis of TiO_2 nanoparticles with a nanostructured morphology and characteristic elemental composition, suitable for adsorption applications.

The SEM images of banana peel (Fig. 7a–c) depict a heterogeneous, rough, and fibrous surface characteristic of lignocellulosic biomass. The micrographs display layered, wrinkled textures with porous, fibrillar networks, indicating numerous cavities and irregular channels that function as potential adsorption sites. These morphological features, combined with a surface area of approximately 13 $m^2.g^{-1}$, improve the accessibility of active sites and

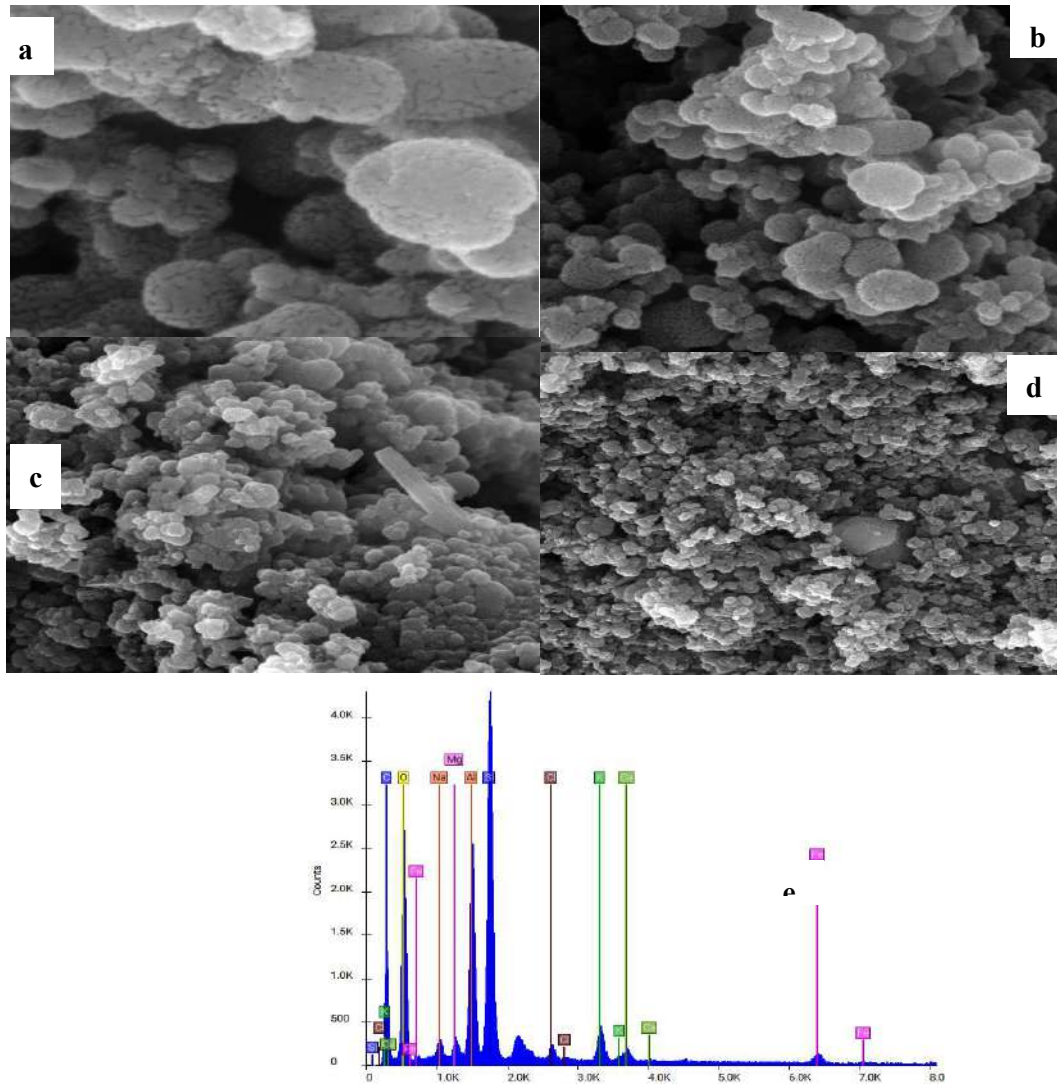


Fig. 5a-e: Scanning electron microscopy of iron oxide.

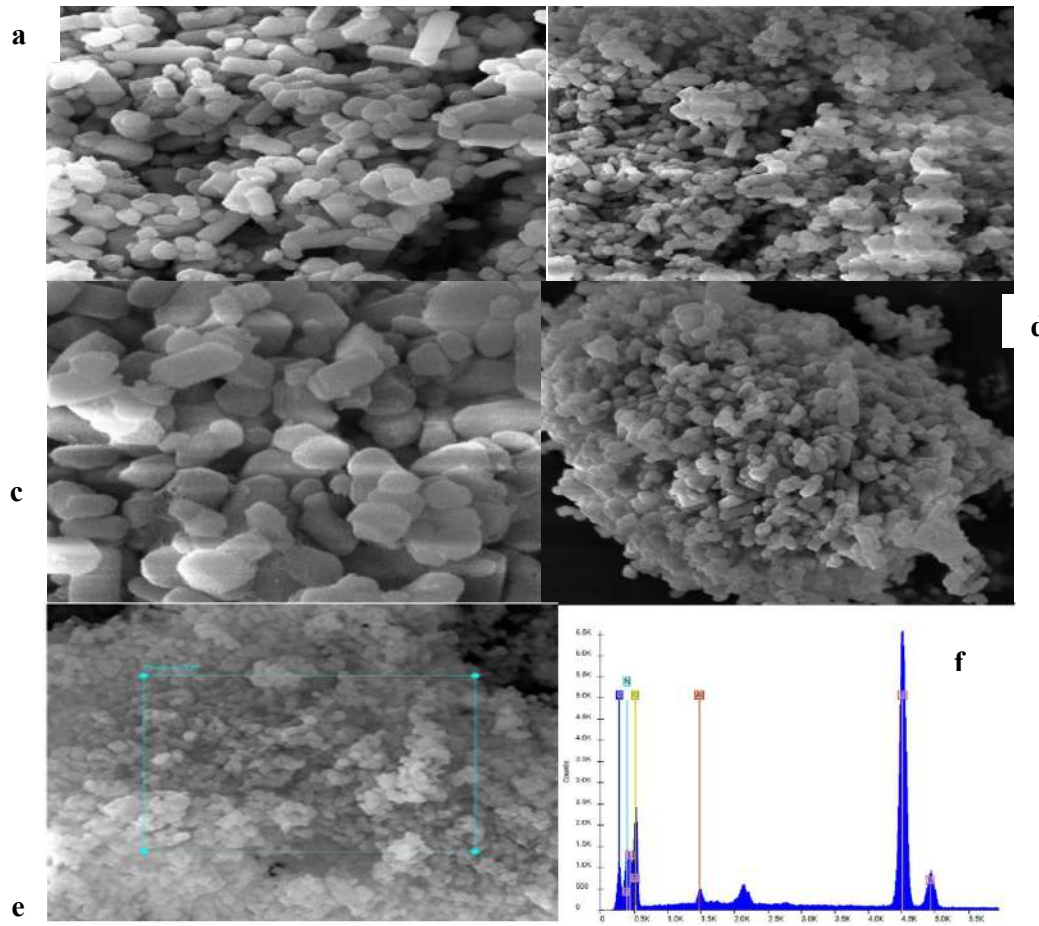


Fig. 6: SEM micrographs and EDS spectrum of titanium dioxide (TiO2) adsorbent.

promote pollutant diffusion within the adsorbent matrix. The EDS spectrum (Fig. 7d) confirms that carbon (C) and oxygen (O) are the predominant elements, consistent with the presence of cellulose, hemicellulose, and lignin, along with minor inorganic elements from the natural biomass or introduced during activation. Overall, SEM–EDS analysis demonstrates that the banana peel-based adsorbent exhibits a rough, porous structure, moderate surface area, and diverse elemental composition, making it an effective and sustainable material for adsorption and water purification.

3.1.4. Surface Area and Porosity Analysis (BET/BJH)

The surface area and pore characteristics of Fe_3O_4, TiO_2, and banana peel were analyzed using nitrogen adsorption–desorption (BET/BJH) at 77 K (Fig. 8). The isotherms display type IV behavior with hysteresis loops, indicating mesoporous structures. Fe_3O_4 exhibited a high BET surface area of 342.10 $m^2.g^{-1}$, a total pore volume of 0.432 $cm^3.g^{-1}$, and an average pore diameter of 2.94 nm, confirming its mesoporous, nanoscale features. TiO_2 showed a surface area of 172.44 $m^2.g^{-1}$, a pore volume of 0.448 $cm^3.g^{-1}$, and an average pore diameter of 9.96 nm, also within the mesoporous range. Conversely, banana peel had a significantly lower surface area of 22.94 $m^2.g^{-1}$ and pore volume of 0.019 $cm^3.g^{-1}$, consistent with its biomass origin. The high surface areas and nanoscale pore sizes of Fe_3O_4 and TiO_2 support the presence of nanoscale primary particles observed by SEM.

3.1.5. Zeta Potential

Zeta potential analysis was performed to assess the surface charge properties and colloidal stability of the adsorbent materials. As illustrated in Fig. 9, banana peel (BP) displayed a highly negative zeta potential of −29.2 mV, indicating robust electrostatic stability in aqueous suspension. This negative charge is mainly due to the presence of oxygen-containing functional groups such as carboxyl and hydroxyl groups on the banana peel surface. Conversely, TiO_2 and Fe_3O_4 showed low positive zeta potentials of +7.21 mV and +13.5 mV, respectively, implying limited colloidal stability and a higher likelihood of particle aggregation in water. The more negative surface charge of BP underscores

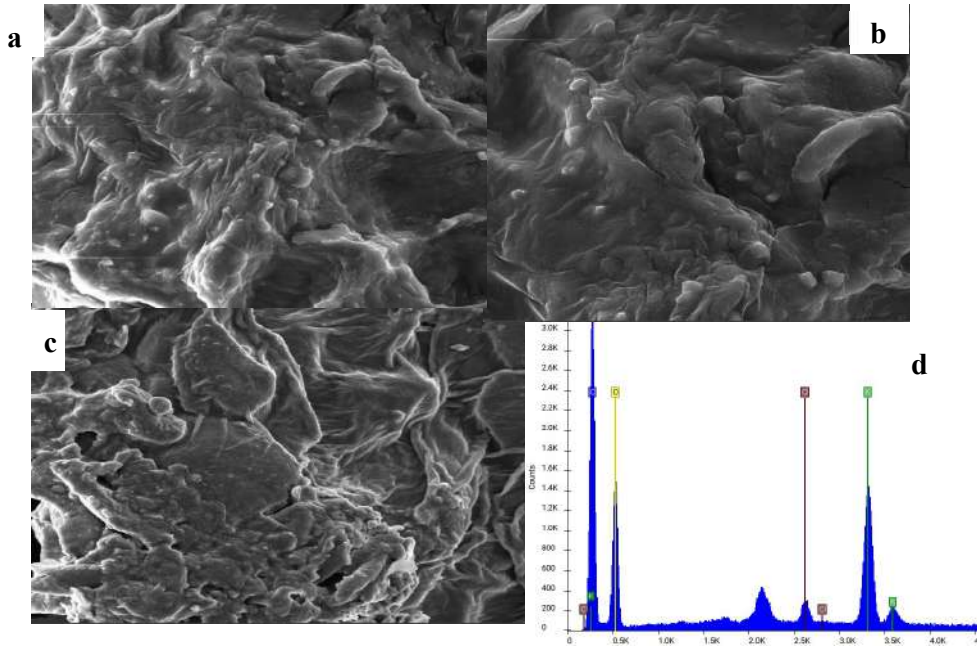


Fig. 7a-d: SEM micrographs and EDS spectrum of banana peel (BP)-based. adsorbent.

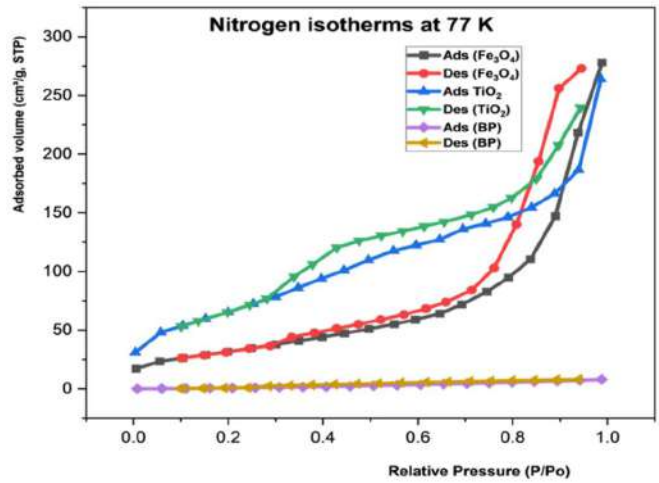


Fig 8: N_2 adsorption-desorption isotherms and BJH/BET textural parameters of the materials at 77 K.

its potential to improve surface stability and the adsorption efficiency of composites when combined with inorganic nanoparticles. These results validate the use of banana peel as a biopolymeric modifier to enhance the dispersion and electrostatic characteristics of Fe_3O_4- and TiO_2-based adsorbents for water and wastewater treatment.

3.1.6. VSM Analysis

The magnetic properties of iron oxide and TiO_2 were examined using a vibrating sample magnetometer (VSM). The hysteresis loop of iron oxide (Fig. 10) displays a narrow S-shaped curve with low coercivity (Hc $\approx$ 80–120 Oe) and minimal remanent magnetization (Mr $\approx$ 5–10 $\times$ 10^{-5} emu.g^{-1}), indicating weak ferrimagnetic behavior. The saturation magnetization (Ms) was found to be approximately 0.0025 emu.g^{-1}. The low Ms value suggests the material has a weak magnetic response, likely due to surface modification and dilution of the magnetic phase within the composite. As a result, the material shows limited magnetic responsiveness rather than practical magnetic separation, and magnetic recovery would only be achievable with a strong external magnetic field at close range (Selim et al. 2023).

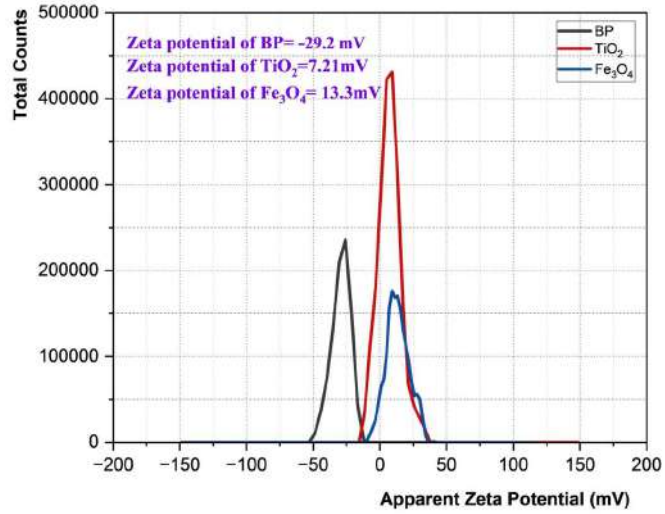


Fig. 9: Zeta potential distribution of Fe_3O_4/TiO_2/BP nanoparticles.

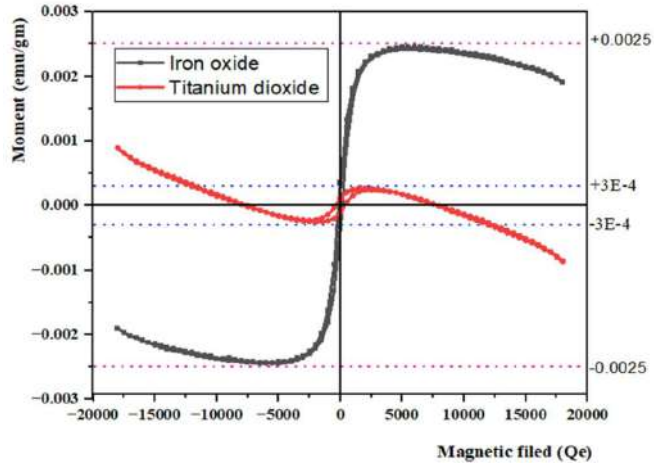


Fig. 10: VSM analysis of iron oxide and titanium dioxide.

Conversely, TiO_2 exhibits an almost linear magnetization curve with negligible coercivity and remanent magnetization, confirming its nonmagnetic nature. Although TiO_2 does not influence the magnetic properties of the composite, its addition enhances the overall adsorption capacity.

3.2. Adsorption Isotherms

The equilibrium adsorption data were modeled using the nonlinear Langmuir, Freundlich, Temkin, and Redlich–Peterson isotherm models (Fig. 11a–e, Table 2) to explore how Cr(VI), Cd(II), and Pb(II) interact with the Fe_3O_4/TiO_2/banana peel nanocomposite. Adsorption efficiency increased with higher adsorbent doses, peaking at 2.0 g, which indicates more active sites are available for metal ion uptake (Foroutan et al. 2022). For Cr(VI), both the Langmuir (R^2 = 0.729, qmax = 14.40 $mg.g^{-1}$) and Freundlich (R^2 = 0.75, KF = 7.12, 1/n = 0.47) models yielded moderate fits, pointing to a mixed adsorption process involving partial monolayer adsorption on a heterogeneous surface. The Freundlich constant (1/n < 1) signifies favorable adsorption. The Redlich–Peterson model (R^2 = 0.73, β = 0.51) further supports this mixed mechanism. For Cd(II), all isotherm models showed low correlation coefficients ($R^2 \leq 0.20$), while for Pb(II), several models produced statistically invalid fits, including negative R^2 values. These outcomes are likely due to nearly complete (~100%) removal efficiencies during experiments, causing equilibrium concentrations to approach zero. Under such conditions, standard adsorption isotherm models cannot reliably fit the data because a clear equilibrium adsorption curve is lacking. Therefore, no definitive adsorption mechanism can be determined for Cd(II) or Pb(II) based on these models, and the parameters should be interpreted with caution.

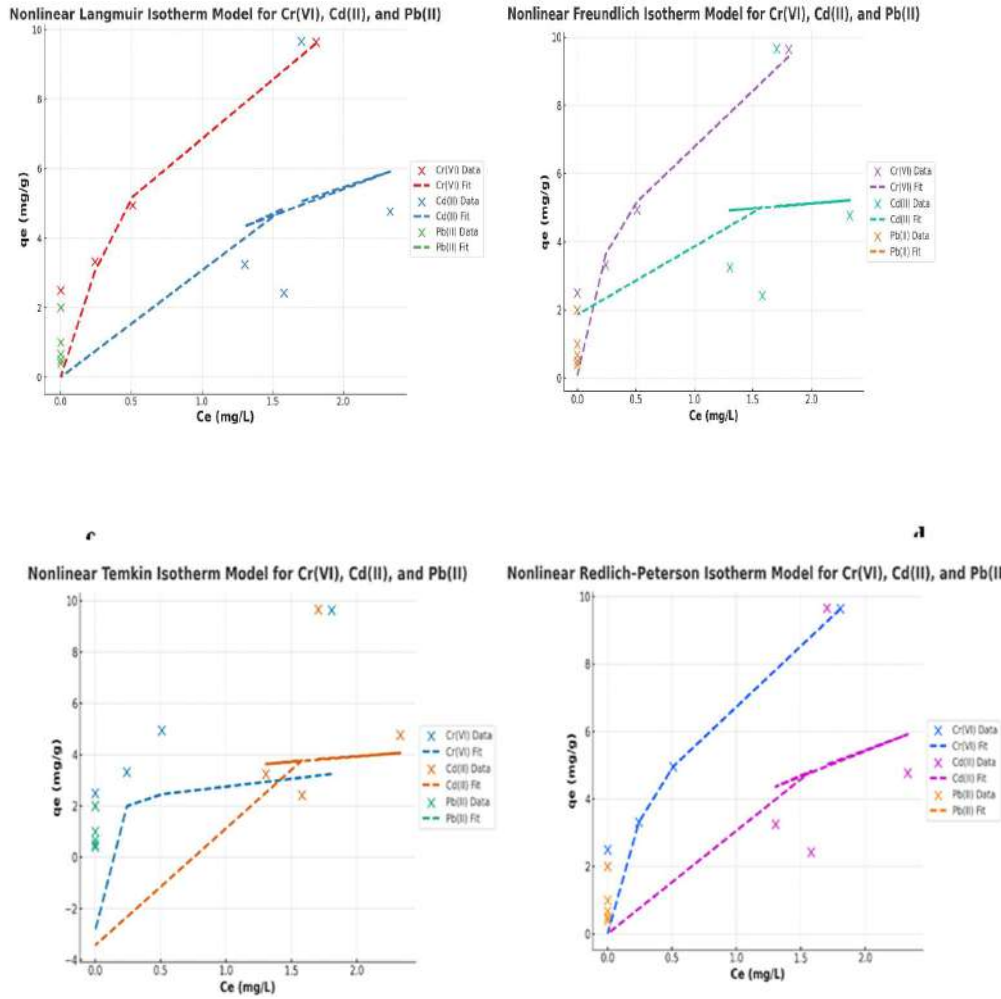


Fig. 11: Adsorption isotherm models (a-Nonlinear Langmuir, b-Nonlinear Freundlich, Nonlinear Temkin, and d-Nonlinear Redlich–Peterson) for the removal of metal ions onto Fe_3O_4/TiO/BP.

Table 2: Adsorption isotherm models and their parameters.

Model	Metal	Model Parameters	R^2	RMSE
Langmuir	Cr(VI)	Q_{max} = 14.3983 mg.g^{-1}, K_L = 1.10588 L.mg^{-1}	0.729	1.44
	Cd(II)	Q_{max} = 10.966 mg.g^{-1}, K_L = 0.50213 L.mg^{-1}	0.134	2.59
	Pb(II)	Q_{max} = 100 mg.g^{-1}, K_L = 10 L.mg^{-1}	-1.966	0.99
Freundlich	Cr(VI)	K_F = 7.12, 1.n^{-1} = 0.47	0.75	1.39
	Cd(II)	K_F = 4.78, 1.n^{-1} = 0.102	0.20	2.49
	Pb(II)	K_F = 27.15, 1.n^{-1} = 0.37	2.22E–	0.58
Temkin	Cr(VI)	AT = 100 L.g^{-1}, bT = 3962.954 J.moL^{-1}	-1.65	4.51
	Cd(II)	AT = 100 L.g^{-1}, bT = 3320.767 J.moL^{-1}	-0.70	3.63
	Pb(II)	AT = 100 L.g^{-1}, bT = 10000 J.moL^{-1}	-12.53	2.13
Redlich–Peterson	Cr(VI)	KR = 100 L.g^{-1}, aR = 13.10 L.mg^{-1}, β = 0.51	0.73	1.43
	Cd(II)	KR = 100 L.g^{-1}, aR = 25.34 L.mg^{-1}, β = 0.49	0.13	2.60
	Pb(II)	KR = 100 L.g^{-1}, aR = 2.99E–05 L.mg^{-1}, β = 1	-2.42	1.07

Overall, only Cr(VI) adsorption could be reasonably described by conventional isotherm models (Langmuir and Freundlich), whereas Cd(II) and Pb(II) exhibited adsorption behaviors beyond the applicability of the tested isotherm models.

The adsorption experiments were carried out in a multicomponent system where Cr(VI), Cd(II), and Pb(II) coexisted and competed for the same surface-active sites on the Fe_3O_4/TiO_2/BP nanocomposite. Consequently, their adsorption behaviors are interdependent and cannot be simply equated to those observed in single-metal systems. Differences in removal efficiency are influenced by factors such as ionic charge, hydrated ionic radius, polarizability, and aqueous speciation. Pb(II) demonstrated the highest affinity for the adsorbent, followed by Cd(II), while Cr(VI), mainly present as anions, showed comparatively weaker adsorption in competition. Although individual isotherm models were used for clarity, the results illustrate the competitive adsorption dynamics in multicomponent conditions. Detailed quantitative modeling of competitive adsorption was beyond this study's scope and should be explored in future research.

3.3. Kinetic Studies

The assessment of adsorbent dosage on adsorption kinetics aimed to simulate practical operating conditions rather than to determine fundamental kinetic constants. As the adsorbent dosage increased, the adsorption capacity (qe, $mg.g^{-1}$) decreased, likely due to a dilution effect and the underutilization of available surface-active sites at higher doses. This typical behavior in batch adsorption systems does not imply a reduction in overall adsorption efficiency or rate.

The kinetic parameters obtained at different adsorbent dosages are not directly compared as intrinsic constants. Instead, kinetic modeling was employed to describe adsorption trends and rate-controlling processes independently at each dosage condition

3.3.1. Kinetic Studies for Chromium (Cr(VI))

The adsorption kinetics of Cr(VI) onto the Fe_3O_4/TiO_2/BP nanocomposite were investigated to elucidate the rate-controlling mechanisms of ion removal. The adsorption capacity increased rapidly during the initial contact period (10–45 min), which can be attributed to the abundance of

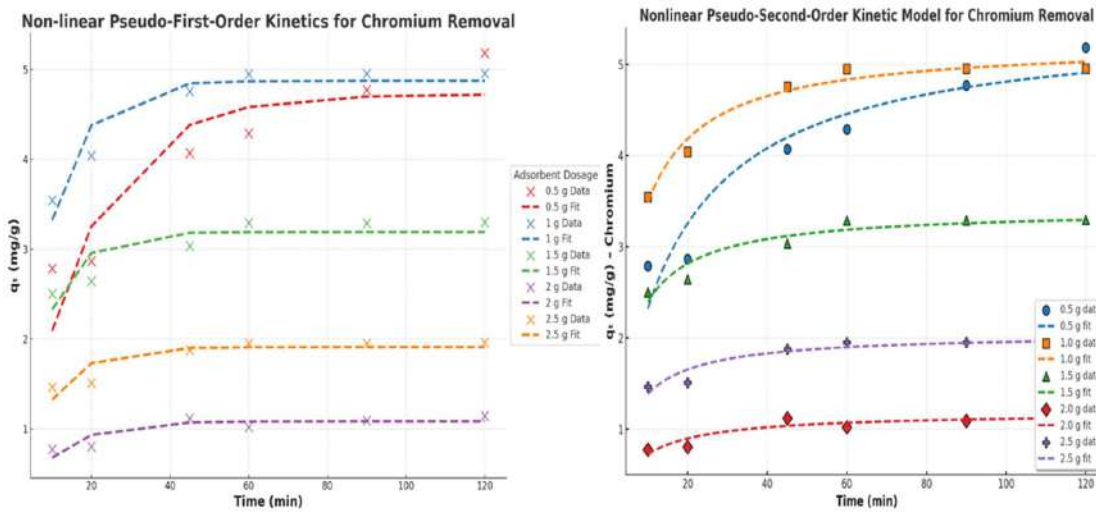


Fig. 12: Nonlinear pseudo-first-order and pseudo-second-order for chromium removal.

Table 3: Nonlinear fitted pseudo-first-order and pseudo-second-order kinetic models for the removal of Chromium ions using different masses of Fe_3O_4/TiO_2/BP.

Mass	Pseudo-first-order				Pseudo-second-order			
	qe [$mg.g^{-1}$]	k1	R^2	RMSE	qe [$mg.g^{-1}$]	k2	R^2	RMSE
0.5g	4.723	0.0584	0.785	0.416	5.46	0.013	0.90	0.286
1g	4.873	0.114	0.893	0.179	5.24	0.038	0.97	0.086
1.5g	3.191	0.131	0.712	0.174	3.41	0.07	0.91	0.1
2g	1.084	0.098	0.735	0.077	1.18	0.133	0.84	0.06
2.5g	1.91	0.118	0.73	0.111	2.05	0.10	0.89	0.071

available surface-active sites and favorable electrostatic interactions between Cr(VI) anions and the positively charged surface of the nanocomposite. As the adsorption process progressed, the uptake rate gradually decreased and eventually reached equilibrium as the available active sites became increasingly occupied, thereby reducing the driving force for mass transfer.

The kinetic data were analyzed using the pseudo-first-order (PFO) and pseudo-second-order (PSO) models (Fig. 12, Table 3). The PSO model provided a better fit to the experimental data, as indicated by higher correlation coefficients (R^2 = 0.84–0.97) and lower RMSE values than those obtained with the PFO model. These results suggest that the adsorption process is predominantly governed by surface-related interactions and the availability of active sites, with chemisorption serving as the primary rate-controlling mechanism rather than diffusion alone.

3.3.2. Kinetic Studies for Cadmium(II)

The time-dependent adsorption of Cd(II) onto Fe_3O_4/TiO_2/BP was examined to evaluate the adsorption rate and controlling processes. Rapid adsorption occurred within the first 20–40 min, corresponding to the occupation of the surface-active sites. As equilibrium was approached, the adsorption rate slowed, likely due to site saturation and increased resistance to mass transfer.

Kinetic modeling using the PFO and PSO equations (Fig. 13, Table 4) showed that the PSO model provided a better fit to the experimental data (R^2 = 0.75, RMSE = 0.0068) than the PFO model. This indicates that Cd(II) adsorption kinetics are influenced by surface interactions and active-site availability. At higher adsorbent dosages, equilibrium was reached more rapidly, which limited the applicability of kinetic modeling under these conditions.

3.3.3. Kinetic Studies for Lead (Pb(II))

The adsorption of Pb(II) onto the Fe_3O_4/TiO_2/BP nanocomposite demonstrated a rapid initial phase, followed by a more gradual approach to equilibrium. This initial fast stage indicates a strong affinity of Pb(II) ions for surface-active sites, while the subsequent slower phase may be due to site saturation and diffusion limitations. Kinetic analysis using the PFO and PSO models (Fig. 14, Table 5) showed that the PSO model best fitted the experimental data, with higher correlation coefficients (R2= 0.87–0.95) and lower RMSE values. This indicates that Pb(II) adsorption kinetics are predominantly governed by surface interactions rather than simple physical diffusion.

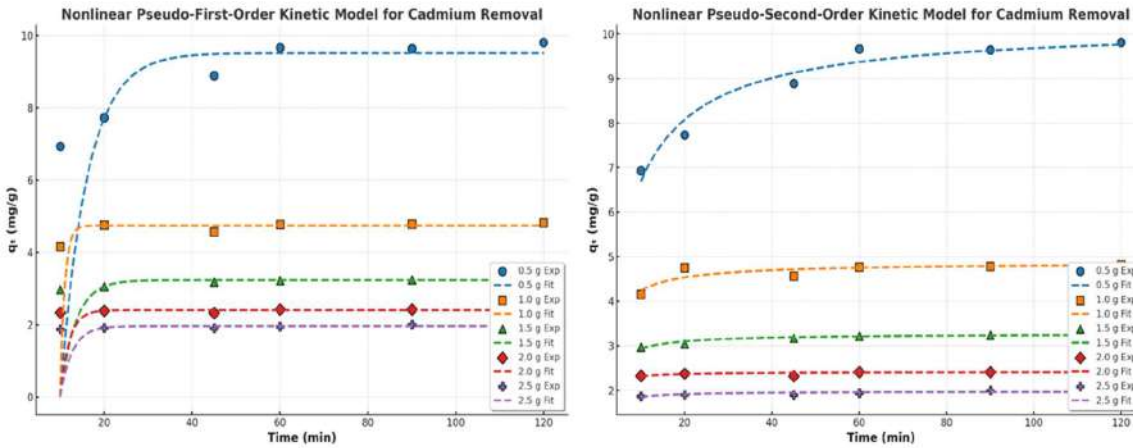


Fig. 13: Nonlinear pseudo-first-order and pseudo-second-order models for cadmium removal.

Table 4: Nonlinear fitted pseudo-first-order and pseudo-second-order kinetic models for the removal of Cadmium ions using different masses of Fe_3O_4/TiO_2/BP.

Mass	Pseudo-first-order				Pseudo-second-order			
	qe [mg.g^{-1}]	k_1 [1.min^{-1}]	R^2	RMSE	qe [mg.g^{-1}]	k_2	R^2	RMSE
0.5g	9.43	0.11	0.82	0.46	10.18	0.019	0.95	0.23
1g	4.75	0.21	0.86	0.09	4.87	0.14	0.76	0.114
1.5g	3.20	0.25	0.64	0.06	3.28	0.27	0.93	0.028
2g	2.40	0.36	0.29	0.037	2.42	1	0.41	0.034
2.5g	1.95	0.31	0.38	0.04	1.98	0.76	0.63	0.03

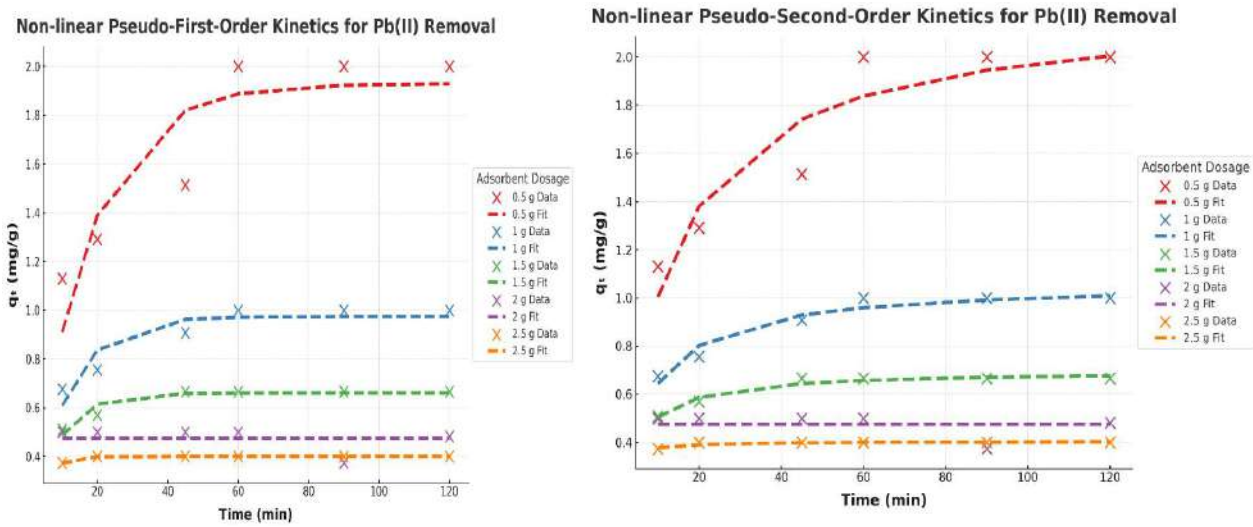


Fig. 14: Nonlinear pseudo-first-order and pseudo-second-order for lead removal.

Table 5: Nonlinear fitted pseudo-first-order and pseudo-second-order kinetic models for the removal of lead ions using different masses of Fe_3O_4/TiO_2/BP.

Mass	Pseudo-first-order				Pseudo-second-order			
	qe [mg.g^{-1}]	k_1 [1.min^{-1}]	R^2	RMSE	qe [mg.g^{-1}]	k_1 [1.min^{-1}]	R^2	RMSE
0.5g	1.93	0.06	0.78	0.17	2.203	0.038	0.87	0.13
1g	0.97	0.1	0.84	0.05	1.06	0.144	0.95	0.03
1.5g	0.66	0.134	0.88	0.02	0.7	0.37	0.96	0.013
2g	0.48	1	~0.00	0.05	0.51	1	~0.00	0.062
2.5g	0.40	0.27	0.99	0.0006	0.43	3.32	0.808	0.017

Different experimental runs were performed to assess how adsorbent dosage influences the rate of adsorption. Typically, the PSO kinetic rate increased with higher dosages. To evaluate the model's accuracy, the equilibrium adsorption capacity predicted by the PSO model at a specific dosage should be compared with the actual batch experimental data obtained at the same dosage. Notably, the equilibrium adsorption capacities tend to decrease as adsorbent dosage increases, likely due to the greater number of available sites, considering the initial heavy metal concentration remains constant.

3.4. Comparative Evaluation with Reported Adsorbents

The Fe_3O_4/TiO_2/BP nanocomposite exhibited high adsorption capacities for Cr(VI), Cd(II), and Pb(II), confirming the synergistic effect of Fe_3O_4 and TiO_2 nanoparticles supported on banana peel biomass. The maximum adsorption capacities of 10.9 mg.g^{-1} for Cd(II) and 100 mg.g^{-1} for Pb(II) obtained in this study are significantly higher than that of raw banana peel (~5.9 mg.g^{-1}) reported by Deshmukh et al. (2017) and are comparable to that of BPB/Fe_3O_4 (~30.3 mg.g^{-1}) reported in the same study. The adsorption performance also remains competitive with more advanced composites, such as BPAC/Al_2O_3–chitosan (~46.9 mg.g^{-1}) and BPB/Fe_3O_4/ZIF-67 (~50.8 mg.g^{-1}), reported by Ramutshatsha-Makhwedzha et al. (2022). Kinetic analysis revealed that adsorption followed the pseudo-second-order (PSO) model, particularly at the 2 g adsorbent dosage, with R^2 values ranging from 0.89 to 0.99 and low RMSE values, indicating that chemisorption, involving electron exchange or complexation with oxygen-containing functional groups, was the predominant adsorption mechanism. Compared with Fe_3O_4–*Actinomucor* sp. composites (qmax = 29.5 mg.g^{-1}) reported by Masoudi et al. (2018), the Fe_3O_4/TiO_2/BP nanocomposite demonstrated superior adsorption capacity while exhibiting similar kinetic behavior.

These findings demonstrate that the Fe_3O_4/TiO_2/BP nanocomposite achieves a favorable balance between adsorption efficiency, structural stability, and a simple, environmentally friendly synthesis route, making it a promising low-cost adsorbent for the removal of heavy metals from aqueous systems.

5. CONCLUSIONS

This study successfully synthesized and evaluated a Fe_3O_4/TiO_2/banana peel (BP) nanocomposite for removing Cr(VI),

Cd(II), and Pb(II) from water. Characterization confirmed the presence of functionalized magnetic surfaces with high reactivity and structural stability. Adsorption data fit best with the Langmuir and Redlich–Peterson models, suggesting that metal ions were primarily adsorbed as a monolayer on uniform active sites. Kinetic results aligned with the pseudo-second-order model, indicating that chemisorption involving valence forces or surface complexation controlled the process. The maximum adsorption capacities—14.4 $mg.g^{-1}$ for Cr(VI), 10.9 $mg.g^{-1}$ for Cd(II), and 100 $mg.g^{-1}$ for Pb(II)—were comparable to or better than those of similar nanocomposites. These findings show that the Fe_3O_4/TiO_2/BP nanocomposite is an effective, magnetically separable, and eco-friendly material for heavy metal removal, promising for water treatment applications and sustainable waste utilization.

6. REFERENCES

Deshmukh, P.D., Khadse, G.K., Shinde, V.M. and Labhasetwar, P., 2017. Cadmium removal from aqueous solutions using dried banana peels as an adsorbent: Kinetics and equilibrium modeling. *Journal of Bioremediation & Biodegradation*, 8(3), p.1000395. [DOI]

FAO of the United Nations, 2024. FAO Statistical Yearbook 2024 reveals critical insights on the sustainability of global agriculture, food security, and the importance of agrifood systems in employment. *2024 Statistical Yearbook*, 2024. [DOI]

Foroutan, R., Peighambardoust, S.J., Mohammadi, R., Peighambardoust, S.H. and Ramavandi, B., 2022. Cadmium ion removal from aqueous media using banana peel biochar/Fe_3O_4/ZIF-67. *Environmental Research*, 211, p.113020. [DOI]

Gupta, S.S., Al Kausor, M. and Chakrabortty, D., 2025. Banana peel as potential bioadsorbent toward removal of emerging contaminants from wastewater for sustainable environment: A review. *Chemical Papers*, 79(5), pp.2717-2750. [DOI]

Keerthana, B.G.T., Solaiyammal, T., Muniyappan, S. and Murugakoothan, P., 2018. Hydrothermal synthesis and characterization of TiO_2 nanostructures prepared using different solvents. *Materials Letters*, 220, pp.20-23. [DOI]

Lellala, K., Behera, S.K., Srivastava, P., Saeed, W.S., Haidyrah, A.S. and Burile, A.N., 2024. Fe_3O_4 nanoparticles decorated on N-doped graphene oxide nanosheets for elimination of heavy metals from industrial wastewater and desulfurization. *Diamond and Related Materials*, 150, p.111746. [DOI]

Liew, R.K., Nam, W.L., Chong, M.Y., Phang, X.Y., Su, M.H., Yek, P.N.Y., Ma, N.L., Cheng, C.K., Chong, C.T. and Lam, S.S., 2018. Oil palm waste: An abundant and promising feedstock for microwave pyrolysis conversion into good quality biochar with potential multi-applications. *Process Safety and Environmental Protection*, 115, pp.57-69. [DOI]

Masoudi, R., Moghimi, H., Azin, E. and Taheri, R.A., 2018. Adsorption of cadmium from aqueous solutions by novel Fe3O4- newly isolated Actinomucor sp. bio-nanoadsorbent: Functional group study. *Artificial Cells, Nanomedicine and Biotechnology*, 46(sup3), pp.S1092-S1101. [DOI]

Mehmood, K. and Dhanya, W.M., 2025. Unlocking the potential of banana peel bioactives: Extraction methods, benefits, and industrial applications. *Discover Food*. [DOI]

Mishra, A., Kumari, M., Swati, Kumar, R., Iqbal, K. and Thakur, I.S., 2022. Persistent organic pollutants in the environment: Risk assessment, hazards, and mitigation strategies. *Bioresource Technology Reports*, 19, p.101143. [DOI]

Mishra, S., Prabhakar, B., Kharkar, P.S. and Pethe, A.M., 2023. Banana peel waste: An emerging cellulosic material to extract nanocrystalline cellulose. *ACS Omega*, 8(1), pp.8-13. [DOI]

Mor, S. and Ravindra, K., 2023. Municipal solid waste landfills in lower- and middle-income countries: Environmental impacts, challenges and sustainable management practices. *Process Safety and Environmental Protection*, 174, pp.510-530. [DOI]

Otieno, A.O., Home, P.G., Raude, J.M., Murunga, S.I., Ngumba, E., Ojwang, D.O. and Tuhkanen, T., 2021. Pineapple peel biochar and lateritic soil as adsorbents for recovery of ammonium nitrogen from human urine. *Journal of Environmental Management*, 293, p.112794. [DOI]

Pokharel, P., Kwak, J.H., Ok, Y.S. and Chang, S.X., 2018. Pine sawdust biochar reduces GHG emissions by decreasing microbial and enzyme activities in forest and grassland soils in a laboratory experiment. *Science of the Total Environment*, 625, pp.1247-1256. [DOI]

Ramutshatsha-Makhwedzha, D., Mbaya, R. and Mavhungu, M.L., 2022. Application of activated carbon banana peel coated with Al2O3-chitosan for the adsorptive removal of lead and cadmium from wastewater. *Materials*, 15(3), p.860. [DOI]

Razzak, S.A., Faruque, M.O., Alsheikh, Z., Alsheikhmohamad, L., Alkuroud, D., Alfayez, A., Hossain, S.M.Z. and Hossain, M.M., 2022. A comprehensive review on conventional and biological-driven heavy metals removal from industrial wastewater. *Environmental Advances*, 7, p.100168. [DOI]

Selim, M.M., El-safty, S. and Tounsi, A., 2023. Review of the impact of the external magnetic field on the characteristics of magnetic nanofluids. *Alexandria Engineering Journal*, 76, pp.75-89. [DOI]

Sial, T.A., Khan, M.N., Lan, Z., Kumbhar, F., Ying, Z., Zhang, J., Sun, D. and Li, X., 2019. Contrasting effects of banana peels waste and its biochar on greenhouse gas emissions and soil biochemical properties. *Process Safety and Environmental Protection*, 122, pp.366-377. [DOI]

Smyth, S., 2024. Waste management in developing countries: Challenges and solutions. *Journal of Waste Management and Environmental Sustainability*, 9(3), p.350. [DOI]

Sossou, K., Bala Prasad, S., Agbotsou, K.E., Saidou Souley, H. and Mudigandla, R., 2024a. Characteristics of landfill leachate and leachate treatment by biological and advanced coagulation processes: Feasibility and effectiveness – An overview. *Waste Management Bulletin*, 2(2), pp.181-198. [DOI]

Sossou, K., Prasad, S.B., Agbotsou, E.K. and Saidou Souley, H., 2024b. Evaluation of the performance of magnetic zeolite nanocomposites in removing various water contaminants as heavy metals, organic pollutants, and emerging contaminants: A review. *Next Nanotechnology*, 6, p.100075. [DOI]

Strategies, E.F., Ayach, J., Malti, W.E., Duma, L., Lalev, J., Ajami, M.A., Hamad, H. and Hijazi, A., 2024. Comparing conventional and advanced approaches for heavy metal removal in wastewater treatment: An in-depth review. *Journal of Environmental Science and Technology*, 45(2), pp.112-128.

Suttiponparnit, K., Jiang, J., Sahu, M., Suvachittanont, S., Charinpanitkul, T. and Biswas, P., 2011. Role of surface area, primary particle size, and crystal phase on titanium dioxide nanoparticle dispersion properties. *Nanoscale Research Letters*, 6(1), p.27. [DOI]

Togun, H., Basem, A., Abdulrazzaq, T., Biswas, N., Abed, A.M., Dhabab, J.M., Mohammed, H.I., Sharma, B.K., Paul, D. and Barmavatu, P., 2025. Current developments in the use of nanotechnology to enhance the generation of sustainable bioenergy. *Sustainable Materials and Technologies*, 43, p.e01266. [DOI]

Zanganeh, S., Kajbafvala, A., Zanganeh, N., Molaei, R., Bayati, M.R., Zargar, H.R. and Sadrnezhaad, S.K., 2011. Hydrothermal synthesis and characterization of TiO_2 nanostructures using LiOH as a solvent. *Advanced Powder Technology*, 22(3), pp.336-339. [DOI]

Nature Environment and Pollution Technology
An International Quarterly Scientific Journal

p-ISSN: 0972-6268
(Print copies up to 2016)
e-ISSN: 2395-3454

Vol. 25 | No. 3 | Article ID D1893 | 2026

Original Research Paper

https://doi.org/10.46488/NEPT.2026.v25i03.D1893

Open Access Journal

Application of Principal Component Analysis (PCA) and Interpolated Spatial Distribution Maps in Soil Quality Control of Dragon Fruit Farms in Tay Ninh Province, Vietnam

Nguyen Van Phuong†, Tong Hai Minh and Le Hong Thia
Institute of Environmental Science, Engineering & Management, Industrial University of Ho Chi Minh City, 70000, Vietnam
†Corresponding author: Nguyen Van Phuong; nguyenvanphuong@iuh.edu.vn

Abbreviation: Nat. Env. & Poll. Technol.
Website: www.neptjournal.com

Received: 20-12-2025
Revised: 17-02-2026
Accepted: 26-02-2026

Key Words:

Dragon fruit
Soil quality index (SQI)
Principal Component Analysis (PCA)
Minimum dataset (MDS)
Soil quality control

Citation for the Paper:

Phuong, N.V., Minh, T.H. and Thia, L.H., 2026. Application of Principal Component Analysis (PCA) and interpolated spatial distribution maps in soil quality control of dragon fruit farms in Tay Ninh Province, Vietnam. *Nature Environment and Pollution Technology*, 25(3), D1893.

Note: From 2025, the journal has adopted the use of Article IDs in citations instead of traditional consecutive page numbers. Each article is now given individual page ranges starting from page 1.

Copyright: © 2026 by the authors
Licensee: Technoscience Publications
This article is an open access article distributed under the terms and conditions of the Creative Commons Attribution (CC BY) license (https://creativecommons.org/licenses/by/4.0/).

ABSTRACT

Accurate and timely assessment of soil quality is essential for sustainable farming and efficient agricultural management. The Soil Quality Index (SQI) is heavily influenced by fluctuations in physical and chemical soil indicators. Twelve composite soil samples were collected from the dragon fruit cultivation area in Tay Ninh, Vietnam. The dataset included eleven soil parameters: pH, electrical conductivity (EC), total organic carbon (TOC), cation exchange capacity (CEC), available phosphorus (P_av), ammonium (NH4+), bulk density, particle density, clay, silt, and sand. Principal Component Analysis (PCA) was employed to identify the Minimum Dataset (MDS) and determine parameter weights. These were combined with land index scores to estimate the SQI. Additionally, a spatial distribution map of SQI was created using the Inverse Distance Weighting (IDW) method in ArcGIS 10.8. Results showed that the MDS is influenced by four principal components, which explain 89.02% of the total data variance. Key parameters include CEC, P_av, EC, and pH, with weights of 0.37, 0.26, 0.22, and 0.15, respectively. The average soil quality score was 41.6%, with 58.3% classified as degraded. The study demonstrated that combining PCA and GIS provides a comprehensive and intuitive approach to SQI evaluation. Furthermore, developing agronomic maps based on large sample sizes supports sustainable agricultural management, as evidenced by these research findings.

1. INTRODUCTION

Soil quality determines the ability of soil to support plant health, maintain productivity, and sustain farmers' livelihoods and economic stability (Rajput et al. 2023). Comprehensive monitoring of soil health and a thorough understanding of soil indicators and their essential functions are critical for developing effective solutions and policies aimed at sustainable land management (Ţopa et al. 2025).

Various approaches have been established to quantify and monitor soil quality based on the calculation of indices, including the Soil Quality Index (SQI), Soil Health Index (SHI), and Soil Sustainability Index (SSI), which are used as decision-support tools (Damiba et al. 2024). However, none of these indices has been widely accepted for soil quality assessment, possibly because of the complexity and heterogeneity of soil systems. Three approaches, namely the Total Data Set (TDS), Expert Data Set (EDS), and Minimum Data Set (MDS), are commonly used for soil quality assessment (Damiba et al. 2024). In the TDS approach, the SQI is calculated as the average score of all selected indicators. In the EDS approach, indicator weights are assigned based on expert knowledge, although sufficient information is often unavailable for all soil indicators. In contrast, the MDS approach is based on Principal Component Analysis (PCA). Compared with the TDS and EDS approaches, the MDS requires less intensive field and laboratory work, thereby reducing both time and cost (Damiba et al. 2024).

In addition, many studies have focused on individual physical and chemical indicators, although these may provide an incomplete assessment because many soil properties result from interactions among several processes. In some studies, biological indicators have been ignored or excluded (Damiba et al. 2024, Ṭopa et al. 2025). Priority soil indicators are generally selected based on the following criteria: ease of measurement, rapid analysis, low cost, applicability under field conditions, and sensitivity to changes in management practices (Ṭopa et al. 2025). Common soil indicators used in soil quality assessment include physical properties such as bulk density, particle density (specific gravity), water retention, and the percentages of clay, sand, and silt, as well as chemical properties including pH, electrical conductivity (EC), organic matter, cation exchange capacity (CEC), NH_4^+, available phosphorus (P_av), copper, and zinc (Abdel-Fattah et al. 2021, Hanif et al. 2025, Rajput et al. 2023, Van 2025).

The MDS-based SQI calculation method is currently the most widely used because of its flexibility, quantitative nature, and ease of application. Statistical techniques such as PCA and Pearson correlation analysis are commonly employed to develop the MDS (Rajput et al. 2023, Ṭopa et al. 2025, Van 2025). This method provides not only an SQI value but also a minimum set of soil parameters for monitoring soil health (Rajput et al. 2023). PCA is a valuable statistical tool for data reduction and improving model efficiency. It removes correlated variables, enhances the statistical significance of selected indicators, and minimizes multicollinearity. By transforming high-dimensional datasets into a smaller number of principal components, PCA reduces the number of variables included in the model, thereby improving computational efficiency and facilitating data visualization and interpretation (Abdel-Fattah et al. 2021). The Inverse Distance Weighting (IDW) interpolation method in ArcGIS 10.8 is widely used to estimate SQI values at unsampled locations based on surrounding sample points and to map the spatial distribution of soil quality (Abdel-Fattah et al. 2021, Kahsay et al. 2025).

Tay Ninh Province is the second-largest dragon fruit-producing province in Vietnam, with more than 7,000 ha under cultivation (Mai et al. 2025). The cultivated area is characterized by acid sulfate soils within the Vam Co River basin. However, soil quality management in this dragon fruit-growing region still lacks effective solutions to ensure sustainable production, including precision farming and modern management practices. Therefore, this study combines PCA and Geographic Information Systems (GIS) to identify key soil quality indicators and simulate the spatial variation of SQI in dragon fruit farms in Tay Ninh Province, Vietnam, using a dataset comprising 11 soil parameters: pH,

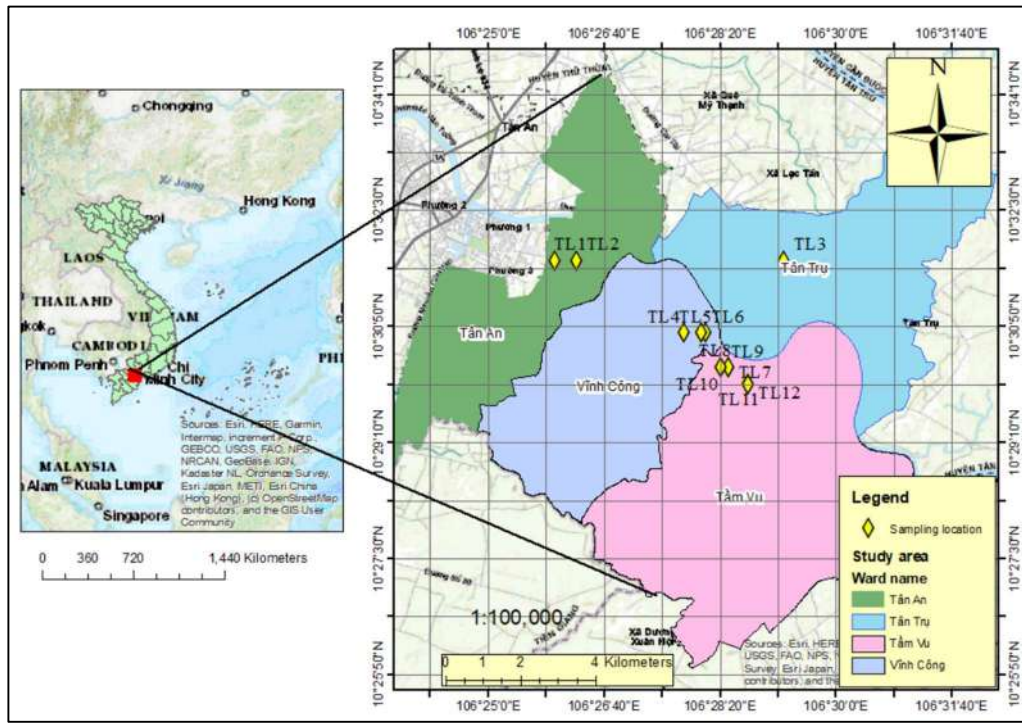


Fig. 1: Map of sampling locations in dragon fruit farms in Tay Ninh, Vietnam (TL1 to TL12 are 12 composite samples collected in the dragon fruit farms, Tay Ninh, Vietnam).

EC, TOC, P_av, NH_4^+, bulk density (d), particle density (D), clay content, silt content, sand content, and CEC.

2. MATERIALS AND METHODS

2.1. Field Sampling

In January 2024, sixty soil samples were collected from dragon fruit farms in Tay Ninh province to form twelve composite samples (see Fig. 1). Each selected area, roughly 4 km² (400 hectares), displayed the greatest homogeneity in dragon fruit tree age and color. Within each zone, a sampling site of at least 1.5 hectares was designated. Soil samples were extracted at a depth of 0-30 cm, the layer most indicative of soil quality dynamics. The sampling employed a composite method: in each area exceeding 1.5 hectares, samples were taken from the four corners and the center along the diagonal. The collected soil was naturally dried, ground finely, and sieved through a 2 mm mesh before analyzing eleven soil parameters: pH, electrical conductivity (EC), total organic carbon (TOC), cation exchange capacity (CEC), available phosphorus (P_av), ammonium (NH4+), bulk density, particle density, clay, silt, and sand.

2.2. Analytical Methods

The soil properties were determined using standardized methods. Soil particle density (d) was determined according to TCVN 6863:2001, pH and electrical conductivity (EC) were measured following ISO 10390:1993, bulk density (D) was determined according to TCVN 8305:2009, total organic carbon (TOC) was analysed using the Walkley–Black method, available phosphorus (P_av) was determined using the Olsen method, ammonium (NH_4^+) was determined following the method of Baethgen & Alley (1989), soil texture was analyzed using the hydrometer method (George 1962), and cation exchange capacity (CEC) was determined using the ammonium acetate method according to TCVN 8568:2010. Analytical-grade reagents, including H_2SO_4, $K_2Cr_2O_7$, $Fe(NH_4)_2(SO_4)_2 \cdot 6H_2O$, Na_3PO_4, $SnCl_2$, and $(NH_4)_6Mo_7O_{24} \cdot 4H_2O$ (Merck, Germany, and China), were used for all laboratory analyses.

2.3. Soil Quality Assessment

Principal Component Analysis (PCA) is a multivariate statistical technique employed for data reduction by simplifying data structure through the extraction of principal components (PCs) and analyzing the orthogonal relationships among variables. Following PCA, the Soil Quality Index (SQI) is determined through a series of steps, which include standardizing variables, constructing a correlation matrix, identifying principal components and their explained variance, calculating indicator weights, analyzing factor loadings, and ultimately computing the SQI (Aisah et al. 2025, Damiba et al. 2024). Since soil indicators are measured in different units, they are standardized to a 0–1 scale to facilitate comprehensive soil quality assessment and to ensure all indicators contribute equally (Damiba et al. 2024). Based on reference values and expert judgment, three common scoring functions, linear or non-linear, are used: "more is better," "optimal range," and "less is better" (Bünemann et al. 2018). In this study, the "more is better" scoring function was applied to relevant soil indicators and is given by Equation (1) (Bandyopadhyay & Maiti 2021).

$$S_i = \frac{X}{X_{max}} \quad ...(1)$$

Where X, Xmax, and Xmin are the measured value, the maximum value, and the minimum value. Si is the score of indicator i. Non-linear functions, including pH, EC, clay, silt, and sand, and linear (NH4+, P_av, TOC, CEC, the more the better), the less the better (bulk density, particle density), are presented in detail in Table 1 (Damiba et al. 2024, Kahsay et al. 2025)

For the soil indices: "less is better" is described in formula (Eq. 2):

$$S_i = \frac{X_{min}}{X} \quad ...(2)$$

For the non-linear scoring function, the soil parameters are converted according to the S-shaped curve equation; formula (Eq. 3) is as follows:

$$S_i = \frac{a}{\left[1 + \left(\frac{X_i}{X_{imean}}\right)^b\right]} \quad ...(3)$$

Where Xi is the measured value, Ximean is the average value, and Xopt is the optimal value (Table 1). Slope b = -2.5 (more is better), b = +2.5 (less is better) và Xo (Damiba et al. 2024, Kahsay et al. 2025)

A Pearson correlation matrix was generated to evaluate the relationships among the variables. Correlation coefficients

Table 1: Components of the scoring function.

Indices	Scoring curve	Xmax	Xmin	Xopt
Sand [%]	Optimum	90.00	6.00	36
Silt [%]	Optimum	50.00	4.00	30
Clay [%]	More is better	84.00		
D [$g.cm^{-3}$]	Less is better	66.00	0.89	
pH [H_2O]	Optimum	9.62	5.04	7.00
EC [$dS\ m^{-1}$]	Less is better	2	0.001	1
TOC [%]	More is better	5.96		
P_av [$mg.kg^{-1}$]	More is better	58.89		
CEC [$cmoL.kg^{-1}$]	More is better	61.98		

range from −1 to +1, where the magnitude indicates the strength of the relationship and the sign denotes its positive or negative nature. These correlations serve as a foundation for the subsequent Principal Component Analysis (PCA). PCA reduces the dataset's dimensionality by transforming the original variables into a set of uncorrelated principal components (PCs) that explain most of the original variance. Variables with the highest loadings on these PCs are considered the most influential parameters affecting agricultural land quality (Rangel-Peraza et al. 2017). Communalities represent the percentage of variance each variable explains in the PCs. PCs with eigenvalues greater than 1 and accounting for at least 10% of the data's variation are retained. From these, a Minimum Data Set (MDS) is derived by selecting variables with significant factor loadings. These influential variables have either the greatest weights on their respective PCs or factor loadings within 10% of the highest loading (Abdu et al. 2023, Damiba et al. 2024). When multiple indicators are grouped within the same PC, the correlation matrix is used to assess inter-variable relationships ($p < 0.05$). If the correlation is strong ($r > 0.5$), the indicator with the highest factor loading is chosen. If the correlation is weak ($r < 0.5$), all indicators are retained (Damiba et al. 2024).

2.4. SQI Calculation and Classification

Calculate the Soil Quality Index Plus (SQI_Plus), formula 4 (Eq. 4) (Damiba et al. 2024)

$$SQI_{Plus} = \frac{\sum_{i=1}^{n} S_i}{n} \quad ...(4)$$

SQI is calculated according to formula (Eq. 5):

$$SQI = \sum_{i=1}^{n} W_i . S_i \quad ...(5)$$

In which: n is the total number of related indicators, Wi is the weight of PCi, and Wi is calculated according to formula (Eq. 6) (Damiba et al. 2024). Where PCi is the rotated load of principal component i and SPC is the total rotational load.

$$W_i = \frac{PC_i}{\sum PC} \quad ...(6)$$

Classification for SQI levels was assessed according to the scale used by Li et al, where SQI>0.8 (very good), 0.7-0.8 (good), 0.6-0.7 (moderate), 0.4-0.6 (degraded), and <0.4 (poor) (Li et al. 2024)

2.5. Data Processing

To ensure reliability, each analysis was performed in triplicate, and the mean, standard deviation, and range were calculated using Excel. Data suitability for PCA was assessed using Bartlett's test and the Kaiser-Meyer-Olkin (KMO) measure, where values above 0.5 are considered acceptable, and Pearson correlation analysis was used to examine the relationships among soil indices using SPSS 23.0 software (Abdel-Fattah et al. 2021, Plonsky 2015). The spatial distribution map of the SQI was generated using ArcGIS 10.8 and the inverse distance weighting (IDW) interpolation method.

3. RESULTS AND DISCUSSION

3.1. Some Soil Properties in the Study Area

The results of the determination of 11 soil physicochemical properties in the dragon fruit-growing area of Tay Ninh, Vietnam, are presented in Table 2. Specifically, the pH values ranged from 6.07 to 7.21, with an average value of 6.48, indicating that the soil pH of the study area is highly suitable for plant growth (Mukherjee & Lal 2014). This suggests that farmers are aware of the importance of controlling soil pH, although previous studies have shown that the soils in this area are generally characterized as acid sulfate soils (pH 4.0–5.4) (Mai et al. 2025, Van 2025).

The results showed that the study area was characterized by low soil EC, with an average value of 0.31 mS cm^{-1}, ranging from 0.16 to 0.45 mS cm^{-1}. According to Mukherjee and Lal, EC values of 0.2–0.5 mS cm^{-1} are considered most suitable for crop cultivation (Mukherjee & Lal 2014). The average TOC content was 3.28%, ranging from 1.80 to 5.04%, indicating a medium to high organic matter content (Mukherjee & Lal 2014). However, because dragon fruit is a perennial crop, insufficient application of organic amendments by farmers may lead to a decline in soil organic matter over time.

The CEC of the study area varied widely, ranging from 11.1 to 33.7 cmoL.kg^{-1} soil, with an average value of 22.5 cmoL.kg^{-1}. These results were similar to those reported for soils in Ben Tre, Vietnam, where CEC ranged from 19.0 to 28.8 cmoL.kg^{-1} (Van 2025). The average available P content was 37 mg.kg^{-1}, ranging from 12 to 66 mg.kg^{-1}, which was lower than that reported for durian-growing soils, where available P ranged from 25.4 to 117.1 mg.kg^{-1} (Van 2025). This difference may be attributed to the different phosphorus requirements of each crop, as well as differences in nutrient management practices associated with production costs.

The average NH_4^+ content was 114 mg.kg^{-1}, ranging from 44 to 148 mg.kg^{-1}, indicating that the NH_4^+ content was similarly high compared with that of neighboring soils reported in a previous study (Van 2025). The lowest NH_4^+ concentration was observed in soil sample TL6, where the crop had just been harvested, whereas the highest

Table 2: Soil physical and chemical indices in the study area.

	pH	EC mS cm^{-1}	TOC %	CEC cmoL.kg^{-1}	P_av mg.kg^{-1}	NH_4^+ mg.kg^{-1}	d g.cm^{-3}	D g.cm^{-3}	Clay %	Silt %	Sand %
TL1	6.17	0.35	3.62	11.1	57	125	2.35	1.06	13	28	60
SD	0.01	0.03	0.14	0.5	8	1	0.13	0.01	1	1	2
TL2	7.15	0.28	3.16	15.7	20	137	2.67	0.91	18	23	60
SD	0.06	0.03	0.16	0.7	1	2	0.07	0.01	1	1	3
TL3	6.92	0.29	3.48	22.5	28	104	2.55	0.98	25	18	58
SD	0.04	0.00	0.24	0.8	6	6	0.02	0.01	1	1	3
TL4	6.77	0.32	4.88	24.7	57	148	2.33	1.03	28	18	55
SD	0.02	0.01	0.16	0.9	2	9	0.16	0.01	1	1	2
TL5	6.60	0.38	4.00	22.5	51	143	2.21	1.01	25	18	58
SD	0.00	0.01	0.28	0.8	3	3	0.09	0.00	1	1	2
TL6	6.46	0.16	3.02	20.4	53	44	2.73	1.15	23	13	65
SD	0.06	0.02	0.02	0.0	2	7	0.02	0.03	1	1	3
TL7	6.32	0.22	2.78	33.7	23	63	2.43	1.10	38	15	48
SD	0.05	0.01	0.10	0.8	1	2	0.04	0.01	1	1	2
TL8	6.25	0.31	3.27	29.3	42	90	2.08	1.01	33	13	55
SD	0.01	0.01	0.13	0.8	6	9	0.01	0.08	1	1	2
TL9	6.45	0.44	3.18	22.5	37	121	2.57	0.92	25	18	58
SD	0.04	0.02	0.18	0.1	2	4	0.02	0.05	1	1	3
TL10	6.22	0.35	3.18	24.7	36	135	2.22	1.05	28	18	55
SD	0.09	0.03	0.18	0.2	1	5	0.11	0.03	1	1	2
TL11	6.31	0.33	2.90	22.5	16	116	2.26	0.91	25	18	58
SD	0.04	0.02	0.10	0.3	1	4	0.22	0.01	1	1	3
TL12	6.12	0.36	1.83	20.4	20	138	2.72	0.93	23	13	65
SD	0.04	0.01	0.03	0.5	8	2	0.01	0.01	1	1	3
Min	6.07	0.16	1.80	11.1	16	44	2.04	0.87	13	13	48
Max	7.21	0.45	5.04	33.7	57	148	2.75	1.19	38	28	65
Average	6.48	0.31	3.28	22.5	37	114	2.43	1.01	25	17	58

SD: standard deviation.

concentration was recorded in sample TL4 during the fruit development stage.

Soil particle density ranged from 2.04 to 2.75 $g.cm^{-3}$, with an average value of 2.43 $g.cm^{-3}$. Soil bulk density ranged from 0.87 to 1.19 $g.cm^{-3}$, corresponding to light- to medium-textured soils, which are common in the Mekong Delta region of Vietnam (Van 2025). The clay, silt, and sand contents ranged from 13 to 38%, 13 to 28%, and 48 to 65%, respectively. The soil texture was classified as loam, which is suitable for cultivation.

3.2. Pearson Correlation Analysis

The correlation coefficients among the soil parameters are presented in Table 3. Soil pH showed low correlations with all other soil parameters. This indicates that the application of alkaline materials, such as lime (CaO and $CaCO_3$), for pH control and regular soil management has little impact on other soil parameters. This finding is consistent with the soil pH results (Table 2), which showed only minor variations in pH.

Soil EC showed a significant positive correlation ($p < 0.05$) with NH_4^+ ($r = 0.80$). The results indicate that the application of nitrogen fertilizers contributed to an increase in the concentration of soluble salts in the soil. Soil TOC was strongly correlated with available P ($r = 0.65$, $p < 0.01$), suggesting that the mineralization of organic matter contributed to an increase in available P through desorption. The significant variation in TOC was attributed to differences

Table 3: Correlation coefficients of soil parameters.

	pH	EC	TOC	P_av	NH_4^+	d	D	% clay	% silt	% sand	CEC
pH	1										
EC	-0.165	1									
TOC	0.454**	0.150	1								
P_av	-0.036	0.002	0.654**	1							
NH_4^+	0.176	0.799**	0.308	0.012	1						
D	-0.259	0.286	0.373*	0.254	0.171	1					
D	0.244	0.580**	-0.210	-0.559**	0.563**	-0.117	1				
% clay	-0.162	-0.212	-0.039	-0.202	-0.376*	0.344*	-0.229	1			
% silt	-0.073	-0.125	-0.030	-0.225	-0.275	0.283	-0.087	0.945**	1		
% sand	-0.323	-0.343*	-0.417*	-0.131	-0.507**	-0.052	-0.197	0.621**	0.698**	1	
CEC	-0.163	-0.220	-0.055	-0.210	-0.386*	0.331*	-0.224	0.999**	0.949**	0.639**	1

**. Correlation is significant at the 0.01 level (2-tailed); *. Correlation is significant at the 0.05 level (2-tailed)

in organic matter management strategies in crop production (Topa et al. 2025).

CEC showed significant positive correlations ($p < 0.01$) with clay ($r = 1.00$), silt ($r = 0.95$), and sand ($r = 0.64$). The results indicate that soil texture strongly influenced soil CEC. Similar findings were reported by Kawaguchi and Kyuma, who suggested that clay minerals explain more than 80% of the variation in CEC, whereas the contribution of organic matter is not statistically significant in paddy soils of tropical Asia (Kawaguchi & Kyuma 1975).

3.3. Principal Component Analysis

Table 4 presents the Bartlett and KMO test results of the total data set (TDS). Bartlett test shows a significance level <0.0001 and an observed chi-square value (607.619), p-value = 0.000 < 0.05, which indicates that the variables are significantly correlated with each other, and the data are suitable for PCA analysis. In addition, the KMO value is also above 0.538 (>0.50), confirming that the sample size is reliable enough for factor analysis. These results confirm that the data set meets the conditions for performing PCA. (Abdel-Fattah et al. 2021).

The relationship between eigenvalues and principal components (PCs) is illustrated in Fig. 2. The analysis identified four PCs with eigenvalues greater than 1, specifically, 4.12, 2.19, 2.14, and 1.35 that together explain over 89.02% of the variance in the original data (Table 5). The contribution levels of these PCs are 33.2%, 22.7%, 19.9%, and 13.2%, respectively (Table 5).

Table 4: Bartlett and KMO test.

Kaiser-Meyer-Olkin Measure of Sampling Adequacy.		0.538
Bartlett's Test of Sphericity	Approx. Chi-Square	607.619
	df	55
	Sig.	0.000

W_PC1, W_PC2, W_PC3, and W_PC4 are the weights of the respective PCs, calculated according to Eq. 6.

PC1 explained 33.2% of the total variance. Parameters with absolute loading values > 0.6 included CEC, clay, silt, sand, and NH_4^+, with loadings of 0.916, 0.909, 0.864, 0.817, and −0.659, respectively, indicating that these parameters made major contributions to PC1 (Table 6). Among them, CEC had the highest loading value, whereas the loading values of clay and silt were within 10% of the CEC loading value and were therefore considered for selection (Abdu et al. 2023, Damiba et al. 2024). However, these two indices were significantly correlated ($P < 0.01$) with CEC, with correlation coefficients (r) of 1.00 and 0.95, respectively (Table 3), and were therefore excluded to avoid multicollinearity (Damiba et al. 2024). Consequently, only CEC was retained as the representative variable for PC1. The results showed that PC1 represents the soil texture component, characterizing the weathering process of the parent material and the effects of soil erosion, which may be caused by rainfall or irrigation.

PC2 explained 22.7% of the total variance. Parameters with loading values > 0.6 included P_av, TOC, and bulk density (D), with loadings of 0.861, 0.830, and 0.643, respectively. Among these, P_av had the highest loading value, while the loading value of TOC was within 10% of that of P_av; therefore, these two parameters were considered for PC2. However, a strong correlation was observed between P_av and TOC ($r = 0.654$, $p < 0.01$, Table 3), and only P_av was retained as the representative variable for PC2 (Damiba et al. 2024). The results indicated that available P was mainly

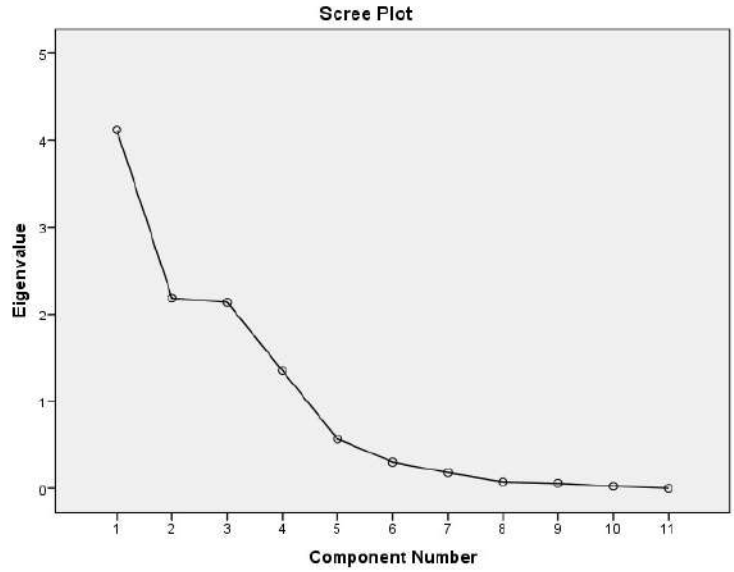


Fig. 2: Eigenvalues by Principal Components.

Table 5: PCs explain total variance.

Component	Initial Eigenvalues			Rotation Sums of Squared Loadings		
	Total	% of Variance	Cumulative %	Total	% of Variance	Cumulative %
1	4.118	37.439	37.439	3.655	33.223	33.223
2	2.185	19.867	57.306	2.497	22.703	55.926
3	2.136	19.420	76.725	2.184	19.850	75.776
4	1.352	12.295	89.020	1.457	13.244	89.020
5	0.568	5.159	94.179			
6	0.302	2.744	96.924	W_PC1	0.37	
7	0.180	1.637	98.560	W_PC2	0.26	
8	0.075	0.681	99.241	W_PC3	0.22	
9	0.059	0.538	99.780	W_PC4	0.15	
10	0.024	0.220	100.000			
11	2.588E-05	.000	100.000			

Extraction Method: Principal Component Analysis.

Table 6: Component matrix.

	Component			
	1	2	3	4
pH	-0.294			0.932
EC	-0.474		**0.762**	-0.294
TOC	-0.268	0.830	0.241	0.369
P_av	-0.188	**0.861**	-0.181	-0.197
d	0.174	0.526	0.588	-0.294
% silt	0.864		0.416	0.210
CEC	0.916		0.334	0.135
% sand	0.817	-0.193		-0.116
D	-0.393	-0.643	0.535	0.204
% clay	0.909		0.343	0.135
NH_4^+	-0.659		0.652	

Extraction Method: Principal Component Analysis.

derived from fertilizer application. However, because the study soils are acidic and have a high phosphorus fixation capacity, the presence of organic matter may contribute to increasing the availability of phosphorus. Therefore, PC2 can be considered representative of the combined effects of phosphorus and organic matter.

PC3 accounted for 19.9% of the total variance. Parameters with loading values > 0.6 included EC and NH_4^+, with loadings of 0.762 and 0.652, respectively. Among these, EC had the highest loading value, while the loading value of NH_4^+ was within 10% of that of EC; therefore, these two parameters were considered for PC3. However, EC and NH_4^+ were strongly correlated (r = 0.799, p < 0.01, Table 3), and only EC was retained as the representative variable for PC3 (Damiba et al. 2024). PC3 is considered to represent soil mineralization and ammonium nitrogen application.

PC4 explained 13.2% of the total variance. Soil pH was the only parameter with a loading value of 0.932 (Table 6) and was therefore retained as the representative variable for PC4 (Damiba et al. 2024). PC4 is considered to represent the application of soil amendments, mainly lime, for soil pH management, according to information obtained from farmers. PC1, PC2, PC3, and PC4, represented by CEC, P_av, EC, and pH, respectively, were selected as the Minimum Data Set (MDS), with a cumulative contribution of 89.02%.

The weighted values (W_PC), representing the contribution of each principal component, were calculated using Eq. 6. The resulting weights were 0.37, 0.26, 0.22, and 0.15 for PC1, PC2, PC3, and PC4, respectively (Table 6). The general formula for calculating the SQI (Eq. 5) for the sampling locations in the study area is presented in Eq. 7:

$$SQI = \sum_{i=1}^{n} W_i . S_i = 0.37 * S_{CEC} + 0.26 * S_{P_{av}} + - 0.22 * S_{EC} + 0.15 * S_{pH} \quad ...(7)$$

Calculate Si scores for soil indices: Table 7 presents the results of Si scoring using linear, non-linear, and optimized scoring functions (Eq. 1, Eq. 2, and Eq. 3). The findings indicate that, except for soil particle density and bulk density Si scores, both exceeding 0.5 with ranges of 0.75 to 0.98 and 0.76 to 0.96 respectively, most other soil indices exhibit significant fluctuations and signs of degradation, with scores below 0.5. The pH scores, ranging from 0.46 to 0.56, are concerning and warrant close monitoring. Notably, indices with considerable variations include EC (0.16 to 0.70), P_av (0.25 to 0.87), NH4+ (0.28 to 0.94), CEC (0.31 to 0.87), and clay (0.33 to 1.00). These variations may serve as indicators of soil index degradation.

This study estimated the SQI of 12 Dragon Fruit cultivation areas using two calculation methods: the Average Addition SQI_Plus (derived from Eq. 4) and the PCA analysis SQI_PCA (from Eq. 7), as shown in Fig. 3. The SQI_Plus has an average of 0.65, ranging from 0.57 to 0.75, with the lowest in sample TL 2 and the highest in TL 4. The SQI_PCA ranges from 0.43 to 0.69, with an average of 0.57, also lowest in TL 2 and highest in TL 4 (Fig. 3). The two methods show highly consistent variation in SQI values, despite differences in their specific results. Both methods support the same overall assessment of SQI. Notably, SQI_PCA values are consistently lower than SQI_Plus, likely

Table 7: Si calculation results based on soil index scoring functions.

	pH	EC	TOC	P_av	NH_4^+	d	D	clay	silt
TL 1	0.47	0.56	0.72	0.87	0.80	0.87	0.82	0.33	0.31
TL 2	0.56	0.43	0.63	0.31	0.87	0.76	0.96	0.47	0.51
TL 3	0.54	0.44	0.69	0.42	0.67	0.80	0.89	0.67	0.72
TL 4	0.53	0.52	0.97	0.87	0.94	0.88	0.85	0.73	0.76
TL 5	0.51	0.61	0.79	0.77	0.91	0.92	0.87	0.67	0.72
TL 6	0.50	0.16	0.60	0.81	0.28	0.75	0.76	0.60	0.66
TL 7	0.48	0.28	0.55	0.34	0.40	0.84	0.80	1.00	0.87
TL 8	0.48	0.49	0.65	0.64	0.58	0.98	0.86	0.87	0.83
TL 9	0.50	0.70	0.63	0.56	0.77	0.80	0.95	0.67	0.72
TL 10	0.47	0.56	0.63	0.54	0.86	0.92	0.83	0.73	0.76
TL 11	0.48	0.52	0.58	0.25	0.74	0.91	0.96	0.67	0.72
TL 12	0.46	0.58	0.36	0.30	0.88	0.75	0.94	0.60	0.66
Min	0.46	0.16	0.36	0.25	0.28	0.75	0.76	0.33	0.31
Max	0.56	0.70	0.97	0.87	0.94	0.98	0.96	1.00	0.87
Average	0.50	0.49	0.65	0.56	0.72	0.85	0.87	0.67	0.68

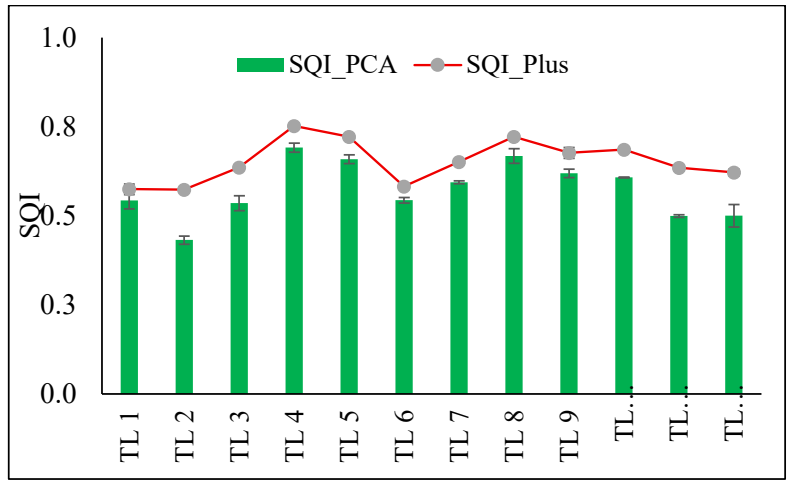
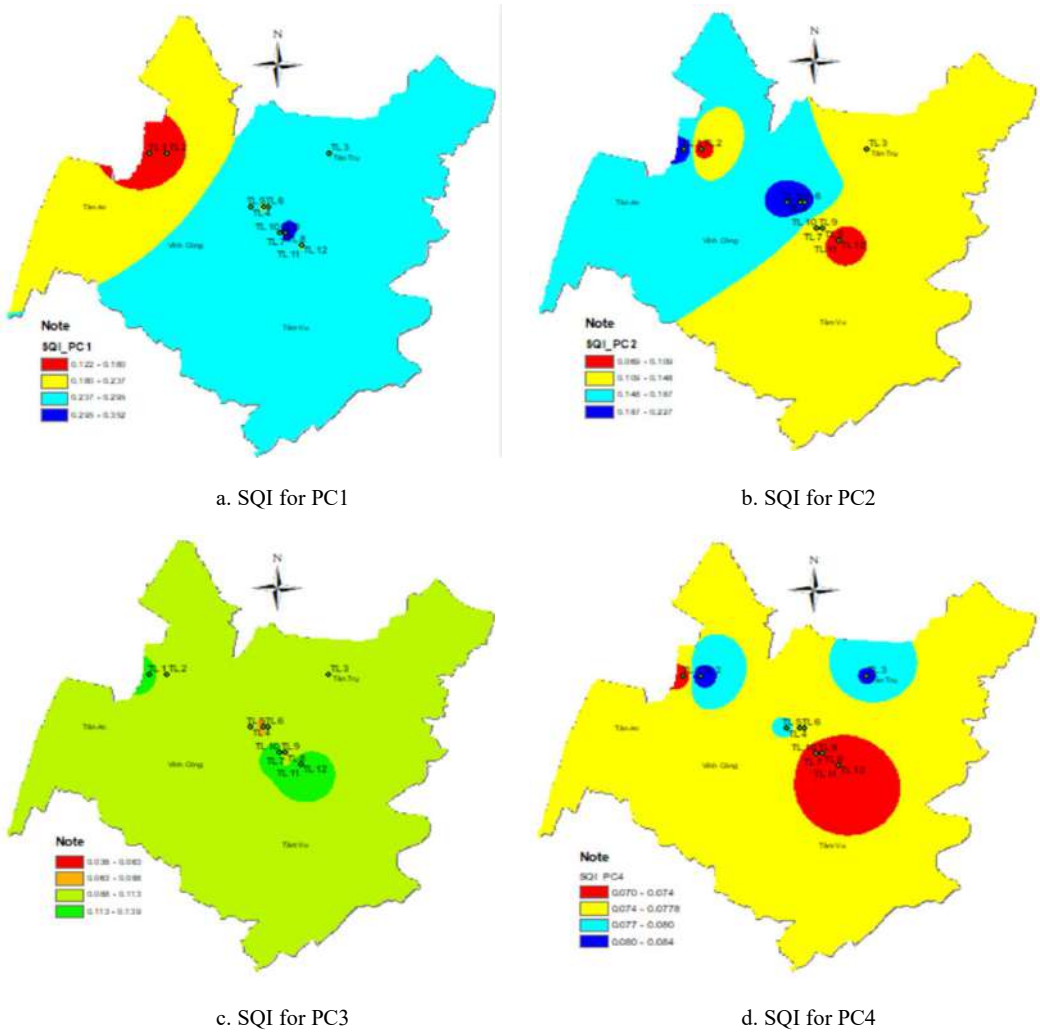


Fig. 3: SQI estimation results of soil samples by 2 methods (Additive method and PCA).



a. SQI for PC1

b. SQI for PC2

c. SQI for PC3

d. SQI for PC4

Fig. 4: SQI for each Principal Component.

due to the influence of highly correlated parameters causing multicollinearity in the calculation.

According to the classification scale used in Li et al.'s study, SQI_Plus classified three samples—TL 4, TL 5, and TL 8—as being in good condition (SQI > 0.7), representing 25%. Six samples fall into the average condition range (SQI 0.6 to 0.7), accounting for 50%, while three samples, TL 1, TL 2 and TL 6, are degraded (SQI 0.4 to 0.6), making up 25%. In contrast, SQI_PCA indicates no soil samples are in good condition, five are in the average range (41.6%), and seven are degraded (58.3%). These findings suggest that SQI_PCA is more appropriate for managing soil quality degradation risks. The soil quality across the studied farms tends to decline, possibly due to recent decreases in dragon fruit prices, which have reduced investments in soil care, improvement, and nutrition. Field observations also reveal that most farms have been cultivated for over a decade, and fragmented cultivation has resulted in a mix of soil qualities, both good and poor (Fig. 3). This variability poses a risk to sustainable agriculture. ble agriculture.

3.4. Mapping: Spatial Interpolation Analysis

Soil Quality Index (SQI) mapping was conducted using the IDW interpolation method in ArcGIS 10.8 to assess the spatial variation of soil quality across the study area based on SQI estimates. As shown in Fig. 4a, SQI_PC1 indicated that samples TL1 and TL2, located west of the dragon fruit plantations, had lower values than other farms, correlating with low clay content and signs of erosion caused by improper irrigation practices and overly strong hoses, as observed in the field. The SQI values for PC2 (Fig. 4b) revealed that the central zone (samples TL11, TL12) and the western zone (TL1) require management interventions, such as the addition of phosphorus and organic matter to enhance soil quality. In Fig. 4c, the SQI values for PC3 in the central (TL10, TL11, TL12) and western (TL1) regions were low, indicating the need to regulate the excessive use of mineral fertilizers like ammonium nitrogen. Instead, increasing organic matter to manage nitrogen levels is recommended. Finally, Fig. 4d demonstrated that the central and western parts of the study area exhibited low SQI values, signifying poor soil pH regulation that warrants closer attention.

Fig. 5 illustrates that the soil quality in the central growing region predominantly falls into the medium category, showing signs of degradation. In contrast, the western area exhibits poor soil quality, indicated by sites TL1 and TL2. These western samples correspond to recently converted dragon fruit cultivation zones where farmers are actively managing soil conditions. The central region also contains areas with lower soil quality, such as sample TL6 (see Fig. 5). The findings demonstrate that the Soil Quality Index (SQI) is influenced by soil properties, crop age, and

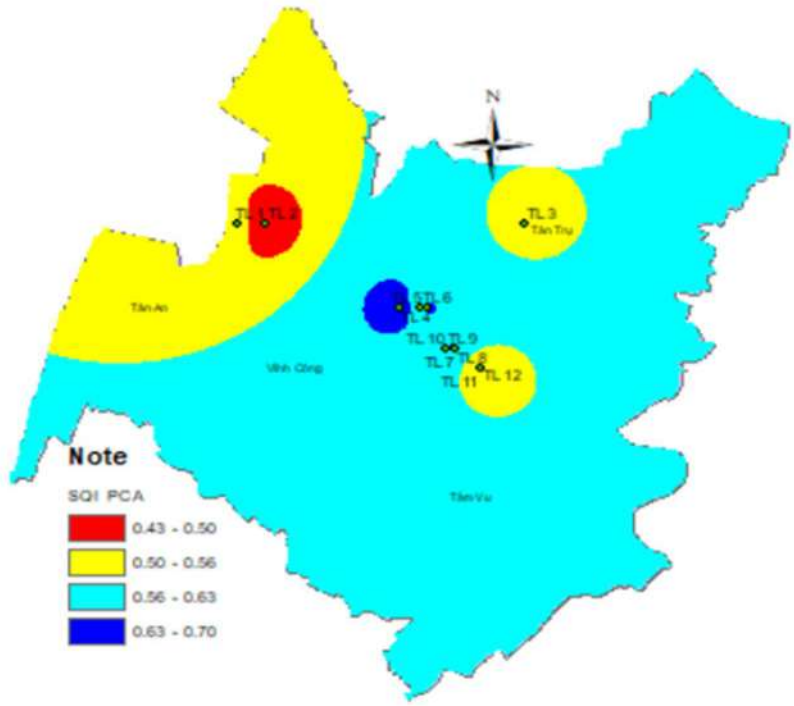


Fig. 5: Spatial distribution map of SQI values according to PCA in dragon fruit farms.

farmers' experience. Implementing a soil quality index distribution map can serve as a valuable tool for managers to identify soil degradation trends early.

4. CONCLUSIONS

Agricultural practices play a crucial role in shaping soil health by impacting its physical, chemical, and fertility attributes. This study assesses the soil quality index (SQI) based on the physico-chemical properties of soil in dragon fruit farms in Tây Ninh, Vietnam. Principal component analysis (PCA) combined with GIS mapping was used to visualize the spatial distribution of SQI. The minimum data set (MDS) derived from PCA explained 89.0% of the total variance, with four principal components contributing 33.2%, 22.7%, 19.9%, and 13.2%, respectively. Key parameters such as cation exchange capacity (CEC), available phosphorus (P_av), electrical conductivity (EC), and pH were selected as representative variables with weights of 0.37, 0.26, 0.22, and 0.15. SQI values calculated through PCA revealed improved risk management, with 41.6% of soils classified as high quality and 58.3% as degraded. These findings demonstrate that integrating PCA and GIS provides an effective approach for detecting soil degradation trends in areas of intensive perennial crop cultivation.

5. ACKNOWLEDGEMENTS

This research was conducted with the support of students majoring in Land Management, Course 16. We also express our deep gratitude to the reviewers for their in-depth comments, which contributed significantly to improving the manuscript.

6. REFERENCES

Abdel-Fattah, M.K., Mohamed, E.S., Wagdi, E.M., Shahin, S.A., Aldosari, A.A., Lasaponara, R. and Alnaimy, M.A., 2021. Quantitative evaluation of soil quality using Principal Component Analysis: The case study of El-Fayoum depression, Egypt. *Sustainability*, 13(4), p.1824. [DOI]

Abdu, A., Laekemariam, F., Gidago, G. and Getaneh, L., 2023. Explaining the soil quality using different assessment techniques. *Applied and Environmental Soil Science*, 2023. [DOI]

Aisah, B.N., Ikhwani, A.T., Setiawan, A.B., Purwantoro, A., Respatie, D.W., Ambarwati, E., Anggraeni, L., Teo, C.H., Setyawan, C. and Khamidah, A., 2025. Assessment of F_5 mungbean genotypes from intergeneric hybridization with common bean for agronomic performance, heritability, variance components, and genetic uniformity. *Caraka Tani: Journal of Sustainable Agriculture*, 40(3), pp.347-360. [DOI]

Baethgen, W. and Alley, M., 1989. A manual colorimetric procedure for measuring ammonium nitrogen in soil and plant Kjeldahl digests. *Communications in Soil Science and Plant Analysis*, 20(9-10), pp.961-969.

Bandyopadhyay, S. and Maiti, S.K., 2021. Application of statistical and machine learning approach for prediction of soil quality index formulated to evaluate trajectory of ecosystem recovery in coal mine degraded land. *Ecological Engineering*, 170, p.106351. [DOI]

Bünemann, E.K., Bongiorno, G., Bai, Z., Creamer, R.E., De Deyn, G., de Goede, R., Fleskens, L., Geissen, V., Kuyper, T.W., Mäder, P., Pulleman, M., Sukkel, W., van Groenigen, J.W. and Brussaard, L., 2018. Soil quality – A critical review. *Soil Biology and Biochemistry*, 120, pp.105-125. [DOI]

Damiba, W.A.F., Gathenya, J.M., Raude, J.M. and Home, P.G., 2024. Soil quality index (SQI) for evaluating the sustainability status of Kakia-Esamburmbur catchment under three different land use types in Narok County, Kenya. *Heliyon*, 10(5), p.e27219.

George, J., 1962. Hydrometer method improved for making particle size analyses of soils. *Agron J*, 54, pp.464-465.

Hanif, S., Ali, S., Chaudhry, A.H., Sial, N., Marium, A. and Mehmood, T., 2025. A review on soil metal contamination and its environmental implications. *Nature Environment and Pollution Technology*, 25(1), Article ID D1684. [DOI]

Kahsay, A., Haile, M., Gebresamuel, G. and Mohammed, M., 2025. Developing soil quality indices to investigate degradation impacts of different land use types in Northern Ethiopia. *Heliyon*, 11(1), p.e41052.

Kawaguchi, K. and Kyuma, K., 1975. Paddy soils in tropical Asia: Part 3. Correlation and regression analyses of the soil data. *South East Studies*, 13(1), pp.97-118.

Li, Y., Zhao, H., Liu, J., Chaonan, C. and Yuxuan, G., 2024. A framework for selecting and assessing soil quality indicators for sustainable soil management in waste dumps. *Scientific Reports*, 14(1), p.8491. [DOI]

Mai, T.D., Dinh, H.H.D., Ha, N.S. and Nguyen, C.K., 2025. Expanding export markets for Vietnamese dragon fruit. *International Journal of Scientific Research and Management (IJSRM)*, 13(4), pp.245-260.

Mukherjee, A. and Lal, R.L., 2014. Comparison of soil quality index using three methods. *PLoS ONE*, 9(8), p.e105981. [DOI]

Plonsky, L., 2015. Advancing quantitative methods in second language research. In: *Routledge Handbook of Second Language Research*. Routledge, pp.145-165.

Rajput, R., Patley, S., Choudhary, B. and Gupta, S., 2023. Assessment and comparison of soil quality using Principal Components Analysis (PCA) & Expert Opinion (EO) methods in different rice-based cropping systems in Alfisol. *Journal of the Indian Society of Soil Science*, 71(3), pp.287-297.

Rangel-Peraza, J.G., Padilla-Gasca, E., López-Corrales, R., Medina, J.R., Bustos-Terrones, Y., Amabilis-Sosa, L.E., Rodríguez-Mata, A.E. and Osuna-Enciso, T., 2017. Robust soil quality index for tropical soils influenced by agricultural activities. *Journal of Agricultural Chemistry and Environment*, 6, pp.199-221.

Ţopa, D.-C., Căpşună, S., Calistru, A.-E. and Ailincăi, C., 2025. Sustainable practices for enhancing soil health and crop quality in modern agriculture: A review. *Agriculture; Basel*, 15(9), p.945.

Van, P.N., 2025. Assessing soil health through multivariate analysis: A focus on durian cultivation in Cho Lach, Ben Tre Province, Vietnam. *Vietnam Journal of Agricultural Sciences*, 8(2), pp.115-128.

Nature Environment and Pollution Technology
An International Quarterly Scientific Journal

p-ISSN: 0972-6268
(Print copies up to 2016)
e-ISSN: 2395-3454

Vol. 25 | No. 3 | Article ID B4400 | 2026

Review Research Paper

https://doi.org/10.46488/NEPT.2026.v25i03.B4400

Open Access Journal

Assessment of Electric Two-Wheelers: A Narrative Review of Technological Trends, Market Growth, and Policy Drivers Associated with Environmental Concerns

Saibal Maitra† and Sarita Sachdeva
Manav Rachna International Institute of Research and Studies, Sector 43, Delhi-Surajkund Road, Faridabad-121004, Haryana, India
†Corresponding author: Saibal Maitra; saibal.maitra04@gmail.com

Abbreviation: Nat. Env. & Poll. Technol.
Website: www.neptjournal.com

Received: 06-10-2025
Revised: 29-12-2025
Accepted: 05-01-2026

Key Words:

Battery technology
Electric two-wheelers
Lifecycle assessment
Policy incentives
Sustainable mobility

Citation for the Paper:

Maitra, S. and Sachdeva, S., 2026. Assessment of electric two-wheelers: A narrative review of technological trends, market growth, and policy drivers associated with environmental concerns. *Nature Environment and Pollution Technology*, 25(3), B4400. https://doi.org/10.46488/NEPT.2026.v25i03. B4400

Note: From 2025, the journal has adopted the use of Article IDs in citations instead of traditional consecutive page numbers. Each article is now given individual page ranges starting from page 1.

Copyright: © 2026 by the authors
Licensee: Technoscience Publications
This article is an open access article distributed under the terms and conditions of the Creative Commons Attribution (CC BY) license (https://creativecommons.org/licenses/by/4.0/).

ABSTRACT

Electric two-wheelers (E2Ws) are key components in decarbonizing urban transportation. Their sustainability implications across different economic contexts remain uneven and are insufficiently synthesized. This review evaluates the sustainability of E2Ws across different economic contexts by synthesizing technological, environmental, market, and policy evidence. Databases such as Scopus, Web of Science, ScienceDirect, and IEEE Xplore were searched for peer-reviewed articles published between January 2015 and September 2025. A structured narrative review approach was applied, and data were synthesized across the technological, environmental, market, and policy dimensions. Studies were categorized according to economic context, including advanced economies (Europe and North America), large emerging economies (China and India), and rapidly motorizing emerging economies (e.g., Vietnam and Southeast Asia). The synthesized evidence focused on battery technologies, regenerative braking systems, charging models, and life cycle sustainability under different electricity mixes. The evidence synthesis found that while E2Ws consistently reduce operational greenhouse gas emissions. Overall sustainability outcomes are strongly influenced by the impacts of battery manufacturing, recycling infrastructure availability, and policy coherence. These findings provide transferable, evidence-based insights to support policymakers and industry stakeholders in accelerating sustainable E2W deployment across both mature and emerging markets.

1. INTRODUCTION

The rapid urbanization of the 21st century has intensified the global demand for sustainable, efficient, and cost-effective transportation modes. In this context, electric two-wheelers (E2Ws) have emerged as a critical component of the global mobility transition, particularly in densely populated countries where two-wheelers form the backbone of daily transportation (Hiep et al. 2023). With over 1.2 billion motor vehicles in use worldwide and projections indicating a rise to two billion by 2035, the decarbonization of personal transport is increasingly urgent, particularly in the face of rising greenhouse gas emissions, energy insecurity, and deteriorating air quality (Raza et al. 2025). Two-wheelers dominate the vehicle fleets of many developing economies. In India alone, over 187 million two-wheelers are in operation, accounting for more than 70% of the country's total registered vehicles (Jindel et al. 2022). Their affordability, maneuverability, and fuel efficiency render them indispensable for short- and medium-distance commuting. However, the heavy dependence on internal combustion engine (ICE)-based two-wheelers has exacerbated fossil fuel consumption and environmental pollution (Liu et al. 2024). Globally, the transport sector is responsible for nearly 24% of the direct CO_2 emissions from fuel combustion (Solaymani 2019). Personal mobility accounts for a significant share of CO_2 emissions. E2W are powered primarily by lithium-ion

(Li-ion) battery systems (Nayak et al. 2023). They offer a promising alternative with the potential to reduce emissions and noise pollution, contingent on the electricity generation mix and usage patterns.

The technological evolution of E2Ws has been largely attributed to improvements in battery chemistry, regenerative braking, and compact motor design. Innovations in battery swapping and fast charging infrastructure have further enhanced their usability (Ahmad et al. 2020). These developments, along with government incentives and environmental directives, have spurred market growth in key regions of the globe, such as China, India, the European Union, and North America. For instance, China's aggressive policy push and domestic manufacturing ecosystem have resulted in over 300 million E2Ws on its roads (Zuev et al. 2019). This growth illustrates a scale-driven adoption model that has proven effective under specific regulatory, manufacturing and infrastructure conditions. Lifecycle assessments (LCA) indicate that while E2Ws significantly reduce tailpipe emissions, their sustainability advantage is moderated by upstream emissions from electricity generation and battery manufacturing (Ahmadzadeh et al. 2025). Additionally, the lack of robust end-of-life recycling mechanisms for Li-ion batteries poses a growing environmental concern that must be addressed.

Despite the rapid global growth of E2Ws, sustainability assessments remain fragmented across regions, technologies, and policy environments, with most existing studies confined to single-country analyses or isolated themes. Such fragmentation limits the transferability of insights across economies at different stages of their development. This narrative review addresses this gap by critically assessing E2W sustainability using a comparative economy-based framework and synthesizing evidence across four key dimensions: technological advancement, environmental performance, economic viability, and policy intervention. Countries are classified into advanced economies, large emerging economies, and rapidly motorizing emerging economies to enable cross-economy comparisons and policy learning. Special emphasis is placed on major E2W markets such as India, China, and Vietnam as representative emerging economies with high two-wheeler dependency, where affordability, policy design, and grid carbon intensity critically shape adoption outcomes (Hiep et al. 2023, Kim et al. 2025). By integrating technological, environmental, market, and policy perspectives within this comparative framework, the review aims to provide actionable insights for policymakers, manufacturers, and researchers seeking to accelerate a scalable, inclusive, and sustainable transition toward electric two-wheeler mobility.

2. REVIEW METHODOLOGY

The literature was retrieved from Scopus, Web of Science, ScienceDirect, IEEE Xplore, and Google Scholar, covering publications from January 2015 to September 2025. Search strings included combinations of "electric two-wheelers," "electric motorcycles," "battery technology," "lifecycle assessment," "policy incentives," and "market adoption." Studies were included if they addressed at least one of the following dimensions: technology, environmental performance, market dynamics, and policy frameworks. Grey literature was excluded, except where official policy documents were necessary for contextual understanding. Rather than statistical aggregation, thematic synthesis representing thematic relevance, geographic diversity, and policy significance was conducted to provide a cross-regional comparison.

3. TECHNOLOGICAL DEVELOPMENTS IN E2WS

Technological advancements in two-wheelers have led to the E2W revolution. The development of lead-acid-powered two-wheelers to high-performance Li-ion-based vehicles represents a significant leap in energy efficiency. Core technological components, such as battery innovations, motor configurations, and charging technologies, play a significant role in enhancing the performance and sustainability of E2Ws. The advanced E2W is an architecture with a robust user interface, integrated with IoT, telematics, and advanced battery packs with a regenerative braking system (Fig. 1).

3.1. Battery Innovations

The industry has largely transitioned from valve-regulated lead-acid and nickel-metal hydride batteries to Li-ion chemistries because of their higher energy densities, which range from 150–250 $Wh.kg^{-1}$ (Kumar et al. 2023). They have a longer cycle life, ranging from 1,000 to 2,000 cycles, and superior charge/discharge efficiency. Among Li-ion variants, lithium iron phosphate (LFP) and nickel manganese cobalt (NMC) are the most widely adopted for two-wheelers (Walvekar et al. 2022). LFP batteries are characterized by strong thermal and chemical stability and operate in the temperature range of −20°C to 60°C. This temperature range makes them suitable for high-ambient-temperature regions such as India and Southeast Asia (Zhao et al. 2024). In contrast, NMC batteries provide higher energy densities (180–250 Wh kg^{-1}) and operate optimally within −10°C to 50°C temperature range. At the materials level, LFP cathodes employ stable olivine crystal structures with reported particle sizes in the 100–300 nm range, whereas NMC cathodes utilize layered oxide structures of ~200–500 nm that enhance

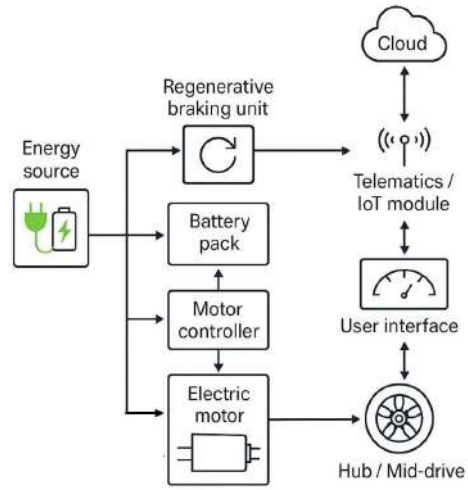


Fig. 1: System architecture of electric two-wheelers.

lithium diffusion but increase sensitivity to thermal and structural stress (Padhi et al. 1997, Xu et al. 2012)

Solid innovations have provided alternatives, such as solid-state batteries, which replace liquid electrolytes with solid electrolytes. They offer higher energy densities, which may exceed 400 $Wh.kg^{-1}$ (Xiao et al. 2020). Sodium-ion (Na-ion) batteries are also gaining attention as low-cost, resource-abundant options. They offer moderate energy densities (100–160 $Wh.kg^{-1}$) and improved thermal stability (Voß et al. 2025). From a life cycle perspective, battery manufacturing accounts for a substantial share of total E2W greenhouse gas emissions, contributing approximately 30–45% of cradle-to-gate emissions, depending on the chemistry and energy source (Ellingsen et al. 2016).

Although commercial deployment is still limited by high production costs and material challenges, companies such as Toyota and CATL have reported significant breakthroughs that could reach the E2W market within the next five years. Another key development is the modular and swappable battery designs. Battery swapping technologies can reduce downtime and permit smaller and lighter battery packs in fleet and shared mobility applications (Vallera et al. 2021). This architecture is beneficial for shared mobility and commercial fleet applications, where uptime is critical. Likewise, advancements in battery management systems (BMS) have significantly improved real-time monitoring and charge balancing. Modern BMS units use AI and cloud-based telematics to optimize the charging behavior, predict faults, and extend the battery lifespan (Nyamathulla & Dhanamjayulu 2024). Thermal management remains a critical focus in high-temperature areas. Cooling solutions, such as phase-change materials, air ducts, and liquid-cooled enclosures, are being developed to maintain optimal operating temperatures (Zonouzi et al. 2024). Innovations in recyclability, cobalt-free chemistries, and green synthesis routes drive improvements in battery lifecycle sustainability. Startups and research institutions are investing in closed-loop recycling techniques that use hydrometallurgy and direct cathode regeneration. A comparative summary of evolving battery technologies used in E2Ws is presented in Table 1.

3.2. Charging Technologies

Charging infrastructure is a critical enabler of widespread electric E2W adoption in the country. E2Ws primarily rely on three charging modalities: slow charging, fast charging, and battery swapping. Each offers distinct benefits and use-case suitability (Al-Saadi et al. 2021). Slow charging is based on Level 1 or Level 2 AC systems. These systems use 230V single-phase AC outlets with onboard chargers rated between 250 W and 1.5 kW (Gnann et al. 2019). It takes approximately 4 to 6 h for a full charge, although the overall charging time also depends on the battery capacity. Slow charging maintains battery longevity owing to lower thermal stress and minimal overvoltage risks. However, the extended charging time can be a limitation for fleet-based applications or high utilization scenarios.

Fast charging uses DC charging protocols such as CHAdeMO or CCS2. These systems deliver power in the range of 3–22 kW for two-wheelers (Tu et al. 2019). Battery chemistries, such as lithium-titanate in conjunction with thermal management systems, have enabled E2Ws to safely achieve an 80% state-of-charge in under 30 min (Hussain et al. 2024). Nonetheless, fast charging can accelerate battery degradation if not properly managed by the BMS, thus requiring trade-offs between speed, cost, and battery health. Battery swapping is an emerging solution

Table 1: Comparative summary of battery technologies used in electric two-wheelers.

Battery Type	Chemistry	Energy Density [Wh.kg^{-1}]	Cycle Life (cycles)	Safety	Advantages	Limitations	Typical Application Stage
Lead-Acid	$PbSO_4$	30–50	300–500	Low (acid leakage, gas release)	Low cost, easy recycling	Heavy, short lifespan, slow charging	Legacy models (China, India - low speed)
Nickel Metal Hydride	NiMH	60–80	500–800	Moderate	Better than lead-acid, moderate cost	Memory effect, lower energy density	Early transition models
Lithium Cobalt Oxide	$LiCoO_2$	150–200	500–1000	Low to moderate (thermal instability)	High energy density	Poor thermal stability, expensive cobalt content	Limited two-wheeler use (mainly consumer electronics)
Lithium Iron Phosphate	$LiFePO_4$	90–160	2000–4000	High (excellent thermal stability)	Long cycle life, safer, wide temperature tolerance	Lower energy density	Dominant for E2Ws in India, China
Lithium Nickel Manganese Cobalt	$Li(NiMnCo)O_2$	150–250	1500–3000	Moderate (improved BMS needed)	High energy density, good power output	Complex thermal management	Premium E2Ws, motorcycles
Solid-State	Solid electrolyte (various chemistries)	300–400+	3000–5000+	Very high	High energy density, very safe, fast charging	Expensive, limited commercialization	R&D phase, emerging
Sodium-Ion	Na-based compounds	100–160	2000+	High (chemically stable)	Low cost, resource abundance	Lower energy density, early stage	Experimental, potentially low-cost future alternative

with demonstrated viability in selected urban logistics, ride-sharing, and commercial fleet contexts, subject to standardization and infrastructure density (Ahmad et al. 2020, Vallera et al. 2021). In this approach, depleted battery packs are replaced with fully charged units at designated swapping stations, reducing the "charging" time to less than five minutes. Battery-as-a-service (BaaS) models decouple battery ownership from vehicles, thereby reducing upfront costs and addressing range anxiety. Companies such as Gogoro, NIO, and Ola Electric have deployed modular and interoperable battery platforms to promote standardization and network scalability (Boti et al. 2024). The integration of smart charging systems is gaining momentum. These systems use Internet of Things (IoT) platforms and communication protocols, such as the Open Charge Point Protocol, to enable load balancing, dynamic pricing, and grid-friendly demand response. Vehicle-to-grid (V2G) capabilities, though nascent in two-wheelers, hold potential for grid stabilization during peak load conditions

3.3. Electric Motor and Powertrain Systems

Electric motors are the core propulsion components of E2Ws. Modern E2Ws predominantly employ brushless DC (BLDC) motors and permanent-magnet synchronous motors (PMSMs) (Prabhu et al. 2023). BLDC motors provide simplified control, whereas PMSMs provide superior efficiency at higher speeds. An improved design of the electric motor is prudent for efficient deployment. For example, hub motors dominate the low-cost segment because of their space efficiency and reduced transmission losses (Madichetty et al. 2021). However, they often exhibit lower heat dissipation and are limited in terms of torque output. In contrast, mid-drive motors are attached to a gear system (Choudhary et al. 2023). This integration allows for better torque multiplication and load distribution. Motor controllers play a pivotal role in regulating the torque, speed, and efficiency by precisely modulating the current and voltage. Field-oriented control and direct torque control perform dynamic responses under varying loads and terrain conditions. Inverters utilizing SiC or gallium nitride power devices have also been introduced to increase the switching frequency and reduce thermal losses (Suthar et al. 2025). Integrated motor-controller units reduce the component count and wiring complexity, thereby improving reliability and reducing manufacturing costs. Moreover, intelligent thermal management systems employing active air or liquid cooling are being incorporated to mitigate heat buildup during high-demand operations, particularly in tropical environments.

The performance of E2W powertrains is often evaluated based on metrics such as torque density (Nm.kg^{-1}), power-to-weight ratio, efficiency curves across speed-load profiles,

and thermal stability (Kumaresan & Rammohan 2024). Innovations in rare-earth magnet technology, winding topologies, and core material selection have continued to improve these metrics. Recent advances in axial flux motor designs are also attracting attention due to their flat geometry, high torque output, and suitability for compact vehicular platforms (Gadiyar et al. 2023).

3.4. Regenerative Braking and Energy Recovery

Regenerative braking is a mechanism by which the kinetic energy of a vehicle is converted back into electrical energy and stored in the battery (Yang et al. 2024). This is achieved by operating an electric motor as a generator during deceleration. The harvested energy is rerouted through a bidirectional inverter and managed by the BMS to safely recharge the battery (Wager et al. 2018). In E2W, regenerative braking can contribute approximately 10–20% of the overall energy recovery under urban stop-and-go driving conditions. The degree of energy recovery depends on factors such as vehicle speed, mass, terrain, braking intensity, and the regenerative braking algorithm implemented by the control unit of the vehicle. This recovery typically corresponds to approximately 5–15 $Wh.km^{-1}$ of reclaimed energy, depending on the vehicle mass, average speed of 20–40 km h^{-1}, braking intensity, and control strategy implemented by the motor controller and battery management system. Higher recovery efficiencies have been reported in dense urban traffic and delivery-use cycles, whereas lower gains have been observed under steady-speed or highway-like conditions, where braking opportunities are limited. Modern E2Ws use variable levels of regenerative braking, either preset or user-adjustable, to balance the braking smoothness with the energy recovery performance. Although regenerative braking adds a layer of complexity to the drivetrain, the benefits in energy efficiency are substantial.

3.5. IoT Integration, BMS and Telematics

The integration of smart technologies, such as GPS navigation, remote diagnostics, and ride behavior analytics, into E2Ws is playing a growing role in enhancing safety, efficiency, and user experience. These features are enabled by IoT platforms and embedded telematics. IoT integration helps E2Ws build cloud platforms and infrastructure systems. As these smart technologies are embedded with sensors and microcontrollers, they continuously monitor vehicle parameters such as the battery state of charge, motor temperature, and fault codes (Nayak et al. 2023). This information is transmitted to cloud servers via cellular or low-power, wide-area networks. Thus, vehicle health, geofencing, and OTA software updates were ensured. Similarly, the BMS regulates the charging and discharging processes to ensure optimal battery performance (Thangavel et al. 2023). The BMS models also support estimation models for the state of health, state of energy, and remaining useful life, which are essential for managing battery degradation and planning maintenance or replacements.

Telematics further extends the capabilities of E2Ws by employing cloud analytics (Kirushanth & Kabaso 2020). This allows improvements in functionalities, such as routing optimization, energy consumption monitoring, and scheduling downtime for charging or maintenance. In addition, the aggregation of telematics data across users helps in understanding traffic management at the macro level. In the emerging frontier, AI-powered edge computing on E2W controllers has been tested for low-latency decision-making without reliance on constant cloud connectivity (Ming 2023).

Synthesis across technological dimensions indicates a pronounced regional differentiation in E2W development pathways. Advanced economies prioritize high-performance battery chemistries, fast-charging compatibility, and digitally integrated powertrains with mature infrastructure and a higher consumer willingness to pay. In contrast, large emerging economies, such as China and India, emphasize cost optimization and scalable manufacturing to support mass adoption. Rapidly motorizing economies, such as Vietnam and parts of Southeast Asia, predominantly adopt entry-level E2W technologies that balance affordability and basic connectivity. These comparisons indicate that technological sustainability in E2Ws is not solely determined by component performance but also by the alignment between battery design, charging strategy, digital integration, and the economic and policy context in which deployment occurs.

4. ENVIRONMENTAL PERFORMANCE AND LIFECYCLE SUSTAINABILITY

The technological configuration of E2Ws outlines their environmental and life-cycle sustainability outcomes. E2Ws are widely promoted as sustainable alternatives to ICE vehicles. However, the environmental benefits of E2Ws must be assessed from raw material extraction to end-of-life disposal (Fig. 2). This section evaluates the environmental footprint of E2Ws, focusing on greenhouse gas (GHG) emissions, air quality, noise pollution, and battery disposal challenges.

4.1. Lifecycle Emissions and Carbon Footprint

Compared to ICE two-wheelers, E2Ws produce zero tailpipe emissions (García-Afonso & González-Díaz 2023). According to LCA studies, battery E2Ws can reduce GHG emissions by 50% to 70% per kilometre travelled, depending

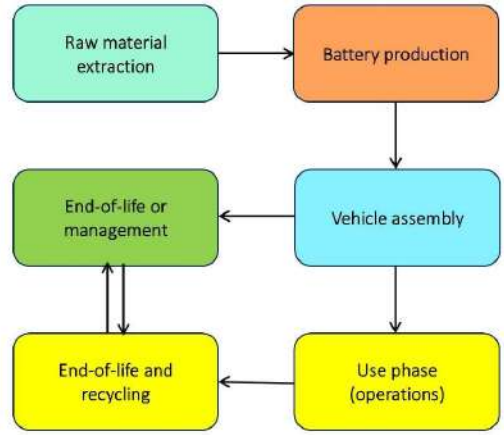


Fig. 2: Life cycle assessment of electric two-wheelers.

on the source of electricity used for charging (Ahmadzadeh et al. 2025). In regions powered by renewable energy (e.g., hydro, solar, or wind), the emission reduction is even more pronounced. However, in coal-dependent countries such as India and China, the upstream emissions from electricity generation partially offset the tailpipe benefits. The manufacturing phase, particularly of Li-ion batteries, is energy-intensive and contributes a considerable share of overall emissions. Despite this, the operational phase of E2Ws can offset the initial carbon debt over time through lower energy consumption and higher efficiency, with compensation periods varying according to electricity grid intensity, vehicle utilization, and battery chemistry.

Beyond carbon emissions, E2Ws contribute meaningfully to improved air and acoustic quality (Münder & Carbon 2022). By eliminating combustion-based exhaust, E2Ws significantly reduce the release of fine particulate matter. These particulate matters, such as PM2.5 and PM10, nitrogen oxides, and other hazardous pollutants, are major contributors to respiratory illnesses and cardiovascular disorders (Henning 2024). This is important in urban centers of low- and middle-income countries, where obsolete emission standards prevail. Furthermore, the quiet operation of electric motors mitigates urban noise pollution. While beneficial, this near-silent performance has also raised pedestrian safety concerns, leading some jurisdictions to mandate minimum noise levels for electric vehicles to alert passersby, particularly the visually impaired (Pardo-Ferreira et al. 2020).

4.2. Battery Disposal and Recycling Concerns

The end-of-life management of batteries is a significant environmental concern. Li-ion batteries contain toxic and rare metals such as cobalt, nickel, and lithium, which pose ecological risks if not recycled properly (Piątek et al. 2021). The inadequate recycling infrastructure in many countries has led to improper disposal practices. For instance, landfilling and incineration can result in groundwater contamination and the generation of hazardous waste. Efforts are underway to establish closed-loop recycling systems and second-life applications for used EV batteries. In India, policy frameworks under the Battery Waste Management Rules (2025), released by the Ministry of Environment, Forest, and Climate Change, India, aim to promote extended producer responsibility and safe collection, disassembly, and material recovery (Central Pollution Control Board 2025). Technologies such as hydrometallurgical and pyrometallurgical recycling are being developed to extract critical minerals efficiently and safely (Sethurajan et al. 2019).

4.3. Sustainability Trade-Offs and Regional Disparities

The sustainability profile of E2Ws is highly dependent on the context. In countries with greener electricity grids, strong recycling systems, and robust policy support, E2Ws offer substantial and long-term benefits. In contrast, in regions lacking renewable energy infrastructure and battery recycling facilities, the full environmental potential of E2Ws is unrealized. Furthermore, the global reliance on resource-intensive battery materials raises ethical and ecological questions related to mining practices and supply chain sustainability, particularly in resource-rich but economically vulnerable regions, such as the Democratic Republic of the Congo (for cobalt) (Feng et al. 2023).

4.4. Raw Materials and Resource Extraction

The production of lithium-ion (Li-ion) batteries requires raw materials such as lithium, cobalt, nickel, manganese, and graphite. These minerals are primarily sourced from geologically concentrated regions, such as lithium from South America's "Lithium Triangle," cobalt from the

Democratic Republic of Congo, and nickel from Indonesia and the Philippines. Mining operations in these areas raise concerns regarding ecological degradation (Piatek et al. 2021). Extraction processes are energy- and water-intensive. This tedious processing contributes to a notable upstream carbon footprint even before manufacturing begins. The lack of stringent environmental regulations in many mineral-rich countries exacerbates the sustainability dilemma. While efforts are underway to encourage responsible sourcing initiatives, government initiatives have also been implemented to encourage researchers and manufacturers to explore next-generation battery chemistries, such as solid-state batteries or Na-ion alternatives.

4.5. Waste Conservation Strategies

Significant waste is generated through metal processing, component molding, and battery cell fabrication during manufacturing. As end waste has significant environmental implications, manufacturers are gradually adopting lean manufacturing practices and zero-waste production targets. At the post-consumer stage, the focus shifts to waste conservation through reuse, repurposing, and recycling. One promising approach that is gaining prominence is the repurposing of used EV batteries for stationary energy storage (Sethurajan et al. 2019). This extends the utility of batteries before they enter recycling channels and reduces the pressure on raw material extraction. Eco-design principles are gaining traction, encouraging modular vehicle architectures that facilitate easy component recovery. Regulatory bodies mandate manufacturers to establish take-back schemes and eco-labeling for tracking. These strategies support a shift from a linear "take-make-dispose" model to a closed-loop, resource-efficient E2W ecosystem.

Cross-economy synthesis of environmental performance reveals that life cycle sustainability outcomes vary significantly by regional context. In advanced economies, E2Ws achieve faster carbon payback periods and greater net emission reductions. In large emerging economies, operational emission benefits are partially offset by grid carbon intensity and battery manufacturing emissions, shifting the sustainability emphasis toward battery longevity and recycling efficiency. Rapidly motorizing economies exhibit the highest marginal mitigation potential owing to heavy two-wheeler reliance; however, environmental gains remain constrained by limited recycling infrastructure and fossil-dominated power systems. These inferences highlight that the environmental advantages of E2Ws are contingent on systemic factors that extend beyond vehicle technology alone.

5. MARKET DYNAMICS AND ADOPTION TRENDS

Although environmental performance determines sustainability potential, market dynamics ultimately govern the scale and pace of E2W adoption. The global E2W market has witnessed a significant surge in recent years (Fig. 3). This surge was induced by increasing environmental awareness, regulatory support, and advances in battery and motor technologies. Although traditional ICE two-wheelers still dominate global sales, E2Ws are rapidly gaining market share. This section explores market trends, adoption patterns, regional comparisons, and consumer behavior that shape the evolving E2W landscape.

The E2W market was valued at approximately USD 15.5 billion in 2017, with forecasts projecting growth to USD 30 billion by the end of 2025, at a compound annual growth rate of over 7.5% (Nayak et al. 2023). The market surge is due to rising fuel prices, urban air quality mandates, and favorable government incentives. Asia-Pacific dominates the E2W market, with China alone accounting for over 300 million E2Ws in operation (He et al. 2022, Li et al. 2018). This

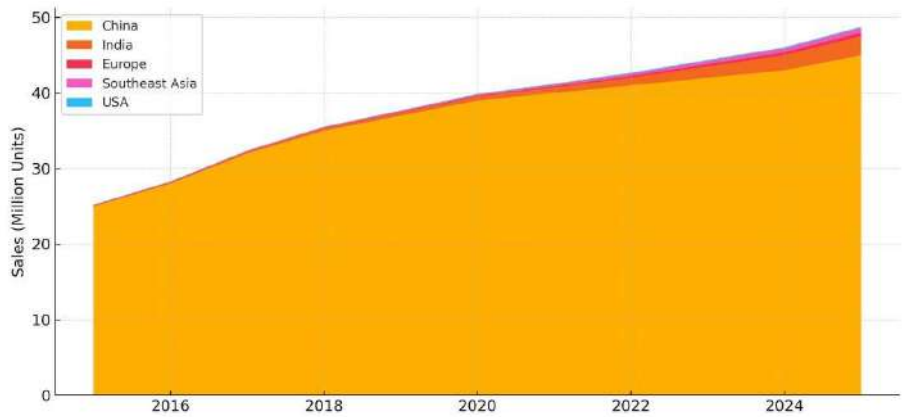


Fig. 3: Global electric two-wheeler sales (2016-2024).

is possible because of the supported regulatory mandates, domestic battery production, and aggressive urban transport policies (Wu et al. 2021). India is emerging as a pivotal region for E2W growth, owing to its status as the world's largest two-wheeler market by volume (Chaturvedi et al. 2022). With over 187 million two-wheelers in circulation and a high dependence on ICE scooters and motorcycles, India presents both challenges and opportunities for electric mobility. The implementation of national programs such as FAME-I and FAME-II, coupled with state-level incentives and tax rebates, has catalyzed the growth of domestic players, such as Ather Energy, Ola Electric, Hero Electric, and TVS (Singh et al. 2022). In contrast, adoption in Europe and North America is relatively moderate but accelerating owing to climate commitments, fuel economy regulations, and urban low-emission zones (Knez et al. 2019). Countries such as the Netherlands, Germany, and France have seen an increased uptake of electric mopeds and shared micro-mobility solutions (Razmjoo et al. 2022). In the United States, although adoption remains niche, innovative startups and rideshare platforms are expanding the E2W footprint, particularly in cities with sustainability mandates (Jenn et al. 2018).

5.1. Regional Adoption Patterns

The adoption of E2Ws varies significantly across different regions. In China, the E2W market is the most mature and expansive. With over 300 million E2Ws in operation, China accounts for more than 80% of the global E2W sales (Ou et al. 2021). This dominance is attributed to early policy interventions, extensive subsidies, and the rapid deployment of charging and battery-swapping infrastructure. The success of leading manufacturers such as Yadea, Aima, and Niu Technologies has further strengthened China's position as a global hub for both domestic consumption and export of E2Ws. In India, the E2W market has shown promising growth, despite infrastructural and regulatory challenges. India's two-wheeler dominance in the global ICE market is now translating into a shift towards electrification, driven by start-ups such as Ather Energy and Ola Electric and established players such as Hero Electric and TVS (Gupta & Anand et al. 2025). Localized production mandates and state-level subsidies have further accelerated market penetration, particularly in metropolitan regions and among last-mile delivery operators. European countries, particularly the Netherlands, France, Germany, and Spain, are witnessing a steady rise in E2W adoption as part of broader climate action strategies and sustainable mobility plans (Razmjoo et al. 2022). Growth is primarily concentrated in urban areas, where strict emissions regulations, congestion charges, and dedicated bike lanes create a conducive environment for electric mobility. Unlike Asia, in Europe, E2W is frequently positioned as a lifestyle or eco-conscious choice. Several governments provide purchase incentives and tax rebates, whereas shared mobility companies such as Lime and Tier have integrated E2Ws into their micro-mobility fleets (Lime 2025). In the United States, E2W adoption remains relatively niche but is growing steadily, especially in coastal urban centers such as San Francisco, New York, and Los Angeles (Onat et al. 2018). Regulatory support, such as grants for electric vehicle infrastructure, is uneven across states but is improving. The market is primarily led by high-end manufacturers such as Zero Motorcycles and new entrants offering affordable urban commuting options. The Southeast Asian market, comprising countries such as Vietnam, Thailand, and Indonesia, shows high latent potential owing to the dominant role of two-wheelers in daily transportation (Kim et al. 2025). However, the uptake of E2Ws is currently hampered by cost sensitivity, limited charging infrastructure, and a lack of localized policy incentives. Nevertheless, increasing investments from regional automotive firms and government-backed pilot projects are beginning to lay the groundwork for broader adoption of hydrogen vehicles.

5.2. Consumer Behavior and Market Segmentation

Consumer behavior is the adoption of E2Ws. Several factors influence the decision to adopt E2Ws. Environmental awareness, operational convenience, and government incentives are the prime deciding factors. In developing markets such as India, Southeast Asia, and parts of Africa, cost sensitivity remains the dominant factor in shaping consumer behavior (Eccarius et al. 2020). Consumers in these regions prioritize the total cost of ownership, factoring in both the initial purchase price and long-term fuel savings. However, range anxiety, limited public charging infrastructure, concerns about battery degradation, and uncertainties surrounding resale value continue to pose psychological barriers. Conversely, in developed markets, environmental concerns increasingly motivate consumers to adopt E2Ws. Here, a segment of environmentally conscious early adopters drives demand, often prioritizing zero-emission credentials, quiet operation, and integration with broader smart mobility ecosystems (Ashok et al. 2024).

The E2W market can be broadly segmented into three principal categories: low-speed, mid-range, and high-performance (Jaiswal et al. 2022). Low-speed electric scooters operating at 25–45 $km.h^{-1}$ are widely adopted for short-distance urban commutes and require minimal licensing and registration in many jurisdictions. This segment is particularly dominant in China. Mid-range commuter E2Ws, operating in the 50–70 $km.h^{-1}$ speed range, represent the largest market segment in countries such as India. These

vehicles cater to mainstream consumers seeking alternatives to ICE motorcycles. High-performance electric motorcycles serve a niche yet rapidly growing segment, primarily in developed economies. These models can exceed 100 $km.h^{-1}$, with ranges surpassing 150 km. They are appealing to users seeking advanced technology, superior acceleration, and recreational value. In parallel, subscription-based ownership, battery leasing, and BaaS are gaining traction among individuals who find personal vehicle ownership impractical or cost-prohibitive. These models help mitigate concerns regarding battery replacement costs and depreciation, further lowering the barriers to entry for prospective E2W users.

Market adoption patterns differ markedly across different economic contexts. China's large-scale manufacturing ecosystem provides rapid diffusion through price compression and infrastructure availability, whereas India's market growth remains highly policy-driven and uneven across states. Emerging economies exhibit high latent demand due to two-wheeler dependence; however, adoption is constrained by affordability, financing access, and charging availability. These findings indicate that market growth is not solely technology-driven but is shaped by institutional and economic conditions.

6. POLICY LANDSCAPE AND INCENTIVE MECHANISMS

Given the observed disparities in market adoption across regions, policy frameworks play a critical role in shaping the deployment trajectories. Government policies, financial incentives, and regulatory frameworks influence the adoption of E2Ws. Given the socioeconomic and infrastructural disparities across countries, policy frameworks vary in scale and scope. This section evaluates policy approaches across economies through three thematic lenses: implementation burden, localizability feasibility, and financial sustainability.

6.1. Fiscal Incentives and Subsidies

Fiscal incentives aim to offset the high upfront costs of E2Ws, which remain a major barrier to adoption. In India, the FAME-I (2015) and FAME-II (2019–ongoing) schemes have stimulated demand through purchase subsidies linked to battery capacity and localization requirements (Saha et al. 2024). Under FAME-II, subsidies of ₹10,000 per kWh are contingent upon 50% component localization, whereas the GST on electric vehicles has been reduced to 5% compared with 28% for ICE two-wheelers (Salman et al. 2018). However, such incentives impose fiscal burdens and raise questions regarding their long-term affordability once subsidies are withdrawn.

Historically, China has provided substantial purchase subsidies, reaching up to 60,000 yuan, coupled with extensive public investment in charging and battery-swapping infrastructure (Zhao et al. 2024). The gradual phase-out of these subsidies reflects concerns over fiscal sustainability, with policy emphasis shifting toward research, development, and domestic battery manufacturing. European countries, such as France, Germany, and Italy, offer targeted purchase incentives and tax deductions, often supplemented by non-monetary benefits, such as parking exemptions (Sheldon & Dua 2019). In the United States, federal tax credits of up to USD 2,500 are complemented by state-level programs and infrastructure funding under the Bipartisan Infrastructure Law (Muehlegger et al. 2022). Across regions, evidence suggests that subsidies accelerate early adoption but yield diminishing returns without parallel infrastructure and market maturation.

6.2. Non-Fiscal Incentives and Urban Policies

Non-fiscal policies enhance the usability and regulatory acceptance of E2Ws but differ in administrative complexity. License exemptions for low-speed E2Ws reduce entry barriers for new users, whereas low-emission and EV-restricted zones in cities discourage ICE use and indirectly promote electrification (Patil & Majumdar 2021). Fleet electrification mandates for delivery and ridesharing services, such as India's 30% electrification target by 2030 (Chaturvedi et al. 2022), demonstrate strong regulatory intent but impose substantial coordination and enforcement burdens, particularly in fragmented governance systems. Therefore, implementation effectiveness is contingent on institutional capacity and urban planning integration, rather than policy ambition alone.

6.3. Localization and Manufacturing Policies

Localization policies seek to reduce import dependence and strengthen domestic supply chains in the country. India's Production Linked Incentive scheme for advanced chemistry cells allocates ₹18,100 crores to stimulate domestic battery manufacturing (Kumar & Shrimali 2020), supported by phased manufacturing programs targeting motors, controllers, and power electronics. China's vertically integrated manufacturing ecosystem, supported by sustained policy backing and market access for firms such as CATL and BYD, has achieved rapid cost reductions and scale advantages (Liu et al. 2019, Li et al. 2022). Comparative evidence indicates that localization success depends on pre-existing industrial capacity and supplier ecosystems; in their absence, localization mandates risk, increasing costs, and delaying the deployment.

6.4. Comparative Effectiveness of Policies

Policy effectiveness varies widely across economies owing to differences in governance structures. China's centralized policymaking has provided rapid scaling and industrial dominance through early ICE restrictions and coordinated manufacturing support (Ou et al. 2021, Zhao et al. 2024). In contrast, India's ambitious but fragmented policy landscape has produced heterogeneous outcomes across states despite national-level incentives (Knez et al. 2019, Gupta & Anand 2025). European approaches have been effective in dense urban contexts but remain limited in scale, while rapidly motorizing economies continue to face gaps in developing stable incentive frameworks. Overall, the evidence suggests that durable E2W adoption emerges not from isolated incentives but from a coherent alignment between fiscal capacity, administrative feasibility, and industrial readiness.

7. KEY CHALLENGES, EMERGING OPPORTUNITIES, AND FUTURE RESEARCH DIRECTIONS

In direct response to the problem (the sustainability of E2W remains fragmented and context-dependent across economies) identified in this review, this section synthesizes the key challenges, emerging opportunities, and future outlook shaping large-scale E2W adoption. Numerous challenges hinder the widespread and sustainable adoption of E2Ws. These challenges span technological, economic, infrastructural, and behavioral dimensions of the industry. A comprehensive understanding of these obstacles is essential for the effective and equitable scaling up of electric mobility solutions (Tarei et al. 2021). Although the global E2W market has demonstrated significant growth, several technical, economic, and institutional barriers continue to constrain the sector's full potential. The high upfront cost of E2Ws remains a persistent obstacle. Although the total cost of ownership of E2Ws is often favorable over the vehicle's lifespan owing to lower fuel and maintenance costs, the initial purchase price is elevated largely owing to the high cost of Li-ion batteries. The cost accounts for approximately 30–40% of the vehicle cost (Patil et al. 2022). Although government subsidies have partially mitigated this burden, many consumers remain price-sensitive.

Charging infrastructure gaps represent another major limitation (Palani et al. 2023). Public charging stations remain concentrated primarily in urban centers, whereas rural and semi-urban regions continue to suffer from inadequate grid access and unreliable electricity supply. Although battery-swapping models offer a promising alternative, the absence of standardized battery formats across manufacturers limits widespread interoperability and scalability. Battery safety and thermal management are also critical concerns (Misar & Thombre 2024). Li-ion battery packs are highly sensitive to environmental conditions, such as temperature, humidity, and overcharging. In hot and humid climates, improper battery management has led to several well-publicized fire incidents that undermine consumer confidence. Range anxiety and battery degradation remain psychological and technical challenges, respectively. Although the E2W range has improved with advances in energy density, many consumers continue to perceive range limitations as a significant risk. Regulatory fragmentation and policy uncertainty hinder consistent growth. Financing barriers further complicate adoption by individual and institutional consumers. Many traditional lenders are reluctant to finance E2Ws because of their relatively untested resale markets and perceived technological risks.

Several emerging trends and untapped opportunities have the potential to accelerate E2W adoption and reshape the global mobility landscape in the next decade. The localization of battery manufacturing and supply chains is emerging. Many countries, such as India, are investing heavily in the domestic production of advanced battery chemistries, supported by government-backed incentive schemes, such as the production-linked incentive program. As battery technologies mature, research into alternative chemistries, such as Na-ion batteries and cobalt-free lithium iron phosphate formulations, is increasing (Chu et al. 2021). Developing circular economy frameworks is another opportunity that can enable battery repurposing in the automotive industry. Technologies such as hydrometallurgical recycling are being actively developed to maximize the recovery rates of critical minerals. The integration of E2Ws with renewable energy systems and smart grids is another area of significant potential (Ismail et al. 2023). The deployment of solar-powered charging stations with net metering and dynamic pricing models can reduce the carbon intensity of charging operations in the long run. Facilities with V2G capabilities could allow E2Ws to serve as distributed storage assets (Shah & Payami 2023). Urbanization and smart city development are also creating new markets for multimodal transport systems, where E2Ws complement mass transit networks as first- and last-mile solutions.

8. LIMITATIONS

This study had certain limitations that should be acknowledged. The analysis used secondary literature and offers qualitative interpretation rather than a quantitative meta-analysis, which may introduce selection or interpretive

bias. In addition, heterogeneity across studies in lifecycle assessment boundaries, grid emission factors, and technology performance metrics limits direct numerical comparability. While substantial literature is available for major markets, empirical evidence from rapidly motorizing economies remains comparatively limited, which may affect the depth of contextual interpretation in these regions. Ongoing advancements in battery chemistry, charging infrastructure, and regulatory frameworks may outpace the temporal coverage of the reviewed literature, meaning that some conclusions reflect current trends rather than long-term, stabilized outcomes.

9. CONCLUSIONS

E2Ws represent a transformative step toward sustainable, affordable, and inclusive mobility. As nations strive to meet climate targets, the electrification of two-wheelers provides a practical and scalable solution. Despite technological advancements and increasing policy support, the widespread adoption of E2Ws faces several challenges. However, ongoing innovations are progressively addressing these issues. Emerging business models enhance convenience and reduce cost barriers. To capitalize on these opportunities, coordinated efforts are required across the policy, industry, and research domains. Localized manufacturing, circular economy practices, renewable energy integration, and data-driven policymaking must be prioritized to accelerate E2W deployment. As cities continue to evolve toward cleaner and smarter mobility systems, E2Ws are poised to play a pivotal role in shaping urban transport.

10. REFERENCES

Ahmad, F., Saad Alam, M., Saad Alsaidan, I. and Shariff, S.M., 2020. Battery swapping station for electric vehicles: Opportunities and challenges. *IET Smart Grid*, 3(3), pp.280–286.

Ahmadzadeh, O., Rodriguez, R., Getz, J., Panneerselvam, S. and Soudbakhsh, D., 2025. The impact of lightweighting and battery technologies on the sustainability of electric vehicles: A comprehensive life cycle assessment. *Environmental Impact Assessment Review*, 110, p.107668.

Al-Saadi, M., Patkowski, B., Zaremba, M., Karwat, A., Pol, M., Chełchowski, Ł., Van Mierlo, J. and Berecibar, M., 2021. Slow and fast charging solutions for Li-ion batteries of electric heavy-duty vehicles with fleet management strategies. *Sustainability*, 13(19), p.10639.

Ashok, K., Tripathi, A. and Arora, S., 2024. What drives and inhibits consumers from adopting electric two-wheelers: A behavioural reasoning theory perspective. *Management and Labour Studies*, (online ahead of print), p.0258042X241292320.

Boti, A.M., Eashwar, M.V., Shekar, H. and Swathika, O.G., 2024. Battery swapping for electric vehicles: Assessing its viability as an alternative or complement to fast charging. In: *2024 3rd Odisha International Conference on Electrical Power Engineering, Communication and Computing Technology (ODICON)*. IEEE, pp.1–6.

Central Pollution Control Board, 2025. Battery Waste Management Rules. Retrieved June 1, 2025, from https://cpcb.nic.in/uploads/hwmd/Battery-WasteManagementRules-2025.pdf

Chaturvedi, B.K., Nautiyal, A., Kandpal, T.C. and Yaqoot, M., 2022. Projected transition to electric vehicles in India and its impact on stakeholders. *Energy for Sustainable Development*, 66, pp.189–200.

Choudhary, A., Mian, T., Fatima, S. and Panigrahi, B.K., 2023. Fault diagnosis of electric two-wheeler under pragmatic operating conditions using wavelet synchrosqueezing transform and CNN. *IEEE Sensors Journal*, 23(6), pp.6254–6263.

Chu, S., Guo, S. and Zhou, H., 2021. Advanced cobalt-free cathode materials for sodium-ion batteries. *Chemical Society Reviews*, 50(23), pp.13189–13235.

Eccarius, T. and Lu, C.C., 2020. Powered two-wheelers for sustainable mobility: A review of consumer adoption of electric motorcycles. *International Journal of Sustainable Transportation*, 14(3), pp.215–231.

Ellingsen, L.A.W., Singh, B. and Strømman, A.H., 2016. The size and range effect: Lifecycle greenhouse gas emissions of electric vehicles. *Environmental Research Letters*, 11(5), p.054010.

Feng, Y., Hu, J., Afshan, S., Irfan, M., Hu, M. and Abbas, S., 2023. Bridging resource disparities for sustainable development: A comparative analysis of resource-rich and resource-scarce countries. *Resources Policy*, 85, p.103981.

Gadiyar, N., Van Verdeghem, J. and Severson, E.L., 2023. A review of axial flux permanent magnet machine technology. *IEEE Transactions on Industry Applications*, 59(4), pp.3920–3933.

García-Afonso, Ó. and González-Díaz, B., 2023. Effectiveness of zero tailpipe vehicles to reduce CO_2 emissions in isolated power systems, a realistic perspective: Tenerife Island test case. *Energy*, 273, p.127211.

Gnann, T., Plötz, P. and Wietschel, M., 2019. Can public slow charging accelerate plug-in electric vehicle sales? A simulation of charging infrastructure usage and its impact on plug-in electric vehicle sales for Germany. *International Journal of Sustainable Transportation*, 13(7), pp.528–542.

Gupta, R. and Anand, A., 2025. Is mobility transition driven by wealth inequality? Evidence from analysis of the electric two-wheelers adoption in India. *Transportation Research Part A: Policy and Practice*, 193, p.104407.

He, H., Sun, F., Wang, Z., Lin, C., Zhang, C., Xiong, R., Deng, J., Zhu, X., Xie, P., Zhang, S. and Wei, Z., 2022. China's battery electric vehicles lead the world: Achievements in technology system architecture and technological breakthroughs. *Green Energy and Intelligent Transportation*, 1(1), p.100020.

Henning, R.J., 2024. Particulate matter air pollution is a significant risk factor for cardiovascular disease. *Current Problems in Cardiology*, 49(1), p.102094.

Hiep, D.V., Tran, N.H., Tuan, N.A., Hung, T.M., Duc, N.V. and Tung, H., 2023. Assessment of electric two-wheelers development in establishing a national e-mobility roadmap to promote sustainable transport in Vietnam. *Sustainability*, 15(9), p.7411.

Hussain, M., Khan, M.K. and Pathak, M., 2024. Thermal management of high-energy lithium titanate oxide batteries using an effective channeled dielectric fluid immersion cooling system. *Energy Conversion and Management*, 313, p.118644.

Ismail, A.A., Mbungu, N.T., Elnady, A., Bansal, R.C., Hamid, A.K. and AlShabi, M., 2023. Impact of electric vehicles on smart grid and future predictions: A survey. *International Journal of Modelling and Simulation*, 43(6), pp.1041–1057.

Jaiswal, D., Deshmukh, A.K. and Thaichon, P., 2022. Who will adopt electric vehicles? Segmenting and exemplifying potential buyer heterogeneity and forthcoming research. *Journal of Retailing and Consumer Services*, 67, p.102969.

Jenn, A., Springel, K. and Gopal, A.R., 2018. Effectiveness of electric vehicle incentives in the United States. *Energy Policy*, 119, pp.349–356.

Jindel, J., Chandra, A., Allirani, H. and Verma, A., 2022. Studying two-wheeler usage in the context of sustainable and resilient urban mobility policies in India. *Transportation Research Record*, 2676(6), pp.424–436.

Kim, H.J., Shrestha, S. and Pranawengkapti, K., 2025. Capacity and market potential for local production and distribution of electric two-wheelers in Southeast Asia, focused on Thailand, Indonesia and Vietnam. *Sustainable Earth Reviews*, 8(1), p.3.

Kirushanth, S. and Kabaso, B., 2020. Design and development of weigh-in-motion using vehicular telematics. *Journal of Sensors*, 2020(1), p.7871215.

Knez, M., Zevnik, G.K. and Obrecht, M., 2019. A review of available chargers for electric vehicles: United States of America, European Union, and Asia. *Renewable and Sustainable Energy Reviews*, 109, pp.284–293.

Kumar, A.R. and Shrimali, G., 2020. Battery storage manufacturing in India: A strategic perspective. *Journal of Energy Storage*, 32, p.101817.

Kumar, P., Bansal, S. and Sonthalia, A., 2023. Introduction to battery systems. In: *Handbook of Thermal Management Systems*. Elsevier, pp.95–118.

Kumaresan, N. and Rammohan, A., 2024. Modeling and performance analysis of an electric two-wheeler on various driving cycles and validation using a performance real-time target machine. *Journal of Energy Storage*, 101, p.113935.

Li, S., Zhu, X., Ma, Y., Zhang, F. and Zhou, H., 2022. The role of government in the market for electric vehicles: Evidence from China. *Journal of Policy Analysis and Management*, 41(2), pp.450–485.

Li, W., Yang, M. and Sandu, S., 2018. Electric vehicles in China: A review of current policies. *Energy and Environment*, 29(8), pp.1512–1524.

Lime, 2025. Electric Access: Lime E-Fleet and More Equity in Smart Mobility. Retrieved June 1, 2025, from https://www.li.me/en-fr/blog/electric-access-lime-e-fleet-more-equity-smart-mobility

Liu, D., Chen, T., Liu, X. and Yu, Y., 2019. Do more subsidies promote greater innovation? Evidence from the Chinese electronic manufacturing industry. *Economic Modelling*, 80, pp.441–452.

Liu, H., Yu, S., Wang, T., Li, J. and Wang, Y., 2024. A systematic review on sustainability assessment of internal combustion engines. *Journal of Cleaner Production*, p.141996.

Madichetty, S., Mishra, S. and Basu, M., 2021. New trends in electric motors and selection for electric vehicle propulsion systems. *IET Electrical Systems in Transportation*, 11(3), pp.186–199.

Ming, G., 2023. Exploration of the intelligent control system of autonomous vehicles based on edge computing. *PLoS ONE*, 18(2), p.e0281294.

Misar, A.E. and Thombre, S.B., 2024. Thermal management of Li-ion battery pack using potting material and air cooling for electric two-wheelers. *Journal of Energy Storage*, 101, p.113760.

Muehlegger, E. and Rapson, D.S., 2022. Subsidizing low- and middle-income adoption of electric vehicles: Quasi-experimental evidence from California. *Journal of Public Economics*, 216, p.104752.

Münder, M. and Carbon, C.C., 2022. Howl, whirr, and whistle: The perception of electric powertrain noise and its importance for perceived quality in electrified vehicles. *Applied Acoustics*, 185, p.108412.

Nayak, A.K., Ganguli, B. and Ajayan, P.M., 2023. Advances in electric two-wheeler technologies. *Energy Reports*, 9, pp.3508–3530.

Nyamathulla, S. and Dhanamjayulu, C., 2024. A review of battery energy storage systems and advanced battery management system for different applications: Challenges and recommendations. *Journal of Energy Storage*, 86, p.111179.

Onat, N.C., Kucukvar, M. and Tatari, O., 2018. Well-to-wheel water footprints of conventional versus electric vehicles in the United States: A state-based comparative analysis. *Journal of Cleaner Production*, 204, pp.788–802.

Ou, S., Hsieh, I.Y., He, X., Lin, Z., Yu, R. and Zhou, Y., 2021. China's vehicle electrification impacts on sales, fuel use, and battery material demand through 2050: Optimizing consumer and industry decisions. *iScience*, 24(11).

Padhi, A.K., Nanjundaswamy, K.S. and Goodenough, J.B., 1997. Phospho-olivines as positive-electrode materials for rechargeable lithium batteries. *Journal of the Electrochemical Society*, 144(4), pp.1188–1194.

Palani, G., Sengamalai, U., Vishnuram, P. and Nastasi, B., 2023. Challenges and barriers of wireless charging technologies for electric vehicles. *Energies*, 16(5), p.2138.

Pardo-Ferreira, M.C., Torrecilla-García, J.A., Heras-Rosas, C.L. and Rubio-Romero, J.C., 2020. New risk situations related to low noise from electric vehicles: Perception of workers as pedestrians and other vehicle drivers. *International Journal of Environmental Research and Public Health*, 17(18), p.6701.

Patil, M., Bandhu Majumdar, B. and Kumar Sahu, P., 2022. A comparative evaluation of the total cost of ownership between electric two-wheelers and motorized two-wheelers from an Indian perspective. *Transportation Research Record*, 2676(5), pp.526–550.

Patil, M. and Majumdar, B.B., 2021. Prioritizing key attributes influencing electric two-wheeler usage: A multi-criteria decision-making (MCDM) approach – A case study of Hyderabad, India. *Case Studies on Transport Policy*, 9(2), pp.913–929.

Piątek, J., Afyon, S., Budnyak, T.M., Budnyk, S., Sipponen, M.H. and Slabon, A., 2021. Sustainable Li-ion batteries: Chemistry and recycling. *Advanced Energy Materials*, 11(43), p.2003456.

Prabhu, N., Thirumalaivasan, R. and Ashok, B., 2023. Critical review on torque ripple sources and mitigation control strategies of BLDC motors in electric vehicle applications. *IEEE Access*, 11, pp.115699–115739.

Raza, M.Y., Wang, W. and Javed, Q., 2025. Decoupling effect and driving factors of transport CO emissions: Modeling and prediction of energy and environmental factors towards Vision-2035 in a developing economy. *Energy Strategy Reviews*, 59, p.101750.

Razmjoo, A., Ghazanfari, A., Jahangiri, M., Franklin, E., Denai, M., Marzband, M., Astiaso Garcia, D. and Maheri, A., 2022. A comprehensive study on the expansion of electric vehicles in Europe. *Applied Sciences*, 12(22), p.11656.

Saha, T., Banerjee, S. and Banerjee, M., 2024. An introspection on FAME India scheme in the light of non-incentivized electric private four-wheelers: Potentials and possibilities. In: *Sustainability in Marketing Practice*. Apple Academic Press, pp.115–130.

Salman, M.M., 2018. Impact of GST on automobile sector with special reference to hybrid & electric cars in India. *Journal of IMS Group*, 15(1).

Sethurajan, M., van Hullebusch, E.D., Fontana, D., Akcil, A., Deveci, H., Batinic, B., Leal, J.P., Gasche, T.A., Ali Kucuker, M., Kuchta, K. and Neto, I.F., 2019. Recent advances on hydrometallurgical recovery of critical and precious elements from end of life electronic wastes – A review. *Critical Reviews in Environmental Science and Technology*, 49(3), pp.212–275.

Shah, V. and Payami, S., 2023. Integrated converter with G2V, V2G, and DC/V2V charging capabilities for switched reluctance motor drive-train based EV application. *IEEE Transactions on Industry Applications*, 59(3), pp.3837–3850.

Sheldon, T.L. and Dua, R., 2019. Measuring the cost-effectiveness of electric vehicle subsidies. *Energy Economics*, 84, p.104545.

Singh, S., Jindel, J., Tikkiwal, V.A., Verma, M., Gupta, A., Negi, A. and Jain, A., 2022. Electric vehicles for low-emission urban mobility: Current status and policy review for India. *International Journal of Sustainable Energy*, 41(9), pp.1323–1359.

Solaymani, S., 2019. CO_2 emissions patterns in 7 top carbon emitter economies: The case of transport sector. *Energy*, 168, pp.989–1001.

Suthar, A.N., Venkataramanaiah, J. and Suresh, Y., 2025. Conventional, wide-bandgap, and hybrid power converters: A comprehensive review. *Renewable and Sustainable Energy Reviews*, 213, p.115419.

Tarei, P.K., Chand, P. and Gupta, H., 2021. Barriers to the adoption of electric vehicles: Evidence from India. *Journal of Cleaner Production*, 291, p.125847.

Thangavel, S., Mohanraj, D., Girijaprasanna, T., Raju, S., Dhanamjayulu, C. and Muyeen, S.M., 2023. A comprehensive review on electric vehicle: Battery management system, charging station, traction motors. *IEEE Access*, 11, pp.20994–21019.

Tu, H., Feng, H., Srdic, S. and Lukic, S., 2019. Extreme fast charging of electric vehicles: A technology overview. *IEEE Transactions on Transportation Electrification*, 5(4), pp.861–878.

Vallera, A.M., Nunes, P.M. and Brito, M.C., 2021. Why we need battery swapping technology. *Energy Policy*, 157, p.112481.

Voß, P., Gruber, B., Mitterfellner, M., Plöpst, J.D., Degen, F., Schmuch, R. and Lux, S., 2025. Benchmarking state-of-the-art sodium-ion battery cells—modeling energy density and carbon footprint at the gigafactory-scale. *Energy & Environmental Science*, 18(17), pp.8104–8129.

Wager, G., Whale, J. and Braunl, T., 2018. Performance evaluation of regenerative braking systems. *Proceedings of the Institution of Mechanical Engineers, Part D: Journal of Automobile Engineering*, 232(10), pp.1414–1427.

Walvekar, H., Beltran, H., Sripad, S. and Pecht, M., 2022. Implications of the electric vehicle manufacturers' decision to mass adopt lithium-iron phosphate batteries. *IEEE Access*, 10, pp.63834–63843.

Wu, Y.A., Ng, A.W., Yu, Z., Huang, J., Meng, K. and Dong, Z.Y., 2021. A review of evolutionary policy incentives for sustainable development of electric vehicles in China: Strategic implications. *Energy Policy*, 148, p.111983.

Xiao, Y., Wang, Y., Bo, S.H., Kim, J.C., Miara, L.J. and Ceder, G., 2020. Understanding interface stability in solid-state batteries. *Nature Reviews Materials*, 5(2), pp.105–126.

Xu, B., Qian, D., Wang, Z. and Meng, Y.S., 2012. Recent progress in cathode materials research for advanced lithium-ion batteries. *Materials Science and Engineering: R: Reports*, 73(5–6), pp.51–65.

Yang, C., Sun, T., Wang, W., Li, Y., Zhang, Y. and Zha, M., 2024. Regenerative braking system development and perspectives for electric vehicles: An overview. *Renewable and Sustainable Energy Reviews*, 198, p.114389.

Zhao, T., Mahandra, H., Marthi, R., Ji, X., Zhao, W., Chae, S., Traversy, M., Li, W., Yu, F., Li, L. and Choi, Y., 2024. An overview on the life cycle of lithium iron phosphate: Synthesis, modification, application, and recycling. *Chemical Engineering Journal*, p.149923.

Zhao, Y., Jian, Z. and Du, Y., 2024. How can China's subsidy promote the transition to electric vehicles? *Renewable and Sustainable Energy Reviews*, 189, p.114010.

Zonouzi, S.A., Yousefi, A., Hosseini, S.H. and Song, M., 2024. Improvement of the thermal management of lithium-ion battery with helical tube liquid cooling and phase change material integration. *Journal of Energy Storage*, 102, p.114113.

Zuev, D., Tyfield, D. and Urry, J., 2019. Where is the politics? E-bike mobility in urban China and civilizational government. *Environmental Innovation and Societal Transitions*, 30, pp.19–32.

Nature Environment and Pollution Technology
An International Quarterly Scientific Journal

p-ISSN: 0972-6268
(Print copies up to 2016)
e-ISSN: 2395-3454

Vol. 25 | No. 3 | Article ID B4402 | 2026

Original Research Paper

https://doi.org/10.46488/NEPT.2026.v25i03.B4402

Open Access Journal

Statistical Modeling Approaches for Nonstationary Flood Frequency Analysis in the Kosi River Basin

Akshay Kumar† and Ramakar Jha
Department of Civil Engineering, National Institute of Technology, Patna, Bihar, India
†Corresponding author: Akshay Kumar; akshayk.phd20.ce@nitp.ac.in

Abbreviation: Nat. Env. & Poll. Technol.
Website: www.neptjournal.com

Received: 13-10-2025
Revised: 18-12-2025
Accepted: 05-01-2026

Key Words:

Flood Frequency Analysis (FFA)
Hydrological risk assessment
Infrastructure design
Stationarity assumption
Nonstationarity
Climate-resilient water management
Flood risk planning

Citation for the Paper:

Akshay Kumar and Jha, R., 2026. Statistical modeling approaches for nonstationary flood frequency analysis in the Kosi River Basin. *Nature Environment and Pollution Technology*, 25(3), B4402. https://doi.org/10.46488/NEPT.2026.v25i03.B4402

Note: From 2025, the journal has adopted the use of Article IDs in citations instead of traditional consecutive page numbers. Each article is now given individual page ranges starting from page 1.

Copyright: © 2026 by the authors
Licensee: Technoscience Publications
This article is an open access article distributed under the terms and conditions of the Creative Commons Attribution (CC BY) license (https://creativecommons.org/licenses/by/4.0/).

ABSTRACT

Flood frequency analysis (FFA) is essential for hydrological risk assessment and infrastructure planning. However, traditional methods often assume stationarity, a premise increasingly challenged by climate change and human activities. This study explores nonstationary FFA in the Kosi River Basin using three approaches: Maximum Likelihood estimation, two-stage regression modeling, and Generalized Additive Models for Location, Scale, and Shape (GAMLSS). Daily flow records were used to extract annual maximum discharges, which were fitted to time-varying Generalized Extreme Value (GEV) models. Results show clear nonstationarity, with rising flood quantiles, especially for the 50- and 100-year return periods. While the Maximum Likelihood and Two-Stage approaches captured linear trends, GAMLSS revealed nonlinear dynamics. Model comparisons via Akaike Information Criterion (AIC) indicated no single method was best overall; multimodel averaging weighted by AIC provided more reliable quantile estimates. Bootstrap resampling confirmed increasing uncertainty with longer return periods and consistently highlighted growing flood risks. Stationary models tended to overestimate current design floods by about 35–40%, risking over-design if stationarity is wrongly assumed. This research illustrates that combining multimodal averaging with bootstrap uncertainty offers a robust framework for nonstationary flood frequency analysis, aiding climate-resilient water management and flood risk planning.

1. INTRODUCTION

Extreme flood events threaten human lives, livelihoods, infrastructure, and ecosystems, especially in flood-prone areas (Hoq et al. 2021). The socio-economic impacts of these events are compounded by rapid urbanization, land-use changes, and increased extreme precipitation due to climate variability and change (Dewan 2015, Khayyam 2020). Reliable flood frequency analysis (FFA) is essential for risk assessment and guiding the design of hydraulic structures, flood defenses, and water management policies (Machado et al. 2015). Traditionally, FFA has assumed stationarity, meaning flood probabilities are considered constant over time. However, growing evidence indicates that this assumption is increasingly invalid due to changing climate conditions, catchment modifications, and human interventions (Cui et al. 2023, Hounkpè et al. 2015). As a result, nonstationary approaches have been developed to explicitly incorporate the temporal variability of extreme hydrological events.

Over the last twenty years, hydrologists have increasingly utilized nonstationary extreme value theory (EVT) to more accurately represent the shifting risks associated with floods (Razmi et al. 2017). Katz et al. (2002) and Coles et al. (2001) established the theoretical groundwork by introducing covariate-dependent Generalized Extreme Value (GEV) models. Later research highlighted the significance of incorporating climate indices, such as ENSO and PDO, or time as covariates to identify trends in flood extremes (Cheng et al. 2014, López & Francés 2013). Comparative analyses indicate that various nonstationary modeling

approaches can produce notably different estimates of return levels, emphasizing the influence of model assumptions on flood risk assessments (Barbhuiya et al. 2023, Debele et al. 2017, Gül et al. 2014, Strupczewski et al. 2001). More recent work recommends multimodel inference and Bayesian model averaging to address structural uncertainties in hydrological extremes (Bhere & Janga Reddy 2025, Cui et al. 2023, Faulkner et al. 2020). Concurrently, bootstrap and Bayesian resampling methods are extensively employed to generate confidence intervals and evaluate uncertainty in non-stationary return level estimates (Kwon et al. 2011, Kwon et al. 2008).

Among various nonstationary methods, the Maximum Likelihood (ML) approach introduces linear trends in GEV parameters, whereas the two-stage method combines regression-based estimation of mean and variance with stationary residual fitting. More adaptable techniques, such as Generalized Additive Models for Location, Scale, and Shape (GAMLSS), enable nonlinear covariate effects on multiple distribution parameters, providing enhanced flexibility for capturing complex hydrological dynamics. Despite their strengths, each method has specific assumptions and limitations (Zhang et al. 2018). Consequently, relying on a single model may result in biased or unstable quantile estimates, especially for higher return periods (de Bruijn et al. 2020, Montello et al. 2022, Rajeshkannan & Kogilavani 2021, Talchabhadel et al. 2023, Zhang et al. 2024, Zheng et al. 2023).

To tackle this challenge, multimodal averaging based on information-theoretic criteria, such as the Akaike Information Criterion (AIC), offers a robust framework for synthesizing multiple models and reducing structural uncertainty (Chow & Watt 1992, Di Baldassarre et al. 2009, Haddad & Rahman 2011, Okoli et al. 2018). Additionally, bootstrap resampling provides a means to quantify estimation uncertainty and develop confidence intervals for non-stationary return levels.

Existing studies on nonstationary flood frequency in the Kosi River Basin and similar monsoon-driven rivers have primarily concentrated on individual modeling approaches or single best-fit models. They have paid limited attention to how model structure and parameter uncertainties jointly influence estimate outcomes. Notably, systematic comparisons of multiple nonstationary estimation methods within a unified framework, as well as the application of information-theoretic multimodel averaging to inform design decisions, remain rare.

This study presents a comprehensive framework for nonstationary flood frequency analysis by explicitly integrating and comparing various statistical methods within a unified model and uncertainty assessment system. Its objectives include (i) evaluating the performance of Maximum Likelihood (ML), Two-Stage, and GAMLSS techniques in modeling annual maximum discharge data, (ii) estimating nonstationary quantiles for return periods of 10, 25, 50, and 100 years, and (iii) assessing model effectiveness using multimodel averaging based on information-theoretic criteria, while quantifying predictive uncertainty with bootstrap confidence intervals. By combining diverse estimation approaches with rigorous uncertainty evaluation, this research aims to overcome the limitations of single modeling techniques, offering more robust and actionable

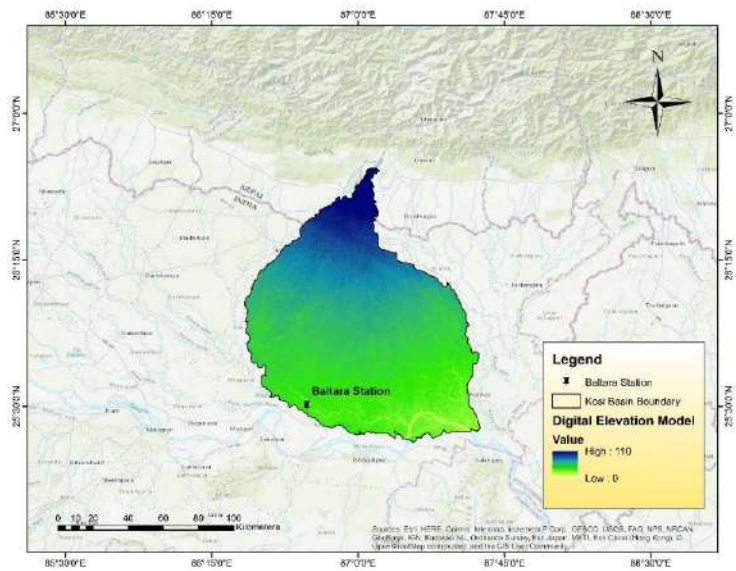


Fig. 1: Study area map showing Baltara station.

insights for flood risk management in dynamic, nonstationary environments.

2. STUDY AREA AND DATA COLLECTION

The Kosi River Basin spans from latitude 25° 21.0' to 26° 21.6' N and longitude 86° 31.8' to 87° 35.4' E. Originating in Tibet, the river flows through Nepal before entering Bihar near Bhimnagar and ultimately merging with the Ganga River near Kurshela (Fig. 1). In Bihar, the river covers a length of 261 km across 10 districts, including Supaul, Saharsa, Madhepura, and Katihar. Located in Bihar's plains, the basin reaches a maximum elevation of 91 meters and features slopes ranging from 0° to 35°. It is vital for agriculture, water supply, and local livelihoods. The climate is tropical monsoon with distinct wet and dry seasons, with most rainfall occurring from June to September.

Daily discharge data were sourced from the Central Water Commission (CWC) for the Baltara gauging station on the Kosi River. Spanning from 1989 to 2022, the dataset encompasses approximately 33 years of continuous observations. The basin exhibits high sensitivity to climate variability, with extreme rainfall events driven by ENSO and other large-scale climate phenomena. Human activities, including land-use changes and agricultural intensification, have also modified catchment responses, highlighting the need for nonstationary flood risk assessment.

3. MATERIALS AND METHODS

Daily discharge records were processed to develop an annual maxima series (AMS), the standard input for extreme value analysis. Initially, the records were examined for completeness and consistency. Years with inadequate daily observations were excluded to avoid bias in estimating the maximum values. Outliers identified through time-series inspection and summary statistics were retained if they represented documented extreme flood events, as removing them would distort the distribution's upper tail, which is essential for flood frequency analysis. Missing values were few and not imputed; instead, years with substantial data gaps were omitted from the AMS. The analysis of the AMS employed nonstationary extreme value frameworks.

3.1. Maximum Likelihood (ML) Estimation

The ML estimation method is widely used for estimating parameters of the Generalized Extreme Value (GEV) distribution under nonstationarity. The GEV distribution is defined as:

$$f\left(x;\mu,\sigma,\xi\right)= \frac{1}{\sigma}\left[1+\xi\left(\frac{x-\mu}{\sigma}\right)\right]^{-1/\xi-1}\exp\left\{-\left[1+\xi\left(\frac{x-\mu}{\sigma}\right)\right]^{-1/\xi}\right\} \quad \ldots(1)$$

where μ is the location parameter, σ > 0 is the scale parameter, and ξ is the shape parameter.

To account for nonstationarity, parameters are modeled as functions of covariates (Z_t). A common formulation is: e.g.:

$$\mu_t=\mu_0+z_t,\quad \sigma_t=\sigma_0\ \exp\left(\sigma_1 z_t\right),\ \xi_t=\xi\left(\text{constant}\right) \quad \ldots(2)$$

Given the relatively short length of the annual maximum series (33 observations), time was selected as the sole covariate in this study to ensure model parsimony and reduce the risk of over-parameterization.

Typically, only μ_t or σ_t are allowed to vary with time (to avoid over-parameterization).In this study, Z_t represents time.

Given a sample $\{x_1, x_2, \quad, x_n\}$ of annual maximum floods, the likelihood function under nonstationarity is

$$L\left(\theta\right)=\prod_{t=1}^{n} f\left(x_t;\mu_t,\sigma_t,\xi\right) \quad \ldots(3)$$

Where $\theta=\left(\mu_0,\mu_t,\sigma_0,\sigma_1,\xi\right)$ is the parameter vector the log -likelihood is

$$l\left(\theta\right)=\sum_{t=1}^{n}\ln f\left(x_t;\mu_t,\sigma_t,\xi\right) \quad \ldots(4)$$

The ML estimates are obtained by solving:

$$\hat{\theta}=\arg\ \max_{\theta}\ l\left(\theta\right) \quad \ldots(5)$$

Once the parameters are estimated, the t-year return level is derived from the quantile function.

$$Q_T=\mu_t-\frac{\sigma_t}{\xi}\left[1-\left\{-\ln(1-1/T\right\}^{-\xi}\right] \quad \ldots(6)$$

This approach enables the calculation of nonstationary flood quantiles that change with covariates like time. Maximum Likelihood (ML) estimation is highly efficient statistically, as it makes full use of all available data and supports likelihood-based inference with flexible covariate inclusion. Nevertheless, it may encounter numerical instability during optimization, be sensitive to sample size and initial parameter guesses, and become more difficult to interpret when multiple covariates are involved.

3.2. Two-Stage Method

The Two-Stage Method offers an alternative to machine learning for nonstationary frequency analysis by dividing the

estimation process into two distinct steps instead of directly fitting the GEV distribution with covariates. Initially, a stationary distribution—typically GEV—is fitted to the data to estimate parameters, which are then used to transform the data into normalized residuals. In the subsequent stage, either the residuals or the distribution parameters are modeled as functions of covariates such as time. This two-step approach reduces computational complexity and facilitates easier interpretation.

Fit the GEV distribution under stationarity:

$$x_t \sim GEV(\mu, \sigma, \xi) \quad \ldots(7)$$

Where μ, σ, ξ are constant parameters estimated using ML or L-moments. Compute the reduced variate (standardized value):

$$y_t = {x_t - \hat{\mu}}/{\hat{\sigma}} \quad \ldots(8)$$

The Two-Stage Method has several advantages over the direct ML approach. It is more computationally efficient because the estimation process is divided into two manageable steps, avoiding complex likelihood optimization with covariates from the start. This division also helps prevent convergence issues that are common in full ML estimation, making the method more stable and easier to implement. Additionally, its interpretability is a key benefit: because regression modeling of parameters occurs separately in the second stage, the effects of covariates on flood frequency can be more clearly understood and communicated. However, this method has some limitations. It is statistically less efficient than ML because it does not utilize all the data in a single, unified estimation, which may reduce precision. If the initial stationary fit is poor, it can introduce bias into the subsequent regression, affecting the accuracy of the nonstationary estimates. Finally, the method does not fully account for parameter uncertainty from the first stage in the second, potentially underestimating variability and leading to overconfident conclusions.

3.3. Generalized Additive Models for Location, Scale, and Shape (GAMLSS)

GAMLSS offers a versatile framework that models all distributional parameters (μ, σ, ξ) as functions of covariates, accommodating both linear and nonlinear (smooth) effects. In this approach, the location parameter was modeled using a quadratic time trend to capture potential nonlinear changes in flood magnitudes, while the scale parameter was modeled with a linear trend. The shape parameter was kept constant to maintain simplicity. The quadratic formulation for the location parameter was chosen to effectively represent nonlinear temporal evolution, balancing model flexibility with parsimony. To ensure numerical stability and parameter identifiability with a limited sample size, the scale parameter was restricted to linear time variation, and the shape parameter was fixed. All parameters were estimated through maximization of the penalized likelihood.

For annual maximum floods:

$$x_t \sim GEV(\mu_t, \sigma_t, \xi_t) \quad \ldots(9)$$

Nonstationary parameter modeling in GAMLSS, parameters are modeled as:

$$\mu_t = \eta_\mu(z_t) = \beta_o^\mu + \sum_j f_j^\mu(z_{jt}) \quad \ldots(10)$$

$$\ln(\sigma_t) = \eta_\sigma(z_t) = \beta_o^\sigma + \sum_j f_j^\sigma(z_{jt}) \quad \ldots(11)$$

$$\xi_t = \eta_\xi(z_t) = \beta_o^\xi + \sum_j f_j^\xi(z_{jt}) \quad \ldots(12)$$

Where $f_j(\bullet)$ are smooth functions (e.g., splines) or linear terms. Covariates z_{jt} include time. In this study, nonstationarity was introduced using time as the sole covariate.

Likelihood Estimation

The GAMLSS log-likelihood is:

$$l(\theta) = \sum_{t=1}^{n} \ln f(x_t | \mu_t, \sigma_t, \xi_t) \quad \ldots(13)$$

with optimization performed using penalized maximum likelihood (PML). Smoothness penalties control overfitting.

Return level for return period T:

$$Q_T(t) = \mu_t - \frac{\sigma_t}{\xi_t}\left[1 - \left(-\ln\left(1 - \frac{1}{T}\right)\right)^{-\xi_t}\right] \quad \ldots(14)$$

This yields time-varying return levels that reflect both linear and nonlinear effects.

The GAMLSS framework offers several key advantages that make it highly effective for nonstationary flood frequency analysis. Its primary strength is its flexibility, enabling it to model nonlinear and non-monotonic trends in the data that simpler models often overlook. Unlike methods that limit covariates to the location parameter alone, GAMLSS allows covariates to influence all three parameters of the GEV distribution, the location (μ), scale (σ), and shape (ξ), providing a more complete picture of non-stationary behavior. Another benefit is the use of penalized likelihood techniques, which regulate the smoothness of the fitted functions and help avoid overfitting, a common issue with flexible models. Additionally, the implementation of smooth functions like splines makes it easier to interpret the effects of covariates visually, helping researchers better

understand and communicate how environmental or climate factors impact flood extremes over time.

Although GAMLSS offers several advantages, it also has notable limitations. The method is computationally intensive, often requiring iterative optimization that can be slow and demanding on resources, especially with large datasets or complex models. Interpreting the results becomes more difficult when multiple smooth terms are included, as the combined effects of nonlinear covariates can be hard to disentangle. Additionally, there is a risk of overfitting with small sample sizes, since the model's flexibility may lead to identifying false patterns as true signals. Because GAMLSS estimates multiple parameters simultaneously, it typically needs a relatively large sample to produce stable estimates and reliable inferences. With limited data, parameter estimates may become unstable, reducing the model's predictive performance. Consequently, results from GAMLSS should be interpreted cautiously, particularly when data are scarce.

3.4. Multimodel Averaging

To reduce dependence on a single model, multimodel averaging was employed using Akaike Information Criterion (AIC) weights:

$$w_m = \frac{\exp\left(-0.5\Delta_m\right)}{\sum_{k=1}^{M}\exp\left(-0.5\Delta_k\right)} \quad \ldots(15)$$

Where $\Delta_m = AIC_m - AIC_{min}$, and M is the number of models. The multimodel return level is then:

$$Q_T^{multi}(t) = \sum_{m=1}^{M} w_m Q_T^{(m)}(t) \quad \ldots(16)$$

with $Q_T^{(m)}(t)$ the return level from the model m.

3.5. Bootstrap Uncertainty Analysis

A nonparametric block bootstrap method was used to assess the uncertainty in the return level estimates. This involved repeatedly resampling the AMS with replacement to create synthetic data sets. Each resampled dataset was then used to refit the models, and the multimodel return levels were recalculated. The distribution of these estimates was used to derive the 95% confidence intervals. This method explicitly accounts for sampling variability and provides robust uncertainty bands around time-varying flood quantiles.

4. RESULTS AND DISCUSSION

4.1. Annual Maximum Series (AMS)

The annual maximum discharge series (AMS) for the Kosi River Basin covered 1989 to 2022, totaling 33 years of data. The series shows significant year-to-year variability, with peak discharges ranging from approximately 766 $m^3.s^{-1}$ to 13,500 $m^3.s^{-1}$ (Table 1). Visual analysis indicated no clear increasing or decreasing trend in the annual maxima, although

Table 1: Summary statistics of annual maximum discharge series.

Statistic	Minimum	Maximum	Mean	Standard Deviation	Skewness	Kurtosis
Value [$m^3.s^{-1}$]	766.24	13,500	6,737.12	2,165.92	0.47	5.44

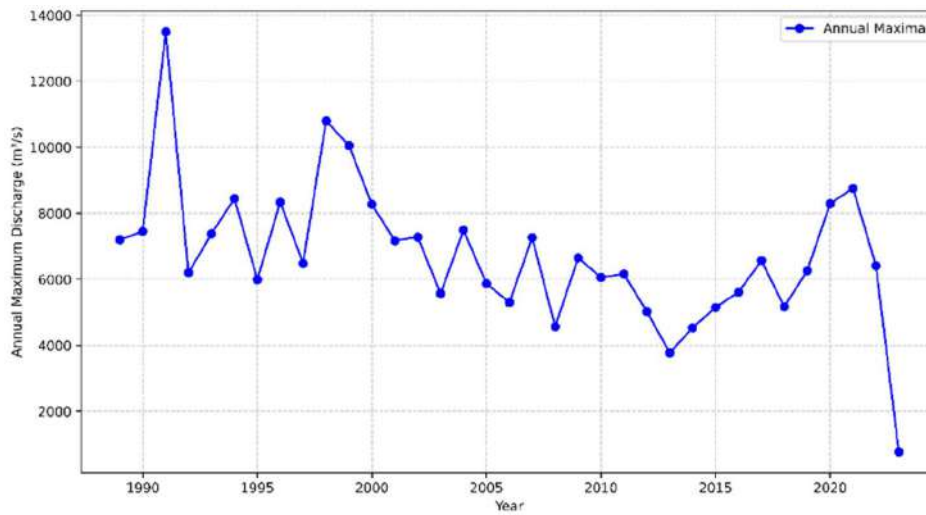


Fig. 2: Time series plot of annual maximum discharge for the Kosi River Basin at the station Baltara.

Table 2: AIC values and normalized weights for ML, Two-Stage, and GAMLSS models.

Model	AIC	Normalized Weight
ML	631.65	0. 70
Two-Stage	1118.09	0.15
GAMLSS	686.81	0.15

notable variability suggested potential nonstationarity (Fig. 2). While the raw AMS data demonstrate considerable interannual fluctuations without a consistent trend, nonstationary analysis indicates rising high-return-period quantiles, reflecting changes in extreme flood events rather than average flow behavior.

4.2. Model Fitting and Information Criteria

Three nonstationary models, Maximum Likelihood (ML), Two-Stage, and GAMLSS, were applied to the AMS using various parameterizations. The model performance was assessed using the Akaike Information Criterion (AIC). The ML-based nonstationary model yielded the lowest AIC, suggesting that it offered the best overall statistical fit among the options (Table 2). Nonetheless, the differences in the AIC weights indicate that no single model clearly outperformed the others, justifying the use of multimodel averaging. Although the ML and Two-Stage models described linear changes in flood behavior, the GAMLSS framework allowed for greater flexibility in capturing nonlinear dynamics, particularly in higher return-period quantiles.

AIC weights showed that no single model dominated across all periods (Table 2), justifying the use of multimodel averaging.

4.3. Time-Varying Flood Quantiles

Nonstationary return levels (T) were estimated for return periods of 10, 25, 50, and 100 years, respectively, as shown in Fig. 3. The maximum likelihood (ML) quantiles showed nearly linear increases over time. The Two-Stage quantiles demonstrated more variability owing to the residual-based variance estimation. The GAMLSS quantiles displayed nonlinear curvature, particularly for higher return periods, indicating increased sensitivity to recent changes in the upper tail of the flood distribution. Multi-model-averaged quantiles provided smoother and more stable estimates by balancing the strengths and weaknesses of the individual models (Fig. 4).

4.4. Bootstrap-Based Uncertainty Bands

A block bootstrap approach was employed to evaluate the predictive uncertainty. For each resampled dataset, the models were refitted, and the multimodel return levels were recalculated. The 95% confidence intervals were obtained from bootstrap distributions. Uncertainty increased with increasing return periods, with the 100-year quantile exhibiting the widest confidence bands. Despite substantial uncertainty at higher return periods, the ensemble of nonstationary models consistently indicates an upward trend in long-period flood quantiles, although the exact extent

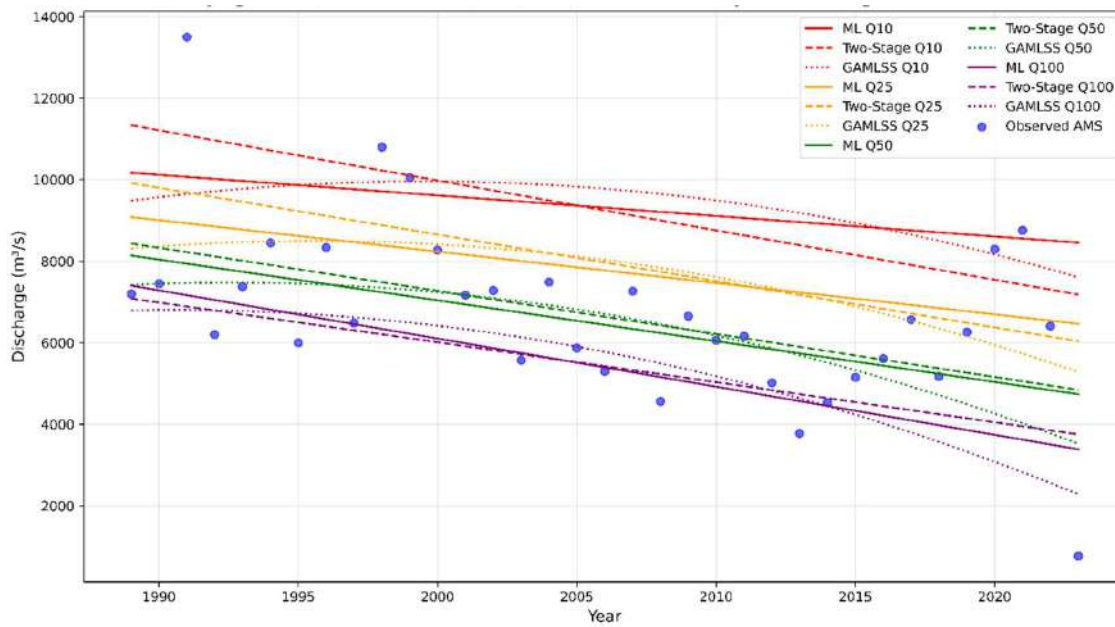


Fig. 3: Time-varying flood quantiles (Q10, Q25, Q50, Q100) estimated by ML, Two-Stage, and GAMLSS models.

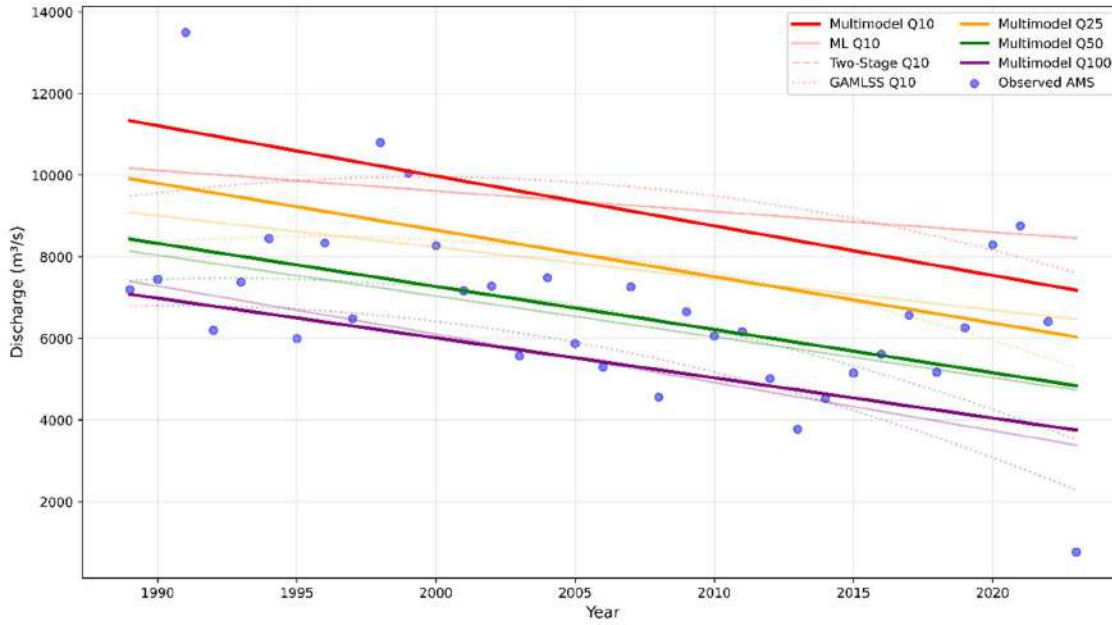


Fig. 4: Multimodel averaged quantiles with individual model contributions highlighted.

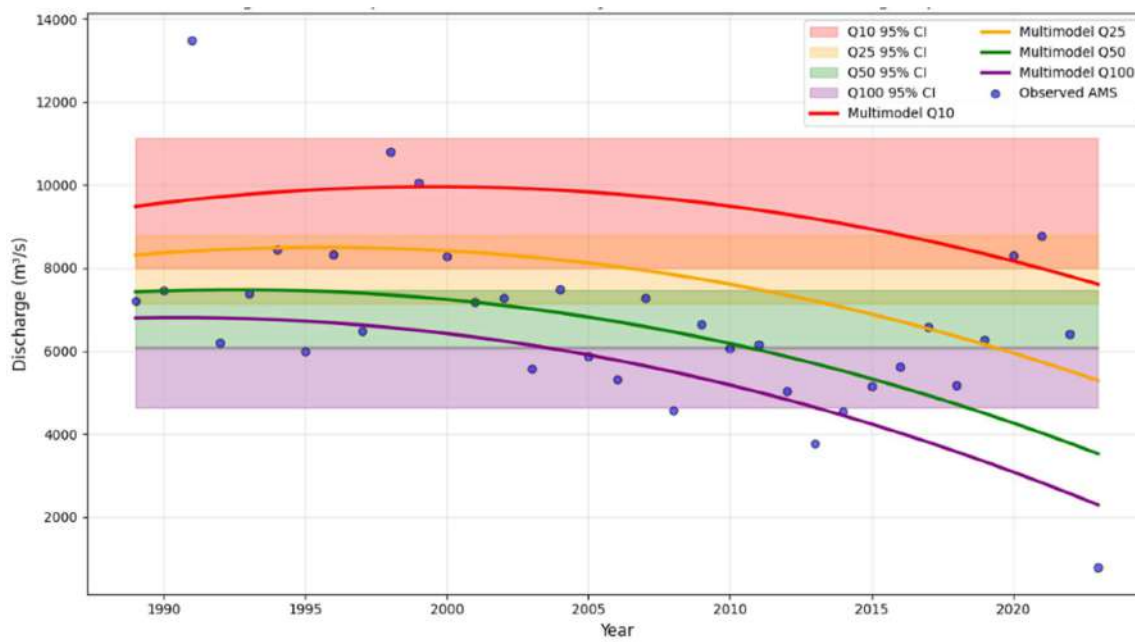


Fig. 5: Bootstrap-based 95% uncertainty bands for multimodel-averaged quantiles.

remains uncertain. The multimodel methodology produced narrower confidence intervals than the single-model estimates, underscoring the benefits of model averaging.

The results highlight the importance of accounting for nonstationarity in flood frequency analysis in the Kosi River Basin. Comparisons with stationary estimates indicated that assuming stationarity led to overestimations of the present-day 50- and 100-year design floods by approximately 40% and 37%, respectively. Although this may result in conservative designs, it also implies potential overdesign and cost inefficiency when nonstationary behavior is ignored.

From a methodological perspective, the integration of multiple nonstationary models, AIC-weighted averaging, and bootstrap uncertainty quantification provides a robust

and defensible framework for flood-risk assessment. These insights are particularly relevant for climate-sensitive basins, where both natural variability and anthropogenic changes contribute to the evolution of floods. To illustrate the differences across the models, we examined the estimated design floods for selected return periods in the most recent decade of the record (2013–2023). Table 3 summarizes the estimates from each method and the multi-model average, along with the bootstrap 95% confidence intervals for the multi-model result.

For the 10-year flood, model estimates ranged from 7,725 $m^3.s^{-1}$ (Two-Stage, which coincided closely with the multi-model average) to 8,681 $m^3.s^{-1}$ (ML), with GAMLSS producing an intermediate estimate of 8,385 $m^3.s^{-1}$, the 95% CI for the multi-model estimate spanned approximately 6,630–11,094 $m^3.s^{-1}$. For the 25-year return level, the ML model yielded approximately 10,463 $m^3.s^{-1}$, and the Two-Stage and multi-model both yielded approximately 8,653 $m^3.s^{-1}$ (indicating that ML's trend led to a higher extrapolation), and GAMLSS yielded approximately 10,755 $m^3.s^{-1}$; the CI was 7,546–16,716 $m^3.s^{-1}$, reflecting greater uncertainty. Divergence between models became more pronounced at the higher return periods: the 50-year flood estimates ranged from 9,242 $m^3.s^{-1}$ (Two-Stage, closely followed by the multi-model average) to 12,744 $m^3.s^{-1}$ (GAMLSS), with ML giving 11,794 $m^3.s^{-1}$. The CI of the multi-model 50-year estimate was wide (approximately 8,078–32,827 $m^3.s^{-1}$), indicative of sparse data in the tails. For the 100-year event, estimates varied between 9,755 $m^3.s^{-1}$ (Two-Stage, ~multi-model) and 14,938 $m^3.s^{-1}$ (GAMLSS), with ML yielding 13,124 $m^3.s^{-1}$, correspondingly, the bootstrap CI for the 100-year multi-model estimate extended from approximately 8,519 to 54,223 $m^3.s^{-1}$. These results highlight both the structural differences among nonstationary models and the growing uncertainty at higher return periods, reinforcing the importance of multi-model averaging and rigorous uncertainty quantification in flood-risk assessment. Relying on a single model may lead to the underestimation or overestimation of flood risk, whereas considering outputs from multiple models offers a more comprehensive view of plausible scenarios.

Bootstrap confidence intervals expand significantly with higher return periods, indicating limited data support in the upper tail and structural differences among models. The particularly wide intervals for 50- and 100-year events highlight the substantial uncertainty in estimating rare floods from short records. These findings emphasize the necessity of multimodel averaging and uncertainty assessment, as relying on a single model can result in either underestimation or overestimation of flood risk.

5. CONCLUSIONS

This study employed three nonstationary flood frequency analysis (FFA) methods—the Maximum Likelihood (ML), a two-stage regression-based estimation, and Generalized Additive Models for Location, Scale, and Shape (GAMLSS)—to analyze the annual maximum discharge data from the Kosi River Basin. The findings clearly indicate nonstationarity, with all models showing increasing trends in flood quantiles, especially for long return periods (50- and 100-year events). While GAMLSS captured nonlinear flood behavior patterns, the ML and Two-Stage approaches offered simpler, yet consistent, trend representations. AIC-based information criteria validated that no single model was consistently superior; therefore, AIC-weighted multimodel averaging provided more reliable and stable flood quantile estimates, reducing dependence on any one model. Bootstrap resampling highlighted increasing uncertainty for longer return periods, emphasizing the difficulty of estimating rare flood events.

Nonetheless, the consistent upward trend across models suggests a robust escalation in flood risk. Importantly, assuming stationarity led to overestimates of current 50- and 100-year flood levels by approximately 37–40%, risking overdesign and increased costs in flood infrastructure, potentially resulting in underestimation of risks if nonstationarity is ignored. These results underscore the need to incorporate nonstationary methods into flood frequency analysis for climate-resilient water resource management, flood protection, and policymaking. The framework can be expanded by integrating climate indices and land-use variables into parameter models, exploring Bayesian hierarchical approaches for uncertainty quantification, applying the methodology across multiple basins to identify regional risk patterns, and using the results for flood hazard mapping and early warning systems.

Table 3: Design flood estimates for the most recent decade (2013–2023) from individual nonstationary models and the multimodel average, with 95% bootstrap confidence intervals.

Return Period	ML [$m^3.s^{-1}$]	Two-Stage [$m^3.s^{-1}$]	GAMLSS [$m^3.s^{-}$]	Multi-model Average (95% CI) [$m^3.s^{-}$]
10-year	8,681	7,725	8,385	7,725 (6,630–11,094)
25-year	10,463	8,653	10,755	8,653 (7,546–16,716)
50-year	11,794	9,242	12,744	9,242 (8,078–32,827)
100-year	13,124	9,755	14,938	9,755 (8,519–54,223)

6. REFERENCES

Barbhuiya, S., Ramadas, M. and Biswal, S.S., 2023. Nonstationary flood frequency analysis: review of methods and models. *River, Sediment and Hydrological Extremes: Causes, Impacts and Management*, pp.271-288. [DOI]

Bhere, S. and Janga Reddy, M., 2025. Multi-covariate non-stationary flood frequency analysis for assessing flood hazard over the Mahanadi River basin, India. *Hydrological Sciences Journal* 1)70), pp.109-93. [DOI]

Cheng, L., AghaKouchak, A., Gilleland, E. and Katz, R.W., 2014. Non-stationary extreme value analysis in a changing climate. *Climatic Change* 2)127), pp.369-353. [DOI]

Chow, K.A. and Watt, W.E., 1992. Use of Akaike information criterion for selection of flood frequency distribution. *Canadian Journal of Civil Engineering* 4)19), pp.626-616. [DOI]

Coles, S., Bawa, J., Trenner, L. and Dorazio, P., 2001. *An Introduction to Statistical Modeling of Extreme Values*. Springer, p.208. [DOI]

Cui, H., Jiang, S., Gao, B., Ren, L., Xiao, W., Wang, M., Ren, M. and Xu, C.-Y., 2023. A method of regional non-stationary flood frequency analysis under the influence of a large reservoir group and climate change. *Journal of Hydrology* 618, p.129255. [DOI]

de Bruijn, J.A., de Moel, H., Weerts, A.H., de Ruiter, M.C., Basar, E., Eilander, D. and Aerts, J.C., 2020. Improving the classification of flood tweets with contextual hydrological information in a multimodal neural network. *Computers & Geosciences* 140, p.104485. [DOI]

Debele, S., Strupczewski, W. and Bogdanowicz, E., 2017. A comparison of three approaches to non-stationary flood frequency analysis. *Acta Geophysica* 4)65), pp.883-863. [DOI]

Dewan, T.H., 2015. Societal impacts and vulnerability to floods in Bangladesh and Nepal. *Weather and Climate Extremes* 7, pp.-36 42. [DOI]

Di Baldassarre, G., Laio, F. and Montanari, A., 2009. Design flood estimation using model selection criteria. *Physics and Chemistry of the Earth, Parts A/B/C* 12-10)34), pp.611-606. [DOI]

Faulkner, D., Warren, S., Spencer, P. and Sharkey, P., 2020. Can we still predict the future from the past? Implementing non-stationary flood frequency analysis in the UK. *Journal of Flood Risk Management* 1)13), p.e12582. [DOI]

Gül, G.O., Aşıkoğlu, Ö.L., Gül, A., Gülçem Yaşoğlu, F. and Benzeden, E., 2014. Nonstationarity in flood time series. *Journal of Hydrologic Engineering* 7)19), pp.1360-1349. [DOI]

Haddad, K. and Rahman, A., 2011. Selection of the best fit flood frequency distribution and parameter estimation procedure: a case study for Tasmania in Australia. *Stochastic Environmental Research and Risk Assessment* 3)25), pp.428-415. [DOI]

Hoq, M.S., Raha, S.K. and Hossain, M.I., 2021. Livelihood vulnerability to flood hazard: understanding from the flood-prone haor ecosystem of Bangladesh. *Environmental Management* 3)67), pp.552-532. [DOI]

Hounkpè, J., Diekkrüger, B., Badou, D.F. and Afouda, A.A., 2015. Non-stationary flood frequency analysis in the Ouémé River Basin, Benin Republic. *Hydrology* 4)2), pp.229-210. [DOI]

Katz, R.W., Parlange, M.B. and Naveau, P., 2002. Statistics of extremes in hydrology. *Advances in Water Resources* 12-8)25), pp.-1287 1304. [DOI]

Khayyam, U., 2020. Floods: Impacts on livelihood, economic status and poverty in the north-west region of Pakistan. *Natural Hazards* 3)102), pp.1056-1033. [DOI]

Kwon, H.-H., Sivakumar, B., Moon, Y.-I. and Kim, B.-S., 2011. Assessment of change in design flood frequency under climate change using a multivariate downscaling model and a precipitation-runoff model. *Stochastic Environmental Research and Risk Assessment* 4)25), pp.581-567. [DOI]

Kwon, H.H., Brown, C. and Lall, U., 2008. Climate informed flood frequency analysis and prediction in Montana using hierarchical Bayesian modeling. *Geophysical Research Letters* 5)35), p.L05404. [DOI]

López, J. and Francés, F., 2013. Non-stationary flood frequency analysis in continental Spanish rivers, using climate and reservoir indices as external covariates. *Hydrology and Earth System Sciences* 8)17), pp.3203-3189. [DOI]

Machado, M.J., Botero, B.A., López, J., Francés, F., Díez-Herrero, A. and Benito, G., 2015. Flood frequency analysis of historical flood data under stationary and non-stationary modelling. *Hydrology and Earth System Sciences* 6)19), pp.2576-2561. [DOI]

Montello, F., Arnaudo, E. and Rossi, C., 2022. Mmflood: A multimodal dataset for flood delineation from satellite imagery. *IEEE Access* 10, pp.96787-96774. [DOI]

Okoli, K., Breinl, K., Brandimarte, L., Botto, A., Volpi, E. and Di Baldassarre, G., 2018. Model averaging versus model selection: estimating design floods with uncertain river flow data. *Hydrological Sciences Journal* 14-13)63), pp.1926-1913. [DOI]

Rajeshkannan, C. and Kogilavani, S., 2021. *Mobile Computing and Sustainable Informatics: Proceedings of ICMCSI 2021*. Springer, pp.489-511. [DOI]

Razmi, A., Golian, S. and Zahmatkesh, Z., 2017. Non-stationary frequency analysis of extreme water level: application of annual maximum series and peak-over threshold approaches. *Water Resources Management* 7)31), pp.2083-2065. [DOI]

Strupczewski, W., Singh, V. and Feluch, W., 2001. Non-stationary approach to at-site flood frequency modelling I. Maximum likelihood estimation. *Journal of Hydrology* 4-1)248), pp.142-123. [DOI]

Talchabhadel, R., Maskey, S., Gouli, M.R., Dahal, K., Thapa, A., Sharma, S., Dixit, A.M. and Kumar, S., 2023. Multimodal multiscale characterization of cascading hazard on mountain terrain. *Geomatics, Natural Hazards and Risk* 1)14), p.2162443. [DOI]

Zhang, T., Wang, Y., Wang, B., Tan, S. and Feng, P., 2018. Nonstationary flood frequency analysis using univariate and bivariate time-varying models based on GAMLSS. *Water* 7)10), p.819. [DOI]

Zhang, Z., Ma, Y. and Liu, P., 2024. A global multimodal flood event dataset with heterogeneous text and multi-source remote sensing images. *Big Earth Data*, pp.1-27. [DOI]

Zheng, X., Duan, C., Chen, Y., Li, R. and Wu, Z., 2023. Disaster loss calculation method of urban flood bimodal data fusion based on remote sensing and text. *Journal of Hydrology: Regional Studies* 47, p.101410. [DOI]

Nature Environment and Pollution Technology
An International Quarterly Scientific Journal

p-ISSN: 0972-6268
(Print copies up to 2016)
e-ISSN: 2395-3454

Vol. 25 | No. 3 | Article ID B4412 | 2026

Original Research Paper

https://doi.org/10.46488/NEPT.2026.v25i03.B4412

Open Access Journal

Spatio-Temporal Distribution and Diversity of Butterflies (Lepidoptera: Papilionoidea) across Biotopes in the Kumaun Division of Western Himalaya: Implications for Habitat Modification and Environmental Monitoring

Surabhi Bisht and Manoj Kumar Arya†

Insect Biodiversity Laboratory, Department of Zoology, D.S.B. Campus, Kumaun University, Nainital-263001, Uttarakhand, India

†Corresponding author: Manoj Kumar Arya; dr.manojkumar19@rediffmail.com

Abbreviation: Nat. Env. & Poll. Technol.
Website: www.neptjournal.com

Received: 13-11-2025
Revised: 02-02-2026
Accepted: 28-02-2026

Key Words:

Biotopes
Conservation
Diversity of butterflies
Environmental monitoring
Lepidoptera
Species richness

Citation for the Paper:

Bisht, S. and Arya, M.K. 2026. Spatio-temporal distribution and diversity of butterflies (Lepidoptera: Papilionoidea) across biotopes in the Kumaun division of Western Himalaya: Implications for habitat modification and environmental monitoring. *Nature Environment and Pollution Technology*, 25(3), B4412. https://doi.org/10.46488/NEPT.2026.v25i03.B4412

Note: From 2025, the journal has adopted the use of Article IDs in citations instead of traditional consecutive page numbers. Each article is now given individual page ranges starting from page 1.

Copyright: © 2026 by the authors
Licensee: Technoscience Publications
This article is an open access article distributed under the terms and conditions of the Creative Commons Attribution (CC BY) license (https://creativecommons.org/licenses/by/4.0/).

ABSTRACT

The abundance and diversity of butterflies in an ecosystem are crucial for informing conservation strategies. This research surveyed butterfly communities across three distinct biotopes in Kumaun, Uttarakhand, India. Random sampling was conducted from March 2023 to February 2024 in agricultural fields, riverine areas, and urban settlements. A total of 94 butterfly species from six families were documented: Nymphalidae (42 species), Pieridae (19), Lycaenidae (17), Papilionidae (08), Hesperiidae (05), and Riodinidae (03). Beta diversity analyses indicated significant variation among biotopes. The riverine habitat exhibited the highest alpha diversity and species richness, followed by urban and agricultural areas. Agricultural land and river catchment site shared the most species, whereas urban and agricultural biotopes showed the least similarity. Butterfly diversity peaked during summer and post-monsoon across all habitats. Seven species are listed under Schedule II, and one under Schedule IV of the Indian Wildlife (Protection) Act, 1972. The decline in butterfly diversity in agricultural landscapes points to habitat loss driven by expanding agricultural frontiers in Nainital district. Overall, the findings underscore the value of butterfly communities as ecological indicators for monitoring habitat changes and environmental health in the Western Himalaya.

1. INTRODUCTION

Habitat heterogeneity significantly influences biodiversity by enhancing niche availability and resource diversity (Bazzaz 1975, Tews et al. 2004, Braga & Diniz 2015). Among terrestrial insects, butterflies from the order Lepidoptera are frequently utilized as ecological indicators because they are easy to monitor and highly responsive to environmental and climate changes (Kocher & Williams 2000). However, ecosystems modified by humans and agricultural landscapes typically prove inadequate for supporting insect diversity, particularly butterflies (Sagwe et al. 2015, Chettri et al. 2018, Samraj & Agnihotri 2021). Landscape degradation driven by rapid climate change, urbanization, and agricultural expansion poses a significant threat to biodiversity (Sagwe et al. 2015, Gallou et al. 2017). Understanding the ecological impacts of habitat loss and fragmentation requires assessing the vulnerability of different biotopes to landscape change (Weißhuhn 2019). Since many butterflies have specific habitat requirements (Leon-Cortes et al. 2004), tracking their abundance and distribution across various biotopes can aid in making timely conservation decisions (Blair & Launer 1997, Munyuli 2013, Fontaine et al. 2016, An & Choi 2021).

The Indian Himalayan Region (IHR) boasts a rich diversity of butterflies. Numerous studies have documented butterfly diversity and habitat associations across both protected and unprotected areas within the IHR (Singh & Bhandari

2003, 2006, Uniyal 2007, Bhardwaj & Uniyal 2011, Sarma et al. 2012, Qureshi et al. 2014, Kumar et al. 2016, Chettri et al. 2018, Paunikar & Sharma 2022). Despite extensive research in the Western Himalaya (Joshi & Arya 2007, Bhardwaj et al. 2012, Kumar et al. 2017, Verma & Arya 2018, Arya et al. 2020a, Samraj & Agnihotri 2021, Verma & Arya 2022), the spatial variation of butterfly assemblages within the Kumun region of Uttarakhand remains insufficiently explored. Similarly, existing records from Nainital district in Kumaun division (Smetacek 2002, 2010, 2011a, 2011b, 2012a, 2012b, Tyagi et al. 2011, Meena & Dayakrishna 2017, Sondhi 2017, Arya et al. 2018, Arya et al. 2020b, Chandra et al. 2023) lack comparative or habitat-based analyses. As a result, systematic documentation of butterfly diversity across the diverse biotopes of the Kumaun Himalaya remains inadequate. Given the scarcity of studies comparing how different biotopes influence butterfly communities seasonally, a detailed assessment is necessary to understand habitat-specific responses. Therefore, this study investigates the effects of habitat simplification on butterfly communities by analyzing (a) species assemblage structure and composition in urban, riverine, and agricultural habitats, (b) seasonal variations in diversity, and (c) the conservation value of these biotopes. The research also evaluates the potential of butterflies as bioindicators of habitat integrity amid expanding agriculture and urban development.

Unlike previous studies from the Kumaun Himalaya, which primarily include checklist-based inventories or site-specific records, this study employs a comparative biotope-based approach to evaluate butterfly assemblages across different land-use systems. It fills this gap by offering a spatio-temporal assessment of butterfly diversity in agricultural, riverine, and urban landscapes within the Kumaun division, providing valuable insights into habitat alteration and its effects on environmental monitoring.

2. MATERIALS AND METHODS

2.1. Study Area

The study area is located in the Kumaun Himalayan region of Uttarakhand, northern India. The district of Nainital, covering 4,251 km², lies at elevations ranging from 151 m to 2,581 m above sea level and is the sixth largest district in the state. It features diverse topographic regions with contrasting landscapes that generate microclimatic variations, which in turn influence soil properties and vegetation patterns. Changes in vegetation, relief, and slope also impact faunal assemblages (Acharya & Vijayan 2015). This study focuses on three structurally distinct biotopes differentiated by elevation, biotic stress levels, vegetation types, and disturbance intensity. These are the Agriculture Biotope, the Riverine Biotope, and the Urban Biotope, situated at approximately 350 m, 950–1,150 m, and 2,100–2,300 m above sea level, respectively (Fig. 1). Due to terrain differences, each biotope experiences variations in rainfall patterns, relative humidity, and monthly temperatures. These climatic parameters were recorded using a digital min/max thermo-hygrometer.

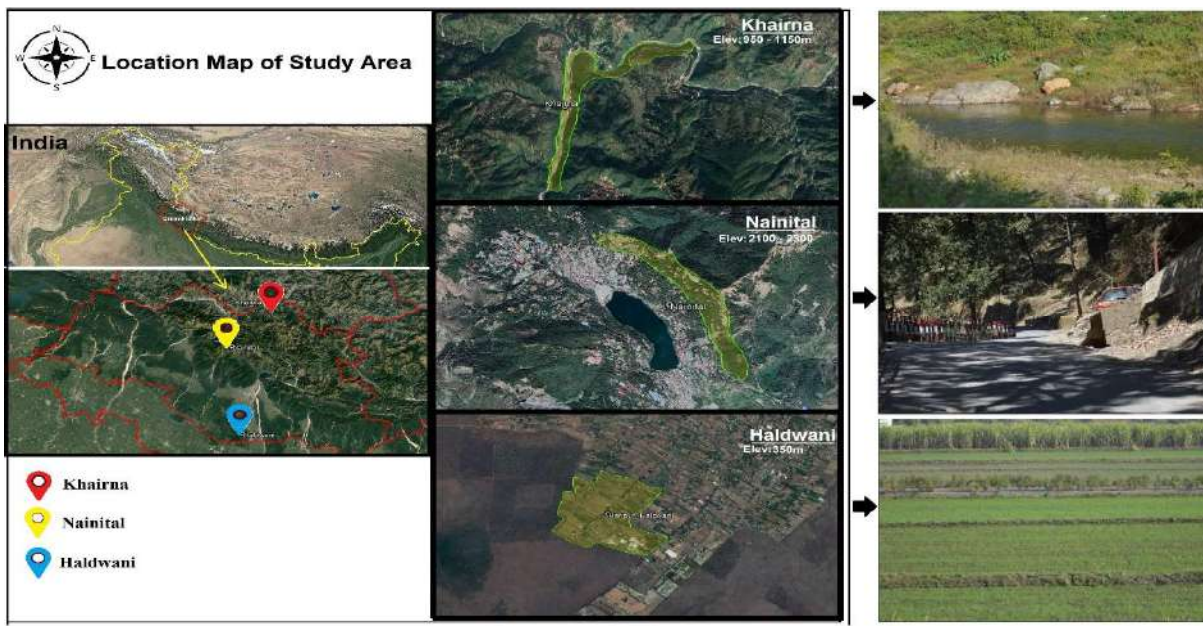


Fig. 1: Map showing selected sampling biotopes ranging in elevational zone from 350-2300m.

2.1.1. Agriculture Biotope (aB)

The study site is situated in Haripur Jamansingh village, Haldwani, characterized by arable lands that reflect a rural environment. The region experiences warmer summers with comparatively higher rainfall than in winters. Annually, kharif crops such as paddy and maize are cultivated, while rabi crops include wheat, sugarcane, pulses, mustard, and *Trifolium alexandrinum*. Additionally, fruit-bearing and ornamental plants along field margins or hedgerows consist of *Catharanthus roseus, Hibiscus, Pyrostegia venusta, Tagetes species, Artocarpus heterophyllus, Mangifera indica, Carica papaya, Punica granatum,* and *Phyllanthus emblica*. Human activities such as surface burning, litter removal, fodder collection, and small-scale construction are prevalent. Butterflies were observed along two transects: one bordering the field margins and another within the crop fields.

2.2.2. Riverine Biotope (rB)

The location is situated along the banks of the Kosi River near Jyari village, Khairna. The riverbed has an average width of about 80 meters and flows in a north-west direction. The region features a mix of broad-leaved and needle-leaved trees, dense shrubs, and ground vegetation. Common tree species planted along the banks include *Cinnamomum tamala, Syzygium cumini,* and *Prunus persica*, while naturally occurring vegetation comprises *Pinus roxburghii, Ricinus communis*, and various *Ficus* species. The shrub and ground layers are dominated by *Berberis asiatica, Callicarpa macrophylla, Lantana camara, Hypericum oblongifolium, Zanthoxylum armatum, Debrigessia longifolia, Ageratina adenophora*, and *Conyza japonica*. The river acts as a boundary, separating a relatively pristine mountainous area on the right bank from a semi-modified landscape on the left bank, which includes small markets and highway crossings. Human activities such as woodcutting for fuel, grazing, fodder collection, and construction along the riverbank have led to alterations in the surrounding forest cover. Butterfly communities were sampled across two transects established on both sides of the Kosi River, providing insight into the local biodiversity.

2.2.3. Urban Biotope (uB)

The urban biotope, belonging to the town of Nainital, represents a highly disturbed landscape characterized by dense human settlements and a rapid influx of tourists. The region has a monsoon-dominated climate, with peak rainfall occurring from mid-June to September. The tree layer consists of a mix of evergreen and deciduous species, including *Acer oblongum, Aesculus indica, Buddleja asiatica, Cupressus torulosa, Quercus leucotricophora, Q. floribunda,* and *Rhododendron arboreum*. Common shrubs and herbs comprise *Berberis sp., Debrigessia longifolia, Pyracantha crenulata, Rubus ellipticus, Ageratina adenophora, Bidens pilosa, Cirsium* sp., *Erigeron* sp., *Rumex nepalensis, Salvia* sp., and *Urtica dioica*. The surrounding forests are often subjected to grazing, as well as fuel wood and fodder collection. The expansion of settlements and occasional forest fires have increased human pressures. Transects were selected to reflect different levels of anthropogenic impact: one experienced recurrent human disturbances, while the other was located in a moderately disturbed area adjacent to forest cover (Table 1).

2.2. Sampling and Identification of Butterflies

Monthly sampling of butterfly species was conducted twice monthly in each biotope from March 2023 to February 2024. Each visit lasted three consecutive days, covering each transect between 08:00 and 15:00. Two 500-meter line transects were established in each biotope, with butterfly counts based on wing morphology performed using the point count method and the modified Pollard Walk Method (Pollard 1977). Due to the varying physiography of the biotopes, transects were strategically placed within a landscape span of approximately 3 km to ensure representative habitat coverage. Along each transect, ten fixed point-count stations were set at regular intervals, with butterfly abundance recorded for five minutes at each station while maintaining a consistent pace within the observer's radius.

Although detectability may differ among biotopes, sampling effort, time of day, transect length, and observation

Table 1: Characteristic features of biotopes selected for butterfly sampling.

Biotope	Location	Elevation [m]	Geographical coordinates	Landscape Element & Vegetation Type	Level of Disturbance
Agriculture (*aB*)	Haldwani	350	29°09'16.1″N Latitude 79°28'40.6″E Longitude	Cultivation fields of cereal and vegetable crops for agricultural practices	Moderate
Riverine (*rB*)	Khairna	950-1150	29°29'56.7″N Latitude 79°30'19.2″E Longitude	Low-lying area Needle and broad-leaved and plantation forests with good cover of grasses	Low
Urban (*uB*)	Nainital city	2100-2300	29°23′ 29.643″ N Latitude 79°28′ 8.436″ E Longitude	Hilly terrain Mixed deciduous forest near human habitation	High

duration were standardized to facilitate comparative analysis. Some cryptic species, such as *Celastrina* spp., *Lethe confusa,* L. *verma,* and *Neptis* spp., which could not be reliably identified in the field from photographs, were collected with butterfly nets, identified, and then released unharmed. No harm was inflicted on any individual during the study. Butterfly identification followed field guides by Kehimkar (2014) and Sondhi and Kunte (2018). The presence of preferred host plants within 2.5 meters of either side of each transect was recorded following Clark et al. (2007).

2.3. Analysis of Data

Five major groups of butterflies were classified based on the occurrence frequency of individuals across all biotopes: Very Rare (1-3 individuals), Rare (4-10 individuals), Uncommon (11-20 individuals), Common (21-40 individuals), and Very Common (>41 individuals). These categories are descriptive and intended to reflect field observations rather than infer the population status of butterflies. To analyze the collected data, the months were grouped into four seasons: (i) summer: March, April, May; (ii) monsoon: June, July, August; (iii) post-monsoon: September, October, November; and (iv) winter: December, January, February.

The functional roles of butterflies, based on information about their larval host plants, were examined using published sources from around the world, including Wynter-Blyth (1957), Veenakumari et al. (1997), Robinson et al. (2023), Smetacek (2011c), Smetacek & Smetacek (2011), Ghorai & Sengupta (2014), Sengupta et al. (2014), Naik & Mustak (2015), Joshi et al. (2016), Nitin et al. (2018), and Sondhi & Kunte (2018). Based on their range of host plant utilization, butterfly species were classified into three categories reflecting host specificity: Monophagous- feeding on plant species within a single genus, Oligophagous- feeding on plant genera within a single family, and Polyphagous- feeding on a diverse array of larval food plants across multiple plant families (Smetacek 2012a).

Using this classification, oligophagous and polyphagous butterflies were regarded as host generalists, whereas monophagous butterflies were considered host specialists. Additionally, the patterns of abundance and species richness across different biotopes and seasons were analyzed separately. A heat map was created to illustrate the seasonal evenness or equitability of species, plotted against normalized abundance—calculated using the formula proposed by Naik et al. (2022). et al. (2022).

$$xi - min(x)/max(x) - min(x)$$

(Where x= absolute frequency and N= total)

The heat map was created to visualize the distribution of butterflies across different seasons, with Hierarchical Cluster Analysis (HCA) conducted to explore relationships between seasons and species assemblages. This analysis utilized normalized abundance data, which is appropriate for presence-absence matrices that display strong seasonal variation. The heat map was generated online using Heatmapper (http://www.heatmapper.ca/, Babicki et al. 2016). Rank-abundance curves illustrating species distribution patterns across various biotopes were produced after log-transforming the abundance data. To evaluate sampling efforts, individual-based rarefaction curves were calculated for each biotope using the software PAST version 3.4 (Magurran 2004, Hammer et al. 2001). Similarly, butterfly diversity among families and biotopes was assessed using alpha diversity indices such as Shannon's Index (Hs) for species diversity (Shannon & Weaver 1949), Simpson's Index (D) for species dominance (Simpson 1949), and Margalef's Index (Hm) for species richness (Margalef 1972), all calculated with PAST 3.4. To compare butterfly richness and abundance across biotopes, One-way ANOVA was performed using SPSS version 22, followed by pairwise comparisons with Tukey's HSD test at a 5% significance level. Additionally, the Jaccard similarity index (J) was employed to measure the similarity in species composition among biotopes based on shared species, using the formula provided by Niwattanakul et al. (2013).

$$(J = a \cup b)/(a \cap b)$$

Where a = the number of species of butterflies present at Site A and b = *the* number of species of butterflies present at Site B.

Bray-Curtis cluster analysis based on single linkage similarity was performed using Biodiversity Pro (Lambshead et al. 1997, McAleece 1998).

3. RESULTS

3.1. Species Richness, Family Composition, and Status of Butterfly Fauna

A total of 94 species, belonging to 66 genera and six families, were identified across the three study sites during the research period. The Nymphalidae family was the most prevalent, representing 44.7% of the species, followed by Pieridae (20.2%), Lycaenidae (18.1%), Papilionidae (8.5%), Hesperiidae (5.3%), and Riodinidae (3.2%). Table 2 presents an inventory of the butterfly species identified, their seasonal abundance, and their polyphagy categories across different biotopes. Fig. 2 highlights some of the notable butterfly species observed during the study.

Out of a total of 94 butterfly species recorded, seven species (*Aporia agathon*, *Ceporia nerissa*, *Euchrysops cnejus*,



Fig. 2: Photo plates of butterflies identified from the study area. (A) *Aglais caschmirensis*. (B) *Danaus chrysippus*, (C) *Vanessa indica*, (D) *Catopsilia pyranthe*, (E) *Eurema laeta*, (F) *Gonepteryx nepalensis*, (G) *Heliophorus sena*, (H) *Lycaena panava*, (I) *Talicada nyseus*.

Table 2: Distribution, species composition, and seasonal abundance of butterfly populations in different biotopes (*aB*, *rB*, *uB*) during the study period.

Family	Scientific Name	(*aB*)				(*rB*)				(*uB*)			
		S	M	PM	W	S	M	PM	W	S	M	PM	W
Nymphalidae	*Acraea issoria* (Hübner) [P]	0	0	0	0	1	2	2	0	1	4	2	1
	Aglais caschmirensis (Kollar) [P]	0	0	0	0	6	8	12	4	34	16	18	8
	Ariadne ariadne (Linnaeus) [M]	2	4	5	3	0	2	5	2	0	0	0	0
	Ariadne merione (Cramer) [O]	2	2	35	31	4	6	20	0	0	0	0	0
	Argynnis hyperbius (Linnaeus) [P]	0	0	1	0	1	0	2	0	1	0	1	0
	Aulocera swaha (Kollar) [M]	0	0	0	0	0	0	0	0	3	2	6	1
	Callerebia annada (Moore) [O]	0	0	0	0	0	0	0	0	8	6	8	0
	Cyrestis thyodamas Doyere [P]	2	1	1	2	2	2	1	1	0	0	0	0
	Danaus chrysippus (Linnaeus) [P]	18	5	14	1	4	5	25	1	9	10	11	0
	Danaus genutia (Cramer) [O]	10	11	11	2	9	2	16	3	6	9	13	0
	Euploea core (Cramer)[P]	3	1	3	1	3	3	0	0	7	2	4	0
	Euthalia aconthea (Cramer) [P]	6	4	3	0	2	2	3	0	0	0	0	0
	Euthalia patala (Kollar) [M]	0	0	0	0	0	0	0	0	2	7	1	0
	Hypolimnas bolina (Linnaeus) [P]	3	6	2	0	1	2	4	0	0	0	0	0
	Issoria issaea (Gray) [P]	0	0	0	0	0	0	0	0	4	1	0	0
	Junonia almana (Linnaeus) [P]	12	5	1	10	16	1	1	1	9	3	3	0
	Junonia iphita (Cramer) [O]	4	0	2	0	5	1	2	0	15	4	1	0

Table Cont....

Family	Scientific Name	(*aB*)				(*rB*)				(*uB*)			
		S	M	PM	W	S	M	PM	W	S	M	PM	W
	Junonia lemonias (Linnaeus) [P]	2	4	5	1	4	1	3	0	3	0	2	0
	Junonia orithya (Linnaeus) [P]	9	6	5	2	5	3	2	0	0	0	0	0
	Kallima inachus (Doyere) [P]	0	0	0	0	4	1	0	0	0	0	0	0
	Kaniska canace (Linnaeus) [P]	0	0	0	0	0	1	0	0	1	0	1	0
	Lasiommata schakra (Kollar) [M]	0	0	0	0	0	0	0	0	5	8	4	0
	Lethe confusa Aurivillus [O]	0	0	0	0	0	1	0	0	1	4	2	0
	Lethe verma (Kollar) [O]	0	0	0	0	0	0	0	0	0	4	2	0
	Melanitis leda (Linnaeus) [O]	0	0	0	0	0	2	0	0	0	4	3	0
	*Mycalesis visala*Moore [O]	1	5	3	1	0	2	1	0	0	0	0	0
	Neptis hylas (Linnaeus) [P]	11	5	8	0	4	0	4	0	9	2	8	1
	Neptis sappho (Pallas) [M]	6	5	8	1	10	1	6	0	0	0	0	0
	Orinoma damaris Gray [M]	0	0	0	0	0	0	0	0	0	0	1	0
	Parantica aglea (Stoll)[O]	2	1	3	0	3	3	5	0	4	6	2	0
	Parantica sita (Kollar)[O]	0	3	3	0	2	2	0	0	2	6	2	0
	Phalanta phalantha (Drury) [P]	0	0	0	0	1	1	27	1	6	0	19	3
	Pseudergolis wedah (Kollar)[O]	0	0	0	0	11	9	8	1	0	0	0	0
	Sephisa dichroa (Kollar) [P]	0	0	0	0	0	0	0	0	1	2	0	0
	Symbrenthia lilaea (Hewitson)[O]	7	2	0	4	1	1	5	0	3	0	9	0
	Tirumala limniace (Cramer)[O]	0	2	0	0	1	1	0	0	0	0	0	0
	Vanessa cardui (Linnaeus) [P]	0	0	0	0	4	0	3	0	14	1	7	0
	Vanessa indica (Herbst) [P]	0	0	0	0	3	0	9	0	26	2	16	4
	Ypthima baldus (Fabricius) [O]	4	14	8	2	2	3	2	2	0	0	0	0
	Ypthima huebneri Kirby[M]	11	14	7	3	4	2	1	0	0	0	0	0
	Ypthima nareda (Kollar) [M]	0	0	0	0	2	1	0	0	0	2	1	0
	Ypthima nikaea Moore[M]	0	0	0	0	0	0	1	0	4	4	3	0
Pieridae	*Aporia agathon* [P]	0	0	0	0	0	0	0	0	16	10	0	0
	Belenois aurota (Fabricius) [P]	8	2	4	1	4	3	1	0	4	0	0	0
	Catopsilia pomona (Fabricius) [O]	14	18	12	6	11	3	11	2	10	6	8	1
	Catopsilia pyranthe (Linnaeus)[O]	9	14	10	16	7	3	9	3	11	6	7	0
	Cepora nerissa (Fabricius) [O]	13	6	3	1	7	1	2	0	0	0	0	0
	Colias erate (Esper)[O]	5	0	1	0	3	1	1	0	5	1	0	0
	Colias fieldii Menetries [P]	27	1	0	0	10	0	0	0	24	4	2	0
	Delias belladonna (Fabricius)[O]	0	0	0	0	3	1	2	0	11	4	2	0
	Eurema andersonii (Moore)[M]	11	1	10	3	3	0	7	0	4	3	2	0
	Eurema blanda (Boisduval) [P]	4	4	6	10	4	2	8	1	0	0	0	0
	Eurema brigitta (Stoll)[P]	8	4	14	4	4	5	11	0	9	5	15	0
	Eurema hecabe (Linnaeus)[O]	24	20	12	24	8	4	12	0	22	7	11	0
	Eurema laeta (Boisduval)[O]	13	6	8	3	6	0	14	2	12	9	14	0
	Gonepteryx nepalensis Doubleday [P]	0	0	0	0	3	0	6	0	7	10	10	2
	Leptosia nina (Fabricius)[P]	1	4	3	3	0	2	1	1	0	0	0	0
	Pareronia hippia (Fabricius)[O]	1	1	4	0	0	2	4	0	0	0	0	0
	Pieris brassicae (Linnaeus) [P]	29	19	20	10	28	10	14	8	29	24	15	2
	Pieris canidia (Linnaeus)[P]	35	17	16	17	32	13	17	8	28	27	20	3

Table Cont....

Family	Scientific Name	(*aB*)				(*rB*)				(*uB*)			
		S	M	PM	W	S	M	PM	W	S	M	PM	W
	Pontia daplidice (Linnaeus)[P]	13	4	2	1	3	0	1	0	1	3	0	0
Lycaenidae	*Catochrysops strabo* (Fabricius)[P]	0	1	4	1	1	0	2	0	0	0	0	0
	Celastrina argiolus (Linnaeus)[P]	0	0	0	0	0	0	0	0	10	6	13	1
	Celastrina huegelii (Moore) [P]	0	0	0	0	0	0	0	0	2	3	9	7
	Celatoxia marginata (de Niceville) [M]	0	0	0	0	0	0	0	0	1	3	6	0
	Euchrysops cnejus (Fabricius) [O]	0	0	7	12	2	0	5	0	0	0	0	0
	Heliophorus moorei (Hewitson) [M]	0	0	0	0	0	0	0	0	0	0	1	0
	Heliophorus sena (Kollar) [P]	0	0	0	0	11	1	8	0	52	24	17	7
	Jamides celeno (Cramer) [P]	2	0	1	0	0	1	2	0	0	0	0	0
	Lampides boeticus (Linnaeus) [O]	11	2	1	0	2	2	2	0	14	3	0	0
	Lycaena panava (Westwood) [M]	0	0	0	0	0	0	0	0	12	38	6	0
	Lycaena phlaeas (Linnaeus) [P]	0	0	0	0	0	0	0	0	2	3	3	0
	Pseudozizzeria maha (Kollar) [P]	27	21	23	9	7	6	6	1	5	2	4	1
	Talicada nyseus (Guerin-Meneville) [O]	20	7	37	21	10	6	14	5	0	0	0	0
	Udara sp. [O]	0	0	0	0	2	1	0	1	1	1	1	0
	Zizeeria karsandra (Moore) [P]	43	18	16	14	5	3	4	2	0	2	2	0
	Zizina otis (Fabricius) [P]	3	2	3	0	2	1	2	0	0	0	0	0
	Zizula hylax (Fabricius) [P]	4	1	2	0	2	0	1	0	0	0	0	0
Papilionidae	*Atrophaneura varuna* (White) [P]	0	0	0	0	0	1	0	0	3	7	5	0
	Byasa polyeuctes (Fruhstorfer)[P]	0	0	0	0	0	0	0	0	4	14	7	0
	Graphium sarpedon (Linnaeus) [P]	0	0	0	0	2	0	0	0	1	2	1	0
	Papilio bianor Cramer [O]	0	0	0	0	7	0	0	0	8	0	0	0
	Papilio demoleus Linnaeus [P]	10	9	3	3	2	2	1	0	4	2	0	0
	Papilio machaon Linnaeus [P]	0	0	0	0	1	0	0	0	2	0	0	0
	Papilio polytes Linnaeus [O]	10	16	14	5	17	12	17	4	9	13	18	0
	Papilio protenor Cramer[P]	0	0	0	0	0	2	0	0	2	1	0	1
Hesperiidae	*Borbo bevani* (Moore) [O]	3	1	5	6	2	2	6	0	1	4	5	0
	Celaenorrhinus munda (Moore) [O]	0	0	0	0	0	0	0	0	0	3	0	0
	Celaenorrhinus pero de Niceville [O]	0	0	0	0	0	0	0	0	1	1	2	0
	Parnara guttatus (Moore) [P]	2	6	6	0	3	2	5	2	0	0	0	0
	Potanthus dara (Kollar)[O]	0	0	0	0	1	3	1	0	0	0	1	0
Riodinidae	*Abisara fylla* (Westwood) [O]	0	0	0	0	1	0	0	0	1	2	0	0
	Dodona Durga (Kollar)[P]	0	0	0	0	0	1	1	0	7	3	2	0
	Zemeros flegyas (Cramer) [M]	1	1	0	0	2	2	0	0	3	0	0	0

Abbreviations: S: Summer, M: Monsoon, PM: Post Monsoon, W: Winter, [M]: Monophagus, [O]: Oligophagus, [P]: Polyphagus (Source: Wynter-Blyth 1957, Sondhi & Kunte 2018, Robinson et al. 2023)

Eurema andersonii, *Euthalia patala*, *Lampides boeticus*, and *Papilio machaon*) are listed under Schedule II of the Indian Wildlife (Protection) Act (1972), with one species, *Euploea core*, classified under Schedule IV. Additionally, 11 species are categorized as "Least Concerned" on the IUCN Red List of Threatened Species (IUCN 2020), including *Belenois aurota, Danaus chrysippus, Euploea core, Eurema brigitta, Graphium sarpedon, Junonia almana, Junonia orithya, Lampides boeticus, Phalanta phalantha, Pontia daplidice,* and *Vanessa cardui*. Table 3 presents the site-wise records of legally protected species observed during the study. Of the 3,592 individuals recorded, 25.53% were very common, 28.72% common, 17.02% uncommon, 23.40% rare, and 5.31% very rare, highlighting the dominance of a few abundant species in the Kumaun region.

Table 3: Status of butterfly species under the Indian Wildlife (Protection) Act, 1972.

Family	Species Name	Biotope			Protection Status IWPA, 1972
		aB	*rB*	*uB*	
Papilionidae	*Papilio machaon*			✓	Schedule-II
Pieridae	*Aporia agathon*			✓	Schedule-II
	Ceporia nerissa	✓			Schedule-II
	Eurema andersonii	✓	✓	✓	Schedule-II
Lycaenidae	*Euchrysops cnejus*	✓	✓		Schedule-II
	Lampides boeticus	✓	✓	✓	Schedule-II
Nymphalidae	*Euthalia patala*			✓	Schedule-II
	Euploea core	✓	✓	✓	Schedule-IV

Abbreviations: *aB*= Agriculture biotope, *rB*= Riverine biotope, *uB*= Urban biotope, ✓= Presence, IWPA: Indian Wildlife (Protection) Act (Source: Anonymous 2006)

Table 4: Variation in diversity indices of butterfly species observed in different biotopes.

Family	Genus	Species	Individuals	Diversity Indices (Hs)		
				aB	*rB*	*uB*
Nymphalidae	29	42	1236	2.77	3.16	2.99
Pieridae	12	19	1319	2.52	2.52	2.46
Lycaenidae	14	17	694	1.67	2.04	1.82
Papilionidae	4	8	242	0.65	0.98	1.67
Hesperiidae	4	5	74	0.69	1.04	1.12
Riodinidae	3	3	27	0	0.95	0.86

The Shannon diversity indices for different butterfly families revealed variations among the biotopes studied (Table 4). Nymphalidae displayed the highest diversity in all biotopes, especially in *rB* (Hs=3.16), indicating that riverine environments support a more diverse butterfly community. Conversely, families Riodinidae and Hesperiidae showed lower diversity indices, likely due to their reduced populations in the current study.

3.2. Relationship between Butterfly Diversity and Biotopes

Across the selected biotopes, 76 butterfly species were documented in the riverine biotope (*rB*), 70 species in the urban biotope (*uB*), and 52 species in the agricultural biotope (*aB*). Species analysis revealed clear differences in assemblages, with steeper upper asymptotic curves observed across all biotopes (Fig. 3). The *aB* and *uB* biotopes reached asymptotes earlier than *rB*, indicating lower species richness. Asymptotic rarefaction curves for all biotopes suggest that sampling efforts were adequate throughout the study and that differences in richness are likely due to ecological variation rather than sampling bias. The one-way ANOVA results showed significant differences in species richness among biotopes (F= 6.130, P < 0.05), emphasizing the

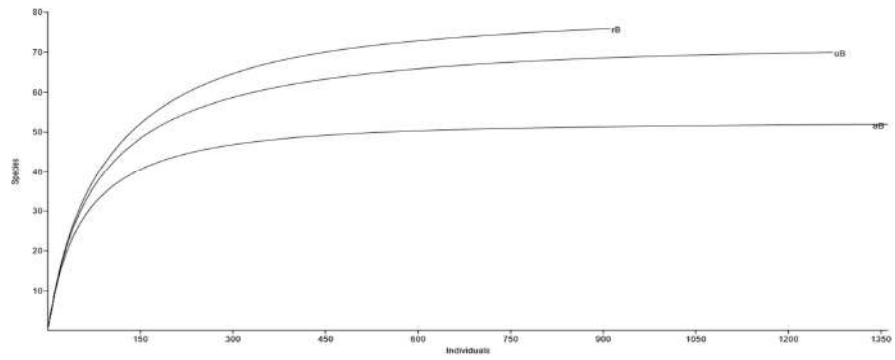


Fig. 3: Individual-based rarefaction curves for butterfly assemblages in different biotope types.

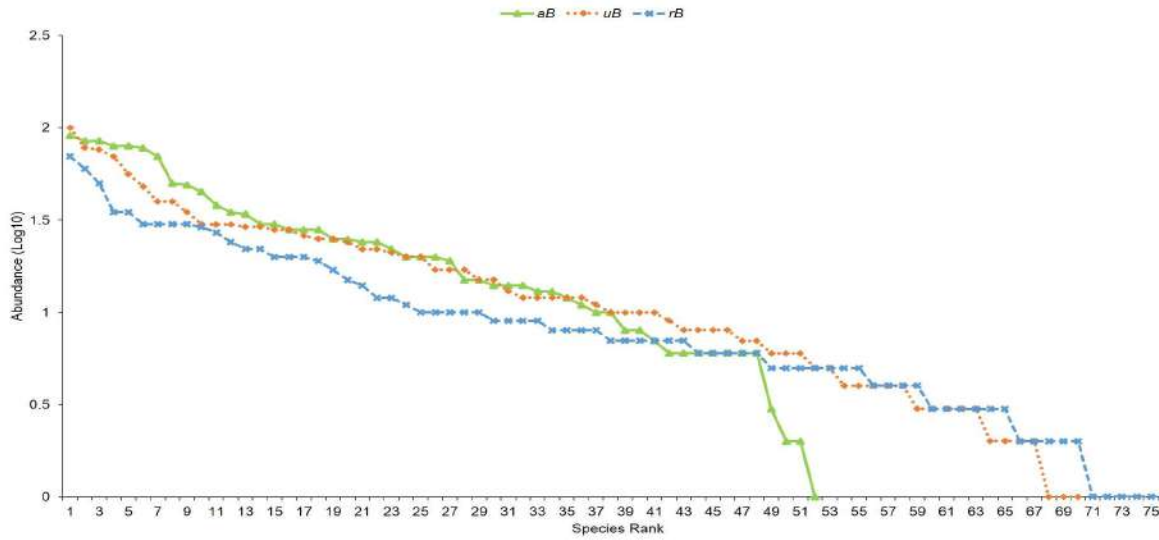


Fig. 4: Rank-abundance curves of butterfly species assemblages in three biotopes.

Table 5: Diversity indices of butterfly communities from the study area.

Diversity indices	*aB*	*rB*	*uB*
Butterfly species	52	76	70
Individuals	1377	929	1286
Dominance_D	0.03	0.02	0.03
Simpson_1-D	0.96	0.97	0.96
Shannon_H	3.57	3.88	3.79
Margalef	7.05	10.97	9.63

impact of land-use and micro-habitat structure on butterfly communities. However, species abundance did not differ significantly (F= 1.722, P > 0.05).

Alpha diversity indices such as Shannon-Wiener alpha diversity (Hs) and Margalef richness (Hm) revealed that the riverine biotope (*rB*) supported the highest level of species diversity and richness, with Hs=3.88 and Hm=10.97. The *uB* followed, with Hs=3.79 and Hm=9.63, while the agriculture biotope (*aB*) exhibited the lowest diversity and richness, with Hs=3.57 and Hm=7.05. Simpson's dominance index (D) was also highest in (*rB*) at 0.97, indicating a community structure that is more even but dominated by a few species (Table 5). The rank abundance plot for *aB* was steeper, suggesting an unequal distribution, whereas the curves for uB and rB displayed smooth patterns, reflecting a more balanced distribution of butterfly assemblages (Fig. 4).

Vegetation heterogeneity across different biotopes significantly influenced butterfly assemblages. Comparative data on larval host plants, collected from studies by prominent researchers, indicated that the butterfly community displayed

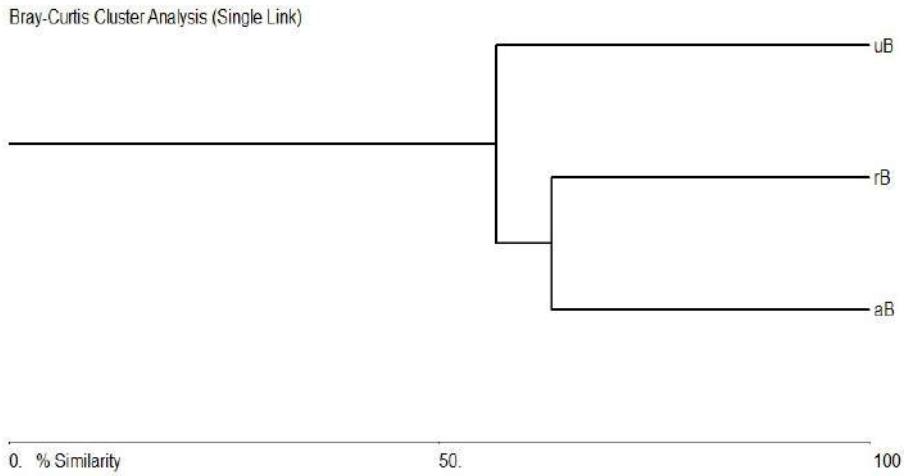
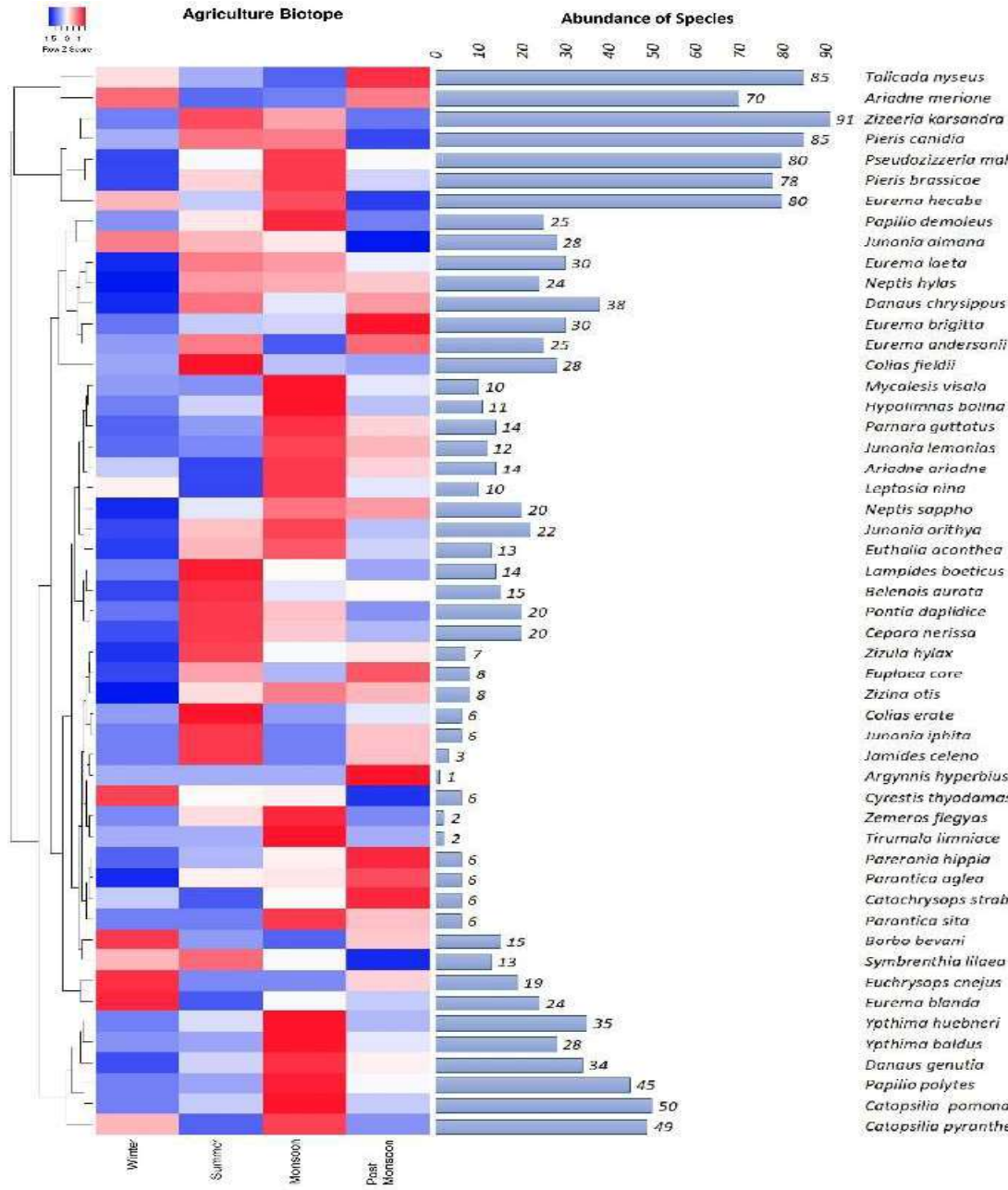


Fig. 5: Bray-Curtis cluster analysis showing similarity of butterfly assemblages across biotopes using single linkage method.

Table 6: Jaccard similarity coefficients among different biotopes.

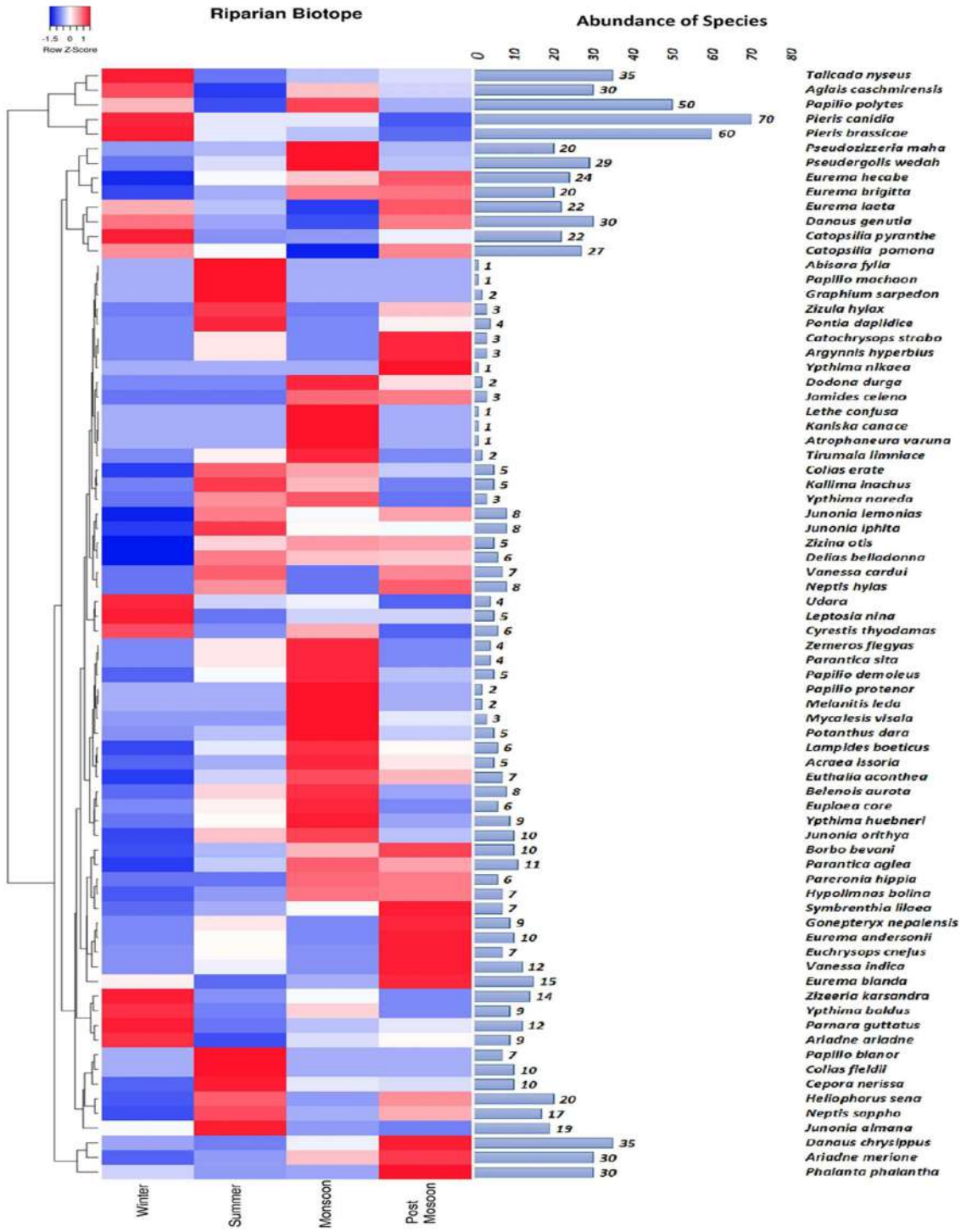
	aB	*rB*	*uB*
aB	*		
rB	0.68	*	
uB	0.32	0.54	*

broad feeding preferences. Out of 94 species, 47 (50%) were polyphagous, 33 (35.1%) were oligophagous, and 14 (14.89%) were monophagous (Table 2). The agricultural biotope had the highest proportion of host generalists at 90.3%, followed by the urban biotope at 84.28%, with only a small fraction (10%) being specialists restricted to forest edges. Conversely, the riverine biotope supported the largest



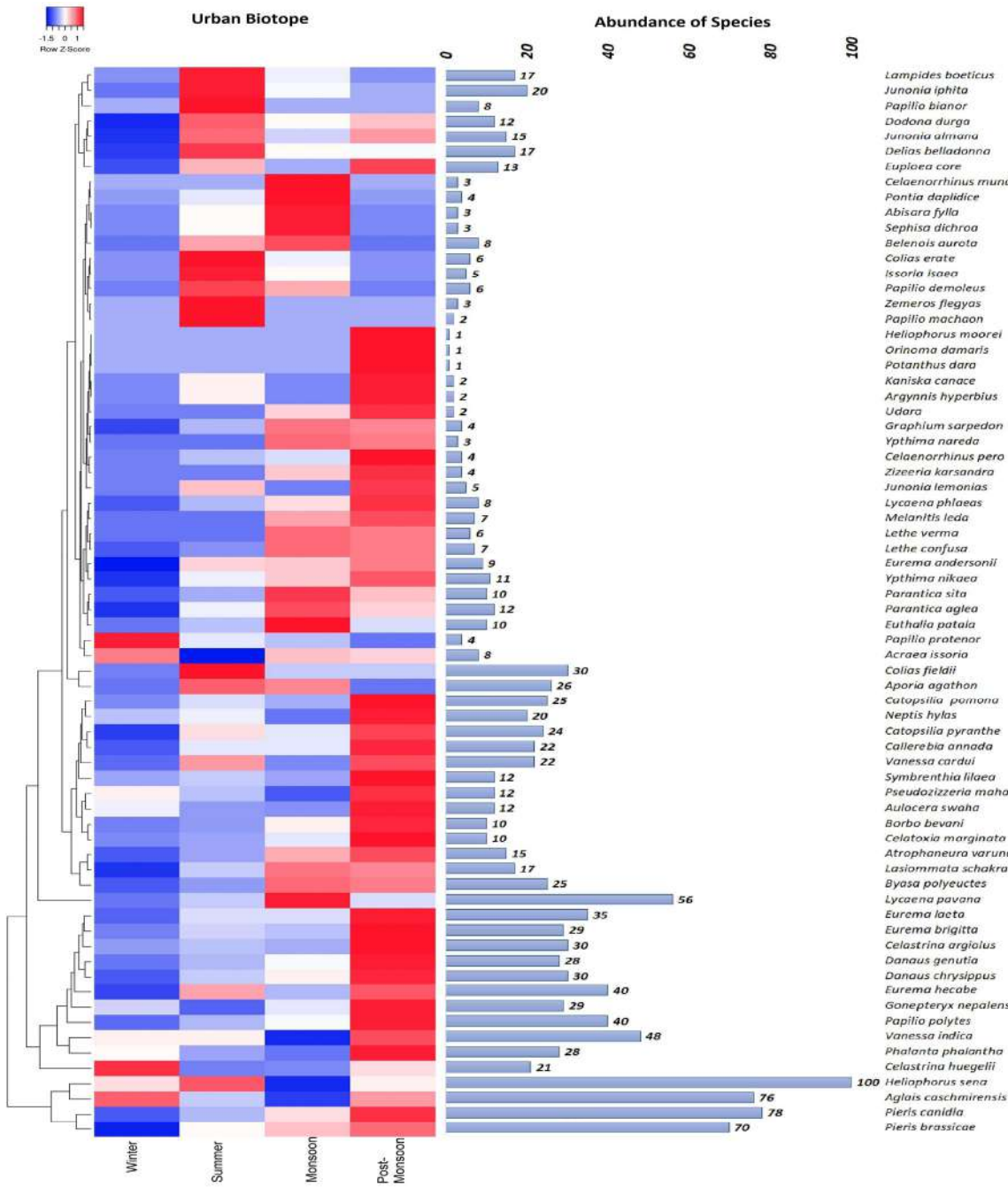
A

Figure Cont....



B

Figure Cont....



C

Fig. 6: Heat map showing patterns of normalized abundance of butterfly species in different seasons at different biotopes during the study period. (A) Agriculture, (B) Riverine, (C) Urban.

proportion of monophagous species (14.47%) among the three biotopes, reflecting relatively undisturbed vegetation.

3.3. Species Diversity and Biotope Association

Single-linkage Bray-Curtis cluster analysis indicated the greatest similarity between riverine and agricultural biotopes at 62.74%, with the urban biotope showing a 56.77% similarity (Fig. 5). There were 52 species common to riverine and agricultural areas, 51 between riverine and urban, and 28 between urban and agricultural biotopes. Based on the

distance matrix and cluster results, Jaccard's coefficient was highest between *aB* and *rB* at 0.68, followed by *rB* and *uB* at 0.54. The lowest similarity index, 0.32, was observed between *aB* and *uB* (Table 6).

3.4. Season-wise Distribution of Butterfly Fauna

The study demonstrated that butterflies across all biotopes exhibited a distinct seasonal pattern, with both overall species richness and individual abundance varying markedly throughout the year. Bi-annual peaks in species richness were observed during the summer (March-May) and post-monsoon (September-November) across all study sites. In contrast, winter showed the lowest richness, primarily due to lower temperatures and limited plant resources. Meanwhile, species abundance reached its highest levels during summer in areas *aB* and *uB*, comprising 33.7% and 40.04% of individuals, respectively, and during the post-monsoon season in *rB*, accounting for 39.7% of individuals.

The heat map illustrating seasonal abundance reveals irregular species occurrences throughout the year (Fig. 6). In panel *aB*, dominant species such as *Zizeeria karsandra, Pieris canidia*, and *Eurema hecabe* were relatively scarce during winters and post-monsoon periods, whereas *Talicada nyseus* and *Ariadne merione* remained comparatively abundant. Twenty-seven species, including *Mycalesis visala, Hypolimnas bolina, Ypthima yubneri,* and *Y. baldus,* peaked during the monsoon and were nearly absent in other seasons.

In *rB*, species distribution appeared to be influenced by river-mediated microclimate. Most species extended across two to three seasons rather than exhibiting strict seasonality. Species such as *Junonia lemonias*, *Zizina otis*, and *Delias belladonna* were present in three seasons, while approximately 24 species, including *Papilio polytes*, *Eurema brigitta*, *Cyrestis thyodamas*, and *Ariadne merione*, were recorded in two seasons.

In *uB*, several dominant species, including *Heliophorus sena, Aglias caschmirensis, Pieris canidia, Vanessa indica,* and *Colias fieldii*, showed biannual peaks, primarily during summer and post-monsoon. Of the 70 species recorded in *uB*, 53 reached peak abundance during the post-monsoon period, suggesting favorable climatic and vegetational conditions.

4. DISCUSSION

Different habitats create unique mosaics that support a variety of butterfly assemblages. The biotopes of the Kumaun region play a significant role in maintaining butterfly diversity. The Nymphalidae family was the most dominant, consistent with findings from other studies (Bhardwaj et al. 2012, Chettri et al. 2018, Verma & Arya, 2018, Samraj & Agnihotri, 2021), exhibiting the highest species richness across all seasons and study sites. Its prevalence may be attributed to the polyphagous nature of its members, which allows them to tolerate disturbances and microclimatic variations. Conversely, the Riodinidae family was the least represented.

The butterfly communities observed across elevations ranging from 350 to 2300 meters above sea level within the Nainital district exhibit greater species richness in the riverine biotope (*rB*). Enhanced habitat heterogeneity, edge interfaces, and stable moisture conditions likely supported a diverse array of larval host plants and adult resources, which is reflected in the higher asymptotic rarefaction curve, rather than any sampling artifacts. Conversely, human activities in other biotopes have simplified their community structures. Several specialist species such as *Pieris canidia*, *P. brassicae*, *Papilio polytes*, *Talicada nyseus*, *Danaus chrysippus*, *Aglais caschmirensis*, *Ariadne merione*, *Danaus genutia*, and *Phalanta phalantha* were more prominent in *rB* (11.84% of total species richness present), suggesting the influence of moderate canopy cover and vegetation composition.

Similarly, in the (*uB*), dominant species included *Heliophorus sena, Pieris canidia, Aglais caschmirensis, P. brassicae, Lycaena panava,* and *Vanessa indica*, constituting 8.57% of the total species. Although situated near forest edges, disturbances such as forest clearings, grazing, roadside traffic, and extreme climatic conditions likely reduced species richness compared to (*rB*). These disturbances favored some disturbance-tolerant generalist species, resulting in higher abundance but lower diversity within the urban biotope.

In agricultural land (*aB*), species richness was reduced, probably due to disturbance factors such as frequency of activities, pesticide application, tillage for pest control, crop harvesting, and periodic surface burning affecting larval food plants. These land use changes may have caused homogenization of species communities, shifting them from less mobile specialists to more mobile generalists, and thereby decreasing functional diversity (Bhardwaj et al. 2012, Börschig et al. 2013, Singh et al. 2017). The dominant generalist species in this biotope included *Zizeeria karsandra, Talicada nyseus, Pieris canidia, Eurema hecabe, Pseudozizeeria maha, Pieris brassicae, Ariadne merione,* and *Catopsilia pomona*. Their polyphagy and higher survival rates contributed to their highest abundance and a steeper rarefaction curve in *aB*. These findings underscore the emerging challenges of agricultural expansion in the rural district area for the first time.

Since the ecology of butterfly communities is influenced by multiple factors, seasonal conditions play a crucial role in determining their life cycle and distribution patterns

(Kunte 1997). Agricultural and urban habitats showed the highest abundance during the summer season, consistent with findings from other studies (Padhye et al. 2006, Parandhaman et al. 2012), possibly due to the presence of diverse vegetation and sequential flowering stages that provide ample food resources. This contrasts with some studies that report higher butterfly numbers during the rainy season (Kunte 1997, Pozo et al. 2008, Hussain et al. 2011, Manwar & Wankhade 2014). Conversely, (*rB*) exhibited greater abundance during the late monsoon, aligning with Gohel & Rava (2019) and Arya et al. (2020b), likely reflecting the availability of host plants. Winter consistently recorded the lowest species richness and abundance across all biotopes. Overall, these spatial and temporal variations highlight the potential of butterfly communities to serve as sensitive ecological indicators of land-use changes in the Kumaun Himalaya.

Under the Indian Wildlife (Protection) Act of 1972, several Schedule II species and one Schedule IV species were recorded. Our study revealed that some legally protected species, such as *Euthalia patala* and *Papilio machaon*, were found as rare or very rare, while few others appeared to be common or very common, such as *Aporia agathon*, *Cepora nerissa*, *Euchrysops cnejus*, *Lampides boeticus*, *Euploea core*, and *Eurema andersonii*. This suggests that these biotopes are crucial for the survival of these threatened species as well, and therefore, vegetation management and conservation should focus on the most preferred plant families.

5. CONCLUSIONS

This study examines the interaction between butterflies and their environment, enabling the assessment of their role as bio-indicators of the ecological health of Himalayan ecosystems amidst increasing disturbances. A total of 30 species, accounting for 31.91% of all species surveyed, were found across all three biotopes, suggesting a broad distribution and stable populations. The findings emphasize the significance of riverine habitats for butterfly diversity, as these areas host the highest number of species and provide well-structured habitats. To reduce the impact of human activities on butterfly populations in urban and agricultural environments, it is crucial to address issues such as habitat degradation and pesticide use, while also involving local communities. Additionally, conserving host tree species and native larval plants along riverbanks, maintaining hedgerows in agricultural fields, and protecting forest-edge microhabitats within urban areas should be prioritized to ensure the sustainability of butterfly diversity.

6. ACKNOWLEDGMENTS

We are thankful to the Head, Department of Zoology, D.S.B. Campus, Kumaun University, Nainital, for encouraging the commencement of this research and necessary facilities. The authors sincerely thank research companions for assistance in the field work and local people for their help during this study. The efforts of various reviewers during the preparation of the manuscript are also acknowledged.

7. REFERENCES

Acharya, B.K. and Vijayan, L., 2015. Butterfly diversity along the elevation gradient of Eastern Himalaya, India. *Ecological Research*, 30(5), pp.909–919. [DOI]

An, J.-S. and Choi, S.-W., 2021. Butterflies as an indicator group of riparian ecosystem assessment. *Journal of Asia-Pacific Entomology*, 24(1), pp.195–200. [DOI]

Anonymous, 2006. *The Wildlife (Protection) Act, 1972*. Natraj Publishers, Dehradun, India, pp.325.

Arya, M.K., Verma, A. and Neha, 2018. Biodiversity assessment of butterflies in Kumaun Lesser Himalayan oak forest for promoting ecotourism at City Nainital. *Journal of Himalayan Ecology and Sustainable Development*, 13(1), pp.75–95.

Arya, M.K., Verma, A. and Tamta, P., 2020a. Diversity of butterflies (Lepidoptera: Papilionoidea) in a temperate forest ecosystem, Binsar Wildlife Sanctuary, Indian Himalayan Region. *Nature Environment and Pollution Technology*, 19(3), pp.1133–1140. [DOI]

Arya, M.K., Dayakrishna and Verma, A., 2020b. Patterns in distribution of butterfly assemblages at different habitats of Corbett Tiger Reserve, Northern India. *Tropical Ecology*, 61(2), pp.180–186. [DOI]

Babicki, S., Arndt, D., Marcu, A., Liang, Y., Grant, J.R., Maciejewski, A. and Wishart, D.S., 2016. Heatmapper: web-enabled heat mapping for all. *Nucleic Acids Research*, 44(W1), pp.W147–W153. [DOI]

Bazzaz, F.A., 1975. Plant species diversity in old-field successional ecosystems in Southern Illinois. *Ecology*, 56(2), pp.485–488. [DOI]

Bhardwaj, M. and Uniyal, V.P., 2011. High-altitude butterfly fauna of Gangotri National Park, Uttarakhand: Patterns in species, abundance, composition and similarity. *ENVIS Bulletin: Arthropods and Their Conservation in India (Insects and Spiders)*, 14(1), pp.38–48.

Bhardwaj, M., Uniyal, V.P., Sanyal, A.K. and Singh, A.P., 2012. Butterfly communities along an elevational gradient in the Tons Valley, Western Himalayas: Implications of rapid assessment for insect conservation. *Journal of Asia-Pacific Entomology*, 15(2), pp.207–217. [DOI]

Blair, R.B. and Launer, A.E., 1997. Butterfly diversity and human land use: Species assemblages along an urban gradient. *Biological Conservation*, 80(1), pp.113–125. [DOI]

Börschig, C., Klein, A.M., von Wehrden, H. and Krauss, J., 2013. Traits of butterfly communities change from specialist to generalist characteristics with increasing land-use intensity. *Basic and Applied Ecology*, 14(7), pp.547–554. [DOI]

Braga, L. and Diniz, I.R., 2015. Importance of habitat heterogeneity in richness and diversity of moths (Lepidoptera) in Brazilian Savanna. *Environmental Entomology*, 44(3), pp.499–508. [DOI]

Chandra, H., Arya, M.K. and Verma, A., 2023. Biodiversity of butterflies (Lepidoptera: Rhopalocera) in the protected landscape of Nandhour, Uttarakhand, India. *Journal of Threatened Taxa*, 15(1), pp.22448–22470. [DOI]

Chettri, P.K., Sharma, K., Dewan, S. and Acharya, B.K., 2018. Butterfly diversity in human-modified ecosystems of southern Sikkim, the Eastern Himalaya, India. *Journal of Threatened Taxa*, 10(5), pp.11551–11565. [DOI]

Clark, P.J., Reed, J.M. and Chew, F.S., 2007. Effects of urbanization on butterfly species richness, guild structure, and rarity. *Urban Ecosystems*, 10(3), pp.321–337. [DOI]

Fontaine, B., Bergerot, B., Le Viol, I. and Julliard, R., 2016. Impact of urbanization and gardening practices on common butterfly communities in France. *Ecology and Evolution*, 6(22), pp.8174–8180. [DOI]

Gallou, A., Baillet, Y., Ficetola, G.F. and Després, L., 2017. Elevational gradient and human effects on butterfly species richness in the French Alps. *Ecology and Evolution*, 7(11), pp.3672–3681. [DOI]

Ghorai, N. and Sengupta, P., 2014. Altitudinal distribution of Papilionidae butterflies along with their larval food plants in the East Himalayan landscape of West Bengal, India. *Journal of Biosciences and Medicines*, 2(1), pp.1–8. [DOI]

Gohel, V.H. and Rava, J.V., 2019. Butterfly diversity, seasonality and status at Junagadh, Gujarat, India. *International Journal of Environment, Ecology, Family and Urban Studies*, 9(2), pp.15–28.

Hammer, O., Harper, D.A.T. and Ryan, P.D., 2001. *PAST: Palaeontological Statistics Software Package for Education and Data Analysis*. Version 3.04. Palaeontologia Electronica, Oslo, Norway. Retrieved May 3, 2025, from https://palaeo-electronica.org/2001_1/past/issue1_01.htm

Hussain, K.J., Ramesh, T., Satpathy, K.K. and Selvanayagam, M., 2011. Seasonal dynamics of butterfly population in DAE Campus, Kalpakkam, Tamil Nadu, India. *Journal of Threatened Taxa*, 3(1), pp.1401–1414. [DOI]

IUCN, 2020. *The Red List of Threatened Species*. Retrieved August 15, 2025, from https://www.iucnredlist.org/

Joshi, P.C. and Arya, M.K., 2007. Butterfly communities along altitudinal gradients in a protected forest in the Western Himalayas, India. *The Natural History Journal of Chulalongkorn University*, 7(1), pp.1–9.

Joshi, R.K., Kapkoti, B., Rawal, R.S., Bhatt, I.D. and Dhyani, P.P., 2016. *Diversity of Butterflies in Surya-Kunj (Contribution to Nature Interpretation and Learning)*. G.B. Pant Institute of Himalayan Environment and Development, Kosi-Katarmal, Almora, Uttarakhand, India, pp.124.

Kehimkar, I., 2014. *The Book of Indian Butterflies*. Bombay Natural History Society and Oxford University Press, Mumbai, pp.497.

Kocher, S.D. and Williams, E.H., 2000. The diversity and abundance of North American butterflies vary with habitat disturbance and geography. *Journal of Biogeography*, 27(4), pp.785–794. [DOI]

Kumar, P., Devi, R. and Mattu, V.K., 2016. Diversity and abundance of butterfly fauna (Insecta: Lepidoptera) of sub-alpine area of Chanshal Valley, District Shimla (Himachal Pradesh). *Journal of Entomology and Zoology Studies*, 4(4), pp.243–247.

Kumar, K., Joshi, P.C. and Arya, M.K., 2017. Variation in population density and biomass of butterflies in Nanda Devi Biosphere Reserve (NDBR), West Himalaya, Uttarakhand. *Journal of Environment and Biosciences*, 31(1), pp.9–16.

Kunte, K.J., 1997. Seasonal patterns in butterfly abundance and species diversity in four tropical habitats in northern Western Ghats. *Journal of Biosciences*, 22(5), pp.593–603. [DOI]

Lambshead, P.J.D., Paterson, G.L.J. and Gage, J.D., 1997. *Biodiversity Professional*. Version 2.0. The Natural History Museum and The Scottish Association for Marine Science, London, pp.156.

Leon-Cortes, J.L., Perez-Espinoza, F., Marin, L. and Molina-Martinez, A., 2004. Complex habitat requirements and conservation needs of the only extant Baroniinae swallowtail butterfly. *Animal Conservation*, 7(3), pp.241–250. [DOI]

Magurran, A.E., 2004. *Measuring Biological Diversity*. Blackwell Publishing, Oxford, U.K., pp.256.

Manwar, N. and Wankhade, V., 2014. Seasonal variation in diversity and abundance of butterflies at Sawanga Vithoba Lake area, District Amravati, Maharashtra, India. *Journal of Biological Sciences*, 14(7), pp.485–493. [DOI]

Margalef, R., 1972. Homage to Evelyn Hutchinson, or why is there an upper limit to diversity? *Transactions of the Connecticut Academy of Arts and Sciences*, 44(1), pp.211–235.

McAleece, N., 1998. *Biodiversity Professional Beta*. The Natural History Museum and The Scottish Association for Marine Science, London, pp.142.

Meena, D.S. and Dayakrishna, 2017. Study on the species composition and status of free-ranging butterflies (Lepidoptera: Rhopalocera) in Pt. G.B. Pant High Altitude Zoo, Nainital, Uttarakhand. *Journal of Entomology and Zoology Studies*, 5(4), pp.1135–1139.

Munyuli, M.B.T., 2013. Drivers of species richness and abundance of butterflies in coffee–banana agroforests in Uganda. *International Journal of Biodiversity Science, Ecosystem Services and Management*, 9(4), pp.298–310. [DOI]

Naik, D. and Mustak, M.S., 2015. Additions to larval host plants of Indian butterflies (Lepidoptera). *Journal of the Bombay Natural History Society*, 112(3), pp.181–183.

Naik, D., Rao, R.S.P., Kunte, K. and Mustak, M.S., 2022. Seasonal dynamics and polyphenism of butterfly communities in the coastal plains of central Western Ghats, India. *Journal of Biosciences*, 47(79), pp.1–13. [DOI]

Nitin, R., Balakrishnan, V.C., Churi, P.V., Kalesh, S., Prakash, S. and Kunte, K., 2018. Larval host plants of the butterflies of the Western Ghats, India. *Journal of Threatened Taxa*, 10(4), pp.11495–11550. [DOI]

Niwattanakul, S., Singthongchai, J., Naenudorn, E. and Wanapu, S., 2013. Using of Jaccard coefficient for keyword similarity. In: *Proceedings of the International MultiConference of Engineers and Computer Scientists*. Vol. I. Hong Kong, pp.1–5.

Padhye, A.D., Dahanukar, N., Paingankar, M., Deshpande, M. and Deshpande, D., 2006. Season and landscape-wise distribution of butterflies in Tamhini, Northern Western Ghats, India. *Zoo's Print Journal*, 21(3), pp.2175–2181. [DOI]

Paunikar, S.D. and Sharma, G., 2022. Butterfly species diversity and distribution in protected forest areas of North-West Himalaya of India. *Biological Forum – An International Journal*, 14(4), pp.1004–1015.

Pollard, E., 1977. A method for assessing changes in the abundance of butterflies. *Biological Conservation*, 12(2), pp.115–134. [DOI]

Pozo, C., Luis-Martínez, A., Llorente-Bousquets, J., Salas-Suárez, N., Maya-Martínez, A., Vargas-Fernandez, I. and Warren, A.D., 2008. Seasonality and phenology of the butterflies (Lepidoptera: Papilionoidea and Hesperioidea) of Mexico's Calakmul region. *Florida Entomologist*, 91(3), pp.407–422.

Parandhaman, D., Sivasankaran, K., Meerasa, M.N. and Ignacimuthu, S., 2012. Diversity of butterflies in different habitats from Tamil Nadu, part of Western Ghats (Lepidoptera: Rhopalocera). *Elixir Applied Biology*, 51, pp.10861–10865.

Qureshi, A.A., Bhagat, R.C. and Bhat, D.M., 2014. Diversity of butterflies (Lepidoptera: Papilionoidea and Hesperioidea) of Dachigam National Park, Jammu and Kashmir, India. *Journal of Threatened Taxa*, 6(1), pp.5389–5392. [DOI]

Robinson, G.S., Ackery, P.R., Kitching, I.J., Beccaloni, G.W. and Hernández, L.M., 2023. *HOSTS – A Database of the World's Lepidopteran Hostplants*. Natural History Museum, London. Retrieved September 30, 2024, from https://data.nhm.ac.uk/dataset/hosts/resource/877f387a-36a3-486c-a0c1-b8d5fb69f85a

Sagwe, R.N., Muya, S.M. and Maranga, R., 2015. Effects of land use patterns on the diversity and conservation status of butterflies in Kisii Highlands, Kenya. *Journal of Insect Conservation*, 19(6), pp.1197–1207. [DOI]

Samraj, J.M. and Agnihotri, M., 2021. Impact of land use pattern and seasonality on butterfly diversity in a sub-tropical Terai Arc Landscape (TAL), Pantnagar, Uttarakhand, India. *Tropical Ecology*, 62(2), pp.301–310. [DOI]

Sarma, K., Kumar, A., Devi, A., Mazumdar, K., Krishna, M., Mu[DOI], P. and Das, N., 2012. Diversity and habitat association of butterfly species in foothills of Itanagar, Arunachal Pradesh, India. *Cibtech Journal of Zoology*, 1(2), pp.67–77.

Sengupta, P., Banerjee, K.K. and Ghorai, N., 2014. Seasonal diversity of butterflies and their larval food plants in the surroundings of Upper

Neora Valley National Park, a sub-tropical broad-leaved hill forest in the Eastern Himalayan landscape, West Bengal, India. *Journal of Threatened Taxa*, 6(1), pp.5327–5342. [DOI]

Shannon, C.E. and Weaver, W., 1949. *The Mathematical Theory of Communication*. The University of Illinois Press, Illinois, pp.144.

Simpson, E., 1949. Measurement of diversity. *Nature*, 163(4148), p.688. [DOI]

Singh, A.P. and Bhandari, R.S., 2003. Butterfly diversity in tropical moist deciduous sal (*Shorea robusta*) forests of Dehradun Valley: The lower Western Himalayas. *The Indian Forester*, 129(10), pp.1257–1269.

Singh, A.P. and Bhandari, R.S., 2006. New additions to the butterflies of Dehradun Valley, the lower Western Himalayas. *The Indian Forester*, 132(6), pp.767–769.

Singh, A., Brar, J.S. and Sarari, P., 2017. Habitat preference of butterflies and moths (Insecta: Lepidoptera) in Talwandi Sabo, Punjab. *Bulletin of Environment, Pharmacology and Life Sciences*, 6(12), pp.67–71.

Smetacek, P., 2002. The genus *Pontia* (Lepidoptera: Pieridae) in the Kumaun Himalaya. *Journal of the Bombay Natural History Society*, 99(2), pp.224–231.

Smetacek, P., 2010. *Ypthima kedarnathensis* Singh, 2007 (Lepidoptera: Nymphalidae: Satyrinae) from the Kumaon Himalaya, India. *Journal of Threatened Taxa*, 2(13), pp.1390–1391. [DOI]

Smetacek, P., 2011a. Detrimental effects of low atmospheric humidity and forest fire on a community of Western Himalayan butterflies. *Journal of Threatened Taxa*, 3(4), pp.1694–1701. [DOI]

Smetacek, P., 2011b. Four new Lycaenid butterfly records from the Kumaon Himalaya, India. *Journal of Threatened Taxa*, 3(2), pp.1555–1558. [DOI]

Smetacek, P., 2011c. On the anomalous altitudinal distribution of West Himalayan Troidini and Papilionini (Papilionidae). *Journal of the Lepidopterists' Society*, 65(2), pp.126–132. [DOI]

Smetacek, P. and Smetacek, R., 2011. Additions to the known larval host plants of Indian Lepidoptera. *Journal of Threatened Taxa*, 3(12), pp.2272–2276. [DOI]

Smetacek, P., 2012a. Butterflies (Lepidoptera: Papilionoidea and Hesperoidea) and other protected fauna of Jones Estate, a dying watershed in the Kumaon Himalaya, Uttarakhand, India. *Journal of Threatened Taxa*, 4(9), pp.2857–2874. [DOI]

Smetacek, P., 2012b. Preimaginal stages of *Graphium (Pazala) eurous caschmirensis* (Rothschild, 1895) (Lepidoptera: Papilionidae) in the Kumaon Himalaya, India. *Nachrichten des Entomologischen Vereins Apollo (News of the Entomological Society Apollo)*, 32(3–4), pp.109–112.

Sondhi, S. and Kunte, K., 2018. *Butterflies of Uttarakhand – A Field Guide*. In: B. Singh and M.P. Singh (eds.). Titli Trust, Dehradun and National Centre for Biological Sciences, Bengaluru, pp.384.

Sondhi, S., 2017. First records of butterflies *Anthene emolus emolus* (Godart, [1824]) (Lepidoptera: Lycaenidae: Polyommatinae) and *Gandaca harina assamica* Moore, [1906] (Lepidoptera: Pieridae: Coliadinae) from Kumaon, Uttarakhand, India. *Journal of Threatened Taxa*, 9(6), pp.10355–10357. [DOI]

Tews, J., Brose, U., Grimm, V., Tielborger, K., Wichmann, M.C., Schwager, M. and Jeltsch, F., 2004. Animal species diversity driven by habitat heterogeneity: The importance of keystone structures. *Journal of Biogeography*, 31(1), pp.79–92. [DOI]

Tyagi, R., Joshi, P.C. and Joshi, N.C., 2011. Butterfly diversity of District Nainital, Uttarakhand, India. *Journal of Environment and Bio-Sciences*, 25(2), pp.273–278.

Uniyal, V.P., 2007. Butterflies in the Great Himalayan Conservation Landscape in Himachal Pradesh, Western Himalaya. *Entomon*, 32(2), pp.119–127.

Veenakumari, K., Mohanraj, P. and Sreekumar, P.V., 1997. Host plant utilization by butterfly larvae in the Andaman and Nicobar Islands (Indian Ocean). *Journal of Insect Conservation*, 1(4), pp.235–246. [DOI]

Verma, A. and Arya, M.K., 2018. A preliminary study on the status and distribution of butterfly fauna in and around the valley of Reetha Sahib, Champawat, Kumaon Himalaya, India. *Journal of Insect Conservation*, 10(1), pp.43–51.

Verma, A. and Arya, M.K., 2022. Butterfly diversity and abundance in a sub-tropical wetland environment of Shyamlatal, Western Himalaya. *Asian Journal of Conservation Biology*, 11(1), pp.26–40. [DOI]

Weißhuhn, P., 2019. Indexing the vulnerability of biotopes to landscape changes. *Ecological Indicators*, 102, pp.316–327. [DOI]

Wynter-Blyth, M.A., 1957. *Butterflies of the Indian Region*. Bombay Natural History Society, Bombay, pp.523.

Nature Environment and Pollution Technology
An International Quarterly Scientific Journal

p-ISSN: 0972-6268
(Print copies up to 2016)
e-ISSN: 2395-3454

Vol. 25 | No. 3 | Article ID D1883 | 2026

Original Research Paper

https://doi.org/10.46488/NEPT.2026.v25i03.D1883

Open Access Journal

Synergy of Corn Cob Biochar Modification in Improving Soil Bulk Density, Porosity, and Water Retention

Budiono[1]†, Irya Ichriani[2], Fakhrur Razie[3] and Sunardi[4]

[1]Doctoral Program of Environmental Sciences, Lambung Mangkurat University, Banjarmasin, South Kalimantan 70124, Indonesia

[2]Soil Science Study Program, Faculty of Agriculture, Lambung Mangkurat University, Banjarmasin, South Kalimantan 70123, Indonesia

[3]Soil Science Study Program, Faculty of Agriculture, Lambung Mangkurat University, Banjarmasin, South Kalimantan 70123, Indonesia

[4]Chemistry Study Program, Mathematics and Natural Science, Lambung Mangkurat University, Banjarmasin, South Kalimantan 70123, Indonesia

†Corresponding author: Author Name; 2241213310057@mhs.ulm.ac.id

Abbreviation: Nat. Env. & Poll. Technol.
Website: www.neptjournal.com

Received: 10-10-2025
Revised: 02-01-2026
Accepted: 13-01-2026

Key Words:

BTJT characteristics
Bulk density
Porosity
Water retention
Co-inoculated Ultisol
Biotron

Citation for the Paper:

Budiono, Ichriani, I., Razie, F. and Sunardi, 2026. Synergy of corn cob biochar modification in improving soil bulk density, porosity, and water retention. *Nature Environment and Pollution Technology*, 25(3), D1883. https://doi.org/10.46488/NEPT.2026.v25i03.D1883

Note: From 2025, the journal has adopted the use of Article IDs in citations instead of traditional consecutive page numbers. Each article is now given individual page ranges starting from page 1.

Copyright: © 2026 by the authors
Licensee: Technoscience Publications
This article is an open access article distributed under the terms and conditions of the Creative Commons Attribution (CC BY) license (https://creativecommons.org/licenses/by/4.0/).

ABSTRACT

This study investigated the characteristics of modified corn cob biochar (BTJT) and its effects on the physical properties of Ultisol soil co-inoculated with BTJT. The material was produced through a synergistic process involving pyrolysis, activation, and immobilization, which combined biochar, nutrients, and biological agents. The research consisted of two experiments: the first analysed the morphological characteristics and specific surface area (SSA) of BTJT pores with three inoculation durations (7, 14, and 21 days), and the second examined soil bulk density, porosity, and water retention after BTJT co-inoculation. A completely randomized design (CRD) with five treatments, three replicates, and three observation periods was applied. The analytical methods included SEM-EDX and BET, with soil parameters comprising bulk density, water content (% volume and % weight), porosity, and water retention. Statistical analyses were conducted using ANOVA-Tukey tests, regression, and correlation analyses with a 5% error margin. The results indicated that BTJT application at 2 $t.ha^{-1}$ significantly decreased bulk density while increasing soil water content, porosity, and water retention. Overall, the study concludes that the synergistic modification of corn cob biochar effectively enhances soil physical properties, recommending the application of BTJT (biotron) at 2 $t.ha^{-1}$ for optimal improvement of Ultisol soil quality.

1. INTRODUCTION

Biochar is a fine-textured, porous, carbon-rich material produced through pyrolysis. BTJT is a composite that integrates biochar, nutrients, and biological agents. Previous research has demonstrated that enriching biochar with organic nutrients consistently enhances soil quality. Thanks to its complex and heterogeneous pore structures, BTJT functions as a carrier medium capable of binding nutrients and biological agents (Allohverdi et al. 2021, Ben-Noah et al. 2021, Deru et al. 2018). Compared to pure biochar (Sepp et al. 2023, Shaheen et al. 2024), BTJT improves the soil's capacity to retain water, air, and nutrients (Raczka et al. 2021, Robinson et al. 2022, Sachdeva et al. 2019). Additionally, biochar enhances soil aeration, which is vital for microbial activity and plant root growth (Quan et al. 2020).

Research on the effectiveness of BTJT in enhancing the physical properties of Ultisol soils—such as bulk density (BD), porosity, and water retention—is limited. This study seeks to fill this knowledge gap by evaluating BTJT's potential as a soil conditioner. The chemical activation process involves lime solution and positive ion activators (catalysts), which are believed to increase pore surface area. Pore

spaces serve as reservoirs for air and water and create a more conducive environment for microbial communities (Pandey et al. 2022). It is also known that unmodified biochar can have diverse effects on soil, plants, and microorganisms (Ottani et al. 2022). Consistent with recent research, applying biochar as a soil amendment has gained increasing attention in soil and environmental studies.

Porosity, water movement, and the availability of space between soil particles and pores are essential physical factors that facilitate root development. These traits are affected by bulk density, a key soil physical property that indicates how tightly soil particles are packed within a given volume (Lei et al. 2022, Liao & Thomas 2019, Liu et al. 2024). Water retention refers to the soil's capacity to hold water against gravity (Lani et al. 2023). The amount of water retained reflects the actual water available at any given moment (Jung et al. 2015, Kiss et al. 2021). This capacity is influenced by soil texture, structure, water-holding ability, and rainfall. Ultisol soils with clay textures typically exhibit higher water retention than sandy soils due to their smaller particle size and greater surface area. Additionally, the presence of soil organic matter can further improve water-holding capacity (Jensen et al. 2020).

Soil water is held by capillary and adsorption forces within the pores of the soil, with bond strength influenced by pore size. Soils containing micropores tend to retain more water, although only a fraction of this water is accessible to plants (Hossain et al. 2020). Various factors, including rainfall, surface water infiltration, evaporation, transpiration, evapotranspiration, soil texture, structure, porosity, and water retention capacity, govern the availability of soil water. (Harish et al. 2022).

2. MATERIALS AND METHODS

2.1. Research Site Description

The field experiment was conducted in a screen house at the Agricultural Training Center (Balai Besar Pelatihan Pertanian, Binuang) under the Ministry of Agriculture of Indonesia. Its coordinates are 3°09′16" S and 115°05′16″ E, at an elevation of 71.7 meters above sea level and approximately 420° from the Earth's horizontal axis. The site is accessible via Google Maps at: https://maps.app.goo.gl/JmwpHRQWjYsLWiWR9

Laboratory analyses were performed at various facilities, including the Soil and Fertilizer, Particle Material, Microbiology, and Postharvest laboratories. The field experiment is scheduled for the rainy season (March–July 2024), with laboratory analyses spanning from March 2024 to May 2025. Weather conditions during the study period can be viewed at https://id.weatherspark.com/y/129103/Cuaca-Rata-rata-pada-bulan-in-Binuang-Indonesia-Sepanjang-Tahun.

2.2. Data Collection

2.2.1. Experiment 1: Characterization of Modified Corn Cob Biochar (BTJT)

The experiment commenced with the preparation of BTJT samples, each weighing 50 g, utilizing three replicates and three different treatments that involved varying soaking (incubation) durations in 2,250 mL of clear $Ca(OH)_2$ solution. The preparation process included physicochemical, chemical, and biological activation of the materials. Chemical activation (Gao et al. 2025) was executed by immersing BTJT powder (450–550°C) (Hafeez et al. 2022) in a CaO solution. This solution was prepared by dissolving 150 g of CaO in 600 mL of distilled water, stirring it with a magnetic stirrer for 60 minutes, and then conducting four activation cycles, each using 575 mL of solution (Ferrarezi et al. 2022). The samples were oven-dried at 105°C for 6 hours (Colucci et al. 2025). Subsequently, they were immersed in the most effective POCH solution for 20 days, with incubation durations of 7, 14, and 21 days (Carril et al. 2024), followed by air-drying for three days at 25–35°C (Ijam 2024). Morphological and surface area analyses were conducted using Scanning Electron Microscopy–Energy Dispersive X-ray (SEM-EDX, JEOL JSM-6510LA) and the Brunauer–Emmett–Teller (BET) method (Chen et al. 2025).

2.2.2. Experiment 2: Soil Quality Characteristics

This experiment involved collecting Ultisol soil samples from a depth of 0–20 cm, with each sample weighing 1,000 g. The samples were arranged in three replicates and subjected to five treatments at three different observation times. Soil sampling was conducted 14 days after co-inoculation with the selected corn cob biochar (BTJ), which had undergone a 7-day inoculation process. The physical properties of the soil were analyzed for parameters including bulk density (BD) (Braz et al. 2025), volumetric water content (% volume, KAV), gravimetric water content (% weight, KAB), and oven-dry soil weight at 105°C for 24 h (BKT). These measurements were obtained through both volumetric and gravimetric methods (Libohova et al. 2018). The parameters—porosity, soil water retention, PD, KAB, KAV, and BD—were calculated using the following equations.

2.3. Particle Density (PD)

Pparticle (PD) = msoil/ volume of soil solids = particle density ($g.cm^{-3}$), commonly assumed to be 2.65 $g.cm^{-3}$ for mineral soils, representing the density of solid soil particles excluding pore spaces.

2.4. Soil Water Content

For gravimetric water content, the wet soil sample (W_1) was weighed, then oven-dried at 105°C for 24 hours or until a constant weight (W_2) was achieved. The formula used was:

Gravimetric Water Content (%weight) = $[(W_1 - W_2)/(W_2) \times 100$ (Braz et al. 2025)

Volumetric water content (%) = Water Content (% by weight) × BD ($g.cm^{-3}$) (Bian et al. 2024)

2.5. Bulk Density (BD)

Pbulk Bulk density (BD) = bulk density ($g.cm^{-3}$), the ratio of the dry weight of the soil to the total volume of the soil, including the volume of pore space or particles (air and water). Bulk density (BD) = Dry soil weight / Soil volume ($g.cm^{-3}$) (Alkharabsheh et al. 2021)

2.6. Porosity (n)

$$n = \text{soil porosity } (cm^3\ cm^{-1} \text{ or } \%)$$

$$n = 1 - (\rho_{particle} \times \rho_{bulk}\text{-}1)$$

$$n\ (\%) = (1 - (\rho_{particle} \times \rho_{bulk}\text{-}1)) \times 100$$

Porosity (%) = (Void Volume/Total Volume) × 100%.

Porosity (%) = (1 - (Bulk Weight/Specific Gravity)) × 100%, which requires measuring the bulk density, emphasizing the total volume, including pores, interparticle voids, and soil specific gravity. The specific gravity of soil particles, without considering pores and interparticle voids, is 2.65 (Ahmad et al. 2023).

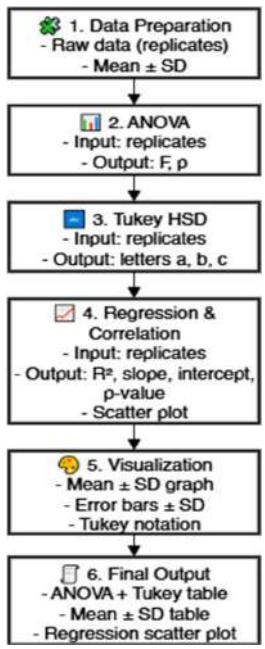


Fig. 1: Statistical analysis flowchart and visualization.

2.7. Data Analysis Methods

All statistical analyses were conducted using IBM SPSS Statistics version 26.0 and Python (Windows) (Fig. 1). An ANOVA was performed, followed by Tukey's post hoc test at a 5% significance level, to detect significant differences, interactions among variables, and correlations between BTJT treatments and soil physical properties. Data visualization, including regression and correlation analyses, was carried out with OriginPro.

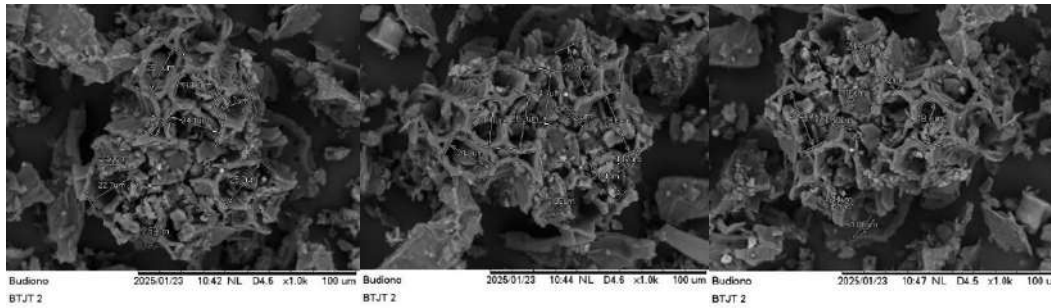
3. RESULTS AND DISCUSSION

3.1. Experiment 1: Characteristics of BTJT

The characterization of BTJT was carried out using Analytical SEM-EDX (JEOL JSM-6510 LA) and the BET method on optimized corn cob biochar (pyrolysis temperature of 450–550°C), which was inoculated in the optimal liquid organic culture (20 days of microbial culture) with incubation periods of 7, 14, and 21 days. The BTJT observation results from three replication points are presented in Figs. 2–4.

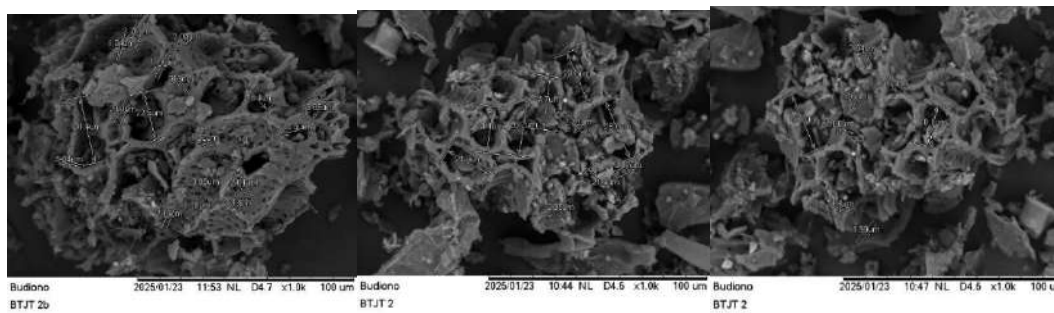
The specific surface area (SSA) of BTJT-7 (7-day co-inoculation) showed an optimal average value of 1.63 $m^2.g^{-1}$, which differed from the values observed for BTJT-14 (14-day co-inoculation) and BTJT-21 (21-day co-inoculation). However, it is important to critically assess whether such a low surface area is sufficient to substantiate the claim of "synergistic modification" made in this study. The term "synergistic modification" suggests a substantial enhancement in the biochar properties, specifically its ability to retain nutrients and water and support microbial life. However, a BET surface area of 1.63 $m^2.g^{-1}$ is relatively low compared to most modified biochars reported in the literature, which often show significantly higher values, typically in the range of 20-100 $m^2.g^{-1}$ depending on the modification method.

Such a low surface area raises questions regarding the effectiveness of the modification process in achieving the claimed synergistic effects. Typically, biochar modification aims to enhance the surface area to increase its porosity, which, in turn, improves its ability to adsorb nutrients and water and facilitates microbial activity. The observed surface area in this study may not be sufficiently high to justify these claims. In this context, it is crucial to emphasize that the BET surface area alone cannot fully explain the soil hydraulic effects, such as water retention and nutrient exchange capacity, especially when the pore size distribution is not considered. The pore size distribution



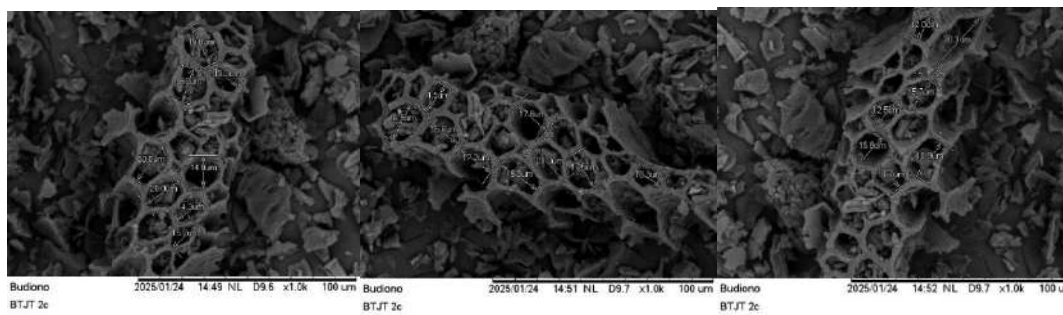
a b c

Fig. 2: BTJT surface structure, 7-day coinoculation duration a) Spot 1 b) Spot 2 c) Spot 3.



a b c

Fig. 3: BTJT surface structure, coinoculation duration 14 days a) Spot 1 b) Spot 2 c) Spot 3.



a b c

Fig. 4: BTJT surface structure, coinoculation duration 21 days: a) Spot 1, b) Spot 2, c) Spot 3.

is a critical factor in determining the ability of biochar to retain water and support microbial colonization, both of which are vital for improving soil structure and fertility. The manuscript does not provide these crucial data, which limits the ability to comprehensively evaluate the true impact of BTJT on soil water retention and other physical properties.

Without pore size distribution data, this study falls short of providing a complete analysis of the hydraulic behavior of biochar in soil. The water retention capacity and porosity depend not only on the surface area but also on the distribution of pore sizes. Pores of different sizes (micropores, mesopores, and macropores) serve distinct functions in retaining water and air and facilitating microbial colonization. Smaller pores may retain more water, but this water may not be readily available to plants. Larger pores facilitate air exchange and microbial activity, which are crucial for maintaining healthy soil. Without this additional

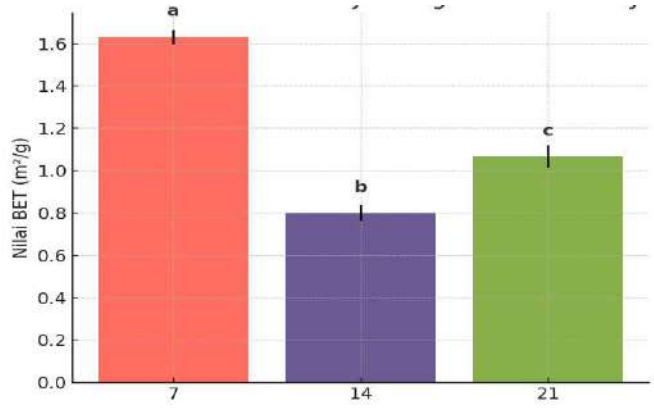


Fig. 5: Differences in specific surface area (SA) of BTJT at various coinoculation durations.

data on the pore size distribution, the claim of synergistic modification in this study remains unsubstantiated.

In summary, although the BET surface area is an important metric, it is not sufficient on its own to explain the observed hydraulic effects of BTJT on soil. The lack of data on pore size distribution significantly weakens the argument for synergistic modification, as it is an essential factor in understanding the role of biochar in improving soil physical properties. For a more comprehensive evaluation, this study should include detailed analyses of pore size distribution and its correlation with soil water retention and other key parameters. This would provide a clearer justification for the claims of synergistic effects and strengthen the manuscript's contribution to this field. The result is presented in Fig. 5.

The result from Fig. 5 shows the BET surface area values (in $m^2.g^{-1}$) of BTJT samples with different co-inoculation durations: 7, 14, and 21 days. The chart indicates the following:

1. The BTJT-7 sample, with a 7-day co-inoculation duration, has the highest BET surface area at around 1.63 $m^2.g^{-1}$, significantly higher than the other two treatments. This suggests that the 7-day inoculation period promotes a more open pore structure, increasing the surface area of the biochar.
2. The BTJT-14 sample, with a 14-day co-inoculation duration, shows a much lower surface area, approximately 0.85 $m^2.g^{-1}$, marked with a "b." This indicates that the longer inoculation time may cause the pores to become filled or blocked, reducing the surface area available for adsorption.
3. The BTJT-21 sample, with a 21-day co-inoculation duration, shows a moderate surface area of about 1.1 $m^2.g^{-1}$, marked with a "c." This suggests that after a longer inoculation period, some of the pores may have reopened, increasing the surface area slightly compared to BTJT-14, but still lower than BTJT-7.

The letters "a," "b," and "c" above the bars indicate statistical differences between the treatments. The significant difference in surface area between BTJT-7 and the other two treatments (14 and 21 days) reflects the influence of the inoculation period on the surface characteristics of biochar, potentially affecting its performance in improving soil properties.

ANOVA revealed a significant difference in the specific surface area (SA) among the three BTJT samples ($F = 292.28$, $p < 0.05$). This difference reflects variations in the pore structure resulting from different co-inoculation durations. A higher SA is positively correlated with the number and openness of pores, which potentially enhances the adsorption capacity of biochar (Sizmur et al. 2017).

Extending the co-inoculation duration from 7 to 14 days caused a significant decrease in the SA of BTJT (Sun et al. 2022, Tamburini 2021, Wang et al. 2021). This suggests that microbial activity and nutrient availability may fill and cover the biochar pores, thereby reducing the BET surface area. BTJT with a 14-day co-inoculation duration (BTJT-14) exhibited the lowest and statistically significant BET value compared to both BTJT-7 and BTJT-21. The SA of BTJT-21 increased again, likely due to the reduction in nutrient availability utilized by microbes within the pore spaces that were previously occupied in BTJT-7 (Wang et al. 2019)

3.1.1. Regression Analysis

BTJT-7 demonstrated the highest potential porosity, resulting in relatively greater adsorption capacity for gas molecules and ions in solution (X. Wang et al. 2024). The regression analysis between BET value

and co-inoculation duration produced the following equation:

$$\hat{Y} = 0.424x + 0.606$$

With a determination coefficient of $R^2 = 0.732$ and p = 0.003, indicating a significant relationship between the two variables. The relationship between BTJT surface area (SA) and co-inoculation duration is illustrated in Fig. 6.

Regression analysis revealed a moderate negative relationship between co-inoculation duration and specific surface area (SA). Increasing the duration from 7 to 14 days significantly reduced SA, whereas at 21 days, the value increased again, although it remained lower than that observed at 7 days (Wei et al. 2023). The Tukey test results indicated that all three co-inoculation durations produced significant differences in SA ($p < 0.05$).

3.1.2. Pearson Correlation

Pearson correlation analysis showed a very strong positive relationship (r = 0.856) with a coefficient of determination (R^2) of 0.44 and a p-value of 0.052, which was close to being significant at the 5% level.

3.1.3. Correlation Analysis

Meanwhile, the correlation analysis based on co-inoculation duration revealed a moderate negative relationship (r = –0.66), indicating that increasing the duration from 7 to 14 days significantly decreased the SA value, whereas at 21 days, the SA increased again but remained lower than that of BTJT-7.

3.2. Experiment 2: Soil Characteristics

Physical analysis of soil was conducted under five BTJT dosage treatments: the control without biochar (B0 = 0 ton·ha^{-1}), a positive control (B1 = 2.0 ton·ha^{-1} of biotron), and three BTJT treatments (B2 = 1.0 ton·ha^{-1}, B3 = 1.5 ton·ha^{-1}, and B4 = 2.0 ton·ha^{-1}). Each treatment was tested in triplicate. The average data analysis from three observation periods (May, June, and July 2024) showed that the application of BTJT significantly affected soil physical properties. These findings indicate that BTJT, particularly at higher doses, has the potential to be an effective soil amendment for improving land resilience against drought stress. The pores within the BTJT serve as spaces that can hold water, air, and nutrients. Treatments B1 (Biotron) and B4 (BTJT at 2 t.ha^{-1}) showed no significant difference, whereas treatments B0, B2, and B3 exhibited significant differences in most parameters, except for bulk density (BD). Previous studies have supported this finding, suggesting that modified biochar possesses pores with larger surface areas. Linear regression analysis has revealed a strong relationship between porosity and soil moisture (Ahmad et al. 2023). Relationship between porosity (%) and gravimetric water content (% by weight). The regression equation obtained was:

$$\hat{Y} = 2.43x + 42.5$$

with a correlation coefficient (r) = 0.849, coefficient of determination (R^2) = 0.721, and $p = 6.27 \times 10^{-5}$, indicatinghighly significant relationship. Where $\hat{Y}$ = water content (% by weight) and x = porosity (Bian et al. 2024).

Relationship between porosity (%) and volumetric water content (% by volume). The regression equation was:

$$\hat{Y} = 1.87x + 10.54$$

with r = 0.681, $R^2 = 0.463$, and p = 0.0052, showing a highly significant positive correlation between porosity and volumetric water content.

Relationship between porosity (%) and bulk density (BD). The regression equation was:

$$\hat{Y} = 0.0265x + 2.65$$

with r = 0.893, $R^2 = 0.797$, and $p = 7.51 \times 10^{-6}$, indicating a strong and significant positive correlation. The higher the soil porosity, the greater its water retention capacity.

Relationship Between Bulk Density (BD), Porosity, and Water Retention. Soils with higher bulk density tend

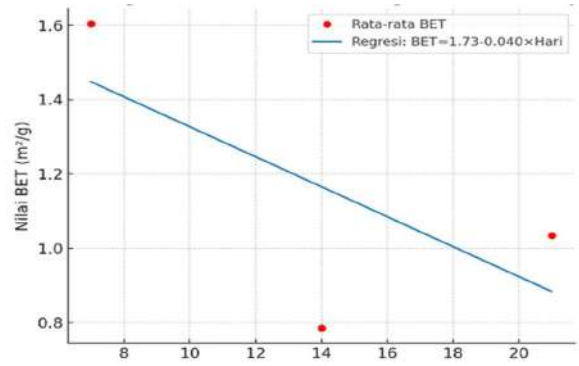


Fig. 6: Linear regression of the relationship between coinoculation duration and SA in BTJT.

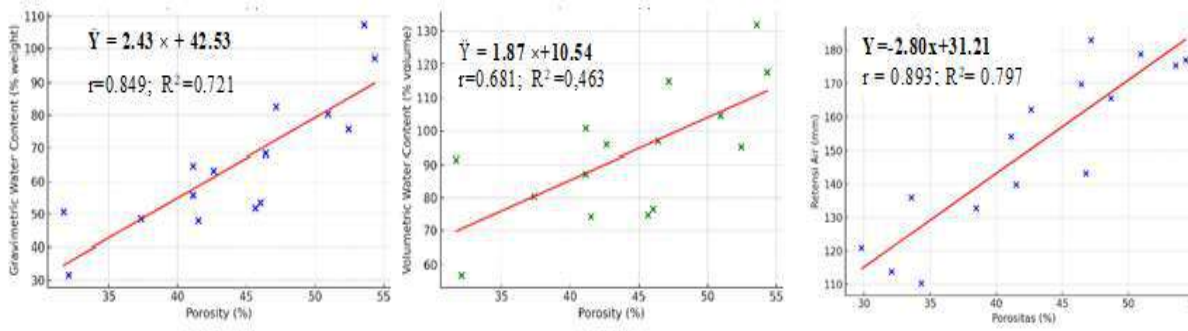


Fig. 7: Relationship of soil porosity with (a) gravimetric water content (% by weight) Vs Porosity, (b) volumetric water content (% by volume) Vs Porosity, (c) Porosity, Retention Vs BD. The red, purple, green, and blue lines show the linear regression equation, while the dots indicate the observed values

to exhibit lower porosity and water retention capacity. Relationship between BD and water retention (%). The regression equation was:

$$\hat{Y} = 105.56x + 310.94$$

With r = –0.893, $R^2 = 0.797$, and $p = 7.5 \times 10^{-6}$, indicating a strong and significant negative correlation, where increased BD leads to reduced soil water retention.

Relationship between BD and porosity (%). The regression equation was:

$$\hat{Y} = 37.73x + 100$$

Overall, the relationships between porosity, soil water content (both gravimetric and volumetric), BD, and water retention show a consistent and statistically significant pattern, as presented in Fig. 7.

Bulk density (BD) is a key indicator of soil physical properties that reflects the degree of particle compaction in a given soil volume. High BD values typically reduce porosity, thereby limiting air and water movement through the soil. The reduction in porosity caused by a high BD also leads to lower water retention, ultimately decreasing the availability of water for plants. The application of biochar has been shown to lower BD by promoting soil aggregation and creating new pores. These changes not only enhance porosity but also improve the soil's ability to retain water against gravitational forces, leading to optimal water retention (Pandey et al. 2022). Thus, the integration of biochar as a soil amendment plays a strategic role in improving soil physical quality, particularly in Ultisol soils, which are generally characterized by high BD, low porosity, and limited water-holding capacity.

The three graphs present the relationships between porosity (%) and various soil properties: gravimetric water content (% by weight), volumetric water content (% by volume), and water retention (%). The first graph shows a strong positive correlation between porosity and gravimetric water content, with a regression equation of $\hat{Y} = 2.43x + 42.53$ and $R^2 = 0.721$, indicating that higher porosity leads to a greater water content by weight. The second graph, showing porosity and volumetric water content, has a moderate positive correlation ($\hat{Y} = 1.87x + 10.54$, $R^2 = 0.463$), suggesting a weaker relationship, where porosity still influences the volumetric water content but with a lower explanatory power. The third graph shows a very strong positive correlation between porosity and water retention ($\hat{Y} = 2.80x + 31.21$, $R^2 = 0.797$), indicating that soils with higher porosity have a significantly higher water retention capacity. These results collectively underscore the critical role of porosity in determining soil water behavior, with higher porosity generally leading to better water retention, although the strength of the correlation varies across different water content measurements.

This study further shows that an increase in BD is negatively correlated with porosity and water retention, consistent with recent findings that soil physical properties, such as density and porosity, strongly influence the availability of aeration space and soil moisture. From an agronomic perspective, increasing porosity means a greater pore space available to retain water and nutrients. This aligns with previous research, which reported that biochar application improves soil structure, reduces BD, and enhances soil water-holding capacity.

5. CONCLUSIONS

The selected co-inoculation duration for corncob biochar (BTJ) was 7 days (BTJT-7), as it produced the highest specific surface area (SA) of 1.63 $m^2.g^{-1}$. The application of BTJT or Biotron at a dosage of 2 $t.ha^{-1}$ had a significant effect on soil physical characteristics, including moisture content (% by weight and volume), bulk density (BD), porosity, and water retention. The treatment sequence began with the control (B0, without BTJT), followed by BTJT-B2

(1 t.ha^{-1}), BTJT-B3 (1.5 t.ha^{-1}), BTJT-B4 (2 t.ha^{-1}), and Biotron (2 t.ha^{-1}). As the dosage increased, improvements in soil physical parameters became more pronounced. Specifically, the application of BTJT (or Biotron) reduced BD, which correlated with increased soil moisture content, porosity, and water retention capacity of the soil. The relationships among the parameters demonstrated moderate to very strong correlations, showing negative interactions with BD and positive interactions with the other parameters. The continuous application of BTJT or Biotron is expected to enhance the overall soil structural stability and resilience, although further long-term studies are needed to explore the chemical and biological aspects of the soil in greater depth.

6. REFERENCES

Ahmad, W., Nepal, J., Zou, Z., Munsif, F., Khan, A., Ahmad, I., Zaheer, S., Khan, M.S., Jadoon, S.A. and Tang, D., 2023. Biochar particle size coupled with biofertilizer enhances soil carbon-nitrogen microbial pools and CO2 sequestration in lentil. Frontiers in Environmental Science, 11, pp.1114728-1114745. [DOI]

Alkharabsheh, H.M., Seleiman, M.F., Battaglia, M.L., Shami, A., Jalal, R.S., Alhammad, B.A., Almutairi, K.F. and Al-Saif, A.M., 2021. Biochar and its broad impacts on soil quality and fertility, nutrient leaching and crop productivity: a review. *Agronomy*, 11(5), pp.11050993-11051010. [DOI]

Allohverdi, T., Mohanty, A.K., Roy, P. and Misra, M., 2021. A review on current status of biochar use in agriculture. *Molecules*, 26(18), pp.26185584-26185600. [DOI]

Ben-Noah, I., Nitsan, I., Cohen, B., Kaplan, G. and Friedman, S.P., 2021. Soil aeration using air injection in a citrus orchard with shallow groundwater. *Agricultural Water Management*, 245, pp.106664-106680. [DOI]

Bian, X., Ren, Z., Zeng, L., Zhao, F., Yao, Y. and Li, X., 2024. Effects of biochar on the compressibility of soil with high water content. *Journal of Cleaner Production*, 434, pp.140032-140050. [DOI]

Braz, G.S., Carvalho, J. do C.L., de Andrade, J.G., Junior, A.T.D., de Lima, R.P., Lima, E.N., Ferreira, O.E., de Oliveira, M.A., Bezerra, A.C. da S. and Machado, A.R.T., 2025. Adsorption of ferrous ions onto phosphoric acid-activated biochar. *Desalination and Water Treatment*, 321, pp.100958-100975. [DOI]

Chen, C., Hu, Y., Ge, Y., Tao, J., Yan, B., Cheng, Z., Lv, X., Cui, X. and Chen, G., 2025. Integrated learning framework for enhanced specific surface area, pore size, and pore volume prediction of biochar. *Bioresource Technology*, 424, pp.132279-132295. [DOI]

Colucci, G., Di Stefano, F., Sacchi, F., Licciardello, M., Tonda-Turo, C., Lavagna, L. and Messori, M., 2025. Bio-based polymer composites obtained by vat photopolymerization of photocurable resins modified with biochar as sustainable filler. *Composites Part A: Applied Science and Manufacturing*, 198, pp.109102-109120. [DOI]

Deru, J.G.C., Bloem, J., de Goede, R., Keidel, H., Kloen, H., Rutgers, M., van den Akker, J., Brussaard, L. and van Eekeren, N., 2018. Soil ecology and ecosystem services of dairy and semi-natural grasslands on peat. *Applied Soil Ecology*, 125, pp.26-34. [DOI]

Ferrarezi, R.S., Lin, X., Gonzalez Neira, A.C., Tabay Zambon, F., Hu, H., Wang, X., Huang, J.H. and Fan, G., 2022. Substrate pH influences the nutrient absorption and rhizosphere microbiome of Huanglongbing-affected grapefruit plants. *Frontiers in Plant Science*, 13, pp.856937-856952. [DOI]

Gao, W., Shi, Y., Zhou, Y., Jia, J. and Chen, S., 2025. Biochar with further enhanced properties prepared by acid base combined pretreatment for removal of water pollutants. *Scientific Reports*, 15(1), pp.19432-19450. [DOI]

Hafeez, A., Pan, T., Tian, J. and Cai, K., 2022. Modified biochars and their effects on soil quality: a review. *Environments*, 9(5), pp.11050060-11050080. [DOI]

Harish, Kumar, P., Kumar, V., Mishra, R.K., Gwag, J.S., Singh, M.K., Singhal, R. and Mukhopadhyay, A.K., 2022. A novel approach to band gap engineering of nano-Ca(OH)2: nanocomposites with Ag2O. *Ceramics International*, 48(23, Part B), pp.35771-35787. [DOI]

Hossain, M.Z., Bahar, M.M., Sarkar, B., Donne, S.W., Ok, Y.S., Palansooriya, K.N., Kirkham, M.B., Chowdhury, S. and Bolan, N., 2020. Biochar and its importance on nutrient dynamics in soil and plant. *Biochar*, 2(4), pp.379-420. [DOI]

Jensen, J.L., Schjønning, P., Watts, C.W., Christensen, B.T. and Munkholm, L.J., 2020. Short-term changes in soil pore size distribution: impact of land use. *Soil and Tillage Research*, 199, pp.104597-104615. [DOI]

Jung, K.W., Hwang, M.J., Jeong, T.U. and Ahn, K.H., 2015. A novel approach for preparation of modified-biochar derived from marine macroalgae: dual purpose electro-modification for improvement of surface area and metal impregnation. *Bioresource Technology*, 191, pp.342-345. [DOI]

Kiss, T., Fórián, S., Szatmári, G. and Sipos, G., 2021. Spatial distribution of microplastics in the fluvial sediments of a transboundary river – a case study of the Tisza River in Central Europe. *Science of the Total Environment*, 785, pp.147306-147325. [DOI]

Lani, N.S., Ngadi, N., Mohammed Inuwa, I., Anako Opotu, L., Zakaria, Z.Y. and Haron, S., 2023. A cleaner approach with magnetically assisted reactor setup over CaO-zeolite/Fe3O4 catalyst in biodiesel production: evaluation of catalytic performance, reusability and life cycle assessment studies. *Journal of Cleaner Production*, 419, pp.138329-138350. [DOI]

Lei, H., Yu, J., Zang, M., Pan, H., Liu, X., Zhang, Z. and Du, J., 2022. Effects of water-fertilizer-air-coupling drip irrigation on soil health status: soil aeration, enzyme activities and microbial biomass. *Agronomy*, 12(11), pp.12112674-12112690. [DOI]

Liao, W. and Thomas, S.C., 2019. Biochar particle size and post-pyrolysis mechanical processing affect soil pH, water retention capacity, and plant performance. *Soil Systems*, 3(1), pp.11030014-11030030. [DOI]

Liu, M., Qiao, P., Shan, Y., Zhang, Z., Pan, P. and Li, Y., 2024. Migration and accumulation simulation prediction of PPCPs in urban green space soil irrigated with recycled water: a review. *Journal of Hazardous Materials*, 476, pp.135037-135055. [DOI]

Ottani, F., Parenti, M., Pedrazzi, S., Moscatelli, G. and Allesina, G., 2022. Impacts of gasification biochar and its particle size on the thermal behavior of organic waste co-composting process. *Science of The Total Environment*, 817, pp.153022-153040. [DOI]

Pandey, M., Tirkey, A., Tiwari, A., Pandey, S.K. and Khan, M.L., 2022. Microbial interaction of biochar and its application in soil, water and air. In: J.A.B.T.-M. and M.B. for G.R. Malik (eds.) *Microbial and Molecular Biotechnology for Green Remediation*. Elsevier, pp.185-203. [DOI]

Quan, G., Fan, Q., Zimmerman, A.R., Sun, J., Cui, L., Wang, H., Gao, B. and Yan, J., 2020. Effects of laboratory biotic aging on the characteristics of biochar and its water-soluble organic products. *Journal of Hazardous Materials*, 382, pp.121071-121090. [DOI]

Raczka, N.C., Piñeiro, J., Tfaily, M.M., Chu, R.K., Lipton, M.S., Pasa-Tolic, L., Morrissey, E. and Brzostek, E., 2021. Interactions between microbial diversity and substrate chemistry determine the fate of carbon in soil. *Scientific Reports*, 11(1), pp.119320-119340. [DOI]

Robinson, D.A., Thomas, A., Reinsch, S., Lebron, I., Feeney, C.J., Maskell, L.C., Wood, C.M., Seaton, F.M., Emmett, B.A. and Cosby, B.J., 2022. Analytical modelling of soil porosity and bulk density across the soil organic matter and land-use continuum. *Scientific Reports*, 12(1), pp.117085-117105. [DOI]

Sachdeva, V., Hussain, N., Husk, B.R. and Whalen, J.K., 2019. Biochar-induced soil stability influences phosphorus retention in a temperate agricultural soil. *Geoderma*, 351, pp.71-75. [DOI]

Sepp, S.-K., Vasar, M., Davison, J., Oja, J., Anslan, S., Al-Quraishy, S., Bahram, M., Bueno, C.G., Cantero, J.J., Fabiano, E.C., Decocq, G., Drenkhan, R., Fraser, L., Garibay Oriel, R., Hiiesalu, I., Koorem, K., Kõljalg, U., Moora, M., Mucina, L. and Zobel, M., 2023. Global diversity and distribution of nitrogen-fixing bacteria in the soil. *Frontiers in Plant Science*, 14, pp.1100235-1100250. [DOI]

Shaheen, J.F., Eniola, J.O. and Sizirici, B., 2024. Adsorption of ibuprofen from aqueous solution by modified date palm biochar: performance, optimization, and life cycle assessment. *Bioresource Technology Reports*, 25, pp.101696-101715. [DOI]

Sizmur, T., Fresno, T., Akgül, G., Frost, H. and Moreno-Jiménez, E., 2017. Biochar modification to enhance sorption of inorganics from water. *Bioresource Technology*, 246, pp.34-47. [DOI]

Sun, M., Liu, X., Shi, K., Peng, F. and Xiao, Y., 2022. Effects of root zone aeration on soil microbes species in a peach tree rhizosphere and root growth. *Microorganisms*, 10(10), pp.110101879-110101895. [DOI]

Tamburini, D., 2021. Analytical pyrolysis applied to the characterisation and identification of Asian lacquers in cultural heritage samples – a review. *Journal of Analytical and Applied Pyrolysis*, 157, pp.105202-105220. [DOI]

Wang, C., Huang, R., Sun, R., Yang, J. and Sillanpää, M., 2021. A review on persulfates activation by functional biochar for organic contaminants removal: synthesis, characterizations, radical determination, and mechanism. *Journal of Environmental Chemical Engineering*, 9(5), pp.1106267-1106285. [DOI]

Wang, L., Wang, Y., Ma, F., Tankpa, V., Bai, S., Guo, X. and Wang, X., 2019. Mechanisms and reutilization of modified biochar used for removal of heavy metals from wastewater: a review. *Science of The Total Environment*, 668, pp.1298-1309. [DOI]

Wang, X., Chen, Z., Wang, C. and Zhang, L., 2024. Ultrahigh and kinetic-favorable adsorption for recycling urea using corncob-derived porous biochar. *Scientific Reports*, 14(1), pp.118131-118150. [DOI]

Wei, B., Peng, Y., Lin, L., Zhang, D., Ma, L., Jiang, L., Li, Y., He, T. and Wang, Z., 2023. Drivers of biochar-mediated improvement of soil water retention capacity based on soil texture: a meta-analysis. *Geoderma*, 437, pp.116591-116610. [DOI]

Nature Environment and Pollution Technology
An International Quarterly Scientific Journal

p-ISSN: 0972-6268
(Print copies up to 2016)
e-ISSN: 2395-3454

Vol. 25 | No. 3 | Article ID B4420 | 2026

Original Research Paper

https://doi.org/10.46488/NEPT.2026.v25i03.B4420

Open Access Journal

Effectiveness of Natural Zeolite and Geo-fabric as Single and Dual Media in Biologically Aerated Filters (BAFs) for Greywater Treatment

Beena P. Nambiar†, Renu Pawels and G. Madhu
School of Engineering, Cochin University of Science and Technology, Kochi, Kerala, India
†Corresponding author: Beena P. Nambiar; beenasaji@gmail.com

Abbreviation: Nat. Env. & Poll. Technol.
Website: www.neptjournal.com

Received: 17-12-2025
Revised: 27-02-2026
Accepted: 01-03-2026

Key Words:

Natural zeolite
Geo-fabric
Biologically aerated filter
Response surface methodology

Citation for the Paper:

Nambiar, B.P., Pawels, R. and Madhu, G., 2026. Effectiveness of natural zeolite and geo-fabric as single and dual media in biologically aerated filters (BAFs) for greywater treatment. *Nature Environment and Pollution Technology*, 25(3), B4420. https://doi.org/10.46488/NEPT.2026.v25i03.B4420

Note: From 2025, the journal has adopted the use of Article IDs in citations instead of traditional consecutive page numbers. Each article is now given individual page ranges starting from page 1.

Copyright: © 2026 by the authors
Licensee: Technoscience Publications
This article is an open access article distributed under the terms and conditions of the Creative Commons Attribution (CC BY) license (https://creativecommons.org/licenses/by/4.0/).

ABSTRACT

The performance of a dual-media biologically aerated filter (NZGF-BAF) incorporating natural zeolite and geo-fabric was studied and compared with single-media BAF systems using only natural zeolite (NZ-BAF) or geo-fabric (GF-BAF) in batch mode. The study examined how hydraulic retention time (HRT), carbon-to-nitrogen (C/N) ratio, aeration rate, and filter depth affected the removal of contaminants such as chemical oxygen demand (COD), biochemical oxygen demand (BOD), ammonia-nitrogen (NH3-N), turbidity, and total dissolved solids (TDS). Results showed that under similar conditions, NZ-BAF and GF-BAF performed similarly in removing COD, BOD, and turbidity, thanks to their larger surface areas, biofilm development, and absorption and adsorption capacities. NZ-BAF was more effective at removing NH3-N due to its ion-exchange properties, while GF-BAF excelled in TDS removal through permeability, adsorption, and bacterial activity. The dual-media NZGF-BAF demonstrated improved removal efficiencies across all contaminants. An optimization study using Response Surface Methodology (RSM) under optimal conditions revealed maximum removal rates of 93% for COD, 98% for BOD, 94% for NH3-N, 93% for turbidity, and 67% for TDS.

1. INTRODUCTION

Aerobic biological processes have been developed in wastewater treatment to lower environmental contaminant levels and efficiently remove most dissolved and suspended organic pollutants through mechanisms such as organic decomposition, surface adsorption, and sedimentation (Huang et al. 2017). Aerobic treatment methods include activated sludge processes, trickling filters, membrane bioreactors (MBRs), moving bed biofilm reactors (MBBRs), and biologically aerated filters (BAF). Both traditional activated sludge and carrier-added activated sludge (CAS) produce excess sludge that must be routinely removed, requiring large liquid-solid separation units. Fixed film techniques tend to nitrify wastewater more effectively than activated sludge methods. Treatment systems like trickling filters and biotowers also need secondary sedimentation to settle waste sludge, making them larger and costlier (Doelle et al. 2020). MBRs are increasingly favored due to their compact size and high effluent quality (Van de Staey et al. 2015), though they face challenges such as membrane fouling, aeration limitations, and high costs. Membranes require frequent chemical cleaning and eventual replacement due to abrasion and declining efficiency (Krzeminski et al. 2012). MBBR systems, despite their benefits, can cause foaming and turbidity from filament growth, which can lead to excessive biomass and reduce void space, impairing oxygen transfer and substrate diffusion. Additionally, the plastic media will eventually need replacement because of wear (Krzeminski et al. 2012).

The BAF system's capability to effectively remove solids, carbon, nitrogen, and phosphorus from wastewaters has established it as a prominent technology in wastewater treatment. This is achieved through the integration of biological

and physical processes, resulting in an effluent suitable for reuse or safe environmental discharge (Mendoza-Espinosa et al. 1999, Jacob et al. 1997). Its compact design, versatility in treating various wastewater types, ease of operation and maintenance, energy efficiency compared to other methods, and its ability to simultaneously eliminate multiple contaminants are some of its key advantages. BAF systems excel at removing organic matter from wastewater due to the high biomass attached to the filter media. This biological treatment efficiently decomposes organic pollutants within a single unit, greatly reducing the organic load (Fu et al. 2016). Additionally, bio-filter systems demonstrate adaptability, functioning effectively across a range of environmental conditions such as pH and temperature changes. This versatility allows their use in diverse climates and geographic regions. The operational flexibility of BAF systems permits modifications to accommodate different influent characteristics, including variations in wastewater composition and flow rates. They typically produce less sludge, simplifying residual sludge management and disposal while reducing environmental impact. Another advantage is that bio-filter systems are environmentally friendly and operate quietly (Nacheva et al. 2008).

Selecting an appropriate support medium is crucial when designing and operating a BAF system. To ensure the discharged effluent is environmentally safe and complies with health and environmental regulations, regulatory bodies establish effluent quality standards. Choosing the right filter media is vital for meeting these standards (Tan et al. 2008). For effective wastewater treatment, media characteristics such as permeability, pore size, and type are essential (Kent et al. 2000, Spychała et al. 2013).

Natural zeolite–based biologically aerated filters (NZ-BAFs) represent an advanced type of submerged biofilter, where natural zeolite serves as the primary support medium. Composed of hydrated alumino-silicates with a honeycomb structure, natural zeolite's three-dimensional network is formed by interconnected tetrahedra of SiO4 and AlO4 linked through shared oxygen atoms (Adam et al. 2023). The substitution of Al3+ ions for Si4+ ions within the lattice creates a negative charge within the tiny pores, establishing effective cation exchange sites (Widiastuti et al. 2011). This property makes natural zeolites particularly selective for cations such as ammonium ions in wastewater. With a high specific surface area and porosity, natural zeolite enhances adsorption capacity and supports biofilm development through bacterial attachment. Larger organic molecules, whether dissolved or colloidal, cannot pass through the zeolite's narrow pores and instead adhere to its surface. Microorganisms, including bacteria, become entrapped within the pores, facilitating microbial activity. Consequently, the extensive surface area allows for a substantial population of active bacteria responsible for degrading organic contaminants in wastewater. The performance of a BAF system is also influenced by the media's size, shape, and surface roughness. The rough surface of zeolite media provides more area for bacterial attachment and biofilm formation (Spychała et al. 2013). Furthermore, the uneven surface of zeolite outperforms spherical media in efficiency. Due to its inertness, low cost, non-metallic, and non-toxic characteristics, natural zeolite is an excellent support medium for wastewater treatment. Although the long-term operation may reduce its effectiveness, natural zeolite's regenerative properties—restored through treatments with NaCl, KCl, acids, or heat—offer additional advantages.

Geo-fabrics are durable polymeric materials designed for a variety of environmental and civil engineering uses. In wastewater treatment, particularly within biofilm reactors, the application of geo-fabrics as support media is an emerging research area. Commonly fabricated from synthetic polymers such as polyester (PET) and polypropylene (PP), geo-fabrics are produced in both woven and non-woven forms. The complex fiber structure of non-woven, needle-punched geo-fabrics has demonstrated exceptional efficiency in capturing suspended solids and larger particles. Due to their superior strength, porosity, flexibility, durability, resistance to environmental factors, and ability to withstand stresses, geo-fabrics are preferred over alternative media such as sand, crushed rock, river gravel, granular activated carbon (GAC), or certain plastics and ceramics (Praveen et al. 2008, Revathi et al. 2016). The large specific surface area of geo-fabrics enhances their effectiveness in filtration and adsorption processes. Their filamentous structure promotes rapid bacterial adhesion and biofilm formation (Alimahmoodi et al. 2012). In wastewater treatments where bacteria play a role in breaking down organic materials, the hydrophilic nature of geo-fabrics further facilitates bacterial attachment. Additionally, the biodegradable and eco-friendly qualities of geo-fabrics help to mitigate environmental impact.

Oxygen plays a crucial role in the decomposition of organic matter (COD and BOD) and in the nitrification process (NH_3-N removal). The efficiency of aerobic bacteria that eliminate pollutants is directly linked to the level of aeration supplied. The BAF system depends on a robust aeration setup, regardless of the support media used, to ensure optimal performance of biological processes, prevent operational issues, and produce high-quality effluent. Proper aeration maintains dissolved oxygen levels and supports the development of bacterial biofilms.

The backwash mechanism in a BAF system is essential for removing biomass and particles from the media surface, preventing clogging, and avoiding mechanical compaction

that could reduce porosity. This process also helps maintain bacterial activity within the biofilm (Charchalac et al. 2015). Proper backwashing reduces energy consumption and extends the treatment cycle. It is important to carefully regulate the frequency of backwashing, as excessive cleaning can decrease biomass and impair bio-filter function. Conversely, infrequent backwashing may limit the removal of BOD and total nitrogen (Xie et al. 2004). Typically, backwashing intervals for some secondary treatment bio-filters range from 24 to 48 hours (Bacquet et al. 1991), while others may only require backwashing every 1-2 weeks to effectively remove excess biomass (Jacob et al. 1997).

This study systematically examines how key operational parameters influence the performance of a bio-adsorption filter (BAF) system that uses dual media—natural zeolite and geo-fabric—compared to single-media setups utilizing only natural zeolite or geo-fabric as biofilm support materials. The treatment effectiveness was evaluated based on the removal of COD, BOD, NH_3–N, turbidity, and TDS from greywater under batch experimental conditions. While most conventional biofilter media achieved satisfactory removal rates for COD, BOD, and turbidity, the efficiencies for NH_3–N and TDS were generally lower and often did not meet permissible discharge standards. The BAF system explored in this research is designed to be a compact, efficient, and cost-effective solution for household greywater treatment, reducing dependence on more advanced and expensive technologies such as ion exchange, ultrafiltration, nanofiltration, distillation, or reverse osmosis.

The operational parameters for the BAF system under investigation include HRT, C/N ratio, aeration rate, and media depth. The system's efficiency under different hydraulic conditions can be assessed by examining fluctuations in HRT, which reflects the contact time between water and microbial biofilm. Monitoring the C/N ratio helps understand nutrient availability and its influence on microbial activity and treatment performance in the dual media BAF. Aeration is vital for maintaining aerobic conditions within the biological filter and promoting the growth of aerobic microorganisms. Optimizing treatment efficiency involves studying how changes in aeration rates impact BAF performance. Additionally, the depth of the filter bed affects microorganism distribution and the contact time between greywater and biofilm. Analyzing the influence of filter depth provides valuable insights into the biofilter's functionality and system design considerations.

The system's optimization was analyzed using Minitab 19, a software that provides a range of data analysis tools through its Response Surface Model (RSM). By applying statistical techniques, mathematical problems are modeled and examined to enhance system performance. RSM offers the key advantage of requiring fewer experimental trials to evaluate multiple factors and their interactions (Jasni et al. 2020, Lin et al. 2010). It is an effective method for understanding how different factors interact and for identifying optimal operating parameters for the BAF system.

2. MATERIALS AND METHODS

2.1. Lab-Scale Setup

A lab-scale bio-filter system was employed to evaluate the feasibility of the proposed single and dual media-based bio-filter configurations. This system was built as a transparent, rigid glass column, allowing visual observation of internal processes. Measuring 150 mm × 150 mm in cross-section and 1200 mm in height, the column's square design provides sufficient capacity for testing. An inlet situated 50 mm from the top and an outlet 50 mm from the bottom enable controlled influent distribution and effluent collection. To ensure uniform distribution of influent and backwash water and to prevent washout, perforated plates are installed at both the top and bottom of the column. Two cubic glass tanks, each measuring 300 mm × 300 mm with a depth of 300 mm, were utilized: one as an equalization tank to supply a steady, regulated flow of greywater to the biofilter, and the other as a settling basin for the collection of treated greywater, allowing suspended solids to settle before disposal or reuse. Influent is pumped into the biofilter column via a submersible pump. Adequate aeration is maintained by an aerator and four evenly spaced air diffusers along the column's depth. To sustain system performance and prevent clogging, a backwash mechanism periodically removes excess biomass and accumulated solids, using the effluent from the settling basin as backwash water, thereby enhancing overall sustainability and efficiency. The schematic of the experimental setup for the BAF system is illustrated in Fig. 1.

2.2. BAF Media

Batch experiments were performed using single- and dual-media BAF filters, comprised of natural zeolite and/or geo-fabric as the filtering media. Natural zeolite, sized between 1-3 mm, was sourced from G. M. Biochem Pvt. Ltd. in Ahmedabad, Gujarat. The non-woven, needle-punched geo-fabric with a GSM of 500 was manufactured by Manas Geo Tech India Pvt. Ltd. in New Delhi, India. Natural zeolites possess a tetrahedral structure, offering high cation exchange, adsorption, and absorption capacities, along with the ability to develop a biofilm on their surface. Geo-fabrics feature a complex, porous structure with high permeability, tensile strength, and porosity, which facilitates microbial growth.

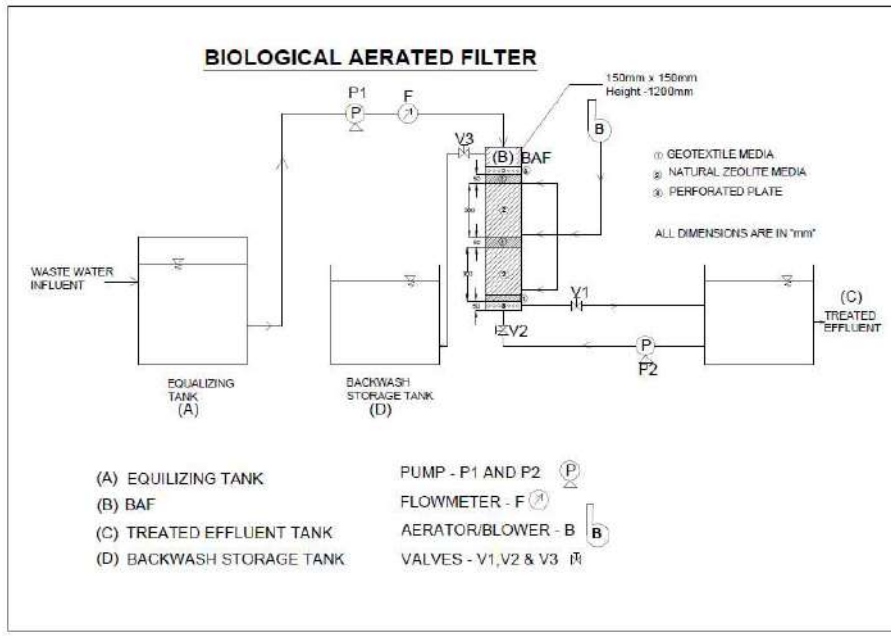


Fig. 1: Experimental setup of the BAF system.

Both materials enable water flow while effectively retaining suspended solids, making them excellent, cost-effective filter media that are easy to handle and install, and resilient against biological degradation and environmental factors.

In the initial series of batch experiments, the BAF system was operated using natural zeolite particles measuring 1-3 mm as the sole filter medium, designated as NZ-BAF. The second series employed only geo-fabric with a density of 500 GSM as the filter medium, labeled GF-BAF. In the third series, a dual media comprising natural zeolite (1-3 mm) and geo-fabric (500 GSM) was used in the BAF system, referred to as NZGF-BAF. The operational conditions remained consistent across all three experimental series.

2.3. Synthetic Greywater Preparation and Analysis

For this study, synthetic greywater was used as the influent to maintain consistent composition and eliminate variability in influent characteristics across the experimental runs conducted for NZ-BAF, GF-BAF, and NZGF-BAF systems. The synthetic greywater was prepared by mixing precise amounts of chemicals such as glucose (300 $mg.L^{-1}$), sodium acetate trihydrate (400 $mg.L^{-1}$), ammonium chloride (225 $mg.L^{-1}$), disodium hydrogen phosphate (150 $mg.L^{-1}$), potassium dihydrogen phosphate (75 $mg.L^{-1}$), and magnesium sulphate (50 $mg.L^{-1}$) with one liter of distilled water. The physicochemical properties of the synthetic greywater, along with their variability—low, high, mean, and standard deviation—are summarized in Table 1. Subsequently, physicochemical parameters were measured before and after treatment to determine the percentage removal of contaminants, following accepted standard methods (APHA 2017).

2.4. Bacterial Inoculation and Acclimation

The prepared synthetic greywater was combined with seed inoculum from the activated sludge of the sewage treatment plant to reduce startup time and promote microbial growth.

Table 1: Characteristics of synthetic greywater used as influent.

Process Parameter	Unit	Number of Samples	Influent Value			
			Low	High	Mean	Standard Deviation
COD	$mg.L^{-1}$	33	368	527	446.2	71.7
BOD	$mg.L^{-1}$	33	203	231	216.2	11.3
NH_3-N	$mg.L^{-1}$	33	15	18	16.42	1.19
Turbidity	NTU	33	46	85	63.5	14
TDS	$mg.L^{-1}$	33	547	609	575.8	24.1

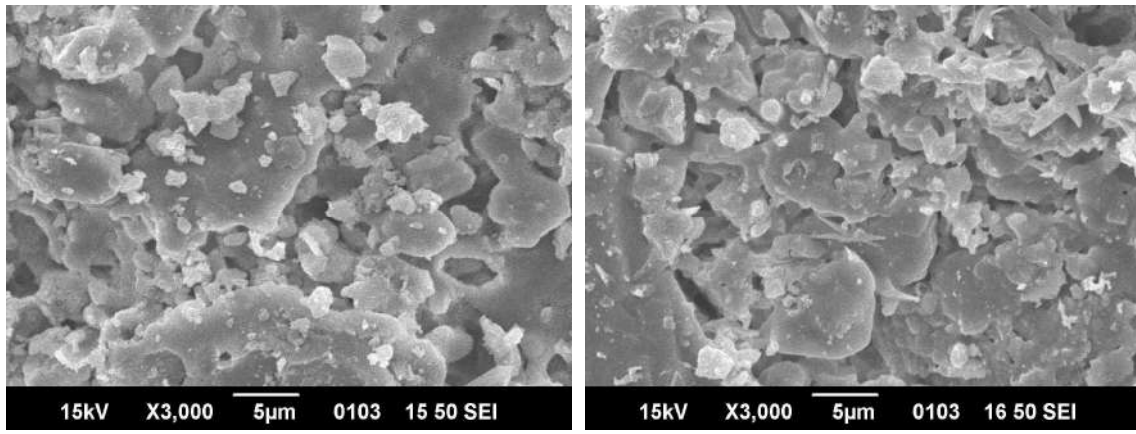
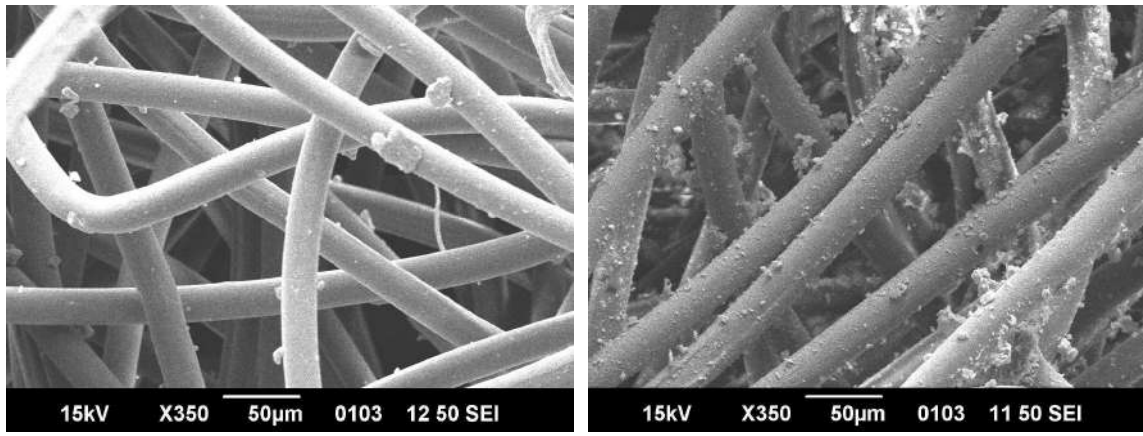


Fig. 2: SEM of natural zeolite 1-3 mm (a) Before treatment (b) After treatment.



(a) (b)

Fig. 3: SEM of geo-fabric media of 500 GSM (a) Before treatment (b) After treatment.

Additionally, nutrients for aerobic bacteria were added to the mixture. Before each experimental series, the respective media underwent a 21-day bacterial acclimation period to support biofilm formation and stabilization. To ensure sufficient oxygen supply, aeration was initially provided at a rate of 15 $L.h^{-1}$. After acclimation, the effluent COD levels remained low and stable, indicating the development of a biofilm on the media.

After the acclimatization phase, each system was operated under various conditions to enhance treatment efficiency and understand the system's sensitivity. The system was maintained at an organic loading rate of 3.95–4.5 kg $BOD.m^{-3}.day^{-1}$, based on initial BOD concentrations of 203 $mg.L^{-1}$ (low) and 231 $mg.L^{-1}$ (high) for synthetic greywater. The performance of single and dual media BAFs was evaluated under similar operational conditions, with variations in HRT, C/N ratio, aeration rate, and filter depth. The following section discusses the results and observations obtained.

3. RESULTS AND DISCUSSION

Batch experiments were conducted using BAF systems with various media configurations, specifically NZ-BAF, GF-BAF, and NZGF-BAF, to compare their treatment effectiveness. Each reactor operated independently under different operational parameters such as HRT, C/N ratio, aeration rate, and filter media depth. The system's performance was evaluated based on removal efficiencies of key parameters, including COD, BOD, NH_3–N, turbidity, and TDS.

To gain a deeper understanding of how media characteristics influence pollutant removal, scanning electron microscopy (SEM) analysis was performed on natural zeolite (particle size 1–3 mm) and geo-fabric (500 GSM) both before and after treatment. The SEM micrographs of natural zeolite and geo-fabric, shown in Fig. 2(a–b) and Fig. 3(a–b), respectively, clearly reveal distinct surface modifications

post-treatment, indicating structural changes linked to biofilm development and contaminant accumulation.

3.1. Assessment of the Performance of BAF Using Single and Dual Media with Natural Zeolite of Size 1-3 mm and/or Geo-fabric of 500 GSM Under Varying Operational Conditions

3.1.1. HRT

For each BAF type—NZ-BAF, GF-BAF, and NZGF-BAF—to assess the impact of HRT on performance and identify the optimal HRT, all other variables such as C/N ratio, aeration rate, and filter medium depth were maintained constant at 6, 65 $L.h^{-1}$, and 70 cm, respectively. In single-media systems, natural zeolite and geo-fabric each occupied a 70 cm filter depth in the NZ-BAF and GF-BAF reactors. The dual-media NZGF-BAF featured a stratified setup, with a 30 cm bottom layer of natural zeolite and a 40 cm top layer of geo-fabric, totaling a 70 cm filter depth. After each operational period, the effluent properties were analyzed. The NZ-BAF was operated by systematically varying HRT values—1 h, 2 h, 3 h, 4 h, and 5 h—repeating the process for GF-BAF and NZGF-BAF. Performance was evaluated based on key process parameters influencing biological treatment: COD, BOD, NH3-N, turbidity, and TDS removal. The highest percentage removal of these parameters was observed at an HRT of 3 h across all BAF systems. At this HRT, removal efficiencies were 85%, 86%, 95%, 76%, and 30% for COD, BOD, NH3-N, turbidity, and TDS in NZ-BAF; 86%, 94%, 77%, 86%, and 63% in GF-BAF; and 91%, 98%, 92%, 91%, and 63% in NZGF-BAF. The variations in removal efficiencies for these parameters at different HRTs for each BAF type are depicted in Fig. 4 (a-c).

In BAF systems, pollutant removal efficiency improves when the HRT is increased from 1 hour to 3 hours. Extending the HRT further to 4 or 5 hours does not significantly enhance pollutant removal, indicating that the optimal HRT is around 3 hours. Initially, organic matter is rapidly eliminated due to the availability of absorbent sites on the filter media, which facilitate efficient adsorption of contaminants. Over time, the removal rate decreases as the active sites become saturated

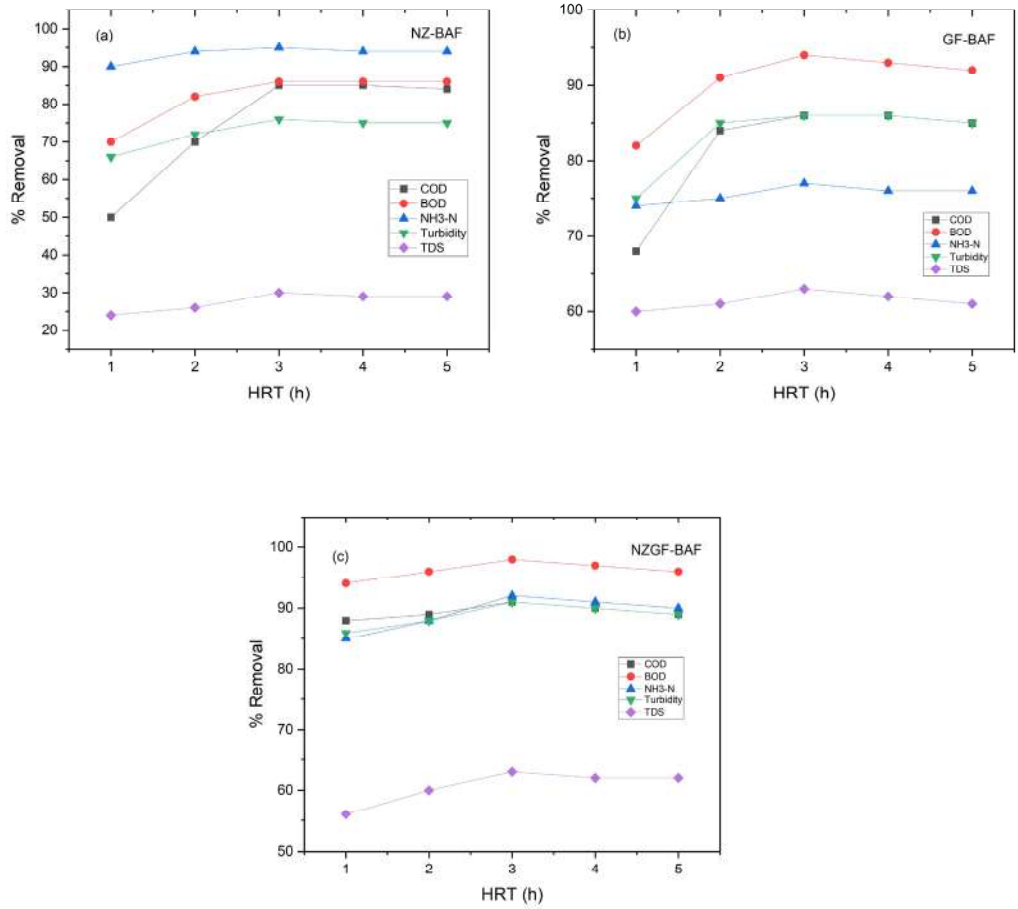


Fig. 4: Effect of the variation in HRT for (a) NZ-BAF, (b) GF-BAF (c) NZGF-BAF.

or deactivated, reducing pollutant removal effectiveness. Shorter HRTs are advantageous because they occupy less space for biofilters, potentially leading to lower building costs for biofiltration systems.

3.1.2. C/N Ratio

The experiments on NZ-BAF, GF-BAF, and NZGF-BAF were carried out with different C/N ratio values, specifically 4, 5, 6, 7, and 8, while maintaining a constant HRT of 3 hours, an aeration rate of 65 $L.h^{-1}$, and a filter depth of 70 cm. These conditions were set to investigate how variations in C/N ratios influence the properties of the effluent. The effluent characteristics were analyzed after each experimental run.

Based on the test results, the highest removal efficiency of contaminants was achieved at a C/N ratio of 6 for NZGF-BAF, NZ-BAF, and GF-BAF. Specifically, for NZGF-BAF, the maximum percentage removals were 93% for COD, 98% for BOD, 92% for NH_3-N, 91% for turbidity, and 66% for TDS. In the NZ-BAF system, the highest removals were 85% for COD, 85% for BOD, 89% for NH_3-N, 78% for turbidity, and 30% for TDS. Meanwhile, the GF-BAF system showed maximum removals of 84% for COD, 91% for BOD, 75% for NH_3-N, 85% for turbidity, and 61% for TDS. The data on contaminant removal across various BAFs and C/N ratios are displayed in Fig. 5(a–c).

Pollutant removal efficiency of the BAFs increased as the C/N ratio rose from 4 to 6. However, removal efficiency began to decline as the C/N ratio reached 6. Consequently, the optimal C/N ratio was found to be 6. The porous nature and large surface area of the natural zeolite and geo-fabric media, which provide ample space for bacterial colonization and pollutant breakdown, enabled effective interaction between organic matter and the media. However, beyond a certain point, the bio-filter's effectiveness declined as organic loading increased.

3.1.3. Rate of Aeration

The systems were operated at various aeration rates (15, 40, 65, 90, and 105 $L.h^{-1}$), with an optimal HRT of 3 hours and a C/N ratio of 6. The media depth remained at 70 cm, consistent with earlier experiments. When compared to NZ-BAF and GF-BAF, the NZGF-BAF system with dual media demonstrated

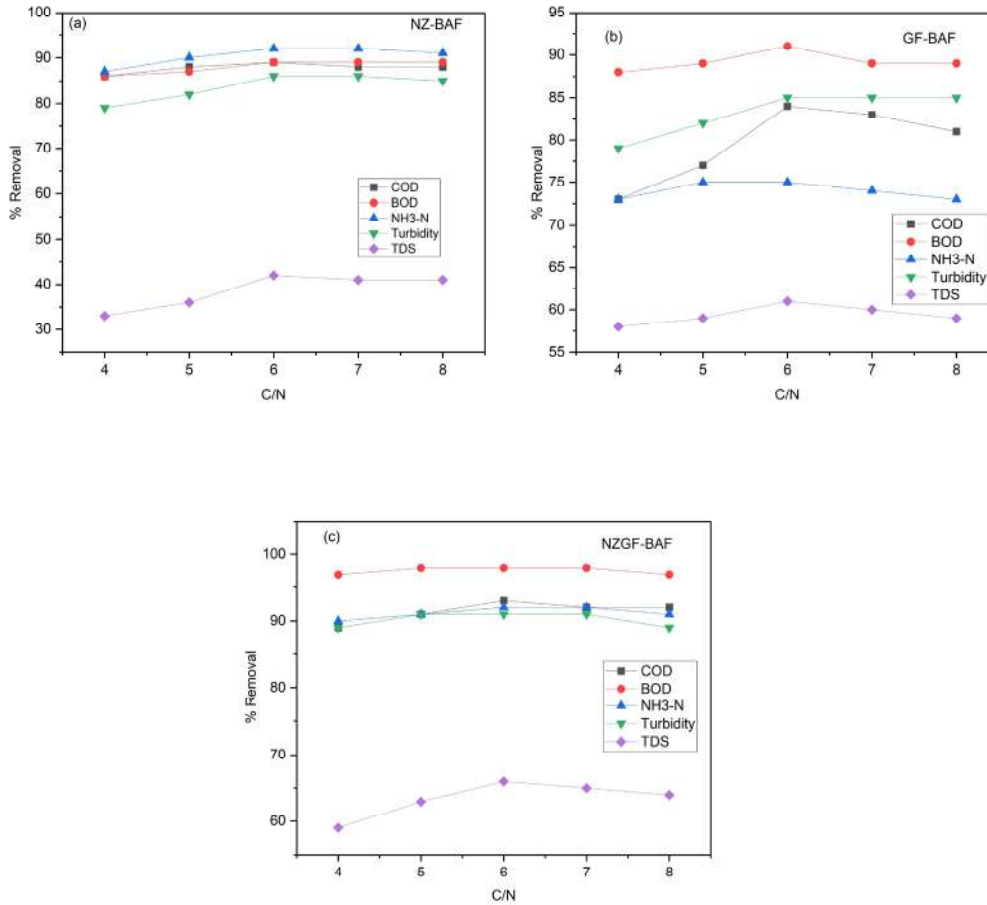


Fig. 5: Effect of various C/N ratios on (a) NZ-BAF, (b) GF-BAF (c) NZGF-BAF.

superior performance at an ideal aeration rate of 65 $L.h^{-1}$. The percentage removal efficiencies for different process parameters across various filter media types and aeration rates are depicted in Fig. 6 (a–c). The NZ-BAF achieved maximum removal rates of 90%, 92%, 96%, 92%, and 49% for COD, BOD, NH_3-N, turbidity, and TDS, respectively. The GF-BAF reported peak removal efficiencies of 90%, 95%, 84%, 88%, and 67% for the same parameters. Notably, the NZGF-BAF yielded the highest removal percentages for COD, BOD, NH_3-N, turbidity, and TDS, which were 93%, 98%, 92%, 91%, and 66%, respectively.

All BAF systems demonstrated improved removal efficiency when aeration was supplied at the optimal rate of 65 $L.h^{-1}$. Increasing the aeration rate to 90 or 115 $L.h^{-1}$ did not yield any noticeable enhancement in system performance. Based on the experimental data, the aeration rate was set at 65 $L.h^{-1}$, indicating that sufficient airflow boosts the metabolic activity of the bacteria.

3.1.4. Depth of Filter

The performance of the BAF system is significantly affected by the choice and properties of the filter media. To investigate how variations in filter depth impact treatment efficiency, reactors were operated with media depths of 60, 70, 80, 90, and 100 cm.

All systems were maintained under previously optimized conditions, including a 3-hour HRT, a C/N ratio of 6, and an aeration rate of 65 $L.h^{-1}$. In the single-media configurations (NZ-BAF and GF-BAF), natural zeolite and geo-fabric, respectively, filled the entire filter depth from 60 to 100 cm. Conversely, the dual-media NZGF-BAF system comprised a fixed 30 cm bottom layer of natural zeolite, with the thickness of the overlying geo-fabric layer varied (30, 40, 50, 60, and 70 cm) to achieve total depths of 60 to 100 cm.

At a filter depth of 80 cm, all three systems demonstrated the highest contaminant removal efficiencies. Fig. 7 (a-c) illustrates the percentage removal of various parameters in relation to filter depth for each system.

At a depth of 80 cm, NZGF-BAF demonstrated superior contaminant removal percentages compared to NZ-BAF and GF-BAF. Specifically, at this total filter depth, NZ-BAF

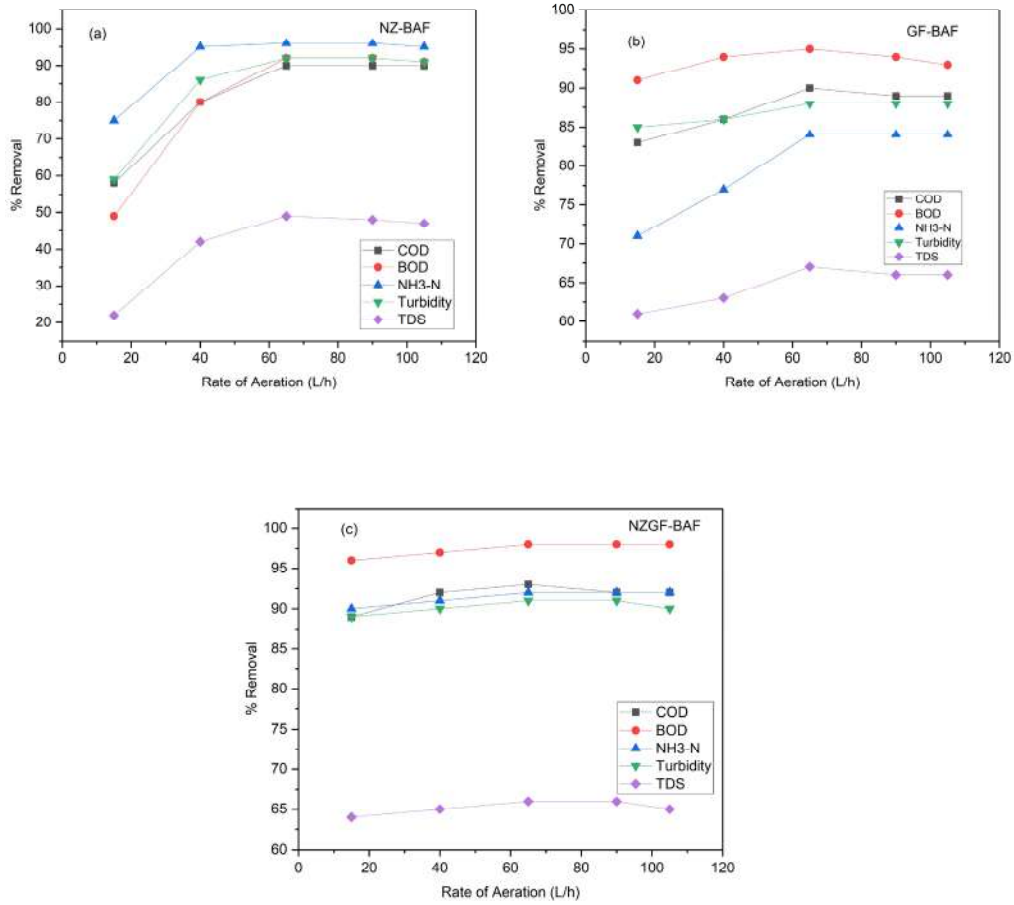


Fig. 6: Effect of various rates of aeration on (a) NZ-BAF, (b) GF-BAF, (c) NZGF-BAF.

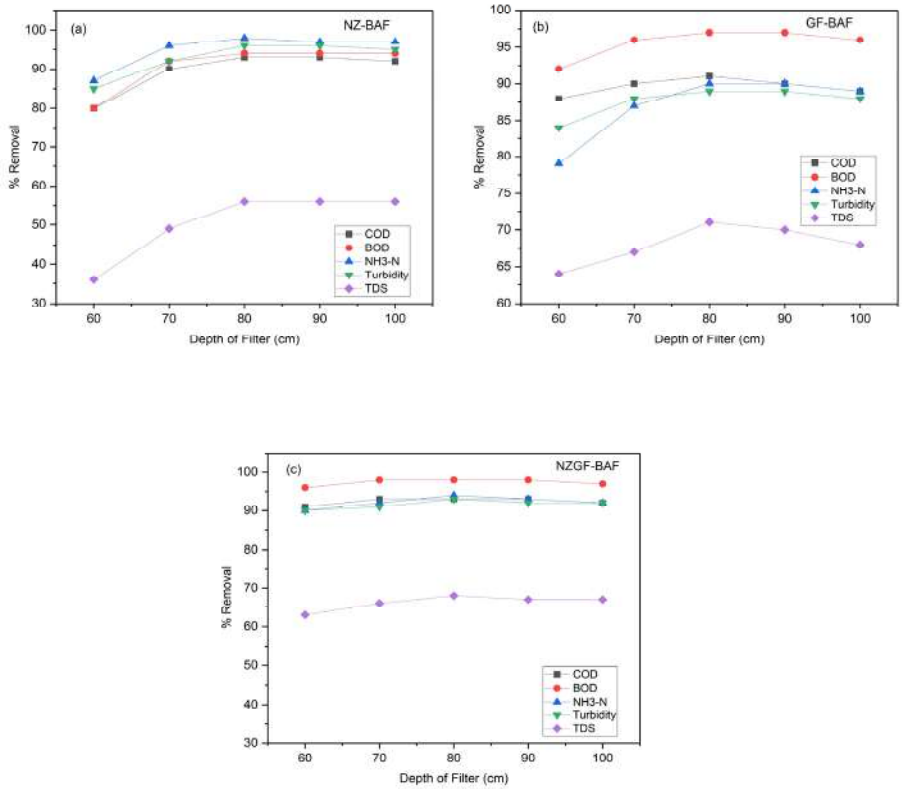


Fig. 7: Effect of variation in the depth of filter on (a) NZ-BAF, (b) GF-BAF, (c) NZGF-BAF.

achieved maximum removal efficiencies of 93% for COD, 96% for BOD, 98% for NH_3-N, 96% for turbidity, and 56% for TDS. GF-BAF recorded removal efficiencies of 91% for COD, 97% for BOD, 90% for NH_3-N, 89% for turbidity, and 71% for TDS. Meanwhile, NZGF-BAF with combined media exhibited maximum removal efficiencies of 93% for COD, 98% for BOD, 94% for NH_3-N, 93% for turbidity, and 68% for TDS.

A higher percentage removal was observed across all process parameters in the BAF systems when the filter bed's depth was increased from 60 cm to 80 cm. However, the improvement in removal efficiency was not significant beyond a depth of 80 cm. Over time, biomass accumulation in the filter bed leads to a decline in the bio-filter's performance. Organic matter buildup in the deeper filter bed results in increased pressure, which can cause uneven distribution of influent and air within the filter bed, as noted by Qamaruz-Zaman et al. (2020).

3.1.5. Media Type

Compared to NZ-BAF and GF-BAF, the NZGF-BAF with dual media exhibited strong performance. The optimal results for NZGF-BAF were achieved at an HRT of 3 hours, a C/N ratio of 6, an aeration rate of 65 $L.h^{-1}$, and a filter depth of 80 cm. Table 2 presents a comparison of the performance of the BAFs based on media types.

The percentage removal of COD, BOD, NH_3-N, turbidity, and TDS for NZ-BAF at an HRT of 3 hours, a C/N ratio of 6, an aeration rate of 65 $L.h^{-1}$, and a filter depth of 80 cm was 93%, 96%, 98%, 96%, and 56%, respectively. Under the same operational conditions, GF-BAF achieved removal efficiencies of 91%, 97%, 90%, 89%, and 71%, respectively. The NZGF-BAF demonstrated the highest removal percentages for COD, BOD, NH3-N, turbidity, and TDS, reaching 93%, 98%, 94%, 93%, and 67%, respectively. Although COD and BOD removals were comparable across NZ-BAF, GF-BAF, and NZGF-BAF, NH_3-N and turbidity removal efficiencies were higher in NZ-BAF due to its ion-exchange properties. Conversely, TDS removal was greater in GF-BAF, attributable to biofilm formation and bacterial

Table 2: Comparison of the performance of BAFs based on media types.

Media Type	Process Parameters				
	COD	BOD	NH_3-N	Turbidity	TDS
NZ-BAF	93%	96%	98%	96%	56%
GF-BAF	91%	97%	90%	89%	71%
NZGF-BAF	93%	98%	94%	93%	67%

activity within the finer pores of the media. Overall, the dual-media NZGF-BAF, combining natural zeolite and geo-fabric, exhibited superior performance in removing all process parameters, leading to further optimization using RSM in Minitab 19.

3.2. Optimization of NZGF-BAF System

Minitab 19 software was utilized to analyze and optimize the performance of the NZGF-BAF system. This version of Minitab supports regression modeling, statistical analysis, and the visualization of relationships between variables. To assess the impact of key independent variables, namely HRT, C/N ratio, aeration rate, and filter depth, on system performance, a total of 30 systematically designed experimental runs were conducted using Central Composite Design (CCD). This approach enables the development of a response surface model (RSM) and facilitates understanding the interactions between critical operational parameters and process parameter removal. The five coded levels and their corresponding experimental ranges for the independent variables are summarized in Table 3.

A regression model is employed to mathematically express the response as a function of the independent variables. The following general quadratic model equation (1) is used to predict and obtain the optimal response.

$$Y = \beta_0 + \sum_{i=1}^{k} \beta_i X_i + \sum_{i=1}^{k} \beta_{ii} X_i^2 + \sum_{i=1}^{k} \sum_{j=1}^{k} \beta_{ij} X_i X_j + \varepsilon \quad \ldots(1)$$

where Y represents the predicted response (% removal), β0 denotes the constant regression coefficient (intercept), βi is the linear coefficient, βii is the quadratic coefficient, and βij signifies the interaction coefficient. Variables i and j are coded values for the independent variables, while k indicates the total number of process variables included in the study.

The equations (2), (3), (4), (5), and (6) represents the second-order quadratic regression models developed using RSM to predict the percentage removal of COD, BOD, NH_3–N, turbidity, and TDS in the NZGF-BAF system as functions of HRT, C/N (C/N ratio), ROA (Rate of Aeration), and DOF (Depth of Filter).

% Removal of COD = 77 + 59.1 HRT - 11.4 C/N - 6.73 ROA+ 4.01 DOF - 8.817 HRT * HRT + 0.065 C/N * C/N + 0.0252 ROA * ROA - 0.02457 DOF * DOF - 1.175 HRT * C/N + 0.390 HRT * ROA - 0.1262 HRT * DOF + 0.179 C/N * ROA + 0.0445 C/N * DOF + 0.0060 ROA * DOF …(2)

% Removal of BOD = 93 + 21.7 HRT - 0.2 C/N- 7.41 ROA+ 5.10 DOF - 9.218 HRT * HRT+ 0.523 C/N * C/N + 0.0370 ROA * ROA - 0.03320 DOF * DOF - 1.225 HRT * C/N + 0.610 HRT * ROA + 0.1900 HRT * DOF + 0.007 C/N * ROA - 0.0055 C/N * DOF - 0.0025 ROA * DOF …(3)

% Removal of NH_3-N = 91+ 21.3 HRT- 1.4 C/N - 7.30 ROA+ 5.07 DOF - 9.211 HRT * HRT+ 0.467 C/N * C/N + 0.0350 ROA * ROA - 0.03298 DOF * DOF - 1.210 HRT * C/N + 0.615 HRT * ROA+ 0.1895 HRT * DOF + 0.036 C/N * ROA - 0.0090 C/N * DOF - 0.0023 ROA * DOF …(4)

% Removal of Turbidity = 76+ 22.4 HRT + 1.1 C/N - 7.13 ROA + 5.03 DOF - 9.220 HRT * HRT+ 0.422 C/N *C/N + 0.0350 ROA * ROA - 0.03268 DOF * DOF - 1.347 HRT * C/N+ 0.611 HRT * ROA+ 0.1903 HRT * DOF + 0.011 C/N * ROA - 0.0063 C/N * DOF - 0.0027 ROA * DOF …(5)

% Removal of TDS = 79 + 36.5 HRT - 5.8 C/N - 5.08 ROA + 2.49 DOF - 10.389 HRT * HRT + 0.636 C/N * C/N + 0.0018 ROA * ROA - 0.02303 DOF * DOF - 4.77 HRT * C/N + 0.834 HRT * ROA + 0.167 HRT * DOF + 0.177 C/N * ROA + 0.069 C/N * DOF + 0.0062 ROA * DOF …(6)

Analysis of Variance (ANOVA) was employed to assess the performance of the NZGF-BAF system utilizing dual media, with results presented in Tables 4 to 8. The developed equation was validated through ANOVA and model adequacy diagnostics, confirming its statistical significance and predictive accuracy.

The p-values derived from the ANOVA tables are instrumental in assessing the significance of the model within the statistical analysis. In this research, all regression models for the process parameters exhibited p-values below the predetermined significance threshold (α = 0.05). Additionally, the linear and quadratic terms for COD, BOD, NH_3-N, turbidity, and TDS each had p-values of 0.000, underscoring the importance of both the primary and quadratic effects of these operating parameters on

Table 3: Five levels and experimental range of independent variables α.

Symbol Coded	Independent Variables (Operational Parameters)	Unit	Range of actual independent variables				
			-α	-1	0	+1	+α
HRT	HRT	h	1.5	2.5	3.5	4.5	5.5
C/N	C/N Ratio	-	4.5	5.5	6.5	7.5	8.5
ROA	Rate of Aeration	$L.h^{-1}$	55	60	65	70	75
DOF	Depth of Filter	cm	60	70	80	90	100

Table 4: ANOVA for percentage removal of COD.

Source of variation	Degrees of freedom [DF]	Sum of squares [SS]	F-value	p-value
Regression	14	1526.77	32.41	0.000
Linear	4	971.17	72.16	0.000
Square	4	524.13	38.94	0.000
Interaction	6	31.46	1.56	0.241
Residual error	12	40.38		
Lack of Fit	10	37.96	3.14	0.266
Pure Error	2	2.42		
Total	26	1567.14		

Table 5: ANOVA for percentage removal of BOD.

Source of variation	Degrees of freedom [DF]	Sum of squares [SS]	F-value	p-value
Regression	14	1618.40	66.26	0.000
Linear	4	947.62	135.79	0.000
Square	4	613.05	87.85	0.000
Interaction	6	57.73	5.52	0.006
Residual error	12	20.94		
Lack of Fit	10	18.52	1.53	0.459
Pure Error	2	2.42		
Total	26	1639.34		

Table 6: ANOVA for percentage removal of NH_3-N.

Source of variation	Degrees of freedom [DF]	Sum of squares [SS]	F-value	p-value
Regression	14	1610.56	63.04	0.000
Linear	4	945.01	129.45	0.000
Square	4	607.29	83.19	0.000
Interaction	6	58.26	5.32	0.007
Residual error	12	21.90		
Lack of Fit	10	19.48	1.61	0.443
Pure Error	2	2.42		
Total	26	1632.46		

treatment performance. Conversely, the interaction term for COD demonstrated less statistical significance ($p = 0.241$), indicating that the combined effects of the factors are comparatively less impactful. The lack-of-fit p-values for COD (0.266), BOD (0.459), NH_3–N (0.443), turbidity (0.439), and TDS (0.205) exceeded 0.05, which suggests that the lack of fit is statistically non-significant and that the quadratic model reliably represents the experimental data. Overall, the developed models are statistically significant, confirming that the chosen independent variables significantly influence the responses—specifically, the removal efficiencies of COD, BOD, NH_3–N, turbidity, and TDS.

Table 7: ANOVA for percentage removal of turbidity.

Source of variation	Degrees of freedom [DF]	Sum of squares [SS]	F-value	p-value
Regression	14	1619.40	60.43	0.000
Linear	4	954.18	124.61	0.000
Square	4	606.10	79.16	0.000
Interaction	6	59.11	5.15x	0.008
Residual error	12	22.97		
Lack of Fit	10	20.46	1.63	0.439
Pure Error	2	2.51		
Total	26	1642.37		

Table 8: ANOVA for percentage removal of TDS.

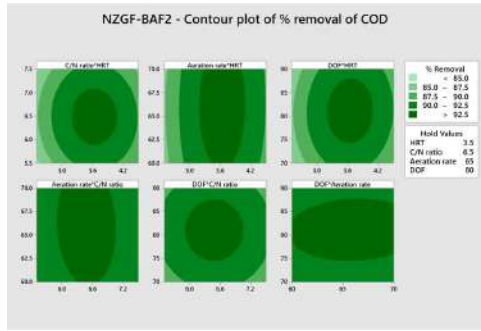
Source of variation	Degrees of freedom [DF]	Sum of squares [SS]	F-value	p-value
Regression	14	2109.27	33.58	0.000
Linear	4	1215.54	67.73	0.000
Square	4	716.78	39.94	0.000
Interaction	6	176.95	6.57	0.003
Residual error	12	53.84		
Lack of Fit	10	51.42	4.25	0.205
Pure Error	2	2.42		
Total	26	2163.11		

Table 9 displays the model summary for the removal efficiencies of COD, BOD, NH_3-N, turbidity, and TDS. The coefficient of determination (R^2) is a statistical metric that assesses how well a model explains the variability in the data. Higher R^2 values indicate better model fit. The models achieved R^2 values of 97.43%, 98.72%, 98.66%, 98.6%, and 97.5% for the removal of COD, BOD, NH_3-N, turbidity, and TDS, respectively. These high R^2 values demonstrate that the models effectively capture the variance in the percentage removal of each parameter. The adjusted R^2 values closely aligned with the R^2 values across all responses, indicating that the models are not overfitted and that the included factors are statistically significant. Similarly, the predicted R^2 values showed reasonable agreement with the adjusted R^2, confirming the models' good predictive ability. Although the predicted R^2 for COD (85.70%) and TDS (86.06%) was slightly lower than for other responses, they still fall within acceptable limits, indicating satisfactory external predictability.

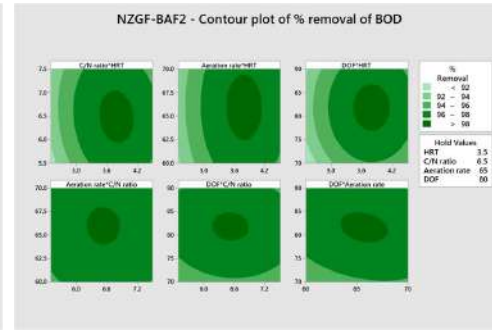
Contour plots derived from the experimental results were utilized to illustrate the responses generated by RSM. These plots depict the simultaneous effects of two variables or operational parameters on the responses. The specific correlations examined include HRT versus C/N ratio, rate of aeration versus C/N ratio, depth of filter versus C/N ratio,

Table 9: Model summary for percentage removal of COD, BOD, NH_3–N, turbidity, and TDS

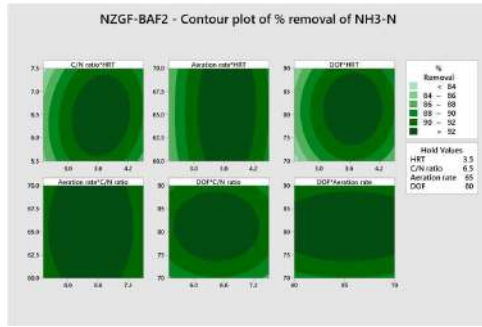
Model Summary for % removal of	Standard Deviation	R^2 [%]	Adjusted R^2 [%]	Estimated R^2 [%]
COD	1.83	97.43	94.42	85.70
BOD	1.32	98.72	97.23	93.16
NH_3–N	1.35	98.66	97.09	92.79
Turbidity	1.38	98.60	96.97	92.48
TDS	2.12	97.50	94.61	86.06



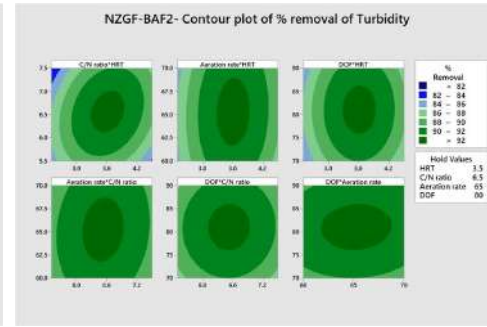
(a)



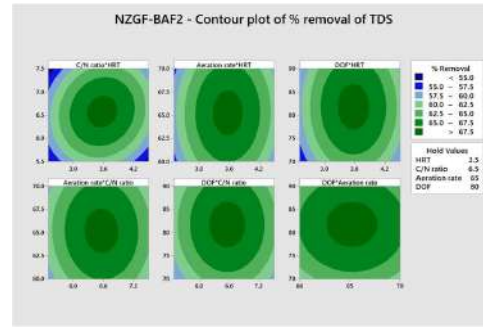
(b)



(c)



(d)



(e)

Fig. 8: Contour plot for percentage removal of (a) COD, (b) BOD, (c) NH_3–N, (d) turbidity, and (e) TDS.

rate of aeration versus HRT, depth of filter versus HRT, and depth of filter versus rate of aeration. These contour plots are shown in Fig. 8 (a–e).

The residual plots in RSM were analyzed to evaluate the adequacy of the model. The normal probability plots for various process parameters are displayed in Fig. 9 (a-e),

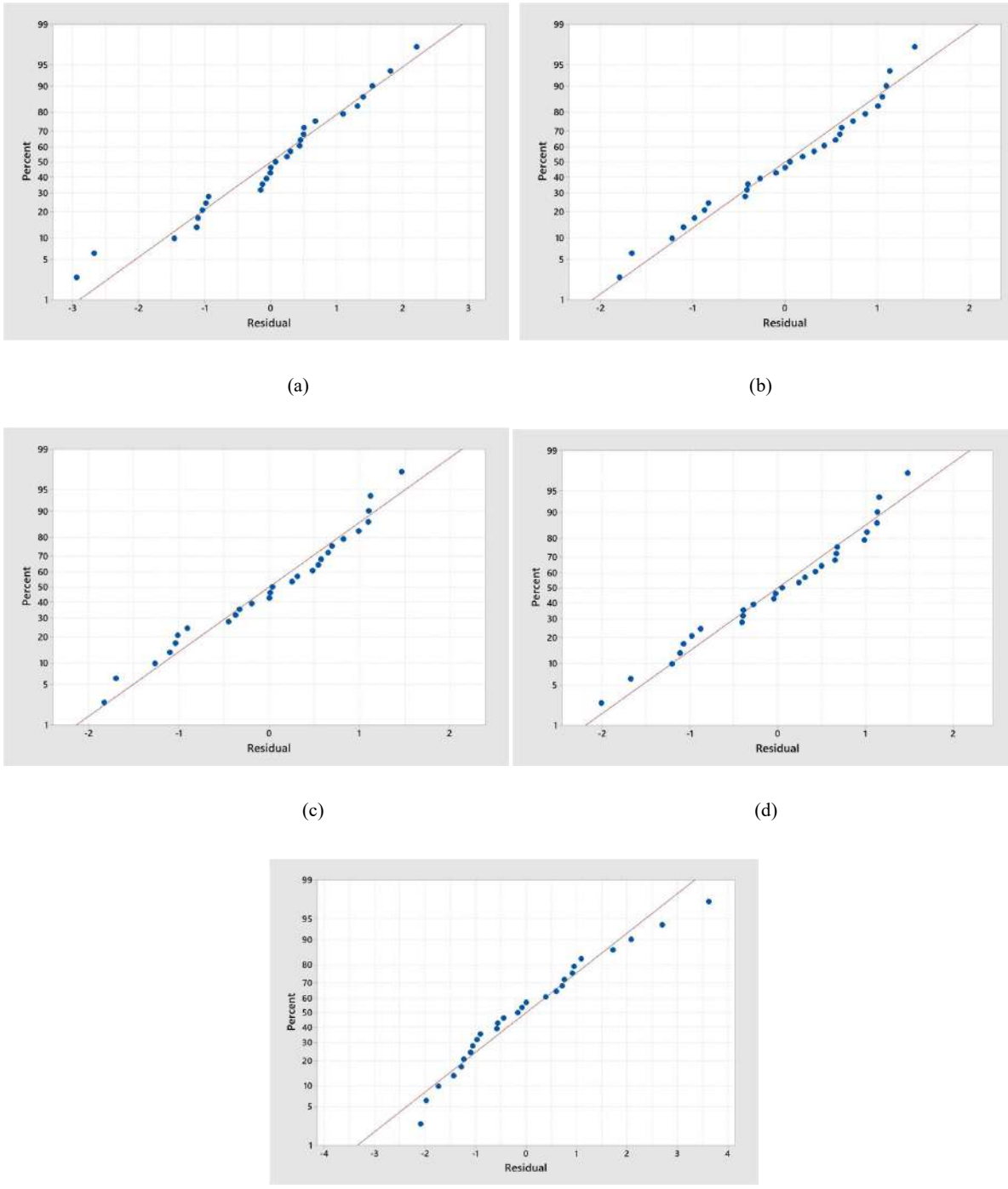


Fig. 9: Residual plot for removal of (a) COD, (b) BOD, (c) NH_3-N, (d) Turbidity and (e) TDS.

indicating that the residuals exhibit a linear pattern. This suggests that the residuals are roughly normally distributed, fulfilling a fundamental assumption of ANOVA and regression analysis.

3.3. Optimized Condition Validation

Based on the results obtained from the RSM optimizer, the maximum percentage removal was achieved for COD, BOD,

Table 10: Comparison of percentage removal for predicted values and experimental results for NZGF-BAF.

Percentage Removal	Process Parameters				
	COD	BOD	NH_3-N	Turbidity	TDS
Theoretically Predicted Value by RSM (%)	94	98	94	93	68
Experimental Value (%)	93	98	94	93	67

NH_3-N, turbidity, and TDS at 93%, 98%, 94%, 93%, and 68%, respectively, under conditions of 3.7 hours HRT, a C/N ratio of 6.5, an aeration rate of 66.2 $L.h^{-1}$, and a filter depth of 81.7 cm. An additional laboratory experiment was conducted under these optimal conditions predicted by the RSM model to evaluate the performance of NZGF-BAF. The final test was performed with the same parameters: HRT of 3.7 h, C/N of 6.5, aeration rate of 66.2 $L.h^{-1}$, and filter depth of 81.7 cm. The experimental results were analyzed and compared to the predicted removal efficiencies provided by the RSM model. These removal percentages are summarized in Table 10. This comparison allows for an assessment of how closely the experimental outcomes align with the model's predictions under optimal conditions. The accuracy of the RSM model in representing system performance can be evaluated by comparing the predicted and experimental data.

4. CONCLUSIONS

The effectiveness of a dual-media biologically aerated filter (BAF), comprising geo-fabric and natural zeolite (NZGF-BAF), was evaluated in this study in comparison to single-media BAFs containing either natural zeolite (NZ-BAF) or geo-fabric (GF-BAF). The performance of these BAF systems in greywater treatment depends on various operational parameters such as hydraulic retention time (HRT), carbon-to-nitrogen (C/N) ratio, aeration rate, and filter depth. The NZ-BAF, using natural zeolite particles of 1-3 mm, and the GF-BAF, with geo-fabric of 500 GSM, showed comparable results in removing COD, BOD, and turbidity. However, due to ion-exchange capabilities, NZ-BAF achieved higher removal of NH_3-N, while GF-BAF excelled in TDS removal owing to permeability, adsorption, biofilm formation, and bacterial activity within the finer pores of its media. The dual media filter, NZGF-BAF, promotes processes such as absorption, adsorption, ion exchange, and biofilm development, leading to enhanced contaminant removal. To optimize the treatment process, Response Surface Methodology (RSM) was employed to determine the optimal operational parameters—HRT, C/N ratio, aeration rate, and filter depth—for maximum removal efficiency of contaminants including COD, BOD, NH_3-N, turbidity, and TDS. Under optimized conditions (HRT of 3.7 hours, C/N ratio of 6.5, aeration rate of 66.2 $L.h^{-1}$, and filter depth of 81.7 cm), the NZGF-BAF system achieved removal efficiencies of 93% for COD, 98% for BOD, 94% for NH_3-N, 93% for turbidity, and 67% for TDS. These results demonstrate that the NZGF-BAF system has significant potential for efficient greywater treatment in controlled laboratory settings. Nevertheless, given the variability of actual greywater composition, further studies involving real greywater under practical conditions are necessary to validate its applicability in real-world scenarios.

5. REFERENCES

Adam, M.R., Othman, M.H.D., Hubadillah, S.K., Abd Aziz, M.H. and Jamalludin, M.R., 2023. Application of natural zeolite clinoptilolite for the removal of ammonia in wastewater. Materials Today: Proceedings, 9, p.72. [DOI]

Alimahmoodi, M., Yerushalmi, L. and Mulligan, C.N., 2012. Development of biofilm on geotextile in a new multi-zone wastewater treatment system for simultaneous removal of COD, nitrogen and phosphorus. Bioresource Technology, 107, pp.78-86. [DOI]

APHA 2017. Standard Methods for the Examination of Water and Wastewater (23rd ed.). American Public Health Association.

Bacquet, G., Joret, J.C., Rogalla, F. and Bourbigot, M.M., 1991. Biofilm start-up and control in aerated biofilter. Environmental Technology, 12(9), pp.747-756. [DOI]

Charchalac Ochoa, S.I., Ushijima, K., Hijikata, N. and Funamizu, N., 2015. Treatment of domestic greywater by geotextile filter and intermittent sand filtration bioreactor. Journal of Water Reuse and Desalination, 5(1), pp.39-49. [DOI]

Doelle, K., Qin, Y. and Wang, Q., 2020. Bio-tower application for wastewater treatment. Journal of Engineering Research and Reports, 11(1), pp.1-7. [DOI]

Fu, L.Y., Wu, C.Y., Zhou, Y.X., Zuo, J.E. and Ding, Y., 2016. Treatment of petrochemical secondary effluent by an up-flow biological aerated filter (BAF). Water Science and Technology, 73(8), pp.2031-2038. [DOI]

Huang, C., Shi, Y., El-Din, M.G. and Liu, Y., 2017. Performance of flocs and biofilms in integrated fixed-film activated sludge (IFAS) systems for the treatment of oil sands process-affected water (OSPW). Chemical Engineering Journal, 314, pp.368-377. [DOI]

Jacob, J., Le Lann, J.M., Pingaud, H. and Capdeville, B., 1997. A generalized approach for dynamic modelling and simulation of biofilters: Application to waste-water denitrification. Chemical Engineering Journal, 65(2), pp.133-143. [DOI]

Jasni, A.B., Kamyab, H., Chelliapan, S., Arumugam, N., Krishnan, S. and Din, M.F.M., 2020. Treatment of Wastewater Using Response Surface Methodology: A Brief Review. CET Journal-Chemical Engineering Transactions, 78, pp.615-632. [DOI]

Kent, T.D., Williams, S.C. and Fitzpatrick, C.S.B., 2000. Ammoniacal nitrogen removal in biological aerated filters: The effect of media size. Water and Environment Journal, 14(6), pp.409-414. [DOI]

Krzeminski, P., Iglesias-Obelleiro, A., Madebo, G., Garrido, J.M., Van Der Graaf, J.H.J.M. and Van Lier, J.B., 2012. Impact of temperature on raw wastewater composition and activated sludge filterability in full-scale MBR systems for municipal sewage treatment. Journal of Membrane Science, 423, pp.348-361. [DOI]

Lin, C.W., Yen, C.H., Lin, H.C. and Tran, D.T., 2010. Response surface optimization of dissolved oxygen and nitrogen sources for the biodegradation of MTBE and BTEX. Biodegradation, 21(3), pp.393-401. [DOI]

Mendoza-Espinosa, L. and Stephenson, T.O.M., 1999. A review of biological aerated filters (BAFs) for wastewater treatment. Environmental Engineering Science, 16(3), pp.201-216. [DOI]

Nacheva, P.M., Chávez, G.M., Zúñiga, M.G., Bustos, C. and Orozco, Y.H., 2008. Comparison of bioreactors with different kinds of submerged packed beds for domestic wastewater treatment. Water Science and Technology, 58(1), pp.29-36. [DOI]

Praveen, A., Sreelakshmy, P.B. and Gopan, M., 2008. Coir geotextile-packed conduits for the removal of biodegradable matter from wastewater. Current Science, 712, pp.655-658. [URL]

Qamaruz-Zaman, N., Yaacof, N. and Kamarzaman, F.F., 2020. The Interaction of Food Industry and Environment . Academic Press, pp. 281-313. [DOI]

Revathi, H.U. and Murthy, S., 2016. Treatment of domestic wastewater using geotextile as a filter media. International Research Journal of Engineering and Technology, 3, p.7. [URL]

Spychała, M., Błażejewski, R. and Nawrot, T., 2013. Performance of innovative textile biofilters for domestic wastewater treatment. Environmental Technology, 34(2), pp.157-163. [DOI]

Tan, H., 2008. An evaluation of biological aerated filtration for wastewater treatment through pilot and laboratory scale experiments. Master's Thesis, Queen's University, Kingston, ON, Canada, 2007.

Van De Staey, G., Smits, K. and Smets, I., 2015. An experimental study on the impact of bioflocculation on activated sludge separation techniques. Separation and Purification Technology, 141, pp.94-104. [DOI]

Widiastuti, N., Wu, H., Ang, H.M. and Zhang, D., 2011. Removal of ammonium from greywater using natural zeolite. Desalination, 277(1-3), pp.15-23. [DOI]

Xie, W., Wang, Q., Song, G., Kondo, M., Teraoka, M., Ohsumi, Y. and Ogawa, H.I., 2004. Upflow biological filtration with floating filter media. Process biochemistry, 39(6), pp.767-772. [DOI]

Nature Environment and Pollution Technology
An International Quarterly Scientific Journal

p-ISSN: 0972-6268
(Print copies up to 2016)
e-ISSN: 2395-3454

Vol. 25 | No. 3 | Article ID B4424 | 2026

Original Research Paper

https://doi.org/10.46488/NEPT.2026.v25i03.B4424

Open Access Journal

Geochemical Fractionation and Internal Loading of Phosphorus in Urban Lake Sediments in Coimbatore, Tamil Nadu, India

Durga M., Nandhini V., Sapna K. and Dhanakumar S.†
Department of Environmental Science, PSG College of Arts & Science, Coimbatore, 641014, Tamil Nadu, India
†Corresponding author: Dhanakumar S; ecodhanan.phd@gmail.com

Abbreviation: Nat. Env. & Poll. Technol.
Website: www.neptjournal.com

Received: 09-01-2026
Revised: 01-03-2026
Accepted: 03-03-2026

Key Words:

Phosphorus fractionation
Eutrophication
Ecological risk
Single pollution index

Citation for the Paper:

Durga, M., Nandhini, V., Sapna, K. and Dhanakumar, S., 2026. Geochemical fractionation and internal loading of phosphorus in urban lake sediments in Coimbatore, Tamil Nadu, India. *Nature Environment and Pollution Technology*, 25(3), B4424. https://doi.org/10.46488/NEPT.2026.v25i03.B4424

Note: From 2025, the journal has adopted the use of Article IDs in citations instead of traditional consecutive page numbers. Each article is now given individual page ranges starting from page 1.

Copyright: © 2026 by the authors
Licensee: Technoscience Publications
This article is an open access article distributed under the terms and conditions of the Creative Commons Attribution (CC BY) license (https://creativecommons.org/licenses/by/4.0/).

ABSTRACT

Phosphorus (P) is primarily released from sediments through the reduction of iron (Fe^{3+}) oxides under anoxic conditions, leading to the dissolution of Fe-bound phosphorus and an increase in dissolved phosphorus in lake water. This study aimed to quantify the major sedimentary phosphorus fractions and assess their ecological risks in Krishnampathy and Singanallur lakes in urban Coimbatore during the post-monsoon season. The sequential extraction method was used to analyze loosely sorbed exchangeable P (NH_4Cl-P), redox-sensitive P (Fe-P), metal oxide-bound P (NaOH-P), calcium-bound P (HCl-P), residual P (Res-P), and total phosphorus (TP). Fe-P and NaOH-P were identified as the dominant fractions in both lakes. Principal component analysis (PCA) was employed to explore the relationship between P fractions and sediment characteristics. Pollution levels, determined using the Single Pollution Index (SPI), were 2.07 for Krishnampathy and 2.14 for Singanallur, indicating serious pollution in both lakes. Surface water phosphorus concentrations were relatively lower, while the distribution of HCl-P and Fe-P was influenced by environmental and geochemical factors. The results suggest that both lakes are at risk of eutrophication. Identifying sedimentary P sources and evaluating ecological risks are crucial for effective restoration and management of these polluted water bodies.

1. INTRODUCTION

Phosphorus (P) is the most critical factor influencing primary productivity in aquatic environments. It is present in lake sediments and the water column, where it continuously undergoes transformation and cycling (Xie et al. 2019). Climate change and human activities exacerbate water scarcity, with the United Nations estimating a 40% shortfall in freshwater availability by 2030 if current trends persist (UN-Water 2023). Lakes and wetlands, vital freshwater sources, are increasingly threatened by eutrophication driven by phosphorus from agricultural runoff and urban pollution, leading to biodiversity loss and ecosystem disturbances (Sharpley et al. 2013, Zhang et al. 2016, Wu & Wang 2017).

Lakes are crucial freshwater ecosystems that offer vital services such as water storage, supporting biodiversity, climate regulation, and recreational activities. Nevertheless, they remain susceptible to nutrient overloads and sediment variations (Mitsch & Gosselink 2015, Rutledge & Chow-Fraser 2019). More than 70% of surface water is contaminated, mainly from agricultural and industrial runoff (CWC 2023). The government has prioritized the restoration of lakes and wetlands as part of sustainable water management efforts, acknowledging their significance in climate regulation and biodiversity preservation (MoEFCC 2023). Freshwater systems, including rivers and wetlands, play a key role in climate regulation, nutrient cycling, and ensuring economic and food security. They face threats from pollution, overextraction, and climate change, underscoring the importance of sustainable management practices (Falkenmark & Rockström 2004, Dingman 2015, Yuan et al. 2019, Camargo et al. 2025).

Sediments form through natural processes and are crucial in aquatic ecosystems by affecting the transport and concentration of pollutants in water bodies (Joshi et al. 2015, Dang et al. 2017, Wang et al. 2021). During deposition, sediments store phosphorus, which can be released under specific physicochemical conditions such as oxygen depletion, pH fluctuations, and changes in oxidation. As they accumulate in lakes and riverbeds, sediments can release pollutants that impact water quality even when external sources are controlled (Dhanakumar et al. 2015, Helfenstein et al. 2018). Additionally, sediments serve as historical records of environmental changes, offering insights into past climate conditions, ecosystem dynamics, and human activities—key for understanding climate change, detecting pollutants, and evaluating land use changes (Hupfer et al. 2019, Heinrich et al. 2021). Lakes, as dynamic ecosystems, play a vital role in global nutrient cycles, especially phosphorus. Eutrophication, primarily caused by untreated sewage, agricultural runoff, and other human activities, leads to elevated phosphorus levels (Parsons et al. 2017, Dhanakumar & Mohanraj 2019). This phenomenon affects roughly 30-40% of the world's freshwater lakes and reservoirs, resulting in biodiversity loss, habitat degradation, declines in fisheries, reduced food security, and economic challenges (Carpenter et al. 1988, Scheffer et al. 2001). Eutrophication also promotes harmful algal blooms, which pose significant health risks and economic costs (Dodds 2002, Paerl & Otten 2013, Wilfert et al. 2018).

Phosphorus diffusion between sediments and surrounding water is a crucial process that regulates internal nutrient cycling. Nutrient enrichment impacts phytoplankton communities, disturbs food webs, and decreases ecosystem resilience (Smith et al. 1999, Walpersdorf et al. 2013). Excess nutrients, particularly nitrogen and phosphorus stemming from agricultural practices, exacerbate eutrophication, leading to harmful algal blooms and ecological disruptions (Anderson et al. 2002, Galloway et al. 2003, Dhanakumar & Mohanraj 2013). Phosphorus present in lake sediments exists in various organic and inorganic forms, each influencing its bioavailability and mobility (Kraal et al. 2017). Sediments act as both a sink and a source of phosphorus, contributing to internal loading that sustains eutrophic conditions even when external inputs decrease (Lijklema et al. 1993, Søndergaard et al. 1996, Rippey et al. 2021). Biogeochemical processes, including redox shifts and pH fluctuations, affect phosphorus release, while climatic factors like temperature and hydrological changes further modulate its behavior (Lepori & Roberts 2015, Saar et al. 2022). For this research, understanding these interactions is vital for designing strategies to mitigate eutrophication and enhance water quality (Wang et al. 2018a, 2018b). Eutrophication remains a significant challenge in lake management worldwide, mainly driven by human activities such as agricultural runoff and urbanization, which elevate phosphorus inputs in water bodies, leading to algal blooms tied to nutrient enrichment, particularly when iron- and manganese-bound phosphorus (Fe-P and NaOH-P) is released into the water column during anoxic conditions in bottom waters (Paerl & Otten 2013, Huang et al. 2020, Lepori & Robert 2015).

Chemical fractionation involves a sequence of extraction steps that depend on how different solid phases react to various extractant solutions (Voegelin et al. 2013). Among the phosphorus fractions, NH_4Cl-P acts as a short-term indicator of phosphorus availability for aquatic organisms (Ajmal et al. 2018). NaOH-P is released into the water column under anaerobic conditions caused by eutrophication, while sediment-bound phosphorus is regarded as a long-term sink for phosphorus (Gérard 2016). HCl-P signifies phosphorus bound to organic matter, which can be liberated through microbial activity. Changes in redox conditions can mobilize phosphorus from its long-term storage form, bound to metal oxides (Li et al. 2015, Barik et al. 2019). Total phosphorus (TP), encompassing both organic and inorganic forms, is used to assess the overall phosphorus content in sediments and their impact on nutrient levels in the water column (Turner et al. 2005, Reddy et al. 2022). Effective lake management and restoration require a comprehensive understanding of these processes, as phosphorus dynamics and water quality are heavily influenced by both internal loading from sediments and external loading from catchment run-off. This study aims to investigate the relationships between various phosphorus fractions and the physico-chemical properties of lake sediments.

2. MATERIALS AND METHODS

2.1. Description of Study Area

Coimbatore is the leading industrial hub in South India. It is situated between 10°55' and 11°10' N latitude and 77°50' and 76°50' E longitude at an elevation of approximately 470 m above sea level. Located along the Noyyal River and encircled by the Western Ghats, the region features around 28 wetlands predominantly fed by the Noyyal River. Sediment samples were collected from two wetlands: Krishnampathy Lake and Singanallur Lake. Krishnampathy Lake, located in the western part of Coimbatore, spans 61 acres and is part of a series of lakes connected to the Noyyal River. Singanallur Lake, situated in Singanallur, covers 1.153 km² with an average depth of 4.25 m. It is divided into two sections: the southern half receives rainwater, while the northern half manages urban and industrial waste (Fig.1).

2.2. Sediment Sampling and Analysis

During the post-monsoon season of 2023, ten sediment samples were collected from each of the Krishnampathy and Singanallur lakes. The top sediment layer, approximately 5 cm thick and situated beneath about 20 cm of water, was gathered using a spade, placed in pre-washed polyethene bags and bottles, and promptly transported to the laboratory. In the lab, the samples were shade-dried at room temperature, ground, and sieved through a 2 mm mesh. The sieved samples were then oven-dried overnight at 108°C to eliminate moisture. A 1:5 sediment-to-water suspension was prepared for pH and electrical conductivity (EC) measurements using potentiometry. Alkalinity was determined via titration with 0.02 N sulfuric acid employing phenolphthalein as an indicator (APHA 2320 B), and chloride concentration was assessed by argentometric titration in the sediment samples, reported as $mg.L^{-1}$ of extract solution following aqueous extraction—these do not reflect bulk sediment chloride content (APHA 4500-Cl-B 2017). Calcium and magnesium levels were analyzed through complexometric titration using the Versanate (EDTA) method. Total organic carbon (TOC) was estimated using the Walkley and Black (1934) method, while total nitrogen (TN) was measured following the procedure described by Jackson et al. (2005).

The alkaline permanganate method was employed to quantify ammoniacal nitrogen. Available phosphorus was extracted using Olsen's method with a sodium bicarbonate solution at pH 8.5, and it was measured spectrophotometrically via the ascorbic acid method. Total phosphorus was determined by molybdenum blue colorimetry after perchloric acid digestion (Grimshaw 1987). Total potassium was measured using a flame photometer after extraction with hydrochloric acid, while available potassium was extracted with neutral ammonium acetate. The cation exchange capacity (CEC) was assessed using the ammonium acetate method as described by Raman and Sathiyanarayanan (2009).

2.3. Multivariate Statistical Analysis

Statistical analysis was performed using IBM SPSS Statistics for Windows, Version 20.0 (IBM Corp., Armonk, NY, USA). The study employed multivariate statistical techniques, including descriptive statistics and Principal Component Analysis (PCA).

2.4. Sequential Extraction Method

Different forms of phosphorus, including readily available, organic, and mineral-bound phosphorus, can be more effectively evaluated concerning soil fertility and environmental concerns such as eutrophication. The sequential extraction method is a laboratory procedure that isolates various phosphorus (P) fractions in sediments using different chemical reagents. This technique, first introduced by Psenner et al. (1984) and subsequently refined by Hupfer

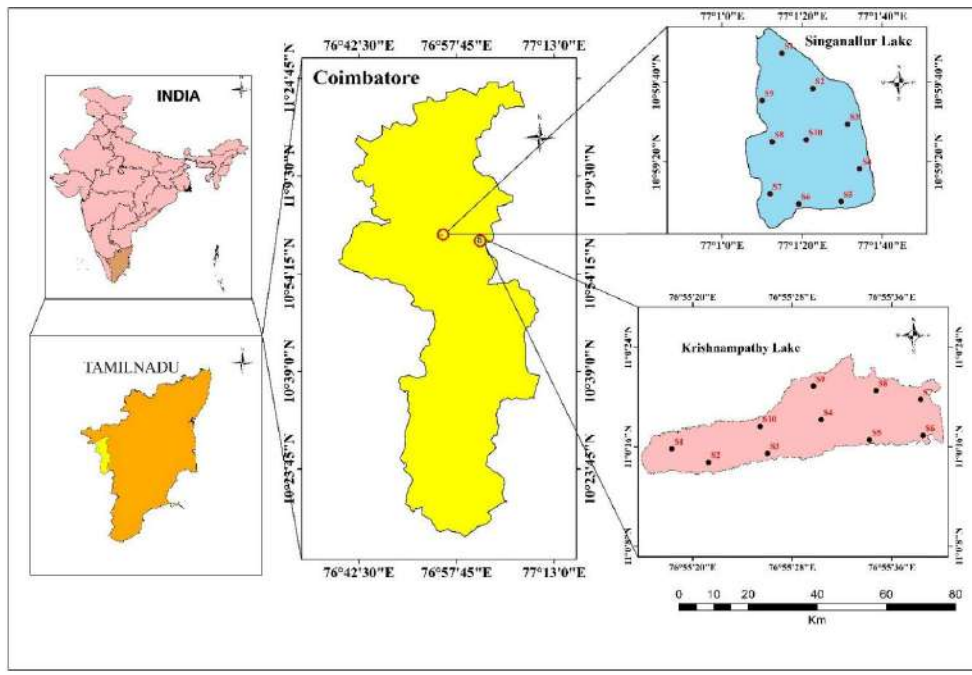


Fig. 1: Study area showing sediment sampling locations in Krishnampathy and Singanallur Lakes.

et al. (1995), improves the extraction process to achieve more accurate phosphorus fractionation. To perform the analysis, 1 gram (1 g) of dry sediment was weighed and placed into a conical flask. Then, 25 mL of 1 M NH4Cl was added, and the mixture was shaken for 2 h. The solution was transferred to a centrifuge tube and centrifuged at 8,000 RPM for 10 minutes. A 10 mL aliquot of the supernatant was collected, to which 2 mL of chloromolybdic acid and a few drops of chlorostannous reductant were added. After 10 minutes, a blue coloration developed, which was then measured spectrophotometrically at 690 nm. This procedure was repeated for subsequent extractants, with slight variations: shaking for 2 h with 1 M NH4Cl, 1 hour with 0.11 M Na-HCO_3/$Na_2S_2O_4$, and 16 h with 0.1 M NaOH and 0.5 M HCl.

2.5. Pollution Assessment

The ecological risk was assessed using a single pollution index based on total phosphorus levels. This index calculates the pollution level within the research area through equation (1). Such an approach allows for quantifying the ecological impact of phosphorus contamination and identifying potential environmental hazards.

$$S_{TP} = \frac{C_{TP}}{C_S} \quad \ldots(1)$$

STP represents the single pollution index, CTP refers to a specific concentration of Total Phosphorus (TP), and CS denotes the standard phosphorus concentration aligned with safe nutrient limits as specified in sediment quality guidelines (SQGs) (Younis et al. 2022). The recommended maximum TP concentration is 600 $\mu g.g^{-1}$, which could pose ecological risks (Barik et al. 2016). Based on the STP index value, Table 1 categorizes risks into four distinct levels.

3. RESULTS AND DISCUSSION

3.1. Descriptive Statistics of Krishnampathy and Singanallur Lakes Sediments

3.1.1. Krishnampathy Lake

Sediment pH ranges from 7.40 to 8.10, with an average of 7.81. These values are characteristic of freshwater systems with carbonate buffering, and they considerably impact microbial activity, metal distribution, and nutrient solubility within sediments (Sayeed et al. 2015). Salinity and ionic concentration, assessed via electrical conductivity (EC), vary from 330 to 800 $\mu S.cm^{-1}$. The sediment alkalinity, ranging from 54.00 to 176.00 $mg.g^{-1}$ as $CaCO_3$, reflects the lake's buffering capacity, primarily due to bicarbonate and carbonate ions. The relatively high alkalinity supports the alkaline pH and indicates a well-buffered aquatic environment. Elevated chloride (Cl) levels, with an average of 168.29 $mg.L^{-1}$ (Table 2), could influence sediment chemistry by modifying ionic interactions and promoting nutrient release from sediment particles. This may also suggest anthropogenic influences such as domestic wastewater or agricultural runoff.

Calcium (Ca) and Magnesium (Mg) are vital bivalent cations, with mean concentrations of 2.46 and 1.34 $mg.L^{-1}$, respectively. The Total Organic Carbon (TOC) varied considerably from 0.3 to 2.43%, averaging 1.45%, indicating a moderate presence of organic matter in the sediment samples. TOC significantly influences microbial activity, sediment quality, and the attachment and movement of nutrients and contaminants. The relatively high organic carbon level points to active detrital input, likely originating from algal production, aquatic plants, and terrestrial runoff (Meyers & Ishiwatari 1993).

Available phosphorus (AP), a crucial macronutrient, exhibits significant variability with concentrations ranging from 311.86 to 791.50 $mg.kg^{-1}$. Its elevated levels are influenced by external sources such as domestic wastewater discharge and agricultural fertilizer application, as well as internal loading processes where phosphorus is released

Table 1: Criteria and factors to evaluate the ecological risk.

Risk level	Value	Pollution assessment
Level I	$S_{TP} < 0.5$	Clean
Level II	$0.5 \leq S_{TP} < 1$	Slightly polluted
Level III	$1 \leq S_{TP} < 1.5$	Moderately polluted
Level IV	$1.5 \leq S_{TP}$	Seriously polluted

(Source: Barik et al. 2016, Younis et al. 2022)

Table 2: Descriptive statistics of sediment characteristics in Krishnampathy Lake.

Parameters	Min	Max	Mean
pH	7.40	8.10	7.81
Electrical conductivity [$\mu S.cm^{-1}$]	330	800	525
Alkalinity [$mg.g^{-1}$ as $CaCO_3$]	54.00	176.00	93.15
Chloride extract concentration [$mg.L^{-1}$]	16	502.52	168.29
Calcium in sediment extract [$mg.L^{-1}$]	1.61	4.26	2.46
Magnesium in sediment extract [$mg.L^{-1}$]	0.97	1.81	1.34
Total organic carbon [%]	0.30	2.43	1.45
Available Phosphorus [$mg.kg^{-1}$]	311.86	791.50	690
Total Phosphorus [$mg.kg^{-1}$]	1125	1417.5	1274.65
Total potassium [$mg.kg^{-1}$]	3500	5100	4200
Available potassium [$mg.kg^{-1}$]	2101.12	2505.44	2275.53
Ammoniacal Nitrogen [$mg.kg^{-1}$]	0.80	4.20	2.99
Total Kjeldhal Nitrogen [$mg.kg^{-1}$]	2.80	4.48	3.58
Cation exchange capacity [$cmoL^{+}.kg^{-1}$]	1.64	6.83	3.99

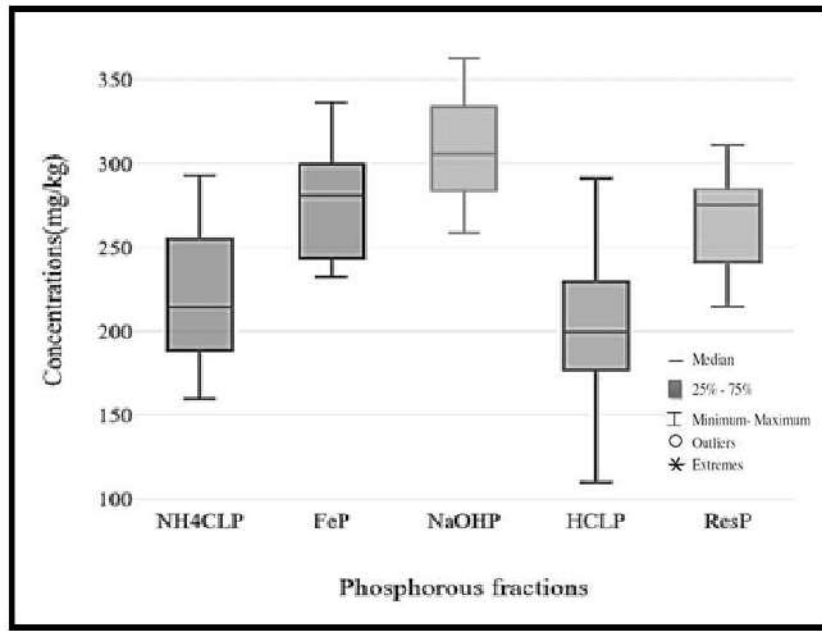


Fig. 2: Phosphorus fractionation concentration mg.kg^{-1} in Krishnampathy Lake.

from sediments under anoxic conditions (Song et al. 2017). Phosphorus predominantly exists in readily available or loosely bound forms rather than in stable, mineralized states, as reflected by the relatively low average total phosphorus (TP) level of 1,274.65 mg.kg^{-1}, with observed values between 1,125 and 1,417.5 mg.kg^{-1}.

The average total potassium (TK) content in the sediments was 4200 mg.kg^{-1}, while the available potassium (AK) varied from 2101.12 to 2505.44 mg.kg^{-1}. The mean concentrations of ammoniacal nitrogen (AN) and Total Kjeldahl Nitrogen (TKN) were recorded as 2.99 and 3.58 mg.kg^{-1}, respectively, indicating the presence of both inorganic and organic nitrogen forms within the sediments. The sediment cation exchange capacity (CEC) ranged from 1.64 to 6.83 cmoL^{+}.kg^{-1}, suggesting a low to moderate potential for nutrient retention. Lower CEC values, often associated with sandy textures, reduced clay content, and limited organic matter, may hinder the sediment's ability to retain essential exchangeable cations such as K^{+}, Ca^{2+}, and Mg^{2+}. Variations in CEC also likely reflect differences in clay mineral composition, organic matter content, and redox-sensitive metal oxides present in the sediments. The analysis of phosphorus fractionation in the sediments offers valuable insights into nutrient mobility and the risk of eutrophication. The distribution of various phosphorus fractions (NH_4Cl-P, Fe-P, NaOH-P, HCl-P, and Res-P) in sediment samples from Krishnampathy Lake is depicted in the box plot shown in Fig. 2.

The NH_4Cl-P, representing readily available phosphorus, ranged from 159.5 to 293.00 mg.kg^{-1}. The highest value suggests the existence of localized hotspots with the potential to release substantial amounts of phosphorus into the upper water layers. This indicates that Krishnampathy Lake remains susceptible to eutrophication, even if external nutrient inputs are managed. The average NH_4Cl-P concentration of 221.13 mg.kg^{-1}, which is widely distributed, reflects variations within this fraction. According to Nishigaki et al. (2018), the lack of dissolved oxygen in water under static or stratified conditions specifically enhances internal nutrient loading. A significant portion of phosphorus is associated with iron oxides, as evidenced by iron-bound phosphorus, which remains potentially bioavailable—especially in reducing conditions where Fe^{3+} reduces to Fe^{2+}, leading to phosphate release into the water column (Xiang et al. 2011). The

Table 3: Mass balance of phosphorus fractions in Krishnampathy Lake sediments.

Parameter	Mean [mg.kg^{-1}]
NH_4Cl–P	221.83
BD–P	278.28
NaOH–P	308.08
HCl–P	202.13
Residual–P	266.52
Sum of Fractions	**1276.84**
Measured TP [Mean]	**1274.65**
Recovery [%]	**100.17%**

distribution of phosphorus fractions in Krishnampathy Lake sediments is summarized in Table 3.

Fe-P concentrations ranged from 232.5 to 336.25 $mg.kg^{-1}$, with an average of 278.68 $mg.kg^{-1}$, indicating phosphorus bound to iron and manganese oxides. Under reducing or anoxic conditions, the reduction of Fe^{3+} and Mn^{4+} to Fe^{2+} and Mn^{2+} facilitates the dissolution of these oxides, leading to the release of bound phosphorus into the overlying water. The relatively high Fe–P levels suggest a significant potential for internal phosphorus loading during periods of low oxygen availability in bottom waters.

Phosphorus associated with humic substances and amorphous aluminum oxides (NaOH–P) exhibited a minimum concentration of 232.50 $mg.kg^{-1}$. This moderately bioavailable fraction can be mobilized through microbial activity, thereby contributing to sustained internal phosphorus loading. HCl–P associated with carbonate and apatite minerals ranged from 110 to 291 $mg.kg^{-1}$. Although this fraction is generally considered stable and less bioavailable, sediment acidification can enhance its solubility and promote phosphorus release into the water column.

Residual phosphorus, predominantly comprising mineral-bound and refractory organic forms, ranged from 214.72 to 311.25 $mg.kg^{-1}$. This indicates a dominance of immobile phosphorus with limited immediate ecological impact. Although mostly non-labile, extended acidification, diagenetic processes, or microbial degradation could gradually increase its mobilization over extended timescales (Cavalcante et al. 2018, Mina Kiani et al. 2023).

TP was observed at a minimum of 1125 $mg.kg^{-1}$ and a maximum of 1417.5 $mg.kg^{-1}$, with an average of 1274.65 $mg.kg^{-1}$. The relatively higher concentrations of NaOH-P and Fe-P suggest that iron- and aluminum-bound phosphorus forms dominate, reflecting potential internal phosphorus loading under reducing conditions. The sediments of the study area location are not only nutrient storage areas, but also potential sources of phosphorus release, as they contain multiple phosphorus forms that can become mobilized under certain environmental conditions. Res-P reflects diverse phosphorus retention in residual forms. The results suggest that the two most common phosphorus fractions in the sediment are NaOH-P and Fe-P, possibly indicating a significant contribution from iron-bound and bioavailable phosphorus. Res-P and NH_4Cl-P are attributed to contributions from recalcitrant and removable phosphorus sources, respectively. The decreased concentration of HCl-P suggests that phosphorus has minimal interaction with carbonate-bound components.

3.1.2. Singanallur Lake

The sediment pH of Singanallur Lake varies from 7.81 to 8.43, with an average of 8.12, indicating slightly alkaline conditions typical of freshwater systems. Such conditions generally promote the precipitation of certain metal ions and phosphorus compounds, influencing nutrient cycling and availability within the sediment (Wu et al. 2014). The freshwater quality of the lake is confirmed by an electrical conductivity with a mean value of 461 $\mu S.cm^{-1}$. Alkalinity ranges from 21.00 to 73.50 $mg.g^{-1}$ as $CaCO_3$. The average chloride (Cl^-) concentration in sediments is 320.77 $mg.L^{-1}$, suggesting significant external inputs rather than retention, as chloride is a highly mobile and conservative ion (Li et al. 2012). The mean concentrations of calcium (Ca) and magnesium (Mg) are 59.48 $mg.L^{-1}$ and 3.20 $mg.L^{-1}$, respectively. Sediments contain a moderate amount of organic carbon, ranging from 0.34 to 2.58%. The average available phosphorus (AP) is 741.01 $mg.kg^{-1}$,

Table 4: Descriptive statistics of sediment characteristics in Singanallur Lake.

Parameters	Minimum	Maximum	Mean
pH	7.81	8.43	8.12
Electrical conductivity [$\mu S.cm^{-1}$]	260	750	461
Alkalinity [$mg.g^{-1}$ as $CaCO_3$]	21.00	73.50	49.35
Chloride extract concentration [$mg.L^{-1}$]	187.11	503.27	320.77
Calcium in sediment extract [$mg.L^{-1}$]	31.18	100.17	59.48
Magnesium in sediment extract [$mg.L^{-1}$]	1.07	7.51	3.20
Total organic carbon [%]	0.34	2.58	1.66
Available Phosphorus [$mg.kg^{-1}$]	294.78	1118.2	741.01
Total Phosphorus [$mg.kg^{-1}$]	1125	1582.5	1287.25
Total potassium [$mg.kg^{-1}$]	3800	5700	5000
Available potassium [$mg.kg^{-1}$]	1800.12	2576.84	2052.54
Ammoniacal Nitrogen [$mg.kg^{-1}$]	3.92	24.64	11.87
Total Kjeldhal Nitrogen [$mg.kg^{-1}$]	11.57	31.14	21.16
Cation exchange capacity [$cmoL^+.kg^{-1}$]	1.82	6.22	3.04

while the total phosphorus (TP) averages 1287.25 mg.kg^{-1}, with a range of 1125 to 1582.5 mg.kg^{-1} (Table 4). Total potassium (TK) has a mean of 5000 mg.kg^{-1}, with values between 3800 and 5700 mg.kg^{-1}. Available potassium (AK) levels vary from 1800.12 to 2576.84 mg.kg^{-1}, averaging 2052.54 mg.kg^{-1}. Ammoniacal nitrogen (AN) ranges from 3.92 to 24.64 mg.kg^{-1}, with a mean of 11.87 mg.kg^{-1}. Total Kjeldahl nitrogen (TKN) ranges from 11.57 to 31.14 mg.kg^{-1}. The cation exchange capacity (CEC) distribution is notably high, with an average of 3.04 cmoL^{+}.kg^{-1} and minimal variation, indicating consistent sediment nutrient retention capacity. The distribution of various phosphorus fractions (NH_4Cl-P, Fe-P, NaOH-P, HCl-P, and Residual-P) in Singanallur Lake sediments is illustrated in the box plot in Fig. 3.

The NH_4Cl-P fraction represents loosely sorbed, exchangeable phosphorus that is highly bioavailable and easily exchanged with the water column. Its average concentration of 204.48 mg.kg^{-1} indicates a significant risk of eutrophication, particularly under low-oxygen conditions (Mahmood et al. 2020). Elevated levels of this phosphorus form suggest a strong potential for resuspension, which can rapidly promote algal blooms, especially in warm, stagnant waters typical of urban lakes. The Fe-P fraction has a minimum observed concentration of 255.75 mg.kg^{-1}. It is sensitive to redox fluctuations and can contribute to internal phosphorus loading by releasing phosphorus into the water column during anoxic conditions (Xu et al. 2014).

The NaOH-P fraction exhibited the highest average concentration at 341.18 mg.kg^{-1} and is primarily associated with organic matter and aluminum compounds. It is moderately bioavailable and somewhat sensitive to

Table 5: Mass balance of phosphorus fractions in Singanallur Lake sediments.

Parameter	Mean [mg.kg^{-1}]
NH_4Cl–P	204.48
BD–P	285.33
NaOH–P	341.19
HCl–P	246.70
Residual–P	269.62
Sum of Fractions	**1347.31**
Measured TP [Mean]	**1347.31**
Recovery [%]	**100.00%**

environmental factors such as pH, redox potential, oxygen levels, and microbial activity. Its release is driven by biogeochemical changes within the sediment (Jiang et al. 2006). The HCl-P fraction, reaching a maximum of 287.50 mg.kg^{-1}, tends to be more stable and less bioavailable. The residual phosphorus fraction, averaging 269.62 mg.kg^{-1}, contains refractory organic and mineral-bound forms that are largely unavailable for biological uptake and reflects long-term phosphorus sequestration. A significant portion of phosphorus exists in potentially mobile forms—NH_4Cl-P, Fe-P, and NaOH-P—indicating their sensitivity to environmental changes (Bańkowska-Sobczak et al. 2020). Although this residual fraction does not directly contribute to eutrophication, it signifies historical nutrient accumulation and the geochemical evolution of the sediment.

NaOH-P exhibits the highest mean concentration, signifying a high availability of phosphorus with minimal variation. In contrast, Fe-P's higher median value and

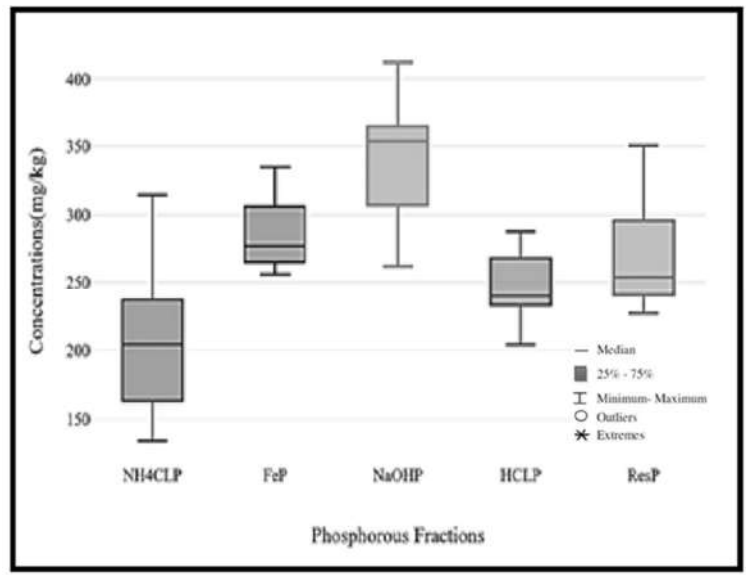


Fig. 3: Phosphorus fractionation concentration mg.kg^{-1} in Singanallur Lake.

wider distribution indicate greater variability in phosphorus content associated with iron minerals. The lowest mean concentration observed in NH_4Cl-P suggests limited amounts of exchangeable phosphorus. The variability of phosphorus related to carbonate is demonstrated by the broader spread and lower mean of HCl-P. Residual phosphorus (Res-P) shows a wide range and an average value, implying that a substantial portion of phosphorus is retained in residual forms across samples with differing concentrations.

Previous studies indicated that sediment phosphorus was predominantly found in the NaOH-P fraction, with total phosphorus (TP) concentrations between 1125 and 1582.5 $mg.kg^{-1}$. Similar findings were reported in Krishnampathy Lake (Søndergaard et al. 2003). Singanallur Lake experiences a greater influx of nutrients than Krishnampathy Lake, suggesting a more significant influence from human activities, including non-point sources like construction debris and household solid waste. The phosphorus fractions' mass balance in Singanallur Lake sediments is detailed in Table 5.

Ecological risk assessment using the single pollution index confirms significant pollution in both lakes, with STP values exceeding level IV (2.07 and 2.14, respectively), indicating high contamination and serious environmental concerns (Younis et al. 2022).

4. CONCLUSIONS

Lake management strategies must be tailored to each site due to the differing ecological and environmental impacts. The management plan for Krishnampathy Lake should prioritize stabilizing Fe-bound phosphorus through reducing internal nutrient loading and limiting organic matter deposition. In contrast, addressing Singanallur Lake's issues involves minimizing external nutrient inputs by improving stormwater management, enhancing wastewater treatment, and promoting greater community involvement. Both urban lakes require targeted restoration efforts and ongoing sediment monitoring to combat eutrophication, restore ecological balance, and preserve water quality.

A comparative evaluation of Singanallur and Krishnampathy Lakes highlights distinct sedimentary and biogeochemical regimes that influence nutrient dynamics. These regimes affect ecosystem functions through the distribution of phosphorus and sediment characteristics. Both lakes exhibit significant phosphorus contamination, especially in NaOH-P and Fe-P fractions, which can degrade water quality under anoxic conditions. Singanallur sediments show higher correlations among total phosphorus, ammoniacal nitrogen, and available phosphorus, but weaker inter-fractional coherence, indicating active internal nutrient recycling. The littoral zones experience greater nutrient mobility due to frequent disturbances and surface inputs, whereas benthic zones maintain more stable, redox-driven phosphorus dynamics, emphasizing the differences between shallow and deep sediment processes. Sediment Pollution Index values categorize both lakes as seriously polluted, with Singanallur affected by external inputs and internal recycling, while Krishnampathy is mainly regulated by Fe–Ca interactions.

Nitrogen cycling and sediment dynamics highlight the importance of site-specific management approaches. Restoration should focus on internal loading pathways by minimizing organic matter and ammoniacal inputs to reduce phosphorus remobilization in Singanallur, and on maintaining oxic bottom conditions to stabilize Fe-bound phosphorus in Krishnampathy. This research offers a scientific foundation for developing targeted eutrophication control strategies based on sediment geochemistry. Implementing these measures will strengthen the resilience of urban freshwater systems, support ecological stability, and protect biological integrity. Without proactive intervention, nutrient enrichment risks accelerating harmful algal blooms, thereby jeopardizing ecosystem health and resilience.

5. ACKNOWLEDGMENTS

The authors thank the PSG College of Arts and Science, Coimbatore, for the support rendered for this research work.

6. REFERENCES

Ajmal, Z., Muhmood, A., Usman, M., Kizito, S., Lu, J., Dong, R. and Wu, S., 2018. Phosphate removal from aqueous solution using iron oxides: adsorption, desorption and regeneration characteristics. *Journal of Colloid and Interface Science*, 528, pp.145-155. [DOI]

American Public Health Association (APHA), American Water Works Association (AWWA), & Water Environment Federation (WEF). (2023). Standard Methods for the Examination of Water and Wastewater (24th ed.). Method 2320 B: Titration Method. APHA, AWWA, WEF, Washington, DC.

American Public Health Association, American Water Works Association, & Water Environment Federation. (2017). Standard Methods for the Examination of Water and Wastewater (23rd ed.). APHA, AWWA, & WEF.

Anderson, D.M., Glibert, P.M. and Burkholder, J.M., 2002. Harmful algal blooms and eutrophication: nutrient sources, composition, and consequences. *Estuaries*, 25(4), pp.704-726. [DOI]

Bańkowska-Sobczak, A., Blazejczyk, A., Eiche, E., Fischer, U. and Popek, Z., 2020. Phosphorus inactivation in lake sediments using calcite materials and controlled resuspension—Mechanism and efficiency. *Minerals*, 10(3), p.223. [DOI]

Barik, S.K., Bramha, S., Bastia, T.K., Behera, D., Mohanty, P.K. and Rath, P., 2019. Distribution of geochemical fractions of Phosphorus and its ecological risk in sediment cores of the largest brackish water lake, South Asia. *International Journal of Sediment Research*, 34(3), pp.251-261. [DOI]

Camargo Hinostroza, S.D., Taza Rojas, C.A., Poma Limache, D.L. and

Poma Romero, C.J., 2025. Determination of the Water Quality Index (ICA-PE) of Lake Chinchaycocha, Junín, Peru. *Nature Environment & Pollution Technology*, 24(2), p.16.

Carpenter, S.R., Caraco, N.F., Correll, D.L., Howarth, R.W., Sharpley, A.N. and Smith, V.H., 1988. Nonpoint pollution of surface waters with phosphorus and nitrogen. *Ecological Applications*, 8(3), pp.559-568. [DOI]

Cavalcante, H., Araújo, F., Noyma, N.P. and Becker, V., 2018. Phosphorus fractionation in sediments of tropical semiarid reservoirs. *Science of the Total Environment*, 619, pp.1022-1029. [DOI]

Central Water Commission 2023. *Annual Report 2022–2023*. Department of Water Resources, River Development and Ganga Rejuvenation, Ministry of Jal Shakti, Government of India. Available at https://cwc.gov.in/sites/default/files/annual-report-cwc-2022-23_2.pdf

Dang, C., Lu, M., Mu, Z., Li, Y., Chen, C., Zhao, F., Yan, L. and Cheng, Y., 2017. Phosphorus fractions in the sediments of Yuecheng Reservoir, China. *Water*, 11(12), p.2646. [DOI]

Dhanakumar, S. and Mohanraj, R., 2013. Fractionation of iron in river-bed sediments: Implications for the assessment of environmental integrity of the Cauvery delta region, India. In: *On a Sustainable Future of the Earth's Natural Resources*. Berlin, Heidelberg: Springer Berlin Heidelberg, pp.123-137. [DOI]

Dhanakumar, S. and Mohanraj, R., 2019. Chromium fractionation in the river sediments and its implications on the coastal environment: a case study in the Cauvery Delta, Southeast Coast of India. In: *Coastal Zone Management*. Elsevier, pp.347-360. [DOI]

Dhanakumar, S., Rutharvel Murthy, K., Mohanraj, R., Kumaraswamy, K. and Pattabhi, S., 2015. Phosphorous fractionation in surface sediments of the Cauvery Delta region, Southeast India. In: *Environmental Management of River Basin Ecosystems*. Cham: Springer International Publishing, pp.477-489. [DOI]

Dingman, S.L., 2015. *Physical Hydrology*. Waveland Press.

Dodds, W.K., 2002. *Freshwater Ecology: Concepts and Environmental Applications*. Elsevier.

Falkenmark, M. and Rockström, J., 2004. *Balancing Water for Humans and Nature: The New Approach in Ecohydrology*. Earthscan.

Galloway, J.N., Aber, J.D., Erisman, J.W., Seitzinger, S.P., Howarth, R.W., Cowling, E.B. and Cosby, B.J., 2003. The nitrogen cascade. *BioScience*, 53(4), pp.341-356. [DOI]

Gérard, F., 2016. Clay minerals, iron/aluminum oxides, and their contribution to phosphate sorption in soils—A myth revisited. *Geoderma*, 262, pp.213-226. [DOI]

Grimshaw, H. M. (1987). The determination of total phosphorus in soils by acid digestion. In *ITE Symposium* (No. 18, pp. 92-95). NERC/ITE.

Heinrich, L., Rothe, M., Braun, B. and Hupfer, M., 2021. Transformation of redox-sensitive to redox-stable iron-bound phosphorus in anoxic lake sediments under laboratory conditions. *Water Research*, 189, p.116609. [DOI]

Helfenstein, J., Tamburini, F., von Sperber, C., Massey, M.S., Pistocchi, C., Chadwick, O.A., Vitousek, P.M., Kretzschmar, R. and Frossard, E., 2018. Combining spectroscopic and isotopic techniques gives a dynamic view of phosphorus cycling in soil. *Nature Communications*, 9(1), p.3226. [DOI]

Huang, L., Sheng, R., Li, Z., Sun, D. and Yan, N., 2020. Comparison of phosphorus fraction in eutrophic lake sediments from the northern hemisphere. *Chemistry and Ecology*, 36(2), pp.100-121. [DOI]

Hupfer, M., Gächter, R. and Giovanoli, R.J.A.S., 1995. Transformation of phosphorus species in settling seston and during early sediment diagenesis. *Aquatic Sciences*, 57(4), pp.305-324. [DOI]

Hupfer, M., Jordan, S., Herzog, C., Ebeling, C., Ladwig, R., Rothe, M. and Lewandowski, J., 2019. Chironomid larvae enhance phosphorus burial in lake sediments: Insights from long-term and short-term experiments. *Science of the Total Environment*, 663, pp.254-264. [DOI]

Jiang, X., Jin, X., Yao, Y., Li, L. and Wu, F., 2006. Effects of oxygen on the release and distribution of phosphorus in the sediments under the light condition. *Environmental Pollution*, 141(3), pp.482-487. [DOI]

Joshi, S.R., Kukkadapu, R.K., Burdige, D.J., Bowden, M.E., Sparks, D.L. and Jaisi, D.P., 2015. Organic matter remineralization predominates phosphorus cycling in the mid-bay sediments in the Chesapeake Bay. *Environmental Science & Technology*, 49(10), pp.5887-5896. [DOI]

Kiani, M., Zrim, J., Simojoki, A., Tammeorg, O., Penttinen, P., Markkanen, T. and Tammeorg, P., 2023. Recycling eutrophic lake sediments into grass production: A four-year field experiment on agronomical and environmental implications. *Science of the Total Environment*, 870, p.161881. [DOI]

Kraal, P., Dijkstra, N., Behrends, T. and Slomp, C.P., 2017. Phosphorus burial in sediments of the sulfidic deep Black Sea: Key roles for adsorption by calcium carbonate and apatite authigenesis. *Geochimica et Cosmochimica Acta*, 204, pp.140-158. [DOI]

Lepori, F. and Roberts, J.J., 2015. Past and future warming of a deep European lake (Lake Lugano): what are the climatic drivers? *Journal of Great Lakes Research*, 41(4), pp.973-981. [DOI]

Li, L., Liu, L., Wang, S., Liu, W., Jiao, L., Yang, Y. and Yang, R., 2015. Spatial distribution of phosphorus fractions in sediment and the potential mobility of phosphorus in Dianchi Lake. *Environmental Earth Sciences*, 74(5), pp.3721-3731. [DOI]

Li, X., Zhou, A., Liu, Y., Ma, T., Liu, C., Liu, L. and Yang, J., 2012. Stable isotope geochemistry of dissolved chloride in relation to hydrogeology of the strongly exploited Quaternary aquifers, North China Plain. *Applied Geochemistry*, 27(10), pp.2031-2041. [DOI]

Lijklema, L., Koelmans, A.A. and Portielje, R., 1993. Water quality impacts of sediment pollution and the role of early diagenesis. *Water Science and Technology*, 28(8-9), pp.1-12. [DOI]

Mahmood, M., Tian, Y., Ma, Q., Ahmed, W., Mehmood, S., Hui, X. and Wang, Z., 2020. Changes in phosphorus fractions and their availability status in relation to long term P fertilization in the loess plateau of China. *Agronomy*, 10(11), p.1818. [DOI]

Ministry of Environment, Forest and Climate Change 2023. *Annual Report 2022–23*. Government of India. Available at : https://www.moef.gov.in/index.php/annual-reports

Mitsch, W.J. and Gosselink, J.G., 2015. *Wetlands*. John Wiley & Sons.

Nishigaki, T., Sugihara, S., Kobayashi, K., Hashimoto, Y., Kilasara, M., Tanaka, H., Watanabe, T. and Funakawa, S., 2018. Fractionation of phosphorus in soils with different geological and soil physicochemical properties in southern Tanzania. *Soil Science and Plant Nutrition*, 64(3), pp.291-299. [DOI]

Paerl, H.W. and Otten, T.G., 2013. Harmful cyanobacterial blooms: causes, consequences, and controls. *Microbial Ecology*, 65(4), pp.995-1010. [DOI]

Parsons, C.T., Rezanezhad, F., O'Connell, D.W. and Van Cappellen, P., 2017. Sediment phosphorus speciation and mobility under dynamic redox conditions. *Biogeosciences*, 14(14), pp.3585-3602. [DOI]

Psenner, R., Pucsko, R. and Sage, M. 1984. Fractionation of organic and inorganic phosphorus compounds in lake sediments, an attempt to characterize ecologically important fractions (Die Fraktionierung Organischer und Anorganischer Phosphorverbindungen von Sedimenten, Versuch einer Definition Okologisch Wichtiger Fraktionen). *Archiv fur Hydrobiologie*, *1*(1).

Qu, Y., Wang, C., Guo, J., Huang, J., Fang, F., Xiao, Y., Ouyang, W. and Lu, L., 2019. Characteristics of organic phosphorus fractions in soil from water-level fluctuation zone by solution 31P-nuclear magnetic resonance and enzymatic hydrolysis. *Environmental Pollution*, 255, p.113209. [DOI]

Raman, N., and Sathiyanarayanan, D. 2009. Physico-Chemical characteristics of soil and influence of cation exchange capacity of soil in and around Chennai. *Rasayan Journal of Chemistry*, 2(4), 875-885.

Reddy, K.R., DeLaune, R.D. and Inglett, P.W., 2022. *Biogeochemistry of Wetlands: Science and Applications*. CRC Press. [DOI]

Rippey, B., Campbell, J., McElarney, Y., Thompson, J. and Gallagher, M., 2021. Timescale of reduction of long-term phosphorus release from sediment in lakes. *Water Research*, 200, p.117283. [DOI]

Rutledge, J.M. and Chow-Fraser, P., 2019. Landscape characteristics driving spatial variation in total phosphorus and sediment loading from sub-watersheds of the Nottawasaga River, Ontario. *Journal of Environmental Management*, 234, pp.357-366. [DOI]

Saar, K., Nõges, P., Søndergaard, M., Jensen, M., Jørgensen, C., Reitzel, K., Jeppesen, E., Lauridsen, T.L. and Jensen, H.S., 2022. The impact of climate change and eutrophication on phosphorus forms in sediment: results from a long-term lake mesocosm experiment. *Science of the Total Environment*, 825, p.153751. [DOI]

Sayeed, M.A., Hossain, M.A.R., Wahab, M.A., Hasan, M.T., Simon, K.D. and Mazumder, S.K., 2015. Water and sediment quality parameters in the Chalan Beel, the largest wetland of Bangladesh. *Chinese Journal of Oceanology and Limnology*, 33(4), pp.895-904. [DOI]

Scheffer, M., 2001. Alternative attractors of shallow lakes. *The Scientific World Journal*, 1(2), pp.254-263. [DOI]

Sharpley, A., Jarvie, H.P., Buda, A., May, L., Spears, B. and Kleinman, P., 2013. Phosphorus legacy: overcoming the effects of past management practices to mitigate future water quality impairment. *Journal of Environmental Quality*, 42(5), pp.1308-1326. [DOI]

Smith, V.H., Tilman, G.D. and Nekola, J.C., 1999. Eutrophication: impacts of excess nutrient inputs on freshwater, marine, and terrestrial ecosystems. *Environmental Pollution*, 100(1-3), pp.179-196. [DOI]

Søndergaard, M., Jensen, J.P. and Jeppesen, E., 2003. Role of sediment and internal loading of phosphorus in shallow lakes. *Hydrobiologia*, 506(1), pp.135-145. [DOI]

Søndergaard, M., Windolf, J. and Jeppesen, E., 1996. Phosphorus fractions and profiles in the sediment of shallow Danish lakes as related to phosphorus load, sediment composition and lake chemistry. *Water Research*, 30(4), pp.992-1002. [DOI]

Song, K., Adams, C.J. and Burgin, A.J., 2017. Relative importance of external and internal phosphorus loadings on affecting lake water quality in agricultural landscapes. *Ecological Engineering*, 108, pp.482-488. [DOI]

Turner, B.L., Cade-Menun, B.J., Condron, L.M. and Newman, S., 2005. Extraction of soil organic phosphorus. *Talanta*, 66(2), pp.294-306. [DOI]

United Nations Environment Programme 2016. *UNEP Frontiers 2016 Report: Emerging issues of environmental concern*. United Nations Environment Programme.

Voegelin, A., Senn, A.C., Kaegi, R., Hug, S.J. and Mangold, S., 2013. Dynamic Fe-precipitate formation induced by Fe (II) oxidation in aerated phosphate-containing water. *Geochimica et Cosmochimica Acta*, 117, pp.216-231. [DOI]

Walkley, A., and Black, I. A. 1934. An examination of the Degtjareff method for determining soil organic matter, and a proposed modification of the chromic acid titration method. *Soil science*, *37*(1), 29-38.

Walpersdorf, E., Koch, C.B., Heiberg, L., O'Connell, D.W., Kjaergaard, C. and Hansen, H.B., 2013. Does vivianite control phosphate solubility in anoxic meadow soils? *Geoderma*, 193, pp.189-199. [DOI]

Wang, J., Huang, T., Wu, Q., Bu, C. and Yin, X., 2021. Sources and cycling of phosphorus in the sediment of rivers along a eutrophic lake in China are indicated by phosphate oxygen isotopes. *ACS Earth and Space Chemistry*, 5(1), pp.88-94. [DOI]

Wang, S., An, J., Wan, Y., Du, Q., Wang, X., Cheng, X. and Li, N., 2018a. Phosphorus competition in bioinduced vivianite recovery from wastewater. *Environmental Science & Technology*, 52(23), pp.13863-13870. [DOI]

Wang, X., Wei, J., Bai, N., Cha, H., Cao, C., Zheng, K. and Liu, Y., 2018b. The phosphorus fractions and adsorption-desorption characteristics in the Wuliangsuhai Lake, China. *Environmental Science and Pollution Research*, 25(21), pp.20648-20661. [DOI]

Wilfert, P., Dugulan, A.I., Goubitz, K., Korving, L., Witkamp, G.J. and Van Loosdrecht, M.C.M., 2018. Vivianite is the main phosphate mineral in digested sewage sludge, and its role in phosphate recovery. *Water Research*, 144, pp.312-321. [DOI]

Wu, T., Zhu, G., Zhu, M., Xu, H., Zhang, Y. and Qin, B., 2020. Use of conductivity to indicate long-term changes in pollution processes in Lake Taihu, a large shallow lake. *Environmental Science and Pollution Research*, 27(17), pp.21376-21385. [DOI]

Wu, X., Jiang, Q. and Ma, T., 2023. Geochemical processes of phosphorusiron on sediment-water interface during discharge of groundwater to freshwater lakes: Kinetic and mechanistic insights. *Science of the Total Environment*, 901, p.165962. [DOI]

Wu, Y., Wen, Y., Zhou, J. and Wu, Y., 2014. Phosphorus release from lake sediments: Effects of pH, temperature and dissolved oxygen. *KSCE Journal of Civil Engineering*, 18(1), pp.323-329. [DOI]

Wu, Z. and Wang, S., 2017. Release mechanism and kinetic exchange for phosphorus (P) in lake sediment characterized by diffusive gradients in thin films (DGT). *Journal of Hazardous Materials*, 331, pp.36-44. [DOI]

Xiang, S.L., 2011. Phosphorus forms and distribution in the sediments of Poyang Lake, China. *International Journal of Sediment Research*, 26(2), pp.230-238. [DOI]

Xie, F., Li, L., Song, K., Li, G., Wu, F. and Giesy, J.P., 2019. Characterization of phosphorus forms in a Eutrophic Lake, China. *Science of the Total Environment*, 659, pp.1437-1447. [DOI]

Xu, N., Chen, M., Zhou, K., Wang, Y., Yin, H. and Chen, Z., 2014. Retention of phosphorus on calcite and dolomite: speciation and modelling. *RSC Advances*, 4(66), pp.35205-35214. [DOI]

Younis, A.M., Soliman, N.F., Elkady, E.M. and Mohamedein, L.I., 2022. Distribution and ecological risk evaluation of bioavailable phosphorus in sediments of El Temsah Lake, Suez Canal. *Oceanologia*, 64(2), pp.287-298. [DOI]

Yuan, H., Li, Q., Kukkadapu, R.K., Liu, E., Yu, J., Fang, H., Li, H. and Jaisi, D.P., 2019. Identifying sources and cycling of phosphorus in the sediment of a shallow freshwater lake in China using phosphate oxygen isotopes. *Science of the Total Environment*, 676, pp.823-833. [DOI]

Zhang, W., Jin, X., Zhu, X. and Shan, B., 2016. Characteristics and distribution of phosphorus in surface sediments of limnetic ecosystem in Eastern China. *PLoS One*, 11(6), p.e0156488. [DOI]

Nature Environment and Pollution Technology
An International Quarterly Scientific Journal

p-ISSN: 0972-6268
(Print copies up to 2016)
e-ISSN: 2395-3454

Vol. 25 | No. 3 | Article ID D1898 | 2026

Original Research Paper

https://doi.org/10.46488/NEPT.2026.v25i03.D1898

Open Access Journal

The Effect of Different Mixtures on Desiccation Crack Behaviour and Hydraulic Stability of a Compacted Liner

Mochamad Arief Budihardjo[1]†, Nita Citrasari[2], Muhammad Altin Massinai[3], Bimastyaji Surya Ramadan[1] and Annisa Sila Puspita[4]

[1]Department of Environmental Engineering, Faculty of Engineering, Universitas Diponegoro, 50275, Indonesia
[2]Department of Biology, Faculty of Science and Technology, Universitas Airlangga, 60115, Indonesia
[3]Department of Geophysics, Faculty of Mathematics and Natural Sciences, Universitas Hasanuddin, 90245, Indonesia
[4]Environmental Sustainability Research Group, Department of Environmental Engineering, Faculty of Engineering, Universitas Diponegoro, Semarang, 50275, Indonesia
†Corresponding author: Mochamad Arief Budihardjo; m.budihardjo@ft.undip.ac.id

Abbreviation: Nat. Env. & Poll. Technol.
Website: www.neptjournal.com

Received: 08-01-2026
Revised: 26-02-2026
Accepted: 02-03-2026

Key Words:

Desiccation crack
Landfill liner
Permeability
Stability
Textile sludge

Citation for the Paper:

Budihardjo, M.A., Citrasari, N., Massinai, M.A., Ramadan, B.S. and Puspita, A.S., 2026. The effect of different mixtures on desiccation crack behaviour and hydraulic stability of a compacted liner. *Nature Environment and Pollution Technology*, 25(3), D1898. https://doi.org/10.46488/NEPT.2026.v25i03.D1898

Note: From 2025, the journal has adopted the use of Article IDs in citations instead of traditional consecutive page numbers. Each article is now given individual page ranges starting from page 1.

Copyright: © 2026 by the authors
Licensee: Technoscience Publications
This article is an open access article distributed under the terms and conditions of the Creative Commons Attribution (CC BY) license (https://creativecommons.org/licenses/by/4.0/).

ABSTRACT

Landfills utilize leachate containment systems featuring a compacted liner layer with low hydraulic conductivity. Typically, the required hydraulic conductivity is ≤ 1 × 10^{-5} cm.s^{-1} for final cover liners and ≤ 1 × 10^{-6} cm/s for bottom liners, to prevent leachate from migrating into surrounding soil and groundwater. This study tested composites made from textile-industry sludge amended with bentonite, lime, and rice husk ash to assess their potential as landfill liner materials. Results indicated that composites with 40% or more bentonite (by mass) mixed with dewatered sludge could meet permeability standards. The addition of 1% lime and 8% rice husk ash further reduced permeability. Incorporating bentonite increased cohesion and lowered the internal friction angle, while lime and rice husk ash raised the internal friction angle and caused fluctuations in cohesion.

1. INTRODUCTION

Leachate is a liquid that percolates through a waste mass, transporting dissolved and suspended substances (Singh & Hendry 2013). To prevent environmental contamination, landfills must be lined with a semi-impermeable barrier designed to contain leachate (Mokhahlane 2013). Many landfills utilize clay liners, which expand when moist and contract when dry (Staub et al. 2011). This swelling and shrinking cycle can compromise the liner's integrity by causing cracks (Chegenizadeh et al. 2025, Vaverková et al. 2018). To minimize cracking, the shrinkage limit for liner materials should not exceed 4% (Maritsa et al. 2016). Consequently, it is crucial to identify a more durable and reliable landfill liner material.

Numerous studies have explored alternative materials, such as coal ash (Nurdin et al. 2016), bentonite (Chaduvula et al. 2017), red mud (Vipulanandan & Leung 1995), among others, to decrease dependence on the overuse of native soil (Puspita et al. 2024). Bentonite is frequently employed as an additive in landfill leachate barriers due to its advantageous properties and low permeability (Kumar & Yong 2002). To reduce costs while satisfying landfill liner performance standards, other materials are often blended with bentonite. In this research, dewatered sludge derived from textile industrial waste serves as the main component, combined with bentonite, lime, and rice husk ash to create a composite layer capable of retaining leachate. Textile industry hazardous waste typically includes sludge or sand that the producer cannot reprocess (Uddin 2021). This waste is generally stored temporarily following incineration before being handed over to a third party.

Consequently, employing dewatered sludge as a landfill liner material necessitates the addition of supplementary materials to enhance its functionality. Ensuring stability is vital in landfill design, impacting both the internal waste mass and the leachate barrier layer (Jones & Dixon 2005, Omidi et al. 1996). The stability of the leachate-retaining layer is inversely related to its permeability (Koerner & Soong 2000). According to standard landfill design practices, the hydraulic conductivity requirement for a compacted final cover liner is usually set at $\leq 1 \times 10^{-5}$ cm.s^{-1}, while bottom liner systems demand a more stringent criterion of $\leq 1 \times 10^{-6}$ cm.s^{-1} to ensure long-term containment effectiveness (Witt & Zeh 2005).

Bentonite demonstrates an exceptionally low permeability coefficient of approximately 1.8×10^{-9} cm.s^{-1}, making it highly effective at preventing leachate infiltration. However, bentonite is highly expansive, shrinking in dry conditions and swelling when exposed to moisture (Holtz 1959). Adding lime has been shown to improve the physical and mechanical properties of the base material, decrease moisture content, and enhance long-term impermeability (Little 1998). When mixed with bentonite for leachate barrier applications, lime can increase the optimum moisture content, lower the maximum dry density, and boost compressive strength (Jain 2024). Additionally, rice husk ash can improve the adsorption of key contaminants such as heavy metals, while reducing permeability and maximum dry density, increasing optimum moisture content, and significantly enhancing compressive strength—up to 200 kN.m^{-2} (Cokca & Yilmaz 2004). This study aims to determine the optimal composition of landfill liner composites made from dewatered sludge amended with bentonite, lime, and rice husk ash. These composites are expected to serve as an alternative material for landfill leachate containment systems.

2. MATERIALS AND METHODS

The samples included dewatered textile-industry sludge waste, bentonite, lime, and rice husk ash (Table 1). The dewatered sludge was sourced from a textile manufacturing plant in Indonesia, while bentonite was obtained from mineral mining facilities. Lime and rice husk ash were purchased commercially. Each material underwent characteristic testing by mixing them at specific compositions. To ensure homogeneous mixtures, the dewatered sludge, bentonite, lime, and rice husk ash were combined using the cone-and-quartering method. The tests conducted included sludge grain size distribution, bentonite swelling, initial moisture content, Atterberg limits, specific gravity, Standard Proctor compaction, and morphological analysis using SEM–EDX.

Table 1: Sample variations.

No	Sample Variation	Variable Code
1	100% S	V1
2	79% S + 20% B + 1% K	V2
3	69% S + 30% B + 1% K	V3
4	59% S + 40% B + 1% K	V4
5	49% S + 50% B + 1% K	V5
6	39% S + 60% B + 1% K	V6
7	71% S + 20% B + 1% K + 8% ASP	V7
8	61% S + 30% B + 1% K + 8% ASP	V8
9	51% S + 40% B + 1% K + 8% ASP	V9
10	41% S + 40% B + 1% K + 8% ASP	V10
11	31% S + 40% B + 1% K + 8% ASP	V11

2.1. Permeability Test

The permeability test was conducted following the falling-head method outlined in AS 1289.6.7.2-2001 (Standards Australia 2001). This technique involves permitting water to pass through a soil specimen connected to a vertical standpipe filled with water. The standpipe is marked with height graduations to enable precise measurement of water level changes and calculation of the volume of water that passes through the soil over time. Before testing, the soil specimen was thoroughly saturated to ensure uniform flow conditions, and the standpipe was filled to a specified initial height. The test began by allowing water to permeate through the soil, with careful observation and recording of the standpipe's water level decline. To ensure consistency and reproducibility, each permeability test was performed in triplicate (n = 3) for each composite variation. The hydraulic conductivity values reported are the average of three independent measurements, with variability expressed as the standard deviation (± SD). The minimal variation among replicates demonstrates the reliability of the falling-head method in assessing the hydraulic performance of the composite materials.

2.2. Desiccation Test

The drying behavior of desiccation cracking was examined in various composite materials under two temperature conditions: a minimum of 25.7°C and a maximum of 40°C. A desiccation test was carried out to identify cracks caused by the drying process and to estimate the hydraulic conductivity of the cracked soil specimen (Puspita et al. 2023). The plate containing dewatered sludge composites with bentonite, lime, and rice husk ash was left to dry, and the changes, including crack formation, were monitored. Photographs of the cracks were captured in both black-and-white and color, then analyzed using MATLAB software to determine the

crack area percentage, which was used to calculate the crack width in the composite layer.

2.3. Direct Shear Test

This test was performed to determine the soil's shear strength parameters, specifically cohesion and the internal friction angle. Shear failure occurred in the soil due to the shear force applied by pushing the upper section. Calculations involved converting normal loads into normal stresses and computing shear force and shear stress. These parameters served as the basis for assessing the shear strength of the composite. A shear stress versus normal stress graph was used to determine the cohesion value and internal friction angle of the composite material. Subsequently, composite stability was evaluated using safety factors. The analysis was conducted with GeoSlope/W employing the Morgenstern–Price method, assuming a 30% slope and a layer thickness of 30 cm × 2.

3. RESULTS AND DISCUSSION

3.1. Characteristic Test

The sieve analysis indicated that 99.62% of the dewatered sludge was classified as sand, with the remaining 0.38% identified as clay and silt. The pure bentonite swelling test revealed a free swell index (FSI) of 390%. Bentonite is known to expand in distilled water, and this expansion helps fill voids between dewatered sludge particles, thereby enhancing soil density (Masihi & Gholikandi 2020, Qin et al. 2023). An FSI of 390% signifies that the bentonite expanded approximately 39 times its original volume. Higher clay content increases soil cohesion and decreases the shear angle (Bozbey & Guler 2006). These effects occur because sand is a non-cohesive soil, especially under dry conditions, and lacks well-defined plasticity boundaries (Nhan et al. 1996, Rubey, 1933). In terms of permeability, a greater sand proportion typically leads to increased permeability (Churchman et al. 2006, Revil & Cathles III, 1999). The Atterberg limit tests showed that not all composite variations demonstrated plastic behavior. Composites with at least 30% bentonite exhibited plasticity, evidenced by their plasticity index. Specifically, the composite with 30% bentonite had a plasticity index between 0.48% and 1.1%, while those with 40%, 50%, and 60% bentonite showed indices of 16.21%, 11.5%, and 14.01%, respectively.

The initial moisture content across all composites ranged from 19.24% to 36.56%. The addition of bentonite caused an increase in moisture content in a non-linear fashion. Lime application also led to a significant rise in moisture content. Conversely, rice husk ash reduced the moisture content compared to the composite containing dewatered sludge, bentonite, and lime. The inclusion of bentonite tended to elevate specific gravity because its swelling fills pores within the dewatered sludge matrix. However, the performance of bentonite was diminished by the addition of lime and rice husk ash, resulting in a subsequent decrease in specific gravity. The Standard Proctor test yielded varying values of optimum moisture content (OMC) and maximum dry density (MDD) among the composites. Notably, composite V1, which lacked bentonite, exhibited the highest OMC and the lowest MDD, reflecting the dewatered sludge's poor water interaction and its need for higher moisture to reach maximum density. The addition of lime increased both OMC and MDD. When rice husk ash was incorporated, OMC decreased while MDD increased, likely due to rice husk ash's role in promoting hardening, thus making the material stiffer and denser. Lime also accelerates hardening, especially before the composite absorbs substantial water.

3.2. Permeability Behavior of the Composites

The initial experiments compared $MgCl_2$ and MgO as sources of magnesium over a pH range of 6–11. The findings showed that $MgCl_2$ consistently surpassed MgO in nutrient removal efficiency. Maximum ammonium reduction was observed at pH 9, while phosphate removal peaked at pH 10. At these optimal conditions, over 70% of phosphate and nearly 60% of ammonium were removed from the solution. The comparatively poorer performance of MgO can be explained by its limited solubility, which results in a slower release of Mg^{2+} ions, delaying nucleation and crystal growth. Conversely, $MgCl_2$ supplies an immediate and high concentration of soluble magnesium, promoting rapid supersaturation and precipitation. The pH dependency aligns with established research indicating that struvite crystallization is heavily influenced by solution chemistry (Petal Battistoni et al. 1997). At near-neutral pH levels (6–7), minimal precipitation occurs due to restricted PO_4^{3-} ion availability. Under highly alkaline conditions (>10.5), the decrease in removal efficiency may be due to competing precipitation of calcium phosphate and amorphous phosphate species. Therefore, pH 9–10 appears to be the optimal range for struvite precipitation in composting leachate, corroborating prior studies on wastewater and digestates (Kabdaslı et al. 2000, Yetilmezsoy & Sapci-Zengin 2009).

The permeability (hydraulic conductivity) test was carried out to assess the composite material's capacity to allow horizontal and lateral water flow through the soil, aiding in the selection of an appropriate composite for a landfill liner (Ng et al. 2016, Scalia IV & Benson 2011). Specimens prepared at the optimal dry density, determined

Table 2: Permeability test results.

No	Sample Variation	Hydraulic Conductivity [cm.s^{-1}]
1	100% S	$(1.36 \pm 0.05) \times 10^{-2}$
2	79% S + 20% B + 1% L	$(6.42 \pm 0.21) \times 10^{-5}$
3	69% S + 30% B + 1% L	$(6.42 \pm 0.18) \times 10^{-5}$
4	59% S + 40% B + 1% L	$(9.79 \pm 0.32) \times 10^{-7}$
5	49% S + 50% B + 1% L	$(1.83 \pm 0.07) \times 10^{-7}$
6	39% S + 60% B + 1% L	$(8.16 \pm 0.29) \times 10^{-7}$
7	71% S + 20% B + 1% L + 8% RHA	$(3.03 \pm 0.11) \times 10^{-5}$
8	61% S + 30% B + 1% L + 8% RHA	$(3.55 \pm 0.13) \times 10^{-5}$
9	51% S + 40% B + 1% L + 8% RHA	$(1.17 \pm 0.04) \times 10^{-6}$
10	41% S + 40% B + 1% L + 8% RHA	$(2.34 \pm 0.08) \times 10^{-6}$
11	31% S + 40% B + 1% L + 8% RHA	$(1.02 \pm 0.03) \times 10^{-6}$

from the Proctor test, were used for the test, which was conducted using the falling-head method. The results of the permeability tests are shown in Table 2.

The decrease in hydraulic conductivity observed in the composite variations is mainly due to microstructural changes within the pore network. Bentonite's swelling capacity plays a key role; when hydrated, bentonite particles expand and fill the voids between dewatered sludge particles, leading to smaller pore sizes and reduced pore connectivity. This swelling markedly restricts water flow pathways and thereby lowers the permeability of the composite materials (Horpibulsuk et al. 2011, Qiang et al. 2014). Additionally, composites containing 30% or more bentonite show an increased plasticity index, which further reduces permeability. Higher plasticity indicates greater water retention and stronger interparticle bonding, impeding the formation of continuous flow channels within the compacted matrix. Consequently, hydraulic conductivity declines as bentonite content increases.

The addition of lime and rice husk ash further alters the pore structure through physicochemical reactions. Lime promotes flocculation and pozzolanic activity, leading to the formation of cementitious compounds such as calcium silicate hydrate (C–S–H) that strengthen interparticle bonds and decrease pore connectivity. Rice husk ash, rich in amorphous silica, reacts with calcium from lime to enhance the composite matrix. These reactions improve the structural integrity and further reduce hydraulic conductivity. However, replacing part of the bentonite with rice husk ash may diminish swelling contributions, which could explain the permeability variations observed across different compositions.

3.3. Desiccation Crack Analysis

Crack testing was performed using MATLAB software, which involved converting the original RGB image into a binary format. The crack area was then determined through the crack intensity factor (CIF) formula, allowing quantification of the crack extent across the entire image. Composite V1, composed of 100% dewatered sludge, could not be assessed in the desiccation test because MATLAB software could not detect any cracks. This limitation is because pure dewatered sludge contains granular particles, commonly known as aggregates, which are dispersed and non-plastic (see Fig. 1). This observation is supported by preliminary grain size analysis, revealing that the dewatered sludge consists of 99.62% sand. Sand is classified as a non-cohesive, easily loosened soil under dry conditions, and therefore lacks plasticity.

For composites other than V1, adding bentonite, lime, and rice husk ash from Day 0 to Day 9 reduced the water content and induced desiccation, leading to cracks on the sample surface at the lowest temperature (25.7°C). The inclusion of bentonite, 1% lime, and 8% rice husk ash also caused a decrease in the CIF value, as depicted in Fig. 2.

The images were taken on the 9th day at the minimum temperature. The CIF values were undefined for V1 and were 0.72% (V2), 2.58% (V3), 2.37% (V4), 2.67% (V5), and 2.78% (V6). For the remaining composites, the CIF values were 0.64% (V7), 2.37% (V8), 1.10% (V9), 1.16% (V10), and 1.20% (V11). The largest CIF value occurred in V6, which consisted of 39% dewatered sludge, 60% bentonite, and 1% lime, while the smallest CIF value occurred in V7, which consisted of 71% dewatered sludge, 20% bentonite, and 1% lime.

The addition of 8% rice husk ash was shown to decrease the CIF value. Incorporating rice husk ash into composites with expansive soils helps reduce the soil's swelling potential. When combined with lime, rice husk ash acts as a binding agent within the aggregate structure (Çoruh &



Fig. 1: Composite V1 from Day 0 to Day 9 (cracks cannot be detected).

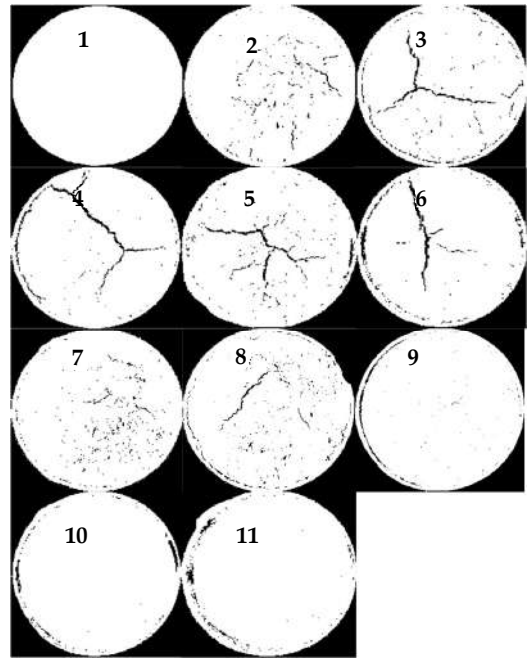


Fig. 2: Binary image of cracks at the minimum temperature on Day 9.

Ergun 2010, Sua-Iam & Makul 2013). This effect is due to the pozzolanic properties of rice husk ash, which react with the expansive soil to create a stiffer, more rigid composite matrix. The silica content in the pozzolanic material reacts with quicklime, improving interparticle bonding and enhancing overall strength. Additionally, rice husk ash helps minimize shrinkage, thus decreasing crack formation within the composite (Amran et al. 2021, Kaya & Durukan 2004). Shrinkage mitigation occurs because rice husk ash reduces the maximum dry density while increasing the optimum moisture content (OMC), leading to a more plastic and workable composite behavior.

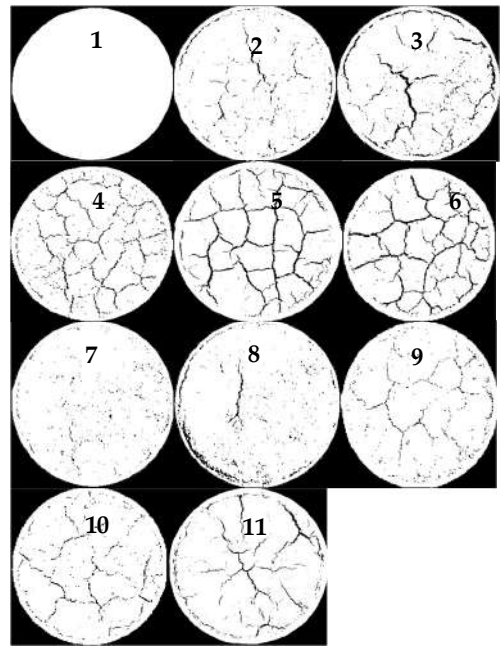


Fig. 3: Binary image of cracks at the maximum temperature on Day 6.

Table 3: Desiccation crack test results.

Variation	CIF [%]	
	27°C	40°C
V1	-	-
V2	2.55	2.25
V3	2.58	4.96
V4	2.38	4.00
V5	2.68	5.70
V6	2.78	6.21
V7	0.64	1.51
V8	2.37	3.10
V9	1.10	2.31
V10	1.16	2.71
V11	1.21	3.41

At an elevated temperature of 40°C, all V2–V11 composite variations containing bentonite, lime, and rice husk ash were tested over a curing period from day 0 to day 6. The results indicate a continuous decrease in moisture content across the V2–V11 samples, leading to desiccation and the subsequent formation of surface cracks, as illustrated in Fig. 3.

Images taken on the 6th day produced CIF values that were undefined for V1 and were 2.25% (V2), 4.96% (V3), 4.00% (V4), 5.70% (V5), 6.21% (V6), 1.51% (V7), 3.10% (V8), 2.31% (V9), 2.71% (V10), and 3.41% (V11). The results of the desiccation crack analysis are presented in Table 3.

At both temperature conditions, composites V2, V8, V9, V10, and V11 demonstrated CIF values below 4%. In contrast, the remaining composites showed CIF values exceeding 4%. The lowest crack intensity was recorded in composite V7, with CIF values of 0.64% at the minimum temperature and 1.51% at the maximum temperature.

3.4. Shear Strength and Stability Analysis

The results indicate that as the bentonite content increased, the internal friction angle generally decreased while cohesion rose. These two parameters are key indicators of the shear strength of the composite materials (Budihardjo et al. 1921). The internal friction angle reflects the stability of the composite in terms of frictional resistance, whereas cohesion represents the bonding force between particles that enhances the material's strength. Notably, the changes in the internal friction angle and cohesion were neither linear nor uniform. The decline in the internal friction angle can be attributed to the fact that bentonite fills the spaces between aggregates, thereby reducing interparticle friction. Conversely, cohesion increased at higher bentonite contents because bentonite functions as a binding agent within the composite structure.

The addition of lime to the composite materials resulted in changes to the internal friction angle and a reduction in cohesion. Lime–aggregate interaction facilitates contact between lime and clay minerals, triggering an ion-exchange reaction that produces calcium silicate gel. This gel, which is insoluble in water, induces particle flocculation, decreasing pore spaces within the aggregates and enhancing overall structural stability (Rubinos et al. 2015). In lime and rice husk ash composites, the internal friction angle increased, while cohesion exhibited irregular fluctuations. These variations in cohesion may be attributed to uneven shear displacement rates, though the overall changes were not significant. The inconsistent and low cohesion response could be due to an imbalanced rice husk ash-to-lime ratio, leading to a non-optimal and uneven reaction across the composite samples.

It was observed that the curing behavior significantly influenced the shear strength parameters, specifically the internal friction angle and cohesion, across all composite variations. When cured using leachate, the composites demonstrated a progressive increase in both parameters over four hours, indicating enhanced mechanical stability and resistance to shear deformation. Simultaneous changes in the internal friction angle and cohesion suggest stronger particle bonding and improved frictional resistance within the composite matrix. The observed increases in shear strength parameters highlight the potential for these composites to serve as leachate-retaining layers. Their ability to maintain and even improve stability under leachate-curing conditions indicates that exposure to leachate does not undermine their structural integrity. Consequently, leachate intrusion will not diminish the composites' mechanical strength, confirming their suitability for long-term use in waste management systems as containment and barrier elements.

The GeoSlope/W analysis aimed to assess the factor of safety of the composite material when used as a leachate barrier layer. The stability was evaluated using the Morgenstern–Price method, considering a 30% slope inclination and a liner thickness of 30 cm (two layers). The model assumed homogeneous material properties derived from laboratory direct shear tests, including cohesion and internal friction angle, without external surcharge or waste overburden pressure. Pore water pressure conditions were simulated under steady-state assumptions, without additional hydraulic head. A slope is deemed stable when the factor of safety exceeds 1.25 (Herrmann et al. 2009). The composites made of dewatered sludge and bentonite generally showed a decreasing trend in factor of safety. For example, the V1 composite, made entirely of 100% dewatered sludge, had

a factor of safety of 14. The high factor of safety values in this study were primarily due to the shallow slope geometry, limited liner thickness, and high cohesion measured under laboratory conditions. These assumptions tend to produce conservative stability results, especially without external loads. The reduction in factor of safety with increasing bentonite content is linked to decreased shear resistance, reflected by lower cohesion and internal friction angles. High safety factors are mainly driven by elevated internal friction angles and cohesion. Conversely, composites with lime and rice husk ash showed a different trend. Adding lime, alone or combined with rice husk ash, increased the factor of safety, reaching a maximum of 21.67. However, this maximum represents idealized conditions and does not consider long-term factors such as waste settlement, dynamic loading, or full saturation, which could lower the safety margin in real-world applications. Additionally, leachate curing contributed to higher factor of safety values, improving cohesion and internal friction angles across all composites. Under the modeled assumptions, all combinations satisfied the stability criteria, indicating a low potential for slope failure in controlled analytical conditions.

3.5. Microstructural Analysis (SEM–EDX)

SEM observations revealed the presence of surface cracks within the composite materials. At higher magnification, micrographs demonstrated that bentonite particles progressively filled and bridged the crack spaces, resulting in a denser and more compact microstructure. This infilling behavior reduced crack continuity and limited the formation of interconnected pore channels, thereby supporting the observed decrease in hydraulic conductivity. However, the addition of lime and rice husk ash altered the swelling behavior of bentonite. The interaction between calcium from lime and silica-rich rice husk ash promoted pozzolanic reactions, leading to the formation of cementitious compounds. EDX analysis confirmed the presence of silica (Si), calcium (Ca), and aluminum (Al), consistent with oxides such as SiO_2, Al_2O_3, and CaO. These components contribute to the development of secondary bonding phases that enhance matrix stiffness and structural integrity. While these reactions improve mechanical strength, they may also partially restrict excessive bentonite swelling, which explains the variation in crack closure observed among different composite formulations. It is important to note that the SEM analysis in this study was primarily qualitative. Quantitative measurements of pore size distribution or crack width were not conducted. Therefore, the SEM–EDX findings serve as microstructural support for the macroscopic permeability and shear strength results, rather than providing direct quantitative evidence. Future research incorporating image-based pore analysis or advanced porosimetry techniques is recommended to better quantify the evolution of the pore network.

3.6. Environmental Risk Considerations

The use of dewatered textile sludge as a component in landfill liner materials warrants careful evaluation of potential

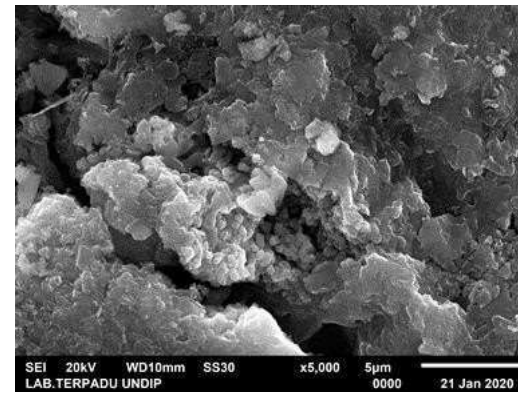


Fig. 4: Composite SEM results.

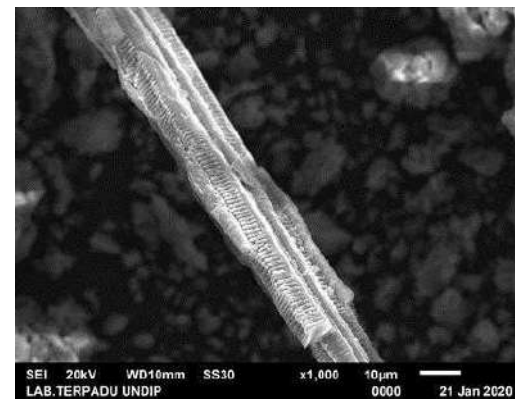


Fig. 5: SEM results of rice husk ash.

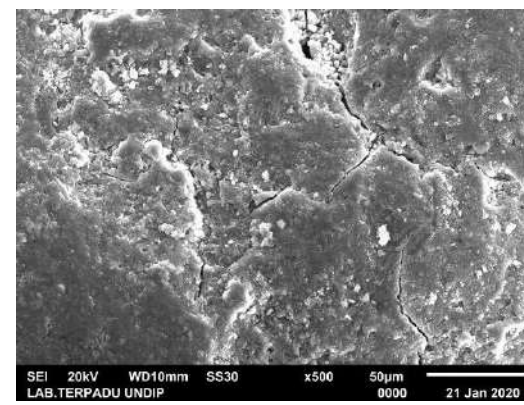


Fig. 6: Composite surface SEM results.

environmental risks. Textile sludge may harbor residual contaminants such as heavy metals, dye compounds, and other industrial by-products, depending on the wastewater treatment processes at the source facility. These contaminants could pose risks if mobilized over long-term field conditions. In this study, leachability tests like the Toxicity Characteristic Leaching Procedure (TCLP) or other standardized methods were not performed, leaving the potential release of heavy metals or other pollutants from the composite liner unquantified. This limitation should be considered when assessing the suitability of the material for large-scale application. Nonetheless, incorporating bentonite, lime, and rice husk ash can aid in contaminant immobilization through various mechanisms. Bentonite's high cation exchange capacity and adsorption potential enable it to retain metal ions within its interlayer structure. Lime increases pH, facilitating the precipitation of metal hydroxides and thus reducing metal solubility. Additionally, pozzolanic reactions between calcium compounds and silica-rich rice husk ash can encapsulate contaminants within a denser cementitious matrix, restricting their mobility. These stabilization processes are well-documented in solidification–stabilization methods for contaminated materials. Future research should incorporate comprehensive leachability evaluations, such as TCLP or long-term column leaching tests, to ensure environmental safety and regulatory compliance of the composite liner. Such studies are crucial to verify that the improved mechanical and hydraulic properties observed also provide adequate environmental protection under operational field conditions.

4. CONCLUSIONS

Dewatered sludge in its pure form exhibits the lowest initial moisture content, the lowest specific gravity, and lacks plasticity. The properties of the composites vary according to the composition and proportion of dewatered textile-industry sludge used. The addition of bentonite, lime, and rice husk ash results in decreased permeability, increased plasticity, and greater shrinkage strength, which can lead to cracking. Incorporating bentonite into dewatered sludge tends to reduce the internal friction angle while increasing cohesion. Conversely, the addition of lime and rice husk ash causes fluctuations in cohesion and elevates the internal friction angle. The safety factor of composites containing bentonite also diminishes. The desiccation process of these composites involves moisture loss during drying, which induces surface cracking. Composites with rice husk ash show lower crack intensity factors, indicating enhanced resistance to desiccation cracking under varying temperature conditions. Variants suitable as alternative cover liners—meeting the shrinkage limit criterion of less than 4% to prevent cracking and having permeability values at or below 1×10^{-5}—include V10 (41% dewatered sludge, 50% bentonite, 1% lime, 8% rice husk ash). For bottom liners, V4 (59% dewatered sludge, 40% bentonite, 1% lime) is recommended. While the mechanical and hydraulic performance of these composites is promising, further study into the leaching and environmental safety of dewatered textile sludge is essential to ensure long-term regulatory compliance. Comprehensive leachability testing is advised prior to field-scale application.

5. ACKNOWLEDGMENT

This study was supported by the Indonesian Collaborative Research Program (PPKI) 2020 (Assignment Letter No. 193.06/UN7.6.1/PP/2020).

6. REFERENCES

Amran, M., Fediuk, R., Murali, G., Vatin, N., Karelina, M., Ozbakkaloglu, T., Krishna, R., Sahoo, A. K., Das, S. K. and Mishra, J., 2021. Rice husk ash-based concrete composites: A critical review of their properties and applications. Crystals, 11(2), p.168. [DOI]

Battistoni, P., Fava, G., Pavan, P., Musacco, A. and Cecchi, F., 1997. Phosphate removal in anaerobic liquors by struvite crystallization without addition of chemicals: preliminary results. *Water Research*, *31*(11), pp.2925-2929. [DOI]

Bozbey, I. and Guler, E., 2006. Laboratory and field testing for utilization of an excavated soil as landfill liner material. *Waste Management*, 26(11), pp.1277-1286. [DOI]

Budihardjo, M.A., Hadiwidodo, M., Wardhana, I.W., Praptomo, E.G., Samadikun, B.P., Puspita, A.S. and Ramadan, B.S., 2021, November. Stability performance of demolition waste composite as landfill liner. In *IOP Conference Series: Earth and Environmental Science*, 896(1), p. 012001. [DOI]

Chaduvula, U., Viswanadham, B. and Kodikara, J., 2017. A study on desiccation cracking behavior of polyester fiber-reinforced expansive clay. *Applied Clay Science*, 142, pp.163-172. [DOI]

Chegenizadeh, A., Puspita, A.S., Budihardjo, M.A. and Nikraz, H., 2025, September. Investigation of Fly Ash-Bentonite Mixture as Waste Containment Liner under Wetting-Drying Cycles. In *IOP Conference Series: Earth and Environmental Science*, 1541(1), p. 012002. [DOI]

Churchman, G., Gates, W., Theng, B. and Yuan, G., 2006. Clays and clay minerals for pollution control. *Developments in Clay Science*, 1, pp.625-675. [DOI]

Cokca, E. and Yilmaz, Z., 2004. Use of rubber and bentonite added fly ash as a liner material. *Waste Management*, 24(2), pp.153-164. [DOI]

Çoruh, S. and Ergun, O. N., 2010. Use of fly ash, phosphogypsum and red mud as a liner material for the disposal of hazardous zinc leach residue waste. *Journal of Hazardous Materials*, 173(1-3), pp.468-473. [DOI]

Herrmann, I., Svensson, M., Ecke, H., Kumpiene, J., Maurice, C., Andreas, L. and Lagerkvist, A., 2009. Hydraulic conductivity of fly ash–sewage sludge mixes for use in landfill cover liners. *Water Research*, 43(14), pp.3541-3547. [DOI]

Holtz, W. G., 1959. *Expansive Clays--Properties and Problems*. Commissioner's Office, Bureau of Reclamation, United States Department of the Interior, pp.58.

Horpibulsuk, S., Yangsukkaseam, N., Chinkulkijniwat, A. and Du, Y. J., 2011. Compressibility and permeability of Bangkok clay compared with kaolinite and bentonite. *Applied Clay Science*, 52(1-2), pp.150-159. [DOI]

Jain, A. K., 2024. Exploring the viability of bentonite-amended blends incorporating marble dust, sand, and fly ash for the creation of an environmentally sustainable landfill liner system. *International Journal of Geo-Engineering*, 15(1), p.16. [DOI]

Jones, D. and Dixon, N., 2005. Landfill lining stability and integrity: the role of waste settlement. *Geotextiles and Geomembranes*, 23(1), pp.27-53. [DOI]

Kaya, A. and Durukan, S., 2004. Utilization of bentonite-embedded zeolite as clay liner. *Applied Clay Science*, 25(1-2), pp.83-91. [DOI]

Koerner, R. M. and Soong, T.-Y., 2000. Leachate in landfills: the stability issues. *Geotextiles and Geomembranes*, 18(5), pp.293-309. [DOI]

Kumar, S. and Yong, W.-L., 2002. Effect of bentonite on compacted clay landfill barriers. *Soil and Sediment Contamination*, 11(1), pp.71-89. [DOI]

Little, D. N., 1998. *Evaluation of Structural Properties of Lime Stabilized Soils and Aggregates*. National Lime Association, pp.98.

Maritsa, L., Tsakiridis, P., Katsiotis, N., Tsiavos, H., Velissariou, D., Xenidis, A. and Beazi-Katsioti, M., 2016. Utilization of spilitic mining wastes in the construction of landfill bottom liners. *Journal of Environmental Chemical Engineering*, 4(2), pp.1818-1825. [DOI]

Masihi, H. and Gholikandi, G. B., 2020. Using acidic-modified bentonite for anaerobically digested sludge conditioning and dewatering. *Chemosphere*, 241, p.125096. [DOI]

Mokhahlane, L., 2013. *Composition and Performance of Multi-Layer Liner Systems to Inhibit Contaminant Transport in a Fly-Ash Dump*. University of the Witwatersrand, pp.189.

Ng, C. W., Coo, J. L., Chen, Z. K. and Chen, R., 2016. Water infiltration into a new three-layer landfill cover system. *Journal of Environmental Engineering*, 142(5), p.04016007. [DOI]

Nhan, C., Graydon, J. and Kirk, D., 1996. Utilizing coal fly ash as a landfill barrier material. *Waste Management*, 16(7), pp.587-595. [DOI]

Nurdin, S., Samang, L., Patanduk, J. and Harianto, T., 2016. Performance of soft soil stabilized by fly ash with natural fiber reinforcement as landfill cover layer. *International Journal of Innovative Research in Advanced Engineering*, 3(12), pp.15-22.

Omidi, G., Prasad, T., Thomas, J. and Brown, K., 1996. The influence of amendments on the volumetric shrinkage and integrity of compacted clay soils used in landfill liners. *Water, Air, and Soil Pollution*, 86(1), pp.263-274. [DOI]

Puspita, A. S., Budihardjo, M. A. and Samadikun, B. P., 2023. Evaluating coconut fiber and fly ash composites for use in landfill retention layers. *Global Nest Journal*, 25(4), pp.1-7. [DOI]

Puspita, A. S., Budihardjo, M. A. and Samadikun, B. P., 2024. Desiccation and crack behavior of modified waste materials–clay mixture as landfill liner: A systematic review. *International Journal of Environmental Science and Technology*, 21(5), pp.5231-5246. [DOI]

Qiang, X., Hai-Jun, L., Zhen-Ze, L. and Lei, L., 2014. Cracking, water permeability and deformation of compacted clay liners improved by straw fiber. *Engineering Geology*, 178, pp.82-90. [DOI]

Qin, S., Cheng, Y. and Zhou, W.-H., 2023. State-of-the-art review on pressure infiltration behavior of bentonite slurry into saturated sand for TBM tunneling. *Smart Construction and Sustainable Cities*, 1(1), p.14. [DOI]

Revil, A. and Cathles Iii, L., 1999. Permeability of shaly sands. *Water Resources Research*, 35(3), pp.651-662. [DOI]

Rubey, W. W., 1933. The size distribution of heavy minerals within a water-laid sandstone. *Journal of Sedimentary Research*, 3(1), pp.3-29.

Rubinos, D., Spagnoli, G. and Barral, M. T., 2015. Assessment of bauxite refining residue (red mud) as a liner for waste disposal facilities. *International Journal of Mining, Reclamation and Environment*, 29(6), pp.433-452. [DOI]

Scalia IV, J. and Benson, C. H., 2011. Hydraulic conductivity of geosynthetic clay liners exhumed from landfill final covers with composite barriers. *Journal of Geotechnical and Geoenvironmental Engineering*, 137(1), pp.1-13. [DOI]

Singh, S. P. and Hendry, M. J., 2013. Solid-phase distribution and leaching behaviour of nickel and uranium in a uranium waste-rock piles. *Water, Air, & Soil Pollution*, 224(1), p.1360. [DOI]

Staub, M. J., Marcolina, G., Gourc, J.-P. and Simonin, R., 2011. An incremental model to assess the environmental impact of cap cover systems on MSW landfill emissions. *Geotextiles and Geomembranes*, 29(3), pp.298-312. [DOI]

Sua-Iam, G. and Makul, N., 2013. Utilization of limestone powder to improve the properties of self-compacting concrete incorporating high volumes of untreated rice husk ash as fine aggregate. *Construction and Building Materials*, 38, pp.455-464. [DOI]

Uddin, F., 2021. Environmental hazard in textile dyeing wastewater from local textile industry. *Cellulose*, 28(17), pp.10715-10739. [DOI]

Vaverková, M. D., Adamcová, D., Radziemska, M., Voběrková, S., Mazur, Z. and Zloch, J., 2018. Assessment and evaluation of heavy metals removal from landfill leachate by Pleurotus ostreatus. *Waste and Biomass Valorization*, 9(3), pp.503-511. [DOI]

Vipulanandan, C. and Leung, M., 1995. Treating contaminated, cracked and permeable field clay with grouts. In: *Geoenvironment 2000: Characterization, Containment, Remediation, and Performance in Environmental Geotechnics*. ASCE, pp.234-249.

Witt, K. and Zeh, R., 2005. Cracks due to desiccation in cover lining systems phenomena and design strategy. In: *Proceedings of the International Workshop LIRIGM*. Grenoble University, France, pp.112-128.

Yetilmezsoy, K. and Sapci-Zengin, Z., 2009. Recovery of ammonium nitrogen from the effluent of UASB treating poultry manure wastewater by MAP precipitation as a slow release fertilizer. *Journal of Hazardous Materials*, 166(1), pp.260-269. [DOI]

Nature Environment and Pollution Technology
An International Quarterly Scientific Journal

p-ISSN: 0972-6268
(Print copies up to 2016)
e-ISSN: 2395-3454

Vol. 25 | No. 3 | Article ID B4419 | 2026

Original Research Paper

https://doi.org/10.46488/NEPT.2026.v25i03.B4419

Open Access Journal

Microbial Interventions for Sustainable Agriculture: Plant Growth-Promoting Rhizobacteria (PGPR) Activity of Isolates of Saline Soils from Karad Taluka, Maharashtra, India

Priyadarshani A. Patil†, Aparna G. Pathade and Girish R. Pathade

Krishna Institute of Science and Technology (Formerly Krishna Institute of Allied Sciences), Krishna Vishwa Vidyapeeth (Deemed to be University), Karad, 415539, Maharashtra, India

†Corresponding author: Priyadarshani A. Patil; pp1655159@gmail.com

Abbreviation: Nat. Env. & Poll. Technol.
Website: www.neptjournal.com

Received: 26-11-2025
Revised: 16-02-2026
Accepted: 19-02-2026

Key Words:

Halotolerant bacteria
Plant growth-promoting rhizobacteria
Bioinoculants
Phosphorus solubilization
Potassium solubilization

Citation for the Paper:

Patil, P.A., Pathade, A.G. and Pathade, G.R., 2026. Microbial interventions for sustainable agriculture: PGPR activity of isolates of saline soils from Karad Taluka, Maharashtra, India. *Nature Environment and Pollution Technology*, 25(3), B4419. https://doi.org/10.46488/NEPT.2026.v25i03.B4419

Note: From 2025, the journal has adopted the use of Article IDs in citations instead of traditional consecutive page numbers. Each article is now given individual page ranges starting from page 1.

Copyright: © 2026 by the authors
Licensee: Technoscience Publications
This article is an open access article distributed under the terms and conditions of the Creative Commons Attribution (CC BY) license (https://creativecommons.org/licenses/by/4.0/).

ABSTRACT

Soil salinity remains a major abiotic factor limiting agricultural productivity worldwide, with the situation worsening in parts of Maharashtra, particularly Karad Taluka. This study examined saline soils from various locations within Karad, assessing their physicochemical properties and isolating indigenous halotolerant bacterial strains that exhibit plant growth-promoting rhizobacterial (PGPR) traits. The soil analysis revealed highly alkaline pH levels (8.8-9.4), elevated sodium concentrations, and deficiencies in organic carbon, nitrogen, and micronutrients. Five halotolerant bacterial isolates (Ko1, Va1, Be1, Vm1, and At1) were obtained and evaluated for PGPR activities such as phosphate and potassium solubilization, nitrogen fixation, indole-3-acetic acid (IAA) production, and siderophore synthesis. All isolates demonstrated positive results in phosphate and potassium solubilization, nitrogen fixation, and IAA production, with four also producing siderophores. Notably, isolates Be1, Vm1, and At1 showed strong performance across multiple traits, highlighting their potential as bioinoculant candidates. These findings suggest that native halotolerant PGPR strains from Karad Taluka could enhance soil fertility, improve nutrient uptake, and support plant growth in saline conditions. Future research including field trials and molecular characterization could facilitate the development of environmentally sustainable microbial formulations for saline agriculture.

1. INTRODUCTION

Soil salinity is a major abiotic factor limiting agricultural productivity worldwide. It affects soil structure, nutrient availability, microbial activity, and plant physiological processes (Butcher et al. 2016, Metternicht & Zinck 2003, Wang et al. 2003). Salinity causes osmotic stress, ion toxicity, and nutrient imbalance, significantly reducing crop growth and yields, particularly in arid and semi-arid regions where poor irrigation practices and excessive fertilizer application accelerate soil degradation (Hailu & Mehari 2021, Hussain et al. 2019, Sultana et al. 2020). In India, approximately 7 million hectares are affected by salinity and sodicity, with secondary salinization increasing in irrigated areas (Mandal et al. 2009, Sharma & Chaudhari 2012). Maharashtra has become a hotspot where intensive farming and inadequate drainage have led to soil alkalinity and nutrient depletion. In Karad Taluka, situated in the Krishna River basin and primarily cultivating sugarcane, soils are increasingly characterized by high pH, sodicity, low organic carbon, and micronutrient deficiencies, threatening long-term soil fertility and crop productivity. Conventional management of saline soils relies heavily on chemical amendments and fertilizers, which often only offer short-term relief and may harm soil biological health further. Plant growth-promoting rhizobacteria (PGPR) present a sustainable alternative by boosting nutrient availability and helping plants withstand stress through mechanisms such as nitrogen fixation, solubilization

of phosphorus and potassium, phytohormone production, and siderophore-mediated iron uptake (Alori et al. 2017, Alori & Babalola 2018, Ambrosini et al. 2016). Numerous studies have shown that halotolerant PGPR can enhance crop performance under saline conditions (Jiang et al. 2018, Krishnamoorthy et al. 2016). However, most research focuses on coastal, desert, or arid ecosystems, with inland saline-alkaline soils remaining underexplored, especially in Western Maharashtra. Additionally, native microbes adapted to local soil conditions are more likely to survive, colonize the rhizosphere, and function effectively as bioinoculants than introduced strains (Trabelsi & Mhamdi 2013, Patil et al. 2024). Despite increasing salinity problems in Karad Taluka, there is a lack of systematic studies connecting soil physicochemical constraints to the functional screening of indigenous halotolerant PGPR.

This study aims to characterize the physicochemical properties of saline soils in Karad Taluka, Maharashtra, and to isolate and assess indigenous halotolerant bacterial strains for key plant growth-promoting traits such as phosphate and potassium solubilization, nitrogen fixation, indole-3-acetic acid production, and siderophore synthesis. By focusing on locally adapted microorganisms, the research seeks to identify potential bioinoculants for the sustainable management and reclamation of inland saline agricultural soils.

2. MATERIAL AND METHODS

2.1. Study Area and Soil Sample Collection

Composite saline soil samples were gathered from eight locations in Karad Taluka (see Fig. 1). Each site was precisely georeferenced with latitude and longitude coordinates. Soil samples were extracted at a depth of 15 cm using a borer. At each site, five subsamples, four from the corners and one from the center, were combined, thoroughly mixed, and reduced to about 100 g by quartering. These samples were stored in sterile polythene bags at low temperature for further analysis (Ghare & Kumbhar 2021, Kekane et al. 2015, Raut & Kurhe 2020).



Fig. 1: Map of Karad Taluka.

2.2. Physicochemical Characterization of Soil Samples

The soil samples were analyzed for a variety of essential physical and chemical parameters to evaluate their fertility and salinity. pH and electrical conductivity (EC) were measured using calibrated digital meters to determine alkalinity and salinity. Organic carbon (OC) was assessed through the dichromate oxidation method, offering insights into soil organic matter content and overall soil health. Nitrogen levels were measured using the Kjeldahl method, phosphorus via the colorimetric molybdenum blue method, and potassium with Atomic Absorption Spectroscopy (AAS). To evaluate soil base saturation and cation balance, secondary nutrients such as calcium and magnesium were determined through EDTA titration. Additionally, micronutrients including iron (Fe), copper (Cu), zinc (Zn), manganese (Mn), boron (B), and sulfur (S) were analyzed using AAS or suitable colorimetric techniques to assess their availability for plant uptake. These analyses provided a comprehensive understanding of the chemical composition and nutritional status of the soil samples (Ghare & Kumbhar 2021, Raut & Kurhe 2020, Panhalkar 1994, Kekane et al. 2015).

2.3. Enrichment, Isolation and Morphological Characterization of Bacterial Isolates

Soil samples were inoculated into nutrient broth containing 7.5% (w/v) NaCl and incubated at 30°C for 48 h under static conditions. The resulting enriched cultures were serially diluted and plated onto nutrient agar with the same salt concentration, then incubated again at 30°C for 48 h (Vazquez et al. 2000). Morphologically distinct colonies were purified through repeated streaking. To assess salt tolerance, purified isolates were evaluated for growth on nutrient agar with increasing NaCl concentrations (0%, 2.5%, 5%, 7.5%, and 10% w/v). These plates were incubated at 30°C for 48–72 h, and growth was qualitatively assessed based on colony formation. Isolates that consistently grew at $\geq$7.5% NaCl were identified as halotolerant and selected for further screening of plant growth-promoting rhizobacteria (Vazquez et al. 2000). Morphological traits, including colony shape, size, margin, elevation, texture, pigmentation, Gram stain, and motility, were recorded.

2.4. Screening for PGPR Traits

The plant growth-promoting traits of the bacterial isolates

were assessed using established microbiological techniques. The Phosphate Solubilization Index (PSI) was determined by cultivating the isolates on Pikovskaya's agar plates for seven days at 28 ± 2°C (Chakdar et al. 2018, Kirui et al. 2022, Mengesha & Legesse 2024). Potassium solubilization was evaluated on Aleksandrov agar medium supplemented with feldspar as a potassium source, and the Potassium Solubilization Index (KSI) was calculated based on the size of the solubilization zone (Verma et al. 2017). To determine nitrogen-fixing ability, isolates were grown on nitrogen-free Ashby's Mannitol agar to demonstrate diazotrophic activity, followed by the acetylene reduction assay for quantification (Tang et al. 2020). IAA production was measured using Salkowski reagent, with results compared to a standard curve for accurate quantification (Patten & Glick 2011). Lastly, siderophore production was assessed on Chrome Azurol S (CAS) agar, where the formation of clear halos around colonies indicated successful siderophore synthesis.

2.5. Controls and Experimental Validation

Uninoculated media were used as negative controls in all biochemical and PGPR assays to ensure their specificity. For qualitative comparisons, previously documented PGPR-positive laboratory strains served as reference standards for phosphate solubilization, IAA production, and siderophore synthesis.

2.6. Molecular Characterization by Using 16S rRNA

The bacterial strains were identified via 16S rRNA gene sequencing. Genomic DNA was isolated and purified using the Thermo Scientific® GeneJet™ Genomic DNA Purification Kit (Youseif 2018).

2.7. Statistical Analysis

All experiments were conducted in triplicate, and results are expressed as mean ± standard deviation. One-way analysis of variance (ANOVA) was used to assess differences in soil physicochemical parameters and PGPR indices, utilizing standard statistical software. A p-value below 0.05 was considered statistically significant.

3. RESULTS

3.1. Physicochemical Properties of Saline Soils

The soils of Karad Taluka display considerable variability in texture, nutrient composition, and chemical characteristics. Predominantly classified as clay loam with 30–38% sand content, these soils exhibit good water retention. As detailed

Table 1(a): Physicochemical properties of saline soils.

Parameters	Permissible level	Belwade Budruk	Vanvasmachi	Dushere	Atake	Khodshi East	Khodshi West	Koparde	Gondi
Soil Texture Composition		Sand 38%, Silt 42%, Clay 20%	Sand 32%, Silt 40%, Clay 28%	Sand , Silt 26%, Clay 6%	Sand 30%, Silt 34%, Clay 36%	Sand 38%, Silt 20%, Clay 42%	Sand 30%, Silt 36%, Clay 34%	Sand 34%, Silt 30%, Clay 36%	Sand 32%, Silt 28%, Clay 40%
Texture		Loam	Clay loam	Clay	Clay loam	Sandy clay	Clay loam	Clay loam	Clay loam
pH	6.5-7.5	9.09	9.2	9.1	8.9	8.9	9.2	8.8	9
Na	0-1	3	4.1	5.4	3.9	3.3	3.2	3.8	3.1
Organic Carbon (%)	0.40-0.60	0.12	0.15	0.14	0.13	0.18	0.16	0.15	0.14
N (kg/ha)	280-420	110	120	105	100	115	118	125	108
P (kg/ha)	14-21	10.5	9.8	9.5	8.9	9.5	9.2	9	8.7
K (kg/ha)	150-200	142	135	138	140	145	148	150	138
Cu (ppm)	0.20-99.99	3.5	3.2	3.4	3.3	3.1	3.2	3	2.9
Fe (ppm)	4.5-9.9	4	3.8	3.7	3.9	3.6	3.7	3.5	3.4
Zn (ppm)	0.61-99.99	0.52	0.48	0.5	0.46	0.44	0.45	0.43	0.41
Mn (ppm)	2.0-99.99	0.28	0.25	0.26	0.24	0.27	0.26	0.25	0.23
Br (ppm)	0.6-0.99	0.75	0.72	0.74	0.7	0.68	0.69	0.72	0.65
S (ppm)	10.-20	9.8	9.2	9.5	9	8.8	8.9	9.1	8.6
$CaCO_3$ (%)	10	10	20	6.1	13.4	6.8	6.6	6.5	6
Water Holding Capacity (%)		20	20	27	20	29	28	27	26

Table Cont....

in Table 1(a, b) and Fig. 2(a–d), they are alkaline (pH 8.8–9.4) with elevated sodium levels (3.0–5.4), raising salinity concerns. Organic carbon content ranges from 0.12% to 0.19%, below the optimal 0.4–0.6%, indicating low organic matter and diminished microbial activity. Nitrogen levels (95–150 kg.ha^{-1}) fall short of the recommended 280–420 kg.ha^{-1}, while phosphorus (8.5–11.2 kg.ha^{-1}) and potassium (132–162 kg.ha^{-1}) are moderate. Copper (2.8–3.8 ppm) and iron (3.3–4.4 ppm) are adequate, whereas zinc (0.41–0.65 ppm) and manganese (0.23–0.38 ppm) are deficient. Sulfur

Table 1(b): Physicochemical properties of saline soils.

Parameters	Permissible level	Karve	Vadgaon Haveli	Chore	Gharewadi	Nandgaon	Shenoli	Kodoli	Mean ± S.D
Soil Texture Composition		Sand 30%, Silt 34%, Clay 36%	Sand 30%, Silt 30%, Clay 40%	Sand 36%, Silt 34%, Clay 30%	Sand 30%, Silt 30%, Clay 40%	Sand 36%, Silt 32%, Clay 32%	Sand 30%, Silt 38%, Clay 32%	Sand 30%, Silt 30%, Clay 40%	
Texture		Clay loam	Clay loam	Clay loam	Clay loam	Clay loam	Clay loam	Clay loam	
pH	6.5-7.5	9.4	9.1	9	8.9	9.2	9.3	9.1	9.08 ± 0.17
Na^+	0-1	3.4	3.2	4.1	4.9	5.3	3.4	4.2	3.89 ± 0.79
Organic Carbon (%)	0.40-0.60	0.19	0.17	0.15	0.13	0.14	0.15	0.16	0.15 ± 0.02
N (kg/ha)	280-420	95	100	102	130	145	138	150	117.4 ± 17.15
P (kg/ha)	14-21	8.5	9	8.8	10.8	11.2	10.5	10.2	9.61 ± 0.85
K (kg/ha)	150-200	132	141	139	155	160	158	162	145.53 ± 9.51
Cu (ppm)	0.20-99.99	2.8	3.2	3.1	3.6	3.8	3.5	3.7	3.29 ± 0.29
Fe (ppm)	4.5-9.9	3.3	3.5	3.6	4.3	4.4	4.2	4.1	3.80 ± 0.34
Zn (ppm)	0.61-99.99	0.42	0.44	0.45	0.6	0.65	0.58	0.62	0.50 ± 0.08
Mn (ppm)	2.0-99.99	0.24	0.25	0.26	0.35	0.38	0.36	0.34	0.28 ± 0.05
Br (ppm)	0.6-0.99	0.63	0.68	0.67	0.8	0.82	0.78	0.79	0.72 ± 0.06
S (ppm)	10.-20	8.4	9	8.7	10.2	10.8	10.4	10.1	9.37 ± 0.73
$CaCO_3$ (%)	10	6.2	16.4	6.3	7	7.2	6.8	7.1	8.83 ± 4.32
Water Holding Capacity (%)		20	29	27	26	25	29	28	25.40 ± 3.56

ppm: Parts per million, kg/ha: Kilogram per hectare,

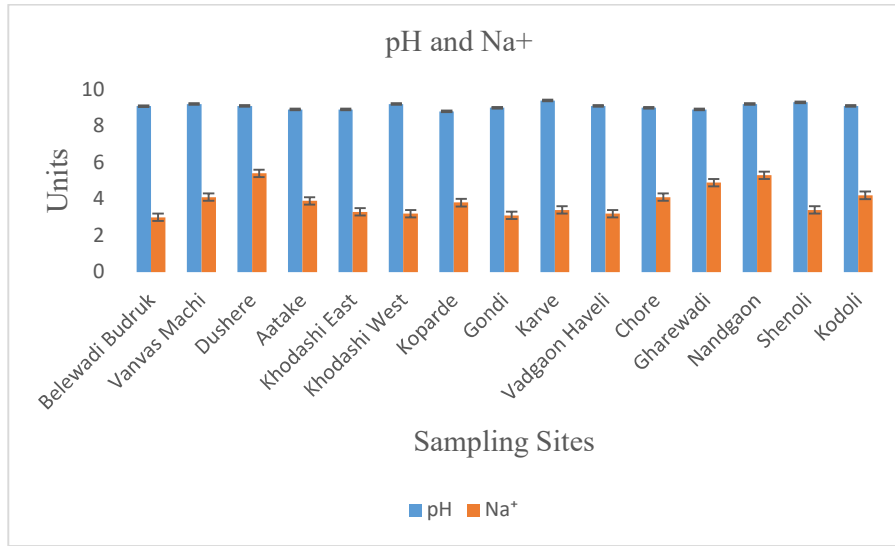


Fig. 2a : pH and Na^+ of soil samples.

Figure Cont....

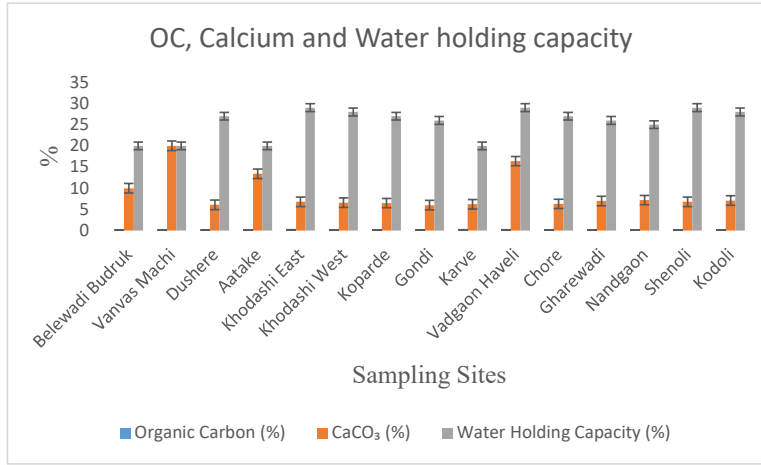


Fig 2b: OC, $CaCO_3$ and water holding capacity of soil samples sites.

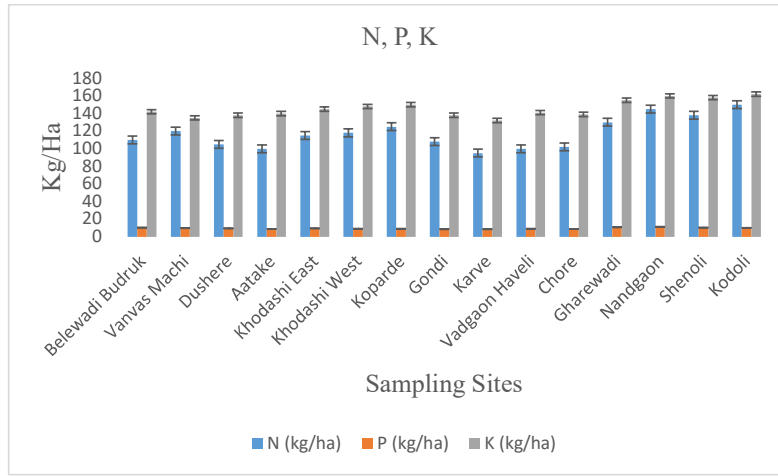


Fig. 2c: N, P, K of soil samples.

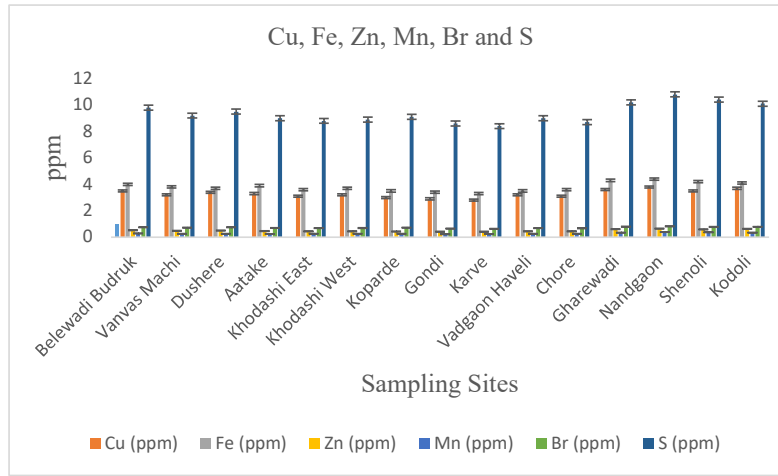


Fig. 2d: Cu, Fe, Zn, Mn, Br and S of soil samples.

(8.4–10.8 ppm) is near the lower threshold, and calcium carbonate (6–16%) is present at moderate levels. Water-holding capacity, ranging from 20% to 29%, correlates with clay content. Overall, these soils are alkaline, low in organic carbon and nitrogen, and moderately rich in nutrients. To enhance soil fertility and productivity, organic amendments and balanced fertilization are essential.

The soils exhibited an average pH of 9.09 with minimal variability (CV = 1.76%), indicating consistent alkalinity across the sampling sites. Sodium levels demonstrated moderate variability (CV = 20.31%), confirming heterogeneous sodicity. Organic carbon content was low, reflecting poor organic matter in the saline soils. Potassium levels remained high and stable, while nitrogen and phosphorus showed moderate fluctuations. Micronutrients such as zinc and manganese also varied, indicating potential deficiencies. Calcium carbonate content was highly variable (CV = 48.24%) due to uneven calcareousness, influencing alkalinity and nutrient availability. Sodicity and soil texture moderately impacted water-holding capacity.

Based on the coefficient of variation (CV), soil pH and the nutrients P, K, Cu, Fe, Br, and S showed low variability (<10%), indicating a uniform distribution across the sites. Organic carbon (OC), nitrogen (N), zinc (Zn), manganese (Mn), and water-holding capacity (WHC) exhibited moderate variability (10–20%), suggesting spatial variation influenced by soil management practices and organic matter content. In contrast, sodium (Na^+) and calcium carbonate ($CaCO_3$) showed high variability (>20%), reflecting heterogeneity in salinity and calcareousness, possibly due to local environmental conditions and parent material. One-way ANOVA for soil pH showed no significant differences among the groups ($F = 2.08$, $p = 0.173$, $p > 0.05$), indicating that pH remained relatively consistent across the sampling locations.

The performance variation among the halotolerant bacterial isolates was linked to their origin in saline-alkaline, nutrient-deficient soils. These soils, characterized by high pH, elevated sodium content, and low organic carbon, favor microorganisms capable of enduring osmotic and ionic stress. Isolates Be1, Vm1, and At1 exhibited enhanced phosphate and potassium solubilization, nitrogen fixation, IAA production, and siderophore secretion, indicating adaptations for nutrient mobilization. In alkaline soils, where phosphorus and potassium often exist in insoluble forms, these microbes have an advantage by increasing nutrient bioavailability. Siderophores likely assist in overcoming iron limitations, while IAA promotes root growth, strengthening plant-microbe interactions. Ko1 did not produce siderophores, suggesting niche specialization. Overall, the variation in functional traits driven by soil conditions indicates that locally adapted, multifunctional isolates are more effective as bioinoculants in saline-alkaline environments, highlighting the importance of selecting region-specific microbial strains.

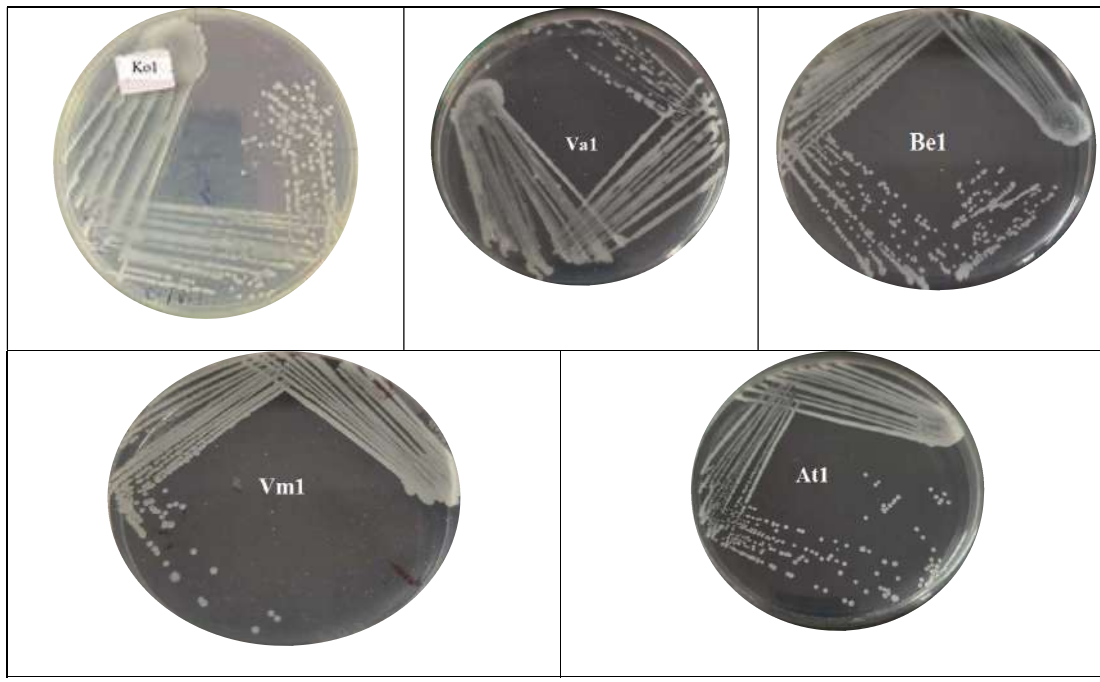


Fig. 3: Bacterial isolates from saline soil samples grown on nutrient agar media at 30°C for 48 hr.

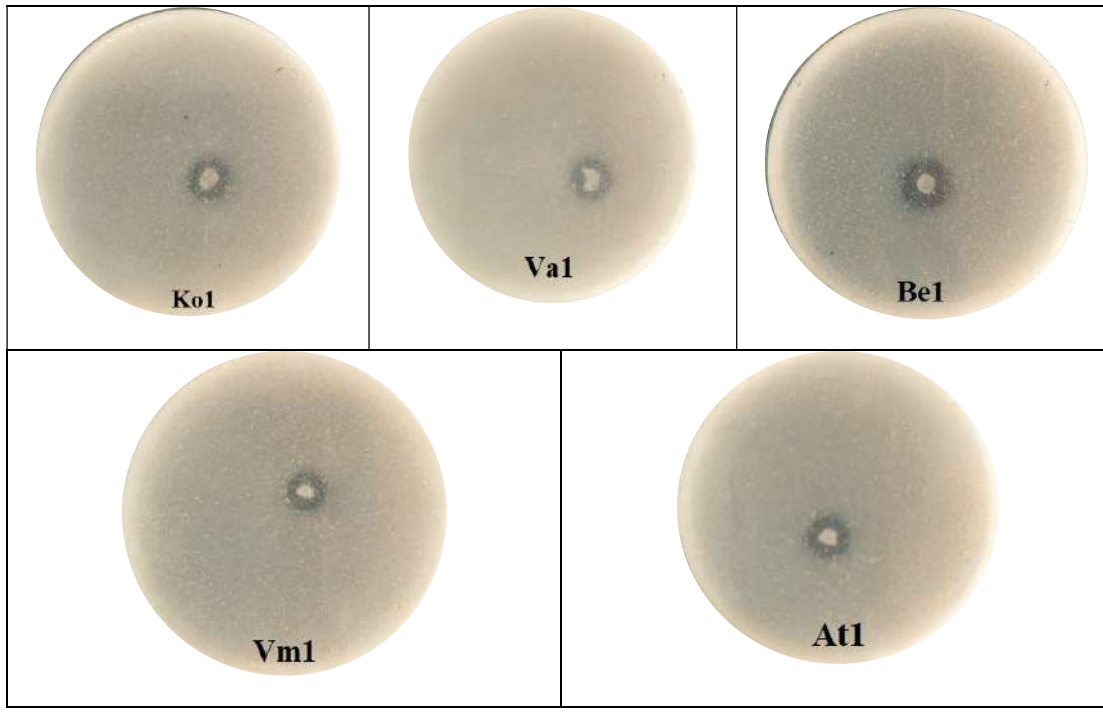


Fig. 4: Phosphate solubilization by isolates on Pikovskaya's medium.

3.2. Morphological Characteristics of Bacterial Isolates

The morphological and microscopic features of five bacterial isolates, i.e., Ko1, Va1, Be1, Vm1, and At1 are detailed in Fig. 3. These isolates were collected from diverse soil samples. All colonies appeared round or circular, varying in size from pinpoint to 1 mm, which reflects differences in growth rates and colony density. Colony colors ranged from white to off-white or transparent, with textures fluctuating from moist and slimy to dry-moist, indicating surface hydration variability. Most colonies were flat to convex with smooth, entire margins, suggesting uniform boundaries without irregularities. Microscopic examination showed that all isolates were Gram-negative, short rods, indicating a dominance of non-spore-forming Gram-negative bacteria in these samples.

3.3. PGPR Activities of Isolates

In laboratory tests, the bacterial isolates displayed a range of plant growth-promoting properties. All isolates demonstrated phosphate solubilisation, evidenced by halo zone formation on Pikovskaya's agar, although their Phosphate Solubilisation Index (PSI) values varied (Fig. 4).

3.3.1. Determination of Phosphate Solubilisation Index

The isolates demonstrating phosphate-solubilizing activity were later assessed for the Phosphate Solubilization Index (PSI) on Pikovskaya's agar. Each bacterial isolate was placed at the center of a Pikovskaya's agar plate and incubated at 28 ± 2°C for five days (Chakdar et al. 2018, Kirui et al. 2022). On the fifth day, the diameters of the bacterial colony and the clear zone surrounding it were measured and used to calculate the PSI using the specified equation (see Table 2).

Phosphate Solubilizing Index (PSI) = Halo zone diameter + Colony diameter/Colony diameter

3.3.2. Determination of Potassium Solubilization Index

Potassium solubilisation was equally effective, evidenced by distinct solubilisation zones on the Aleksandrov medium and measurable Potassium Solubilisation Index (KSI) values (Fig. 5). The isolates demonstrating phosphate-solubilizing activity were further assessed for the Phosphate Solubilization Index (PSI) on Pikovskaya's agar. Each

Table 2: Phosphate solubilization index of isolates.

Sr. No.	Bacterial Isolate	Colony diameter [mm]	Colony +Halozone diameter [mm]	Phosphate Solubilization Index
1.	Ko1	2	9	5.5
2.	Va1	3	9	4.0
3.	Be1	3	15	6.0
4.	Vm1	3	10	4.33
5.	At1	3	11	4.6

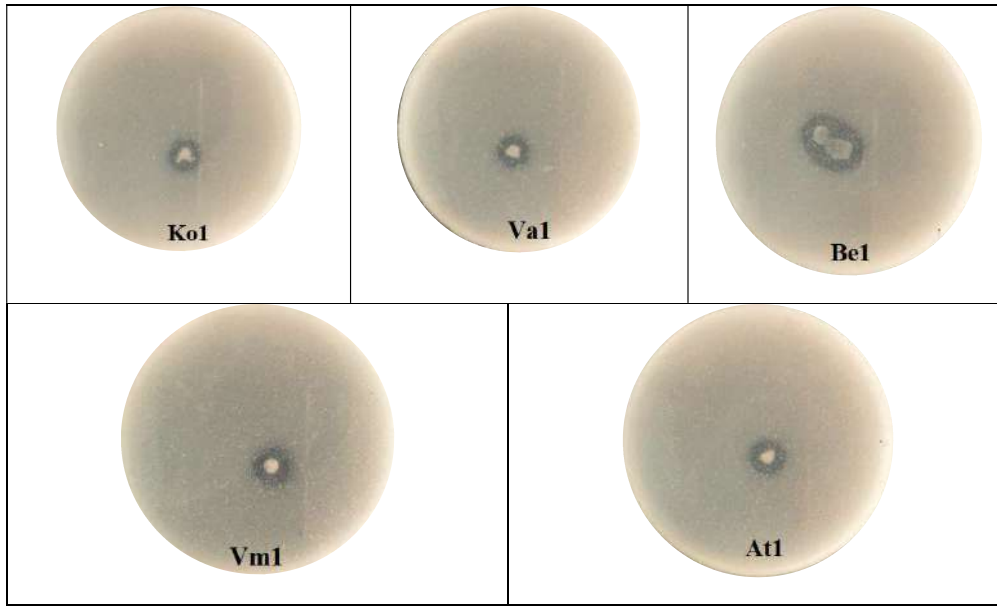


Fig. 5: Potassium solubilization by bacterial isolates on Alexandrov medium.

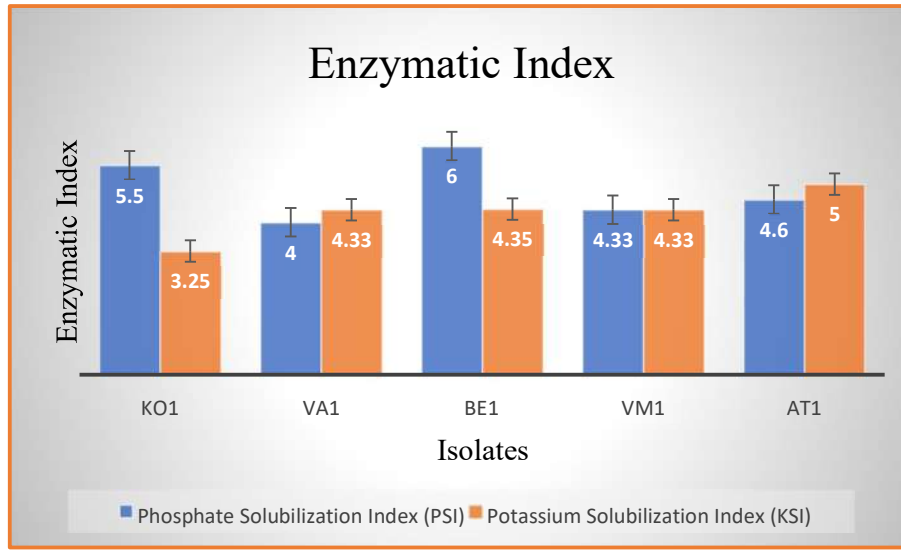


Fig. 6: Enzymatic index of selected isolates.

Table 3: Potassium solubilization index of isolates.

Sr. No.	Bacterial Isolate	Colony diameter [mm]	Colony + Halozone diameter [mm]	Potassium Solubilization Index [PSI]
1.	Ko1	3	9	3.25
2.	Va1	3	10	4.33
3.	Be1	4	13	4.35
4.	Vm1	3	10	4.33
5.	At1	3	12	5.0

bacterial isolate was placed at the center of a Pikovskaya's agar plate and incubated at 28 ± 2°C for five days (Chakdar et al. 2018, Kirui et al. 2022). On the fifth day, the diameters of the bacterial colonies and the clear zones surrounding them were measured to determine the PSI using the specified equation (Table 3 and Fig. 6).

The isolates demonstrated their ability to fix atmospheric nitrogen through growth on Ashby's medium, indicating diazotrophic potential (Fig. 7). Additionally, the development of a distinctive red coloration in the presence of Salkowski

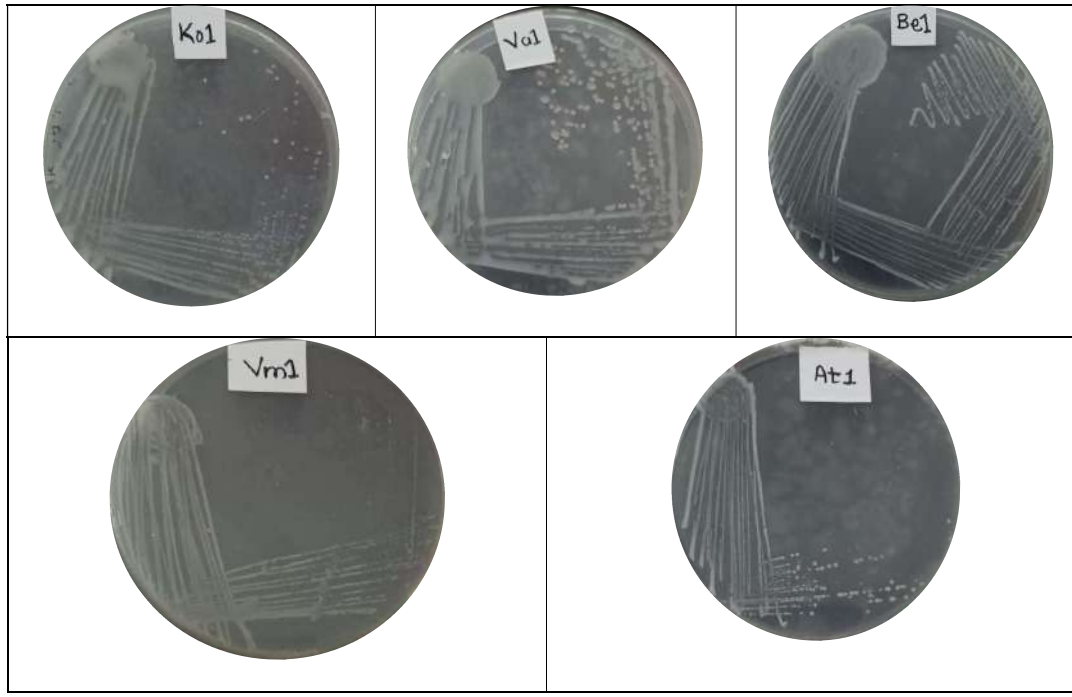


Fig. 7: N_2 Fixation by bacterial isolates on Ashby's medium.

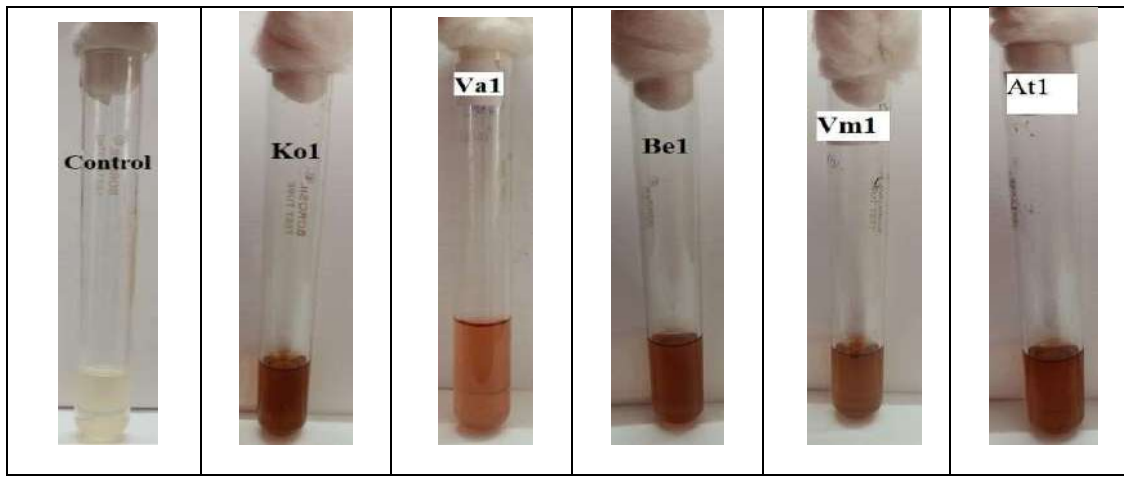


Fig. 8: IAA production by bacterial isolates on LB Broth supplemented with L-tryptophan (0.1%).

reagent confirmed that all isolates tested positive for indole-3-acetic acid (IAA) production (Fig. 8). Finally, four isolates (Va1, Be1, Vm1, and At1) produced siderophores, whereas Ko1 showed no siderophore activity (Fig. 9).

Isolate Be1, Vm1, and At1 among the tested strains exhibited strong multi-trait PGPR activity, including phosphate and potassium solubilization, nitrogen fixation, IAA production, and siderophore production. They emerged as promising candidates for bioinoculant development. The plant growth-promoting rhizobacteria (PGPR) traits of five halotolerant bacterial isolates were systematically evaluated, with results summarized in Table 4. All isolates showed positive activity for phosphate and potassium solubilization, nitrogen fixation, and IAA production, indicating their potential to enhance nutrient availability and promote plant growth in saline conditions. Ko1 displayed activity for all traits except siderophore production, suggesting it supports plant growth through nutrient mobilization and hormone production but may have a limited role in iron chelation. Conversely, Va1, Be1, Vm1, and At1 tested positive for

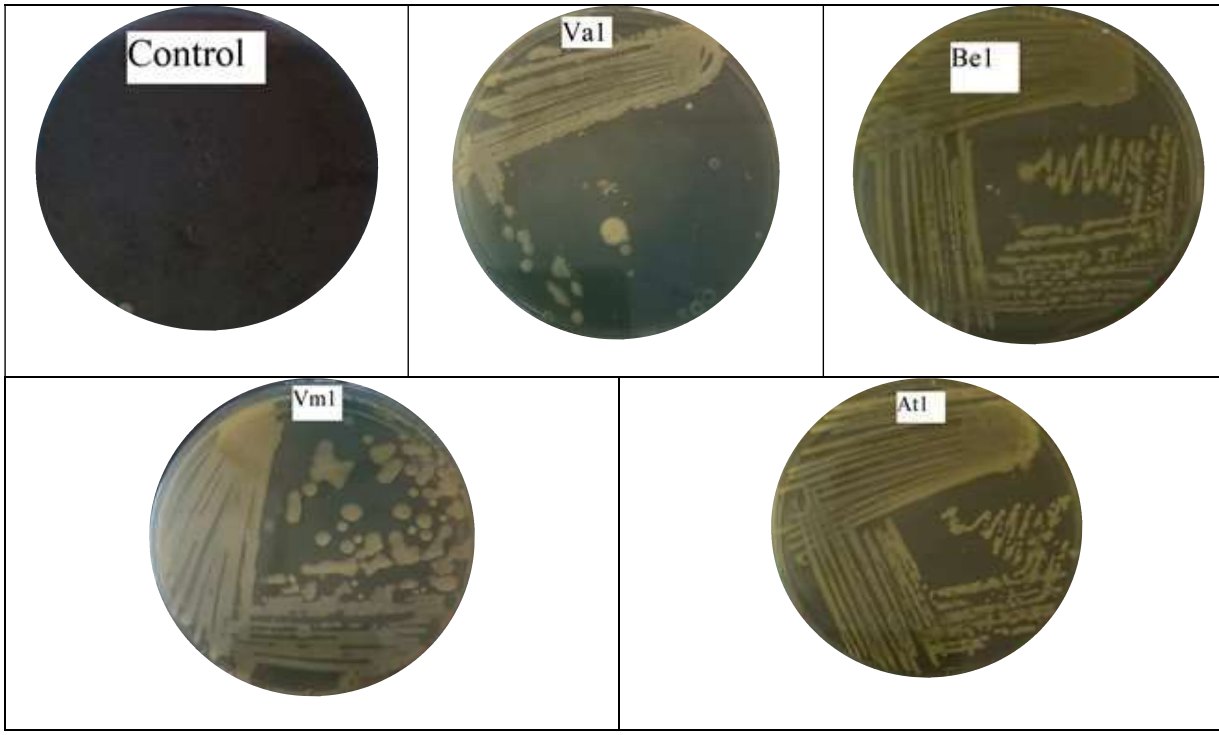


Fig. 9: Production of Siderophores by bacterial isolates on Chrome Azurol S (CAS) agar.

Table 4: Summarized PGPR activity.

Sr. No.	Isolates	P Solubilization	K Solubilization	N_2 Fixation	IAA Production	Siderophore Production
1	Ko1	+	+	+	+	-
2	Va1	+	+	+	+	+
3	Be1	+	+	+	+	+
4	Vm1	+	+	+	+	+
5	At1	+	+	+	+	+

all five PGPR traits, with siderophore production adding to their multifunctional potential and making them strong bioinoculant candidates. Overall, while all isolates show promise, Be1, Vm1, and At1 stand out for their consistent performance across all traits, highlighting their potential in developing microbial bioformulations to boost crop productivity and soil fertility in saline-affected areas.

3.4. Molecular Identification

The genomic DNA of three isolates, At1, Vm1 and Be1, was identified as *Pantoea dispersa, Solibacillus isronensis* and *Pseudomonas putida,* respectively, using the BLASTN tool for 16s rDNA partial gene sequencing (Fig. 10).

4. DISCUSSION

The study isolated indigenous halotolerant bacteria from saline soils in Karad, Maharashtra, demonstrating effective plant growth-promoting capabilities. All strains exhibited traits such as phosphate and potassium solubilization, nitrogen fixation, and IAA production. Additionally, four strains (Va1, Be1, Vm1, and At1) produced siderophores. These salt-adapted microorganisms enhance plant growth under saline conditions.

Soil salinity and sodicity threaten agricultural sustainability by causing land degradation and adversely affecting the soil properties essential for plant growth. Metternicht and Zinck (2003) and Butcher et al. (2016) identified soil salinity as a major constraint on soil fertility. The strongly alkaline and sodic conditions observed in Karad Taluka provide a clear ecological context for the functional traits expressed by the isolated bacteria. The consistent expression of phosphate and potassium solubilization across

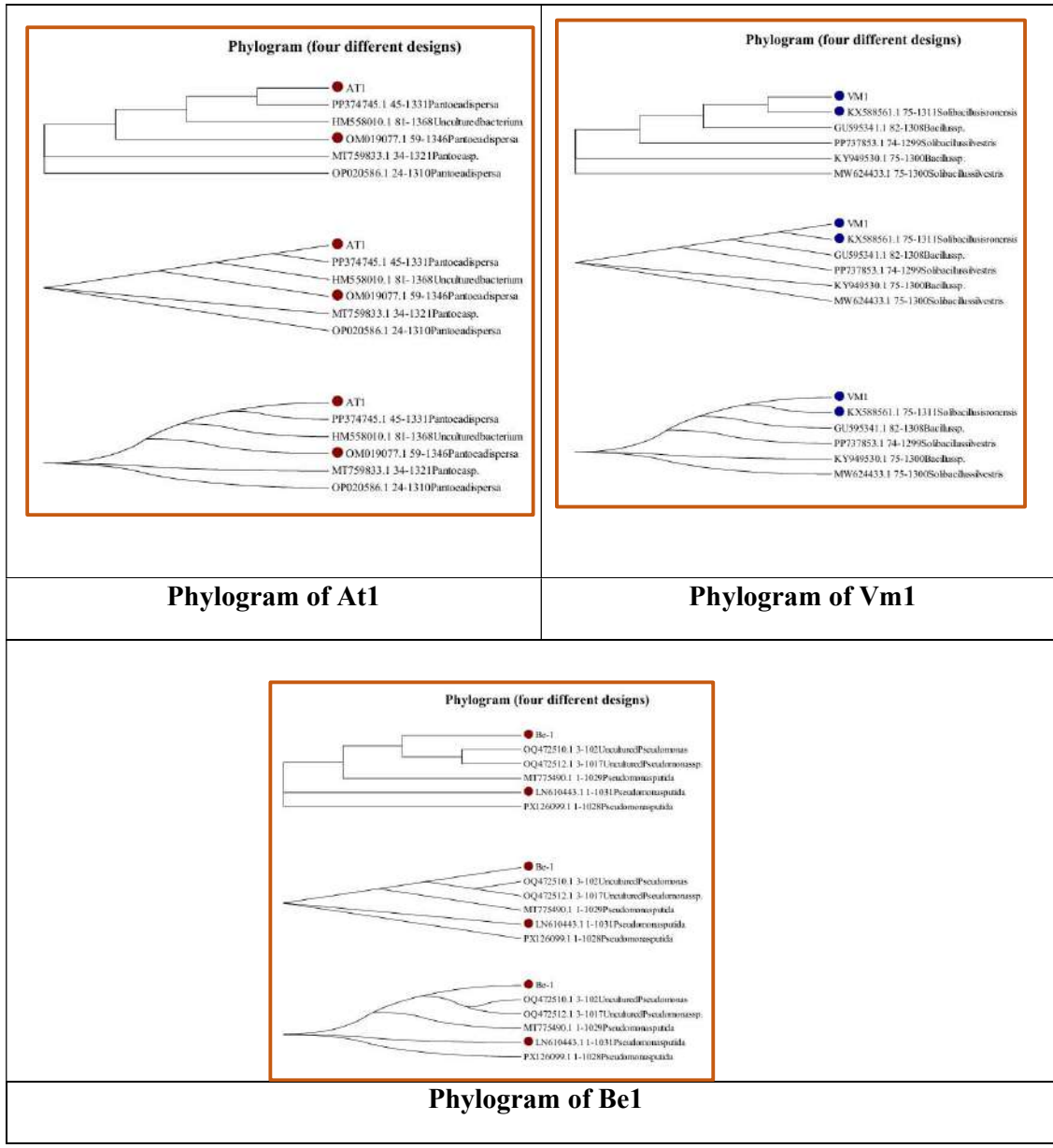


Fig. 10: Phylograms of isolates.

all isolates reflects the selective pressure imposed by alkaline soils, where essential nutrients are largely immobilized and inaccessible to plants. This suggests that nutrient solubilization is not incidental but rather a necessary adaptive trait for microbial persistence in these soils.

Jiang et al. (2018) observed that halotolerant microorganisms from saline soils often demonstrate enhanced mineral solubilization. This accounts for the superior performance of isolates Be1, Vm1, and At1 in phosphate and potassium solubilization tests. These isolates likely have more effective mechanisms for producing organic acids or chelating metals, giving them a competitive edge under nutrient-limited conditions. The narrower functional range of isolate Ko1 suggests niche specialization rather than diminished viability, highlighting the functional diversity within native microbial communities.

Krishnamoorthy et al. (2016) showed that nitrogen-fixing bacteria are more prevalent in salt-affected soils with low organic carbon content. All isolates maintained their diazotrophic ability, indicating an adaptive advantage. In these challenging soils, nitrogen fixation likely compensates for nitrogen scarcity, supporting microbial survival and

maintaining rhizosphere stability. This strategy enhances the ecological importance of these isolates for sustainable nutrient cycling in saline agricultural environments.

Alori & Babalola (2018) highlighted the crucial role of phytohormone-producing PGPR in enhancing root architecture under stress conditions, aligning with the universal IAA production observed in this study. IAA-driven root elongation and branching likely promote increased contact between roots and microbes, as well as more efficient nutrient uptake, thereby supporting stronger microbial colonization in challenging soil environments. This function is especially vital in saline soils, where root growth is often hindered by osmotic stress.

Ambrosini et al. (2016) found that siderophore production enhances microbial competitiveness and promotes iron uptake in plants within alkaline soils, explaining why four isolates exhibited this trait. Due to the significantly reduced iron availability at high pH levels, siderophore synthesis likely boosts both microbial survival and plant nutrition. The lack of siderophore production in isolate Ko1 further indicates a case of functional specialization rather than a shared trait among the isolates.

Hailu & Mehari (2021) and Fahad et al. (2020) noted that salinity stress imposes multiple simultaneous constraints on plants, underscoring the importance of multifunctional PGPR. The superior multi-trait performance of Be1, Vm1, and At1 suggests that functional redundancy across nutrient mobilization, hormone production, and iron acquisition enhances their reliability as bioinoculant candidates for saline-alkaline systems.

Trabelsi & Mhamdi (2013) cautioned that non-native microbial inoculants may disrupt native soil communities, underscoring the importance of using indigenous strains. The isolates identified in this study are adapted to the specific physicochemical constraints of Karad soils, increasing their likelihood of persistence, compatibility, and effectiveness under field conditions.

This study isolated three bacterial strains from the saline soils of Karad Taluka, identified as Pantoea dispersa (At1), Solibacillus isronensis (Vm1), and Pseudomonas putida (Be1) through partial 16S rDNA sequencing. All three species are known for their plant growth-promoting abilities or salt-stress tolerance, positioning them as promising bioinoculants for saline soils. Notably, members of the Pantoea genus, including P. dispersa, are increasingly recognized as salt-tolerant PGPR that enhance plant growth via mechanisms such as phytohormone (e.g., IAA) production, phosphate solubilization, siderophore synthesis, and ACC deaminase activity, which mitigates ethylene-induced stress under saline conditions (Lv 2022).

Costa-Gutierrez et al. (2022) investigated Pseudomonas putida strains and emphasized their significance as plant growth-promoting rhizobacteria in agriculture. Some P. putida strains demonstrate traits such as producing phytohormones, solubilizing nutrients, and effectively colonizing roots. Their review summarized current understanding of P. putida and related strains, highlighting their plant growth-promoting abilities. Overall, the results indicate that soil-driven selection influences PGPR functionality and that native halotolerant bacteria from inland saline-alkaline soils offer a valuable, ecologically compatible resource for sustainable soil management. By directly associating microbial traits with local soil conditions, this study advances the development of practical bioinoculants for saline agriculture, moving beyond generalized PGPR functions.

This study isolated native, salt-tolerant plant growth-promoting rhizobacteria (PGPR) from inland saline-alkaline soils in Maharashtra, a region with limited microbiological research. It found that soils with high alkalinity (pH 8.8–9.4), sodicity, and low organic carbon and nutrient content harbor bacteria that exhibit multiple plant growth-promoting traits. Unlike many previous studies that focused on single traits or non-native strains, these microorganisms demonstrated abilities such as phosphate and potassium solubilization, nitrogen fixation, indole-3-acetic acid production, and siderophore synthesis. Three isolates—Be1, Vm1, and At1—showed all five traits, indicating strong ecological adaptation and resilience. By combining soil physicochemical analysis with microbial functional screening, this research highlights how inland saline soils select for multifunctional PGPR and lays the groundwork for region-specific bioinoculants aimed at enhancing soil fertility and crop yields in salt-affected areas.

5. CONCLUSIONS

The study demonstrated that the saline soils of Karad Taluka are highly alkaline and deficient in nutrients, which restricts agricultural productivity. Nonetheless, indigenous halotolerant bacterial isolates with plant growth-promoting rhizobacteria (PGPR) traits were successfully identified. These isolates effectively solubilized phosphorus and potassium, fixed nitrogen, and produced indole-3-acetic acid (IAA). Three strains—Be1, Vm1, and At1—exhibited all five key PGPR traits, highlighting their strong potential as sustainable bioinoculants. Their application could improve soil fertility and enhance plant tolerance to salinity, offering an eco-friendly alternative to chemical fertilizers. The soils were markedly alkaline, highly sodic, low in organic carbon, and showed variable nutrient levels. Elevated sodium and

calcium carbonate levels primarily compromised soil physical properties and nutrient availability. Sustainable management strategies should include gypsum application, organic matter addition, and site-specific nutrient management. Future research should focus on molecular characterization and field trials to assess these isolates' effectiveness, thereby advancing soil salinity management and boosting crop productivity sustainably.

6. ACKNOWLEDGMENTS

The authors are thankful to Krishna Institute of Science and Technology, Krishna Vishwa Vidyapeeth, Karad for providing the facilities.

7. REFERENCES

Alori, E.T. and Babalola, O.O., 2018. Microbial inoculants for improving crop quality and human health in Africa. *Frontiers in Microbiology*, 9, pp.1–12. [DOI]

Alori, E.T., Dare, M.O. and Babalola, O.O., 2017. Microbial inoculants for soil quality and plant health. In: *Microorganisms for Sustainability*, Springer, pp.281–307. [DOI]

Ambrosini, A., de Souza, R. and Passaglia, L.M.P., 2016. Ecological role of bacterial inoculants and their potential impact on soil microbial diversity. *Plant and Soil*, 400(1–2), pp.193–207. [DOI]

Butcher, K., Wick, A.F., Desutter, T., Chatterjee, A. and Harmon, J., 2016. Soil salinity: A threat to global food security. *Agronomy Journal*, 108(6), pp.2189–2200. [DOI]

Chakdar, H., Dastager, S.G., Khire, J.M., Rane, D. and Dharne, M.S., 2018. Characterization of mineral phosphate solubilizing and plant growth promoting bacteria from termite soil of arid region. *3 Biotech*, 8(11), pp.1–11. [DOI]

Costa-Gutierrez, S.B., Adler, C., Espinosa-Urgel, M. and de Cristóbal, R.E., 2022. Pseudomonas putida and its close relatives: mixing and mastering the perfect tune for plants. *Applied Microbiology and Biotechnology*, *106*(9), pp.3351-3367. [DOI]

Fahad, S., Hasanuzzaman, M., Alam, M., Ullah, H., Saeed, M., Khan, I.A. and Adnan, M., 2020. Environment, climate, plant and vegetation growth. In: *Environment, Climate, Plant and Vegetation Growth*, Springer. [DOI]

Ghare, P.M. and Kumbhar, A.P., 2021. Study on physico chemical parameters of soil sample. *IARJSET*, 8(9), pp.171–187. [DOI]

Hailu, B. and Mehari, H., 2021. Impacts of soil salinity/sodicity on soil-water relations and plant growth in dry land areas: A review. *Journal of Natural Sciences Research*, 12(3), pp.1–10. [DOI]

Hussain, S., Shaukat, M., Ashraf, M., Zhu, C., Jin, Q. and Zhang, J., 2019. Salinity stress in arid and semi-arid climates: Effects and management in field crops. In: *Climate Change and Agriculture*. [DOI]

Jiang, H., Qi, P., Wang, T., Wang, M., Chen, M., Chen, N., Pan, L. and Chi, X., 2018. Isolation and characterization of halotolerant phosphate-solubilizing microorganisms from saline soils. *3 Biotech*, 8(11), pp.1–8. [DOI]

Kekane, S.S., Chavan, R.P., Shinde, D.N., Patil, C.L. and Sagar, S.S., 2015. A review on physico-chemical properties of soil. *International Journal of Chemical Studies*, 3(4), pp.29–32.

Kirui, C.K., Njeru, E.M. and Runo, S., 2022. Diversity and phosphate solubilization efficiency of phosphate solubilizing bacteria isolated from semi-arid agroecosystems of Eastern Kenya. *Microbiology Insights*, 15, pp.1–14. [DOI]

Krishnamoorthy, R., Kim, K., Subramanian, P., Senthilkumar, M., Anandham, R. and Sa, T., 2016. Arbuscular mycorrhizal fungi and associated bacteria isolated from salt-affected soil enhances the tolerance of maize to salinity in coastal reclamation soil. *Agriculture, Ecosystems and Environment*, 231, pp.233–239. [DOI]

Lv, L., Luo, J., Ahmed, T., Zaki, H.E., Tian, Y., Shahid, M.S., Chen, J. and Li, B., 2022. Beneficial effect and potential risk of Pantoea on rice production. *Plants*, *11*(19), p.2608. [DOI]

Mandal, A.K., Sharma, R.C. and Singh, G., 2009. Assessment of salt affected soils in India using GIS. *Geocarto International*, 24(6), pp.437–456. [DOI]

Mengesha, A.S. and Legesse, N.H., 2024. Isolation and characterization of phosphate solubilizing bacteria from the rhizosphere of lentil (Lens culinaris M.). *PLoS ONE*, 19(11), pp.1–17. [DOI]

Metternicht, G.I. and Zinck, J.A., 2003. Remote sensing of soil salinity: Potentials and constraints. *Remote Sensing of Environment*, 85(1), pp.1–20. [DOI]

Panhalkar, S.S., 1994. Assessment of soil salinity in southern Shirol Tahsil of Maharashtra (India) using IDW geospatial techniques. *Journal of Environmental Studies*, 2(3), pp.1–10.

Patil, A., Abhang, R. and Pathade, G., 2024. Development of microbial bioinoculant of soil isolates for the reclamation of salt affected soils from Karad Taluka, Maharashtra, India: A mini review. *Ecology, Environment and Conservation*, 30(Suppl), pp.243–246. [DOI]

Patten, C.L. and Glick, B.R., 2011. Role of bacterial indole-3-acetic acid in plant growth promotion. *Applied and Environmental Microbiology*, 68(8), pp.3795–3801. [DOI]

Raut, R.R. and Kurhe, A., 2020. Studies on soil quality parameters in relation to cropping patterns, micronutrients and pH from Goagalgaon area in Ahmednagar District. *International Journal of Innovative Research in Multidisciplinary Fields*, 30(4), pp.1–9.

Sharma, D.K. and Chaudhari, S.K., 2012. Agronomic research in salt affected soils of India: An overview. *Indian Journal of Agronomy*, 57(3), pp.175–185.

Sultana, S., Paul, S.C., Parveen, S., Alam, S., Rahman, N., Jannat, B., Hoque, S., Rahman, M.T. and Karim, M.M., 2020. Isolation and identification of salt-tolerant plant-growth-promoting rhizobacteria and their application for rice cultivation under salt stress. *Canadian Journal of Microbiology*, 66(2), pp.1–12. [DOI]

Tang, A., Haruna, A.O., Majid, N.M.A. and Jalloh, M.B., 2020. Potential PGPR properties of cellulolytic, nitrogen-fixing, phosphate-solubilizing bacteria in rehabilitated tropical forest soil. *Microorganisms*, 8(3), pp.1–22. [DOI]

Trabelsi, D. and Mhamdi, R., 2013. Microbial inoculants and their impact on soil microbial communities: A review. *BioMed Research International*, 2013, pp.1–11. [DOI]

Vazquez, P., Holguin, G., Puente, M.E., Lopez-Cortes, A. and Bashan, Y., 2000. Phosphate-solubilizing microorganisms associated with the rhizosphere of mangroves in a semiarid coastal lagoon. *Biology and Fertility of Soils*, 30(5–6), pp.460–468. [DOI]

Verma, P., Yadav, A.N., Khannam, K.S., Saxena, A.K. and Suman, A., 2017. Potassium-solubilizing microbes: Diversity, distribution and role in plant growth promotion. *Microorganisms for Sustainability*, 6, pp.125–149. [DOI]

Wang, W., Vinocur, B. and Altman, A., 2003. Plant responses to drought, salinity and extreme temperatures: Towards genetic engineering for stress tolerance. *Planta*, 218(1), pp.1–14. [DOI]

Youseif, S.H., 2018. Genetic diversity of plant growth promoting rhizobacteria and their effects on the growth of maize plants under greenhouse conditions. *Annals of Agricultural Sciences*, 63(1), pp.25-35. [DOI]

Nature Environment and Pollution Technology
An International Quarterly Scientific Journal

p-ISSN: 0972-6268
(Print copies up to 2016)
e-ISSN: 2395-3454

Vol. 25 | No. 3 | Article ID D1899 | 2026

Original Research Paper

https://doi.org/10.46488/NEPT.2026.v25i03.D1899

Open Access Journal

Potential of Struvite Recovery from Compost Leachate Using Multistage Processes

Bimastyaji Surya Ramadan[1]†, Nurani Ikhlas[2], I. D. A. A. Warmadewanthi[3] and Annisa Sila Puspita[1]

[1]Department of Environmental Engineering, Universitas Diponegoro, Semarang, 57127, Indonesia
[2]Environmental Research Center, Semarang, 50266, Indonesia
[3]Department of Environmental Engineering, Research Center for Infrastructure and Sustainable Environment, Institut Teknologi Sepuluh Nopember, Kampus ITS Sukolilo, Surabaya, 60111, Indonesia
†Corresponding author: Bimastyaji Surya Ramadan; bimastyaji@live.undip.ac.id

Abbreviation: Nat. Env. & Poll. Technol.
Website: www.neptjournal.com

Received: 06-01-2026
Revised: 26-02-2026
Accepted: 02-03-2026

Key Words:

Compost leachate
Magnesium precipitation process
Nutrient recovery
Slow-release fertilizer
Struvite crystallization

Citation for the Paper:

Ramadan, B.S., Ikhlas, N., Warmadewanthi, I.D.A.A. and Puspita, A.S., 2026. Potential of struvite recovery from compost leachate using multistage processes. *Nature Environment and Pollution Technology*, 25(3), D1899. https://doi.org/10.46488/NEPT.2026.v25i03.D1899

Note: From 2025, the journal has adopted the use of Article IDs in citations instead of traditional consecutive page numbers. Each article is now given individual page ranges starting from page 1.

Copyright: © 2026 by the authors
Licensee: Technoscience Publications
This article is an open access article distributed under the terms and conditions of the Creative Commons Attribution (CC BY) license (https://creativecommons.org/licenses/by/4.0/).

ABSTRACT

Leachates produced from composting activities often contain high levels of ammonium and phosphate. If left untreated, these compounds can pollute water bodies, but at the same time, they also represent nutrients that could be recovered and reused. This study explored the possibility of transforming composting leachate into struvite, a slow-release fertilizer, by applying sequential recovery processes. Initial characterization of the leachate showed high concentrations of phosphate (1179.8 $mg.L^{-1}$) and ammonium (312.5 $mg.L^{-1}$), while magnesium was almost absent (0.017 $mg.L^{-1}$), confirming the need for external magnesium addition. A series of experiments and PHREEQC simulations were carried out to examine the influence of magnesium sources ($MgCl_2$ and MgO), pH adjustment, molar ratios, and mixing conditions. The results showed that $MgCl_2$ consistently enhanced nutrient removal compared with MgO, with the best outcomes occurring at around pH 9 for ammonium and pH 10 for phosphate. Increasing the magnesium dosing ratio to 5:1:1 further improved precipitation, while controlled mixing (fast followed by slow) supported crystal formation. The presence of struvite crystals confirmed the effectiveness of the process. These findings suggest that composting leachate, which is often considered problematic waste, can be converted into a valuable product while reducing environmental risks.

1. INTRODUCTION

Composting is a widely practiced method for managing organic waste and converting biodegradable materials into stable, humus-like compost that can enhance soil fertility. Despite these benefits, composting processes also generate a significant amount of leachate, a dark and odorous liquid that often contains high levels of organic matter, ammonium, phosphate, and various dissolved ions (Priyambada et al. 2021). If left untreated, this leachate may pose serious environmental problems, including surface water eutrophication, groundwater contamination, and indirect greenhouse gas emissions when it infiltrates anaerobic environments (Puspita et al. 2024). Nitrogen and phosphorus are particularly concerning, as ammonium (NH_4^+) can exert toxic effects on aquatic ecosystems and contribute to nitrate pollution through nitrification, while phosphate (PO_4^{3-}) acts as a limiting nutrient for algal growth and is a major driver of eutrophication in lakes and rivers. However, the same compounds that create environmental hazards also represent valuable resources for agriculture. In the context of phosphorus scarcity and the rising costs of chemical fertilizers, leachate streams with high nutrient concentrations could be reimagined as raw materials for nutrient recovery rather than as pollutants requiring disposal (Ramadan et al. 2024).

One of the most promising approaches for nutrient recovery from wastewater and similar effluents is the crystallization of struvite (magnesium ammonium

phosphate hexahydrate, $MgNH_4PO_4 \cdot 6H_2O$). Struvite is a sparingly soluble crystalline compound that precipitates when magnesium, ammonium, and phosphate ions are present at sufficient concentrations under alkaline conditions. Research on struvite crystallization has gained momentum over the past two decades because of its dual role in both wastewater treatment and resource recovery. On the one hand, struvite formation reduces the concentrations of ammonium and phosphate in effluents, thereby mitigating the risks of eutrophication. On the other hand, the recovered crystals can be directly applied as slow-release fertilizers, providing agronomic benefits such as gradual nutrient release and reduced leaching losses compared with conventional soluble fertilizers. Therefore, struvite recovery has been studied in a wide range of systems, including municipal wastewater treatment plants, anaerobic digestate supernatants, livestock manure effluents, landfill leachates, and various industrial wastewaters (Petal Battistoni et al. 1997, Doyle & Parson 2002, Kabdaslı et al. 2000, Le Corre et al. 2009, Rahman et al. 2014, Yetilmezsoy & Sapci-Zengin 2009). Beyond pollution control, the recovery of phosphorus as struvite also contributes to the broader sustainability agenda, as phosphorus is a finite, non-renewable resource concentrated in a few geographic regions and is subject to long-term depletion risks (Cordell et al. 2009).

However, struvite formation is influenced by multiple operational factors that require careful optimization. Among these, pH is considered the most critical. Numerous studies have reported that struvite crystallization is most favorable under alkaline conditions, generally between pH 8 and 10.5 (Bhuiyan et al. 2007). At lower pH values, phosphate is predominantly present as $H_2PO_4^-$ or HPO_4^{2-}, limiting the availability of PO_4^{3-} ions necessary for precipitation, whereas excessively high pH values can encourage the formation of competing salts, particularly calcium phosphates, which reduce struvite purity. The choice of magnesium source is another decisive factor. Magnesium chloride ($MgCl_2$) is often used in laboratory studies because of its high solubility and reliable release of Mg^{2+} ions, which promotes rapid precipitation. Magnesium oxide (MgO), while less soluble, is cheaper and provides a slower release of magnesium, which, in some contexts, may improve crystal growth. Other alternatives, such as seawater, bittern, and industrial by-products, have also been explored as cost-effective magnesium sources (Doyle et al. 2003, Hutnik et al. 2013, Münch & Barr 2001, Ye et al. 2011). The stoichiometric ratio of magnesium to ammonium and phosphate is theoretically 1:1:1; however, in practice, excess magnesium dosing is frequently applied to overcome losses due to competing reactions and to ensure high recovery efficiencies (Thomas 2007).

Hydrodynamics also plays a vital role in crystallization. Struvite formation begins with supersaturation, followed by nucleation and crystal growth, all of which are strongly affected by mixing intensity. Rapid mixing promotes homogeneity and enhances nucleation; however, excessive turbulence can break crystals or prevent them from growing to a size suitable for recovery. Conversely, gentle, slow mixing provides favorable conditions for crystal aggregation and settling. Several studies have therefore recommended a two-step mixing regime—rapid mixing to initiate nucleation, followed by slow mixing to encourage crystal growth and settling—as the most effective strategy (Wang et al. 2005). In addition, reaction time and sedimentation period determine the extent to which equilibrium is approached, with longer retention times generally improving recovery but also increasing operational costs. Finally, the presence of competing ions, such as calcium, potassium, and sodium, as well as high levels of suspended solids or organic matter, can interfere with the crystallization pathway by either substituting into the crystal lattice or sequestering phosphate and magnesium into alternative compounds (Paolo Battistoni et al. 2001).

Although a large body of work has investigated struvite recovery from sewage sludge liquors, digester supernatants, and livestock effluents, the application of this technique to composting leachate remains relatively underexplored. Composting leachate is a particularly challenging medium because of its highly variable composition, elevated suspended solids content, and fluctuating pH. Mizuta et al. have shown that composting leachate can indeed support struvite precipitation; however, the recovery efficiency is strongly dependent on operating conditions, and the outcomes are less predictable than those in digester or sewage liquors. Unlike more homogeneous wastewaters, composting leachate is influenced by multiple factors, including feedstock composition, composting temperature, and retention time, which affect both the nutrient content and the concentration of interfering compounds. These challenges underline the need for systematic studies to determine how struvite recovery can be optimized specifically for composting leachate streams.

The present study addresses this gap by investigating the potential production of struvite fertilizer from composting leachate through a sequential recovery process. This research combines geochemical modeling using PHREEQC with laboratory-scale experiments to examine the effects of magnesium source, pH, molar ratios, and mixing conditions on struvite formation. Magnesium chloride and magnesium oxide were selected as representative soluble and sparingly soluble magnesium sources, respectively, while the pH was varied between 6 and 11 to capture the full precipitation

window. The molar ratio of Mg: NH_4:PO_4 was systematically increased from 1:1:1 to 5:1:1, and sequential mixing regimes consisting of rapid followed by slow agitation were tested to replicate practical treatment conditions. The reaction times and sedimentation periods were extended to 48 h to examine the kinetics of precipitation. By linking simulation and experimentation, this study identifies the operational windows that maximize ammonium and phosphate recovery while producing visible struvite crystals.

The novelty of this study lies in the following three aspects. First, it applies a sequential mixing framework to composting leachate, a strategy that has rarely been explored for this particular waste stream. Second, it compares two distinct magnesium sources under identical conditions, providing insights into their relative effectiveness in a complex leachate matrix. Third, it integrates PHREEQC simulations with experimental validation, offering both predictive and empirical perspectives on struvite formation. By addressing these aspects, this study contributes to a better understanding of nutrient recovery from composting leachate and highlights the potential for transforming an environmentally problematic waste stream into a valuable slow-release fertilizer resource.

2. MATERIALS AND METHODS

2.1. Data Collection and Characterization

2.1.1. Leachate Characterization

Leachate samples were obtained from a composting facility and stored under cool and dark conditions prior to analysis. Standardized laboratory protocols were followed in accordance with the 24th edition of APHA. The parameters measured included pH, ammonium (NH_4^+), phosphate (PO_4^{3-}), magnesium (Mg^{2+}), total suspended solids (TSS), and selected major ions (Na, K, Ca, and Si). Measurements were performed in duplicate to ensure reproducibility. Initial results showed that the leachate was highly enriched in phosphate (1179.8 mg.L^{-1}) and ammonium (312.5 mg.L^{-1}) but was almost devoid of magnesium (0.017 mg.L^{-1}), confirming the necessity of magnesium supplementation to enable struvite crystallization.

2.2. Experimental Framework

The study design combined thermodynamic modeling with bench-scale jar tests. This dual approach has been widely adopted in struvite research to first predict the precipitation conditions and then validate them experimentally. The geochemical software PHREEQC was used to simulate the leachate composition under varying pH conditions (6–11) and magnesium addition. Simulations were performed using the measured initial concentrations of major ions (NH_4^+, PO_4^{3-}, Mg^{2+}, Ca^{2+}, K^+, Na^+, Si, and F^-) as input parameters, and the thermodynamic database provided in PHREEQC was used to calculate aqueous speciation and mineral saturation indices (SI). Two magnesium sources, $MgCl_2$ (aqueous) and MgO (solid), were modeled to examine differences in solubility and to estimate the saturation index (SI) of struvite, as well as that of potential competing mineral phases (e.g., calcium phosphate phases), under different pH scenarios. The SI values were used to identify the pH range at which struvite precipitation was thermodynamically favorable (SI > 0) and to evaluate potential competition from other mineral species.

Based on the modeling results, laboratory trials were conducted in beakers using controlled mixing regimes. Each run consisted of a rapid-mixing phase at 158 rpm for 1 h, followed by a slow-mixing phase at 30–75 rpm for 1 h. This sequential mixing setup reflects common practice in struvite studies, where rapid mixing promotes supersaturation and nucleation, while slow mixing allows crystal growth. Because the natural magnesium concentration was insufficient, external magnesium was added. The molar ratios of Mg: NH_4:PO_4 were varied systematically from 1:1:1 to 5:1:1. The pH of the leachate was adjusted using NaOH or HCl before the addition of magnesium. The experimental design was guided by the simulation outputs, particularly the predicted struvite saturation window and the influence of magnesium availability on supersaturation. Screening experiments confirmed optimum precipitation near pH 9 for ammonium and pH 10 for phosphate. The mixing times were varied between 20 and 60 min, while the sedimentation period was extended from 20 to 48 h. This approach enabled the analysis of reaction kinetics and the establishment of equilibrium conditions.

2.3. Data Analysis

The ammonium and phosphate removal efficiencies were calculated from the difference between the initial and residual concentrations using the following equation:

$$\text{Removal efficiency } (\%) = C_0 - Ct \times 100 \quad \ldots(1)$$

where C_o is the initial concentration, and C_t is the concentration after treatment. The concentrations were determined spectrophotometrically. Kinetic data were analyzed by plotting the removal efficiency against sedimentation time and fitting regression models. Linear regression was applied as a descriptive tool to illustrate the overall temporal trend of nutrient removal rather than to represent a mechanistic kinetic model of struvite crystallization. Optimal conditions were identified by comparing magnesium sources, pH levels, molar ratios, and mixing regimes. Because struvite precipitation is governed

by non-linear processes, including nucleation, crystal growth, aggregation, and diffusion-controlled mechanisms, the regression analysis was intended to provide comparative trend evaluation only. More advanced kinetic modeling was beyond the scope of the present study and is recommended for future work.

3. RESULTS AND DISCUSSION

3.1. Preliminary Characterization of Composting Leachate

Preliminary analysis of the composting leachate revealed a challenging, nutrient-rich matrix (Table 1). The leachate exhibited an acidic pH of 5.8, high concentrations of phosphate (1179.8 mg.L^{-1}) and ammonium (312.5 mg.L^{-1}), and negligible levels of magnesium (0.017 mg.L^{-1}). In addition, high concentrations of total suspended solids (TSS, 8105 mg.L^{-1}), potassium (5255 mg.L^{-1}), sodium (217.4 mg.L^{-1}), calcium (136.3 mg.L^{-1}), silica (1146 mg.L^{-1}), and fluoride (583 mg.L^{-1}) were detected. This profile confirmed that the leachate is both a pollution concern and a potential nutrient source. The low magnesium concentration indicated that external magnesium addition would be indispensable for inducing struvite precipitation, while the presence of competing cations, such as potassium and calcium, could interfere with crystallization.

The relatively high calcium concentration (136.3 mg.L^{-1}) is particularly important, as Ca^{2+} can compete with Mg^{2+} for phosphate and promote the formation of calcium phosphate phases (e.g., amorphous calcium phosphate or hydroxyapatite), thereby reducing phosphate availability for struvite formation. The extremely high potassium concentration (5255 mg.L^{-1}) increases the ionic strength of the solution, which may reduce ion activity coefficients and consequently lower the effective supersaturation required for struvite nucleation. Although K^+ does not directly participate in struvite formation, elevated ionic strength can influence crystallization kinetics and precipitation efficiency. Silica (1146 mg.L^{-1}) may also contribute to interference, as dissolved silicate species can interact with Mg^{2+} and potentially form magnesium silicate complexes, thereby reducing the free Mg^{2+} fraction available to react with ammonium and phosphate. Similarly, the presence of fluoride (583 mg.L^{-1}) under alkaline conditions may lead to the partial formation of MgF_2 or other magnesium fluoride species, further decreasing magnesium availability.

The very high TSS concentration (8105 mg.L^{-1}) suggests that heterogeneous nucleation and adsorption phenomena are likely to occur. Suspended particles can adsorb phosphate or magnesium ions and may either promote localized nucleation or hinder crystal growth by trapping fine precipitates, thereby affecting sedimentation efficiency. These combined matrix effects help explain the need for excess magnesium dosing and careful pH control observed in the subsequent experiments. Similar characteristics have been observed in leachates from organic waste treatment systems, where nutrient recovery requires chemical supplementation and careful process control (Doyle & Parsons 2002, Le Corre et al. 2009).

3.2. Stoichiometric Analysis and Mass Balance Consideration

The initial nutrient concentrations were converted into molar units to evaluate the stoichiometric feasibility of struvite formation. Ammonium (312.5 mg.L^{-1}) corresponded to 17.36 mmoL.L^{-1}, while phosphate (1179.8 mg.L^{-1}) corresponded to 12.42 mmoL.L^{-1}. Because struvite crystallizes according to a 1:1:1 molar ratio (Mg^{2+}: NH_4^+:PO_4^{3-}), phosphate was identified as the limiting reactant under the initial conditions. Based on this stoichiometry, the maximum theoretical struvite formation was 12.42 mmoL.L^{-1}, equivalent to approximately 3043 mg.L^{-1} of $MgNH_4PO_4{\cdot}6H_2O$. This indicates that, even with sufficient magnesium supplementation, complete ammonium removal was not theoretically achievable because ammonium was present in excess relative to phosphate. The experimental results, showing incomplete phosphate recovery, suggest that matrix effects, including high calcium (136.3 mg.L^{-1}), elevated potassium (5255 mg.L^{-1}), and high suspended solids (8105 mg.L^{-1}), likely reduced the effective availability of phosphate for struvite precipitation. These competing interactions explain why the observed removal efficiencies were lower than the theoretical maximum.

3.3. Effect of Magnesium Source and pH

The first set of experiments compared $MgCl_2$ and MgO as magnesium sources across a pH range of 6–11. The results

Table 1: Preliminary test.

Parameter	Value	Units
pH	5.8	
Phosphate (PO_4)	1179.8	mg.L^{-1}
Ammonia (NH_4)	312.5	mg.L^{-1}
Total Suspended Solids (TSS)	8105.0	mg.L^{-1}
Silica (Si)	1146.0	mg.L^{-1}
Sodium (Na)	217.4	mg.L^{-1}
Calcium (Ca)	136.3	mg.L^{-1}
Potassium (K)	5255.0	mg.L^{-1}
Magnesium (Mg)	0.017	mg.L^{-1}
Fluoride (F)	583.0	mg.L^{-1}

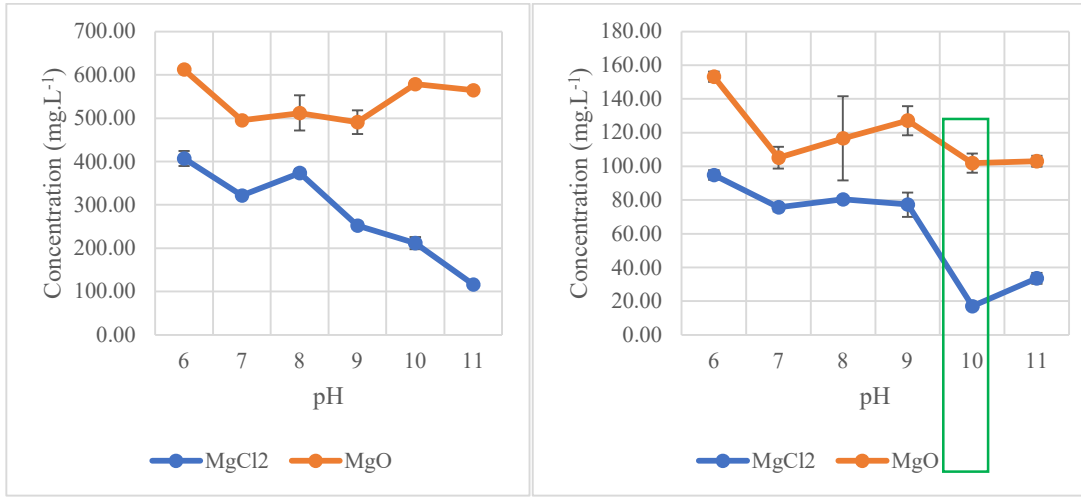


Fig. 1: Effect of magnesium source and pH on ammonia and phosphate reduction.

demonstrated that $MgCl_2$ consistently outperformed MgO in nutrient removal (Fig. 1). For ammonium, the greatest reduction was achieved at pH 9, whereas phosphate removal peaked at pH 10. Under the optimized conditions (pH 10 and an Mg: NH_4:PO_4 molar ratio of 5:1:1 using $MgCl_2$), phosphate removal exceeded 70%, while ammonium removal approached 60%. The lower performance of MgO can be attributed to its limited solubility, which releases Mg^{2+} ions at a slower rate, thereby delaying nucleation and crystal growth. In contrast, $MgCl_2$ provided an immediate and high concentration of soluble magnesium, enabling rapid supersaturation and precipitation. The dependence on pH observed here is consistent with established findings that struvite crystallization is strongly influenced by solution chemistry (Petal Battistoni et al. 1997). At near-neutral pH (6–7), little precipitation occurred because the availability of PO_4^{3-} ions was restricted. Under highly alkaline conditions (pH >10.5), the competing precipitation of calcium phosphate and amorphous phosphate species may explain the decline in removal efficiency. Thus, pH 9–10 can be considered the optimal window for struvite precipitation in composting leachate, consistent with previous studies on wastewater and digestates (Kabdaslı et al. 2000, Yetilmezsoy & Sapci-Zengin 2009).

3.4. Influence of Mg: NH_4:PO_4 Molar Ratios

Following the identification of the optimum pH, the molar ratio of Mg: NH_4:PO_4 was varied between 1:1:1 and 5:1:1. A clear trend was observed: increasing the magnesium dosage enhanced nutrient removal, with the most significant improvement occurring between the 1:1:1 and 3:1:1 ratios (Fig. 2). At ratios beyond 3:1:1, the incremental benefit was smaller, although the maximum removal was achieved at 5:1:1. Ammonium removal increased from approximately 25% at a 1:1:1 ratio to nearly 60% at a 5:1:1 ratio, whereas phosphate removal increased from approximately 40% to more than 70%.

To better represent resource recovery performance beyond percentage removal, phosphorus recovery was estimated based on the initial phosphate concentration (1179.8 $mg.L^{-1}$). At more than 70% phosphate removal, approximately 826 $mg.L^{-1}$ of PO_4^{3-} was recovered from the solution. Assuming complete conversion of the removed phosphate into struvite ($MgNH_4PO_4{\cdot}6H_2O$), the theoretical struvite yield corresponds to approximately 2.1 $g.L^{-1}$, based on stoichiometric conversion (molecular weight of struvite = 245 $g.moL^{-1}$, molecular weight of PO_4^{3-} = 95 $g.moL^{-1}$). This estimation indicates that the process not only reduces nutrient concentrations but also produces a potentially recoverable solid product in the gram-per-liter range. The calculated crystallization yield, relative to the theoretical maximum (based on the limiting phosphate concentration), suggests that a substantial fraction of recoverable phosphorus can be converted into solid form under optimized conditions.

These findings are consistent with the principle that excess magnesium is often required to overcome interference in complex wastewaters (Rahman et al. 2014). Composting leachate, with its high concentrations of calcium, potassium, and suspended solids, likely sequestered some of the added magnesium, reducing the fraction available for struvite formation. Calcium can preferentially bind phosphate to form calcium phosphate phases, while fluoride and silicate species may partially complex with Mg^{2+}, thereby decreasing the effective free magnesium concentration in solution. In addition, the elevated ionic strength caused by high potassium levels may reduce ion activities and lower the

effective supersaturation required for nucleation. Therefore, the observed need for overstoichiometric magnesium dosing can be interpreted as compensation for these competing reactions and activity corrections rather than as a simple deviation from ideal stoichiometry. Excess magnesium addition ensured that sufficient Mg^{2+} remained available to react with NH_4^+ and PO_4^{3-}. Similar requirements for overstoichiometric dosing have been reported for digester liquors (Cordell et al. 2009), landfill leachates (Bhuiyan et al. 2007), and animal manure effluents (Münch & Barr 2001).

3.5. Effect of Mixing Regime

The sequential mixing approach, consisting of rapid mixing (158 rpm) followed by slow mixing, was evaluated by varying the slow-mixing speed from 30 to 75 rpm. The results showed that moderate agitation (approximately 60 rpm) provided the best balance between ammonium and phosphate removal (Fig. 3). At very low speeds (30 rpm), crystal nucleation and aggregation were insufficient, resulting in poor recovery. At very high speeds (75 rpm), shear forces likely disrupted crystal growth and resuspended fine particles, leading to lower sedimentation efficiency.

This behavior underscores the importance of hydrodynamic control during crystallization. Previous studies have shown that rapid mixing promotes homogeneous nucleation, whereas gentle slow mixing supports crystal growth and aggregation into recoverable particles (Hutnik et al. 2013, Ye et al. 2011). The optimum mixing speed of 60 rpm observed here mirrors similar results reported for engineered reactors, where excessively vigorous mixing reduced the struvite particle size and increased washout (Doyle et al. 2003). From an operational perspective, optimizing mixing intensity is also relevant to process efficiency, as excessive agitation may increase energy consumption without proportionally improving nutrient recovery. Therefore, moderate mixing conditions not only enhance precipitation performance but may also contribute to more practical and energy-efficient implementation at a larger scale. Thus, sequential mixing is a promising operational strategy for composting leachate, enabling both nucleation and crystal growth in a controlled manner.

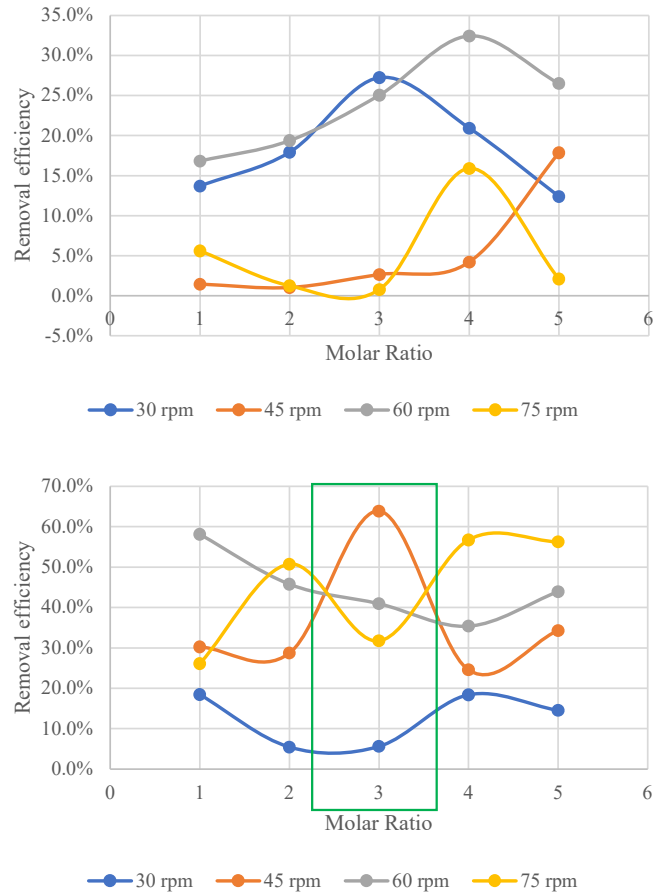


Fig. 2: Influence of molar ratio on ammonia and phosphate removal efficiency.

3.6. Influence of Mixing and Sedimentation Times

The mixing time was varied between 20 and 60 min, while the sedimentation period was extended to 48 h to investigate the precipitation kinetics. The results demonstrated that most nutrient removal occurred within the first 30 min of slow mixing, with only marginal improvements observed beyond this duration (Fig. 4). Sedimentation tests revealed that the removal efficiency increased steadily over time, reaching equilibrium after approximately 24–36 h. The ammonium and phosphate removal efficiencies approached 65% and 75%, respectively, after extended sedimentation.

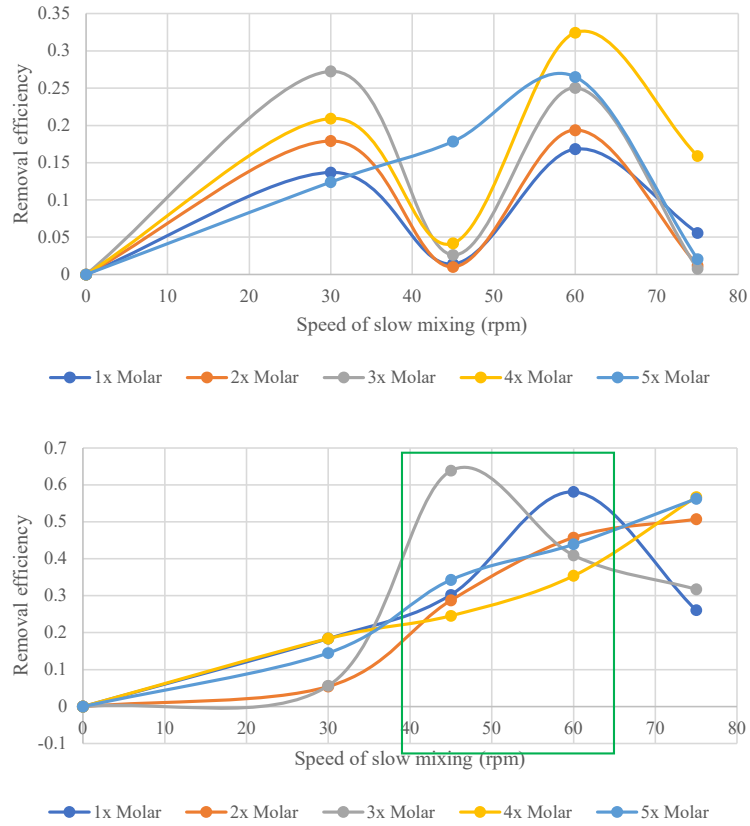


Fig. 3: Influence of mixing regime on ammonia and phosphate removal efficiency.

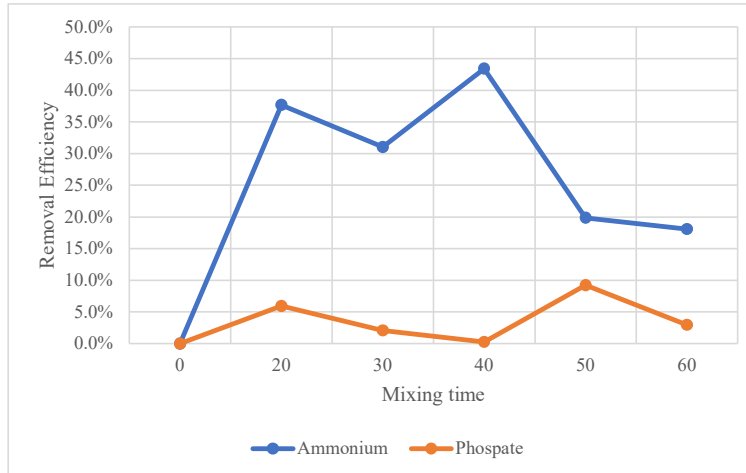


Fig. 4: Influence of mixing and sedimentation times on ammonia and phosphate removal efficiency.

The kinetic profiles suggest that struvite crystallization in composting leachate follows a two-stage process: rapid initial nucleation and crystal growth, followed by slower aggregation and settling. Regression analysis of the removal efficiency versus sedimentation time yielded moderate correlations ($R^2 \approx 0.36–0.40$), reflecting the complexity of the leachate matrix and the competing processes involved. These results are consistent with kinetic studies of struvite formation in other wastewaters, which also reported rapid early-stage precipitation followed by a slower approach to equilibrium (Thomas 2007, Wang et al. 2005).

3.7. Kinetic Rate of Ammonia and Phosphate Precipitation

The choice of magnesium source played an important role. $MgCl_2$ resulted in higher removal efficiencies than MgO, and pH strongly influenced the outcome. The most effective nutrient reduction occurred at pH 9 for ammonium and pH 10 for phosphate. Adjusting the molar ratio showed a clear trend: higher magnesium input promoted more complete precipitation, with significant improvement from 1:1:1 to 5:1:1. The kinetic study investigated how the removal efficiencies of ammonium and phosphate evolved with increasing sedimentation time (0–3000 min, approximately 2 days). It should be noted that the kinetic experiment was conducted under fixed operational parameters and did not necessarily represent the globally optimized pH and molar ratio. As shown in Figure 5, both ammonium and phosphate exhibited a positive trend with increasing sedimentation time, indicating that struvite crystallization and settling continued gradually over time.

For ammonium, the removal efficiency increased from approximately 40 % during the initial measurement to nearly 70% after 3000 min. The linear regression equation ($y = 0.0001x + 0.3589$, $R^2 = 0.3584$) was applied as a descriptive approximation of the overall trend rather than as a mechanistic kinetic model. The relatively low R^2 value indicates that ammonium removal does not follow a strictly linear pattern and that the precipitation kinetics are governed by more complex processes, including nucleation, crystal growth, aggregation, and diffusion limitations. Phosphate removal followed a similar but slower trend, increasing from approximately 20% at the initial measurement to approximately 35% after 3000 min. The regression equation ($y = 7E–05x + 0.2026$, $R^2 = 0.4029$) likewise served only as a simplified representation of the temporal trend. Given the presence of competing ions, such as calcium and potassium, as well as high suspended solids, phosphate precipitation is likely influenced by multiphase reactions and surface-mediated processes rather than by a single linear kinetic pathway. This lower value does not contradict the more than 70% phosphate removal reported under optimized conditions; rather, it reflects the specific operational settings applied during the kinetic experiment.

The R^2 values (0.36 for ammonium and 0.40 for phosphate) indicated only a moderate fit to a linear model, suggesting that the kinetics may not be strictly linear. In reality, struvite precipitation often follows a two-phase process: a rapid nucleation and crystal growth stage within the first hour, followed by a slower approach to equilibrium as supersaturation declines. The scatter observed at shorter times reflected this rapid initial stage, after which a slower linear trend predominated. Overall, the kinetic results highlighted that ammonium removal proceeded more effectively than phosphate removal under the tested conditions. This imbalance is

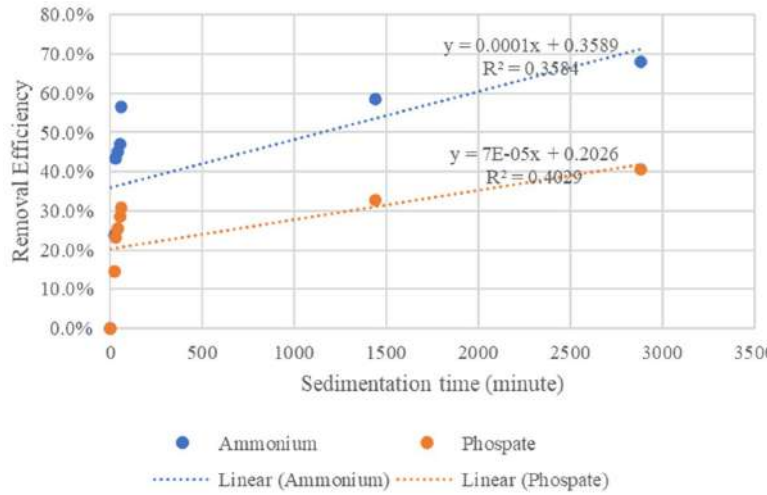


Fig. 5: Kinetic rate of ammonia and phosphate precipitation.

consistent with previous studies showing that phosphate recovery is often more sensitive to competing ions and pH fluctuations.

Although sedimentation was monitored for up to 24-48 h to evaluate equilibrium behavior under batch conditions, this extended settling time was intended for mechanistic observation rather than to represent a practical hydraulic retention time (HRT) for full-scale operation. In engineered struvite reactors, shorter retention times can be achieved through enhanced mixing, seeding, fluidized-bed configurations, sludge recirculation, or improved solid–liquid separation systems. Nonetheless, the gradual increase in both removal efficiencies over time suggests that allowing sufficient contact and settling time improves recovery performance. Future research should focus on reactor design optimization to reduce the HRT while maintaining high supersaturation and efficient crystal harvesting, thereby improving the practical applicability of the process. Future studies should also apply more appropriate kinetic models (e.g., pseudo-first-order, pseudo-second-order, or diffusion-controlled models) to better describe the crystallization mechanism in complex leachate matrices.

3.8. Visual Confirmation of Struvite

Microscopic examination of the precipitates confirmed the formation of crystalline struvite. The recovered solids displayed the typical white, needle-like crystal morphology associated with struvite, providing qualitative evidence that the sequential recovery strategy successfully produced the target compound. Confirmation of the crystalline product is critical, as competing salts, such as amorphous calcium phosphate, can also form under similar conditions. Therefore, this visual confirmation strengthens the conclusion that the observed nutrient removal was predominantly due to struvite precipitation.

Mixing intensity also affected the results. Moderately slow mixing (around 60 rpm) provided a balance between promoting particle collisions and avoiding re-dispersion. Extending the mixing time led to improved precipitation, although the effect leveled off after a certain period. Kinetic analysis suggested that both ammonium and phosphate removal followed a predictable precipitation pattern (Fig. 5), and visual inspection confirmed the formation of struvite crystals (Fig. 6).

3.9. Implications for Nutrient Recovery from Composting Leachate

The results of this study demonstrate that composting leachate, often regarded solely as problematic waste, can be transformed into a valuable resource through sequential struvite recovery. By applying $MgCl_2$ supplementation, controlling the pH within the range of 9–10, and adopting sequential mixing at moderate slow-mixing speeds, significant recovery of ammonium and phosphate was achieved. The production of crystalline struvite highlights the potential for converting nutrient pollution into an agricultural input, aligning with the principles of waste valorization and the circular economy.

Compared with previous work on sewage sludge liquors and digestates, the recovery efficiencies achieved in this study were somewhat lower. This outcome reflects the complexity of composting leachate, which contains higher levels of suspended solids and competing ions. Nonetheless, the ability to recover more than 60% of ammonium and 70% of phosphate under optimized conditions is a promising outcome, particularly given that composting leachate has been underutilized in nutrient recovery research. Mizuta et al. similarly reported that struvite recovery from composting leachate is feasible but requires careful control of operating conditions. The present study adds to the literature by

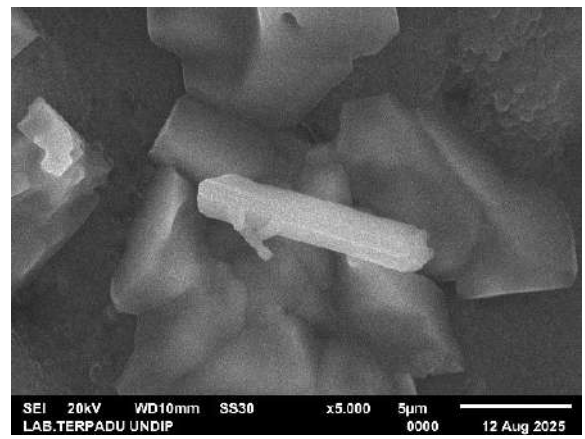


Fig. 6: Struvite crystal formation.

providing a detailed analysis of the magnesium source, mixing regimes, and kinetics, thereby offering practical guidance for potential scale-up.

Although the laboratory results are encouraging, several limitations should be noted. First, the high suspended solids content of composting leachate may require pre-treatment to enhance recovery efficiency and reduce interference. Second, the reliance on chemical magnesium sources such as $MgCl_2$ may limit economic feasibility unless supplemented with low-cost alternatives, such as seawater or industrial by-products. In particular, while increasing the Mg: NH_4:PO_4 ratio to 5:1:1 improved phosphate recovery, the incremental benefit beyond 3:1:1 was comparatively smaller, suggesting diminishing returns relative to magnesium input. This indicates that optimization at lower overstoichiometric ratios may offer a more practical balance between nutrient recovery efficiency and chemical consumption.

Furthermore, residual magnesium concentrations were not quantified in this study; therefore, the extent of unreacted magnesium remaining in solution could not be assessed. Excess magnesium dosing may lead to higher operational costs and potential downstream impacts if it is not recovered or reused. Future studies should therefore evaluate magnesium utilization efficiency (e.g., recovery per mole of magnesium added) and incorporate cost–performance analyses to determine the most economically viable dosing strategy.

Third, the experiments were performed at the bench scale, and scale-up challenges, such as reactor design, continuous operation, and the handling of sludge-like precipitates, remain to be addressed. Therefore, future research should focus on integrating struvite recovery with leachate management systems at composting facilities, exploring the use of alternative magnesium sources, and evaluating the agronomic performance of the recovered struvite as a fertilizer. Techno-economic assessments are also essential to determine the practicality of implementing such recovery systems at full scale. Comprehensive techno-economic assessments are essential to determine the practicality and sustainability of implementing high magnesium dosing strategies at full scale.

4. CONCLUSIONS

This study demonstrated the potential of composting leachate as a nutrient-rich feedstock for struvite precipitation, offering the dual benefits of pollution control and fertilizer production. The initial characterization revealed extremely high concentrations of ammonium (312.5 $mg.L^{-1}$) and phosphate (1179.8 $mg.L^{-1}$), but almost negligible magnesium, confirming the necessity of external magnesium supplementation. Stoichiometric analysis indicated that phosphate (12.42 $mmoL.L^{-1}$) was the limiting reactant relative to ammonium (17.36 $mmoL.L^{-1}$), meaning that complete ammonium removal was theoretically constrained by phosphate availability. Despite the challenging matrix, characterized by high suspended solids, interfering cations, and acidic pH, the sequential recovery strategy proved effective in achieving measurable nutrient removal and the formation of needle-like crystalline precipitates consistent with struvite morphology. However, because no advanced mineralogical characterization (e.g., XRD, FTIR, or SEM-EDS) was performed, the identity of the precipitated phase should be interpreted as indicative rather than as conclusive evidence of pure struvite. The presence of competing ions, such as calcium, suggests that mixed or calcium phosphate phases may also have formed under certain conditions.

The results clearly showed that the choice of magnesium source and pH were decisive factors. $MgCl_2$ consistently outperformed MgO because of its higher solubility, enabling the immediate availability of Mg^{2+} for crystallization. Optimum nutrient recovery occurred at pH 9 for ammonium and pH 10 for phosphate, consistent with the previous literature on struvite solubility while highlighting the narrow operational window required for composting leachate. When the molar ratios were varied, a strong dose–response relationship was observed, with excess magnesium addition ($\geq$3:1:1) being necessary to overcome competition from other ions and to drive the system towards higher supersaturation. Under optimized conditions (pH 10 and Mg: NH_4:PO_4 = 5:1:1 using $MgCl_2$), phosphate removal exceeded 70%, demonstrating the feasibility of achieving high recovery when the operational parameters were carefully controlled.

Mixing-regime experiments confirmed the importance of hydrodynamics. A sequential approach involving rapid mixing followed by moderately slow mixing (approximately 60 rpm) provided the best balance between nucleation and crystal growth. At very low mixing speeds, limited nucleation reduced recovery, whereas at very high speeds, crystal breakage and resuspension diminished sedimentation efficiency. Similarly, the reaction time and sedimentation studies revealed a two-stage kinetic process: rapid initial removal within the first 30 min, followed by slower aggregation and settling over 24–36 h.

In the kinetic experiment conducted under fixed operational parameters, ammonium removal reached nearly 70% after 48 h of sedimentation, while phosphate removal reached approximately 35%. This lower phosphate value reflects the specific experimental conditions applied during the kinetic evaluation and does not contradict the

higher removal observed under optimized settings. The lower phosphate removal reflects the stronger sensitivity of phosphate recovery to matrix interferences. The kinetic results underline that ammonium removal was more efficient than phosphate removal under the tested conditions, a finding consistent with previous studies in which phosphate recovery was suppressed by competing ions such as calcium and potassium. Regression analyses yielded modest R^2 values, indicating that more advanced kinetic models are required to fully capture the complexity of crystallization in such heterogeneous matrices. Nevertheless, the gradual increase in recovery efficiency over time suggests that extended sedimentation could be a practical operational strategy for improving performance. Future studies should incorporate detailed solid-phase characterization and purity analysis to confirm the mineral composition and evaluate the agronomic suitability of the recovered product.

5. ACKNOWLEDGMENTS

Thanks to all the students for contributing to collecting the data. The authors would like to acknowledge the KWEF Board for the Kurita Overseas Research Grant (KORG) 2024 for funding this research with the grant number 24Pid162.

6. REFERENCES

Battistoni, P., De Angelis, A., Pavan, P., Prisciandaro, M. and Cecchi, F., 2001. Phosphorus removal from a real anaerobic supernatant by struvite crystallization. *Water Research*, 35(9), pp.2167-2178. [DOI]

Battistoni, P., Fava, G., Pavan, P., Musacco, A. and Cecchi, F., 1997. Phosphate removal in anaerobic liquors by struvite crystallization without addition of chemicals: preliminary results. *Water Research*, 31(11), pp.2925-2929. [DOI]

Bhuiyan, M., Mavinic, D. and Beckie, R., 2007. A solubility and thermodynamic study of struvite. *Environmental Technology*, 28(9), pp.1015-1026. [DOI]

Cordell, D., Drangert, J.O. and White, S., 2009. The story of phosphorus: global food security and food for thought. *Global Environmental Change*, 19(2), pp.292-305. [DOI]

Doyle, J.D., Oldring, K., Churchley, J., Price, C. and Parsons, S.A., 2003. Chemical control of struvite precipitation. *Journal of Environmental Engineering*, 129(5), pp.419-426. [DOI]

Doyle, J.D. and Parsons, S.A., 2002. Struvite formation, control and recovery. *Water Research*, 36(16), pp.3925-3940. [DOI]

Hutnik, N., Kozik, A., Mazienczuk, A., Piotrowski, K., Wierzbowska, B. and Matynia, A., 2013. Phosphates (V) recovery from phosphorus mineral fertilizers industry wastewater by continuous struvite reaction crystallization process. *Water Research*, 47(11), pp.3635-3643. [DOI]

Kabdaslı, I., Tünay, O., Öztürk, I., Yılmaz, S. and Arıkan, O., 2000. Ammonia removal from young landfill leachate by magnesium ammonium phosphate precipitation and air stripping. *Water Science and Technology*, 41(1), pp.237-240. [DOI]

Le Corre, K.S., Valsami-Jones, E., Hobbs, P. and Parsons, S.A., 2009. Phosphorus recovery from wastewater by struvite crystallization: A review. *Critical Reviews in Environmental Science and Technology*, 39(6), pp.433-477. [DOI]

Mizuta, K., Fujii, T., Ito, R. and Umita, T., 2020. Behavior of nutrients in composting leachate and recovery of ammonium and phosphate as struvite. *Waste Management*, 102, pp.148-156. [DOI]

Münch, E.V. and Barr, K., 2001. Controlled struvite crystallization for removing phosphorus from anaerobic digester sidestreams. *Water Research*, 35(1), pp.151-159. [DOI]

Priyambada, I.B., Widianarko, B., Sasongko, S. and Puspita, A., 2021. Application of Leachate Recirculation on the Concentration of Landfill Gases. In: *IOP Conference Series: Earth and Environmental Science*, 896(1), pp.012034. [DOI]

Puspita, A., Budihardjo, M. and Samadikun, B., 2024. Desiccation and crack behavior of modified waste materials–clay mixture as landfill liner: A systematic review. *International Journal of Environmental Science and Technology*, 21(5), pp.5231-5246. [DOI]

Rahman, M.M., Salleh, M.A.M., Rashid, U., Ahsan, A., Hossain, M.M. and Ra, C.S., 2014. Production of slow-release crystal fertilizer from wastewaters through struvite crystallization–A review. *Arabian Journal of Chemistry*, 7(1), pp.139-155. [DOI]

Ramadan, B.S., Fajar, I. and Puspita, A.S., 2024. Estimating short-lived climate pollutants emission from waste management system in Semarang–a life cycle and material flow analysis. *Ecological Engineering & Environmental Technology*, 25, pp.1-12. [DOI]

Thomas, D.J., 2007. *Maximising Struvite Recovery from Real Wastewater Sources*. PhD Thesis, Cranfield University (United Kingdom).

Wang, J., Burken, J.G., Zhang, X. and Surampalli, R., 2005. Engineered struvite precipitation: Impacts of component-ion molar ratios and pH. *Journal of Environmental Engineering*, 131(10), pp.1433-1440. [DOI]

Ye, Z.-L., Chen, S.-H., Lu, M., Shi, J.-W., Lin, L.-F. and Wang, S.M., 2011. Recovering phosphorus as struvite from the digested swine wastewater with bittern as a magnesium source. *Water Science and Technology*, 64(2), pp.334-340. [DOI]

Yetilmezsoy, K. and Sapci-Zengin, Z., 2009. Recovery of ammonium nitrogen from the effluent of UASB treating poultry manure wastewater by MAP precipitation as a slow release fertilizer. *Journal of Hazardous Materials*, 166(1), pp.260-269. [DOI]

NATURE ENVIRONMENT AND POLLUTION TECHNOLOGY

JOURNAL INFORMATION

Vol. 25, No. 3, September 2026

About the Journal

Nature Environment and Pollution Technology is an international peer-reviewed open-access journal covering environmental science, pollution control, environmental technology, sustainability, and related interdisciplinary research.

Scope

The journal publishes original research and review articles on environmental monitoring, pollution prevention and control, air, water, soil and noise pollution, waste management, environmental technologies, conservation and resource management, toxicology, recycling, environmental policy, and related interdisciplinary areas.

p-ISSN	e-ISSN	PUBLICATION FREQUENCY	WEBSITE
0972-6268	2395-3454	Quarterly	www.neptjournal.com

Open Access

All articles published in Nature Environment and Pollution Technology are freely accessible online through the journal website.

Peer Review

Manuscripts undergo preliminary editorial screening followed by the journal's established peer-review and editorial decision process.

Digital Object Identifier

Individual articles are assigned persistent Crossref Digital Object Identifiers (DOIs) to support citation, linking, and discoverability.

Publication Ethics

NEPT maintains publication policies addressing research integrity, authorship, conflicts of interest, peer review, corrections, and responsible scholarly publishing. Detailed policies are available on the journal website.

Abstracting & Indexing

- Scopus
- Directory of Open Access Journals (DOAJ)
- Zoological Record (Clarivate)
- GEOBASE (Engineering Village)
- CAB Abstracts (CABI)
- Chemical Abstracts Service (CAS)
- AGRIS (FAO)
- CNKI Scholar (China National Knowledge Infrastructure)
- EBSCO Environment Index
- Pollution Abstracts (ProQuest)

For Authors

Guidelines and online submission:
https://editorial.neptjournal.com/index.php/1/about/submissions

Editorial Office

General: contact@neptjournal.com
Operations: operations@neptjournal.com

Published by

Technoscience Publications LLP
Scholarly Publishing
A6/1903, Kumar Prospera, Hadapsar,
Pune-411 028, Maharashtra, India
www.technosciencepub.in